CEAS - AIDAA Conference 2025

Proceedings of the 10th CEAS Aerospace Europe Conference
and 28th AIDAA International Congress.
Held December 1-4, 2025 at the Lingotto Congress Center,
Turin, Italy



Edited by
Erasmo Carrera and Matteo Filippi

M|R|F

CEAS - AIDAA Conference 2025

Proceedings of the 10th CEAS Aerospace Europe Conference 28th AIDAA International Congress. Held December 1-4, 2025 at the Lingotto Congress Center, Turin, Italy

Editors

Erasmo Carrera and Matteo Filippi

Politecnico di Torino
Mechanical and Aerospace Engineering Department, Turin, Italy

Peer review statement

All papers published in this volume of "Materials Research Proceedings" have been peer reviewed. The process of peer review was initiated and overseen by the above proceedings editors. All reviews were conducted by expert referees in accordance to Materials Research Forum LLC high standards.

Copyright © 2026 by authors

Content from this work may be used under the terms of the Creative Commons Attribution 3.0 license. Any further distribution of this work must maintain attribution to the author(s) and the title of the work, journal citation and DOI.

Published under License by **Materials Research Forum LLC**
Millersville, PA 17551, USA

Published as part of the proceedings series
Materials Research Proceedings
Volume 67 (2026)

ISSN 2474-3941 (Print)
ISSN 2474-395X (Online)

ISBN 978-1-64490-424-4 (Print Set)
ISBN 978-1-64490-425-1 (eBook)

This book contains information obtained from authentic and highly regarded sources. Reasonable efforts have been made to publish reliable data and information, but the author and publisher cannot assume responsibility for the validity of all materials or the consequences of their use. The authors and publishers have attempted to trace the copyright holders of all material reproduced in this publication and apologize to copyright holders if permission to publish in this form has not been obtained. If any copyright material has not been acknowledged please write and let us know so we may rectify in any future reprint.

Distributed worldwide by

Materials Research Forum LLC
105 Springdale Lane
Millersville, PA 17551
USA
https://mrforum.com

Manufactured in the United States of America
10 9 8 7 6 5 4 3 2 1

Table of Contents

Preface
Committees

1. Artificial Intelligence, Machine Learning & Data Driven Methods

Detection of Aircraft Spoofing Using the GVA Parameter in ADS-B Data
Jakub TRÝB, Jakub HOSPODKA 2

Immersive Virtual Reality Framework for Lunar Pressurized Rover Training and Interaction
Dario Zamani, Mehran Bahojb Ghalibafan, Marco Crestini, Matteo D'Aquila, Magesh Chandramouli, Alfonso Pagani, Marco Petrolo, Erasmo Carrera 9

Single Controller for Multiple Aircraft by Deep Reinforcement Learning
Fatih Ahmet SARIGUL, Ismail BAYEZIT 15

Comparative Analysis of Generative Data Augmentation Techniques for Aircraft Damage Detection Algorithms: A Case Study
Salvatore MEROLA, Aditi MHATRE, Ann-Kathrin KOSCHLIK, Michele GUIDA, Francesco MARULO 21

Enabling Physics-Based Deep-Learning Thunderstorm Nowcasting for Critical Decision Making in Innovative Air Mobility
Niklas WARTHA, Grigory ROTSHTEYN, Christoph METZL, Tobias BÖLLE 25

Neural Network-Based Prediction of Bursting Events in a Turbulent Channel Flow
Enrico SACCAGGI, Gaetano Maria DI CICCA 31

Deep-Learning-based Dent Detection of Aircraft Surfaces using Synthetic Data
Aditi MHATRE, Salvatore MEROLA, Ann-Kathrin KOSCHLIK, Rebecca RODECK, Gerko WENDE 37

Improving GNSS Positioning Accuracy through Adaptive Weighting and Multipath Isolation
Sebastiano CHIODINI, Andrea VALMORBIDA, Giovanni ANESE, Marco PERTILE, Giada GIORGI, Claudio NARDUZZI, Bortolino SAGGIN 42

Lunar Descent and Landing Via Fusion of Deep Learning-Based Visual Navigation and Moonlight Signals
Michele CERESOLI, Floor MELMAN, Yoann AUDET, Richard SWINDEN, Francesco CAPOLUPO, Michèle LAVAGNA 48

Numerical Assessment of Convective PGMs
Giada COLOMBO, Umberto IEMMA 54

Modelling the Correlation Function of Wall Pressure Fluctuations Under Turbulent Boundary Layers with Machine Learning Methods
Marika DI MEO, Alessandro CASABURO, Arthur Diniz FLOR TORQUATO FERNANDES, Francesco FRANCO 60

Use of Convolutional Neural Networks for Multifidelity CFD Problems
Sebastiano Geremia Isidoro MARCI, Luca MUSCARA, Lorenzo FOLCARELLI, Andrea FERRERO, Filippo MASSENI, Dario Giuseppe PASTRONE 66

Vision-Based Relative Pose Estimation of Space Objects for Proximity Operations Using Lab-Validated Deep Learning
Matteo FORASASSI, Giordana BUCCHIONI, Lorenzo POLLINI 72

Minimum-Energy Trajectory Generation for Quadrotor UAVs Using Basis Functions and Gradient-Based Optimization
Fabio CELANI, Dennis LUCARELLI 78

Tuning Machine Learning Outcomes for Airfoil Aerodynamics Seed Sensitivity in Predictive Performance
Diana-Andreea STERPU, Daniel MĂRIUȚA, Grigore CICAN, Ciprian-Marius LARCO, Lucian-Teodor GRIGORIE 84

Modular OODA-Based Agents for Scalable and Adaptive AI in System-of-Systems Modelling and Simulation
Jorge L. LOVACO, Karl ZUBER, Raghu Chaitanya MUNJULURY, Christopher JOUANNET, Petter KRUS 88

Comparing UAM Demand, eVTOL Design, and Profitability across Metropolitan Regions using Simulation and Optimization
Ansgar KIRSTE, Eike STUMPF 94

2. Aerodynamics & Fluid Mechanics

Wind Tunnel Investigation of Vertical Stabilizer Wedging Angles on the Aerodynamic Performance of a Modular Aircraft Model
Valeria VAVALÀ, Ambra GIOVANNELLI, Tomasz ŁUSIAK 100

Design of a 3D-Printed Modular Airframe with Interchangeable Vertical Stabilizers for Experimental Applications
Valeria VAVALÀ, Ambra GIOVANNELLI, Tomasz ŁUSIAK 106

Effects of Airfoil Trailing Edge Thickness on the Generation of Secondary Tones
Giorgio SANTANATOGLIA, Richard D. SANDBERG, Elnaz HAJIZADEH 112

Computational Analysis of a Multistage Nose Spike to Reduce Drag on a Conceptual Supersonic Transport Aircraft
Joseph Ciano Pinto, Siva Marimuthu, Parvathy Rajendran, Rajadurai Murugesan 119

Computational Analysis to Improve the Aerodynamic Performance of NACA 0012 in Transonic Flow Using Raw Riblet Patterns
Siva MARIMUTHU, Sheikh ISLAM, Parvathy RAJENDRAN, Rajadurai MURUGESAN 125

Advanced Numerical Modeling for Calibration of Heat Flux Sensors for Space Applications
Armando MAIELLO, Orsola PETRELLA, Angela VOZELLA 130

Influence of Variable Camber by Differential Flap Setting on the Aerodynamic Performance in Off-Design Flight Conditions
Katharina Alt, Victoria Schmitz, Jochen Wild, Daniel Reckzeh 136

An Unsteady Lifting-Line Model for Rotors in Forward Flight
Gregorio FRASSOLDATI, Beatrice DE RUBEIS, Giovanni BERNARDINI, Massimo GENNARETTI 142

When Propellant Controls the Spin: Two-Phase Fluid Dynamics and Their Impact on Spacecraft Rotational Stability
Gianni CASSONI, Gianmarco COVETTI, Fabrizio GENNARI, Jacopo SERAFINI 148

Improving Post-Stall Airfoil Performance Using Synthetic Jet-Based Flow Control
Baris GUNGORDU 154

A Comparative Study of Flow-Induced Vibrations by Circular and Polygonal Cylinders Using Lattice Boltzmann and Immersed Boundary Methods
Alessandro TROTTA, Esmaeel MASOUDI, Stefano MELONI, Mahdi AZARPEYVAND, Djamel REZGUI, Stefano UBERTINI, Andrea Luigi FACCI 158

Hot-Wire Velocity Measurements in Subsonic Nozzle Flows: Experimental Test Campaign
R. Camussi, E. De Paola, A. Talamelli, L. Lazzarini, S. Palazzo, F. De Gregorio, K.-S. Rossignol 164

Lattice Boltzmann Simulation of Cylinder-Induced Loads on a Lamina
Alessandro TROTTA, Riccardo GIANSANTE, Stefano MELONI, Carlo AQUILINI, Roberto CAMUSSI, Stefano UBERTINI, Andrea Luigi FACCI 172

Image Segmentation for Leading Edge Experiments of Rocket Fins in an Arc-Heated Wind Tunnel
Oliver ASSENMACHER, Oliver HOHN, Alexander RÜTTGERS, Ali GÜLHAN 177

Assessment of a CFD Solver for Detonation Wave Simulations
BONELLI Francesco, MILIA Davide, NINNI Davide, PASCAZIO Giuseppe, LAERA Davide 183

Comparison of Far-Field Methodologies for Unsteady Low Reynolds Number Flows
Dameon WESTLEY, Lelanie SMITH, Drewan SANDERS, Manuel CARREN˜O RUIZ, Domenic D'AMBROSIO 187

Implicit-Mesh Discontinuous Galerkin Methods for Solving Multiphysics Flow in Lid-Driven Cavities
Niba KAINAT, Vincenzo GULIZZI 193

Analysis of the Wake Vortex Encounter Risk Under Reduced Vertical Separation Enabled by Geometric Altimetry
Tobias BAUER, André KOLOSCHIN 199

Assessment of RANS Turbulence Models for Swept Shock Wave–Boundary Layer Interactions
Andrea PALUMBO, Sergio PIROZZOLI 205

Numerical Simulation of the Effect of Extreme Accelerations on the Sonic Boom Generated by a Circular Cylinder
Roberto Francisco Bobenrieth MISERDA, Braulio Gutierrez PIMENTA, Vinicius Coutinho DA SILVA, Ana Luisa Pereira MALDONADO 211

Numerical Simulation of the Transition from Regular to Mach Reflection of Oblique Shocks
Davide RUOCCHIO, Alberto GUARDONE 217

Use of Matching Pursuit Algorithm for Identification of Aircraft Aerodynamic Coefficients
Mateusz PILECKI, Manfred GAWLAS, Jacek GRZEGORZEWSKI 221

Blockage Effects in Wind Tunnel Experiments of Turbulent Wakes: A Numerical Study
Gianluca PORPORA, Andrea PALUMBO 227

Numerical Simulation of Wall-Bounded Flows with Thermally Perfect Gases
Alessandro AIELLO, Andrea PALUMBO, Gennaro COPPOLA 233

Assessment of Structure-Preserving Methods for LES of Compressible, Wall-Bounded Flows
Giuseppe ILLIANO, Francesco DE VANNA, Gennaro COPPOLA 239

Static and Dynamic Derivatives Estimation of an Image Guided Rocket Using Computational Fluid Dynamics
Karol Bielaszka, Radosław Kamiński, Olgierd Skromak 244

Instability Mechanisms in the Compressible Falkner–Skan Boundary Layers with A Cooled Wall
Hao Li, Franco Auteri 250

Far-Field Exergy-Based Drag Decomposition of a Turbulent Blunt-Body Wake with Hybrid-LES
Justin DU PLESSIS, Drewan SANDERS, Tamas JÓZSA, Tom-Robin TESCHNER 254

The impact of Staggered Fins on Aerodynamic Drag of a Transonic Sounding Rocket
Jakub Antoni JANKIEWICZ, Manfred GAWLAS, Urszula WASILEWSKA 260

3. Aeroacoustics & Noise Control

High-Order Vibroacoustic Modal Analysis of Fluid-Loaded Plates with Simply-Supported and Free Edges
Dario MAGLIACANO, Matteo FILIPPI 267

Noise Robust ML Sunspot Forecasts for Cycle Aware Space Weather Operations in the Cycle 25 Era
Esraa Zeki Mohammed, Ahmed Ghareeb, Mohammed Rashad Baker 271

Aspects Regarding the Implementation, Capture and Measurement of Noise on the Măgurele Air Test Stand
Radu Cristian GABOR, Grigore CICAN, Mihnea GALL 275

Local Noise Dissipation Mechanism and Flow Impedance in Acoustic Liner Grazed by Turbulent Flow and Acoustic Wave
Francesco AVALLONE, Angelo PADUANO, Francesco SCARANO 281

A Novel Multipolar Expansion for Acoustic Footprint Reduced Order Modeling
Giorgio PALMA, Stefano MELONI, Christophe BOGEY, Lorenzo, BURGHIGNOLI, Caterina POGGI, Jacopo SERAFINI 287

Labyrinthine Acoustic Metamaterials for grazing Sound Waves
Giuseppe PETRONE, Alessandro CASABURO, Giuseppe CATAPANE..... 293

Wavenumber-based Reconstruction Methof for the Vibroacoustic Response of Plates under Distorted Similitude
Alessandro CASABURO, Giuseppe PETRONE, Francesco FRANCO, Sergio DE ROSA 298

Effects of Pre-Stressed Conditions on the Dynamic and Acoustic Behavior of Composite Sandwich Panels
Piero CHIAIA, Matteo FILIPPI, Alfonso PAGANI, Erasmo CARRERA 303

The Ffowcs-Williams and Hawkings Analogy for Full Aircraft Noise Prediction
Emanuele STICCHI, Damiano CASALINO, Daniele RAGNI, Francesco AVALLONE..... 308

Multi-Fidelity Numerical Acoustic Optimization of UAV Propellers
Roberto NAVARRO, Luis Miguel GACÍA-CUEVAS, Jorge GARCÍA-TISCAR, Federico Nahuel RAMÍREZ, Marco LAUDATO, Mihai MIHAESCU 314

Auralization and Subjective Evaluation of Air Taxi Noise Events
Teresa MOSES, Michael SCHMÄHL, Mirko HORNUNG 319

Optimal Impedance for Acoustic Liners: From Cremer to Nonlocal Concepts
Emanuele De Bono, Alessandro Casaburo, Giuseppe Petrone, Manuel Collet, Sergio De Rosa 325

Vibration and Noise Analyses of eVTOL Tilting Propeller with Different Anhedral Angles in Low-Speed Flight
Gi-Jeong Park, Hyeok-Jin Son, Jaeheon Jeong, Jae-Sang Park 331

Acoustic Liners for Low-Frequency Sound Absorption: A Preliminary Study
Luigi Maria CARDONE, Giuseppe PETRONE, Alessandro CASABURO, Francesco FRANCO, Sergio DE ROSA 335

Numerical Vibro-Acoustic Characterization of Aerospace Structures Made of Miura-Ori Origami Metamaterial
Martino Carlo MORUZZI, Vasilena Petrova KRALEVA, Matteo FILIPPI, Maria CINEFRA 341

Acoustic Comfort Evaluation in the Passenger Cabin and Cockpit Through a Mixed-Reality Environment
Andrea ALAIMO, Sara BAGASSI, Francesca BRACAGLIA, Erasmo CARRERA, Antonio ESPOSITO, Tommaso FADDA, Matteo FILIPPI, Martino Carlo MORUZZI 346

4. Aeroelasticity & Structural Dynamics

Set-Up of a Generic Aeroelastic Simulation Model for Demonstration and Software Testing Purposes
Francisco CARVALHO, Arne VOSS, Raffaello MARIANI 352

Periodic Ground Resonance Analysis with Harmonic Decomposition
Andrea BASSI, Giuseppe QUARANTA 358

Whirl Flutter: An Experimental, Numerical, and Analytical Study on a Small-Scale Demonstrator
Giusi MAGLIOCCO, Francesco MARULO, Michele GUIDA, Giovanni MARULO, Emilio DI LORENZO 362

Fault Tolerance Analysis of a Double Ailerons Based Adaptive Flutter Suppression System
Carmelo Rosario VINDIGNI, Giuseppe MANTEGNA, Calogero ORLANDO, Andrea ALAIMO 366

Aeroelastic Modeling of Deformable-Airfoil Wings Through Unsteady Lifting-Line Theory
Riccardo GIANSANTE, Giovanni BERNARDINI, Massimo GENNARETTI 370

Aeroelastic Modelling of Highly Deformable Wings in Compressible Flows
Edoardo LEVATI, Igor PAOLINI, Giovanni BERNARDINI, Massimo GENNARETTI 375

Propeller-driven Vibration Testing of Aircraft Wings
Gabriele DESSENA, Alessandro PONTILLO 380

Coupled Thermal-Mechanical Behaviour of Ventilated Brake Discs with Radial Vanes and Lattice Cores: A Preliminary Comparison
Giuseppe MANTEGNA, Calogero ORLANDO, Davide TUMINO, Carmelo Rosario Vindigni, Andrea ALAIMO 384

Trim Analysis of Highly Flexible Aircraft via a Coupled DG-VLM Framework
Elisa TESTAQUATRA, Vincenzo GULIZZI 390

Mid-Fidelity Approaches for the Non-Linear Aeroelastic Assessment of The Pazy Wing
Alessia BOVE, Giuseppe QUARANTA 396

Aeroelastic Evaluation of Dry Wing Effects for Hydrogen Aircraft
Fanglin YU, Mirko HORNUNG 402

Dynamic Modeling of Rotor Damper Configurations for Aeroelastic and Ground Resonance Analysis
Matteo CROCI, Pierangelo MASARATI 408

Investigation of Lift-offset Effect on Performance and Vibratory Loads of a Rigid Coaxial Rotor
Jae-Hee HWANG, Jae-Sang PARK 414

Analysis of Morphing Trailing Edge Flap Effects on Dynamic Stall of the NACA 13112 Airfoil for Helicopter Rotor Blade Applications Using CFD and Experimental Methods
Dorin-Madalin FERARU, Daniel MARIUȚA, Grigore CICAN, Ciprian-Marius LARCO, Lucian-Teodor GRIGORIE 418

5. Aircraft Design, MDO & Performance

A Survey of Advanced Air Mobility Use Cases and Implementation Challenges in Japan: A Systems Approach Perspective
Yusuke Mihara 425

Fire Fighting System Integration on C-27J Aircraft
Francesco GIUGLIANO, Fabio CHIACCHIO, Pierpaolo BORRELLI, Marco DI GIFICO, Rosalia GRAZIANO, Salvatore PANICO 431

Conceptual Design for Uncrewed Combat Aircraft through a Modular Low-Fidelity MDO Workflow
Lorenzo VISCONTI, Giovanni ZIPPA, Paolo BADER 436

Most Promising Technologies and Aircraft Concepts for Environmental Performance Improvements: A Systematic Review
Lukas SÖFFING, Elise SCHEERS, Helen SZÖKE-ERÖS, Lukas WEBER, Pascal BERTRAM, Patrick RATEI 442

Co-design of Aircraft Configuration and Flight Profile for Match-range Operation
Lijing LIU, Christian REYNER, Rhea P. LIEM 448

Design and Optimization of Thin Membrane Tensioning for Deployable Space Antennas
Lorenzo MARTINAZZOLI, Mena PALMIERI, Susanna LAURENZI 453

Aero-Propulsive Modeling and System Identification of a Distributed Electric Propulsion Flying Model
Giorgio FILIPPOLI, Niko TERZAROLI, Beniamino M. PERRI, Lorenzo MASSA, Stefano CACCIOLA, Lorenzo TRAINELLI Carlo E. D. RIBOLDI 457

Exploring Box-Wing Configurations for Next-Generation Firefighting Aircraft
Giuseppe Palaia, Karim Abu Salem, Andrea Fasolis, Erasmo Carrera 463

Systematic Aircraft Propulsive System Generation for Sizing, Evaluation and Selection
Enzo DELLA BELLA, Valérie POMMIER-BUDINGER, Scott DELBECQ, Joël JEZEGOU, Marija JANKOVIC, Alain LEFEBVRE 469

Aerodynamic Efficiency of Longitudinally Unstable Tailless Aircraft
Stefan RIETHAUSEN, David LUNDSTRÖM, Petter KRUS 475

An Energy-Centric Approach for Evaluating Climate Impact Levers in Conceptual Aircraft Design
Kristina MAZUR, Mirko HORNUNG 481

A Modular Life Cycle Assessment Framework for Novel Aircraft Configurations and Sustainable Aviation Fuels
Kristina MAZUR, Katrin BISTRECK, Christina ERBSKORN, Mirko HORNUNG 487

Validation of High-Fidelity Multidisciplinary Maneuver Simulations with Flight Test Data from DLR Dassault Falcon 2000LX ISTAR
Martin BAUER, Johan Moritz FELDWISCH, Philipp MÜHLMANN 493

A Simulation-Coupled Concurrent Engineering Approach to Next-Generation Low-Cost Counter-UAV Missiles
Vincenzo Jr. DI ROSA, Francesco GASPERINI, Matteo GIANNITTI, Michele GUIDA, Simone GUBBIONI, Emanuele COFANI 499

Enhancements in the Aircraft Preliminary Design Methodologies: Adoption of Sustainable High-Fidelity Simulations
Federico CARLINI, Marco BASAGLIA, Luca BATTAGLIA, Elisa GARBI, Simone GENOVESE, Rocco GENTILE, Chiara LA GUARDIA, Angela SCARDIGLI, Lorenzo VISCONTI, Giovanni ZIPPA 504

Wind Gust Spectral Analysis with Aeolus Observations: Insights from a Transatlantic Route
Marianna VALENTE, Giuseppe PALAIA, Alfonso PAGANI, Erasmo CARRERA 510

Preliminary Design of Advanced Wing for an Ultra Efficient Regional Aircraft
Giovanni Marco CAROSSA, Elena RONCOLINI, Tomás Eugenio CÁRDENAS MUTIS, Francesco TOFFOL, Sergio RICCI 516

Investigation of the Influences of Different Booster Recovery Methods on Air Traffic
Antonio DEPARDON, Jonas LANGNER, Thomas FEUERLE, Carsten WIEDEMANN, Simona SILVESTRI 522

Assessing Synergies Between Truss-Braced Wings, Liquid Hydrogen Propulsion, and Open Rotors in Conceptual Aircraft Design
Lucas KUGLER, Michael KOTZEM, Sebastian WÖHLER, Thomas ZILL 528

Development of a Flying Platform to Study Three-Surface Configurations with Redundant Longitudinal Control
Stefano Cacciola, Carlo E.D. Riboldi, Carlo Fazioli, Leonardo Filippello, Francesco Rosato 534

Analysis of LTO Cycle Emissions as Results of Aircraft Operations in the Vicinity of Torino Caselle Airport
Edoardo Blanco, Davide Ferretto 540

Analysis of CO_2 Emissions and Cost Resulting from the Adoption of Sustainable Aviation Fuels by Medium Range Aircraft in Different World Regions
Angela Bozzaotre, Davide Ferretto 546

Synthesizing Aircraft System Specifications with Document-Managed Large Language Model Outputs from One-Shot System Inquiry Prompt Chain
Vinicius Kaster MARINI, Petter KRUS 552

AI-Driven Pre-Design Predictions of a 90-Passenger Hybrid-Electric Aircraft
Erick ESPINOSA-JUÁREZ, Álvaro GÓMEZ-RODRÍGUEZ, Felix MARTINEZ-RIOS, Christopher JOUANNET, Kristian AMADORI 558

GPU-Accelerated CABARET Simulations of Distributed Propulsion for UAM
Hussain A. ABID, Igor SOLNTSEV, Andrea RAPISARDA, Hassan A. ABID, Sergey A. KARABASOV, E. DE PAOLA, Luana Georgiana STOICA, Giorgia CAPOBIANCHI, Alessandro DI MARCO, R. CAMUSSI 564

6. Propulsion, Energy & Combustion

Experimental Characterization of Ageing Phenomena in Li-Po Battery Packs for Lightweight UAV Applications
Aleksander SUTI, Gianpietro DI RITO, Aurélien REYSSET 572

Comprehensive Modelling for Electric Machine Sizing and Performance Estimation in Aerospace Applications Enhancing Static and Dynamic Simulation
Victor J. BAHRS, Katharina KOLO, Stefanie DE GRAAF 577

Modelling the Transient Behavior of Heat Exchangers in Aircraft Engine Preliminary Design
Aytunc YILDIRIM, Marc SCHMELCHER, Alexander GÖRTZ 583

Suitability Assessment and Potential Use Case Definition for the Application of Electric Energy Carriers in Electrified Aircraft
Maurice Lucas DOERNTE, Florian FRANKE, Stefan KAZULA 589

Experimental Study of Vibration Levels in Microjet Engine Prototype Considering Venturi Intake Influence
Cornel-Mihai TĂRĂBÎC, Andrei-George TOTU, Grigore Cican 595

The GREEN FOXFIRE Project: Sustainable Hybrid Propulsion for CubeSats Based on Paraffin/HTPB
Daniele TORTORICI, Sasi Kiran PALATEERDHAM, Antonella INGENITO, Alessandro MONTANARO, Daniele PIAZZULLO, Luigi ALLOCCA 601

Off-Design Performance Consequences of Design Payload and Range Requirements for SPPH Hybrid-Electric Aircraft
Maurice F.M. HOOGREEF 607

Engineering Polyimide Materials for Moon Exploration Missions: Intrinsic Self-Healing and Shape Memory Properties via Supramolecular Interactions
Francesca BLONDELLI, Elisa TOTO, Guido SACCONE, Nunzia FAVALORO, Maria Gabriella SANTONICOLA 614

Sustainable Hydrogen-Rich Polymer Blends for Advanced Space Radiation Shielding
Elisa TOTO, Francesca BLONDELLI, Lorenzo FERRI, Susanna LAURENZI, Maria Gabriella SANTONICOLA 620

Numerical Investigation of the Applicability of a Single Ramp Supersonic Inlet for Ramjet Propulsion
Franciszek Dominik TOMCZAK 626

Operational Envelope of an EAD Thruster Under Varying Pressure and Humidity
Davide USUELLI, Andrea AVALLI, Raffaello TERENZI, Stefano TROVATO, Marco BELAN 632

Advanced Mesh Grid Geometries for EAD Thrusters: An Experimental Approach
Stefano TROVATO, Raffaello TERENZI, Davide USUELLI, Marco BELAN 638

Sustainable Aircraft Propulsion with Four Energy Sources
Salvatore Trepiccione, Giuseppe Grazioso, Fabrizio Nicolosi 644

Automated Flight Testing of a Distributed Electric Propulsion Flying Model
Lorenzo TRAINELLI, Giorgio FILIPPOLI, Niko TERZAROLI, Beniamino M. PERRI, Stefano CACCIOLA, Carlo E. D. RIBOLDI 650

Development of an Autonomous Flight Control System for a Distributed Electric Propulsion Flying Model
Giorgio FILIPPOLI, Beniamino M. PERRI, Niko TERZAROLI, Lorenzo TRAINELLI, Stefano CACCIOLA, Carlo E. D. RIBOLDI 656

Preliminary Sizing of Airport Infrastructures for Refuelling Hydrogen-Powered Aircraft
Lorenzo Trainelli, Gabriele Sirtori, Carlo E.D. Riboldi, Giorgio Filippoli, Stefano Cacciola 662

A Breguet Range Formulation for Liquid Hydrogen-Powered Aircraft
Giuseppe PALAIA, Karim ABU SALEM, Erasmo CARRERA 666

Defining Control Loops for a Fuel Cell Powered Aeronautic Propulsion System
Rudy CEPEDA-GOMEZ 672

Analyzing the Eco-Design Approach for an Innovative In-Space Propulsion System
Daniele Ferrara, Michele Trovato, Angelo Minotti, Antonio Casimiro Caputo, Paolo Cicconi 677

Reduced-Order Dynamic Modelling of the Wankel Engine Employed in the Hybrid Propulsion System of a Lightweight Helicopter UAV
Gianpietro DI RITO, Alessandro MAZZONE, Andrea NESCI, Eugenio ROVERA, Valerio BONINI 683

Preliminary Safety Assessment of the Propulsion Power Management System of a Hybrid-Electric Regional Aircraft
Gianpietro DI RITO, Aleksander SUTI 689

Hydrogen-Enriched and Plasma-Assisted Flames for Lean Blow-Out Control in a Swirl-Stabilized Burner
Maria Grazia DE GIORGI, Pasquale DI GLORIA, Sara BONUSO, Ekin Can KARASU 695

Numerical Modeling and Validation of a Water Electrolysis Propulsion System for CubeSats
Raviteja VEMULA, Pratyush Kumar SINGH, Maria Grazia DE GIORGI 701

Propeller Aerodynamics Under Non-Uniform Inflows
Sara MONTAGNER, Manuel ZANNONE, Jacopo SERPIERI, Gioacchino CAFIERO 707

Thermo-structural Design of Composite Pressure Vessels for Hydrogen Aircraft
Luigi Maria CARDONE, Vittorio MEMMOLO 713

Configuration Analysis and Impeller Design for an Oxidizer Pump in Small Liquid Rocket Engines
Miłosz KOZYCZ1 718

AI-Driven Inverse Constrained Design for Turbine Optimization
Francesco PORTA, Sergio LAVAGNOLI 724

Enabling Aerospace Electrification by means of Scale-Resolved Battery Simulation
Max OKRASCHEVSKI, Janina DREWS, Steffen REHSE, Dana SCHONVOGEL, Ralf SCHMIDT, Tom BOENKE, Holger ALTHUES, Arnulf LATZ, Timo DANNER 730

Experimental Flow Characteristics of Turbine Stator Well with Honeycomb and Labyrinth Structures
Jiahua LIU, Zeyu WU, Dongdong LIU, Nan CAO, Xiang LUO 735

Development and Characterization of Solid Propellants Based on Environmentally Friendly Sugar and Oxidants for Aerospace Applications
Gerardo Raúl CABALLERO MORALES, Italo Paolo AMBROSIO HUANAY 741

Design of a Low Power Anode Layer Hall Thruster
Ivana SETTEMBRE, Davide PICCIAU 747

Comparative Analysis of Copper Hairpin Motors and Cryogenic Pure-Aluminum Litz-Wire Motors for Hybrid-Electric Aircraft Propulsion
Xinjun Liu, Thomas Schriefer, Andreas Lindner, Maximilian Hofmann 751

Retrofitting a Hairpin Stator Winding Aircraft Propulsion Motor with a Superconducting Rotor
Andreas Lindner, Xinjun Liu, Daniel Walch 757

7. UAV, UAM & Rotorcraft Systems

Shuttle Drone Control with Airflow Disturbance Compensation for Cooperative Target Capture
António S. Costa, Bruno J. N. Guerreiro 765

Towards Cooperative Guidance in Air-Defense: Extending Weapon-Target Assignment into the Mid-Course Phase
Ole OSTERMANN, Johannes AUTENRIEB, Carsten SCHWARZ 771

Simulation-Based Development of a Forward-Motion Mid-Air Deployment System for Fixed-Wing UAVs from Quadrotor Platforms
Paul Olanifimihan OKE, Yingsong GU 777

Electric Powered Helicopter: From Concept to Feasibility
Elif Hazal ÇELİKCAN, Ahmad HAMMAD, Michail TSAGKARIS 782

Application of Control Barrier Functions to Avoid Vortex Ring State in Unmanned Helicopters
Emilia ISBONO, Mark SPILLER, Philipp SCHITZ 788

Anti-Windup Compensator Design for Fixed-Tilt Multirotors with Interaction Capabilities
Dharani JAYANNA, Davide INVERNIZZI, Daniele MAGLIORE, Simone PANZA, Marco LOVERA 794

Ground Effect in Thrust-Lift Conversion using the Deflected Slipstream Concept in Martian Conditions
Wei HAN, Manuel CARREÑO RUIZ, Domenic D'AMBROSIO 800

Learning-Based Quadrotor Tracking Control Using Recursive Gaussian Processes
Alessandro LUPATINI, Giovanni GOZZINI, Alessandro NAZZARI, Roberto RUBINACCI, Marco LOVERA 806

Perception Aware Quadrotor Control: An Experimental Evaluation
Lidia PEREZ, Alessandro NAZZARI, Roberto RUBINACCI, Davide INVERNIZZI..... 812

eVTOLs in Inter-Hospital Medical Transport: A Simulation Based Scenario Analysis for Bavaria
Benedikt M. DREYER, Sophie F. ARMANINI 817

An Extensible Drone Framework for In-flow Disturbance Analysis
Benedetta NOVELLI, Stefano MELONI, Diego PENNINO, Alessandro TROTTA..... 822

Aerodynamic Performance Characterization of UAV Propellers via Blade Element Momentum Theory including Post-Stall Behaviour
Marco LUCARINI, Gianpietro DI RITO, Simone CAMARRI, Marco NARDESCHI..... 827

Assessing the Technical-Economic Feasibility of Unmanned Airships: Methodology and Case-Studies
Carlo E.D. RIBOLDI, Luca FANCHINI 833

Identification of Airship Aerodynamic Models from Flight Data: Preliminary Investigation and Identifiability Analysis
Carlo E.D. RIBOLDI, Stefano CACCIOLA, Yan POZHANKA, Mostafa HASSANALIAN 839

Reinforcement Learning-Based Bezier Airship Hull Optimization: A Data-Driven Framework for Shape Adaptation Under Aerodynamic Constraints
Qian ZHAO, Carlo Emanuele Dionigi RIBOLDI..... 846

CFD-Based Estimation of Added-Mass and Aerodynamic Derivatives in Heave Motion for a Hybrid Closed-Wing HAPS
Eleonora RICCIO, Alessandro CERESA, Vincenzo Rosario BARANIELLO, Giuseppe PERSECHINO, Francesco TUFANO, Domenico COIRO..... 850

A Novel Approach to Quantify Counter-Drone System Effectiveness Against UAS Swarms
Dani HOTTERS, Nikolaos KALLIATAKIS, Felix KUHNERT, Prajwal Shiva PRAKASHA, Ries VAN HEUR, Buse KAYA 856

8. Guidance, Navigation & Control

Performance Assessment of a Multi-Step Guidance and Control Architecture for Approach and Capture of a Tumbling Space Target
Agostino MADONNA, Giuseppe NAPOLANO, Alessia NOCERINO, Roberto OPROMOLLA, Giancarmine FASANO, Michele GRASSI 862

Enhancing Incremental NDI Control with L1 Adaptive Augmentation in a Longitudinal Autopilot
Giorgio RAOS, Giovanni GOZZINI, Davide INVERNIZZI 868

Adaptive Augmentation of Incremental NDI Laws with Systematic H∞ Synthesis
Giulio FRANCESCHINI, Giorgio RAOS, Giovanni GOZZINI, Davide INVERNIZZI 874

From Strain Measurements to Rotor Blade Shape and Loads Reconstruction: The BeSaME Project
Pierangelo MASARATI, Emanuele CASCIARO, Alessandro COCCO, Roman SUTOV, Paolo BETTINI, Alex ZANOTTI, Giovanni BERNARDINI, Francesco LIGUORI, Jacopo SERAFINI, Claudio PASQUALI 880

Hierarchical Task-Priority Tracking Control in Space Robots
Pietro BRUSCHI, Davide INVERNIZZI 885

Enabling Onboard Analytical Batch Filtering for Angles-Only Navigation to Non-Cooperative Space Targets
Alessandro SCALVINI, Giacomo BORELLI, Gabriella GAIAS 891

Hardware-in-the-Loop Implementation of a Fixed-Point Controller for Boresight Stabilization of Magnetorquer-Only Satellites
Emre SAYIN, Stefano CARLETTA, Fabio CELANI 897

Single Agent On-Orbit Inspection: Energy-Awareness, Data Down-linking and Orbital Exploration via Deep-Q-Learning
Augustin DAY, Francesco Paolo SALZO, Gabriele GEMIGNANI, Stéphanie LIZY-DESTREZ, Giordana BUCCHIONI 902

A Decentralized Cluster-based Approach for Multi-Agent On-Orbit Inspection
Francesco Paolo SALZO, Pasquale FERRARA, Giordana BUCCHIONI 908

Nonlinear Simulation of Aircraft Terminal Maneuvers Including Gear Dynamics and Ground Effect
Stefano CACCIOLA, Andrea CALABRIA 913

Precise Orbit Determination of Satellites with Low-Cost, Single Frequency Receivers in raPPPid
Hoor BANO, Marcus Franz WAREYKA-GLANER, Gregor MÖLLER 919

9. Space Systems, GNC & Orbital Operations

GeoScout: Architecture for Piggyback Interplanetary CubeSats
Lorenzo OLIVIERI, Alessandro FRANCESCONI, Matteo MASSIRONI 926

Mission Design and Enabling Technologies for a LEO-to-MEO Dual-Phase CubeSat Mission: The BOREALIS Platform
Lorenzo Nardi, Fabio Curti, Stefano Carletta, Parsa Abbasrezaee, Lorenzo Thomas Contessa, A. Di Serafino, Vahid Omrani, Domenico Caputo, Giovanni Palmerini, Nicola Lovecchio, Sahithi Sriramoju, VS Siva Sankaram Emani, Nunzio Burgio, Giulia Petrucci, Riccardo Mazzotti, Mara Mirasoli, Fabio Lorenzini, Matteo Mergé, Augusto Nascetti 930

Autonomous Detection of Satellite Orbital Anomalies Through Statistical Behavioural Analysis
Pietro RUSSO, Giorgio ISOLETTA, Roberto OPROMOLLA, Giancarmine FASANO..... 936

Enhancing Space Manipulator Fault Tolerance for In-Orbit Servicing through Meta-Reinforcement Learning
Matteo D'AMBROSIO, Michèle LAVAGNA 942

Estimating the Probability of Close Approaches Generated by an In-Orbit Fragmentation via Monte Carlo-Based Approach
Yeerang Lim, Camilla Colombo 948

Multidisciplinary Design and Optimization of Suborbital Transatmospheric Vehicles
Pierluigi DELLA VECCHIA, Luca FALCONE, Agostino DE MARCO, Fabrizio NICOLOSI, Giulio AVANZINI, Mario DI RENZO, Donatella PASSIATORE, Danilo ZONA 954

A Modular and Scalable Validation Framework for Planetary Rovers: Application to the ARDITO System
Amalia Dellacasa, Gianmarco Polvani, Leonardo Maria Festa, Fabrizio Stesina..... 960

Aerodynamic Characterization of Fin Configuration for VLEO Attitude Stabilization
Vincenzo Maria CANNAVALE, Mattia ILLIANO, Tobia Armando LA MARCA, Maria Daniela GRAZIANO, Elisa CAPELLO, Michele GRASSI..... 966

GRIAL: A High-Fidelity Simulator of Orbital Forces and Torques
Valerio LEVI, Adrián DE ANDRÉS TIRADO, Miguel GUEREÑU MIRA 972

Forecasting a Complete Picture of Future Launches in Terms of Orbital Region and Physical Parameters
Wiebke RETAGNE, Camilla COLOMBO 994

Baseline Values and Sensitivity Analysis of the THEMIS Space Debris Index
Daniel LÜCK, Andrea MUCIACCIA, Martina RUSCONI, Camilla COLOMBO..... 1000

Formation Flying Strategies for Small Distributed SAR Satellites: A Trade-Off between Stability and Performance
Maria SALVATO, Antonio GIGANTINO, Gianluca COPPA, Francesca PELLICCIA, Maria Daniela GRAZIANO, Alfredo RENGA..... 1006

Development of a Robotic Testbed and Initial Testing for Machine Learning-Based Spacecraft Pose Estimation
Alessandro LOTTI, Dario MODENINI, Paolo TORTORA 1012

Chemical Emissions and Near-Field Dispersion of Suborbital Carriers in Conceptual Design
Fabrizio BORGNA, Roberta FUSARO, Davide FERRETTO, Sara GNACCARINI, Nicole VIOLA 1018

Galileo Space Service Volume Analysis for Earth Orbit Rising Missions
Andrea PICCOLO, Francesco MENZIONE 1024

Safe Reinforcement Learning for Autonomous and Constraint-Aware Earth Observation Satellite Scheduling
Fabio FAVARETTO, Claudio RONCHETTI, Guido VOLPI 1030

Rendezvous in Low-Lunar-Orbit from Gateway via Low-Thrust Nonlinear Control
Edoardo Maria LEONARDI, Mauro PONTANI, Paolo TEOFILATTO 1036

Conjunction Risk Reduction in LEO through Onboard Optical Processing
Giulio Campiti, Alessandra Colucci, Giuseppe Brunetti, Caterina Ciminelli 1042

Trajectory Design, Stability, and Maintenance Analysis of Quasi-Satellite-Orbits in Martian Moons Environment
Enrico BELLONI, Fabrizio Maccari, Michèle LAVAGNA 1048

Remote sensing use in Insurance Companies to Manage Natural Disasters Policies – IRIDE Constellation Case Study
Ludovica LOCATELLI, Giuseppe DI BELLA, Franco BERNELLI-ZAZZERA 1054

Experimental Validation of Initial Orbit Determination of Resident Space Objects Using Probabilistic Admissible Regions
Bart KIEBOOM, Martin MICHEL, Urs HUGENTOBLER 1059

Impact assessment of perturbations on the orbit control in a Near-Zero Inclination Geosynchronous Synthetic Aperture Radar
Francesca PELLICCIA, Alfredo RENGA, Matteo MONTI, Andrea MONTI-GUARNIERI, Giovanni Paolo BLASONE, Simona ZOFFOLI 1065

Digital Twins and Modelling for Spacecraft Science Operations: Application to Surface Interaction and Sampling on Small Solar-System Bodies
Iosto FODDE, Fabio FERRARI, Franco Bernelli ZAZZERA 1071

The Legal Conundrum of Mega-Constellations: A Call for a Sustainable Space Governance Framework
Margherita PENNA 1077

Adaptive Sliding Mode for Agile Attitude Tracking in a High-Precision Modelled VLEO Environment
Pierantonio BERTUCCIO, Vincenzo Maria CANNAVALE, Mattia ILLIANO, Tobia Armando LA MARCA, Mauro MANCINI, Maria Daniela GRAZIANO, Elisa CAPELLO, Michele GRASSI 1083

A Heterogeneous Multi-robot Framework for Cooperative Lunar Exploration
Riccardo Caccavale, Stefano Ciaravino, Alberto Finzi, Vincenzo Lippiello, Giuseppe Rauso 1089

Integrated Active Vibration Control and Structural Health Monitoring of Flexible Spacecraft Panels
Muhammad Faisal NADEEM, Sajid RAFIQUE 1095

Nonlinear Orbit Control for Small Satellite Missions with Hardware-In-The-Loop Testing
Virna SISTI, Stefano CARLETTA, Mauro PONTANI, Paolo TEOFILATTO..... 1101

Tensor Modeling of Zero-Sum Games for In-Orbit Servicing Operations with Collision Avoidance
Stefano CARLETTA, Alfonso FARINA, Giovanni B. PALMERINI,
Francesco DE ANGELIS 1107

Efficient Information Routing for Constellations with Satellite Clusters via Static Digraph
Giulio DE ANGELIS, Matteo GUCCINI, Stefano CARLETTA, Mauro PONTANI,
Paolo TEOFILATTO 1114

Orbit Data Analysis of LAGEOS and LARES 2 Space Missions
Ignazio CIUFOLINI, Claudio PARIS, Darpanjeet DEKA, Emiliano ORTORE,
Antonio PAOLOZZI 1120

Design of Responsive Space-Based Observation Systems with Integrated Collision Risk Consideration
Yifan CAI, Camilla COLOMBO 1125

Estimation and Prediction of Long-duration Aerodynamic Drag Effect on Floating LEO Debris using the EDAC-adapted Model
Victor U. J. NWANKWO, Jens BERDERMANN, Timothy N. KODIKARA,
Frank HEYMANN William DENIG..... 1131

Reconfiguration and Optimization of Lunar Navigation Satellite Constellation Targeting South Hemisphere
Shuo YANG, Rui ZHONG, Franco BERNELLI ZAZZERA..... 1140

Multi-Hitchhiking Strategies Using Advanced Tether Materials for Enhanced Deep Space Exploration
Valentina NASTI, Giorgio ISOLETTA, Giancarmine FASANO, Michele GRASSI 1146

A Compensation Strategy for Cases of Divergence in Angle of Arrival Measurements Due to Satellite Attitude
Marcello ASCIOLLA, Angela CRATERE, Francesco DELL'OLIO..... 1153

A Multi-Constellation Approach to Space-Based RF Emissions Monitoring Through Opportunistic Satellite Cluster Collisions in LEO
Marcello ASCIOLLA, Francesco MENZIONE, Angela CRATERE,
Francesco DELL'OLIO..... 1158

10. Structures, Materials & Manufacturing

Open-Source Path Planning for Spot, Line, and Contour Strategies in E-PBF Additive Manufacturing
Anton Wiberg, Pritwish Tarafder, Karin Wennersten, Jinghao Xu, Johan Moverare..... 1165

Low-Velocity Impact Analysis of Composite Plates using the Hashin 3D Criterion and Layer-Wise Models
Marco PETROLO, Matteo FILIPPI, Erasmo CARRERA, Chiara FRANCESCHINI, Elisa TORTORELLI 1171

Accuracy Prediction of Higher-Order Structural Theories for 1D Aerospace Structures Using Neural Networks
Marco Petrolo, Alfonso Pagani, Erasmo Carrera, Giulio Candita 1176

Adaptive Multi-Fidelity Framework for Defect and Damage Tolerant Composite Structures
Dario Zamani, Chiara Franceschini, Marco Petrolo, Alfonso Pagani, Erasmo Carrera..... 1181

Geometrically Non-Linear Thermo-Elastic Analysis of Variable Angle Tow Composite Plates Thorugh Layerwise Models
Francesca Bracaglia, Alfonso Pagani, Enrico Zappino, Erasmo Carrera..... 1187

Multiscale Optimization of Composite Wings Through Global-Local High-Order Modeling
Spyridon KILIMTZIDIS, Dario ZAMANI, Giuseppe PALAIA, Karim ABU SALEM, Alfonso PAGANI, Vassilis KOSTOPOULOS, Spyridon PSARRAS 1192

Experimental Study on Rotational Heat Transfer in Rib-pin Composite Trapezoidal Channels with Varied Rib Configurations
Chenghua ZHU, Hao LI, Jiale WANG, Jie WEN..... 1198

Understanding Strength reduction in Aerospace Composites Structures: The Role of Delamination
Abrar H. BALUCH 1204

Failure Analysis of Deployable Thin-Shell Space Structures Using Refined One-Dimensional Finite Elements
Daniele SCANO, Riccardo Augello, Erasmo CARRERA, Francesco LATINI, Marco PETROLO..... 1210

Virtual Modeling of The Curing Process of Composite Aerospace Components Using Coupled Multiphysics Models
M. SANTORI, E. ZAPPINO, N. ZOBEIRY, M. PETROLO 1215

A Multi-Fidelity Gaussian Process Framework for Predicting Process-Induced Deformations in Composites
K. JOHNSON, M. SANTORI, E. ZAPPINO, N. ZOBEIRY, M. PETROLO 1220

Numerical-Experimental Approach for Simplified Aerospace Structures' Testing Using the Eulerian Video Magnification Technique
Giusi MAGLIOCCO, Salvatore MEROLA, Michele GUIDA, Francesco MARULO..... 1225

Experimental Investigation of Energy Dissipation in BCC and Wavy-BCC Lattice Structures under Drop-Weight Impact Testing
Giuseppe Iacolino, Davide Tumino, Calogero Orlando, Giuseppe Mantegna, Giuseppe Catalanotti, Emilio V. González, Andrea Alaimo 1229

Global-Local Modelling with Node Dependent Kinematics and Arbitrary Displacement Fields for Plates
Daniele SCANO, Erasmo CARRERA, Enrico ZAPPINO 1235

Global–Local Optimization of Composite Structures Using Unified High-Order Finite Element Models
Alex Pereira do Prado, Dario Zamani, Alfonso Pagani, Erasmo Carrera, Saullo G. P. Castro, Roeland De Breuker, Pedro Higino Cabral 1240

Post-Buckling Behaviour of a Multi-Stable Composite Stiffened Specimen under Low-Cycle Fatigue – A Preliminary Study
Xi LI, Chiara BISAGNI 1246

Evaluation of the Mechanical Properties of Ultrathin CNTs Reinforced Composites for Deployable Structures
Lorenzo MARTINAZZOLI, Flavia PALMERI, Susanna LAURENZI 1250

Regolith-Induced Abrasion as a Critical Challenge for Lunar Materials: Experimental Insights on Fiber Reinforced Composites and Polyethylene
Marta BALESTRA, Susanna LAURENZI, Andrea DI BENEDETTO, Antonia SIMONE 1255

Preliminary Design of a Platinum Wire Temperature Sensor for Martian Atmosphere Monitoring Using Additive Manufacturing Technologies
Elisabetta DOLEJSI, Davide TONELLI, Bortolino SAGGIN, Francesca FERRI, Alessio ABOUDAN, Carlo BETTANINI, Giacomo COLOMBATTI 1260

Multifunctional Gels for Strain Sensing and Radiation Shielding in Space
Lucia LAMBERTINI, Maria Gabriella SANTONICOLA, Susanna LAURENZI 1266

Flexible Poly(Vinyl Alcohol) Gels for Radiation Shielding in Next-Generation Spacesuits
Lucia LAMBERTINI, Maria Gabriella SANTONICOLA, Susanna LAURENZI 1272

Conceptual Structural Design of a Pressurized Inflatable and Deployable Habitat Optimized for Lunar Surface Missions
Alfonso CAIAZZO, Giuseppe PETRONE, Alessandro CASABURO, Sergio DE ROSA, Francesco FRANCO 1278

Non-Equilibrium Thermochemical Models for the Characterization of Titan Atmospheric Entry Under Hypersonic Conditions
Antonio NARRACCI, Francesco BONELLI, Davide NINNI, Gianpiero COLONNA, Annarita LARICCHIUTA, Giuseppe PASCAZIO 1283

Toward Vibration-Based Damage Detection: Nonlinear Modal Damping Estimation in Delaminated Structures
Shabnam KIASAT, Ali SALEHZADEH NOBARI, Matteo FILIPPI, Erasmo CARRERA 1287

Comparative Analysis of Nonlinear Effects in Debonded Structures under Deterministic and Stochastic Excitations
Shabnam KIASAT, Matteo FILIPPI, Ali SALEHZADEH NOBARI, Erasmo CARRERA 1292

Preliminary Fatigue Life Prediction of Composite Wing under Gust Spectrum Loads Using a CUF-Based Approach
Elisa TORTORELLI, Marianna VALENTE, Giuseppe PALAIA, Erasmo CARRERA..... 1298

Novel Curvilinear 2|3D Unified Finite Element Formulations for the Analysis of Complex Shell Structures
Piero CHIAIA, Maria CINEFRA, Erasmo CARRERA..... 1304

Functionally Graded TPMS Structures for Boundary Layer Suction on a Swept Wing
Jan KUBE, Lajos FOHLMEISTER, Rolf RADESPIEL, Christian HÜHNE 1310

High-Order Kinematic Coupling of Embedded Fiber and Matrix Ensembles Using a Unified Variational Approach
Alberto RACIONERO SÁNCHEZ-MAJANO, Alfonso PAGANI 1314

Damage Localization Accuracy in Probabilistic Imaging Techniques based on Guided Ultrasonic Waves
Francesco GASPERINI, Vittorio MEMMOLO, Fabrizio RICCI..... 1319

Preliminary Study on the Design of a Fragmentation Warhead and Damage Simulation using FEM Models
Francesco GASPERINI, Matteo GIANNITTI, Michele GUIDA, Simone GUBBIONI, Emanuele COFANI 1325

Maintaining Multistability in Cured Shapes of Series-Connected Unsymmetrical Laminates with Clamped Edges
P. R. MANU, B. N. RAO, P. M. ANILKUMAR..... 1331

Constrained Surrogate-based Optimisation for Finite Element Model Updating
Eduardo LARREA HERRANZ, Gabriele DESSENA..... 1336

Smart Composite for Structural Health Monitoring: Using Copper Wires for Strain Sensing
Antonio Paolo Fontanella, Matteo Febo, Ester D'Accardi, Davide Palumbo, Umberto Galietti, Francesco Ciampa, Maria Cinefra..... 1341

Nonlinear Post-Buckling Analysis of Variable Cross-Section Beams Using the Carrera Unified Formulation
Antonio Paolo Fontanella, Tommaso Sironi, Piero Chiaia, Maria Cinefra, Alfonso Pagani 1347

Fatigue Cracking Analysis by Coupled 3D Peridynamics and 1D High Order Refined Elements
Qiang ZHANG, Alfonso PAGANI, Xiang LIU, Wei ZHOU, Jiahui SHEN 1353

High-Order Multiscale Thermo-Elastic Analysis of a Triangular Sub-Array with Dielectric Patches
Rebecca MASIA, Irene IZZO, Alfonso PAGANI, Enrico ZAPPINO, Ryo HIGUCHI,

Xin LU, Erasmo CARRERA 1358

Variational Asymptotic Micromechanics of Piezoelectric Composites Using Carrera Unified Formulation
Alfonso PAGANI, Rebecca MASIA, Enrico ZAPPINO 1364

Thermal and CUF-Based Decoupled Thermo-Elastic Analysis of a Microstrip Patch Antenna Circuit for Radar Applications
Rebecca MASIA, Federico ZOPPI, Alfonso PAGANI, Enrico ZAPPINO, Erasmo CARRERA 1369

Magnetically Targeted Microcapsules to Enhance Self-Healing Behaviour of High-Performance Polymers Designed to Withstand Moondust Environment
Guido SACCONE, Elisa TOTO, Nunzia FAVALORO, Marianna RINALDI, Maria Gabriella SANTONICOLA 1374

Novel Modeling Technique of Metamaterials Using One-Dimensional Finite Elements
Riccardo Augello, Erasmo Carrera 1379

Component-Wise Beam Modelling of Sandwich Panels with Arbitrary Core Topologies
Erasmo Carrera, Karim Abu Salem, Riccardo Augello 1384

Folding Simulation of Flat Arrays Using Refined Beam Finite Elements
Riccardo Augello, Erasmo Carrera 1387

The Effect of TVAC Cycles on Physical Properties and Morphology of Alumina Coated AA7075 via Hard Anodization and Pulsed Laser Deposition: A Comparative Study for Space Applications
Andrea SEMERARO, Luca GIULIANI, Emanuele Nicolò PIZZO, Federico PICCAGLI, Diego SCACCABAROZZI, Chiara MARTINA, Marco G. BEGHI, Fabio DI FONZO, Nicola CEFIS 1391

The Effect of TVAC Cycles on Mechanical Properties of Coated AA7075 via Hard Anodization and Pulsed Laser Deposition: A Comparative Study for Space Applications
Emanuele Nicolò PIZZO, Luca GIULIANI, Andrea SEMERARO, Andrea RAYMOND, Federico PICCAGLI, Diego SCACCABAROZZI, Nora LECIS, Chiara MARTINA, Fabio DI FONZO, Nicola CEFIS 1397

A Simplified Modelling Strategy for the Analysis of Lattice Structures with Manufacturing Defects
Davide Lorenzo CAPPA, Riccardo VESCOVINI 1402

Dynamic Characterization of Compliant Wheel for Martian Rover: ARDITO
Enrico SABBATINI, Damiano CARRA, Enrico ZAPPINO 1407

A Multiscale Approach for the Thermo-Hydraulic and Structural Performance Prediction of Compact Cross Flow Heat Exchangers
Girindra RAMGOBIN, Harvey THOMPSON, Amirul KHAN, Martin MUIR, Gregory de BOER 1412

Assessment of CUF-Based Variable-Section 1D Finite Elements for the Nonlinear Analysis of a Wingbox Structure
Francesco Mario Antonio MITROTTA, Antonio Paolo FONTANELLA, Maria CINEFRA, Rauno CAVALLARO 1416

Peridynamic Modeling of Nearly-Incompressible Soft Materials for Aerospace Systems
Francesco SCABBIA, Vito DIANA, Francesca FANTONI, Mirco ZACCARIOTTO, Ugo GALVANETTO 1422

Computationally Efficient Fracture Modeling Using a Hybrid Peridynamic Formulation
Mirco ZACCARIOTTO, Sebastiano GALEAZZO, Francesco SCABBIA, Ugo GALVANETTO 1427

Structural Batteries for Aeronautical Applications: A Multidisciplinary Analysis of Integration and Multifunctional Performance
M. MANGONE, S. MALLARDO, C. B. NIUTTA, A. CIAMPAGLIA, M. GUIDA, P. RUSSO, G. SANTAGATA, R. CIARDIELLO, F. MARULO, G. BELINGARDI 1432

Design and Prototyping of a Lunar Rover Wheel Using Additive Layer Manufacturing
Gaetano IPPOLITO, Rosario BORRELLI, Stefania FRANCHITTI, Marco RUSSO, Nunzia FAVALORO 1438

Numerical Modeling and Fabrication of Hybrid Metal-Ceramic Structures for Space Applications Using FDM Additive Manufacturing
Enrico ZAPPINO, Matteo FILIPPI, Alfonso PAGANI 1444

Fatigue Life Estimation in Frequency-Domain of Composite and Metallic Structures via CUF and Dirlik's Method
Elisa TORTORELLI, Giuseppe PALAIA, Erasmo CARRERA 1450

11. Human Factors, Cockpit & Operations

Application of Random Forest and HRV Analysis for Real-Time Pilot Mental Workload Monitoring: Toward an Intelligent Cockpit Support System
Carmelo Rosario VINDIGNI, Giuseppe IACOLINO, Antonio ESPOSITO, Calogero ORLANDO, Andrea ALAIMO 1456

Data-Driven Detection of Pilot-Induced Oscillations using Principal Component Analysis
André L. A. PALADINI, Raghu Chaitanya MUNJULURY, Daniel DREWIACKI, Petter KRUS, Jorge Henrique BIDINOTTO 1460

Integrated Rotorcraft Stability through Pilot Biomechanics: A Human Factors Perspective
Andrea ZANONI, Pierangelo MASARATI 1466

DLR Project NICo – Feasibility Study of an Alternate Airport Assistant for Pilots Deciding Where to Divert
Joan Iñaki GONZÁLEZ CABEZA, Sören PETERSEN, Jan-Philipp BUCH,

Dominik NIEDERMEIER, Matthias WIES, Anne PAPENFUß 1471

Visual Monitoring Behavior in Dual- and Reduced-Crew Configurations During Abnormal Events
Nicola PUCA, Marco POGLIANO, Gabriele LUZZANI, Giorgio GUGLIERI, Danilo DEMARCHI 1475

Continuous Time Estimation of Pilot Biodynamic Response for Vertical Bounce Coupling Assessment
Tommaso ARESI, Andrea ZANONI, Pierangelo MASARATI 1481

Navigating the New Frontier: The EU Space Act and its Impact on the European Aerospace Sector
Cecilia NOTA 1487

12. Systems Engineering, Digital Twins & Simulation

From Flight Test to a Simulator Model - System Identification of the ISTAR Research Aircraft
Christian RAAB, Anton DILCHER 1494

Another F-16 Simulation? A User-Friendly Julia, MATLAB, and Simulink Flight Simulation Package Suitable for Undergraduate Teaching
Duc NGUYEN, Mark LOWENBERG 1500

Integrated Model-Based Systems Engineering methodology for design, analysis and simulation of an Environmental Control and Life Support System for an Analog Habitat
Giacomo LUCCISANO, Loris GIANNINI, Nicole VIOLA, Roberta FUSARO 1505

Integrating Scenario-Based Life Cycle Assessment into Model-Based Systems Engineering for Space Exploration Systems Design
Giacomo LUCCISANO, Fabrizio BORGNA, Roberta FUSARO, Nicole VIOLA 1512

iDREAM 2.0: A Paradigm Shifts Towards Reusable Space Systems
Antonio GREGORIO, Roberta FUSARO, Nicole VIOLA, Davide FERRETTO, Giuseppe NARDUCCI, Valeria BORIO, Giacomo LUCCISANO, Marco VERRASCINA, Giuseppe DE BARI 1518

Digital Twinning for Onboard Health Monitoring of Solar Panels for Space Exploration Missions
Sachin SOLANKI, Francesco DI FIORE, Laura MAININI 1524

Temporal Decoupling of Weakly Coupled Systems in Hybrid Co-Simulation
Erik ROSENLUND, Robert HÄLLQVIST, Robert BRAUN, Petter KRUS 1530

An Experimental Co-Simulation Engine for Advanced Cyber-Physical Systems (CPS) Scheduling and Digital Twin Evaluation
Erik ROSENLUND, Robert HÄLLQVIST, Robert BRAUN, Petter KRUS 1537

Communication Architectures for System-of-Systems Engineering
Jorge L. LOVACO, Karl ZUBER, Raghu Chaitanya MUNJULURY, Petter KRUS 1544

Extended Reality Technologies for enhanced Public Acceptance of Urban Air Mobility: insights on the State of the Art
Millene GOMES ARAUJO, Francesca DE CRESCENZIO, Francesca STARITA, Giuseppe DI PELLEGRINO 1549

Urban Air Mobility: Trends and Economic Perspective in Europe and Italy
Gabriele LECIS, Leonardo CORBO, Francesca DE CRESCENZIO, Millene GOMES ARAUJO 1554

An Extended Reality-based Platform for Digital Twin applications in Urban Air Mobility and Advanced Air Mobility: Framework proposed within MOST Project
Francesca DE CRESCENZIO, Millene GOMES ARAUJO, Sara BAGASSI, Fabrizio LAMBERTI, Filippo Gabriele PRATTICO', Domenico ACCARDO, Claudia CONTE, Lorenza SABATINO, Marco BAZZANI 1559

FORTUNA: Design, Integration and Testing of a Technology Demonstrator for Space Exploration Rover
Enrico SABBATINI, Ludovica GIACCONI, Fabrizio STESINA, Stefano GIULIANELLI, Damiano CARRA, Massimiliano MORELLI, Federico FANTASTICO 1563

Ontology-Assisted Aircraft Cabin Design: A Data-Driven Approach Using Language Models
Raghu Chaitanya MUNJULURY, Jorge LOVACO, Ludvig KNÖÖS FRANZÉN, Petter KRUS 1568

Development of a Flexible Flight Simulation Design and Test Environment
Peter THOMAS, Joanna RAWSKA 1574

Keyword Index

Preface

The CEAS/AIDAA Conference 2025 was held in Turin, Italy, from December 1 to 4, 2025, co-organized by the Council of European Aerospace Societies (CEAS) and the Italian Association of Aeronautics and Astronautics (AIDAA).

The conference provided an international forum for researchers, engineers, and professionals to present and discuss recent advances in aerospace science and engineering. The program covered a broad range of topics, reflecting the diversity and evolving challenges of the aerospace sector.

The editors wish to thank the authors, reviewers, and members of the organizing and scientific committees for their valuable contributions to the conference's success.

Turin, Italy
December 2025

Committees

Conference Chairs

- Cornelia Hillenherms, German Aerospace Center – CEAS President
- Erasmo Carrera, Politecnico di Torino – AIDAA President

Executive Committee

- Andrea Alaimo – CEAS Director General
- Riccardo Augello – AIDAA Member
- Erasmo Carrera – AIDAA President
- Rosanna Daly – Conference Lead and UK Director, Advanced Business Events
- Nunzia Favaloro – Chair of the AIDAA Communication Committee
- Matteo Filippi – Politecnico di Torino – AIDAA Member
- Cornelia Hillenherms – German Aerospace Center, CEAS President
- Lukasz Kiszkowiak – Acting Editor-in-Chief, CEAS Quarterly Bulletin
- Erika Manis – Piemonte Agency
- Philip Nickenig – CEAS Vice-President Finance
- Giuseppe Palaia – Politecnico di Torino – AIDAA Member
- Beata Wierzbińska-Prus – CEAS Secretary

Scientific Committee (Scientific Board)

- Cornelia Hillenherms, German Aerospace Center – CEAS President
- Erasmo Carrera, Politecnico di Torino – AIDAA President
- Sergio De Rosa, Editor-in-Chief, *Aerotecnica Missili & Spazio*
- Marco Petrolo, Managing Editor, *Aerotecnica Missili & Spazio*
- Markus Fischer, Editor-in-Chief, *CEAS Aeronautical Journal*
- Janko Kreikemeier, Managing Editor, *CEAS Aeronautical Journal*
- Franco Bernelli, Editor-in-Chief, *CEAS Space Journal*
- Andrea Dieball, Managing Editor, *CEAS Space Journal*
- Johan Steelant, Managing Editor, *CEAS Space Journal*

Scientific Committee

- Christina Ahremark, The Swedish Armed Forces
- Andrea Alaimo, University of Enna Kore
- Tommaso Andreussi, Sant'Anna School of Advanced Studies
- Sophie Armanini, Imperial College London
- Riccardo Augello, Politecnico di Torino
- Giulio Avanzini, Università del Salento
- Ivano Benedetti, University of Palermo
- Carlo Bettanini, Università di Padova
- Chiara Bisagni, Politecnico di Milano
- Roberto Camussi, Roma Tre University
- Erasmo Carrera, Politecnico di Torino

- Damiano Casalino, TU Delft
- Matteo Ceriotti, University of Glasgow
- Andreas Chiaranda, ARTEC GmbH
- Maria Cinefra, Politecnico di Bari
- Camilla Colombo, Politecnico di Milano
- Jonathan Cooper, University of Bristol
- Francesca De Crescenzio, University of Bologna
- Emanuele Luigi De Angelis, University of Bologna
- Sarita Dara, Civil Aviation Authority, New Zealand
- Sam Diserens, UK Civil Aviation Authority
- Lorenzo Dozio, Politecnico di Milano
- Umut Durak, DLR
- Gerhard Ebenhoch, DGLR Technical Committee
- Antonio Esposito, University of Enna Kore
- Nunzia Favaloro, CIRA
- Jürgen Fecher, Zeppelin NT
- Matteo Filippi, Politecnico di Torino
- Roberta Fusaro, Politecnico di Torino
- Gabriella Gaias, Politecnico di Milano
- Thomas Geyer, DLR
- Tomasz Grabowski, Warsaw University of Technology
- Derek Greer, Flexible Executive Insights
- David Hansell, Irish Aviation Authority
- Albert S.J. van Heerden, University of Glasgow
- Cornelia Hillenherms, DLR
- Eric Hoffman, Eurocontrol
- Robert Hällqvist, SAAB Aeronautics
- Łukasz Kiszkowiak, Military University of Technology
- Petter Krus, Linköping University
- Philipp Krämer, Duale Hochschule Baden-Württemberg
- Ugo Lafont, ESA ESTEC
- Jianglin Lan, University of Glasgow
- Christian Langenbach, DLR
- Rhea Liem, Imperial College London
- Pierluigi Di Lizia, Politecnico di Milano
- Linghai Lu, Cranfield University
- Michele Maestrini, Politecnico di Milano
- Laura Mainini, Imperial College London
- Siva Marimuthu, University of Staffordshire
- Francesco Marulo, University of Naples Federico II
- Pierangelo Masarati, Politecnico di Milano
- Franco Mastroddi, Sapienza University of Rome
- Kristian Mears, Royal Air Force
- Joris Melkert, TU Delft
- Mihai Mihaescu, KTH Royal Institute of Technology
- Alberto Milazzo, University of Palermo
- Raghu Munjulury, Linköping University

- Björn Nagel, DLR
- Manju Nanda, National Aerospace Laboratories
- Duc Nguyen, University of Bristol
- Melike Nikbay, Istanbul Technical University
- Calogero Orlando, University of Enna Kore
- Alfonso Pagani, Politecnico di Torino
- Giuseppe Palaia, Politecnico di Torino
- Giovanni Palmerini, Sapienza University of Rome
- Antonio Paolozzi, Sapienza University of Rome
- Giuseppe Pascazio, Politecnico di Bari
- Marilena Pavel, TU Delft
- Anastasia Pesce, European Space Agency
- Marco Petrolo, Politecnico di Torino
- Fabrizio Ponti, University of Bologna
- Giuseppe Quaranta, Politecnico di Milano
- Carlo Riboldi, Politecnico di Milano
- Sergio De Rosa, University of Naples Federico II
- Karim Abu Salem, Politecnico di Torino
- Francesco Sanfedino, ISAE-SUPAERO
- Raffaele Savino, University of Naples Federico II
- Kaushil Solanki, Stirling Dynamics Ltd.
- Svjetlana Stekovic, Linköping University
- Jochen Wild, DLR
- Mohammad Yazdani-Asrami, University of Glasgow
- Mirco Zaccariotto, Università di Padova
- Enrico Zappino, Politecnico di Torino
- Tao Zhang, University of Glasgow

Editors

Erasmo Carrera, Politecnico di Torino – AIDAA President
Matteo Filippi, Politecnico di Torino – AIDAA Member

Artificial Intelligence, Machine Learning & Data Driven Methods



Materials Research Proceedings 69 (2026) 2-8 https://doi.org/10.21741/9781644904251-1

Detection of Aircraft Spoofing Using the GVA Parameter in ADS-B Data

Jakub TRÝB[1,a*], Jakub HOSPODKA[1,b]

[1]Czech Technical University in Prague, Department of Air Transport, Horská 3, Prague, Czechia

[a]jakub.tryb@cvut.cz, [b]hospodka@fd.cvut.cz

Keywords: GNSS Interference, ADS-B, GVA, Aircraft Navigation, Spoofing

Abstract. GNSS interference, including jamming and spoofing, represents a growing challenge to aviation safety. These disruptions critically impact systems reliant on accurate positional and altitude data, such as Enhanced Ground Proximity Warning Systems (EGPWS). Spoofing, in particular, can cause severe anomalies in aircraft position and altitude data, leading to erroneous system responses. This paper investigates the potential application of the GVA (Geometric Vertical Accuracy) parameter, derived from ADS-B data, as a means of detecting GNSS interference, with a specific focus on its relevance for EGPWS functionality. More than 110 flights were analysed, comparing GVA parameter behaviour in regions with and without reported GNSS interference. Regions of suspected interference were identified using NOTAMs, reports, and algorithms from SkAI Data Services. The analysis focuses on the correlation between GVA anomalies and known GNSS disruption events, examining altitude discrepancies (GNSS versus barometric altitude) and positional anomalies (e.g., erratic movements, off-route positioning, and sudden location shifts). The methodology includes data preprocessing to isolate flights affected by interference, statistical analysis of GVA fluctuations, and graphical representation of observed trends. Flights from interference-free areas served as a baseline for comparison. The results indicate that GVA anomalies are consistently associated with regions of reported GNSS spoofing. Spoofing events manifest as significant discrepancies in aircraft position and GVA altitude. The discussion highlights the implications of these findings for operational safety. The study emphasizes the potential for integrating GVA-based detection methods, enabling these systems to act as supplementary indicators of GNSS interference. Limitations of the study, including a gap in critical coverage that partially limits the completeness of the analysis and the reliance on available ADS-B data, are acknowledged, along with suggestions for future research. This study demonstrates the feasibility of using ADS-B parameters, the GVA, as an indirect method for detecting GNSS interference. Future work will focus on expanding the dataset to include flights from additional regions, refining detection algorithms, and exploring the integration of these methods into operational aviation systems. By addressing GNSS interference at a system level, this research aims to contribute to the development of robust solutions that enhance aviation safety in an increasingly challenging navigation environment.

Introduction

Global Navigation Satellite Systems (GNSS) form the backbone of modern civil aviation, supporting safety-critical applications such as ADS-B and RNAV [1], [2]. This strong dependence, however, introduces vulnerabilities to radio-frequency interference, particularly jamming and spoofing [3], [4]. While jamming typically results in a denial of service, spoofing is more hazardous as it generates counterfeit signals that mislead receivers without necessarily triggering immediate alarms [5]–[7]. Recent reports confirm that large-scale GNSS interference has become an active and globally relevant aviation safety issue [8], [9].

ADS-B broadcasts include integrity indicators defined in RTCA DO-260B and EUROCAE ED-102A standards [11], [12], such as the Geometric Vertical Accuracy (GVA). While parameters

Content from this work may be used under the terms of the Creative Commons Attribution 3.0 license. Any further distribution of this work must maintain attribution to the author(s) and the title of the work, journal citation and DOI. Published under license by Materials Research Forum LLC.

such as NACp have been investigated for interference detection [13], [14], the behaviour of GVA during GNSS spoofing remains insufficiently explored. A robust consistency reference can be obtained by comparing GNSS-derived geometric altitude with barometric altitude, which is independent of GNSS and therefore immune to spoofing effects [15].

This paper investigates the combined use of altitude discrepancy between barometric and GNSS-derived altitude and the GVA parameter as indicators of GNSS spoofing. Using ADS-B data from over 110 flights obtained from the OpenSky Network, nominal operations are compared with flights affected by suspected spoofing. The objective is to assess whether GVA provides meaningful supplementary information, particularly in subtle spoofing scenarios where altitude discrepancies remain small, thereby enhancing situational awareness of GNSS integrity degradation.

- **Data Source and Flight Selection**

ADS-B data were obtained from the OpenSky Network, a large-scale open air-traffic surveillance infrastructure composed of distributed ground-based receivers [16], [17]. The dataset covers the period from January 2024 to January 2025 and consists of more than 110 anonymized commercial flights operating in multiple airspace regions. The analysed dataset was divided into reference flights operating under nominal GNSS conditions and flights suspected of GNSS spoofing based on independent operational reports and the SKAI Data Services monitoring platform [18]. All aircraft identifiers and operational details were fully anonymized. Each ADS-B message provides barometric altitude, GNSS-derived geometric altitude, quality indicators, and precise time tags, forming the basis of the vertical-consistency analysis.

- **Altitude Consistency Metric**

The detection approach is based on the physical independence between barometric altitude and GNSS-derived geometric altitude. While barometric altitude is derived from onboard pressure sensors and is immune to GNSS interference, the geometric altitude directly depends on the integrity of the satellite navigation solution [15].

For each ADS-B message, the instantaneous altitude discrepancy was computed as

$$\Delta h(t) = h_{baro}(t) - h_{GNSS}(t) \quad (1)$$

where h_{baro} represents the barometric altitude and h_{GNSS} the geometric altitude derived from GNSS. Based on reference-flight behaviour and standard operational tolerances [1], a conservative detection threshold of $|\Delta h| > 200$ft was adopted.

- **Geometric Vertical Accuracy (GVA) Parameter**

The Geometric Vertical Accuracy (GVA) parameter transmitted in ADS-B Version 2 messages was analysed as a supplementary indicator. According to the RTCA DO-260B / EUROCAE ED-102A standard, GVA is a 2-bit indicator expressing the 95% confidence bound of the GNSS-derived vertical position [11], [12].

***Table 1** – GVA parameter encoding (95% confidence bound)*

Encoding	Meaning
0	Unknown or ≥ 150 m
1	< 150 m
2	< 45 m
3	< 15 m

Since GVA is derived from the internal receiver figure-of-merit models, it may not directly reflect malicious spoofing scenarios. Therefore, GVA is evaluated strictly as a complementary indicator and always interpreted jointly with the altitude discrepancy Δh.

- **Data Preprocessing and Quality Control**

All data processing was performed using MATLAB R2024b [19]. ADS-B messages with missing altitude or time information were removed. All timestamps were converted to Coordinated Universal Time (UTC), and both barometric and geometric altitudes were converted to feet to ensure consistency with aviation standards [1], [20]. The altitude discrepancy Δh was then computed for each time step using (1). For each flight, three synchronized time series were evaluated: barometric altitude, GNSS-derived geometric altitude, and $\Delta\, h$. These quantities were jointly visualized to assess the magnitude, duration, and temporal evolution of vertical inconsistencies. In parallel, GVA time series were analysed to evaluate their response to detected altitude anomalies. The classification of spoofed flights was validated by cross-comparison with independently reported spoofing intervals from monitoring services [18]. This external information was used solely for validation and not as a primary detection criterion.

Results – Altitude and GVA Analysis

The results of the combined analysis of altitude discrepancies and the ADS-B-reported GVA parameter are presented in this section. The results are organized from reference flights under nominal GNSS conditions to progressively more pronounced spoofing scenarios, highlighting both strong and subtle manifestations of GNSS integrity degradation.

- **Reference Flights – Nominal GNSS Operation**

Reference flights unaffected by spoofing or other forms of interference are used to establish a baseline for nominal GNSS behaviour, characterized by close agreement between barometric and GNSS-derived geometric altitude and stable GVA values throughout the flight.

Figure 1 – Reference flight under nominal GNSS conditions showing close agreement between barometric and GNSS-derived geometric altitude and stable GVA values.

Materials Research Proceedings 69 (2026) 2-8 https://doi.org/10.21741/9781644904251-1

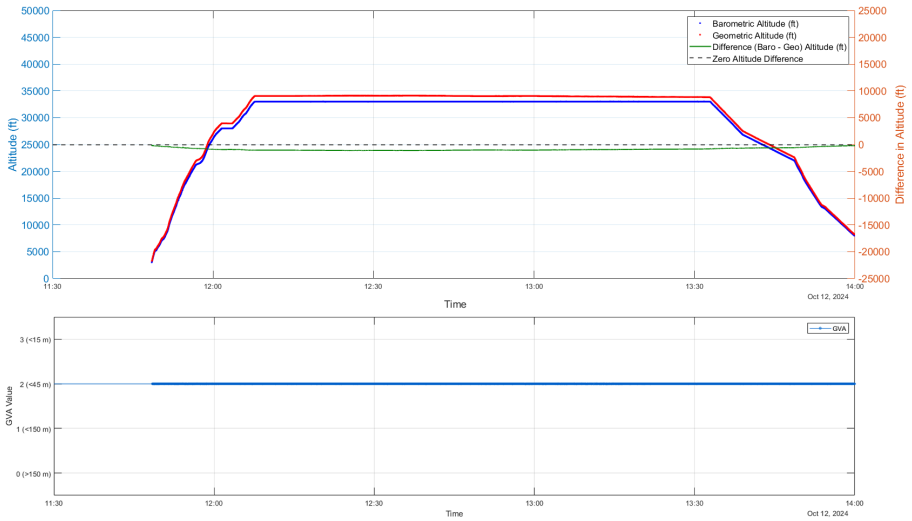


***Fig. 1** – Reference flight under nominal GNSS conditions*

- **Strong GNSS Spoofing – Large Vertical Discrepancies**

Flights affected by strong GNSS spoofing exhibit pronounced and persistent separation between barometric and GNSS-derived geometric altitude. These events are characterized by a sudden onset of large altitude discrepancies Δh, typically exceeding the 200 ft detection threshold, and persisting over extended time intervals.

Figure 2 – Spoofed flight A showing a large and persistent vertical discrepancy between barometric and GNSS-derived altitude, accompanied by a temporary interruption of ADS-B reporting during the cruise-to-descent transition.

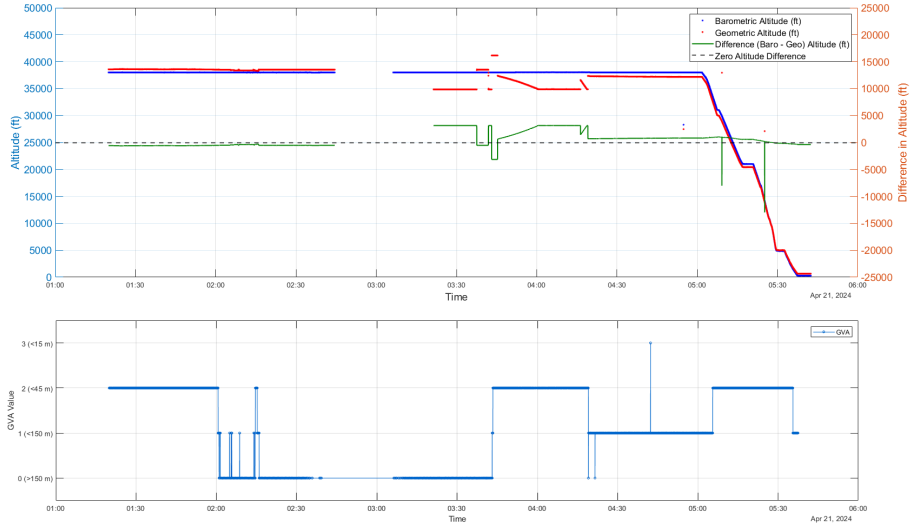


***Fig. 2** – Spoofed flight A (strong vertical discrepancy)*

Figure 3 – Spoofed flight B illustrating intermittent and discontinuous GNSS-derived altitude behaviour, visible as increased scatter and reduced temporal continuity, followed by the development of a sustained vertical discrepancy during descent.

Materials Research Proceedings 69 (2026) 2-8 https://doi.org/10.21741/9781644904251-1

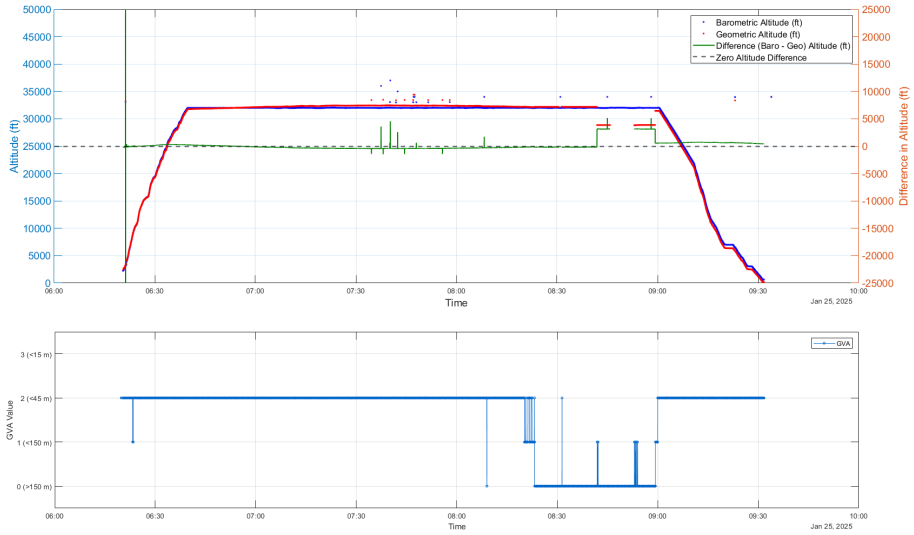


***Fig. 3** – Spoofed flight B (intermittent GNSS behaviour)*

- **Directional Properties of Altitude Discrepancies**

A consistent directional tendency in altitude discrepancies was observed across the analysed spoofed flights. In most strong spoofing cases, barometric altitude exceeded the GNSS-derived geometric altitude during peak discrepancy intervals, indicating a systematic downward bias of the spoofed GNSS solution. In a smaller subset of cases, the opposite behaviour was observed, with geometric altitude exceeding barometric altitude, suggesting upward manipulation of the GNSS solution. This directional asymmetry indicates that spoofing scenarios are not random but follow specific interference patterns.

- **Subtle Spoofing – GVA Response Below the Δh Threshold**

Not all spoofing events produce large vertical deviations. A subset of affected flights exhibits altitude discrepancies that remain below the 200 ft detection threshold throughout the flight. In these cases, the primary indication of degraded GNSS integrity is provided by changes in the GVA parameter rather than by Δh alone.

Figure 4 – Spoofed flight C exhibiting minimal vertical discrepancy remaining below the 200 ft threshold, while GVA indicates degraded GNSS integrity during the affected interval.

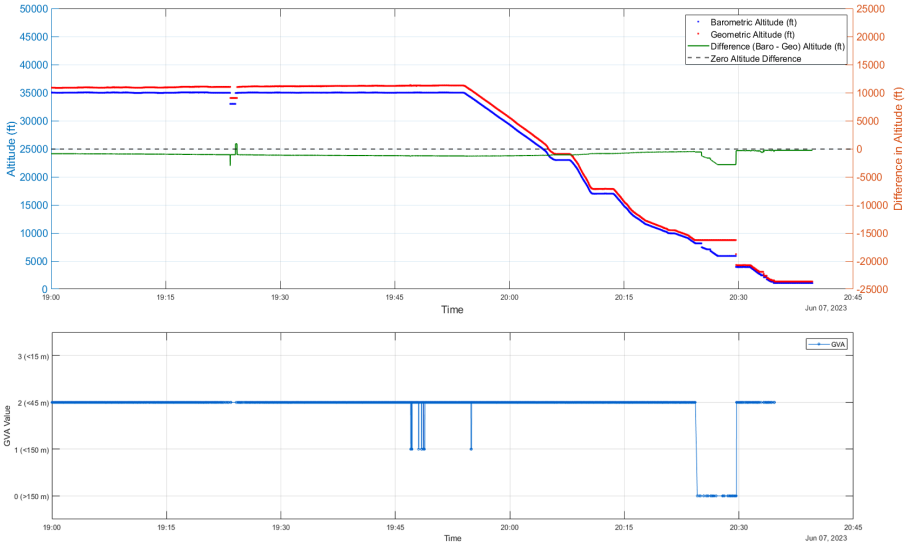


***Fig. 4** – Spoofed flight C (subtle spoofing)*

Discussion

The presented results demonstrate that vertical consistency analysis based on barometric and GNSS-derived geometric altitude provides a physically interpretable indicator of GNSS spoofing. Large spoofing events are clearly manifested as persistent altitude discrepancies exceeding the selected 200 ft threshold. In these cases, the onset of spoofing is typically abrupt and remains detectable over extended time intervals. More importantly, the analysis shows that the GVA parameter provides complementary information in cases where altitude discrepancies remain below the detection threshold. In such subtle spoofing scenarios, GVA degradation often precedes or accompanies minor vertical inconsistencies, indicating a deterioration of GNSS solution integrity that would otherwise remain undetected using altitude comparison alone. The results further indicate that spoofing-induced altitude deviations exhibit non-random directional properties, suggesting structured interference mechanisms rather than stochastic navigation errors. While GVA is not a direct spoofing detector, its joint interpretation with altitude consistency significantly improves situational awareness regarding GNSS integrity. It should be noted that ADS-B-based detection methods are inherently limited by message availability, update rates, and receiver-dependent quality indicators. Consequently, the presented approach is intended as a supplementary integrity-monitoring tool rather than a standalone detection system.

Conclusion

This study evaluated the feasibility of using ADS-B-reported Geometric Vertical Accuracy (GVA) in combination with barometric–GNSS altitude consistency as an indirect indicator of GNSS spoofing. The analysis of more than 110 operational flights demonstrated that strong spoofing events are reliably detectable through large and persistent vertical discrepancies, while subtle spoofing scenarios can be identified through characteristic changes in the GVA parameter.

The results confirm that GVA does not act as a standalone spoofing detector but provides valuable complementary information when interpreted jointly with physically independent altitude sources. This combined approach enables the detection of integrity degradation even in cases where altitude discrepancies remain within nominal operational limits. Future work will focus on expanding the dataset to additional geographic regions, refining quantitative detection thresholds, and integrating other ADS-B quality indicators to improve robustness. The presented methodology contributes to the development of passive, data-driven GNSS integrity monitoring techniques that can enhance aviation safety in environments affected by satellite navigation interference.

Acknowledgements

This work was supported by the Ministry of the Interior of the Czech Republic, grant No. VK01030071 – "*Aviation resilience against GNSS and ADS-B spoofing*" and Czech Technical University school grant reference SGS25/107/OHK2/2T/16.

References

[1] ICAO, Annex 10 - Aeronautical Telecommunications, Volume I - Radio Navigation Aids, International Civil Aviation Organization, Montréal, Canada, 2018.

[2] Parkinson, B. W., Spilker, J. J. (eds.), Global Positioning System: Theory and Applications, Volume I, American Institute of Aeronautics and Astronautics, Washington, DC, 1996.

[3] Kaplan, E. D., Hegarty, C. J. (eds.), Understanding GPS/GNSS: Principles and Applications, 3rd ed., Artech House, Norwood, MA, 2017.

[4] Humphreys, T. E., Detection Strategy for Cryptographic GNSS Anti-Spoofing, IEEE Transactions on Aerospace and Electronic Systems, Vol. 49, No. 2, 2013, pp. 1073-1090. https://doi.org/10.1109/TAES.2013.6494400

[5] Psiaki, M. L., Humphreys, T. E., GNSS Spoofing and Detection, Proceedings of the IEEE, Vol. 104, No. 6, 2016, pp. 1258-1270. https://doi.org/10.1109/JPROC.2016.2526658

[6] Montgomery, P. Y., Humphreys, T. E., Ledvina, B. M., A Multi-Antenna Defense: Receiver-Autonomous GPS Spoofing Detection, Inside GNSS, Vol. 4, No. 2, 2009, pp. 40-46.

[7] Tippenhauer, N. O., Pöpper, C., Rasmussen, K. B., Čapkun, S., On the Requirements for Successful GPS Spoofing Attacks, Proceedings of the 18th ACM Conference on Computer and Communications Security, Chicago, IL, 2011, pp. 75-86. https://doi.org/10.1145/2046707.2046719

[8] European Union Aviation Safety Agency (EASA), GNSS Interference - Operational Guidance, Safety Information Bulletin No. 2022-02, Cologne, Germany, 2022.

[9] International Air Transport Association (IATA), GNSS Interference and Aviation Safety, IATA Guidance Material, Montréal, Canada, 2023.

[10] FAA, Automatic Dependent Surveillance-Broadcast (ADS-B) Services, Federal Aviation Administration, Washington, DC, 2020.

[11] RTCA, Minimum Operational Performance Standards for 1090 MHz Extended Squitter Automatic Dependent Surveillance-Broadcast (ADS-B) and Traffic Information Services - Broadcast (TIS-B), RTCA DO-260B, Washington, DC, 2009.

[12] EUROCAE, Minimum Operational Performance Specification for 1090 MHz Extended Squitter ADS-B and TIS-B, ED-102A, EUROCAE, Saint-Denis, France, 2009.

[13] Schäfer, M., Lenders, V., Martinovic, I., Experimental Analysis of Attacks on Next Generation Air Traffic Communication, Applied Cryptography and Network Security (ACNS), Lecture Notes in Computer Science, Vol. 8479, 2014, pp. 253-271. https://doi.org/10.1007/978-3-642-38980-1_16

[14] Strohmeier, M., Smith, M., Schäfer, M., Lenders, V., Assessing the Impact of GNSS Spoofing on ADS-B, Proceedings of the 2018 IEEE/AIAA Digital Avionics Systems Conference (DASC), London, UK, 2018.

[15] Kayton, M., Fried, W. R., Avionics Navigation Systems, 2nd ed., John Wiley & Sons, New York, 1997. https://doi.org/10.1002/9780470172704

[16] Schäfer, M., Strohmeier, M., Lenders, V., Martinovic, I., Bringing Up OpenSky: A Large-Scale ADS-B Sensor Network for Research, Proceedings of the 13th International Symposium on Information Processing in Sensor Networks (IPSN), Berlin, Germany, 2014, pp. 83-94. https://doi.org/10.1109/IPSN.2014.6846743

[17] OpenSky Network, "The OpenSky Network - A Swiss Non-Profit Association," https://opensky-network.org, accessed Jan. 2025.

[18] SkAI Data Services GmbH, GNSS Interference Monitoring Platform, Germany, 2024.

[19] MATLAB, version R2024b, The MathWorks Inc., Natick, MA, USA, 2024.

[20] ICAO, Procedures for Air Navigation Services - Aircraft Operations (PANS-OPS), Doc 8168, Volume I, International Civil Aviation Organization, Montréal, Canada, 2018.

Materials Research Proceedings 69 (2026) 9-14 https://doi.org/10.21741/9781644904251-2

Immersive Virtual Reality Framework for Lunar Pressurized Rover Training and Interaction

Dario Zamani[1,a *], Mehran Bahojb Ghalibafan[2,b], Marco Crestini[1,c], Matteo D'Aquila[1,d], Magesh Chandramouli[3,e], Alfonso Pagani[1,f], Marco Petrolo[1,g], and Erasmo Carrera[1,h]

[1]MUL 2 Lab, Department of Mechanical and Aerospace, Engineering, Politecnico di Torino, Corso Duca degli, Abruzzi 24, 10129 Turin, Italy

[2]Department of Architecture, Construction and Design, Politecnico di Bari, Via Edoardo Orabona 4, 70126 Bari, Italy

[3]Computer Graphics Technology, Purdue University Northwest, 2200 169th Street Hammond, IN, USA

[a]dario.zamani@polito.it, [b]m.bahojbghalibafan@studenti.poliba.it, [c]marco.crestini@studenti.polito.it, [d]matteo.daquila@studenti.polito.it, [e]mchandr@pnw.edu, [f]alfonso.pagani@polito.it, [g]marco.petrolo@polito.it, [h]erasmo.carrera@polito.it

Keywords: Virtual Reality, Lunar Pressurized Rover, Immersive Simulation, Digital Twin, Astronaut Training, 3D Modeling

Abstract. This work presents an immersive Virtual Reality framework integrated into a digital twin architecture for the Lunar Pressurized Rover (LPR). The system enables both dynamic simulation of rover operations on simulated lunar terrain and static exploration of its internal layout. Users can interact in real time with cockpit controls, onboard systems, and functional subsystems such as navigation, power, and life support. The framework supports astronaut training, ergonomic assessment, and early design validation, offering a human-centered, cost-effective tool for developing and testing future lunar exploration vehicles.

Introduction

The development of Lunar Pressurized Rovers (LPR) necessitates innovative approaches to design, validation, and training, given the absence of prior operational experience, test campaigns, or physical prototypes [1-2]. To address these challenges, this work presents an immersive virtual environment integrated into a full digital twin architecture, enabling human-centered design exploration, interactive control simulation, and early design insight [3-4].

The virtual platform supports two complementary modes: dynamic simulation and static exploration. In the dynamic simulation mode, users operate a fully interactive digital replica of the LPR within a simulated lunar terrain (Fig. 1). The interface includes cockpit-mounted VR menus for real-time interaction with rover systems. The primary control panel allows users to initiate the rover, toggle between gear modes (Park, Neutral, Drive, and Reverse), and activate auxiliary systems, including Cruise Control and All-Wheel Steering (AWS). A secondary menu enables in-depth interaction with navigation, lighting, onboard cameras, power management, and telemetry displays, including speed, battery status, oxygen level, acceleration, wheel torque, and center of mass tracking. These features provide a realistic operational environment for astronaut and operator training, system diagnostics, and scenario testing [5-6].

Content from this work may be used under the terms of the Creative Commons Attribution 3.0 license. Any further distribution of this work must maintain attribution to the author(s) and the title of the work, journal citation and DOI. Published under license by Materials Research Forum LLC.

Materials Research Proceedings 69 (2026) 9-14 https://doi.org/10.21741/9781644904251-2

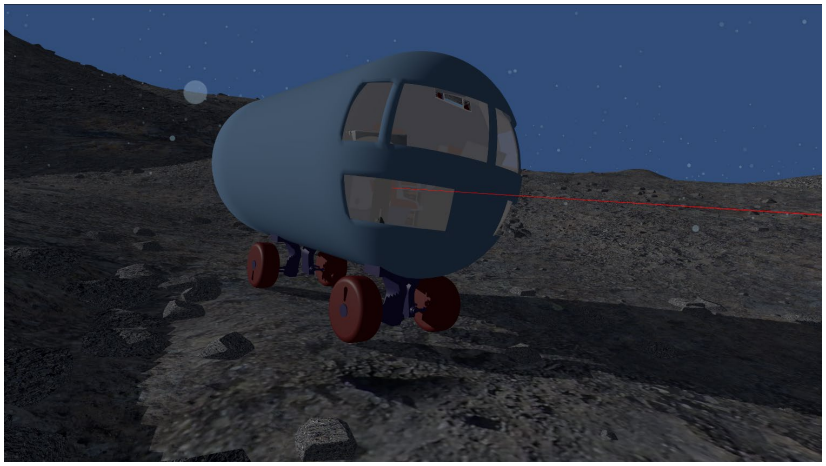


Figure 1. Simulated lunar terrain used in the dynamic mode for immersive operation of the Lunar Pressurized Rover (LPR), enabling real-time interaction with rover systems and environmental navigation.

The static exploration mode focuses on internal layout and functional inspection. Based on a functional flow diagram depicted in Fig. 2, the LPR is decomposed into five subsystems: cockpit, scientific workspace, EVA interface and airlock, crew and utility section, and emergency systems. Each subsystem is modeled with interactive elements and associated tasks, allowing users to explore the internal environment, interact with displays and equipment, and assess ergonomic configuration [7]. The cockpit section includes two reclining seats, multi-functional displays for navigation and system control, and a panoramic viewing system with integrated cameras (Fig. 3). The scientific workspace enables procedural interaction for tasks such as lunar sample handling, analysis, and storage.

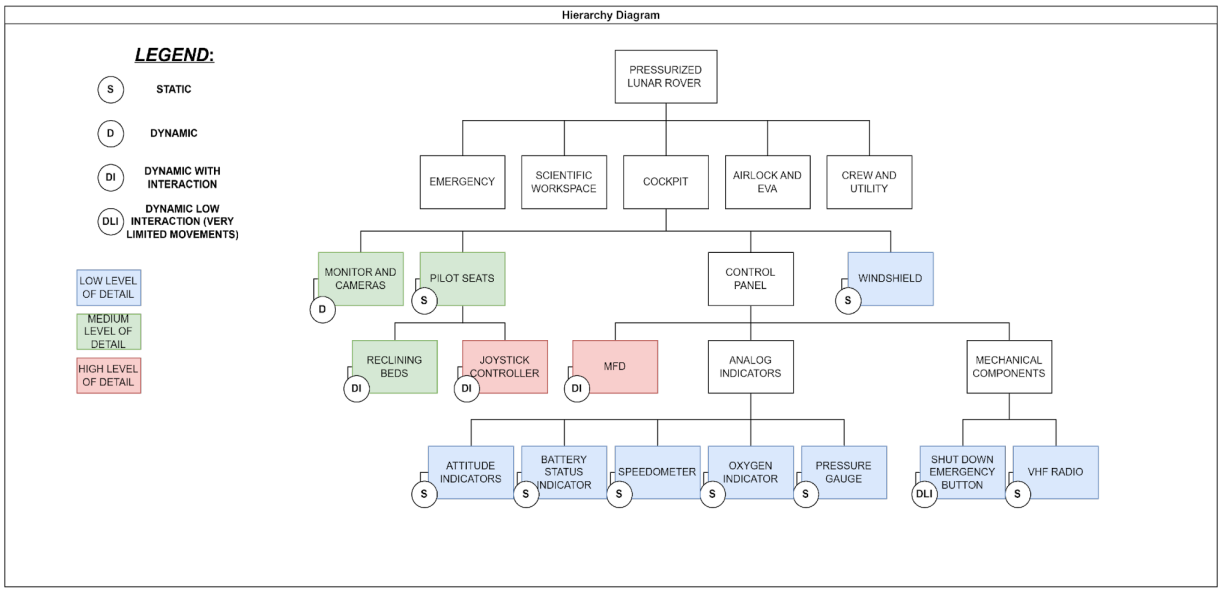


Figure 2. Hierarchical functional diagram of the pressurized lunar rover, showing subsystem decomposition and classification of components by interaction type (static, dynamic, interactive) and simulation detail level.

Together, these two modes provide an integrated environment for both system-level prototyping and mission-specific training [8]. The use of VR from the early stages of design provides a precise spatial perception of volumes and interfaces, which is critical in the absence of physical mock-ups. Human factors are integrated directly through spatial interaction and real-time feedback,

Materials Research Proceedings 69 (2026) 9-14 https://doi.org/10.21741/9781644904251-2

improving the placement and accessibility of control systems [9]. Moreover, the virtual model can serve as the front end of a complete digital twin, enabling predictive maintenance through the real-time overlay of telemetry and diagnostic data [10]. This supports fault detection, system health monitoring, and mission planning with a proactive approach to rover operations.

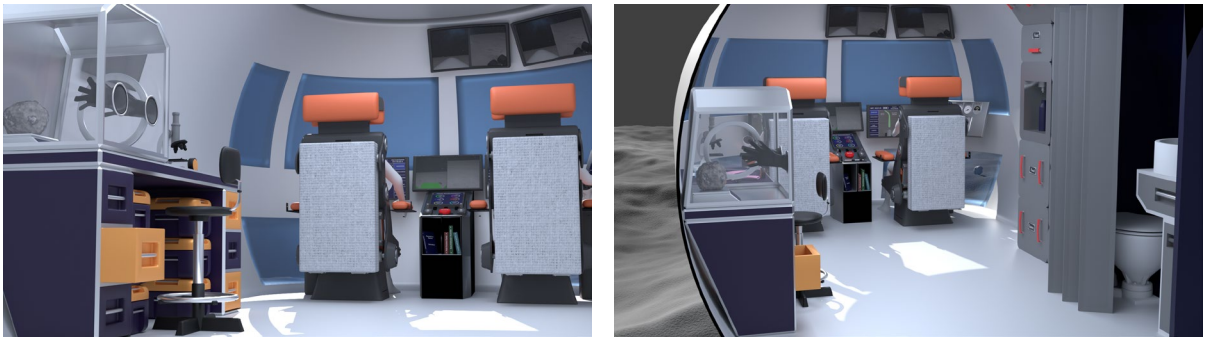


Figure 3. Interior rendering of the pressurized lunar rover showing the cockpit and scientific workspace. The configuration displays ergonomic seating, panoramic screens, multifunctional displays, and a dedicated area for lunar sample analysis and storage.

Cockpit Virtual Environment

One important section of the static exploration mode is the cockpit. In this area, users perform a sequence of tasks aimed at preparing the system for the lunar surface exploration mission. The first step is to perform a functional analysis to break down the cockpit into subsections; after a few iterations the component level is reached. The modeling phase is based on the items identified in the previous step, using aircraft and space systems as a reference for the necessary mesh detailing. Another important topic is the arrangement of elements around the seats: the first inspiration comes from a plane control panel, with a very high level of redundancy, then followed by a more automotive-centered layout, with less redundant components and with a higher distinction between the two crew members' functions. It is also essential to add ergonomic considerations to ensure that every object the crew must interact with is within reach and the configuration is guided by a principle of priority and frequency of use. The last important point is the creation of materials, aiming at reproducing the look and feel of a real environment to increase the sense of immersion. Before focusing on the actual software implementation, extensive preproduction work must be done to identify the precise input-output sequence that users will perform. This process has major impact on the time spent developing the simulation: very detailed studies for every single subtask to be achieved lead to a smoother implementation job. Virtual reality development focuses on establishing an effective interaction between users and the system's interface in front of them. C# scripts are the main way to bring models into life. The simulation is organized as follows: a script, called user interface manager, rules over the instruction messages that show up to guide the players; a second key script is the multi-functional display manager, it controls the navigation within the main interactable display. Additional scripts are created to provide specific methods needed during certain tasks or special out-of-nominal conditions. The result of this work is a sequence of five tasks, with instructions following the users along their path and marking the completion of each single required activity. The first one asks users to turn on the multi-functional display for the first time and to perform a check of the life-support system's status; two problems arise during the inspection of the menu, but users have the necessary support to solve them. The second task focuses on setting up the external camera views in the screens located in the cockpit around the pilot seat, serving as aid during the driving. The third guides the trip planning via the navigation menu and teaches users how to display all the critical data to be accessed during the

rover's movement. Other two tasks demonstrate the configuration of the sleeping area and how to handle an emergency.

Unity Simulation

Unity was selected as the development environment due to its real-time rendering capabilities, integrated physics engine, VR compatibility, and versatility in simulating interactive systems. Given that stakeholder training represented a primary project objective, Unity's C# scripting environment enabled the development of customized interaction logic to enhance user engagement, manoeuvrability, and system responsiveness. A dedicated simulation terrain was constructed to evaluate rover performance under lunar like operational conditions. As illustrated in Fig. 4 an interactive menu system designed for a better manipulation. The system includes a main menu, where user can monitor the speed, time, energy level and Oxygen level. A lighting setup designed to imitate the lighting conditions on the Moon, with three groups of lights: wheel lights, interior lights, and headlights. A multi-camera system is also implemented, giving the user side-mirror views, wheel-mounted camera views, and a 360-degree camera for better awareness of the surroundings. In addition, a power-management panel allows the user to adjust the rover's power based on the situation, with numeric input controls to improve accuracy. A navigation display shows the path already travelled by using the stored movement data, and the data-logging system records important values such as position, velocity, acceleration, and each wheel's torque. The user can start or stop the simulation at any time, and the recorded data are exported as a .xlsx file for further analysis. All features are integrated into a VR interactive menu, where the right-hand controller is used for acceleration and braking, and the left-hand controller is used to interact with the menu, giving the user intuitive and efficient control during the simulation. These sections are integrated into an interactive menu accessible through the Meta Quest 2 VR headset. To ensure effective control of both the menu and the rover, the VR controllers are configured to provide maximum ease of use and operational efficiency. The right-hand controller is assigned to control the rover's acceleration and braking, while the left-hand controller is used to interact with the on-screen menu and its functions.

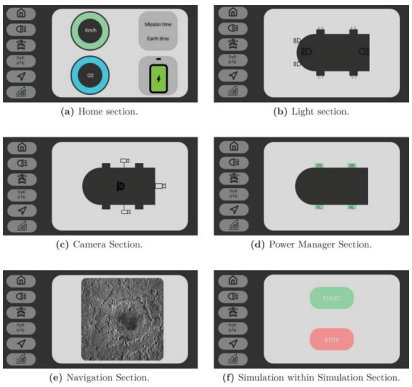


Figure 4. The interactive menu of the Roover.

Scientific Workspace Virtual Environment

The scientific workspace is the LPR's onboard workbench used in static exploration to inspect internal layout, equipment, and conduct moon sample analysis experiments. In this mode, users can explore the laboratory and interact with instruments to complete the related tasks. The workspace is modeled around a workbench equipped with different useful tools for measurement and inspection, a microscope, and a local monitor for task prompts and readouts. A sealed chamber (glovebox) with integrated gloves enables manipulation of regolith while preventing dust

dispersion inside the rover (Fig. 4). Visual fidelity focuses on highly interactive tools, including baked textures for regolith to preserve surface detail in real time. As with the cockpit, the scientific workspace was first decomposed through a functional analysis. Before implementation, a detailed input–output storyboard was created for each subtask (inputs: grabs, button presses, tool contacts; outputs: UI prompts, instrument readings, state changes). This upfront mapping shortened implementation time and ensured that every interaction in VR corresponds to an explicit, verifiable outcome. As seen in the previous section, the task sequence is implemented in Unity through C# scripts that manage state transitions and user interactions. A VR storyboard shows the workspace as a sequence of tightly scoped training tasks whit event-driven scripts that handle collisions, grabs and UI prompts:

- Sample selection & setup: The user opens the sealed box UI, selects a sample/object set, and confirms to lock into glovebox view with the chosen items inside.
- Weighing, sizing, and subdivision: Inside the glovebox, the trainee weighs the sample (balance readout on UI), measures dimensions, fractures it with a hammer, and repeats measurements on fragments—all with immediate UI feedback.
- Microscope analysis: After exiting glovebox view, a selected fragment is placed in the microscope; here it's possible to zoom/rotate controls for close inspection and to gather more data.
- Data capture & verification: Results are recorded in a notebook UI; a "Check Answers" step flags correct/incorrect entries and reports a score on the bench monitor.
- Emergency drill (workspace-linked): If an onboard alert triggers, the trainee leaves the bench, wears a suit in a prescribed order, and returns to diagnose the fault via the workspace monitor, reinforcing cross-section readiness while remaining anchored to lab operations.



Figure 4. VR rendering of the sealed-box interior showing the sample measurement and tool selection. The configuration displays interactive hands, various instruments, and a panel for choosing what to bring inside the box.

Conclusions

By integrating immersive simulation, functional modeling, and predictive analytics, the proposed framework reduces development time and costs, enhances system reliability, and facilitates real-time operational decision-making in planetary surface missions. The developed virtual environments for the cockpit and scientific workspace demonstrate how VR can effectively support human-centered design, procedure validation, and astronaut training. The approach enables early evaluation of ergonomics, system accessibility, and task sequences before physical prototypes exist. Future developments will extend the framework toward a fully integrated digital twin with real-time telemetry, haptic feedback, and interactive mission simulations.

Acknowledgments
This study was carried out within the Space It Up project funded by the Italian Space Agency, ASI, and the Ministry of University and Research, MUR, under contract n. 2024-5-E.0 - CUP n. I53D24000060005.

References

[1] M. Bhardwaj, V. Bulsara, D. Kokan, S. Shariff, E. Svarverud, and R. Wirz, "Design of a Pressurized Lunar Rover", NASA Technical Report NAS 1.26:192033, 1992.

[2] M. Interbartolo, W. O'Neill, and A. Chandler, "Forging Lunar Pressurized Rovers for Artemis," in 2024 IEEE Aerospace Conference, 2024, pp. 1-9. https://doi.org/10.1109/AERO58975.2024.10521267

[3] L. Hochberg, "Exploring the Role of Simulation-Based Design Principles in Support of Transportation and Material Handling Activities for the Lunar Mission", IEEE International Conference on Systems, Man and Cybernetics (SMC), 2019. https://doi.org/10.1109/SMC.2019.8914298

[4] M. Daniele, G. Quaranta, P. Masarati, and A. Zanoni, "Pilot-in-the-loop simulation of helicopter-ship operations using virtual reality," Aerotec. Missili Spaz., vol. 99, pp. 53-62, 2020. https://doi.org/10.1007/s42496-020-00037-3

[5] V. Garg, V. Singh, and L. Soni, "Preparing for Space: How Virtual Reality is Revolutionizing Astronaut Training", IEEE International Conference for Women in Innovation, Technology & Entrepreneurship (ICWITE), Bangalore, India, 2024, pp. 78-84. https://doi.org/10.1109/ICWITE59797.2024.10503238

[6] A. D. Garcia, J. Schlueter, and E. Paddock, "Training Astronauts using Hardware-in-the-Loop Simulations and Virtual Reality" NASA Johnson Space Center, Virtual Reality Laboratory, Houston, United States.

[7] M. Chandramouli, 3D Modeling & Animation: A Primer, 1st ed., CRC Press, 2021. https://doi.org/10.1201/9780429186349-1

[8] E. L. Seedhouse, "Avatar Influence and Cognitive Performance in a Virtual Spacecraft Environment: A Pilot Study," Aerotec. Missili Spaz., 2025. https://doi.org/10.1007/s42496-025-00274-4

[9] G. Franchini, B. Tuberga, and M. Chiaberge, "Advancing lunar exploration through virtual reality simulations: a framework for future human missions" Proc. Int. Astronautical Congress, 2024. https://doi.org/10.52202/078372-0023

[10] A. E. M. Casini, P. Maggiore, N. Viola, V. Basso, M. Ferrino, J. A. Hoffman, and A. Cowley, "Analysis of a Moon outpost for Mars enabling technologies through a Virtual Reality environment" Acta Astronautica, vol. 143, pp. 353-361, 2018. https://doi.org/10.1016/j.actaastro.2017.11.023

Materials Research Proceedings 69 (2026) 15-20 https://doi.org/10.21741/9781644904251-3

Single Controller for Multiple Aircraft by Deep Reinforcement Learning

Fatih Ahmet SARIGUL[1,a] and Ismail BAYEZIT[1,b,*]

[1]Istanbul Technical University, Faculty of Aeronautics and Astronautics, 34469, Maslak, Istanbul, Turkey

[a]sarigul20@itu.edu.tr, [b]bayezit@itu.edu.tr

Keywords: AI-Based Control, Generalized Flight Control, Deep Reinforcement Learning (DRL), Fixed-Wing Aircraft Control

Abstract. This study introduces a DRL-based controller for multiple fixed-wing aircraft without model-specific tuning. The proposed system is trained using Proximal Policy Optimization (PPO) and is enhanced by algorithmic strategies such as multi-model training and kinematics-based reward shaping to ensure generalization across diverse platforms. It is compared with a conventional method to see if the generalized controller maintains high control performance at the level of an aircraft-specific design. This approach presents an adaptable alternative to conventional control design, offering resilience to configuration changes, and providing reduced dependency on the model.

Introduction

This work proposes a new approach to flight control by making it more general rather than being aircraft-specific. In this sense, a single controller can handle multiple aircraft's control by itself without any reconstruction or recalibration. It is expected that such a controller can be used like a plug-and-play system across aircraft platforms that are distinct in many ways. In other words, this controller is not specific to any of the aircraft worked on but general for all of them.

The generalized control concept can offer numerous advantages over conventional methods such as scalability, adaptability, reduced maintenance and tuning, lower development costs, and reduced dependency on specific models. This new design logic, unlike conventional aircraft-specific control system design, provides two important innovations to flight control. First, such a control system can be used for more than one aircraft. Second, such a controller can show good control performance even in the face of unknown or previously unseen flight dynamics. On the other hand, this approach may raise questions about optimality, which is the main advantage of aircraft-specific control design.

Background

As an initial step, to construct a testbed environment for the proposed control system design, five distinct fixed-wing aircraft models shown in Fig. 1 have been selected.

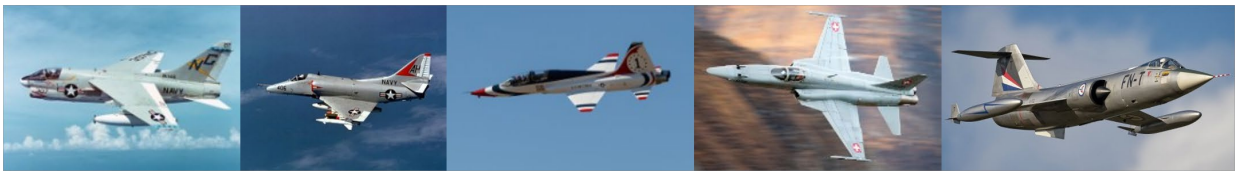


Figure 1: Five aircraft models

These models provide a good base for the multiple aircraft definition since they clearly present different dynamics, and also for generalization concept because they are similar due to being military aircraft. Besides that, they have already been subjected in a valuable work called "Aircraft

Content from this work may be used under the terms of the Creative Commons Attribution 3.0 license. Any further distribution of this work must maintain attribution to the author(s) and the title of the work, journal citation and DOI. Published under license by Materials Research Forum LLC.

Materials Research Proceedings 69 (2026) 15-20 https://doi.org/10.21741/9781644904251-3

Stability and Control Data" conducted by Gary L. Teper in 1969 [1]. This paper contains useful data including aerodynamic derivatives and coefficients obtained from mostly wind tunnel tests. This facilitates the aircraft modeling process and increases the fidelity. However, this paper is not the only source of the data because there are some missing parts. Therefore, computational tools such as DATCOM [2] and OpenVSP [3] have also been used in compiling the required data. Table 1 shows the data sources for the aircraft models;

Table 1: Main source of aerodynamic data for aircraft models

Aircraft	Data Source
A-7A	Teper
A-4D	Teper
T-38	Teper + DATCOM
F-5A	OpenVSP
F-104	Teper + OpenVSP

Other missing parameters which will be used in the flight simulation have been estimated by using standard analytical methods [4, 5]. Using low fidelity computational tools and analytical estimation methods can cause loss in fidelity for the modeling process. However, this is not important in the sense of this work because these models will be sufficient as long as they properly represent aircraft dynamics and they are different. Different sizes, shapes, and body-wing-tail configurations shown in Fig. 2 ensure that these are distinct models, and they will show different flight behaviors.

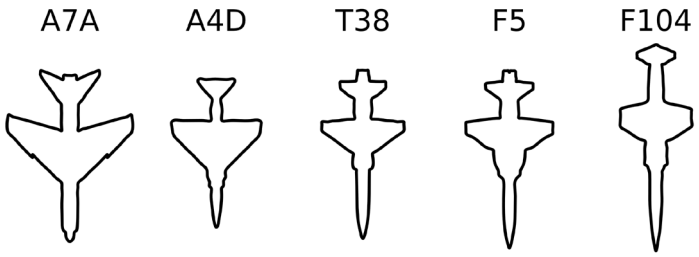


Figure 2: Five models at the same length scale

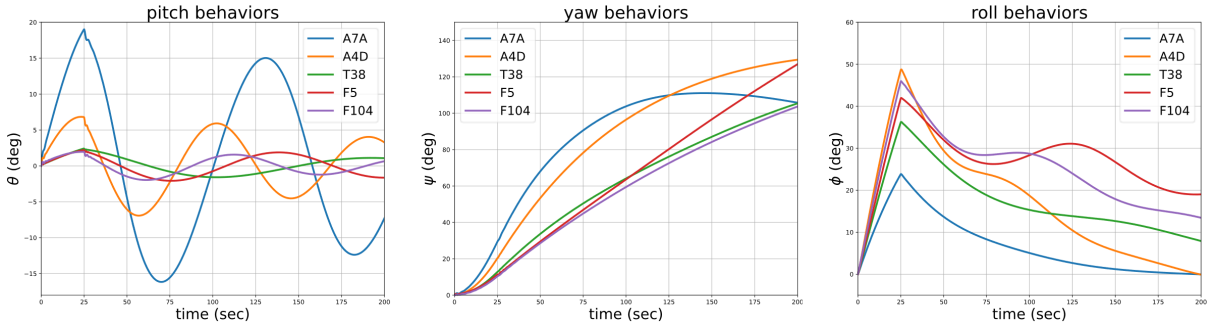


Figure 3: Aircraft behaviors in terms of Euler angles

How different these aircraft behave either in the presence or absence of control input can be seen in Fig. 3 where first 25 seconds the elevator, rudder and ailerons are held at 5, 5, and 3 degrees deflections, respectively and then released. These plots show that neither natural behaviors nor the control input reactions are the same for all the models nevertheless there is a general pattern.

Materials Research Proceedings 69 (2026) 15-20 https://doi.org/10.21741/9781644904251-3

Methodology

In this work, a DRL-based control approach is used in which a control agent is trained by using the PPO algorithm [6]. The learning procedure as an Markov Decision Process MDP [7] is integrated with the flight simulation where the aircraft's equation of motion with 6 degree of freedom is solved by Runge-Kutta [8] integration. This process can be seen below in Fig. 4;

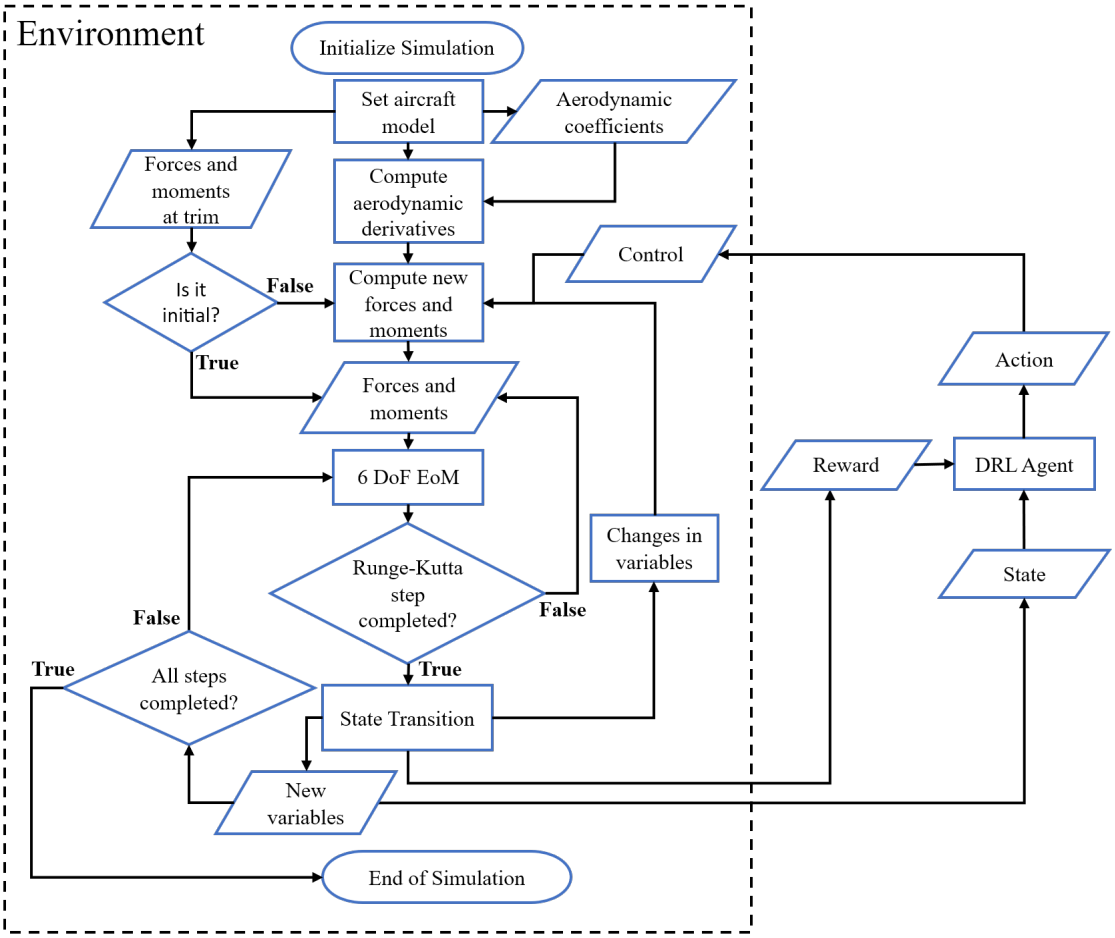


Figure 4: MDP with flight simulation environment

Since the task is attitude control, the difference between Euler angles and reference (desired) angles are used as state parameters. It becomes directly Euler angles themselves where the reference values are zeros. However, this state definition is too instantaneous and does not give much information about the kinematics. For this reason besides the current Euler angles, previous Euler angle values are also added as state parameters to get information about direction and the change of angles. Also, action space is already predetermined as control inputs which are elevator, throttle, aileron and rudder change. The reward function is defined in terms of norm of the state vectors since this vector gives us the proximity to the desired values.

$$S = [\theta_c \quad \psi_c \quad \phi_c \quad \theta_p \quad \psi_p \quad \phi_p] \tag{1}$$

$$A = [\delta e \quad \delta T \quad \delta a \quad \delta r] \tag{2}$$

Materials Research Proceedings 69 (2026) 15-20 https://doi.org/10.21741/9781644904251-3

$$R = \left(\frac{1}{s}\right) - s \quad \text{where} \quad s = \text{norm}(S) \tag{3}$$

Results

The results are obtained for two tasks which are leveling and turning. In leveling, the aircraft start with deflected Euler angles from trim point and the controller tries to bring them back to zero. It can be considered as stabilization and thus the controller fulfills the stability augmentation task here. When the aircraft are left to their own devices for 10 degrees distributed angles, they behave as shown in Fig. 5;

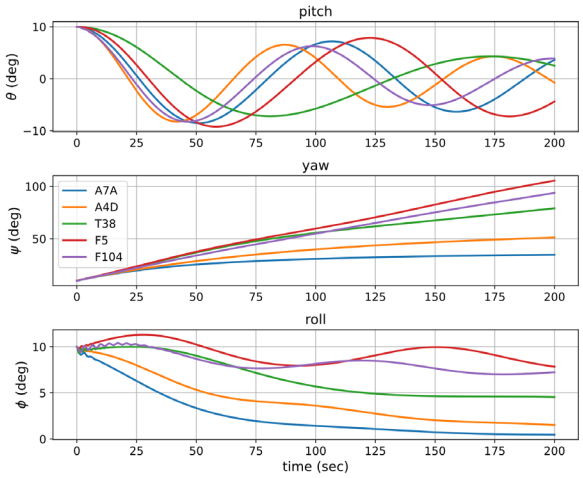


Figure 5: Stick-free motion in the presence of distribution

When the single DRL control agent steps in, it works for all five aircraft as shown in Fig. 6;

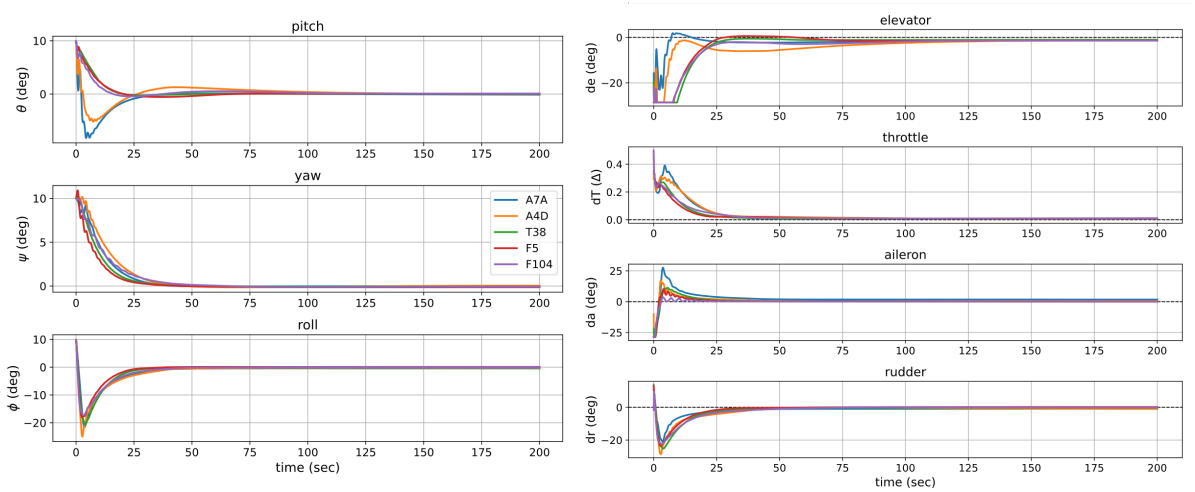


Figure 6: Stability augmentation with DRL controller

The controller is also tested for a task where the agent needs to bring Euler angles to predefined values and hold them there. This makes the aircraft turn their heading to a certain direction.

Materials Research Proceedings 69 (2026) 15-20 https://doi.org/10.21741/9781644904251-3

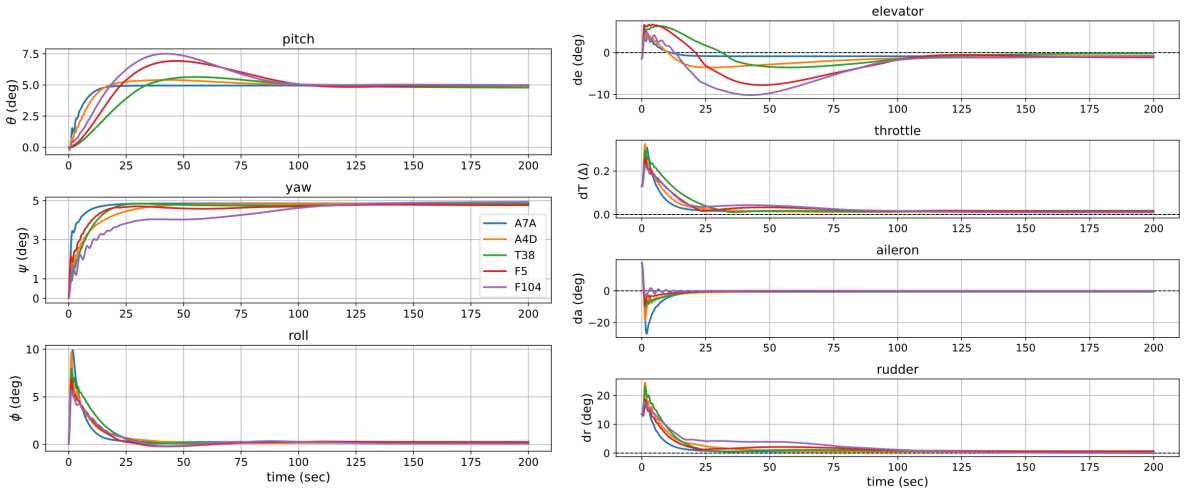


Figure 7: Turning control with DRL controller

The above results in Fig. 7 show that a single control agent can be used for control of multiple aircraft. On the other hand, we also need to test control performance for the DRL agent. For this reason, the A7A aircraft is taken as the sample and the DRL based controller is compared with an LQR controller. As seen in Fig. 8 the DRL-based controller can show performance at the level of the LQR controller, however making it generalized for multiple aircraft has caused some changes in performance. This trade-off between optimality and adaptability can be considered acceptable when taking account that a single controller can handle five aircraft.

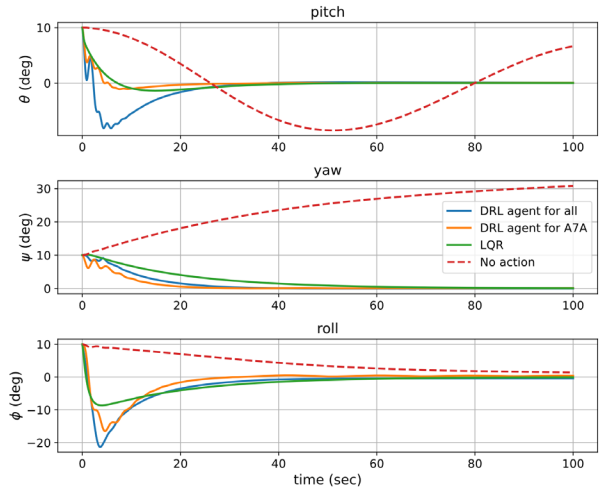


Figure 8: Comparison with LQR for A7A

Conclusion

This study has demonstrated that a single DRL-based controller trained via multi-model learning can effectively manage attitude control tasks for multiple fixed-wing aircraft without making model-specific adjustments. Though the generalized controller has exhibited a compromise in optimality compared to an aircraft-specific LQR controller, this trade-off is acceptable given the significant gain in adaptability and scalability. Overall, the results confirm that DRL offers a promising path toward generalized flight control that reduce dependence on individual models.

Acknowledgments
This research study is conducted at the ITU Model-Based Design and Control Systems Laboratory. This project is financially supported by the Scientific Research Projects Coordination Unit of Istanbul Technical University (ITU) Research Fund with Project ID: 47556.

References

[1] G.L. Teper, Aircraft stability and control data, No. NASA-CR-96008 (1969)

[2] J.E.Williams, and S.R. Vukelich, The USAF stability and control digital DATCOM, Volume I Users manual, No. AFFDLTR793032 VOL1 (1979). https://www.pdas.com/datcom.html

[3] R.A. McDonald, J.R. Gloudemans, Open vehicle sketch pad: An open source parametric geometry and analysis tool for conceptual aircraft design, AIAA SciTech 2022 Forum, p. 0004 (2022). https://doi.org/10.2514/6.2022-0004

[4] R.C. Nelson, Flight stability and automatic control, Vol. 2. New York: WCB/McGraw Hill, 1998.

[5] R.A. MacDonald, M. Garelick, J. O'grady, Linearized mathematical models for De Havilland Canada'Buffalo and Twin Otter'STOL transports. No. TSCFAA718 (1971).

[6] J. Schulman, F. Wolski, P. Dhariwal, A. Radford, O. Klimov, Proximal policy optimization algorithms, arXiv preprint arXiv:1707.06347 (2017). https://doi.org/10.48550/arXiv.1707.06347

[7] R.S. Sutton, A.G. Barto, Reinforcement learning: An introduction, Vol. 1, no. 1. Cambridge: MIT press, 1998.

[8] J.C. Butcher, Numerical methods for ordinary differential equations, second ed., John Wiley & Sons, 2008, pp. 137-317

Materials Research Proceedings 69 (2026) 21-24 https://doi.org/10.21741/9781644904251-4

Comparative Analysis of Generative Data Augmentation Techniques for Aircraft Damage Detection Algorithms: A Case Study

Salvatore MEROLA[1,a *], Aditi MHATRE[2,b], Ann-Kathrin KOSCHLIK[2,c], Michele GUIDA[1,d], and Francesco MARULO[1,e]

[1]University of Naples Federico II – Dept. of Industrial Engineering, Naples, Italy

[2]German Aerospace Center (DLR) - Institute of Maintenance, Repair and Overhaul, Hamburg, Germany

[a]salvatore.merola@unina.it, [b]aditi.mhatre@dlr.de, [c]Ann-Kathrin.Koschlik@dlr.de, [d]michele.guida@unina.it, [e]francesco.marulo@unina.it

Keywords: Aircraft Maintenance, Generative AI, Data Augmentation, Computer Vision, Digital Optics

Abstract. This study addresses the challenge of limited annotated data in aircraft surface damage detection by evaluating generative models for data augmentation. Conducted within the CINNABAR 2 project with DLR MRO institute in Hamburg (DE), it compares Generative Adversarial Networks (GANs) and Diffusion Models for producing realistic synthetic images. Real data are collected from smartphones, DSLRs, and robotic camera systems. Image quality is assessed using the Learned Perceptual Image Patch Similarity (LPIPS) metric and visual inspection. Results indicate that Diffusion Models outperform GANs, achieving a lower LPIPS score and better detection metrics, demonstrating superior realism, diversity, and suitability for enhancing deep learning model training.

Introduction

A major limitation affecting the accuracy and generalization of deep learning algorithms in object detection tasks, such as aircraft surface damage detection, is the scarcity of annotated training data [1]. In industrial applications, particularly in safety-critical fields like aerospace, creating large, high-quality datasets is both costly and time-consuming. The diversity of defect types, materials, lighting conditions, and imaging perspectives further complicates data collection, as these factors significantly impact model performance [2]. When datasets are insufficient or unbalanced, AI algorithms often fail to generalize beyond their training domain. Therefore, developing comprehensive datasets that capture a broad spectrum of damage appearances and acquisition conditions—such as variations in illumination, resolution, surface texture, and viewing angle—is essential for effective model training. However, achieving such diversity manually is often impractical. To address this challenge, recent research has explored the use of generative models to address the lack of annotated data in structural damage detection [3] to augment limited datasets for multiclass structural damage classification, obtaining limited results in terms of accuracy in the subsequent testing phase for damage detection algorithms.

Methodology

This study investigates two different generative strategies for augmenting training datasets to make a comparison between them. First, Generative Adversarial Networks (GANs) [4] employ a dual-network architecture where a generator produces synthetic images, and a discriminator learns to distinguish between real and fake samples. The process begins with configuration and initialization, where the generator (G), discriminator (D), and perturbation module are initialized along with key hyperparameters (learning rate, number of steps, perturbation strength). The training loop iterates until convergence; within each iteration, the discriminator update phase

Content from this work may be used under the terms of the Creative Commons Attribution 3.0 license. Any further distribution of this work must maintain attribution to the author(s) and the title of the work, journal citation and DOI. Published under license by Materials Research Forum LLC.

Materials Research Proceedings 69 (2026) 21-24 https://doi.org/10.21741/9781644904251-4

(performed for multiple steps per loop) involves generating fake images, sampling real images, performing adversarial training on real data, and computing the discriminator loss on both real and fake samples. The adversarial training component introduces perturbations to real images to enhance discriminator robustness and reuses the perturbed data efficiently across discriminator updates. In the generator update phase, the generator produces fake images to fool the discriminator, and its weights are updated based on the discriminator's feedback. The loss and stability emphasize training balance, combining discriminator and generator losses without requiring additional normalization or large batch sizes. The convergence/termination stage monitors performance metrics such as FID and IS, stopping training once convergence or saturation is reached.

The second approach, Diffusion Models [5], synthesizes images by iteratively denoising random noise, effectively reversing a diffusion process that gradually corrupts data. As the previous algorithm setup, the process begins with configuration, including specification of training parameters, dataset paths, and device selection. The pretrained model is then loaded, comprising components such as the Stable Diffusion pipeline, CLIP tokenizer, U-Net network with Low Ranking Adaption (LoRA) layers, Variational Auto Encoder (VAE), frozen text encoder, and DDPM scheduler. Next, LoRA configuration defines which attention layers to adapt and sets hyperparameters such as rank and dropout. The dataset and dataloader stage involve loading and augmenting image–prompt pairs for training. The training setup specifies optimization settings, including the AdamW optimizer, learning rate scheduler, and early stopping. During the training loop, images are encoded using the VAE, prompts are tokenized, noise is added and predicted by the U-Net, and model weights are updated based on MSE loss between predicted and target noise. Finally, the model saving stage stores the best-performing model, including the trained U-Net and LoRA configuration files.

As a case study, this work is conducted within the scope of the CINNABAR 2 [6] project, in collaboration with the DLR Institute of Maintenance, Repair and Overhaul – Department of Process Optimization and Digitalization in Hamburg, Germany. The test study focuses on a representative structural component of a commercial aircraft — specifically, a section of a medium-range commercial aircraft wing — used to simulate real-world inspection scenarios. To assess the impact of different image acquisition conditions, three imaging systems are used to collect real data:

- *Smartphone camera*, representing low-cost, flexible field inspections.
- *Digital Single-Lens Reflex (DSLR) camera*, providing high-resolution, professional-grade imagery.
- *Robotic arm* with a mounted camera

The images collected are used to build a dataset of 50 images with different subjects; the main goal is to have an *Image-to-Image (*Img2img*)* model able to generate new damage starting from existing ones in different poses, colors, illumination, and scenes. To do so, both algorithms previously described are trained using similar training options (Table 1).

Table 1 - Training option for Diffusion algorithm (left) and GAN algorithm (right)

	Diffusion model	**GAN model**
N. of epochs	100	1000
Batch size	4	4
Image size [pixel]	512x512	512x512
Learning rate	0.0001	0.0002

Materials Research Proceedings 69 (2026) 21-24 https://doi.org/10.21741/9781644904251-4

Results

The LPIPS metric is used to compare the performance of the two algorithms. The Learned Perceptual Image Patch Similarity (LPIPS) metric is a perceptual measure designed to quantify the similarity between two images in a way that aligns more closely with human visual judgment than traditional pixel-based metrics. LPIPS evaluates differences in feature representations extracted from intermediate layers of convolutional neural networks pretrained on large-scale image datasets. These deep features capture structural and semantic content that humans are sensitive to, such as textures, edges, and object parts. A lower LPIPS score indicates higher perceptual similarity between two images, while higher values suggest greater visual differences. This makes LPIPS widely applicable in the evaluation of generative models, image restoration, and data augmentation tasks. The results obtained are reported in Fig. 1 and Fig.2. The synthetic images generated by Diffusion Models are more suitable for data augmentation purposes, as indicated by their LPIPS average score of 0.2707 (versus GAN model LPIPS average score: 0.5797). For this reason, it is decided to use a diffusion model to generate 100 synthetic images to compare the performance of a damage detection algorithm trained on a mixed dataset (real images + synthetic images) with the performance of the same algorithm trained only on real images. YOLOv11 is chosen as the damage detection algorithm. YOLOv11 is the latest iteration in the You Only Look Once (YOLO) series, developed by Ultralytics [7]. It is designed to offer high performance across a range of computer vision tasks, including object detection and image classification. Two datasets are therefore prepared: the first containing 50 real images (real dataset) and the second containing 50 real images and 100 synthetic images (real + fake dataset). Both are split into 80%/20% for the training/validation phase, using only real images for the validation phase in both cases. The results are evaluated in terms of Precision, Recall, mean Average Precision at 50% Intersection over Union (mAP50), and mAP50-95 (Table 2). More details about its use for Damage Detection can be found in [8].

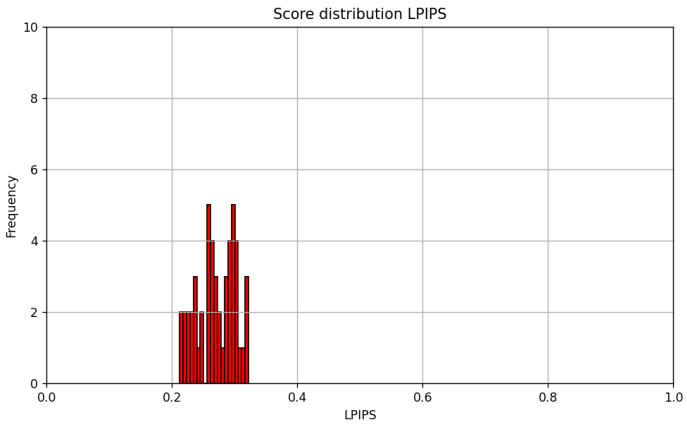


Fig. 1 - Score distribution LPIPS for Diffusion model

Table 2 - Evaluation metrics for real image dataset and real + fake image dataset

	Box P	**Box R**	**mAP50**	**mAP50-95**
Real	0.81	0.85	0.837	0.421
Real + Fake	0.978	0.889	0.951	0.586

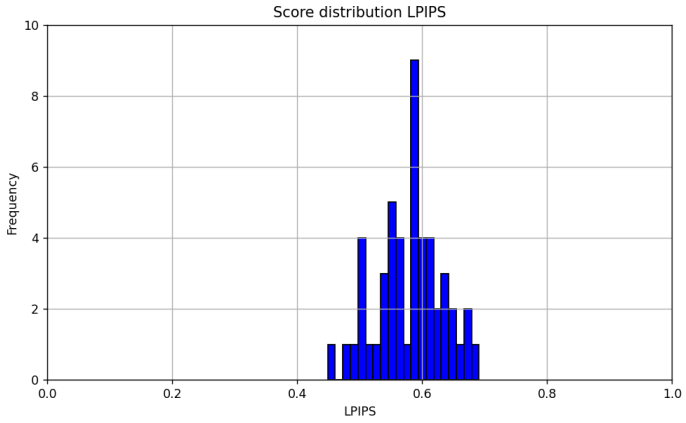


Fig. 2 - Score distribution LPIPS for GAN model

Conclusion

The comparison between the two training strategies demonstrates the clear benefit of augmenting real data with synthetic samples. The model trained exclusively on real images achieved a reasonable balance between precision and recall but struggled with bounding box accuracy. In contrast, the model trained on the mixed dataset showed a notable improvement across all metrics: it is more reliable in its predictions, slightly more sensitive in detecting true cases, and produced more accurate localizations. These results show that synthetic data can effectively complement limited real datasets, minimize false positives while improving overall detection performance, and generalize to real-world circumstances.

References

[1] S.E.Whang, Y. Roh, H. Song, et al. Data collection and quality challenges in deep learning: a data-centric AI perspective. The VLDB Journal 32, 791-813 (2023). https://doi.org/10.1007/s00778-022-00775-9

[2] S.U.G. Hyontai. Performance of machine learning algorithms and diversity in data. In MATEC web of conferences (2018, Vol. 210, p. 04019). EDP Sciences. https://doi.org/10.1051/matecconf/201821004019

[3] K. Dunphy, M. N. Fekri, K. Grolinger, A. Sadhu. Data augmentation for deep-learning-based multiclass structural damage detection using limited information. 2022. Sensors, 22(16), 6193. https://doi.org/10.3390/s22166193

[4] L. Bingchen, et al. Towards Faster and Stabilized GAN Training for High-fidelity Few-shot Image Synthesis. ICLR. 2021.

[5] B. Trabucco, K. Doherty, M. Gurinas, R. Salakhutdinov. Effective data augmentation with diffusion models (2023). arXiv preprint arXiv:2302.07944.

[6] A.K. Koschlik, F. Rauscher, M. J. Scott, S. Merola, H. Meyer, W. Verhagen, G. Wende. Digital Twins for Aircraft Structural Inspections: Enhancing Dent Detection (2025). In Proceedings of 21st Australian International Aerospace Congress, 24-26 March 2025, Melbourne & Avalon.

[7] G. Jocher, J. Qiu. Ultralytics YOLO v11 v.11.0.0 (2024).

[8] Mhatre, S. Merola, A.K. Koschlik, R. Rodeck, G. Wende. Deep-Learning-based Dent Detection of Aircraft Surfaces using Synthetic Data (2025). Proceedings of 28th AIDAA International Congress & 10th CEAS Aerospace Europe Conference.

Materials Research Proceedings 69 (2026) 25-30 https://doi.org/10.21741/9781644904251-5

Enabling Physics-Based Deep-Learning Thunderstorm Nowcasting for Critical Decision Making in Innovative Air Mobility

Niklas WARTHA[1,a *], Grigory ROTSHTEYN[2,b], Christoph METZL[1,c] and Tobias BÖLLE[1,d]

[1]Institut für Physik der Atmosphäre, Deutsches Zentrum für Luft- und Raumfahrt, Oberpfaffenhofen, Germany

[2]Unisphere GmbH, Constance, Germany

[a]niklas.wartha@dlr.de, [b]grigory.rotshteyn@unisphere.de, [c]christoph.metzl@dlr.de, [d]tobias.boelle@dlr.de

Keywords: Nowcasting, IAM, Thunderstorms, Deep Learning

Abstract. Adverse weather events constitute a major contributor to delays of aircraft. Thunderstorms, and accompanying effects, are frequently considered most hazardous to aircraft. Spatiotemporally highly resolved short-term forecasting of thunderstorms is possible from remote sensing data and has previously proven beneficial for commercial aircraft operations. This work demonstrates the potential of thunderstorm nowcasting in the innovative air mobility (IAM), by incorporating a physics-based deep-learning approach in an operational IAM flight planning platform. Operators benefit from more accurate and higher-resolved thunderstorm information, translating into smarter, safer, and more efficient operations and flight planning. Ultimately, a higher number of safe IAM operations can be realized.

Introduction

Atmospheric phenomena play a major role in air traffic management and flight planning, significantly contributing to delays. EUROCONTROL reports a 48%-increase in weather related delays in their civil aviation network from the years 2023 to 2024, resulting in a total of nearly 7 million delay minutes [1]. Commonly, numerical weather predictions (NWP) are employed to anticipate weather events. However, recurrently their spatiotemporal resolution proves insufficient. Furthermore, computational complexity of NWP models disallows frequent forecast updates, particularly hindering accurate predictions for short lead times. The need for accurate and very short-term forecasts, also called nowcasts, of aviation-relevant weather phenomena has been established throughout the past years [2]. With climate change, the frequency and severity of extreme weather events are expected to increase [3], further emphasizing the need for nowcasting. Besides civil aviation, the demand for Innovative Air Mobility (IAM) is expected to grow in passenger and cargo transportation [4]. To this day only few weather nowcasting studies have been performed for the IAM. For instance, Chrit and Majdi [5] performed wind and turbulence nowcasting. Particularly the IAM is expected to benefit from weather nowcasting: their operation is tied to versatility, short flight times and routes. Thus, the spatiotemporal scales are significantly smaller than global NWP can offer today. Thunderstorms and accompanying effects are particularly hazardous for small air vehicles, e.g., drones (here analogous to IAM). Lightning strikes, heavy precipitation, strong winds, and hail may affect drones far more than experienced by conventional aircraft.

To the authors' knowledge, for the first time this paper investigates the operational potential of nowcasting thunderstorms for IAM-sector in comparison to NWP implementations. A particular focus is put on the automatization of flight planning and increasing its efficiency. A physics-based machine learning (ML) model, the advection-informed neural network (AINN) [6], and the flight

Content from this work may be used under the terms of the Creative Commons Attribution 3.0 license. Any further distribution of this work must maintain attribution to the author(s) and the title of the work, journal citation and DOI. Published under license by Materials Research Forum LLC.

Materials Research Proceedings 69 (2026) 25-30 https://doi.org/10.21741/9781644904251-5

planning platform NOVA [7] by Unisphere are employed. The nowcasting model is prototypically integrated into the NOVA platform. NWP and nowcasting forecasts are compared via representative case studies, which confirm the added value of nowcasting for IAM. The remainder of this paper is structured as follows: the two main methods, NOVA and the AINN, are detailed. Afterwards, two case studies validate the potential of thunderstorm nowcasting in an IAM flight planning platform. Lastly, conclusions are provided.

Methods

NOVA [7] for planning IAM flights. The NOVA platform, developed by Unisphere, is a simulation-based digital co-pilot for IAM operations, offering advanced automation in flight planning, risk assessment, and regulatory compliance. NOVA applies Smart 4D Trajectory technology to evaluate weather impacts, battery performance, and global navigation satellite system reliability along planned flight paths, thereby supporting scalable and safe beyond visual line-of-sight operations. Within NOVA, aircraft performance, route geometry, and user-defined operational limits are combined with meteorological data to assess flight feasibility over a planning horizon of up to seven days. The system presents results through an automated traffic-light scheme (green/yellow/red) that compares forecast conditions against configurable thresholds for parameters such as wind, precipitation, temperature, visibility, and other operator-defined limits. Presently, weather-related risk assessment in NOVA relies on NWP data provided by the European Centre for Medium-Range Weather Forecasts (Integrated Forecast System) at a horizontal resolution of approximately 9 km resolution (≈ 0.1 deg), with new hourly forecasts issued every six hours. Because NWP data alone has limited ability to represent rapidly developing convective phenomena, operators complement NOVA's automated evaluation by inspecting radar imagery, which is available as an integrated visualization layer within the platform. This manual review of thunderstorm activity currently informs final go/no-go decisions. Integrating nowcasting into NOVA will replace this manual radar interpretation with an automated, short-term convective risk assessment, enhancing the reliability and efficiency of mission planning. Satellite-based thunderstorm nowcasting is embedded into NOVA as illustrated in Fig. 1 - this enables global nowcasting coverage (unlike radar).

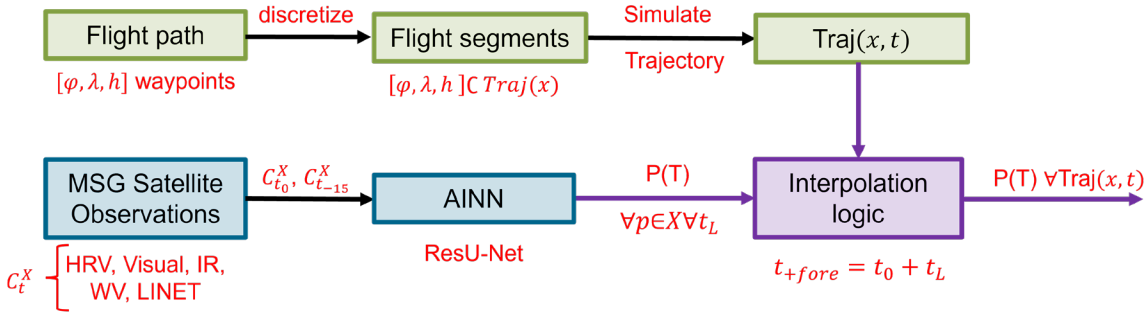


Figure 1 - AINN (blue) integration into NOVA (green). Purple represents the integration.

NOVA components are marked in green, first defining the desired flight path according to the latitude (φ), the longitude (λ), and the altitude (h), after which the complete flight path is discretized into flight segments. Along these segments, the flight trajectory (Traj) is simulated i.e., a time component is added.

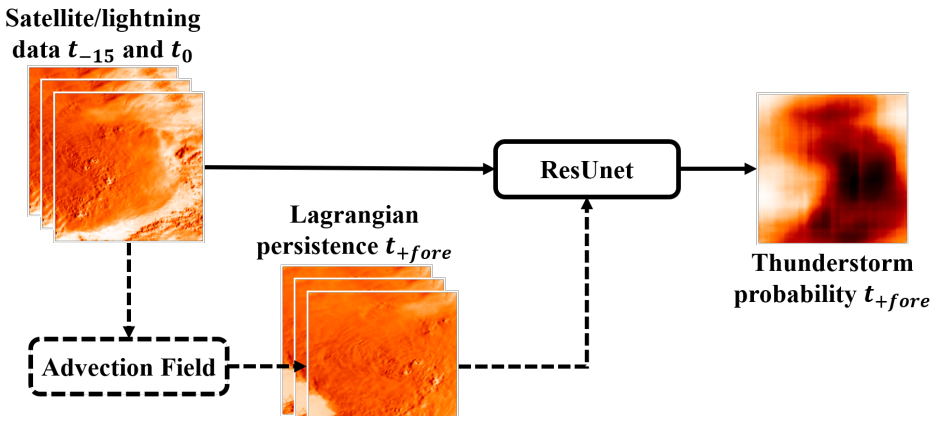


Figure 2 - AINN value chain. The employed BNN is represented by solid arrows only. [6]

Physics-based ML thunderstorm nowcasting [6]. Conventional operational nowcasting algorithms rely on advection and empirical rules from optical flow considerations in remote sensing imagery [8]. In recent years data-driven nowcasting, particularly ML models, achieved promising results. Metzl et al. [6] developed the AINN model depicted in Fig. 2. It is based on geostationary satellite and ground-based lightning data. The input for our task are the latest two observations (at t_0 and t_{-15}) of four Meteosat Second Generation (MSG) satellite [9] channels (C: HRV, VIS008, IR108, WV062) with a minimum temporal and spatial resolution of 15 min and ≈ 3 − 5 km (the HRV channel has a resolution of ≈ 1 km), respectively, aggregated lighting observations from the lightning detection network (LINET) [10], and the Lagrangian persistence advection field of all input channels for the desired forecast time (dashed arrows in Fig. 2). A ResU-Net [11] constitutes the heart of the AINN, delivering pixel-wise (p) calibrated thunderstorm probabilities P(T) as output. It solves a semantic segmentation task with binarized LINET data as ground truth, given its detection efficiency of over 95% and the 150 m spatial accuracy. For both the input and ground truth, each lightning stroke is grouped into 15-min bins and covers a disc with a 15-km radius. For each lead time t_L, i.e., 30 min, 60 min, 90 min, 120 min, 150 min, 180 min, one ResU-Net is trained for a 1024 × 1024 grid with a 0.0125-deg spacing (≈ 1 km) centered around the European Alps (25 crops of size X: 256 × 256 are individually processed). Data from May to October in 2018 and 2019 are employed for model training, validation, and testing. Metzl et al. [6] differentiate between the AINN (all arrows in Fig. 2) and the so-called baseline neural network (BNN) (only the solid lines in Fig. 2). They find that for lead times (fore in Fig. 2) up to 2 h, the difference in nowcasting skill between the AINN and BNN is negligible, with only a minor skill deficit by the latter for larger lead times. For the present study we thus consider the BNN sufficient. At present NOVA interpolates thunderstorm probabilities in a nearest-neighbor and linear fashion for the spatial and temporal domains, respectively.

Case Studies

June 18, 2019: Nowcasting solves NWP uncertainty. We demonstrate how nowcasting can automatically support NWP forecasts in NOVA. A drone is scheduled to fly across Lake Constance as drawn in Fig. 3 (≈ 30 km distance, ≈ 20 min duration) with a take-off time t_{TO} at 19:40 UTC from Constance. Forty minutes prior (19:00 UTC) the drone operator wishes to make a go/no-go decision for the flight and runs NOVA to obtain a flight recommendation. At that time, LINET observations of the past three hours (see Fig. 4 left) reveal large thunderstorm cells approaching from the south-west of Lake Constance. NOVA's NWP forecasts predict a thunderstorm probability between 40% - 50% along the flight distance D_F (see Fig. 5). These values do not allow

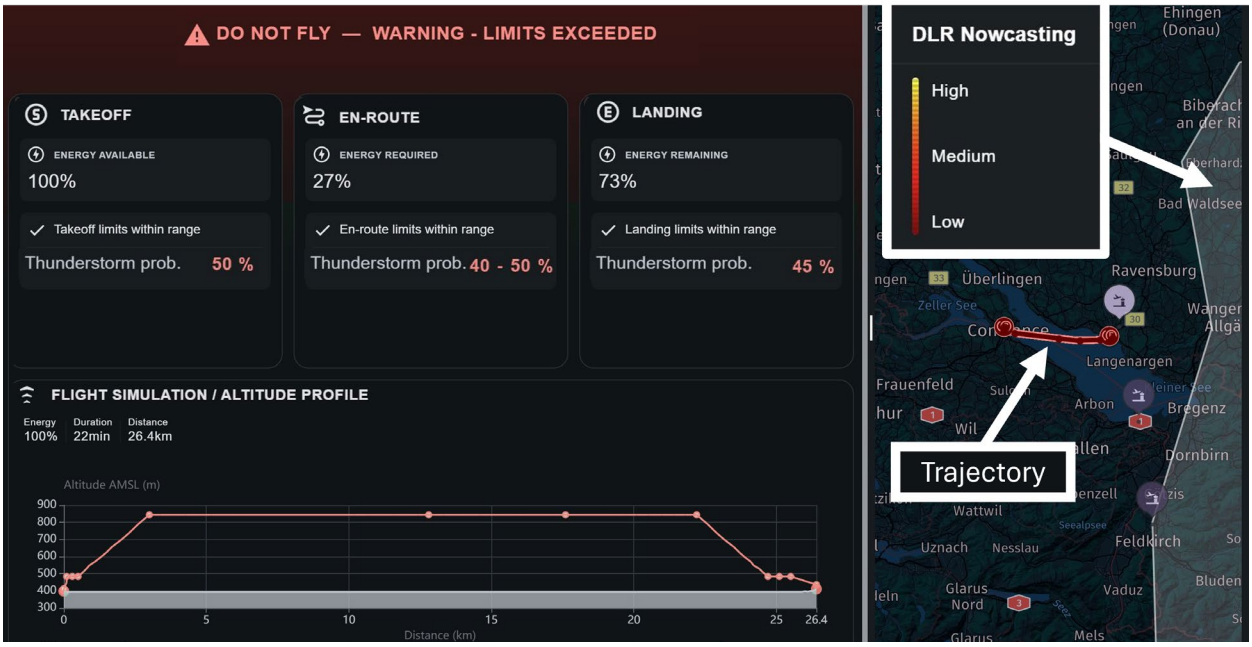


Figure 3 - NOVA interface. Overview of the critical simulation parameters (left) and the drone flight trajectory across Lake Constance, Germany (right).

for an obvious go/no-go decision and thus NOVA recommends to not fly. Instead of canceling the flight, we additionally run our nowcasting tool (NWC). Precise thunderstorm nowcasts are provided for t_{TO}, as plotted in Fig. 5 - a near zero thunderstorm probability is predicted along the complete flight distance. Thunderstorms predicted by the nowcasting are drawn on the map in Fig. 3. The right of the map is marked as very dangerous (white layer), the flight trajectory is clear. These results align well with lightning observations (Fig. 4 right) from post-analysis. At already 19:00 UTC our nowcasts predict that the thunderstorm cells will morph around the south-east of Lake Constance, while the north-west area of the lake (the area containing the flight trajectory) remains safe to fly. The NWP model is unable to resolve the convective cell as necessary and instead marks the complete lake area as potentially containing thunderstorms. The added value of the automatic nowcast is evident: tactical planning of drone flights is increased.

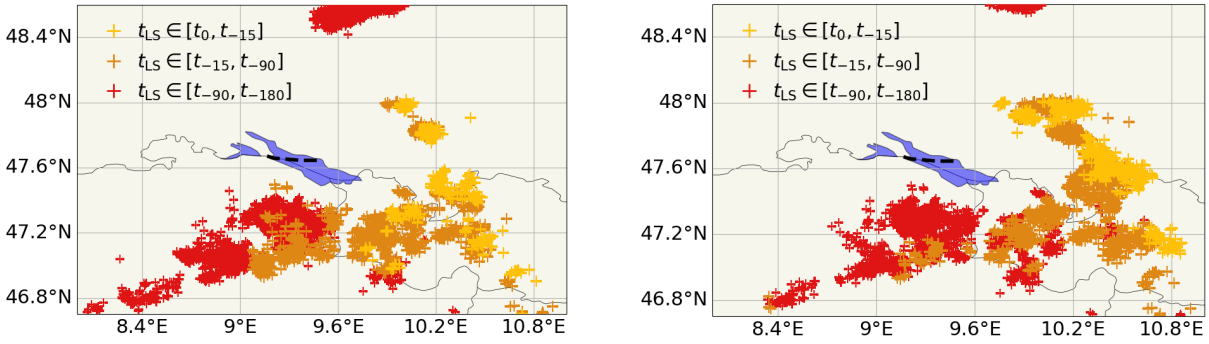


Figure 4 - Lightning strikes (LS) at 19:00 UTC (left) and 19:40 UTC (right) near the flight trajectory (dashed line). Symbols represent lightning strikes during the past 15 − 180 min.

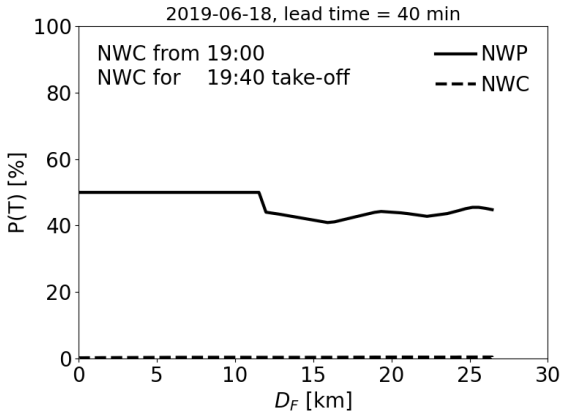


Figure 5 - Thunderstorm probabilities for DF by NWP (solid) and NWC (dashed) estimated 40 min ahead of t_{TO}. NWP and NWC probabilities are not directly comparable.

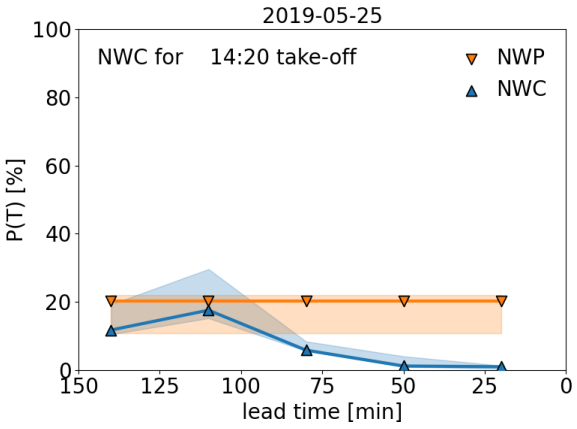


Figure 6 - Median thunderstorm probabilities for the flight trajectory (with 5% and 95% percentiles) by NWP and NWC, which are not directly comparable.

May 25, 2019: High spatiotemporal resolution enables reliable flight planning. The same flight trajectory is assumed. NOVA, with our nowcasting tool, is run at 30-min intervals prior to take-off planned for 14:20 UTC, given that a first run indicated the possibility of thunderstorm occurrence. Indeed, a significant convective cloud front is observed to approach from the north-west at these early times. While NWP continues to provide uncertain thunderstorm probabilities, Figure 6 illustrates the advantage of the nowcasting (lead time here refers to the nowcast computation time prior to take-off). As take-off approaches, the nowcasting thunderstorm probabilities diminish, which is owed to the high temporal resolution of the data. Just under one hour prior to take-off, the thunderstorm probability is near zero. Post-analysis of observations confirm that no thunderstorm occurred for the planned flight trajectory and time - the main cell re-routed north of Lake Constance. This study emphasizes the necessity for high temporal resolution in weather forecasts for the IAM.

Summary

A first investigation and feasibility study to automatize thunderstorm nowcasting for the IAM was presented. A novel machine learning nowcasting model was embedded in an IAM flight planning platform. Case studies showcase the benefit of thunderstorm nowcasting for the IAM. Flights that previously had to be canceled can be conducted safely with our automatic nowcasting. It is also expected that hazardous flights are avoided by detecting thunderstorm cells in regions marked as safe-to-fly by NWP forecasts. Manual monitoring of radar imagery is no longer necessary for flight operators. A great potential is seen for thunderstorm nowcasting to improve flight planning. In future, dynamic flight re-routing is also considered plausible with this high-resolution nowcasting tool.

References

[1] S. Moore and Y. Portillo. Managing adverse weather in the European air traffic network, May 2025. [Available from https://www.eurocontrol.int/sites/default/files/2025-05/eurocontrol-2025-fireside-chat-moore-portillo.pdf]

[2] C. Forster, A. Ritter, S. Gemsa, A. Tafferner, and D. Stich. Satellite-based real-time thunderstorm nowcasting for strategic flight planning en route. J. Air Transp., 24(4):113–124, October 2016. https://doi.org/10.2514/1.d0055

[3] N. Diffenbaugh, M. Scherer, and R. Trapp. Robust increases in severe thunderstorm environments in response to greenhouse forcing. Proc. Natl. Acad. Sci., 110(41):16361–16366, September 2013. https://doi.org/10.1073/pnas.1307758110

[4] S. Xiang, A. Xie, M. Ye, X. Yan, X. Han, H. Niu, Q. Li, and H. Huang. Autonomous eVTOL: A summary of researches and challenges. Green Energy Intell. Transp., 3(1):100140, February 2024. https://doi.org/10.1016/j.geits.2023.100140

[5] M. Chrit and M. Majdi. Operational wind and turbulence nowcasting capability for advanced air mobility. Neural Comput. Appl., 36(18):10637–10654, March 2024. https://doi.org/10.1007/s00521-024-09614-0

[6] C. Metzl, K. Vahid Yousefnia, R. M¨uller, V. Poli, M. Celano, and T. B¨olle. Physical scales matter: The role of receptive fields and advection in satellite-based thunderstorm nowcasting with convolutional neural networks. Artif. I. Earth Syst., 4(4), October 2025. https://doi.org/10.1175/aies-d-25-0035.1

[7] Unisphere GmbH. NOVA operations platform. https://unisphere.io/solutions/nova-operations-platform/, 2025.

[8] Y. Wang, E. De Coning, W. Jacobs, P. Joe, L. Nikitina, R. Roberts, J. Wang, and J. Wilson. Guidelines for nowcasting techniques. Technical report, World Meteorological Organization, 2017. WMO-No. 1198. [Available from https://library.wmo.int/viewer/55666/download?file=WMO-1198-2017_en.pdf&type=pdf&navigator=1]

[9] J. Schmetz, P. Pili, S. Tjemkes, D. Just, J. Kerkmann, S. Rota, and A. Ratier. Supplement to an introduction to Meteosat second generation (MSG): SEVIRI calibration. Bull. Am. Meteorol. Soc., 83(7):992–992, July 2002. https://doi.org/10.1175/bams-83-7-schmetz-2

[10] H. Betz, K. Schmidt, P. Laroche, P. Blanchet, W. Oettinger, E. Defer, Z. Dziewit, and J. Konarski. LINET—an international lightning detection network in Europe. Atmos. Res., 91(2–4):564–573, February 2009. https://doi.org/10.1016/j.atmosres.2008.06.012

[11] Z. Zhang, Q. Liu, and Y. Wang. Road extraction by deep residual U-Net. IEEE Geosci. Remote Sens. Lett., 15(5):749–753, May 2018. https://doi.org/10.1109/lgrs.2018.2802944

Materials Research Proceedings 69 (2026) 31-36 https://doi.org/10.21741/9781644904251-6

Neural Network-Based Prediction of Bursting Events in a Turbulent Channel Flow

Enrico SACCAGGI[1,a *] and Gaetano Maria DI CICCA[1,b]

[1]Department of Mechanical and Aerospace Engineering, Politecnico di Torino, Corso Duca degli Abruzzi 24, Torino, Italy

[a]enrico.saccaggi@polito.it, [b]gaetano.dicicca@polito.it

Keywords: Wall Turbulence, Flow Control, Machine Learning

Abstract. This study investigates the use of a hybrid architecture of a Feed-forward Neural Network (FNN) combined with the Proper Orthogonal Decomposition (POD) to estimate the effect of control on sweep events within the context of an opposition control strategy. The experiments were carried out in a fully turbulent channel flow with a friction Reynolds number of 365. The POD was conducted to reduce the database dimensionality, and then a FNN was trained to predict the non-normalized spatial modes matrix, subsequently allowing the reconstruction of the Conditionally Averaged Sweep Event (CASE). The results demonstrate that the hybrid neural network is capable of reproducing the control signature for different actuation parameters with an accuracy comparable to a conventional neural network, while requiring approximately 90 times fewer trainable parameters.

Introduction

Choi et al. [1] through direct numerical simulations, demonstrated that the opposition control technique can achieve skin-friction reductions up to 25% by applying wall blowing and suction with velocities equal in magnitude but opposite in direction to those at a prescribed wall-normal location. Wind tunnel experiments reported in [2, 3] further demonstrated that real-time opposition control, implemented through wall-normal jet actuation to block high-speed fluid motions during sweeps, effectively mitigates the intensity of these events. In recent years, data-driven models have shown success in estimating the response of control systems to given actuation parameters. A FNN was implemented in [4] to predict the effect of actuation parameters on the CASE. The objective of the present work is to extend that study by reducing the dimensionality of the FNN by changing the model architecture. Furthermore, the possibility of further reducing the dimensionality is explored through the use of a hybrid POD-FNN, which first predicts the non-normalized spatial modes matrix of the POD and then reconstructs the CASE, while maintaining nearly the same accuracy.

Experimental setup

The experiments were conducted in an 8-meter-long duct with a 7 cm x 30 cm rectangular cross-section (aspect ratio equal to 4.28). The center-line velocity was set to $U_0 = 3.22$ m/s corresponding to a friction velocity of $u_\tau = 0.16$ m/s and a resulting friction Reynolds number of $Re_\tau = 365$. Two hot-wire probes were employed, each connected to a Dantec 55M10 CTA Standard Bridge anemometer. Both probes featured a sensitive tungsten wire with a diameter of 5 μm and a length of 1.25 mm. The upstream probe, a Dantec 55P11, was positioned at $x^+ = -65$ and $y^+ = 15$, while the downstream probe, a Dantec 55P15 boundary-layer type, was mounted on a two-axis stand. The superscript + denotes quantities in wall units. Following [3], sweep events were detected in real time using the velocity-gradient technique applied to the streamwise velocity signal acquired from the upstream probe. An analog differentiator computed the gradient from the hot-wire anemometer voltage output, and a comparator identified events

Content from this work may be used under the terms of the Creative Commons Attribution 3.0 license. Any further distribution of this work must maintain attribution to the author(s) and the title of the work, journal citation and DOI. Published under license by Materials Research Forum LLC.

Materials Research Proceedings 69 (2026) 31-36 https://doi.org/10.21741/9781644904251-6

when the time derivative exceeded a threshold. The threshold was calibrated to match the event count from the variable interval time averaging method [5] with k=1.0 and averaging time T^+=10. A detected sweep event generated a TTL signal sent to an Arduino Uno Rev3 board, introducing a delay ΔT to take into account convection time and actuator response time. The delayed TTL signal triggered a signal generator to produce a single-period sine wave of frequency f and voltage amplitude $\hat{A}$, amplified to drive a loudspeaker. The loudspeaker produced a jet through a 1 mm diameter orifice (corresponding to about 11 viscous units). The rear probe velocity signal was acquired and conditionally averaged to visualize the sweep event.

Database description and model creation

The database used in this study is the one presented by [4], constructed by varying the control parameters. The objective is to predict the longitudinal component of the velocity signal for the controlled CASE, $\hat{u}_c \in \mathbb{R}^{1\times n_t}$, using as inputs the actuation parameters and the longitudinal component of the velocity signal for the uncontrolled CASE, $\hat{u}_{nc} \in \mathbb{R}^{1\times n_t}$, where $n_t = 750$ is the number of points in the conditionally averaged window and corresponds to 139 viscous units. Let the control triplet be denoted as θ, characterized by actuation frequency f, voltage amplitude $\hat{A}$, and delay time ΔT. A total of $n_d = 130$ control triplets were sampled to construct the input part of the dataset using a Latin Hypercube Sampling technique within the space 30÷60 Hz, 50÷75mV_{pp} and 0.15÷3ms for frequency, voltage amplitude and delay time respectively. For each dataset sample, $\hat{u}_c(\theta)$ was experimentally evaluated after a conditional sampling of the rear probe velocity signal acquired at $x^+ = 65$ and $y^+ = 15$. The resulting dataset was divided into training and validation subsets, containing 80% and 20% of the data respectively, and normalized to have all the features in the range between 0 and 1. A FNN with a reduced number of trainable parameters compared to the model proposed in [4] was adopted to predict the control effect on the CASEs.

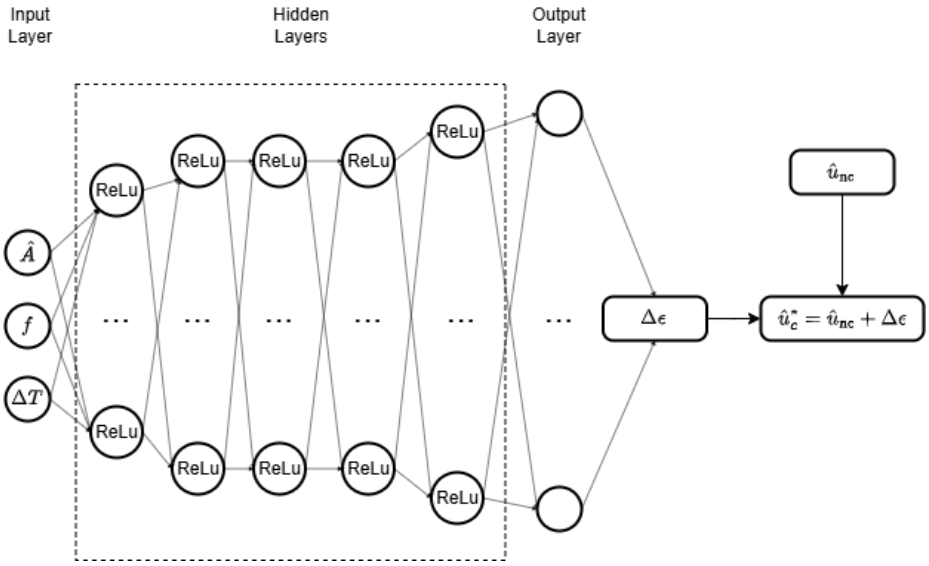


Figure 1. FNN structure used to predict the longitudinal component of the velocity signal for the controlled CASE $\hat{u}_c^*$ based on the control parameters and the longitudinal component of the velocity signal for the uncontrolled CASE, $\hat{u}_{nc}$.

The network architecture here implemented, is illustrated in Fig. 1 and comprises 5 hidden layers of dimension (16, 32, 32, 32, 64) followed by an output layer which produces as output $\Delta\epsilon$. $\Delta\epsilon$ is then added to $\hat{u}_{nc}$ to give the predicted controlled CASE signal, represented as $\hat{u}_c^*$ for a given triplet θ. The hyperparameters of the network, including learning rate, batch size, and activation

Materials Research Proceedings 69 (2026) 31-36 https://doi.org/10.21741/9781644904251-6

functions, are the same as [4]. This network will be referred to hereafter as $\mathcal{N}$. Similar results to those obtained with the network presented in [4] were achieved using $\mathcal{N}$, which features a deeper architecture with fewer neurons, leading to a reduction in the number of trainable parameters from approximately 225,000 to 53,000 (over four times fewer).

Hybrid POD-FNN model

To further reduce the size of the model, it is possible to decrease the dimensionality of the output part of the dataset. The first step is therefore to compress this dataset from $\widehat{\boldsymbol{U}}_{\boldsymbol{c}} \in \mathbb{R}^{n_d \times n_t}$ to $\widetilde{\widehat{\boldsymbol{U}}}_{\boldsymbol{c}} \in \mathbb{R}^{n_d \times n_r}$ where $n_r \ll n_t$ denotes the reduced temporal dimension of the output part of the dataset. POD [6] was then applied to decompose the dataset according to:

$$\widehat{\boldsymbol{U}}_{\boldsymbol{c}} = \boldsymbol{\phi}\boldsymbol{\Sigma}\boldsymbol{\psi}^{\boldsymbol{T}}, \quad (\mathbf{1})$$

where $\boldsymbol{\phi} \in \mathbb{R}^{n_d \times n_d}$ denotes the matrix of pseudo-spatial basis vectors, $\boldsymbol{\Sigma} \in \mathbb{R}^{n_d \times n_d}$ is the singular value matrix, and $\boldsymbol{\psi} \in \mathbb{R}^{n_t \times n_d}$ is the matrix of the temporal modes. A reduced-order approximation of the dataset, retaining only the first n_r most energetic modes, is given by:

$$\widetilde{\widehat{\boldsymbol{U}}}_{\boldsymbol{c}} = \widetilde{\boldsymbol{\phi}}\widetilde{\boldsymbol{\Sigma}}\widetilde{\boldsymbol{\psi}}^{\boldsymbol{T}}, \quad (\mathbf{2})$$

where $\widetilde{\boldsymbol{\phi}} \in \mathbb{R}^{n_d \times n_r}$, $\widetilde{\boldsymbol{\Sigma}} \in \mathbb{R}^{n_r \times n_r}$ and $\widetilde{\boldsymbol{\psi}} \in \mathbb{R}^{n_t \times n_r}$ contains only the first n_r columns or singular values. Analysis reveals that retaining only the first 7 modes (n_r = 7) is sufficient to capture more than 99% of the total energy. A reconstruction of $\hat{u}_c$ taking into account only the first 7 modes is presented in Fig. 2.

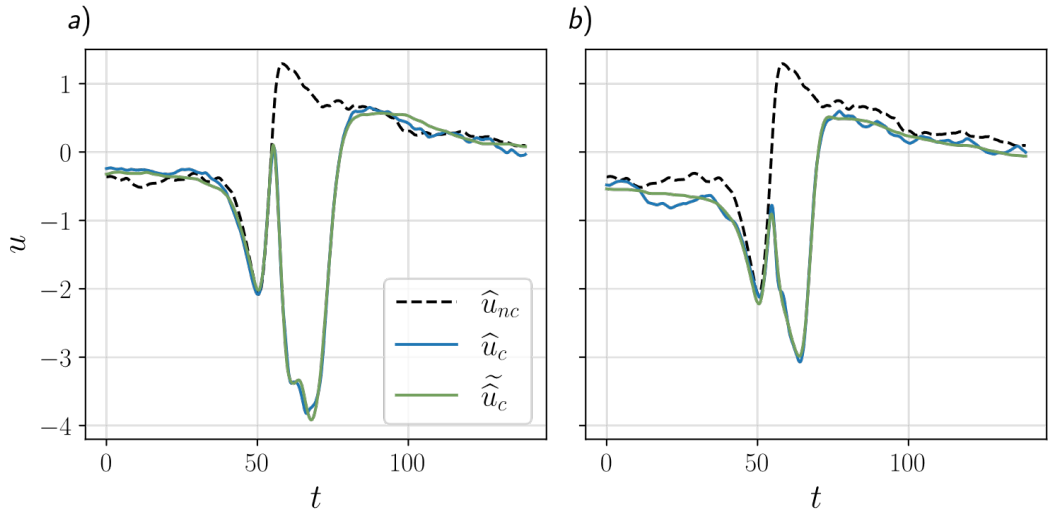


Figure 2. Longitudinal component of the velocity signal (in viscous units) for the CASEs. The superscript + is here omitted for both u and t. The black dashed lines and the blue continuous lines represent the experimentally sampled uncontrolled and controlled CASE, respectively. The green lines indicate the reconstructed CASE with the first 7 POD modes.
a) $\theta = [33.3\ Hz,\ 56.44\ mV_{pp},\ 0.65\ ms]$, *b)* $\theta = [52.49\ Hz,\ 61.59\ mV_{pp},\ 0.95\ ms]$.

Relying on this low-dimensional representation, it becomes possible to predict $\widetilde{\boldsymbol{\alpha}} = \widetilde{\boldsymbol{\phi}}\widetilde{\boldsymbol{\Sigma}} \in \mathbb{R}^{n_d \times n_r}$ from the input-parameter dataset $\boldsymbol{X} \in \mathbb{R}^{n_d \times n_i}$, where n_i=3 denotes the number of control parameters, and subsequently reconstruct $\tilde{\hat{u}}_c$ using regressors such as decision trees [7] or XGBoost regressors [8]. Although this strategy is computationally lightweight, it suffers from significant issues related to the regularization of the cost function when predicting the coefficients of $\widetilde{\boldsymbol{\alpha}}$ since each coefficient must be weighted. An alternative approach that avoids a direct regularization is to predict the coefficients of $\widetilde{\boldsymbol{\alpha}}$ using a FNN, then reconstruct $\tilde{\hat{u}}_c$ and compare the reconstruction with $\hat{u}_c$ within the loss function. In this case, the regularization is implicitly

Materials Research Proceedings 69 (2026) 31-36 https://doi.org/10.21741/9781644904251-6

enforced by the training procedure. A schematic of this hybrid POD–FNN architecture is shown in Fig. 3**.** Different architectures of the hybrid POD–FNN model were evaluated by varying the number of neurons per layer and the number of hidden layers. The learning rate and weight decay were kept identical to those used to train $\mathcal{N}$, while a greater number of training epochs (30000 vs 10000) was adopted since the model contains fewer trainable parameters. In addition an early stopping criterion was implemented to avoid overfitting [9].

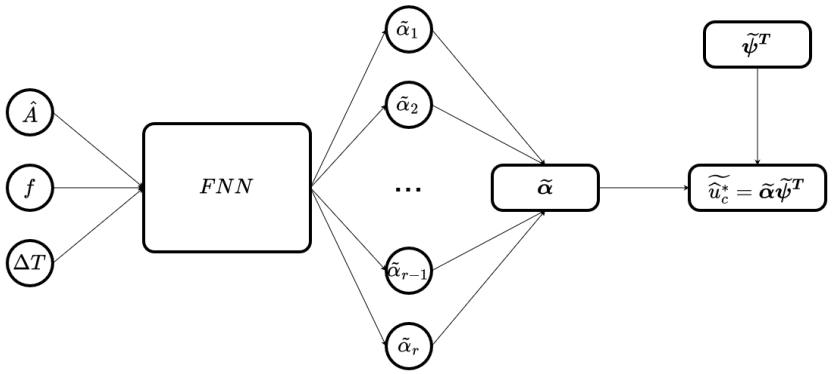


Figure 3. Schematic of the hybrid POD-FNN model. Inputs are the actuation parameters and the temporal modes. Outputs are the predicted controlled CASEs.

Models were assessed on the validation dataset using R^2 and the adjusted R^2 named R^2_{adj} as metrics [10]. R^2_{adj} accounts for the number of trainable parameters and thus penalizes excessively large networks. In Table 1, the metrics R^2 and R^2_{adj} are reported for the tested architectures identified through the sequence (*a, b, c*) where *a* is the number of neurons in the first hidden layer, *b* in the second, and *c* in the third. As expected, R^2 increases with the number of parameters. Conversely, R^2_{adj}, increases up to the architecture (8, 16, 16), named $\widetilde{\mathcal{N}}$, and then slightly decreases, even though the R^2 continues to improve. This behavior reflects the penalization term included in R^2_{adj}, whose denominator increases more rapidly than the improvement in the R^2 value due to the higher amount of trainable parameters. A comparison between the CASEs predicted by $\mathcal{N}$ and $\widetilde{\mathcal{N}}$ for the inputs in the validation dataset is shown in Fig. 4. The measured quantity to be approximated by the FNN, $\hat{u}_c$, is represented by a solid blue line, while the solid red and green lines correspond to the predicted controlled CASE obtained by $\mathcal{N}$ and $\widetilde{\mathcal{N}}$, denoted as $\hat{u}_c^*$ and $\tilde{\hat{u}}_c^*$, respectively. The comparison between the two curves indicates that both networks successfully capture the dynamics of the system, providing an accurate representation of the controlled sweep event. While $\mathcal{N}$ is slightly more accurate than $\widetilde{\mathcal{N}}$, as reflected by its R^2 value of 0.977 compared to 0.976 for $\widetilde{\mathcal{N}}$, this marginal improvement comes at the cost of a model over 90 times larger in terms of trainable parameters.

Materials Research Proceedings 69 (2026) 31-36 https://doi.org/10.21741/9781644904251-6

Table 1. Comparison between different hybrid POD-FNN models in terms of network architectures, number of parameters, and performance metrics, sorted by the number of parameters. The metrics were computed using the validation dataset.

Architecture	Params	R^2	R^2_{adj}
(4, 4)	71	0.963	0.963
(4, 4, 4)	91	0.965	0.965
(4, 8)	119	0.971	0.971
(8, 8)	167	0.972	0.972
(4, 8, 8)	191	0.974	0.973
(8, 8, 8)	239	0.974	0.974
(8, 16)	295	0.975	0.974
(16, 16)	455	0.975	0.974
(8, 16, 16)	567	0.976	0.975
(16, 16, 16)	727	0.974	0.973
(16, 32)	839	0.975	0.974
(32, 32)	1415	0.974	0.972
(16, 32, 32)	1895	0.976	0.973
(32, 32, 32)	2471	0.976	0.972
(32, 64)	2695	0.975	0.972
(32, 64, 64)	6855	0.976	0.963

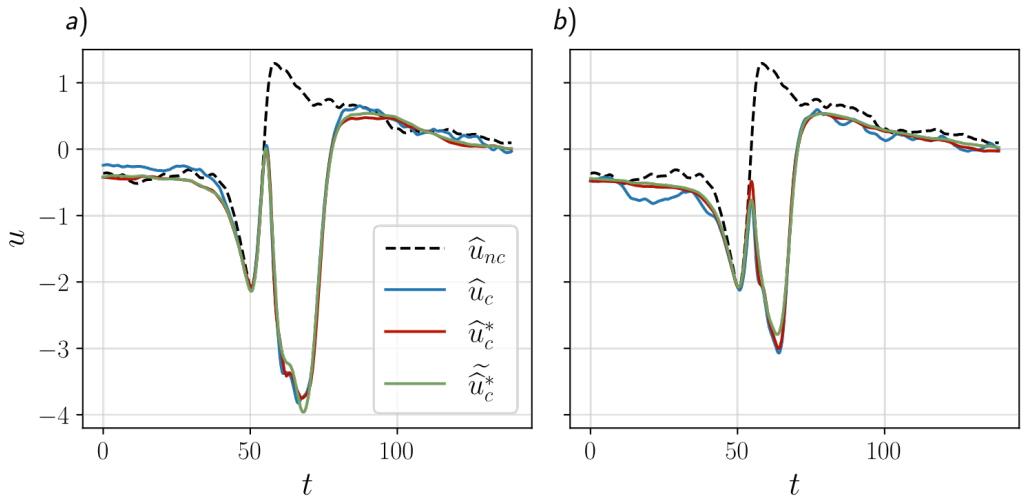


Figure 4. Evaluation of $\mathcal{N}$ and $\widetilde{\mathcal{N}}$ in the validation dataset. The black dashed line represents the uncontrolled CASE. The blue lines corresponds to the experimentally sampled controlled CASEs. The red and green lines indicate the predicted controlled CASEs with $\mathcal{N}$ and $\widetilde{\mathcal{N}}$ respectively. a) $\theta = [33.3\ Hz,\ 56.44\ mV_{pp},\ 0.65\ ms]$, b) $\theta = [52.49\ Hz,\ 61.59\ mV_{pp},\ 0.95\ ms]$.

Conclusion

In the context of opposition control, and with the goal of predicting the controlled CASE more efficiently, the first step consisted in improving the network architecture used in [4], thus reducing the number of trainable parameters by a factor of approximately four. Subsequently, aiming for an even more lightweight model, a POD analysis was performed, revealing that only 7 modes are

sufficient to capture 99% of the output dataset energy. Building on this insight, a significantly smaller FNN was trained, featuring roughly 90 times fewer trainable parameters than those adopted in $\mathcal{N}$ while achieving a comparable R^2 value.

Acknowledgments
This publication is part of the project PNRR-NGEU which has received funding from the MUR – DM 118/2023. We acknowledge the work of the student Arthur Pierre Philippe Nuvoloni for his help in defining the architecture of network $\mathcal{N}$.

References

[1] H. Choi, P. Moin, and J. Kim. Active turbulence control for drag reduction in wall bounded flows. J. Fluid Mech., 75:262, 1994. https://doi.org/10.1017/S0022112094000431

[2] H. Rebbeck and K.-S. Choi. Opposition control of near-wall turbulence with a piston-type actuator. Phys. Fluids, 13(8):2142-2145, 2001. https://doi.org/10.1063/1.1381563

[3] H. Rebbeck and K.-S. Choi. A wind-tunnel experiment on real-time opposition control of turbulence. Phys. Fluids, 18:035103, 2006. https://doi.org/10.1063/1.2173295

[4] E. Saccaggi and G. M. Di Cicca. Application of a neural network for predicting the control effect on sweep events in a fully turbulent channel flow. In AIAA AVIATION FORUM AND ASCEND2025, Las Vegas, NV, USA, July 2025. American Institute of Aeronautics and Astronautics (AIAA). AIAA 2025-3022. https://doi.org/10.2514/6.2025-3022

[5] R. F. Blackwelder and R. E. Kaplan. On the wall structure of the turbulent boundary layer. J. Fluid Mech., 76(1):89-112, July 1976. https://doi.org/10.1017/S0022112076003145

[6] G. Berkooz, P. Holmes, and J. L. Lumley. The proper orthogonal decomposition in the analysis of turbulent flows. Annu. Rev. Fluid Mech., 25:539-575, 1993. https://doi.org/10.1146/annurev.fl.25.010193.002543

[7] J. R. Quinlan. Induction of decision trees. Machine learning, 1(1):81-106, 1986. https://doi.org/10.1023/A:1022643204877

[8] T. Chen and C. Guestrin. Xgboost: A scalable tree boosting system. In Proceedings of the 22nd ACM SIGKDD International Conference on Knowledge Discovery and Data Mining, 785-794, 2016. https://doi.org/10.1145/2939672.2939785

[9] L. Prechelt. Early stopping-but when?. In: Neural Networks: Tricks of the trade. Berlin, Heidelberg: Springer Berlin Heidelberg, 2002. p. 55-69. https://doi.org/10.1007/3-540-49430-8_3

[10] M. Ezekiel and K. A. Fox. Methods of correlation and regression analysis. Linear and curvilinear, 1959.

Materials Research Proceedings 69 (2026) 37-41 https://doi.org/10.21741/9781644904251-7

Deep-Learning-based Dent Detection of Aircraft Surfaces using Synthetic Data

Aditi MHATRE[1,a *], Salvatore MEROLA[2,b], Ann-Kathrin KOSCHLIK[1,c], Rebecca RODECK[1,d] and Gerko WENDE[1,e]

[1]German Aerospace Center (DLR) – Institute of Maintenance, Repair, and Overhaul, Hamburg, Germany

[2]University of Naples Federico II – Dept. of Industrial Engineering, Naples, Italy

[a]aditi.mhatre@dlr.de, [b]salvatore.merola@unina.it, [c]ann-kathrin.koschlik@dlr.de, [d]rebecca.rodeck@dlr.de, [e]gerko.wende@dlr.de

Keywords: Aircraft Surface Inspection, Dent Detection, Deep Learning, Aircraft Maintenance, Visual Check, Generative AI

Abstract. Detecting and localizing dents on aircraft surfaces is crucial for maintaining their structural integrity. However, this task can be challenging for humans as dents are not very prominent to the naked eye and require the assistance of light reflections to reveal the damages across the surface. Latest state-of-the-art technologies such as lasers or cameras digitize this step, however the workload is shifted to identifying the dents in the virtual image. The integration of deep-learning methodologies can help automate dent detection. This study compares two object detection architectures: You Look Only Once (YOLOv11) and RealTime DETection TRansformer (RT-DETR) for dent detection. A high-quality dent dataset is prepared, consisting of real and synthetic images of common long- and mid-range aircraft fuselages, to train and test the models. The results indicate that YOLOv11 marginally outperforms RT-DETR in detecting dents with a mean accuracy precision (mAP50) score of 0.66 against the mAP50 value of 0.57 for RT-DETR.

Introduction

Dents are one of the most common damages found in aircraft surfaces that are caused by external forces and affect the structural integrity. These dents need to be classified based on their size, shape, and location to assess their severity and guide maintenance decisions [1,2]. This inevitable inspection process is performed manually by technicians, and requires a significant number of work hours. Unlike other types of defects like scratches or corrosion, dents are more difficult to detect visually as there is usually no prominent change in colour [3]. Inspectors must rely on close observation and additional lighting, which can lead to eye fatigue and missed detections. Introducing deep-learning methodologies offers a promising solution by automatically detecting dents on large aircraft surfaces with high accuracy, reducing human errors and inspection time. However, most existing studies focus on larger dents and are constrained by limited training datasets for dents, which hinders the models' ability to learn diverse dent features [3,4]. This study aims to identify the most suitable approach for detecting dents with the help of light reflections, serving as the Region of Interest (ROI) for further damage assessment and decision-making. This case study focuses on dent detection on aircraft structures using visual images. In addition to the accuracy of the models, it is required that the algorithms are fast and efficient, enabling them to operate in real-time. To address this, our study implements and compares the object detection architectures, YOLOv11[1] and the RT-DETR [5]. One of the key contributions of our work is the generation of an enriched dent dataset, consisting of both real images of dents and synthetic images generated with the help of generative AI models, improving the overall results

[1] YOLOv11: github.com/ultralytics/ultralytics

Content from this work may be used under the terms of the Creative Commons Attribution 3.0 license. Any further distribution of this work must maintain attribution to the author(s) and the title of the work, journal citation and DOI. Published under license by Materials Research Forum LLC.

Materials Research Proceedings 69 (2026) 37-41 https://doi.org/10.21741/9781644904251-7

Methodology

The YOLOv11 is a versatile foundational model that is adept at object detection and instance segmentation, and suitable for real-time applications. It is available in different model sizes allowing it to cater to diverse computing environments. Similarly, RT-DETR is another state-of-the-art model in this domain, which is an end-to-end Transformer-based detector. These models are the current state-of-the-art in real-time object detection, which provide a good trade-off between accuracy and speed, making them suitable for aircraft inspection. To train the models, we prepared a high-quality dent dataset, which contains 1166 annotated images of dents across various aircraft parts including wing sections of B737 and A380. The dataset is prepared by combining the 614 real images and 552 synthetic images, which are generated with the help of a Diffusion model [6, 7], an image-to-image model. The real images capture artificial impacts created on a B737 wing section [2], and various dents caused due to hailstorms on a slat section of an A380. These images are captured under varying light conditions to replicate the diverse illumination found in aircraft visual inspections, including natural light and flashlights as well as photos from different angles. This helps capture the effect of specular light reflections across the surface to highlight dents on reflective materials and help recognize dents more accurately.

Various image acquisition methods are employed to collect the images, namely a smartphone camera, an Intel RealSense camera mounted on an inspection robot, and a digital single-lens reflex (DSLR) camera. To further augment the dataset for training, we generate synthetic images based on 276 out of 614 real images, with two synthetic images being generated for every real image, leading to a total of 552 synthetic images. More details can be found in [7]. The annotated labels on the dataset were “dent” and “no_dent”. The “no_dent” is introduced to label other types of defects such as corrosion or peeling paint to differentiate it from dents. Some sample images of the dataset are showcased in Table 1. The dataset is split into train and test datasets in a ratio of 80:20, with all the synthetic images being assigned to the training subset and only real images being used for the test subset. In total, the training dataset consisted of 933 images and the test dataset contained 233 images. To optimize training, we leveraged pre-trained YOLOv11 and RT-DETR models, which were initially trained on the popular COCO (Common Objects in Context)[2] dataset. The NVIDIA GeForce RTX 4070 SUPER GPU is utilized to finetune these pre-trained models for our specific task. The training process involved 200 epochs with a learning rate of 0.001.

Results and Discussion

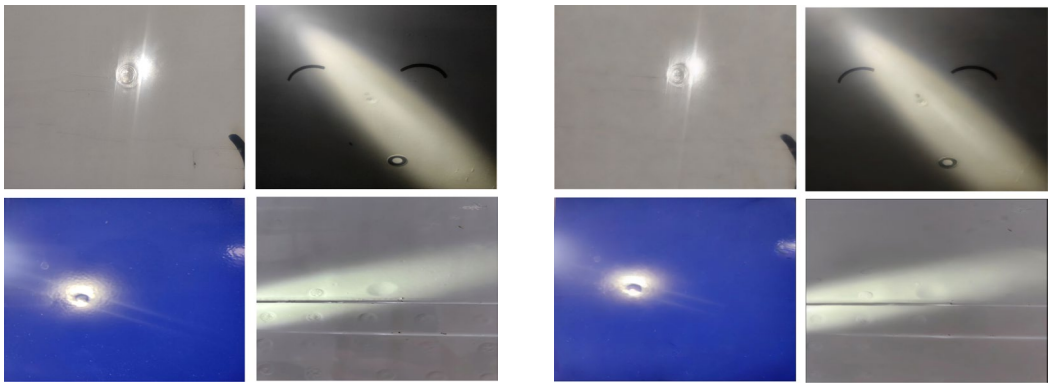
After training the models for 200 epochs on the training dataset, they are evaluated on the test dataset in two ways: quantitatively and qualitatively. For the quantitative method, the mean accuracy precision of the model predictions was compared with the ground truth labels to evaluate how accurately the model localized the dents. There are two variations of mAP used to evaluate the results: mAP50 and mAP50-95, which are both valued in the range of 0–1, where a higher value indicates a better model accuracy. The mAP50 is calculated at an intersection over union (IoU) threshold of 0.5. In the mAP50-95 metric, the model’s average performance is taken across IoU thresholds from 0.5 to 0.95 in steps of 0.05. Due to this difference in the calculation, the scores of mAP50 are generally higher than mAP50-95. The quantitative results for the models are summarized in Table 2. The YOLOv11 has a mAP50 score of 0.64 and mAP50-95 of 0.27. After training the RT-DETR with the same learning rate and epochs as the YOLOv11, it achieved a mAP50 score of 0.57 and a corresponding mAP50-95 value of 0.23. Compared to other existing studies [4], where the performance for dent identification was around 0.5, our approach achieved a higher score of 0.64, indicating an improvement in dent detection accuracy.

[2] https://cocodataset.org

Materials Research Proceedings 69 (2026) 37-41 https://doi.org/10.21741/9781644904251-7

Table 1: Overview of dent dataset showing real and synthetic images under different lighting.

(a) Real Images (left box) vs. Synthetic Images (right box).



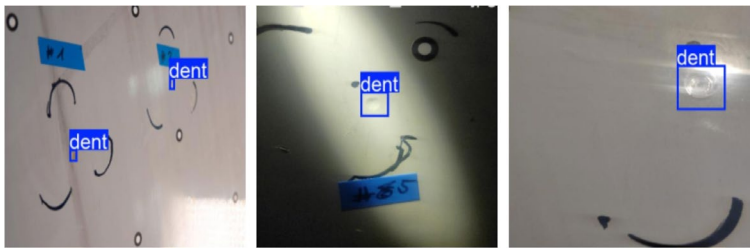
(b) Effect of light reflections across dented surface in real images.



Table 2: Quantitative results for the accuracy precision of the models.

Model	mAP50	mAP50-95
YOLOv11	0.64	0.27
RT-DETR	0.57	0.23

The qualitative method involves observing the bounding box predictions of the models, and comparing them against the annotated labels of the test dataset. The models predict bounding boxes along with a prediction label and a corresponding confidence score for each detected dent. The confidence score is in the range of 0–1 to indicate the probability of the classification being correct. A comparison of the ground truth labels against the dent predictions of YOLOv11 and RT-DETR is shown in Fig.1.

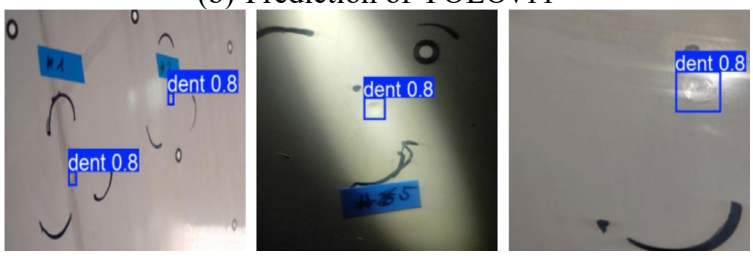


(a) Ground Truth of Test Dataset

Materials Research Proceedings 69 (2026) 37-41 https://doi.org/10.21741/9781644904251-7



(b) Prediction of YOLOv11



(c) Prediction of RT-DETR

Figure. 1: Comparison of (a) ground truth labels against dent detection predictions of (b) YOLOv11 and (c) RT-DETR.

Based on the tests conducted, both YOLOv11 and RT-DETR demonstrated a high degree of accuracy in detecting dents across aircraft surfaces, with the YOLOv11 achieving marginally better results compared to RT-DETR. It was also observed that the introduction of synthetic images for training helped improve the accuracy of both the models as compared to when they were only trained on real images. As real images are used to generate more training images, the damages produced in the synthetic images are very similar to the dents found in a real scenario with pixel-level deviations. This introduces the required variation needed in a training dataset to enable better training of the models. The unique illumination modes employed during image capture enabled the models to comprehend the diverse ways dents can appear under different environmental conditions. This is observed in Table 1(b), where the left image reveals dents due to the gap in the line of light as it deviates around the dent, creating a stark contrast. The right image showcases shadows around the curve and partial illumination of the dent, resulting in a more nuanced representation. This approach helps develop a deeper understanding of how environmental factors influence dent appearance as well as recognize the variations in lighting conditions during inspections.

Conclusion

In this study, two deep-learning models, YOLOv11 and RT-DETR, are trained on a novel dent dataset to develop a dent detection system for aircraft damage assessment. A diverse dataset comprising real and synthetic images was used, captured under varying light conditions to account for the impact of specular light reflections on dent visibility. Comparative evaluation of YOLOv11 and RT-DETR models showed that YOLOv11 outperformed RT-DETR, albeit with a modest margin. The findings contribute to the existing literature on dent detection using deep-learning methods and highlight the effectiveness of synthetic images in datasets for more comprehensive understanding of lighting effects on surface features. Future work can build upon this work by expanding the dataset to include more synthetic images for training deep-learning architectures and exploring the use of light reflections to reveal damages.

References

[1] R. Arora, V. Bhatia and S. Sidharth. Military Aircraft Surface Defect Detection Using Machine Learning (2024). International Conference on Computing, Sciences and Communications (ICCSC), pp. 1-6. https://doi.org/10.1109/ICCSC62048.2024.10830372

[2] A.K. Koschlik, M. J. Scott, T. Keser, F. Rauscher, H. Meyer, W. Verhagen, P. Marzocca, F. Raddatz, and G. Wende. Mixed reality for aircraft structural dent and buckle non-destructive evaluation (2024). In 34th Congress of the International Council of the Aeronautical Sciences, ICAS 2024. Congress of the International Council of the Aeronautical Sciences.

[3] A. Plastropoulos, K. Bardis, G. Yazigi, N.P. Avdelidis, and M. Droznika. Aircraft Skin Machine Learning-Based Defect Detection and Size Estimation in Visual Inspections. Technologies 12, no. 9 (2024): 158. https://doi.org/10.3390/technologies12090158.

[4] P. Shailaja and S. Padmanabhan. A Survey on Autonomous Damage Detection on Aircraft Surfaces using Deep Learning Models (2022). 2022 6th International Conference on Computing Methodologies and Communication (ICCMC), Erode, India. pp. 1135-1140, doi:10.1109/ICCMC53470.2022.9753755.

[5] Y. Zhao, W. Lv, S.L. Xu, J.M. Wei, G.Z. Wang, Q.Q. Dang, Y. Liu, and J. Chen. DETRs Beat YOLOs on Real-time Object Detection (2024). 2024 IEEE/CVF Conference on Computer Vision and Pattern Recognition (CVPR), pp. 16965-16974. https://doi.org/10.1109/CVPR52733.2024.01605.

[6] R. Rombach, A. Blattmann, D. Lorenz, P. Esser, and B. Ommer. High-Resolution Image Synthesis with Latent Diffusion Models. 21st IEEE/CVF Conference on Computer Vision and Pattern Recognition (CVPR), pp. 10674-10685. https://doi.org/10.1109/CVPR52688.2022.01042.

[7] S. Merola, A. Mhatre, A.K. Koschlik, M. Guida, and F. Marulo. Comparative Analysis of Generative Data Augmentation Techniques for Aircraft Damage Detection Algorithms: A Case Study (2025). Proceedings of 28th AIDAA International Congress & 10th CEAS Aerospace Europe Conference.

Materials Research Proceedings 69 (2026) 42-47 https://doi.org/10.21741/9781644904251-8

Improving GNSS Positioning Accuracy through Adaptive Weighting and Multipath Isolation

Sebastiano CHIODINI[1,2,a *], Andrea VALMORBIDA[1,2,b], Giovanni ANESE[1,2,c], Marco PERTILE[1,2,d], Giada GIORGI[3,e], Claudio NARDUZZI[3,f] and Bortolino SAGGIN[1,2,g]

[1]Dept. of Industrial Engineering (DII) - University of Padova, Italy

[2]CISAS 'Giuseppe Colombo' - University of Padova, Italy

[3]Dept. of Information Engineering (DEI), University of Padova, Italy

[a]sebastiano.chiodini@unipd.it, [b]andrea.valmorbida@unipd.it, [c]giovanni.anese@phd.unipd.it, [d]marco.pertile@unipd.it, [e]giada.giorgi@unipd.it, [f]claudio.narduzzi@unipd.it, [g]bortolino.saggin@unipd.it

Keywords: GNSS Positioning, Multipath Mitigation, Adaptive Weighting, Code-Minus-Carrier

Abstract. This work addresses the challenge of multipath interference in Global Navigation Satellite System (GNSS) positioning. An approach is proposed to improve accuracy through adaptive weighting strategies and multipath isolation techniques. Weighting methods based on elevation and carrier-to-noise ratio (C/N0) are employed, and this strategy is combined with a multipath detection technique using the Code-minus-carrier (CMC) rate of change. The method is tested using a Piksi Multi GNSS Module, with data processed using Standard Point Positioning (SPP) techniques. An 8-state filter based on a Position-Velocity (PV) model is implemented for dynamic state estimation. Experiments in static and dynamic scenarios demonstrate significant improvements in positioning accuracy.

Introduction

GNSS is critical for autonomous guidance, providing accurate positioning and timing. However, multipath remains a challenging error source, occurring when signals reach the receiver via multiple paths, leading to interference and range errors. Robust integrity measures are essential for detecting and identifying outliers and unmodeled errors [1]. Weighting residuals with appropriate variance models can significantly improve positioning accuracy, particularly by accounting for the elevation dependence of pseudorange errors [2]. Proper modeling of measurement variances, using dual-frequency iono-corrected code-minus-carrier combinations and Bayesian analysis, can help characterize multipath effects and develop more accurate error models [3]. In this work, we present a characterization of pseudorange errors based on both satellite elevation and C/N0. Our analysis shows that lower elevation angles generally correspond to increased pseudorange noise. Moreover, we observe that C/N0 is low not only for low-elevation satellites but also in cases of multipath or other disturbances, suggesting that C/N0 may capture a broader range of error sources compared to elevation alone. These observations motivate the use of pseudorange measurement weighting strategies in the position estimation stage. Specifically, we have chosen to test these weighting techniques within an Extended Kalman Filter position-velocity (PV) model [4]. Additionally, we employ CMC analysis to detect multipath effects, as proposed by [5]. By examining the time-differenced CMC (TDCMC), we establish thresholds for multipath detection based on satellite elevation. This allows for the identification and potential exclusion of measurements significantly affected by multipath. Our experimental results compare the performance of C/N0-based and elevation-based weighting schemes for pseudorange measurements within the Extended Kalman

Content from this work may be used under the terms of the Creative Commons Attribution 3.0 license. Any further distribution of this work must maintain attribution to the author(s) and the title of the work, journal citation and DOI. Published under license by Materials Research Forum LLC.

Filter (EKF). The integration of CMC-based multipath detection with these weighting strategies is also evaluated.

Methodology

In this chapter, we present a two-step approach to enhance GNSS positioning accuracy. First, we conduct a characterization of pseudorange errors, analyzing their relationship with both satellite elevation and CN/0. The receiver position has been kept fixed and known during the characterization phase. Subsequently, we implement this error model within an EKF framework. The model is used to differentially weight pseudorange measurements in the EKF, optimizing the integration of satellite observations based on their expected error characteristics.

Pseudo range Characterization. Let us define the code observable:

$$R_i = \rho_i + c(dt_r - dt_i) + Tr_i + I_i + MP_i + \varepsilon_i \quad (1)$$

where the subscript i refers to the i-th satellite, ρ_i is the geometric distance between the satellite and the receiver's position, R_i is the GNSS code observation, cdt_r is the receiver clock offset delay, cdt_i is the satellite clock offset delay, Tr_i stands for the tropospheric effects, I_i gathers the ionospheric effects, ε_i constitutes the remaining errors in the code observations. The following errors: leap seconds, relativistic effects, satellite clock drift, Sagnac effect, Timing Group Delay (TGD) correction and satellite movement have been corrected. The ionospheric correction has been performed using the ionosphere-free combination of f_{L1} and f_{L2}, and the tropospheric correction using the delay model of [6]. We have considered a series of pseudorange errors $\varepsilon_{i,j}$, where i represents the i-th satellite and j represents the j-th observation. These errors are assumed to follow a normal distribution with zero mean and variance $\sigma^2(\theta)$, where θ is the elevation of the i-th satellite corresponding to that pseudorange observation. This can be expressed as $\varepsilon_{i,j} \sim \mathcal{N}(0, \sigma^2(\theta))$. Additionally, we have also considered the distribution $\mathcal{N}(0, C/N0)$, where $C/N0$ is the carrier-to-noise density ratio associated with the pseudorange observation.

For pseudorange weighting, we have considered the following variance models as in [3]:

$$\sigma^2(\theta) = a + \frac{b}{\sin\theta} \qquad \sigma^2(C/N0) = c + d \cdot 10^{-C/N0/10} \quad (2)$$

Estimation of multipath with Code Minus Carrier techniques. In addition to the code observable (Equation 1), let us define the carrier phase observable Φ_i for the i-th satellite:

$$\Phi_i = \rho_i + c(dt_r - dt_i) + Tr_i - I_i + \lambda N_i + mp_i + \zeta_i \quad (3)$$

where λ is the wavelength of the carrier signal, N_i is the integer ambiguity, and ζ_i represents the noise and multipath effects. To estimate multipath effects, first, the CMC observable is computed by subtracting the phase measurements from the code measurements (eq. 4), then, to remove the carrier phase ambiguity term (λN_i), the rate of change of multipath and noise is obtained by differencing consecutive CMC measurements (eq. 5):

$$\mathrm{CMC}_i = R_i - \Phi_i = 2I_i - \lambda N_i + MP_i - mp_i + \varepsilon_i - \zeta_i \quad (4)$$

$$\Delta\mathrm{CMC}_{i,k} = \frac{1}{\Delta t}\left(\mathrm{CMC}_{i,k} - \mathrm{CMC}_{i,k-1}\right) = 2\dot{I}_{i,k} + \dot{MP}_{i,k} + \dot{\varepsilon}_{i,k} \quad (5)$$

Materials Research Proceedings 69 (2026) 42-47 https://doi.org/10.21741/9781644904251-8

where k represents the epoch index. To characterize the behavior of $\sigma_{\Delta CMC}$ in low multipath environments, an analysis has been conducted in an open sky static scenario. Then the standard deviation of ΔCMC has been calculated as a function of the elevation angle of the satellite θ. Based on this characterization, we defined a multipath detection threshold empirically as $T_k = 3\sigma_{\Delta CMC}(\theta)$. When the absolute value of ΔCMC exceeds this threshold, it indicates a high probability of significant multipath effects on the measurement.

Extended Kalman Filter Implementation. The adopted filter is an 8-state filter based on a Position-Velocity (PV) model where the acceleration is assumed to be white noise and the velocity and position are estimated as random-walk processes. The state vector $\mathrm{x_k}$ consists of the receiver's position (x, y, z), velocity $(\dot{x}, \dot{y}, \dot{z})$, clock bias ct_r, and clock drift $c\dot{t_r}$. In the prediction phase, we estimate the state $\hat{\boldsymbol{x}}_{k|k-1}$ and the state covariance matrix $\boldsymbol{P_{k|k-1}}$ as follows:

$$\hat{\boldsymbol{x}}_{k|k-1} = \boldsymbol{A}_k \hat{\boldsymbol{x}}_{k-1|k-1} \qquad \boldsymbol{K_k} = \boldsymbol{P_{k|k-1}} \boldsymbol{H_k^T} \left(\boldsymbol{H_k} \boldsymbol{P_{k|k-1}} \boldsymbol{H_k^T} + \boldsymbol{R_k}\right)^{-1}$$

$$\boldsymbol{P_{k|k-1}} = \boldsymbol{A}_k \boldsymbol{P_{k-1|k-1}} \boldsymbol{A_k^T} + \boldsymbol{Q_k} \qquad \hat{\boldsymbol{x}}_{k|k} = \hat{\boldsymbol{x}}_{k|k-1} + \boldsymbol{K_k} \left(\boldsymbol{z_k} - \boldsymbol{h}\left(\hat{\boldsymbol{x}}_{k|k-1}\right)\right)$$

$$\boldsymbol{P_{k|k}} = (\boldsymbol{I} - \boldsymbol{K_k} \boldsymbol{H_k}) \boldsymbol{P_{k|k-1}} \tag{5}$$

where $\boldsymbol{A}_k$ is the state transition matrix, $\boldsymbol{Q_k}$ is the covariance matrix of the process noise, $\boldsymbol{K_k}$ is the Kalman gain, $\boldsymbol{H_k}$ is the measurement matrix, $\boldsymbol{R_k}$ is the measurement noise covariance matrix, $\boldsymbol{z_k}$ is the measurement vector, and $h(\cdot)$ is the measurement function. The measurement function $\boldsymbol{h}\left(\hat{\boldsymbol{x}}_{k|k-1}\right)$ represents the expected pseudorange measurements $\hat{\rho}_i$ for each satellite i, calculated as the geometric distance between the receiver position $\boldsymbol{r}_r$ and the satellite position $\boldsymbol{r}_i$, plus the receiver clock bias δt_r: $\hat{\rho}_i = \|\boldsymbol{r}_r - \boldsymbol{r}_i\| + c\delta t_r$. The noise covariance measurement matrix $\boldsymbol{R_k}$ has only diagonal elements σ_i^2 that represent the variance of the pseudorange measurement for each satellite i, as determined from the previous characterization. The observations corresponding to signals for which multipath has been identified using the ΔCMC threshold criterion are eliminated from the measurement vector $\boldsymbol{z_k}$ and the corresponding rows and columns are removed from the measurement noise covariance matrix $\boldsymbol{R_k}$.

Results

The experiments were conducted using the Piksi Multi GNSS Module (https://www.swiftnav.com/piksi-multi). Figure 1 presents the pseudorange code error profiles during the acquisition phase, with each line representing a different visible satellite. The data were acquired on July 18, 2025, at a location with latitude 45.411955° and longitude 11.898037°, focusing on GPS L1 and L2 signals. The graph displays the $\varepsilon_{i,j}$ values as calculated in equation (1). Moreover, Figure 1 provides a skyplot representation of the visible satellites, with the color of each marker indicating the C/N0, higher C/N0 values generally correspond to more reliable pseudorange measurements.

Materials Research Proceedings 69 (2026) 42-47 https://doi.org/10.21741/9781644904251-8

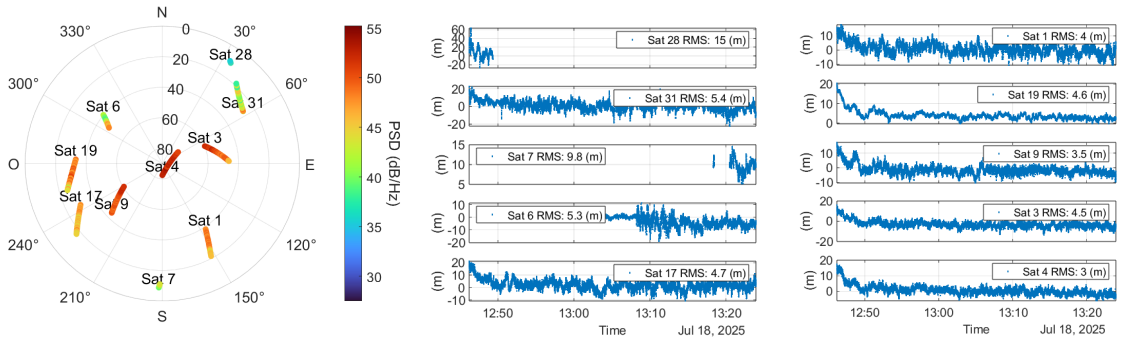


Figure 1 (Left) Skyplot of visible satellites. The C/N0 is visualized for each satellite. (Middle-Right) Pseudorange code error profiles during the acquisition phase for each visible satellite.

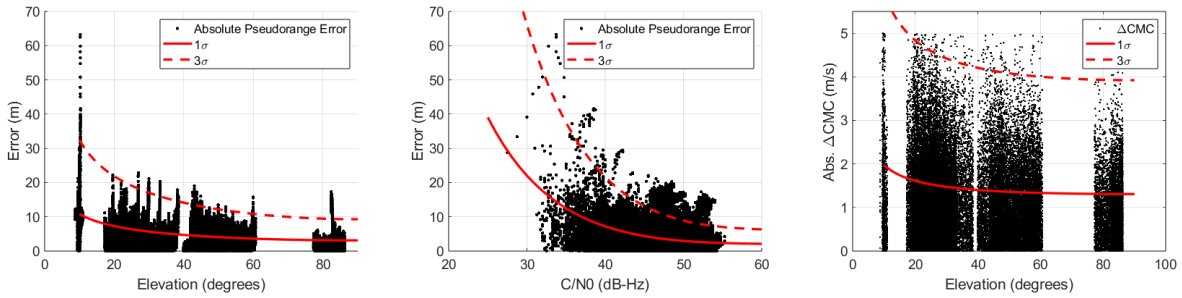


Figure 2 Statistical Characterization of Pseudorange Errors: Standard deviation of pseudorange error as a function of satellite elevation ($\boldsymbol{\theta}$) (left) and as a function of C/N0 (middle). (right) Absolute $\boldsymbol{\Delta CMC}$ as a function of satellite elevation.

Figure 2 presents the characterization of pseudorange errors $\varepsilon_{i,j}$ as a function of θ and the C/N0. It is evident that pseudorange accuracy tends to degrade at lower elevation angles, which is expected due to increased atmospheric path delays and multipath effects. Similarly, Figure 2 shows the standard deviation of the pseudorange error as a function of the C/N0. This plot demonstrates that higher C/N0 values generally correspond to lower pseudorange errors. From fitting the models in Eq. 2 to the variance found for each bin, the following variance models $\sigma^2(\theta) = -13 + 23/\sin\theta$ and $\sigma^2(C/N0) = 4 + (693^2)10^{-C/N0/10}$ have been obtained, these models have been used during the weighting phases.

The performance of the proposed method was evaluated under both static and dynamic conditions to assess its robustness and accuracy across various scenarios. The static test, performed in open sky and low-multipath environment, was conducted on July 18, 2025, from 13:27 to 13:39 UTC. This test used a precisely known reference position with coordinates latitude 45.411733 ° and longitude 11.899049 °, located in Parco Europa, Padova, Italy. Figure 3 presents the normal probability plots of positioning errors for the tested models: constant variance, elevation-weighted variance, C/N0-weighted variance, and C/N0-weighted variance with multipath isolation. The results shows that incorporating variance models significantly enhances the accuracy of localization. The C/N0-weighted variance model exhibits superior performance, yielding a distribution that more closely adheres to the theoretical normal distribution. However, in this scenario, the isolation of multipath effects does not significantly improve the performance of the C/N0-weighted variance model.

Materials Research Proceedings 69 (2026) 42-47 https://doi.org/10.21741/9781644904251-8

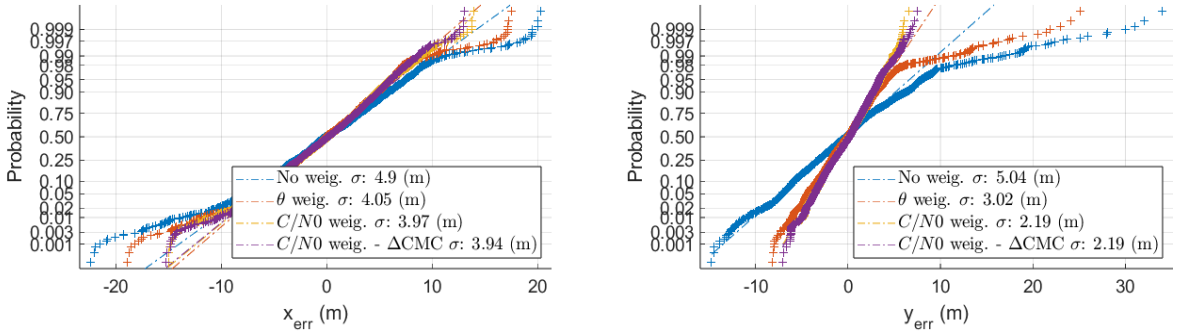


Figure 3 Normal probability plots assessing the distributional characteristics of positioning errors.



Figure 4 (Left) Comparison of trajectories reconstructed using EKF. (Right) Trajectory traveled and sections in which the presence of multipath was identified.

To assess the algorithm's performance under more challenging and realistic conditions, a dynamic test was conducted. This test involved the reconstruction of a trajectory that encompassed both open-sky environments and areas with significant building presence. Figure 4 presents the comparison of the reconstructed trajectories during this test. The blue trajectory represents the path reconstructed using an EKF with constant pseudorange variance. The orange and yellow trajectory respectively shows the results obtained using the elevation-weighted and the C/N0-weighted variance models. The purple trajectory shows the C/N0-weighted variance models combined with the multipath isolation performed with the $\Delta\boldsymbol{CMC}$ analysis. A detailed examination of the trajectories reveals that the C/N0-weighted variance model yields better results, particularly in areas prone to multipath effects. The analysis of the $\Delta\boldsymbol{CMC}$ appears to effectively identify the presence of multipath-affected zones. However, the improvement in the trajectory reconstruction is relatively small, indicating that the C/N0-based weighting scheme already mitigates the undesirable effects of multipath to a significant extent.

Conclusions

This study presents a comprehensive analysis of GNSS pseudorange errors and their impact on positioning accuracy, focused on the effectiveness of different variance models in an EKF framework. The results show the advantage of employing adaptive weighting strategies based on satellite elevation and C/N0 in both static and dynamic scenarios. Pseudorange error characterization revealed strong correlation with elevation and C/N0, providing a basis for developing more accurate variance models. The C/N0-weighted variance model outperformed constant variance and elevation-weighted models, particularly in multipath-prone environments. $\Delta\boldsymbol{CMC}$ seems to successfully identifying areas impacted by multipath. Nonetheless, the enhancement in trajectory reconstruction is minor, suggesting that, for the testes scenario, the C/N0-based weighting scheme reduces the negative effects of multipath on its own.

Acknowledgment
Project BIRD239711-Enhancing Remote Sensing Capabilities: Integrating Multispectral Sensor Suite on a Rover for Robust Fiducial Reference Measurements financially supported by BIRD 2023 Research Program of University of Padova.

References

[1] Hewitson, S., & Wang, J. (2007). GNSS receiver autonomous integrity monitoring with a dynamic model. The Journal of Navigation, 60(2), 247-263. https://doi.org/10.1017/S0373463307004134

[2] Kost, O., Dun'ık, J., Straka, O., & Daniel, O. (2023). Identification of GNSS measurement error: From time to elevation dependency. IEEE Transactions on Aerospace and Electronic Systems, 59(6), 8931-8943. https://doi.org/10.1109/TAES.2023.3315727

[3] Medina, Daniel, et al. "Determination of pseudorange error models and multipath characterization under signal-degraded scenarios." Proceedings of the 31st International Technical Meeting of the Satellite Division of the Institute of Navigation, ION GNSS+ 2018. 2018. https://doi.org/10.33012/2018.16094

[4] Brown, R. G. and Hwang, P. Y. C. (1996) Introduction to Random Signals and Applied Kalman Filtering, 3rd ed., Wiley, New York

[5] M. Caamano, O. G. Crespillo, D. Gerbeth and A. Grosch, "Detection of GNSS Multipath with Time-Differenced Code-Minus-Carrier for Land-Based Applications," 2020 European Navigation Conference (ENC), Dresden, Germany, 2020, pp. 1-12. https://doi.org/10.23919/ENC48637.2020.9317340

[6] Collins, J., 1999. Assessment and Development of a Tropospheric Delay Model for Aircraft Users of the Global Positioning System. M.Sc.E. thesis, Department of Geodesy and Geomatics Engineering Technical Report No. 203, University of New Brunswick, Fredericton, New Brunswick, Canada.

[7] Sarunic, P. W. (2016). Development of GPS receiver Kalman Filter algorithms for stationary, low-dynamics, and high-dynamics applications (No. DSTGroupTR3260).

Materials Research Proceedings 69 (2026) 48-53 https://doi.org/10.21741/9781644904251-9

Lunar Descent and Landing Via Fusion of Deep Learning-Based Visual Navigation and Moonlight Signals

Michele CERESOLI[1,a,*], Floor MELMAN[2], Yoann AUDET[2], Richard SWINDEN[2], Francesco CAPOLUPO[2] and Michèle LAVAGNA[1]

[1]Department of Aerospace Science and Technology, Politecnico di Milano, Via La Masa 34, 20156, Milan, Italy

[2]European Space Research and Technology Centre (ESTEC), European Space Agency, Keplerlaan 1, 2201AZ, Noordwijk, The Netherlands

[a]michele.ceresoli@polimi.it

Keywords: Lunar Landing, Vision-Based Navigation, Moonlight, Deep-Learning

Abstract. The renewed momentum in lunar exploration has driven the development of dedicated lunar communication and navigation infrastructures such as the European Space Agency's Moonlight Lunar Communication and Navigation System (LCNS). In this context, landing operations are key mission phases that enable humans and scientific experiments to reach the Moon surface. However, recent crashes of both public and private missions have highlighted how challenging and complex such operations are. As such, this work investigates the achievable navigation performance of a lunar lander targeting the Moon's South Pole through the integration of One-Way Ranging signals from LCNS and Deep Learning–based Vision-Based Navigation measurements, showcasing the benefits that the fusion of these two distinct type of measures can bring.

Introduction

Planetary landings represent a very challenging scenario for Guidance, Navigation and Control (GNC) systems. Indeed, due to a combination of fast-landing dynamics, communication delays, and restricted coverage of landing areas, real-time ground control is often limited or impractical. Recent attempts to land on the lunar surface have further highlighted the need for an autonomous and reliable GNC module. Thus, to support these missions, the European Space Agency (ESA) is currently developing the Moonlight Lunar Communication and Navigation System (LCNS) that will provide GNSS-like signals enabling One-Way Ranging (OWR) for future lunar users. However, as the constellation will be gradually deployed, an initial key challenge will be the limited availability of such signals with respect to well-established Earth GNSS systems. Within this context, current and future landing missions rely on Vision-Based Navigation (VBN) techniques to estimate the state of the lander while minimizing the overall size, weight and power of the GNC subsystem. As such, this study aims to showcase the performance and robustness improvements that the integration of radiometric OWR signals with AI-based VBN techniques can bring to landing vehicles.

Landing Trajectory

The considered mission scenario consists in the spacecraft descent from the pericenter of an elliptical Low Lunar Orbit (LLO) (100×30 km altitude) to touchdown at a targeted landing site close to the Lunar South Pole. The trajectory reproduces the common scheme of lunar landings and begins with the Main Braking Burn (MBB), where the engines are initiated at full thrust to reduce the orbital velocity. This maneuver lasts until the lander reaches the Pitch-Up Gate (PGA), at an altitude of about 1 km, where thrust is re-oriented towards the vertical direction and the Hazard Detection and Avoidance (HDA) sensors and routines are activated. A final powered

Content from this work may be used under the terms of the Creative Commons Attribution 3.0 license. Any further distribution of this work must maintain attribution to the author(s) and the title of the work, journal citation and DOI. Published under license by Materials Research Forum LLC.

Materials Research Proceedings 69 (2026) 48-53 https://doi.org/10.21741/9781644904251-9

descent is foreseen for the last few hundreds of meters and ends before the final vertical descent at the Vertical Gate (VGA), where the horizontal velocity becomes null.

The trajectory was generated following the expected profile of the Argonaut mission [1], using an indirect optimization technique for the main braking phase, and a semi-analytical guidance for the final approach [2]. The lander is assumed to have an initial mass of 7000 kg, a maximum thrust of 18000 N, and a specific impulse of 330s. The entire descent duration is of 584s. The target landing site has been selected near the Sverdrup crater, in proximity of the South Pole, at approximately 153° W and 88° S.

The dynamical model used to simulate the true lander dynamics includes most of the major perturbations that are relevant in a lunar scenario and that affect the navigation accuracy. Specifically, it accounts for the gravitational point-mass accelerations due to the Earth, Sun and Moon as well as the effects of the irregular lunar gravity field. The latter are modelled using a spherical harmonic expansion up to 120×120 degree and order. On the other hand, control errors are assumed null.

On-board Sensors

The lander is equipped with a monocular camera to acquire navigation images and with two antennas to retrieve the LCNS signals. An Inertial Measurement Unit (IMU) is instead used to retrieve both acceleration and angular velocity readings. Finally, a star tracker enables precise attitude measurements, with an accuracy up to 10 arcseconds. A brief overview of the mathematical modeling of each sensor is provided hereafter.

Inline with previous work [3], the LCNS constellation is comprised of 4 satellites deployed on 4 distinct Elliptical Lunar Frozen Orbits (ELFO). The constellation parameters are based on internal Moonlight studies and are designed to optimize the South Pole visibility. All satellites are deployed on orbits with a 24-hours orbital period and a nominal eccentricity of 0.63.

The Signal-in-Space Error (SISE) is modeled using a realistic Orbit Determination and Time Synchronization (ODTS) simulator [4], which provides the time series of the errors in each satellite's position, velocity, and clock states. The user on-board clock is modelled using a two-state clock model, in which the frequency deviation is originated from two types of noise, a White Frequency Modulation (WFM) and a Random Walk Frequency Modulation (RWFM). The standard deviations of the noises are based upon a space-qualified OCXO, inline with previous studies [3]. The LCNS receiver is designed to track the LunaNet AFS signal specifications using Delay Locked Loop (DLL) and Frequency Locked Loop (PLL) techniques, providing as an output the pseudorange and doppler quantities with respect to each visible LCNS satellite. The standard DLL and FLL equations are used to characterize the pseudorange and measurement noises. The patterns for the transmitting and receiving antennas are also based upon the on-going Moonlight studies [3,4].

A high-fidelity model is used to account for the measurement errors that real IMUs are subject to, including non-orthogonalities, scale factor, bias and noise errors. The parameters are loosely based upon the flight-proven LN-200HPS model from Northrop Grumman.

A monocular camera is installed on the side of the lander, at angle of 22.5° with respect to the face normal, ensuring constant visibility of the Moon surface throughout the spacecraft descent. The camera is based upon the standard pinhole model, with a 640×640 resolution and a Field-of-View (FOV) of 45°. Images of the Moon surface are generated using the in-house rendering software presented in [5]. Two distinct pipelines are used to process the acquired images.

Materials Research Proceedings 69 (2026) 48-53 https://doi.org/10.21741/9781644904251-9

Navigation Filter Architecture

The navigation module consists of an Extended Kalman Filter (EKF) to estimate the absolute inertial position and velocity of the lander together with the LCNS OWR receiver clock bias and drift, and a Multiplicative Extended Kalman Filter (MEKF) to estimate the lander inertial attitude and gyroscope bias. An overview of the entire navigation module is given by Figure 1.

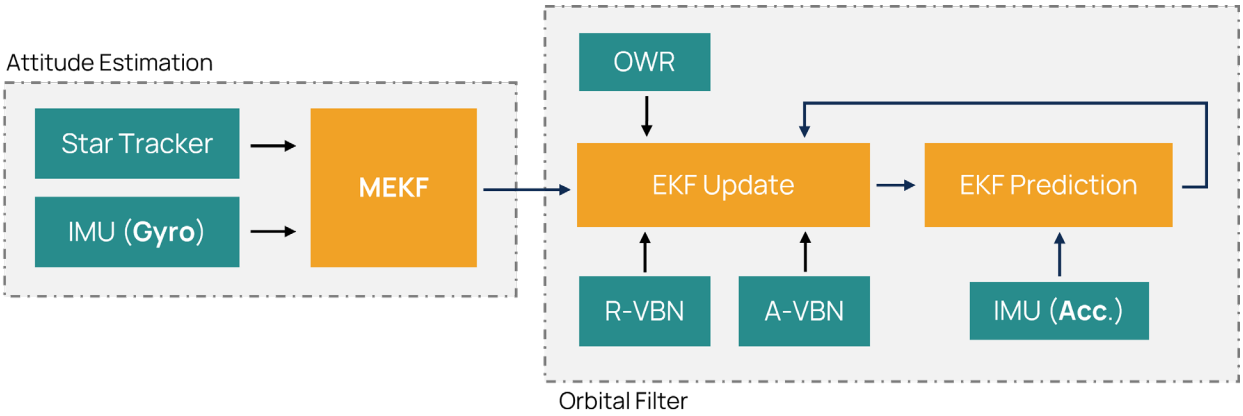


Figure 1: High-level overview of the navigation block interfaces.

The Absolute Vision Based Navigation (A-VBN) module uses Moon impact craters as landmarks, comparing them with a dedicated on-board crater catalogue to retrieve absolute estimates of the lander position. The adopted catalogue is derived from the global Robbins catalogue [6], which has been expanded by manually mapping all the visible craters along the expected spacecraft groundtrack. A Deep Neural Network (DNN) based upon the YOLOv11n architecture is used to identify the bounding box surrounding each crater. Subsequently the crater shape is fitted with an ellipse and matched against the crater database to retrieve its selenographic coordinates. The crater matching algorithm is based upon an iterative direct matching strategy, which leverages the estimated spacecraft position and orientation to project onto the image plane the on-board catalogue. Detected and projected craters are then transformed into bivariate Gaussian Probability Density Functions (PDFs), and their similarity is quantified through the Gaussian Angle distance. A RANSAC-based outlier rejection strategy is then used to identify potential wrong matches. Finally, the resulting pairs of detected and projected craters are used to assemble a Perspective-n-Crater (PnC) problem, which leverages the known spacecraft orientation and the full information from the crater shapes to compute an estimate of the spacecraft position with respect to the Moon-fixed frame [7]. The M-estimator SAmple Consensum (MSAC) algorithm is used to further mitigate the impact of outliers.

On the other hand, the Relative Vision Based Navigation (R-VBN) module integrates multiple-view geometry and deep-learning to estimate the direction of motion of the lander from one image frame to the other. It leverages SuperPoint, a deep-learning based feature extractor [8] to identify 2D features in the images, which are then matched using a brute-force approach. Using the known spacecraft attitude a system of equations enforcing the epipolar constraint is then assembled and solved for the relative camera translation direction [7]. To enhance robustness, MSAC is again adopted to reject potential outliers from the identified 2D features pairs.

Both the EKF and the MEKF filters are executed at 10 Hz, with the IMU measurements sampled at the same frequency. On the other hand, due to the post-processing requirements, the A-VBN position estimate is assumed to be available at a frequency of 0.1 Hz and with a delay of 10s (i.e., the measurement at time k is associated to the pose the spacecraft had 10 seconds before k), while the R-VBN measures are given at a frequency of 0.5 Hz. Finally, the OWR pseudorange and

Materials Research Proceedings 69 (2026) 48-53 https://doi.org/10.21741/9781644904251-9

Doppler signals are ingested at 1 Hz and fused using a tightly-coupled approach. Stochastic Cloning (SC) is used to handle both delayed and relative measurements by making two independent copies of the position states, each synchronized to the associated measurement. A simplified dynamic model is used to predict the inertial position and velocity of the lander, which uses a 40×40 expansion of the Moon gravity field. For the process noise, the global contribution of unmodelled dynamic accelerations and IMU biases is assumed to behave as a First-Order Gauss-Markov (FOGM) processes, following the Dynamic Model Compensation (DMC) algorithm. On the other hand, the process noise of the clock states assumes the clock drift is also driven by a FOGM, while the clock bias is the integral of the drift plus a Gaussian noise term.

Results and Discussion

A Montecarlo simulation with 200 samples has been performed for two distinct scenarios, with 2 and 3 visible LCNS satellites, respectively. The results in terms of 3D position error are reported in Figure 2. In both cases the final navigation error is very small, under 7m (99th) with 2 satellites and smaller than 5m (99th) with 3. A comparison between the two also highlights a faster convergence when 3 satellites are available, as well as the maximum error being smaller than 40m with respect to the 50m achieved when only 2 LCNS signals are tracked.

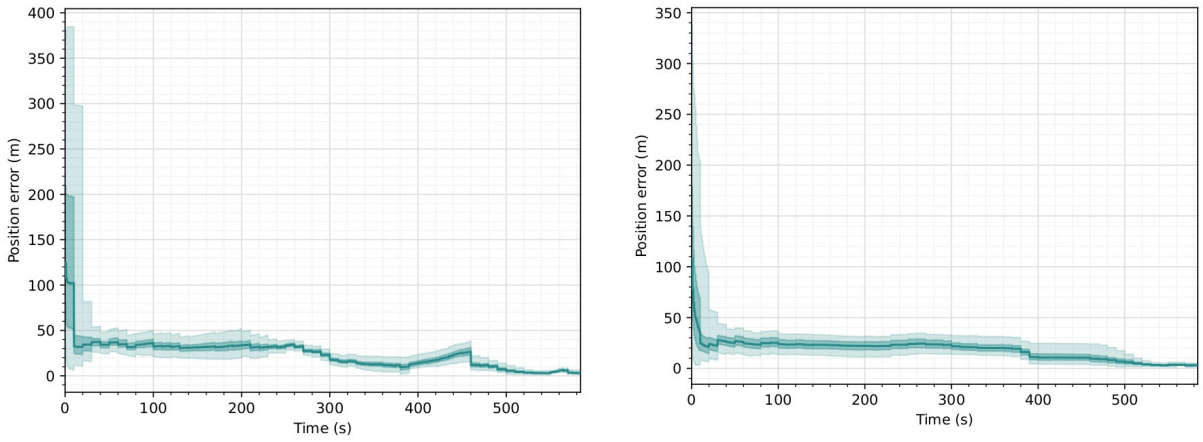


Figure 2: 3D position error throughout the descent with 2 (left) and 3 (right) LCNS satellites in visibility

The benefits of merging VBN and OWR measurements can be further appreciated by comparing the results in Figure 2 with those in Figure 3, which reports the Montecarlo simulations when VBN-only measures are considered. Indeed, despite the VBN-only solution already provides a satisfactory final navigation error below 20m (99th), the addition of OWR measurements further improves this result, reducing the maximum navigation error after the initial convergence from 100m to around 50m. Moreover, these added signals can also prove beneficial when above areas that are either not covered by the on-board crater catalogues or are characterized by unfavorable illumination conditions, scenarios in which the VBN may struggle to provide meaningful measures.

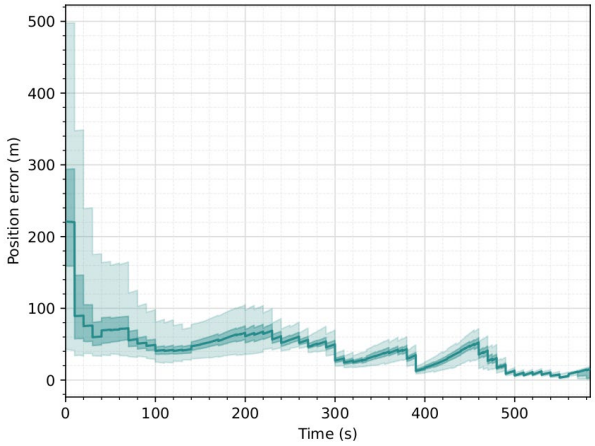


Figure 3: 3D position error throughout the descent trajectory with VBN-only measurements

On the other hand, it is well known that for OWR measures, a minimum of 4 visible satellites is requested to compute a position-fix. In this regard, these simulations highlight that the addition of VBN measurements allows a stable navigation solution to be computed even with limited LCNS availability.

Conclusions

The International Space Exploration Coordination Group (ISECG) has quantified 90m as a threshold for the maximum landing uncertainty with respect to the target location that guarantees the safety of the operations. This contribution shows that the fusion of vision-based and radiometric data from the proposed LCNS constellation is capable of meeting this strict navigation requirement over a candidate landing site at the Lunar South Pole. Moreover, it highlights the robustness of the solution even when only a portion of the LCNS satellites is visible.

References

[1] F. Capolupo, A. Rinalducci, Descent & Landing Trajectory Guidance Algorithms with Divert Capabilities for Moon Landing, AIAA Scitech Forum, 2024 https://doi.org/10.2514/6.2024-0086

[2] P. Lunghi, P. Di Lizia, R. Armellin, M. Lavagna, Semi-analytical adaptive guidance computation for autonomous planetary landing.

[3] Y. Audet, M. Ceresoli, F. Melman, D. Psychas, R. Swinden, C. Stallo, J. Ventura-Traveset, Assessment of lunar users' PVT performances tightly coupling Moonlight signal with IMU, MDPI (2025)

[4] Y. Audet, F. Melman, D. Psychas, R. Swinden, J. Ventura-Traveset, Positioning of a Lunar Lander Using a Dedicated Lunar Communication and Navigation System Assuming Realistic ODTS Performances, Engineering Proceedings, MDPI (2025) https://doi.org/10.3390/engproc2025088074

[5] M. Ceresoli, S. Silvestrini, M. Lavagna, Optical Image Generation Through Digital Terrain Models for Autonomous Lunar Navigation, Aerospace, MDPI (2025) https://doi.org/10.3390/aerospace12020092

[6] S. Robbins, A new global database of lunar impact craters¿ 1-2 km, Journal of Geophysical Research: Planets, Wiley Online Library, 2019, pp. 871-892 https://doi.org/10.1029/2018JE005592

[7] J. Christian, H. Derksen, R. Watkins, Lunar crater identification in digital images, The Journal of Astronautical Sciences, Springer, 2021, pp. 1056-1144 https://doi.org/10.1007/s40295-021-00287-8

[8] D. DeTone, T. Malisiewicz, A. Rabinovich, Proceedings of the IEEE conference on computer vision and pattern recognition workshop, 2018, pp. 224-236.

Materials Research Proceedings 69 (2026) 54-59 https://doi.org/10.21741/9781644904251-10

Numerical Assessment of Convective PGMs

Giada COLOMBO[1,a *] and Umberto IEMMA[1,b]

[1]Department of Civil, Computer Science and Aeronautical Technologies Engineering, Roma Tre University, Rome, Via Vito Volterra 62, 00146, Italy

[a]giada.colombo@uniroma3.it, [b]umberto.iemma@uniroma3.it

Keywords: Metamaterials, Acoustic Metacontinuum, Spacetime, Metasurfaces, Convective Metasurfaces

Abstract. Acoustic metamaterials enable advanced wavefront control, offering compact and lightweight solutions for noise reduction in aeronautical applications. As thin metasurface, they can be integrated onto existing structures, like nacelle intakes or control surfaces, to absorb or redirect acoustic energy. However, performance degrades in the presence of a background flow due to the change in the mechanism of propagation of the acoustic perturbation. To address this, a spacetime-based analytical framework incorporates flow effects in the medium design by introducing spacetime coordinate transformations. The mathematical tools of differential geometry extend the applicability of static designs to convective environments. This study evaluates the performance of a convective phase gradient metasurface based on a space-coiled, 8-unit cell design, optimised for frequency robustness. Numerical solutions obtained in the frequency domain aim to assess the capability of a flow-corrected design in maintaining wave deflection under grazing flow.

Introduction

Metamaterials have revealed themselves to be a powerful technology to achieve the full control of moulding wavefronts, a task hard to accomplish with the existing materials due to the limitations of their material properties. By intending the meta-device as a three-dimensional composite of periodic or non-periodic structure, tailored responses to specific excitations are affordable [1]. Therefore, exotic wave manipulations (*i.e.*, metabehaviours) can be realised, and in the context of aeronautical applications, acoustic metamaterials appear as a promising strategy for noise abatement purposes [2]. The interest in this advanced technology solution is increased by the possibility of generating exotic wave manipulation with light and compact solutions that do not penalise the weight nor the size of the aircraft. In this fashion, the meta-device appears in the form of a metasurface - *i.e.*, a thin distribution of a material – [3] that can be implemented as a superficial treatment of the already existing surfaces of the airfoil, thus representing an acceptable solution that does not require the innovation of the aircraft concept and layout.

Such could be used to generate absorption of the acoustic energy or the steering of the wavefront in a target direction [2, 4]. The solution is mainly implemented in the nacelle intakes [5], but it could also be applied on the flight control surfaces. However, the topic still captures the research efforts' interest since, in aeronautics, it is not possible to neglect the interaction effects between acoustic waves and the complex background field that develops from the fluid-structure interaction. This coupling alters the propagation mechanism of the acoustic perturbation, causing metadevices to lose their effectiveness in manipulating acoustic wavefronts [6,7]. Different research groups tried to overcome such limitations, introducing correction factors in the design parameters [8,9,10]. Nevertheless, it is believed that the solution can be found in the analytical framework proposed in 2020 in Iemma and Palma [11] based on the combination of the acoustic metacontinuum model of Norris [12] and the spacetime reinterpretation of the convective phenomena [13, 14]. Indeed, spacetime curvature is generated whenever the propagating medium

Content from this work may be used under the terms of the Creative Commons Attribution 3.0 license. Any further distribution of this work must maintain attribution to the author(s) and the title of the work, journal citation and DOI. Published under license by Materials Research Forum LLC.

manifests anisotropic acoustic parameter distribution or whenever there is convection. Therefore, it appears reasonable to describe the phenomenon in a (3+1)-dimensional differential manifold, where the equations governing the acoustic perturbation propagation show up in a conservative form. Based on these observations, it is possible to introduce the background flow information into the analytic design of the acoustic metacontinuum by exploiting the formal invariance of the governing equations to spacetime change of coordinates. The approach has already been tested on a cloaking benchmark in a context of high-fidelity models for the hosting fluid and experimentally realisable Gaussian-beam acoustic sources [15], where some correction defect is still present in the convective design. However, it is also proven that the approach is not influenced by the specific acoustic mirage aimed at, but limited solely by the possibility of including general flow conditions through the specific spacetime mapping used [16]. Therefore, in the present work, the performance of convective phase gradient metasurfaces (PGMs) is evaluated.

Analytical Modelling of a Convective PGM

The acoustic metasurface considered is in a space-coiled solution, which guarantees the compactness of the device, and it is based on a unit cell of eight units [17]. The building blocks operate in a 2π phase range, and their performances are optimised in the sense that their dependency on the frequency of the incoming wave is minimised. Therefore, the optimum design proposed in [18] is associated with the constructive parameters of the eight-block unit cell that provides an equispaced phase delay in the scattered field. The acoustic behaviour of this assembly is then associated with the behaviour of an equivalent acoustic metafluid model. Hence, the framework relies on the extended continuum model of Norris in [12] (*acoustic metacontinuum*) whose governing equation for the acoustic fluctuation propagation is in terms of pseudo-pressure, and, in the present test case, it assumes the form

$$\partial_{tt} p + K \nabla \cdot (\boldsymbol{\rho}^{-1} \nabla p) = 0, \tag{1}$$

by having addressed the anisotropic material parameter distribution of the device to the inertia tensor $\boldsymbol{\rho}$, and being K the space-varying function for the bulk modulus. The metafluid cell can mimic the acoustic behaviour of the original cell by properly defining $\boldsymbol{\rho}$ and K through the following coordinate transformation

$$x = X, \quad y - y_0 = \frac{l_{mf}}{l_{eq}}(Y - Y_0), \quad z = Z \qquad \text{with} \quad Y_0 < Y < l_{eq}, \tag{2}$$

with l_{eq} the equivalent length of a straight channel associated with the space-coiled cell, and l_{mf} is the arbitrarily chosen thickness for the equivalent metafluid domain. Therefore, the parameters in Eq. (1) are specified by the deformation gradient tensor $\boldsymbol{F}$ associated with the transformation in Eq. (2), as

$$K = K_0 \det(\boldsymbol{F}), \quad \boldsymbol{\rho} = \rho_0 det(\boldsymbol{F})(\boldsymbol{V}\boldsymbol{V}^T)^{-1}, \tag{3}$$

with K_0 and ρ_0 the referenced values for the metacontinuum to fulfil the impedance matching condition with the external conventional fluid, and avoid any unwanted reflection.

In [18], the consistency of the results obtained concerning the implementation of the whole architecture has already been proven through a cost-efficient optimization framework. Nevertheless, the device maintains its performance if it is set to operate in a quiescent medium. Therefore, the work aims at assessing the performances of an aeroacoustic PGM whose static design is the one obtained in [18] and represented by Eqs. (1) and (2), and where the background

flow features are included through the spacetime framework proposed in [11]. Specifically, by moving in a $(3+1)$-dimensional differential manifold, it is possible to recast Eq. (1) as

$$\partial_\mu (W^{\mu\nu} \partial_\nu p) = 0, \tag{4}$$

where $\boldsymbol{\partial}$ is the fourth-dimensional nabla differential operator, and $\boldsymbol{W}$ is the second-order tensor enclosing the metric information associated with the propagating mechanism of the acoustic perturbation. The adaptation of the static design is thus provided by the introduction of the Prandtl-Glauert transformation that, in a spacetime formalism, assumes the form

$$\xi_0' = \beta \xi_0 + M_\infty \xi_2', \quad \xi_1' = \xi_1, \quad \xi_2' = \frac{\xi_2}{\beta}, \quad \xi_3' = \xi_3, \tag{5}$$

being $\beta = \sqrt{1 - M_\infty^2}$ the Prandtl-Glauert contraction factor along the y direction. Equation (5) associates a propagation uniformly convected by the free stream with an equivalent isotropic pattern field. Therefore, if $\boldsymbol{\Lambda}$ represent the Jacobian matrix for Eq. (5), then its inverse must be implemented to adapt the acoustic metacontinuum design enclosed in $\boldsymbol{W}$ to convective environments

$$\boldsymbol{W}_c = \boldsymbol{\Lambda}^{-1} \boldsymbol{W} \boldsymbol{\Lambda}^{-T}, \tag{6}$$

being $\boldsymbol{W}_c$ the spacetime-corrected tensor enclosing the new metacontinuum design where the background flow characteristics captured by $\boldsymbol{\Lambda}^{-1}$ are accounted for.

Numerical Results

To assess the performance of the resulting convective PGM, numerical simulations are performed in the frequency domain through a commercial FEM solver. The test case chosen sees a rectangular domain addressed to the external conventional fluid, modelled as a linearised potential fluid, and with which the metadevice is in communication. A plane wave is proceeding from right to left and is impinging on the left boundary where the metacontinuum is disposed. A uniform background flow of Mach 0.3 from top to bottom is introduced to include the effect of a grazing flow. The simulations are performed in the frequency domain, with a working frequency of $f = 857.5\ [Hz]$ that corresponds to a wavelength of $\lambda = 0.4\ [m]$, which is one-tenth the distance between the left and right boundaries of the domain. Perfectly Matched Layers (PML) surround the boundaries in communication with conventional fluid. Figure 1 assesses the equivalence of the performances in static conditions ($M_\infty = 0$), with the reflected wave correctly deflected downward for both configurations. However, the introduction of the grazing flow associated with a Mach number of 0.3 and indicated by the red arrows in Fig. 2, causes a substantial reduction ability of the static design to perform the expected extraordinary reflection (see Fig. 2a). On the other hand, the adapted design can maintain the deflection of the wavefronts in the lower part of the domain (see Fig. 2b). Unwanted reflections are observed in the upper part of the computational domain. They are likely related to numerical artefacts, such as imperfect absorption in the PML region or the limited domain extent.

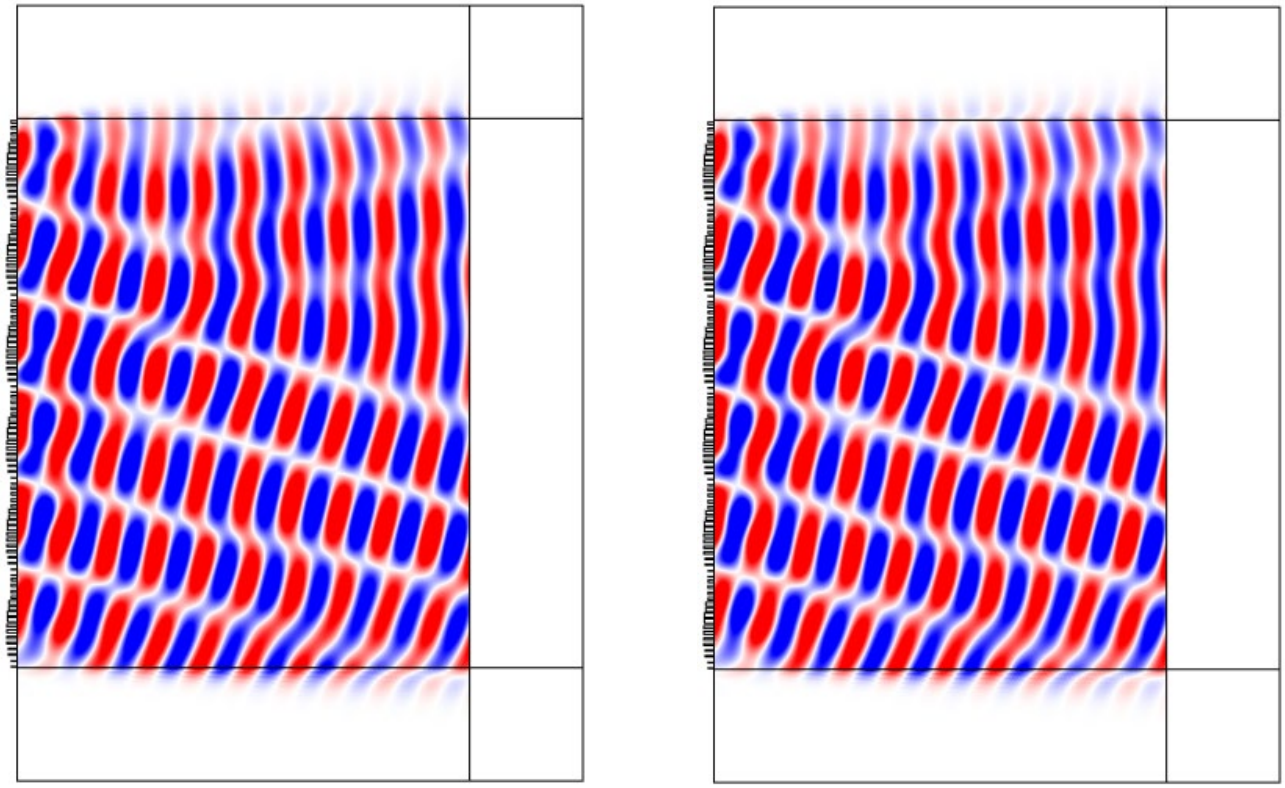
Conclusions

An analytically adapted design for a metasurface performing extraordinary reflection has been numerically evaluated. The spacetime framework used to derive the PGM design is independent of the specific acoustic mirage aimed at. In fact, concerning the state of the art where spacetime transformations are applied on a cloaking benchmark, here the spacetime-corrected

Materials Research Proceedings 69 (2026) 54-59 https://doi.org/10.21741/9781644904251-10

metacontinuum is used to recover the performance decay of a static PGM. The numerical simulations presented in this work corroborate this assumption by displaying a pressure field that maintains the expected deflection towards the lower part of the domain, even in the presence of a grazing flow. Still, the resulting device should be tested in its sensitivity to the frequency emissions, to assess whether the optimised static design maintains its robustness to the frequency of the incoming wave.

Aknowledgements
This work is supported by the European Commission through Project eVTOLUTION (eVTOL mUlti-fideliTy hybrid desIgn and Optimization for low Noise and high aerodynamic performance), call HORIZON-CL5-2023-D5-01, Grant agreement No. 101138209.



(a) (b)

Figure 1: PGMs acoustic pressure field for Mach 0.0 - Static metacontinuum model in 1a and spacetime corrected metacontinuum in 1b

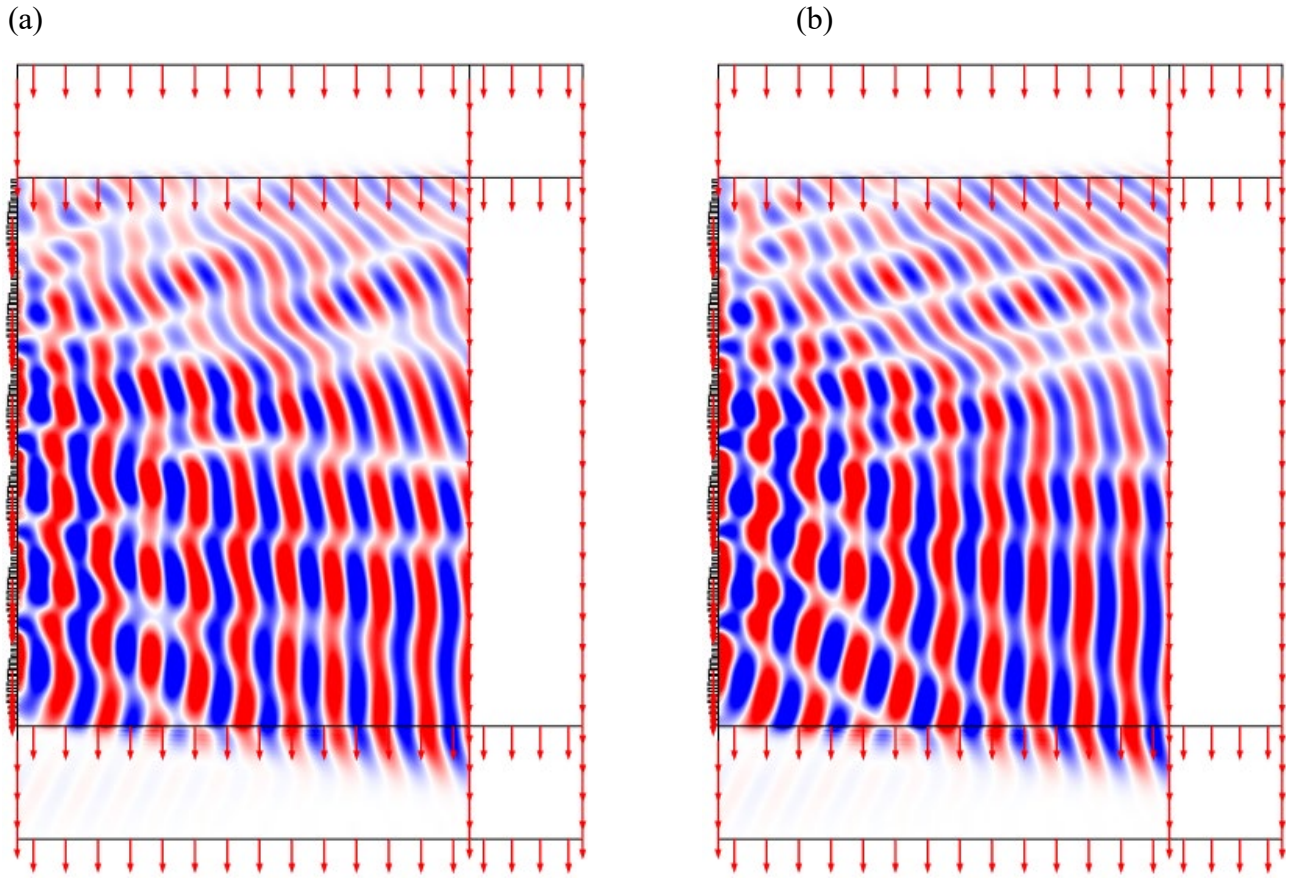


Figure 2: PGMs acoustic pressure field for Mach 0.3 - Static metacontinuum model in 2a and spacetime corrected metacontinuum in 2b

References

[1] T. J. Cui, D. R. Smith, and R, Liu, Metamaterials - Introduction to metamaterials. Boston, Ma: Springer US, 2010.

[2] G. Palma, , H. Mao, L. Burghignoli, P. Göransson and U. Iemma, Acoustic metamaterials in aeronautics, Applied Science, 8 (2018), 971-989. https://doi.org/10.3390/app8060971

[3] G. Palma, and L. Burghignoli, On the integration of acoustic phase-gradient metasurfaces in aeronautics, International Journal of Aeroacoustics, 19 (2020) 294-310. https://doi.org/10.1177/1475472X20954404

[4] P. Cobo, H. Ruiz, A. Julian, Double-Layer Microperforated Panel/Porous Absorber as Liner for Anechoic Closing of the Test Section in Wind Tunnels, AAuA, 96 (2010), 914-922. https://doi.org/10.3813/AAA.918350

[5] G. Palma, L. Burghignoli and U. Iemma, A framework for micro-perforated absorbers optimization, Proc. 29th Int. Congr. Sound Vibr., Prague, Czech Republic : ICSV (2023).

[6] K. Hyunsu and S. Ahmet, Acoustic performance of Helmholtz resonator with flow, JVNV, 7 (2011), 285-305. https://doi.org/10.1504/IJVNV.2011.043191

[7] M. Li, H. J. Wu, and Y. X. Yuan, Metasurface zero-impedance matching mechanism for aerodynamic noise reduction, JSV, 536 (2022), 117147- 117161. https://doi.org/10.1016/j.jsv.2022.117147

[8] Y. He, Z. Siyang and X. Huang, Extensions to the acoustic scattering analysis for cloaks in non-uniform mean flows, JASA, 146 (2019), 41-49. https://doi.org/10.1121/1.5115046

[9] H. Ryoo and W. Jeon, Effect of compressibility and non-uniformity in flow on the scattering pattern of acoustic cloak. Sci. Rep., 7 (2017), 2125- 2136. https://doi.org/ 10.1038/s41598-017-02143-y

[10] U. Iemma, Theoretical and numerical modelling of acoustic metamaterials for aeroacoustic applications, Aerospace, 3 (2016), 15-34. https://doi.org/10.3390/aerospace3020015

[11] U. Iemma, and G. Palma, Design of metacontinua in the aeroacoustic spacetime, Scientific Reports, 10 (2020), 18192- 18202. https://doi.org/10.1038/s41598-020-74304-5

[12] A. N. Norris, Acoustic cloaking theory, R. Soc. A : Math. Phys. Eng. Sci., 464 (2008), 2411-2434. https://doi.org/10.1098/rspa.2008.0076

[13] C. García-Meca, S. Carloni, C. Barceló, G. Jannes, J. Sánchez-Dehesa, and A. Martínez, Analogue Transformation in Physics and their Application to Acoustics, Sci. Rep., 3 (2013), 2009-2014. https://doi.org/10.1038/srep02009

[14] M. Visser, Acoustic propagation in fluids: an unexpected example of Lorentzian geometry, (1993), 1-11. https://doi.org/10.48550/arXiv.gr-qc/9311028

[15] G. Colombo, G. Palma and U. Iemma, Numerical Aeroacoustic Assessment of a Metacontinuum Device Impinged by a Laser-Generated Sound Source, J. Eng., (2024), 1-11. https://doi.org/10.1155/2024/5421663

[16] G. Colombo and U. Iemma, Assessment of the performances and limitations of spacetime convective corrections for acoustic metacontinua design, Sci. Rep, 15 (2025), 7827 -7839. https://doi.org/10.1038/s41598-025-92264-6

[17] G. Palma, I. Cioffi, F. Centracchio, L. Burghignoli, and U. Iemma, Steering of Acoustic Reflection from Metasurfaces through Numerical Optimization, Proc. 25th AIAA/CEAS Aeroacoustic Conf., Delft, The Netherlands: The American Inst. of Aeroacoustics and Aeronautics, (2019), 1-10

[18] G. Palma and U. Iemma, A metacontinuum model for phase gradient metasurfaces. Sci. Rep., 13 (2023), 13038 - 13049. https://doi.org/10.1038/s41598-023-39956-z

Materials Research Proceedings 69 (2026) 60-65 https://doi.org/10.21741/9781644904251-11

Modelling the Correlation Function of Wall Pressure Fluctuations Under Turbulent Boundary Layers with Machine Learning Methods

Marika DI MEO[1,a], Alessandro CASABURO*[1,b], Arthur Diniz FLOR TORQUATO FERNANDES[1,2,c], Francesco FRANCO[1,d]

[1]Pasta-Lab, Department of Industrial Engineering (DII), University of Naples Federico II, Via Claudio 21, 80125 Naples, Italy

[2]SUPMICROTECH, Université de Framche-Comté, Rue de l'Épitaphe 26, Besançon, France, 25000

[a]marik.dimeo@studenti.unina.it, [b]alessandro.casaburo@unina.it, [c]arthurdiniz.flortorquatofernandes@unina.it, [d]francof@unina.it

Keywords: Turbulent Boundary Layer, Wall-Pressure Fluctuations, Chase Model, Deep Learning, Transformers

Abstract. The structural vibrations and aerodynamic noise induced by the wall-pressure fluctuations due to a turbulent boundary layer have received great attention in recent years. Nowadays, the prediction of the vibroacoustic response of structures subjected to this type of source relies on the use of statistical quantities and semi-empirical spectral models in the frequency-wavenumber domain. This work explores machine learning techniques to reconstruct the complex coherence function from the structural response. The behaviour of a rectangular plate under stochastic loading is simulated using the Chase model for four flow conditions, and the resulting response at grid points is used to train an encoder-only transformer. The results show that the algorithm satisfactorily reproduces the Chase-like coherence trends at all the flow conditions.

Introduction

The interest of all major sectors of transportation engineering in the effects of the turbulent boundary layer (TBL) and resulting wall-pressure fluctuations (WPFs) has grown in recent years, as the generated dynamic loads induce mechanical vibrations and structural noise [1]. Being far from negligible, the structural noise has a detrimental impact on the acoustic comfort of passengers and crew members, whereas structural vibrations may impair the operating life of the system.

The investigation of these issues is still nowadays an intrinsically complex challenge. The stochastic nature of the WPFs can be described only through statistical quantities, such as mean-square pressure or two-points correlation functions, typically modelled via semiempirical formulations based on a combination of theoretical assumptions and experimental observations. Several methods have been proposed in literature ranging from mathematically simple formulations to analytically more complex descriptions, like Chase model [2], which offers great accuracy at the cost of an increased number of empirical constants, to be determined experimentally. The Chase model describes the two-points pressure spectrum, which is the product between the auto-spectrum, conveying the amplitude information, and the coherence function, carrying the spatial information, therefore essential for the accurate estimation of the load distribution over the structural domain.

The objective of this work is to exploit the potential of deep learning techniques to reconstruct the Chase-like coherence function of the two-point spectra of TBL-induced WPFs from the structural response of a plate subjected to TBL loading. The main aim is to assess whether a data-driven algorithm can be trained to learn and reproduce the behavior of this function, therefore enabling the reconstruction of the pressure field over a structure subjected to random loading.

Content from this work may be used under the terms of the Creative Commons Attribution 3.0 license. Any further distribution of this work must maintain attribution to the author(s) and the title of the work, journal citation and DOI. Published under license by Materials Research Forum LLC.

Materials Research Proceedings 69 (2026) 60-65 https://doi.org/10.21741/9781644904251-11

Machine learning has already been applied to reconstruct models of TBL-induced WPFs [1, 3], however its use was limited to the reconstruction of real-valued functions. This work proposes an encoder-only transformer to reconstruct the complex coherence function, treated as a sequence in the machine learning sense [4], starting from response data and flow conditions.

Encoder-only transformer and dataset

The deep learning method chosen for this activity is an encoder-only transformer (EOT) [5, 4], preferred to other methods as the problem at hand requires a direct mapping over a fixed frequency grid, the encoder block has substantially a fixed structure, reducing the hyperparameter tuning to a limited number of global variables, and the multi-head self-attention mechanism allows to model explicitly long-range dependencies, rather than focusing on local patterns. Fig. 1 displays the structure of an encoder-only transformer.

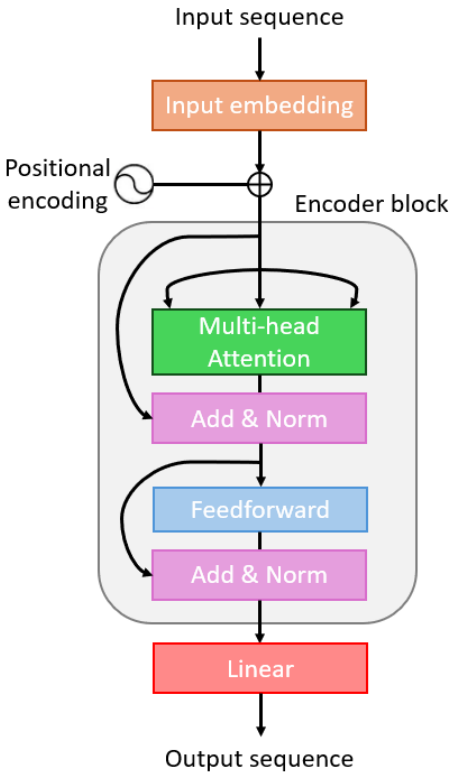


Figure 1 - Structure of the encoder-only transformer.

The test case is a rectangular, plexiglas plate with dimensions 0.58×0.20×0.003 m^3, subjected to a TBL loading at four different flow conditions and clamped boundary conditions. The numerical mesh is made of 29 × 10 grid points. Modal analysis is performed, and the estimated mode shapes are used to calculate the structural response under stochastic load, representative of a TBL excitation described by Chase model, with parameters, flow characteristics and approach reported in Ciappi et al. [6] and Casaburo et al. [1]. These results are used as part of the dataset.

The input to the transformer consists of both scalar and sequential features. The scalar input comprises nine quantities: the nondimensional x and y coordinates of the two points, the nondimensional stream- and cross-wise distances, the flow speed outside the boundary layer, the friction velocity, and the boundary-layer thickness. These are followed by six sequences of length 100, given by the amplitude and phase of the structural response autospectrum at each of the two points. To better exploit the phase information and avoid discontinuities, each phase sequence is split into two sequences defined by its cosine and sine. The output of the transformer consists of two sequences of length 100, representing the real and imaginary parts of the coherence function.

Materials Research Proceedings 69 (2026) 60-65 https://doi.org/10.21741/9781644904251-11

This choice is motivated by the strong instability of the phase sequence and to limit the output prediction to only two sequences, instead of three, which would be required if a sine/cosine transform were applied directly to the coherence phase. The dataset is augmented by considering all possible pairs of grid points, discarding symmetric pairs and all cases in which the response is identically zero due to the boundary conditions. For each flow condition, 39,402 observations are provided, resulting in a full dataset with size 157,608 × 809. The dataset is polluted with 5% magnitude Gaussian noise and is split into a training set, containing the observations from three flow conditions, and a test set, containing an unseen flow condition. This setup is more appropriate to assess the generalization capability of the transformer, since mixing all flow conditions across the training and test sets would lead to information leakage and overestimated performances. For the same reason, standardization is performed using only the statistical estimators computed on the training set.

The optimal transformer for the task at hand has the hyperparameters and training settings summarized in Table 1. While the initial values were chosen according to rules of thumb from the literature [5], the final configuration was determined by analysing the training and test errors.

Table 1 - Hyperparameters and training settings of the encoder-only transformer.

Training settings	Value
Model dimension	160
Scalar embedding dimension	64
Sequence embedding dimension	96
Batch size	128
Dimension feedforward network	768
Dropout ratio	0.1
Number of encoder layers	8
Number of attention heads	4
Weight decay	0.015
Number of epochs	100
Gradient accumulation factor	2
Ratio of used datasets	0.25

Both the real and imaginary parts of the coherence function exhibit a variable-length tail with values close to zero, which biases the training loss. In fact, even an initial and trivial prediction close to zero already yields a low average error, providing a weak learning signal on the non-zero part of the coherence and limiting the model's ability to improve. For this reason, being $\tilde{E}(f)$ the normalized energy of the signal in frequency, every output sequence is modulated with weights $w(f)$ defined as

$$w(f) = 0.1 + 0.9\tilde{E}(f) \tag{1}$$

Huber loss with $\delta = 0.25$ is adopted for training, and AdamW is used as optimizer to obtain a more interpretable and effective weight-decay behaviour [7]. The learning rate is controlled by a scheduler that first applies a warm-up phase, in order to prevent exploding gradients during the initial epochs and to mitigate the sensitivity of transformers to the initial learning rate. After the warm-up, a cosine decay schedule is employed for fine tuning. Optimizer stability is further improved through gradient accumulation. Additional mechanisms introduced to reduce weight noise and overfitting include dropout, exponential moving averaging of the weights, and stochastic weight averaging.

Materials Research Proceedings 69 (2026) 60-65 https://doi.org/10.21741/9781644904251-11

Validation of transformer performances

The training and generalization capabilities of the transformer are assessed through four tasks, each training the model on three flow conditions and testing it on the fourth, which is excluded from the training set. The average training and test errors over three runs for each task are reported in Fig. 2. While the training errors (Fig. 2, left) show similar decreasing trends as the number of epochs increases, the test errors (Fig. 2, right) strongly depend on the specific task. Lower test errors are obtained when the 30 kn and 35 kn flow conditions are used as test cases, whereas for 25 kn and 40 kn the test error tends to increase and then plateau, leading to overall lower performance. This behaviour is expected: generalizing to flow conditions at the extremes of the considered range is more challenging for deep learning models. The numbers in the right plot indicate the best epoch.

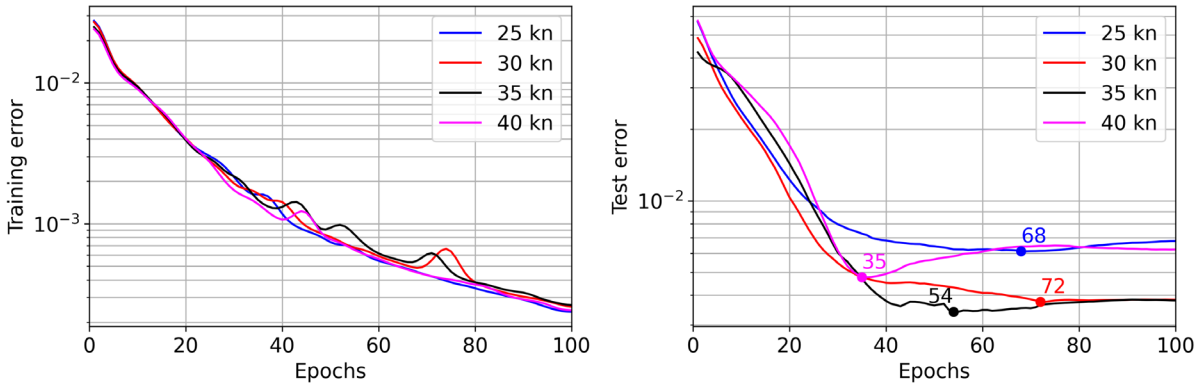


Figure 2 - Average training and test errors for each flow condition. Left: training error. Right: test error.

The reconstruction of the real and imaginary parts for four observations, each corresponding to a pair of points at different distances at 35 kn, is shown in Fig. 3, where the target sequences are compared with those predicted by the transformer at the best epoch. Further confirmation of the transformer's performance is provided in the left part of Fig. 4, which shows the magnitude of the coherence function, a representation closer to those commonly reported in the scientific literature. The target sequence is estimated with the Chase model. The stream- and cross-wise distances (ξ, η) are in meters, and they are indicated, along with the flow stream direction, in the right part of Fig. 4. The predictions shown in Figs. 3-4 are consistent with the test errors reported in Fig. 2 and further confirm the reliability of the encoder-only transformer architecture.

Conclusions

An encoder-only transformer is trained to reconstruct the Chase-like complex coherence function of the TBL-induced WPFs acting on a rectangular plate, starting from structural response and flow conditions data. Four tasks are performed, each one using three flow conditions for training and one condition for testing. The overall performances are satisfactory, as the chosen architecture provides good reconstruction of the output sequences, even for flow conditions at the boundaries of the considered range. These results pave the way for further generalization tests and the introduction of experimental measurements.

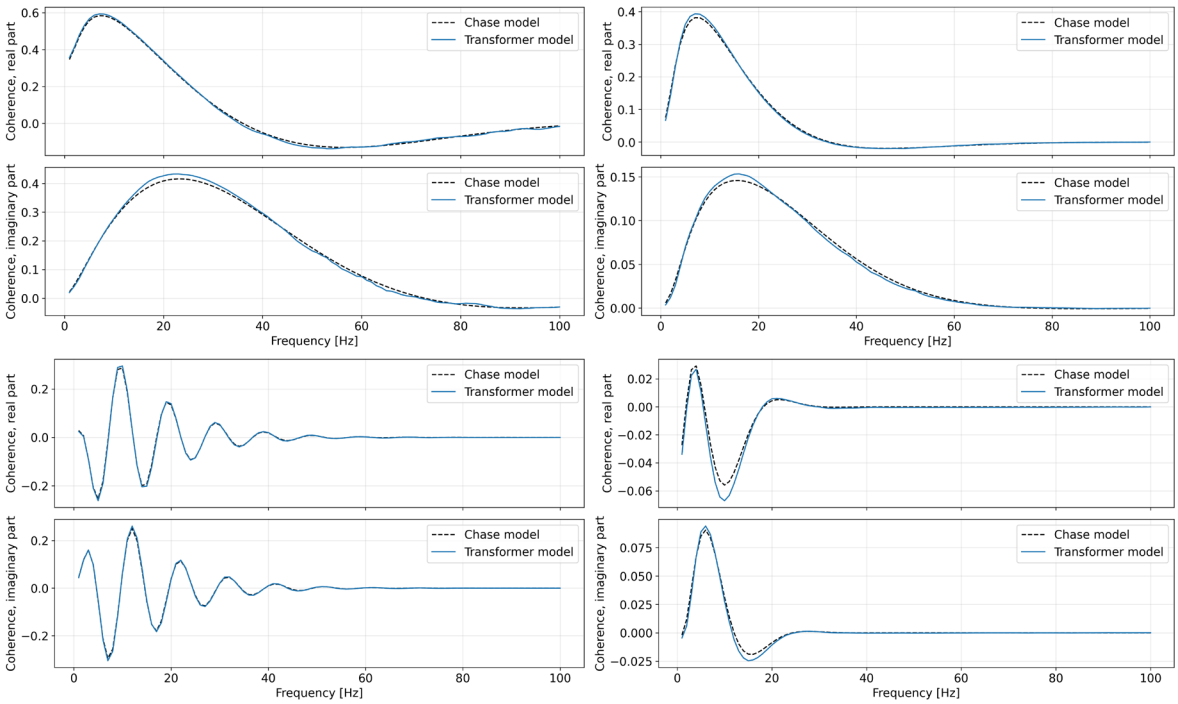


Figure 3 - Comparison between target and predicted real and imaginary parts of the complex coherence function. Top-left: Sample 1, (ξ, η) = (0.021, 0.022). Top-right: Sample 2, (ξ, η) = (0.021, -0.044). Bottom-left: Sample 3, (ξ, η) = (0.311, 0.044). Bottom-right: Sample 4, (ξ, η) = (0.124, 0.133).

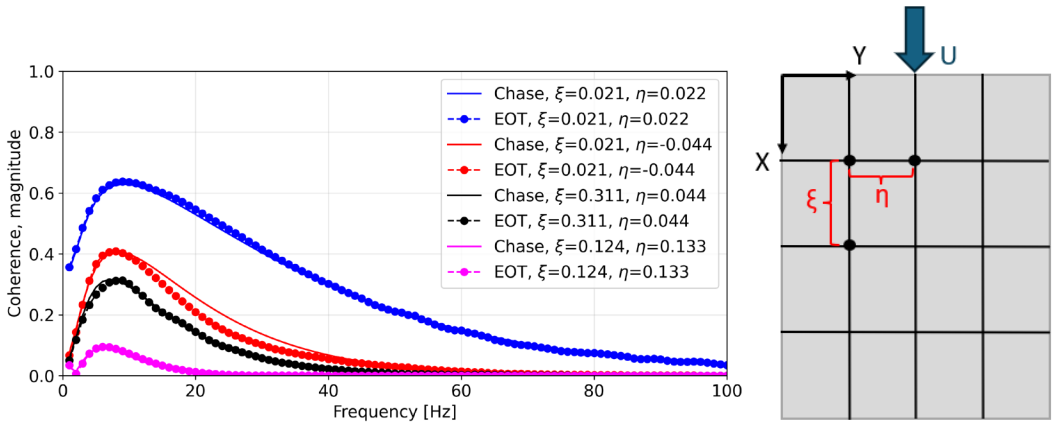


Figure 4 - Left: magnitude of coherence function, comparison between Chase model and the prediction of the EOT. Right: sketch of the plate, with flow stream direction and distances (ξ, η).

References

[1] A. Casaburo, G. Petrone, E. Ciappi, F. Franco, S. De Rosa, Data-Driven Symbolic Regression for the Modelling of Correlation Functions of Wall Pressure Fluctuations Under Turbulent Boundary Layers, in C. Doolan, D. Moreau, A. Wills (Eds.), Flinovia – Flow Induced Noise and Vibration Issues and Aspects – IV. FLINOVIA 2023, Springer Cham, 2025, pp. 277-304, https://doi.org/10.1007/978-3-031-73935-4 14

[2] D. M. Chase, Modeling the wavevector-frequency spectrum of turbulent boundary layer wall pressure, Journal of Sound and Vibration 70(1), 29-67 (1980), https://doi.org/10.1016/0022-460X(80)90553-2

[3] J. Dominique, J. Van den Berghe, C. Schram, M. A. Mendez, Artificial neural networks modeling of wall pressure spectra beneath turbulent boundary layers, Physics of Fluids, 34(3), 035119 (2022), https://doi.org/10.1063/5.0083241

[4] S. Raschka, Y. Liu, V. Mirjalili, Machine Learning with PyTorch and Scikit-Learn, 2022, Packt, Birmingham.

[5] A. Vaswani, N. Shazeer, N. Parmar, J. Uszkoreit, L. Jones, A. N. Gomez, L. Kaiser, I. Polosukhin, Attention Is All You Need, in I. Guyon, U. Von Luxburg, S. Bengio, H. Wallach, R. Fergus, S. Vishwanathan, R. Garnett (Eds.) 31st Conference on Neural Information Processing Systems (NIPS). Advances in Neural Information Processing Systems. Vol. 30, 2023, Curran Associates, Inc., 1706.03762.

[6] E. Ciappi, F. Magionesi, S. De Rosa, F. Franco, Hydrodynamic and hydroelastic analyses of a plate excited by the turbulent boundary layer, Journal of Fluids and Structures, 25(2), 321-342 (2009), https://doi.org/10.1016/j.jfluidstructs.2008.04.006

[7] I. Loshchilov, F. Hutter, Decoupled Weight Decay Regularization, in International Conference on Learning Representations (ICLR), 2019, https://doi.org/10.48550/arXiv.1711.05101

Materials Research Proceedings 69 (2026) 66-71 https://doi.org/10.21741/9781644904251-12

Use of Convolutional Neural Networks for Multifidelity CFD Problems

Sebastiano Geremia Isidoro MARCI[1,a *], Luca MUSCARA[1,b], Lorenzo FOLCARELLI[1,c], Andrea FERRERO[1,d], Filippo MASSENI[1,e] and Dario Giuseppe PASTRONE[1,f]

[1]Politecnico di Torino, Dipartimento di Ingegneria Meccanica e Aerospaziale, Corso Duca degli Abruzzi 24, 10129 Torino, Italy

[a]sebastiano.marci@polito.it, [b]luca.muscara@polito.it, [c]lorenzo.folcarelli@polito.it, [d]andrea_ferrero@polito.it,[e]filippo.masseni@polito.it, [f]dario.pastrone@polito.it

Keywords: Convolutional Neural Networks (CNN), U-Net, Computational Fluid Dynamics (CFD), Field Reconstruction, Super-Resolution, Multifidelity

Abstract. In recent years, there has been a growing interest in applying deep learning techniques to Computational Fluid Dynamics (CFD), particularly for accelerating simulations and enhancing data resolution. This work explores the use of Convolutional Neural Networks (CNNs) to reconstruct high-resolution CFD fields from low-resolution inputs. A U-Net architecture was selected due to its proven ability to capture both global context and fine-scale features through its encoder–decoder structure combined with skip connections, facilitating detailed reconstructions. The study focuses on two canonical CFD problems: a bump-in-a-duct configuration and a hydrogen combustion chamber. These cases were chosen to encompass both non-reactive and reactive flow regimes and to test the generalization capability of the model under different physical conditions. The network was trained to predict high-resolution pressure, axial velocity, and heat of reaction fields from their corresponding low-resolution versions, thus performing a super-resolution task. Due to the limited size of the available dataset, several regularization techniques were employed to improve model robustness, including Dropout layers and Batch Normalization. Additionally, different data normalization strategies were tested, such as Z-normalization and Min–Max scaling, to enhance training stability and ensure faster convergence. A multi-network approach was also developed to separately handle the prediction of pressure fields and that of axial velocity and heat release rate, mitigating the risk of feature mixing and allowing each network to specialize in learning specific patterns. The datasets were generated using two solvers: a custom Fortran-based code solving the non-dimensional Euler equations, and the commercial CFD software Ansys Fluent for more complex reactive flow simulations. This combination enabled the creation of a multifidelity database, covering a wide range of fluid dynamic behaviors and ensuring better generalization capabilities during training and validation phases. The training process involved careful hyperparameter optimization, early stopping strategies, and loss function selection to prevent overfitting and maximize prediction quality. Quantitative assessments demonstrated prediction errors on the order of a few percent, while qualitative analyses confirmed the ability of the models to accurately reconstruct the flow structures, even in complex reacting flows. The final phase of the project focused on identifying potential future developments of the proposed framework, particularly exploring the capability of the U-Net architecture to address a broader class of problems. One promising direction involves extending the methodology to correct two-dimensional solutions in order to approximate three-dimensional flow fields. This approach consists of training the network with the 2D planes extracted from the full 3D simulations. Furthermore, techniques such as data augmentation could be implemented to improve the model's generalization and robustness. The main contribution of this work includes the dataset generation, the design and implementation of the U-Net architecture, the training framework, and the

Content from this work may be used under the terms of the Creative Commons Attribution 3.0 license. Any further distribution of this work must maintain attribution to the author(s) and the title of the work, journal citation and DOI. Published under license by Materials Research Forum LLC.

Materials Research Proceedings 69 (2026) 66-71 https://doi.org/10.21741/9781644904251-12

performance evaluation. The results highlight the promising role of CNN-based surrogate models in enhancing CFD simulation capabilities and accelerating future engineering workflows by enabling fast and accurate predictions across different fidelity levels.

Introduction

Deep learning approaches are increasingly used to complement conventional CFD [1] solvers, aiming to accelerate simulations, reduce computational costs, and improve data resolution [2]. Convolutional Neural Networks (CNNs), with their strong capability in pattern recognition and feature extraction, have shown potential in reconstructing high-fidelity flow fields from coarse data. This study applies a U-Net-based CNN architecture to perform a super-resolution task on CFD fields. The goal is to recover high-resolution distributions flow field from their corresponding low-resolution counterparts.

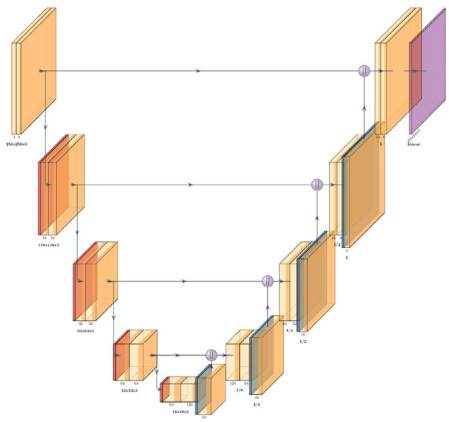


Figure 1 : The U-net structure.

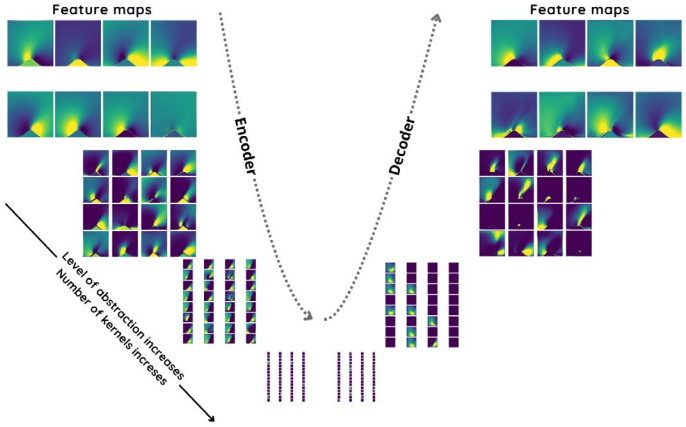


Figure 2: Feature maps extracted during training.

The classic U-Net [3] (Fig. 1) follows a symmetric **encoder-decoder** structure with **skip connections**. It consists of two main parts:

- **Contracting path (encoder)**: this path captures context through successive applications of *convolutions*, each followed by a non-linear *activation function* and a *max-pooling* operation for downsampling. With each downsampling step, the number of feature channels doubles.
- **Expanding path (decoder)**: this path performs *upsampling* of the feature maps using interpolation methods (e.g., nearest-neighbor, or bilinear) followed by convolutional layers. Each step halves the number of channels and concatenates the result with the corresponding feature maps from the contracting path (skip connections). This fusion helps the network localize features accurately.

The network ends with a 1x1 convolution to map the last layer feature vector to the desired number of output classes or regression values. This architecture allows the U-Net to combine coarse contextual information with fine spatial details.

Core Operations in U-Net

The U-Net architecture relies on a sequence of well-established operations in deep learning, we treated many of them in the previous section:

Materials Research Proceedings 69 (2026) 66-71 https://doi.org/10.21741/9781644904251-12

- **Convolution**: each convolutional layer applies learnable filters (typically 3x3) to the input feature maps. At the beginning of training the kernel are randomly weighted. The output of this operation is a set of output channels known as **feature maps**.
- **Max Pooling**: a downsampling operation where a window (commonly 2x2) slides over the input, and only the maximum value within the window is retained.
- **Upsampling**: In the decoder, spatial resolution is restored using learned upsampling, typically with *nearest neighbor* or *bilinear interpolation*, followed by convolutional layers to refine the features.
- **Concatenation (also known as Skip Connections)**: Skip connections link encoder and decoder features at equal resolutions, preserving spatial details and aiding gradient flow. They prevent vanishing gradients, enhance training efficiency, and merge low-level and high-level information, enabling precise segmentation even with few labeled samples.

A python framework (Fig. 3) has been written in order to:

- Import CFD scenes from the solver and interpolate them onto a uniform grid.
- Crop a subregion of interest and apply a mask for out-of-domain points if needed.
- Normalize the dataset using different strategies.
- Train the U-net with two approaches:
  1. Run a single U-net model for all fields.
  2. Run separate U-net models for each field.
- Correct the low-fidelity simulation, denormalize the output, and interpolate back to the original grid.

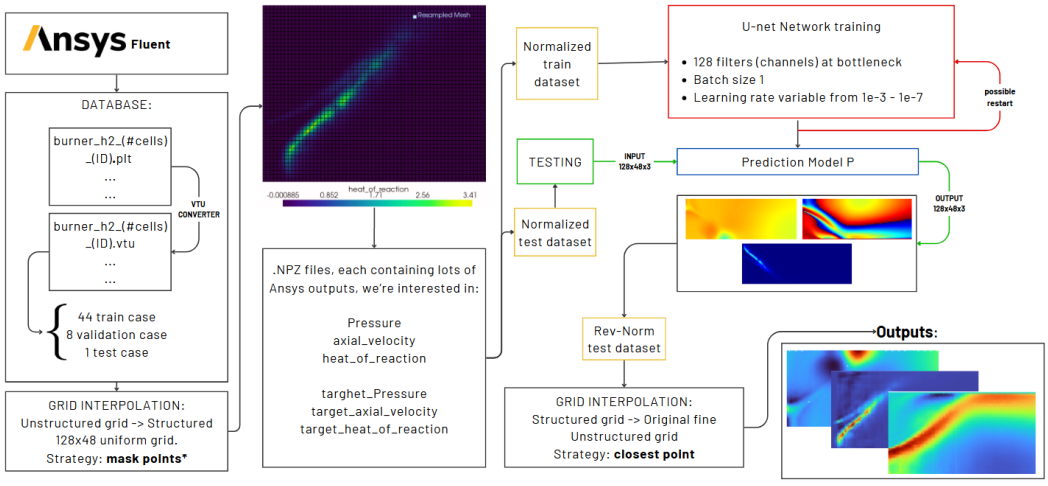


Figure 3 : The workflow of the framework

Two test cases were selected to validate the framework: a non-reactive "bump-in-a-duct" configuration and a reactive hydrogen burner [4], representing a multifidelity scenario that combines Euler or RANS-based simulations.

Materials Research Proceedings 69 (2026) 66-71 https://doi.org/10.21741/9781644904251-12

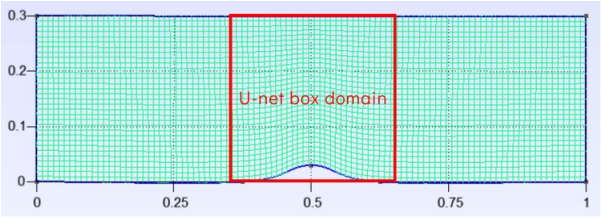


Figure 4 : Bump - low fidelity mesh (3k nodes)

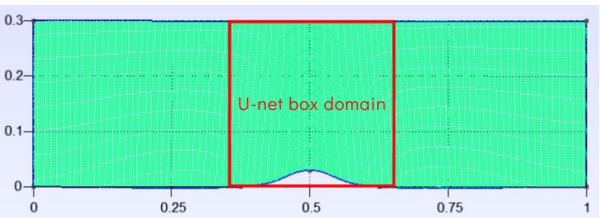


Figure 5 : Bump - high fidelity mesh (30k nodes)

Methodology

The database was generated using two distinct CFD solvers. The non-reactive dataset derives from a Fortran-based Euler code, while the reactive one comes from Ansys Fluent [5] simulations of a lean premixed hydrogen–air burner. The high-resolution fields were downsampled to generate corresponding low-fidelity maps, producing paired inputs and targets for network training. The U-Net architecture employed consists of an encoder–decoder structure with skip connections linking corresponding layers. These connections preserve spatial information that would otherwise be lost during the downsampling process. The encoder extracts global flow patterns, and the decoder reconstructs localized structures, such as shocks or flame fronts. Regularization was introduced via Dropout and Batch Normalization layers to enhance model generalization. A multi-network configuration was adopted to separately predict flow fields, avoiding feature maps interference.

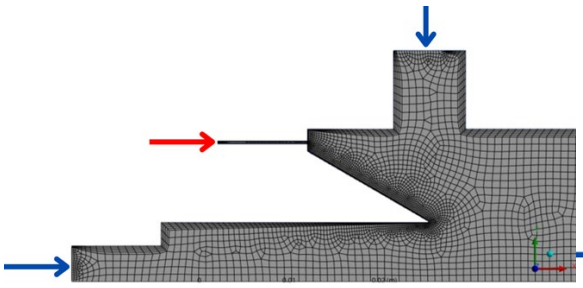


Figure 6: Hyd. burner - Low fidelity mesh (40k nodes)

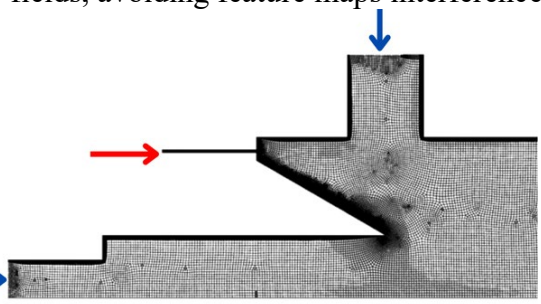


Figure 7 : Hyd. burner - high fidelity mesh (200k nodes)

Results and Discussion

Due to the limited size of the dataset, several combinations of batch size, dropout, and hyperparameters were tested, until good results have been reached. The trained networks achieved accurate reconstructions across both test cases. For the bump-in-a-duct case, the predicted wall-pressure distributions closely matched the high-fidelity results (Fig. 8). In the reactive burner case, the U-Net reproduced consistent with the high-fidelity reference solution (Fig. 9). The proposed framework successfully captured both global and local flow features, proving robust despite the dataset limitations. The analysis also highlighted the advantages of the multi-network configurations, which improved stability and accuracy for the different physical quantities.

Materials Research Proceedings 69 (2026) 66-71 https://doi.org/10.21741/9781644904251-12

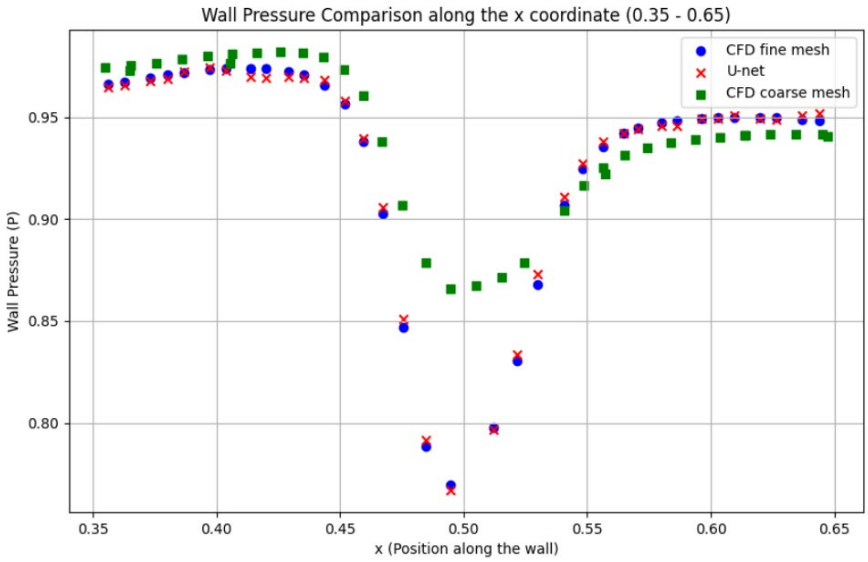


Figure 8 : Reconstruction of the high-fidelity wall pressure in the bump-in-a-duct configuration.

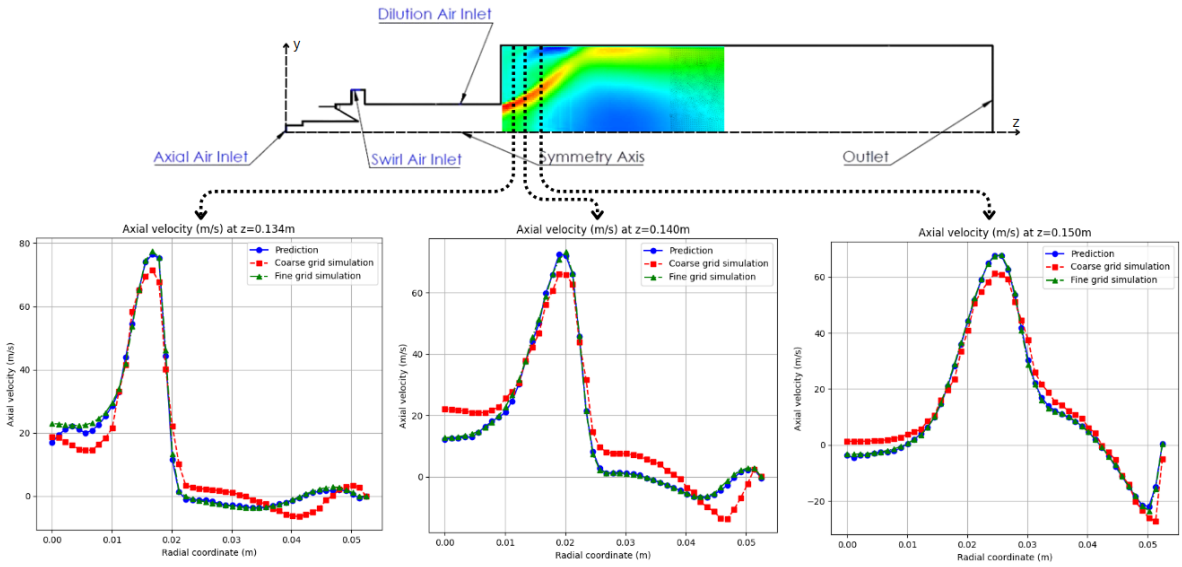


Figure 9 : Reconstruction of the high-fidelity velocity field for the hydrogen burner case. Radial profiles are shown at three different axial positions.

Conclusions

A Convolutional Neural Network based on the U-Net architecture was developed and applied to the reconstruction of high-resolution CFD fields from low-resolution data under multifidelity conditions. The method effectively recovered detailed pressure, velocity, and heat of reaction (for the specific case of the combustor) distributions across different flow regimes. Future work will focus on extending the approach to three-dimensional field correction and on implementing data augmentation strategies to improve generalization.

References

[1] O. Ronneberger, P. Fischer, T. Brox, U-Net: Convolutional networks for biomedical image segmentation, Medical Image Computing and Computer-Assisted Intervention (MICCAI), Springer, 2015, pp. 234–241. https://doi.org/10.1007/978-3-319-24574-4_28

[2] N. Thuerey, K. Weißenow, L. Prantl, X. Hu, Deep learning methods for Reynolds-averaged Navier–Stokes simulations of airfoil flows, AIAA Journal 58 (1) (2020) 25–36. https://doi.org/10.2514/1.J058291

[3] L. Muscarà, M. Cisternino, A. Ferrero, A. Iob, F. Larocca, A comparison of local and global strategies for exploiting field inversion on separated flows at low Reynolds number, Applied Sciences 14 (18) (2024) 8382. https://doi.org/10.3390/app14188382

[4] L. Folcarelli et al., Multifidelity modeling of a lean premixed swirl-stabilized hydrogen burner with axial air injection, AIAA SciTech 2025 Forum, Paper 0941, 2025. https://doi.org/10.2514/6.2025-0941

[5] ANSYS Inc., ANSYS Fluent Student, Release 2024 R1, Canonsburg, PA, USA, 2024. Available at: https://www.ansys.com/academic/students/ansys-fluent-student

Materials Research Proceedings 69 (2026) 72-77 https://doi.org/10.21741/9781644904251-13

Vision-Based Relative Pose Estimation of Space Objects for Proximity Operations Using Lab-Validated Deep Learning

Matteo FORASASSI[1,a*], Giordana BUCCHIONI[1,b], Lorenzo POLLINI[1,c]

[1]Department of Information Engineering, University of Pisa, Via G. Caruso 16,56122, Pisa, Italy

[a]matteo.forasassi@phd.unipi.it, [b]giordana.bucchioni@unipi.it, [c]lorenzo.pollini@unipi.it

Keywords: Pose, Computer Vision, YOLO, Synthetic Dataset, Extended-Kalman-Filter, Lab-Testing, Sim2Real

Abstract. This paper presents a scalable framework for real-time, 6-DOF pose estimation of uncooperative space objects using monocular cameras. We address dataset scarcity by generating mission-specific synthetic data augmented with style randomization to mitigate domain shift. A lightweight YOLOv11n-pose model extracts keypoints, which feed into a RANSAC-PnP solver for initial pose estimation, refined through an Extended Kalman Filter leveraging rigid body dynamics. Validation against synthetic sequences and laboratory experiments with a 1:1 replica demonstrates mean orientation errors of 3.9° and translation errors of 1.1%, matching state-of-the-art performance. The pipeline maintains robustness under challenging lighting conditions and domain shift, achieving ~50 fps on GPU and ~5 fps on CPU, enabling deployment on resource-constrained platforms for on-orbit servicing and debris removal missions.

Introduction

In the context of the actual space environment characterized by growing congestion due to the rise of the new space economy, autonomous pose estimation of unprepared/uncooperative space objects represents a critical bottleneck for next-generation space missions, from debris removal to on-orbit servicing. While active sensors offer reliable localization, their power requirements make monocular cameras coupled with deep learning the preferred solution [1]. However, this approach faces the critical challenge of requiring thousands of training images, often not publicly available and hence replaced by synthetically generated datasets which inevitably create a performance gap when deployed in real scenarios. This gap in literature is referred to as the sim-to-real (sim2real) gap [2]. While more mature domains, like maritime, medical or automotive, have developed mitigation strategies to the sim2real gap using domain-specific Generative Adversarial Networks (GAN) [3] or using a limited subset of real data [4] in training the intrinsic complexity of the space domains makes such mitigations challenging to apply. On the space application matter, recent solutions proposed leverages texture randomization [2] and online refinement [5] to adapt the model to the distinctive optical features of real space imagery (e.g. contrast, illumination, saturation etc.). Nevertheless, pose estimation is often not addressed as a whole but rather analysed separately, leaving integration and deployment matters unsolved.

This work utilizes deep learning tools to efficiently tackle this challenge, presenting a scalable, low-cost framework that leverages Commercial-Off-The-Shelf (COTS) solutions to enable real-time pose estimation of unprepared/uncooperative Space Resident Objects (SROs). Deep learning techniques were chosen given that traditional methods rely heavily on hand-crafted features that are easily compromised by texture-less surfaces, lighting variations, and occlusions – conditions inherent to uncooperative/unprepared targets. Our approach addresses the challenge of limited space-domain datasets while maintaining the accuracy and time sensitiveness required for mission-critical applications. Our contributions are threefold: (1) we leverage Blender, a free software, to generate mission-tailored synthetic datasets that are subsequently enhanced using domain-agnostic style transfer as well as physics-driven test sequences; (2) we train a COTS YOLO11n-pose

Content from this work may be used under the terms of the Creative Commons Attribution 3.0 license. Any further distribution of this work must maintain attribution to the author(s) and the title of the work, journal citation and DOI. Published under license by Materials Research Forum LLC.

Materials Research Proceedings 69 (2026) 72-77 https://doi.org/10.21741/9781644904251-13

Convolutional Neural Network (CNN) to locate landmarks in real-time and estimate SRO pose using Perspective-n-Point (PnP) algorithms coupled with a physics-aware Extended Kalman Filter (EKF); and (3) we provide a preliminary validation of the entire framework with representative laboratory imagery, demonstrating practical applicability for space missions.

Methods

Our pipeline starts with developing a CAD model of the mission-specific SRO, in our case a platform with a core and two solar panels – easily modifiable for specific needs. The object's dimensions were kept below 10 cm in order to be easily manufactured in full scale, via 3-D printing, for later real imagery validation [6]. The model is imported in Blender [7] and representative textures are applied to the different surfaces. The camera is modelled with a 5.2×7.1 mm sensor and 3 mm focal length *f* yielding a wide yet undistorted Field-of-View (>100°): this design choice was made to obtain an apparent target size resembling that of the same target but at a longer distance with a longer *f* or of a scaled-up target at a longer distance with the same *f*. Rendering is automated by positioning the camera in spherical coordinates (θ, φ, r) relative to the target object at the origin, with a varying radial distance $r \in [600,\ 3000]$ mm and angular coordinates incrementally varying by $\Delta\theta, \Delta\varphi = 1°$ per frame, to generate labels of target-camera poses and keypoint positions. Images were augmented with imaging artifacts: (i) Gaussian noise with standard deviation $\sigma \sim U(0.0,0.5)$, (ii) lateral chromatic aberration simulated by independently translating red and blue channels by $\Delta x, \Delta y \sim U(-5, +5)$ pixels while maintaining the green channel as reference, and (iii) randomized gamma correction $\gamma \sim U(0.4,1.4)$and exposure $E \sim U(0.4,1.4)$. Additional stochastic effects included glow and color adjustments applied probabilistically to enhance photorealistic diversity. This yields a dataset of 56000 labelled 1920x1080 px images which are additionally randomly sampled (1 out of 5) and augmented with domain-agnostic style transfer [8] by randomizing low-level features while maintaining high-level semantic content to increment robustness of the model to domain shift (Figure 1).

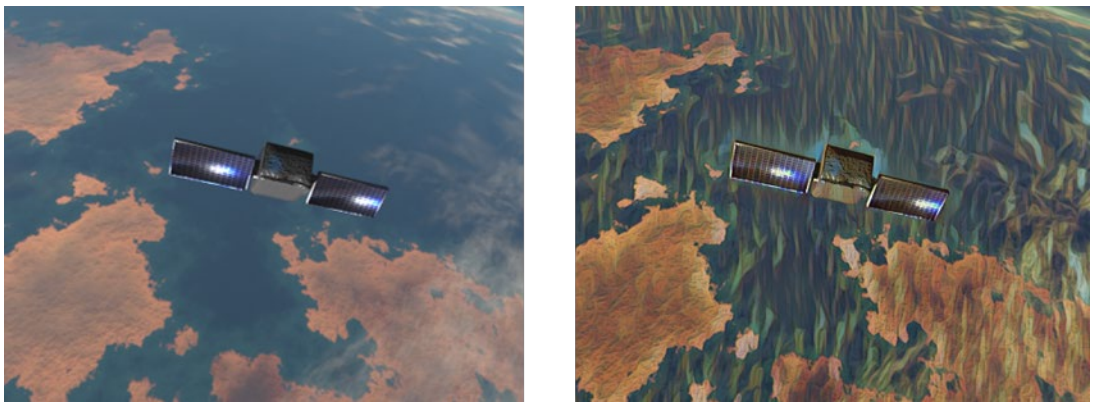


Figure 1 Sample of rendered dataset and its augmented version

The dataset obtained is used to train a YOLO11n-pose model [9]. Among the possible CNN-based architectures (HRnet, R-CNN, Fast R-CNN), YOLO was chosen for its capability to deliver accuracy levels comparable to larger models [10] while retaining real-time latency values. Indeed, as anticipated, this consideration was made relatively to a possible implementation of the pipeline for actual navigation purposes, where inference time, as well as computational power, is a significant factor. The training suite is derived from the state-of-the-art Ultralytics [11] implementation, with a key modification performed related to the Object Keypoint Similarity (OKS) loss function (1)

Materials Research Proceedings 69 (2026) 72-77 https://doi.org/10.21741/9781644904251-13

$$OKS = \sum_i \frac{\exp\left(\frac{d_i^2}{2s^2\sigma_i^2}\right)\delta(v_i>0)}{\sum_i \delta(v_i>0)} \quad (1)$$

where d_i is the Euclidean distance between the predicted and ground truth locations for keypoint i, s is the object scale, σ_i is a per-keypoint sigma value encoding annotation difficult and represents a per-keypoint standard deviation parameter, δ (v_i >0) is 1 if the keypoint is visible and 0 otherwise. In particular σ_i associated to keypoints located in the core structure – less prone to symmetry ambiguity – was decreased with respect to the outer keypoints to prioritize their accurate localization during training, improving overall pose stability. The trained model output a bounding box and the 2D pixel coordinates (and confidence) for all 20 keypoints.

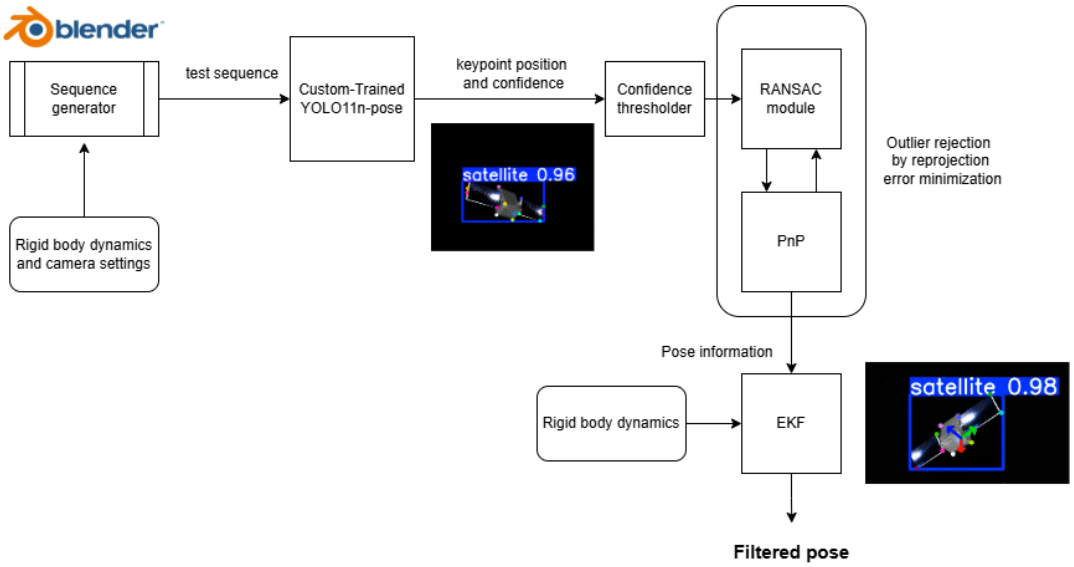


Figure 2 Pose estimation pipeline

As depicted in Figure 2, the high-confidence set of 2-D coordinates obtained from YOLO is fed into a combined RANSAC – Perspective-n-Point (RPnP) block for the first estimate of the pose. The RANSAC module works iteratively as a watchdog for possible outliers. Indeed, the module samples randomly a subset of the 2-D keypoints provided and the PnP module, implementing Efficient-PnP [12], obtain a pose which in turn is used to evaluate the reprojection error e_r. Keypoints with e_r larger than a certain threshold are labelled as outliers and are not used in the subsequent pose estimation steps. The RANSAC process continues until a predetermined level of confidence, calculated as in [13], is reached. The final pose, consisting of a translation vector and a quaternions quartet describing the relative asset of the RSO, is used as measurement input to an EKF which incorporates the rigid body dynamics typical of an uncontrolled tumbling object in space. The EKF's prediction step propagates the satellite's 19 elements state (position, orientation, angular velocity, linear velocity, inertia tensor) using Euler's equations for rigid body dynamics. This filtering step (running at 100Hz, with 10Hz measurements) rejects spurious measurements and provides a stable pose estimate even if the RPnP block temporarily fails ensuring smooth and physically-consistent tracking. The introduction of an EKF in our method make it different from several solutions in literature which are intended for single shot pose estimation [1]. This choice is motivated by a focus on the practical implementation of the estimation pipeline rather solely on its performance.

Results

The proposed pipeline was tested with both synthetic and real imagery. Relatively to synthetic testing, three sequences of 800 frames each were generated using Blender and simulated the

Materials Research Proceedings 69 (2026) 72-77 https://doi.org/10.21741/9781644904251-13

approach of a servicing spacecraft to a tumbling SRO. The dynamics of the SRO, which rotates with angular velocities ω up to 0.5 radians/s along the three axes according to Euler laws for rigid bodies $I\,I\dot{\omega} + \omega \times (I\omega) = \tau$ with inertia tensor when impacted by a debris applying a torque τ, is constant across the three scenarios while the motion of the chaser is defined to expose the pipeline to a wider range of conditions. According to standardized metrics [1], the translation error is calculated as $e_t = \left|t_{est} - t_{gt}\right|_2$ and the normalized translation error as $\overline{e_t} = e_t / \left|t_{gt}\right|_2$ while the orientation error is calculated as the angular distance between the unit quaternions representing the estimated target rotation with respect to the camera frame q_{est}^{bc} and the true rotation with respect to the camera frame q_{true}^{bc} as $e_q = 2 \cdot \arccos\left(\left|\langle q_{est}^{bc}, q_{true}^{bc}\rangle\right|\right)$. The following Table 1 summarizes the conditions as well as the results of the synthetic experiments for both RANSAC-PnP (RPnP) and filtered estimations.

Table 1 Experiments condition and results

Exp.	Range	Closing speed	Tgt. Cond.	Mean $\overline{e_t}$		Mean e_q	
				EKF	RPnP	EKF	RPnP
Nr.1	2.5 – 1.3 m	0.015 m/s	Nominal (f=3 mm)	1.64%	2.4%	3.9°	5.38°
Nr.2	50 – 30 m	0.25 m/s	Nominal (f=60 mm)	1.13%	1.41%	4.41°	4.76°
Nr.3	2.5 – 1.3 m	0.015 m/s	Damaged (f=3 mm)	3.18%	5.45%	7.8°	14.60°

The experiments were conducted on different hardware platforms, in order to evaluate both the portability of the framework and the capability to provide real-time results also on CPUs while retaining the accuracy levels obtained until now. The models were optimized using the OpenVINO™ toolkit for inference on Intel CPUs.

Table 2 Inference time (ms) on different hardware with input dimensions in brackets

Hardware	Pythorch (1920x1080)	OpenVINO™ FP32 (1920x1080)	OpenVINO™ FB32 (1132×640)	OpenVINO™ FB32 (640×640)
Nvidia GPU V100	10.3	/	/	/
Xeon® CPU	158.50	52.09	/	/
Intel® Core® i7 10th gen CPU	945.23	549.21 (453.33 for FP16)	198.32	181.27

Table 2 presents the inference time measured in different hardware conditions. It is worth noting that in all the cases presented aside from that of the last column the errors obtained varied of 0.5% with respect to the benchmark condition (i.e. Pytorch model with input 1920x1080).

For real imagery validation, videos were recorded using a 1:1 replica of the Blender-designed RSO. The mock-up featured a reflective coating simulating spacecraft thermal insulation and PVC-covered solar panels to reflect direct light. Orbital conditions were simulated by suspending the target against a black background to minimize shadows, with motion induced by manual push. The suspension constrained rotation to the local vertical axis only. Background imperfections (reflections, stains) provided additional complexity for testing keypoint extraction robustness. Frames captured with a GoPro Hero 7 White varied in initial target orientation and lighting conditions (diffused or direct).

Quantitative analysis of the two scenarios revealed that frames with diffused light exhibited stable low-luminance conditions (mean=21.73±0.90) with full dynamic range utilization (254.6±0.5). In contrast, direct light frames showed significantly higher temporal variability (mean luminance=19.39±5.47) with largely fluctuating contrast (0.818±0.138) and dynamic range (247.7±33.3). In both set of frames Shannon entropy of the intensity histogram remains low (~4.6

bits), indicating limited tonal gradations. Examples of diffuse and direct light frames are reported in Figure 3.

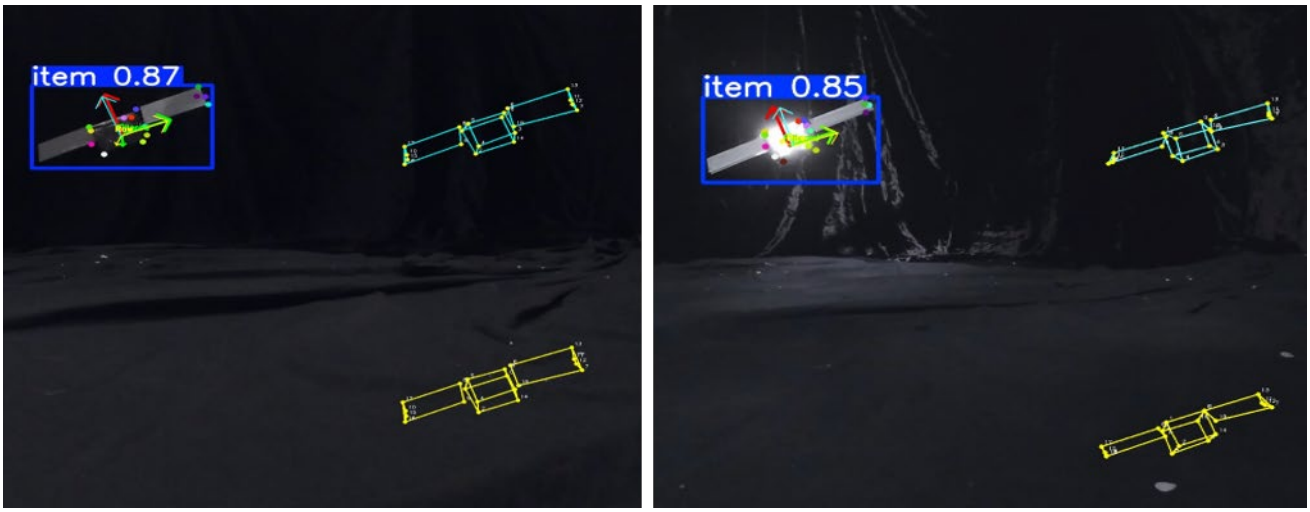


Figure 3 Example of diffused (sx) and direct light (dx) imagery. In cyan the silhouette of the pose from RPnP estimation and in yellow from RPnP-EKF combined estimation

Relatively to the diffused light subset (716 frames), the mean orientation error e_q for RPnP is 21.16° while for EKF is 11.30. The mean normalized translation error $\bar{e_t}$ for RPnP is 6.7% while for EKF is 4.6%. Relatively to the direct light subset (350 frames), the results obtained shows lower adaptability because the model struggles to provide coherent keypoints location across subsequent frames given the extreme variability of lighting conditions. Indeed, mean e_q for RPnP is 77.18° while the mean e_q for EKF is 68.51° given that the filter cannot properly initialize. Relatively to the normalized translation error $\bar{e_t}$, RPnP is 19.5% while for EKF is 4.9%. The experiments showed that the integration of an EKF can dramatically increase the performance of the system specifically in conditions where a slight domain shift can be appreciated. This benefit is strongly marked in the improvement of e_q for the diffused light subset as well as in the synthetic scenario where a damaged target is present. Similarly, an improvement for $\bar{e_t}$ can be seen in the direct light scenario. The direct light scenario was a useful case-study to steer future works, in order to address cases where target features are partially obscured by harsh illumination conditions.

Conclusions

This paper introduced a scalable framework for real-time 6-DOF pose estimation of uncooperative space objects using monocular vision and deep learning. By combining synthetic dataset generation with style randomization, the estimation pipeline composed of a YOLO11n-pose model and a coupled PnP-EKF block achieved state-of-the-art performance with mean orientation errors of 3.9° and translation errors of 1.1% on synthetic sequences. Laboratory validation demonstrated successful sim-to-real transfer under diffused lighting, with the EKF significantly improving robustness. Real-time performance across hardware platforms (~50 fps GPU, ~5 fps CPU) enables deployment on resource-constrained spacecraft for proximity operations and debris removal. While strong and direct illumination revealed limitations requiring further investigation including study on on-line adaptation, the results validate the practical applicability of COTS-based solutions for autonomous space missions.

References

[1] M. Kisantal, S. Sharma, T. H. Park, D. Izzo, M. Märtens, and S. D'Amico, "Satellite Pose Estimation Challenge: Dataset, Competition Design, and Results," *IEEE Transactions on*

Aerospace and Electronic Systems, vol. 56, no. 5, pp. 4083–4098, Oct. 2020, doi: 10.1109/TAES.2020.2989063.

[2] T. H. Park, S. Sharma, and S. D'Amico, "Towards Robust Learning-Based Pose Estimation of Noncooperative Spacecraft," Sep. 01, 2019, *arXiv*: arXiv:1909.00392. https://doi.org/10.48550/arXiv.1909.00392

[3] B. Joshi *et al.*, "DeepURL: Deep Pose Estimation Framework for Underwater Relative Localization," in *2020 IEEE/RSJ International Conference on Intelligent Robots and Systems (IROS)*, Oct. 2020, pp. 1777–1784. https://doi.org/10.1109/IROS45743.2020.9341201

[4] T. R. Lenhard, A. Weinmann, K. Franke, and T. Koch, "SynDroneVision: A Synthetic Dataset for Image-Based Drone Detection," in *2025 IEEE/CVF Winter Conference on Applications of Computer Vision (WACV)*, Feb. 2025, pp. 7637–7647. https://doi.org/10.1109/WACV61041.2025.00742

[5] T. H. Park and S. D'Amico, "Robust multi-task learning and online refinement for spacecraft pose estimation across domain gap," *Advances in Space Research*, vol. 73, no. 11, pp. 5726–5740, Jun. 2024, doi: 10.1016/j.asr.2023.03.036

[6] M. Forasassi, Bucchioni, G, and Pollini, Lorenzo, "Vision-based relative navigation system for autonomous proximity orbital operations," in *Materials Research Proceedings*, Jul. 2024, pp. 150–153. https://doi.org/10.21741/9781644903193-33

[7] D. P. Rohe and E. M. C. Jones, "Generation of Synthetic Digital Image Correlation Images Using the Open-Source Blender Software," *Exp Tech*, vol. 46, no. 4, pp. 615–631, Aug. 2022, https://doi.org/10.1007/s40799-021-00491-z

[8] P. T. Jackson, A. Atapour-Abarghouei, S. Bonner, T. P. Breckon, and B. Obara, "Style Augmentation: Data Augmentation via Style Randomization," in *Proceedings of the IEEE/CVF Conference on Computer Vision and Pattern Recognition (CVPR) Workshops*, Jun. 2019.

[9] D. Maji, S. Nagori, M. Mathew, and D. Poddar, "YOLO-Pose: Enhancing YOLO for Multi Person Pose Estimation Using Object Keypoint Similarity Loss," in *2022 IEEE/CVF Conference on Computer Vision and Pattern Recognition Workshops (CVPRW)*, New Orleans, LA, USA: IEEE, Jun. 2022, pp. 2636–2645. https://doi.org/10.1109/cvprw56347.2022.00297

[12] J. Redmon, S. Divvala, R. Girshick, and A. Farhadi, "You Only Look Once: Unified, Real-Time Object Detection," presented at the Proceedings of the IEEE Conference on Computer Vision and Pattern Recognition, 2016, pp. 779–788.

[11] G. Jocher, J. Qiu, and A. Chaurasia, *Ultralytics YOLO*. (Jan. 2023). [Online]. Available: https://github.com/ultralytics/ultralytics

[12] V. Lepetit, F. Moreno-Noguer, and P. Fua, "EPnP: An Accurate O(n) Solution to the PnP Problem," *Int J Comput Vis*, vol. 81, no. 2, pp. 155–166, Feb. 2009, https://doi.org/10.1007/s11263-008-0152-6

[13] M. A. Fischler and R. C. Bolles, "Random Sample Consensus: A Paradigm for Model Fitting with Applications to Image Analysis and Automated Cartography," in *Readings in Computer Vision*, M. A. Fischler and O. Firschein, Eds., San Francisco (CA): Morgan Kaufmann, 1987, pp. 726–740. https://doi.org/10.1016/B978-0-08-051581-6.50070-2

Materials Research Proceedings 69 (2026) 78-83 https://doi.org/10.21741/9781644904251-14

Minimum-Energy Trajectory Generation for Quadrotor UAVs using Basis Functions and Gradient-Based Optimization

Fabio CELANI[1,a *] and Dennis LUCARELLI[2,b]

[1]School of Aerospace Engineering, Sapienza University of Rome, Via Salaria 851, 00138 Roma, Italy

[2]Department of Physics, American University, 4400 Massachusetts Avenue NW, Washington, DC, 20016, USA

[a]fabio.celani@uniroma1.it, [b]dlucarelli@gmail.com

Keywords: Trajectory Optimization, Quadrotor UAV, Minimum Energy, Slepian Sequences, Differentiable Programming

Abstract. A quadrotor Unmanned Air Vehicle (UAV) consumes considerable energy in its rotors. Due to the limited payload of the UAV, the on-board batteries are small and have limited capacity. Thus, generating minimum-energy trajectories is of great importance to increase quadrotor UAV flight time. This work proposes a novel method for generating optimal energy trajectories for a quadrotor UAV subject to spatial constraints. The objective is to drive the vehicle from an initial hovering condition to a desired final hovering condition, flying within assigned boundaries and avoiding obstacles, while minimizing the energy expended by the rotors. In this work the quadrotor thrusts are expressed as linear combinations of orthonormal basis functions, and the trajectory planning problem is formulated as an optimization problem in which the weights of the basis expansion are the decision variables. The proposed approach is validated by a numerical example in which the optimization problem is solved by using a gradient-based local optimization algorithm with the gradients computed by employing the differentiable programming technique.

Introduction

Many real-world applications of UAVs require operation in environments characterized by boundaries and obstacles, including inspection, transportation, surveillance, and search and rescue activities. Trajectory generation (or motion planning) is critically important in these scenarios [1].

Quadrotors play a primary role among UAVs. Their motion is controlled by varying the rotational speeds of four rotors which modify the thrusts generated by each of the four propellers. A quadrotor UAV consumes considerable energy through its rotors. Due to the limited payload capacity, onboard batteries are small and have limited storage capability. Thus, the generation of energy-minimizing trajectories is of paramount importance for increasing quadrotor UAV flight time.

This work proposes a novel method for generating optimal energy trajectories for a quadrotor UAV subject to spatial constraints. The objective is to drive the vehicle from an initial hovering condition to a desired final hovering condition, flying within assigned boundaries and avoiding obstacles, while minimizing the energy expended by the rotors.

Quadrotor Model

In a quadrotor UAV four identical rotors and propellers are located at the vertices of a square and generate a thrust and torque normal to the plane of the square (see Fig. 1).

Content from this work may be used under the terms of the Creative Commons Attribution 3.0 license. Any further distribution of this work must maintain attribution to the author(s) and the title of the work, journal citation and DOI. Published under license by Materials Research Forum LLC.

Materials Research Proceedings 69 (2026) 78-83 https://doi.org/10.21741/9781644904251-14

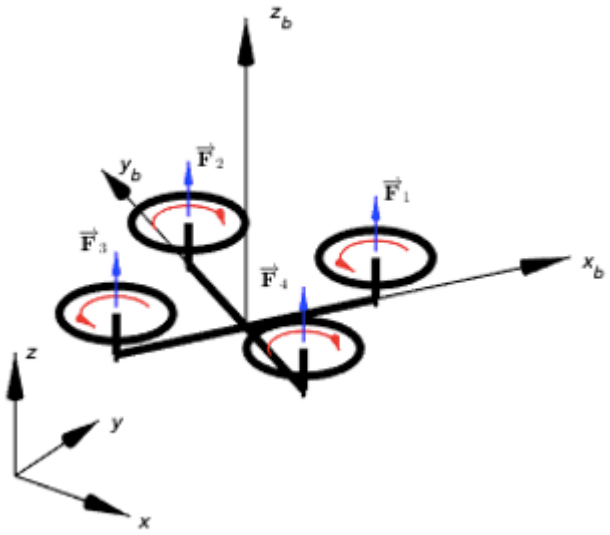


Figure 1: Sketch of a quadrotor

Choose a right-handed inertial reference frame $\{x,y,z\}$ with the z axis pointing upward, and a right-handed body frame $\{x_b,y_b,z_b\}$. The origin of the body frame is located at the center of mass of the vehicle. The first and the second axes $x_b\, y_b$, lie in the plane defined by the centers of the four rotors. The third axis z_b is normal to this plane. The following conventions are assumed for the rotors and propellers, and the thrust and moment that they exert on the quadrotor UAV. Assume that the thrust of each propeller is directly controlled, and the direction of the thrust of each propeller is normal to the quadrotor plane. Let F_j $j = 1,...,4$ be the projection along z_b of the thrust generated by propeller j . Propellers 1 and 3 are assumed to generate positive F_1 and F_3 when rotating counterclockwise. Propellers 2 and 4 do the same when rotating clockwise. The projection of the total thrust along z_b is given by $F_{tot} = \sum_{j=1}^{4} F_j$. Assume that the torque generated by each propeller is directly proportional to its thrust. Since it is assumed that propellers 1 and 3 rotate counterclockwise when they generate positive F_1 and F_3, and propellers 2 and 4 rotate clockwise when they generate a positive F_2 and F_4 , the torque generated by the j-th propeller along z_b can be written as $T_j = (-1)^j cF_j$ where $c > 0$ is a coefficient. Let d denote the distance from the center of mass to the center of each rotor, and let $\mathbf{M}$ denote the body coordinates of the total moment applied to the quadrotor with respect to its center of mass. Thus, obtain

$$\begin{bmatrix} F_{tot} \\ \mathbf{M} \end{bmatrix} = \mathbf{HF} \tag{1}$$

with

$$\mathbf{H} = \begin{bmatrix} 1 & 1 & 1 & 1 \\ 0 & d & 0 & -d \\ -d & 0 & d & 0 \\ -c & c & -c & c \end{bmatrix} \quad \mathbf{F} = \begin{bmatrix} F_1 \\ F_2 \\ F_3 \\ F_4 \end{bmatrix} \tag{2}$$

The equations of motion of the quadrotor UAV can be written as follows

Materials Research Proceedings 69 (2026) 78-83 https://doi.org/10.21741/9781644904251-14

$$\dot{\mathbf{p}} = \mathbf{v}$$

$$\dot{\mathbf{v}} = -g\mathbf{e}_3 + \frac{F_{tot}}{m}\mathbf{R}\mathbf{e}_3 \tag{3}$$

$$\dot{\mathbf{R}} = \mathbf{R}\,\boldsymbol{\omega}^{\times}$$

$$\mathbf{J}\dot{\boldsymbol{\omega}} = -\boldsymbol{\omega}^{\times}\mathbf{J}\boldsymbol{\omega} + \mathbf{M}$$

in which m is the mass, **J** is the inertia matrix, **p** and **v** are the position and velocity of the center of mass resolved in the inertial frame, **R** is the rotation matrix that transforms a column matrix of body coordinates into the corresponding column matrix of inertial coordinates, **ω** is the angular velocity resolved in body frame, $\boldsymbol{\omega}^{\times}$ denotes the matrix associated to **ω** to perform the cross-product operation, g is the gravity acceleration, and $\mathbf{e}_3=[0\ 0\ 1]^T$.

Minimum Energy Trajectory

In the proposed approach for trajectory generation, the flight time t_f is fixed along with the following initial conditions

$$\mathbf{p}(0) = \mathbf{p}_i \quad \mathbf{v}(0) = \mathbf{0} \quad \mathbf{R}(0) = \mathbf{R}_z(\psi_0) \quad \boldsymbol{\omega}(0) = \mathbf{0} \tag{4}$$

where $\mathbf{R}_z(\psi_0)$ represents a rotation ψ_0 about the z axis. The following desired final conditions are given

$$\mathbf{p}(t_f) = \mathbf{p}_f \quad \mathbf{v}(t_f) = \mathbf{0} \quad \mathbf{R}(t_f) = \mathbf{I}_{\mathbf{3}\times\mathbf{3}} \quad \boldsymbol{\omega}(t_f) = \mathbf{0} \tag{5}$$

Obstacles and boundaries are present in the flight space leading to a constraint of the following type

$$\mathbf{c}_{\text{obs}}(\mathbf{p}(t)) \leq \mathbf{0} \quad 0 \leq t \leq t_f \tag{6}$$

The objective is determining a thrust input **F**(t) defined over the interval [0 t_f] such that the corresponding position **p**(t), velocity **v**(t), attitude **R**(t), and angular velocity $\boldsymbol{\omega}$(t) satisfy the final conditions in Eq. (5) and the boundaries and obstacles constraint in Eq. (6).

It is important to select a trajectory that saves the energy spent by the rotors so to increase the autonomy of the UAV. The expression of the actual energy due to rotors is quite complex. Thus, it becomes hard to perform optimization using that cost index. However, intuitively the actual energy is related to the "energy" of the thrust **F** generated by the propellers which is given by

$$\int_0^{\mathrm{t_f}} ||\,\mathbf{F}(\mathrm{t})||^2 \mathrm{dt} \tag{7}$$

which measures the "energy" related to the control action performed by the propellers. However, for the trajectory generation problem studied in this work, it seems more appropriate to consider as cost function the "energy" related to the control action performed by the propellers required to

Materials Research Proceedings 69 (2026) 78-83 https://doi.org/10.21741/9781644904251-14

move the UAV away from a hovering condition since the UAV must be hovering at the initial and final time of its flight. Since in hovering condition $F_j(t) = mg/4$ j = 1,2,3,4 the following cost index is considered

$$\mathcal{E} = \int_0^{t_f} \left\| \mathbf{F}(t) - \frac{mg}{4}\mathbf{e} \right\|^2 dt \tag{8}$$

with $\mathbf{e}=[1\ 1\ 1\ 1]^T$.

Trajectory Generation Using Basis Functions

In this work trajectory generation is performed by first expressing the propellers thrusts as follows

$$F_j(t) = \frac{mg}{4} + \sum_{k=1}^{M} \alpha_{jk} u_k(t) \quad j = 1,2,3,4 \tag{9}$$

for a set of M basis functions $u_k(t)$ $k=1,\ldots,M$ $0 \le t \le t_f$. The basis functions must satisfy the following end-point conditions $u_k(0)= u_k(t_f)=0$. The latter conditions guarantee the fulfilment of the following equations $F_j(0) = F_j(t_f) = mg/4$ j=1,2,3,4 which are required for having the UAV hovering at the initial and final times.

The trajectory generation problem is formulated as a nonlinear programming problem in which the decision variables are the weights α_{jk} in Eq. (9). The cost index is given by Eq. (8). Achieving the desired final position, final velocity, final attitude, and final angular velocity is enforced through the following four scalar equality constraints

$$\left\|\mathbf{p}(t_f) - \mathbf{p}_f\right\|^2 = 0 \quad \left\|\mathbf{v}(t_f)\right\|^2 = 0 \quad 3 - \mathrm{tr}[\mathbf{R}(t_f)] = 0 \quad \left\|\boldsymbol{\omega}(t_f)\right\|^2 = 0 \tag{10}$$

where tr denotes the trace of a matrix. The boundaries and obstacles constraints are expressed as in Eq. (6).

Numerical Example

The proposed method is applied to the following numerical example. The mass of the UAV is m = 0.5 kg, its inertia matrix is equal to $\mathbf{J}$ = diag [0.0622 0.0733 0.0964] kg m^2, $c = 5\cdot10^{-3}$ m, d = 0.2 m (see Eq. (2)). The boundary constraint $z \ge 0$ is introduced since plane z = 0 corresponds to the ground. The initial and desired final positions are given by $\mathbf{p}_i=[0.5\ 0\ 1]^T$ m $\mathbf{p}_f=[0.5\ 1.5\ 4]^T$ m. A box-shaped obstacle is present in between those positions. Four vertices of the obstacle are on the ground and have the following coordinates $\mathbf{w}_1=[0.25\ 0.75\ 0]^T$ $\mathbf{w}_2=[0.75\ 0.75\ 0]^T$ $\mathbf{w}_3=[0.25\ 1.25\ 0]^T$ $\mathbf{w}_4=[0.75\ 1.25\ 0]^T$. The remaining four vertices are at the height of 6 m. The flight time is t_f=3 s.

To generate the trajectory by using the proposed approach, the interval $0 \le t \le t_f$ is discretized into N = 300 equal segments defining $\Delta = t_f/N$ and $t_l = (l-1)\Delta$ $l = 1,\ldots,N+1$. Consequently, the equations of motion in Eq. (3) are discretized and the boundary and obstacle constraints in Eq. (6) are enforced only at discrete times t_l. The basis functions $u_k(t)$ k = 1,...,M are obtained by defining samples $u_k(t_l)$ and applying a zero-order hold interpolation. The samples $u_k(t_l)$ are chosen as the so-called Slepian sequences [2]. These sequences are parameterized by their length N set to 300, and by the half-bandwidth parameter $W \in [0\ 0.5]$. In this numerical study, the first M = 6 Slepian sequences with W = 0.02 are considered.

Materials Research Proceedings 69 (2026) 78-83 https://doi.org/10.21741/9781644904251-14

The resulting nonlinear programming problem is solved numerically by using a local gradient-based optimization. The computation of gradients is carried out by using the differentiable programming technique also known as automatic differentiation. Differentiable programming is neither a symbolic computer algebra system nor a method that relies on finite-difference numerical derivatives. Rather, differentiable programming systems provide numerical expressions of analytic derivatives and a seamless framework for implementing the chain rule from differential calculus.

The time evolutions of the four rotor thrusts F_j $j = 1,...,4$ are showcased in Fig. 2. The corresponding path followed by the center of mass is displayed in Fig. 3.

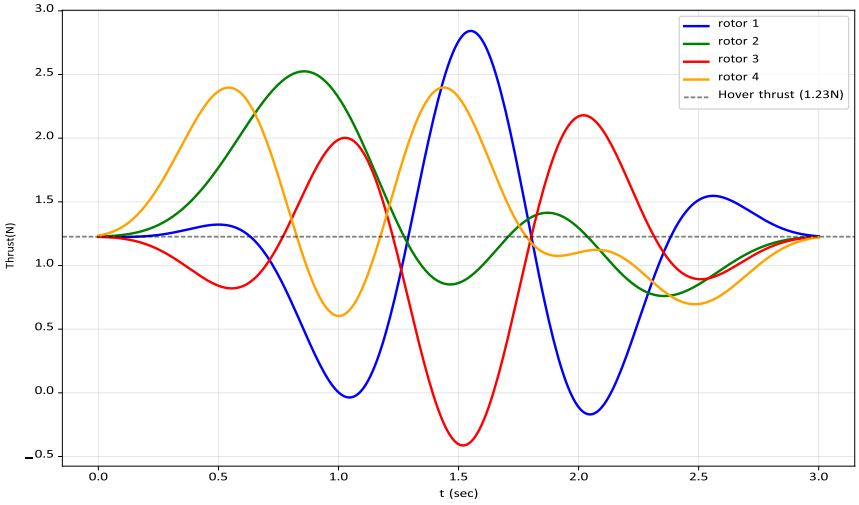


Figure 2: Time evolutions of the thrusts

The final values satisfy the following equalities

$$\| \mathbf{p}(t_f) - \mathbf{p}_f \| = 1.25 \cdot 10^{-6}\,\text{m} \quad \|\mathbf{v}(t_f)\| = 1.22 \cdot 10^{-4}\,\text{m/s}$$
$$3 - \text{tr}(\mathbf{R}(t_f)) = 1.35 \cdot 10^{-10} \quad \|\boldsymbol{\omega}(t_f)\| = 1.46 \cdot 10^{-8}\,\text{deg/s} \tag{11}$$

The distance from the box-shaped obstacle changes with time as indicated in Fig. 4.

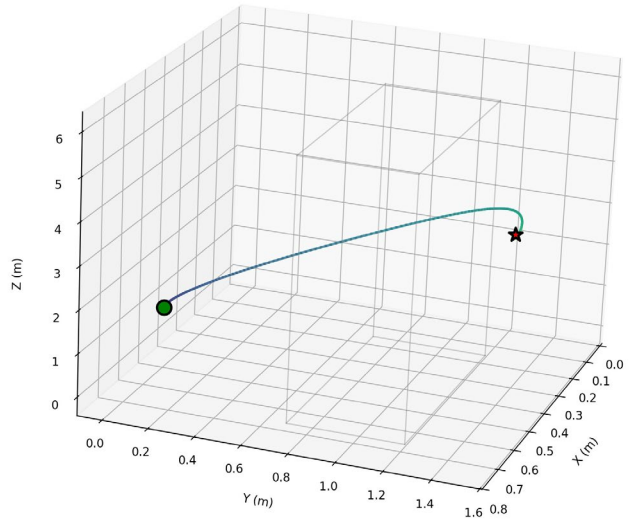


Figure 3: Path followed by the center of mass (green circle = initial position, red star = final position)

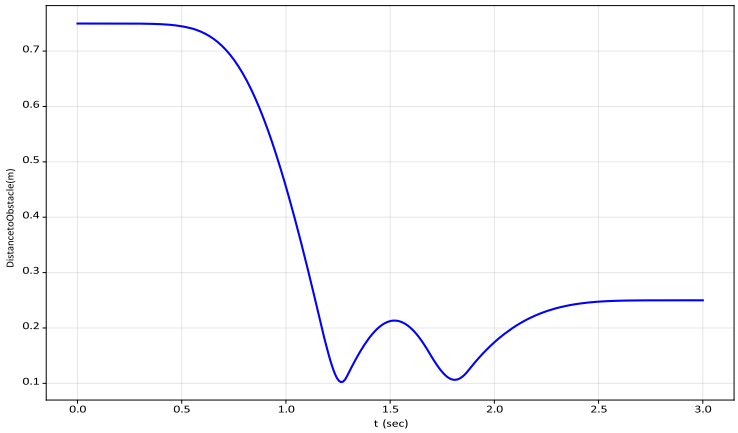


Figure 4: Time evolution of the distance to the box-shaped obstacle

Concluding Remarks

The trajectory generation approach for quadrotor UAVs presented in this work provides a systematic method for determining trajectories from a given hovering condition to a desired hovering condition with fixed flight time including spatial constraints while minimizing the energy spent by the rotors. The method relies on a basis function expansion of the propellers thrust and in solving a nonlinear programming problem using a gradient-based method. A numerical example has shown the effectiveness of the proposed approach.

References

[1] W. Sun, and A. L'Afflitto, A survey of guidance, navigation, and control systems for autonomous multi-rotor small unmanned aerial systems, Annual Reviews in Control 52 (2021) 390–427. https://doi.org/10.1016/j.arcontrol.2021.10.013

[2] D. Slepian, Prolate spheroidal wave functions, Fourier analysis, and uncertainty-V: the discrete case, Bell System Technical Journal 57 (1978) 1371-1430. https://doi.org/10.1002/j.1538-7305.1978.tb02104.x

Materials Research Proceedings 69 (2026) 84-87 https://doi.org/10.21741/9781644904251-15

Tuning Machine Learning Outcomes for Airfoil Aerodynamics Seed Sensitivity in Predictive Performance

Diana-Andreea STERPU[1,a*], Daniel MĂRIUȚA[2,b], Grigore CICAN[1,3,c], Ciprian-Marius LARCO[2,d] and Lucian-Teodor GRIGORIE[1,e]

[1]Faculty of Aerospace Engineering, National University of Science and Technology POLITEHNICA Bucharest, 060042 Bucharest, Romania

[2]Department of Aircraft Integrated Systems and Aviation, Military Technical Academy "Ferdinand I" Bucharest, 050141 Bucharest, Romania

[3]Romanian Research and Development Institute for Gas Turbines—COMOTI, 220D Iuliu Maniu, 061126 Bucharest, Romania

[a]sterpudianaandreea@gmail.com, [b]daniel.mariuta@mta.ro, [c]grigore.cican@upb.ro, [d]ciprian.larco@mta.ro, [e]teodor.grigorie@upb.ro

Keywords: Aerodynamic Prediction, Machine Learning, Random Seed Initialization, Ensemble Modelling, Airfoil Performance, Seed Sensitivity, Model Reproducibility, Pseudo-Random Number Generator

Abstract. Accurate aerodynamic performance prediction remains critical in preliminary design and optimization workflows. This study proposes a hybrid deep learning framework that combines convolutional neural networks (CNNs), operating directly on raw airfoil geometries, with two fully connected branches that process engineered shape descriptors and flow parameters such as angle of attack and Reynolds number. This model is trained on a high-resolution dataset generated via XFOIL simulations, covering 91 NACA 4-digit airfoils across 200 aerodynamic conditions each, spanning Reynolds numbers from 500,000 up to 5,000,000 and angles of attack between -5˚ and 14˚. A key novelty introduced in this work is the investigation of how random seed initialization influences predictive accuracy. In machine learning, a random seed is a fixed numerical input that initializes the pseudo-random number generator responsible for operations such as weight-initialization and data shuffling. While typically treated as a background setting, the *seed plays a critical role in defining the starting conditions of model training* and can directly influence final performance outcomes. Results show that models with identical architecture and data can differ in performance by up to 250% depending solely on the seed used during training. To mitigate this variability, ensemble strategies based on seed diversity were also explored, leading to greater consistency and generalization. The top-performing single-seed model tested (seed 0) achieved a mean absolute percentage error (MAPE) of 1.1% for lift coefficient and 0.57% for drag coefficient, with R^2 values of 0.9998 and 0.9954, respectively. The best ensemble built from three diverse seeds (C2) achieved slightly higher generalization: 1.43% MAPE C_L, 1.19% MAPE C_D, with R^2 values of 0.9999 and 0.9968. All models tested, spanning ten seeds and five ensembles, achieved R^2 scores exceeding 0.97. The results emphasize that treating seed selection as a fixed default can overlook significant variability, and that ensemble calibration can serve as a robust strategy to improve prediction reliability.

Introduction

Machine learning (ML) is increasingly used in aerodynamic prediction as a data-driven framework capable of learning the complex relationships between geometry, flow conditions, and aerodynamic performance. Various ML architectures, including convolutional neural networks [1], multilayer perceptron (MLPs) [2], and ensemble strategies [3], have been explored for

Content from this work may be used under the terms of the Creative Commons Attribution 3.0 license. Any further distribution of this work must maintain attribution to the author(s) and the title of the work, journal citation and DOI. Published under license by Materials Research Forum LLC.

Materials Research Proceedings 69 (2026) 84-87 https://doi.org/10.21741/9781644904251-15

aerodynamic performance estimation. These studies demonstrate the potential of ML to bridge the gap between accuracy and computational efficiency, which represents the primary downside of traditional computational fluid dynamic (CFD) tools [4, 5].

Despite this progress, one important factor has been largely overlooked: *the influence of random seed initialization*. In ML, seeds determine weight initialization, data shuffling, and training dynamics. Although seeds are typically fixed for reproducibility, their role as an active parameter influencing accuracy and stability has not been systematically investigated in aerodynamic applications. This present study investigates the influence of random seed sensitivity on the results obtained from an identical machine learning architecture. The initial scope was to calibrate the model in a fully reproducible manner; however, the process revealed significant variations in performance caused solely by the seed selection. Under identical data and architecture, prediction errors *varied by up to 250% depending only on the random seed selection.* In common ML libraries, *the seed is a 32-bit unsigned integer*, which translated into over four billion possible initialization states, therefore an exhaustive sweep is infeasible. In this study, an intentional but limited sampling of seeds was used to capture representative variability while keeping the analysis computationally practical.

By *recognizing seed selection as a design parameter* rather than a procedural formality, this study reinforces the reliability of machine learning-based aerodynamic prediction and establishes concrete guidelines for their consistent integration into aerodynamic design workflows.

Methodology

Following earlier CFD-based analyses of airfoil aerodynamics [6], the study focuses on adopting a machine learning approach to mitigate the computational cost challenge. Therefore, as presented in detail in [7], the methodology is built on a self-generated database of NACA four-digit airfoils. A total of 112 geometries were considered, of which 91 were used for training and 21 were excluded for independent testing. For each airfoil, aerodynamic data was collected from XFOIL simulations at Reynolds numbers between 0.5 and 5 million (in steps of 0.5 million) and angles of attack from -5˚ up to 14˚, resulting in approximately 18,200 samples. Each sample corresponds to an airfoil evaluated under a specific combination of flow conditions and geometric parameters, including lift and drag coefficients, coordinate distributions, Reynolds number, angle of attack, and engineered features such as maximum thickness and camber.

The proposed model employs a hybrid neural network architecture designed to capture both geometric and aerodynamic relationships. The airfoil geometry is processed through a one-dimensional convolutional branch that extracts local contour features from coordinate points. In parallel, a dense network interprets flow parameters – angle of attack and Reynolds number – while a second dense branch encodes engineered shape descriptors such as maximum thickness and camber. The three latent representations are then merged into a unified feature space, enabling the network to learn coupled geometric-aerodynamic interactions. The fused output is directed toward two dedicated prediction heads for lift and drag coefficients. This setup represents the single-seed configuration, where one model is trained with a specific initialization state. In the ensemble approach, several identical networks with the same architecture are trained independently using different random seeds, and their predictions are averaged to obtain a more stable result. The difference between the single-seed and ensemble configurations is illustrated in Figure 1, where the ensemble approach combines multiple independently trained single-seed models to produce an average prediction.

Materials Research Proceedings 69 (2026) 84-87 https://doi.org/10.21741/9781644904251-15

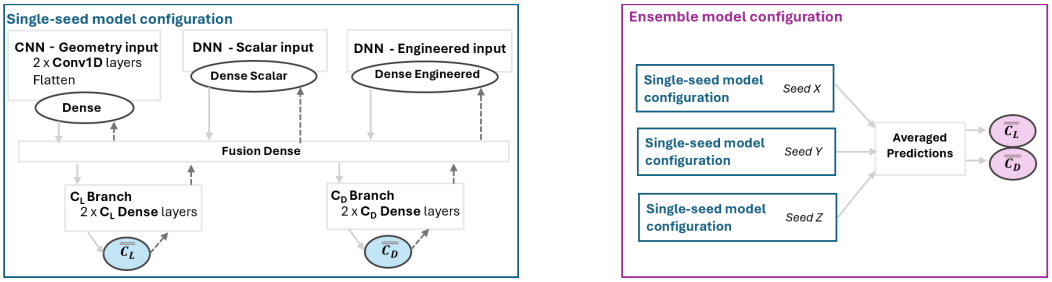


Figure 1. Single-seed and ensemble configurations of the hybrid CNN–DNN model

In order to analyze seed variability, three groups of experiments were defined: *Group A*, using consecutive seeds (42-46) to test local stability; *Group B*, using diverse seeds (0, 1, 123, 777, 999) to explore broader variability; and *Group C*, consisting of ensembles formed from three independently trained models with different seeds to evaluate robustness through averaging.

Results and Discussion

Experiments with individual seeds, as presented in Table 1, show that lift predictions remain generally stable across different initializations, with mean absolute percentage error between 1.1-1.9%. In contrast, drag predictions are highly sensitive, with errors ranging from 0.57% up to 2.02%. From Groups A and B, the best performer was seed 0, with achieved C_L MAPE of 1.1% and C_D MAPE of 0.57%, corresponding to R^2 values above 0.995. The worst performer was seed 45, with C_L MAPE of 1.86% and C_D MAPE of 1.92%, alongside noticeably lower R^2 for drag. This comparison shows that simply *changing the seed can significantly increase the prediction error*, despite using identical data and architecture. Across all tested cases, *error variation reached up to 250%* (e.g. MAPE C_D values varying from 0.57% on Group B, Seed 0 to 2.02% on Group A, Seed 43), confirming that seed initialization is a non-negligible factor in aerodynamic ML prediction.

Table 1. Performance metrics of single-seed models across Groups A and B

Single seeds	MAPE C_L	MAPE C_D	R^2 C_L	R^2 C_D
Group A, Seed 42	1.33%	1.07%	0.9998	0.9933
Group A, Seed 43	1.41%	2.02%	0.9996	0.98
Group A, Seed 44	1.67%	0.84%	0.9998	0.9909
Group A, Seed 45	1.86%	1.92%	0.9998	0.9784
Group A, Seed 46	1.27%	1.19%	0.9998	0.99
Group B, Seed 0	1.10%	0.57%	0.9998	0.9954
Group B, Seed 1	1.97%	0.99%	0.9998	0.9938
Group B, Seed 123	1.08%	1.54%	0.9999	0.9855
Group B, Seed 777	1.78%	1.70%	0.9998	0.9861
Group B, Seed 999	1.65%	0.58%	0.9998	0.9974

From Group C, as presented in Table 2, the most effective ensemble, C2 (610, 987, 75025), achieved C_L MAPE of 1.43% and C_D MAPE of 1.19%, delivering smoother R^2 values across all test airfoils compared to single seeds. By contrast, C1 (17, 89, 257) was the weakest ensemble, with overall errors around 2.2%. In the case of Ensemble C3, the lift coefficient error (MAPE 2.72 %) was approximately 46 % higher than the worst-performing single-seed model, indicating the possible presence of an unfavourable or “black swan” seed within the configuration. The ensemble output represents the mean of predictions from independently trained models. While

mathematically this is a simple average, the resulting predictions could be more accurate because random seed and underestimations cancel each other out.

Table 2. Performance metrics of ensemble models across Group C

Ensembles	**MAPE C_L**	**MAPE C_D**	**R^2 C_L**	**R^2 C_D**
C1 = (17, 89, 257)	1.78%,	2.62%	0.9998	0.9887
C2 = (610, 987, 75025)	1.43%	1.19%	0.9999	0.9968
C3 = (2^8, 2^{16}, $2^{32}-1$)	2.72%	1.08%	0.9998	0.997
C4 = (0, 123, 999)	1.82%	1.46%	0.9999	0.9936
C5 = (43, 45, 777)	1.55%	2.01%	0.9999	0.9893

The simulations confirm that random seed initialization is not a mere implementation detail but a *parameter with a measurable impact on machine learning-based aerodynamic prediction*. Within the tested range, certain seeds yielded better accuracy on the lift branch, while others performed more effectively on the drag branch, showing that initialization can influence each output differently. To mitigate these variations, a *weighted ensemble strategy* could be developed in future work, assigning greater influence to seeds that perform best on specific aerodynamic coefficients. Given that the random seed space spans billions of initialization states, exhaustive exploration is infeasible. This highlights the importance of adopting deliberate sampling and ensemble strategies to balance reproducibility with the computational efficiency expected from machine learning approaches.

References

[1] Andrés-Pérez, E.; Paulete-Periáñez, C. On the Application of Surrogate Regression Models for Aerodynamic Coefficient Prediction. Complex Intell. Syst. 2021, 7, 1991–2021. https://doi.org/10.1007/s40747-021-00307-y

[2] Zuo, K.; Bu, S.; Zhang, W.; Hu, J.; Ye, Z.; Yuan, X. Fast Sparse Flow Field Prediction around Airfoils via Multi-Head Perceptron Based Deep Learning Architecture. Aerospace Sci. Technol. 2022, 130, 107942.

[3] Bakar, A.; Li, K.; Liu, H.; Xu, Z.; Alessandrini, M.; Wen, D. Multi-Objective Optimization of Low Reynolds Number Airfoil Using Convolutional Neural Network and Non-Dominated Sorting Genetic Algorithm. Aerospace 2022, 9, 35. https://doi.org/10.3390/aerospace9010035

[4] Galeazzo, F.C.C.; Garcia-Gasulla, M.; Boella, E.; Pocurull, J.; Lesnik, S.; Rusche, H.; Bnà, S.; Cerminara, M.; Brogi, F.; Marchetti, F.; et al. Performance Comparison of CFD Microbenchmarks on Diverse HPC Architectures. Computers 2024, 13, 115. https://doi.org/10.3390/computers13050115

[5] Cooper-Baldock, Z.; Vara Almirall, B.; Inthavong, K. Speed, Power and Cost Implications for GPU Acceleration of Computational Fluid Dynamics on HPC Systems. arXiv 2024, Preprint arXiv:2404.02482.

[6] Sterpu, D.-A.; Măriuța, D.; Grigorie, L.-T. A UDF-Based Approach for the Dynamic Stall Evaluation of Airfoils for Micro-Air Vehicles. Biomimetics 2024, 9, 339. https://doi.org/10.3390/biomimetics9060339

[7] Sterpu, D.-A.; Măriuța, D.; Cican, G.; Larco, C.-M.; Grigorie, L.-T. Machine Learning Prediction of Airfoil Aerodynamic Performance Using Neural Network Ensembles. Appl. Sci. 2025, 15, 7720. https://doi.org/10.3390/app15147720

Materials Research Proceedings 69 (2026) 88-93 https://doi.org/10.21741/9781644904251-16

Modular OODA-Based Agents for Scalable and Adaptive AI in System-of-Systems Modelling and Simulation

Jorge L. LOVACO[1,a *], Karl ZUBER[1,b *], Raghu Chaitanya MUNJULURY[1,2,c], Christopher JOUANNET[1,2,d] and Petter KRUS[1,e]

[1]Department of Management and Engineering, Linköping University, Olaus Magnus väg, Linköping, Sweden

[2]Saab Aeronautics, Bröderna Ugglas gata, Linköping, Sweden

[a]jorge.lovaco@liu.se, [b]karl.zuber@liu.se, [c]raghu.munjulury@liu.se, [d]christopher.jouannet@liu.se, [e]petter.krus@liu.se

Keywords: System-of-Systems, Agent-Based Modelling and Simulation, OODA Loop, Wildfire Suppression, Collaborative AI

Abstract. Agent-Based Modelling and Simulation (ABMS) is widely used in System-of-Systems (SoS) studies to represent constituent systems operating in dynamic environments. However, the absence of standardised agent architectures hinders scalability, behaviour traceability, and comparative evaluation of emergence, coordination, and operational performance. This work introduces a modular agent design based on Observe–Orient–Decide–Act (OODA) loops as a framework for SoS simulations, enabling transparent information flow and Artificial Intelligence (AI) integration at the decision layer. A wildfire suppression scenario is used for the study, modelling firefighting crews, aircraft, helicopters, bulldozers, and an incident commander as OODA-driven agents. Results show that OODA-based agents exhibit coherent and traceable team behaviours, adaptive task switching, and communication-driven coordination, supporting the study of emergence and interoperability in SoS operations. The Decision stage is designed for future improvements in the form of learning-based AI and Large Language Models to enhance autonomy and operational fidelity.

Introduction

The advancements of Artificial Intelligence (AI) are opening new possibilities in the field of product development. A proper understanding of the complexity of a new product and all its subsystems could greatly benefit from the new AI-enabled technologies. Systems Engineering is strongly correlated with the product development process as it provides standardised methods and tools to handle the complexity of the new system in a traceable manner [1].

For the proper generation of requirements, it is important to have a clear idea and understanding of how the new system will operate and interact with other systems.

Background

System of Systems (SoS) analysis is a valuable tool for finding needs and capabilities that will be translated into requirements for new systems [2]. Communication, interoperability and performance are some of the several key aspects analysed for the collection of constituent systems that form the SoS. For these analyses, ABMS is typically used, as the resources needed to evaluate a complete operation with several constituent systems in a complex and dynamic environment can become exorbitant [3]. The focus of ABMS is the evolution and interactions of large-scale complex systems, which is also the main concern of SoS analysis. The agents in the model are a representation of the constituent systems within an SoS. The agents are implemented to mimic the capabilities and behaviours of the systems during the execution of a mission. Their behaviours will be affected by the interactions they have with one another and with the environment. This is a key

Content from this work may be used under the terms of the Creative Commons Attribution 3.0 license. Any further distribution of this work must maintain attribution to the author(s) and the title of the work, journal citation and DOI. Published under license by Materials Research Forum LLC.

Materials Research Proceedings 69 (2026) 88-93 https://doi.org/10.21741/9781644904251-16

part of the SoS simulation and analysis, as the interactions and behavioural changes might lead to emergent behaviours that are very difficult to predict.

Contribution

The present work considers the use of the Observe-Orient-Decide-Act (OODA) loop as the standard method for Agent-Based Modelling oriented towards SoS analysis. The OODA loop was originally proposed for military operations [4], but it provides a flexible structure for implementing agents and their behavioural rules that is easily relatable to operational guidelines. Moreover, the use of OODA loops is considered a step towards more generalised and agnostic frameworks for representing different systems. The OODA loop can be mapped into agent behaviour rules:

1. Observe: agents acquire information using sensors and external inputs.
2. Orient: agents use the observed data and compare it with the situational context.
3. Decide: decision-making logic selects optimal actions in response to the information propagated from the orientation phase.
4. Act: actions are executed, influencing the agents' state, the other agents and the system environment.

This approach is considered as a manner to ease the characterisation of SoS architectures in simulations, increases operational fidelity, and improves the scalability by allowing variable forms of AI to be included in the Decision phase of the loop.

Study Case

A wildfire suppression scenario is used as a case study. In this context, multiple constituent systems will be included: bulldozers, water bomber aircraft, helicopters, ground teams, and an incident commander are modelled as agents. Each of the agents will be implemented from an embedded base OODA and loop extended to their own characteristics. The agents' behaviour will change dynamically depending on the information that they receive through communication. They will decide and act depending on the information, situation and assigned tactics. The proposed implementation structure is expected to help capture emergent effects from coordinated strategies, communication, and allow for different levels of AI sophistication to be used in the agents' decision-making processes. This generalised approach enables the flexible testing of diverse AI models, SoS architectures and their impact on system performance and operational safety. By providing an adaptable and scalable agent modelling structure oriented for SoS, the OODA-loop method helps to improve fidelity of simulations for complex missions, leaving the increment in computational resources dependent only on the sophistication of the AI used.

Implementation

The implementation of the agents attempts to follow OODA loops in such a way that, in the Decision step of the loop, different forms of AI could be used for extending the implementation. The steps of the loop perform were implemented as follows:

- Observe (perception/inputs): Agents gather data from the world current state such fire grid, distance fields, costs, terrain multipliers, fuel state, etc. This is done via the shared memory in terms of the software implementation.
- Orient (context building/interpretation): Agents derive context from observations: compare terrain costs, possible routes, inaccessible-gap flags, live metadata from the quadrants that split the map into a grid, or day/night thresholds for tactics. The special case is the incident commander agent world picture, who depends on the communication and information from

Materials Research Proceedings 69 (2026) 88-93 https://doi.org/10.21741/9781644904251-16

other agents to know who is where, what is left to do, assignment counts, local completed sets, and finish-and-exit targets.

- Decide (select behaviour): The choice of what to do is mainly done by the commander:
  - Assigns targets (quadrants) and tracks completion of tasks.
  - Implemented rule tables for choosing points of interest and suppression strategy.
  - Switches between main and alternative tactics given thresholds and time-of-day.

  All agents can take decisions to some extent, and it is this step of the OODA loop that is open to the inclusion of advanced forms of AI.
- Act (executes task): Movements are done by the agents using path planning (A* search algorithm and direct-path checks) [5], and they perform tasks such as apply suppression over cells (which updates on-fire pixels) or transport other agents (this task is only realizable by helicopters). In the case of low fuel, the perform actions for returning to base and refuel.

The OODA loop shown in Fig. 1 is the most basic form of it, but there are versions where intents have been added between Orient and Decide, with continuous evaluation of knowledge and beliefs, in order to separate desires and orders [6].

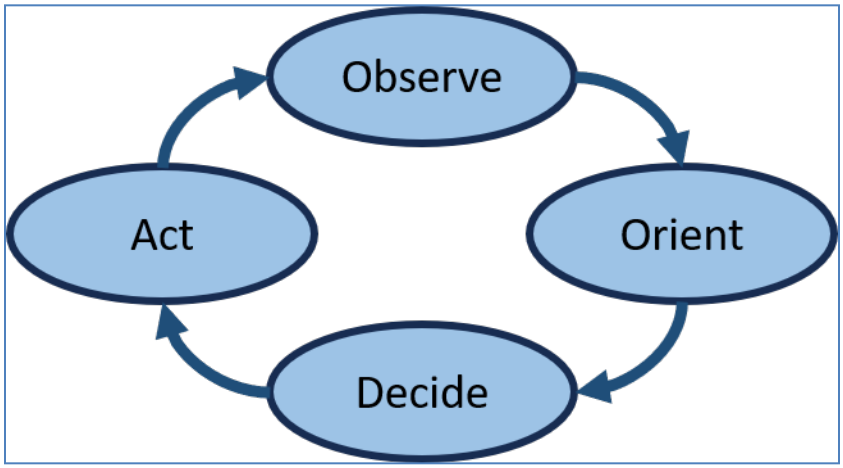


Figure 1: Observe-Orient-Decide-Act loop used by agents.

Discussion

The agent-based model with the agents based on the OODA loop allowed to represent important topics for studying SoS. Collaboration and communication to reach a common goal are particularly difficult, as any form of information exchange for taking decisions based on prior knowledge require to use some form of AI. For the present case, decision trees have been used, which limit the decision capabilities and are considered an AI in narrow form. However, the results were satisfactory since agents performing tasks are aware of their surroundings and react and communicate to events.

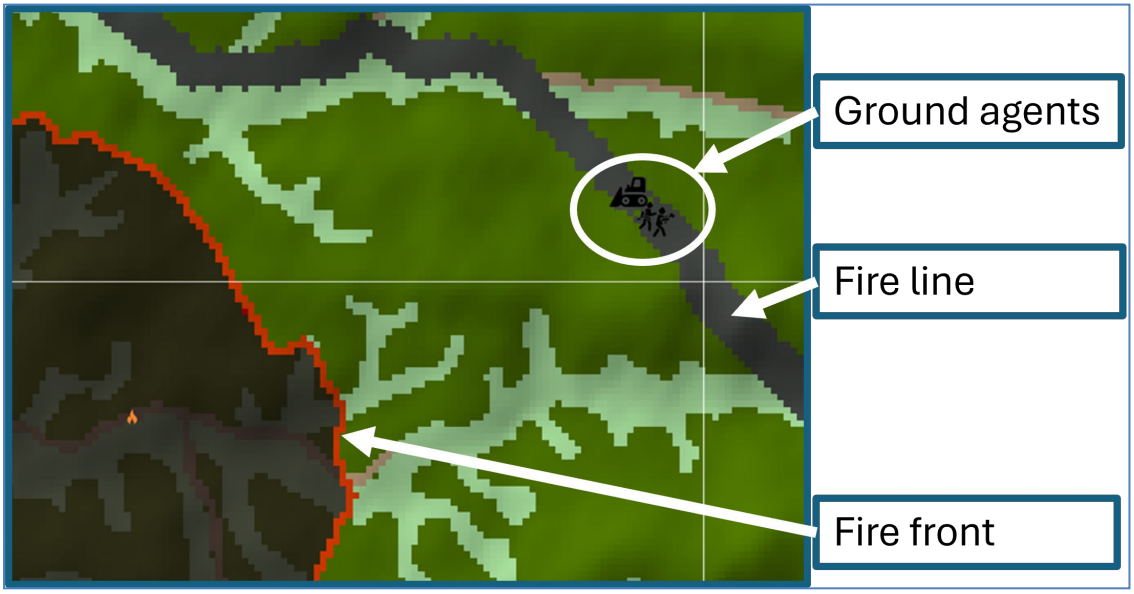


Figure 2: Agents collaborating during a simulation of a wildfire suppression case.

An example of this can be seen in Fig. 2, where ground agents are working for closing a fire line to stop the fire front from spreading. The agents are assigned to a location by the commander agent to create the fire line in a certain direction. The simulation showed that, if they observe another agent working in the line and they close it, they stop the current action, communicate the completion and request another task. In the example of the figure the bulldozer will drive to a different location and the firefighters will request transport to their next location. The implementation, nevertheless, is still the most basic form of OODA loops with a very simple form of intelligence, which in terms of operational credibility can generate situations that would be open to debate with stakeholders and experts. For example, when many firefighters are assigned to work on a line at a certain area, they try to work in parallel, leading to situations where they become less efficient due to a lack of advanced forms of planning.

A further advantage of the OODA-based agent design is that it enables traceability of decisions and actions during the simulation. Each stage of the loop generates information that is exchanged and recorded between agents, forming a continuous flow of observations, decisions, and actions. These communications are automatically stored in a text-based log, creating a chronological record of assignments, acknowledgements, and task completions (see Table 1). This allows reconstruction of how the commander's decisions propagate through the SoS and how agents respond to changing conditions. The sequence also supports post-simulation analysis of coordination efficiency, task timing, and communication reliability, which are essential for validating and improving the models.

Table 1: Agents communication during a simulation of a wildfire suppression case.

Time (hh:mm:ss)	**Sender**	**Receiver**	**Message Summary**
15:03:30	Commander	Hotel-1	Assigned suppress in Q53
15:03:30	Commander	Sierra-1	Assigned suppress in Q53; helper
16:05:43	Hotel-2	Commander	Reported Q53 task complete
16:10:04	Sierra-2	Commander	Reported Q53 task complete

The modular OODA structure also strengthens how communication is modelled across architectural layers of a System of Systems. By explicitly separating Observation, Orientation,

Decision, and Action, it defines clear points where information must be exchanged between agents and higher-level systems. This mirrors real operational architectures, where systems contribute to and depend on shared situational awareness. In this way, OODA provides a unifying logic that links system-level design with software and agent-based implementation. Each message or data exchange can be associated with a stage of the Decision cycle, improving consistency between intent and execution while enhancing interpretability of communication behaviours.

Despite these advantages, some limitations remain. The conceptual OODA framework is flexible and continuous, allowing entities to operate at different speeds, but in the agent-based simulation all loops run synchronously on a shared time step. This simplifies computation yet limits realism, as agents react simultaneously rather than at their own decision rates. In real operations, commanders and field units act asynchronously, and these temporal differences shape coordination and response dynamics. Future work should introduce variable or event-driven update cycles so that agents process information and decide independently while maintaining coordinated communication within the OODA framework.

Conclusion and Future Work

The implemented model has shown that using OODA loops as framework results in agents with behaviours that are closer to those of humans. The different steps in the loop can be implemented separately, making the code easier to maintain and understand. Moreover, the information that is propagated from one step to the next of the loop can be traced, making it possible to understand if the amount of shared is correct, which pieces must be communicated and how this affects the behaviour of an agent representing a constituent system. For an SoS, where there are many interactions that results in its overall behaviour, it is important to understand what the constituent systems need from the group and what they bring to the group value.

The Decision part of the loop is the most relevant part for including different levels of AI as future work. Starting from a narrow form of AI, different methods can be used, such as Machine Learning, for training agents in a certain situation. However, this would be a very challenging task. Following the case of a fire suppression operation, firefighters and pilots are trained in real life both as individuals and as a group, but they also need to follow the orders of a commander. It is then important to be able to include communication into the training, so they learn by using both individual and group knowledge. With the recent advancements in AI, the OODA loops could also include image recognition or forms of Large-Language Models for including outputs similar to human communication, which brings another layer to the research about relevant communication and information in SoS, in order to avoid miscommunication or knowledge gaps that will affect the group performance and the resilience of the SoS.

Acknowledgments

The research presented in this paper has been performed in the framework of the COLOSSUS project (Collaborative System of Systems Exploration of Aviation Products, Services and Business Models) and has received funding from the European Union Horizon Europe programme under grant agreement No. 101097120. The Swiss participation in the Colossus project is supported by the Swiss State Secretariat for Education, Research and Innovation (SERI) under contract number 22.00609. The authors would also like to acknowledge the Swedish Innovation Agency (VINNOVA) and The Swedish Defence Materiel Administration (FMV) for financial support through the grant 2019-05371. Finally, the authors want to acknowledge the insightful discussions about the topic with Kristian Amadori.

References

[1] Brusa, E., Cal'a, A., & Ferretto, D. (2018). Systems engineering and its application to industrial product development. Cham: Springer International Publishing. https://doi.org/10.1007/978-3-319-71837-8

[2] DeLaurentis, D. A., Moolchandani, K., & Guariniello, C. (2022). System of systems modeling and analysis. CRC Press. https://doi.org/10.1201/9781003231011

[3] Murphy, K. J., Ciuti, S., & Kane, A. (2020). An introduction to agent-based models as an accessible surrogate to field-based research and teaching. Ecology and evolution, 10(22), 12482-12498. https://doi.org/10.1002/ece3.6848

[4] Enck, R. E. (2012). The OODA loop. Home Health Care Management & Practice, 24(3), 123-124. https://doi.org/10.1177/1084822312439314

[5] Russell, S. J., Norvig, P. (2018). Artificial intelligence a modern approach (4th ed.). Boston: Pearson.

[6] Silvander, J., & Angelin, L. (2019). Introducing intents to the OODA-loop. Procedia Computer Science, 159, 878-883. https://doi.org/10.1016/j.procs.2019.09.247

Materials Research Proceedings 69 (2026) 94-98 https://doi.org/10.21741/9781644904251-17

Comparing UAM Demand, eVTOL Design, and Profitability across Metropolitan Regions using Simulation and Optimization

Ansgar KIRSTE[1,a,*] and Eike STUMPF[1]

[1]RWTH Aachen University, Institute of Aerospace Systems, Wuellnerstrasse 7, 52062 Aachen, Germany

[a]kirste@ilr.rwth-aachen.de, research@ilr.rwth-aachen.de

Keywords: Advanced Air Mobility (AAM), eVTOL (Electric Vertical Take-Off and Landing), Agent-Based Simulation, Demand Estimation, Transportation Economics

Abstract. We develop an integrated methodology at the UAM fleet level combining multi-agent transport simulation (MATSim) with profit optimization. The approach is applied to three simulation scenarios (Los Angeles, Kyoto, Rhine-Ruhr) with varying network sizes, ticket prices, and eVTOL vehicle characteristics. Demand surrogates are analyzed for large-scale simulation prediction. Results of all scenarios indicate that profitable UAM operations by 2030 require autonomous flight, scenario specific ticket pricing, and efficient eVTOL designs.

Introduction

With ongoing development of electric vertical take-off and landing (eVTOL) vehicles, certifications for U-Space operations, and battery technologies, the feasibility of Urban Air Mobility (UAM) applications is increasing. In passenger transport, this potential is mainly based on travel time savings, but high costs are limiting the future market potential. Consequently, cost optimization approaches are needed at the strategic and operational levels. These include optimized vertiport station placement, configuration and size of the eVTOL fleet, and ticket pricing. In previous studies, several simulations and optimization models have been introduced and applied to individual use cases. Particularly relevant are agent-based transport systems that incorporate both time savings and costs for UAM and ground-based transport modes in a comprehensive modeling environment [1].

A comprehensive analysis of UAM further requires consideration of overlapping research areas: aerodynamic performance of eVTOL vehicles, dispatching within overall demand scenarios, acceptance respectively user preferences, air traffic management, battery technologies and sustainability, vertiport placement and operation, and certification of partially autonomous fleets [2, 3].

In recent research, comprehensive system definitions have been introduced, specifically for UAM and AAM (Advanced Air Mobility – which also includes logistics operations, medical care, and search and rescue applications). These methodological frameworks are called system-of-system approaches or UAM ecosystem analyses, both of which specify the air transportation system [4, 5].

There is a research gap in the comparability of previous UAM studies on air transportation system level, including UAM market potential studies. This work aims to first establish a generally applicable evaluation methodology for UAM and then apply it to various metropolitan regions in a global context.

Methodology

To address both aspects of comprehensive large-scale simulation and specific optimization for profitability, the methodology is divided into three steps: (1) UAM demand simulation, (2) profit maximization, and (3) resulting UAM evaluation. These steps enable modeling between eVTOL

Content from this work may be used under the terms of the Creative Commons Attribution 3.0 license. Any further distribution of this work must maintain attribution to the author(s) and the title of the work, journal citation and DOI. Published under license by Materials Research Forum LLC.

Materials Research Proceedings 69 (2026) 94-98 https://doi.org/10.21741/9781644904251-17

vehicle design and the overall transportation system, including competing modes of transportation within metropolitan areas. Consequently, the existing transportation network and conceptualized eVTOL vehicles are input to the UAM ecosystem. Figure 1 shows the modular structure.

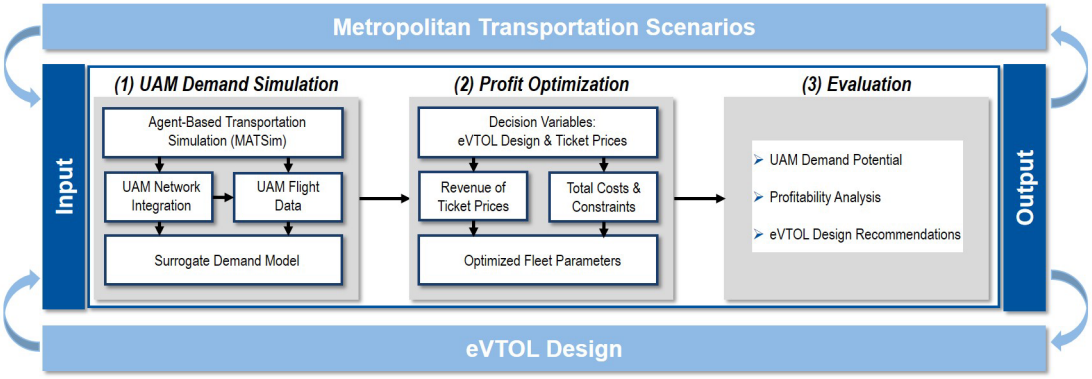


Figure 1. Methodology for modular evaluation of different UAM demand scenarios.

First, existing ground-based demand scenarios from metropolitan regions are considered and evaluated using Multi-Agent Transport Simulation (MATSim) [6]. To create demand-efficient vertiport networks, potential UAM candidate flights are analyzed with k-means clustering. Since UAM only enables travel time savings over medium to long distances, a lower boundary is relevant as input for k-means clustering, which can be set to 15 kilometers based on previous studies. In the next step, the simulation of UAM demand is carried out using MATSim UAM extension. Further modeling includes UAM ticket prices, eVTOL vehicle range limitations, and specific speeds on the UAM network links. Through iterative simulation, in which agents test different modes of transport with temporal and spatial variations, the overall benefit of the agents' daily schedules is optimized. These comparable and reproducible UAM flight data can be extended to demand surrogate models using larger randomized UAM input datasets [7]. Table 1 summarizes default settings and value ranges.

Table 1. Parameter input for surrogate demand models.

parameter	unit	default	value range
fixed price	€	10	[0, 30]
variable price	€/pkm	1.50	[0.80, 2.5]
range	km	200	[20, 200]
cruise speed	m/s	85	[25, 85]

Second, UAM demand data is input to profit optimization, where eVTOL vehicle concepts, battery masses, horizontal flight speed, and ticket prices are decision variables. The revenue is generated by the ticket prices of the UAM flights operated, while the costs are modeled as total costs of ownership from the perspective of a fleet operator, including energy, maintenance, batteries, vehicle acquisition, vertiport operations, air traffic management, charging, and vertiport infrastructure.

Third, the simulated UAM flight data have an optimum point that the operator aims to achieve. Sensitivities of the technology assumptions are added for further profit analyses. eVTOL design recommendations are derived from vehicle-specific decision variables. These in turn represent input for vehicle design as a further loop in the overall methodology.

Study

Simulation. The open-source population data from the following simulation scenarios is used for the UAM demand analysis: Los Angeles [8], Kyoto [9], and Rhine-Ruhr [10, 11]. The latter is

Materials Research Proceedings 69 (2026) 94-98 https://doi.org/10.21741/9781644904251-17

considered a comparison scenario together with analyses that have been carried out recently [12, 13]. Accordingly, the same default settings are used.

Network analysis. K-means clustering of 1% population data for mobility routes over 15 km is used as the initial UAM network to exclude short-distance biases. For the Los Angeles simulation scenario, this results in around 124,000 trips, with an average distance of 9.5 km and a median of 5.6 km. For the Kyoto simulation scenario, this results in around 11,000 trips, with an average distance of 11 km and a median of 3.9 km, which is due to the reduced network size. The Rhine-Ruhr simulation scenario is medium-sized with around 24,000 UAM candidate trips.

UAM network analysis. Figure 2 shows (a) an efficient and high density UAM station network, (b) the coverage of all simulated flight distances, and (c) flight counts. This results in regression functions, with polynomial and exponential approaches having a coefficient of determination (R^2) of 0.99. Estimated power-law scaling for vertiports $n \in [0,100]$ result:

$$(1)\ \text{distance}(n) = 2.32\ n^{0.823}$$
$$(2)\ \text{count}(n) = 1.84\ n^{0.871}$$

The sublinear elasticities (0.823 and 0.871) are consistent with network scaling effects. The reference network of 55 vertiports accounts for 70% of total demand. For the smaller simulation scenario Kyoto, the coefficients of determination are around 0.82 with an indicated target network size of 15 to 25 vertiports.

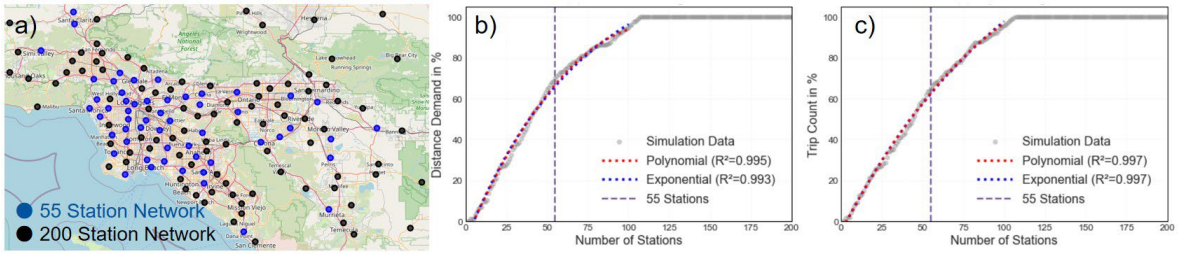


Figure 2. UAM network size effects for simulation scenario Los Angeles.

UAM demand analysis. The surrogate demand models for count and distance are derived from 40 randomized simulations and 150 iterations per scenario, considering Table 1. Comparing these simulation scenarios, it can be shown that the average coefficients of determination are around 0.8, with flight count, larger scenarios, and polynomial models of higher accuracy. The demand surrogate models are linearized and passed on to the profit optimizer.

Profitability analysis. For technology assumptions for the year 2030, this results in feasible business cases. Table 2 shows the resulting key fleet level characteristics. A comparison of the current eVTOL designs indicates that the Joby S4 is the best performing vehicle. The vehicle's study ranges vary less between simulation scenarios than ticket prices.

Table 2. Results of fleet level profit analyses.

parameter	Rhine-Ruhr	Los Angeles	Kyoto
network size	55	100	15
fixed ticket price	12 €	17 €	10 €
variable ticket price	1 €/pkm	1.70 €/pkm	1.15 €/pkm
eVTOL design	Joby S4	Joby S4	Joby S4
study range	95 km	125 km	90 km
2025 profit potential	no	no	no
2030 profit potential	yes	yes	yes*

2025 (2030) assumptions are piloted (autonomous) operation and 250 (400) Wh/kg.
*Kyoto profitability depends on reduced network size (15 stations), extended network analysis indicates marginal viability.

Discussion

UAM demand modeling. The introduced methodology enables consistent and reproducible simulation of demand data using MATSim UAM. Although simple linear regression modeling is possible as an interface for profit optimization, polynomial regression modeling is more accurate. A more detailed analysis with larger data sets and more feature parameter variations is relevant. The simulation studies show a relevant difference between UAM candidate stations and demand-efficient UAM networks, which highlights UAM fleet simulation as key aspect in the methodology.

UAM profitability. It can be stated that autonomous flight operations are necessary and ticket prices comprising fixed and variable prices are profit-enhancing. This enables greater demand over longer distances in all scenarios. The highest ticket prices in the simulation scenario Los Angeles result from (i) the generally higher price structure in California, (ii) greater UAM distances, and (iii) less competition from public transport. The latter is more relevant in both the Kyoto and Rhine-Ruhr scenarios.

eVTOL designs. Cost-efficient vehicles at the UAM fleet level require low energy consumption for longer distances, efficient hovering, and the possibility of passenger pooling to reduce fleet size and maintenance costs. These requirements are best met by the Joby S4, which also offers the advantage of a high cruise speed.

Summary

We develop a modular evaluation framework that enables a consistent comparison of UAM business cases across metropolitan regions. We combine surrogate modeling of agent-based demand simulations to account for system complexity. The study demonstrates that autonomous operations and scenario specific ticket pricing are critical success factors, with the Joby S4 emerging as the most cost-efficient vehicle design across all analyzed scenarios. Regional differences in optimal ticket pricing reflect variations in travel distances and public transport competition, highlighting the need for region-specific UAM business models.

Acknowledgement

Computations were performed with computing resources granted by RWTH Aachen University under projects rwth1250 and rwth1619.

This paper was presented at the CEAS/AIDAA 2025 conference in Turin, Italy.

CRediT authorship contribution statement

Ansgar Kirste: Conceptualization, Data curation, Formal analysis, Investigation, Methodology, Software, Validation, Visualization, Writing – original draft, Writing – review & editing. **Eike Stumpf:** Conceptualization, Funding acquisition, Supervision, Validation, Writing – review & editing.

Funding

This work builds upon the results and models developed during the PhD-program “ACCESS!”, which was supported by the funding scheme “NRW Forschungskollegs” by the Ministry of Culture and Science of the German State of North Rhine-Westphalia (Grant no. 321-8.03.07-127598). Although this program provided foundational support for earlier research, the current study was conducted independently and without direct involvement from the earlier funding source.

Competing interests

The authors declare no competing interests.

References

[1] R. L. Rothfeld, M. Balac, K. O. Ploetner, and C. Antoniou. Agent-based simulation of urban air mobility. 2018 Modeling and Simulation Technologies Conference, 2018. https://doi.org/10.2514/6.2018-3891

[2] L. Kiesewetter, K. Shakib, P. Singh, M. Rahman, B. Khandelwal, S. Kumar, and K. Shah. A holistic review of the current state of research on aircraft design concepts and consideration for advanced air mobility applications. Progress in Aerospace Sciences, 142:100949, 2023. https://doi.org/10.1016/j.paerosci.2023.100949

[3] A. P. Cohen, S. A. Shaheen, and E. M. Farrar. Urban air mobility: History, ecosystem, market potential, and challenges. IEEE Transactions on Intelligent Transportation Systems, 22(9), 2021. https://doi.org/10.1109/TITS.2021.3082767

[4] F. Causa and G. Fasano. Multiobjective modular strategic planning framework for low-altitude missions within the urban air mobility ecosystem. IEEE Transactions on Aerospace and Electronic Systems, 60(1):474–489, 2024. https://doi.org/10.1109/TAES.2023.3324625

[5] S. Wandelt and C. Zheng. Toward smart skies: Reviewing the state of the art and challenges for intelligent air transportation systems (IATS). IEEE Transactions on Intelligent Transportation Systems, 25(10):12943–12953, 2024. https://doi.org/10.1109/TITS.2024.3415588

[6] A. Horni, K. Nagel, and K. W. Axhausen. The multi-agent transport simulation MATSim. Ubiquity Press, London, 2016. https://doi.org/10.5334/baw

[7] A. Kirste and E. Stumpf. Multidisciplinary optimization of advanced air mobility fleet operations. AIAA SciTech 2025 Forum, 2025. https://doi.org/10.2514/6.2025-2170

[8] Institute of Transportation Studies, University of California, Davis and Transport Systems Planning and Transport Telematics, Technische Universität Berlin. MATSim open Los Angeles scenario v1.0 – data repository, 2024. https://svn.vsp.tu-berlin.de/repos/public-svn/matsim/scenarios/countries/us/los-angeles/los-angeles-v1.0/

[9] Transport Systems Planning and Transport Telematics, Technische Universität Berlin. MATSim open Kyoto scenario – data repository, 2024. https://svn.vsp.tu-berlin.de/repos/public-svn/matsim/scenarios/countries/jp/kyoto/

[10] Transport Systems Planning and Transport Telematics, Technische Universität Berlin. MATSim open Ruhrgebiet scenario v1.1 – data repository, 2024. https://svn.vsp.tu-berlin.de/repos/public-svn/matsim/scenarios/countries/de/ruhrgebiet/ruhrgebiet-v1.1-1pct/

[11] D. Ziemke, I. Kaddoura, and A. Agarwal. Entwicklung eines regionalen, agentenbasierten Verkehrssimulationsmodells zur Analyse von Mobilitätsszenarien für die Region Ruhr. In: Heike Proff (Ed.), Mobilität in Zeiten der Veränderung. Springer Fachmedien Wiesbaden, 2019. https://doi.org/10.1007/978-3-658-26107-8_29

[12] A. Kirste and E. Stumpf. Modeling and analysis of dynamic pricing potential for urban air mobility operations. AIAA Aviation 2024 Forum, 2024. https://doi.org/10.2514/6.2024-3938

[13] A. Kirste and E. Stumpf. Development of a generalized eVTOL vehicle cost model for urban air mobility operations. Journal of the Air Transport Research Society, 5:100082, 2025. https://doi.org/10.1016/j.jatrs.2025.100082

Aerodynamics & Fluid Mechanics



Materials Research Proceedings 69 (2026) 100-105 https://doi.org/10.21741/9781644904251-18

Wind Tunnel Investigation of Vertical Stabilizer Wedging Angles on the Aerodynamic Performance of a Modular Aircraft Model

Valeria VAVALÀ[1,2,a *], Ambra GIOVANNELLI[1,b] and Tomasz ŁUSIAK[2,c]

[1]Department of Industrial, Electronic and Mechanical Engineering, University of Roma Tre, Via Vito Volterra 62, 00146 Rome, Italy

[2]Department of Thermodynamics, Fluid Mechanics and Aviation Propulsion Systems, Lublin University of Technology, Nadbystrzycka 36 St., 20 – 618 Lublin, Poland

[a]val.vavala@stud.uniroma3.it, [b]ambra.giovannelli@uniroma3.it, [c]t.lusiak@pollub.pl

Keywords: Aircraft, Airplane, Modular Design, Simulation, Stabilizer, Aerodynamic, Wind Tunnel, Sting Software, Wedging Angles

Abstract. The article reports the experimental findings of a 3D-printed modular airframe with interchangeable stabilizers tested in a wind tunnel. In particular, it describes how variations in the stabilizer geometry affect the aerodynamic performance of the airframe. Parameters of measurement (airflow velocity, air density, slope angle, and sideslip) were put into the Sting program for accurate data acquisition during the test campaigns. The Sting software, realised in Gdynia (Poland) in 2018, is useful to run calibration sequences and keep measurement biases under a minimum value as well as to enable real-time model simulations and data analyses. The wind tunnel used was a closed-circuit modular tunnel with a 2400 mm fan, which is capable of generating air velocities up to 60 m/s, with a modular chamber design enabling a variety of test objects. The chosen setup allowed for measurements at an airflow velocity of 27–29 m/s, which is typical of small-scale aerodynamic testing, while allowing accurate force and moment readings. The model was studied in a wind tunnel where test campaigns were carried out to see how stabilizer configurations affect aerodynamic performance metrics like lift, drag, and side forces. As a result, the test data have been processed and analysed to find key aerodynamic results, which were then compared across different stabilizer setups to check their performance and compare several stabilisers' configurations, highlighting those ones that improve aerodynamic stability and efficiency.

Introduction

This article is a comprehensive overview of the analysis and tests made on a PLA modular model of a 1:10 scaled gyroplane inspired by the Gyroplane I-28 ILOT [1], the Carter Copter Gyrocopter [2], and the T6 Aduster gyroplane [3] with the aim of increasing the amount of data relating to the aerodynamic behaviour of the model to speed up design optimization processes. The model construction and numerical analyses were presented in a previous article [4] where is carefully described the design and the construction of a 3D-printed modular airframe with interchangeable vertical stabilizers. Particular attention was on the post-processing in order to create a solid piece ready to be used in wind tunnel tests. The modular construction applied is an innovation that enables systematic aerodynamic performance investigation of vertical stabilizer effects.

The wind tunnel

The wind tunnel is horizontally-oriented and equipped with two interchangeable measurement chambers. The high-speed test section, with an internal dimension of 1275 × 1415 mm, allows flow velocities up to 60 m/s, while the larger environment test section, the one used in this research with dimension of 1800 × 2000 mm, has a maximum velocity of 30 m/s. In Figure 1 a wind tunnel overview is given.

Content from this work may be used under the terms of the Creative Commons Attribution 3.0 license. Any further distribution of this work must maintain attribution to the author(s) and the title of the work, journal citation and DOI. Published under license by Materials Research Forum LLC.

Materials Research Proceedings 69 (2026) 100-105 https://doi.org/10.21741/9781644904251-18



Fig. 1 View of the wind tunnel

Both test sections are particularly suited to measure accurately aerodynamic forces and pressures on whole aircraft models, as well as to:

• Optimize object shapes for aerodynamic drag reduction and flight characteristics improvement.

• Analyze the influence of airflow on structural stability, critical for aircraft, race cars, bridges, and skyscrapers.

• Study aerodynamic properties like lift, drag, and aerodynamic moments varying the slope angle and airflow speeds.

The tunnel circuit consists of four 90° bends, each of which has flow-guide palisades fitted to provide even flow and minimal pressure losses. The drive system is an axial fan with a diameter of 2.4 m located within a streamlined casing to reduce aerodynamic disturbances, with the heat dissipation being directed out of the tunnel. There is an air cooler ducted in position between the third diffuser and the first low-velocity bend in effort to control the air temperature during prolonged operation. To ensure good quality flow in the test section, a honeycomb straightener and a velocity-stabilizing screen set are positioned upstream of the contraction and ground-layer formation duct. The tunnel body is composed of a modular framework. The overall size of the tunnel is 18.7 m long, 7.4 m wide, and 3.3 m high (3.7 m with support pillars). The structure offers excellent flow quality, such as a core velocity uniformity of more than 0.6 m/s, a turbulence intensity of less than 0.3%, and a maximum angularity of the flow of less than 0.3° in vertical and horizontal directions. At maximum airspeed, the Reynolds number based on a reference length of 1 m is below 2×10^5, and this offers uniform test conditions for both fundamental research on boundary-layer development and applied, involving aerodynamic loads, flutter behaviour, and flow-structure dynamics. These conditions are at the base of precise aerodynamic measurements.

Model assembly

The model assembly included several accurate procedures. It begins with the mounting of the tail part of the airframe, along with the first set of tested vertical stabilizers with a wedging angle of 0°. Place the prepared part of the model on the strain gauge transducer of the wind tunnel requires high precision due to the sensitivity of the measuring device [5]. When the tail section is placed, it is screwed in place with a hex socket screw as reported in Figure 2 (a-b-c). In order to eliminate possible air turbulence, which may appear due to the gaps in the connected elements, insulating tape is used. During the assembly of individual sets of vertical stabilizers, the method of their protection was modified. The original idea was to use cotter pins or pins made of wire with a diameter of 2 mm to prevent the stabilizers from falling out during measurements. However, due to the difficulty of pulling out these cotter pins, they were replaced with wood screws. Thanks to this modification, the strain gauges of the measuring scale are exposed to much less vibrations.

Materials Research Proceedings 69 (2026) 100-105 https://doi.org/10.21741/9781644904251-18

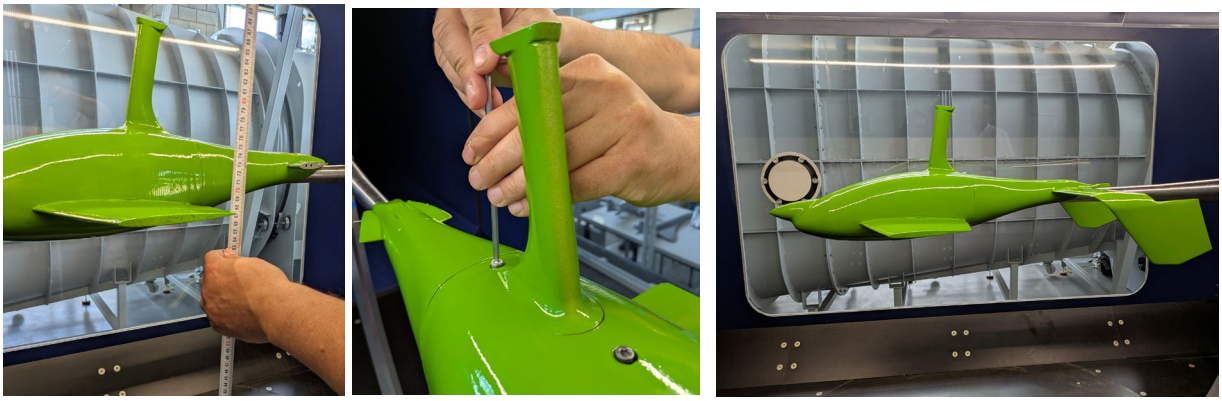


Fig. 2a,2b,2c Assembly and placement on the wind tunnel stand

To prevent the screws from causing unnecessary resistance and air turbulence, the holes were chamfered on the surface of the ballasts so that the screw head could be flush with the surface of the element.

Measurement procedure

Measurements were taken at a constant airflow speed, varying the angle of attack (α) and sideslip angle (β) systematically to cover a wide range of flight conditions.

The aerodynamic forces and moments recorded during testing were processed to calculate standard coefficients (Cx, Cy, Cz) and performance ratios (like Cz/Cx), creating a detailed aerodynamic profile for each configuration.

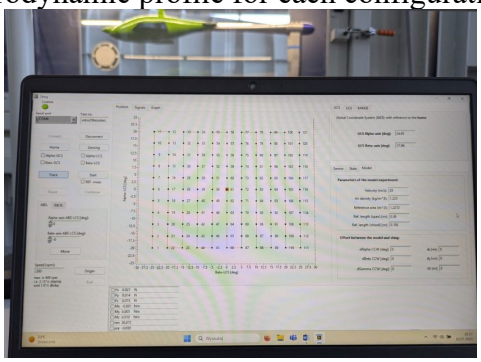


Fig. 3 View of the STING software during measurements



Fig. 4 View of the wind tunnel control panel

The STING software [6, 7] a data acquisition and calibration environment, has been developed to support six-component force balances in wind tunnel testing. It allows for a direct comparison between experimental data and predictions based on aerodynamic models, reducing post-processing time and improving the repeatability of measurements. The Sting software was used to handle measurement control and data collection, including automatic calibration (tare) for each stabilizer configuration, from -15° to +15° in 5° increments, including a baseline with no stabilizers, and for data acquisition (air flow velocity, air density, slope angle and slide, etc.).

The measurements were carried out using: Air velocity: 29 m/s; Slope angle α in the range of ±20° with increments of 2.5°; Glide angle β in the range of ±25°with increments of 5°.

Therefore, according to the abovementioned parameters, 121 measurement conditions were acquired by the STING program (Figure 3).

Later, is the tare calibration was carried out. It consists in going through all measurement points without the tunnel fan running eliminating the effect of the model's weight on the measurements.

Materials Research Proceedings 69 (2026) 100-105 https://doi.org/10.21741/9781644904251-18

Taring was done individually for each set of stabilizers. Once taring was completed [8], the side panel of the test stand was sealed, and the measurement series began. On the tunnel control panel, the predefined value of the airflow speed was set (Figure 4).

The results were collected as data file easy to be processed into tables and graphs. Forces and moments acting on the model were analyzed. The reference system applied is shown in Figure 5.

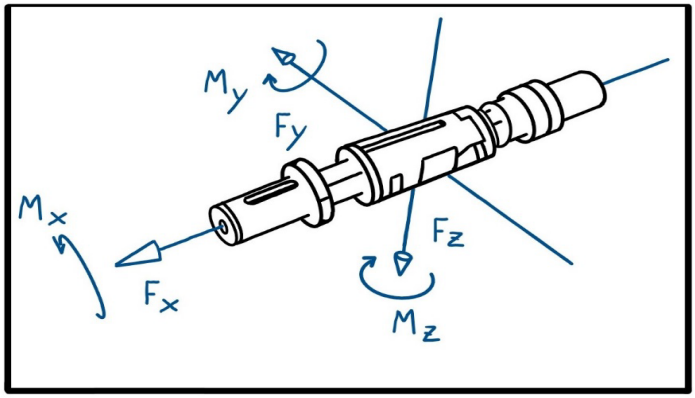


Fig. 5 Diagram of aerodynamic moments and forces in relation to the measuring element of the aerodynamic of the wind tunnel

Measurements results and analysis

During this research, several relevant values were achieved. In particular drag coefficient C_x, lift coefficient Cz, side force coefficient Cy and force ratio Cz/Cx [9] in addition to axis forces and moments were calculated for each slope angle using the equations reported below. [10, 11]. The tests did not take into account the influence of propellers or rotor windage.

1. Drag coefficient equation (C_x)

$$\mathbf{C_x = \frac{2F_x}{\rho V^2 S}} \tag{1}$$

Where $\mathbf{F_x}$ is the aerodynamic drag force, **ρ** the air density, **V** the air flow velocity and **S** the reference area of the model.

2. Lift coefficient equation (C_z)

$$C_z = \frac{F_z}{\frac{1}{2}\rho V^2 S} \tag{2}$$

Being F_z the aerodynamic lift, ρ the air density, V the air flow speed, and S the reference model surface, respectively.

3. Side force coefficient equation (C_y)

$$C_y = \frac{F_y}{\frac{1}{2}\rho V^2 S} \tag{3}$$

Where F_y is the aerodynamic side force, **ρ** the air density, **V** the air flow velocity and **S** the reference area of the model.

4. Force ratio equation (E)

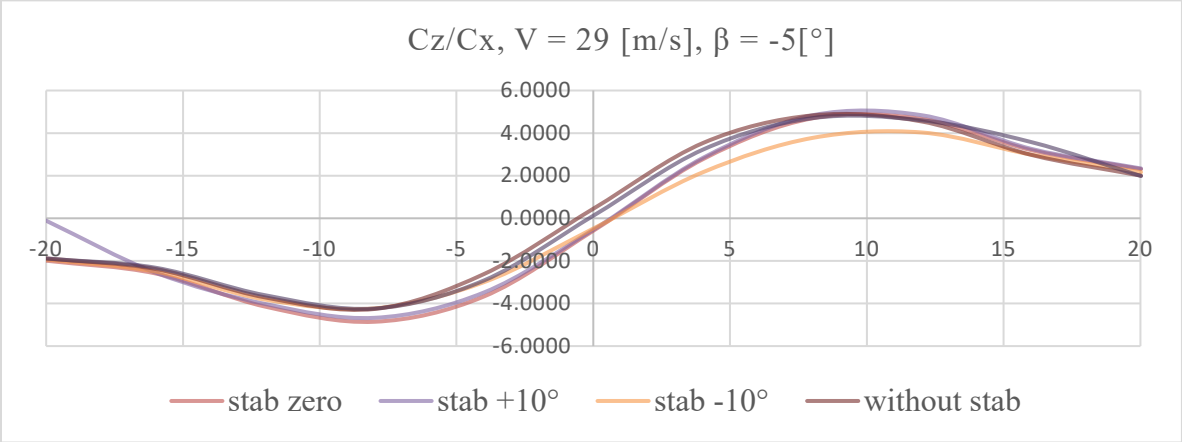
$$E = \frac{C_z}{C_x} \tag{4}$$

Being C_z the lift coefficient and C_x the drag coefficient.

Materials Research Proceedings 69 (2026) 100-105 https://doi.org/10.21741/9781644904251-18

The calculations were made using the results for the sliding angles β from -20° to +20° and the air flow velocity equal to V = 29 m/s, with the stabilizer settings shown in Table 1 and connected with the following stabilizer angles: Stabilizer angle = 0°; Stabilizer angle = +15°; Stabilizer angle = -15°; Without stabilizer.

Table 1 Example of graph obtained analysing force ratio at a sliding angle of -5° and at a velocity of 29 [m/s]



Conclusions

Based on the tests carried out in the wind tunnel, it was possible to analyze the different effects connected with the modifications of the basic configuration.

The more the wedge angle increases, the higher the stability and aerodynamic efficiency are. Such an effect can be observed in the lift/drag ratio, despite this involves a reduction in the optimal slope angle.

Asymmetric flow tests, i.e. with $\beta \neq 0$, show a small yaw moment coefficient. However, it can be noticed that as the drift angle increases, a strong roll moment is generated, which is accentuated as the slope angle increases, highlighting a strong lateral instability. Furthermore, the drift angle leads to an increase in drag, lateral force, and lift, with a consequent reduction in pitch moment.
With the use of smaller stabilizers, a reduced stability can be observed. Increasing the drift angle partially improves stability, which confirms the need for larger tail surfaces.

In symmetrical flights, increasing the surface area of the horizontal tailplane improves longitudinal stability. In addition, there is an increase of approximately 10% in the lift coefficient and its drift, while the angle of lift remains unchanged.

In asymmetric flows, the tailplane area has minimal effects on the aerodynamic coefficients in conditions of drift and zero slope angle. What would make a difference, increasing both horizontal stability and lateral force, is the possibility of adding a ventral fin below the fuselage.
In conclusion, it can be observed that the optimal configuration requires sufficiently large tail planes [12] and a positive wedge angle to ensure stability and efficiency.

Overall, the wind tunnel tests provided a quality dataset for the evaluation of vertical stabilizers' contribution to the control of aerodynamic performance.

The systematic method ensured comparability among configurations, and experimental setup precision minimized measurement uncertainty. The findings offer application in the optimization of stabilizer design for model aircraft and as a validation reference for numerical models.

To sum up, this research provides insights for the researcher in the aerodynamic domain of aircraft stabilizers by detailing the latest techniques in aerodynamic flow analysis. These results aim to deepen the understanding of stabilizer-induced aerodynamic behavior in small-scale aircraft. By measuring how changes in wedging angles affect key aerodynamic parameters, this research offers useful data for improving tail design in both academic and industrial settings.

Additionally, the methodology used, which involved models and systematic wind tunnel testing, can serve as a guide for future aerodynamic studies.

Acknowledgments
The present study was carried out under the Erasmus+ Program. In particular, the Authors want to thank the Lublin University of Technology, and the University of Roma Tre for their kind support.

References

[1] S. Cieślak, W. Krzymień, Drivetrain Noise of the Gyroplane I-28, Transactions of the Institute of Aviation, vol. 230, 2013, pp. 31–50. https://ilot.lukasiewicz.gov.pl/wp-content/uploads/2020/03/230-03.pdf

[2] J. Carter, Development and Flight Testing of the CarterCopter Technology Demonstrator (CCTD), Carter Aviation Technologies Technical Report, 2005.

[3] T6 “Aduster” Gyroplane – Technical Specifications and Performance Data, Aviation Artur Trendak, Product Technical Sheet, 2016. https://trendak.eu/t6-aduster

[4] V. Vavalà, A. Giovannelli, T. Łusiak, Design of a 3D-printed modular airframe with interchangeable vertical stabilizers for experimental applications, Proceedings of the AIDAA International Conference on Aeronautics and Astronautics, 2025, Paper ID 736.

[5] Chernyshev, S.L., Lyapunov, S.V. & Wolkov, A.V. Modern problems of aircraft aerodynamics. Adv. Aerodyn. 1, 7 (2019). https://doi.org/10.1186/s42774-019-0007-6

[6] MIKOM Systemy Pomiarowe, STING – Six-Component Aerodynamic Balance Software, Technical Product Documentation, Gdynia, 2018. https://mikom.pl/sting

[7] Łukasiewicz Research Network – Institute of Aviation, Wind Tunnel Test Equipment and Data Acquisition Systems, Laboratory Technical Catalogue, Warsaw, 2021. https://ilot.lukasiewicz.gov.pl

[8] *J.Barlow, W.H.Rae, A.Pope*, Low speed wind tunnel testing a wiley-interscience publication,1999

[9] Kumar, J.K.A., Prabhu, K.S., Veerendra, A.S. et al. A comprehensive review of aerodynamic performance evaluation for aircraft wings and engines: insights into experimental, numerical, and theoretical approaches. AS (2025). https://doi.org/10.1007/s42401-025-00366-w

[10] Hao D, Zhang L, Yu J, Mao D. Modeling of unsteady aerodynamic characteristics at high angles of attack. Proceedings of the Institution of Mechanical Engineers, Part G: Journal of Aerospace Engineering. 2018;233(6):2291-2301. https://doi.org/10.1177/0954410018776527

[11] Voevodin, A.V., Efremov, A.A. & Soudakov, V.G. Numerical and experimental study of the aerodynamics of a civil-aircraft model at high angles of attack and during rotation. Thermophys. Aeromech. 30, 1–12 (2023). https://doi.org/10.1134/S0869864323010018

[12] Natella, M. & De Breuker, Roeland. (2019). The effects of a full-aircraft aerodynamic model on the design of a tailored composite wing. CEAS Aeronautical Journal. 10. https://doi.org/10.1007/s13272-019-00366-5

Materials Research Proceedings 69 (2026) 106-111 https://doi.org/10.21741/9781644904251-19

Design of a 3D-Printed Modular Airframe with Interchangeable Vertical Stabilizers for Experimental Applications

Valeria VAVALÀ[1,2,a *], Ambra GIOVANNELLI[1,b] and Tomasz ŁUSIAK[2,c]

[1]Department of Industrial, Electronic and Mechanical Engineering, University of Roma Tre, Via Vito Volterra 62, 00146 Rome, Italy

[2]Department of Thermodynamics, Fluid Mechanics and Aviation Propulsion Systems, Lublin University of Technology, Nadbystrzycka 36 St., 20 – 618 Lublin, Poland

[a]val.vavala@stud.uniroma3.it, [b]ambra.giovannelli@uniroma3.it, [c]t.lusiak@pollub.pl

Keywords: Aircraft, Gyroplane, Aerodynamic, 3D Printing, PLA Filament, FDM Technology, Modular Design, Vertical Stabilizers, Various Angles of Attack

Abstract. The optimization of aircraft stability and aerodynamic performance is a key aspect of modern aerospace engineering, especially concerning vertical stabilizers, which are essential for maintaining yaw stability and controlling sideslip during flight. To enable adequate analysis regarding performance, stability, and control, a validated aerodynamic model of the aircraft has been created. The main goal of the study is to evaluate how stabilizer shape affects the aerodynamic traits of the airframe. In this paper it is examined a detailed view of the modular aircraft model, which was created, to ensure accurate and repeatable results, using computer-aided design (CAD) software and manufactured with fused deposition modelling (FDM) 3D printing using polylactic acid (PLA) material. This method provided a balance between strength and flexibility, allowing for precise reproduction of complex parts while reducing material waste. The modular design of the airframe enabled quick swapping of stabilizer components, making systematic and comparative analysis across different setups easier and ensuring consistent measurements under the same conditions. This research discusses the aerodynamic features of an aircraft model with modular, interchangeable vertical stabilizers set at different wedging angles. In total, there are seven pairs of easily replaceable elements. The model has been obtained in order to be used to perform tests in the wind tunnel. To sum up this research provides an airframe model construction and design traded off additive manufacturing effectiveness with attention to post-processing in order to create a solid experimental piece. Modular construction is an applied innovation that enables systematic aerodynamic performance investigation of vertical stabilizer effects.

Introduction

Airplanes and helicopters have been studied exhaustively, to the point of becoming a standard and well-established area of modern aviation. Nevertheless, ultralight aircraft such as the gyroplane, which offer significantly lower operational and maintenance costs, have always been quite underrated.

Despite their remarkable characteristics such as a rotor, similar to that of a helicopter, which generates lift through autorotation, and as an engine-driven propeller, similar to an airplane's, which provides thrust, the gyroplane has spent nearly a century in the shadow of both airplanes and helicopters [1].

In recent years, instead, there has been a renewed interest in gyroplanes, due to their safety, simplicity of use and price as well as their ability to take off and land short distances, which makes them best for recreational, training and potential urban mobility applications.

Content from this work may be used under the terms of the Creative Commons Attribution 3.0 license. Any further distribution of this work must maintain attribution to the author(s) and the title of the work, journal citation and DOI. Published under license by Materials Research Forum LLC.

Materials Research Proceedings 69 (2026) 106-111 https://doi.org/10.21741/9781644904251-19

The model design

In this paper, the design and the manufacture of a modular scaled model of a gyroplane is presented in order to analyze how different stabilizers influence the aerodynamics of the aircraft.

The initial gyroplane used as reference was the I-28 (Fig.1), designed by Sieć Badawcza Łukasiewicz – the Polish Institute of Aviation known as iLOT- in 2010 as part of the project named "Technology for implement a new type of rotorcraft into commercial practice" [2] and, lately, manufactured in 2012 through a collaboration with the Aviation Arthur Trendak [3].

The I-28 is a two-seat gyroplane featuring a 6-meter-long fuselage. It is equipped with a two-blade, ground-driven prerotational rotor, with the drive shaft divided by universal joints and guided within the rotor pylon. Propulsion is provided by a 110 kW diesel engine driving a propeller with a diameter of 1.73 m.

The I-28 was later modified through the addition of wings by Carter Aviation Technologies, and this configuration, known as CarterCopter (fig.2), was used as the starting point for the analysis in this work.

The CarterCopter prototype was developed to prove the slow rotor compound technology, which consists of slowing the rotor during the cruise and letting the wings supply the majority of lift as speed increases.



Fig.1 Gyrocopter I-28



Fig.2 CarterCopter gyrocopter

The practical result was visible in the value of the advance ratio μ – the relationship between the aircraft's forward speed and the tip speed of its rotor blades.

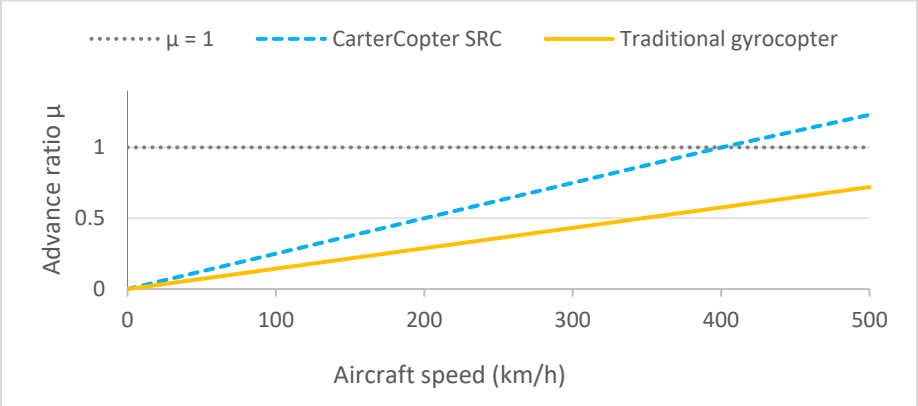
In conventional helicopters, μ was typically around 0.3-0.4. Trying to push a helicopter faster would run into serious problems as the retreating blade stalls - no more lift contribute - and the advancing blade approaches supersonic speed - huge drag and instability.

The CarterCopter, instead, became the first rotorcraft in history capable of obtaining = 1, its airspeed was equal to the rotor tip speed (table 1).

This innovation showed that with a slowed rotor and fixed wings, it is possible to fly much faster than with a helicopter while still having short or vertical takeoff and landing [4].

This research was focused on creating a model to perform systematic tests on its aerodynamic properties. The prototype was designed trying to maintain scaled geometric similarity, consider the Reynolds number consistently within the limits of the wind tunnel, and preserve the relative proportions of key aerodynamic surfaces.

Table 1. Comparison of Advance ratio μ



Computational geometry

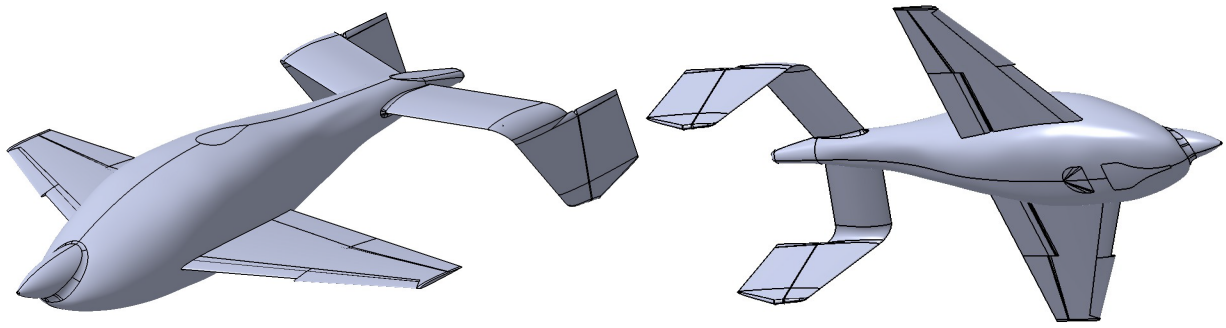


Fig 4-5 Different views of the model in the CAD software

The solid geometry was then imported to Design Modeler in ANSYS Workbench, where further simplifications were performed for the mesh quality enhancement. These included reducing fragmented surfaces, healing irregularities, eliminating sharp angles, and smoothing edges. Tools such as Repair, Merge, Hard Edges, Holes, Spikes, and Faces were used to improve geometric consistency.

Then, the model was discretized based on tetrahedral elements, whose size, number, and quality were checked as influential parameters on simulation accuracy.

A mesh sensitivity analysis was conducted to access the effect of the element density on aerodynamic predictions. On the half-height geometry, a mesh of 0.98 million elements under-predicted drag by 39% and lift by 52% in comparison with a refined mesh of 1.67 million elements. Further refining the mesh to 2.46 million elements reduced differences to approximately 1% in drag and 7% in lift and was considered appropriate for the objectives of the present study.

In the initial design phase, it was recommended the fuselage to be redesigned for improved aerodynamics. More precisely, provisions for enhancing fuselage airflow, especially aft of the nacelles and wing–fuselage junctions, were included. These were intended to eliminate adverse force gradients on the horizontal stabilizer, so that the overall performance was improved.

Construction

Particular relevance was given to the model creation phase, essential for reliable prototype's tests and evaluate its effectiveness.

A modular design approach was adopted instead of constructing a single, fixed-geometry model to allow the analysis of different stabilizer deflection angles (± 15, 10 and 5 degrees [6]).

Materials Research Proceedings 69 (2026) 106-111 https://doi.org/10.21741/9781644904251-19

The modularity of the prototype facilitates an easy replacement and adjustment of stabilizers and an identical testing across configurations. This offered not just improved efficiency of experimentation but also comparability of results.

Before testing, the model was printed using Fused Deposition Modelling (FDM) technology. The process consists in heating Polylactic Acid (PLA) filaments, extruding them through a nozzle and depositing layer by layer on a worktable.

The resulting 3D draft model made up of several elements is reported in Figure 6.

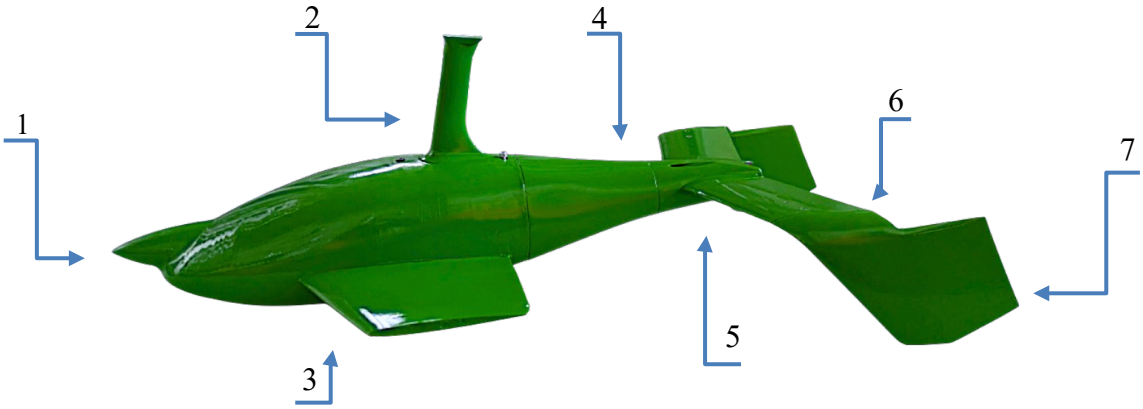


Fig. 6 Division of the gyroplane into individual components: 1- nose, 2- mast ,3- left wing, 4- first half of the tail, 5-second half of the tail, 6- horizontal stabilizers, 7- vertical stabilizers

The model went through a rigorous process of refinement to prevent interference during testing and to ensure precise alignment and smooth connections.

All the elements were refined [7], removing support structures, sanding in multiple stages, filling surfaces, and applying primers and varnishes.

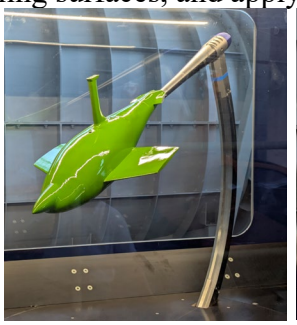




Fig.7-8 Different views of the printed model on the wind tunnel stand first without and then with stabilizer



Fig. 9 Cuboid-shape core on the wind tunnel stand

Finally, the main structural element of the tail was connected to the core, located at the front of the model as reported in Figures 7 and 8.

A special profiled socket for a metal sleeve was provided into the cuboid-shaped core. Such a sleeve is an adapter to connect the model to the wind tunnel balance system as shown in Figure 9. The upper part of the tail consists of two halves, allowing the connection of the main element of the tail with the horizontal stabilizers.

The vertical stabilizers, which are the main subject of the study, were arranged in interchangeable pairs with deflection angles ranging from ±15 degrees (every 5 degrees).

There are seven pairs of easily replaceable elements, which are placed directly on the horizontal stabilizers via an insertion element and secured using metal cotter pins.

Materials Research Proceedings 69 (2026) 106-111 https://doi.org/10.21741/9781644904251-19

Although considerable attention was paid to manufacturing accuracy, minor surface irregularities were detected. Consequently, further steps as rough machining, surface finishing, and painting were carried out to ensure aerodynamic smoothness and dimensional precision.

Turbulence Modelling and Numerical Approach

Preliminary numerical studies were carried out using Ansys Fluent. The applied turbulence model was the SST (Shear Stress Transport) [8] one, to reduce the computing effort. The numerical model capable of obtaining results such as drag coefficient, pressure distribution, and vortices extremely close to what would realistically occur in flight.

The study considers the results of numerical tests of aerodynamic loads on a 1:10 scale model of the gyroplane fuselage and for actual geometry. The tests carried out on the fuselage do not take into account the influence of operating propellers and the aerodynamic drag of the rotor. The aerodynamic characteristics necessary for analyzing the longitudinal and directional stability of the gyroplane have been obtained. All forces and moments are calculated in the velocity system. During the calculations, the following parameters were considered: speed of 29 m/s, air density of 1,225 kg/m³, reference span length of 0.36 m, and reference chord length of 0.193 m.

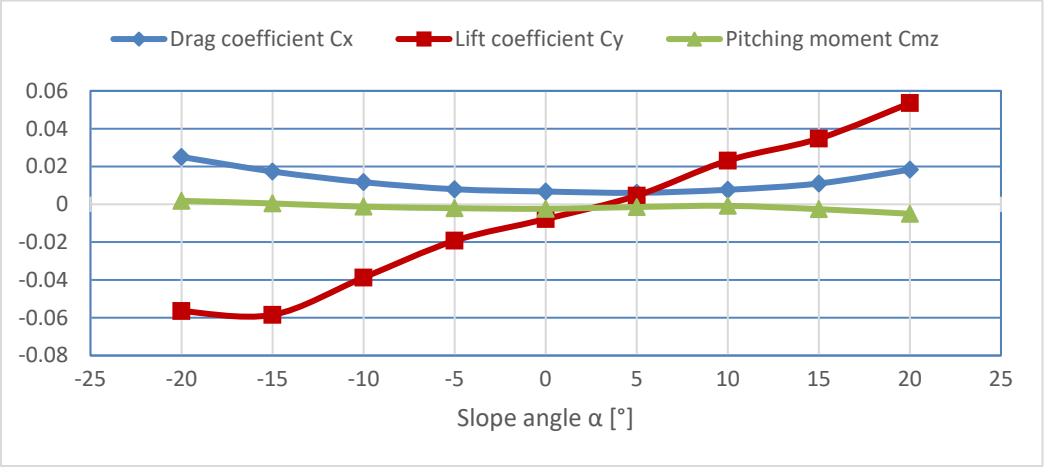


Fig.10 Drag, lift and pitching moment varying the slope angle

Figure 10 shows the main results. In particular, the coefficients of drag, lift, and the pitching moment are reported as a function of the slope angle (α) from -20° to +20° for the tail-pinned gyro [9].

The measurement area of the object under examination is of 1,2272 m², to which a velocity condition (velocity input) has been assigned at the inlet and a pressure condition (pressure output) at the outlet. The remaining walls are recorded as walls, including the surfaces of the gyroplane fuselage.

The analyses were conducted as a pressure-based model, variable in time and at steady state. Air was the fluid flowing through the test object, but an incompressible flow was assumed, and the material definition assumed an ideal incompressible gas. This simplification is acceptable if the flow velocity is less than 0.3 Mach. In the case under consideration, for the assumed temperature of T-288 K, the limit value is 367.4 km/h (the speed of sound for these conditions is 340 m/s, or 1,224.6 km/h).

Conclusions

In this overview paper, the historical background was presented that led to the design and construction of an innovative gyroplane model equipped with different stabilizers to be tested into a wind tunnel. Particular attention was paid to the model modularity, which was strictly connected to the research needs. Moreover, preliminary 3D numerical analyses were carried out, applying

the commercial tool Ansys Fluent, to estimate drug, lift and pitching moment of the gyroplane under several slope angles. On the basis of the promising numerical results, the study will be carried on testing the gyroplane into a wind tunnel, comparing the effect of several stabilizers.

Acknowledgments
The present study was carried out under the Erasmus+ Program. In particular, the Authors want to thank the Lublin University of Technology, and the University of Roma Tre for their kind support.

References

[1] Jategaonkar, R. V. (2023). Aerodynamic Modeling and System Identification from Flight Data. Journal of Aerospace Sciences and Technologies, 57(1), 1–16. https://doi.org/10.61653/joast.v57i1.2005.674

[2] Łukasiewicz Research Network, Institute of Aviation, Technology for implementing in the economic practice of a new type of rotorcraft, Project Documentation Report, Warsaw, 2010. https://ilot.lukasiewicz.gov.pl

[3] A. Artur Trendak & Son Aircraft Manufacturer, Company Profile and Gyroplane Production Overview, Corporate Technical Publication, 2014. https://trendak.eu

[4] Aşkan, Abdulhalim & Tangöz, Selim & Konar, Mehmet. (2022). An investigation of aerodynamic behaviours and aerodynamic performance of a model wing formed from different profiles. The Aeronautical Journal. 127. 1-22. https://doi.org/10.1017/aer.2022.85.

[5] Kandemir C. Barış Sabuncuoğlu (2020) Weight optimization of an aircraft wing composite rib using finite element method. Master thesis, School of Science and Engineering of Hacettepe University.

[6] Jakub Szczepaniak (2023) Aerodynamic analysis of a rotorcraft in a wind tunnel using wing elements, Master thesis, Lublin University of Technology, Poland.

[7] Tomasz Markiewicz (2023) Comparative analysis of experimental research of an aircraft model with armament components, Lublin University of Technology, Poland.

[8] F.R. Menter, Two-Equation Eddy-Viscosity Turbulence Models for Engineering Applications, AIAA Journal, vol. 32, no. 8, 1994, pp. 1598–1605. https://doi.org/10.2514/3.12149

[9] Asaro, S., & Vos, R. (2025). Synthesis of the Aerodynamic Model of a Flying Wing Aircraft. In AIAA Science and Technology Forum and Exposition, AIAA SciTech Forum 2025 Article AIAA 2025-0852 (AIAA Science and Technology Forum and Exposition, AIAA SciTech Forum 2025). American Institute of Aeronautics and Astronautics Inc. (AIAA). https://doi.org/10.2514/6.2025-0852

Materials Research Proceedings 69 (2026) 112-118 https://doi.org/10.21741/9781644904251-20

Effects of Airfoil Trailing Edge Thickness on the Generation of Secondary Tones

Giorgio SANTANATOGLIA[1,a *], Richard D. SANDBERG[1,b], Elnaz HAJIZADEH[1,c]

[1]Department of Mechanical Engineering, Faculty of Engineering and IT, The University of Melbourne, Parkville, Victoria, 3010, Australia

[a]g.santanatoglia@student.unimelb.edu.au, [b]richard.sandberg@unimelb.edu.au, [c]ellie.hajizadeh@unimelb.edu.au

Keywords: Aeroacoustics, Computational Methods, Boundary Layer Separation, Vortex Shedding

Abstract. New noise regulations are issued to respond to the expected impact of a massive exploitation of drones in the urban environment. The small size and low flight speed of drones is related to flight regimes characterised by low Reynolds numbers with ignorable compressibility effects. This has recently raised interest in the study of noise generated by transitional airfoils at moderate angles of attack. Where distinct narrow-band frequency peaks, which are perceived as a pitching sound over the broadband noise, are known to arise. Therefore, raising concerns in the design of quieter drones. The current research studies the effects of the airfoil trailing edge thickness on the generation of secondary tones. The flow around a NACA 0012 airfoil and the associated acoustic signature are studied with 2D DNS for six different values of the airfoil trailing edge thickness at $\mathrm{Re}=2.0\times10^5$, $\mathrm{Ma}=0.1$, $\mathrm{AoA}=2.0°$. The role played by the trailing edge thickness in establishing a reattachment region downstream of the laminar separation bubble on the airfoil pressure side is shown. For the first time it is demonstrated that the presence of such reattachment region just upstream of the airfoil trailing edge leads to non-negligible differences in the airfoil acoustic signature. Furthermore, an existing acoustic sharpness criterion is revised considering the presence of the reattachment region. Finally, the fluid dynamics behind the generation of the side tones is described.

Introduction

Airfoil self-noise typically shows a broadband character [1]. But varying the airfoil trailing edge thickness, mechanisms related to the flow dynamics behind the generation of tones are promoted differently. Therefore, airfoils with a sharper trailing edge emit more tonal noise because of the vortex shedding becoming more predominant, while airfoils with a sharper trailing edge are more broadband. Blake conducted an experimental campaign [2] to derive an empirical parameter [3] to determine when an airfoil can be considered acoustically sharp, given different free-stream flow conditions and airfoil trailing edge geometries. But the difficulty in describing the airfoil acoustic signature emerges at moderate Reynolds numbers [4] and at low angles of attack [5, 6], when distinct narrow-band frequency peaks between 20 and 30 dB above the background level [5] arise. The existence of such discrete frequency tones was firstly identified in the early 1970s in [7, 8, 9]. In the pioneering research by Paterson et al. [10] a characteristic *ladder-type* structure in the tonal frequencies with tones undergoing jumps as the free-stream velocity changes was identified. The main aerodynamic source of tones was addressed by Tam [11] to be found in disturbances of the Tollmien-Schlichting instability waves. Lowson et al. [12] concluded for the first time that the appearance of tones is related to the presence of a laminar separation bubble on the airfoil pressure side. With Nash et al. [4] remarking that it is the close proximity of the separation bubble to the airfoil trailing edge the sufficient condition, and not the presence of separation alone. The role of

Content from this work may be used under the terms of the Creative Commons Attribution 3.0 license. Any further distribution of this work must maintain attribution to the author(s) and the title of the work, journal citation and DOI. Published under license by Materials Research Forum LLC.

Materials Research Proceedings 69 (2026) 112-118 https://doi.org/10.21741/9781644904251-20

the angle of attack on the generation of tones was studied by Plogmann et al. [6]. And the role of the Mach number on the laminar separation bubble was recently studied by Pröbsting et al [13].

Numerical solver

High-fidelity 2D compressible Direct Numerical Simulations (DNS) are run in *HiPSTAR*, a *High-Performance Solver for Turbulence and Aeroacoustics Research*. The numerical solver uses an explicit 4th-order central standard-difference scheme with a five-point stencil for spatial discretisation furtherly implemented with a Carpenter boundary scheme, and a 4th-order-accurate five-stage Runge-Kutta integration scheme.

The free-stream conditions are defined by Prandtl number $Pr = 0.70$, Sutherland's dimensionless temperature $S/T_\infty = 0.3686$, Reynolds number $Re = 2.0 \times 10^5$, Mach number $Ma = 0.1$, angle of attack $AoA = 2.0°$. All variables are dimensionless, with the airfoil chord as the reference length.

Grid and boundary conditions

The computational domain is made of three independent structured meshes coupled using a stable overset technique. Specifically, an outer background cartesian mesh discretising the far-field, an O-grid discretising the region around the airfoil, a fish-tail mesh discretising the airfoil wake-region.

In total, the overall grid points are about 10.5 million.

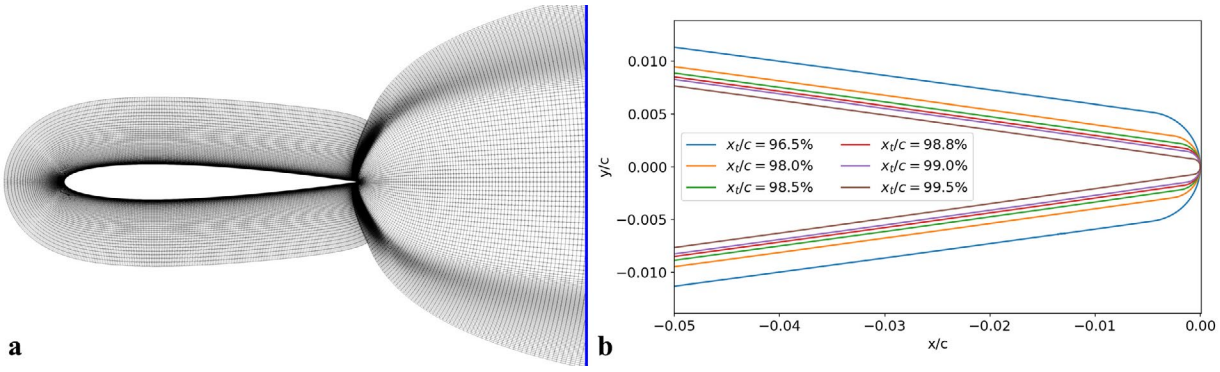


Figure 1 (a) O-grid and part of the fish-tail mesh, (b) comparison of the airfoil trailing edge for different cases.

The free-stream flow is enforced on the outer boundaries by Dirichlet boundary conditions. Reflections from the airfoil's wake are dampened out by zonal characteristic boundary condition on the right outer boundary. Reflections from the acoustic waves are dampened out by integral characteristic boundary conditions (*sponges*) on the remaining outer borders.

The trailing edge of the airfoil is rounded off with a tangential circle to the local surface at a distance x_t/c from the airfoil leading edge, as reported in *table 1* for the six cases. The airfoil is then rescaled to a unitary chord length. The resulting airfoil trailing edges are shown in *figure 1(b)*.

Table 1 Location of the airfoil trailing edge round-off [1st row]and related airfoil trailing edge thickness [2nd row].

x_t/c	0.965	0.980	0.985	0.988	0.990	0.995
$h/c\ [\times 10^{-3}]$	9.9174	5.7239	4.3012	3.4544	2.8737	1.4457

The hydrodynamic and acoustic fields are recorded in a time interval long 30 flow-through-time units after convergence is reached.

Materials Research Proceedings 69 (2026) 112-118 https://doi.org/10.21741/9781644904251-20

Results

A laminar separation bubble (LSB) is present on both airfoil sides.

In general, the separation point moves toward the leading edge with a bigger displacement than the one of the reattachment point. The remarkable phenomenon shown in *figure 2* is that a reattachment region is present on the airfoil pressure side in close proximity of the airfoil trailing edge for the cases $x_t/c \geq 0.988$.

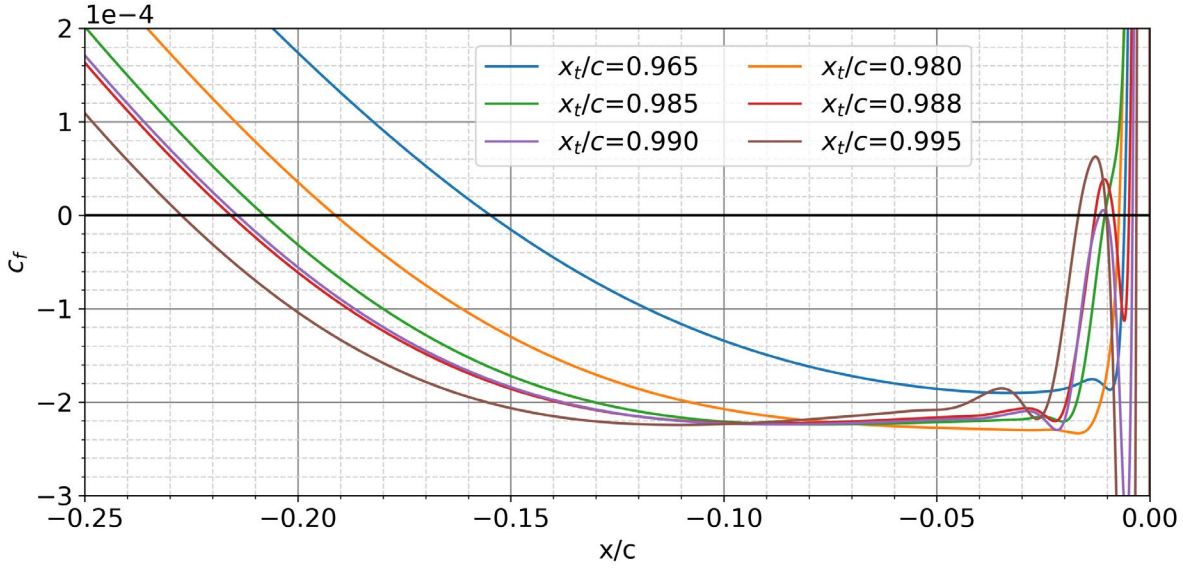


Figure 2 Local chord-wise distribution of the skin-friction coefficient on the airfoil pressure side.

Blake's acoustic sharpness criterion $(h/c)/\delta^*_{tot}$ is given by the ratio of the trailing edge thickness and the displacement thickness measured on both airfoil sides at the trailing edge [3]. A criterion is missing for *laminar* airfoils with a blunt trailing edge described by a local circular arc.

Table 2 Blake's acoustic sharpness parameter [3] calculated for the DNS cases.

x_t/c	0.965	0.980	0.985	0.988	0.990	0.995
$(h/c)\ /\delta^*_{suc}\ [\times 10^{-1}]$	7.633	4.058	2.998	2.377	1.935	0.957
$(h/c)\ /\delta^*_{pres}\ [\times 10^{-1}]$	6.047	2.877	1.968	1.522	1.291	0.609
$(h/c)\ /\delta^*_{tot}$	1.3680	0.6935	0.4966	0.3899	0.3226	0.1565

Therefore, the parameter is calculated for the six DNS cases (*table 2*). The local-reconstruction method proposed in [14] was used to calculate the boundary layer thickness. Given the difference in magnitude and the accountability of different phenomena happening on the two airfoil sides, it is here proposed that the parameter should be calculated separately for the two airfoil sides. For the flow conditions at hand, transition between cases without and with reattachment happens at $(h/c)\ /\delta^*_{pres} \approx 0.197$. With side tones radiated often for cases with a smaller value. The ratio of the same parameter calculated at the trailing edge and at the separation point for the transitional case is 1.946. With cases radiating side tones having a bigger ratio.

The different hydrodynamic fields on the airfoil pressure side are associated with different acoustic fields. With the directivity curves, shown in *figure 3(a)*, that do not simply scale, given a different airfoil trailing edge thickness. The main directivity angle does not change notably. But it is observed that the blunter the airfoil trailing edge, the more directional the overall acoustic signature is. A second lobe is more evident for airfoils without a reattachment region on the pressure side because of the absence of interference by additional side tones. Indeed, the missing lobe becomes evident for all the cases when the directivity plot is filtered in a band-pass interval

centred at the unstable frequency of the suction-sided laminar separation bubble, as shown in *figure 3(b)*.

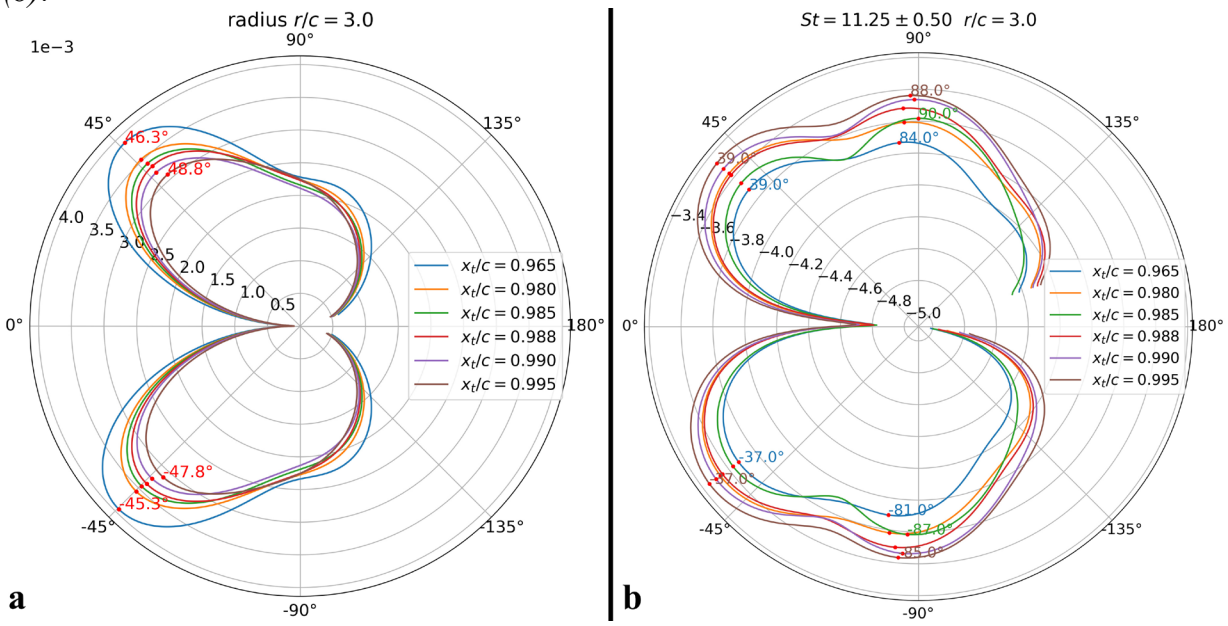


Figure 3 Directivity plot of the root-mean-squared pressure fluctuations recorded at a distance $r/c = 3.0$ from the airfoil trailing edge: (a) non-filtered, (b) filtered around the Tollmien-Schlichting frequency.

High frequency second tones are observed to be radiated *often* only for the cases with a reattachment region on the airfoil pressure side. This is visible in the instantaneous dilatation field, as shown in *figure 4(a)*. And since the time derivative of density balances the divergence of the velocity field, which can be used to visualise the acoustic field, the high-frequency second tones become visible in the power spectral density of the time-derived pressure fluctuations as well, as shown in *figure 4(b)*. With some peaks at higher frequencies and an evident lower decay rate for airfoils exhibiting a pressure-sided reattachment region.

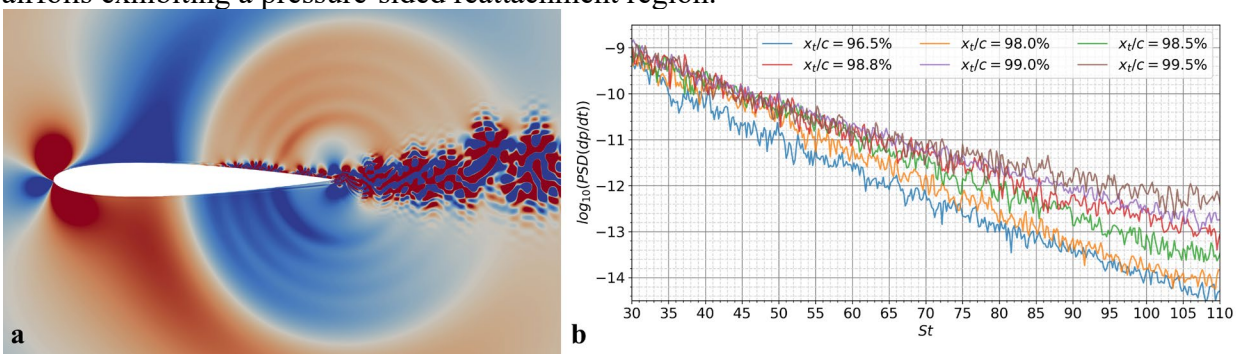


Figure 4 (a) Side tones visible in the instantaneous dilatation field. Range is chosen to highlight the second tones, with the side effect of the wake and laminar separation bubble on the airfoil suction side that look noisier than they are. (b) Power spectral density of the time-derived pressure recorded at $(x/c, y/c)=(0.0;1.0)$, calculated applying the Welch method with a Hann window long 5 flow-through-time units and 50% overlap.

High frequency *consecutive* secondary tones are seen to arise from the interaction of one or two eddies in close proximity of the airfoil trailing edge, with the latter acting as a scattering source. This is visible in *figure 5*. Here a vortex is growing in the recirculation region downstream of the trailing edge, thanks to the locally re-attached flow downstream of the laminar separation bubble

Materials Research Proceedings 69 (2026) 112-118 https://doi.org/10.21741/9781644904251-20

on the airfoil pressure side. When a local region of opposite sign of vorticity, which follows the vortex just shedded from the suction-side, slips over the mentioned small vortex. The pressure fluctuations related to the interaction of these two local concentrations of vorticity of opposite sign is scattered by the trailing edge in high-frequency side tones.

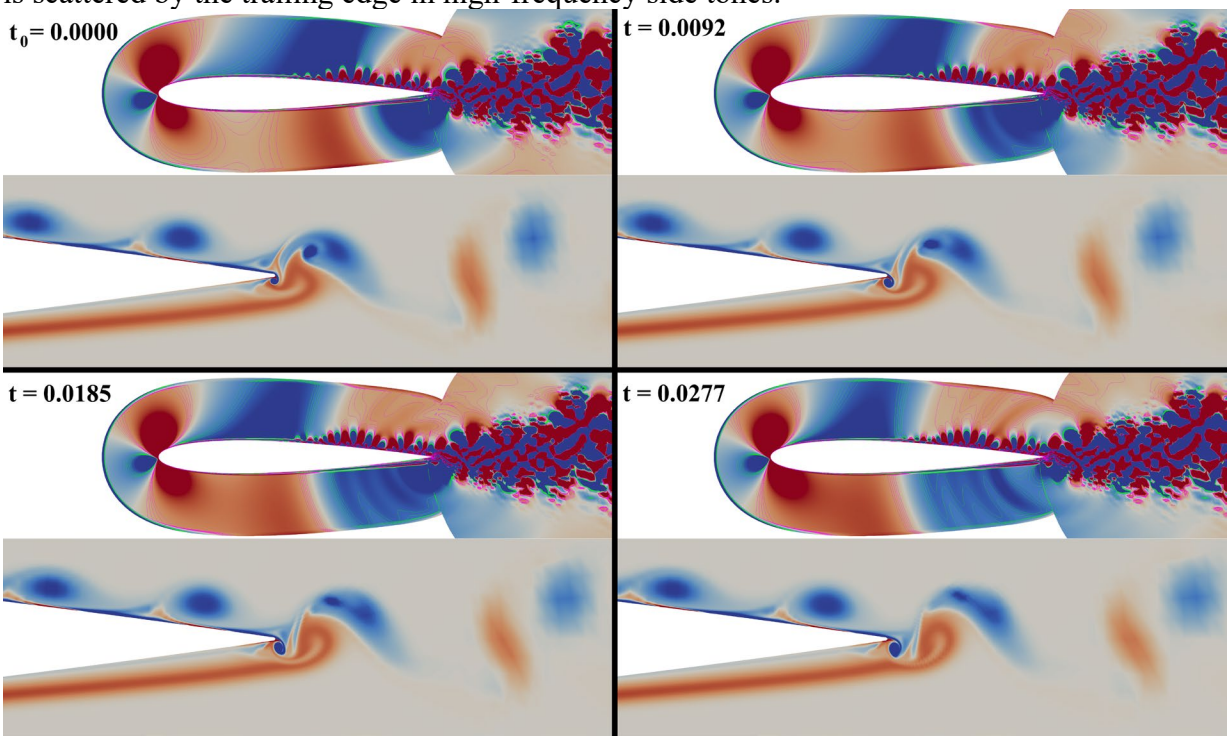


Figure 5 Interaction of vortices behind the generation of high-frequency side tones for the sharpest airfoil trailing edge case. Spatial distribution of the divergence of the velocity vector [upper row] and of its vorticity [bottom row].

A *single* secondary tone is observed to be emitted *rarely* in the cases without a reattachment region for the laminar boundary layer developing on the airfoil pressure side. In this case (*figure 6*), the tone is generated by the spinning of a vortex at the trailing edge. This vortex sheds in phase opposition with respect to the incoming vortex convected from the suction side. Therefore, the incoming vortex does not scatter energetically at the trailing edge and the associated tone is quieter.

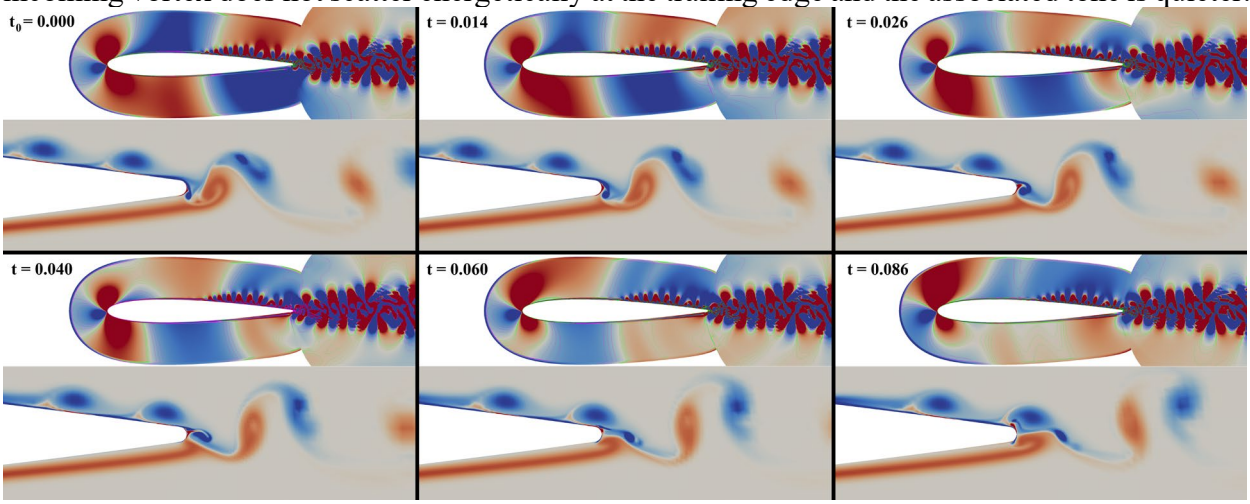


Figure 6 Interaction of vortices behind the generation of high-frequency side tones for the bluntest airfoil trailing edge case. Spatial distribution of the divergence of the velocity vector [upper row] and of its vorticity [bottom row].

Conclusions

At a moderate Reynolds number and for a nearly incompressible flow, varying the airfoil trailing edge thickness while keeping unitary chord length allows the laminar flow to reattach on the airfoil pressure side. The present paper shows for the first time how the presence of a reattached laminar flow is associated with a different acoustic field. Therefore, existing empirical parameters aimed at determining when an airfoil can be considered acoustically sharp or not do not consider such phenomenon. Specifically, the acoustic field changes because of the presence of additional secondary tones. Sharper cases with a reattachment region promote different interactions between vortices rolled up from the laminar separation bubbles on the two airfoil sides and convected past the airfoil trailing edge. These eddy-with-eddy self-sustained interactions generate high-frequency secondary consecutive tones. On the contrary, the absence of such interactions in cases without a reattachment, make secondary single tones possible only rarely and due to a non-self-sustained offset in the main shedding frequency.

Acknowledgements

The bulk of the computing time of the simulations was provided by the *LIEF HPC-GPGPU* Facility hosted at the University of Melbourne and by the *Pawsey Supercomputing Center* in Perth, thanks to the Australian *National Computational Merit Allocation Scheme*.

References

[1] T. Brooks, D. Pope e M. Marcolini, «Airfoil self-noise and prediction.,» NASA Reference Publication 12181, 1989.

[2] W. K. Blake e J. L. Gershfeld, «The Aeroacoustics of Trailing Edges,» in Frontiers in Experimental Fluid Mechanics. Lecture Notes in Engineering, 1989. https://doi.org/10.1007/978-3-642-83831-6_10

[3] W. Blake, «Mechanics of flow-induced sound and vibration, vol II,» Applied Mathematics and Mechanics, Frenkiel, FN and Temple, Academic Press, 1986, pp. 423-430.

[4] E. C. Nash, M. V. Lowson e A. McAlpine, «Boundary-layer instability noise on aerofoils,» Journal of Fluid Mechanics, n. 382, pp. 27-61, 1999. https://doi.org/10.1017/S002211209800367X

[5] A. McAlpine, E. C. Nash e M. V. Lowson, «On the generation of discrete frequency tones by the flow around an airfoil,» Journal of Sound and Vibration, vol. 5, n. 222, pp. 753-779, 1999. https://doi.org/10.1006/jsvi.1998.2085

[6] B. Plogmann, A. Herrig e W. Würz, «Experimental investigations of a trailing edge noise feedback mechanism on a NACA 0012 airfoil,» Exp. Fluids, vol. 54, n. 1480, 2013. https://doi.org/10.1007/s00348-013-1480-z

[7] D. L. Smith, A. R. Bayer, R. D. Talmadge e R. P. Paxon, «Test report on measurements of the radiated noise from a Schweizer 2-32 sailplaine with and without a wing mounted multi-strut assembly,» Air Force Flight Dynamics Laboratory (U.S.), 1973.

[8] L. T. Clark, «The radiation of sound from an airfoil immersed in a laminar flow,» J. Eng. Power, vol. 93, n. 4, pp. 366-376, 1971. https://doi.org/10.1115/1.3445595

[9] A. S. Hersh e R. E. Hayden, «Aerodynamic sound radiation from lifting surfaces with and without leading edge serrations,» Technical Report CR1144370, NASA, 1971.

[10] R. W. Paterson, P. G. Vogt e M. R. Fink, «Vortex noise of isolated airfoils,» Journal of Aircraft, vol. 10, n. 5, pp. 296-302, 1973. https://doi.org/10.2514/3.60229

[11] C. K. W. Tam, «Discrete tones of isolated airfoils,» The Journal of the Acoustical Society of America, vol. 55, n. 6, pp. 1173-1177, 1974. https://doi.org/10.1121/1.1914682

[12] M. Lowson, S. Fiddes e E. Nash, «Laminar boundary layer aero-acoustic instabilities,» AIAA, 1994-358, 32nd Aerospace Sciences Meeting and Exhibit. https://doi.org/10.2514/6.1994-358

[13] S. Pröbsting, Y. Yang, H. Zhang, P. Li, Y. Liu e Y. Li, «Effect of Mach number on the aeroacoustic feedback loop generating airfoil tonal noise,» Physics of Fluids, vol. 34, n. 9, 2022. https://doi.org/10.1063/5.0107181

[14] K. P. Griffin, L. Fu e P. Moin, «General method for determining the boundary layer thickness in nonequilibrium flows,» Phys. Rev. Fluids, vol. 6, n. 2, pp. 024608-024631, 2021. https://doi.org/10.1103/PhysRevFluids.6.024608

Materials Research Proceedings 69 (2026) 119-124 https://doi.org/10.21741/9781644904251-21

Computational Analysis of a Multistage Nose Spike to Reduce Drag on a Conceptual Supersonic Transport Aircraft

Joseph Ciano Pinto[1,a], Siva Marimuthu[1,b*], Parvathy Rajendran[2,c], Rajadurai Murugesan[3,d]

[1]Department of Engineering, University of Staffordshire, Stoke on Trent, United Kingdom

[2]School of Aerospace Engineering, University Sains Malaysia, Seberang Perai, Malaysia

[3]Department of Aeronautical Engineering, Nitte Meenakshi Institute of Technology, Bengalore, India

[a]Josephpinto002@gmail.com, [b]siva.marimuthu@staffs.ac.uk, [c]aeparvathy@usm.my, [c]mrajadurai700@gmail.com

Keywords: Aerodynamics, Supersonic Aircraft, Drag Reduction, Nose Spike

Abstract. Supersonic commercial aircraft have the potential to greatly reduce global travel times, but key challenges, such as high fuel consumption due to increased drag at supersonic speed, remain a barrier to commercial feasibility. In this study, a Concorde-like delta wing aircraft was modelled and analysed using ANSYS Fluent at different Mach numbers, such as Mach 0.8, 1.02,1.5 and 2. During supersonic flight, significant aerodynamic drag is generated primarily due to wave drag. A multi-stage nose spike was designed and tested to reduce the drag. Results indicate that a stage 4 spike reduced the total drag by 4.23% at Mach 1.5, and the Lift to Drag ratio has increased by 3.9%. The simulation results were compared and validated against results from a previous research paper It is recommended that at subsonic speed, the spike be retracted in position 1, position 2 is optimal for transonic speeds, and position 4 performs best at supersonic speeds.

Introduction

Commercial supersonic flight ended with the Concorde retirement in 2003 after nearly three decades of operation with British Airways and Air France. Despite its technological success, Concorde faced two major challenges the sonic boom, which restricted supersonic flight over land and high operating costs due to poor fuel efficiency. Both issues arise from the physics of supersonic flight, as an aircraft approaches and exceeds Mach 1, which is the speed of sound, the air in front of the aircraft begins to compress, resulting in the formation of shock waves. These shock waves not only produce a sonic boom but also introduce a component of drag known as wave drag, which can increase the total drag by more than 50% [1]. This significant increase in drag is responsible for the poor fuel efficiency of supersonic flight. There is renewed interest in the commercial supersonic market, with companies such as Boom Supersonic actively working to bring back supersonic commercial flight. The market is projected to be valued at USD 70 billion by 2034 [2]. However, aviation currently contributes approximately 2.5% of global carbon emissions, highlighting the need for a solution to make commercial supersonic travel environmentally viable [3].

Improving fuel efficiency and reducing drag in supersonic flight was greatly advanced by the development of the area rule in the 1950s[4]. This rule demonstrates that the significant increase in drag at transonic and supersonic speeds is heavily influenced by the longitudinal distribution of the cross-sectional area. A smooth and gradual change in cross-sectional area will minimise the increase in drag. [5]Supersonic fuselage designs often include a bottleneck section near the wings to reduce the change in cross-sectional area distribution. While it is effective at reducing drag,

Content from this work may be used under the terms of the Creative Commons Attribution 3.0 license. Any further distribution of this work must maintain attribution to the author(s) and the title of the work, journal citation and DOI. Published under license by Materials Research Forum LLC.

Materials Research Proceedings 69 (2026) 119-124 https://doi.org/10.21741/9781644904251-21

such a design compromises the cabin layout and limits the number of passenger seats [6] creating challenges for commercial aviation. [7]Variable sweep wings allow an aircraft to optimise performance at low and high Mach numbers. The wings sweep back to reduce the cross-sectional area change as the Mach number increases. However, the mechanisms are heavy, complex and difficult to maintain. [8]Extended nose designs, such as the NASA X-59, reduce the strength of the initial shock by distributing it along the length of the nose. Such a design does, however, limit pilot visibility, which is essential for certification in commercial applications. An alternative approach is the use of a slender retractable nose spike, [9] Gulfstream Aerospace has previously experimented with an extendable nose boom concept that extends in front of the fuselage at high speeds to break up the strong initial shock into subsequent smaller shocks, and the spike would be retracted at lower speeds, such as for take-off and landing. Gulfstream developed this concept to avoid impacting the internal cabin and cargo space. The concept was tested in an F15 platform, but its application for commercial supersonic aircraft has not been analysed. This study will examine the aerodynamic benefits of a multi-stage spike in reducing drag for supersonic transport aircraft. A simplified Concorde-type model will be analysed using computational fluid dynamics with baseline lift and drag values evaluated at Mach 0.8,1.02,1.5 and 2. Testing done by Gulfstream showed that while a single stage spike reduced the initial overpressure, multistage spikes effectively split the primary shock, lowering peak overpressure [10] .

Design

The baseline configuration was derived from a Concorde-type design from a previous analysis [11]. The long and slender fuselage, along with the ogive delta, was designed on Fusion 360 with the NACA 64A210 aerofoil being utilised. The Fuselage section was generated from longitudinal and cross-sectional sketches, which were mirrored about the centreline. The final base model measured 62 m in length. The wing geometry was produced by lofting the aerofoil section with the leading and trailing edge curves. The final wingspan measures 25.46 m Finally, the vertical stabiliser and the engine inlets were modelled. For computational fluid dynamics (CFD), all components were unified into a single body and uniformly scaled down by a factor of 1:10. The scaled-down dimension measures 6.2 m in length and a span of 2.54 m. This was done to reduce the computational time and allow for a denser mesh. A multistage nose spike consisting of four different stages was designed with the modification beginning from the approximate location of the bulkhead in front of the cockpit. The retracted stage measures 0.69 m in length with a radius of 224mm, while the fully extended stage measures 2.59 m in length. The spike proportions were based on a ratio derived from Gulfstream Aerospace. Figure 1 show the base and the multistage spike configurations and figure 2 shows the four different spike stages.

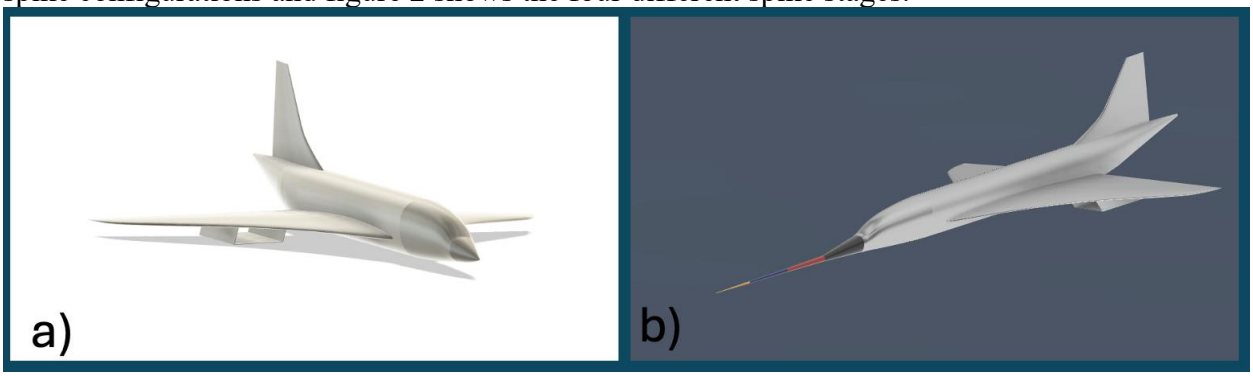


Figure 1 a) Base configuration b) Multi-Stage spike configuration

Materials Research Proceedings 69 (2026) 119-124 https://doi.org/10.21741/9781644904251-21

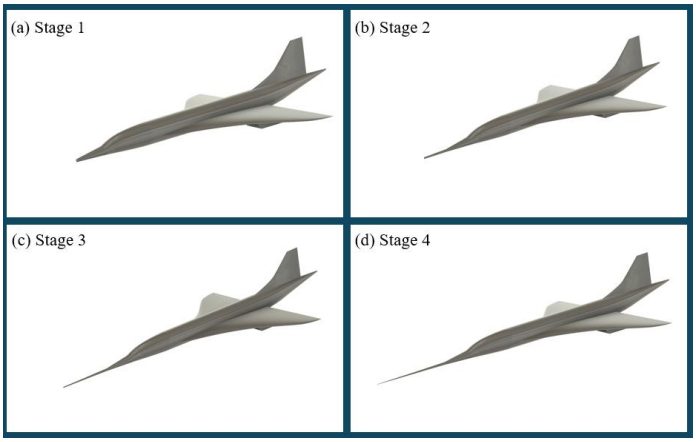


Figure 2 Four different Spike Stages

Computational Analysis

ANSYS Fluent was used to conduct the CFD simulation. The aircraft model geometry was imported into Design Modeller, and a C-Type domain was generated 40 m upstream and 60 m downstream. The aircraft model was subtracted from the domain using a Boolean command. The mesh generation was carried out using Fluent's watertight meshing. A poly hexacore mesh was used, and an inflation layer with 20 layers and a target wall y+ of 5 was applied to accurately resolve the boundary layer. The final mesh contained approximately 800,000 cells with an average orthogonal quality and skewness of 0.97 and 0.0024, respectively. A mesh-independent study was performed to ensure the accuracy of the results. The simulations were performed using a steady-state density-based solver. The K -ω SST turbulence model was employed as it is good at capturing the boundary layer Curvature correction and compressibility effect were enabled to improve accuracy[12]. The ideal gas model and Sutherland viscosity model were used to model the air properties. The Boundary conditions include a pressure far field and a pressure outlet based on the simulation setting from a base reference paper. The aircraft surface was defined as a no-slip wall. The operating conditions were based on standard atmospheric data at four Mach numbers 0.8,1.02,1.5 and 2. All cases were analysed at a 5-degree angle of attack. The implicit solver was used along with Solution steering to improve convergence and stability. The lift and drag coefficient was analysed and compared against the base reference paper to validate the results, following which the multi-stage spike was implemented and analysed under the simulation conditions from table 1 .

Table 1 Simulation conditions

Mach number	Angle of attack (degrees)	Altitude (m)	Temperature (K)	Pressure (Pa)	Density ($Kg.m^{-3}$)
0.8	5	5090	255.09	53402	0.7359
1.02	5	7940	236.60	35961	0.5248
1.5	5	18288	216.65	7231.20	0.1206
2	5	18288	216.65	7231.20	0.1206

Materials Research Proceedings 69 (2026) 119-124 https://doi.org/10.21741/9781644904251-21

Results

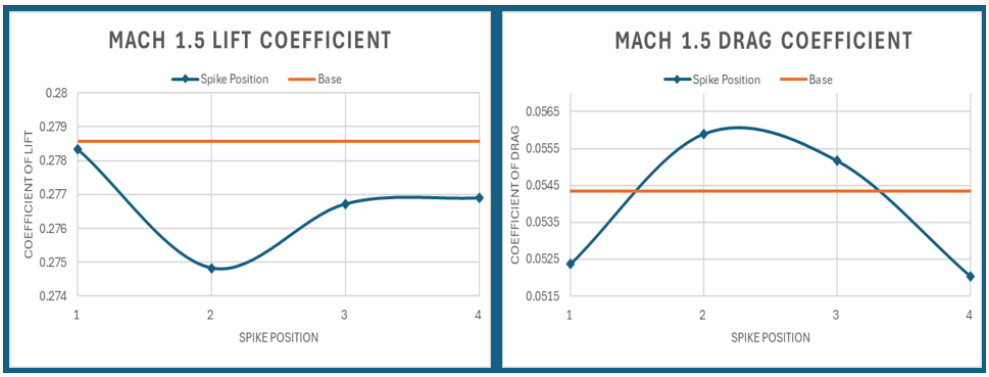


Figure 3 Lift and Drag Coefficient

At Mach 1.5, the baseline configuration produced a lift coefficient of 0.2786. With spike position 1, lift decreased marginally to 0.2783, a 10% decrease. The lowest lift was observed at position 2, while positions 3 and 4 had only a 0.6% decrease in lift relative to the baseline
In terms of drag, the baseline coefficient was 0.0543. Spike 1 reduced drag to 0.524, representing a 3,6% improvement. Position 4 achieved the greatest drag reduction with a 4.2% decrease in the drag coefficient. Considering both lift and drag, position 4 produced the most favourable lift-to-drag ratio. Thus, spike position 4 was identified as the most aerodynamically effective configuration at Mach 1.5

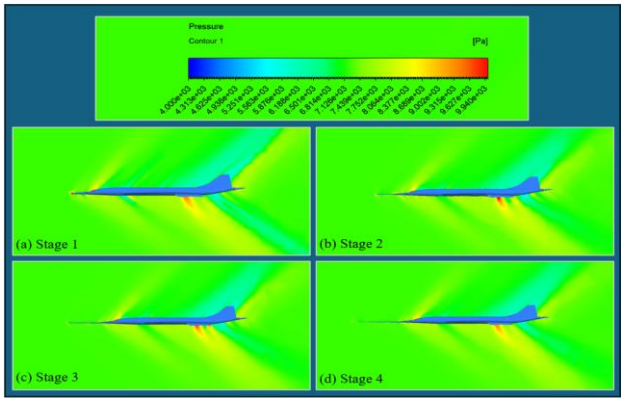


Figure 4 Spike stages pressure contours

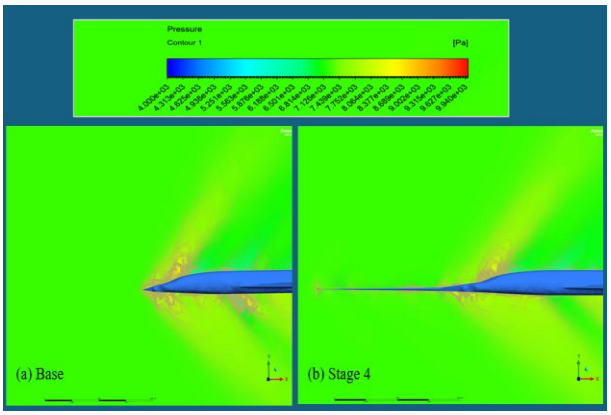


Figure 5 Nose Close-up Pressure Contours

The pressure contours in figure 4 further support these results. Across all supersonic cases, shock waves originated at the nose of the aircraft, with the shock deflection angle increasing as the Mach number increased. However, their intensity diminished progressively with the extension of the spike. The stage 4 configuration displayed notably weaker and more diffuse shocks, indicating improved shock mitigation at higher Mach numbers. Pressure distribution ranged between 4000 Pa and 9000 Pa. Overall, the analysis demonstrates that a multistage spike can efficiently reduce drag and improve aerodynamic efficiency at supersonic speeds.

A more detailed comparison in figure 5 of the baseline configuration with the stage 4 spike configuration clearly shows the representation of the shockwaves. The colour scale ranges from 4000 Pa in blue to 9000 Pa in red, with the green corresponding to approximately 7000 Pa, the atmospheric pressure at an altitude of 18000 m. In the base configuration, a strong singular shock was observed at the nose of the aircraft. The pressure contour in this region reaches close to 8800 Pa, significantly above the standard atmospheric pressure. This concentrated rise in pressure is a characteristic of wave drag due to the formation of a strong supersonic shock. By contrast, in the stage 4 spike configuration, instead of a single strong shock, there are multiple weaker shocks

distributed along the length of the spike. These shocks appear to not coalesce, resulting in a lower intensity. This diffusion of the shock strength indicates improvements in reducing the wave drag and the overall total drag on the aircraft. Analysing the Lift to drag ratio across 4 different Mach numbers and spike positions, at Mach 0.8, the baseline achieves the highest L/D However, using a spike reduces the efficiency in subsonic Mach numbers. In the transonic regime, Mach 1.02 spike position 2 provides a 1.5% increase in the L/D. At supersonic Mach numbers, spike position 4 increases the L/D by 3.9% at Mach 1.5 and 0.38% at Mach 2. Based on these results, the spike should remain retracted at subsonic speeds, partially extended to position 2 at transonic speeds and fully extended at position 4 in supersonic flight to maximise aerodynamic efficiency and reduce drag, which will contribute to lower fuel consumption and emissions.

The results were validated against values from a previous study. Comparing the values at Mach 1.5, the coefficient values from the analysis deviated by only 3.77% and 5.54 % for the lift and drag coefficient values, respectively, from the reference study. Additionally, a mesh-independent study was conducted to ensure that the mesh quality did not affect the results, as can be seen in figure 6

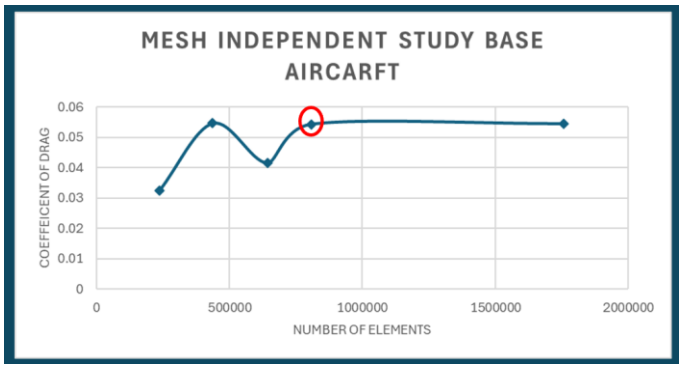


Figure 6 Mesh Independent Study

Conclusion

This study investigated the aerodynamic performance of a supersonic transport aircraft using a multi-stage nose spike to reduce total drag. Using CFD simulation in Ansys Fluent at Mach numbers 0.8,10.2,1.5 and 2, the lift and drag coefficients were analysed along with pressure contours. Results indicate that while the spike reduces efficiency in subsonic conditions. At Mach 1.5, the stage 4 position reduces drag by 4.23% and improves the lift to drag ratio by 3.9%. Pressure contours indicate that the spike diffuses the strong nose shock into multiple weaker shocks, reducing the drag. These results highlight the potential of a multistage nose spike for enhancing the aerodynamic performance and reducing drag and fuel consumption for future supersonic passenger aircraft.

References

[1] Boom Supersonic, "Aerodynamics 101: The Shape of Supersonic," 2022. Available: https://boomsupersonic.com/flyby/aerodynamics-101-the-shape-of-supersonic#:~:text=Pressure%20waves%20form%20in%20front,%2C%20100%25%2C%20or%20more

[2] A. Shivarkar, "Commercial supersonic aircraft market size, share and trends 2025 to 2034," 2025Available: https://www.precedenceresearch.com/commercial-supersonic-aircraft-market#:~:text=The%20global%20commercial%20supersonic%20aircraft%20market%20size%20was%20estimated%20at,4.30%25%20from%202025%20to%202034

[3] National Academies of Sciences, Engineering, and Medicine et al, Commercial Aircraft Propulsion and Energy Systems Research. (1st ed.) 2016Available: https://nap.nationalacademies.org/23490. DOI: 10.17226/23490

[4] J. G. Leishman, Introduction to Aerospace Flight Vehicles. 2023Available: https://eaglepubs.erau.edu/introductiontoaerospaceflightvehicles/

[5] K. Mizobata, T. Mio and K. Miyamoto, "Drag Reduction on the Basis of the Area Rule of the Small-Scale Supersonic Flight Experiment Vehicle Being Developed at Muroran Institute of Technology (Second Report)," Aerospace, vol. 11, (9), pp. 777, 2024. Available: https://www.proquest.com/docview/3110282765. DOI: 10.3390/aerospace11090777

[6] Available: https://ntrs.nasa.gov/citations/20080004528, 1999

[7] Radhakrishnan P et al, "Aerodynamic Performance Analysis of a Variable Sweep Wing for Commercial Aircraft Applications," ACS Journal for Science and Engineering, vol. 1, (1), pp. 31–37, 2021. Available: https://acsjse.in/index.php/acsjse/article/download/5/5. DOI: 10.34293/acsjse.v1i1.5

[8] A. Donaldson. (Jan 14). NASA, Lockheed Martin Reveal X-59 Quiet Supersonic Aircraft. Available: https://www.nasa.gov/news-release/nasa-lockheed-martin-reveal-x-59-quiet-supersonic-aircraft/

[9] F. Simmons III and D. Freund, "Quiet Spike(TM): The Design and Validation of an Extendable Nose Boom Prototype," AIAA Paper, 2007. Available: https://www.proquest.com/docview/30106560

[10] Donald Howe, "Improved sonic boom minimization with extendable nose spike," in 43rd AIAA Aerospace Sciences Meeting and ExhibitAnonymous . DOI: 10.2514/6.2005-1014

[11] A. Aprovitola et al, "Aerodynamic Analysis of a Supersonic Transport Aircraft at Low and High Speed Flow Conditions," Aerospace, vol. 9, (8), pp. 411, 2022. Available: https://www.proquest.com/docview/2706028797. DOI: 10.3390/aerospace9080411

[12] ANSYS. Fluent User's Guide. Available: https://ansyshelp.ansys.com/public/account/secured?returnurl=/Views/Secured/corp/v242/en/flu_ug/flu_ug.html.

Materials Research Proceedings 69 (2026) 125-129 https://doi.org/10.21741/9781644904251-22

Computational Analysis to Improve the Aerodynamic Performance of NACA 0012 in Transonic Flow Using Raw Riblet Patterns

Siva MARIMUTHU[1,a *], Sheikh ISLAM[1,b], Parvathy RAJENDRAN[2,c], Rajadurai MURUGESAN[3,d]

[1]Department of Engineering, University of Staffordshire, Stoke on Trent, United Kingdom

[2]School of Aerospace Engineering, University Sains Malaysia, Seberang Perai, Malaysia

[3]Department of Aeronautical Engineering, Nitte Meenakshi Institute of Technology, Bengaluru, India

[a]siva.marimuthu@staffs.ac.uk, [b]sheikh.islam@staffs.ac.uk, [c]aeparvathy@usm.my, [c]mrajadurai700@gmail.com

Keywords: Computational Analysis, Viscous Drag, Raw-Riblets, Surface Pattern

Abstract. Emission reduction is of global importance and a big challenge in the aviation industry. In this research project, the emission issue was addressed aerodynamically by improving the performance of wings in transonic flow. This improvement was achieved by implementing a Raw-riblet pattern at different locations on the top surface of the wing as this showed higher values of viscous drag. Viscous drag is a large composition of total drag and reducing them will help to reduce the fuel consumption of aircraft and effectively reduce the carbon emissions. Two types of designs named Low-depth (0.305) and Low-depth (0.455) patterns were developed based on the 'Raw Riblet'. Computational analyses were carried out in the commercial code FLUENT with the help of the Spalart-Allmaras turbulence model to capture the viscous drag issues on the normal NACA 0012 wing at different angles of attack and solved them using the biomimetic patterns implemented. It was evidenced in this research work that the Low-depth (0.455) Raw Riblet pattern could reduce a significant amount of viscous drag on the NACA wing when compared to the Low-depth (0.305) pattern. Compatibility tests were done to check the suitability and stability of the model and mesh, respectively, and compared them to the experimental results. This research demonstrated the potential of surface texture-based solutions for aerodynamic design improvement and emission reduction.

Introduction

Commercial aviation has grown every year. Airbus has forecasted 43420 new aircraft deliveries between 2025 and 2044 [1]. This will increase aviation emissions in near future. Xueli et al., mentioned in their work that carbon emissions are a concern in the aviation industry [2]. Carbon emission from commercial aviation is expected to contribute 25% of overall emissions by 2050 [3]. It is essential that this issue needs to be addressed. Feuvre [4] stated that the aviation industry is committed to reducing carbon emissions by 50% in the year 2050. To mitigate this issue, a number of research are still carried out in the areas of propulsion, aerodynamics, structures, aircraft design and beyond. Capoccitti et al., [5] discussed about three important areas for researchers to look at in order to reduce the use of fossil fuels. They are structural (weight), propulsion (engine) and aerodynamic improvements. Out of these three elements, aerodynamic improvement was selected in this research project and it can be achieved by reducing drag on aircraft [6]. The longest phase of a commercial aircraft is the cruise and in that flight phase, the amount of skin-friction drag generation would be as high as 50% of total drag [7]. Skin friction drag, which is also known as viscous drag, is generated because of the contact (sliding motion, especially) between the aerodynamic body and air particles. Kumar et al., [8] reviewed five types of viscous drag reduction

Content from this work may be used under the terms of the Creative Commons Attribution 3.0 license. Any further distribution of this work must maintain attribution to the author(s) and the title of the work, journal citation and DOI. Published under license by Materials Research Forum LLC.

Materials Research Proceedings 69 (2026) 125-129 https://doi.org/10.21741/9781644904251-22

methods and concluded that surface morphology is the most reliable method because it has been verified both computationally and experimentally. Liu et al., [9] proved in their research work that the surface structures could reduce the disturbances in the fluid flow. Lloyd et al., [10] mentioned in their research that shark-skin mimicked structures have evolved as a mechanism to reduce skin friction. The most common method used to develop a surface structure is biomimetics. In this method, the solutions are observed and mimicked from nature to solve the issues in engineering sciences. Our previous research works on shark skin inspired surface patterns had proved that a significant amount of drag reduction could be achieved in airflow [11-14]. Hence, in this research, the same 'Raw Riblet' pattern was implemented on the chosen wing surface (especially, where the issues identified) in different ways to reduce the skin friction drag, which is the main aim of this research.

Computational Design

Using the coordinates from airfoiltools.com [15], the NACA 0012 aerofoil was generated in the SolidWorks software and it was then extruded into a three-dimensional model, as shown in Fig. 1(a). In previous research work [11], the Raw Riblet (RR) pattern, which is shown in Fig. 1(b), was developed using the scanning microscopic image of a Requiem shark. This RR pattern was then implemented on the NACA 0012 wing surface in two different positions based on the issues observed. Fig. 1(c) depicts the implemented hollow RR pattern near the leading edge with a cut-depth of 0.455 metres from the top to mid-surface and hence, called a one low depth RR (1-LRR, 0.455) model. Similarly, another design was made by reducing the cut-depth from 0.455 to 0.305 metres for analysing the influence of depth in the performance of the RR pattern and hence, called the one lower depth RR (1-LRR, 0.305) model, which is shown in Fig. 1(d). All these designs were then exported to IGES format and imported into ANSYS.

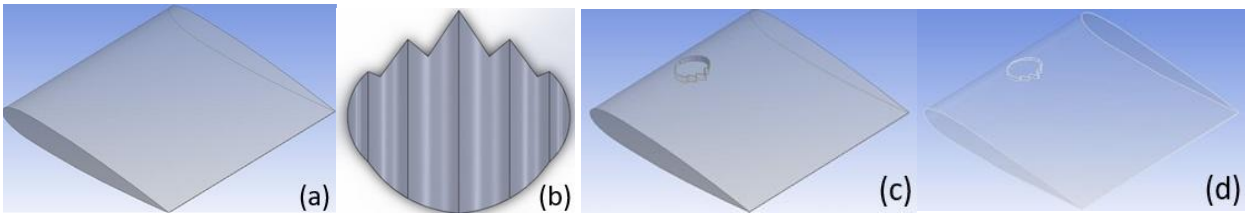


Figure 1. (a) NACA 0012, (b) Top view of RR[11], (c) 1-LRR (.455), (d) 1-LRR (0.305)

Computational Analysis

The three-dimensional NACA 0012 wing was imported into ANSYS Design Modeler and a computational domain was created. With the use of the Boolean tool, the solid boundary and wing were defined. This was then read into Mesh, where all the solid surfaces of the wing were named as top, bottom, trailing edge and riblets. The outer computational domain was considered the control volume, through which the air flows. Higher order elements and program-controlled automatic inflation were opted to minimise the errors and not inflate the selected boundaries, respectively. Most of the settings were set to default and the mesh was generated with 1.9 million nodes and 1.3 million elements. Quality check was carried out and the meshed design was brought into Fluent and the polyhedral mesh was selected, which helped reduce the element size, nodes and computational time. The Spalart-Allmaras viscous model was chosen as it involves the solution of the kinematic turbulent viscosity transport equation only, and it agrees well with experimental results [16]. Hence, less effort is required to solve when compared to other models. As the Eulerian approach was selected, the angle of flow was modified. A coupled solution method was chosen and discretization variables were defined as second order to reduce the time in solving the equations and then the iterations were done. These simulations were repeated for different angles of attack (0^0, 3^0, 6^0, 9^0, 12^0), in the 0.8 Mach number flow, which matched the cruise speed

Materials Research Proceedings 69 (2026) 125-129 https://doi.org/10.21741/9781644904251-22

of commercial flights in general. The same computational simulation procedure was repeated for 1-LRR (0.455) and 1-LRR(0.305) models.

Results and Discussion

Outputs such as lift coefficient and viscous drag values were noted at the end of analyses. Based on the comparison between the lift coefficient results, which is shown in Fig. 2(a), it was observed that both 1-LRR(0.455) and 1-LRR(0.305) had generated the same levels of lift at 3^0, 6^0, 9^0 and slightly lesser levels of lift at 0^0 and 12^0, when compared to the NACA 0012. These are acceptable levels and thus demonstrate potential in biomimetic designs. Similarly, comparing the viscous drag results against angle of attack, as shown in Fig. 2(b), it was identified that both biomimetic designs performed very well in reducing the drag when compared to the original wing at all of angles of attack. When the angle of attack was increased, the rate of viscous drag reduction was observed largely in both biomimetic designs.

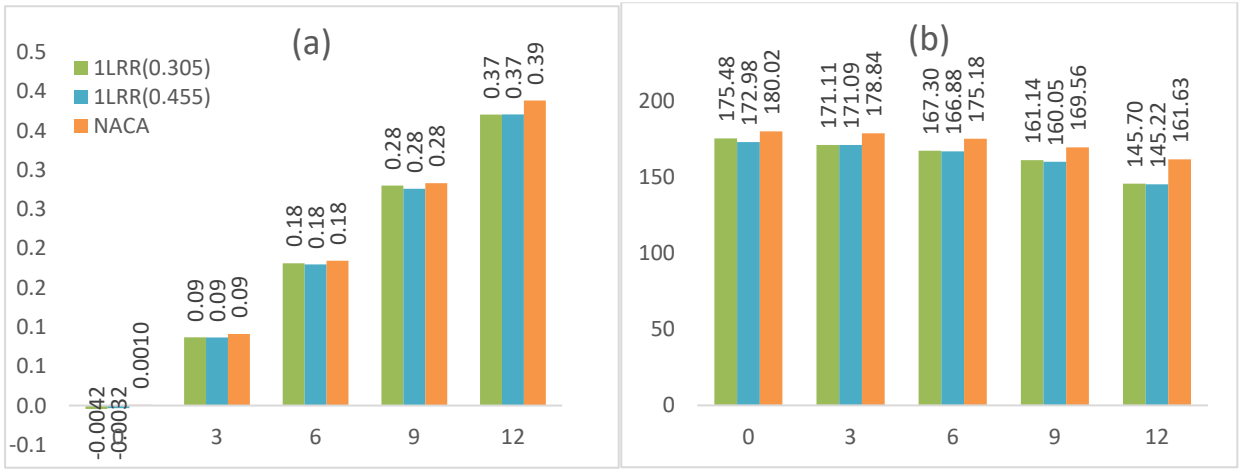


Figure 2. (a) Lift Coefficient Vs Angle of Attack, (b) Viscous Drag Vs Angle of Attack

1-LRR (0.455) reduced the viscous drag between the range 3.91 and 10.15 % from 0^0 to 12^0 angles of attack. Although 1-LRR(0.305) model has reduced the drag in the range of 2.52 to 9.85%, it is still a bit less than the deeper 1-LRR (0.455) model. For example, at 12^0 angle of attack, NACA 0012's top surface has medium and low values of skin friction drag as shown in Fig. 3(a). This is higher when compared to both biomimetic designs. Fig. 3(b) and (c) illustrate the skin friction contours of 1-LRR(0.455) and 1-LRR(0.305), respectively. From these figures, it can be noted that the skin friction distribution values on 1-LRR(0.455) were much lower compared to those on 1-LRR(0.305). This is due to the differences in the depths of the hollow raw riblet patterns applied on the models. The hollow pattern enabled the reversed flow at high angles of attack to circulate, lift, re-reverse/straighten and join the mainstream flow. This reduced the disturbance in the flow, which led to a reduction in the skin-friction coefficient.

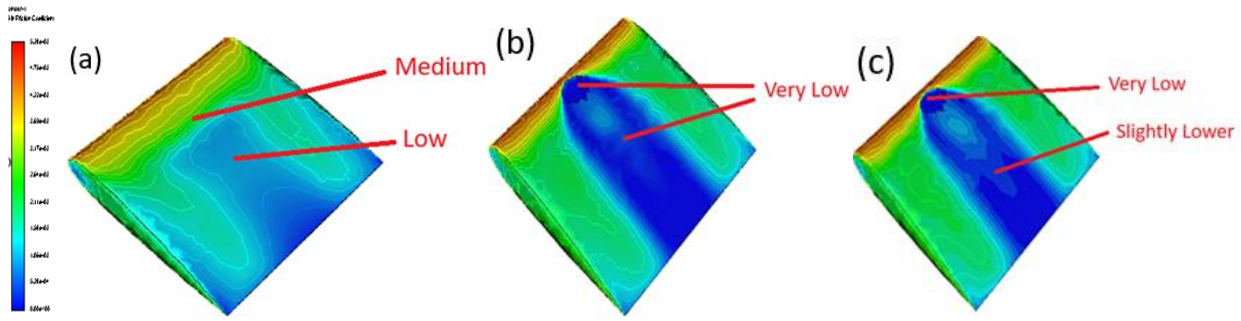


Figure 3. Skin Friction Contour at 12^0: (a) NACA 0012, (b) 1-LRR (0.455), (c) 1-LRR (0.305)

Validation

Validation tests were carried out to verify the accuracy of the procedure and results. In the model compatibility test, many viscous models such as K-epsilon, K-omega, Transition K-Kl-omega and Spalart Allmaras were used to analyse the NACA 0012, separately, to find a suitable turbulence model for this research. Eventually, the Spalart Allmaras was selected as it resulted in closer agreement with experimental values. In order to find a suitable mesh, a grid compatibility test was conducted. This was done by meshing the NACA 0012 model with their control volume at different mesh element sizes, such as 0.3, 0.4, 0.5, 0.6, 0.7, 0.8, 0.9, 1, 1.5 and 2 and solving them in Fluent. Additionally, a grid independence test was carried out to ensure the stability of the results. Based on these tests, a 0.5 mesh element size was chosen as it agreed well with the experimental values and had used them the mesh procedure.

Conclusion

As aimed, the viscous drag reduction was achieved in both models using the biomimetic pattern. Especially, the 1-LRR(0.455) model achieved a maximum of 10.15% viscous drag reduction at 120 angle of attack in the transonic flow regime. This aerodynamic improvement would help reduce the fuel consumption requirements and hence, emissions. Overall, this research has proved the potential in the hollow biomimetic raw riblet pattern in reducing the viscous drag and improving the wing aerodynamics. Technical elements such as structural strength of the wing, experimental modelling and tests are to be explored in the future for further enhancement of this work and bringing this idea into reality.

References

[1] Information on https://www.airbus.com/en/products-services/commercial-aircraft/global-market-forecast.

[2] Xiong, X., Song, X., Kaygorodova, A., Ding, X., Guo, L. and Huang, J., Aviation and carbon emissions: Evidence from airport operations, Journal of Air Transport Management, 109, p.102383, (2023), https://doi.org/10.1016/j.jairtraman.2023.102383

[3] Graver, B., and Zhang, K., CO2 emissions from commercial aviation 2018, The International Council on Clean Transportation, pp. 1- 13, (2019).

[4] Feuvre, P.L., Are aviation biofuel is ready for take off?, (2019), https://www.iea.org/commentaries/are-aviation-biofuels-ready-for-take-off.

[5] Capoccitti, S., Khare, A., and Mildenberger, U., Aviation industry - mitigating climate change impacts through technology and policy, Journal of Technology Management and Innovation, pp. 66-75, (2010).

[6] Nath, D.S., Pujari, P.C., Jain, A. et al., Drag reduction by application of aerodynamic devices in a race car, Advances in Aerodynamics, 3, 4 (2021), https://doi.org/10.1186/s42774-020-00054-7.

[7] Ricco, P., Stoke, M., and Leschziner, M.A., A review of turbulent skin-friction drag reduction by near-wall transverse forcing, Progress in aerospace sciences, pp.1-137, (2021).

[8] Kumar, S., Pandey, K.M., and Sharma, K.K., Advances in drag-reduction methods related with boundary layer control – A review, Materials Today: Proceedings 45, pp. 6694-6701, (2021).

[9] Liu, Q., Zhong, S., and Li, L., Effects of Bio-inspired micro-scale surface patterns on the profile losses in a linear cascade, Journal of Turbomachinery, 141(12): 121006, (2019).

[10] Lloyd, C.J., Peakall, J., Burns, A.D., Keevil, G.M., Dorrell, R.M., Wignall, P.B., and Fletcher T.M., Hydrodynamic efficiency in sharks: the combined role of riblets and denticles, Bioinspiration and Biomimetics, 16 (4), pp. 1-17, (2021).

[11] Marimuthu, S., and Chinnathambi, D., Computational analysis of biomimetic butterfly valve, Bioinspired, Biomimetic and Nanobiomaterials, 9 (4): 223–232, (2020), https://doi.org/10.1680/jbibn.20.00027.

[12] Marimuthu, S., Natarajan, S., Ramesh R., and Murugesan, R., Hollow Three-dimensional Model for Fuel Reduction in Aviation Industry, International Journal on Interactive Design and Manufacturing, (2022), https://doi.org/10.1007/s12008-022-00883-4.

[13] Marimuthu, S., Al-Rabeei, S., and Boha, H-A., Three-dimensional analysis of biomimetic aerofoil in transonic flow, Biomimetics (MDPI), 7(1), 20, (2022), https://doi.org/10.3390/biomimetics7010020.

[14] Marimuthu, S., and Chinnathambi, D., Computational Analysis to Enhance the Compressible Flow over an Aerofoil surface, Aircraft Engineering and Aerospace Technology, 93(5), 925-934, (2021), https://doi.org/10.3390/biomimetics7010020.

[15] Information on http://airfoiltools.com/.

[16] Pellerin, N., Leclaire, S., and Reggio, M., An implementation of the Spalart–Allmaras turbulence model in a multi-domain lattice Boltzmann method for solving turbulent airfoil flows. Computers & Mathematics with Applications, 70(12), pp.3001–3018, (2015), https://doi.org/10.1016/j.camwa.2015.10.006.

Materials Research Proceedings 69 (2026) 130-135 https://doi.org/10.21741/9781644904251-23

Advanced Numerical Modeling for Calibration of Heat Flux Sensors for Space Applications

Armando MAIELLO[1,a *], Orsola PETRELLA[1,b] and Angela VOZELLA[1,c]

[1]CIRA, Via Maiorise, 1, 81043 Capua CE, Italy

[a]a.maiello@cira.it, [b]o.petrella@cira.it, [c]a.vozella@cira.it

Keywords: Gardon Gauge, Calibration, Heat Flux, Sensor, Laser

Abstract. Sensor calibration is important for validity of data acquired during experimental testing. Heat flux sensors, used in the SCIROCCO experimental facility at CIRA, are critical to ensure that thermodynamic conditions comparable to those typical of re-entry maneuvers are achieved. This work aims to develop a numerical model for sensor simulation. A preliminary analysis has shown good response of the model to variation of flux diameter. The model will be used to investigate the implications and limits of using a continuous laser as a reference thermal source for sensor calibration to create an experimental setup for future activities.

Introduction

Extreme thermodynamic conditions achieved during re-entry from space require careful design and testing of vehicle components. Among them, structural safety of Thermal Protection Systems is fundamental to ensure safety of crew and payloads. Their experimental characterization is performed through testing in Plasma Wind Tunnels, like the SCIROCCO facility at the Italian Aerospace Research Centre (CIRA) [1], in which high-enthalpy levels are achieved to reproduce re-entry conditions using plasma flows [2].

During such tests, thermal heat flux must be measured with high accuracy to increase the reliability of test data and hence components. Gargon Gauges (GGs) are considered as the most reliable and accurate sensors, and they can operate over a wide range of heat flux intensities, reaching up to 3000 kW/m^2 [3]. A standard calibration procedure is still missing, and those existing fail in achieving heat flux intensities comparable to those generated during re-entry maneuvers. Most of them are based on blackbody radiation as a thermal source under vacuum conditions to minimize convective heat, while other procedures have been developed or are under investigation [4]-[6]. The main limits to be faced are the high energy consumption, the low accuracy deriving from poorly known energy of the thermal source and the lack of repeatability.

The aim of this work is to develop an advanced numerical model of a complete GG that can be used to investigate an innovative calibration procedure currently being developed at CIRA. The calibration procedure employs a laser as a well-defined thermal source to calibrate GGs in a repeatable, accurate, sustainable and safe manner. The emitted power can be accurately measured using a thermal sensor for low power lasers and the laser is subsequently used for GG calibration, as schematically shown in Fig. 1.

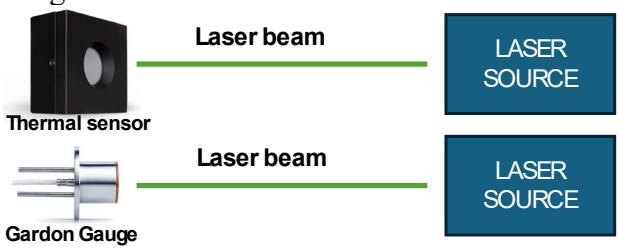


Fig. 1 – Schematization of laser power characterization for GG calibration.

Content from this work may be used under the terms of the Creative Commons Attribution 3.0 license. Any further distribution of this work must maintain attribution to the author(s) and the title of the work, journal citation and DOI. Published under license by Materials Research Forum LLC.

Materials Research Proceedings 69 (2026) 130-135 https://doi.org/10.21741/9781644904251-23

Theoretical background

GG sensors consist of a thin electrical insulating disk in which a thermopile, composed of constantan and copper, is arranged along a circular path, forming the sensitive element (SE) of the sensor. The disk is coated with a high-emissivity black paint that maximizes absorptivity, improving sensor sensitivity. The SE is mounted in a brass body that serves as both a mechanical support and a heat sink, thanks to its integrated water-cooling circuit, which maintains a fixed perimeter temperature of the SE. The structure of the sensor is schematized in Fig. 2. The incident flux is absorbed by the SE and the heat is distributed through conduction creating a radial temperature distribution. The perimeter of the SE is kept at fixed temperature by the brass body. The heat flux measurement is realized by sensing the electric voltage generated by the thermopile based on the Seebeck effect [7].

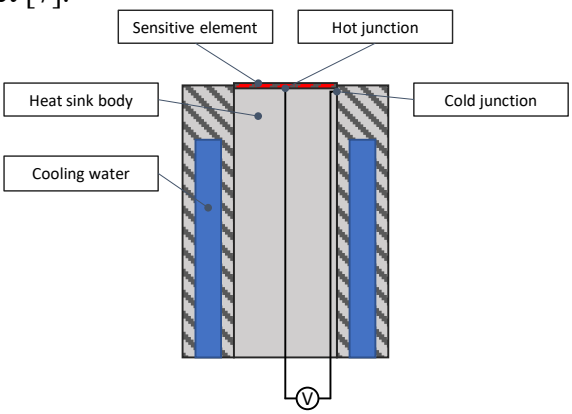


Fig. 2 – GG operational scheme.

Numerical methodology

The sensor was modelled to simulate its thermoelectric behavior under steady-state heat flux conditions representing the laser input energy. The model was created by leveraging the Mechanical module in Ansys Workbench, employing Finite Element Analysis (FEA) to solve the governing equations of heat transfer and thermoelectric phenomena. To create a highly detailed model, a real sensor was sectioned and its geometry was reproduced in the model allowing detailed representation of the SE, the brass body and the cooling system, as reported in Fig. 3.

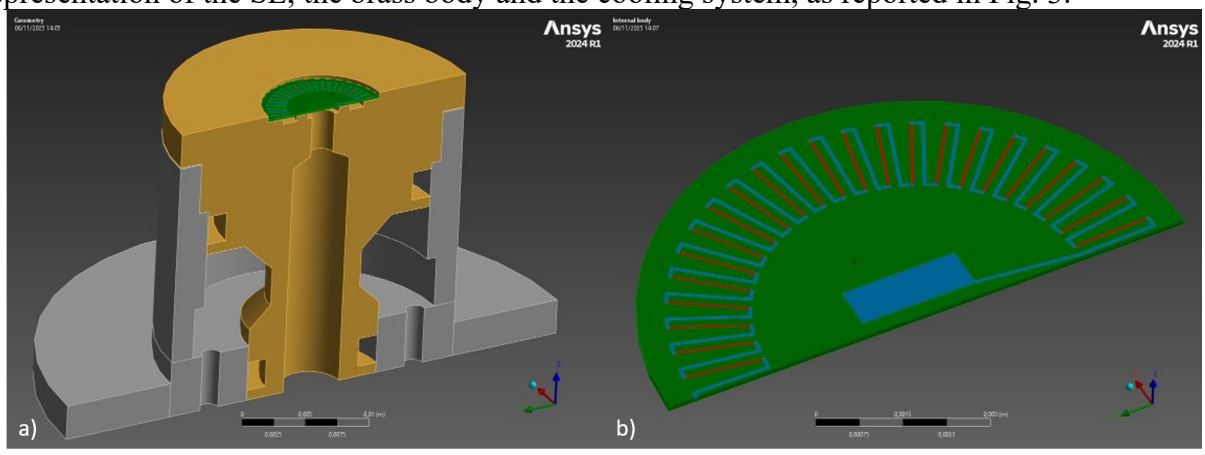


Fig. 3 - Model geometry: a) entire model; b) SE detail showing thermopile layout (copper in blue and constantan in red).

Material properties were included in the model in temperature dependent tables, using data from scientific literature [8]-[16]. Boundary conditions include convective heat transfer from the water-cooling circuit, with the heat transfer coefficient estimated using the Dittus-Boelter correlation for pipes and the flat plate correlation for the cavity, averaged over the heat exchange surface; radiative

Materials Research Proceedings 69 (2026) 130-135 https://doi.org/10.21741/9781644904251-23

heat flux is calculated providing emissivity of material and setting a fixed ambient temperature; the heat flux modeling the laser was imposed on the upper surface of the SE with varying diameter (spanning from 7 to 10 mm) for fixed power intensity equal to 0.4 W. The main parameters of the model are resumed in Table 1. The model considers half sensor with proper boundary conditions (e.g. adiabatic surfaces for heat exchange), as perfect symmetry can be exploited to reduce simulation time without affecting the results. The lower surface of the SE is also considered adiabatic, as the real sensor has insulating material to minimize the heat flux across SE thickness.

Table 1: Geometric dimensions and material properties used in the model.

Parameter	Value	Unit
SE diameter	10	[mm]
Body diameter	25.4	[mm]
Body total height	22.4	[mm]
Flange diameter	43.9	[mm]
Flange height	3	[mm]
Internal diameter, larger	11.6	[mm]
Internal diameter, smaller	2	[mm]
Convective heat exchange surface	129.21	[mm^2]
Sensor volume	6317.7	[mm^3]
Convective heat coefficient	1535	[$W/(m^{2*}K)$]
Body emissivity	0.07	[-]

Model Results

The model facilitates a better understanding of physics within the sensor about temperature and voltage behavior. In Fig. 4 is reported the temperature distribution of the sensor when the heat flux diameter is equal to the SE's diameter. The simulation confirms that the body and the SE's perimeter are almost at 20 °C. The slight increase in SE's perimeter temperature should be accounted for during sensor calibration to accurately estimate the calibration uncertainty.

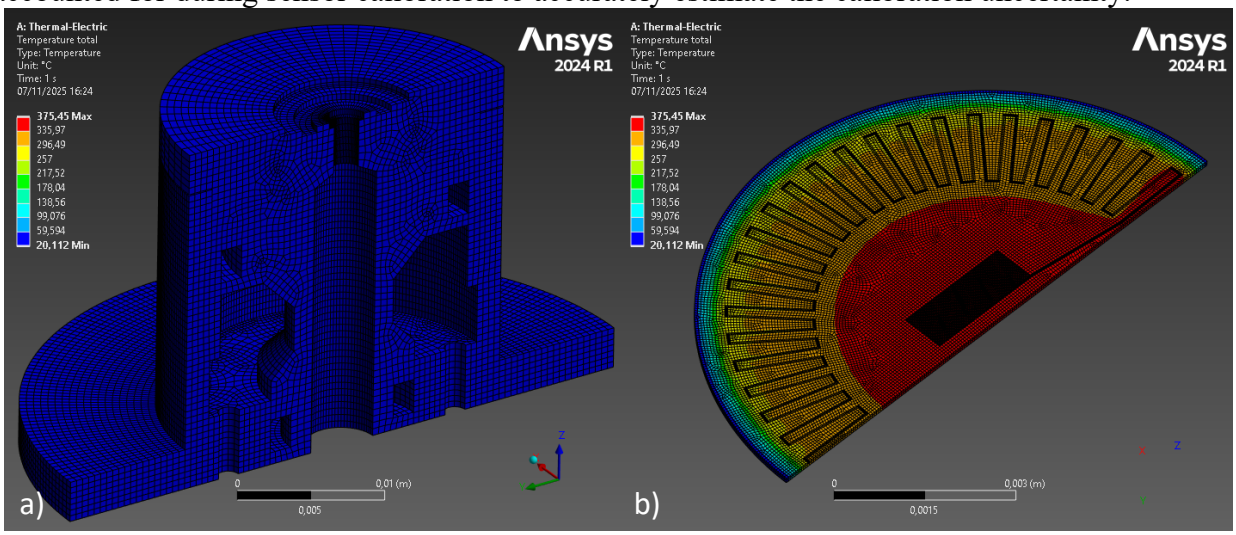


Fig. 4 – Temperature field of the sensor: a) body; b) SE.

By modifying the flux diameter with constant power, the thermopile shows an increase in maximum temperature at the center and a decrease of the temperature closer to the border (Fig. 5). Even if the temperature is higher for a diameter of 7 mm and equal to 491.43 °C, the maximum value is below the maximum temperature allowed by the manufacturer, which is equal to 600 °C [17]. That is reflected in the output voltage, plotted in Fig. 6 as the difference between the voltage

Materials Research Proceedings 69 (2026) 130-135 https://doi.org/10.21741/9781644904251-23

of the central region and that of the transversal surface of the copper wire cut from the plane of symmetry. Initially, a reduction of flux diameter leads to an increase of voltage. That is ascribable to the increase of temperature of the central region and the reduction of temperature of the border region that is no longer directly hit by the flux. When the diameter reaches 7 mm, the voltage starts to decrease, due to the radiative loss deriving from the elevated temperature achieved in this case, which reduces the overall flux flowing in the sensor.

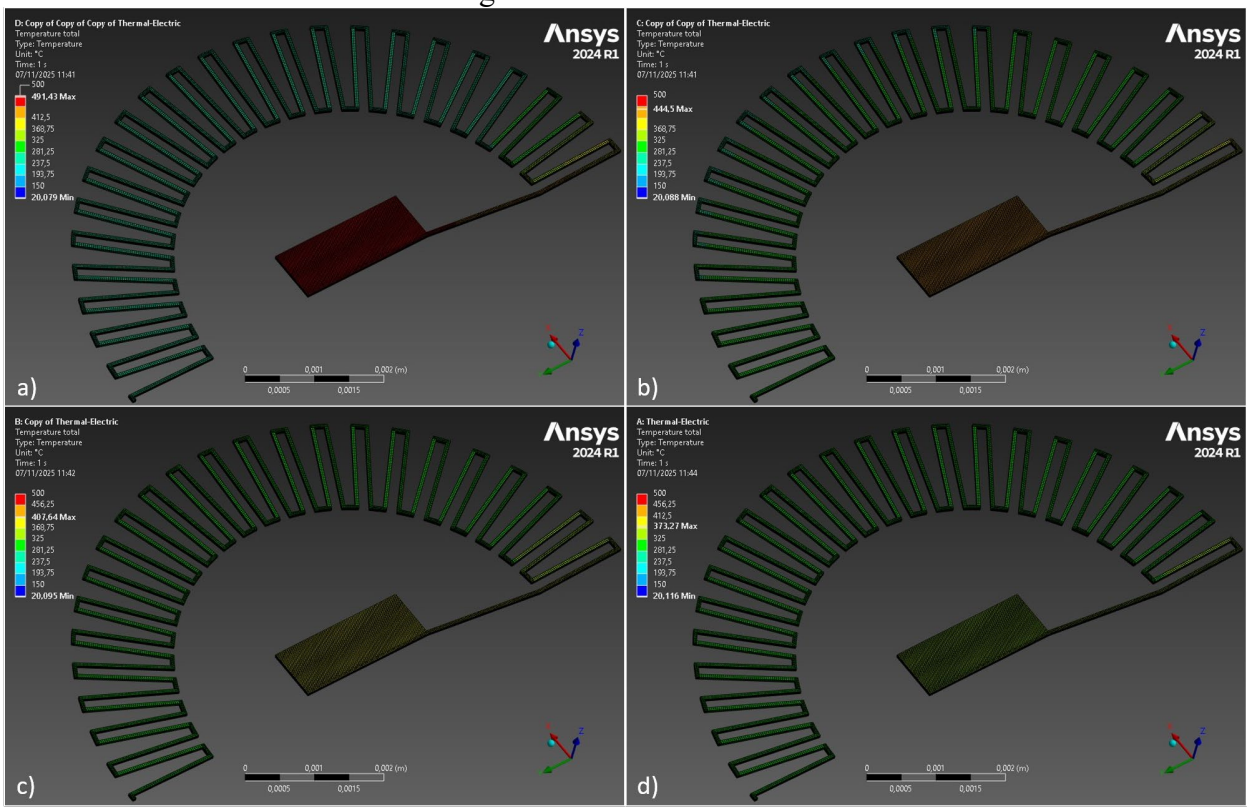


Fig. 5 – Temperature distribution of the thermopile for varying flux diameter at fixed power: a) 7 mm; b) 8 mm; c) 9 mm; d) 10 mm.

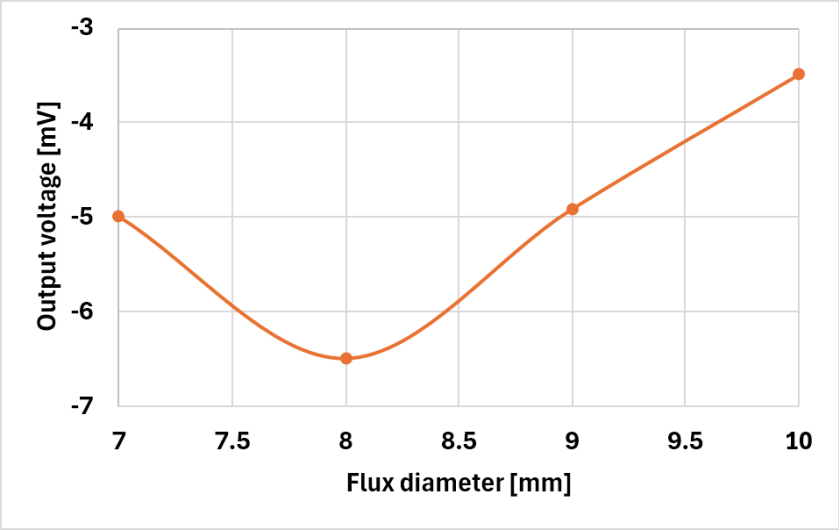


Fig. 6 – Output voltage against flux diameter at fixed power.

Conclusions

An advanced numerical model of a GG sensor has been developed using a real sensor to obtain all the fundamental information regarding its geometry. Material properties and boundary conditions

have been obtained from scientific literature or estimated based on typical experimental setups. The model provides data and information regarding the thermoelectrical phenomena within the sensor, such as the temperature distribution and the output voltage.

Future activities will investigate the influence and implications of using a laser as a thermal source for calibration of these sensors, guiding in the preparation of an experimental test bench for calibration activities.

References

[1] Purpura, C., De Filippis, F., Barrera, P., & Mandanici, D. (2008). Experimental characterisation of the CIRA plasma wind tunnel SCIROCCO test section. Acta Astronautica, 62(6-7), 410-421. https://doi.org/10.1016/j.actaastro.2008.01.008

[2] Borrelli, R., & Martucci, A. (2011). SCIROCCO plasma wind tunnel: synergy between numerical and experimental activities for tests on aerospace structures. In Wind Tunnels and Experimental Fluid Dynamics Research. IntechOpen. https://doi.org/10.5772/21125

[3] Guillot, E., Alxneit, I., Ballestrin, J., Sans, J. L., & Willsh, C. (2014). Comparison of 3 heat flux gauges and a water calorimeter for concentrated solar irradiance measurement. Energy Procedia, 49, 2090-2099. https://doi.org/10.1016/j.egypro.2014.03.221

[4] Pitts, W. M., Murthy, A. V., de Ris, J. L., Filtz, J. R., Nygård, K., Smith, D., & Wetterlund, I. (2006). Round robin study of total heat flux gauge calibration at fire laboratories. Fire Safety Journal, 41(6), 459-475. https://doi.org/10.1016/j.firesaf.2006.04.004

[5] Ballestrìn, J., Estrada, C. A., Rodríguez-Alonso, M., Perez-Rabago, C., Langley, L. W., & Barnes, A. (2004). High-heat-flux sensor calibration using calorimetry. Metrologia, 41(4), 314. https://doi.org/10.1088/0026-1394/41/4/013

[6] McLaughlin, L., Laubscher, H. F., Nguyen, J., Banh, L., & Konings, J. (2023). Development of Readily Available & Robust High Heat Flux Gardon Gauges. In SolarPACES Conference Proceedings (Vol. 2). https://doi.org/10.52825/solarpaces.v2i.892

[7] Stathopoulos, P., Hofmann, F., Rothenfluh, T., & von Rohr, P. R. (2012). Calibration of a gardon sensor in a high-temperature high heat flux stagnation facility. Experimental Heat Transfer, 25(3), 222-237. https://doi.org/10.1080/08916152.2011.609631

[8] Lanc, Z., Zeljković, M., Živković, A., Štrbac, B., & Hadžistević, M. (2018). Determination of emissivity of brass alloy using infrared thermographic technique. Original scientific paper Izvirni znanstveni članki, 65(3), 115-122. https://doi.org/10.2478/rmzmag-2018-0019

[9] Jose, A., Bekal, S., Shanubhogue, U. D., & Gurukrishna, K. (2024). Development and Analysis of Current Collectors for Proton Exchange Membrane Fuel Cells. Advances in Science and Technology. Research Journal, 18(6). https://doi.org/10.12913/22998624/192333

[10] Abadlia, L., Gasser, F., Khalouk, K., Mayoufi, M., & Gasser, J. G. (2014). New experimental methodology, setup and LabView program for accurate absolute thermoelectric power and electrical resistivity measurements between 25 and 1600 K: Application to pure copper, platinum, tungsten, and nickel at very high temperatures. Review of Scientific Instruments, 85(9). https://doi.org/10.1063/1.4896046

[11] Vasileiou, A. N., Vosniakos, G. C., & Pantelis, D. I. (2015). Determination of local heat transfer coefficients in precision castings by genetic optimisation aided by numerical simulation. Proceedings of the Institution of Mechanical Engineers, Part C: Journal of Mechanical Engineering Science, 229(4), 735-750. https://doi.org/10.1177/0954406214539468

[12] Muta, H., Kurosaki, K., Uno, M., & Yamanaka, S. (2003). Thermoelectric properties of constantan/spherical SiO2 and Al2O3 particles composite. Journal of alloys and compounds, 359(1-2), 326-329. https://doi.org/10.1016/S0925-8388(03)00295-0

[13] Guan, A., Wang, H., Jin, H., Chu, W., Guo, Y., & Lu, G. (2013). An experimental apparatus for simultaneously measuring Seebeck coefficient and electrical resistivity from 100 K to 600 K. Review of Scientific Instruments, 84(4). https://doi.org/10.1063/1.4798647

[14] Marushin, L. A., & Tikhonova, D. A. (2019, December). Heat transfer in materials with a disordered structure. In Journal of Physics: Conference Series (Vol. 1399, No. 5, p. 055005). IOP Publishing. https://doi.org/10.1088/1742-6596/1399/5/055005

[15] Schuster, C. E., Vangel, M. G., & Schafft, H. A. (2001). Improved estimation of the resistivity of pure copper and electrical determination of thin copper film dimensions. Microelectronics Reliability, 41(2), 239-252. https://doi.org/10.1016/S0026-2714(00)00227-4

[16] Burova, Z., Kovtun, S., Dekusha, L., & Vasilevskaya, V. (2023). Methodology for designing precision sensors which using in thermal conductivity measurement systems. In Systems, Decision and Control in Energy IV: Volume I. Modern Power Systems and Clean Energy (pp. 223-238). Cham: Springer Nature Switzerland. https://doi.org/10.1007/978-3-031-22464-5_12

[17] https://www.hukseflux.com/uploads/product-documents/SBG_series_manual_v2303_0.pdf.

Materials Research Proceedings 69 (2026) 136-141 https://doi.org/10.21741/9781644904251-24

Influence of Variable Camber by Differential Flap Setting on the Aerodynamic Performance in Off-Design Flight Conditions

Katharina Alt[1,a *], Victoria Schmitz[1,b], Jochen Wild[1,c] and Daniel Reckzeh[2,d]

[1]German Aerospace Center (DLR), Institute of Aerodynamics and Flow Technology, Lilienthalplatz 7, 38102 Braunschweig, Germany

[2]Airbus Operations GmbH, Airbus-Allee 1, 28199 Bremen, Germany

[a]katharina.alt@dlr.de, [b]victoria.schmitz@dlr.de, [c]jochen.wild@dlr.de, [c]daniel.reckzeh@airbus.com

Keywords: Off-Design, Variable Camber, Differential Flap Setting

Abstract. The present investigations analyze the influence of Variable Camber by Differential Flap Setting (DFS) on the aerodynamic performance of the DLR-F25 configuration in off-design flight conditions. Therefore, trailing edge (TE) flap deflections at the design point (h = 35000 ft) and off-design point (h = 29000 ft) are studied. The aim of the research at hand is to identify the optimal flap deflection angle for the corresponding flight conditions and thus to distinguish the difference in the aerodynamics due to DFS.

Introduction

Air traffic is responsible for approximately 3.5% of the global climate effect, consisting of CO_2-based and non-CO_2-based emissions, such as contrails and contrail-cirrus [1]. In combination with the annual growth in air traffic of approx. 2% [2], the necessity of the reduction of climate impacting emissions is increased. Furthermore, the growth in air traffic increases the importance of vertical leveling of aircraft. Subsequently, the investigation of the aerodynamic performance on multiple flight levels, should be considered in the aircraft design. Currently, the design process of an aircraft focuses on the cruise design point and only a performance driven altitude step to compensate aircraft weight variation due to fuel burn. Further analysis of the flight conditions in reduced flight levels, described as off-design conditions, is still necessary.

As part of the LuFo project AirTiMe, the aim of the present work is to analyze the aerodynamics of the DLR-F25 configuration (Figure 1) in off-design conditions. To improve the aerodynamic performance of the aircraft while operating in off-design conditions, DFS can be applied, which applies differential position of the TE devices. Due to DFS, the shock impact positions as well as the circulation distribution over the wing is influenced so that the aircraft flight performance (L/D over Mach or Lift Coefficient C_L) can be improved.

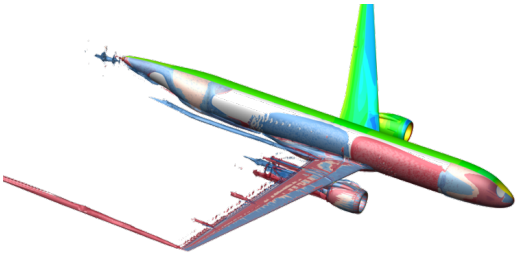


Fig. 1: Flow topology of DLR-F25.

To fulfill the aim of the present work, the aerodynamic performance of the configuration in the cruise design point, 35000 ft, serves as a reference (Mission Scenario 1 (MS1)). Three additional MS considering different off-design parameters evaluate the influence of Mach number, True Airspeed (TAS) and C_L on the aerodynamic performance of the configuration, when the flight level is reduced to 29000 ft. In MS2, the Mach number of MS1 is kept constant. In MS3, the TAS is kept constant, which leads to a reduced Mach number. In MS4, the Mach number is reduced to

Content from this work may be used under the terms of the Creative Commons Attribution 3.0 license. Any further distribution of this work must maintain attribution to the author(s) and the title of the work, journal citation and DOI. Published under license by Materials Research Forum LLC.

Materials Research Proceedings 69 (2026) 136-141 https://doi.org/10.21741/9781644904251-24

0.68 in order to keep C_L of the reference scenario is constant. The flight conditions of these considered MS are listed in Table 1.

Table 1: Flight conditions of MS.

		MS1	MS2	MS3	MS4
Altitude	h [ft]	35000	29000		
Mach number	M [-]	0.78		0.76	0.78
True Air Speed	TAS [m/s]	231.36	237.54	231.36	206.81
Lift Coefficient	C_L [-]	0.592	0.449	0.473	0.592

Configuration DLR-F25

The short-medium range transport aircraft configuration DLR-F25 is used in the study at hand. The configuration includes multiple moveable devices [3]. In Figure 2, the moveable layout of the DLR-F25 is visualized. It includes the two different types of moveables: three segmented Adaptive Dropped Hinge Flap (Inboard flap (IB), Flaperon 1 (F1), Outboard flap (OB)) and two segmented Plain Flap (Flaperon 2 (F2), Flaperon 3 (F3)), which are collectively used. The configuration considered here contains neither a horizontal nor a vertical tail plane.

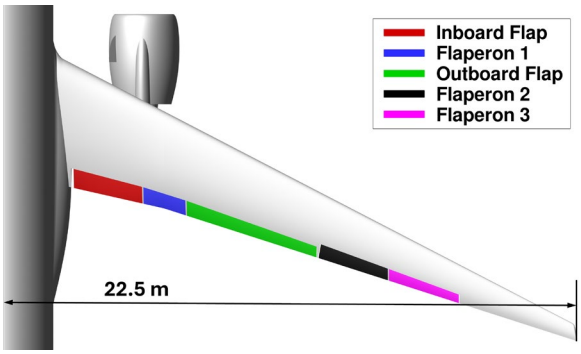


Fig. 2: Moveable layout of DLR-F25.

Methodology

The design space is explored by a Design of Experiment (DoE) sampling. Within this design space, the TE devices are deflected in a range of δ = -3° to 3° in the present investigations. To create the DoE, a Sobol's sequence [4] algorithm is used. In the end, a combination of 109 different TE deflection combinations are included within the DoE.

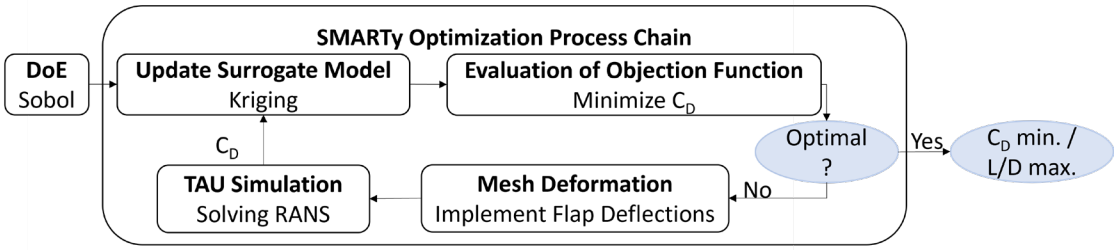


Fig. 3: SMARTy optimization process chain.

The computational grid is generated with the use of ANSA [5] and the TE flap deflections are implemented by the use of mesh deformation technique.

For aerodynamic analysis the DLR TAU code that solves the steady compressible RANS equations [6] has been applied to the different configurations. Within the CFD simulations, the Spalart-Allmaras turbulence model in its negative formulation is used.

The TAU simulations are set up to reach the constant target lift coefficient C_L. The Surrogate Modeling for AeRo Data Toolbox (SMARTy) is a modular python package and forecasts aerodynamic data based on high-fidelity CFD simulations [7]. The Toolbox is used for the implementation of Surrogate Based Optimization (SBO) processes. Based on the DoE the in Figure 3 illustrated optimization process chain is implemented to find the optimal DFS. The DFS is defined as optimal if the configuration achieves a minimum drag coefficient C_D or maximum lift-to-drag ratio L/D, which is equivalent because of the constant C_L in the TAU simulations.

Materials Research Proceedings 69 (2026) 136-141 https://doi.org/10.21741/9781644904251-24

Computational Results

In this section, the influence of Variable Camber by DFS on the aerodynamic performance in off-design flight conditions is discussed. For the off-design analysis, the flight level (FL) is reduced by 6000 ft. The reduced FL, leads to a reduced air density and temperature which influences the Mach number, the TAS, and C_L as it is the case for MS2 to MS4. With a reduced C_L, the Angle of Attack (AoA) is reduced as well in the off-design (MS2, MS3). When C_L remains unchanged, the Mach number is reduced (MS4), due to which the AoA is increased to reach the targeted C_L. The implementation of TE deflections further influences the circulation distribution and AoA. Due to a positive flap deflection, the camber of the wing is increased and thus locally increases the lift. A reduced local lift is implemented by negative flap deflection angles. The optimal DFS depends on the flight conditions and varies between the MS. The simulations show, that for each MS, the inboard flaps (IB, F1, OB) are deflected negatively and the outboard flaps F2 and F3 are deflected positively to improve the aerodynamic performance. The increased L/D indicates the improvement of the aerodynamic performance. The optimal configuration contains the optimal DFS which were found either from an optimization of the surrogate model based on the initial DoE or from the simulation results of the initial DoE. For MS2 a full SBO cycle with refinement of the surrogate model was performed to assess the predictive quality of the surrogate model. The comparison of the result of the SBO and the direct evaluation of the sample points in the DoE resulted in a difference of less than 1 drag count (10^{-4}). Because of this, the optimal configuration of MS3 and MS4 was found by a direct analysis of the DoE. The TE deflection angles of each moveable as well as the resulting flight parameters are listed in Table 2.

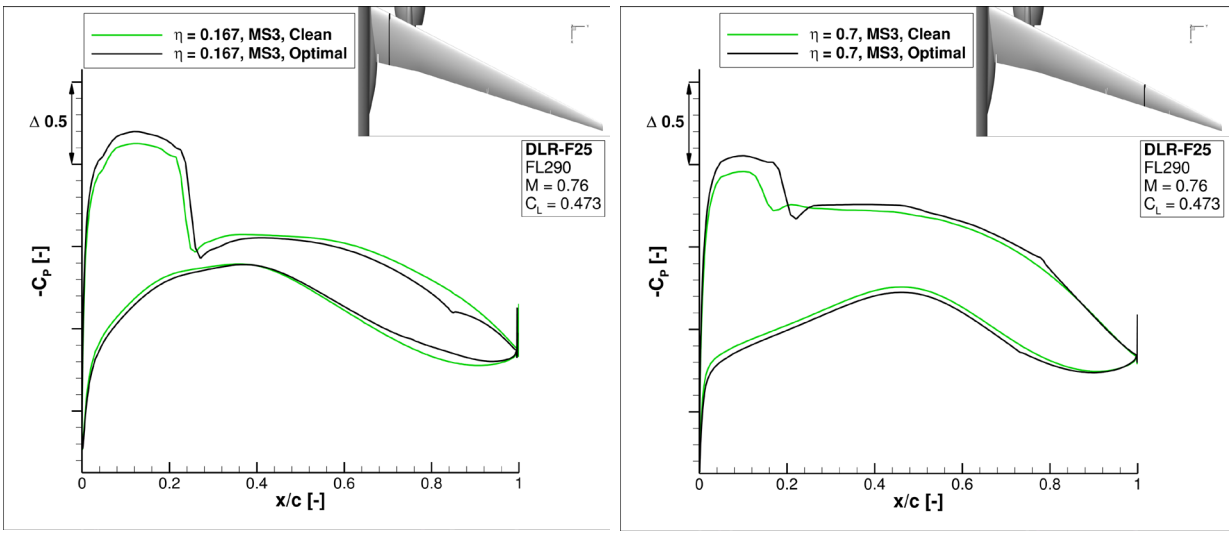
Table 2: Flight parameters of each MS - clean config. vs. config. with optimal DFS.

	Config.	δ_{IB} [°]	δ_{F1} [°]	δ_{OB} [°]	$\delta_{F2,3}$ [°]	α [°]	C_L $[\cdot 10^{-2}]$	C_D $[\cdot 10^{-4}]$	L/D [-]
MS1	Clean	0	0	0	0	1.59	59.2	283	20.87
	Optimal	-0.3	-0.8	-0.5	1.6	1.62	59.2	282	20.96 (+Δ0.43%)
MS2	Clean	0	0	0	0	0.64	44.9	235	19.09
	Optimal	-2.6	-2.8	-1.7	0	1.32	44.9	231	19.42(+Δ1.62%)
MS3	Clean	0	0	0	0	0.94	47.3	239	19.83
	Optimal	-1.7	-1.7	-2.2	0.9	1.45	47.3	236	20.04(+Δ1.11%)
MS4	Clean	0	0	0	0	2.28	59.2	269	21.94
	Optimal	-2.1	-2.1	0.2	2.1	2.48	59.2	268	22.07(+Δ0.59%)

The influence of the DFS on the aerodynamics is similar for each MS, regardless of the optimal TE deflection angles. Because of this, the change due to DFS is highlighted in the following paragraphs using MS3.

Materials Research Proceedings 69 (2026) 136-141 https://doi.org/10.21741/9781644904251-24

In Figure 4 the pressure distributions at two different spanwise positions of the optimal configuration are compared to the clean configuration, that does not include TE deflections. The pressure distribution at η = 0.4 is illustrated in Figure 4a and at η = 0.7 in Figure 4b. The AoA of MS3 is increased by implementing DFS. Due to this, the suction peek is more pronounced at both wing segments. Furthermore, the shock wave system is influenced. In- (η = 0.167) and outboard (η = 0.7), the shock wave is intensified and shifted downstream compared to the clean configuration. In combination with the increased pressure on the bottom of the wing near the leading edge, the pressure difference is locally increased. In the rear part of the wing sections, the pressure difference between upper and lower side of the wing is reduced for x/c > 0.5 at the inboard segment and remains higher or unchanged at the outboard segment. At the inboard segment η = 0.167, the slice cuts through the negative deflected inboard flap of the DLR-F25 as well. The negative flap deflection leads to a deceleration of the flow in front of the flap bend (x/c ≈ 0.85), due to which the pressure is increased locally on the upper side of the wing. However, on the lower side of the wing, the pressure is slightly reduced. At the outboard segment η = 0.7, the positive deflection of F2 and F3 further reduce the pressure on the upper side and increase the pressure on the lower side. Overall, the center of pressure is shifted upstream, which reduces the rear loading of the wing.



(a) η = 0.176 *(b) η = 0.7*

Fig. 4: Pressure distributions.

Materials Research Proceedings 69 (2026) 136-141 https://doi.org/10.21741/9781644904251-24

The circulation distributions of the optimal configuration are compared to the clean configuration in Figure 5. The circulation Γ of the flaps (dashed lines) depends on the flap deflection angle. As it was shown in the pressure distributions, a negative flap deflection leads to a reduction of Γ and a positive flap deflection, as it is necessary for the optimal configuration for F2 and F3, increases Γ. The changes in the spanwise load distribution are also reflected in the overall load distribution for wing and flaps (solid lines). The inboard load reduction and outboard load augmentation shifts the center of pressure to the wing tip. Due to this, the load distribution is shifted closer to an elliptical load distribution, which is resulting in a reduced induced drag.

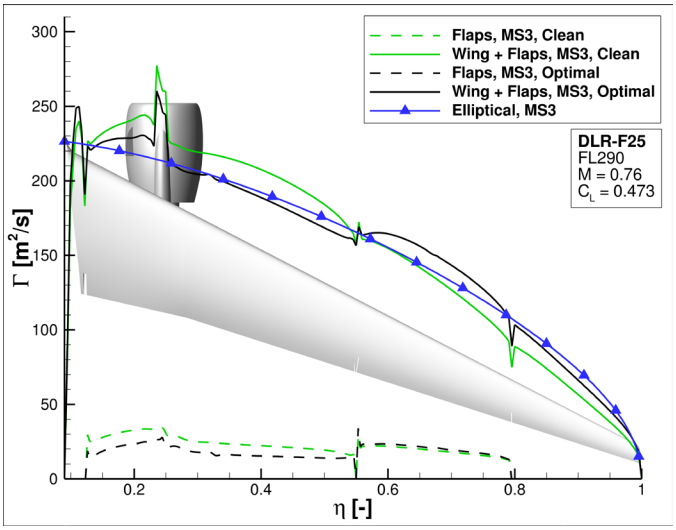


Fig. 5: Circulation distribution, MS3.

In Figure 6 the lift-to-drag ratio of the clean configuration in each MS and the possible improvement by DFS implementation is illustrated. In the design point (MS1), DFS can slightly improve the aerodynamic performance. In the off-design (MS2, 3, 4) the improvement reached by DFS is higher:

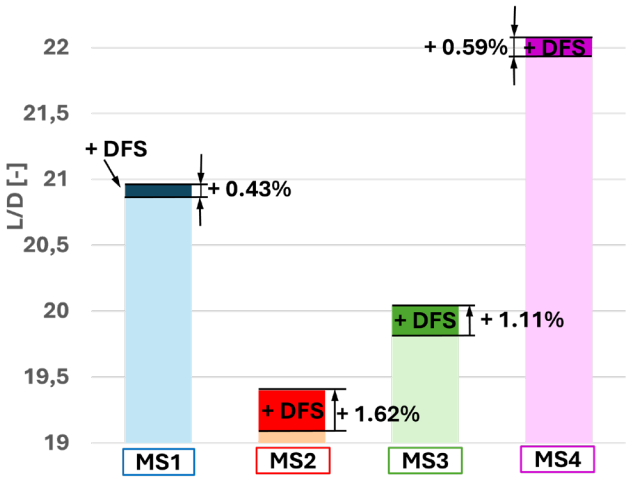


Fig. 6: DFS improvements.

MS2, the scenario at same Mach number shows the lowest aerodynamic performance, but the highest potential of DFS. This can be attributed that due to the higher dynamic pressure, the AoA is reduced by approximately 1° and the wing is operated away from the optimal design point.

MS4, the scenario at the same lift coefficient, shows an increased aerodynamic performance even without DFS. The improvement may be attributed to reduced wave drag at lower Mach number.

Summing up, the DFS is more beneficial at low AoA. This may be that the circulation distribution adaptation is more sensitive at low AoA or, conversely, as soon as C_L is high the load redistribution due to DFS is less sensitive.

Summary

In the current work the influence of DFS on the aerodynamic performance in off-design flight conditions were investigated. The off-design was defined as a flight level reduction by 6000 ft. For the investigations the transport aircraft configuration DLR-F25 was used.

The aerodynamic performance was evaluated based on the lift-to-drag ratio of each configuration. Implementing DFS during cruise, is able to improve the aerodynamic performance. Regardless of the flight conditions, it has been shown that a negative flap deflection in the inboard area and a positive flap deflection in the outboard area of the wing produce optimum aerodynamic

performance. A positive deflection increases the camber of the wing locally, due to which the local contribution of lift is increased. A negative deflection reduces the lift generation locally by implementing a negative camber line. In general, the ideal DFS leads to a shift of the spanwise circulation distribution towards an elliptical distribution, which is resulting in a reduced induced drag.

The results of the present study provide a basis for further studies on flight route adaptation with the motivation to reduce non-CO_2-based emissions.

Acknowledgment

The presented work is partially funded by the Federal Ministry for Economic Affairs and Climate Action (BMWK) as part of the LuFo VI-3 project AirTiMe, funding reference: 20A2201A. The results shown here were achieved as part of a master's thesis at the Institute of Jet Propulsion and Turbomachinery of the TU Braunschweig. The authors gratefully acknowledge the scientific support and HPC resources provided by the German Aerospace Center (DLR). The HPC systems CARA and CARO are partially funded by the Saxon State Ministry for Economic Affairs, Labour and Transport, the Ministry of Science and Culture of Lower Saxony, and the BMWK. The DLR-F25 is a conceptual design of an advanced short-to-medium-range airliner provided by DLR. It features an initial shape of a very high-aspect-ratio wing and was developed as a challenge for high-fidelity disciplinary and multi-disciplinary preliminary design. The development was funded by the BMWK as part of the LuFo project VIRENFREI.

References

[1] D.S. Lee, et al.: The contribution of global aviation to anthropogenic climate forcing for 2000 to 2018, Atmospheric Environment, Vol. 244, 2021. https://doi.org/10.1016/j.atmosenv.2020.117834.

[2] EUROCONTROL: EUROCONTROL Forecast Update 2024-2030. https://www.eurocontrol.int/publication/eurocontrol-forecast-2024-2030-autumnupdate (visited: 09.09.2025), 2024.

[3] S. W¨ohler, J. H¨aßy, V. Kriewall: Establishing the DLR-F25 as a Research Baseline Aircraft for the Short-Medium Range Market in 2035, ICAS Conference, 2024.

[4] M. Hadigol, A. Doostan: Least squares polynomial chaos expansion: A review of sampling strategies. Vol. 332, 2018. – pp. 382–407. https://doi.org/10.1016/j.cma.2017.12.019. ISSN 0045–7825.

[5] V. Skaperdas, N. Ashton: Development of high-quality hybrid unstructured meshes for the GMGW-1 workshop using ANSA, AIAA 2018-0660. 2018 AIAA Aerospace Sciences Meeting. 2018.

[6] D. Schwamborn, T. Gerhold, R. Heinrich: The DLR TAU-Code: Recent Applications in Research and Industry. ECCOMAS CFD 2006 Conference, 2006.

[7] P. Bekemeyer, et al.: Data-Driven Aerodynamic Modeling Using the DLR SMARTy Toolbox, AIAA AVIATION 2022 Forum, Chicago, IL, USA, 2022. https://doi.org/10.2514/6.2022-3899.

Materials Research Proceedings 69 (2026) 142-147 https://doi.org/10.21741/9781644904251-25

An Unsteady Lifting-Line Model for Rotors in Forward Flight

Gregorio FRASSOLDATI[1,a *], Beatrice DE RUBEIS[1], Giovanni BERNARDINI[1] and Massimo GENNARETTI[1]

[1]Department of Civil, Computer Science and Aeronautical Technologies Engineering, Roma Tre University, Rome, Italy

[a]gregorio.frassoldati@uniroma3.it

Keywords: Unsteady Aerodynamics, Rotor Aerodynamics, Rotary Wing, Küssner-Schwarz, Free-Wake, Generalized Lifting Line Theory

Abstract. This study presents a time-marching lifting-line algorithm to predict the unsteady aerodynamics of rotors. Validation studies employing purely harmonic and damped oscillatory wing and blade motions have demonstrated the solver's ability to accurately and stably predict unsteady loads. Augmenting the free and prescribed wake solvers recently developed, this method extends their time-marching framework to rotary wing applications in forward flight. In the present formulation, wake-induced velocities are evaluated via a free-wake model, while sectional forces are computed via Küssner-Schwarz unsteady theory. The bound circulation is derived by an unsteady Kutta-Joukowski relation. From there, both load and circulation equations are cast into state-space form. A vital modification for rotating blades is the careful definition of the reduced frequency, dealing with the accuracy of the prediction of dynamic loads and circulation.

Introduction

Lifting-line models remain widely used in industrial rotorcraft applications [1] because they offer a favorable cost–accuracy trade-off and allow seamless integration with structural and inertial models. At the same time, their computational efficiency makes them a natural choice for optimization studies, which are essential during the early phases of aircraft design.

The model presented here extends analytical aerodynamic methods to modern free-wake lifting-line solvers, thereby combining computational efficiency with numerical corrections that enhances robustness and load-prediction accuracy.

The application to forward flight represents the most recent challenge addressed by the model, which has already been validated on finite wings [2] and proprotors in axial flight [3]. The flexible formulation adopted granted the possibility to investigate a range of different reduced frequencies in both studies, always providing accurate predictions when compared to fully three-dimensional boundary element method simulations. The enhancements are especially evident when compared to the application of a canonical lifting-line model in which the unsteady prediction is recovered solely through the action of the numerical wake.

In doing so, the proposed approach bridges, in a novel fashion, the gap between simplified formulations and fully three-dimensional computational methods, enabling accurate predictions of unsteady loads without the prohibitive cost of high-fidelity CFD simulations. The resulting framework provides a versatile foundation for future aeroelastic and aeroacoustic analyses of rotorcraft operating in complex flight conditions.

Theoretical Formulation

The proposed *Unsteady Lifting Line Theory* (ULLT) introduces several novel elements to produce a comprehensive and self-consistent framework for predicting unsteady loads on lifting bodies across arbitrary flight conditions.

Content from this work may be used under the terms of the Creative Commons Attribution 3.0 license. Any further distribution of this work must maintain attribution to the author(s) and the title of the work, journal citation and DOI. Published under license by Materials Research Forum LLC.

Materials Research Proceedings 69 (2026) 142-147 https://doi.org/10.21741/9781644904251-25

Küssner-Schwarz Model. The aerodynamic forces on each section of a lifting body can be determined accurately for arbitrary body motions and inflow conditions using the Küssner–Schwarz solution [4] [5]. By contrast, alternative formulations impose assumptions on the downwash distribution—for example, constant or linear profiles [6] – or prescribe specific gust shapes acting on the airfoil [7] [8] [9].

Here, the time reformulated Küssner–Schwarz model developed in [2] is considered, where, using a rational approximation of the lift deficiency function and performing an inverse Fourier transform of both circulatory and noncirculatory generalized aerodynamic loads, a time-domain, state-space formulation of aerodynamic loads of the following type is obtained

$$\begin{cases} \boldsymbol{f}(\tau) = 2b\rho V^2[\boldsymbol{CB}\ddot{\boldsymbol{q}} + (\boldsymbol{CA}+\boldsymbol{DB})\dot{\boldsymbol{q}} + \boldsymbol{DAq} + \boldsymbol{C}\dot{\boldsymbol{t}} + \boldsymbol{Dt} + \boldsymbol{g}(\ddot{r} - (z_1+z_2)\dot{r} + z_1 z_2 r)] \\ \ddot{r} - (\sigma_1+\sigma_2)\dot{r} + \sigma_1\sigma_2 r = \boldsymbol{l}^T\dot{\boldsymbol{q}} + \boldsymbol{h}^T\boldsymbol{q} + \gamma \end{cases} \quad (1)$$

where τ is the non-dimensional time variable, defined as $\tau = V/b$, with V the body velocity and b the airfoil semichord, $\boldsymbol{t}$ is a N-component vector and γ is a scalar whose expressions are given by:

$$\begin{cases} t_n(y,t) = -\frac{1}{\pi V}\int_{-1}^{1}\frac{\cos n\theta(\xi)}{\sqrt{1-\xi^2}}v_i(x(\xi),y,t)d\xi \\ \gamma(y,t) = -\frac{1}{\pi V}\int_{-1}^{1}\frac{\sqrt{1-\xi^2}}{1-\xi}v_i(x(\xi),y,t)d\xi \\ \text{for } n = 0,1,\dots,N \end{cases} \quad (2)$$

For the definition of the other symbols in Eq. 1, the reader is referred to [2].

With respect to the canonical formulation for the sectional loads of Küssner-Schwarz model, we include three-dimensional effects into the sectional solution accounting for the effects of the wake-induced velocity.

This is achieved by numerically evaluating the chordwise distribution caused by the trailing vortices, since the effects of the shed vortices are already accounted for in Küssner-Schwarz theory. The contributions of the shed vorticity can be reintroduced when the wake differs from the thin and straight vortex sheet assumed by the analytical model; in our case, the best effects are found reintroducing it after 1/4 of the revolution.

The suitable integration of sectional loads given in Eq. 1 along the span gives the total loads acting over the body.

Extension to Rotary-Wing Aerodynamics. To extend the application of the presented unsteady aerodynamic formulation to rotors in hovering or axial flight, we have to assess the spanwise variation of the sectional reduced frequency. That is due to the radial variation of the undisturbed flow velocity (for instance, $V = \Omega r$ in hovering flight, with Ω and r denoting, respectively, rotor angular speed and radial position of the section). Therefore, a global reduced frequency is introduced, along with local rescaling of the reduced frequency, of zeroes and poles of the rational approximations of the lift deficiency function and Kutta-Joukowski transfer function (closely to what is done for tapered wings [10]) is performed. The particular case of rotors in forward flight can be approached in two different ways. The first approach is to keep the scaling of poles and zeroes constant, thus using an average scaling over the entire rotor revolution. The second approach involves considering the scaling to vary at each timestep. The scaling ratio is computed

Materials Research Proceedings 69 (2026) 142-147 https://doi.org/10.21741/9781644904251-25

by comparing the local velocity experienced by each airfoil with the reference hovering tip speed, thereby allowing the poles and zeros to evolve harmonically over the revolution.

This second approach, even if not mathematically exact, is the one that provided the best results, and therefore the one adopted in this study.

Numerical Results

References are The numerical investigation aims to assess the proposed ULLT formulation in terms of its aerodynamic and aeroacoustic results against a widely validated Boundary Element Formulation suited to analyzing thick bodies in unsteady motion in potential flows [11].

The reference rotor is a scaled version of the BO105 helicopter main rotor, exactly like the one used in HELINOISE test campaign [12]. The setup is summarized in Table 1. The forward flight case selected for this study is the #508, characterized by effective tip-path-plane angle $\alpha_{TPP} = -14.63°$ and advance ratio $\mu = 0.148$.

Table 1: Rotor Data

Radius	2.0 [m]
Chord	0.121 [m]
Twist Ratio	-4.0 [deg/m]
Null Twist	@0.70R
Root Cutout	0.22R
Airfoil	NACA23012
Pre-cone	2.5 [°]
RPM	1040

The shape and spatial development of Figure 1 is guaranteed by the free wake algorithm that enhances the velocity distribution required for the proper modeling even in this ULLT method. A solution computed via the Boundary Element Method solver (described in [13]), trimmed around the experimental values of integral forces and moments, is used as benchmark. From its results are derived the commands and the inputs of the aerodynamic simulation performed with the ULLT model.

Materials Research Proceedings 69 (2026) 142-147 https://doi.org/10.21741/9781644904251-25

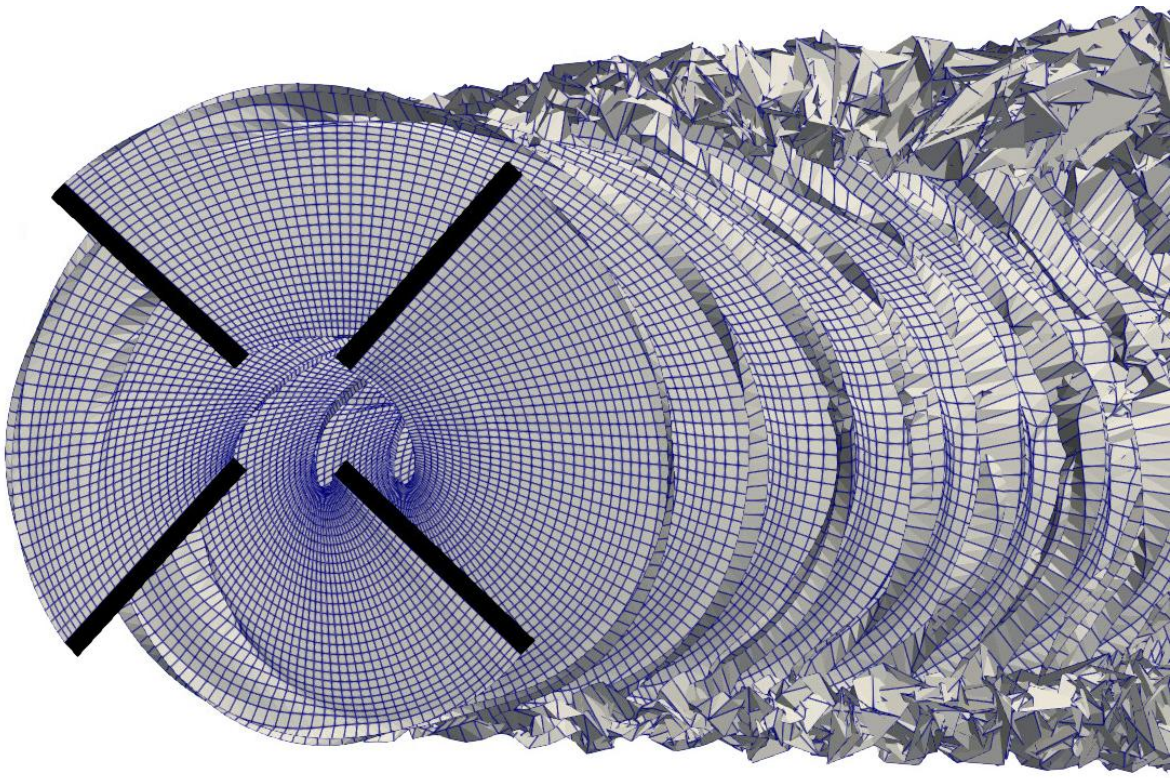


Figure 1: Free Wake Shape for ULLT Rotor Simulation

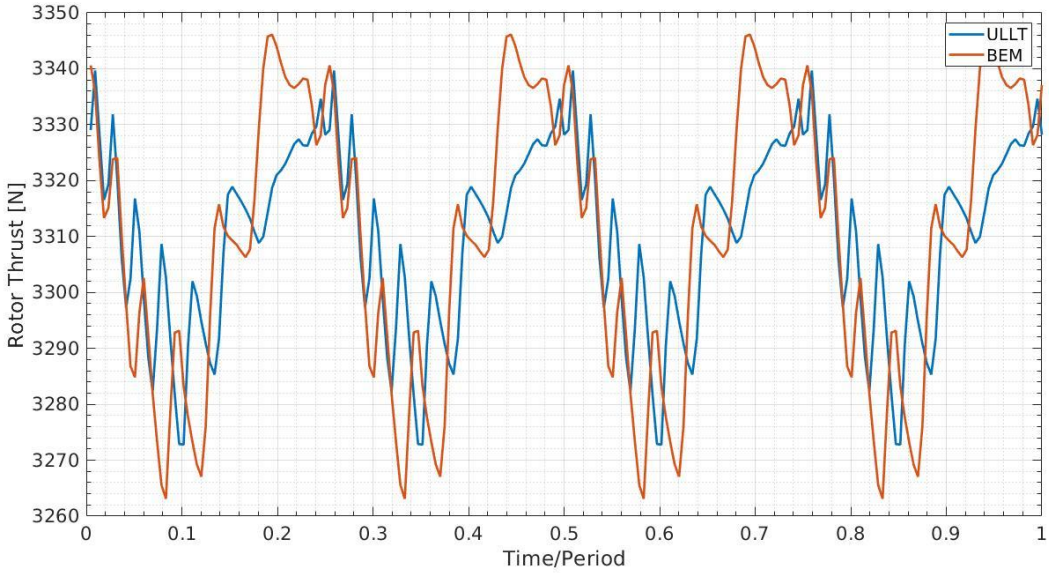


Figure 2: Rotor Thrust Time History Comparison

The single-revolution thrust time history shows a strong correlation between the ULLT and BEM solutions: both free-wake implementations reproduce similar higher-order oscillations while the dominant low-frequency 4/rev blade harmonic is clearly present; the principal discrepancy is that the BEM solution attains the upper envelope of the main harmonic earlier and at a higher magnitude than ULLT, a difference possibly attributable to thickness contributions in the BEM formulation and three-dimensional phenomena unmodeled by the lifting-line approach.

Materials Research Proceedings 69 (2026) 142-147 https://doi.org/10.21741/9781644904251-25

The plotted single-revolution thrust trend demonstrates that both models capture the low-frequency envelope and the dominant forcing, with the 4/rev blade contribution appearing as the principal harmonic in both traces. Higher-order oscillatory content produced by the free-wake algorithms is similar in phase and frequency, which indicates that wake-induced unsteady loading is consistently represented across the two solvers.

Finally, the aeroacoustic analysis is performed using the compact-source version of the Farassat 1A formulation, which enables the radiated noise to be evaluated from the knowledge of the spanwise distribution of the section aerodynamic loads [14]. This implies that this aeroacoustic formulation is well-suited to be coupled with the aforementioned aerodynamic solver. Specifically, for the microphone of the HELINOISE database located at -3.99 [m], -2.70 [m], and -2.30 [m] with respect to the rotor hub (considering an upward z axis and a forward x axis), the time history of the rotor radiated noise, evaluated using the spanwise load distribution from the present ULLT solver, is compared with the BEM results, validated in [15].

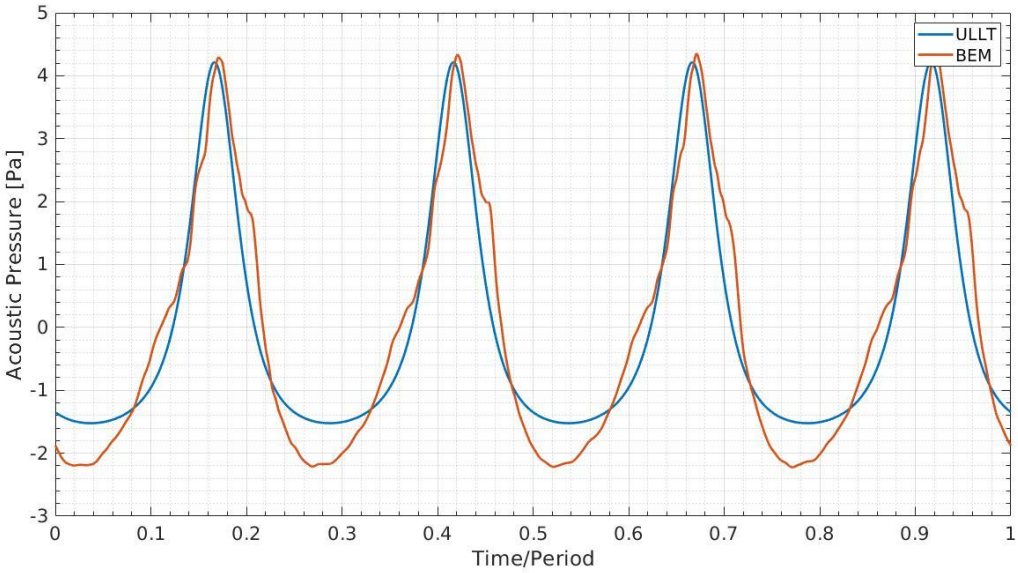


Figure 3: Loading-Noise Acoustic Footprint at Chosen Microphone

As can be seen from figure Figure 3, the ULLT solver accurately captures the loading contribution to noise, producing acoustic traces whose time history and dominant harmonic content closely match those of the validated BEM solution. Given the nature of the ULLT solver, for a proper assessment of accuracy, the contribution of thickness noise was disregarded in this evaluation.

The ULLT predictions accurately reproduce the phase and amplitude of the main low-frequency harmonics (particularly the 4/rev component), yielding a waveform over a single rotor revolution that closely matches the reference data. This confirms that the ULLT approach reliably maps spanwise load distributions into acoustic output, thus once again validating the methodology for predicting the aerodynamic loads on rotor blades.

Conclusions

The methodology presented in this study allows for a novel kind of simulation for unsteady aerodynamics of rotors. The forward flight validation test case shows the potentiality of this application and the validity of the model extension to forward flight cases, where most elements, namely the Küssner-Schwarz model in time and the reduced frequency scaling, are stretched at the edge of their applicability. Nonetheless, the results in terms of load prediction and noise estimation

confirm a very good accuracy, using a full three-dimensional boundary element method solver as benchmark.

References

[1] A. Cocco, A. Savino, A. Colli, P. Masarati and A. Zanotti, "A non-linear unsteady vortex-lattice method for rotorcraft applications," The Aeronautical Journal, vol. 128, no. 1328, 2024. https://doi.org/10.1017/aer.2024.55

[2] G. Frassoldati, R. Giansante, G. Bernardini and M. Gennaretti, "Unsteady Lifting-Line Free-Wake Aerodynamic Modeling for Morphing Wings," Aerospace, vol. 11, 2024. https://doi.org/10.3390/aerospace11090745

[3] G. Frassoldati, G. Bernardini and M. Gennaretti, "An Innovative Lifting-Line Model for Proprotors in Axial Flight," in 51st European Rotorcraft Forum, Venice, Italy, 2025.

[4] H. G. Küssner and I. Schwarz, "The Oscillating Wing with Aerodynamically Balanced Elevator," NACA, 1941.

[5] Y. C. Fung, An Introduction to the Theory of Aeroelasticity, New York: Dover Publications, Inc., 1993.

[6] T. Theodorsen, "General Theory of Aerodynamic Instability and the Mechanism of Flutter," NACA, 1935.

[7] W. R. Sears, "Some Aspects of Non-Stationary Airfoil Theory and Its Practical Application," Journal of Aeronautical Sciences, vol. 8, no. 3, pp. 104-108, 1941. https://doi.org/10.2514/8.10655

[8] J. P. Giesing, W. P. Rodden and B. Stahl, "Sears Function and Lifting Surface Theory for Harmonic Gust Fields," Journal of Aircraft, vol. 7, no. 3, pp. 252-255, 1970. https://doi.org/10.2514/3.44155

[9] H. G. Küssner, "Summary Report on the Nonstationary Lift of Wings," Luftfahrtforschung, 1936.

[10] M. Gennaretti, Fundamentals of Aeroelasticity, Springer Nature, Switzerland AG, 2024. https://doi.org/10.1007/978-3-031-53379-2

[11] M. Gennaretti and G. Bernardini, "Novel boundary integral formulation for blade-vortex interaction aerodynamics of helicopter rotors," AIAA Journal, vol. 45, no. 6, pp. 1169-1176, 2007. https://doi.org/10.2514/1.18383

[12] H. Heller, W. Splettstoesser, V. Kloeppel and F. Cenedese, "HELINOISE - The European Community Rotor Acoustics Research Program," AIAA Journal, 1993. https://doi.org/10.2514/6.1993-4358

[13] M. Gennaretti, G. Bernardini, J. Serafini and G. Romani, "Rotorcraft Comprehensive Code Assessment for Blade-Vortex Interaction Conditions," Aerospace Science and Technology, vol. 80, pp. 242-246, 2018. https://doi.org/10.1016/j.ast.2018.07.013

[14] G. Bernardini, M. Gennaretti and C. Testa, "Spectral-boundary-integral compact-source formulation for aero-hydroacoustics of rotors," AIAA Journal, vol. 54, no. 11, pp. 3349-3360, 2016. https://doi.org/10.2514/1.J054923

[15] M. Gennaretti, B. De Rubeis, C. Poggi and G. Bernardini, "Deformable-boundary integral formulation for the solution of arbitrarily-forced acoustic wave equation," Journal of Sound and Vibration, vol. 591, 2024. https://doi.org/10.1016/j.jsv.2024.118618

Materials Research Proceedings 69 (2026) 148-153 https://doi.org/10.21741/9781644904251-26

When Propellant Controls the Spin: Two-Phase Fluid Dynamics and Their Impact on Spacecraft Rotational Stability

Gianni CASSONI[1,a,*], Gianmarco COVETTI[1,b], Fabrizio GENNARI[2,c], and Jacopo SERAFINI[1,d]

[1]Department of Civil, Computer Science and Aeronautical Technology Engineering, Roma Tre University, Via Vito Volterra 62 00146 Rome, Italy

[2]Thales Alenia Space Italia, via Saccomuro 24, 00131 Rome, Italy

[a]gianni.cassoni@uniroma3.it, [b]gia.covetti@stud.uniroma3.it, [c]fabrizio.gennari@thalesaleniaspace.com, [d]serafini@uniroma3.it

Keywords: Fluid Dynamics, Rigid-Body Dynamics, Slosh Dynamics, OpenFOAM, Spacecraft Control

Abstract. Internal fluid rotation and slosh in spacecraft tanks produce time-varying torques and changes in effective inertia that directly affect a satellite's rotational dynamics. For small tanks or low fluid mass fractions, these effects can be treated as perturbations, approximated by simple slosh modes, or even considered negligible noise. However, when tanks are large relative to the vehicle's structural mass, the fluid's inertia and unsteady torques can alter the rotational equilibrium and its stability. This work examines how rotating internal fluid motion affects spacecraft attitude stability, with particular attention to the minimal axis instability phenomenon, in which a body containing a cavity filled with a two-phase fluid shift from rotating about its axis of minimum inertia to rotating about its axis of maximum inertia as the fluid dissipates energy, and the consequences of that behaviour for rotation-sensitive missions. The objective is to establish a connection between viscous boundary-layer dissipation mechanisms, the minimal axis instability phenomenon, and the relative time scale, which also depends on the fill level.

Introduction

Modern satellite missions have become increasingly complex and ambitious, often requiring spacecraft to carry significantly more fuel than during the early stages of the space era [7]. Liquid propellants are widely used in many space applications, particularly for high altitude and long duration missions [2]. In such satellites, the propellant can account for a substantial portion of the total mass, often around 40% of the initial launch mass [6]. This large amount of onboard fuel, which remains in a partially filled state for most of the mission duration, gives rise to complex fluid-structure interactions. For rotating spacecraft, this can be seen in changes to the effective inertia tensor as the fluid redistributes and in a moment opposite to the rotation, if it is not rotating about the greatest principal axis of inertia. These unsteady hydrodynamic loads may adversely affect the stability and controllability of the spacecraft. Flight experiments and flight-scale tests have long shown that internal fluid motion can couple strongly to spacecraft attitude: for example, the Wet Satellite Model (WSM) flight experiment produced a measurable minimal axis instability [9]. One criterion to characterize the effect of the fluid is an equivalent timescale, obtained by comparing the angular momentum of the rigid-body with the torque exerted by the fluid on the rigid-body. A convenient estimate is

$$\tau \approx \frac{rigid-body\ angular\ momentum}{characteristic\ fluid\ torque} = \frac{m_b \mathrm{L}^2 \Omega}{M_G^E}$$

Content from this work may be used under the terms of the Creative Commons Attribution 3.0 license. Any further distribution of this work must maintain attribution to the author(s) and the title of the work, journal citation and DOI. Published under license by Materials Research Forum LLC.

Materials Research Proceedings 69 (2026) 148-153 https://doi.org/10.21741/9781644904251-26

where ME denotes the characteristic viscous torque. In practice, the most at-risk satellites satisfy two conditions: a large fluid-structure momentum ratio and a short τ. The characteristic time scale τ is interpreted as the duration over which dissipative fluid torques redistribute angular momentum between the fluid and the rigid body sufficiently to shift the stable rotation of the composite body from the minimum to the maximum inertia axis. This differs from the classical Ekman spin-down time [10], which quantifies only the timescale for transient fluid motion to relax to a quasi-steady internal flow state. To estimate the viscous wall torque, let where M_G^E denotes the characteristic viscous torque. In practice, the most at-risk satellites satisfy two conditions: a large fluid-structure momentum ratio and a short τ. The characteristic time scale τ is interpreted as the duration over which dissipative fluid torques redistribute angular momentum between the fluid and the rigid body sufficiently to shift the stable rotation of the composite body from the minimum to the maximum inertia axis. This differs from the classical Ekman spin-down time [10], which quantifies only the timescale for transient fluid motion to relax to a quasi-steady internal flow state. To estimate the viscous wall torque, let

$$\Omega = \max\{\omega_x(t_0), \omega_y(t_0), \omega_z(t_0)\}.$$

Classical Ekman-layer theory, for Geophysical Fluid Dynamics, requires a small Rossby number $Ro \ll 1$, where $Ro = U/(L\,\Omega)$, so that nonlinear advection is negligible and the Coriolis-driven boundary layer controls the viscous torque [1]. In low-gravity spacecraft tanks, centrifugal effects are largely absorbed into the hydrostatic pressure and the static free-surface shape, but centrifugal and gyroscopic effects can be non-negligible. For the small-rotation regime considered here, a typical Rossby number may be $Ro \sim 1$. Therefore, the near-wall velocity is treated as a small perturbation to the background rotation. In a coupled rigid-body–fluid problem, the perturbation amplitude is defined from the instantaneous slip between the solid body and the fluid. It is expressed as

$$\alpha(t) = \left|\Omega_b(t) - \Omega_f(t)\right|, \quad U(t) \sim \alpha(t) L\Omega \sim L\left|\Omega_b(t) - \Omega_f(t)\right|$$

where $\Omega_b(t)$ is the instantaneous angular velocity of the rigid body and $\Omega_f(t)$ is the mean angular velocity of the fluid bulk. Using the Ekman thickness

$$\delta_E \sim \frac{r\nu}{\Omega}$$

and estimating the wall shear as $\tau_w \sim C_\tau \mu U/\delta_E$, and taking the torque as shear area lever arm, one obtains

$$M_G^E \sim C_\tau \alpha(t) \rho \nu^{1/2} L^4 \Omega^{3/2}$$

with $\mu = \rho\nu$. For two-phase flows, an interfacial torque must be added, which depends on the level of fill, the mobility of the interface, and the surface tension.

Methodology

The numerical simulations for the fluid were performed in the inertial frame using the Arbitrary Lagrangian-Eulerian (ALE) formulation of the Navier-Stokes equations with the VOF method for the two-phase interface. Within this framework, mesh motion was accounted for through the relative convective flux $(\boldsymbol{V} - \boldsymbol{V}_m)$, where $\boldsymbol{V}_m$ denotes the local mesh velocity. The rigid-body motion library was modified to prescribe cavity rotation, ensuring that the mesh boundaries followed the imposed motion in a kinematically consistent manner. It is important to note that no additional Coriolis or centrifugal source terms were introduced in this approach, as the frame is inertial. Nevertheless, the effects of rotation were still captured. The methodology follows the established ALE framework [4, 5, 1, 8].

Materials Research Proceedings 69 (2026) 148-153 https://doi.org/10.21741/9781644904251-26

$$\left.\frac{\partial(\rho \boldsymbol{V})}{\partial t}\right|_{\chi} + \nabla \cdot \rho \boldsymbol{V} \otimes (\boldsymbol{V} - \boldsymbol{V}_m) = -\nabla p + \mu \Delta \boldsymbol{V}, \qquad in\ \Omega, \qquad (1)$$

$$\nabla \cdot (\boldsymbol{V} - \boldsymbol{V}_m) = 0, \qquad in\ \Omega, \qquad (2)$$

where χ is the fixed reference coordinate system. The boundary condition on the moving walls is the no-slip

$$\boldsymbol{V} = \boldsymbol{V}_{wall} = \boldsymbol{V}_m, \qquad in\ \partial\Omega_{wall}$$

The dynamic equations of motion of the tank, are the following [3]

$$m_b \dot{\boldsymbol{V}}_{\boldsymbol{G}} = \boldsymbol{F}^{\boldsymbol{E}} = \boldsymbol{R}_{I\to B} \int_{\partial\Omega_{wall}} (p\,\mathbf{I} - \mu\,(\nabla \boldsymbol{V} + (\nabla \boldsymbol{V})^T) \cdot \mathbf{n}\, dS, \qquad (3)$$

$$\boldsymbol{J}_G \dot{\boldsymbol{\omega}} + \boldsymbol{\omega} \times \boldsymbol{J}_G \boldsymbol{\omega} = \boldsymbol{M}_G^E = \boldsymbol{R}_{I\to B} \int_{\partial\Omega_{wall}} \boldsymbol{r}_G \times (p\,\mathbf{I} - \mu\,(\nabla \boldsymbol{V} + (\nabla \boldsymbol{V})^T) \cdot \mathbf{n}\, dS, \qquad (4)$$

Where m_b and $\boldsymbol{J}_G$ are the tank mass and inertia tensor, $\boldsymbol{V}_G$ is the center of mass velocity, and $\boldsymbol{r}_G$ is the vector pointing to the tank internal surface points from the center of mass. The incompressible two-phase Navier-Stokes equations are solved using OpenFOAM, while the rigid-body equations of motion are integrated through a custom Python script. The iteration scheme for the fluid rigid-body interaction has been implemented in a strong coupling, in which the rigid-body motion exchanges information with the fluid multiple times until a convergence criterion is reached for the wall forces.

Results and Discussion

To investigate the influence of two-phase fluid dissipation on rotational stability, a rectangular tank with dimensions $L \times W \times H = 1.2 \times 0.8 \times 0.2$ m was considered. The liquid phase was modeled as water ($\rho_l = 1000$ kg m^{-3}, $\mu_l = 1 \times 10^{-3}$ Pa s) and the gas phase as air. All cases were initialized with the body rotating about the minimum-inertia axis, J_x. The rigid-body angular momentum about the initial spin axis was $H_b = J_x\,\Omega = 10$ kg m$^2 \times \Omega$ rad/s $= 10\,\Omega$ kg m^2/s The torque prefactor (without $C_\tau\alpha$) was estimated as $\sqrt{\nu} = \sqrt{(1 \times 10^{-6})} = 0.001$ m^2/s$^{1/2}$, $L^4 = 1.2^4 = 2.0736$, and $\rho\sqrt{\nu} = 1000 \times 0.001 = 1$, giving $M_G^E \sim C_\tau \rho \sqrt{\nu} L^4 \Omega^{3/4} \approx \left(C_\tau \alpha \Omega^{3/4}\right) \times 2.0736$ N m, and the corresponding timescale:

$$\tau = \frac{H_b}{M_G^E} \approx \frac{10\Omega}{(C_\tau \alpha \Omega^{3/2}) 2.0736} \approx \frac{4.8225}{C_\tau \alpha \Omega^{1/2}}\ \text{s}$$

In the simulation, the Rossby number was estimated as $\text{Ro} \sim 0.05 - 0.1$. The slip ratio was approximated as$\alpha \sim \text{Ro}$, and assuming $C_\tau \sim O(1)$, the viscous coupling was $C_\tau\alpha \sim \text{Ro}$. Therefore, for $\text{Ro} \sim 0.05$, $C_\tau\alpha \sim 0.05$, and for $\text{Ro} \sim 0.1$, $C_\tau\alpha \sim 0.1$. Two sets of numerical experiments were performed. In the first series, the fill level was fixed at 50% while the initial angular velocity about the minimum-inertia axis was varied. This sweep showed that higher initial rotation rates converged more rapidly to rotation about the maximum-inertia axis (i.e., the axis switch occurred sooner) due to increased fluid torque, as shown in Fig. 1. In the second series, the initial angular velocity was held constant while the fill ratio was varied. Changing the fill modified the free-surface geometry and the gas– liquid interaction, which affected the effective viscous coupling (apparent viscous timescale) and, consequently, the dissipation-driven dynamics, as illustrated in Fig. 2. The timescale, τ , was similar to that observed in the simulation of a tank full of water with a Rossby number of

Materials Research Proceedings 69 (2026) 148-153 https://doi.org/10.21741/9781644904251-26

Ro ~ 0.01. The dimensional analysis was performed without accounting for the interface, which could modify the dissipation by increasing the effective area of the fluid over which the torque was applied.

Table 1 Dissipation-driven timescale τ for different spin rates Ω and coupling strengths $C = C_\tau \alpha$.

Ω [rad/s]	τ (C= 1.0) [s]	τ (C= 0.1) [s]	τ (C = 0.01) [s]
0.50	6.82	68.20	682.00
1.00	4.82	48.23	482.25
2.50	3.05	30.50	305.00
5.00	2.16	21.57	215.67
10.00	1.53	15.25	152.50

Summary

The results confirmed that two-phase fluid dissipation plays a role in determining spacecraft rotational stability. Higher initial spin rates or stronger viscous coupling led to faster axis switching, while reduced fill levels or weaker coupling increased the timescale for dissipation-driven reorientation. Overall, the timescale τ provides a practical metric for assessing susceptibility to the minimal axis instability phenomenon in a variety of spacecraft designs.

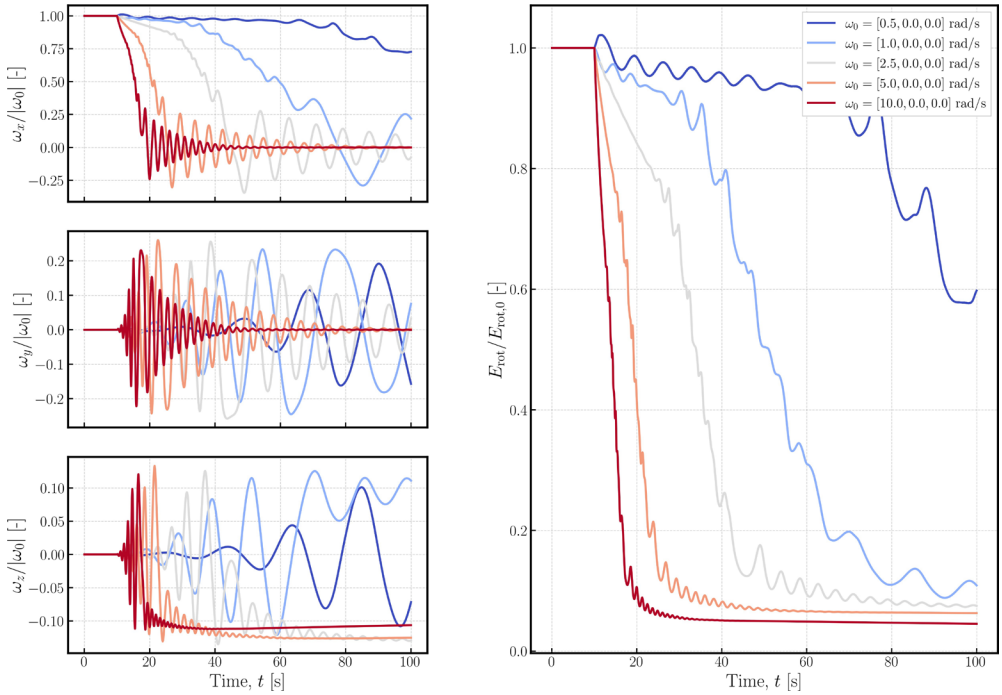


Figure 1: Time evolution of the angular velocity for different initial rotation rates at a fill level of 50%. The principal moments of inertia satisfy $J_z < J_y < J_x$.

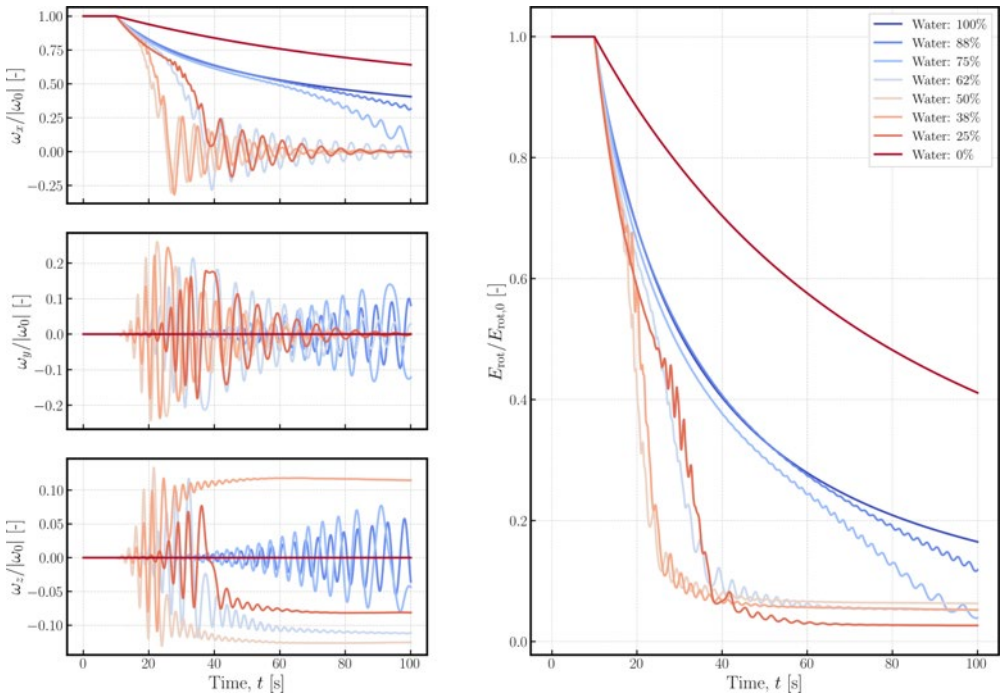


Figure 2: Time evolution of the angular velocity for different fill levels, with an initial angular velocity of 5 rad/s. The principal moments of inertia satisfy y $J_z < J_y < J_x$.

References

[1] Donea, J., Huerta, A., Ponthot, J.-P., and Rodríguez-Ferran, A. (2004). Arbitrary lagrangian-eulerian methods. Encyclopedia of computational mechanics. https://doi.org/10.1002/0470091355.ecm009

[2] Gasbarri, P., Sabatini, M., and Pisculli, A. (2016). Dynamic modelling and stability parametric analysis of a flexible spacecraft with fuel slosh. Acta Astronautica, 127:141-159. https://doi.org/10.1016/j.actaastro.2016.05.018

[3] Gerrits, J. and Veldman, A. (2003). Dynamics of liquid-filled spacecraft. Journal of Engineering Mathematics, 45(1):21-38. https://doi.org/10.1023/A:1022055916067

[4] Hirt, C. W., Amsden, A. A., and Cook, J. L. (1974). An arbitrary lagrangian-eulerian computing method for all flow speeds. Journal of Computational Physics, 14(3):227-253. https://doi.org/10.1016/0021-9991(74)90051-5

[5] Hughes, T. J. R., Liu, W. K., and Zimmermann, T. K. (1981). Lagrangian-eulerian finite element formulation for incompressible viscous flows. Computer Methods in Applied Mechanics and Engineering, 29(3):329-349. https://doi.org/10.1016/0045-7825(81)90049-9

[6] Luo, H., Zhang, R., and Weng, D. (2016). Mitigation of liquid sloshing in storage tanks by using a hybrid control method. Soil Dynamics and Earthquake Engineering, 90:183-195. https://doi.org/10.1016/j.soildyn.2016.08.037

[7] Riel, T., Sinn, A., Schwaer, C., Ploner, M., and Schitter, G. (2019). Iterative trajectory learning for highly accurate optical satellite tracking systems. Acta Astronautica, 164:121-129. https://doi.org/10.1016/j.actaastro.2019.07.012

[8] Tuković, Z. and Jasak, H. (2012). A moving mesh finite volume interface tracking method for surface tension dominated interfacial fluid flow. Computers & Fluids, 55:70-84. https://doi.org/10.1016/j.compfluid.2011.11.003

[9] Vreeburg, J. P. B. (1991). Investigations preparatory to the Wet Satellite Model Experiment. Presented at the International Symposium on Hydromechanics and Heat/Mass Transfer in Microgravity, Perm-Moscow, USSR, 6-12 Jul. 1991.

[10] Greenspan, H. P. (1969). The theory of rotating fluids. Cambridge University Press. https://doi.org/10.1002/sapm196948119

[11] Cushman-Roisin, B. and Beckers, J.-M. (2011). Chapter 4 - equations governing geophysical flows. In Cushman-Roisin, B. and Beckers, J.-M., editors, Introduction to Geophysical Fluid Dynamics, volume 101 of International Geophysics, pages 99-129. Academic Press. https://doi.org/10.1016/B978-0-12-088759-0.00004-3

Materials Research Proceedings 69 (2026) 154-157 https://doi.org/10.21741/9781644904251-27

Improving Post-Stall Airfoil Performance Using Synthetic Jet-Based Flow Control

Baris GUNGORDU[1,a *]

[1]Middle East Technical University, Kalkanlı, Güzelyurt, Mersin 10, 99738, Türkiye

[a]gbaris@metu.edu.tr

Keywords: Aerodynamics, Active Flow Control, Computational Fluid Dynamics

Abstract. This study numerically investigates the aerodynamic performance of a NACA0012 airfoil equipped with a leading-edge synthetic jet actuator at a Reynolds number of $1.35x10^5$. The analysis was conducted at a fixed angle of attack of 16° to represent post-stall flow conditions. Two-dimensional unsteady, incompressible Reynolds-Averaged Navier-Stokes equations were solved using a commercial finite-element solver, and the baseline results were validated against available experimental data. The effects of actuation frequency and jet velocity ratio on aerodynamic characteristics were examined. Results indicate that actuation frequency plays a dominant role in flow control effectiveness. At twice the natural wake frequency ($2f_c$), the synthetic jet substantially improved aerodynamic efficiency, increasing the lift-to-drag ratio by up to 34.1% compared to the baseline case. These findings demonstrate the strong potential of synthetic jet actuators for mitigating flow separation and enhancing post-stall performance in future low-energy aerodynamic applications.

Introduction

The global aviation industry, while facilitating rapid transportation and economic development, has also become a notable source of anthropogenic climate change. Recent analyses indicate that commercial aviation contributes about 2.4% of total global CO_2 emissions [1]. A considerable share of this impact originates from aerodynamic inefficiencies, particularly drag-induced fuel consumption during cruise flight [2]. Consequently, many studies have focused on improving aerodynamic performance by reducing drag and increasing the lift-to-drag ratio as part of a broader effort toward sustainable aviation.

Flow separation is among the key causes of aerodynamic inefficiency. It occurs when the boundary layer loses momentum and detaches from the surface under adverse pressure gradients, leading to a marked increase in pressure drag and loss of lift, especially at high angles of attack or during unsteady manoeuvres. Traditional passive flow control methods—such as vortex generators, winglets, and riblets—have been widely applied to alleviate flow separation; however, they lack adaptability to varying flow conditions and flight regimes [3]. In contrast, active flow control (AFC) techniques provide real-time control over the flow field. Among these, synthetic jet actuators (SJAs) have drawn significant attention as a compact, energy-efficient, and geometry-preserving solution [1,9]. By producing zero-net-mass-flux oscillatory jets, SJAs can re-energize the boundary layer and delay separation without requiring an external air supply [4]. These features make them highly suitable for sustainable aircraft applications, enabling performance enhancement with minimal design compromise [5,6]. The jet produced by an SJA is typically described by a sinusoidal velocity profile characterized by its peak jet velocity (U_{jet}) and actuation frequency (f_a).

This study presents a numerical investigation of an NACA0012 airfoil equipped with a single synthetic jet actuator using a commercial finite-element-based solver. The objective is to evaluate aerodynamic improvements, particularly the lift-to-drag ratio, under post-stall conditions. Although the broader motivation relates to the development of energy-efficient flow control

Content from this work may be used under the terms of the Creative Commons Attribution 3.0 license. Any further distribution of this work must maintain attribution to the author(s) and the title of the work, journal citation and DOI. Published under license by Materials Research Forum LLC.

Materials Research Proceedings 69 (2026) 154-157 https://doi.org/10.21741/9781644904251-27

strategies for emission reduction, the current work focuses on the aerodynamic effects at a single angle of attack of 16°.

Model, Computational Methods and Validation

The airfoil has a chord length (c) of 0.15 m and a free-stream flow Reynolds number of parallel to the experimental validation study by Lee and Gerontakos [7]. For the NACA0012 airfoil, incompressible Reynolds-Averaged Navier-Stokes (RANS) was solved over time numerically as the Mach number of the free-stream flow, $M_\infty < 0.3$. The numerical study utilized a 2-D geometry for the airfoil, and $k-\omega$ SST turbulence model was employed. A C-type grid was used with a size of 20c x 20c. The time step of the simulation is $\Delta t = 1\text{x}10^{-4}$, and the total time is set to t = 10 seconds. The solver is using a 2nd order accurate discretization for space and time. The lift and drag coefficients are the time-average values, disregarding the first second. A mesh grid independence test was conducted to ensure that the mesh grid does not affect the results.

Figure 1a illustrates the NACA0012 airfoil with mesh, and Figure 1b presents the illustration of the synthetic jet actuator, which is located near the leading edge of the upper surface, where the orifice mid-point is located at x/c = 5.33%. The synthetic jet actuator is modelled as a velocity boundary condition to mimic the piezoelectric diaphragm and has the same dimensions as reported in the work of Gungordu et al. [4,9].

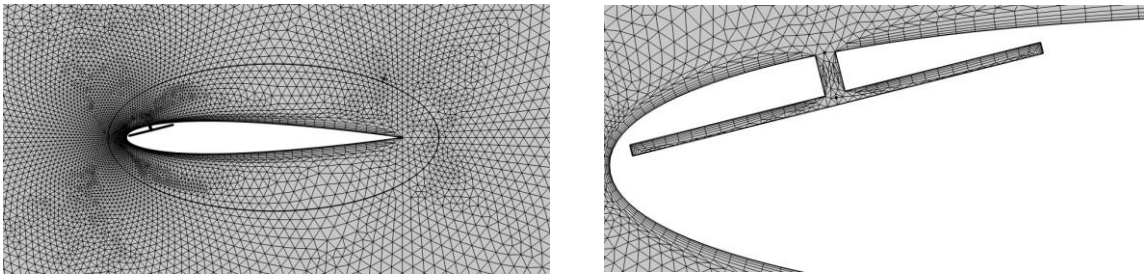


Figure 1: (a) NACA0012 Airfoil with mesh (left) (b) Magnified view of the synthetic jet actuator in the airfoil (right)

The base-flow (i.e., no flow control) lift coefficient results of the airfoil for various angles of attack at a Reynolds number of 1.35×10^5 were taken from the experimental study of Lee and Gerontakos [8]. The results revealed that the accuracy of the numerical study exceeds 95% across the entire angle-of-attack sweep when compared with the experimental data. For the present investigation, the angle of attack of the NACA0012 airfoil was fixed at α = 16°, at which a strong wake formation accompanied by vortex shedding is observed. By performing a power spectral density analysis of the wake using a virtual pressure probe, the characteristic vortex shedding frequency (f_c) was identified as 34.2 Hz. Accordingly, the oscillation frequency of the synthetic jet actuator was selected within this range. The synthetic jet actuation frequency (f_a) was varied as 0.5 f_c, f_c, and 2 f_c.

Results and Discussion

Table 1 summarizes the principal numerical results for the simulated flow-control cases at a fixed angle of attack of 16°. The reported parameters include the velocity ratio (V.R.; defined as the ratio of peak orifice-exit jet velocity to free-stream velocity), synthetic jet actuation frequency, lift-to-drag ratio, the corresponding baseline lift-to-drag ratio without flow control, and the relative percentage difference.

The aerodynamic performance of the airfoil exhibits a clear dependence on both the velocity ratio (V.R.) and the actuation frequency (f_a). At V.R. = 1.0, increasing the actuation frequency leads to a progressive improvement in the lift-to-drag ratio, with C_l/C_d increasing from 3.76 to

4.30, corresponding to a maximum enhancement of 7.1% relative to the baseline. As the velocity ratio increases to V.R. = 1.8, the influence of actuation frequency becomes more pronounced, with the maximum C_l/C_d reaching 5.28 at $2f_c$, representing a 34.1% improvement.

For both velocity ratio cases, actuation frequency of $0.5f_c$ provides only minor or negligible improvements, whereas the intermediate frequency (f_c) results in moderate gains. Overall, the results demonstrate that higher velocity ratios and higher actuation frequencies consistently produce stronger flow-control authority, leading to substantial improvements in aerodynamic efficiency, particularly at $f_a = 2f_c$.

Table 1: *Aerodynamic performance for different velocity ratios and actuation frequencies*

Case	V.R.	Actuation Frequency (f_a)	C_l/C_d	Baseline C_l/C_d	Difference (%)
1	1.0	0.5 f_c	3.76	3.94	−4.5
2	1.0	f_c	4.11	3.94	4.4
3	1.0	2 f_c	4.30	3.94	7.1
4	1.8	0.5 f_c	3.94	3.94	0
5	1.8	f_c	4.84	3.94	23.1
6	1.8	2 f_c	5.28	3.94	34.1

Conclusions

This numerical study investigated the aerodynamic effects of a synthetic jet actuator located at the leading edge of a NACA 0012 airfoil under post-stall flow conditions. The results demonstrate that the actuation frequency is the dominant parameter governing aerodynamic performance. At half of the characteristic wake frequency ($0.5\ f_c$), the actuator provided limited benefits and, in some cases, reduced the lift-to-drag ratio due to intensified vortex shedding. Near the characteristic frequency (f_c), moderate improvements of approximately 4–7% were observed. The most significant performance gains occurred when the actuation frequency was twice the wake frequency ($2\ f_c$), where the lift-to-drag ratio increased by up to 34.1% compared with the baseline case.

In the present study, the synthetic jet actuator was modelled using a prescribed velocity boundary condition at the orifice to emulate the oscillatory jet generated by a piezoelectric diaphragm. While this approach captures the primary aerodynamic effects of synthetic jet actuation, it does not fully represent the coupled structural–fluid–acoustic behaviour of a real piezoelectric actuator. Future work should therefore incorporate a fully coupled physical model of the piezoelectric diaphragm and cavity dynamics to provide a more realistic representation of actuator performance. In addition, extending the numerical framework to three-dimensional simulations would enable the investigation of spanwise effects, three-dimensional vortex structures, and their influence on flow-control effectiveness under realistic operating conditions.

References

[1] L. Wang, X. Li, H. Zhu, Improvement of poststall performance of NACA 0015 airfoil using virtual tubercles constructed by synthetic jets, Journal of Aerospace Engineering (ASCE) 37 (2024) 04024043. https://doi.org/10.1061/JAEEEZ.ASENG-5243

[2] International Council on Clean Transportation, ICCT Annual Report 2020, Washington, DC, USA, (2021), 1-32. https://theicct.org/publications/icct-annual-report-2020/

[3] M.A. Boukenkoul, F.C. Li, M. Aounallah, A 2D simulation of the flow separation control over a NACA0015 airfoil using a synthetic jet actuator, IOP Conference Series: Materials Science and Engineering 187 (2017) 012007. https://doi.org/10.1088/1757-899X/187/1/012007

[4] F. Aguirre-Villegas, B. Miranda-Godoy, L. Silva-Llanca, Harnessing the jet-flap effect: Enhancing lift with synthetic jets, International Journal of Mechanical Sciences 304 (2025) 110677. https://doi.org/10.1016/j.ijmecsci.2025.110677

[5] B. Güngördü, M. Jabbal, A. A. Popov, Enhancing jet velocity and power conversion efficiency of piezoelectric synthetic jet actuators, AIAA Journal 61 (2023) 4321-4331. https://doi.org/10.2514/1.J062930

[6] A. Glezer, Some aspects of aerodynamic flow control using synthetic-jet actuation, Philosophical Transactions of the Royal Society A 369 (2011) 1476-1494. https://doi.org/10.1098/rsta.2010.0374

[7] D. You, P. Moin, Active control of flow separation over an airfoil using synthetic jets, Journal of Fluids and Structures 24 (2008) 1349-1357. https://doi.org/10.1016/j.jfluidstructs.2008.06.017

[8] T. Lee, P. Gerontakos, Investigation of flow over an oscillating airfoil, Journal of Fluid Mechanics 512 (2004) 313-341. https://doi.org/10.1017/S0022112004009851

[9] B. Gungordu, M. Jabbal, A.A. Popov, Structural-fluidic-acoustic computational modelling and experimental validation of piezoelectric synthetic jet actuators, International Journal of Heat and Fluid Flow 104 (2023) 109215. https://doi.org/10.1016/j.ijheatfluidflow.2023.109215

Materials Research Proceedings 69 (2026) 158-163 https://doi.org/10.21741/9781644904251-28

A Comparative Study of Flow-Induced Vibrations by Circular and Polygonal Cylinders Using Lattice Boltzmann and Immersed Boundary Methods

Alessandro TROTTA[1, *], Esmaeel MASOUDI[2], Stefano MELONI[1], Mahdi AZARPEYVAND[2], Djamel REZGUI[2], Stefano UBERTINI[1], and Andrea Luigi FACCI[1]

[1]Department of Economics, Engineering, Society and Business Organization, University of Tuscia, 01100 Viterbo, Italy

[2]School of Civil, Aerospace and Design Engineering, University of Bristol, Queen's Building, University Walk, Bristol. BS8 1TR, United Kingdom

alessandro.trotta@unitus.it

Keywords: Fluid-Structure Interaction, Lattice Boltzmann, Immersed Boundary, Large Eddy Simulation, Vortex Induced Vibration, Polygonal Cylinders

Abstract. Fluid–Structure Interaction plays a critical role in many engineering applications, particularly in the aerospace and aeronautics sectors. In this context, the interaction between fluid flow and bluff bodies is often used to model key aircraft components. While extensive research has been conducted on simple geometries such as circular and square cylinders, polygonal bodies remain comparatively understudied. To address this gap, the Lattice Boltzmann Method with a Multiple-Relaxation-Time collision operator is employed in combination with a Large Eddy Simulation approach based on the Smagorinsky model. This setup is used to simulate the flow past circular and hexagonal cross-section cylinders under two different orientations and in various flow conditions. The Immersed Boundary Method is applied here to represent efficiently the boundary. The study moves investigating the vortex-induced vibrations problem at a Reynolds number of 200, considering a low density ratio between the solid and the fluid density. Results show that the orientation of the hexagonal cylinder strongly affects the wake formation in both stationary and vibrating cases.

Introduction

Understanding the flow behavior around bluff bodies is critically important, particularly in the context of Fluid–Structure Interaction (FSI) problems. In aeronautical applications, components such as engine mounts or landing gear assemblies often act as bluff bodies, causing airflow separation and the formation of vortices. Gaining a detailed understanding of these flow patterns is therefore essential for optimizing designs and reducing the fatigue loads induced by the unsteady flow. Similarly, in the energy sector, understanding the flow pattern is essential to improve the energy efficiency; for instance, in wind farms, downstream turbines are significantly influenced by the wakes generated by the upstream turbines.

To investigate these phenomena, bluff bodies are frequently modeled using simple geometries, such as cylinders with circular or polygonal cross-sections, cubes, spheres, or thin flat plates inclined at specific angles. These idealized shapes provide a practical way to study the fundamental flow behavior around non-streamlined objects while capturing the key mechanisms of separation and vortex formation. Several authors systematically investigated these geometries both experimentally and numerically, with particular emphasis on the influence of cross-sectional shape and incidence angle on the flow characteristics [1, 2, 3]. Specifically, polygonal cross-section

Content from this work may be used under the terms of the Creative Commons Attribution 3.0 license. Any further distribution of this work must maintain attribution to the author(s) and the title of the work, journal citation and DOI. Published under license by Materials Research Forum LLC.

Materials Research Proceedings 69 (2026) 158-163 https://doi.org/10.21741/9781644904251-28

cylinders introduce geometric asymmetries compared to classical circular cylinders, arising from the number of edges and the incidence angle with respect to the free-stream direction [4, 5].

In this work, the Lattice Boltzmann Method (LBM) is adopted with the Multiple Relaxation Time (MRT) collision operator, chosen for its superior numerical stability and accuracy, particularly at high Reynolds numbers, compared to the classical Single Relaxation Time (SRT) approach. Specifically, the present study employs a Large Eddy Simulation (LES) approach based on the Smagorinsky Subgrid-Scale model [6] to investigate both the flow past circular and hexagonal cross-section cylinders. The near-wall eddy viscosity is modeled using the Van Driest function [7].

The Immersed Boundary Method (IBM) is then employed in a three-dimensional LBM framework to efficiently represent complex and moving geometries.

In Section 2, the numerical model is presented which includes a brief description of the employed LBM scheme, followed by an outline of the LES approach, and concluding with the formulation of the IBM. In Section 3 results obtained with the present algorithm are then presented.

Numerical modeling

The LBM is a numerical approach for simulating fluid flows based on the evolution of particle distributions on a discrete lattice. The discrete form of the governing equation can be written as:

$$f_i(\boldsymbol{x}_f + \boldsymbol{c}_i\Delta t, t + \Delta t) = f_i(\boldsymbol{x}_f, t) + \Omega_i(\boldsymbol{x}_f, t)\Delta t + F_i(\boldsymbol{x}_f, t)\Delta t \quad (1)$$

where $f_i(\boldsymbol{x}_f, t)$ represents the distribution functions associated to pre-determined lattice directions $\boldsymbol{c}_i$, $\Omega_i(\boldsymbol{x}_f, t)$ and $F_i(\boldsymbol{x}_f, t)$ are the MRT collision operator and the source term respectively [8].

In Eq. (1), the source term $F_i(\boldsymbol{x}_f, t)$ accounts for internal or external forces acting on the fluid. Among the various forcing schemes available in the literature the present approach adopts Guo's forcing scheme [9].

To handle high Reynolds number flows, rather than employing an excessively fine mesh to resolve all the small turbulent scales, a LES approach based on the Smagorinsky subgrid scale model has been integrated in the present algorithm. This approach allows to model small scale structures while large energy containing turbulent structures, strongly influenced by the geometrical shape of the obstacle, are directly resolved [10, 11, 12]. To account for near-wall effects, Van Driest damping function is then used to let the turbulent viscosity exponentially damp to zero close to the wall.

Finally, to deal with stationary and moving complex geometries within the fluid domain, the IBM, a non-body conformal grid methodology, is adopted. Two different grid systems are used, the Eulerian grid for the fluid which is stationary and the Lagrangian mesh used for the immersed object. The presence of the obstacle in the flow field is then modeled through a force density added in the fluid governing equations in order to satisfy the no-slip condition on the boundary [13, 14, 15]. In this work the Direct-force IB formulation proposed by Kang and Hassan in [13] is used; the diffuse interface scheme is then adopted to represent the boundary.

Furthermore, the D3Q19 lattice stencil is employed, with periodic boundary conditions applied in the spanwise direction to simulate an infinitely long cylinder, while Neumann boundary conditions are imposed on the top and bottom boundaries.

Results

The three-dimensional algorithm has been validated against literature data for flow past a circular cylinder at various Reynolds numbers, using drag and lift coefficients C_d and C_l, and Strouhal number St as benchmark quantities, as summarized in Table 1.

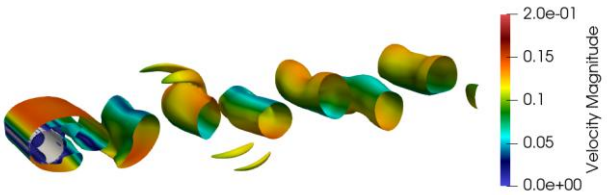
Materials Research Proceedings 69 (2026) 158-163 https://doi.org/10.21741/9781644904251-28

Table 1 Circular cylinder: comparison of C_d, C_l, and St, between present simulations and literature.

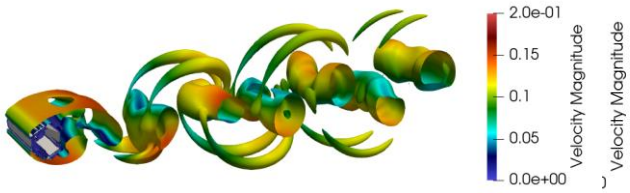
	Re = 20			Re = 100		
	C_d	C_l	St	C_d	C_l	St
Present	2.208	-	-	1.489	±0.386	0.165
Kang et al. [13]	2.09	-	-	-	-	-
Hu et al. [16]	2.21	-	-	1.418	±0.367	0.166
Cheylan et al. [17]	-	-	-	1.42	±0.33	0.166
	Re = 200			Re = 500		
	C_d	C_l	St	C_d	C_l	St
Present	1.496	±0.748	0.192	1.314	±0.332	0.201
Hu et al. [16]	1.394	±0.712	0.195	-	-	-
Lai et al. [18]	1.44	-	0.184	-	-	-
	Re = 1000					
	C_d	C_l	St			
Present	1.178	±0.170	0.211			
Lei et al. [19]	1.10	±0.319	0.203			
Cao et al. [20]	1.095	±0.177	0.217			

Contour maps of the wakes for the three stationary geometries at Re = 200 are shown in Fig. 1 where the Q-criterion is used to identify vortical structures, which are colored by the magnitude of the lattice velocity.

A distinct secondary vortex with higher energy content characterizes the face oriented hexagonal cylinder compared to the other configurations, likely as a result of a different flow separation induced by the geometry's orientation. In contrast, the edge oriented hexagonal cylinder behaves similarly to the circular cylinder, probably due to its lower azimuthal separation point.



(a)



(b) (c)

Figure 1 Wake visualization using Q-criterion: stationary case, (a) circular cylinder, (b) edge oriented hexagonal cylinder, (c) face oriented hexagonal cylinder

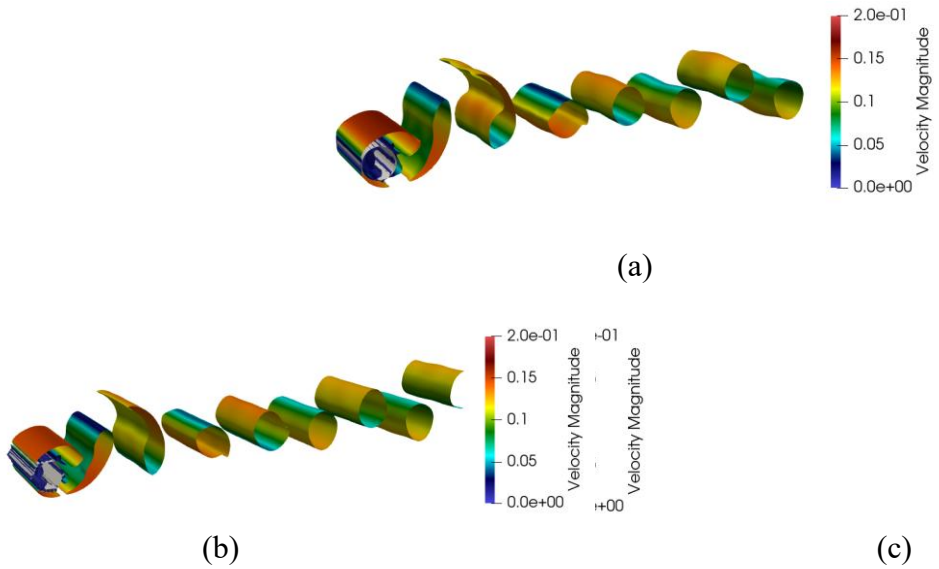


Figure 2 Wake visualization using Q-criterion: VIV case, (a) circular cylinder, (b) edge oriented hexagonal cylinder, (c) face oriented hexagonal cylinder

The wakes of the vibrating geometries at Re = 200 are visualized using the Q-criterion in Fig. 2. Compared to the stationary cases, the circular cylinder and the edge oriented hexagonal cylinder shed vortices that are strongly distorted by the vibration, after which the two single vortices formed during one shedding cycle develop along the centerline without the significant deformation observed in the stationary configuration. The face oriented hexagonal cylinder, on the other hand, exhibits a different pattern, with two pair of primary coherent structures formed in same shedding cycle no longer aligned with the wake centerline and secondary vortices displaying a more elongated shape Fig. 2c.

Conclusions

In this paper, we propose a 3D algorithm based on the coupling between the IBM and the LBM-MRT to investigate Fluid-Structure Interaction problems. The IBM allows for accurate evaluation of the forces exerted on the solid structure. Validation against the benchmark case of flow past a circular cylinder over a range of Reynolds numbers shows a very good agreement.

The analysis is further extended to hexagonal cross-sectional cylinders with different orientations. Comparison of the wake structures reveals that the edge oriented hexagonal cylinder and the circular cylinder exhibit similar wake characteristics, featuring deformed coherent vortices convected along the streamwise direction. In contrast, the face oriented hexagonal cylinder undergoes an earlier transition to three-dimensional vortex formation, characterized by the appearance of secondary vortices superimposed on strongly deformed primary coherent structures.

The investigation is subsequently extended to vibrating configurations. While the circular cylinder and the edge oriented hexagonal cylinder generate comparable wakes with stretched vortices, the face oriented hexagonal cylinder produces elongated vortices that propagate along the streamwise direction, with two pair of primary coherent structures no longer aligned with the centerline.

References

[1] Hao Cheng, Esmaeel Masoudi, Yu Liu, and Lian Gan. On the asymmetric vortex evolution in the near wake behind polygonal cylinders in an incident flow. Ocean Engineering, 307:118142, 2024. https://doi.org/10.1016/j.oceaneng.2024.118142

[2] Esmaeel Masoudi, Lian Gan, and David Sims-Williams. Large eddy simulation of incident flows around polygonal cylinders. Physics of Fluids, 33(10), 2021. https://doi.org/10.1063/5.0063046

[3] Hatef A Khaledi and Helge I Andersson. On vortex shedding from a hexagonal cylinder. Physics Letters A, 375(45):4007-4021, 2011. https://doi.org/10.1016/j.physleta.2011.09.046

[4] Qingyang Wang, Lian Gan, Shengjin Xu, and Yu Zhou. Vortex evolution in the near wake behind polygonal cylinders. Experimental Thermal and Fluid Science, 110:109940, 2020. https://doi.org/10.1016/j.expthermflusci.2019.109940

[5] SJ Xu, WG Zhang, L Gan, MG Li, and Y Zhou. Experimental study of flow around polygonal cylinders. Journal of fluid mechanics, 812:251-278, 2017. https://doi.org/10.1017/jfm.2016.801

[6] Joseph Smagorinsky. General circulation experiments with the primitive equations: I. the basic experiment. Monthly weather review, 91(3):99-164, 1963. https://doi.org/10.1175/1520-0493(1963)091<0099:GCEWTP>2.3.CO;2

[7] Edward R Van Driest. On turbulent flow near a wall. Journal of the aeronautical sciences, 23(11):1007-1011, 1956. https://doi.org/10.2514/8.3713

[8] S Succi. The Lattice Boltzmann Equation for Fluid Dynamics and Beyond. Oxford University Press, 2001. https://doi.org/10.1093/oso/9780198503989.001.0001

[9] Zhaoli Guo, Chuguang Zheng, and Baochang Shi. Discrete lattice effects on the forcing term in the lattice boltzmann method. Physical review E, 65(4):046308, 2002.

[10] Bernardus J Geurts. Elements of direct and large eddy simulation. RT Edwards, Inc, 2003.

[11] Stephen B Pope. Turbulent flows. Measurement Science and Technology, 12(11):2020-2021, 2001. https://doi.org/10.1088/0957-0233/12/11/705

[12] Pierre Sagaut. Large eddy simulation for incompressible flows: an introduction. Springer Science & Business Media, 2005.

[13] Shin K Kang and Yassin A Hassan. A comparative study of direct-forcing immersed boundary-lattice boltzmann methods for stationary complex boundaries. International Journal for Numerical Methods in Fluids, 66(9):1132-1158, 2011. https://doi.org/10.1002/fld.2304

[14] Roberto Verzicco. Immersed boundary methods: Historical perspective and future outlook. Annual Review of Fluid Mechanics, 55(1):129-155, 2023. https://doi.org/10.1146/annurev-fluid-120720-022129

[15] A Trotta, S Meloni, G Falcucci, S Ubertini, and AL Facci. An immersed boundary formulation for lattice boltzmann simulations of low-reynolds fluid-structure interaction problems. Physics of Fluids, 37(3), 2025. https://doi.org/10.1063/5.0256946

[16] Yang Hu, Haizhuan Yuan, Shi Shu, Xiaodong Niu, and Mingjun Li. An improved momentum exchanged-based immersed boundary-lattice boltzmann method by using an iterative technique. Computers & Mathematics with Applications, 68(3):140-155, 2014. https://doi.org/10.1016/j.camwa.2014.05.013

[17] Isabelle Cheylan, Julien Favier, and Pierre Sagaut. Immersed boundary conditions for moving objects in turbulent flows with the lattice-boltzmann method. Physics of Fluids, 33(9), 2021. https://doi.org/10.1063/5.0062575

[18] Ming-Chih Lai and Charles S Peskin. An immersed boundary method with formal second-order accuracy and reduced numerical viscosity. Journal of computational Physics, 160(2):705-719, 2000. https://doi.org/10.1006/jcph.2000.6483

[19] Chengwang Lei, Liang Cheng, and Ken Kavanagh. Spanwise length effects on three-dimensional modelling of flow over a circular cylinder. Computer methods in applied mechanics and engineering, 190(22-23):2909-2923, 2001. https://doi.org/10.1016/S0045-7825(00)00272-3

[20] Shuyang Cao, Shigehira Ozono, Yukio Tamura, Yaojun Ge, and Hironori Kikugawa. Numerical simulation of reynolds number effects on velocity shear flow around a circular cylinder. Journal of Fluids and structures, 26(5):685-702, 2010. https://doi.org/10.1016/j.jfluidstructs.2010.03.003

Materials Research Proceedings 69 (2026) 164-171 https://doi.org/10.21741/9781644904251-29

Hot-Wire Velocity Measurements in Subsonic Nozzle Flows: Experimental Test Campaign

R. Camussi[1,a *], E. De Paola[1,b], A. Talamelli[2,c], L. Lazzarini[2,d], S. Palazzo[3,e], F. De Gregorio[3,f] and K.-S. Rossignol[4,g]

[1]Department of Civil, Computer Science and Aeronautical Technologies Engineering, University of Roma Tre, Italy

[2]Department of Industrial Engineering / CIRI Aerospace, University of Bologna, Italy

[3]Centro Italiano Ricerche Aerospaziali – CIRA, Italy

[4]Institute of Aerodynamics und Flow Technology, Department of Technical Acoustics, German Aerospace Center (DLR), Germany

[a]roberto.camussi@uniroma3.it, [b]elisa.depaola@uniroma3.it, [c]alessandro.talamelli@unibo.it, [d]lorenzo.lazzarini@unibo.it, [e]s.palazzo@cira.it, [f]f.degregorio@cira.it, [g]Karl-Stephane.Rossignol@dlr.de

Keywords: Turbulent Jet; UAV; Flow Measurements

Abstract. Understanding the development of turbulent jets in subsonic nozzles is essential for improving jet noise prediction models and for validating high-fidelity numerical simulations in aerospace applications. Within the framework of the NATO STO AVT-415 activity, a dedicated experimental campaign was carried out at the Italian Aerospace Research Center (CIRA) to investigate the velocity field and turbulence characteristics at the inlet and exit of a novel subsonic nozzle configuration using hot-wire anemometry (HWA). The results offer a comprehensive description of the flow evolution downstream of the nozzle exit and a detailed characterization of the turbulence properties upstream of the nozzle. These measurements are of significant importance for establishing accurate boundary conditions in numerical simulations.

Introduction

The need for optimizing performances of Unmanned Air Vehicles (UAV) in military and civil applications requires the use of advanced computational studies providing both the aerodynamic and the aeroacoustic behavior in particular in the region close to the exhaust of the propulsion system.

The main objective of the *NATO STO AVT-415* group is to investigate intake and exhaust sound radiation of a UCAV-type military vehicle and to evaluate low-noise nozzle concepts by means of dedicated experiments and numerical simulations. The configuration under investigation is the so called DLR-F24 MULDICON that has been thoroughly described in [1, 2, 3, 4]. This specific wind tunnel model is designed around the concurrent agile (unmanned) NATO air vehicle design, the MULDICON UCAV configuration (MULti-Disciplinary CONfiguration)[1]. The original MULDICON UCAV planform design, which originates from NATO AVT-251 [1], was adopted. AVT-251 was not about designing a competitive UCAV but rather aimed at improving earlier designs while moving towards a realistic flyable vehicle. The configuration was slightly modified to allow the integration of an intake and an exhaust channel necessary for the conduction of the experiments [4]. For experimental purposes, the original MULDICON platform remained untouched while the centre body design by FOI (Swedish Defence Research Agency) was selected [5]. This design has a thicker centre-body, leaving more room for the intake and exhaust channels. The system is equipped with a non-axisymmetric nozzle that features an elliptical cross-section at

Content from this work may be used under the terms of the Creative Commons Attribution 3.0 license. Any further distribution of this work must maintain attribution to the author(s) and the title of the work, journal citation and DOI. Published under license by Materials Research Forum LLC.

Materials Research Proceedings 69 (2026) 164-171 https://doi.org/10.21741/9781644904251-29

its interface with the settling chamber and a gradual transition into a high-aspect-ratio rectangular exit section.

While acoustic tests and numerical simulations on this configuration have been carried out in the past, a comprehensive aerodynamic characterisation has never been performed so far. Due to the complexity of the settling chamber and of the nozzle geometry, detailed measurements of velocity and turbulence statistics are essential for the understanding of the flow physics and for the assessment of the boundary conditions used in the numerical approaches.

The main scope of the present activity is to provide an extensive aerodynamic description of the flow in the intake and in the region downstream of the nozzle exit. To this purpose, an extensive measurement campaign has been carried out at the Italian Aerospace Research Centre (CIRA) by means of hot-wire anemometry. In parallel, the nozzle surface pressure distribution has been investigated in order to ensure the repeatability of the test conducted at DLR. The experimental tests provided mean velocity profiles along with higher-order statistics for different positions at the inlet and outlet regions and different Mach numbers.

Experimental set-up

The DLR-F24 Muldicon model was originally designed for use in the anechoic test section of the DNW-NWB (see ref. 4), and a proper setup has been arranged at CIRA to provide the air supply and mass flow control. A picture illustrating the pressure supply arrangement is presented in *Figure 1*. The pneumatic flow system is equipped with a pressure valve regulator, temperature, pressure and mass flow sensors. The operative inlet pressure is maintained by an active closed-loop control. Temperature, mass flow and pressure are measured during the full test.

A cross-cut view through the model centre is shown in *Figure 2*, making visible the arrangement of all components and the detailed contours of the intake duct and nozzle. The section area distribution of the nozzle duct is given in *Figure 3*. The nozzle is equipped with 36 static pressure taps distributed on streamwise-aligned lines on the upper and lower walls of its duct, at the nozzle symmetry plane. Seven pressure taps are spread out streamwise, three taps on each side of the centre line at the 200 mm position (see *Figure 4*). The pressure taps at positions 300 mm, 320 mm and 340 mm are located beneath the exchangeable lower wall plate. Pressure measurements. were carried out by a PSI8400 system. Two differential EPS modules with full-scale values of ± 5 psid and ± 15 psid, respectively, were used.

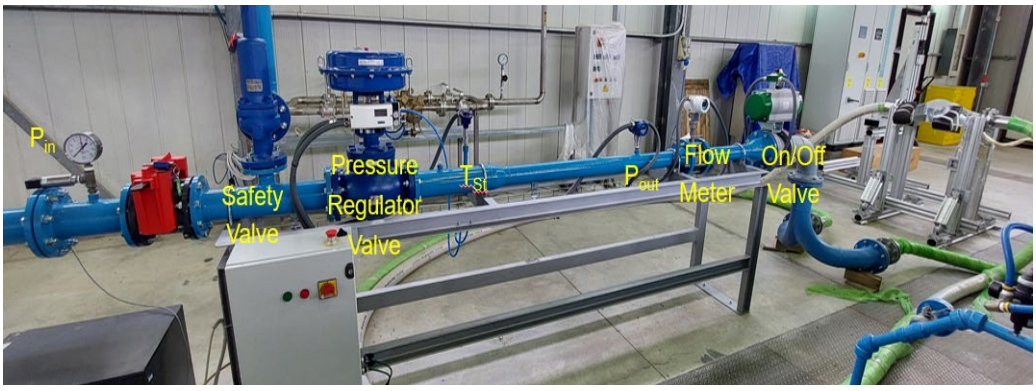


Figure 1 – Picture of the pressure supply system

At the 30 mm position on the upper wall, a 4 mm circular opening is foreseen for the insertion of a hot-wire probe. The probe is tightly held in place using a tight screw-on fitting. The probe mounted at the nozzle entrance is visible in *Figure 5*.

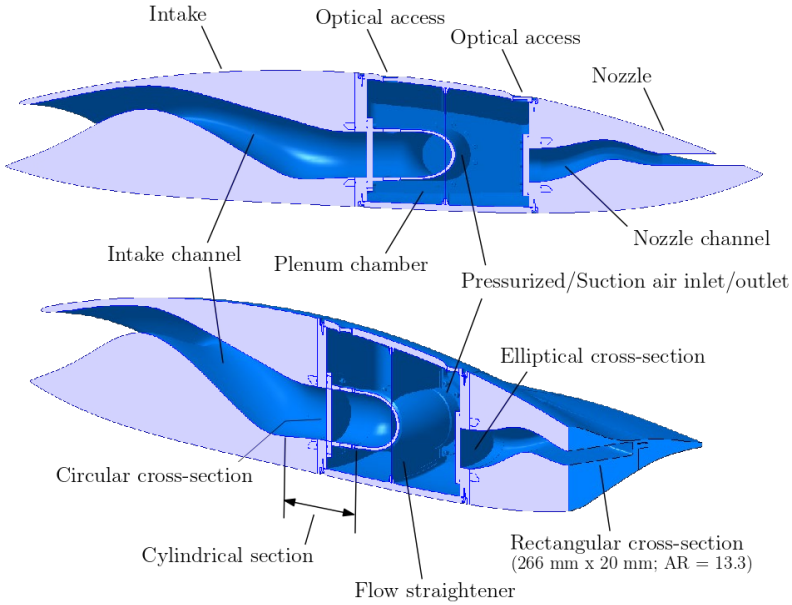


Figure 2. Section view of the DLR-F24 Muldicon model

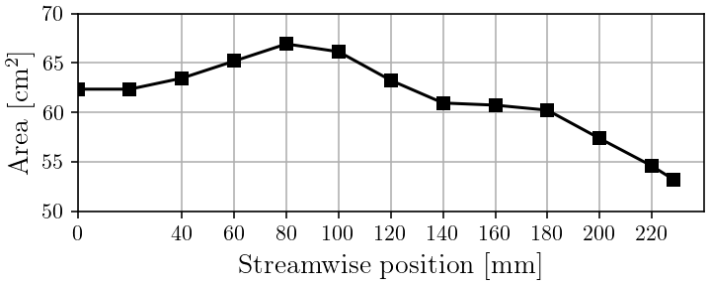


Figure 3. Nozzle duct cross-section area distribution

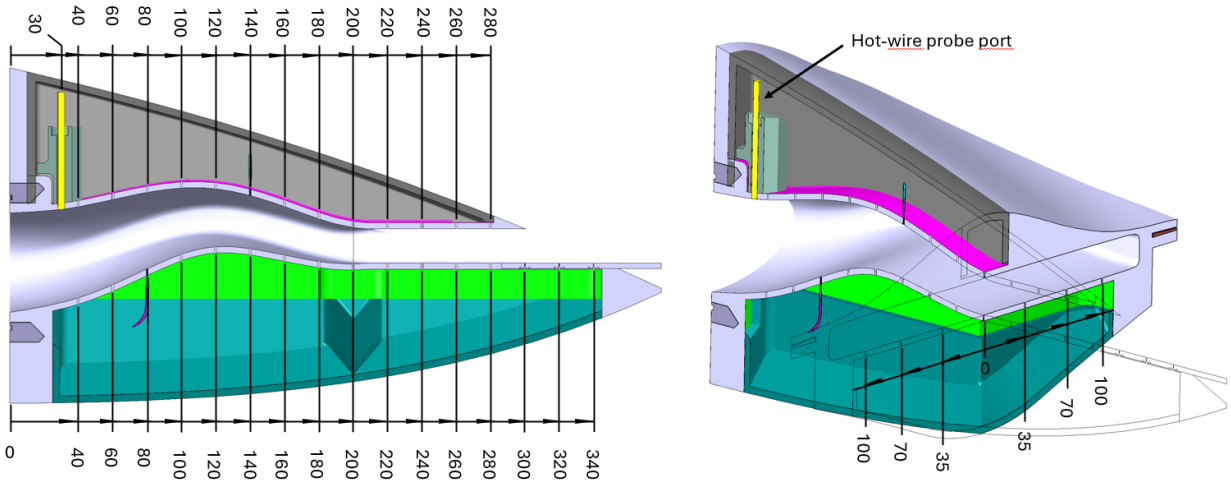


Figure 4. Centre line section (left) and cross-section (right) showing the static pressure taps positions and hot-wire probe port position

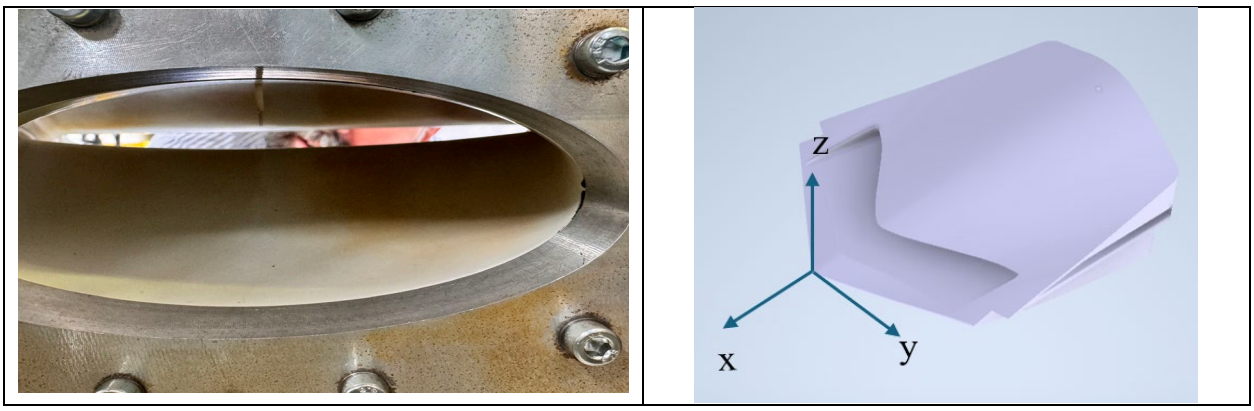


Figure 5: Set-up of the Hot-Wire probe mounted at the nozzle inlet and the reference system adopted for the hot wire positioning in the outer region

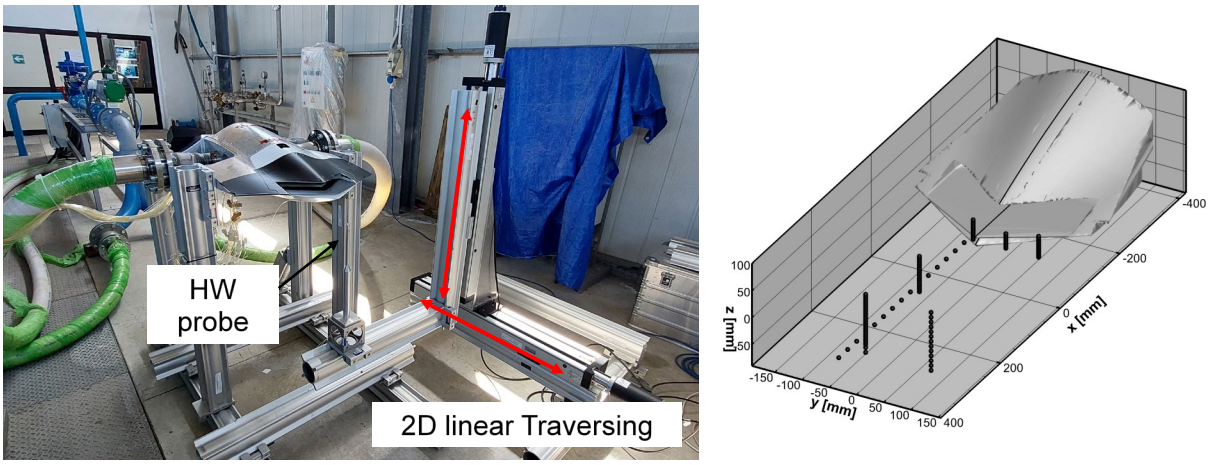


Figure 6 - Sketch of the setup and measured points

The pneumatic pressure system has been designed and installed in CIRA for the purposes of reproducing the same conditions tested in [4]. Preliminary tests have been carried out to verify the response of the pneumatic system and the similarity of the results against data achieved at DNw-NWB.

The nozzle geometry is described in detail in [4], and it features an elliptical cross-section at its interface with the settling chamber, which gradually transitions into a high-aspect-ratio rectangular exit section (266 mm × 20 mm, AR = 13.3).

Measurements have been carried out for subsonic Mach numbers of 0.5 and 0.66. To this end, a Dantec 5-channel Constant Temperature Anemometry (CTA) system was employed with single-component plated tungsten wire probes (5 µm diameter, 1.25 mm length), mounted on a two-dimensional traversing system (*Figure 6*). The setup allowed precise spatial scanning of the jet flow field at specific downstream locations; more than 220 spatial positions were investigated at different coordinates. An overview of the measurement spatial distribution is shown in *Figure 6*. The origin of the reference system was located at the lower tip of the nozzle outlet, with the x-axis directed toward the flow direction, the z-axis upward and vertically directed, and the y-axis oriented as the rule of the right-hand rule.

The probes featured a frequency response of up to 400 kHz in CTA mode. Calibration was conducted in controlled conditions to ensure accurate measurements up to 300 m/s. Velocity signals were acquired over 1.5 seconds at a 30 kHz sampling rate, enabling detailed analysis of both mean flow and turbulence fluctuations.

Materials Research Proceedings 69 (2026) 164-171 https://doi.org/10.21741/9781644904251-29

Results

Three axial positions downstream of the nozzle (x = 0 mm, x = 180 mm, and x = 360 mm) were investigated, with velocity profiles acquired along the z-axis to characterize the jet development. The resulting axial velocity distributions are presented in Figure 7 for the two Mach numbers. At each position, maximum velocity values, Uc, are found near the jet centerline, decreasing with distance from the nozzle exit due to jet spreading. The profiles at x=0 are sharp and narrow, reflecting a thin shear layer, while downstream locations show broader, lower peaks, consistent with turbulent jet decay. By measuring Uc/2 it is possible to assess the jet spreading. The figures show that the jet spreads more rapidly in the case of M=0.66, indicating stronger initial momentum and increased entrainment.

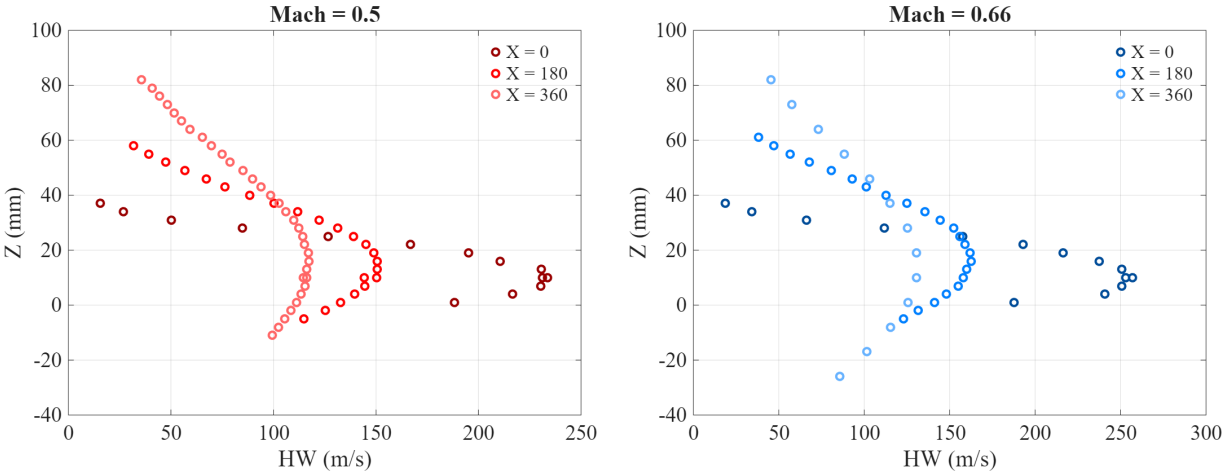


Figure 7 – Axial velocity profiles

Figure 88 shows the standard deviation of the velocity fluctuations along the z-axis. In all cases, the fluctuations exhibit minima at the jet centerline and maxima near to the center of the shear layer, where turbulence intensity is highest due to the strong velocity gradients between the jet core and the ambient flow [5, 6, 7]. The centerline velocity decay, represented as inverse velocity versus axial distance, confirms a monotonic decrease and hints at a slight jet deflection.

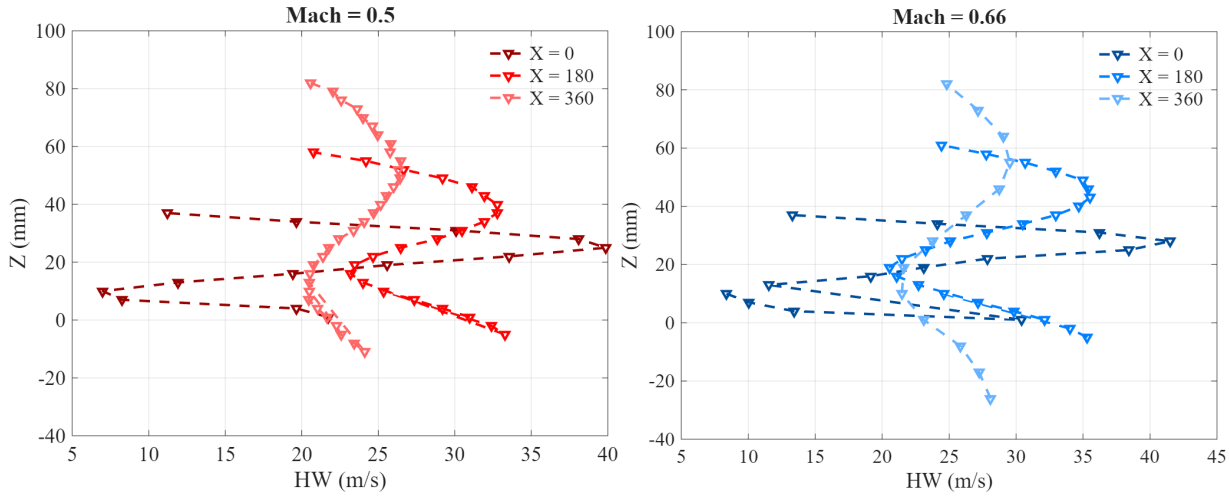


Figure 8 – Standard deviation of the axial velocity

Materials Research Proceedings 69 (2026) 164-171 https://doi.org/10.21741/9781644904251-29

In addition to the downstream measurements, the inlet turbulence conditions were assessed by installing three turbulence-generating grids upstream of the nozzle: fine (0.035 mm × 0.1 mm), intermediate (1 mm × 1 mm), and coarse (2 mm × 2 mm). Hot-wire measurements were performed inside the settling chamber for Mach numbers 0.5, 0.66, and 0.74. These measurements aimed to quantify the turbulence levels introduced by each grid before entering the nozzle.

The turbulence intensity was found to be highest for the coarse grid, decreasing with the intermediate and fine grids, as depicted in Figure 9.

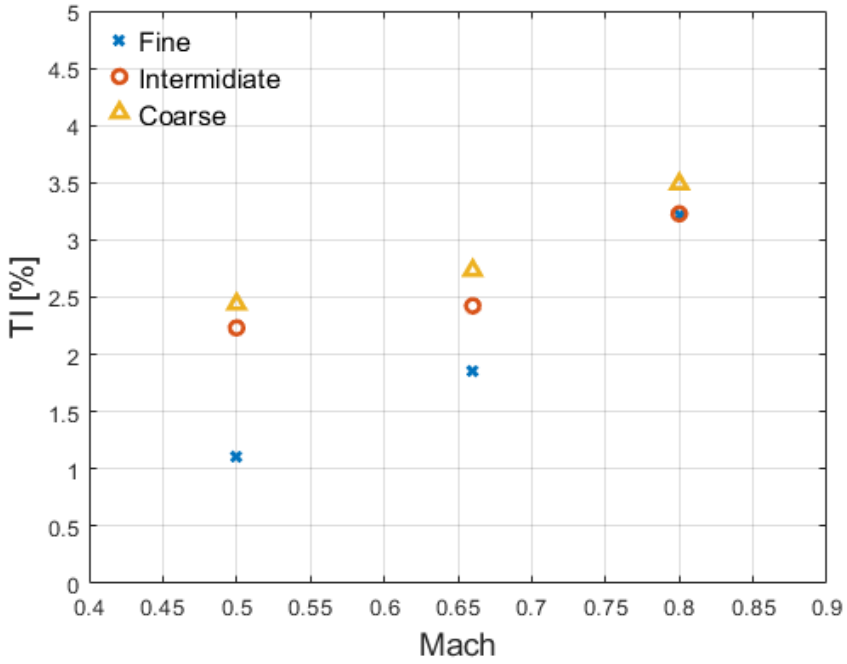
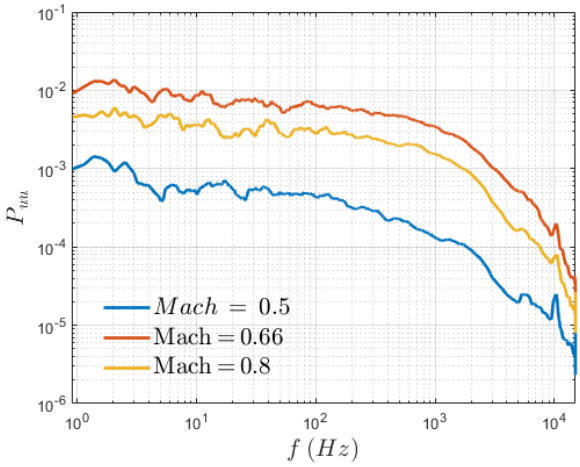


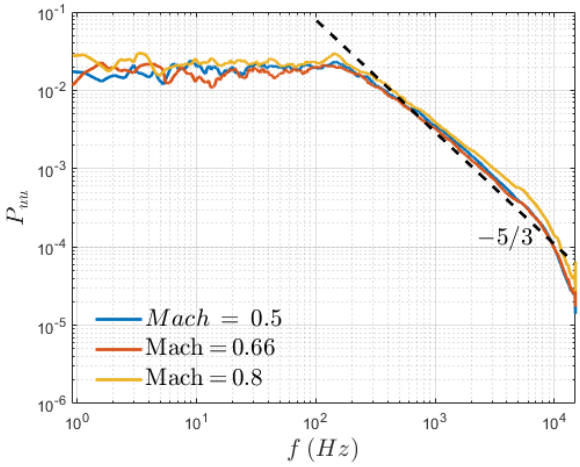
Figure 9 - Turbulence intensity comparison for the three grids

This effect seems to decrease when increasing the Mach number increases and further investigations are needed to clarify this behaviour. As illustrated in Figure 10, power spectral density (PSD) analysis further corroborates these trends: the coarse grid shows a significant shift of energy toward lower frequencies, indicating the presence of large-scale, energetic turbulent structures. These differences in inflow turbulence are expected to impact the downstream jet development and provide valuable reference data for numerical validation.

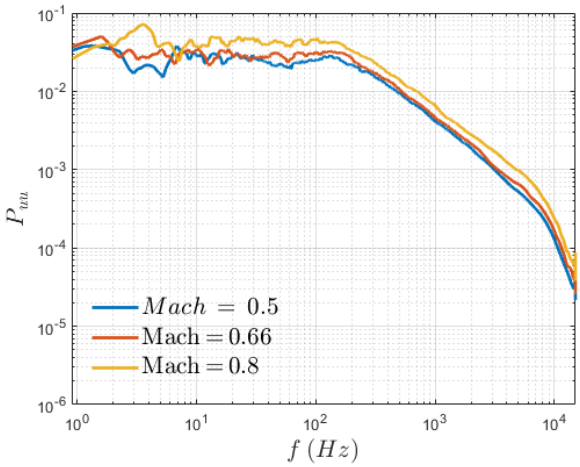
Materials Research Proceedings 69 (2026) 164-171 https://doi.org/10.21741/9781644904251-29



a) Fine grid



b) Intermediate grid



c) Coarse grid

Figure 10 - PSD evaluated for the different grids

Conclusions

An extensive hot-wire test campaign was successfully completed, confirming expected behaviors in jet development and offering a robust dataset for future comparisons with CFD and Large-Eddy Simulations (LES). Upcoming work will include Particle Image Velocimetry (PIV) measurements and expanded numerical analyses using the experimental database as validation.

References

[1] Liersch, C. M., Cummings, R. M., Schütte, A., Vormweg, J., Maye, R. G., & Jeans, T. L. (2020). Multi-disciplinary design and performance assessment of effective, agile NATO air vehicles. Aerospace Science and Technology, 99, 105764. https://doi.org/10.1016/J.AST.2020.105764

[2] Nangia, R., Ghoreyshi, M., van Rooij, M. P. C., & Cummings, R. M. (2019). Aerodynamic design assessment and comparisons of the MULDICON UCAV concept. Aerospace Science and Technology, 93, 105321.

[3] Zenkner, S., Trost, M., Becker, R., & Voß, C. (2019). Preliminary engine design and inlet optimization of the MULDICON concept. Aerospace Science and Technology, 93, 105318. https://doi.org/10.1016/J.AST.2019.105318

[4] Rossignol, K. S., & Delfs, J. (2023). Acoustic Radiation from an Integrated High Aspect Ratio Rectangular Nozzle with Co-Flow. In AIAA Aviation 2023 Forum (p. 4179).

[5] H. Edefur and M. H. Tormalm, "Design and Integration of a Low Observable Intake for the MULDICON Platform," in AIAA Applied Aerodynamics Conference, Atlanta, USA, 2018.

[6] Hussein, H. J., Capp, S. P., & George, W. K. (1994). Velocity measurements in a high-Reynolds-number, momentum-conserving, axisymmetric, turbulent jet. Journal of Fluid Mechanics, 258, 31–75.

[7] Panchapakesan, N. R., & Lumley, J. L. (1993). Turbulence measurements in axisymmetric jets of air and helium. Part 1. Air jet. Journal of Fluid Mechanics, 246, 197–223.

[8] Kolmogorov, A. N. (1941). The local structure of turbulence in incompressible viscous fluid for very large Reynolds numbers. Doklady Akademii Nauk SSSR, 30, 301–305.

Materials Research Proceedings 69 (2026) 172-176 https://doi.org/10.21741/9781644904251-30

Lattice Boltzmann Simulation of Cylinder-Induced Loads on a Lamina

Alessandro TROTTA[1, *], Riccardo GIANSANTE[1], Stefano MELONI[1], Carlo AQUILINI[2], Roberto CAMUSSI[3], Stefano UBERTINI[1], and Andrea Luigi FACCI[1]

[1]Department of Economics, Engineering, Society and Business Organization, University of Tuscia, 01100 Viterbo, Italy

[2]Airbus Defence and Space GmbH, 85077, Manching, Germany

[3]Department of Civil, Computer Science and Aeronautical Technologies Engineering, Roma Tre University, 00146, Rome, Italy

alessandro.trotta@unitus.it

Keywords: Fluid-Structure Interaction, Lattice Boltzmann, Immersed Boundary, Large Eddy Simulation, Vortex Induced Vibration

Abstract. In this work, the Lattice Boltzmann Method based on the Multiple Relaxation Time collision operator is employed to solve the governing fluid flow equations. The method is coupled with the Immersed Boundary Method , a robust meshless approach that represents the geometry of interest on a grid distinct from that used for solving the fluid equations. The interaction between the fluid and the solid boundary is modeled through a body force term, which is transferred between the two grid systems via a Dirac delta function. This coupling enables accurate simulation of fluid–structure interactions involving complex geometries. Within this framework, a Large Eddy Simulation approach is implemented using the Smagorinsky subgrid-scale model, allowing the study of high Reynolds number flow regimes without the need for excessive grid refinement. The study then examines the interaction between a circular cylinder and a lamina at a fixed Reynolds number of 10^4.

Introduction

In modern civil aircraft, landing gears are still critical components for designers, with the main goals to resist the heaviest loads, be the lightest, occupy the smallest volume possible, and meet the safety requirements. Moreover, they are non-redundant, unlike almost the entirety of the other aircraft components, which are designed to ensure the vehicle's correct functionality even after a break.

Retractable landing gears are particularly susceptible to fluid-induced vibrations, not only when deployed but also when retracted, especially in cases of improper closure of the front landing gear hatch. In such scenarios, the flow released by the landing gear generates fluid structures across a range of scales, whose interactions play a critical role in shaping the unsteady aerodynamic loading on nearby surfaces, such as the landing gear door. While large-scale vortices cause global pressure fluctuations, smaller-scale structures contribute to high-frequency vibrations. A thorough understanding of these multi-scale interactions is essential for accurately predicting structural response and assessing the risk of fatigue damage.

Within this context, different Computational Fluid Dynamics (CFD) approaches involving Finite Volume (FV) discretization are employed in the literature [1, 2, 3, 4].

In the present study, the Lattice Boltzmann Method (LBM) with a Multiple Relaxation Time (MRT) collision operator is employed to solve the fluid dynamics equations and coupled with the Immersed Boundary Method (IBM), a meshless approach using distinct grids for the fluid and solid domains. The body–fluid interaction is modeled through a body force term exchanged

Content from this work may be used under the terms of the Creative Commons Attribution 3.0 license. Any further distribution of this work must maintain attribution to the author(s) and the title of the work, journal citation and DOI. Published under license by Materials Research Forum LLC.

Materials Research Proceedings 69 (2026) 172-176 https://doi.org/10.21741/9781644904251-30

between the grids via a Dirac delta function, allowing accurate simulation of complex geometries [5]. A Large Eddy Simulation (LES) framework based on the Smagorinsky subgrid-scale model is incorporated to capture high Reynolds number regimes without excessive grid refinement. Model validation is conducted on the benchmark case of flow past a circular cylinder.

The study then examines the interaction between a cylinder and a rigid lamina fixing the Reynolds number at 1×10^4. The cylinder-lamina configuration may represent a simplified model of the aerodynamic interaction between the landing gear and the adjacent door. The lamina, modeled as a rigid wall-like surface, captures the essential flow mechanisms (i.e. vortex shedding, wake interaction, and unsteady pressure loads) that occur when the landing gear flow impinges on the nearby structures in real aircraft configurations. The high temporal and spatial resolution of the LBM–IBM framework enables detailed analysis of multiscale flow structures and their coupling with the lamina. Finally, the lamina is allowed to vibrate freely, and its distance from the cylinder is varied to investigate fluid–structure interactions and vortex-induced effects.

The paper is structured as follows: Section 2 details the numerical modeling, Section 3 discusses the obtained results, and Section 4 provides the concluding remarks.

Numerical modeling

In the present work, the LBM is used to model fluid flows. The Lattice Boltzmann Equation can be written in its discrete form as:

$$f_i(\boldsymbol{x}_f + \boldsymbol{c}_i\Delta t, t + \Delta t) = f_i(\boldsymbol{x}_f, t) + \Omega_i(\boldsymbol{x}_f, t)\Delta t + F_i(\boldsymbol{x}_f, t)\Delta t \quad (1)$$

where $f_i(\boldsymbol{x}_f, t)$ represents the distribution functions associated to pre-determined lattice directions $\boldsymbol{c}_i$, $\Omega_i(\boldsymbol{x}_f, t)$ and $F_i(\boldsymbol{x}_f, t)$ are the MRT collision operator and the source term respectively. The latter term represents the internal or external forces acting on the fluid and it is modeled using Guo's forcing approach [6, 7].

The LBM is further improved to handle high Reynolds number flows using a LES approach based on the Smagorinsky subgrid scale model. This model is then coupled with the Van Driest damping function to let the turbulent viscosity exponentially damp to zero close to the wall. This approach allows using a coarser mesh reducing computational cost directly resolving large energy containing structures while small scale structures are only modeled [8, 9, 10].

Finally, the IBM is adopted to deal with stationary and moving complex geometries within the fluid domain. Two different grid systems are used, a Lagrangian mesh free to move within the fluid domain used to model the geometry and a stationary cartesian grid for the fluid domain. A force density added in the fluid governing equations is used to model the presence of the obstacle [11, 12, 5]. In this work the diffuse interface scheme based on the IB formulation proposed by Kang and Hassan in [13] is adopted to represent the boundary.

Furthermore, the D3Q19 lattice stencil is employed, with periodic boundary conditions to simulate a lamina and cylinder infinitely long in the spanwise direction, while Neumann boundary conditions are imposed on the top and bottom boundaries.

Results

The first part of the results focuses on the validation of the three-dimensional algorithm against reference data from the literature, using the canonical test case of flow past a circular cylinder at a Reynolds number of 1×10^4. The two-dimensional velocity field is shown Fig. 1a, while Fig. 1b presents the wake visualization using the Q-criterion colored by the lattice velocity magnitude. As expected, a distinct Kármán vortex street develops downstream, with coherent vortices convecting in the freestream direction.

Subsequently, the configuration involving a cylinder with a side-mounted lamina is investigated at the same Reynolds number of 1×10^4. The lamina is characterized by an aspect ratio of L/H = 15, where L denotes its streamwise length and H its height. The upper surface of the lamina is

Materials Research Proceedings 69 (2026) 172-176 https://doi.org/10.21741/9781644904251-30

positioned one cylinder diameter below the lower surface of the cylinder. This arrangement enables the analysis of the interaction between the cylinder wake and the nearby laminar structure, providing further insight into the algorithm's ability to reproduce complex three-dimensional flow features.

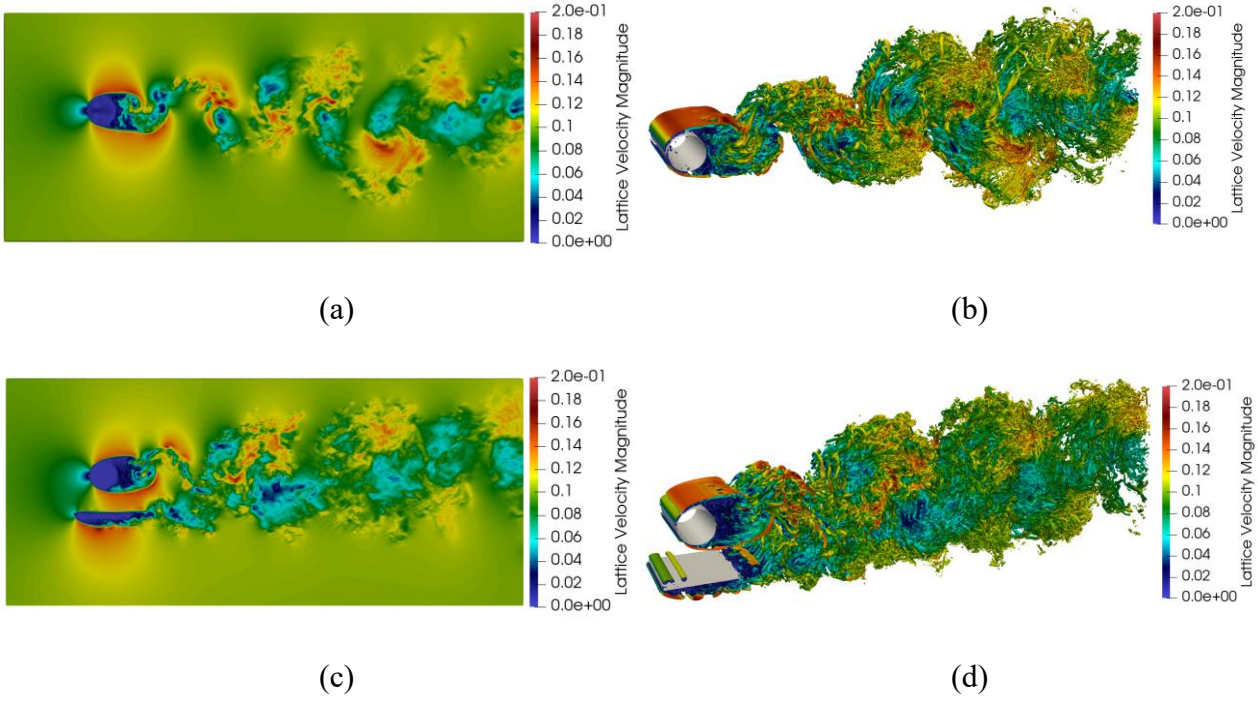
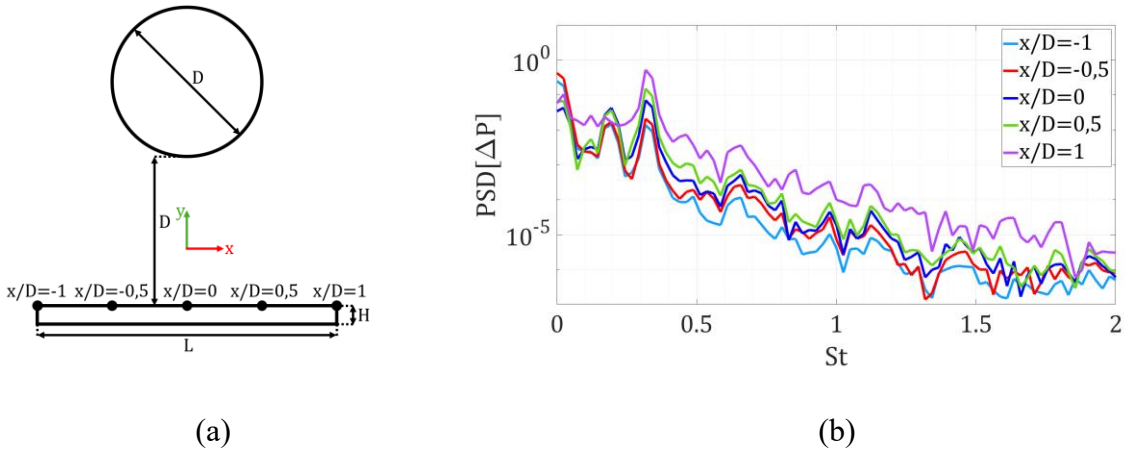


Figure 1 Isolated Cylinder wake: (a) 2D lattice velocity map, (b) Q-criterion; Cylinder with lamina wake (c) 2D lattice velocity map, (d) Q-criterion

The corresponding two-dimensional velocity map, expressed in lattice units, is presented in Fig. 1c. It can be observed that the flow initially separates at the leading edge but rapidly reattaches to the lamina surface due to the influence of the cylinder, which appears to delay flow separation. Further downstream, the wake development is clearly affected by the presence of the lamina, which constrains the wake when compared to the isolated cylinder case. This effect is even more evident in Fig. 1d where the Q-criterion colored by the lattice velocity magnitude reveals the vortical structures. The thin lamina generates additional small-scale vortices that strongly interact with those shed by the cylinder, thereby disturbing their development downstream.

The analysis was further extended to investigate the unsteady wall-pressure load on the lamina by monitoring five discrete points, as schematically illustrated in Fig. 2a. The corresponding unsteady pressure spectra, computed using Welch's method [14], are shown in Fig. 2b. As expected, moving from the leading edge to the trailing edge of the lamina, the broadband power spectral density (PSD) level increases as a consequence of the flow development over the surface. Two distinct peaks are visible in the spectra at different Strouhal numbers: a first peak at $St = 0.19$ corresponding to the vortex-shedding frequency of the circular cylinder, in good agreement with previous studies investigating the effect of the gap between a cylinder and a plane boundary [15, 16].



(a) (b)

Figure 2 (a) Schematic view of the virtual probe positions, (b) Unsteady pressure spectra

Furthermore, the peak intensity progressively diminishes from the leading to the trailing edge, where it becomes indistinguishable, possibly as a consequence of the enhanced broadband energy content induced by the flow grazing along the plate surface. A secondary peak at $St = 0.3$ is consistently detected across all virtual probes, becoming the dominant frequency contribution at $x/D = 1$ This secondary frequency is presumably related to the finite length and aspect ratio of the lamina. However, further analysis is required to confirm this hypothesis.

Conclusions

In this study, the flow around a cylinder with a side-mounted lamina was investigated at a Reynolds number of 1×10^4 using a three-dimensional numerical algorithm that couples the IBM with the LBM-MRT. The computational approach was first validated through the classical benchmark case of flow past a circular cylinder at the same Reynolds number. Subsequent analysis focused on the unsteady pressure loads acting on a thin lamina positioned one diameter away from the cylinder surface, aligned with the freestream flow (zero incidence angle). Comparison of the wake structures for the two configurations clearly highlights the influence of the lamina on wake development. Specifically, the presence of the lamina restricts the motion of vortices that the cylinder sheds, thereby altering the dynamics of the downstream flow. Spectral analysis of the unsteady pressure loads over the lamina surface reveals two distinct frequency components. The first, at $St = 0.19$ corresponds to the characteristic vortex shedding frequency of the cylinder. The second, at $St = 0.3$ becomes increasingly dominant near the trailing edge of the lamina and is likely associated with the finite length and aspect ratio of the lamina itself. These findings highlight the strong coupling between wake dynamics and wall-induced flow confinement. Future work will extend the analysis to configurations with a freely vibrating lamina, to further assess the role of fluid–structure interaction in the onset of flow-induced vibrations.

References

[1] Qing-Li Dong, He-Yong Xu, and Zheng-Yin Ye. Numerical investigation of unsteady flow past rudimentary landing gear using ddes, les and urans. Engineering Applications of Computational Fluid Mechanics, 12(1):689-710, 2018. https://doi.org/10.1080/19942060.2018.1510791

[2] Giuliano De Stefano, Nunzio Natale, Giovanni Paolo Reina, and Antonio Piccolo. Computational evaluation of aerodynamic loading on retractable landing-gears. Aerospace, 7(6), 2020. https://doi.org/10.3390/aerospace7060068

[3] Andreas Lintermann and Wolfgang Schröder. Lattice-boltzmann simulations for complex geometries on high-performance computers. CEAS Aeronautical Journal, 11:745-766, 2020. https://doi.org/10.1007/s13272-020-00450-1

[4] Huixue Dang, Jiang Xu, Wei Wang, Xiaochen Wang, Bin Li, Ruizhi Cao, Liuhong Kang, and Zhichun Yang. Numerical study on the unusual vibration load characteristics and mechanisms of the front landing gear compartment. Aerospace, 10(12), 2023. https://doi.org/10.3390/aerospace10120999

[5] A Trotta, S Meloni, G Falcucci, S Ubertini, and AL Facci. An immersed boundary formulation for lattice boltzmann simulations of low-reynolds fluid-structure interaction problems. Physics of Fluids, 37(3), 2025. https://doi.org/10.1063/5.0256946

[6] Zhaoli Guo, Chuguang Zheng, and Baochang Shi. Discrete lattice effects on the forcing term in the lattice boltzmann method. Physical review E, 65(4):046308, 2002. https://doi.org/10.1103/PhysRevE.65.046308

[7] S Succi. The Lattice Boltzmann Equation for Fluid Dynamics and Beyond. Oxford University Press, 2001. https://doi.org/10.1093/oso/9780198503989.001.0001

[8] Edward R Van Driest. On turbulent flow near a wall. Journal of the aeronautical sciences, 23(11):1007-1011, 1956. https://doi.org/10.2514/8.3713

[9] Stephen B Pope. Turbulent flows. Measurement Science and Technology, 12(11):2020-2021, 2001. https://doi.org/10.1088/0957-0233/12/11/705

[10] Pierre Sagaut. Large eddy simulation for incompressible flows: an introduction. Springer Science & Business Media, 2005.

[11] Luoding Zhu, Guowei He, Shizhao Wang, Laura Miller, Xing Zhang, Qian You, and Shiaofen Fang. An immersed boundary method based on the lattice boltzmann approach in three dimensions, with application. Computers & Mathematics with Applications, 61(12):3506 - 3518, 2011. https://doi.org/10.1016/j.camwa.2010.03.022

[12] Roberto Verzicco. Immersed boundary methods: Historical perspective and future outlook. Annual Review of Fluid Mechanics, 55(1):129-155, 2023. https://doi.org/10.1146/annurev-fluid-120720-022129

[13] Shin K Kang and Yassin A Hassan. A comparative study of direct-forcing immersed boundary-lattice boltzmann methods for stationary complex boundaries. International Journal for Numerical Methods in Fluids, 66(9):1132-1158, 2011. https://doi.org/10.1002/fld.2304

[14] Stefano Meloni, Anderson R Proença, Jack LT Lawrence, and Roberto Camussi. An experimental investigation into model-scale installed jet-pylon-wing noise. Journal of FluidMechanics, 929:A4, 2021. https://doi.org/10.1017/jfm.2021.831

[15] XK Wang and SK Tan. Near-wake flow characteristics of a circular cylinder close to a wall. Journal of Fluids and Structures, 24(5):605-627, 2008. https://doi.org/10.1016/j.jfluidstructs.2007.11.001

[16] SJ Price, D Sumner, JG Smith, K Leong, and MP Paidoussis. Flow visualization around a circular cylinder near to a plane wall. Journal of Fluids and Structures, 16(2):175-191, 2002. https://doi.org/10.1006/jfls.2001.0413

Materials Research Proceedings 69 (2026) 177-182 https://doi.org/10.21741/9781644904251-31

Image Segmentation for Leading Edge Experiments of Rocket Fins in an Arc-Heated Wind Tunnel

Oliver ASSENMACHER[1,a *], Oliver HOHN[2,b], Alexander RÜTTGERS[1,c] and Ali GÜLHAN[2,d]

[1]German Aerospace Center (DLR) – Institute of Software Technology, High-Performance Computing Department, Linder Höhe, 51147 Cologne, Germany

[2]German Aerospace Center (DLR) – Institute of Aerodynamics and Flow Technology, Supersonic and Hypersonic Technologies Department, Linder Höhe, 51147 Cologne, Germany

[a]oliver.assenmacher@dlr.de, [b]oliver.hohn@dlr.de, [c]alexander.ruettgers@dlr.de, [d]ali.guelhan@dlr.de

Keywords: Machine Learning, Computer Vision, High enthalpy, Arc-Heated Wind Tunnel

Abstract. Leading edges of rocket fins made from glass fibre composites were tested in the arc-heated wind tunnel L2K at the German Aerospace Center (DLR) under continuous high-enthalpy flow conditions. Under these aerothermal loads, the leading edge undergoes significant shape deformation, and pyrolysis-induced melt products accumulate on the sides of the fin. Video recordings of the experiments were captured and analysed to track the deformation of the leading edge and the formation of melt products at the sides of the fin. Computer vision algorithms for image segmentation are applied to this data to detect for each frame the region of the image that corresponds to the leading edge and the melt products, respectively. Ultimately, the goal of this analysis is to quantify the deformation of the leading edge and the formation of melt products over the duration of the experiment. The task of image segmentation is performed with a convolutional neural network, based on the U-Net architecture and the neural network approach is compared to a simple threshold procedure. Both methods are able to separate the images into the relevant regions, but the approach using thresholds struggles with the high variation in illumination along the fin and underestimates the amount of melt. Furthermore, the separation between melt and leading edge is difficult to achieve correctly with a threshold. In contrast, the U-Net approach agrees better with manual labels in both regards on unseen test frames. This improved fidelity in the detection of the leading edge and the melt products aids in the automatic analysis of these wind tunnel experiments.

Introduction

Wind tunnel experiments are an important intermediate step between simulation and flight experiments because they provide real experimental data under realistic conditions without the associated costs of a full flight experiment, enabling the validation of simulation results and the preparation of flight missions. These experiments generate a wealth of data which creates opportunities for applying modern data science methods to extract additional insights. For example, computer vision algorithms developed over the past decade can aid significantly in analysing image data that would otherwise require manual inspection. One such application is the automatic segmentation of video data from experiments with leading edges of rocket fins in an arc-heated wind tunnel at DLR Cologne. The goal in this task is, separating each frame of a video into distinct image regions, to enable further downstream analysis such as tracking the deformation of the leading edge. In this paper, a neural network-based approach for this problem is presented, which compares favourably with simpler threshold-based methods.

Content from this work may be used under the terms of the Creative Commons Attribution 3.0 license. Any further distribution of this work must maintain attribution to the author(s) and the title of the work, journal citation and DOI. Published under license by Materials Research Forum LLC.

Materials Research Proceedings 69 (2026) 177-182 https://doi.org/10.21741/9781644904251-31

The paper is organized as follows: First the methods are explained, which includes the experimental setup and the use of neural networks for image segmentation. Then, the results of this method are presented, including a quantitative and qualitative evaluation, as well as a comparison to an optimal threshold-based approach. Finally, some conclusions and an outlook for future work is given.

Methods

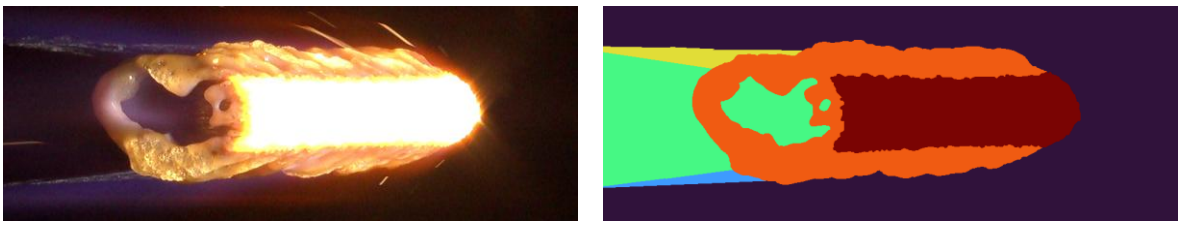
Experimental Setup. The video data, analysed in this study, were recorded during experiments in the arc-heated wind tunnel L2K at DLR Cologne with rocket fin leading edges made from glass fibre composites. These tests are intended to evaluate the suitability of different materials for hypersonic flight conditions by exposing the test specimen to thermal loads comparable to those observed in real flight experiments. Detailed descriptions of the test facilities can be found in [3,4,5]. The experimental conditions are summarized in Table 1, which mirror those of an analogues test campaign with wood fibre materials [1]. The leading edge undergoes significant deformation during these experiments and a total mass loss of 15.8% was recorded. Furthermore, melt products accumulate on the sides of the fin. During the experiment the leading edge is recorded with a video camera, Fig. 1 (a) shows one frame from this video recording. The topic of the present work is the algorithmic analysis of this video data.

Table 1: Experimental conditions

Flow Parameter	Value
Total gas mass flow [g/s]	50
Air mass flow [g/s]	2
Nitrogen mass flow [g/s]	48
Total enthalpy h_0[MJ/kg]	6.85
Stagnation pressure p_s[hPa]	89
$h_0 \cdot \sqrt{p_s}$	64.6
Nozzle configuration (throat/exit diameter) [mm]	29/100
Distance from nozzle exit [mm]	120
Test duration [s]	120

Image Segmentation. A commonly used step in the algorithmic analysis of image data is separating the image into distinct regions, so called classes, with some specific application defined meaning. The result of this step is called a segmentation or mask, which contains for each pixel in the input image the index identifying the class this pixel belongs to. In this work, the input images are the video frames from the wind tunnel experiments described in the previous subsection. The six image regions that are to be distinguished are: background, the three visible sides of the fin (downward, frontward, upward), melt products and leading edge. For the sake of brevity, the classes will be referred to as background, down, front, up, melt and edge, respectively, in the remainder of the paper.

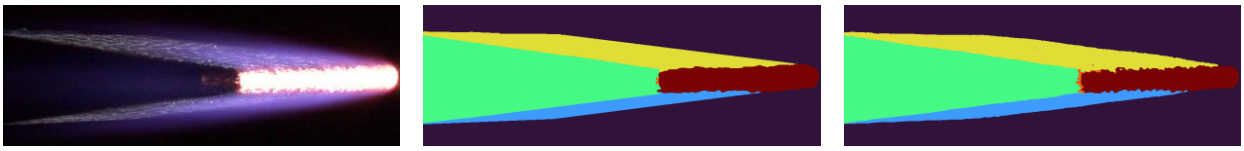
Materials Research Proceedings 69 (2026) 177-182 https://doi.org/10.21741/9781644904251-31



(a) Video frame *(b) Manual segmentation*

Fig. 1: Manually created segmentation. The classes are: background (dark blue), downward side (light blue), frontward side (green), upward side (yellow), melt products (orange) and leading edge (red).

Intersection over Union. To assess the accuracy of an image segmentation algorithm, manual segmentations of some of the images are created first. These can then be used to compute the Intersection over Union (IoU) metric for algorithmically created segmentations. The IoU is computed for each class separately, by counting the number of pixels in the intersection of manual and algorithmic segmentation and dividing by the number of pixels in the union of both segmentations for this class. This fraction is 1 if both algorithm and human labels agree perfectly and it is 0 if the two segmentations are completely disjoint for this class. The background class will be excluded, when computing the IoU, because the IoU for the background heavily depends on how the images are cropped around the object of interest.



(a) Video frame *(b) Manual segmentation* *(c) Neural network prediction*

Fig. 2: Earliest manually labelled frame.

Neural Networks for Image Segmentation. Neural networks have been successfully applied for image segmentation in several domains, such as medical images [2] and high-speed combustion videos [6]. Typically, this is treated as a supervised machine learning problem, which means that a set of training examples of images with corresponding segmentations has to be created first. For example, Fig. 2 shows one such training example, where the different regions of the leading edge were manually annotated. Furthermore, a neural network architecture must be defined to compute the probabilities that each pixel belongs to each of the different classes for a given input image, depending on a set of parameters. In this study, a U-Net architecture is used, which was first proposed for the analysis of medical images [2]. Ultimately, the goal is then, to find a setting for the parameters of the neural network such that the resulting probabilities match the provided segmentations on the training set as closely as possible. This is achieved by applying stochastic gradient descent, or variants thereof, to a minimization problem based on the training data, the network architecture and a loss function, which quantifies the discrepancy between the computed class probabilities and the manual annotations. Finally, after computing a setting for the parameters, which minimizes the total loss on the training set, the neural network with these specific parameter values can be applied to images outside of the training set to obtain for each pixel in the image an estimate of how likely this pixel belongs to each of the different classes. A segmentation can then be obtained by determining the most likely class for each pixel. Fig. 2 shows a comparison of the manual and the neural network-computed segmentation for one of the video frames.

Data augmentation. Machine learning methods that use neural networks are often limited by the quantity and quality of the available training data. Since each image in the training dataset must

be annotated manually, it can be very time-consuming to create a sufficiently large dataset for applying a neural network based method. A common approach to reduce the number of necessary training examples is to apply data augmentation during training. This involves applying random transformations to the input data during training that either preserve the correctness of the corresponding labels, or transform the labels as well. For image segmentation, for example, small changes in brightness usually do not affect the accuracy of the segmentation. On the other hand, if the images are rotated by a small angle, then the segmentations can be rotated in the same way to preserve their correctness. Adding small perturbations like this, while preserving the correctness of the labels, can significantly improve the robustness and accuracy of the resulting prediction model.

Results

Cross Validation. To evaluate the performance of this neural network approach, a 4-fold cross validation is performed on a dataset of 20 manually labelled images. This involves randomly splitting the dataset into four folds, training four U-Net models and leaving one fold out each time. This process was repeated for five different random seeds, resulting in a total of 20 trained models. The 15 images used for training each model are processed 1000 times each with a new randomly sampled data augmentation applied to the image every time. The models are then evaluated on the fold that was left out during their training. Finally, the average Intersection over Union (IoU), as described in the previous section, is computed for each random seed across all 20 images and Table 2 shows the minimum, maximum and mean of the average IoU across the 5 different random seeds. The performance across the different random seeds, and thus different ways of splitting the data, is relatively stable for all the classes. The largest variation can be observed in the segmentation quality of the melt products which varies from 0.7844 to 0.8160 and this is also the class, for which the model performs the worst in general. Examining the accuracies for each frame, cf. Fig. 3, reveals that the main reason for the lower average IoU in the melt class is that this class is segmented poorly in the initial frames.

As can be seen in Fig. 2, there is basically no melt product visible yet at the beginning of the video and because the IoU is a relative error measure, even small absolute errors can lead to a very low IoU.

Table 2: IoU of neural network predictions across 5 different random seeds.

	Down	Front	Up	Melt	Edge
Minimum	0.8258	0.9074	0.8649	0.7844	0.9610
Maximum	0.8516	0.9179	0.8932	0.8160	0.9667
Mean	0.8350	0.9145	0.8811	0.8062	0.9649

Comparison with Optimal Thresholds. The performance of the neural network approach is further evaluated by comparing it to a simple threshold method. To this end, a segmentation pipeline consisting of three stages, pre-processing (optional Gaussian blur and selection of colour channel or greyscale), threshold (global or adaptive) and post-processing (optional morphological transformation) is used. These stages are first applied to determine the leading edge segmentation and are then repeated in a second step for the melt region. The other classes are omitted for this comparison because in practice the edge and melt are the most relevant. The stages each contain several free parameters that have to be chosen, e.g. the value of the threshold or the radius of several sliding-window type filters. To provide an upper bound for the accuracy of this method, an exhaustive brute-force search to determine the optimal value for all free parameter is performed. This search is done once for each annotated image, separately, and once for all images simultaneously. The accuracy of the resulting methods is shown in Table 3 and compared to the average accuracy of the neural network approach. This comparison shows that computing the

Materials Research Proceedings 69 (2026) 177-182 https://doi.org/10.21741/9781644904251-31

parameters once for all images leads to a significant drop in segmentation quality compared to computing them for each image separately, in particular for the melt products. Furthermore, the neural network approach outperforms even the optimal threshold for each image on average.

Table 3: Intersection over Union (IoU) for different methods.

	Threshold	Threshold (per frame)	Neural network (Mean)
Melt	0.6374	0.7589	0.8062
Edge	0.9326	0.9580	0.9649

Additionally, Fig. 3 shows how the methods compare for each frame by plotting the IoU over the experiment duration. Only in the very beginning do the threshold methods perform better than the neural network, though all methods see a significant drop in accuracy for the earliest frames. For most of the experiment duration, the neural network approach outperforms both threshold-based methods.

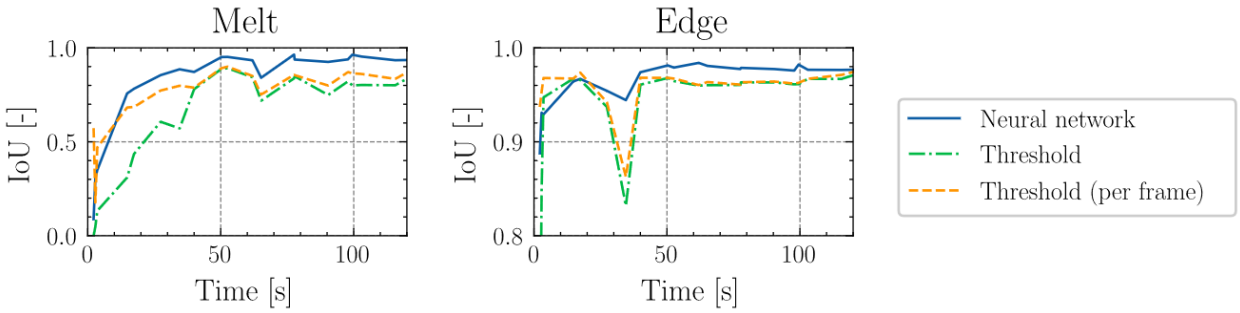
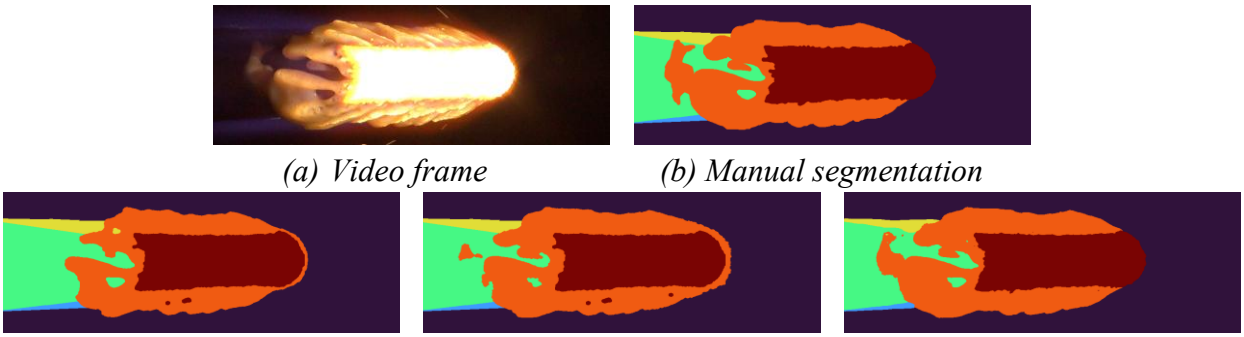


Fig. 3: IoU over time for different segmentation methods.

Fig. 4 depicts the segmentations produced by each method for one frame of the video. One can see, that the threshold method struggles with separating the leading edge from the melt products. Furthermore, parts of the melt products can not be properly detected by a threshold due to the high variation in illumination in the image.



(a) Video frame *(b) Manual segmentation*

(c) Threshold *(d) Threshold (per frame)* *(e) Neural network prediction*

Fig. 4: Comparison of different segmentation methods.

It should be highlighted that to compute the optimal threshold a manual segmentation of that specific frame is needed, rendering this approach useless in practice. Therefore, it is only a theoretical upper bound of what can be achieved with a simple threshold. Conversely, the neural network is evaluated only on frames that were not part of its training set, which means that these segmentations can be computed for other frames without manual segmentation.

Conclusion

A neural network-based approach for image segmentation of videos frames from experiments with a rocket fin leading edge in an arc-heated wind tunnel is presented. This approach is compared

with a simple threshold method, where the parameters, such as the threshold value, are chosen optimally. This serves as a theoretical upper bound on the performance of a simple threshold, as computing the optimal parameters requires the ground truth. Nonetheless, the neural network approach consistently outperforms the simpler threshold method across several random seeds.

In future work, this improved segmentation accuracy will be combined with 3D information about the camera position/rotation to enable downstream tasks, such as quantifying the volume of melt products at the side of the fin or tracking the deformation of the leading edge.

Acknowledgments
The research was carried out under the project Advanced Technologies for High Energetic Atmospheric Flight of Launcher Stages (ATHEAt) by the German Aerospace Center (DLR).

References

[1] R. Günther, O. Hohn, H. Unbehaun, O. Drescher, H. Weihs, Wood Fibre Materials on Hot Sounding Rocket Structures, 2nd International Conference on Flight Vehicles, Aerothermodynamics and Re-entry Missions & Engineering (FAR), Heilbronn, 2022.

url: https://elib.dlr.de/200779/

[2] O. Ronneberger, P. Fischer, T. Brox, U-Net: Convolutional Networks for Biomedical Image Segmentation, in: N. Navab, J. Hornegger, W. Wells, A. Frangi (Eds.) Medical Image Computing and Computer-Assisted Intervention – MICCAI 2015, Springer, Cham, 2015,

pp. 234-241. https://doi.org/10.1007/978-3-319-24574-4 28

[3] A. Gülhan, B. Esser, Arc-Heated Facilities as a Tool to Study Aerothermodynamics Problems of Reentry Vehicles, in: D. Marren, F. Lu (Eds.) Advanced Hypersonic Test Facilities, American Institute of Aeronautics and Astronautics, Reston, 2002, pp. 375-403. https://doi.org/10.2514/5.9781600866678.0375.0403

[4] A. Gülhan, B. Esser, U. Koch, K. Hannemann, Mars Entry Simulation in the Arc Heated Facility L2K, in: R.A. Harris (Ed.) Fourth Symposium on Aerothermodynamics for Space Vehicles, European Space Agency, Capua, 2002, pp. 665-672.

url: https://adsabs.harvard.edu/full/2002ESASP.487..665G

[5] A. Gülhan, B. Esser, U. Koch, Experimental Investigation of Reentry Vehicle Aerothermodynamic Problems in Arc-Heated Facilities, J. Spacecr. Rockets Vol. 38 Nr.2 (2001) 199-206. https://doi.org/10.2514/2.3670

[6] O. Assenmacher, R. Gelain, A. Rüttgers, A. Petrarolo, P. Hendrick, Convolutional neural networks for image analysis of high-speed videos from two slab burners, Acta Astronaut. Vol. 219 (2024) 931-940. https://doi.org/10.1016/j.actaastro.2024.04.005

Materials Research Proceedings 69 (2026) 183-186 https://doi.org/10.21741/9781644904251-32

Assessment of a CFD Solver for Detonation Wave Simulations

BONELLI Francesco[1,a *], MILIA Davide[1,b], NINNI Davide[1,c], PASCAZIO Giuseppe[1,d], LAERA Davide[1,e]

[1]DMMM & CEMeC, Politecnico di Bari, Via Re David 200, Bari, 70125, Italy

[a]francesco.bonelli@poliba.it, [b]d.milia@studenti.poliba.it, [c]davide.ninni@poliba.it, [d]giuseppe.pascazio@poliba.it, [e]davide.laera@poliba.it

Keywords: ZND Detonation, Reacting Flows, Shock-Combustion Interaction

Abstract. This work assesses the capabilities of an innovative fluid dynamics solver, originally developed to deal with high-enthalpy flows in the context of hypersonic planetary entry, and now applied to simulate problems involving complex interactions between strong shock waves and combustion processes. With a view toward future simulations of rotating detonation combustors, the solver accuracy is assessed by considering 1D and 2D detonation fronts.

Introduction

Over the years, Rotating Detonation Engines (RDEs) have become very attractive in the field of aerospace propulsion due to their high efficiency and mechanical simplicity [1,2]. Moreover, Rotating Detonation Combustors (RDCs), the core component of RDEs, have aroused a growing interest in the field of energy generation as a promising solution to the rising energy demand, climate change, and increasing pollution, all of which threaten human well-being and health.

The main characteristic of such devices is the detonation-based combustion, which, on one hand, is the key feature enabling higher efficiency, and on the other hand, introduces several challenges.

In the aerospace field, RDEs represent an evolution of Pulse Detonation Engines (PDEs) which in turn evolved from pulsejets. These systems can achieve higher efficiency with respect to turbojets, since the pressure gain during the combustion process leads to the Fickett-Jacobs thermodynamic cycle [3]. RDEs retain the advantages of PDEs while employing a continuous combustion process that eliminates the drawbacks associated with intermitted operation. However, the apparent simplicity of these systems hides several issues related to the intrinsic complexity of the supersonic combustion process [4]. Thus, to ensure proper engine operation, a multidimensional numerical solver capable of handling highly compressible flows in chemical non-equilibrium, and capturing complex shock and expansion waves structures, is required.

In this context, the aim of the present work is to extend the capabilities of the Damiso solver [5,6] to deal with detonative combustion. This solver has been developed to simulate high enthalpy flows in thermochemical non-equilibrium, leveraging GPU computational power.

In the present study, the solver has been verified by comparing the results of a 1D detonation with the Zel'dovich–von Neumann–Döring (ZND) solution obtained using CANTERA [7].

Subsequently, 2D simulations of a detonation front have been performed in order to highlight the code's capability to capture multidimensional detonation structures [2,3].

Governing Equations and Numerical Method

The flow field is simulated by solving the Navier–Stokes equations for a multicomponent reacting mixture in chemical non-equilibrium. The system of equations is discretized using a cell-centered finite-volume approach. To deal with the stiffness associated with chemical reactions, an operator-splitting strategy is adopted, separating fluid dynamics from chemistry. The homogeneous system of fluid-dynamic equations is solved first.

Content from this work may be used under the terms of the Creative Commons Attribution 3.0 license. Any further distribution of this work must maintain attribution to the author(s) and the title of the work, journal citation and DOI. Published under license by Materials Research Forum LLC.

Materials Research Proceedings 69 (2026) 183-186 https://doi.org/10.21741/9781644904251-32

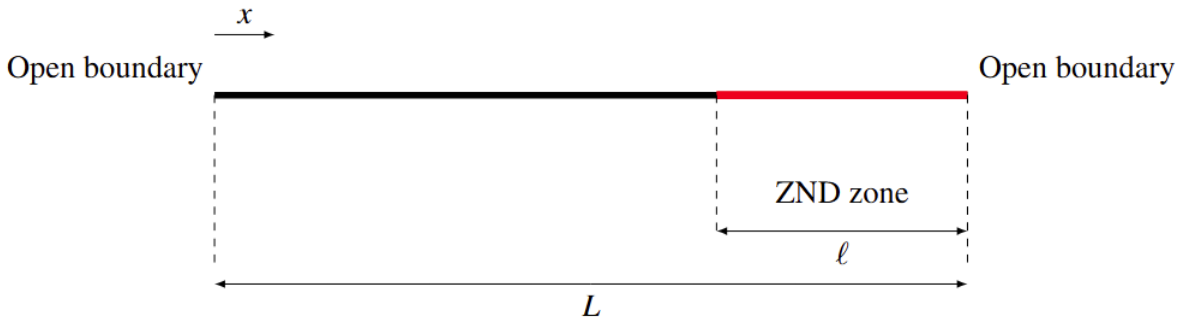


Fig. 1 1D domain for the simulation of the detonation in the lab frame with Damiso.

For this step, the method of lines is employed to separate time and space discretization. First, surface fluxes are computed by employing the Steger and Warming flux vector splitting in combination with a MUSCL (Monotonic Upstream-centered Scheme for Conservation Laws) reconstruction of primitive variables, in order to achieve second-order accuracy. Subsequently, time integration is performed using a third-order Runge–Kutta scheme. Finally, the solution of species partial densities is updated by solving a system of ODEs accounting for the chemical source terms, where an implicit iterative Gauss–Seidel scheme is employed to handle stiffness. Further details can be found in [5,6].

Results

Following the work of Strempfl et al. [2,8], the capabilities of Damiso have been verified by performing a 1D detonation test case, whose results have been compared with those obtained with the well-know and reliable toolbox CANTERA using the Shepherd ToolBox [9].

A hydrogen-air mixture with initial conditions of T_{init} = 300 K, P_{init} = 101325 Pa and an equivalence ratio of ϕ=0.9 was considered [8]. To reduce the computational cost, the 1-step chemical scheme developed by Strempfl et al. [2,8] was employed.

$$H_2 + 0.5O_2 \rightleftharpoons H_2O. \quad (1)$$

Specifically, in Refs. [2,8], the H_2O formation enthalpy at 0 K (-226.8 *kJ/mol*), the Arrhenius pre-exponential factor ($5.3 \cdot 10^{10}$ $1/\left(\sqrt{mol\ cm^{-3}}s\right)$) and the activation energy (18000.0 *cal/mol*) were tuned and optimized in order to match the Chapman–Jouguet detonation speed (D_{CJ}) and the half-reaction thickness obtained with detailed mechanisms.

The CANTERA toolbox was employed to obtain a 1D ZND solution in the detonation-wave reference frame. This solution was then employed as the initial condition for the 1D Damiso simulation in the laboratory frame.

Figure 1 shows the 1D computational domain adopted in Damiso. The total length is $L = 2 \cdot 10^{-3}$ m, whereas the ZND initial solution (in red) extends over $\ell = 7 \cdot 10^{-4}$ m. The CANTERA solution was imposed after transforming the velocity from the detonation to the laboratory frame as:

$$u_{lab}(x) = D_{CJ} - u_{det\text{-}frame}(x), \quad (2)$$

where D_{CJ} = 1920.02 m/s.

The left portion of the domain (in black) represents the region of the fresh, unreacted mixture, which is initially at rest. A uniform mesh with a 6000 cells has been employed.

In order to verify the accuracy of the Damiso solver, the ZND detonation structure was allowed to evolve in time. Therefore, the steady detonation-frame solution provided by CANTERA was compared with the unsteady laboratory-frame solution computed by Damiso.

Materials Research Proceedings 69 (2026) 183-186 https://doi.org/10.21741/9781644904251-32

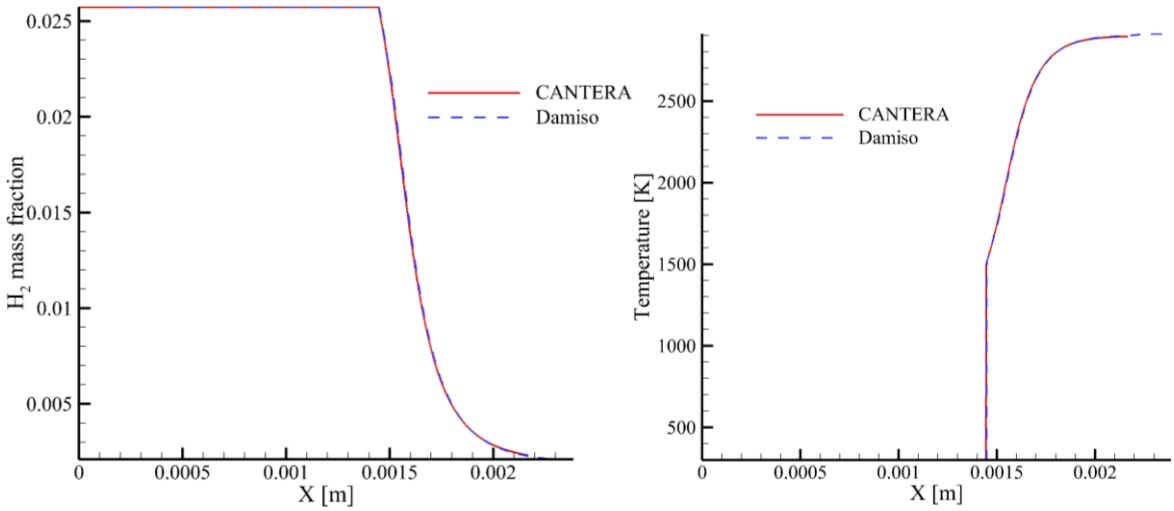


Fig. 2 1D ZND comparison: H_2 mass fraction (left) and temperature (right) profiles.

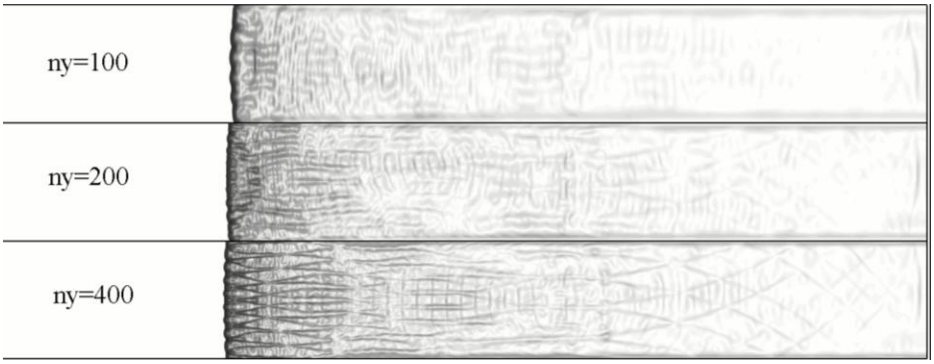


Fig. 3 2D ZND solution for different grid size resolutions along the transverse direction: magnitude of the density gradient.

The comparison is provided in Figs. 2 (left) and (right), showing the H_2 mass-fraction and temperature profiles, respectively. The Damiso solution, taken at a generic time instant, shows excellent agreement with the CANTERA reference solution.

Once the Damiso accuracy had been verified, a 2D detonation tube test case was simulated. The initial conditions are the same of the 1D case, but the computational domain now has L=0.5 m, $\ell=1\cdot10^{-2}$ m, and it extends in the transverse direction for an height of $H=3\cdot10^{-2}$ m. In order to investigate the influence of grid resolution, three uniform meshes with different resolutions were considered. The number of cells along the x-direction is 6000, while three different discretizations have been used along the y-direction, with 100, 200, and 400 cells, respectively. These configurations allow an evaluation of how the numerical resolution affects the morphology of the detonation cells and their spatial periodicity. As in the 1D case, the steady solution obtained with CANTERA was interpolated and imposed on the right side of the domain to initialize the thermochemical profile of the ZND region. In this configuration, however, the detonation front was not initialized as planar, but as a sinusoidal wave with a wavelength equal to one-quarter of the domain height. This choice, promotes the development of transverse instabilities from the very beginning, favoring the rapid formation of the cellular structure of the detonation and reducing the transition from a planar wave to an unstable front.

Figure 3 shows the contour plot of the density-gradient magnitude. The simulations demonstrate that, as the number of cells increases along the transverse direction, the cellular pattern becomes progressively more defined and detailed. The higher resolution enables a more accurate

representation of local instabilities and of the transverse waves that characterize the detonation front.

Summary

In this work, the Damiso solver, originally devised for hypersonic flow simulations, has been assessed for detonation processes. The solver has been verified by comparing the results of a 1D ZND detonation with those obtained using the CANTERA toolbox. Finally, a simulation of a 2D ZND detonation has been performed, demonstrating the capability of the solver to identify the characteristic detonation structures.

Acknowledgement

F. Bonelli, D. Ninni, G. Pascazio and D. Laera were partially supported by the Italian Ministry of Education, University and Research under the Program Department of Excellence Legge 232/2016 (Grant No. CUP - D93C23000100001).

References

[1] I.J. Shaw, J.A. Kildare, M.J. Evans, A. Chinnici, C.A. Sparks, et al. (2019). A theoretical review of rotating detonation engines. In Direct Numerical Simulations: An Introduction and Applications, ed. S Rao.London: IntechOpen.

[2] P. Strempfl, O. Dounia, D. Laera, & T. Poinsot. Effects of mixing assumptions and models for LES of hydrogen-fueled rotating detonation engines. International Journal of Hydrogen Energy, 62 (2024) 1-16. https://doi.org/10.1016/j.ijhydene.2024.03.033

[3] P.C. Nassini (2021). High-fidelity numerical investigations of a hydrogen rotating detonation combustor. PhD Thesis, Università degli studi di Firenze.

[4] V. Raman, S. Prakash, & M. Gamba. Nonidealities in rotating detonation engines. Annu. Rev. Fluid Mech. , 55(1) (2023) 639-674. https://doi.org/10.1146/annurev-fluid-120720-032612

[5] G. Pascazio, D. Ninni, F. Bonelli, G. Colonna, Hypersonic flows with detailed state-to-state kinetics using a GPU cluster. In Plasma Modeling (Second Edition): Methods and applications. IOP Publishing. Bristol, UK, 2022, pp. 10-1–10-41. https://doi.org/10.1088/978-0-7503-3559-1

[6] F. Bonelli, D. Ninni, A. Narracci, G. Colonna, & G. Pascazio. Assessment of a consistent multi-internal-temperature kinetic model for hypersonic neutral air flows using a finite volume solver. Computers & Fluids, 106796 (2025). https://doi.org/10.1016/j.compfluid.2025.106796

[7] D.G. Goodwin, R.L. Speth, H.K. Moffat, & B.W. Weber. Cantera: An object-oriented software toolkit for chemical kinetics, thermodynamics, and transport processes. (2018) https://www.cantera.org

[8] P. Strempfl, LES of Rotating Detonation Engines: sensitivity and Physics. 2024. PhD Thesis. Université de Toulouse.

[9] S. Browne, J. Ziegler, and J. Shepherd (2008). “Numerical solution methods for shock and detonation jump conditions”. GALCIT report FM2006, 6, p. 90.

Materials Research Proceedings 69 (2026) 187-192 https://doi.org/10.21741/9781644904251-33

Comparison of Far-Field Methodologies for Unsteady Low Reynolds Number Flows

Dameon WESTLEY[1], Lelanie SMITH[1], Drewan SANDERS[2], Manuel CARREN˜O RUIZ[3]*, and Domenic D'AMBROSIO[3]

[1]University of Pretoria, South Africa

[2]Cranfield University, United Kingdom

[3]Politecnico di Torino, Italy

*manuel.carreno@polito.it

Keywords: Far-Field, Power Balance Method, Momentum Decomposition, Energy Decomposition, Exergy Decomposition, Thermodynamic Methods, Unsteady CFD, STAR CCM+

Abstract. Low Reynolds number (Re) flows in the range of 1000-10000 are common in applications such as Micro Aerial Vehicles (MAVs), Martian flight, and high-altitude terrestrial flight. The flow around conventional airfoils in this regime exhibits periodic vortex shedding with spanwise coherence at low angles of attack (AoA). These simple cases are very useful for testing and implementing unsteady far-field force decomposition methods within commercial CFD software. In this work, a conventional NACA 0012 airfoil at Re = 5000 and an AoA of 6° was analyzed using time-accurate Navier-Stokes simulations in the commercial CFD code STAR-CCM+. The resulting flow fields were subjected to different far-field analyses based on unsteady thermodynamic approaches and extended mechanical energy balances to include unsteady terms and exergy additions. Near-field drag was compared with various far-field drag predictions, and several decompositions are proposed to isolate the energy, exergy, and thermodynamic contributions to the overall far-field drag. This constitutes the first study of its kind comparing unsteady thermodynamic, mechanical-energy-based, and exergy-based decomposition approaches.

Introduction

Initially conceptualized by Desterac and Van der Vooren [1], far-field methods enable the non-intrusive analysis of bodies in motion, providing information that cannot necessarily be obtained through near-field methods. These advantages, together with the growing emphasis on integrated airframe-propulsion configurations, have led to the continued development of various far-field drag analysis approaches. Many of these methodologies have undergone extensive validation in the steady domain. Drela [2] first derived the mechanical-energy-based power balance decomposition method, which was later extended by Sanders and Laskaridis [3] to employ an absolute reference frame. Arntz et al. [4] further expanded this formulation to include additional exergy terms. Similarly, Toubin [5] developed the momentum-based thermodynamic methods to their current unsteady form. However, these far-field approaches have so far been tested only to a limited extent in the unsteady domain. The Reynolds number range of 1000 - 10000 is commonly used for unsteady cases because the flow around wings in this regime exhibits spanwise-coherent vortex shedding at low to moderate angles of attack. Such flow conditions resemble those encountered by Micro Aerial Vehicles (MAVs), biological insects, and vehicles in Martian flight. Unsteady cases involving fixed- angle-of-attack wings offer suitable testing conditions for far-field methods, as they allow transient flow behavior with unsteady vortex shedding features to be analyzed on fixed grids. This configuration provides relative simplicity, low computational cost,

Content from this work may be used under the terms of the Creative Commons Attribution 3.0 license. Any further distribution of this work must maintain attribution to the author(s) and the title of the work, journal citation and DOI. Published under license by Materials Research Forum LLC.

Materials Research Proceedings 69 (2026) 187-192 https://doi.org/10.21741/9781644904251-33

and clearly defined downstream coherent structures that facilitate the assessment and comparison of unsteady far-field decomposition methodologies.

Methodology

A NACA 0012 airfoil at an angle of attack (AoA) of 6° was analysed using Star CCM+ using an unstructured C-type domain grid at a Reynolds number of 5000 and a Mach number of 0.2, with velocity inlet and pressure outlet boundary conditions. Mesh, domain, and time- independence studies indicated near-field convergence at a mesh size of 1.4 million cells, a domain radius of 100 chord lengths, and a time-step size of 0.0025 c/V_∞, ensuring a convective CFL number below 1 throughout the computational domain. To ensure accurate far-field resolution, the mesh was further refined to 2,097,000 cells. A second-order coupled laminar solver with second-order implicit dual time-stepping was employed, with five inner iterations per time step being sufficient to reduce residuals by two to three orders of magnitude. The wall y^+ value was kept below 0.1 for all simulations. A series of control volumes (CVs) were subsequently defined to analyze and compare far-field methods, as shown in Figure 1, where the CV sizes are non-dimensionalised by the airfoil chord length.

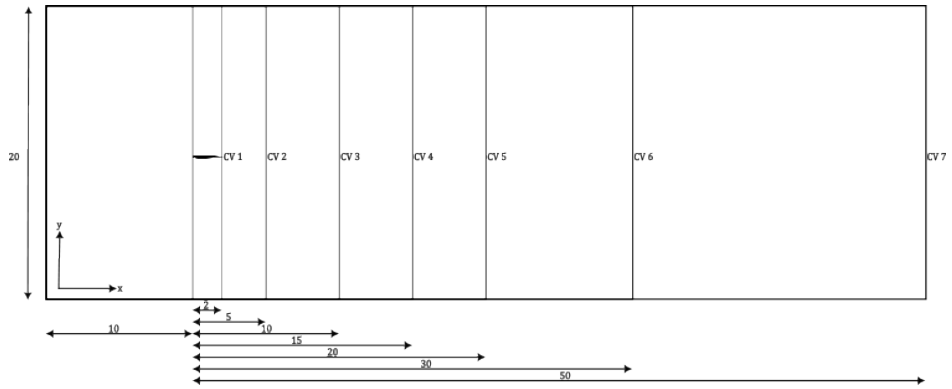


Figure 1: Control Volumes used in Far-Field Analysis of Airfoil

Far-Field energy decompositions were based on the Absolute Reference Frame (ARF) derivation introduced by Sanders and Laskaridis [3], extended here with an additional time-dependent term to account for the inherent unsteadiness of transient flows. This leads to Eq. (1), where the near-field encompasses all propulsive and drag-related elements, while the far-field balances the near-field through a series of energy-based components. As the present test case does not include any propulsive elements, only the near-field body-force term, $F_B \cdot U$, is considered. The far-field terms consist of the volumetric integrals of the rate of change of kinetic energy, $\frac{dE_k}{dt}$, viscous dissipation, Φ, and compression work, Θ, together with the mechanical energy flux across the control volume (CV) surfaces, $\boldsymbol{\mathcal{E}_{WP}}$. The latter can be further decomposed into streamwise (E_a), transverse (E_v), pressure (E_p), and viscous (E_τ) energy components.

$$\overbrace{-\underbrace{\iint \left[p_G \boldsymbol{V'_{cs}} + \bar{\bar{\tau}} \cdot \boldsymbol{V'_{cs}}\right] \cdot dS_B}_{\mathcal{P}_S} + \underbrace{\iiint p\boldsymbol{f} \cdot \boldsymbol{V'} d\mathcal{V}}_{\mathcal{P}_f} + \underbrace{\iint \left[p_G \boldsymbol{V}_\infty + \bar{\bar{\tau}} \cdot \boldsymbol{V}_\infty\right] \cdot \boldsymbol{dS}_B}_{\mathbf{F}_B \cdot U} + \underbrace{\iiint p\boldsymbol{f} \cdot \boldsymbol{V}_\infty d\mathcal{V}}_{\mathbf{F}_f \cdot U}}^{Near\ Field} +$$

$$= \overbrace{\underbrace{\frac{d}{dt}\iiint \frac{\boldsymbol{V}^2}{2}\rho d\mathcal{V}}_{\frac{d\dot{E}_k}{dt}} + \underbrace{\iint \left[\left(\frac{\boldsymbol{V}^2}{2}\rho \boldsymbol{V'}\right) + p_G \boldsymbol{V} - \bar{\bar{\tau}} \cdot \boldsymbol{V}\right] \cdot \boldsymbol{dS_{TP}}}_{\boldsymbol{\mathcal{E}_{WP}}} + \underbrace{\iiint -\boldsymbol{p_G} \nabla \cdot \boldsymbol{V} d\mathcal{V}}_{\Theta} + \underbrace{\iiint \bar{\bar{\tau}} : \nabla \boldsymbol{V} d\mathcal{V}}_{\Phi}}^{Far\ Field} \qquad (1)$$

Far-field exergy decompositions extend the unsteady energy-based formulations by in-corporating the second law of thermodynamics and introducing the concepts of exergy and anergy

Materials Research Proceedings 69 (2026) 187-192 https://doi.org/10.21741/9781644904251-33

into the energy-based framework. First conceptualized by Arntz [4], the derivation shown in Eq.(2) follows a slightly modified approach, using Eq.(1) in the Absolute Reference Frame (ARF) as its starting point.

$$\overbrace{\mathcal{P}_S + \mathcal{P}_f + \underbrace{\iint [p_G \boldsymbol{V}_\infty + \bar{\bar{\tau}} \cdot \boldsymbol{V}_\infty] \cdot \boldsymbol{dS}_B}_{\mathbf{F}_B \cdot U} - \underbrace{\iint \left(1 - \frac{T_\infty}{T}\right) \boldsymbol{q} \cdot \boldsymbol{dS_B}}_{\dot{\chi}_{\boldsymbol{q}}} - \underbrace{\iiint \left(1 - \frac{T_\infty}{T}\right) \rho \dot{q}\, d\mathcal{V}}_{\dot{\chi}_{\dot{q}}}}^{Near\ Field}$$
$$= \overbrace{\underbrace{\frac{d\dot{\mathrm{E}}_k}{dt} + \frac{d}{dt}\iiint \rho \dot{\chi}_s d\mathcal{V}}_{\dot{\chi}_v} + \underbrace{\iint \rho \dot{\chi}_s \boldsymbol{V}' \cdot \boldsymbol{dS_{TP}}}_{\dot{\chi}_{th}} + \underbrace{\boldsymbol{\mathcal{E}_{WP}}}_{\dot{\chi}_m} + \underbrace{\iiint \frac{T_\infty}{T} \bar{\bar{\tau}} : \nabla \boldsymbol{V} d\mathcal{V}}_{\dot{\mathrm{A}}_\Phi} + \underbrace{\iiint T_\infty \mathcal{K} \left(\frac{\nabla \mathrm{T}}{T}\right)^2 d\mathcal{V}}_{\dot{\mathrm{A}}_{\nabla T}}}^{Far\ Field} \quad (2)$$

An alternative family of far-field approaches is based on momentum decompositions. In particular, we present a variation of the unsteady thermodynamic method proposed by Toubin [5], itself derived from the original formulation of Destarac and Van der Vooren [1]. In this approach, a thermodynamic definition of velocity is introduced to define an irreversible velocity component, shown in Eq.(3), which enables the separation of the convective part of the momentum flux. Equation (4) presents a two-component decomposition that divides the far-field drag into unsteady induced drag and viscous drag, the two components expected in a subsonic case without body motion. In the present work, a single integration volume is used; consequently, the unsteady term is fully included in the viscous drag. This differs from the approach of Toubin [5], in which multiple volumes are defined to isolate the various phenomenological drag components.

$$u_{irr} = u_\infty \sqrt{1 + \frac{2\Delta H}{u_\infty^2} + \frac{2}{(\gamma - 1) M_\infty^2} \left(e^{\frac{\gamma - 1 \Delta s}{\gamma \ r}} - 1\right)} \quad (3)$$
$$\text{Near Field Drag}$$

$$\overbrace{\underbrace{\iint (p - p_\infty)(i \cdot n) dS_a}_{Pressure\ Drag} - \underbrace{\iint (\tau_x \cdot n) dS_a}_{Shear\ Drag}}^{Far\ Field\ Drag}$$
$$= \underbrace{\iint -\rho(u - u_{irr}) q - (p - p_\infty) i) \cdot n) dS_e}_{Unsteady\ Induced\ Drag\ (C_{D_{ui}})} + \underbrace{\iint -\rho(u_{irr} - u_\infty) q + \tau_x \cdot n) dS_e - \iiint \frac{\partial \rho(-u_\infty)}{\partial t} d\mathcal{V}}_{Viscous\ Drag\ (C_{D_v})} \quad (4)$$

Results

Figure 2 shows the energy-based decomposition results with downstream wake planes located 10 and 30 chord lengths from the airfoil leading edge, while Fig. 3 presents the corresponding exergy-based decomposition results. Figure 4 then illustrates the momentum-based decom- position results. Here, *t* denotes the fraction of time within a drag-wave cycle, *T*. The average near-field drag coefficient was 0.078454, differing by only 0.32*,* % from the results of Carren˜o Ruiz and D'Ambrosio [6]. All sets of results were found to be in close agreement with the near-field drag and provided complementary data, offering additional insight into the flow field around the airfoil. Table 1 summarizes the average far-field drag results and their relative errors with respect to the near-field drag coefficient, confirming that the overall unsteady far-field methods effectively reproduce near-field values.

Decomposing the energy- and exergy-based results provides valuable insight into the energy and exergy released into the flow field by the asymmetric vortex shedding process, with the mechanical energy flux in particular highlighting the downstream evolution of vortices. The fluctuations in mechanical energy represent recoverable energy carried by vortices crossing the downstream wake plane. As the mechanical energy components dissipate further down- stream, they are replaced by the viscous/anergy dissipation, while the volumetric change in kinetic energy acts as an unsteady correction term that maintains phase synchronization with the near-field drag.

Materials Research Proceedings 69 (2026) 187-192 https://doi.org/10.21741/9781644904251-33

It is important to note that the decline in the amplitude of the mechanical energy flux fluctuations from CV 3 to CV 6 reflects the progressive breakdown of vortices downstream of the airfoil. At the wake plane of CV 6, almost no coherent vor- tex structures are observed, as indicated by the minimal fluctuations in mechanical energy crossing the surface boundaries.

Table 1: Time Averaged Far-Field Drag Coefficients and Relative Error of the Near-Field Drag Coefficient

CV Name	Energy c_d	% error	Exergy c_d	% error	Momentum c_d	% error
CV 3	0.078281	-0.22	0.078157	-0.38	0.078624	+0.22
CV 6	0.079224	+0.98	0.079112	+0.84	0.078614	+0.21

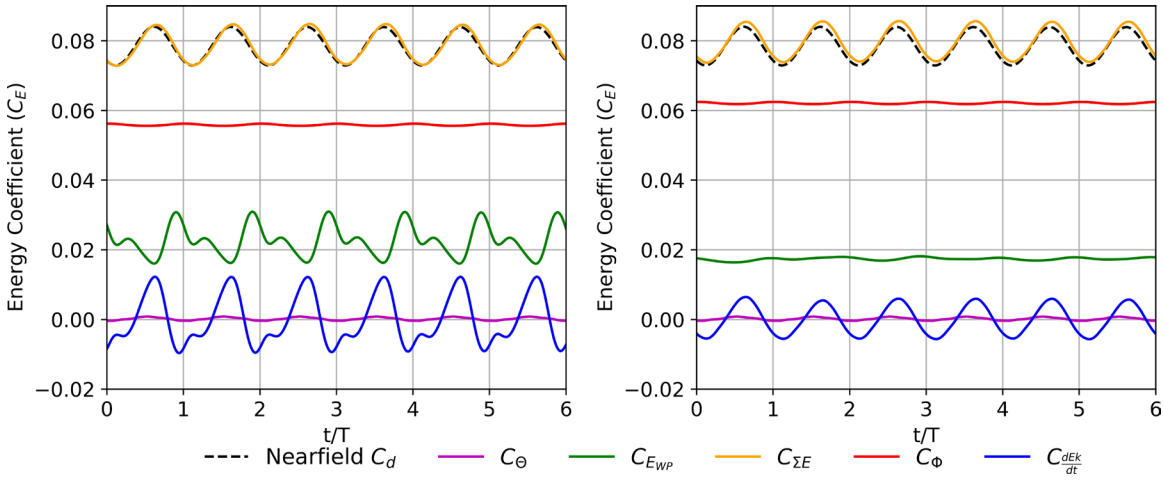


Figure 2: Energy Decompositions, with CV 3 on the left and CV 6 on the right

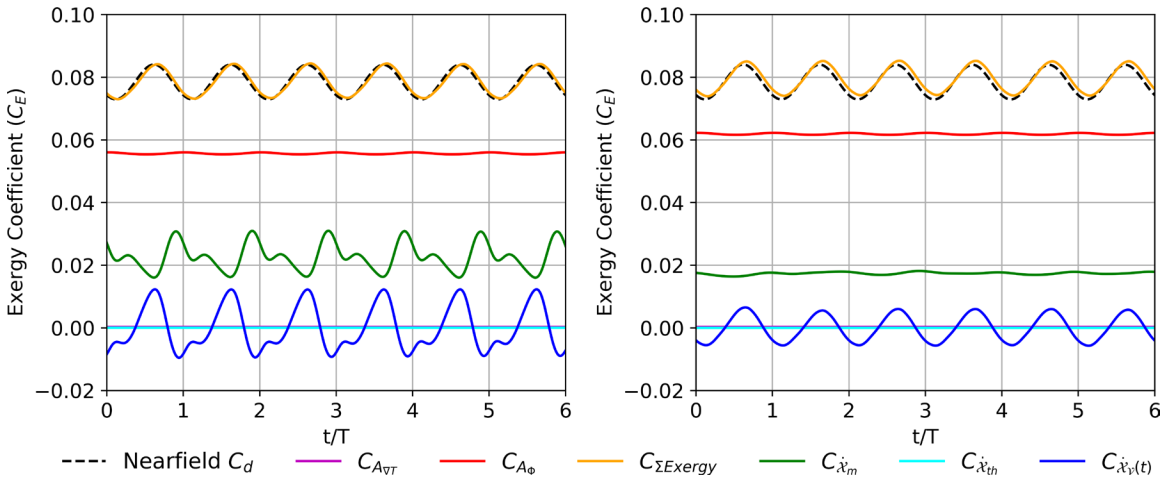


Figure 3: Exergy Decompositions, with CV 3 on the left and CV 6 on the right

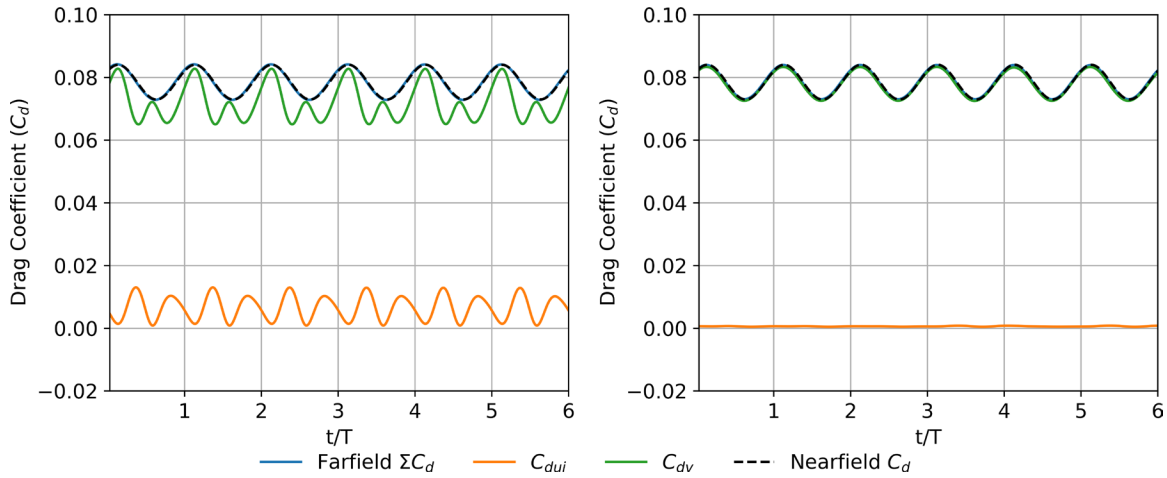


Figure 4: Momentum Decompositions, with CV 3 on the left and CV 6 on the right

The momentum balance provides a reasonable overall estimate of far-field drag in both probed control volumes. Decomposing this total value reveals significant differences in the viscous and unsteady induced components of drag between the two control volumes. CV 3, located closer to the airfoil, still captures the contribution of vortex shedding to the unsteady induced drag. In contrast, CV 6 extends 30 chord lengths downstream of the trailing edge, where the vortices have been subjected to numerical and, to a lesser extent, physical dissipation. It is noteworthy that this vortex decay does not affect the accuracy with which far-field approaches reproduce the near-field drag. Instead, it results in a redistribution of unsteady induced drag into viscous drag, in a manner similar to that observed for the energy- and exergy-based balances.

Conclusions

A NACA 0012 airfoil flying at a Reynolds number of 5000 under Martian atmospheric conditions was analysed using energy-, exergy-, and momentum-based far-field drag decomposition methods. All three far-field approaches yielded overall drag values within 0.25, % of the near-field results, while also providing complementary insights into the drag breakdown. This initial study offers a useful validation of the capabilities of different far-field formulations to analyze naturally unsteady vortex-shedding scenarios of lifting airfoils using the commercial CFD solver STAR-CCM+. The main challenge and primary source of discrepancies in implementing this methodology within a commercial solver lies in the computation of surface integrals in wake planes, where steep gradients can lead to interpolation errors.

This test case enables unsteady far-field formulations in the absolute reference frame to be assessed without the added complexity of mesh motion or turbulence modeling. Unlike traditional postprocessing methods, the far-field equations have been implemented directly within STAR-CCM+, removing the need to export data from the CFD solver for exter- nal processing. This significantly reduces data-storage requirements, as the data can be processed on the fly rather than saved and exported at each timestep for postprocessing. Future work will focus on a detailed comparison of the decompositions and on identifying the interconnections, strengths, and limitations of the proposed approaches.

References

[1] Destarac, D., and Van Der Vooren, J., “Drag/thrust analysis of jet-propelled transonic transport aircraft; Definition of physical drag components,” Aerospace Science and Technology, Vol. 8, No. 6, 2004, pp. 545-556 https://doi.org/10.1016/j.ast.2004.03.004

[2] Drela, M., “Power Balance in Aerodynamic Flows,” AIAA Journal, Vol. 47, No. 7, 2009, pp. 1761–1771. https://doi.org/10.2514/ 1.42409, URL https://doi.org/10.2514/1.42409

[3] Sanders, D. S., and Laskaridis, P., “Full-aircraft energy-based force decomposition applied to boundary-layer ingestion,” AIAA Journal, Vol. 58, No. 10, 2020, pp. 4357–4373

[4] Arntz, A., Atinault, O., Merlen, A., “Exergy-based formulation for aircraft aeropropulsive performance assessment: Theoretical development,” AIAA Journal, Vol. 53,. No 6, 2015,

pp. 1627-1639. https://doi.org/10.2514/1.J053467

[5] Toubin, H., Bailly, D., and Costes, M., “Improved unsteady far-field drag breakdown method and application to complex cases,” AIAA Journal, Vol. 54, No. 6, 2016, pp. 1907–1921

[6] Carren˜o Ruiz, M., D’Ambrosio, D. “Implicit and Explicit Large Eddy Simulations in Martian Aerodynamics.” In AIAA AVIATION 2025 Forum. Las Vegas, NV, AIAA-2025- 3585. https://doi.org/10.2514/6.2025-3585

Materials Research Proceedings 69 (2026) 193-198 https://doi.org/10.21741/9781644904251-34

Implicit-Mesh Discontinuous Galerkin Methods for Solving Multiphysics Flow in Lid-Driven Cavities

Niba KAINAT[1,a] and Vincenzo GULIZZI[1,b *]

[1]Department of Engineering, Università degli Studi di Palermo, Italy

[a]niba.kainat@unipa.it, [b]vincenzo.gulizzi@unipa.it

Keywords: Implicit-Mesh Discontinuous Galerkin Method, High-Order Accuracy, Lid-Driven Cavity Problem, Incompressible Navier-Stokes Equations

Abstract. In this contribution, a novel computational framework for incompressible flow with multi-physics coupling in lid-driven cavities is presented. The framework is based on the implicit-mesh discontinuous Galerkin method, a computational approach that combines an implicit representation of the fluid domain and the variable-order accurate discontinuous Galerkin formulation. The framework falls within the class of embedded-boundary approaches, which are based on the use of an easy-to-generate background grid that is intersected with the domain of analysis to generate the mesh. This allows a simpler mesh generation phase with respect to body-fitted mesh strategies. The use of a discontinuous Galerkin formulation ensures a high-order accurate solution of the problem, even in proximity of generally shaped mesh elements that stem from the mesh generation procedure. A lid-driven cavity benchmark problem is considered to assess the capability and confirm the accuracy of the proposed framework.

Introduction

The interaction between a flow and a cavity is characteristic of many engineering applications, ranging from high-speed flows in combustors [1] and over fuselage bays [2,3] to low-speed flows in the thermal management systems of electronic devices [4]. For these problems, numerical methods are often employed to investigate how the cavity geometry influences flow behavior and key quantities of interest, such as acoustic emissions or heat flux. However, exploring the full range of design parameters requires analyzing multiple meshes for the fluid domain, a process that can be more time-consuming than the analysis itself.

In general, numerical methods for solving partial differential equations in complex domains can be categorized into two main approaches: those based on body-fitted meshes and those using background structured meshes combined with embedded boundaries. Most commercial computational fluid dynamics software libraries adopt the former approach, which, while highly flexible in handling irregular geometrical features, requires significant effort and expertise to generate high-quality mesh elements. In contrast, embedded-boundary (EB) methods construct the mesh by intersecting the domain with an easy-to-generate background grid. This approach simplifies the domain discretization process and is particularly efficient for dynamic adaptive mesh refinement strategies [5]. However, EB methods have traditionally been implemented within finite volume schemes [6,7], which typically achieve only up to second-order accuracy with very few exceptions. For example, very recently, Overton-Katz et al. [8] presented a fourth-order accurate embedded-boundary finite volume scheme for the Stokes flow equations, employing an extended-stencil least-squares reconstruction technique.

Content from this work may be used under the terms of the Creative Commons Attribution 3.0 license. Any further distribution of this work must maintain attribution to the author(s) and the title of the work, journal citation and DOI. Published under license by Materials Research Forum LLC.

Materials Research Proceedings 69 (2026) 193-198 https://doi.org/10.21741/9781644904251-34

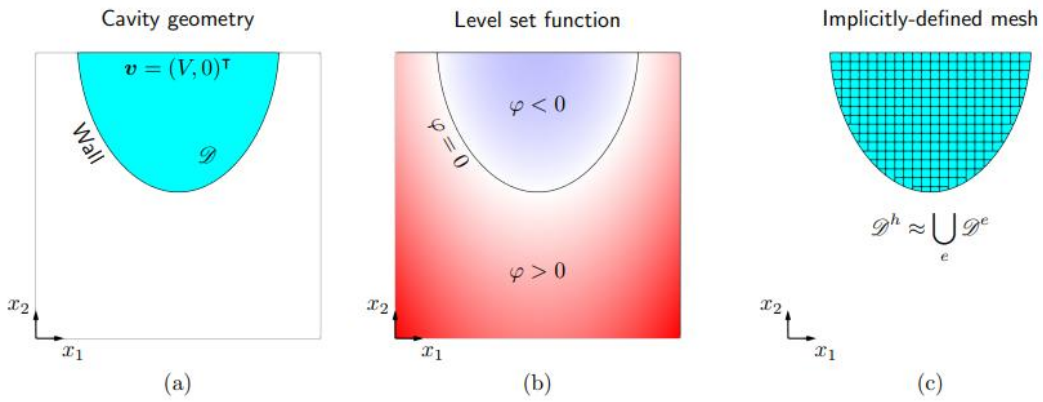


Fig. 1 (a) Geometry and boundary conditions of a lid-driven cavity problem. (b) Implicit geometry representation via a level set function φ. (c) Implicitly-defined mesh of the cavity of Fig. (a).

Discontinuous Galerkin (DG) methods are a viable alternative to finite volume methods as they offer high-order accuracy, local conservation properties, *hp*-adaptivity, and blockstructured mass matrices regardless of the choice of discretization. In fact, DG methods enable high-order accuracy when employed in combination with EB representations as demonstrated in problems related to elastic wave propagation [10], incompressible flow [9] and compressible flow [5].

In this contribution, DG methods are employed in combination with an EB approach to study incompressible flow with multi-physics coupling in lid-driven cavities. The proposed methodology is referred to as implicit-mesh DG method because the considered cavities are represented implicitly by suitably defined level set functions. The lid-driven cavity problem is considered as it represents a classic benchmark in fluid dynamics for code validation, offering a simple setup able to reproduce flow phenomena such as recirculating vortexes, shear layers, corner singularities, and instabilities [11].

Problem statement

Let us consider a lid-driven cavity problem, as shown in Fig. 1(a) , which generally involves of a fluid domain whose top boundary is a lid with a prescribed tangential motion and remaining boundaries are walls featuring a no-slip boundary condition.

The fluid within the cavity is assumed to be governed by the steady Navier-Stokes equation in the laminar regime, which consist of the continuity equation

$$\frac{\partial v_k}{\partial x_k} = 0 \tag{1}$$

and the momentum equation

$$\rho v_k \frac{\partial v_i}{\partial x_k} + \frac{\partial p}{\partial x_i} = \frac{\partial \tau_{ki}}{\partial x_k} + s_i. \tag{2}$$

In Eq. 1 and Eq. 2, x_k is the k -th component of the space location vector, $v_k$is the k -th component of the velocity vector, ρdenotes the fluid density,$p$is the pressure, andτ_{ki}denotes the ki -th component of the viscous stress tensor given by

Materials Research Proceedings 69 (2026) 193-198 https://doi.org/10.21741/9781644904251-34

$$\tau_{ki} = \mu\left(\frac{\partial v_i}{\partial x_k} + \frac{\partial v_k}{\partial x_i}\right) \tag{3}$$

being μ the fluid viscosity. On the other hand, in Eq. 2, s_i denotes i -th component of a generic source vector. For example, considering the Boussinesq approximation for natural convection, the term $s_i$may be written as $s_i = \rho g_i \beta_\vartheta \vartheta$, where $g_i$is the i -th component of gravity acceleration vector, $\beta_\vartheta$is coefficient of volumetric thermal expansion, and $\vartheta \equiv T - T_{ref}$denotes the temperature fluctuation with respect to a reference temperature T_{ref}. In such a case, the pressure $p$appearing in Eq. 2 must be considered as a modified pressure accounting for the gravitational potential, and an additional equation must be included to model the temperature fluctuation field ϑ. Considering the energy equation within the Boussinesq approximation, the following equation is coupled to Eq. 1 to Eq. 2 to account for the transport of ϑ

$$v_k \frac{\partial \vartheta}{\partial x_k} = \alpha \frac{\partial^2 \vartheta}{\partial x_k \partial x_k} \tag{4}$$

where $\alpha$is the thermal diffusivity.

Similar source terms can be added to Eq. 2 and similar transport equations can be considered to account for additional species, such as the presence of humidity.

Implicit-mesh discontinuous Galerkin formulation

The implicit-mesh discontinuous Galerkin formulation for solving Eq. 1 to Eq. 4 is presented in this section. First, it is noted that the equations can be written in compact notation via the following expression

$$-\frac{\partial \Sigma_k}{\partial x_k} + \Psi = 0 \tag{5}$$

where

$$\Sigma_k \equiv \begin{pmatrix} 0 \\ \tau_{k1} - p\delta_{k1} \\ \tau_{k2} - p\delta_{k2} \\ \alpha \frac{\partial \vartheta}{\partial x_k} \end{pmatrix} \quad \text{and} \quad \Psi \equiv \begin{pmatrix} \frac{\partial v_k}{\partial x_k} \\ \rho v_k \frac{\partial v_1}{\partial x_k} + \rho g_1 \beta_\vartheta \theta \\ \rho v_k \frac{\partial v_2}{\partial x_k} + \rho g_2 \beta_\vartheta \theta \\ v_k \frac{\partial \vartheta}{\partial x_k} \end{pmatrix} \tag{6}$$

Here Σ_k and Ψ are functions of the unknown field vector $U$and its gradients, where $U \equiv (v_1, v_2, p, \vartheta)^T$. The system of equations given in Eq. 5 is closed by providing suitable boundary conditions. In case of the lid-driven cavity problem, Dirichlet boundary conditions are provided for the velocity, whereas either prescribed-temperature (i.e.Dirichlet) or prescribed-flux (i.e.Neumann) boundary conditions can be provided for the temperature fluctuation field.

It is then possible to show that the DG weak form associated with Eq. 5 reads as follows: find U^hsuch that $B(V, U^h) = L(V, \bar{U}, \bar{T}) \forall V \in \mathcal{V}^{hp}$,being $\mathcal{V}^{hp}$the space of discontinuous polynomial vector fields, where

$$\begin{aligned} B(V, U^h) \equiv & \int_{\mathcal{D}^h} \left(\frac{\partial V^T}{\partial x_k} \Sigma_k + V^T \Psi\right) dV + \\ & - \int_{\mathscr{J}^h} \left([\![V^T]\!]_k \{\Sigma_k\} + \{\Pi_k^T\} [\![U^h]\!]_k \right) dS + \int_{\mathscr{J}^h} [\![V^T]\!]_k \mu [\![U^h]\!]_k dS + \\ & - \int_{\mathscr{B}_D^h} \left(n_k V^T \Sigma_k + \Pi_k^T U^h n_k\right) dS + \int_{\mathscr{B}_D^h} V^T \mu U^h dS \end{aligned} \tag{7}$$

Materials Research Proceedings 69 (2026) 193-198 https://doi.org/10.21741/9781644904251-34

and

$$L(V,\overline{U},\overline{T}) \equiv \int_{\mathscr{B}_N^h} V^T\,\overline{T}\,dS - \int_{\mathscr{B}_D^h} \Pi_k^T\,\overline{U} n_k dS + \int_{\mathscr{B}_D^h} V^T\,\mu\overline{U}\,dS. \quad (8)$$

In Eq. 7 and Eq. 8, the terms $[\![\bullet]\!]_k$ and $\{\bullet\}$denote the jump and average operators, respectively, whereas the integrals over $\mathcal{D}^h$,$\mathscr{I}^h$,$\mathscr{B}_D^h$and $\mathscr{B}_N^h$are usually referred to as broken integrals and must be intended as the sum over the mesh elements of the integrals computed over each element domain and boundary; for instance, $\int_{\mathcal{D}^h} \bullet\, dV \equiv \sum_e \int_{\mathcal{D}^e} \bullet^e\, dV$, where $\mathcal{D}^e$is the domain of the generic mesh element. Additionally, n_k is the k -th component of the unit normal of the fluid boundary, while Π_k is a symmetrization vector and μ is a penalization matrix that are typical of DG formulations. Further detail on the employed notation can be found in Ref. [12].

The DG formulation introduced above is valid regardless of the type of mesh elements that are chosen to discretize the fluid domain. In this work, the implicitly-defined mesh technique developed in Ref. [5,10] is employed. In particular, the cavity domain is implicitly-defined by a level set function φ such that the domain cavity is identified by the region where φ is negative and its walls are identified by $\varphi = 0$. The level set function is defined in a background rectangle and the intersection between the rectangle and the region $\varphi < 0$identifies the lid of the cavity. As an example, the level set function employed to define the cavity in Fig. 1(a) is shown in Fig. 1(b). Then, to generate the mesh, a background grid is generated using the background rectangle and is intersected with the level set function to generate the implicitly-defined mesh. Fig. 1(c) shows the implicitly-defined mesh of the the cavity of Fig. 1(a).

Results

An example of the capability of the proposed methodology is shown in Fig. 2, where the solution associated with a lid-driven triangular cavity problem is reported. Fig. 2(a) shows the considered geometry, which is represented implicitly by the level set function $\varphi(x) = \frac{2H|x_1|}{L} - x_2$, where H and L are the height and the width, respectively, of the cavity. The associated implicitly-defined mesh is displayed in Fig. 2(b), where it is possible to notice the shape of the elements in proximity of the wall boundaries, obtained as a result of a cell-merging procedure implemented to avoid overly small cut cells. Fig. 2(c) and Fig. 2(d) report the contour plot of the velocity magnitude and the streamlines obtained with the present framework for two values of the Reynolds number $Re \equiv VH/(3\nu)$, namely

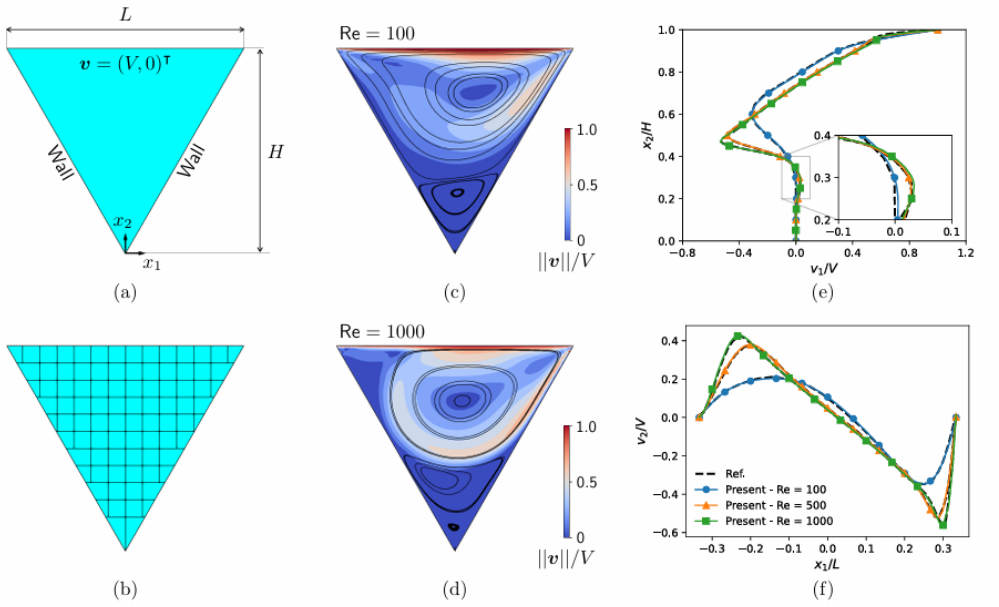


Fig. 2: Implicit-mesh DG solution of the lid-driven triangular cavity problem. (a) Geometry. (b) Implicitly-defined mesh. (c) Contour plot of the velocity magnitude and streamlines for $Re = 100$. *(d) Contour plot of the velocity magnitude and streamlines for* $Re = 1000$. *(e) Profile of the velocity component* v_1 *along the height of the cavity at* $x_1 = 0$. *(f) Profile of the velocity component* v_2 *along the width of the cavity at* $\frac{x_2}{H=\frac{2}{3}}$. *Reference results are taken from Ref. [13].*

$Re = 100$ and $Re = 1000$, respectively, being ν the kinematic viscosity of the fluid. Eventually, Fig. 2(e) and Fig. 2(f) show the profile of the velocity component v_1 along the height of the cavity at $x_1 = 0$ and profile of the velocity component v_2 along the width of the cavity at $\frac{x_2}{H=\frac{2}{3}}$, respectively, along with reference results (the thick dashed lines) taken from Ref. [13]. The comparison confirms the accuracy and the potential of the proposed formulation.

Conclusions

A novel computational framework for the incompressible flow in lid-driven cavity has been presented. The framework is based on combined use of the the implicitly-defined mesh technique to generate the fluid domain partition and the discontinuous Galerkin method to solve the governing equations with high-order accuracy. Numerical results have been presented for the lid-driven flow in a triangular cavity, confirming the accuracy of the proposed formulation. Currently, the method is being extended to account for the multi-physics coupling between temperature, humidity and mass transfer in cavities with general shapes.

References

[1] Zhao, G. Y., Sun, M. B., Song, X. L., Li, X. P., & Wang, H. B.: Experimental investigations of cavity parameters leading to combustion oscillation in a supersonic crossflow, Acta Astronautica, 155 (2019), 255–263. https://doi.org/10.1016/j.actaastro.2018.12.011

[2] Lawson, S. J., & Barakos, G. N.: Review of numerical simulations for high-speed, turbulent cavity flows, Progress in Aerospace Sciences, 47(3) (2011), 186–216. https://doi.org/10.1016/j.paerosci.2010.11.002

[3] Neri, E., Kennedy, J., & Bennett, G. J.: Bay cavity noise for full-scale nose landing gear: a comparison between experimental and numerical results, Aerospace Science and Technology, 72 (2018), 278–291. https://doi.org/10.1016/j.ast.2017.11.016

[4] Nimmagadda, R., Reuven, R., Asirvatham, L. G., & Wongwises, S.: Thermal management of electronic devices using gold and carbon nanofluids in a lid-driven square cavity under the effect of variety of magnetic fields, IEEE Transactions on Components, Packaging and Manufacturing Technology, 10(11) (2020), 1868–1878. https://doi.org/10.1109/TCPMT.2020.3008786

[5] Gulizzi, V., Almgren, A. S., & Bell, J. B.: A coupled discontinuous Galerkin-Finite Volume framework for solving gas dynamics over embedded geometries. Journal of Computational Physics, 450, (2022), 110861. https://doi.org/10.1016/j.jcp.2021.110861

[6] Graves, D., Colella, P., Modiano, D., Johnson, J., Sjogreen, B., & Gao, X.: A cartesian grid embedded boundary method for the compressible Navier–Stokes equations. Com munications in Applied Mathematics and Computational Science, 8(1), (2013), 99-122. http://dx.doi.org/10.2140/camcos.2013.8.99

[7] Trebotich, D., & Graves, D.: An adaptive finite volume method for the incompressible Navier–Stokes equations in complex geometries. Communications in Applied Mathemat ics and Computational Science, 10(1), (2015), 43-82. http://dx.doi.org/10.2140/camcos.2015.10.43

[8] Overton-Katz, N., Gao, X., Guzik, S., Antepara, O., Graves, D. T., & Johansen, H.: A fourth-order embedded boundary finite volume method for the unsteady Stokes equations with complex geometries. SIAM Journal on Scientific Computing, 45(5), (2023), A2409–A2430. https://doi.org/10.1137/22M1532019

[9] Saye, R.: Implicit mesh discontinuous Galerkin methods and interfacial gauge methods for high-order accurate interface dynamics, with applications to surface tension dynamics, rigid body fluid–structure interaction, and free surface flow: Part I, Journal of Computational Physics, 344 (2017), 647–682. https://doi.org/10.1016/j.jcp.2017.04.076

[10] Gulizzi, V., & Saye, R.: Modeling wave propagation in elastic solids via high-order accurate implicit-mesh discontinuous Galerkin methods, Computer Methods in Applied Mechanics and Engineering, 395 (2022), 114971. https://doi.org/10.1016/j.cma.2022.114971

[11] Albensoeder, S., Kuhlmann, H. C., & Rath, H. J.: Three-dimensional centrifugal-flow instabilities in the lid-driven-cavity problem, Physics of Fluids, 13(1) (2001), 121–135. https://doi.org/10.1063/1.1329908

[12] Gulizzi, V., Benedetti, I., & Milazzo, A.: An implicit mesh discontinuous Galerkin formu lation for higher-order plate theories. Mechanics of Advanced Materials and Structures, 27(17), (2020), 1494-1508. https://doi.org/10.1080/15376494.2018.1516258

[13] Mai-Duy, N., & Tran-Cong, T.: A high-order upwind control-volume method based on integrated RBFs for fluid-flow problems. International journal for numerical methods in fluids, 67(12), (2011), 1973-1992. https://doi.org/10.1002/fld.2477

Materials Research Proceedings 69 (2026) 199-204 https://doi.org/10.21741/9781644904251-35

Analysis of the Wake Vortex Encounter Risk Under Reduced Vertical Separation Enabled by Geometric Altimetry

Tobias BAUER[1,a *], André KOLOSCHIN[1,b]

[1]German Aerospace Center (DLR), Institute of Flight Systems, Lilienthalplatz 7, 38108 Braunschweig, Germany

[a]tobias.bauer@dlr.de, [b]andre.koloschin@dlr.de

Keywords: Wake Turbulence, Wake Vortex, Wake Vortex Encounter, Aircraft Separation Minima

Abstract. As the current requirements of at least 1000 ft vertical separation between aircraft in en-route airspace are mainly determined by the limited accuracy of barometric altimetry, a study has been performed whether these separation minima might be reduced to 500 ft with usage of geometric altimetry. Thus, allowing smaller nominal vertical distances between flight paths, it is to be expected that the risk (in frequency of occurrence and severity) of wake vortex encounters increases. The present study, using a comparative fast-time simulation of traffic at European level for two full-day scenarios, indeed confirms a relative encounter risk increase by a factor of 3 to 4 across all severities (as expressed by the magnitude of the circulation encountered), with this factor being largely independent of the wind situation. Consequently, the exploration of mitigation means such as conditional application of reduced vertical separation or tactical wake conflict prediction tools should be undertaken as part of further development of the concept.

Motivation

In order to increase capacity in en-route airspace and therefore reduce the need for detours, thus contributing to a more environmentally friendly aviation, a reduction of the vertical separation minima has been considered as a part of the research project *Green-GEAR* (Green Operations with Geometric Altitude, Advanced Separation & Route Charging Solutions). Currently, within the so-called RVSM (Reduced Vertical Separation Minima) airspace between flight levels (FLs) 290 to 410 inclusive, a minimum vertical separation of 1000 ft between aircraft is applied. The new RVSM 2 concept [1] aims to reduce this separation minimum to 500 ft while at the same time increasing the upper applicability limit to FL 600, enabled by the usage of geometric altimetry, i.e. usage of GNSS vertical positions, instead of barometric altimetry. In view of the fact that the main contributor to the current value for the minimum vertical separation is the comparatively large allowance for the barometric altimetry system error (ASE), its decrease should be feasible when geometric altimetry is employed.

Geometric altitude reference in cruise implies no longer following the isobaric altitudes that are consistent with aircraft performance, resulting on average in penalties in fuel use as expectable [2,3]. On the other hand, besides the capacity increase reducing the need for detours, the finer granularity of available flight levels could allow flights to operate closer to their optimum altitudes than today, counteracting and possibly outweighing the penalties [4].

A reduction of aircraft separation minima would obviously impact flight safety so that a safety case including consideration of the risks of aircraft collisions under nominal and non-nominal conditions and of wake turbulence encounters is required. The Green-GEAR project has conducted a preliminary safety study for the RVSM 2 concept [5,6]; the results of the wake turbulence risk assessment are presented in this paper. While out of scope here, we note that the aircraft collision risk for RVSM 2 is acceptable under certain conditions [5].

Content from this work may be used under the terms of the Creative Commons Attribution 3.0 license. Any further distribution of this work must maintain attribution to the author(s) and the title of the work, journal citation and DOI. Published under license by Materials Research Forum LLC.

Materials Research Proceedings 69 (2026) 199-204 https://doi.org/10.21741/9781644904251-35

Background and Prior Work

A wake turbulence encounter is a possibly hazardous situation for an aircraft, but such encounters cannot be completely avoided by procedural means alone if any airspace capacity is to be maintained. Existing (procedural) separation minima have been initially defined at ICAO level using expert judgement more than 50 years ago [7], and the only modifications for en-route airspace implemented so far have been the increased horizontal separation from the Boeing B757-300 and the new SUPER wake vortex class (currently only populated by the Airbus A380) and the introduction of RVSM between FLs 290 and 410. Studies for wake vortex risk in the en-route flight phase are scarce (e.g. [8-10] for North American airspace, [11,12] for European airspace) and with the exception of [10] concern the status quo. Due to limited monitoring and reporting of wake vortex encounters, it is difficult to quantify whether the studies correctly estimate their frequency and severity. Especially concerning the latter, it can be observed that the crossing of a wake where forces or moments beyond the aircraft's control capabilities could be generated needs to be regarded as hazardous from a safety point of view *in the absence of further information*, but these effects may only persist for a fraction of a second and need not lead to relevant consequences on practical operations [6].

Method

The analysis is based on a fast-time simulation using a software toolbox [13,14] that had been previously developed and now has been improved. The fast-time simulation uses trajectory data generated from submitted flight plans and meteorological data, in this case from the German COSMO-EU numerical weather prediction model, as input. As there is no (planned) traffic yet adhering to the new flight levels, a corresponding modification of altitudes has been employed for the RVSM 2 scenario, cf. Fig.°1, that also serves to concentrate the traffic around the most popular flight levels, effectively locally increasing traffic density. ASE, different for barometric and geometric altimetry, and flight technical error (FTE) are modelled to obtain actual flight altitudes from nominal ones [6]. The simulation calculates probabilistic corridors with an elliptical shape that contain the wake vortices with a high probability using the well-established P2P model [15,16] that also models the evolution of these wake corridors over time. A semi-deterministic approach (the initial conditions for aircraft trajectories and meteorological parameters are assumed as known in the simulation, while uncertainties in atmospheric effects and consequently wake evolution are modelled) ensures realistic corridor sizes with the proper probability distribution of parameters. The traffic scenario is then evaluated with respect to crossings of the aircraft trajectories with these wake corridors. The final step is a hazard assessment based on the SHAPe model [17-19], which uses the roll control ratio (RCR) as the most relevant parameter and has been integrated into the simulation as part of this work.

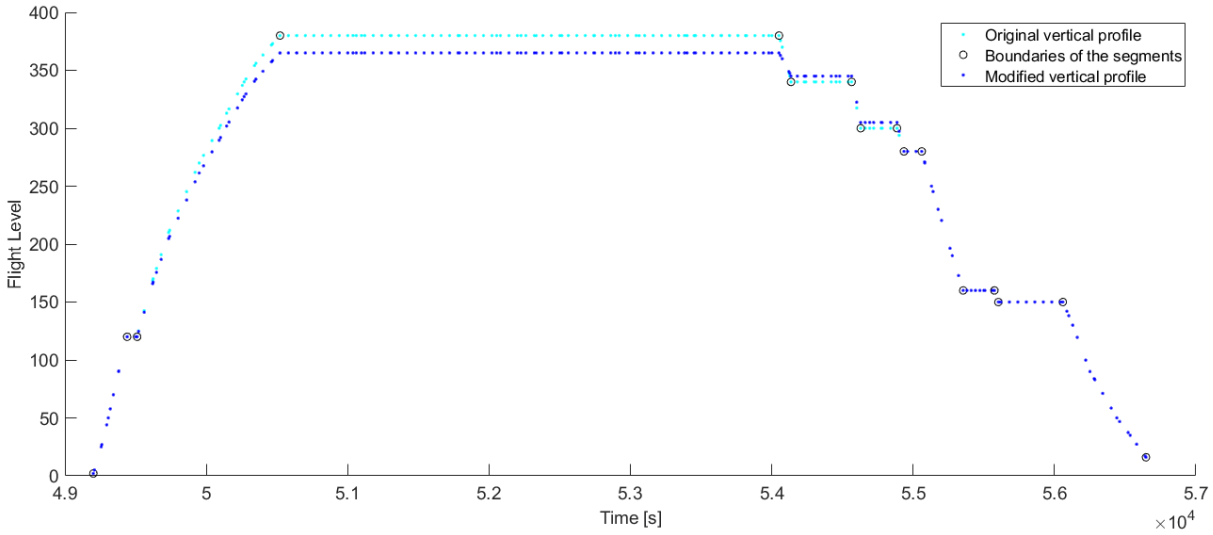


Fig.°1: sample of adapted fight profile, moving horizontal segments to new flight levels

Two full-day scenarios with traffic samples for the whole European airspace (more than 20000 trajectories each) have been analysed in this study: one day with relatively low wind speeds and one day with relatively high wind speeds at the relevant altitudes, as the wind situation strongly influences the horizontal movement of wake vortices and therefore the probability of wake encounters. Both scenarios have been analysed in a baseline version using barometric altimetry and 1000 ft minimum vertical separation in the RVSM airspace as it is used today and in a modified version using geometric altimetry and 500 ft minimum vertical separation as it might be used in the RVSM 2 airspace in the (far) future. Due to limitations of the meteorological data input driver, scenarios from 2014 (14th Feb and 3rd June) were used. The observed increase of traffic densities since then, or even until a possible introduction of RVSM 2, is not modelled, which is believed acceptable as the relevant question is the relative change of encounter risk.

Results

The results show that a reduction of the vertical separation to 500 ft leads to an increase of the number of wake encounters approximately by a factor of 3 to 4 over the full range of encountered circulation values, as shown in Fig.°2 for both scenarios. The figure only contains encounters where the magnitude of the encountered circulation in relation to the respective aircraft's capability to deal with it (as assessed by the SHAPe method) is high enough that the situation cannot be *guaranteed* to be safe. The high-wind-speed scenarios show a smaller overall number of encounters, which can be explained with the higher wind speeds moving the wake vortices away from the generator aircraft's trajectories in many situations so that other aircraft on the same trajectory do not encounter them. Aircraft on adjacent trajectories can encounter wake vortices as a result of strong crosswinds, but overall, the reduction of the number of wake encounters on same trajectory outweighs this effect. Despite the overall number of encounters being very different in the two wind scenarios, the relative increase between baseline and modified separations is approximately the same.

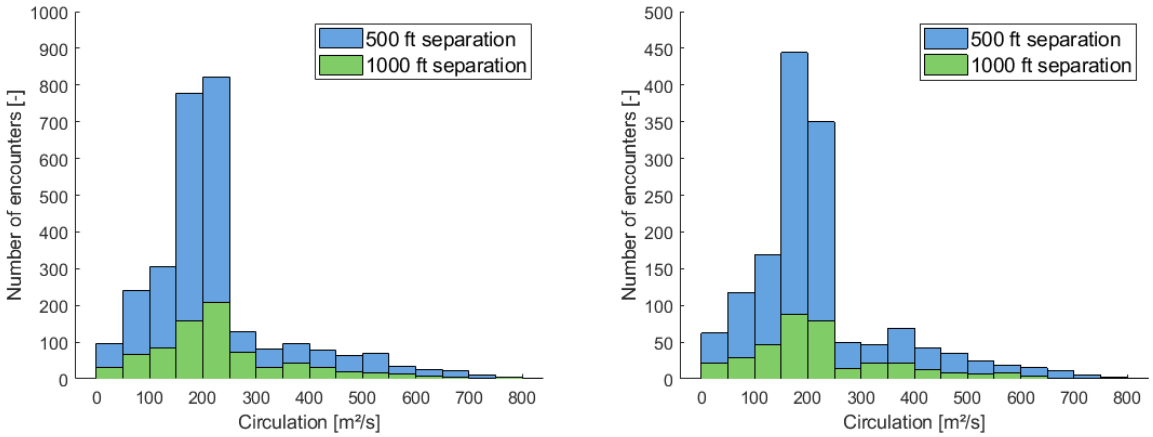


Fig.°2: Distribution of the encountered circulation in the low-wind-speed (left) and high-wind-speed scenario (right). Note the different vertical scaling.

An analysis of the aircraft separations at the start times of the wake encounters revealed that in the scenario with 500 ft vertical separation, most encounters happen 500 ft below the wake generating aircraft at a horizontal separation between 5 and 20 NM. In the scenario with 1000 ft vertical separation, far less encounters happen 1000 ft below the wake generating aircraft at a similar horizontal separation. Therefore, it can be concluded that the wake encounters 500 ft below the wake generating aircraft are not shifted from 1000 ft below to 500 ft below when changing the vertical separation, but instead, these are nearly exclusively additional encounters that would not happen with 1000 ft separation as used today. This is plausible because, even though wake vortices can descend more than 1000 ft (in some cases even 2000 ft [20]), they descend less than 1000 ft most of the time.

Conclusions and Further Work

As *Green-GEAR* is an exploratory research project with a relatively low TRL (Technology Readiness Level), some limitations of the fidelity of the results have to be accepted, notably due to restrictions in traffic flow modelling. Nevertheless, as many additional effects with respect to prior work have been modelled in relatively high detail, and large-scale scenarios have been used for the simulations, at least the relative results can be considered as representative.

With that caveat in mind, we find a substantial increase in the number of wake encounter occurrences with no significant change in average severity as expressed by the magnitude of the circulation encountered. In fact, there is an increase of the number of encounters in all ranges of circulation values, with a comparatively higher increase for lower circulation values (see again Fig.°2) so that the average is, if only slightly, decreased. The overall result means an increase in wake encounter risk (substantially increased frequency of occurrence at virtually unchanged average severity) and as such is not unexpected considering the nature of wake vortex transport and evolution. We therefore note a substantial relative decrease in wake turbulence safety.

Prior activities modifying separation standards have adopted a comparative approach, demonstrating no (unfavourable) change of risk through a new concept of operation – this is not the case here. However, with no official definition of a target level of safety (TLS) for the wake encounter risk, nor any means of quantification for the encounter severity defined by regulation, a formal statement that the new situation would be unsafe cannot be made at this point. It is reasonable to assume though that it would not be acceptable without modifications. Remedies can be mitigation means and/or limiting conditions for its application. Indeed, further analysis of the results especially regarding particular aircraft (category) pairings, relative flight path geometries or weather situations is desirable, so as to possibly identify criteria when or where the new

separation standards could be applied safely, or should not be applied. An alternative approach could be the introduction of a safety net: analogous to the Airborne Collision Avoidance System (ACAS) and Air Traffic Control's short-term conflict alert (STCA), a ground-based or airborne predictive tool to identify and prevent potentially hazardous wake encounters [21] could be employed, potentially rendering large benefits as operational limits, and thus capacities, would no longer need to be dictated by the worst-case assumption. Such a tool could already contribute to increase the safety of operations under current separation rules.

Acknowledgements and Disclaimer
The following colleagues from the Royal NLR have been leading in the development of the RVSM 2 concept within the Green-GEAR project (in alphabetical order): Ingmar Boshuizen; Patrick Jonk; Bart Klein Obbink; Job Smeltink.

Furthermore, the authors gratefully acknowledge support and advice received from the following colleagues for the presented work (in alphabetical order): Frank Holzäpfel, DLR Atmospheric Physics (P2P vortex model); Alexander Lau, DLR Air Transport (Network Flow environment and trajectory data provision); Carsten Schwarz, DLR Flight Systems (SHAPe severity assessment method); Majed Swaid, DLR Air Transport (wind data analysis); Kianusch Vahid Yousefnia, DLR Atmospheric Physics (NWP data processing).

This paper is based on work performed in the SESAR 3 Exploratory Research Project „Green-GEAR", which has received funding from the SESAR 3 Joint Undertaking (JU) under grant agreement no. 101114789. Views and opinions expressed are however those of the authors only and do not necessarily reflect those of the European Union or SESAR 3 JU. Neither the European Union nor the SESAR 3 JU can be held responsible for them.

References

[1] P. Jonk, I. Boshuizen, A. Koloschin, B. Klein Obbink, J. Smeltink and T. Bauer, "SESAR 3 ER 1 Green-GEAR – D4.6 – Final OSED – Separation Minima", ed. 03.00, 25th June 2025, https://doi.org/10.3030/101114789 → Results → Deliverables.

[2] D. Nelson, R.M. Donaghey, J. Melendez, D. Zapata Arenas, P. Rouquette, D. Vechtel, A. Koloschin and T. Bauer, "SESAR 3 ER 1 Green GEAR – D3.3 – ERR – Geometric Altimetry", ed. 01.00, 28th February 2025, https://doi.org/10.3030/101114789 → Results → Deliverables.

[3] D. Vechtel, About the Influence of the Use of Geometric Altimetry on Cruise Flight Efficiency, submitted to CEAS Aeronautical Journal.

[4] T. Bauer, P. Jonk, I. Boshuizen and L. Castelli, "SESAR 3 ER 1 Green-GEAR – D4.7 – ECO-EVAL – Separation Minima", ed. 01.00, 28th May 2025, https://doi.org/10.3030/101114789 → Results → Deliverables.

[5] P. Jonk, B. Klein Obbink, J. Smeltink and I. Boshuizen, "SESAR 3 ER 1 Green-GEAR – D4.3 – RVSM 2 Safety Case", ed. 01.00, 28th February 2025, https://doi.org/10.3030/101114789 → Results → Deliverables.

[6] T. Bauer, A. Koloschin, P. Jonk, I. Boshuizen, B. Klein Obbink and J. Smeltink, "SESAR 3 ER 1 Green-GEAR – D4.4 – ERR – Separation Minima", ed. 01.00, 30th May 2025, https://doi.org/10.3030/101114789 → Results → Deliverables.

[7] ICAO, Doc 4444, Procedures for Air Navigation Services (PANS) – Air Traffic Management. International Civil Aviation Organization, 16th Edition, 2016.

[8] ICAO, Doc 9574, Manual on a 300 m (1 000 ft) Vertical Separation Minimum Between FL 290 and FL 410 Inclusive. International Civil Aviation Organisation, Third edition, 2012.

[9] U. Schumann and R. Sharman, “Aircraft Wake-Vortex Encounter Analysis for Upper Levels”, Journal of Aircraft 2015 52:4, 1277-1285, https://doi.org/10.2514/1.C032909.

[10] Z. Fan, N. Schroeder, D. Swol and A. Trani, "Potential wake turbulence encounters analysis in current and NextGen flight operations," 2013 Integrated Communications, Navigation and Surveillance Conference (ICNS), Herndon/VA, 2013, pp. 1-7, https://doi.org/10.1109/ICNSurv.2013.6548576.

[11] A.A. Woodfield, “En-route encounters with wake vortices, and the implications of reduced vertical separation minima RVSM”. 1999. Woodfield Aviation Research Report No. 9901.

[12] J. Busto and S. Ruiz, “Final Project Report”. SESAR 2020 R-WAKE Deliverable D2.1, ed.01.00.00, 2018, https://doi.org/10.3030/699247 → Results → Deliverables.[13] A. Koloschin, Modellkopplung zur Vorhersage von en-route Wirbelschleppeneinflügen für Luftverkehrsflusssteuerungsmaßnahmen im europäischen Luftraum. Internal Report, DLR-IB-328-2017-4 and Master thesis, Hamburg University of Technology, 2017.

[14] A. Lau, J. Berling, A. Koloschin, F. Holzäpfel, F. Linke and K. Wicke, Ground-based Wake Vortex Prediction in the En-route European Airspace, AIAA 2018-2879, AIAA AVIATION Forum, June 25-29, 2018, Atlanta/GA, https://doi.org/10.2514/6.2018-2879.

[15] F. Holzäpfel, A Probabilistic Two-Phase Wake Vortex Decay and Transport Model, Journal of Aircraft, Vol. 40, 2003, pp. 323-331, https://doi.org/10.2514/2.3096.

[16] F. Holzäpfel, Probabilistic Two-Phase Aircraft Wake-Vortex Model: Further Development and Assessment, Journal of Aircraft, Vol. 43, 2006, pp. 700-708, https://doi.org/10.2514/1.16798.

[17] K.-U. Hahn, C. Schwarz and H. Friehmelt, A simplified hazard area prediction (SHAPe) model for wake vortex encounter avoidance. ICAS 2004, Yokohama, 29.08. – 03.09.2004. proceedings: Edinburgh, 2004.

[18] C. Schwarz, K.-U. Hahn and D. Fischenberg, Wake Encounter Severity Assessment Based on Validated Aerodynamic Interaction Models. AIAA ASE Conference 2010, August 02-05. 2010, Toronto, Kanada.

[19] C. Schwarz and K.-U. Hahn, Simplified Hazard Area Prediction Method – SHAPe. Internal Report, DLR-IB 111-2011/31, Braunschweig, 2011.

[20] A. Brown & F. Holzäpfel, Case Studies in Modelling Cruise-generated trailing Vortices”. AIAA Aviation forum and ASCEND 2024, July 29 – August 2, 2024, Las Vegas/NV, https://doi.org/10.2514/6.2024-3773.

[21] T. Bauer, D. Vechtel, F. Abdelmoula and Th. Immisch, In-Flight Wake Encounter Prediction with the Wake Encounter Avoidance and Advisory System (WEAA). 6th AIAA Atmospheric and Space Environments Conference, AVIATION 2014, Atlanta/GA, 16.-20.06.2014, Paper AIAA-2014-2333.

Materials Research Proceedings 69 (2026) 205-210 https://doi.org/10.21741/9781644904251-36

Assessment of RANS Turbulence Models for Swept Shock Wave–Boundary Layer Interactions

Andrea PALUMBO[1,a *], Sergio PIROZZOLI[1,b]

[1]Sapienza Università di Roma, Dipartimento di Ingegneria Meccanica e Aerospaziale, Via Eudossiana 18, Roma, Italy

[a]andrea.palumbo@uniroma1.it, [b]sergio.pirozzoli@uniroma1.it

Keywords: Computational Fluid Dynamics, Supersonic/Hypersonic Flows, Shock Wave-Boundary Layer Interaction, Turbulence Modelling

Abstract. In this work, we carry out Reynolds-Averaged Navier-Stokes (RANS) simulations of the three-dimensional interaction between an oblique shock wave and a supersonic turbulent boundary layer. The analysis focuses on the canonical case of three-dimensional interaction with cylindrical symmetry, obtained by adding a crossflow velocity component to the incoming boundary layer, resulting in a two-dimensional, three-component (2D/3C) flow. In the RANS framework, the 2D/3C flow assumption leads to a simplified set of equations, which can be efficiently solved in a two-dimensional domain. The RANS results are compared with previous high-fidelity data-sets in the same flow conditions for two values of the sweep angle. It is shown that the RANS approach is able to predict the increased size of the interaction region for the swept case, in agreement with previous literature findings. However, we observe noticeable differences between RANS and DNS in the streamwise distributions of wall quantities.

Introduction

Recent years have seen a renewed interest in the development of air-breathing vehicles for supersonic/hypersonic flight. Commercial interest in hypersonic aircraft for intercontinental flight and the resurgence of world-wide military threats have pushed momentum into the high-speed aerospace research. The main challenges associated with the design of high-speed aerodynamic systems are related to the intense wall friction, heat flux and thermo-mechanical loads generated by the interaction between the vehicle and the surrounding flow. Improved understanding of the fluid-dynamic phenomena occurring in this regime is therefore necessary to provide fast and accurate design tools [1]. In this context, it is expected that computational fluid dynamics (CFD) should play a pivotal role, as using it would allow massive cost reductions if compared with full-scale experiments.

A well-known phenomenon in high-speed aerodynamics is related to the interaction between shock waves and turbulent boundary layers developing along the aircraft external walls (shock wave-boundary layer interaction, SBLI). SBLI often results in extensive flow separation, leading to aerodynamic efficiency loss, control reversal, wall heat transfer increase, and structural vibrations. Recently, high-fidelity numerical simulations have allowed to obtain important physical insights on this topic, and to shed light on the origin of shock-induced low-frequency oscillations [2]. However, direct numerical simulations (DNS) and wall-resolved large eddy simulations are typically characterized by very strict grid resolution requirements [3], which lead to very high computational costs, thereby hindering their use as a design tool.

A low-cost solution for the analysis of high-speed flows would be to extend Reynolds-averaged Navier-Stokes (RANS) turbulence models, which have been the workhorse of low-speed aerodynamic design for the last decades, to the hypersonic regime. However, there are several arguments against the use of RANS models in high-speed cases. First, turbulence models have been originally calibrated for incompressible flows, and they generally have significant loss of

Content from this work may be used under the terms of the Creative Commons Attribution 3.0 license. Any further distribution of this work must maintain attribution to the author(s) and the title of the work, journal citation and DOI. Published under license by Materials Research Forum LLC.

Materials Research Proceedings 69 (2026) 205-210 https://doi.org/10.21741/9781644904251-36

accuracy when dealing with the strong temperature/density gradients occurring in diabatic high-speed conditions and/or in presence of SBLIs [4]. In addition, the vast majority of SBLIs are inherently three-dimensional, as the shock impingement line is rarely orthogonal to the incoming flow. The reliability of RANS models is entirely questionable in those cases, due to numerical issues in managing shock-dominated, three-dimensional flows and due to the intrinsic approximation of the Boussinesq gradient-viscosity hypothesis.

Based on the previous discussion, we deem very important to assess the performance of RANS models in simple three-dimensional SBLIs before applying them to real-world applications. In this work, we carry out a series of RANS simulations of three-dimensional SBLIs in supersonic regime. Specifically, we focus on a canonical configuration, namely the swept oblique shock reflection, which has been recently investigated through wind tunnel experiments [5] and high-fidelity numerical simulations [6,7,8]. As previous studies have demonstrated an increasing trend of the length of the interaction region with the sweep angle, it would be important that RANS models are able to replicate this behaviour.

Numerical setup

The analysis of the swept interaction between an oblique shock and a supersonic, turbulent boundary layer is carried out using the open-source code OpenFOAM. The density-based transient solver *rhoCentralFoam* is used to deal with the flow configuration under study in a finite-volume framework. The numerical setup used in this work is sketched in figure 1: an oblique shock of wave angle β impinges onto a flat plate and interacts with a turbulent boundary layer, whose streamwise direction is not orthogonal to the shock impingement line.

Following previous work on this topic, the swept interaction is obtained by adding a crossflow component to the upstream boundary layer at the inflow, making it swept by an angle γ_0 with respect to the x axis. On the other hand, the impinging shock wave is generated by a compression wedge of dihedral angle 2θ, whose lower surface is numerically treated as an inviscid wall (using a slip condition for the velocity) and constitutes part of the top boundary of the domain. The wedge geometry is properly designed to have shock impingement onto the flat plate at $x_{imp} = 64\ \delta_0$ (where δ_0 is the boundary layer thickness at the inflow plane). The flat plate is treated as an isothermal, nominally-adiabatic wall, as its temperature is set to the adiabatic wall temperature upstream of the shock $T_{aw,0} = T_0[1 + r\,(\gamma_g-1)/2\ M_0^2]$ (where γ_g is the heat transfer coefficient ratio, r the recovery factor, $M_0 = M_{0,x}\cos(\gamma_0)$ the free-stream Mach number and T_0 the inflow free-stream temperature). A turbulent boundary layer profile of thickness δ_0 is introduced at the inflow plane, with its wall-normal distributions of the thermo-fluid-dynamic variables being taken from a precursor simulation. Non-reflecting boundary conditions are imposed on the free portions of the top boundary and the outlet ($x=L_x$).

Materials Research Proceedings 69 (2026) 205-210 https://doi.org/10.21741/9781644904251-36

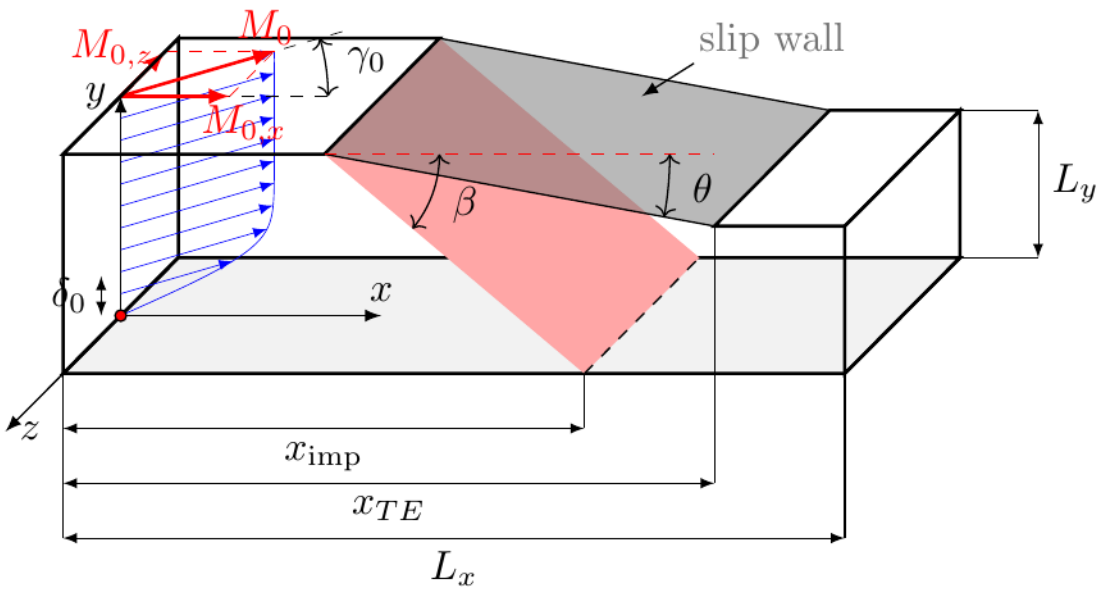


Figure 1 - Schematic of numerical simulations: δ_0 is the incoming boundary layer thickness, γ_0 is the incoming flow skew angle, β is the shock angle, θ the deviation angle, x_{imp} the nominal location of the shock impingement, x_{TE} the wedge trailing edge location.

It can be easily recognized that the SBLI configuration under study, despite being inherently three-dimensional, is statistically homogeneous along the *z*-direction. This feature yields a two-dimensional, three-component (2D/3C) flow behaviour, which provides a strong simplification for RANS modelling. In this framework, RANS equations can be recast in a simplified system of equations (infinite swept model, [9]), which can be solved in a two-dimensional domain at a very reduced computational cost. In this work, the 2D/3C swept model is solved using the following procedure: at each time step, we solve the two-dimensional continuity equation and the momentum equation in the longitudinal plane *(x,y)*. Then, the crossflow velocity component *w* is solved as a separate thermo-fluid-dynamic variable governed by a simplified momentum equation, which is mutually coupled with the longitudinal flow dynamics through the energy equation and the turbulence model. The numerical solution is then marched in time until a steady state is obtained.

The 2D/3C RANS equations are discretized and solved using an in-house modification of the aforementioned *rhoCentralFoam* flow solver. The turbulent flows considered in this work are solved using a RANS approach, based on the Spalart-Allmaras turbulence model. The flow conditions match previous DNS by our research group [7]: the *x*-projected Mach number is selected as $M_{0,x} = 2.28$, and two sweep angles, $\gamma_0=\{0°,30°\}$, are considered. The inflow Reynolds numbers $Re_{\delta 0}= \rho_0 u_0 \delta_0/\mu_0$ of the computations are chosen such as the same value of the Reynolds number $Re_{\delta 2}= \rho_0 u_0 \delta_2/\mu_w \approx 1100$ (where δ_2 is the boundary layer momentum thickness) is obtained at a reference location just upstream of the interaction region. It is worthwhile remarking that the same approach was followed in the reference DNS study.

Materials Research Proceedings 69 (2026) 205-210 https://doi.org/10.21741/9781644904251-36

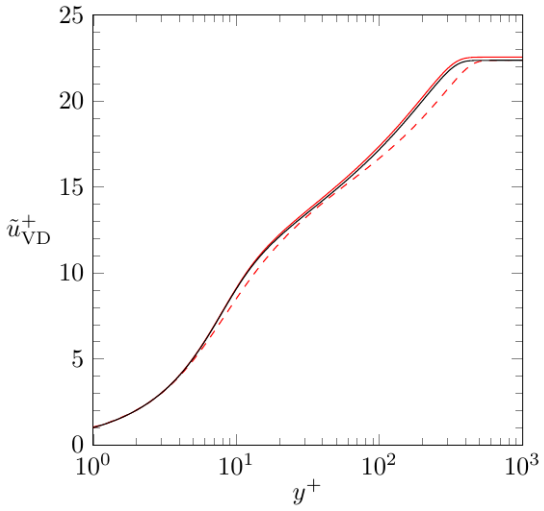


Figure 2 - Wall-normal profiles of Van Driest transformed velocity in the free-stream direction at a reference location upstream of the shock. Solid lines denote the results of the present RANS simulations, a dashed line denote Favre-averaged velocity obtained by DNS [7]. A red solid line is used for the unswept RANS case, a black solid line denotes the swept RANS case.

It can be noticed that the free-stream Mach number M_0 is different for the two simulations (M_0 = 2.28 for the unswept case, $M_0 \approx 2.63$ for the swept one), which yields a larger value of the ratio T_w/T_e for the swept case. Previous studies on the configuration considered in this work have demonstrated that this fact has a significant effect on the flow behaviour in the interaction region [10].

Results

The validity of the present numerical setup is first assessed by inspecting the wall-normal velocity distributions at the reference location. Figure 2 compares the inner-scaled velocity profiles along the free-stream direction obtained by RANS with the Favre-averaged velocity of the DNS dataset at the same location. Despite the different free-stream Mach numbers considered, it is shown that the RANS velocity profiles basically overlap, which is a result of fixing the same $\mathrm{Re}_{\delta 2}$ at the reference location. Overall, the RANS profiles are in good agreement with the DNS data-sets, which allows to state that the turbulence model is able to obtain reliable results in the zero-pressure-gradient region.

Wall pressure streamwise distributions (scaled by the inflow pressure) are depicted in figure 3 (top panel), along with the time-averaged wall pressure data obtained by DNS. It can be observed that all streamwise profiles have similar trends, with a steep increase at the onset of the interaction region and a pressure plateau just upstream of the inviscid impingement line position. All simulations slowly reach the pressure ratio given by the inviscid shock relations before the end of the computational domain.

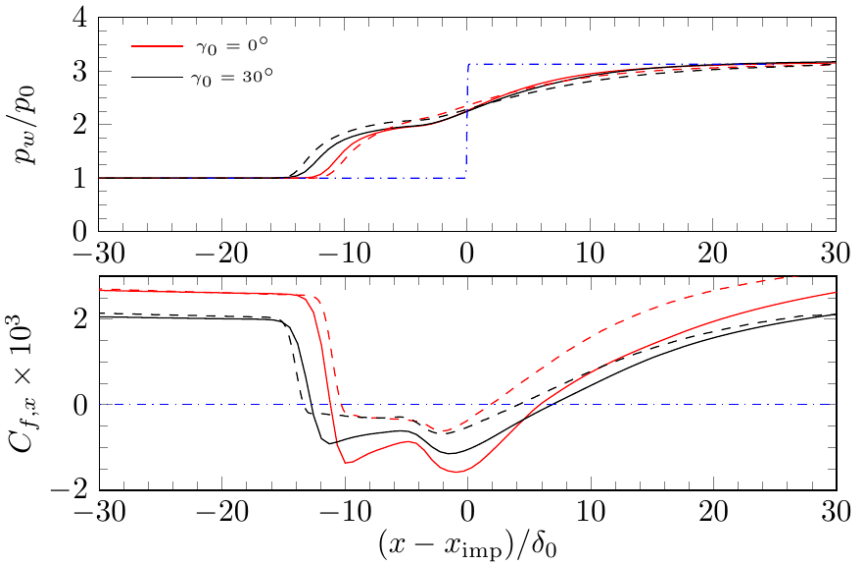


Figure 3 - Streamwise distributions of wall pressure (top) and x-projected friction coefficient (bottom). Solid lines denote the results of the present RANS simulations, dashed lines denote DNS data-sets [7]. Red lines indicate unswept interactions, black lines denote swept interactions. The blue dash-dotted line in the top panel ndicates the inviscid shock solution. The blue-dash-dotted line in the bottom panel represents $C_{f,x}$=0.

A closer look to the RANS pressure distributions past the nominal impingement line reveals that the swept case approaches the inviscid pressure jump more slowly than the unswept one, meaning that the interaction region is larger in the former case. Interestingly, the same trend is observed for the DNS data-set, meaning that RANS models are able to predict the slower relaxation towards the inviscid pressure value that is typical of swept interactions. However, it can be observed that the RANS turbulence model is not able to predict accurately the anticipated shift in the upstream influence observed by DNS in the swept case. In addition, the plateau region observed by the RANS computations is not in good agreement with the DNS data-set, and flow relaxation is retarded in RANS computations. Overall, it can be stated that the leading-order effect of sweep in this configuration, namely the increase in the size of the interaction region, is qualitatively well predicted by RANS. However, there are relatively large discrepancies between the present RANS results and the corresponding DNS data-sets, which are possibly due to the RANS inaccuracy in handling even the two-dimensional case.

Those remarks are further substantiated by the analysis of the x-projected wall friction coefficient, shown in figure 3, bottom panel. It can be observed that RANS models succeed in predicting the increased size of the separation region for the swept case. However, the streamwise length of the separation bubbles is clearly over-predicted, as the result of retarded reattachment. Moreover, the swept RANS case is characterized by retarded flow separation if compared with DNS, which confirms the previous conclusion that the modification of the upstream influence typically observed in swept interactions is not quantitatively retrieved by RANS.

Conclusions

A canonical three-dimensional shock-wave/turbulent boundary layer interaction has been examined using RANS simulations. The comparison between the present RANS results and previous DNS simulations in the same flow conditions has allowed to assess the validity of turbulence models in this regime. The analyses of the wall pressure distribution and the friction coefficient have shown that the RANS models appear to retrieve some salient features of swept interactions (for instance, the increased length of the interaction region in the swept case). Nonetheless, we found significant discrepancies between RANS and DNS for this kind of flow.

The present work emphasizes possible inconsistencies in the use of standard RANS models for high-speed separated flows in two- and three-dimensional configurations. Future work on this topic will extend the present study to a wider range of Mach and Reynolds numbers and will explore other RANS models.

References

[1] D. Sziroczak, H. Smith, A review of design issues specific to hypersonic flight vehicles. Progress in Aerospace Sciences, 84, 1-28 (2016). https://doi.org/10.1016/j.paerosci.2016.04.001

[2] N. T. Clemens, V. Narayanaswamy, Low-frequency unsteadiness of shock wave/turbulent boundary layer interactions. Annual Review of Fluid Mechanics, 46(1), 469-492 (2014). https://doi.org/10.1146/annurev-fluid-010313-141346

[3] A. Ceci, A. Palumbo, S. Pirozzoli, Grid Resolution Requirements for DNS of Shock/Boundary-Layer Interactions. Computers & Fluids, 106892 (2025). https://doi.org/10.2139/ssrn.5271692

[4] C. J. Roy, F. G. Blottner, Review and assessment of turbulence models for hypersonic flows, Progress in Aerospace Sciences 42(7-8), 469-530 (2006). https://doi.org/10.1016/j.paerosci.2006.12.002

[5] S. Padmanabhan, J. C. Maldonado, J. A. Threadgill, J. C. Little, Experimental study of swept impinging oblique shock/boundary-layer interactions. AIAA Journal 59(1), 140-149 (2021). https://doi.org/10.2514/1.J058910

[6] S. Lee, A. Gross, Numerical investigation of sweep effect on turbulent shock-wave boundary-layer interaction, AIAA Journal 60(2), 712-730 (2022). https://doi.org/10.2514/1.J060794

[7] A. Ceci, A. Palumbo, J. Larsson, S. Pirozzoli, On low-frequency unsteadiness in swept shock wave-boundary layer interactions, Journal of Fluid Mechanics 956, R1 (2023). https://doi.org/10.1017/jfm.2023.2

[8] A. Ceci, A. Palumbo, J. Larsson, S. Pirozzoli, Low-frequency unsteadiness in hypersonic swept shock wave-boundary layer interactions, Physical Review Fluids 9(5), 054603 (2024). https://doi.org/10.1103/PhysRevFluids.9.054603

[9] S. Bourgault-Côté, S. Ghasemi, A. Mosahebi, É. Laurendeau, Extension of a two-dimensional Navier-Stokes solver for infinite swept flow, AIAA Journal 55(2), 662-667 (2017) https://doi.org/10.2514/1.J055139

[10] J. Larsson, V. Kumar, N. Oberoi, M. Di Renzo, S. Pirozzoli, Large-Eddy Simulations of Idealized Shock/Boundary-Layer Interactions with Crossflow, AIAA Journal 60(5), 2767-2779 (2022). https://doi.org/10.2514/1.J061060

Materials Research Proceedings 69 (2026) 211-216 https://doi.org/10.21741/9781644904251-37

Numerical Simulation of the Effect of Extreme Accelerations on the Sonic Boom Generated by a Circular Cylinder

Roberto Francisco Bobenrieth MISERDA[1,a *], Braulio Gutierrez PIMENTA[1,b], Vinicius Coutinho DA SILVA[1,c], and Ana Luisa Pereira MALDONADO[2,d]

[1]Computational Aeroacoustics Laboratory, University of Brasilia, Brasilia, DF, 70910-900, Brazil

[2]Arup Acoustics, Manchester, M1 3BN, United Kingdom

[a]rfbm@unb.br, [b]brauliogp@unb.br, [c]viniciuscoutinho04@gmail.com, AnaLuisa.Maldonado@arup.com

Keywords: Circular Cylinder, Sonic Boom, Extreme Accelerations, Numerical Simulation

Abstract. The effect of extreme accelerations, namely 10^2 g, 10^3 g, and 10^4 g, on the intensity of the sonic boom generated by a circular cylinder accelerated from rest to a Mach number equal to 5 is investigated by a numerical simulation that uses a moving-body immersed boundary methodology, allowing to naturally capture the pressure level fluctuations generated over nearby stationary observers positioned in the opposite and orthogonal directions relative to the cylinder velocity. The compressible and unsteady Euler equations are numerically solved in a computational domain that is discretized using a finite-volume formulation. The cylinder moves through a regular Cartesian mesh where specific boundary conditions are applied to the immersed boundary volumes during the acceleration period. These boundary conditions are associated with the effect of the acceleration levels on the thermodynamic gradients in the normal direction over the surface of the cylinder. The numerical results show that the acceleration levels significantly influence the amplitude of the sonic boom measured by a stationary observer positioned in the opposite direction to the movement of the cylinder. However, they also show that the acceleration levels do not have any measurable influence on the intensity of the sonic boom measured by a stationary observer positioned in a direction orthogonal to the cylinder velocity.

Numerical Method and Boundary Conditions for Accelerating Bodies

The fundamental physics of inviscid, unsteady and compressible flows are modeled by the Euler equations, and the numerical method used in this work to solve them using a finite-volume discretization with a moving immersed-boundary approach is presented in detail by Miserda et al. [1]. To impose boundary conditions on the surface of accelerating bodies, the velocity of the fluid, $\mathbf{u}$, on the solid surface is decomposed into normal (subscript n) and tangential (subscript t) components as

$$\mathbf{u} = u\mathbf{i} + v\mathbf{j} = \mathbf{u}_n + \mathbf{u}_t = u_n\mathbf{n} + u_t\mathbf{t}, \tag{1}$$

where $\mathbf{i}$ and $\mathbf{j}$ are the unit vectors in Cartesian coordinates and $\mathbf{n}$ and $\mathbf{t}$ are the local unit vectors in the normal and tangential directions relative to the solid surface. Since the impenetrability condition on the solid surface establishes that the normal component of the fluid velocity must be equal to the normal component of the velocity of the moving body, v_{n_B}, the normal component of the velocity on the surface is given by

$$u_n = v_{n_B}. \tag{2}$$

It is important to note that for a static body, $v_{n_B} = 0$, and that for moving bodies the normal component of the velocity is simply given by

Content from this work may be used under the terms of the Creative Commons Attribution 3.0 license. Any further distribution of this work must maintain attribution to the author(s) and the title of the work, journal citation and DOI. Published under license by Materials Research Forum LLC.

Materials Research Proceedings 69 (2026) 211-216 https://doi.org/10.21741/9781644904251-37

$$v_{n_B} = \mathbf{v}_B \cdot \mathbf{n}, \tag{3}$$

where $\mathbf{v}_B$ is the instantaneous velocity of the moving body.

However, thermodynamic properties are independent of the frame-of-reference of the observer, and the thermodynamic boundary conditions at the surface of an accelerating body immersed in a stagnant fluid must be the same as the boundary conditions for a static body that is immersed in an accelerating fluid, since the only difference between the two cases is the frame-of-reference. For this reason, the thermodynamic boundary conditions are deduced for the latter case and then applied for the first one. The boundary condition for the static pressure on the wall of a stationary body immersed in an accelerating flow is obtained considering the momentum equation in the normal direction

$$\frac{\partial}{\partial t}(\rho\, u_n) + \frac{\partial}{\partial x_n}(\rho\, u_n u_n) + \frac{\partial}{\partial x_t}(\rho\, u_n u_t) = -\frac{\partial p}{\partial x_n} + f_n, \tag{4}$$

where f_n is the normal component of the volume pseudo-force imposed on the entire flow to accelerate it from stagnation condition to operational condition. This local normal component is given by $f_n = \rho[(\mathbf{u}_\infty/t_a) \cdot \mathbf{n}]$, being $\mathbf{u}_\infty$ the free-flow velocity after the acceleration period. It is important to mention that after the acceleration time t_a, the value of the pseudo-force is $f_n = 0$.

Expanding all the terms of Eq. (4) and applying the impenetrability condition, $u_n = v_{n_B}$, for a stationary body,

$$v_{n_B} = \frac{\partial v_{n_B}}{\partial t} = \frac{\partial v_{n_B}}{\partial x_n} = \frac{\partial v_{n_B}}{\partial x_t} = 0, \tag{5}$$

immersed in an accelerating flow, yields

$$\frac{\partial p}{\partial x_n} = f_n. \tag{6}$$

The entropy relation for an ideal and calorically perfect gas is given by Anderson [2] as

$$ds = \left(\frac{c_p}{T}\right) dT - \left(\frac{R}{p}\right) dp, \tag{7}$$

is also valid in the outward normal direction from the wall, yielding

$$\frac{\partial s}{\partial x_n} = \left(\frac{c_p}{T}\right)\frac{\partial T}{\partial x_n} - \left(\frac{R}{p}\right)\frac{\partial p}{\partial x_n}. \tag{8}$$

By imposing the isentropic boundary condition in the normal direction,

$$\frac{\partial s}{\partial x_n} = 0, \tag{9}$$

in conjunction with the pressure boundary conditions obtained previously and the state equation for an ideal gas, $p = \rho RT$, Eq. (8) results in the temperature boundary condition,

Materials Research Proceedings 69 (2026) 211-216 https://doi.org/10.21741/9781644904251-37

$$\frac{\partial T}{\partial x_n} = \left(\frac{1}{c_p\ \rho}\right) f_n. \tag{10}$$

Differentiating the state equation for an ideal gas in the normal direction,

$$\frac{\partial p}{\partial x_n} = \frac{\partial}{\partial x_n}(\rho R T) = R\rho \frac{\partial T}{\partial x_n} + RT \frac{\partial \rho}{\partial x_n}, \tag{11}$$

results in the density boundary condition,

$$\frac{\partial \rho}{\partial x_n} = \left(\frac{1 - R/c_p}{RT}\right) f_n. \tag{12}$$

For a termically and calorically perfect gas, the relation between internal energy and temperature is given by $e = c_v T$. Deriving this relation in the normal direction and using Eq. (10) yields

$$\frac{\partial e}{\partial x_n} = \left(\frac{c_v}{c_p\ \rho}\right) f_n. \tag{13}$$

Numerical Setup

The numerical simulations are performed using a two-dimensional domain where the characteristic length of the setup, $D = 10$ m, is the diameter of the circular cylinder. The regular computational domain extends $30D$ in the horizontal direction, x, and $300D$ in the vertical direction, y. The diameter of the cylinder is discretized using 256 finite volumes, resulting in a regular Cartesian grid that has 589.82×10^6 of them. The initial undisturbed pressure and temperature for the whole domain are 1.01325×10^5 Pa and 3.0×10^2 K, resulting in a cylinder Mach number of 5 after the acceleration period to a maximum vertical velocity of 1,735.94 m/s. The cylinder is initially stationary and is positioned at $x = 15D$ and $y = 15D$. After the acceleration period, it is in the same horizontal position, but at $y = 168.59D$ for 10^2 g, $y = 30.36D$ for 10^3 g, and $y = 16.54D$ for 10^4 g. The boundary conditions for accelerating bodies were implemented in the Virtual Aeroacoustic Tunnel (VAT) code, developed and maintained by the Computational Aeroacoustics Laboratory (CAALab) of the University of Brasilia (UnB). The VAT code uses a hybrid MPI/OpenACC parallel processing paradigm to numerically solve the Euler equations [1], allowing a parallel execution using six NVIDIA GeForce RTX 4090, while using simple-precision floating point arithmetic (FP32). Using these computational resources, 2.44×10^{10} degrees of freedom are solved per second of wall-clock.

Materials Research Proceedings 69 (2026) 211-216 https://doi.org/10.21741/9781644904251-37

Aeroacoustic Fields and Pressure Signals

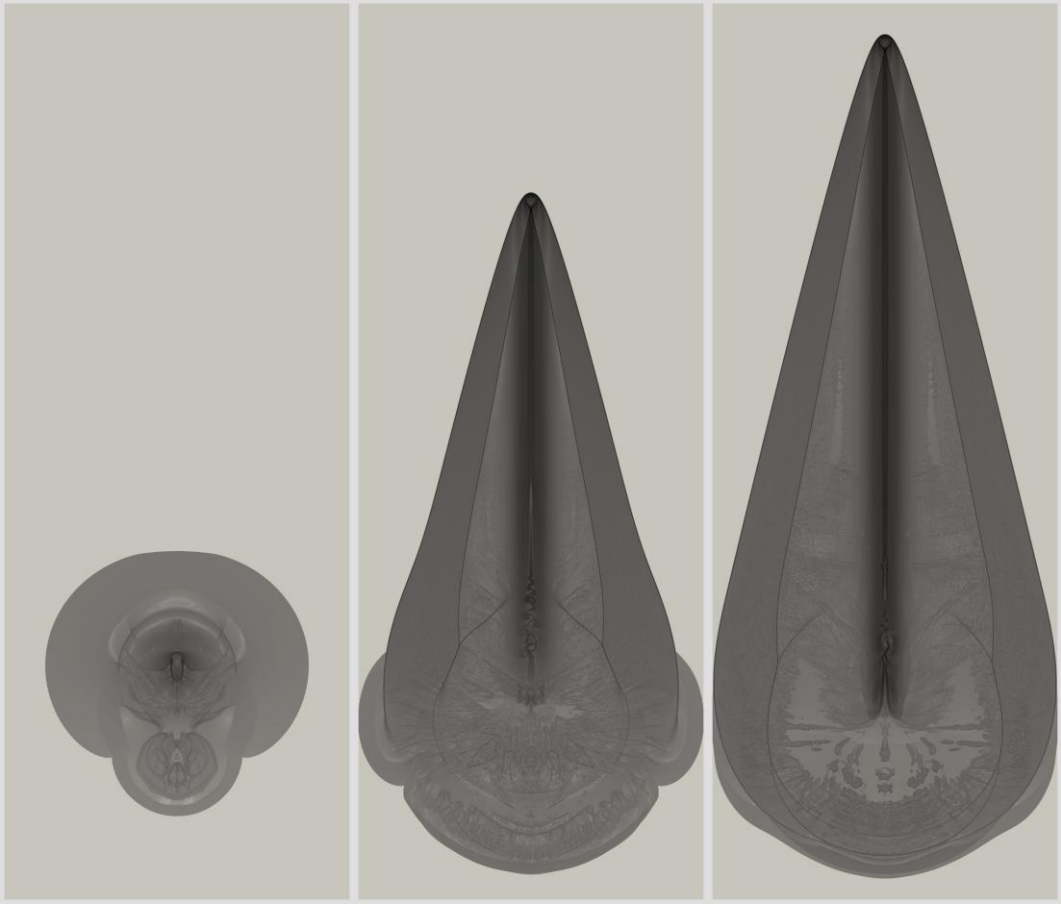


Figure 1: Comparative visualization of the aeroacoustic field using the variable $\beta_T = |\nabla T|^{1/10}$ at the same elapsed time, 0.354 s, for 10^2 *g* (left), 10^3 *g* (center), and 10^4 *g* (right).

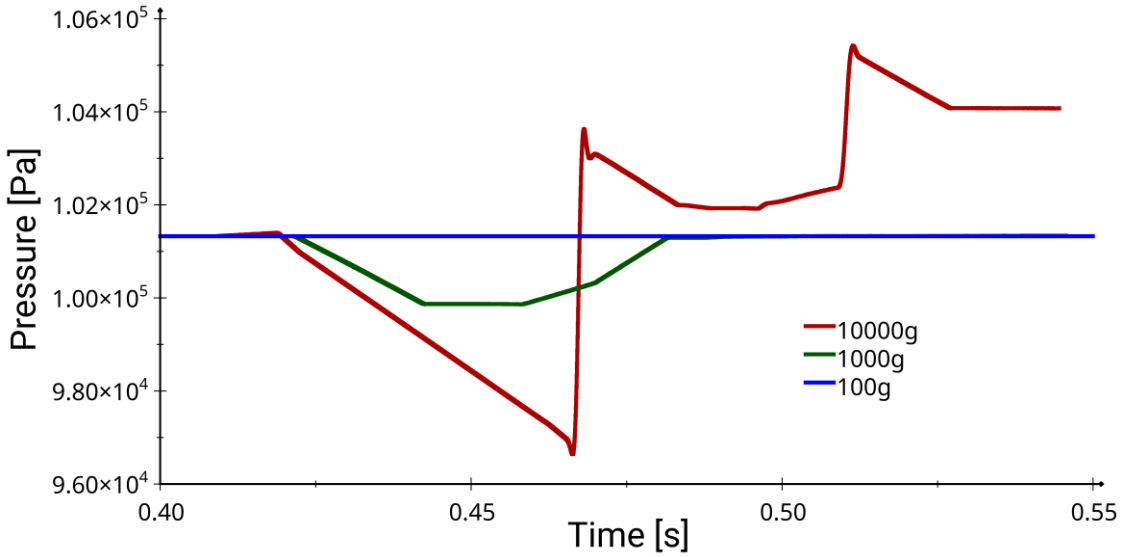


Figure 2: Pressure signal at the center of the bottom edges of the regular computational domains shown in Fig. 1.

Materials Research Proceedings 69 (2026) 211-216 https://doi.org/10.21741/9781644904251-37

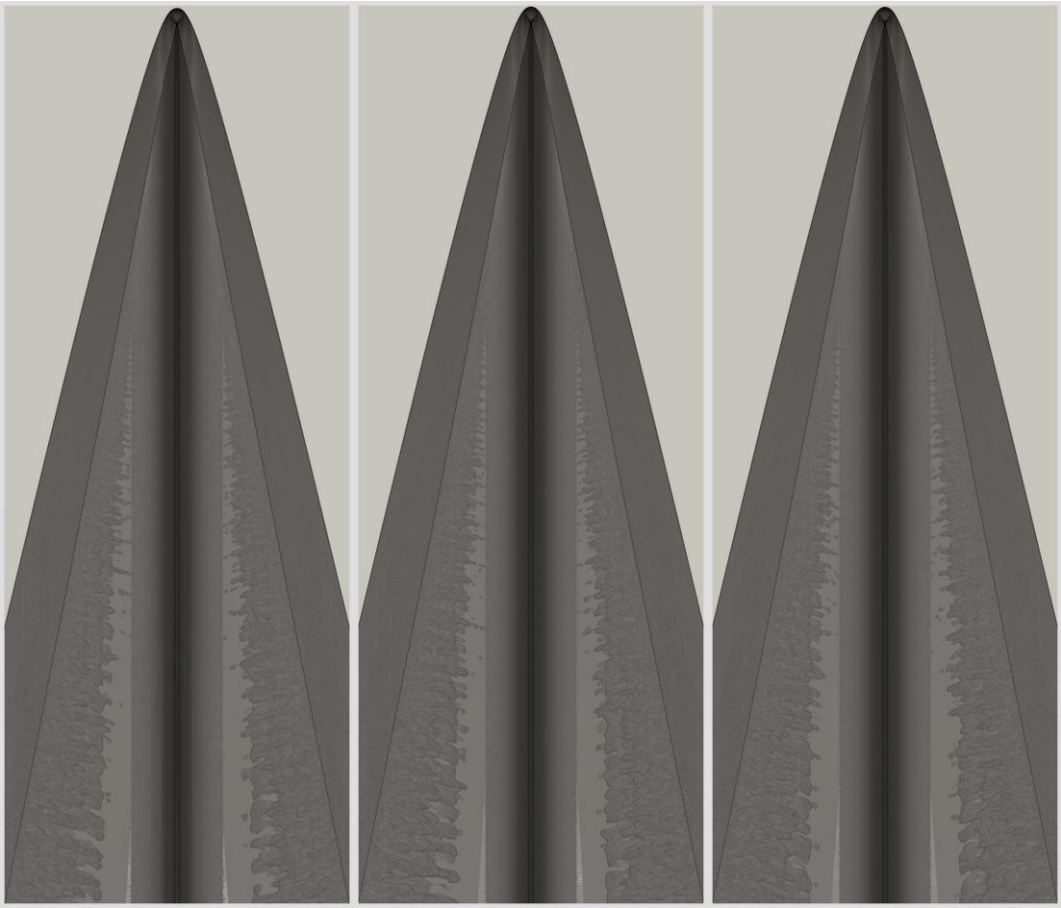


Figure 3: Comparative visualization of the aeroacoustic field using the variable $\beta_T = |\nabla T|^{1/10}$ at the same cylinder position, $y = 260.74D$, for 10^2 g (left), 10^3 g (center), and 10^4 g (right).

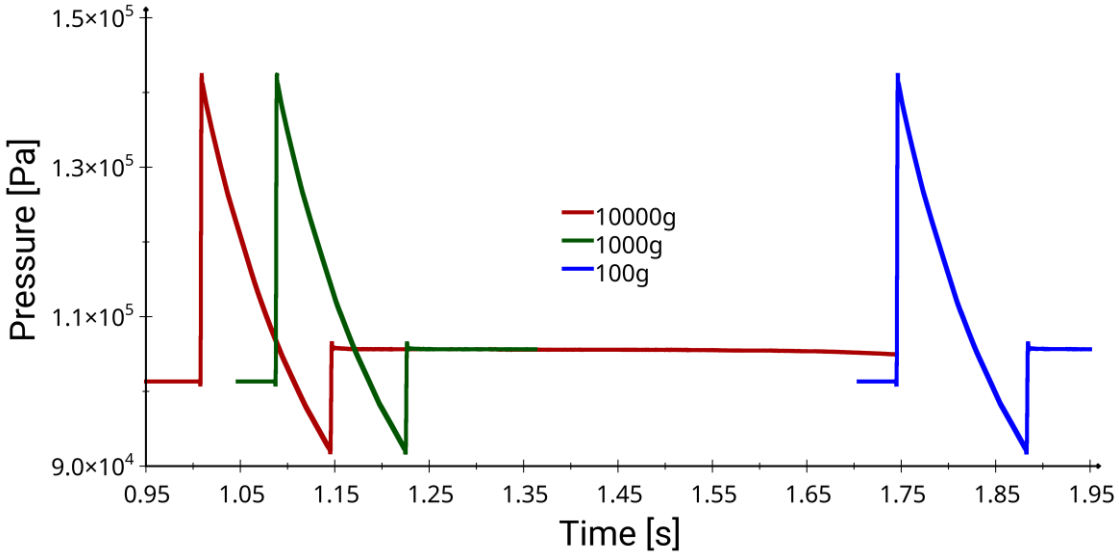


Figure 4: Pressure signal at coordinates $(30D, 135D)$ *associated with the passage of the shock-wave systems shown on each of the regular computational domains of Fig. 3.*

Summary

The numerical results show that the acceleration levels significantly influence the amplitude of the pressure fluctuations measured by a stationary observer positioned in the opposite direction to the movement of the cylinder (Fig. 2), at a distance $15D$ from its initial position. However, they also show that acceleration levels do not have any measurable influence on the intensity of pressure fluctuations measured by a stationary observer that is positioned, at a distance $15D$, in a direction that is orthogonal to the trajectory of the cylinder after it reaches Mach 5 (Fig. 4).

References

[1] R.F.B. Miserda, B.G. Pimenta, L.S. da Rocha, Numerical Simulation of Rotor-Stator Interaction Noise in Transonic Cascades, Journal of Propulsion and Power, Vol. 36, No. 3, May-June 2020. https://doi.org/10.2514/1.B37627

[2] J.D. Anderson, Modern Compressible Flow: With Historical Perspective, second ed., McGraw-Hill Publishing Company, New York, 1990

Materials Research Proceedings 69 (2026) 217-220 https://doi.org/10.21741/9781644904251-38

Numerical Simulation of the Transition from Regular to Mach Reflection of Oblique Shocks

Davide RUOCCHIO[1,a *] and Alberto GUARDONE[1,b]

[1]Department of Aerospace Science and Technology, Politecnico di Milano, Italy

[a]davide.ruocchio@mail.polimi.it, [b]alberto.guardone@polimi.it

Keywords: Oblique Shock Reflection, Transition Criteria, SU2, Mach Stem

Abstract. We use a rectangular computational domain to study numerically the transition from regular to Mach reflection of oblique shock waves in steady The SU2 solver is used to solve the 2D Euler equation, where the desired shock conditions are obtained by imposing suitable boundary conditions. Results for the Mach stem height compare fairly well with those obtained on the conventional wedge geometry. Accurate Mach stem height requires a domain large enough to resolve the sonic throat.

Introduction

Oblique shock reflections are either regular reflections (RR) or irregular reflections (IR), further classified as Mach (MR), von Neumann (vNR), Guderley (GR) and Vasilev (VR) reflections [1]. Possible criteria for the transition between regular and Mach reflections are the detachment condition [2], the sonic condition [3], and the von Neumann condition [4]. RR can only exist below the detachment condition and MR only above the von Neumann condition. Both RR and MR are stable within the dual-solution domain. Identifying the correct transition point remains a challenge, but a length-scale criterion suggests that the sonic and the von Neumann conditions should be preferred, depending on the initial state of the flow [1].

Experiments conducted by Hornung and Robinson recorded transition at the von Neumann condition, supporting the length-scale principle [5]. Hysteresis effects, first discussed by Hornung et al. [3], were reproduced experimentally by Chpoun et al. [6]. Hysteresis was also observed in 2D numerical simulations, with the transition from RR to MR occurring at detachment, while the transition from MR to RR occurs closer to the von Neumann condition [7]. The discrepancy between numerical simulations and experiments lies in the strong three-dimensionality of the process. Small perturbations may also trigger the transition [8].

The geometry of the domain influences the transition and the shape of the reflection [9]. This study employs numerical simulations of oblique shock wave reflections to examine the transition in steady flows across different domain geometries and to define the optimal approach for obtaining consistent and reliable results.

Methodology

Euler 2D simulations were performed using SU2, an open-source CFD suite combined with the in-house adaptive mesh refinement tool Darwin. Unstructured triangular grids were generated using the in-house mesh software uhMesh.

The domain (Fig. 1) is rectangular: pre-shock inlet conditions are imposed on the left boundary, the bottom boundary is the symmetry plane where reflection occurs, while the right boundary is the outlet. The top boundary is divided into two segments: the shock is generated by imposing the post-shock state computed using the Rankine-Hugoniot jump conditions on the foremost segment (or gap); the aftermost segment is a wall.

Content from this work may be used under the terms of the Creative Commons Attribution 3.0 license. Any further distribution of this work must maintain attribution to the author(s) and the title of the work, journal citation and DOI. Published under license by Materials Research Forum LLC.

Materials Research Proceedings 69 (2026) 217-220 https://doi.org/10.21741/9781644904251-38

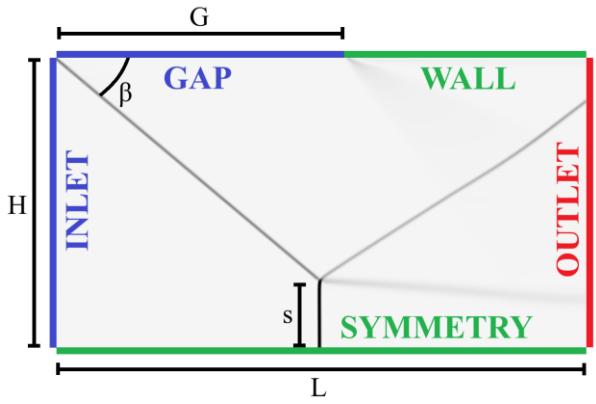


Figure 1: Numerical domain.

Table 1: Grid convergence.

Cell size h/H	Mach stem height s/H	Percentage variation
0.0100	0.223	–
0.0070	0.231	3.6
0.0050	0.238	3.0
0.0035	0.242	1.7
0.0025	0.244	0.8

The starting grid size is h/H = 0.05 as a balance between the advantage of better catching the transition at earlier steps of the iterations and the computational time. The mesh undergoes six levels of refinement. Mesh refinement is only used to assess the transition, but not when measuring the Mach stem height. In this case, a cell size of h/H = 0.005 is selected after performing a grid convergence study with parameters M_0 = 2.9, β = 40 deg, G/H = 1, reported in Table 1. Mach numbers range from 2 to 6, and incident shock angles from 31 degrees to 43 degrees.

Results

The simulation domain can be related to a corresponding configuration (Fig. 2) in which the shock is generated by the presence of a wedge by purely geometrical considerations, for any initial condition. In Fig. 3, a comparison of the normalized Mach stem heights in the two setups shows the expected agreement.

MR are not self-similar, thus requiring to define a length scale for a stable solution [8]. An expansion fan forms at the leading edge of the top wall and impinges on the slip line originating at the triple point of the MR. The region below the slip line behaves as a converging-diverging duct, selecting the required length scale [5]. The interaction of the expansion fan with the slip line can be controlled by changing the gap-to-height ratio, which is equivalent to changing the relative size of the wedge in the conventional configuration. As also observed by Bai [10], the Mach stem height is found to change linearly with the gap-to-height ratio as long as the fan does not interact with the incident shock, but uniquely with the reflected shock. The domain must be large enough to solve the sonic throat below the slip line to consistently predict the MR geometry (Fig. 4).

Conclusions

This numerical study investigates the transition of oblique shock reflections using a rectangular computational domain as an alternative geometry of generating the shock by imposing suitable boundary conditions. A constant number of elements between the symmetry plane and the wall is key to consistent, comparable results. This approach allows the use of fewer elements compared

Materials Research Proceedings 69 (2026) 217-220 https://doi.org/10.21741/9781644904251-38

to domains including wedges while preserving the overall number of cells when solving a wider range of initial conditions.

Reproducing accurate and reliable simulations can support theoretical findings, while also helping to predict the shape of shock reflections.

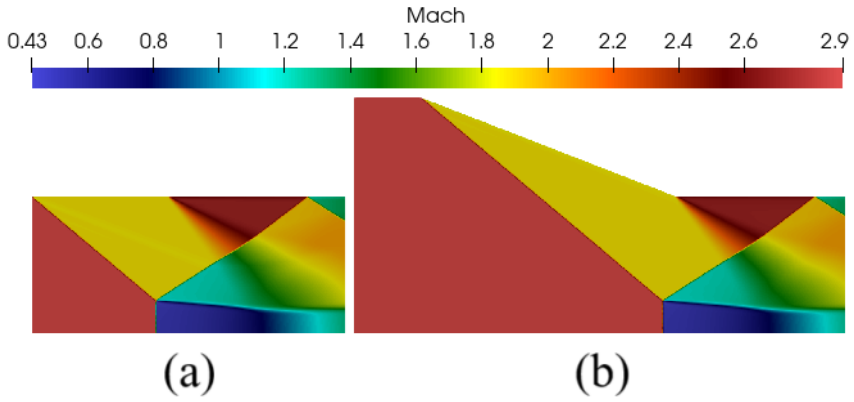


Figure 2: Rectangular domain (a) and corresponding domain with wedge (b) for M_0 = 2.9, β = 40 deg, G/H = 1.

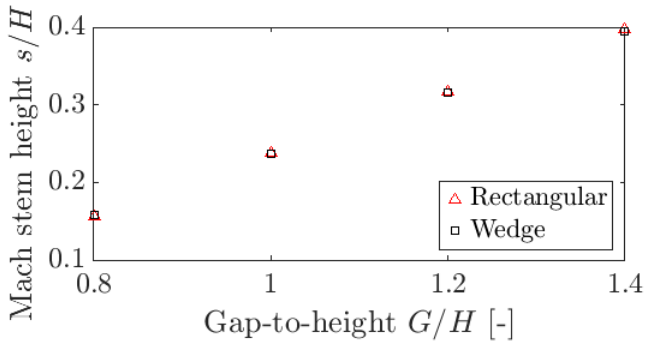


Figure 3: Comparison between the Mach stem height resolved in the rectangular domain and the domain with wedge (M_0 = 2.9, β = 40 deg).

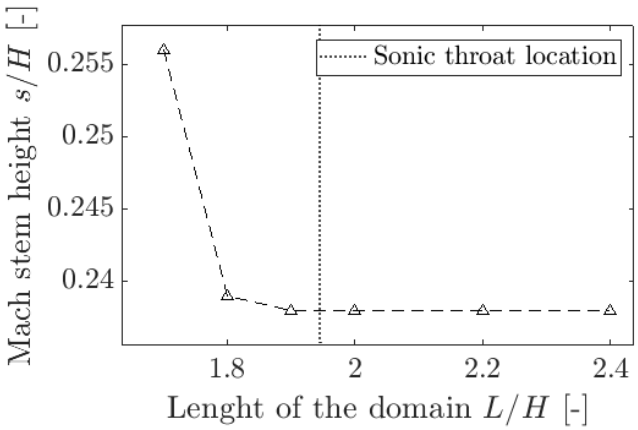


Figure 4: Mach stem height compared to the length of the domain. The height becomes constant only when the sonic throat is included inside the domain (M0 = 2.9, β = 40 deg, G/H = 1).

References

[1] G. Ben-Dor, Shock wave reflection phenomena, second ed., Springer Berlin, Heidelberg, 2007. https://doi.org/10.1007/978-3-540-71382-1

[2] J. von Neumann, Collected works, volume IV, Pergamon Press, Oxford, 1963.

[3] H.G. Hornung, H. Oertel, R.J. Sandeman, Transition to Mach reflexion of shock waves in steady and pseudosteady flow with and without relaxation, J. Fluid Mech. 90 (1979) 541-560. https://doi.org/10.1017/S002211207900238X

[4] L.F. Henderson, A. Lozzi, Experiments on transition of Mach reflexion, J. Fluid Mech. 68 (1975) 139-155. https://doi.org/10.1017/S0022112075000730

[5] H.G. Hornung, M.L. Robinson, Transition from regular to Mach reflection of shock waves Part 2. The steady-flow criterion, J. Fluid Mech. 123 (1982) 155-164. https://doi.org/10.1017/S0022112082003000

[6] A. Chpoun, G. Ben-Dor, Numerical confirmation of the hysteresis phenomenon in the regular to the Mach reflection transition in steady flows, Shock Waves 5 (1995) 199-203. https://doi.org/10.1007/BF01419001

[7] A. Chpoun, D. Passerel, H. Li, G. Ben-Dor, Reconsideration of oblique shock wave reflections in steady flows. Part 1. Experimental investigation, J. Fluid Mech. 301 (1995) 19-35. https://doi.org/10.1017/S0022112095003776

[8] M.S. Ivanov, D. Vandromme, V.M. Fomin, A.N. Kudryavtsev, A. Hadjadj, D.V. Khotyanovsky, Transition between regular and Mach reflection of shock waves: new numerical and experimental results, Shock Waves 11 (2001) 199-207. https://doi.org/10.1007/PL00004075

[9] J. Vuillon, D. Zeitoun, G. Ben-Dor, Reconsideration of oblique shock wave reflections in steady flows. Part 2. Numerical investigation, J. Fluid Mech. 301 (1995) 37-50. https://doi.org/10.1017/S0022112095003788

[10] C.-Y. Bai, Z.-N. Wu, A Study of the dependence of the Mach stem height on the trailing edge height, Fluids 6 (2021) 313. https://doi.org/10.3390/fluids6090313

Materials Research Proceedings 69 (2026) 221-226 https://doi.org/10.21741/9781644904251-39

Use of Matching Pursuit Algorithm for Identification of Aircraft Aerodynamic Coefficients

Mateusz PILECKI[1,a*], Manfred GAWLAS[1,b], and Jacek GRZEGORZEWSKI[2,c]

[1]PWr in Space, Faculty of Information and Communication Technology, 27 Wybrzeże Wyspiańskiego St., 50-370 Wrocław, Poland

[2]Faculty of Electronics, Photonics and Microsystems Technology, 27 Wybrzeże Wyspiańskiego St., 50-370 Wrocław, Poland

[a]279994@student.pwr.edu.pl, [b]279722@student.pwr.edu.pl, [c]jacek.grzegorzewski@pwr.edu.pl

Keywords: System Identification, Aerodynamics, Matching Pursuit

Abstract: This paper describes a novel use of the Matching Pursuit (MP) algorithm, originating in signal processing literature, in identifying aerodynamic coefficients as functions of wind and control surface deflection angles from Computational Fluid Dynamics (CFD) simulations results, as well as comparing MP to other commonly used methods of system identification. Due to the high number of variables that parametrise the aerodynamic coefficients of actuated airframes, traditional methods suffer from the so-called "curse of dimensionality", which requires a very large sample size for satisfactory identification. If the coefficient functions are known to be sparse in terms of an assumed function basis, MP lowers the number of samples needed to identify these coefficients down to a much more tractable size. As long as the function basis used is differentiable and continuous, the estimated coefficients will be as well, giving a form that is particularly convenient from a control system design perspective. The paper is structured as follows: the first section describes the definition of the problem. The second section details the Matching Pursuit approach in the context of identifying the aerodynamic forces and moments acting on a rigid body. The third section briefly states on traditionally used methods and how MP might perform better. Finally, MP is applied to CFD dataset obtained for canard-actuated sounding rockets created in collaboration of Attitude Control System Project of the PWr in Space Student Scientific Association with KTH Student Scientific Association Æsir under the UNITE! Program.

Introduction

Accurate knowledge of aerodynamic coefficients is essential for aircraft and flight control system design. These coefficients describe the relationship between aerodynamic forces and moments with respect to flight conditions and control inputs. However, due to the nonlinear nature of aerodynamic behavior, especially under real flight conditions, the precise estimation of these parameters remains a challenging and tedious task [1].

In this paper the algorithm called Matching Pursuit (MP) [2] is used for aerodynamic coefficient identification for canard-controlled student-built rockets . The analysis focuses on the accuracy and computational efficiency of the MP-based approach relative to the conventional least square estimation technique.

Problem definition

The objective of this study is to develop a sparse, continuous and differentiable representation of the aerodynamic coefficient functions for a rocket with movable canards. The model is based on a set of simulation data consisting of around 500 data points obtained from low- fidelity CFD simulations based on Spalart-Allmaras model [3, 4] that describes how input parameters affect aerodynamic forces and torques. Table 1 summarizes the input and output variables considered in the simulations.

Content from this work may be used under the terms of the Creative Commons Attribution 3.0 license. Any further distribution of this work must maintain attribution to the author(s) and the title of the work, journal citation and DOI. Published under license by Materials Research Forum LLC.

Materials Research Proceedings 69 (2026) 221-226 https://doi.org/10.21741/9781644904251-39

Table 1: Summary of Input and Output Parameters

Symbol	Description	Units
Input Variables		
C_{zp}, C_{zm}, C_{yp}, C_{ym}	Canard deflection angles (pos./neg. Y,Z)	[deg]
M	Mach number	[-]
α	Angle of attack	[deg]
β	Sideslip angle	[deg]
Output Variables		
F_x, F_y, F_z	Aerodynamic forces (body axes)	[N]
T_x, T_y, T_z	Aerodynamic torques (body axes)	[N * m]

Figures 1 and 2 illustrate the rocket geometry and canard orientation in the *X-Z* and *X-Y* planes, respectively.

For the present analysis, the Mach number is assumed constant, as variations in M within the considered flight regime should have a limited influence on the relative trends of the aerodynamic coefficients. Furthermore, while the aerodynamic forces generated directly by canard deflections are negligible in comparison to those produced by the main rocket body, their contribution to the aerodynamic torques is significant due to the distance of the canards to the center of mass of the. Consequently, the focus is placed on accurately capturing the torque effects induced by canard motion, while the corresponding force variations are neglected.

In this work, we also restrict the identification to static aerodynamic coefficients. Modeling dynamic effects would require time-dependent simulations and substantially higher computational resources, which are beyond the current scope of this study and are left for future work [5].

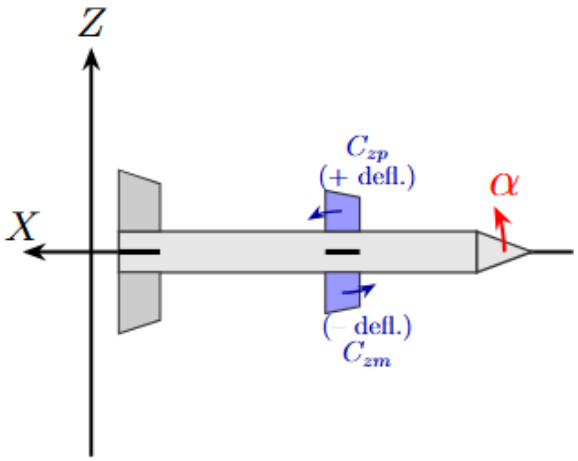


Figure 1: Rocket side view (X-Z plane)

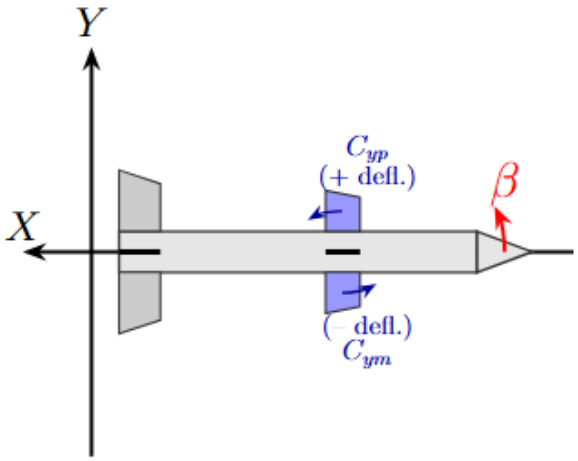


Figure 2: Rocket side view (X-Y plane)

Matching Pursuit for Aerodynamic Functions

In the MP framework, each aerodynamic coefficient function $f(x)$ (with x denoting angles and deflections) is treated as a "signal" to be approximated. We choose a dictionary $D = \{g_\gamma\}$ of smooth basis trigonometric functions. MP then proceeds by initializing the residual $R^0 f = f$ and iteratively selecting atoms that maximize the correlation with the residual. At iteration m, MP picks the atom g_{γ_m} satisfying

Materials Research Proceedings 69 (2026) 221-226 https://doi.org/10.21741/9781644904251-39

$$\gamma_m = \arg\max_{\gamma \in \Gamma} \left| \left\langle R^m f, g_\gamma \right\rangle \right|, \tag{1}$$

then updates the approximation via

$$f \approx \sum_{m=0}^{M} \left\langle R^m f, g_{\gamma_m} \right\rangle g_{\gamma_m}, \qquad R^{m+1} f = R^m f - \left\langle R^m f, g_{\gamma_m} \right\rangle g_{\gamma_m}. \tag{2}$$

This process is repeated until the residual norm is negligible or a maximum number of atoms M is reached. Variables used to construct atoms are described in table 2.

Table 2: Variable Definitions and Derived Parameters

Symbol	Definition	Description
Primary Variables		
a	α	Alpha angle (symbolic)
b	β	Beta angle (symbolic)
A	$\sqrt{\alpha^2 + \beta^2}$	Total angular magnitude
Derived Delta Parameters		
d_p	$\frac{C_{zp} + C_{yp} + C_{zm} + C_{ym}}{4}$	Average of all measurements
d_q	$\frac{C_{zp} - C_{zm}}{2}$	Half difference (Z-axis pair)
d_r	$\frac{C_{yp} - C_{ym}}{2}$	Half difference (Y-axis pair)

Because we use smooth, differentiable atoms, the fitted coefficient functions are themselves continuous and differentiable. In practice, MP was applied to CFD-generated force/torque dataset for rocket models. The algorithm produced very high R^2 fits for most force/torque components, yielding explicit series of trigonometric terms (see example table 3) that smoothly capture the input--output relationships. Thus MP provides a sparse, analytic model of the aerodynamics that is easy to evaluate and differentiate.

For this usage, the function dictionary D is constructed from a basis of trigonometric functions. A distinct dictionary is defined for each of the six aerodynamic coefficients (F_x, F_y, F_z, T_x, T_y, T_z), as each coefficient is modeled as a function of a different subset of the input variables defined in Table 2. For an aerodynamic coefficient f that depends on a set of d input variables, such as (α, β, A) for the force components, the dictionary is formed by the tensor product of one-dimensional function sets. For each variable x_k in the input set (e.g., $x_1 = \alpha$, $x_2 = \beta$, $x_3 = A$), we define a basis with a maximum frequency F_{max}:

$$B_k = \{1\} \cup \{\cos(j \cdot x_k)\}_{j=1}^{F_{max}} \cup \{\sin(j \cdot x_k)\}_{j=1}^{F_{max}} \tag{3}$$

The full dictionary D_f for the coefficient f is the set of all possible products where one function is chosen from each corresponding basis B_k:

$$D_f = \left\{ g(x) = \prod_{k=1}^{d} \phi_k(x_k) \;\middle|\; \phi_k \in B_k \right\} \tag{4}$$

To manage this large dictionary computationally, each atom $g_\gamma \in D_f$ is identified by a unique integer index γ. This index is mapped to a specific combination of trigonometric functions using a mixed-radix conversion, where the base is $b = 2F_{max} + 1$. This allows any atom in the high-

Materials Research Proceedings 69 (2026) 221-226 https://doi.org/10.21741/9781644904251-39

dimensional dictionary to be generated on-the-fly from a single integer, avoiding the need to store the entire dictionary in memory.

Traditional Identification Methods

The Least Squares (LS) method is one of the most frequently employed approaches for aerodynamic coefficient identification due to its simplicity and well-established statistical foundation. LS has been extensively used in estimating lateral–directional derivatives and other aerodynamic coefficients from various data [6, 7].

Despite these advantages, the LS method presents several limitations when applied to aerodynamic system identification. It relies on the assumption that the model structure is correctly specified and linear in its parameters—an assumption that may not hold for the inherently nonlinear aerodynamic phenomena observed in flight dynamics. Important limitation is that the classical LS formulation assumes error-free independent variables, an assumption that is rarely valid in practical flight-test scenarios, where sensor noise and measurement uncertainties can lead to biased parameter estimates [1, 7].

To address some of these shortcomings, the Matching Pursuit (MP) method offers an alternative perspective on coefficient identification. MP iteratively selects basis functions from a predefined dictionary to minimize the residual error at each step [2, 8]. Moreover, MP naturally promotes sparsity by retaining only the most relevant terms, which can enhance interpretability and prevent overfitting in complex aerodynamic models. Finally, its flexible dictionary structure allows for the inclusion of nonlinear terms, providing a more adaptable framework for capturing nonlinear aerodynamic effects compared to the strictly linear LS approach. Therefore, while LS remains an established baseline method, the MP approach may offer potential advantages in contexts where nonlinearity, collinearity, and measurement uncertainty limit the accuracy of traditional least-squares estimation.

Application of Matching Pursuit

Finally, MP is applied to CFD simulation data obtained for a canard-actuated sounding rocket created in collaboration with KTH Student Scientific Association Æsir under the UNITE! Program. The results from the function identification are visible in table 3 and figure 3.

Table 3: Calculated expressions for forces and torques

Component	Mathematical Expression	R^2
F_x	$0.23\cos\left(\sqrt{\alpha^2+\beta^2}\right)\cos(2\alpha)\cos(\beta)$	0.5014
F_y	$-7.6\,cos(\alpha)\sin(\beta)$	0.9725
F_z	$7.2\,cos(\beta)\sin(\alpha)$	0.9815
T_x	$0.018\,cos\left(8\sqrt{\alpha^2+\beta^2}\right)\cos(4\alpha)\sin(7\delta_p)$	0.4158
T_y	$-0.63\cos(4\beta)\sin(\alpha)-0.21\sin(2\delta_r)\cos(3\alpha)\cos(\beta)$	0.9535
T_z	$0.72\cos(3\alpha)\sin(\beta)+0.43\cos(4\beta)\cos(3\alpha)\sin(\delta_q)$	0.9700

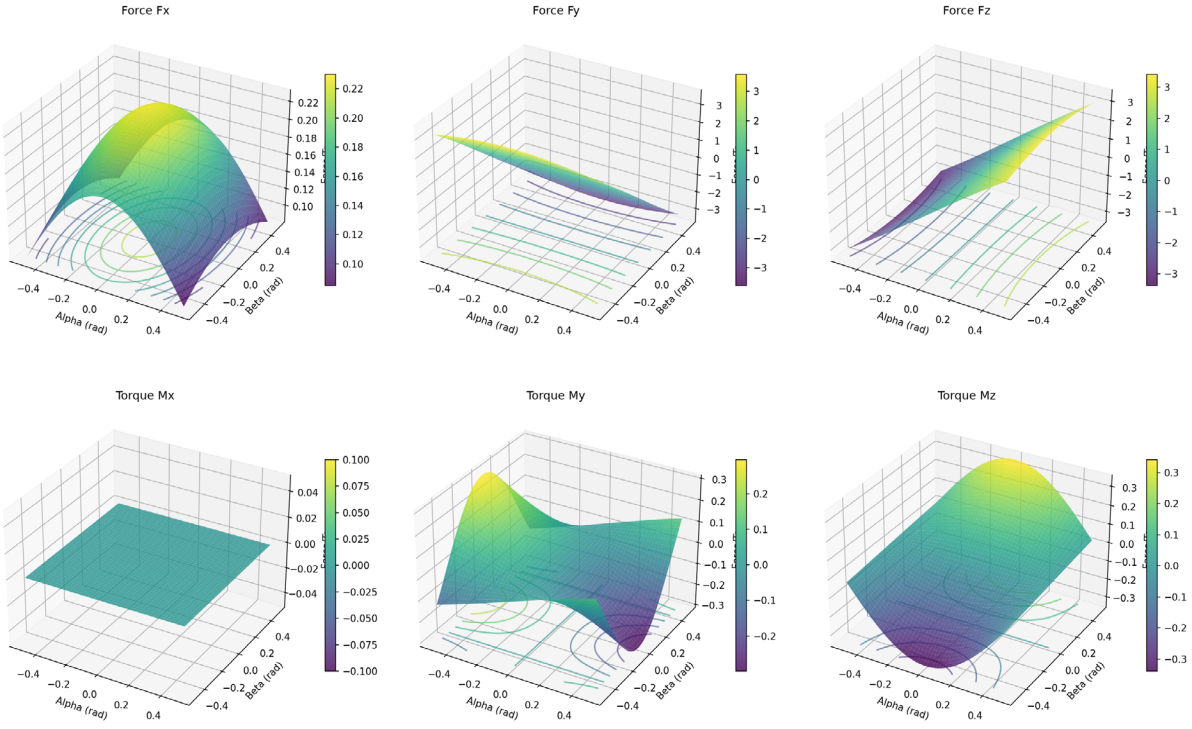


Figure 3: Aerodynamic coefficients visualization as functions of α, β for δ_p, δ_q, $\delta_r = 0$

Discussions

The preliminary results demonstrate that the Matching Pursuit (MP) framework is a promising approach for constructing aerodynamic coefficient functions. The method effectively identifies functions while maintaining interpretability and differentiability. However, further testing is required across a wider range of aerodynamic conditions and control settings. Future work should focus on expanding the dictionary to include a richer and more redundant set of basis functions, which may improve the accuracy and flexibility of the approximations.

Acknowledgements

We would like to express our gratitude to the Services And Networking TechnologieS Laboratory (SANTOS Lab) operating within the Department of Computer Science and Systems Engineering at Wroc law University of Science and Technology for their support in providing the computational resources necessary to carry out the simulations used in this article.

References

[1] M. Albisser, Identification of aerodynamic coefficients from free flight data. Theses, Universit'e de Lorraine, July 2015.

[2] S. Mallat and Z. Zhang, "Matching pursuits with time-frequency dictionaries," IEEE Transactions on Signal Processing, vol. 41, no. 12, pp. 3397-3415, 1993. https://doi.org/10.1109/78.258082

[3] P. R. Spalart and S. R. Allmaras, "A one-equation turbulence model for aerodynamic flows," in 30th Aerospace Sciences Meeting and Exhibit, 1992. https://doi.org/10.2514/6.1992-439

[4] B. Baran, "Skrypt obliczenia numeryczne (cfd)." Lecture script, Wroc law University of Science and Technology.

[5] R. Tamai and S. Nonaka, "A study on unsteady aerodynamics modeling for a slender body," in Proceedings of the 3rd International Conference on Flight Vehicles, Aerother-modynamics and Re-entry (FAR), (Arcachon, France), The University of Tokyo and ISAS/JAXA, 2025-05-18/2025-05-22.

[6] R. Kumar and A. K. Ghosh, "Estimation of lateral-directional aerodynamic derivatives from flight data using conventional and neural based methods," The Aeronautical Journal, vol. 118, no. 1210, p. 1453-1479, 2014. https://doi.org/10.1017/S0001924000010149

[7] Z. Mohamed, A. Mohamed, F. Khaled, A. Souhila, and B. N. Sarah, "Application of the total least squares estimation method for an aircraft aerodynamic model identification," World Academy of Science, Engineering and Technology, International Journal of Mechanical, Aerospace, Industrial, Mechatronic and Manufacturing Engineering, vol. 10, pp. 1152-1161, 2016.

[8] V. N. Temlyakov, "Greedy approximation," Acta Numerica, vol. 17, p. 235-409, 2008. https://doi.org/10.1017/S0962492906380014

Materials Research Proceedings 69 (2026) 227-232 https://doi.org/10.21741/9781644904251-40

Blockage Effects in Wind Tunnel Experiments of Turbulent Wakes: A Numerical Study

Gianluca PORPORA[1,a *] and Andrea PALUMBO[1,b]

[1]Dipartimento di Ingegneria Meccanica e Aerospaziale, Sapienza Università di Roma, Via Eudossiana 18, 00184 Roma, Italy

[a]gianluca.porpora@uniroma1.it, [b]andrea.palumbo@uniroma1.it

Keywords: Computational Fluid Dynamics, Separated Flows, Wind Tunnel Blockage

Abstract. In many industrial applications, turbulent flow past bluff bodies separates, causing aerodynamic forces unsteadiness, structural vibrations, and noise. Wind tunnel experiments are commonly used to study wake dynamics, evaluate aerodynamic coefficients and perform spectral analyses. However, wind tunnel walls may significantly alter the wake topology, thereby leading to biased measurements. Predictive formulae for the effect of confinement are mainly available for simple bodies, such as circular and square cylinders. This study investigates the influence of wall confinement on the turbulent wake behind a missile-shaped airfoil using unsteady Reynolds-averaged Navier–Stokes (URANS) simulations. The analysis is performed at moderate Reynolds numbers and for various blockage ratios. Results show that drag, lift fluctuations, and shedding frequency all increase monotonically with blockage ratio. These findings extend previous observations on laminar confined wakes to turbulent bluff-body wakes, underscoring the importance of designing proper wind tunnel experiments.

Introduction

Flow unsteadiness behind bluff bodies is a critical issue in aerospace applications, as the shedding of vortical structures can affect vehicle performance, structural integrity, and generate acoustic emissions. Those phenomena are often the effects of vortical structures generated in the separated region behind the body. Numerous passive and active flow-control strategies have been proposed, whose design requires accurate knowledge of the characteristic frequency and spatial pattern of the wake structures.

Wind tunnel experiments have been the main source of knowledge about separated flows behind bluff bodies. However, the physical significance of those studies may be questioned when the separated flow dynamics is strongly influenced by the bounding walls of the test section. As demonstrated in [1], lateral walls can strongly affect experimental measurements, as confinement modifies both the mean flow topology and the large-scale wake dynamics. Moreover, blockage effects may alter vortex shedding frequencies, distort aerodynamic forces, and even promote coherent structures that are absent in unconfined conditions. Those long standing issues have been the object of several studies, as recently reviewed by [2].

Extensive studies have been performed for canonical geometries such as circular [3, 4, 5] and square [6, 7, 8] cylinders. Those studies span a very wide range of flow conditions, from very low-Reynolds number laminar flows, to subcritical/supercritical turbulent flow regimes. All those studies do recognize a strong effect of blockage on aerodynamic coefficients and their characteristic frequency (which is properly scaled to form a non-dimensional group, known as Strouhal number). By contrast, other geometries as elongated or rectangular bluff bodies have received less attention, despite their relevance for practical aerodynamic design. Addressing the lack of research on this topic may be particularly important because accurate wind tunnel measurements must account for confinement effects while still satisfying similarity laws.

Content from this work may be used under the terms of the Creative Commons Attribution 3.0 license. Any further distribution of this work must maintain attribution to the author(s) and the title of the work, journal citation and DOI. Published under license by Materials Research Forum LLC.

Materials Research Proceedings 69 (2026) 227-232 https://doi.org/10.21741/9781644904251-40

In this study, unsteady Reynolds-averaged Navier–Stokes (URANS) simulations are em ployed to characterize the influence of wall confinement on the turbulent wake past a D shaped cylinder in subcritical conditions. Fully resolved simulations as direct numerical simulations or wall-resolved large eddy simulations would be computationally prohibitive, and dedicated experimental facilities quite demanding. In this sense, URANS computations provide a low-fidelity tool, able to obtain the unsteady distributions of drag and lift coeffi cients in relatively short time and with good accuracy. Blockage ratio, defined as the ratio between the thickness of the body and the wind tunnel crosswise width, is varied between 2% and 25%. The present study allows a systematic assessment of confinement effects in turbulent bluff-body wakes and provides insights for the design and interpretation of wind tunnel experiments. Specifically, we aim at investigating confinement effects on the time averaged value of the drag, lift fluctuations variance, and Strouhal number.

Methodology

The two-dimensional turbulent wake behind a thick flat plate in a confined wind tunnel is numerically analyzed by means of URANS simulations. The flow configuration under study is sketched in Fig. 1. It consists of an elongated D-shaped cylinder with aspect ratio $A = c/H = 10$, where *c* is the chord length and *H* is the trailing edge thickness. The longitudinal axis of the body lies along the mid-plane of a two-dimensional plane channel. The leading edge of the body is rounded in the form of a semi-ellipse, transitioning into a thick flat plate that terminates with a blunt trailing edge. This setup mimics the longitudinal mid-plane of a wind tunnel configuration, where the test model spans the full tunnel width in the spanwise direction.

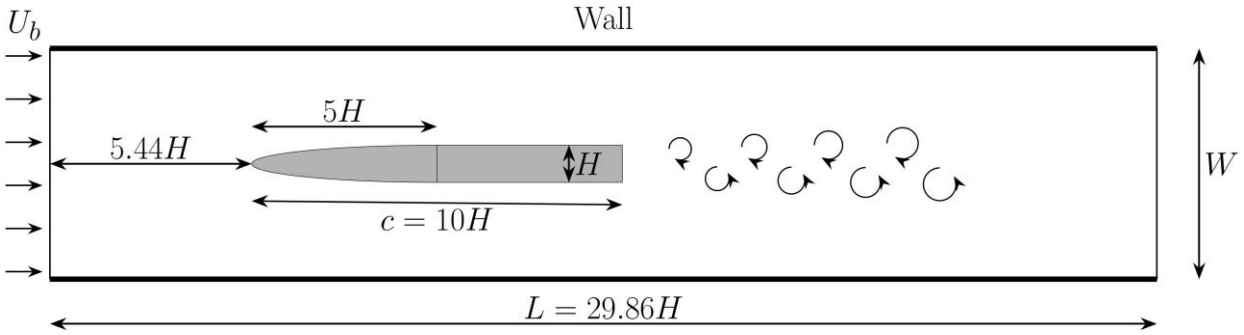


Figure 1: Sketch of the numerical setup and main notation used in this study.

The computational domain extends for a $L = 29.86H$ length in the streamwise direction, while the transverse width W is varied to analyze blockage effects. The plate leading edge is placed $5.44H$ downstream from the inflow section, where a uniform velocity profile is imposed. The governing equations considered in this work are the incompressible Navier-Stokes equations, made dimensionless using the bulk velocity U_b and the plate thickness H. This configuration is completely characterized by two non-dimensional parameters, namely the Reynolds number $Re = U_b H/\nu$ and the blockage ratio $B = H/W$. A fixed Reynolds number of $Re = 32000$ is considered in this work, with blockage ratios varying in the range $2\% < B < 25\%$ ($W/H \in [4,50]$). The present numerical setup allows direct comparison with the previous work [9], which investigated the same configuration, at the same Reynolds numbers for a single blockage ratio $B \approx 0.16$.

Simulations are performed with the OpenFOAM solver *pimpleFoam* [10] using the $k-\omega$ SST model [11]. Body-fitted meshhed are generated with the native OpenFOAM mesher *snappyHexMesh*. Fig. 2 shows the numerical mesh used to investigate the confined flow at $B = 0.16$. The figure highlights the wake refinement and the prismatic layers introduced on the body and the wind tunnel lateral walls. Near-wall mesh clustering ensures resolutions of $y^+ \approx 1$ on the

Materials Research Proceedings 69 (2026) 227-232 https://doi.org/10.21741/9781644904251-40

lateral walls and $y^+ \approx 0.5$ on the body. Within this framework, governing equations are spatially discretized using second-order schemes for p and U, whereas turbulent quantities are discretized using first-order upwind schemes. Time integration is performed with a second-order implicit scheme. Pressure-velocity coupling is handled with the PIMPLE algorithm, which merges the SIMPLE (semi-implicit method for pressure linked equations) and PISO (pressure implicit with split operator) [12]. At the inlet, a uniform velocity is prescribed, whereas the turbulent variables are obtained by fixing the inflow turbulence intensity to 2%.

The main output of the work ist o quantify blockage effects on the aerodynamic force coefficients, namely the aerodynamic drag coefficient $C_D = 2D/(\rho U_B^2 H)$ and the aerodynamic lift coefficient $C_L = 2L/(\rho U_B^2 H)$. Those quantities are obtained as the projection oft he aerodynamic force along the x and y axes. In this work, we mainly refer to the time-averaged drag coefficient $\overline{C_D}$, the lift coefficient root-mean square C_L' and their characteristic Strouhal number $S_t = fH/U_b$. The aerodynamic coefficients are sampled once the flow have reached a saturated vortex-shedding regime, and the Strouhal number is obtained as the peak of the lift frequency spectra.

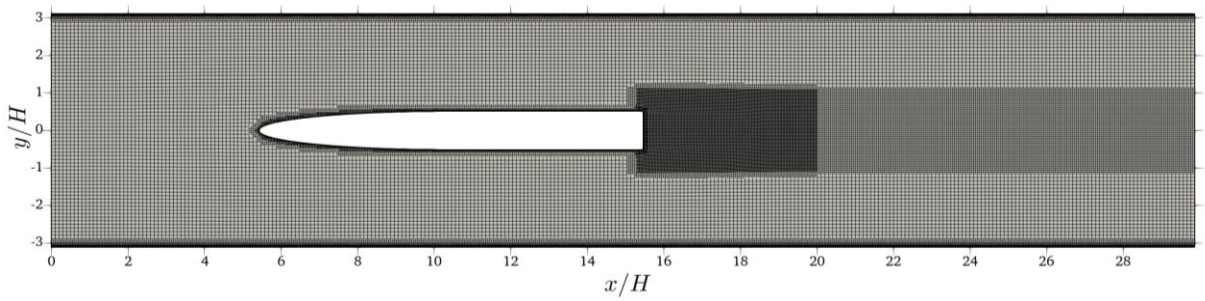


Figure 2: Mesh employed for the numerical analysis. Blockage ratio B=0.16.

Results

Fig. 3 shows the variation of the mean drag coefficient $\overline{C_D}$, with blockage ratio. We can distinguish two different trends as B is increased. For low blockage ratios ($B < 0.04$), $\overline{C_D}$ remains nearly constant. Outside of this range, the drag coefficient start deviating from its unconfined value, with an increasing slope as B increases. The present trend appears to be in very good agreement with the previous simulation by [9] in the same flow conditions.

The difference between the confined and the unconfined drag coefficient value exceed 3% for $B > 6\%$. Similar results have been reviewed by [2] for circular and square cylinders in both laminar and turbulent regimes. Hence, the present geometry appears to follow the same trend shown in those cases. However, for the thick D-shaped plate the viscous contribution to $\overline{C_D}$ should be larger than in the circular cylinder case making a direct quantitative comparison non readily available.

Materials Research Proceedings 69 (2026) 227-232 https://doi.org/10.21741/9781644904251-40

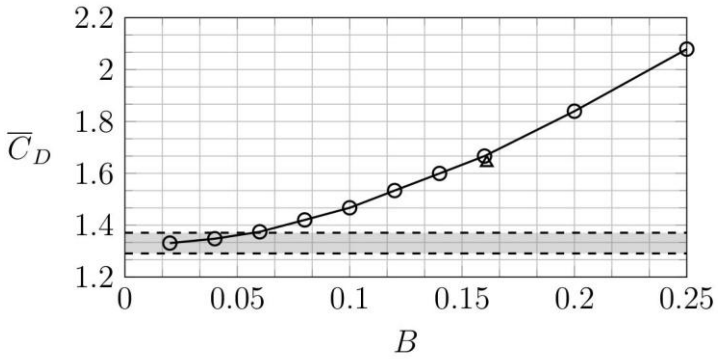


Figure 3: Time-averaged drag coefficient as function of blockage ratio B. Dashed lines represent ±3% difference band with respect to $\overline{C_D}$ at B=0.02. A triangle mark denotes the URANS results by [9] at B=1/6.2.

Fig.4 shows the standard deviation of the lift coefficient, C_L', which quantifies the intensity of unsteady lift fluctuations induced by vortex shedding, as a function of the blockage ratio B. For small blockage ratios $B < 0.04$, the variation of fluctuating lift coefficient remains weak, whereas at higher blockage ratios the growth becomes stronger, reflecting the increasing influence of wall confinement. The growth is monotonic, indicating that confinement amplifies the strength of the periodic vortex shedding, thereby increasing the unsteady aerodynamic loads on the body. This result is in very good agreement with turbulent wakes at subcritical Reynolds number (as reported in [2]) and, as expected, in contrast with laminar wakes and turbulent wakes in supercritical conditions.

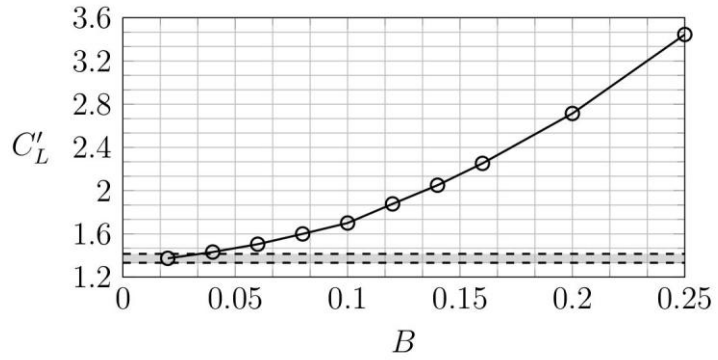


Figure 4: Lift coefficient root-mean-square C_L' as a function of blockage ratio B. Dashed lines represent ±3% difference band with respect to C_L' at B=0.02.

The dependence on B of the Strouhal number St is illustrated in Fig.5. The value of the Strouhal number is in excellent agreement with the experimental value found by [9] using particle image velocimetry (triangle mark in Fig.5). The present results show that St increases monotonically with B. Specifically, for very low blockage ratios $B < 0.1$, St is weakly influenced by confinement, consistent with observations summarized in [2]. The overall observed trend in Strouhal number well conforms with previous findings from circular and square cylinders in both laminar and turbulent regimes.

Finally, Fig. 6 shows an instantaneous snapshot of the vorticity field for $B = 0.16$. The classical vortex shedding is still visible, however their trajectory is closer to the x axis if compared with unconfined flow. A large amount of vorticity is also observed next to the wind tunnel walls, which is connected to boundary layer thickening and instantaneous lift-off of fluid from the near-wall region.

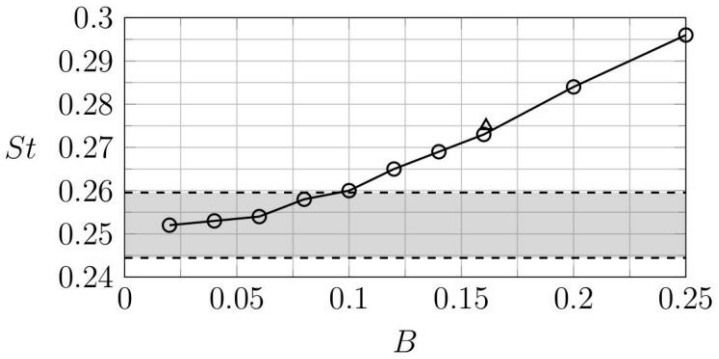


*Figure 5: Stouhal number as a function of blockage ratio **B**. Dashed lines represent ±3% difference band with respect to St at B=0.02. The triangle marker reports the experimental value of the Strouhal number obtained by [9].*

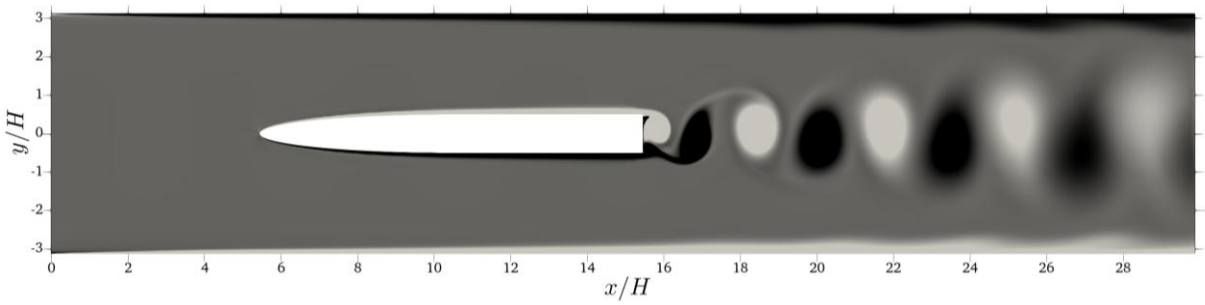


Figure 5: Instantaneous snapshot of flow vorticity for the B=16% case (extrema of the color map are 1.5, black and -1.5, white).

Conclusions

The present study quantified the influence of wall confinement on the turbulent wake past a missile-shaped airfoil using URANS simulations. The mean drag coefficient, lift coefficient and fluctuations, and Strouhal number all increase monotonically with blockage ratio. For low blockage ratios ($B < 0.1$), mean drag and shedding frequency remain within a $\pm 3\%$ band, indicating negligible confinement effects. At higher blockage ratios ($B > 0.1$), the aerodynamic coefficients and Strouhal number are markedly affected by the wind tunnel walls. These results provide a practical reference for estimating the influence of confinement in wind tunnel experiments of non-canonical bluff bodies in turbulent channels.

References

[1] G.S. West, C.J. Apelt, The effects of tunnel blockage and aspect ratio on the mean flow past a circular cylinder with Reynolds numbers between 104 and 105, Journal of Fluid Mechanics, 114 (1982) 361-377 https://doi.org/10.1017/S0022112082000202

[2] R. Mondal, M.M. Alam, Blockage effect on wakes of various bluff bodies: A review of confined flow, Ocean Engineering, 286 (2023) 115592 https://doi.org/10.1016/j.oceaneng.2023.115592

[3] J.-H. Chen, W.G. Pritchard, and S.J. Tavener, Bifurcation for flow past a cylinder between parallel planes, Journal of Fluid Mechanics, 284, 23-41, 1995 https://doi.org/10.1017/S0022112095000255

[4] M. Sahin and R.G. Owens, A numerical investigation of wall effects up to high blockage ratios on two-dimensional flow past a confined circular cylinder, Physics of Fluids, 16(5), 1305-1320, 2004 https://doi.org/10.1063/1.1668285

[5] S. Singha, K.P. Sinhamahapatra, Flow past a circular cylinder between parallel walls at low Reynolds numbers, Ocean Engineering, 37(8-9) (2010) 757-769 https://doi.org/10.1016/j.oceaneng.2010.02.012

[6] M. Breuer, J. Bernsdorf, T. Zeiser, F. Durst, Accurate computations of the laminar flow past a square cylinder based on two different methods: lattice-Boltzmann and finite volume, International Journal of Heat and Fluid Flow, 21(2) (2000) 186-196 https://doi.org/10.1016/S0142-727X(99)00081-8

[7] S. Turki, H. Abbassi, S. Ben Nasrallah, Effect of the blockage ratio on the flow in a channel with a built-in square cylinder, Computational Mechanics, 33(1) (2003) 22-29 https://doi.org/10.1007/s00466-003-0496-2

[8] Patil, P. P. and Tiwari, S., Effect of blockage ratio on wake transition for flow past square cylinder, Fluid Dynamics Research, 40(11-12), 753, 2008 https://doi.org/10.1016/j.fluiddyn.2008.04.001

[9] M. Carini, C. Airiau, A. Debien, O. Léon, J.O. Pralits, Global stability and control of the confined turbulent flow past a thick flat plate, Physics of Fluids, 29(2) (2017) https://doi.org/10.1063/1.4974069

[10] OpenFOAM web page: www.openfoam.org

[11] F.R. Menter, Two-equation eddy-viscosity turbulence models for engineering applications, AIAA Journal, 32 (8) (1994) 1598-1605 https://doi.org/10.2514/3.12149

[12] R.I. Issa, Solution of the implicitly discretised fluid flow equations by operator-splitting, Journal of Computational Physics, 62 (1) (1986) 40-65 https://doi.org/10.1016/0021-9991(86)90099-9

Materials Research Proceedings 69 (2026) 233-238 https://doi.org/10.21741/9781644904251-41

Numerical Simulation of Wall-Bounded Flows with Thermally Perfect Gases

Alessandro AIELLO[1,a *], Andrea PALUMBO[2,b] and Gennaro COPPOLA[1,c]

[1]Federico II University of Naples, Naples, Italy

[2]Sapienza University of Rome, Rome, Italy

[a]alessandro.aiello@unina.it, [b]andrea.palumbo@uniroma1.it, [c]gennaro.coppola@unina.it

Keywords: Compressible Flows, Wall-Bounded Flows, Thermally Perfect Gases, Structure-Preserving

Abstract. The present study addresses the numerical simulation of wall-bounded flows with thermally perfect gases using structure-preserving spatial discretizations. The supersonic turbulent boundary layer and channel flow are chosen as numerical flow cases to highlight the differences with respect to the widely used calorically perfect gas model when relatively high temperature ranges are present. Specifically, we compare literature results obtained for air flows with the ones carried out for carbon-dioxide, which is likely to be treated as a thermally perfect gas in high-temperature cases. Results show non-negligible physical differences with the reference cases, and the numerical treatment of the convective terms of the integrated equations is taken into account as well.

Introduction

Supersonic wall-bounded flows are among the most extensively studied physical configurations and encompass a wide range of applications, including the aerodynamics of supersonic and hypersonic vehicles, aerospace propulsion and aerothermal heating and heat transfer. In most applications, when the working fluid is air, it is well known that the calorically perfect (CP) hypotheses hold, up to negligible differences, in a wide range of Mach numbers, even when strongly diabatic walls are studied [1]. However, dependency of specific heat capacities on temperature becomes relevant when chemical species with several thermodynamic degrees of freedom are considered; for instance, the case of carbon-dioxide represents a fitting example of a nonpolar molecule whose heat capacities strongly vary within temperature, and it is widely studied for applications like atmospheric re-entry. In this context, Direct Numerical Simulations (DNS) represent a powerful and reliable tool when it comes to build a physical understanding of configurations with severe thermo-fluid dynamic conditions, especially within an *ad hoc* numerical treatment of the discretized equations that aims to consistently represent important properties and symmetries of the continuous system also in the discrete framework [2]. In this work, computations of high-speed wall bounded flows are carried out with thermally perfect (TP) gas laws in the open-source, GPU-accelerated code STREAmS 2.1 [3]. We consider both channel flows and turbulent boundary layer, with the latter case being compared with the literature results in [1].

Organization of the Text

The three-dimensional Navier-Stokes equations are solved for a viscous, heat-conducing, Newtonian fluid

$$\partial_t \rho + \partial_{x_j}(\rho u_j) = 0 \tag{1}$$

Content from this work may be used under the terms of the Creative Commons Attribution 3.0 license. Any further distribution of this work must maintain attribution to the author(s) and the title of the work, journal citation and DOI. Published under license by Materials Research Forum LLC.

Materials Research Proceedings 69 (2026) 233-238 https://doi.org/10.21741/9781644904251-41

$$\partial_t(\rho u_i) + \partial_{x_j}\left(\rho u_j u_i + p\delta_{ij}\right) - \partial_{x_j}\tau_{ij} - f_1\delta_{i1} = 0 \quad (2)$$

$$\partial_t(\rho E) + \partial_{x_j}\left(\rho u_j H\right) - \partial_{x_j}\left[\left(u_j\tau_{ij} - q_j\right)\right] + \Phi - f_1 u_1 = 0 \quad (3)$$

with ρ the density of the fluid, u_i the Cartesian components of the velocity field, p the thermodynamic pressure, $E = e + u_i u_i/2$, the total energy and $H = E + p/\rho$ the total enthalpy. The standard constitutive relation are assumed for the dissipative part of the stress tensor $\tau_{ij} = \mu\left(\partial_{x_j}u_i + \partial_{x_i}u_j - 2/3\ \partial_{x_k}u_k\delta_{ij}\right)$, and the heat flux $q_j = -k\partial_{x_j}T$. Dynamic viscosity μ depends on temperature according to the Sutherland's law, whose general expression is $\mu/\mu_e = (T/T_e)^{1/2}(1 + C/T_e)/(1 + C/T)$, and it is linked to the thermal conductivity $\mu c_p\ /Pr$, with C the Sutherland's constant and the subscript "e " to indicate the asymptotic conditions. Finally, $T_e = 298.15$ K and Prandtl number is $Pr = 0.72$. The production terms Φ, f_i will only be taken into account to simulate compressible channel flows with a constant bulk temperature and mass flow rate. The system is closed upon specification of the equation of state $p = \rho RT$ and the relation that links internal energy to intensive thermodynamic variables, which, for thermally perfect gases, takes the form $de = c_v(T)dT$. Given the Mayer's relation $c_p - c_v = R$, the functional law for $c_v(T)$ is assumed from the 7-coefficient polynomial fittings of the NASA Glenn Coefficients [4].

Numerical treatment of the system of equations Eqs. (1) - (3) is carried out in a semi-discretized framework, where the spatial discretization enforces the Kinetic-Energy Preserving (KEP) property for all the compared simulations, such that the total energy equation is represented by the sum of the contributions of the (induced) kinetic energy and internal energy [2,5]. Additionally, a novel Entropy-Conserving (EC) formulation is considered [6], where the internal energy equation is discretized to ensure exact entropy-conservation by convection, that is no spurious contributions occur from the convective terms for interior points.

Given this background, Tab.1 reports the physical parameters and the computational setup for the presented simulations. The viscous scaling is given by the standard definitions $\delta_v = \nu_w/u_\tau$, $u_\tau = (\tau_w/\rho)^{1/2}$, with the subscript "$w$ " denoting conditions at the wall. Thus, we have$\Delta x^+ = \Delta x/\delta_v$ and $\Delta z^+ = \Delta z/\delta_v$, which are discretized with evenly-spaced points, and $\Delta y^+ = \Delta y/\delta_v$ clustered near the walls. To generate a turbulent inflow for the boundary layer case, the recycling-rescaling procedure in STREAmS is employed, setting the recycling plane at $x_{rec} = 80\delta_{in}$. Profiles and statistics are computed at $Re_\tau = \delta/\delta_v \approx 450$ with δ being the boundary layer thickness, to carry out the comparison with the results in [1]. On the other hand, the supersonic channel flow case is performed at a constant mass flow rate and enabling the cooling term Φ in total energy equation to keep the bulk temperature constant. As far as it concerns notations, we use the symbol $\overline{\phi}$ to denote the both in time and in spanwise direction - assuming homogeneity along z -direction itself- while the Favre averaging will be denoted as $\tilde{\phi} = \overline{\rho\phi}/\overline{\rho}$ for which we denote $\phi = \tilde{\phi} + \phi''$ instead of the standard Reynolds' decomposition.

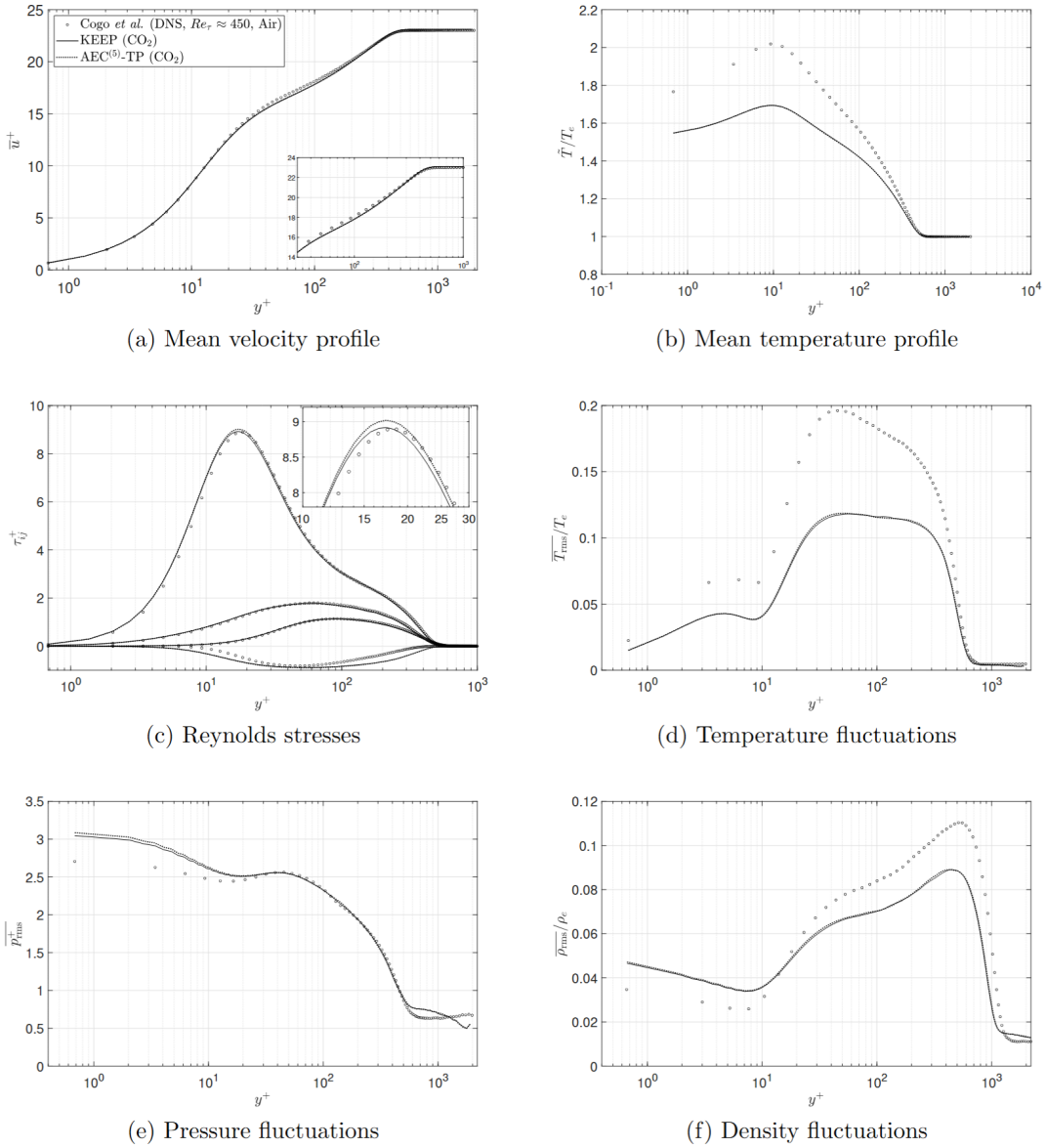
Materials Research Proceedings 69 (2026) 233-238 https://doi.org/10.21741/9781644904251-41

Table 1: *Indication of the main flow and computational parameters for supersonic boundary layer at $M_e = 4.0$ (BLM4) and supersonic channel flow at $M_b = 2.0$ (CFM2). The definitions for the Mach numbers employed are $M_e = U_e/\sqrt{\gamma_e R\, T_e}$ and $M_b = U_b/\sqrt{\gamma_b R T_b}$. Recovery temperature, T_r, is likewise derived from the isentropic relations $T_r/T_e = 1 + rM_e^2(\gamma_e - 1)/2$ for the boundary layer case and, dually, $T_r/T_b = 1 + rM_b^2(\gamma_b - 1)/2$ for the channel flow case, with $r = P\, r^{1/3}$ the recovery factor. Finally, h is the half-height of the channel.*

	Gas	M	Re_τ	T_w/T_r	L_x	L_y	L_z	Δx^+	Δy_w^+	Δz^+
BLM4–CP	Air	4.0	443.6	0.44	$100\delta_{in}$	$15\delta_{in}$	$9\delta_{in}$	4.4	0.7	3.9
BLM4–TP	CO_2	4.0	443.5	0.44	$100\delta_{in}$	$12\delta_{in}$	$8\delta_{in}$	7.3	0.7	4.1
CFM2–CP	CH_4	2.0	215	0.36	$4\pi h$	$2h$	$2\pi h$	7.6	0.4	3.8
CFM2–TP	CH_4	2.0	215	0.36	$4\pi h$	$2h$	$2\pi h$	7.6	0.4	3.8

Results and discussion

Fig.1 shows both velocity and temperature profiles, where the TP case is carried out with both the built-in "KEEP" discretization in STREAmS, EC for ideal gases only, and the EC formulation specifically designed for TP gases. Inner-scaled velocity profiles present an upward shift with respect to the incompressible log-law, which is due to the combined effects of compressibility and heat transfer at the wall. On the other hand, Fig.1(b) shows that air and CO_2, given the same asymptotic conditions, produce remarkably different temperature distributions. Specifically, higher values of c_p lead to smaller temperature variations. The region associated to larger $\partial_y T$ is indeed the one that better highlights the effects of the variable $c_p(T)$. Looking at Fig.1(b)-(d), the logarithmic layer and the buffer layer are the ones that exhibit the strongest deviation from the ideal gas behaviour, especially in temperature fluctuations, whose peaks appear to largely differ. Density fluctuations behave similarly, while pressure fluctuations have also been reported, showing higher values for the TP case around 15 % at the wall. As far as it concerns the role of the numerical discretization, the KEEP scheme and the Asymptotically Entropy-Conserving (AEC) [7] only differ in the treatment of the energy equation, and research is ongoing to understanding the impact on the final results, already observed for higher-order statistics. To check the generality of the previous results, we observe that similar trends are found for the channel flow case, although both physical and computational parameters are different. This time we carry out a comparison with the same chemical specie, once modelled as a CP gas and once as a TP gas. For the CP test, γ is evaluated at bulk temperature and kept constant. Results are shown in Fig.2, with the same definitions for scaling described in Fig.1. Given the more extreme cold wall conditions considered for the channel flow, the higher variation of $c_p(T)$ for methane and the lower Reynolds number, differences between the two gas models are emphasized in this case, still holding the same trend shown for the boundary layer simulations. A final, noteworthy observation addresses the effect of the heat capacities on the skin friction coefficients, defined as $c_f = 2\overline{\tau_w}/(\rho_e U_e^2)$ - for boundary layer, $\rho_b U_b^2$ used for channels instead - and the heat transfer coefficient $B_q = \overline{q_w}/\overline{\rho_w} c_p u_\tau T_w$.



(a) Mean velocity profile

(b) Mean temperature profile

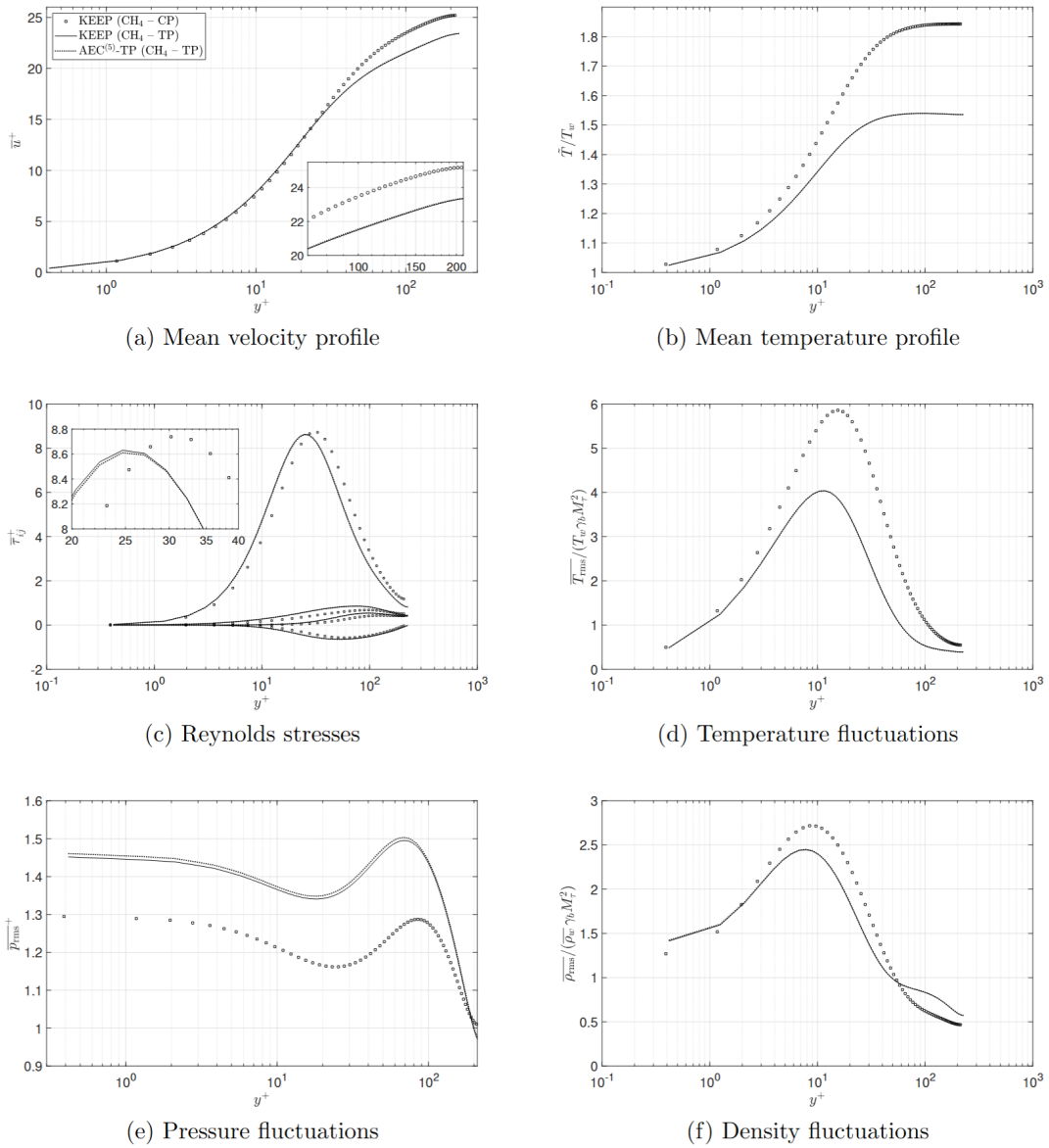
(c) Reynolds stresses

(d) Temperature fluctuations

(e) Pressure fluctuations

(f) Density fluctuations

Figure 1. *Thermo-fluid dynamic profiles for the supersonic boundary layer. Reynolds stresses are reported in viscous units as* $\tau_{ij}^+ = \overline{\rho}\,\widetilde{u_i'' u_j''}\,/\rho_w u_\tau^2$ *while thermodynamic fluctuations are expressed as root mean squares.*



(a) Mean velocity profile (b) Mean temperature profile

(c) Reynolds stresses (d) Temperature fluctuations

(e) Pressure fluctuations (f) Density fluctuations

Figure 2. T*hermo-fluid dynamic profiles for the supersonic channel flow. Scalings are performed with* $\gamma_b = \gamma(T_b)$ *to standardize comparisons between the two different thermodynamic models. Friction Mach number is defined, as usual, as* $M_\tau = u_\tau/(\gamma_b R T_w)$.

While we have not identified a general behaviour for the first one yet, exhibiting a variation with respect to the CP case within a range of ± 10 % in the second one tends to be closer to zero for higher values of $c_p$at the wall, consistent with the linear relation between the heat flux and the temperature variation, $\delta q = c_p dT$. Further research is however required to characterize both the physical and the numerical aspects of new thermodynamic frameworks.

Summary

We have presented simulations of wall-bounded supersonic flows using thermally perfect gas models and an *ad hoc* numerical formulation implemented in highly scalable GPU-based codes. Such results have been compared with the classical calorically perfect gas cases. Significant physical differences were observed, indicating that the calorically perfect gas assumption proves too restrictive in such configurations. Further research is ongoing to achieve improved modeling and numerical characterizations.

References

[1] M. Cogo, U. Baù , M. Chinappi, M. Bernardini, F. Picano, Assessment of heat transfer and Mach number effects on high-speed turbulent boundary layers. Journal of Fluid Mechanics. 2023;974:A10. https://doi:10.1017/jfm.2023.791

[2] C. De Michele, G. Coppola, Numerical treatment of the energy equation in compressible flows simulations, Computers & Fluids, Volume 250, 2023, 105709, ISSN 0045-7930, https://doi.org/10.1016/j.compfluid.2022.105709.

[3] F. Salvadore, G. Soldati, A. Ceci, G. Rossi, A. Memmolo, G. Della Posta, D. Modesti, S. Sathyanarayana, M. Bernardini, S. Pirozzoli, STREAmS-2.1: Supersonic turbulent accelerated Navier-Stokes solver version 2.1, Computer Physics Communications, Volume 314, 2025, 109652, ISSN 0010-4655, https://doi.org/10.1016/j.cpc.2025.109652.

[4] B. J. McBride, M. J. Zehe, S. Gordon, NASA Glenn Coefficients for Calculating Thermodynamic Properties of Individual Species, Technical444 Report, Glenn Research Center, Cleveland, Ohio, 2002. URL: https://ntrs.nasa.gov/api/citations/20020085330/downloads/445 20020085330.pdf.446

[5] C. De Michele, G. Coppola, Asymptotically entropy-conservative and kinetic-energy preserving numerical fluxes for compressible Euler equations, Journal of Computational Physics, Volume 492, 2023, 112439, ISSN 0021-9991, https://doi.org/10.1016/j.jcp.2023.112439.

[6] A. Aiello, C. De Michele, G. Coppola, Entropy conservative discretization of compressible Euler equations with an arbitrary equation of state, Journal of Computational Physics, Volume 528, 2025, 113836, ISSN 0021-9991, https://doi.org/10.1016/j.jcp.2025.113836.

[7] A. Aiello, C. De Michele, G. Coppola, Formulation of entropy-conservative discretizations for compressible flows of thermally perfect gases, Journal of Computational Physics (under review), https://doi.org/10.48550/arXiv.2507.08115

Materials Research Proceedings 69 (2026) 239-243 https://doi.org/10.21741/9781644904251-42

Assessment of Structure-Preserving Methods for LES of Compressible, Wall-Bounded Flows

Giuseppe ILLIANO[1,a], Francesco DE VANNA[2,b] and Gennaro COPPOLA[1,c *]

[1]Università degli Studi di Napoli "Federico II", Napoli, Italy

[2]Università degli Studi di Padova, Padova, Italy

[a]giuseppeilliano75@gmail.com, [b]francesco.devanna@unipd.it, [c]gcoppola@unina.it

Keywords: Kinetic Energy Preserving Schemes, Entropy Conservative Fluxes, Large Eddy Simulation, Compressible Turbulence, High-Order Methods, GPU-Accelerated CFD

Abstract. Structure-preserving schemes have emerged as a powerful tool for simulating compressible, wall-bounded turbulence, offering improved robustness and physical fidelity. By preserving key invariants—such as kinetic energy and entropy—at the discrete level, these methods enhance numerical stability and accuracy in challenging flow regimes. This work evaluates the performance of a high-order, GPU-accelerated solver employing entropy-conservative and kinetic-energy-preserving fluxes in DNS and LES of turbulent boundary layers. Results demonstrate improved alignment with benchmark data and highlight the potential of structure-preserving schemes in capturing complex interactions between compressibility, turbulence, and wall effects in high-fidelity simulations.

Introduction

The numerical simulation of turbulent compressible flows plays a pivotal role in advancing aerospace engineering and fluid dynamics. These flows are characterized by complex interactions between turbulence, compressibility effects (such as shock waves and acoustic propagation), and wall-bounded behavior, posing challenges for computational modeling. Despite significant progress in computational power, reliably capturing such phenomena remains difficult due to the combined effects of high computational cost, numerical instability, and the need for physical accuracy. The recent availability of high-performance computing (HPC) platforms, including GPU-based architectures, has enabled more detailed simulations such as Direct Numerical Simulation (DNS) and Large Eddy Simulation (LES), making it increasingly feasible to study these flows with high fidelity.

A critical element in the successful simulation of compressible turbulence is the choice of numerical scheme, particularly in the discretization of convective fluxes. Classical methods may introduce spurious dissipation or numerical artifacts that compromise the physical accuracy of the solution. In response, several structure-preserving schemes have emerged. Kinetic Energy Preserving (KEP) schemes aim to retain the divergence structure of the convective term in the kinetic energy equation, thus enhancing robustness and suppressing unphysical energy growth [1]. Entropy Conservative (EC) schemes take this further by preserving entropy at the discrete level through non-linear flux formulations, although this often comes at the expense of higher computational cost. To mitigate this, research has explored low-cost asymptotic approximations [2]. Additionally, Pressure Equilibrium Preserving (PEP) methods are designed to suppress spurious pressure oscillations—an issue that can be critical in shock-dominated or multi-physics scenarios [3]. Despite extensive theoretical development, the application of these schemes to realistic wall-bounded flows remains relatively limited in the engineering community.

This study investigates the impact of structure-preserving numerical schemes, including KEP, EC, and PEP methods, on the LES of turbulent, compressible, wall-bounded flows. Unlike prior

Content from this work may be used under the terms of the Creative Commons Attribution 3.0 license. Any further distribution of this work must maintain attribution to the author(s) and the title of the work, journal citation and DOI. Published under license by Materials Research Forum LLC.

Materials Research Proceedings 69 (2026) 239-243 https://doi.org/10.21741/9781644904251-42

works, focused primarily on theoretical benchmarks, the present analysis emphasizes practical application in large-scale simulations using GPU-accelerated solvers over a spatial developing turbulent boundary layer, a canonical configuration that represent the prototype of all external and internal aerodynamics problems. We demonstrate that these schemes improve the accuracy of turbulence statistics and reduce numerical artifacts, particularly for those associated with thermal quantities and in coarse-grid LES regimes where the scheme behavior strongly influences the solution. Thus, results confirm that high-order, structure-preserving discretizations play a critical role in enhancing both the reliability and predictive power of compressible turbulence simulations.

The remainder of the paper is organized as follows. Section *Theoretical Background* introduces the minimal theory illustrating structure-preserving schemes. Section *Numerical setup and computational results* summarizes the main findings while Section *Conclusions* states the conclusive remarks.

Theoretical Background

The discretization of compressible flow equations requires particular attention to the convective terms, which play a crucial role in ensuring the physical fidelity and numerical stability of the solution. The general convective term in compressible Navier-Stokes equations takes the form

$$\mathsf{C}_{\rho\phi} = \frac{\partial \rho u_i \phi}{\partial x_i}, \tag{1}$$

where ϕ is 1, u_j or E in the mass, momentum or total energy equations, respectively. A typical discretization for compressible flows requires that convective terms in Eq. 1 are expressed as a difference of numerical fluxes, i.e. in the form

$$\mathsf{C}^{i}_{\boldsymbol{\rho\phi}} = \frac{\mathbf{1}}{\boldsymbol{\Delta x_i}}\left(\boldsymbol{\mathcal{F}}^{\boldsymbol{i+\frac{1}{2}}}_{\boldsymbol{\rho\phi}} - \boldsymbol{\mathcal{F}}^{\boldsymbol{i-\frac{1}{2}}}_{\boldsymbol{\rho\phi}}\right), \tag{2}$$

where $\mathcal{F}_{\rho\phi}$ denotes the numerical flux across control volume interfaces. When the discretization of the convective term $\mathsf{C}_{\rho\phi}$ can be expressed as in Eq. 2, the quantity $\rho\phi$ is globally preserved by convection, and the divergence structure of Eq. 1 is mimicked at discrete level. However, preserving this structure in the continuity, momentum, and total energy equations does not automatically guarantee numerical robustness or accuracy. Particular attention must also be devoted to the conservation of derived physical quantities, such as kinetic energy, pressure, and entropy.

The kinetic energy balance in the inviscid limit is expressed as

$$\frac{\partial(\rho u_i^2/2)}{\partial t} + \frac{\partial(\rho u_j u_i^2/2)}{\partial x_j} + u_j \frac{\partial p}{\partial x_j} = 0, \tag{3}$$

which again exhibits a convective term in the conservative form of Eq. 1. To automatically retain this structure at the discrete level, it can be shown that a coordinate specification of the fluxes in mass and momentum equations is required. In particular, the numerical flux in the momentum equation should have the form [4]

$$\mathcal{F}_{\rho u} = \mathcal{F}_{\rho}\bar{u}, \tag{4}$$

Materials Research Proceedings 69 (2026) 239-243 https://doi.org/10.21741/9781644904251-42

where $\bar{u} = (u_i + u_{i+1})/2$ is the arithmetic mean and $\mathcal{F}_\rho$ is the mass flux. Schemes satisfying Eq. 4 are referred to as *Kinetic Energy Preserving* (KEP), and are known to improve the stability and robustness of scale-resolved simulations [1].

Another important property is the *Pressure Equilibrium Preserving* (PEP) condition, which ensures that initially uniform pressure and velocity fields remain unaltered during the evolution; an analytical property of the compressible Euler equations allowing the existence of traveling density-wave solutions. Violation of the PEP condition at discrete level can lead to the emergence of spurious pressure waves and nonphysical behavior. As discussed in [3], if the pressure equation is discretized in place of the total energy equation, this property is naturally satisfied. When total or internal-energy equations are employed, a more complex compatibility condition between the fluxes in mass and internal energy equations needs to be satisfied.

A third desirable property is that of *Entropy Conservation* (EC), which is particularly relevant in the context of under-resolved compressible turbulence. In the inviscid limit, the entropy equation reads

$$\frac{\partial \rho s}{\partial t} + \frac{\partial \rho u_j s}{\partial x_j} = 0, \tag{5}$$

where $s = \log(p/\rho^\gamma)$ for a calorically perfect gas. The nonlinear nature of this relation poses challenges for the design of discretizations that satisfy Eq. 5 at the discrete level. One possible strategy relies on the use of logarithmic means in the definition of fluxes [5]. However, despite their theoretical appeal, these flux formulations are computationally expensive due to the evaluation of transcendental functions. To reduce computational cost, alternative schemes have been proposed that replace the logarithmic mean with truncated series expansions, achieving *Asymptotic Entropy Conservation* (AEC) with significantly lower computational overhead [2,3]. These formulations preserve the leading-order entropy consistency while maintaining compatibility with the KEP and PEP frameworks. Their low-cost implementation makes them particularly attractive for high-fidelity simulations, including DNS and LES, of compressible wall-bounded turbulence.

Table 1 provides a selection of some popular and more recent structure-preserving schemes available in the literature and tested in this paper. All the formulations have numerical fluxes calculated by using only algebraic operations, and satisfy the Kinetic Energy Preserving (KEP) property. The recently proposed AEC schemes are also PEP and recovers the EC property in the limit $N \to \infty$. The schemes in Table 1 are recalled and analyzed in [2] and [3], where the references to the original papers can also be found.

In Table 1, the notation is as follows: $\bar{\phi}^H = \phi_i \phi_{i+1}/(2\bar{\phi})$ denotes the harmonic mean and the hat operator is defined as $\hat{\phi} = \delta\phi/(\phi_{i+1} + \phi_i)$. The symbol $\overline{\overline{\phi\psi}} = (\phi_i\psi_{i+1} + \phi_{i+1}\psi_i)/2$ denotes the product mean associated with the advective formulation $\phi\partial\psi + \psi\partial\phi$ [4]. In the scheme definitions, N indicates the order of the truncated series expansion, while $\mathcal{F}^*_{\rho E}$ refers to the total energy flux including the (conservative) pressure contribution.

Materials Research Proceedings 69 (2026) 239-243 https://doi.org/10.21741/9781644904251-42

Table 1. Summary of some numerical fluxes for the convective term and their properties.

Scheme	$\mathcal{F}_\rho$	$\mathcal{F}^*_{\rho E}$	*PEP*	*AEC*
JP	$\bar{\rho}\,\bar{u}$	$\mathcal{F}_\rho \overline{H}$	✗	✗
KEEP	$\bar{\rho}\,\bar{u}$	$\mathcal{F}_\rho \left(\bar{e} + \frac{u_i u_{i+1}}{2}\right) + \overline{\overline{pu}}$	✗	✗
AEC^0	$\bar{\rho}\,\bar{u}$	$\mathcal{F}_\rho \left(\bar{e}^H + \frac{u_i u_{i+1}}{2}\right) + \overline{\overline{pu}}$	✓	✗
AEC$^{(N)}$	$\bar{\rho}\,\bar{u}\frac{1}{\sum_{n=0}^{N}\frac{\hat{\rho}^{2n}}{2n+1}}$	$\mathcal{F}_\rho \left(\bar{e}^H \sum_{n=0}^{N} \frac{\hat{e}^{2n}}{2n+1} + \frac{u_i u_{i+1}}{2}\right) + \overline{\overline{pu}}$	✓	✓

Numerical setup and computational results

To evaluate the impact of structure-preserving schemes on the prediction of thermal and dynamic quantities in compressible wall-bounded turbulence, we perform WRLES of a supersonic boundary layer at $M_\infty = 2$ using the GPU-accelerated solver URANOS [6,7]. Turbulent inflow conditions are generated at $Re_{\tau,0} = 450$ and statistics are collected downstream where $Re_\tau = 840$. The domain size is $L_x \times L_y \times L_z = (150 \times 10 \times 10)\delta_0$, discretized with $N_x = 2048$, $N_z = 256$, and $N_y = 384$ points. Uniform spacing is used in the streamwise and spanwise directions, while a hyperbolic-sine stretching is applied in the wall-normal direction for adequate near-wall resolution. Boundary conditions are periodic in z, adiabatic no-slip at the wall, and fully 3D Navier–Stokes Characteristic Boundary Conditions (NSCBC) at the top and outlet. The subgrid-scale model is WALE [6], chosen for its compatibility with compressible flows and improved near-wall behavior. Initialization and inflow generation strategies follow Refs. [6,7].

Fig. 1 provides the results of the analysis. It is observed that the introduction of these advanced schemes brings clear benefits in capturing pressure and temperature fluctuations, particularly PEP in the former case and AEC in the latter. It should be emphasized that both KEEP and AEC0, although strictly not EC, are documented to have good entropy conservation properties, and exhibit good performance in reproducing temperature fluctuations; this has also been shown in Refs. [3,2] for the Eulerian case. No significant advantages are observed in terms of velocity profiles or Reynolds stresses. Overall, the scheme that shows the poorest performance is JP, which does not satisfy the PEP or AEC properties.

Conclusions

In this work, a range of structure-preserving schemes for the discretization of convective terms in the compressible Navier–Stokes equations has been presented and critically analyzed. Unlike much of the existing literature, which focuses on idealized or inviscid test cases, these schemes were assessed in the context of high-fidelity LES of wall-bounded, supersonic turbulent flows. The results demonstrate that structure-preserving formulations—particularly those satisfying pressure-equilibrium and entropy-consistency properties—offer benefits in capturing pressure and temperature fluctuations. These quantities are crucial for a wide range of engineering applications, such as heat transfer prediction, noise generation, and shock–boundary-layer interactions. The observed improvements highlight the relevance of these methods beyond theoretical analysis, reinforcing their applicability to realistic turbulent flow simulations.

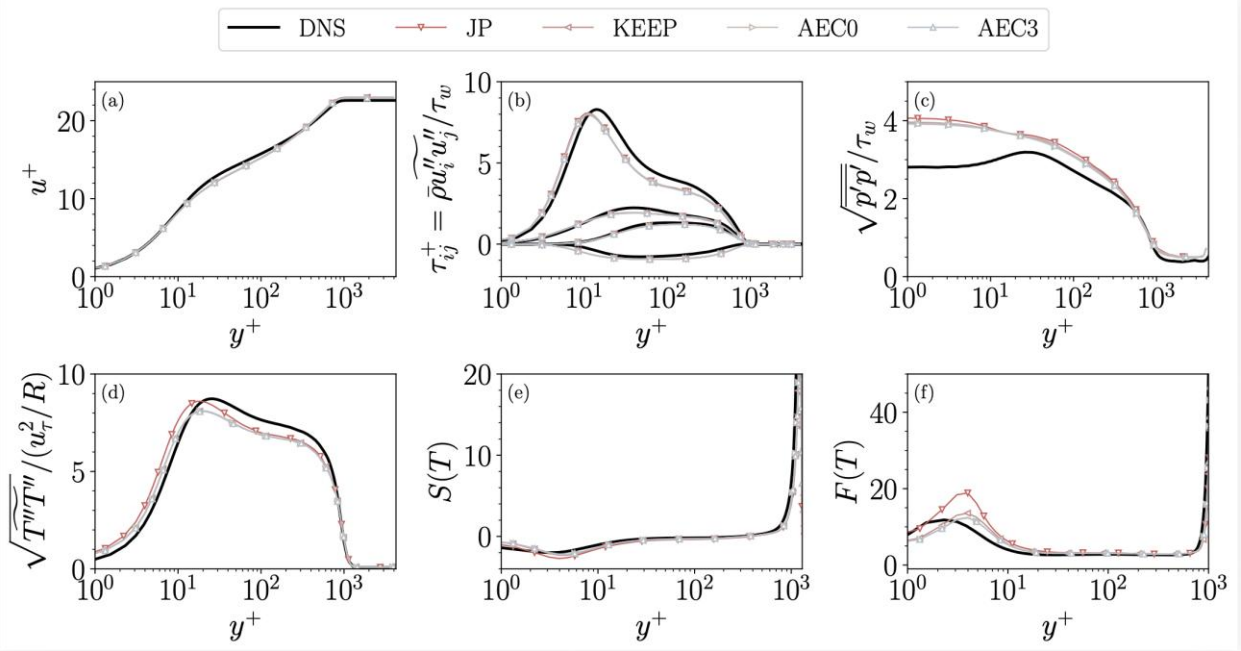


Figure 1. WRLES of a turbulent boundary layer at $M_\infty = 2$ and $Re_\tau = 840$. Distributions of (1a) mean velocity, (1b) Reynolds stresses, (1c,d) root-mean-square of pressure and temperature fluctuations, and (1e,f) skewness and flatness of temperature fluctuations, plotted against y^+. All results are compared with DNS data from Ref. [8]. Favre decomposition is denoted by $\tilde{\phi} = \overline{\rho\phi}/\bar{\rho}$ and $\phi = \tilde{\phi} + \phi''$.

References

[1] G. Coppola, F. Capuano, S. Pirozzoli, L. De Luca, Numerically stable formulations of convective terms for turbulent compressible flows, J. Comput. Phys. 382 (2019) 86-104. https://doi.org/10.1016/j.jcp.2019.01.007
[2] C. De Michele, G. Coppola, Asymptotically entropy-conservative and kinetic-energy preserving numerical fluxes for compressible Euler equations, J. Comput. Phys. 492 (2023) 112439. \href{https://doi.org/10.1016/j.jcp.2023.112439
[3] C. De Michele, G. Coppola, Novel pressure-equilibrium and kinetic-energy preserving fluxes for compressible flows based on the harmonic mean, J. Comput. Phys. 518 (2024) 113338. https://doi.org/10.1016/j.jcp.2024.113338
[4] C. De Michele, G. Coppola, Numerical treatment of the energy equation in compressible flow simulations, Comput. Fluids 250 (2023) 105709. https://doi.org/10.1016/j.compfluid.2022.105709
[5] H. Ranocha, Comparison of some entropy conservative numerical fluxes for the Euler equations, J. Sci. Comput. 76 (2018) 216-242. https://doi.org/10.1007/s10915-017-0618-1
[6] F. De Vanna, F. Avanzi, M. Cogo, S. Sandrin, M. Bettencourt, F. Picano, E. Benini, URANOS: A GPU-accelerated Navier–Stokes solver for compressible wall-bounded flows, Comput. Phys. Commun. 287 (2023) 108717. https://doi.org/10.1016/j.cpc.2023.108717
[7] F. De Vanna, G. Baldan, URANOS-2.0: Improved performance, enhanced portability, and model extension towards exascale computing of high-speed engineering flows, Comput. Phys. Commun. 303 (2024) 109285. https://doi.org/10.1016/j.cpc.2024.109285
[8] S. Pirozzoli, M. Bernardini, Turbulence in supersonic boundary layers at moderate Reynolds number, J. Fluid Mech. 688 (2011) 120-168. https://doi:10.1017/jfm.2011.368

Materials Research Proceedings 69 (2026) 244-249 https://doi.org/10.21741/9781644904251-43

Static and Dynamic Derivatives Estimation of an Image Guided Rocket Using Computational Fluid Dynamics

Karol Bielaszka[1,a *], Radosław Kamiński[1,b] and Olgierd Skromak[1,c]

[1]Students' Space Association, Warsaw University of Technology, Nowowiejska 21/25, 00-665 Warsaw, Poland

[a]karol.bielaszka.stud@pw.edu.pl, [b]radoslaw.kaminski4.stud@pw.edu.pl, [c]olgierd.skromak.stud@pw.edu.pl

Keywords: CFD, Aerodynamics, Steering, Dynamic Response

Abstract. FOK 2 is the second iteration of the FOK rocket developed by the Students' Space Association at the Warsaw University of Technology. It is an aerodynamically controlled, subsonic rocket powered by a solid rocket motor with an impulse of 1000 Ns. The second iteration differs from the first by employing a seeker, which houses a vision system, instead of a von Karman nosecone. Such drastic changes in the geometry necessitate the re-examination of the rocket's aerodynamics. Since FOK 1 missions were relatively simple [1], there was no need to perform computational analysis of the rocket's dynamic coefficients [2]. FOK 2's mission is more involved: guidance towards a target using visual navigation. Numerous flight simulations and prior flight tests must be conducted to ensure the mission's success. Having precise aerodynamics, including static and dynamic coefficients, enables good predictive capabilities of the simulations, which allow the design of the guidance and steering algorithms. This is especially important for ensuring both mission success and the safety of the flight test. While static coefficients are relatively straightforward to obtain, dynamic ones require including the motion of the rocket, which demands the usage of the Unsteady Reynolds-Averaged Navier Stokes model. In this paper, the FOK 2's aerodynamics have been investigated. Both static and dynamic derivatives were calculated. Static analysis was performed for a range of Mach numbers, angles of attack and canard deflection configurations. The generated data served as a basis for conducting the dynamic analysis. The process of obtaining dynamic derivatives differs significantly from the one used to obtain static ones, thus the influence of the canards' deflection rate on the rocket's loads will be investigated. As the end goal is to provide an accurate model for controlling a guided rocket, especially in the later phases of flight, where the reaction time is very low and the response of the missile to canard input may sometimes not reach a steady state, more attention must be focused on the oscillations induced by canard motion. Some efforts regarding this can be found in: [3]. In the case of FOK 2, transient analysis was used to study the dynamic response of the rocket under rolling motion. The canards were dynamically deflected, and the angular response was examined in relation to signals of varying frequencies. The performance of the model created as a result of the conducted analysis has been evaluated using flight data and compared against the prior model [1]. Expanding the accuracy of the aerodynamic model used in the association through the application of transient analysis has been a major leap in the numerical capabilities available and has furthered the efforts into creating an accurate guidance system at hand.

Introduction

FOK 2 is a an aerodynamically controlled missile equipped with an optoelectronic seeker developed by the Student's Space Association at Warsaw University of technology since 2021 [4]. It is steered using 4 independently controlled canards placed in front of the rocket's centre of mass (Fig. 1a). The missile is capable of steering itself both in pitching/yawing motion or rolling one. This paper focuses on the control of the missile in the roll axis.

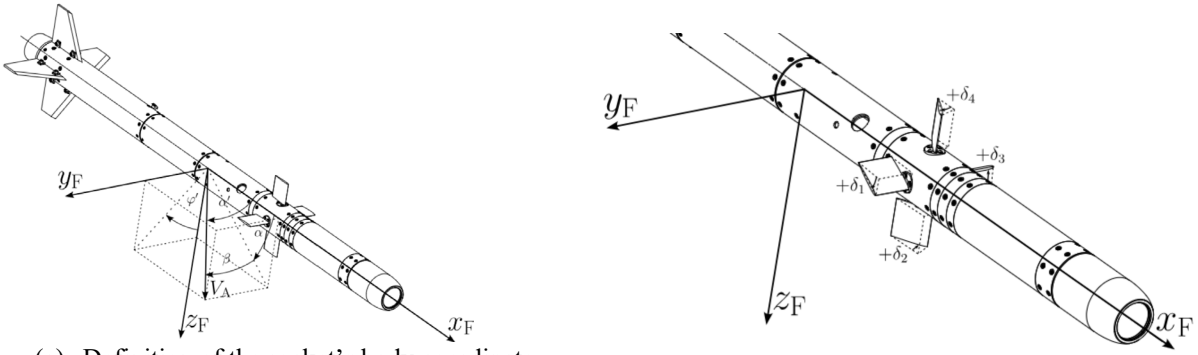
Content from this work may be used under the terms of the Creative Commons Attribution 3.0 license. Any further distribution of this work must maintain attribution to the author(s) and the title of the work, journal citation and DOI. Published under license by Materials Research Forum LLC.

Materials Research Proceedings 69 (2026) 244-249 https://doi.org/10.21741/9781644904251-43

In order to accurately reproduce the flight in simulation, it is necessary to analyse both static aerodynamic coefficients and dynamic ones. In light of the fact that the object of analysis is the impact of canards on the dynamic coefficients, it was established that the coefficients would be determined from the constant angular velocity of the canards for varying canard configurations, roll angular velocity and angles of attack of the rocket.

Case description

The simulations were done in ANSYS Fluent and the viscous model chosen was the Spalart-Allmaras model, due to its low processing costs from it being a one-equation model. During the simulation, the rocket's canards were moved step by step up to their maximum deflection angle of ±10◦ (Fig. 1b). The frame of reference around the rocket was also rotated to simulate rolling motion, with the fluid angle at the inlet being changed to provide a varying angle of attack (Fig. 1a).



(a) Definition of the rocket's body coordinate frame and incidence angles

(b) Definition of the canards' deflection angle

Figure 1: Aerodynamic definitions, as shown in [5]

Due to limitations in the interface method, the geometry near the canards had to be simplified and the canard was modelled separately with a gap of 0.25 mm between it and the main fuselage. This allowed for the creation of a rotating mesh interface between the fluid domain and the canards (Fig. 2). The mesh (Fig. 3) has approximately seven million cells, in accordance with y+ values that are less than one.

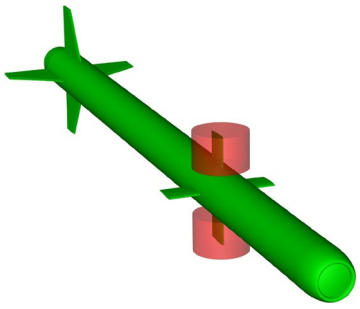
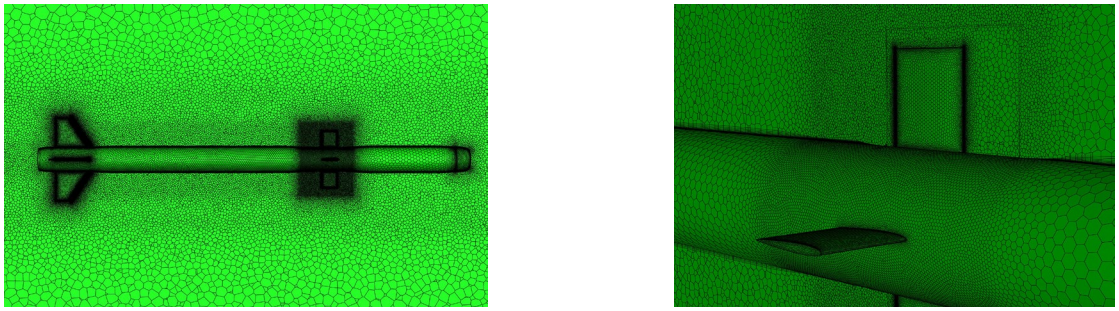


Figure 2: Rocket geometry, with red interface zones

Materials Research Proceedings 69 (2026) 244-249 https://doi.org/10.21741/9781644904251-43



(a) Rocket mesh (b) Canards' mesh

Figure 3: Mesh used in calculations

Chosen from previous flights of the rocket are the different input variables for the simulation. Those are:

- Mach number Ma = 0.4
- Angular velocity of the canards ωc = 2 rad/s
- Angular velocity of the rocket ωr = {0, 0.5, 1} rad/s
- Angle of attack α = {0, 2, 4, 6, 8, 10}°

Model Validation

To assess the validity of the case setup, a standardised geometry – the generic Army-Navy finner missile (ANF) of length 600mm, as in [6]. The mesh used was also similar, with the leading and trailing edges on the canards and fins sized to 0.08mm, with the face sizing from 1mm to 6mm on the body. As in the final model, the coefficients were calculated with a moving reference frame.

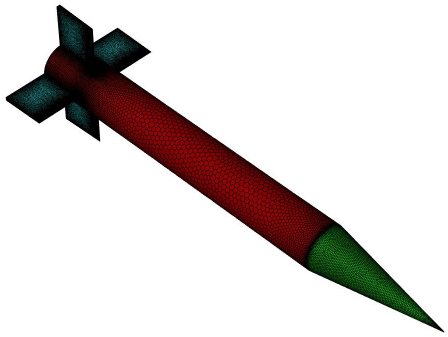


Figure 4: ANF rocket mesh

Even though the model used was different (Spalart Allmaras rather than K-ω), the obtained results of the rolling moment coefficient Clp calculated from (Eq. 1) aligned with the ones in the paper, as shown in Fig. 5, where Cl is the rolling moment in a given case and Cl0 is the rolling moment for a nonrotating case (in cases where the canards were not deflected, this moment is assumed to be zero, as the rocket is symmetric.

$$C_{lp} = \frac{2|v|}{Pd_{\text{ref}}} C_l - C_{l_0} \quad (1)$$

Materials Research Proceedings 69 (2026) 244-249 https://doi.org/10.21741/9781644904251-43

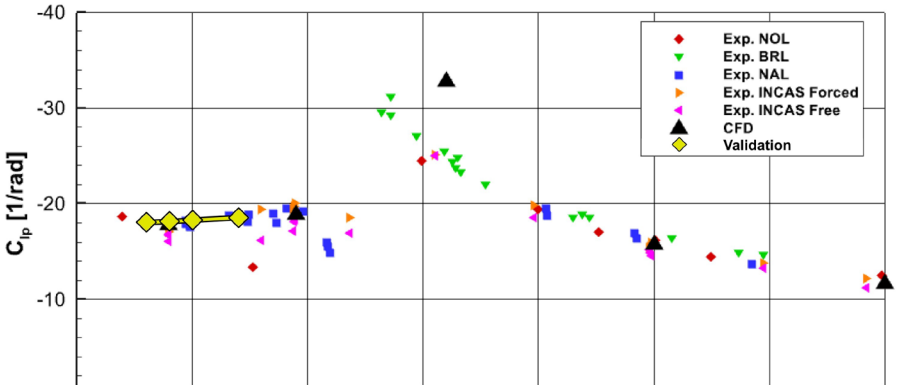
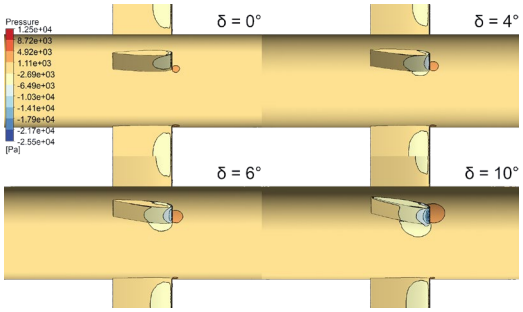


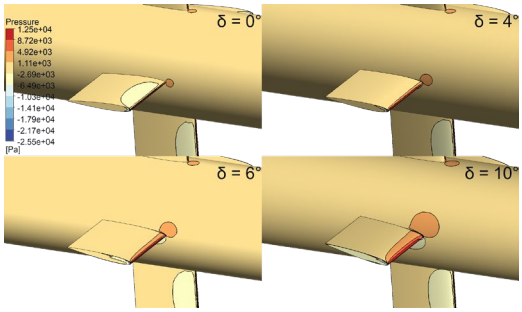
Figure 5: Graph of Clp versus the mach number as per [6]. The validation results are shown in yellow

Calculation results

As illustrated in Figure 6, it is evident that the area of reduced pressure on one side of the canard increases in proportion to the augmented deflection angle of the canard. A similar phenomenon occurs on the other side, where the area of higher pressure increases in size. It has been determined that, commencing at deflection angle 6 degrees, an area of underpressure is observed on the canard's side face. This phenomenon may be attributed to the strengthening of edge vortices, which initiate their influence on the lateral face once a critical deflection angle is reached.



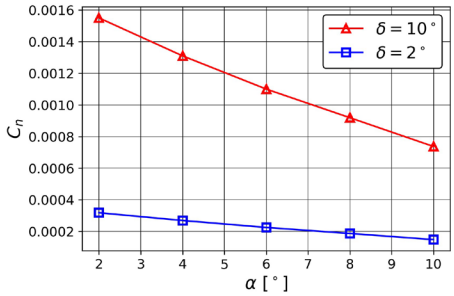
(a) Underpressure side



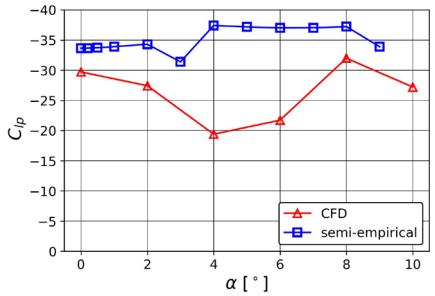
(b) Overpressure side

Figure 6: Pressure contours for different canards' deflections, Ma = 4 , $\alpha = 0°, \omega_r = 1 \frac{rad}{s}$

The yaw calculations yielded results that are to be expected – the canards being less efficient at higher angles of attack as well as the yaw moment rising linearly, as we are dealing with small deflections, as seen in Fig. 7a and 7b. The calculations also showed a present non-linearity in the rolling moment coefficient due to roll rate. This was also (more qualitatively than quantitatively) reflected in the data from other, non-empirical models. The calculated coefficients were also used to simulate the rocket in a rolling manoeuvre and compare the model to a real world test. The results shown in Fig. 9 are very promising, showing significant improvement over the previous model shown in green.



(a) Cn vs α for canard deflections 2◦ and 10◦



(b) Cn vs canard deflection at α=0

Figure 7: Yaw moment graphs

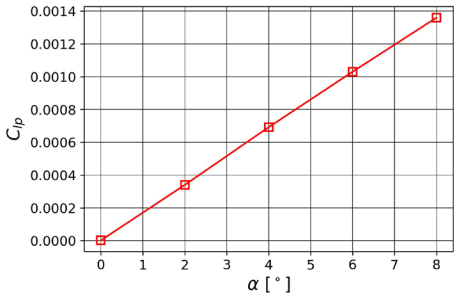


Figure 8: Graph of C_{lp} versus α at no canard deflection

Summary

Overall, this study presented a computational framework for analysing the aerodynamic behaviour of the FOK rocket. If more simulations were to be performed on a wider scope, a dynamic model of the rocket could be obtained. The approach offers a basis for future refinements in geometry, turbulence modelling, and higher-fidelity unsteady simulations.

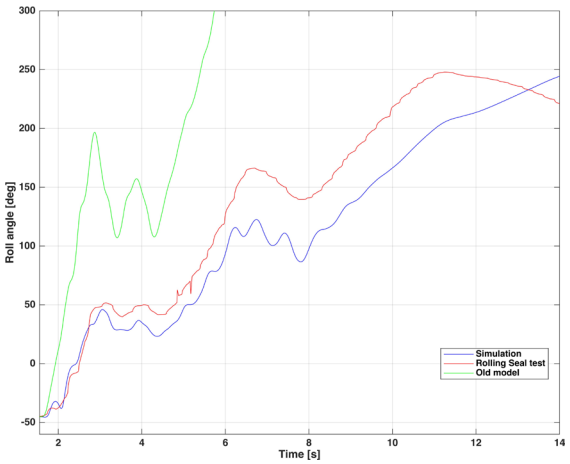


Figure 9: Comparison of real world data to a rocket simulation using the calculated coefficients.

Acknowledgments

This project was supported by the grant of the Ministry of Science and Higher Education of Poland awarded to Warsaw University of Technology as part of the “Supporting students to improve their competences and skills” program. The calculations were carried out with the support of the Interdisciplinary Centre for Mathematical and Computational Modelling at the University of Warsaw (ICM UW).

References

[1] Sahbon, N. et al. “A CFD Study of the Aerodynamic Characteristics of Twardowsky and FOK Rockets”. In: Transactions on Aerospace Research Volume 2022 (Mar. 2022), p. 1. https://doi.org/10.2478/tar-2022-0003

[2] Li, R., Li, D., Fan, J. “Dynamic Response Analysis for a Terminal Guided Projectile With a Trajectory Correction Fuze”. In: IEEE Access 7 (2019), pp. 94994–95007. https://doi.org/10.1109/ACCESS.2019.2928718

[3] Miedziński, D. et al. “Missile Aerodynamics Model Identification Using Flight Data”. In: 2023 IEEE Aerospace Conference. 2023, pp. 1–12. https://doi.org/10.1109/AERO55745.2023.10115928

[4] Miedziński, D. et al. “Preliminary design of a homing rocket using image recognition”. In: Proceedings, International Astronautical Congress. 2021.

[5] Skromak, O. “Study of the control actuation system of a rocket using Hardware-in-the-Loop method”. Engineering Thesis. Warsaw University of Technology, 2025.

[6] Bunescu, I. et al. “Numerical Study of the Basic Finner Model in Rolling Motion”. In: Aerospace 12.5 (2025). https://doi.org/10.3390/aerospace12050371

Materials Research Proceedings 69 (2026) 250-253 https://doi.org/10.21741/9781644904251-44

Instability Mechanisms in the Compressible Falkner–Skan Boundary Layers with A Cooled Wall

Hao Li[1,a *] and Franco Auteri[1,b]

[1]Department. of Aerospace Science and Technology, Politecnico di Milano, Via La Masa 34, 20156 Milano, Italy

[a]10968983@polimi.it, [b]franco.auteri@polimi.it

Keywords: Falkner-Skan Boundary Layer, Hypersonic Flow, Spectral Method, Linear Stability Analysis, Energy Analysis

Abstract. We study the stability of compressible Falkner Skan boundary layers over a wedge at hypersonic speeds (target location $Ma_e = 7$). For a cooled wall with temperature ratio $T_{ratio} = 0.25$ (wall temperature scaled by the corresponding adiabatic value), we compute accurate basic solution via Laguerre spectral method and perform a temporal linear stability analysis to locate the critical Reynolds number Re_c and streamwise wavenumber α_c. A key result is quite unexpected: as the favorable pressure-gradient parameter β increases, Re_c decreases (from 115.3 at $\beta = 0$ to 83.5 at $\beta = 0.3$), opposite to the classical incompressible Falkner-Skan boundary layer. In contrast, for an adiabatic wall ($T_{ratio} = 1$), Re_c increases with β (from 107.7 to 153.1), recovering the classical behavior. A fluid–thermodynamic energy decomposition shows that vortical contributions to the instability are predominantly stabilizing, whereas the thermal and acoustic contributions strengthen with β under cooled wall conditions, thereby lowering the stability threshold.

Introduction

The Falkner–Skan equation, introduced by Falkner and Skan in 1930 [1], provides similarity solutions work for boundary layers over wedges subject to pressure gradients depending on the parameter β. While the incompressible case is classical, its compressible counterpart in hypersonic regimes remains less explored. We employ a Laguerre spectral method based on modified Laguerre bases [2] to solve both the base flow as well as the linear stability equations in a temporal setting. By satisfying the far-field boundary condition naturally, this method avoids the singularities of mapping [3] and the domain-size-dependent truncation error [4], delivering spectral accuracy on semi-infinite domains. After a high-accuracy basic solution is obtained, we apply the temporal linear stability analysis [5] to determine Re_c and α_c for adiabatic and cooled walls. For the latter, we interpret the observed trends using a fluid–thermodynamic energy decomposition [6] that separates the perturbation energy into vortical, thermal, and acoustic energy components.

Theory and Numerical Methods

Referring to the work of A. F. Stephansen and L. Quartapelle [7], the compressible Falkner- Skan boundary layer equation is shown as follows:

$$\begin{cases} f'''(\eta) + f(\eta)f''(\eta) + \beta\left(g(\eta) - f'^2(\eta)\right) = 0, \\ g''(\eta) + Prf(\eta)g'(\eta) = 2(1 - Pr)\left(f'(\eta)f''(\eta)\right)', \end{cases} \tag{1}$$

where $f(\eta)$ and $g(\eta)$ represent the dimensionless stream function and total enthalpy, respectively. The parameter β denotes the pressure-gradient factor, while the Prandtl number Pr is fixed at $Pr = 0.72$ in the present study. The corresponding boundary conditions are:

Content from this work may be used under the terms of the Creative Commons Attribution 3.0 license. Any further distribution of this work must maintain attribution to the author(s) and the title of the work, journal citation and DOI. Published under license by Materials Research Forum LLC.

Materials Research Proceedings 69 (2026) 250-253 https://doi.org/10.21741/9781644904251-44

$$\begin{cases} f(0) = 0, f'(0) = 0, \lim_{\eta\to\infty} f'(\eta) = 1, \\ g(0) = g_{\text{wall}}(\text{isothermal wall}), \lim_{\eta\to\infty} g(\eta) = 1. \end{cases} \tag{2}$$

After computing the basic solution, a linear stability analysis is carried out following Malik [5] to extract the critical curve (Re, α). To interpret the physics, we adopt the fluid– thermodynamic decomposition of Unnikrishnan and Gaitonde [6].

Results and Discussion

Table 1: Summary of flow parameters at the inlet for different pressure-gradient parameters β. (The subscript 'e0' indicates external conditions evaluated at the inlet).

β	ρ_e [kg/m^3]	μ_{e0} [kg/[m·s]]	T_{e0} [K]	Ma_{e0}	P_{e0} [Pa]	U_{e0} [m/s]
0.000	0.0175	0.00000504	74.0740	7.000	371.626	1207.636
0.100	0.1169	0.00001082	158.416	4.500	5315.808	1135.316
0.200	0.3031	0.00001505	231.884	3.500	20170.761	1068.337
0.300	0.8824	0.00002099	355.556	2.500	90043.072	944.928

The inlet parameters listed in Table 1 correspond to different pressure-gradient factors β. They are selected so that, for each case, the external flow conditions at the target location (Ma_e = 7) match those of the Blasius flow (β = 0). Particularly, the wall temperature T_{wall} (cold wall) is obtained by T_{wall} = 0.25 T_{adb}, where T_{adb} is defined as$T_{adb} = T_e(1 + Pr^{1/2}(\gamma\text{-}1)\, Ma_e^2/2)$. With a cooled wall ($T_{ratio}$ = 0.25), increasing the favorable pressure-gradient parameter from β = 0 to 0.3 lowers the critical Rynolds number from Re_c = 115.3 to 83.5 (Fig.1), in contrast with the classical incompressible Falkner-Skan boundary layer where Re_c increases with β. The critical wavenumber α_c also decreases with β, indicating longer wavelengths at the onset of instability, while the shape of the neutral curves is independent of β, suggesting a common instability mechanism. For an adiabatic wall (T_{ratio} = 1) opposite trend is observed as shown in Table 2. Re_c rises from 107.7 to 153.1 as β increases from 0 to 0.3 (≈42%). α_c grows slightly (0.082→0.085), in line with the incompressible case, highlighting the important role of wall temperature in hypersonic boundary-layer flows.

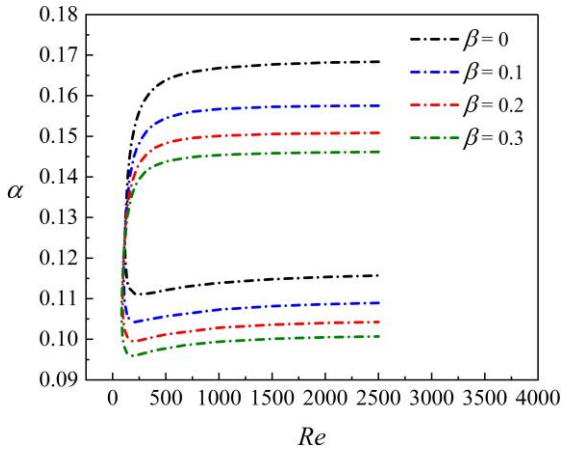


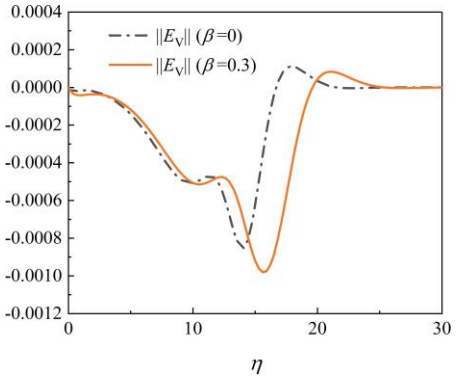
Figure 1: Neutral stability curves for four pressure-gradient parameters β, plotted in theReynolds number–streamwise wavenumber (Re-α) plane (T_{ratio} = 0.25, Pr = 0.72, Ma_e = 7)

Materials Research Proceedings 69 (2026) 250-253 https://doi.org/10.21741/9781644904251-44

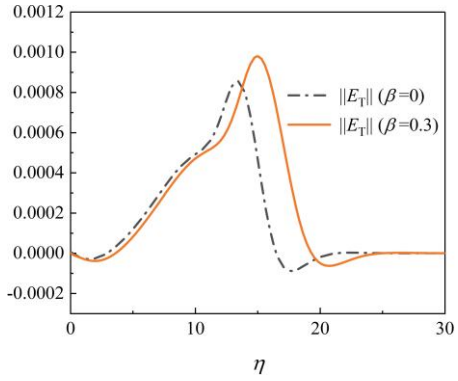
Table 2: Critical parameters for an adiabatic wall T_{ratio} = 1 with pressure-gradient parameters β = 0, 0.1, 0.2, and 0.3.

β	Re_c	α_c
0.000	107.7	0.082
0.100	125.3	0.083
0.200	140.3	0.084
0.300	153.1	0.085

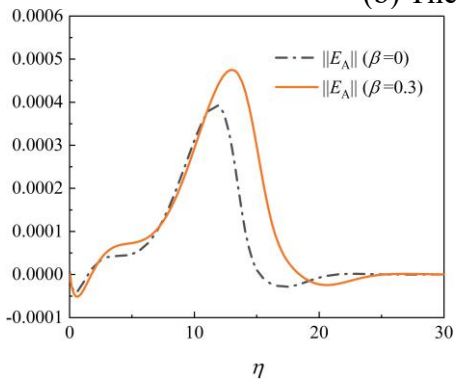
To elucidate the physics behind the surprising decrease of Re_c with increasing β under a cooled-wall condition, we employ a fluid-thermodynamic decomposition as shown in Fig. 2, which compares the spatial distributions of the perturbation-energy components: vortical (E_V), thermal (E_T), and acoustic (E_A). The vortical contribution E_V is negative over most of the boundary-layer thickness and reaches its largest magnitude in the outer region, indicating a stabilizing effect. By contrast, the compressible E_T and E_A are predominantly positive and peak toward the outer edge, thereby supplying energy to the disturbance and enhancing the instability. Under the cooled-wall condition (T_{ratio} = 0.25), increasing the favorable pressure-gradient from β = 0 to β = 0.3 amplifies the compressible components: both E_T and E_A show higher peaks and wider positive support. This shift increases the perturbation energy gain and leads to the reduction in Re_c observed as β grows.



(a) Vortical energy



(b) Thermal energy



(c) Acoustic energy

Figure 2: Comparison of the perturbation energy components E_V (vortical), E_T (thermal), and E_A (acoustic) for β = 0 and β = 0.3 (cooled wall with T_{ratio}=0.25).

Summary
We analyzed hypersonic ($Ma_e = 7$) compressible Falkner-Skan boundary layers under cooled ($T_{ratio} = 0.25$) and adiabatic ($T_{ratio} = 1$) wall conditions. Using a spectral discretization for the basic solution and linear stability analysis, we mapped the neutral curves in the Re-α plane for $\beta \in [0, 0.3]$. A robust unexpected trend emerges for cooled walls, where Re_c decreases when β increases—while in the adiabatic case the classical increase is observed. The decomposition of perturbation energy indicates stabilization of the vortical contribution and a destabilization of the thermal/acoustic contributions with increasing β, which explains the decreases in the instability threshold.

References

[1] Falkner, V. M., and S. W. Skan, Aero. Res. Coun. Rep. and Mem., No. 1314 (1930).

[2] Shen, J., Stable and efficient spectral methods in unbounded domains using Laguerre functions, SIAM J. Numer. Anal. 38 (2000) 1113-1133. https://doi.org/10.1137/S0036142999362936

[3] Buffett, B. A., Numerical solution of boundary-layer problems, Geophys. J. Int. 126 (1996) 291-295. https://doi.org/10.1111/j.1365-246X.1996.tb05288.x

[4] Boyd, J. P., Rangan, C., Bucksbaum, P. H., Pseudospectral methods on a semi-infinite interval with application to the hydrogen atom: a comparison of the mapped Fourier-sine method with Laguerre series and rational Chebyshev expansions, J. Comput. Phys. 188 (2003) 56-74. https://doi.org/10.1016/S0021-9991(03)00127-X

[5] Malik, M. R., Numerical methods for hypersonic boundary-layer stability, J. Comput. Phys. 86 (1990) 376-413. https://doi.org/10.1016/0021-9991(90)90106-B

[6] Unnikrishnan, S., and D. V. Gaitonde, Interactions between vortical, acoustic and ther- mal components during hypersonic transition, J. Fluid Mech. 868 (2019) 611-647. https://doi.org/10.1017/jfm.2019.176

[7] Stephansen, A. F., Solving the similarity equations for compressible flow with Pr = 1, Master's thesis, Politecnico di Milano, Milan, 2019.

Materials Research Proceedings 69 (2026) 254-259 https://doi.org/10.21741/9781644904251-45

Far-Field Exergy-Based Drag Decomposition of a Turbulent Blunt-Body Wake with Hybrid-LES

Justin DU PLESSIS[1], Drewan SANDERS[1,b,*], Tamas JÓZSA[1,c], and Tom-Robin TESCHNER[1,d]

[1]Cranfield University, United Kingdom

[b]d.s.sanders@cranfield.ac.uk, [c]tamas.jozsa@cranfield.ac.uk, [d]tom.teschner@cranfield.ac.uk

Keywords: Exergy-Balance, Drag Decomposition, IDDES, Vortex Shedding

Abstract This study investigates the application of the exergy balance to an unsteady turbulent wake using a Hybrid-LES methodology. A circular cylinder at Re = 5000 is simulated in ANSYS Fluent using IDDES, and the far-field exergy balance is evaluated across multiple control volumes to assess its accuracy and behaviour in a turbulent regime. The closest control volume shows reasonable agreement with the near-field drag with an error of 3.58%, but a progressive underestimation develops as the Trefftz plane is positioned further downstream. Analysis of the drag power components indicates that the reduction in mechanical exergy is not compensated by an equivalent increase in viscous dissipation, suggesting that part of the mechanical energy is being artificially dissipated or not fully captured within the IDDES framework. The findings highlight the sensitivity of exergy-based drag decomposition to numerical error in turbulent flows and provide a basis for future work aimed at identifying error sources and mitigating these errors.

Introduction

The accurate evaluation and decomposition of aerodynamic forces remains a key challenge in the design and optimisation of efficient vehicles. Traditional near-field methods based on surface integration can only recover pressure and viscous drag and cannot separate thrust from aerodynamic contributions, motivating the development of far-field, control-volume-based approaches.

Several formulations have been proposed, including the momentum balance of Destarac and van der Dooren [1] and Drela's mechanical energy balance [2], each providing improved physical insight, but limited in their treatment of thermodynamic effects. More recently, the exergy balance introduced by Arntz et al. [3] has become the preferred method, as it incorporates temperature gradients, entropy production, and all irreversible losses, offering a complete thermodynamic picture of drag generation [3, 4]. Its recent applications [5, 6] have demonstrated strong potential in steady state flows. Furthemore Ruscio et al.'s transient vortex-shedding study [7] and studies by du Plessis [8] and Westley [9] have demonstrated its capabilities and high accuracy in periodically repeating transient flows.

Outside aerospace, Norman and Howard [10] recently applied the mechanical energy balance to a road vehicle using a DES methodology, noting acceptable agreement with nearfield forces, but also increased error compared to previous studies. This increase in error was determined to be a result of a non-physical loss of mechanical energy due to numerical diffusion, highlighting the need to further examine these balances in hybrid-RANS-LES methods.

This work extends the use of the exergy balance to an unsteady turbulent wake using a Hybrid-LES methodology. A circular cylinder at Re = 5000 is selected as a continuation of Ruscio's study, where periodic vortex shedding transitions into a turbulent wake. The aim of this study is to provide a preliminary assessment of the accuracy and behaviour of the exergy balance within a

Content from this work may be used under the terms of the Creative Commons Attribution 3.0 license. Any further distribution of this work must maintain attribution to the author(s) and the title of the work, journal citation and DOI. Published under license by Materials Research Forum LLC.

Materials Research Proceedings 69 (2026) 254-259 https://doi.org/10.21741/9781644904251-45

hybrid-RANS-LES framework, and to generate reference results that help identify sources of artificial energy loss, informing future aerodynamic design workflows.

Methodology

The time-resolved incompressible Navier–Stokes simulation is performed in ANSYS Fluent 2024R2 using IDDES with the k–ω SST model in the near-wall region. A pressure-based solver with non-iterative time advancement and fractional-step pressure–velocity coupling is employed. The simulation consists of a cylinder of Diameter $0.01m$ in an incompressible flow at Reynolds number $Re = 5000$, while a time step of $\Delta t = 1.6096 \times 10 - 5\, s$ is used to maintain a maximum CFL ≈ 1.

A grid convergence study is conducted using the time-averaged nearfield drag coefficient (C_d NF). The selected 11.8×10^6 cell mesh yields $C_d = 1.0306$ and $St = 0.2085$, in close agreement with values of Massey [11] and Roshko [12] (3% and 0.7% error respectively). The domain extends 15D upstream, 20D downstream, and uses a span AR = 2.5 with periodic spanwise boundaries.

The exergy formulation used in this study is adapted from Arntz's work to operate in the Absolute Reference Frame (ARF) rather than the Relative Reference Frame (RRF) typically used in CFD. As detailed by Lamprakis, Sanders and Laskaridis [13], this change in reference frame provides a more intuitive and physically meaningful interpretation of work done, since the body is viewed as performing work on the flow rather than vice versa. The transformation is achieved through the velocity shift in Equation 1, where V denotes the ARF velocity and V' the RRF velocity.

$$V = V' - V\infty \tag{1}$$

As the test case is an adiabatic flow around a no-slip stationary wall, and features no source terms, the balance can be simplified to only represent the drag power. The simplified balance is presented in equation 2, where the left hand side represents the near-field drag power, while the right hand side represents the far-field recoverable energy (exergy $[\dot{X}]$) and the irreversibly lost energy (anergy $[\dot{\mathcal{A}}]$).

$$\overbrace{\iint \left(p_g \mathbf{V}_\infty - \bar{\bar{\tau}} \cdot \mathbf{V}_\infty\right) \cdot d\mathcal{S}_{\mathcal{B}}}^{\text{Near-Field Drag Power}} = \overbrace{\frac{d}{dt}\iiint \left(\rho \frac{\mathbf{V}_\infty{}^2}{2}\right) d\mathcal{V} + \frac{d}{dt}\iiint \rho \mathcal{X}_s d\mathcal{V}}^{\text{Far-}Field\ Exergy} + \overbrace{\iint \rho \mathcal{X}_s \mathbf{V}' \cdot \mathbf{d}\mathcal{S}_{\mathcal{TP}}}^{\dot{X}_{th}}$$
$$+ \overbrace{\iint \left(\frac{\mathbf{V}^2}{2}\rho \mathbf{V}' + p_g \mathbf{V} - \bar{\bar{\tau}} \cdot \mathbf{V}\right) \cdot d\mathcal{S}_{\mathcal{TP}}}^{\text{Far-Field Exergy}} + \overbrace{\iiint \frac{T_\infty}{T}\left(\bar{\bar{\tau}} : \nabla \mathbf{V}\right) d\mathcal{V}}^{\text{Far-Field Anergy}} + \overbrace{\iiint T_\infty \mathcal{K}\left(\frac{\nabla T}{T}\right) d\mathcal{V}} \tag{2}$$

Figure 1 shows a 2-dimensional example of how the balance is applied to a selected Control Volume (CV) and Trefftz Plane (TP) during the simulation. This study focuses on three distictly sized CV's where the distance W is shown in Table 1.

Table 1: Control Volume Dimensions

CV	TP Distance (W)
CV1	2.5D
CV2	5D
CV3	10D

Materials Research Proceedings 69 (2026) 254-259 https://doi.org/10.21741/9781644904251-45

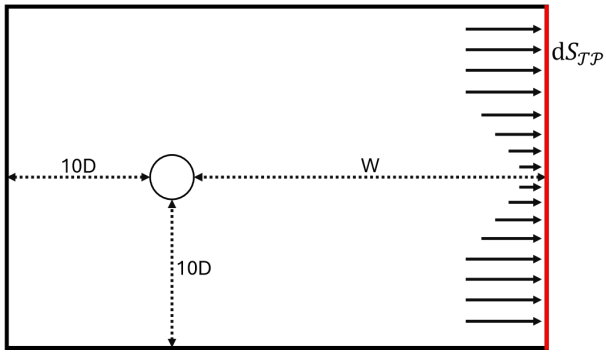


Figure 1: Control Volume Diagram

Results

To investigate the effect of CV size on the accuracy of the balance, the near-field drag coefficient was compared with the exergy-based prediction at the three CV's, as shown in Table 2. The results show reasonably good agreement at the closest control volume, with progressively larger errors as the Trefftz plane is positioned further downstream.

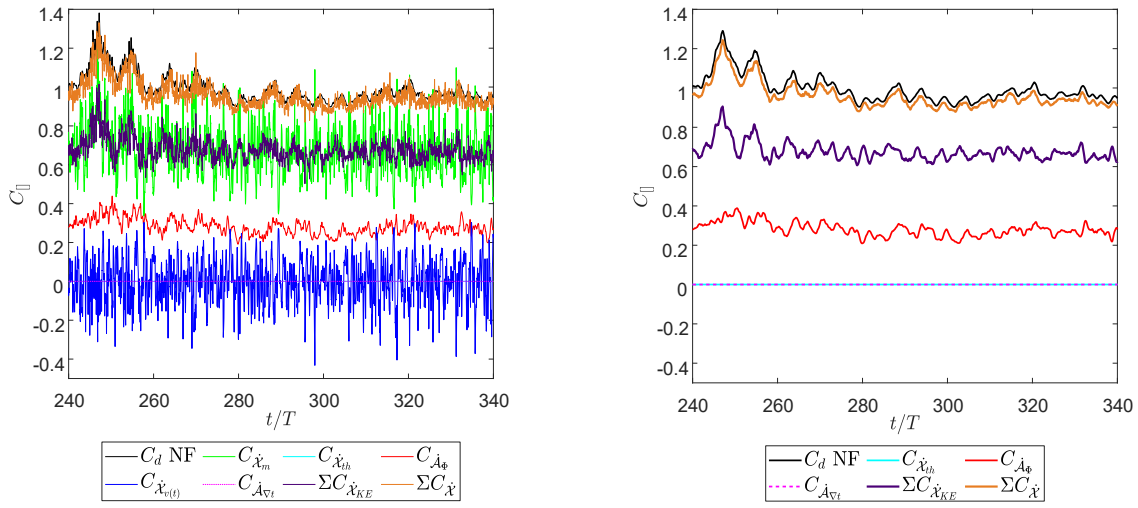
Table 2: Time Averaged C_d Comparison for final 100 Shedding Cycles

Location	**NF**	**CV1**	**CV2**	**CV3**
C_d	0.9971	0.9614	0.9244	0.8880
% Error	-	3.58	7.29	10.94

Overall, the results in Table 2 indicate that the error is not solely a consequence of grid stretching. Even at CV1, where the Trefftz plane is positioned very close to the body, a noticeable deviation from the near-field drag is already present. This suggests that a portion of the missing mechanical energy originates in the near-field itself, likely due to numerical diffusion, with grid stretching further amplifying the error as the control volume is extended downstream.

To further assess the nature of the drag being produced, the individual components of the drag power at CV1 were evaluated, as shown in Figure 2. The raw data (Figure 2a) shows the drag power being dominated by heavy fluctuations in mechanical exergy contributions ($\dot{X}_m$ and $\dot{X}_{(v)t}$), due to the highly turbulent nature of the wake. These terms are summed together to give a representative contribution of the mechanical exergy on the drag ($\Sigma\dot{X}_{KE}$). The filtered results in Figure 2b highlight how at the close control volume the drag is entirely composed of mechanical exergy ($\Sigma\dot{X}_{KE}$) and viscous dissipation ($\dot{\mathcal{A}}_\Phi$).

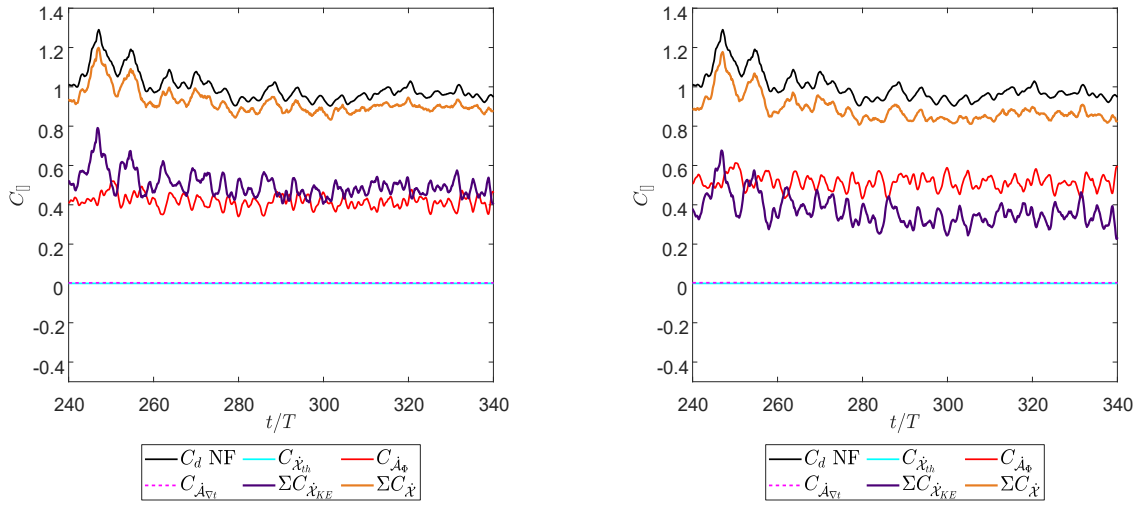
Materials Research Proceedings 69 (2026) 254-259 https://doi.org/10.21741/9781644904251-45



(a) Raw (b) Filtered

Figure 2: Drag Power Decomposition at CV1

The transfer of mechanical exergy to viscous dissipation is visualised in the plots for CV2 and CV3 (Figures 3a and 3b), where it can be seen how the mechanical energy component reduces with increasing CV size, while the energy is transferred to viscous dissipation. It is also noted how the amount of error between the NF C_d and total far-field balance increases with distance but remains as a constant underestimation as distance increases.



(a) CV2 Filtered (b) CV3 Filtered

Figure 3: Drag Power Decomposition at CV2 and CV3

To quantify how the mechanical exergy is transferred across the control volumes, the net change in $\Sigma\dot{X}_{KE}$ and viscous dissipation ($\dot{\mathcal{A}}_\Phi$) between successive CVs is shown in Figure 4. The results make it clear that the reduction in mechanical exergy does not correspond to an equal increase in viscous dissipation. Instead, a portion of the mechanical energy appears to be dissipated or lost without being recovered through $\dot{\mathcal{A}}_\Phi$. This imbalance indicates that part of the energy transfer is being artificially damped or is not correctly accounted for within the hybrid RANS-LES framework, explaining the increasing underestimation of the C_d from the exergy balance as the CV size increases.

Materials Research Proceedings 69 (2026) 254-259 https://doi.org/10.21741/9781644904251-45

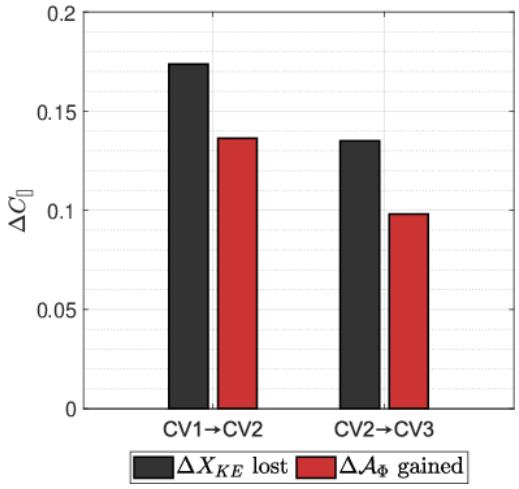


Figure 4: Change in Exergy and Anergy Between CV's

Conclusion

This study has successfully demonstrated the application of the exergy balance to an unsteady turbulent wake using a Hybrid-LES methodology to assess its behaviour and accuracy. The results show that reasonable agreement with the near-field drag is achieved at a small control volume, but a persistent underestimation develops as the Trefftz plane is moved downstream. Examination of the drag power components further reveals that the loss of mechanical exergy is not matched by a corresponding rise in viscous dissipation, indicating that part of the mechanical energy is being artificially damped or not properly captured within the hybrid RANS-LES framework. The exact source of this numerical dissipation remains unclear, with grid stretching a likely contributor in the far-field, but not explaining the imbalance on the small control volume. Future work will focus on better understanding the source of the error.

Acknowledgments

This work was funded by the Ford Motor Company via a University Research Grant-EXTPART-1195 entitled "Control Volume Method Development for Improved Aero Investigations".

References

[1] Destarac D, Vooren JVD. Drag/thrust analysis of jet-propelled transonic transport aircraft; Definition of physical drag components. Aerospace Science and Technology. 2004;8:545-56. https://doi.org/10.1016/j.ast.2004.03.004

[2] Drela M, Kohler TJ. Power balance in aerodynamic flows. AIAA Journal. 2009 7;47:1761-71 https://doi.org/10.2514/1.42409

[3] Arntz A, Atinault O, Merlen A. Exergy-based formulation for aircraft aeropropulsive performance assessment: Theoretical development. AIAA Journal.

[4] Berhouni I, Bailly D, Petropoulos I. On the Definition of Exergy in the Field of Aerodynamics. AIAA Journal. 2023 10;61:4356-66. https://doi.org/10.2514/1.J062833

[5] Zhao W, Zhang Y, Wu J. Energy-Based Aerodynamic Analysis on the Blended-Wing- Body Aircraft with Boundary Layer Ingestion. International Journal of Aerospace Engineering. 2022;2022. https://doi.org/10.1155/2022/6452099

[6] Sanders DS, Laskaridis P. Full-aircraft energy-based force decomposition applied to boundary-layer ingestion. AIAA Journal. 2020;58:4357-73. https://doi.org/10.2514/1.J058695

[7] Ruscio JP, Duplaa S, Aguirre MA, Aero A, Binder N. Exergy analysis of unsteady flow around an adiabatic cylinder in vortex shedding condition. In: 56th International Symposium of Applied Aerodynamics. 3AF; 2022.

[8] du Plessis, J. (2025). Application of Energy and Exergy Balances to Drag Decomposition in Unsteady Incompressible Flows [MSc Thesis]. Cranfield University

[9] Westley, D. (2025). Development of Unsteady Energy and Exergy-Based Drag Decomposition Techniques [MSc. Thesis]. University of Pretoria

[10] Norman, P. and Howard, K., "A Mechanical Energy Control Volume Approach Applied to CFD Simulations of Road Vehicles," SAE Int. J. Adv. & Curr. Prac. in Mobility 7(1):532-545, 2025, https://doi.org/10.4271/2024-01-2524. https://doi.org/10.4271/2024-01-2524

[11] Massey BS. Mechanics of Fluids [Internet]. 1970. Available from: https://www.taylorfrancis.com/books/mono/10.1201/9781315272542/mechanics-fluids- bernard-massey-john-ward-smith

[12] Roshko A. On the Development of Turbulent Wakes from Vortex Streets. California Institute of Technology; 1954. Available from: https://ntrs.nasa.gov/citations/19930092207.

[13] Lamprakis I, Sanders DS, Laskaridis P. Fundamental Concepts of Boundary-Layer Ingestion Propulsion. Journal of Aircraft. 2025 5:1-22. https://doi.org/10.2514/1.C037675

Materials Research Proceedings 69 (2026) 260-265 https://doi.org/10.21741/9781644904251-46

The impact of Staggered Fins on Aerodynamic Drag of a Transonic Sounding Rocket

Jakub Antoni JANKIEWICZ[1,a*], Manfred GAWLAS[2,b] and Urszula WASILEWSKA[1,c]

[1]PWr in Space, Faculty of Mechanical and Power Engineering, Wrocław University of Science and Technology 27 Wybrzeże Stanisława Wyspiańskiego St. 50-370 Wrocław, Poland

[2]PWr in Space, Faculty of Information and Communication, Technology Wrocław University of Science and Technology 27 Wybrzeże Stanisława Wyspiańskiego St. 50-370 Wrocław, Poland

[a]jjankiewicz5@gmail.com, [b]manfredgawlas12@gmail.com, [c]ula.was033@gmail.com

Keywords: Aerodynamics, Computational Fluid Dynamics, Drag Reduction, Rocket Wave Drag, Fluid Mechanics, Offset Rocket Fins

Abstract. Sounding rockets are unmanned rockets which carry instruments to perform experiments during their suborbital flights. These rockets are typically equipped with fins to ensure stability throughout the ascent. The fins, however, can be a significant source of wave drag, especially at transonic Mach numbers. Increased drag can lead to reduced apogee, decreased velocity, greater fuel consumption, increased drag-induced stresses, and overall performance degradation. The purpose of this study is to investigate the effect of longitudinal fin offset on the aerodynamic drag of a transonic sounding rocket. The use of staggered tail sections and their impact on drag, especially in rocketry, remains largely unexplored and warrants further investigation. Therefore, in this study, three-dimensional, compressible computational fluid dynamics (CFD) analyses in Ansys Fluent were conducted. The simulations were performed using Reynolds-Averaged Navier-Stokes (RANS) equations and the k-ω SST turbulence model. A preliminary stability analysis was also performed. The rocket under analysis features two pairs of fins, mounted near the bottom of the rocket, 90° apart, with one pair longitudinally offset. This staggered configuration alters the cross-sectional area distribution which more closely aligns with the transonic area rule, promoting wave drag reduction. The results demonstrate a significant aerodynamic drag reduction at transonic Mach numbers. The findings provide insight for researchers aiming to optimize fin configurations for improved aerodynamic efficiency and higher apogee in sounding rocket designs.

Introduction

The concept of staggered tail sections has been explored and used primarily in aircraft design to improve aerodynamic efficiency at transonic and supersonic speeds [1,2]. However, its application in sounding rockets remains largely unexplored. The staggered fin configuration, shown in Fig. 1, modifies the rocket's cross-sectional area distribution [2,3], aligning it more closely with the transonic area rule, which leads to lower wave drag.

In this study, the concept is tested using computational fluid dynamics (CFD) to assess the impact of longitudinally offset fins on aerodynamic drag [4] of a rocket moving at a Mach number (M) equal to one.

Content from this work may be used under the terms of the Creative Commons Attribution 3.0 license. Any further distribution of this work must maintain attribution to the author(s) and the title of the work, journal citation and DOI. Published under license by Materials Research Forum LLC.

Materials Research Proceedings 69 (2026) 260-265 https://doi.org/10.21741/9781644904251-46

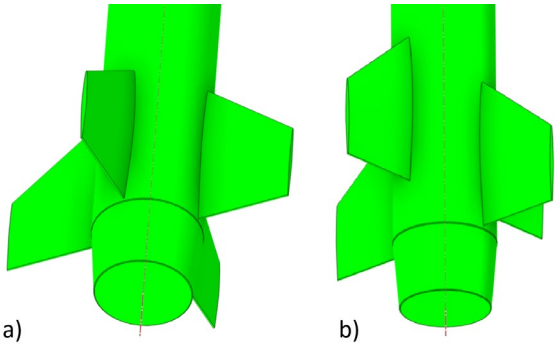


Figure 1: Comparison of rocket tails a) with a traditional fin configuration b) with staggered fins.

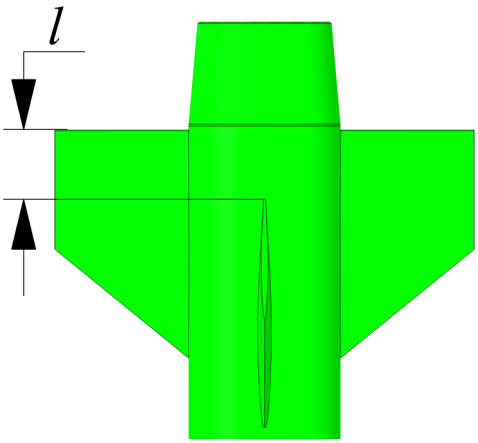


Figure 2: Rocket tail with staggered fins with the offset length l.

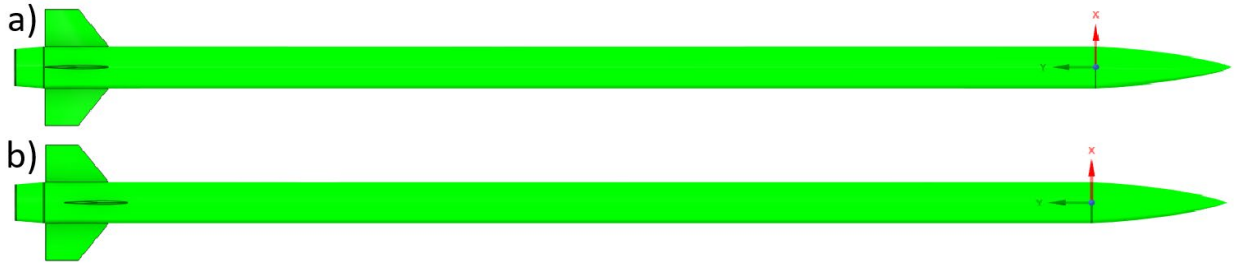


Figure 3: 3D model of the tested rocket a) with a traditional fin configuration b) with staggered fins. The rockets are identical besides the offset fins.

Methodology

The tested rocket had a length l_r of 4.5 m and a diameter of 0.152 m. The rocket included a set of four identical fins with a trapezoidal planform and NACA 66-006 symmetrical aerofoil. Additionally, for $l = 40\%$ of root chord, an additional simulation was conducted with a modified fin which's semi-span was increased to 145 mm to compensate for the decrease in aerodynamic stability around one of the axes. With baseline fin, the stagger was causing stability margins around one of the axes to decrease by 73 mm. Stability analysis was conducted using *OpenRocket* software [5,6]. Baseline fin dimensions are shown in Table 1.

Table 1: Baseline fin dimensions

Semi-span [mm]	Root chord (c) [mm]	Tip chord [mm]	Leading edge sweep angle [°]
135	230	120	39.2

The computer-aided design (CAD) models of the rocket and fluid domain were created using *Ansys SpaceClaim*. The computational domain was a rounded cylinder with the dimensions of: $2l_r$ upstream from rocket nose, $5l_r$ downstream, and a radius of $2l_r$. The domain with boundary conditions can be seen in Fig. 4.

Materials Research Proceedings 69 (2026) 260-265 https://doi.org/10.21741/9781644904251-46

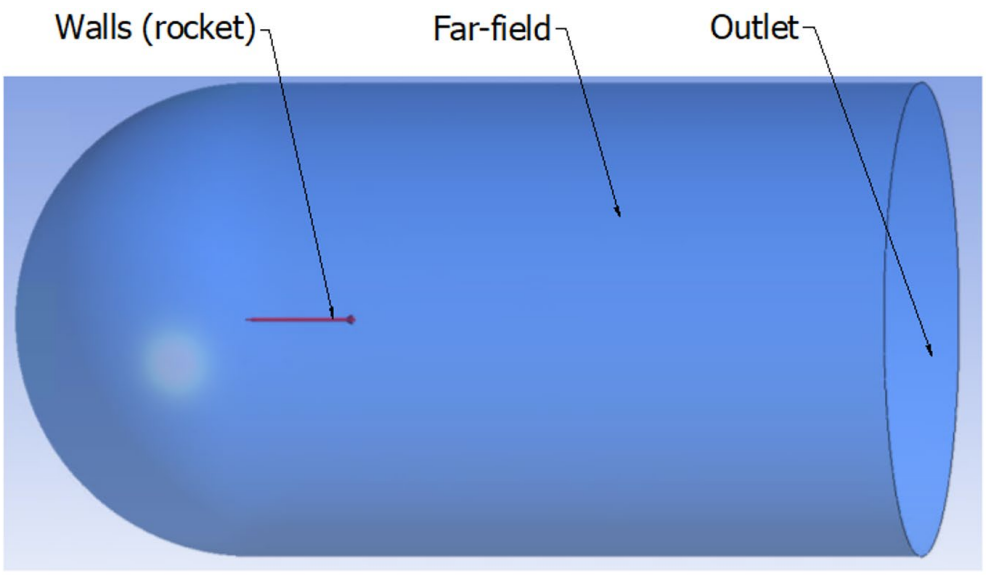


Figure 4: Computational domain with boundary conditions.

The fluid domain was discretized using *Ansys Fluent with Meshing* software into an unstructured hexahedra-based mesh. Mesh resulted in y^+ values seen in Table 2.

Table 2: Maximum and average values of y_+. The values are within the recommended range for the k-ω SST turbulence model [7].

y^+_{max}	y^+_{avg}
1.41	0.61

To ensure the results are not mesh dependent, a mesh sensitivity study was conducted (see Table 3). Medium mesh was selected.

Calculations were performed in *Ansys Fluent* using Reynolds-Averaged Navier-Stokes equations and the k-ω SST turbulence model. The density-based solver was employed for all cases to account for compressibility effects present at $M > 0.3$ [8,9].

Table 3: Mesh independence study results.

Grid size	Cell count	C_D	ΔC_D [%]
Coarse	6.08×10^6	0.6158	4.99
Medium	11.6×10^6	0.5839	-0.45
Fine	15.7×10^6	0.5866	-

Results

In total, 6 simulations were performed with l ranging from 0% to 50%c resulting in a maximum drag coefficient C_D (reduction of 14.5% at 50%c (0.499 compared to 0.584). On all simulations C_D was observed to decrease with the increase of l (see Fig. 6). Two simulations were conducted at 40%c, one with a baseline fin and one with the fin modified by increasing its semi-span to account for the stability margin decrease around one of the axes. Modified fin at 40%c increased

Materials Research Proceedings 69 (2026) 260-265 https://doi.org/10.21741/9781644904251-46

C_D from 0.521 to 0.530 allowing a net drag decrease of 9.3% compared to the rocket without staggered fins.

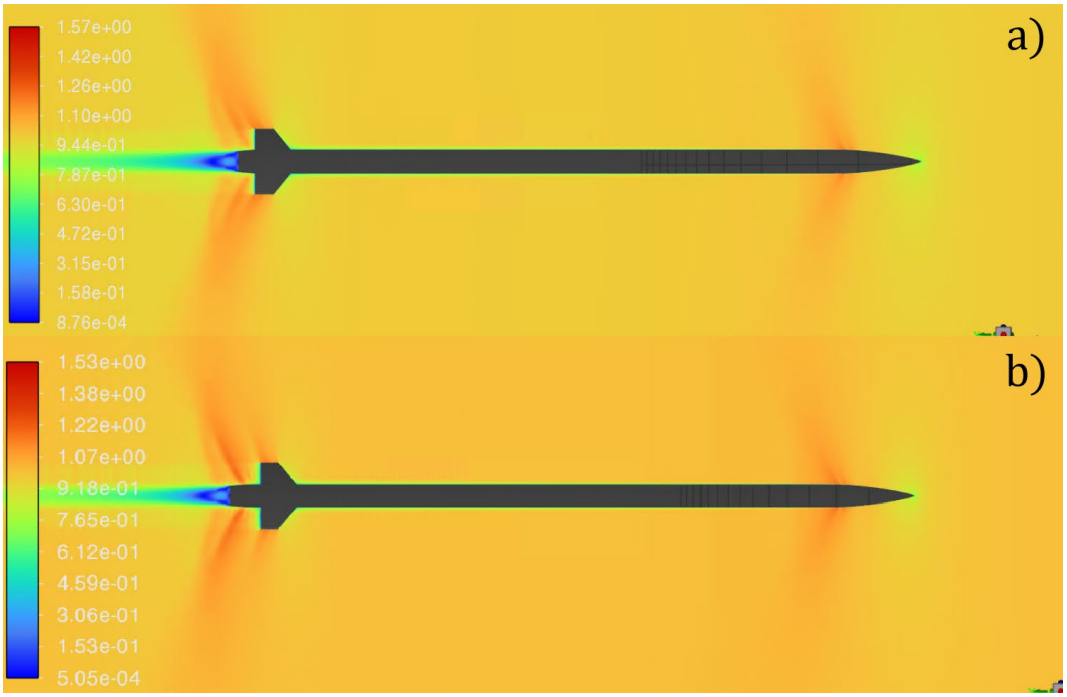


Figure 5: Contours of Mach number at M = 1 for a) a rocket with traditional fins b) a rocket with staggered fins ($l = 40$).

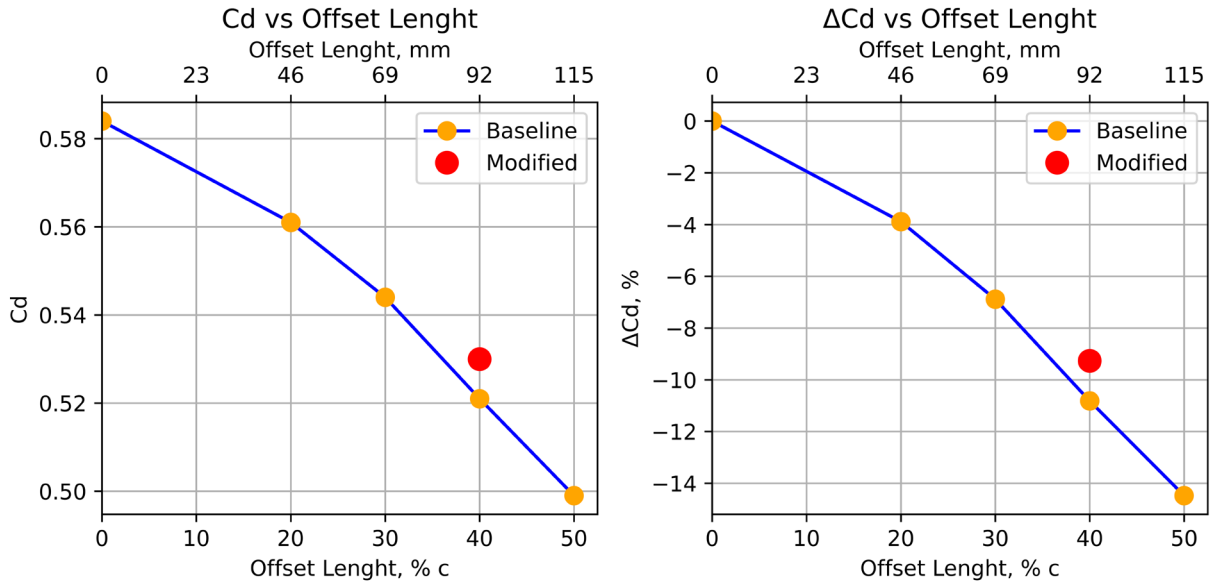


Figure 6: Plots of C_D against l (left) and difference in C_D (ΔC_D) compared to a traditional rocket (right). Modified denotes the result for the fin with increased semi-span to account for decreased stability margin around one of the axes.

Discussion

The results presented in this study clearly indicate a significant relationship between fin offset and the aerodynamic drag experienced by the rocket. The observed trend wherein an increase in l

corresponds to a decrease in total drag has profound implications for future rocket design and mission performance.

A reduction in aerodynamic drag directly translates to several key performance benefits. Most notably, it implies lower overall fuel consumption, as less thrust is required to overcome air resistance during atmospheric ascent. This efficiency gain could, in turn, enable rockets to achieve higher apogees, increase their effective range, or carry heavier payloads with the same fuel load. Furthermore, lower drag-induced stresses on the airframe could enhance structural margins, improve reliability, and potentially reduce manufacturing costs by allowing for a lighter structure.

While these findings are promising, they also open new avenues for future investigation. A next step would be to analyze the effect of fin stagger on aerodynamic drag across different Mach number values.

Moreover, the current study was conducted using a specific rocket configuration. To generalize these findings, it is imperative to test the observed effect across a wider variety of designs, particularly those with different fin planform shapes, sizes and aerofoils.

Finally, while this work focused primarily on aerodynamic performance, a preliminary stability analysis was also conducted. It is recognised that such modification of a rocket might warrant a more rigorous follow-up. Future research should, therefore, include an in-depth assessment of the impact of fin stagger on aerodynamic stability.

Acknowledgements
The re We would like to express our gratitude to the Services And Networking TechnOlogieS Laboratory (SANTOS Lab), operating within the Department of Computer Science and Systems Engineering at Wrocław University of Science and Technology, for their support in providing the computational resources necessary to carry out the simulations presented in this article.

References

[1] B. Burley, James R. II Berrier, "Effects of tail span end empennage arrangement on drag of a typical single-engine fighter aft end (NASA technical paper 2352)," NASA Scientific and Technical Information Branch, 1984. https://ntrs.nasa.gov/api/citations/19870001405/downloads/19870001405.pdf.

[2] K. S. Jones, W. T. Abdol-Hamid, "Computational analysis of drag reduction techniques for afterbody/nozzle/empennage configurations," SAE Technical Paper Series. Aerospace Technology Conference and Exposition. SAE International., 1991. https://doi.org/10.4271/912127

[3] Z.-T. L. . S.-S. C. . M.-L. J. . Z.-H. G. . Z.-Y. L. . J.-F. L. . L. Xie, "Supersonic low-boom and low-drag coupled area rules for transport efficient design.," Physics of Fluids, vol. 37, no. 7, 2025. https://doi.org/10.1063/5.0271721

[4] F. Wang, I. Animasaun, and T. Muhammad, "Recent advancements in fluid dynamics: Drag reduction, lift generation, computational fluid dynamics, turbulence modelling, and multiphase flow," Arabian Journal for Science and Engineering, vol. 49, no. 10237-10249, 2024. https://doi.org/10.1007/s13369-024-08945-3

[5] R. Nanditta, "Structural design and analysis of high-powered model rockets using open-rocket," International Journal of Engineering Research, vol. 6, no. 2456-1290, 2021.

[6] S. Niskanen, "Development of an open source model rocket simulation software," m.sc. thesis, Helsinki University of Technology, 2009.

[7] B. Baran, "Skrypt obliczenia numeryczne (CFD)." Lecture script, Wroc law University of Science and Technology, 2024.

[8] P. H. Zipfel, Modeling and Simulation of Aerospace Vehicle Dynamics. American Institute of Aeronautics and Astronautics, 2014. https://doi.org/10.2514/4.102509

[9] N. Sahbon, S. Murpani, M. Michałów, D. Miedziński, and M. Sochacki, "A cfd study of the aerodynamic characteristics of twardowsky and fok rockets," Transactions on Aerospace Research, vol. Volume 2022, p. 1, 03 2022. https://doi.org/10.2478/tar-2022-0003

Aeroacoustics & Noise Control



Materials Research Proceedings 69 (2026) 267-270 https://doi.org/10.21741/9781644904251-47

High-Order Vibroacoustic Modal Analysis of Fluid-Loaded Plates with Simply-Supported and Free Edges

Dario MAGLIACANO[1,a *] and Matteo FILIPPI[1,b]

[1]Department of Mechanical and Aerospace Engineering, Politecnico di Torino, Corso Duca degli Abruzzi 24, 10129, Turin (TO), Italy

[a]dario.magliacano@polito.it, [b]matteo.filippi@polito.it

Keywords: Vibroacoustics, Carrera Unified Formulation, Lagrange Polynomials, Taylor Expansion, Simply-Supported Boundary, Free Edge, Fluid-Structure Interaction, Modal Assurance Criterion, High-Order Finite Elements

Abstract. A higher-order Carrera Unified Formulation is presented for fluid-loaded slender plates, employing orthogonal Lagrange and total-degree Taylor polynomials to capture cross-sectional kinematics. Comparison with three-dimensional finite-element models shows that moderate-order Lagrange expansions predict coupled eigenfrequencies with an error of less than 1%. In contrast, fourth- and fifth-order Taylor models achieve engineering accuracy with approximately 100 times fewer degrees of freedom. Parametric studies reveal that changing the lateral boundaries from simply supported to free lowers the fundamental frequency by approximately 3% and accentuates in-plane motion, especially in the mid-frequency range where plate and cavity modes coalesce. The method thus offers an efficient and validated alternative to complete 3-D analysis, with future extensions envisioned for nonlinear effects, damping layers, and gradient-based design optimization.

Introduction

Lightweight aircraft panels and launch-vehicle fairings often operate in strong fluid-structure interaction (FSI) regimes where classical first-order theories become inaccurate [1][2]. Recent Carrera Unified Formulation (CUF) studies have demonstrated rapid convergence for composite beams and shells [3][4]. By adopting a structured ML pipeline, a reliable predictive methodology for structural health monitoring was derived, following the strategy proposed by Magliacano *et al.* [5]. Nevertheless, realistic edge constraints and mid-frequency validation remain open issues [6][7][8]. This comprehensive framework represents a natural evolution of the authors' previous studies on FS systems with clamped or cantilever boundary conditions [9] and delivers a self-contained, substantially novel contribution.

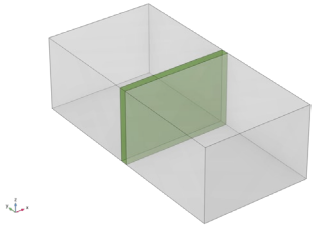


Figure 1: Schematic of the model domains; the aluminum plate is green, while the air volumes are gray.

Methodology

Cross-sectional displacements and pressure fields are approximated by linear, quadratic, or cubic Lagrange polynomials, or, for the uncoupled domains, by total-degree Taylor polynomials up to

Content from this work may be used under the terms of the Creative Commons Attribution 3.0 license. Any further distribution of this work must maintain attribution to the author(s) and the title of the work, journal citation and DOI. Published under license by Materials Research Forum LLC.

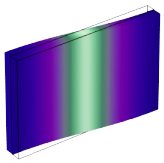
Materials Research Proceedings 69 (2026) 267-270 https://doi.org/10.21741/9781644904251-47

fifth order. The axial field employs one-dimensional Lagrangian elements, allowing the formulation to recover three-dimensional behavior hierarchically [10].

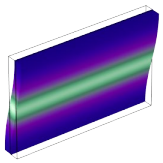
A 15[cm]×10[cm] aluminum plate of thickness 1[cm] is surrounded by 15[cm] air layers on both faces, as illustrated in Figure 1, following ISO 9613-1 guidelines. Reference three-dimensional solutions are obtained with Comsol Multiphysics 6.2.

Results and Discussion

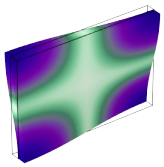
The predictive capability of the higher-order scheme is assessed by juxtaposing *in-vacuo* solutions with those of the fully coupled fluid–structure model. The analysis focuses on (i) the global downshift of the eigenvalue spectrum caused by added mass, and (ii) the preservation of modal shape integrity, paying special attention to the influence of realistic edge constraints. The Lagrange LE9B3 expansion is singled out because it reproduces the three-dimensional benchmark while keeping the numerical cost moderate.



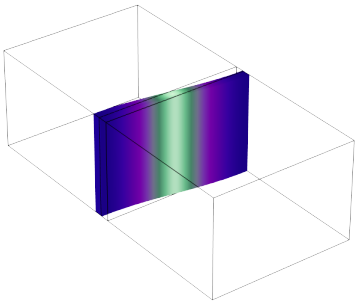
2nd modal shape of the in vacuo *model, 1079[Hz].*



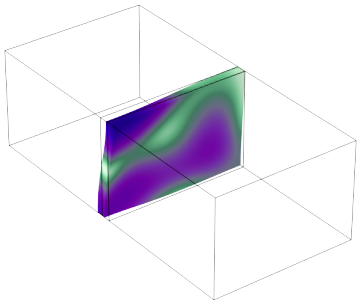
3rd modal shape of the in vacuo *model, 2408[Hz].*



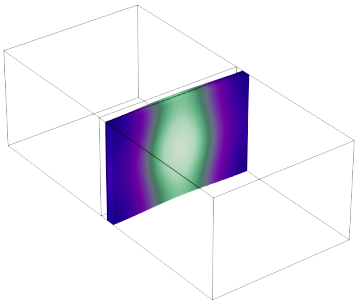
4th modal shape of the in vacuo *model, 3454[Hz].*



2nd modal shape of the coupled model, 1079[Hz].



3rd modal shape of the coupled model, 2138[Hz].



4th modal shape of the coupled model, 2139[Hz].

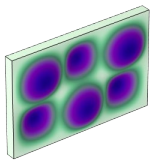
Figure 2: Comparison of the first three non-rigid modal shapes between in vacuo (displacement) and coupled (displacement-pressure) models. Aluminum material, simply supported structural, and absorbing fluid boundary conditions.

Acoustic loading produces a mode-dependent frequency reduction: the fundamental pair remains virtually unchanged, whereas higher modes experience a drop of up to 20%. Mode shapes plotted in Figure 2 retain their nodal patterns, confirming that the hierarchical CUF kinematics accurately captures fluid–structure coupling without sacrificing shape fidelity.

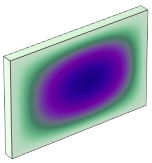
Releasing the lateral restraints lowers the first significant eigenfrequency from 2140[Hz] to 2073[Hz], a reduction of roughly 3% in line with the expected loss of bending stiffness. Despite

Materials Research Proceedings 69 (2026) 267-270 https://doi.org/10.21741/9781644904251-47

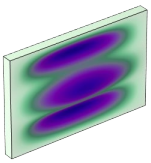
this shift, Figure 3 shows that the modes remain bending-dominated; only a mild intensification of in-plane displacements is observed near the free edges.



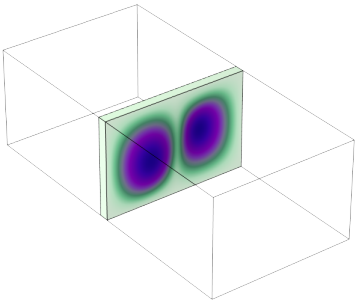
7th modal shape of the in vacuo *model, 2081[Hz].*



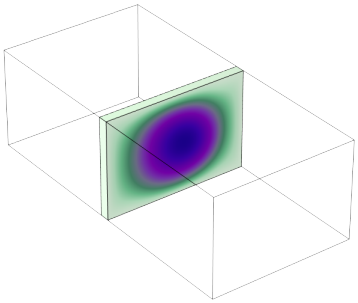
8th modal shape of the in vacuo *model, 2298[Hz].*



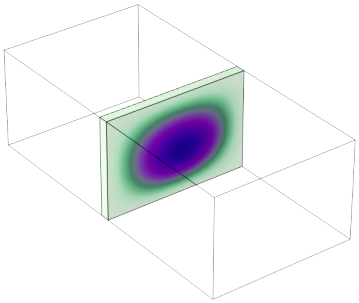
9th modal shape of the in vacuo *model, 4742[Hz].*



7th modal shape of the coupled model, 2079[Hz].



8th modal shape of the coupled model, 2138[Hz].



9th modal shape of the coupled model, 2140[Hz].

Figure 3: Comparison of the first three non-rigid modal shapes between in vacuo (displacement) and coupled (displacement-pressure) models. Aluminum material, free structural, and absorbing fluid boundary conditions.

The fluid medium produces a pronounced added-mass effect, shifting the plate's eigenfrequencies to lower values compared with the *in vacuo* case and activating additional hybrid resonance modes. Numerical results confirm that the CUF-based formulation retains high fidelity while achieving marked computational savings: high-order cross-sectional expansions cut the number of required degrees of freedom by up to two orders of magnitude yet still yield mesh-independent predictions. This approach makes it attractive for large-scale or high-frequency analyses under stringent resource constraints. Across all test cases, the model reproduces benchmark data with excellent accuracy, displays robust convergence, and faithfully captures the essential physics of fluid-structure interaction.

Conclusions

The present research confirms that high-order CUF elements [11], when combined with a weak interface coupling, provide a numerically parsimonious yet accurate tool for fluid-loaded plate analysis. Frequency errors stay below 1% with two orders of magnitude fewer unknowns than complete three-dimensional meshes. This efficiency paves the way for integration into multi-disciplinary optimization loops.

Acknowledgments
The authors acknowledge the support of the Italian Ministry of University and Research (MUR) and the Sustainable Mobility Center (MOST) through the project PNRR - M4C2 - CNMS - Spoke 1, funded under the scheme CN00000023 - PNRR - M4C2 Inv. 1.4 (grant no. 55-PRR22-1155-22-GG002138).

References

[1] Carrera, E., Zappino, E.: Carrera unified formulation for free-vibration analysis of aircraft structures. AIAA Journal 54(1), 280–292 (2016). https://doi.org/10.2514/1.J054265

[2] Magliacano, D., Ouisse, M., Khelif, A., De Rosa, S., Franco, F., Atalla, N.: Computation of wave dispersion characteristics in periodic porous materials modeled as equivalent fluids. pp. 4741–4751. 28th International Conference on Noise and Vibration Engineering (ISMA 2018), Leuven (Belgium) (2018)

[3] Pagani, A., Carrera, E.: Unified formulation of geometrically nonlinear refined beam theories. Mechanics of Advanced Materials and Structures 25(1), 15–31 (2018). https://doi.org/10.1080/15376494.2016.1232458

[4] Magliacano, D., Ouisse, M., Rosa, S., Franco, F., Khelif, A.: Investigations about the modelling of acoustic properties of periodic porous materials with the shift cell approach. pp. 1112–1123. 9th ECCOMAS Thematic Conference on Smart Structures and Materials (SMART 2019), Paris (France) (2019)

[5] Magliacano, D., Tufano, V., Letizia, A., Sessa, B., Filippi, M.: Data-driven failure criteria prediction in composite wing boxes using machine learning. Composite Structures 363 (2025). https://doi.org/10.1016/j.compstruct.2025.119675

[6] Casaburo, A., Magliacano, D., Petrone, G., Franco, F., de Rosa, S.: Optimizing the acoustic properties of a meta-material using machine learning techniques. pp. 1948–1959. 50th International Congress and Exposition of Noise Control Engineering (INTERNOISE 2021), Washington (USA) (2021). https://doi.org/10.3397/IN2021-2294. Paper number 2294

[7] Catapane, G., Magliacano, D., Petrone, G., Casaburo, A., Franco, F., De Rosa, S.: Labyrinth resonator design for low-frequency acoustic meta-structures. Mechanisms and Machine Science 125 MMS, 681–694 (2022). https://doi.org/10.1007/978-3-031-15758-5_70

[8] Winter, R., Norambuena, M., Sinske, J., Zettel, S.: High-resolution vibroacoustic characterization of dlr's falcon 2000lx istar aircraft. CEAS Aeronautical Journal 14, 953–963 (2023). https://doi.org/10.1007/s13272-023-00676-9

[9] Magliacano, D.: High-order vibroacoustic modal analysis framework for fluid-structure coupling. Aerospace 12(11) (2025). https://doi.org/10.3390/aerospace12110994

[10] Filippi, M., Magliacano, D., Petrolo, M., Carrera, E.: Variable-kinematics finite elements for propagation analyses of two-dimensional waveguides. In: 30th AIAA/CEAS Aeroacoustics Conference, 2024 (2024). https://doi.org/10.2514/6.2024-3078

[11] Filippi, M., Magliacano, D., Petrolo, M., Carrera, E.: Wave propagation in prestressed structures with geometric nonlinearities through carrera unified formulation. AIAA Journal 63(1), 292–308 (2025). https://doi.org/10.2514/1.J064695

Materials Research Proceedings 69 (2026) 271-274 https://doi.org/10.21741/9781644904251-48

Noise Robust ML Sunspot Forecasts for Cycle Aware Space Weather Operations in the Cycle 25 Era

Esraa Zeki Mohammed[1,a *], Ahmed Ghareeb[2,b] and Mohammed Rashad Baker[3,c]

[1]Higher Institute of Communication, ITPC, Ministry of Communications, Iraq

[2]Department of Mechanical Engineering, College of Engineering, University of Kirkuk, Iraq

[3]Department of Software, College of Computer Science and Information Technology, University of Kirkuk, Iraq

[a]esraa@uokirkuk.edu.iq, [b]aghareeb@uokirkuk.edu.iq, [c]mohammed.rashad@uokirkuk.edu.iq

Keywords: Solar Cycle Prediction, Machine Learning, Symbolic Regression, Stacked Ensemble, Space Weather Forecasting, Noise Robustness, Satellite-Drag Mitigation

Abstract. Accurate monthly solar activity forecasting is vital for satellite operations and ionospheric modeling. We developed a lightweight, interpretable machine-learning framework using the complete SILSO record (1749–2024) to predict the 13-month smoothed sunspot number (SSN) for solar cycles 20–24 and the rising phase of cycle 25. We tested linear regression, tree-based models, their stacked ensemble, and a symbolic regressor, assessing robustness by injecting Gaussian noise (σ = 0, 1, 3 SSN) in to training data. Across 75 experiments, median performance was r^2 = 0.86 and RMSE< 31 SSN. The framework delivers deep-learning-class accuracy with negligible computational overhead and full transparency, offering an operationally practical tool as solar cycle 25 approaches its peak.

Introduction and Related Works

Solar activity (sunspots, flares, CMEs) impacts critical infrastructure like power grids, satellites, and GNSS, necessitating accurate 13-month smoothed SSN forecasts [1]-[3], especially given societal risks like geoelectric hazards and GNSS degradation [4]-[6]. Recent SSN forecasting increasingly uses diverse hybrid and ensemble ML models (e.g., XG-SN, LSTMs) and physical proxies [7]-[12], while NOAA's operational nonlinear forecast [2] and physics-based precursors [13] remain strong comparators. However, few studies report per-cycle generalization. Grounded in SILSO V2.0 [10] and the SWPC context [5],[4], our work addresses this gap by presenting a compact, cycle-aware ML pipeline. This framework (i) contrasts transparent linear baselines with stacked ensemble and symbolic regression, (ii) reports per-cycle R^2/RMSE across Cycles 21–24, and (iii) stress-tests robustness to label-noise.

Methodology

1. Data and Feature Engineering

We utilized the monthly 13-month smoothed International Sunspot Number (V2.0, WDC-SILSO) for cycles 21–24 (1976–2019), training models on past data (raw data: SN_m_tot_V2.0.csv) via an expanding one-step-ahead setup with per-cycle metrics. A compact, interpretable regressor for smoothed SSN (y_t) was built using z-scored features, including: SSN lags (6, 12, 24 months), rolling statistics, cycle phase (raw, normalized, asymmetric), 11-year sine/cosine harmonics, and interaction terms.

2. Models

In this study we three models, these models are: (a) LinearReg: A ridge-regularized linear baseline predicting smoothed SSN from all features, penalizing large coefficients to prevent overfitting. (b) Stacked: A stacked ensemble combining diverse base learners (e.g., Elastic Net, Gradient-Boosted Trees, RF) using a ridge meta-learner, trained on K out-of-fold (OOF) predictions from expanding windows to prevent leakage. (c) Symbolic: Symbolic regression using a small operator set (add,

Content from this work may be used under the terms of the Creative Commons Attribution 3.0 license. Any further distribution of this work must maintain attribution to the author(s) and the title of the work, journal citation and DOI. Published under license by Materials Research Forum LLC.

Materials Research Proceedings 69 (2026) 271-274 https://doi.org/10.21741/9781644904251-48

subtract, multiply, etc.), selecting compact formulas via a Pareto trade-off between prediction error and complexity.

3. Training, Settings, Hyper-parameter Tuning and Evaluation Metrics

Training utilized an expanding-window cross-validation setup to generate one-step-ahead monthly predictions for solar cycles 21–24. Hyperparameters were tuned for each model-ridge/elastic net for linear, boosted/random forests for trees, and population-based search for symbolic regression-with early stopping based on validation RMSE. Light Gaussian noise was added during training for robustness. All features were z-scored per window, using a fixed scaler for validation and test months. Performance was assessed using "per-cycle metrics," specifically calculating the RMSE and the R^2 independently for each cycle.

Results and Discussion

1. Overall accuracy

Across Cycles 21–24, LinearReg achieved R^2 = 0.876 / RMSE = 23.28 SSN, Stacked = 0.878 / 23.17 SSN (≈0.5% gain), and Symbolic = 0.856 / 25.04 SSN, showing all models perform well with Stacked only slightly ahead. As shown in Fig. 1(a–b), rolling means and short lags are highly collinear (ρ ≈ 0.92–0.98) while CyclePhase adds complementary cues (ρ ≈ 0.3), justifying ridge regularization. Linear and Stacked capture cycle peaks and troughs closely, whereas Symbolic appears smoother and slightly off near extrema.

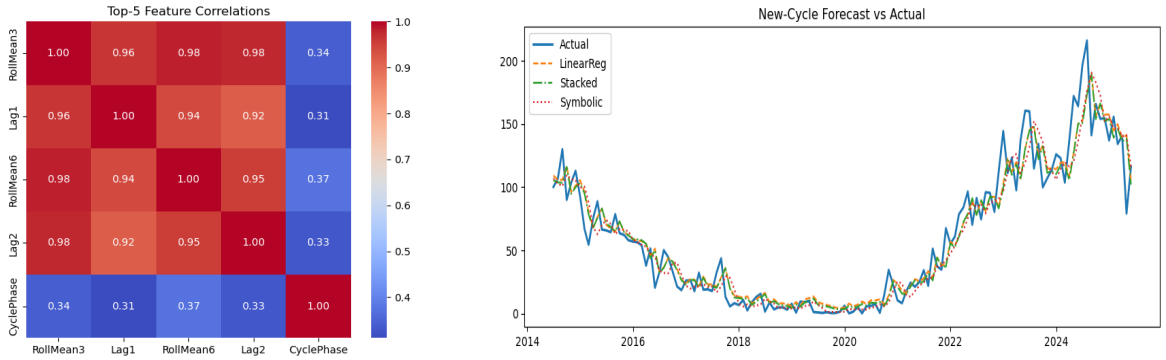


Fig. 1(a):*Collinearity Among Lag/Trend and Cycle-Phase Features,* ***(b)****Monthly SSN Forecasts vs. SILSO Truth During the Cycle-24 Minimum and Rise to Cycle-25 (2014–2025)*

2. Per-cycle behavior

Cycle-level R^2 is stable across methods: in Cycles 21–23, Stacked is about +0.001–0.003 over LinearReg, while in Cycle 24 they are essentially tied. The Symbolic model is competitive (≈0.86–0.87 in Cycles 21–23; ≈0.833 in Cycle 24) but consistently below LinearReg/Stacked, and per-cycle RMSE likewise shows small gains for Stacked—most evident in higher-amplitude cycles; while Symbolic carries a modest penalty; see Fig. 2(a) for R^2 and Fig. 2(b) for RMSE.

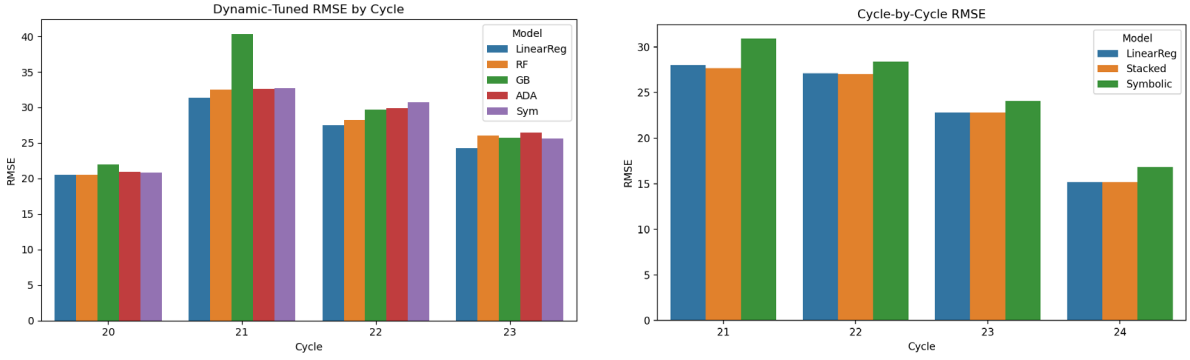


Fig. 2*.Cycle-by-Cycle RMSE (a) Dyanamic (b) Static Settings, Cycles (21–24)*

Materials Research Proceedings 69 (2026) 271-274 https://doi.org/10.21741/9781644904251-48

As shown in Figs. 2, RMSE decreases with declining cycle amplitude (≈28–31 SSN in C21 to ≈15–17 in C24). Stacking slightly improves accuracy in strong cycles, while Symbolic regression trades precision for simplicity. Under dynamic tuning, Linear and RF remain most consistent (R^2 ≈ 0.82–0.88), Gradient Boosting spikes in C21, and Symbolic overestimates peaks as tree ensembles occasionally overshoot.

3. Computation versus benefit

LinearReg runs ~0.018s per cycle versus ~35.6s for Stacked and ~28.8s for Symbolic—about 2,000× and 1,650× slower; while Stacked cuts average RMSE by <0.5% and Symbolic is modestly worse. Per-cycle results mirror this: Stacked offers tiny gains in C21–C23 and ties Linear in C24, whereas Symbolic is consistently slower and less accurate, as shown in Table (1).

Table 1: Per-Cycle Accuracy and Runtime for Monthly Smoothed Sunspot Number Predictions

Cycle	Linear (RMSE / R^2 / s)	Stacked (RMSE / R^2 / s)	Symbolic (RMSE / R^2 / s)
21	27.98 / 0.885 / 0.03	27.65 / 0.888 / 34.67	30.9 / 0.86 / 28.9
22	27.11 / 0.879 / 0.01	27.02 / 0.880 / 37.07	28.36 / 0.867 / 28.85
23	22.82 / 0.878 / 0.02	22.80 / 0.878 / 35.04	24.06 / 0.864 / 28.86
24	15.19 / 0.864 / 0.01	15.19 / 0.864 / 35.75	16.83 / 0.833 / 28.7

4. Interpretation of the symbolic form

The optimal symbolic expression reduces to a quasi-linear, interpretable ARX-style law combining lag-1 and lag-2 SSN, a minor cycle-phase correction, and 11-year harmonics (sine/cosine), utilizing inputs for SSN lags (X_3, X_4) and cycle phase (X_5). This simplicity mirrors the high performance of LR and explains why the Stacked ensemble yields only marginal gains without exogenous precursors. At the monthly horizon, the most predictive content is already captured by autoregressive memory plus smooth cycle phase and seasonality.

5. Operational alignment and robustness

Per-cycle reporting matches operational reality shown in Fig.3, and under label-noise stress (σ=0–3 SSN) the linear model shifts by less than one SSN while the stacked ensemble keeps its slight edge. Across Cycles 20–23, all models retain high fit (R^2≈0.80–0.88) with RMSE tracking amplitude; light noise (σ=1) regularizes (damping GB Cycle-21 spike), σ=3 raises errors but preserves rankings. Linear and AdaBoost (RF close) are most stable, Symbolic is consistent but higher RMSE—supporting L2-style regularization or light target jitter for robust monthly updates.

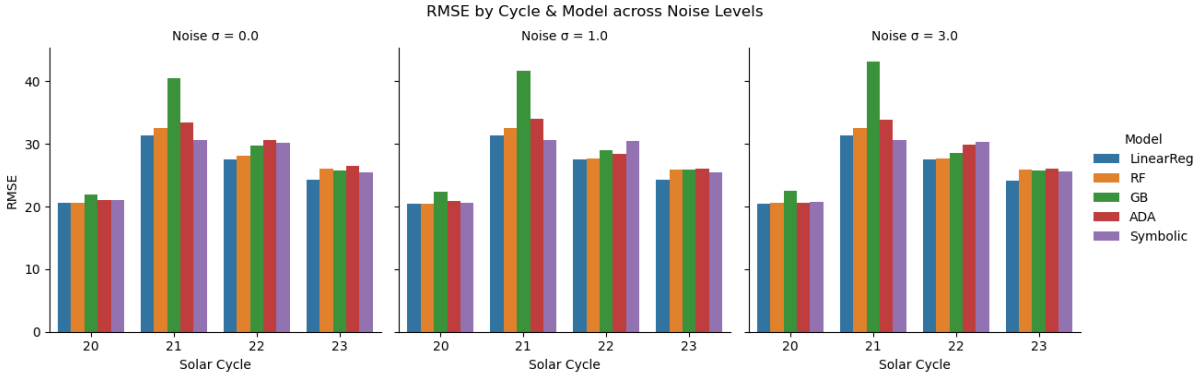


Fig 3. *Noise-Robustness Across Solar Cycles: RMSE vs. Label-Noise Levels (σ∈{0, 1, 3})*

Regularized linear models on lags/phase/Fourier are a strong monthly SSN default; stacking is worthwhile mainly with strong cycles or added covariates due to compute cost, while symbolic models aid auditability and physics insight. Our study used SSN-only features; future work should add physical precursors and include phase-specific and peak-timing metrics to pinpoint operational value.

Conclusion

We developed a lightweight, interpretable framework for monthly 13-month smoothed SSN forecasting (Cycles 20–24, rise of 25) using endogenous predictors (lags, rolling means, harmonics, time/phase). We compared linear regression, tree-based models (RF/GB/ADA), a stacked ensemble, and symbolic regression, testing robustness via Gaussian label noise. Across 75 runs, median performance was $R^2 \approx 0.86$ (RMSE <31SSN). Linear regression proved near-optimal (Cycle-24 RMSE ≈15–24), while stacking offered minor RMSE gains at high compute cost. Symbolic regression was competitive ($R^2 > 0.83$) but missed peaks. Errors scaled with amplitude; light noise regularized. Linear models are favored operationally. Future work should add physics-based inputs and peak-timing metrics.

References

[1] K. Petrovay, "Solar cycle prediction," Living Reviews in Solar Physics, vol. 17, no. 2, 2020. https://doi.org/10.1007/s41116-020-0022-z

[2] L. A. Upton and D. H. Hathaway, "Solar Cycle Precursors and the Outlook for Cycle 25," J. Geophys. Res.: Space Physics, vol. 128, no. 11, e2023JA031681, 2023. https://doi.org/10.1029/2023JA031681

[3] NOAA/NWS SWPC, "NOAA forecasts quicker, stronger peak of solar activity," Dec. 19, 2023.

[4] J. J. Love, D. A. Jonas, and A. Kelbert, "Mapping a Magnetic Superstorm: March 1989 Geoelectric Hazards in the United States," Space Weather, vol. 20, no. 5, 2022. https://doi.org/10.1029/2021SW003030.

[5] W. Nie et al., "The Mechanism for GNSS-Based Kinematic Positioning Degradation at High Latitudes Under the March 2015 Great Geomagnetic Storm," Space Weather, vol. 20, no. 6, 2022. https://doi.org/10.1029/2022SW003132

[6] V. Lanabere, Y. Y. Podladchikova, E. I. Gordeev, A. Wintoft, and M. Palmroth, "Characterizing the distribution of extreme geoelectric field gradients in North America," J. Space Weather Space Clim., vol. 14, 2024, Art. 12. https://doi.org/10.1051/swsc/2024012.

[7] X. Su, B. Liang, S. Feng, Y. Cai, W. Dai, and Y. Yang, "Solar cycle prediction using a combinatorial deep learning model," Mon. Not. R. Astron. Soc., vol. 527, no. 3, pp. 5675–5682, 2024. https://doi.org/10.1093/mnras/stad3451

[8] H. Zhu, W. Zhu, and M. He, "Predicting Solar Cycle 25 Using an Optimized Long Short-Term Memory Model Based on Sunspot Area Data," Adv. Space Res., vol. 71, no. 8, pp. 3521–3534, 2023. https://doi.org/10.1016/j.asr.2023.02.025

[9] WDC-SILSO, "Sunspot Number graphics (daily, monthly, 13-month smoothed)," accessed Sept. 2025. [Online]. Available: https://www.sidc.be/SILSO/ssngraphics

[10] J.-V. Rodríguez, V. M. Sánchez Carrasco, I. Rodríguez-Rodríguez, A. J. Pérez Aparicio, and J. M. Vaquero, "Hemispheric Sunspot Number Prediction for Solar Cycles 25 and 26 Using Spectral Analysis and Machine Learning Techniques," Solar Physics, vol. 299, no. 116, 2024. https://doi.org/10.1007/s11207-024-02363-2

[11] D. Sierra-Porta, M. Tarazona-Alvarado, and D. D. Herrera Acevedo, "Predicting sunspot number from topological features in spectral images I: Machine learning approach," Astronomy and Computing, vol. 48, p. 100857, 2024. https://doi.org/10.1016/j.ascom.2024.100857

[12] V. Kumar, "Enhancing Solar Cycle 25 and 26 Forecasting with Vipin-Deep-Decomposed-Recomposed Rolling-window (vD2R2w) Model on Sunspot Number Observations," Solar Physics, vol. 299, no. 147, 2024. https://doi.org/10.1007/s11207-024-02389-6

[13] M. S. Miesch et al., "Solar Cycle Prediction at NOAA's Space Weather Prediction Center," Space Weather, 2025. https://doi.org/10.1029/2025SW004444

Materials Research Proceedings 69 (2026) 275-280 https://doi.org/10.21741/9781644904251-49

Aspects Regarding the Implementation, Capture and Measurement of Noise on the Măgurele Air Test Stand

Radu Cristian GABOR[1,a*], Grigore CICAN[2,b], Mihnea GALL[3,c]

[1]Romanian Air Force 90th Airlift Base "Comandor Aviator Gheorghe Bănciulescu" Otopeni; 1 Zborului Street, 075150 Otopeni, Romania

[2]Faculty of Aerospace Engineering National University of Science and Technology POLITEHNICA of Bucharest; 313 Independence Blvd. Bucharest, District 6, 060042, Romania

[3]Romanian National Research & Development Institute for Gas Turbine - COMOTI; 220D Iuliu Maniu Blvd. Bucharest, District 6, 061126, Romania

[a]gabor.radu.cristian@gmail.com, [b]mihnea.gall@comoti.ro, [c]grigore.cican@upb.ro

Keywords: Air Injection System, Noise, Acoustics, Chevron Nozzles, Test Stand

Abstract. This paper presents a comprehensive analysis of the air supply system implemented at the Măgurele Air Test Stand, an essential infrastructure for experimental research in noise reduction devices for turbojet engines. The paper meticulously details the system configuration, component integration, instrumentation, and control methodologies designed to simulate realistic engine operating conditions, including subsonic and transonic flow regimes. Experimental procedures focused on evaluating system stability, thermal response, and pressure regulation accuracy, providing critical data for validating the performance of a home-developed air injection system aimed at noise suppression through fluidic chevron simulation. The experimental air supply system at the Măgurele Air Test Stand has proven to be a critical infrastructure for advanced research in noise reduction technologies for turbojet engines. Its precise flow control, robust safety mechanisms, and modular design establish it as an indispensable asset for dynamic experimental setups involving pressure-gain combustion and detonation-based propulsion studies. Therefore, this paper serves not only as a detailed documentation of the existing experimental setup but also as a compulsory reference for future research activities, ensuring that all subsequent experimental investigations build upon a validated and thoroughly characterized technical foundation.

Introduction

The air supply system serves as the backbone for all experimental tests that involve high-frequency ignition, pressure gain cycles, and visual flow analysis through Schlieren techniques. Its role is not just to provide a stable airflow, but also to ensure the correct thermal and pressure conditions that allow a realistic simulation of engine operations [1].

Through its modular design, it enables researchers to simulate various flow configurations, including subsonic, transonic, and limited supersonic regimes. Additionally, the system is designed with full safety interlocks and redundant control paths to avoid hazardous over-pressurization or thermal damage during long-duration tests [2,3]. The air supply system implemented at the experimental testing facility located at Măgurele plays a central role in enabling pulsed detonation and pressure-gain combustion studies [4].

This report provides a detailed technical breakdown of the high-pressure air system, incorporating static documentation and experimental configurations from validated articles [5,6]. Additional systematization and augmentation were applied to adapt the report for personal use, specifically to test the ability of my jet nozzle to reduce noise by a certain number of decibels.

Content from this work may be used under the terms of the Creative Commons Attribution 3.0 license. Any further distribution of this work must maintain attribution to the author(s) and the title of the work, journal citation and DOI. Published under license by Materials Research Forum LLC.

Materials Research Proceedings 69 (2026) 275-280 https://doi.org/10.21741/9781644904251-49

System configuration

The design further integrates a safety buffer before entering the experimental section. This is implemented using a high-precision needle valve that regulates backpressure while ensuring no significant temperature drop across the bypass module. The system also features real-time feedback loops integrated into the PLC software. These are responsible for performing corrective actions in less than 100 ms, which is essential when testing dynamic systems such as pulsed detonation combustors. Moreover, the use of high-quality stainless steel piping, flexible joints, and vibration dampers ensures mechanical robustness, particularly in tests involving rapid pressure oscillations.

The system architecture of the Măgurele test stand consists of a high-pressure compressor (11 bar nominal, 1.2 kg/s peak output), two buffer tanks: 500 L (x1), 1000 L (x1), max pressure: 12 bar, an electric heater unit: OSRAM SYLVANIA SFI-8D-192-38, 5 kW, flow sensors: CS Instruments VA500, pressure sensors: WIKA Digital PG + backup Bourdon gauge, temperature sensors: K-type thermocouples, control valves: Burkert Type 8802, 3-way modulating, one data acquisition: NI CompactDAQ + LabVIEW interface, one PLC: Siemens S7-1200 with PID logic, some emergency stop and safety relief systems and connecting pipes, gaskets and nipples



Fig. 1. Air supply line components

The core of the air line is built around a compressor that maintains a maximum absolute pressure of 11 bar. Compressed air is stored in buffer tanks (500L and 1000L) to ensure flow stability. Flow is managed via motorized three-way valves and throttling valves that direct the airflow either to the experimental area or through a heating loop that includes an OSRAM SYLVANIA SFI-8D-

Materials Research Proceedings 69 (2026) 275-280 https://doi.org/10.21741/9781644904251-49

192-38 electric resistor heater. The bypass mechanism allows switching between heated and ambient air flows without interrupting the experiment.

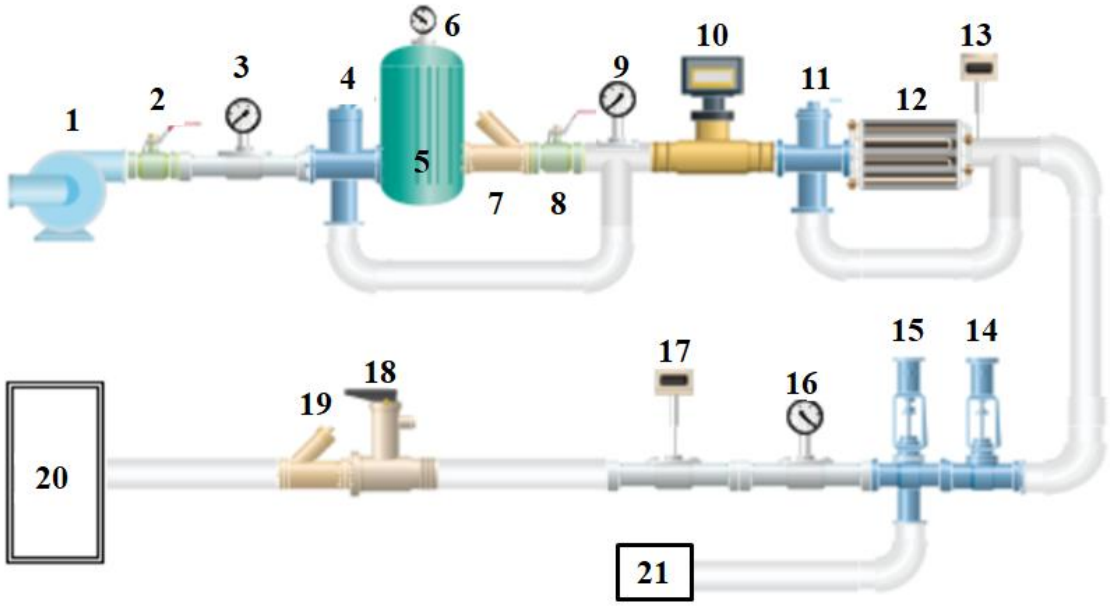


Fig. 2. Graphic diagram of the air supply line (1-compressor; 2-adjustment tap; 3,6,9-pressure gauge; 4,11,15-three way valve; 5-tank; 7,19-one way valve; 8,14-adjustment valve; 10-flow meter; 12-heater;13-temperature sensor; 16-thermometer; 17-gauge; 18-safety valve; 20-experimental zone; 21-atmospheric exhaust).

In addition to what was listed above, the system will also have a home-made injection air system designed especially for this research. The flange is 3D printed from PLA and the air injection system is made of a 15 mm diameter pipe, welded together with eight other pipes with an internal diameter of 4 mm that can be oriented at various angles in order to simulate the fluidic chevrons.



Fig. 3. The home-made injection air system in different views.

Instrumentation and monitoring

From a control systems standpoint, the instrumentation is coupled with a time-synchronized logging unit that records at 1 kHz sampling frequency. This resolution ensures precise matching between physical events (e.g., spark ignition, shock wave propagation) and measured signals (pressure, temperature, flow). Sensor calibration is performed prior to every test session using

NIST-traceable calibration units to ensure traceability and data integrity. An online dashboard is also available for operators to visualize trends and receive system alarms in real-time.

A combination of flow, temperature, and pressure sensors are distributed along the line to ensure accurate parameter tracking. These include:

- Thermocouples for upstream and downstream thermal monitoring.
- Pressure gauges (pre- and post-regulation).
- CS Instruments VA500 flowmeter for mass flow measurement.

All sensors are integrated with a PLC-based data acquisition and control system, which also handles PID regulation for fine-tuned valve adjustment and interlocking safety logic.

Experimental results (Calibrations and checks)

Initial tests conducted using the air test bench focused on system stability, pressure regulation accuracy, and temperature response when switching between bypass and heating modes.

The following results summarize key performance indicators recorded during these runs.

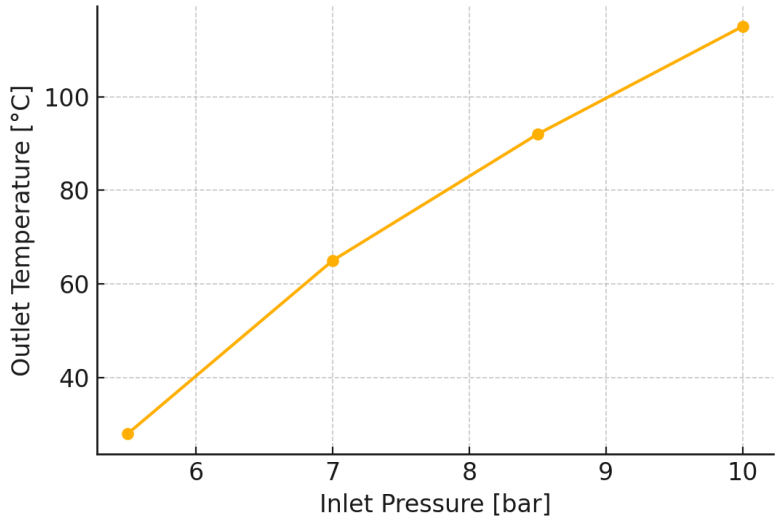


Fig. 4. Variation of outlet temperature with inlet pressure (heater active)

Additional validation tests were performed using stepped flow rate increments to determine the response time and thermal inertia of the system under various loads.

The bypass and heater loop were cycled to simulate real experimental transitions. It was observed that the heater exhibited a delay of 8–12 seconds before stable output.

Three full cycles under 7.5 bar inlet pressure yielded:

- Flow rate fluctuation: ±1.5%
- Temperature deviation: ±3.2 °C
- Pressure consistency: ±0.2 bar

These confirm the system's reliability under both steady-state and transient flow scenarios.

The home-made injection air system designed especially for this research was tested under pressure from 9 bar to almost atmospheric pressure. The results can be seen in the graph below, from which it can be concluded that there are no inappropriate variations or choked elements in the air flow through the eight ducts.

After connecting the air supply line to my air injection system with 8 tubes fed from a compressor to practically simulate fluid chevrons, several tests will be carried out and the resulting total noise as well as the distribution of the jets will be measured with a sound level meter. I will use a Schlieren-type system for viewing the jets and the tests will be performed on different configurations of reactive nozzles with a smaller or larger number of chevrons.

Materials Research Proceedings 69 (2026) 275-280 https://doi.org/10.21741/9781644904251-49

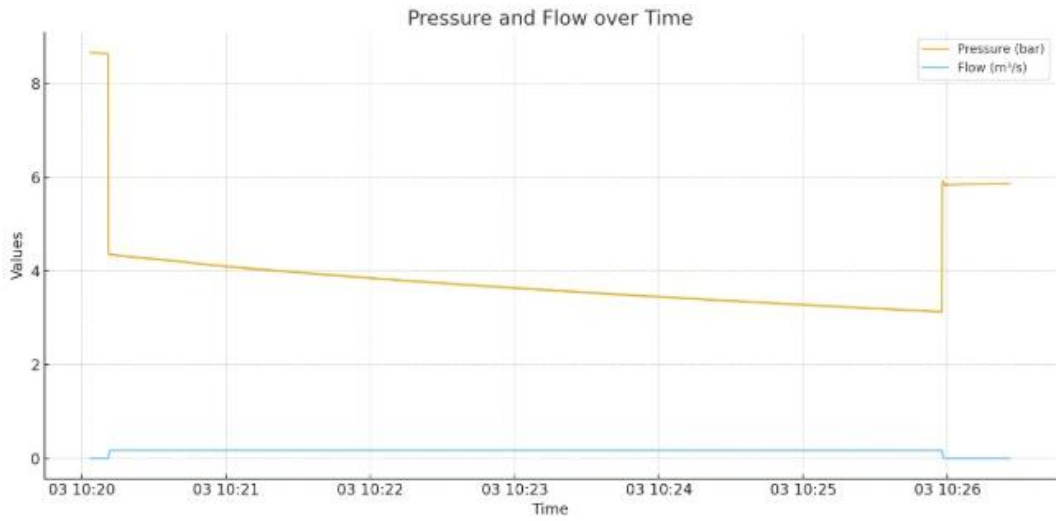


Fig. 5. Variation of the pressure air flow through the air injection system

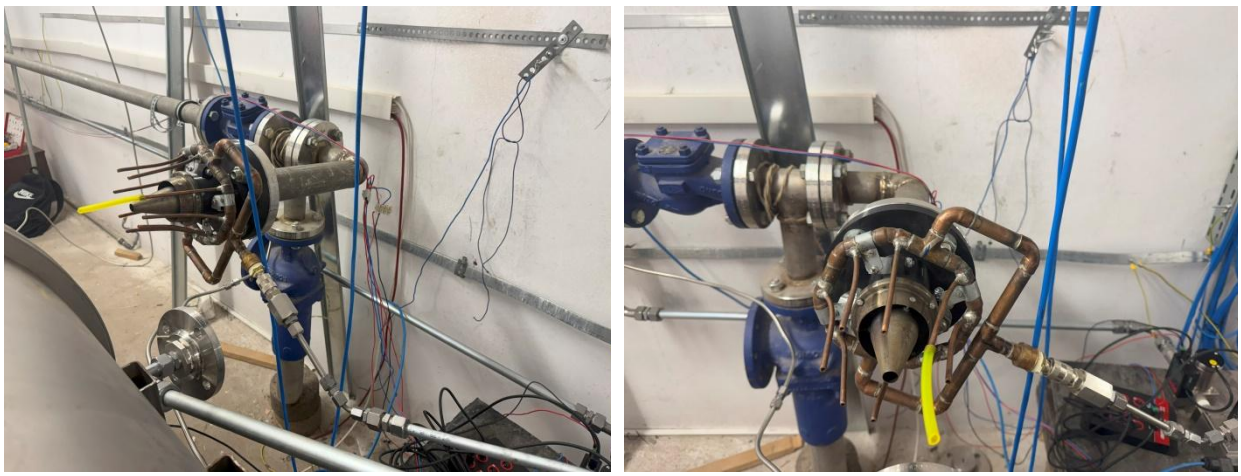


Fig. 6. The final assembly of the system

Future research directions

Unfortunately, the validation tests performed affected the inner section of the 3D printed PLA flange, yielding unsatisfactory results.

To overcome this situation, we have already made an improved flange, which can be seen in the following figure. This is the third version of the flange and should withstand the pressure and thermal inertia of the system under various loads.



Fig. 7. The third version of the home-made injection air system in different views

Future developments of the air supply system aim to improve measurement resolution, system modularity, and enable advanced measurments of total noise of the system. Key upgrades under consideration include:

- Integration of real-time gas composition sensors for exhaust analysis
- Installation of a mass spectrometry module for hydrogen leak detection
- Implementation of automatic flow balancing between dual feed lines
- Expansion of data acquisition channels to >50 for multipoint instrumentation

Furthermore, a comparison between the real data obtained from the practical tests will be compared with the data from the CFD analysis performed on the same model in ANSYS. Several tests will be carried out and the resulting total noise as well as the distribution of the jets will be measured with a sound level meter. I will use a Schlieren-type system for viewing the jets and the tests will be performed on different configurations of reactive nozzles with a smaller or larger number of chevrons orientated at different angles.

Summary

The system in use at the Măgurele facility is a robust and adaptable high-pressure air supply configuration capable of supporting advanced experimental combustion research. Its architecture emphasizes flow control precision, safety redundancy, and modular design suited for rapid changes in experimental needs. In future upgrades, the integration of mass spectrometry for gas composition and high-speed thermographic cameras will further expand the diagnostic capabilities of the air supply system. In parallel, the facility's modular design makes it possible to introduce scramjet or rotating detonation test modules without major structural changes to the existing infrastructure. Through careful design and system validation, the air line at Măgurele has demonstrated reliability, safety, and flexibility for advanced propulsion experiments.

References

[1] A. V. Cojocea et al., “Experimental Investigations of Hydrogen Fuelled Pulsed Detonation Combustor”, ASME Turbo Expo 2022. https://doi.org/10.1115/GT2022-82393

[2] B. Callender, E. Gutmark, and S. Martens, “A comprehensive study of fluidic injection technology for jet noise reduction”, AIAA-2007-3608, 2007. https://doi.org/10.2514/6.2007-3608

[3] M. Massey et al., “Effect of Chevrons on Jet Noise Reduction,” AIAA Journal, 2019. https://doi.org/10.3390/aerospace11060465

[4] A. Bogoi et al., “Experimental Pressure Gain Analysis of Pulsed Detonation Engine,” Aerospace, vol. 11, no. 6, p. 465, 2024.

[5] NASA Tech Briefs, “Fluidically Enhanced Nozzles for Noise Suppression,” 2021.

[6] J. D. Bridges and C. A. Brown, “Parametric Testing of Chevron Nozzles,” NASA TM-2004-213107.

Materials Research Proceedings 69 (2026) 281-286 https://doi.org/10.21741/9781644904251-50

Local Noise Dissipation Mechanism and Flow Impedance in Acoustic Liner Grazed by Turbulent Flow and Acoustic Wave

Francesco AVALLONE[1,a,*], Angelo PADUANO[1,b], and Francesco SCARANO[1,c]

[1]Department of Mechanical and Aerospace Engineering, Politecnico di Torino, Corso Duca degli Abruzzi 24, 10129, Torino, Italy

[a]francesco.avallone@polito.it, [b]angelo.paduano@polito.it, [c]francesco.scarano@polito.it

Keywords: Aeroacoustics, Acoustic Liner, Turbulent Flows

Abstract. The acoustic energy dissipation mechanisms of a single-degree-of-freedom liner under grazing turbulent flow are investigated using high-fidelity lattice-Boltzmann very-large-eddy simulations. Viscous and vortex-shedding contributions are quantified through stress-based integration and Howe's energy corollary. Results confirm that grazing flow modifies local shear structures and enhances dissipation at more downstream locations. The evolving flow field alters liner impedance and shifts the balance between viscous and vortical losses, emphasizing the importance of flow development in liner characterization.

Introduction

Acoustic liners are widely used in aircraft engines to mitigate fan noise, which has become a dominant source in modern ultra-high-bypass-ratio configurations. The simplest liner, a single-degree-of-freedom (SDOF) design, consists of a perforated face sheet backed by a cavity and behaves as a Helmholtz resonator. Its acoustic response is typically characterized through the impedance, which depends on geometric parameters, sound pressure level (SPL), and flow conditions. While the dissipation mechanisms of SDOF liners under purely acoustic excitation are well understood, their behavior under realistic conditions—where strong acoustic waves interact with high-speed grazing turbulent flow—remains only partially characterized.

In the absence of flow, dissipation arises from viscous losses and vortex shedding within the orifices. However, when grazing flow is present, additional nonlinear effects modify the impedance. The coupling between flow topology, boundary layer state, and acoustic-induced motion within the orifices plays a critical role in determining the overall energy dissipation.

This study investigates the relative contributions of viscous and vortex-shedding mechanisms to acoustic energy dissipation in an SDOF liner, including the effects of streamwise flow development. Dissipation due to viscous effects is quantified following Ref. [1], while vortex-induced dissipation is evaluated using Howe's energy corollary [2, 3]. High-fidelity lattice-Boltzmann very-large-eddy simulations (LB/VLES) of a fully resolved liner geometry, representative of a geometry investigated at the Federal University of Santa Catarina [4], are employed. The results provide new insights into how the development of the grazing flow alters local flow structures and the balance between viscous and vortex-shedding dissipation mechanisms.

Methodology

Following the formulation in Ref. [1], the instantaneous viscous dissipation rate, $D(t)$, is obtained by integrating the stress tensor over the orifice wall region where a boundary-layer-like flow develops

$$D(t) = \iint_{walls} \sigma_{ij} \frac{\partial u_i}{\partial x_j} dxdy \quad (1)$$

Content from this work may be used under the terms of the Creative Commons Attribution 3.0 license. Any further distribution of this work must maintain attribution to the author(s) and the title of the work, journal citation and DOI. Published under license by Materials Research Forum LLC.

Materials Research Proceedings 69 (2026) 281-286 https://doi.org/10.21741/9781644904251-50

where the stress tensor is defined as

$$\sigma_{ij} = \mu\left(\frac{\partial u_i}{\partial x_j} + \frac{\partial u_j}{\partial x_i}\right) \tag{2}$$

and μ is the dynamic viscosity. To capture the periodic variation over the acoustic cycle, *D(t)* is phase-averaged with respect to the excitation phase ϕ. The time-averaged viscous energy dissipation per unit area is then

$$E_{viscous} = \frac{1}{T}\int_0^T D(t)dt \tag{3}$$

providing a measure of viscous losses under both linear and nonlinear acoustic conditions. The conversion of acoustic energy into vortical motion is quantified using Howe's energy corollary [2, 3]. The instantaneous power density exchanged between the acoustic and vortical fields is given by

$$\Pi_g = \rho_0(\boldsymbol{\omega} \times \boldsymbol{u}') \cdot \boldsymbol{u}_{ac} \tag{4}$$

where ρ_0 is the mean density, $\boldsymbol{\omega}$ the vorticity, $\boldsymbol{u}' = \boldsymbol{U} + \boldsymbol{u}_{aero} + \boldsymbol{u}_{ac}$ the total velocity field, where $\boldsymbol{u}_{ac}$ is the acoustic-induced velocity, $\boldsymbol{U}$ is the time-averaged velocity and $\boldsymbol{u}_{aero}$ is the turbulent velocity fluctuation.
The total acoustic-to-vorticity energy transfer within the orifice is

$$\Pi(t) = \iint_{orifice} \Pi_g dxdy \tag{5}$$

where positive values indicate absorption of acoustic energy by the vortical field, and negative values indicate acoustic generation. The mean energy exchanged over one oscillation period is expressed as

$$E_{shedding} = \frac{1}{T}\int_0^T \Pi(t)dt \tag{6}$$

To evaluate Howe's corollary, the acoustic-induced velocity must be isolated from turbulent fluctuations associated with grazing flow. Spectral Proper Orthogonal Decomposition (SPOD) is employed following Ref. [5]. SPOD extracts coherent, energy-dominant modes from statistically stationary flow data, combining the advantages of POD and DMD. The MATLAB routines of Ref. [6] are used to perform the decomposition and velocity reconstruction. A reduced-order model is built from the leading SPOD mode within a narrow frequency band centered on the forcing frequency, yielding the coherent, phase-locked acoustic-induced velocity field. This reconstructed velocity represents the dominant coherent component relevant to acoustic–flow coupling and dissipation, rather than the irrotational part of the flow obtained through a Helmholtz decomposition.
The local flow impedance is obtained by computing at each point in the fluid domain the ratio

$$\frac{S_{pp}(f)}{S_{pv}(f)} \tag{6}$$

where $S_{pp}(f)$ is the auto-spectrum of the pressure and $S_{pv}(f)$ is the cross-spectrum between the pressure signal and the vertical velocity component. The real part of the ratio is the

Materials Research Proceedings 69 (2026) 281-286 https://doi.org/10.21741/9781644904251-50

local flow resistance, while the imaginary part is the local flow reactance. In the following, the flow resistance at a frequency equal to that of the acoustic plane wave is shown.

Test case

The simulations were conducted in a rectangular duct with the liner mounted on the upper wall. An acoustic liner with a rounded orifice geometry, as the one described as scanned in Ref. [7], is investigated. The liner has 11 cavities in the streamwise direction. A zig-zag trip upstream generated turbulence, while sponge layers at the outlet prevented reflections. The inlet Mach number was M=0.3 (U_0 = 110 m/s) or M=0. Periodic lateral boundaries reproduced the experimental setup. A variable-resolution mesh (Δx = 0.02d near orifices, 40 cells across diameter) was used. Flow-only simulations were run until convergence, after which plane acoustic waves were imposed using the OptydB toolkit. This two-step LBM-VLES approach efficiently captured nonlinear flow-acoustic coupling at 145 dB and 1400Hz.

Results

Fig. 1 reports the phase-averaged acoustic dissipation rate obtained through both viscous and vortex-shedding mechanisms. The top figures refer to the case in the absence of flow, while the bottom ones refer to the case with the grazing turbulent flow. In each subfigure, three cavities, i.e., the most upstream (cavity 1), the central one (cavity 6), and the most downstream (cavity 11), are shown.

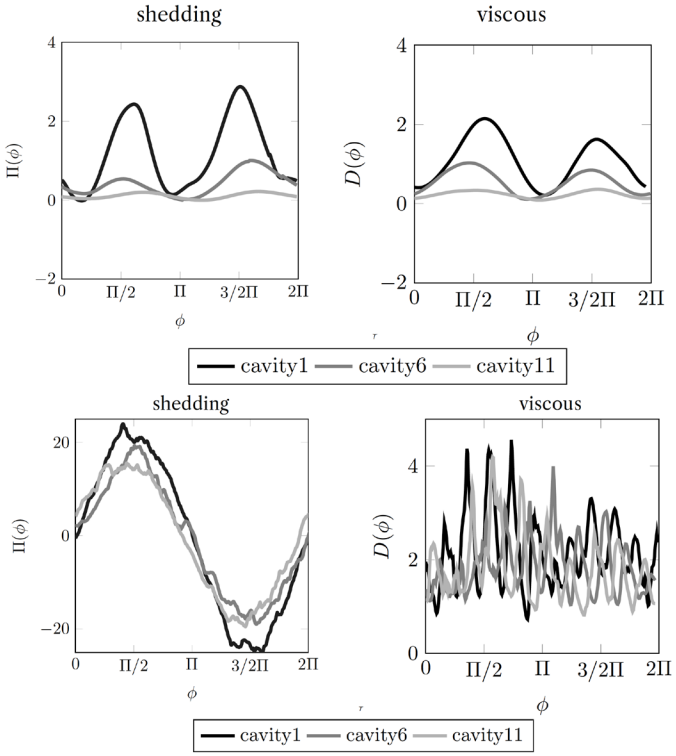


Figure 1. Phase averaged shedding and viscous dissipation in the absence (top) and in the presence of grazing turbulent flow (bottom). SPL equal to 145dB and frequency equal to 1400Hz.

In the absence of grazing turbulent flow, both acoustic energy dissipation mechanisms contribute similarly. In particular, acoustic energy is dissipated during both the inflow and outflow phases in a similar way. However, at more downstream cavities, the rate of dissipation for both mechanisms diminishes. This is due to the reduction of acoustic amplitude in the streamwise direction.

Materials Research Proceedings 69 (2026) 281-286 https://doi.org/10.21741/9781644904251-50

In the presence of the grazing flow, differences between the two acoustic dissipation mechanisms are present. The rate of dissipation due to vortex shedding exhibits a positive rate, i.e., noise dissipation, during the inflow and a negative one, i.e., noise generation, during the outflow phase. The possible reason is that during the outflow phase, the acoustic-induced velocity ejected by the cavity interacts with the convecting turbulent flow, thus generating vorticity responsible for noise generation. When comparing different cavities, it can be observed that the maximum and minimum values at the first cavity are larger than at the more downstream ones. This can be caused by the flow development and the consequent reduction of the shear layer strength over the orifices, as reported in Ref. [7]. On the other hand, the contribution due to viscous effects is always positive, and minor differences are found between cavities. The high-frequency fluctuations visible in the figures are due to amplified acoustic fluctuations caused by a resonant cavity depth noise [7]. The total balance, including both noise dissipation mechanisms, is positive, i.e., noise reduction. Fig. 2 (left) reports the integrated rate of dissipation of the two noise dissipation mechanisms at different cavities, while Fig. 2 (right) reports the sum of the two contributions. It is interesting to notice that the sound energy dissipation varies differently between the cases with and without turbulent grazing flow. As a matter of fact, without grazing flow, the acoustic dissipation decreases at more downstream cavities because of the streamwise reduction of the SPL; conversely, it increases in the presence of flow caused by the streamwise development of the turbulent flow and shear strength over the orifices. These findings confirm that it is essential to account for the development of the flow when computing impedance in grazing flow facilities.

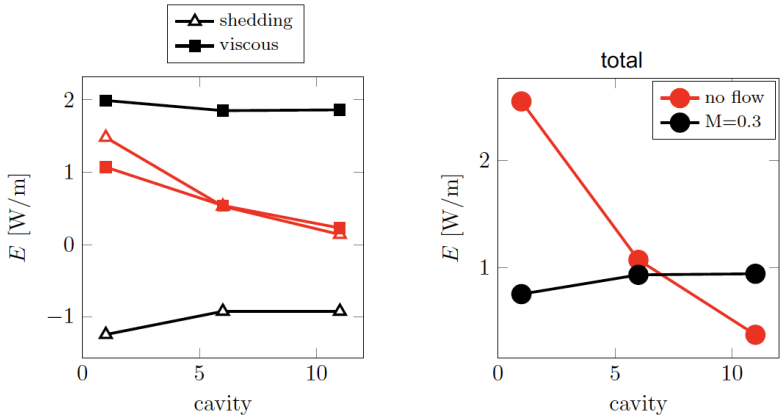


Figure 2. (left) Contribution of the energy dissipation through viscous and vortex shedding for the injection (full symbol) and ejection (empty symbol). (Right) Total energy dissipated with and without grazing flow.

To confirm the above statement, the real and imaginary parts of the flow impedance, named resistance and reactance, at the frequency of interest are shown in Fig. 3. The top figures display results for the grazing flow case, while the bottom ones display the no-flow case.

In the presence of turbulent grazing flow, it can be noticed that the flow field within the channel can be split into two parts: for $0.5<y/H<0$ or $5<y/\delta^*<0$, where H is the half channel heigh and δ^* the boundary layer displacement thickness upstream of the liner, the local effects of the facesheet orifice and of the solid surfaces between cavities are clearly visible, demonstrating that the liner is locally perturbing the flow. Conversely, for $y/H<0.5$ or $y/\delta^*<5$, local effects are not visible. This suggests that at this location, the assumption of uniform impedance is more valid. However, it can be observed that there is a change in the fluid flow resistance in the streamwise direction

Materials Research Proceedings 69 (2026) 281-286 https://doi.org/10.21741/9781644904251-50

with larger variations close to x/L=0 where L is the liner length. This finding suggests that the change in the flow over the facesheet orifices, as explained before, modifies the local flow impedance, which flattens at approximately x/L>0.5. Similar findings are found for the flow reactance in the presence of flow. Results are different without flow, where the localized impact of the vortex shedding, which penetration decreases in the streamwise direction because of the lower SPL, is visible. However, the two regions, differently from what is found with grazing flow, cannot be distinguished.

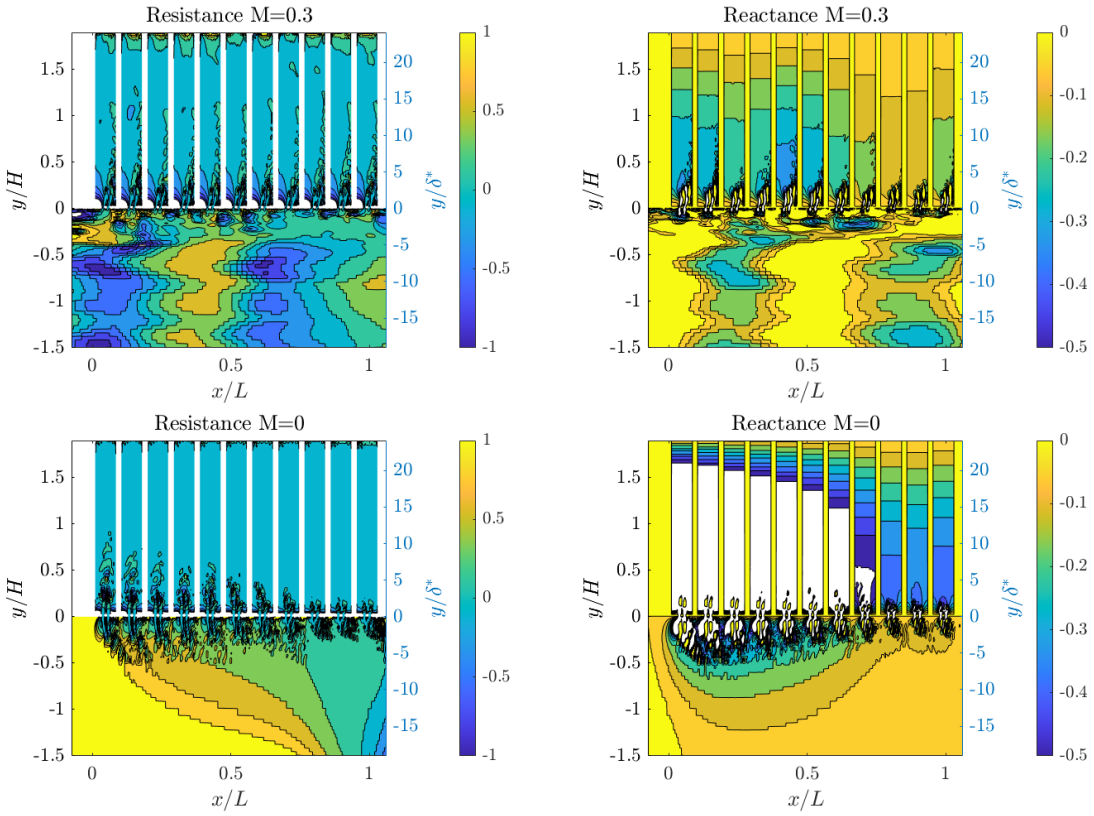


Figure 3. Flow resistance components with (top) and without (bottom) grazing flow.

Conclusions

This study investigates the impact of the flow development over an acoustic liner on both the acoustic energy dissipation and the flow impedance. It is found that the acoustic dissipation increases in the streamwise direction, reaching a plateau. This is due to the change in the shear strength over the liner orifice. As a consequence, the flow impedance changes in the streamwise direction, thus resulting in a larger variation at the interface between the solid and lined surfaces. It is also found that, in the presence of the flow, the local effects of the flow through the orifices are less visible at y/H < 0.5. Future studies on a longer liner with more geometries and acoustic conditions will shed further light on what is presented in this paper.

Acknowledgment

The authors are co-funded by the European Union (ERC, LINING, 101075903). Views and opinions expressed are, however, those of the authors only and do not necessarily reflect those of the European Union or the European Research Council. Neither the European Union nor the granting authority can be held responsible for them.

References

[1] Christopher K. W. Tam and Konstantin A. Kurbatskii. Microfluid Dynamics and Acoustics of Resonant Liners. AIAA Journal, 38(8):1331-1339, August 2000. https://doi.org/10.2514/2.1132

[2] M. S. Howe. Contributions to the theory of aerodynamic sound, with application to excess jet noise and the theory of the flute. Journal of Fluid Mechanics, 71(4):625-673, October 1975. https://doi.org/10.1017/S0022112075002777

[3] M.S. Howe. The dissipation of sound at an edge. Journal of Sound and Vibration, 70(3):407-411, June 1980. https://doi.org/10.1016/0022-460X(80)90308-9

[4] N.T. Quintino, L.A. Bonomo, J.A. Cordioli, M.G. Jones, B.M. Howerton, D.M Nark, and F. Avallone. Comparison of Impedance Eduction Test Rigs with Different Boundary-Layer Profiles. AIAA Journal, 2025. https://doi.org/10.2514/1.J065173

[5] Oliver T. Schmidt and Tim Colonius. Guide to Spectral Proper Orthogonal Decomposition. AIAA Journal, 58(3):1023-1033, March 2020. https://doi.org/10.2514/1.J058809

[6] Aaron Towne, Oliver T. Schmidt, and Tim Colonius. Spectral proper orthogonal decomposition and its relationship to dynamic mode decomposition and resolvent analysis. Journal of Fluid Mechanics, 847:821-867, July 2018. https://doi.org/10.1017/jfm.2018.283

[7] Angelo Paduano, Francesco Scarano, Julio Cordioli, Damiano Casalino, and Francesco Avallone. On the impact of the turbulent grazing flow development on the acoustic response of an acoustic liner. arXiv preprint arXiv:2507.22714, 2025. https://doi.org/10.1017/jfm.2026.11544

Materials Research Proceedings 69 (2026) 287-292 https://doi.org/10.21741/9781644904251-51

A Novel Multipolar Expansion for Acoustic Footprint Reduced Order Modeling

Giorgio PALMA[1,a], Stefano MELONI[2,b], Christophe BOGEY[3,c], Lorenzo BURGHIGNOLI[4,d], Caterina POGGI[4,e], and Jacopo SERAFINI[4,f*],

[1]National Research Council-Institute of Marine Engineering, Via di Vallerano 139, 00128 Roma, Italy

[2]Università della Tuscia, Dipartimento di Economia, Ingegneria, Società e Impresa, 01100 Viterbo, Italy

[3]Laboratoire de Mécanique des Fluides et d'Acoustique, LMFA, UMR 5509, 69130 Ecully, France

[4]Università degli Studi Roma Tre, Dipartimento di Ingegneria Civile, Informatica e delle Tecnologie Aeronautiche, Via Vito Volterra 62, 00146 Roma, Italy

[a]giorgio.palma@cnr.it, [b]stefano.meloni@unitus.it, [c]cristophe.bogey@ec-lyon.fr, [d]lorenzo.burghignoli@uniroma3.it, [e]caterina.poggi@uniroma3.it, [f]jacopo.serafini@uniroma3.it

Keywords: Aeroacoustics, Reduced Order Modeling, Jet Noise, BVI, Equivalent Sources

Abstract. High-fidelity computational aeroacoustic simulations are often too computationally expensive for rapid evaluation of aircraft noise, especially when assessing full-system acoustic footprints during operations. This work introduces a physics-informed multipolar-expansion methodology that generates equivalent acoustic sources capable of accurately reproducing complex pressure fields in both near- and far-field regions at a fraction of the computational cost. The method employs expansions from monopoles to higher-order terms for noise modeling and prediction, using spherical harmonics as a complete basis of the Helmholtz equation. Acoustic moments coefficients are identified through linear regression analysis of pressure data obtained from numerical or experimental sampling, enabling the accurate reconstruction of the acoustic field once the coefficients are determined. The methodology is assessed using two representative aeroacoustic problems: a helicopter rotor operating in Blade–Vortex Interaction conditions and a subsonic jet at Mach 0.9 with varying nozzle temperatures. The results show excellent agreement with reference data, maintaining amplitude accuracy up to the far field while drastically reducing computational time. The proposed reduced-order model demonstrates strong robustness and generalizability, offering a fast and physically grounded tool for aerodynamic optimization, real-time control, and digital-twin frameworks, enabling efficient and scalable noise prediction in complex aeroacoustic environments.

Introduction

High-fidelity computational aeroacoustic simulations are prohibitively expensive for rapid evaluation of noise propagation from aeronautical sources [1], especially when assessing the acoustic footprint of complete aircraft in operational phases [2]. Many recent papers have focused on developing metamodels for acoustic problems to reduce this computational burden [3, 4]. This work presents a physics-informed multipolar-expansion methodology that generates equivalent acoustic sources capable of accurately reproducing the complex pressure field in both near-field and far-field regions, with a low computational cost. The source of interest may be the entire aircraft or single components (rotors, engines), since the equivalent sources can also be used in scattering problems.

Content from this work may be used under the terms of the Creative Commons Attribution 3.0 license. Any further distribution of this work must maintain attribution to the author(s) and the title of the work, journal citation and DOI. Published under license by Materials Research Forum LLC.

Materials Research Proceedings 69 (2026) 287-292 https://doi.org/10.21741/9781644904251-51

Building upon the framework introduced in [5], this work extends the use of spherical harmonics as a complete basis for solving the Helmholtz equation, providing an efficient and physically grounded representation of acoustic fields. The core idea of the proposed approach is to identify the acoustic moment coefficients through a linear regression procedure applied to pressure data sampled at a set of control points, which can be obtained either numerically or experimentally. The methodology follows a structured sequence of steps. First, a training set is defined by collecting pressure values on grids surrounding the emitting source, at all frequencies of interest. Then, a suitable multipolar expansion is selected: typically centered on, or aligned with, the symmetry axis of the source. The expansion coefficients are estimated by minimizing the mean square error between the reconstructed and sampled pressures, using the Moore–Penrose pseudoinverse of the measurement matrix. Once these coefficients are determined, the model can predict the acoustic pressure distribution at arbitrary spatial locations, both in the near and far field. To evaluate the accuracy and generalizability of the proposed procedure, two representative aeroacoustic test cases are considered: the noise footprint generated by a rotor operating under Blade-Vortex Interaction conditions, and the sound radiation from a round free jet in a high-subsonic regime. In both cases, the results demonstrate excellent agreement with reference data, showing accurate reproduction of noise amplitudes up to the far field. Moreover, once the multipolar coefficients are available, the acoustic field can be evaluated in milliseconds across thousands of observer positions, highlighting the computational efficiency of the approach.

Multipolar expansion

This work proposes to approximate the reference acoustic field with a series Nexp of multipolar linear expansions of arbitrary order N, each one defined by elementary sources using spherical harmonics as a basis [6] ($e^{i\omega t}$ time convention):

$$p(r,\phi,\theta,\omega) = \sum_{i=0}^{N_{exp}} \sum_{l=0}^{N} \sum_{m=-l}^{l} A_{l,m}^{i} Y_{l,m}(\phi_i,\theta_i) h_l^{(2)}(\kappa r_i)$$

where $\kappa = \omega/c$, $h_l^{(2)}(x)$ is the l-th order spherical Hankel function of the second kind, providing the radial dependence of the solution, and the real (Laplace's) spherical harmonics $Y_{l,m}$ of degree l and order m are a set of functions orthonormal over a sphere, obtained as the angular-dependent portion of the solution of Laplace's operator in spherical coordinates [5]. In this work, multiple multipolar expansions are introduced along the jet axis line, extending in from the nozzle exit up to z_{max} .

For simplicity, all the expansions share the same order N. Each i-th spherical harmonic multipolar expansion involves $L_{ind} = \sum_{m=0}^{N} 2m + 1$ independent sources. Hence, the total number of free parameters in the model is $a = N_{exp} L_{ind}$, namely the coefficients $A_{l,m}^{i}$, which are adjustable to tune the equivalent sources to reproduce the acoustic field produced by the actual sources. To define the values of the coefficients of the expansions $A_{l,m}^{i}$, some monitoring points where the acoustic field is known are defined. Those are subdivided into two sets: the first, Q, contains q points, whose acoustic measurements will be used to *train* the multipolar model; the second, S, contains s points, whose acoustic pressures are only used to *validate* the performance of the equivalent source model at different locations not used in its training. To retrieve the coefficients $A_{l,m}^{i}$ of the approximation in eq. (1), the difference between the reference acoustic field and the field produced by the multipolar expansions is minimized in a least square sense. Since the position of the equivalent sources is fixed, the problem can be conveniently formulated in matrix form as:

$$\mathrm{V}_Q \mathbf{x} = \mathbf{b}_Q$$

Materials Research Proceedings 69 (2026) 287-292 https://doi.org/10.21741/9781644904251-51

Where $\boldsymbol{x} \in \boldsymbol{C}^{\boldsymbol{a}}$ collects the $\boldsymbol{N}_{\text{exp}}\boldsymbol{L}_{\text{ind}}$ coefficients $\boldsymbol{A}_{\boldsymbol{l},\boldsymbol{m}}^{\boldsymbol{i}}$; the vector $\boldsymbol{b}_{\boldsymbol{Q}} \in \boldsymbol{C}^{\boldsymbol{q}}$ collects the values of the reference field at all the monitoring points Q; and the complex-valued terms resulting from the evaluation of each spherical harmonics term $\boldsymbol{Y}_{\boldsymbol{l},\boldsymbol{m}}(\boldsymbol{\phi}_{\boldsymbol{i}},\boldsymbol{\theta}_{\boldsymbol{i}})\boldsymbol{h}_{\boldsymbol{l}}^{(\boldsymbol{2})}(\boldsymbol{\kappa r}_{\boldsymbol{i}})$ at the Q monitoring points populate the matrix $\boldsymbol{V}_{\boldsymbol{Q}} \in \boldsymbol{C}^{\boldsymbol{q}\times\boldsymbol{a}}$. The number of monitoring points in the training set limits the maximum order of the multipolar expansion as the system is solved using a Moore-Penrose pseudo-inverse (the condition $\boldsymbol{q} > \boldsymbol{a}\left(\boldsymbol{N},\boldsymbol{N}_{\text{exp}}\right)$ - ideally $\boldsymbol{q} \gg \boldsymbol{a}(\boldsymbol{N},\boldsymbol{N}_{\text{ind}})$ - has to be satisfied), namely:

$$\mathbf{x} = \mathbf{V}_{\boldsymbol{Q}}^{\dagger}\mathbf{b}_{\boldsymbol{Q}} = \left(\mathbf{V}_{\boldsymbol{Q}}^{*}\mathbf{V}_{\boldsymbol{Q}}\right)^{-\mathbf{1}}\mathbf{V}_{\boldsymbol{Q}}^{*}\mathbf{b}_{\boldsymbol{Q}}$$

where the superscript $*$ indicates the complex conjugate operation. Then, the acoustic pressure at the validation points $\widehat{\boldsymbol{b}}_{\boldsymbol{S}}$ is obtained by:

$$\widehat{\boldsymbol{b}}_{\boldsymbol{S}} = \mathbf{V}_{\boldsymbol{S}}\,\mathbf{x}$$

where $\boldsymbol{V}_{\boldsymbol{S}} \in \boldsymbol{C}^{\boldsymbol{s}\times\boldsymbol{a}}$ is the matrix collecting the evaluation of each spherical harmonics term $\boldsymbol{Y}_{\boldsymbol{l},\boldsymbol{m}}(\boldsymbol{\phi}_{\boldsymbol{i}},\boldsymbol{\theta}_{\boldsymbol{i}})\boldsymbol{h}_{\boldsymbol{l}}^{(\boldsymbol{2})}(\boldsymbol{\kappa r}_{\boldsymbol{i}})$ at the S validation points.

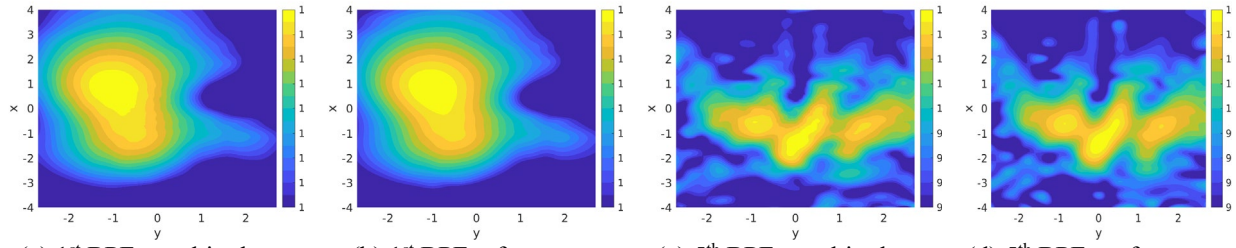
Results on landing helicopter rotor model

In this test case, a single multipolar expansion ($\boldsymbol{N}_{\boldsymbol{exp}} = \mathbf{1}$) is used to model the noise footprint of the scaled-down baseline version (BL) of the hingeless four-bladed main rotor of the Bo-105 helicopter. The rotor, investigated in the HART II test campaign [7, 8, 9], has a radius of R = 2 m, a blade chord length of c = 0.121 m, a linear twist of $\boldsymbol{\theta}_{\boldsymbol{tw}} = -\mathbf{8}$ deg/R, and rotates at Ω = 109.12 rad/s. The rotor is also subjected to a free stream (advance ratio equal to 0.15, shaft angle of 5.3 deg) as in a descent flight.

The numerical data set for the identification of the multipolar expansion consists of the numerical results presented in [10].In particular, the complex-valued acoustic pressure on a carpet of virtual microphones placed under the rotor and the fuselage, at a distance of 2.215 m, is extracted for the first five multiples of the blade passing frequency (BPF) and used as reference pressure fields for the multipolar approximation. A convergence analysis has allowed us to consider N = 20 as the converged value. The good quality of the prediction obtained with N = 20 is demonstrated by the comparison between the reference and the reconstructed field shown in Fig. 1. In particular, the reconstructed acoustic fields using N = 20 are almost indistinguishable from the reference data for the first two BPF multiples, and negligible differences are present at higher frequencies (comparisons are shown in the Supplementary Information up to the fifth BPF multiple). In general, higher BPFs show multiple peaks in the directivity pattern, progressively narrower in space. Reproducing such pressure fields requires higher orders of the multipolar expansion to be used.

In this case, the model benefits from training points at various distances from the multipolar source, as they lie on a planar surface. This distribution helps the multipoles in obtaining a good approximation of the radial propagation of noise. At the same time, however, the multipolar expansion does not have information about the whole directivity, but only on a spherical sector as defined by the planar array of virtual microphones. Hence, when interrogated on points outside the bounding box of the original data set, the model tries to extrapolate information with poor results. This limitation is well known for interpolative models and can be overcome using training points covering the entire spherical angle surrounding the sources of the expansion, which, however, were not available in this case.

Materials Research Proceedings 69 (2026) 287-292 https://doi.org/10.21741/9781644904251-51



(a) 1st BPF - multipolar (b) 1st BPF reference (c) 5th BPF - multipolar (d) 5th BPF - reference

Figure 1: comparison between reconstructed (fig. 1a, and 1c), and reference (fig. 1b, and 1d) sound pressure levels for the HART II test case for the first (1a and 1b) and fifth BPFs (1c and 1d), for $N = 20$.

Results on jet noise

Large Eddy Simulations of round free jets at a Reynolds number $Re = 10^5$ and Mach number $M = 0.9$ have been used for the analysis reported in this paper. The jets originate from a short pipe nozzle at the inlet of which a boundary layer velocity profile is prescribed [11, 12, 13]. An in-house solver, based on the three-dimensional filtered compressible Navier–Stokes equations in cylindrical coordinates, has been used to perform the LES simulations. The LESs were carried out using grids containing an amount of points ranging between 250 million and 1 billion, with low-dissipation finite-difference schemes and relaxation filtering as a subgrid-scale dissipation model [11]. The LES are detailed at length in several references [14, 15, 13]. Data from a fixed nozzle-exit turbulence intensity $TI = 9\%$, and three thermal conditions were considered, corresponding to nozzle-exit temperatures of $T = T_a$, $T = 1.5\ T_a$, and $T = 2.25\ T_a$, with T_a being the ambient temperature, were used in this work. The dataset consists of pressure time series recorded over a domain extending in the streamwise direction from $x = 0$ to $x/D = 20$, and in the radial direction from $r/D = 0.5$ (nozzle centerline) to $r/D = 3$, where D denotes the jet exit diameter. After transforming the signals in the frequency domain, four values of Strouhal number ($Sr = 0.25$, 0.5, 0.75, 1) are considered. The number of multipolar sources is fixed to $N_{exp} = 6$ equally distributed along the jet axis up to $z_{max} = 15D$. Each multipolar source included monopolar, dipolar, and quadrupolar terms only, $N = 2$. For each Sr, a ROM is built, using the absolute value of the axial pressure distribution at $r/D = 2$ and $r/D = 2.5$ as training data. The prediction of the resulting model is validated against axial pressure data at $r/D = 3$. The training set includes multiple axial lines at various azimuthal angles ϕ spaced by $\Delta\phi$ to give information about the axial symmetry of the jet in the training phase. The axial symmetry of the ROM prediction improves as $\Delta\phi$ decreases; however, reducing $\Delta\phi$ below 15 deg does not yield further improvements with the current settings of N_{exp}, N, and z_{max}. Despite using information at multiple azimuthal lines in the training, the model could not achieve perfect axial symmetry due to the truncated nature of the multipolar expansion. Nevertheless, the difference for a fixed axial position along the azimuthal angular direction is very limited. Results are shown in Fig. 2: the ROM predictions are presented using a solid line for the mean azimuthal value and a shaded area representing a ±STD range. The prediction is good for the points outside the jet core. The points farther from the nozzle may fall inside the jet mixing region, where the noise cannot be approximated by a simple propagation, resulting in higher errors. This is particularly evident for the $r/D = 2$ case.

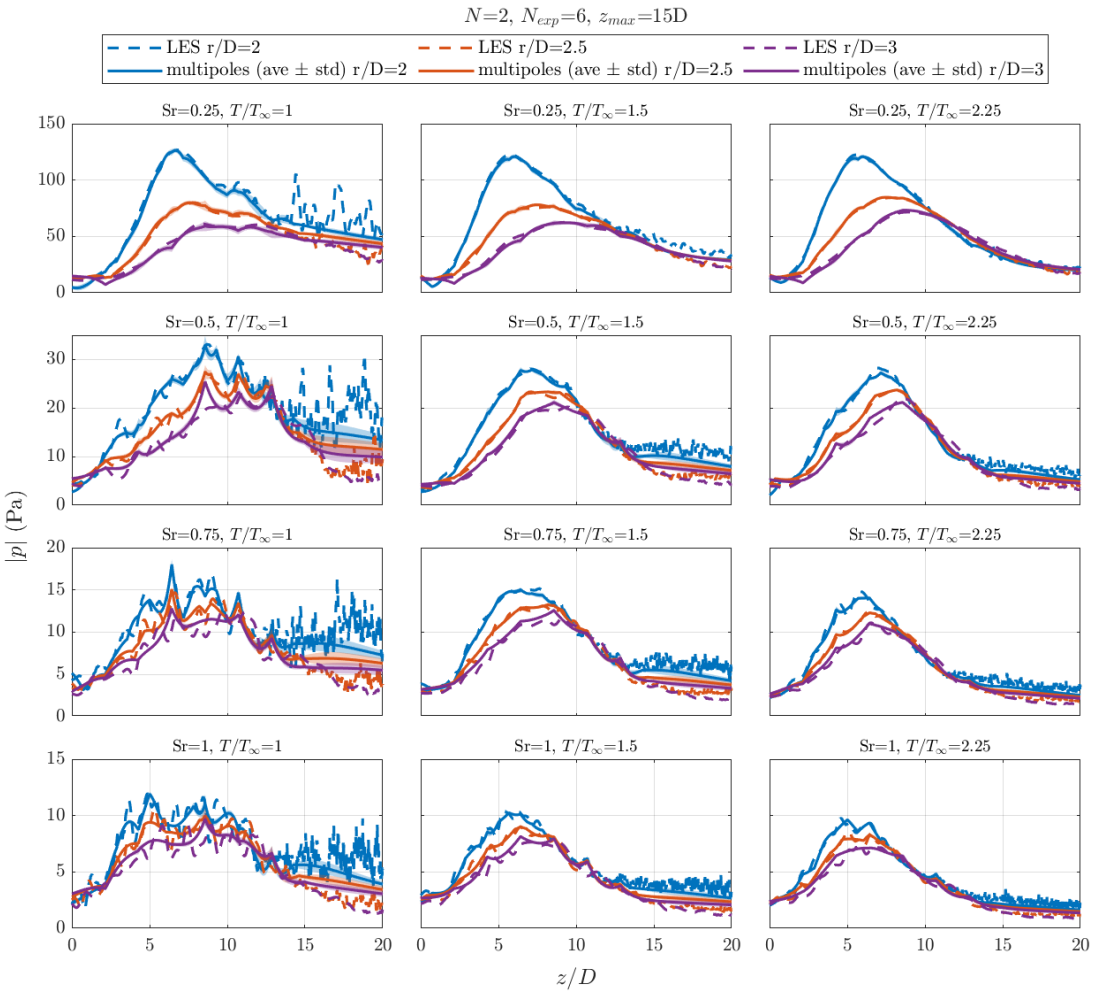


Figure 2: absolute value of pressure, comparison between LES and multipolar reconstruction, $N = 2$, $N_{exp}=6$, $z_{max} = 15D$.

Final remarks

This work investigated the applicability and performance of multipolar expansion techniques for the reduced-order modeling of complex aeroacoustic fields. Two representative configurations were analyzed: the scaled-down baseline version of the Bo-105 hingeless four-bladed main rotor tested in the HART II experimental campaign, and subsonic turbulent round jets computed via high-fidelity Large Eddy Simulations (LES). For the Bo-105 rotor, a single multipolar expansion accurately reproduced the reference acoustic fields, showing excellent agreement for the first two BPF harmonics and capturing key directivity features at higher harmonics. For subsonic jets, six multipolar sources were used to mimic the axially distributed characteristics of jet noise sources, with monopole, dipole, and quadrupole terms capturing key acoustic features across different thermal conditions

References

[1] A. Filippone, "Aircraft noise prediction," Progress in Aerospace Sciences, vol. 68, pp. 27-63, 2014 https://doi.org/10.1016/j.paerosci.2014.02.001

[2] M. Gennaretti, G. Bernardini, J. Serafini, A. Anobile, and S. Hartjes, "Helicopter noise footprint prediction in unsteady maneuvers," International Journal of Aeroacoustics, vol. 16, no. 3, pp. 165-180, 2017. https://doi.org/10.1177/1475472X17709927

[3] B. Aflalo, D. Ferrari, et al., "Metamodeling techniques applied to aircraft noise prediction," Blucher Mechanical Engineering Proceedings, vol. 1, no. 1, pp. 5018-5033, 2012. https://doi.org/10.5151/meceng-wccm2012-20194

[4] C. Poggi, M. Rossetti, J. Serafini, G. Bernardini, M. Gennaretti, and U. Iemma, "Neural network meta-modelling for an efficient prediction of propeller array acoustic signature," Aerospace Science and Technology, vol. 130, p. 107910, 2022. https://doi.org/10.1016/j.ast.2022.107910

[5] G. Palma, L. Burghignoli, C. Poggi, and J. Serafini, "Multipolar expansion for aircraft noise equivalent sources," Aerospace Science and Technology, vol. 155, 2024. https://doi.org/10.1016/j.ast.2024.109629

[6] E. G. Williams, "Chapter 6 - spherical waves," in Fourier Acoustics (E. G. Williams, ed.), pp. 183-234, London: Academic Press, 1999. https://doi.org/10.1016/B978-012753960-7/50006-1

[7] B. G. van der Wall, "2nd hhc aeroacoustic rotor test (hart ii)-part i: Test documentation," tech. rep., US Army AFDD, NASA Langley, DLR, ONERA and DNW, 2003.

[8] B. G. van der Wall, C. L. Burley, Y. Yu, H. Richard, K. Pengel, and P. Beaumier, "The hart ii test - measurement of helicopter rotor wakes," Aerospace Science and Technology, vol. 8, no. 4, p. 273-284, 2004. https://doi.org/10.1016/j.ast.2004.01.001

[9] B. G. van der Wall and C. L. Burley, "2nd hhc aeroacoustic rotor test (hart ii)-part ii: representative results," tech. rep., US Army AFDD, NASA Langley, DLR, ONERA and DNW, 2005.

[10] M. Gennaretti, G. Bernardini, J. Serafini, and G. Romani, "Rotorcraft comprehensive code assessment for blade-vortex interaction conditions," Aerospace Science and Technology, vol. 80, pp. 232-246, 2018. https://doi.org/10.1016/j.ast.2018.07.013

[11] C. Bogey, O. Marsden, and C. Bailly, "Large-eddy simulation of the flow and acoustic fields of a reynolds number 105 subsonic jet with tripped exit boundary layers," Physics of Fluids, vol. 23, p. 035104, 2011. https://doi.org/10.1063/1.3555634

[12] C. Bogey, O. Marsden, and C. Bailly, "Influence of initial turbulence level on the flow and sound fields of a subsonic jet at a diameter-based reynolds number of 105," Journal of Fluid Mechanics, vol. 701, p. 352-385, 2012. https://doi.org/10.1017/jfm.2012.162

[13] S. Meloni, R. Camussi, and C. Bogey, "An analysis of the effect of the jet initial conditions on the wavelet separated near-field acoustic pressure," Theoretical and Computational Fluid Dynamics, vol. 39, no. 1, p. 5, 2025. https://doi.org/10.1007/s00162-024-00727-9

[14] G. Palma, S. Meloni, R. Camussi, U. Iemma, and C. Bogey, "Data-driven multiobjective optimization of wave-packets for near-field subsonic jet noise," AIAA Journal, vol. 61, no. 5, pp. 2179-2188, 2023. https://doi.org/10.2514/1.J062261

[15] G. Palma, S. Meloni, R. Camussi, U. Iemma, and C. Bogey, "Subsonic jet noise prediction in near and far field with optimized wave-packet approach," AIAA Journal, vol. 62, no. 11, pp. 4144-4152, 2024. https://doi.org/10.2514/1.J064232

Materials Research Proceedings 69 (2026) 293-297 https://doi.org/10.21741/9781644904251-52

Labyrinthine Acoustic Metamaterials for grazing Sound Waves

Giuseppe PETRONE[1,a *], Alessandro CASABURO[1,b] and Giuseppe CATAPANE[1,c]

[1]Laboratory for Promoting experiences in Aeronautical STructures and Acoustics, Department of Industrial Engineering, Universita degli Studi di Napoli Federico II, Via Claudio 21, Napoli, 80125, Italy

[a]giuseppe.petrone@unina.it, [b]alessandro.casaburo@unina.it, [c]giuseppe.catapane@unina.it

Keywords: Acoustic Metamaterial, Labyrinth, Transmission Loss, Grazing Waves

Abstract. This study presents a novel acoustic liner configuration developed using additive manufacturing, which enables precise geometric control. The proposed design modifies traditional honeycomb sandwich structures with microperforated plates (MPPs) by integrating a labyrinth channel inside the honeycomb core. MPPs provide both structural integrity and acoustic functionality by serving as inlets to the labyrinth, inducing thermal and viscous dissipation. A numerical model was developed in COMSOL Multiphysics using the Pressure Acoustics module, with MPPs modeled through dedicated boundary conditions and thermo-viscous effects applied to cavity walls. The predicted Transmission Loss results were validated experimentally using an impedance tube with grazing incidence. Numerical and experimental data showed good agreement, confirming the reliability of the model and demonstrating that the proposed liner achieves Noise Transmission Loss (NSTL) values exceeding 50 dB at the first resonance frequency. These promising results highlight the potential of this configuration for future aero-acoustic applications.

Introduction

The evolution of aircraft engines, characterized by large bypass ratios, will require advancements in liner designs to have an acceptable value of noise reduction, in a different frequency range and reduced space for which the current acoustic liner concept may be not sufficient [1] (Fig. 1). For this reason, novel configurations are object of research, such as variable depth liners [2], distributed face-sheets [3], slanted septum embedded [4, 5].

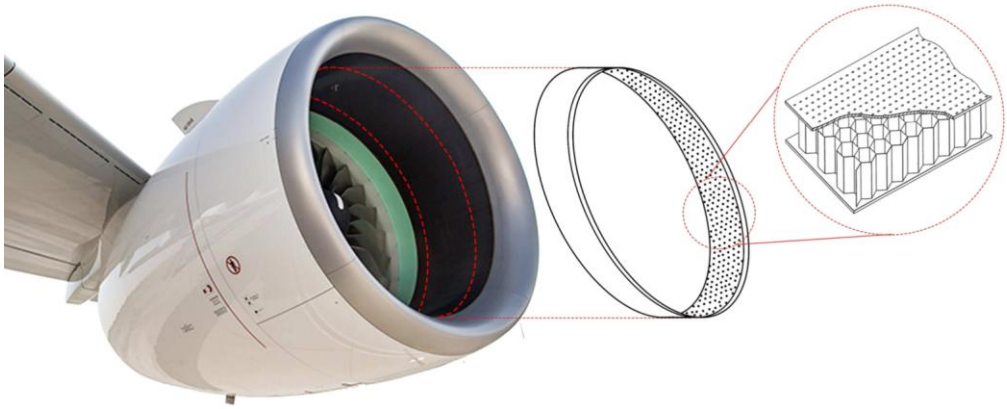


Figure 1 - Conventional liner [1]

To achieve good acoustic performances in a reduced space is a huge challenge, and the use of additive manufacturing technologies provides some flexibility in designing the final test article with specific characteristics. In this paper, a novel configuration of acoustic liner is proposed. The test article consists in a modification of the actual design of the conventional liners, consisting in

Content from this work may be used under the terms of the Creative Commons Attribution 3.0 license. Any further distribution of this work must maintain attribution to the author(s) and the title of the work, journal citation and DOI. Published under license by Materials Research Forum LLC.

Materials Research Proceedings 69 (2026) 293-297 https://doi.org/10.21741/9781644904251-52

sandwich structures with a honeycomb core embedded in microperforated plates (MPPs). In particular, a labyrinth has been drawn and built in the honeycomb removing a small part of a cell wall from the internal honeycomb (Fig. 2), which mitigates tonal noise [6]. MPPs are fundamental to close the test article for structural integrity, and the holes work as inlet for the labyrinth, introducing at same time thermal and viscous dissipation.

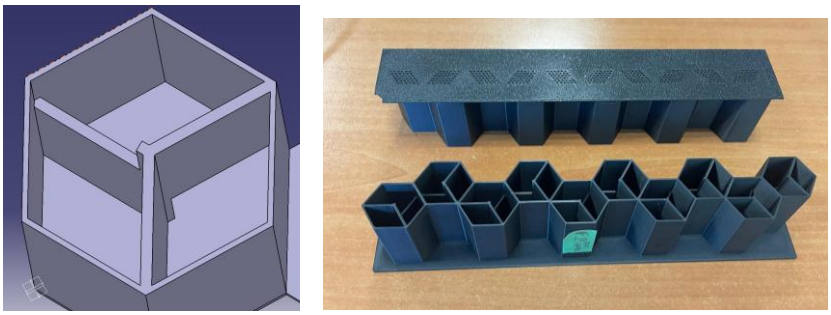


Figure 2 - acoustic metamaterial for liners

A numerical model has been first developed using COMSOL Multiphysics software (Fig. 3). Both the impedance tube and honeycomb cavities have modelled the Pressure Acoustics module in which the MPP is modelled with MPP boundary condition, while the Thermo-viscous Boundary Layer Impedance boundary condition is applied to the remaining walls. The results, in terms of Transmission Loss, carried out from numerical model (Fig. 4a) have been compared and validated with the ones coming from experimental tests in an impedance tube with grazing incidence holder (Fig. 4b).

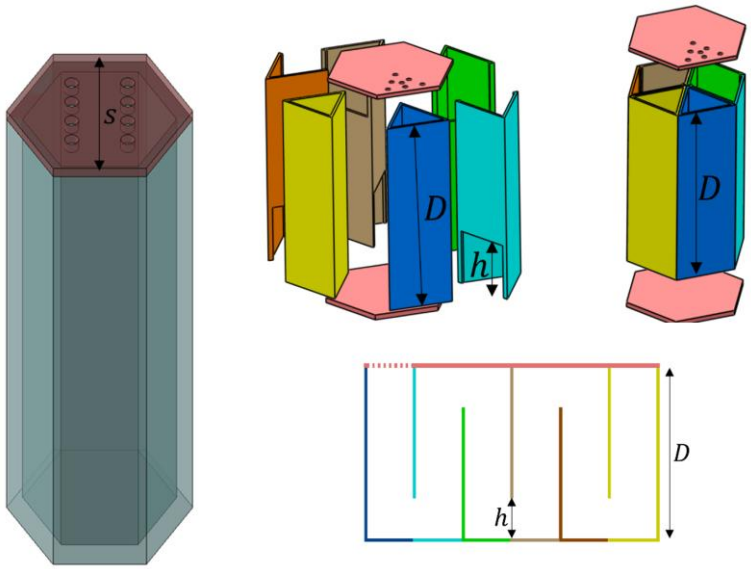


Figure 3 - numerical model of the unit cell of the proposed liner

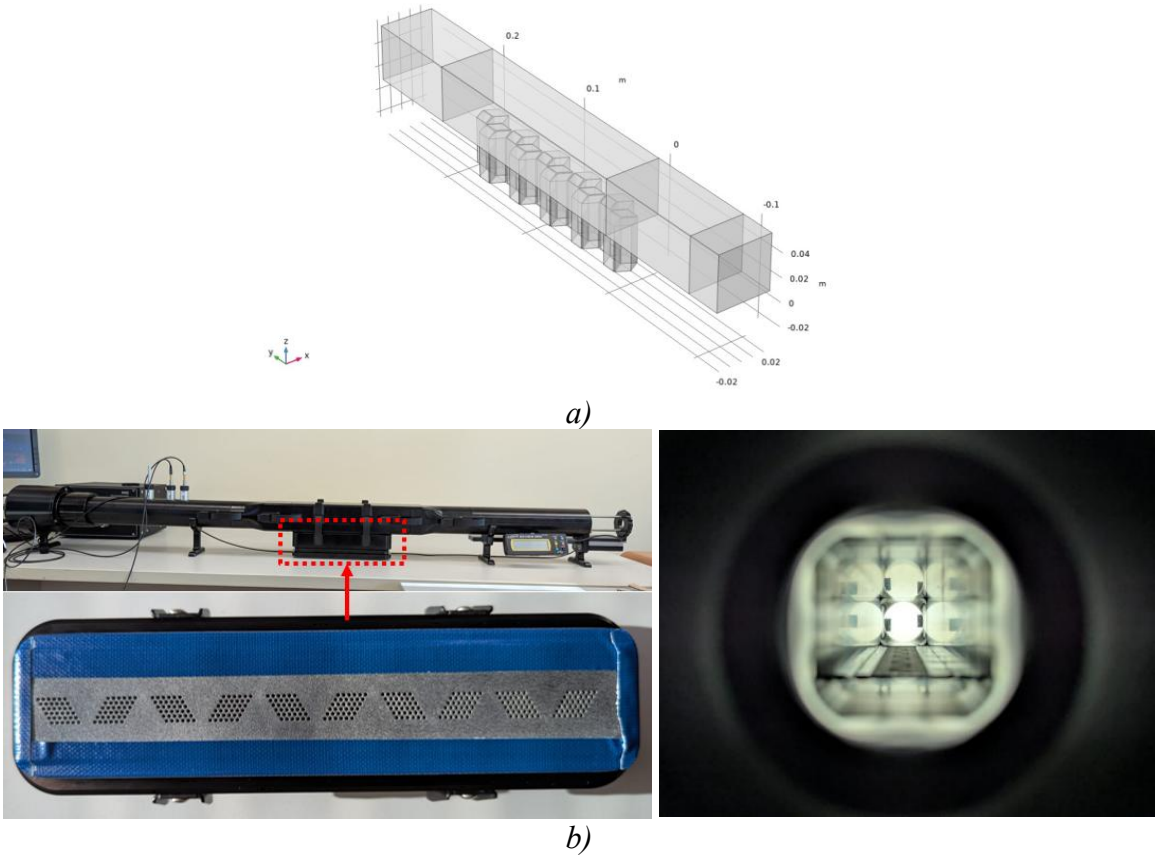


Figure 4 - Impedance tube with grazing incidence holder: a) numerical model and b) experimental tool

A comparison of numerical and experimental results carried out from the standard liner is reported in Fig. 5 and it can be noted that there is a good overlap of the two curves, which means that the numerical model.

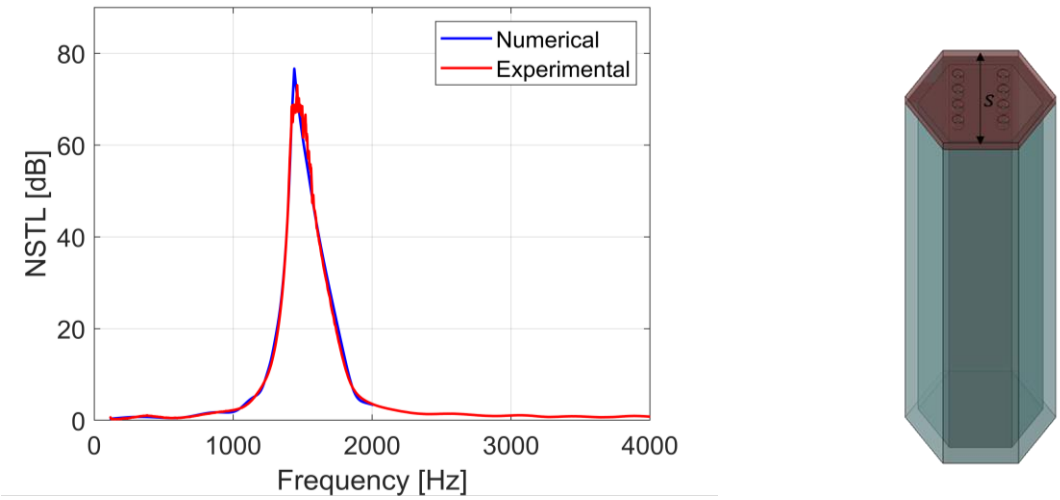


Figure 5 - Numerical and experimental comparison of NSTL of a standard liner

In Fig. 6. the same comparison for the proposed liner is reported and once it can be highlighted a good overlap of the curves, the numerical and experimental ones, especially for the first peak

followed by a small shift for the other two peaks at higher frequencies probably due to manufacturing defects. Moreover, the proposed liner show high acoustic performances with more peaks respect the standard ones, according to the effect of the labyrinth, and with values of NSTL high, more than 50 dB at the first frequency.

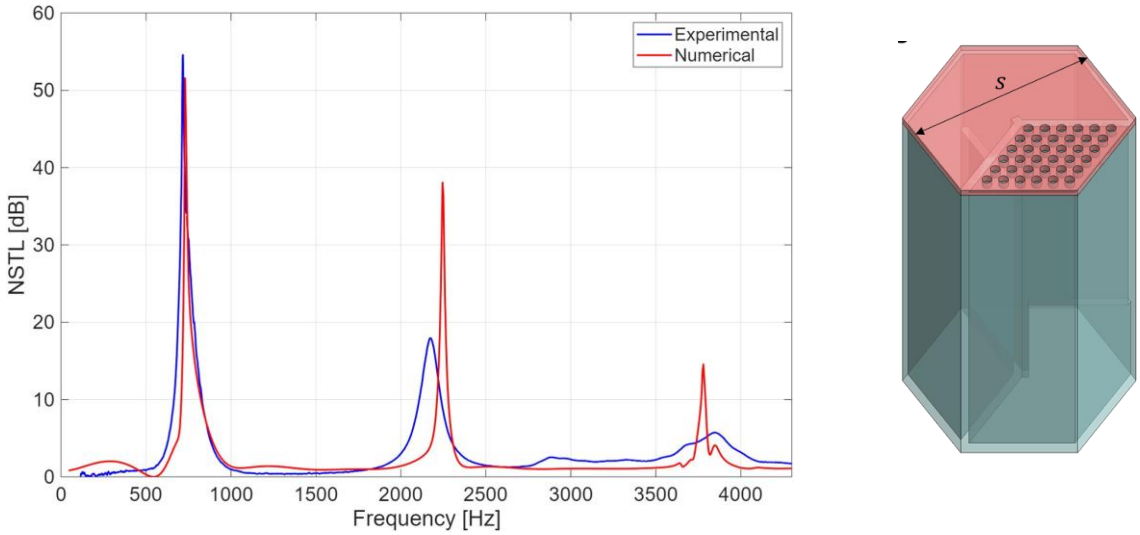


Figure 6 - Numerical and experimental comparison of NSTL of the proposed acoustic liners

Conclusion

This work introduced a novel acoustic liner configuration based on labyrinthine metamaterials, manufactured through additive techniques that enable high geometric precision and design flexibility. By integrating a labyrinth channel within a conventional honeycomb core closed by microperforated plates (MPPs), the proposed concept enhances acoustic absorption through combined thermal and viscous dissipation mechanisms.

Numerical simulations performed with COMSOL Multiphysics showed good agreement with experimental results obtained from grazing incidence impedance tube tests, confirming the reliability of the developed model. The proposed liner demonstrated superior acoustic performance compared to the standard configuration, achieving Noise Transmission Loss (NSTL) values above 50 dB at the first resonance frequency and exhibiting multiple attenuation peaks due to the labyrinth structure.

These preliminary findings highlight the effectiveness and potential of the proposed labyrinthine liner concept for advanced aero-acoustic applications. Future work will focus on further optimization of the geometry, detailed parametric analyses, and experimental validation under more representative operating conditions to support integration into real aeronautical systems.

Acknowledgments

The authors acknowledge the support of the Italian Ministry of Education, University and Research (MIUR) through the project DAMA, funded under the scheme PRIN-2022 – grant agreement No. 20229PLCAC.

References

[1] DL. Sutliff, DM Nark, MG Jones, Multi-degree-of-freedom liner development: Concept to flight test, International Journal of Aeroacoustics, 20, 5-7 (2021), 792-825. https://doi:10.1177/1475472X211023860

[2] M.B. Galles, M.G. Jones and D.M. Nark, An Initial Assessment of Variable Depth Liner Optimization for Ducted Proprotor Applications, AIAA 2022-2821. 28th AIAA/CEAS Aeroacoustics 2022 Conference (2022), https://doi.org/10.2514/6.2022-2821.

[3] M.C. Brown and M.G. Jones, Evaluation of Variable Facesheet Liner Configurations for Broadband Noise Reduction, AIAA 2020-2616, AIAA AVIATION 2020 FORUM, (2020), https://doi.org/10.2514/6.2020-2616

[4] S. Palani, P. Murray, A. McAlpine, K. Knepper and C. Richter, Experimental and numerical assessment of novel acoustic liners for aero-engine applications, In 28th AIAA/CEAS Aeroacoustics 2022 Conference. American Institute of Aeronautics and Astronautics (2022), https://doi.org/10.2514/6.2022-2900

[5] S. Palani, P. Murray, A. McAlpine, D. Sasaki and C. Richter, Slanted septum and multiple folded cavity liners for broadband sound absorption, International Journal of Aeroacoustics, 20, 5-7 (2021), pp. 633–661, https://doi.org/10.1177/1475472X211023835

[6] G. Catapane, G. Petrone, O. Robin, K. Verdiere, Coiled quarter wavelength resonators for low-frequency sound absorption under plane wave and diffuse acoustic field excitations, Applied Acoustics, 209 (2023), 109402, https://doi.org/10.1016/j.apacoust.2023.109402

Materials Research Proceedings 69 (2026) 298-302 https://doi.org/10.21741/9781644904251-53

Wavenumber-based Reconstruction Methof for the Vibroacoustic Response of Plates under Distorted Similitude

Alessandro CASABURO[1,a *], Giuseppe PETRONE[1,b], Francesco FRANCO[1,c], and Sergio DE ROSA[1,d]

[1]Pasta-Lab, Department of Industrial Engineering (DII), University of Naples Federico II, Via Claudio 21, 80125 Naples, Italy

[a]alessandro.casaburo@unina.it, [b]giuseppe.petrone@unina.it, [c]francof@unina.it, [d]sergio.derosa@unina.it

Keywords: Wavenumber Space, Vibroacoustics, Isotropic Plates, Distorted Similitude

Abstract. Similitude methods are an important tool to address typical obstacles of structural testing, such as impractically large dimensions relative to laboratory space, as well as excessive cost and time. However, methods in the literature typically require the fulfillment of similitude conditions to achieve accurate, reliable reconstructions of full-scale responses. The approach proposed here overcomes this limitation by exploiting the dispersion relation to link the frequency scale factor to the wavenumber scale factor, the latter estimated from the model's mode shapes via a wavenumber transform, finally obtaining local scale factors to apply to each eigensolution. Numerical validation on two distorted models under simply supported boundary condition shows accurate reconstructions, supporting the robustness of the method.

Introduction

Similitude theory is widely used across many engineering branches, as testing scaled models, rather than full-scale prototypes, leads to cost reduction, lower complexity, and time savings [1], with significant impact not only on experimental testing, but also on numerical simulations [2]. In fact, similitude methods, rooted in this theory, enable the reconstruction of the structural response (whether static, dynamic, or due to impacts, etc.) of the prototype from that of the scaled model. Over the past seventy years, several methods have been proposed, such as dimensional analysis (DA) based on Buckingham's Π Theorem [3], similitude theory applied to governing equations (STAGE) [4], asymptotically scaled modal analysis (ASMA) [5], and sensitivity analysis (SA) [6].

The majority of these methods rely on the definition of scale factors, scaling laws and similitude conditions, the latter being mandatory requirements to fulfil to achieve the complete similitude condition. In this case, the scale factors are invariant terms enabling the mapping from the model to the prototype's behaviour through univocal scaling laws. However, when even one similitude condition is violated, the scaling laws are no more unique, with consequent reduction of the predictive capabilities of any similitude method.

When attempting the reconstruction of the structural response in frequency domain, the similitude methods proposed up to now fail to address the issue of distorted similitudes as the invariance of the scale factors cannot account for the changes of the modal sequence. The shift of the modes becomes more pronounced with larger geometrical distortions. This issue is of particular relevance, as distorted models may be the only solution to meet manufacturing limits and errors, as well as limited size of testing facilities [1].

The method herein proposed aims at reconstructing the dynamic response of isotropic thin plates under distorted similitude. The method exploits the spatial vibration pattern of mode shapes and their transform to the wavenumber space to determine ad hoc scaling factors for each natural frequency. Therefore, the scale factors of the natural frequencies and, consequently, of the frequency response are no more invariants, rather they act locally on each eigensolution.

Content from this work may be used under the terms of the Creative Commons Attribution 3.0 license. Any further distribution of this work must maintain attribution to the author(s) and the title of the work, journal citation and DOI. Published under license by Materials Research Forum LLC.

Materials Research Proceedings 69 (2026) 298-302 https://doi.org/10.21741/9781644904251-53

Moreover, the derivation of the scaling laws relies only on very general expressions, such as the dispersion relation and the equation of the bending waves in thin plates, that do not involve dependencies on the boundary conditions, and do not lead to the imposition of similitude conditions. The entire procedure can be carried out only knowing geometrical and material properties of the prototype, and it requires only the response characteristics of the scaled model.

Derivation of the scaling laws

The convention on the scale factors r used in this work is the following:

$$r_X = \frac{X_p}{X_m} \tag{1}$$

where X denotes a generic physical variable, the subscript p refers to the prototype, and m to the model.

The equation of the bending waves speed c_b in thin isotropic plates [7] can be written in terms of scale factors as

$$r_{c_b} = \left(\frac{r_D}{r_\rho r_h}\right)^{1/4} r_\omega^{1/2} \tag{2}$$

where D is the bending stiffness, ρ is the mass per unit volume, h is the plate thickness, and ω is the angular frequency. Applying the same procedure on the dispersion relation leads to

$$r_{c_b} = r_c r_k = \left(\frac{r_D}{r_\rho r_h}\right)^{1/4} r_\omega^{1/2} r_k = \left(\frac{r_D}{r_\rho r_h}\right)^{1/2} r_k^2 \tag{3}$$

where k is the wavenumber.

Eq. 3 allows to estimate the frequency scale factor once the wavenumber scale factor is known. When $k = k_{m,n}$, i.e., when the wavenumber is equal to the modal wavenumber, then Eq. 3 provides the scale factor of the natural frequency associated with the mode (m, n), provided the modal wavenumber scale factor is known for both prototype and model. While the model's modal wavenumbers are available from experiments or numerical simulations, typical operating conditions of similitude methods assume that only the prototype's geometry and material properties are known, with no information about its frequency response. This issue can be easily bypassed by noting that, for a plate with length a and width b, the wavevector components along the sides of the plate (assumed parallel to the x and y axes) scale as $k_x \propto 1/a$ and $k_y \propto 1/b$, so that

$$r_{k_x} = \frac{k_{x_p}}{k_{x_m}} = \frac{a_m}{a_p} = \frac{1}{r_a} \tag{4}$$

Consequently, the x component of the wavevector of the prototype can be estimated as

$$k_{x_p} = \frac{k_{x_m}}{r_a} \tag{5}$$

and the y component can be estimated in a similar fashion through the width scale factor r_b.

Once the natural frequency scale factor is known, the velocity frequency response can be reconstructed through the scaling law [8]

Materials Research Proceedings 69 (2026) 298-302 https://doi.org/10.21741/9781644904251-53

$$r_V = \frac{1}{r_M r_\omega} \tag{6}$$

where V is the velocity, and M is the mass of the plate, provided that the corresponding frequency range is remodulated with the right frequency scale factor.

Numerical validation of the proposed method

The procedure is numerically validated on three plates under simply supported boundary conditions. The plates are prototype (P), model with small distortion (SD), and model with large distortion (LD). The geometrical characteristics of the plate are summarized in Table 1.

Table 1 - Dimensions of the plates and corresponding scale factors.

Plate ID	a [m]	b [m]	h [m]	r_a	r_b	r_h	r_a/r_b
P	0.658	0.478	0.0025	-	-	-	-
SD	0.616	0.382	0.002	0.94	1.25	1.25	0.75
LD	0.585	0.273	0.002	1.125	1.751	1.25	0.64

To ensure a satisfactory estimation of the wavevector components, the same mesh with 66 × 48 elements is applied to all the plates. Numerical modal and frequency response analyses are performed, and the mode shapes of the plates are processed through 2D Fast Fourier Transform with padding factor 100 to estimate the spectrum in the wavenumber space. The modal wavevector component along the x direction is calculated as [9]

$$k_m = k_z - \frac{2\pi}{a} \tag{7}$$

with k_z indicating the wavenumber corresponding to the first zero of the spectrum along the $x > 0$ semiaxis. The wavenumber component k_n can be determined analogously introducing the width b.

Fig. 1 displays the results of the reconstruction of the natural frequencies of the model SD (top row) and LD (bottom row) within the 0-500 Hz frequency range. In particular, the figures on the left column compare three sets of frequencies: the prototype, the model, and the prototype reconstructed from the model. The figures on the right column show histograms of the error distribution. The percent MAE (Mean Absolute Error) is the chosen metric. The results indicate low reconstruction error, within the 0%-0.3% and 0%-0.5% ranges for the models SD and LD, respectively.

The reconstruction of the root mean square (RMS) velocity is shown in Fig. 2 for SD and LD models, respectively. Due the local nature of the scale factors, both the frequency range and the velocity amplitude must be remapped peak by peak. The overall accuracy of the reconstruction is very good, with slight discrepancies in amplitude due to sampling matters rather than shortcomings of the method.

Materials Research Proceedings 69 (2026) 298-302 https://doi.org/10.21741/9781644904251-53

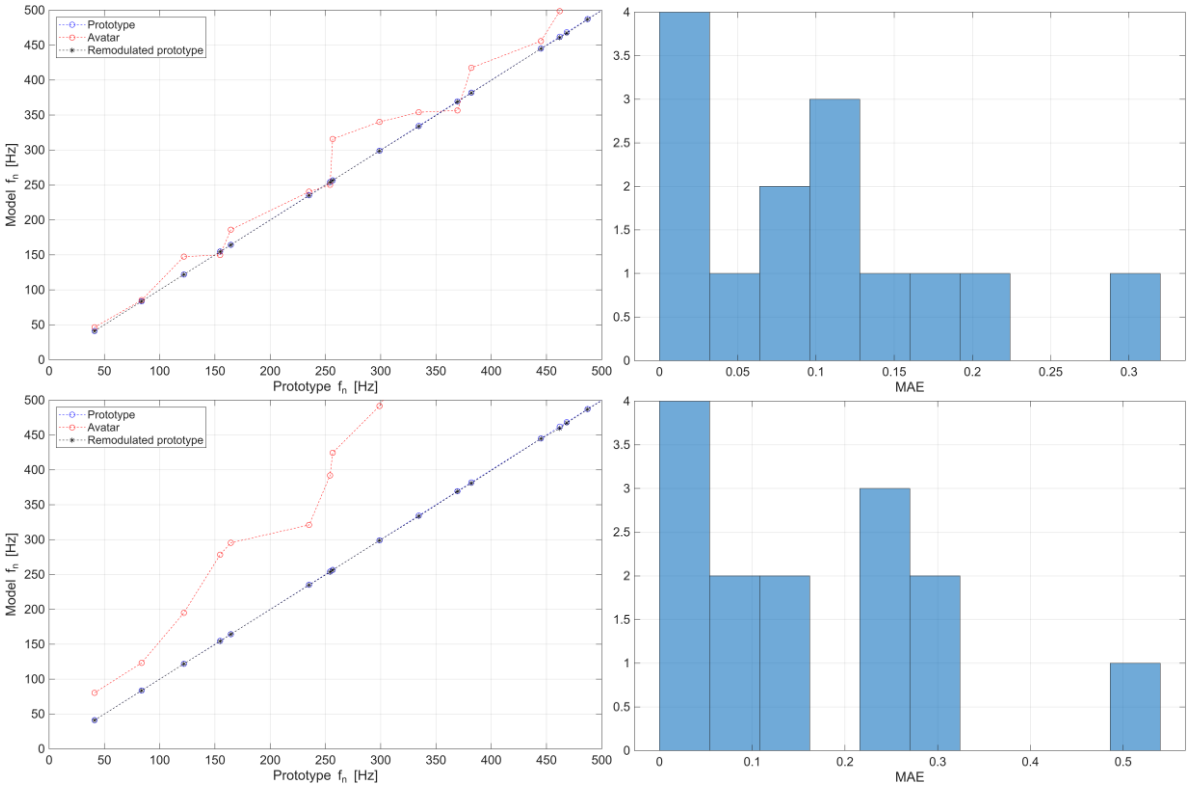


Figure 1 - Remodulation of natural frequencies and corresponding errors. Top-left: natural frequencies of P, SD, and remodulated P. Top-right: error histogram of the remodulated frequencies from SD. Bottom-left: natural frequencies of P, LD, and remodulated P. Bottom-right: error histogram of the remodulated frequencies from LD.

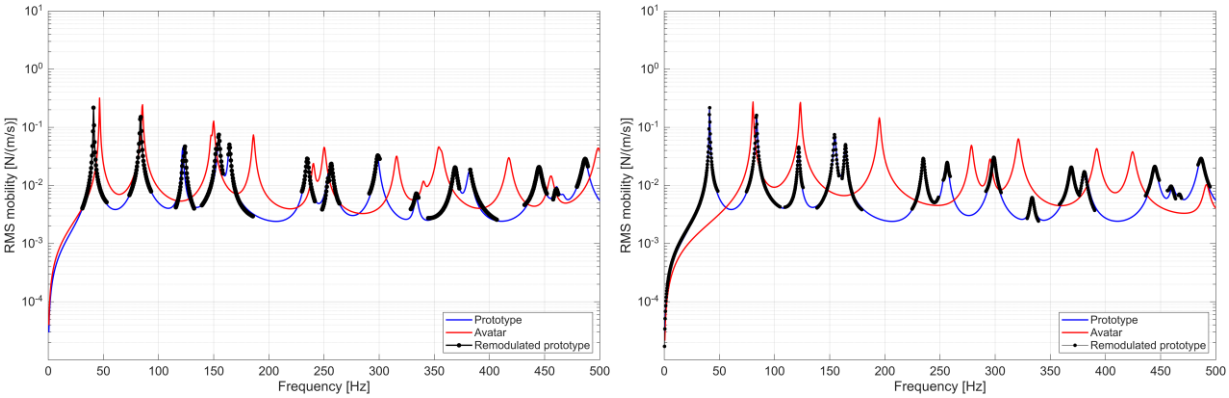


Figure 2 - Reconstruction of the RMS velocity. Left: SD model. Right: LD model.

Conclusions

This work proposes a wavenumber-based method to reconstruct the structural response of plates under distorted similitude. By applying a 2D spatial Fourier transform to the plates' mode shapes, the modal wavevector of the mode and its scale factor are estimated, then the scale factor of each natural frequency is obtained via dispersion relation. Numerical tests on two plates, exhibiting small and large distortions, yield accurate reconstructions, indicating that the method is both robust and reliable. The approach rests on general relationships (dispersion relation and bending-wave speed), avoiding boundary condition-dependent expressions. Finally, it requires only prototype scaling information (geometry and/or material properties), with no need for response data, which makes the method easy to implement and suitable in operating conditions.

References

[1] A. Casaburo, G. Petrone, F. Franco, S. De Rosa, A Review of Similitude Methods in Structural Engineering, Applied Mechanics Reviews 71(3) (2019), 030802, https://doi.org/10.1115/1.4043787

[2] S. De Rosa, F. Franco, A Scaling Procedure for the Response of an Isolated System with High Modal Overlap Factor, Mechanical Systems and Signal Processing 22(7): 1549-1565 (2008), https://doi.org/10.1016/j.ymssp.2008.01.007

[3] E. Buckingham, On Physically Similar Systems; Illustrations of the Use of Dimensional Analysis, Physical Review 4(4):345-376 (1914), https://doi.org/10.1103/PhysRev.4.345

[4] S. J. Kline, Similitude and Approximation Theory, McGraw-Hill, New York, 1965.

[5] S. De Rosa, F. Franco, F. Ricci, F. Marulo, First Assessment of the Scaling Procedure for the Evaluation of the Damped Structural Response, Journal of Sound and Vibration 204(3): 540-548 (1997), https://doi.org/10.1006/jsvi.1996.0910

[6] C. Adams, J. Bös, E. M. Slomski, T. Melz, Scaling Laws Obtained From a Sensitivity Analysis and Applied to Thin Vibrating Structures, Mechanical Systems and Signal Processing 110: 590-610 (2018), https://doi.org/10.1016/j.ymssp.2018.03.0325

[7] L. Cremer, M. Heckl, B. A. T. Petersson, Structure-Borne Sound. Structural Vibrations and Sound Radiation at Audio Frequencies. Third edition, Springer-Verlag Berlin, Heidelberg, 2005, https://doi.org/10.1007/b137728

[8] S. De Rosa, F. Franco, V. Meruane, Similitudes for Structural Response of Flexural Plates", Proceedings of the Institution of Mechanical Engineers, Part C: Journal of Mechanical Engineering Science 230(3): 174-188 (2015), https://doi.org/10.1177/095440621557243

[9] M. R. Shepherd, S. A. Hambric, Comment on plate modal wavenumber transforms in Sound and Structural Vibration [Academic Press (1987, 2007)] (L), Journal of Sound and Vibration 132(4): 2155-2157 (2012), https://doi.org/10.1121/1.4747012

Materials Research Proceedings 69 (2026) 303-307 https://doi.org/10.21741/9781644904251-54

Effects of Pre-Stressed Conditions on the Dynamic and Acoustic Behavior of Composite Sandwich Panels

Piero CHIAIA[1,a *], Matteo FILIPPI[1,a], Alfonso PAGANI[1,a] and Erasmo CARRERA[1,a]

[1]Department of Mechanical and Aerospace Engineering, Polytechnic of Turin, Corso Duca degli Abruzzi 24, 10129 Torino, Italy

[a]piero.chiaia@polito.it, [b]matteo.filippi@polito.it, [c]alfonso.pagani@polito.it, [d]erasmo.carrera@polito.it

Keywords: Sandwich Panel, Higher-Order Models, Dynamic Analysis, Vibroacoustic Analysis

Abstract. Lightweight sandwich panels are widely used in aeronautical engineering for their high specific strength, stiffness, and multifunctional performance. Their applications have expanded from interior components to secondary and even primary load-bearing structures, as they offer excellent acoustic insulation and cabin noise and vibration reduction. Recent research focuses on enhancing acoustic performance through modified core materials, geometries, or absorptive layers. The present work is devoted to the development of high-fidelity multilayered plate models within the Carrera Unified Formulation (CUF) methodology, including the description of the physical nonlinearities of soft cores using a hyperelastic constitutive law. Within this framework, the linearized modal and frequency response analyses of lightweight sandwich structures with soft cores are proposed, examining the influence of prestress on natural frequencies, transmission ratios, and overall dynamical properties.

Introduction

Lightweight sandwich panels have been increasingly adopted in aeronautical engineering due to their excellent specific strength and stiffness, as well as their potential for multi-functional performance [1]. Sandwich panels in aircraft are also typically employed for their notable acoustic performance, providing better sound and vibration insulation, as well as noise isolation and absorption [2]. The enhanced acoustic properties expressed by the core (honeycomb, foam, acoustic liners, etc.) and face sheets are typically measured by metrics like sound transmission loss (STL), thus, several solutions and designs have been proposed to enhance the performance of such structures in various applications.

Due to the complexity of the involved structures, numerical simulations based on the Finite Element Method have emerged as a common approach, as they provide a flexible and efficient tool for the complex dynamic characterization of such structures (vibrations, frequency response) and design investigations [3], effectively including material anisotropy, boundary conditions, viscoelasticity, and frequency-dependent core behavior [4,5]. To simulate these features, high-fidelity models have been proposed within the well-established Carrera Unified Formulation (CUF) framework, where 2D plate models with three-dimensional capabilities for the dynamic analysis of multilayered sandwich structures have been shown to be effective [6,7]. These high-fidelity FE models, based on higher-order kinematics and structural theory, provide reliable results for static, modal, and dynamic behavior, as shown in many works [8,9].

In addition, the prestress condition in sandwich structures plays a critical role in enhancing acoustic isolation; it can affect the natural frequencies, mode shapes, and dynamical properties of the panel, thereby improving the acoustic performance and sound transmission loss (STL) of the structure. These features can also be used as tuning parameters to tailor acoustic performance,

Content from this work may be used under the terms of the Creative Commons Attribution 3.0 license. Any further distribution of this work must maintain attribution to the author(s) and the title of the work, journal citation and DOI. Published under license by Materials Research Forum LLC.

Materials Research Proceedings 69 (2026) 303-307 https://doi.org/10.21741/9781644904251-54

modify the structure's damping characteristics, and reduce wave transmission. Moreover, prestress can induce beneficial geometric stiffening, which limits large-amplitude vibrations and enhances structural integrity or creates frequency band gaps.

Higher-order structural theories

The Unified Formulation for development of higher-order plate theories has been already established in the literature, and here extended to the analysis of multilayered sandwich plates in pre-stressed conditions. The linearized frequency response analysis is exploited in a numerical framework adopting higher-order multilayered plate (2D) models, defined under the CUF formalism: :

$$\boldsymbol{u}(x,y,z) = F_\tau(z)\boldsymbol{u}_\tau(x,y) = F_\tau(z)N_i(x,y)\boldsymbol{u}_{\tau i} \quad \tau = 1,\dots,\mathrm{M}, \quad i = 1,\dots,\mathrm{N_n} \tag{8}$$

where M is the related to the order of the structural theory adopted, $\boldsymbol{F_\tau(z)}$ is the set of expansion functions, representing the theory of structure approximation, $\boldsymbol{N_i(x,y)}$ is the set of 2D shape functions of the discrete $\mathrm{N_n}$ finite nodes along the mid-surface, and finally $\mathbf{u_{\tau i}}$ is the vector of generalized displacement component.. In the present work, Lagrange Expansion (LE) class are considered, starting from the set of Lagrange's polynomials [6].

Governing equations

The equilibrium equations for the static and linearized frequency response analysis are carried out by means of the Principle of Virtual Displacements (PVD), written as:

$$\delta\mathcal{L}_{ine} + \delta\mathcal{L}_{int} = \delta\mathcal{L}_{ext} \tag{1}$$

where $\boldsymbol{\delta\mathcal{L}_{ine}}$ is the virtual variation of the work done by inertial forces, $\boldsymbol{\delta\mathcal{L}_{int}}$ and $\boldsymbol{\delta\mathcal{L}_{ext}}$ represents instead the virtual variation of the internal strain energy and work done by the external forces, respectively. Adopting the same indices notation introduced for the displacement field also for the Green-Lagrange strain tensor and the virtual quantities, one can derive the FN (Fundamental Nuclei) of the internal and external forces vector and mass matrix, obtaining the matrix form of the governing equation.

$$\delta\boldsymbol{u}_{sj}: \ \boldsymbol{M}^{\tau sij}\ddot{\boldsymbol{u}}_{\tau i} + \boldsymbol{F}_{int}^{sj} = \boldsymbol{F}_{ext}^{sj} \ \rightarrow \ \boldsymbol{M}\ddot{\boldsymbol{u}} + \boldsymbol{F}_{int} = \boldsymbol{F}_{ext} \tag{9}$$

The nonlinear governing equation is then linearized to implement an incremental numerical solver based on path-following constraints. Through a Taylor expansion truncated at the first order, one can derive the incremental equation:

$$\boldsymbol{M}\Delta\ddot{\boldsymbol{u}} + \boldsymbol{K}_T\Delta\boldsymbol{u} = -\boldsymbol{\phi}_{res}(\boldsymbol{u}_0, \ddot{\boldsymbol{u}}_0, \boldsymbol{p}_0) + \boldsymbol{I}\Delta\lambda\boldsymbol{p}_{ref} \tag{9}$$

Finally, imposing a harmonic solution of the type $\boldsymbol{\Delta u = \Phi e^{i\omega t}}$ when an harmonic load of the type $\boldsymbol{p_{ref} = \bar{p}e^{i\omega t}}$ the frequency response problem around pre-stressed conditions are obtained, that provides the amplitude of the displacements $\boldsymbol{\Phi}$ around the computed non-trivial equilibrium state for each excitation frequency $\boldsymbol{\omega}$:

$$(\boldsymbol{K}_T - \omega^2\boldsymbol{M})\boldsymbol{\Phi} = \bar{p} \tag{9}$$

The analysis of multilayered structures via higher-order finite elements based on CUF has already been established in many works, including also physical nonlinearities.

Numerical results

The proposed approach is applied to the analysis of a multilayered sandwich structure with a natural rubber-like core and composite skin, evaluating its dynamic properties via frequency response analysis under various pre-stressed conditions. The proposed case studies have been

Materials Research Proceedings 69 (2026) 303-307 https://doi.org/10.21741/9781644904251-54

proposed by Selvaraj et al. [10]. A composite plate of length L = 300 mm, width B = 300 mm and overall thickness H = 10.05 mm is considered, with two laminated skins of thickness h_s = 2.01 mm made of natural composites with lamination 0°/90°/0° and core with thickness $h_c = 6.03$ mm. The resulting structure is then a final composite laminate with stacking sequence 0°/90°/0°/rubber-core/0°/90°/0°. The material constants adopted in the case of natural composite for the skin sheets are $E_1 = 5.16$ GPa, $E_2 = 4.70$ GPa, $\nu_{12} = 0.15$, $G_{12} = 0.81$ GPa and $\rho = 1197$ kg/m^3. Different from the reference work, the core layer is modeled using the Neo-Hookean hyperelastic model [11], with calibrated constants matching the original infinitesimal elastic constants, namely $\mu = 1.61$ MPa and $k = 10.72$ MPa. In all the models considered, a single parabolic LE2 model per layer will be adopted, for a total of seven LE2 elements along the through-the-thickness discretization. Figure 1 shows the graphical representation of the geometrical features and finite element model adopted.

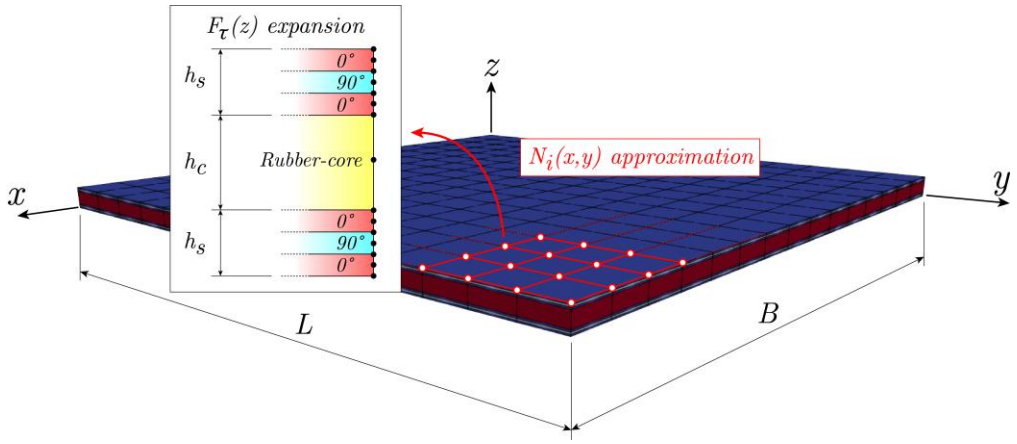


Figure 1: Rubber-core sandwich plate: geometrical features and finite element approximation

The first analysis addressed is the modal analysis of the plate in a clamped-free-free-free (CFFF) configuration, validating the proposed approach and investigating the influence of the mid-surface discretization on the results. Table 1 shows the first five natural frequencies of the CFFF plate, comparing the results obtained against the available literature reference ones, including the relative percentage difference between the 2D CUF results and the actual reference, reported in brackets

Table 1: *Rubber-core sandwich plate: first five natural frequencies for various FE approximations [Hz]. Comparison between 2D CUF results and available literature results.*

Mesh	Mode 1	Mode2	Mode 3	Mode 4	Mode 5	DOFs
10x10 Q9	$25.89^{0.271\%}$	$39.24^{0.203\%}$	$94.66^{1.886\%}$	$114.45^{0.728\%}$	$128.75^{0.885\%}$	19485
15x15 Q9	$25.85^{0.116\%}$	$39.14^{0.457\%}$	$94.10^{2.497\%}$	$114.04^{1.084\%}$	$128.57^{1.023\%}$	43245
20x20 Q9	$25.84^{0.077\%}$	$39.11^{0.534\%}$	$93.92^{2.653\%}$	$113.86^{1.240\%}$	$128.50^{1.077\%}$	75645
Ref. [1]	25.82	39.32	96.48	115.29	129.99	-

For the considered discretizations, furthermore, the nonlinear static analysis of the clamped plate for an applied pressure at the top surface in the transversal direction is considered, to analyze the influence of highly-deformed states and pre-stress effects to the linearized frequency response analysis. Adopting instead the 20x20 Q9 + 7 LE2 discretization, also the linearized vibration problem is solved around specific equilibrium conditions. The results for both these analysis are proposed in Fig. 2, uniquely defined introducing the tangent stiffness matrix at the specific equilibrium point reported and applying a load variation of $\bar{p} = 1$ Pa. All the results are measured at the tip free-end point, at location $x = L$, $y = B/2$ and $z = H$, as reported in Fig. 1. The

equilibrium path instead is reported in terms of transversal displacement u_z measured at the same location.

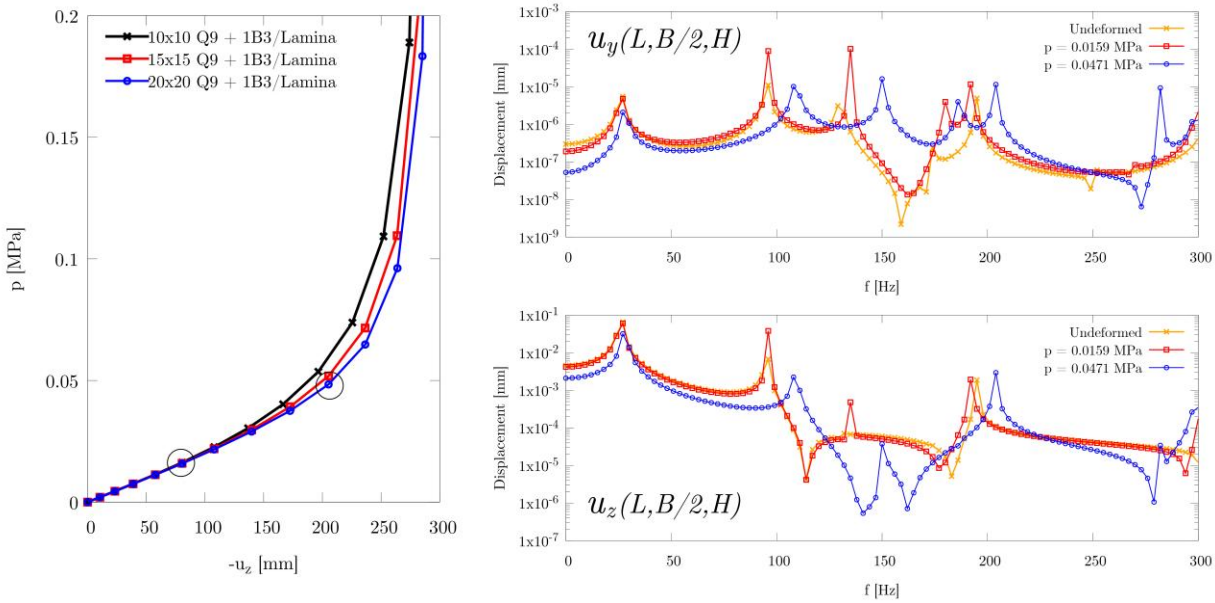


Figure 2: Rubber-core sandwich plate: static and linearized frequency response analysis. Comparison between higher-order 2D CUF solutions and influence of pre-stressed condition on the dynamic response around highly-deformed states.

Conclusions

This manuscript discusses the implementation of linearized frequency response analysis for the mechanical characterization of composite sandwich plate with soft cores, implementing physical nonlinearities to accurately represent the complex response of the core layer. The linearized dynamic problem around a generic non-trivial equilibrium state is solved implementing a finite element procedure that exploits the adoption of higher-order CUF-based finite element, an efficient tool for the generation of accurate and efficient numerical models for multilayered plate structures based on higher-order theory of structure approximation. The proposed results suggest the consistency of the proposed approach and the capabilities of the modeling strategies when coupled problems are considered. In particular, the effects of pre-stressed conditions on the frequency response analysis are analyzed, including the evolutions of resonance peaks and dynamic properties for varying pre-stressed states.

References

[1] Castanie B., Bouvet C. and Ginot M. "Review of composite sandwich structure in aeronautic applications", Composites Part C: Open Access, 2020, 10(4), 1543. https://doi.org/10.1016/j.jcomc.2020.100004

[2] Chuwkuemeke W.I., Marek P., and Stanislaw W. "Comparative Study of Sound Transmission Losses of Sandwich Composite Double Panel Walls", Applied Science , Aug. 2020. https://doi.org/10.3390/app10041543

[3] Khaniki H.B., Ghayesh M.H., Chin R. and Hussain S. " Nonlinear continuum mechanics of thick hyperelastic sandwich beams using various shear deformable beam theories", Continuum Mechanics and Thermodynamics, 2022, Vol. 34. https://doi.org/10.1007/s00161-022-01090-y

[4] Hemmatian M. and Sedaghati R. "Vibro-acoustic topology optimization of sandwich panels partially treated with MR fluid and silicone rubber core layer", Smart Mater. Struct. 26, 2017. https://doi.org/10.1088/1361-665X/aa908b

[5] De Rosa S., Koopmann G. and Marulo F. "First Steps Towards a Digital Plane Wave Superposition Method for Vibroacoustic Problems", Aerotecnica Missili & Spazio, Vol. 97, pages 13-18, 2018. https://doi.org/10.1007/BF03404760

[6] Carrera E., Abu Salem K., Augello R. “Free vibration analysis of sandwich plates by component-wise approach, Thin-Walled Structures, Vol. 218, 114062, 2025. https://doi.org/10.1016/j.tws.2025.114062

[7] Abu Salem K., Augello R., Carrera E. " Component-wise modelling of core and skin in sandwich structures using a single refined beam finite element ", Mechanics of Advanced Materials and Structures , 2025. https://doi.org/10.1080/15376494.2025.2458237

[8] Pagani A., Chiaia P., Carrera E. " Vibration of solid and thin-walled slender structures made of soft materials by high-order beam finite elements ", International Journal of Non-Linear Mechanics, Vol. 160, 104634, 2024. https://doi.org/10.1016/j.ijnonlinmec.2023.104634

[9] Moruzzi M.C., Cinefra M. and Bagassi S. "Analysis of an Acoustic Monopole Source in a Closed Cavity via CUF Finite Elements", Aerotecnica Missili & Spazio, Vol. 101, pages 371–385, 2022. https://doi.org/10.1007/s42496-022-00129-2

[10] Selvaraj R., Maneengam A., Sathiyamoorthy M. "Characterization of mechanical and dynamic properties of natural fiber reinforced laminated composite multiple-core sandwich plates", Composite Structures, Vol. 284, 115141, 2022. https://doi.org/10.1016/j.compstruct.2021.115141

[11] Smith M. " ABAQUS/Standard User’s Manual ", Version 6.9. Dassault Syst`emes Simulia Corp, United States, 791 2009.

Materials Research Proceedings 69 (2026) 308-313 https://doi.org/10.21741/9781644904251-55

The Ffowcs-Williams and Hawkings Analogy for Full Aircraft Noise Prediction

Emanuele STICCHI[1,a *], Damiano CASALINO[1,b], Daniele RAGNI[1,c] and Francesco AVALLONE[2,d]

[1]Delft University of Technology, Flow Physics and Technology Department, Kluyverweg 1, 2629 HS Delft, The Netherlands

[2]Polytechnic University of Turin, Department of Mechanical and Aerospace Engineering, Corso Duca degli Abruzzi 24, Torino, 10129, Italy

[a]e.sticchi@tudelft.nl, [b]d.casalino@tudelft.nl, [c]d.ragni@tudelft.nl, [d]francesco.avallone@polito.it

Keywords: Aeroacoustics, Acoustics Analogy, Aircraft Noise

Abstract. This study investigates the influence of different Ffowcs Williams and Hawkings (FW–H) formulations on far-field noise prediction for a propeller-driven strut-braced wing aircraft. High-fidelity flow data were obtained using the Lattice–Boltzmann Very-Large-Eddy Simulation (LB-VLES) solver PowerFLOW®, and acoustic predictions were carried out using the permeable-surface, solid-surface, and volumetric FW–H analogies included in the $Opty\partial B$™ toolkit. Results show that the permeable formulation reproduces both the amplitude and directivity of the dominant tonal lobes in good agreement with the noise directly extracted from the CFD simulation. The solid formulation, instead, exhibits discrepancies in regions exposed to the impingement of propeller-generated sound waves, where pressure fluctuations are detected but not correctly propagated. The volumetric approach, while computationally demanding, provides valuable physical insight by confirming the absence of actual radiating sources on that part of the fuselage. For similar configurations, the permeable formulation represents the most reliable and computationally efficient choice for predicting far-field noise.

Introduction

The prediction of far-field aircraft noise has become a critical component in the design of next-generation low-noise aircraft. Most aeroacoustic simulations rely on acoustic analogies, with the Ffowcs Williams–Hawkings (FW-H) method being a standard in both academia [1] and industry [2].

Two main formulations of the FW-H method are commonly employed: the solid surface formulation, which records pressure fluctuations on the aircraft surface, and the permeable surface formulation, which samples the data on a surface located within the flow, enclosing the entire noise-generating region, and capturing both surface and volume sources [3]. Each has its own practical advantages and theoretical limitations. Recent studies have provided valuable insights into the performance of both approaches. For instance, Spalart et al. [4] emphasized the sensitivity of the permeable formulation to numerical errors and surface placement, while Ribeiro et al. [2] showed that even in large-scale simulations, solid surface methods can lead to overprediction or misidentification of key sources, particularly in the presence of shielding and complex geometries.

In this context, this work aims to assess the performance of the solid and permeable FW-H formulations when applied to a high-fidelity simulation of a propeller-driven regional aircraft with a strut-braced wing configuration. The simulation is carried out using the LBM-VLES solver PowerFLOW®, and results are assessed in terms of their acoustic directivity, spectral content and noise source density.

Content from this work may be used under the terms of the Creative Commons Attribution 3.0 license. Any further distribution of this work must maintain attribution to the author(s) and the title of the work, journal citation and DOI. Published under license by Materials Research Forum LLC.

Materials Research Proceedings 69 (2026) 308-313 https://doi.org/10.21741/9781644904251-55

The manuscript is organized as follows: first, the methodology is described; next, the results of the analysis are discussed; finally, the main conclusions are presented.

Methodology

The flow field was computed using the flow solver PowerFLOW®, version 6-2022-R3 from 3DS Dassault Systèmes, which implements the Lattice-Boltzmann Method (LBM). The software used has been extensively used to accurately predict noise generated in complex flow problems, including full-vehicle configurations [5], and propulsion systems [6] [7]. A detailed description of the solver can be found in Ref. [8]. For the present computation, the high-subsonic solver, extended to transonic regime, is used.

Far-field noise predictions were obtained using three approaches: the permeable-surface formulation of the FW–H analogy ($Opty\partial B$-FWHFREQ™), the solid formulation ($Opty\partial B$-SOLID™), and the complete volumetric analogy ($Opty\partial B$-LIGHTHILL™). The solid surface consisted in the aircraft surface. The permeable surface was defined as an offset from the aircraft plus a cylinder, which includes the propeller's wake, to reduce spurious noise sources. Three equally shaped FW-H surfaces, placed 25 cm apart, were used to average noise signals. For the full volumetric formulation, the integration domain corresponds to the volume enclosed by the previously defined permeable surface. The tailored Green's function was obtained using the quasi-Dirac pulse method described in Ref. [9]. Since acoustic reciprocity does not hold in a rotating frame, the local rotating frame (LRF) associated with the propeller was excluded from the volume integral and accounted for through an additional permeable surface surrounding the LRF. The additional Green's-function simulation required about 5k CPU-h compared to the 70k CPU-h for the main run. The subsequent volumetric FW–H calculation, performed for one microphone over a narrow frequency range, lasted around three hours on a fat node of the Dutch national supercomputer Snellius (dual AMD EPYC Rome 7H12 @ 2.6 GHz, 128 cores, 1 TiB RAM). Consequently, the full spectrum is not shown in the next section, and only source-localization results are presented for this case.

Results

An overview of the instantaneous flow field is provided in Fig. 1, which shows a λ_2 isosurface coloured by the velocity magnitude and normalized by the freestream value. The insets in the top-left and top-right corners highlight the interaction of the tip vortices with the wing and the strut, respectively. This visualization intends to introduce the reader to the aerodynamic features underlying the acoustic mechanisms under investigation. A more detailed flow analysis is intentionally omitted to comply with the page limitations and to maintain focus on the acoustic analogy assessment.

Materials Research Proceedings 69 (2026) 308-313 https://doi.org/10.21741/9781644904251-55

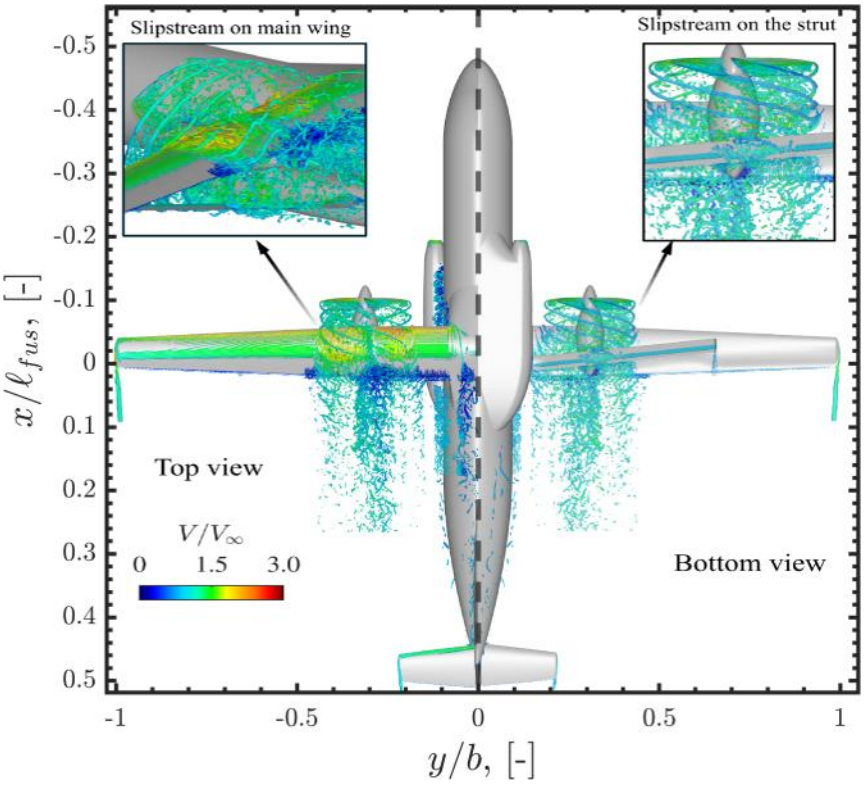


Figure 1: Isosurface of λ_2 colored by the magnitude of velocity, V, normalized by the cruise speed, V_∞.

Figure 2(a) shows the aircraft geometry, the FW–H integration surface, and the microphone array used for the acoustic analysis. The Overall Sound Pressure Level (OASPL) at the microphone locations for both FW–H formulations, compared with the direct noise extracted from the simulation, is displayed in Fig. 2(b). The permeable formulation shows good agreement with the direct results, except in the angular regions upstream and downstream (grey areas in the Fig. 2(b)), likely due to the impingement of the propeller wake on the FW–H surface. Despite these local deviations, the overall agreement is very satisfactory, confirming the reliability of the results obtained with the permeable formulation. In contrast, the solid formulation exhibits a marked discrepancy, particularly at $\theta = 250°$, where it fails to reproduce the acoustic lobe. To investigate this discrepancy, Fig. 3 shows the sound pressure spectra at the microphone located at $\theta = 250°$. The results obtained with the permeable formulation are compared with those from the solid formulation, which is also decomposed into its individual surface contributions. The spectra show that the solid formulation underpredicts both the first and second Blade-Passing-Frequency (BPF) tones. Focusing on the first BPF, it can be seen that the fuselage contribution has an intensity comparable to that of the propeller. A phase analysis, not shown here for conciseness, shows that these two signals are nearly out of phase at the first BPF, resulting in a destructive interference between the fuselage and propeller contributions.

Materials Research Proceedings 69 (2026) 308-313 https://doi.org/10.21741/9781644904251-55

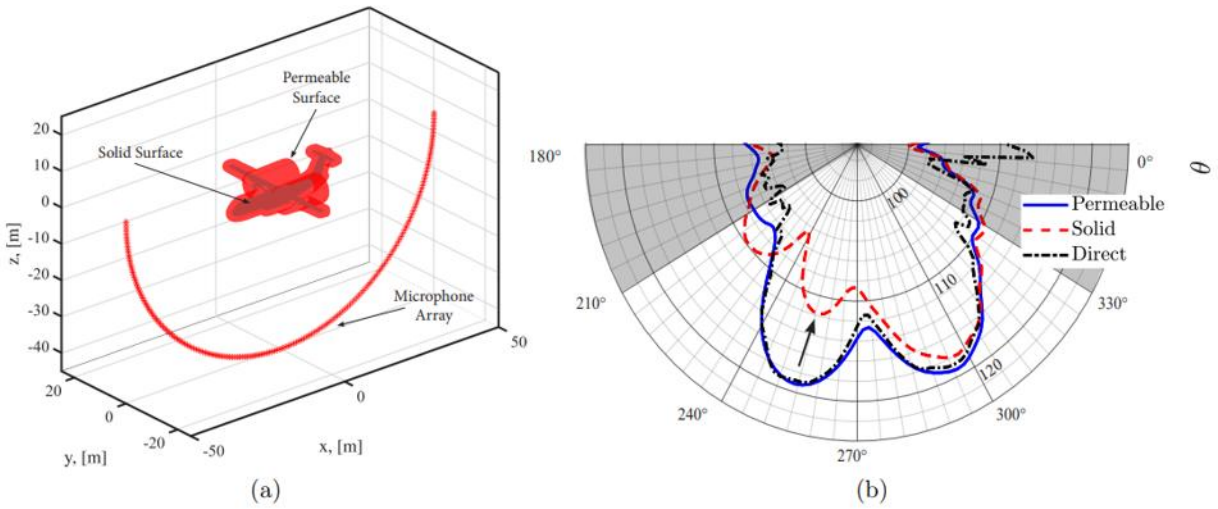


Figure 2: (a) Far-field directivity arc together with the aircraft geometry and the FWH surface used for the analyses. (b) Comparison between the noise computed by means of solid and permeable FWH formulation.

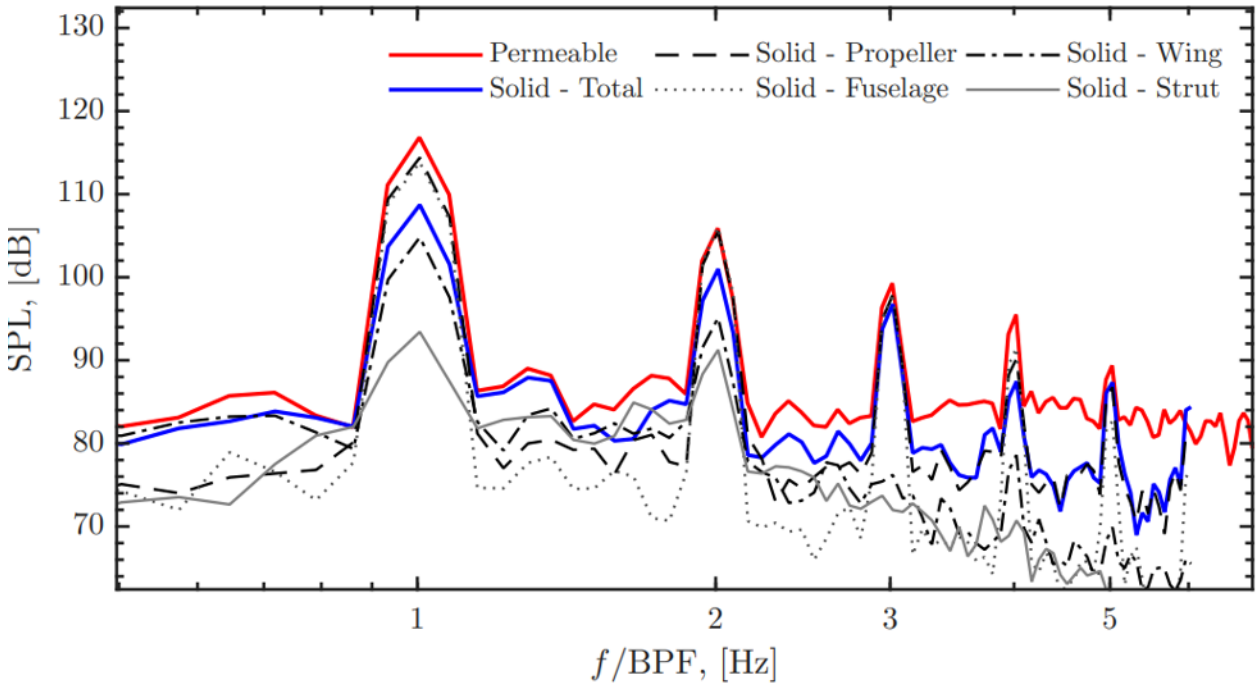


Figure 3: Sound level spectra at the microphone located at θ = 250◦ . Comparison between Permeable and Solid FWH formulation.

Furthermore, the inspection of the acoustic source amplitude per unit area obtained with the solid formulation (see Fig. 4(a)) shows that this contribution originates from the upper side of the fuselage sponson. In fact, the fuselage sponson is exposed to the impingement of the propeller-generated sound waves during rotation, resulting in high pressure fluctuations sampled on the solid surface.

Figure 4(b) shows the noise sources computed using the volumetric FW–H analogy at the first BPF. According to this formulation, the main source is the propeller. However, this contribution is not shown in the Fig. 4(b) since the local rotating frame is excluded from the integration volume (see Sec. Methodology). The secondary volumetric sources, displayed as isosurfaces of noise

Materials Research Proceedings 69 (2026) 308-313 https://doi.org/10.21741/9781644904251-55

source amplitude per unit volume, show pronounced distortion effects on the wing and strut, while no contribution from the fuselage sponson is observed. This comparison suggests that the solid formulation identifies apparent sources on surfaces affected by the impingement of acoustic waves, as its propagation model does not account for local flow refraction. In contrast, the permeable and volumetric formulations correctly interpret these fluctuations as non-radiating. In addition, it is worth noting that no source appears on the lateral side of the fuselage in Fig. 4(a), indicating that the discrepancy occurs only when the reflecting surface is oriented with its normal in the observer direction.

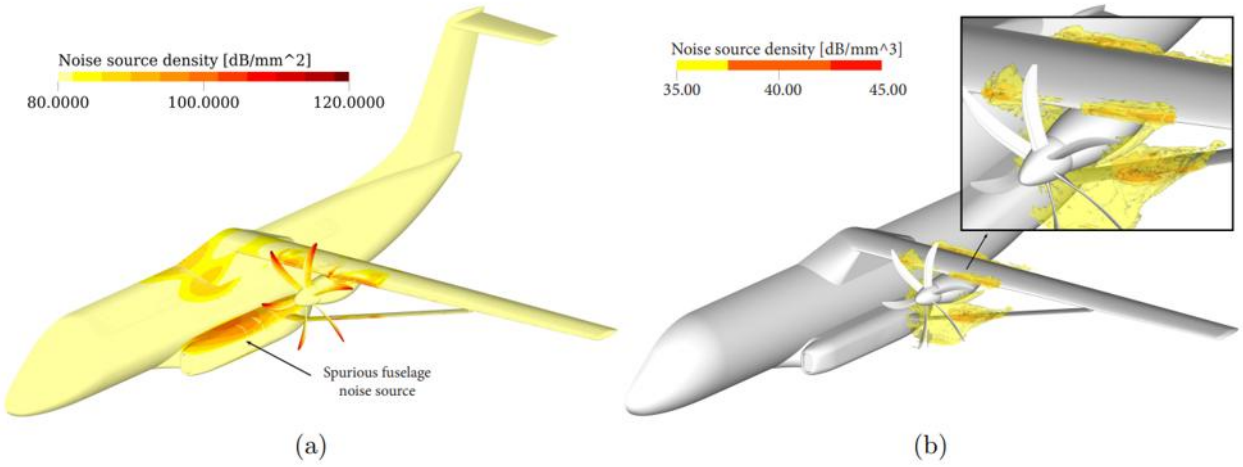


Figure 4: Noise source density at the first BPF computed with (a) solid FW-H formulation and (b) the volumetric acoustic analogy.

Conclusion

The study presented a comparative assessment of three acoustic analogy formulations: permeable FW–H, solid FW–H, and volumetric FW-H applied to the prediction of far-field noise from a propeller-driven strut-braced wing aircraft. The flow field was computed using the Lattice–Boltzmann solver PowerFLOW®.

The results show that the permeable formulation provides a consistent agreement with the noise extracted from the CFD simulation, accurately reproducing both the directivity and amplitude of the dominant acoustic lobes. The solid formulation, instead, exhibits discrepancies in regions influenced by the impingement of sound waves generated by the propeller, such as on the fuselage sponson. In these areas, pressure fluctuations are detected but are not correctly propagated as acoustic waves, since the underlying propagation model does not account for local flow refraction. This interpretation is supported by the volumetric FW–H analysis, which confirms that no actual radiating sources are present in those regions.

Although the volumetric approach offers valuable physical insight, it is computationally expensive and not feasible when many microphones or frequency bands are of interest. The permeable formulation is therefore recommended for practical far-field predictions, while caution should be exercised with the solid formulation in regions affected by strong mean-flow gradients or acoustic reflections.

Acknowledgments

The authors gratefully acknowledge financial support from the Clean Aviation Joint Undertaking under the HERWINGT project (grant agreement No. 101102010).

The authors also thank SURF for the support in using the National Supercomputer Snellius (grant no. EINF-13850).

References

[1] C. Teruna, F. Manegar, F. Avallone, D. Ragni, D. Casalino and T. Carolus, "Noise reduction mechanisms of an open-cell metal-foam trailing edge," Journal of Fluid Mechanics, vol. 898, p. A18, September 2020. https://doi.org/10.1017/jfm.2020.363

[2] A. F. Ribeiro, M. R. Khorrami, R. Ferris, B. König and P. A. Ravetta, "Lessons learned on the use of data surfaces for Ffowcs Williams-Hawkings calculations: Airframe noise applications," Aerospace Science and Technology, vol. 135, April 2023. https://doi.org/10.1016/j.ast.2023.108202

[3] J. E. Ffowcs Williams and D. L. Hawkings, "Sound generation by turbulence and surfaces in arbitrary motion," Philosophical Transactions of the Royal Society of London. Series A, Mathematical and Physical Sciences, vol. 264, no. 1151, pp. 321-342, 1969. https://doi.org/10.1098/rsta.1969.0031

[4] . P. R. Spalart, K. V. Belyaev, M. L. Shur, M. Strelets and A. K. Travin, "On the differences in noise predictions based on solid and permeable surface Ffowcs Williams-Hawkings integral solutions," International Journal of Aeroacoustics, vol. 18, no. 6-7, pp. 621-646, 2019. https://doi.org/10.1177/1475472X19878934

[5] C. Teruna, L. Rego, D. Casalino, D. Ragni and F. Avallone, "A Numerical Study on Aircraft Noise Mitigation Using Porous Stator Concepts," Aerospace, vol. 9, no. 2, 2022. https://doi.org/10.3390/aerospace9020070

[6] D. Casalino, F. Avallone, I. Gonzalez-Martino and D. Ragni, "Aeroacoustic study of a wavy stator leading edge in a realistic fan/OGV stage," Journal of Sound and Vibration, vol. 442, pp. 138-154, 2019. https://doi.org/10.1016/j.jsv.2018.10.057

[7] D. Casalino, A. Hazir and A. Mann, "Turbofan Broadband Noise Prediction Using the Lattice Boltzmann Method," AIAA Journal, vol. 56, no. 2, pp. 609-628, 2018. https://doi.org/10.2514/1.J055674

[8] E. Fares , B. Duda, A. F. Ribeiro and B. König, "Scale-resolving simulations using a lattice Boltzmann-based approach," CEAS Aeronautical Journal, vol. 4, no. 9, pp. 721-733, 2018. https://doi.org/10.1007/s13272-018-0317-0

[9] G. Romani and D. Casalino, "On the Use of Acoustic Analogy and Scale-resolving Turbulent Flow Computations for Noise Sources Identification," in 30th AIAA/CEAS Aeroacoustics Conference, Rome, 2024. https://doi.org/10.2514/6.2024-3243

Materials Research Proceedings 69 (2026) 314-318 https://doi.org/10.21741/9781644904251-56

Multi-Fidelity Numerical Acoustic Optimization of UAV Propellers

Roberto NAVARRO[1,a], Luis Miguel GACÍA-CUEVAS[1,b], Jorge GARCÍA-TISCAR[1,c *], Federico Nahuel RAMÍREZ[1,d], Marco LAUDATO[2,e], and Mihai MIHAESCU[2,f]

[1]CMT - Clean Mobility & Thermofluids, Universitat Politècnica de València, Camino de Vera, 46022 Valencia, Spain

[2]FLOW Research Center, Department of Engineering Mechanics, KTH Royal Institute of Technology, Stockholm, SE-10044, Sweden

[a]ronagar1@mot.upv.es, [b]luiga12@mot.upv.es, [c]jorgarti@mot.upv.es, [d]fera1@mot.upv.es, [e]laudato@kth.se, [f]mihaescu@kth.se

Keywords: Noise, UAS, Drones, AAM, VPM, CFD

Abstract. In this work, we propose a multi-fidelity approach to optimize the geometry of a small fixed-pitch propeller to reduce its acoustic impact. This way, the advantages of low-fidelity methods (low cost and fast results) can be combined with those of higher-order ones (better resolution and more reliable results) to obtain an optimized solution within a reasonable timeframe. We train a fully connected network surrogate that maps propeller geometry (chord and twist) and thrust to optimal rotating speed, torque, and sound pressure level (SPL) at the blade passing frequency (BPF) at 17 different angles, and benchmark it on three datasets: low-order blade element momentum theory (BEMT), higher-order vortex particle method (VPM), and a balanced Mixed set.

Introduction

Advanced Air Mobility (AAM) has experienced significant development in recent years, and this trend is expected to continue [1]. Among these developments, small electric Unmanned Aerial Vehicles (UAVs) promise to improve small cargo transport, such as last-mile shipping, medical emergency delivery, surveillance, traffic management, etc. However, some drawbacks also emerge, including security risks and environmental impact. Among these drawbacks, one of the most important is noise pollution, which can contribute to reducing social acceptance.

Propellers are the primary noise source in small electric UAVs. Thus, reducing the noise produced by the propellers is the best approach to mitigate the acoustic footprint of UAVs and, therefore, facilitate their social acceptance [2]. These fixed-pitch propellers typically operate at low Reynolds regimes and Mach numbers below 0.3, setting them apart from traditional aircraft propellers. As a result, certain complex phenomena may gain importance, such as laminar-turbulent transitions and the emergence of laminar separation bubbles. For this reason, low-order models cannot always fully predict the complex aero-acoustic processes involved.

Numerical models and validation

The proposed numerical models are a combination of Blade Element Momentum Theory (BEMT) and the Hanson model [3], implemented as an in-house code, as the low-fidelity approach; and a reformulated Vortex Particle Method (VPM), implemented in FLOWUnsteady [4] as a mid and high-fidelity model —depending on the number of particles—, coupled to a Ffowcs-Williams and Hawkings (FW-H) solver to compute the acoustics. A fourth, high-fidelity Finite Volume Method (FVM) model, implemented in OpenFOAM, was also tested, using the improved delayed detached eddy simulation (IDDES) technique coupled again with the FW-H method.

Content from this work may be used under the terms of the Creative Commons Attribution 3.0 license. Any further distribution of this work must maintain attribution to the author(s) and the title of the work, journal citation and DOI. Published under license by Materials Research Forum LLC.

The main advantage of the proposed methodology is that the same common propeller plain text description file is used as an input for all the fidelity levels, and a custom toolchain has been implemented to programmatically simulate each fidelity level. In the case of the FVM-CFD method, which of course requires the actual geometry to be meshed, advantage is taken of NASA's Open-VSP software [5] to automatically build an STL format representation of the propeller, which is then meshed and solved by OpenFOAM.

To validate the models, a commercial propeller (XOAR 9x7") was also tested in the anechoic chamber available at the CMT Institute, to provide experimental validation to the proposed numerical approaches. As can be seen in Figure 1, which focuses on the Blade Passing Frequency tonal noise, good agreement is found for this acoustic feature at the propeller plane (0º), and some of the downstream orientations (-30º and -60º). However, as expected, upstream acoustic propagation in the propeller axis direction (90°) was not achieved by either the low-fidelity model or the mid-fidelity VPM settings. Increasing the VPM fidelity level, or switching to the FVM approach, yielded good agreement even in the 90º direction. However, the FVM model required significantly more computational resources than the VPM approach, and therefore, it was not used in this work.

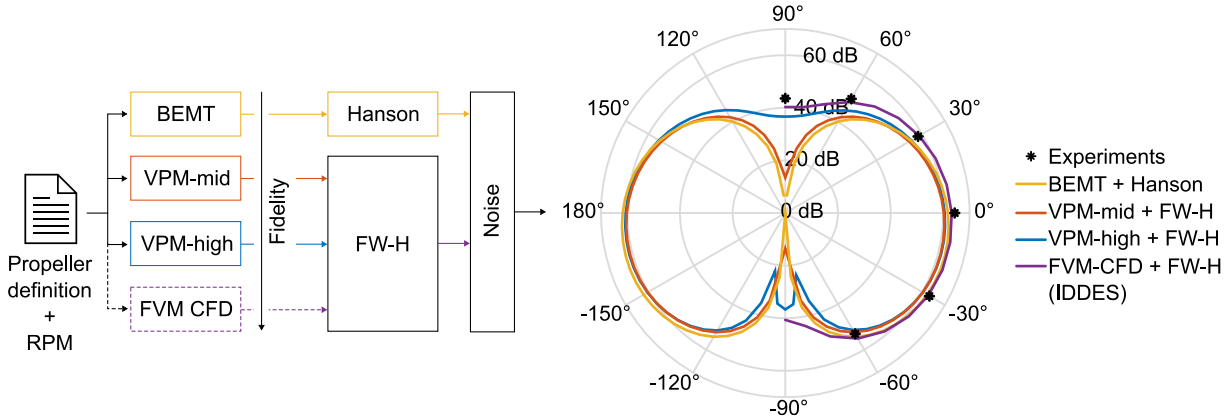


Figure 1: Experimental validation of Sound Pressure Level directivity at Blade Passing Frequency

Surrogate model, training datasets, and performance assessment

In order to avoid running the numerical model for each optimization step, we then train a data–driven surrogate that maps UAV propeller inputs to operating and acoustic outputs. The input vector $\mathbf{x} \in \mathrm{R}^7$ contains three geometric dimensions [m], three installation angles [°], and target thrust [N]. The geometric parameters define the chord and twist angle of the blade at 10%, 70%, and 100% of the blade span. The output vector $\mathbf{y} \in \mathrm{R}^{19}$ contains the optimal rotational speed ω [rpm], torque [Nm], and the SPL value [dB] at the BPF at 17 different locations (equispaced 10º from -80º to 80º at a 2m radius). Angles are encoded as $\{\sin \theta_i, \cos \theta_i\}$ to avoid wrap–around, and all features/targets are standardized (z–score) using training statistics.

We use a compact fully connected network that maps the preprocessed inputs (three geometry dimensions, thrust, and three angles encoded as sin / cos) to the outputs (optimal ω, torque, and 17 SPL values). The architecture has four hidden layers with widths [256, 256, 128, 64], ReLU activations, and a linear output layer. Inputs and targets are standardized (z-score) using training statistics only. Models are trained with Adam (10^{-3}) to minimize MSE, using a 70/15/15 train/validation/test split, batch size 128, and up to 200 epochs. We apply *ReduceLROnPlateau* (factor 0.5, patience 10, min lr = 10^{-6}) and *EarlyStopping* (patience 20, restoring the best weights); the best checkpoint by validation loss is used for testing. We report MSE/MAE on the held-out test set, and per-output errors in physical units after inverse scaling with the stored target mean and standard deviation.

Materials Research Proceedings 69 (2026) 314-318 https://doi.org/10.21741/9781644904251-56

Evaluation protocol. We consider three training sets: (i) BEMT (low fidelity), (ii) VPM (mid fidelity), and (iii) Mixed (balanced union of BEMT and VPM). These datasets are computed using a Clark-Y as the airfoil of the propeller. The hi-fi VPM setting is reserved for analysis of the optimized case due to longer computing times. Each case is split 70/15/15 into train/validation/test, trained with a fully-connected neural network (FCN), and evaluated on its own held-out test split. Reported metrics are RMSE/MAE in physical units per output; SPL rows are aggregated across the 17 angles using mean/median/95th percentile (see Fig. 2, left plot).

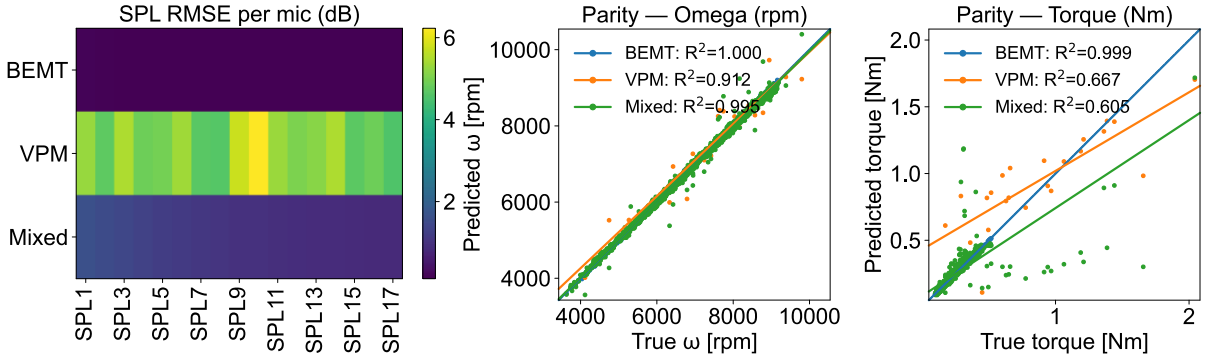


Figure 2: Surrogate evaluation results. Per-microphone SPL RMSE (dB) for the three surrogates (left). BEMT exhibits uniformly small errors, VPM shows systematically larger errors across every angle position, and the Mixed model lies in between with sub-1.5 dB errors across most microphones. Parity plot for rotational speed (center) and torque (right). Points are colored by surrogate, solid lines are least-squares fits. For rotational speed, the Mixed model closely tracks BEMT and remains near-unbiased across the range, while VPM shows a mild slope bias; for the torque it only partially mitigates the intercept bias but retains slope shrinkage.

Table 1 summarizes test performance. The BEMT-only model attains very low errors (e.g. SPL mean RMSE 0.130 dB). Including VPM data makes the learning problem harder: the VPM-only model shows larger errors and lower SPL R^2 (mean 0.699), consistent with a more complex input–output mapping and broader dynamic range. The Mixed model trades a small degradation relative to BEMT (SPL mean RMSE 0.971 dB; Δ Mixed–BEMT = 0.842 dB; SPL mean R^2 = 0.984) for substantially improved robustness across fidelity sources. For operating metrics, the same trend holds ($RMSE_\omega$: 24.9 rpm BEMT vs. 79.2 rpm Mixed; $RMSE_\tau$: 0.002 Nm BEMT vs. 0.074 Nm Mixed). Overall, the Mixed surrogate remains accurate (sub-1.5 dB at the 95th percentile across microphone locations) while generalizing across the two simulation schemes.

Table 1: Test performance of the three surrogates. SPL rows are aggregated across 17 microphones.

	BEMT	VPM	Mixed	Δ Mixed–BEMT
$RMSE_\omega$ [rpm]	24.932	440.657	79.238	54.306
$RMSE_\tau$ [Nm]	0.002	0.281	0.074	0.071
SPL RMSE (mean) [dB]	0.130	5.116	0.971	0.842
SPL RMSE (median) [dB]	0.124	5.016	0.882	0.758
SPL RMSE (95th pct) [dB]	0.164	5.839	1.403	1.239
SPL $\overline{R^2}$ (mean)	1.000	0.699	0.984	-0.016

For the rotational speed ω (see Fig. 2, center plot), the BEMT surrogate is nearly perfect and the Mixed model remains close to the identity ($R^2 \approx 0.996$), indicating that combining fidelities preserves high accuracy for operating speed. The VPM-only model shows a slope < 1 with a positive intercept, consistent with a mild high-end underprediction. For torque (see Fig. 2, right plot), BEMT again aligns with $y=x$ ($R^2 \approx 1$), whereas both VPM and Mixed display slope shrinkage

(≪ 1) and lower R^2 (~ 0.63–0.67), pointing to a systematic domain shift or coverage mismatch in torque across fidelities. The Mixed model reduces the intercept bias relative to VPM but still underestimates high torques. These trends suggest using a domain flag and/or per-domain target normalization, additional high-torque samples, torque-weighted loss to correct residual calibration differences between BEMT and VPM, or the addition of higher fidelity levels.

Propeller optimization results

Once the multifidelity surrogate model was built, a Pareto front was generated using a genetic optimization algorithm based on the surrogate model. In this optimization, as in the surrogate, the required thrust and propeller diameter are fixed. To compare against a single-fidelity surrogate, the Pareto front is also generated using only the BEMT-trained surrogate. The Mixed model results in some discontinuities, probably due to the training dataset and mixing procedure as outlined above. More crucially, there are differences in trends towards both extremes of the front, highlighting the importance of considering multifidelity models.

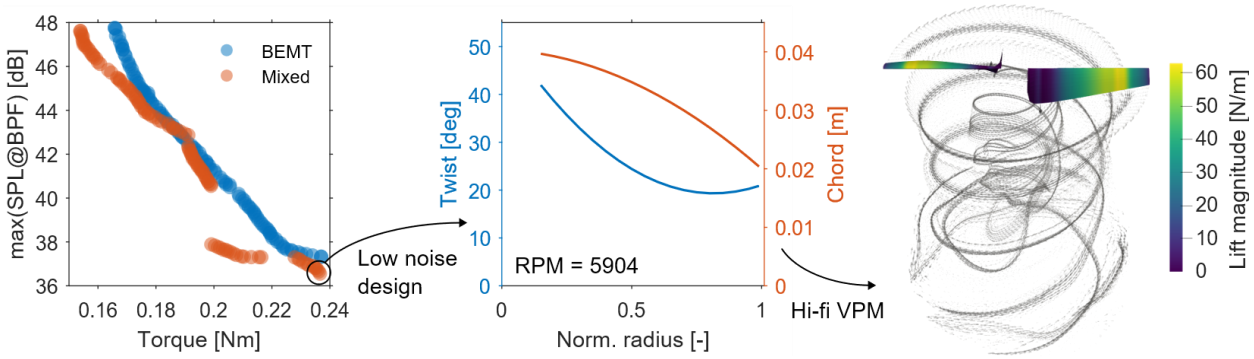


Figure 3: Pareto front resulting from a genetic optimization algorithm, proposed propeller geometry for reduced noise emissions, and sample result from the high-fidelity VPM simulation.

As an example of such optimized designs, the geometric distribution of the Pareto front extreme resulting in a lower BPF sound pressure level is shown in the center plot of Figure 3, together with the required RPMs as computed by the surrogate. This data was then used to run the high-fidelity VPM model, leveraging the unified propeller representation. A sample result from this high-fidelity model is shown in the right plot of Figure 3.

Conclusions and future works

In this work, a methodology for simulating a propeller with varying levels of fidelity (BEMT, VPM with mid and high fidelity, and full FVM CFD) from the same geometric definition has been demonstrated and experimentally validated for a 9-inch commercial propeller.

This methodology has been used to generate two datasets using the two fastest fidelity levels. This datasets has been used to build and validate a compact FCN surrogate for UAV propeller aerodynamics–acoustics with three approaches (only using the BEMT dataset, only using the VPM one, or mixing both); the BEMT model gives the best in-domain accuracy, while the Mixed model retains high fidelity across sources with a modest error increase (torque remains the most sensitive to domain shift).

Discrepancies have been observed between the model results, mainly in the torque obtained, which is substantially higher when using VPM compared to BEMT for some geometries. These discrepancies will be studied to determine whether they are due to limitations in the models for certain geometries, whether they also appear in higher-order models, and whether they can be resolved by fine-tuning the lower-order models.

To further close the gap between the surrogate and higher-order models, we plan to adopt *transfer learning*: pre-train on the large BEMT set and then fine–tune on higher fidelity levels by

restarting from the BEMT weights with a reduced learning rate and early stopping. This methodology can be further extended to consider higher-fidelity VPM settings or the high-fidelity FVM IDDES solver, by taking advantage of the common geometric representation and processing toolchain developed in this work.

Acknowledgements
This work was partly sponsored by grant PID2022-142018OA-I00 *Experimental and Numerical Optimization to Lower UAV Acoustical pollution (ENOLA)* funded by MCIU/AEI/ 10.13039-501100011033 and by ERDF, EU. F. N. Ramírez is supported by grant PREP202-000221 funded by MCIU/AEI/10.13039-501100011033 and by "ESF Investing in your future". J. García-Tíscar also acknowledges the support of the MCIU through the José Castillejo grant CAS23/00244.

References

[1] McKinsey & Company. Study on the societal acceptance of urban air mobility in Europe. EASA report, American Institute of Aeronautics and Astronautics, July 2021.

[2] Edoardo Grande, Gianluca Romani, Daniele Ragni, Francesco Avallone, and Damiano Casalino. Aeroacoustic Investigation of a Propeller Operating at Low Reynolds Numbers. *AIAA Journal*, 60(2):860–871, 2022. https://doi.org/10.2514/1.J060611

[3] Donald B. Hanson. Helicoidal surface theory for harmonic noise of propellers in the far field. *AIAA Journal*, 18(10):1213–1220, 1980. https://doi.org/10.2514/3.50873

[4] Eduardo J. Alvarez, Judd Mehr, and Andrew Ning. *FLOWUnsteady: An Interactional Aerodynamics Solver for Multirotor Aircraft and Wind Energy*.

[5] Robert A McDonald and James R Gloudemans. Open vehicle sketch pad: An open source parametric geometry and analysis tool for conceptual aircraft design. In *AIAA SciTech 2022 Forum*, page 0004, 2022. https://doi.org/10.2514/6.2022-0004

Materials Research Proceedings 69 (2026) 319-324 https://doi.org/10.21741/9781644904251-57

Auralization and Subjective Evaluation of Air Taxi Noise Events

Teresa MOSES[1,a *], Michael SCHMÄHL[1,b] and Mirko HORNUNG[1,c]

[1]Technical University of Munich, Boltzmannstraße 15, 85748 Garching, Germany

[a]teresa.moses@tum.de, [b]michael.schmaehl@tum.de, [c]mirko.hornung@tum.de

Keywords: Auralization, Air Taxi, Perceptual Noise Assessment, Urban Air Mobility

Abstract. To integrate human perception into the noise assessment of novel aircraft concepts, researchers resort to auralizations based on simulated noise-source data. This study presents a workflow for auralizing level flyovers of representative Urban Air Mobility vehicles for a stationary ground observer, based on noise source data generated via Computational Fluid Dynamics. The framework incorporates established methods for signal synthesis, spreading losses, atmospheric absorption, and Doppler shift, while enabling the imitation of rotational speed variations, spatialization via head-related transfer functions, and the addition of background noise. A listening test examined how these stimuli affect perceived annoyance. All three factors had a significant impact, with more realistic audio rendering consistently leading to lower ratings.

Introduction

Traditional noise assessment within the aviation sector is often based solely on compliance with regulatory sound level metrics, such as the maximum A-weighted sound pressure level ($L_{A,max}$) or the Sound Exposure Level (SEL) [1]. While a general trend of increasing annoyance with higher noise metric level exists, it does not ultimately hold true when comparing sounds with different characteristics. As demonstrated by the psychoacoustic hearing test conducted in [2], a drone flyover and a car drive-by with the same SEL can evoke different levels of perceived annoyance. Drone flyovers were generally rated as more annoying, partly because of their unfamiliar sound. In view of introducing new aircraft concepts, this finding underscores the need to incorporate subjective evaluations of aviation noise into aircraft design.

Subjective annoyance ratings can be obtained via listening tests. The corresponding audios are either based on measurements or generated via auralization - a technique that transforms simulated noise sources at vehicle level into a full acoustic pressure-time signal at an observer location [1]. A general workflow for the auralization of flyovers has been established in [1-4]. Accordingly, such a state-of-the-art auralization framework for level steady-state flyovers of two representative Urban Air Mobility (UAM) vehicles is presented herein. Assuming a stationary observer on the ground, a set of auralized scenarios is selected for a listening test campaign to investigate the effects of rotational speed (RPM) variations, spatialization, and background noise (BGN) on the perceived annoyance of a flyover event.

Methodology

The auralization workflow comprises three main stages: (1) noise signal generation, (2) propagation modeling, and (3) perceptual rendering. The workflow implemented here is depicted in Fig. 1 and concisely explained in the following.

Generation of the Emitted Signal. The emitted acoustic pressure signal of a level steady-state flyover is constructed from two components: the noise sources, in the form of a noise sphere storing the time-dependent acoustic pressure $p'(t)$ over a range of emission angles, and the aircraft's flight trajectory, described by a sequence of waypoints. Since measurement data for UAM vehicles are scarce, the noise spheres were derived from Computational Fluid Dynamics (CFD) simulations, focusing on the resolution of tonal noise sources [5]. To investigate the

Content from this work may be used under the terms of the Creative Commons Attribution 3.0 license. Any further distribution of this work must maintain attribution to the author(s) and the title of the work, journal citation and DOI. Published under license by Materials Research Forum LLC.

Materials Research Proceedings 69 (2026) 319-324 https://doi.org/10.21741/9781644904251-57

perceptual impact of RPM variations, two types of noise spheres were generated: one containing the acoustic pressure over a single blade-passing frequency (BPF) period, and another storing the pressure over five rotor revolutions. The latter includes apparent RPM variations arising from unsteady thrust-induced pressure fluctuations captured by the CFD simulation. Although these are not true RPM changes, they perceptually mimic such variations.

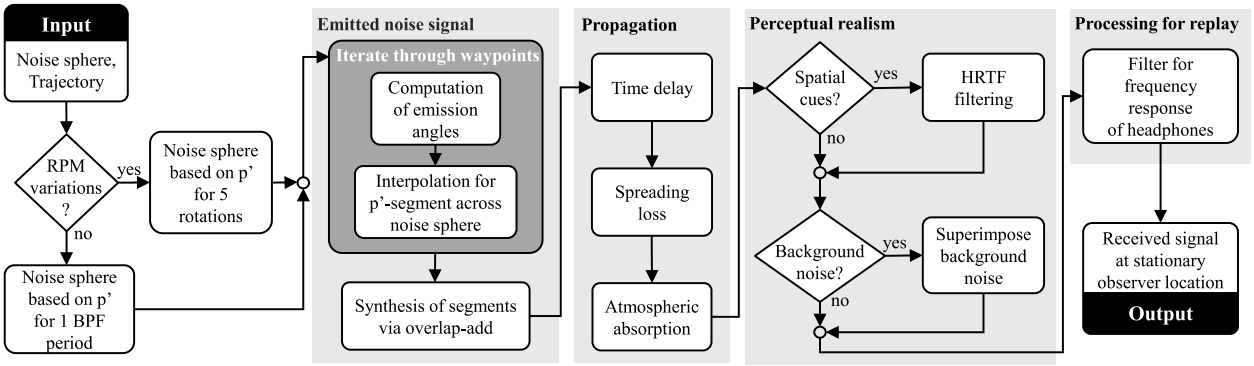
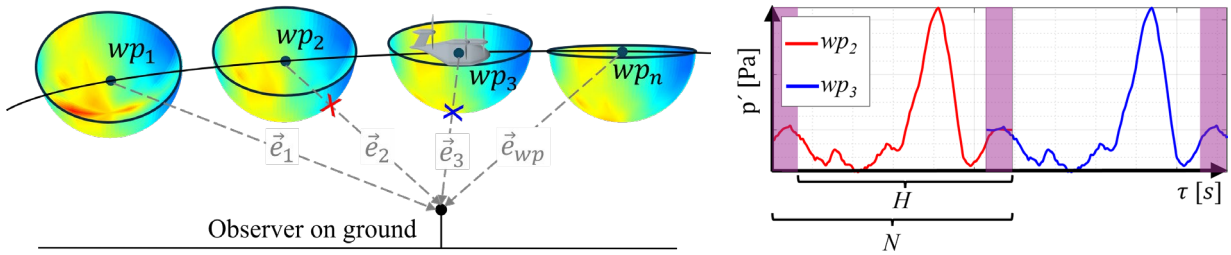


Figure 1: Flow diagram of the auralization workflow, where p' represents the emitted acoustic pressure extracted from the noise source sphere.

At each waypoint, the noise sphere is positioned and oriented along the local flight path. Then, the emission vector $\vec{e}_{wp}$, being the shortest vector between waypoint wp and observer, is computed. Its intersection with the noise sphere determines the query coordinates for a 2D-spline interpolation to extract a short pressure segment from the noise source data (marked with an 'x' for $\vec{e}_2$ and $\vec{e}_3$ in Fig. 2a). While not guaranteeing perfect phase coherence between neighboring data points on the noise sphere, this time-domain interpolation offers efficient and perceptually smooth results for the intended application.



(a) (b)

Figure 2: (a) shows the extraction of waypoint-specific pressure segments p', with $\vec{e}_{wp}$ as emission vector of waypoint wp. (b) visualizes the cross-fade OLA synthesis. τ, H, and N denote emission time, hop size, and segment length. The overlap region is shown in purple.

The interpolated segments are then concatenated to form a continuous emission signal using a cross-fade overlap-add (OLA) method [6]. This implies that consecutive segments overlap by 1/8 of the hop size H, i.e., the number of samples by which the signal synthesis advances. It is derived from $\Delta\tau_{wp} \cdot f_s$, with $\Delta\tau_{wp}$ being the waypoint time step, set to 1 BPF period, and $f_s = 44.1$ kHz as the desired sampling frequency. This results in an effective pressure segment length of $N = H + H/8$ (see Fig. 2b). If the interpolated p'-snippet is shorter than N, it is wrapped using shape-preserving cubic interpolation to ensure smooth continuity and phase alignment with the preceding segment. If the snippet exceeds N, the following segment resumes from the endpoint index of the previous extraction. Within the overlap region (highlighted purple in Fig. 2b), complementary Hann windows are applied before addition to guarantee a smooth transition between segments.

Materials Research Proceedings 69 (2026) 319-324 https://doi.org/10.21741/9781644904251-57

Propagation Mechanisms. Under free-field conditions, three propagation mechanisms altering the amplitude and spectral content of the emitted signal were implemented: time delay, spherical spreading, and atmospheric absorption. The arrival time at the observer is obtained by the summation of emission time and sound propagation time, where the latter is determined by the instantaneous distance between source and observer, divided by the speed of sound [4]. The amplitude attenuation with distance follows the inverse-distance law [3]. Frequency-dependent atmospheric absorption is modeled according to [7], assuming a uniform standard atmosphere (15°C, 1 atm, 70% relative humidity) [4].

Rendering for Perceptual Realism. To generate a spatially realistic auditory impression, a set of Head-Related Transfer Functions (HRTFs) from [8] is applied to the propagated signal. HRTFs represent the acoustic filtering introduced by the listener's head, torso, and pinnae, thereby enabling the perception of sound source direction. The implementation was performed in the frequency domain using a segment-wise convolution approach. Each audio segment is Hann-windowed, transformed to the frequency domain, filtered with observer angle- and orientation-dependent HRTFs for both ears, and converted back to the time domain. Before segments are recombined, a second Hann window is applied for smooth synthesis via OLA. The large overlap of $0.75 \cdot N$ ensured compliance with the constant OLA constraint [6], to ensure artifact-free signal reconstruction. Optionally, BGN can be superimposed onto the synthesized flyover audio. In cases where the BGN is binaural but the flyover signal is not HRTF-processed, both BGN channels are averaged to obtain a compatible track prior to mixing.

Listening Test Campaign. The auralization workflow was implemented for 9 flyover scenarios combining different vehicle types, trajectory definitions, and BGN settings (refer to Fig. 4). The operational conditions of the reference vehicles are listed in Table 1. Three left-to-right flight paths were considered: a direct overhead flyover, one passing 200 m in front of, and one 500 m behind the observer. Three BGN conditions were considered: 'none', 'busy street', and 'suburb', with the latter two tracks obtained from [9]. For every scenario, four audio variations were produced by toggling the inclusion of RPM variations and HRTF processing (on/off combinations), leading to a total of 36 audios. To ensure playback compatibility, monaural tracks were duplicated into two identical channels. Each flyover audio was trimmed to a total duration of 35 s, starting 15 s before and ending 20 s after the occurrence of $L_{A,max}$. For smooth playback, 2s fade-in and fade-out ramps were applied.

Table 1: Tilt-rotor and multicopter air taxi operational parameters for cruising flight.

	Speed [m/s]	Altitude [m]	RPM [min^{-1}]	Number of rotors [-]
Tilt-rotor	77.77	305	1002.5	6
Multicopter	25.00	305	1900.0	18

The listening test included 24 participants, rating the perceived annoyance of each flyover on a 7-point scale (1 = not annoying, 7 = very annoying). The presentation order of the audio samples was randomized, including two repeated samples to assess response consistency. Playback was conducted using Beyerdynamic DT 1990 PRO MK II headphones. Hence, the recordings were equalized to the headphones' frequency response before being played back through a HEAD acoustics SQadriga III audio interface and amplifier.

Data Post-processing. For the analysis, the first five audio ratings of each participant were excluded to eliminate potential outliers related to participants' initial adaptation to the stimuli and their expectations. To present the results, the arithmetic mean of the annoyance ratings of all participants was plotted against the corresponding audio SELs. These were computed from the average of the left and right audio channels.

Materials Research Proceedings 69 (2026) 319-324 https://doi.org/10.21741/9781644904251-57

Results and Discussion

Following [2], Fig. 3 analyzes the linear relationship between noise metric level and annoyance rating, distinguishing between vehicle type and BGN. Across the full dataset, no clear linear trend is apparent. The linear fit, shown as a dashed line, yields a squared correlation coefficient of R^2 =0.08. This indicates that only 8% of the variance in annoyance rating can be explained by this regression line [2], meaning that a linear fit fails to capture the underlying trend. Notably, the 'busy street' condition consistently produces lower ratings for a given SEL. The corresponding data points rather appear as "outliers", motivating a shift of focus to the subset considering only the BGN scenarios 'none' and 'suburb'. The linear relationship improves substantially, as indicated by the dotted fit achieving $R^2 = 0.78$. The complex 'busy street' environment likely distracts listeners, and possible masking effects partially obscure the aircraft sound, reducing its perceptual prominence. This leads to lower perceived annoyance and, presumably, to a less predictable regression model. Overall, this indicates that ambient noise has a systematic and measurable effect on perceived annoyance.

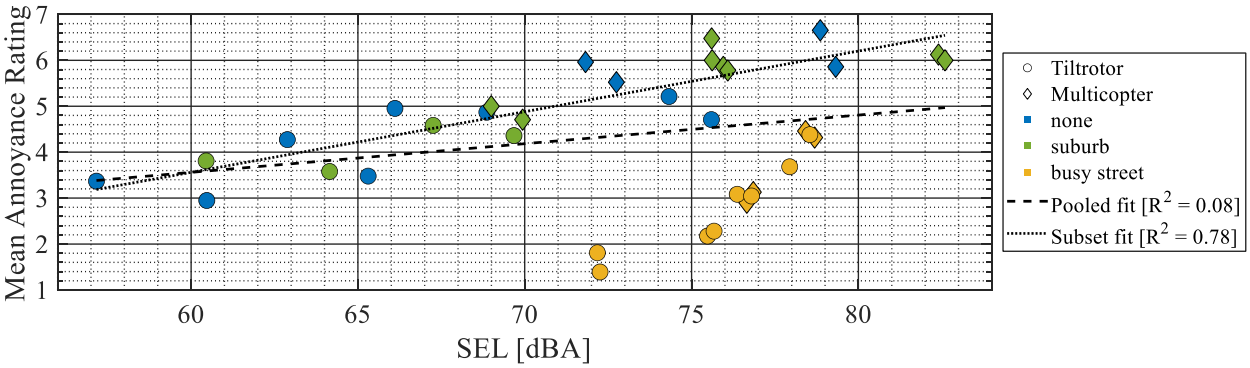


Figure 3: Mean annoyance rating versus SEL by aircraft type and BGN setting, with linear fits for the pooled data and for the subset excluding 'busy street' BGN.

Figure 4 reorganizes the data by scenario and stimuli to evaluate the effects of spatialization and RPM variations on the annoyance rating. Scenarios are labeled A – I and color-coded, with the RPM-off/HRTF-off conditions (●) marked by the corresponding letters. Focusing on spatialization, HRTF-processed audios (♦ and ▲) consistently exhibit lower SELs than unprocessed ones (● and ■), a consequence of the spatial filtering that reduces the acoustic energy reaching the observer. Excluding scenarios A and F, spatialization also leads to lower annoyance ratings, as seen when comparing HRTF-off versus HRTF-on conditions for the same RPM model (● vs. ♦, or ■ vs. ▲). Considering RPM variations, scenarios that include them are generally rated less annoying, despite showing higher SEL values. This is apparent when comparing RPM-off and RPM-on audios within an HRTF setting (● vs. ■, or ♦ vs. ▲). Exceptions occur for scenarios E and H, both featuring the 'busy street' BGN, a complex acoustic environment previously shown to deviate from overall trends. Nevertheless, these findings suggest that monotone sounds are perceived as more disturbing, whereas introducing realistic RPM fluctuations reduces perceived annoyance. When both models - HRTF and RPM - are activated simultaneously (▲), all scenarios show lower SELs and annoyance ratings compared to the default case (●). This underlines the importance of incorporating realistic acoustic and spatial cues in noise simulations to better reflect actual listening conditions and to foster public acceptance of emerging aircraft concepts.

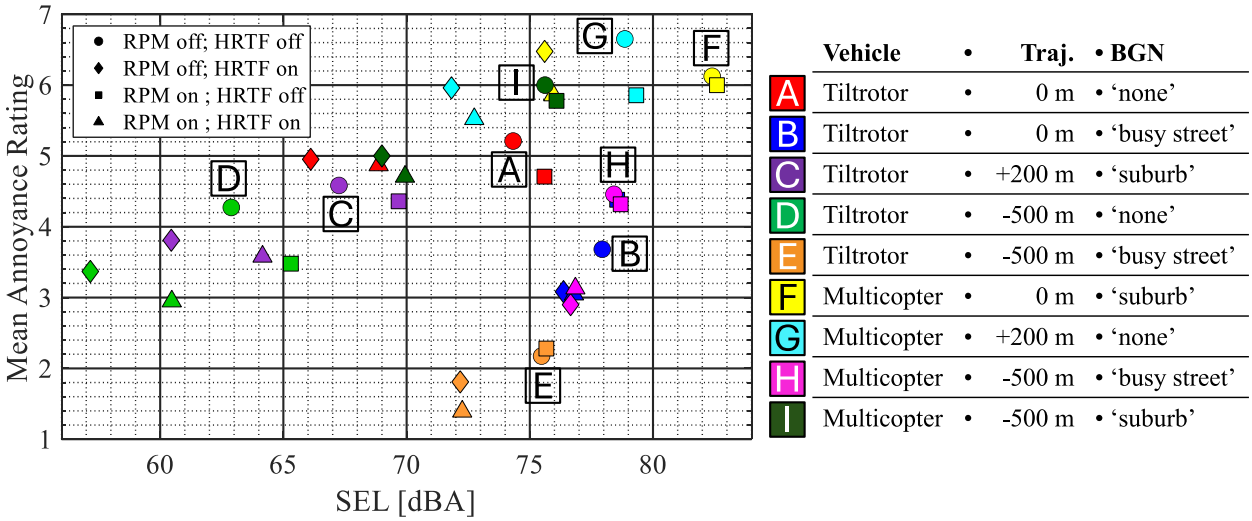


Figure 4: Mean annoyance ratings plotted against SEL, categorized by scenario, RPM model, and spatialization condition.

Conclusion

This study used a state-of-the-art auralization framework to examine the effects of spatialization, RPM variations, and background noise on perceived annoyance of UAM flyovers. Listening tests with 24 participants showed that audios including spatialization reduced the SEL and annoyance ratings. Realistic RPM variations further lowered perceived annoyance, despite slightly higher SELs, highlighting that perception can differ from objective sound levels. Background noise, particularly complex environments like busy streets, masked aircraft sounds and reduced annoyance, demonstrating the role of environmental context. The combination of HRTF processing and RPM variations yielded the lowest annoyance, confirming that investing in accurate, reality-close auralization models is worthwhile, as realistic scenarios reduce annoyance and can support public acceptance of UAM concepts.

References

[1] Stephen Rizzi, "Toward Reduced Aircraft Community Noise Impact via a Perception-Influenced Design Approach". In: INTER-NOISE and NOISE-CON Congress and Conference Proceedings. Vol. InterNoise16. Hamburg: Institute of Noise Control Engineering, 2016, pp. 220–244.

[2] Andrew W. Christian and Randolph Cabell. "Initial Investigation into the Psychoacoustic Properties of Small Unmanned Aerial System Noise". In: 23rd AIAA/CEAS Aeroacoustics Conference. American Institute of Aeronautics and Astronautics, June 2017. https://doi.org/10.2514/6.2017-4051.

[3] Stephen A. Rizzi and Abhishek K. Sahai. "Auralization of air vehicle noise for community noise assessment". In: CEAS Aeronautical Journal 10.1 (Mar. 2019), pp. 313–334. https://doi.org/10.1007/s13272-019-00373-6.

[4] Stephen Rizzi and Brenda Sullivan. "Synthesis of Virtual Environments for Aircraft Community Noise Impact Studies". In: 11th AIAA/CEAS Aeroacoustics Conference. American Institute of Aeronautics and Astronautics, May 2005. https://doi.org/10.2514/6.2005-2983.

[5] Teresa Baerens, Michael Schmähl, and Mirko Hornung. "Noise Modeling of a Tilt-Rotor Air Taxi Configuration Utilizing a Hybrid Acoustic Analogy Approach". In: Proceedings of the

Vertical Flight Society 80th Annual Forum. The Vertical Flight Society, May 2024, pp. 1–17. https://doi.org/10.4050/f-0080-2024-1085.

[6] Julius Orion I. I. I. Smith. Spectral audio signal processing. Stanford, Calif.: Stanford University, CCRMA, 2011. 654 pp. ISBN: 9780974560731.

[7] Acoustics - Attenuation of sound during propagation outdoors - Part1: Calculation of the absorption of sound by the atmosphere. online. Tech. rep. International Organization for Standardization (ISO), 1993.

[8] Ramona Bomhardt, Matias de la Fuente Klein, and Janina Fels. “A high-resolution head-related transfer function and three-dimensional ear model database”. In: Proceedings of Meetings on Acoustics. Acoustical Society of America, 2016, p. 050002. https://doi.org/10.1121/2.0000467.

[9] Pixabay. url: https://pixabay.com/sound-effects/ (visited on 10/31/2025).

Materials Research Proceedings 69 (2026) 325-330 https://doi.org/10.21741/9781644904251-58

Optimal Impedance for Acoustic Liners: From Cremer to Nonlocal Concepts

Emanuele De Bono[1,a *], Alessandro Casaburo[1,b], Giuseppe Petrone[1,c], Manuel Collet[2,d] and Sergio De Rosa[1,e]

[1]Laboratory for Promoting experiences in Aeronautical STructures and Acoustics, Department of Industrial Engineering, Universita degli Studi di Napoli Federico II, Via Claudio 21, Napoli, 80125, Italy

[2]Ecole Centrale de Lyon, CNRS, ENTPE, LTDS, UMR5513, 69130 Ecully, France

[a]emanuele.debono@unina.it, [b]alessandro.casaburo@unina.it, [c]giuseppe.petrone@unina.it, [d]manuel.collet@ec-lyon.fr, [e]derosa@unina.it

Keywords: Acoustic Liners, Cremer Impedance, Nonlocal, Noise Control, Advection Boundary Law

Abstract. The Cremer impedance is, so far, the only analytical result concerning optimal locally reacting impedances for acoustic liners. Nevertheless, the unfulfillment of the reality condition makes the Cremer impedance unachievable in a broadband sense. Moreover, the maximization of the attenuation of the principal duct mode in an infinite lined duct, as in Cremer, does not take into account the influence of backward reflection at the interface between rigid and lined portions of the duct. Therefore, the actual optimal impedance for locally reacting liners is usually obtained by numerical optimization of the insertion loss. Nevertheless, leveraging nonlocality, both in active and passive acoustic metamaterials, has allowed to achieve anomalous reflection, dispersion tailoring, higher isolation and nonreciprocity. These extraordinary control capabilities should be explored to conceive innovative concepts towards generalized impedance behaviours, where also nonlocality is contemplated and optimized. This paper first questions the optimality of Cremer-like impedances, and then it investigates an alternative boundary operator taking into account nonlocal interactions in the acoustic liner.

Introduction

The noise transmission mitigation in waveguides by parietal acoustic treatment interests heating and air-conditioning ventilation systems and aircraft turbofan engines. Its main challenge is the need to provide noise attenuation along the direction which is parallel to the surface where acoustic liner is applied. This is necessary as the liner should have minimal impact on the aerodynamic flow going through the duct. The Cremer's optimal impedances [4, 19, 18] are analytical solutions to the problem of maximizing the attenuation of specific duct-modes in an infinite waveguide. This problem is formulated in the frequency domain, and indeed, unfortunately, leads to non-real impedance operators, in the sense that their inverse Fourier transform does not produce a real function in the time domain (the reality condition [17] is unfulfilled). Therefore, the Cremer impedance can only be achieved at discrete frequencies [12, 1]. Moreover, the Cremer's impedance is not optimal for maximizing the Insertion Loss (IL) out of a finite size lined segment, as it will be shown below. Meanwhile, the progress in impedance control strategies has allowed to digitally program the impedance of an Electroacoustic Liner (EL) as an array of tunable Electroacoustic Resonators [3, 2, 11]. The model-inversion strategy has been employed for controller to synthesize nonlinear behaviours at low excitation amplitudes [8, 5, 15, 14, 16], or a nonlocal (generalized) impedance, as the so-called Advection Boundary Law (ABL) [13, 6, 10, 9, 7]. In this contribution, we first demonstrate the non-optimality of Cremer local impedance for

Content from this work may be used under the terms of the Creative Commons Attribution 3.0 license. Any further distribution of this work must maintain attribution to the author(s) and the title of the work, journal citation and DOI. Published under license by Materials Research Forum LLC.

Materials Research Proceedings 69 (2026) 325-330 https://doi.org/10.21741/9781644904251-58

scattering problems (Section 1), then we demonstrate how the potentialities of locally-reacting liners can be enlarged by including nonlocal interactions as in the ABL (Section 2). Finally, conclusions are given in Section 3.).

On the optimality of the Cremer local impedance operator

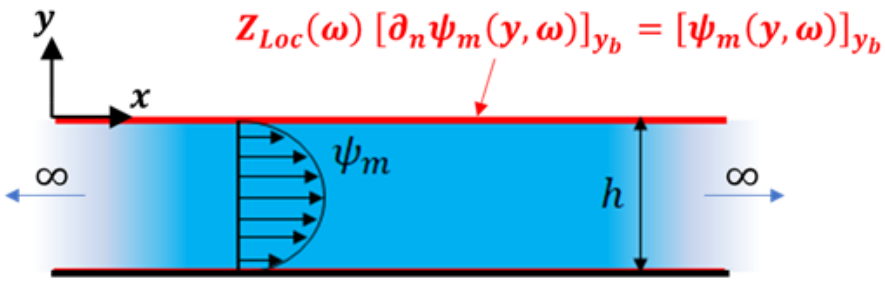


Figure 1: Problem for analytical optimization of $\boldsymbol{Z_{Loc}(\omega)}$ studied by Cremer, Tester and Spillere [4, 19, 18].

Fig. 1 sketches the 2D problem studied in [4, 19, 18] to find the analytical optimum of $\boldsymbol{Z_{Loc}(\omega)}$, defined as the ratio between the local pressure p(ω) and normal velocity $v_y(\omega)$ on the boundary $y = y_b$. The function $\psi_m(y,\omega)$ refers to the duct mode m describing the pressure distribution along the cross-section of the waveguide, which is solution of the dispersion problem of the wave equation coupled with the boundary condition given by the impedance operator of the liner. The corresponding eigen-function, is the duct-mode wave number $k_{x,m}(\omega)$. The solutions of such dispersion problem form a basis to the pressure $p(\omega,x,y)$ (see Eq. (1)), inside the duct of infinite size along x, lined on the top wall, for all $x \in R$, by the local impedance $Z_{Loc}(\omega)$.

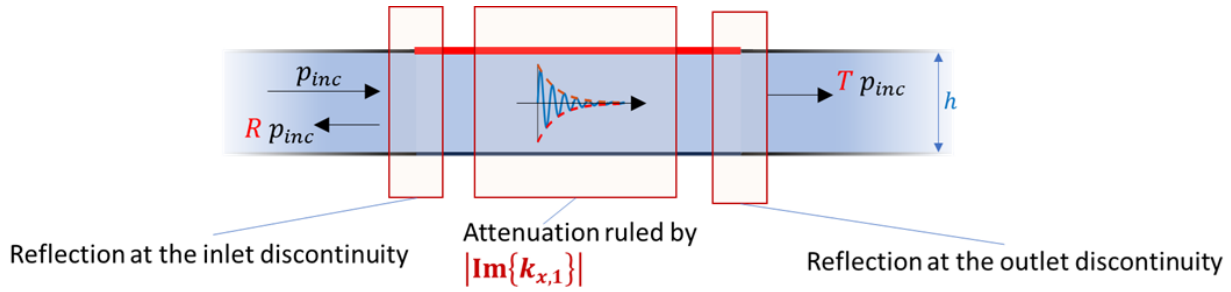


Figure 2: Scattering problem, defining the reflection R and transmission T coefficients.

$$p(\omega,x,y) = \sum_m \psi_m(y,\omega)e^{-jk_x(\omega)x} \quad . \tag{1}$$

Cremer and the others looked for the value of $Z_{Loc}(\omega)$ producing the highest attenuation along x in the sense of the highest value of $|\mathrm{Im}\{k_{x,m}(\omega)\}|$, with m the lowest duct mode of interest. The optimal dimensionless impedance $\zeta_{Loc} = \frac{Z_{Loc}}{\rho_0 c_0}$ (with $\rho_0 c_0$ the characteristic impedance of air) providing the maximum value of $|\mathrm{Im}\{k_{x,1}(\omega)\}|$ (where $k_{x,1}$ corresponds to the least attenuated duct mode), found in [4, 19], has the form:

$$\zeta_{Loc}(\omega) = \zeta_{Cre}(\omega) = (a_{Cre} - jb_{Cre})\frac{k_0 h}{\pi}, \tag{2}$$

with $a_{Cre} \approx 0.929$ and $b_{Cre} \approx 0.744$ according to the corrections of [19]. This analytical value

Materials Research Proceedings 69 (2026) 325-330 https://doi.org/10.21741/9781644904251-58

provides the merging of the least attenuating dispersion solution $k_{x,1}$, with $k_{x,2}$, where the subscript numbering $m = 1, 2, \ldots$ is according to growing $|\mathrm{Im}\{k_{x,m}(\omega)\}|$. Nevertheless, such optimization does not take into account the finiteness of the lined segment in actual scattering problems, where reflections at the discontinuities play a crucial role. Fig. 2 sketches the scattering problem, with $p_{inc}(\omega)$ the incident, $R(\omega)p_{inc}(\omega)$ the reflected, and $T(\omega)p_{inc}(\omega)$ the transmitted pressure fields' amplitudes. The definition of the scattering coefficients R(ω) and T(ω) follow. We solve, by Finite Elements, the scattering problem in a 2D waveguide of crosssection size $h = 0.11$ m, with the upper wall lined for an extension of $L = 0.25$ m, by a Single- Degree-Of-Freedom local impedance $\zeta_{SDOF}(\omega) = m_d j\omega + r_d + k_d/j\omega$, where m_d, r_d and k_d the dimensionless acoustical mass, stiffness and resistance. Fig. 3 shows the scattering solutions for varying r_d, along with the scattering solutions obtained by the Cremer impedance defined above. The scattering coefficients are provided in terms of $IL = 10\log_{10}\left(\frac{1}{|T|^2}\right)$, $|R|^2$ and $\alpha = 1 - |T|^2 - |R|^2$. It is clear that the Cremer impedance does not maximize IL. Reasonably, the Cremer impedance shows to be mostly related to the highest α.

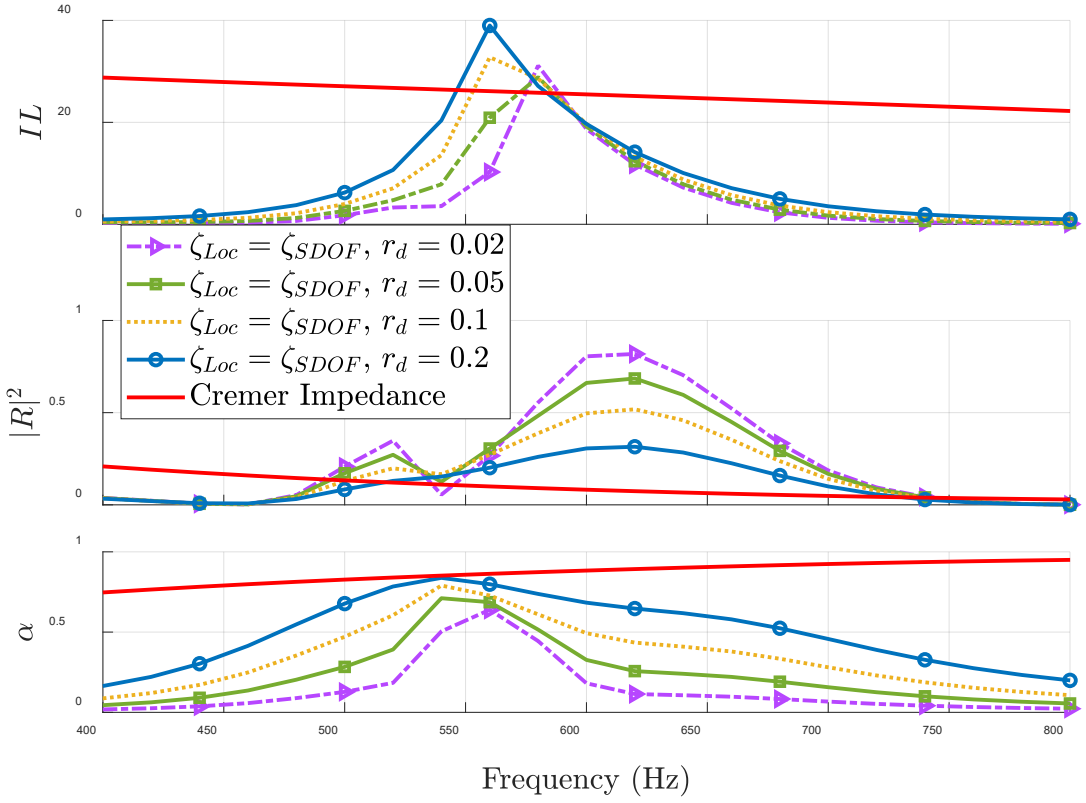


Figure 3: Scattering coefficients in case of a SDOF local impedance liner, with varying resistance, compared to the Cremer outcomes.

A nonlocal impedance operator

In this section we introduce the ABL non-local impedance operator, as an extension of the classical local impedance one, along the boundary $y = y_b$ and $x \in [0, L]$:

$$\rho_0 c_0 \zeta_{Loc}(\omega) j\omega v_n(x,\omega) = j\omega p(x,\omega) + U_b \partial_x p(x,\omega), \tag{3}$$

where $U_b = M_b c_0$, called the advection speed on the boundary, multiplies the x-gradient of pressure ∂xp(x, ω). Fig. 4 compares the scattering coefficients obtained by applying the ABL, with

those featured by the Cremer impedance. Notice that, for $M_b = 0$, we retrieve a classical local impedance operator, and in Fig. 4, this is set in such a way to achieve the Cremer value at the resonance $f_t = \frac{\sqrt{\frac{k_d}{m_d}}}{2\pi}$. The case with $M_b = 0.5$ features the highest IL, demonstrating the importance of including nonlocal terms in programmed generalized impedances.

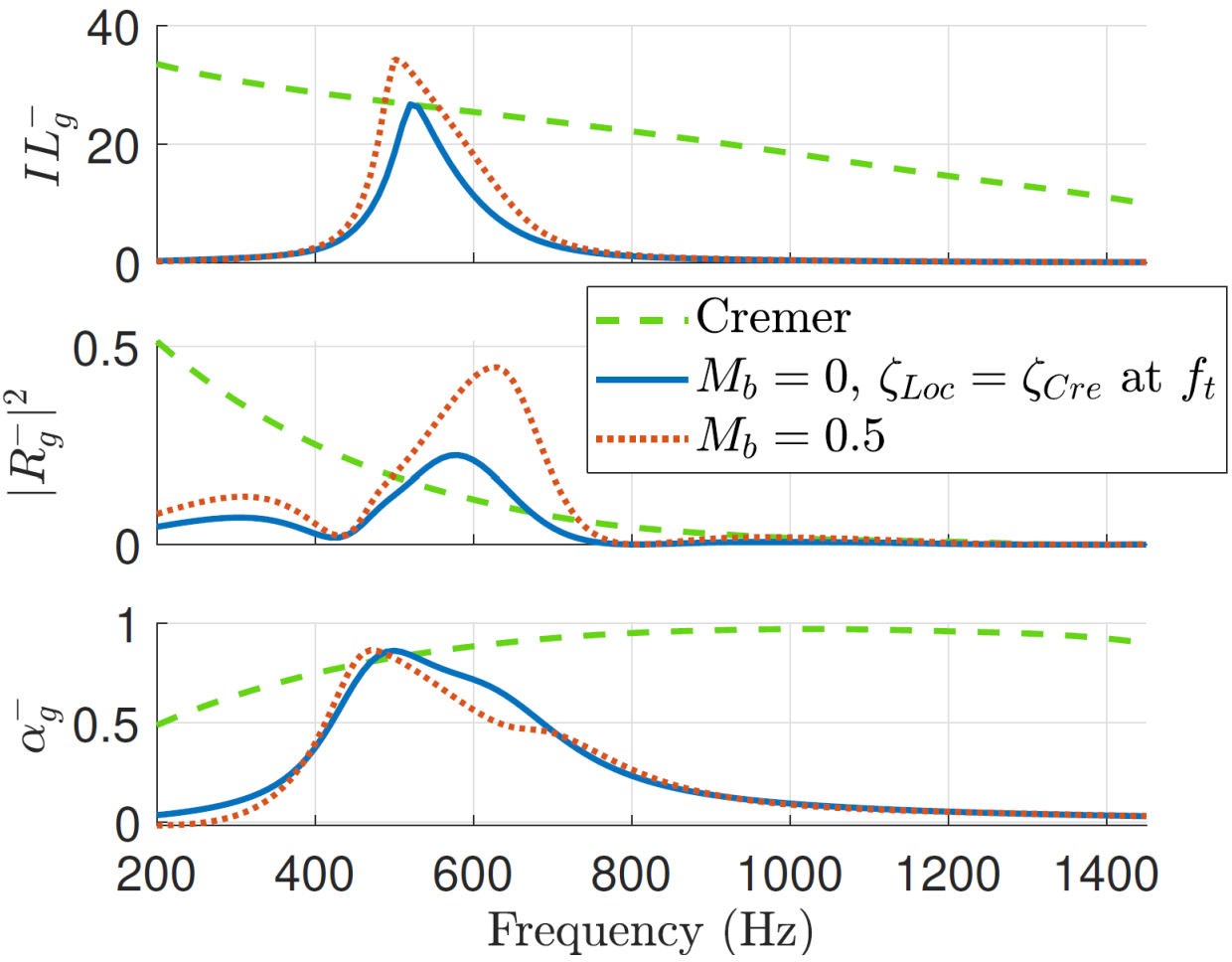


Figure 4: Scattering coefficients in case of the ABL, with varying Mb, compared to the Cremer outcomes.

Conclusions

In this contribution, we have showed the non-optimality of the Cremer impedance for the scattering problem faced with low resistive SDOF resonators, and nonlocal boundary operators. The ABL, as the first form of nonlocal boundary operator synthesized by the programmable EL, indicates the importance of nonlocality to overcome the classical optimal solutions for acoustic liners.

References

[1] Benjamin Betgen. Comportement d'un absorbant actif en écoulement: étude théorique et expérimentale. PhD thesis, 2010.

[2] K. Billon, E. De Bono, M. Perez, E. Salze, G. Matten, M. Gillet, M. Ouisse, M. Volery, H. Lissek, J. Mardjono, and M. Collet. In flow acoustic characterisation of a 2D active liner with local and non local strategies. Applied Acoustics, 191:108655, 2022. https://doi.org/10.1016/j.apacoust.2022.108655

[3] E De Bono, M Collet, G Matten, S Karkar, H Lissek, M Ouisse, K Billon, T Laurence, and M Volery. Effect of time delay on the impedance control of a pressure-based, current-driven Electroacoustic Absorber. J. Sound Vib., 537:117201, 2022. https://doi.org/10.1016/j.jsv.2022.117201

[4] L Cremer. Theory regarding the attenuation of sound transmitted by air in a rectangular duct with an absorbing wall, and the maximum attenuation constant produced during this process. Acustica, 3(1):249, 1953.

[5] Camila Elizabeth da Silveira Zanin, Aurélie Labetoulle, Emanuele De Bono, Emmanuel Gourdon, Manuel Collet, and Alireza Ture Savadkoohi. Experimental evidences of nonlinear programmable electroacoustic loudspeaker. Building Acoustics, 30(3):249-263, 2023. https://doi.org/10.1177/1351010X231184040

[6] E De Bono, M Collet, and M Ouisse. The Advection Boundary Law in absence of mean flow: Passivity, nonreciprocity and enhanced noise transmission attenuation. Journal of Sound and Vibration, page 118603, 2024. https://doi.org/10.1016/j.jsv.2024.118603

[7] E. De Bono, M. Collet, 'E. Salze, M. Ouisse, M. Gillet, H. Lissek, J. Mardjono, K. Billon, and M. Volery. Advection Boundary Law for sound transmission attenuation of plane and spinning guided modes. In Forum Acusticum, pages 6065-6069, 2024. https://doi.org/10.61782/fa.2023.0573

[8] E. De Bono, M. Morell, M. Collet, E. Gourdon, A. Ture Savadkoohi, M. Ouisse, and C. H. Lamarque. Model-inversion control to enforce tunable Duffing-like acoustical response on an Electroacoustic resonator at low excitation levels. Journal of Sound and Vibration, 570:118070, feb 2024. https://doi.org/10.1016/j.jsv.2023.118070

[9] Emanuele De Bono, Manuel Collet, Kevin Billon, Edouard Salze, Herv'e Lissek, Maxime Volery, Morvan Ouisse, and Jacky Marjono. Smart Acoustic Lining for UHBR Technologies Engine Part 2: Acoustic Treatment at the Intake of a Scaled Turbofan Nacelle. In 30th AIAA/CEAS Aeroacoustics Conference (2024), page 3304, 2024. https://doi.org/10.2514/6.2024-3304

[10] Emanuele De Bono, Manuel Collet, Morvan Ouisse, Edouard Salze, Maxime Volery, Hervé Lissek, and Jacky Mardjono. The Advection Boundary Law in presence of mean flow and plane wave excitation: Passivity, nonreciprocity and enhanced noise transmission attenuation. Journal of Sound and Vibration, page 119293, 2025. https://doi.org/10.1016/j.jsv.2025.119293

[11] Emanuele De Bono, Edouard Salze, Manuel Collet, Martin Gillet, Morvan Ouisse, Maxime Volery, Herv'e Lissek, and Jacky Mardjono. Experimental assessment of a programmable Electroacoustic Liner in a representative turbofan facility. Applied Acoustics, 240:110896, 2025. https://doi.org/10.1016/j.apacoust.2025.110896

[12] A W Guess. Calculation of perforated plate liner parameters from specified acoustic resistance and reactance. Journal of Sound and Vibration, 40(1):119-137, 1975. [13] Sami Karkar, Emanuele De Bono, Manuel Collet, Gael Matten, Morvan Ouisse, and Etienne Rivet. Broadband Nonreciprocal Acoustic Propagation Using Programmable Boundary Conditions: From Analytical Modeling to Experimental Implementation. Physical Review Applied, 12(5):054033, nov 2019. https://doi.org/10.1103/PhysRevApplied.12.054033

[14] Maxime Morell, Manuel Collet, Emmanuel Gourdon, Alireza Ture Savadkoohi, and Emanuele De Bono. Experimental validation of the analytical modelling of a digitally created

duffing acoustic nonlinear oscillator at low amplitudes. Mechanics & Industry, 26:2, 2025. https://doi.org/10.1051/meca/2024036

[15] Maxime Morell, Emmanuel Gourdon, Manuel Collet, Alireza Ture Savadkoohi, Emanuele De Bono, and Claude-Henri Lamarque. Towards digitally programmed nonlinear electroacoustic resonators for low amplitude sound pressure levels: Modeling and experiments. Journal of Sound and Vibration, 584:118437, 2024. https://doi.org/10.1016/j.jsv.2024.118437

[16] Maxime Morell, Aurélie Labetoulle, Emmanuel Gourdon, Emanuele De Bono, Manuel Collet, and Alireza Ture Savadkoohi. On the programming of cubic acoustic resonator with periodic time-dependent coefficient. Communications in Nonlinear Science and Numerical Simulation, page 108972, 2025. https://doi.org/10.1016/j.cnsns.2025.108972

[17] Sjoerd W Rienstra. Fundamentals of duct acoustics. Von Karman Institute Lecture Notes, 2015.

[18] Andre M N Spillere and Julio A Cordioli. Optimum acoustic impedance in circular ducts with inviscid sheared flow: Application to turbofan engine intake. Journal of Sound and Vibration, 443:502-519, 2019. https://doi.org/10.1016/j.jsv.2018.12.007

[19] B.J. Tester. The optimization of modal sound attenuation in ducts, in the absence of mean flow. Journal of Sound and Vibration, 27(4):477-513, apr 1973. https://doi.org/10.1016/S0022-460X(73)80358-X

Materials Research Proceedings 69 (2026) 331-334 https://doi.org/10.21741/9781644904251-59

Vibration and Noise Analyses of eVTOL Tilting Propeller with Different Anhedral Angles in Low-Speed Flight

Gi-Jeong Park[1,a *], Hyeok-Jin Son[1,b], Jaeheon Jeong[2,c], and Jae-Sang Park[1,d]

[1]Chungnam National University, Daejeon, Korea

[2]Korea Aerospace Research Institute, Daejeon, Korea

[a]rlwjd04046@gmail.com, [b]so7230052@gmail.com, [c]jhj123@kari.re.kr, [d]aerotor@cnu.ac.kr

Keywords: Electric Vertical Take-Off and Landing (eVTOL), Tiltrotor, Blade-Vortex Interaction (BVI), Hub Vibratory Loads, BVI Noise, Anhedral Angle

Abstract. In this study, a notional eVTOL tiltrotor model is developed and analyzed using the rotorcraft comprehensive analysis code, CAMRAD II, to investigate the effects of blade tip anhedral angles (Γ = 0°, 15°, and 25°) on hover performance, rotor hub vibratory loads, and BVI noise at a low-speed descending flight condition (C_T/σ=0.107, μ=0.15, and α_s=+6°)**.** For the hover performance the model with Γ=25° showed a 1.54% lower rotor power than the baseline model with Γ=0°**.** In the low-speed descend flight, the model with Γ=25° reduces hub Vibration Index (VI) by 21.24% compared to the baseline model. Furthermore, BVI noise is predicted using the CII-Sound code based on the FW-H equation, the baseline result shows a maximum BVI noise of 91.3dB, the case with Γ=25° yields the BVISPL of 88.7dB, a 2.62dB reduction compare to the baseline value

Introduction

Electric Vertical Take-Off and Landing (eVTOL) aircraft are being intensively developed for Urban Air Mobility (UAM), which is regarded as the next generation of air transportation [1,2]. The configurations of eVTOL aircraft are categorized into three types: Multicopter, Lift + Cruise, and Vectored Thrust [3]. Among these, vectored thrust aircraft use mixed RPM and pitch controls along with variable tilting angles, which enables various flight modes such as helicopter, airplane, and transition modes.

eVTOL aircraft require low vibration and low noise compared to conventional rotorcraft. In particular, during low-speed flights, rotors experience Blade-Vortex Interaction (BVI). BVI occurs when vortices approach the rotor blades, and its intensity increases when tip vortices collide with subsequent blades [4]. This interaction results in unsteady pressure fluctuations on the blades, causing severe rotor vibration and noise. Therefore, a study on rotor vibration and noise caused by the BVI phenomenon is required for eVTOL aircraft.

This study investigates the change in vibration and noise induced by BVI when applying different blade tip anhedral angles to a notional eVTOL tiltrotor (Figure 1). An aeromechanics model is developed using CAMRAD II, a rotorcraft comprehensive analysis code. Furthermore, BVI noise is predicted with CII-Sound, a rotorcraft noise analysis code, utilizing the CAMRAD II prediction results. The present paper summarizes the authors' recent work [5]; therefore, further detailed explanation and more results can be found in the reference [5].

Content from this work may be used under the terms of the Creative Commons Attribution 3.0 license. Any further distribution of this work must maintain attribution to the author(s) and the title of the work, journal citation and DOI. Published under license by Materials Research Forum LLC.

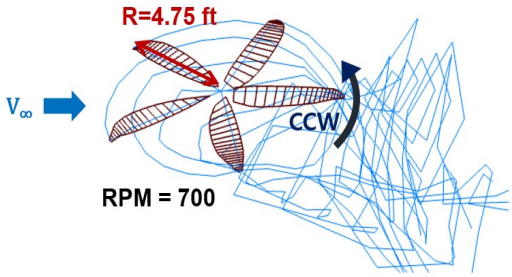


Figure 1. A notional eVTOL tiltrotor model

Methodology

Based on the reference [6], anhedral angles (Γ) of 0°, 15°, and 25° are applied at the 94% of blade radius. The blade sectional properties for the present proprotor model are obtained from a 1/4-scaled model of the V-22 Osprey tiltrotor (R=4.75 ft, [7]), with the geometric scaling considering different blade chord lengths. Each blade is modeled with seven finite beam elements for the blade structural dynamics modeling. For unsteady rotor aerodynamics using the second-order lifting-line theory, 19 aerodynamic panels are applied per blade. The Selig stall-delay model represents stall delay phenomena caused by a large built-in twist angle, and a general free-wake model is used for the rotor wake. This study assumes that the present model uses electromechanical actuators to control both collective and cyclic pitch motions of the blades for tiltrotor trim. The rotor, for a given flight speed (advance ratio, μ) and rotor shaft tilting angle (α_s), is trimmed to match the assumed rotor thrust and 1P lateral and longitudinal flapping angles of 0°.

Results

Figure 2 presents the hover performance (rotor power) analysis results obtained when different anhedral angles are considered for the eVTOL tiltrotor. The model with Γ=25° shows a 1.54% lower rotor power than the baseline model with Γ=0°. Therefore, these results indicate that the anhedral angle enhances hover performance. Figure 3 shows the hub vibratory loads in low-speed descending flight (C_T/σ=0.107, μ=0.15, and α_s=+6°), using the Vibration Index (VI). As the anhedral angle increases, VI decreases; therefore, the model with an anhedral angle of Γ=25° shows a 21.24% lower VI than the baseline model.

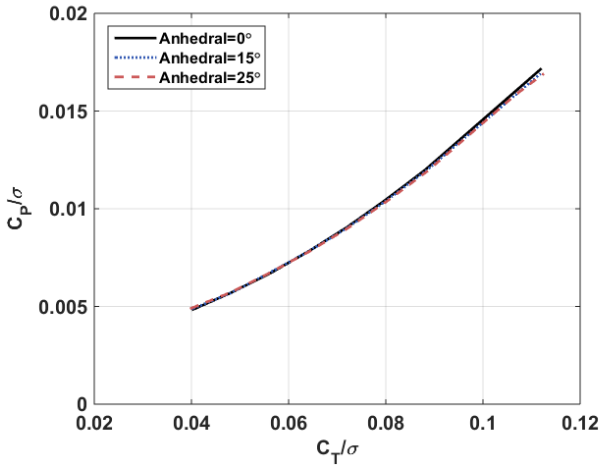


Figure 2. Rotor power in hover

Materials Research Proceedings 69 (2026) 331-334 https://doi.org/10.21741/9781644904251-59

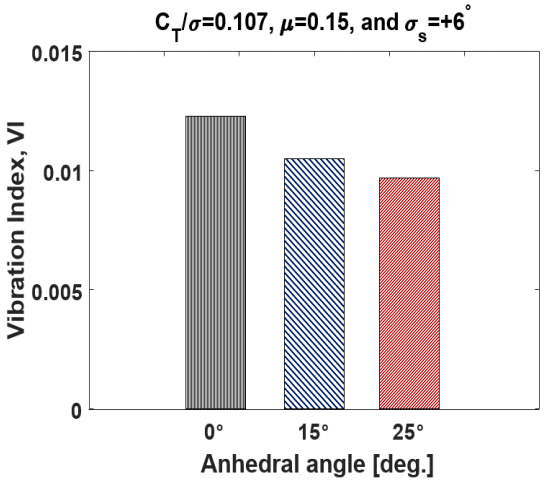
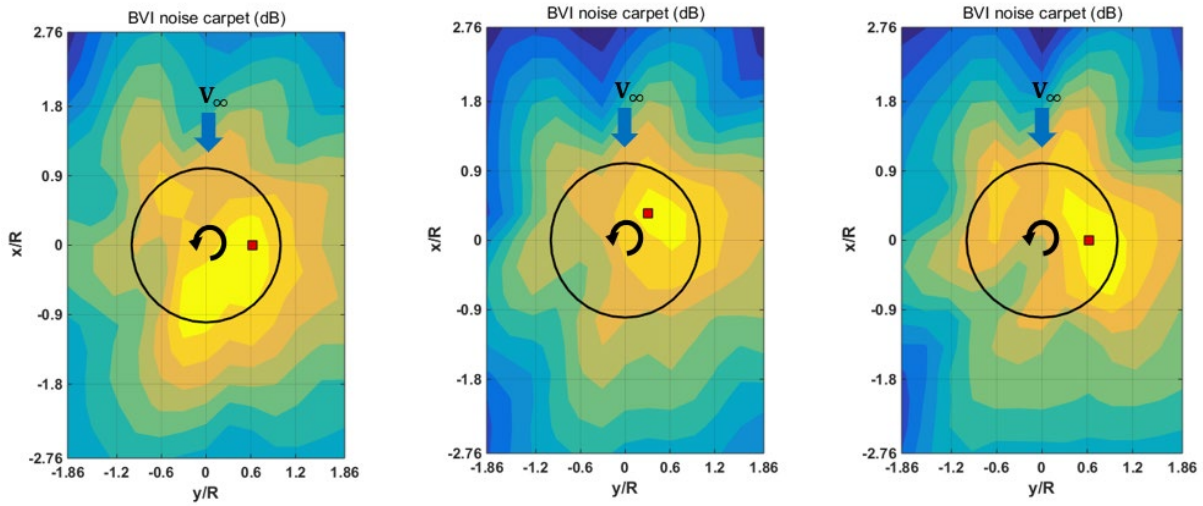


Figure 3. Vibration Index (VI) in low-speed descending flight (helicopter mode)

The CII-Sound code based on the Ffowcs Williams and Hawkings (FW-H) formulation is applied to predict BVI noise with different anhedral angles at a low-speed dsecending flight condition in helicopter mode (C_T/σ=0.107, μ=0.15, and α_s=+6°). BVISPL is determined by applying bandpass filtering to the acoustic analysis results in the 5th to the 42th Blade Passage Frequency (BPF) range. Figure 4 displays the BVI noise carpets for the eVTOL tiltrotor with different anhedral angles. While the baseline result shows a maximum BVISPL of 91.3 dB, the Γ=25° case yields 88.7 dB, a 2.62 dB reduction. This clearly indicates that an anhedral angle at the blade tip significantly reduces the eVTOL tiltrotor BVI noise. Furthermore, the locations of maximum BVISPL vary with the different anhedral angles, indicating changes in the directivity.



(a) Γ =0° (Max. BVISPL=91.3 dB) **(b) Γ=15° (Max. BVISPL=89.3 dB)** **(c) Γ =25° (Max. BVISPL=88.7 dB)**

Figure 4. BVI noise carpets in low-speed descending flight (helicopter mode)

Summary

This study developed a notional eVTOL tiltrotor model using the rotorcraft comprehensive analysis code, CAMRAD II, to investigate the effects of blade tip anhedral angles (Γ = 0°, 15°, and 25°). In hover flight, the model with Γ=25° showed a 1.54% lower rotor power than the baseline model with Γ=0°. In the low-speed descend flight (C_T/σ=0.107, μ=0.15, and α_s=+6°), the

model with Γ=25° reduced hub Vibration Index (VI) by 21.24% compared to the baseline model. Furthermore, BVI noise predicted with the CII-Sound code decreased from 91.3 dB for the baseline model to 88.7 dB for the model with Γ = 25°, with a 2.62 dB reduction. Therefore, applying blade tip anhedral to an eVTOL tiltrotor improved hover performance while simultaneously reducing hub vibratory loads and BVI noise during low-speed descending flight.

Acknowledgments
This research was supported by Basic Science Research Program funded by Ministry of Science and ICT (2021R1A5A1031868).

References

[1] A. Straubinger, R. Rothfeld, M. Shamiyeh, K. D. Büchter, J. Kaiser, and K. O. Plötner, "An overview of current research and developments in urban air mobility–setting the scene for UAM introduction," *Journal of Air Transport Management*, vol. 87, 101852, 2020. https://doi.org/10.1016/ j.jairtraman.2020.101852

[2] A. Abu Zaid, B. E. Y. Belmekki, and M. S. Alouini, "eVTOL communications and networking in UAM: requirements, key enablers, and challenges," *IEEE Communications Magazine*, vol. 61, no. 8, pp. 154-160, 2023. https://doi.org/10.1109/MCOM.004.2300061

[3] J. Su, H. Huang, H. Zhang, Y. Wang, and F. Y. Wang, "eVTOL performance analysis: A review from control perspectives," *IEEE Transactions on Intelligent Vehicles*, vol. *9*, no.5, pp. 4877-4889, 2024. https://doi.org/10.1109/TIV.2024.3387405

[4] J. Wu, O. Stalnov, W. Chen, Z. Yang, and X. Huang, "Transient analysis of blade-vortex interaction noise," *Aerospace Science and Technology*, vol. 120, 107294, 2022. https://doi.org/10.1016/j.ast.2021.107294

[5] G. J. Park, H. J. Son, J. H. Jeong, and J. S. Park,"Vibration and BVI noise analyses of eVTOL tiltrotors in low-speed descending flight," *Journal of Aerospace System Engineering*, Under Review, 2025.

[6] J. Bevirt, E. Stilson, A. Stoll, and G. V. Mikic, "Electric tiltrotor aircraft," U.S. Patent Application US 2021/0253237 A1, 2021.

[7] U. J. Hwang, J. S. Park, and M. K. Lee, "A validation study on the performance and load analyses of tiltrotors in wind tunnel," *Journal of the Korean Society for Aeronautical and Space Sciences*, vol. 51, no. 1, pp. 57–66, 2023. https://doi.org/10.5139/JKSAS.2023.51.1.57

Materials Research Proceedings 69 (2026) 335-340 https://doi.org/10.21741/9781644904251-60

Acoustic Liners for Low-Frequency Sound Absorption: A Preliminary Study

Luigi Maria CARDONE[1,a *], Giuseppe PETRONE[1,b], Alessandro CASABURO[1,c], Francesco FRANCO[1,c] and Sergio DE ROSA[1,d]

[1]University of Naples Federico II, via Claudio 21, 80125 Naples

[a]luigimaria.cardone@unina.it, [b]giuseppe.petrone@unina.it, [c]alessandro.casaburo@unina.it, [d]francesco.franco@unina.it, [e]sergio.derosa@unina.it

Keywords: Absorption Coefficient, Honeycomb Structures, Comsol Multiphysics, Acoustic Liner

Abstract. With growing global awareness of environmental impacts from the transport sector, significant attention is now being directed at reducing noise emissions. In aviation, the dominant source of noise emissions is the engine, which produces intense acoustic energy during take-off and landing phases, often exceeding 140 dB close to the source. Efforts to address this issue are increasingly tied to advancements in propulsion technologies, particularly novel propulsion systems such as electric and hybrid-electric engines are altering the noise signature of aircraft and rendering conventional noise reduction technologies less effective. This study proposes an innovative acoustic liner design based on modified honeycomb sandwich structures. The objective is to enhance low-frequency sound absorption performance while ensuring the design remains suitable for industrial application in nacelle liners and other aircraft interior components. In the proposed design, a standard honeycomb strut is retained but modified by reducing the inlet hole diameter, thereby tuning the system's resonance behavior. This reduction causes a downshift in the peak absorption frequency, enabling better performance in the low-frequency range (below 1000 Hz), which is critical for jet engine noise. By varying geometrical parameters—such as cell size, wall thickness, and perforation diameter—the frequency response can be tailored to target specific tonal components of engine noise

Introduction

In response to growing concerns about environmental impact, the European community has introduced increasingly stringent regulations aimed at reducing CO_2 emissions and minimizing aircraft noise during takeoff and landing phases [1]. One of the primary sources of such noise is the aircraft engine. To address this, acoustic liners are employed to attenuate the tonal components of fan noise. These liners are typically constructed as sandwich structures, consisting of a rigid bottom panel—often perforated or slotted for drainage—a honeycomb core with defined hexagonal geometry, and a micro-perforated sheet that seals the structure[2, 3] as visible in Fig.1.

Content from this work may be used under the terms of the Creative Commons Attribution 3.0 license. Any further distribution of this work must maintain attribution to the author(s) and the title of the work, journal citation and DOI. Published under license by Materials Research Forum LLC.

Materials Research Proceedings 69 (2026) 335-340 https://doi.org/10.21741/9781644904251-60

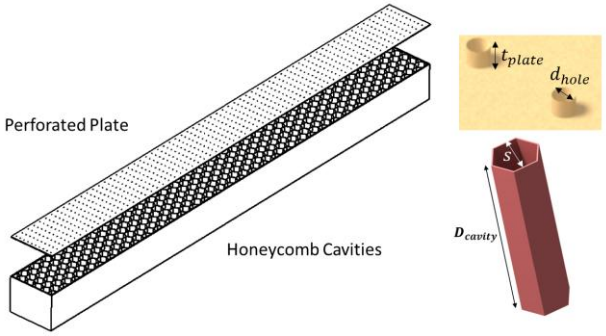


Fig. 1:Example of a liner section (left-hand side) with perforated facesheet and honeycomb cavities backed by rigid walls, with single cell of perforated plate plus honeycomb

The sound absorption mechanism of these liners is fundamentally based on Helmholtz resonator principles. By adjusting parameters such as the flat-to-flat dimension of the honeycomb cells (s), the cavity depth ($D_$cavity), the diameter of the perforations ($d_$holes), and the thickness of the plates ($T_$plates), the resonance frequencies can be tuned to coincide with tonal sources like Blade Passing Frequencies, thereby reducing acoustic disturbances. These structures are strategically installed in the engine intake area, where space constraints—especially at the bypass outlet—necessitate compact designs. As engine bays are increasingly optimized for lower emissions, higher bypass ratios (e.g., GE9X.) are becoming more common [4].

Beyond aviation, acoustic liners are also utilized in various sectors such as helicopter cabin noise reduction, automotive interiors, and offshore installations, all sharing similar manufacturing and structural concepts[5;6;7]. Enhancing these liners within the strict confines of aeronautical standards can thus yield benefits across multiple industries. Recent advancements in 3D printing have opened new possibilities for designing complex geometries that significantly improve acoustic performance. The concept proposed in this study is to retain the conventional honeycomb manufacturing process while innovating its internal configuration. For this preliminary investigation, a simplified model is adopted where each cell lacks internal substructures and is tuned to a single frequency, effectively functioning as a large cavity.

The structure of the paper is as follows: it begins with a description of the numerical methodology, followed by the experimental procedures and results, and concludes with the main findings.

Numerical model and experimental setup

To correctly validate the experimental setup, a digital twin of the initial stage of the impedance tube experiments was first created. In the laboratory, alongside the Mecanum Alpha-cabin, there is a 44 mm impedance tube from the same manufacturer. This tube size matches perfectly with the dimensions of a single cell of the device, making it ideal for preliminary analysis. To ensure that the device was properly tuned to the target frequency of 500 Hz, a digital model replicating the laboratory tube was developed using the COMSOL Multiphysics simulation environment. Several analyses were performed to investigate how variations in specific geometric control parameters influence the position of the absorption coefficient peak. The model structure utilized two acoustic modules from the Acoustics Interfaces package—Pressure Acoustics and Thermo-Viscous Acoustics. This combination was selected to balance computational efficiency with physical accuracy, ensuring that the simulated setup closely replicated the real experimental apparatus. The Pressure Acoustics module was employed to model the impedance tube and the honeycomb cavities, with a Plane Wave Radiation boundary condition applied on the side opposite to the sample placement (see Fig. 2(a)).

Materials Research Proceedings 69 (2026) 335-340 https://doi.org/10.21741/9781644904251-60

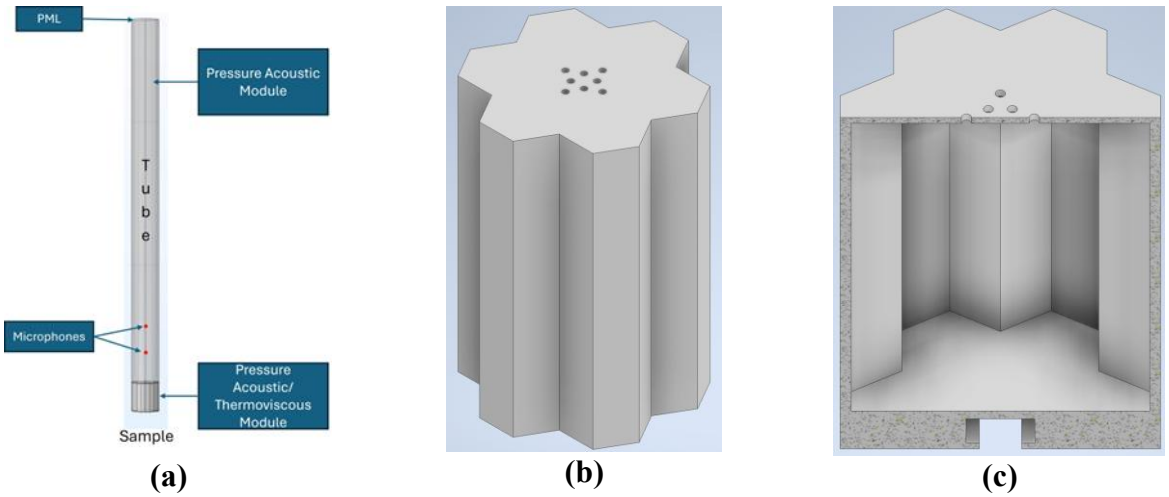


Fig. 2: (a) Digital Twin Impedance tube in Comsol Multiphysics; (b) Cad sample model; (c) Section of the sample

For the perforated plate, the Thermo-Viscous Acoustics module was used to accurately capture acoustic behavior in small-scale geometries. Although this module incurs a higher computational cost than the simpler Pressure Acoustics module, it is essential for detailed analysis of the hole regions. All structural domains and walls were assumed to be acoustically rigid. A comprehensive description of the boundary conditions and physics implementation can be found in the COMSOL Multiphysics Acoustics Module User Guide [8].

At this stage, the investigation focuses exclusively on the acoustic performance of the proposed device. The results obtained from the simulations are presented in the following section, alongside those from the Alpha-cabin experiments. Once the geometry and effectiveness of the digital model were validated, physical testing within the cabin commenced. It is important to note that the impedance tube and the Alpha-cabin determine the absorption coefficient using different methodologies. The impedance tube technique determines the sound absorption coefficient by analyzing the pressure variations of incident and reflected acoustic waves. This is achieved through the evaluation of the complex reflection coefficient, which is derived using the following standard expression:

$$\boldsymbol{R = \frac{H_{12} - e^{-jk_0 s}}{e^{jk_0 s} - H_{12}} \cdot e^{2jk_0 x_1}} \tag{1}$$

In this formulation, $\boldsymbol{H_{12}}$denotes the complex acoustic transfer function measured between microphones 2 and 1. Corrections for amplitude and phase discrepancies are applied using the switched microphones method. The term $\boldsymbol{k_0}$represents the wave number under plane wave excitation conditions, as outlined in standardized methodologies [9,10].

The sound absorption coefficient under plane wave excitation is subsequently evaluated using the relation

$$\boldsymbol{\alpha = 1 - |R|^2} \tag{2}$$

Conversely, the Alpha-cabin estimates the absorption coefficient—known as $\boldsymbol{\alpha_{sabine}}$—based on the reverberation time of the room, denoted as T_{60}. The subscript "60" refers to a 60 dB decay within a reference volume. Consequently, as shown in the results section, α_Sabine values can exceed 1.

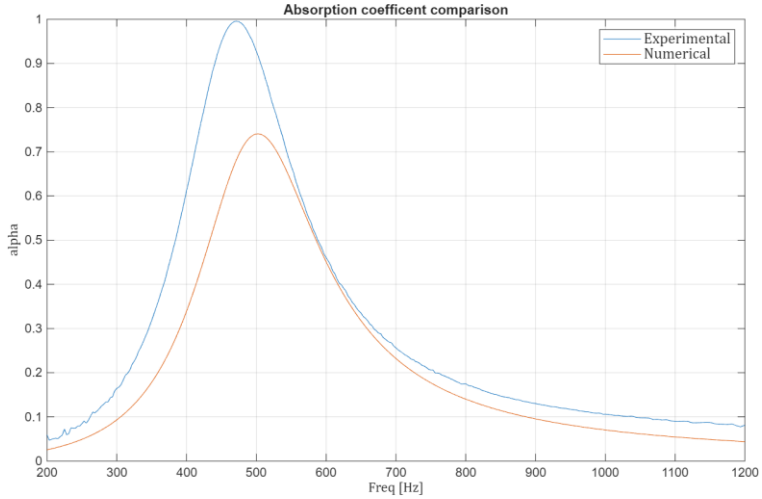
$$\boldsymbol{\alpha_{sabine} = \frac{0.966}{S}\left(\frac{1}{T_1} - \frac{1}{T_0}\right)} \qquad \boldsymbol{T_i = 0,16\frac{V}{S\bar{a}}} \tag{3}$$

Materials Research Proceedings 69 (2026) 335-340 https://doi.org/10.21741/9781644904251-60

From the Sabine formulation in possible to understand that the absorption coefficients is referred to a surface and could be more than 1. This is not a physical inconsistency but rather a reflection of the different evaluation methodology used.

Experimental results

Following the validation of the numerical model, experimental verification was performed on the fabricated samples to substantiate the computational results. Acoustic characterization was carried out using two distinct measurement techniques, the first employing an impedance tube in accordance with ASTM E1050 and ISO 10534-2 standards. The comparison presented in the figure 3(a) demonstrates an excellent correspondence between the numerical predictions and the experimental measurements obtained in our laboratory. This strong agreement substantiates the accuracy and robustness of the proposed model, thereby validating its applicability to other multi-tonal configurations beyond the scope of the present study.



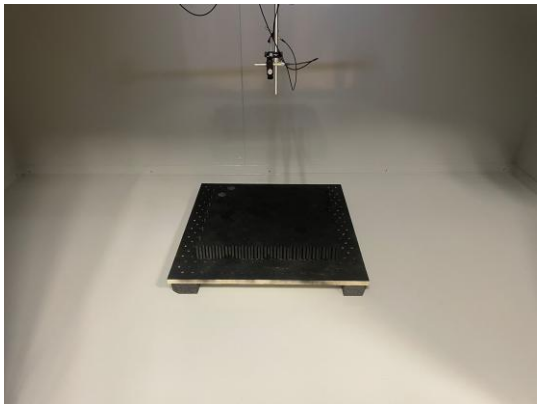
(a)



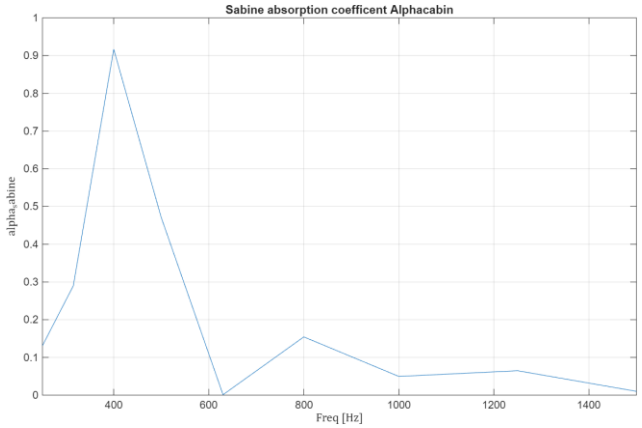
(b)

Fig. 3:(a) Numerical and Experimental absorption curve comparison; (b) 3D printed model

After validating the performance of the individual samples, the study progressed to the second phase. A total of 250 unit cells were 3D-printed and subsequently mounted onto an 18 mm thick marine plywood panel. This panel served as a means of minimizing potential vibrations of the single element induced by the acoustic field within the cabin. Prior to testing, the cabin was acoustically mapped to determine the optimal measurement locations. The analysis indicated that positioning the panel at the geometric center—equidistant from the surrounding boundaries as visible in figure 4a—was most effective in mitigating edge effects. The experimental tests were then conducted, and the corresponding results are presented in the diagram below.



(a)



(b)

Fig. 4: (a) Experimental set-up for Alpha Cabin Mecanum; (b) Sabine absorption coefficient diagram

A noticeable discrepancy was observed between the results obtained using the impedance tube and those recorded in the cabin environment. Although the resonators were specifically designed to absorb sound at 500 Hz, the diagram in Fig. 4b reveals no absorption peak at this frequency. Instead, the only discernible peak appears at 400 Hz. Following a series of investigations conducted in collaboration with the cabin manufacturer's team, it was hypothesized that an interaction may exist between the first modal shape of the cabin and the resonators. This phenomenon has not been previously encountered, likely due to the novelty of testing resonant cavity materials tuned to frequencies near the lower limit of the cabin's measurement capabilities. A similar condition is discussed in the work of Strasberg [11]. Further investigations are deemed necessary to accurately validate the performance of the proposed samples.

Conclusion

In summary, the numerical model has demonstrated a strong capability to accurately predict the behavior of the samples tested in the impedance tube. The observed discrepancies between the numerical and experimental curves are primarily attributed to the manufacturing process, which, for reasons of expediency and prototyping, currently relies on 3D printing. The adoption of higher-grade materials is expected to significantly reduce these discrepancies, as suggested by the comparison shown in Figure 3b. Additional configurations, including multi-tonal designs, have already been developed and validated both numerically and experimentally—through impedance tube testing and a more advanced experimental campaign conducted in the anechoic wind tunnel at TU Delft. However, the acoustic behavior of these samples under a diffuse sound field remains to be thoroughly investigated. This condition is particularly critical, as it would enable the validation of these devices not only for use in nacelle liners but also for interior aircraft cladding and other applications where enhanced acoustic comfort is required through structurally advanced solutions.

References

[1] Kreimeier, M., Stumpf, E., and Gottschalk, D., Economical assessment of air mobility on demand concepts with focus on Germany, 2016. https://doi.org/10.2514/6.2016-3304

[2] Liu, X., Zhao, D., Guan, D., Becker, S., Sun, D., and Sun, X., "Development and progress in aeroacoustic noise reduction on turbofan aeroengines," Progress in Aerospace Sciences, Vol. 130, 2022, p. 100796. https://doi.org/10.1016/j.paerosci.2021.100796

[3] Sutliff, D. L., Nark, D. M., and Jones, M. G., "Multi-degree-of-freedom linerdevelopment:Concept to flight test," InternationalJournal of Aeroacoustics, Vol. 20, No. 5-7, 2021, pp. 792–825. https://doi.org/10.1177/1475472X211023860

[4] GE9X," https://www.geaerospace.com/propulsion/commercial/ge9x, 2023.

[5] Li, C., Lu, Y., Lan, C., and Wang, Y., "Noise Reduction in Helicopter Cabins Using Microperforated Panel Composite Sound Absorption Structures," Applied Sciences, Vol. 13, No. 14, 2023. https://doi.org/10.3390/app13148153

[6] Jonza, J., Yoo, T., Herdtle, T., Kalish, J., Gerdes, R., and Eichhorn, G., "Acoustically Absorbing Lightweight Thermoplastic Honeycomb Panels," INTER-NOISE and NOISE- CON Congress and Conference Proceedings, Vol. 254, No. 2, 2017, pp.210–219.

[7] Cardone, L. M., Catapane, G., & Petrone, G. (2024). Innovative honeycomb design for low frequency applications. In 30th AIAA/CEAS Aeroacoustics Conference (2024) (p. 3079).

[8] "Acoustics Module User's Guide, COMSOL Multiphysics 6.0," https://doc.comsol.com/6.0/doc/com.comsol.help.aco/AcousticsModuleUsersGuide.pdf, 2023. (Accessed: 24/11/2023).

[9] ASTM E1050-19, "Standard Test Method for Impedance and Absorption of Acoustical Materials Using a Tube, Two Microphone and a Digital Frequency Analysis System," Standard, ASTM International, 2019.

[10] ISO 10534-2, "Determination of sound absorption coefficient and impedance in impedance tubes — Part 2: Transfer- function method," Standard, International Organization for Standardization, 1998.

[11] M. Strasberg, D. Feit, Vibration damping of large structures induced by attached small resonant structures, J. Acoust. Soc. Am. 99 (1996) 335–344.

Materials Research Proceedings 69 (2026) 341-345 https://doi.org/10.21741/9781644904251-61

Numerical Vibro-Acoustic Characterization of Aerospace Structures Made of Miura-Ori Origami Metamaterial

Martino Carlo MORUZZI[1,a,*], Vasilena Petrova KRALEVA[2,b], Matteo FILIPPI[3,c], Maria CINEFRA[2,d]

[1]University of Bologna, Department of Industrial Engineering, Forlì, Italy

[2]Polytechnic University of Bari, Department of Mechanics, Mathematics and Management, Bari, Italy

[3]Polytechnic University of Turin, Department of Mechanical and Aerospace Engineering, Turin, Italy

[a]martinocarlo.moruzzi@unibo.it, [b]vasilena.kraleva@poliba.it, [c]matteo.filippi@polito.it, [d]maria.cinefra@poliba.it

Keywords: Origami, Acoustic Metamaterial, Carrera's Unified Formulation, Wave Finite Element Method

Abstract The objective of this work is to define a method for evaluating the dynamic characteristics of a Miura-origami acoustic metamaterial panel. The metamaterial must be able to absorb the noise generated by an aircraft and shield the passenger cabin from it. The Miura-origami metamaterial is a periodic corrugated plate. The acoustic properties can be derived from the calculation of the dispersion curves, given the mechanical properties of the structure. The former are obtained using the Wave Finite Element Method, the latter using a Layer-Wise approach based on Carrera's Unified Formulation. The method is applied to a starting configuration of the metamaterial's unit cell.

Introduction

Acoustics, a branch of physics concerning the generation, propagation, detection, and conversion of sound waves, is playing an increasingly important role in modern engineering. With the advent of acoustic metamaterials (AMMs), the manipulation of complex sound and vibrations has become possible. Due to their distinctive engineering properties determined by the precisely structured geometries at the macro level, they have been artificially designed to address the noise and vibrations problem which cannot be solved with naturally occurring materials and are often used for efficient sound absorption and insulation as well as negative refraction, wave steering, and filtering.

AMM for aeronautical use has been developed in various studies [1, 2, 3], particularly for low-frequency noise, which is the primary source of noise in an aircraft. The advantage is the possibility of obtaining efficient, lightweight materials. In particular, AMM panels can be inserted into the cavity between the fuselage and the cabin as the core of a sandwich, replacing the traditional material [4, 5] (usually Nomex). In this case, the AMM must also guarantee a minimum level of mechanical strength. In this work, Miura-origami-shaped panels were chosen [6]. These materials are suitable for insertion into a sandwich and offer various production options for different materials, ranging from plastics to carbon fiber.

The presence of complete and partial bandgaps will be evaluated employing the wave finite element method (WFE) [7, 8]. The developed method enables the calculation of dispersion curves for periodic materials. The structure is described according to the Carrera's Unified Formulation (CUF) framework for beams, plates, and shells, which embeds a wide class of powerful refined 2D plate theories exploiting the finite element (FE) approximation

Content from this work may be used under the terms of the Creative Commons Attribution 3.0 license. Any further distribution of this work must maintain attribution to the author(s) and the title of the work, journal citation and DOI. Published under license by Materials Research Forum LLC.

Materials Research Proceedings 69 (2026) 341-345 https://doi.org/10.21741/9781644904251-61

[9].

Among these, layer-wise (LW) approaches, that suppose the composite structure as made of independent layers so that it is possible to have a 3D description of the stress-strain state in the material, makes it possible to evaluate the power radiated by the plate in a given layer, so the one opposite to the layer on which the acoustic wave breaks. LW theories have also been proved to be able to model the vibro-acoustic behaviour of structures with low computational costs and high accuracy, particularly in the case of multilayer orthotropic materials, which gives the opportunity for future developments in the manufacturing and analysis of the Miura-Ori structure as a carbon fibre reinforced polymer (CFRP) composite material. Finally, numerical simulations will be validated against experimental results, conducted by impedance tube system and anechoic chamber.

In conclusion, the development and characterization of an acoustic origami-inspired metamaterial is proposed in this work in order to address the noise and vibration problem in aircraft cabins. The aim is to obtain an accurate evaluation of the dynamic behaviour of an ABS Miura-Ori plate, an origami-inspired acoustic metamaterial, parametrized according to the unit cell shown in Fig. 1.

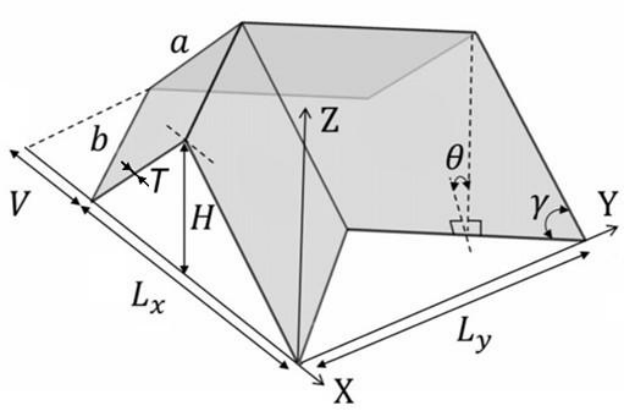


Figure 1: Periodic unit cell of the Miura-Ori plate.

Wave finite element and numerical approximation

The WFE is a powerful tool for understanding the energy transfer mechanism of a structure. This method has gained popularity in the study of infinite periodic structures, enabling the calculation of dispersion curves [10].

Considering a $x - y$ plate made of an infinite periodic repetition of unit cells with N degrees of freedom (DOFs) and assuming both forces and displacements are harmonic in time, the kinematic field is described in the frequency domain by the following relation:

$$(\boldsymbol{K} - \omega 2\boldsymbol{M})\boldsymbol{q} = \boldsymbol{F} \qquad \widetilde{\boldsymbol{D}}(\omega)\boldsymbol{q} = \boldsymbol{F} \tag{1}$$

with **K**, **M** being the $N \times N$ stiffness and mass matrices, and **q** and **F** the $N \times 1$ nodal displacement and external forces vectors. The angular frequency is ω. The mass and stiffness matrices are merged in the dynamic stiffness matrix $\widetilde{\boldsymbol{D}}$.

According to the Bloch's theorem, due to the periodicity of the medium and the equilibrium of the forces, the propagation of the free waves depends only on the reduced displacement vector $\widetilde{\boldsymbol{q}}$:

$$\boldsymbol{q} = \boldsymbol{R}\widetilde{\boldsymbol{q}} \qquad \boldsymbol{R}'\boldsymbol{F} = 0 \tag{2}$$

where **R** is the periodicity matrix and $\mathbf{R}'$ is the conjugate transpose of **R**. Combining Eq. 2 in Eq. 1, the generalized dispersion eigenvalue problem is obtained:

Materials Research Proceedings 69 (2026) 341-345 https://doi.org/10.21741/9781644904251-61

$$\left(\boldsymbol{R}'\widetilde{\boldsymbol{D}}(\boldsymbol{\omega})\boldsymbol{R}\right)\widetilde{\boldsymbol{q}} = \boldsymbol{0} \tag{3}$$

in which $\widetilde{\boldsymbol{D}}$ is a function of the wave numbers k_x and k_y ($\lambda_x = e^{-jk_x\Delta x}$ and $\lambda_y = e^{-jk_y\Delta y}$, where Δ_x and Δ_y are the dimensions of the unit cell in x and y).

Solving the problem for λ_y with a direct approach (providing ω and λ_x), Eq. 3 becomes a quadratic equation:

$$\left(\boldsymbol{A_2}\lambda_y^2 + \boldsymbol{A_1}\lambda_y + \boldsymbol{A_0}\right)\widetilde{\boldsymbol{q}} = 0 \tag{4}$$

The full definition of the matrices for different finite elements is reported in [7, 8].

According to the CUF, the displacement vector **u** for a plate in the finite element approximation is written as:

$$\mathbf{u}(x,y,z,t) = F_\tau(z)N_i(x,y)q_{i\tau}(t), \quad 1 \le i \ge n_e, \quad 1 \le \tau \ge M \tag{5}$$

with $F_\tau(z)$ the thickness functions, $N_i(x,y)$ the Lagrangian finite element shape functions. The order of the shape function is defined by the number of nodes in the element, n_e (i is the nodal index in the element), while the order of the thickness depends on the number M which define the structural theory (τ is the nodal index through the thickness). The WEM has been already validated in [8] for different thickness functions. In this work, Lagrange polynomials are used.

Case study

In this work, the use of WEM is extended to a corrugated metamaterial plate. The unit cell, derived from [6], is shown in Fig. 1. As a case study, an ABS (Young modulus E =2.2 GPa, Poisson ratio ν = 0.35 and density ρ =1040 kg/m^3) cell is used for future experimental comparisons, with a thickness of 1.5 mm and dimensions as shown in Tab 1. The FEM analysis is made using 16 quadrangular elements with four nodes Q4 (four Q4 per face) and three nodes along the thickness (LW2). To manage the edges, the formulation in [11] is used, which allows for unconventional, distorted 3D elements (a combination of 2D FEM and 1D thickness functions). The periodic conditions are shown in Fig. 2. The problem has 19 independent nodes, with a total of 171 DOFs. Results are calculated from 0 Hz to 20000 Hz. The dispersion curves of the real part of the wave number are reported in Fig. 3 and Fig. 4 for k_x and k_y respectively.

Table 1: Dimension of the unit cell in Fig. 1. Lengths are in mm and angles in degrees.

L_x	L_y	V	H	T	a	b	θ	γ
59.9	52.5	26.7	26.5	1.5	40.0	40.0	60	42

Materials Research Proceedings 69 (2026) 341-345 https://doi.org/10.21741/9781644904251-61

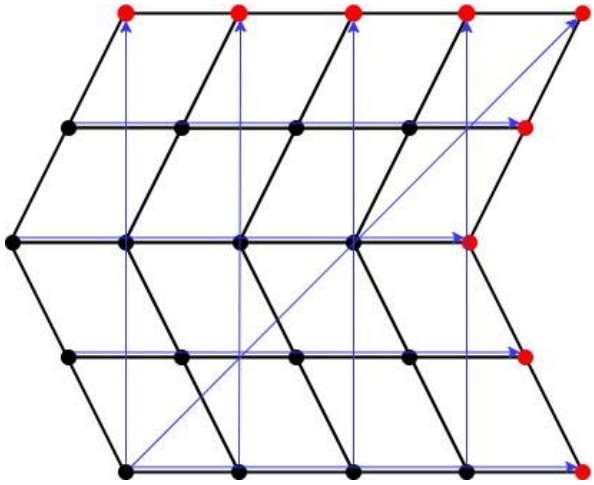


Figure 2: Periodic boundary conditions applied to the unit cell. Black nodes are independent, red dependent and the arrows show the dependency.

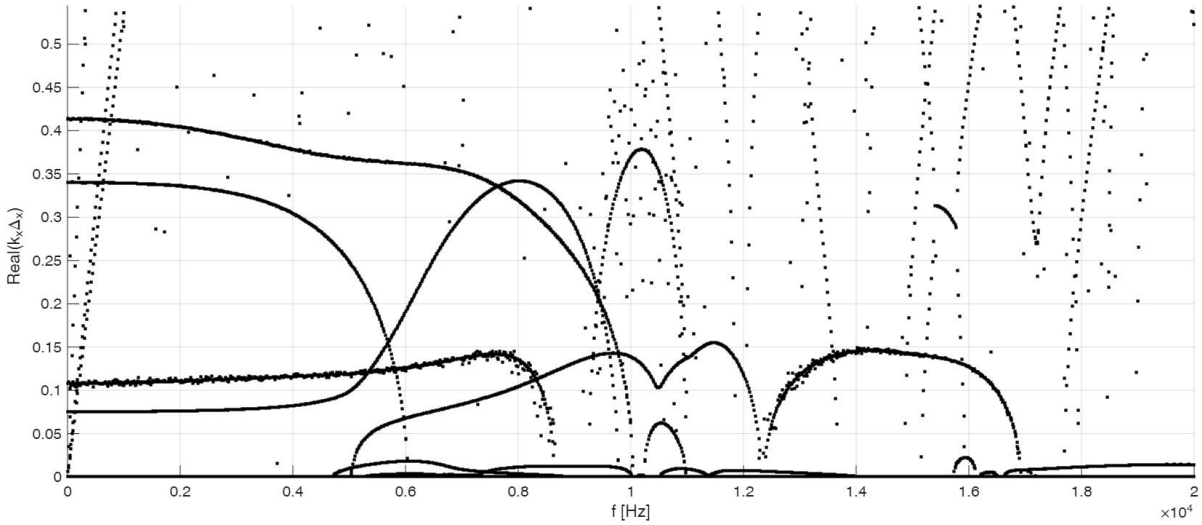


Figure 3: Real part of the dispersion curve in x.

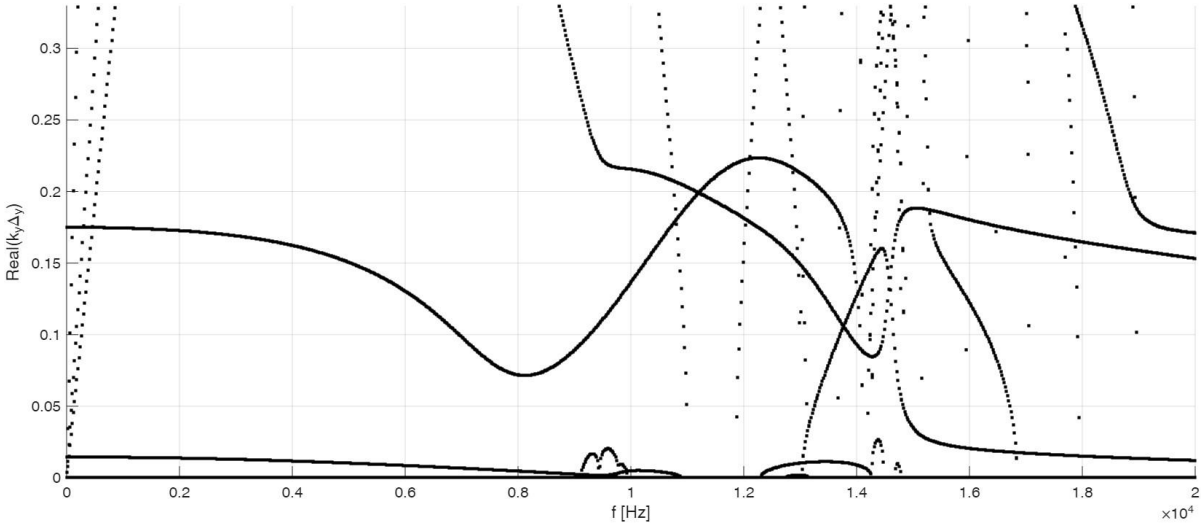


Figure 4: Real part of the dispersion curve in y.

Conclusions

Thanks to WFE, it is possible to calculate dispersion curves for a periodic material. In this work, we combine the potential of a LW approach with that of WFE to calculate dispersion curves for a corrugated metamaterial. A future development will be to calculate transmission loss based on the results obtained.

Acknowledgments

This work has been supported by the project ”Advanced numerical models for the vibro-acoustic characterization of aerospace structures made of metamaterials”, funded by the MIUR Progetti di Ricerca di Rilevante Interesse Nazionale (PRIN), bando 2022.

References

[1] G. Palma, H. Mao, L. Burghignoli, P. Goransson, U. Iemma. Acoustic Metamaterials in Aeronautics. Appl. Sci. (2018) 8, 971. https://doi.org/10.3390/app8060971

[2] L.M. Cardone, G. Catapane, G. Petrone, S. De Rosa, A. Squillace, L. Landolfi, A. L.H.S. Detry. Acoustic Characterization of Metamaterial Structures Fabricated via Foamed Filament 3D Printing, AIAA 2024-3080 (2024). https://doi.org/10.2514/6.2024-3080

[3] M. Cinefra, G. D'Amico, A.G. De Miguel, M. Filippi, A. Pagani, E. Carrera. Efficient numerical evaluation of transmission loss in homogenized acoustic metamaterials for aeronautical application, Applied Acoustics (2020) 164, 107253. https://doi.org/10.1016/j.apacoust.2020.107253

[4] M.C. Moruzzi, M. Cinefra, S. Bagassi. Vibroacoustic analysis of an innovative windowless cabin with metamaterial trim panels in regional turboprops. Mechanics of Advanced Materials and Structures (2019) 28(14), 1509-1521. https://doi.org/10.1080/15376494.2019.1682729

[5] G. Catapane, D. Magliacano, G. Petrone, A. Casaburo, F. Franco, S. De Rosa, Transmission Loss Analyses on Different Angular Distributions of Periodic Inclusions in a Porous Layer (2021) Aerotecnica Missili & Spazio, Vol. 100, pp. 363-373. https://doi.org/10.1007/s42496-021-00101-6

[6] X. Zhang, X. Huang, G. Lu. Tunable bandgaps and acoustic characteristics of perforated Miura-ori phononic structures, International Journal of Mechanical Sciences (2023). https://doi.org/10.2139/ssrn.4347055

[7] B.R. Mace, E. Manconi. Modelling wave propagation in two-dimensional structures using finite element analysis, Journal of Sound and Vibration, (2008) 318, 4-5, 884-902. https://doi.org/10.1016/j.jsv.2008.04.039

[8] M. Filippi, D. Magliacano, M. Petrolo, E. Carrera. Variable-Kinematics Finite Elements for Propagation Analyses of Two-Dimensional Waveguides, AIAA 2024-3078 (2024). https://doi.org/10.2514/6.2024-3078

[9] E. Carrera, M. Cinefra, M. Petrolo, E. Zappino. Finite element analysis of structures through unified formulation, Wiley (2014). https://doi.org/10.1002/9781118536643

[10] V. Cool, E. Deckers, L. Van Belle, C. Claeys. A guide to numerical dispersion curve calculations: Explanation, interpretation and basic Matlab code, Mechanical Systems and Signal Processing (2024) 215, 111393. https://doi.org/10.1016/j.ymssp.2024.111393

[11] M.C. Moruzzi, M. Cinefra, S. Bagassi. Free vibration of variable-thickness plates via adaptive finite elements, Journal of Sound and Vibration (2024) 577, 118336. https://doi.org/10.1016/j.jsv.2024.118336

Materials Research Proceedings 69 (2026) 346-350 https://doi.org/10.21741/9781644904251-62

Acoustic Comfort Evaluation in the Passenger Cabin and Cockpit Through a Mixed-Reality Environment

Andrea ALAIMO[1,a], Sara BAGASSI[2,b], Francesca BRACAGLIA[3,c], Erasmo CARRERA[3,d], Antonio ESPOSITO[1,e], Tommaso FADDA[2,f], Matteo FILIPPI[3 g], Martino Carlo MORUZZI[2,h,*]

[1]Faculty of Engineering and Architecture, Kore Università di Enna, Enna, Italy
[2]University of Bologna, Department of Industrial Engineering, Forlì, Italy [3]Polytechnic University of Turin, Department of Mechanical and Aerospace Engineering, Turin, Italy

[a]andrea.alaimo@unikore.it, [b]sara.bagassi@unibo.it, [c]francesca.bracaglia@polito.it, [d]erasmo.carrera@polito.it, [e]antonio.esposito@unikore.it, [f]tommaso.fadda2@unibo.it, [g]matteo.filippi@polito.it, [h]martinocarlo.moruzzi@unibo.it

Keywords: Aircraft Noise, Auralisation, Cabin Design, Virtual Reality

Abstract This work develops a method for converting the results of vibroacoustic numerical simulations into virtual perceived noise. The goal is to evaluate solutions for reducing noise in passenger cabins in virtual mock-ups using a user-centred approach. Passengers wearing augmented reality headsets are immersed in the cabin environment, both visually and auditorily. This article describes the virtual auralisation process and presents a case study of a business jet cabin to evaluate the quality of the developed method.

Introduction

The acoustic footprint of an aircraft not only affects the structure through vibrations, but also plays a key role in the flight experience in the passenger cabin and the cockpit. In the former, the problem mainly concerns user comfort [1], although novel aircraft configurations could bring noise levels above the recommended thresholds; in the latter, in addition to the comfort problem, excessive noise levels could compromise pilot performance and increase pilot workload. For these reasons, users should take a central role in assessing interior noise for new aircraft configurations or evaluating the effectiveness of new acoustic solutions. Nevertheless, noise impact assessment has been conventionally carried out using human-based metrics, i.e. comparing measured noise levels with parameters derived from physical and physiological laws and data from experience. While this assessment method can be valid for regulatory compliance, it fails to assess qualitatively the impact of noise variation on users. To make a qualitative and reliable evaluation of the effect of an acoustic variation on passengers and crew, users need to be directly involved in the design and evaluation process, thus using a human-centred approach. Studies have already been carried out in the comfort assessment field utilising this type of approach [2]. In particular, the evaluation must pass through the "immersion" of the user in the environment by constructing a mock-up. Given the complexity of creating an aircraft cabin and considering the acoustic aspect, it is preferable to use virtual mock-ups, which guarantee less time and cost and greater flexibility in trying out different designs and acoustic solutions [3, 4]. This aspect proves essential in preliminary design phases. The present work aims to define a human-centred approach for assessing interior noise in the passenger cabin and cockpit [5, 6]. The origin of the noise, or instead of its variation, can be manifold; in this study, we focus on a decrease given by applying acoustic metamaterials capable of absorbing certain frequency bands. Given the acoustic footprint of the aircraft, the aim is to construct a virtual mock-up containing both the visual layer (what the user sees), defined by the cabin design, and the auditory layer (what the user hears). The former is conventionally called visualisation; similarly, the latter is called auralisation [7]. In addition, to increase the realism of the experience by incorpoating the inertial effects of flight, and

Content from this work may be used under the terms of the Creative Commons Attribution 3.0 license. Any further distribution of this work must maintain attribution to the author(s) and the title of the work, journal citation and DOI. Published under license by Materials Research Forum LLC.

Materials Research Proceedings 69 (2026) 346-350 https://doi.org/10.21741/9781644904251-62

to avoid having to virtualise the cockpit due to the complexity of both design and gestures, the virtual environment is implemented within a full-motion flight simulator, in which both the cockpit and a section of the passenger cabin are present. The core objective is to import the numerical results into the virtual environment and then deploy the virtual environment in head-mounted display [8, 9]. The integration of the simulation data is achieved by condensing some of the numerical data issues, i.e. acoustic pressures as a function of frequency and position in the aircraft:

- The results are in the frequency domain and therefore need to be returned to the time domain with the inverse of the Fourier transform and then converted to an audible audio format.
- Some simplifications are made in numerical simulation, particularly on sound sources and frequency range. This compromises the realism of the generated audio files, which are thus used as filters applied to a baseline noise to avoid having an unrealistic audio track or one with anomalous sound levels. This process is possible by knowing the actual tracks of the aircraft or, in general, of the most relevant sources (e.g. the engine).

The primary objective of this work is to validate the methodology and feasibility of the cabin virtualisation process, focusing on the realism of both visual and aural components. A secondary goal is to assess the effectiveness of the implemented soundproofing solutions in a preliminary manner. The final design was deployed on a Microsoft™ HoloLens 2 Augmented Reality (AR) device, chosen for its 3D rendering capabilities, world-locking features, and integrated spatial audio system. The cabin layout was designed as a CAD model and imported into Unity, where it was refined using a scanned 3D model of cabin section represented in the full-motion aircraft simulator at Enna Kore University.

Auralisation process.

The auralisation workflow consists of three stages:

- The aircraft's acoustic footprint is obtained through numerical analyses estimating cabin sound pressure distributions across frequency, used to evaluate soundproofing materials.
- Simulation results are processed to obtain impulsive responses in the time domain (IRs), thus convolved with the dry sound of an aircraft engine, generating convolved sounds, which are integrated into the virtual aircraft model.
- Participants experience both visual and acoustic stimuli representative of a cruise flight phase in an immersive virtual environment, enabling subjective assessment of realism and comfort.

Vibroacoustic analysis is performed over a representative half-section of the aircraft cabin, corresponding to the flight simulator at the Enna Kore University. The vibroacoustic model is reduced to a half longitudinal section for symmetry optimisation. The cabin walls are modelled as an external 3 mm-thick aluminium panel (equivalent to the thickness of a real panel plus ribs and frames), jointed with an internal 24 mm soundproofing panel. Two solutions are compared, using Nomex and an acoustic metamaterial as the soundproofing material of the panels of the cabin. To simulate an impulsive analysis, the simulation utilises a point source emitting modal frequency sound (one frequency at a time) over a range of 20 Hz to 1000 Hz, with a constant step size of 5 Hz up to 500 Hz and of 20 Hz up to 1000 Hz. The source is positioned externally to the cabin, at a location equivalent to the engine position on the real aircraft. Probes placed at key cabin locations record complex acoustic pressure values at each location, representative of the transfer function of the cabin footprint. The analyses are performed based on the data in for the metamaterial, panels of melamine foam with cylindrical inclusions of aluminum, that was already tested in a fuselage environment in [10, 11]. The metamaterial is developed to absorb low-frequency noise, and for this reason, FEM is chosen as the numerical solution and COMSOL Multiphysics® as software. Once

Materials Research Proceedings 69 (2026) 346-350 https://doi.org/10.21741/9781644904251-62

the analysis is performed for both materials, these frequency-domain data are then converted into time-domain IRs via inverse real FFT to enable audio convolution. The data are interpolated on a uniform grid, smoothed to highlight the overall transmission characteristics, and band-limited to 14 kHz. A global normalisation is applied across the two analyses to prevent clipping in the final audio files, ensuring consistency between Nomex and metamaterial measurements and retaining the respective soundproofing capacities. The resulting IRs are exported as 48 kHz WAV files and convolved with a dry source signal toobtain simulated audio outputs:

$$y(t) = s(t) \cdot h(t) \tag{1}$$

The two convolved sound sets (Nomex and metamaterial) are further refined for seamless looping and prepared for integration.

The processed sounds are integrated into Unity to create a coherent audio-visual experience. Probe positions from the vibroacoustic model are used to position corresponding sound sources in Unity as shown in Fig. 1. Each probe features two audio sources reproducing the Nomex or metamaterial convolved sound obtained for that location, respectively. Each set of sounds relates to a specific audio group in the sound mixer. Application commands enable toggling among the two audio groups at runtime, allowing the user to hear the different sound presets for each solution, one at a time. The cabin geometry is that of a business jet, developed as part of the European CASTLE (CAbin Systems design Toward passenger welLbEing) project. Only a section with three seats and other design elements is used.

The active audio group's volume distribution is controlled through Gaussian interpolation based on the user's (camera) position relative to each probe. Each probe contributes proportionally to the total perceived sound according to its distance from the user. A global normalisation ensures that the sum of all source volumes equals unity, reflecting the fact that the probes represent measurement points inside the cabin, rather than physical sound emitters, thus no distance-based absolute attenuation is applied. Since point sources are used, the sound is rendered in the entire cabin.

The final application is deployed on HoloLens 2 and spatially aligned with an equivalent simulator for testing, ensuring the virtual seats are positioned in alignment with their real-world counterparts.

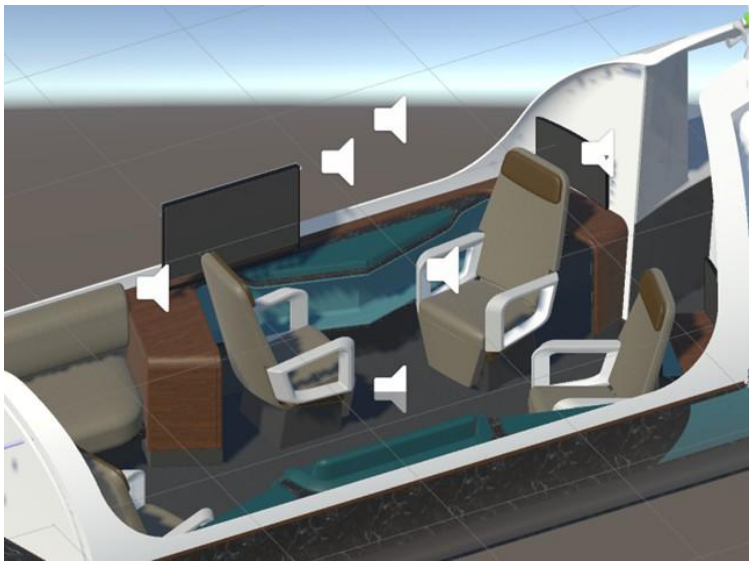


Figure 1: Unity model, with an array of six sound sources, corresponding to the probes of the vibroacoustic analysis, surrounding the cabin section used for the test.

Materials Research Proceedings 69 (2026) 346-350 https://doi.org/10.21741/9781644904251-62

User Testing Experiment Design.

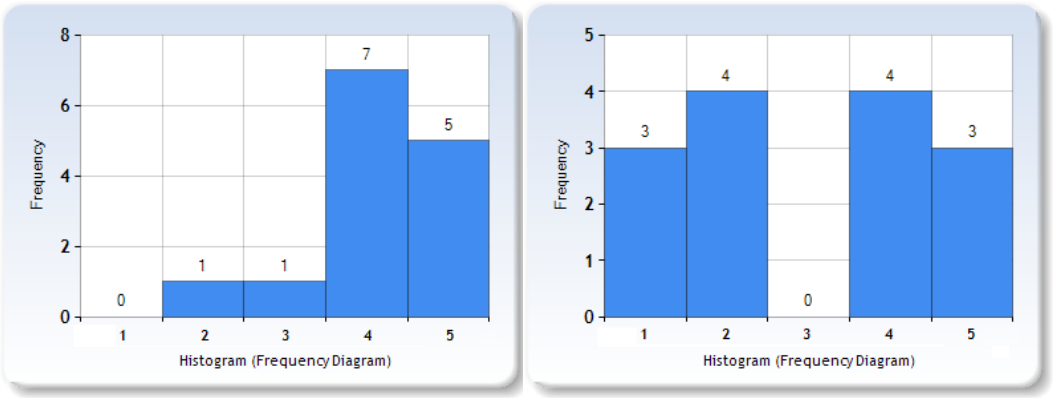
The user testing phase evaluates the realism of the virtualised cabin and user perception of acoustic treatments. A within-subjects design is adopted, where each participant experiences both the Nomex and one of the two available metamaterial conditions, with the order of presentation of the solution changed between participants to minimise habituation effects. Each participant completes two sessions, one for each of the two presented conditions: first, seated for two minutes, and then walking through the virtual cabin for two minutes. After both sessions, users complete Likert-scale (from 1 to 5) questionnaires to assess the perceived realism of the visual and aural layers, as well as the differences between acoustic configurations.

The questions and answers for each participant are reported in the Tab. 1, along with their mean value.

The realism of the scenarios is satisfying, with a mean value above 4 and low standard deviation below 1. Participants are also able to perceive the difference in sound between the two scenarios, as reported in Fig. 2(a). This difference is expressed in a decrease in low-frequency noise. The main problem lies in understanding which of the noises is louder, with about half of the participants incorrectly assigning the difference in noise, Fig. 2(b). The results give a perfect average of 3 and a standard deviation of 1.57. The reasons for this can be found in the exposure time which is very short.

Table 1: Results of the questionnaires, using Likert-scale where 1 is the minimum (Strongly disagree) and 5 the maximum (Strongly agree). The first scenario, panel in Nomex, is the louder than the second, panel in metamaterial.

	1	**2**	**3**	**4**	**5**	**6**	**7**	**8**	**9**	**10**	**11**	**12**	**13**	**14**	**Mean**
The business jet cabin is realistic	4	4	4	5	4	5	5	5	3	5	4	4	5	5	4.43
The sound faithfully reproduces that of a real airplane.	3	4	5	5	4	3	5	5	5	4	3	4	5	4	4.21
When moving around the cabin, the sound/noise is smooth and realistic.	4	4	5	5	5	4	4	5	5	4	5	4	5	4	4.50
The two scenarios have different noise levels.	4	2	4	4	5	3	4	5	5	4	5	4	5	4	4.14
In the first scenario, the noise is louder than in the second.	5	2	2	2	5	1	4	1	5	2	4	4	1	4	3.00



(a) (b)

Figure 2: The results for the last two questions in Tab. 1. (a) The two scenarios have different noise levels. (b) In the first scenario, the noise is louder than in the second.

Conclusions

The method presented starts from a numerical simulation and basic audio to recreate internal noise through signal convolution. The results show that the noise is realistic, but future experimental campaigns are needed to test its use in assessing acoustic comfort.

Acknowledgements

This work has been supported by the project ”TWINCRAFT - Digital Twin for Human-Centred Design of Future Aircraft”, funded by the MIUR Progetti di Ricerca di Rilevante Interesse Nazionale (PRIN) Bando 2022 - grant 2022LXKA3R.

References

[1] V. Mellert, I. Baumann, N. Freese, R. Weber. Impact of sound and vibration on health, travel comfort and performance of flight attendants and pilots. Aerospace Science and Technology (2008) 12(1):18-25. https://doi.org/10.1016/j.ast.2007.10.009

[2] P. Vink, C. Bazley, I. Kamp, M. Blok. Possibilities to improve the aircraft interior comfort experience. Appl Ergon (2011) 43(2):354-359. https://doi.org/10.1016/j.apergo.2011.06.011

[3] F. De Crescenzio, S. Bagassi, F. Starita. Preliminary user centred evaluation of regional aircraft cabin interiors in virtual reality. Scientific Reports (2021) 11(1):9662. https://doi.org/10.1038/s41598-021-89098-3

[4] S. Jonckheere, J. Cardenuto, T. van Putten, H. B'eriot, E. Deckers. Efficient auralization of vibro-acoustic systems with trim packages. ISMA2022 (2022).

[5] A. Alaimo, S Bagassi, E.. Carrera, T. Fadda, M.C. Moruzzi. Design and development of the visual and auditory layer for different cabin/cockpit layout. 34th Congress of the International Council of the Aeronautical Sciences (2024).

[6] R. Pieren, I. Le Griffon, L. Bertsch, Axel Heusser, F. Centracchio, D. Weintraub, C. Lavandier, B. Sch¨affer, Perception-based noise assessment of a future blended wing body aircraft concept using synthesized flyovers in an acoustic VR environment-The ARTEM study, Aerospace Science and Technology (2024) Volume 144 108767. https://doi.org/10.1016/j.ast.2023.108767

[7] M. Vorlaender, J. Summers. Auralization: Fundamentals of Acoustics, Modelling, Simulation, Algorithms, and Acoustic Virtual Reality. The Journal of the Acoustical Society of America (2008) 123, 4028. https://doi.org/10.1121/1.2908264

[8] A. Allen, S. Krishnamurthy. A hybrid transfer function procedure for broadband auralization within small flight vehicle interiors. INTER-NOISE and NOISE-CON Congress and Conference Proceedings (2023) 266, 927-937. https://doi.org/10.3397/NC_2023_0110

[9] A. Bolduc, P.A. Gauthier, A. Berry. Auralization of vibroacoustic models in engineering using Wave Field Synthesis: Application to plates and transmission loss, Journal of Sound and Vibration (2017) Volume 410, 64-86. https://doi.org/10.1016/j.jsv.2017.08.025

[10] M.C. Moruzzi, M. Cinefra, S. Bagassi. Vibroacoustic analysis of an innovative windowless cabin with metamaterial trim panels in regional turboprops. Mechanics of Advanced Materials and Structures (2019) 28(14), 1509-1521. https://doi.org/10.1080/15376494.2019.1682729

[11] M. Cinefra, G. D'Amico, A.G. De Miguel, M. Filippi, A. Pagani, E. Carrera, Efficient numerical evaluation of transmission loss in homogenized acoustic metamaterials for aeronautical application, Applied Acoustics (2020) Volume 164, 107253. https://doi.org/10.1016/j.apacoust.2020.107253

Aeroelasticity & Structural Dynamics



Materials Research Proceedings 69 (2026) 352-357 https://doi.org/10.21741/9781644904251-63

Set-Up of a Generic Aeroelastic Simulation Model for Demonstration and Software Testing Purposes

Francisco CARVALHO[1,a *], Arne VOSS[2,b] and Raffaello MARIANI[1,c]

[1]KTH Royal Institute of Technology, Division of Aerospace, Moveability and Naval Architecture, Stockholm, Sweden

[2]DLR - German Aerospace Center, Institute of Aeroelasticity, Göttingen, Germany

[a]franciscomcpbcarvalho@gmail.com, [b]arne.voss@dlr.de, [c]rmariani@kth.se

Keywords: Aeroelasticity, Maneuver Loads, Gust Loads, Flutter, DC-3, Loads Kernel

Abstract. This work presents the development and comprehensive analysis of an open-source aeroelastic model for the Douglas DC-3 with some modifications. The model serves as a platform for software testing, capturing essential aeroelastic phenomena. It features a conventional configuration with two engines, control surfaces, and a wing with a leading-edge sweep angle of 15.5°, dihedral angle of 5° and aspect ratio of 9.2, operating in a subsonic regime. The development process included finite element modeling using beam elements, aerodynamic modeling with the Doublet Lattice Method (DLM), and mass modeling with a dedicated fuel mass model. Trim case analyses were performed using both *Loads Kernel* and SOL144 in *MSC Nastran*, revealing significant differences between rigid and flexible configurations. Maneuver load analyses were conducted exclusively using *Loads Kernel*. Additionally, gust loads were studied using the (1-cos) Discrete Gust Model, demonstrating coupling with the short-period mode due to high static margin. Flutter checks showed matching results between *Loads Kernel* and *MSC Nastran*, with flutter speeds of 195 m/s and 203 m/s, respectively, confirming the model's plausibility for aeroelastic analysis.

Introduction

The sparseness of open-source generic aeroelastic simulation models poses a significant challenge, as existing options are invariably limited. For demonstration and software testing, it is essential to have a generic model that includes key aircraft components and balances simplicity with fidelity. FERMAT, based on the NASA Common Research Model (CRM) [1,2], resembles a wide-body transport aircraft. However, its design for Mach $Ma = 0.85$ introduces transonic complexities — such as shock-induced separation and nonlinearities — that affect flutter boundaries and reduce its suitability for demonstration. It also lacks flexibility to tune properties or exaggerate effects to highlight aeroelastic phenomena. The Active Aeroelastic Aircraft Structures (3AS) project [3] explored active aeroelastic concepts across several aircraft types, but the models were only shared among project partners. Furthermore, the Aeroelastic Prediction Workshop (AePW) [4] used the Benchmark Supercritical Wing (BSCW), which includes only a wing model. To address this gap, an aeroelastic model of the Douglas DC-3 has been meticulously established. It serves as a demonstrative platform for software testing, supporting both the Deutsche Zentrum für Luft- und Raumfahrt (DLR) in-house tool *Loads Kernel* [5] and *MSC Nastran* [6]. This model fills a critical need by offering a publicly available, representative aeroelastic platform. It supports further development and highlights the role of Aeroelasticity in Aircraft Design, Performance, and Flight Dynamics, particularly the interplay between unsteady flow and flexible structures, and the differences between rigid and flexible configurations.

Content from this work may be used under the terms of the Creative Commons Attribution 3.0 license. Any further distribution of this work must maintain attribution to the author(s) and the title of the work, journal citation and DOI. Published under license by Materials Research Forum LLC.

Materials Research Proceedings 69 (2026) 352-357 https://doi.org/10.21741/9781644904251-63

Aircraft Selection

To ensure the generality and representativeness of the aeroelastic model, an existing aircraft was selected based on specific requirements, with minor modifications introduced to highlight aeroelastic phenomena. The selected aircraft needed to balance simplicity and complexity while capturing relevant aeroelastic effects. Key criteria included: a conventional configuration; non-rectangular wing with significant leading edge sweep (Λ_{LE}), dihedral (Γ), washin/washout (Φ), cambered airfoil, and aspect ratio AR > 8; conventional or T-tail empennage; standard control surfaces (excluding flaps); a maximum of two engines; subsonic flight regime (Ma < 0.6); public availability of geometric, aerodynamic, structural, and performance data; and clear aeroelastic phenomena such as wing bending, torsion, and flutter. The Douglas DC-3 was selected as it best met all criteria. Its historical relevance and widespread use further support its suitability. The DC-3 is a low-wing, all-metal monoplane with retractable landing gear, powered by two Pratt & Whitney R-1830 engines. It features a cruise speed of 339 km/h, a range of 2,540 km, and a wing with a 15.5 ° sweep and 5 ° dihedral, and an aspect ratio of 9.2.

Aeroelastic Model

Structural Modeling

The finite element model (FEM) of the Douglas DC-3 was developed using DLR's in-house tool *ModGen* [7]. The lifting surfaces were modeled as beam elements along the Load Reference Axis (LRA), with stiffness properties assigned via *Python* scripts. Each wing was divided into 30 sections, with cross-sectional properties calculated based on spars, skin, and stringers. Stringer effects were included using an equivalent stiffness method to ensure realistic bending and torsional behavior. All structural components were assumed to be made of a single aluminum alloy, with typical properties: density 2710 kg/m³, Young's modulus 70 GPa, shear modulus 26.9 GPa, and Poisson's ratio 0.3. The fuselage was simplified as a rigid body with distributed grid points to preserve dynamic characteristics. Engines and empennage were connected to the aircraft via rigid elements to ensure consistent load transfer and structural integrity. The model was tuned iteratively to match reference mass and stiffness distributions, providing a reliable foundation for aeroelastic analysis. Fig. 1 illustrates the structural discretization used in the model, along with the positions of the LRA, the leading edge (LE), and the trailing edge (TE).

Mass Modeling

Mass estimation for each aircraft component was performed using statistical methods based on historical data and geometric parameters, following guidelines from Raymer, Torenbeek and Anderson [8,9,10]. A scaling factor was applied to align the total estimated mass with the aircraft known empty weight. Component masses were distributed across structural nodes using weighted averages based on cross-sectional areas. Wing-like components were assigned mass along the LRA, while fuselage mass was distributed over 11 nodes. System masses — including landing gear, avionics, and furnishings — were placed according to reference data and aircraft layout. Fuel modeling was handled separately using *ModGen*, with discretized fuel tanks per wing to capture mass and inertia effects. Fig. 2 illustrates the complete mass distribution used in the aeroelastic model.

Aerodynamic Modeling

The aerodynamic model was developed using the Doublet Lattice Method (DLM). This approach requires the construction of an aerodynamic mesh composed of quadrilateral panels. While the DLM enables modeling of control surface motions, its accuracy in capturing control surface effects is influenced by discretization, often necessitating empirical corrections [11]. To ensure accuracy, the meshing process must be performed rigorously. The aerodynamic mesh was generated using *ModGen*. Fig. 3 presents the final aerodynamic mesh for the Douglas DC-3 model.

Materials Research Proceedings 69 (2026) 352-357 https://doi.org/10.21741/9781644904251-63

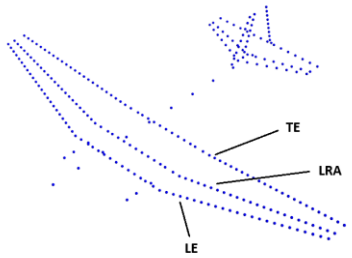


Figure 1: Structural discretization.

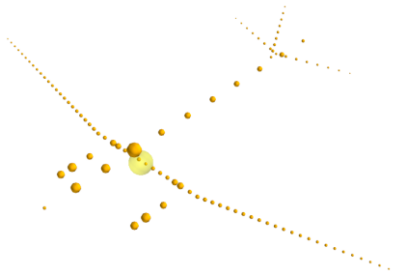


Figure 2: Mass discretization.

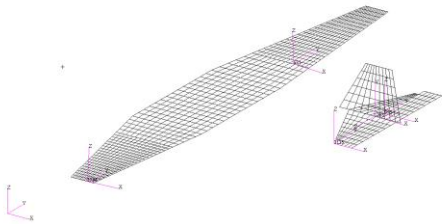


Figure 3: Aerodynamic panels.

More Flexible Models

The models of the Douglas DC-3 were modified to enhance aeroelastic effects. Compared to the original, the final modified model incorporates reduced wing stiffness, updated inertial properties, and a repositioned elastic axis (LRA). These changes were introduced to amplify the coupling between bending and torsion and to ensure that elastic deformation contributes meaningfully to aerodynamic behavior. In this model, the elastic contribution to the total lift coefficient reached approximately 4.7%, a significant increase compared to 0.7% observed in the original configuration. For all aeroelastic analyses, the selected mass configuration corresponds to the Maximum Take-Off Weight (MTOW), due to its significant structural deformations, representing a critical test case. The first flexible eigenmode of the final model appears at 3.17 Hz. This frequency does not fall in the range expected for an aircraft of similar size and weight but is comparable to a larger (and more flexible) passenger transport aircraft, reflecting the intentional tuning of the model.

Results

Trim Cases

Using the mass and stiffness matrices exported from *MSC Nastran*, the trim conditions for the Douglas DC-3 model were computed using both *Loads Kernel* and *MSC Nastran* (SOL144). Three trim cases were analyzed at a True Airspeed (TAS) of 70 m/s and Flight Level FL000: horizontal level flight ($n_z = 1$), push-down maneuver ($n_z = -1$), and pull-up maneuver ($n_z = 2.5$), based on CS-25 certification specifications [12]. Trim results showed close agreement between both tools, with minor differences due to modeling approaches. *Loads Kernel* uses a modal approach requiring convergence, with 71 eigenmodes found sufficient. Additionally, *MSC Nastran* assumes no elastic deformation at the wing root, while *Loads Kernel* allows it, complicating direct comparisons in the flexible case. Aeroelastic effects were significant: In horizontal level flight, *Loads Kernel* showed a 26.6% increase in trim angle of attack due to flexibility, and a 5.22% reduction in lift coefficient. Fig. 4 illustrates the elastic deformation of the wing for each trim case. The maximum vertical displacement reached 1.55 m at the wing tip during the pull-up maneuver, remaining within linear elasticity limits. The elastic twist varied across the span, with a maximum of -1.98º at the tip, affecting lift distribution and overall performance.

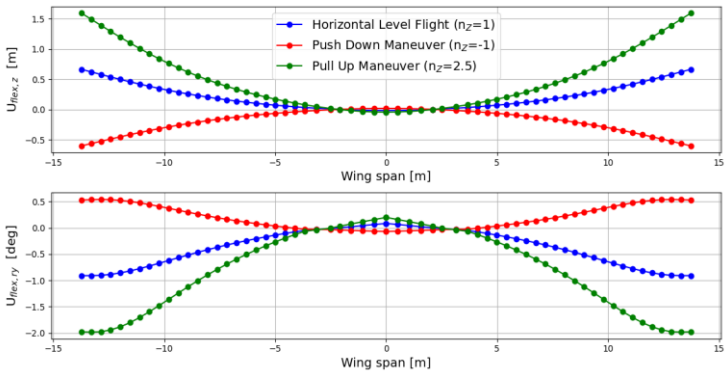


Figure 4: Loads Kernel elastic deformation of the wing at True Airspeed (TAS) of 70 m/s, Flight Level FL000, M3 for the final modified aeroelastic model.

Maneuver Loads

Maneuver loads were computed using *Loads Kernel*, considering critical cases for structural sizing. The flight conditions are the same as those used in trim cases. The maneuvers analyzed include: (1) horizontal level flight ($n_z = 1$), (2) push-down ($n_z = -1$), (3) pull-up ($n_z = 2.5$), and (4) and (5) roll maneuvers. Although CS-25 Amendment 28 [12] defines a roll rate of 5.45º/s, a more representative rate of 20º/s over 3 seconds was applied. Section loads were derived from integrated nodal loads at 16 monitoring stations per wing. The quantities of interest are bending moment M_x, torsional moment M_y, and shear force F_z, based on the coordinate system defined in Fig. 3. Given the validated agreement with *MSC Nastran*, only *Loads Kernel* results are presented. Observing the 1-D Envelopes (Fig. 5), maneuver (3) produced the highest negative bending moment at the wing root, while maneuver (2) induced the highest positive moment. Torsional moment M_y showed a change in critical load case near the wing kink, influenced by elastic twist deformation (Fig. 4). Maneuvers (4) and (5) contributed significantly to torsional loads in the outboard wing sections. Shear force F_z followed a similar trend to M_x, with peak values occurring near the wing root.

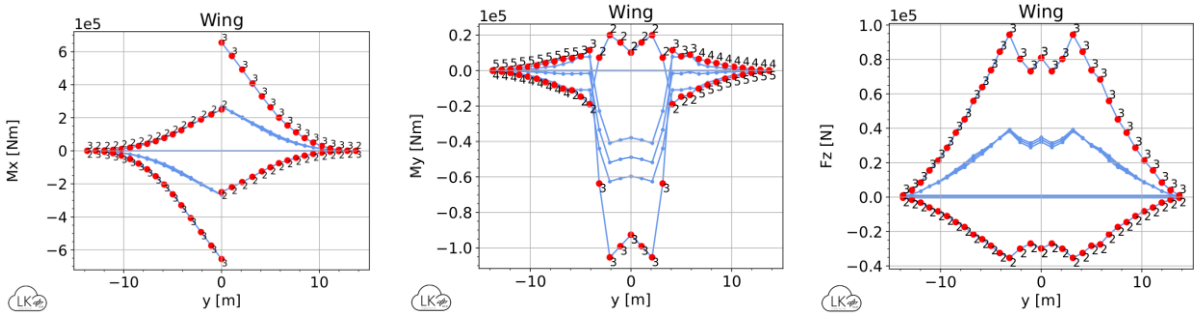


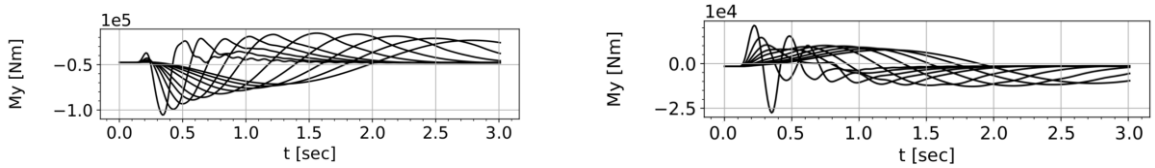
Figure 5: 1-D envelope of bending moment M_x, torsional moment M_y and shear force F_z.

Gust Loads

Gust loads were analyzed using the (1-cos) Discrete Gust Model implemented in *Loads Kernel*, under the same flight conditions as the maneuver loads. Gust profiles at sea level were defined according to CS-25.341 [12], covering the required certification spectrum. One-dimensional and two-dimensional load envelopes were computed similarly to maneuver loads, with focus placed on the time-domain response. The bending moment M_x over time showed similar positive and negative peak magnitudes, with the highest peak occurring for a gust gradient of H = 23 m, deviating from empirical predictions that suggest H = 44 m. The shear force F_z followed the same trend as M_x. The torsional moment M_y (Fig. 6) exhibited larger negative peaks, with the highest arising from H = 9 m. Oscillations observed at the wing kink for this gust gradient suggest

Materials Research Proceedings 69 (2026) 352-357 https://doi.org/10.21741/9781644904251-63

excitation of an eigenmode near 3.3 Hz, close to the first symmetric wing bending mode (3.17 Hz). This behavior is attributed to low torsional stiffness and the aft location of wing mass points relative to the LRA, resulting in strong bending-torsion coupling. Further simulations revealed coupling between gusts and the short-period flight mechanics mode due to high static margin. Reducing the static margin to approximately 10% modified the moment and force responses, leading to distinct positive and negative peak magnitudes and shifting the highest peak to a gust gradient between H = 37 m and H = 51 m, aligning with empirical expectations.



(a) Wing root. (b) Wing kink.

Figure 6: Torsional moment M_y over time for different gust gradients.

Flutter Check

Flutter check was performed using both *Loads Kernel* and *MSC Nastran* (SOL145), applying the pk-method at flight level FL000. Both tools identified the first unstable mode as the pure symmetrical torsion mode, with flutter speeds of 195 m/s in *Loads Kernel* and 203 m/s in *MSC Nastran*. A second mode became unstable at 262 m/s and 256 m/s, respectively. These flutter speeds are outside the flight envelope (Never exceed speed V_{NE} = 119.72 m/s) but remain within the subsonic regime (Ma < 0.6), as intended.

Conclusion and Outlook

This work develops the Douglas DC-3 aeroelastic model, bridging the identified knowledge gap with a comprehensive and open-source platform for demonstration and testing. The model, which balances complexity and simplicity, underscores the importance of aeroelasticity in aircraft design and stability. It captures key phenomena such as wing bending, torsion, and flutter, and was validated through trim, maneuver, gust, and flutter analyses using both *Loads Kernel* and *MSC Nastran*, showing consistent results across tools.

References

[1] T. Klimmek, Parametric Set-Up of a Structural Model for FERMAT Configuration for Aeroelastic and Loads Analysis, ASDJournal, Vol. 3, No. 2, 2014, pp. 31-49.

[2] M. B. Rivers, NASA Common Research Model: A History and Future Plans, NASA Langley Research Center, Hampton, VA 23681.

[3] J. Schweiger, A. Suleman, S. Kuzmina, V. Chedrik, MDO Concepts for an European Research Project on Active Aeroelastic Aircraft, 2002. https://doi.org/10.2514/6.2002-5403 https://doi.org/10.2514/6.2002-5403

[4] J. Heeg, P. Chwalowski, S. Kuzmina, D. M. Schuster, Plans and Example Results for the 2nd AIAA Aeroelastic Prediction Workshop, 2015. https://doi.org/10.2514/6.2015-0437

[5] A. Voß, Loads Kernel User Guide Version 1.04s, Deutsches Zentrum für Luft und Raumfahrt, Institute of Aeroelasticity, Göttingen, 2020.

[6] MSC.Software Corporation, MSC Nastran 2023.1 Quick Reference Guide, 2023.

[7] T. Klimmek, ModGen User's Manual, Version 2023-01-17, 2023.

[8] D. Raymer, Aircraft Design: A Conceptual Approach, AIAA Education Series, Washington D.C., 1996.

[9] E. Torenbeek, Synthesis of Subsonic Aircraft Design, 3rd ed., Delft University Press, Delft, 1986.

[10] R. Anderson, Weight Estimation Methods, Unpublished Notes, Design Branch, Air Force Flight Dynamics Laboratory, Wright-Patterson AFB, Ohio, July 1973.

[11] E. Albano and W. Rodden, A Doublet-Lattice Method for calculating the lift distribution on oscillating surfaces in subsonic flow, AIAA Journal, Vol. 2, No. 7, 1969, pp. 279-285. https://doi.org/10.2514/3.5086

[12] European Union Aviation Safety Agency (EASA), Certification Specifications and Acceptable Means of Compliance for Large Aeroplanes (CS-25), 2007.

Materials Research Proceedings 69 (2026) 358-361 https://doi.org/10.21741/9781644904251-64

Periodic Ground Resonance Analysis with Harmonic Decomposition

Andrea BASSI[1,a *], Giuseppe QUARANTA[1,b]

[1]Dipartimento di Scienze e Tecnologie Aerospaziali, Politecnico di Milano, Via La Masa 34, 20156 Milano, Italy

[a]andreabassi249@gmail.com, [b]giuseppe.quaranta@poilimi.it

Keywords: Rotorcraft Stability, Ground Resonance, Linear Time-Periodic Systems, Floquet Method, LTI Harmonic Decomposition

Abstract. Ground resonance is a rotorcraft instability that involves an interaction between the rotor and its support, consisting of the fuselage and the landing apparatus. In cases where the rotor lacks symmetry, the equations of motion are periodic. This paper compares the classic time-periodic Floquet approach to investigate stability with the truncated linear time-invariant harmonic decomposition. Then, various cases are presented dealing with variations in some basic rotor characteristics, such as the number of blades. These findings show the capacity of the decomposition to represent time-periodic modes and present a criterion for the optimal application of this decomposition, which is extremely advantageous because it leads to a linear model for further analyses.

Introduction

Ground resonance is an instability caused by the coupling between structural vibrations and the periodic inertia forces originating from the lead-lag degrees of freedom of helicopter blades. This phenomenon is avoided through dampers connecting each blade with the rotor mast (or with another blade for interblade configurations). This problem was first studied by Coleman and Feingold [1], then the analysis was generalised by Hammond [2] for cases where the formulation cannot be reduced to a linear time-invariant form, typically if nonsymmetric behaviour is analysed, i.e. the failure of a single lag damper, take-off or landing scenarios involving wind or uneven surfaces. As periodic coefficients appear in the equations, modal analysis is more complex, especially in the context of preliminary design or nonlinear stability.

The following sections explain briefly the classic Floquet method and the novel harmonic decomposition. After that, a succinct overview of the rotor model is provided, with a focus on multiblade coordinates. Subsequently, results are shown for a four-bladed rotor with one inoperative damper, followed by a discussion of rotors with more failed dampers, different damper attachment and a changed number of blades. Conclusively, the relationship between the number of rotor blades, multiblade coordinates and modal participation is highlighted to delineate a reasonable criterion to apply the harmonic decomposition.

Modal analysis of periodic systems and linear time-invariant formulation

Floquet analysis for linear time-periodic systems. The Floquet approach, as formulated by Peters et al. [3], enables the stability analysis of Linear Time-Periodic (LTP) systems. Let a LTP system be defined as $d\{x(t)\}/dt = [A(t)]\{x(t)\}$, with $[A(t)] = [A(t+T)]$, i.e. periodic of period T. If the transition matrix $[\Phi(t)]$ is defined as $\{x(t)\} = [\Phi(t)]\{x(0\}$, then the stability of the system may be discerned from the eigenvalues of $[\Phi(T)]$, the *characteristic multipliers* Λ, or from the *characteristic exponents* $\eta = 1/T\ log(\Lambda) = \lambda + i\omega$. ω is not unique (the complex logarithm is multi-valued), as any integer multiple of $\Omega = 2\pi/T$ may be added without loss of meaning of the solution. Nonetheless, LTP stability is based on λ or $|\Lambda|$, which are uniquely defined. In particular, the system is unstable if at least one $\lambda > 0$.

Content from this work may be used under the terms of the Creative Commons Attribution 3.0 license. Any further distribution of this work must maintain attribution to the author(s) and the title of the work, journal citation and DOI. Published under license by Materials Research Forum LLC.

Materials Research Proceedings 69 (2026) 358-361 https://doi.org/10.21741/9781644904251-64

LTI Harmonic decomposition. Lopez and Prasad [4] propose a linear time-invariant *Harmonic Decomposition* (HD) of an LTP system (where $\psi = \Omega t$), with the state vector expanded as:

$$\{x\} = \{x^0\} + \sum_{n=1}^{N_H} \quad \{x^{nc}\} cos(n\psi) + \{x^{ns}\} sin(n\psi) \tag{1}$$

N_H is arbitrary and must be chosen properly, since $N_H \to \infty$ causes the HD modes to tend exactly to the LTP modes, whereas truncation to a finite number of harmonics leads to approximation.

A possible criterion for minimum N_H is based on the modal participation of the different harmonics to states and modes.

After differentiating in time Eq. (1) and substituting it in the system equations, integration is performed over one revolution for the average term x^0; whereas the system equations are multiplied by $cos(j\psi)$ or $sin(j\psi)$ with $j = 1, \ldots, N_H$ and integrated over one rev to obtain the equations for x^{jc} and x^{js}. This formulation is computationally efficient, as the integration of the matrix terms may be substituted with the Fourier series expansion of $[A]$. The eigenvalues of the system are *equivalent to the Floquet exponents of the LTP system* ([4]).

Modal participation. After presenting the HD, modal participation [3,4] is introduced to provide an in-depth assessment of the harmonic content of modes. The modal participation of the n-th harmonic to the j-th state and k-th mode is defined as:

$$\phi_{j,k,n} = |c_{j,k,n}| / \sum_l \quad |c_{j,k,l}|, \quad -N_H \leq l \leq N_H \tag{2}$$

where $c_{j,k,n}$ is the n-th harmonic coefficient of the Fourier series expansion of $V_{j,k}(t)$, the j-th state of the k-th LTP eigenvector.

Given the equivalence of the LTI HD formulation to the LTP problem, the k-th LTI HD eigenvector contains the Fourier coefficients directly and can be used alternatively to compute the modal participation. The addition of integer multiples of Ω to the imaginary part of η, or equivalently the choice of the modes associated with higher harmonics in the LTI HD, does not change the harmonic content of the modes, rather their numbering, i.e. the value of n is shifted.

Ground resonance model and multiblade coordinates

The rotor model is originally from [2]. The j-th blade is linked to a rigid arm with a hinge, which allows a lag motion ζ_j. All blades constitute the rotor, spinning with a constant angular speed Ω. The arm is connected to the rotor mast and the structure of the rotorcraft, referred to as the "hub", whose dynamics is represented through two damped harmonic oscillators. This simple model encapsulates the dynamic interactions causing ground resonance. This system is unstable and requires additional dampers mounted between each blade and the rotor head (Hub-to-Blade or H2B) or between adjacent blades (Blade-to-Blade or B2B). The full derivation of all model equations, with both damper connections, is discussed in Bassi [5].

Notably, periodic coefficients, linking the hub equations to the blade ones, emerge in the system matrices whenever asymmetry is present. Unless the hub is symmetric, and all blades and dampers are equal, they cannot be deleted. Moreover, as the equations of the blades are in a rotating frame, while the hub ones are in a fixed frame, they may all be written in a fixed frame through multiblade coordinates (MBC). The j-th lag angle ζ_j is expressed as the sum of collective and cyclic coordinates:

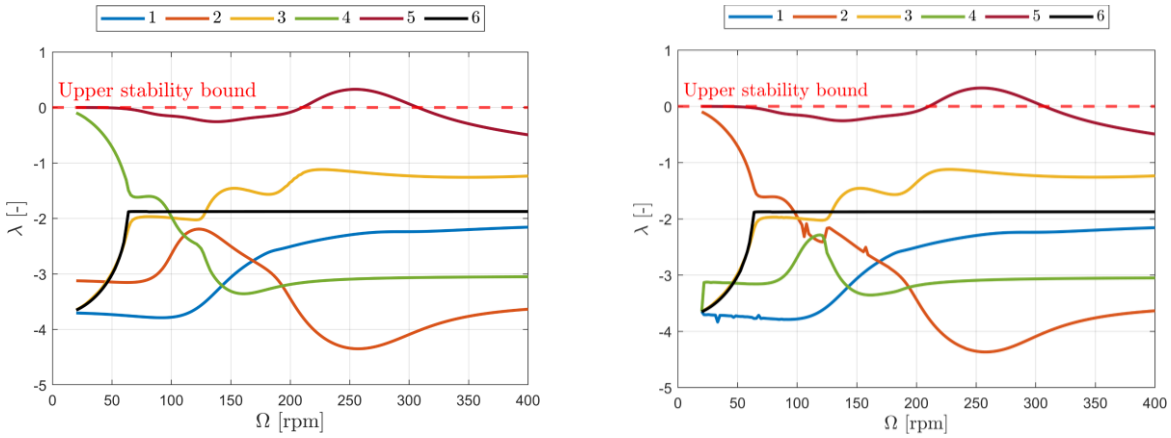
$$\zeta_j = Z_0 + Z_d(-1)^j + \sum_{n=1}^{N*} \quad Z_{nc} cos(n\psi_j) + Z_{ns} sin(n\psi_j) \tag{3}$$

Materials Research Proceedings 69 (2026) 358-361 https://doi.org/10.21741/9781644904251-64

with $\psi_j = \Omega t + (2\pi)/N_b(j-1), j = 1,\ldots,N_b$, and $N^* = (N_b - 1)/2$ for odd N_b (Z_d is absent), while $N^* = N_b/2 - 1$ for even N_b.

Stability of rotors and modal participation

Four-bladed rotor stability. The results of Fig. 1 deal with the hub-to-blade rotor with four blades, first presented in [2]. One of the blade dampers is inactive, so periodic coefficients appear. The time-periodic equations are harmonically decomposed up to the first harmonic, i..e $N_H = 1$ in Eq. (1). The system is correctly predicted to be unstable. The two approaches provide the same modes as in [2], except at low RPM, where the continuation algorithm tracks differently.



(a) HD modes *(b) Floquet modes*

Figure 1: Comparison of modes, 4 blades, H2B dampers

Modal participation in different rotors. Modal participation is computed in both configurations, then with a different number of inoperative dampers, and finally with different numbers of bladesN_b. For LTP modes, the principal logarithm is employed, whereas the modes in Fig. 1 are used in the HD case, thus achieving the same numbering for the harmonics.

The results for the 4-bladed rotor are also achieved with the two damper configurations, as well as when two adjacent or opposite dampers fail. Therefore, damper attachment and functionality do not affect modal participation. Regarding the variation of N_b, the harmonics with the highest modal participation in the unstable mode are reported in Table 1. Notably, all other modes never have harmonics higher than those in the table. To draw a link with the number of sinusoidal terms in the multiblade coordinates, the variable N^* from Eq. 2 is reported for each N_b, alongside the minimum N_H required to have a good approximation as in Fig. 1.

The conclusion is that the harmonic decomposition must contain at least as many harmonics as the cyclic terms in the MBC to approximate LTP modes.

Materials Research Proceedings 69 (2026) 358-361 https://doi.org/10.21741/9781644904251-64

Table 1: Modal participation to unstable mode

N_b	3 or 4		5 or 6		7 or 8	
N^*	*1*		*2*		*3*	
min N_H	*1*		*2*		*3*	
States	Z_{1c}, Z_{1s}, x_H, y_H	Z_0, Z_d	Z_{2c}, Z_{2s}	Other	Z_{3c}, Z_{3s}	Other
Harm. with max $\phi_{j,k,n}$	*+1/-1*	0	*+2/-2*	As $N_b = 3,4$	*+3/-3*	As $N_b =$ 3,4,5,6

Conclusion

The harmonic decomposition has been presented alongside its time-periodic counterpart, the Floquet method. The first provides an excellent approximation of modal damping if the proper number of harmonic terms has been employed, which in turn is determined from the number of cyclic coordinates in the MBC. In conclusion, the HD successfully and reliably approximates LTP modes, providing an ever-useful linear time-invariant representation.

References

[1] R. P. Coleman, A. M. Feingold, Theory of self-excited mechanical oscillations of helicopter rotors with hinged blades, In No. NACA-TN-3844 (1957).

[2] E. C. Hammond, An application of Floquet theory to prediction of mechanical instability, Journal of the American Helicopter Society, 19(4) (1974), 14-23. https://doi.org/10.4050/JAHS.19.14

[3] D. A. Peters, S. M. Lieb, L. A. Ahaus, Interpretation of Floquet Eigenvalues and Eigen vectors for Periodic Systems, Journal of the American Helicopter Society, 56(3) (2011), 1-11. https://doi.org/10.4050/JAHS.56.032001

[4] M. J. Lopez, J. V. R. Prasad, Linear Time Invariant Approximations of Linear Time Periodic Systems, Journal of the American Helicopter Society, (2017) 62(1), 1-10. https://doi.org/10.4050/JAHS.62.012006

[5] A. Bassi, Periodic ground resonance analysis with non-linear elements, (2025). https://hdl.handle.net/10589/234428

Materials Research Proceedings 69 (2026) 362-365 https://doi.org/10.21741/9781644904251-65

Whirl Flutter: An Experimental, Numerical, and Analytical Study on a Small-Scale Demonstrator

Giusi MAGLIOCCO[1,a *], Francesco MARULO[1,b], Michele GUIDA[1,c], Giovanni MARULO[2,d], Emilio DI LORENZO[3,e]

[1]University of Naples Federico II – Dept. of Industrial Engineering, Naples, Italy

[2]Dream srl – Boscotrecase (NA), Italy

[3]Siemens Digital Industries Software, Interleuvenlaan 68, 3001 Leuven, Belgium

[a]giusi.magliocco@unina.it, [b]francesco.marulo@unina.it, [c]michele.guida@unina.it, [d]nanni.marulo@hotmail.it, [e]emilio.dilorenzo@siemens.com

Keywords: Whirl Flutter, Experimental Modal Analysis (EMA), Operational Modal Analysis (OMA), Aeroelasticity

Abstract. Whirl flutter is a critical aeroelastic instability arising from the coupling of aerodynamic, structural, and gyroscopic effects in turboprop propulsion systems. This work investigates the phenomenon through analytical, numerical, and experimental approaches using a Whirl Flutter Small-Scale Demonstrator (WFSD). The demonstrator reproduces the dynamic behaviour of a turboprop configuration with two degrees of freedom, namely pitch and yaw. Analytical models based on strip theory, numerical simulations performed in MSC NASTRAN, and wind tunnel tests were used to evaluate natural frequencies and aeroelastic stability. The results show a strong correlation among the three methodologies, validating the modelling framework and providing reliable data to support the design of safer and more efficient propeller-driven systems.

Introduction

Whirl flutter is a complex and critical aeroelastic instability that arises from the dynamic interaction between unstable aerodynamic forces, structural rigidities, and gyroscopic inertial effects in engine-propeller systems elastically mounted on aircraft [1][2]. Its understanding and mitigation have historically been of paramount importance, especially after significant accidents involving turboprop aircraft in the 1960s [1][3][4][5]. To ensure the safety and reliability of modern propulsion systems, a thorough knowledge of this phenomenon is indispensable. This study aims to address this challenge through a comprehensive multidisciplinary survey, which harmonises and validates the results obtained from analytical analyses, numerical simulations, and experimental tests. At the heart of the research is the Whirl Flutter Small-Scale Demonstrator (WFSD)(Fig.1), a small-scale physical demonstrator designed to accurately replicate the dynamic and aeroelastic behaviour of a turboprop propulsion system under critical flight conditions. The model is based on a two-degree-of-freedom (2DOF) configuration with a rigid propeller, which includes pitch and yaw freedoms, elastically constrained by a spring system [6]. The design of the demonstrator considers crucial details such as materials and spring specifications to ensure that natural frequencies and vibration modes are consistent with those of a full-scale system [6]. During the tests, the stiffness of the springs, and thus their tension, was varied using a position variator. Configurations corresponding to positions 1 and 14 were tested, this means the two ends of the demonstrator's stay.

Content from this work may be used under the terms of the Creative Commons Attribution 3.0 license. Any further distribution of this work must maintain attribution to the author(s) and the title of the work, journal citation and DOI. Published under license by Materials Research Forum LLC.

Materials Research Proceedings 69 (2026) 362-365 https://doi.org/10.21741/9781644904251-65

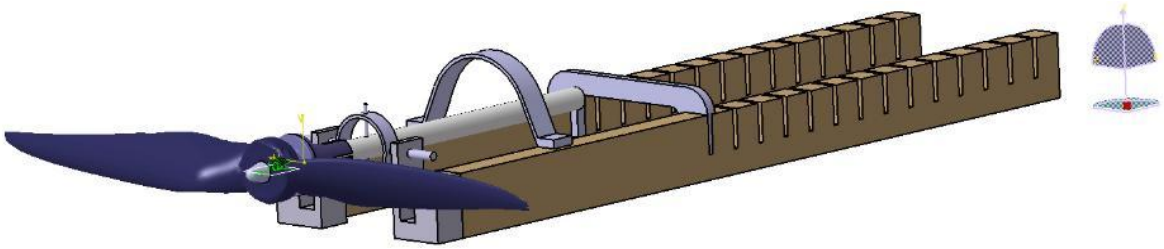


Figure 1 - Whirl Flutter Small-Scale Demonstrator

Methodology

The study combines analytical, numerical, and experimental methods to capture the essential features of the whirl flutter phenomenon and validate the results across the different approaches. The analytical investigation starts from a 2DOF model and employs strip theory to predict the natural frequencies and vibration modes of the system. This part of the study examines the influence of key structural and aerodynamic parameters for a more accurate representation of propeller performance [4]. In parallel, an in-depth numerical analysis is conducted using a finite element model (FEM) for flutter analysis in NASTRAN (SOL 145) [7]. This implementation builds upon the work of Rodden and Rose, who developed a preprocessor to include aerodynamic and gyroscopic forces of the propeller and nacelle in flutter analysis. Their approach enables the modelling of the propeller in Nastran as a point mass using the CONM2 card, with torsional springs defined on the Y and Z axes via the CELAS2 cards, and structural damping on the propeller attachment using the CDAMP1 and PDAMP cards. The model accounts for the flexibility of the shaft and the real distribution of the masses, which are crucial for a faithful representation of the system. Simulations are performed at various speeds and use the FLUTTER PK option to carry out the flutter analysis using the P-K method. A key objective is the generation of Campbell diagrams, enabling the analysis of the behaviour of natural whirl frequencies (backward and forward) as a function of the propeller's rotational speed. These models also allow the extraction of stiffness and aerodynamic damping matrices for different flight conditions.

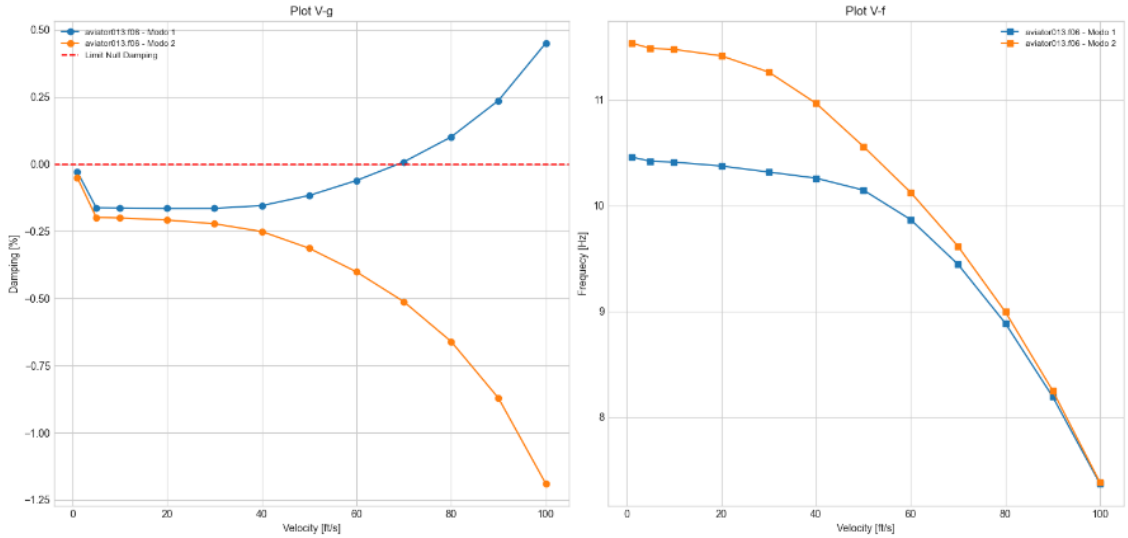


Figure 2 – VGF plot of the Model

The experimental phase is divided into two distinct phases. Initially, the tests are performed via an Experimental Modal Analysis (EMA) on the fixed-helix demonstrator. EMA was carried out in still air using an instrumented hammer to excite the structure. Accelerometers placed at selected locations on the nacelle and propeller hub measured the response. The analysis provided the natural frequencies and mode shapes of the demonstrator, allowing validation of the inertial and elastic

Materials Research Proceedings 69 (2026) 362-365 https://doi.org/10.21741/9781644904251-65

characteristics of the model. Operational Modal Analysis (OMA) was subsequently conducted in an open-circuit wind tunnel. During these tests, the stiffness configuration (positions 1 and 14), airflow velocity, and propeller rotational speed were systematically varied. The demonstrator was mounted on an aluminium support frame designed to minimise mechanical interference with the system dynamics. These tests enabled the identification of the whirl modes and the experimental assessment of aeroelastic stability.



Figure 3 – Test setup

Results

Table 1 presents a comparison between numerical and experimental results. The measured natural frequencies show excellent agreement with the FEM predictions, with deviations below 1%. This confirms the accuracy and reliability of the developed models.

Table 1 – Results of Numerical- Experimental Comparison.

	Flutter Velocity [ft/s]	Pitch Freq. [Hz]	Yaw Freq. [Hz]	Err %
Numerical	68.4	9.71	9.52	1.03
Experimental	68.0	9.61	9.61	0.95

The Campbell diagrams derived from the numerical simulations effectively captured the evolution of the forward and backward whirl modes with increasing propeller rotational speed. The backward whirl frequency decreased with speed, while the forward mode increased, approaching the rotational frequency line at higher RPM. Experimental results confirmed these trends. Increasing the spring stiffness (from position 1 to 14) caused an upward shift in both pitch and yaw natural frequencies and delayed the approach to the whirl-flutter boundary. The measured damping behaviour was consistent with theoretical expectations, showing a stabilising effect as stiffness increased. Overall, the analytical, numerical, and experimental results demonstrated strong consistency. The validated FEM and analytical models accurately reproduced the system

dynamics, confirming that the WFSD successfully emulates the aeroelastic coupling typical of turboprop configurations.

Conclusion

The present work provided an integrated analytical, numerical, and experimental investigation of whirl flutter on a small-scale demonstrator. The WFSD has demonstrated to be a useful tool for simulating the coupled aeroelastic behaviour of turboprop propulsion systems. The excellent agreement between FEM predictions and wind tunnel measurements validates the adopted modelling approach and demonstrates the robustness of the experimental methodology. These results represent a significant step toward the reliable prediction and control of whirl flutter phenomena in propeller-driven aircraft. Future developments will focus on refining the aerodynamic modelling, incorporating nonlinear effects, and expanding the test matrix to include higher rotational speeds and different propeller geometries and configurations.

References

[1] Proceedings of Symposium on Aaeroelastic & Dynamic Modeling Technology, RTD-AIA(Research & Technology Division Aerospace Industries Association); RTD - TDR- 63-4197 Part I

[2] Jr. Abbott, T. Frank, H. Kelley, N. Hampton, D. Kenneth. Investigation of propeller-power-plant autoprecession boundaries for a dynamic-aeroelastic model of a four-engine turboprop transport airplane. 1963.

[3] P. Hylton. Analyzing a simple prop-whirl-flutter model using modern analysis tools. In: IJME Intertech 2006 international conference, New Jersey, USA. 2006.

[4] J. Čecrdle. Whirl flutter of turboprop aircraft structures. Elsevier, 2023.

[5] R. Kvaternik, G. Kohn, Jerome S. An experimental and analytical investigation of proprotor whirl flutter. 1977.

[6] G.M Gagliardi, D. Marano, F. Marulo. Numerical and experimental investigation of whirl flutter characteristics in a small-scale demonstrator. Journal of Aerospace Engineering, 2022, 35.3: 04022025. https://doi.org/10.1061/(ASCE)AS.1943-5525.0001422

[7] Ted Rose and Bill Rodden. Propeller/Nacelle Whirl Flutter Addition to MSC/Nastran. Technical report, The MacNeal-Schwendler Corporation, March 1989

Materials Research Proceedings 69 (2026) 366-369 https://doi.org/10.21741/9781644904251-66

Fault Tolerance Analysis of a Double Ailerons Based Adaptive Flutter Suppression System

Carmelo Rosario VINDIGNI[1,a *], Giuseppe MANTEGNA[1,b], Calogero ORLANDO[1,c], and Andrea ALAIMO[1,d]

[1]Department of Engineering and Architecture, Kore University of Enna, 94100, Enna, Italy

[a]carmelorosario.vindigni@unikore.it, [b]giuseppe.mantegna@unikore.it, [c]calogero.orlando@unikore.it, [d]andrea.alaimo@unikore.it

Keywords: Flutter Suppression System, Double Ailerons Wing, Adaptive Control, Fault Tolerance

Abstract. This work presents a fault-tolerance analysis of an adaptive control scheme for flutter suppression using multiple control surfaces. The proposed architecture is designed to exploit the distributed actuation capabilities of modern wings to enhance performance and reliability in realistic flight conditions. By employing an adaptive control technique, the system continuously adjusts to variations in flight dynamics without requiring prior knowledge of the complete aeroelastic model. Practical challenges, such as actuator faults and external disturbances, are explicitly addressed, contributing to the development of more robust and fault-tolerant flutter suppression strategies. The methodology is demonstrated on a representative system modeled using a low-order aeroelastic beam formulation based on Euler–Bernoulli beam theory and strip theory aerodynamics, and is suitable for extension to higher-fidelity models.

Introduction

The aviation industry is moving towards lightweight, high-aspect-ratio wing designs to improve fuel efficiency and reduce CO_2 emissions. While slender wing structures offer aerodynamic advantages, they are also more susceptible to aeroelastic instabilities such as flutter, posing significant limitations on their operational envelope. Adaptive control strategies have attracted growing interest due to their capability to manage the highly dynamic, speed-dependent behavior of aeroelastic systems [1]. These methods offer robustness to modeling uncertainties and flight condition variations, but so far, their application has primarily been restricted to low-order aeroelastic models. Furthermore, only a limited number of studies have investigated the integration of multiple control surfaces in adaptive flutter suppression architectures [2]. This work contributes in this framework by presenting a fault-tolerance analysis of an adaptive control scheme for flutter suppression using multiple control surfaces. The architecture is designed to exploit the distributed actuation potential of modern wings, with a focus on improving performance and reliability in realistic flight scenarios. Relying on adaptive control techniques, the system dynamically adjusts to changes in flight conditions and structural properties without requiring full knowledge of the aeroelastic model in advance. Additionally, the proposed approach takes into account practical considerations such as actuator faults and external disturbances, contributing to the development of more fault-tolerant and robust flutter suppression systems. The methodology is suitable for application to higher-fidelity aeroelastic models, moving closer to implementation on actual aircraft configurations.

Materials and method

The aeroelastic plant, representing a modified Goland's wing [3] equipped with double aileron, is modeled exploiting a low order aeroelastic beam formulation [4] based on Euler-Bernoulli beam

Content from this work may be used under the terms of the Creative Commons Attribution 3.0 license. Any further distribution of this work must maintain attribution to the author(s) and the title of the work, journal citation and DOI. Published under license by Materials Research Forum LLC.

Materials Research Proceedings 69 (2026) 366-369 https://doi.org/10.21741/9781644904251-66

theory and strip theory aerodynamics which allows to cast the aeroelastic equations in the following state space form

$$\begin{cases} \dot{X} = \mathrm{A}X + \mathrm{B}u + \mathrm{B}^{g}w_{g} \\ Y = \mathrm{C}X \end{cases}. \quad (1)$$

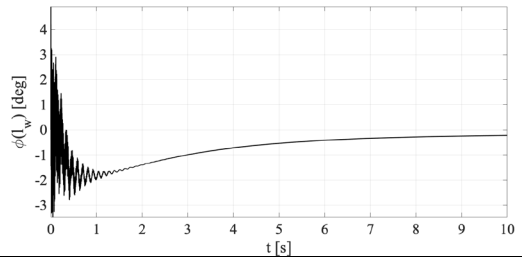
where A is the dynamic matrix, B is the control-state matrix, B^{g} is the gust influence matrix, C is assumed as an identity matrix in the hypothesis of ideal sensors that directly measure the structural displacements of interest, the control input vector u collects the ailerons commanded deflections, and w_g is the gust disturbance [5]. Loss of aileron effectiveness is taken into account by means of an effectiveness factor α_{f} that multiplies the transfer functions related to eq. 1 linking the inboard or outboard aileron deflection with the structural displacements. The Adaptive control scheme generates the control input by processing the wing tip torsion measurement $\phi(\mathrm{l_w})$, which is augmented with the output of a parallel feedforward compensator needed to fulfill the passivity requirements of the adaptive controller [6,7]. Specifically, the augmented plant meets the passivity requirements for velocity values below $U_f^{CL} = 190.6m/s$, which represents the ideal flutter boundary of the closed loop system.

The adaptive controller invariant gains were tuned by means of a Population Decline Swarm Optimization $\mathrm{P_DSO}$ algorithm [8]. The objective function was the Integral of Time Absolute Error ITAE of the wing tip torsion angle, which was computed considering the plant at the open loop flutter speed $U_f = 109.5m/s$ subjected to a pulse disturbance on the wing tip torsion rate of amplitude 100 rad/s and width 0.001 s. The optimized adaptive controller was then tested in a flight scenario involving a 1-cosine gust disturbance and loss of actuator effectiveness considering the wing flying at U_f^{CL}. The obtained results in terms of ITAE, maximum transverse displacement at the tip $w(l_w)$, maximum inboard aileron deflection δ^{in}, and maximum outboard aileron deflection δ^{out} are summarized in Table 1.

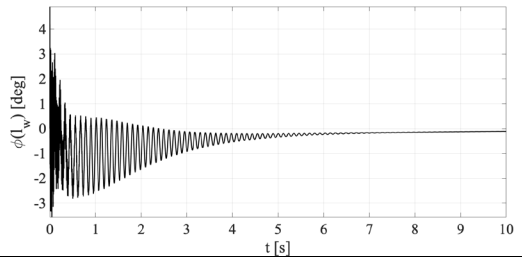
Table 1: Fault tolerance analysis results

Case	α_f^{in}	α_f^{out}	ITAE [rad-s]	Max$[w(l_w)]$ [m]	Max(δ^{in}) [deg]	Max(δ^{out}) [deg]
1	1.0	1.0	23.6	0.060	20	5.8
2	0.5	1.0	12.6	0.067	20	6.7
3	1.0	0.5	59.2	0.090	20	14.2
4	0.5	0.5	unstable	-	-	-
5*	0.0	1.0	245.0	0.200	52.3	40.0
6	1.0	0.0	unstable	-	-	-

The system maintains stable and acceptable performance when the inner aileron experience 50% loss of effectiveness. In this case, the reduction in ITAE observed between the first and second cases is attributed to the oscillatory nature of the response in the second scenario, as shown in Figure 1. Although the system exhibits increased oscillations, the error tends to decay more rapidly over time, resulting in a lower accumulated time-weighted error. In contrast, the first case presents a smoother, more damped response, but with a sustained deviation from the desired setpoint, leading to a higher ITAE.



(a) Fault-free scenario



(b) Inner aileron partial loss $\alpha_f^{in} = 0.5$

Figure 1: Wing tip torsion displacement

A reduction in the effectiveness of the outer aileron significantly degrades system performance, as indicated by the increase in ITAE and tip deflection. Simultaneous degradation of both ailerons and complete failure of the outer one lead to instability, demonstrating the key role of the outer control surface. It is worth noting that, in the case of complete failure of the inner aileron the system exhibits poor performance with large control surface deflections, but the system is still able to damp out the vibrations of the linear aeroelastic plant.

Conclusions

This work investigated the flutter suppression capabilities of a simple adaptive control strategy implemented on a wing configuration with double ailerons. The fault tolerance analysis demonstrated that the flutter suppression system exhibits greater robustness to partial loss of effectiveness in the inner ailerons than in the outer ones. While moderate inner actuator degradation may even improve the ITAE index due to a more oscillatory yet convergent response, outer actuator degradation significantly degrades performance and leads to larger wing-tip deflections. Complete or simultaneous failures ultimately result in instability, highlighting the critical importance of actuator redundancy. These findings emphasize that maintaining at least partial availability of both actuator groups is essential to ensure closed-loop stability and acceptable performance in flutter suppression.

References

[1] E. Livne, "Aircraft active flutter suppression: State of the art and technology maturation needs," Journal of Aircraft, vol. 55, no. 1, pp. 410-452, 2018. https://doi.org/10.2514/1.C034442

[2] L. Zhang and Y. Zhao, "Adaptive feed-forward control for gust load alleviation on a flying-wing model using multiple control surfaces," Aerospace, vol. 10, no. 12, p. 981, 2023. https://doi.org/10.3390/aerospace10120981

[3] M. Goland, "The flutter of a uniform cantilever wing," 1945. https://doi.org/10.1115/1.4009489

[4] C. R. Vindigni, G. Mantegna, C. Orlando, A. Alaimo, and M. Berci, "A refined aeroelastic beam finite element for the stability analysis of flexible subsonic wings," Computers & Structures, vol. 307, p. 107618, 2025. https://doi.org/10.1016/j.compstruc.2024.107618

[5] R. L. Bisplinghoff, H. Ashley, and R. L. Halfman, Aeroelasticity. Courier Corporation, 2013.

[6] I. Barkana, "Output feedback stabilizability and passivity in nonstationary and nonlinear systems," International Journal of Adaptive Control and Signal Processing, vol. 24, no. 7, pp. 568-591, 2010. https://doi.org/10.1002/acs.1149

[7] I. Barkana, "Simple adaptive control-a stable direct model reference adaptive control methodology-brief survey," International Journal of Adaptive Control and Signal Pro-cessing, vol. 28, no. 7-8, pp. 567-603, 2014. https://doi.org/10.1002/acs.2411

[8] C. R. Vindigni and C. Orlando, "A gain scheduling control of incompressible airfoil flutter tuned by the population decline swarm optimizer-pdso," Aerotecnica Missili & Spazio, vol. 99, no. 1, pp. 3-16, 2020. https://doi.org/10.1007/s42496-019-00032-3

Materials Research Proceedings 69 (2026) 370-374 https://doi.org/10.21741/9781644904251-67

Aeroelastic Modeling of Deformable-Airfoil Wings Through Unsteady Lifting-Line Theory

Riccardo GIANSANTE[1,a *], Giovanni BERNARDINI[2,b], and Massimo GENNARETTI[2,c]

[1]Department of Economics, Engineering, Society, and Business Organisation, University of Tuscia, Viterbo, 01100, Italy

[2]Department of Civil, Computer Science and Aeronautical Technologies Engineering, Roma Tre University, Rome, 00146, Italy

[a]riccardo.giansante@unitus.it, [b]giovanni.bernardini@uniroma3.it, [c]massimo.gennaretti@uniroma3.it

Keywords: Unsteady Aerodynamics, Aeroelasticity, State-Space, Lifting-Line Theory, Morphing Wings, Paper Flutter, Flag Flutter, Finite Element Method

Abstract. This paper presents a state-space formulation for the aeroelastic stability analysis of deformable-airfoil wings. The proposed approach couples the wing structural dynamics modeled as a cantilever plate (through an FEM approach) with aerodynamic loads computed through an Unsteady Lifting-Line Theory (ULLT), which evaluates the unsteady sectional loads using the Küssner-Schwarz and accounts for wake effects through the Biot–Savart law. The corresponding bound circulation is obtained via the Kutta–Joukowski theorem extended to unsteady flows. The distributed aerodynamic loads are projected onto the shape functions introduced in a Galërkin solution approach, thus yielding an aerodynamic operator expressed through transcendental transfer functions, which is then approximated into a rational state-space form. This enables straightforward aeroelastic stability assessment through eigenvalue analysis and provides a framework suitable for control design. The model's accuracy is validated using the paper flutter problem, whose aeroelastic behavior is representative of deformable-airfoil wings.

Introduction

Engineers have traditionally designed aircraft to perform optimally under specific conditions, but this approach has become restrictive as aviation technology advances. Inspired by birds and insects, which naturally change wing shape for both efficient flight and agile maneuvering, researchers have increasingly explored the concept of morphing aircraft, which are capable of real-time shape adaptation to improve performance across multiple flight conditions. While morphing is not new, as seen in the Wright Brothers' wing-warping system and modern high-lift devices, recent research has formalized morphing into categories such as planform, out-of-plane, and airfoil morphing, with camber morphing being the most widely studied [1,2]. Numerous designs, including compliant and composite-based morphing airfoils, have been developed and modeled to optimize aerodynamic efficiency and stability. Aeroelastic modeling has also played a key role in analyzing and optimizing these systems for stability and performance. Interestingly, similar aeroelastic phenomena appear in other fields as well, such as medical research on snoring, where the soft palate behaves like a flexible plate, and industrial challenges like paper or flag flutter.

The present paper aims to develop a state-space formulation for studying the aeroelastic stability of deformable-airfoil wings or camber-morphing wings, a subcase of the more general morphing wings category. Throughout the years, various models have been proposed to evaluate the aerodynamic loads, from high-fidelity CFD approaches to low-fidelity

Content from this work may be used under the terms of the Creative Commons Attribution 3.0 license. Any further distribution of this work must maintain attribution to the author(s) and the title of the work, journal citation and DOI. Published under license by Materials Research Forum LLC.

Materials Research Proceedings 69 (2026) 370-374 https://doi.org/10.21741/9781644904251-67

analytical formulations. In the present paper, a novel aeroelastic tool is proposed, obtained by coupling the structural dynamics model with the aerodynamic loads evaluated by an Unsteady Lifting-Line Theory (ULLT), developed for the unsteady aerodynamics of camber morphing wings. The aerodynamic three-dimensional solver recently presented by the authors [3,4,5,6] is based on the analytical Küssner-Schwarz theory for the evaluation of the sectional unsteady aerodynamic loads, coupled with the application of the Biot-Savart law for determining the wake inflow due to the trailed vorticity. The extension to unsteady aerodynamics of the Kutta-Joukowski theorem is also applied to determine the sectional bound circulation from the knowledge of the evolution of the sectional circulatory lift [7]. The generalized aerodynamic loads forcing the structural dynamics are obtained by projections of the airfoil distributed loads onto suitable shape functions introduced in the Galërkin solution approach. These are related to the corresponding Lagrangian coordinates through transcendental transfer functions of the reduced frequency, collected in the aerodynamic matrix. Thus, the rational matrix approximation of the latter is applied in order to describe the aerodynamic operator in a state-space form, from which the state-space aeroelastic model is readily determined. This state-space aeroelastic formulation is very convenient since it allows the study of the aeroelastic stability through eigenproblem solution and can be straightforwardly applied for control purposes. The accuracy of the overall aeroelastic model will be assessed by comparison with experimental/numerical data regarding the specific test case of paper flutter (also known as flag flutter), an industrial problem that limits the speed of printing machines, which is widely documented in the literature from both numerical and experimental perspectives (see for example [8,9]) and whose aeroelastic behavior is closely related to the ones of deformable-airfoil wings.

Observing that literature results on paper flutter are typically related to one-dimensional approximation of the structural dynamics coupled with a two-dimensional description of the aerodynamic loads account for only shed wake vorticity, the numerical investigation examines the effects on the aeroelastic simulation given by including the wake trailed vorticity and modeling the structure as a flat plate through an FEM tool.

Aeroelastic Model based on the ULLT approach

In this work, the aeroelastic operator for morphing wings is derived by applying a frequency-domain Unsteady Lifting Line Theory solver, ULLT, suitable for the analysis of unsteady aerodynamics of morphing wings with deformable camber. The model, recently presented in the work [5] as an extension of the previously published ULLT for non-morphing wings [10], is based on the evaluation of the pressure distribution along the whole wing through the analytical Küssner-Schwarz theory for unsteady flows [11,12], which is then integrated to obtain the generalized loads as projections onto the shape functions used to express the wing deformation in a Galërkin approach. The Küssner-Schwarz theory is the perfect choice for the aerodynamic study of camber morphing wings, since it is a linear aerodynamic theory, for incompressible, potential flows providing the airfoil pressure loads generated by an arbitrary distribution of downwash, thus representing the extension of the Theodorsen theory to deformable camber airfoils. While the shed vorticity is already analytically included in the Küssner-Schwarz theory (through the well-known Theodorsen function [13]), the Biot-Savart law is used to determine the wake trailed vorticity effects on the sectional downwash appearing in the Küssner-Schwarz theory. The wake vorticity released by the lifting body is determined from the relation between the sectional bound circulation and the sectional circulatory lift provided by the extension of the Kutta-Joukowski theorem to unsteady linear aerodynamics presented in [7], which closes the loop of the aerodynamic system.

This aerodynamic solution approach yields the following relation between the M generalized aerodynamic forces, **f**, and the M Lagrangian coordinates, **q**, of the structural dynamics problem

Materials Research Proceedings 69 (2026) 370-374 https://doi.org/10.21741/9781644904251-67

$$\tilde{\mathbf{f}} = \mathbf{E}(\mathrm{k})\,\tilde{\mathbf{q}} \tag{1}$$

where k is the reduced frequency and $\mathbf{E}$ is the transcendental [M × M] aerodynamic matrix, that collects the aerodynamic frequency response functions (see [5] and [10] for details).

The presence of the transcendental contributions comes from three sources: *i*) the exponential contribution due to the delays appearing in the Biot-Savart law used to evaluate the downwash generated by the wake trailed vorticity (the vorticity at a given wake point corresponds to the vorticity released by the trailing edge when passing at that point), *ii*) the Theodorsen lift deficiency function used to evaluate the coefficients a_n of the Küssner-Schwarz theory (see [11, 12] for more details), and *iii*) the frequency response function, G(k), of the unsteady Kutta-Joukowski theorem (see [7]). This implies that, in this form, the aerodynamic matrix is unsuitable for aeroelastic stability analyses and control applications.

To overcome this difficulty, it is convenient to apply the following rational-matrix approximation of the aerodynamic matrix along the imaginary axis of the complex plane

$$\mathrm{E(k)} \cong (\mathrm{ik})^2\mathrm{A}_2 + \mathrm{ikA}_1 + \mathrm{A}_0 + \mathrm{Q(ikI - A)^{-1}R} \tag{2}$$

where $\mathbf{A}_2$, $\mathbf{A}_1$ and $\mathbf{A}_0$ are [M × M] matrices, $\mathbf{A}$ is a diagonal [N_p × N_p] matrix, where N_p is the number of aerodynamic poles that can be arbitrarily increased to better approximate the aerodynamic transfer functions, whereas $\mathbf{Q}$ is a [M × N_p] matrix and $\mathbf{R}$ is a [N_p × M] matrix. These constant-coefficient matrices can be determined by a least-square approximation technique [14,15].

Thus, the combination of Eq. (2) with (1), followed by the transformation into the time domain yields, for $\tau = t\,V/b$ (being t the dimensional time, V the velocity and b the semi-chord),

$$\begin{cases} \mathbf{f}(\tau) = \mathbf{A_2}\,\ddot{\mathbf{q}} + \mathbf{A_1}\,\dot{\mathbf{q}} + \mathbf{A_0}\,\mathbf{q} + \mathbf{Q}\,\mathbf{r} \\ \dot{\mathbf{r}} = \mathbf{A}\,\mathbf{r} + \mathbf{R}\,\mathbf{q} \end{cases} \tag{3}$$

where $\mathbf{r}$ denotes the vector of the N_p additional aerodynamic states introduced by the rational contribution in Eq. (2).

Equation (3) represents the state-space model of the wing generalized aerodynamic loads derived from the frequency-domain ULLT solver, suitable for aeroelastic stability analyses and control purposes once coupled with a structural dynamics operator. Previous analyses were accomplished by approximating the lifting body as a semi-infinite thin plate (namely, a cantilever beam with the inclusion of the Poisson ratio) [3]. In the present work, a complete cantilever plate is considered in order to better simulate the phenomenon of the paper flutter. To this aim, mass and stiffness matrices relative to the cantilever plate, respectively $\mathbf{M}$ and $\mathbf{K}$, are determined by a Finite Element Method (FEM) approach (specifically, the commercial software Inventor Nastran). The corresponding eigenvectors are applied to determine the approximated natural modes of vibration of the structure, which, in turn, are used as the shape functions of the Galërkin approach. The complete aeroelastic system defined in a state-space form reads

$$\begin{cases} \mathbf{M}\,\ddot{\mathbf{q}} + \mathbf{K}\,\dot{\mathbf{q}} = \mathbf{A_2}\,\ddot{\mathbf{q}} + \mathbf{A_1}\,\dot{\mathbf{q}} + \mathbf{A_0}\,\mathbf{q} + \mathbf{Q}\,\mathbf{r} \\ \dot{\mathbf{r}} = \mathbf{A}\,\mathbf{r} + \mathbf{R}\,\mathbf{q} \end{cases} \tag{4}$$

from which the velocity and frequency of flutter are determined through a standard eigen- value analysis.

Numerical Investigations

The numerical results presented in this section are obtained by three different applications of the aeroelastic model, whose accuracy is assessed by comparison with the experimental benchmark of Huang [8]. It considers a thin rectangular aluminum plate, with a span length

Materials Research Proceedings 69 (2026) 370-374 https://doi.org/10.21741/9781644904251-67

of 6 cm and four different values of the chord: 4, 6, 8, 10 cm. Along with the complete ULLT aerodynamic model coupled with the plate structural operator, a simplified version of it, not including the trailed vorticity effects, is considered. This last model consists of a strip-theory (S-T) approach based on the Küssner-Schwarz theory, and it is coupled with both the beam-like and plate modeling of the structure, in order to evaluate the resulting prediction discrepancies.

The results, for both the flutter velocity and frequency, are shown in Fig. 1. First, note the excellent accuracy of flutter frequency predicted by all the aeroelastic models considered, resulting from the comparison with the experimental. On the other hand, the flutter velocity prediction is less accurate, with a slightly better accuracy of the ULLT with respect to the S-T. This means that, although the trailed vorticity effect has an important role in the aerodynamic model, other phenomena not captured by the ULLT model could have a more significant influence on the aeroelastic stability.

The slight difference between the results obtained by beam and plate structural modeling is also noticeable. The correlation between the flutter frequencies of the analyzed configurations and their natural vibration frequencies shows that the critical frequency practically corresponds to the frequency of vibration of the second natural vibration mode of the beam model. This confirms the validity of the aeroelastic tool based on the simpler description of the structural dynamics operator. The analyses indicate that flutter instability primarily occurs in symmetric bending vibration modes, for which aerodynamic forces are uniformly distributed along the direction orthogonal to the undisturbed flow, coupling between aerodynamic forces and structural deformations is stronger, and more efficient energy transfer and accumulation until the flutter threshold occurs. In contrast, antisymmetric modes experience partial force cancellation, reducing energy transfer and delaying instability.

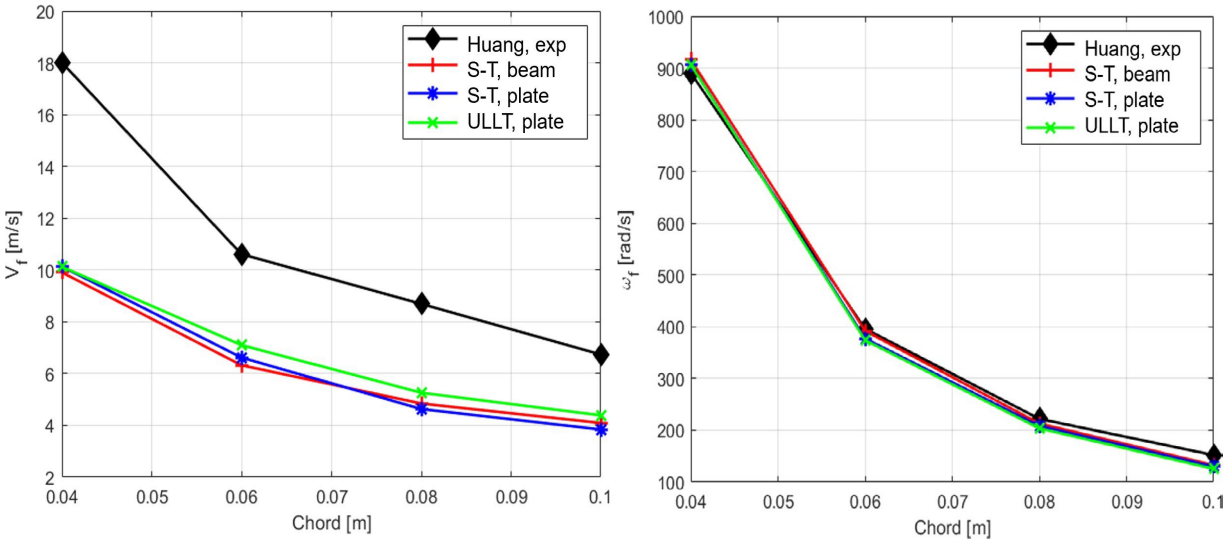


Figure 1: Velocity and frequency of flutter as functions of the chord length. Comparison between strip-theory results for both beam and plate models, ULLT results including the trailed vorticity, and the experimental data by Huang [8].

Conclusions

A state-space formulation for the aeroelastic stability analysis of deformable-airfoil wings has been presented. It relies on a ULLT aerodynamic solver based on the Küssner-Schwarz theory for the evaluation of the sectional aerodynamic loads, on the unsteady Kutta–Joukowski theorem for the definition of the bound circulation from the circulatory lift, and on the Biot–Savart law for the inclusion of the wake trailed vorticity effects. Considering a paper flutter problem, the comparison of the outcomes of the present model with experimental data from

the literature showed very good accuracy in terms of flutter frequency prediction. Less accurate is the prediction of the flutter velocity. The effect of the trailed vorticity seems to be marginal for the examined problem, and, at the same time, the prediction accuracy seems to be scarcely affected by the improvement of the structural operator (from beam-like to plate modeling), since the identified flutter mode is close to the second mode of vibration of the cantilever beam.

References

[1] S. Barbarino, O. Bilgen, R. M. Ajaj, M. I. Friswell, and D. J. Inman. A review of morphing aircraft. Journal of Intelligent Material Systems and Structures, 22(9):823–877, 2011, https://doi.org/10.1177/1045389X11414084

[2] R. M. Ajaj, M. S. Parancheerivilakkathil, M. Amoozgar, M. I. Friswell, and W. J. Cantwell. Recent developments in the aeroelasticity of morphing aircraft. Progress in Aerospace Sciences, 120:100682, 2021, https://doi.org/10.1016/j.paerosci.2020.100682

[3] R. Giansante, G. Bernardini, and M. Gennaretti. Finite-state aeroelastic modelling of morphing wing through unsteady lifting-line theory. In 34th Congress of the International Council of the Aeronautical Sciences (ICAS 2024), 2024

[4] G. Frassoldati, R. Giansante, G. Bernardini, and M. Gennaretti. Unsteady lifting-line free-wake aerodynamic modeling for morphing wings. Aerospace, 11(9), 2024, https://doi.org/10.3390/aerospace11090745

[5] R. Giansante, G. Bernardini, and M. Gennaretti. Unsteady lifting-line theory for camber morphing wings state-space aeroelastic modeling. AIAA Journal, 62(12):4654–4664, 2024, https://doi.org/10.2514/1.J064329

[6] R. Giansante, G. Bernardini, and M. Gennaretti. State-space lifting line aerodynamic modelling for aeroelasticity of camber morphing wings. In AIAA AVIATION 2023 Forum, https://doi.org/10.2514/6.2023-3372

[7] M. Gennaretti and R. Giansante. Kutta-joukowski theorem for unsteady linear aerodynamics. AIAA Journal, 60(10):5779–5790, 2022, https://doi.org/10.2514/1.J061894

[8] L. Huang. Flutter of cantilevered plates in axial flow. Journal of Fluids and Structures, 9(2):127–147, 1995, https://doi.org/10.1006/jfls.1995.1007

[9] Y. Watanabe, K. Isogai, S. Suzuki, and M. Sugihara. A theoretical study of paper flutter. Journal of Fluids and Structures, 16(4):543–560, 2002, https://doi.org/10.1006/jfls.2001.0436

[10] R. Giansante, G. Bernardini, and M. Gennaretti. Frequency-domain lifting-line aerodynamic modelling for wing aeroelasticity. Applied Sciences, 12(23), 2022, https://doi.org/10.3390/app122312204

[11] H.G. Küssner and I. Schwarz. The oscillating wing with aerodynamically balanced elevator. Technical Report No.991, NACA, 1941.

[12] Y. C. Fung. An Introduction to the Theory of Aeroelasticity. Dover Publications, Inc., New York, 1993.

[13] T. Theodorsen. General theory of aerodynamic instability and the mechanism of flutter. NACA TR-496, 1935.

[14] R. Gori, J. Serafini, M. Molica Colella, and M. Gennaretti. Assessment of a state-space aeroelastic rotor model for rotorcraft flight dynamics. CEAS Aeronautical Journal, 7:405–418, 2016, https://doi.org/10.1007/s13272-016-0196-1

[15] E. Sambenedetto, R. Giansante, G. Bernardini, and M. Gennaretti. A state-space aeroservoelastic model for deformable airfoils. In Online Symposium on Aeroelasticity, Fluid-Structure Interaction, and Vibrations, pages 184 – 191, 14 - 15 October 2021.

Materials Research Proceedings 69 (2026) 375-379 https://doi.org/10.21741/9781644904251-68

Aeroelastic Modelling of Highly Deformable Wings in Compressible Flows

Edoardo LEVATI[1,a*], Igor PAOLINI[1,b], Giovanni BERNARDINI[1,c] and Massimo GENNARETTI[1,d]

[1]Department of Civil, Computer Science and Aeronautical Technologies Engineering, Roma Tre University, Rome, Italy

[a]edoardo.levati@uniroma3.it, [b]igo.paolini@stud.uniroma3.it, [c]giovanni.bernardini@uniroma3.it, [d]massimo.gennaretti@uniroma3.it

Keywords: Wing Aeroelasticity, Potential Flows, Compressible Flows, High Deformable Wings

Abstract. This work presents a methodology for the aeroelastic analysis of a highly de- formable wing in compressible flow. The aim is to define a design tool for innovative, highly deformable aeronautical configurations, in which nonlinearities in the structural operator and the effects of body and wake deformation in the compressible-flow aerodynamic operator are significant and play a crucial role in simulating the aeroelastic behavior.

Introduction

Recent advances in aeronautical engineering have increasingly focused on novel structural concepts featuring highly flexible lifting surfaces, for which significant geometric deformations occur during flight due to aerodynamic and structural interactions. These solutions, often adopted to improve aerodynamic efficiency and adaptability to varying operational conditions, introduce new design challenges. In particular, the interaction between aerodynamic forces and the significant elastic response of the structure makes aeroelasticity crucial, especially when assessing flutter and dynamic stability conditions. The aeroelastic analysis is of paramount importance to ensure the safety and good performance of novel aircraft configurations, requiring advanced predictive models and a deep understanding of fluid-structure coupling mechanisms [1, 2].

Aeroelastic analyses can be accomplished through experimental campaigns [3] or by employing theoretical-numerical models [4]. While experiments provide direct and tangible data, they often demand substantial resources and offer limited flexibility. Theoretical-numerical models, on the other hand, allow for the exploration of a wide range of operating conditions and structural configurations, offering predictive tools that are valuable during the design and optimization phases, although necessarily affected by a given degree of approximation. This work presents the development and application of a theoretical-numerical model for the aeroelastic analysis of a flexible wing, with the aim of identifying aeroelastic response and flutter conditions.

The aeroelastic model is obtained by coupling a geometrically nonlinear structural dynamics model for a bending-torsion beam [5] with the aerodynamic loads evaluated using a free-wake panel method solver. This solver is based on a novel boundary integral formulation for the solution of compressible potential flows around deforming lifting bodies, recently introduced by the authors [6]. It pays particular attention to the inclusion of body deformation and free-wake description, since these factors strongly affect the aerodynamic loads prediction and therefore the aeroelastic response. The aeroelastic coupling is based on a Galerkin approach and solved via a time-marching method, since the wing structural model and the free wake formulation introduce structural and aerodynamic nonlinearities that cannot be treated in the frequency domain.

The first section presents the aeroelastic model, whereas the second discusses the numerical investigation, which aims to validate the developed aeroelastic solver against literature results, and

Content from this work may be used under the terms of the Creative Commons Attribution 3.0 license. Any further distribution of this work must maintain attribution to the author(s) and the title of the work, journal citation and DOI. Published under license by Materials Research Forum LLC.

Materials Research Proceedings 69 (2026) 375-379 https://doi.org/10.21741/9781644904251-68

to assess the impact of including deformations and compressible aerodynamic effects on the wing aeroelastic response.

Aeroelastic model

This section presents the methodology used to develop the aeroelastic model for flexible wings subjected to moderate bending (in-plane and out-of-plane) and torsion displacements. The wing is modeled as a straight, slender, homogeneous, and isotropic beam undergoing moderate displacements, with geometric and mechanical properties that vary along its span. The aerodynamic forces are evaluated using a compressible potential-flow model.

Structural dynamics model. To derive the structural dynamic model of the wing, the space-time partial differential equations presented in Ref. [5] are considered, referring to the case of a bi-directional bending and torsion beam, namely a beam subject to in-plane bending, out-of-plane bending, and torsion about the elastic axis.

For the solution procedure, spatial integration of the structural-aerodynamic coupled model is performed using the Galerkin method, with shape functions corresponding to the natural modes of vibration of the uncoupled linear bending and torsional uniform beam models, with clamped-free boundary conditions. The method allows the transformation of the system of space-time partial differential equations into a set of ordinary differential equations in time

$$\mathbf{M}\,\ddot{\mathbf{x}}(t) + \mathbf{K}\big(\mathbf{x}(t)\big)\mathbf{x}(t) = \mathbf{f}(t) \tag{1}$$

where $\mathbf{M}$ is the mass matrix, $\mathbf{x}$ is the vector of the Lagrangian coordinates (time-variant coefficients of the linear combination of shape functions providing the beam bending and torsion displacements) and $\mathbf{K}\big(\mathbf{x}(\mathrm{t})\big) = \mathbf{K_L} + \mathbf{K_{NL}}(\mathbf{x}(\mathrm{t}))$ is the stiffness matrix, which is linear combination of a linear stiffness matrix $\mathbf{K_L}$ and a non linear contribution $\mathbf{K_{NL}}$. In addition, $\mathbf{f}$ is the vector collecting the generalized aerodynamic forces.

Aerodynamic model. The generalized aerodynamic forces are obtained by solving a compressible potential-flow problem around lifting bodies.

To perform an accurate simulation taking into account wing deformation and wake vorticity evolution, the boundary integral equation formulation proposed in Ref. [6] is adopted, with the wake contribution expressed in terms of the material wake description proposed in that work. The formulation includes kinematic and geometric terms that account for the deformation of the boundary surfaces, making it particularly suitable for aeroelastic analyses, where both the lifting body and the wake can deform.

The velocity potential is solved using a zero-order panel method, which yields the following solution of the problem

$$\phi_k = B_{kn}\,\psi_n + C_{kn}\,\phi_n + D_{kn}\dot{\phi}_n + F_{km}\Delta\phi_m \tag{2}$$

where ϕ_k and ϕ_n represent the velocity potential at the receiving points and at the panel centroids, respectively, ψ_n denotes the normalwash at the panel centroids as determined from the imposition of the impermeability boundary condition, while $\Delta\phi_m$ are velocity potential discontinuities evaluated at the centroids of the wake panels. The influence coefficients B_{kn}, C_{kn}, D_{kn} refer to the lifting body, while F_{km} corresponds to the wake contributions.

The computed velocity potential distribution over the body is then used to derive the generalized aerodynamic forces, $\mathbf{f}$, via the application of the unsteady, non-linear, Bernoulli theorem.

Numerical results

This section presents the numerical results obtained by using the aeroelastic model in Eq.

(1). The main objective of the numerical investigation is the assessment of the influence of the effects of the inclusion of body and wake deformations in the aeroelastic formulation in terms of

Materials Research Proceedings 69 (2026) 375-379 https://doi.org/10.21741/9781644904251-68

predicted aeroelastic stability boundaries. This is accomplished by comparisons with the results given by aeroelastic stability analysis based on the compressible-flow velocity potential formulation valid for undeformed wing surfaces presented in [7]. Moreover, the comparison with the results of the aeroelastic stability analysis performed by using an incompressible-flow model is also presented.

The aeroelastic model presented in Eq. (1) is non-linear, and thus, to evaluate the flutter stability, a time-marching scheme is used.

The numerical investigation deals with the Goland's wing model [8]. It is important to note that the structural dynamics model of Goland's wing is linear (with in-plane bending displacement neglected), but, however, the deformation of the wing is taken into account along with the wake surface deformation, and thus a time-marching scheme is requested.

Table 1 presents a comparison between the flutter speeds reported in the literature and those obtained by using the present model (PM). The comparison is carried out both under the assumption of a rigid-body aerodynamic formulation (Rig.), as described in [7], where the deformation is considered only in the definition of the impermeability boundary condition (rigid body and fixed flat wake are considered), and under the assumption of deformable surfaces by employing the aerodynamic formulation given in Eq. (2), in which the influence aerodynamic coefficients are time-dependent (due to the deformation of body and wake).

The results show excellent agreement between the data reported in the literature and those obtained by using the aeroelastic model developed in this work.

It is worth noting that the predictions based on the incompressible flow assumption tend to be more conservative than those considering flow compressibility. The flutter phenomenon depends, of course, on the dynamics of the aerodynamic loads, and particularly to their phase shift with respect to the dynamic response of the structure. Although the amplitude of the aerodynamic loads is typically higher in the compressible-flow case compared to the incompressible-flow one, the presence of a transmission delay contributes to postponing the onset of the aeroelastic instability.

Table 1: Velocity flutter comparison between present model and literature results

Model	Flutter Velocity
Wang et al. [9]	163.8 *m/s*
Zaero [9]	174.3 *m/s*
Murua et al. [10]	165 *m/s*
Werter et al. [11]	168.4 *m/s*
PM Rig. Inc.	173 *m/s*
PM Rig. Comp.	186 *m/s*
PM Def. Inc.	164 *m/s*
PM Def. Comp.	170 *m/s*

Figure 1 shows the aeroelastic stability limit as a function of the altitude. Changing altitude affects both air density and speed of sound, thereby modifying the magnitude of the unsteady aerodynamic loads as well as the transmission delay. The aim is to investigate how compressibility affects the stability boundary.

The formulation based on compressible flow, except at very high altitudes, yields less conservative predictions compared to the incompressible case. Furthermore, the formulation accounting for surface deformations anticipates the onset of instability. This is due to the geometric deformation of the body and wake, which alters the vorticity distribution in the flow field, and thus the magnitude and phase of the aerodynamic loads.

Materials Research Proceedings 69 (2026) 375-379 https://doi.org/10.21741/9781644904251-68

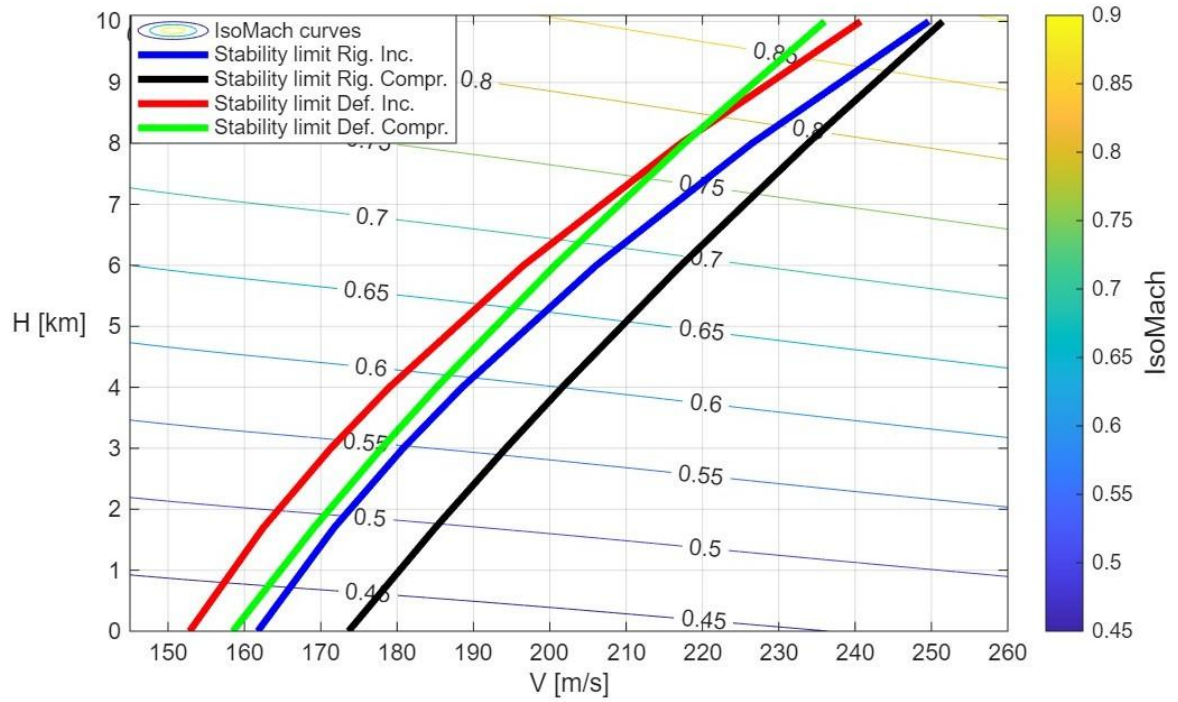


Figure 1: Flutter stability limit .vs. altitude

Conclusions

In this work, a non-linear model for the aeroelastic analysis of highly deformable wings has been presented.

The wing structural dynamics has been modeled using an equivalent bending-torsion beam representation, with clamped-free boundary conditions. Aerodynamic forces have been described through a panel method for the solution of compressible potential flows around lifting bodies, able to account for significant wing deformations and the evolution of the wake sur- face due to the self-induced velocity field.

The main objective of the numerical investigation has been the assessment of the influence of wing and wake deformations on the predicted aerodynamic loads and thus on the wing aeroelastic response. Specifically, the aeroelastic outcomes from the panel method, including wing and wake deformations (free-wake analysis), are compared with those deriving from the panel method that considers wing deformations only in terms of their effect on the impermeability boundary conditions. This comparison has revealed a difference of approximately 10% between the aeroelastic stability boundaries given by the two models analyzed. It is important to highlight that the deformable model generally predicts a lower flutter speed, thus showing that the simpler model does not provide conservative stability predictions. Furthermore, the aeroelastic results of the incompressible flow model have been considered. They show that although the compressible model generates aerodynamic loads with higher amplitudes, aeroelastic instability occurs at higher speeds compared to those of the incompressible case. This behavior is attributed to the transmission delays inherent in the compressible model, which introduce a phase shift between the aerodynamic loads and the dynamic response, postponing the onset of flutter instability.

References

[1] M. Gennaretti, A. Corbelli, and F. Mastroddi. A comparison among some aeroelas- tic models for the stability analysis of a flap-lag-torsion helicopter rotor in hover. In EUROPEAN ROTORCRAFT FORUM, volume 26, pages 68–68. AAAF; 1998, 2000, http://hdl.handle.net/20.500.11881/515.

[2] P. Prapamonthon, B. Yin, G. Yangi, M. Zhang, and P. Lu. Recent progress in flexibility effects on wing aerodynamics and acoustics. Proceedings of the Institution of Mechanical Engineers, Part C: Journal of Mechanical Engineering Science, 235(2):208–244, 2021, https://doi.org/10.1177/0954406220932208.

[3] A. Drachinsky, O. Avin, D.E. Raveh, Y. Ben-Shmuel, and M. Tur. Flutter tests of the pazy wing. AIAA Journal, 60(9):5414–5421, 2022, https://doi.org/10.2514/1.J061717.

[4] M. Gennaretti and G. Bernardini. Aeroelastic response of helicopter rotors using a 3d unsteady aerodynamic solver. The Aeronautical Journal, 110(1114):793–801, 2006, https://doi.org/10.1017/S0001924000001664.

[5] D.H. Hodges and R.A. Ormiston. Stability of elastic bending and torsion of uniform cantilever rotor blades in hover with variable structural coupling. NASA Technical Note TN D-8192, NASA, 1976.

[6] E. Levati, C. Pasquali, G. Bernardini, and M. Gennaretti. A boundary integral equation formulation for potential compressible flows around deformable bodies. 34th Congress of the International Council of the Aeronautical Sciences, 2024.

[7] L. Morino, G. Bernardini, and M. Gennaretti. A boundary element method for the aero-dynamic analysis of aircraft in arbitrary motions. Computational Mechanics, 32:301– 311, 2003, https://doi.org/10.1007/s00466-003-0487-3.

[8] M. Goland. The flutter of a uniform cantilever wing. Journal of Applied Mechanics, 12(4):A197–A208, 1945, https://doi.org/10.1115/1.4009489.

[9] Z. Wang, PC. Chen, DD. Liu, DT. Mook, and MJ. Patil. Time domain nonlinear aeroelastic analysis for hale wings. In 47th AIAA/ASME/ASCE/AHS/ASC structures, structural dynamics, and materials conference 14th AIAA/ASME/AHS adaptive structures conference 7th, page 1640, 2006, https://doi.org/10.2514/6.2006-1640.

[10] J. Murua, R. Palacios, and JMR. Graham. Assessment of wake-tail interference effects on the dynamics of flexible aircraft. AIAA journal, 50(7):1575–1585, 2012, DOI: 10.2514/1.J051543.

[11] NPM. Werter and R. De Breuker. A novel dynamic aeroelastic framework for aeroelastic tailoring and structural optimisation. Composite Structures, 158:369–386, 2016, https://doi.org/10.1016/j.compstruct.2016.09.044.

Materials Research Proceedings 69 (2026) 380-383 https://doi.org/10.21741/9781644904251-69

Propeller-driven Vibration Testing of Aircraft Wings

Gabriele DESSENA[1,a *] and Alessandro PONTILLO[2,b]

[1]Department of Aerospace Engineering, Universidad Carlos III de Madrid, Av. de la Universidad 30, 28911 Leganés, Madrid, Spain

[2]School of Engineering, University of the West of England, Frenchay Campus, Coldharbour Lane, Bristol, BS16 1QY, UK

[a]GDessena@ing.uc3m.es, [b]Alessandro.Pontillo@uwe.ac.uk

Keywords: Propeller-driven Vibration Testing, Modal Analysis, Flexible Wings, Operational Modal Analysis, Experimental Structural Dynamics

Abstract. This study details the development and initial validation of a newly introduced modal testing method, called Propeller-Driven Vibration Testing (PVT), designed for validating aircraft wing dynamics. Ground vibration testing (GVT) is crucial for aircraft certification, but it is often costly and time-consuming. By utilising the operational modal analysis (OMA) principle, PVT leverages the forces generated by an aircraft propeller running to excite the wing structure, potentially streamlining the GVT process. The research specifically examines a flexible wing model spar, constructed from Aluminium 7075-T6, excited by varying propeller speeds. Seven distinct vibration tests were conducted, including a baseline case without propeller rotation and numerous configurations with the propeller spinning at different throttle settings. Results demonstrate the feasibility of PVT in assessing dynamic characteristics, indicating that this method could significantly reduce the duration and resources needed for traditional GVT, thereby optimising the certification timeline for future electrical regional aircraft designs.

Introduction

Ground vibration testing (GVT) is a pivotal part of the aircraft certification process [1]. As such, complex and lengthy testing campaigns are usually needed, lasting weeks and involving intricate setups [2]. These make GVT expensive and time-consuming. In addition, recent advances in materials and aircraft design have highlighted that this process cannot always be considered fully linear. Nonlinearities arise from the interaction of subparts and geometrical effects [3]. Nevertheless, these are not considered in this work, as in typical operational scenarios, civil aircraft operate in the linear regime.

For these reasons, a series of approaches have been proposed to increase the efficiency of the GVT process. In particular, the Taxi Vibration Testing (TVT) [4] has received some attention over the last 20 years. The procedure proposed in TVT is to use the aircraft taxing on a taxiway or runway, uneven by definition, as a source of input for the excitation of an aircraft during a dynamic test. Within TVT, two approaches are sought: the (i) towing-based, as shown in [5], and the (ii) active taxing, through the aircraft own propulsion. A demonstrator-scale example of the latter is shown in [6].

The idea behind the PVT is that, with the race towards electric regional aircraft, it can serve as an additional tool for the dynamic validation of the aircraft system, freeing pressure, time, and money from the GVT. This would allow practitioners to streamline the verification process for certification, as it is foreseen to shorten the dynamic testing campaign.

In this work, the concept of PVT is preliminarily validated on the flexible wing model spar from the Experimental Flight Dynamics Testing for Highly Flexible Aircraft project at the University of Bristol [7]. First, the wing spar is tested with the propeller off to define a baseline case. Then,

Content from this work may be used under the terms of the Creative Commons Attribution 3.0 license. Any further distribution of this work must maintain attribution to the author(s) and the title of the work, journal citation and DOI. Published under license by Materials Research Forum LLC.

Materials Research Proceedings 69 (2026) 380-383 https://doi.org/10.21741/9781644904251-69

the test is carried out with a series of different input voltages, resulting in different Revolutions per Minute (RPMs). Finally, a propeller voltage sweep is conducted.

In the following sections, the experimental setup and specimen are described, followed by the introduction and discussion of the results.

Materials and Methods

The wing spar considered in this work spans 80 cm (out of the 7 cm constrained end) and has a constant thickness of 2.3 mm. The specimen is made out of Aluminium 7075-T6, thus yielding typical Aluminium properties for density, Young's modulus, shear modulus, and Poisson's ratio. The spar planform is characterised by four distinct sections, shown in Figure 1 alongside their dimensions.

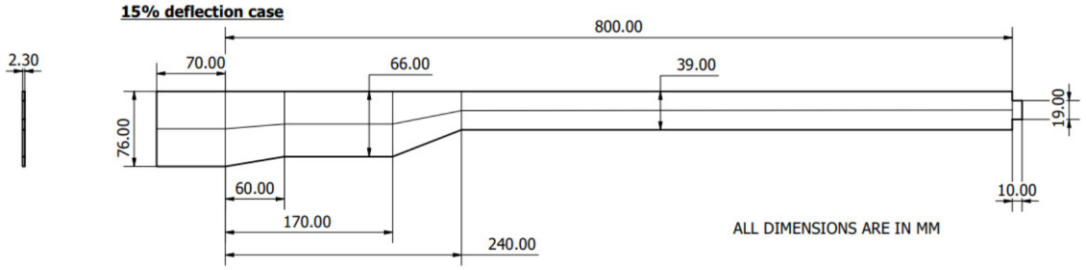


Figure 1 Flexible wing spar geometry (retrieved from [7]).

The constrained root is secured to a wall mount, providing the spar a cantilever beam-like setup. Furthermore, the spar is fitted with an in-house designed and manufactured motor bracket, positioned at 32 cm from the tip. The bracket is 3D printed using a carbon-reinforced nylon filament. A TMOTOR AS2317 electric motor, with a two-blade 8-inch propeller, is attached to the bracket. The motor is driven by a Favourite FVT 50A BLHeli_32 electronic speed control unit, connected to a lithium polymer 3S LiPo battery and to a receiver. This is, in turn, linked to a radio controller. The spar-bracket-motor assembly is instrumented with seven mono-axial accelerometers, five of which have a nominal sensitivity of approximately 100 mVg^{-1} and the remaining two have a sensitivity of 10 mVg^{-1}. The latter are placed in the accelerometer row at the spar tip. The accelerometers and motor bracket location are shown in Figure 2.

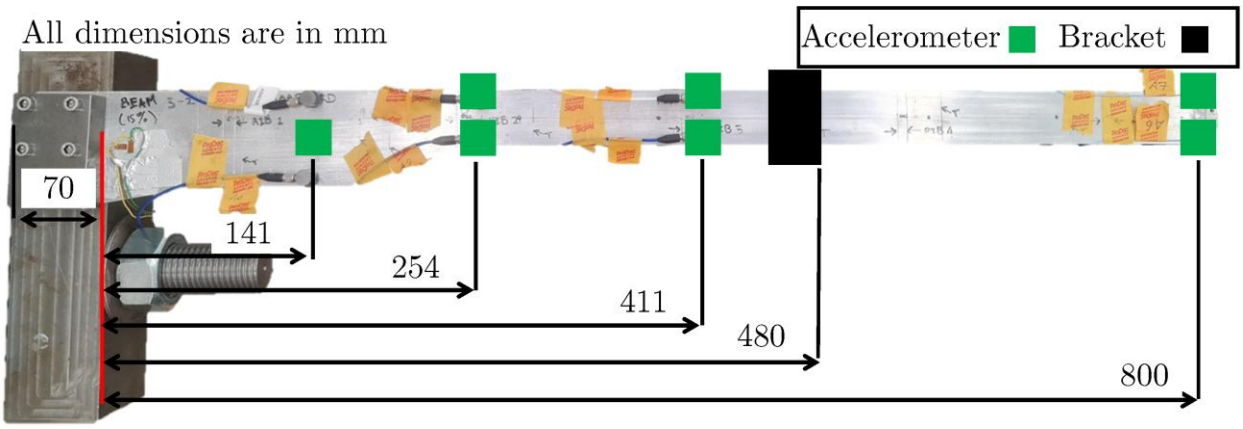


Figure 2 Experimental setup. Any distortion in the image is due to camera lens effects only.

Seven different vibration tests were carried out on the spar-bracket-motor-propeller assembly. One with the motor not spinning (i), while, in the remaining cases, the motor spins at five different fixed rates (25, 37.5, 50, 62.5, 75% throttle - cases ii-vi respectively). A final case was conducted

Materials Research Proceedings 69 (2026) 380-383 https://doi.org/10.21741/9781644904251-69

for an up-and-down sweep, where the throttle position is varied, ideally, linearly between 12.5 and 77.5% (vii).

In test (i), the assembly is excited with two impulses delivered with two subsequent hammer hits, such that the second hammer hit happens after the free-decay response of the first is fully damped. Only the seven output signals of the accelerometers labelled in Figure 2 are recorded at any time. The motor-off test lasts roughly $T_d \approx 120$ s, while in tests ii-vi $T_d \approx 300$ s. The sweep up and down test lasts approximately 600 s. All tests are sampled at a frequency $f_s = 1066$ Hz.

Results

The results from the seven tests are presented in Figure 3, which shows the Average Normalised Power Spectral Density (ANPSD) of the seven channels for each test for clarity.

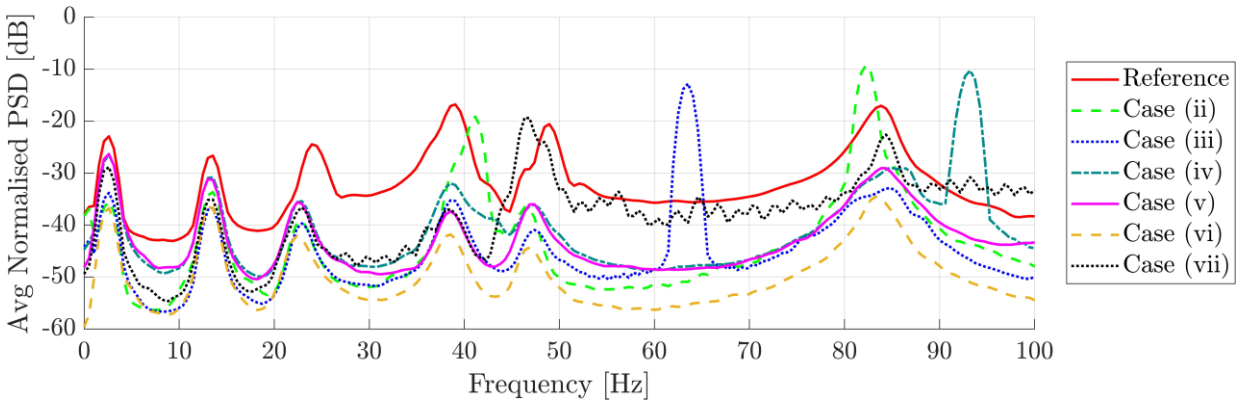


Figure 3 ANPSD of all cases tested via impulse testing and PVT.

The impulse test with the engine off and the propeller stationary, shown in Figure 3 (red), serves as the reference. As shown, all test conditions exhibit ANPSD peaks consistent with those of the reference case. Therefore, the same modes are observed irrespective of the test configuration, supporting the suitability of PVT for the modal analysis of flexible wings. However, some limitations remain. For throttle settings of 50% or less, the harmonics of the spinning propeller interfere with the measurements, which are visible at approximately 42, 63, 84, and 94 Hz in cases ii–iv. By contrast, for higher throttle settings, the dominant harmonics lie above 100 Hz, outside the frequency range analysed.

Since propeller harmonics are not always known *a priori*, case vii employs an up-down sinusoidal sweep in PVT to avoid harmonic overlap. This strategy is effective, although it yields a noisier PSD estimate than the fixed-throttle tests. This might be attributed to the fact that the sweep had to be carried out *manually*, without the aid of an external controller to regulate its rate.

Conclusions and Future Work

In this work, the viability of a new vibration testing technique applied to aeronautical components, namely Propeller-driven Vibration Testing (PVT), is proposed. The proposed method aims at using the aircraft or wing propeller as a source of excitation for the system modal analysis. The PVT is preliminary validated on a flexible wing spar equipped with an electrical motor driving a propeller. Method challenges have been identified in the propeller harmonics, which can be mitigated by using higher motor throttle settings, which push the harmonics to higher frequencies, or by implementing a throttle sweep strategy. Thus, proving the PVT as a viable vibration testing technique.

Future work includes extracting modal parameters, including mode shapes, from the response data. Furthermore, it involves the setup of a test bench with a fully controllable and verifiable throttle sweep rate, running the test on a flexible wing, including its skin, to study the effects of

aerodynamics on the PVT, and then transitioning to a full small form factor aircraft, such as a small unmanned aerial vehicle.

Aknowledgements
The authors thank Prof Mark H. Lowenberg from the School of Civil, Aerospace and Design Engineering at the University of Bristol for kindly allowing the use of the wing spar, which was designed and manufactured within the EPSRC Experimental Flight Dynamics Testing for Highly Flexible Aircraft project grant ref. EP/T018739/1. Furthermore, the first author is supported by the grants for research activity of young PhD holders, part of the Universidad Carlos III de Madrid Own Research Program (TOMA - Tangential interpolation for Operational Modal Analysis project).

References

[1] De Florio F. Airworthiness. Elsevier; 2011. https://doi.org/10.1016/C2010-0-65567-2

[2] Peeters B, Debille J, Climent H. Modern Solutions for Ground Vibration Testing of Small, Medium and Large Aircraft. SAE Int J Aerosp 2008;1:2008-01–2270. https://doi.org/10.4271/2008-01-2270

[3] Lubrina P, Giclais S, Stephan C, Boeswald M, Govers Y, Botargues N. AIRBUS A350 XWB GVT: state-of-the-art techniques to perform a faster and better GVT campaign. In: Allemang R, editor. Top. Modal Anal. II, Vol. 8. Conf. Proc. Soc. Exp. Mech. Ser., vol. 45, Orlando, FL.: Springer, Cham; 2014, p. 243–56. https://doi.org/10.1007/978-3-319-04774-4_24

[4] Govers Y, Sinske J, Schwochow J, Jelicic G, Buchbach R, Springer J, et al. Efficient ground vibration testing of aircraft based on output-only modal analysis during taxi. 58th AIAA/ASCE/AHS/ASC Struct. Struct. Dyn. Mater. Conf., Reston, Virginia: American Institute of Aeronautics and Astronautics; 2017, p. 1–11. https://doi.org/10.2514/6.2017-1824

[5] Pagani A, Azzara R, Carrera E, Zappino E. Static and dynamic testing of a full-composite VLA by using digital image correlation and output-only ground vibration testing. Aerosp Sci Technol 2021;112:106632. https://doi.org/10.1016/j.ast.2021.106632

[6] Al-bess L, Khouli F. Experimental Investigation of a Flexible Airframe Taxiing Over an Uneven Runway for Aircraft Vibration Testing. SAE Int J Aerosp 2024;17:01-17-02–0013. https://doi.org/10.4271/01-17-02-0013

[7] Banneheka Navaratna PD, Pontillo A, Rezgui D, Lowenberg MH, Neild SA, Cooper JE. Design and Assessment of Subscale Flexible High Aspect Ratio Cantilever Wings. AIAA SCITECH 2022 Forum, vol. 1305, Reston, Virginia: American Institute of Aeronautics and Astronautics; 2022. https://doi.org/10.2514/6.2022-1305

Materials Research Proceedings 69 (2026) 384-389 https://doi.org/10.21741/9781644904251-70

Coupled Thermal-Mechanical Behaviour of Ventilated Brake Discs with Radial Vanes and Lattice Cores: A Preliminary Comparison

Giuseppe MANTEGNA[1,a*], Calogero ORLANDO[1,b], Davide TUMINO[1,c], Carmelo Rosario Vindigni[1,d] and Andrea ALAIMO[1,e]

[1]Department of Engineering and Architecture, Kore University of Enna, Cittadella Universitaria, 94100, Enna, EN, Italy

[a]giuseppe.mantegna@unikore.it, [b]calogero.orlando@unikore.it, [c]davide.tumino@unikore.it, [d]carmelorosario.vindigni@unikore.it, [e]andrea.alaimo@unikore.it

Keywords: Ventilated Brake Disc, Radial Vane, BCC Lattice, WBCC Lattice, Thermalmechanical Analysis

Abstract Brake discs are critical components during a vehicle's braking phase. To dissipate the heat generated, ventilated discs are commonly employed. Among these, radial vane configurations are widely adopted due to their effective cooling performance and relatively simple manufacturability. This work presents a preliminary comparison between a conventional radial vane disc and lattice cores ventilated disc. Specifically, a coupled steady-state thermal-mechanical analysis is conducted to assess the radial and circumferential temperature distributions, as well as the thermal stresses, during a hard braking event. The steadystate assumption is adopted as a first approximation to evaluate the thermo-mechanical behaviour of the two configurations. The results show that the lattice core disc has a lower maximum temperature and a more uniform thermal distribution, suggesting an improved heat dissipation capability compared with the conventional design.

Introduction

Brake discs are critical components during a vehicle's braking phase. Friction between the pads and the disc slows the vehicle and converts kinetic (and, where relevant, potential) energy into heat. A large fraction of this energy, up to 90%, is absorbed by the disc and must be appropriately dissipated to avoid local overheating, which can lead to wear, oxidation, and thermal fatigue [1–4]. To better dissipate heat, ventilated discs with radial or curved vanes are widely used for their superior cooling performance. During rotation, air is drawn into the disc by centrifugal forces and guided through the vanes, promoting forced convection and improving thermal dissipation [5,6].

Recently, lattice structures have gained increased attention in various engineering fields due to their tunable thermo-mechanical properties at low mass [7–10]. Among these, BodyCentred Cubic (BCC) lattices are a common choice, as they are easy to manufacture, can be designed for specific stiffness, and provide a high surface-area-to-mass ratio.

This work compares three brake disc designs: a conventional radially-ventilated disc, a disc with a Body-Centred Cubic (BCC) lattice core, and a novel lattice configuration featuring BCC unit cells with curved struts referred to as Waved Body-Centred Cubic (WBCC) [11]. To isolate geometric effects, the different designs have the same core mass. Given the geometric complexity of the lattice structures, a preliminary steady-state, coupled thermomechanical analysis is conducted. Although simplified, this approach enables a direct comparison of heat-dissipation and structural behaviour under identical loads and boundary conditions.

The study evaluates the discs' effectiveness by examining temperature and stress fields along the radial, circumferential, and through-thickness directions.

Content from this work may be used under the terms of the Creative Commons Attribution 3.0 license. Any further distribution of this work must maintain attribution to the author(s) and the title of the work, journal citation and DOI. Published under license by Materials Research Forum LLC.

Materials Research Proceedings 69 (2026) 384-389 https://doi.org/10.21741/9781644904251-70

Steady-state thermo-mechanical model

The transient energy equation $\rho c_p \frac{\partial T}{\partial t} = \nabla \cdot (k \nabla T)$ derived from the Fourier's law for a steady-state analysis simplifies to:

$$\nabla \cdot (k \nabla T) = 0 \tag{1}$$

In this study, both internal heat generation and radiation effects are neglected. However, the frictional heating at the pad-disc interface and the convective dissipation to the surrounding air must be accounted for. The local frictional heat flux at the interface is:

$$q''_{fric}(r) = \eta \mu p(r) V(r), \quad \text{with} \quad V(r) = \omega r \tag{2}$$

where η is the the heat-partition ratio into the disc, μ is the friction coefficient between the pad and the disc, p is the normal pressure applied to the pads, $V(r)$ is the sliding velocity retrieved from the angular velocity ω and the radius r of the disc.

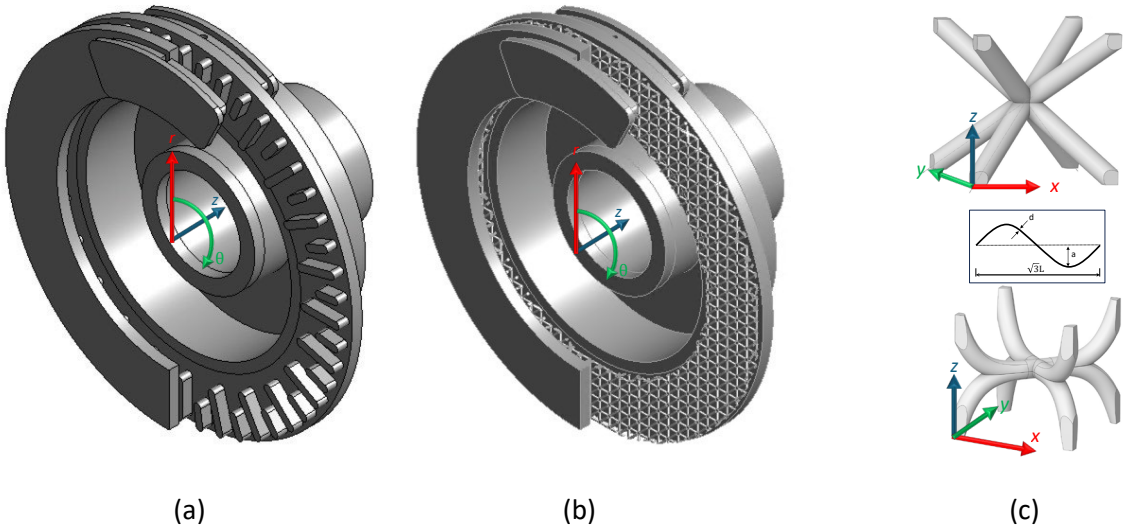
Defining h as the convective heat coefficient, the convective heating flux is:

$$q''_{conv} = h(r)(T - T_\infty) \tag{3}$$

Keeping μ, p, ω, h constant, the study simulates a constant friction power, pressure on the pads, angular velocity, and convective exchanges to isolate the effect of core geometry on temperatures and stresses.

Geometry and numerical model

The analyses were performed on a ventilated brake disc featuring three different cores designs: a conventional radial vane core, a BCC lattice core, and a Waved Body-Centred Cubic lattice core. The three configurations, reported in Figure 1, are characterised by the same mass to have a direct comparison of their thermo-structural performance. The WBCC structure is derived from the BCC cell by introducing sinusoidally curved struts with a wave amplitude of $a = 1.5$ mm. Unlike the BCC lattice, which is intrinsically isotropic, the WBCC cell exhibits directional dependence. In this study, only the WBCC configuration with its z-axis aligned with the disc thickness direction is considered.



(a) (b) (c)

Figure 1: Brake disc model (top half disc hidden for clarity). (a) Radial vane, (b) Lattice core and (c) BCC and WBCC unit cell detail

Materials Research Proceedings 69 (2026) 384-389 https://doi.org/10.21741/9781644904251-70

The simulations were conducted using ANSYS Workbench 2022 R1.

Gray cast iron, commonly used in automotive applications, was assigned to the disc, while the brake pads are assumed as an elastomer and modelled with a linear elastic material. The material properties are reported in Table 1.

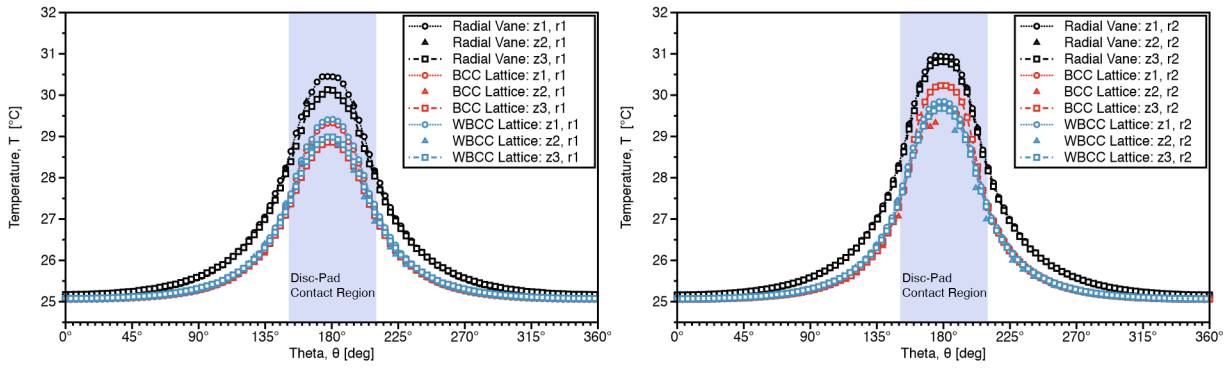
Table 1: Material properties

Property	Brake Disc and Core	Brake Pads
Density, ρ [kg/m^3]	7200	2045
Young's Modulus, E [GPa]	110	0.8
Poisson's Ratio, v [-]	0.28	0.34
Thermal Conductivity, k [W/(m °C)]	53	0.84
Specific heat constant pressure, c_p [J/(kg °C)]	586	1000
Convective heat transfer coefficient, h [W/(m^2 °C)]	50	50

A constant angular velocity of 55 rad/s was applied to the disc, while a force of 50,000 N was applied to each brake pad. The frictional contact between the pads and the disc was defined with a coefficient of $\mu = 0.25$. Through an APDL script, the heat-partition ratio η was set to 0.9. To evaluate heat dissipation, a convective heat transfer coefficient of 50 W/(m^2 °C) was applied to all external and internal surfaces of the disc and pads models. This simplified approach, using a uniform coefficient, allows for a direct comparison of the core architectures by isolating the effects of internal thermal conduction and surface area. Ambient temperature was set to 25 °C for all components.

Results and Discussion

All results are evaluated at three specific depths within the disc: on the external surfaces of the core under the inner and outer disc z_1 and z_3, and at the mid-plane of the core z_2. In addition, three radial positions are considered along the friction track: r_1, located near the inner edge of the brake pad; r_2, at the pad's mid-radius; and r_3, close to the outer edge. Finally, the distributions are assessed over the entire circumferential angle of the disc to capture the full tangential variation of temperature and stress fields. The circumferential temperature distributions are compared in Figure 2.



Materials Research Proceedings 69 (2026) 384-389 https://doi.org/10.21741/9781644904251-70

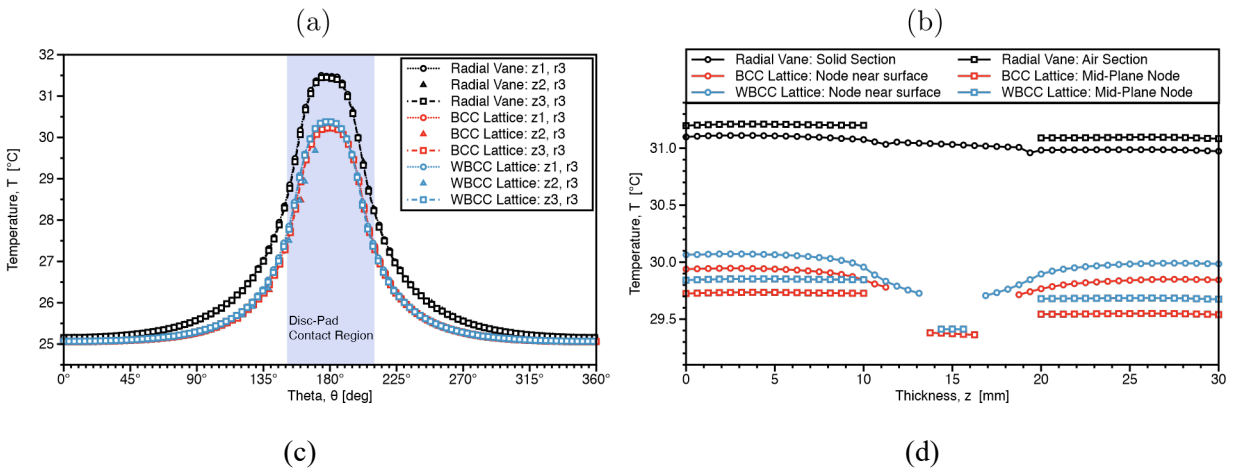


Figure 2: (a)-(c) Circumferential temperature distributions at different radial and depth locations. (d) Through-thickness temperature profiles at r_2 near $\theta \approx 180°$

All the temperature profiles in Figure 2(a)-(c) exhibit a single symmetric peak centred within the highlighted light-blue region, corresponding to the pad-disc contact area. The BCC and WBCC lattice configurations consistently show lower peak temperatures than the conventional radial-vane core, with nearly identical values to each other. Both lattice designs reduce the maximum temperature by about 6%. This trend aligns with their larger surface area, as the convective power scales with $Q_{conv} \approx \int(h, \Delta T)dA$. The lattice configurations also feature a narrower width peak, indicating a more localised heat sink due to enhanced heat extraction near the hot sector, which sharpens the thermal profile and limits circumferential diffusion. At all circumferential locations, the through-thickness temperature trends are similar across the three designs, with the surfaces (z_1, z_3) warmer than the mid-plane (z_2). Figure 2(d) illustrates this behaviour at two points near the pad centre $(r_2, \theta \approx 180°)$. In the radial-vane disc, these positions correspond to a solid vane and an adjacent ventilated channel, while in the lattice configurations they coincide with the strut junction nodes—one at the disc surfaces and the other at the core mid-plane. Consistent with the previous plots, the through-thickness profiles reveal small but systematic differences, with the radial-vane disc remaining slightly hotter than the lattice designs.

Finally the Von Mises stress map distributions on the disk-pad contact surface for the three design is shown in Figure 3(a)-(c). On the disc-pad contact face, the equivalent von Mises stresses concentrate in the hot sector beneath the pad. The radial-vane core shows the highest peak ($\approx$ 28.2 MPa), with a uniform broad distribution under the contact. The BCC lattice lowers the peak to $\approx$ 22.0 MPa (about 23% reduction compared to the radial-vane), while the WBCC has the greatest reduction with of about 35% compared to the standard configuration. In both lattice designs the high-stress zone is more confined, in accordance with the lower, sharper temperature peaks observed earlier. Away from the contact sector, the stresses remain low across all designs. Overall, the lattices mitigate peak stress on the pad-disc surface, with the WBCC providing the largest reduction.

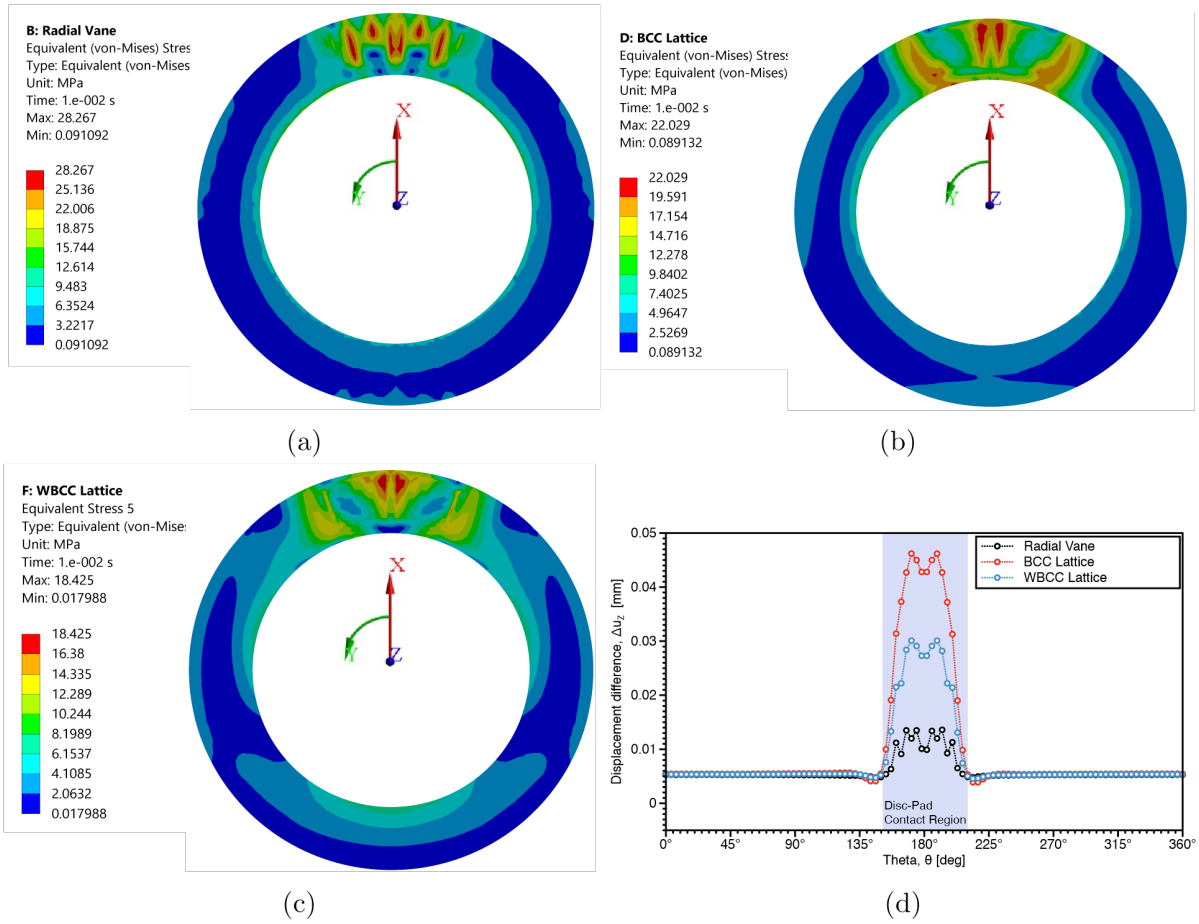


Figure 3: Circumferential equivalent (von Mises) stress distribution: (a) Radial Vane, (b) BCC Lattice, (c) WBCC lattice. (d) Core face distance difference comparison

Figure 3(d) shows the face-to-face core displacement difference, Δu_z. The BCC lattice shows the largest displacement which results in the lowest stiffness of the three configurations. The WBCC design, on the other hand, has an intermediate behaviour, while the standard radial configuration is the smallest. Overall, the radial core is approximately three time stiffer than the BCC and approximately two times stiffer than the WBCC configuration.

Conclusions

In this preliminary comparison of different cores for ventilated vane brake discs, lattice designs, particularly WBCC, improved the thermal properties by lowering peak temperatures and localizing the heat sink, though at the cost of reduced disc stiffness. Further analyses are needed to better evaluate the thermo-mechanical properties.

References

[1] David Phan and Dino Kondyles. Rotor design and analysis; a technique using computational fluid dynamics (CFD) and heat transfer analysis. Technical report, SAE Technical Paper, 2003. https://doi.org/10.4271/2003-01-3303

[2] Thomas J Mackin, Steven C Noe, KJ Ball, BC Bedell, DP Bim-Merle, MC Bingaman, DM Bomleny, GJ Chemlir, DB Clayton, HA Evans, et al. Thermal cracking in disc brakes. Engineering Failure Analysis, 9(1):63-76, 2002. https://doi.org/10.1016/S1350-6307(00)00037-6

[3] Qifei Jian and Yan Shui. Numerical and experimental analysis of transient temperature field of ventilated disc brake under the condition of hard braking. International Journal of Thermal Sciences, 122:115-123, 2017. https://doi.org/10.1016/j.ijthermalsci.2017.08.013

[4] Dejian Meng, Xiangxin Zeng, Lijun Zhang, and Birui Li. A novel approach to analyzing thermoelastic behavior of brake disc under the combined action of thermal and mechanical loads. Mechanical Systems and Signal Processing, 224:112155, 2025. https://doi.org/10.1016/j.ymssp.2024.112155

[5] David A. Johnson, Bryan A. Sperandei, and Ross Gilbert. Analysis of the flow through a vented automotive brake rotor. Journal of Fluids Engineering, 125(6):979-986, 01 2004. https://doi.org/10.1115/1.1624426

[6] Ali Belhocine and M Bouchetara. Thermal behavior of full and ventilated disc brakes of vehicles. Journal of Mechanical Science and Technology, 26(11):3643-3652, 2012. https://doi.org/10.1007/s12206-012-0840-6

[7] Giuseppe Iacolino, Giuseppe Mantegna, Emilio V Gonz'alez, Giuseppe Catalanotti, Calogero Orlando, Davide Tumino, and Andrea Alaimo. Low-Velocity Impact Behavior of PLA BCC Lattice Structures: Experimental and Numerical Investigation with a Novel Dimensionless Index. Materials, 2025. https://doi.org/10.3390/ma18194574

[8] G Mantegna, CR Vindigni, D Tumino, C Orlando, and A Alaimo. Comparison of lattice core topologies in sandwich structures. Materials Research Proceedings, 37, 2023. https://doi.org/10.21741/9781644902813-64

[9] Jean Ernot, Patrick G Verdin, Hayder Ahmad, and Philip Indge. Analytical and numerical predictions of the thermal performance of multi-layered lattice structures. International Journal of Heat and Mass Transfer, 145:118752, 2019. https://doi.org/10.1016/j.ijheatmasstransfer.2019.118752

[10] Jian Liu, Mengyao Xu, Rongdi Zhang, Xirui Zhang, and Wenxiong Xi. Progress of porous/lattice structures applied in thermal management technology of aerospace applications. Aerospace, 9(12):827, 2022. https://doi.org/10.3390/aerospace9120827

[11] Davide Tumino, Andrea Alaimo, Giuseppe Mantegna, Calogero Orlando, and Stefano Valvano. Mechanical properties of bcc lattice cells with waved struts. International Journal on Interactive Design and Manufacturing (IJIDeM), 18(8):5823-5836, 2024. https://doi.org/10.1007/s12008-023-01359-9

Materials Research Proceedings 69 (2026) 390-395 https://doi.org/10.21741/9781644904251-71

Trim Analysis of Highly Flexible Aircraft via a Coupled DG-VLM Framework

Elisa TESTAQUATRA[1,a], Vincenzo GULIZZI[1,b*]

[1]Department of Engineering, Università degli Studi di Palermo, Italy

[a]elisa.testaquatra@unipa.it, [b]vincenzo.gulizzi@unipa.it

Keywords: Flexible Aircraft, Hyperelasticity, Nonlinear Trim, Discontinuous Galerkin Method, Vortex Lattice Method

Abstract. An original computational framework for the trim analysis of highly-flexible aircraft is presented in this work. The framework is based on the combination of a discontinuous Galerkin (DG) method and a non-planar Vortex Lattice Method (VLM). The DG method is employed for solving three-dimensional finite-strain, whereas the non-planar VLM is employed for solving potential-flow aerodynamics of the deformed structure. The DG-VLM coupling is performed by considering the forces generated by the vortexes as energetically equivalent to body forces acting on the structure. The framework is validated by considering the finite-strain response of a cantilever beam, the finite-strain response of a highly flexible wing, and the angle of attack and elevator deflection at longitudinal trim condition of an aircraft featuring the same highly flexible wing.

Introduction

Over the past years, research on High Aspect Ratio Long Endurance (HALE) aircraft has been of particular interest, as high-aspect-ratio wings provide greater aerodynamic efficiency, reducing fuel consumption and extending endurance. However, high-aspect-ratio wings may undergo large deformations and rotations, which can significantly affect their aerodynamic characteristics. For this reason, the analysis and design of vehicles featuring such type of wings, including the aspects related to their flight mechanics performances, must be performed accounting for fluid-structure interaction effects.

Numerical methods are often necessary as analytical solutions are seldom available, especially in the regime of large deformations and rotations. Recently, several approaches have been proposed to solve the aeroelastic problems of highly flexible aircraft. Murua and Palacios [1] developed a computational framework based on a geometrically exact beam model and the Unsteady Vortex Lattice Method (UVLM). Zhang et al.[2] developed a 3D co-rotational beam framework, coupling the structural dynamics with unsteady aerodynamics. Drachinsky and Raveh [3] employed the modal rotation method to capture large deformations through spatial derivatives of mode shapes. Medeiros and Cesnik [4] proposed a reduced-order geometrically nonlinear formulation, accounting large deformation effects on both inertia and stiffness terms.

This contribution presents a novel computational framework for the aeroelastic analysis of highly flexible aircraft based on finite-strain elasticity and potential-flow aerodynamics. The framework is based on the coupling between a discontinuous Galerkin (DG) method for solving finite-strain total-Lagrangian elasticity and a non-planar Vortex Lattice Method (VLM) for solving potential flow aerodynamics. The framework is validated considering the finite-strain response of a cantilever beam and the finite-strain response of a highly flexible wing. Then, the framework is employed to study the longitudinal trim of an aircraft featuring a high-aspect-ratio wing. Numerical results are presented by comparing the computed values of angle of attack and elevator deflection at trim condition upon considering a rigid wing, an elastic wing undergoing small deformations, and an elastic wing undergoing large deformations.

Content from this work may be used under the terms of the Creative Commons Attribution 3.0 license. Any further distribution of this work must maintain attribution to the author(s) and the title of the work, journal citation and DOI. Published under license by Materials Research Forum LLC.

Materials Research Proceedings 69 (2026) 390-395 https://doi.org/10.21741/9781644904251-71

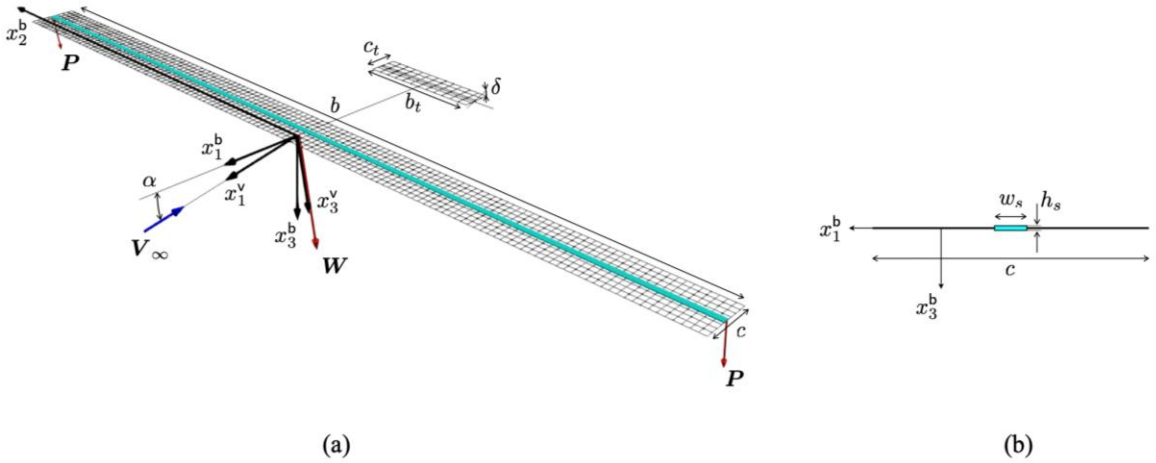


Figure 1: (a) Geometry of the flexible aircraft. (b) Load-bearing rectangular cross section of the main wing.

Problem statement

Let us consider the longitudinal behavior an aircraft modeled by a main wing and a horizontal tail, as shown in Fig.(1a). The span and the chord of the main wing are denoted by b and c, respectively, while the span and the chord of the horizontal tail are denoted by b_t and c_t, respectively. The main wing has a load-bearing rectangular cross section of density ρ_s, width w_s, and thickness h_s, that is placed at 50% of the wing's chord; see Fig.(1b). The entire horizontal tail is supposed to be a rigid movable surface that can rotate of an angle δ around an axis placed at 0.39% of its chord. The aircraft is assumed to be in horizontal flight at a speed V_∞ and angle of attack α within a fluid whose density is denoted by ρ_∞.

The flexible part of the aircraft is the load-bearing cross-section of the main wing, which is made of an isotropic material identified by Young's modulus E and Poisson's ratio v. Two different elastic behaviors are considered for the main wing cross section, namely a linear elastic behavior within the small-deformation hypothesis and a hyper-elastic behavior accounting for large deformations and rotations. In the former case, the deformation of the main wing is obtained by solving the equations of linear elasticity combined with a constitutive behavior that can be written as $\boldsymbol{\sigma} = \boldsymbol{C\varepsilon}$, where $\boldsymbol{\sigma}$ and $\boldsymbol{\varepsilon}$ are vectors collecting the stress and strain components, respectively, in Voigt notation, and $\boldsymbol{C}$ is the associated matrix of elastic coefficients for isotropic materials. On the other hand, in the hyper-elastic case, the deformation of the main wing is obtained by solving the equations of finite-strain elasticity in combination with a constitutive behavior of the form $\boldsymbol{S} = \boldsymbol{CE}$, where $\boldsymbol{S}$ and $\boldsymbol{E}$ are vectors collecting the second Piola-Kirchhoff stress components and the Green-Lagrange strain components, respectively, in Voigt notation, whereas, following the Saint Venant–Kirchhoff model, $\boldsymbol{C}$ is the same matrix of elastic coefficients employed in the small-strain case.

The loads acting on the wing structure consist of its weight, a load $\boldsymbol{P}$ placed at each tip of the wing, and the aerodynamic loads deriving from the interaction with the fluid.

DG-VLM formulation

The solution of the aeroelastic problem introduced in the preceding section is performed by combining a DG formulation for solving finite-strain elasticity and a non-planar VLM for solving potential-flow aerodynamics. In this section, the solution of finite-strain is reported, whereas the solution of the rigid and small-strain problems can be obtained as special cases.

Following Gulizzi et al.[5], it is possible to show that the DG weak form associated to the finite-strain elastic behavior of the wing structure can be stated as follows: find $\boldsymbol{\varphi}$, being $\boldsymbol{\varphi}$ the

Materials Research Proceedings 69 (2026) 390-395 https://doi.org/10.21741/9781644904251-71

approximated deformation mapping, such that $B(\boldsymbol{V},\boldsymbol{\varphi}) = F(\boldsymbol{V},\boldsymbol{b_0})\ \forall \boldsymbol{V} \in \boldsymbol{V}^{hp}$, being $\boldsymbol{V}^{hp}$ the space of discontinuous polynomial vector fields, where

$$B(\boldsymbol{V},\boldsymbol{\varphi}) \equiv \int_{\mathcal{D}^h} \frac{\partial \boldsymbol{V}^T}{\partial x_k}\frac{\partial w}{\partial \boldsymbol{F}_k} - \int_{\mathcal{J}^h}\left(\llbracket \boldsymbol{V}\rrbracket_k^T\left\{\frac{\partial w}{\partial \boldsymbol{F}_k}\right\} + \{\boldsymbol{\Pi}_k^T\}\llbracket\boldsymbol{\varphi}\rrbracket_k\right) + \int_{\mathcal{J}^h}\mu\llbracket\boldsymbol{V}\rrbracket_k^T\llbracket\boldsymbol{\varphi}\rrbracket_k + \\ - \int_{\mathfrak{B}_D^h}\left(\boldsymbol{V}^T\ \frac{\partial w}{\partial \boldsymbol{F}_k}n_k + \boldsymbol{\Pi}_k^T n_k\boldsymbol{\varphi}\right) + \int_{\mathfrak{B}_D^h}\mu\boldsymbol{V}^T\boldsymbol{\varphi} \qquad (1)$$

and

$$F(\boldsymbol{V},\boldsymbol{b}) \equiv \int_{\mathcal{D}^h}\boldsymbol{V}^T\boldsymbol{b} \qquad (2)$$

In Eq.(1), w denotes the solid strain energy function, $\boldsymbol{F}_k$ denotes the k-th column of the deformation gradient tensor, n_k is the k-th component of the unit normal of the solid boundary, while $\boldsymbol{\Pi}_k$ is a symmetrization vector and μ is a penalization parameter that are typical of DG formulations. Additionally, the integrals appearing in Eq.(1) are referred to as broken integrals and must be intended as the sum over the mesh elements of the integrals computed over each element domain and boundary. See Ref.[5] for further details.

Eventually, Eq.(2) accounts for the loads acting on the wing structure and includes those stemming from gravity, the concentrated loads at the wing tips and the aerodynamic loads, which are computed solving a non-planar VLM system where the vortexes deform with the structure [6].

Upon introducing the DG structural degrees of freedom that are collected in the vector $\boldsymbol{X}$ and the VLM degrees of freedom that collected in the vector $\boldsymbol{\Gamma}$, the final system of equations governing the aeroelastic problem can be written as

$$\begin{cases}\boldsymbol{R}_S(\boldsymbol{X},\boldsymbol{\Gamma}) = \boldsymbol{0}\\ \boldsymbol{R}_A(\boldsymbol{X},\boldsymbol{\Gamma}) = \boldsymbol{0}\end{cases} \qquad (3)$$

where $\boldsymbol{R}_S(\boldsymbol{X},\boldsymbol{\Gamma})$ denotes the equations associated with the structural problem and $\boldsymbol{R}_A(\boldsymbol{X},\boldsymbol{\Gamma})$ denotes the equations associated with the aerodynamic problem. This system of equations is solved via a Newton-Raphson approach.

Results

In the first set of tests, an isolated half-wing with a load P placed at its tip is considered. The wing is clamped at its root and has a square cross section, i.e., $ws = hs$. Two lengths are considered, namely $b/2 = L = 10w_s$ and $b/2 = L = 100w_s$. The deformation of the structure using a kinematic model featuring a third-order approximation along the cross section and fifth-order approximation along the span. The obtained results are reported in Fig.(2) for the two lengths in terms of u_z/L versus $PL^2/(EI)$, where I is the moment of inertia of the cross section. The comparison with the results available in the literature [7,8] confirms the capability of the proposed framework to capture finite-strain bending behaviors.

Materials Research Proceedings 69 (2026) 390-395 https://doi.org/10.21741/9781644904251-71

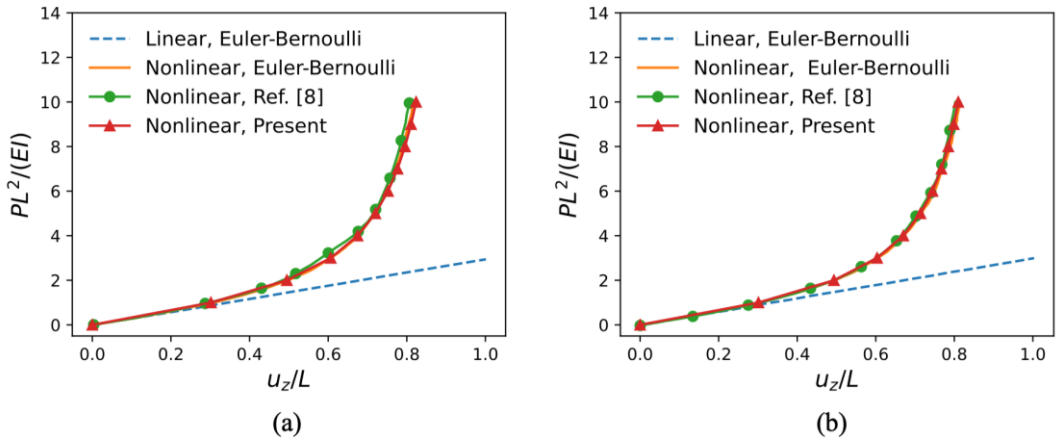


Figure 2: Vertical displacement of a cantilever beam under finite deformations due to a tip load.

In second set of tests, the developed framework is employed to compute the aeroelastic response of a half-wing clamped at its root in terms of tip displacement versus wind speed. The wing is modeled under the small-strain hypothesis and under the finite-strain hypothesis. The geometrical and material properties of the considered wing can be found in Ref.[9]. The wing tip displacement as a function of the flow speed is reported in Fig.(3) for an angle of attack of 0.4°. The results obtained using the linear model and the nonlinear model are compared with the results (both numerical and experimental) provided in Ref.[9]. As shown in figure, it is possible to notice how the linear and nonlinear models agree for low speed, while they start to provide different results for a flow speed V_∞ approximately above 31 m/s, when the geometric nonlinearities become dominant. In particular, the linear models provide a tip displacement that tends to infinity as the flow speed approaches the divergence speed. Such a divergent behavior is not present in the results obtained by the nonlinear models, which remain much closer to the experimental results, confirming that the use of a finite-strain model is essential for accurately capturing the aeroelastic behavior of a highly flexible wing.

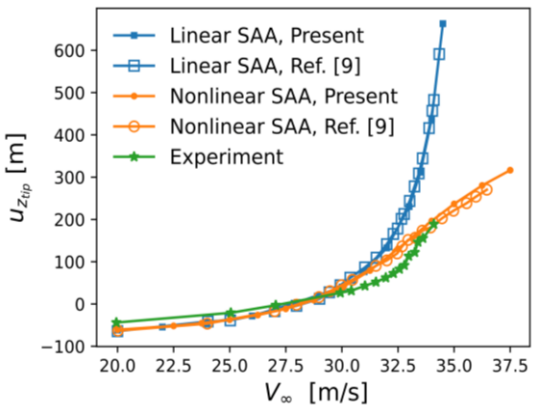


Figure 3: Wing tip displacement versus wind speed for a highly-flexible wing.

Eventually, the framework is employed to compute longitudinal trim conditions in terms of angle of attack and elevator deflection of an aircraft featuring the same highly flexible wing considered for the previous set of tests. The geometrical properties of the entire aircraft can be found in Ref.[10]. Table (1) reports the obtained values of angle of attack α and elevator deflection δ at longitudinal trim condition for $V_\infty = 25$ m/s in the cases the wing is considered rigid or highly flexible. An error of approximately 10% is observed with the results provided in the literature.

Table 1: Angle of attack α and elevator deflection δ at longitudinal trim condition for an aircraft featuring a highly-flexible wing for V_∞ = 25 m/s.

	Present		Ref.[10]	
	α [°]	δ [°]	α [°]	δ [°]
Rigid	3.77	-1.97	3.76	-1.98
Flexible	2.88	-1.99	3.22	-1.81

Conclusions

A novel computational framework for the trim analysis of highly-flexible aircraft has been presented. The novelty of the framework is the combined use of a discontinuous Galerkin method for solving finite-strain elasticity and a non-planar Vortex Lattice Method for solving potential-flow aerodynamics of the deformed structure. The capabilities of the framework have been assessed by analyzing the finite-strain bending of a cantilever beam subject to a tip load, the finite-strain aeroelastic response of an isolated wing, and the longitudinal trim of an aircraft featuring a highly-flexible wing. A satisfactory comparison between the results obtained with the present framework and the results available in the literature, which consist of both numerical and experimental results, has been observed. Currently the framework is being extended to consider different kinematic approximations, more complex internal structures and materials, and a wider range of flight conditions.

Acknowledgments

This work has been supported by the project “Hydro-dynamic devices for micro-particle trapping and vibrational energy harvesting (HYDRA)”, CUP B53D23005770006, funded by Next Generation EU - PNRR M4 - C2 - investimento 1.1: Fondo per il Programma Nazionale di Ricerca e Progetti di Rilevante Interesse Nazionale (PRIN) - PRIN 2022 cod.2022AALLEC.

References

[1] J. Murua, R. Palacios, J. M. R. Graham, Applications of the unsteady vortex-lattice method in aircraft aeroelasticity and flight dynamics, Progress in Aerospace Sciences. 55 (2012) 46-72. https://doi.org/10.1016/j.paerosci.2012.06.001

[2] C. Zhang, Z. Zhou, X. Zhu, L. Qiao, A comprehensive framework for coupled nonlinear aeroelasticity and flight dynamics of highly flexible aircrafts, Applied Sciences. 10(3)(2020) 949. https://doi.org/10.3390/app10030949

[3] A. Drachinsky, D. E. Raveh, Nonlinear aeroelastic analysis of highly flexible wings using the modal rotation method, AIAA Journal. 60(5) (2022) 3122-3134. https://doi.org/10.2514/1.J061065

[4] R. R. Medeiros, C. E. Cesnik, E.B. Coetzee, Computational aeroelasticity using modal-based structural nonlinear analysis, AIAA Journal. 58(1) (2020) 362-371. https://doi.org/10.2514/1.J058593

[5] V. Gulizzi, I. Benedetti, A. Milazzo, Discontinuous Galerkin methods for solids and structures, Comprehensive Structural Integrity 2nd edition, Oxford: Elsevier, (2023) 348-377. https://dx.doi.org/10.1016/B978-0-12-822944-6.00024-4

[6] V. Gulizzi, I. Benedetti, Computational aeroelastic analysis of wings based on the structural discontinuous Galerkin and aerodynamic vortex lattice methods, Aerospace Science and Technology, 144 (2024) 108808. https://doi.org/10.1016/j.ast.2023.108808

[7] K. E. Bisshopp, D. C. Drucker, Large deflection of cantilever beam, Quarterly of applied mathematics. 3(3) (1945) 272-275. https://www.jstor.org/stable/43633516

[8] A. Pagani, R. Augello, E. Carrera, Frequency and mode change in the large deflection and post-buckling of compact and thin-walled beams, Journal of Sound and Vibration. 432 (2018) 88-104. https://doi.org/10.1016/j.jsv.2018.06.024

[9] C. Xie, L. Wang, C. Yang, Y. Liu, Static aeroelastic analysis of very flexible wings based on non-planar vortex lattice method, Chinese Journal of Aeronautics. 26(3) (2013) 514- 521. https://doi.org/10.1016/j.cja.2013.04.048

[10] C. Yang, L. Wang, C. Xie, Y. Liu, Aeroelastic trim and flight loads analysis of flexible aircraft with large deformations, Science China Technological Sciences. 55(10) (2012) 2700-2711. https://doi.org/10.1007/s11431-012-4912-8

Materials Research Proceedings 69 (2026) 396-401 https://doi.org/10.21741/9781644904251-72

Mid-Fidelity Approaches for the Non-Linear Aeroelastic Assessment of The Pazy Wing

Alessia BOVE[1,a *] and Giuseppe QUARANTA[1,b]

[1]Department of Aerospace Science and Technology, Politecnico di Milano, Via La Masa 34, 20156 Milano, Italy

[a]alessia.bove@polimi.it, [b]giuseppe.quaranta@polimi.it

Keywords: Aeroelasticity, Limit Cycle, Panel Method, Vortex Lattice, Pazy Wing

Abstract. Predicting the non-linear aeroelastic behavior of very flexible structures and the limit cycle oscillations that often develop is a challenge. This work investigates the nonlinear aeroelastic behavior of the Pazy Wing to determine the nature of its LCOs by coupling a nonlinear structural beam model with different mid-fidelity aerodynamic methods: the vortex lattice method and the panel method. The results demonstrate that the limit cycle originates from nonlinear structural effects, rather than aerodynamic nonlinearities. While both methods successfully predict the onset of the phenomenon, this study highlights that only the panel method accurately estimates the oscillation amplitude when compared to experimental data. This underscores the fundamental role of 3D aerodynamic effects, which are underestimated by the vortex lattice. The study therefore provides clear guidance for selecting efficient models, recommending the coupling of a nonlinear structural model with 3D aerodynamics as the optimal approach for a correct assessment of LCO severity.

Introduction

Due to increasing interest in the first decade of the 21st century for HALE (High Altitude Long Endurance) aircraft handling a plurality of goals, the aerospace industry, also driven by the need for greener, lightweight, therefore more elastic vehicles, started developing flying machines characterized by extremely slender wings. Due to their elongated shape, such components are exceptionally flexible, reaching an in-flight deflection up to 25% of their semispan, thus posing new challenges in the estimation of aircraft's flutter boundaries. Moreover, it may happen that such large deflections bring the structure out of the linear deformation field, making it necessary to establish some ad hoc tools to investigate how this impacts the dynamic behavior of said component. In these kind of design, it may occur, for example, that divergent modes lead to Limit Cycle Oscillations (LCOs), a nonlinear phenomenon characterizing post-flutter structural behavior, which, depending on the cycle amplitude, may cause structural failure. An essential step in the assessment of novel nonlinear models is wind tunnel testing, allowing to gather data for computational models' validation. With this aim, the *Pazy Wing*, designed to experience deformation up to the 50% of its semi-span, was built at Technion [1]. It manifested both hard and soft flutter, and several LCOs. In particular, there is a Hump Mode region that is a speed bounded region of instability where the wing experiences LCOs. However, increasing the airspeed past this region, the wing regains stability, until it gets into an unbounded oscillation that is denominated Hard Flutter. The purpose of the present study is to evaluate if this nonlinear aeroelastic behavior can be assessed using mid-fidelity approaches. Additionally, by using these simulations, this work aimed at assessing the nature of such LCOs, trying to discriminate if they are dominated by structural or aerodynamic nonlinearities or by both. A reduced order structural model, namely a beam, was created in MBDyn [2] and loaded using three different aerodynamic models: strip theory, Vortex Lattice Method (VLM) and Panel Method (PM) [3]. In the VLM method, the lifting wing is represented by a line where at each section is associated an airfoil with certain lift, drag,

Content from this work may be used under the terms of the Creative Commons Attribution 3.0 license. Any further distribution of this work must maintain attribution to the author(s) and the title of the work, journal citation and DOI. Published under license by Materials Research Forum LLC.

Materials Research Proceedings 69 (2026) 396-401 https://doi.org/10.21741/9781644904251-72

and moment characteristics curves, which can be linear or nonlinear. Whenever the associated vorticity changes along the line, the system will generate a vortex particle that is released in the wake. In contrast, the PM method does not relay on the characteristics of the airfoils, but represents the lift produced by the wing through local vorticity distributions on the surface represented through panels [4].

Models and Methods

The beam model, implemented in MBDyn, is composed of 16 structural dynamic nodes that lye along the y-direction. Inertia and stiffness characteristics were determined by a previous study, which started from a detailed Finite Element Method (FEM) model of the wing [5]. The MBDyn representation was validated by means of comparison of the predicted frequencies and modes with the same quantity identified in both the wind tunnel tests and the paper [5]. The results of this comparison are reported in Table 1.

Table 1: Eigenfrequencies from Wind Tunnel Test (WTT), MBDyn and UM/NAST models.

Mode	MBDyn [Hz]	WTT [Hz]	UM/NAST [Hz]
OOP1	4.22	4.17	4.22
OOP2	28.29	28.3	28.37
T1	41.46	41.3	40.72
OOP3	81.99	81.5	82.48
IP	108.57	N.A.	108.65

The first aerodynamic model used, directly implemented in MBDyn, was the strip theory, used with and without a tip loss correction [6]. Then, the coupling through DUST [3] software was performed to use the PM and the VLM, with and without nonlinear corrections.

Initially, the static deformed shape obtained, in terms of the tip torsion angle and the out-of-plane bending, was compared with the wind tunnel tests data to validate the different approaches used. Here in Figures 1-2 the results of the comparison at a single angle of attack $\alpha = 5°$. More results can be found in Ref. [7]. No significant differences were shown between the various methods adopted and the WTT data, with an exception only for the stip-theory model.

Materials Research Proceedings 69 (2026) 396-401 https://doi.org/10.21741/9781644904251-72

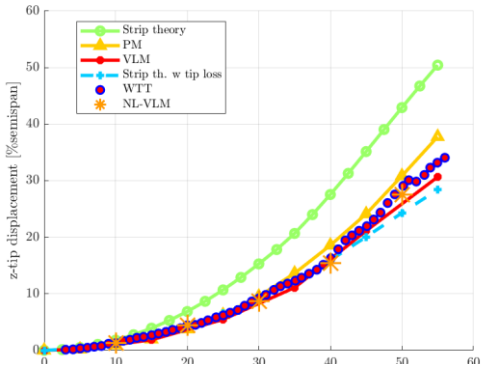


Figure 1: Out of plane tip displacement - comparisons at α = 5°.

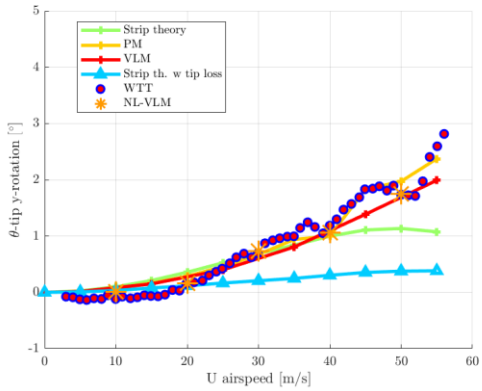


Figure 2: Tip torsional rotation - comparisons at α = 5°.

Looking at the torsion angle of the tip reported in Fig. 2, it is visible that the WTT data are also less regular than the bending ones, due to the relevant difficulties encountered during the collection of the experimental data. The VLM and PM results appeared to be more coherent with the experimental results than the strip-theory ones, especially in the high-speed range. Therefore, the strip theory model was deemed unsuitable for performing an accurate aeroelastic analysis. Thus, the following studies were deepened only through the VLM and PM aerodynamic models.

Results

All results are discussed in a comparative way among the different methods and where several cases, varying U or α, were investigated, just one will be reported here (more in [7]). Since the simulations, due to software capabilities, were all performed in time domain, the stability limits were identified by looking at oscillations in the tip vertical position, using a pseudo-experimental approach. The studies were then deepened by performing a post-processing of simulation results in the frequency domain. The nonlinear correction of the VLM was used in the determination of the Hump mode region, but, since no significant difference was displayed, nor in terms of oscillations or boundaries with respect to the simple VLM, said model was not deepened any further.

Hard flutter. Figure 3 displays a graph that shows the hard flutter onset point for both VLM and PM. The simulations were run at α = 1° and significant differences between the two results were shown. The VLM underpredicts the static deformed shape above certain speed values (see Fig. 1), leading to an increase in the estimated speed at the flutter boundary. A detailed analysis showed that the PM method predicted the hard flutter onset at 84.83 m/s. Although experimental data are not available for comparison, the individuated stability boundary is coherent with what found in other numerical studies [1], [5], [8].

Materials Research Proceedings 69 (2026) 396-401 https://doi.org/10.21741/9781644904251-72

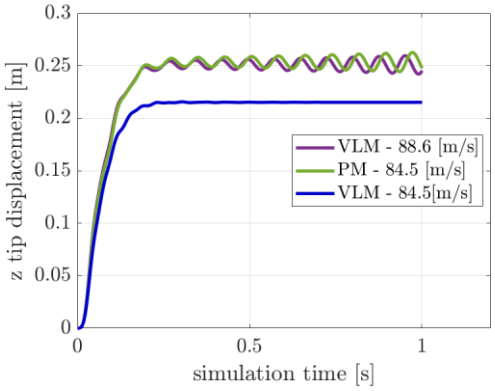


Figure 3: Hard Flutter: onset - comparison of time responded at different speeds.

Hump mode. For what concerns instead the investigation of the hump mode boundaries, similar analyses were performed.

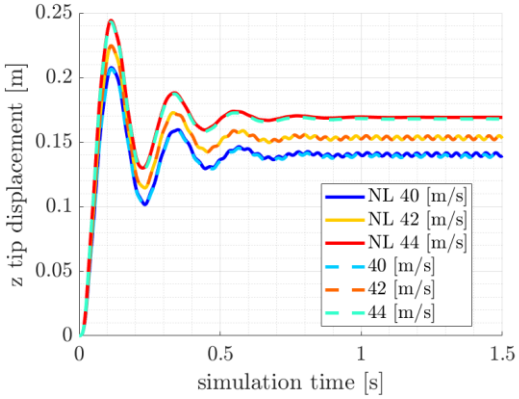


Figure 4: Hump Mode boundaries: VLM and NL-VLM comparisons α = 7°.

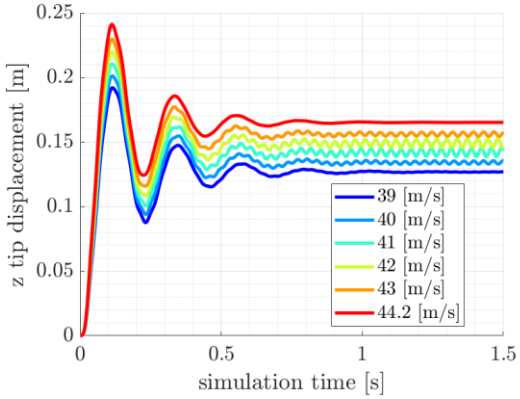


Figure 5: Hump mode boundaries: results of PM α = 7°.

Figure 4 displays the soft flutter region in the prescribed α and U, retrieved by means of the VLM with and without considering its nonlinear correction (i.e., the stall region for the lift coefficient). No significant differences are visible between the two models. Therefore, the nonlinear aerodynamic effects do not seem to play a determinant role in the individuation of the hump mode boundaries, or in the determination of the amplitudes of the oscillations. Figure 5 shows the hump mode boundaries identified at α = 7° through the PM. No significant differences are identified in terms of stability limits.

With the aim of validating the obtained results, while assessing at the same time which modes were coalescing, giving birth to the instability, a frequency study, by means of a perturbation analysis, was conducted. This investigation was carried out for a variety of velocities and angles to understand when, for different deformed shapes, the modes coalesced, leading to null damping ξ. The results of this set of analyses are summarized in Fig. 6, which shows a good agreement among the information retrieved in the frequency and time domains. Finally, the unstable regions, identified using PM and VLM are overlapped in Fig. 7, showing limited differences in the full envelope of conditions.

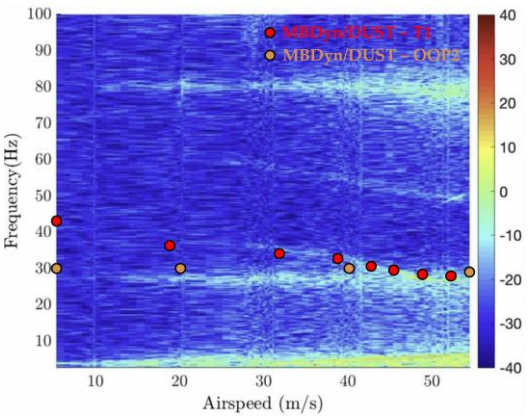


Figure 6: OOP2-T1 modes frequency oscillation at different speeds.

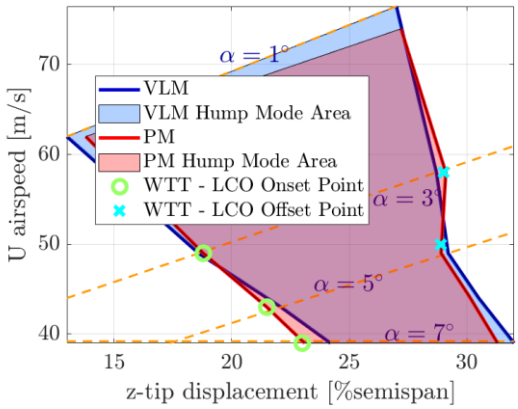


Figure 7: Hump mode area comparison.

Post-flutter behavior. With the aim of investigating the post flutter behavior, two simulations were run in the mid of the hump mode speed range, using both the PM and the VLM. Figure 8 at α = 7° shows that the PM predicts an amplitude that is closer to the experimental one.

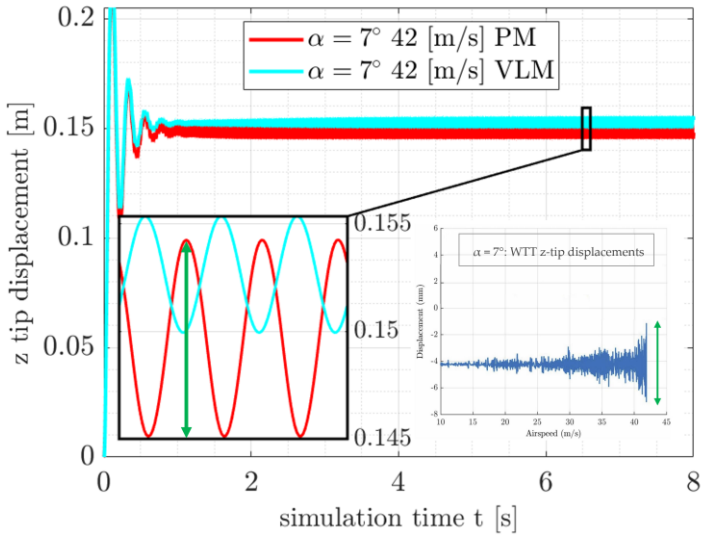


Figure 8: Post flutter wing tip oscillation at α = 7° in the hump mode range.

Also, at α = 5° the oscillations tend to stabilize into a limit cycle of about 8 mm (see [7]). In both cases a significant difference in the resulting amplitude of the LCO by VLM and PM is shown. Given the results related to vertical tip displacement with the VLM and NL-VLM models, as also reported in Fig. 4, it is clear that the amplitude of the oscillations is independent of nonlinear aerodynamic effects. Consequently, the magnitude mismatch cannot be attributed to these effects. Results from the wind tunnel tests present good agreement in terms of oscillations size with those retrieved through the PM, therefore, it is possible to say that such a difference in the amplitude of the motion can be attributed to 3D aerodynamic effects, which are correctly caught by the PM, but are not correctly detected by the VLM or its nonlinear correction, since it remains locally a bi-dimensional method.

Conclusions

This study focused on the nature of LCOs in the Pazy Wing through a comparative analysis of mid-fidelity aeroelastic models. The main conclusion is that the LCOs exhibited by the wing are primarily driven by structural nonlinearities. This finding is supported by the fact that both the VLM and the PM, when coupled with a non-linear structural model, were able to predict the onset of oscillations, regardless of the inclusion of nonlinear aerodynamic corrections. However, a critical distinction emerged in the assessment of the severity of the phenomenon. Only the Panel Method showed quantitative agreement with the experimental data regarding the oscillation amplitude. In contrast, the VLM consistently underestimated this amplitude. This discrepancy is attributed to the PM's ability to capture three-dimensional aerodynamic effects, which prove to be fundamental in determining the post-flutter response but cannot be adequately modelled by a two-dimensional approach like the VLM.

Consequently, for engineering applications requiring a reliable yet computationally efficient prediction of the aeroelastic behavior of very flexible wings, the use of nonlinear structural models paired with 3D aerodynamic methods, such as the PM, is recommended. Employing simpler models, while correctly identifying instabilities, carries the risk of underestimating the severity of the oscillations, and therefore the operational safety of the aircraft.

References

[1] O. Avin, D. Raveh, A. Drachinsky, Y. Ben-Shmuel, M. Tur, (2022). ”Experimental Aeroelastic Benchmark of a Very Flexible Wing”, AIAA Journal, Vol.60(3). https://doi.org/10.2514/1.J060621

[2] P. Masarati, M. Morandini, P. Mantegazza, (2014). ”An Efficient Formulation for General Purpose Multibody/Multiphysics Analysis”, ASME Journal of Computational and Nonlinear Dynamics, Vol. 9(4). https://doi.org/10.1115/1.4025628

[3] M. Tugnoli, D. Montagnani, M. Syal, G. Droandi, A. Zanotti, A. (2021). ”Mid-fidelity approach to aerodynamic simulations of unconventional VTOL aircraft configurations”, Aerospace Science and Technology, Vol. 115. https://doi.org/10.1016/j.ast.2021.106804

[4] J. Katz, A. Plotkin, (2001). Low-speed aerodynamics, Cambridge University Press.

[5] C. Riso, C. Cesnik, (2023). ”Impacts of Low-Order Modeling on Aeroelastic Predictions for Very Flexible Wings”, Journal of Aircraft, Vol.60(3). https://doi.org/10.2514/1.C036869

[6] L. Prandtl (1919). ”G¨ottinger Klassiker der Stromungsmechanik”, Bd. 3. pp. 89-92

[7] A. Bove (2025). ”Mid-fidelity approaches for the nonlinear aeroelastic assessment of the Pazy Wing”, Thesis, Politecnico di Milano.

[8] Norberto Goizueta, Andrew Wynn, Rafael Palacios, Ariel Drachinsky, Daniella E. Raveh (2022). ”Flutter Predictions for Very Flexible Wing Wind Tunnel Test”, Journal of Aircraft, Vol.59(4). https://doi.org/10.2514/1.C036710

Materials Research Proceedings 69 (2026) 402-407 https://doi.org/10.21741/9781644904251-73

Aeroelastic Evaluation of Dry Wing Effects for Hydrogen Aircraft

Fanglin YU[1,a *] and Mirko HORNUNG[2,b]

[1]Chair of Aircraft Design, Technical University of Munich, Boltzmannstrasse 15, 85748 Garching b. München, Germany

[a]fanglin.yu@tum.de, [b]mirko.hornung@tum.de

Keywords: Hydrogen Aircraft, Dry Wing, Aeroelasticity, Structural Sizing, Load Analysis

Abstract. Hydrogen aircraft eliminate the beneficial inertial relief provided by wing fuel storage, substantially increasing structural loads. This study quantifies the resulting penalties for a "dry wing" through detailed aeroelastic simulation and a two-stage structural sizing. A kerosene-fueled reference aircraft wing and a dry wing variant were analyzed using the FAST toolchain and NASTRAN optimization based on critical load cases. Results show that removing wing fuel increased shear forces and root bending moments by up to 48% and 25%, respectively. To satisfy all design constraints, the final optimized dry wing box required significant reinforcement, resulting in a 8.4% weight penalty. This work provides essential quantitative data and insights specific to the dry wing configuration, crucial for early-stage hydrogen-powered aircraft design.

Introduction

Climate change has become a critical concern. The aviation industry faces particular scrutiny due to its significant carbon footprint and the complexity of decarbonization. Reducing carbon emissions is now an urgent priority for aviation, especially given the long turnover times associated with aircraft fleets. Aligning with the ambitious goals set forth by the Flightpath 2050 initiative, the aviation industry aims to reduce CO_2 emissions by 75%, NO_X emissions by 90%, and the noise footprint by 60% by 2050, relative to the levels recorded in the year 2000 [1].

However, the incremental improvements in aircraft efficiency seen over recent decades will no longer be sufficient to meet future targets. Both Boeing and Airbus project that global air traffic, measured in revenue passenger kilometers, will double within the next two decades [1]. This anticipated growth in demand is expected to outweigh the emissions reductions achieved through technological advancements alone [2]. Consequently, without more transformative innovations and comprehensive systemic changes, the efficiency gains may be eclipsed by the expansion of air travel, emphasizing the need for more radical solutions.

Hydrogen-powered aircraft represent a promising solution for decarbonization. During flight, hydrogen-powered aircraft produce zero CO_2 emissions. Hydrogen can be produced through electrolysis using electricity from renewable sources. Hydrogen-powered aviation is predicted to be the most cost-effective and sustainable pathway to achieving carbon-neutral air travel in the long term [3].

However, hydrogen as a fuel presents significant challenges, particularly in terms of storage, due to its different properties compared to traditional Jet-A fuel. While liquid hydrogen has a high gravimetric energy density of 33.3 kWh/kg compared to kerosene's 12 kWh/kg [1], it requires approximately four times more volume.

The large volume requirement and geometric constraints imposed by cryogenic insulation make traditional wing fuel tanks unsuitable for hydrogen storage. External wing-mounted hydrogen tanks are not viable for commercial aircraft, as the drag penalty outweighs any mass savings from the inertial relief provided by the tanks [4]. Several studies [5–7] suggest that integrating the fuel tank into the fuselage appears to be the most viable solution for hydrogen-powered aircraft.

Content from this work may be used under the terms of the Creative Commons Attribution 3.0 license. Any further distribution of this work must maintain attribution to the author(s) and the title of the work, journal citation and DOI. Published under license by Materials Research Forum LLC.

Materials Research Proceedings 69 (2026) 402-407 https://doi.org/10.21741/9781644904251-73

Most research on hydrogen-powered aircraft has focused on fuel storage solutions. However, publications on the structural impact of transitioning from kerosene to hydrogen remain limited. Without fuel in the wing—and thus the loss of inertial relief—aircraft designers face the challenge of heavier wing structures, particularly as future wings are likely to feature higher aspect ratios for aerodynamic efficiency.

Several research projects are currently exploring this topic. One such project is the UP Wing initiative under Clean Aviation. Méheut explored the strut-braced hydrogen dry wing concept using multidisciplinary optimization [8].

In the DLR EXACT project, long-range hydrogen aircraft are being investigated. A conceptual load analysis performed using the tool LOADzero revealed that the wings of hydrogen-powered aircraft experience 20% higher shear force and 15% greater root bending moment compared to kerosene-powered aircraft [9]. These findings highlight the necessity for more detailed investigations into the impact of fuel absence on wing structures, as the analysis relied on analytical methods.

This paper quantitatively assesses the wing weight penalties in hydrogen-powered aircraft using high-fidelity aeroelastic simulation and structural sizing.

Aircraft Models

This study uses an A320-like reference configuration developed by Bauhaus Luftfahrt (BHL). This configuration, featuring a winglet and utilizing aluminum as the primary material, was designed using the BHL in-house tool, BLADE, and adheres to the same top-level requirements as the A320. The full geometry is shown in Fig. 1.

To isolate and quantify the effects of the missing fuel mass inside of wing, a dry wing configuration is introduced. This configuration is based on the reference aircraft but converts the wing-borne kerosene fuel into an equivalent hydrogen mass that is relocated to the fuselage. Critically, the wing planform and all other parameters are kept identical to the reference model. This setup enables a focused evaluation, separating the dry wing effect from other influencing design factors.

The aeroelastic model is automatically generated using the in-house multi-fidelity toolchain, the *Flexible Aero-Structural Toolbox* (FAST). The FAST toolchain automates FEM generation (Beam and Shell) and provides versatile analysis capabilities.



Figure 1: Reference Aircraft.

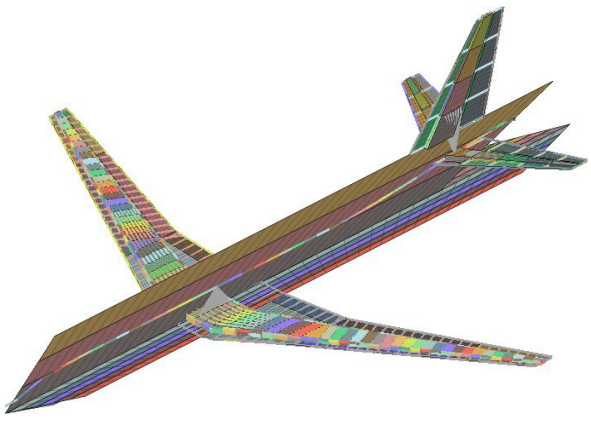


Figure 2: Aeroelastic model of reference configuration.

Given the primary focus on the wing's behavior, the wing box is modeled using shell elements, while stiffeners and stringers are represented by beam elements. To reduce computational cost and modeling effort, the fuselage structure is simplified to a rigid beam.

Materials Research Proceedings 69 (2026) 402-407 https://doi.org/10.21741/9781644904251-73

Non-structural masses (e.g., engine and landing gear) are accounted for in the model. The fuel mass is represented by concentrated mass elements: for the wet wing (reference configuration), mass is distributed along the wing span; for the dry wing configuration, this mass is placed in the fuselage.

For the aerodynamic side, a full-aircraft model based on the Doublet Lattice Method (DLM) is employed. This model covers the complete aircraft and ensures direct compatibility with the NASTRAN solver format required for the aeroelastic analysis. The resulting full aeroelastic model is illustrated in Fig. 2.

Methodology

To systematically evaluate the dry wing effect and quantify the impact of losing fuel inertial relief on the load-bearing wing box, a structural sizing analysis is required. This process necessitates the prior identification of critical design load cases.

Determining load cases for structural sizing typically requires a comprehensive analysis across the full flight envelope and all mass configurations, resulting in hundreds of simulations. However, since this study aims to assess the dry wing effect rather than conduct an exhaustive certification-level analysis, a simplified approach is adopted. Only steady maneuver loads are simulated for one representative mass configuration.

The representative mass configuration selected is the maximum take-off mass with full payload and the center of gravity positioned at 15% mean aerodynamic chord. This specific case typically represents the most demanding mass configuration with regard to steady maneuvers.

In total, 60 maneuver load cases were simulated, including 2.5g pull-up, −1g push-over, and 1.67g roll maneuvers. All cases adhere to the certification specification (CS) 25 [10] flight envelope boundaries and maneuvering load factor limits across a range of speeds and altitudes.

Following the simulation, the load results are post-processed to generate load envelopes. The most critical load cases are subsequently extracted from these envelopes and used as inputs for the structural sizing process.

Structural sizing of the wing was performed in two sequential stages using NASTRAN's SOL200 optimization module. This two-stage approach ensures a minimal-mass design that satisfies material strength, buckling, and aeroelastic stability requirements. To reduce computational effort and the number of design variables, the geometry of stiffeners and stringers was held constant and not included in the optimization. The design variables are defined as the thicknesses of the primary structural elements (spars, ribs, and skins).

Stage 1: Strength and Buckling Sizing. The objective of the first stage was to minimize the wing's structural mass subject to material strength and buckling criteria. Static analysis and linear buckling analysis were performed under the critical loads derived from the load analysis process. The optimization problem for this stage is formulated as:

$$\begin{aligned} \text{minimize} \quad & \mathrm{m}(\mathrm{t}) \\ \text{subject to} \quad & \sigma(\mathrm{t}) \leq \frac{\sigma_{\text{ultimate}}}{1.5} \\ & \lambda \geq 1.4 \end{aligned}$$

Here, t represents the thickness of the structural elements (the design variables), and the objective function $\mathrm{m}(\mathrm{t})$ is the total mass of the wing structure. The constraints limit the von Mises stress $\sigma(\mathrm{t})$ to be less than the ultimate allowable stress σ_{ultimate} divided by a safety factor of 1.5, and ensure the linear buckling factor λ is greater than or equal to 1.4. A safety factor of 1.4 was selected for the buckling analysis, a slightly less conservative value than 1.5, given that linear buckling analysis inherently provides a conservative estimate compared to nonlinear methods. The

Materials Research Proceedings 69 (2026) 402-407 https://doi.org/10.21741/9781644904251-73

optimization monitored the first 10 buckling modes to ensure both global and local criteria were satisfied.

Following the initial sizing, a comprehensive aeroelastic analysis was conducted to ensure the wing's stability and preclude hazardous phenomena such as aileron reversal, divergence, and flutter. This evaluation is essential for meeting CS-25 requirements [10], which mandate stability up to $1.15V_D$ or $1.15M_D$.

To satisfy the subsonic-only validity of NASTRAN's DLM, the simulation was performed at sea level at a Mach number of approximately 0.70. This condition was selected to achieve a high dynamic pressure, where the possibility of aeroelastic instabilities is highest.

For flutter and divergence analyses, NASTRAN's Solution 145 was employed. A non-matched point flutter analysis was performed using the PK solver with a fixed Mach number and a fixed density ratio. The analysis utilized 40 structural modes and assumed 2% structural damping, with a reduced frequency range from 0.0001 to 10.0 to cover all frequencies of interest. The extremely low end of this range was specifically intended to capture potential divergence.

For the aileron reversal check, NASTRAN's Solution 144 was used. The aileron effectiveness, η_{ail}, is defined as the negative ratio of the roll coefficient due to aileron deflection (Cl_{δ_a}) to the roll coefficient due to rolling (roll damping, Cl_p). The aileron effectiveness should remain positive.

Stage 2: Aeroelastic-Constrained Sizing. As the initial sized model demonstrated a failure in the aileron reversal check, a subsequent structural sizing optimization was performed. The objective function remained the minimization of structural weight. However, this second-stage optimization was constrained by the aileron effectiveness. The structural properties resulting from the first sizing served as the lowest bound for the design variables in this new optimization. This allowed the optimizer only to increase thicknesses to satisfy the new aeroelastic constraint while ensuring the final structural design maintained a minimal weight that satisfied all criteria.

Results

The comparison between the reference aircraft and the dry wing configuration is carried out in two main steps.

The first step compares the maximum loads on the wing structure. This provides an initial, quantitative indication of the consequences of losing fuel inertial relief, which, in the reference configuration, helps to alleviate structural stress.

Fig. 3 and 4 show the load envelopes derived from the reference model and the dry wing model. A significant increase in internal loads is observed for the dry wing: a 48% increase in shear force (F_z) and a 25% increase in bending moment (M_x) are noted.

The thickness distributions resulting from the two-stage structural sizing process are presented

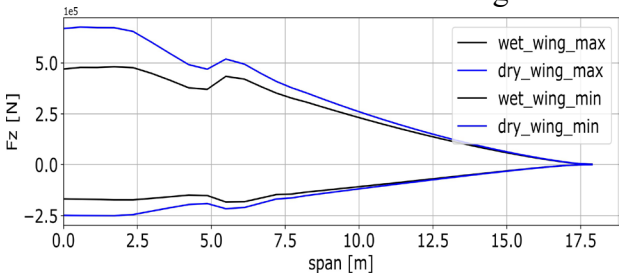


Figure 3: Comparison of shear force.

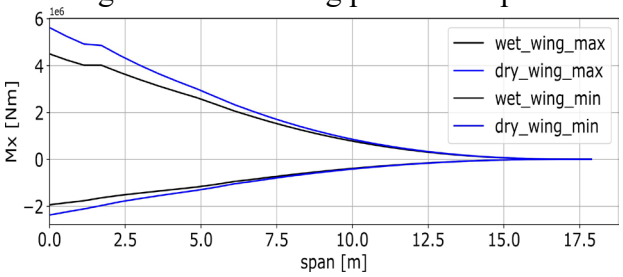


Figure 4: Comparison of bending moment.

in Fig. 5 and 6. The results show a noticeable increase in thickness for the dry wing configuration compared to the wet wing, particularly evident in the upper skin. This reinforcement is required to compensate for the missing inertial relief from the wing-borne fuel mass.

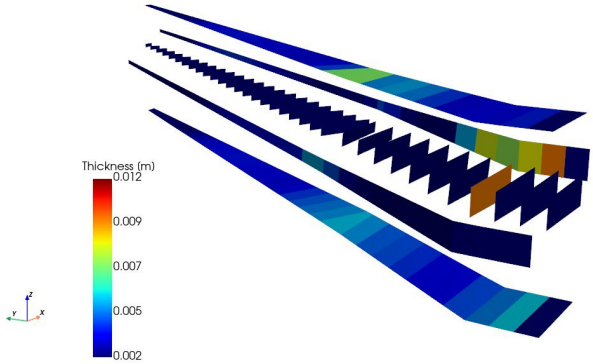


Figure 5: Thickness distribution of wet wing.

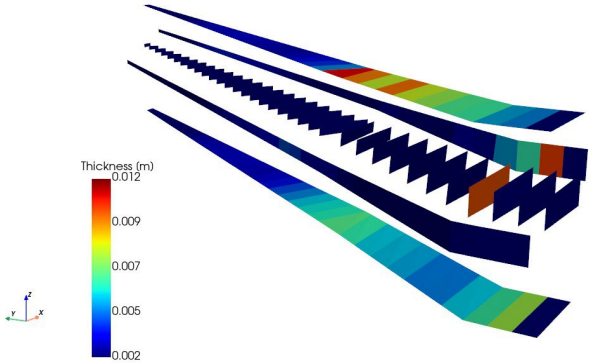


Figure 6: Thickness distribution of dry wing.

Furthermore, due to the swept wing geometry at the wing kink, stresses are not distributed evenly across the wing box. This non-uniformity results in a triangular stress redistribution area near the wing root, which necessitates a clear increase in the thickness of the skin, spars, and ribs in this specific region. Higher stresses are also concentrated toward the rear spar due to shear lag effects, which contributes to the higher required thickness in that location.

The final optimal wing box weight from the completed two-stage sizing process for the dry wing is 4373 kg, compared to 4034 kg for the wet wing.

Conclusion and Outlook

The structural and aeroelastic impact of a dry wing hydrogen concept is quantified using a two-stage optimization. Load analysis showed a significant increase in internal loads of wingbox, specifically a 48% increase in shear force and a 25% increase in bending moment over the wet wing. Structural reinforcement was required to satisfy strength, buckling, and the critical aileron reversal constraint. This resulted in a 8.4% weight penalty for the dry wing, directly quantifying the structural enforcement needed for the hydrogen concept.

Future work will focus on expanding the analysis beyond static maneuvers to include dynamic load cases, specifically incorporating gust load to identify critical load case. Furthermore, the load analysis will be refined by assessing various mass configurations across the full flight envelope. Finally, a parametric study is planned to gain crucial insights into how the wing aspect ratio influences the structural and aeroelastic performance of the dry wing concept.

References

[1] C. Winnefeld et al. "Modelling and Designing Cryogenic Hydrogen Tanks for Future Aircraft Applications". In: Energies 11.1 (Jan. 2018), p. 105. https://doi.org/10.3390/en11010105

[2] E. J. Adler et al. "Hydrogen-Powered Aircraft: Fundamental Concepts, Key Technologies, and Environmental Impacts". In: Progress in Aerospace Sciences 141 (Aug. 2023), p. 100922. https://doi.org/10.1016/j.paerosci.2023.100922

[3] D. Timmons et al. "Economics of Aviation Fuel Decarbonization: A Preliminary Assessment". In: Journal of Cleaner Production 369 (Oct. 2022), p. 133097. https://doi.org/10.1016/j.jclepro.2022.133097

[4] F. Healy et al. "Wing Mounted Hydrogen Fuel Tanks: Mitigating the Aeroelastic Penalties of Dry Wing Configurations?" In: IFASD. 2024.

[5] D. Silberhorn et al. "Assessment of Hydrogen Fuel Tank Integration at Aircraft Level". In: Deutscher Luft- Und Raumfahrtkongress. 2019.

[6] F. M. Troeltsch et al. "Hydrogen Powered Long Haul Aircraft with Minimized Climate Impact". In: AIAA AVIATION 2020 FORUM. VIRTUAL EVENT: American Institute of Aeronautics and Astronautics, June 2020. https://doi.org/10.2514/6.2020-2660

[7] G. Onorato et al. "Assessment of Hydrogen Transport Aircraft: Effects of Fuel Tank Integration". In: CEAS Aeronautical Journal 13.4 (Oct. 2022), pp. 813-845. https://doi.org/10.1007/s13272-022-00601-6

[8] M. Méheut et al. "Strut-Braced Dry Wing Concept for Hydrogen-Powered Aircraft". In: ICAS. 2024.

[9] T. Hecken et al. "Conceptual Loads Assessment of Aircraft with Fuselage Integrated Liquid Hydrogen Tank". In: DLRK. 2022.

[10] Certification Specification 25.

Materials Research Proceedings 69 (2026) 408-413 https://doi.org/10.21741/9781644904251-74

Dynamic Modeling of Rotor Damper Configurations for Aeroelastic and Ground Resonance Analysis

Matteo CROCI[1,a] and Pierangelo MASARATI[1,b,*]

[1]Department of Aerospace Science and Technology, Politecnico di Milano, via La Masa 34, Milano, Italy

[a]matteo6.croci@mail.polimi.it, [b]pierangelo.masarati@polimi.it

Keywords: Interblade Damper, Helicopter Rotor, Ground Resonance

Abstract. This paper presents the formulation and sensitivity analysis of ground resonance stability in rotorcraft equipped with unconventional lead-lag damping configurations, including the inter-blade and the recently proposed inter-2-blade arrangements. The developed framework enables consistent linearization of the coupled rotor-airframe system and supports comparison of the stability performance of conventional and novel damper configurations.

Introduction

Ground Resonance (GR) is a dynamic instability typical of helicopters, caused by the adverse coupling between the cyclic lead-lag motion of the blades and the motion of the airframe acting as a flexible support. It arises when the frequency of the slow first-order cyclic lead-lag mode approaches that of either the longitudinal (pitch) or lateral (roll) airframe motion [1].

Helicopter rotors are commonly equipped with damping devices to prevent such instability. The most conventional configuration employs dampers directly connecting each blade to the hub (BTH). Alternative arrangements connect the blades in different ways, often bypassing the hub. Among these, the "inter-blade" (IB) configuration couples adjacent blades, while the "inter-2-blade" (I2B) configuration connects non-adjacent blades [2, 3]. These concepts offer potential advantages partly explored in earlier studies.

The objectives of this work are:

- to develop a framework describing the exact kinematics of damper activation as a function of blade motion,
- to couple the consistently linearized damper-blade kinematics with industry-grade rotorcraft aeroelastic solvers,
- to formulate a consistent sensitivity analysis of the GR eigensolution,
- to assess the stability performance of the three configurations (BTH, IB, I2B), including selected damper-failure conditions.

The GR problem is analyzed by linearizing about steady reference equilibrium conditions.
The kinematics are derived by consistently linearizing a geometrically exact multibody model. For the nominal isotropic rotor, the system obtained through the multiblade coordinate transformation is linear and time-invariant and is treated using standard eigenanalysis.

Blade Lag Dynamics. Following Coleman's formulation [1], the linearized lead-lag dynamics of the *m*th blade in a rotor with three or more blades is expressed as

$$I_\xi \ddot{\xi}^{(m)} + \left(eS_\xi \Omega^2 + k_\xi\right) \xi^{(m)} = \tau_{\text{damper}}^{(m)} - S_\xi \ddot{y} \cos\psi_m + S_\xi \ddot{x} \sin\psi_m \qquad (1)$$

with $m = 1..N_b$, and the damping torques are

Content from this work may be used under the terms of the Creative Commons Attribution 3.0 license. Any further distribution of this work must maintain attribution to the author(s) and the title of the work, journal citation and DOI. Published under license by Materials Research Forum LLC.

$$\tau_{\text{damper}}^{(m)} = -c_\xi \begin{cases} \dot{\xi}^{(m)} & \text{BTH} \\ 2\dot{\xi}^{(m)} - \dot{\xi}^{(m-1)} - \dot{\xi}^{(m+1)} & \text{IB} \\ 2\dot{\xi}^{(m)} - \dot{\xi}^{(m-2)} - \dot{\xi}^{(m+2)} & \text{I2B} \end{cases} \tag{2}$$

Equation (1) is azimuth-dependent because the forcing terms associated with the airframe roll and pitch through the corresponding lateral and longitudinal accelerations depend on the blade azimuth $\psi_m = \psi + 2\pi\, m/N_b$.

Multiblade Coordinates. For identical, equally spaced blades (isotropic rotor), introducing the multiblade (Coleman) transformation eliminates azimuth dependence:

$$\xi^{(m)} = \xi_0 + \sum_{n=1}^{\text{fix}((N_b-1)/2)} [\cos(n\psi_m)\xi_{nc} + \sin(n\psi_m)\xi_{ns}] + (-1)^m \xi_{N_b/2} \tag{3}$$

The last term applies only to even N_b. The transformation can be written compactly as

$$\boldsymbol{\xi}_b = \mathbf{T}(\psi)\boldsymbol{\xi} \qquad \dot{\boldsymbol{\xi}}_b = \dot{\mathbf{T}}(\psi)\boldsymbol{\xi} + \mathbf{T}(\psi)\dot{\boldsymbol{\xi}} \qquad \ddot{\boldsymbol{\xi}}_b = \ddot{\mathbf{T}}(\psi)\boldsymbol{\xi} + 2\dot{\mathbf{T}}(\psi)\dot{\boldsymbol{\xi}} + \mathbf{T}(\psi)\ddot{\boldsymbol{\xi}} \tag{4}$$

Here, $\boldsymbol{\xi}$ denotes the multiblade coordinates, $\boldsymbol{\xi}_b$ the individual blade coordinates, and $\mathbf{T}(\psi)$ the azimuth-dependent transformation matrix.

Coupled Rotor-Airframe Equations. After algebraic manipulation, the coupled rotor-airframe equations can be expressed as

$$\begin{bmatrix} N_bI_\xi/2 & 0 & 0 & N_bS_\xi/2 \\ 0 & N_bI_\xi/2 & -N_bS_\xi/2 & 0 \\ 0 & -N_bS_\xi/2 & M_x + N_bM_b & 0 \\ N_bS_\xi/2 & 0 & 0 & M_y + N_bM_b \end{bmatrix} \begin{Bmatrix} \ddot{\xi}_{1c} \\ \ddot{\xi}_{1s} \\ \ddot{x} \\ \ddot{y} \end{Bmatrix}$$

$$+ \begin{bmatrix} N_b\Xi_\clubsuit c_\xi/2 & N_bI_\xi\Omega & 0 & 0 \\ -N_bI_\xi\Omega & N_b\Xi_\clubsuit c_\xi/2 & 0 & 0 \\ 0 & 0 & C_x & 0 \\ 0 & 0 & 0 & C_y \end{bmatrix} \begin{Bmatrix} \dot{\xi}_{1c} \\ \dot{\xi}_{1s} \\ \dot{x} \\ \dot{y} \end{Bmatrix}$$

$$+ \begin{bmatrix} N_b\left[\Xi_\clubsuit k_\xi + (eS_\xi - I_\xi)\,\Omega^2\right]/2 & N_b\Xi_\clubsuit c_\xi\Omega/2 & 0 & 0 \\ -N_b\Xi_\clubsuit c_\xi\Omega/2 & N_b\left[\Xi_\clubsuit k_\xi + (eS_\xi - I_\xi)\,\Omega^2\right]/2 & 0 & 0 \\ 0 & 0 & K_x & 0 \\ 0 & 0 & 0 & K_y \end{bmatrix} \begin{Bmatrix} \xi_{1c} \\ \xi_{1s} \\ x \\ y \end{Bmatrix} = \begin{Bmatrix} 0 \\ 0 \\ 0 \\ 0 \end{Bmatrix} \tag{5}$$

with $\Xi_{\text{BTH}} = 1$, $\Xi_{\text{IB}} = 2(1 - \cos(2\pi/N_b))$, and $\Xi_{\text{I2B}} = 2(1 - \cos(4\pi/N_b))$, the latter two for ideal damping, i.e., directly proportional to the respective combinations of blade rotation.

The remaining multiblade coordinates remain decoupled from the airframe and are not discussed here. In the IB and I2B configurations, the collective motion receives no damping, and higher-order cyclic or reactionless I2B equations experience reduced damping compared with IB and BTH [3].

Damper Activation Kinematics. In practical designs, the damper activation depends on the relative motion of the blades through nonlinear kinematic relationships. Let $\varphi^{(m)}$ denote the activation of the mth damper (relative rotation or displacement),

$$\boldsymbol{\phi}^{(m)}\left(\mathbf{x}^{(m)}, \boldsymbol{\xi}_b\right) = \mathbf{0} \tag{6}$$

that represents the scleronomic constraint equations, where $\mathbf{x}^{(m)}$ collects the internal coordinates of the damper, with $\varphi^{(m)} = \varphi^{(m)}(\mathbf{x}^{(m)})$ (without excessive loss of generality, $\varphi^{(m)}$ can directly be an element of $\mathbf{x}^{(m)}$, or a linear combination, $\varphi^{(m)} = \mathbf{C}\,\mathbf{x}^{(m)}$; in the following, the superscript (m) will be

Materials Research Proceedings 69 (2026) 408-413 https://doi.org/10.21741/9781644904251-74

omitted for ease of notation). $\boldsymbol{\phi}$ contains as many equations as internal coordinates $\mathbf{x}$. The blade rotations, $\boldsymbol{\xi}_b$, are the independent variables. Equation (6) is solved to determine $\mathbf{x}$ as a function of $\boldsymbol{\xi}_b$, and thus determine the reference configuration of the damper system for a given reference blade lag rotation.

Linearization of Eq. (6) around the reference configuration yields

$$\Delta\mathbf{x} = -\boldsymbol{\phi}_{/\mathbf{x}}^{-1}\boldsymbol{\phi}_{/\boldsymbol{\xi}_b}\Delta\boldsymbol{\xi}_b \qquad \text{and} \qquad \Delta\varphi = -\mathbf{C}\boldsymbol{\phi}_{/\mathbf{x}}^{-1}\boldsymbol{\phi}_{/\boldsymbol{\xi}_b}\Delta\boldsymbol{\xi}_b = \boldsymbol{\Psi}\Delta\boldsymbol{\xi}_b \tag{7}$$

where submatrix $\boldsymbol{\phi}_{/\mathbf{x}}$ of the constraint Jacobian matrix is square by assumption and invertible as long as the closed kinematic chain it describes is not in a singular configuration. In the ideal BTH case, $\boldsymbol{\Psi}_i^{(m)} = \delta_{im}$, where δ_{im} is Kronecker's operator; in the ideal IB case, $\boldsymbol{\Psi}_i^{(m)} = \delta_{im}$ and $\boldsymbol{\Psi}_{i+1}^{(m)} = -\delta_{im}$; finally, in the ideal I2B case, $\boldsymbol{\Psi}_{i-1}^{(m)} = \delta_{im}$ and $\boldsymbol{\Psi}_{i+1}^{(m)} = -\delta_{im}$.

Damper Contribution to Virtual Work. The virtual work of the mth damper is

$$\delta\mathcal{W}_{\text{damper}}^{(m)} = -\delta\varphi\left(c_\varphi\Delta\dot{\varphi} + k_\varphi\Delta\varphi\right) = -\delta\boldsymbol{\xi}_b^{\mathsf{T}}\boldsymbol{\Psi}^{\mathsf{T}}\left(c_\varphi\boldsymbol{\Psi}\Delta\dot{\boldsymbol{\xi}}_b + k_\varphi\boldsymbol{\Psi}\Delta\boldsymbol{\xi}_b\right) \tag{8}$$

where c_φ and k_φ are the linearized viscous and elastic characteristics of an elastomeric damper. In the ideal case, $c_\xi \equiv c_\varphi$ and $k_\xi \equiv k_\varphi$, whereas in practical cases, the kinematics of the lag activation mechanism hidden in $\boldsymbol{\Psi}$ need to be used.

Using the same reference configuration for all blades (e.g., the same reference lead-lag angle), the kinematic problem is solved for just one damper, and the same expression of Eq. (8) for the virtual work is used for all, simply changing the indexes of the involved blade rotations in $\boldsymbol{\xi}_b$. Stacking all dampers yields

$$\delta\mathcal{W}_{\text{dampers}} = \sum_m \delta\mathcal{W}_{\text{damper}}^{(m)} = -\delta\boldsymbol{\xi}_b^{\mathsf{T}}\mathbf{B}^{\mathsf{T}}\left(c_\varphi\mathbf{B}\Delta\dot{\boldsymbol{\xi}}_b + k_\varphi\mathbf{B}\Delta\boldsymbol{\xi}_b\right) \tag{9}$$

where

$$\mathbf{B}^{\mathsf{T}} = [\boldsymbol{\Psi}^{(1)^{\mathsf{T}}}, \ldots, \boldsymbol{\Psi}^{(N_b)^{\mathsf{T}}}]$$

A kinematically and energetically consistent definition of damper activation does not alter the structure of Eq. (5), only affecting the coefficients $\Xi_\clubsuit$. It also affects the remaining rotor equations, which, however, remain decoupled from the airframe motion.

Sensitivity of Eigensolution. Equation (5) can be written as

$$\left(s^2\mathbf{M}_c + s\mathbf{C}_c + \mathbf{K}_c\right)\mathbf{z} = \mathbf{0} \tag{10}$$

where $\mathbf{z}$ is the eigenvector and s the eigenvalue.

The sensitivity of the ℓth eigenpair to a generic parameter p is obtained by differentiating Eq. (10) and the L^∞ normalization condition $\mathbf{n}^{\mathsf{T}}\mathbf{z} = 1$ ($\mathbf{n} = [0, \ldots, 1, \ldots 0]^{\mathsf{T}}$) with respect to p, i.e.,

$$\begin{bmatrix} \left(s_\ell^2\mathbf{M}_c + s_\ell\mathbf{C}_c + \mathbf{K}_c\right) & \left(2s_\ell\mathbf{M}_c + \mathbf{C}_c\right)\mathbf{z}_\ell \\ \mathbf{n}^{\mathsf{T}} & \end{bmatrix} \begin{Bmatrix} \mathbf{z}_{\ell/p} \\ s_{\ell/p} \end{Bmatrix} = \begin{Bmatrix} -\left(s_\ell^2\mathbf{M}_{c/p} + s_\ell\mathbf{C}_{c/p} + \mathbf{K}_{c/p}\right)\mathbf{z}_\ell \\ 0 \end{Bmatrix} \tag{11}$$

If the damper kinematics depend on p, the corresponding derivatives include

$$\Delta\varphi_{/p} = -\mathbf{C}\boldsymbol{\phi}_{/\mathbf{x}}^{-1}\left(\boldsymbol{\phi}_{/\boldsymbol{\xi}_b p} - \boldsymbol{\phi}_{/\mathbf{x}p}\boldsymbol{\phi}_{/\mathbf{x}}^{-1}\boldsymbol{\phi}_{/\boldsymbol{\xi}_b}\right)\Delta\boldsymbol{\xi}_b = \boldsymbol{\Psi}_{/p}\Delta\boldsymbol{\xi}_b \tag{12}$$

while for parameters directly affecting system matrices, the computation is straightforward.

Damper Failure. If one or more dampers fail, the problem becomes time-periodic. Its stability can be studied using the Floquet-Lyapunov method [4], and its sensitivity can be derived following the procedure in [5].

Results

Realistic IB and I2B layouts, adapted from existing designs, are shown in Fig. 1. In the IB configuration (left), a rotational damper is attached to blade m and linked to blade $m + 1$ through

Materials Research Proceedings 69 (2026) 408-413 https://doi.org/10.21741/9781644904251-74

a rigid connection. The model is treated as two-dimensional for clarity, but has also been implemented in 3D. Each sub-assembly consists of a blade, a damper, and a connecting link between the damper and the preceding blade, for a total of three bodies and nine DoF, eight of which are eliminated by the four hinges, leaving one DoF, the blade rotation. Each closed loop consists of four bodies and 12 DoF, 10 of which are eliminated by the five hinges, corresponding to a five-bar mechanism. Prescribing the rotations of the blades makes the problem kinematically determined. Using data from [6], the transmission ratio is $\boldsymbol{\Psi}(m, m+1) = [-1.5045, 0.6320]$, which differs notably from the ideal $[-1, 1]$.

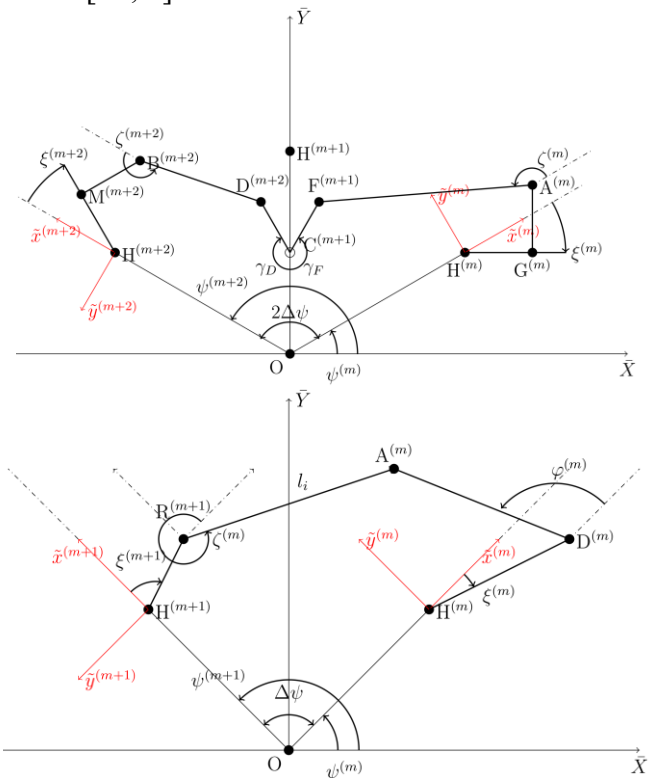


Figure 1: Realistic configurations: inter-blade (left) and inter-2-blade (right).

Figure 2 presents the coupled rotor-airframe eigensolution for the IB configuration. The top-left panel shows the real parts of all eigenvalues; the top-right highlights the critical mode (real and imaginary parts), the slow cyclic eigenvalue, which becomes unstable slightly above $\Omega_{100\%}$. The bottom panels show its sensitivity to the stiffnesses (left) and dampings (right) of the damper and the link's elastomeric bearings.

Using sensitivity analysis, equivalent BTH and I2B models were tuned by continuation. The equivalent BTH configuration was matched by adjusting k_ξ and c_ξ to reproduce the same slow cyclic eigenvalue as the IB case at $\Omega_{100\%}$. The equivalent I2B model was tuned by adjusting also other kinematic parameters to match the slow cyclic and also the collective eigenvalue, which is undamped in the ideal IB and I2B cases.

Figure 3 compares the real parts of the eigenvalues for the IB (left), I2B tuned for slow cyclic (center), and I2B tuned for both slow cyclic and collective modes (right) at $\Omega_{100\%}$. The results demonstrate strong similarity and comparable GR stability among the configurations.

Finally, results obtained with a detailed rotor and airframe aeroelastic model implemented in MASST [7], a general-purpose rotorcraft aeroelasticity tool, confirm the observed trends.

Materials Research Proceedings 69 (2026) 408-413 https://doi.org/10.21741/9781644904251-74

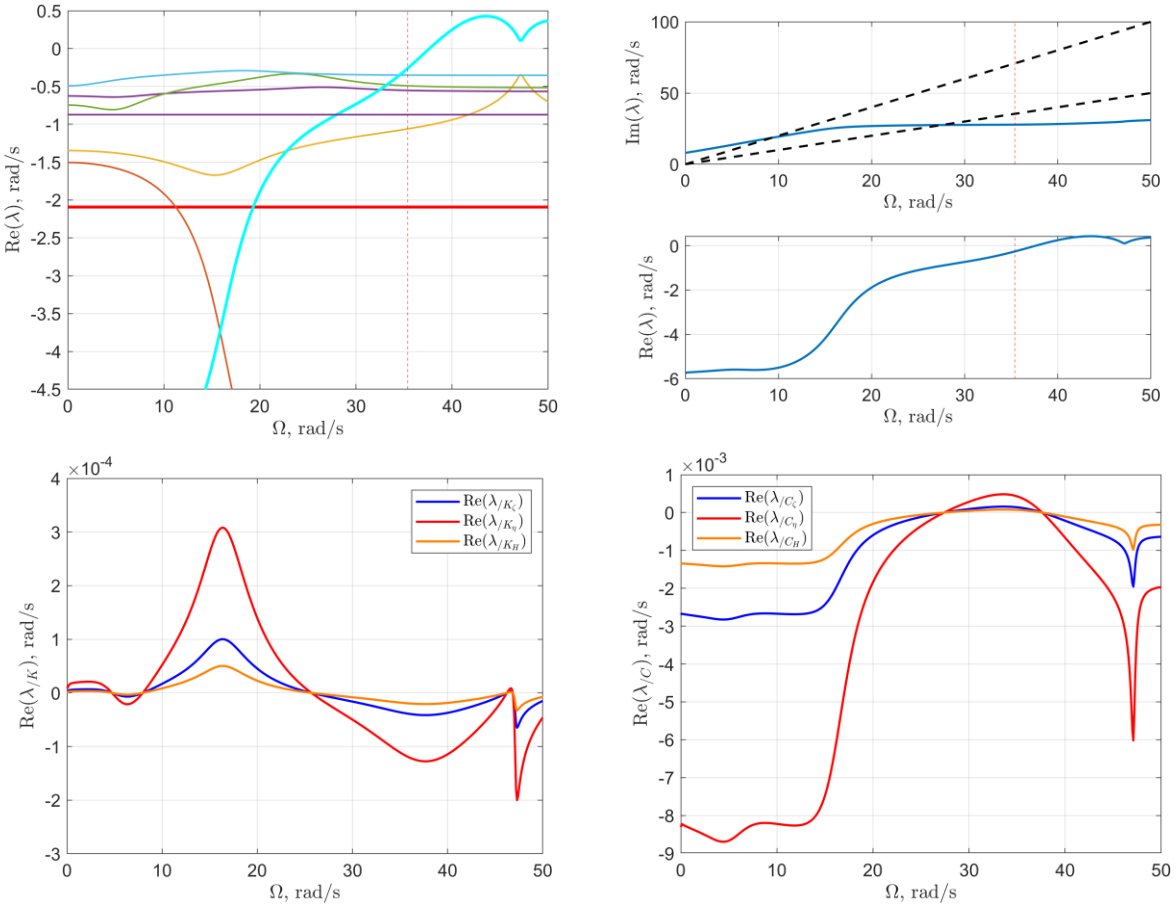


Figure 2: Realistic IB configuration: Re(s) ↖, critical Re(s) and Im(s) ↗, Re(s$_k$) ↙, Re(s$_c$) ↘.

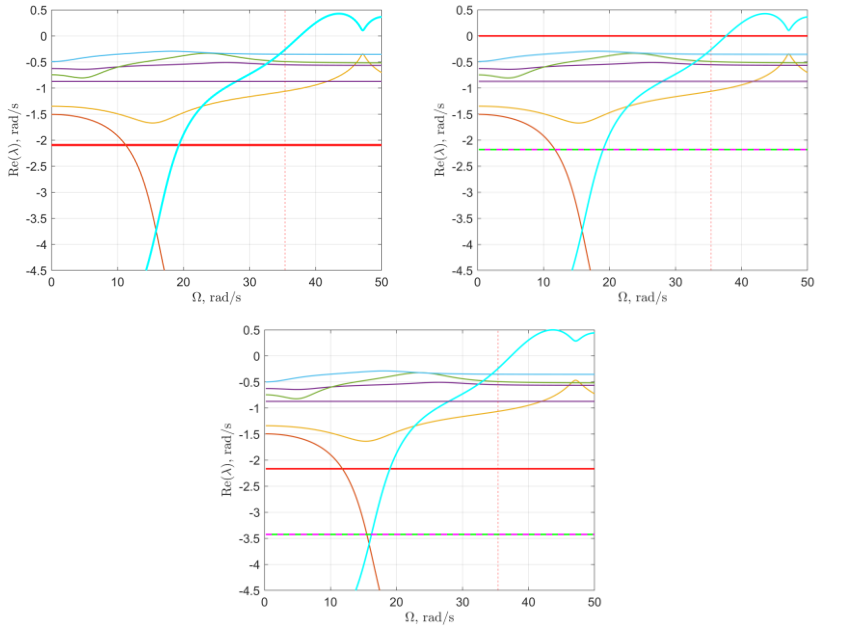


Figure 3: Comparison of configurations: IB (left), I2B tuned for slow cyclic (center), and for slow cyclic and collective (right).

References

[1] Robert P. Coleman. Theory of self-excited mechanical oscillations of hinged rotor blades. ARR 3G29, NACA, July 1943.

[2] Pierangelo Masarati and Leonardo Frison. Rotore per elicottero a smorzamento migliorato, 2021. Italian Patent No. 102021000018017

[3] Leonardo Frison, Andrea Zanoni, and Pierangelo Masarati. The inter-2-blade lead-lag damper concept. In 78th Forum of the Vertical Flight Society, Fort Worth, TX, USA, May 20–22, 2022. https://doi.org/10.4050/F-0078-2022-17524

[4] C. Eugene Hammond. An application of Floquet theory to prediction of mechanical instability. Journal of the American Helicopter Society, 19(4):14–23, 1974. https://doi.org/10.4050/JAHS.19.14

[5] Aykut Tamer and Pierangelo Masarati. Periodic stability and sensitivity analysis of rotating machinery. In Proceedings of the 9th International Conference on Rotor Dynamics IFToMM ICORD 2014, Milan, Italy, Sept. 22–25, 2014. https://doi.org/10.1007/978-3-319-06590-8_170

[6] Matteo Croci. Ground resonance sensitivity study for unconventional damper configurations. Master's thesis, Politecnico di Milano, 2025.

[7] Pierangelo Masarati, Vincenzo Muscarello, and Giuseppe Quaranta. Linearized aeroservoelastic analysis of rotary-wing aircraft. In 36th European Rotorcraft Forum, pages 099.1–10, Paris, France, September 7–9, 2010.

Materials Research Proceedings 69 (2026) 414-417 https://doi.org/10.21741/9781644904251-75

Investigation of Lift-offset Effect on Performance and Vibratory Loads of a Rigid Coaxial Rotor

Jae-Hee HWANG[1,a *], and Jae-Sang PARK[1,b]

[1]Chungnam National University, Republic of Korea

[a]ghkdnonon7@gmail.com, [b]aerotor@cnu.ac.kr

Keywords: Rigid Coaxial Rotor, Lift-Offset, Aerodynamic Performance, Hub Vibratory Loads, Pitch-Link Vibratory Loads

Abstract. This study investigates the hub and pitch-link vibratory loads of a generic lift-offset coaxial rotor, using the comprehensive rotorcraft analysis code, CAMRAD II. The analysis results indicate that increasing the lift-offset leads to a reduction in the hub vibratory load (VI) and pitch-link vibratory loads at 250 knots. Furthermore, the rotor aerodynamic performance improves with increasing lift-offset.

Introduction

In recent years, the rotorcraft community has actively pursued the development of rotorcraft with enhanced high-speed and long-range flight capabilities. Lift-offset compound helicopters adopt the Advancing Blade Concept (ABC) to achieve superior high-speed performance. However, the lift-offset coaxial rotor (or rigid coaxial rotor) requires short inter-rotor spacing between the upper and lower rotors, demanding highly stiff blades that generate significant vibrations in high speed flights. The airframe vibrations from the rotor hub vibratory loads cause various problems, such as limited maximum flight speed, increased mechanical fatigue, and passenger discomfort. In addition, the severe pitch-link vibratory loads should be investigated since the pitch-link is an important component of a rotor control system to control blade pitch motions. The analysis examines the effects of pitch-link stiffness on rotor aerodynamic performance, hub vibratory loads, and pitch-link forces at various flight speeds, and investigates the influence of lift-offset on them at a flight speed of 250 knots.

Analytical Methods

The modeling and analysis are conducted based on the authors' previous studies [1, 2], in which the modeling and analysis of the lift-offset rotor were validated against wind tunnel test results. This study employs the generic lift-offset coaxial rotor developed in the authors' previous work [3] which is similar to the SB>1 Defiant rigid coaxial rotor (Figure 1). CAMRAD II is utilized for the rotor aeromechanics modeling and analyses. Blade structural dynamics is modeled using eight nonlinear beam elements per blade. The rotor control system, including pitch-links, pitch-horns, and swashplates, is also incorporated into the model. For unsteady rotor aerodynamics, 25 aerodynamic panels for a blade are employed, based on the second-order lifting-line theory and an airfoil table lookup. Furthermore, a general free-wake model is applied to account for the aerodynamic interference between the upper and lower rotors. With six pitch control angles (θ_0^U, θ_{1C}^U, θ_{1S}^U, θ_0^L, θ_{1C}^L, θ_{1S}^L), the rotor is trimmed to match the assumed rotor thrust, hub roll moments prescribed using an assumed lift-offset value, zero hub pitch moments, and zero torque of a coaxial rotor.

The analysis examines the effects of pitch-link stiffness values (K_{pl}) and lift-offsets on rotor aerodynamic performance, hub vibratory loads, and half peak-to-peak pitch-link forces.

Content from this work may be used under the terms of the Creative Commons Attribution 3.0 license. Any further distribution of this work must maintain attribution to the author(s) and the title of the work, journal citation and DOI. Published under license by Materials Research Forum LLC.

Materials Research Proceedings 69 (2026) 414-417 https://doi.org/10.21741/9781644904251-75

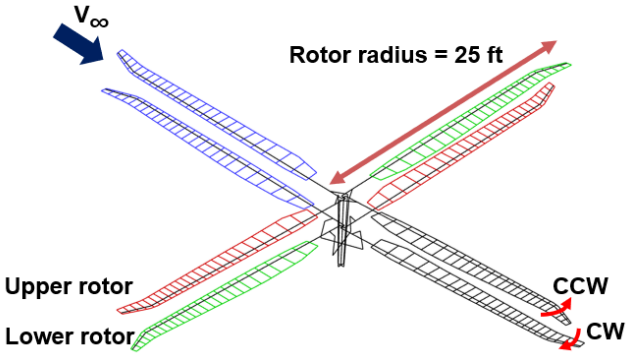


Figure 1. CAMRAD II model for lift-offset coaxial rotor

Results

Fan plot

The natural frequencies of a rotating blade are analyzed in terms of the rotor rotational speed to investigate the structural dynamics of the present lift-offset rotor with different pitch-link stiffness values. As seen in the figure, the first torsion mode (1T) frequency decreases as the pitch-link stiffness (K_{pl}) decreases; however, due to the extremely high blade stiffness (rigid blades), it still exhibits high natural frequency values exceeding 10P (where 1P = 1/rev is a nondimensional rotor speed).

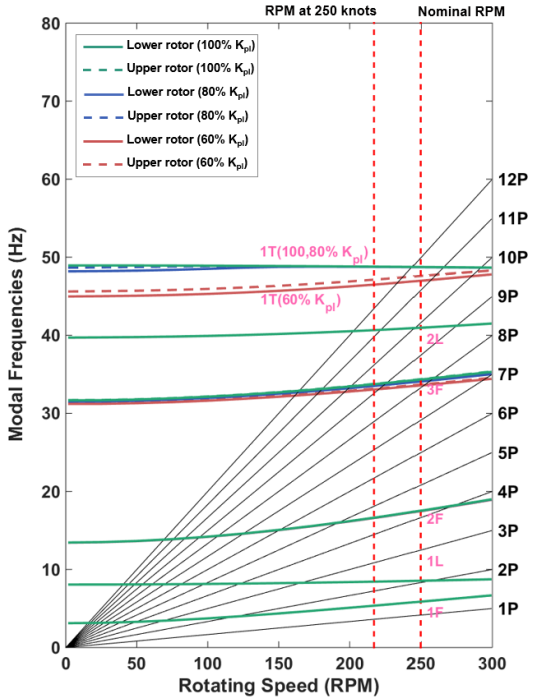


Figure 2. Natural frequencies of a rotating blade for the lift-offset coaxial rotor (in vacuum)

Analysis with various pitch-link stiffness values

As the pitch-link stiffness (K_{pl}) decreases, the rotor aerodynamic performance (rotor effective lift-to-drag ratio, L/D_e) in forward flight is not altered significantly (Figure 3); however, the hub vibratory loads (Vibration Index, VI) and pitch-link forces (1/2 peak-to-peak forces) increase (Figure 4).

Materials Research Proceedings 69 (2026) 414-417 https://doi.org/10.21741/9781644904251-75

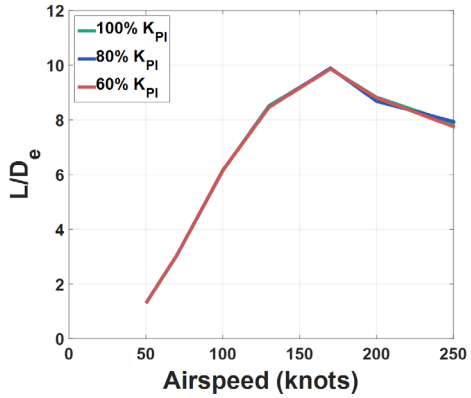


Figure 3. Aerodynamic performance with different pitch-link stiffness values; rotor effective lift-to-drag-ratios (L/D_e)

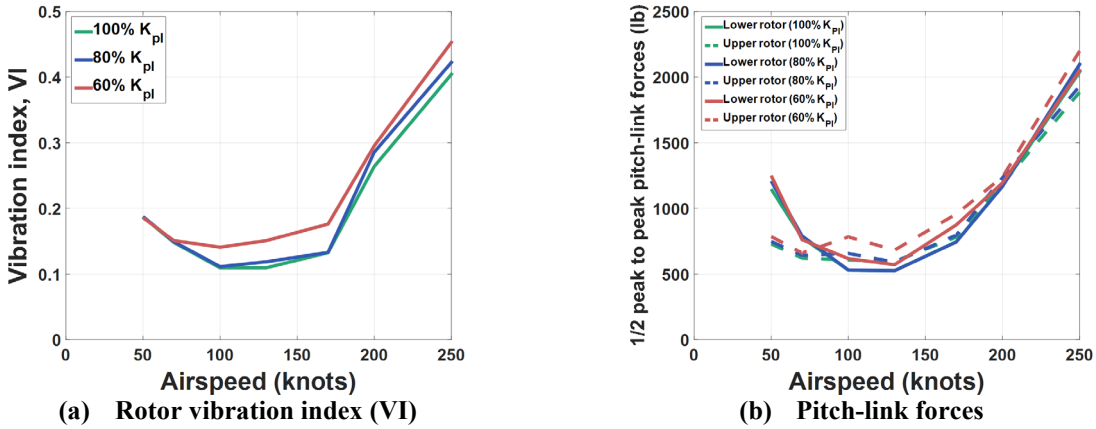


Figure 4. Hub vibratory loads and pitch-link forces with different pitch-link stiffness values

Analysis with various lift-offset values

Forward flight performance and vibratory loads of the lift-offset coaxial rotor are investigated in Figures 5 and 6 at a flight speed of 250 knots. In these examples the baseline pitch-link stiffness (100% K_{pl}) and various lift-offset values of 0.1, 0.2, and 0.3 are considered to analyze the effect of lift-offset. Figure 5 illustrates the variations of the rotor effective lift-to-drag ratio (L/D_e) in terms of the lift-offset value. As the lift-offset increases, the L/D_e is observed to increase; therefore, the aerodynamic performance is improved. Furthermore, the hub vibratory load (VI) and pitch-link force both decrease as the lift-offset increases, as shown in Figure 6.

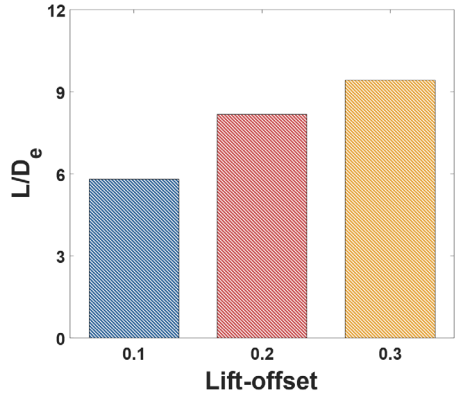
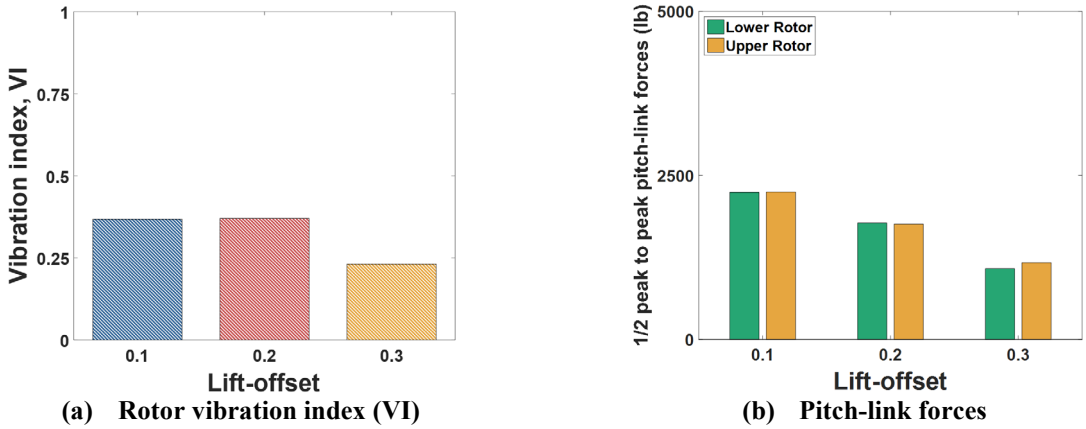


Figure 5. Aerodynamic performance with different lift-offset values at 250 knots; rotor effective lift-to-drag-ratios (L/D_e)



(a) Rotor vibration index (VI) **(b) Pitch-link forces**

Figure 6. Hub vibratory loads and pitch-link forces with different lift-offset values at 250 knots

Conclusions

In this work, the performance and vibratory loads of a generic lift-offset coaxial rotor were investigated with various pitch-link stiffness and lift-offset values. This study utilized the rotorcraft comprehensive analysis code, CAMRAD II, to investigate the performance, hub vibratory loads, and pitch-link forces for the lift-offset coaxial rotor. The rotor aerodynamic performance in forward flight remained unchanged with varying pitch-link stiffnesses (100%, 80%, and 60% K_{pl}); however, hub vibratory loads and pitch-link forces both increased when using lower pitch-link stiffness. Furthermore, at 250 knots, a higher lift-offset value improved aerodynamic performance and decreased hub vibratory loads and pitch-link forces of the lift-offset coaxial rotor.

Acknowledgments

This work was supported by Korea Research Institute for defense Technology planning and advancement (KRIT) grant funded by the Korea government (DAPA (Defense Acquisition Program Administration) (No. KRIT-CT-22-082, Design/Manufacturing Technology of Rigid Coaxial Rotor System for High-Speed Compound Helicopter, 2025, contribution rate 100%).

References

[1] Y. B. Lee, and J. S. Park, “Validation for Performance and Hub Vibratory Load Analyses of Lift-offset Coaxial Rotors in Wind-Tunnel Tests,” Journal of The Korean Society for Aeronautical and Space Sciences, Vol. 50, No. 7, July 2022, pp. 497-505. https://doi.org/10.5139/JKSAS.2022.50.7.497

[2] S. B. Lee, Y. B. Lee, and J. S. Park,” Validation Study on Pitch-link Vibratory Loads of a Rigid Coaxial Rotor in Wind-Tunnel Tests,” Journal of The Korean Society for Aeronautical and Space Sciences, Vol. 52, No. 1, July 2024, pp. 47-56. https://doi.org/10.5139/JKSAS.2024.52.1.47

[3] J. H. Hwang, S. B. Lee, and J. S. Park, “Performance and Vibratory Load Analyses of a Rigid Coaxial Rotor with Lift-offset,” Journal of The Korean Society for Aeronautical and Space Sciences, 2026, Accepted for Publication. https://doi.org/10.5139/JKSAS.2026.54.3.275

Materials Research Proceedings 69 (2026) 418-423 https://doi.org/10.21741/9781644904251-76

Analysis of Morphing Trailing Edge Flap Effects on Dynamic Stall of the NACA 13112 Airfoil for Helicopter Rotor Blade Applications Using CFD and Experimental Methods

Dorin-Madalin FERARU[1,a*], Daniel MARIUȚA[2,b], Grigore CICAN[1,3,c], Ciprian-Marius LARCO[2,d] and Lucian-Teodor GRIGORIE[1,e]

[1]Faculty of Aerospace Engineering, National University of Science and Technology POLITEHNICA Bucharest, 060042 Bucharest, Romania

[2]Department of Aircraft Integrated Systems and Aviation, Military Technical Academy "Ferdinand I" Bucharest, 050141 Bucharest, Romania

[3]Romanian Research and Development Institute for Gas Turbines—COMOTI, 220D Iuliu Maniu, 061126 Bucharest, Romania

[a]ferarumadalin96@gmail.com, [b]daniel.mariuta@mta.ro, [c]grigore.cican@upb.ro, [d]ciprian.larco@mta.ro, [e]teodor.grigorie@upb.ro

Keywords: Morphing Airfoil, Dynamic Stall, Trailing Edge Flap, CFD Validation, Mesh Topology, Aerodynamic Coefficients, Moving Reference Frame, NACA 13112, Adaptive Geometry, Rotorcraft Aerodynamics

Abstract. High-fidelity modeling of unsteady aerodynamic phenomena is critical for the development of next-generation rotor blades and morphing airfoils. This study examines the unsteady flow over four representative 3D morphing NACA 13112 airfoil sections, each associated with a blade of the IAR 330 PUMA main rotor and pitching about an axis located at 25% of the chord. Simulations conducted at Mach 0.38 replicate hover conditions and capture the dominant unsteady mechanisms governing dynamic stall. Wind-tunnel measurements were used exclusively to validate the baseline airfoil section, confirming the accuracy of the numerical predictions. Two morphing strategies were investigated. The first employed pre-morphed CAD geometries generated in CATIA for trailing-edge flap (TEF) deflections ranging from −20° to +20°, using a fixed flap-chord fraction of 0.75c. The second implemented dynamic morphing via compiled user-defined functions (UDFs) in conjunction with CATIA-generated bodies corresponding to various flap-chord lengths. The angle of attack followed a sinusoidal variation between −3° and +18°, while a dedicated UDF imposed TEF rotation within the same deflection range. The flap motion was applied in antiphase to the pitching cycle, and a dynamic mesh continuously updated the geometry, enabling a realistic representation of unsteady morphing effects across all blade sections. For static validation, unstructured O-grid and C-grid meshes were generated and compared against wind-tunnel data. For dynamic simulations, an unstructured mesh featuring a fixed outer domain and a rotating inner rotor domain was employed to resolve cyclic pitching, flap motion, and rotor-induced flow interactions. The numerical setup used a Moving Reference Frame at 265 rpm and a sliding-mesh interface to capture relative domain motion. Parametric studies demonstrate that TEF amplitude and flap-chord fraction have a significant impact on the unsteady aerodynamic response. Dynamic morphing effectively delays stall, reduces unsteady loads, and enhances aerodynamic damping, highlighting its potential for improving the stability and performance of future rotor systems.

Introduction

Aerodynamic research plays a crucial role in understanding and optimizing the performance of lifting surfaces, encompassing both fixed wings and rotary blades. Such analyses form the

Content from this work may be used under the terms of the Creative Commons Attribution 3.0 license. Any further distribution of this work must maintain attribution to the author(s) and the title of the work, journal citation and DOI. Published under license by Materials Research Forum LLC.

Materials Research Proceedings 69 (2026) 418-423 https://doi.org/10.21741/9781644904251-76

foundation for validating aerodynamic theories and for designing engineering solutions that improve safety, structural integrity and efficiency under various flight regimes. Experimental campaigns, notably those involving the ONERA M6 wing, have yielded comprehensive insights into transonic flow phenomena over swept wings and remain essential benchmarks for the validation of computational fluid dynamics (CFD) models [1–3].

Wind tunnel experimentation continues to serve as a cornerstone in aerodynamic performance assessment. However, confined test sections inherently introduce boundary effects and wall interference, which can distort flow characteristics and alter pressure distributions. Computational analysis has therefore become an essential complementary approach, offering the capability to resolve complex and unsteady flow structures with both flexibility and accuracy. Early numerical investigations on the NACA 0012 and S809 airfoils have demonstrated the strong influence of Reynolds number, reduced frequency, and pitch-axis position on vortex evolution, as well as on the corresponding lift and moment coefficients [4,5].

Dynamic stall represents a critical aerodynamic phenomenon in rotorcraft operation, arising when the angle of attack on the retreating blade exceeds the static stall threshold. This unsteady process induces the formation of leading-edge vortices that cause abrupt variations in lift, drag, and pitching moment, often resulting in significant vibration, structural loading, and potential aeroelastic instabilities. Extensive experimental and computational investigations have examined dynamic stall on pitching airfoils, finite wings, and rotating blades, emphasizing the combined influence of blade–vortex interactions, rotational acceleration, and three-dimensional flow development on the overall aerodynamic response.

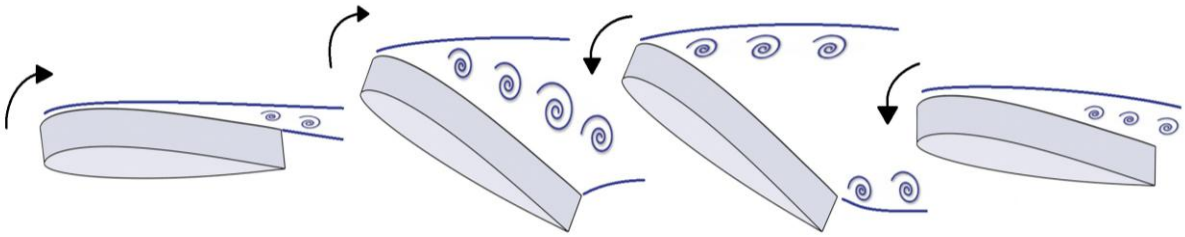


Fig. 1. Dynamic stall stages

The present work investigates the unsteady aerodynamics of three-dimensional morphing NACA 13112 airfoil sections representative of the IAR 330 PUMA main rotor. Wind-tunnel measurements were employed to validate the baseline geometry and establish the reliability of the numerical approach. Following this validation, CFD simulations were carried out to examine both pre-morphed and dynamically morphed configurations. The study focuses on how variations in flap-chord fraction and trailing-edge flap deflection influence lift and drag, with the broader aim of evaluating their effects on aerodynamic performance and dynamic stall behavior under rotor-relevant operating conditions.

Methodology

The baseline NACA 13112 geometry was generated in CATIA from discrete coordinate data. A 1:5-scale model derived from this geometry was CNC-machined for wind-tunnel testing and subsequently used to validate the steady-state CFD results, while the dynamic morphing geometries were likewise constructed in CATIA for the transient simulations.

Steady-State Analysis. To analyze the influence of grid topology on steady-state CFD accuracy, two unstructured mesh strategies were developed. The O-grid topology wraps the mesh concentrically around the airfoil, providing excellent orthogonality near the wall and facilitating accurate resolution of the viscous sublayer and boundary layer. In contrast, the C-grid topology

features an open downstream region that allows the mesh to extend naturally past the trailing edge, improving wake resolution and enabling more accurate capture of trailing-edge vortices.

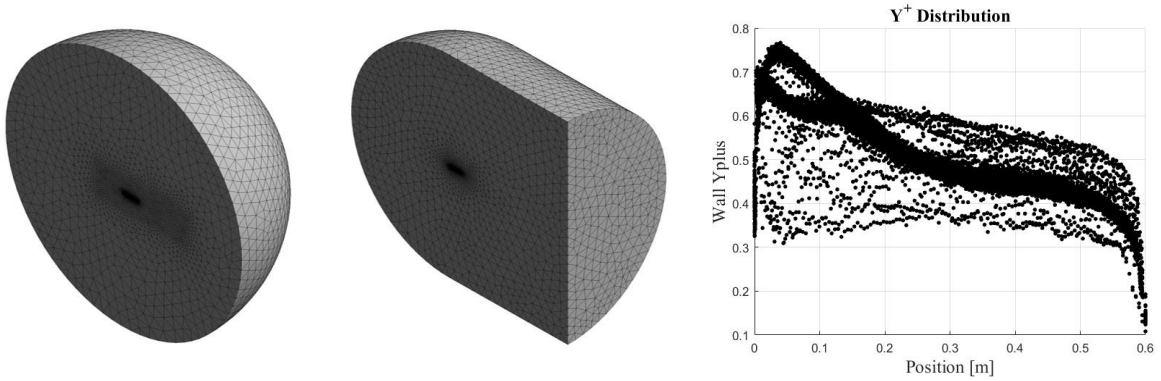


Fig. 2. Unstructured mesh with boundary-layer inflation corresponding to $y^+ \approx 1$, including C-grid and O-grid blocks around the airfoil.

The turbulence model adopted was the Spalart–Allmaras (S–A) one-equation model. Regarding physical models, compressibility effects were introduced using the ideal gas law, while viscosity variations were accounted for through Sutherland's law.

Dynamic Analysis. The mesh comprises a fully unstructured background grid combined with refined cylindrical sub-domains around the four blade sections. Each section includes multiple inflation layers to accurately resolve near-wall gradients and capture the unsteady boundary-layer behavior during dynamic pitching motion. This mesh strategy ensures numerical stability and sufficient spatial resolution for transient flow separation, dynamic stall development, and vortex convection.

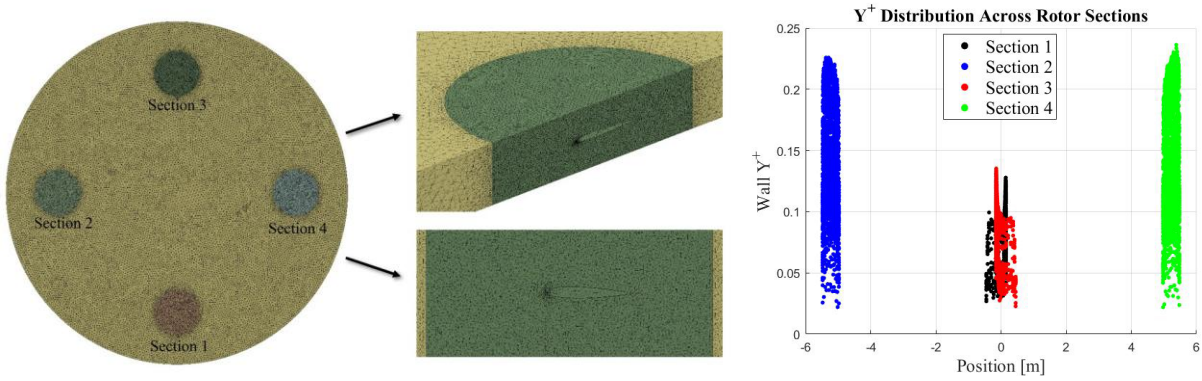


Fig. 3. Unstructured computational mesh with boundary-layer inflation corresponding to $y^+ \approx 1$ used in the transient CFD simulations.

A transient CFD analysis was conducted employing the SST k–ω turbulence model. Four airfoil sections, positioned at a radial distance of 4975 mm from the rotor hub, were examined under operating conditions corresponding to a rotor speed of 265 rpm. Each section featured a chord length of 600 mm and a span of 500 mm, matching the geometric characteristics used in the experimental model.

Materials Research Proceedings 69 (2026) 418-423 https://doi.org/10.21741/9781644904251-76

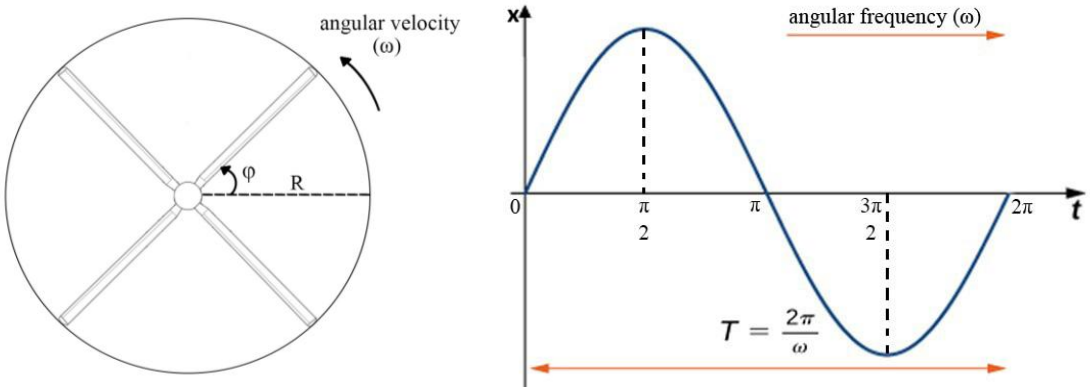


Fig. 4. Circular motion; Simple harmonic motion.

Results and discussion

Steady-State Results. The results indicate that the choice of grid topology has a significant influence on the prediction of lift and drag in the vicinity of stall. The C-grid mesh provides a smoother resolution of the suction-side flow curvature and consequently captures flow separation earlier, producing aerodynamic trends that align more closely with the experimental measurements, particularly in the post-stall regime. In contrast, the O-grid mesh, although accurate at low angles of attack, slightly underpredicts the drag increase and delays the onset of stall compared with both the C-grid results and the experimental data.

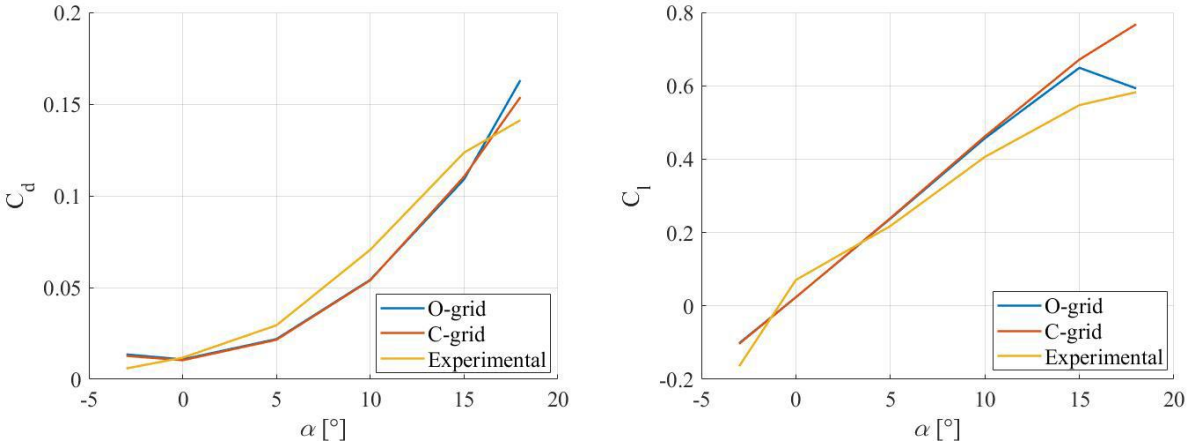


Fig. 5. Grid topology influence on aerodynamic coefficients with experimental validation.

The CFD results were validated against experimental data obtained from wind-tunnel tests conducted on the CNC-machined aluminum airfoil model. The comparison of aerodynamic coefficients showed a consistently good agreement between the numerical predictions and the measurements, confirming the reliability of the computational approach across the stall regime.

Dynamic Results. The transient CFD results in Fig. 6 illustrate the evolution of lift and drag during the first rotor revolution for the morphed airfoil sections subjected to different flap deflection angles β. The aerodynamic response exhibits periodic oscillations driven by the time-varying angle of attack and unsteady rotor-induced loading, with each section showing a distinct phase shift. The curves display key signatures of dynamic stall, including a delayed stall onset and pronounced overshoots in lift and drag as the leading-edge vortex develops and convects downstream. During the downstroke, the delayed load recovery generates the characteristic hysteresis loops in Cl and Cd, highlighting the strong unsteady aerodynamic effects acting on the morphing configurations.

Materials Research Proceedings 69 (2026) 418-423 https://doi.org/10.21741/9781644904251-76

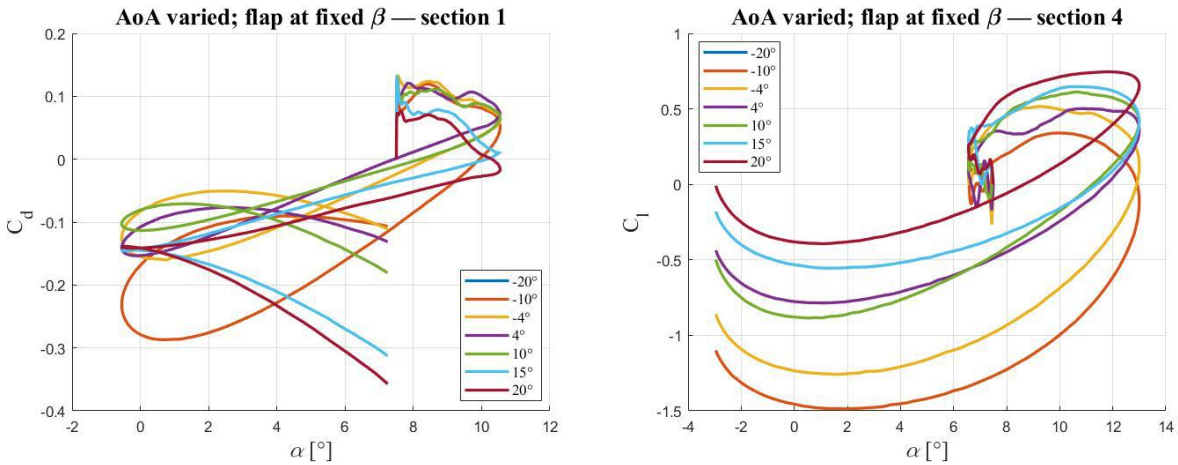


Fig. 6. Aerodynamic coefficients obtained during the first rotor revolution, highlighting the variation with angle of attack (α).

The aerodynamic loops obtained during the third rotor revolution exhibit increased distortion as the flap deflection β varies, reflecting stronger nonlinear behavior and enlarged hysteresis cycles. In this configuration, both the angle of attack and the flap motion vary sinusoidally, with the flap operating in antiphase relative to the airfoil pitching motion. Larger flap amplitudes amplify the peak aerodynamic loads and shift the stall onset, whereas smaller amplitudes produce tighter loops with smoother recovery. These trends underline the high sensitivity of the dynamic stall process to active trailing-edge morphing. As the rotor motion reaches a mature state, the signals show sharper oscillations and more pronounced extrema—particularly for higher β values—indicating the intensified unsteady vortex dynamics governing the flow.

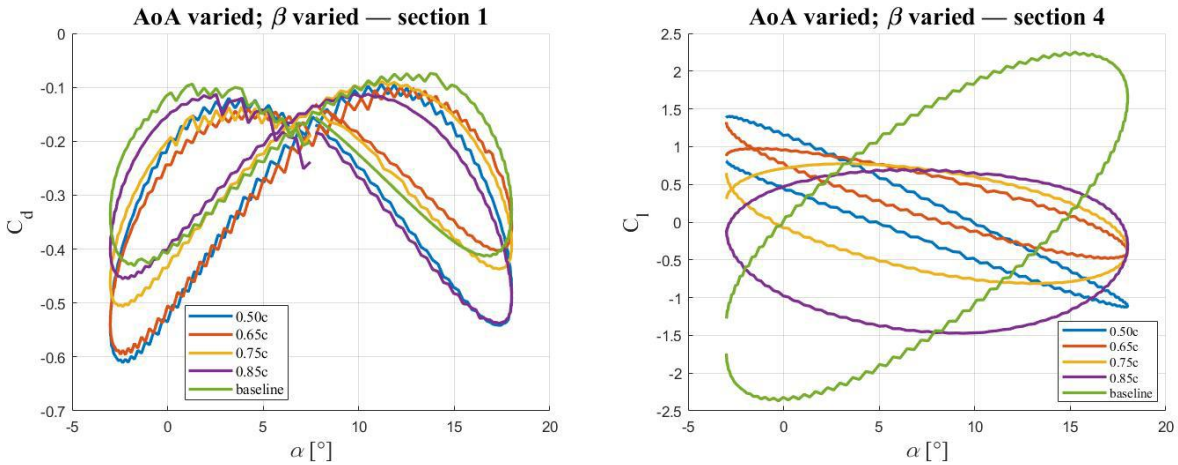


Fig. 7. Aerodynamic coefficients obtained during the third rotor revolution, highlighting the variation with angle of attack (α).

The time histories in Fig. 8 clearly reflect the sinusoidal kinematics imposed by the UDF, which become fully established by the third rotor revolution. The periodic variation of angle of attack and the antiphase flap motion produce smooth, repeatable oscillations in both lift and drag. Differences between flap-chord ratios are evident through the modulation of amplitude and waveform shape, showing how the imposed morphing law directly governs the temporal aerodynamic response.

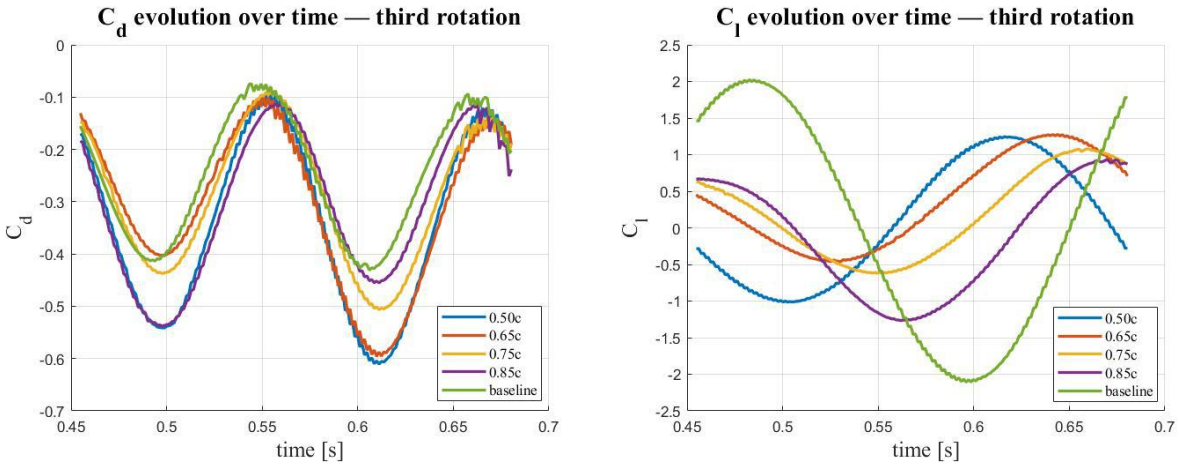


Fig. 8. Aerodynamic coefficients during the third rotor revolution: drag coefficient (Cd) for blade section 1 and lift coefficient (Cl) for blade section 4.

Conclusions

The CFD methodology showed good agreement with wind-tunnel measurements, confirming its capability to accurately predict the aerodynamic behavior of the NACA 13112 sections across pre-stall and post-stall regimes.

The sinusoidal pitch–flap kinematics imposed by the UDF, with the flap operating in antiphase to the airfoil, generated stable and repeatable unsteady responses by the third rotor rotation, clearly governing the temporal evolution of lift and drag.

Variations in flap-chord fraction and deflection angle β strongly influenced the dynamic stall characteristics, affecting stall onset, peak loads, and the extent of hysteresis across all sections.

Among the tested morphing configurations, the 0.75c flap-chord ratio yielded the highest lift-to-drag efficiency, particularly at mid-range angles of attack in the pre-stall regime.

The combined experimental and CFD investigations demonstrated a coherent and validated framework for assessing trailing-edge morphing on helicopter rotor blade sections, supporting its potential for enhancing rotorcraft aerodynamic performance.

References

[1] Cambier, L., and Gazaix, M., "ElsA: An Efficient Object-Oriented Solution to CFD Complexity," 2002. https://doi.org/10.2514/6.2002-108

[2] Schmitt, V., and Charpin F., "Pressure Distributions on the ONERA-M6-Wing at Transonic Mach Numbers," 1979.

[3] Durrani, N., and Qin, N., "Comparison of RANS, DES and DDES Results for ONERA M-6 Wing at Transonic Flow Speed Using an In-House Parallel Code," 2011. https://doi.org/10.2514/6.2011-190

[4] Battisti, L., Benini, E., Brighenti, A., Raciti Castelli, M., Dell'Anna, S., Dossena, V., Persico, G., Schmidt Paulsen, U., and Pedersen, T. F., "Wind Tunnel Testing of the DeepWind Demonstrator in Design and Tilted Operating Conditions," Energy, Vol. 111, 2016. https://doi.org/10.1016/j.energy.2016.05.080

[5] Bianchini, A., Balduzzi, F., Ferrara, G., Ferrari, L., Persico, G., Dossena, V., and Battisti, L., "Detailed Analysis of the Wake Structure of a Straight-Blade H-Darrieus Wind Turbine by Means of Wind Tunnel Experiments and Computational Fluid Dynamics Simulations," Journal of Engineering for Gas Turbines and Power, Vol. 140, No. 3, 2018. https://doi.org/10.1115/1.4037906

Aircraft Design, MDO & Performance



Materials Research Proceedings 69 (2026) 425-430 https://doi.org/10.21741/9781644904251-77

A Survey of Advanced Air Mobility Use Cases and Implementation Challenges in Japan: A Systems Approach Perspective

Yusuke Mihara[1,a *]

[1]Shizuoka Institute of Science and Technology, Shizuoka, Japan

[a]mihara.yusuke@sist.ac.jp

Keywords: Advanced Air Mobility, System Design, Holistic Systems Approach, Use Case Analysis

Abstract. Advanced Air Mobility (AAM) is envisioned as a new form of aerial transportation designed to move people efficiently at low altitudes. The goal of AAM is to democratize access to air travel. Nevertheless, its realization depends not solely on vehicle technology but on a holistic systems approach that integrates vehicles, infrastructure, and operations. This paper discusses representative AAM use cases in Japan, focusing on air taxis and medical emergency transport, and identifies current issues toward establishing a holistic system design.

1. Introduction

Advanced Air Mobility (AAM) is envisioned as a new form of aerial mobility designed to transport people efficiently through the air [1]. Its key features include electrification, automation, and vertical take-off and landing (VTOL) capability [2]. The goal of AAM is to democratize air travel in lower altitudes. In Japan, AAM is referred to as "flying cars" due to its envisioned role in everyday transport and its potential market scale comparable to the automotive industry [3].

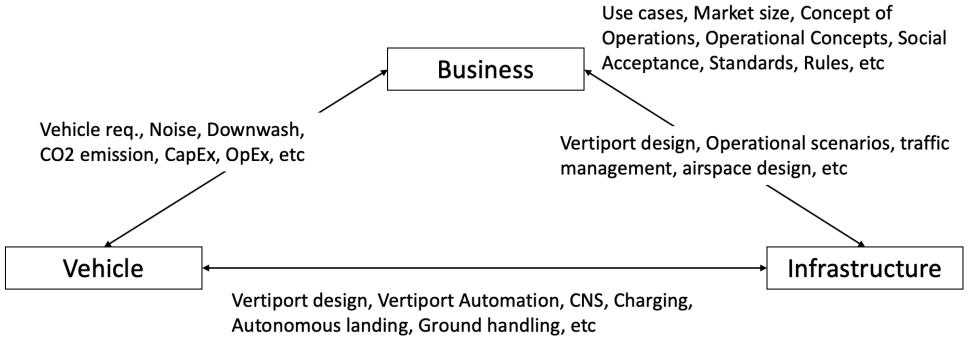


Fig.1. Socio-Technical System Design of AAM

Implementing AAM in society requires more than combining technologies such as batteries, automation, and sensors. It demands a holistic system design that includes vehicles, supporting infrastructure, and their operational use cases. Fig.1 shows that an AAM system is decomposed into vehicle, infrastructure, and business. The AAM system exhibits the interdependent relationships among Vehicle, Infrastructure, and Business in the AAM ecosystem, where each domain influences the others through technical, operational, and economic parameters such as requirements, design, operational concepts, and regulatory frameworks. Moreover, AAM must coexist with UAVs, VFR vehicles like helicopters, and IFR aircraft, making it a component within a larger system of systems (SoS). Thus, a systems approach is essential to understand and implement AAM effectively.

The AAM concept gained momentum following the 2016 Uber Elevate white paper [4], with most developments focused on realizing urban air taxis. A systems approach has been applied in

Content from this work may be used under the terms of the Creative Commons Attribution 3.0 license. Any further distribution of this work must maintain attribution to the author(s) and the title of the work, journal citation and DOI. Published under license by Materials Research Forum LLC.

Materials Research Proceedings 69 (2026) 425-430 https://doi.org/10.21741/9781644904251-77

the U.S. and Germany to evaluate the feasibility of UAM operational concepts [5,6,7]. However, these studies mainly target air taxi use cases.

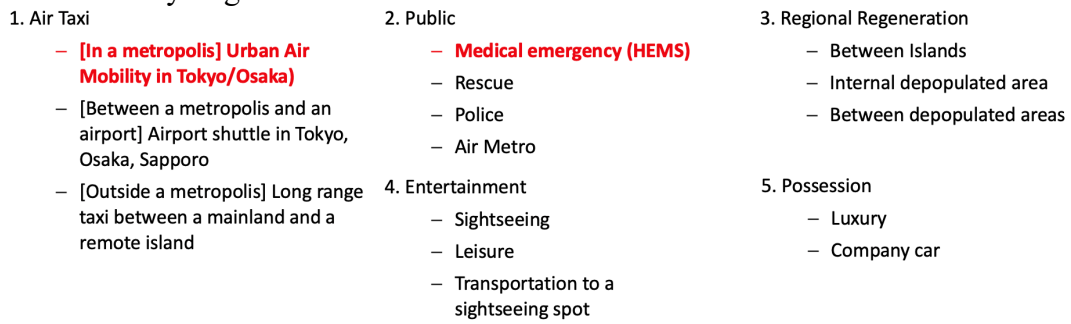


Fig.2. Potential AAM Use Cases (Applications) in Japan

This paper discusses air taxis and medical emergency application of representative AAM use cases, with the purpose of identifying conventional challenges. While AAM applications range from air taxis and rural mobility to public services and tourism, written in Fig. 2, this paper focuses on two representative cases: air taxi and medical emergency transport due to their high potential. Each case is analysed in terms of stakeholders, operational areas, routes, concepts of operation, and current transportation issues. A holistic framework is used to map use case challenges across technological, social, economic, and environmental dimensions.

2. Advanced Air Mobility

Although the term “Flying Car” is widely used in Japan, its definition can be interpreted from four perspectives, as shown in Fig.3 [3]. First, it refers to eVTOLs—the mainstream design type—but can also include hybrid or short takeoff and landing (STOL) models that fall outside this category [8]. Second, it can be defined from the purpose perspective—as an air mobility system enabling point-to-point transportation. However, Japan’s limited land area restricts the number of available takeoff and landing sites, necessitating the use of existing heliports or the construction of new vertiports. Third, it can describe roadable aircraft, combining both automotive and aeronautical functionalities, as seen in designs like PAL-V, Klein Vision, and Terrafugia. Yet, these models often rely on internal combustion engines and tend to be larger than eVTOLs, making them less dominant. Fourth, it can be framed as Urban Air Mobility (UAM), emphasizing the use case of air taxis in metropolitan areas. Nevertheless, the applications of AAM (or flying cars) are not limited to intra-urban air taxi services alone. In summary, AAM—often termed the “flying car” in Japan—can be broadly understood as an emerging form of air mobility that seeks to realize an aerial transportation economy operating within the low-altitude range of approximately 150 to 1,000 meters.

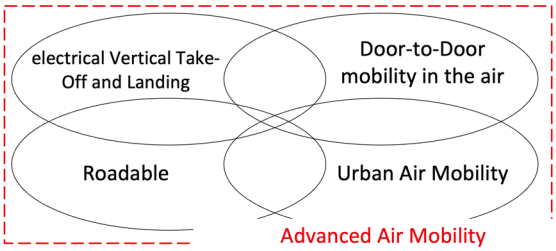


Fig. 3. A Definition of Advanced Air Mobility

3. Potential Use Cases

3.1 Air Taxi

Air taxi use cases can be classified into three categories. In the Uber Elevate White Paper, the feasibility of air taxi operations within Los Angeles was analyzed based on large-scale mobility

data [4]. Air taxis can be categorized into intra-urban, inter-urban, and extra-urban operations. This paper discusses only an intra-urban operation.

Within urban areas, existing transportation modes include trains, subways, buses, and conventional taxis. Indeed, in major metropolitan areas such as Tokyo, road congestion significantly affects travel time reliability. Most citizens rely on public transportation for commuting or daily travel, and long-distance, high-fare trips are relatively uncommon in such cities. In Tokyo, these typically occur only when individuals miss the last train at night. Analysis of operational data from Tokyo's taxi network indicates that trips costing over 5,000 yen and lasting more than 30 minutes account for approximately 7–12% of all rides [9]. Assuming that 3–5% of these customers switch to AAM, the estimated intra-Tokyo demand for air taxi services would be roughly 60–100 trips per day [4].

However, there are substantial challenges in establishing takeoff and landing sites in dense urban environments like Tokyo. Currently, there are only six public and private heliports within the city [10]. Japan's high-rise buildings, which maximize limited land by expanding office and residential spaces vertically, often include emergency landing pads or rescue areas [11]. Buildings exceeding 100 meters in height are required to allow helicopter landings during emergencies such as fires, while those between 31 and 100 meters are recommended to include hovering-based rescue spaces. Given the expected weight of AAM vehicles, such infrastructure may offer limited takeoff and landing potential [9]. Nonetheless, converting existing emergency heliports directly into operational vertiports would be challenging due to issues such as access routes, landing area dimensions, and approach angles. Any plan to enable AAM operations on rooftops would therefore require redevelopment projects that explicitly incorporate vertiport functionality from the design stage.

The size constraints of potential vertiports also influence aircraft configuration. For example, compact multi-rotor type designs such as EHang's coaxial-rotor systems are advantageous for small footprints but are limited in speed. In contrast, winged configurations—such as vectored-thrust or lift-plus-cruise types—achieve higher cruising speeds but require larger landing areas. Conventional helicopters remain costly both in terms of acquisition and operation [12]. While airworthiness certification is essential for ensuring safety, the economic feasibility of air taxi operations ultimately depends on reducing vehicle costs and improving battery performance.

Airspace design also presents critical challenges. Since March 2020, a new south-wind landing route for Tokyo International Airport (Haneda) has been in use, operating daily between 3 p.m. and 7 p.m. This route passes over central Saitama Prefecture (3,000–5,000 ft) and central Tokyo (3,000–4,500 ft) before reaching Haneda [13]. Consequently, the available airspace for urban flight operations has become more restricted. Furthermore, areas such as the Imperial Palace and the National Diet Building are politically sensitive and likely to be no-fly zones. The establishment of dedicated UAM corridors in the 150–1,000 m altitude range could enable AAM to operate within exclusive airspace. Nevertheless, with existing air traffic around Haneda's southbound route, any air taxi service must address not only safety but also aesthetic and privacy concerns. Building social consensus among AAM stakeholders and urban residents is thus indispensable.

3.2 Helicopter Emergency Medical Service (HEMS)

In Japan, a helicopter emergency medical service (HEMS), commonly known as the Doctor-Heli, has been in operation since 2001. The program was initiated in response to the lack of sufficient aerial medical transport capabilities revealed during the 1995 Great Hanshin-Awaji Earthquake. As of today, 57 aircraft operate across Japan's 47 prefectures, providing rapid transport of physicians to emergency scenes. Each helicopter is equipped with essential medical instruments and pharmaceuticals required for initial treatment. In 2022 alone, the Doctor-Heli system recorded 29,245 operational missions [14,15].

When an emergency occurs, the system is activated through a request from a local fire department command center following a 119 emergency call. A helicopter carrying both a flight physician and a flight nurse is dispatched from a base hospital. Simultaneously, local fire units transport the patient by ambulance to a designated rendezvous point, where the helicopter lands to either transfer medical staff or transport the patient directly to the hospital [14].

Public emergency ambulance services in Japan are free of charge, and the same applies to Doctor-Heli operations. However, each aircraft incurs an annual operational cost of approximately 250 million yen—including lease fees, pilot salaries, fuel, maintenance, and insurance. The average cost per sortie is estimated at 460,000 yen [14]. Due to these high operational expenses, the sustainability of the program is dependent on government subsidies, and its long-term viability remains uncertain.

Recently, discussions have emerged regarding the use of electric AAM (Advanced Air Mobility) vehicles as a complementary solution to Doctor-Heli operations. Strong requests from flight physicians, along with the public nature of the service, have facilitated social acceptance, especially regarding noise concerns. The primary objective of the Doctor-Heli is to minimize the time to first contact between medical staff and patients. In the initial stage of AAM implementation, a two-seat configuration—carrying a pilot and a physician—could be deployed, with patient transport handled by ground ambulances.

Operational data analyses indicate that compact, low-cost vehicles with a range of approximately 50 km and a maximum speed of 150 km/h are desirable [16]. Based on cost modeling from existing aircraft and operational cost structures, a fixed-wing configuration could achieve a unit cost around 100 million yen and a direct operating cost (DOC) of approximately 50,000 yen per flight hour [16]. However, these estimates assume economies of scale at a production level exceeding 100 units per year and the use of existing lithium-ion batteries; current market prices are several times higher. Thus, both battery performance improvement and reductions in capital (CapEx) and operating expenditures (OpEx) are essential for AAM to contribute effectively to the sustainability of HEMS operations.

Doctor-Heli helicopters typically meet patients at rendezvous points—designated open spaces such as riverbanks, parks, or school grounds. The MD902, a helicopter known for its low vibration, is commonly used for this purpose in Japan. With a maximum takeoff weight of approximately 2.8 tons, its relatively high disk loading produces considerable rotor downwash, generating dust and debris that can affect nearby residents [16]. Firefighters often spray water on the ground prior to landing to mitigate this effect. In contrast, a two-seat AAM vehicle would likely have a maximum takeoff weight below 2 tons, potentially improving social acceptability due to reduced downwash and noise [16]. In fact, Joby Aviation's demonstration flight planned for the 2025 Osaka Expo aims to showcase the quiet operation of electric eVTOLs, which emit no engine noise. Moreover, the required landing area is another critical issue. If AAMs can operate from smaller landing zones, the number of feasible rendezvous points will increase, reducing the time needed to reach patients. However, even compact eVTOLs—whether fixed-wing or multi-rotor configurations—are not necessarily smaller than helicopters. Among current designs, multi-rotor types such as EHang's coaxial-rotor eVTOL could potentially land in spaces as small as a supermarket or convenience store parking lot [17]. Such capability would substantially expand the network of accessible emergency landing sites, enhancing response time and system efficiency for future medical AAM operations.

4. Discussion

4.1 Use Case Challenges

Although AAM is often envisioned around the high-profile air taxi concept in megacities, focusing exclusively on dense metropolitan areas or congested airports may hinder near-term feasibility.

The development of AAM should therefore begin with simpler, regionally adaptable use cases where airspace and public acceptance barriers are lower—such as emergency medical services, logistics, or island and rural mobility. These applications can serve as testbeds for regulatory learning and operational validation.

4.2 Vehicle Challenges

From a technological perspective, three issues dominate AAM vehicle development. First, energy storage remains a major bottleneck. While lithium-ion batteries have enabled early eVTOL prototypes, their energy density is insufficient for longer missions. Even with anticipated progress in solid-state batteries, range and endurance remain uncertain, particularly under Japan's humid climate and safety regulations. Second, vehicle cost—both in acquisition (CapEx) and operation (OpEx)—must be significantly reduced to achieve business viability. Economies of scale will take time to emerge; therefore, lightweight materials, modular manufacturing, and shared-use business models are essential. Third, automation technologies such as autonomous or supervised takeoff and landing must mature to reduce pilot workload, minimize human error, and enable scalable operations. Safety certification of such autonomy functions will require new standards that balance aviation-grade reliability with automotive-level cost efficiency.

4.3 Infrastructure Challenges

Infrastructure constraints represent another major barrier to AAM implementation. First, airspace management must evolve from traditional VFR/IFR to include Digital Flight Rules (DFR) and defined low-altitude corridors that ensure safe coexistence with helicopters, drones, and conventional aircraft. Japan's complex airspace, particularly around Tokyo and Haneda Airport, already imposes strict altitude and routing limits that restrict UAM operations. Second, vertiport availability remains limited. Current heliports and emergency rooftop pads are insufficient for regular AAM use, as they lack proper approach paths, passenger access routes, and safety clearances. Future urban development must therefore incorporate vertiport-ready building designs. Third, social acceptance will depend on noise mitigation and visual integration with urban environments. Although electric propulsion reduces acoustic signatures, community-level engagement will be necessary to establish operational trust and regulatory approval.

5. Conclusion

This study examined two representative use cases of Advanced Air Mobility (AAM) in Japan through a systems approach perspective. The analysis demonstrated that AAM is not merely a new aviation technology but rather a system of systems that integrates vehicles, infrastructure, operations, regulations, and social acceptance in a highly interdependent manner.

For future research, a quantitative evaluation framework should be established that links the sequence of use case definition → technical specifications → adoption probability modeling → estimation of economic impacts. Such a systems-based framework would enable multi-dimensional assessment of AAM feasibility under regional conditions and support decision-making for both technology development and policy design.

Acknowledgement

The author gratefully acknowledges the financial support of the Keio University Flying Car Research Laboratory.

References

[1] W. Johnson, and C. Silva, "NASA concept vehicles and the engineering of advanced air mobility aircraft", The Aeronautical Journal, Vol.126, p.59-91, 2022. https://doi.org/10.1017/aer.2021.92

[2] Ministry of Economics, Trade, and Industry, "Concept of Operations for Advanced Air Mobility", Public-Private Council for Air Mobility Revolution, 2024.

[3] M. Nakano, et al, "The Mechanism of Flying Cars: How System Design Integrating Technology and Service Drives a Mobility Revolution", The Daily Industry News, 2019.

[4] J. Holden, and N. Goel, "Fast-forwarding to a future of on-demand urban air transportation", Uber Elevate, 2016.

[5] P. Vascik, and J. Hansman, "Scaling constraints for urban air mobility operations: Air traffic control, ground infrastructure, and noise", 2018 aviation technology, integration, and operations conference, p.3849, 2018. https://doi.org/10.2514/6.2018-3849

[6] D. Gunady, S. Patel, and D. DeLaurentis, "A system-of-systems approach to analyzing future advanced air mobility cargo operations", IEEE 17th Annual System of Systems Engineering Conference, p.368-373, 2022. https://doi.org/10.1109/SOSE55472.2022.9812637

[7] A. Kirste, E. Stumpf, "Multidisciplinary Optimization of Advanced Air Mobility Fleet Operations", AIAA SCITECH 2025 Forum, 2025. https://doi.org/10.2514/6.2025-2170

[8] The Vertical Flight Society, "eVTOL Aircraft Directory", eVTOL.news, 2025.

[9] Y. Mihara, M. Nakano, " Modelling and Simulation of the Impulsive Load in the Emergent Landing of an Urban Air Mobility for Designing a Safe Vertiport", The Japan Society for Aeronautical and Space Sciences, Vol.69, No.3, p.98-104, 2021. https://doi.org/10.2322/jjsass.69.98

[10] Ministry of Land Infrastructure, Transport and Tourism East Japan Civil Aviation Bureau, "Airport and Heliport List", https://www.cab.mlit.go.jp/tcab/conditions/02.html, Access 2025-11-08, 2025.

[11] Tokyo Fire Department, "Establishment of standards for rooftop emergency takeoff/landing areas", https://www.tfd.metro.tokyo.lg.jp/lfe/office_adv/heri_chaku.html, Access 2025-11-08, 2022.

[12] Y.Mihara, P. Pawnlada, M. Nakano, et al, " Cost analysis of eVTOL configuration design for an air ambulances system in Japan", Council of Engineering Systems Scholars and Universities 2021. https://doi.org/10.5703/1288284317285

[13] Ministry of Land, Infrastructure and Transport, "Haneda Airport for Tomorrow", https://www.mlit.go.jp/koku/haneda/public/pdf/haneda_Pamphlet_english_vol2.pdf, Access 2025-11-08, 2020

[14] Emergency Medical Network of Helicopter and Hospital, "What is a Doctor Helicopter?", https://hemnet.jp/know-about, Access 2025-11-08, 2024.

[15] Y.Motomura, et al, "Changes in doctor helicopter activities and air medical transport in large-scale disasters in Japan", Japan Journal of Disaster Medicine, Vol.29, No.1, 2024.

[16] Y.Mihara, M.Nakano, et al, "Airframe design optimization and simulation of a flying car for medical emergencies", International Journal of Automation Technology, Vol.16, No.2, p.183-196, 2022. https://doi.org/10.20965/ijat.2022.p0183

[17] A.Nakamoto, et al, "Analysis of Newly Available Takeoff and Landing Sites for Emergency Medical Flying Cars", Journal of Japanese Society for Aeromedical Services, Vol.26, No.1, 2025.

Materials Research Proceedings 69 (2026) 431-435 https://doi.org/10.21741/9781644904251-78

Fire Fighting System Integration on C-27J Aircraft

Francesco GIUGLIANO[1,a *], Fabio CHIACCHIO[1,b], Pierpaolo BORRELLI[1,c], Marco DI GIFICO[2,d], Rosalia GRAZIANO[2,e] and Salvatore PANICO[1,f]

[1]Leonardo Aeronautics, Aircraft Business Unit, Viale dell'Aeronautica SNC, 80038 Pomigliano d'Arco, Italy

[2]Leonardo Aeronautics, Aircraft Business Unit, Corso Francia 426, 10146 Torino, Italy

[a]francesco.giugliano02@leonardo.com, [b]fabio.chiacchio@leonardo.com, [c]pierpaolo.borrelli@leonardo.com, [d]marco.digifico@leonardo.com, [e]rosalia.graziano@leonardo.com, [f]salvatore.panico@leonardo.com

Keywords: Fire Fighting, System Integration, Aircraft Capability Enhancing, Virtual Modelling, Computational Fluid Dynamics, Flight Testing Optimization

Abstract. The C-27J Fire Fighting program was born from the growing need in the fight against forest fires for a fixed-wing platform that is complementary to the Canadair fleet (CL-415) in a national and international context. It aims to create a firefighting version of the C-27J transport aircraft through the integration of an additional module and the related certification and industrialization, enhancing its multi-role capability. The work aims at presenting the modelling, simulation and testing activity performed in 2024 through the integration of a prototypical System on C-27J. The analytical approach developed and validated during this phase will be used to support the development of the first series unit of the System, where issues in terms of Centre of Gravity excursion will be more important because of the increase in payload.

Introduction

During 2024, the development activity related to the integration of a pressurized Fire Fighting System on the Leonardo C-27J® cargo aircraft in order to increase its multi-role capability was completed.

This activity consisted of the design, manufacturing and testing of a System suitable for market needs in terms of capabilities, performances and costs. System integration on C-27J did not require A/C modification (only control panel installation in central console and connections with A/C power supply are required).

The first chapter of this project (called POC = Proof Of Concept) regarded a feasibility phase, performed with a prototypical System, aimed at investigating the main aspects related to the integration of such a System on the C-27J and the verification of target performances. During this phase, particular attention and efforts have been devoted to the following aspects:

- Controllability and Handling Qualities (HQ) of the aircraft in the presence of the asymmetric thrust (up to 50 kN) generated by the System during the pressurized drop
- Verification of the aircraft's Centre of Gravity (CoG) under all operational conditions on the ground and in flight in the presence of the sloshing phenomena of the retardant fluid contained in the System tank (payload of 5500 liters).

Particular attention was paid to the verification of the CoG as preliminary assessments highlighted the risk of exceedance from the flight envelope due to the possible transfer of fluid from the discharge duct to the tank under intermediate fill conditions.

Content from this work may be used under the terms of the Creative Commons Attribution 3.0 license. Any further distribution of this work must maintain attribution to the author(s) and the title of the work, journal citation and DOI. Published under license by Materials Research Forum LLC.

Materials Research Proceedings 69 (2026) 431-435 https://doi.org/10.21741/9781644904251-78

System Modelling

HQ and CoG aspects were predicted during the development phase through modelling and simulation:

- Geometric modelling of the fluid volume using CAD software "CATIA V5" for static centering analysis with respect to the aircraft Weight & Balance (W&B) envelope
- Study of sloshing phenomena and design solutions for their containment (baffles for fluid oscillations damping in the tank and check-valve between the discharge pipe and tank to inhibit pouring occurrence) through fluid dynamics simulations with CFD software "STAR CCM+" (see Fig. 1)
- Development of an algorithm in MATLAB Simulink for the Flight Engineering Simulator able to reproduce the behavior of the liquid in the tank.

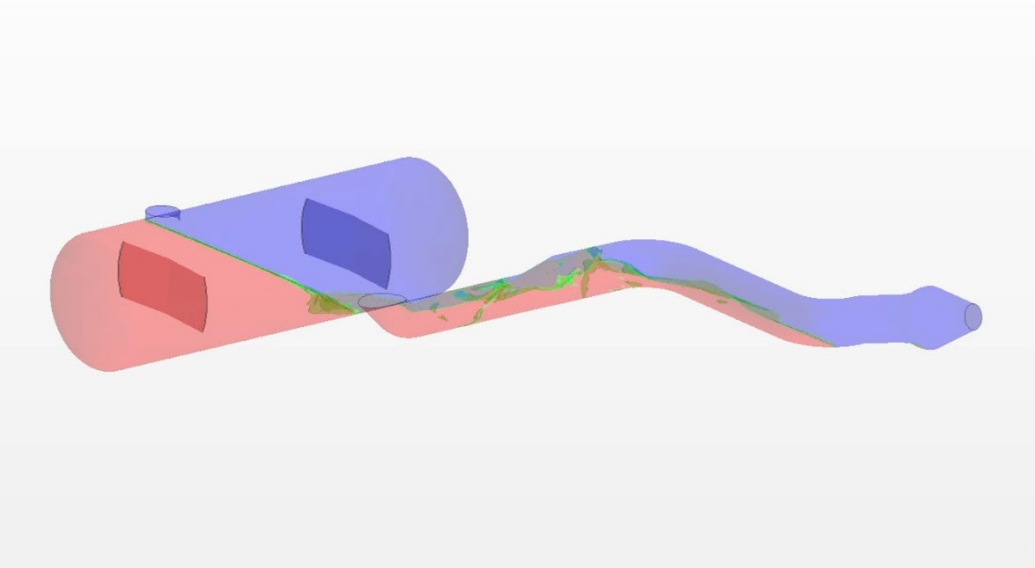


Figure 1: System at a representative instant during sloshing simulation

CFD simulations were carried out in order to reproduce the liquid transfer phenomena from the discharge pipe to the tank that static analyses are unable to capture. The results of these simulations were used to calibrate the constants of the pendulum equation on which the virtual digital model of the System is based:

$$m_{tank} \cdot \ddot{\theta} + c \cdot \dot{\theta} + k \cdot \theta = \frac{m_{tank} \cdot g}{l} \cdot \left(\frac{n_X}{n_Z} \cdot \cos\theta + \sin\theta \right) \quad (1)$$

Where:

- n_X, n_Y and n_Z are the load factors along X, Y and Z axis respectively (input parameters);
- $g = 9.81 \ \frac{m}{s^2}$ is the gravitational acceleration;
- m_{tank} indicate the liquid mass contained in the tank (output parameter);
- c, k and l are the damping, the stiffness and the length associated to the pendolum model;
- $\dot{\theta}$ and $\ddot{\theta}$ are respectively the angular speed and the acceleration of the apparent pitch angle $\theta = \tan^{-1}\left(\frac{n_X}{n_Z}\right)$ experienced by the aircraft.

Eq. 1 obtains the longitudinal CoG coordinate of the tank:

$$X_{tank} = l \cdot \cos\theta \quad (2)$$

Materials Research Proceedings 69 (2026) 431-435 https://doi.org/10.21741/9781644904251-78

The performed analyses allowed to:

- Discard the hypothesis of introducing a check-valve (which would have negatively affected System performance and aircraft safety)
- Support the clearance issuance and the Permit to Fly (PtF) request.

Next, an incremental approach was defined to safely perform the flight activity starting from a full-fill condition, validating the analysis results and progressively reducing the quantity through the following process:

1. Conduction of braking taxi tests up to the Rejected Take-Off (RTO) condition with tank in intermediate fill conditions for model validation
2. Execution of flight test with tank in full condition
3. CFD model validation using data acquired during the test like accelerations and tank liquid level measurements (see Fig. 2)
4. Prediction of the results of the next flight with reduced quantity in terms of dynamic behavior of the liquid and CoG displacement
5. Verification of absence of CoG exceedances with respect to the flight envelope
6. Repetition of steps 2-5 with progressively reduced quantities.

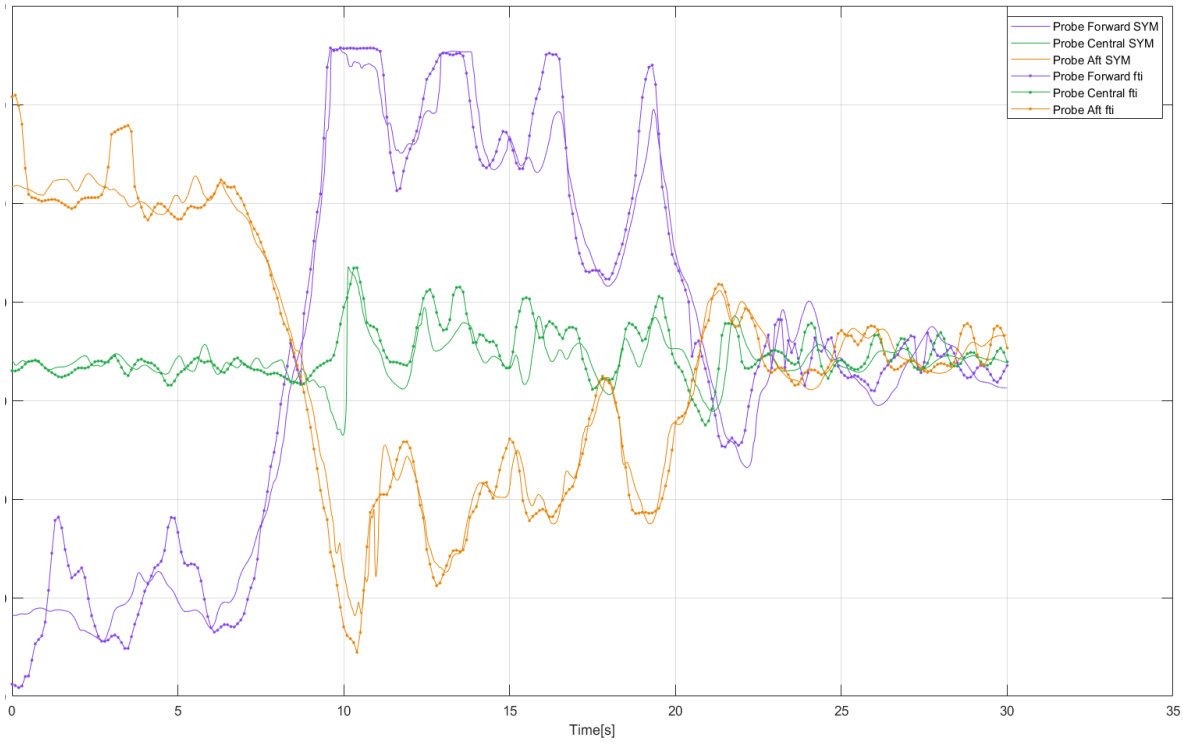


Figure 2: Comparison between measures of tank probes acquired during a test and results of CFD simulation

The results of the experimental campaign made it possible to remove the full tank limitation and validate the virtual model of the System, which demonstrated high reliability in predicting the dynamic behavior of the liquid and the performance of the System.

The analytical approach developed and validated during the PoC phase will be used to support the development of the first series unit of the System (called System Version 1 = SV1), where issues in terms of CoG will be more important as a result of the increase in payload up to 7500 liters.

Materials Research Proceedings 69 (2026) 431-435 https://doi.org/10.21741/9781644904251-78

Performance Measurement

From the performance point of view, it was verified during the testing phase by conducting ground and flight tests:

- Ground functional tests on the aircraft under all operational and emergency conditions
- In-flight functional tests with water and retardant under all operational and emergency conditions at a safe altitude
- Flight tests with water and retardant (see Figure 3) to measure performance in terms of Ground Pattern Coverage (GPC 1 = 1 gallon/100 squared feets) at 60-100 feets above the ground
- Flight testing by performing maneuvered drops under conditions similar to those experienced in an operational scenario based on what the Fire Fighting end-users reported during the demo campaigns.



Figure 3: C-27J Fire Fighter dropping retardant on the test range

System performance was measured using dedicated Flight Test Instrumentation (FTI) improving existing methods ([1], [2]). It consisted of 400 smart cups arranged to form a grid, of which they constitute the nodes, that maps the surface affected by the drop. The units are connected via radio to a master unit, which allows measurement management, data collection and system diagnostic. The master unit provides in output a coverage report with values expressed in GPC.

During this activity, it was necessary to demonstrate the achievement of GPC 6 performance, which guarantees the effectiveness of the Fire Fighting System against medium and heavy smash fires [3]. According to the criteria defined by the Interagency Airtanker Board [4], with a payload of 5500 liters the GPC 6 target is achieved when a minimum length of line of 140 ft is produced on ground. This result was successfully achieved and overcome during the experimental campaign (see Fig. 4).

Materials Research Proceedings 69 (2026) 431-435 https://doi.org/10.21741/9781644904251-78

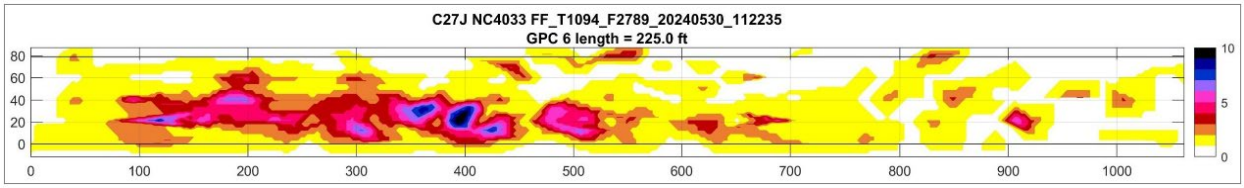


Figure 4: GPC footprint measured with dedicated FTI after a drop on test range (flight direction from right to left)

Conclusions and Next Steps

During 2024, the development activity related to the integration of a prototypical Fire Fighting System on C-27J in order to increase its multi-role capability was completed. HQ and CoG aspects were predicted through modelling and simulation. The virtual model of the System, calibrated with CFD simulations and implemented at the Flight Engineering Simulator, was validated via flight tests and allowed to gradually remove liquid filling limitation. In addition, System performance was successfully verified, using dedicated FTI improving existing methods. The analytical approach developed and validated during this phase will be used to support the development of the first series unit of the System, where issues in terms of CoG excursion will be more important because of the increase in payload.

References

[1] A. Suter, Drop testing airtankers: a discussion of the cup-and-grid method, 2000

[2] A. Suter, Gum-Thickener Study - Drop Test for Firefighting Operations, Marana, AZ, 2017

[3] G. Johnson, C. Jordan, Ground Pattern Performance of the Marsh Turbo Thrush, Airtanker Drop Guides, 0057-2835-MTDC, April 2000

[4] Procedures and Criteria for the Interagency Airtanker Board (IAB), 2013

Materials Research Proceedings 69 (2026) 436-441 https://doi.org/10.21741/9781644904251-79

Conceptual Design for Uncrewed Combat Aircraft through a Modular Low-Fidelity MDO Workflow

Lorenzo VISCONTI[1,a,*], Giovanni ZIPPA[2,b], Paolo BADER[1,c]

[1]Leonardo Aeronautics, Aircraft Business Unit, corso Francia 426, 10146 Torino, Italy

[2]Leonardo Aeronautics, Aircraft Business Unit, via P. Foresio, 1, 21040 Venegono Superiore, Italy

[a]lorenzo.visconti@leonardo.com, [b]giovanni.zippa@leonardo.com, [c]paolo.bader@leonardo.com

Keywords: Multidisciplinary Design Optimization (MDO), Plug and Play Architecture, Design of Experiments (DOE), Initial Design Point (IDP), Radar Cross Section (RCS)

Abstract. An automated Multidisciplinary Design Optimization (MDO) process has been developed to support the conceptual design of uncrewed combat aircraft. This methodology integrates low-fidelity simulations to enable fast design space exploration, facilitating informed trade-offs between key engineering disciplines such as aerodynamics, weight estimation, and propulsion. It was chosen as the validation exercise a typical aircraft configuration for Loyal Wingman class, also in view to explore the design space of baseline configuration reflecting platform as Kratos XQ-58A, Boeing MQ-28, and others, Among the investigated layouts, the V-tail merged as a promising layout, offering maneuverability, scalable payload capacity, and low radar observability.The process architecture foresees to start with the parametric CAD modeling of a conceptual configuration (e.g., V-tail). Geometry is automatically generated through scripting based on modifiable input variables, ensuring real-time synchronization with analytical modules. This tight integration allows for continuous geometry control and significantly reduces iteration time. The overall architecture is modular: each block (aerodynamics, weights, propulsion, etc.) is independent and replaceable, allowing seamless updates or substitutions without disrupting the full system. The workflow can incorporate commercial tools, open-source software, or in-house developments. A key advantage lies in the system's ability to perform multi-objective optimization via automated Design of Experiments (DoE). Results are evaluated using performance indicators (KPIs), enabling the identification of an optimized baseline configuration consistent with project constraints. Compared to traditional approaches, this solution offers: wide design space exploration in short timeframes, minimal computational requirements (workstation-executable), immediate readiness for configurational multi-objective trade-off analysis and sensitivity mapping. The workflow is structured to feed into high-fidelity design phases, ensuring continuity between conceptual and preliminary design while reducing data loss and transition time.

1. Introduction

The current aerospace landscape is witnessing a paradigmatic shift toward unmanned combat aircraft as autonomous systems capable of operating in high-threat environments. This transformation requires innovative design methodologies that can rapidly explore vast design spaces to identify the most performing configurations that comply with customer goals. The V-tail configuration has emerged as a particularly promising architecture, offering several distinctive advantages: examples include avionics and armament payload capacity (internal and external), and a predisposition to medium-high maneuverability with a two surfaces only as empennages. This aspect introduces benefits also from the low observability standpoint: V-tail configurations present canted flat surfaces, contributing to radar cross section reduction across the waterline when appropriately optimized.

Content from this work may be used under the terms of the Creative Commons Attribution 3.0 license. Any further distribution of this work must maintain attribution to the author(s) and the title of the work, journal citation and DOI. Published under license by Materials Research Forum LLC.

Materials Research Proceedings 69 (2026) 436-441 https://doi.org/10.21741/9781644904251-79

This work presents a comprehensive multidisciplinary workflow specifically adapted for conceptual design, incorporating a modular architecture that enables plug-and-play integration of multidisciplinary analysis modules. The framework is based on the necessity of rapid design space exploration, integration of stealth considerations from conceptual phases, and transition from low-fidelity conceptual models to high-fidelity detailed analyses.

2. Methodology and Architecture of the Workflow

2.1 Adaptation of the Low-Fidelity Workflow for Specific Configurations

The developed process begins with the reconstruction of a conceptual model geometry, which serves as a baseline. This geometry is then parametrized using a set of geometric relationships that define each aircraft component (e.g., fuselage, wing, V-tail) based on a set of input variables. These formulas automatically update the geometry whenever parameters are modified. This approach ensures that the parameters of each design are immediately available to the analytical and numerical modules within the workflow, which directly derive the inputs generated by the parametric script.

Therefore, the model geometry automatically updates based on changes in design parameters. The availability of a framework with seamless integration of typical Preliminary Design models reduces iteration times and improves design flexibility.

2.2 Plug-and-Play Modular Architecture with RCS Integration

A distinctive feature of the proposed workflow resides in its plug-and-play modular architecture, conceived to enable rapid reconfiguration of disciplinary blocks without compromising the overall process integrity. The baseline chain can be modified through standardized input-output interfaces. Each block is interchangeable, allowing adaptation of the process fidelity level according to design requirements. A typical workflow in shown in *Figure 1*.

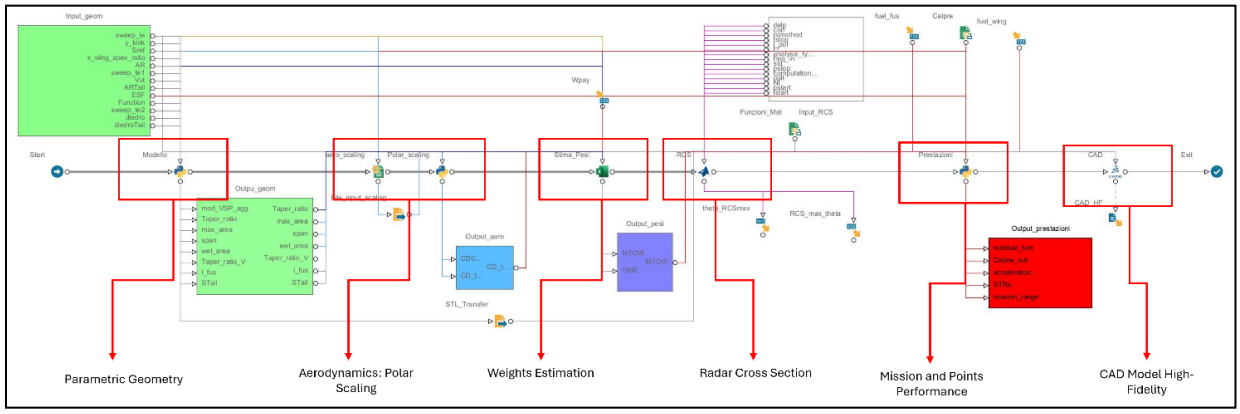


Figure 1 Multidisciplinary Workflow to Define a Design Envelope

For example, the aerodynamic block based on parametric scaling of baseline performance can be replaced with a VLM or panel method (*VSPAERO* or *FlightStream*), directly calculating the characteristics of each geometry instead of relying on a baseline scaled according to handbook methods.

The innovation of this integrated process does not reside in the individual solvers employed, but in the possibility of increasing or reducing fidelity on demand. By defining a priori the necessary inputs and outputs of each module (coherent variable names, uniform units of measurement, shared reference systems), it is possible to integrate new software into the workflow without having to redesign the global architecture. The algorithm is prone to reuse and scalability to different aircraft classes, following appropriate geometry parametrization.

Materials Research Proceedings 69 (2026) 436-441 https://doi.org/10.21741/9781644904251-79

The integration of RCS as a native discipline further expands the capabilities of conceptual design. Unlike traditional workflows, where stealth considerations are often deferred to subsequent phases with consequent design compromises, in this case RCS is treated as an interchangeable module. Based on the design stage, it can be evaluated with rapid physical-optics tools (e.g., *PoFACETS*) or with high-fidelity commercial codes.

2.3 Geometric Continuity from Low to High Fidelity

An aspect of the developed framework is the implementation of a parametric bridge to the *CATIA* CAD environment, which ensures geometric continuity from low-fidelity conceptual models to high-fidelity detailed design phases.

The CAD model in *CATIA* is parametrized upstream without resorting to scripts, but rather by applying the same parameter definition methodology used in the low-fidelity *OpenVSP* model. In this way, variables such as reference surface, aspect ratio, leading edge sweep, or tail configurations are defined in a coherent and unambiguous manner, ensuring alignment between geometries of different fidelity.

This bridge proves particularly useful in two cases:

- when it is desired to rapidly verify a design point already identified in the conceptual phase, transferring it without manual reconstructions toward the high-fidelity domain.
- when it is desired to integrate processes of different fidelity, for example using the parametric CAD geometry as input for commercial asymptotic RCS analysis codes, to evaluate low observability at low frequencies with greater accuracy.

In this way, the entire flow allows seamless transition from rapid conceptual generation to detailed engineering validation (CFD, FEM, RCS), maintaining geometric coherence, parameter traceability, and drastically reducing times and risks of manual reconstruction.

3. Loyal Wingman V-Tail Case Study

The developed workflow was applied to a Loyal Wingman case study with a V-tail configuration (as shown in *Figure 2*) for rapid definition of the design envelope.

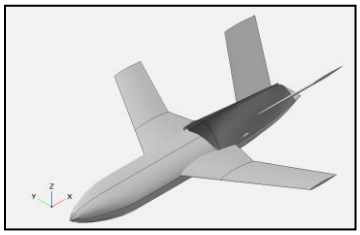


Figure 2 OpenVSP model of the Loyal Wingman

3.1 Process Timeline and Phases

One of the primary strengths of the developed process lies in its time efficiency, enabling complete execution on a single workstation. This is possible because the low-fidelity modules do not require extensive computational resources. The time constraint is critical during conceptual phases, where fast turnaround times are key factors for rapid iterations with stakeholders and support requirement definition. The algorithm employed by the workflow is outlined below:

- Parametrization and Input Preparation: this phase begins with a OpenVSP model configuration representing the conceptual layout (V-tail, flying wing, etc.), in which the geometric configuration (wing, fuselage, tail) is parametrized and the baseline reference datasets (aerodynamics, propulsion, weight) are established.
- DOE Generation and Initial Design Space Exploration: after completing the parametric definition, a Design of Experiments (DOE) is automatically generated based on

Materials Research Proceedings 69 (2026) 436-441 https://doi.org/10.21741/9781644904251-79

predefined criteria (e.g., Uniform Latin Hypercube, Full Factorial, etc.). Each DOE point is processed through the computational chain, yielding key performance indicators (KPIs).

- Design Space Evaluation with Performance Constraints for Design Zone Definition.

The IDP definition workflow including preparation typically requires two weeks. In the Loyal Wingman case *OpenVSP* model development takes 3 days, parameterization 2 days, dataset assembly 2 days and initial data analysis with baseline verification 7 days, followed by a full factorial DOE of at least 100 designs to secure design-zone accuracy.

These durations assume an existing parametric CATIA model which yields a forty-percent reduction in total timeline compared to development from scratch, since geometric logic and formulas are already available. The process duration remains largely invariant across aircraft configurations because low-fidelity methods rely on statistical and analytical techniques rather than iterative solvers; only the drag-polar extent varies for supersonic cruise, which demands a greater computation time.

3.2 Results

The design space exploration was conducted through a Design of Experiments (DOE) employing a full-factorial algorithm for the geometric input parameters that most significantly influence point performance. Two key variables were identified: the reference wing area, varied within a range of –30% to +40% relative to the baseline, and the Engine Scale Factor (ESF), varied by ±20%. The results are visualized in *Figure 3* using contours on thrust to weight ratio and wing loading graphs. The point performance metrics evaluated for this aircraft are mission range, sustained turn ratio, and ceiling.

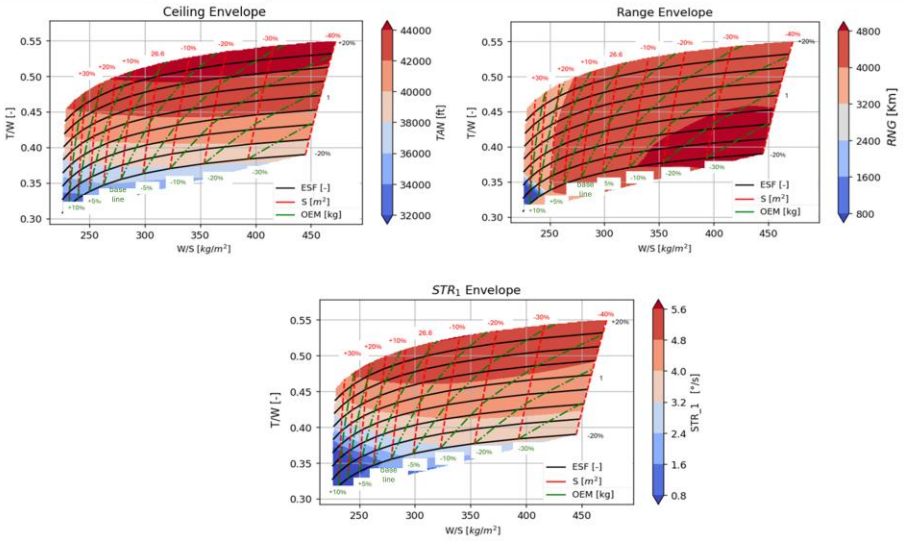


Figure 3 Point performance contours in correlation with input variables

Each design envelope represents a specific aircraft performance contour. Varying the wing area and ESF values allows visualization of trade-offs among different performance metrics. For example, a higher ESF improves sustained turn ratio and turn ceiling but penalizes mission range due to increased engine fuel consumption and weight penalty. *Figure 4* illustrates the radar cross-section analysis results. The employed methodology yields robust insights into shaping behavior trends, supplying critical guidance for directing design choices toward geometries that optimize stealth performance.

Materials Research Proceedings 69 (2026) 436-441 https://doi.org/10.21741/9781644904251-79

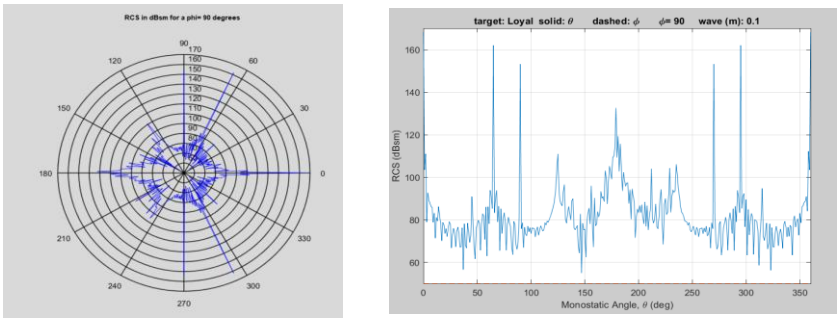


Figure 4 RCS signal of one of the generated DOE points.

Finally, the analysis identifies a design zone, shown in green in Figure 55, that satisfies all constraints. This zone therefore constitutes the design space in which ceiling, range, and sustained turn ratio meet or exceed baseline values, and RCS does not exceed the baseline maximum.

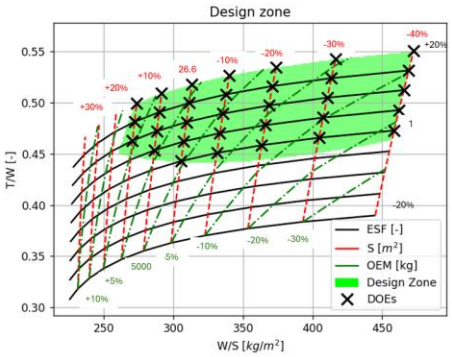


Figure 5 Final design region with overlay of data points generated through Design of Experiments (DOE)

4. Conclusion

The automated workflow represents a conceptual design methodology, addressing key challenges in defining the design space. The integration of a plug-and-play modular architecture with RCS analysis and CAD integration enables rapid exploration of the design space. The introduction of:

- A modular architecture of interchangeable blocks that clearly separates interfaces and methods, allowing rapid substitution.
- Parametric integration of preliminary RCS evaluation already from the conceptual phases, eliminating traditional discontinuities between aerodynamic design and stealth considerations. The main purpose of this assessment is to understand the criticalities of the geometrical configuration, rather than the absolute value of RCS (which would require more in-depth definitions of local geometries, like steps and gaps, and the application of RAM materials and coatings).
- A methodological bridge between low and high fidelity via CAD integration, which removes geometric inconsistencies and reduces validation times between different analysis methods for each discipline.
- A process for defining the design envelope within two weeks.

The workflow establishes a foundation for integrated design methodologies, providing the aerospace industry the tools required to address increasingly complex design challenges. The primary value lies not in the single final configuration, but in the ability to generate a design

envelope rapidly while maintaining continuity toward advanced simulations, and ensuring traceability, reusability, and accuracy throughout the entire development process.

References

[1] K. M. Mull, «Expanded MDO for Effectiveness Based Design Technologies: The EXPEDITE Program and Successes with ESTECO Technologies,» American Institute of Aeronautics and Astronautics, Inc., Orlando, FL, 6-10 January 2020. https://doi.org/10.2514/6.2020-1390

[2] D. P. Raymer, Aircraft Design: A Conceptual Approach - 6th edition, Reston, Virginia: American Institute of Aeronautics & Astronautics, September 30, 2018.

[3] L. Visconti, «Ottimizzazione multidisciplinare di un velivolo fighter nella fase di progetto preliminare,» Master thesis developed at Leonardo Aeronautics - Aircraft Business Unit, Torino, 2024.

[4] J. R. Martins et A. Ning, Engineering Design Optimization, Cambridge University Press, 2021. https://doi.org/10.1017/9781108980647

Materials Research Proceedings 69 (2026) 442-447 https://doi.org/10.21741/9781644904251-80

Most Promising Technologies and Aircraft Concepts for Environmental Performance Improvements: A Systematic Review

Lukas SÖFFING[1,a *], Elise SCHEERS[1,b], Helen SZÖKE-ERÖS[2,c], Lukas WEBER[2,d], Pascal BERTRAM[2,e], Patrick RATEI[2,f]

[1]Royal Netherlands Aerospace Centre (NLR), Anthony Fokkerweg 2, Amsterdam, The Netherlands

[2]German Aerospace Centre (DLR), Institute of System Architectures in Aeronautics, Hein-Saß-Weg 22, Hamburg, Germany

[a]Lukas.Soffing@nlr.nl, [b]Elise.Scheers@nlr.nl, [c]Helen.Szoeke-Eroes@dlr.de, [d]Lukas.Weber@dlr.de, [e]Pascal.Bertram@dlr.de, [f]Patrick.Ratei@dlr.de

Keywords: Environmental Performance Improvement, Roadmaps, Aircraft Technologies, Aircraft Concepts

Abstract. A systematic review of the most promising technologies and aircraft concepts for reaching climate-neutral aviation is presented, based on a technology scouting for classification and benchmarking of their environmental performance. In a first step, a heuristic approach is used to analyse existing technology roadmaps on reducing environmental impact. The main levers commonly identified are technology advancements, operational measures, sustainable aviation fuel and demand management. The aircraft technologies from the aviation roadmaps are classified in a technology taxonomy in the categories aerodynamics, structural, systems and propulsion technologies and the entry-into-service is visualised in technology roadmaps. In a second step, an overview and categorisation of recent developments in advanced and disruptive (regional, short/medium and long-range) aircraft concepts is compiled. Environmental performance improvements can reach up to 40-50% (kerosene fuel burn and CO_2) and 70% (NO_X) compared to older reference aircraft, with reductions dependent on reference aircraft age. Hydrogen combustion offers zero CO_2 while hydrogen fuel cells offer zero CO_2 and NO_X emissions. Different architectures are used for various ranges: Blended wing body and tube and wing (long-range), tube and wing (regional), and box-wing, double-bubble, strut-braced wing and tube and wing (short/medium range). While it is not possible to attribute a single reduction potential to a single technology feature, the most promising fuels are kerosene (conventionally, or in combination with batteries or fuel cells), sustainable aviation fuel and hydrogen. From the propulsion concepts, innovative turbofans (e.g. ultra-high bypass ratio turbofans) and innovative engines (e.g. hybrid-electric fans) had large improvements. In the field of aerodynamics, most applied technologies are high aspect ratio wings, riblets and laminar flow control, furthermore most concepts applied composite materials. For some aircraft concepts the climate impact was measured using climate metrics like ATR100 or GWP100, revealing trade-offs between fuel burn and climate impact or NO_X emissions.

Introduction

The aviation sector moves towards climate neutral aviation, with the goal of reaching Net Zero CO_2 emissions in 2050 [1, 2, 3]. Therefore, technological advancements are needed to reduce fuel burn and the resulting emissions. In Europe, Clean Aviation will contribute to Europe's climate neutrality by developing and implementing aircraft new technologies [4]. The concepts of a hybrid electric regional aircraft and short/medium range aircraft, both with a tube and wing architecture, have the overall target of a 30% CO_2 emission reduction compared to an aircraft with 2020 state-

Content from this work may be used under the terms of the Creative Commons Attribution 3.0 license. Any further distribution of this work must maintain attribution to the author(s) and the title of the work, journal citation and DOI. Published under license by Materials Research Forum LLC.

Materials Research Proceedings 69 (2026) 442-447 https://doi.org/10.21741/9781644904251-80

of-the-art technology. A hydrogen-powered aircraft, either with H_2 direct combustion or a fuel cell-powertrain, would lead to 100% in-flight CO_2 reductions. The objective of the Clean Aviation project CLAIM is to translate these goals into tangible (climate) metrics and recommend an assessment methodology. As an input for a performance assessment of Clean Aviation-like aircraft concepts, a technology scouting has been performed to classify and benchmark technologies and aircraft concepts in terms of environmental performance, providing guidance for future research and deployment efforts.

In this paper the most promising aircraft technologies for emission savings are investigated by reviewing recent technology roadmaps [5]. Additionally, it compares the potential of sized aircraft concepts with different architectures and utilised technologies on an aircraft basis and linking the improvement potential to the utilised technologies [6].

Methods

A literature research was conducted to identify key trends and developments in aircraft technologies. The scouting of technology roadmaps comprised roadmaps, aviation strategies, pathways and projections from international authorities, government agencies and (non-) governmental associations. The roadmaps[1] and the mentioned technologies are classified along a defined taxonomy, to enable a fast analysis and comparison. The categories are: aerodynamics, propulsion, systems, structural, architecture/concepts, air traffic management (ATM) and (Aero) Acoustics. Information is collected on the entry-into service, interdependencies, technology readiness level (TRL), market segment, estimated market penetration and considered benefits. The results are saved in a technology database which enables the analysis and comparison of the different technologies, the identification of more progressive and conservative sources, key technologies and technology groups.

In a second step, a structured literature review on advanced and disruptive aircraft concepts was performed, considering research programs, research papers and commercial developments.

For an aircraft concept to be included in this assessment, its environmental performance must be defined relative to a reference aircraft. This can be determined through indicators such as fuel burn reduction, CO_2 or NO_X emissions, or an overall climate impact evaluated using dedicated climate metrics. The concepts were then categorised by study context, aircraft class, aircraft architecture, fuel/energy source, propulsion concept, aerodynamic concepts, and structural concepts. The collected data was analysed to provide insights into the potential environmental improvement of these advanced and disruptive aircraft concepts.

Results

All roadmaps recognise current challenges in aviation with the overall goal to decouple future growth from emissions and their resulting climate effects. The main levers are technology advancements, consisting of fuel efficiency increase and a shift towards zero carbon technologies, operational measures, SAF deployment and demand management. Without economic measures, net zero CO_2 emissions will not be reached within the sector by 2050. Non-CO_2 emissions are mostly only incorporated as a future goal and more mitigation measures are needed to reach net zero climate impact of aviation.

Through an in-depth analysis of the technologies, a database of 117 technologies, architectures, and concepts was established. Some technologies are specific to individual market segments, while others can be applied across multiple aircraft types. The technology references (if given) also vary from technologies from the year 2000 and technologies about to enter service or currently in service. Generally, there is an agreement on which type of future aircraft concepts are needed, however the expected entry-into-service (EIS) date varies:

- Sub-regional zero-carbon electric aircraft (EIS 2029-2030)

[1] The list of investigated roadmaps can be found in the CLAIM D3.1 report [5].

Materials Research Proceedings 69 (2026) 442-447 https://doi.org/10.21741/9781644904251-80

- Regional aircraft (hybrid electric EIS 2029-2040 or zero-carbon EIS 2036-2040)
- Narrow body aircraft (ultra-efficient EIS 2033-2040 or zero-carbon EIS 2042-2050)
- Wide body aircraft (ultra-efficient EIS 2042-2050 or zero-carbon EIS 2050)

The key technology groups are hybridisation and electrification, sustainable aviation fuel (SAF) upscaling, (liquid) hydrogen aircraft enabling technologies (direct combustion, fuel cell propulsion), ATM and operational technologies, and knowledge and research needs (especially for non-CO_2, fuel characteristics and operations).

Along with the most frequently mentioned technologies, technology roadmaps were developed. An example[2] for the group 'Propulsion Technologies' is given in Figure 1, where the new technologies are matched with the future aircraft type that they could be deployed on and an estimation of the entry-into-service (EIS) is given.

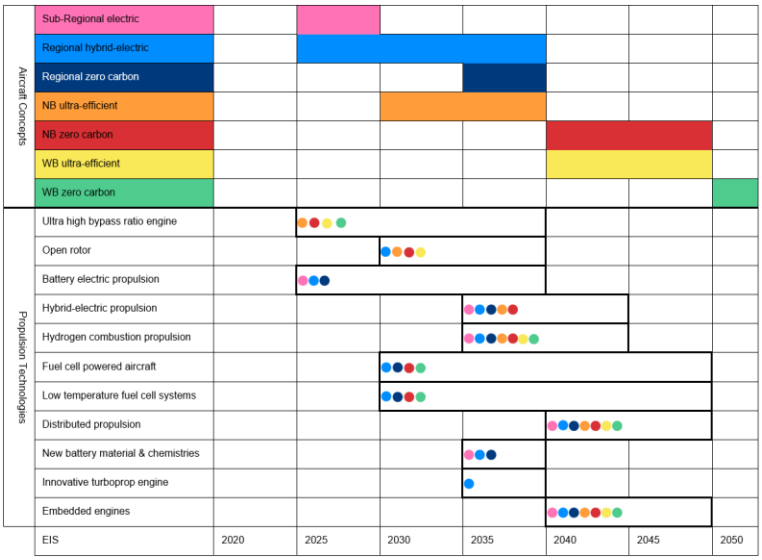


Figure 1: Roadmap for propulsion technologies

In the second step, 161 disruptive or advanced aircraft concepts[3] were found and analysed with respect to climate impact parameters fuel burn, CO_2 emissions, NO_X emissions and other climate metrics. The reported kerosine fuel burn reductions were up to 40-50% compared to traditional reference aircraft (EIS before 2015). Smaller gains were observed compared to state-of-the-art reference aircraft (EIS between 2015 and 2025), and even smaller gains compared to future reference aircraft (EIS after 2025). This is due to the fact that the more recent or future reference aircraft already include technology advancements with the connected benefits in fuel burn reductions. For some aircraft concepts, the fuel burn even slightly increases which stems from a trade-off with other climate effects.

The overview of CO_2 emission reductions in Figure 2 looks similar as the kerosene fuel burn reductions, because for aircraft concepts that only use kerosene or SAF[4] (and potentially batteries) as fuel, the reduction of kerosene fuel burn equals the reduction of CO_2. However, hydrogen aircraft stand out, as they lead to a 100% CO_2 reduction potential.

[2] More roadmaps for aerodynamic, system, structural and ATM technologies can be found in the CLAIM D3.1 report [5].
[3] The list of investigated aircraft concepts can be found in Appendix B of the CLAIM D3.2 report [6].
[4] Tank-to-wake emissions of SAF are taken into account, not considering well-to-tank CO_2 reductions and a possibly higher energy content of SAF.

Materials Research Proceedings 69 (2026) 442-447 https://doi.org/10.21741/9781644904251-80

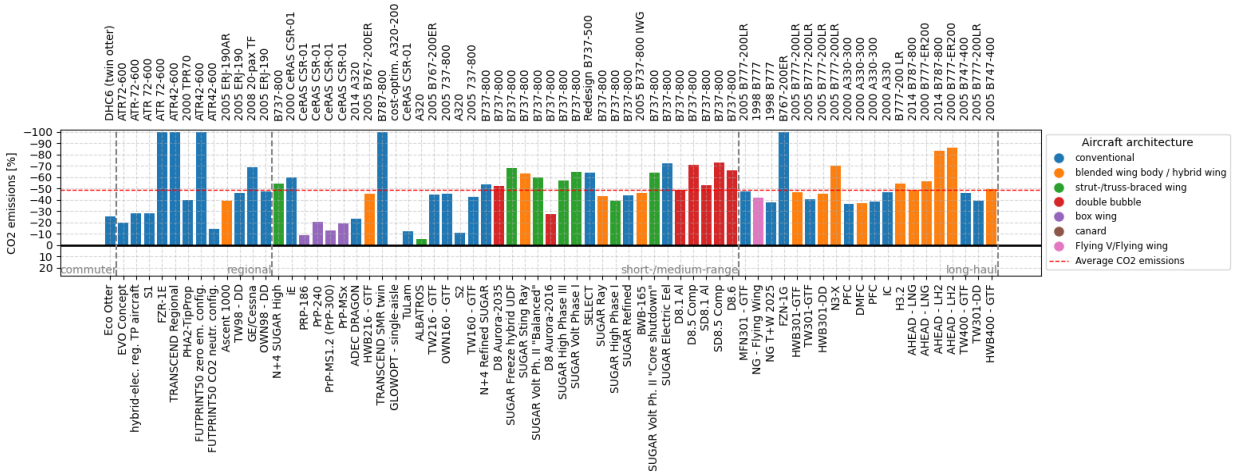


Figure 2: CO_2 emissions compared to traditional reference aircraft (EIS before 2015)

For NO_X emissions, reductions up to 70-80% were found compared to traditional reference aircraft (EIS before 2015). A plausible explanation for the high reduction values is that the NO_X reductions were a specific target for a subset of the investigated aircraft concepts. A few concepts lead to higher NO_X emissions due to trade-offs with CO_2 emissions.

It is hard to attribute general emission reductions to specific aircraft technology features and architectures. Some concepts apply only one or a few new technologies while other concepts have the intention to include a large number of technologies that are realistic for a future EIS. The aircraft concepts with several technologies are conceptualised to explore the possibilities of environmental impact reduction or to assess the integration and interaction of the different technologies. The relationship between the aircraft architecture and kerosene fuel burn reduction potential is complex, as multiple factors have an influence, such as energy carrier, aerodynamics, propulsion and structural advanced technology. From the overview, e.g. in Figure 2, it is not possible to identify one specific aircraft architecture that clearly leads to higher environmental performance improvements. One can observe that the blended wing body aircraft architecture and tube and wing architecture are mostly used for long-range aircraft and that commuter and regional aircraft mostly use a tube and wing architecture. For short/medium range aircraft more different aircraft architectures are explored such as tube-and-wing, box-wing, double-bubble or strut-braced wing aircraft architectures.

To identify promising technologies heat maps are used, an example is given in Figure 3. The heat map shows which technologies are utilised on which aircraft concepts and in which combinations the technologies are deployed. The metric, either kerosene fuel burn, CO_2 emissions or NO_X emissions, is visualised in a colour scheme, which is identical for each concept(/row), as it is not possible to attribute a single reduction potential to a single technology feature.

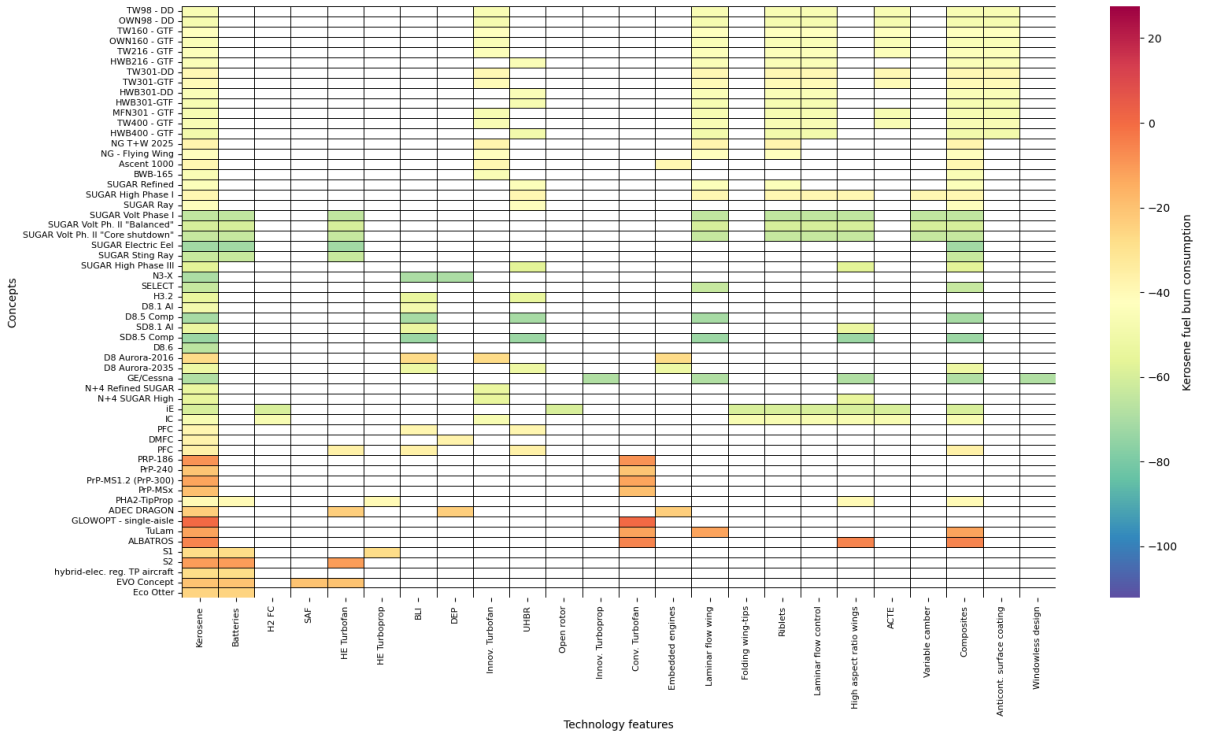


Figure 3: Heat map of the effect of technology features on fuel burn consumption compared to traditional reference aircraft (EIS before 2015)

The most promising fuels include sustainable aviation fuel (SAF) and hydrogen, while even kerosene-powered aircraft (either conventionally, or in combination with batteries or fuel cells) showed significant performance improvements. From the propulsion concepts, innovative turbofans (such as ultra-high bypass ratio turbofans), innovative engines (e.g. hybrid-electric fans) and to a certain extend the aero-propulsive concept of boundary-layer ingestion (BLI) had large improvements. For regional concepts, the hybrid electric powertrain enables distributed electric propulsion. In the field of aerodynamics, most applied technologies are high aspect ratio wings, drag reduction (e.g. riblets for skin friction drag reduction) and laminar flow control which can be well combined with high aspect ratio wings. In terms of structural technologies, the most concepts applied composite materials. Some concepts even include improvements in operations and from air traffic management (ATM) in their environmental reduction potential.

Discussion

Some of the roadmaps are more conservative whereas others are more progressive in the estimations. The entry-into-service window of a technology can be large or vary according to the source. Older sources, and the most progressive ones even foresee the EIS of some technologies in the timeframe 2025-2030 which seems questionable with today's knowledge.

The energy carrier strongly influences the CO_2 and NO_X reduction potential with hydrogen and batteries reducing CO_2 emissions by 100%. Purely battery-electric concepts were beyond the scope of this study, as they are currently hindered by the substantial weight penalty and energy density constraint of batteries.

The data of aircraft concepts was derived from conceptual studies in which usually low-fidelity methods are used. This leads to uncertainties, which can only be reduced during later design stages.

For some aircraft concepts the climate impact was measured with a climate metric such as ATR100 or GWP100. In some cases, trade-offs between total climate impact and fuel burn (with resulting CO_2 emissions) or between NO_X emissions and fuel burn reduction (either kerosene or

hydrogen) occurred, which can lead to the deterioration of one assessment value while another one is optimised.

The here presented technology scouting of the most promising aircraft technologies served as an input for a performance assessment of Clean Aviation-like aircraft concepts, using the climate metrics ATR100 and EGWP100, showing how climate metrics can be used to benchmark and monitor new aircraft concepts and technologies [7]. Furthermore, this systematic review can provide guidance for future research and deployment.

Funding

This research has been performed in the frame of the CLAIM project (Clean Aviation Support for Impact Monitoring), which is funded by the European Union Clean Aviation Joint Undertaking program, under Grant Agreement No. 101140632.

References

[1] ICAO, "Report on the Feasibility of a Long-Term Aspirational Goal (LTAG) for International Civil Aviation CO2 Emission Reductions," International Civil Aviation Organization Committee on Aviation Environmental Protection, 2022.

[2] NLR & SEO, "Destination 2050 - A Route to Net Zero European Aviation," Royal Netherlands Aerospace Centre NLR, Amsterdam, the Netherlands, 2021.

[3] EASA, EEA, EUROCONTROL, "European Aviation Environmental Report," 2022.

[4] Clean Aviation, "Strategic Research and Innovation Agenda - Towards Disruptive Technologies for new Generation Aircraft by 2035," 2024.

[5] H. Szöke-Erös, P. Ratei, L. Weber, L. Söffing and M. Solazzo, "CLAIM D3.1 - Heuristics Approach for Environmental Impact Assessment of Technology Roadmaps and Technology Taxonomy & Mapping," 2024.

[6] L. Söffing, E. Scheers, M. Solazzo, V. Villani, L. Travascio, L. Weber, P. Bertram and P. Ratei, "CLAIM D3.2 - Advanced/Disruptive Aircraft Concepts and Architectures, Purpose-Built Research Infrastructures, and Advanced Aeronautical Research and Technology," 2025.

[7] P. Bertram, T. Lefebvre, L. Söffing, S. Zhukovska, V. Grewe and P. Ratei, "CLAIM D3.3 - Performance Analysis of Aircraft Concepts," 2025.

Materials Research Proceedings 69 (2026) 448-452 https://doi.org/10.21741/9781644904251-81

Co-design of Aircraft Configuration and Flight Profile for Match-range Operation

Lijing LIU[1,a], Christian REYNER[1,b] and Rhea P. LIEM[2,c*]

[1]The Hong Kong University of Science and Technology, Clear Water Bay, Hong Kong SAR, 999077

[2]Imperial College London, South Kensington Campus, London SW7 2AZ, United Kingdom

[a]lliubo@connect.ust.hk, [b]creyner@connect.ust.hk, [c]r.liem@imperial.ac.uk

Keywords: Match-Range Operation, Flight Profile Optimization, Aircraft Sizing

Abstract. The close coupling between aircraft system and operations is often overlooked in design frameworks, where most of them are focused on optimizing one aspect while keeping the other fixed, potentially yielding sub-optimum fuel efficiency during real world operations. This paper introduces an aircraft design optimization approach that simultaneously considers both the aircraft configuration and flight profile during the on-design process. The effectiveness of this approach is demonstrated through a comparative fuel consumption analysis using historical flight data from 2019 to 2020. This analysis provides insights into achieving greater fuel efficiency in actual operations by employing the most optimal combination of aircraft configuration and flight mission profile.

Introduction

All manuscripts must be in English, also the table and figure text. The interconnectedness between aircraft configuration designs and operations calls for the simultaneous consideration of the two systems in achieving global optimum convergence [1] within an operation-aware aircraft design optimization process. However, most of the ex- isting design platforms focus solely on optimizing one aspect while keeping the other fixed, at the expense of suboptimal fuel efficiency in real-world operational scenarios. Ideally, air- craft should be operated following the match-range concept [2], where an aircraft is operated closer to its mission range by optimizing operational practices—which likely results in lower fuel consumption and reduced trip time, leading to decreased direct operating costs (DOC). However, this concept may not be practical with the limited fleet composition that airlines operate with, where a few aircraft types are operated for a wide range of flight missions.

To assist the match range operation, we propose a co-design optimization approach to simultaneously consider both the aircraft configuration and flight profile during the on- design process—by taking into account the aircraft's expected operations learned from data. Specifically, a data-driven analysis model will be utilized to generate the top-level aircraft requirements (TLARs) for design specifications and a segmented reference mission profile as the operational constraints in flight simulation. Subsequently, geometry and mass coupling will be performed to estimate the size and structural weight of the aircraft in each of the optimization iterations. An operation-based flight profile optimization method will then be applied to the mission analysis model to estimate the optimum fuel performance for the current designed configuration.

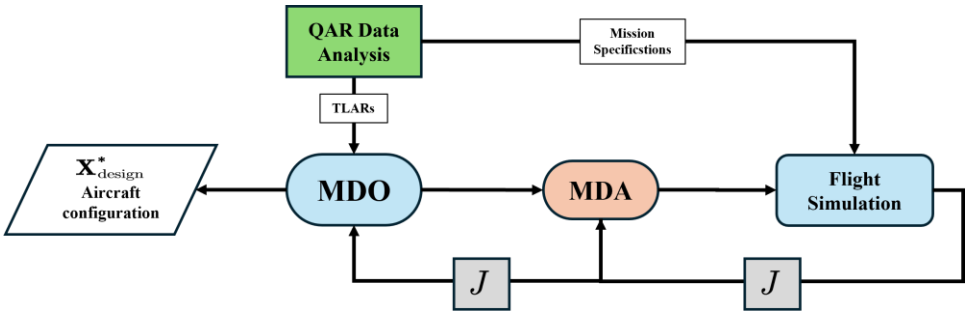
Organization of the Text

Section Headings. The section headings are in boldface capital and lowercase letters. Second level headings are typed as part of the succeeding paragraph (like the subsection heading of this paragraph). The proposed method in this study is built upon an aircraft design platform called the Multidisciplinary Airplane Research Integrated Library (MARILib)[1]. MARILib is a fully open-

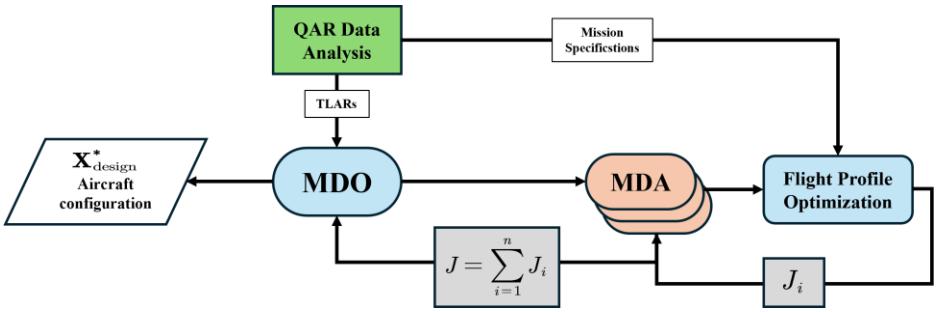
Content from this work may be used under the terms of the Creative Commons Attribution 3.0 license. Any further distribution of this work must maintain attribution to the author(s) and the title of the work, journal citation and DOI. Published under license by Materials Research Forum LLC.

Materials Research Proceedings 69 (2026) 448-452 https://doi.org/10.21741/9781644904251-81

source design optimization framework that includes models from various disciplines, and is highly adaptable for modifications [3]. The schematic of the design optimization structure in MARILib is shown in **Fig. 1a**. In the base framework, wing area $S_{\text{wing}} \in \mathbb{R}$ and reference thrust $T_{\text{ref}} \in \mathbb{R}$ are optimized for one of the objective functions $J \in \mathbb{R}$, which can be maximum takeoff weight (MTOW), mission fuel, CO_2 emission, cash operating cost, or DOC. This base framework can design an aircraft specifically optimized for a fixed design mission. **Fig. 1b** shows the proposed framework structure developed and used in this study, which is built upon MARILib and incorporates three key enhancements: 1) our in-house flight data analysis module [4] to generate mission specification and operational constraints for high-fidelity flight simulation, 2) bi-level structure allowing for simultaneously optimizing aircraft configuration and flight profile, and 3) the functionality to allow for multi-mission based optimization if the aircraft's intended operations cover more than one mission range.



(a) Base framework



(b) Proposed framework

Figure 1: Schematic flowcharts of design optimization processes.

In our framework, two design variables—i.e., reference wing area and thrust—are considered in the fuel consumption minimization problem at the design mission range. A generalized optimization formulation for the proposed framework is shown below,

$$\begin{aligned} \min_{\mathbf{X}_{\text{design}} \in \{(S_{\text{Wing}}, T_{\text{ref}})\}} \quad & J(\mathbf{X}_{\text{design}}, \mathbf{X}_{\text{TLARs}}) \\ \text{s.t.} \quad & \mathbf{g}(\mathbf{X}_{\text{design}}, \mathbf{X}_{\text{TLARs}}) - \mathbf{g}^{\text{Constraint}} \leq 0, \quad \mathbf{g} = \{g_j \mid j = 1, \ldots, 6\} \\ & \mathbf{X}_{\text{design}_{\min}} \leq \mathbf{X}_{\text{design}} \leq \mathbf{X}_{\text{design}_{\max}} \end{aligned} \tag{1}$$

where $\mathbf{X}_{\text{design}}$ represents design variables and $\mathbf{X}_{\text{TLARs}}$ are the fixed inputs other than design variables, including TLARs and default configuration parameters that users can change.

$J(\mathbf{X}_{\text{design}}, \mathbf{X}_{\text{TLARs}})$ represents the objective function for optimization, which refers to fuel consumption value(s) in this study.

Materials Research Proceedings 69 (2026) 448-452 https://doi.org/10.21741/9781644904251-81

The flight profile optimization (FPO) module within each multidisciplinary design analysis (MDA) iteration is set up based on our previous work [5]. The schematic representation of the method used to obtain the optimal trajectory under constrained conditions is illustrated in **Fig. 2**. Preprocessed flight data are utilized to establish operational constraints for each flight phase, including flight speeds and altitudes. These constraints are analyzed using a mission analysis (MA) model to determine the climb fuel consumption (m_{fuel_1} in **Fig. 2**) and the flight states at the top of constant CAS climb segment [6]. Afterwards, the optimal cruise profile and fuel consumption (m_{fuel_2} in **Fig. 2**) during the cruise segment are determined by a continuous cruise climb operation (CCO) model, which is followed by the MA to solve the fuel consumption and flight dynamics for the rest of the flight phases (m_{fuel_3} in **Fig. 2**).

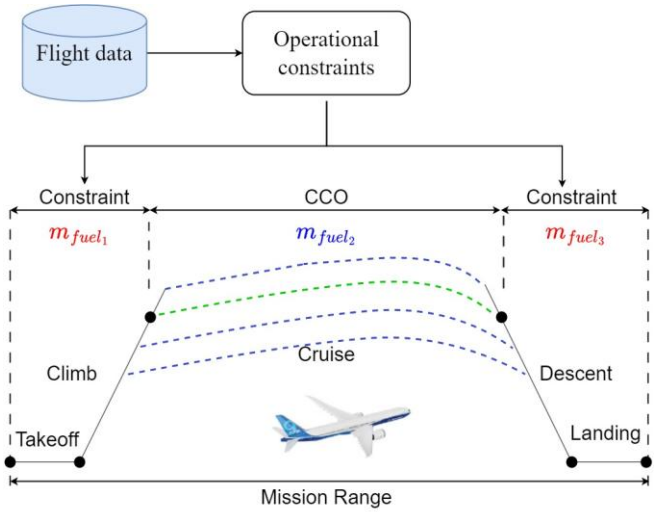


Figure 2: Schematic of the FPO method.

In the current framework, FPO is defined as an optional function for users. In the following section, we will compare the FPO-based (co-design) and FPO-free (fixed-operation profile) design optimization results to show the effectiveness of the co-design structure.

Results and Discussion

To demonstrate the benefits of the proposed method in this study, we conduct FPO-based and FPO-free design optimizations for three different-range missions. The mission scenarios are derived from flight data analysis using the eXtreme Gradient Boosting (XGboost) flight classification model as presented in [6]. The reference routes are from Hong Kong International Airport (HKG) to Taiwan Taoyuan International Airport (TPE) for the short-haul mission, Singapore Changi Airport (SIN) for the medium-haul mission, and to Heathrow Airport, London (LHR) for the long-haul mission.

The FPO-free design optimization results for the three missions are presented in **Table 1**. As the fuselage size depends only on the number of passengers, all three aircraft have the same fuselage size. There is no significant difference in wing area as the fuselage size is the same. However, longer mission range results in larger wing area. Longer mission range implies more fuel to carry, which leads to heavier weight, higher thrust, and higher lift from larger wing area and to the base aircraft (Boeing 777-300ER) operating the same mission. The greater improvement for shorter ranges can be attributed to the fact that the Boeing 777-300ER is designed for long-range operations---the operational optimality diminishes as the range deviates from its match range.

Materials Research Proceedings 69 (2026) 448-452 https://doi.org/10.21741/9781644904251-81

Table 1: Design optimization result (FPO-free).

Category	Item	HKG-TPE	HKG-SIN	HKG-LHR
Engine	Reference thrust (N)	298,793	420,753	481,866
	Bypass ratio	9	9	9
Wing	Wing area (m^2)	414.34	436.81	457.90
	Wing span (m)	61.07	62.70	64.20
Weight	MTOW (kg)	175,218	208,904	283,180
	MLW (kg)	175,210	205,498	237,743
	OEW (kg)	124,328	144,526	167,980
	MEW (kg)	120,481	137,100	145,627
Performance	Fuel consumption reduction (%)	20.45	9.15	2.53

The FPO-based design optimization results are presented in Table 2. Compared to the FPO-free design, all three aircraft configurations exhibit reductions in both reference thrust and wing area. This sizing reduction can be attributed to the decreased fuel consumption achieved through flight profile optimization within the same mission, which consequently reduces the required aircraft size while maintaining operational feasibility. It can be seen that the integration of FPO with the aircraft design optimization process demonstrates strong synergistic effects—the FPO leads to reduced fuel consumption, which enables smaller aircraft dimensions; conversely, the smaller aircraft size further expands the boundary of achievable fuel consumption improvements. This positive feedback loop enhances overall optimization effectiveness. Regarding fuel consumption reduction, the benefit of incorporating FPO is most pronounced for the HKG-LHR mission. The additional fuel savings achieved through FPO-based design optimization are 0.51%, 2.17%, and 3.73% for HKG-TPE, HKG-SIN, and HKG-LHR missions, respectively. This increasing trend correlates with mission range, as FPO is inherently more effective for longer-range operations where cruise range are larger.

Table 2: Design optimization result (FPO-based).

Category	Item	HKG-TPE	HKG-SIN	HKG-LHR
Engine	Reference thrust (N)	298,032	419,065	480,000
	Bypass ratio	9	9	9
Wing	Wing area (m^2)	414.34	435.90	455.36
	Wing span (m)	61.07	62.63	64.02
Performance	Fuel consumption reduction (%)	20.96	11.32	6.26

Conclusion

In this study, we propose an integrated framework for co-optimizing aircraft configuration and flight mission profile to achieve the "truly" global optimal design for specified mission(s). The results demonstrate that, compared to FPO-free design, the co-design approach yields aircraft with smaller dimensions for the same mission requirements—this reduction in size can be interpreted as achieving a better match-range for the designed aircraft. In the future, we will try to simultaneously optimize multiple operational conditions to address the complex and diverse operational requirements encountered in real-world scenarios.

References

[1] E. N. Van, D. Alazard, C. D¨oll, and P. Pastor, “Co-design of aircraft vertical tail and control laws using distributed electric propulsion,” IFAC-PapersOnLine, vol. 52, no. 12, pp. 514–519, 2019. https://doi.org/10.1016/j.ifacol.2019.11.295

[2] R. Miller, E. Whittington, S. Gabra, P. Hodgson, J. Green, J. Kho, J. Smith, and D. Singh, “Five years to chart a new future for aviation: The 2030 sustainable aviation goals,” tech. rep., AIA, University of Cambridge, 2024. https://report.aiazero.org/, Last accessed on 2025-06-27

[3] T. Y. Druot, M. Belleville, P. Roches, F. Gallard, N. Peteilh, and A. Gazaix, “A multidisciplinary airplane research integrated library with applications to partial turboelectric propulsion,” in AIAA Aviation 2019 Forum, p. 3243, 2019. https://doi.org/10.2514/6.2019-3243

[4] L. Liu, D. Kim, C. Reyner, and R. P. Liem, “Data-driven multi-range mission-based overall aircraft conceptual design optimization,” in Proceedings of the 34th Congress of ICAS, (Florence, Italy), September 2024.

[5] L. Liu, C. Reyner, and R. P. Liem, “Operation-based fight profile optimization with continuous cruise climb operations,” in AIAA AVIATION FORUM AND ASCEND 2025, p. 3815, 2025. https://doi.org/10.2514/6.2025-3815

[6] D. Kim, A. Seth, and R. P. Liem, “Data-enhanced dynamic flight simulations for flight performance analysis,” Aerospace Science and Technology, vol. 121, p. 107357, 2022. https://doi.org/10.1016/j.ast.2022.107357

Materials Research Proceedings 69 (2026) 453-456 https://doi.org/10.21741/9781644904251-82

Design and Optimization of Thin Membrane Tensioning for Deployable Space Antennas

Lorenzo MARTINAZZOLI[1,a], Mena PALMIERI[1,b] and Susanna LAURENZI[1,c *]

[1]Department of Astronautical Electrical and Energy Engineering, Sapienza University of Rome, Via Salaria 851-881, Rome, 00138, Italy

[a]lorenzo.martinazzoli@uniroma1.it, [b]palmieri.1714494@studenti.uniroma1.it, [c]susanna.laurenzi@uniroma1.it

Keywords: Foldable Antennas, Deployable Structures, Tensioning System, Thin Membranes

Abstract. Thin and ultra-thin materials, such as Kapton foils or thin spread-tow carbon fabrics, are increasingly employed in spacecraft systems due to their low weight and high flexibility, which are suitable features for deployable reflector structures. However, these devices require a uniformly tensioned surface to ensure optimal signal reflection, which represents a challenging achievement due to the wrinkle formation induced by the tensioning process. This study investigates numerically and experimentally the mechanical behaviour of triangular Kapton foils subjected to a 3-point tensioning configuration. Moreover, a one-shot manufacturing process is proposed to realize the cable-membrane interface, conceived for minimizing surface defects and keeping membrane integrity.

Introduction

In recent years, ultra-thin materials have been increasingly employed in spacecraft systems, both for the realization of structural components and operational instruments. The main advantage of these devices lies in their high structural flexibility and low weight, features that are appealing for the development of compact structures capable of expanding once in orbit [1-4]. Such systems are well-suited for the development of foldable antennas, which often require a large, well-tensioned surface for effective signal transmission and reception. However, the requirements for low mass, high mechanical performance and resistance to the space environment are particularly stringent, limiting the choice of appropriate materials. Kapton foils are commonly used in these applications due to their favourable mechanical properties, low density, and thermal resistance [5,6]. Typically, Kapton foils are manufactured with thicknesses on the order of tenths of micrometres, allowing for efficient folding and unfolding, as controlled by the deployment mechanisms. Generating a uniform stress field inside large-scale surfaces is a challenging goal to achieve, as it is strongly dependent on material elastic properties, thickness, geometry and tension method. Therefore, a high level of accuracy in the tensioning process is essential, especially to avoid formation of wrinkles, which represent out-of-plane wavy deformations of the membrane, compromising its proper performance as a reflector [7,8]. Studying the effects of the cable-membrane interface on surface tensioning is one of the goals of the present research. Experimental tests were performed on reduced scale triangular Kapton foils, studying how the interface affects out-of-plane deformations. Such a junction was realized with a one-shot manufacturing process, avoiding any drilling operation to attach the cables. In addition, a numerical model was designed to replicate the tests and study more in depth the surface behaviour under in-plane loads. The aim is to develop a reliable numerical model suitable for scaling up the analysis to full-size membranes of different configurations.

Content from this work may be used under the terms of the Creative Commons Attribution 3.0 license. Any further distribution of this work must maintain attribution to the author(s) and the title of the work, journal citation and DOI. Published under license by Materials Research Forum LLC.

Materials Research Proceedings 69 (2026) 453-456 https://doi.org/10.21741/9781644904251-82

Experimental study

To analyse the effects of the tensioning method on triangular Kapton foils, a one-shot manufacturing process was designed to realize the samples. Particularly, the aim was to co-bond the Kapton layer and the Kevlar cables in a single thermal cycle for efficient tensile load transfer. To this end, a hydraulic press with heating plates was used to reach the temperature for the curing cycle. Samples were obtained by cutting the Kapton foil (Dupont^{TM}) as triangles with edges of 20 cm and placing triangular patches of AF163-2K structural adhesive (3M^{TM}), with selected shapes, over the foil corners. Kevlar cables were then placed between 2 layers of adhesive. Material properties are summarized in Table 1, where Kevlar ones are taken from literature [9,10]. Such a manufacturing process avoids the need to drill the Kapton in the reinforced area to attach the tensioning cables, as is commonly done in similar applications, thereby establishing a non-invasive technique. For experimental tests, we have selected Kapton foils with a thickness of 2 MIL, ensuring low weight and flexibility at the same time. Experimental tests focused on the shape and size of the adhesive patches to minimize wrinkles formation. A simple triangular shape and a sector-like shape were adopted: the former to reproduce traditional supports used up to date, the latter to get a different load direction on the vertex, as shown in Fig.1, determining variations on the deformation field.

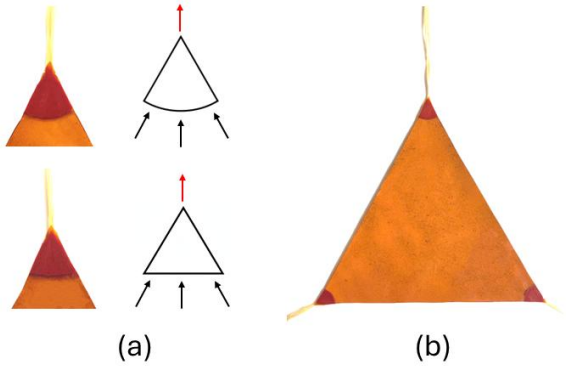


Fig. 1 Adhesive shape comparison (a) and finished Kapton test sample (b).

***Table. 1** Membrane and cables properties.*

	Kapton	**Kevlar**
Tensile modulus **[GPa]**	2.76	62
Poisson's ratio	0.34	0.36
Thickness **[µm]**	50.8 (2 mil)	-
Density **[kg/m^3]**	1420	1440

Later, cables are fixed on 3D printed supports, in such a way that the tension was equally distributed on the 3 vertices and adapted to Shimadzu AGS-X 10KN tensile machine. Tests were conducted at 2 mm/min, supported by a DIC optical system to monitor micro-displacements in the membrane. Results showed high load capacity of the interface, reaching over 300 N total load keeping the integrity of the membrane. An adhesive patch of 15 mm edge was observed to be the minimum size required to achieve adequate adhesion at high tensile loads. For smaller dimensions, there is a progressive detachment of the patches from the membrane and a clear formation of wrinkles near the vertices. In Fig.2 the out-of-plane displacement was analysed at low and high level of tensioning, respectively at 30 N and 300 N of total load, for both the adhesive shapes. Results highlight a flatter surface at low tension levels, generating depression regions near the corners. Such a behaviour is slightly reduced by the curved adhesive shape at 30 N of load, whereas an opposite outcome is observed at higher loads. Indeed, the curved triangle induces a much more pronounced bending of the membrane edges compared to the traditional shape.

Materials Research Proceedings 69 (2026) 453-456 https://doi.org/10.21741/9781644904251-82

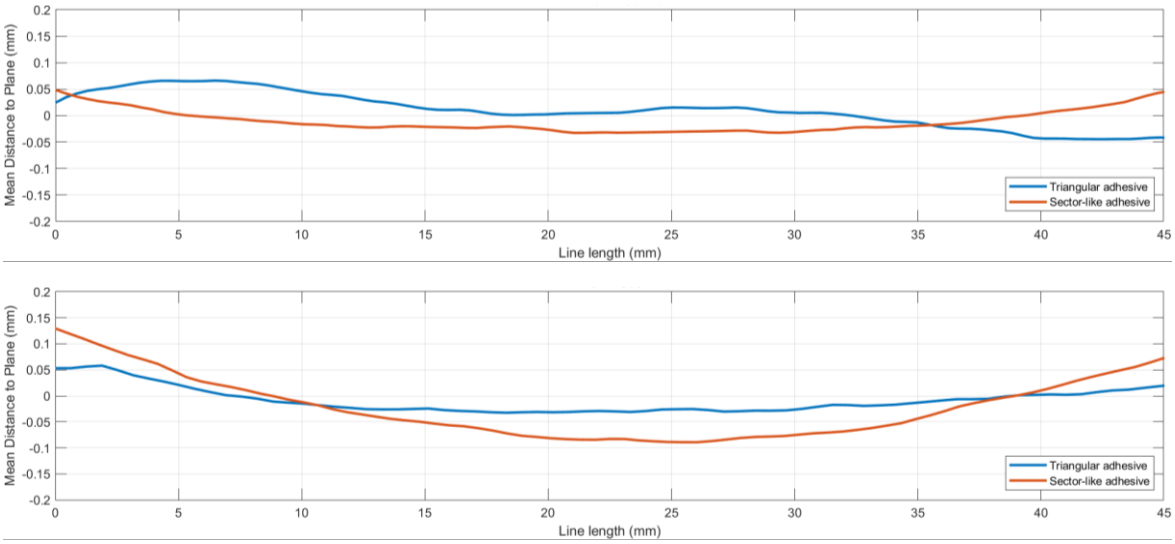


Fig. 2 Out-of-plane deformation of the membrane along side-to-side path at 30 N (top) and 300 N (bottom) total load.

Computational study

The numerical model was implemented on the finite element program ABAQUS and consists of a triangular Kapton membrane, reproducing lab scale experimental tests. The membrane was modelled as a 3D deformable shell, composed of 7500 S8R5 elements, with a structured meshing technique. For the cables truss elements (T3D2) were adopted, with a discretization of one element per cable. The external nodes of the cables were fixed, while the other end is joined to membrane vertices. Following the work of Galhofo et al., the compression state is firstly evaluated to observe the regions where buckling may occur [11]. With a pre-stress of 12.7 MPa on each cable, the membrane is subjected to an internal stress of 42 KPa, while compression regions are observed near the corners, as shown in Fig.3, and it is precisely in these areas that wrinkles appear during in-plane tensioning.

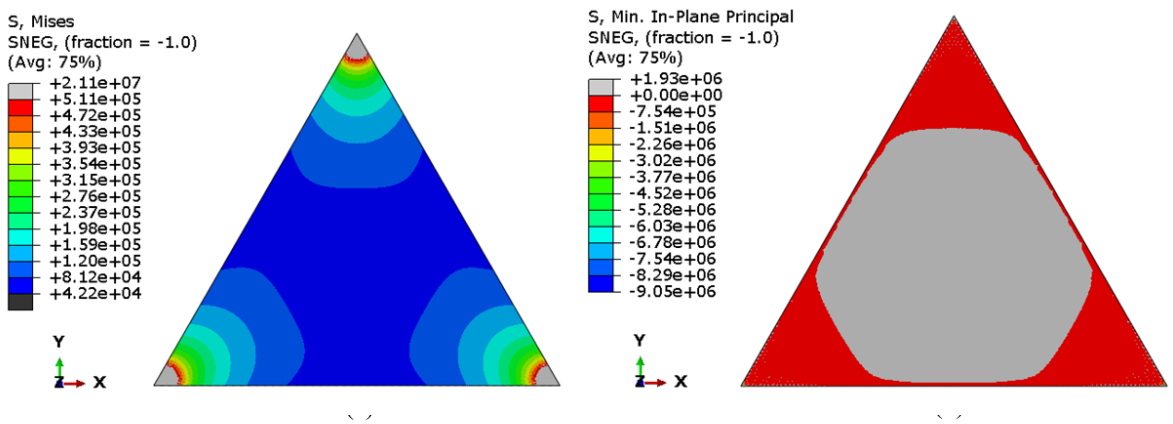


Fig. 3 Membrane's internal stress (a) and compression regions - in red - and tension region -in grey - at pre-tensioning configuration (b).

Conclusions

In this work, the structural response of a Kapton membrane to in-plane tensioning is investigated, both numerically and experimentally, aiming to reduce wrinkles formation. Lab-scale Kapton triangles of 20 cm per side have been bonded with Kevlar cables in a one-shot manufacturing process, using an epoxy structural adhesive, providing a non-invasive solution for membrane-cable interface. The adhesive was cut in two different shapes to analyse variations in the material behaviour. Experimental results highlighted an excellent resistance of the adhesive, reaching more than 100 N on each cable, establishing an effective manufacturing process. Additionally, from DIC correlation, limited out-of-plane deformations were observed for both the interface shapes, keeping wrinkles under a value of 10^{-5} m. Numerical simulations were performed for a comparison with experimental results. Here, the compression regions were emphasized, corresponding to the corners of the membrane. Such a stress configuration will be replicated in a buckling analysis to understand the wrinkles formation and evolution. Further analysis of the numerical model is planned, focused on better simulate the boundary conditions of the adhesive and on proportionally scale the model to greater membrane dimensions.

References

[1] SHINDE, Swapnil D.; UPADHYAY, Sanjay H. The novel design concept for the tensioning system of an inflatable planar membrane reflector. Archive of Applied Mechanics, 2021, 91.4: 1233-1246. https://doi.org/10.1007/s00419-020-01841-w

[2] XIE, Chao, et al. Design and demonstration of a roll-out membrane antenna based on thin-walled deployable composite booms. Thin-Walled Structures, 2024, 205: 112486. https://doi.org/10.1016/j.tws.2024.112486

[3] WILKIE, William K. Overview of the nasa advanced composite solar sail system (acs3) technology demonstration project. In: AIAA SciTech 2021 forum. 2021. p. 1260. https://doi.org/10.2514/6.2021-1260

[4] MALLIKARACHCHI, H. M. Thin-walled composite deployable booms with tape-spring hinges. 2011. PhD Thesis. https://doi.org/10.2514/6.2011-2019

[5] LIU, Y. A. N.; LIU, YANZHEN. Experimental research on uniaxial tensile mechanical properties of Kapton foils. Journal of Polymer Research, 2022, 29.7: 271. https://doi.org/10.1007/s10965-022-03123-1

[6] LIU, Yan; LIU, Yanzhen; LIN, Guochang. Uniaxial tensile mechanical tests of Kapton foil at high-low temperature conditions. Aircraft Engineering and Aerospace Technology, 2021, 93.6: 1043-1051. https://doi.org/10.1108/AEAT-02-2021-0031

[7] BONIN, A. S.; SEFFEN, K. A. De-wrinkling of pre-tensioned membranes. International Journal of Solids and Structures, 2014, 51.19-20: 3303-3313. https://doi.org/10.1016/j.ijsolstr.2014.05.001

[8] Galhofo, D., Duarte, A. P., & Silvestre, N. (2025, July). Preventing wrinkling in Kapton solar sails through graphene reinforcement. In Structures (Vol. 77, p. 108931). Elsevier. https://doi.org/10.1016/j.istruc.2025.108931

[9] Information on https://www.qnityelectronics.com/content/dam/electronics/amer/us/en/electronics/public/documents/en/EI-10206-Kapton-HN-Data-Sheet.pdf

[10] Taleghani, B., Sleight, D., Muheim, D., Belvin, K., & Wang, J. (2003). Assessment of analysis approaches for solar sail structural response. Paper presented at the 39th AIAA/ASME/SAE/ASEE Joint Propulsion Conference & Exhibit. https://doi.org/10.2514/6.2003-4796

[11] GALHOFO, Diogo, et al. Structural behaviour of pre-tensioned solar sails. Thin-Walled Structures, 2022, 181: 110007. https://doi.org/10.1016/j.tws.2022.110007

Materials Research Proceedings 69 (2026) 457-462 https://doi.org/10.21741/9781644904251-83

Aero-Propulsive Modeling and System Identification of a Distributed Electric Propulsion Flying Model

Giorgio FILIPPOLI[1,a*], Niko TERZAROLI[1,b], Beniamino M. PERRI[1,c], Lorenzo MASSA[1,d], Stefano CACCIOLA[1,e], Lorenzo TRAINELLI[1,f] and Carlo E. D. RIBOLDI[1,g]

[1]Department of Aerospace Science and Technology, Politecnico di Milano, Via G. La Masa 34, Milano, Italy

[a]giorgio.filippoli@polimi.it, [b]niko.terzaroli@mail.polimi.it, [c]beniaminomaria.perri@polimi.it, [d]lorenzo1.massa@mail.polimi.it, [e]stefano.cacciola@polimi.it, [f]lorenzo.trainelli@polimi.it, [g]carlo.riboldi@polimi.it

Keywords: Distributed Electric Propulsion, Model Identification, Automated Flight Test Procedures, Aero-Propulsive Coupling

Abstract. This contribution illustrates a novel approach to aero-propulsive modeling and system identification for Distributed Electric Propulsion (DEP) aircraft. The placement of multiple propellers along the wing leading edge significantly alters the flow field, affecting both performance and flying qualities. A direct modeling approach based on simplified theoretical formulations is insufficient to accurately predict the complex behavior of the aircraft. Therefore, model identification is necessary to achieve some insight on the phenomenon. Based on the identified model, the aim is twofold: to generalize the modeling for aircraft design and analysis, and to develop a high-fidelity simulation tool for control law synthesis and advanced applications. The flight test campaign supporting the identification activities was carried out through fully automated flight tests using the scaled DEP demonstrator SwitchMaster, as discussed in [1].

Introduction

Distributed Electric Propulsion (DEP) represents a promising solution among unconventional aircraft design concepts, because the interaction between the propellers and the wing is exploited in the attempt of increasing the overall aerodynamic performance [2]. DEP offers several benefits in efficiency, control authority and system redundancy.

However, the aerodynamic coupling between propeller slipstreams and the airframe introduces strong nonlinearities that challenge conventional modeling techniques. To address this challenge, a dedicated research effort has been conducted at the Politecnico di Milano using the SwitchMaster demonstrator, an electrically powered, radio controlled aircraft featuring six propellers distributed along the leading edge of the wing.

Earlier studies [1, 3, 4] focused on the design, preliminary flight testing, and the development of an autonomous flight control framework based on a Total Energy Control System (TECS). Building on that foundation, the present work focuses on identifying a complete aero-propulsive model from flight data. The identification campaign was conducted using an autonomous flight test procedure designed to systematically excite the aircraft's dynamic modes under different blowing conditions. The identified model captures the impact of distributed propellers on stability and control derivatives, providing a formulation for subsequent simulation and control studies.

This paper details the applied methodology and estimation techniques, discusses DEP-specific identification challenges and shows results illustrating propeller-induced aerodynamic effects.

Content from this work may be used under the terms of the Creative Commons Attribution 3.0 license. Any further distribution of this work must maintain attribution to the author(s) and the title of the work, journal citation and DOI. Published under license by Materials Research Forum LLC.

Materials Research Proceedings 69 (2026) 457-462 https://doi.org/10.21741/9781644904251-83

Aero-Propulsive Modeling

DEP introduces a strong coupling between aerodynamic and propulsive effects due to the blowing phenomenon, where the propeller slipstream accelerates the local airflow over the wing. This increases lift but also alters drag and aerodynamic moments, leading to a complex interaction in which aerodynamic and thrust contributions cannot be easily separated. While this coupling poses modeling and control challenges, it also offers opportunities for improved performance and innovative control strategies.

The identification campaign was performed exclusively under the Collective Thrust Control (CTC) conditions, with all propellers operating at the same rotational speed and producing equal thrust. The reference model adopted for parametric identification is a non-linear formulation of conventional fixed-wing aircraft dynamics. The propeller advance ratio, $J = \frac{U}{nd}$, where U is airspeed, n the propeller rotational speed and d the diameter, quantifies the influence of propeller-induced blowing relative to aircraft airspeed.

Aerodynamic coefficients in the equations of motion follow standard constitutive relationships:

$$C_{(.)_{(.)}} = C_{(.)_0} + C_{(.)_\alpha}\,\alpha + C_{(.)_{\hat{q}}}\,\hat{q} + C_{(.)_{\delta_e}}\,\delta_e + C_{(.)_{\alpha^2}}\,\alpha^2 \qquad \text{longitudinal}$$

$$C_{(.)_{(.)}} = C_{(.)_0} + C_{(.)_\beta}\,\beta + C_{(.)_{\hat{p}}}\,\hat{p} + C_{(.)_{\hat{r}}}\,\hat{r} + C_{(.)_{\delta_a}}\,\delta_a + C_{(.)_{\delta_r}}\,\delta_r \qquad \text{lateral-directional}$$

In the previous identification campaign [4], performed manually without the support of an automatic flight testing system, stability and control derivatives were found to vary with the propeller advance ratio J. Accordingly, each derivative is expressed as:

$$C_{(.)_{(.)}}(J) = C^{unb}_{(.)_{(.)}} + \Delta C_{(.)_{(.)}}(J)$$

where $C^{unb}_{(.)_{(.)}}$ denotes the unblown value, i.e., evaluated with $J \to \infty$ and $\Delta C_{(.)_{(.)}}(J)$ the blowing-induced contribution.

System Identification

The flight test methodology, including automated excitation maneuvers and trim management through the Total Energy Control System (TECS), followed the approach outlined in [5, 6]. The identification aimed at estimating the stability and control derivatives $C_{(.)_{(.)}}(J)$, including the propeller blowing effects $\Delta C_{(.)_{(.)}}(J)$.

The identification process involved two main steps: first, solving the Equation-Error Method (EEM) for each selected maneuver, and second, applying the Output-Error Method (OEM) [7]. The EEM provided initial parameter estimates by minimizing the squared differences between modeled and measured aerodynamic coefficients, using a least-squares solution. These estimates served as initial guesses for the OEM, which refined the parameters by minimizing, through an optimization problem, a cost function quantifying the difference between measured and model-predicted outputs, such as airspeed, angular rates and attitude angles. The cost function, expressed as a weighted sum of squared output errors over the maneuver duration, provides a quantitative measure of model fidelity. In the OEM, initial conditions were also treated as optimization variables to account for small state uncertainties, and parameters were normalized by their initial estimates to improve numerical conditioning. The optimization, performed via the *fmincon* algorithm, included physical bounds to avoid unrealistic solutions and local minima.

Compared to the EEM, the OEM provided higher fidelity and dynamic consistency, as illustrated in Fig. 1, which reports a representative elevator doublet maneuver. The simulated responses using OEM parameters showed a markedly improved match with measured data. Fig. 2 further shows that OEM-based simulations closely match the measured motion states and aerodynamic coefficients.

Materials Research Proceedings 69 (2026) 457-462 https://doi.org/10.21741/9781644904251-83

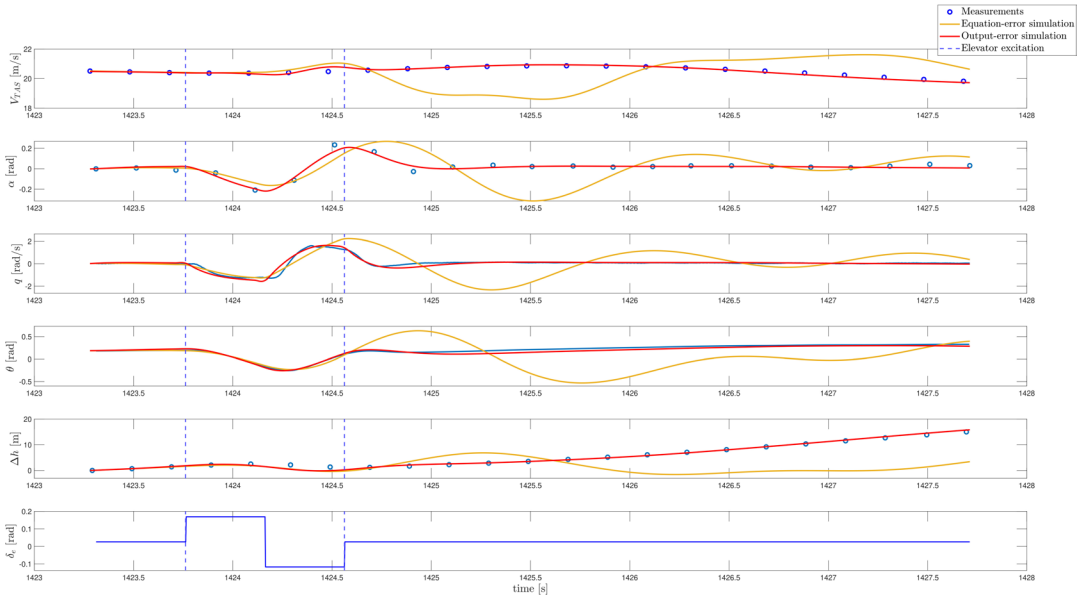


Figure 1: Longitudinal output time histories from measured data, simulated with Equation Error and Output-Error results.

Results

The identified aerodynamic derivatives were analyzed to evaluate the impact of propeller blowing on the aircraft's longitudinal and lateral-directional dynamics. Stability and control derivatives were identified for each stabilized maneuver, defined by its trim advance ratio J_{TRIM} and angle of attack α_{TRIM}. The resulting derivatives were plotted as functions of J and grouped into clusters based on α_{TRIM}, facilitating the interpretation of their trends across different flight conditions.

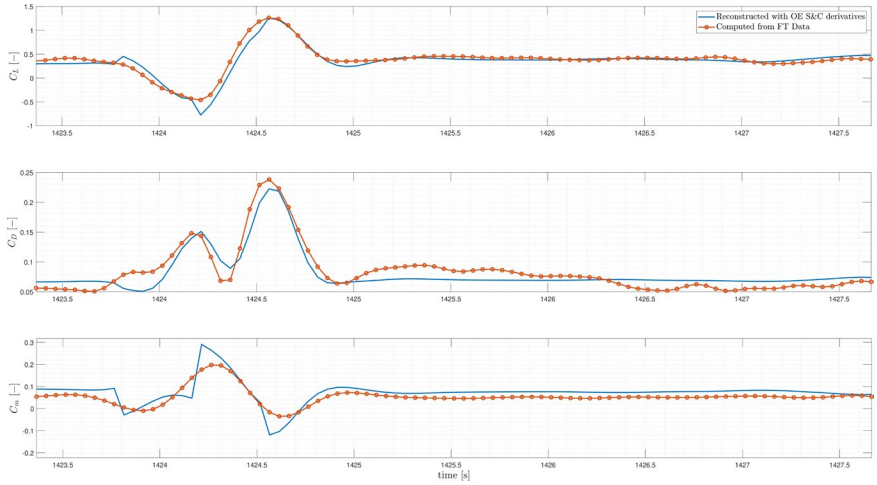


Figure 2: Comparison of longitudinal aerodynamic coefficient time histories, computed from the identified model (blue) and the flight data (red).

Several derivatives showed a clear exponential dependence on J: C_{L_0}, C_{m_0}, $C_{m_{\hat{q}}}$ and $C_{m_{\delta_e}}$ for the longitudinal dynamics, and C_{S_β}, C_{l_β}, C_{n_β} and $C_{l_{\delta_a}}$ for the lateral-directional dynamics.

The remaining terms exhibited only random fluctuations around a mean value, indicating negligible sensitivity to the blowing effect. Derivatives exhibiting a dependence on J were fitted using exponential functions $C(J) = C_\infty + p_1 e^{-p_2 J}$, or, in some cases, the sum of two exponential terms, where C_∞ denotes the asymptotic unblown value ($J \to \infty$).

Materials Research Proceedings 69 (2026) 457-462 https://doi.org/10.21741/9781644904251-83

As shown in Fig. 3, the lift coefficient increases with the blowing effect, thus at low J. In the unblown condition, data scattering led to adopting the mean value as representative. Improved accuracy is expected from refining the glide test procedure to ensure that the autopilot maintains properly trimmed flight conditions even without engine thrust. Variations in pitching moment derivatives mainly result from increased dynamic pressure at low J and from slipstream-tail interactions causing additional downwash.

In the lateral-directional dynamics, the derivatives linked to sideslip (C_{S_β}, C_{l_β}, C_{n_β}) show an exponential dependence on J due to propeller slipstream effects on the fuselage and vertical tail. Among the control derivatives, $C_{l_{\delta_a}}$ is the most affected, as the slipstream enhances ailerons effectiveness and roll control at low J.

Overall, the identified exponential trends confirm the strong aero-propulsive coupling introduced by DEP and offer a quantitative foundation for modeling and control analysis.

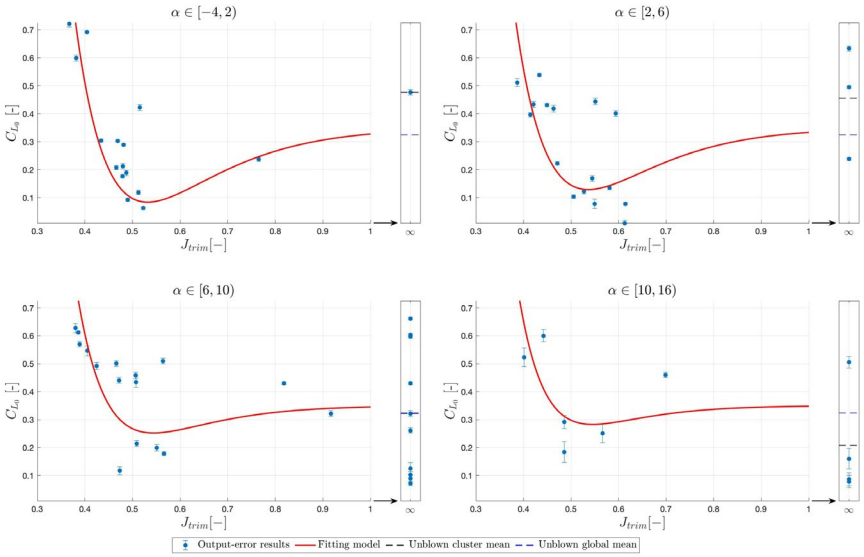


Figure 3: Trends of C_{L_0} with respect to J_{trim} divided into α_{trim} clusters.

Semi-Local Model Identification

The aerodynamic model obtained by fitting the clustered stability and control derivatives from the Output-Error identification was defined as the parametric global model, representing a generalized formulation compared to the local models, which are specifically optimized for each maneuver.

A refinement step followed, reapplying the Output-Error identification while constraining selected high-confidence parameters to the corresponding values from the global model within the equations of motion. In particular, C_{L_0} and C_{m_0} were fixed for the longitudinal dynamics, and C_{S_β} and $C_{l_{\delta_a}}$ for the lateral-directional dynamics, based on a trial-and-error tuning. The rest of the identification process remained unchanged, with derivatives estimated for each maneuver and fitted using exponential or mean-value models, depending on their sensitivity to J. The resulting formulation has been defined as semi-local model, since combines global constraints on selected derivatives with local estimation of the remaining ones. As shown in Fig. 4, it provides a more interpretable trend of the derivatives with respect to propeller advance ratio, compared to both the local and global models, confirming the enhanced predictive capability of this hybrid identification approach.

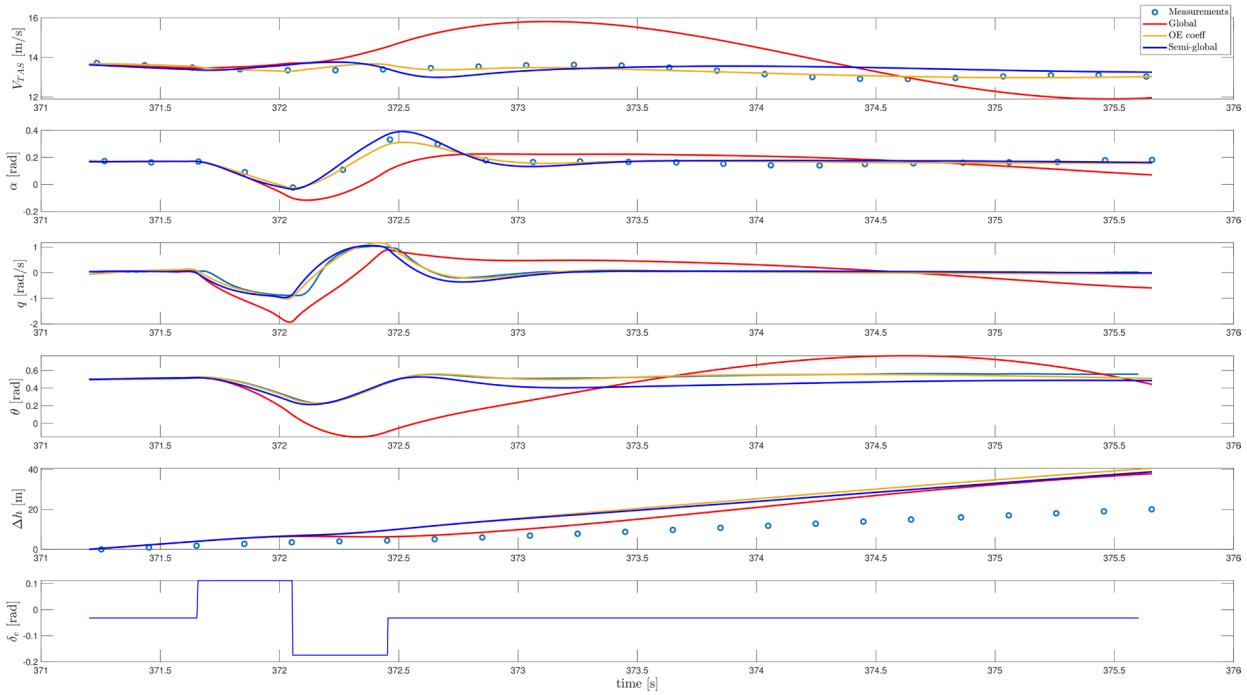


Figure 4: Longitudinal output time histories from measured data, simulated with Output-Error results and with global and semi-global fitted models.

Conclusions and Future Developments

This study presented an aero-propulsive identification methodology for a Distributed Electric Propulsion aircraft, integrating Equation-Error and Output-Error techniques within an autonomous flight testing framework. Applied to the SwitchMaster demonstrator, the approach successfully captured the non-linear aero-propulsive coupling introduced by the propeller slipstream and its impact on stability and control derivatives, leading to the development of both global and semi-global models. The semi-global formulation, incorporating selected global constraints, showed improved consistency and predictive accuracy, confirming its suitability for control-oriented applications.

Future work will extend the identification process by combining all maneuvers within similar α_{TRIM} ranges into a single optimization, where J-dependent derivatives are constrained to follow exponential laws. Successful convergence would validate the exponential dependence on the advance ratio and reinforce the robustness of the proposed aero-propulsive model.

References

[1] Cacciola S., Filippoli G., Perri B. M., Riboldi C. E. D., Terzaroli N., Trainelli L., "Autonomous Flight Tests of a Distributed Electric Propulsion Demonstrator Based on a Total Energy Control System", 11th European Conference for Aeronautics and Aerospace Sciences (EUCASS), Rome, Italy, 2025.

[2] Hoogreef M.F.M., de Vries R., Sinnige T. and Vos R., "Synthesis of aero-propulsive interaction studies applied to conceptual hybrid-electric aircraft design", AIAA Scitech 2020 Forum, Orlando, USA, January 6–10, 2020. https://doi.org/10.2514/6.2020-0503

[3] Trainelli L., Riboldi C. E. D., Cacciola S., "Design, Implementation and Testing of a Distributed Electric Propulsion Demonstrator", 2023 Annual Society of Flight Test Engineers European Chapter Symposium, Rome, Italy, May 16-17, 2023.

[4] Cacciola S., Bottà L., Riboldi C. E. D., Trainelli L., “Identification of the Impact of Blowing on the Aerodynamic Model of an Airplane with Distributed Electric Propulsion”, 34th ICAS Congress, Firenze, Italy, September 9-13, 2024.

[5] Trainelli L., Filippoli G., Terzaroli N., Perri B. M., Cacciola S., Riboldi C. E. D., “Automated Flight Testing of a Distributed Electric Propulsion Flying Model”, 10th CEAS Aerospace Europe Conference / 28th AIDAA International Congress, Turin, Italy, December 1–4, 2025.

[6] Filippoli G., Perri B. M., Terzaroli N., Trainelli L., Cacciola S., Riboldi C. E. D., “Development of an Autonomous Flight Control System for a Distributed Electric Propulsion Flying Model”, 10th CEAS Aerospace Europe Conference / 28th AIDAA International Congress, Turin, Italy, December 1–4, 2025.

[7] Vladislav Klein and Eugene A. Morelli, “Aircraft system identification: theory and practice”, AIAA education series, Reston, American Institute of Aeronautics and Astronautics, 2006, isbn: 978-1-56347-832-1.

Materials Research Proceedings 69 (2026) 463-468 https://doi.org/10.21741/9781644904251-84

Exploring Box-Wing Configurations for Next-Generation Firefighting Aircraft

Giuseppe Palaia[1,a *], Karim Abu Salem[1,b], Andrea Fasolis[1,c] and Erasmo Carrera[1,d]

[1]Polytechnic of Turin, Corso Duca degli Abruzzi 24, 10129, Torino, Italy

[a]giuseppe.palaia@polito.it, [b]karim.abusalem@polito.it, [c]andrea.fasolis@studenti.polito.it, [d]erasmo.carrera@polito.it

Keywords: Box-Wing, Firefighting, MDO, Multidisciplinary, Aircraft Design, Optimization

Abstract: This research introduces an integrated, physics-based framework for the conceptual design and multidisciplinary optimization of next-generation aerial firefighting aircraft adopting a box-wing configuration. The study is motivated by the increasing frequency and intensity of wildfires, which call for novel aviation solutions with improved performance, payload capacity, and mission efficiency. Box-wing architectures, featuring two main lifting surfaces connected by vertical tip wings, offer promising aerodynamic benefits, including drag reduction and increased payload capability, and may serve as a viable alternative to conventional monoplane layouts in demanding aerial firefighting operations. The aeromechanic design of this innovative concept has been carried out through a vortex lattice method-based numerical optimization procedure; the structural design and weight estimation of the lifting-system has been performed by means of a physics-based ad hoc developed stick model. A conceptual design framework, integrating also propulsive design, mission simulation, and performance assessment, has been finally integrated, providing a platform for box-wing scooper conceptual design. The results highlight the potential of the box-wing in the context of aerial firefighting, mainly related to its increased lifting capability if the same wingspan of a conventional tube-and-wing aircraft is considered.

Introduction

Wildfires, although natural phenomena, have become increasingly intense due to climate change and urbanization, posing a growing threat to ecosystems and human settlements [1]. Rising temperatures and urban expansion amplify both the risk and the complexity of fire control, highlighting the need for innovative technological solutions, including the development of next-generation firefighting aircraft designed for more effective interventions. A scooper aircraft is a firefighting airplane designed to collect large amounts of water directly from lakes, rivers, or seas while flying at low altitude [2]. Equipped with retractable scoops and amphibious hulls, it can quickly refill and drop water to suppress wildfires efficiently. The objective of the study is to develop a parametric and flexible conceptual design tool capable of generating and evaluating candidate box-wing aircraft architectures starting from high-level mission and operational requirements. The box-wing configuration consists of two main horizontal lifting surfaces connected at the tips by properly designed vertical wings [3,4]. The main advantages of this configuration compared to a conventional aircraft lie in its ability to minimise induced drag [5] and in the possibility of increasing its lifting capacity while maintaining the same wingspan [6].

While closed-wing systems have been studied in academic aerodynamics, their application to specialized mission aircraft, such as aerial firefighting platforms, remains an open research field. By combining mission-specific requirements, parametric modelling, and cross-disciplinary coupling in a single toolchain, this study provides a foundation for evaluating the true potential of box-wing designs in this applied aviation context.

Content from this work may be used under the terms of the Creative Commons Attribution 3.0 license. Any further distribution of this work must maintain attribution to the author(s) and the title of the work, journal citation and DOI. Published under license by Materials Research Forum LLC.

Materials Research Proceedings 69 (2026) 463-468 https://doi.org/10.21741/9781644904251-84

Methodology

The design framework adopts a Multidisciplinary Design Optimization (MDO) approach [7], enabling the concurrent management of heterogeneous subsystems and the iterative refinement of key design variables. The core of the framework is a set of modular disciplinary blocks, each based on simplified analytical, semi-empirical, numerical formulations derived from first principles. These blocks are structured to allow incremental fidelity upgrades, enabling coupling with high-resolution simulation tools as needed. The current implementation includes:

- **Aerodynamics and Flight Stability**: aeromechanic design is based on vortex lattice models and semi-empirical corrections for parasite and interference drag for box-wing lifting system. A numerical optimization procedure supports variables as aspect ratio, twist, taper, dihedral, sweep, and wings positioning, allowing exploration of multiple lifting system geometries under consistent design conditions and constraints. Details on the box-wing aeromechanic optimization procedure are available in refs. [8-10]. The optimization process provides as output a large number of possible box-wing planforms (an example in Fig. 1), among which the designer can select a specific configuration fulfilling pre-defined performance target. Detailed study on longitudinal stability and controllability is integrated in the lifting system design, see ref. [11]. In the present case the aircraft wingspan is set equal to that of the Viking CL-415, as the primary goal is to obtain a box-wing aircraft having the same overall size of a consolidated competitor, but with higher operating capabilities, i.e. larger water load.

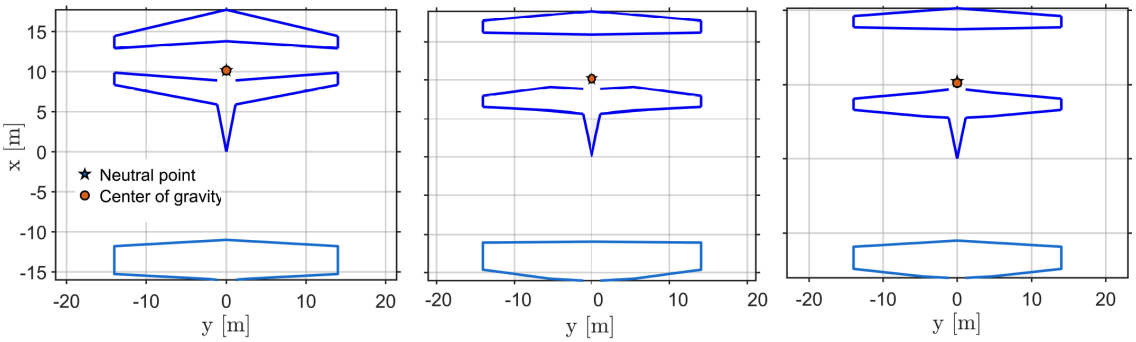


Figure 1. Subset of possible output of the aerodynamic optimization procedure.

- **Propulsion Sizing**: the matching chart tool has been adopted for the installed power sizing. The canonical power relations, for each flight conditions, have been adopted, see ref. [12]. In addition, the scooping phase has been modelled, as it could represent a limit sizing condition for the propulsion system, see the illustrative example proposed in Fig. 2. For the scooping phase, the power requirement mainly depends on the geometric parameters describing the aircraft hull, summarized in Fig. 3.

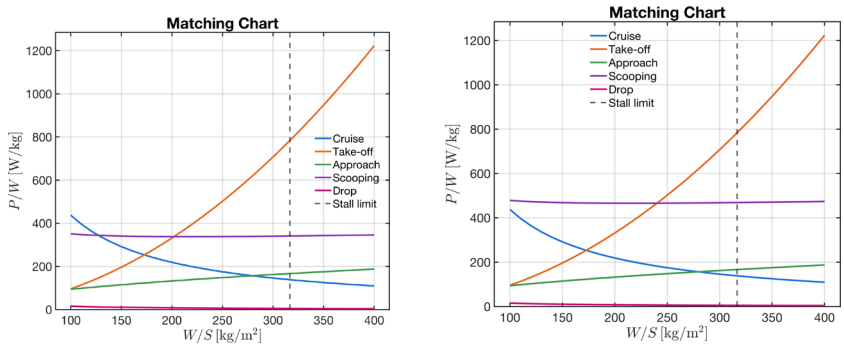


Figure 2. Matching chart for a scooper aircraft with different scooping conditions.

Materials Research Proceedings 69 (2026) 463-468 https://doi.org/10.21741/9781644904251-84

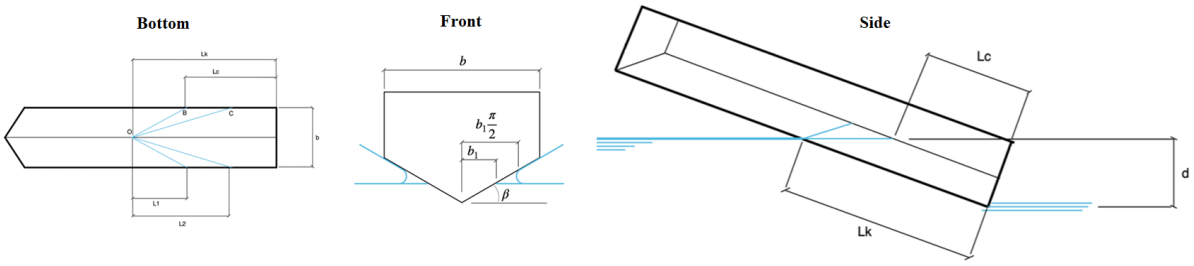


Figure 3. Illustrative scheme of the main hull dimensions.

- **Structural Sizing**: this module aims at designing the lifting system primary structures, calculating bending and torsional loads on the main wings elements using beam theory and simplified loading models. Particular attention is given to the closed-loop load paths in the box-wing arrangement and their impact on stiffness and weight. Indeed, in a conventional wing, an initial assessment of structural sizing can be obtained by modelling the wing as a cantilever beam subjected to design loads. In the box-wing case, however, the lifting system is overconstrained to the fuselage, see ref. [13,14], making the system statically indeterminate and the development of an analytical model more complex. To address this, the wing structure was modelled as a beam discretized into a number of elements defined in three-dimensional space, see Fig. 4. After applying the sizing loads, a simplified wing-box model was used to compute stress, enabling the determination of the required equivalent skin thickness to ensure adequate structural strength under the sizing loads, with the prescribed safety factor.

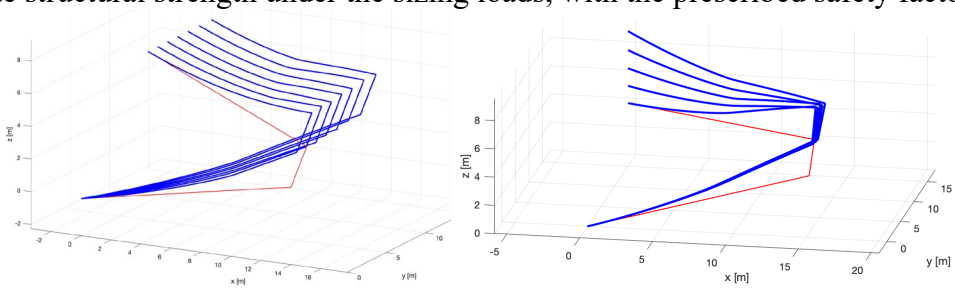


Figure 4. Stick model for the primary box-wing lifting structure.

- **Mission Modelling and Drop Envelope Analysis**: this module provides the time simulation of the flight profiles, including water drop fire zones. The simulation is made by means of Euler integration of aircraft equation of motion, considered as a point mass. The impact of repeated load cycles and water release on overall mission performance is captured, mainly in terms of fuel consumption and residual endurance. Fig. 5 reports illustrative profiles of power, aircraft trajectory, and weight evolution during a standard mission.

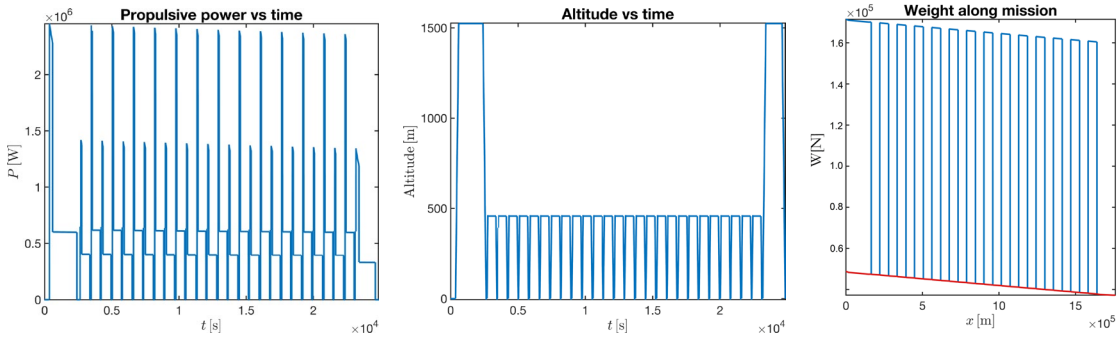


Figure 5. Power profile (left), trajectory (centre), weight profile (right).

Materials Research Proceedings 69 (2026) 463-468 https://doi.org/10.21741/9781644904251-84

- **Mass Budget Estimation:** this module estimates component-level mass breakdowns using both physics-based assessments and statistical correlations, and evaluates centre-of-gravity location and excursion during water load and release phases. The model accounts for tank placement and structural reinforcements due to sloshing and dynamic loads. As a final output of the MDO loop, the module aggregates the contributions of all subsystems and provides verification against take-off weight targets, regulatory limits, and payload-to-weight efficiency.

Each module communicates with the others via a centralized data structure, enabling full coupling and iterative convergence of design parameters. The system is designed to be reconfigurable, supporting both baseline studies of reference architectures and exploration of unconventional layouts for the box-wing family. The framework, sketched in Fig. 6 also includes capabilities for trade-off analysis and multi-objective optimization, allowing the user to evaluate performance trends across families of solutions.

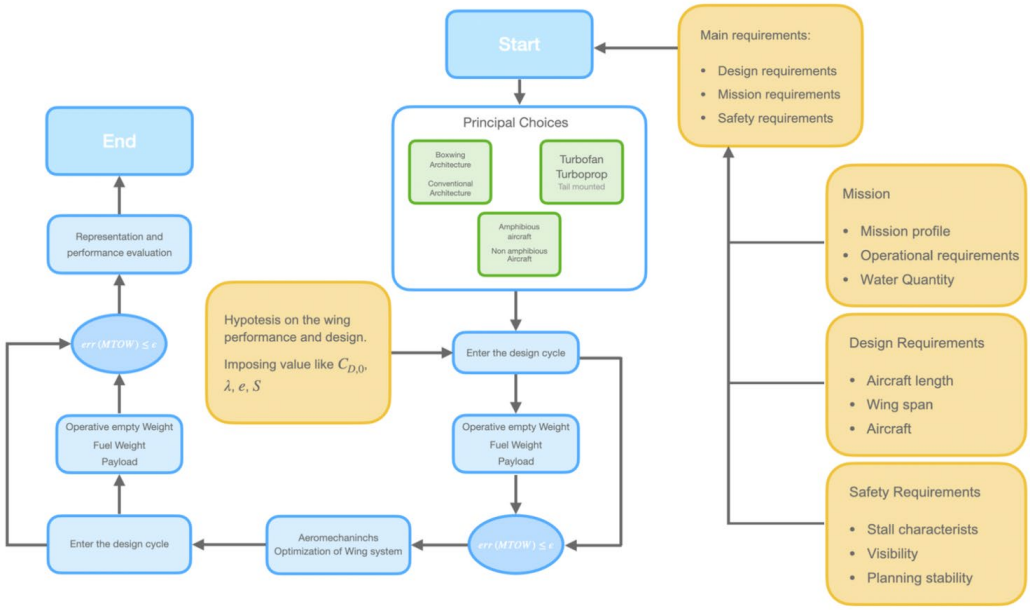


Figure 6. General scheme of the developed aircraft design framework.

Preliminary results

One of the selected criteria for comparative study between conventional and box-wing scooper aircraft is the total amount of water that can be dropped during a single mission, which is a key factor for this class of aircraft. A preliminary proposed box-wing concept has a water capacity of 12500 kg, maintaining the same wingspan of the conventional competitor, with a elongated and widened fuselage necessary to integrate the larger water tank; this philosophy is the same applied to the medium-range box-wing concept proposed in ref. [6]. A simplified sketch is provided in Fig. 7. The increase in drag caused by the larger fuselage is compensated by the reduction in induced drag provided by the box-wing configuration. The adoption of the box-wing configuration provides a clear advantage in reducing the overall dimensions for the same payload capacity, allowing the use of existing infrastructures designed for the CL-415 while doubling the aircraft water load capability; CL-415 maximum water loading capability is indeed equal to 6000 kg [15]. Attempting to reach the same payload increase with a conventional wing layout would require a much larger aircraft, especially with a larger wingspan. As a side effect, the configuration also improves aerodynamic efficiency, which, although not the main focus of the project, helps reduce fuel consumption and extend mission range, leading to improved firefighting performance.

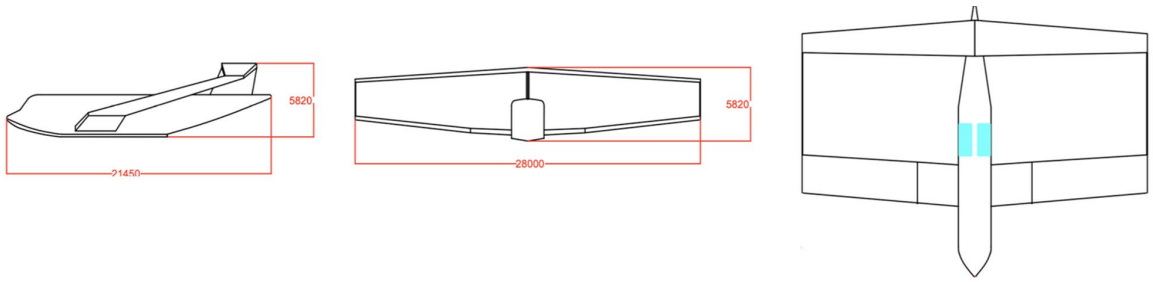


Figure 7. Simplified scheme of a possible solution of box-wing scooper aircraft. The units are mm.

Conclusions

This work presented a multidisciplinary, physics-based framework for the conceptual design and optimization of firefighting aircraft adopting a box-wing configuration. The developed tool demonstrated the ability to integrate aerodynamic, structural, and propulsive models within an integrated design environment, enabling the consistent assessment of unconventional aerodynamic layouts against mission-driven constraints. Preliminary results confirm that the box-wing architecture can substantially enhance lifting capability while maintaining the same overall wingspan of reference aircraft such as the CL-415, thus allowing higher water loads without requiring larger infrastructures or operational envelopes. The reduction in induced drag contributes to both aerodynamic and energetic efficiency, indirectly extending endurance during repetitive firefighting missions The developed framework establishes a solid foundation for future research on advanced firefighting box-wing architectures. Upcoming work will focus on a systematic exploration of the box-wing design space to identify the most promising trade-offs between aerodynamic efficiency, structural weight, and mission performance. This process will enable the selection of optimal configurations suitable for high-fidelity refinement and detailed development. Coupling with CFD and FEM tools will further enhance the predictive accuracy of the framework and support the transition from conceptual design to comprehensive multidisciplinary optimization of future firefighting aircraft.

References

[1] J.G. Pausas, J.E Keeley, Wildfires and global change, Frontiers in Ecology and the Environment 19 (2021) 387-395. https://doi.org/10.1002/fee.2359

[2] K. Rokhsaz, L. Kliment, J. Nelson, Flight Loads Analysis of CL-415 Scoopers, AIAA Aviation 2022 Forum (2022). https://doi.org/10.2514/6.2022-4015

[3] K. Abu Salem, G. Palaia, A. Frediani, E. Carrera, The box-wing configuration: a critical review of design approaches and applications, Progress in Aerospace Sciences (2025). https://doi.org/10.1016/j.paerosci.2025.101108

[4] A. Frediani, V. Cipolla, E. Rizzo, The PrandtlPlane configuration: overview on possible applications to civil aviation, Variational Analysis and Aerospace Engineering: Mathematical Challenges for Aerospace Design, Springer, Boston, MA, 2012. https://doi.org/10.1007/978-1-4614-2435-2_8

[5] A. Frediani, G. Montanari, Best wing system: an exact solution of the Prandtl's problem. Variational Analysis and Aerospace Engineering. Springer Optimization and Its Applications, Springer, New York, NY, 2009. https://doi.org/10.1007/978-0-387-95857-6_11

[6] K. Abu Salem, V. Cipolla, G. Palaia, V. Binante, D. Zanetti, A physics-based multidisciplinary approach for the preliminary design and performance analysis of a medium

range aircraft with box-wing architecture, Aerospace 8 (2021). https://doi.org/10.3390/aerospace8100292

[7] G. La Rocca, M.J. Van Tooren, Knowledge-based engineering approach to support aircraft multidisciplinary design and optimization, Journal of aircraft 46 (2009) 1875-1885. https://doi.org/10.2514/1.39028

[8] K. Abu Salem, G. Palaia, M. Carini, M. Méheut, M. Maganzi, C. Falcone, A CFD-based collaborative approach for box-wing aircraft aerodynamic assessment: the PARSIFAL study case, Aerotecnica Missili & Spazio 102 (2023) 385-407. https://doi.org/10.1007/s42496-023-00172-7

[9] E. Rizzo, A. Frediani, Application of optimisation algorithms to aircraft aerodynamics, Variational Analysis and Aerospace Engineering, Springer Optimization and its Applications, Springer, New York, NY, 2009. https://doi.org/10.1007/978-0-387-95857-6_23.

[10] K. Abu Salem, G. Palaia, V. Cipolla, V. Binante, D. Zanetti, M.R. Chiarelli, Tools and methodologies for box-wing aircraft conceptual aerodynamic design and aeromechanic analysis, Mechanics & Industry 22 (2021). https://doi.org/10.1051/meca/2021037

[11] K. Abu Salem, G. Palaia, A.A. Quarta, M.R. Chiarelli, Preliminary analysis of the stability and controllability of a box-wing aircraft configuration, Aerospace 10 (2023). https://doi.org/10.3390/aerospace10100874

[12] J.D. Mattingly, W.H. Heiser, D.H. Daley, Aircraft Engine Design, 3rd ed, American Institute of Aeronautics and Astronautics: Washington, DC, USA, 2018. https://arc.aiaa.org/doi/book/10.2514/4.105173

[13] M.P. Scardaoni, M. Montemurro, E. Panettieri, PrandtlPlane wing-box least-weight design: a multi-scale optimisation approach, Aerospace Science and Technology 106 (2020). https://doi.org/10.1016/j.ast.2020.106156

[14] G. Palaia, K. Abu Salem, V. Binante, E. Carrera, Metamodeling approach for wing structural sizing of box-wing aircraft, Journal of Aircraft (2025) 1-10. https://doi.org/10.2514/1.C038131

[15] C. Calbrix, A. Stoukov, A. Cadiere, B. Roig, D. Legendre, Numerical simulation of aerial liquid drops of Canadair CL-415 and Dash-8 airtankers, International journal of wildland fire, 32 (2023), 1515-1528. https://doi.org/10.1071/WF22147

Materials Research Proceedings 69 (2026) 469-474 https://doi.org/10.21741/9781644904251-85

Systematic Aircraft Propulsive System Generation for Sizing, Evaluation and Selection

Enzo DELLA BELLA[1,2,3,a *], Valérie POMMIER-BUDINGER[1,b], Scott DELBECQ[1,c], Joël JEZEGOU[1,d], Marija JANKOVIC[2,e] and Alain LEFEBVRE[3,f]

[1]Fédération ENAC ISAE-SUPAERO ONERA, Université de Toulouse, 10 avenue Marc Pélegrin, Toulouse, France

[2]Laboratoire Génie Industriel, CentraleSupélec, Université Paris-Saclay, 91190 Gif-sur Yvette, France

[3]Safran Tech, 78772 Châteaufort, Magny-Les-Hameaux, France

[a]enzo.della-bella@isae-supaero.fr, [b]valerie.budinger@isae-supaero.fr, [c]scott.delbecq@isae-supaero.fr, [d]joel.jezegou@isae-supaero.fr, [e]marija.jankovic@centralesupelec.fr, [f]alain.lefebvre@safrangroup.com

Keywords: System Architecture, Automatic Architecture Generation, Safety, Aircraft Design, Hybrid-Electric Aircraft

Abstract. To mitigate the projected increase in emissions of the aeronautical sector, companies investigate novel propulsive systems. Three main aspects are considered: energy sources (e.g., electricity, hydrogen), powertrain technologies and equipment (e.g., fuel cells, smart motors), and propulsive architectures (e.g., series/parallel hybrid-electric, distributed propulsion). The need to study these alternatives results in a vast design space, as each potential solution has benefits and drawbacks. To facilitate the exploration of the design space, this paper presents a methodology to generate, evaluate and select aircraft propulsive architectures. The application of the method to design the propulsive system of a twin-engine commuter aircraft illustrates its capabilities. It enables easy comparison between propulsive architectures, hybridization strategies and technology assumptions.

Introduction

The aeronautical sector contributes to approximately 2.5% of the global greenhouse emissions [1]. Moreover, these contributions are expected to increase in the next decades [2]. To mitigate this impact, the members of the International Civil Aviation Organization (ICAO) have an objective to reach net zero emissions by 2050. Several levers will be necessary to reach this goal, such as improvements in technology and optimization of traffic management. This work focuses on technological enhancement, more specifically aircraft propulsion systems, considering three categories of decision-making levers coordinated through a systematic approach: the type of energy sources (e.g., electricity, drop-in fuel, hydrogen), the powertrain equipment and technologies considered (internal combustion engines, fuel cells, smart motors) and the propulsive architecture (e.g., hybrid-electric series/parallel, distributed propulsion).

The literature shows that numerous propulsive architectures are investigated for the purpose of decarbonizing air transport by increasing energy efficiency or the usage of less carbon intensive energy carriers [3]. Several studies explore the viability of hybrid-electric configurations [4–6]. Two types of hybridization are considered: series or parallel. The former consists of connecting a generator to the turbine in order to produce electricity, while the latter relies on separate electrical and thermal chains [3]. Hybridization may also be combined with other innovative technologies and configurations, such as distributed propulsion [7] or blended wing body aircraft [8]. Another potential solution for decarbonation is hydrogen-based propulsion. The hydrogen can either be

Content from this work may be used under the terms of the Creative Commons Attribution 3.0 license. Any further distribution of this work must maintain attribution to the author(s) and the title of the work, journal citation and DOI. Published under license by Materials Research Forum LLC.

Materials Research Proceedings 69 (2026) 469-474 https://doi.org/10.21741/9781644904251-85

used for combustion directly [9–11], which eliminates the emission of CO_2 during flight, or to produce electricity via fuel cells [12,13], thus removing both NO_x and CO_2 emissions in flight. Studies suggest that fuel cell may be well-suited for small aircraft, whereas larger aircraft are more likely to require hydrogen combustion, as the higher efficiency of fuel cell powertrains does not compensate for their limited power density [3,14].

This diversity of energy sources, powertrain equipment and propulsive architectures expands the propulsive system design space significantly. Furthermore, according to the state of the art, hybrid-electric and fuel cell configurations appear to increase aircraft weight, but have a better carbon intensity. Thus, trade-offs are required to find the most appropriate solution in each technological scenario. In this context, automatic generation of propulsive architectures for their simulation and evaluation enables a broader range of potential solutions to be explored more rapidly than with the usual process. The aim of this work is to introduce a tool to systematically generate, evaluate and select propulsive system architectures. This tool is meant to help system architects in the exploration of the design space and in their decision-making process.

Proposition of a workflow to generate, evaluate and select propulsive architectures

The workflow is illustrated in Fig. 1 and consists of the following three major steps: propulsive architecture generation, systematic evaluation and selection of the most promising architectures.

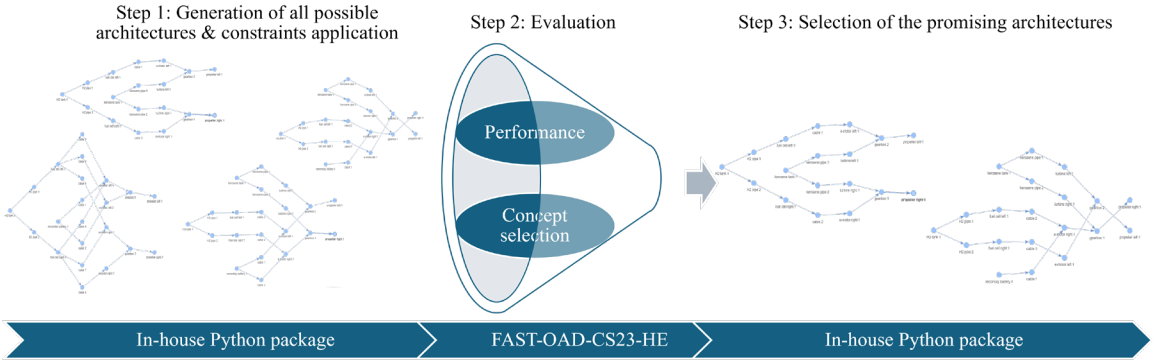


Fig. 1: Proposed workflow

The first step is the generation of the architectures. It explores all the decisions concerning the three decision-making levers mentioned in the introduction. The architecture generation algorithm, implemented as an in-house Python package, uses matrices [15] and combinatorial methods to explore the design space systematically, thus returning all possible propulsive system configurations with respect to the functional architecture and components compatibility. The exhaustive nature of the generation ensures the reproducibility of the process. The algorithm enumerates the propulsive system architectures and filters them using a sequence of constraints to ensure their validity according to relevant system safety requirements addressing the probability of occurrence of failure conditions related to loss of thrust failure scenarios. They verify the failure rate of the architectures using the minimal cut sets method [16] and the power loss associated with the failure of key components, such as power sources.

In the second step, the pre-selected architectures are evaluated one by one on a predetermined mission. This includes the sizing of the components of the propulsive system, and the estimation of the global energy performance of the aircraft. The overall aircraft evaluation is performed from scratch for each architecture to ensure a representative design. The open-source Python framework FAST-OAD-CS23-HE [17], which allows the preliminary design and analysis of hybrid-electric general aviation aircraft, was chosen to conduct this evaluation. It provides the flexibility necessary to evaluate the diverse architectures generated during the first step of the workflow. Extensive data

Materials Research Proceedings 69 (2026) 469-474 https://doi.org/10.21741/9781644904251-85

is available after the simulation, among which the mass breakdown of the aircraft and some performance figures (e.g., energy consumption, emissions).

Finally, these data are processed by an in-house Python algorithm that achieves the final selection according to predefined criteria characterized by metrics. They include, but are not limited to, the maximum take-off mass (MTOM), the operating empty mass, the energy and fuel consumption, and the CO_2 emissions for a typical mission. Even though this paper focuses on the evaluation and the selection of the propulsive configurations, the metrics concern the aircraft. Indeed, the design of a propulsive system cannot be separated from the design of the entire aircraft, as the mass and energy consumption of the aircraft are intertwined in a sizing loop.

Case study: twin-engine commuter aircraft

The tool presented in the previous section was used to design a twin-engine commuter aircraft, with either a conventional thermal propulsive system or a hybrid-electric configuration. Hybrid-electric systems present an additional variability with the number of batteries used and the way they are connected to the electric motors. Indeed, multiple batteries may be used, for instance to satisfy quantitative safety objectives from small airplanes certification requirements, and each battery may be connected to one or several electric motors. In this study, we consider either one or two batteries, each connected to either one or both electric motors. The aircraft is based on the geometry of the Daher Kodiak 100. However, the propulsion system is switched from a single- to a twin-engine layout, as illustrated in Fig. 2.

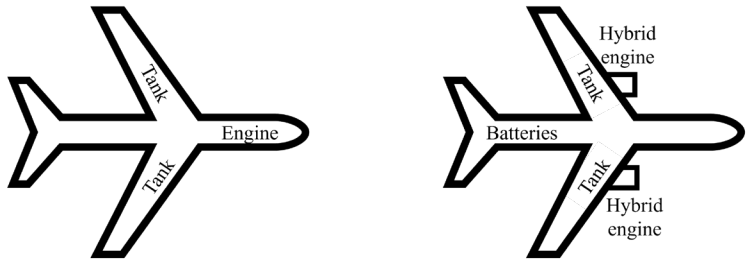


Fig. 2: Propulsive layout of the conventional Kodiak 100 (left) and of the twin-engine Kodiak 100 considered for this study (right)

Table 1 presents the top-level aircraft requirements considered for the sizing, with multiple options for the range. They were identical for all the propulsive architectures generated. In particular, the possible ranges were tested for each configuration. In addition, the tool supports multiple technology scenarios. This work specifically studies the influence of battery specific energy. The values considered are in Table 2. Scenario 1 represents state-of-the-art batteries, and scenarios 2 and 3 represent different levels of technology improvements, in line with values from battery technologies reviews [18,19].

Table 1: Aircraft requirements and mission definition

Range [NM]	**Cruise speed [kt]**	**Cruise altitude [ft]**	**Payload [kg]**
200, 300, 500, 700, 800, 1000	120	10000	400

Table 2: Battery specific energy scenarios

Scenario	1	2	3
Battery specific energy [Wh/kg]	250	500	1000

For each hybrid architecture, multiple hybridization strategies are considered. In this paper, hybridization ratio is defined as a fixed percentage of electric power over thermal power for each flight phase. In FAST-OAD-CS23-HE, the mission is divided into four phases (climb, cruise,

Materials Research Proceedings 69 (2026) 469-474 https://doi.org/10.21741/9781644904251-85

descent and reserves). The hybridization strategies chosen for this study follow the same split. Five hybridization ratios were considered (5%, 10%, 15%, 25% and 50%), combined with four combinations of phases: climb, climb-descent, climb-descent-reserves, and full mission.

The generation algorithm found, after the constraints, 9 architectures (1 thermal and 8 hybrid-electric) in 2 seconds. Combined with the 3 technology scenarios and 20 hybridization strategies, a total of 481 configurations (one thermal and 160 hybrid-electric for each scenario) were submitted for sizing and evaluation with FAST-OAD-CS23-HE. For reference, the computation time to size and evaluate all the configurations on a laptop using 11-core multiprocessing varies from 2 to 3 hours depending on the range, as the convergence is faster for shorter ranges.

Table 3 presents the overall results of the simulation. The first metric considered is the number of configurations that led to a successful sizing of the aircraft. For short ranges, up to 300 NM, sizing an aircraft is possible for 473 of the 481 configurations, at constant payload but with an increase in MTOM. The remaining 8 are hybrid configurations with a constant 50% hybridization in scenario 1. As the range increases, the number of feasible configurations decreases. As expected, the number of feasible configurations decreases faster for state-of-the-art batteries (scenario 1) than for the two future technology assumptions (scenarios 2 and 3). The second metric used in this work is the number of points on the Pareto front of each scenario, relative to two parameters: MTOM and emissions. In scenario 1, for all ranges, only one point is on the Pareto front: the kerosene configuration. Thus, state-of-the-art batteries do not allow for a hybrid configuration to improve the emissions on the considered missions. In scenarios 2 and 3, multiple hybrid configurations are on the Pareto fronts. As range increases, the number of points decreases, until no hybrid configurations are Pareto-optimal. Such a table shows up to which range hybrid-electric configurations are interesting compared to conventional propulsive systems for a given technology improvement scenario.

Table 3: Number of Pareto-optimal solutions / number of feasible solutions

Range [NM]	**200**	**300**	**500**	**700**	**800**	**1000**
Scenario 1	1/152	1/152	1/144	1/138	1/138	1/136
Scenario 2	7/160	5/160	1/152	1/152	1/152	1/145
Scenario 3	15/160	11/160	11/160	7/159	3/160	1/154

The selection process is based on Pareto fronts. Fig. 3 presents the Pareto front of emissions over the mission versus MTOM obtained for a range of 300 NM. They are normalized using the kerosene configuration as reference. The emissions are computed using the French electric mix for hybrid architectures. The graph highlights the impact of the battery specific energy on the performance of the configurations. The point of minimum MTOM (in green on the graph) corresponds to the conventional kerosene configuration. As the only variability in terms of technology assumptions is the specific energy of the batteries, this point is identical for all three scenarios. For scenario 1 (in green), none of the hybrid architectures are optimal. However, several architectures can bring improvements in terms of emissions in the more favorable scenarios 2 and 3 (in red and blue, respectively). The results also show that for both scenarios 2 and 3, a hybridization strategy increasing electrical energy consumption results in a reduction of emissions. The corresponding increase in MTOM depends on the technology assumptions.

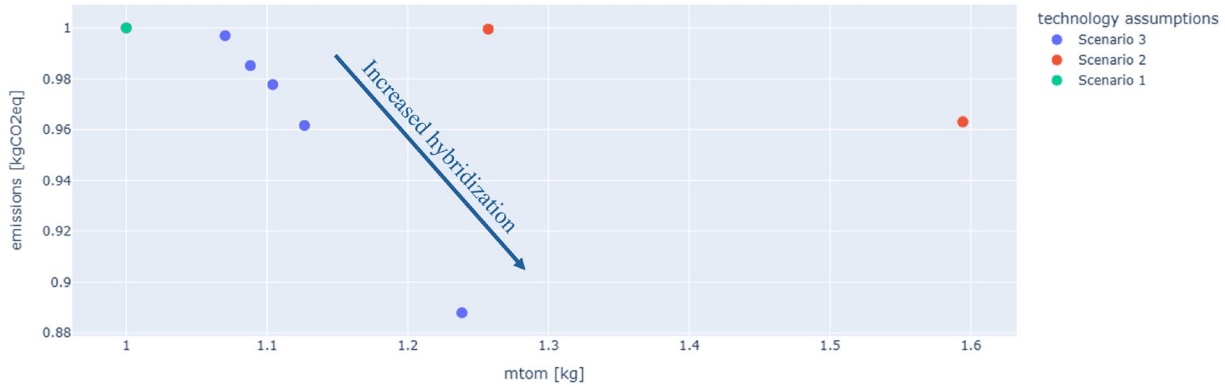


Fig. 3: Pareto front for a 300 NM range

This process provides interesting results. However, it presents some limitations. First, the sizing of the horizontal tail is not covered, which impacts the controllability of the aircraft. Furthermore, this work focuses only on hybridization with batteries. In future work, the scope will be extended to hybridization with hydrogen fuel cells.

Conclusion

This paper proposes a tool to assist system architects in the design of innovative aircraft propulsive systems. A matrix-based methodology is implemented to generate propulsive architectures systematically. A set of constraints is then verified to ensure compliance with reliability requirements. The second step is to size and evaluate the remaining architectures using the open-source aircraft sizing tool FAST-OAD-CS23-HE. The most promising architectures are then selected. An application on the propulsive system of a twin-engine commuter aircraft is presented. It investigated the feasibility of a battery-kerosene hybrid-electric configuration compared to the conventional kerosene propulsive system, with the inclusion of three technology assumptions regarding battery specific energy. The results show that batteries with the current level of technology cannot be used to reduce emissions for the considered missions. However, a reduction can be achieved with higher battery specific energy, and this reduction increases with higher degrees of hybridization. Perspectives for future work include a more complete aircraft design process, with the consideration of horizontal tail sizing, the addition of hydrogen-based propulsive systems, and an application to a regional aircraft.

References

[1] Delbecq, S., Fontane, J., Gourdain, N., Planès, T., and Simatos, F., 2023, "Sustainable Aviation in the Context of the Paris Agreement: A Review of Prospective Scenarios and Their Technological Mitigation Levers," Progress in Aerospace Sciences, **141**, p. 100920. https://doi.org/10.1016/j.paerosci.2023.100920

[2] ICAO, "Trends in Emissions That Affect Climate Change." [Online]. Available: https://www.icao.int/environmental-protection/Pages/ClimateChange_Trends.aspx.

[3] Sirtori, G., Aigner, B., Wehrle, E., Riboldi, C. E. D., and Trainelli, L., 2025, "Innovative Aircraft Propulsive Configurations: Technology Evaluation and Operations in the SIENA Project," Aerospace, **12**(3). https://doi.org/10.3390/aerospace12030240

[4] Antcliff, K., Guynn, M., Marien, T., Wells, D., Schneider, S., and Tong, M., 2016, "Mission Analysis and Aircraft Sizing of a Hybrid-Electric Regional Aircraft." https://doi.org/10.2514/6.2016-1028

[5] Riboldi, C. E. D., 2018, "An Optimal Approach to the Preliminary Design of Small Hybrid-Electric Aircraft," Aerospace Science and Technology, **81**, pp. 14–31. https://doi.org/10.1016/j.ast.2018.07.042

[6] Moebs, N., Eisenhut, D., Windels, E., Pols, J., and Strohmayer, A., 2022, "Adaptive Initial Sizing Method and Safety Assessment for Hybrid-Electric Regional Aircraft," Aerospace, **9**, p. 150. https://doi.org/10.3390/aerospace9030150

[7] Balack, P., Atanasov, G., and Zill, T., 2023, "Architectural Trade-Offs for a Hybrid-Electric Regional Aircraft." https://doi.org/10.13009/EUCASS2023-463

[8] Patel, S., Ahuja, J., Ragauss, E., Gladin, J., and Mavris, D., 2024, "Development of a Blended Wing Body Aircraft with Hydrogen-Electric Hybrid Distributed Propulsion." https://doi.org/10.2514/6.2024-0282

[9] Guo, Y., Chow, J., Chen, H., Qiao, X., and Fan, C., 2024, "Conceptual Design and Optimization of a Hydrogen-Powered Aircraft with a Dorsal Tank Layout," Journal of Physics: Conference Series, **2882**(1), p. 012022. https://doi.org/10.1088/1742-6596/2882/1/012022

[10] Nguyen Van, E., Gauvrit-Ledogar, J., Julien, C., Paluch, B., Ruan, J. L., and Moens, F., 2024, "Impact of Hydrogen Fuel on Overall Design of Transport Aircraft," *ICAS 2024*, Florence, Italy. [Online]. Available: https://hal.science/hal-04778307

[11] O'Sullivan, G., Horvat, A. B., Jézégou, J., Carrasco, B. J., and André, R., 2025, "Hydrogen Aircraft, Technologies and Operations Towards Certification Readiness Level 1," Aerospace, **12**(6). https://doi.org/10.3390/aerospace12060490

[12] Marinaro, G., Di Lorenzo, G., and Antonio, P., 2022, "From a Battery-Based to a PEM Fuel Cell-Based Propulsion Architecture on a Lightweight Full Electric Aircraft: A Comparative Numerical Study," Aerospace, **9**. https://doi.org/10.3390/aerospace9080408

[13] Vonhoff, G. L. M., 2021, "Conceptual Design of Hydrogen Fuel Cell Aircraft," TU Delft. [Online]. Available: https://resolver.tudelft.nl/uuid:8bd63dec-b67b-496b-92bc-3d5c07ff859f

[14] Aigner, B., Wehrle, E., Struiwig, W., Sirtori, G., Riboldi, C. E. D., and Trainelli, L., 2023, "Consideration of Technology Scalability in the Design of Electric Propulsion System Architectures." https://doi.org/10.13009/EUCASS2023-273

[15] Bryant, C., Mcadams, D., Stone, R., Kurtoglu, T., and Campbell, M., 2005, "A Computational Technique for Concept Generation," *ASME 2005 International Design Engineering Technical Conferences & Computers and Information in Engineering Conference*, Long Beach, California USA. https://doi.org/10.1115/DETC2005-85323

[16] Billinton, R., and Allan, R. N., 1992, *Reliability Evaluation of Engineering Systems: Concepts and Techniques*, Springer, Boston, MA.

[17] Lutz, F., Jezegou, J., Budinger, M., and Reysset, A., 2025, "Open-Source Framework for Sizing Hybrid and Electric General Aviation Aircraft," Journal of Aircraft, **62**(2), pp. 381–395. https://doi.org/10.2514/1.C038004

[18] Pattanayak, T., and Mavris, D., 2025, "Battery Technology for Sustainable Aviation: A Review of Current Trends and Future Prospects," Applied Energy, **397**, p. 126356. https://doi.org/10.1016/j.apenergy.2025.126356

[19] Townsend, A., Jiya, I. N., Martinson, C., Bessarabov, D., and Gouws, R., 2020, "A Comprehensive Review of Energy Sources for Unmanned Aerial Vehicles, Their Shortfalls and Opportunities for Improvements," Heliyon, **6**(11), p. e05285. https://doi.org/10.1016/j.heliyon.2020.e05285

Materials Research Proceedings 69 (2026) 475-480 https://doi.org/10.21741/9781644904251-86

Aerodynamic Efficiency of Longitudinally Unstable Tailless Aircraft

Stefan RIETHAUSEN[1,a *], David LUNDSTRÖM[1,b] and Petter KRUS[1,c]

[1]Linköping University, Department of Management and Engineering, Fluid and Mechatronic Systems, SE-581 83 Linköping, Sweden

[a]stefan.riethausen@liu.se, [b]david.lundstrom@liu.se, [c]petter.krus@liu.se

Keywords: Tailless Aircraft, Stability Augmentation, Unmanned Aerial Vehicle, Aerodynamic Efficiency, Flight Testing

Abstract. A tailless unmanned aerial vehicle (UAV) to measure the efficiency difference of stable and augmented unstable flight was developed, built and flown. An overview of the UAV and its systems is given along with the test flight procedure. The measurements are then compared between stable and augmented unstable configuration to draw conclusions.

Introduction

Rapid developments in hardware and software over the last decades have improved UAVs flight characteristics, autonomous capabilities and operational efficiency, making them a viable option for a wide range of applications. Tailless aircraft and flying wings are an attractive category of UAVs due to their structural simplicity and resulting robustness, as well as their potential for reduced parasitic drag. However, the compromises required to achieve longitudinal stability in these configurations, such as wing twist or reflex airfoils, reduce aerodynamic efficiency. By instead discarding inherent stability in favour of an unstable design with active stabilisation, these drawbacks can be avoided and conventional high-performance airfoils can be used. This approach potentially enables a tailless UAV to be more efficient than conventional configurations. An unstable tailless UAV was first designed and flown by S. Morris, R. Miley and D. Larkin in 1987 [1]. In a theoretical study S. Morris also found that a tailless aircraft with an augmentation system could result in a 13% reduction in drag compared to a non-stabilised tailless aircraft with the same handling qualities [2]. Similarly, a study by I. L. Ashkenas and D. H. Klyde found a potential improvement in range by 14% at best cruise altitude of an unstable flying wing compared to a stable configuration [3].

In order to test the above hypothesis a UAV test platform and control system have been developed to measure the efficiency difference between stable and augmented unstable flight. To measure the efficiency, the UAV was outfitted with instruments to measure the power consumption of its propulsion system, flight control system and actuators, as well as attitude, barometric altitude, airspeed and GNSS data.

Method

Test Aircraft. The test aircraft is a conventional tailless aircraft of moderate aspect ratio and without sweep, shown in Fig. 1. It has a mass of 1.92 kg, wingspan of 1.904 m and wing area of 0.5712 m^2. The centre of mass can be shifted from 77 mm to 106 mm, which corresponds to a shift in static margin from 5.18% to -4.40%.

Content from this work may be used under the terms of the Creative Commons Attribution 3.0 license. Any further distribution of this work must maintain attribution to the author(s) and the title of the work, journal citation and DOI. Published under license by Materials Research Forum LLC.

Materials Research Proceedings 69 (2026) 475-480 https://doi.org/10.21741/9781644904251-86

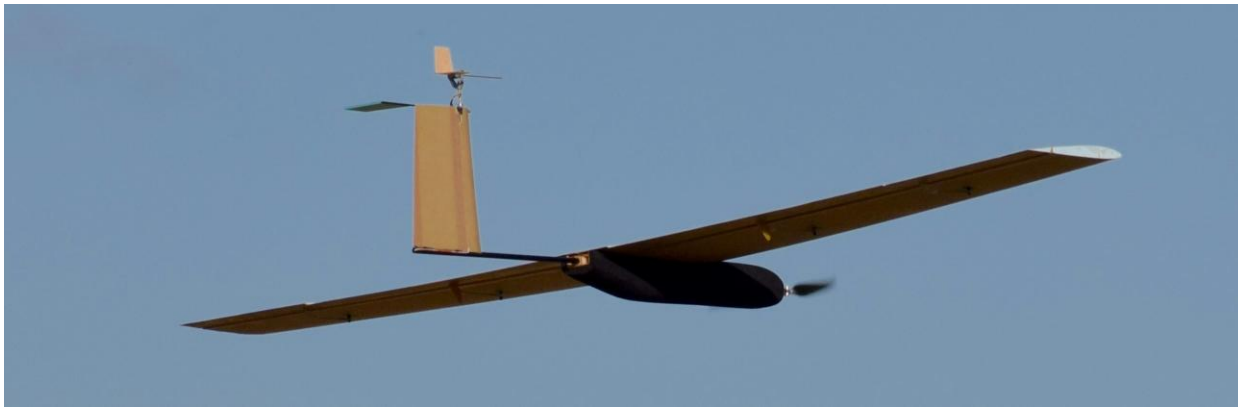


Figure 1: test aircraft

In order to balance the aircraft in statically stable configuration, an airfoil with a positive pitching moment is required. The test aircrafts airfoil (TAA) is a custom low camber and low moment airfoil. By deflecting the flap, the pitching moment coefficient can be increased to that of a high-performance reflex airfoil (HS-117) without large performance penalties, as shown in Fig. 2 [4, 5].

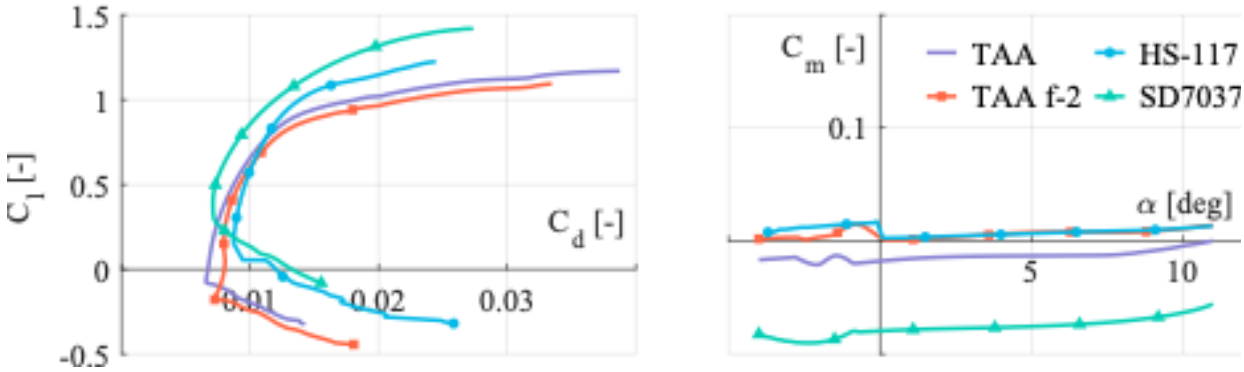


Figure 2: airfoil data (XFOIL simulation, Re = 3× 10^5)

The test aircrafts system diagram is shown in Fig. 3. Its propulsion side consist of a T-Motor MT2814 770 kV, aero-naut CAMcarbon 11 × 6" propeller with a 52 mm centre hub, 40 A Turnigy Plush electronic speed controller and a 4-cell 2.7 Ah lithium-polymer battery. The power consumption of the propulsion side was measured by the autopilots on-board current and voltage sensor, using the standard calibration parameters given by the manufacturer.

The autopilot is a Matek Systems H743-WLITE running Ardupilot v4.5.7 and used for automatic circling and data recording. Stabilisation of the aircraft in pitch is achieved through a custom flight controller, using a combination of pitch rate and angle of attack from its own set of sensors. Besides the on-board sensors, an external GNSS module (Matek Systems M10Q-5883), an airspeed sensor based on a Sensirion SDP31 with a pressure range of ±500 Pa, and an external current sensor to measure the power consumption of the actuator side are connected to the autopilot. The airspeed sensor was calibrated with the GNSS speed in automatic circle flight. Calibration of barometric altitude is done automatically by the autopilot at bootup. The actuator side consist of two Dualsky AS82MG servos used for the ailerons, two Align DS535 servos used for the pitch control flaps and a 2-cell 1 Ah lithium-polymer battery. The current sensor to measure the flight control battery power consumption is an Allegro Microsystems ACS71240KEXBLT-010B3 with a range of ±10 A on a carrier board made by Pololu. The flight control battery voltage was measured on the battery side of the sensor carrier PCB through one of the autopilots analogue

Materials Research Proceedings 69 (2026) 475-480 https://doi.org/10.21741/9781644904251-86

to digital converter inputs. The scaling parameters for the autopilots sensor inputs were calculated from sensor characteristics given by the manufacturer.

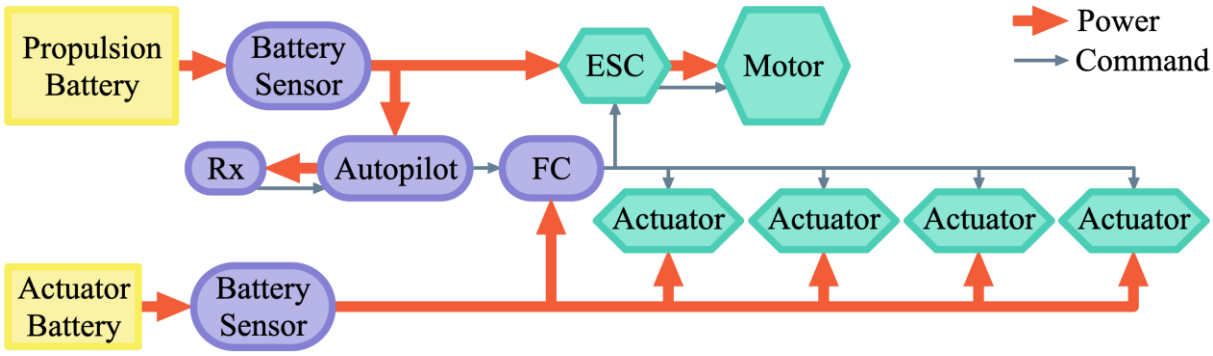


Figure 3: system diagram of the test aircraft

Test Flights. Each test flight consisted of three phases. The take-off and landing were controlled manually, while the measurement phase was controlled by the autopilot. After engagement of the automatic mode, the aircraft climbs to a set altitude and circles the point of engagement with a radius of 100 m while keeping the barometric altitude and airspeed constant at 80 m and 13 m/s. When the flight time reached 15 min, the last circle was completed and the automatic mode disengaged. After the landing the batteries were replaced and the centre of mass shifted to the alternate position for the next flight. The turnaround time between test flights was approximately 10 to 15 min.

Results

The test flights were conducted over three consecutive days. To process the data, the test flights were trimmed to the measurement phase and until airspeed and barometric altitude are stable. The points of largest longitude were then used to divide the test flights into circles and further trim the beginning and end of the flight. In total 34 test flights were conducted, amounting to 284 and 287 circles in unstable and stable configuration. The mean and median power draw per circle were calculated and are shown in histograms in Fig 4. Additionally, histograms of pitch and roll attitude, as well as barometric altitude and airspeed measurements are shown in Fig. 5. Mean, standard deviation, median and interquartile range values are listed in Table 1 and Table 2. The Fourier transform of pitch and roll attitude data is shown in Fig. 6.

Materials Research Proceedings 69 (2026) 475-480 https://doi.org/10.21741/9781644904251-86

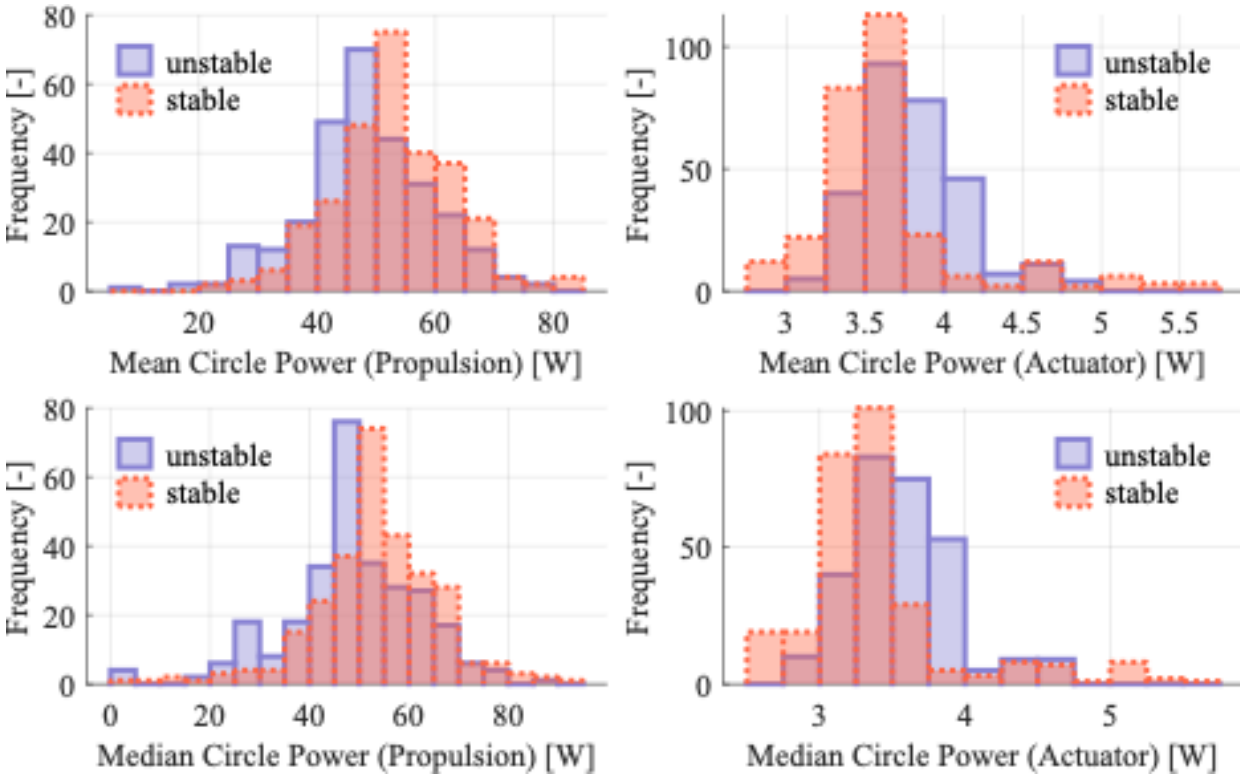


Figure 4: circle power histograms

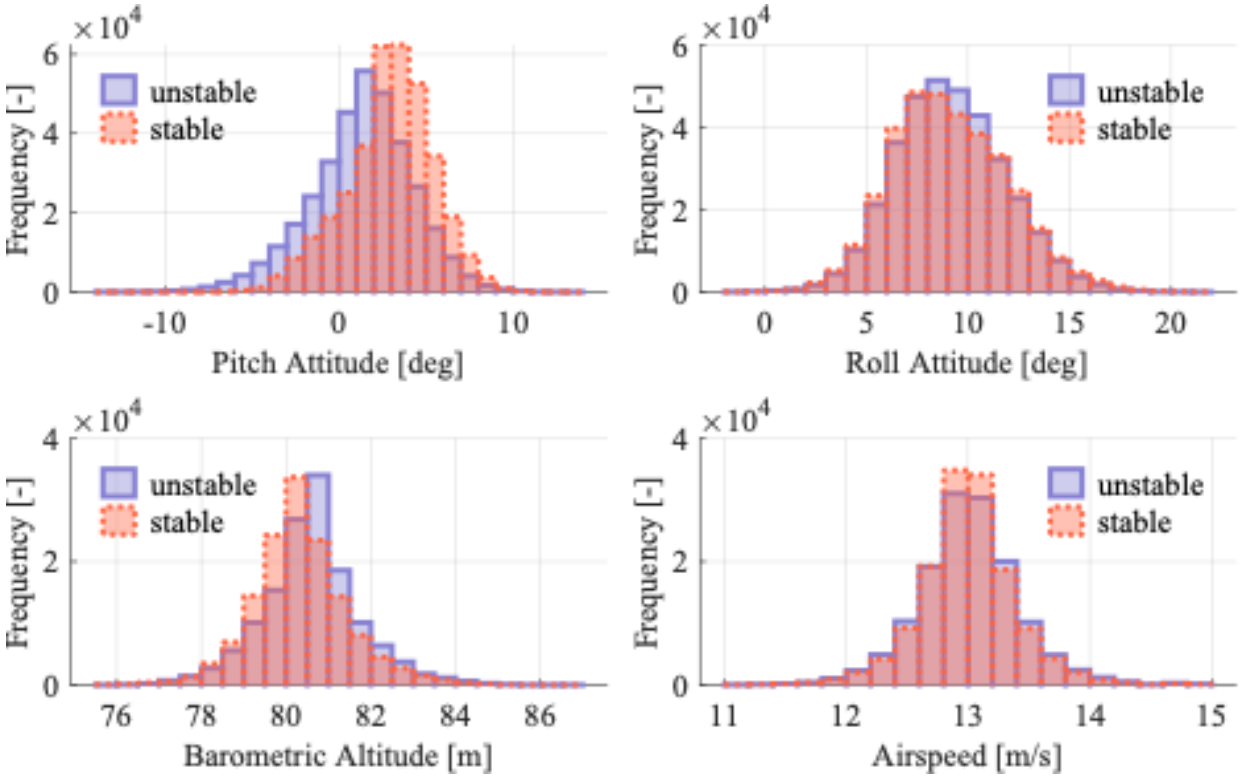


Figure 5: attitude, altitude and airspeed histograms

Materials Research Proceedings 69 (2026) 475-480 https://doi.org/10.21741/9781644904251-86

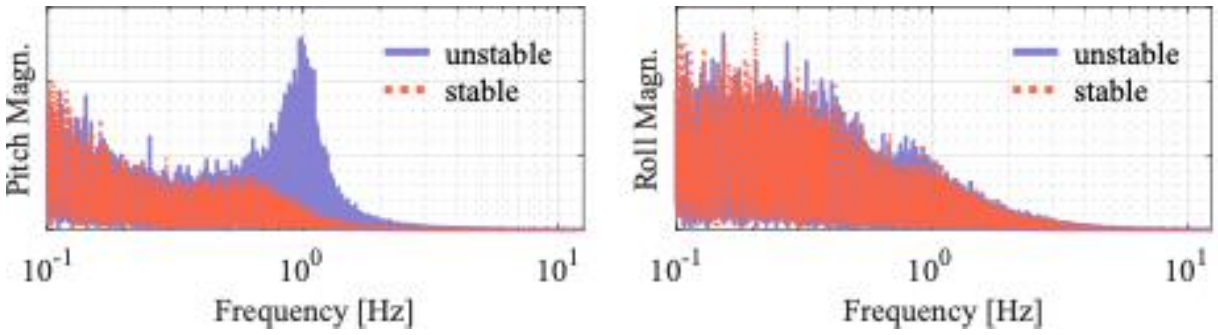


Figure 6: Fourier transform of pitch & roll attitude

Table 1: mean & standard deviation

	Mean		Standard Deviation	
	unstable	stable	unstable	stable
Mean Circle Power (Propulsion) [W]	48.34	52.87	10.99	10.12
Mean Circle Power (Actuator) [W]	3.80	3.64	0.33	0.50
Circle Duration [s]	49.25	49.19	1.07	1.20
Pitch Attitude [deg]	1.29	2.90	2.95	2.50
Roll Attitude [deg]	9.14	9.15	2.69	2.87
Airspeed [m/s]	13.01	13.00	0.42	0.40
Barometric Altitude [m]	80.60	80.34	1.15	1.12

Table 2: median & interquartile range

	Median		Interquartile Range	
	unstable	stable	unstable	stable
Median Circle Power (Propulsion) [W]	48.21	53.21	14.89	13.11
Median Circle Power (Actuator) [W]	3.52	3.30	0.44	0.38
Circle Duration [s]	49.22	48.98	1.40	1.44
Pitch Attitude [deg]	1.50	3.08	3.61	3.07
Roll Attitude [deg]	9.01	8.92	3.63	3.97
Airspeed [m/s]	13.00	13.00	0.47	0.41
Barometric Altitude [m]	80.60	80.27	1.20	1.24

Discussion

When comparing roll attitude, barometric altitude, airspeed and circle duration, it can be seen, that there are only minor differences between the two configurations. However, during the test flights in unstable configuration, an occasional oscillation in pitch was observed. This oscillation is visible through a distinct peak at 1 Hz in the Fourier transform of the pitch attitude data when compared to the stable configuration, see Fig. 6. The initial design of the aircraft and augmentation system did not include the autopilot and its sensors, which increased the mass of the aircraft by over 10%. The addition also decreased the static margin from -3.74% to -4.40%. Furthermore, the autopilot includes a stabilisation loop at lower rate, and test flights were performed in the lower half of the augmentation systems design speed range. Therefore, the controller gains are likely not optimal and a potential source for the oscillation. Comparing the distributions of pitch attitude data, no significant impact of the oscillation besides a small increase in standard deviation and interquartile

range is visible. In case the oscillation has an impact, it likely decreases the performance due to the dynamic loading of the wing and resulting increased average drag.

When comparing the actuator power draw, an increase is visible for the unstable configuration. This effect is to be expected as a consequence of the augmentation system correcting small disturbances, that would otherwise be damped by the aircrafts natural stability. The aforementioned oscillation possibly increase the actuator power draw further due to the resulting large control surface deflections and thus greater actuator loads. Comparing the propulsion power draw, a decrease by over 4 W is visible for the unstable configuration. Combining the propulsion and actuator power draw, the unstable configuration is at least 8% more efficient than the stable configuration. In addition, the efficiency of electronic speed controller and motor generally decreases at lower duty cycles [6]. This would result in a greater difference of the aerodynamic efficiency of the two configurations compared to the measured difference in power draw. Since the aircraft was to be flown both stable and unstable, a compromise in the airfoil selection had to be made. Generally, conventional airfoils tend to perform better than reflex airfoils, as visible in Fig. 2. Since unstable flight enables the use of conventional airfoils for tailless aircraft, it is likely that the use of such an airfoil would increase the performance difference further.

Conclusion

Efficiency measurements of a tailless aircraft in stable and unstable augmented configuration have been performed. The aircraft is at least 8% more efficient in unstable configuration at the tested airspeed of 13 m/s. Compromises in the aircrafts design point towards a possible further increase in efficiency of an augmented unstable tailless aircraft over a conventional stable design.

References

[1] Unstable Tailless Demonstrator, https://www.youtube.com/watch?v=JfKrUbJYk74, retrieved 2025.11.10

[2] S.J. Morris, Integrated Aerodynamics and Control System Design for Tailless Aircraft, AIAA Guidance, Navigation and Control Conference, Hilton Head Island, South Carolina, 1992, p. 4604. https://doi.org/10.2514/6.1992-4604

[3] I. L. Ashkenas, D. H. Klyde, Tailless aircraft performance improvements with relaxed static stability, NASA-CR-181806, 1989

[4] Reflex Airfoil Database, https://www.aerodesign.de/profile/profile_sp.htm, retrieved 2025.11.10

[5] UIUC Airfoil Database, https://m-selig.ae.illinois.edu/ads/coord_database.html, retrieved 2025.11.10

[6] D. Lundström, K. Amadori, P. Krus, Validation of Models for Small Scale Electric Propulsion Systems, 48th AIAA Aerospace Sciences Meeting Including the New Horizons Forum and Aerospace Exposition, 2010, p. 483. https://doi.org/10.2514/6.2010-483

Materials Research Proceedings 69 (2026) 481-486 https://doi.org/10.21741/9781644904251-87

An Energy-Centric Approach for Evaluating Climate Impact Levers in Conceptual Aircraft Design

Kristina MAZUR[1,a,*], and Mirko HORNUNG[1,b]

[1]Technical University of Munich, Chair of Aircraft Design, Bolzmannstr. 15, 85748 Garching, Germany

[a]kristina.mazur@tum.de, [b]mirko.hornung@tum.de

Keywords: Aircraft Design, Energetic Assessment, Climate Impact Assessment, Fractional Change

Abstract. Achieving net-zero emissions in aviation by 2050 requires systematic evaluation of emerging mitigation measures. Based on full pre-studies, this paper presents a methodological shift from complex approaches toward a sensitivity assessment. Building on the hypothesis that energy demand is the dominant cause of climate impact, a first-order approach is developed. It determines fractional change functions for mission energy and global warming potential depending on key aircraft and mission parameters. Based on a wide-body case study (70 missions and ten aircraft variants), the mission energy function results in a high goodness-of-fit and includes elasticity coefficients, which are statistically significant. Extended by a simplified climate impact model, the global warming potential function indicates a two-third contribution from fuel-related emissions (CO_2, H_2O, NO_x), with the remaining related to aircraft-induced cloudiness.

Introduction

Sustainability is one of the defining challenges shaping the future of aviation. For that, mitigation strategies, such as new aircraft concepts and technologies, have to be assessed in the early stages of conceptual aircraft design. While Life Cycle Assessment (LCA) provides a holistic framework for comparing strategies, its application in conceptual design is hindered by high complexity and data uncertainties. The reliance on numerous, often unavailable, inputs make the prediction of reliable absolute impact values - such as the climate impact in kg CO2-equivalent - a significant challenge, potentially obscuring the key drivers of change and leading to conclusions that are not robust. To address this, this paper introduces a methodological shift from absolute quantification to a sensitivity assessment. We propose a simplified, first-order framework *LEVER* (Low-fidelity Energy-based Valuation for Emission Reduction), built on the central hypothesis that ”energy demand is key”. By using a fractional change approach, the model is designed to provide clear, intuitive insights into fundamental design trade-offs. The research question is therefore:

Can a simplified, fractional change, energy-centric approach provide clear and intuitive insights for comparing the climate impact of future aircraft concepts?

To answer this question, this paper is structured in four objectives: (1) to research existing approaches and mitigation measures; (2) to develop a model of the aviation system’s energy and climate footprint; and (3) to present a case study for the wide-body aircraft cluster.

State-of-the-Art

Existing Approaches. The standard holistic approach is Life Cycle Assessment (LCA), as defined by ISO 14040. It is designed to evaluate multiple environmental stressors - such as climate change, resource depletion, and land use - across a product’s entire life cycle. However, this multi-indicator strength also poses challenges when applied to conceptual aircraft design [1, 2]. To address this complexity, three main categories of models have emerged. The first comprises streamlined LCA approaches, which preserve the multi-phase structure of a full assessment but rely on aggregated

Content from this work may be used under the terms of the Creative Commons Attribution 3.0 license. Any further distribution of this work must maintain attribution to the author(s) and the title of the work, journal citation and DOI. Published under license by Materials Research Forum LLC.

Materials Research Proceedings 69 (2026) 481-486 https://doi.org/10.21741/9781644904251-87

or simplified data (e.g. [3, 4]). These tools are complemented by detailed, phase-specific process models (e.g., [5]). In contrast, parametric, first-order models adopt a different philosophy. Isikveren [7] presents a fractional change model for assessing the impact of parametric variations on aircraft performance and geometry, providing a fast estimation for conceptual design studies. The Aviation Integrated Model (AIM) [6] applies parametric methods to capture the interactions between aircraft technology, operations, and atmospheric effects, enabling system-level environmental assessments of the aviation sector.

Mitigation Measures. In line with global climate goals, the aviation sector has outlined a roadmap toward net-zero CO2 emissions by 2050. Mitigation strategies are generally defined in four sections [8]: technological advancements, operational improvements, sustainable aviation fuels (SAF), and market-based measures. *Technology* measures include next-generation aircraft designs, lightweight materials, advanced aerodynamics, and more efficient propulsion systems, including hybrid-electric and hydrogen concepts. *Operational strategies* focus on improved air traffic management, optimized flight trajectories, and enhanced ground operations. *SAF* aims to replace fossil fuels as low-carbon alternatives derived from biomass or renewable electricity, while *market-based measures* (Carbon Offsetting and Reduction Scheme for International Aviation (CORSIA) or emissions trading systems) address residual emissions that cannot be eliminated through technological means.

Methodology and Validation

The framework LEVER adopts the philosophy of parametric, first-order models.

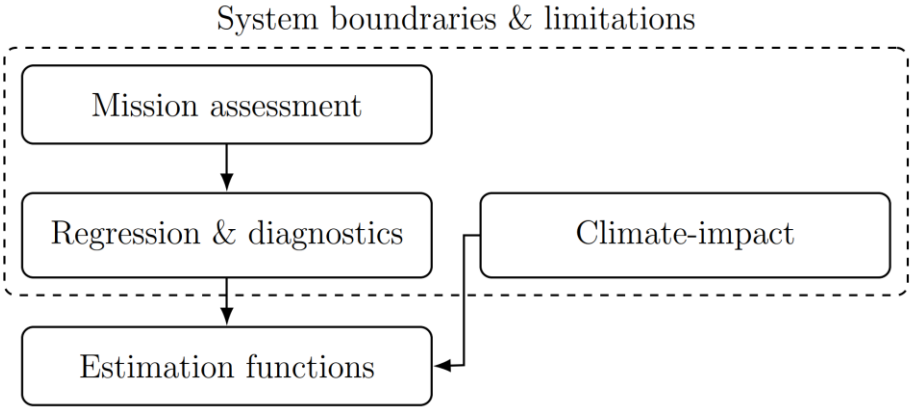


Fig. 1: LEVER workflow.

The methodology is shown in Fig. 1 and includes:

- *System boundaries*: We concentrate on aircraft operations (tank-to-wake, TtW).
- *Mission assessment*: The model processes aircraft, engine, and mission datasets based on publicly available data to estimate the selected key parameters. Empirical equations, additional mission performance assumptions, and energy balance calculations are added. The dataset is input for the regression.
- *Regression and diagnostics*: Log-log regression is applied with a 20% test split to determine elasticity. Diagnostics include R^2 and p-value.
- *Climate-impact*: The global warming potential with a time horizon of 100 years GWP_{100} is used. CO_2, NO_x, and H_2O are considered as well as aircraft-induced cloudiness (AIC).
- *Estimation functions*: We use two metrics ($\triangleleft$ adopted from [7]): 1) $\triangleleft E_{mission}$ as fractional change of mission energy, 2) $\triangleleft GWP_{100}$ as fractional change of global warming.
- *Limitations*: The regression model is applied for aircraft whose payload-range diagrams are sufficiently similar to justify a local linear approximation. Fractional change in mission energy

Materials Research Proceedings 69 (2026) 481-486 https://doi.org/10.21741/9781644904251-87

is assumed equivalent to elasticity, which is valid for small changes. As presented in the results, the use case is wide body aircraft flying > 4000 NM (from A330-300 to 747-400). Climate impact is focused on cruise-only operations and assumes an altitude of 39000 ft. HC, CO, and SO_x are neglected.

Mission assessment, regression & diagnosis. The goal is to derive the following:

$$\triangleleft E_{mission} = \alpha_1 \cdot \triangleleft m_{TO} + \alpha_2 \cdot \triangleleft R + \alpha_3 \cdot \triangleleft TSFC_{cr} + \alpha_4 \cdot \triangleleft L/D_{cr}, \quad (1)$$

with α as regression coefficients, Emission as mission energy, m_{TO} as take-off mass, $TSFC_{cr}$ as cruise thrust specific fuel consumption, L/D_{cr} as cruise lift-to-drag ratio, R as range. These parameters are aligned with the Coffin-Breguet equation (speed omitted as a constant in the data). Note that the parameters are dimensionless due to $\triangleleft x = \Delta x/x_0$ as fractional change [7]. Since $\ln(x/x_0) = \ln(1 + \triangleleft x) \approx \triangleleft x$ for small changes, $\ln(E_{mission}/E_0) = \sum \beta_i \ln(x_i/x_{i0})$ is locally identical to the linearized relation $\triangleleft Emission = \sum \beta_i \triangleleft x_i$. Consequently, the coefficients α represent the same elasticities as those obtained from the log–log regression β, which are interpretable as percentage sensitivities.

To derive the function and regression coefficients, data is required. The mission assessment model processes the following based on literature and publicly available data from Aircraft Commerce to estimate the parameters:

- *Mission data* containing equivalent still air distance (ESAD), block time & fuel, passenger number, cargo payload, taxi time, reserve rules (incl. alternate distance),
- *Aircraft data* providing mass breakdown (operating empty mass (OEM), maximum take-off mass (MTOM), maximum payload, fuel capacity, design range, engine variant),
- *Engine data* specifying type, bypass ratio, and empirical constants for $TSFC_{cr}$.

m_{TO} is assumed as the sum of OEM, payload, block fuel (without taxi-in), and reserve fuel. Reserve fuel is calculated with 5% trip fuel, a 30 min holding at FL150 at 20 kg/min and alternate airport flight at 5 kg/NM (data estimates based on UNICADO-LR-01 [10]). Range is equivalent to ESAD. $TSFC_{cr}$ is estimated based on Howe [9] at FL390 and M0.84 (altitude and speed not specifically provided in source). L/D_{cr} is calculated under the same operating conditions. Steady state flight is assumed:

$$\triangleleft L/D_{cr} = \frac{m_{midcruise} \cdot g}{\dot{m}_{cr}/TSFC_{cr}}, \quad (2)$$

with $m_{midcruise}$ as mid-cruise aircraft mass (OEM plus payload, reserve, descent, and 50% cruise fuel), g as gravitational constant, and $\dot{m}_{cr}$ as cruise fuel flow. m_{cr} and t_{cr} are assumed as block fuel and time, excluding taxi and descent (1800 ft/min descent rate, 8 min for approach/landing, fuel flow at 35 kg/min). The climb segment was initially heuristically estimated, but tests have shown that omitting it results in a minor error.

Climate Impact Model. For each flight mission, the model computes the Absolute Global Warming Potential $AGWP_{100}$ (100-year horizon) as the time-integrated radiative forcing associated with in-flight emissions. This is then expressed as equivalent CO_2 mass GWP_{100}. The formulation accounts for the main contributors - CO_2, H_2O, NO_x, and aircraft-induced cloudiness (AIC).

To calculate AGWP and GWP, the radiative forcing at time t is used as the sum of altitude-dependent responses for each contributor i:

$$RF_{tot}(t) = m_{CO2}\, RF_{CO2}(t) + m_{H2O}\, s_{H2O}\, RF_{H2O}(t) + m_{NOx}[s_{O3S}\, RF_{O3S}(t) + s_{O3L,CH4}(RF_{O3L}(t) + RF_{CH4}(t))] + r_{cruise}\, s_{AIC}\, RF_{AIC}(t), \quad (3)$$

where m_i are the emitted masses (or cruise distance for AIC), and $s_i(h)$ are altitude-dependent forcing factors [13]. The short-lived species (O_3 short, H_2O, and AIC) are treated as one-year box forcings, while the long-lived species (CO_2, CH_4, O_3 long) follow exponential impulse–response functions. Integrating the response over the time horizon H yields the AGWP for each species:

$$AGWP_{100,tot} = \int_0^H RF_{tot}(t)dt = \sum_i m_i \int_0^H RF_{tot}(t)dt.\ GWP_{100} = \frac{AGWP_{100,tot}}{AGWP_{100,CO2}}. \quad (4)$$

Emission masses are computed from mission fuel and engine data:

- CO_2 and H_2O from stoichiometric oxidation EI_{CO2} = 3.16 kg/kg fuel and EI_{H2O} = 1.23 kg/kg fuel.
- NO_x from the Boeing Fuel Flow Method 2 (BFFM2)[14], using sea-level emission indices $EI_{SL,NOx}$ from ICAO engine databank. The method converts in-flight fuel flow to sea-level equivalent conditions by applying altitude and humidity corrections:

$$m_{NOx} = EI_{SL,NOX} \left(\frac{\delta^{1.02}}{\theta^{3.3}}\right)^{0.5} e^{H} m_f, \quad (5)$$

with δ, θ, and H as pressure ratio, temperature ratio, and altitude.

For simplicity, $r_{cruise} \approx R$ and a constant cruise altitude of FL390 are assumed, which fixes the forcing factors $s_i(h)$ and NO_x altitude correction. $\int RF_i(t)\,dt$ are calculated as constant multipliers k_i, yielding:

$$GWP_{100,TtW} = (k_{CO2} + k_{H2O} + k_{NOx}) m_f + k_{AIC}\, R. \quad (6)$$

This linearized model allows to formulate $\gamma_i = GWP_i/GWP$, which represents the fractional share of each species in total GWP:

$$\triangleleft GWP_{100,TtW} = (\gamma_{CO2} + \gamma_{H2O} + \gamma_{NOx}) \triangleleft m_f + \gamma_{AIC} \triangleleft R. \quad (7)$$

Wide Body Case Study

The aircraft considered for this study are 777-200 (GE90, PW4000, Trent 800), 787-8/9/10 (Genx, Trent), A330-200/300, 747-400, A350-900/1000. In total, 69 missions are evaluated [11, 12]. The input data ranges are OEM [t]∈ [116.7, 188], ESAD [NM]∈ [3928, 7190], and payload [t] ∈ [25.6, 120] (A330 to 747). The calculated parameter are for TFSC [kg/s/N] = 1.68 · 10−5 ± 3.69 · 10−7 (mean) ∈ [1.64 · 10−5, 1.77 · 10−5] and L/D= 19.7 ± 2.1 (mean) ∈ [16.0, 22.9] (with ±1σ), resulting in

$$\triangleleft E_{mission} = 0.957 \triangleleft m_{TO} + 0.808 \triangleleft R + 0.916 \triangleleft TSFC_{cr} - 0.851 \triangleleft L/D_{cr}. \quad (8)$$

Each coefficient can be interpreted as elasticity - accordingly, a 1% improvement in cruise lift-to-drag ratio reduces mission fuel by roughly 0.85%, and a 1% higher specific fuel consumption raises it by 0.92%. All coefficients are statistically significant ($p < 0.001$), with high $R^2 = 0.964$.

It should be noted that since L/D_{cr} and $TSFC_{cr}$ are reconstructed via inverse mission analysis, the regression serves as a validation of the internal consistency rather than an independent discovery of airframe performance. For $GWP_{TtW,100}$, the average emissions contributions were derived from all missions as

$$\begin{aligned} \triangleleft \boldsymbol{GWP_{100,TtW}} &= (\boldsymbol{\gamma_{CO2} + \gamma_{H2O} + \gamma_{NOx}}) \\ &\cdot (\mathbf{0.957} \triangleleft \boldsymbol{m_{TO}} + \mathbf{0.808} \triangleleft \boldsymbol{R} + \mathbf{0.916} \triangleleft \boldsymbol{TSFC_{cr}} - \mathbf{0.851} \triangleleft \boldsymbol{L/D_{cr}}) \\ &\quad + \boldsymbol{\gamma_{AIC}} \triangleleft \boldsymbol{R}. \end{aligned} \tag{9}$$

with $\gamma_{CO2} = 0.366$, $\gamma_{H2O} = 0.003$, $\gamma_{NOx} = 0.352$, and $\gamma_{AIC} = 0.279$. This indicates that approximately two-thirds of the total GWP stems from fuel-related effects (CO_2, H_2O, and NO_x), while aircraft-induced cloudiness (AIC) contributes the remaining one-third. The very small share of H_2O reflects the low radiative forcing efficiency of water vapor compared to CO_2 and NO_x under typical cruise conditions.

Conclusion and Future Work

This study presents a simple, relative energy-centric approach that provides intuitive insight into comparing climate impacts for wide-body derivatives. The framework showed the impact of the key aircraft parameters take-off mass, range, TSFC, and lift-to-drag ratio on the global warming potential. Based on the derived sensitivities, a 1% increase of these parameters leads to +0.69%, +0.86%, +0.66%, and -0.61% change in GWP_{100}, respectively. This approach focuses on mitigation technology that enhances aircraft parameters. Future work can be an extension that includes the well-to-tank energy and climate impacts to address the benefits and drawbacks of the SAF mitigation measure.

Additionally, this approach can be applied to other aircraft categories such as turboprop, regional jets, narrow bodies, and other energy carriers such as hydrogen. This requires additional assumptions and modeling, including LTO emissions. Using aircraft design environments, such as UNICADO [10], enables detailed validation of the mission energy estimation. Furthermore, incorporating error propagation enables a more rigorous assessment of uncertainties, thereby enhancing the robustness and interpretability of the results.

References

[1] D. Keiser, L. H. Schnoor, B. Pupkes, M. Freitag, Life cycle assessment in aviation: A systematic literature review of applications, methodological approaches and challenges, in: Journal of Air Transport Management 110 (2023). https://doi.org/10.1016/j.jairtraman.2023.102418

[2] K. Mazur, M. Saleh, M. Hornung, Integrating Life Cycle Assessment in Conceptual Aircraft Design: A Comparative Tool Analysis. Aerospace, 11(1), 101 (2024). https://doi.org/10.3390/aerospace11010101

[3] K. SchÄfer. Methode zur ökologischen Bewertung von Flugzeugkonzepten. Dissertation, RWTH Aachen (2018).

[4] K. Kossarev, A. E. Scholz, P. Egerer, M. Hornung, Comparison of Environmental Life Cycle Impact Assessment Methods for Future Aircraft Designs, in: AIAA AVIATION 2022 Forum (2022). https://doi.org/10.2514/6.2022-3659

[5] A. Rahn, K. Wicke, G. Wende, Using Discrete-Event Simulation for a Holistic Aircraft Life Cycle Assessment, in: Sustainability, 14(17) (2022). https://doi.org/10.1016/j.ast.2018.06.020

[6] L. M. Dray, P. Krammer, K. Doyme, B. Wang, K. A. Zayat, A. O'Sullivan, A. W.Schäfer, AIM2015: Validation and initial results from an open-source aviation systems model, in: Transport Policy, vol. 79 (2019). https://doi.org/10.1016/j.tranpol.2019.04.013

[7] A. Isikveren, Parametric Modeling Techniques in Industrial Conceptual Transport Aircraft Design, SAE Technical Paper 2003-01-3052 (2003). https://doi.org/10.4271/2003-01-3052

[8] ATAG. Waypoint 2050: Aviation: Benefits Beyond Borders, 2.ed (2021).

[9] D. Howe, Aircraft Conceptual Design Synthesis, in: Professional Engineering Published, London and Bury St Edmunds, UK (2000).

[10] Information on https://unicado.pages.rwth-aachen.de/unicado.gitlab.io/

[11] A350-900/-1000 fuel burn & operating performance, in: Aircraft Commerce, Issue No.121, Dec. 2018.

[12] 777 fuel burn performance, in: Aircraft Commerce, Issue No. 60, Oct./Nov. 2008.

[13] K. Dahlmann, Eine Methode zur effizientn Bewertung von Maßnahmen zur Klimaoptimierung des Luftverkehrs, Dissertation, Ludwig-Maximilians-Universität (2011).

[14] D. DuBois, G. C. Paynter, Fuel Flow Method2 for Estimating Aircraft Emissions, in: SAE International, Vol.115 (2006).

Materials Research Proceedings 69 (2026) 487-492 https://doi.org/10.21741/9781644904251-88

A Modular Life Cycle Assessment Framework for Novel Aircraft Configurations and Sustainable Aviation Fuels

Kristina MAZUR[1,a,*], Katrin BISTRECK[2,b], Christina ERBSKORN[1,c], and Mirko HORNUNG[1,d]

[1]Technical University of Munich, Chair of Aircraft Design, Bolzmannstr. 15, 85748 Garching, Germany

[2]Hamburg University of Technology, Institute for Air Transportation Systems, Harburger Schloßstraße 22A, 21079 Hamburg, Germany

[a]kristina.mazur@tum.de, [b]katrin.bistreck@tuhh.de, [c]christina.erbskorn@tum.de, [d]mirko.hornung@tum.de

Keywords: Life Cycle Assessment, Sustainable Aviation Fuel, Aircraft Design

Abstract. This work presents a modular framework for environmental impact assessment in conceptual aircraft design, developed within the UNICADO environment. The new architecture decouples individual life cycle phases and has been extended to various Sustainable Aviation Fuel (SAF) pathways. This enhanced flexibility enables a more robust and holistic trade-off analysis of an aircraft's environmental footprint early in the design process. The case study of UNICADO-LR-01 presents results on cumulative energy demand shares for each life cycle activity. Additional results reveal that the life cycle phases operations (62.0, 78.4, 84.6%) and energy carrier production (29.6, 14.3, 9.9%) are most dominant in terms of energy, CO_2, and NO_x, respectively. Results from SAF pathways suggest a shift towards the energy carrier production phase.

Introduction

The aviation industry is focusing increasingly on mitigating its environmental impact. Initiatives such as "Fly the Green Deal" [1] are being developed to promote sustainable aviation. The measures considered include novel aircraft configurations and sustainable aviation fuels, which could reduce climate impact compared to traditional fossil fuels. To appropriately assess these measures, a holistic approach in terms of a life cycle assessment (LCA) within the earliest stage of conceptual aircraft design has to be considered.

Most existing aircraft design and assessment tools are either not open code, lack flexibility for quick studies, or do not consider life cycle assessment evaluations at all. FAST (Future Aircraft Sizing Tool) [2] focuses on sizing and performance analysis for conventional and electrified aircraft without LCA evaluation. *AeroMAPS* [3] and *CASCADE* [4] serve as scenario-exploration frameworks for air transport decarbonization strategies, but provide little detail on aircraft life cycle phases. Tools such as *AD-LCA* Excel/Matlab methodology [5] and ecological assessment [6, 10] suffer from monolithic architectures that lack the flexibility required for advanced aircraft concepts and emerging technologies. And while offering LCA frameworks such as *qUWick* [7], *ecoLYFE* [8], or *AEco* [9], the implementations are not openly accessible to the broader research community.

To address this, an extensible *assessment framework* is being developed within the open-source conceptual aircraft design environment UNICADO [10]. As a use case, a long-range aircraft is assessed with multiple sustainable aviation fuel (SAF) pathways.

Methodology

Assessment Framework. The foundation for this work is the *ecological assessment* tool based on [6] (detailed documentation see [10]). While providing a solid basis for life cycle emissions and

Content from this work may be used under the terms of the Creative Commons Attribution 3.0 license. Any further distribution of this work must maintain attribution to the author(s) and the title of the work, journal citation and DOI. Published under license by Materials Research Forum LLC.

Materials Research Proceedings 69 (2026) 487-492 https://doi.org/10.21741/9781644904251-88

impact assessment, the original tool was built with a monolithic architecture. This posed challenges within the UniSELECT project [11], as its goal is a climate-efficient long-range aircraft considering disruptive technologies (e.g., open rotor), configurations (e.g., blended-wing body), or operations (e.g., stopover flights). The former logic is shown in Fig. 1 (left). The tool provides a single interface for inputs and focuses on internal calculations. It includes a database of materials, fuels, and primary energy factors, as well as methods for the cradle-to-grave (from development to end-of-life) inventory and impact assessment (air quality index calculation and application of an altitude-dependent climate model to evaluate average temperature response).

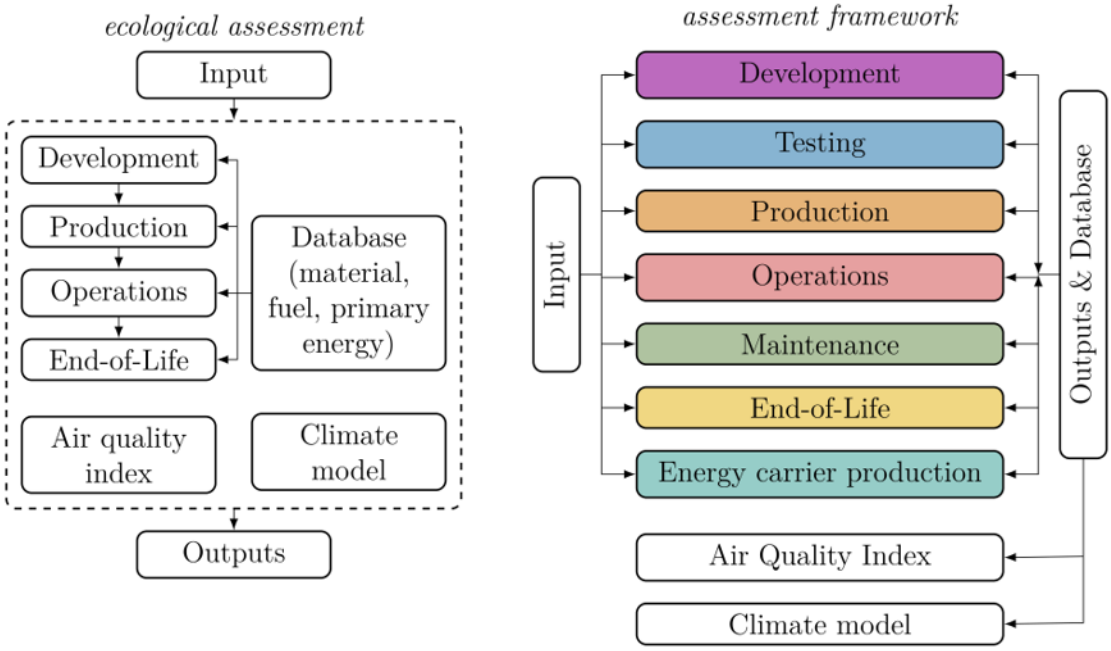


Fig. 1: Comparison of life cycle assessment tool by Schäfer (left, based on [6]) and assessment framework in UNICADO (right).

To address this issue, the tool was restructured into a modular *assessment framework* (right in Fig. 1). It treats each phase as individual stand-alone modules that have individual in- and output interfaces. This enables the exchange of phase-specific methods, e.g., by replacing the simplified electricity demand model in the development phase with more sophisticated data or higher fidelity methods. Additionally, several tools are split, e.g., the operations phase is divided into operations, maintenance procedures, and energy carrier production. The input settings are extended, e.g., Boeing Fuel Flow Method 2. For details, it refers to the open-source documentation [10].

Assessment Manager. To orchestrate the *assessment framework*, a manager tool was developed. This tool is integrated into the aircraft design platform (RCE) of UNICADO, enabling the connection of aircraft design results to the assessment. The data is exchanged with the common exchange file format (XML). Additionally, each tool has its own configuration file that varies depending on input settings (e.g., hours of system integration tests).

Sustainable Aviation Fuels. SAFs are one primary measure for decarbonization. Several production pathways are included in the *assessment framework*, such as Alcohol-to-Jet (AtJ), Hydroprocessed Esters and Fatty Acids (HEFA), Power-to-Liquid (PtL), and Biomass Gasification with Fischer-Tropsch (Gas+FT). For details, refer to [12].

Results and Discussion

A case study is presented of the long-range aircraft design UNICADO-LR-01 (Release 0.8.1). It is a kerosene-burning tube-and-wing turbofan configuration for 300 passengers and entry-into-

Materials Research Proceedings 69 (2026) 487-492 https://doi.org/10.21741/9781644904251-88

service 2020. The use case is the design mission with 6700 NM range with 77.8 t block fuel (details see aircraft references documentation [10]). Note that the results relate to the aircraft's lifetime with 369 flights/year for 30 years assuming:

- energy (heat, electricity) for personnel/offices developing the aircraft,
- energy (heat, electricity, fuel) for multiple tests & for additional test aircraft and engine (its production and end-of-life is allocated to testing),
- material and energy (heat, electricity, fuel) producing one aircraft (material production, component manufacturing, transport to assembly site, electric and heat energy needed for manufacturing & assembly personnel),
- fuel for operating an aircraft during its lifetime (total number of flights in its operating duration),
- material and energy (heat, electricity) maintaining an aircraft during its lifetime,
- energy for producing the required fuel (e.g., kerosene for flights, kerosene for transport during disposal, diesel during transportation to the final assembly site).

Fig. 2 shows the cumulative energy demand (CED) results for all phases. In the *development* phase, the impact is driven by electricity and heat demand for the offices with the primary energy demand for electricity being the highest share. In the *testing* phase, the energy for the test aircraft production (2 for fatigue, 6 for flight tests) requires 30% of the total testing CED. Both the material production (22%) and the component manufacturing (38%) dominate the *production* phase. To be noted is that the primary scrap is recycled (e.g., for aluminum, a scrap ratio of 0.85 and a recovery rate of 0.9 is assumed). In *operations*, the landing and take-off cycle is with 1% negligible in terms of energy. The dominant phase in maintenance is the spare part production (88%). The *end-of-life* phase includes both energy credit as well as demand. The credit due to material is five times higher than the energy required for recycling, incineration, and landfill. While the phases *testing*, *operations*, *production*, and *end-of-life* require energy carriers (kerosene, diesel), only the first two are relevant with 4% and 96%, respectively.

Materials Research Proceedings 69 (2026) 487-492 https://doi.org/10.21741/9781644904251-88

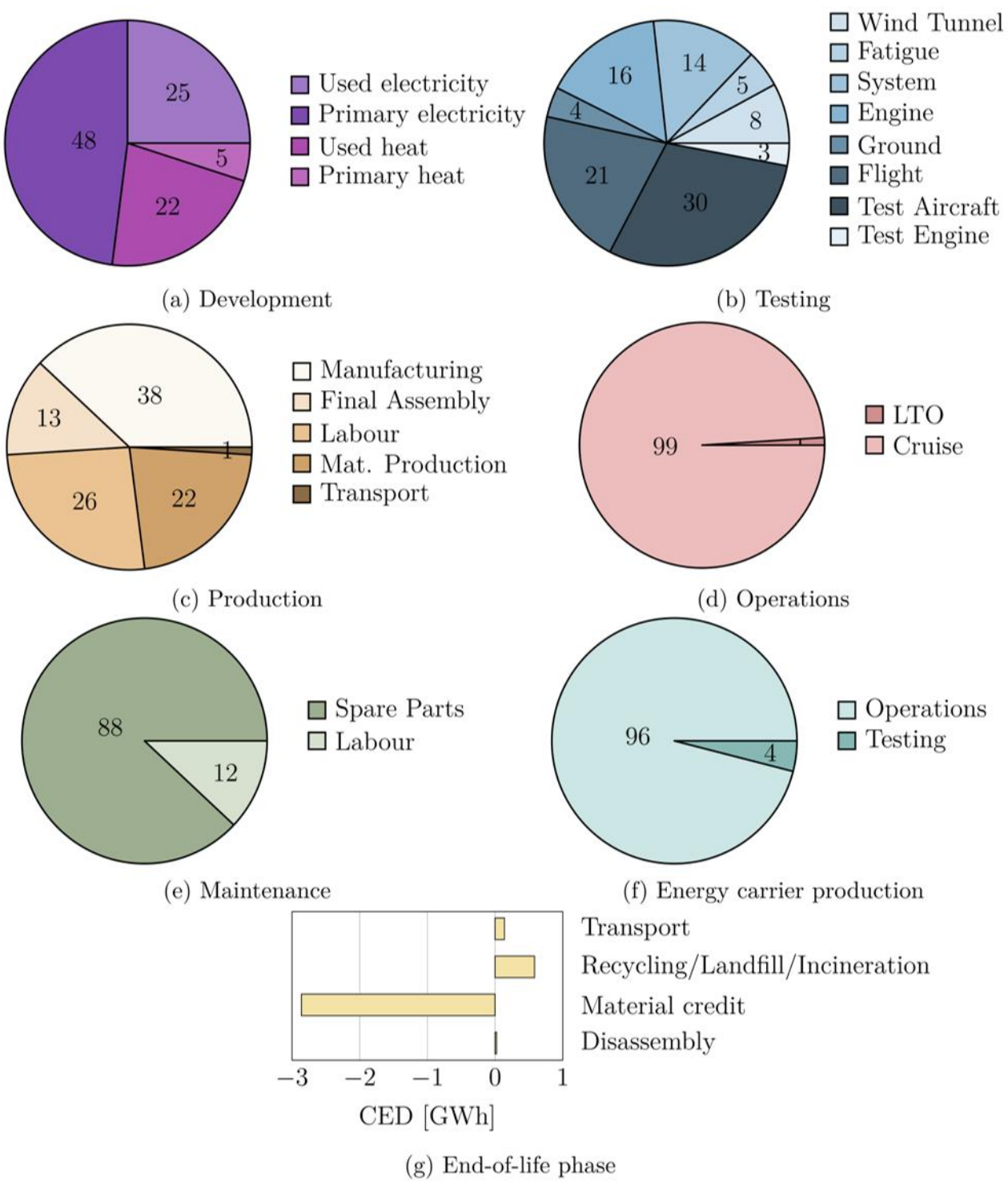


Fig. 2: Cumulative energy demand shares for life cycle phases of UNICADO-LR-01.

Table 1 shows how the individual phases contribute to the total impact with respect to CED, CO_2, and NO_x. The most influential phase is operations, followed by energy carrier production. This is due to the scaling to the entire service life (single mission operation requires 3.35 TJ which is < 1% of development CED). The total life cycle global warming potential (GWP) results in 93 gCO_2eq per MJ fuel burned during the operational flights (only CO_2 considered, cf. 89 gCO_2eq/MJ according to CORSIA [14]).

Materials Research Proceedings 69 (2026) 487-492 https://doi.org/10.21741/9781644904251-88

Table 1: Cumulative energy demand and emissions (CO_2, NO_x) inventory results for UNICADO-LR-01 lifetime.

	CED [%]	CO2 [%]	NOx [%]
Development	1.0	0.8	0.2
Testing	6.2	5.7	4.9
Production	0.3	0.2	0.1
Operations	62.0	78.4	84.6
Maintenance	0.9	0.6	0.2
End-of-Life	0.0	0.0	0.0
Energy carrier production	29.6	14.3	9.9
Total	**56.8 PJ**	**3.24 Tg**	**13.7 Gg**

Switching to SAF affects both dominant life cycle phases of aviation energy demand. Table 2 shows that the conversion efficiency of the different production pathways varies widely between 13.8% and 55.6%, reflecting substantial energy losses during synthesis and upgrading (note that a high efficiency does not automatically imply a low CED, since it depends on the primary energy factors; compared to fossil kerosene PEF = 1.24, efficiency = 80%). CORSIA eligibility (10% reduction to the fossil baseline) can thus only be achieved if biogenic CO_2 sources, renewable electricity, or carbon capture technologies (e.g., direct air capture) are applied to offset the combustion-related impact.

Table 2: Process energy efficiency and tank-to-wake global warming potential with and without offset.

	Energy efficiency [%]	GWP [g CO_2eq/MJ]	GWP (no offset)[2] [g CO_2eq/MJ]
AtJ (Alcohol-to-Jet)	35.5	45.7	153
HEFA	55.6	16.2	86.9
PtL[1](Power-to-Liquid)	13.8	22.6/513	91/522
Gasification +Fischer-Tropsch	27.2	4.52	266

[1] PtL electricity from wind or current German electricity mix.
[2] Biogenic offset for HEFA, AtJ, Gas+FT & DAC for PtL.

Conclusion and Future Work

This work has presented a fully modular and extensible Life Cycle Assessment framework in UNICADO. By decomposing the monolithic legacy tool into a suite of modules orchestrated by an assessment manager, the new architecture provides the flexibility required for holistic trade-off analyses of novel aircraft and fuel technologies such as SAF. Future work will focus on expanding the library of impact assessment methods like CED and ReCiPe midpoint categories to translate the calculated inventories into a broader range of environmental damage categories.

References

[1] Fly the Green Deal : Europe's vision for sustainable aviation, Amt für Veröffentlichungen der Europäischen Union, 2022. https://doi.org/10.2777/732726

[2] P. Mokotoff, M. Arnson, Y.-C. Wang, G. Cinar, FAST: A Future Aircraft Sizing Tool for Conventional and Electrified Aircraft Design, in: AIAA SciTech 2025 Forum (2025). https://doi.org/10.2514/6.2025-2374

[3] T. Planès, S. Delbecq, A. Salgas, AeroMAPS: a framework for performing multidisciplinary assessment of prospective scenarios for air transport, in: Journal of Open Aviation Science, 1(1) (2023). https://doi.org/10.59490/joas.2023.7147

[4] Information on https://cascade.boeing.com.

[5] K. Kossarev, A. E. Scholz, P. Egerer, M. Hornung, Comparison of Environmental Life Cycle Impact Assessment Methods for Future Aircraft Designs, in: AIAA AVIATION 2022 Forum (2022). https://doi.org/10.2514/6.2022-3659

[6] K. Schäfer, Conceptual Aircraft Design for Sustainability, Dissertation, RWTH Aachen (2018).

[7] E. Dallara, J. Kusnitz, M. Bradley, Parametric Life Cycle Assessment for the Design of Aircraft, in: SAE Int. J. Aerosp. 6(2)(2013). https://doi.org/10.4271/2013-01-2277

[8] A. Rahn, K. Wicke, G. Wende, Using Discrete-Event Simulation for a Holistic Aircraft Life Cycle Assessment, in: Sustainability, 14(17), 10598 (2022). https://doi.org/10.3390/su141710598

[9] G. Parolin, A. T. Borges, L. C.C. Santos, A. V. Borille, A tool for aircraft eco-design based on streamlined Life Cycle Assessment and Uncertainty Analysis, in: Procedia CIRP, Volume 98 (2021). https://doi.org/10.1016/j.procir.2021.01.152

[10] Information on https://unicado.pages.rwth-aachen.de/unicado.gitlab.io [Accessed on 23.10.2025].

[11] F. Schültke, E. Stumpf, UniSELECT - Development of a Climate Efficient Long-Range Aircraft Configuration, in: Deutscher Luft- und Raumfahrtkongress Hamburg (2024).

[12] C. Erbskorn, Life Cycle Assessment of Sustainable Aviation Fuels, Research Internship, Technical University of Munich (2025). https://mediatum.ub.tum.de/doc/1835252/1835252.pdf

[13] E. Schwartz Dallara, Aircraft Design for Reduced Climate Impact, Dissertation, Stanford University (2011).

[14] M. Prussi, U. Lee, M. Wang, R. Malina, H. Valin, F. Taheripour, C. Velarde, M. D. Staples, L. Lonza, J. I. Hileman, CORSIA: The first internationally adopted approach to calculate life-cycle GHG emissions for aviation fuels. Renewable and Sustainable Energy Reviews, (2021) 150(111398). https://doi.org/10.1016/j.rser.2021.111398

Materials Research Proceedings 69 (2026) 493-498 https://doi.org/10.21741/9781644904251-89

Validation of High-Fidelity Multidisciplinary Maneuver Simulations with Flight Test Data from DLR Dassault Falcon 2000LX ISTAR

Martin BAUER[1,a *], Johan Moritz FELDWISCH[2,b] and Philipp MÜHLMANN[3,c]

[1]German Aerospace Center (DLR), Institute of Aerodynamics and Flow Technology, Lilienthalplatz 7, 38108, Braunschweig, Germany

[2]German Aerospace Center (DLR), Institute of Aeroelasticity, Bunsenstraße 10, 37073, Göttingen, Germany

[3]German Aerospace Center (DLR), Institute of Aerodynamics and Flow Technology, Lilienthalplatz 7, 38108, Braunschweig, Germany

[a]Ma.Bauer@dlr.de, [b]Johan.Feldwisch@dlr.de, [c]Philipp.Muehlmann@dlr.de

Keywords: Virtual Flight Testing, Certification By Analysis, Simulation-Based Certification, Full-Scale Flight Validation Data, Digital Twin, CFD, Aeroelasticity, Maneuver Simulation

Abstract. This paper presents a validation of high-fidelity aeroelastic maneuver simulations using experimental data of the DLR Falcon 2000 ISTAR aircraft in a clean cruise configuration from the HighFly MaGE flight test campaign. The dynamic open-loop maneuver simulations of the flexible free-flying aircraft are achieved with the DLR multidisciplinary process chain UltraFLoads, which can combine a flight dynamics model with a CFD flow solver (URANS with the DLR TAU-Code) and an unsteady structural modal analysis computed from the FE NASTRAN model. Pull-up and push-down and bank-to-bank maneuver simulations of different flight points are investigated (subsonic and transonic). The static pressure distributions on three chordwise wing sections and global flight dynamic quantities are compared with experimental data. Three pressure distributions on the right wing of the ISTAR aircraft were dynamically measured during the MaGE flight campaign using pMEMS sensors (Micro Electro Mechanical System).

Introduction

The central goal in current aviation research and development is to increase the efficiency of aircraft and reduce their environmental impact. Achieving these goals is supported by the ability to accurately and quickly analyse aircraft characteristics, including flight performance, flight loads, aeroelastic phenomena, flight control, and stability. Continuous development in high-performance calculations enables the application of high-fidelity numerical methods such as computational fluid dynamics (CFD), computational structural mechanics (CSM), thermodynamic engine models, and flight dynamics models, and their integration into multidisciplinary analysis. These methods can be used at early design stages and for virtual flight tests during certification by analysis. Virtual flight tests as part of the aircraft development digitalization should enable faster, safer, and more cost-effective progress of new technologies towards climate-neutral air transport.

To validate virtual flight test methods and models, comparisons with experimental data are required. This was the goal of the DLR project HighFly (High-Speed Inflight Validation) 2018–2023 [1]. In this project, comprehensive flight test data in the high-speed range and at the edge of the flight envelope of the new DLR research aircraft Dassault Falcon 2000LX ISTAR (In-flight Systems & Technology Airborne Research) [2] were provided. The ISTAR measurement instruments of the flight campaign MaGE (Maneuvers at the Border of the Envelope) are depicted in Fig. 1. With the measured flight data, the validation of simulation models for virtual flight testing and the quantification of numerical uncertainties are carried out.

Content from this work may be used under the terms of the Creative Commons Attribution 3.0 license. Any further distribution of this work must maintain attribution to the author(s) and the title of the work, journal citation and DOI. Published under license by Materials Research Forum LLC.

Materials Research Proceedings 69 (2026) 493-498 https://doi.org/10.21741/9781644904251-89

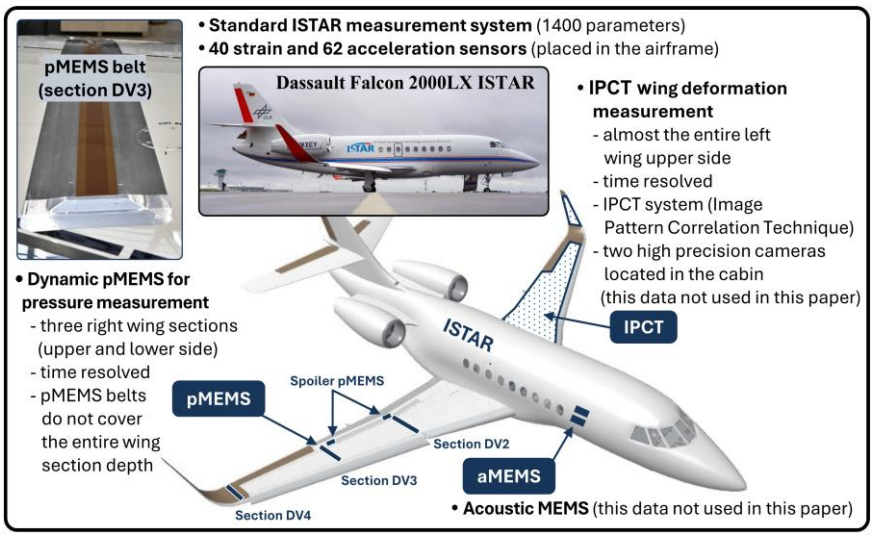


Fig. 1 DLR research aircraft Dassault Falcon 2000LX ISTAR with MaGE measurement instruments (project HighFly)

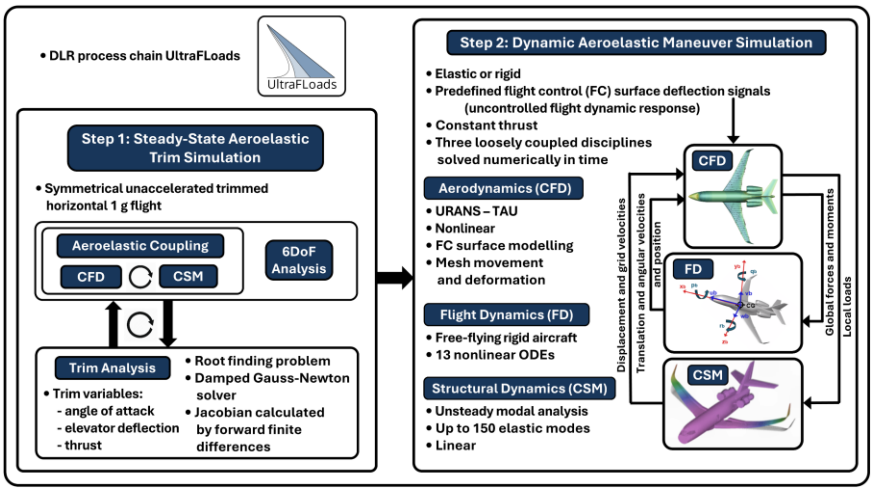


Fig. 2 UltraFLoads process of dynamic open-loop maneuver simulation

The first steady-state trimmed aeroelastic simulations and elastic dynamic maneuver simulations of the ISTAR aircraft with detailed descriptions of the individual numerical models and analysis were published in [3]. The first validation of the steady-state trimmed aeroelastic simulations with HighFly flight data was published in [4], where pressure distributions, trim variables, and elastic wing deformation were compared. These steady-state simulations serve as an initial solution for the dynamic maneuver simulations, which are introduced together with their validation in this paper.

Simulation Process Chain, Numerical Models, and Analysis

For maneuver simulations of the ISTAR aircraft, the UltraFLoads (UFL) process chain is used. It has been developed at the DLR Institute of Aeroelasticity in Göttingen. Fig. 2 schematically shows the overall UltraFLoads computation process. The first step is to trim the free-flying, elastic aircraft in a unaccelerated 1g horizontal flight. The second step, the open-loop dynamic maneuver simulation with predefined control surface deflections, starts from the trimmed state. The aircraft rigid body motion (flight dynamics) and the flexible degrees of freedom (structural modal analysis) are combined into one decoupled set of first-order ordinary differential equations, which is enabled

Materials Research Proceedings 69 (2026) 493-498 https://doi.org/10.21741/9781644904251-89

by the mean-axis condition. The equations are solved by the implicit linear multistep Adams-Moulton method, and their results are loosely coupled with the TAU-URANS simulation. The CFD mesh deformation based on RBF (Radial Basis Function) is performed at every time step (flight control surface deflections and aircraft elastic deformation) and the TAU-URANS simulation considers grid velocities due to mesh deformation and rigid body motion (ALE formulation).

Fig. 3 gives basic information about the CFD and CSM models and simulations of the ISTAR aircraft. More detailed information about these models can be found in [3]. A general description of UltraFLoads' architecture and capabilities can be found in [5], and three UltraFLoads applications are presented in [6, 7].

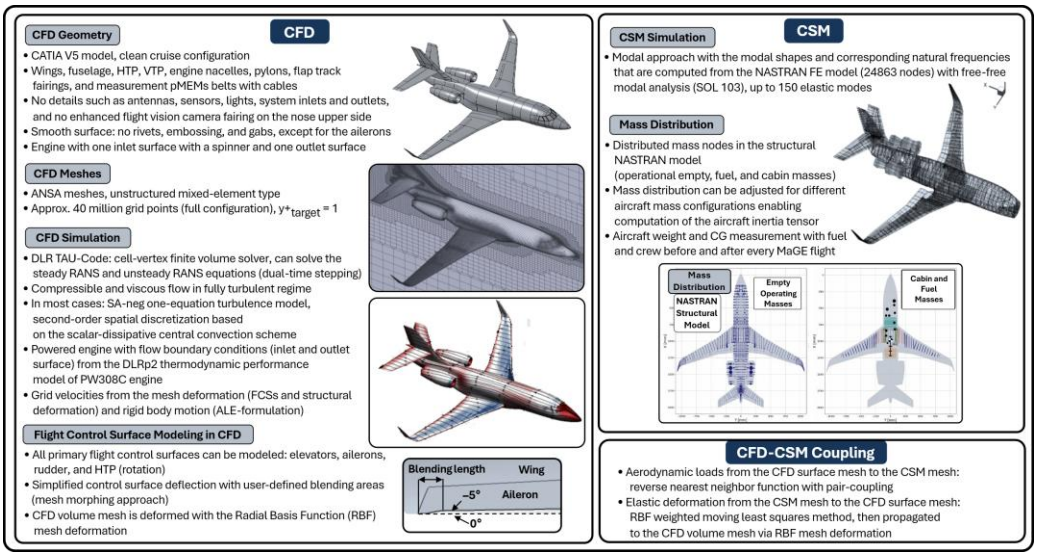


Fig. 3 CFD and CSM models and analysis of ISTAR

Results of Validation of Dynamic Maneuver Simulations with MaGE Flight Data

This section presents the first validation results of the dynamic maneuver simulations of the ISTAR aircraft against the MaGE flight data. It consists of three maneuvers (two pull-up and push-down maneuvers and one bank-to-bank maneuver), plotted in Figs. 4, 5, and 6. Local static pressure distributions on three wing sections (DV2, DV3, and DV4) at three time points, along with a few selected global flight dynamic variables, are depicted: red lines represent simulations, and blue solid lines and blue points represent flight measurement data. Dashed blue lines representing accuracy criteria from the Manual of Criteria for the Qualification of Flight Simulation Training Devices [8] are added to the diagrams. This ICAO document contains different criteria for different types of maneuvers. The following criteria are selected for the presented variables: ±1.0° angle of attack, ±0.1 g load factor, ±3 kt (±1.54 m/s) true air speed, ±2°/s pitch rate, ±1.5° pitch angle, ±2° roll angle, and ±2°/s roll rate. These flight simulator criteria can serve here as a preliminary accuracy assessment of the virtual flight tests. Figs. 4 and 5 also show the simulation wing upper side with surface pressure distribution for the initial trimmed flight state. A description of the simulation input parameter settings (such as Mach number, flight altitude, weight, and CG), a description of the CFD wing geometry details (pMEMS belts and cables), and a detailed comparison of the simulation results and the measurement data of the trimmed steady flight states (wing pressure distributions, trim variables, and wing elastic deformation) is presented in Section 3 in [4]. During the MaGE flight campaign, the dynamic maneuvers were flown manually in the calmest possible atmosphere without an autopilot and with a constant thrust setting.

Materials Research Proceedings 69 (2026) 493-498 https://doi.org/10.21741/9781644904251-89

The simulation results for the subsonic pull-up and push-down maneuver with only elevator deflection at a Mach number of 0.46 (Fig. 4) agree very well with the measured flight data. The most significant deviations in the static pressure distributions are observed at the wing section DV4 (the most outboard section), where the largest wing deformation occurs. The depicted simulation and measurement pressure distributions show local effects (local pressure peaks) at the beginnings and ends of all the pMEMS belts, which are caused by the leading and trailing ramps of the pMEMS belts with a thickness of 2 mm (also observed in Fig. 5).

Generally, a good correlation is observed in the transonic pull-up and push-down maneuver at a Mach number of 0.78 (Fig. 5), where only the elevator is deflected in the simulation. A minor tolerance violation of the simulation load factor can be observed in some areas. The pressure distributions show the largest deviations on the upper side of DV3, which is partially due to the absence of local spanwise surface waves on the wing in this region compared to the real aircraft (this deviation is described in Section 3.2 in [4]). Other larger deviations are visible in the front part of the DV4 lower side at time point 3, where the boundary layer separation appears in the simulation.

Fig. 6 presents only a comparison of the global flight dynamics parameters for the transonic bank-to-bank maneuver (+67º to −63º) at a Mach number of 0.78, with the ailerons and elevator deflected in the simulation. For roll rate and roll angle, the simulation values are within certain areas on the edge of the tolerance range (the highest deviation for roll angle is approximately 2º), but overall good agreement is observed.

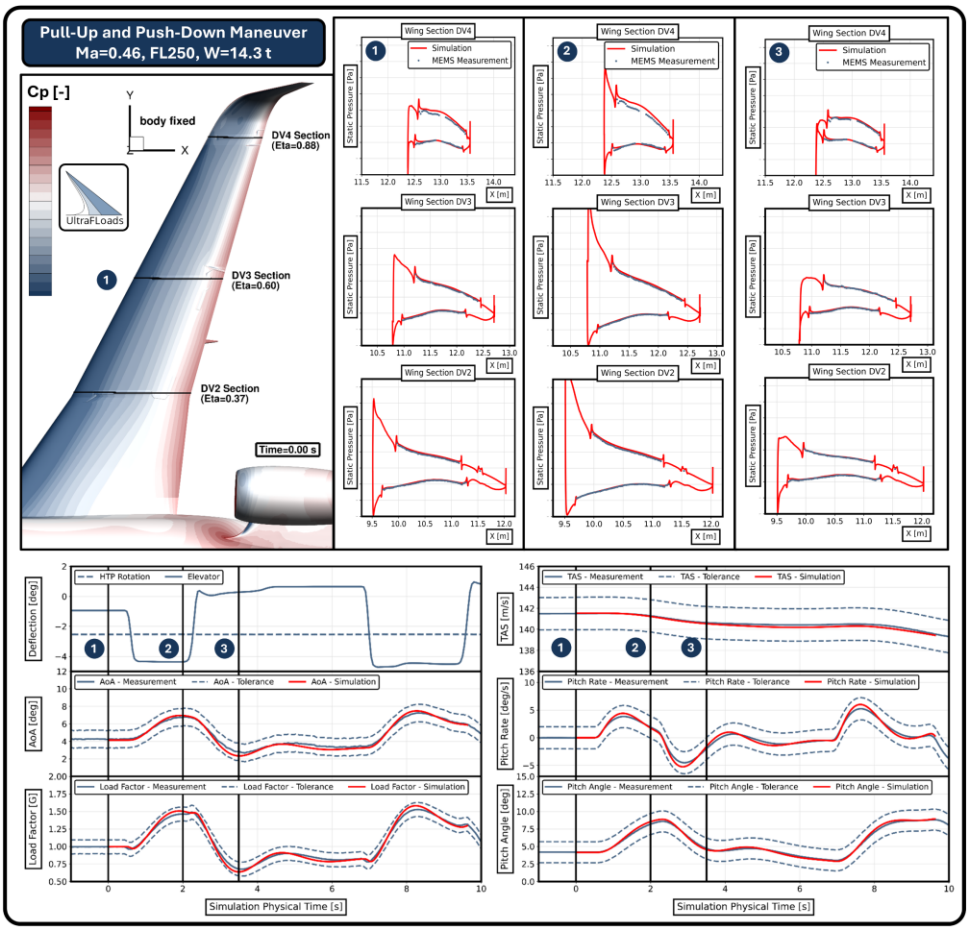


Fig. 4 Pull-up and push-down maneuver – Ma=0.46, FL250

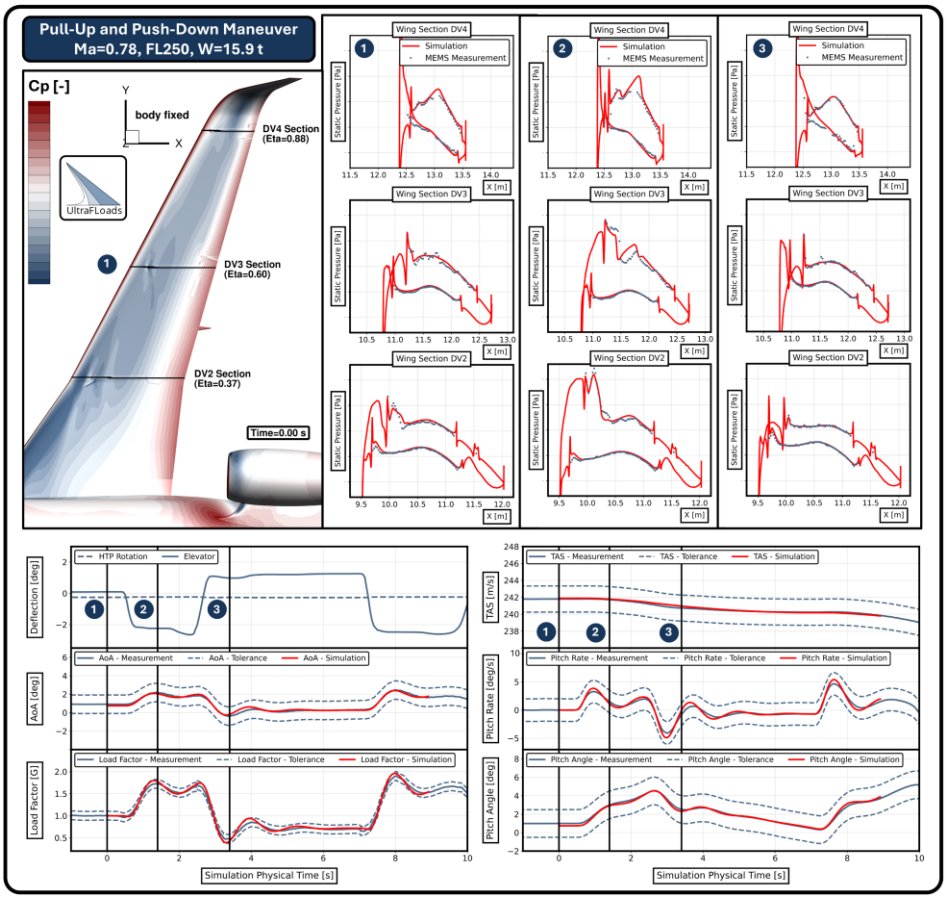


Fig. 5 Pull-up and push-down maneuver – Ma=0.78, FL250

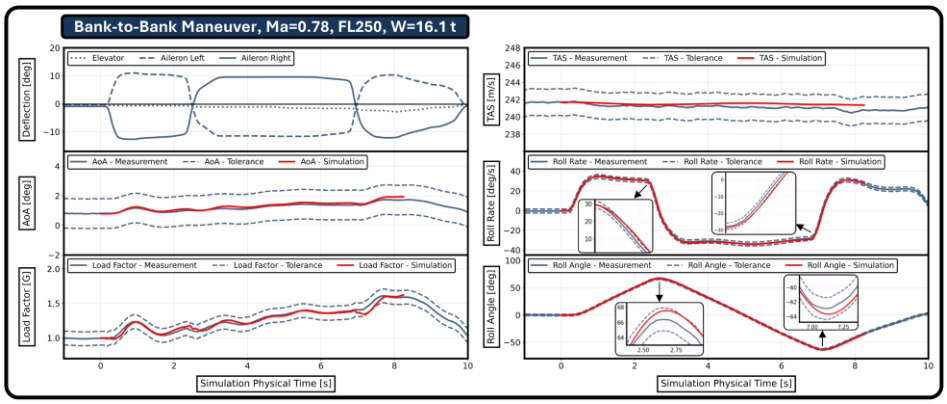


Fig. 6 Bank-to-bank maneuver – Ma=0.78, FL250

All presented UltraFLoads maneuver simulations are computed on the DLR HPC cluster CARO. The presented simulations with the CFD mesh with approximately 40 million points take about 330h on 480 CPUs on CARO (simulation physical time of approximately 9s, simulation time step of 0.0025s).

Summary and Outlook

In this paper, validation results for the first set of dynamic maneuver simulations, using experimental data from the DLR Falcon 2000LX ISTAR aircraft in clean cruise configuration during the HighFly flight campaign MaGE, are presented. This validation of pull-up and push-down and bank-to-bank maneuver simulations for Ma=0.46 and 0.78 shows a sufficient qualitative

correspondence between the simulations and measured data for the presented parameters (wing static pressure distributions and global flight dynamic quantities).

Further validation with MaGE flight data of different dynamic maneuvers will be performed in the next step. These will be more critical flight maneuvers: higher Mach numbers (closer to the maximum operating Mach number), higher flight altitudes, and maneuvers with a buffet onset (a light buffet onset occurred during some MaGE maneuvers). The influence of variations in different numerical parameters (CFD parameters, turbulence models, mesh resolution, inflow Mach number, weight, CG position, aircraft inertia properties, and elasticity variation) will be investigated.

Future DLR projects on validating virtual flight tests and certification by analysis are planned. The aircraft Falcon 2000LX ISTAR will be used again and will be equipped with a nose boom featuring more accurate measurement sensors, and additional pMEMS sensors could be installed on both sides of the aircraft, including the tail surfaces.

Acknowledgements
The authors gratefully acknowledge the scientific support and HPC resources provided by the German Aerospace Center (DLR). The HPC system CARO is partially funded by "Ministry of Science and Culture of Lower Saxony" and "Federal Ministry for Economic Affairs and Climate Action".

References

[1] DLR Institute of Aerodynamics and Flow Technology: HighFly - Aerodynamics, aeroelasticity, structures and propulsion on the ISTAR research aircraft. https://www.dlr.de/en/as/research-and-transfer/projects/highfly Accessed 09 November 2025

[2] German Aerospace Center (DLR): ISTAR Dassault Falcon 2000LX D-BDLR. https://www.dlr.de/en/research-and-transfer/research-infrastructure/research-aircraft-fleet/istar-dassault-falcon-2000lx-d-bdlr Accessed 09 November 2025

[3] Bauer, M., Feldwisch, J.M.: High-Fidelity Multidisciplinary Maneuver Simulations of the Falcon 2000LX ISTAR. CEAS Aeronaut J (2025). https://doi.org/10.1007/s13272-025-00849-8

[4] Bauer, M., Feldwisch, J.M., Mühlmann, P., Kirmse, T. (accepted for publication): Validation of High-Fidelity Aeroelastic Simulations with Flight Test Data from Dassault Falcon 2000LX ISTAR. CEAS Aeronaut J (2025).

[5] Feldwisch, J.M., Bauer, M.: UltraFLoads: A Simulation Suite and Framework for High-Fidelity Flight Loads. Aerospace 2023, 10, 273. https://doi.org/10.3390/aerospace10030273

[6] Feldwisch, J.M., Schulze, M.: High-Fidelity Aeroelastic Loads Calculation for a Transport Aircraft Configuration Including Pitch and Roll Maneuvers. In: Dillmann, A., Heller, G., Krämer, E., Wagner, C. (eds) New Results in Numerical and Experimental Fluid Mechanics XIII. STAB/DGLR Symposium 2020. Notes on Numerical Fluid Mechanics and Multidisciplinary Design, vol 151. Springer, Cham. https://doi.org/10.1007/978-3-030-79561-0_50

[7] Zimmer, M., Feldwisch, J.M., Ritter, M.: Coupled CFD-CSM Analyses of a Highly Flexible Transport Aircraft by Means of Geometrically Nonlinear Methods. In: 19. International Forum on Aeroelasticity and Structural Dynamics, Madrid, 13-17 Juni 2022.

[8] International Civil Aviation Organization: Manual of Criteria for the Qualification of Flight Simulation Training Devices. 2015. Kap. Part II Appendix B. isbn: 978-92-9249-761-3.

Materials Research Proceedings 69 (2026) 499-503 https://doi.org/10.21741/9781644904251-90

A Simulation-Coupled Concurrent Engineering Approach to Next-Generation Low-Cost Counter-UAV Missiles

Vincenzo Jr. DI ROSA[1,a *], Francesco GASPERINI[1,b *], Matteo GIANNITTI[1,c], Michele GUIDA[1,d], Simone GUBBIONI[2,e], Emanuele COFANI[2,f]

[1]University of Naples Federico II, Department of Industrial Engineering, Naples, Italy

[2]MBDA, Lethality Section, Rome, Ital

[a]vincenzo.dirosa@studenti.unina.it, [b]fr.gasperini@studenti.unina.it, [c]m.giannitti@studenti.unina.it, [d]michele.guida@unina.it, [e]simone.gubbioni@mbda.it, [f]emanuele.cofani@mbda.it

Keywords: Concurrent Engineering, Preliminary Missile Design, Counter-UAV Systems, Kill Probability (P_k), Simulation and Off-Design Analysis

Abstract. The activities are based on the Sagittarius project, which introduces a simulation-coupled concurrent engineering framework for the preliminary design of a low-cost surface-to-air missile aimed at countering small hostile drones. The methodology integrates guidance, propulsion, aerodynamics, structures, and lethality within a unified workflow, enabling continuous exchange of boundary conditions and performance constraints across subsystems. Trajectory simulations are employed to validate the missile performance against representative mission scenarios, while warhead lethality and structural analyses are iteratively harmonized with aerodynamic and propulsion requirements to maintain design coherence. A reference case involving a target UAV flying at 60~m/s, positioned 8000~m from the defended zone and 5000~m in altitude, was used to assess nominal behavior and off-design robustness. Results demonstrate that the integrated workflow achieves consistent performance and high kill probability across different operational profiles, highlighting the benefits of multidisciplinary coupling in early-stage design. The proposed approach emphasizes the importance of scenario-driven, simulation-based interaction between subsystems as a key enabler for affordable and adaptable Counter-UAV missile solutions.

Introduction

The rapid proliferation of unmanned aerial vehicles (UAVs) and loitering munitions has reshaped modern warfare, introducing new paradigms in surveillance, reconnaissance, and tactical engagement. Their low cost, agility, and swarm capability have increased the complexity of airspace protection, as small UAVs can operate at low altitude with limited radar visibility, posing asymmetric threats to both military and civilian infrastructures [1, 2].

Conventional defense systems, conceived for high-value targets, are economically unsustainable against large numbers of inexpensive drones. Consequently, research has focused on affordable short-range missile systems capable of ensuring reliable interception performance [3]. These systems must guarantee adaptability to diverse UAV classes and flight profiles, requiring advanced detection, guidance, and control strategies.

Addressing these challenges demands an integrated approach combining aerodynamic, structural, guidance, and propulsion design under a unified optimization framework. Modern missile development therefore relies on simulation-driven, multidisciplinary environments that enable concurrent progress across domains, accelerating design and improving overall coherence [4].

Content from this work may be used under the terms of the Creative Commons Attribution 3.0 license. Any further distribution of this work must maintain attribution to the author(s) and the title of the work, journal citation and DOI. Published under license by Materials Research Forum LLC.

Materials Research Proceedings 69 (2026) 499-503 https://doi.org/10.21741/9781644904251-90

Within this context, *Project SAGITTARIUS* was developed at the University of Naples Federico II, in collaboration with MBDA Roma, as a next-generation surface-to-air missile optimized for Counter-UAV missions (Fig. 1). The project applies a simulation-coupled concurrent engineering framework in which all primary subsystems—guidance, propulsion, aerodynamics, structures, and lethality—are developed in parallel through iterative data exchange and mission-driven constraints.

This paper outlines the design rationale and integrated workflow of the *SAGITTARIUS* project, demonstrating how scenario-based simulations and subsystem interaction lead to a coherent and adaptable missile configuration.



Figure 1: SAGITTARIUS Missile Design.

Methodology

The development of the *SAGITTARIUS* missile followed a concurrent engineering workflow aimed at ensuring tight integration among all subsystems from the earliest design phases. Each discipline was developed in parallel, with continuous data exchange and validation loops driven by mission-level simulations. The overall workflow is illustrated in Fig. 2.

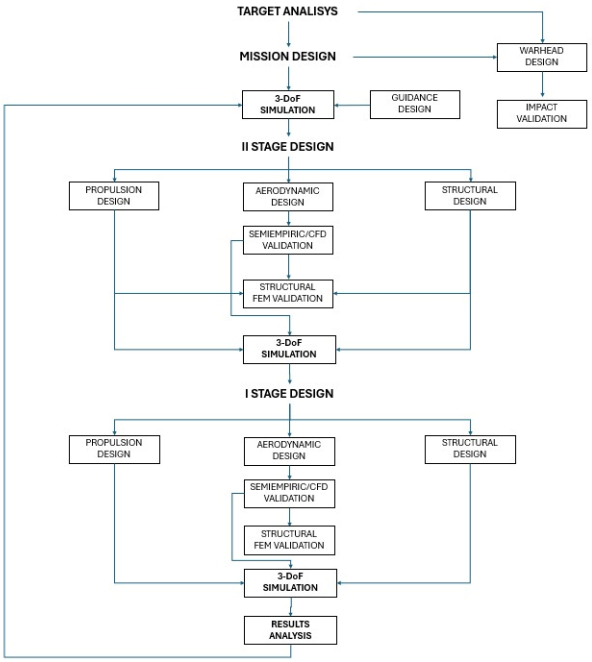


Figure 2: Concurrent engineering workflow adopted for the SAGITTARIUS missile design.

The process began with a comprehensive target analysis, defining the physical and operational characteristics of hostile UAVs, such as velocity range, altitude, and representative geometry.

Materials Research Proceedings 69 (2026) 499-503 https://doi.org/10.21741/9781644904251-90

These parameters guided the mission design, establishing engagement requirements including an interception range of 8 km, target altitude of 5 km, and velocity of 60 m/s.

A 3-Degree-of-Freedom (3-DoF) trajectory simulation was employed to assess mission feasibility and derive key metrics—acceleration limits, flight path, and kill probability (P_k). The simulation outputs served as boundary conditions for subsystem design, while the guidance and control logic were developed in parallel using a Proportional Navigation (PN) scheme integrated into the model.

The second-stage design followed a concurrent approach, combining propulsion, aerodynamic, and structural development. Propulsion parameters such as thrust and burn time were refined through iterative feedback with trajectory results. Aerodynamics were assessed using semi-empirical and CFD-based analyses, whereas FEM simulations validated the structural response of major components. Each iteration of the 3-DoF model ensured alignment between subsystem performance and mission objectives. After the second stage was finalized, its output conditions—velocity, attitude, and altitude—were transferred as inputs for the first-stage design, optimized to provide adequate thrust and stability during launch while maintaining overall mission coherence.

Missile Design & Reference Scenario

The interceptor was conceived as a compact, two-stage subsonic missile optimized for short-range air defense against small UAVs and loitering munitions. The architecture couples a booster stage for initial acceleration with a sustain stage for cruise and terminal engagement, balancing mass distribution, propulsion performance, and aerodynamic stability. The configuration was defined through a concurrent engineering process harmonizing subsystem constraints derived from trajectory simulations. The resulting main geometric and mass properties are summarized in Table 1.

Table 1: Principal characteristics (II stage / I stage / Total).

Characteristic	*II Stage (Sustain)*	*I Stage (Booster)*	*Total (Missile)*
Total mass	11.224 kg	5.470 kg	16.694 kg
Propellant mass	2.524 kg	1.288 kg	3.812 kg
Diameter	0. 0806 m	0.0806 m	0.0806 m
Length	0. 976 m	0.456 m	1.432 m
Reference Area S_{ref}	0.005 m^2	0.005 m^2	0.005 m^2
Nominal Thrust	150 N	3626.5 N	-
Average burn time	30.0 s	0.8201 s	-

The design workflow employs a hybrid MATLAB/Simulink environment coupling a 3-Degree-of-Freedom (3-DoF) trajectory solver with guidance, control, and propulsion modules. The booster provides initial conditions to the sustain stage, whose dynamics include aerodynamic forces, gravity, and actuator response. Launch geometry is computed through an *auto-aiming* routine solving the relative motion with gravity correction. Guidance follows a Proportional Navigation (PN) law generating commanded accelerations, converted into fin deflections by the autopilot. The simulation ends when the range-to-target R drops below 1 m or interception becomes unfeasible, providing data for subsystem sizing and P_k estimation.

The reference mission involves a small UAV flying at constant altitude and speed toward a protected area, representing a typical Counter-UAV engagement. The target travels at 60 m/s and 5000 m altitude, starting 8000 m from the defended zone on a 180° inbound heading. The protected area radius is 3 km, defining the interception boundary for neutralizing the threat. Fig. 3 shows the nominal engagement, highlighting missile and target trajectories together with the corresponding P_k evolution, confirming full interception and stable guidance under nominal conditions.

Materials Research Proceedings 69 (2026) 499-503 https://doi.org/10.21741/9781644904251-90

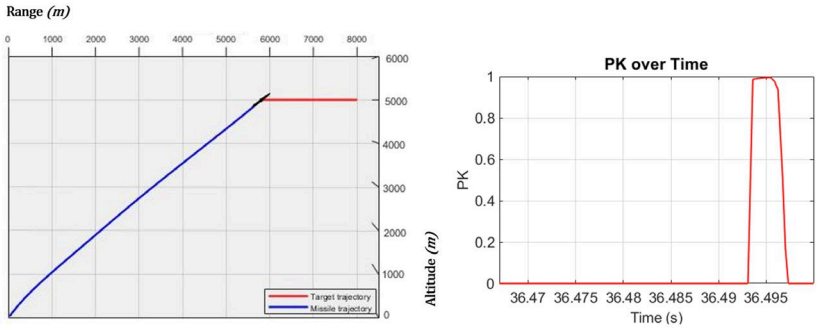


Figure 3: Nominal engagement scenario with time evolution of P_k.

Off-Design Conditions

To assess the robustness of the *SAGITTARIUS* missile, several off-design simulations were conducted by varying the target geometry and initial conditions, while keeping control laws and propulsion settings identical to the nominal case. This allowed the evaluation of guidance adaptability and overall system performance under realistic deviations from design conditions. Here two of these cases are represented.

The first configuration reproduces a *shallow dive attack*, with the target descending at 30° from 5000 m altitude and 8000 m ground distance at 60 m/s (Fig. 4). The interceptor adapts its trajectory through a progressive climb, completing the engagement after about 35 s with stable guidance and nearly unitary lethality ($P_k \approx 1$). The second case simulates a *close-range engagement*, with the UAV starting 3000 m from the launch point at 5500 m altitude (Fig. 5). Despite higher maneuver demand and shorter flight time (~33 s), the missile maintains control stability and achieves $P_k \approx 0.9$, confirming adequate energy and guidance margin.

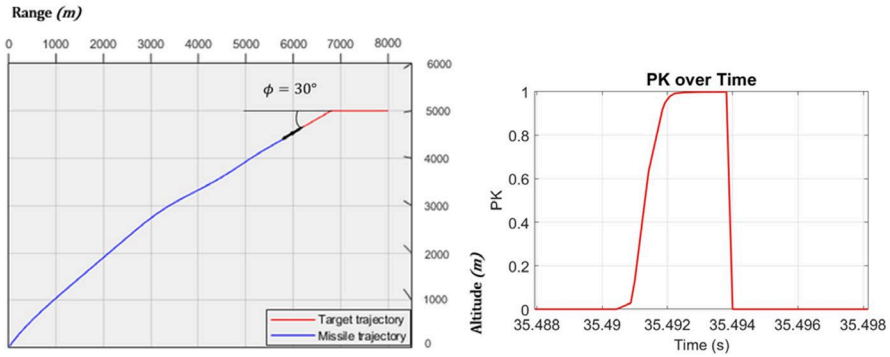


Figure 4: Off-design scenario 1 (Shallow dive approach) with time evolution of P_k.

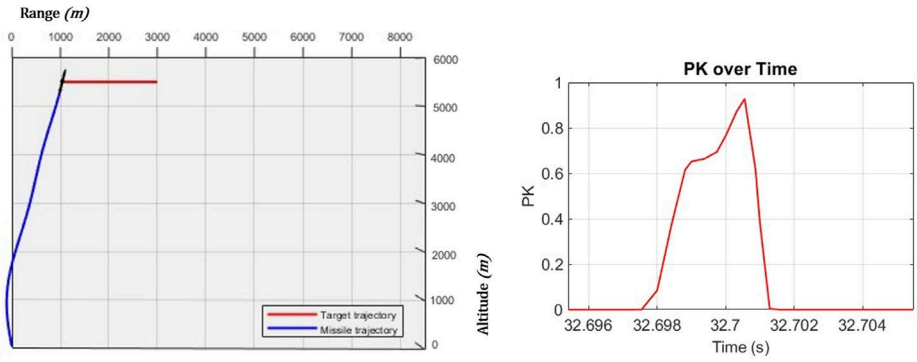


Figure 5: Off-design scenario 2 (Close-range engagement) with time evolution of P_k.

Conclusions

The *SAGITTARIUS* validated a simulation-driven, concurrent engineering framework for the preliminary design of Counter-UAV missile systems. The integrated workflow ensured coherence among propulsion, aerodynamics, structures, guidance, and lethality, maintaining performance consistency across nominal and off-design scenarios.

Results confirmed stable guidance, aerodynamic efficiency, and high lethality under varied mission geometries, demonstrating the robustness of the proposed approach. The methodology proved effective in enabling reliable and adaptable missile configurations through early multidisciplinary coupling.

References

[1] O. Molloy, How are drones changing modern warfare?, Australian Army Research Centre, Land Power Forum, 2024. https://researchcentre.army.gov.au/library/land-power-forum/how-are-drones-changing-modern-warfare

[2] C. Marino, Send in the drones, Army AL&T Magazine, 2024. https://www.army.mil/article/280609/

[3] H. González Jorge, E. Aldao, G. Fontenla Carrera, F. Veiga López, E. Balvís, and E. Ríos Otero, Counter Drone Technology: A Review, Preprints, 2024, 10.20944/preprints202402.0551.v1.

[4] M. Zakeri, M. Nosratollahi, and A. Novinzade, Multi-Disciplinary System Design Optimization of a Launch Vehicle Upper-Stage, Journal of Aerospace Technology and Management 9(1) (2017) 48–62.

Materials Research Proceedings 69 (2026) 504-509 https://doi.org/10.21741/9781644904251-91

Enhancements in the Aircraft Preliminary Design Methodologies: Adoption of Sustainable High-Fidelity Simulations

Federico CARLINI[1,a,*], Marco BASAGLIA[2,b], Luca BATTAGLIA[1,c], Elisa GARBI[2,d], Simone GENOVESE[1,e], Rocco GENTILE[3,f], Chiara LA GUARDIA[1,g], Angela SCARDIGLI[4,h], Lorenzo VISCONTI[3,j] and Giovanni ZIPPA[2,i]

[1]ESTECO, Trieste, Italy

[2]Leonardo Aeronautics, Venegono Superiore, Italy

[3]Leonardo Aeronautics, Torino, Italy

[4]OPTIMAD, Torino, Italy

[a]carlini@esteco.com, [b]marco.basaglia@leonardo.com, [c]battaglia@esteco.com, [d]elisagiulia.garbin@leonardo.com, [e]genovese@esteco.com, [f]rocco.gentile@leonardo.com, [g]laguardia@esteco.com, [h]scardigli@esteco.com, [j]lorenzo.visconti@leonardo.com, [i]giovanni.zippa@leonardo.com

Keywords: Aircraft Preliminary Design, Multi-Disciplinary Optimization, Reduced Order Model (ROM), Proper Orthogonal Decomposition (POD)

Abstract. Aircraft preliminary design requires the capability of rapidly exploring several different configurations without compromising the accuracy of the different physics involved, such as aerodynamics, structural analysis and low observability. In this work we propose a multi-fidelity methodology combining analysis with different levels of fidelity, where the high-fidelity is meant to be supported by Reduced Order Models (ROM). The purpose is to significantly accelerate the decision process, increasing the quality of the design already in the preliminary phases. Inspired by a previous ESTECO's experience [1], the methodology is applied by Leonardo Aeronautics in a study-case based on an example configuration of a fighter jet. The ultimate goal is to include this methodology among the tools available for preliminary aircraft design [2]. The design workflow begins with a conceptual phase that involves the rapid generation of several configurations through low-fidelity simulations. The purpose is not only to get a preliminary evaluation of the performances and requirements compliance, but also to find a region of interest in the input domain where to concentrate the analysis effort. In this region, we developed a Design of Experiments (DOE) Table containing different possible aircraft configurations to perform the high-fidelity simulations for the two selected physics: CFD for the aerodynamics and electromagnetic fields for the estimation of the radar cross-section (RCS). The resulting set is used as a training set for the development of the non-intrusive ROM models. This approach enables a detailed exploration of the solution space with limited computational costs, making it possible to converge on engineering-feasible configurations within the timeframes of the preliminary design phase.

Introduction

Engineering design processes commonly incorporate high-fidelity solvers to facilitate the acquisition of solutions characterised by high resolution. While the efficacy of these methodologies has been demonstrated, they are associated with a considerable computational cost. In the aerospace and defence sector, where rapid design iteration is paramount, this computational burden poses a substantial challenge, particularly in the initial stages of development that necessitate extensive parametric studies. Reduced order modelling represents a promising alternative to address these limitations. The purpose of this study is to demonstrate that, in a preliminary phase, ROM can act as an enabler for optimisation, reducing the quantity on high-

Content from this work may be used under the terms of the Creative Commons Attribution 3.0 license. Any further distribution of this work must maintain attribution to the author(s) and the title of the work, journal citation and DOI. Published under license by Materials Research Forum LLC.

Materials Research Proceedings 69 (2026) 504-509 https://doi.org/10.21741/9781644904251-91

fidelity simulations while maintaining sufficient accuracy for decision-making. To do so, we apply the methodology to a design process carried out by the Leonardo S.p.A. aircraft preliminary design team. The original design process consists of several distinct phases, all integrated and automated through modeFRONTIER and VOLTA. The process starts with a parametric CAD model of the aircraft generated in CATIA V5, followed by a meshing step performed in ANSA BETA CAE. Subsequently, the CFD simulation is conducted in Ansys Fluent, and finally, a low-observability study is carried out in Ansys HFSS. The entire process for a single design lasts four hours on an HPC node with 48 CPUs showing an evident limitation to perform a multi-objective optimization within the industry timing. The output of interest for the CFD simulation includes the pressure and shear stress fields on the aircraft surface, whereas the electromagnetic result is the Mono-static RCS Total signal. This highlights the need to develop a surrogate model that preserves the space resolution of the Full-Order Model (FOM) to enable the analysis of physical phenomena, including flow separation and shock waves.

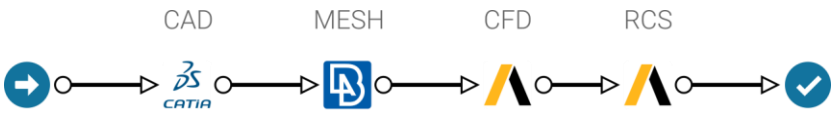


Figure 1: Original design process

Reduced Order Models have emerged as a strategy to approximate the behaviour of complex systems with significantly reduced computational effort. The classification of ROMs is typically divided into two categories: intrusive and non-intrusive. While the intrusive operate directly on the governing equations, requiring modification of the underlying solver, non-intrusive ROMs treat the solver as a black-box and consider only input-output data for training. Among non-intrusive techniques, Proper Orthogonal Decomposition (POD) is one of the most widely used. The system extracts dominant modes from a set of high-fidelity solution snapshots and projects new queries onto this reduced space. When combined with interpolation schemes such as Radial Basis Functions (RBF), POD-based ROMs can reconstruct flow fields across a range of geometric parameter variations. This technique relies on matrix operations on the training samples, and consequently, it is required that training designs have equal dimension. For the CFD, this means that the fields must be defined on the same number of mesh nodes, that the meshes need to be topologically equivalent.

Low-fidelity Exploration

In the initial study phase, we explore a large number of configurations with a dual purpose: to perform a sensitivity analysis on the input variables and to identify a promising region for a high-fidelity optimization. Low-fidelity simulations, although simplified, are sufficiently accurate to capture general performance trends, providing valuable insight to set up the optimization problem. Aerodynamics is computed through a simulation based on the Vortex Lattice Method (VLM), while the electromagnetic analysis, relies on a high-frequency faceted scattering model. This exploration determines the input variables that most influence the performance metrics of interest and finds a design region that best balances: weight reduction, improved aerodynamic efficiency allowing for a smaller engine and reduced peak in the RCS. Additionally, we apply performance constraints to improve the Specific Turn Rate (STR) at two target altitudes and across multiple Mach numbers. The most relevant input variables and the variation limits are respectively: Reference Surface Area (Sref) in the range [65, 75], Aspect Ratio (AR) in the range [2.6, 3.1], Leading Edge Sweep Angle in the range [36, 46], and Thickness-to-Chord Ratio (tc) in the range [4, 5].

Materials Research Proceedings 69 (2026) 504-509 https://doi.org/10.21741/9781644904251-91

Table 1: Input Domain

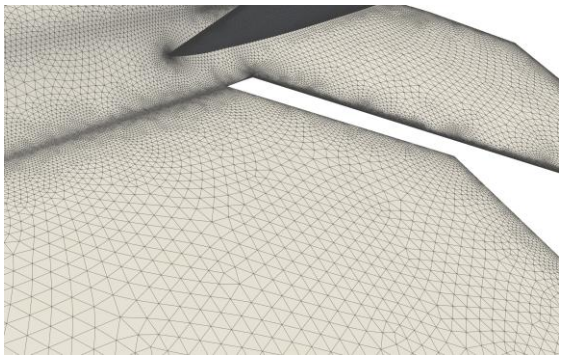
Input variables	Lower Bound	Upper Bound
Sref	65	75
AR	2.6	3.1
Sweep Angle LE Wing	36	46
Thickness wing root	4	5

High-fidelity

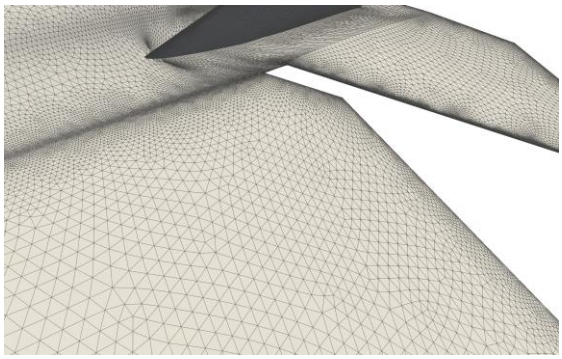
The High-Fidelity simulations are used to create a representative dataset for the region identified in the former phase; this dataset serves for the training of the ROM models. To distribute the data set uniformly, we used a Uniform Latin Hypercube (ULH) as the DOE algorithm. A DOE table of 40 configurations is set up directly in modeFRONTIER, which orchestrates the whole design process and enables to apply advanced sampling techniques to add new points at the training dataset during the ROM's quality assessment phase. Since the CFD and RCS simulations are performed on the same starting geometry, but they do not depend one to the other, they can be run in parallel.

Registration and Mapping - CFD

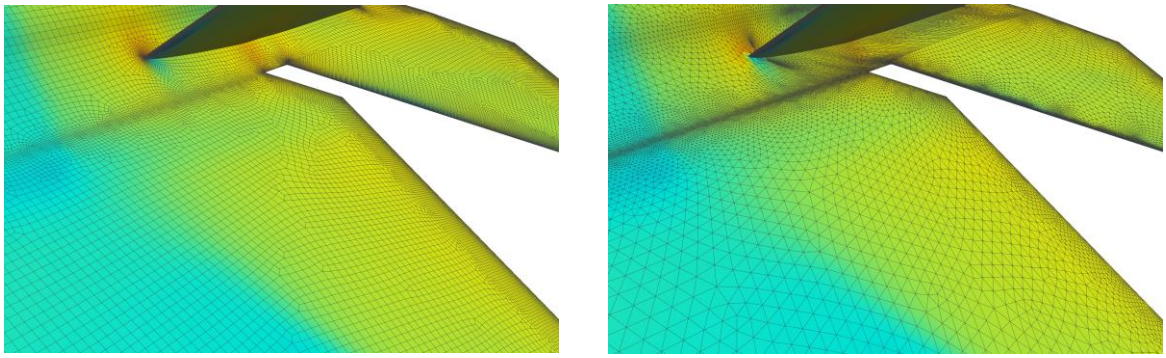
As stated previously, the ROM used in this study requires field data of equal dimensions to create the snapshot matrix. Consequently, the resulting fields: pressure and skin friction, must be mapped on the same reference mesh morphed on different geometries. The original framework did not incorporate mesh morphing; instead, it involved a meshing phase for each geometry resulting from the parametric CAD model, thus yielding to typical CFD meshes with variable number of cells. To adapt to this framework, we integrated a mesh morphing procedure that adjusts a reference surface mesh to the geometries produced from the parametric model. This step, designated as "registration", necessitates a modification to the original modeFRONTIER workflow: the definition of Surface IDs and the export of the resulting surface mesh. This process enables Mimic, ESTECO's proprietary software, to identify the features and edges between the surface IDs for each input geometry, thus determining the computation of the deformation fields between them. Iterating this procedure among all the designs allows to collect all the so-called registered meshes, i.e. the baseline mesh overlapping with each different geometric configuration (Figure 2: a - b). The selection of the baseline mesh is crucial in this context. We chose the geometry with the largest reference surface to prevent certain elements from being enlarged during morphing, thus losing mesh resolution. After the registration phase, each field derived from CFD simulations is mapped from the original computational mesh to the corresponding registered mesh (Figure 2: c - d).



(a) Baseline Mesh



(b) Registered Mesh

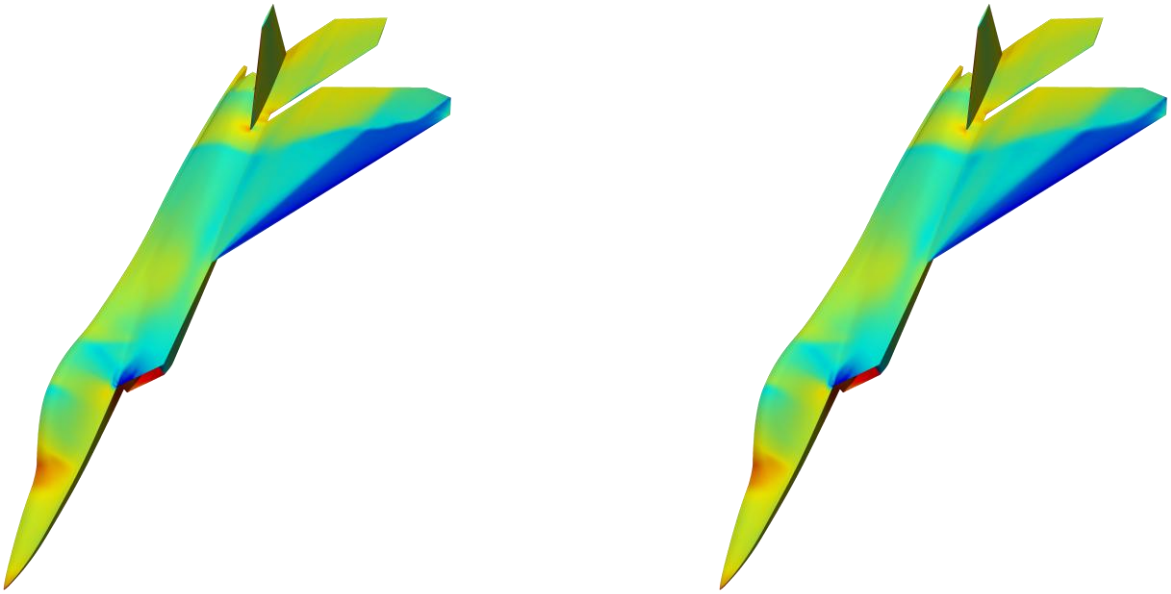


(c) Original Pressure Field (d) Mapped Pressure Field

Figure 2: Registration and mapping

ROM Model - CFD

As previously stated, the ROM used in this study is based on POD techniques and nonlinear regression models, such as RBF [3].



(a) High fidelity pressure field (b) Predicted pressure field

Figure 3: Comparison between the pressure field from the CFD and the ROM model

The generation of a solution for a new geometry is simplified by predicting, using regression models, the relevant expansion's coefficients of the POD. The training phase is performed through a dedicated ROM training node in modeFRONTIER. Through this node we can control the POD energy, the validation strategy and the regressor configuration.

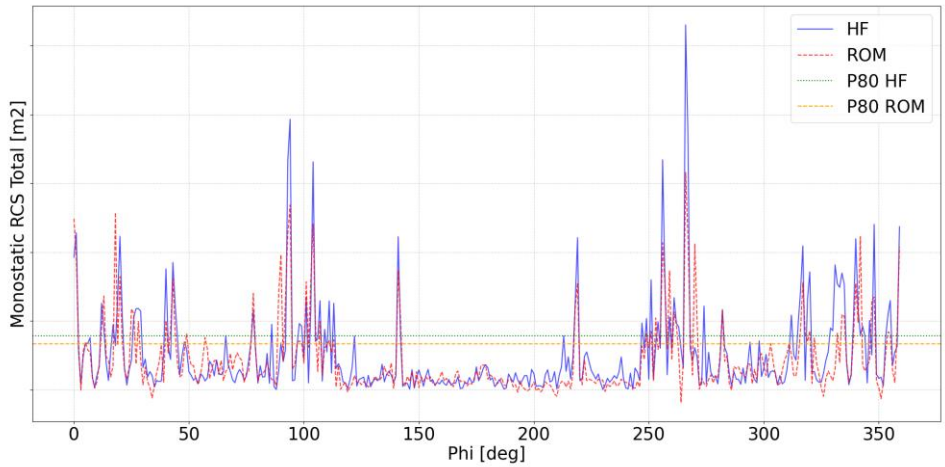
The validation estimates the ROM's quality by calculating the projection and the validation error for each design in the validation set. The figure 3 shows a qualitative comparison between the pressure field obtained from the CFD simulation and the one predicted with the ROM model.

ROM Model - RCS

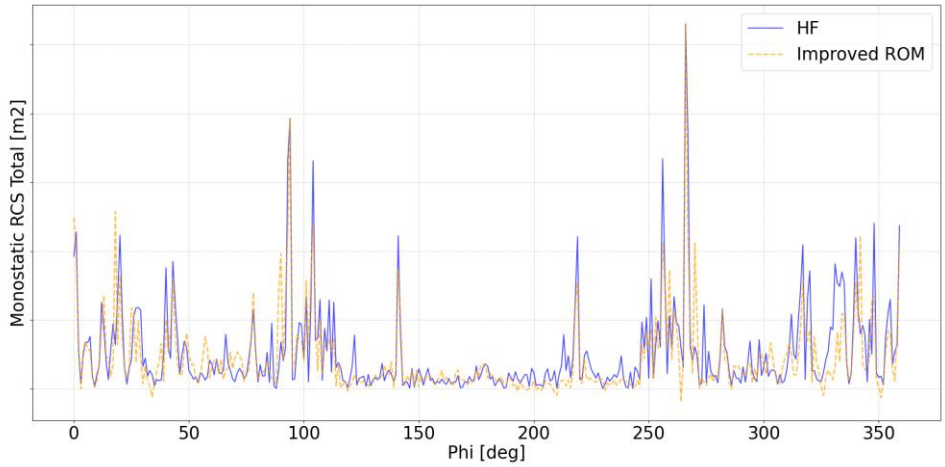
In the case of the RCS simulation, the ROM model predicts the Mono-static RCS Total, considering fixed values for the frequency and the elevation angle (θ) of the incident wave direction. Unlike the previous two cases, here the quantity is not predicted for a point on the mesh but for a given azimuth angle (ϕ). The ROM model therefore aims to predict the Mono-static RCS

Materials Research Proceedings 69 (2026) 504-509 https://doi.org/10.21741/9781644904251-91

Total signal as the azimuth angle varies from 0 to 360 degrees. The highly non-linear behaviour of RCS signals represents a particularly challenging case for prediction using a ROM model.



(a) Predicted RCS signal



(b) Improved prediction RCS signal

Figure 4: Predicted and Improved RCS

The ROM model trained only the initial DOE of 40 designs has a very high projection error, indicating that the starting dataset was insufficient to achieve an accurate representation. For this reason, an additional 60 configurations were added for the only RCS simulation, using modeFRONTIER's Incremental Space Filler algorithm based on Voronoi–Delaunay tessellation. These new points made it possible to significantly reduce both projection and prediction errors. As shown in Figure 4-a, the model still struggles to accurately predict peak values. With the aim of correcting the highest peaks value, a second ROM model was trained on the reordered peaks. The two ROM models were then combined for the final signal prediction, as shown in Figure 4-b.

Optimization

The trained ROM models can ultimately be used within modeFRONTIER as replacement to CFD and RCS simulations. A dedicated node allows for straightforward use of the ROM models and seamless integration with other disciplines in the design process. The optimization considers the same variables and input domain of the high-fidelity, and three objective functions: minimization of the drag coefficient (CD), maximization of the lift coefficient (CL), and minimization of the maximum peak of the RCS signal. The DOE of high-fidelity designs is used as first generation for

the NSGA-II genetic algorithm. The algorithm evolves over 20 generations, evaluating a total of 400 designs. The optimization yields a Pareto front of optimal designs, from which three configurations were selected, each representing a good balance between the objectives. Finally, the three selected designs were validated using high-fidelity simulations.

Summary

This case study highlighted how ROM models can enable optimization during the preliminary design phase of an aircraft, drastically reducing simulation times. The short training times and the relatively small number of designs required to create the training dataset allow the overall timeframe to fit within the constraints of the preliminary design phase. The modifications to the framework already used by the Leonardo team were acceptable, demonstrating the potential for adopting such a tool. There are numerous opportunities for future developments, both in improving the ROM model (through techniques such as error-based adaptive sampling) and in expanding the methodology to additional disciplines, ultimately enabling an effective optimization framework.

References

[1] Mull, K. M. (2020). Expanded MDO for Effectiveness Based Design Technologies: The EXPEDITE Program and Successes with ESTECO Technologies. https://doi.org/10.2514/6.2020-1390

[2] Visconti, L. (2024). Ottimizzazione multidisciplinare di un velivolo fighter nella fase di progetto preliminare – Tesi di Laurea presso Leonardo Velivoli.

[3] Bui-Thanh, T., Damodaran, M., and Willcox, K. (2003). Proper Orthogonal Decomposition Extensions for Parametric Applications in Compressible Aerodynamics. In 21st AIAA Applied Aerodynamics Conference. Orlando, FL. AIAA 2003-4213. https://doi.org/10.2514/6.2003-4213

Materials Research Proceedings 69 (2026) 510-515 https://doi.org/10.21741/9781644904251-92

Wind Gust Spectral Analysis with Aeolus Observations: Insights from a Transatlantic Route

Marianna VALENTE[1,a *], Giuseppe PALAIA[1,b], Alfonso PAGANI[1,c], Erasmo CARRERA[1,d]

[1]Department of Mechanical and Aerospace Engineering, Polytechnic of Turin, Corso Duca degli Abruzzi 24, 10129 Torino, Italy

[a]marianna.valente@polito.it, [b]giuseppe.palaia@polito.it, [c]alfonso.pagani@polito.it, [d]erasmo.carrera@polito.it

Keywords: Remote Sensing, Aviation, Satellite, Spectral Analysis

Abstract. This study explores the use of ESA's Aeolus satellite data to characterize wind gusts along a transatlantic flight corridor. A dedicated framework was developed to extract the power spectral density (PSD) of wind signals from temporally discontinuous satellite observations, enabling PSD-based gust characterization using spaceborne Doppler lidar data along operational flight routes. The proposed framework extracts and preprocesses wind data from ESA's Aeolus mission and applies Fourier-based spectral analysis to obtain the PSD of the signal, which is then fitted using two different approaches: a classical von Kármán turbulence model and a data-driven optimization method. Results reveal deviations from the von Kármán spectrum, highlighting regional variability and demonstrating the potential of spaceborne Doppler wind lidar for global gust characterization and improved aviation safety modeling.

Introduction

Space technologies play an increasingly vital role in sustainable development, driven by innovation and the widespread use of satellite services [1]. Earth Observation (EO) systems are key, supporting disaster management, environmental monitoring, and climate adaptation [2]. EO capabilities, especially satellite constellations and real-time data, enable high-frequency, wide-area observations suited to operational needs [3]. These are crucial in atmospheric science, where accurate wind measurements improve weather forecasts and climate models. ESA's Aeolus mission, the first to provide global wind profile data via space-based Doppler lidar, marked a milestone, offering new insights into atmospheric dynamics [4]. However, despite extensive use of satellite wind products in meteorology and climate studies, their exploitation for aeronautics, particularly for gust load assessment, is still largely unexplored. Wind gusts pose significant challenges for flight safety, passenger comfort, and aircraft integrity. Accurate gust characterization is vital for aircraft design and certification.

Traditionally, gust spectra are derived from dedicated flight-test campaigns, which are costly, geographically constrained, and limited to regions frequently flown by commercial traffic. The emergence of advanced EO platforms, such as the Copernicus Sentinel missions, may open new opportunities to complement in situ data with continuous, high-resolution atmospheric observations, offering a promising avenue for improving gust load prediction and hazard monitoring in aviation [5]. In parallel, the increasing vertical integration of New Space companies, spanning upstream, midstream, and downstream activities, amplifies the ability to harness EO data in operational aerospace applications [6]. Within this evolving framework, ESA's Aeolus mission stands out as a unique opportunity to extend wind and turbulence monitoring to remote and oceanic regions beyond the reach of aircraft-based sensing.

This study utilizes data from ESA's Aeolus satellite during a transatlantic flight to analyze wind gusts. A framework is developed to derive the PSD from the wind temporal signal, providing a

Content from this work may be used under the terms of the Creative Commons Attribution 3.0 license. Any further distribution of this work must maintain attribution to the author(s) and the title of the work, journal citation and DOI. Published under license by Materials Research Forum LLC.

Materials Research Proceedings 69 (2026) 510-515 https://doi.org/10.21741/9781644904251-92

detailed characterization of wind gusts. The proposed framework extracts and preprocesses wind data from ESA's Aeolus mission and applies Fourier-based spectral analysis [7] to obtain the PSD of the signal, which is then fitted using two different approaches: (i) a parametric function based on the von Kármán turbulence model, and (ii) a data-driven approach from [8]. Notably, the latter approach, unlike the model-based fit, involves solving an optimization problem to maximize the R^2 between the PSD and the fitting curve without assuming an a-priori mathematical function. This comparison helps evaluate whether the von Kármán turbulence model adequately describes the wind gust signals.

This paper is structured as follows: Section 1 provides an overview of the Aeolus mission and the extracted data; Section 2 outlines the adopted methodology; Section 3 presents some preliminary results; and finally, Section 4 concludes the paper by summarizing the main findings.

Aeolus

The Aeolus mission, developed by the ESA, represented a technological milestone in atmospheric observation by delivering the inaugural global wind profile measurements from space through the Atmospheric Laser Doppler Instrument (ALADIN). Operating in a sun-synchronous low Earth orbit at an approximate altitude of 320 km, Aeolus achieved near-global coverage. It emitted ultraviolet laser pulses at 355 nm to detect the Doppler shift in the light backscattered by air molecules and aerosols. These measurements facilitated the estimation of both the line-of-sight (LOS) and horizontal line-of-sight (HLOS) wind components, which are vital for meteorological analyses.

Because Aeolus operates in a sun-synchronous Low Earth Orbit and measures winds along its ground track (see Figure 1), each location is observed only during short temporal windows. Consequently, each surface point is sampled only during the orbital pass, resulting in a dataset that is temporally sparse and spatially irregular.

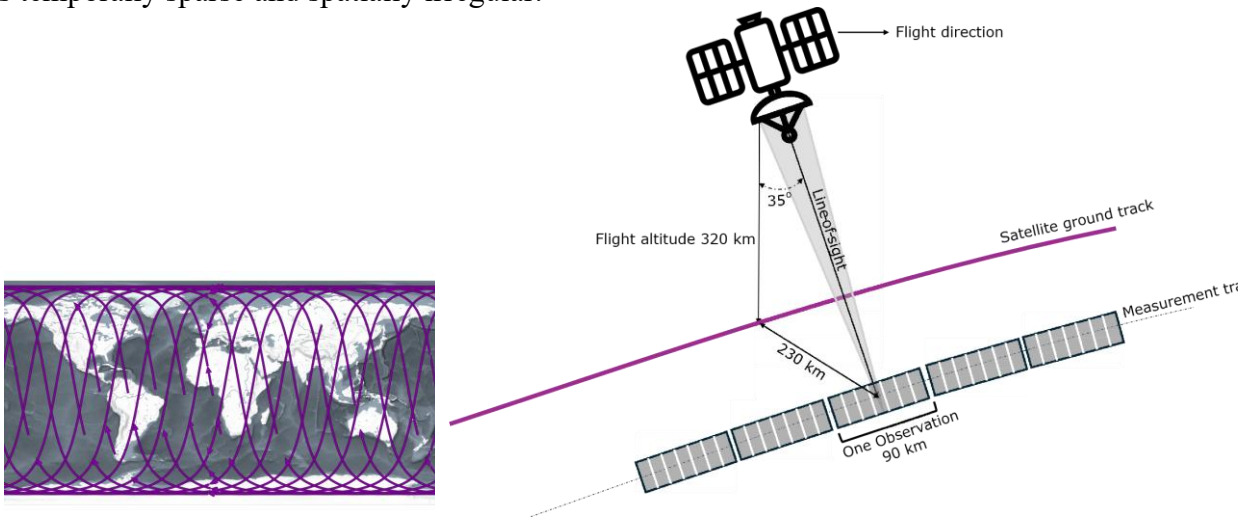


Figure 1. Aeolus' ground track in one day (left). Schematic view of Aeolus measurement geometry (right).

These characteristics prevent the direct application of standard spectral analysis procedures and require dedicated preprocessing before PSD estimation.

From an analytical perspective, these characteristics pose significant challenges for spectral analyses and time-domain studies of atmospheric dynamics. The gaps and irregular sampling intervals necessitate the adoption of specific pre-processing and reconstruction techniques before extracting spectral information such as the PSD of wind gusts. Despite these constraints, Aeolus data offer a unique opportunity to explore global wind variability, providing valuable input for

Materials Research Proceedings 69 (2026) 510-515 https://doi.org/10.21741/9781644904251-92

turbulence characterization and gust modelling in regions where conventional in-situ measurements are unavailable.

Methodology

This section outlines the methodology used to analyze the wind data collected from the Aeolus satellite. The approach follows the general framework shown in Figure 2. Once the signal has been extracted, time intervals with no data are removed, and the remaining intervals are concatenated into a uniformly sampled sequence. Welch's method is then applied to estimate the PSD. Subsequently, the fitting model is applied.

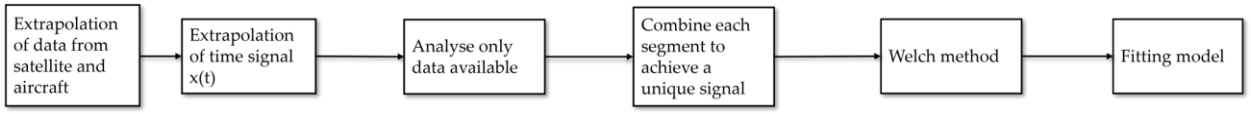


Figure 2. Workflow adopted in the proposed methodology.

Fitting Model

To accurately determine a representative curve of the PSD, the data have been fitted using a model based on the von Kármán equation, a renowned mathematical representation for the PSD of vertical and horizontal wind gust [9]. Eq. 1 is used for vertical wind gusts

$$\mathrm{PSD_{vk}}(f_k)=\frac{\sigma^2 L}{\pi V}\frac{1+\frac{8}{3}\left(1.339\frac{2\pi L}{V}f\right)^2}{\left[1+\left(1.339\frac{2\pi L}{V}f\right)^2\right]^{\frac{11}{6}}} \quad (1)$$

in which σ represents the root mean square of the vertical wind speed, L denotes the turbulence scale, and V is the air speed. The von Kármán model is calibrated using two key parameters: L and σ. The parameter L determines the frequency at which the slope of Eq. 1 increases, providing insight into how gust properties vary spatially, and it is influenced by factors such as altitude. Meanwhile, the parameter σ quantifies turbulence intensity, which depends on the average wind speed and altitude. These parameters are estimated using a non-linear least squares optimization approach to determine the PSD curve that best fits the data, based on the von Kármán equation. Eq. 2 is the parametric equation used in the optimization:

$$\mathrm{PSD_{vk}}(f_k)=a\frac{1+\frac{8}{3}(bf)^2}{\left[1+(bf)^2\right]^{\frac{11}{6}}} \quad (2)$$

with $a=\frac{\sigma^2 L}{\pi V}$ and $b=1.339\frac{2\pi L}{V}$.

While the von Kármán model is widely used in the aeronautical industry for sizing aircraft structural components, it is essential to note that recent climate changes have increased the frequency of hazardous phenomena [10]. Consequently, the von Kármán model may no longer effectively describe such complex and evolving phenomena. In this work, an alternative approach is introduced. This new model, called *agnostic* because it does not depend on a specific pre-existing equation, aims to determine the best-fit curve directly from data without relying on a predefined formula. The process begins by identifying a polygonal chain, followed by an optimization procedure to find the best-fit curve. The key steps to determine the polygonal chain are as follows: i) a set of n points, equally spaced on a logarithmic frequency scale, is defined; ii) for each point is calculated a specific frequency f_n and a corresponding value on the y-axis y_n is

Materials Research Proceedings 69 (2026) 510-515 https://doi.org/10.21741/9781644904251-92

assigned; iii) the polygonal chain is defined by the union of *n-1* segments that connect the n points, with each segment connecting two consecutive points.

The error e_k between the polygonal chain and the PSD is defined according to Eq. 3, where y_k represents the value of the polygonal chain at the *k-th* frequency f_k.

$$e_k = y_k - PSD(f_k) \tag{3}$$

Once the polygonal chain is defined, an optimization problem is carried out according to Eq. 4

$$\begin{cases} \min \dfrac{\sum_{k=0}^{N-1} e_k^2(y_n)}{\sum_{k=0}^{N-1}\left(PSD(f_k) - \frac{1}{N}\sum_{j=0}^{N-1} PSD(f_j)\right)} \\ y_{min} \leq y_n \leq y_{max} \end{cases} \tag{4}$$

The objective function chosen for the optimization problem is the complement of (R^2), as shown in Eq. 4. The design variables are the *y* coordinates y_n of the *n* points in the polygonal chain, with the upper bound y_{max} and lower bound y_{min} depending on the data used. The optimization utilizes gradient-based algorithms, along with a multi-start approach, to find a solution close to the global minimum. The output of the optimization algorithm is the polynomial chain that best fits the data. The shape of this curve varies with the number of points *n,* which is discussed in the next section.

Results

This section presents the main results, specifically considering one of the busiest routes, namely the transatlantic route, the data collected by Aeolus between 2019 and 2022 was used to compare the two fitting models presented in the previous sections.

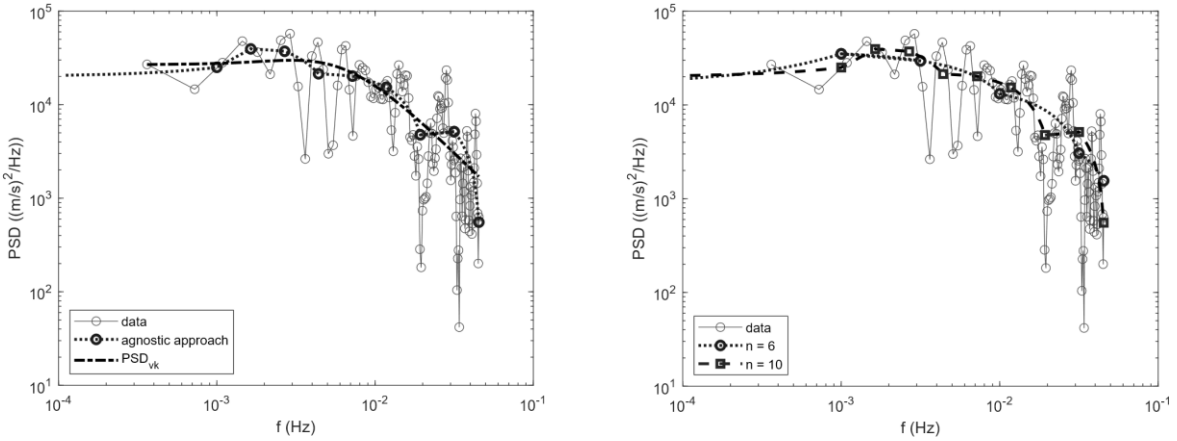


Figure 3. Comparison between the two fitting models, using 10 points for the agnostic approach. $R^2 = 0.54$ for von Kármán fitting and $R^2 = 0.59$ for the agnostic approach (left). Comparison using the agnostic fitting model but varying the points. $R^2 = 0.55.

Specifically, once the data were extracted and Welch's method was applied to derive the PSDs, the two fitting models were applied. Figure 3 shows the results on the data collected in the area from 50° to 55° North and from 33° to 43° West, during July and August 2021, at an altitude of 10 km.

Results indicate that both models capture the PSD trend with comparable accuracy. In this specific region (50°–55°N, 33°–43°W), the von Kármán model remains valid, likely because the model was historically derived from transatlantic flight-test campaigns.

Conclusion

This study demonstrates that ESA's Aeolus satellite observations can be used effectively for spectral analysis of wind gusts along transatlantic routes. A dedicated framework was developed to address challenges from Aeolus's irregular and non-uniform data, allowing for the estimation of the PSD of atmospheric wind signals using spaceborne Doppler lidar data

The comparison between the classical von Kármán turbulence model and a data-driven agnostic fitting approach offered important insights into wind gust spectra characterization. Results in the North Atlantic show both models can reproduce observed PSD trends with similar accuracy. This confirms the von Kármán model's relevance in regions where it was originally developed, while also highlighting the agnostic method's ability to adapt to various atmospheric conditions without relying on fixed assumptions.

This work demonstrates that satellite-based wind measurements can extend turbulence characterization globally. Integrating Aeolus data into gust models can improve aviation safety, aircraft design, and risk assessment, especially in data-scarce oceanic and remote regions. Future work aims to analyze different atmospheric layers, seasons, and areas. These efforts will help create a global turbulence database, aiding scientific research and aerospace safety by addressing atmospheric variability challenges.

Acknoledgment

This study was carried out within the Space It Up project funded by the Italian Space Agency, ASI, and the Ministry of University and Research, MUR, under contract n. 2024-5-E.0 - CUP n. I53D24000060005.

References

[1] Marianna Valente, Federico Caviggioli, and Lara Agostini. "Space economy and sustainability: A systematic review". In: Sustainable Development 33.4 (2025), pp. 4922– 4959. https://doi.org/10.1002/sd.3383

[2] Dominik Starzmann et al. "Design study of a camera system for Earth observation as a payload on the small satellite ROMEO". In: CEAS Space Journal 17.5 (2024), pp. 839–853. https://doi.org/10.1007/s12567-024-00582-8

[3] Radhika Kandepi et al. "Agile earth observation satellite constellations scheduling for large area target imaging using heuristic search". In: Acta Astronautica 219 (2024), pp. 670–677. https://doi.org/10.1016/j.actaastro.2024.03.027

[4] Gordon G. Shepherd. "Development of wind measurement systems for future space missions". In: Acta Astronautica 115 (2015), pp. 206–217. https://doi.org/10.1016/j.actaastro.2015.05.015

[5] David S. Lee et al. "Aviation and global climate change in the 21st century". In: Atmospheric Environment 43.22–23 (2009), pp. 3520–3537. https://doi.org/10.1016/j.atmosenv.2009.04.024.

[6] Marco Bartolini. "The Vertical Integration in the NewSpace". In: Aerotecnica Missili e Spazio 100 (2025). https://doi.org/10.1007/s42496- 025- 00271- 7. url: https://link.springer.com/article/10.1007/s42496-025-00271-7

[7] P. Welch. "The use of fast Fourier transform for the estimation of power spectra:A method based on time averaging over short, modified periodograms". In: IEEE Transactions on Audio and Electroacoustics 15.2 (1967), pp. 70–73. https://doi.org/10.1109/TAU.1967.1161901

[8] E. Carrera et al. "A preliminary methodology to assess gust spectra via satellite data". In: Advances in Aircraft and Spacecraft Science 12.1 (2025), pp. 25–43. https://doi.org/10.12989/aas.2025.12.1.025

[9] F. M. Hoblit. Gust loads on aircraft: Concepts and applications. AIAA Education Series. Washington, D.C.: American Institute of Aeronautics and Astronautics, 1988. isbn: 978-0-930403-45-4.

[10] Luke N. Storer, Philip G. Gill, and Paul D. Williams. “Multi-model ensemble predictions of aviation turbulence”. In: Meteorological Applications 26.3 (2019), pp. 416–428. https://doi.org/10.1002/met.1772

Materials Research Proceedings 69 (2026) 516-521 https://doi.org/10.21741/9781644904251-93

Preliminary Design of Advanced Wing for an Ultra Efficient Regional Aircraft

Giovanni Marco CAROSSA[1,a *], Elena RONCOLINI[1,b], Tomás Eugenio CÁRDENAS MUTIS[1,c], Francesco TOFFOL[1,d] and Sergio RICCI[1,e]

[1]Dipartimento di Scienze e Tecnologie Aerospaziali, via La Masa 34, 20156, Milano, Italy

[a]giovannimarco.carossa@polimi.it, [b]elena.roncolini@polimi.it, [c]tomaseugenio.cardenas@mail.polimi.it, [d]francesco.toffol@polimi.it, [e]sergio.ricci@polimi.it

Keywords: Clean Aviation, Ultra Efficient Regional Aircraft, Preliminary Design

Abstract. Under the HERWINGT project, a comprehensive trade-off study was performed to assess advanced wing concepts for a next-generation regional aircraft, referred to as the Ultra Efficient Regional Aircraft (UERA). The investigation focused on aeroelastic implications of increasing wing aspect ratio up to 16, with the goal of reducing fuel burn, while limiting the structural weight growth driven by higher loads. Parametric analyses have been conducted along with the assessment of a load alleviation system. Study results provided wing structural and aero-servo-elastic requirements fundamental for the experimental demonstration phase, based on wing gust load alleviation system, to be tested inside POLIMI wind tunnel.

Introduction

Climate change has become a central rationale for disruptive technologies in the aviation field. In 2023, air transport was responsible for 2.5% of total CO_2 emissions [1]. The worsen scenario if contrails are kept into consideration, leading aircrafts to be responsible for 4% of global warming [2]. To mitigate the negative environmental impact of human-related activities, the European Union (EU) has settled an agreement - Green Deal - to reach net zero emissions by year 2050 [3]. The Clean Aviation Joint Undertaking was created to research new aviation technologies compliant with the climate crisis. In this context, the *Hybrid-Electric Regional Architecture* (HERA) project - coordinated by Leonardo (A/C Division), and the *Hybrid Electric Regional Wing Integration Novel Green Technologies* (HERWINGT) project - coordinated by Airbus Defence and Space, started in January 2023. The aim is to study a new regional aircraft configuration capable of reducing the emissions both flight-related and technology-based [4, 5]. Hybrid electric propulsion is introduced by batteries and Sustainable Aviation Fuels (SAFs). Aerodynamics efficiency is reached through high Aspect Ratio (AR) wing along with morphing control surfaces, to reduce drag. Since increasing wing AR leads to an increase in wing loads and, consequently, in wing structural mass, additional control surfaces with Load Alleviation (LA) purposes are considered.

The present work focuses on preliminary design of high AR wing for such aircraft, summarized in the following.

1. A reference aircraft - ATR72-600 - has been designed. The model is referenced throughout the work as ATR72-like.
2. The ATR72-like has been modified to account for the presence of batteries and lower fuel mass. The updated model is named UERA-like.

Content from this work may be used under the terms of the Creative Commons Attribution 3.0 license. Any further distribution of this work must maintain attribution to the author(s) and the title of the work, journal citation and DOI. Published under license by Materials Research Forum LLC.

Materials Research Proceedings 69 (2026) 516-521 https://doi.org/10.21741/9781644904251-93

3. A parametric analysis has been computed on the UERA-like configuration, increasing wing AR and assessing its effect on sizing and loads. The set of obtained models are UERAAR, with AR substituted by its value (e.g. UERA16, for AR=16).

On such models, a LA system has been introduced through an additional wing control surface, here referenced as Load Control (LC) tab, along with the conventional aileron. Static aeroelastic analyses have been computed for different deflections - considered positive as the control surface goes downward - of LC tab, also coupled with ailerons, to quantify potential wing root load alleviations.

Models

The adopted tool to generate and analyze models in the current work is NeoCASS, an open-source code developed at POLIMI [6, 7, 8]. The procedure starts with the definition of geometry, maneuvers compliant with the certification regulations (EASA CS23, CS25) and mass configurations. Aerodynamics is modeled through Vortex Lattice Method (VLM), while structure is represented by beam elements. The sizing process leads to a stick model, whose inertia and stiffness distributions are evaluated through a physics-based approach. NeoCASS allows to compute trim, modal and flutter analyses, but also dynamic responses to gust or control deflections.

ATR72-like model. Starting from ATR72-600 public data, the ATR72-like model has been sized. The analyzed configuration considers a 72 passengers cabin arrangement, total fuel mass of 5000 [kg] - entirely stored in wing tanks - and aluminum alloy as material. Table 1 presents some data concerning the wing. The reference model has AR=12.

Table 1: Wing data for ATR72-like

Area	61 [m^2]
AR	12 [-]
Kink 1	0.176 [-]
Taper tip	0.59 [-]

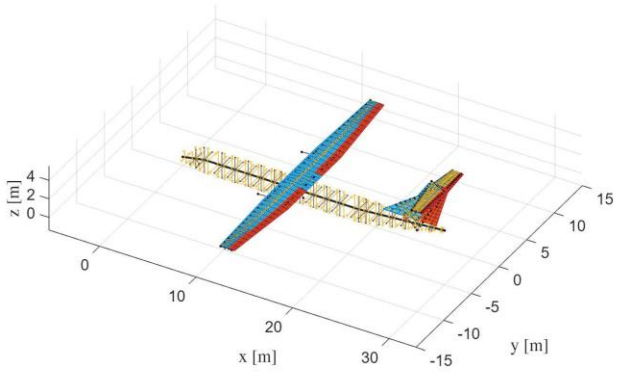


Figure 1: ATR72-like model

Sizing has been computed considering EASA CS25 maneuvers, for 4 mass configurations: Maximum Take-Off Weight (MTOW), Maximum Landing Weight (MLW), Maximum Zero Fuel Weight (MZFW) and Operative Empty Weight (OEW). The sizing results in terms of total masses are reported in Table 2, while Fig. 1 shows the aeroelastic model.

Materials Research Proceedings 69 (2026) 516-521 https://doi.org/10.21741/9781644904251-93

Table 2: Sized total masses for ATR72-like

MTOW	23000 [kg]
MLW	22350 [kg]
MZFW	21000 [kg]
OEW	13600 [kg]

UERA-like. As anticipated, ATR72-like model has been modified into UERA-like to account for the presence of the hybrid propulsive system of HERA aircraft, including two concentrated masses (the batteries) inside rear and forward portions of the fuselage, while fuel mass has been reduced of 70%. ATR72-like geometry has been kept unchanged.

Total masses obtained for UERA-like model are reported in Table 3. The last column represents the increase obtained with respect to the values of Table 2.

Table 3: Sized total masses of UERA-like, compared to ATR72-like

MTOW	27420 [kg]	+16%
MLW	27220 [kg]	+18%
MZFW	25920 [kg]	+19%
OEW	18520 [kg]	+26%

UERA with increased AR (UERAAR). To improve aerodynamic efficiency, a possible option is to increase wing AR. Indeed, the induced drag coefficient is inversely proportional to wing AR, as reported in Eq. 1.

$$c_{D_i} = \frac{c_L^2}{\pi e AR} \tag{1}$$

Nevertheless, this has an impact on wing loads and consequently on wing weight. To alleviate the excess of loading, LA systems can be implemented. They consist of dedicated control surfaces, generally placed close to the wing tip to increase their effectiveness in load redistribution. In principle, if the sizing is recomputed including the presence of such devices, wing weight can be kept limited. A quantification of these concepts is given in the current work, for different wing ARs.

Starting from UERA-like model, only wing planform has been adjusted to reach the desired values of ARs, as reported in Fig. 2 left. Also wing aileron and LC tab are displayed, with the former kept fixed for all the models. Sizing procedure is the same adopted for ATR72-like and UERA-like models. The results can be found in Fig. 2 right, where the induced drag coefficient has been estimated following Eq. 1 and, concerning the total masses, just MTOW has been reported for simplicity. As expected, as AR increases, MTOW increase, while c_{D_i} decrease. The data have been a-dimensionalized for the values correspondent to AR=12 model (i.e. UERA-like). Maxima deviations are reached for UERA16.

Materials Research Proceedings 69 (2026) 516-521 https://doi.org/10.21741/9781644904251-93

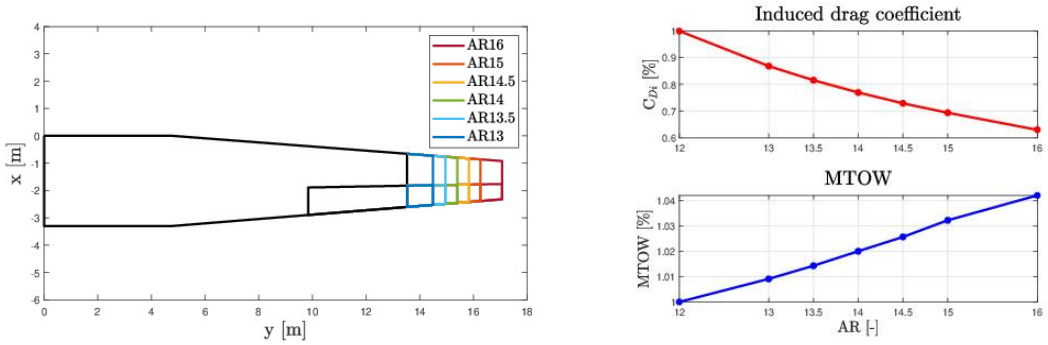


Figure 2: UERAAR, effects of wing AR on wing planform (left) and on induced drag coefficient and MTOW (right)

Analyses

To show the static effect of LA system, a pull-up maneuver at cruise design point has been computed for UERA-like model (black). Then, the same analysis has been applied to UERA16 in three different conditions: without any deflection of the LC tab (red); with $\delta_{LC_{tab}}$=10 [deg] (orange); with $\delta_{LC_{tab}}$=10 [deg] coupled with δ_{ail}=5 [deg] (yellow). These results, normalized for the wing root loads of UERA-like configuration, are shown in Fig. 3. As one can notice, for both bending and torsion, the increase in wing AR leads to a higher root load (red curve is higher than black one). A deflection of LC tab produces the expected load alleviations, bringing root torsional moment to even lower values than the reference one. The situation is even better if a deflection of the LC tab is combined to a deflection of ailerons.

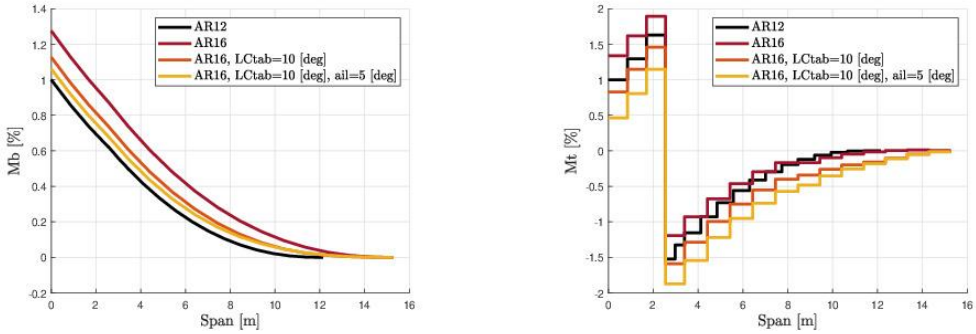


Figure 3: Effect of LC tab deflection on UERA16's bending moment (left) and torque (right)

Table 4 summarizes the root load alleviations obtained for different LC tab and aileron deflections, for UERA16, expressed as percentage of UERA-like root loads. Looking at the trend, it is possible to reach and reduce further the wing root loads with higher deflections.

LA systems are particularly suited when a gust is encountered during flight. This situation must be addressed carefully especially for future aircrafts, since, due to climate change, atmospheric turbulence is changing [9], and the probability to encounter a hard gust will increase. As anticipated, NeoCASS allows to compute also gust responses. In general, this kind of analyses are conducted simultaneously with the design of a control law - as it was done e.g. in [10] - whose output is the evolution of the LC tab deflection that matches the desired load alleviation level. These analyses are currently under investigation.

A preliminary estimation of the effectiveness of control surfaces deflection on Wing Root Bending Moment (WRBM) and Wing Root Torsion Moment (WRTM) is provided in Fig. 4, where

Materials Research Proceedings 69 (2026) 516-521 https://doi.org/10.21741/9781644904251-93

the Transfer Functions (TF) between the wing root load and a unitary gust, a unitary aileron deflection and a unitary LC tab deflection, for UERA16, are presented. Figure 4 left shows that aileron deflection is more effective on bending than LC tab. The opposite is valid for torsion: the blue peak at torsional frequency in Fig. 4 right is much larger than the black one.

Table 4: Root load alleviation, UERA16

$\delta_{LC_{tab}}$ [deg]	δ_{ail} [deg]	M_b [%]	M_t [%]
0	0	+27.3	+17.3
5	0	+19.9	+8.3
10	0	+12.6	-0.6
10	5	+6.1	-46

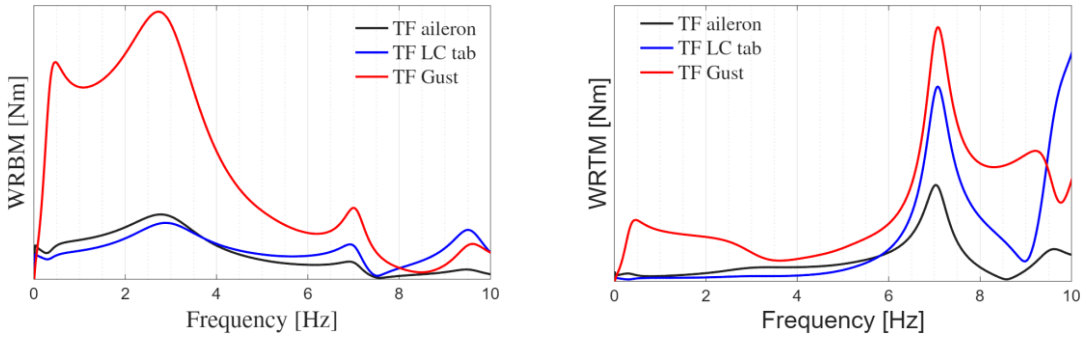


Figure 4: Transfer functions for UERA16, WRBM (left) and WRTM (right)

Conclusions and Future Work

Different models have been created and analyzed, with varying wing AR. The highest aerodynamic efficiency has been reached for UERA16, along with the highest wing root internal actions. An additional control surface has been introduced to alleviate such loads. Static analyses showed promising load reductions, within reasonable LC tab and aileron deflections. A control law for Gust Load Alleviation (GLA) is under investigation, along with the creation of the wing aero-servo-elastic experimental model, to be gust tested inside POLIMI Wind Tunnel.

Acknowledgements

This study is part of the Hybrid Electric Regional Wing Integration Novel Green Technologies (HERWINGT) project. This project has received funding from the Clean Aviation Joint Undertaking under the European Union's Horizon Europe research and innovation program under grant agreement ID 101102010. Views and opinions expressed are however those of the authors only and do not necessarily reflect those of the European Union or the Clean Aviation Joint Undertaking. Neither the European Union nor the granting authority can be held responsible for them.

References

[1] «Tracking Aviation,» [Online]. Available: https://www.iea.org/energy-system/transport/aviation.

[2] M. Klöwer, M. R. Allen, D. S. Lee, S. R. Proud, L. Gallagher e A. Skowron, «Quantifying aviation's contribution to global warming,» Environmental Research Letters, vol. 16, n. 10, p. 104027, 2021. https://doi.org/10.1088/1748-9326/ac286e

[3] «The European Green Deal: striving to be the first climate-neutral continent,» [Online]. Available: https://commission.europa.eu/strategy-and-policy/priorities-2019-2024/european-green-deal_en.

[4] «HERWINGT: Hybrid Electric Regional Wing Integration Novel Green Technologies,» [Online]. Available: https://herwingt-project.eu/home.

[5] «HERA: Hybrid Electric Regional Architecture,» [Online]. Available: https://project-hera.eu/home.

[6] L. Cavagna, S. Ricci e L. Travaglini, «NeoCASS: An Integrated Tool for Structural Sizing, Aeroelastic Analysis and MDO at Conceptual Design level,» in Progress in Aerospace Sciences, vol. 47, 2011. https://doi.org/10.2514/6.2010-8241

[7] L. Cavagna, S. Ricci e L. Riccobene, «Structural Sizing, Aeroelastic Analysis, and Optimization in Aircraft Conceptual Design,» Journal of Aircraft, vol. 48, pp. 1840--1855, 2011. https://doi.org/10.2514/1.C031072

[8] L. Cavagna, S. Ricci e L. Travaglini, «Aeroelastic Analysis and Optimization at Conceptual Design Level Using NeoCASS Suite,» in Collection of Technical Papers - AIAA/ASME/ASCE/AHS/ASC Structures, Structural Dynamics and Materials Conference, 2011. https://doi.org/10.2514/6.2011-2079

[9] L. N. Storer, P. D. Williams e P. G. Gill, «Aviation turbulence: dynamics, forecasting, and response to climate change,» Pure and Applied Geophysics, vol. 176, n. 5, pp. 2081--2095, 2019. https://doi.org/10.1007/s00024-018-1822-0

[10] F. Fonte, S. Ricci e P. Mantegazza, «Gust load alleviation for a regional aircraft through a static output feedback,» Journal of Aircraft, vol. 52, n. 5, pp. 1559--1574, 2015. https://doi.org/10.2514/1.C032995

Materials Research Proceedings 69 (2026) 522-527 https://doi.org/10.21741/9781644904251-94

Investigation of the Influences of Different Booster Recovery Methods on Air Traffic

Antonio DEPARDON[1,a *], Jonas LANGNER[2,b], Thomas FEUERLE[2,c], Carsten WIEDEMANN[1,d], and Simona SILVESTRI[1,e]

[1]Institute of Space Systems, Technische Universität Braunschweig, Hermann-Blenk-Str.23, 38108 Braunschweig, Germany

[2]Institute of Flight Guidance, Technische Universität Braunschweig, Hermann-Blenk-Str.27, 38108 Braunschweig, Germany

[a]antonio.depardon@tu-braunschweig.de, [b]jonas.langner@tu-braunschweig.de, [c]t.feuerle@tu-braunschweig.de, [d]c.wiedemann@tu-braunschweig.de, [e]simona.silvestri@tu-braunschweig.de

Keywords: Reusable Launcher, Booster Recovery, Air Traffic

Abstract. To ensure economic access to space, re-using rocket boosters can be one key-element. In comparison to expendable boosters, reusable boosters need to perform additional flight maneuvers, resulting in different airspace demand. As a safety measure for air traffic, airspaces in which spacecraft operate are temporarily closed. Such airspace closures pose an additional challenge for planning flights and airspace capacities. The influence of different booster recovery methods on the airspace closure dimensions are investigated in a collaborative study between TU Braunschweig and DLR SART. Further, the effects of such closures on air traffic are analyzed. As a first proof of concept, this paper applies the developed methodology to quantify airspace closures and associated costs per affected aircraft for two scenarios. While demonstrating the capabilities of the methodology, its limitations and intended improvements are stated and discussed.

Introduction

The reusability of rockets has become crucial considering the cost advantages such systems show in comparison to expendable rockets. Although Europe's current launchers, Ariane 6 and Vega C, are still designed as expendable vehicles, concept studies for a European reusable launcher are already underway. As an example, the ENTRAIN study [1, 2] performed by the DLR SART investigates different rocket designs for a successor of Ariane 6 with a reference mission of delivering 7500 kg to a geostationary-transfer orbit (GTO). Besides various propellant combinations, different booster recovery designs are investigated like the downrange landing (DRL) of the booster on a barge, and the so-called in-air-capturing (IAC) recovery method. While the DRL method is already successfully operated by companies like SpaceX, the IAC method is still under development. This method foresees the capture of the booster after its ballistic flight and its subsequent towing of the rocket stage to a designated runway by an aircraft.

Because space vehicles are certified under a higher acceptable-risk standard than conventional aircraft, spaceflight operations are segregated from air traffic through temporary airspace closures. Such airspace closures are also denoted as Aircraft Hazard Area (AHA) and Temporary Flight Restriction (TFR). The ENTRAIN study enables direct comparison of reusable rocket designs and their booster recovery methods resulting in a different demand for airspace closures. The investigation of the needed airspace closure size for different booster recovery methods and potentially varying resulting impacts on air traffic is part of a collaboration between TU Braunschweig and DLR SART. In this paper, the preliminary procedure to perform this research is introduced and encountered limitations are discussed.

Content from this work may be used under the terms of the Creative Commons Attribution 3.0 license. Any further distribution of this work must maintain attribution to the author(s) and the title of the work, journal citation and DOI. Published under license by Materials Research Forum LLC.

Materials Research Proceedings 69 (2026) 522-527 https://doi.org/10.21741/9781644904251-94

Methodology

To assess the results of the rocket design dependent AHAs, a seven-step process must be conducted for each investigated rocket design. This process is introduced in Fig. 1.

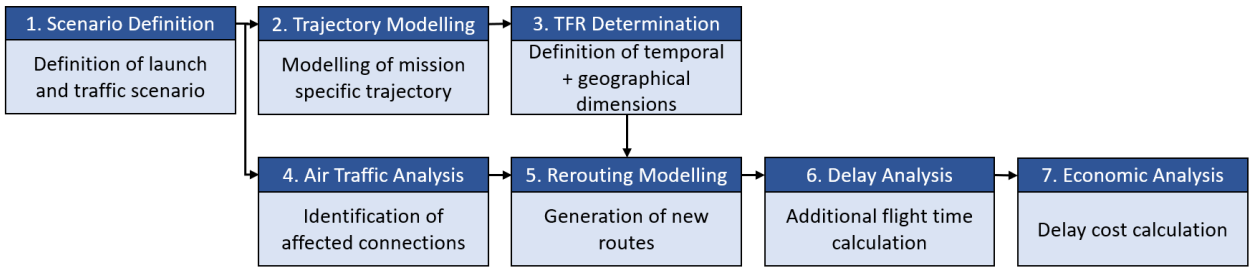


Figure 1 Process of determining additional costs for airlines from AHAs.

In the first step, the launch scenario comprising rocket-specific aspects like booster recovery method and propellants as well as mission-specific parameters including the target orbit and launch site is generated. In this paper, launches from Guyana Space Center (GSC) into GTO with an IAC and DRL rocket configuration propelled by methane and liquid oxygen are taken as scenarios. Based on existing trajectory data for the scenarios, the TFRs are determined in step two and three. In this first iteration, the temporal aspect of the TFR is not analyzed, but is intended to be further investigated in later research iterations. In addition to the TFRs, in the fourth step, an air traffic analysis for the launch scenario is conducted to obtain an overview about potentially affected flights. Such flights are then selected for the re-routing modelling in the fifth step. In the remaining two steps, the additional flight time of the rerouted flights along with the resulting delay costs are computed. Important aspects of the general approach are described in the following paragraphs.

Airspace closure definition

The airspace closures are determined in a conservative approach, accounting for the worst-case scenario. This scenario reflects in-flight fragmentations of the rocket stages and the resulting fallout of debris. In this study, the two graphs representing the ENTRAIN IAC and DRL ascent as well as booster trajectories shown in Fig. 2 are the baseline for the analysis.

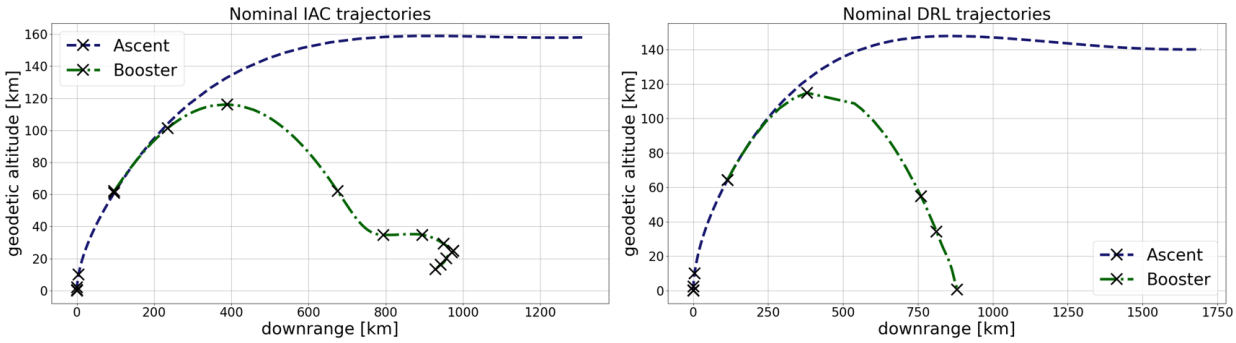


Figure 2 Trajectories of DRL and IAC rocket and booster configurations with the simulated breakup points marked with crosses.

Along the predefined points on the trajectories that are marked with crosses in the diagrams, fragmentation events are modelled. A fragmentation is a stochastic event that generates debris that is ejected during the event. The stochastic behavior means that the exact number of debris, their physical properties as well as the ejection direction and velocity of each fragment cannot be predicted in advance. Models to simulate such events are working on a stochastic foundation. In this work, the ballistic coefficients (the main physical property) are based on the Columbia

Materials Research Proceedings 69 (2026) 522-527 https://doi.org/10.21741/9781644904251-94

fragmentation catalogue and the ejection directions and velocities are determined with the NASA standard breakup model [3, 4]. Simulating the fragmentation event only once is not sufficient to determine TFRs due to the unpredictable behavior of the resulting fallout. To account for this, the potential fallout must be assessed with Monte Carlo-like approaches by simulating the stochastic fragmentation and propagation of the fragments several times. In this study, three independent fragmentation events per breakup point are modelled, resulting in 9133 fragments per breakup point for the whole DRL scenario. In the IAC scenario, only one breakup event per booster breakup point was modelled due to time constraints.

The resulting fragments are numerically propagated under the influence of gravity and aerodynamic drag (wind is neglected) until they either impact the ground or reach a maximum flight time of 24 hours. The resulting fallout distributions are then superposed, and the width and length of the AHA are estimated with the fragment density over longitude and latitude. The AHA boundaries are defined so that the longitude and latitude spans comprise 99.999 % of the debris. Figure 3 shows on the left side the impact areas and resulting AHAs of the IAC and on the right side of the DRL superposed fragmentation scenarios. For comparison purposes, the TFRs obtained from [5, 6] during the last Ariane V flight (*VA 261*) and the first Ariane VI flight (*VA 262*) are included in the graphic.

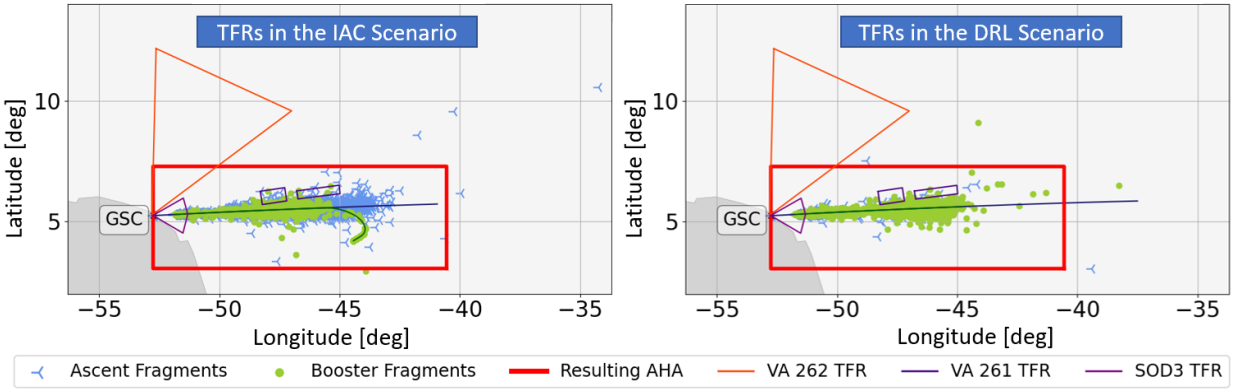


Figure 3 IAC and DRL determined AHAs with fragment distribution and reference AHA

In the first iteration presented in this paper, the AHA is implemented as a simple rectangular defined by the longitude and latitude threshold determined to contain 99.999 % of the debris. This conservative approach does not consider the increasing downfall area with the altitude of the rocket that leads to funnel-formed downfall area during a rocket launch. In real rocket launches, this behavior is converted into funnel-formed AHAs like in the *VA 262* TFR shown in Fig. 3. In the *VA 261* launch, the funnel-formed TFR *SOD3* is implemented in the near-field of the launch site. Such funnel-formed AHA designs for the near-field could also be used in later iterations to reduce the impact on traffic flying around the AHA close to launch site.

Traffic and cost analysis

The AHAs prohibit aircraft from flying through the airspace. To identify flights that normally would fly through the affected airspace, the publicly accessible ADS-B database from flightradar24 [7] was used. The data showed that besides traffic from and to Cayenne, routes between North America and Brazil, North America and South Africa as well Europe and South-America can be affected. The available flight data showed that some flights presented a significant deviation from the great circle distance between the airports. Several reasons like weather, airline specific operational regulations, other airspace closures or in-air re-routings from air traffic controllers can lead to such longer routes. Whether these longer paths were part of the original flight plans cannot be inferred from the available traffic data. To allow for a more representative

Materials Research Proceedings 69 (2026) 522-527 https://doi.org/10.21741/9781644904251-94

comparison, the great circle distance between the city pairs are used as baseline for the further investigations. Flights are only considered if the great circle line between the airports crosses the determined AHAs. For further analysis, two selected city pairs from the traffic scenario are taken for the delay and cost determination.

The re-routing is implemented with a single re-routing point that is first approached by the aircraft on its way from the departure to the destination airport. In the first iteration presented in this paper, the corner points of the AHA are used as re-routing point. The corner point allowing the plane to fly around the AHA in the shortest possible additional distance is selected as re-routing point. This re-routing algorithm represents the best-case delay scenario with the least possible flown extra distance. In future research iteration, existing airways and waypoints could be used for improved re-routing algorithms targeting for more realistic results. The flown rerouted distance is determined based on great circle distance sections between the departure and destination airports and the re-routing point. The original and rerouted trajectories of the two flights as well as their great circle lines for the IAC TFR are shown in Fig. 4.

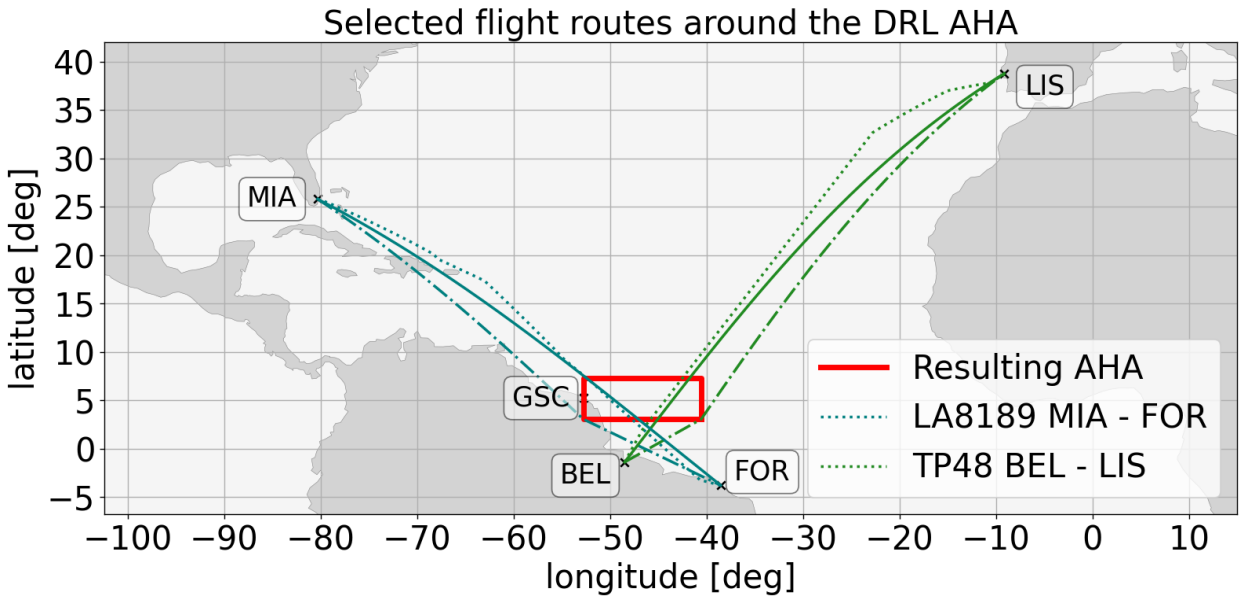


Figure 4 Impact of the IAC AHA on the two reference flights showing the reference flight routes as dotted lines, the great circle connection as line, and the rerouted flight routes as dash-dotted lines.

The flight delay due to the AHA is determined based on the obtained additional flight distance. It is assumed that the aircraft fly with cruise speed on the additional flight sections. The resulting delay costs are interpolated based on the average en-route delay cost values from Westminster University [8, 9]. The delay cost values for the Boeing *B787-9* is not included in this reference. Therefore, the mean value of the two cost values from *B767-300* and *B747-400* was used to estimate the cost value of the *B787-9*. To improve the cost calculation, a more precise approach for aircraft types that are not included in [8, 9] should be developed that also accounts for inflation.

Discussion of the results

The obtained flown distances, delays and resulting additional costs for the IAC TFR scenario are introduced in Table 1 and for the DRL TFR scenario in Table 2. In the IAC scenario, the flight between Belem and Lisbon shows an increased route length of about 1.5 % resulting into a delay of seven minutes. For the Miami - Fortaleza flight, the route length almost increases by one percent. The additional costs for the second flight are estimated to be higher than in the other flight.

Considering the different aircraft sizes, the resulting higher costs for the *B787-9* are deemed to be realistic.

Table 1 Obtained results from the IAC AHA rerouting scenario

Flight number	Connection	Aircraft type	Great circle distance [km]	Rerouted distance [km]	Delay [minutes]	Additional costs [€]
TP 48	BEL-LIS	A321-LR	6007	6099	7	478
LA 8189	MIA-FOR	B787-9	5572	5633	4	576

In the DRL scenario, the resulting additional flown distances are each less than one percent of the original flown distance. The resulting delay of four minutes can be expected to be compensated for by increasing the cruise speed of the aircraft. Therefore, in reality it can be estimated that the delay is eliminated in the end. The here investigated GTO launch scenarios from GSC show in general a low impact on air traffic. In the scenarios, the sustainability gain through the booster recovery does not significantly affect air traffic. Further investigation of these two and other scenarios must be performed to generate more data to fully address the stated research topic.

Table 2 Obtained results from the DRL AHA rerouting scenario

Flight number	Connection	Aircraft type	Great circle distance [km]	Rerouted distance [km]	Delay [minutes]	Additional costs [€]
TP 48	BEL-LIS	A321-LR	6007	6052	4	240
LA 8189	MIA-FOR	B787-9	5572	5623	4	576

Summary

In this work, an approach to determine the influences of different reusable rocket designs on the air traffic is introduced. A first methodology iteration is performed for an IAC and DRL booster recovery scenario launching from GSC into a GTO. These launch scenarios showed to have a low impact on air traffic as the investigated flights are long-distance flights with sufficient flight time to compensate for the delays. In general, more simulations per scenario should be conducted to ensure the data quality. The here performed analysis and its results are a proof of concept of the developed methodology. Further, encountered challenges of the methodology are described and a outlook for later iterations is sketched. For example, the current fragmentation model shows limitations as its components are intended to simulate other events than rocket fragmentations during launch. By implementing a better suited fragmentation model and including a propitiated wind model, the simulation results are expected to be closer to reality. The introduced investigation approach lays the foundation for future research.

Acknowledgements

The authors would like to thank the whole DLR SART team for providing the ENTRAIN trajectory data.

This research is funded by the Deutsche Forschungsgemeinschaft (DFG, German Research Foundation) - 441090785.

References

[1] I. Dietlein, L. Bussler, S. Stappert, J. Wilken, and M. Sippel, Overview of system study on recovery methods for reusable first stages of future European launchers, CEAS Space J, vol. 17, no. 1, pp. 71-88, 2025, doi: 10.1007/s12567-024-00557-9. https://doi.org/10.1007/s12567-024-00557-9

[2] S. Stappert, I. Dietlein, J. Wilken, L. Bussler, and M. Sippel, Options for future European reusable booster stages: evaluation and comparison of VTHL and VTVL return methods, CEAS

Space J, vol. 17, no. 1, pp. 155-175, 2025, doi: 10.1007/s12567-024-00571-x. https://doi.org/10.1007/s12567-024-00571-x

[3] J. R. Barry, D. R. Jenkins, D. J. White, P. A. Goodman, L. A. Reingold, A. H. Simon, and C. M. Kirchhoff. Columbia accident investigation board report, volume 2. Columbia Accident Investigation Board, 2003.

[4] N. L. Johnson, P. H. Krisko, J.-C. Liou, and P. D. Anz-Meador. Nasa's new breakup model of evolve 4.0. Advanced Space Research, (Vol. 28, No. 9), 2001. https://doi.org/10.1016/S0273-1177(01)00423-9

[5] Information on https: https://skyvector.com/

[6] Information on https: https://notams.aim.faa.gov/notamSearch/nsapp.html

[7] Information on https://www.flightradar24.com

[8] A. J. Cook and G. Tanner 2015 European airline delay cost reference values - updated and extended values (Version 4.1) Tech. rep.

[9] A. J. Cook, G. Tanner and T. Bolic D3.2 Industry briefing on updates to the European cost of delay. Tech. rep. BEACON Consortium

Materials Research Proceedings 69 (2026) 528-533 https://doi.org/10.21741/9781644904251-95

Assessing Synergies Between Truss-Braced Wings, Liquid Hydrogen Propulsion, and Open Rotors in Conceptual Aircraft Design

Lucas KUGLER[1,a *], Michael KOTZEM[1,b], Sebastian WÖHLER[1,c] and Thomas ZILL[1,d]

[1]DLR Institute for System Architectures in Aeronautics, Hein-Saß-Weg 22, 21129 Hamburg, Germany

[a]lucas.kugler@dlr.de, [b]michael.kotzem@dlr.de, [c]sebastian.woehler@dlr.de, [d]thomas.zill@dlr.de

Keywords: Overall Aircraft Design, Truss-Braced-Wing Open-Rotor, Liquid-Hydrogen

Abstract. This study investigates the synergistic potential of integrating truss-braced wings, liquid hydrogen propulsion, and open rotor technology in a potential next-generation short-medium-range aircraft. Through exploration of the possible design space, the combined impact on aerodynamic efficiency, structural weight, and emissions reduction is evaluated. The analysis demonstrates that the synergistic combination of technologies can significantly reduce fuel consumption and climate impact while maintaining competitive performance metrics. This work provides a foundation for future sustainable aircraft development by optimizing the interactions of these advanced technologies.

Introduction

Addressing the air transport sector's target of reducing its climate impact will require the next generation of commercial airliners to achieve significantly higher energy efficiency [1]. To reach this goal, several levers are available: reducing the mass of the airframe or improving the aerodynamic efficiency can lower the required thrust; improved engine efficiency can reduce the energy consumption per unit thrust; alternative energy carriers can reduce the climate impact per unit energy consumed. In this study, three technologies which act on those levers have been selected based on their relevance for a potential next generation-aircraft on the short-medium-range (SMR) market:

On the airframe side, the truss-braced wing (TBW) has emerged as a promising alternative to the conventional tube-and-wing configuration: The addition of a strut enables higher aspect ratio wings, which improve the aerodynamic efficiency of the aircraft. This benefit comes with its drawbacks and challenges, but recent advancements in digital design methods demonstrated their maturity for tackling the challenges specific to TBW aircraft operating in the transonic regime [2, 3, 4].

On the propulsion side, efficiency gains have traditionally been gained in particular by increasing the bypass-ratio of turbofan engines. While this trend could be pursued further, this comes at the cost of an increased nacelle size and weight; the conventional turbofan architecture is therefore being challenged by the open-rotor technology: by combining a large-diameter unducted fan with a stator stage for swirl-recovery, very high bypass-ratios and therefore efficiency are anticipated [5, 6], while circumventing the nacelle drag and mass penalties, as well as the integration challenges of UHBR engines.

On the energy carrier side, liquid hydrogen direct combustion has emerged as the most serious

Content from this work may be used under the terms of the Creative Commons Attribution 3.0 license. Any further distribution of this work must maintain attribution to the author(s) and the title of the work, journal citation and DOI. Published under license by Materials Research Forum LLC.

Materials Research Proceedings 69 (2026) 528-533 https://doi.org/10.21741/9781644904251-95

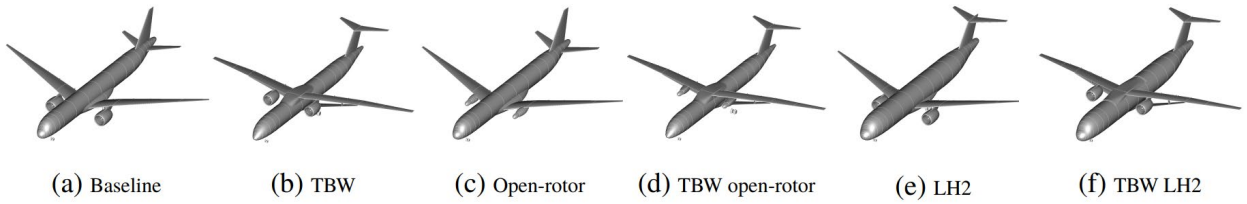


Figure 1: Axonometric view of the different configurations investigated.

contender to kerosene for all but the regional market segment. While it promises a significant reduction of the climate impact, the large tank volume necessary is detrimental to the overall efficiency of such aircraft.

Yet individually, none of these technologies are sufficient to meet the industry-wide climate targets on their own, and it remains to be seen which combination is the most promising. This study aims to address this question by investigating the interactions between the above-mentioned technologies.

Methods

The investigation is conducted with the German Aeropace Center's overall aircraft design process, as described in detail by Wöhler et al. [7]. This design framework is built around different tools exchanging information via the CPACS data format [8] combined into a workflow, which can be divided into three main parts: openAD is the central overall aircraft design and synthesis tool, which initializes the design according to the user-defined top-level aircraft requirements based on low-fidelity conceptual design methods. The resulting data is then processed by a series of higher fidelity tools in an iterative loop. The results of the analyses are fed back into openAD to adjust the initial design until convergence between the low- and higher-fidelity tools is reached. Finally, a post-processing phase ensues, in which the payload-range characteristics are computed, as well as the performance for the evaluation mission.

The capabilities of openAD have been extended to handle truss-braced wing configurations [9]. To this effect, the wing mass model of Chiozzotto [10] is implemented. This method is combined with the equation presented by Gur et al. [11] to account for the mass of folding wing-tips. Interference drag is considered through a surrogate model of CFD simulations [12], calibrated to wind tunnel test results [13]. The design lift coefficient of the strut in cruise condition can be varied, and is accounted for in the lift and drag predictions. Lastly, a simple method to consider the impact of a natural laminar flow (NLF) wing was incorporated.

The LH2-configurations are based on the assumptions and technology choices described by Kotzem et al. [14]: the cryogenic hydrogen tanks are rear-fuselage mounted, with an increased fuselage diameter housing an 8-abreast cabin to keep the fuselage slenderness ratio within reasonable bounds. The tank sizing tool chain is described by Burschyck et al. [15]. The cryogenic hydrogen tank is made of aluminium with a foam insulation architecture. Additionally, a mid-fidelity fuselage structure sizing tool chain is used to account for the effect of the LH2 tanks on the fuselage structure.

The Open-Rotor configurations are based on the findings of Ritter [5], and feature a 4 m diameter 12-blade propeller, and a 13-blade stator stage of the same diameter. The wing integration is of podded type, meaning that there is no separate pylon component. While it is planned to further extend the workflow in the future by tailoring the propeller to each design point, fixed propeller characteristics are currently assumed throughout the design space. A combined mass of 2800 kg for the propeller and stator is assumed, as well as a propeller efficiency of 81% with an activity factor of 180.

Materials Research Proceedings 69 (2026) 528-533 https://doi.org/10.21741/9781644904251-95

Table 1 Summary of aircraft top-level requirements

Requirement	Value		Requirement	Value	
Passengers	239		Max. operating altitude	12192	m
Design payload	25000	kg	Approach speed	136	knt
Design range	4630	km	Cruise Mach-number	0.78	
Evaluation range	1482	km	Wingspan (folded)	36	m
Take-off field length	2200	m	Wingspan (extended)	52	m

The study focuses on the short-to-medium range aircraft segment, with the Airbus A321 selected as the reference aircraft. Top-level aircraft requirements are detailed in Table 1.

While the comparison with the reference aircraft allows assessing the potential improvements against current in service aircraft types, the improvements of the individual technology bricks are can be assessed by comparison against the Baseline aircraft, which represents the anticipated state of the art for an entry-into-service in 2035, accounting for existing trends in technology maturation, but no significant architectural changes. The baseline used in this project is the DLR-F25 [16]. It notably features a 45 m span composite wing with an aspect ratio of 15.5 (these values will be varied in this study), as well as ultra-high bypass-ratio turbofan engines.

Results

The combinations of the 3 technologies to be investigated results in 7 possible configurations to be optimized in addition to the baseline.

This leads to a large design space where each configuration can potentially have different optima. Therefore, instead of manually optimizing each configuration, the approach selected is to perform parameter sweeps of key driving parameters to gain a generalized understanding of the behaviour of the different combinations of technologies. The main parameters selected for this study are the aspect ratio and wing loading, as these two parameters have a strong impact on all aspects of the aircraft design, including the aerodynamics, flight performance, engine sizing, and structural mass of the aircraft. The selected metrics are the block energy on an 800 nm evaluation mission, as an indicator for the fuel costs and in service emissions, and the operating empty mass (OEM), as it strongly correlates to the airframe acquisition and maintenance costs. The constraint on approach speed was not enforced on the individual designs, but rather used as a constraint on the feasible design space. This allows to assess the potential impact of an increase in approach speed, or alternatively of the installation of more advanced high-lift systems.

Figure 2 shows the results of the parameter sweeps for the different configurations. The following observations can be made based on these results: Generally, it is noticeable that despite the aggressive upper bound for the aspect ratio, there is no distinct optimum value after which an increase in aspect ratio is detrimental to the aircraft performance. This can be explained by the fact that the wing mass model has been evaluated outside the bounds of the data it was trained on, and fails to capture all the constraints and adverse effects linked to wings of very high slenderness. This limitation in the model must be taken into account in the interpretation of the data.

For all configurations, it is clearly visible that the fuel consumption is more sensitive to aspect ratio than to wing loading, indicating clearly that high-aspect ratio wings are one of the main lever to increase the efficiency of future aircraft configurations. The OEM on the other hand shows a higher sensitivity to the wing-loading: this metric is the main driver for favouring designs with smaller wings. Additionally, the optimum wing loading for fuel efficiency falls within the upper and lower bounds imposed by the constraint of the approach speed and maximum altitude for all configurations. Indeed, low wing-loadings lead to high thrust requirements at the top of climb,

Materials Research Proceedings 69 (2026) 528-533 https://doi.org/10.21741/9781644904251-95

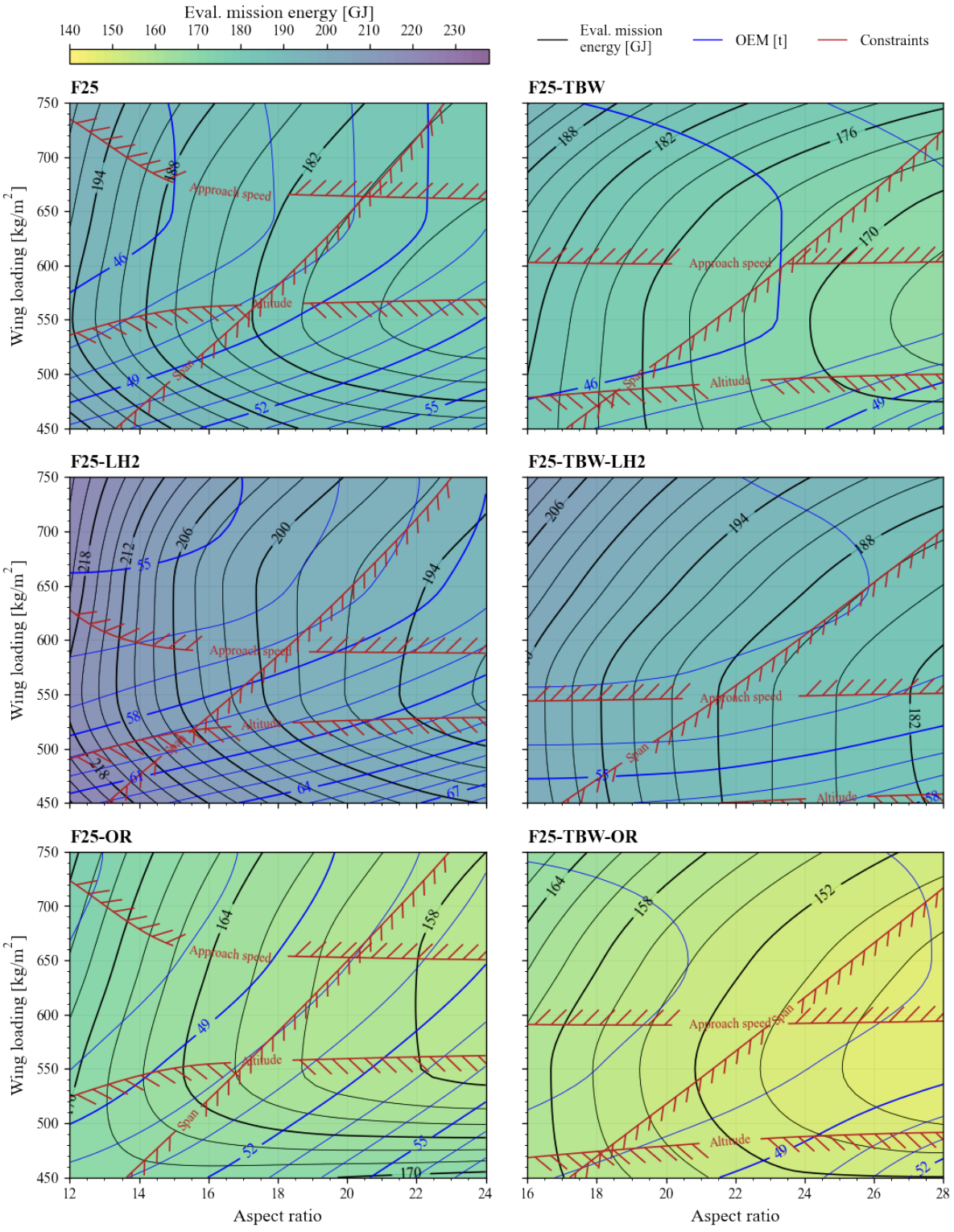


Figure 2 Contour plots of block energy on a 800 nm mission and OEM for the different configurations, as a function of aspect ratio and wing loading. The red lines represent the different constraints restricting the feasible design space.

while high wing-loadings lead to increased takeoff thrust requirements, in both cases leading to

Materials Research Proceedings 69 (2026) 528-533 https://doi.org/10.21741/9781644904251-95

Table 2 Summary of aircraft results. Deltas are relative to the F25 baseline design.

	F25	OR		TBW		TBW-OR		LH2		TBW-LH2	
Parameter			*Δ%*		*Δ%*		*Δ%*		*Δ%*		*Δ%*
MTOM [t]	86.3	86.7	*+0,4*	84.3	*-2,3*	84.6	*-2,0*	88.6	*+2,6*	83.4	*-3,3*
OEM [t]	46.3	48.3	*+4,3*	45.5	*-1,7*	47.3	*+2,1*	57.9	*+25,1*	53.1	*+14,7*
L/D	20.3	20.7	*+1,8*	21.9	*+7,7*	22.3	*+9,9*	19.7	*-2,8*	19.8	*-2,3*
Aspect ratio	16	16	*+0,0*	20	*+25,0*	20	*+25,0*	16	*+0,0*	20	*+25,0*
W/S [kg/m2]	650	650	*+0,0*	550	*-15,4*	550	*-15,4*	550	*-15,4*	550	*-15,4*
Block energy [GJ]	185	164	*-1,3*	175	*-5,4*	153	*-17,3*	204	*+10,1*	190	*+2,9*

oversized engines due to inadequate matching of the high- and low-speed performance. Generally, all SAF-powered configurations show a trend of increasing optimal wing loading

with increasing aspect ratio. This trend is however not visible for the LH2 aircraft, which show a relatively constant optimum wing loading, albeit at a lower wing loading than the SAF-powered equivalents. This lower wing loadings can be explained by the higher OEM which, given an identical optimum lift coefficient and engine thrust lapse, requires a larger wing to cruise at the optimum altitude.

Table 2 shows a summary of metrics for point designs selected according to the constraints defined in Table 1. In addition, the aspect ratio was limited to 16 for the cantilever wing and 20 for the TBW to keep the design in a realistic range despite the limitations of the mass model. The results for the energy consumed on the evaluation mission show the compounding effects of the technologies: combining the TBW with the open-rotor yields a performance effect larger than the sum of the individual contributions. In particular, the LH2 designs have particularly high snowball effects, as any reduction in fuel consumption leads to smaller tanks, and therefore to a reduction of fuselage length and drag. Consequently, adding a truss braced wing to the LH2 design yields a 7.3 % fuel burn reduction, instead of 5.4 % when the TBW is added to the SAF configuration. While the results for the OR-LH2-TBW configuration are not yet available, it is anticipated that the addition of the open-rotor will further narrow the gap between the LH2- and SAF-configuration.

Conclusions

In this study, the effect on fuel burn efficiency and OEM of the integration of truss-braced wings, liquid-hydrogen propulsion, and open-rotors on a potential next generation SMR aircraft were investigated across a range of aspect ratios and wing loadings. The results of this study show that for the considered technologies, all combinations are feasible under the given requirements. They further show that there is compounding effect between the technologies, opening the possibility of substantial performance gains relative to the baseline design, and further demonstrate that the LH2 configuration benefit more strongly of this compounding effect than the SAF configurations.

Supported by:



on the basis of a decision
by the German Bundestag

In future work, the limitations of the methods will be addressed by including higher-fidelity tools to increase the confidence in the results throughout the design space, in particular regarding the wing mass estimation and the propeller design. Additionally, detailed climate impact assessments including non-CO2 effects (contrails) will be performed for each configuration, such as to allow a holistic understanding of their respective total climate impact.

References

[1] IATA, IATA technology roadmap 2013. 2013.

[2] G. G. Carrier et al., “Multidisciplinary analysis and design of strut-braced wing concept for medium range aircraft,” in AIAA SCITECH 2022 forum, American Institute of Aeronautics and Astronautics. https://doi.org/10.2514/6.2022-0726.
[3] T. Chau and D. W. Zingg, “Aerodynamic optimization and fuel burn evaluation of a transonic strut-bracedwing single-aisle aircraft,” Journal of Aircraft, pp. 1–21, 2023. https://doi.org/10.2514/1.C037158.
[4] E. Moerland, R.-G. Becker, and B. Nagel, “Collaborative understanding of disciplinary correlations using a low-fidelity physics-based aerospace toolkit,” CEAS Aeronautical Journal, vol. 6, no. 3, pp. 441–454, 2015. https://doi.org/10.1007/s13272-015-0153-4.
[5] J. Ritter, “Design and assessment of open rotor aircraft conceps,” Master Thesis, Universität Stuttgart; Institut für Flugzeugbau, Stuttgart, 01.05.2023.
[6] C. Diette, “Open fan engine architecture for next generation SMR,” in 33rd congress of the international council of the aeronautical sciences, 2022. Available: https://icas.org/ICAS_ARCHIVE/ICAS2022/data/papers/ICAS2022_0925_paper.pdf
[7] S. Woehler, G. Atanasov, D. Silberhorn, B. Fröhler, and T. Zill, “Preliminary aircraft design within a multidisciplinary and multifidelity design environment,” in Proceedings of aerospace europe conference, 2020.
[8] M. Alder, E. Moerland, J. Jepsen, and B. Nagel, “Recent advances in establishing a common language for aircraft design with cpacs,” 2020, Available: https://elib.dlr.de/134341/
[9] L. Kugler, “Design and assessment of transonic truss-braced wing aircraft concepts,” Universität Stuttgart, 2023. Available: https://elib.dlr.de/200716/
[10] G. Pinho Chiozzotto, “Improving aircraft conceptual design with methods for wing loads, aeroelasticity and mass estimation,” Dissertation, Technische Universität Berlin, Berlin, 08.11.2018.
[11] O. Gur, M. Bhatia, W. H. Mason, J. A. Schetz, R. K. Kapania, and T. Nam, “Development of a framework for truss-braced wing conceptual MDO,” Structural and Multidisciplinary Optimization, vol. 44, no. 2, pp. 277–298, 2011. https://doi.org/10.1007/s00158-010-0612-9.
[12] R. K. Duggirala, C. J. Roy, and J. A. Schetz, “Analysis of interference drag for strut-strut interaction in transonic flow,” AIAA Journal, vol. 49, no. 3, pp. 449–462, 2011. https://doi.org/10.2514/1.45703.
[13] C. K. Droney, A. J. Sclafani, N. A. Harrison, A. D. Grasch, and M. D. Beyar, “Subsonic ultra green aircraft research: Phase III – mach 0.75: Transonic truss-braced wing design.” NASA, Boeing Research and Technology. Available: https://ntrs.nasa.gov/citations/20205005698
[14] R. A. L. Wilson and R. I. Jones, “Project design studies on aircraft employing natural and assisted laminar flow technologies,” SAE Transactions, vol. 104, pp. 1571–1582, 1995
[15] M. A. Kotzem, S. Wöhler, T. Burschyk, C. Hesse, S. Hellbrück, and T. Zill, “Conceptual aircraft design of a research baseline with direct liquid hydrogen combustion,” in 34th congress of the international council of the aeronautical sciences, ICAS 2024, 2024. Available: https://elib.dlr.de/208298/
[16] T. Burschyk, D. Silberhorn, J. Wehrspohn, M. Kühlen, and T. Zill, “Scenario-based implications of liquid hydrogen storage tank insulation quality for a short-range aircraft concept,” in AIAA AVIATION 2023 forum, Reston, Virginia: American Institute of Aeronautics and Astronautics, 2023. https://doi.org/10.2514/6.2023-3522.
[17] S. Wöhler, J. Häßy, and V. Kriewall, “Establishing the DLR-F25 as a research baseline aircraft for the shortmedium range market in 2035,” in Proceedings of the 34th congress of the international council of the aeronautical sciences (ICAS), florence, italy, 2024, pp. 9–13.

Materials Research Proceedings 69 (2026) 534-539 https://doi.org/10.21741/9781644904251-96

Development of a Flying Platform to Study Three-Surface Configurations with Redundant Longitudinal Control

Stefano Cacciola[1,a *], Carlo E.D. Riboldi[1,b], Carlo Fazioli[1]
Leonardo Filippello[1], Francesco Rosato[1]

[1]Department of Aerospace Science and Technology, Politecnico di Milano, Milan, Italy

[a]stefano.cacciola@polimi.it, [b]carlo.riboldi@polimi.it

Keywords: Three-Surface Airplane, Redundant Longitudinal Control, Flight Testing, CFD, FlightStream

Abstract. Improvements in aviation are typically driven by innovative propulsion systems and unconventional configurations. However, since these novel technologies often require a significant leap to become industrially viable, less demanding alternatives can be profitably explored through intelligent adaptations of existing configurations. Three-surface airplanes can be considered as a realistic alternative to conventional back-tailed airplanes, particularly because this configuration allows for trim optimization to minimize drag, provided both the canard and tail are equipped with movable surfaces enabling redundant longitudinal control. The focus of this paper is twofold. First, it aims to provide the first field demonstration of the possible benefits of the three-surface configurations with redundant longitudinal control over equivalent back-tailed airplanes. Second, it presents a preliminary comparison between test data and numerical results obtained from a CFD simulation campaign.

Introduction

Improvements in aviation are typically driven by innovative propulsion systems and unconventional configurations. However, these novel technologies require significant changes in the way we design, build, and operate aircraft. Just consider the substantial modifications to the supply chain and storage systems at airports that may be required by a massive use of hydrogen as aircraft propellent. In this context, interesting and less demanding alternatives can be found by intelligent adaptations of conventional configurations [1, 2, 3].

Among all, three-surface airplanes can be considered as a realistic alternative to conventional back-tailed airplanes. Recently (see Ref.[4] and [5]), a three-surface configuration was employed to demonstrate the potential benefit of the redundant longitudinal control: when both the canard and tail have a movable part, the longitudinal trim, i.e. the equilibrium of vertical forces and moments about the pitch axis, becomes overdetermined: there is an infinite possible combination of canard and elevator deflections which can trim the airplane. This allows one to select the couple of elevator and canard deflections associated with an optimum of a particular merit function, such as for example the overall drag. As reported in preliminary works [4, 5], a comparison between a standard back-tailed four-seat propeller-driven aircraft and an equivalent three-surface aircraft with redundant longitudinal control predicted that the latter configuration exhibits a 4% improvement in the maximum lift-to-drag ratio, potentially leading to comparable fuel savings. It is noteworthy that such an improvement could be achieved through a relatively minor change to the airframe design, especially if compared to more impactful alternatives such as box-wing or blended-wing airplanes.

Building on this promising analysis, we are developing a flying prototype to demonstrate the effectiveness of three-surface configuration with redundant longitudinal control through a dedicated flight experimentation. To achieve this, we first designed a reference back-tailed

Content from this work may be used under the terms of the Creative Commons Attribution 3.0 license. Any further distribution of this work must maintain attribution to the author(s) and the title of the work, journal citation and DOI. Published under license by Materials Research Forum LLC.

Materials Research Proceedings 69 (2026) 534-539 https://doi.org/10.21741/9781644904251-96

prototype optimized for a standard mission of a scaled remote-controlled airplane. Next, we turned the reference aircraft into an equivalent three-surface aircraft, featuring the same wing, fuselage, static margin, and empennage volume. For a given canard of a specific surface, the tail area must be reduced to maintain the same empennage volume and the wing shifted backward to keep the static margin unaltered. Both canard and tail are equipped with movable surfaces, yielding the desired redundancy in the longitudinal trim.

A parallel study was also performed based on Computational Fluid Dynamics (CFD) analyses. In particular, both airplane configurations (two- and three-surface) were modeled through a panel method-based tool, FlightStream [6], to compute the aerodynamic steady coefficients, C_L, C_D and $C_{\mathcal{M}_G}$, as functions of the angle of attack and the deflections of both control surfaces. The obtained aerodynamic database was then used to perform the comparison between the simulated data and the measured quantities obtained through the testing campaign of both airplanes.

Both the experimental and numerical studies on the scaled demonstrator provided evidence that the three-surface configuration with redundant longitudinal control is associated with a significant increase in the maximum lift-to-drag ratio over an equivalent back-tailed airplane, quantified in about 20%. The reasons for this improvement, still to be better understood, are manifold. First, by appropriately configuring the area and location of the lifting surfaces, it is possible to trim the aircraft such that all wings (main wing, tail and canard) generate positive lift. This leads to lower angles of attack and to a corresponding reduction in the overall airplane drag. Second, there could be a beneficial aerodynamic interaction between the canard and the wing, because the outer sections of the main wing experience upwash flow components entailed by the tip vortices of the forward surface. Third, redundant control allows one to optimize the aircraft trim across all flight conditions by directly setting the lift of all surfaces, as also reported in [4, 5, 7]. The study presented in this paper represents the extension of the work object of [8].

Experimental and numerical study on three-surface configurations with redundant control

In the present section, the procedure to design and build the equivalent two- and three-surface airplanes with redundant longitudinal control is first presented. Next, the process of modeling the aircraft in FlightStream is described.

First, it is necessary to define how the equivalence between a three-surface and reference back-tail airplane is established. Among all possible criteria, static margin and tail volume represent two parameters expected to strongly influence equilibrium, stability and maneuverability. Hence, in a preliminary design context, one may envision that airplanes with the same stability margin and tail volume should meet the same mission and design requirements. Accordingly, we first design a conventional aft-tailed aircraft and then convert it into an equivalent three-surface configuration, following the criteria, previously mentioned.

The design process for both prototypes utilized Digital Datcom [9] coupled with downwash/upwash models [10, 11] to render the aerodynamics of the reference and equivalent three-surface aircraft. The reference back-tail airplane was designed to perform a usual mission for remote-controlled demonstrators, as reported in [8]. In order to design the three-surface airplane, one has to find suitable values for the canard area S_C, the tail area S_T, the incidence of the canard i_C, and the location of the aerodynamic center of the wing x_{AC^w}. In doing so, one may consider that in the case of redundant longitudinal control lift C_L and pitch moment $C_{\mathcal{M}_G}$ coefficients are both functions of the angle of attack α, the elevator deflection δ_E and the canard deflection δ_C, as

$$\begin{cases} C_L = C_{L_\alpha}\alpha + C_{L_{\delta_E}}\delta_E + C_{L_{\delta_C}}\delta_C + C_{L_0}, \\ C_{\mathcal{M}_G} = C_{\mathcal{M}_{G_\alpha}}\alpha + C_{\mathcal{M}_{G_{\delta_E}}}\delta_E + C_{\mathcal{M}_{G_{\delta_C}}}\delta_C + C_{\mathcal{M}_{G_0}}. \end{cases} \quad (1)$$

Materials Research Proceedings 69 (2026) 534-539 https://doi.org/10.21741/9781644904251-96

When it comes to evaluating the vertical and pitch moment equilibrium, one immediately recognizes that there are infinite possible solutions for α, δ_E and δ_C. Each combination of these trim variables is associated with a drag coefficient $C_D = C_D(\alpha, \delta_E, \delta_C)$, that can be computed again using Datcom. The redundancy in the trim is leveraged to minimize drag across all speeds, resulting in quasi-linear relationships between the angle of attack, the canard and elevator deflections as function of the overall lift coefficients C_L^*, indicated as $\alpha = \alpha^*(C_L^*)$, $\delta_E = \delta_E{}^*(C_L^*)$ and $\delta_C = \delta_E{}^*(C_L^*)$ [4, 8]. The trimmed polar is than computed as,

$$C_D = C_D\left(\alpha^*(C_L^*), \delta_E^*(C_L^*), \delta_C^*(C_L^*)\right). \quad (2)$$

The design of the three-surface model, i.e. the selection of the values for canard area S_C, tail area S_T, canard incidence i_C and wing location x_{AC^W}, is carried out by maximizing the maximum lift-to-drag ratio of the trimmed polar, constrained by the reference static margin and tail volume.

Fig. 1 shows a picture of the two equivalent designs and reports the expected increase in the maximum lift-to-drag ratio of the trimmed polar as function of the canard surface, demonstrating that the three-surface prototype could feature an increment of almost 3%. The demonstrators were then built to allow for an experimental campaign aimed at providing evidence of the goodness of the proposed configuration. The flying platform was also given a name: Aether (Airplane in Three-Surface Configuration with Redundant Longitudinal Control). The Aether features a wingspan of 1.5 m and weighs 3.5 kg. Fig. 2 displays two pictures of the two airplanes during flight tests.

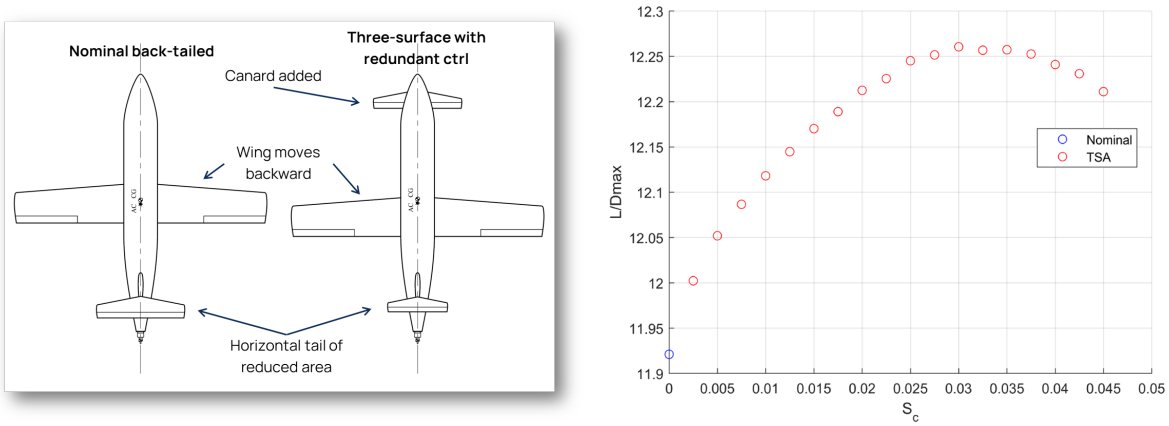


Figure 1: View of reference back-tailed (Nominal) and equivalent three-surface (TSA) airplanes (left). The three-surface airplane features a canard surface of 0.03 m2, associated with the optimal lift-to-drag ratio.

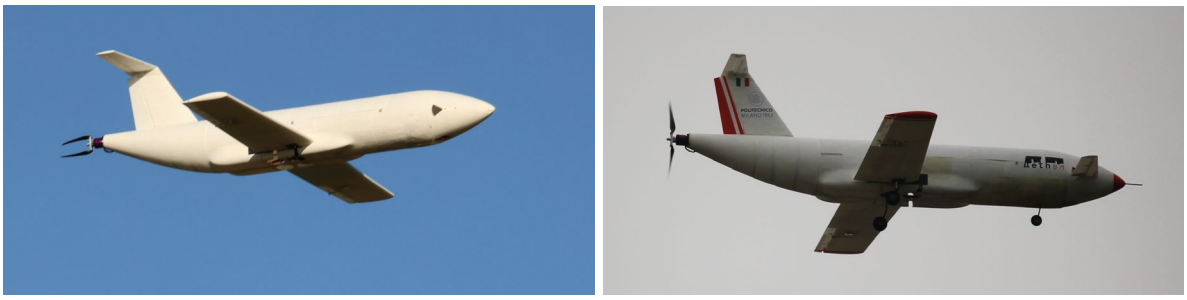


Figure 2: The Aether platform in two- (left) and three-surface (right) configuration, during flight tests.

The external shape of the aircraft is 3D-printed and connected to some carbon-fiber-made structural elements which provide stiffness to the system. The control of the platform is managed by the Pixhawk device and PX4 autopilot software. The system also integrates retractable landing

Materials Research Proceedings 69 (2026) 534-539 https://doi.org/10.21741/9781644904251-96

gears, off-the-shelf motors for the deflection of control surfaces and an electric motor linked to a propeller. A nose-mounted pitot tube, an inertial measurement unit (accelerometers and gyros) and GPS enable the measurement of the key flight mechanics variables. Telemetry, batteries and the remote-control unit complete the hardware setup.

The test campaign, aimed at determining and comparing the polars of both aircraft, was performed between March 2025 and June 2025. It initially focused on estimating the neutral point of the two-surface reference aircraft so as to impose a static margin of 12% through the introduction of an appropriate ballast. Finally, a series of gliding flights at varying speeds was conducted to allow the quantification of the polar. The same procedure was applied to the three-surface aircraft; however, in this case, gliding flights were also performed for several canard deflections chosen a priori. This resulted in multiple trimmed drag polars, each parameterized by the corresponding canard deflection. During each gliding flight, the aircraft speed and position were recorded using the pitot tube and GPS, respectively, enabling the estimation of glide angle. The glide angle and the speed measurements easily provided the lift-to-drag ratio and the lift coefficients (and consequently the drag coefficients), through the standard flight mechanics model of steady gliding flight to enable the estimation of the trimmed aerodynamic polar.

In parallel with the execution of flight tests, the software FlightStream was also used to model both demonstrators, with the goal of supporting the interpretation of the flight testing results. FlightStream is described as a modernized panel method that includes enhancements over other vortex lattice techniques associated with an increased accuracy in the results. For this reason and for its capability to model in a simple way the control surface motion, it was chosen in this study. With its reduced computational expense compared to traditional Navier-Stokes solvers, panel methods offer a good trade-off between fidelity and solver runtime.

FlightStream was then used to derive a complete aerodynamic dataset encompassing the lift, drag and pitch moment coefficients as functions of all trim variables, i.e. the couple α and δ_E for the reference airplane, and the triplet α, δ_E and δ_C in the case of redundant longitudinal control. Afterwards, the aerodynamic dataset was used to compute the equilibrium of the airplane for the same speed and static margin recorded in the experimentation. Although the adopted procedure could produce less accurate results than just running the simulations for the experimentally recorded trim variables, it was considered preferable due to, first, the inherent mismatches between the demonstrator and the numerical model and, second, to some uncertainties in the recorded angles of attack and control deflections during the experimental campaign.

Results

Experimental data were filtered and thoroughly analyzed to yield the polars of both airplanes. Similarly, numerical data were analyzed to ensure convergence of the solutions and used to derive the numerical trimmed polars for comparison with the experimental data.

Fig. 3 displays the experimental polar data of the two-surface reference airplane (thick dashed black line) and the three-surface one for three different canard deflections (thin solid lines). Each marker represents the flight data while the lines show the corresponding quadratic fittings. From this plot, it can be observed that the three-surface airplane with redundant longitudinal control exhibits lower drag within a lift coefficient range of 0.25 to 0.7, resulting in an increase in the maximum lift-to-drag ratio of approximately 19%, significantly higher than the one predicted by the flight mechanics models developed in the design phases.

To assess the accuracy of the two numerical methods against the flight data, Tab. 1 presents the induced drag coefficients k_2 of a parabolic polar approximation, fitted to both real and simulated dataset. The results indicate that Datcom tends to better capture the parasitic drag, while FlightStream performs more accurately in estimating the lift-induced component.

Materials Research Proceedings 69 (2026) 534-539 https://doi.org/10.21741/9781644904251-96

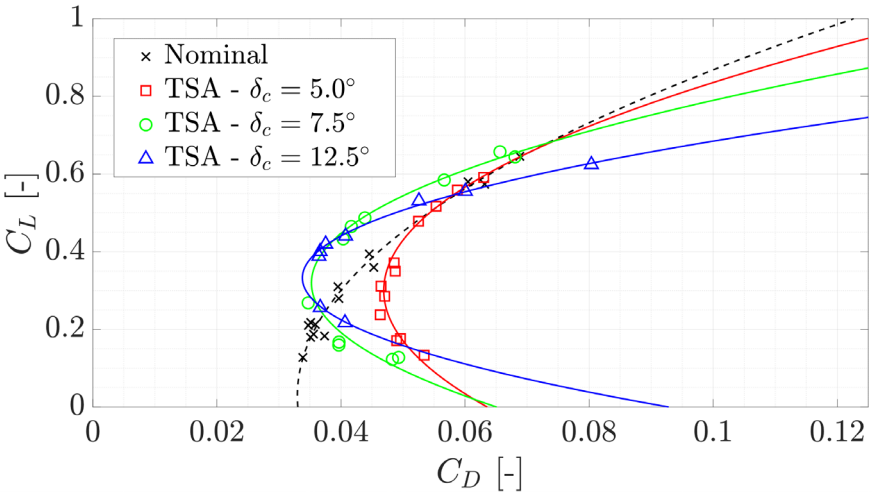


Figure 3: Polar data obtained from flight tests for the for two-surface (black dashed line) and three-surface airplane (solid lines and markers) for different canard deflections.

Table 1: Experimental and numerical polar comparison in terms of fitting coefficients.

	Two-surface k_2	**Three-surface** ($\delta_c = 7.5$ deg) k_2
Experimental data	0.095	0.293
Datcom	0.049	0.055
FlightStream	0.132	0.172

Conclusions and outlook

This study provides the first experimental evidence that a three-surface configuration with redundant longitudinal control can deliver improved aerodynamic performance over equivalent standard back-tailed airplanes. Complementary CFD simulations using FlightStream also estimated higher lift-to-drag ratios, supporting the experimental findings. There are still some non-negligible discrepancies in the matching between numerical and simulation data, particularly evident in the three-surface case. Such a mismatch can be due to multiple sources: incorrect treatment of the wake interaction among the wings in the numerical tools, geometric deviation between the modeled airplanes and the manufactured ones or deterministic biases in the outputs of the sensors used during the experiments. The continuation of this work will aim to address these modeling gaps, possibly through a new set of experimental data and a refinement of the numerical simulations.

Acknowledgement

The authors would like to thank Alexander Heidebrecht and Carmine Varriale from the Department of Flight Performance and Propulsion, TU Delft, Delft, The Netherlands, for their valuable discussions and insightful comments on the topic of this work.

References

[1] T. Goetzendorf-Grabowski, Flight dynamics of unconventional configurations. Progress in Aerospace Science (2023), 137, 100885-1-19, https://doi.org/10.1016/j.paerosci.2023.100885

[2] P.D. Bravo-Mosquera, F.M. Catalano, D.W. Zingg, Unconventional aircraft for civil aviation: A review of concepts and design methodologies. Progress in Aerospace Science (2022), 131, 1008131-1-29, https://doi.org/10.1016/j.paerosci.2022.100813

[3] J.W. Gallman, S.C. Smith, I.M. Kroo, Optimization of joined-wing aircraft. Journal of Aircraft (1993), 30, 897–905, https://doi.org/10.2514/3.46432

[4] S. Cacciola, C.E.D. Riboldi, M. Arnoldi, Three-surface model with redundant longitudinal control: modeling, trim optimization and control in a preliminary design perspective, Aerospace (2021), 8, 139-1-28. https://doi.org/10.3390/aerospace8050139

[5] S. Cacciola, C.E.D. Riboldi, C. Spitale, Steady analysis of three-surface airplanes: improving the aerodynamic performance through redundant longitudinal control, 34th Congress of the International Council of the Aeronautical Sciences (2024), Florence, Italy.

[6] Altair FlightStream, (2025) https://altair.com/altair-flightstream.

[7] C. Varriale, T. Lombaerts, G. Looye, Direct Lift Control: A review of its principles, merits, current and future implementations, Progress in Aerospace Sciences (2025), 152. 101073-1-25, https://doi.org/10.1016/j.paerosci.2024.101073

[8] S. Cacciola, C. Fazioli, L. Filippello, C.E.D. Riboldi, Design and Testing of a Three-Surface Demonstrator with Redundant Longitudinal Control, 11th European Conference for AeroSpace Sciences, EUCASS (2025), Rome, Italy.

[9] R.D. Fink, The USAF stability and control Digital Datcom, McDonnell Douglas Astronautics Company (1978), Technical report AFFDL-TR-79-3032.

[10] S. Corcione, G. Bonavolontà, A. De Marco, F. Nicolosi, Downwash modelling for three-lifting-surface aircraft configuration design, Chinese Journal of Aeronautics (2023) 36, 161-173. https://doi.org/10.1016/j.cja.2023.03.035

[11] D. Levy, Prediction of average downwash gradient for canard configurations. 30th Aerospace Sciences Meeting and Exhibit (2012), Reno, NV, USA

Materials Research Proceedings 69 (2026) 540-545 https://doi.org/10.21741/9781644904251-97

Analysis of LTO Cycle Emissions as Results of Aircraft Operations in the Vicinity of Torino Caselle Airport

Edoardo Blanco[1,a] and Davide Ferretto[1,b *]

[1]Department of Mechanical and Aerospace Engineering, Politecnico di Torino, Corso Duca degli Abruzzi 24, 10129, Torino, Italy

[a]s347182@studenti.polito.it, [b]davide.ferretto@polito.it

Keywords: LTO Cycle, Pollutant Emissions, Boeing Fuel Flow Method, Aircraft Operations, Environmental Impact

Abstract. This paper proposes a methodology based on the Boing Fuell Flow Method 2 (BFFM2) in order to assess non-CO2 emissions resulting from the analysis of real-life aircraft Landing and Take-Off (LTO) cycles. The method is validated exploiting, as case study, the operational procedures in the vicinity of Torino Caselle airport, in the north-west part of Italy. Notably, this study focuses on the analysis of the individual operational procedures, including Standard Instrument Departures (SIDs), Standard Terminal Arrivals (STARs) and Approaches, published by the Italian Air Navigation Service Provider (ENAV), in order to assess the expected level of emissions for nominal trajectories, potentially identifying those flight legs which can be more relevant in terms of impact on air quality. This may open up for suggestions about updates to the procedures themselves, according to a trade-off with actual flown distance (i.e. fuel consumption), also looking at the most congested trajectories.

Introduction

The mitigation of aviation's environmental impact is a key requirement to ensure the sustainable growth of the sector, in line with regulatory demands and the continuous increase in air traffic. Following the goals of the 2015 COP 21 Paris Agreement [1], the International Civil Aviation Organization (ICAO) adopted the Carbon Offsetting and Reduction Scheme for International Aviation (CORSIA) [2], as part of the Long-Term Aspirational Goal (LTAG) [3] defined by the Committee on Aviation Environmental Protection (CAEP).

While CO2 reduction is critical in order to reduce global climate impact, the influence of non-CO2 emissions and, notably, Unburned Hydrocarbons (HC), Carbon Monoxide (CO) and Nitrogen Oxides (NOx) [4], directly affects air quality around airports. To quantify these pollutants, ICAO established an engines certification procedure based on standard operating points of the Landing and Take-Off (LTO) cycle [5], with results collected in a continuously updated database [6].

To extend such certification data beyond LTO conditions, Boeing introduced the Fuel Flow Method 2 (BFFM2) [7], which uses semi-empirical correlations to estimate continuous in-flight emissions. Compared to more detailed methods (such as P3T3 [8]), BFFM2 offers a simpler yet effective framework, which has been applied also to non-conventional configurations [9]. These approaches have since enabled preliminary assessments of local environmental impacts by combining traffic data with airport-specific characteristics and operational patterns [10, 11, 12].

This paper proposes a methodology based on the BFFM2 in order to assess non-CO2 emissions resulting from the analysis of real-life aircraft LTO cycles. The method is validated exploiting, as case study, the operational procedures in the vicinity of Torino Caselle airport, in the north-west part of Italy. Notably, this study focuses on the analysis of the operational scenario, including Standard Instrument Departures (SIDs), Standard Terminal Arrivals (STARs) and Approach procedures, published by the Italian Air Navigation Service Provider (ENAV) [13], in order to assess the expected level of emissions for nominal trajectories. The main goal is to provide a

Content from this work may be used under the terms of the Creative Commons Attribution 3.0 license. Any further distribution of this work must maintain attribution to the author(s) and the title of the work, journal citation and DOI. Published under license by Materials Research Forum LLC.

Materials Research Proceedings 69 (2026) 540-545 https://doi.org/10.21741/9781644904251-97

preliminary evidence of the impact of current operational procedures on air quality, which can be used as basis for a potential update of the trajectories, also considering a trade-off with actual flown distance (i.e. fuel consumption), especially looking at the most congested paths (according to open flight tracking data).

The paper is organized as follows: after this short introduction, a methodological section is presented, with the aim of describing the approach used for the collection of flight data and the implementation of the BFFM2. A section including the main results is then described, with focus on emissions computed for all SIDs and STARs/Approaches. Ultimately, a short summary collects the main outcomes of the work and paves the way for future research.

Methodology

The modeling approach adopted in this work relies on dedicated datasets assembled to characterize inbound and outbound traffic, engine performance, and mission profiles. These inputs were used to estimate non-CO2 emissions in the proximity of Torino Caselle International Airport (LIMF) through the implementation of BFFM2 method.

The structure of such database was divided in three main, branches (Fig. 1): a collection of all information related to standard departure and arrival procedures (SIDs/STARs) involving the airport and derived by official documentation released by ENAV [13]; a catalog of aircraft engines performance across specific regimes obtained from the ICAO Engine Data Bank [6]; a flight database obtained from the sampling of a time frame that could be considered unaffected by bias due to traffic seasonal peaks, thanks to open tracking services.

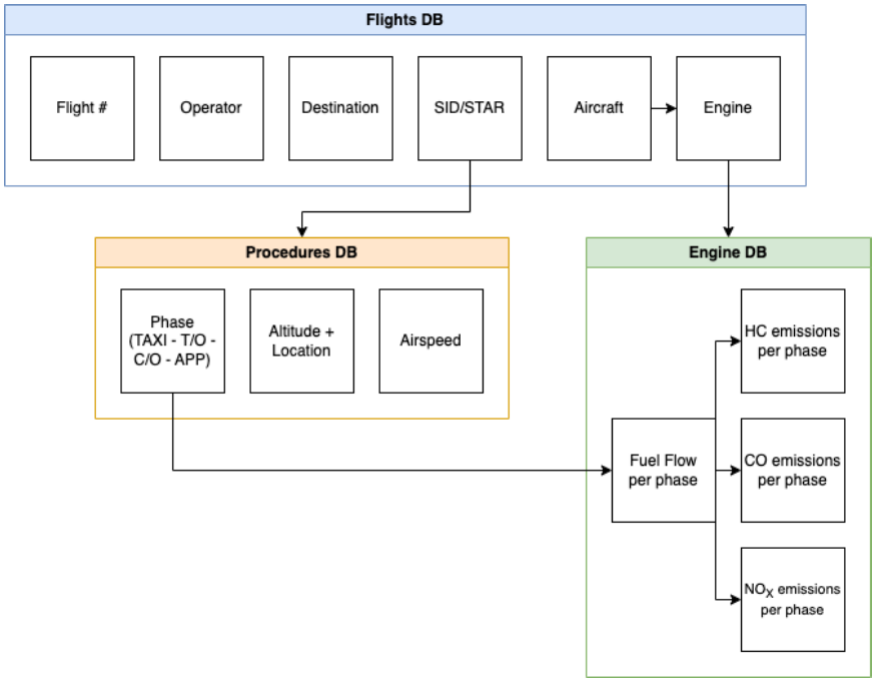


Figure 1: Datasets exploited and related links

Basic data specific to flights was collected exploiting the web based Flightradar24© service. The determination of aircraft model for each LTO cycle created an unambiguous link between the propulsive database, through the determination of the model, and number of installed engines. Furthermore, visual inspections of flight paths enabled the recognition of the actual procedures and consequent mission profiles followed. Samples presenting mismatches between actual tracks and official procedures were excluded from the study. In fact, differently from other works available in literature, such as [12], this paper does not exploit flight tracking service as unique

Materials Research Proceedings 69 (2026) 540-545 https://doi.org/10.21741/9781644904251-97

source of data to build the reference trajectory, but only as verification mean to quantify the usage of the operational procedures. Undoubtedly, in order to start an informed decision making process for procedures update, aimed at improving air quality around the regions affected by air operations, it is important to refer, in the first place, to the official procedures representing the intended paths published by the Authority, rather than looking only at flown trajectories, which may be affected by episodic bias, as well as tracking errors.

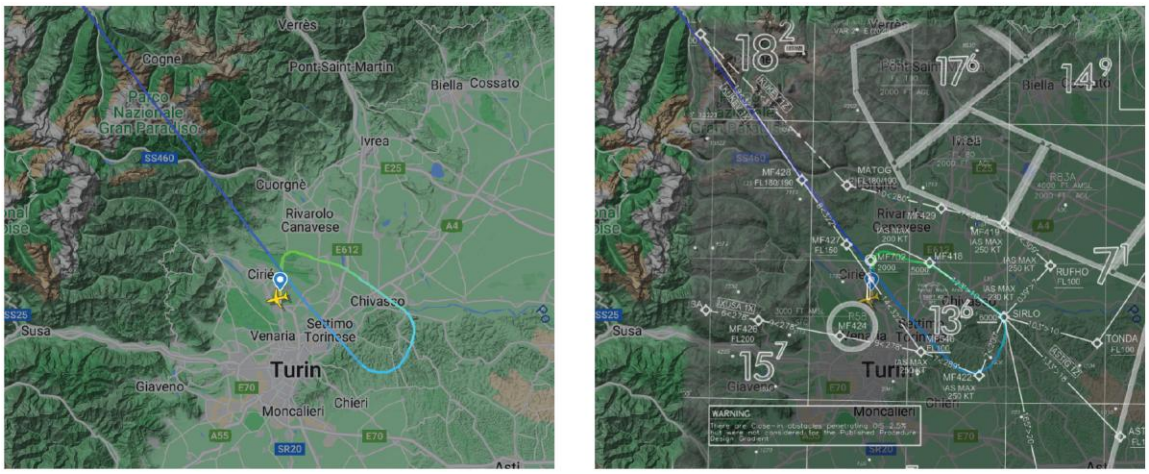


Figure 2: Example of valid trajectory (sources: FlightRadar24) and its adherence to official procedures [13]

The estimation of non-CO2 emissions was then carried out, as already mentioned, using the BFFM2 [7], a semi-empirical approach developed to extrapolate certification data to the entire operational envelope of the engine. The method establishes correlations between fuel flow rate and Emission Indices (EI), allowing the calculation of pollutant mass flows under arbitrary operating conditions. For each i-th pollutant, the emission index EI_i [g/kg_fuel], at a given operating point, is expressed as a function of the reference emission index at equivalent sea-level static conditions ($EI_{i,ref}$) (Eq. 1 to 3), associated, exploiting the data in the ICAO Databank [6], to the reference fuel flow rate $\dot{m}_{f,ref}$ (Eq. 4) computed by translating the actual rate $\dot{m}_f$ (in flight) to sea-level conditions as well.

$$EIHC = EIHC_{ref} \cdot \frac{\theta_{amb}^{3.3}}{\delta_{amb}^{1.02}} \tag{1}$$

$$EICO = EICO_{ref} \cdot \frac{\theta_{amb}^{3.3}}{\delta_{amb}^{1.02}} \tag{2}$$

$$EINO_x = EINO_{x_{ref}} \cdot \sqrt{\frac{\delta_{amb}^{1.02}}{\theta^{3.3}}} \cdot e^{H} \tag{3}$$

$$\dot{m}_{f,ref} = \frac{\dot{m}_f}{\delta_{amb}} \cdot \theta_{amb}^{3.8} \cdot e^{0.2 \cdot M} \cdot r \tag{4}$$

where δ_{amb} and θ_{amb} are ambient pressure and temperature ratios, M is the Mach number and H is a humidity correction factor. The reference flow rate is also multiplied by a coefficient r, which accounts for installation and bleed air extraction losses. Representative values of r for the different operating regimes are reported in Table 1.

Materials Research Proceedings 69 (2026) 540-545 https://doi.org/10.21741/9781644904251-97

Table 1: Correction coefficients $\boldsymbol{r}$ *for fuel flow*

	Idle	Approach	Climb-Out	Take-Off
Throttle [%]	7	30	85	100
r [-]	1.100	1.020	1.013	1.010

The methodology was applied to Torino Caselle International Airport (LIMF), selected as a representative regional hub characterized by mixed short and medium-haul operations. A traffic sample was collected for a reference period between 8-14 March 2024, chosen to minimize seasonal biases and ensure a statistically representative dataset. The resulting dataset included 232 departures and arrivals, covering 14 different aircraft/engine combinations. For each mission profile, the BFFM2 model was applied to compute continuous emission indices and pollutant mass flows up to 10,000 ft, thus extending the conventional LTO cycle and enabling the assessment of local air quality impacts in the airport surroundings. The equations were implemented in a Python model, allowing the automated processing of flight data and the discrete estimation of emissions at specific waypoints along each trajectory.

Results

The model application yielded quantitative estimates of HC, CO and NOx emissions for the reference time frame. Results are presented in terms of average emission rates per flight and their spatial distribution with respect to airport surroundings, according to the SIDs (Fig. 3) and STARs (Fig. 4) respectively followed.

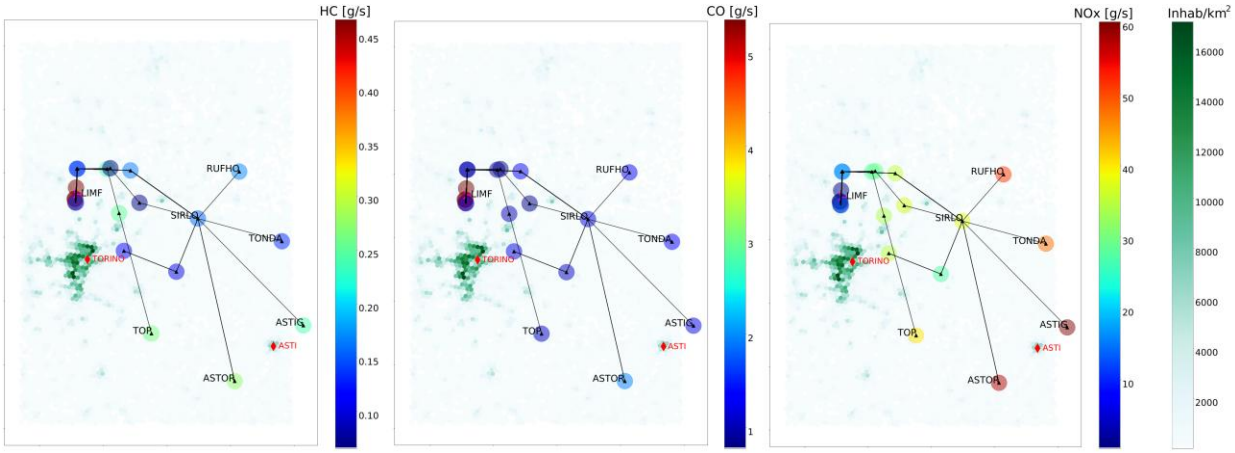


Figure 3: Visualization of emission rates according to SIDs (overlaid with population density)

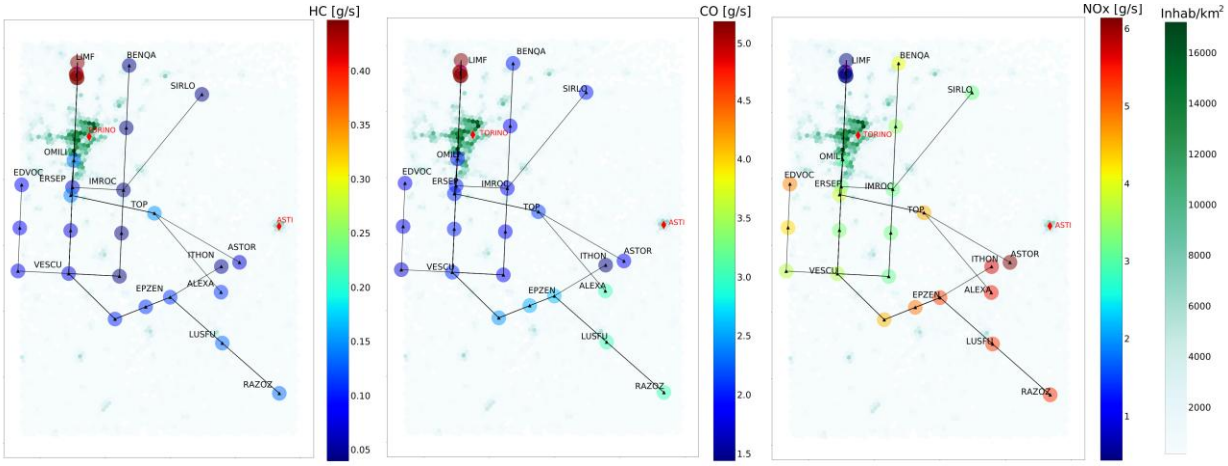


Figure 4: Visualization of emission rates according to STARs/Approaches (overlaid with population density)

Analysis of the emission profiles indicates that more than 50% of HC and CO emissions occur during ground operations (idle and taxi), with a marked reduction at take-off, where maximum thrust is applied. This confirms their nature as incomplete combustion products. In contrast, NOx production showed a strong dependence on altitude and engine thrust. Emission rates for NOx at take-off represented in fact approximately 15% of the peak values observed during climb-out segments around 10,000 ft, where temperatures and pressures combination in the combustor favour NOx formation. The spatial mapping of emission sources across procedures highlights that instantaneous peaks of NOx are concentrated along departure and initial arrival corridors, whereas HC and CO remain localized in the immediate airport vicinity. When overlaid with population density data, the results reveal that the areas most affected by pollutant emission sources are generally displaced from the most densely populated districts of Turin. This may be favourable from an exposure perspective, as the strongest sources are far from densely populated areas, even though a dispersion analysis is required to evaluate the true impact on ground, also according to meteorological data.

Summary

This work exploits the Boeing Fuel Flow Method 2 (BFFM2) in order to evaluate non-CO2 effects on local air quality referring to real world navigation and traffic data. The method is validated with reference to the Landing and Take-Off (LTO) cycles associated to operations in the vicinity of Torino Caselle International Airport (LIMF). In this case, results show that the positioning of emission sources along the trajectories is located far from densely populated areas, with the majority of HC and CO emitted on ground (on airport premises), while NOx have peaks at higher altitudes. The work confirms that this approach can be effectively adopted to potentially consider updates to operational procedures, in order to account for local air quality impact, even though dispersion analyses are needed, as future works, to better assess the distribution of pollutants with time, making benefit of meteorological data.

References

[1] The Paris Agreement. 2015. Available online: https://unfccc.int/process-andmeetings/the-paris-agreement (accessed on 29 July 2025)

[2] International Civil Aviation Organization (ICAO). Consolidated Statement of Continuing ICAO Policies and Practices Related to Environmental Protection—Global MBM Scheme, 2016

[3] International Civil Aviation Organization (ICAO). Report on the feasibility of a Long-Term Aspirational Goal (LTAG) for international civil aviation CO2 emission reductions. CAEP,

March 2022. https://www.icao.int/environmentalprotection/LTAG/Pages/LTAGreport.aspx (Accessed on 29 July 2025).

[4] M. Masiol, R. M. Harrison. Aircraft engine exhaust emissions and other airport-related contributions to ambient air pollution: A review. Atmospheric Environment, 95, pp. 409-405, 2014. http://dx.doi.org/10.1016/j.atmosenv.2014.05.070

[5] International Civil Aviation Organization. (2017). Annex 16 to the Convention on International Civil Aviation: Environmental protection (Vol. II, Aircraft engine emissions). Montréal, Canada.

[6] ICAO Aircraft Engine Emissions Databank (06/2025). Available online: https://www.easa.europa.eu/en/domains/environment/icao-aircraft-engine-emissionsdatabank (accessed on 29 July 2025).

[7] D. Du Bois, G. C. Paynter. Fuel flow method 2 for estimating aircraft emissions (SAE Technical Paper 2006 01 1987). Warrendale, PA: SAE International, 2006.

[8] V. J. Sarli, D. C., Eiler. Effects of operating variables on gaseous emissions. In Proceedings of the Air Pollution Control Association Speciality Conference on Air Pollution Measurement Accuracy As It Relates to Regulation Compliance, New Orleans, LA, USA, 26 October 1975. https://www.icao.int/environmentalprotection/LTAG/Pages/LTAGreport.aspx (Accessed on 29 July 2025).

[9] R. Fusaro, N. Viola, D. Galassini. Sustainable Supersonic Fuel Flow Method: An Evolution of the Boeing Fuel Flow Method for Supersonic Aircraft Using Sustainable Aviation Fuels. Aerospace, 8(11), 331, 2021. https://doi.org/10.3390/aerospace8110331

[10] A. Unal et al. Airport related emissions and impacts on air quality: Application to the Atlanta International Airport. Atmospheric Environment, 39, pp. 5787-5798, 2005. https://doi.org/10.1016/j.atmosenv.2005.05.051

[11] H. Lee, S. C. Olsen, D. J. Wuebbles, D. Youn. Impacts of aircraft emissions on the air quality near ground. Atmospheric Chemistry and Physics, 13, pp. 5505-5522, 2013. https://doi.org/10.5194/acp-13-5505-2013

[12] K. Sanajou, O. Tchepel. Modelling of Aircraft Non-CO2 Emissions Using Freely Available Activity Data from Flight Tracking. Sustainability, 16, 2558, 2024. https://doi.org/10.3390/su16062558

[13] Italy's Aeronautical Information Service Provider (AISP). https://www.enav.it/en/what-we-do/we-create-solutions-for-internationalmarkets/informazioni-aeronautiche/aip-italia (accessed 29 July 2025).

Materials Research Proceedings 69 (2026) 546-551 https://doi.org/10.21741/9781644904251-98

Analysis of CO2 Emissions and Cost Resulting from the Adoption of Sustainable Aviation Fuels by Medium Range Aircraft in Different World Regions

Angela Bozzaotre[1,a] and Davide Ferretto[1,b *]

[1]Department of Mechanical and Aerospace Engineering, Politecnico di Torino, Corso Duca degli Abruzzi 24, 10129, Torino, Italy

[a]s316752@studenti.polito.it, [b]davide.ferretto@polito.it

Keywords: Sustainable Aviation Fuels, CO2 Emissions, Cost Analysis, Life-Cycle Assessment, Environmental Impact

Abstract. This paper aims at evaluating the potential impact on CO2 emissions and cost as result of the exploitation of different kinds of SAFs, around different regions of the world. The study focuses, on one side, on the life-cycle emissions of the fuel, from production to aircraft operations, considering medium range flights from main hubs in Europe, United States, Brazil and Australia. This analysis makes benefit from a literature review on SAF producers around the world. The study of production processes allows in fact to identify the predicted life-cycle emissions of the specific fuel blend, up to the operational phase, also thanks to the adoption of the ICAO Carbon Emissions Calculator (ICEC). In parallel, an assessment of the cost associated to the use of SAF is also carried out, in comparison with conventional kerosene, along the years, up to 2050. Previsions on cost-per-kg of the different fuels are provided, taking into account the impact of the improvement of production process and increase of production quantity, together with inflation. The study demonstrates that, even if an increase of cost-per-kg for the fuel is always present, according to the predicted scenarios, the cost associated to the abatement of CO2 through the exploitation of SAFs has the potential of matching the equivalent cost of CO2 quotas in case an equivalent EU Emissions Trading System (ETS) is present, also considering the reduction of direct emissions over SAF lifecycle.

Introduction

Aviation de-carbonization has been an increasing worldwide effort for many years. In fact, even though commercial aircraft operations account for only 2% of global CO2 emissions, and 10% of overall transport means [1], their contribution is expected to grow due to the increase in traffic demand. During the last decade, also as result of the goals identified within the 2015 COP 21 Paris Agreement [2], the progressive reduction of CO2 emissions has been formalized within a roadmap named Carbon Offsetting and Reduction Scheme for International Aviation (CORSIA) [3] by the International Civil Aviation Organization (ICAO), being in line with net-zero 2050 objective of the Long Term Aspirational Goal (LTAG) [4] proposed by the Committee on Aviation Environmental Protection (CAEP). As demonstrated in [5], emissions reduction can be achieved by introducing new aircraft and powerplant technologies, new fuels, as well as improved operations and Air Traffic Management (ATM). Notably, the most relevant contribution to de-carbonization is associated to the introduction of new fuels capable of either reducing their carbon footprint acting on a more sustainable life-cycle, while maintaining similar operations. This challenge can be actually addressed exploiting the so-called Sustainable Aviation Fuels (SAFs), most of which are produced thanks to organic feedstocks (biofuels) or advanced technologies associated to renewable energy sources and carbon-capture strategies (synthetic fuels), which can replace conventional kerosene (Jet A) as drop-in blends.

Content from this work may be used under the terms of the Creative Commons Attribution 3.0 license. Any further distribution of this work must maintain attribution to the author(s) and the title of the work, journal citation and DOI. Published under license by Materials Research Forum LLC.

Materials Research Proceedings 69 (2026) 546-551 https://doi.org/10.21741/9781644904251-98

Worldwide fleets are dominated by single-aisle short and medium range aircraft (70%), mostly flying along 2000 km routes [6]. This accounts for 65% of CO2 emissions of global aviation, while wide-body airliners flying long-range represent 30%, followed by regional and commuter services [6]. Acting on medium range aircraft is thus the priority to start make the difference. Notably, in the European market, the ReFuel EU plan [7], as part of "Fit for 55", aims at progressively substituting traditional kerosene with SAF in the amount of 2% by 2025, 6% by 2030 and 70% by 2050, which are considered mandatory targets for the airlines.

In this context, this paper aims at evaluating the potential saving in CO2 emissions as result of the exploitation of different kinds of SAFs, according to feedstocks and production processes, around different regions of the world. The study focuses on the life-cycle emissions of the fuel, from production to aircraft operations, considering medium range flights from main hubs in Europe, United States, Brazil and Australia. The work makes benefit from a literature review on SAF producers around the world, and it includes a brief analysis of the most promising production processes. On the other hand, the ICAO Carbon Emissions Calculator (ICEC) [8] is adopted to quantify the emissions for the flights considered within the study.

In parallel, an assessment of the cost associated to the use of SAF is also carried out, in comparison with conventional kerosene, along the years, up to 2050. Previsions on cost-per-kg of the different fuels are provided, leveraging information coming from the literature. A trade-off between emissions and cost is provided, with reference to the competitiveness of the exploitation of SAFs for CO2 abatement process in terms of cost per equivalent CO2 emission, if compared to traditional CO2 mitigation measures based on EU Emissions Trading System (ETS).

After this introduction, a methodological section is presented in order to describe the approach used for the determination of traffic demand for medium-range flight over different regions, as well as to present the results of the review about most adopted SAFs production processes around the globe, and related emissions/costs, hypothesizing a worldwide increase in SAF share according to the ReFuel EU-like plan. Then, a results section is provided to show the outcome of this analysis, also combining the data about emissions and cost in order to assess the competitiveness of SAFs adoption to comply with CO2 mitigation constraints if compared to the use of EU ETS. A summary section concludes the paper, paving the way for future works.

Methodology

As starting point of the workflow, an estimation of traffic demand is performed looking at the world regions previously specified (i.e. Europe, United States, Brazil and Australia), respectively in 2025, 2030 and 2050. The time span is selected in order to be in line with the goals of a ReFuel EU-like plan. References and literature models [9-10] are used in order to derive average traffic in million flights per year, as indicated in Table 1, looking at medium-range category.

Table 1: Hypotheses on traffic data (million flights per year)

Region	2025	2030	2050
Europe	2.02	2.24	2.67
USA	4.77	5.37	7.78
Brazil	0.32	0.44	0.93
Australia	0.66	0.72	1.01

Then, a set of relevant city pairs connected through medium-range flights is selected according to the information provided in [11], in order to consider the most representative missions for each world region. As result, an average value of distance vs fuel consumption is derived, taking into account a constant energy per unit mass of the fuel, equal to 43 MJ/kg, independently from the

Materials Research Proceedings 69 (2026) 546-551 https://doi.org/10.21741/9781644904251-98

blend actually used (SAFs and conventional kerosene have very similar lower heating values). Results of this approach are shown in Table 2.

Table 2: Average fuel quantity for medium range flight in different regions

	Europe	**USA**	**Brazil**	**Australia**
Fuel quantity per flight [kg]	10,685	11,800	10,310	11,000

Moreover, a literature review about the main SAFs producers and production processes around the world is performed, with the aim of determining the most relevant SAFs categories in the different regions and the related feedstocks used for the production. This step is crucial since emissions associated to fuel lifecycle are very specific depending on the type of fuel, production process and feedstock, as well as on the actual region in which they are produced. As result, the data collected in Table 3 have been derived, looking at studies [12] and information provided in literature by the most relevant companies listed in [11].

Table 3: Emissions per unit energy for main SAF type produced in different regions

Region	**Emissions per unit energy [gCO2eq/MJ]**	**(Fuel type) Feedstock**
Europe	19.51	(HEFA) – Agricultural residues, used cooking oil, fatty acid distillate
USA	24.54	(ATJ) – Switchgrass, muscanthus, corn grain, sugarcane
Brazil	44.48	(ETJ) – Forestry residues, corn grain, sugarcane
Australia	23.64	(ATJ) – Switchgrass, muscanthus, poplar, forestry residues, agricultural residues

Resulting emissions per unit energy (gCO2eq/MJ) of the different fuels take already into account production phase as well as operations (i.e. combustion), so they can directly be used for the estimation of the overall lifecycle emissions when applied to the operational context specified in Table 2 (since they are proportional to the quantity of fuel used). Emissions per unit energy can be compared with the standard value of 89 gCO2eq/MJ traditionally adopted for Jet A. As it can be seen, SAF are around 20 – 25 gCO2eq/MJ in most regions, benefitting from the adoption of feedstocks for the production of HEFA or ATJ, with the exception of Brazil, where the use of forestry residues for ETJ production may strongly increase the carbon footprint.

The overall quantity of CO2eq produced during the lifecycle can be computed according to (1). The computation shall take into account the amount of SAF blend specified by ReFuel EU (ϕ) for 2025, 2030 and 2050, respectively equal to 2%, 6% and 70% of the total mixture.

In parallel to emissions evaluation, it is also important to assess the economic impact of SAF adoption, especially looking at the operational costs of blends.

$$kg_{CO2_{eq_{yr}}} = \left(\left(\frac{kg_{CO2_{eq}}}{MJ}\right)_{SAF} \cdot \phi_{yr} + \left(\frac{kg_{CO2_{eq}}}{MJ}\right)_{Jet\ A} \cdot (1 - \phi_{yr})\right) \cdot \left(\frac{MJ}{kg}\right)_{fuel} \cdot m_{fuel_{flight}} \cdot n_{flights_{yr}} \quad (1)$$

According to the information present in [11-14], for the different world regions, considering the type of SAF described in Table 3, the costs reported in Table 4 apply for the different years used as reference in the study. The total Direct Operating Cost (DOC) for fuel can then be computed according to (2).

Materials Research Proceedings 69 (2026) 546-551 https://doi.org/10.21741/9781644904251-98

Table 4: Fuel cost [€/kg] in different regions

Years	Europe		USA		Brazil		Australia	
	Jet A	**SAF**	**Jet A**	**SAF**	**Jet A**	**SAF**	**Jet A**	**SAF**
2025	0.74	1.59	0.75	1.95	0.76	2.04	0.71	2.10
2030	0.77	1.41	0.78	1.73	0.80	1.73	0.75	1.89
2050	0.85	1.29	0.86	1.55	0.88	1.54	0.82	1.53

$$DOC_{fuel_{yr}} = \left(\left(\frac{€}{kg} \right)_{SAF_{yr}} \cdot \phi_{yr} + \left(\frac{€}{kg} \right)_{Jet\ A_{yr}} \cdot (1 - \phi_{yr}) \right) \cdot m_{fuel_{flight}} \cdot n_{flights_{yr}} \quad (2)$$

Ultimately, it is possible to relate costs and equivalent CO2 emissions for the different scenarios in order to estimate the cost associated to emissions reduction through the exploitation of SAFs. This relative cost (in €/kgCO2eq), specific for each year and world region, can be obtained by dividing the cost of fuel and the quantity of emissions, and it shall be computed incrementally, as differential cost, comparing the situation of the target year (i.e. the one under investigation) and a reference year (i.e. current situation or, in general, previous situation in which SAF exploitation is lower) in order to assess the viability of the solution. The mathematical relationship is shown in (3), where, for example, if the aim is to compute the cost per equivalent CO2 emission in 2030, if compared to the same value in 2025, taking into account aforementioned blend shares, i-th is 2030 and (i-1)th is 2025.

$$Cost_{CO_2eq} = \frac{DOC_{fuel_{yr_i}} - DOC_{fuel_{yr_{i-1}}}}{kg_{CO_2eq_{yr_{i-1}}} - kg_{CO_2eq_{yr_i}}} \quad (3)$$

In order to understand the cost-effectiveness of this measure, notwithstanding the obvious benefit in terms of absolute emissions, as specified in the next section, it is possible to compare the result with the relative cost of emissions abatement measures based on equivalent EU ETS. The cost of CO2 emissions on ETS-like quota allocation is also function of the related year, so an extrapolation of reference values used for this study are reported in Table 5 [5]. The application of ReFuel-EU-like plan as well as of an equivalent EU-ETS scheme is a strong hypothesis since different world regions would require specific policy making actions in order to obtain effective outcome, depending on the specific scenario.

Table 5: Reference value of cost for 1 tonn of CO2 in the EU ETS scheme

	2025	**2030**	**2050**
EU ETS – Cost per tonn of CO2 [€/tonn CO2]	78	101	188

The results in the next section shall then not be treated as universally applicable, but just as a starting point for the refinement of the theoretical approach.

Results

According to the methodology described in the previous section, total emissions trends per year, for the different world regions, can be shown in Fig. 1 (left). As it can be seen, after a couple of years, the adoption of SAF is generally beneficial for what concerns overall emissions quantity, expect for the Brazilian scenario, where the adoption of ETJ obtained from forestry residues do not ensure a positive abatement along the years. A similar trend summarizing the cost escalation due to the introduction of SAF blends, is shown in Fig. 1 (right), neglecting taxes. As it can be

Materials Research Proceedings 69 (2026) 546-551 https://doi.org/10.21741/9781644904251-98

seen, the exploitation of SAF has a negative impact on cost, since a general increase is present, with differences depending on SAF types and world regions.

The cost-effectiveness related to CO2 compensation exploited through SAFs introduction, in comparison with conventional EU ETS scheme adoption for CO2 quota compensation, is shown in Fig. 2. As it can be seen, a progressive adoption of SAF may allow to match the expenses associated to CO2 compensation through equivalent EU ETS scheme with time. The breakeven point (i.e. where the different lines matches the cyan one) depends on the scenario considered for the different regions and the type of SAFs.

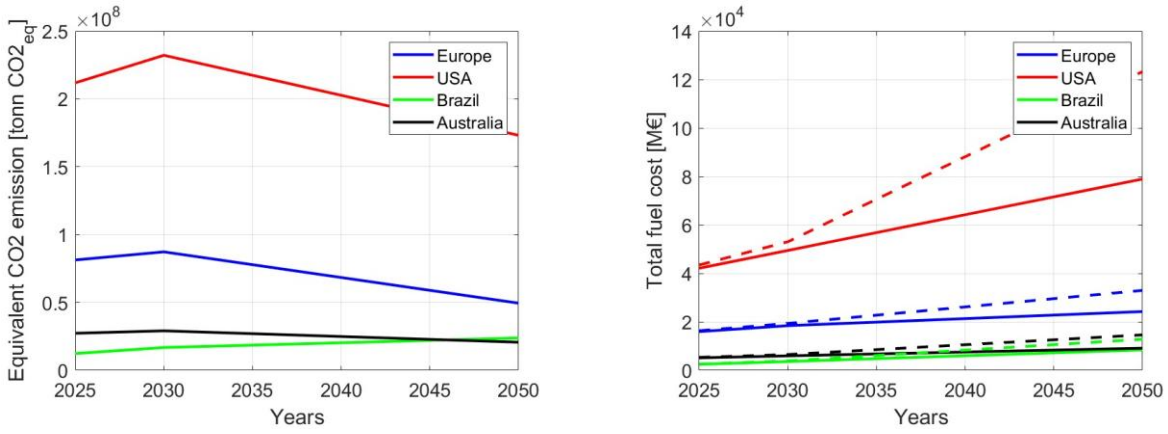


Figure 1: Total equivalent CO2 emissions (left) and total fuel cost (blends) (right) over the years

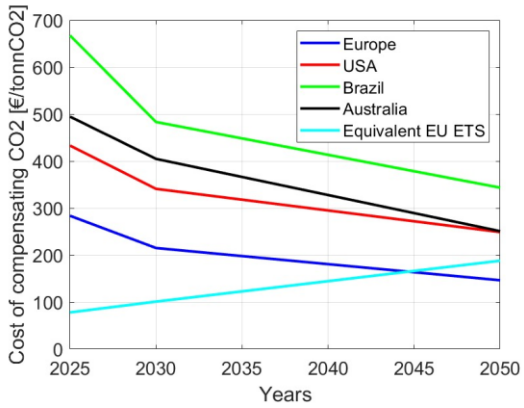


Figure 2: Cost per CO2 emissions and comparison between SAF adoption and EU ETS-like compensation

Summary

The methodology described in this paper demonstrates how to rapidly assess the impact of the progressive SAFs introduction in aviation on emissions and costs, according to international roadmaps, such as ReFuel-EU. The methodology is based on four main steps, consisting respectively in evaluation of traffic, analysis of SAFs production processes and feedstocks, assessment of cost associated to SAFs introduction and cost-effectiveness evaluation through the analysis of the trade-off between cost escalation and emissions reduction resulting from the increase in SAF blends over the years. Results demonstrate that different world regions shall be analyzed adopting different assumptions and policies, considering their specific needs and socio-economic situation. However, the results show that incremental introduction of SAFs in Europe can contribute, over the years, to a sensible reduction of CO2 emissions and that the cost associated to the introduction of new fuel can be competitive with reference to the traditional CO2 quota

allocation based on EU ETS scheme in the long term. Future works shall deal with detailed analyses on different world regions, as well as with assessment of the principles behind the ETS-like schemes in order to improve the cost-effectiveness evaluation.

References

[1] H. Ritchie. Sector by sector: where do global greenhouse gas emissions come from? Our World in Data, 2020. https://ourworldindata.org/ghg-emissions-by-sector (acc. on 30 July 2025)

[2] The Paris Agreement. 2015. https://unfccc.int/process-and-meetings/the-paris-agreement (acc. on 29 July 2025).

[3] International Civil Aviation Organization (ICAO). Consolidated Statement of Continuing ICAO Policies and Practices Related to Environ. Prot. - Global Market-Based Measure, 2016

[4] International Civil Aviation Organization (ICAO). Feasibility of a Long-Term Aspirational Goal (LTAG) for international aviation CO2 emission reductions. CAEP, 2022. https://www.icao.int/environmental-protection/LTAG/Pages/LTAGreport.aspx (acc. on 29 July 2025).

[5] European Aviation Safety Agency. European Aviation Environmental Report 2025. EASA, 2025. https://www.easa.europa.eu/en/domains/environment/eaer (acc. 30 July 2025)

[6] Clean Sky 2. Hydrogen-powered aviation. A fact-based study of hydrogen technology, economics and climate impact by 2050. Clean Sky 2 JU, 2020

[7] European Commission – Mobility and Transport. ReFuel EU Aviation. EC, 2025. https://transport.ec.europa.eu/transport-modes/air/environment/refueleu-aviation_en (acc. 30 July 2025)

[8] International Civil Aviation Organization. ICAO Carbon Emiss. Calc. Method v13.1, 2024

[9] H. Jung. Airport Industry Outlook: Past, Present and Future. Aviation Data Analysis Seminar, Airport Council International, 2024.

[10] FAA FY2024 – 2044 Aerospace Forecast, Federal Aviation Administration, 2024.

[11] A. Bozzaotre. MSc Thes.: Assessment of CO2 emissions and cost-benefit analysis of medium-range commercial aircraft powered by Sustainable Aviation Fuel, Polit. di Torino, 2025.

[12] Z. Song, Z. Li and Z. Liu. Comparison of Emission Properties of Sustainable Aviation Fuels and Conventional Aviation Fuel: A Review, Applied Sciences, 14, 2024. https://doi.org/10.3390/app14135484

[13] M. Braun, W. Grimme and K. Oesingmann. Pathway to net zero: Reviewing sustainable aviation fuels, environmental impacts and pricing, Journal of Air Trans. Manag., vol. 117, 2024. https://doi.org/10.1016/j.jairtraman.2024.102580

[14] N. Detsios, S. Theodoraki, L. Maragoudaki, K. Atsonios, G. Panagiotis and N. Orfanoudakis. Recent Advances on Alternative Aviation Fuels/Pathways: A Critical Review, Energies, 2023. https://doi.org/10.3390/en16041904

Materials Research Proceedings 69 (2026) 552-557 https://doi.org/10.21741/9781644904251-99

Synthesizing Aircraft System Specifications with Document-Managed Large Language Model Outputs from One-Shot System Inquiry Prompt Chain

Vinicius Kaster MARINI[1,a *], Petter KRUS[2,b]

[1]Dept of Mechanical Engineering, Centre of Technology, Federal University of Santa Maria, Brazil

[a]vinicius.marini@ufsm.br, [b]petter.krus@liu.se

Keywords: Aircraft System Design, System Context Input, Human-Machine Collaboration, Large Language Models

Abstract. Human-machine collaboration on systems design as well as on systems operation aims to face the intricacy and complexity of novel systems with artificial intelligence. This work aims to display a human-machine collaboration approach by front-end aircraft system design aiming to maintain human ownership and leverage artificial intelligence capabilities. Here, large language models (LLMs) gather information on system design to documental quality, to be reviewed and augmented with supervision by engineers. The study involves the following steps: firstly, a review on examples of using LLMs; then, prompt modelling on a search-and-rescue mission example; then, generating document-managed conversations.

Introduction

The complexity of automation in aircraft draws interest on human-machine interfaces as a matter of concern for aircraft systems engineering. The arrival of *artificial intelligence* (AI) as a component in aircraft automation requires an evolved perspective about *human-machine collaboration* to ensure the newly implemented systems can offer predictable and robust performance [1].

However, the implementation of AI to augment the control chains of novel aircraft systems also has implications that extend back to the design process. The realization of efficiencies from AI-enabled and connected smart devices entails added complexity and intricacy in the development of system designs as multi-domain system stacks [2].

This contribution aims to demonstrate an approach to human-machine collaboration making use of *large language models* (LLMs) to gather information on system design and yield work products with document quality, to be reviewed and augmented with supervision by engineers. It builds upon using *standard chatbox* tools [3] towards experimenting with a *custom chatbox* about how it affords interacting with LLMs onto traceable output.

About large language models (LLMs)

The prospects of using *large language models* (LLMs) attract attention to their use within systems engineering and design. Through the use of the transformer mechanism to neural networks [4], newer LLMs came with *problem-solving* abilities. This enables the prospect of generative AI (GenAI), regarding their ability to yield knowledge in its answers [5]. However, they have drawn criticism upon their lack of *matter-of-factness* [6], thereby with limited use for assurance cases of complex systems [7].

Content from this work may be used under the terms of the Creative Commons Attribution 3.0 license. Any further distribution of this work must maintain attribution to the author(s) and the title of the work, journal citation and DOI. Published under license by Materials Research Forum LLC.

Materials Research Proceedings 69 (2026) 552-557 https://doi.org/10.21741/9781644904251-99

At the same time, their ability to compute language could support aircraft and aerospace design where traditional design automation methods have so far fallen short when the scope of inquiry is carefully managed [8]. Attempts at using LLMs to compute system design use embedded training patterns to yield deliverables, with examples reviewed on the following use cases [3]:

a) Processing of mission and design requirements,
b) Generation of structured system models,
c) Engineering assessment of hazards and assurance cases.

Common conclusions from these examples regard the remarkably short timeframe to building *reasonable* outputs. However, the quality of LLM-supported work products suffers from incompleteness to scope, or inaccuracy to intent, or non-compliance to rules. This means the usage of LLMs as GenAI tools requires attention by engineers about generating content upstream and downstream; The indiscriminate use of GenAI content without proper scrutiny results in the *workslop* phenomenon [9] with negative effects to productivity due to the rework needed.

Scope of work

We perform exploratory research on the use of LLMs in systems engineering, to understand *human-machine collaboration* with generative AI. The study illustrated in Figure 1 departs from the literature review onto experimenting with a prompt chain into developer-*standard chatbox*. Then, a *custom chatbox* is set to enable *human-in-the-loop* involvement in the inquiry process, to provide specification-quality outcomes from LLMs.

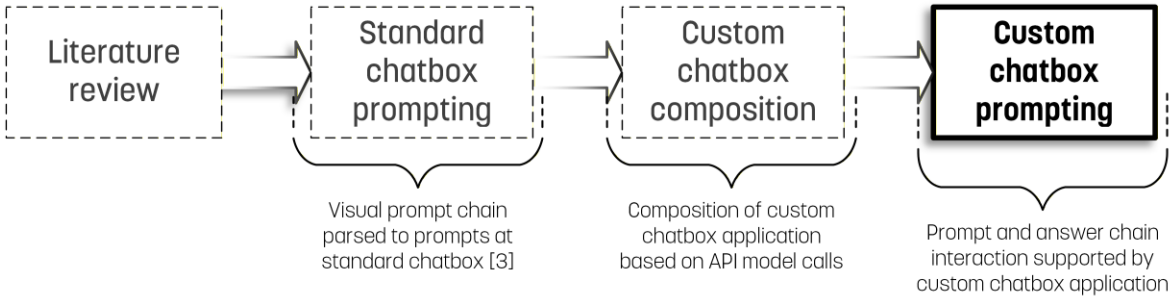


Figure 1 – Stepwise development of the study

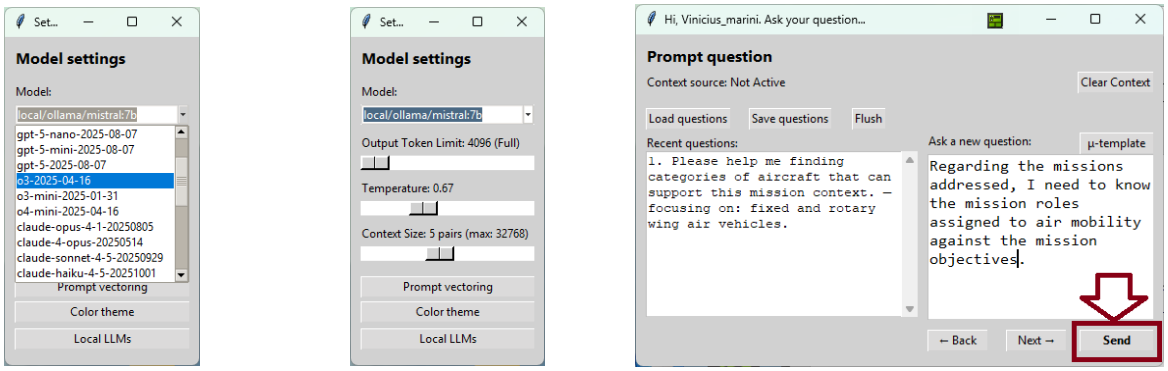
Visual concept mapping enables shaping the prompt question pathway, parsed onto topic questions and split in manageable chunks. This enables the buildup of conversation context in pre-specification level [3]. The conversation policy requires awareness to language processing and takes significant context space. While compliant to policy, standard chatbox responses require effort to monitor policy compliance and perform content review.

The custom chatbox

A *custom chatbox* application allows forwarding a planned question chain to a sequence of prompts at a LLM of choice through API calls. LLM model setup functionality is intended to augment the usability of the chatbox format towards better management of prompting and content review. The application is also intended to handle the streaming of context-supported and traceable answer content for editing and local saving.

The experimentation with standard chatbox resources [3] led to the understanding the need for improved human-machine interaction upon performing chained prompt inquiries. Here, Figure 2 displays the user interface approaches for selecting the intended model and performing/managing questions. It provides means to select the specific model for asking the questions (a), configuring context usage and temperature (b), and entering questions at the selected LLM (c).

Materials Research Proceedings 69 (2026) 552-557 https://doi.org/10.21741/9781644904251-99



a) Selecting model *b) Model selected* *c) Question history and next*

Figure 2 – Entering context information to prompt the selected LLM.

The model setting window (a, b) enables the choice of LLM and parameters on which to call it into *API calls*. The question window has a *question history* section (c) intended to manage the prompt chain, and a *single prompt* section to set one-time and recurring prompt questions. Figure 3 displays the setting of these different components for each model call requested through the *Send* button: the global prompt (a) to provide recurring instructions; the actual question in (b); and the boundary context prompt (c) as exemplar in each few calls.

Figure 3 shows the application windows including the question box (left), the prompt vectoring box (center) and the answer box (right). After setting up the intended model and adding the global and context in the question box (left), then it is possible to add *prompt vectors*[1], and choose between a single combined question or a batch prompt of several answers, each covering a different aspect. Here, question and prompt vectoring boxes allow including *µ-Templates*[2] as exemplars making part of the prompt [8].

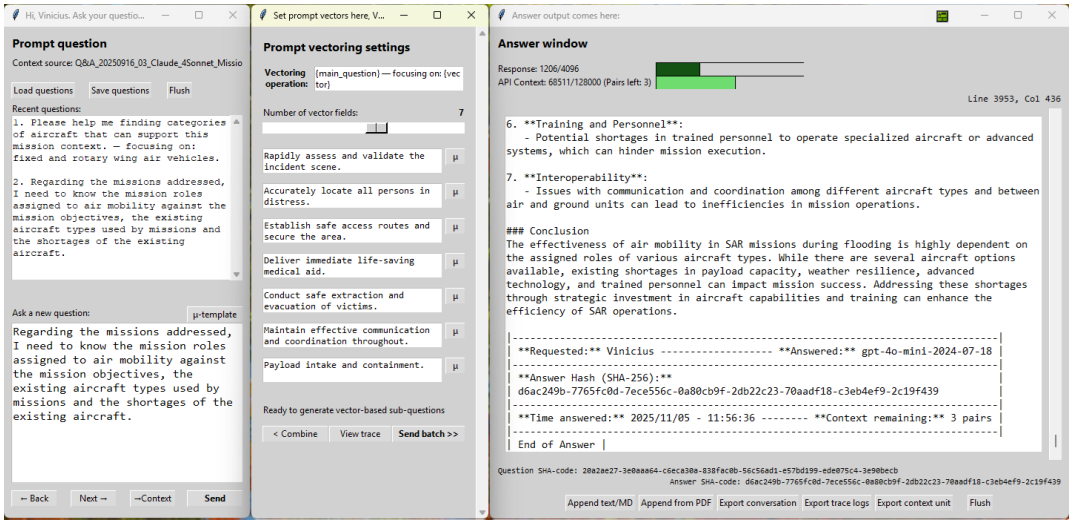


Figure 3 – Entering context information to prompt the selected LLM.

[1] *Prompt vectors* compose the prompt with aspect fields along a main question statement, intended to *steer* the answer to one or more specifics of the main question. Maintaining them along a question string enables *swimlaning* of related issues across specifics within the context window.

[2] *µ-Templates* (*micro-templates*) [8] are specific text or code snippets bringing in exemplars to the prompt, effectively enabling *one-shot* and *few-shot* prompting [10] with instances that the selected model is intended to follow and apply in generating its answer.

Materials Research Proceedings 69 (2026) 552-557 https://doi.org/10.21741/9781644904251-99

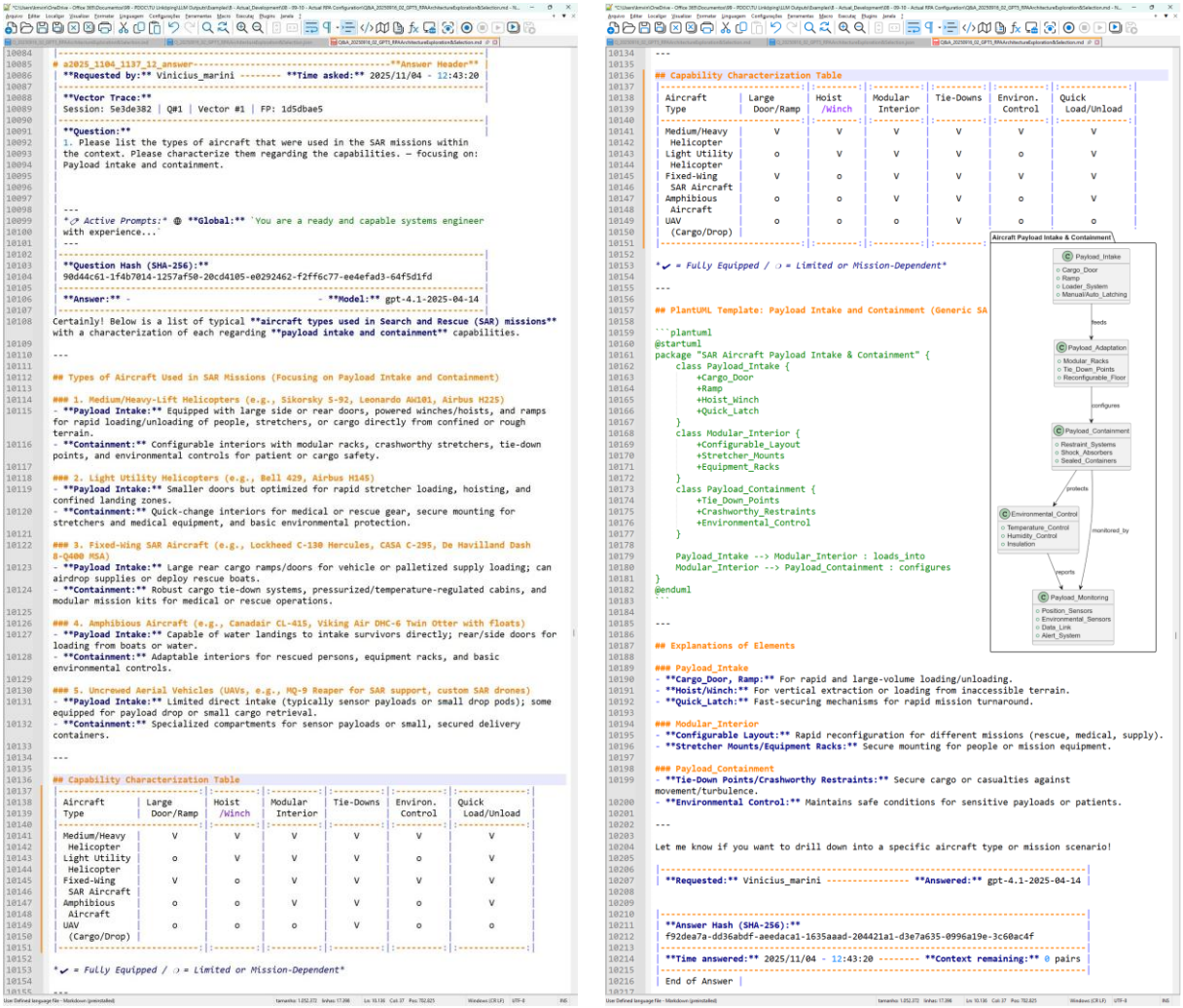
The answer window allows the addition of context references along with *μ-Templates*; here, token counting enables the verification of the ongoing context performance against the capabilities of the selected model. The sizing of individual answers and the API context in use allows estimating the LLM capability resources available in providing an answer. Here, prompt vectoring enables the choice between a combined single question/answer and a batch of question/answer pairs where each will focus a specific aspect.

The case study

This contribution will display the application and its use, with particular focus on the interface channels and the authentication information, towards mission and system design. The mission case is a large-scale flood [11] that occurred between April and June of 2024 with 100 municipalities affected, 600.000 displaced victims and 183 casualties.

Such large-scale and the urgency open prospects for enhancing aerial mobility, with the aim to simplify and leverage aircraft systems for large-scale lifting and medevac operations. Here, the mission context and the stakeholder needs have been established through a chain of prior questions, considering issues previously engaged with the use of standard chatbox input [3].

The resulting documentation from answers is in display by Figure 4.



a) First page with answer header *b) Second page with system model*

Figure 4 – Entering context information to prompt the selected LLM.

Figure 4 shows a saved answer about payload intake and containment capabilities for SAR aircraft. The synthesis of the specification benefits from context intakeStarting with a survey of aircraft design categories and existing products, the answer then characterises the capabilities per aircraft design category. Then it presents a *PlantUML* model (with graphic as reference) of the intended aircraft capabilities and concludes the specification with explaining capability highlights.

The answer includes authentication information in who requested information and the model providing the answers, including SHA-256 traceability codes for question and answer. The recording of the prompt chain - including vectors - enables reproducing the questions a number of times. However, long prompt chains - especially those involving the selection of batch prompts from vectoring - will also generate long conversations, which require significant workload for review.

Discussion

With Figure 4 shown as a single answer in a chain, the scope and sequence of questions shall be planned [3] with regard to reviewing workload. Our prompt composition approach provides some complementary resources to support this. Global and context prompts with guidelines help pre-organizing answer structure and focus, whereas *μ-Templates* constrain the LLM output to specific modelling guidelines.

Nevertheless, the use of LLMs to generating architecture models still requires review on the text and especially about codeblock output. The results have shown enough quality to be useful with replacement/incremental additions, without extensive refactoring.

Conclusion

The article focuses the synthesis of system design specifications for aircraft in displaying a human-machine collaboration interface. The proposed solution departs from the usual chatbox format, with generating system design specifications through a context assembly framework that manages requests to the model and enables curating the answer content.

Acknowledgment

This contribution is supported through a grant by the Brazil-Sweden Innovation Partnership in Aerospace Engineering through the MCTI-CNPq-CISB-Saab AB call 37/2023, with hosting by Linköping University at Sweden.

References

[1] P. Millot and G. A. Boy, ‘Human-machine cooperation: a solution for life-critical Systems?’, *WORK: A Journal of Prevention, Assessment & Rehabilitation*, vol. 41, no. S1, pp. 4552–4559, Mar. 2012. https://doi.org/10.3233/WOR-2012-0033-4552

[2] M. Törngren and P. T. Grogan, ‘How to Deal with the Complexity of Future Cyber-Physical Systems?’, *Designs*, vol. 2, no. 4, p. 40, Oct. 2018. https://doi.org/10.3390/designs2040040

[3] V. K. Marini, J. Alfredson, and P. Krus, ‘Context of collaborative human-machine systems architecture design for enhanced functionality awareness and balanced command and control authority’, in *FT2025: Proceedings of the 12th Swedish Aerospace Technology Congress*, Stockholm: Linköping University Press, Oct. 2025. https://doi.org/https://doi.org/10.3384/wcc215.1192

[4] A. Vaswani *et al.*, ‘Attention is all you need’, *Advances in neural information processing systems*, vol. 30, 2017.

[5] W. X. Zhao *et al.*, ‘A Survey of Large Language Models’, Mar. 11, 2025, *arXiv*: arXiv:2303.18223. https://doi.org/10.48550/arXiv.2303.18223

[6] M. T. Hicks, J. Humphries, and J. Slater, ‘ChatGPT is bullshit’, *Ethics Inf Technol*, vol. 26, no. 2, p. 38, Jun. 2024. https://doi.org/10.1007/s10676-024-09775-5

[7] M. S. Graydon and S. M. Lehman, ‘Examining Proposed Uses of LLMs to Produce or Assess Assurance Arguments’, National Aeronautics and Space Administration, Technical memorandum NASA/TM–20250001849, Mar. 2025.

[8] P. Krus, ‘Large language model in aircraft system design’, in *ICAS Proceedings, 34th Congress of the International Council of the Aeronautical Sciences*, Florence, Italy: The International Council of the Aeronautical Sciences, Oct. 2024, pp. 1–13.

[9] K. Niederhoffer, G. R. Kellerman, A. Lee, A. Liebscher, K. Rapuano, and J. T. Hancock, ‘AI-Generated “Workslop” Is Destroying Productivity’, *Harvard Business Review*, Sep. 25, 2025. Accessed: Nov. 06, 2025. [Online]. Available: https://hbr.org/2025/09/ai-generated-workslop-is-destroying-productivity

[10] D. C. Schmidt, J. Spencer-Smith, Q. Fu, and J. White, ‘Towards a Catalog of Prompt Patterns to Enhance the Discipline of Prompt Engineering’, *Ada Lett.*, vol. 43, no. 2, pp. 43–51, Jun. 2024. https://doi.org/10.1145/3672359.3672364

[11] I. T. Simoes-Sousa, C. M. L. Camargo, J. Tavora, A. Piffer-Braga, J. T. Farrar, and T. M. Pavelsky, ‘The May 2024 Flood Disaster in Southern Brazil: Causes, Impacts, and SWOT-Based Volume Estimation’, *Geophysical Research Letters*, vol. 52, no. 4, p. e2024GL112442, 2025. https://doi.org/10.1029/2024GL112442

Materials Research Proceedings 69 (2026) 558-563 https://doi.org/10.21741/9781644904251-100

AI-Driven Pre-Design Predictions of a 90-Passenger Hybrid-Electric Aircraft

Erick ESPINOSA-JUÁREZ[1,a *], Álvaro GÓMEZ-RODRÍGUEZ[2,b], Felix MARTINEZ-RIOS[3,c], Christopher JOUANNET[1,d] and Kristian AMADORI[1,e]

[1]Linköping University, 581 83 Linköping, Sweden

[2]Universidad Politécnica de Madrid, 28040 Madrid, Spain

[3]Universidad Panamericana, 03920 Mexico City, Mexico

[a]erick.espinosa.juarez@liu.se, [b]alvaro.gomez.rodriguez@upm.es, [c]fmartin@up.edu.mx, [d]christopher.jouannet@liu.se, [e]kristian.amadori@liu.se

Keywords: Artificial Intelligence, Aircraft Conceptual Design, Fully Electric Aircraft, Hybrid-Electric Aircraft, Correlation Analysis, Singular Value Decomposition (SVD)

Abstract. As the numerous aircraft concepts using electric or hybrid-electric propulsion remain at low technology readiness levels, there are no operational statistical data, and information on these concepts is comparatively scarce. The objective of this study is to explore alternative methods for early-stage estimations by evaluating and comparing design parameter predictions derived from conventional statistical methods and artificial intelligence (AI) for a 90-passenger hybrid-electric aircraft. The findings highlight the potential of AI as a tool for the early phases of aircraft conceptual design.

Introduction

Electrified aircraft propulsion remains in its early development phase due to technological, operational, and economic limitations. As these aircraft may have significantly different design characteristics when compared with conventionally powered aircraft, novel approaches for their design are required. To deal with these differences and the aforementioned data limitations, the present study explores alternative methods for early-stage parameter estimations of a 90-passenger hybrid-electric aircraft. Taking the number of passengers as the single input, estimations of key design parameters were obtained and compared from both statistical data and predictions generated by artificial intelligence (AI), proposing the use of AI as a supporting tool for initial parameter estimations in conceptual design.

Methodology

Design parameters of 52 fully electric (FE) and hybrid-electric (HE) aircraft concepts, chosen by relevance under the authors' criteria, were collected in a database whose extract is shown in Table 1. These parameters included the propulsion type, certification sought, number of passengers, maximum take-off mass (MTOM), wing loading (W/S), power-to-weight ratio (P/W) and battery mass fraction (BMF). The certification appears in Table 1 as CS-25, CS-23 or Light Sport Aircraft (LSA), which includes both general aviation and experimental categories. For turboelectric configurations lacking batteries (denoted T), BMF values were logged as 0* and were not included in any further analysis. Some parameters were directly reported by designers, while others were inferred. Those that were neither directly nor indirectly available in the sources were left blank (shown in red in Table 1). The methodologies applied to the collected data to support early-stage estimation of key parameters are now described.

Content from this work may be used under the terms of the Creative Commons Attribution 3.0 license. Any further distribution of this work must maintain attribution to the author(s) and the title of the work, journal citation and DOI. Published under license by Materials Research Forum LLC.

Materials Research Proceedings 69 (2026) 558-563 https://doi.org/10.21741/9781644904251-100

Table 1 Extract of the electric and hybrid-electric aircraft concepts database. 0 denotes no battery for turboelectric (T) types of aircraft (not used in further analysis). Red cells indicate missing values.*

Aircraft	Type	Cert	PAX	MTOM [ton]	(W/S) [kg/m²]	(P/W) [kW/kg]	BMF
AEA-800	FE	CS25	180	109	868	0.13	0.44
Wright Spirit	FE	CS25	100				
Volt Air	FE	CS25	33	33			
DEP Tw'otter	FE	CS23	19	5.67	145		0.62
EL19	FE	CS23	19	8.62	222	0.17	0.45
ERA	FE	CS23	19	8.60	141	0.09	
E10	FE	CS23	10	3.50	201	0.15	0.29
Alice	FE	CS23	9	8.17	359	0.18	0.51
eCaravan	FE	CS23	9	4.50	173	0.17	0.32
EL-2 Goldfinch	FE	CS23	9	1.40	78	0.11	
SwitchMaster	FE	CS23	2	1.07	68	0.08	0.48
SCEPTOR	FE	LSA	4	1.18	80	0.10	0.34
Alpha Electro	FE	LSA	2	0.57	60	0.15	0.33
eDA40	FE	LSA	2	1.31	98	0.10	0.23
Velis Electro	FE	LSA	2	0.60	63	0.10	0.33
X-57 Maxwell	FE	LSA	2	1.36	219	0.13	0.33
E-fan	FE	LSA	2	0.55		0.11	0.45
E-Genious	FE	LSA	2	0.95	65	0.06	0.35
Extra 300	FE	LSA	2	1.00	92	0.26	
ACCEL	FE	LSA	1	1.25	177	0.60	0.39
Antares	FE	LSA	1	0.66	52	0.06	0.20
Electraflyer C	FE	LSA	1	0.28	19	0.05	0.20
BHL A320PHE	HE	CS25	180	74.02	644	0.13	0.12
SUGAR N+4	HE	CS25	154	61.88	491	0.09	0.16
Sugar VOLT	HE	CS25	154	68.04	496	0.18	0.18
A320-200PHE	HE	CS25	150	77.00	644	0.03	

Aircraft	Type	Cert	PAX	MTOM [ton]	(W/S) [kg/m²]	(P/W) [kW/kg]	BMF
A320neoPHE	HE	CS25	150	79.00	644		
EVE	HE	CS25	150	69.13	504		0.15
STARC-ABL	HE	CS25	150	60.50	576	0.09	
ATR-72HE	HE	CS25	70	28.50	376	0.17	0.16
E-fan X	HE	CS25	70	38.40	497	0.24	0.05
PEGASUS	HE	CS25	48	18.14	333	0.10	0.33
REG-C	HE	CS25	40	21.30	493	0.19	0.17
REG-R	HE	CS25	40	22.64	345	0.12	0.14
ES-30	HE	CS25	25	21	303	0.17	0.24
ES-19	HE	CS25	19	8.60		0.19	0.19
Eco Otter SX	HE	CS23	19	5.67	145	0.18	
ZA-10	HE	CS23	12	5.22	186	0.19	0.27
Eco Caravan	HE	CS23	9	4.00	154	0.14	0.32
Tailwind	HE	CS23	9	5.00	224	0.10	
Cassio	HE	CS23	6	5.00	267	0.08	
Ecopulse	HE	CS23	4	3.35	186	0.28	0.14
Electric Eel	HE	CS23	3	2.00	107	0.17	0.24
P2010 H3PS	HE	LSA	4	1.22	88	0.11	0.13
Panthera	HE	LSA	3	1.32	117	0.15	0.08
DA-36 E-Star	HE	LSA	2	0.80	52	0.09	0.13
Crop Duster	HE	LSA	1	3.36	134	0.24	0.36
CENTRELINE	T	CS25	340	229	644	0.08	0*
SUSAN	T	CS25	180	69.84	559	0.29	0*
DRAGON	T	CS25	150	58.85	482	0.33	0*
ECO-150	T	CS25	150	63.33	560	0.25	0*
SMC-R	T	CS25	150	79	294	0.25	0*

The use of correlation and regression analyses constitutes a proven approach in aircraft conceptual design, as seen in design manuals [1, 2] and in recent research works [3, 4, 5], where the sample Pearson Correlation Coefficient, r_{xy}, has been used to explore the strength of linear relationships between pairs of variables [4, 5]. The statistical basis of this coefficient can be found in [6]. Aside from measuring the strength of the linear relationship through its numeric value, this sample coefficient can be used to make inferences on the population correlation coefficient ρ_{xy}. Of particular interest is the hypothesis test to check whether the obtained value of r_{xy} is such that a statistically significant correlation can be inferred for the population. This test can be undertaken through the statistic [6]:

$$t = \frac{r(n-2)^{0.5}}{(1-r^2)^{0.5}} \sim t(n-2) \qquad (1)$$

Materials Research Proceedings 69 (2026) 558-563 https://doi.org/10.21741/9781644904251-100

Which follows a Student's t-distribution with $(n-2)$ degrees of freedom. As this is a two-tailed distribution, the obtained p-value should be compared with half of the level of significance, α, that has been determined for the case study. Here, a value of α = 0.05 has been chosen, representing a 5% chance of making a Type I error. This choice has been made considering that in aircraft conceptual design an error of around 10–15 % can be accepted [1, 2], which is later refined in further design stages. Thus, the cut-off p-value would be 0.025 for the hypothesis test, where larger probabilities would result in the conclusion that no linear correlation can be assumed for the population in view of the results, whereas smaller probabilities would lead towards rejecting the null hypothesis and accepting that a statistically significant linear correlation may be inferred.

The second statistical method used was the Singular Value Decomposition (SVD) analysis described in [7]. It takes the intrinsic correlations between aircraft design parameters and transforms these into a smaller set of synthetic orthogonal parameters ordered by importance. This allows complex relationships to be approximated by only a few parameters. For the matrix-shaped dataset X, there exists a decomposition of the form:

$$X = s \times w \times V^T \quad (2)$$

Where s is an orthogonal input vector, w is a diagonal matrix with the singular values ordered by importance which weights how dominant design variables are. V is an orthogonal matrix that rotates the coordinate system from the original axes into the new axes. The matrix X gets transformed and centred to a base-2 log-scale for manipulation and then converted back to its original scale. An important limitation of this specific analysis is that they cannot handle missing data, and so any element with an incomplete row (at least one cell marked in red in Table 1) must be discarded. Consequently, the sample size is reduced, thus affecting the hypothesis testing and the statistical significance of the results. The following studies have focused on the first two categories due to their higher number of aircraft. Although the certification sought is critical for estimations of design parameters, no further category subdivisions were made in this study due to the mentioned limited sample size. For example, there is a single CS-25 compliant FE aircraft with full rows, which would make an analysis using these subdivisions impossible with the available data.

Lastly, queries to six Large Language Models (LLMs) were performed, namely Wolfram GPT, Meta Llama 3.2, Microsoft Copilot, ChatGPT o1, ChatGPT 4o, and ChatGPT 4o with Canvas. To account for the stochastic variability of the outputs, 28 queries per LLM were performed under four conditions: (i) without providing Table 1 in a single session, (ii) without providing Table 1 with a new fresh session for each run, (iii) providing Table 1 in a single session, and (iv) providing Table 1 with a fresh session for each run. The query performed was always the same: "*Give me the estimation for MTOM (in kg), cruise speed (in knots), Wing loading (in kg/m2), power to weight ratio (in kW/kg) and battery mass fraction for a HYBRID-ELECTRIC 90 PASSENGER AIRCRAFT."* The results totalled 168 answers for each parameter. The cruise speed was omitted from the analysis given its low impact as a design driver.

Results

Fig. 1 shows a correlation matrix where each combination between row and column corresponds to a pair of variables, with the Pearson Correlation Coefficient printed, with the main diagonal (where each variable is compared with itself) showing the corresponding histograms. The cells where the value of the Pearson Coefficient falls below the lower limit to achieve a p-value of 0.025 are shaded in a diagonal pattern, representing correlations whose statistical significance cannot be ascertained through the aforementioned hypothesis test. The limit values are r = 0.514 for a sample of 15 aircraft in the FE case, and a value of r = 0.482 for a sample of 17 aircraft in the HE case. Fig. 2 shows a heatmap of the values of the Pearson Coefficient with the corresponding p-values.

Materials Research Proceedings 69 (2026) 558-563 https://doi.org/10.21741/9781644904251-100

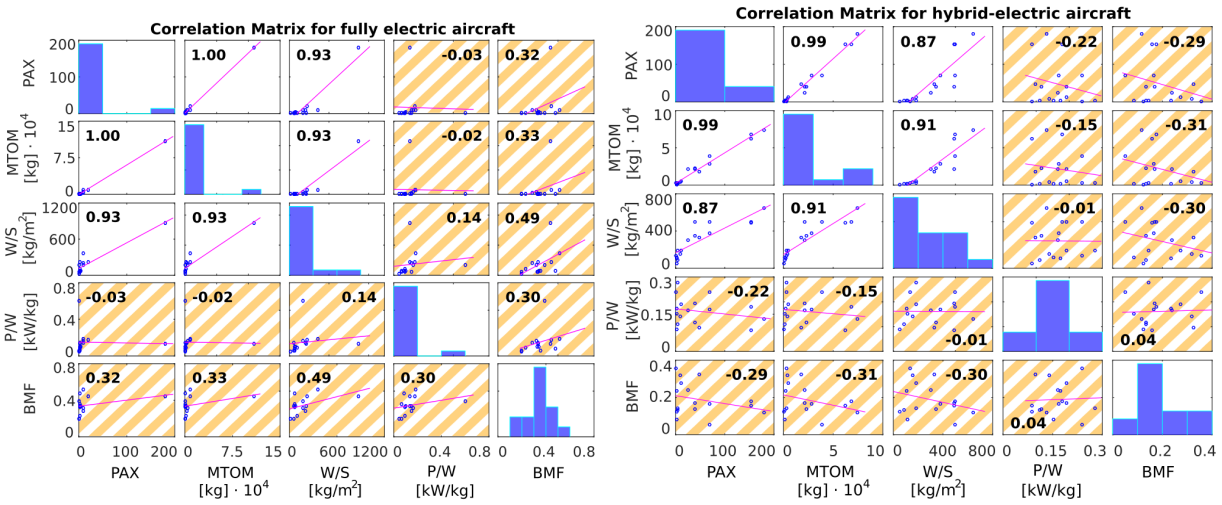


Figure 1: Correlation plots for fully electric aircraft (left) and hybrid-electric aircraft (right). Cells with shaded diagonals are correlations with low statistical significance.

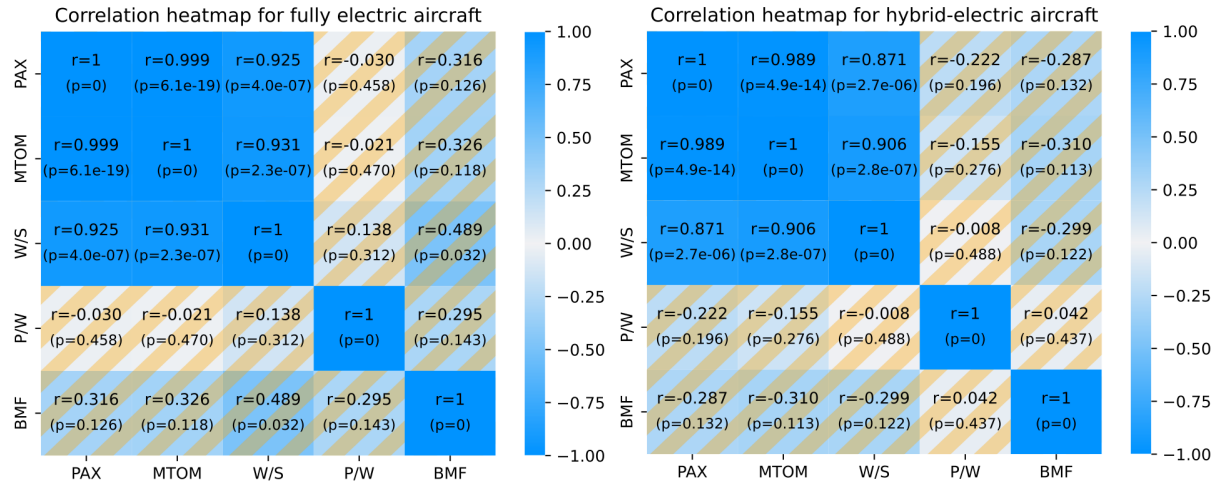


Figure 2: Heatmap of the Pearson Correlation Coefficient for fully electric aircraft (left) and hybrid-electric aircraft (right), with the corresponding p-values shown below in each case.

Regarding the SVD results, the predictions of the design parameters using 90 PAX as the only input are summarized in Table 3 for datasets including only full electric (FE), only hybrid-electric (HE), and both (FE+HE). Regarding the responses from the LLMs, Fig. 4 shows the distribution charts of the query responses for each model grouped by parameter. Wider areas represent higher data density, the central continuous line marks the median, the dashed lines indicate the first and third quartiles, and the dots individual points.

Table 2 SVD results using 90 PAX as input.

Type	MTOM [kg]	W/S [kg/m2]	P/W [kW/kg]	BMF
FE	61 275	820	0.22	0.47
HE	44 289	516	0.17	0.15
FE+HE	45 076	536	0.17	0.17

Materials Research Proceedings 69 (2026) 558-563 https://doi.org/10.21741/9781644904251-100

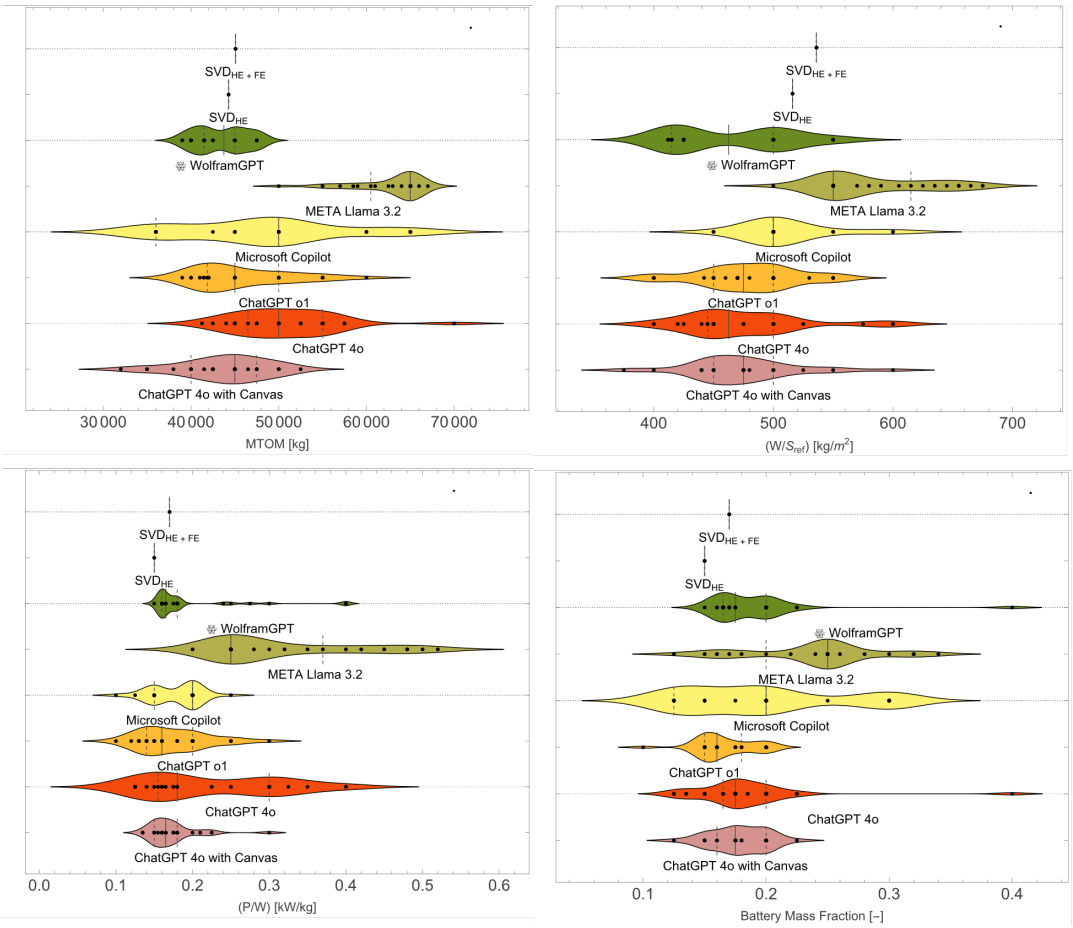


Figure 4: Distribution charts of query responses from LLMs with SVD results for HE.

Discussion

With respect to the results of the correlation analysis, for both samples, very strong correlations can be seen among the number of passengers, MTOM, and W/S, fitting the conventionally-powered trends seen in previous research [3]. It should be noted that a single data point can be seen far from most of the other aircraft in the FE case (see Fig. 1), since this point corresponds to the only large transport category aircraft found within this powerplant type. By analysing the main group of points, the existence of a linear trend has been checked for them, but further study would be worthwhile to examine the influence of the furthest data point on the correlation of the whole group. As for the BMF correlation difference between FE and HE categories, it could be deduced that, when moving to higher passenger numbers, designers of HE aircraft might favour higher fuel mass fractions rather than battery mass to limit the increase in overall mass of the aircraft. However, FE aircraft possess low specific energy and therefore the battery mass increases faster than other mass elements of the aircraft, resulting in a higher BMF. These trends are in line with the current approach of favouring HE over FE aeroplanes for commuter and larger transport categories for the present battery state of the art. Nevertheless, it should be noted that from a statistical standpoint, the correlations of BMF in both cases would not be sufficiently strong to support their statistical significance through the hypothesis test. Larger samples reduce the value of the cut-off Pearson Coefficient following the statistical test commented beforehand, thus an increase in the database in future work, depending on the variation in the results, could serve to substantiate the significance of the correlations from a statistical standpoint.

In the case of the power-to-weight ratio, very weak correlations are observed in almost all cases. This is in part due to the fact of different battery energy densities being assumed by designers,

with values ranging from 250 up to 1500 Wh/kg, which has a direct impact in these powerplant-related variables. This is another reason why range was not included in the analysis, since the same aeroplane with different energy densities assumed would have significantly different ranges and performance. For the SVD analysis, the results from Table 3 agree with the trends from the correlation analysis. The fact that the number of passengers has the highest weight in all cases suggests that estimating other design parameters based solely on the number of passengers is reasonable. For electric aircraft, the large predictions for a 90 PAX design may result from not distinguishing certification categories, as the SVD uses data from all CS-25, CS-23, and LSA compliant aircraft to make the prediction. A larger dataset could enable this differentiation in future work. For HE aircraft, average values from the AI responses are comparable in most cases to the results from the statistical analysis. Considering that in aircraft conceptual design an error of around 10–15% can be accepted [1, 2], usage of AI to complement pre-design studies appears viable. Nonetheless, the spread of the predictions evidences the need to query the LLM multiple times to avoid obtaining an outlier if this method were to be used.

Conclusion

A dataset comprising 52 aircraft concepts was compiled for correlation and Singular Value Decomposition (SVD) analyses, whose results were compared with the responses of six large language models. Insights revealed that there are moderate to strong correlations among various parameters selected for the study. The SVD analysis indicates that the number of passengers was the dominant factor in determining other design parameters. AI predictions showed average values comparable to the results from the statistical analysis, although exhibiting a large scatter. For the aircraft types studied here, the use of the statistical test to check the significance of the Pearson Correlation Coefficient, the SVD analysis to discover underlying trends, and the exploration of LLM queries for parameter estimation constitute novel contributions of this research. The study therefore explores the possibility of using artificial intelligence not as inspiration or as an active decision-maker, but rather as an aid that complements pre-design statistical analysis.

References

[1] Torenbeek, E. (1982). Synthesis of subsonic airplane design. Dordrecht, Springer

[2] Raymer, P. D. (2018). Aircraft design: A conceptual approach (6th ed.). Reston, VA, United States: American Institute of Aeronautics and Astronautics (AIAA).

[3] Marinus, B. G., & Quodbach, L. (2020). Data and design models for civil turbopropeller aircraft. Journal of Aircraft, 57(6). Reston, VA, United States: American Institute of Aeronautics and Astronautics (AIAA). https://doi.org/10.2514/1.C035271

[4] Mitridis, D., Kapsalis, S., Terzis, D., & Panagiotou, P. (2023). An evaluation of fixed-wing unmanned aerial vehicle trends and correlations with respect to NATO classification, region, EIS date and operational specifications. Aerospace, 10(4), 382. Basel, Switzerland: MDPI.

[5] Bajwa, O. I., Baluch, H. A., & Saeed, H. A. (2024). Machine learning approach for predicting key design parameters in UAV conceptual design. Ain Shams Engineering Journal, 15(9), 102932. Amsterdam, Netherlands: Elsevier. https://doi.org/10.1016/j.asej.2024.102932

[6] Mason, R. L., Gunst, R. F., & Hess, J. L. (1989). Statistical design and analysis of experiments. New York, NY, United States: John Wiley & Sons.

[7] Krus, P. (2016). Models based on singular value decomposition for aircraft design. In Proceedings of the Swedish Aerospace Technology Congress, Solna, Stockholm, Sweden.

Materials Research Proceedings 69 (2026) 564-570 https://doi.org/10.21741/9781644904251-101

GPU-Accelerated CABARET Simulations of Distributed Propulsion for UAM

Hussain A. ABID[1,2,a], Igor SOLNTSEV[2], Andrea RAPISARDA[3], Hassan A. ABID[4], Sergey A. KARABASOV[1,2], E. DE PAOLA[5], Luana Georgiana STOICA[5], Giorgia CAPOBIANCHI[5], Alessandro DI MARCO[5], R. CAMUSSI[5]

[1]School of Engineering and Materials Science, Queen Mary University of London, Mile End Road, London, E1 4NS, UK

[2]GPU-prime Ltd, Cambridge, UK

[3]Department of Civil, Environmental and Mechanical Engineering, University of Trento, Via Mesiano, 77, 38123 Trento, IT

[4]Department of Aerospace Engineering, King Fahd University of Petroleum and Minerals (KFUPM), Dhahran, Saudi Arabia

[5]Department of Engineering, Roma Tre University, Via Vito Volterra, 62, Rome, 00146, RM, Italy

[a]h.abid@qmul.ac.uk

Keywords: Distributed Propulsion, Urban Air Mobility, CABARET Method, Large Eddy Simulation, Rotating Meshes, Aeroacoustics, Trailing-Edge Serrations

Abstract. Urban Air Mobility (UAM) vehicles rely on distributed propulsion (DP) to achieve efficiency, control authority, and compact integration with lifting surfaces. The close spacing of multiple rotors, however, intensifies installation effects that elevate tonal and broadband noise. This work presents a high-fidelity Large Eddy Simulation (LES) study using the CABARET method on rotating meshes to quantify aeroacoustic and aerodynamic sensitivities of a three-propeller DP configuration. The campaign varies: (i) central-rotor axial position ($\Delta x = \{-0.2Db, 0, +0.2Db\}$), (ii) inter-rotor phase angle ($0°, 45°, 90°, 135°$), and(iii) blade trailing-edge geometry (baseline vs. sawtooth serrations). Band-limited overall sound pressure level (BL OASPL) is evaluated on a probe plane under the array between the 1st and 6th blade-passing frequencies. Key findings are: (a) serrations consistently reduce area-averaged and maximum BL OASPL by up to 2.4 dB, most notably around 90◦ phase; (b) moving the central rotor closer to the wing increases thrust coefficient by ≈ 7.8%, indicating a beneficial rotor–wing interaction akin to ground effect; (c) the aerodynamic penalty of serrations is modest and attributable to effective area loss near the tip. Flow visualizations show serrations disrupt spanwise coherence and trailing-edge vortex organization, explaining the observed acoustic benefits. The results highlight the importance of joint optimization of geometry and phasing to deliver quieter, efficient DP systems for UAM.

1. Introduction

UAM concepts increasingly adopt DP to distribute thrust and to leverage propeller–wing interaction for lift augmentation and control [1, 2, 3, 4]. Compact layouts, however, amplify noise through periodic wake–airframe interactions (tonal peaks at blade-passing harmonics) and broadband mechanisms associated with boundary-layer and wake turbulence [5, 6, 7, 8]. Prior work shows strong sensitivity of noise directivity and level to rotor placement and phasing relative to wings [9, 10, 11]. Passive serrated trailing edges, inspired by owl feathers, can reduce scattering efficiency and spanwise coherence [12, 13, 14, 15, 16, 17, 18]. Here we assess, within one

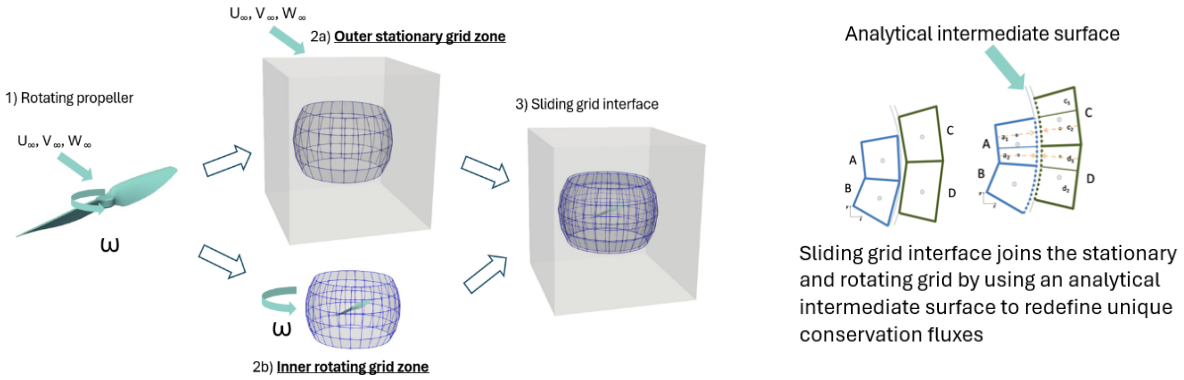
Content from this work may be used under the terms of the Creative Commons Attribution 3.0 license. Any further distribution of this work must maintain attribution to the author(s) and the title of the work, journal citation and DOI. Published under license by Materials Research Forum LLC.

Materials Research Proceedings 69 (2026) 564-570 https://doi.org/10.21741/9781644904251-101

consistent LES framework, how axial position, phase, and serrations jointly govern the aeroacoustic signature of a representative three-rotor DP system based on TU Delft experiments [19].

2. Numerical Methodology

We employ a GPU-accelerated CABARET LES on rotating meshes [19, 20, 21, 22, 23]. Sliding interfaces conserve fluxes via a super-mesh projection and compact sub-cell reconstructions, preserving the dispersion and dissipation properties of the base scheme while avoiding re-meshing.



(a) Rotating and stationary zones with sliding interface. (b) *Analytical interface for conservative fluxing.*

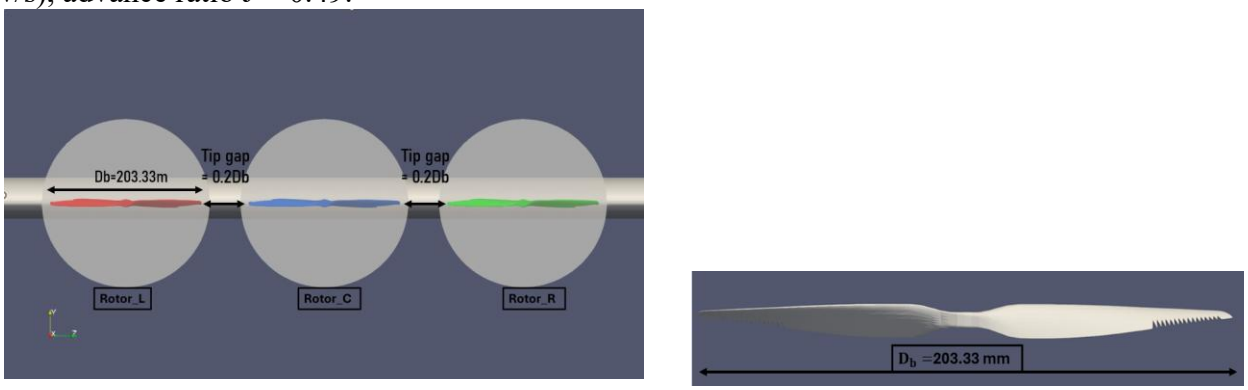
Figure 1: CABARET LES rotating-mesh formulation.

2.1 LES CABARET Solver

An improved-dispersion variant and asynchronous time-stepping enhance accuracy and efficiency. Wall modelling adopts Reichardt's law; the solver is MPI parallel and GPU-resident to minimize turnaround time. Prior validations include a single propeller in boundary-layer ingestion configurations [24].

2.2 Test Cases and Parametric Study

Three identical two-bladed Mejzlik propellers of diameter $D_b = 203.33\,mm$ are aligned span-wise and located 220 mm upstream of a wing leading edge; the central rotor (Rotor$_C$) translates axially by $\pm 0.2D_b$, while lateral rotors remain fixed. The phase of Rotor$_C$ relative to the others is set to 0◦, 45◦, 90◦, 135◦. Serrations (sawtooth, 16 wedges from r = 63.5–88.5 mm, depth 2.32 mm, spacing ≈ 1.55 mm) follow guidelines in [14]. Operating point: U∞ = 30 m/s, n = 5730 RPM (95.5 rev/s), advance ratio J = 0.49.



(a) Three-rotor configuration upstream of the wing. *(b) Serrated trailing-edge geometry.*

Figure 2: Configuration and serration concept used in the study.

Materials Research Proceedings 69 (2026) 564-570 https://doi.org/10.21741/9781644904251-101

2.3 Numerical grid
ANSYS ICEM generates hexahedral meshes with rotating zones around each rotor and a stationary outer domain. The domain extends $5D_b$ upstream and $10D_b$ downstream of the wing. Grids contain ~ 5.1M cells (serrated) and ~ 4.9M (baseline), refined near blades, wakes, and the wing.

2.4 Noise footprint of the DEP system
Pressure probes populate a plane at z = $-1D_b$ beneath the array to evaluate BL OASPL between the 1st and 6th BPFs. We report (i) area-averaged BL OASPL and (ii) maximum BL OASPL across all probes.

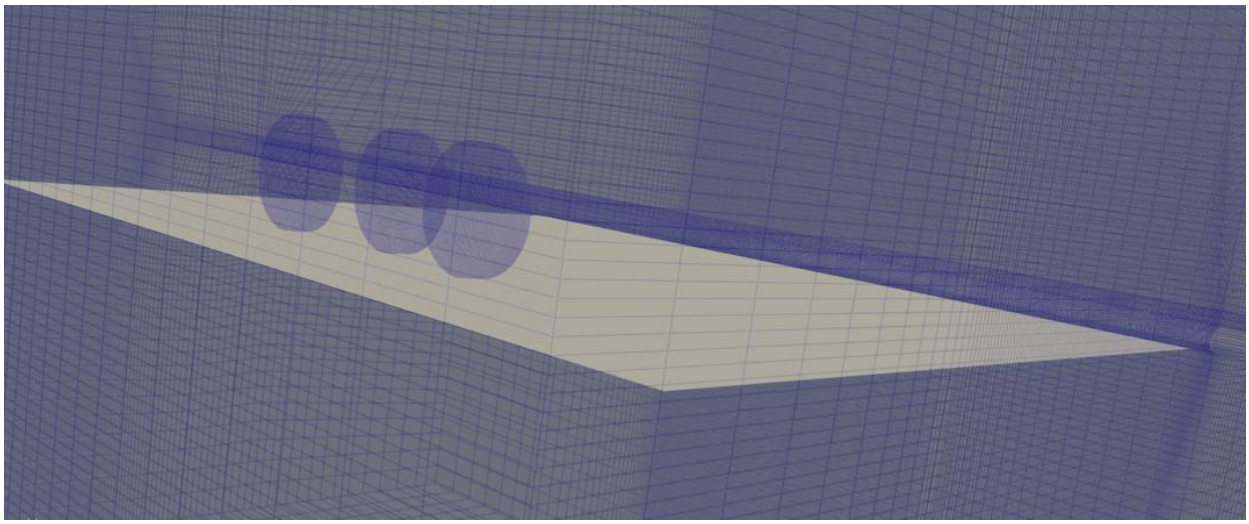


Figure 3: Probe plane used for BL OASPL evaluation beneath the rotors.

3. Results and Discussion

3.1 Aerodynamic Results
Rotor performance is characterized by thrust and torque coefficients:

$$C_T = \frac{T}{\rho n^2 D^4}, \qquad C_Q = \frac{T}{\rho n^2 D^5} \tag{1}$$

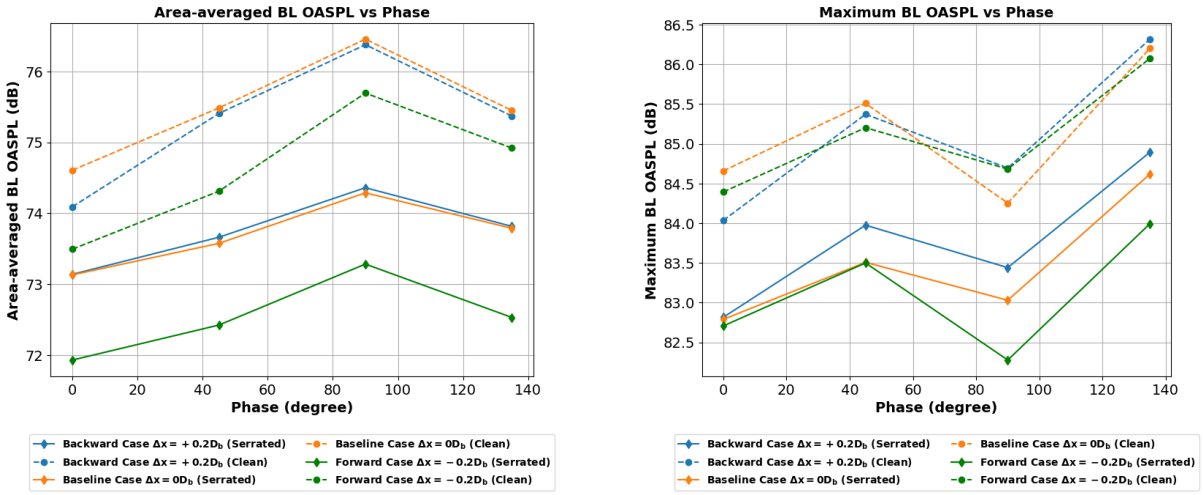
At fixed RPM and J, axial translation of Rotor$_C$ modulates rotor–wing interaction. Bringing Rotor$_C$ closer to the wing increases C_T by ≈ 7.8% relative to the baseline, consistent with an effective ground-effect mechanism that boosts induced velocities and pressure recovery below the disk. Phase primarily affects unsteady interference rather than mean thrust; thus, C_T is comparatively insensitive to phase. Serrations slightly reduce C_T (and C_Q) due to effective area loss near the tip, matching the expected aerodynamic trade-off.

3.2 Flow Field
Baseline blades shed coherent trailing-edge and tip structures whose interaction with the wing drives unsteady loading. Serrations fragment large coherent vortices into weaker, shorter-coherence structures, reducing spanwise correlation of surface pressure fluctuations. The resulting wake has diminished organized content at BPF harmonics, a precondition for lower tonal and mid-to-high-frequency broadband emissions.

3.3 Acoustic Pressure Fluctuations
Figure 4 summarizes BL OASPL trends versus phase for axial positions. Serrations reduce both area-averaged and maximum BL OASPL across all cases, with the largest benefit near 90°. Forward axial offset ($\Delta x = -0.2D_b$) generally yields the lowest BL OASPL; the backward case shows smaller gains, indicating geometry-dependent engagement of the serration mechanism with

Materials Research Proceedings 69 (2026) 564-570 https://doi.org/10.21741/9781644904251-101

installation effects. The peak reduction of ≈ 2.4 dB aligns with small-scale experimental ranges in the literature for sawtooth treatments [25, 26, 27] and with analytical predictions of coherence suppression [28, 29, 30, 31].



(a) Area-averaged BL OASPL vs. phase. *(b) Maximum BL OASPL vs. phase.*

Figure 4: Noise metrics for baseline and serrated blades across axial positions.

4. Conclusion

A GPU-accelerated CABARET LES framework was applied to a three-rotor DP system typical of UAM installations. We varied axial position, inter-rotor phase, and trailing-edge geometry to isolate drivers of aeroacoustic performance. Serrated trailing edges achieved up to 2.4 dB reductions in both maximum and area-averaged BL OASPL, with strongest gains near 90◦ phase. Moving the central rotor closer to the wing increased C_T by ≈ 7.8%, evidencing beneficial rotor–wing coupling; serrations incurred a modest aerodynamic penalty.

Flow analyses support a mechanism of reduced spanwise coherence and disrupted vortex organization. The combined results indicate that optimizing rotor placement, phasing, and serration geometry is essential to simultaneously mitigate noise and retain efficiency in DP architectures. Future work will extend to alternative serration metrics, flap-equipped wings, and advance-ratio sweeps to map robustness across flight phases.

5. Additional work to be reported on full paper

Noise directivity results of the above considered three propeller-wing configurations will be compared with the available experimental results of the 3D wing-flap and three electric motor-driven propellers in a similar ‘puller’ propeller setup. The latter setup corresponds to the recent H2020 CS2 European project VENUS, which investigated methodologies and tools to enable a concurrent design approach for both the aerodynamics and aeroacoustics of aircraft focusing on DEP. The details about the work are presented in DePaola et al. [32] The experimental tests comprise both measurements of acoustics and aerodynamics. A particular finding of the VENUS campaign was that the largest effect on DP noise was due to the propeller wake interaction with the deployed wing flap. Therefore, the best noise reduction was found for the propellers positioned closest to the wing.

In comparison with the VENUS configuration, the ENODISE setup does not include a deployed flap, and the best reduction there appears to correspond to the largest distance between the propellers in the forward staggered configuration. Nevertheless, regardless of the specific propeller/wing geometry details it is interesting to compare the acoustic directivity of the overall noise reduction achieved by changing the propeller installation with respect to the wing in the

ENODISE and VENUS DP configurations. This comparison will be performed for similar offset phase angles of the central propeller, with and without applying the noise reduction technique (trailing edge serrations) in case of the ENODISE propellers. Details will be reported in the full paper along with the LES grid sensitivity study.

In addition, aerodynamic performance of different DEP configurations corresponding to the ENODISE setup will be analyzed as well as the far-field noise will be computed based on the Ffwocs Williams-Hawkings's method. This will allow us to assess the trade-off between the aerodynamic and the aeroacoustic performance for the considered ENODISE DEP configuration, like the experimental investigation in the VENUS project.

References

[1] Nicholas K Borer, Michael D Patterson, Jeffrey K Viken, Mark D Moore, Joe Ben Bevirt, Alex M Stoll, and Andrew R Gibson. Design and performance of the NASA sector distributed electric propulsion flight demonstrator. In 16th AIAA aviation technology, integration, and operations conference, page 3920, 2016. https://doi.org/10.2514/6.2016-3920

[2] Jean Hermetz, Michael Ridel, and Carsten Doll. Distributed electric propulsion for small business aircraft a concept-plane for key-technologies investigations. In ICAS 2016, 2016.

[3] Reynard de Vries, Nando van Arnhem, Tomas Sinnige, Roelof Vos, and Leo L. M. Veldhuis. Aerodynamic interaction between propellers of a distributed-propulsion system in forward flight. Aerospace Science and Technology, 118:107009, 2021. https://doi.org/10.1016/j.ast.2021.107009

[4] Michael D Patterson, Joseph M Derlaga, and Nicholas K Borer. High-lift propeller system configuration selection for NASA's sector distributed electric propulsion flight demonstrator. In 16th AIAA aviation technology, integration, and operations conference, page 3922, 2016. https://doi.org/10.2514/6.2016-3922

[5] Hyun D. Kim, Aaron T. Perry, and Phillip J. Ansell. A Review of Distributed Electric Propulsion Concepts for Air Vehicle Technology.

[6] Tian Zhou and Rami Fattah. Tonal noise acoustic interaction characteristics of multi-rotor vehicles. In 23rd AIAA/CEAS Aeroacoustics Conference, page 4054, 2017. https://doi.org/10.2514/6.2017-4054

[7] J. Thauvin, Guillaume Barraud, Marc Budinger, Xavier Roboam, Dimitri Leray, and Bruno Sareni. Hybrid regional aircraft: A comparative review of new potentials enabled by electric power. In 52nd AIAA/SAE/ASEE joint propulsion conference, page 4612, 2016. https://doi.org/10.2514/6.2016-4612

[8] J. E. Barker, A. Zarri, J. Christophe, and C. F. Schram. Numerical investigation of tonal noise emissions from propeller-wing aerodynamic and acoustic interactions. In AIAA Aviation 2023 Forum, 2023. https://doi.org/10.2514/6.2023-4056

[9] Tomas Sinnige, Nando van Arnhem, Tom C. A. Stokkermans, Georg Eitelberg, and Leo L. M. Veldhuis. Wingtip-mounted propellers: Aerodynamic analysis of interaction effects and comparison with conventional layout. Journal of Aircraft, 56(1):295-312, 2019. https://doi.org/10.2514/1.C034978

[10] Andrea Zarri, Athanasios Koutsoukos, and Francesco Avallone. Aerodynamic and acoustic interaction effects of adjacent propellers in forward flight. In 29th AIAA/CEAS Aeroacoustics Conference, page 4489, 2023. https://doi.org/10.2514/6.2023-4489

[11] Z. Yang, M. Meinke, and W. Schroder. Numerical analysis of propeller-airfoil interaction in a distributed propulsion system using a hybrid les and fw-h approach. In AIAA Aviation Forum, page 3211, 2024. https://doi.org/10.2514/6.2024-3211

[12] M. S. Howe. Aerodynamic noise of a serrated trailing edge. Journal of Fluids and Structures, 5(1):33-45, 1991. https://doi.org/10.1016/0889-9746(91)80010-B

[13] M. S. Howe. Noise produced by a sawtooth trailing edge. The Journal of the Acoustical Society of America, 90(1):482-487, 1991. https://doi.org/10.1121/1.401273

[14] M. Gruber. Airfoil noise reduction by edge treatments. PhD thesis, University of Southampton, 2012.

[15] B. Lyu, M. Azarpeyvand, and S. Sinayoko. Prediction of noise from serrated trailing edges. Journal of Fluid Mechanics, 793:556-588, 2016. https://doi.org/10.1017/jfm.2016.132

[16] T. P. Chong and A. Vathylakis. On the aeroacoustic and flow structures developed on a flat plate with a serrated sawtooth trailing edge. Journal of Sound and Vibration, 354:65-90, 2015. https://doi.org/10.1016/j.jsv.2015.05.019

[17] C. Arce-Leo'n, R. Merino-Mart'ınez, D. Ragni, F. Avallone, and M. Snellen. Boundary layer characterization and acoustic measurements of flow-aligned trailing edge serrations. Experiments in Fluids, 57(182), 2016. https://doi.org/10.1007/s00348-016-2272-z

[18] T. P. Chong, P. F. Joseph, and M. Gruber. Airfoil self-noise reduction by non-flat plate type trailing edge serrations. Applied Acoustics, 74(4):607-613, 2013. https://doi.org/10.1016/j.apacoust.2012.11.003

[19] I. Solntsev, A Chintagunta, A Markesteijn, and S Karabasov. Cabaret on rotating meshes. Elsevier Applied Mathematics and Computation, 2023. https://doi.org/10.1016/j.amc.2023.127871

[20] Anton P. Markesteijn and Sergey A. Karabasov. Cabaret solutions on graphics processing units for NASA jets: Grid sensitivity and unsteady inflow condition effect. Comptes Rendos M'ecanique, 346(10):948-963, 2018. Jet noise modelling and control Modelisation et controle du bruit de jet. https://doi.org/10.1016/j.crme.2018.07.004

[21] Vasily A. Semiletov and Sergey A. Karabasov. A volume integral implementation of the Goldstein generalized acoustic analogy for unsteady flow simulations. Journal of Fluid Mechanics, 853:461-487, 2018. https://doi.org/10.1017/jfm.2018.572

[22] Georgy A. Faranosov, Vasily M. Goloviznin, Sergey A. Karabasov, Vasily G. Kondakov, Victor F. Kopiev, and Mihail A. Zaitsev. Cabaret method on unstructured hexahedral grids for jet noise computation. Computers and Fluids, 88:165-179, 2013. https://doi.org/10.1016/j.compfluid.2013.08.011

[23] V.A. Semiletov and S.A. Karabasov. Cabaret scheme for computational aero acoustics: Extension to asynchronous time stepping and 3d flow modelling. International Journal of Aeroacoustics, 13(3-4):321-336, 2014. https://doi.org/10.1260/1475-472X.13.3-4.321

[24] Hussain Ali Abid, Sergey A. Karabasov, Annabel P. Markesteijn, and Igor Solntsev. Numerical investigation of propeller boundary layer ingestion noise using cabaret on rotating meshes. In 30th AIAA/CEAS Aeroacoustics Conference, Rome, Italy, June 2024.

[25] Weicheng Ning, Shaohong Jia, Hongyu Wang, Zhe Chen, and Bing Yang. An experimental study on small UAV propellers with serrated trailing edges. AIAA Journal, 2017. UAV-scale tests showed 0.9-1.6dB noise reduction. https://doi.org/10.2514/6.2017-3813

[26] Weicheng Xue et al. An experimental study of noise reduction in wind turbine airfoils with serrated trailing edges. arXiv preprint arXiv:2307.12188, 2023. Sawtooth serrations reduced noise by 2.7-3.0dB with thrust preservation.

[27] A. Rapisarda, L. Sangiuliano, L. D'Alessandro, and N. M. Pugno, Bio-inspired rotor designs: enhancing thrust, energy efficiency, and noise reduction,' Bioinspiration & Biomimetics, Nov. 28, 2025. https://doi.org/10.1088/1748-3190/adf6f8

[28] B. Lyu, Mahdi Azarpeyvand, and Samuel Sinayoko. Prediction of noise from serrated trailing-edges. Journal of Fluid Mechanics, 793:1-29, 2016. Analytical model predicts noise reduction up to 10dB at 90°. https://doi.org/10.1017/jfm.2016.132

[29] D. J. Moreau and C. J. Doolan. Noise-reduction mechanism of a flat-plate serrated trailing edge. AIAA Journal, 51(10):2513-2524, 2013. https://doi.org/10.2514/1.J052436

[30] Samuel Sinayoko, B. Lyu, and M. Azarpeyvand. Prediction of noise from serrated trailing-edges (AIAA 2015). AIAA/CEAS Aeroacoustics Conference, 2015. Provided advanced analytical model validating serration performance.

[31] F. Avallone, W. C. P. Van der Velden, D. Ragni, and D. Casalino, Noise reduction mechanisms of sawtooth and combed-sawtooth trailing-edge serrations. Journal of Fluid Mechanics, 848:560-591, 2018. Confirmed geometry- and phase-dependent trends. https://doi.org/10.1017/jfm.2018.377

[32] Emanuele De Paola, Andrea Di Marco, Laurentiu G. Stoica, Luca Falcini, and Roberto Camussi. Experimental investigation on a side-by-side twin rotor system in pusher configuration. In INTER-NOISE and NOISE-CON Congress and Conference Proceedings, volume 265, pages 5862-5872, 2023. https://doi.org/10.3397/IN_2022_0870

Propulsion, Energy & Combustion



Materials Research Proceedings 69 (2026) 572-576 https://doi.org/10.21741/9781644904251-102

Experimental Characterization of Ageing Phenomena in Li-Po Battery Packs for Lightweight UAV Applications

Aleksander SUTI[1,a *], Gianpietro DI RITO[1,b] and Aurélien REYSSET[2,c]

[1]Dept. of Civil and Industrial Engineering, University of Pisa, Pisa, Italy

[2]Dept. of Mechanical Engineering, Université de Toulouse, UPS, INSA, ISAE-SUPAERO, MINES-ALBI, CNRS, ICA, Toulouse, France

[a]aleksander.suti@dici.unipi.it, [b]gianpietro.di.rito@unipi.it, [c]a_reysse@insa-toulouse.fr

Keywords: Li-Po Battery Pack, Performance Testing, Ageing, Propulsion, UAV, eVTOL

Abstract. The performance of electric UAVs largely depends on the efficiency of their onboard energy storage systems. In battery-powered propulsion, maximizing battery life and flight time is a key function of the Battery Management System (BMS). This study presents an ageing test campaign to characterize the State of Health (SOH) of a Li-Po battery pack. The tests use a current load profile derived from a flight simulator that models UAV longitudinal dynamics, propulsion, and onboard systems for realistic current demand. When predefined ageing indicators, such as reduced end-of-mission voltage variation, exceed set thresholds, Hybrid Pulse Power Characterization (HPPC) tests are conducted to characterize the battery at different ageing states. The resulting parameters support dynamic battery modelling at various ageing stages.

Introduction

Within the broader goals of global transport decarbonization, the electrification of propulsion systems for airborne vehicles remains a critical challenge, significantly affecting flight performance (e.g., endurance) and reliability. Electrification efforts are primarily focused on Unmanned Aerial Vehicles (UAVs) since they not only serve as effective platforms for prototyping advancements for future manned systems, but have also gained increasing attention due to their wide range of applications [1] and economic advantages [2].

In particular the endurance is predominantly influenced by the onboard energy storage system. Li-Po batteries, lead the market for small UAVs due to their favourable balance of energy density (approximately 100–200 Wh/kg) and power density (around 200–1000 W/kg), which better suits the demands of UAVs applications [3], [4], [5], [6]. Moreover, since battery performance can significantly vary based on their condition and operating environment [5], energy storage module, which is usually composed of multiple batteries connected in series and parallel, is usually equipped with a Battery Management System (BMS) which primary objective is to optimize battery utilization aiming to extend battery cycle life and flight time, while ensuring the safety and reliability of battery operation [7]. In particular, among all the batterie states, the State Of Charge (SOC), the State of Temperature (SOT) and the State of Health play a crucial role in the performance of lithium batteries [8], [9], [10]. Consequently, to ensure operation within a safe and optimal range, the monitoring section of BMSs must be capable of estimating the battery states.

In a previous work [11], the authors developed a State of Charge (SOC) and State of Temperature (SOT) estimator based on model-based observer algorithms. To now enable the development of a State of Health (SOH) estimator, it is necessary to characterize the battery pack under ageing conditions [12], [13]. Therefore, this study focuses on the design and testing of procedure for the ageing characterization of a 6-cell, 22.2 V, 2000 mAh Li-Po battery pack used in a 25 kg dual electric Vertical Take-Off and Landing (eVTOL) UAV.

Content from this work may be used under the terms of the Creative Commons Attribution 3.0 license. Any further distribution of this work must maintain attribution to the author(s) and the title of the work, journal citation and DOI. Published under license by Materials Research Forum LLC.

Materials Research Proceedings 69 (2026) 572-576 https://doi.org/10.21741/9781644904251-102

The manuscript is organized as follows: Section 2 provides a description of the system; information on the experimental test plan and test setup are proposed in section 3. Finally, the result section shows an excerpt of the experimental test and the ageing results.

System description

The reference eVTOL UAV, shown schematically in Figure 1, is a 25 kg hybrid copter-plane designed for VTOL and forward flight. It features two groups of non-tilting rotors: eight motors for vertical take-off, landing, and low-speed control, and two motors for forward flight. The propulsion system includes ten fixed-pitch, two-blade APC 18x5.5MR propellers, each driven by its own ESC. Power is supplied by a Battery Pack System (BPS) consisting of 18 parallel-connected batteries. Additional components include onboard systems and payload (absorbing 250 W), a BMS and a Flight Control Computer.

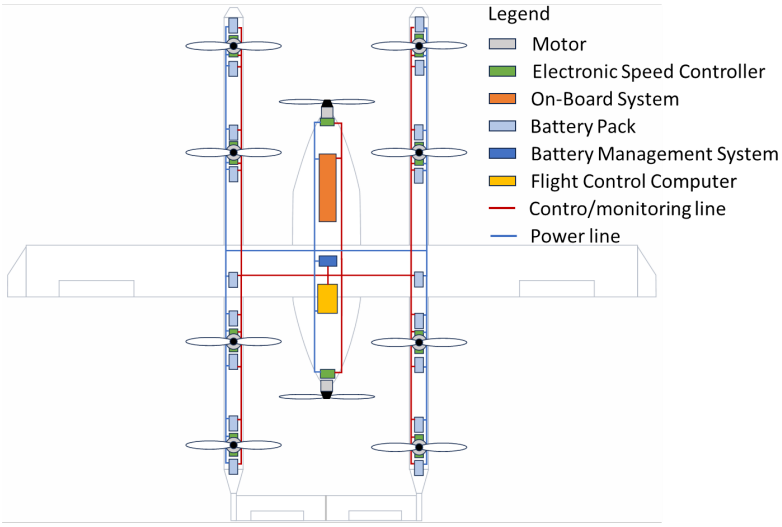


Figure 1. Conceptual schematic of the reference eVTOL UAV (top view).

Test plan and experimental set-up

To create a suitable database for the development of a SOH observer, HPPC tests and flight mission simulations have been combined, by evaluating internal resistance, capacity, and voltage response at various SOCs to identify key battery model parameters [14], [15]. Throughout the tests, the battery operates in a thermal chamber to control the environmental conditions. The ageing is monitored by tracking voltage drops at the end of missions and temperature rises between cycles. When these indicators exceed predefined thresholds, HPPC tests are performed to assess the impact of ageing on capacity and internal resistance, supporting the development of an accurate SOH estimator. The test setup, illustrated in Figure 2, also includes an electronic load simulator (Electronic Power Unit, EA-EL 9000 DT 500W), which applies the current load for the battery and provides voltage and current feedbacks. The data acquisition and the monitoring of the battery is managed by the Electronic Control & Monitoring Unit, featuring an NXP S32K144EVB microcontroller, an MCP4725 DAC for analog signal control, and eight Type-T thermocouples with MAX6675 modules for temperature sensing. Test logic, monitoring algorithms, and protection routines are developed and deployed in the MATLAB/Simulink environment.

Materials Research Proceedings 69 (2026) 572-576 https://doi.org/10.21741/9781644904251-102

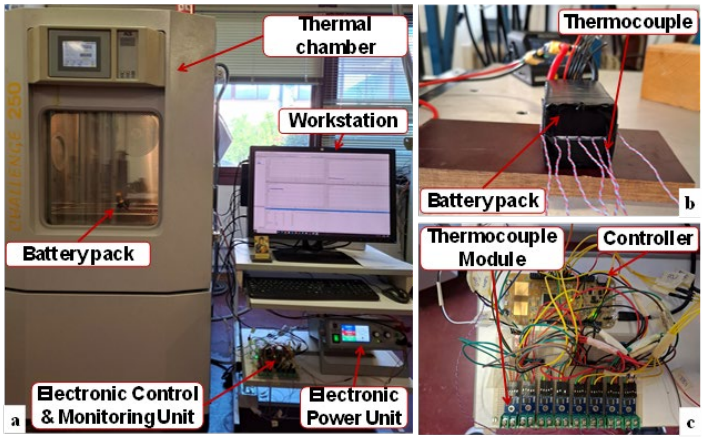


Figure 2. Experimental set-up (a) with focus on battery pack(b) and on Electronic Control & Monitoring Unit (c).

Results

An excerpt of the test campaign outputs is reported in Figure 3 in terms of current, voltage and the battery temperatures along the cells for a flight mission simulation. while reports. From the thermal-related measurements, it appears that the thermal stress experienced by the third cell is higher than the one of the other cells. This condition could lead to accelerated ageing over time and, in the short term, this causes a faster discharge rate due to the reduced internal resistance at higher temperatures. The battery capacity and the internal resistance with the ageing cycles are reported in Figure 4. The internal resistance trend with the temperature confirms literature results [14], [15]. Similarly the total capacity trend with the ageing cycles is coherent with the maximum number of cycles of the reference battery technology.

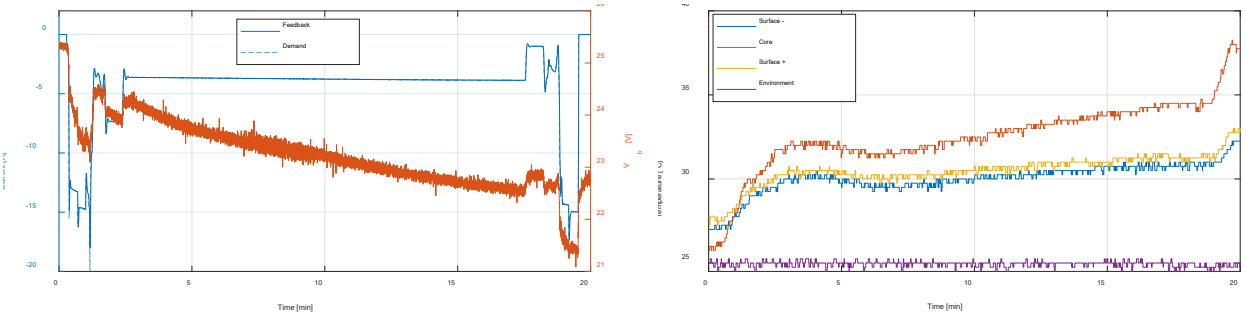


Figure 3. Flight mission time histories: (left) current input and terminal voltage; (right) temperatures.

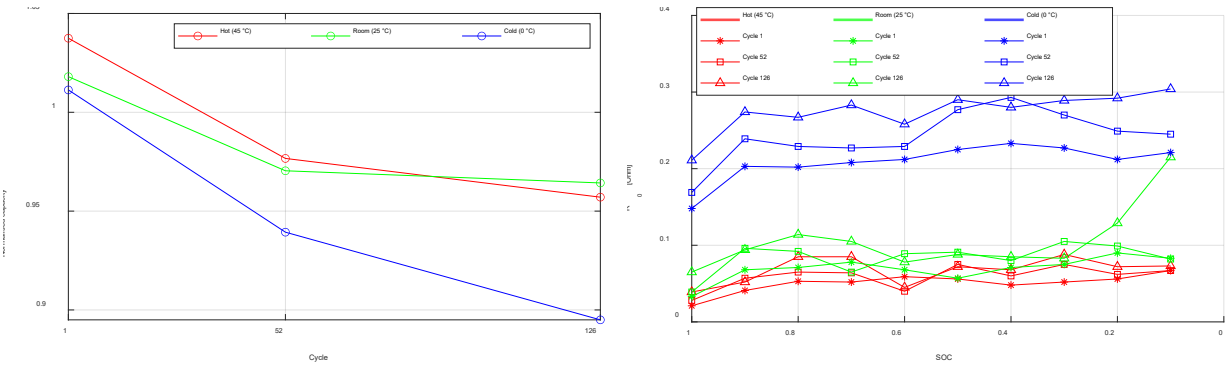


Figure 4. Battery pack parameters with ageing cycles: (left) total capacity, (right) internal resistance.

Summary

An experimental test setup for the performance characterisation of a Li-Po battery pack in terms of temperature and ageing is presented. The battery pack, designed for a 25 kg eVTOL UAV, is subjected to repeated discharge cycles based on the flight mission load profile of the reference UAV. The results show that, after approximately 130 flight missions, the internal resistance increases by about 15 %, particularly at low temperatures. Similarly, under cold conditions, the capacity decreases by roughly 10 %. The identified parameters will be employed in the development of a model-based monitoring system for the online estimation of the battery states.

References

[1] G. Nugroho, Y. D. Hutagaol, and G. Zuliardiansyah, "Aerodynamic Performance Analysis of VTOL Arm Configurations of a VTOL Plane UAV Using a Computational Fluid Dynamics Simulation," *Drones*, vol. 6, no. 12, p. 392, Dec. 2022. https://doi.org/10.3390/drones6120392

[2] R. Dianovský, P. Pecho, M. Bugaj, and J. Jackuliak, "Economic efficiency comparison of unmanned aerial vehicles with conventional and alternative propulsion systems," *Transportation Research Procedia*, vol. 81, pp. 307–317, 2024. https://doi.org/10.1016/j.trpro.2024.11.032.

[3] S. Jiao, G. Zhang, M. Zhou, and G. Li, "A Comprehensive Review of Research Hotspots on Battery Management Systems for UAVs," *IEEE Access*, vol. 11, pp. 84636–84650, 2023. https://doi.org/10.1109/ACCESS.2023.3301989

[4] M. N. Boukoberine, Z. Zhou, and M. Benbouzid, "A critical review on unmanned aerial vehicles power supply and energy management: Solutions, strategies, and prospects," *Appl Energy*, vol. 255, p. 113823, Dec. 2019. https://doi.org/10.1016/j.apenergy.2019.113823.

[5] A. G. Olabi *et al.*, "Battery thermal management systems: Recent progress and challenges," *International Journal of Thermofluids*, vol. 15, p. 100171, Aug. 2022. https://doi.org/10.1016/j.ijft.2022.100171

[6] G. Di Rito, A. Suti, A. Ricci, R. Galatolo, and G. Mattei, "Experimental characterisation of Li-Po battery packs and BLDC machines for hybrid propulsion systems of lightweight UAVs," in *2022 IEEE 9th International Workshop on Metrology for AeroSpace (MetroAeroSpace)*, IEEE, Jun. 2022, pp. 49–53. doi: 10.1109/MetroAeroSpace54187.2022.9856056

[7] S. Jiao, G. Zhang, M. Zhou, and G. Li, "A Comprehensive Review of Research Hotspots on Battery Management Systems for UAVs," *IEEE Access*, vol. 11, pp. 84636–84650, 2023. https://doi.org/10.1109/ACCESS.2023.3301989

[8] Y. W. Son, D. Kang, and J. Kim, "Passive battery thermal management system for an unmanned aerial vehicle using a tetrahedral lattice porous plate," *Appl Therm Eng*, vol. 225, p. 120186, May 2023. https://doi.org/10.1016/j.applthermaleng.2023.120186

[9] Q. L. Yue, C. X. He, M. C. Wu, and T. S. Zhao, "Advances in thermal management systems for next-generation power batteries," *Int J Heat Mass Transf*, vol. 181, p. 121853, Dec. 2021. https://doi.org/10.1016/j.ijheatmasstransfer.2021.121853

[10] F. S. Hwang *et al.*, "Review of battery thermal management systems in electric vehicles," *Renewable and Sustainable Energy Reviews*, vol. 192, p. 114171, Mar. 2024. https://doi.org/10.1016/j.rser.2023.114171

[11] A. Suti, M. Budinger, G. Di Rito, and A. Reysset, "Development and HIL validation of observer-based monitoring algorithms of battery packs for eVTOL UAV applications," *Appl Energy*, vol. 401, p. 126637, Dec. 2025. https://doi.org/10.1016/j.apenergy.2025.126637

[12] D. Chrenko, M. Fernandez Montejano, S. Vaidya, and R. Tabusse, “Aging Study of In-Use Lithium-Ion Battery Packs to Predict End of Life Using Black Box Model,” *Applied Sciences*, vol. 12, no. 13, p. 6557, Jun. 2022. https://doi.org/10.3390/app12136557

[13] S. Barcellona, M. Brenna, F. Foiadelli, M. Longo, and L. Piegari, “Analysis of Ageing Effect on Li-Polymer Batteries,” *The Scientific World Journal*, vol. 2015, no. 1, Jan. 2015. https://doi.org/10.1155/2015/979321

[14] A. Suti, G. Di Rito, and G. Mattei, “Development and Experimental Validation of Novel Thevenin-Based Hysteretic Models for Li-Po Battery Packs Employed in Fixed-Wing UAVs,” *Energies (Basel)*, vol. 15, no. 23, p. 9249, Dec. 2022. https://doi.org/10.3390/en15239249

[15] A. Suti, G. Di Rito, and G. Mattei, “Heuristic Estimation of Temperature-Dependant Model Parameters of Li-Po Batteries for UAV Applications,” in *2023 IEEE 10th International Workshop on Metrology for AeroSpace (MetroAeroSpace)*, IEEE, Jun. 2023, pp. 269–274. https://doi.org/10.1109/MetroAeroSpace57412.2023.10190045

Materials Research Proceedings 69 (2026) 577-582 https://doi.org/10.21741/9781644904251-103

Comprehensive Modelling for Electric Machine Sizing and Performance Estimation in Aerospace Applications Enhancing Static and Dynamic Simulation

Victor J. BAHRS[1,a *], Katharina KOLO[1,b] and Stefanie DE GRAAF[1,c]

[1]German Aerospace Center (DLR), Institute of Electrified Aero Engines, Cottbus, Germany

[a]victor.bahrs@dlr.de, [b]katharina.kolo@dlr.de, [c]stefanie.degraaf@dlr.de

Keywords: Mathematical Model, Steady-State Approximation, Transient Performance Estimation, Clean Aviation, Electric Aircraft

Abstract. In order to evaluate the potential of different electrified aircraft propulsion system topologies, accurate and efficient sizing models as well as performance evaluation techniques are necessary. To accommodate for this, the presented study introduces a comprehensive methodology for electric machine sizing and performance estimation. Therein, static and dynamic modelling approaches are combined to investigate both steady-state operation as well as the transient behaviour. The dynamic model is verified against the already validated static one and both models are used for the simulation of a realistic test case from the literature, showing very good agreement for the steady-state operation phases while highlighting key differences during transient operation. Based on these results, the presented study enables a detailed static and dynamic performance analysis of electric machines while coupling it to the sizing process.

Introduction

To effectively address climate change, the transportation sector must achieve a substantial reduction in greenhouse-gas emissions. In aviation, a considerable portion of these emissions originates from the carbon-based fuels that power today's propulsion systems. One promising pathway to limit this impact is the development of novel propulsion technologies, such as using electrically driven propellers. Particularly for aircraft operating up to the regional market, electrically supported or electric-driven concepts are drawing research attention as they hold the potential to lower the carbon footprint while maintaining operational efficiency and performance [1], [2]. Besides full-electric powertrain concepts which are solely powered by electric energy, hybrid-electric or more-electric propulsion systems arise as intermediate step for electrification – especially for aircraft classes beyond the regional sector [2]. One approach for electrifying conventional aircraft engines was presented by the NASA in their Turbine Electrified Energy Management (TEEM) [3]. In this concept, electric machines are placed on either the low-pressure shaft, the high-pressure shaft or on both shafts to support and optimize the gas turbine operation. The electric machines are meant to draw power from or supply power to the shaft dependent on the flight phase to power secondary aircraft systems and optimize the turbine operation. In addition, the electric machines should also be used for shifting safety margins in critical flight phases, such as the stall margin while rapidly powering the turbine up or down. As this represents a highly transient operation of the electric machines, e.g. increasing its torque supply from 0 to over 250 Nm within seconds [4], the dynamic performance behaviour of the machine needs to be assessed based on its initial design. Therefore, this study introduces a comprehensive methodology which includes both the initial sizing of an electric machine sizing as well as the performance estimation for steady-state and transient operation, which can be applied to such use cases.

Content from this work may be used under the terms of the Creative Commons Attribution 3.0 license. Any further distribution of this work must maintain attribution to the author(s) and the title of the work, journal citation and DOI. Published under license by Materials Research Forum LLC.

Materials Research Proceedings 69 (2026) 577-582 https://doi.org/10.21741/9781644904251-103

Methodology

To facilitate the preliminary sizing of an electric machine, a static model of a permanent magnet synchronous machine (PMSM) is used. The model published by Bahrs *et al.* [5] allows for preliminary machine sizing with a high degree of detail. Therein, the most important parts of the machine are sized individually while taking their interdependencies as well as an initial performance estimation into account. Furthermore, the analytical character of the model allows for computationally inexpensive calculations and is therefore optimal for fast investigations of numerous propulsion system architectures in early design phases. To enhance the coupling of this steady-state model with a transient counterpart, its formulation was updated to represent a non-linear mathematical model. Therein, the objective is defined as

$$min\ F\left(\eta, h_{sl}, N_t, \lambda, \hat{B}_{gap}\right) = \left[\left(\frac{\eta-\tilde{\eta}\left(\eta,N_t,\lambda,\hat{B}_{gap}\right)}{\tilde{\eta}\left(\eta,N_t,\lambda,\hat{B}_{gap}\right)}\right)^2 + \left(\frac{h_{sl}-\widetilde{h_{sl}}\left(\eta,h_{sl},N_t,\lambda,\hat{B}_{gap}\right)}{\widetilde{h_{sl}}\left(\eta,h_{sl},N_t,\lambda,\hat{B}_{gap}\right)}\right)^2 + \left(\frac{N_t-\widetilde{N_t}\left(\eta,N_t,\lambda,\hat{B}_{gap}\right)}{\widetilde{N_t}\left(\eta,N_t,\lambda,\hat{B}_{gap}\right)}\right)^2 + \left(\frac{\hat{B}_{gap}-\widetilde{\hat{B}_{gap}}(h_{sl})}{\widetilde{\hat{B}_{gap}}(h_{sl})}\right)^2\right] \quad . \tag{1}$$

which represents the iterative character of the sizing detailed in [5]. Initial values for the efficiency η, the sleeve thickness h_{sl}, the number of stator turns N_t, the relative length λ and the peak air gap flux density $\hat{B}_{gap}$ must be set to initiate the sizing, but they are refined based on the results of the sizing process. Therefore, the main goal of the objective function is to find a valid design of an electric machine given a set of boundary conditions and requirements. Using $\eta, h_{sl}, N_t, \lambda$ and $\hat{B}_{gap}$ as model variables, the constraints from Eq. (2) - (5) and the sizing equations from Bahrs *et al.* [5], a valid preliminary design is achieved by solving the objective function in Eq. (1)

$$\text{s.t.} \quad \tilde{\eta}\left(\eta, N_t, \lambda, \hat{B}_{gap}\right) = \frac{P_{\text{mech}}}{P_{\text{mech}} + P_{\text{loss}}\left(\eta, N_t, \lambda, \hat{B}_{gap}\right)} \tag{2}$$

$$\widetilde{h_{sl}}\left(\eta, h_{sl}, N_t, \lambda, \hat{B}_{gap}\right) = -\frac{m_{\text{mag}}\left(\eta, h_{sl}, N_t, \lambda, \hat{B}_{gap}\right) r_{sl}\left(\eta, N_t, \lambda, \hat{B}_{gap}\right) \omega^2}{\pi\, l_{\text{rot}} \left(\rho_{sl}\, r_{sl}^2\left(\eta, N_t, \lambda, \hat{B}_{gap}\right) \omega^2 - \frac{\sigma_{y,sl}}{K_{sl}}\right)} \tag{3}$$

$$\widetilde{N_t}\left(\eta, N_t, \lambda, \hat{B}_{gap}\right) = \frac{S_{ph,Co}\left(\eta, N_t, \lambda, \hat{B}_{gap}\right)}{S_w\left(\eta, N_t, \lambda, \hat{B}_{gap}\right)} \tag{4}$$

$$\widetilde{\hat{B}_{gap}}(h_{sl}) = \frac{B_r}{1 + \frac{h_{\text{gap}}(h_{sl})}{h_{\text{mag}}}} \quad . \tag{5}$$

As detailed in [5], m_{mag} represents the combined mass of the magnets, r_{sl} the inner radius of the sleeve, ω the angular speed of the machine and l_{rot} the length of the rotor. The density, yield stress and safety factor of the sleeve are denoted by $\rho_{sl}, \sigma_{y,sl}$ and K_{sl} respectively. Furthermore, $S_{ph,Co}$ and S_w are the usable cross section area in the slots of one phase and area of one wire, respectively, while B_r represents the remanent magnet flux density, h_{gap} the air gap thickness and h_{mag} the thickness of the magnets.

Besides the sizing, the analytical model can be used for steady-state performance estimation of the machine for different operating points as well. Therefore, Eq. (2) contains the static efficiency relations that are relevant for the performance analysis. In addition to the geometric dependencies, the efficiency also depends on the current i and the angular rotational speed ω [5]. Consequently,

the efficiency expression in Eq. (2) can be rewritten for static models with arbitrary but fixed geometric parameters $\eta, N_t, \lambda, \hat{B}_{gap}$ and a given mechanical power $P_{\text{mech}}(\omega)$ as

$$\eta(i,\omega) = \frac{P_{\text{mech}}(\omega)}{P_{\text{mech}}(\omega) + P_{\text{loss}}(i,\omega)} \quad , \tag{6}$$

where $P_{\text{mech}}(\omega) = M_L \cdot \omega$ with the load torque M_L.

The power losses $P_{\text{loss}}(i,\omega)$ are in particular composed of current dependent copper losses $P_j(i)$, speed dependent mechanical losses $P_{\rho w}(\omega)$ and iron losses P_{vu} which are constant with respect to both i and ω. Following Bahrs *et al.* [5], these contributions can be expressed as

$$P_{\text{loss}}(i,\omega) = P_j(i) + P_{vu} + P_{\rho w}(\omega)\,, \quad \text{with} \tag{7}$$

$$P_j(i) = R_S\, i^{\top} i \quad \text{and} \tag{8}$$

$$P_{\rho w}(\omega) = \frac{\pi}{32}\, k_{\text{rou}}\, C_{M1}(\omega)\, \rho_{\text{air}}\, \omega^3\, d_{\text{rot}}^4\, l_{\text{rot}} + \frac{1}{64}\, C_{M2}(\omega)\, \rho_{\text{air}}\, \omega^3 \left(d_{\text{rot}}^5 - d_{\text{sha}}^5\right) \,. \tag{9}$$

In addition to this static model, a dynamic model is created to analyse the transient efficiency and operation of the machine as a function of time t using machine parameters obtained by the initial sizing. Therefore, the time-dependent form of the efficiency relation in Eq. (6) is examined. The temporal influence is mainly determined by the variables current $i(t)$, angular speed $\omega(t)$ and rotor angle $\theta(t)$, which arise as solution of the differential equation system of the PMSM. In the present study, the electric frequency is assumed to be constant, wherefore the iron losses P_{vu} are treated as constant values as well. For models that also allow variations in the excitation frequency, extensions of the iron-loss model and of the stator-resistance term R_S must be taken into account. By employing the three-phase back electro-magnetic force (EMF) voltages $e(t)$ equations as

$$e(t) = -\psi_f\, N_{pp}\, \omega(t) \begin{pmatrix} \sin\left(N_{pp}\, \theta(t)\right) \\ \sin\left(N_{pp}\, \theta(t)\right) - \frac{2}{3}\pi \\ \sin\left(N_{pp}\, \theta(t)\right) - \frac{4}{3}\pi \end{pmatrix} \tag{10}$$

a dynamic expression for the mechanical power in terms of the flux-linkage constant ψ_f and the number of pole pairs N_{pp} is obtained:

$$P_{\text{mech}}\big(i(t), \omega(t), \theta(t)\big) = e^{\top}(t)\, i(t) \quad . \tag{11}$$

The dynamic efficiency equation for given initial values $[i_0, \omega_0, \theta_0]$ can be written as

$$\eta\big(i(t), \omega(t), \theta(t)\big) = \frac{P_{\text{mech}}\big(i(t), \omega(t), \theta(t)\big)}{P_{\text{mech}}\big(i(t), \omega(t), \theta(t)\big) + P_{\text{loss}}\big(i(t), \omega(t)\big)} \quad , \quad \text{with} \tag{12}$$

$$\frac{di(t)}{dt} = \frac{1}{L_S}\big(v(t) - R_S\, i(t) - e(t)\big) \quad , \tag{13}$$

$$\frac{d\omega(t)}{dt} = \frac{1}{J}\left(\frac{e^{\top}(t)\, i(t)}{\omega(t)} - M_L(t)\right) \quad , \tag{14}$$

$$\frac{d\theta(t)}{dt} = \omega(t) \quad . \tag{15}$$

Materials Research Proceedings 69 (2026) 577-582 https://doi.org/10.21741/9781644904251-103

whereby $i(t), v(t), e(t) \in \mathbb{R}^3$ and $\omega(t), \theta(t), M_L(t) \in \mathbb{R}\ \forall t \in \mathbb{R}$. The set of equations (13) - (15) constitutes a phase-resolved dynamic model of the PMSM [7], [8].

A fundamental distinction of the dynamic model to its static counterpart is that the mechanical power of the machine is no longer prescribed as the desired input, but rather arises as the solution of the governing differential equation (cf. Eq. (11)). In addition, the differential equation model must be augmented with a speed- and current-control law, which is realised by basic proportional-integral (PI) controllers in the present study.

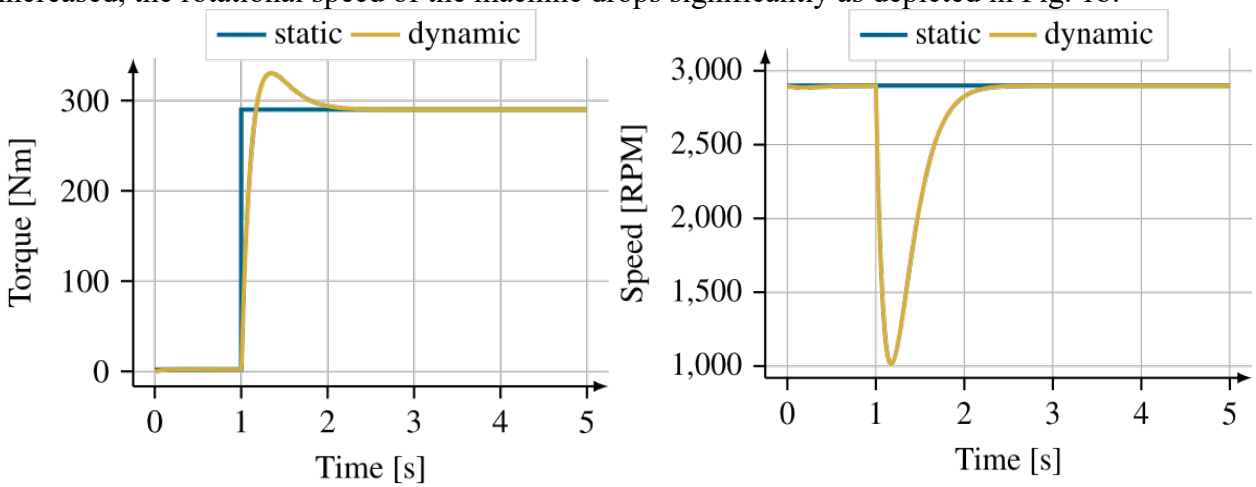
Results

To validate the dynamic model against the static one, different operating points as parts of a realistic load profile for an aviation application are simulated. To enable the analysis of the dynamic behaviour a discrete step increase of the load torque M_L is considered as test case. Based on the take-off phase from the mission profile compiled in [6], a torque increase from 2 to 290 Nm at 2900 RPM is simulated. Followed by the machine sizing for the given set of torque and speed requirement, both models are applied to calculate the efficiency of the machine throughout the simulation. Therein, the machine parameters listed in Table 1 are used to characterise the dynamic model, whereas R_S and J are directly calculated based on the sized machine while L_S and ψ_f are selected as academic values appropriate for the machine size and operation.

Table 1: Machine parameters used for dynamic model

Parameter	Symbol	Value	Unit
Phase resistance	R_S	0.03539	Ω
Phase inductance	L_S	0.001	H
Flux-linkage	ψ_f	0.4	Wb
Rotor inertia	J	0.094	kg m^2

Fig. 1 shows the resulting torque and speed profile of the selected test case for both static and dynamic model. While the step in the mechanical torque at $t = 1$ s is directly transferred into the static model, a clear difference to the dynamic behaviour can be seen. As the mechanical torque is increased, the rotational speed of the machine drops significantly as depicted in Fig. 1b.



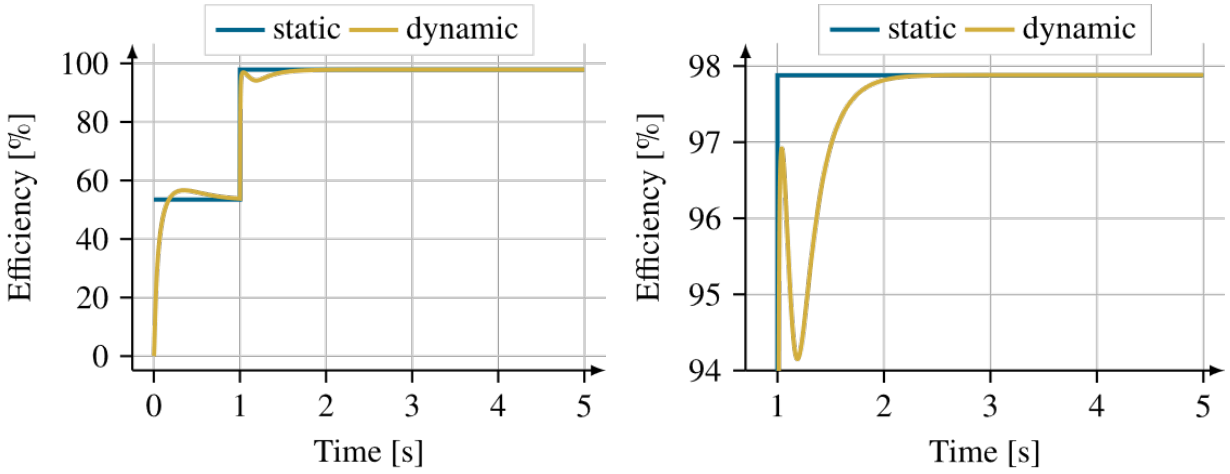
(a) Electromagnetic torque profile (b) Rotational speed profile

Fig. 1: Comparison of results for torque (a) and speed (b) for static and dynamic machine model

Materials Research Proceedings 69 (2026) 577-582 https://doi.org/10.21741/9781644904251-103

Using the PI controllers within the dynamic model, both speed and torque are effectively regulated to achieve their respective target values by increasing the phase currents in the machine. Accordingly, the results of both the electromagnetic torque and the rotational speed match between both models after approximately 2.5 s.

A similar behaviour can be observed for the efficiency calculated with both models, as depicted in Fig. 2.



(a) Complete efficiency profile (b) Efficiency after torque step

Fig. 2: Comparison of efficiency results for static and dynamic machine model

The divergence between the calculated efficiency of both models has to be examined in two different areas, namely before and after the torque step increase at $t = 1$ s (cf. Fig. 2a). Up until the torque increase the initial start of the electric machine is visible in the efficiency of the dynamic model. While the initial speed is set to the target speed of 2900 RPM, the torque and, subsequently, the power start at zero. During the first second of the simulation the initial torque of 2 Nm has to be build up which leads to the deviations in the calculated efficiency. As the machine reaches its steady-state operation shortly before the torque increase, the efficiencies predicted by the two models are matching at $t = 1$ s.

As shown in detail in Fig. 2b, the performance estimation of both models deviate again following the torque increase at $t = 1$ s. Referring to Fig. 1, the speed and torque of the machine must be controlled in the dynamic model to reach the desired targets. Accordingly, the transient power and performance of the machine differ from the nominal steady-state operation, resulting in a reduced efficiency in the transient phase. Initially, the mechanical power P_{mech} is increasing faster than the power losses P_{loss}, which results in a temporary efficiency peak directly after $t = 1$ s before the efficiency drops intermittently. After the local minimum has been reached around $t = 1.2$ s, the dynamic efficiency starts to increase again. Eventually, the predictions of the efficiency start to converge after $t = 2$ s and match for the remainder of the simulation beyond $t = 2.5$ s.

Summary and Outlook

This paper presents an integrated methodology for sizing electric machines and predicting their performance. By coupling the dynamic model with the previously developed static model, it captures both steady-state and transient behavior. Using a benchmark case from the literature, the models are cross-validated against each other showing excellent agreement in steady-state operation and clearly revealing differences during transients as expected. Future studies will improve the interdependence between dynamic model and the preliminary design of the machine.

Namely, important machine parameters such as the phase inductance L_S and flux-linkage constant ψ_f can be linked to the sizing, while the rotor inertia J should also factor in the inertia moment of all connected parts – for instance, the propeller. Furthermore, additional use cases such as the TEEM concept [4] or the over-torque behaviour of a machine will be analysed.

References

[1] Schäfer, A., et al. Technological, economic and environmental prospects of all-electric aircraft. Nature Energy. 4, 160-166 (2019) https://doi.org/10.1038/s41560-018-0294-x

[2] Sahoo, S., Zhao, X., & Kyprianidis, K. A Review of Concepts, Benefits, and Challenges for Future Electrical Propulsion-Based Aircraft. Aerospace, 7(4), 44. (2020) https://doi.org/10.3390/aerospace7040044

[3] Culley, D. E., Kratz, J. L. & Thomas, G. L. Turbine electrified energy management (TEEM) for enabling more efficient engine designs. AIAA 2018-4798. (2018) https://doi.org/10.2514/6.2018-4798

[4] Kratz, J. L., Culley, D. E., & Thomas, G. L. Evaluation of electrical system requirements for implementing turbine electrified energy management. AIAA/IEEE Electric Aircraft Technologies Symposium (2019) https://doi.org/10.2514/6.2019-4502

[5] Bahrs, V., Staggat, M. & Enghardt, L. Analytical model for electric machine sizing in electrified aviation. Deutsche Gesellschaft für Luft- und Raumfahrt-Lilienthal-Oberth e.V., (2022)

[6] Bahrs, V. J., Broumand, M., Kolo, K., Arenas, O. & de Graaf, S. Assessment of General Aviation Electrified Aircraft Powertrain Based on Simulation and Experiment, IEEE/AIAA Transportation Electrification Conference and Electric Aircraft Technologies Symposium (2025) https://doi.org/10.1109/ITEC63604.2025.11098111

[7] Kleimaier, A. Modellierung der PMSM im uvw-System, Deutsche Nationalbibliothek (2021)

[8] Pillay, P., Krishnan, R. Modeling of permanent magnet motor drives. IEEE Transactions on industrial electronics, (1988) https://doi.org/10.1117/12.942973

Materials Research Proceedings 69 (2026) 583-588 https://doi.org/10.21741/9781644904251-104

Modelling the Transient Behavior of Heat Exchangers in Aircraft Engine Preliminary Design

Aytunc YILDIRIM[1,a *], Marc SCHMELCHER[1,b] and Alexander GÖRTZ[1,c]

[1]DLR - German Aerospace Center, Institute of Propulsion Technology, Cologne, Germany

[a]aytunc.yildirim@dlr.de, [b]marc.schmelcher@dlr.de, [c]alexander.goertz@dlr.de

Keywords: Aero Engines, Heat Exchangers, Transient Modelling, Hydrogen Conditioning, Response Time, Wall Thermal Inertia, Residence Time

Abstract. Compact heat exchangers must be integrated into advanced aero-engine concepts; therefore, thorough analysis is needed in the preliminary phase. This work advances an early aero-engine heat-exchanger design tool by extending methods beyond stationary analyses to fully transient operation. Flight conditions change within seconds during maneuvers, so pressures, temperatures, and mass flows on both sides of a heat exchanger vary simultaneously. Steady analyses cannot capture response times, while many transient models treat only single-inlet disturbances or simple layouts. High-fidelity simulations are also too slow for broad design sweeps of the preliminary phase. The proposed tool retains the three-dimensional, cell-based framework and solves an unsteady wall energy balance with finite differences to represent thermal inertia. Between cells, fluid enthalpy information is propagated using the concept of residence time, allowing for arbitrary, coupled inlet ramps. Validation against a Modelica benchmark model shows close agreement for fluid temperatures. Runtime remains in minutes on modest hardware, enabling rapid exploration of the parameter space. A multipass counter-crossflow hydrogen conditioner is further evaluated for a Go-Around maneuver, revealing a lag between boundary changes and temperature propagation, as well as a nonlinear dependence of transient duration on ramp time.

Introduction

Implementing concepts like hydrogen combustion and hybrid-electric requires novel aeroengine architectures and advanced heat exchangers. At DLR's Institute of Propulsion Technology, the PreHEAT tool is being developed for preliminary heat-exchanger design [1]. It employs a cell-based framework that enables rapid parameter changes and, by assembling simple flow cells, analysis of complex geometries. Prior to this work, capabilities were limited to steady-state P-NTU calculations at the cell level. While the industry typically optimizes for steady operation, unsteady behavior can be critical, necessitating estimates of how boundary condition changes affect performance and how much time remains to avert system-level impacts. In 1992, Spiga et al. analyzed the step response in a crossflow heat exchanger, considering the finite heat capacity of the wall [2]. In 2003, Yin et al. presented an analytical solution for a heat exchanger scenario where one fluid maintains a constant temperature, while the other fluid experiences temperature changes along the heat exchanger [3]. In 2021, Yang et al. introduced a transient analytical model for heat exchangers with counterflow geometries, using Laplace transformations to determine the temperature response for each fluid and wall [4]. When examining the analytical models presented in the literature, it is observed that most analytical works have focused on simple flow configurations. These works with simple geometries could be used as the building blocks in the PreHEAT code's cell-level hierarchy. However, in many cases of transient behavior analysis of aircraft heat exchangers, there are simultaneous and combined boundary condition changes on both fluid side inlets. These combined shifts are expected to occur during the transition between different flight phases. Hence, it is not feasible to implement each analytical solution found in the literature as a separate switch case in the cell-level hierarchy. Instead, the developed methodology

Content from this work may be used under the terms of the Creative Commons Attribution 3.0 license. Any further distribution of this work must maintain attribution to the author(s) and the title of the work, journal citation and DOI. Published under license by Materials Research Forum LLC.

Materials Research Proceedings 69 (2026) 583-588 https://doi.org/10.21741/9781644904251-104

takes into account the wall thermal inertia at the cell level, with an energy balance along the wall. Additionally, the thermal disturbance introduced at the boundaries is then propagated according to the fluid's residence time and the simulation time steps. Due to the preliminary design focus, the PreHEAT code has been reutilized and expanded to integrate these physical principles effectively while prioritizing simulation speed.

Methodology

As a starting point, the steady-state PreHEAT solver was looped over varying inlet conditions to compare its behavior with the desired dynamic response. It was observed that boundary changes propagated instantaneously through the exchanger, indicating the need for a mechanism that de-celerates information propagation. It was also observed that wall thermal inertia was neglected in the P-NTU calculations, necessitating an unsteady wall energy balance to capture the physical lag. These two aspects could be addressed within two hierarchical levels of the code structure, namely the heat-exchanger and cell levels. The cell-level hierarchy calculates the heat transfer in simple geometries using the P-NTU method for each cell. The second level of the hierarchy is at the heat-exchanger level, considering the configuration of each cell in a flow geometry [1]. PreHEAT produces a result data object, which contains both the geometry and simulation results. In the transient modeling, each result data object represents a single time step of the dynamic simulation. The result data list enables transient boundary conditions to be defined at each time step, ensuring the delayed propagation of inlet changes through the heat exchanger. It is also essential for obtaining fluid state information from previous time steps at both hierarchy levels.

Heat Exchanger Level Hierarchy. In a discretised geometry, each cell has two residence times, one for each side, defined as the average time a fluid particle spends. Inlet disturbances should influence downstream cells only after a time proportional to their residence times. The methodology considers changes in inlet mass flow rate, temperature, and pressure. Two modeling assumptions are introduced. First, mass-flow-rate change affects all cells immediately along the flow direction, assuming incompressible flow. While this assumption is not strictly valid when the cold side is gaseous, it remains acceptable for preliminary design. Once the incompressible- flow assumption is adopted, a second assumption is that pressure drop and pressure information also propagate instantaneously within each cell. Once mass-flow-rate and pressure propagation is handled, thermal information propagation is considered. Direct temperature propagation is avoided because temperature remains constant during phase change. Instead, enthalpy flows, $\dot{H} = \dot{m}h$, are used. Since the specific enthalpy, h, continues to evolve through phase change, it serves as a robust carrier of thermal information. State transfer between connected cells is organized through a result list that stores, for every time step, the fluid states of cells and the intermediate connector states.

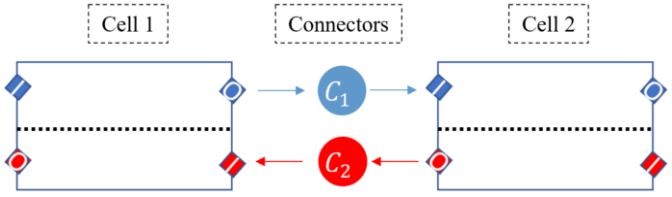


Figure 1: Example configuration for counter-flow with cells and connectors.

An example counter-flow configuration can be seen in Fig. 1. Focusing on the cold (blue) side, Cell 1 is upstream, and connector C_1 Cell 1's outlet to Cell 2's inlet. The key concept is that the connector (ghost) state may differ from the upstream outlet. At each time step, the upstream cell is solved first; then the connector state is updated; finally, the downstream inlet takes the connector state. With incompressible flow assumption, the upstream outlet pressure and mass-flow-rate is

Materials Research Proceedings 69 (2026) 583-588 https://doi.org/10.21741/9781644904251-104

assigned directly to connector and downstream inlet. Weighted update of specific enthalpy enforces delayed propagation of information:

$$h_{con}^{n} = {(h_{con}^{n-1}\dot{m}_{con}^{n-1}/\Delta t + h_{up}^{n}\dot{m}_{up}^{n}/t_{res,up}^{n})}\Big/{(\dot{m}_{con}^{n-1}/\Delta t + \dot{m}_{up}^{n}/t_{res,up}^{n})}. \quad (1)$$

Here, superscripts denote time steps; “con” and “up” refer to connector and upstream-outlet states; Δt is the simulation time step; $t_{res,up}$ is the upstream cell’s residence time. The ${}^{1}/_{\Delta t}$ weight scales information from the previous time level, while ${}^{1}/_{t_{res}}$ scales information arriving from the previous spatial location. Those scaling terms are constructed from internal energy balance equation of a fluid control volume, in which diffusive term is neglected:

$$\frac{\partial T}{\partial t} + u\frac{\partial T}{\partial x} = q'_{ex,i} \quad (2)$$

The balance equation indicates a relation between unsteady term, advection term, and external heat transfer rate. The influence of the unsteady term scales with ${}^{1}/_{\Delta t}$. On the other hand, the advection term’s effect scales with the residence time expressed as ${}^{u}/_{\Delta x} = {}^{1}/_{t_{res}}$. These scaling factors are used in Eq. 1. Consequently, higher upstream mass flow accelerates the connector-enthalpy change, whereas lower mass flow slows it. The smoothing inherent in Eq. 1 yields physically consistent transition curves and reduces time-step-related numerical instabilities, while enabling coupled inlet ramps to propagate across complex cell networks with controlled delay.

Cell Level Hierarchy. Transient cell-level modeling can involve conduction along the heat exchanger wall with Neumann boundary conditions, which are heat fluxes from both fluid sides. Let us assume a one-dimensional wall with thickness $2\Delta x$ discretised as three nodes at the hot side, mid-plane and cold side. One can write internal energy balance equation for each node with unsteady term and diffusion term; followingly, rewrite them in the finite difference form. Finite difference form of energy balance equation for mid-plane node is written as such:

$$\frac{T_{wall,mid}^{n+1} - T_{wall,mid}^{n}}{\Delta t} = \kappa\frac{T_{wall,out}^{n+1} - 2{\cdot}T_{wall,mid}^{n+1} + T_{wall,in}^{n+1}}{\Delta x^2}. \quad (3)$$

In this equation, $T_{wall,mid}^{n+1}$ and $T_{wall,mid}^{n}$ represent the temperatures at the midpoint of the wall at times $n + 1$ and n, respectively. κ is thermal diffusivity which includes thermal conductivity, k, specific heat capacity, c_p, and density of wall, ρ; hence, one considers wall thermal inertia. The left-hand side uses a first-order, forward finite difference scheme. The term Δt is the time step, and Δx is the spatial step size along the wall. Considering heat fluxes through the boundaries of wall control volume, linear equation system can be build in the form of $Ax = b$:

$$\begin{bmatrix} 1+\frac{2\kappa\Delta t}{\Delta x^2} & -\frac{2\kappa\Delta t}{\Delta x^2} & 0 \\ -\frac{\kappa\Delta t}{\Delta x^2} & 1+\frac{2\kappa\Delta t}{\Delta x^2} & -\frac{\kappa\Delta t}{\Delta x^2} \\ 0 & -\frac{2\kappa\Delta t}{\Delta x^2} & 1+\frac{2\kappa\Delta t}{\Delta x^2} \end{bmatrix} \begin{bmatrix} T_{wall,in}^{n+1} \\ T_{wall,mid}^{n+1} \\ T_{wall,out}^{n+1} \end{bmatrix} = \begin{bmatrix} T_{wall,in}^{n} + \frac{2\kappa\Delta t}{\Delta x\cdot k} q''_{hot} \\ T_{wall,mid}^{n} \\ T_{wall,out}^{n} + \frac{2\kappa\Delta t}{\Delta x\cdot k} q''_{cold} \end{bmatrix} \quad (4)$$

Time steps for the temperature values are intentionally selected as they appear in Eq. 4 to construct an implicit finite difference scheme. Right-hand side is known, and one solves this equation system by using Gaussian elimination for the wall temperature values of next time step.

Materials Research Proceedings 69 (2026) 583-588 https://doi.org/10.21741/9781644904251-104

Validation & Results

In the literature, various papers have utilized numerical models created in the Modelica environment to validate their analytical models [3, 4]. This work applies the same approach. A benchmark numerical model or concentric double pipe counterflow arrangements is created within the Modelica environment. An example configuration is shown in Fig. 2, and the geometrical and material details are provided in Table 1. In the methodology, two different hierarchy levels are explained. First, changes to the heat exchanger level hierarchy are implemented in the code, along with the residence time calculations for the cells. A good level of agreement is observed between the Modelica and PreHEAT results, with the implementations only on the heat exchanger level hierarchy. Cell- level calculations are conducted using the P-NTU method in those prior observations. Then, implementations on the cell-level hierarchy are applied to the code to include the wall thermal inertia. As expected, a much better agreement is observed in the results, but this comes with the cost of higher computation times. Both in Modelica and PreHEAT, ramps are applied linearly in 5 seconds starting at $t = 150s$.



Figure 2: Configuration for counter-flow with cells.

Table 1: Benchmark model geometry and material data.

	Tube Diameter [m]	Tube Length [m]	Heat Transfer Area [m^2]	Flow Area [m^2]
Inner Pipe	0.020	2.00	1.25E-01	3.14E-04
Outer Pipe	0.034	2.00	1.38E-01	5.20E-04
	Thermal Conductivity [W/(m · K)]	**Thickness** [m]	**Specific Heat Capacity** [J/(kg · K)]	**Density** [kg/m^3]
Wall Properties	9800.0	0.001	434.0	8440.0

In Figure 3, temperature results for multi ramp case are plotted at two spatial points along the two-meter-long pipe: $x = 0.5m$ and $x = 1.5m$. For each spatial point, three different results are provided: one from Modelica, another from the PreHEAT using the P-NTU method at the cell level, and a third that incorporates Wall Thermal Inertia (WTI) into the cell-level hierarchy. Inner side inlet temperature decreased from $50°C$ to $20°C$, while outer pipe inlet temperature is decreased from $90°C$ to $70°C$. Inner side mass-flow-rate is decreased from $60^L/_h$ to $30^L/_h$, while outer pipe mass-flow-rate is increased from $60^L/_h$ to $120^L/_h$. Pressure values of both side are constant at $1atm$. Also, heat transfer coefficients are held constant at 100 $^W/_{m^2 \cdot K}$. For the inner flow, temperatures start to increase slightly at the beginning since the volumetric flow rate of the inner pipe decreases, and its effect is immediate along the pipe. However, the decrease in the inner flow's inlet temperature starts to impact temperature values along the pipe according to the residence time of the inner flow. Again, both versions of PreHEAT start to react quicker than the benchmark model when the temperature values decrease. However, the WTI version captures almost exact dynamic response characteristics with the Modelica before the transient phase ends.

Materials Research Proceedings 69 (2026) 583-588 https://doi.org/10.21741/9781644904251-104

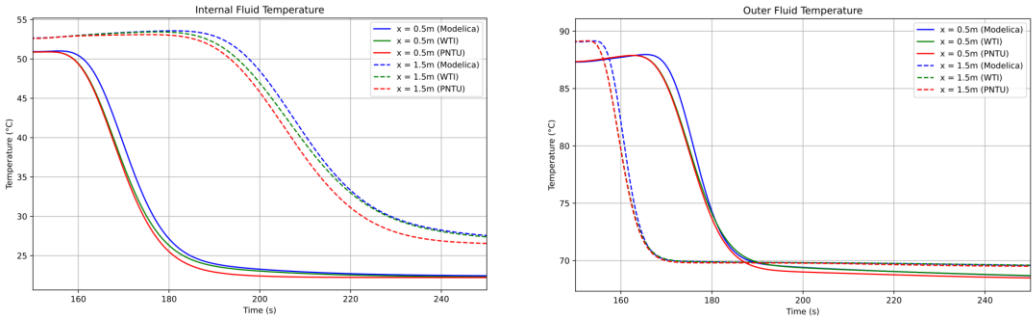


Figure 3: Temperature values of Modelica and PreHEAT models for multi-ramp.

At the outer flow temperature results, both PreHEAT models perform well. Again, the WTI version catches almost the same characteristics as the Modelica before the transient phase ends. Once the validation with benchmark assessed, as a demonstration case, the dynamic response of a hydrogen conditioning heat exchanger is presented. Görtz et al. proposed a turbofan engine layout for hydrogen combustion, and its integration with heat exchangers is illustrated in Fig. 4 [5]. Detailed geometry and material properties can be found in that article. A part of the compressed air is utilized to heat the liquid hydrogen before it is pumped into the combustion chamber. In the simulated Go-Around maneuver, the operating point (OP) Maximum-Take-Off

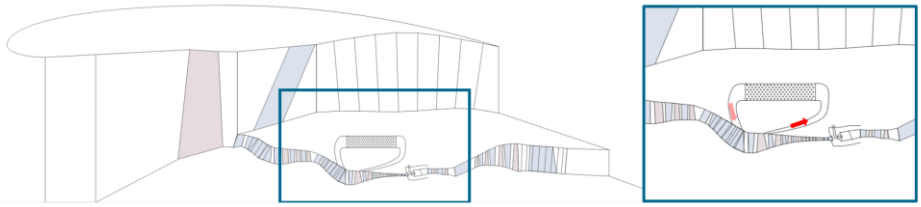


Figure 4: Heat Exchanger Integration Concept for Hydrogen Conditioning [5].

(MTO) is reached in 5 seconds, starting from the Approach OP. Accordingly, inlet boundary conditions for the air and hydrogen sides are provided in the Table 2. Ramp starts at 0.5 seconds, follows a linear characteristic, and ends at 5.5 seconds. In Fig. 5, two snapshots of the transient simulation are shown. The one on the left shows the temperatures along the tube at t = 1 second, and the other plot at t = 3 seconds. In both snapshots, initial and final temperature characteristics are plotted with the OP names. In many transient modeling studies, one should verify that the simulation terminates at the intended final OPs, meaning that the propagated temperature profile along the heat exchanger converges to the last steady-state profile. The developed PreHEAT transient model fulfills this requirement. In Fig. 5, one can also observe the temperature profile of the heat exchanger wall. In this demonstration case, wall thermal inertia is taken into account. Hence, the increases in hot-side temperature do not immediately affect the hydrogen temperature, and a non-linear dynamic response is observed. Together with the increase in temperature of the hot-side inlet, the mass-flow rates also increase, creating less time for heat transfer. As a result, a decrease in cold side temperatures are observed.

Table 2: Go-Around Manoeuvre: Inlet Conditions for Hydrogen and Air.

		Hydrogen		Air	
Inlet Property	**[unit]**	**Approach**	**MTO**	**Approach**	**MTO**
Mass Flow Rate	[kg/s]	6.3E-03	4.6E-02	1.7E-01	5.8E-01
Temperature	[K]	20.0	20.0	337.7	459.0
Pressure	[Pa]	5000000.0	5000000.0	175564.4	444828.6

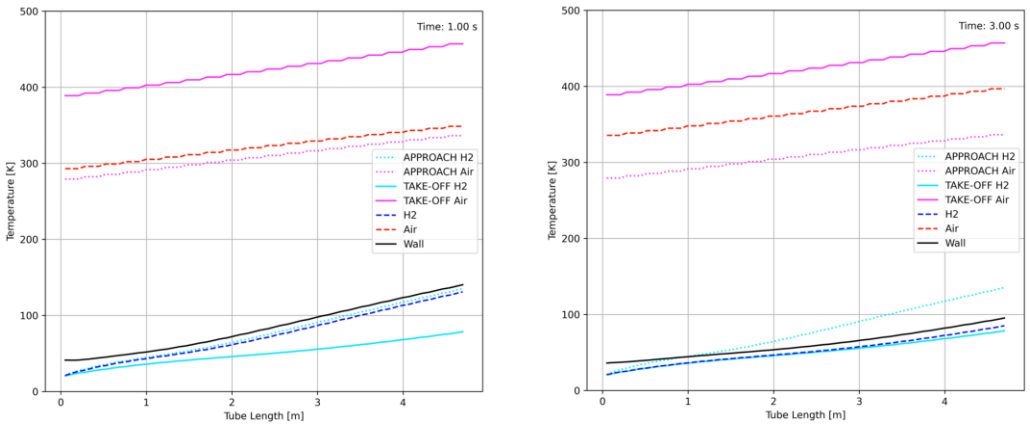


Figure 5: Temperatures along the heat exchanger at $t = 1s$ and $t = 3s$.

Conclusion

The proposed transient model attains the accuracy and computational efficiency required for preliminary design across complex geometries and operating conditions. A residence-time/step-size methodology, derived from simplified energy balances, is embedded within PreHEAT's heat-exchanger level hierarchy. Advective and unsteady internal-energy terms are treated via a weighted formulation. At the cell level, wall thermal inertia is incorporated using finite differences. This hybrid analytical–numerical framework extends PreHEAT for fast transient modelling. Validation against a concentric flow configuration benchmark with simultaneous inlet temperature and mass-flow perturbations indicates excellent agreement in temperature propagation along the pipe. Inlet-temperature changes propagate with a delay due to the residence times of the fluids and wall thermal inertia. Go-Around case study of hydrogen conditioning heat exchanger reveals that hydrogen temperatures approach almost steady profiles before the boundary ramps are completed, indicating the need for transient analysis in aero-engine context.

References

[1] M. Schmelcher, J. Häßy, A. Görtz, M. El-Soueidan, Methods for the preliminary design of heat exchangers in aircraft engines, Volume 5: Cycle Innovations. Turbo Expo (2023), https://doi.org/10.1115/GT2023-102959

[2] M. Spiga, G. Spiga, Step response of the crossflow heat exchanger with finite wall capacitance, International Journal of Heat and Mass Transfer, 35 (1992), https://doi.org/10.1016/0017-9310(92)90290-9

[3] J. Yin, M.K. Jense, Analytic model for transient heat exchanger response, International Journal of Heat and Mass Transfer, 46 (2003), https://doi.org/10.1016/S0017-9310(03)00118-2

[4] R. Yang, C.T. Tran, A. Zoughai, An analytical model to study the dynamic response of heat exchanger network, International Journal of Heat and Mass Transfer 176 (2021), https://doi.org/10.1016/j.ijheatmasstransfer.2021.121461

[5] A. Görtz, K. Kyprianidis, D. Bermperis, Implementation of intercompressor cooling in the cycle analysis of hydrogen powered gas turbine engines using scalable heat exchanger maps, Journal of Engineering for Gas Turbines and Power 147 (2025), https://doi.org/10.1115/1.4069486

Materials Research Proceedings 69 (2026) 589-594 https://doi.org/10.21741/9781644904251-105

Suitability Assessment and Potential Use Case Definition for the Application of Electric Energy Carriers in Electrified Aircraft

Maurice Lucas DOERNTE[1 *], Florian FRANKE[1] and Stefan KAZULA[1]

[1]German Aerospace Center (DLR), Institute of Electrified Aero Engines, Lieberoser Straße 13a, 03046 Cottbus, Germany

[a]maurice.doernte@dlr.de

Keywords: More Electric Aircraft, Electrical Energy Storage System, Battery, Flywheel, Supercapacitor, Aircraft Subsystems, Suitability Analysis, Sustainable Aviation

Abstract. The emerging electrification of aircraft aims to extensively reduce emissions. One near term mitigation strategy can be the implementation of electrical energy storage systems (EESSs) such as batteries, flywheels and supercapacitors to power subsystems of more electric aircraft. However, these EESSs are subjected to various advantages and drawbacks. Therefore, this study provides a detailed assessment of the suitability of integrating these systems into aircraft applications. For this purpose, aircraft design criteria relevant for the analysis are derived and their relative importance is determined through pairwise comparison. To ensure comparability among the subsystems, they are categorized based on their operating time. The subsequent rating of the EESSs suggests, that supercapacitors may be best suited to short- and medium-duration operations, while batteries seem to be more beneficial for long-duration applications. However, flywheels appear to be unsuitable for either. For further assessing the feasibility of integrating EESSs in aircraft, the weight penalty associated to each system can be investigated.

Introduction

Over recent decades, global warming has become a major challenge. The aviation industry contributes around 2.5% of global CO_2 emissions, a number expected to rise [1]. To address this, new propulsion concepts such as all-electric (AEA), hybrid-electric, turbo-electric, and more-electric aircraft (MEA) have been introduced. In the AEA concept, all energy for thrust and subsystems is supplied by electrical energy storage systems (EESSs) [2]. These can be battery- (BSs), flywheel- (FSs), and supercapacitor-systems (SCSs).

An exploration of the future aircraft concepts reveals that, in advanced electrified configurations beyond the MEA, BSs are typically considered [3]. They usually outperform other storage technologies in terms of mass specific energy (SE), and their lower mass specific power (SP) is offset by the total capacity of the installed BSs. However, current state of the art (SoA) EESSs still require improvements in SE to meet even short-range aircraft mission demands [4].

Thus, in the near term, electrifying subsystems of MEA may offer promising potential for reducing emissions. These are typically powered by generators [5], but integrating EESSs could lower fuel burn and enable new use cases Especially, the high SP of supercapacitors and flywheel systems may be particularly beneficial for short, power-intensive operations such as actuation. Several studies have examined EESSs for propulsion support or powering aircraft electrical subsystems (AESs) [6–8]. Nonetheless, factors such as safety, SE, and SP must be considered, and a detailed assessment of EESSs suitability for MEA applications is still lacking in the literature.

Consequently, this study covers such an evaluation and rating of EESSs according to their suitability for aircraft applications. First, it presents the SoA performance characteristics of the EESSs. Then, it discusses aircraft secondary power consumers. Finally, the EESSs options are rated according to their suitability for operating these AESs. Therefore, relevant criteria for aircraft applications are derived, and their relative importance is determined through pairwise comparison.

Content from this work may be used under the terms of the Creative Commons Attribution 3.0 license. Any further distribution of this work must maintain attribution to the author(s) and the title of the work, journal citation and DOI. Published under license by Materials Research Forum LLC.

Materials Research Proceedings 69 (2026) 589-594 https://doi.org/10.21741/9781644904251-105

State of the art

Batteries, flywheels, and supercapacitors each offer distinct advantages in terms of their performance parameters, while the most significant are the SP and SE. Due to their electrochemical nature, BSs can store comparatively larger amounts of energy per unit weight than other technologies [9–11]. Conversely, SCSs excel at delivering very high power outputs because of their ability to discharge stored electrons almost instantaneously, making them well suited for meeting peak power demands [12, 13]. On the contrary, BSs demonstrate comparatively moderate SP, while SCSs typically exhibit low SE [12, 14]. FSs, on the other hand, are usually recognized for offering a balanced compromise, with SP and SE values that lie between those of BSs and SCSs [9].

In addition to their high energy density, BSs are susceptible to external factors such as temperature changes, which can result in degradation and, in extreme cases, thermal runaway. To protect the system, energy and temperature management systems are required [15]. Furthermore, extracting the materials required for production can be hazardous and recycling remains difficult. Nevertheless, they remain widely available, cost-effective, and relatively easy to integrate into aircraft through modular designs [10]. FSs, on the other hand, must meet stringent safety standards due to their high-speed rotating components, and their installation can be complex, particularly because the system's moment of inertia requires careful compensation [8]. Additionally, high self-discharge losses and power control elements must be considered [14]. Nonetheless, FSs offer strong resilience against external environmental influences, require minimal maintenance, and contain no hazardous materials, offering favorable recyclability [9, 14]. SCSs, despite being disadvantaged by low energy density and moderate self-discharge, share many of the benefits of BSs, such as availability and ease of integration due to modular configuration. Although elevated temperatures may degrade the electrolyte, SCSs are not prone to thermal runaway. However, to prevent the system from overcharging and thus bursting, an energy management system is required [12]. Beyond that, many of the system's components are non-hazardous and recyclable [16]. Table 1 summarizes the SP and SE of the EESSs, also considering cycle life, daily losses, cycle efficiency, and response time. Reported values for the systems may differ across references as a result of technological evolution and variations in research focus. Nevertheless, the order of magnitude is similar, and the data is provided for guidance [9–14, 17, 18].

For comparison purposes, the available specific energy of jet fuel can be assumed to be approximately 6.5 kWh/kg [8]. Furthermore, the integration of an EESSs may lead to a fuel penalty if the fuel savings do not offset the additional system mass [19]. Therefore, incorporating an EESSs into aircraft requires a comprehensive assessment of the resulting increase in fuel consumption.

Table 1 *State of the art performance characteristics of energy storage systems*

EESS	SP [kW/kg]	SE [Wh/kg]	Cycle Life	Loss [%/d]	Eff. [%]	Rp. time [s]
BS	0.3–0.5 [10]	250–400 [10]	10^3 [14]	< 0.1 [13]	~ 95 [13]	< 1 [13]
FS	1–2 [11]	20–80 [11]	10^6 [14]	50–100 [13]	80–95 [9]	~ 0.01 [13]
SCS	1–10 [12]	1–10 [12]	10^6 [14]	0.4–5 [17]	95–98[18]	< 0.01 [13]

In conventional aircraft, secondary (non-propulsive) systems, or subsystems, are often operated using either pneumatic or hydraulic energy, both extracted from the aircraft engine. Current trends aim to replace these systems with electrical ones to enhance efficiency, reduce weight, and/or increase mission range [20]. The corresponding power requirements range from a few kilowatts up to several hundred kilowatts. As a result, the total electrical load of the aircraft increases. Multiple studies estimated the required power for the AESs, aiding in determining the electrical energy demand of MEA [21–24]. As some of the advantages and disadvantages of the EESSs strongly correlate with the operating time, it is essential to define groups of AESs operating under similar conditions. Therefore, three groups are established: short-duration operations lasting up to

Materials Research Proceedings 69 (2026) 589-594 https://doi.org/10.21741/9781644904251-105

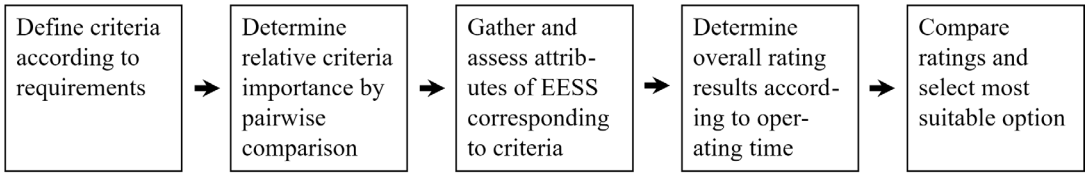


Fig. 1 *Evaluation process for rating the EESS suitability, adopted from[25]*

one minute, medium-duration operations ranging from one minute to 15 minutes, and long-duration operations covering all operations beyond that.

In the realm of short-duration operations, representative power consumers are the landing gear actuation, door actuation, thrust reverse actuation and the engine starter. To eliminate the hydraulic system and thereby improve efficiency and safety, electromechanical actuators are being developed as replacements for hydraulic components, with the first commercial implementations already in use [23, 24]. In comparison, the engine starter in MEA is powered by an electric motor instead of using pressurized air [24]. For medium-duration applications, the ice protection system and electric taxiing may be considered. Among the relevant long-duration electrical loads are the environmental control system, flight control system, and miscellaneous systems such as the galley.

Methodology

The first step of building a basis for the suitability analysis is the aforementioned categorization of the AESs with respect to their operating times. Subsequently, the relative suitability rating of each EESSs in terms of the derived evaluation criteria and with regard to the time categories is determined. A general evaluation process to identify suitable EESSs is shown in Fig. 1.

At this preliminary stage of the assessment conducted here, it is necessary to employ an evaluation method that will facilitate an initial estimation of suitability. Therefore, the EESSs are benchmarked using evaluation criteria. These criteria are derived according to aircraft design requirements and their relative importance is determined using weighted point rating [26]. The criteria are defined as follows and are adapted from Franke et al. [25]:

1. *Short Term Performance (ST):* Fast power handling ability
2. *Long Term Performance (LT):* High time independent energy supply
3. *Ease of Integration (I):* Necessary integration efforts
4. *Safety (S):* Safe and reliable operation of aircraft, vulnerability of the system to failure, failure probability and severity
5. *Cost (C):* Cost of development, manufacturing and maintenance
6. *Sustainability (U):* Reducing the emission impact of aircraft and resource conservation

Table 2 lists the results from the criteria weighting using a color coding to illustrate the different operating time categories. Here, performance and safety emerge as the most important criteria.

Table 2 *Criteria weighting according to the time categories using pairwise comparison*

Criteria	ST			LT			I			S			C			U			Weighting		
ST	-	-	-	2	1	0	2	2	0	1	1	0	2	2	0	2	2	1	0.30	0.27	0.03
LT	0	1	2	-	-	-	0	2	2	0	1	1	0	2	2	1	2	2	0.03	0.27	0.30
I	0	0	2	2	0	0	-			0			1			2			0.17	0.10	0.17
S	1	1	2	2	1	1	2			-			2			2			0.30	0.27	0.30
C	0	0	2	2	0	0	1			0			-			1			0.13	0.06	0.13
U	0	0	1	1	0	0	0			0			1			-			0.07	0.03	0.07

Color coding: green = short-duration ($t \leq 1$min); blue = medium-duration (1min $< t \leq 15$ min); red = long-duration (15 min $< t$); Values: row criterion is more important than column criterion = 2, equally important = 1, less important = 0

Materials Research Proceedings 69 (2026) 589-594 https://doi.org/10.21741/9781644904251-105

Results and discussion

Table 3 *Relative Rating of EESSs with respect to aircraft design criteria and time domain*

Criteria	Battery	Flywheel	Supercapacitor
Shor Term Performance (ST)	moderate SP, moderate reaction time	high SP, fast rection time	very high SP, very fast reaction time
	o	+	+ +
Long Term Performance (LT)	high SE, excellent long-term storage, low self-discharge	moderate SE, high self-discharge	very low SE, self-discharge
	+ +	–	–
Ease of Integration (I)	modular configuration, thermal and energy management required	compensation of rotor inertia required, bulky design, safety and control equipment required	modular configuration, implementation of energy management required
	o	–	o
Safety (S)	risk of fire due to thermal runaway, sensitive to external influences, emergency energy storage	severe safety hazard due to material rupture, high resilience against external influences, quick short term power supply	no thermal runaway, quick short term power supply
	o	o	+
Cost (C)	available, high TRL, mass production, exchange every few months, exchange of whole module	high manufacturing cost, low maintenance cost, easy part exchange, rare system replacement	vastly available, high TRL, mass production, exchange after years, exchange of whole module
	+	+	+
Sustainability (U)	relatively short lifetime, resource extraction harmful, recycling difficult	almost infinite lifetime with maintenance, no hazardous materials, good recyclability	long lifetime, almost no hazardous materials
	–	+	+
Rating	0.53	0.65	0.67	0.58	0.51	0.44	0.77	0.67	0.57

Symbols: – – = 0, – = 1, o = 2, + = 3, + + = 4; SE: specific energy, SP: specific power

The assessment of the EESSs according to each criterion and the corresponding relative ratings are outlined in Table 3. The relative rating is obtained following the process defined in [25, 26]. It can be observed, that the SCSs show a good overall rating for most of the criteria, while BSs and FSs exhibit rather moderate results. In the case of BSs, the major positive contributing factors are the excellent long-term energy storage capability and their availability. This is opposed by a moderate SP, a low cycle life, low recyclability and safety concerns due to the risk of thermal runaway and degradation. SCSs on the other hand exhibit an excellent SP, cycle life and a rather low risk of failure, while the technology is vastly available as well. However, they are subjected to a very low SE making them unsuitable for high energy applications.

Despite the fact that FSs are usually recognized for combining both a good SP and SP, in the context of the suitability analysis, this type of EESSs demonstrates limited performance. The results indicate that SCSs and BSs are the most suitable systems for empowering MEA. For comparison, Lukic et al. investigated the integration of both for covering the energy demand of aircraft taxiing [6]. The study demonstrated the promising opportunities arising from the combination of BSs and SCSs. This hybrid approach appears particularly well suited for medium-duration operation, as both systems exhibited comparable rating for this time domain. A similar benefit was also reported by Gladin et al. [7]. In contrast, Frederick et al. pointed out that the anticipated increase in the SE of FSs may surpass that of BSs at some point [8]. However, due to rotor material scaling limitations, these developments seem to be of theoretical nature for now. Hence, focusing on SCSs and BSs for aircraft applications seems to be the most reasonable choice.

Conclusion

This study analyses the suitability of batteries, flywheels and supercapacitors for supplying energy to AESs in electrified aircraft. The AESs are categorized by operating time to enable comparison. Based on aircraft design requirements, evaluation criteria are derived and weighted using pairwise comparison. The suitability of different electrical energy storage systems (EESSs) across operating time categories is then assessed against these criteria. The results show that supercapacitors are well suited for short- and medium-duration operations, while batteries appear most suitable for long-duration applications. In contrast, the use of flywheels in aircraft is limited by moderate specific energy, safety concerns, and installation constraints.

Overall, the specific energy of all examined EESSs remains significantly lower than that of jet fuel. Additionally, a potential fuel penalty due to the added weight of EESSs must be considered. This penalty occurs when the mass of the energy carrier exceeds the fuel saved through energy substitution. Therefore, future work should include preliminary sizing of EESSs based on current performance data and an estimation of the resulting fuel penalty.

References

[1] European Union Aviation Safety Agency, *European aviation environmental report 2025*, 2025.

[2] B. J. Brelje *et al., Electric, hybrid, and turboelectric fixed-wing aircraft: A review of concepts, models, and design approaches*, Prog. Aerosp. Sci., vol. 104, 2019. https://doi.org/10.1016/j.paerosci.2018.06.004

[3] National Academies of Sciences, Engineering, and Medicine, *Commercial Aircraft Propulsion and Energy Systems Research: Reducing Global Carbon Emissions.* Washington, D.C.: The National Academies Press, 2016. https://doi.org/10.17226/23490.

[4] L. Tom *et al., Commercial Aircraft Electrification—Current State and Future Scope*, Energies, vol. 14, 2021. https://doi.org/10.3390/en14248381

[5] A. Barzkar *et al., Electric Power Systems in More and All Electric Aircraft: A Review*, IEEE Access, vol. 8, 2020. https://doi.org/10.1109/ACCESS.2020.3024168

[6] M. Lukic *et al., Analysis of Energy Storage System Requirements for Aircraft Electric Taxiing Operations*, IECON 2019-45th Annual Conference of the IEEE Industrial Electronics Society, 2019. https://doi.org/10.1109/IECON.2019.8926797

[7] J. C. Gladin *et al., A Comparison of Hybrid Electric Propulsion Architectures for Civil Aircraft*, AIAA AVIATION 2023 Forum, 2023. https://doi.org/10.2514/6.2023-4502

[8] Z. J. Frederick *et al., Design Exploration of a Mild Hybrid Electrified Aircraft Propulsion Concept*, AIAA AVIATION 2023 Forum, 2023. https://doi.org/10.2514/6.2023-4226

[9] K. Xu *et al., A Review of Flywheel Energy Storage System Technologies*, Energies, vol. 16, 2023. https://doi.org/10.3390/en16186462

[10] M. Armand *et al., Lithium-ion batteries - Current state of the art and anticipated developments*, J. Power Sources, vol. 479, 2020. https://doi.org/10.1016/j.jpowsour.2020.228708
[11] A. Aghmadi *et al., Energy Storage Systems: Technologies and High-Power Applications*, Batteries, vol. 10, 2024. https://doi.org/10.3390/batteries10040141
[12] K. Dissanayake *et al., A review of supercapacitors: Materials, technology, challenges, and renewable energy applications*, J. Energy Storage, vol. 96, 2024. https://doi.org/10.1016/j.est.2024.112563
[13] P. Kurzweil *et al., Elektrochemische Speicher*. Wiesbaden: Springer Fachmedien Wiesbaden, 2018. https://doi.org/10.1007/978-3-658-21829-4
[14] M. Hedlund *et al., Flywheel Energy Storage for Automotive Applications*, Energies, vol. 8, 2015. https://doi.org/10.3390/en81010636
[15] S. Mallick *et al., Thermal behaviour and thermal runaway propagation in lithium-ion battery systems – A critical review*, J. Energy Storage, vol. 62, 2023. https://doi.org/10.1016/j.est.2023.106894
[16] C. L. Pastra *et al.,* "Projecting Key Performance Parameters for Electric Powertrain Components through 2050 for Aerospace Applications," in *AIAA Aviation Forum*, San Diego, 2023.
[17] K. Liu *et al., Recent research advances of self-discharge in supercapacitors: Mechanisms and suppressing strategies*, J. Energy Chem., vol. 58, 2021. https://doi.org/10.1016/j.jechem.2020.09.041
[18] A. D. Jagadale *et al., Review—Mitigating Supercapacitor Self-Discharge Through Strategic Materials Modification*, J. Electrochem. Soc., vol. 168, 2021. https://doi.org/10.1149/1945-7111/ac275d
[19] H. Kühnelt *et al., Structural Batteries for Aeronautic Applications*, Transport Research Arena Conference, 2025. https://doi.org/10.1007/978-3-031-89444-2_36.
[20] P. Thalin, *Fundamentals of Electrical Aircraft*. Warrendale, PA: SAE International, 2018. https://doi.org/10.4271/r-462
[21] V. Voth *et al., Estimating Aircraft Power Requirements: A Study of Electrical Power Demand Across Various Aircraft Models and Flight Phases*, Aerospace, vol. 11, 2024. https://doi.org/10.3390/aerospace11120958
[22] T. Lampl *et al., Parameterized Flight Mission for Secondary Power Requirement Estimations of Commercial Transport Aircraft*, 17th AIAA Aviation Technology, Integration, and Operations ConferenceAt: Denver, Colorado, 2017. https://doi.org/10.2514/6.2017-3066.
[23] A. T. Johnson, *Electric Thrust Reverser Actuation Systems*, SAE International, 2002. https://doi.org/10.4271/2002-01-2950
[24] I. Chakraborty *et al., An integrated approach to vehicle and subsystem sizing and analysis for novel subsystem architectures*, Proc. Inst. Mech. Eng., Part G: J. Aerosp. Eng., vol. 230, 2016. https://doi.org/10.1177/0954410015594399
[25] F. Franke *et al., Elaboration and outlook for metal hydride applications in future hydrogen-powered aviation*, Aeronaut. j., vol. 128, 2024. https://doi.org/10.1017/aer.2024.53
[26] G. Pahl *et al., Engineering Design*. London, s.l.: Springer London, 2013. https://doi.org/10.1007/978-1-4471-3581-4

Materials Research Proceedings 69 (2026) 595-600 https://doi.org/10.21741/9781644904251-106

Experimental Study of Vibration Levels in Microjet Engine Prototype Considering Venturi Intake Influence

Cornel-Mihai TĂRĂBÎC[1,2,a *], Andrei-George TOTU[2,b] and Grigore Cican[1,c]

[1]National University of Science and Technology POLITEHNICA, 313 Independence Blvd. Bucharest, District 6, RO-060042, Romania

[2]COMOTI - Romanian Research and Development Institute for Gas Turbines Blvd. Iuliu Maniu, Nr. 220D, District 6, RO-061126, Romania

[a]cornel.tarabic@comoti.ro, [b]andrei.totu@comoti.ro, [c]grigore.cican@upb.ro

Keywords: Microjet Prototypes, Experimental Testing, Venturi Intake, Structural Dynamics

Abstract. This paper presents a study on the functionality of a microjet engine prototype, developed by COMOTI - Romanian Research and Development Institute for Gas Turbines focusing on vibration, FFT analysis and speed extraction across all four operating regimes. Despite the compact size, the microjet engines are emerging as a solution for propulsion units for drones, small electrical generator unit or other particular application for civil and military domain. However, even at this scale, prototype designs can exhibit significant vibration levels that compromise structural integrity, mission reliability and the functionality in terms of performance. During these experiments, three single axis accelerometers from PCB were mounted on the metal structure supporting the engine and one triple axis accelerometer was mounted on the engine, near the compressor in a relatively cool region of the flow path. The experimental campaign aimed to evaluate the influence of intake geometry on the vibrational behavior of the engine. Two configurations were tested: one equipped with a Venturi-type air intake and one with a direct open inlet, lacking any aerodynamic shaping at the compressor entry. The test stand was realized using compactDAQ hardware from National Instruments with LabVIEW software for main and auxiliary parameters and PCB accelerometers with Dewesoft software for vibration levels and speed extraction.Results showed that the venturi intake can influence the vibrational levels for the engine during start-up, idle, working and shutdown regimes compared with the second configuration, without the venturi intake.

Introduction

Microjet engines have gained increased attention in recent years due to their compact size, relatively low maintenance cost, lower NO_x emissions, high specific power and the compatibility for both civil and military applications, represent a promising solution for propulsion systems in UAVs [1], small to medium portable power generation units combined with cogeneration systems for heat and electrical generation [2] or other application where the report from weight to size reduction is a critical requirement [3]. Compared to the large gas turbines using jet as a source of force, microjet engines face unique challenges arising from the small scale, which include high sensitivity to intake conditions (ambient pressure, temperature or humidity), lower thermal inertia and most importantly, increased susceptibility to vibration related issues [4].

One factor that can strongly influence microjet functionality is the extremely high range of shaft speed, which can exceed 100.000 [RPM]. At such rotational speeds, even small mechanical or aerodynamic asymmetries can generate significant vibrational dynamics [5]. The consequences of vibration phenomena are particularly critical, as they can compromise structural integrity, reduce overall performance, accelerate mechanical fatigue of internal components, and shorten bearing

Content from this work may be used under the terms of the Creative Commons Attribution 3.0 license. Any further distribution of this work must maintain attribution to the author(s) and the title of the work, journal citation and DOI. Published under license by Materials Research Forum LLC.

Materials Research Proceedings 69 (2026) 595-600 https://doi.org/10.21741/9781644904251-106

life. Furthermore, excessive vibration can induce instabilities in the compressor or turbine stages, originating from rotor-stator misalignments, aerodynamic flow disturbances, or resonance phenomena [6].

The development of microjet engines therefore requires dedicated test benches that combine advanced instrumentation, robust data acquisition systems, and appropriate mechanical support structures for the engine under investigation [7]. In this context, vibration analysis represents a crucial step in the development and validation process. Beyond simple monitoring, advanced signal processing techniques such as FFT analysis enable the identification of characteristic frequency components linked to rotor dynamic and structural behavior. Moreover, vibration signals can also be exploited for indirect speed extraction, providing redundancy to traditional measurement system and enabling insights into transient engine regimes.

The present study focuses on the vibrational behavior of a microjet engine prototype, developed by INCDT COMOTI, with particular emphasis on the influence of intake geometry. By employing multiple PCB accelerometers both triaxial and single axis, in different location on the engine and its support structure, the analysis aims to provide a deeper understanding of how the intake can affect vibration levels across all operating regimes, using Dewesoft DAQ and software.

Experimental setup and test methodology

The experimental campaign was conducted on a microjet engine prototype developed by e National Research and Development Institute for Gas Turbines (COMOTI). The engine is a single-shaft configuration, consisting of a radial-flow compressor, annular combustion chamber, single-stage axial turbine and an exhaust nozzle. All components are directly mounted on the same shaft, resulting in a compact and mechanically simple architecture that is representative of current microjet engine designs [8].

Two intake models were investigated in order to assess their influence on the vibrational behavior of the microjet engine, besides the parameters measured from the main DAQ. The first configuration employed a Venturi intake, specifically engineered to provide aerodynamic shaping of the incoming airflow. The venturi geometry was expected to improve the acceleration and conditioning the air, before it reaches the compressor to improve the stability and efficiency for both compressor and burning chamber. This component also introduces additional structural mass close to the engine, which could affect local vibration levels during testing. The second configuration consisted of a direct open inlet, in which the compressor entry was left exposed without any flow-shaping component. This arrangement represented the simplest possible intake solution, eliminating the aerodynamic and structural influence of the venturi intake. The absence of flow conditioning can increase the sensitivity to ambient conditions and introduce higher levels of turbulence at the compressor intake, that can affect the vibration levels during testing.

The data acquisition was designed to provide high-resolution and synchronized measurements of all relevant parameters during the microjet testing phase. For the main parameters, the inputs and outputs for the auxiliary systems (pressurized air, fuel and gas) and microjet engine, a cDAQ system was developed from National Instruments, equipped with 8 modules. The software that handles the inputs, outputs and automated algorithm was developed in LabVIEW and can operate on all regimes, including start-up, idle, working and shutdown regime, including protection for the engine. For vibration, a Sirius Dewesoft data acquisition system was installed, equipped with PCB mono axial and triaxial acceleration sensors.

Materials Research Proceedings 69 (2026) 595-600 https://doi.org/10.21741/9781644904251-106

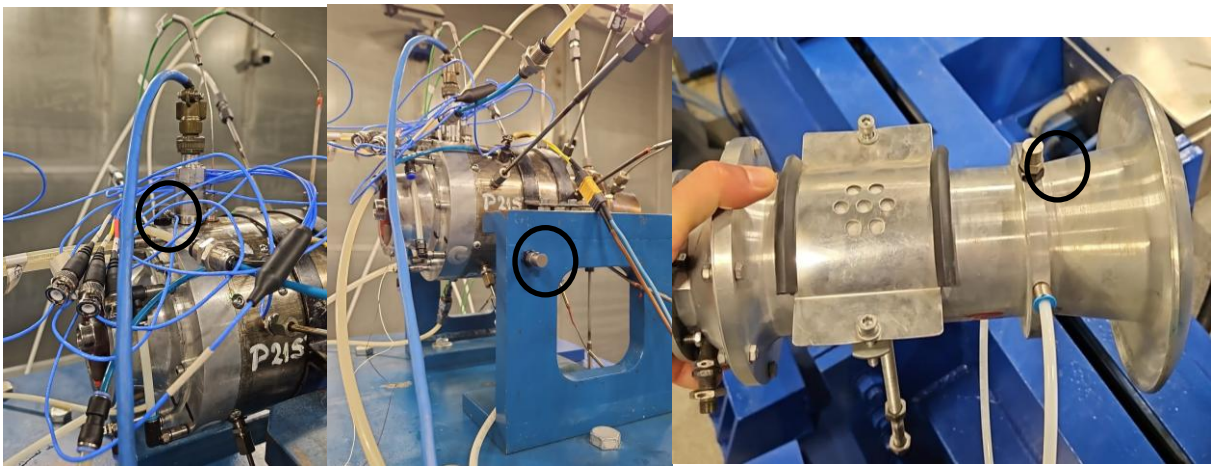


Figure 1. Engine triaxial vibration sensor (The left picture), Engine support monoaxial vibration sensor (Middle picture) and Venturi intake monoaxial vibration sensor (Right picture).

The test bench was equipped with a dedicated control setup, capable of adjusting fuel flow with a P control and monitoring the engine's operating regime. Instrumentation included sensors, for thrust, shaft speed, temperatures, pressures, fuel flows, vibration, placed at strategic points along the engine.

Results

To evaluate the influence of intake geometry on engine dynamics, vibration velocity measurement was recorded for both cases, with and without the intake installed. The speed regimes are based on the speed extracted from vibration using exact-frequency function from Dewesoft. Based on the common regimes, the data was extracted and presented in Table 1 for both configurations and Y axis, on engine and intake.

Table 1. Engine data for both configurations based on Y axis.

Speed [RPM]	Equipped with venturi intake		Without venturi intake	
	Engine Y [mm/s]	Venturi intake [mm/s]	Engine Y [mm/s]	Venturi Intake Y [mm/s]
27300	3.10	1.10	2.91	-
34500	3.13	2.91	2.82	-
39700	4.76	2.82	3.71	-
45130	7.24	5.61	3.11	-
50000	21.77	7.28	25.57	-
52000	26.76	8.30	-	-

Fig. 2 and Fig. 3 presents the vibration and speed evolution of the microjet engine prototype under two intake configurations. In the first case in Fig. 2, with the venturi intake installed, the plots show a more structured vibration response across the different operating regimes, with distinct peaks emerging during acceleration phases and a correlation with shaft speed increases (upper plot). The additional measurement channel (middle plot) also highlights fluctuations captured at the intake, indicating that the venturi introduces measurable vibrational dynamics in the engine.

Materials Research Proceedings 69 (2026) 595-600 https://doi.org/10.21741/9781644904251-106

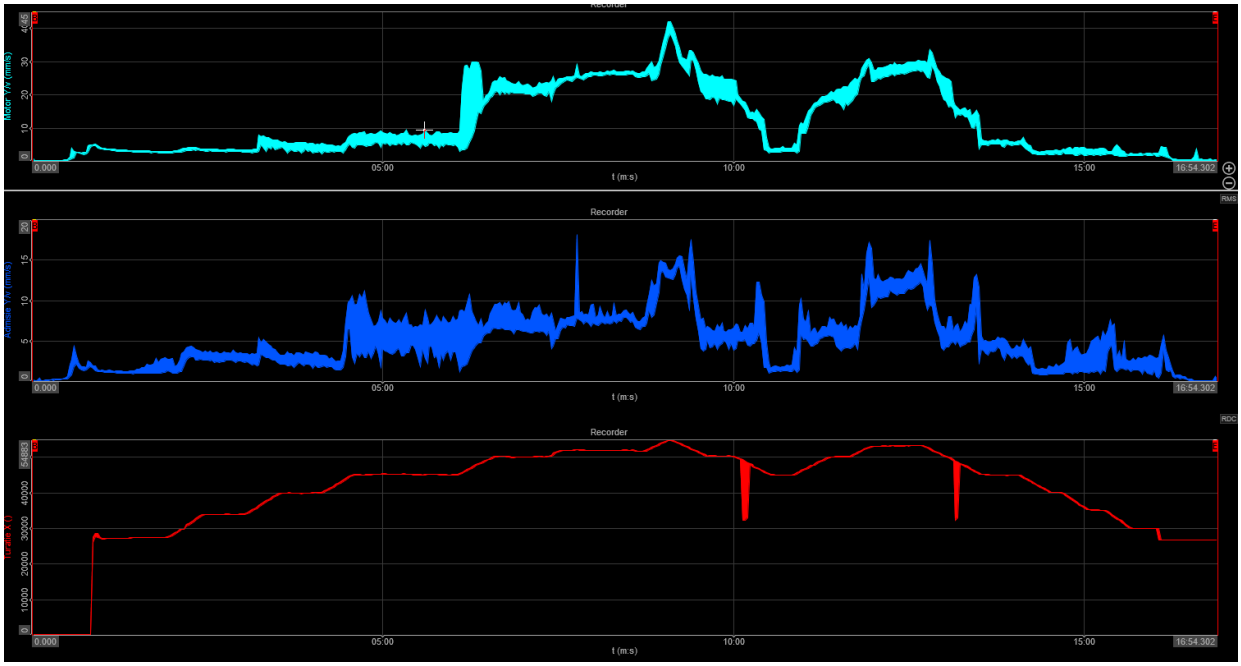


Figure 2. Velocity level for Engine Y, for Intake Y and Speed during test with venturi intake

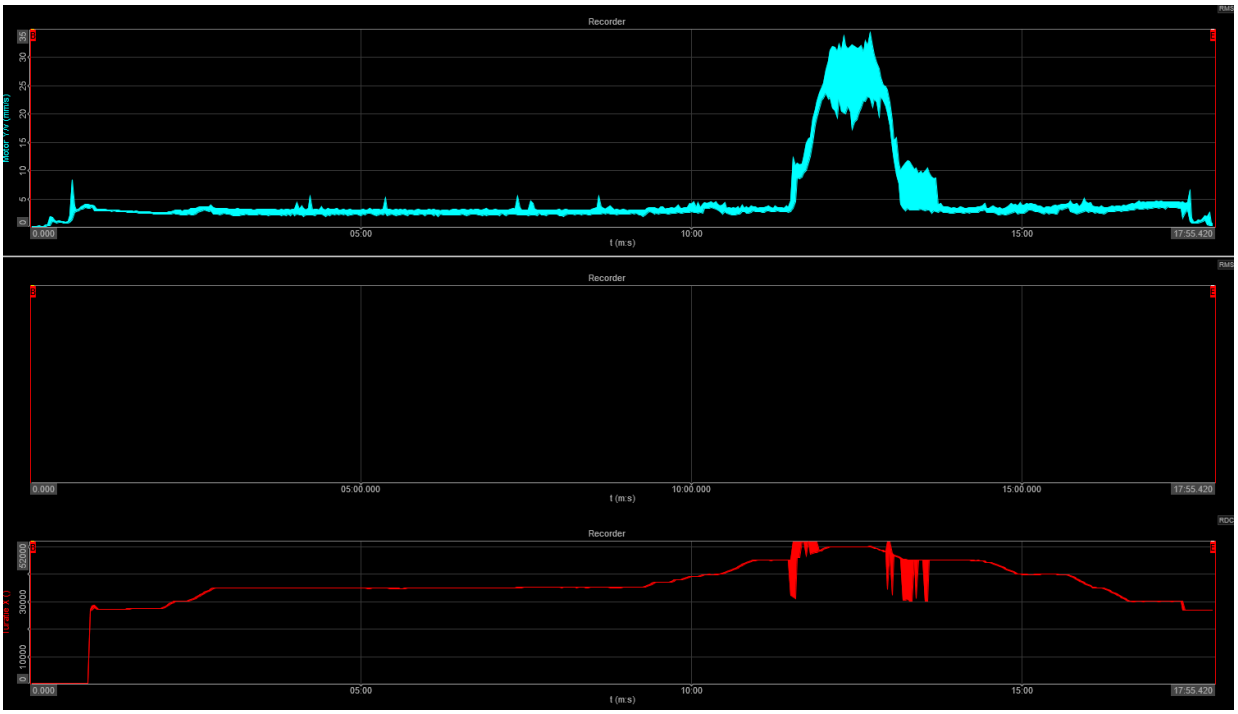


Figure 3. Velocity level for Engine Y and Speed during test without venturi intake

In second case, Fig. 3, without the venturi intake, the vibration response appears simpler, without an increase in the shaft speed and a critical section during high speeds of the engine.

In addition to the velocity measurements, an order tracking analysis was carried out for both the engine and intake. The order maps show that the fundamental order and two harmonics are present in the set frequency interval of 0 – 2000 [Hz]. Setting the shaft speed on minimum and maximum measured, corelated with the main data acquisition system, Fig. 4 and Fig 5. presents the order tracking analysis for both cases. It is shown that the first configuration implies more

structural lines that are pronounced in the intake section and that will influence the vibration levels on the engine.

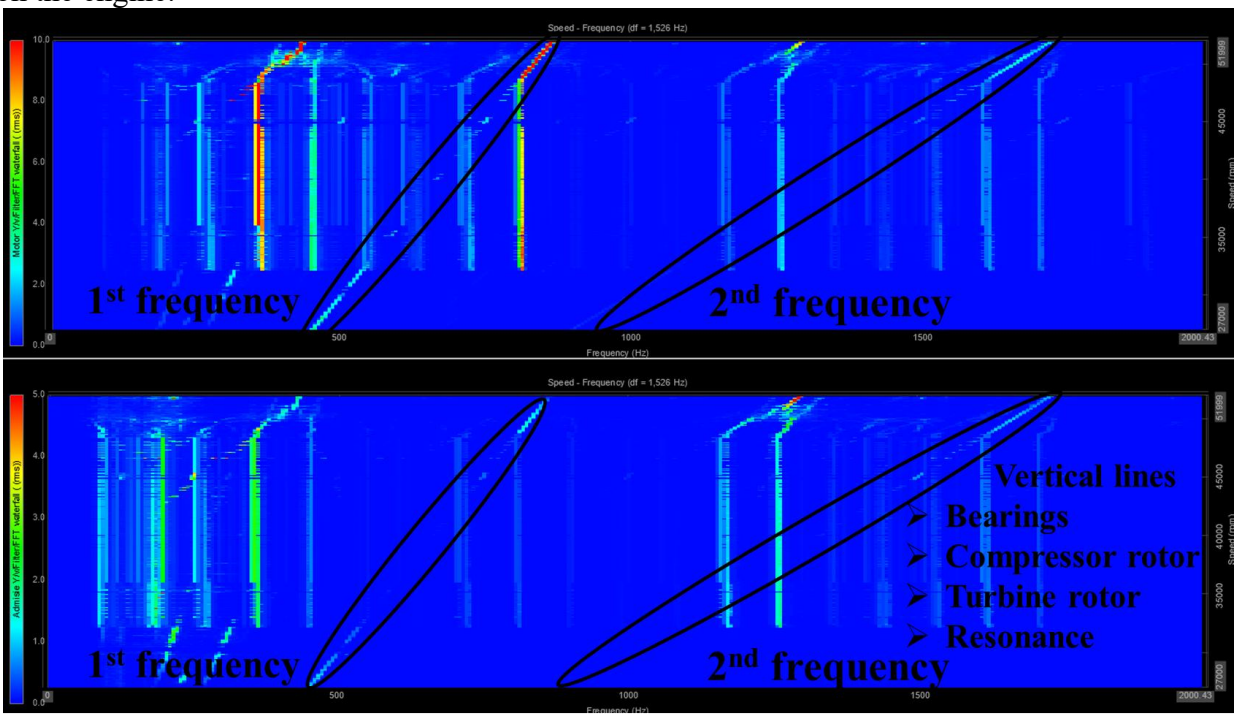


Figure 4. Order tracking for Engine Y and Venturi Y during test with venturi intake

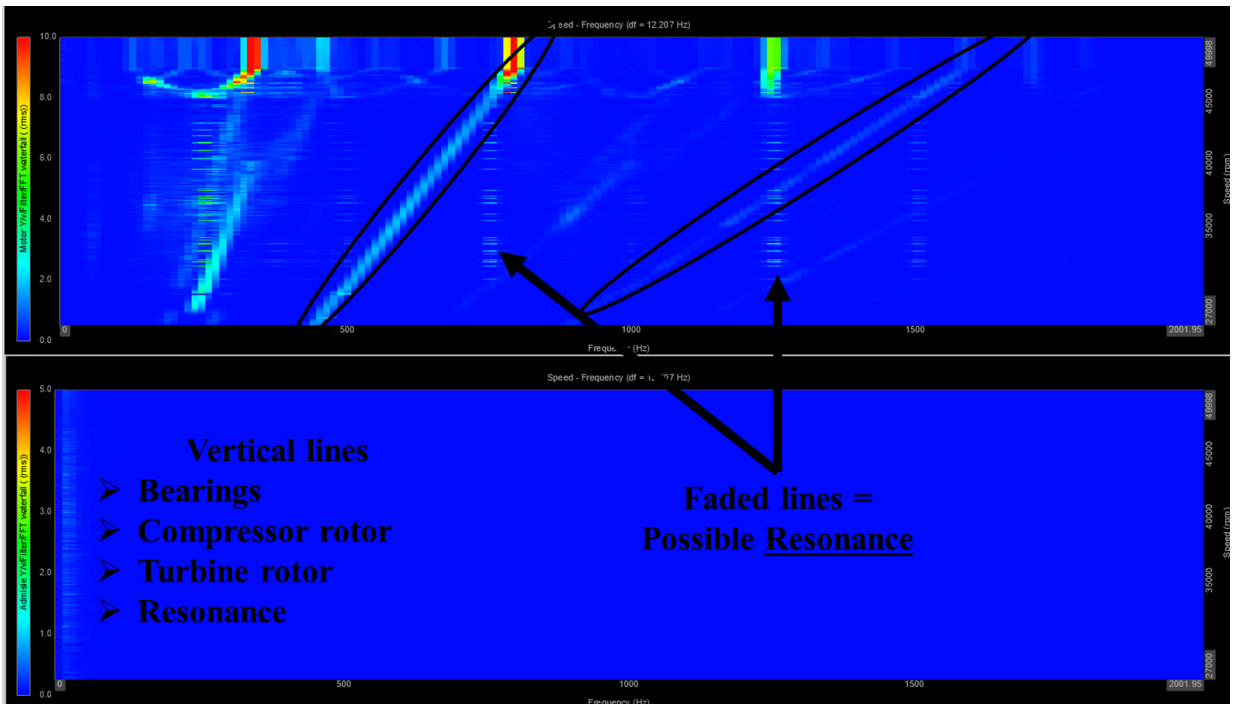


Figure 5. Order tracking for Engine Y and Venturi Y during test without venturi intake

On the other hand, without the intake, most of the structural lines disappear at lower regimes, following the fundamental order at higher regimes.

Conclusion and discussion

The comparative analysis of the two operating configurations highlights a notable influence of the intake geometry on the microjet engine's vibration response. When the venturi intake is used, the

vibration velocity on the engine casing increases progressively in shaft speed, showing a consistent upward trend that becomes irregular at high speeds. In contrast, the second intake configuration results in lower vibration amplitudes at lower operating regimes, with a distinct critical point observed at maximum speed, associated with an unstable dynamic. Order tracking indicates that the venturi intake can introduce specific structural vibrational frequencies, potentially affecting the engine's performance under these conditions comparing to the second configuration, where a part of the frequency lines are not visible.

Summary

This paper describes the experimental setup and procedures used to evaluate a vibrational behavior of a microjet engine prototype developed by COMOTI - Romanian Research and Development Institute for Gas Turbines. A few operating regimes were investigated, combining accelerometer measurements and order tracking to capture vibration velocity and harmonic content. The results indicate that intake geometry has a clear influence on the dynamic response of the engine, with differences becoming more pronounced at higher operating regimes.

Acknowledgements

The data presented and analyzed in this report were obtained with the help of COMOTI's Research and Experiments Center in the field of Acoustic and Vibrations staff and facility.

References

[1] Catana, R.M.; Cican, G.; Badea, G.-P. Thermodynamic Analysis and Performance Evaluation of Microjet Engines in Gas Turbine Education. Appl. Sci. 2024, 14, 6754. https://doi.org/10.3390/app14156754

[2] Banihabib, R.; Assadi, M. The Role of Micro Gas Turbines in Energy Transition. Energies 2022, 15, 8084. https://doi.org/10.3390/en15218084

[3] Amici, C.; Ceresoli, F.; Pasetti, M.; Saponi, M.; Tiboni, M.; Zanoni, S. Review of Propulsion System Design Strategies for Unmanned Aerial Vehicles. Appl. Sci. 2021, 11, 5209. https://doi.org/10.3390/app11115209

[4] Rossi, I., & Traverso, A. (2018). AMBIENT TEMPERATURE IMPACT ON MICRO GAS TURBINES: EXPERIMENTAL CHARACTERIZATION. Acta Polytechnica CTU Proceedings, 20, 78-85. https://doi.org/10.14311/APP.2018.20.0078

[5] G. Żywica, T. Z. Kaczmarczyk, Breńkacz, M. Bogulicz, A. Andrearczyk, and P. Bagiński, "Investigation of dynamic properties of the microturbine with a maximum rotational speed of 120 krpm – predictions and experimental tests," Journal of Vibroengineering, Vol. 22, No. 2, pp. 298–312, Mar. 2020, https://doi.org/10.21595/jve.2019.20816

[6] Heng, X.; Zhang, H.; Wang, A.; Zhang, W. The Effect of Support Misalignment on Vibration Characteristics of Aero-Engine Rotor Systems under Ultra-High Operating Speeds. Machines 2024, 12, 669. https://doi.org/10.3390/machines12100669

[7] Tărăbîc, C.M.; Cican, G.; Olariu, C.; Dediu, G.; Catană, R.M. Test Stand for Microjet Engine Prototypes. Machines 2024, 12, 688. https://doi.org/10.3390/machines12100688

[8] Tărăbîc, C.M.; Olariu, C.; Cican, G.; Dediu, G.; Secăreanu, R.A.; Suciu, C.P.; Hank, A. Instrumentation and data acquisition system for microjet engines—Prototypes. Turbo 2023, X, 1.

Materials Research Proceedings 69 (2026) 601-606 https://doi.org/10.21741/9781644904251-107

The GREEN FOXFIRE Project: Sustainable Hybrid Propulsion for CubeSats Based on Paraffin/HTPB

Daniele TORTORICI[1,a], Sasi Kiran PALATEERDHAM[1,b], Antonella INGENITO[1,c *], Alessandro MONTANARO[2,d], Daniele PIAZZULLO[2,e], Luigi ALLOCCA[2,f]

[1]School of Aerospace Engineering, Sapienza University of Rome, Via Salaria 851, 00138 Rome, Italy

[2]National Research Council (CNR) - STEMS, Via Marconi 4, 00125 Naples, Italy

[a]daniele.tortorici@uniroma1.it, [b]sasikiran.palateerdham@uniroma1.it, [c]antonella.ingenito@uniroma1.it, [d]alessandro.montanaro@stems.cnr.it, [e]daniele.piazzullo@stems.cnr.it, [f]luigi.allocca@stems.cnr.it

Keywords: Hybrid Rocket Propulsion, Green Propellants, Paraffin/HTPB Fuel Blends, Mission Design

Abstract. The growing relevance of small satellites in space exploration, which in 2023 accounted for 97% of all spacecraft launched worldwide, requires addressing the challenges of propulsion miniaturization. To meet these needs, the GREEN FOXFIRE (Green Fuel and OXidizer For Innovative hybrid Rocket Engines) project investigates compact, efficient, and environmentally responsible hybrid systems, aiming to develop a sustainable hybrid rocket engine (HRE) capable of inserting a 24U CubeSat into Martian orbit from an Earth-orbit transfer. In this work, the performance of paraffin/HTPB fuel blends using gaseous oxygen as oxidizer was evaluated through a combination of numerical simulations and experimental ballistic tests. Paraffin offers high regression rates but limited mechanical strength, whereas HTPB improves structural integrity with lower combustion efficiency. Blended formulations (70/30, 50/50, 35/65, and 25/75 paraffin/HTPB ratios) were analyzed using NASA's Chemical Equilibrium with Applications (CEA) code and validated experimentally. Results confirmed that paraffin enhances regression rate and combustion efficiency, while HTPB contributes to mechanical robustness. Preliminary design activities also included a four-cluster thruster configuration with dual oxidizer tanks optimized for CubeSat mission requirements. Overall, the study demonstrates the feasibility of green hybrid propulsion as an enabling technology for interplanetary small-satellite missions, combining environmental sustainability with system scalability and performance.

Introduction

The rise of small satellites has reshaped space missions: from under 2% of total launch mass in 2013 to 97% of spacecraft by 2023 [1,2]. This miniaturization demands compact and efficient propulsion systems. Rocket engines are typically classified as solid, liquid, or hybrid. Solid motors are simple and reliable but lack controllability. Liquid engines offer precise thrust control but involve complex systems and hazardous propellants. Hybrid rocket engines (HRE) combine a solid fuel with a liquid or gaseous oxidizer, offering a compromise between safety, simplicity, and controllability.

Unlike traditional spacecrafts' mono- and bi-propellant systems that often rely on toxic substances like hydrazine [3], HRE can use greener propellants such as paraffin and nitrous oxide, reducing environmental and health risks [4].

Within this context, the GREEN FOXFIRE project proposes a hybrid propulsion system designed to insert a 24U CubeSat into Martian orbit. The mission profile was preliminarily

Content from this work may be used under the terms of the Creative Commons Attribution 3.0 license. Any further distribution of this work must maintain attribution to the author(s) and the title of the work, journal citation and DOI. Published under license by Materials Research Forum LLC.

Materials Research Proceedings 69 (2026) 601-606 https://doi.org/10.21741/9781644904251-107

analyzed to define performance requirements, leading to the development of a four-thruster configuration optimized for the spacecraft's mass, geometry, and delta-V needs [5].

To meet these demands with a sustainable approach, GREEN FOXFIRE investigates paraffin (P) and hydroxyl-terminated polybutadiene (HTPB) as solid fuels, paired with nitrous oxide (N_2O) and gaseous oxygen (O_2) as oxidizers. Paraffin offers high regression rates but lacks mechanical strength, while HTPB provides structural integrity with lower combustion efficiency [6,7]. Blending these fuels in various ratios (e.g., 70/30, 50/50, 35/65, 25/75) enables tailored performance characteristics suited to mission constraints. This integrated strategy supports the broader goal of enabling efficient, green propulsion for small-scale interplanetary exploration.

This work focuses on O_2 as oxidizer and integrates numerical simulations using NASA's Chemical Equilibrium with Applications (CEA) software and experimental ballistic testing to evaluate combustion behavior, regression rates, and performance metrics.

Fuel Preparation and Test Methodology

This study employs paraffin ($C_{28}H_{58}$) and HTPB ($C_{10}H_{15.4}O_{0.007}$) as solid fuels. HTPB is synthesized using poly bd® R45 V resin, with dioctyl adipate (DOA), toluene diisocyanate (TDI), and glycerol as additives to enhance flexibility and curing properties. Fuel blends were prepared with varying paraffin content, from 100% paraffin (100P) to 0% paraffin (0P), to assess the influence of composition on both material and combustion properties. All fuel formulations were tested using gaseous oxygen as oxidizer to evaluate the effects of fuel blending on combustion performance. Nitrous oxide will be introduced in future phases of the study.

Thermochemical analyses were performed using NASA's CEA software to predict the combustion behavior of the paraffin–HTPB blends. The simulations provided key performance parameters, including adiabatic flame temperature (T_{flame}), characteristic velocity (C*), and specific impulse (Isp). Simulations were conducted across a range of chamber pressures (50, 40, 30, 20, 10, and 5 bar) and oxidizer-to-fuel (O/F) ratios (0.5 to 7).

To experimentally evaluate the combustion performance of the paraffin–HTPB fuel blends, ballistic tests were conducted in the ASP Laboratory-scale hybrid rocket motor (Fig. 1). The setup included a thrust stand-mounted motor, an oxidizer feed line with a stainless-steel axial flow injector, a pyrotechnic igniter and a NI lab view based data acquisition system. The combustion chamber measures 240 mm in length and 80 mm in diameter and is equipped with a convergent-divergent nozzle featuring a 12 mm throat and semi-angles of 45° (convergent) and 13° (divergent).

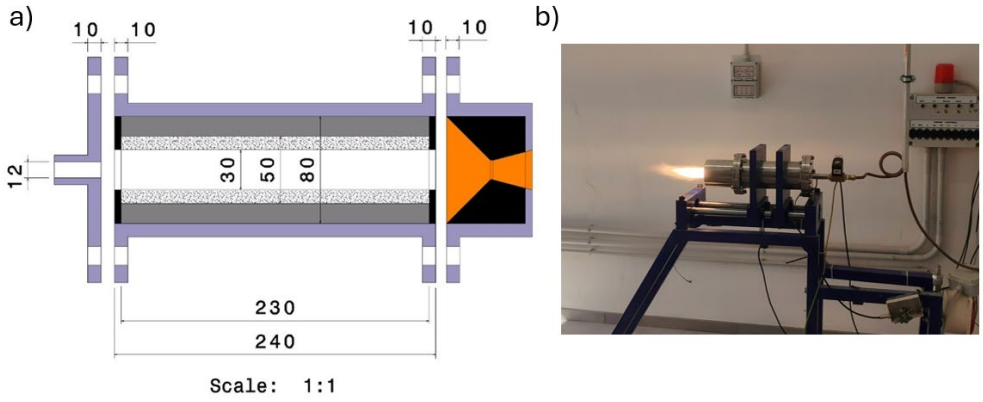


Fig. 1. HRE at the School of Aerospace Engineering: (a) motor schematic; (b) operational phase.

Each firing test lasted 5 or 10 seconds, with oxidizer flow regulated by a pressure controller and solenoid valve. After each test, the fuel grain was extracted and weighed to determine mass loss.

Materials Research Proceedings 69 (2026) 601-606 https://doi.org/10.21741/9781644904251-107

The regression rate ($\dot{\mathbf{r}}$) was calculated using the weight loss method, based on the difference between initial and final fuel mass ($\mathbf{m_b}$), burn duration ($\mathbf{t_b}$), and port geometry using port area diameter before ignition ($\mathbf{d_{ig}}$) and after burning ($\mathbf{d_b}$), using the following equations [8]:

$$\dot{r} = \frac{d_b - d_{ig}}{2t_b} \tag{1}$$

$$d_b = \sqrt{d_{ig}^2 + \frac{m_b}{\frac{\pi}{4}\rho_f l_f}} \tag{2}$$

$$G_{ox} = \frac{\dot{m}_{ox}}{\frac{\pi}{4}\left(\frac{d_b + d_{ig}}{2}\right)^2} \tag{3}$$

ρ_f and l_f refer to the fuel density and grain length, respectively, while $\dot{m}_{ox}$ and G_{ox} denote the oxidizer mass flow and oxidizer mass flux rate.

Theoretical Results

The CEA analyses were performed using five fuel combinations (100P, 70P, 35P, 25P, 100HTPB) and six pressures (from 5 to 50 bar), across O/F ratios ranging from 0.5 to 7. Fig. 2 presents the adiabatic flame temperature for the investigated pressures as a function of O/F ratio. All fuels show low adiabatic flame temperatures at low O/F (<2) due to insufficient oxidizer and incomplete combustion.

Maximum temperatures (of order of 2900 K) are observed between O/F 2–4. This range is coherent with stoichiometric ratios found in literature that are 3.4 for O_2/P combustion [9] and 2.95 for O_2/HTPB combustion [10], respectively, where combustion is nearly complete. Beyond this range, excess oxidizer lowers flame temperature. As shown by the temperature trend (T25P > T35P > T70P > T100P), fuels with higher hydrogen content exhibit lower flame temperatures at low and mid O/F ratios, indicating a greater oxidizer demand for complete combustion.

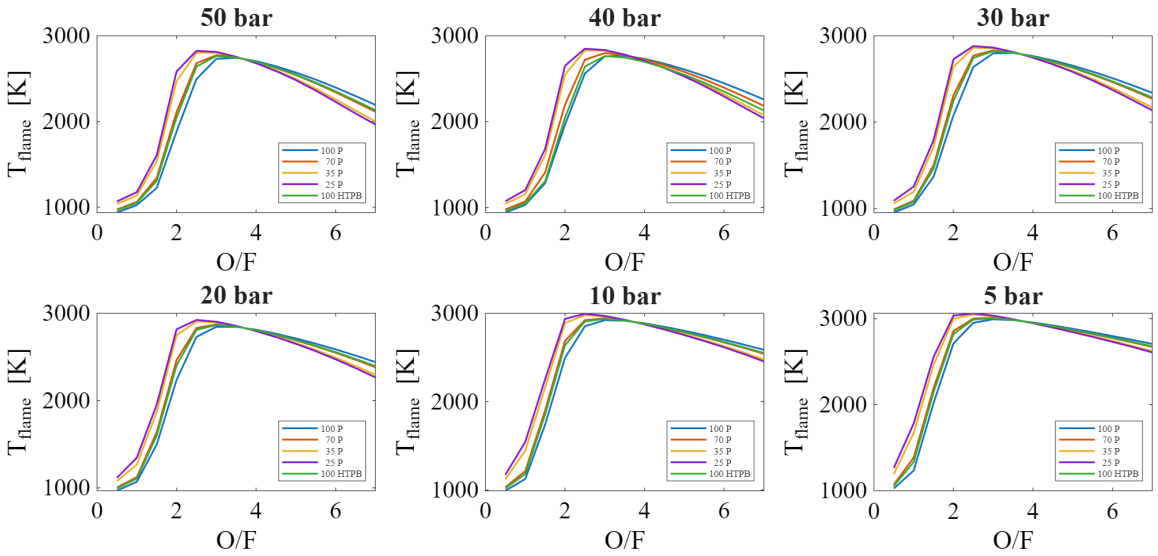


Fig. 2. CEA adiabatic flame temperature, for investigated fuels, as a function of O/F for various pressures.

Between 100P and 100HTPB, the latter exhibits higher flame temperatures at low to mid O/F due to its lower hydrogen content and better reactivity with limited oxidizer. At high O/F, the temperature trend reverses: T100P > T100HTPB > T70P > T35P > T25P.

Materials Research Proceedings 69 (2026) 601-606 https://doi.org/10.21741/9781644904251-107

Regarding characteristic velocity (C*, plots in Fig. 3), low O/F ratios yield lower values due to incomplete combustion. The optimal range for C* (1700 m/s for 25P to 1900 m/s for 100P) is O/F 2–2.5. Across all O/F values, 100P shows higher C* than 100HTPB (1800 m/s).

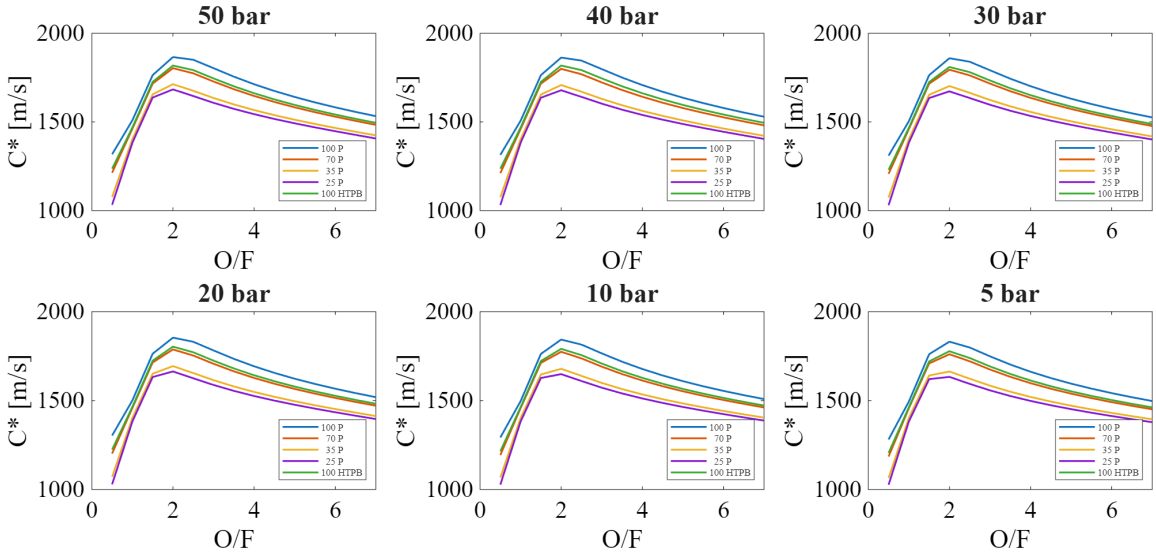


Fig. 3. CEA characteristic velocity, for investigated fuels, as a function of O/F for various pressures.

Specific impulse follows the C* trend, being lower at low O/F ratios due to incomplete combustion, peaking near stoichiometric conditions (O/F 2–3), and decreasing with excess oxidizer. Fig. 4 reports the peak specific impulse values for various propellants as a function of chamber pressure. The plot highlights how Isp decreases with lower pressure, as reduced pressure promotes product separation, thereby diminishing both thrust and specific thrust.

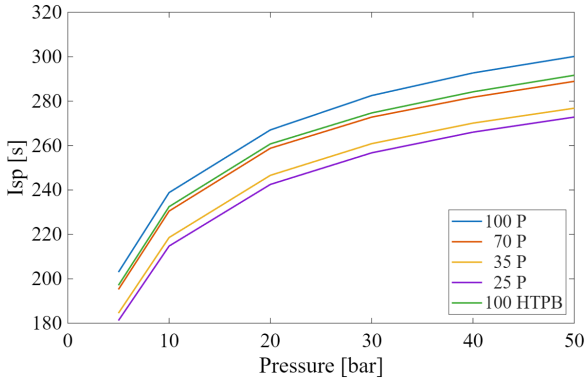


Fig. 4. CEA specific impulse, for investigated fuels, as a function pressure at stoichiometric O/F.

Experimental Results

The ballistic tests (Table 1) were conducted at the ASP Laboratory (Fig. 1). Pure paraffin fuel exhibited the highest regression rate (0.9 mm/s) at the lowest oxidizer mass flux (25.25 kg/m²·s), with a final port diameter of 47.8 mm. In contrast, blended fuels showed reduced regression rates, clustering around 0.3–0.4 mm/s despite varying HTPB content. The 25P and 0P formulations reached 0.4 mm/s, while 35P, 50P, and 70P blends maintained 0.3 mm/s across different mass fluxes. These results indicate a general decline in regression rate with increasing oxidizer mass flux and highlight the trade-off introduced by HTPB: although it lowers regression rates, it enhances structural integrity.

Materials Research Proceedings 69 (2026) 601-606 https://doi.org/10.21741/9781644904251-107

Table 1. Data from ballistic testing.

Fuel	Gox [kg/(m^2·s)]	O_2 mass [g]	Grain initial mass [g]	Grain final mass [g]	ṙ [mm/s]	Final port diameter [mm]	O/F
100 P	25.25	300	820	600	0.9	47.8	1.4
70 P	35.40	140	780	745	0.3	33.5	4.0
50 P	25.36	100	800	766	0.3	33.4	2.9
35 P	30.52	120	812	779	0.3	33.3	3.6
25 P	30.24	120	829	793	0.4	33.6	3.3
0 P	27.56	110	743	708	0.4	33.8	3.1

The motor firing sequence included ramp-up, steady-state, and cut-off phases, as illustrated in Fig. 5. After ignition, a rapid pressure spike was followed by combustion stabilization around 0.5 s. During steady-state operation, 100P fuel delivered the highest performance, reaching ~3.5 bar chamber pressure and 3500–4000 g thrust. Blends like 25P and 35P sustained ~3.0 bar and ~2500–3000 g thrust, while 50P and 70P showed intermediate and stable behavior, respectively.

The 0P formulation matched or exceeded the 50P blend, achieving ~3.5 bar and ~5000 g thrust. All fuels exhibited a sharp drop in pressure and thrust during the cut-off phase, marking complete flameout.

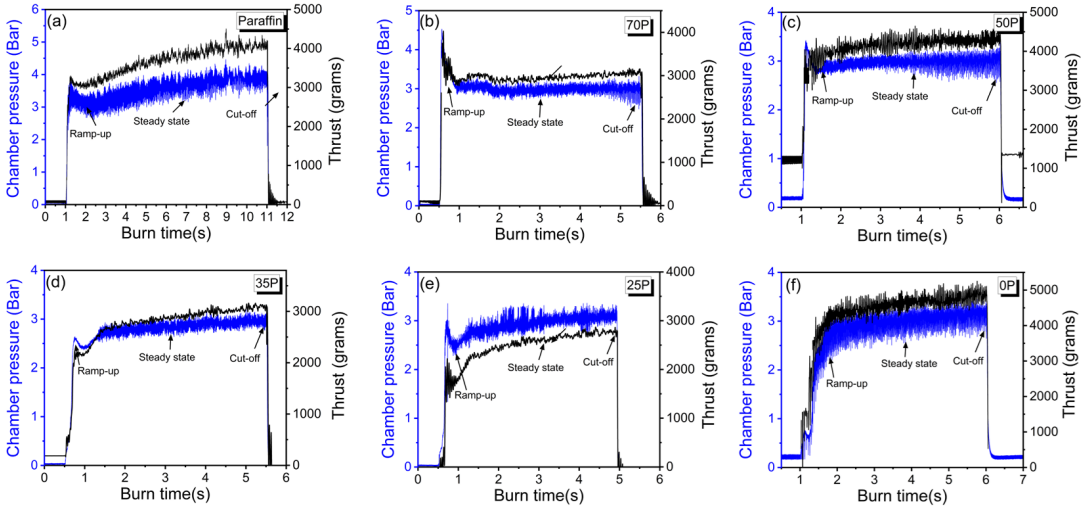


Fig. 5. Combustion chamber pressure and thrust profile for 100P (a), 70P (b), 50P (c), 35P (d), 25P (e), and 0P (f) combustion with gaseous oxygen.

Conclusion

The GREEN FOXFIRE project aims to demonstrate the feasibility of sustainable hybrid propulsion for small satellite missions, specifically targeting Mars orbit insertion for a 24U CubeSat. Through a combination of numerical simulations and ballistic testing, paraffin–HTPB fuel blends paired with gaseous oxygen were shown to offer a viable balance between combustion efficiency and structural integrity. Pure paraffin achieved the highest regression rates (0.9 mm/s), while HTPB contributed to mechanical robustness. During steady-state operation, thrust levels were ~3500–4000 g for 100P, ~3000 g for 70P and 50P, ~2500–3000 g for 35P and for 25P, and ~5000 g for 0P. Performance metrics such as adiabatic flame temperature, characteristic velocity, and specific impulse confirmed optimal combustion near stoichiometric O/F ratios, with pressure-dependent enhancements. The successful integration of a multi-thruster configuration and oxidizer injection system will support the potential of this green hybrid architecture for future interplanetary missions.

Acknowledgement
The authors acknowledge the GREEN FOXFIRE (Green Fuel and OXidizer For Innovative hybrid Rocket Engines) project, a joint research initiative between Sapienza University of Rome and the STEMS group of CNR Naples, funded under Italy's PRIN 2022 program, for its financial support.

References

[1] Weston, S. V., Burkhard, C. D., Stupl, J. M., Ticknor, R. L., Yost, B. D., Austin, R. A., ... & Soto, L. S. (2025). State-of-the-art small spacecraft technology.

[2] Bryce and Space Technology. "SmallSat by the Numbers, 2024." Accessed September 08, 2025. [Online] Available at: https://brycetech.com/reports/reportdocuments/Bryce_Smallsats_2024.pdf

[3] Niemeier, J. K., & Kjell, D. P. (2013). Hydrazine and aqueous hydrazine solutions: evaluating safety in chemical processes. Organic Process Research & Development, 17(12), 1580-1590. https://doi.org/10.1021/op400120g

[4] Montanaro, A., Piazzullo, D., Tortorici, D., Ingenito, A., & Allocca, L. (2026). Green rocket propulsion: overview of nitrous oxide applications with emphasis on hybrid systems. Fuel, 406, 137036. https://doi.org/10.1016/j.fuel.2025.137036

[5] Tortorici, D., Ingenito, A., Piazzullo, D., Allocca, L. & Montanaro, A. Design of a 24U-cubesat hybrid rocket engine for insertion in Mars orbit., presented in 12TH IAA Symposium on the future of space exploration (2025).

[6] Pal, Y., Mahottamananda, S. N., Palateerdham, S. K., Subha, S., & Ingenito, A. (2021). Review on the regression rate-improvement techniques and mechanical performance of hybrid rocket fuels. FirePhysChem, 1(4), 272-282. https://doi.org/10.1016/j.fpc.2021.11.016

[7] Palateerdham, S. K., Ingenito, A., & Ciprioti, S. (2020). Experimental investigation of the paraffin thermomechanical properties and hybrid rocket engine performance for different fuel grain formulations. MS Thesis. https://doi.org/10.13140/RG.2.2.25305.29280

[8] Palateerdham, S. K., Tortorici, D., Ingenito, A. Thermo-Mechanical Characterization and Combustion Analysis of HTPB/Paraffin Wax blended Hybrid Rocket. Presented in HiSST: 4th International Conference on High-Speed Vehicle Science & Technology. HiSST-2025-324 (2025).

[9] Migliorino, M. T., Bianchi, D., & Nasuti, F. (2020). Numerical analysis of paraffin-wax/oxygen hybrid rocket engines. Journal of Propulsion and Power, 36(6), 806-819. https://doi.org/10.2514/1.B37914

[10] George, P., Krishnan, S., Varkey, P. M., Ravindran, M., & Ramachandran, L. (2001). Fuel regression rate in hydroxyl-terminated-polybutadiene/gaseous-oxygen hybrid rocket motors. Journal of Propulsion and Power, 17(1), 35-42. https://doi.org/10.2514/2.5704

Materials Research Proceedings 69 (2026) 607-613 https://doi.org/10.21741/9781644904251-108

Off-Design Performance Consequences of Design Payload and Range Requirements for SPPH Hybrid-Electric Aircraft

Maurice F.M. HOOGREEF[1,a *]

[1]Delft University of Technology, Faculty of Aerospace Engineering, Kluyverweg 1, 2629HS Delft, The Netherlands

[a]m.f.m.hoogreef@tudelft.nl

Keywords: Aircraft Design, Hybrid-Electric Aircraft, Off-Design Performance

Abstract. This article illustrates the variations in off-design performance for a serial-parallel partial hybrid regional aircraft when varying design range or payload. It leverages recent work exploring off-design performance of hybrid electric aircraft and shows the impact of TLAR selection on the operational bandwidth of such aircraft. The latter is important to exploit installed battery capacity, especially when considering a tighter coupling between conceptual aircraft design and strategic airline planning. Comparisons are made to baseline kerosene aircraft, designed for identical TLAR flying identical missions. Results highlight the importance of TLAR selection to achieve both operational flexibility and fuel savings, especially concerning the selection of design range, payload and battery supplied power ratio.

Introduction and motivation

Aircraft electrification is considered as one of the pathways to address the environmental targets. Among targeted solutions distinctions can be made between so-called mild and heavy hybrids (typically including a battery and combustion engine), as well as fully electric designs.

Design solutions typically evaluate performance for a single design mission. However, especially for hybrid-electric aircraft, off-design performance becomes interesting from the perspective of leveraging installed battery capacity for shorter missions or missions with less payload. Such off-design performance is important if we consider the typical average usage of aircraft, see for example the study by [1] or [2]. Recent studies investigating off-design performance of hybrid-electric aircraft ([3], [4], [5], [6]) show potential benefits/penalties on aircraft performance across the payload-range diagram for hybrid-electric aircraft.

Studies coupling aircraft design with strategic airline planning indicate that a tighter coupling can achieve emission benefits at little consequence for profitability. ([7], [8]). These studies, however, also indicate that aircraft design points in terms of, for example, payload and range should be coupled with strategic airline planning where including off-design performance is essential to find more sustainable designs.

However, we may wonder how the off-design performance is impacted by the chosen design point, and whether it is possible to achieve a larger bandwidth leveraging installed battery capacity. This study addresses these points for the most promising hybrid-electric architecture found in a comparative study for off-design performance of various hybrid-electric powertrain architectures [6]; the serial/parallel partial hybrid (SPPH) (as defined by [9]).

Method

The studies presented in this article use the same method as outlined in *[6]*. It relies on a conceptual aircraft design framework *[10]*, adapted to analyze hybrid-electric aircraft according to the methods by *[11]* and *[12]*. As the control variables for the hybrid-electric powertrain allow for infinitely many possible combinations, a strategy is used that is maximizing the battery supplied power in cruise (whilst considering the operating limits of all powertrain components) to leverage

Content from this work may be used under the terms of the Creative Commons Attribution 3.0 license. Any further distribution of this work must maintain attribution to the author(s) and the title of the work, journal citation and DOI. Published under license by Materials Research Forum LLC.

Materials Research Proceedings 69 (2026) 607-613 https://doi.org/10.21741/9781644904251-108

the efficiency of the electric part of the powertrain. Ideally, the gas turbine is downsized to its cruise condition, with the battery complementing it to meet other design constraints, and the battery providing a constant positive amount of power during the cruise phase. Though not necessarily optimal, this strategy allows for a consistent comparison.
The SPPH powertrain operates two propulsor paths. In this particular article, a single propeller (on each wing) is attached on the primary path, and three distributed electrical propellers are on the secondary path. To minimize powertrain mass, conversion losses should be minimized by choosing a strategy that is "decoupling" the two branches of the SPPH powertrain. Decoupling results in minimizing EM1 in Figure 1, thereby minimizing the mass of this powertrain component and minimizing conversion losses. For more details, the reader is referred to *[6]*.

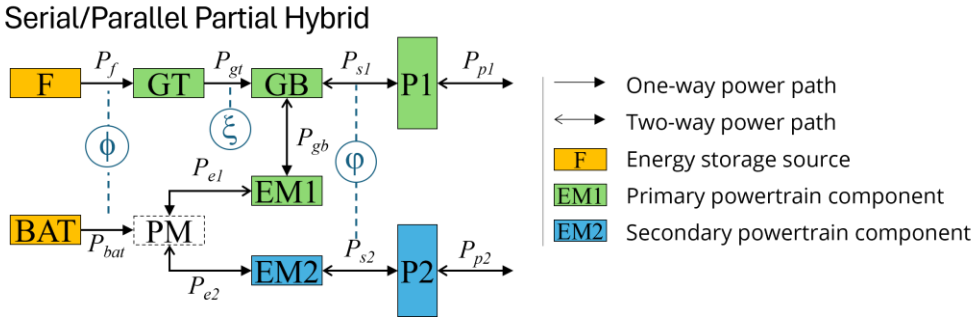


Figure 1 – Serial/Parallel Partial Hybrid (SPPH) powertrain architecture

Analysis and results

A sweep of design payload, at constant design range, and a sweep of design range at constant design payload has been performed for regional SPPH aircraft, along with kerosene baselines for identical top-level aircraft requirements (TLARs), based on the ATR 72-600. The baseline kerosene and SPPH versions are sized for 70 passengers (100kg each, plus 500kg additional cargo mass) and a design range of 926km. For SPPH aircraft a cruise battery supplied power ratio (φ*) of 10% or 20% is used, with a shaft power ratio (ψ) of 30% or 50%, respectively. TLARs and technology scenario (2035 entry into service, battery at 340 Wh/kg usable pack level and 20% maximum depth of discharge) are detailed in [6]. Note that all comparisons are made to baseline kerosene aircraft flying identical off-design missions. Analyses are presented graphically in terms of delta fuel consumption with respect to the kerosene aircraft and in terms of cruise supplied power ratio (maximizing usage of installed battery capacity).

Off-design performance sensitivity to design range

The baseline design point (70 pax, 926km) has been varied to 648, 1019 and 1111km, for the same design payload. Off-design performance is illustrated in Figures 2-5 in terms of delta fuel consumption with respect to kerosene baselines for an SPPH with design $\varphi^* = 10\%$, designed for identical TLAR flying the same off-design missions. Figures 6-9 show the cruise supplied power split for these aircraft.

The figures show a quickly narrowing band of fuel reduction when increasing design range for operational flexibility. Interestingly, it is possible to increase the cruise supplied power ratio for both shorter and longer off-design missions for longer design range. This highlights the impact of MTOM on the absolute fuel consumption as the larger electrification is not reflected in delta fuel consumption. It also marks the importance of the selection of the design TLARs when balancing operational flexibility and fuel efficiency.

Materials Research Proceedings 69 (2026) 607-613 https://doi.org/10.21741/9781644904251-108

SPPH φ=10%, ψ = 30% variable design range delta fuel contours.*

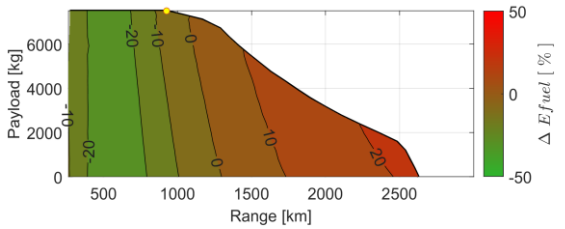


Figure 2 – Design point 70PAX @926km

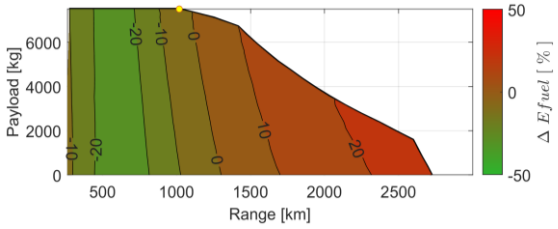


Figure 3 – Design point 70PAX @1019km

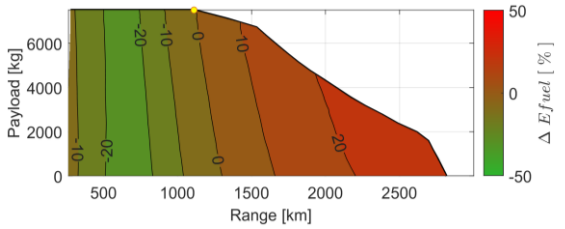


Figure 4 – Design point 70PAX @1111km

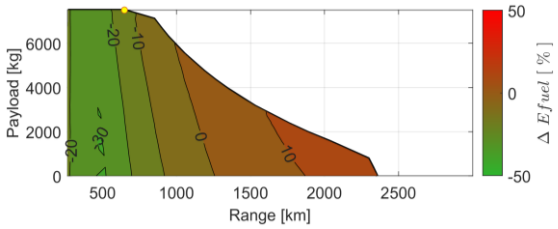


Figure 5 – Design point 70PAX @648km

SPPH φ=10%, ψ = 30% variable design range cruise supplied power split contours.*

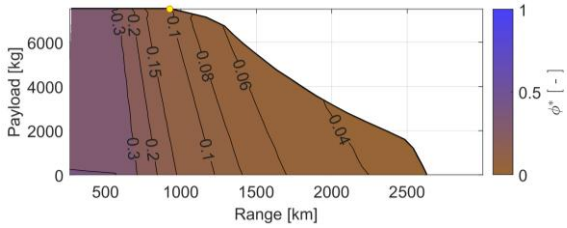


Figure 6 – Design point 70PAX @926km

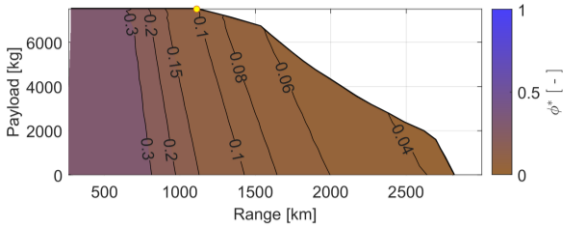


Figure 7 – Design point 70PAX @1019km

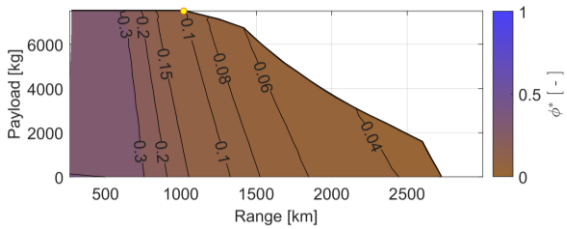


Figure 8 – Design point 70PAX @1111km

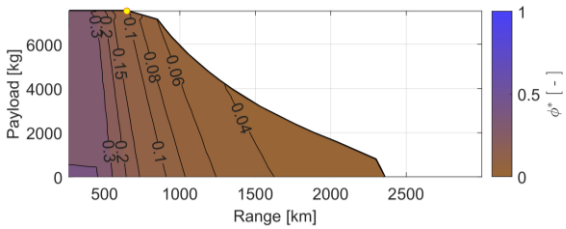


Figure 9 – Design point 70PAX @648km

Figures 10 – 13 and 14-17 illustrate the same comparison for of a SPPH aircraft with design *φ* = 20%*. These figures show two clear additional trends; (1) operational flexibility in terms of range is greatly reduced and (2) these heavier hybrids offer significant relative fuel savings over almost their entire payload range envelope. This illustrates an important design trade-off.

Materials Research Proceedings 69 (2026) 607-613 https://doi.org/10.21741/9781644904251-108

SPPH φ=20%, ψ = 50% variable design range delta fuel contours.*

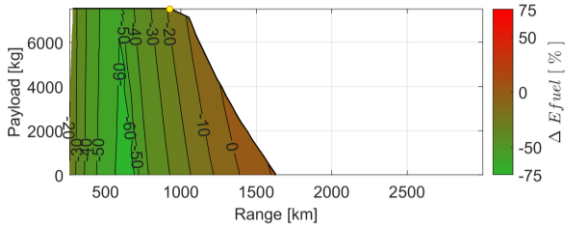


Figure 10 – Design point 70PAX @926km

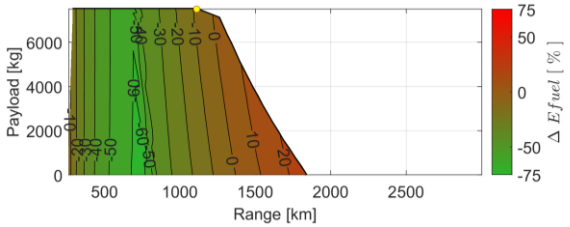


Figure 11 – Design point 70PAX @1019km

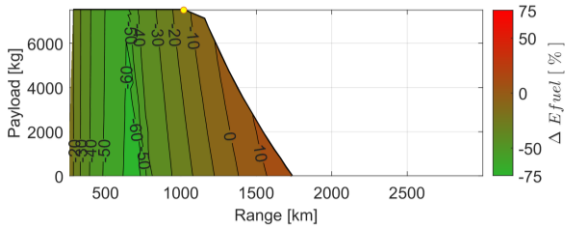


Figure 12 – Design point 70PAX @1111km

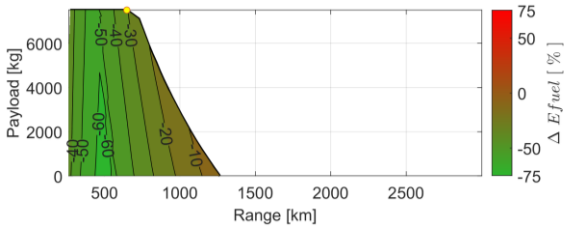


Figure 13 – Design point 70PAX @648km

SPPH φ=20%, ψ = 50% variable design range cruise supplied power split contours.*

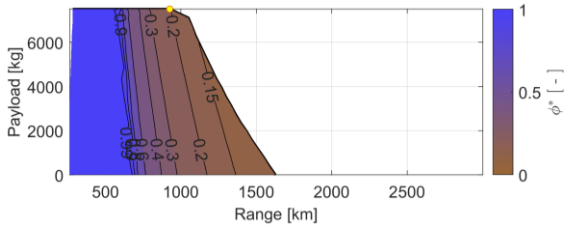


Figure 14 – Design point 70PAX @926km

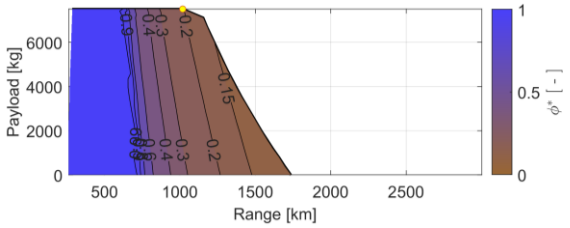


Figure 15 – Design point 70PAX @1019km

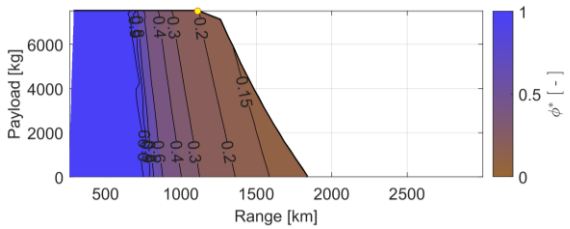


Figure 16 – Design point 70PAX @1111km

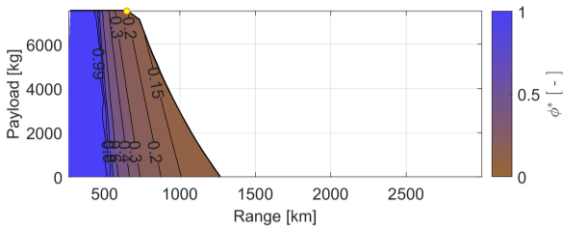


Figure 17 – Design point 70PAX @648km

Off-design performance sensitivity to design payload

The baseline design point (70 pax, 926km, 500kg extra cargo) has been varied to 40, 50 and 80 passengers. Off-design performance is illustrated in Figures 18-21 in terms of delta fuel consumption for a design $\varphi^* = 10\%$ with respect to kerosene baselines, designed according to the same requirements, flying the same off-design missions. Figures 22-25 show the cruise supplied power split.

Increased payload offers both operational flexibility and increased electrification over a larger bandwidth of missions. In fact, the cruise supplied power split can be higher for more ranges and the increased payload does not seem to penalize the relative energy saving (compared to identically designed kerosene aircraft). This seems to confirm the possibility to design for larger design payloads, when a 36 meter span limit is no longer a concern [13] [14].

Materials Research Proceedings 69 (2026) 607-613 https://doi.org/10.21741/9781644904251-108

SPPH φ=10%, ψ = 30% variable design payload delta fuel contours.*

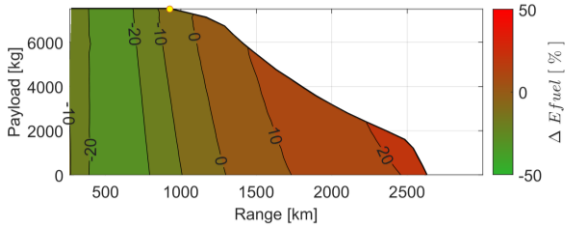


Figure 18 – Design point 70PAX @926km

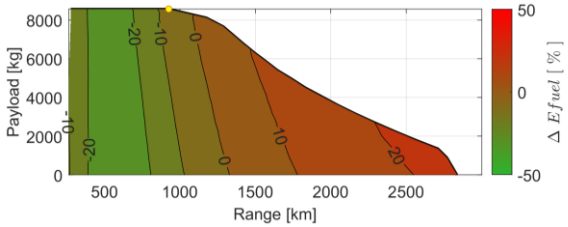


Figure 19 – Design point 40PAX @926km

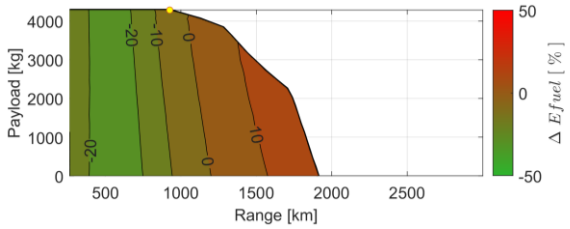


Figure 20 – Design point 80PAX @926km

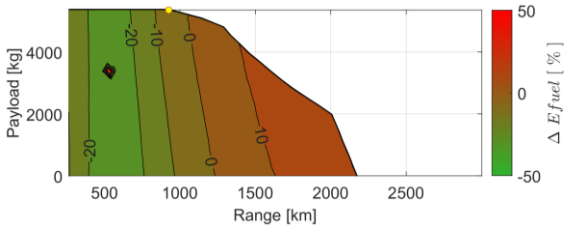


Figure 21 – Design point 50PAX @926km

SPPH φ=10%, ψ = 30% variable design payload cruise supplied power split contours.*

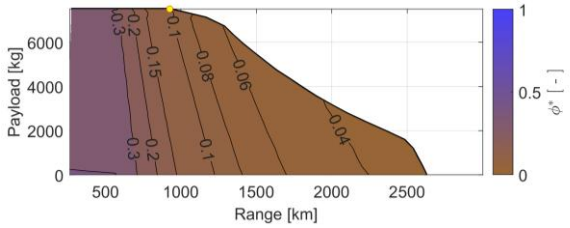


Figure 22 – Design point 70PAX @926km

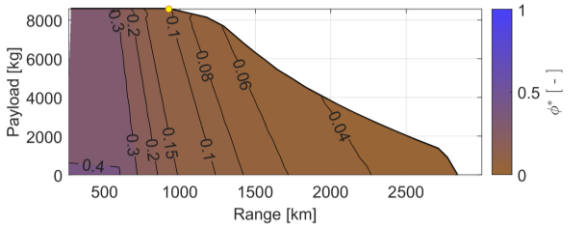


Figure 23 – Design point 40PAX @926km

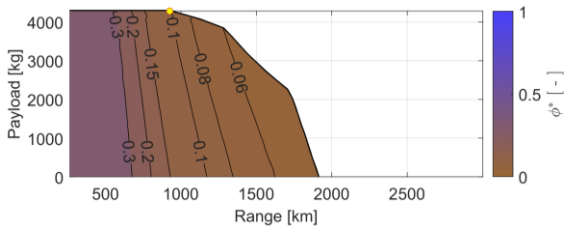


Figure 24 – Design point 80PAX @926km

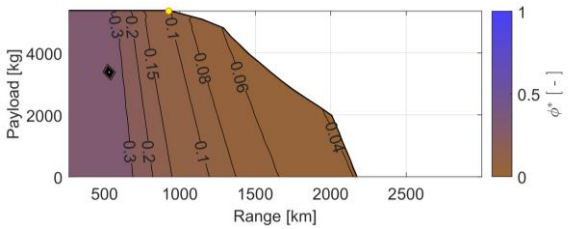


Figure 25 – Design point 50PAX @926km

Similar studies for *SPPH with design φ*=20%*, as illustrated in Figures 26 – 29 and Figures 30 – 33, respectively, confirm that the relative fuel saving is (almost) not penalized by design payload. Additionally, they offer significant relative fuel consumption benefits over almost their entire payload-range diagram. However, the range flexibility seems much less sensitive to design payload as the powertrain mass is more dominant on MTOM than payload. Consequently, the larger payload variant does not offer much more range flexibility anymore.

Materials Research Proceedings 69 (2026) 607-613 https://doi.org/10.21741/9781644904251-108

SPPH φ=20%, ψ = 50% variable design payload delta fuel contours.*

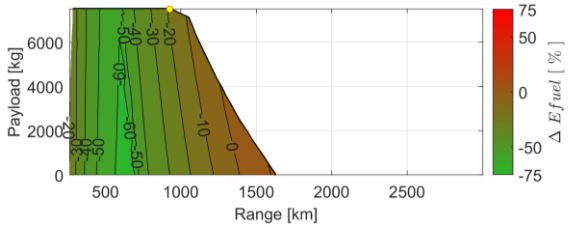


Figure 26 – Design point 70PAX @926km

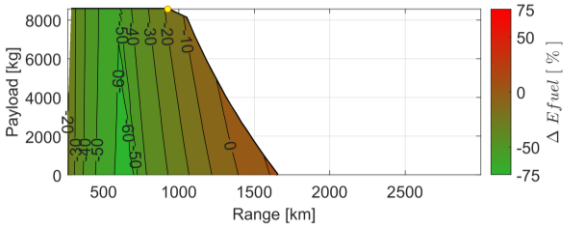


Figure 27 – Design point 40PAX @926km

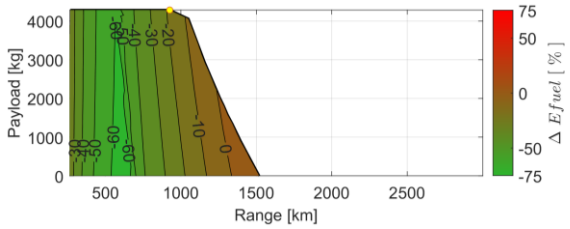


Figure 28 – Design point 80PAX @926km

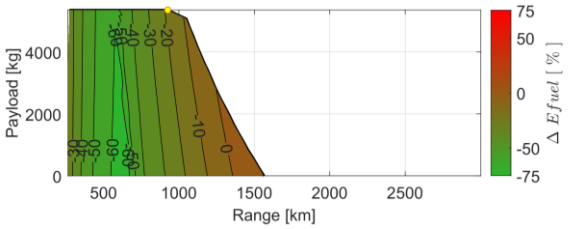


Figure 29 – Design point 50PAX @926km

SPPH φ=20%, ψ = 50% variable design payload cruise supplied power split contours.*

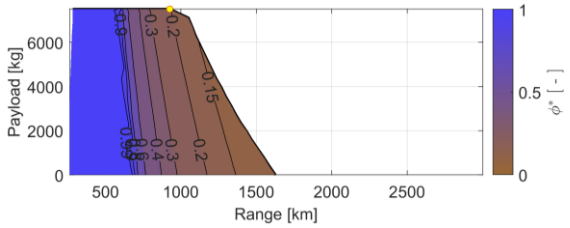


Figure 30 – Design point 70PAX @926km

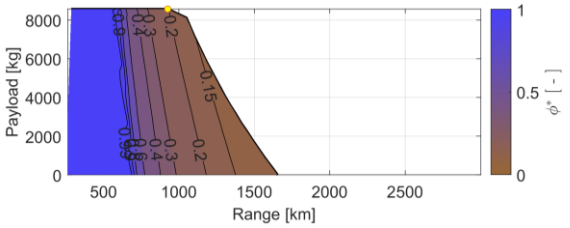


Figure 31 – Design point 40PAX @926km

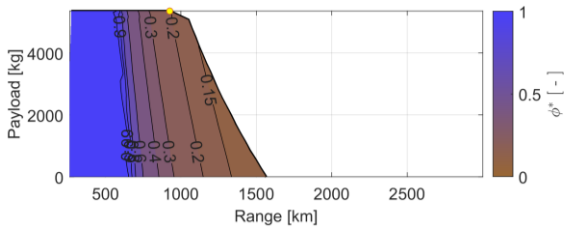


Figure 32 – Design point 80PAX @926km

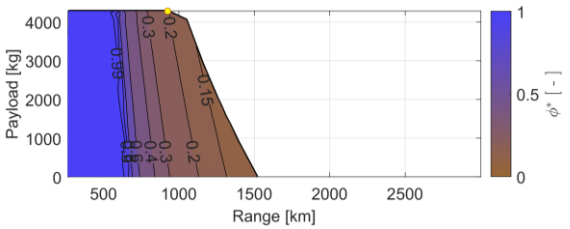


Figure 33 – Design point 50PAX @926km

Conclusions

A sweep of design payload, at constant design range, and a sweep of design range at constant design payload was performed for regional SPPH aircraft (with design supplied power ratio of 10% and 20%), along with kerosene baselines for identical TLARs, flying identical missions. Results illustrate quickly narrowing bands of fuel reduction potential when increasing design range. Heavier hybrids demonstrate that operational flexibility in terms of range is greatly reduced when increasing design supplied power ratio although they offer significant relative fuel savings over almost their entire payload range envelope. This illustrates an important design trade-off. Increased payload offers both operational flexibility and increased electrification over a larger bandwidth of missions for light hybridization. Increased payload does not seem to penalize the relative energy saving compared to kerosene aircraft (with same TLARs and flying identical missions). However, heavier hybrids with increased payload do not offer more range flexibility anymore as the powertrain mass becomes dominant on MTOM.

Acknowledgements
This research was partially funded by the “CHYLA” project, which received funding from the European Union’s Horizon 2020 research and innovation program under Grant Agreement No. 101007715. Special thanks go to Dr. Vincent Bonnin whose efforts made these studies possible.

References
[1] B. Graver, D. Rutherford and S. Zheng, "CO2 emissions from commercial aviation: 2013, 2018, and 2019.," 2020. https://theicct.org/publications/co2-emissions-commercial-aviation-2020.
[2] A. T. Isikveren, S. Kaiser, C. Pornet and P. C. Vratny, "Pre-design strategies and sizing techniques for dual-energy aircraft," Aircraft Engineering and Aerospace Technology, vol. 86, p. 525–542, September 2014. https://doi.org/10.1108/AEAT-08-2014-0122.
[3] G. E. Wroblewski and P. J. Ansell, "Mission Analysis and Emissions for Conventional and Hybrid-Electric Commercial Transport Aircraft," Journal of Aircraft, vol. 56, pp. 1200-1213, 2019. https://doi.org/10.2514/1.C035070.
[4] G. Palaia and K. A. Salem, "Mission Performance Analysis of Hybrid-Electric Regional Aircraft," Aerospace, vol. 10, p. 246, March 2023. https://doi.org/10.3390/aerospace10030246.
[5] D. Quillet, V. Boulanger and D. Rancourt, "Off-Design Performance Analysis of a Parallel Hybrid Electric Regional Turboprop Aircraft," Journal of Aircraft, p. 1–11, 2023. https://doi.org/10.2514/1.C036927.
[6] V. O. Bonnin and M. F. M. Hoogreef, "Exploration of Off-Design Performance for Hybrid Electric Regional Aircraft," Journal of Aircraft, vol. 62, no. 4, pp. 876-895, 2025. https://doi.org/10.2514/1.C037893.
[7] M. Hoogreef, N. Zuijderwijk, E. Scheers, P.-J. Proesmans and B. F. Santos, "Coupled Hybrid & Electric Aircraft Design and Strategic Airline Planning," in AIAA AVIATION 2023 Forum, 2023. https://arc.aiaa.org/doi/abs/10.2514/6.2023-3869.
[8] S. C. Antunes, P.-J. Proesmans, B. F. Santos, M. Hoogreef and S. Birolini, "Multidisciplinary Coupling for Hybrid-Electric Aircraft Design and Strategic Airline Planning Including Off-Design Performance," in AIAA SCITECH 2025 Forum, 2025. https://arc.aiaa.org/doi/abs/10.2514/6.2025-2375.
[9] Felder, James L., "NASA Electric Propulsion System Studies," 2015. https://ntrs.nasa.gov/citations/20160009274.
[10] R. J. M. Elmendorp, R. Vos and G. La Rocca, "A Conceptual Design and Analysis Method for Conventional and Unconventional Airplanes," in ICAS Congress 2014, 2014. https://repository.tudelft.nl/record/uuid:1dc55ce5-18c3-4986-b668-f70d9b24aac0.
[11] R. de Vries, "Hybrid-Electric Aircraft with Over-the-Wing Distributed Propulsion: Aerodynamic Performance and Conceptual Design," 2022. https://resolver.tudelft.nl/uuid:ef87dc11-e7b2-4726-a41f-28588d64c58d.
[12] F. Orefice, S. Corcione, F. Nicolosi, D. Ciliberti and G. D. Rosa, "Performance Calculation for Hybrid-Electric Aircraft integrating Aero-Propulsive Interactions," in AIAA Scitech 2021 Forum, 2021. https://arc.aiaa.org/doi/abs/10.2514/6.2021-1640.
[13] V. Bonnin, M. Hoogreef and R. de Vries, "Distributed Hybrid-Electric Propulsion Benefits for Span-Limited Aircraft," in AIAA SCITECH 2023 Forum, 2023. https://arc.aiaa.org/doi/abs/10.2514/6.2023-2098.
[14] R. Wolleswinkel, R. de Vries, M. F. M. Hoogreef and R. Vos, "A New Perspective on Battery-Electric Aviation, Part I: Reassessment of Achievable Range," in AIAA Scitech 2024 Forum, 2024. https://doi.org/10.2514/6.2024-1489.

Materials Research Proceedings 69 (2026) 614-619 https://doi.org/10.21741/9781644904251-109

Engineering Polyimide Materials for Moon Exploration Missions: Intrinsic Self-Healing and Shape Memory Properties via Supramolecular Interactions

Francesca BLONDELLI[1,a], Elisa TOTO[1,b], Guido SACCONE[2,c], Nunzia FAVALORO[2,d], Maria Gabriella SANTONICOLA[1,e*]

[1]Department of Chemical Engineering Materials Environment, Sapienza University of Rome, Via del Castro Laurenziano 7, 00161 Rome, Italy

[2]Italian Aerospace Research Centre, Via Maiorise, 81043, Capua, Italy

[a]francesca.blondelli@uniroma1.it, [b]elisa.toto@uniroma1.it, [c]g.saccone@cira.it, [d]n.favaloro@cira.it, [e]mariagabriella.santonicola@uniroma1.it

Keywords: Polyimide; Self-Healing Properties; Shape Memory Ability; Supramolecular Interactions; Lunar Exploration Missions

Abstract. Polyimides are a well-established class of high-performance polymers known for their excellent thermal and chemical stability, mechanical robustness, low outgassing, and radiation resistance. These properties have made polyimides essential in aerospace applications, both for systems operating in low Earth orbit and for those used in long-term exploration missions. In recent years, polyimides have attracted growing interest for planetary exploration, particularly for lunar missions. The critical challenges of these missions include mechanical abrasion from regolith dust and the extreme temperature fluctuations. These conditions can damage exposed surfaces and compromise system performance. To overcome these challenges, self-healing materials represent a promising strategy, enabling polymers to autonomously repair mechanical damage and thereby enhance the reliability and operational lifetime of spacecraft components.

Introduction

Among the different classes of high-performance polymers, polyimides (PIs) are recognized as one of the most reliable options for aerospace applications. Their combination of thermal and chemical stability, mechanical strength, low outgassing, and resistance to radiation has made PIs widely used in many aerospace systems, from satellites in low Earth orbit (LEO) to components for future lunar missions [1, 2]. For LEO applications, PIs are commonly used as insulating layers in multi-layer insulation systems and as protective coatings against atomic oxygen erosion, which can severely degrade polymeric surfaces [3]. This class of polymers also finds application in flexible solar arrays, solar sails, and high-temperature adhesives [3]. In recent years, PIs have attracted growing interest for their applications in planetary missions, especially for lunar exploration missions. The critical challenges of these missions, such as mechanical abrasion from regolith dust, demand materials that can withstand harsh environments while maintaining structural integrity. Indeed, the surfaces of exposed materials may suffer progressive damage, for instance due to the accumulation and adhesion of abrasive lunar dust [4, 5]. This phenomenon can degrade the surface, and compromise the functionality of systems, posing a risk to mission success.

Over the last decade, self-healing materials have gained increasing interest in the aerospace field, thanks to technological advances that allow the development of systems able of repairing mechanical damage [6]. Integrating these materials into the design of spacecraft components can enhance structural integrity, safety, and mission reliability, extending the operational lifetime of space systems [7, 8]. Based on this ability, self-healing mechanisms are classified as intrinsic or extrinsic [9]. Extrinsic self-healing refers to systems in which the healing agents are embedded

Content from this work may be used under the terms of the Creative Commons Attribution 3.0 license. Any further distribution of this work must maintain attribution to the author(s) and the title of the work, journal citation and DOI. Published under license by Materials Research Forum LLC.

Materials Research Proceedings 69 (2026) 614-619 https://doi.org/10.21741/9781644904251-109

within the material structure, typically stored in microcapsules networks that release the agent upon damage [10]. Intrinsic self-healing mechanisms do not require healing agents. They are typically based either on dynamic covalent chemistry, such as Diels–Alder reactions, dynamic urea and imine bonds, or on supramolecular interactions, including H-bonding, van der Waals forces, hydrophobic interactions, π–π stacking, and interdiffusion mechanisms [11]. According to the type of recovery process, self-healing materials are autonomous and non-autonomous [9]. Non-autonomic self-healing materials require an external trigger, like heat. Autonomic self-healing materials do not require any additional external trigger, but the damage itself is the stimulus for the healing [9].

In this context, the development of PI with self-repair capabilities and shape memory behaviour is a promising strategy to enhance the resilience and longevity of components during long-term exploration missions. This work focuses on the design, synthesis and characterization of flexible supramolecular PI materials with non-autonomous intrinsic self-healing and shape-memory properties. These results highlight the strong potential of polyimide systems engineered via supramolecular interactions to act as multifunctional materials for future space missions.

Experimental section

Polyimide synthesis. Three types of PIs were synthesized under an argon atmosphere via the polycondensation reaction between the same aromatic fluorinated dianhydride and two different diamines (one aliphatic and one aromatic). The corresponding diamine(s) were dissolved in a mixed DMAc/IPA solvent under mechanical stirring, and a stoichiometric amount of dianhydride was subsequently added to the solution. The reactions were carried out for 24 h at room temperature. After reaction, the solutions were heated in oven to evaporate the solvent. Finally, a thermal imidization process was optimized to obtain homogeneous PIs membranes (thickness ~ 300 μm).

Characterization methods. Density was measured by the hydrostatic weighing method in ultrapure water using the Sartorius YDK01 kit [2]. The wettability was assessed using the DataPhysics OCA15 PRO tensiometer, and the surface free energies (SFE) was calculated following the Owens–Wendt method [2]. In order to assess the self-healing behaviour of materials, optical images were acquired using a Leica polarized light microscope (DMLP series, Leica Microsystems, Germany). The sample surfaces were mechanically scratched with a scalpel, simulating external mechanical damage that may occur during exploration missions. Subsequently, the samples were heated at different temperatures (T = 50 °C and 150 °C). The two temperatures were chosen to provide a representation of the thermal conditions encountered on the lunar surface. Images were acquired immediately after the mechanical damage and subsequently after the repair induced by heat exposure.

Results and discussion

The fully aromatic PI is referred to as PI-1 (Fig.1a), the supramolecular semi-aromatic PI containing an aliphatic diamine and the same aromatic dianhydride as PI-2 (Fig.1b), and the supramolecular copolyimide prepared from both an aliphatic and an aromatic diamine with the same aromatic dianhydride as coPI-3 (Fig.1c).

Materials Research Proceedings 69 (2026) 614-619 https://doi.org/10.21741/9781644904251-109

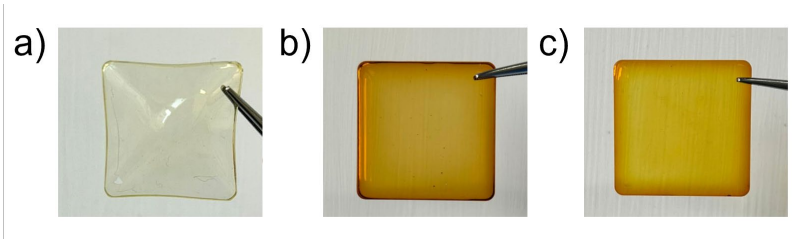


Fig.1 *a) Fully aromatic polyimide PI-1, b) semi-aromatic polyimide PI-2, and c) semi-aromatic copolyimide coPI-3 membranes obtained after thermal treatment.*

The density values of PI-1, PI-2, coPI-3 are reported in Table 1. The analysis indicates that the density decreases from 1.452 g·cm^{-3} (PI-1) to 1.107 g·cm^{-3} (PI-2) and 1.154 g·cm^{-3} (coPI-3) with the introduction of the aliphatic diamine. This reduction can be attributed to the lower packing efficiency and higher free volume associated with the flexible aliphatic segments. The reduction in density contributes to lowering payload mass, a key factor in spacecraft design and mission cost efficiency.

The WCA and the SFE with its dispersive (γ^d) and polar (γ^p) components are reported in Table 1. The wettability analysis unveiled the high level of hydrophobicity for all samples, with WCA ≥ 100°. The SFE showed a noticeable decrease, from 30.08 mJ m^{-2} for PI-1 to 24.69 mJ m^{-2} for PI-2, due to the introduction of the aliphatic diamine. The increase of hydrophobicity and the decrease of surface energy play a crucial role in dust mitigation. The reduction in SFE as it decreases the van der Waals and electrostatic forces responsible for lunar dust adhesion. Consequently, materials with higher hydrophobicity and lower SFE are less inclined to particle accumulation. In addition, hydrophobicity represents a critical requirement for space materials, as it effectively mitigates moisture uptake. Indeed, during ground handling and launch, materials may absorb water from the terrestrial environment, which in orbit can sublimate under specific conditions and generate structural defects.

Table 1. *Density, WCA, SFE with dispersive (γ^d) and polar (γ^p) components, for the aromatic PI-1 and the semi-aromatic PI-2 and cPI-3 samples.*

Sample	Density [g cm^{-3}]	WCA [°]	SFE [mJ m^{-2}]	γ^d [mJ m^{-2}]	γ^p [mJ m^{-2}]
PI-1	1.452 ± 0.024	100.0 ± 0.8	30.08	29.02	1.06
PI-2	1.107 ± 0.021	103.7 ± 2.3	24.69	23.75	0.94
coPI-3	1.154 ± 0.063	101.1 ± 1.6	25.07	24.03	1.04

Fig.2 shows the optical images of the materials surface immediately after the damage and subsequently after the repair induced by heat exposure. For brevity, only two representative samples (PI-1 and PI-2) at one self-healing temperature (T = 150 °C) are shown. The fully fluorinated aromatic PI-1 exhibited no self-healing (Fig.2a). Indeed, even after 40 min, the cut is still clearly visible. The same behavior was also observed at T = 50 °C. Fig. 2b shows the intrinsic self-healing behavior of PI-2 upon heating at T = 150 °C, where the damage disappears immediately.

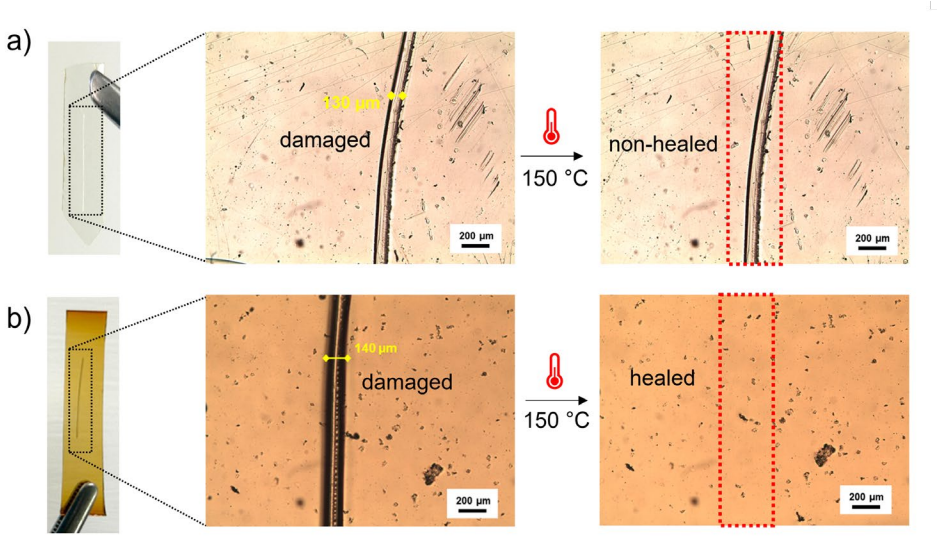


Fig.2 *Optical microscopy images of cut surfaces (left) and their response after heating at 150 °C (right). a) Aromatic PI-1, which does not self-heal even after 40 min, and b) semi-aromatic PI-2, showing rapid intrinsic self-healing within few seconds.*

Overall, all semi-aromatic PIs developed in this work exhibit intrinsic self-healing ability, and the repair process becomes progressively faster with increasing temperature, reaching healing times of only a few instants under elevated conditions (T = 150 °C). An increase in temperature enhances the segmental mobility of the polymer chains, allowing them to diffuse more across the damaged interface. Also, dynamic supramolecular bonds become more reactive, as higher thermal energy facilitates their reversible recombination. At T = 50 °C, PI-2 required approximately 20 min to restore the damaged area, whereas coPI-3 exhibited much faster recovery, completing the healing process in less than 20 s. When the temperature was increased to 150 °C, both materials healed significantly faster, with PI-2 achieving complete recovery in under 1 min and coPI-3 in less than 10 s. These results clearly indicate that higher temperatures enhance chain mobility and dynamic bond exchange, leading to accelerated self-repair. The self-healing rate is a critical factor for space applications, where rapid recovery from mechanical damage is essential to maintain structural integrity and functionality in harsh environments. Indeed, materials exhibiting fast self-healing can significantly enhance the reliability and lifetime of spacecraft components.

The supramolecular semi-aromatic PIs (PI-2 and coPI-3) developed in this work exhibit also shape memory behavior, being capable of recovering their original shape after deformation. Fig. 3 shows a schematic representation of the shape memory behaviour of PI-2. Specifically, the sample is deformed (Fig.3a) and subsequently recovers its original shape (Fig.3b-c), with the recovery time decreasing as the temperature increases.

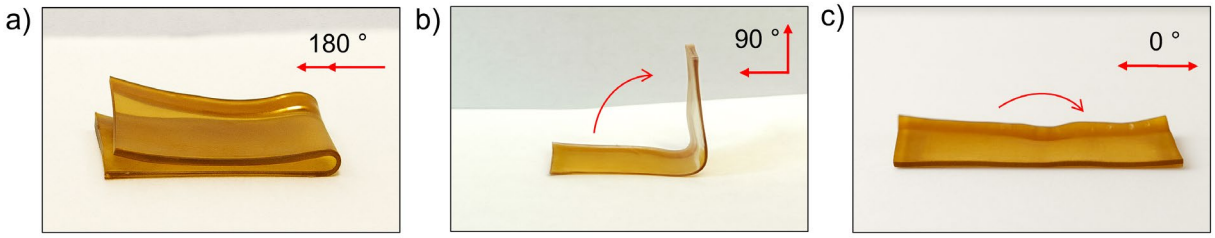


Fig.3 *Representative illustration of the shape memory behaviour of PI-2. a) The sample is deformed to 180°; b) bent to 90°, with a recovery time dependent on temperature; c) recovery of the original flat shape (0°). The images highlight the high elasticity and excellent shape recovery ability of the material after deformation.*

The test was carried out at 50 °C and 150 °C. The fully aromatic sample does not exhibit shape memory behaviour, as it is unable to recover its original shape after deformation. For both supramolecular materials, at T = 50 °C, the restoration process requires approximately 10 s, while at higher temperatures (T = 150 °C) it occurs instantly. This thermally induced response highlights the presence of dynamic reversible interactions within the polymer network, which enable rapid and efficient shape recovery. The shape memory process occurs even at room temperature, although the complete restoration may require up to 20 min for PI-2 and coPI-3. This behaviour is particularly advantageous for space applications, where shape memory capability can be exploited for deployable structures and adaptive components. Moreover, shape memory polymers could be integrated into deployable components, antennas, solar arrays, or dust-mitigation systems, where controlled deformation and recovery are crucial for operation and compact storage during launch.

Conclusions

Fully aromatic (PI-1) and supramolecular semi-aromatic (PI-2 and coPI-3) materials with a thickness of approximately 300 µm were successfully fabricated in DMAc/IPA. All materials exhibited low density, particularly in the case of polyimides containing aliphatic diamine. High hydrophobicity was observed for all materials, while the surface free energy decreased for the supramolecular polyimides. These characteristics are particularly relevant for space applications, as low density contributes to mass reduction, while hydrophobicity minimizes moisture uptake, preventing defect formation during mission operations. Moreover, a low surface free energy helps reduce lunar dust accumulation on the surface. Optical microscopy revealed the ability of the semi-aromatic materials to fully recover their morphology after mechanical damage, with healing efficiency strongly dependent on temperature. Higher temperatures enhanced chain mobility and dynamic bond exchange, leading to faster repair. The semi-aromatic PIs developed in this work also demonstrate shape memory behavior suitable for advanced space applications. Their thermally triggered recovery allows compact storage and autonomous deployment of structural elements, reducing both mass and mechanical complexity in spacecraft design. This functionality, combined with intrinsic self-healing capability, provides a dual advantage for long-duration missions where maintenance and repair are particularly challenging.

Acknowledgements

F.B. is supported by a PNRR PhD scholarship (D.M. 117/2023) co-funded by Sapienza University of Rome and the Italian Aerospace Research Centre (CIRA).

References

[1] I. Gouzman, E. Grossman, R. Verker, N. Atar, A. Bolker, N. Eliaz, Advances in Polyimide-Based Materials for Space Applications, Adv. Mater. 31 (2019) 1807738. https://doi.org/10.1002/adma.201807738

[2] F. Blondelli, E. Toto, S. Botti, F. Bonfigli, S. Laurenzi, M.G. Santonicola, Polyimide/graphene Nanocomposites for Space Applications: Potential Antibacterial Coatings for Human Exploration Missions, Acta Astronaut. 238 Part A (2026) 957-965. https://doi.org/10.1016/j.actaastro.2025.09.074

[3] Y. Zhang, S. Dai, Z. Yin, et al., Integration Fabrication of Polyimide Composite Films for Aerospace Applications, SmartMat. 5 1225, (2024). https://doi.org10.1002/smm2.1225

[4] F. Blondelli, G. Saccone, N. Favaloro, E. Toto, M.G. Santonicola, Poly(Imide-Siloxane) Copolymer Materials for Lunar Dust Mitigation: Synthesis and Characterization of Surface Properties, Macromol. Symp., https://doi.org/10.1002/masy.70246

[5] L. H. Lee, Adhesion and Cohesion Mechanisms of Lunar Dust on the Moon's Surface, J. Adhes. Sci. Technol. 9 (2012) 1103–1124. https://doi.org/10.1163/156856195X00932

[6] F. Blondelli, G. Saccone, N. Favaloro, E. Toto, M.G. Santonicola, Polyimide-based Materials with Self-healing Properties for Lunar Exploration Mission, Proceedings of the 75th International Astronautical Congress (IAC 2024), Materials and Structures Symposium, vol. 2, pp. 1167-1174. https://doi.org/10.52202/078369-0124

[7] L. Pernigoni, U. Lafont, A.M. Grande, Self-healing Materials for Space Applications: Overview of Present Development and Major Limitations, CEAS Space J. 13 (2021) 341–352. https://doi.org/10.1007/s12567-021-00365-5

[8] M. Goyal, S. N. Agarwal, N. Bhatnagar, A Review on Self-healing Polymers for Applications in Spacecraft and Construction of Roads, J. Appl. Polym. Sci. 139.37 (2022). https://doi.org/10.1002/app.52816

[9] M.D. Hager, P. Greil, C. Leyens, S. van der Zwaag, U.S. Schubert, Self-Healing Materials, Adv. Mater. 22 (2010) 5424-5430. https://doi.org/10.1002/adma.201003036

[10] I. L. Hia, V. Vahedi, P. Pasbakhsh, Self-Healing Polymer Composites: Prospects, Challenges, and Applications, Polymer Reviews 56(2) (2016) 225–261. https://doi.org/10.1080/15583724.2015.1106555

[11] S.R.M. Paladugu, P.S.R. Sreekanth, S.K. Sahu, K. Naresh, S.A. Karthick, N. Venkateshwaran, M. Ramoni, R.A. Mensah, O. Das, R. Shanmugam, Comprehensive Review of Self-Healing Polymer, Metal, and Ceramic Matrix Composites and Their Modeling Aspects for Aerospace Applications, Materials 15 (2022) 8521. https://doi.org/10.3390/ma15238521

Materials Research Proceedings 69 (2026) 620-625 https://doi.org/10.21741/9781644904251-110

Sustainable Hydrogen-Rich Polymer Blends for Advanced Space Radiation Shielding

Elisa TOTO[1,a], Francesca BLONDELLI[1,b], Lorenzo FERRI[1,c], Susanna LAURENZI[2,d], Maria Gabriella SANTONICOLA[1,e*]

[1]Department of Chemical Engineering Materials Environment, Sapienza University of Rome, Via del Castro Laurenziano 7, 00161 Rome, Italy

[2]Sapienza Aerospace Structures Laboratory, Via Salaria 851-881, 00138 Rome, Italy

[a]elisa.toto@uniroma1.it, [b]francesca.blondelli@uniroma1.it, [c]lorenzo.ferri@uniroma1.it, [d]susanna.laurenzi@uniroma1.it, [e]mariagabriella.santonicola@uniroma1.it

Keywords: Space Radiation Shielding, Hydrogen-Rich Polymers, Polymer Blends, Boron-Containing Compounds, Numerical Simulations

Abstract. Radiation exposure is one of the main obstacles to long-term human space exploration. Beyond Earth's atmosphere, astronauts are subjected to galactic cosmic rays and solar particle events, which can cause severe biological damage. The development of lightweight and efficient shielding materials is therefore crucial to ensure crew safety during missions in low Earth orbit and on the lunar surface. This study investigates hydrogen-rich polymer blends based on polyethylene and newly developed polyimides synthesized through environmentally sustainable, green-solvent routes. Polyimides exhibit excellent thermal resistance, mechanical robustness, and structural integrity at elevated temperatures, properties that complement the hydrogen-rich shielding capabilities of polyethylene. Radiation transport simulations were conducted using NASA's OLTARIS tool to evaluate exposure conditions in both low Earth orbit and lunar environments. The combination of polyethylene with advanced polyimides and boron-containing additives, such as boric acid, results in hybrid materials that are effective in radiation attenuation while remaining lightweight, flexible, and mechanically durable. These multifunctional composites represent promising candidates for integration into personal protective equipment and other shielding systems essential for future human space missions.

Introduction

Human space exploration is progressing toward missions of increasing duration and complexity, ranging from extended operations in low Earth orbit (LEO) to long-term habitation on the Moon and future expeditions to Mars. One of the major challenges to these endeavors is the hazardous radiation environment encountered beyond Earth's protective atmosphere and magnetic field. Astronauts operating in space are continuously exposed to a complex spectrum of ionizing particles, primarily galactic cosmic rays (GCRs) and solar particle events (SPEs), capable of penetrating spacecraft structures and biological tissues. These interactions can lead to ionization, molecular damage, and biological effects, such as acute radiation syndromes, degenerative pathologies, and an elevated lifetime cancer risk [1].

In LEO, astronauts are partially shielded by Earth's magnetic field, although radiation levels remain substantially higher than those at Earth's surface. In contrast, on the Moon, the absence of geomagnetic protection exposes crews directly to cosmic and solar radiation, resulting in a significantly harsher radiative environment for both human health and material integrity. The development of advanced shielding solutions is therefore a fundamental prerequisite for ensuring the safety, reliability, and long-term sustainability of human operations beyond Earth orbit.

Content from this work may be used under the terms of the Creative Commons Attribution 3.0 license. Any further distribution of this work must maintain attribution to the author(s) and the title of the work, journal citation and DOI. Published under license by Materials Research Forum LLC.

Materials Research Proceedings 69 (2026) 620-625 https://doi.org/10.21741/9781644904251-110

Traditional metallic shields, though structurally robust, tend to generate secondary radiation when interacting with high-energy ions, thereby reducing their overall effectiveness. Hydrogen-rich polymers, composed of low atomic number elements, have emerged as promising alternatives due to their high efficiency in attenuating charged particles and minimizing secondary radiation [2,3]. Among them, polyethylene (PE) has long been considered a benchmark material for radiation protection because of its high hydrogen content, low density, and ease of processing. However, PE alone suffers from limited thermal stability and mechanical strength, restricting its use in demanding space environments.

To overcome these limitations, this study explores hybrid polymeric systems that combine PE with newly synthesized polyimides (PIs) obtained via environmentally sustainable, green-solvent routes [4]. Polyimides exhibit outstanding thermal resistance, mechanical robustness, and radiation tolerance, making them ideal candidates to complement the shielding performance of PE. The addition of boron-containing compounds, such as boric acid (BA), further enhances protection through neutron capture, providing a more comprehensive response to the mixed radiation fields typical of both LEO and lunar environments [5].

Radiation transport simulations were carried out using NASA's OLTARIS tool to model particle interactions and organ dose deposition under realistic mission scenarios. The synergistic integration of hydrogen-rich PE, high-performance polyimides, and boron-based additives results in hybrid materials that combine radiation attenuation efficiency with excellent thermal stability, mechanical reliability, and low density. These multifunctional composites are particularly suited for use in personal protective equipment and modular shielding systems for future human space missions.

Numerical simulations

Numerical simulations were carried out using NASA's on-line tool for the assessment of radiation in space (OLTARIS), considering both the LEO and lunar environments. The computational geometry was modeled as a spherical shell composed of an internal cavity with a radius of 150 cm, surrounded by an external shielding layer made of the investigated material, with areal densities ranging from 0 to 30 g/cm². The shielding effectiveness was determined based on the cross-sectional properties of each configuration, derived from the material's chemical composition and density. Since radiation absorption strongly depends on body morphology and tissue composition, anatomical differences between male and female bodies were taken into account. To represent the biological models accurately, the male adult voxel (MAX) and female adult voxel (FAX) phantoms developed by Kramer et al. were considered as reference anthropomorphic geometries [6,7]. Specifically, both models were applied for LEO simulations, while only the MAX phantom was used for the lunar environment. The simulations yielded the total effective dose equivalent (TEDE) calculated at the phantom's center using three-dimensional radiation transport analyses.

For the LEO analysis, orbital parameters representative of the International Space Station (ISS) were adopted, corresponding to a circular orbit at 400 km altitude and 51.6° inclination. Radiation exposure was evaluated over a one-year mission duration to estimate the cumulative dose from GCRs, SPEs, trapped particles, and albedo neutrons. The AP8 MAX model was used to describe trapped protons [8], while galactic cosmic radiation spectra were represented using the BON2020 model [9]. For the lunar environment, the BON2020 GCR model corresponding to the 2010 solar minimum was applied [9]. Radiation effects were evaluated over a one-year mission duration to assess cumulative exposure from GCRs on the human body [10].

Results and discussion

Fig. 1 shows the total effective dose equivalent (TEDE) obtained for the main reference materials (aluminium, liquid water, and polyethylene) and for the PE/PI-based blends, evaluated using both

Materials Research Proceedings 69 (2026) 620-625 https://doi.org/10.21741/9781644904251-110

MAX and FAX anthropomorphic phantoms under LEO conditions. For all investigated materials and both body models, the analysis demonstrates a consistent decrease in TEDE with increasing areal density. The reduction follows a nonlinear trend, characterized by a steep decline at low areal depths and a gradual attenuation at higher thicknesses, reflecting the progressive moderation of primary and secondary radiation components. Among the materials analyzed, a clear difference in shielding performance is observed, with aluminium showing the lowest effectiveness and polyethylene the best performance, which is consistent with its well-known role as a benchmark hydrogen-rich material for space radiation protection. Liquid water and PE/PI-based materials exhibit intermediate behavior, with water showing slightly lower TEDE values at higher areal densities because of its greater hydrogen content.

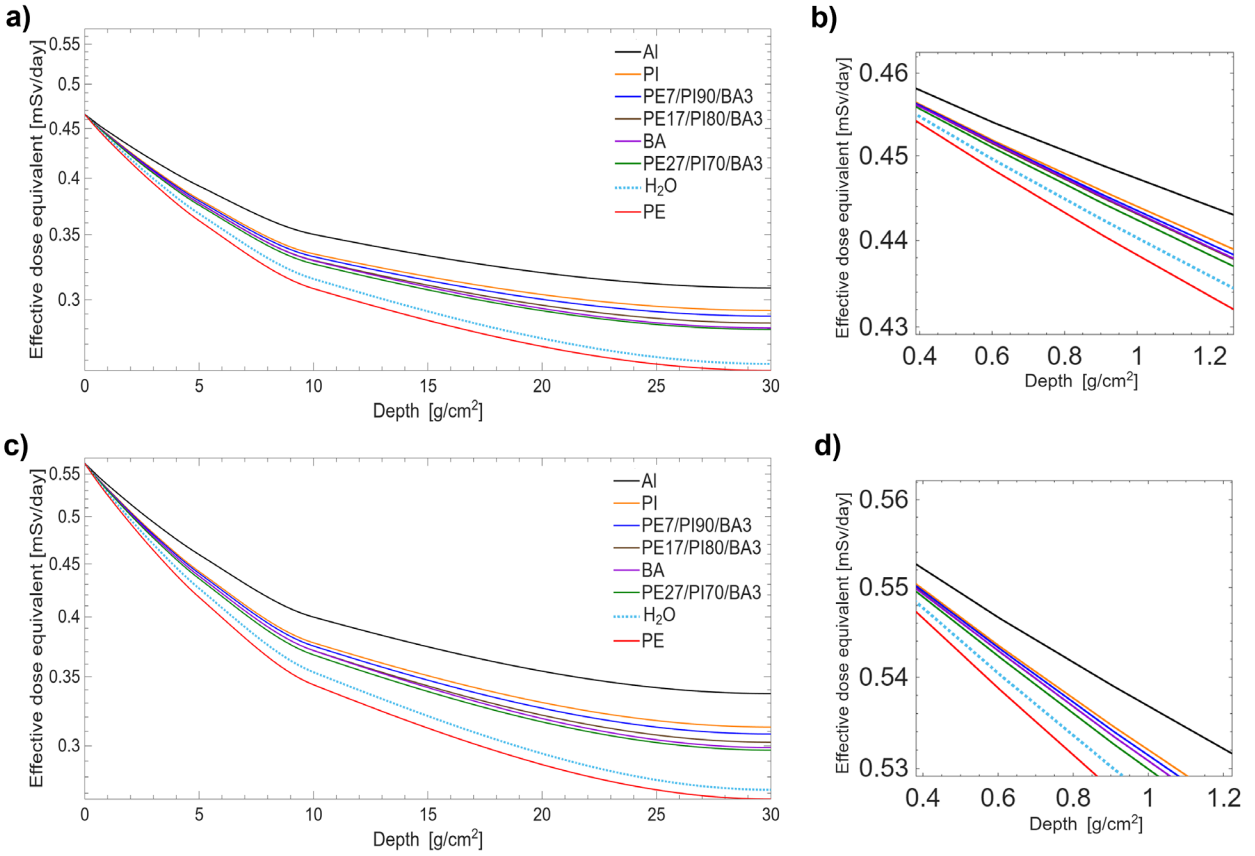


Fig. 1. *TEDE as function of the areal depth in LEO environment for a) MAX and c) FAX human phantom models; b,d) enlarged area of the plots in the depth range 0.4 – 1.2 g/cm².*

The comparison between the MAX and FAX phantoms reveals that the female model consistently receives higher radiation doses than the male model, with an increased exposure risk for women. Consequently, optimized protective strategies, such as localized thickening of spacesuit shielding or habitat walls, may be required to ensure equivalent safety margins for female astronauts.

The stochastic health effects of radiation were evaluated by comparing the TEDE obtained after a one-year exposure at shielding thicknesses of 0.5 and 1.0 g/cm² with the permissible limits defined by the National Council on Radiation Protection and Measurements (NCRP) report No. 167. In this analysis, the PE/PI/BA material with a 27:70:3 ratio was selected for its high hydrogen concentration. The corresponding TEDE values are summarized in Table 1 for both MAX and FAX phantoms. According to the NCRP guidelines for astronauts aged approximately thirty years,

Materials Research Proceedings 69 (2026) 620-625 https://doi.org/10.21741/9781644904251-110

the career dose limits are 620 mSv for males and 470 mSv for females, representing the most restrictive scenario for human space missions.

Table 1. *Total effective dose equivalent after one-year mission in LEO for both MAX and FAX human phantom models considering the PE/PI/BA material with 0.5 and 1.0 g/cm² of areal depth.*

Analysis model	Depth in PE27/PI70/BA3 [g/cm²]	Total effective dose equivalent after one year [mSv]
MAX	0.5 (0.4 cm)	165.4
MAX	1.0 (0.8 cm)	161.5
FAX	0.5 (0.4 cm)	199.1
FAX	1.0 (0.8 cm)	193.4

Results unveiled that the PE/PI/BA material provide substantial radiation attenuation, maintaining TEDE values below the NCRP thresholds even at a minimum thickness of 0.5 g/cm². In the lunar environment, the TEDE values reported in Fig. 2 for the MAX phantom show a progressive decrease in radiation dose with increasing areal depth for all analyzed materials, consistent with the attenuation behavior previously observed under LEO conditions.

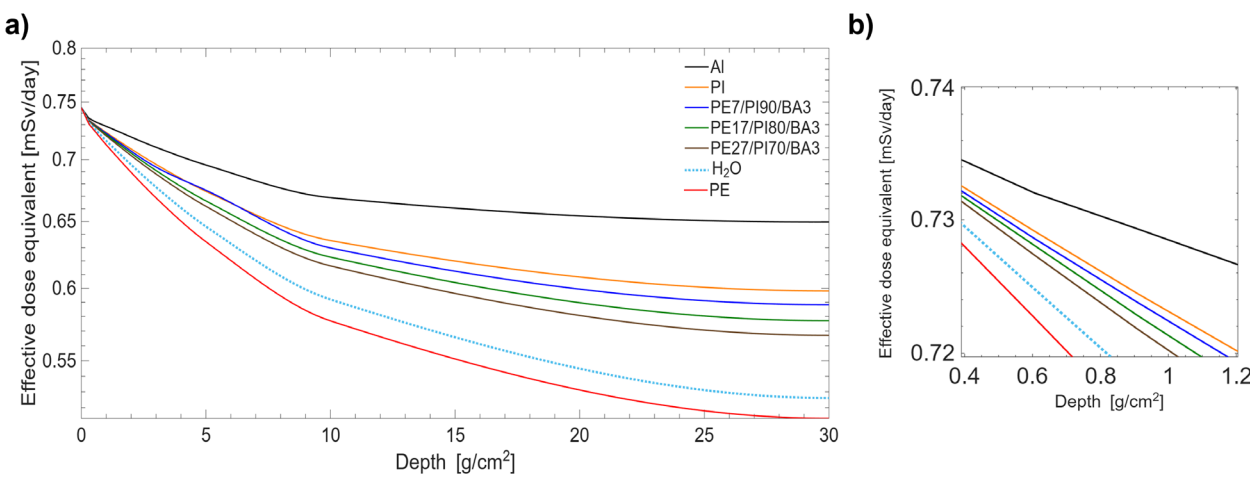


Fig. 2. *a) TEDE as function of the areal depth in lunar environment for MAX human phantom model; b) enlarged area of the plot in the depth range 0.4 – 1.2 g/cm².*

As expected, aluminum exhibits the poorest shielding capability, while PE provides the most effective attenuation owing to its high hydrogen content. The PE/PI/BA materials show intermediate performance between these two reference materials, closely approaching that of PE, and outperforming both pure PI and aluminum. As shown in Table 2, PE/PI/BA materials with ratios of 7:90:3, 17:80:3, and 27:70:3 demonstrated comparable radiation-shielding performance. In particular, TEDE values remain below the career dose limit of 620 mSv, thereby enabling safe exposure durations equivalent to missions of up to two years. Overall, the numerical simulation results underscore the suitability of PE/PI/BA materials as lightweight, efficient, and adaptable candidates for radiation protection in both LEO and lunar environments.

Table 2. *Total effective dose equivalent after one-year mission in the lunar environment for MAX human phantom model considering different PE/PI/BA materials with 0.5 and 1.0 g/cm^2 of areal depth.*

Material	Depth [g/cm^2]	Total effective dose equivalent after one year [mSv]
PE7/PI90/BA3	0.5 (0.4 cm)	266.6
	1.0 (0.7 cm)	263.7
PE17/PI80/BA3	0.5 (0.4 cm)	266.4
	1.0 (0.8 cm)	263.3
PE27/PI70/BA3	0.5 (0.4 cm)	266.2
	1.0 (0.8 cm)	262.9

Conclusions

This study assessed the radiation-shielding performance of hydrogen-rich PE/PI/BA materials through numerical simulations using NASA's OLTARIS tool under both LEO and lunar conditions. The findings show that combining polyethylene with thermally stable and mechanically robust polyimides, together with boric acid as a neutron-absorbing additive, yields hybrid materials that exhibit radiation shielding properties while maintaining low density. The obtained TEDE values remain below NCRP dose limits even at minimal areal densities, allowing safe exposure durations equivalent to up to three years in LEO and two years on the lunar surface. Overall, the PE/PI/BA materials can be considered promising candidates for integration into lightweight and multifunctional shielding components, such as personal protective equipment and modular systems, in future human space missions.

Acknowledgements

This study was carried out within the Space It Up project funded by the Italian Space Agency, ASI, and the Ministry of University and Research, MUR, under contract n. 2024-5-E.0 - CUP n. I53D24000060005.

References

[1] M. Maalouf, M. Durante, N. Foray, Biological effects of space radiation on human cells: history, advances and outcomes, J. Radiat. Res. 52 (2011) 126–146. https://doi.org/10.1269/jrr.10128

[2] S. Laurenzi, G. De Zanet, M.G. Santonicola, Numerical investigation of radiation shielding properties of polyethylene-based nanocomposite materials in different space environments, Acta Astronaut. 170 (2020) 530–538. https://doi.org/10.1016/j.actaastro.2020.02.027

[3] E. Toto, L. Lambertini, S. Laurenzi, M.G. Santonicola, Recent advances and challenges in polymer-based materials for space radiation shielding, Polymers 16 (2024) 382. https://doi.org/10.3390/polym16030382

[4] E. Toto, S. Laurenzi, R.C. Pellegrini, E. Cavallini, M.G. Santonicola, Eco-friendly synthesis of high-performance polyimide materials using bio-based greener solvents: towards sustainable technologies in space environment, Mater. Today Sustain. 25 (2024) 100657. https://doi.org/10.1016/j.mtsust.2023.100657

[5] R.N. Yastrebinsky, A.V. Yastrebinskaya, A.I. Gorodov, A.V. Akimenko, Polymer boron-containing composite for protecting astronauts of manned orbital stations from secondary neutron radiation, J. Compos. Sci. 8 (2024) 372. https://doi.org/10.3390/jcs8090372

[6] R. Kramer, J. Vieira, H. Khoury, F. Lima, D. Fuelle, All about MAX: a male adult voxel phantom for Monte Carlo calculations in radiation protection dosimetry, Phys. Med. Biol. 48 (2003) 1239–1262. https://doi.org/10.1088/0031-9155/48/10/301

[7] R. Kramer, H. Khoury, J. Vieira, E. Loureiro, V. Lima, F. Lima, G. Hoff, All about FAX: a Female Adult voXel phantom for Monte Carlo calculation in radiation protection dosimetry, Phys. Med. Biol. 49 (2004) 5203–5216. https://doi.org/10.1088/0031-9155/49/23/001

[8] F.F. Badavi, K.J. West, J.E. Nealy, J.W. Wilson, B.L. Abrahms, N.J. Luetke, A dynamic/anisotropic low Earth orbit (LEO) ionizing radiation model, NASA Technical Paper NASA/TP-2006-214533 (2006).

[9] T.C. Slaba, K. Whitman, The Badhwar–O'Neill 2020 GCR model, Space Weather 18 (2020). https://doi.org/10.1029/2020SW002456

[10] A. Adamczyk, M. Clowdsley, G. Qualls, S. Blattnig, K. Lee, D. Fry, N. Stoffle, L. Simonsen, T. Slaba, S. Walker, E. Zapp, Full mission astronaut radiation exposure assessments for long-duration lunar surface missions, in: Proc. IEEE Aerospace Conf. (2011) 1–15. https://doi.org/10.1109/AERO.2011.5747250

Materials Research Proceedings 69 (2026) 626-631 https://doi.org/10.21741/9781644904251-111

Numerical Investigation of the Applicability of a Single Ramp Supersonic Inlet for Ramjet Propulsion

Franciszek Dominik TOMCZAK[1,a *]

[1]Łukasiewicz Research Network, Institute of Aviation, Warsaw, Poland

[a]Franciszek.Tomczak@ilot.lukasiewicz.gov.pl

Keywords: Supersonic Inlet, External Compression Inlet, Strong Oblique Shock Wave, Total Pressure Recovery, Ramjet Propulsion, Numerical Simulation (CFD)

Abstract. In this work, we investigate the applicability and performance limitations of a single-ramp, external-compression inlet for ramjet propulsion over a range of supersonic Mach numbers. The current work examines the use of strong oblique shocks instead of terminal normal shocks to enhance inlet performance and reduce the total pressure losses in simplified geometries. A combined analytical and numerical approach is used. Oblique shock theory and the Oswatitsch criterion for optimal multi-shock compression are employed to estimate the performance limitations of the multi-ramp configuration. The analytical predictions are then validated using high-fidelity CFD simulations performed with ANSYS Fluent. The results show that the single-ramp inlets are efficient at lower supersonic speeds (up to approximately Mach 2) due to the use of a strong oblique terminal shock. However, their efficiency deteriorates rapidly at higher Mach numbers, significantly increasing the total pressure losses. Analytical models slightly overpredict pressure recovery by 1.5–2% compared to numerical results. The current work aims to provide insight into the performance envelope of simplified inlet geometries for high-speed air-breathing propulsion systems. The research demonstrates the benefits and trade-offs of various ramp designs and highlights the necessity of more complex geometries, such as multi-ramp designs, for efficient operation at Mach numbers exceeding 2. These findings can support the optimization of a ramjet inlet design and provide guidelines for the development of future propulsion systems.

Introduction

External-compression inlets have been widely studied and successfully employed in high-speed applications, from supersonic aircraft to ramjet-powered cruise missiles. They are attractive due to their relatively simple geometry, predictable starting behavior, and robust operating characteristics. Compared with more advanced inlet configurations, such as divergentless, mixed-compression, or fully internal compression inlets, external compression designs are less efficient in terms of total pressure recovery. Nonetheless, their structural simplicity and reliability make them appealing for practical systems [1-3].

One way to simplify the external-compression inlets is to reduce the number of ramps, which directly affects the inlet's size, drag, and overall performance. Traditional studies focus on multi-ramp designs with carefully tuned ramp angles to balance the total pressure recovery across stages [4]. However, to the best of the author's knowledge, the case of a single ramp inlet utilizing a strong oblique shock as the terminal shock instead of the conventional normal shock has not been explored in the literature. This study focuses on designing a supersonic inlet with a targeted mass flow rate of approximately 1 [kgs^{-1}], which results in a correspondingly small capture area. Inlet geometries with such low mass flow rates present substantial technical challenges that are inadequately documented in the open literature.

Despite their lower efficiency, single ramp external compression inlets offer practical advantages. They are simple to design and can reduce the overall drag due to a smaller capture

Content from this work may be used under the terms of the Creative Commons Attribution 3.0 license. Any further distribution of this work must maintain attribution to the author(s) and the title of the work, journal citation and DOI. Published under license by Materials Research Forum LLC.

Materials Research Proceedings 69 (2026) 626-631 https://doi.org/10.21741/9781644904251-111

ratio. These factors motivate the present feasibility study of single ramp external compression inlets across various Mach numbers, highlighting their potential for cost-effective and compact high-speed propulsion systems, such as ramjets.

Methodology

The analytical formulation in this study is developed under the classical assumptions of steady, adiabatic, inviscid, two-dimensional flow of a perfect gas with a constant specific heat ratio. These assumptions simplify the governing equations and allow for the use of the well-established oblique shock and isentropic flow relations. Within this framework, the inlet geometry can be approximated with reasonable accuracy while preserving physical insight.

In the proposed inlet design, the weak-shock solution is followed by a strong oblique shock to reduce total-pressure losses. Static pressure, temperature, and density ratios are obtained from the standard shock-jump relations. For multi-shock configurations, the *Oswatitsch condition* [4] provides an optimization criterion, i.e. maximum total-pressure recovery is achieved when all shocks are of equal strength, which is equivalent to ensuring that the normal components of the Mach number upstream of each shock are identical. In practice, the design is carried out iteratively by adjusting the initial assumptions on the freestream Mach number until a target condition is satisfied, namely $M > 1.3$ at the diffuser exit. This results in well-balanced shock strengths and improved inlet performance. The inlet geometry was adapted from published work with simplifications introduced for small-scale application purposes [5].

Numerical Model

Simulations were conducted in ANSYS Fluent using the density-based solver. Gas density was calculated from the ideal gas law, while dynamic viscosity was evaluated using Sutherland's law.

A two-dimensional structured mesh was generated with refined near-wall spacing to achieve $y^+ < 1$. The computational domain was extended in all directions, with the additional spacing set equal to the inlet height. Three meshes consisting of approximately 130,000, 200,000 and 300,000 elements were tested. A grid independence study showed that the difference in bleed flow rate between medium- and fine-resolution grids was less than 1%, and total pressure recovery was not sensitive for the mesh study. The medium-density mesh was, therefore, selected as a trade-off between accuracy and efficiency.

A turbulence model sensitivity study was performed using the *RNG k-ε*, *k-ω*, and *SST k-ω* models. The predicted flow characteristics showed no significant differences among the different setups. Based on existing recommendations [6-8], the *SST k-ω* model was selected for the current study.

During the initial 10,000 iterations, the spatial discretization was set to First-Order Upwind to ensure numerical stability. The scheme was then switched to Second-Order Upwind for another 15,000 iterations, where face values were reconstructed using a multidimensional linear approach, thereby increasing spatial accuracy.

For the full multigrid initialization (FMG), the Courant–Friedrichs–Lewy (CFL) number was fixed at 0.05. During the solution process, ANSYS Fluent dynamically adjusted the Courant number, progressively increasing it to a maximum of 2.5 in response to residual stabilization. This adaptive strategy provides a trade-off between numerical stability and computational efficiency.

To model the freestream, a pressure far-field boundary condition was applied. This requires specifying the static pressure, Mach number, and static temperature. The pressure outlet boundary condition was used to represent both the downstream outflow and the bleed outflow; static pressure was prescribed. At the main inlet exit, a pressure boundary condition was imposed to enforce a choked flow condition. For this boundary, static pressure and total temperature were specified, stabilizing the internal shock system and maintaining the goal mass flow rate. The numerical study

Materials Research Proceedings 69 (2026) 626-631 https://doi.org/10.21741/9781644904251-111

was carried out for three freestream Mach numbers: 1.5, 2.0, and 2.5, under the conditions listed in Table 1.

Table 1: Flow conditions of the proposed supersonic inlets. Key parameters besides Mach numbers include freestream pressure, freestream temperature, turbulent kinetic energy, specific dissipation rate, and design mass flow rate, from which inlet and exit pressure and total temperature were prescribed, as well as bleed flow rate.

p_s [kPa]	T_s [K]	k $[m^2s^2]$	ω $[s^{-1}]$	$\dot{m}$ $[kgs^{-1}]$	$\dot{m}_{bleed}$ [%]
101.325	288.15	1735.708	$1.188 * 10^{-7}$	1.0	5

Results

The primary motivation for employing the single compression ramp lies in its geometric and aerodynamic simplicity. In contrast, external compression inlets utilizing multiple ramps typically generate a larger total flow deflection, which, although beneficial for achieving higher pressure recovery, increases the inlet capture area. Since the capture area is directly associated with inlet drag, becomes a critical factor in the inlet design. Figure 1 presents the results obtained using the Oswatitsch condition, which constrains the Mach number to $M = 1.3$ downstream of the final ramp. This condition provides a useful benchmark for evaluating the balance between compression efficiency and drag penalties in different inlet configurations. Therefore, a direct connection between the combined ramp angle and efficiency can be seen. This occurs because a specific Mach number is required to sustain a strong oblique shock wave after the external compression ramps. As the number of shocks increases, the net total pressure loss per shock decreases, resulting in a higher total deflection angle of the external diffuser.

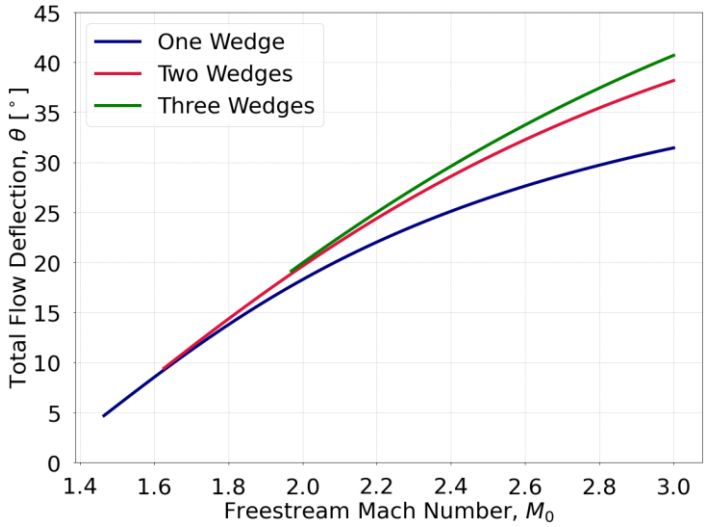


Figure 1: The characteristic of the total flow deflection angle to the Mach number, calculated for different ramp numbers by the Oswatitsch condition.

The MIL-E-5008B standard is employed to estimate the possible operating range for inlets with different numbers of compression ramps. Figure 2 illustrates the results of an analytical calculation based on the assumption of equal pressure-recovery shocks for varying free-stream Mach numbers, with the Mach number constrained after the final shock constrained to $M = 1.3$. The results reveal that a single-ramp inlet can be used effectively up to approximately $M = 1.85$, a double-ramp configuration extends the applicability to approximately $M = 2.5$. A triple-ramp inlet exceeds this standard over the Mach number range of interest. These findings emphasize the role of multi-ramp compression in expanding the operational envelope of supersonic inlets, while maintaining compliance with performance standards.

Materials Research Proceedings 69 (2026) 626-631 https://doi.org/10.21741/9781644904251-111

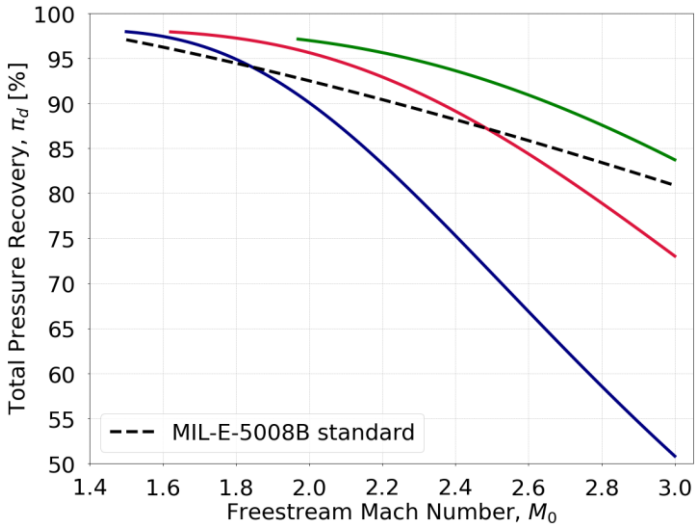


Figure 2: The total pressure recovery characteristic as a function of the Mach number, calculated using the Oswatitsch condition for different ramp numbers. The results are compared to the MIL-E-5008B standard is presented as dashed line.

Table 2 summarizes the results of the present study, which combines the MIL-E-5008B standard with analytical predictions and numerical simulations for three representative Mach numbers and three inlet configurations. For $M = 1.5$, the two- and three-ramp configurations could not be designed according to the Oswatitsch condition for the desired ramp Mach number. The single ramp configuration meets the standard only at that Mach number.

For the remaining Mach number range, the performance drops significantly below the standard. The two ramps configuration falls below the standard for both Mach numbers within the operating range. The three-ramp configuration exceeds the standard at $M = 2.0$, where analytical and numerical calculations are in good agreement. The comparatively high performance of the inlet is primarily due to the use of a strong oblique shock. Furthermore, it is important to emphasize that the analytical model consistently overpredicts the recovery efficiency by approximately 1.5-2%, when compared to numerical simulations. This indicates relatively close agreement between the analytical and numerical estimates. Therefore, the analytical tool can be used with reasonable accuracy, reducing process time by orders of magnitude while preserving an acceptable level of detail for design optimization.

Table 2: The table reports the total pressure recovery ratio for each configuration, expressed as a percentage. Values without markings correspond to the MIL-E-5008B standard. Values with a (′) correspond to analytical calculations, whereas values with a (″) correspond to numerical results. The results demonstrate that the proposed single ramp configuration achieves superior performance at lower Mach numbers. A clear trend of increased performance can be seen with an increased ramp number.

M	π_d	Single ramp		Double ramp		Triple ramp	
		π_d'	π_d''	π_d'	π_d''	π_d'	π_d''
1.5	97.06%	98.50%	97.12%	-	-	-	-
2.0	92.50%	90.25%	88.19%	93.28%	91.59%	93.98%	93.44%
3.0	87.03%	74.27%	73.00%	86.56%	85.02%	90.57%	87.01%

Materials Research Proceedings 69 (2026) 626-631 https://doi.org/10.21741/9781644904251-111

Concluding Remarks

The present study demonstrates that the single-ramp external compression inlet performs sufficiently good over a limited range of supersonic conditions. Specifically, at Mach 1.5 the inlet exceeds the adopted performance standards, indicating robust total pressure recovery. Even at Mach 2.0, the inlet maintains acceptable performance levels. Minor geometric optimizations, such as adjusting the cowl lip angle or throat section parameters, could elevate their efficiency to closely match or surpass established benchmarks. However, performance at Mach 2.5 reveals a critical limitation, that is the inlet experiences a 14% loss in the total pressure. This renders the inlet unsuitable for high-speed applications without a significant redesign.

The performance of the two-ramp configurations falls slightly below the standard, while the three-ramp configurations exceed it. For Mach numbers 2, therefore the use of a double ramp configuration appears to be unjustified. The reason for this is that the two ramp configuration does not meet performance requirements; see Table 2. On the other hand, concerning the performance gain, the three-ramp configuration is preferable; if simplicity of the design is prioritized, then the single-ramp inlet might be considered for application at approximately Mach 2. Nevertheless, the size of the inlet increases with the two- and three-ramp configurations, consistent with the literature on the practical limitations of external compression inlets within the Mach 2.5–3.0 range.

Furthermore, the results corroborate the broader consensus that even strong oblique shock wave, which promise high efficiency, begin to lose their effectiveness at higher Mach numbers for single and double configurations.

In summary, single-ramp inlets show promise for moderate supersonic speeds, offering efficient performance with relatively simple geometry. However, their performance is significantly constrained beyond Mach 2.5 due to the increased total pressure losses as well as reduced inlet efficiency. More advanced inlet configurations, such as multi-ramp designs, provide superior total-pressure recovery and enhanced operational flexibility. This is achieved by distributing compression across multiple weaker shocks and enabling better control over shock position. These geometries mitigate total pressure losses and flow distortion issues, making them better suited for sustained operation in the Mach 2.5–3.0 range.

Disclaimer



Co-funded by the European Union. Views and opinions expressed are however those of the author(s) only and do not necessarily reflect those of the European Union or OCCAR. Neither the European Union nor the granting authority can be held responsible for them.

The European Hypersonic Defence Interceptor (EU HYDEF) is a project co-funded by the European Union, under the European Defence Fund, and Belgium, Germany, Norway, Poland and Spain. OCCAR has been entrusted the management of the EU HYDEF project by the European Commission (EC) and the Participating States.

References

[1] P. Xie, Y. Liu, W. Yuan, An investigation on bleed flow control of an axisymmetric supersonic intake based on parametric outline optimization design, Aerospace Science and Technology, 159 (2025) 110027. https://doi.org/10.1016/j.ast.2025.110027

[2] S. Farokhi, Aircraft engine inlets and nozzles, in: Aircraft Propulsion, 2nd ed., John Wiley & Sons, Ltd, Chichester (UK), (2014) pp. 327-427.

[3] J. W. Slater, Design and analysis tool for external-compression supersonic inlets, 50th AIAA Aerospace Sciences Meeting, (2012). https://doi.org/10.2514/6.2012-16

[4] K. Oswatitsch, Pressure recovery for missiles with reaction propulsion at high supersonic speeds (The efficiency of shock diffusers), Forschungen und Entwicklungen des Heereswaffenamtes, Issue: 1005, Reprinted as NACA-TM-1140, (1947).

[5] J. W. Slater, Design factors for two-dimensional, external-compression supersonic inlets, AIAA, 2020-2090, High Speed Inlets, (2020). https://doi.org/10.2514/6.2020-2090

[6] H. Yuan, F. Liu, X. Wang, Z. Zhou, Design and analysis of a supersonic axisymmetric inlet based on controllable bleed slots, Aerospace Science and Technology, 118 (2021) 106229. https://doi.org/10.1016/j.ast.2021.107008

[7] H. C. Yuan, J. S. Zhang, Y. F. Wang, G. P. Huang, Experimental and numerical investigation on a supersonic inlet with large bleed window, The Aeronautical Journal, 126 (2022) 1352-1374. https://doi.org/10.1017/aer.2021.76

[8] W. Z. Xie, W. Yang, Y. Jin, S. Yang, C. Zeng, S. Guo, Prediction of self-starting limit of two-dimensional supersonic inlets considering viscous effects, Aerospace Science and Technology, 106 (2020) 106229. https://doi.org/10.1016/j.ast.2020.106229

Materials Research Proceedings 69 (2026) 632-637 https://doi.org/10.21741/9781644904251-112

Operational Envelope of an EAD Thruster Under Varying Pressure and Humidity

Davide USUELLI[1,a,*], Andrea AVALLI[1,b], Raffaello TERENZI[1,c], Stefano TROVATO[1,d], Marco BELAN[1,e]

[1]Politecnico di Milano, Via La Masa 34, 20156, Milan, Italy

[a]davide.usuelli@polimi.it, [b]andrea3.favalli@polimi.it, [c]raffaello.terenzi@polimi.it, [d]stefano.trovato@polimi.it, [e]marco.belan@polimi.it

Keywords: EAD Thruster, Corona Discharge, Pressure, Humidity, Performance

Abstract. A wire-to-grid electroaerodynamic (EAD) thruster is experimentally investigated under varying environmental conditions. Experiments are conducted in a low-pressure chamber to assess the influence of ambient pressure p and relative humidity RH on device performance. The key performance metrics considered are corona current i_c, the thrust density T/A, and the thrust-to-power ratio T/P. Experimental results indicate that decreasing pressure negatively affects all performance indicators while reducing the ignition threshold. Additionally, both current consumption and ignition voltage exhibit a parabolic dependence on relative humidity.

1. Introduction

Electroaerodynamic (EAD) thrusters are emerging as a promising technology for aerospace applications, particularly for lighter-than-air (LTA) vehicles such as airships [1]. These air-breathing devices offer several advantages, including zero emissions, low acoustic noise and the absence of moving parts. Although various EAD thruster concepts exist, they all rely on a common operating principle: two electrodes supplied with a high DC voltage generate a sufficiently asymmetric electric field such that air is ionized at the emitter and drifts toward the collector. The resulting interaction between ions and neutral molecules produces an ionic wind and generates thrust [2]. The performance of EAD thrusters is influenced by environmental conditions such as temperature, pressure and humidity, which can significantly alter their operational characteristics [3,4,5]. In this work, the performance of a gridded EAD thruster developed at Politecnico di Milano within the framework of the EU-funded I-PROP project is experimentally investigated as a function of two environmental variables, namely ambient pressure p and humidity.

2. Experimental Setup

The experimental campaign was conducted in a grounded cylindrical steel chamber capable of sustaining pressures down to a few pascals. The desired pressure level was achieved using a single-stage rotary vane pump connected to a lateral port. The corona voltage was monitored using a voltage divider connected in parallel with the thruster, while the corona current i_c was measured using a contactless probe. Thrust was measured with a load cell and humidity was determined from the output of a dew-point temperature sensor. The water vapor content inside the chamber was reduced using silica gel and increased through controlled water evaporation.

Low-voltage connections (load cell, dew-point sensor, and ground lines) were routed through a feedthrough and EMI-shielded to prevent signal degradation. The voltage supplied by the 0–30 kV DC power supply was delivered to the thruster through a dedicated high-voltage feedthrough. A ballast resistor with resistance $R_b = 1$ MΩ was connected in series for safety purposes.

Content from this work may be used under the terms of the Creative Commons Attribution 3.0 license. Any further distribution of this work must maintain attribution to the author(s) and the title of the work, journal citation and DOI. Published under license by Materials Research Forum LLC.

Materials Research Proceedings 69 (2026) 632-637 https://doi.org/10.21741/9781644904251-112

Analog outputs were acquired using a data acquisition system at a sampling frequency $f_s = 25$ kHz over an observation time $T_{obs} = 2$ s, and subsequently processed in Python. A schematic of the setup is presented in Figure 1. Further details about the instrumentation can be found in [6].

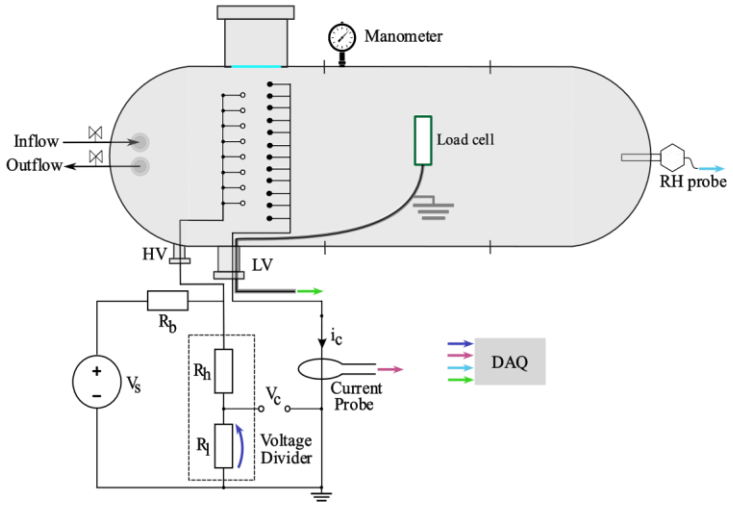


Figure 1 — Schematic diagram of the test facility. Colored arrows indicate acquired signals.

A dedicated test rig was designed to house the wire-to-grid thruster inside the chamber. The adopted thruster configuration replicates the one presented in [6]. The load cell was installed vertically and connected to the test rig through a single-point attachment, while its base was secured to a grounded iron platform. A counterbalancing arm was added to offset the cantilever moment and prevent overload. A schematic view of the complete test rig is shown in Figure 2.

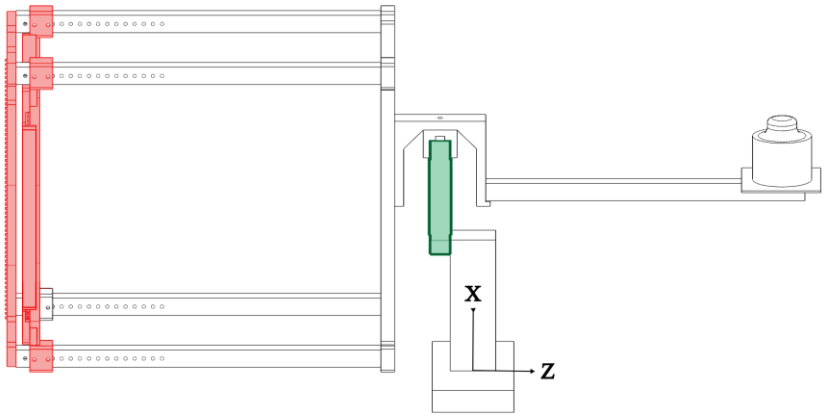


Figure 2 — Complete test rig: the EAD thruster is highlighted in red, while the load cell is depicted in green.

The tested pressure levels ranged from 101 kPa down to 20 kPa. Absolute humidity values between 5 and 20 g/m^3 were achieved, corresponding to relative humidity levels of approximately 20–80%. Temperature could not be actively controlled during the campaign but was continuously monitored and showed no significant variation; it was therefore treated as constant. Thrust, voltage

Materials Research Proceedings 69 (2026) 632-637 https://doi.org/10.21741/9781644904251-112

and current measurements were obtained as the difference between the thruster-on and thruster-off signals. Multiple acquisitions were averaged to obtain the final measurement values. Measurement uncertainty was propagated using the root-sum-square method.

3. Results

The outcomes of the experimental campaign are reported in three parts: the ignition voltage V_{ign}, which sets the lower limit of the thruster's electrical envelope, is addressed first; second, the influence of the tested variables on the corona current i_c is examined; finally, the performance is evaluated through the thrust density T/A, which is an index of thruster compactness, and the thrust-to-power ratio T/P, representative of efficiency.

Ignition Voltage

The ignition voltage is found to be a monotonic function of pressure, as shown in Figure 3. Experimental data are interpolated using a model function resembling Peek's law.

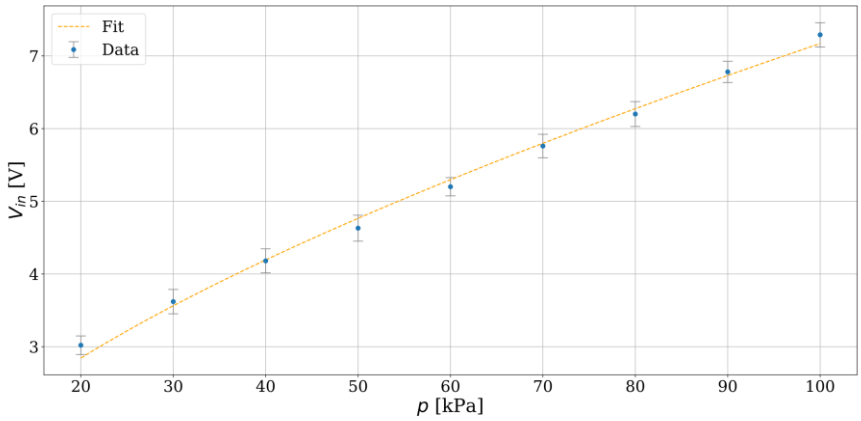


Figure 3 — V_{ign} as a function of pressure p.

The effect of humidity on the ignition voltage is shown in Figure 4. Experimental data are well fitted by a parabolic trend, in agreement with previous findings reported in the literature [7].

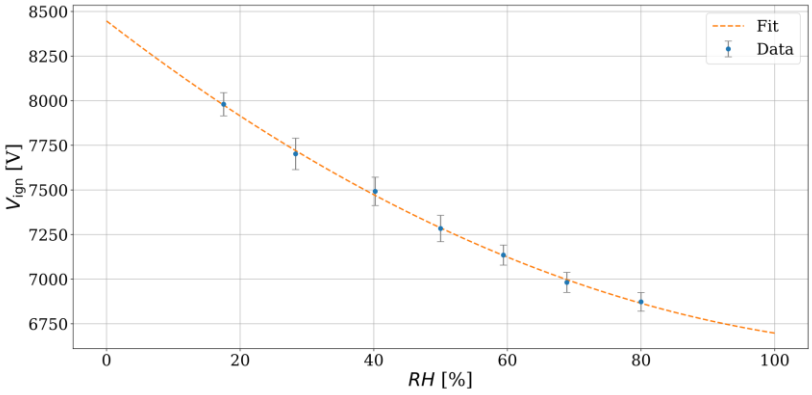


Figure 4 — V_{ign} as a function of humidity.

Corona Current

The corona current increases as pressure decreases, as highlighted in Figure 5, due to the dependence of ion mobility on pressure [8]. The corona current exhibits a parabolic dependence

Materials Research Proceedings 69 (2026) 632-637 https://doi.org/10.21741/9781644904251-112

on humidity, as shown in Figure 6 for three different voltage levels. This behavior is attributed to the combined effects of variations in both ignition voltage and ion mobility.

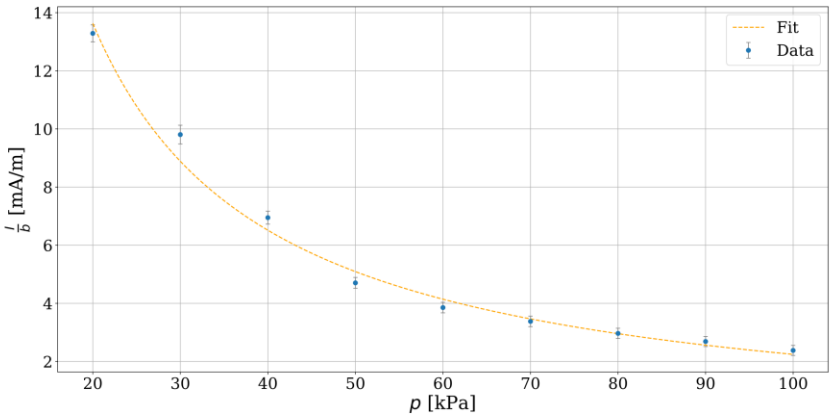


Figure 5 — Corona current i_c as a function of pressure p.

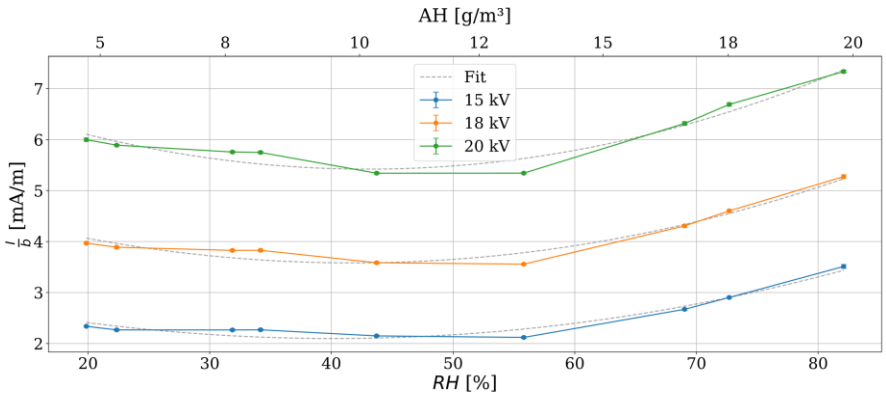


Figure 6 — Corona current i_c as a function of relative humidity RH and absolute humidity AH.

Thrust Density and Thrust-to-Power Ratio

Thrust density exhibits a linear dependence on pressure as shown in Figure 7, resulting from the dependence of the collision frequency νon the gas density ρ. As the gas becomes rarefied, the probability of ionizing collisions decreases, despite the greater ion availability associated with lower ignition voltages, which drives a reduction in space charge density. In other words, although ionization is easier to initiate at lower pressures, the number of effective ionizing collisions decreases, thereby reducing the momentum transfer which is the main mechanism of thrust generation. The corona current, as well as the corona power P, decreases proportionally to $1/p$; the combination of this dependence with the scaling of the generated thrust explains the behavior of T/P, which tends to zero as $p \to 0$, as shown in Figure 8. This is expected, since fewer neutral particles are available at lower pressure levels, resulting in null thrust production regardless of the consumed power. The dependence of thrust density and thrust-to-power ratio on humidity does not exhibit any significant variation, as the measurements acquired at different humidity levels fall within the uncertainty bands.

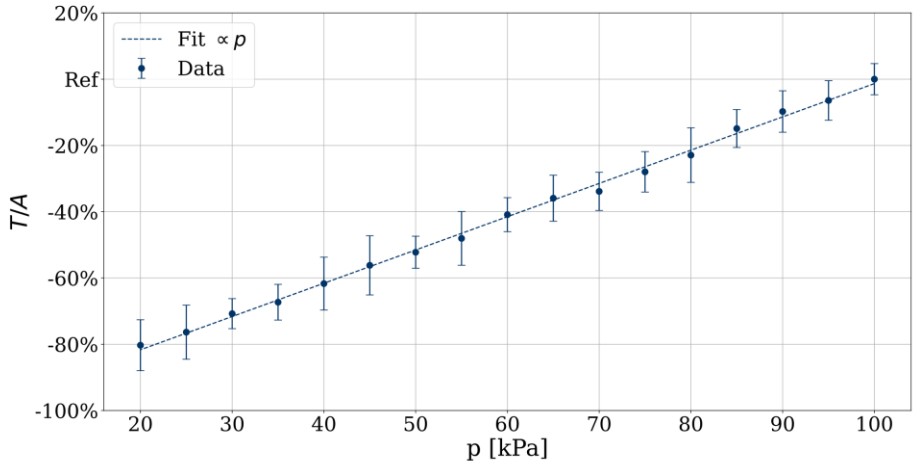


Figure 7 — Thrust density T/A as a function of pressure p.

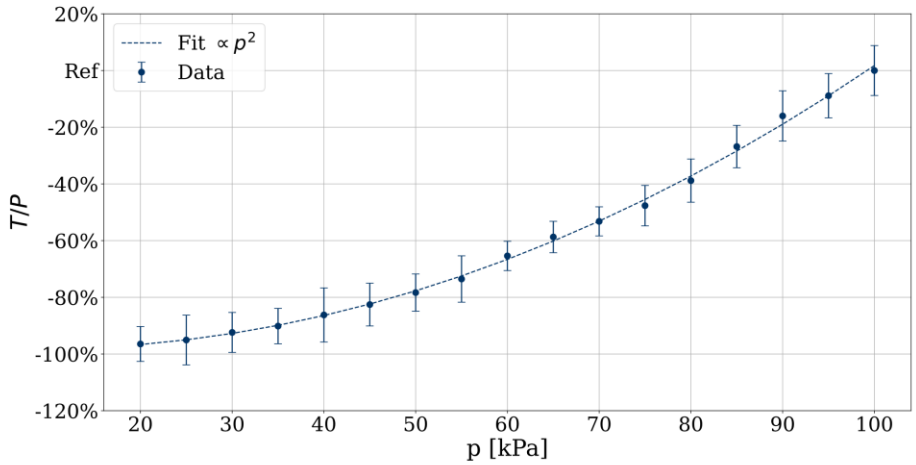


Figure 8 — Thrust-to-power ratio T/P as a function of pressure p.

4. Conclusions

This study experimentally investigates the performance of electroaerodynamic thrusters under varying ambient pressure $p$and relative humidity RH. Experiments are conducted in a low-pressure chamber with controlled environmental conditions. Thrust is measured using a load cell, while corona voltage and current are obtained using a voltage divider and a contactless probe, respectively. Results show that the ignition voltage increases with both pressure and relative humidity, with variations reaching up to 25% between dry and saturated air. A reduction in pressure leads to a decrease in thrust density and thrust-to-power ratio proportional to p and p^2, respectively, while the corona current increases inversely with pressure. These trends are primarily driven by changes in ion mobility and space-charge density. Finally, the corona current is found to scale approximately with RH^2, due to the combined effects of humidity-induced variations in both ignition voltage and ion mobility.

Acknowledgments

This project has received funding from the European Union's *Horizon Europe Research and Innovation Programme* under Grant Agreement No. 101098900. The views and opinions expressed are solely those of the authors and do not necessarily reflect those of the European Union

or the European Innovation Council and SMEs Executive Agency (EISMEA). Neither the European Union nor the granting authority can be held responsible for them.

References

[1] Riboldi C E D, Belan M, Cacciola S, Terenzi R, Trovato S, Usuelli D and Familiari G 2024 Aerospace 11 590 https://doi.org/10.3390/aerospace11070590

[2] Fridman A and Kennedy L A 2004 Plasma Physics and Engineering 1st ed (Boca Raton: CRC Press) https://doi.org/10.1201/9781482293630

[3] Grosse S, Benard N and Moreau E 2025 Current, thrust, and power of a corona discharge plasma thruster at tropospheric altitude vol 58 p 095201 https://doi.org/10.1088/1361-6463/ad9d54

[4] Khomich V, Malanichev V and Rebrov I 2021 Electrohydrodynamic thruster for near-space applications vol 180 pp 141-148 https://doi.org/10.1016/j.actaastro.2020.12.002

[5] Zhao Y, Chen S, Li K, Wang T and Wang F 2024 Influence of humidity and air pressure on thrust characteristics of ion wind propulsion systems vol 57 https://doi.org/10.1088/1361-6463/ad60d8

[6] Usuelli D, Terenzi R, Trovato S and Belan M 2025 Atmospheric EAD grid thruster performance: a theoretical-experimental approach on geometry and pressure effects submitted to Journal of Physics D: Applied Physics https://doi.org/10.1088/1361-6463/ae251d

[7] Zavilopulo A, Chipev F and Shpenik O 2005 Technical Physics 50 402-407 https://doi.org/10.1134/1.1901776

[8] Terenzi R, Trovato S, Usuelli D and Belan M 2025 Atmospheric electroaerodynamic thrusters with grid collectors submitted to Nature Scientific Reports https://doi.org/10.1038/s41598-025-25308-6

Materials Research Proceedings 69 (2026) 638-643 https://doi.org/10.21741/9781644904251-113

Advanced Mesh Grid Geometries for EAD Thrusters: An Experimental Approach

Stefano TROVATO[1,a *], Raffaello TERENZI[1,b], Davide USUELLI[1,c] and Marco BELAN[1,d]

[1]Politecnico di Milano, Via La Masa 34, 20156, Milan, Italy

[a]stefano.trovato@polimi.it, [b]raffaello.terenzi@polimi.it, [c]davide.usuelli@polimi.it, [d]marco.belan@polimi.it

Keywords: EHD Atmospheric Propulsion, Grid Collectors, Double-Level Collectors, Blade Collectors, Green Propulsion

Abstract. This work presents an experimental study of ion thrusters for atmospheric flight, with a focus on the research for an optimal configuration of the collectors. Based on a recent study that demonstrated the advantages of EHD grids as a replacement for classical airfoil shaped ion collectors, test campaigns were carried out with the aim of finding configurations that would further improve their performance in terms of thrust density and thrust-to-power ratio. The main topic of the work is the investigation on the benefits of using a double level of grid collectors, representing the proof of concept for the final examined configuration, which involves the use of metal blade collectors, replacing the classic wires. This latest development could in fact be the ideal solution for practical applications, given the constructional and operational advantages.

Introduction

Ion propulsion is a novel technology for atmospheric applications [1,2], it exploits a high voltage difference between the electrodes to ionize the air and accelerate the ions through the resulting electric field, thus creating thrust through the collision with neutral molecules. The simplest form of EAD thrusters employs the corona effect [3] as the ionization source, enabled thanks to the different geometry of the two electrodes. The emitting electrode must have a high electric field in its surroundings to ionize the air, which is achieved by employing physically small conductive objects as emitters. These should possess regions with a small curvature radius where intense electric field gradients can develop, therefore overcoming the breakdown electric field for air and generating ions. Notable examples include wires with a diameter in the range of tens of micrometers, pins, blades, or sawtooth-shaped electrodes. The collecting electrode should instead inhibit ionization in its surrounding region, which is typically obtained using larger objects as collectors, such as plates [4], large diameter cylinders [5] or metallic airfoils [6]. What is necessary for an efficient ion thruster is the asymmetry of the electric field between the electrodes, which may also be achieved employing the same physical objects for emitters and collectors but in a different spatial density and therefore employing the shielding effect, thus enabling the concept of grid collectors, which may employ the same wires as the emitting electrode. As a result of a recent study that demonstrated the great performance advantages of wire grids as a replacement for classical airfoil-shaped ion collectors, previously established as the canonical geometry for atmospheric ion thrusters, comprehensive test campaigns were carried out with the aim of finding configurations that would further improve their performance in terms of thrust density and thrust-to-power ratio, the two main parameters that characterize the performance of an EAD thruster [7], the first representing an index of compactness and the second one of efficiency. This endeavor has been promoted by the need of minimizing the thruster's drag coefficient, which severely limits the maximum operating velocity of an ion thruster [8], defined as the maximum velocity for which an ion thruster generates positive net thrust, a crucial parameter for any future practical application

Content from this work may be used under the terms of the Creative Commons Attribution 3.0 license. Any further distribution of this work must maintain attribution to the author(s) and the title of the work, journal citation and DOI. Published under license by Materials Research Forum LLC.

Materials Research Proceedings 69 (2026) 638-643 https://doi.org/10.21741/9781644904251-113

of this technology, such as airships [9]. Two possible configurations are here presented to limit the aerodynamic drag generated by a single-level mesh grid collector. A first solution would be using a double level of collectors with the second row in the wake of the first one, therefore reducing the overall drag coefficient. This approach represents the electrical analogue as proof of concept for the final examined configuration, which involves the use of metal blade collectors, replacing the classical wires. This latest development aims to become the ideal solution for practical applications, given the construction and operational advantages paired with the performance improvements of the novel grid collectors, extended to higher velocities. The main geometrical parameter of interest is the grid density, which, for a single-level grid collectors corresponds to the aerodynamic blockage ratio of the grid itself. Previous studies have indicated that a minimum grid density is necessary for the thruster to function efficiently, after which a plateau for all main performance parameters is found, albeit with an increasing drag created by the collectors, which mainly hampers performance in non-zero velocity conditions. The effective grid density of double-level collectors was found to be the sum of its two constitutive levels, thereby allowing a lower blockage ratio and drag for the same grid density and performance, thus becoming promising for practical applications. Blade collectors would be a further aerodynamic improvement, as they substitute the cylindrical wires with ultra-thin metal strips. An overall three-fold thrust increase compared to the baseline configuration found in literature is possible with these types of collectors.

Theoretical aspects

In order to facilitate a direct comparison of the performance of the tested configurations with each other and with other types of thrusters, it is possible to introduce dimensionless coefficients, which remove the dependence of the results on the characteristic dimensions and test voltages. The following three coefficients, obtained in a parallel study currently in its publication process [10], will be utilized:

- Thrust density coefficient (C_{TA}).

$$C_{TA} = \frac{T\chi d}{A\epsilon_0 p V_c \Delta V} \tag{1}$$

- Thrust-to-power ratio coefficient (C_{TP}).

$$C_{TP} = \frac{9T\chi\mu_0 V_c}{8P_c p^2 d^2} \tag{2}$$

- Corona current coefficient (C_c)

$$C_c = \frac{I_c}{\frac{9}{8}\epsilon_0\mu_0\frac{V_c\Delta V}{d^3}} \tag{3}$$

In order to provide a description of the behavior of EAD grid thrusters, it is necessary to introduce parameters that are specific to these systems, related to the geometry of the configurations under consideration. In particular, since both the distance between the wires and their diameter may vary between tests, the grid density parameter ρ_c has been introduced, following the same definition as in [11]. For tests involving double-level collectors, the calculation of ρ_c is derived as the sum of the contributions of the individual grids ρ_{c1} and ρ_{c2}, which are separated by a distance h, regardless of the orientation of the wires at the two levels, such that:

$$\rho_c = \rho_{c1} + \rho_{c2} \tag{4}$$

Materials Research Proceedings 69 (2026) 638-643 https://doi.org/10.21741/9781644904251-113

It has to be pointed out that, in the case of the double-level configuration, the parameter ρ_c defined above has a strictly electrical significance and does not reflect the total blockage ratio of the two collector grids. Previous experimental campaigns have demonstrated that ρ_e and ρ_c are the geometric parameters that most influence the performance of grid ion thrusters. The subsequent results will present the evolution of the dimensionless performance parameters of the thruster as ρ_e and ρ_c vary. For blade collectors the mesh density parameter is again equivalent to the blockage ratio, such that:

$$\rho_c = \frac{t}{s_b} \tag{5}$$

Where t is the blades thickness, here fixed at 0.1 mm and S_b is the spacing between the parallel blades.

Experimental setup

Different custom setups have been designed and built to accommodate the three different configurations (Fig. 1 shows the double-level collectors setup as an example) to be compared in this work, all retaining the same Power Supply Unit (PSU) and nominal geometrical parameters such as frontal area and inter-electrodes gap d (defined as the distance between the emitters plane and the closest point of the collectors, thus being applicable for all configurations). The setup is then mounted on a high precision scale to read the thrust produced T, obtained subtracting the different loads on the balance with the thruster powered on and off. At the same time the corona voltage V_c and corona current I_c are acquired through a voltage divider in parallel with the thruster and a shunt resistor in series with the collector on the ground return path respectively. More details about the setup may be found in [11], which shares the same equipment and measurement techniques.

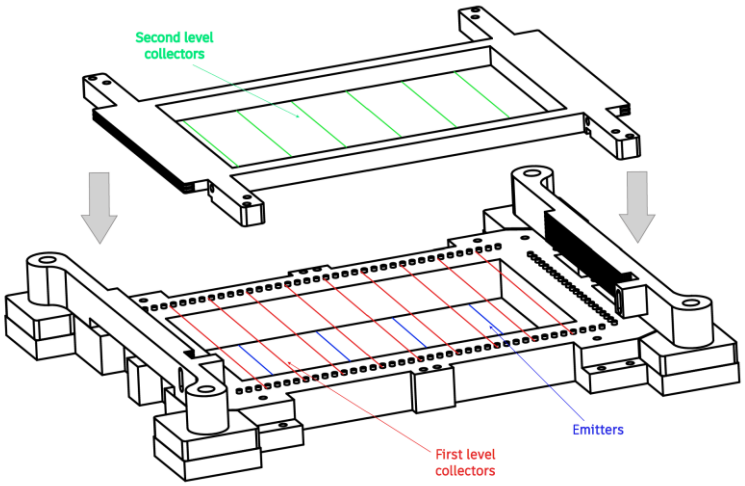


Figure 1: Double-level collectors setup.

Results

In this section the three configurations, namely the original grid collector thruster and the two novel configurations here presented (double-level grid collectors and blade collectors) are compared employing the different performance coefficients at varying grid density levels (ρ_c, defined specifically for each configuration). All the configurations show the typical behavior of mesh grid thrusters, showing a low performance and high power consumption at low grid densities and then improving and finally reaching a plateau at higher grid densities, representing the region where the thruster works as intended with no reverse corona forming, ionization happening

Materials Research Proceedings 69 (2026) 638-643 https://doi.org/10.21741/9781644904251-113

exclusively at the emitters and the collectors functioning as an equipotential plate. The generated thrust actually decreases at very high mesh densities due to the increasing aerodynamic drag generated by the increasingly more numerous collectors. The regression line of all the points inside the plateau of a given configuration are representative of the drag coefficient of that configuration, with the double-level collectors (especially when the second level is exactly in the wake of the first one) and the blade collectors showing a lower drag coefficient compared to the original single-level grid thruster, thus being better suited for high-velocity applications, while retaining the same or even slightly superior static performance. In particular, Fig. 2 shows how the thrust coefficient varies for the different configurations, comparing the novel geometries at different distances h for the double-level collectors setup and different blade chords c for the blade collectors with the classic single-level grid collector design found in [11], displayed at varying emitter densities ρ_e. It has been confirmed that all configurations require a minimum mesh density in order to achieve optimum performance levels, this being confirmed also for the other performance indicators, as in Fig. 3 for the thrust-to-power coefficient and in Fig. 4 for the corona current coefficient, reiterating the presence of adverse reverse corona effects at insufficient grid densities. Outliers in the double-level collectors setup are relative to configurations with increasing drag, i.e. when the second level does not lie in the wake of the first one.

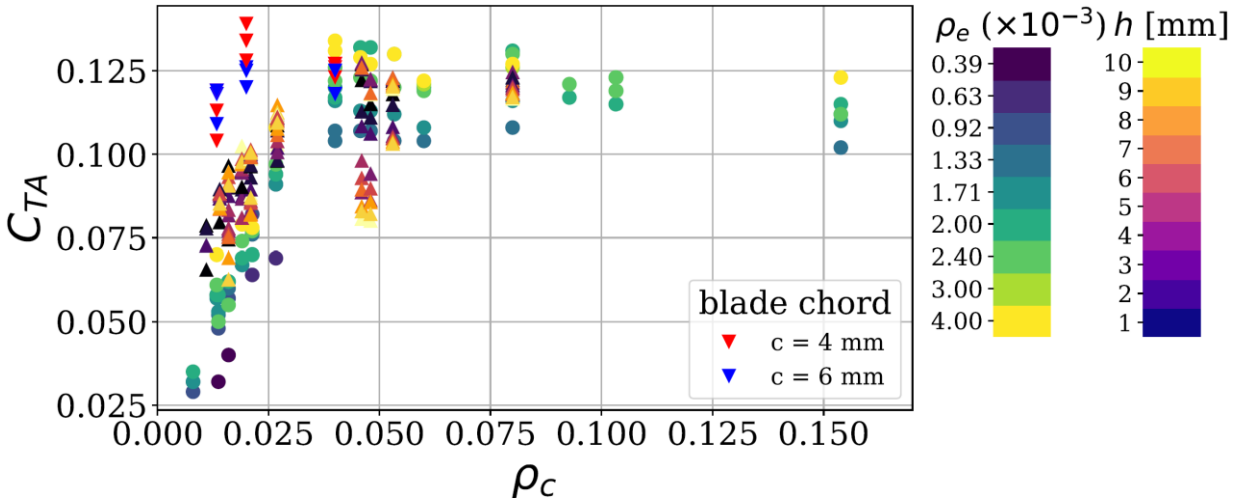


Figure 2: C_{TA} for different configurations at varying grid density (ρ_c).

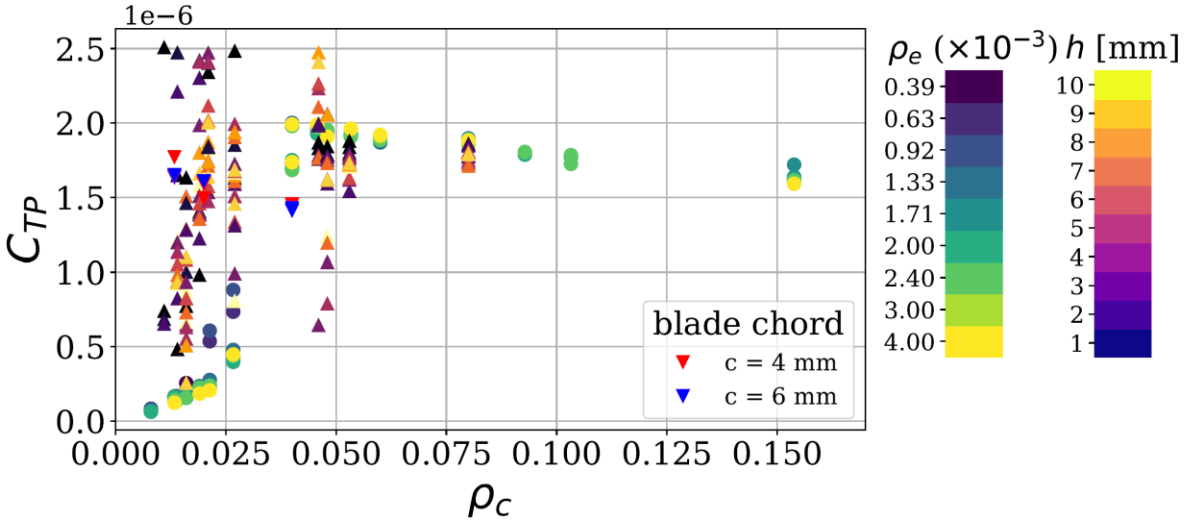


Figure 3: C_{TP} for different configurations at varying grid density (ρ_c).

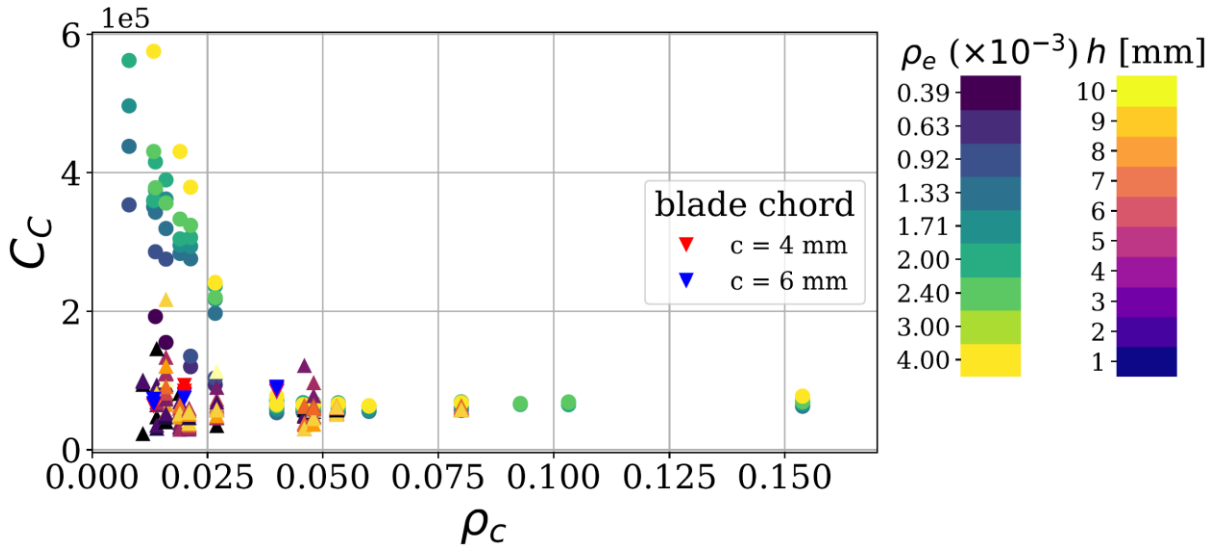


Figure 4: C_c for different configurations at varying grid density (ρ_c).

References

[1] H. Xu et al., Flight of an aeroplane with solid-state propulsion, Nature, vol. 563, no. 7732, pp. 532-535, Nov. 2018. https://doi.org/10.1038/s41586-018-0707-9

[2] V. Y. Khomich and I. E. Rebrov, In-atmosphere electrohydrodynamic propulsion aircraft with wireless supply onboard, J. Electrostatics, vol. 95, pp. 1-12, Oct. 2018. https://doi.org/10.1016/j.elstat.2018.07.005

[3] A. Fridman and L. Kennedy, Plasma Physics and Engineering. New York, NY, USA: Taylor & Francis, 2004. https://doi.org/10.1201/9781482293630

[4] M. Kaci, H. Ait Said, A. Laifaoui, M. Aissou, H. Nouri, and Y. Zebboudj, Investigation on the corona discharge in blade-to-plane electrode configuration, Brazilian J. Phys., vol. 45, no. 6, pp. 643-655, Dec. 2015. https://doi.org/10.1007/s13538-015-0357-4

[5] E. Moreau, N. Benard, J.-D. Lan-Sun-Luk, and J.-P. Chabriat, Electrohydrodynamic force produced by a wire-to-cylinder DC corona discharge in air at atmospheric pressure, J. Phys. D: Appl. Phys., vol. 46, no. 47, Nov. 2013, Art. no. 475204. https://doi.org/10.1088/0022-3727/46/47/475204

[6] M. Belan, L. Arosti, R. Polatti, F. Maggi, S. Fiorini, and F. Sottovia, A parametric study of electrodes geometries for atmospheric electrohydrodynamic propulsion, J. Electrostatics, vol. 113, Sep. 2021, Art. no. 103616. https://doi.org/10.1016/j.elstat.2021.103616

[7] O. Kahol, M. Belan, M. Pacchiani, and D. Montenero, Scaling relations for the geometry of wire-to-airfoil atmospheric ionic thrusters, J. Electrostatics, vol. 123, May 2023, Art. no. 103815. https://doi.org/10.1016/j.elstat.2023.103815

[8] S. Trovato, R. Terenzi, D. Usuelli, and M. Belan, Wind tunnel testing and performance modeling of an atmospheric ion thruster, J. Phys. D: Appl. Phys. 58 015201, Oct. 2024 https://doi.org/10.1088/1361-6463/ad7d9c

[9] C. E. D. Riboldi et al., Preliminary sizing of high-altitude airships featuring atmospheric ionic thrusters: An initial feasibility assessment, Aerospace, vol. 11, no. 7, p. 590, Jul. 2024. https://doi.org/10.3390/aerospace11070590

[10] D. Usuelli, A. Favalli, R.Terenzi, S. Trovato and M. Belan, Atmospheric EAD grid thruster performance: a theoretical-experimental approach on geometry and pressure effects, Under review on J. Phys. D: Appl. Phys.

[11] R. Terenzi, S. Trovato, D. Usuelli and M. Belan, Atmospheric electroaerodynamic thrusters with grid collectors, Accepted on Sci. Rep.

Materials Research Proceedings 69 (2026) 644-649 https://doi.org/10.21741/9781644904251-114

Sustainable Aircraft Propulsion with Four Energy Sources

Salvatore Trepiccione[1,a *], Giuseppe Grazioso[1,b] and Fabrizio Nicolosi[1,c]

[1]University of Naples Federico II, Department of Industrial Engineering, Via Claudio, 21, Naples, 80125, NA, Italy

[a]salvatore.trepiccione@unina.it, [b]giuseppe.grazioso@unina.it, [c]fabrizio.nicolosi@unina.it

Keywords: Hybrid-Electric Aircraft, Sustainable Propulsion Systems, Energy Management, Mission Simulation

Abstract. In response to the aviation sector's decarbonization goals, particularly the European Union's 2050 net-zero target, this study proposes an advanced hybrid-electric propulsion system for regional aircraft integrating four energy sources to enhance energy efficiency and environmental sustainability. Building upon a prior three-source model comprising a gas turbine, a hydrogen fuel cell, and one lithium-ion battery, this work introduces a second battery to create a four-source Serial-Parallel-Partial Hybrid (SPPH) architecture. The powertrain includes two 2,550 kW gas turbines (specific fuel consumption: 0.213 kg/kWh during cruise), two 1,500 kW hydrogen fuel cells (55% peak efficiency), and two lithium-ion batteries: a power-oriented 100 kWh unit (C-rate: 2 h^{-1}, 96% efficiency) designed for transient power demands, and a 300 kWh energy-optimized unit (C-rate: 0.33 h^{-1}, 96% efficiency) intended for steady operating phases such as cruise. A throttle-based control algorithm dynamically allocates power among the different energy sources according to mission requirements, ensuring optimal energy management and thermal balance. Simulations of regional aircraft missions demonstrate the advantages of the proposed configuration compared with its three-source predecessor. The dual-battery system enables targeted energy deployment: the high-power battery supports takeoff and climb phases, while the energy-oriented battery sustains cruise operations, reducing gas turbine and fuel cell loads during transient conditions. This results in lower fuel consumption, reduced thermal peaks, and extended component lifetime. Furthermore, the architecture improves redundancy, fault tolerance, and overall system resilience. Environmental benefits include reduced CO_2 and NO_x emissions enabled by the integration of hydrogen fuel cells and the strategic reduction of gas turbine utilization. Compatibility with renewable energy sources for battery charging and hydrogen production further strengthens the sustainability potential of the proposed system. The four-source hybrid-electric architecture therefore represents a promising pathway toward cleaner regional aviation, offering enhanced efficiency, operational flexibility, and improved integration with future green energy infrastructures.

Introduction

The aviation industry is under increasing pressure to reduce its environmental impact, especially with the European Union's aim of achieving net-zero CO_2 emissions by 2050 [1, 2]. Achieving this aim will necessitate the innovation and implementation of new propulsion technologies. An hybrid-electric aircraft architecture integrates conventional gas turbine engines with one or more electrical power sources, such as batteries, fuel cells, allowing for flexible distribution of energy according to De Vries et al. [3]. Such architectures aim to reduce emissions, and enable the use of renewable energy vectors. Recent studies have explored hybrid-electric configurations ranging from various topologies, demonstrating the potential for energy savings and emission reductions across regional and short-haul aircraft missions, as highlighted by Yuanyuan Li et al. and Nasoulis et al. [4, 5]. However, most state-of-the-art systems focus on single battery packs, which limits possible mission strategies. The present work extends the tri-source architecture proposed by

Content from this work may be used under the terms of the Creative Commons Attribution 3.0 license. Any further distribution of this work must maintain attribution to the author(s) and the title of the work, journal citation and DOI. Published under license by Materials Research Forum LLC.

Materials Research Proceedings 69 (2026) 644-649 https://doi.org/10.21741/9781644904251-114

Grazioso et al. [6], which couples fuel cells and batteries with conventional thermal engines, by adding an additional battery element as a fourth energy source. Among the various possible architectural combinations, one was chosen that allows for independent management of individual battery packs, ensuring more efficient energy distribution during all phases of flight and supporting sustainable regional aviati on missions.

Generalizing hybrid-electric powerplant system

The tri-source architecture discussed in [6], which includes only one battery element, has inherent limitations. When batteries of different types are used, this configuration cannot manage them effectively, making it necessary to adopt the four-source architecture. The powertrain model is characterized by gas turbine engines, fuel cell systems and two separate battery elements [7]. One objective of such a system could be to ensure independent control of two different battery packs, such as a power-sized battery and an energy-sized battery. The hybrid electric architecture in

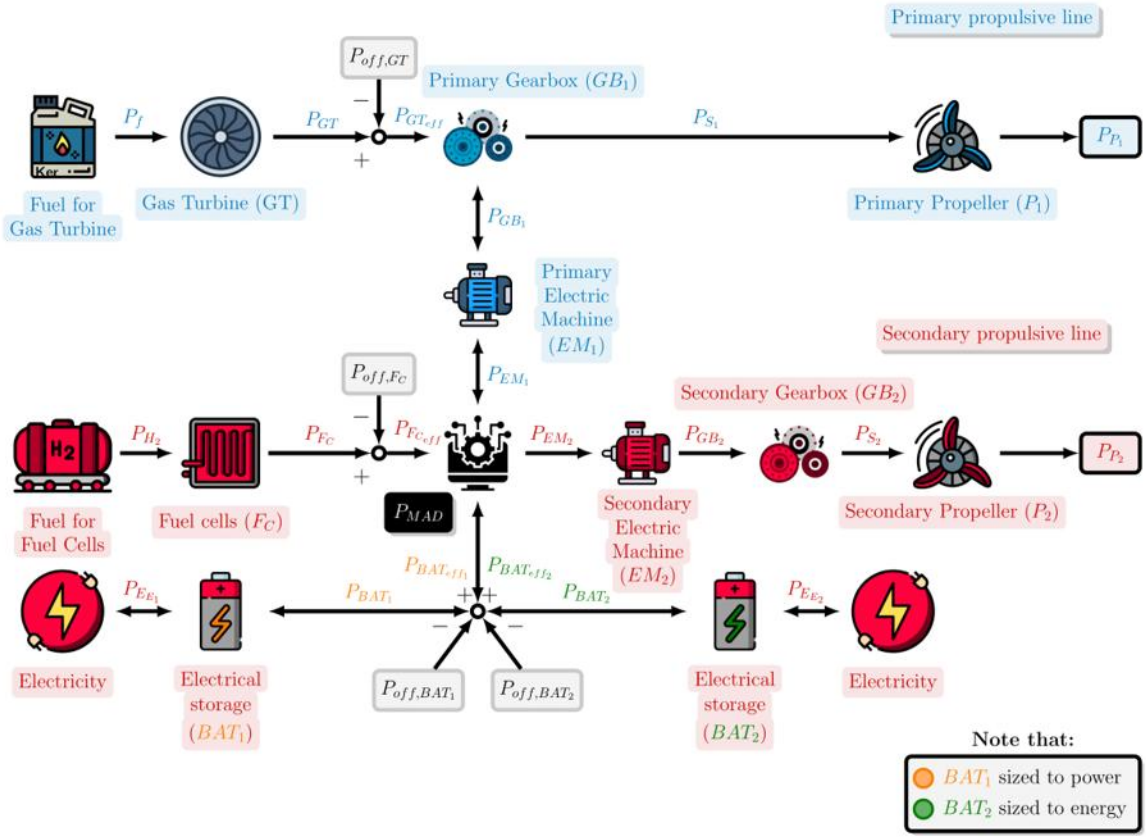


Figure 1 supports multiple operating modes, shown by double arrowheads indicating electric machines that can act as generators or motors, and batteries that can charge or discharge.

Materials Research Proceedings 69 (2026) 644-649 https://doi.org/10.21741/9781644904251-114

Table 1: Hybrid-electric powerplant system specifications.

Component	Parameter	Value	Units	Notes
Gas turbine engine	Quantity	2	-	-
	Max power	2,550	kW	per unit
	SFC	0.213	kg/kWh	cruise
	Total power	5,100	kW	combined
Fuel cell system	Quantity	2	-	-
	Max power	1,500	kW	per unit
	Efficiency	55	%	@ peak power
	Total power	3,000	kW	combined
Primary battery system	Quantity	1	-	-
	Capacity	100	kWh	-
	Max C-rate	2.0	h^{-1}	-
	Efficiency	96	%	-
Secondary battery system	Quantity	1	-	-
	Capacity	300	kWh	-
	Max C-rate	0.33	h^{-1}	-
	Efficiency	96	%	-

Case study: regional transport aircraft

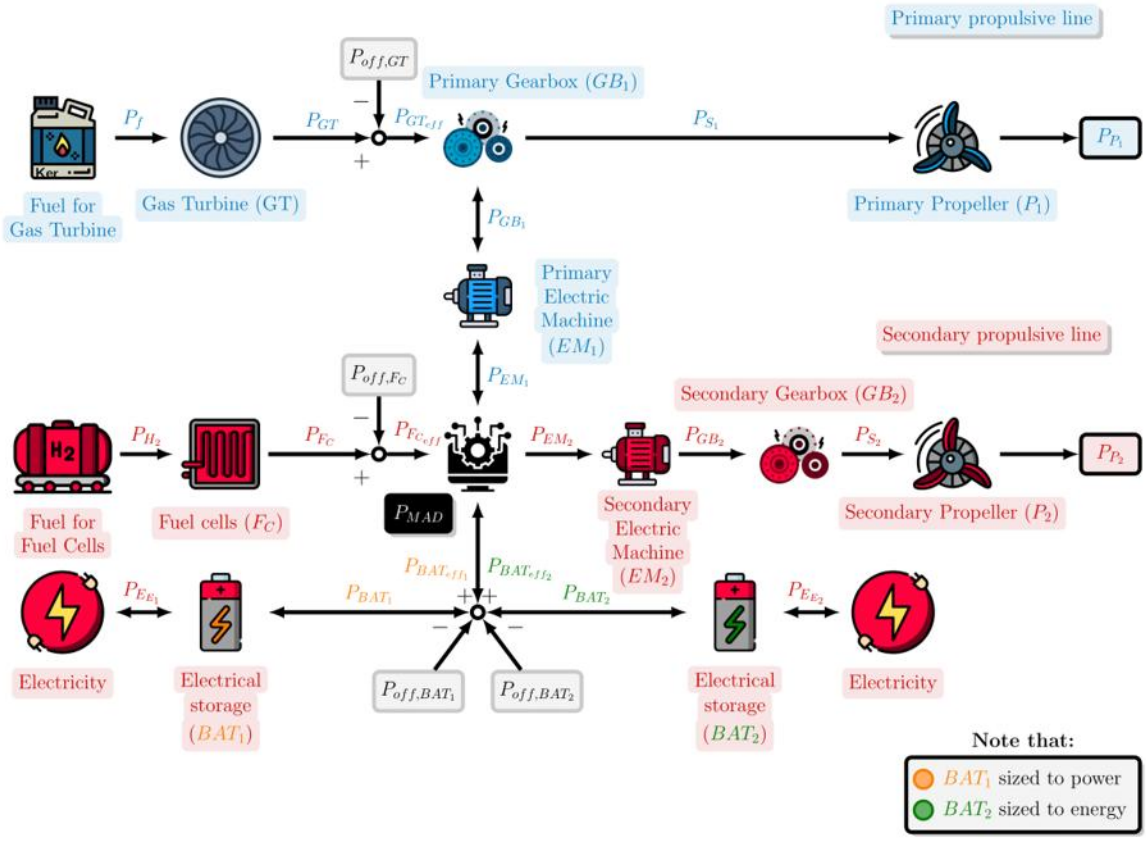


Figure 1: Logic diagram of the four source hybrid-electric architecture (SPPH configuration).

The proposed regional transport aircraft is designed to carry 80 passengers (at an average weight of 110 kg each) over a range of 600 nmi. Both takeoff and landing field lengths are approximately

Materials Research Proceedings 69 (2026) 644-649 https://doi.org/10.21741/9781644904251-114

1,400 m. The aircraft is expected to cruise at 300 KTAS at FL250 and achieve a climb from FL150 to FL250 in 20 minutes at maximum takeoff mass. Fuel reserves are sized to cover a 100 nmi diversion, 30 minutes of holding, and 5 % additional trip fuel. The minimum and maximum state of the charge are set respectively to 20% and 80% for both battery packs in order to preserve the element life cycle.

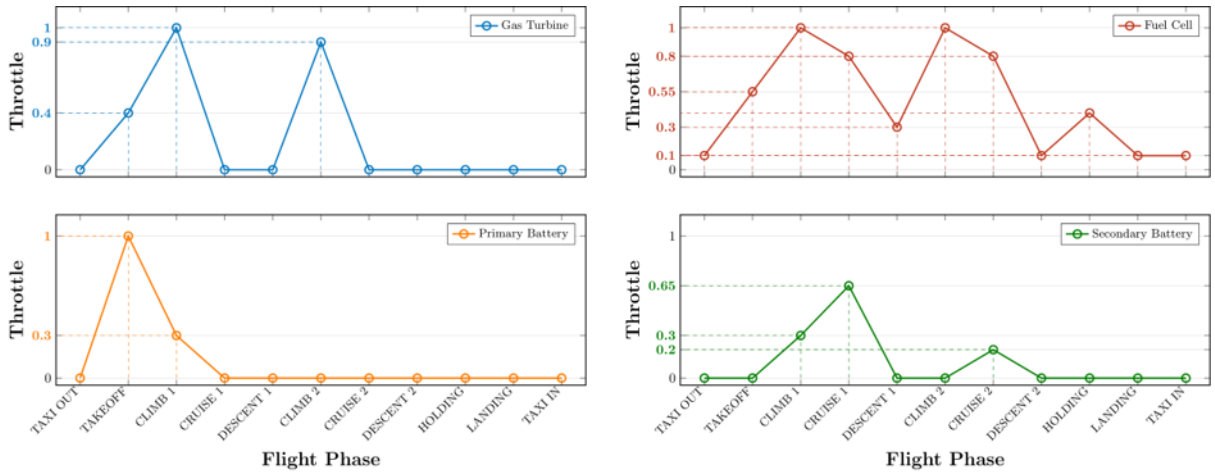


Figure 2: Powerplant throttles settings for the selected mission profile.

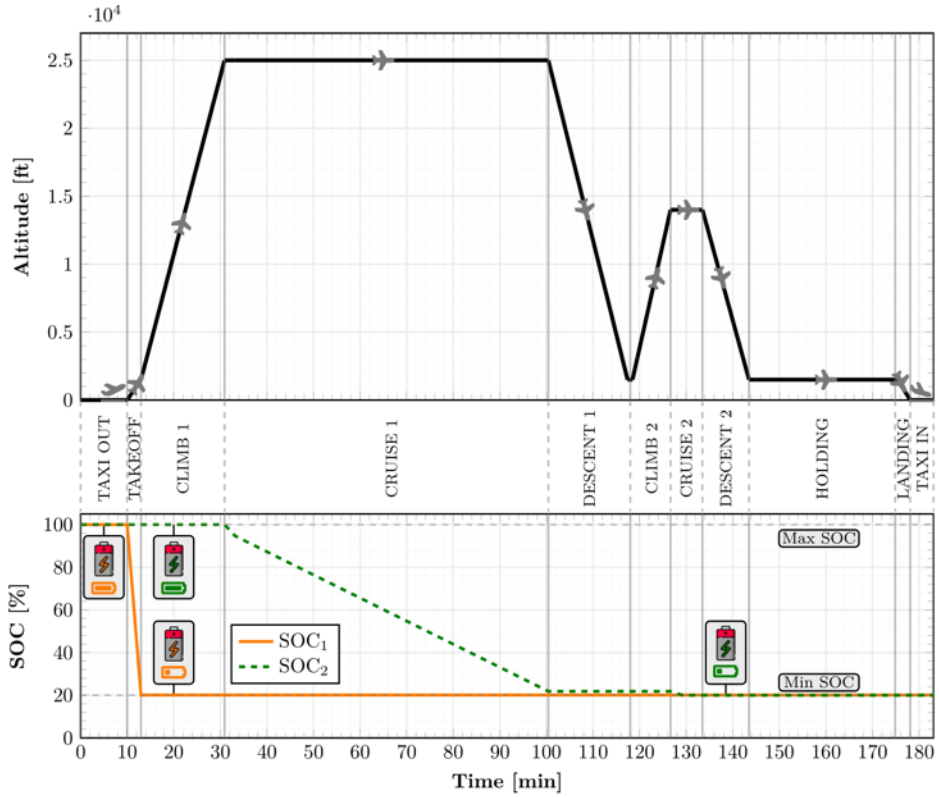


Figure 3: Mission profile and state of charge. Phases number 1 indicates block, instead number 2 stands for diversion.

The four-sources model uses an architecture inspired by the more general serial parallel partial hybrid (SPPH), regulated by energy flow equations and a throttle-based power management algorithm to dynamically respond to mission power requirements. The high- power battery (primary battery), characterized by a high discharge rate (c-rate) and lower capacity, is mainly

Materials Research Proceedings 69 (2026) 644-649 https://doi.org/10.21741/9781644904251-114

depleted during the takeoff phase, when the peak power demand is at its highest. In contrast, the energy-optimized battery (secondary battery), with higher capacity and lower discharge rate, supports power delivery throughout the cruise phase of the mission, when a constant and continuous power supply is essential. The targeted use of each battery based on its functional strength improves the overall energy handling of the powertrain.

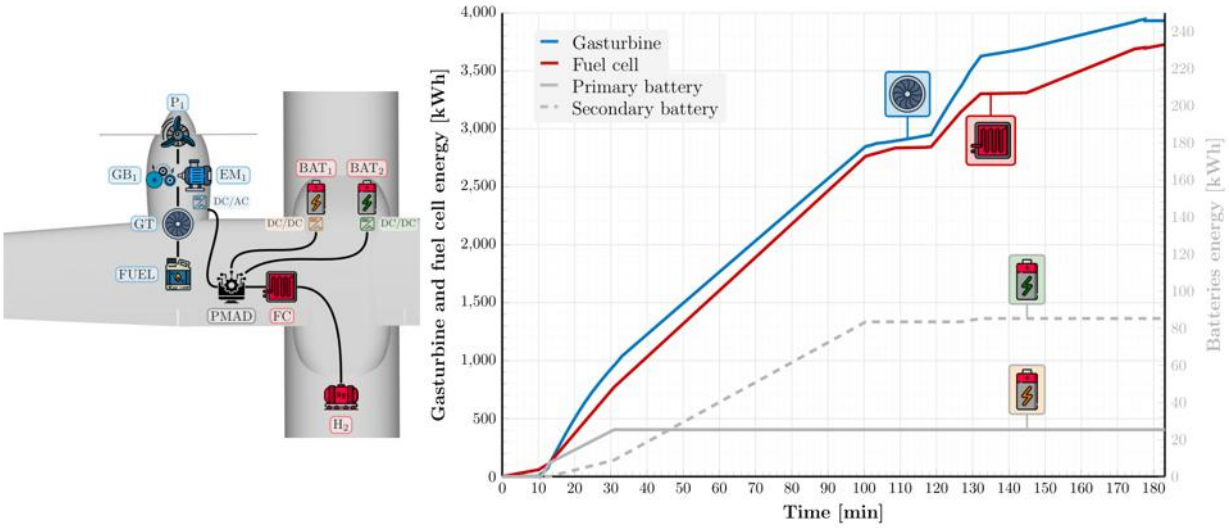


Figure 4: Actual hybrid aircraft configuration integrating four power sources (left), and the corresponding energy profile for each source throughout the mission (right).

Table 2: Mission range 600 nmi.

	Mission analysis results	Units
Block Kerosene fuel	637.36	[kg]
Block H_2 fuel	188.59	[kg]
Final primary battery SOC	20	[%]
Final secondary battery SOC	20	[%]
Block time	125.15	[min]

Table 3: Advantages and shortcomings of chosen hybrid powerplant architecture.

	Description
Advantages	Greater operational flexibility
	Reduced dependence on turbine and fuel cell during transient phases, leading to lower fuel consumption and smoother power delivery.
	Use of smaller, specific batteries minimizes energy waste compared to a single oversized pack.
Shortcomings	Increased system weight.
	More complex architecture in terms of control, maintenance, integration, and cooling.
	Hydrogen production and storage may still be associated with certain emissions.

Acknowledgments
The research presented in this paper has been performed in the framework of the HERA project (Hybrid Electric Regional Aircraft) and has received funding from the European Union Clean Aviation Program under grant agreement n°101102007.Please note that Figures have been designed using resources from Flaticon.com.







References

[1] B. Baptiste, N. Alexandros, G. Ajay, K. Konstantinos and e. al, "A multi-model analysis of the EU's path to net zero," Joule, vol. 7, no. 12, pp. 2760-2782, 2023. https://doi.org/10.1016/j.joule.2023.11.002

[2] E. C. a. D.-G. f. R. Innovation, Fly the Green Deal - Europe's vision for sustainable aviation, Publications Office of the European Union, 2022.

[3] R. de Vries, M. Brown and R. Vos, "Preliminary Sizing Method for Hybrid-Electric Distributed-Propulsion Aircraft," Journal of Aircraft, vol. 56, pp. 1-17, 10 2019. https://doi.org/10.2514/1.C035388

[4] Y. Li, Z. Hu, Y. Zhang, J. Li, L. Xu and M. Ouyang, "Optimal performance and preliminary parameter matching for hydrogen fuel cell powertrain system of electric aircraft," eTransportation, vol. 21, p. 100342, 2024. https://doi.org/10.1016/j.etran.2024.100342

[5] C. Nasoulis, G. Protopapadakis, E. Ntouvelos, Gkoutzamanis and e. al., "Environmental and techno-economic evaluation for hybrid-electric propulsion architectures," The Aeronautical Journal, vol. 127, no. 1317, p. 1904-1926, 2023. https://doi.org/10.1017/aer.2023.27

[6] G. Grazioso, M. Di Stasio, F. Nicolosi and S. Trepiccione, "A mathematical model for hybrid-electric propulsion system for regional propeller-driven aircraft," Energy Conversion and Management: X, vol. 26, p. 100957, 2025. https://doi.org/10.1016/j.ecmx.2025.100957

[7] N. U. K. F.M., G. R. Mohammad, S. A.S.M. and M. Nirmal, "Maximizing energy density of lithium-ion batteries for electric vehicles: A critical review," Energy Reports, vol. 9, pp. 11-21, 2023. https://doi.org/10.1016/j.egyr.2023.08.069

Materials Research Proceedings 69 (2026) 650-655 https://doi.org/10.21741/9781644904251-115

Automated Flight Testing of a Distributed Electric Propulsion Flying Model

Lorenzo TRAINELLI[1,a *], Giorgio FILIPPOLI[1,b], Niko TERZAROLI[1,c], Beniamino M. PERRI[1,d], Stefano CACCIOLA[1,e], and Carlo E. D. RIBOLDI[1,f]

[1]Department of Aerospace Science and Technology, Politecnico di Milano, Via G. La Masa 34, Milano, Italy

[a]lorenzo.trainelli@polimi.it, [b]giorgio.filippoli@polimi.it, [c]niko.terzaroli@mail.polimi.it, [d]beniaminomaria.perri@polimi.it, [e]stefano.cacciola@polimi.it, [f]carlo.riboldi@polimi.it

Keywords: Distributed Electric Propulsion, Aero-Propulsive Interaction, Automated Flight Testing, Model Identification

Abstract. This work presents the development and implementation of a fully automated flight testing methodology for the SwitchMaster, a Distributed Electric Propulsion (DEP) demonstrator designed to investigate aero-propulsive coupling effects. Previous manual flight campaigns were limited by variability in trim conditions and inconsistent excitation inputs, constraining both data quality and the range of blowing conditions achievable in flight. The proposed framework integrates mission design, nonlinear Simulink simulation, Software-in-the-Loop validation and autonomous flight through the onboard PX4 autopilot, forming a coherent and reusable flight test suite. A total of 38 autonomous missions and 141 maneuvers were conducted across an expanded envelope of airspeeds and climb angles, enabling exploration of blowing regimes previously inaccessible. Automated trim acquisition and maneuver execution significantly improved repeatability and reduced variability in key stability and control derivatives, yielding clearer trends with the propeller advance ratio J and enhancing subsequent model-identification fidelity. The methodology provides a robust foundation for future DEP research, control-law development and aero-propulsive modelling.

Introduction

Distributed Electric Propulsion (DEP) represents one of the most promising technological pathways for future sustainable aviation. By distributing multiple propellers along the wing, DEP enables aero-propulsive coupling effects that can enhance lift, modify stability characteristics and introduce new opportunities for vehicle control. The SwitchMaster demonstrator (Fig. 1), a scaled aircraft equipped with six wing-mounted electric motors, was developed within this broader research effort to experimentally investigate these phenomena. Previous work focused on establishing the AeroSwitch [1] concept and on developing modeling strategies capable of capturing the influence of the propeller advance ratio J on aerodynamic derivatives [2]. These studies demonstrated the potential of DEP architectures but also highlighted the need for more refined flight data to support accurate model identification.

In this context, the present contribution describes the transition from manual to automated flight testing, providing the methodological foundations required to acquire consistent, repeatable and high-quality flight data, widening the spectrum of the conditions to be tested with respect to previous campaigns. The development of an autopilot, based on a Total Energy Control System [3], and the associated control logic is addressed in a complementary article [4], while another contribution focuses on advanced modeling and identification techniques [5]. Here, attention is devoted to the experimental framework that supports those efforts, with particular emphasis on trim stabilization, maneuver execution and the resulting improvements in data fidelity.

Content from this work may be used under the terms of the Creative Commons Attribution 3.0 license. Any further distribution of this work must maintain attribution to the author(s) and the title of the work, journal citation and DOI. Published under license by Materials Research Forum LLC.

Materials Research Proceedings 69 (2026) 650-655 https://doi.org/10.21741/9781644904251-115



Figure 1: The SwitchMaster before a test flight.

Limitations of manual Flight Testing

Initial test campaigns relied on a remote pilot to perform trim and excitation maneuvers [6]. Although adequate for preliminary qualitative analyses, manual piloting introduced intrinsic variability that limited the reliability of the collected data. Achieving a stable trim condition requires finely balancing airspeed, climb angle and control surface deflections, a task that proved difficult to perform consistently across multiple repetitions. Even small deviations in the steady-state flight condition resulted in significantly different levels of propeller blowing and, consequently, different values of the aerodynamic coefficients at the start of each maneuver.

Similarly, manual execution of elevator, aileron or rudder doublets and 3-2-1-1 inputs leads to variations in amplitude, timing and input shape, reducing the effectiveness of the excitation and making it challenging to isolate specific dynamic modes such as the short-period and Dutch-roll.

Moreover, high-blowing conditions typically require trimming the aircraft in steep climbs, a regime that was difficult to maintain manually with sufficient precision. These limitations motivated the development of a fully automated testing system, capable of reproducible trim settings and consistent maneuver execution across the entire test matrix.

Automated Flight Test Framework

To address these challenges, a complete automated testing framework was developed, integrating mission planning, autonomous flight control and maneuver execution into a unified methodology. A nonlinear simulator built in MATLAB/Simulink, incorporating flight dynamics, aerodynamics and autopilot logic, served as the foundational tool for mission design. This simulator allowed the prediction of trim points across a wide range of airspeeds and climb angles, ensuring that each combination corresponded to a feasible steady-state flight condition.

Onboard, the aircraft relied on a customized autopilot system capable of reaching and maintaining precise trim values of airspeed and climb angle. Once stabilized, the controller executed predefined excitation maneuvers while following programmed flight paths. Only the essential aspects of this control architecture are recalled here, as the detailed implementation is discussed separately; the focus of this article remains on its role within the experimental process. Importantly, automation allowed not only superior data quality but also access to flight regimes previously unreachable.

Flight Test Planning and Mission Design

Mission profiles were designed to span the entire range of propeller advance ratio J relevant for the aero-propulsive characterization of the SwitchMaster. For each airspeed setpoint, several climb

Materials Research Proceedings 69 (2026) 650-655 https://doi.org/10.21741/9781644904251-115

and descent angles were selected to vary blowing intensity while remaining within the limits of the aircraft performance and battery endurance. The simulator was used to calculate the expected mission duration, the time required to reach trim conditions and the geometry of the flight path, including straight segments and turns. Fig. 2 illustrates a representative mission profile generated during simulation.

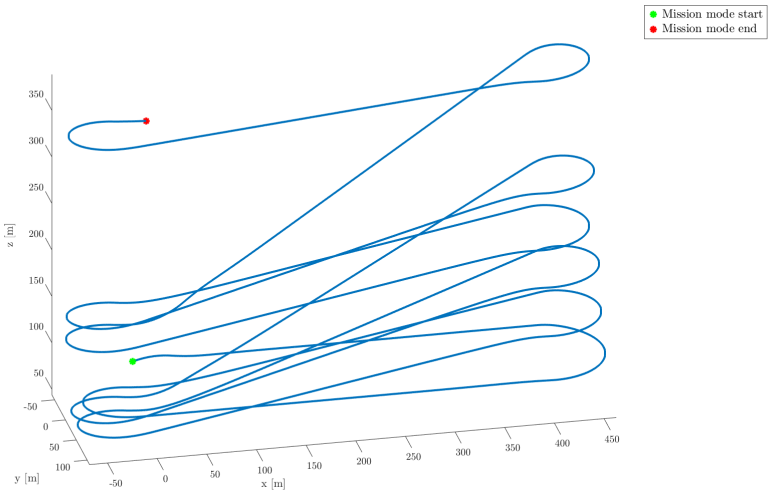


Figure 2: Example of a simulated mission.

This approach ensured that each mission could be completed safely, with sufficient energy margins for contingencies. The resulting mission plans were translated into MAVLink-compatible files and uploaded directly to the aircraft, enabling fully autonomous execution without the need for manual intervention (except for takeoff and landing).

Automated maneuver execution and environment

Once the aircraft reached the prescribed trim state, the system evaluated the tolerances on airspeed and climb angle before triggering the selected maneuver. The maneuvers included elevator doublets, ailerons and rudder doublets, 3-2-1-1 sequences and combined inputs. Each excitation was parameterized to deliver consistent spectral content close to the natural frequencies of the relevant dynamic modes.

The execution took place at the Mach Aurora airfield, east of Milan, where the flight path was designed to account for nearby obstacles and geometric constraints. During each maneuver, the autopilot temporarily suspended TECS and other modules regulation, applied the commanded input and then allowed the aircraft to settle, ensuring clear observation of both forced and free responses. Fig. 3 shows a typical elevator doublet executed during a stabilized descent.

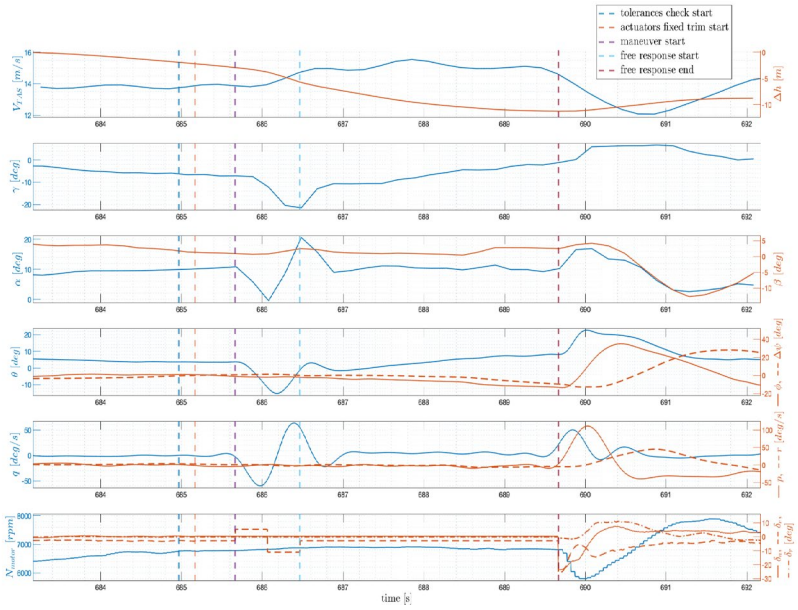


Figure 3: Elevator doublet time histories during stabilized descent.

The improvement in input precision achieved through automation is evident when comparing automated and manual doublets. Fig. 4 illustrates this contrast, highlighting the superior repeatability and stability obtained through autonomous maneuver execution.

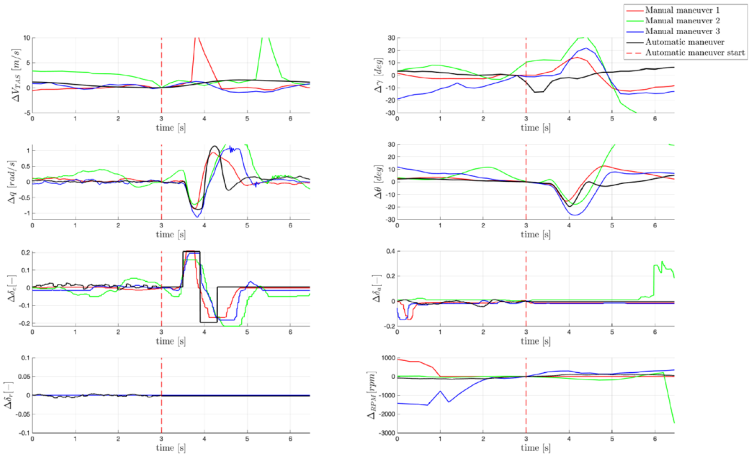


Figure 4: Comparison between manual and automated elevator doublets.

Beyond enabling automated trim acquisition and maneuver execution, the methodology developed in this work effectively constitutes a coherent and reusable flight testing suite specifically tailored for DEP aerodynamic and aero-propulsive investigations. The suite integrates all stages of the experimental workflow into a unified process, ensuring continuity between mission design, simulation and real-flight execution. Mission profiles are first generated and analyzed within a nonlinear MATLAB/Simulink environment, where the complete aeromechanical model of the SwitchMaster and the high-level autopilot logic are used to predict trim feasibility, expected values of the advance ratio J, maneuver windows and total mission duration. The same missions are then replicated in a Software-in-the-Loop environment based on Gazebo, enabling verification of the flight path, software testing and safety protections within a physics-based simulation prior to deployment.

Once validated, the mission and software build is transferred unchanged to the real aircraft and executed by the onboard PX4 autopilot, ensuring full traceability between predicted and observed

aircraft behavior. This integrated workflow provides a robust methodological backbone for conducting systematic DEP flight test campaigns and ensures that variations observed in aerodynamic coefficients derive from physical effects rather than inconsistencies in piloting or test execution.

Safety Checks

Following an accident during a test flight [7], the safety architecture of the system was substantially reinforced. Prior to each maneuver, the autopilot verified that the computed control surface offsets required to maintain trim remained within acceptable bounds. If the aileron or rudder offsets exceeded these thresholds, the maneuver was not initiated, even if all other conditions were satisfied.

During maneuvers, additional protections monitored attitude limits, aborting the excitation if excessive roll or pitch angles were reached. In addition, there were checks on altitude, airspeed, vertical speed and horizontal limits, plus a manual switch for the pilot to interrupt a maneuver and possibly regain manual control. These safeguards contributed to the integrity of the test campaign, ensuring both the safety of the vehicle and the consistency of the logged dataset.

Flight test campaign and data acquisition strategy

The final campaign included the setpoints listed in Table 1, covering airspeeds between approximately 12 m/s and 20 m/s and climb angles from about −15° to +40°. This structure enabled the acquisition of data in conditions of descent, level flight, moderate climb and steep climb, the latter being particularly valuable for exploring strong blowing conditions.

Table 1: Tested flight conditions.

Airspeed setpoint [m/s]	Angle of Climb setpoint [deg]
20, 18	40, 30, 20
16, 14	10, 0, -5
13, 12	-10, -15, glide

Between February and June 2025, a total of 38 autonomous missions were executed, yielding 141 valid maneuvers. These included elevator doublets, 3-2-1-1 sequences and combined ailerons and rudder doublets, each initiated from a stable trim condition. The avionics suite, comprising PX4 inertial sensors, GPS, Pitot probe, telemetry and RC link, provided comprehensive logging of all variables required for model identification.

All logs were stored in *.ulg* files for offline processing. The consistency of the trim states and the precision of the maneuver execution rapidly became evident when comparing automated data with that obtained during earlier manual tests.

Results and impact on model identification

The transition to automated testing produced a clear and quantifiable improvement in the quality of the recorded data. Time histories of doublets and 3-2-1-1 inputs exhibited sharply defined input profiles with uniform amplitude and timing. The stabilization preceding each maneuver was markedly more precise, resulting in consistent initial conditions even across different days and environmental conditions.

These enhancements translated directly into improvements in system identification. The reduced variability in the experimental data led to tighter clustering of aerodynamic derivatives, clearer trends with the propeller advance ratio J and more reliable application of both Equation-Error and Output-Error methods. Particularly, coefficients such as C_{m0} and selected lateral-directional derivatives displayed smoother and more physically interpretable behaviors, reinforcing the validity of the underlying modelling assumptions. The automated framework thus

proved essential for obtaining the fidelity required to advance the aero-propulsive modelling of DEP configurations.

Conclusions

The automated flight testing methodology presented in this work represents a significant advancement in the experimental analysis of DEP aircrafts. By eliminating the variability inherent in manual piloting and enabling consistent execution of trim and excitation maneuvers, the framework provides a robust foundation for accurate model identification.

Together with ongoing developments in modelling and control, the results obtained from this campaign contribute to a broader effort aimed at understanding and exploiting the unique characteristics of Distributed Electric Propulsion. Future work will extend this methodology to expanded flight envelopes, advanced control strategies and more refined modelling approaches, further strengthening the experimental basis for DEP technologies.

References

[1] D. Pasquali, A. Santeramo, L. Alberti, M. Tombolini, L. Trainelli, C.E.D. Riboldi, Distributed Electric Propulsion Aircraft Simulating a Single Propeller Aircraft, European Patent EP21725107.3 (published December 11, 2024; priority date May 8, 2020).

[2] S. Cacciola, G. Filippoli, B.M. Perri, C.E.D. Riboldi, N. Terzaroli, L. Trainelli, Autonomous Flight Tests of a Distributed Electric Propulsion Demonstrator Based on a Total Energy Control System, 11th European Conference for Aeronautics and Aerospace Sciences (EUCASS), Rome, Italy, 2025.

[3] L.F. Faleiro, A.A. Lambregts, Analysis and Tuning of a 'Total Energy Control System' Control Law Using Eigenstructure Assignment, Aerospace Science and Technology 3 (3) (1999) 127–140. https://doi.org/10.1016/S1270-9638(99)80037-6

[4] G. Filippoli, B.M. Perri, N. Terzaroli, L. Trainelli, S. Cacciola, C.E.D. Riboldi, Development of an Autonomous Flight Control System for a Distributed Electric Propulsion Flying Model, 10th CEAS Aerospace Europe Conference / 28th AIDAA International Congress, Turin, Italy, December 1–4, 2025.

[5] G. Filippoli, N. Terzaroli, B.M. Perri, S. Cacciola, C.E.D. Riboldi, L. Trainelli, Aero-Propulsive Modeling and System Identification of a Distributed Electric Propulsion Flying Model, 10th CEAS Aerospace Europe Conference / 28th AIDAA International Congress, Turin, Italy, December 1–4, 2025.

[6] S. Cacciola, L. Bottà, C.E.D. Riboldi, L. Trainelli, Identification of the Impact of Blowing on the Aerodynamic Model of an Airplane with Distributed Electric Propulsion, 34th ICAS Congress, Florence, Italy, September 9–13, 2024.

[7] G. Filippoli, L. Trainelli, N. Terzaroli, B.M. Perri, Accident Investigation and Lessons Learnt during an Automated Flight Test Campaign of a Distributed Electric Propulsion Demonstrator, Flight Test Safety Committee Workshop, Trieste, 2025.

Materials Research Proceedings 69 (2026) 656-661 https://doi.org/10.21741/9781644904251-116

Development of an Autonomous Flight Control System for a Distributed Electric Propulsion Flying Model

Giorgio FILIPPOLI[1,a*], Beniamino M. PERRI[1,b], Niko TERZAROLI[1,c], Lorenzo TRAINELLI[1,d], Stefano CACCIOLA[1,e] and Carlo E. D. RIBOLDI[1,f]

[1]Department of Aerospace Science and Technology, Politecnico di Milano, Via G. La Masa 34, Milano, Italy

[a]giorgio.filippoli@polimi.it, [b]beniaminomaria.perri@polimi.it, [c]niko.terzaroli@mail.polimi.it, [d]lorenzo.trainelli@polimi.it, [e]stefano.cacciola@polimi.it, [f]carlo.riboldi@polimi.it

Keywords: Distributed Electric Propulsion, Flight Control System, Automated Flight Testing, Model Identification

Abstract. The scope of this work is the realization of a fully automated testing campaign, through the development of an autonomous Flight Control System (FCS), in order to support the model identification of a Distributed Electric Propulsion (DEP) scaled demonstrator. The autopilot has been used to follow a GPS trajectory, reach trim conditions, execute the required maneuvers, define and tune specific control actions and carry out automatic safety checks. The chosen software environment is PX4, an open-source professional autopilot, which has been extended and customized to carry out the flight operations needed for parametric identification, while fulfilling functional and safety-related requirements. In addition, a simulation environment has been set up for software testing and pre-flight configuration. The result is a fully automated platform for flight testing and advanced research within DEP models.

Introduction

In earlier works [1], a parametric model identification of a DEP flying model, the SwitchMaster, was carried out, leading to a numerical definition of its stability and control derivatives. Besides, it was observed how the blowing effect on the wings impacts several derivatives, which in particular can have an exponential growth as the blowing intensifies, due to the aero-propulsive coupling generated by the faster air flow on the wings with respect to that along the fuselage. The blowing can be quantified in terms of propellers advance ratio $J = \frac{V}{nD}$, where V is the true airspeed, n is the propellers rotational speed and D the propellers diameter. In fact low J values, that can be achieved at low airspeed and high propellers rotational speed, correspond to high blowing, and vice versa. The unblown case, defined as $J \to +\infty$, can be obtained by gliding. However, the main limitation of this work was the difficulty to have good trim conditions and a precise execution of the maneuvers, especially at high climb angles which are required to experiment high blowing, mainly due to the manual remote piloting. Hence, it was necessary to develop an autopilot to support the realization of a fully automated testing campaign and then improve the quality of the data collected to feed the model identification process, leading to a more realistic estimated DEP model.

System Requirements Analysis

Following a standard software engineering procedure, it was started defining the Goals of the System and the Domain Assumptions, which are hypotheses assumed to hold about the environment and the user's behavior. With this procedure, the System Requirements can be defined, being essentially conditions that the System must satisfy to reach the Goals, assuming true the Domain Assumptions. The main Goal can be expressed as follows:

Content from this work may be used under the terms of the Creative Commons Attribution 3.0 license. Any further distribution of this work must maintain attribution to the author(s) and the title of the work, journal citation and DOI. Published under license by Materials Research Forum LLC.

Materials Research Proceedings 69 (2026) 656-661 https://doi.org/10.21741/9781644904251-116

The System must be able to reach trim conditions at any feasible combination of J and α, holding V_{TAS} and γ setpoints while following a GPS flight plan, then executing safely and autonomously all the needed maneuvers for parametric identification.

Hence, here are provided some examples of the Requirements that had to be satisfied, which led to significant changes and extensions of PX4:

1. The System must be able to execute climb and descent, following a climb angle γ setpoint defined by the User. The level flight should be treated as a particular case with $\gamma = 0$ deg.
2. Multiple circuits could be executed in automatic flight, following a GPS flight plan, and along each straight leg of the circuit one climb angle has to be scheduled.
3. After each climb or descent, the aircraft smoothly stabilizes at a given altitude, defined in the loaded flight plan. If that altitude cannot be reached within the given leg length, then it proceeds following the next waypoint, loitering to the final altitude if needed.
4. A Glide Mode has to be available, as a special case of descent, in which the aircraft keeps the motors at zero power and follows only a V_{TAS} setpoint, thus ignoring γ.
5. During each leg of the circuit, the System must be able to check whether trim conditions have been reached and maintained for a minimum time, then executes the scheduled maneuver automatically. During the whole maneuver duration, the autopilot must remain disengaged, as the control system should operate in open-loop. In addition, the control surfaces not involved in the excitation input at a certain time, must remain locked at a fixed computed trim value. However, the correction of the bank angle by the autopilot during longitudinal maneuvers could be tolerated in certain cases. When it is done, including the required free response time, the autopilot regains control and continues with the flight plan.
6. The System must provide a wide list of maneuvers, basically doublets and 3-2-1-1 involving all the control surfaces (elevator, ailerons and rudder), selectable from the ground station parameters menu. Each maneuver must be configurable at runtime, to comply with the parametric identification process and follow the flight campaign planning.
7. There must be automatic controls to abort an ongoing maneuver, or to prevent its beginning, whenever anomalous conditions are sensed in flight, like low airspeed and altitude, critical attitude and others. The maneuvers must also be interrupted when the aircraft is near to the altitude setpoint or to the next GPS waypoint. In addition, at any time the Test Pilot must be able to interrupt a maneuver and possibly regain manual control. The Glide Mode should be subjected to similar safety checks.

As a result of the requirements analysis, many functionalities have been progressively developed: Gamma Mode, Glide Mode, Trim conditions evaluation, Maneuver launch and execution, Maneuver aborting, Safety features, Control surfaces trim computation, Maneuver testing on the ground, TECS Stand-by Mode and Failure injection.

Control System Development

PX4 Autopilot consists of two main layers: the Flight Stack is an estimation and flight control system layer, while the Middleware is a general robotics layer that can support any type of autonomous robot, providing internal/external communication and hardware integration [2]. The Flight Stack is composed of many modules. The most important ones are Commander, Navigator, Position Control, Attitude Controller and Control Allocator, which are also shared by almost any airframe. For the fixed-wing configuration, there is also a Total Energy Control System (TECS), that is the core library of the PX4 Flight Stack.

Materials Research Proceedings 69 (2026) 656-661 https://doi.org/10.21741/9781644904251-116

In order to implement the above functionalities, three major PX4 modules were modified: Position Control, TECS and Control Allocator. The newly introduced Position Control sends to the TECS the altitude, climb rate and true airspeed setpoints, plus a message for Glide Mode triggering, along with many other flight data and information. The climb rate setpoint, when present, is derived from the scheduled γ_{sp}, by the simple relation: $\dot{h}_{sp} = V_{TAS}^{sp}\, sin(\gamma_{sp})$.

The Position Control can also start and abort the maneuvers, when needed, using a dedicated message. The main output of the TECS is the couple thrust setpoint T_{sp} in percentage and pitch angle setpoint θ_{sp}, in radians. Then, the Attitude Controller, which has not been modified, transforms the Euler Angles setpoint into an angular acceleration setpoint vector, in body frame, while leaving the thrust setpoint as it is. A standard geometrical turn coordination algorithm is also exploited, to compute the optimal yaw rate setpoint from the roll and pitch angles. Finally, the Control Allocator takes in input the angular acceleration vector and thrust setpoints and applies the Allocation Algorithm, to compute the actuator input values normalized between -1 and 1 (0 and 1 for the motors). These, are then converted by a driver into PWM signals for the servos and UAVCAN values to be sent to the Electronic Speed Controllers.

For the development of the control system to be used in the testing campaign, it was decided not to completely replace the existing TECS [2], but to extend it and make it able to support the requirements and the introduced functionalities. This, mainly due to compatibility and integration with the existing software reasons, which lead to several advantages in terms of reliability and effectiveness of the new system. The general functioning of the Total Energy Control System is described in various other works [3], among which an earlier implementation in Simulink used for the definition of an automated testing campaign within the SwitchMaster project [4, 5]. The specific original PX4 implementation can be found in the related documentation [6]. In this work, it is described the development of an Extended TECS, realized by adding to the original multiple new inner states.

As described by the finite state automaton in Fig. 1, from Normal Mode the TECS can go to Glide Mode by reading a specific message, coming from the Position Control, as long as the climb rate setpoint does not exist. In this mode, the throttle setpoint is zero and the energy weights are set to give maximum priority to the Kinetic Energy Rate, while the Potential Energy Rate is ignored. This, because during a glide only the V_{TAS} setpoint should be followed, acting on the pitch output, whereas the vertical speed at trim conditions is dependent on the speed.

Climb and Sink Modes are activated when exists an altitude rate setpoint positive or negative, respectively, coming from Position Control. They are the two states supporting the Gamma Mode, with the level flight, namely $\gamma = 0°$, included into the climb case. An altitude margin h_m is derived from the climb rate setpoint and a fixed time margin t_m, and corresponds to the Δh where the TECS starts reducing the climb rate to stabilize at the final altitude setpoint.

To achieve this, a gain k_h is computed as altitude error divided by altitude margin, then constrained between 0 and 1. Hence, when the distance in altitude to the setpoint goes below the margin (in climb coming from below the setpoint and vice versa), the gain starts decreasing from 1 to 0. Then, the nominal climb rate is reduced gradually, multiplying it by k_h, effectively stabilizing the aircraft near the altitude setpoint. The Stand-by Mode is an extra condition that can be activated in all the cases where a maneuver can be triggered, so in each of the previous modes but the Normal one, and allows to keep the TECS integrator states steady during the maneuvers, thus preventing saturation due to error increase caused by the disengaged control action.

Materials Research Proceedings 69 (2026) 656-661 https://doi.org/10.21741/9781644904251-116

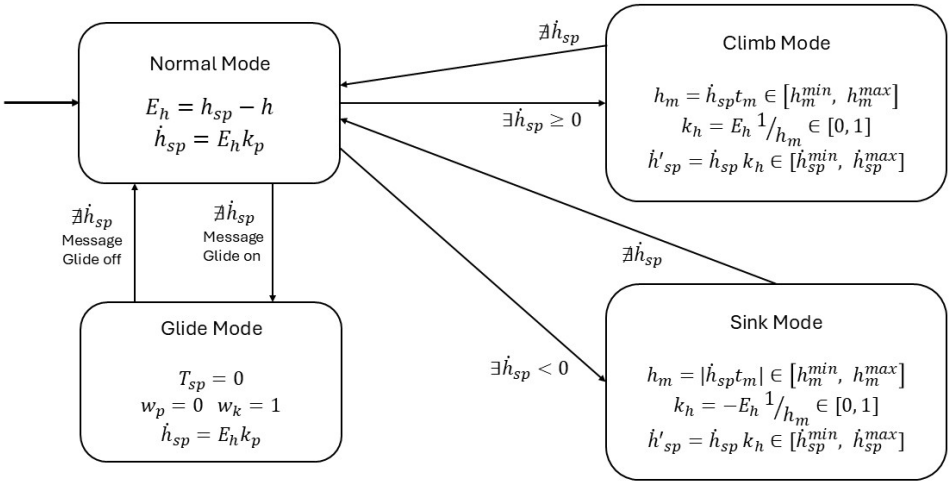


Figure 1: Simplified finite state automaton of the Extended TECS.

At each call of the main Position Control procedure, the system checks whether the distance between previous and next waypoint is greater or equal than a fixed minimum distance, defined as a parameter. Along with the distance, also the difference in altitude is evaluated: if the difference is positive, meaning that there is a climbing path between the waypoints, then it activates the Climb Mode, otherwise it goes towards the glide/sink branch, while the level path is included into the climb case. The Position Control scheduler then evaluates the current γ angle and computes the climb rate setpoint to be sent to the TECS. The case of $\gamma < 0$ (usually set to -1) is reserved for the triggering of the Glide Mode, whereas in each other case a positive angle is inserted as parameter in the system. In Normal Mode, the original PX4 algorithm is used, with altitude setpoints forming a linear trajectory between the aircraft and the next waypoint and the climb rate setpoint is computed by the TECS from the altitude error.

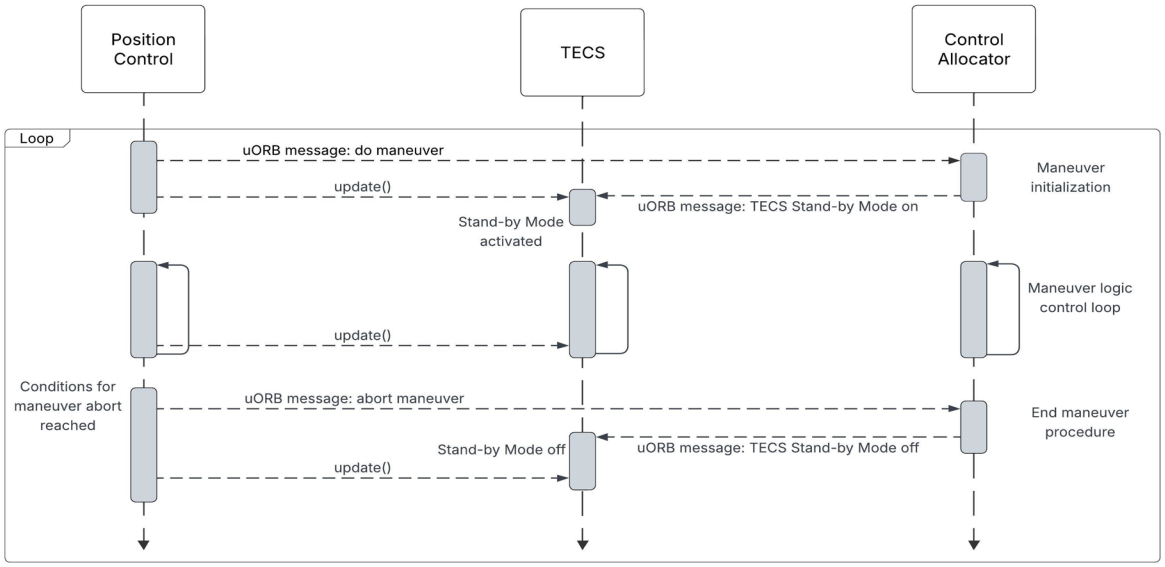


Figure 2: Sequence diagram describing the communication during a maneuver.

The other fundamental operations performed by the Position Control are trim conditions evaluation and safety checks. Regarding the trim evaluation, errors on γ and true airspeed with respect to the setpoint are continuously evaluated during the Climb and Sink modes, usually activated on the straight leg of the circuit [7], whereas in glide the only error considered is that on airspeed. Subsequently, as soon as the errors have been staying inside fixed thresholds for a

Materials Research Proceedings 69 (2026) 656-661 https://doi.org/10.21741/9781644904251-116

minimum user-defined time, the selected maneuver (such as an elevator doublet) is launched, by sending a specific message to the Control Allocator, as shown in Fig. 2. For what concerns the safety checks, they are similarly scheduled at each call of the Position Control procedure, as detailed in the next paragraph.

Finally, the modified procedures of the Control Allocator module are in charge of selecting and executing the commanded maneuver, configured by specific system parameters, through the manipulation of the actuator input values. In addition, a trim control value is computed for all the control surfaces and motors as a mean value of the sampled inputs immediately prior to the maneuver beginning and is used as a fixed offset to be maintained for the whole duration, including the final free response time. Hence, within this period of time the Control Allocator ignores all the inputs coming from the autopilot, realizing an open-loop behavior, plus initiates and ends the TECS Stand-by Mode, by sending a proper message. In this way, the maneuver execution is managed independently of the higher layer autopilot modules, which enables a responsibility decoupling and a safer logic. The sequence diagram in Fig. 2 describes the communication scheme among these modules throughout the maneuver execution.

Safety Features

Numerous automatic safety checks have been implemented and extended throughout the testing campaign, which in general do not require the pilot intervention and give control back to the autopilot, in case critical or upset conditions are sensed during the maneuvers or glide. The Position Control schedules these control procedures periodically, through the analysis of altitude, airspeed, sink rate, GPS position and attitude in real time. If a maneuver has to be aborted, the Position Control sends a message to the Control Allocator, which interrupts it in case it is still ongoing. The Control Allocator can also prevent the maneuver initiation in the case of out-of-bound ailerons or rudder trim computation. Lastly, the pilot can use two manual switches mapped on the remote control, one safety switch to override the maneuver logic and go back to automatic flight and a standard mode switch to activate the manual flight and immediately regain control, in which case the maneuvers and glide are always aborted.



Figure 3: The SwitchMaster demonstrator.

Conclusions and Future Developments

This work represents a remarkable advancement in the field of DEP advanced research and parametric model identification, since it has produced a complete platform for autonomous and safe flight testing of DEP demonstrators. The better quality of the trim conditions and executed maneuvers, made possible by the features implemented, allows an improved system identification process with respect to that performed with manual piloting [8]. The simulation and software testing subject, part of this project and as much important as the FCS development, will be dealt with in future publications, as it deserves a separate and exhaustive discussion.

In future developments, the whole FCS could be further extended with new functionalities and a more effective control action, starting from a better tuning of the TECS gains and the refinement of the control logic in glide, which in some cases showed poor performance.

In addition, a Total Heading Control System [9] is being evaluated to integrate the sideslip angle estimation into the yaw rate control logic of the Attitude Controller, in order to achieve a better turn coordination. Finally, the FCS should be generalized and adapted to models different from the DEP one, to obtain a portable platform which could support the automatic flight testing of other airframes, possibly also in general aviation. This could involve a change of the underlying software and hardware environment to become feasible.

References

[1] Cacciola S., Bottà L., Riboldi C. E. D., Trainelli L., "Identification of the Impact of Blowing on the Aerodynamic Model of an Airplane with Distributed Electric Propulsion", 34th ICAS Congress, Firenze, Italy, September 9-13, 2024.

[2] PX4 Documentation. Architectural Overview. Url: https://docs.px4.io/main/en/concept/architecture.html.

[3] A.A. Lambregts, "TECS Generalized Airplane Control System Design – An Update", 2013 EAS conference on Guidance, Navigation and Control, Delft, The Netherlands. https://doi.org/10.1007/978-3-642-38253-6_30

[4] Lorenzo Germinario. Identification of the Aerodynamics of a Distributed Electric Propulsion Demonstrator: Towards the Definition of a Fully Automated Testing Campaign. Url: https://www.politesi.polimi.it/handle/10589/219028.

[5] Cacciola S., Filippoli G., Perri B. M., Riboldi C. E. D., Terzaroli N., Trainelli L., "Autonomous Flight Tests of a Distributed Electric Propulsion Demonstrator Based on a Total Energy Control System", 11th European Conference for Aeronautics and Aerospace Sciences (EUCASS), Rome, Italy, 2025.

[6] PX4 Documentation. Controller Diagrams. Url: https://docs.px4.io/main/en/flight_stack/controller_diagrams.html.

[7] Trainelli L., Filippoli G., Terzaroli N., Perri B. M., Cacciola S., Riboldi C. E. D., "Automated Flight Testing of a Distributed Electric Propulsion Flying Model", 10th CEAS Aerospace Europe Conference / 28th AIDAA International Congress, Turin, Italy, December 1–4, 2025.

[8] Filippoli G., Terzaroli N., Perri B. M., Massa L., Trainelli L., Cacciola S., Riboldi C. E. D., "Aero-Propulsive Modeling and System Identification of a Distributed Electric Propulsion Flying Model", 10th CEAS Aerospace Europe Conference / 28th AIDAA International Congress, Turin, Italy, December 1–4, 2025.

[9] Lambregts A., "THCS generalized airplane control system design". In: 2013 CEAS conference on guidance, navigation and control, Delft, The Netherlands, 10–12 April 2013. https://doi.org/10.1007/978-3-642-38253-6_30

Materials Research Proceedings 69 (2026) 662-665 https://doi.org/10.21741/9781644904251-117

Preliminary Sizing of Airport Infrastructures for Refuelling Hydrogen-Powered Aircraft

Lorenzo Trainelli[1,a*], Gabriele Sirtori[2,b], Carlo E.D. Riboldi[1,c], Giorgio Filippoli[1,d], Stefano Cacciola[1,e]

[1]Department of Aerospace Science and Technology (DAER), Politecnico di Milano, Milan, Italy

[2]Fédération ENAC ISAE-SUPAERO ONERA, Université de Toulouse, Toulouse, France

[a]lorenzo.trainelli@polimi.it, [b]gabriele.sirtori@polimi.it, [c]carlo.riboldi@polimi.it, [d]giorgio.filippoli@polimi.it, [e]stefano.cacciola@polimi.it

Keywords: Hydrogen-Powered Aircraft, Airport Infrastructure

Abstract. This paper illustrates a general methodology aimed at coping with the need to preliminarily assess the feasibility, cost and performance of a future commercial aviation system based on hydrogen as the in-flight energy source. The methodology is devoted to the preliminary sizing of the complex airport infrastructure needed to service hydrogen-powered airliners, namely on-site generator and liquefier, storage tank, and dispensing units, providing an optimal solution in terms of acquisition and operating costs, and eventually hydrogen cost "at the pump". A sensitivity analysis shows how the system performs in off-design conditions, with the price of the various components needing to be shared by a smaller hydrogen production.

Introduction

A revolution in future civil aviation is currently being envisaged through the switching of the current jetliner fleet to hydrogen-powered aircraft, seeking a significant reduction of the environmental impact of commercial air transport. While the technology of hydrogen propulsive systems is currently undergoing research and initial development, making the implementation of suitable airframes reasonably likely in the next decades, another significant hurdle for the entry-into-service of such a fleet is posed by the need to provide the required quantity of hydrogen at airports. Therefore, a methodology to estimate the infrastructural needs is essential to support feasibility analysis and scenario studies towards the fleet switching from kerosene- to hydrogen-powered airliners. Similarly to what was accomplished for the preliminary sizing of a battery-recharging airport equipment[1], this paper introduces a methodology to preliminarily size an infrastructure devoted to the on-site production, storage and delivery of liquid hydrogen.

The sizing is based on an optimal procedure that, based on the flight scheduling at a given airport, computes the need for hydrogen generation, liquefaction, storage and just-in-time distribution to each aircraft, by minimizing the total cost of acquisition and operation of the hydrogen plant and thus of the fuel. Grid electricity cost day variations are considered, as well as other factors impacting costs and operations. The hydrogen needs for each aircraft model are computed by using a dedicated preliminary sizing methodology that allows substituting current aircraft models with performance-equivalent hydrogen-powered ones [2].The process not only delivers the overall sizing of the hydrogen generator, liquefier, cryogenic tank and of the set of dispensing units, but also provides the optimal time scheduling of hydrogen mass flows across the various components of the infrastructure.

A similar approach is shown in [3], which identifies that hydrogen can be delivered as a liquid or a gas to the airport, or produced on-site, with the last two instances requiring on-site liquefaction. After being stored as a liquid at the airports, the cryogenic fuel can be delivered via LH2 tank trucks or an airport pipeline infrastructure, with aircraft serviced by dispensing trucks.

Content from this work may be used under the terms of the Creative Commons Attribution 3.0 license. Any further distribution of this work must maintain attribution to the author(s) and the title of the work, journal citation and DOI. Published under license by Materials Research Forum LLC.

Materials Research Proceedings 69 (2026) 662-665 https://doi.org/10.21741/9781644904251-117

The former is more flexible and economical for airports with annual demands below 125 kt of LH2. In contrast, the latter is economically viable for airports with higher demands, offering faster and safer refueling. The expected hydrogen price will be between 2.6 and 3.9 $/kgH2 for a 2050 time horizon, depending on the airport size and refueling layout. For a large airport, 69 % of the hydrogen cost at refueling is represented by the GH2 supply, followed by 25 % for the liquefaction. The remainder is represented by storage, dispenser and pipeline costs.

Besides the methodology description, presented in ch. 2, an example application and sensitivity studies referred to existing international airports with actual aircraft movements are discussed in ch. 3.

Methodology

The objective of the work presented here is to size the main elements of an airport hydrogen refueling facility in support to hydrogen-powered airliners. This allows to quantify the required electricity supply, with a view to the foreseen adoption of this fuel in place of jet-fuel for commercial aircraft operations. The developed methodology is called Airport Hydrogen Refueling Equipment Sizing (AHRES). The airport refueling station includes three main elements:

- The generator, consisting of an electrolyzer, a buffer tank, and a liquefier, where, starting from liquid water, hydrogen is obtained through an electrolysis process powered by electric energy from the grid or from a local renewable electricity plant; the gas is then cooled to cryogenic temperatures for storage in liquid form;
- The storage tank which accumulates the hydrogen produced earlier than it is required, e.g., during a time slot when electricity is cheaper, so that there is enough of it stored to refuel departing aircraft;
- Dispensing units that pump liquid hydrogen from the storage tank to the aircraft tank.

Details on the cost of the components implemented within AHRES can be found in *[4] [5]*.
The preliminary sizing of an airport's hydrogen refueling infrastructure, characterized by a large number of variables and parameters, is approached as an optimization problem. Thus, a cost function, representing the daily cost of the system as the sum of the costs of its components and cost of electricity and power, is defined. The cost function is minimized while all relevant constraints are satisfied. The constraints of the optimizer aim to ensure that the problem properly reflect real-world operations: maximum capacity of the ground and aircraft tanks is respected, there is enough availability of hydrogen and dispensing units for each departure, the electrolyzer is always running at least at its minimum production rate.

The solution of the problem, based on the daily schedule of the busiest day of operations at the selected airport, details the nominal production rate of the hydrogen generator and liquefier, the size of the cryogenic ground tank, the number of required dispensing units and the detailed refueling time history over the considered time frame. The selection of the busiest day ensures that the refueling system is properly sized for the traffic received at the airport. The ultimate output is the cost of 1 kg of hydrogen.

Results

Here results considering the Milan Malpensa short-haul flights are presented, as both the airport operator [6] and one of the main airlines [7] have shown particular interest in developing climate-neutral flight technologies. In particular, the busiest day of operations (Most Demanding Day – MDD) in 2022 showed 239 short-haul flights, all considered in the following analysis. Namely, two pricing models for electricity have been introduced, enabling the comparison of the sizing with a fixed electricity rate or with cheaper prices at night. Table 1 details the results. The main differences between the mono- and dual-rate electricity cost simulations are the operation and sizing of the hydrogen generator and the size of the tank. The overall daily costs to support the hydrogen production plant, including the cost of the components, the peak power, and the

Materials Research Proceedings 69 (2026) 662-665 https://doi.org/10.21741/9781644904251-117

electricity, increase by 7.7% going from a mono- to a dual-rate electricity cost. The lower electricity costs permitted by the dual-rate scenario (-4.9%) are outbalanced by an increased maximum power (+81.4%), generator (+85.3%), and tank (+125.6%) costs. The hydrogen cost increases by 7.3%, going from 4.104 €/kg to 4.405 €/kg.

Table 1: Comparison of the results for Milan Malpensa considering mono- and dual-rate

Indicator	Mono-rate	Dual-Rate	Change[%]
Cost function [€/day]	$1.70 \cdot 10^{+6}$	$1.83 \cdot 10^{+6}$	7.7
Consumed energy [kWh/day]	$2.57 \cdot 10^{+7}$	$2.58 \cdot 10^{+7}$	0.3
Electricity cost [€/day]	$1.45 \cdot 10^{+6}$	$1.38 \cdot 10^{+6}$	-4.9
Max. power [kW]	$1.07 \cdot 10^{+6}$	$1.94 \cdot 10^{+6}$	81.4
Power cost [€/day]	$8.94 \cdot 10^{+4}$	$1.62 \cdot 10^{+5}$	81.4
H2 production [kg/day]	$4.14 \cdot 10^{+5}$	$4.16 \cdot 10^{+5}$	0.3
GNR cost [€/day]	$1.42 \cdot 10^{+5}$	$2.63 \cdot 10^{+5}$	85.3
Max mass in ST [kg]	$1.14 \cdot 10^{+5}$	$2.58 \cdot 10^{+5}$	125.6
Boil-off mass [kg]	$1.14 \cdot 10^{+3}$	$2.58 \cdot 10^{+3}$	125.6
ST cost [€/day]	$6.26 \cdot 10^{+3}$	$1.41 \cdot 10^{+4}$	125.6
Number of DU [-]	9	9	–
DU cost [€/day]	$9.47 \cdot 10^{+3}$	$9.47 \cdot 10^{+3}$	0.0
Cost of 1 kg of LH2 [€/kg]	4.104	4.405	7.3

The lowest obtained hydrogen pricing (4.10 €/kg for the Malpensa mono-rate scenario) is in line with the information presented by McKinsey in their 2021 Hydrogen Insight Report [8], which shows the price of 1 kg of green hydrogen in the range of 3.5-4.8 $/kg (3.2-4.3 €/kg) for 2023. The cost of energy is also coherent across the two models, with ours considering 0.0565 €/kWh and [8] a range of 25-73 $/MWh (0.023-0.067 €/kWh).

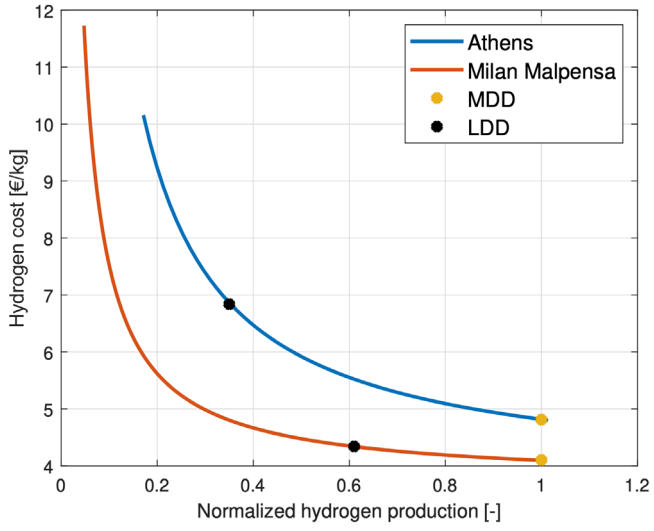


Figure 1: Variation of the cost of 1 kg of hydrogen as a function of the normalized production level.

Since the refueling system has been sized considering the busiest day, it is relevant to assess the impact on the hydrogen price on off-design conditions, with a lower required production. Figure 1 shows how the price of 1 kg of hydrogen for the considered scenario and for a smaller

airport sized for regional hydrogen-powered operations only. The Least Demanding Day (LDD) is also shown, indicating the day with the least operations. It is acceptable that larger plants work at 30% of their nominal capacity, with the cost of 1 kg of hydrogen rising to 5 €/kg. For smaller plants, the price is already high at the nominal production level, therefore an oversizing will make innovative aircraft not competitive with conventional ones in terms of fuel cost.

conclusion

This paper presents the AHRES methodology, whose objective is to optimize the sizing of a hydrogen production plant at airports, developed with the objective of supporting hydrogen-powered aircraft. A proper assessment of the impact on supporting infrastructures for hydrogen flights is important, in order to facilitate a smooth entry into service of novel aircraft. In fact, all the aviation stakeholders have the common objective of reducing the environmental impact of air transport: to achieve this, parallel development of hydrogen aircraft and of the refuelling infrastructures at airports is necessary, as the introduction of hydrogen as the main energy carrier onboard aircraft will represent a complete revolution for the aeronautical sector. The presented methodology is capable of sizing the generator, tank and amount of dispensing units necessary to support a given schedule while optimizing the overall cost. Particularly, the explication of the mathematical modeling and constraints and the application to selected scenarios are introduced. The results, with the cost of 1 kg of hydrogen being the ultimate indicator, are comparable with scenarios presented in the literature.

References

[1] Trainelli L., Salucci F., Riboldi C.E.D., Rolando A. et Bigoni F., «Optimal Sizing and Operation of Airport Infrastructures in Support of Electric-Powered Aviation,» Aerospace, 8 (40), pp. 1-29, 2021. https://doi.org/10.3390/aerospace8020040

[2] Aigner B., Garcia Garriga A., Sirtori G., Riboldi C. E. D., Trainelli L., et al. «Overview and preliminary results of the scalability investigation of hybrid Electric concepts for next-generation aircraft (SIENA) project,» Journal of Physics: Conference Series, 2023. https://doi.org/10.1088/1742-6596/2526/1/012017

[3] Hoelzen J., Flohr M., Silberhorn D., et al. «H2-powered aviation at airports - Design and economics of LH2 refueling systems,» Energy Conversion and Management: X, 14:100206, ISSN 2590-1745. doi: 10.1016/j.ecmx.2022.100206., 2022. https://doi.org/10.1016/j.ecmx.2022.100206

[4] Clean Hydrogen, « GB decision no. Clean Hydrogen-GB-2022-02,» Strategic research and innovation agenda 2021-2027, 2022.

[5] W. Amos, «Costs of storing and transporting hydrogen,» National Renewable Energy Lab, 1999. https://doi.org/10.2172/6574

[6] SEA Milan Airports, «Sustainability report 2022».

[7] easyJet, « Annual report 2022.,» 2023.

[8] McKinsey Company, «Hydrogen insights: A perspective on hydrogen investment, market development and cost competitiveness.,» 2022.

[9] G. Brewer, Hydrogen aircraft technology., CRC Press, 1991.

Materials Research Proceedings 69 (2026) 666-671 https://doi.org/10.21741/9781644904251-118

A Breguet Range Formulation for Liquid Hydrogen-Powered Aircraft

Giuseppe PALAIA[1,a*], Karim ABU SALEM[1,b] and Erasmo CARRERA[1,c]

[1]Polytechnic of Turin, Corso Duca degli Abruzzi 24, 10129, Torino, Italy

[a]giuseppe.palaia@polito.it, [b]karim.abusalem@polito.it, [c]erasmo.carrera@polito.it

Keywords: Hydrogen, Breguet, Aircraft Design, Green Aviation

Abstract. This work proposes a modified Breguet-type range formulation for liquid hydrogen-powered aircraft during cruise. While hydrogen enables CO_2-free propulsion and significantly reduces NO_x emissions, its low volumetric energy density requires cryogenic storage, introducing thermomechanical challenges and boil-off losses. Current simulation frameworks can accurately model coupled heat and mass transfer inside the tank but are computationally expensive. The proposed formulation is derived from a surrogate model trained on a structured design of experiments using high-fidelity tank simulations that account for venting pressure, fill level, insulation configuration, and tank geometry. The resulting model, expressed as a modification of the well known Breguet equation taking venting losses into account, achieves a prediction error below 8% for short tanks, demonstrating both accuracy and generalization capability. The final analytical formulation preserves physical interpretability while reducing computational effort, making it suitable for early-stage sizing and trade-off studies of hydrogen-powered aircraft.

Introduction

The aviation sector is facing increasing pressure to reduce its environmental impact and contribute to climate-neutral mobility. Recent studies highlight that future commercial aviation will require disruptive solutions rather than incremental improvements to achieve meaningful emission reductions [1-3]. Among emerging propulsion technologies, hydrogen has gained strong interest due to its ability to eliminate CO_2 emissions during flight and significantly reduce NO_x formation when properly integrated into propulsion architectures [4]. Despite its high gravimetric energy density, liquid hydrogen (LH_2) presents a major challenge due to its low volumetric energy density, which necessitates cryogenic storage in insulated tanks [4,5]. Cryogenic conditions introduce complex thermodynamic phenomena such as boil-off and venting, which affect the quantity of usable fuel and, consequently, the achievable cruise range. Detailed simulation frameworks can model these coupled heat- and mass-transfer processes [6,7], but their computational cost may limit their applicability in conceptual aircraft design. Therefore, simplified yet physically consistent range formulations are required to enable rapid early-stage trade-off studies.

Material and Methods

The study adopts a workflow consisting of three main blocks, depicted in Fig. 1:

- Reference aircraft selection: the aircraft main parameters, such as aerodynamics, propulsion settings, mission profile, and weight breakdown, are defined;
- Tank geometry and main parameters: tank geometry and position can be arbitrarily defined; in the illustrative example proposed in this work, a cylindrical tank with hemispherical end-caps and located in the aft fuselage, is selected; its cross section is coincident with the fuselage cross-section;
- Mission performance analysis: the aircraft flight profile and tank internal thermodynamics are co-simulated over the cruise phase of the mission to assess usable LH_2, boil-off losses, weight evolution, and fuel flow. The remaining liquid hydrogen is checked against a minimum reserve threshold. Once the threshold is satisfied, achievable range is computed.

Content from this work may be used under the terms of the Creative Commons Attribution 3.0 license. Any further distribution of this work must maintain attribution to the author(s) and the title of the work, journal citation and DOI. Published under license by Materials Research Forum LLC.

Materials Research Proceedings 69 (2026) 666-671 https://doi.org/10.21741/9781644904251-118

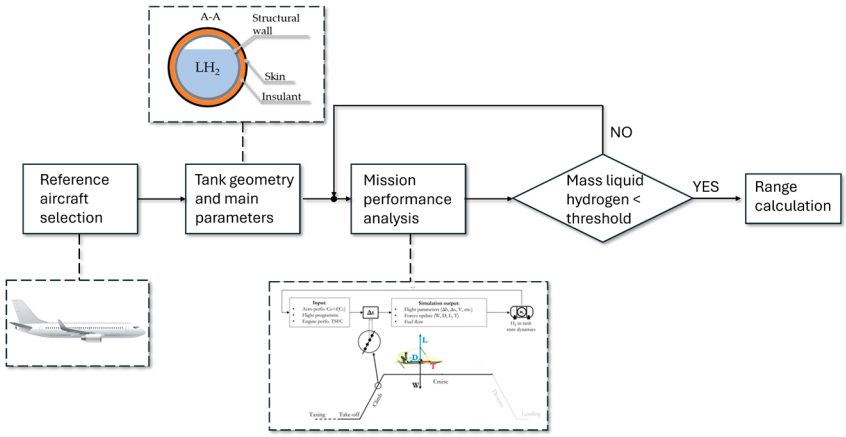


Figure 1. Workflow to assess LH_2 aircraft range.

Reference aircraft selection. The reference aircraft is defined as a short/medium-range twin-engine transport aircraft. Aerodynamic, propulsion and mass characteristics are known at the beginning of the workflow; in the considered study case, the aircraft characteristics are fixed, allowing the tank behaviour to be isolated as the only design variable during the mission simulations. The aerodynamic model adopts a classical parabolic drag polar, where drag is expressed as a combination of zero-lift drag and induced drag. Wing geometry and aerodynamic efficiency parameters (such as wing aspect ratio and Oswald factor) are selected to be representative of a tube-and-wing single-aisle commercial aircraft. The propulsion system assumes a hydrogen-fuelled turbofan with thermodynamic efficiency comparable to that of a conventional kerosene engine, consistently with the assumptions in ref. [7]. As a consequence, the thrust specific fuel consumption of the hydrogen engine is scaled based on the relative energy densities of the fuels, according to Eq. (1); all reference parameters are reported in Table 1.

$$c_{LH2} = c_{ker} E_{ker} / E_{LH2} \quad (1)$$

Table 1. Main data of reference aircraft.

CATEGORY	PARAMETER	SYMBOL	VALUE	UNIT
FLIGHT CONDITION	Cruise altitude [8]	h	11 000	m
	Cruise Mach number [8]	M	0.80	–
	Wing reference area [9]	S	122.4	m²
	Fuselage equivalent diameter [9]	D	4	m
AERODYNAMICS	Zero-lift drag coefficient [8]	C_{D0}	0.02	–
	Oswald efficiency factor [8]	e	0.8	–
	Aspect ratio [9]	AR	9.5	–
PROPULSION	Kerosene-based TSFC [8]	c_{ker}	0.50	1/h
	LH_2 TSFC (Eq. (1))	c_{LH2}	0.18	1/h
	Energy density kerosene [4]	E_{ker}	12	MWh
	Energy density LH_2 [4]	E_{LH2}	33	MWh

Tank geometry and main parameters. The liquid-hydrogen storage system is modelled as a cylindrical cryogenic tank with hemispherical end-caps, installed in the aft fuselage. The tank is composed of three concentric layers: a load-bearing structural shell that determines the internal volume to host hydrogen, a foam-based insulation layer surrounding the structural shell to limit heat transfer from the aircraft environment, and a thin outer skin enclosing and protecting the insulation, and providing mechanical integration with the surrounding fuselage structure. The

Materials Research Proceedings 69 (2026) 666-671 https://doi.org/10.21741/9781644904251-118

internal volume contains two regions, the lower liquid hydrogen portion and an upper vapour ullage, whose height varies during cruise according to boil-off rate and venting. A representative cross-section of the tank is shown in Fig. 2.

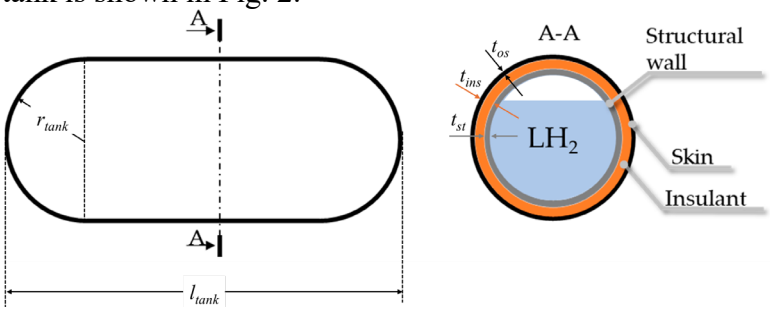


Figure 2. Simplified schema of the liquid hydrogen tank.

All parameters related to tank geometry are summarized in Table 2, and, by using well known geometric relationships of solids, it is possible to derive additional geometrical parameters such as internal volume.

Table 2. Main data of LH2 tank.

CATEGORY	PARAMETER	SYMBOL	MATERIAL	VALUE	UNIT
GEOMETRY	Tank length	l_{tank}	–	[5, 16]	m
	Tank radius	r_{tank}	–	2	m
	Structural layer thickness	t_{st}	Aluminium Alloy 2219	10	mm
	Insulation thickness	t_{ins}	Polystyrene foam	[20, 240]	mm
	Outer skin thickness	t_{os}	Aluminium Alloy 2219	2	mm
THERMODYNAMICS	Venting pressure	P_v	–	1.59	bar

Mission performance analysis. The mission module computes the evolution of aircraft mass, fuel consumption, and tank thermodynamic state during the cruise phase. The analysis is performed through a time-marching integration, where the aircraft equations of motion and the cryogenic tank thermal model are solved simultaneously at each time step Δt. The procedure is detailed in refs. [7,10]. The time evolution of the system is computed using the forward Euler method. Three hypotheses are assumed to model aircraft mission: *(i)* aircraft is modelled as a point mass, *(ii)* quasi-steady flight conditions, meaning that accelerations are negligible over each integration step, *(iii)* the motion is confined to the vertical plane, as a direct consequence, lateral dynamics is not considered. According to the above hypotheses, Eq. (2) describes the equilibrium equation during cruise phase where L, D, and W are aircraft lift, drag and weight respectively, and T is engine thrust. Eq. (3) assesses the distance x travelled by the aircraft, V is the aircraft speed, and t is time.

$$\begin{cases} L = W \\ T = D \end{cases} \tag{2}$$

$$x(t+\Delta t) = x(t) + V\Delta t \tag{3}$$

The tank internal simulation module is based on the coupled heat- and mass-transfer framework described in ref. [7]. At each time step of the mission analysis, the model computes the heat entering the tank through external convection and thermal radiation at the outer protective skin, and conduction through the insulation layer. As heat is transferred to the liquid hydrogen, a portion

Materials Research Proceedings 69 (2026) 666-671 https://doi.org/10.21741/9781644904251-118

of the liquid evaporates, increasing the vapour mass in the ullage region. The evaporation process causes a rise in the internal pressure. Whenever the internal pressure exceeds the venting threshold, the simulation procedure computes the mass of gaseous hydrogen that must be vented to restore the pressure to its allowable value. At each time step the following sequence is executed: *(i)* the aircraft lift and engine thrust are computed by Eq. (2), *(ii)* the fuel consumption $\dot{W}_{LH2}$ requested by the engine is computed by Eq. (4), *(iii)* the tank thermal model computes boil-off and possible venting mass flow rate $\dot{W}_{vent}$, *(iv)* the aircraft weight is updated based on Eq. (5).

$$\dot{W}_{LH2}=c_{LH2}T \tag{4}$$

$$\dot{W} = \dot{W}_{LH2} + \dot{W}_{vent} \tag{5}$$

Table 3 details the initial condition of the simulation, specifically the parameter f_f indicates the amount of internal volume of the tank occupied by the liquid hydrogen, and it is assumed that the tank internal pressure is close to the venting pressure.

Table 3. Initial conditions of the simulation.

CATEGORY	PARAMETER	SYMBOL	VALUE	UNIT
AIRCRAFT	Initial weight	W_i	70000	kg
TANK	Initial LH_2 volume percentage	f_f	0.95	-
	Initial tank internal pressure	P_i	$0.99P_v$	bar

Surrogate modelling and range formulation. To derive a preliminary mathematical formulation (i.e. a modified Breguet range equation) several simulations were carried out by varying two parameters, tank length and insulation thickness, according to the boundaries defined in Table 1. This is an initial simplified illustrative example of the procedure, that can be extended to a broader set of sampling variables. For each couple (t_{ins}, l_{tank}), the workflow depicted in Fig. 1 computes the aircraft range, the amount of hydrogen burned in the engine and vented in each time step of the cruise phase. The total hydrogen mass flow lost by the aircraft is computed by Eq. (5), so it is possible to define an equivalent thrust specific fuel consumption c_{eq} which can be computed by Eq. (6).

$$c_{eq}=\frac{\dot{W}_{LH2} + \dot{W}_{vent}}{T}=c_{LH2}+c_{vent} \tag{6}$$

c_{eq} varies over time because venting events depend on the tank thermodynamics, which changes during cruise phase. Its time-average over the cruise phase, denoted by $\bar{c}_{eq}$, is used in a Breguet-type formulation for range calculation (X), as detailed in Eq. (7).

$$X=\frac{V}{\bar{c}_{eq}}\frac{L}{D}\ \log\left(W_i/W_f\right) \tag{7}$$

where W_i and W_f are the aircraft weight at the beginning and at the end of cruise. A subset of simulated configurations is used to estimate $\bar{c}_{eq}$ and identify a compact analytical expression relating tank length and insulation thickness according to Eq. (8).

$$\bar{c}_{eq} = c_{LH2}+\bar{c}_{vent} = c_{LH2}+k\left(\frac{t_{ins}}{t_0}\right)^{\alpha}\left(\frac{l}{l_0}\right)^{\beta} \tag{8}$$

The coefficients k, α, and β are identified by applying a non-linear least square method and minimizing the squared difference between the range calculated by Eq. (7) and the range computed by Eq. (3) over a calibration subset of configurations. Reference scales t_0 and l_0 (medians of Table 2) are used for normalization. The remaining simulations are used to validate Eq. (7).

Materials Research Proceedings 69 (2026) 666-671 https://doi.org/10.21741/9781644904251-118

Results

This section presents a selection of the most representative results. Fig. 3-left illustrates the effect of tank geometry and insulation on hydrogen venting losses. The contour map shows the total mass of liquid hydrogen expelled during the mission as a function of tank length and insulation thickness. Configurations characterized by long tanks with limited insulation experience the highest venting. In these cases, the increase in external surface area relative to the stored volume results in greater heat entry, which accelerates liquid-vapor state change and triggers venting. Increasing the insulation thickness markedly reduces heat transfer and venting, while shorter tanks tend to be less sensitive to insulation because of their lower exposed area. Fig. 3-right introduces a new performance indicator, named the Propulsive Energy Utilization Factor Ψ, and defined according to Eq. (9).

$$\Psi = E_m / E_{LH2,0} \tag{9}$$

E_m is the energy spent to fly, and $E_{LH2,0}$ is the chemical energy stored in liquid hydrogen at departure. This factor measures the fraction of the initial energy load that is ultimately exploited for propulsion, inherently accounting for both boil-off and venting losses. The contour map shows that Ψ increases as venting decreases: configurations with thicker insulation and optimized tank geometry retain a larger portion of the stored energy, yielding higher propulsive utilization. Conversely, thermal-inefficient configurations waste energy through venting, resulting in lower Ψ.

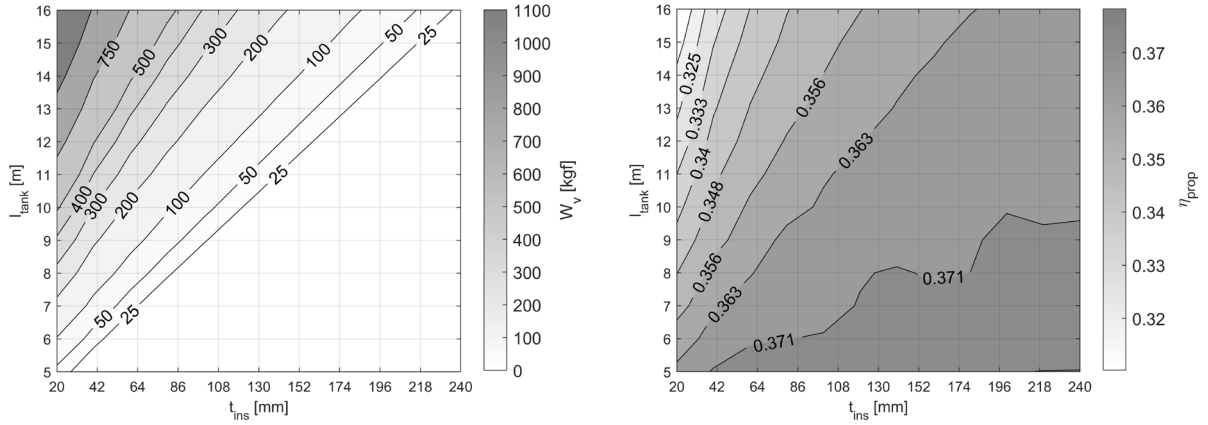


Figure 3. Vented mass (left) and efficiency (right) varying tank length and insulant thickness.

Based on the grid-search procedure, the optimal parameters for the modified Breguet formulation are $k = 0.0126$, $\alpha = -0.62$, $\beta = 1$. Table 4 reports the comparison between some cases of the mission-simulated range and the range predicted by the modified Breguet equation on the validation set. The validation results show that the modified Breguet formulation provides accurate predictions and the maximum error is below 7%. The current formulation captures geometric and thermal effects but additional physical parameters are necessary for a complete formulation. The refinement of the model is ongoing.

Table 4. Comparison between some cases of the mission-simulated range and the range predicted by the modified Breguet equation.

l_{tank} [m]	t_{ins} [mm]	x (simulation) [km]	X (Breguet) [km]	X-x [km]	X-x [%]
5	40	2998	2910	-87	-2.92
7	100	4367	4287	-80	-1.84
9	80	6043	5910	-133	-2.20
11	80	7625	7436	-189	-2.47
13	80	9182	8949	-233	-2.54
15	20	10410	9688	-722	-6.93
15	140	10292	10045	-247	-2.40

Summary

This work presented the initial foundation for the extrapolation of a modified Breguet-type formulation able to predict the cruise range of liquid hydrogen-powered aircraft while accounting for boil-off and venting losses. A coupled mission-tank simulation framework was used to generate high-fidelity data, from which an equivalent fuel consumption term was derived and expressed as a function of tank geometry and insulation. Validation against full mission simulations shows that the formulation provides accurate range predictions with a maximum error below 7%. Future developments will expand the surrogate formulation to include additional design variables and mission phases.

References

[1] A. Ficca, F. Marulo, A. Sollo, An open thinking for a vision on sustainable green aviation, Progress in Aerospace Sciences 141 (2023). https://doi.org/10.1016/j.paerosci.2023.100928
[2] F. Afonso, et al., Strategies towards a more sustainable aviation: A systematic review, Progress in Aerospace Sciences 137 (2023). https://doi.org/10.1016/j.paerosci.2022.100878
[3] L.M. Cardone, G. Petrone, S. De Rosa, et al., Review of the Recent Developments About the Hybrid Propelled Aircraft, Aerotec. Missili Spaz. 103 (2024) 17–37. https://doi.org/10.1007/s42496-023-00173-6
[4] E.J. Adler, J.R.R.A. Martins, Hydrogen-powered aircraft: Fundamental concepts, key technologies, and environmental impacts, Progress in Aerospace Science 141 (2023). https://doi.org/10.1016/j.paerosci.2023.100922
[5] S. Bagarello, D. Campagna, I. Benedetti, A survey on hydrogen tanks for sustainable aviation, Green Energy and Intelligent Transportation (2024). https://doi.org/10.1016/j.geits.2024.100224
[6] E.J. Adler, J.R.R.A Martins, Liquid Hydrogen Tank Boil-off Model for Design and Optimization, Journal of Thermophysics and Heat Transfer 39 (2025). https://doi.org/10.2514/1.T7005
[7] V. Cipolla, D. Zanetti, K. Abu Salem, V. Binante, G. Palaia, A Parametric Approach for Conceptual Integration and Performance Studies of Liquid Hydrogen Short–Medium Range Aircraft, Applied Sciences 12 (2022). https://doi.org/10.3390/app12146857
[8] D.P. Raymer, Aircraft Design: A Conceptual Approach, AIAA Education Series, 6th ed., 2018.
[9] Civil Jet Aircraft Design – Aircraft Data File (Elsevier/Butterworth-Heinemann) - Appendice "Aircraft Data File: Airbus Aircraft. Information on: https://booksite.elsevier.com/9780340741528/appendices/data-a/table-1/table.htm
[10] G. Palaia, K. Abu Salem, E. Carrera, Preliminary Performance Analysis of Medium-Range Liquid Hydrogen-Powered Box-Wing Aircraft, Aerospace 11 (2024). https://doi.org/10.3390/aerospace11050379

Materials Research Proceedings 69 (2026) 672-676 https://doi.org/10.21741/9781644904251-119

Defining Control Loops for a Fuel Cell Powered Aeronautic Propulsion System

Rudy CEPEDA-GOMEZ[1,a *]

[1]DLR Institute of Electrified Aero-Engines, Leiberoser Straße 13a, 03046 Cottbus, Germany

[a]rudy.cepedagomez@dlr.de

Keywords: FADEC, Electric Propulsion, Control Loops

Abstract. The main function of the Full-Authority Digital Engine Controller in turbofan engines is to ensure that the thrust required by the aircraft is provided while avoiding exceedances on engine parameters. Limits on maximum and minimum values of shaft speeds, temperatures, and pressures are defined to protect the engine from damage and to ensure its correct operation. The maximum available thrust becomes a function of environmental variables like altitude, ambient pressure and temperature, and of some operational parameters such as airspeed and auxiliary power demands (air conditioning, anti-ice, etc). This work explores the definition of similar control loops for an electric power train. It is assumed that the main source of energy is a hydrogen fuel cell and that it is supported by a battery to shave power demand peaks at certain phases of flight. A top-down methodology is used, in which the different operational scenarios (both steady-state and transient) are considered and the management problem for each one is discussed.

Introduction

The main function of the propulsion system of an aircraft is to provide thrust. Since this variable cannot be normally measured directly, Full-Authority Digital Engine Control (FADEC) systems are designed to regulate a variable that can be correlated with thrust. In turbofan engines, the Engine Pressure Ratio (EPR) or the fan rotational speed (equivalent to the speed of the low pressure shaft, NLP) are commonly used to this end, with the fuel mass flow rate being used as manipulated variable. Other engine actuators such as the compressor stator vanes and bleed valves, are usually scheduled in open-loop to maintain the operational margins of the engine.

The EPR or NLP demand is set by the FADEC based on the Power Lever Angle (PLA), which is the main interface between pilot and the engine control system, and depending on the difference between demand and current value, a fuel flow command is issued. This command, however, may be limited by a set of protection rules which, due to safety and operability restrictions, regulate excessive transients and other engine limits which could lead to compressor stalls and surges or other failures in the engine. Upper limits are commonly in place for shaft speeds (NHP, NLP), for the compressor discharge pressure (P30), for turbine temperature, and for the acceleration and deceleration during transient maneuvers. Minimum limiters on P30 and NHP are used to ensure that the engine does not flame out, and usually correspond to certain pre-determined idle schedules. The selection process follows a min/max approach, and is schematically shown in Fig. 1, which has been adapted from [1].

In an (Hybrid)-Electric Aircraft Propulsion ((H)-EAP) system, the propeller rotational speed and its pitch angle, if it is variable, are the parameters to be regulated to set the thrust. Controlling these two parameters based on pilot's input is a relatively straightforward task, considering that an electric motor is a very simple machine for which a high level of understanding has been already achieved. However, depending on the specific architecture of a H-EAP system, the control task can be way more complex than in a turbofan engine, since a larger number of subsystems need to be controlled. Furthermore, a generic architecture for such a controller is not possible, given the fact that there are many different ways of arranging an (H)-EAP: pure electric with batteries, turbo-

Content from this work may be used under the terms of the Creative Commons Attribution 3.0 license. Any further distribution of this work must maintain attribution to the author(s) and the title of the work, journal citation and DOI. Published under license by Materials Research Forum LLC.

Materials Research Proceedings 69 (2026) 672-676 https://doi.org/10.21741/9781644904251-119

electric with or without batteries, parallel-hybrid, series-hybrid, etc. The control challenges posed by H-EAP systems are the main topic in [2]. The authors of that work, however, focus mainly on hybrid electric systems, in which a turbomachine still provides a certain amount of the power required.

The present work considers the particularities of controlling a very specific architecture: a pure EAP in which the energy comes from a hydrogen fuel cell and a battery is used for power shaving. The problem of energy and power management for such a propulsion system has already been treated in the literature. An implementation point of view is considered for example in [3], where a module to essentially control the flow of energy between fuel cell, motor and battery is described. A methodology for energy management based on heuristic rules is shown in [4], whereas [5] treats the problem using dynamic programming.

The following section of the paper describes the EAP system that is addressed in this work. After that, the control loops that are considered necessary for normal operation of this plant are described. The paper is closed with a conclusion section in which the main points of the work a re-stated and brief discussion of the future work to be developed is performed.

The System under Consideration

This paper considers an EAP composed by an electric machine actuating a propeller. The energy for the motor is provided by an electrical power distribution system, whose main task is to manage the flow of energy between the machine and the main two sources of power: a battery and a hydrogen fuel cell. It is assumed that only the battery can have a bi-directional flow of energy, i.e., it can be charged or discharged during the operation, acting either as a sink or source of energy. The fuel cell only provides energy, and the electrical machine is limited to operate as a motor, so no energy recovery from windmilling is considered.

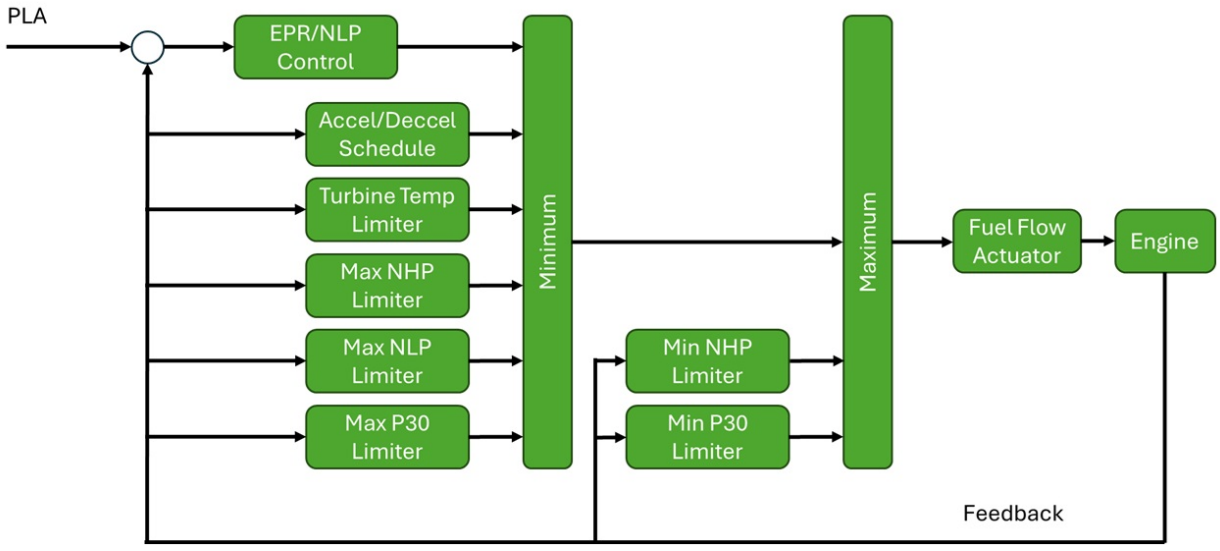


Figure 1: Standard Control Laws for a Turbofan Engine

Materials Research Proceedings 69 (2026) 672-676 https://doi.org/10.21741/9781644904251-119

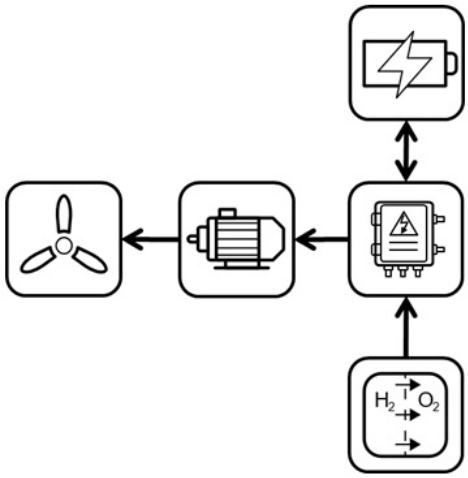


Figure 2: Generic Structure of a Battery/Fuel Cell Electric Power Train

A generic diagram of the architecture of such a system is shown in Fig. 2, from which the multivariable nature of the control problem becomes evident. While the PLA command defining the demanded thrust directly translates into a set point for the speed/torque of the electric motor, it is not immediately clear how the power required for this should flow from the two sources. The definition of the appropriate set points for the other main components, namely the battery management, the fuel cell, and the power distribution systems, is not a straightforward task and requires a careful design.

The different components of the system are sized during the EAP design process to achieve a certain performance during most critical static operating points. For example, the fuel cell could be sized to achieve its highest efficiency at the standard power level needed by the aircraft during cruise, whereas the battery would have enough storage capacity to provide the extra energy needed to maintain take-off power for the required time [6]. While very important for the tuning of the control loops, this sizing is not that crucial for the architectural definition presented in the next section.

Control Loops for the EAP System

A max/min approach, similar to that of used in turbofan engines and shown in Fig. 1, is also proposed for the EAP. The proposed control logic is presented in Fig. 3. The way the limiters act and interact is however different, due to the increased complexity of the system and its individual subsystems.

Steady State Loops. An example schedule for power split between the battery and the fuel cell depending on the demanded propulsive power can be seen in Fig. 4, which has been adapted from [2]. In this case, the fuel cell is sized such that it can provide alone up to 67% of the maximum rated power. This point would probably be the Maximum Continuous power (MCT) rating of the EAP. To reach the full power, the Battery is needed, but this level of thrust could only be maintained for as long as the battery still has sufficient charge. This would be the case during take-off or a go-around maneuver. For power demands below MCT, the fuel cell has extra power capacity, which can be used to charge the battery in phases of flight that not require extreme power.

The power that can be delivered by the fuel cell or the battery at a given instant, however, is not constant. It will be limited by factors such as the Outside Air Temperature (OAT), which affects the effectiveness of the thermal management systems of the power sources. The states of charge (SoC) and health (SoH) of the battery will also act as limiters for the power available. The thermal challenges are usually addressed by the control system of turbofan engines by means of de-rating the maximum available thrust. When the OAT is below the value for which the turbine would reach its thermal limit, the maximum thrust is available. For OAT values beyond this, the

Materials Research Proceedings 69 (2026) 672-676 https://doi.org/10.21741/9781644904251-119

maximum available thrust is reduced proportionally. In the case of an EAP, these limitations are more dynamic, since they depend on more factors and affect several different components.

Transient Loops. One of the advantages of electric motors over turbomachines are their faster dynamics. An electric machine can change its speed almost instantaneously. These fast dynamics, however, cannot be followed up by a fuel cell, whose electrochemical processes have a large inertia and very long time constants. To have time to adjust the power delivered by the fuel cell, the transients have to be absorbed by the battery. The transient control loops will ensure that the battery provides the extra power needed during acceleration maneuvers, and absorbs the surplus power during deceleration.

Idle Limiter. Contrary to internal combustion engines, electric motors do not need to remain on when not needed, wasting energy while idling. Fuel Cells, however, need to provide at least a minimum amount of power required by its auxiliary systems and the aircraft. This minimum fuel cell power requirement plays a role similar to the idle limiters in turbofan controls. Any excess in power can be used to charge the battery when the conditions allow it.

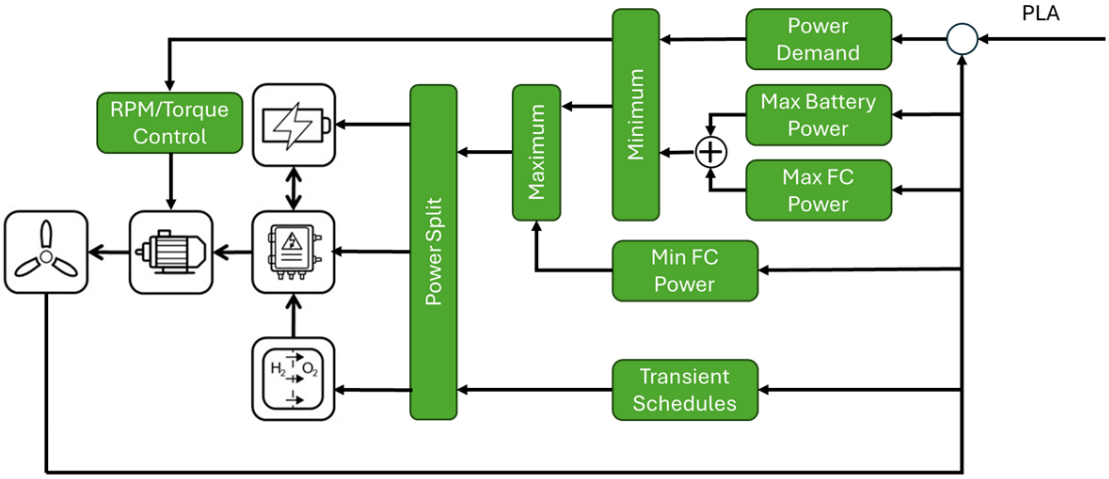


Figure 3: Proposed Set of Control Laws for an Electric Aircraft Propulsion System

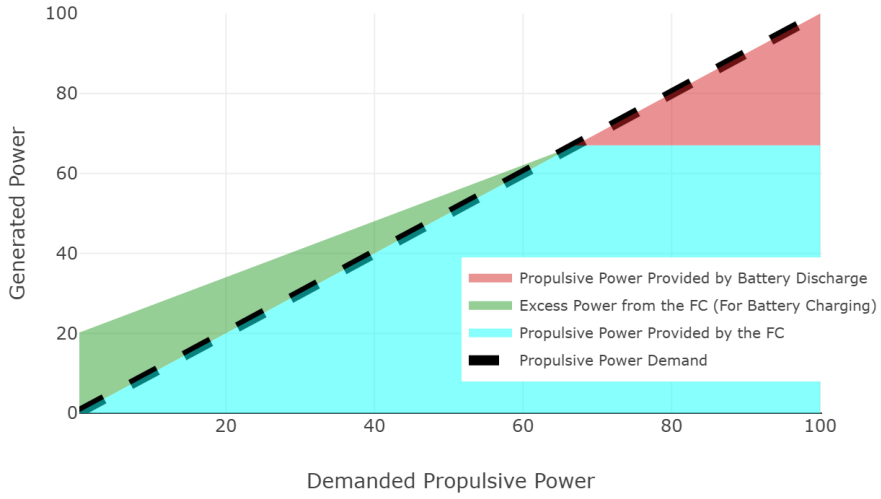


Figure 4: Example of a Schedule for Power Split According to Demanded Propulsive Power

Closing Remarks and Future Work

This work discussed some of the control challenges presented by an Electric Aircraft Propulsion system powered by a combination of fuel cell and battery. An architectural design of such a system

is proposed, discussing which control laws are considered necessary for the correct operation of the system. The factors which would limit the available thrust are mentioned and their effect in the design of the control loops are also considered.

The next steps are the detailed design of such control loops for an exemplary system. This includes the definition of numerical values for parameters such as the different required power levels and the minimum and maximum limiters, but also numerical targets regarding required acceleration times, contingency ratings, and other needs imposed, for example, by certification requirements. The specific control algorithms to be used for the definition of the loops, and the hardware and software architectures needed to implement the logic in an actual system, are also topics of extreme interest, which will be addressed in future works.

It must be stated again, that the generalization of such a control architecture is an almost impossible task, since each electrified topology would require specific considerations. A *one-size-fits-all* solution cannot be achieved.

Acknowledgement
This work has been financed by the DLR project SyneLa: *Synergien und Interaktionen in elektrifizierten Luftfahrtantrieben*.

References

[1] J. Connolly, J. Csank, and A. Chicatelli, Advanced Control Considerations for Turbofan Engine Design, 52nd AIAA/SAE/ASEE Joint Propulsion Conference. July 25-27 (2016). https://doi.org/10.2514/6.2016-4653

[2] D. Simon, J. Connolly, and D. Culley, Control Technology Needs for Electrified Aircraft Propulsion Systems, ASME Turboexpo. June (2019). https://doi.org/10.1115/GT2019-91413

[3] P. Hoenicke, D. Ghosh, A. Muhandes, S. Bhattacharya, C. Bauer, J. Kallo, and C. Willich, Power management control and delivery module for a hybrid electric aircraft using fuel cell and battery, Energy Conversion and Management. 244 (2021) https://doi.org/10.1016/j.enconman.2021.114445

[4] T. Marzougui, E. Solano Saenz, and M. Bareille, A Rule-Based Energy Management Strategy for Hybrid Powered eVTOL, Journal of Physics: Conference Series, 2526 (1), (2023) https://doi.org/10.1088/1742-6596/2526/1/012024

[5] U. M. Ferruli, M. Tipaldi, P. R. Massenio, and D. Naso, Energy Management System of a Fuel-Cell Hybrid Electric Aircraft Based on Dynamic Programming, Proccedings of the 16th International Conference on Information Technology and Electrical Engineering. October (2024). https://doi.org/10.1109/ICITEE62483.2024.10808922

[6] V. P. Joshi, R. Cepeda-Gomez, and T. F. Geyer, Optimal Sizing and Energy Management of a Battery To Support a Fuel Cell Powered Regional Electric Aircraft During Take-Off, AIAA Aviation Forum and ASCEND. June (2024) https://doi.org/10.2514/6.2024-3702

Materials Research Proceedings 69 (2026) 677-682 https://doi.org/10.21741/9781644904251-120

Analyzing the Eco-Design Approach for an Innovative In-Space Propulsion System

Daniele Ferrara[1,2,a *], Michele Trovato[1,b], Angelo Minotti[2,c], Antonio Casimiro Caputo[1,d] and Paolo Cicconi[1,e]

[1]Università degli Studi Roma Tre, Dipartimento di Ingegneria Industriale, Elettronica e Meccanica, Via Vito Volterra 62, 00146, Rome, Italy

[2]MIPRONS S.r.l., Via Riccardo Morandi snc, 00034, Colleferro, Rome, Italy

[a]daniele.ferrara@uniroma3.it, [b]michele.trovato@uniroma3.it, [c]angelo.minotti@miprons.com, [d]antoniocasimiro.caputo@uniroma3.it, [e]paolo.cicconi@uniroma3.it

Keywords: Eco-Design, Sustainable Space Propulsion Systems, Water Electrolysis

Abstract. In the context of the New Space Economy, sustainability has become a key driver for the development of next-generation space systems. The growing intensity of orbital activity is pushing space stakeholders to align future missions with global environmental goals, guided by space agencies and inspired by best practices from other industrial sectors. This paper proposes an eco-design workflow to support the design of in-space propulsion systems, focusing on an innovative patented water-electrolysis concept. The objective is to ensure high technical performance while integrating environmental sustainability considerations from the earliest design phases. Preliminary benchmark results on propellant production impacts offer a first perspective on how sustainability assessments can guide the design of advanced propulsion technologies.

Introduction

Sustainability is increasingly recognized as a strategic priority in the space sector, which historically has lacked alignment with ecological and long-term impact considerations. Although no specific environmental regulations currently exist for space activities, growing efforts are being made to raise awareness and reduce the environmental footprint of space systems design [1].

Major research efforts currently focus on satellite constellations in Low Earth Orbit (LEO), due to the already high number of operational satellites and the expected increase driven by the wide range of services offered at these altitudes [2]. This scenario has significant implications for both the orbital environment, where space debris and end-of-life management are critical issues, and the terrestrial environment, affected by development, production, launch, ground operations, and re-entry activities; both dimensions must be preserved for a truly sustainable space sector.

Recent studies on rocket launchers highlight the complexity of applying eco-design principles to space systems, due to the significant uncertainties in modeling emissions across different atmospheric layers and in characterizing the environmental behavior of the unique manufacturing processes and materials [3]. These challenges are also relevant for in-space propulsion systems. These are directly affected by the ongoing shift toward sustainable space development, particularly through the transition toward "green" propellants as alternatives to conventional options such as toxic hydrazine or expensive, resource-intensive xenon [4].

Frameworks to account for sustainability in space system design, with a specific focus on space propulsion, have already been proposed: Canepari *et al.* [5] developed a tool to select the most suitable propulsion system for different in-space mission scenarios, based on four figures of merit namely performance, cost, reliability, and environmental performance; Wilson *et al.* [6] proposed replacing hydrazine-based propulsion with a "green" chemical propellant, namely LMP-103S, for their case-study mission. Although this change reduced operational hazards, it resulted in a burden

Content from this work may be used under the terms of the Creative Commons Attribution 3.0 license. Any further distribution of this work must maintain attribution to the author(s) and the title of the work, journal citation and DOI. Published under license by Materials Research Forum LLC.

Materials Research Proceedings 69 (2026) 677-682 https://doi.org/10.21741/9781644904251-120

shift at the propellant production stage rather than a net improvement in overall environmental performance. Across these studies, Life Cycle Assessment (LCA) is commonly employed as a methodological tool to quantify environmental burdens and identify key hotspots for improvement. Most recent analyses implement the European Space Agency (ESA) LCA guidelines and database, the first eco-instruments developed explicitly for space applications [7].

It is important to highlight that the propulsion architectures analyzed in recent studies are based on existing technologies (i.e., *as-is* systems) and their environmental performance is evaluated *ex post*. To date, there are few studies addressing the sustainability-oriented design of novel in-space propulsion technology concepts. The goal of this work is therefore to introduce an engineering eco-design workflow that supports the early development of a novel water electrolysis propulsion concept from both technical and environmental perspectives.

The following section outlines the proposed workflow and describes the case study, followed by results and discussions. The paper ends with conclusions and a description of future work directions.

Methodology and Materials

Product design is inherently an interdisciplinary iterative process that evolves from a conceptual stage toward detailed specification. In eco-design, this evolution entails that, alongside technical requirements, early decisions on materials and processes are made and progressively refined through manufacturing routes, geometries, masses, and interfaces. Design for Environment (DFE) is an established industrial eco-design practice aimed at reducing environmental impact while improving cost and quality [8]. Its principles provide a reference for integrating environmental considerations into the engineering design of space systems.

When designing novel and innovative products, the product structure and complete material list are not yet defined in the early design phase. Consequently, conducting a rigorous LCA study as required by ISO 14040 and ISO 14044 is challenging due to the lack of comprehensive and well-defined information. However, environmental criteria can still be integrated from the very beginning using complementary approaches such as streamlined and Fast-Track LCA, supported by benchmarking, literature analysis, lookup tables (e.g., eco-cost indicators), and material selection software such as Cambridge Engineering Selector [9]. These methods enable parallel progress in data collection and design exploration, following an iterative cycle that continues until the detailed design stage. Moreover, they can provide sufficiently accurate results to support design decisions and accelerate the transition toward prototyping.

Workflow. Fig. 1 illustrates the proposed workflow integrating life-cycle environmental considerations into the engineering design process of innovative in-space propulsion systems. As in any design process, technical requirements are first derived from external and internal inputs, including stakeholder needs, applicable standards and regulations, and the technological concept itself (e.g., from patents). Establishing a Design Reference Mission (DRM) provides the common basis for both the system sizing and the LCA framework, including the definition of the functional unit, system boundaries, and goal and scope. These elements are expected to evolve iteratively at each design loop, depending on the specific design inputs; however, the system-level definition and its design objective should remain consistent to ensure traceability and comparability of results. From the DRM, mission goals determine sizing parameters such as propellant mass, system architecture, and mission duration. Additionally, including the emerging New Space design drivers as input ensures compliance with current development scenarios [10]. The following engineering design stages include iterations for requirement analysis and system modeling through functional allocation and product tree definition [11]. The subsequent stage integrates the typical steps of LCA, adapting them at each iteration to the current level of detail and accuracy. In the first analysis, openLCA 2.5.0 and the Ecoinvent v3.10 database (APOS) are used.

Materials Research Proceedings 69 (2026) 677-682 https://doi.org/10.21741/9781644904251-120

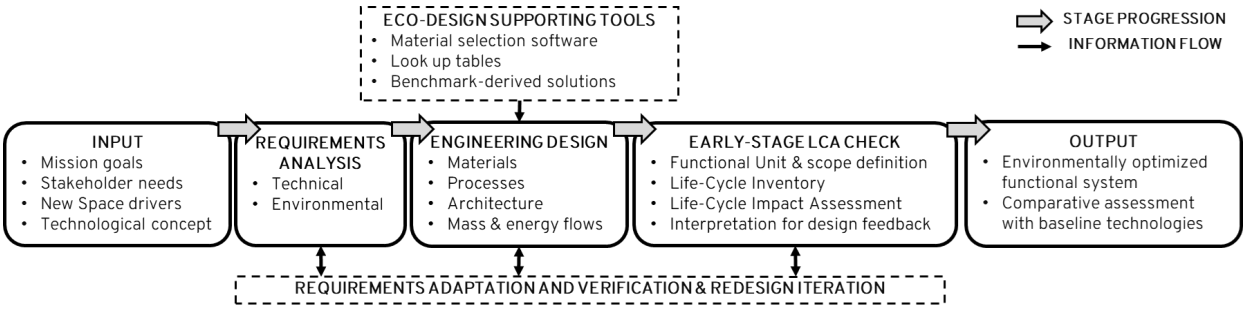


Figure 1: Proposed eco-design workflow for the early-stage development of innovative in-space propulsion systems.

Within the information flow, the iteration loop includes both technical and eco-design refinement, ensuring that environmental feedback informs engineering choices. The design phase is over when both performance and environmental requirements are satisfied in accordance with the defined goals, verified through analysis, demonstration, or testing within a rapid prototyping approach. The findings are finally benchmarked against publicly available data from existing propulsion solutions to investigate the potential of the proposed case study.

Case study. This study focuses on an industrial in-space propulsion concept that uses water as propellant, protected by patent WO 2019/0212347A1 [12]; Fig. 2 illustrates the minimal functional architecture: it consists of a modular unit capable of delivering high thrust by splitting water into hydrogen and oxygen on demand via electrolysis directly in orbit and subsequently combusting the resulting gas mixture. The system is designed to maximize propulsion efficiency and combustion performance within a compact size, making it particularly suitable for small satellite applications. Water is an environmentally benign monopropellant option: it is non-toxic, inert, widely available, inexpensive, storable, and has a favorable density. While the concept of water electrolysis propulsion dates to the 1970s, technological progress, together with the evolving needs of the New Space sector, now make this solution both technically and economically viable.

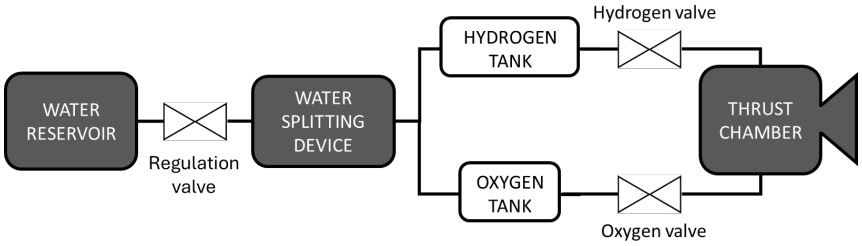


Figure 2: Scheme of the minimal functional architecture of the water-electrolysis high thrust propulsion system based on the patent WO 2019/021234 [12].

Motivation of the work. The patented water-electrolysis propulsion concept is a promising candidate for high-performance and environmentally aware in-space propulsion. Nevertheless, its potential can only be fully realized through an eco-design approach that integrates technical performance and environmental criteria from the outset. This case study applies the workflow in Fig. 1, supported by preliminary LCA, to guide the development of the system in Fig. 2 and provide an early quantitative basis for sustainability-driven design decisions.

Results and Discussion

As LEO missions are among the most critical from a sustainability perspective, the DRM has been defined with reference to such a scenario. Furthermore, the selected mission parameters are representative of an actual mission under investigation for this case study. Table 1 summarizes the main DRM parameters.

Materials Research Proceedings 69 (2026) 677-682 https://doi.org/10.21741/9781644904251-120

Table 1: Design Reference Mission (DRM) main parameters.

Mission parameter	Value
Mission type	Orbit maintenance and collision avoidance
Orbit	Low Earth Orbit (LEO)
Δv budget [m/s]	100
Satellite dry mass [kg]	150
Nominal lifetime [years]	7

The main functional unit is defined as *one propulsion system able to perform the DRM reported in Table 1*. Full system boundaries and full scope will be defined as the design matures and the conceptual architecture, transport scenarios, and life-cycle stages become better defined, following the iterative approach suggested in [9]. In this first design iteration, the study adopts a system boundary limited to the initial life-cycle stage, namely the *production of propellant quantities for the selected DRM (cradle-to-gate)*. The system boundary does not include space-grade conditioning (final purification, tank filling, etc.), which may be modelled in a separate analysis. Focusing on the production phase isolates the upstream contribution of the propellant, the key element characterizing a space propulsion system. Production impacts are expected to reveal the potential environmental advantages of a water electrolysis-based solution, subject to the assumptions on energy supply and process modelling.

The early LCA scope is defined as a *comparison between water-electrolysis, xenon-based Hall Effect, and hydrazine monopropellant propulsion alternatives*, offering a preliminary benchmark against conventional systems. Propellant masses required to achieve the mission are computed using Tsiolkovsky's rocket equation, assuming an appropriate specific impulse for each technology; see Eq. 1, where m_p is the propellant mass, m_f the satellite dry mass, Δv the mission velocity budget, I_{sp} the specific impulse, and g_0 the standard gravity. The resulting propellant masses are reported in Table 2 together with the specific impulse.

$$m_p = m_f(e^{\frac{\Delta v}{I_{sp} g_0}} - 1). \quad (1)$$

Table 2: Propellant masses required to meet the DRM for each propulsion system.

Propulsion system type	Specific impulse [s]	Propellant mass [kg]
Hydrazine monopropellant thruster	220	7.1
Xenon-based Hall Effect Thruster	1300	1.2
Water-electrolysis propulsion system	300	5.2

The preliminary results for propellant production are shown in Fig. 3 and refer to five impact categories and corresponding LCIA (Life-Cycle Impact Assessment) methods recommended by ESA [6,7]. The results are scaled with respect to xenon production. Each production process was modelled in openLCA for the propellant masses in Table 2: hydrazine (Raschig process), xenon (cryogenic air separation), and deionized water (ion exchange) as proxies, representing large-scale European production (Switzerland excluded only for water for dataset availability).

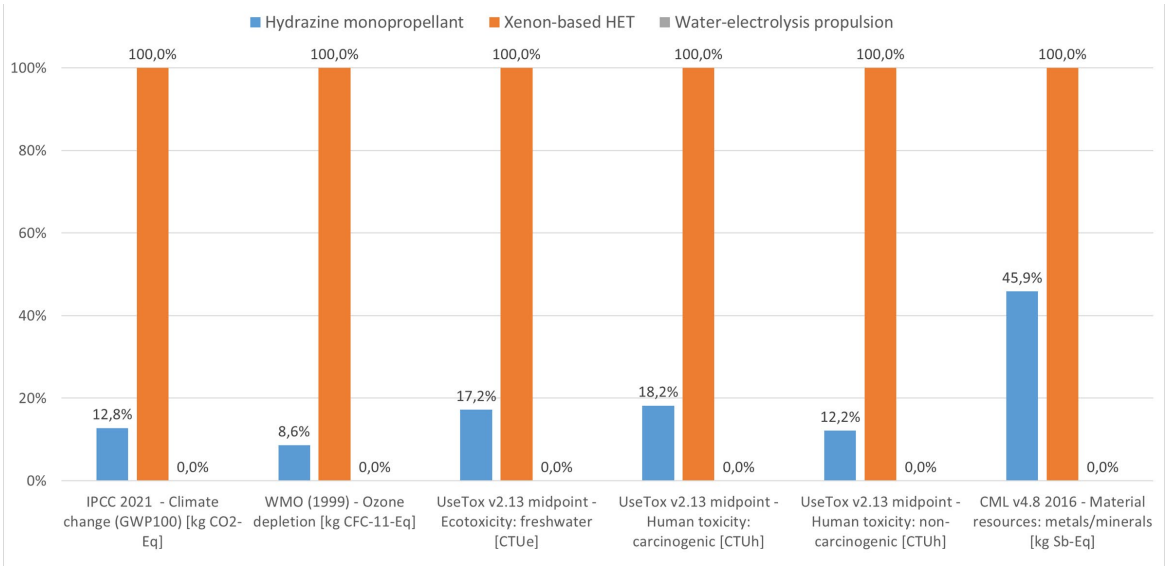


Figure 3: Preliminary LCIA comparison for the production of propellant masses required by the DRM. Modelling in openLCA 2.5.0 using Ecoinvent v3.10 (APOS, Europe).

These results confirm that the environmental burden associated with the production of deionized water in large-scale European processes is negligible, corresponding to a relative impact close to 0% compared to xenon within the scope of this analysis (Fig. 3). In contrast, xenon production exhibits the highest environmental impact among the three investigated propulsion systems. This aspect becomes particularly relevant when designing large-scale LEO constellations, as the advantages of carrying smaller propellant quantities using HETs may be offset by the xenon's high manufacturing footprint. Hydrazine, on the other hand, despite being more hazardous than xenon and less mass-efficient, shows comparatively lower impacts (ranging from 9% to 46%). However, this apparent advantage is expected to diminish once downstream life-cycle stages (handling, transport, and refueling) are included. This is due to the toxic nature of the propellant, which entails specific safety procedures and equipment for storage and operations, increasing both mission costs and lead times. In light of these preliminary findings, the environmental impact of water during the production phase is negligible, confirming its potential to enhance the mission's overall sustainability.

Conclusions

This study introduces a workflow for the early sustainable design of a water-electrolysis propulsion system. The preliminary LCA analysis focused on comparing the production process of three space propellants: water, hydrazine, and xenon. The initial results indicate that conventional propellants are increasingly misaligned with the perspective of a sustainable space sector, supporting the rationale for continued investment in water-propulsion as an effective alternative. Future work will extend the analysis to the main components and life-cycle phases of the innovative water-electrolysis propulsion solution to verify whether it maintains the environmental advantages highlighted in this study and to integrate economic and social considerations.

Acknowledgements

This doctoral project was activated under The Italian Ministry of University and Research—Ministerial Decree 117/2023, resources based on PNRR, Mission 4, component 2 "From Research to Business"—Investment 3.3 "Introduction of innovative doctorates that meet the innovation needs of businesses and promote the hiring of researchers from businesses", with the contribution and involvement of MIPRONS S.r.l..

References

[1] L. Miraux, A.R. Wilson, G.J. Dominguez Calabuig, Environmental sustainability of future proposed space activities, Acta Astronaut. 200 (2022) 329–346. https://doi.org/10.1016/j.actaastro.2022.07.034

[2] S.T. Kumaran, C. Tan, M. Emes, Quantifying the environmental impacts of manufacturing Low Earth Orbit (LEO) satellite constellations, Sustainability 16 (2024) 9431. https://doi.org/10.3390/su16219431

[3] L. Miraux, L. Pineau, P. Noir, Parametric Life Cycle Assessment of a space launch service based on a LOx/biomethane semi-reusable launcher, in: 73rd Int. Astronaut. Congr., 2022, Paris, France. https://hal.science/hal-04274253

[4] J. Muñoz Tejeda, A. Schwertheim, A. Knoll, Water as an environmentally friendly propellant for a multi-functional spacecraft architecture, Int. J. Energetic Mater. Chem. Propuls. 22 (2022) 21–33. https://doi.org/10.1615/IntJEnergeticMaterialsChemProp.v22.i2.20

[5] L. Blondel-Canepari, A. Tacchi, A. Pasini, Development of a propulsion system analysis tool for quick global performance evaluation of a kick stage mission scenario, in: AIAA SCITECH 2024 Forum, AIAA SciTech Forum, American Institute of Aeronautics and Astronautics, 2024. https://doi.org/10.2514/6.2024-1368

[6] A.R. Wilson, M. Vasile, C. Maddock, K. Baker, Implementing life cycle sustainability assessment for improved space mission design, Integr. Environ. Assess. Manag. 19 (2023) 1002–1022. https://doi.org/10.1002/ieam.4722

[7] European Space Agency, Space System Life Cycle Assessment (LCA) Guidelines, Handbook ESSB-HB-U-005, ESA, Paris, 2016.

[8] K.T. Ulrich, S.D. Eppinger, Product Design and Development, sixth ed., McGraw-Hill Education, New York, 2016.

[9] J. Vogtlander, LCA: A Practical Guide for Students, Designers and Business Managers, sixth ed., VSSD, Delft, 2023.

[10] D. Ferrara, P. Cicconi, A. Minotti, M. Trovato, A.C. Caputo, New Space engineering design: Characterization of key drivers, Appl. Sci. 15 (2025) 8138. https://doi.org/10.3390/app15158138

[11] D. Ferrara, P. Cicconi, A. Minotti, M. Trovato, M. Amicarelli, A.C. Caputo, A design framework for the development of an innovative water-electrolysis space propulsion system, Procedia CIRP 136 (2025) 856–861. https://doi.org/10.1016/j.procir.2025.08.146

[12] MIPRONS S.r.l., Space propulsion system, WO2019021234A1 (2019). https://patents.google.com/patent/WO2019021234A1/en

Materials Research Proceedings 69 (2026) 683-688 https://doi.org/10.21741/9781644904251-121

Reduced-Order Dynamic Modelling of the Wankel Engine Employed in the Hybrid Propulsion System of a Lightweight Helicopter UAV

Gianpietro DI RITO[1,a *], Alessandro MAZZONE[1,b], Andrea NESCI[2,c], Eugenio ROVERA[2,d] and Valerio BONINI[2,e]

[1]Università di Pisa – Dipartimento di Ingegneria Civile e Industriale, Pisa, Italy

[2]Leonardo Helicopters Division, Leonardo S.p.A., Rome, Italy

[a]gianpietro.di.rito@unipi.it, [b]alessandro.mazzone@phd.unipi.it, [c]andrea.nesci@leonardo.com, [d]eugenio.rovera@leonardo.com, [e]valerio.bonini@leonardo.com

Keywords: UAV Propulsion, Wankel Engine, Modelling and Simulation, Testing, Sustainable Propulsion, Helicopters

Abstract. This work deals with the development of a reduced-order dynamic model of a Wankel rotary engine for the propulsion of a lightweight helicopter UAV, to be used for in-flight health-monitoring. The model, which is real-time executable by the on-board electronics of the UAV, includes the simulation of mechanical power generation, intake manifold pressure dynamics, fuel flow consumption, and thermal transfer in the combustion chamber. Aiming to develop a simulator based on physical principles, a correlation analysis among the experimental measurements obtained by endurance tests has been carried out, up to select the states and the inputs of the model sections and to identify their parameters via ordinary least square method. Simulation demonstrates to satisfactorily reproduce the experimental behaviour (maxima errors are lower than 5%), when the engine works near its nominal operating conditions, i.e. at constant rotor speed, while the model errors increase (up to 30%) during the transients from/to warm-up phases.

Introduction

The interest in the development of hybrid-electric powertrain for efficiency enhancement, noise abatement and reduction of pollutants emission of UAV propulsion systems is continuously increasing in the aeronautical sector [1]. The hybridization of UAV propulsion has found fertile ground due to the promises of extended endurance and lower fuel consumption combined with emissions abatement and thermal signature minimization, resulting in a solution that is attractive for both civil and military applications [2, 3, 4]. Wankel rotary engines [5] have emerged as a viable solution for the internal combustion power source in hybrid-electric configurations [6], given their high-power density, extreme compactness, and lower noise emission with respect to conventional reciprocating engines [7]. The application background of rotary engines is undoubtedly poorer than that of four-pistons engines and extended dissertations are not available in literature. Mean Value Engine Models (MVEMs) have been developed for Wankel engines [8], but their effectiveness strongly depends on detailed knowledge of geometry, size, and operating conditions [9, 10], so that they are not suitable for control design or digital twin development, which requires real-time execution capabilities. Within this context, this paper deals with the development and experimental validation of a reduced-order model of a Wankel engine, using as a case study the one employed in the propulsion system of a lightweight helicopter UAV by Leonardo Elicotteri. In the initial architecture layout, the propulsion system integrates a Wankel engine mechanically coupled to a mixing unit whose output shaft rotates synchronously with the engine shaft. This shaft is connected to the drive system, enabling power distribution to the helicopter rotors and it is then connected to the driving system allowing distribution of power to the helicopter rotors. The engine shaft can be decoupled from the mixing unit during idling or

Content from this work may be used under the terms of the Creative Commons Attribution 3.0 license. Any further distribution of this work must maintain attribution to the author(s) and the title of the work, journal citation and DOI. Published under license by Materials Research Forum LLC.

Materials Research Proceedings 69 (2026) 683-688 https://doi.org/10.21741/9781644904251-121

warm-up phases. An innovative version is under evaluation, in which an electric motor will be integrated with a downsized version of the Wankel engine to achieve a hybrid-electric configuration.

Materials and methods

Experimental set-up

The modelling and simulation activities have been supported by the availability of an experimental database related to endurance tests, in which the propulsion system is required to operate under three different loads scenarios, referred to take-off at maximum weight, cruise at maximum speed and cruise at nominal speed, respectively.

During the tests, the propulsion system was equipped with sensors providing:

- throttle valve opening
- fuel flow
- air-to-fuel ratio
- angular speed of the engine
- manifold air pressure
- temperatures of external air, exhaust gas and coolant
- external load applied to the mixing unit output shaft
- angular speed of the mixing unit output shaft

Model sections and identification technique

The Wankel engine model has been developed including the following sections:

- mechanical power generation
- fuel flow consumption
- intake manifold pressure dynamics
- thermal transfer in the combustion chamber

For each section of the model, a correlation analysis among the available measurements from tests was conducted, identifying physically-based relationships between inputs (e.g. throttle valve opening) and dynamic states (e.g. shaft speed, manifold air pressure, etc.). The parameters of model sections were then identified via Ordinary Least Squares (OLS) technique [11]. According to OLS, if the linearly dependence of a quantity Y on data x and z through unknown parameters $\beta_0, \beta_1, \beta_2$

$$Y = \beta_0 + \beta_1 x + \beta_2 z \tag{1}$$

is applied to a vast dataset of measurements, the following relationship is obtained:

$$\begin{bmatrix} Y_1 \\ \vdots \\ Y_n \end{bmatrix} = \begin{bmatrix} 1 & x_1 & z_1 \\ \vdots & \vdots & \vdots \\ 1 & x_n & z_n \end{bmatrix} \begin{bmatrix} \beta_0 \\ \beta_1 \\ \beta_2 \end{bmatrix} \rightarrow \boldsymbol{f} = \boldsymbol{M}\ \boldsymbol{c} \tag{2}$$

Thus, the vector $\boldsymbol{c}$ of unknown parameters can be determined by

$$\boldsymbol{c} = (\boldsymbol{M^T M})^{-1} \boldsymbol{M^T f} \tag{4}$$

Mechanical power generation

The correlation analysis pointed out that the engine torque has a strong correlation with the throttle valve opening and (at weaker level) engine speed. Therefore, the torque for the Wankel engine of the propulsion system has been modelled as:

$$T_W(\tau, \omega) = a_1\left[1 + \gamma_1\left(\omega - \omega_{ref}\right)\right]\tau + a_2\left[1 + \gamma_2\left(\omega - \omega_{ref}\right)\right]\tau^2 \tag{5}$$

Materials Research Proceedings 69 (2026) 683-688 https://doi.org/10.21741/9781644904251-121

where T_W is the torque in Nm, τ is the throttle opening percentage (from 0 to 100); ω is the angular speed in rad/s, while a_k and γ_k are unknown model parameters (k=1,2).
By assuming a rigid transmission from the Wankel engine to the system output shaft, we have

$$\omega_a = \omega_b = \omega \tag{5}$$

and the momentum equation at the output shaft becomes:

$$J_o\dot{\omega} = T_W + T_L - B_f\omega \tag{6}$$

In Eq. (6), T_L is the external load, while J_o, the equivalent system inertia, and B_f , the viscous coefficient, are unknown model parameters. Substituting Eq. (4) in Eq. (6), we obtain:

$$J_o\dot{\omega} = a_1\left[1+\gamma_1\left(\omega-\omega_{ref}\right)\right]\tau + a_2\left[1+\gamma_2\left(\omega-\omega_{ref}\right)\right]\tau^2 + T_L - B_f\omega \tag{7}$$

Using Eq. (7), a two-step identification has been carried out:

1. in steady-state conditions, i.e. $\dot{\omega} \approx 0 \ \ and \ \ \left|\omega-\omega_{ref}\right| < 0.01$, for the identification of the parameters $B_f, \mathrm{a}_1, \mathrm{a}_2$.
2. in transient conditions near the nominal speed: $\dot{\omega} \neq 0 \ \ and \ \ \left|\omega-\omega_{ref}\right| < 0.1$, for the identification of the parameters J_o, γ_1, γ_2 identification.

Fuel flow consumption and intake manifold air pressure
Both fuel flow and manifold air pressure signals exhibited a strong correlation with throttle valve opening and engine angular speed was again found, so that the following models have been used:

$$\dot{m}_f(\tau,\omega) = \phi_0 + \phi_1\left[1+g_1\left(\omega-\omega_{ref}\right)\right]\tau + \phi_2\left[1+g_2\left(\omega-\omega_{ref}\right)\right]\tau^2 \tag{8}$$

$$P_m(\tau,\omega) = \psi_0 + \psi_1\left[1+k_1\left(\omega-\omega_{ref}\right)\right]\tau + \psi_2\left[1+k_2\left(\omega-\omega_{ref}\right)\right]\tau^2 \tag{9}$$

where $\dot{m}_f$ is the fuel flow in kg/s, P_m is the manifold pressure in Pa, while ϕ_0, ϕ_1, ϕ_2 and ψ_0, ψ_1, ψ_2 are unknown model parameters to be identified in steady-state conditions, while g_1, g_2 and k_1, k_2 in transient conditions.

Thermal transfer in the combustion chamber
The temperature dynamics in the combustion chamber has finally been modelled via an energy balance applied to the chamber control volume, Fig. 1.

$$I_t\dot{\theta}_e = \dot{m}_f LHV - T_w\omega + B_f\omega^2 - k_c(\theta_e-\theta_c) - \dot{m}_f c_v(1+\lambda)\theta_x \tag{10}$$

where θ_e , θ_c and θ_x are the engine chamber, the coolant and the exhaust gas temperatures in °K, LHV is the fuel lower heating value in J/kg, $\boldsymbol{c_v}$ is the specific heat at constant volume in J/kg°K, and λ is the air-to-fuel ratio, while I_t and k_c are unknown model parameters.

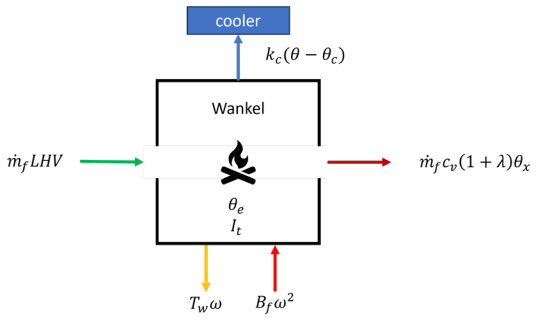


Figure 1 – Energy flows in the combustion chamber control volume.

Materials Research Proceedings 69 (2026) 683-688 https://doi.org/10.21741/9781644904251-121

Results and discussion

A comparison between simulation and experimental results are summarized from Fig. 2 to Fig. 4. When simulating the operation near the nominal speed, the model exhibits a strong matching with experiments (Figs. 2-3). As highlighted by Fig. 3, the model errors are small throughout the test in nominal operative condition. The detailed comparison in Fig. 4 permits to confirm the satisfactory accuracy of the developed model.

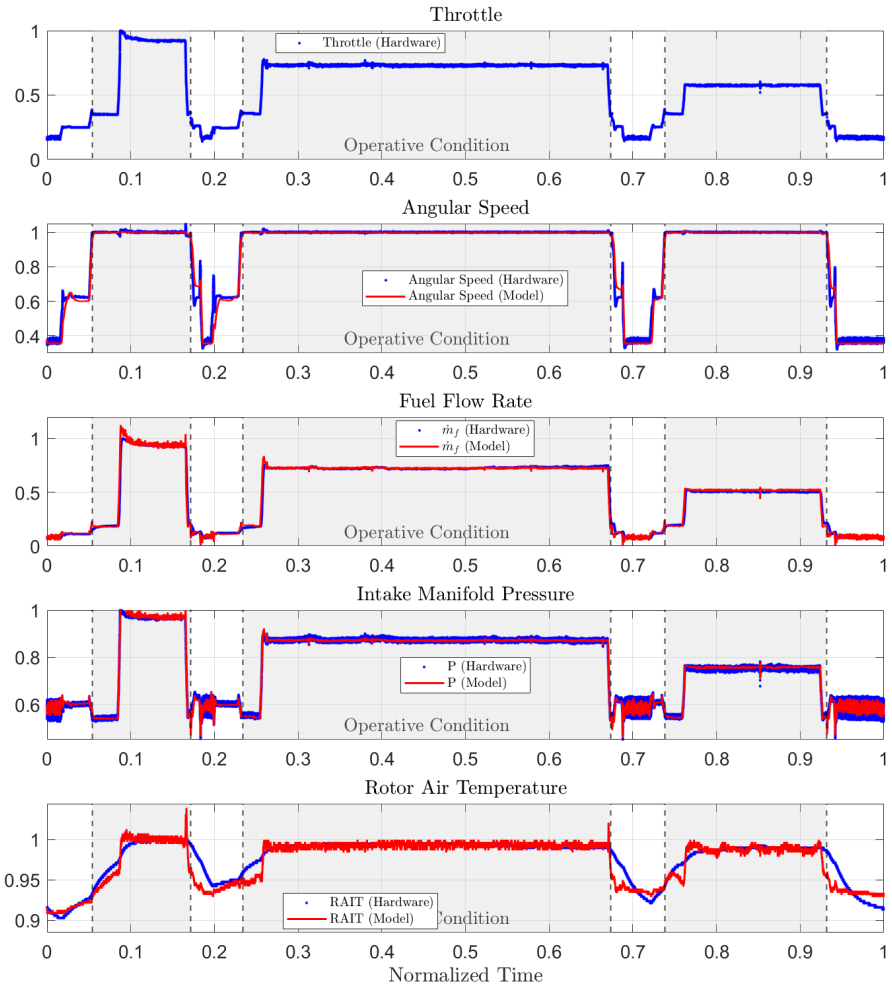


Figure 2 - Comparison of simulation and experiments related to Wankel engine dynamics (normalized data): throttle (top), shaft speed, fuel flow, intake pressure, engine temperature (bottom)

Materials Research Proceedings 69 (2026) 683-688 https://doi.org/10.21741/9781644904251-121

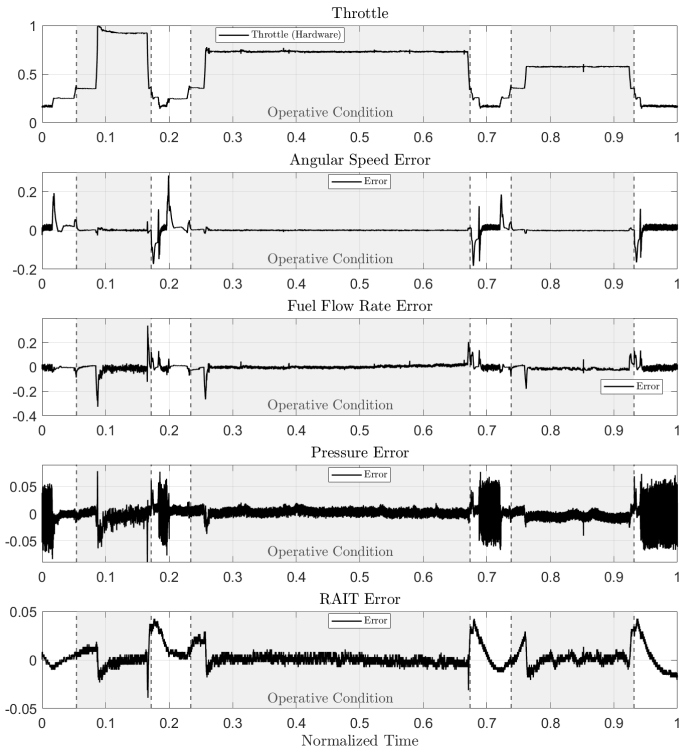


Figure 3 – Model errors related to Wankel engine dynamics (normalized data): shaft speed (top), fuel flow, intake pressure, engine temperature (bottom).

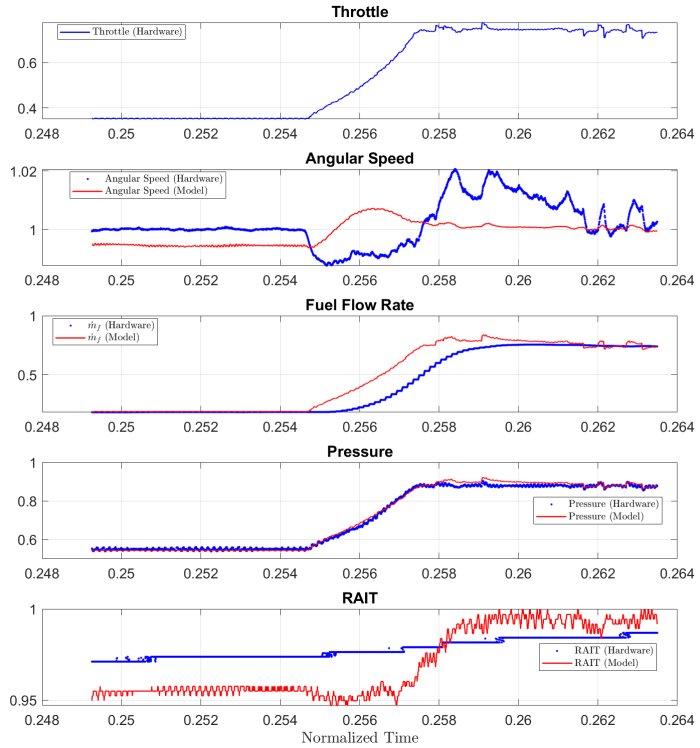


Figure 4 - Comparison of simulation and experiments related to Wankel engine dynamics (normalized data): throttle (top), shaft speed, fuel flow, intake pressure, engine temperature (bottom).

References

[1] "Destination 2050-A route to net zero European aviation." Accessed: Feb. 25, 2024. [Online]. Available: https://www.destination2050.eu/

[2] R. Hiserote and F. Harmon, "Analysis of Hybrid-Electric Propulsion System Designs for Small Unmanned Aircraft Systems," in *8th Annual International Energy Conversion Engineering Conference*, Reston, Virigina: American Institute of Aeronautics and Astronautics, Jul. 2010. https://doi.org/10.2514/6.2010-6687

[3] J. Y. Hung and L. F. Gonzalez, "On parallel hybrid-electric propulsion system for unmanned aerial vehicles," *Progress in Aerospace Sciences*, vol. 51, pp. 1–17, May 2012. https://doi.org/10.1016/j.paerosci.2011.12.001

[4] Joachim Schömann, "Hybrid-Electric Propulsion Systems for Small Unmanned Aircraft," Ph.D. Dissertation, Technischen Universität München, 2014.

[5] Harris Edward Dark, *The Wankel Rotary Engine: Introduction and Guide*. 1992. Accessed: Sep. 20, 2024. [Online] https://books.google.it/books/about/The_Wankel_Rotary_Engine.html?id=L6hUyQEACAAJ&redir_esc=y

[6] T. Donateo, A. Ficarella, and C. L. De Pascalis, "Energy management-based design of a Wankel hybrid-electric UAV," *Aircraft Engineering and Aerospace Technology*, vol. 92, no. 5, pp. 701–715, May 2020. https://doi.org/10.1108/AEAT-06-2019-0117.

[7] C. Ji, H. Wang, C. Shi, S. Wang, and J. Yang, "Multi-objective optimization of operating parameters for a gasoline Wankel rotary engine by hydrogen enrichment," *Energy Convers Manag*, vol. 229, p. 113732, Feb. 2021. https://doi.org/10.1016/j.enconman.2020.113732.

[8] A. S. Chen *et al.*, "Control-Oriented Modelling of a Wankel Rotary Engine: A Synthesis Approach of State Space and Neural Networks," Apr. 2020. https://doi.org/10.4271/2020-01-0253

[9] G. Vorraro, M. Turner, and J. W. G. Turner, "Testing of a Modern Wankel Rotary Engine - Part I: Experimental Plan, Development of the Software Tools and Measurement Systems," Jan. 2019. https://doi.org/10.4271/2019-01-0075

[10] G. Vorraro, J. W. G. Turner, and S. Akehurst, "Testing of a Modern Wankel Rotary Engine - Part III: Firing Condition Analysis," Mar. 2022. https://doi.org/10.4271/2022-01-0591

[11] Goldberger, *Econometric Theory*, 10th ed. 1964.

Materials Research Proceedings 69 (2026) 689-694 https://doi.org/10.21741/9781644904251-122

Preliminary Safety Assessment of the Propulsion Power Management System of a Hybrid-Electric Regional Aircraft

Gianpietro DI RITO[1,a *] and Aleksander SUTI[1,b]

[1]Università di Pisa – Dipartimento di Ingegneria Civile ed industriale
Largo Lucio Lazzarino 2, 56122, Pisa (Italy)

[a]gianpietro.di.rito@unipi.it, [b]aleksander.suti@dici.unipi.it

Keywords: Aircraft Electrification, Hybrid Propulsion, Power Management Systems, Reliability, Safety, Functional Hazard Analysis

Abstract. The development and the technological demonstration of Hybrid-Electric Propulsion Systems (HEPSs) represent fundamental steps towards more sustainable air transports, especially with reference to regional applications. Beyond performance aspects, the reliability and safety of the electrical power devices integrated in the HEPSs are still far to be substantiated, especially with reference to Li-Ion batteries and fuel cells. In addition, due to the presence of multiple power paths, a safety-critical element of all HEPSs is the power management system, defining the torque split among sources and monitoring the health-state of subsystems. This work presents the preliminary Functional Hazard Assessment of the power management system of a 2-MW HEPS with hydrogen fuel cells for regional aircrafts, developed within the context of the EU-funded AMBER project, launched in 2023 and part of the Clean Aviation program. The activity conducts to the identification of the most critical failure conditions of the HEPS power management system, which can bring up to hazardous consequences (depending on the mission phase), and to the proposal of possible enhancements of the system architecture aiming to mitigate or eliminate the failure effects.

Introduction

Environmental sustainability is nowadays one of the most crucial challenges of aviation industry, which is striving to validate technologies capable of reducing aircraft noise and Greenhouse Gas (GHG) emissions [1]. In this context, the development and the technological demonstration of Hybrid-Electric Propulsion Systems (HEPSs) represent fundamental steps towards more sustainable air transports, especially with reference to regional applications [2-7], To address such issue, the EU-funded AMBER project has been launched in 2023 as part of the Clean Aviation program [8], aiming to mature, integrate and validate a 2-MW HEPS powered by hydrogen fuel cells. The main goal of the AMBER project is to reduce the fuel burn and the GHG emissions by at least 30% at aircraft level, compared to 2020 state-of-art [9]. The HEPSs essentially try to combine and balance the advantages of electric propulsion in terms low noise emissions and high power efficiency with those of Internal Combustion Engines (ICEs) in terms of long flight endurance, high power density and proven reliability [10]. Actually, beyond performance aspects, the reliability and safety of electrical propulsion systems are still far to be substantiated, especially with reference to energy storage devices [11]. In HEPSs with hydrogen fuel cells, multiple power paths can be used for propulsion, so that a power management system is needed to define the torque split among sources, while monitoring the health-state of critical subsystems (e.g. Li-ion batteries and fuel cells) and estimating the pollutant emissions [12]. In the AMBER HEPS, this task is allocated to the so-called Supervisory and Hierarchical Control System (SHCS) and this work presents the Functional Hazard Assessment (FHA) [13, 14], referred to a preliminary architecture of the system, aiming to highlight its potentialities and limitations for the airworthiness certification [15-17].

Content from this work may be used under the terms of the Creative Commons Attribution 3.0 license. Any further distribution of this work must maintain attribution to the author(s) and the title of the work, journal citation and DOI. Published under license by Materials Research Forum LLC.

Materials Research Proceedings 69 (2026) 689-694 https://doi.org/10.21741/9781644904251-122

The paper is articulated as follows: in the first section, a brief description of the AMBER HEPS and its main components is provided. In the second part, the methodology for the FHA development is briefly recalled, by defining the system functional requirements, the mission profile, the failure types and the related severities. In the third section, an excerpt of the HEPS SHCC FHA table is reported, by highlighting the most critical failure conditions and proposing possible enhancements in the system architecture.

Materials and Methods

System description

In the AMBER twin-engine aircraft, the HEPS is made of two assemblies, each one dedicated to one of the two engine. The main components of each HEPS assembly are, Figure 1:

- ICE, composed of Gas Turbine (GT) and related FADEC
- electric propulsion system, composed of
  - Electric Motor (EM) subsystem, including
    - a three-phase permanent magnets synchronous electric machine
    - Electronic Control Unit (EM ECU)
    - Electronic Power Unit (EM EPU)
    - Thermal Management System (EM TMS)
  - fuel cell subsystem, including
    - hydrogen tank
    - Fuel Cell (FC)
    - Master Electronic Control Unit (FC M-ECU)
    - secondary ECUs (Fuel Cell Control)
    - Thermal Management System (FC TMS)
  - battery subsystem, including
    - Battery Pack
    - Electronic Control Unit (BS ECU)
    - Thermal Management System (BS TMS)
- SHCS, composed of:
  - Supervisory and Hierarchical Controller (SHC)
  - Fault Detection, Isolation and Accommodation Control Unit (FDIA-CU)
  - Power Fault Compensation Control Unit (PFC-CU)
- Electric Power Distribution (EPD) module
- Propeller Actuators and Sensors (PAS) module
- clutch and gearbox connecting the ICE and EM output shafts to the propeller in parallel torque-summing configuration

Concerning the interfaces, each assembly receives commands from the Power Lever Angle (PLA) module (in the AMBER aircraft, it is the basic pilot interface with the HEPS to define, depending on the mission phase, the propulsion request) and exchanges data with avionics and the SHCS of the other HEPS assembly. In addition, the SHCS can communicate with the maintenance ECU, when connected.

Materials Research Proceedings 69 (2026) 689-694 https://doi.org/10.21741/9781644904251-122

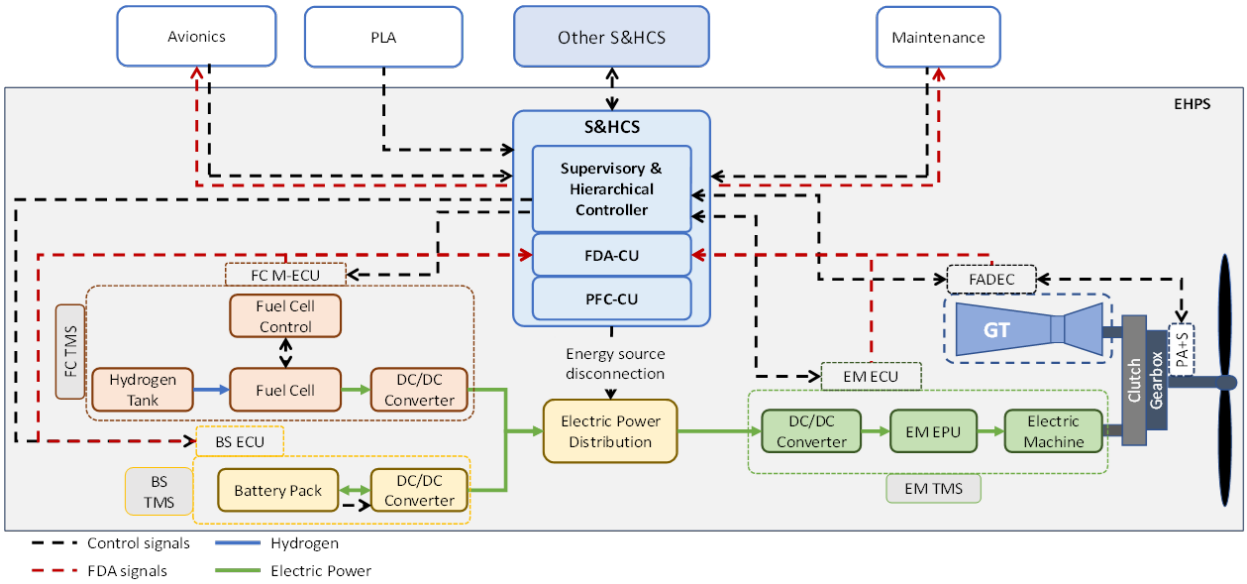


Figure 1. Architecture of one of the two HEPS assemblies of the AMBER regional aircraft.

Aircraft and HEPS mission profile

Due to the double power source, the HEPS mission profile has been constructed starting from the mission of a typical regional aircraft and defining the power demands limits on the two propulsion sources, up to identify the HEPS Operating Modes (OMs).

As pointed out in Table 1, the following OMs have been defined:

- *Check-in*, in which the SHCS validates the HEPS health-state and manages the power-up operation;
- *Eco*, in which the SHCS manages the power demands to minimize the noise and CO2 emissions of the HEPS, by limiting the GT power demand;
- *Boost*, in which the SHCS manages the power demands to maximize thrust while optimizing the HEPS efficiency;
- *Cruise*, in which the SHCS manages the power demands to maximize range or endurance, while optimizing the HEPS efficiency;
- *Hold*, in which the SHCS manages the power demands to maintain the thrust demand while cooling the electrical systems (the EM power demand is limited).

Table 1 - Mission phases (with related FHA ID), OMs and power demand limits.

Mission phase	FHA ID	OM	Power demand limits	
			GT	EM
Power-on	a	Check-in	Full	Full
Taxi-out	b	Eco	Limited	Full
Take-off	c	Boost	Full	Full
Climb	d	Boost	Full	Full
Acceleration	e	Boost	Full	Full
Cruise	f	Cruise	Limited	Full
Acc/dec	g	Boost	Full	Full
Descent	h	Hold	Full	Limited
Approach/landing	i	Hold	Full	Limited
Taxi-in	j	Hold	Full	Limited
Power-off	k	Check-out	Full	Full

Materials Research Proceedings 69 (2026) 689-694 https://doi.org/10.21741/9781644904251-122

Functional requirements of the HEPS SHCS

The SHCS functional requirements have been identified starting from aircraft- and engine-level requirements, up to allocate the following first-level capabilities:

- communication with external systems (avionics, PLA, SHCS of the other HEPS assembly, maintenance ECU);
- communication with HEPS subsystems;
- diagnosis of HEPS major faults;
- management of the propulsion power.

Failure types and severity categories

To develop the FHA, generalized Failure Types (FT) have been addressed, i.e.:

- *total loss* (FT1), i.e. a complete inability of implementing the function under exam, for the whole duration of the examined mission phase;
- *incorrect operation* (FT2), including partial and/or intermittent loss of a function, i.e. the function can be achieved with limited effectiveness for the whole duration of the mission phase and/or it can be achieved only for a limited duration of the mission phase;
- *inadvertent activation* (FT3), applicable to functions the implementation of which requires the pilots' intervention, in case that it unintentionally occurs.

Concerning the severity classification of the failures, it has been defined by evaluating the failure effects on aircraft, flight crew and passengers as recommended by [17], as well as on the propulsion system [15].

Results and discussion

The FHA demonstrated that only total losses (FT1) can determine a large reduction of aircraft safety margin. In particular, hazardous consequences can derive from two failures (Table 2):

- the inability to shut down the HEPS in case of emergency, caused by a total loss of communication with avionics (SHCS.116.1), impeding the pilots to send commands to the HEPS SHCS, or a total loss of the SHCS power management functions, once a shut-down command is received (SHCS.416.1)
- the inability to perform FDIA via in-flight BIT against propeller overspeed (SHCS.321.1c-i), thrust deviation (SHCS.322.1c-i), power deviation (SHCS.323.1c-i), overheating (SHCS.324.1c-i) or anomalous vibrations (SHCS.325.1c-i), in case that the fault occurs

Concerning the major consequences, the FHA identified 31 failure conditions, which can be essentially grouped into the following categories (Table 2):

- failure leading to the shutdown of one of the two HEPS power lines when the full power is requested to both GT and EM, causing a one-side inopera-tive condition (e.g. SHCS.113.1c-d, SHCS.113.2c-d)
- failure leading to the incorrect power management of the HEPS power lines (e.g. SHCS.114.1f, SHCS.114.2f, SHCS.414.1f, SHCS.414.2f)
- the inability to restore the HEPS functionality after an inadvertant shutdown (e.g. SHCS.116.3c-i) or an erroneous mode selection (e.g. SHCS.113.3b, SHCS.114.3b-e, SHCS.115.3b-g)
- a total loss or incorrect operation of all the SHCS power management func-tions, except the emergency shutdown (e.g. SHCS.411.1a, SHCS.411.2a, SHCS.412.1b, SHCS.412.2b, etc.). It is worth noting that these failure condi-tions, in conjunction with loss of protection against thrust deviation can lead to significant thrust in the opposite direction (HAZ)

Table 2 - Severity classifications with related FHA ID.

Failure ID from FHA	Description (Capability to…)	Severity	MTBF [FH^{-1}]
SHCS.116.1	… communicate with avionics for selecting the HEPS OM: Check-out	HAZ	10^{-7}
SHCS.321.1c-i	… perform FDIA via in-flight BIT to protect against propeller overspeed		
SHCS.322.1c-i	… perform FDIA via in-flight BIT to protect against thrust deviation		
SHCS.323.1c-i	… perform FDIA via in-flight BIT to protect against power deviation		
SHCS.324.1c-i	… perform FDIA via in-flight BIT to protect against overheating		
SHCS.325.1c-i	… perform FDIA via in-flight BIT to protect against anomalous vibrations		
SHCS.416.1	… manage the propulsion power demands once selected the OM: Check-out		
SHCS.113.1c-d **SHCS.113.2c-d** **SHCS.113.3b**	… communicate with avionics for selecting the HEPS OM: Boost	MAJ	10^{-5}
SHCS.114.1f **SHCS.114.2f** **SHCS.114.3b-e**	… communicate with avionics for selecting the HEPS OM: Cruise		
SHCS.115.1h-j **SHCS.115.2h-j** **SHCS.115.3b-g**	… communicate with avionics for selecting the HEPS OM: Hold		
SHCS.116.2c-i **SHCS.116.3b-i**	… communicate with avionics for selecting the HEPS OM: Check-out		
SHCS.321.2c-i **SHCS.321.3c-i**	… perform FDIA via in-flight BIT to protect against propeller overspeed		
SHCS.322.2c-i **SHCS.322.3c-i**	… perform FDIA via in-flight BIT to protect against thrust deviation		
SHCS.323.2c-i **SHCS.323.3c-i**	… perform FDIA via in-flight BIT to protect against power deviation		
SHCS.324.2c-i **SHCS.324.3c-i**	… perform FDIA via in-flight BIT to protect against overheating		
SHCS.325.2c-i **SHCS.325.3c-i**	… perform FDIA via in-flight BIT to protect against anomalous vibrations		
SHCS.411.1a **SHCS.411.2a**	… manage the propulsion power demands once selected the OM: Check-in		
SHCS.412.1b **SHCS.412.2b**	… manage the propulsion power demands once selected the OM: Eco		
SHCS.413.1c-e,g **SHCS.413.2c-e,g**	… manage the propulsion power demands once selected the OM: Boost		
SHCS.414.1f **SHCS.414.2f**	… manage the propulsion power demands once selected the OM: Cruise		
SHCS.415.1h-j **SHCS.415.2h-j**	… manage the propulsion power demands once selected the OM: Hold		

Funding
The project is supported by the Clean Aviation Joint Undertaking and its members in the framework of Grant Agreement n° 101102020 – AMBER. Funded by the European Union. Views and opinions expressed are however those of the author(s) only and do not necessarily reflect those of the European Union or Clean Aviation Joint Undertaking. Neither the European Union nor the granting authority can be held responsible for them.





References

[1] Fleming, G. G.; de Lépinay, I.; Schaufele, R. "Environmental Trends in Aviation to 2050", ICAO 2022 Environmental Report. https://www.icao.int/environmental-protection/Pages/Environmental-Trends.aspx (accessed online on November 2025).
[2] Zaporozhets, O.; Isaienko, V.; Synylo, K. "PARE preliminary analysis of ACARE FlightPath 2050 environmental impact goals", CEAS Aeronautical Journal, Vol. 12, 2021, pp. 653–667, https://doi.org/10.1007/s13272-021-00525-7
[3] Delbecq, S.; Fontane, J.; Gourdain, N.; Planès, T.; Simatos, F. "Sustainable aviation in the context of the Paris Agreement: a review of prospective scenarios and their technological mitigation levers", Progress in Aerospace Sciences, Vol. 141, 2023, n. 100920, https://doi.org/10.1016/j.paerosci.2023.100920
[4] Ansell, P. J. "Review of sustainable energy carriers for aviation: benefits, challenges, and future viability", Progress in Aerospace Sciences, Vol. 141, 2023, n. 100919, https://doi.org/10.1016/j.paerosci.2023.100919
[5] Kusmierek, A.; Galinski, C.; Stalewski W. "Review of the hybrid gas-electric aircraft propulsion systems versus alternative systems", Progress in Aerospace Sciences, Vol. 141, 2023, n. 100925, https://doi.org/10.1016/j.paerosci.2023.100925
[6] Ficca, A.; Marulo, F.; Sollo, A. "An open thinking for a vision on sustainable green aviation", Progress in Aerospace Sciences, Vol. 141, 2023, n. 100928, https://doi.org/10.1016/j.paerosci.2023.100928
[7] Adler, E. J.; Martins J. R. R. A. "Hydrogen-powered aircraft: fundamental concepts, key technologies, and environmental impacts" Progress in Aerospace Sciences, Vol. 141, 2023, n. 100922, https://doi.org/10.1016/j.paerosci.2023.100922
[8] CORDIS EU research results - innovAtive deMonstrator for hyBrid-Electric Regional application (AMBER), Fact sheet, Project description https://cordis.europa.eu/project/id/101102020 (accessed online on November 2025).
[9] Clean Aviation - innovAtive deMonstrator for hyBrid-Electric Regional application (AMBER), https://www.clean-aviation.eu/amber (accessed online on November 2025).
[10] Cameretti, M.C.; Del Pizzo, A.; Di Noia, L.P.; Ferrara, M.; Pascarella, C. "Modeling and investigation of a turboprop hybrid electric propulsion system", Aerospace 2018, 5, 123. https://doi.org/10.3390/aerospace5040123
[11] C. Motte et al. "Functional hazard assessment of the propulsion control system designed for a small hybrid electric aircraft". In Proceedings of Global Power and Propulsion Society, GPPS, Chania22, September 12th–14th, 2022.
[12] L. Serrao et al. "Open issues in supervisory control of hybrid electric vehicles: a unified approach using optimal control methods", Oil & Gas Science and Technology, Vol. 68, n. 1, 2013, pp.23-33, https://doi.org/10.2516/ogst/2012080
[13] SAE ARP4761A, "Guidelines and methods for conducting the safety assessment process on civil airborne systems and equipment", SAE International, 2023.
[14] SAE ARP4754B, "Guidelines for development of civil aircraft and systems", SAE International, 2023.
[15] EASA CS-E, "Certification specifications for engines", Amendment 3, European Aviation Safety Agency (EASA), 2010.
[16] EASA CS-P, "Certification specifications for propellers", Amendment 1, European Aviation Safety Agency (EASA), 2006.
[17] EASA CS-25, "Certification specifications for large aeroplanes", European Aviation Safety Agency (EASA), 2003.

Materials Research Proceedings 69 (2026) 695-700 https://doi.org/10.21741/9781644904251-123

Hydrogen-Enriched and Plasma-Assisted Flames for Lean Blow-Out Control in a Swirl-Stabilized Burner

Maria Grazia DE GIORGI[1,a *], Pasquale DI GLORIA[2,b], Sara BONUSO[3,c], Ekin Can KARASU[1,d]

[1]Department of Engineering for Innovation, University of Salento, Via per Monteroni, 73100 Lecce, Italy

[a]mariagrazia.degiorgi@unisalento.it, [b]pasquale.digloria@unisalento.it, [c]sara.bonuso@unisalento.it, [d]ekincan.karasu@unisalento.it

Keywords: Hydrogen Enrichment, Plasma-Assisted Combustion, Lean Blowout, Flame Stability, Methane-Hydrogen Flames

Abstract. Hydrogen enrichment increases the reactivity of methane flames but can reduce stability under lean conditions, limiting operability. This work investigates the enhancement of lean blowout (LBO) limits in methane-hydrogen blends through plasma-assisted combustion in a swirl-stabilized combustor at fixed thermal power. Experiments were performed with fuel mixtures containing 0%, 30%, 40%, 60%, 80%, and 100% H_2 by volume. While higher hydrogen content enhances flame reactivity, it also progressively reduces stability under lean operation. The application of non-thermal plasma was found to significantly extend the LBO limits across all tested blends by $\Delta\phi_{LBO} \approx 0.04$, effectively stabilizing hydrogen-enriched flames. These results highlight the potential of plasma-assisted combustion to improve flame operability and enable low-emission performance in lean hydrogen-containing fuel mixtures.

Introduction

Hydrogen is increasingly recognized as a promising fuel due to its zero carbon emissions during combustion. Its use is rapidly expanding as a key strategy to reduce CO_2 output in both energy production and transportation [1]. Upon combustion, H_2 primarily forms water, making it an environmentally friendly alternative to fossil fuels. While the long-term objective is the transition to 100% green hydrogen, in the short term blending hydrogen with natural gas, mainly methane, offers a practical approach to partially lower CO_2 emissions in gas turbines and industrial burners. Modern combustion systems are designed for "fuel flexibility," i.e., the capability to safely operate with varying hydrogen content, accommodating fluctuations in renewable energy availability [2]. Hydrogen differs significantly from methane in its combustion characteristics, exhibiting a much higher laminar flame speed (SL = 2.5 m/s for H_2 vs. 0.3 m/s for CH_4) [3]. These features enhance reaction rates but can make flame stabilization more difficult, particularly under lean conditions. Furthermore, hydrogen flames achieve higher adiabatic temperatures, potentially increasing NO_x formation; however, lean premixed operation can limit thermal NO_x due to lower oxygen availability and shorter residence times.

Several studies have explored how hydrogen enrichment affects methane flames in swirl-stabilized and dual-fuel burners. Marragou et al. [4] investigated flame stabilization regimes and pollutant emissions in a CH_4/H_2 dual swirl low-NOx burner. Patel et al. [5] analyzed hydrogen's impact on swirling and non-swirling methane flames. Kwak et al. [6] and Li et al. [7] studied the forced response of H_2/CH_4 flames in dual-nozzle swirl-stabilized setups. An et al. [8] examined flame stabilization mechanisms and shape transitions in a 3D-printed H_2-enriched CH_4/air low-swirl burner. Guo et al. [9] focused on the effect of hydrogen on swirl/bluff-body lean premixed flames, considering mixtures with ZH_2 = 0%, 40%, and 80%. Collectively, these works show that while hydrogen increases flame reactivity, it can also enhance dynamic instabilities.

Content from this work may be used under the terms of the Creative Commons Attribution 3.0 license. Any further distribution of this work must maintain attribution to the author(s) and the title of the work, journal citation and DOI. Published under license by Materials Research Forum LLC.

Materials Research Proceedings 69 (2026) 695-700 https://doi.org/10.21741/9781644904251-123

Despite these insights, the combined effects of hydrogen enrichment on flame behavior under partially premixed and swirl-stabilized conditions, particularly regarding flame stability and lean blowout (LBO), remain incompletely understood. Non-thermal plasma (NTP) systems such as dielectric barrier discharges (DBD) or nanosecond pulsed discharges operate at reduced electric fields of E/N = 100–300 Td and can promote oxidation reactions by directly generating O*, H*, and OH* radicals. Previous works [10-13] demonstrated that nanosecond discharges accelerate ignition kinetics and lower LBO thresholds. However, few studies have explored the combined effects of hydrogen enrichment and plasma activation in swirl-stabilized combustors. To address this gap, the present study examines methane flames with varying hydrogen content and evaluates how plasma-assisted combustion can improve LBO limits. Experiments were carried out with fuel blends containing 0%, 30%, 40%, 60%, 80%, and 100% H_2 by volume in a swirl-stabilized combustor. The focus is on understanding flame stabilization and operability under lean conditions, providing guidance for the development of hydrogen-enriched, low-emission combustion systems.

Experimental Setup

Flame stabilization at different levels of hydrogen enrichment was studied using an atmospheric-pressure swirl-stabilized burner. The setup consists of a central fuel injector mounted on a support nozzle and a quartz-windowed combustion chamber that allows for high-resolution optical access, as illustrated in Fig. 1.

Swirled flames were produced using an air-blast nozzle with an effective outlet area of 319 mm^2, representative of the geometric scale typical of aero-engine combustors, similar to the configuration reported by Kasabov et al. [14]. The nozzle includes two concentric air swirlers: Swirler 1 with a geometric swirl number of 0.76 and Swirler 2 with a swirl number of 0, followed by an air diffuser. Methane and hydrogen were injected axially through a central tube, while primary and secondary air streams were supplied through separate inlets located in the lower and upper sections of the nozzle holder.

The setup was enclosed in a Faraday cage to prevent interference from electromagnetic fields generated by the plasma discharge. The plasma actuator consists of a needle with a diameter of 1 mm and a length of 46 mm, positioned at the center of the nozzle with a blunt tip angle of 90°, serving as the high-voltage (HV) electrode. The nozzle itself acted as the grounded (GND) electrode. Experiments were performed at an inlet air temperature of 298 K. Fuel flow rates were adjusted for each case to maintain a constant thermal power of 4.6 kW. Fuel compositions ranged from pure methane to pure hydrogen, with intermediate blends containing 30%, 40%, 60%, and 80% hydrogen by volume. A summary of all operating conditions is provided in Table 1.

Materials Research Proceedings 69 (2026) 695-700 https://doi.org/10.21741/9781644904251-123

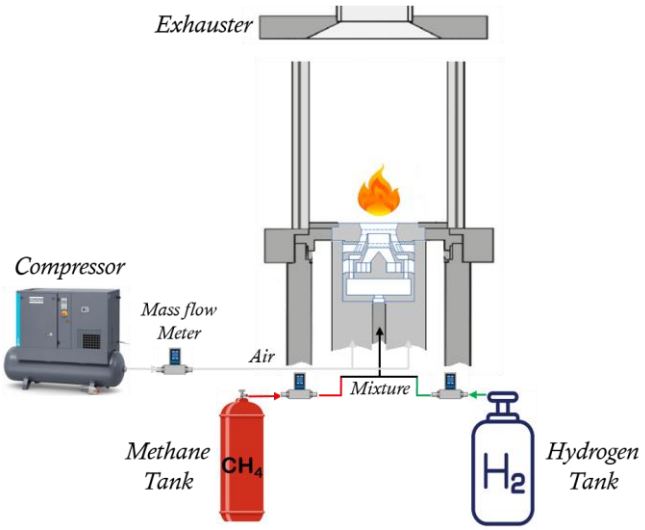


Fig. 1 Experimental Set-Up

Table 1 Experimental conditions

Case	H_2 volume [%]	Thermal Power [kW]	CH_4 [Nm^3/h]	H_2 [Nm^3/h]
1	0%	4.6	0.5	0
2	30%		0.44	0.2
3	40%		0.41	0.3
4	60%		0.35	0.5
5	80%		0.23	0.9
6	100%		0	1.6

Flame Characterization with H_2 Addition

The effect of hydrogen enrichment on flame structure was investigated by analyzing the spatial distribution of chemiluminescence intensity for different fuel mixtures. Fig. 2 shows representative flame images for three of the tested cases: pure methane (0% H_2), and blends with 30% and 40% hydrogen by volume. The images reveal a clear trend in flame morphology as the hydrogen content increases.

In the pure methane case (Test 1), the flame exhibits a moderately broad shape with less intense emission. Introducing 30% hydrogen (Test 2) results in a more compact and brighter flame, indicating higher reaction rates and increased flame stability. At 40% hydrogen (Test 3), the flame becomes even more intense and well-defined, suggesting that hydrogen enrichment enhances combustion reactivity and reduces geometric irregularities.

Materials Research Proceedings 69 (2026) 695-700 https://doi.org/10.21741/9781644904251-123

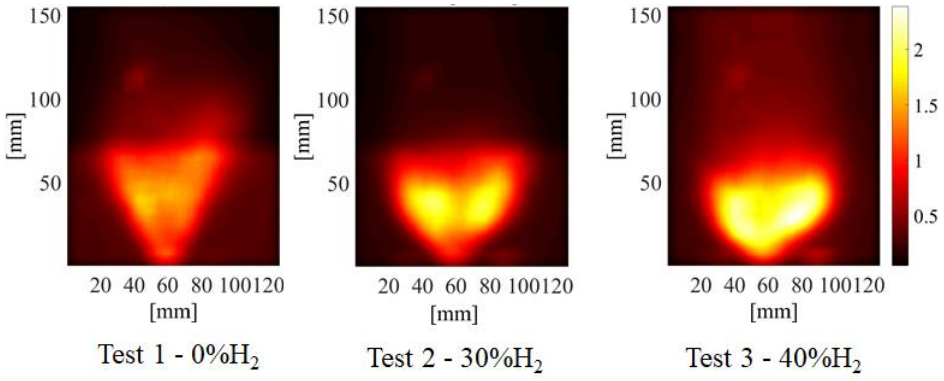


Fig. 2 Chemiluminescence imaging of broadband signals, reported as mean fields from pure methane to 40% hydrogen by volume.

Plasma-Assisted Combustion and LBO Improvement

For each hydrogen-containing fuel blend, combustion was investigated under the application of non-thermal plasma at different intensity levels, corresponding to 25%, 40%, 50%, and 75% of the generator's maximum amplitude. The electrical set-up consisted of HV sinusoidal amplifier, a current transformer, and a high voltage (HV) probe and an oscilloscope. The HV generator supplies the voltage in sinusoidal waveform *V(t)* at different amplitudes and a constant frequency of about 20 kHz.

The plasma application enhanced flame stability and extended lean blowout limits across all tested H_2/CH_4 mixtures, as shown in Fig. 3.

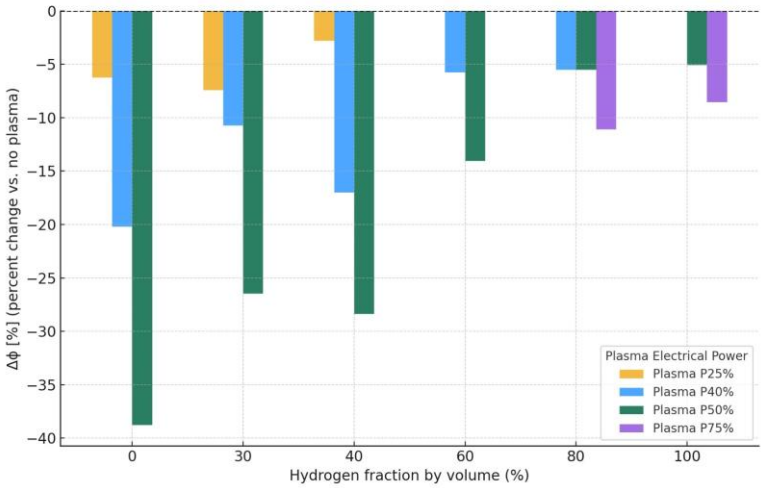


Fig. 3 Variation of LBO Equivalence Ratio with Plasma Activation

The effect of plasma on lean blowout was evaluated by measuring the percentage variation of the equivalence ratio ($\Delta\phi$) relative to the no-plasma case as a function of hydrogen fraction in the CH_4/H_2 mixture. Negative $\Delta\phi$ values indicate enhanced flame stability, allowing combustion at leaner conditions. All plasma-assisted conditions show negative $\Delta\phi$, confirming that the plasma stabilizes the flame. The stabilizing effect generally increases with plasma power, reaching a maximum around 50% of the generator amplitude (P50%), while higher power (P75%) produces a slightly smaller improvement, suggesting possible saturation or less efficient energy use. The effect is most pronounced at low to moderate H_2 fractions (0–40%), where plasma-generated radicals (H*, O*, OH*) significantly enhance reaction rates and flame stability. At high H_2 fractions (≥80%), the mixture is already highly reactive, and the additional contribution of plasma becomes less relevant. In summary, at 30–40% H_2, plasma power levels of 25–40% reduce the

LBO threshold by 10–20%, while higher power levels (50–75%) achieve reductions exceeding 30%. Overall, these results highlight the effectiveness of non-thermal plasma in extending lean blowout limits, particularly for moderately hydrogen-enriched methane flames.

Conclusions

This study demonstrates that hydrogen enrichment increases methane flame reactivity but reduces stability under lean conditions. Plasma-assisted combustion effectively extends lean blowout limits across all tested H_2/CH_4 blends, with the strongest stabilizing effect observed at low to moderate hydrogen fractions. Plasma-generated radicals accelerate reaction kinetics, improving flame stability and operability without requiring additional thermal power. These findings highlight the potential of non-thermal plasma as a tool to enhance combustion of hydrogen-enriched fuels and support the development of low-emission, lean-burning combustion systems.

Acknowledgements

This work was provided within the framework of the FFLECS Project funded by the European Union's Horizon Europe research and Innovation programme under Grant Agreement No 101096436 (CUP F83C23003480006). Views and opinions expressed are, however, those of the author(s) only and do not necessarily reflect those of the European Union or the granting authority. Neither the European Union nor the granting authority can be held responsible for them.



Additional support was provided by the PINUT project, funded by the European Union – NextGenerationEU, within the National Recovery and Resilience Plan (PNRR), Mission 4, Component 2, Investment 1.4, as part of the Sustainable Mobility Center initiative (Project CN_00000023, CUP: B43C22000440001).

Additional funding was provided by project GRACE, funded by the European Union – NextGenerationEU – National Recovery and Resilience Plan (PNRR) – Mission 4, Component 2, Investment 1.4 – Project CN_00000023 entitled 'Sustainable Mobility Centre CUP': F83C22000720001. Views and opinions expressed are, however, those of the author(s) only and do not necessarily reflect those of the European Union or the Secretariat-General, Directorate-General for Research, European Commission. Neither the European Union nor the European Commission can be held responsible for them.



References

[1] Amin M, Shah HH, Iqbal MA. Barriers to sustainable hydrogen production through renewable energy processes and their environmental impacts. Sustainable Energy Technologies and Assessments 72 (2024) 104075. https://doi.org/10.1016/j.seta.2024.104075

[2] Pan H, Geng S, Yang H, Zhang G, Bian H, Liu Y. Influence of H2 blending on NOx production in natural gas combustion: Mechanism comparison and reaction routes. International Journal of Hydrogen Energy 48 (2023) 784–797, ISSN 0360-3199. https://doi.org/10.1016/j.ijhydene.2022.09.251

[3] Liu Y, Zhang Y, Liu X, Liu Z, and Che D, Experimental and numerical investigation on premixed H2/air combustion, International Journal of Hydrogen Energy 2016;41(24): 10496-10506. https://doi.org/10.1016/j.ijhydene.2016.01.049

[4] Marragou S, Magnes H, Poinsot T, Selle L, Schuller T. Stabilization regimes and pollutant emissions from a dual fuel CH4/H2 and dual swirl low NOx burner. International Journal of Hydrogen Energy 2022; 47:19275–19288. https://doi.org/10.1016/j.ijhydene.2022.04.033

[5] Patel V, Shah R. Effect of hydrogen enrichment on combustion characteristics of methane swirling and non-swirling inverse diffusion flame. International Journal of Hydrogen Energy 2019; 44, 28316-28329. https://doi.org/10.1016/j.ijhydene.2019.09.076

[6] Kwak S, Choi J, Ahn M, Yoon Y. Effects of hydrogen addition on the forced response of H2/CH4 flames in a dual-nozzle swirl-stabilized combustor. International Journal of Hydrogen Energy 2022;47, 28139-28151. https://doi.org/10.1016/j.ijhydene.2022.06.117

[7] Li D, Wang R, Yang G, Wan J. Effect of hydrogen addition on the structure and stabilization of a micro-jet methane diffusion flame. International journal of Hydrogen Energy 2021; 46:5790-5798. https://doi.org/10.1016/j.ijhydene.2020.11.034

[8] An Q. et al., Flame stabilization mechanisms and shape transitions in a 3D printed, hydrogen enriched, methane/air low-swirl burner, International Journal of Hydrogen Energy 2021;46:14764-14779, https://doi.org/10.1016/j.ijhydene.2021.01.112

[9] Guo S, Wang J, Zhang W, Zhang M, Huang Z. Effect of hydrogen enrichment on swirl/bluff-body lean premixed flame stabilization International Journal of Hydrogen Energy 2020;45:10906-10919, https://doi.org/10.1016/j.ijhydene.2020.02.020

[10] Starikovskiy, A., & Aleksandrov, N. (2013). Plasma-assisted ignition and combustion. Progress in Energy and Combustion Science, 39(1), 61–110. https://doi.org/10.1016/j.pecs.2012.05.003

[11] Mehdi, G., Fontanarosa, D., Bonuso, S., De Giorgi, M.G. Ignition thresholds and flame propagation of methane–air mixture: detailed kinetic study coupled with electrical measurements of the nanosecond repetitively pulsed plasma discharges. Journal of Physics D: Applied Physics 55, 315202 (2022). https://doi.org/10.1088/1361-6463/ac6f2c

[12] Mehdi, G., De Giorgi, M.G., Bonuso, S., Shah, Z.A., Cinieri, G., Ficarella, A. Comparative analysis of flame propagation and flammability limits of CH_4/H_2/air mixtures with or without nanosecond plasma discharges. Aerospace 10, 224 (2023). https://doi.org/10.3390/aerospace10030224

[13] De Giorgi, M. G., Di Gloria, P., & Ficarella, Advanced multiscale modal and frequency analysis of swirling spray flame near to lean blowout. Case Studies in Thermal Engineering, (2024) 60, 104651. https://doi.org/10.1016/j.csite.2024.104651

[14] Kasabov P, Zarzalis N, Habisreuther P. Experimental Study on Lifted Flames Operated with Liquid Kerosene at Elevated Pressure and Stabilized by Outer Recirculation, Flow Turbulence and Combustion 2013; 90(3):605-619, https://doi.org/10.1007/s10494-013-9444-1

Materials Research Proceedings 69 (2026) 701-706 https://doi.org/10.21741/9781644904251-124

Numerical Modeling and Validation of a Water Electrolysis Propulsion System for CubeSats

Raviteja VEMULA[1,a *], Pratyush Kumar SINGH[1,b] and Maria Grazia DE GIORGI[1,c]

[1]University of Salento, Lecce, Italy

[a]raviteja.vemula@studenti.unisalento.it, [b]pratyushkumar.singh@studenti.unisalento.it, [c]mariagrazia.degiorgi@unisalento.it

Keywords: Water Electrolysis Propulsion (WEP), CubeSat, Micro Propulsion, Green Propellant, Proton Exchange Membrane (PEM) Electrolysis

Abstract This work presents the conceptual design and numerical modeling of a electrolysis based water propulsion system tailored for CubeSat applications. A Python based simulation framework models the complete electrolyze–store–burn cycle, integrating a Proton Exchange Membrane (PEM) electrolyzer, gas storage reservoirs, a catalytic ignition chamber, and an isentropic nozzle expansion stage. The system evaluated over an input power range of 3.95–9.7 W, with electrolyzer efficiencies ranging from 71% to 76%. At optimal conditions (P_c = 6 bar, T_c = 3300 K), the quasi-steady nozzle model predicts a theoretical specific impulse of 450.3 s. However, realistic pulsed operation includes startup and shutdown transients that reduce the effective specific impulse to 405 s approximately 10% performance penalty. Each operational cycle consumes around 1.25 g of water, producing sufficient thrust for CubeSat scale maneuvers. These performance metrics demonstrate alignment with small satellite propulsion requirements. The integrated model offers a foundational tool for linking electrochemical generation with thrust performance, supporting future development of green, multi-mode micro propulsion systems for agile CubeSat missions.

Introduction

The rapid growth of CubeSat missions has increased demand for compact, safe, and energy efficient propulsion systems. Traditional chemical and electric thrusters, designed for larger spacecraft, often exceed CubeSat limits in mass, complexity, and safety. This has led to a shift toward green propulsion technologies using nontoxic propellants. Water has recently become a strong candidate due to its availability, stability, and ease of handling. Electrolysis allows water to be split into hydrogen and oxygen, stored and combined to produce thrust an approach known as Water Electrolysis Propulsion (WEP).

Table 1: Summary of Representative Water Based Micro propulsion Studies.

Reference	Power[W]	Thrust+[N]	I_{sp} [s]	Propellant
Hwang et al. (2022) [1]	4.0 ~12	1.0	~430	H_2/O_2 (Electrolysis)
Porter et al. (PTD-1 / HYDROS-C) [2]	0.5 ~10	0.8	~300	Water (HYDROS-C)
Pothamsetti & Thangavelautham (2016) [3]	10.0 ~15	8.5	~420	Photovoltaic Electrolysis
This Work	4.0 ~10	0.9	~450	Water (PEM Electrolyzer)

This method combines electric and chemical propulsion, offering a clean, reusable solution for small satellites. Missions like NASA's HYDROS and PTD-1 [4], along with lab studies by Hwang et al. [1] and others [3], have demonstrated the feasibility of water-based propulsion. Table 1,

Content from this work may be used under the terms of the Creative Commons Attribution 3.0 license. Any further distribution of this work must maintain attribution to the author(s) and the title of the work, journal citation and DOI. Published under license by Materials Research Forum LLC.

Materials Research Proceedings 69 (2026) 701-706 https://doi.org/10.21741/9781644904251-124

summarizes key system performances, highlighting the balance between power, thrust, and efficiency.

System Architecture and Modeling

The proposed Electrolysis-based water propulsion system Propulsion (WEP) system is structured around four modular sub systems in Table 2, Each module is integrate into a Python based simulation pipeline that models the complete electrolyze–store–burn cycle, including mass and energy transfers. Key modeling assumptions include ideal gas behavior, quasi steady state operation, complete combustion, adiabatic nozzle expansion, and negligible heat losses.

Table 2: Subsystem Functions and Governing Equations in WEP Model

Subsystem	Inputs	Output and Equations
PEM Electrolyzer	Electrical power (P_{in}), current (I), current efficiency(η_c)	Hydrogen production rate: $\dot{n}H_2 = \eta_C \frac{1}{2F}$
		System efficiency: $\eta_{sys} = \frac{\dot{n}_{H_2} \cdot \mathrm{HHV}_2}{P_{in}}$
Gas Storage Unit	Molar flow rates ($\dot{n}H_2O_2$), Temperature(T)	Tank pressure: $P = \frac{nRT}{V}$ (Ideal Gas Law)
Catalytic Ignition Chamber	Tank pressure (P), temperature (T), catalyst mass (m_{cat})	Ignition delay:$\tau_{ign} = \frac{m_{cat}}{Ae^{-Ea/(RT)C_r}}$
		Combustion chamber pressure (P_c), temperature (T_c)
Nozzle Expansion	P_C, T_c, heat capacity ratio (γ), throat area (A_t)	Choked mass flow rate: $\dot{m} = \frac{P_C A_t}{\sqrt{Tc}} \sqrt{\frac{\gamma}{R}} \left(\frac{2}{r+1}\right)^{\frac{r+1}{2(r-1)}}$

PEM Electrolyzer Operation and Propellant Generation: The PEM electrolyzer splits water into hydrogen and oxygen in a 2:1 stoichiometric ratio of $2H_2O \rightarrow 2H_2 + O_2$.Hydrogen production follows Faraday's law, scaling linearly with stack current. The system efficiency, based on the Higher Heating Value (HHV) of hydrogen, improves from 71% to 76% across an input power range of 3.96–9.70 W. At 9.7 W over 45 minutes, the system consumes 1.255 g of water, producing 140.4 mg of H_2 and 1.114 g of O_2, stored at 5.67 bar. The specific impulse defined as:

$$I_{sp} = \frac{V_e}{g_0} \quad (1)$$

where V_e is the exhaust velocity, derived from nozzle thermodynamics. Total thrust is:

$$F = mV^{\cdot} + (pe - pa)Ae \quad (2)$$

with the pressure term clamped to ensure physical consistency during low-pressure operation.

Transient Efficiency and Impulse Modeling. While steady-state predictions suggest $i_{sp} = 450.3s$, practical pulsed operation yields $I_{sp,eff} = 450.3s$ due to transient effects. The thrust follows a trapezoidal profile comprising: (i) ignition delay τ_{ign} = 61.7 ms (at ϕ = 0.5), (ii) steady combustion plateau, and (iii) tail-off $\tau_{tailoff} \approx$ 138 ms. Impulse per pulse is approximated by integrating thrust over time:

Materials Research Proceedings 69 (2026) 701-706 https://doi.org/10.21741/9781644904251-124

$$I_{bit} = \int_0^{t_{burn}} F(t)dt \quad (3)$$

assuming a trapezoidal thrust profile with a linear ramp up(startup), steady plateau and linear decay(shutdown) then the impulse per pulse will be:

$$I_{bit} = \frac{1}{2}F \cdot \tau_{ign} + \mathrm{F} \cdot \left(t_{burn} - \tau_{ign} - \tau_{tailoff}\right) + \frac{1}{2}F \cdot \tau_{tailoff} \quad (4)$$

Transient efficiency is defined as:

$$\eta_{transient} = \frac{\tau_{ign}+\tau_{tailoff}}{2t_{burn}} \quad (5)$$

reaching ~ 98% at t_{burn} = 5 s and dropping to ~ 67% for short 0.3 s pulses. The ignition delay varies quadratically with equivalence ratio:

$$\tau_{ign}(\phi) = k_{scale}\,(-0.4394\phi^2 + 0.9357\phi + 0.4087) \quad (6)$$

Electrolysis to Thrust Performance: To quantify system level performance, a detailed parametric analysis was conducted across input power levels, focusing on a 45-minute accumulation window. Once the tank pressure reaches the design threshold of 6 bar, combustion is initiated in a catalyst assisted ignition chamber. Solenoid valves deliver 50ms gas pulses, triggering ignition with a 61.7ms delay. The resulting combustion raises the chamber temperature to approximately 3300 K, producing a choked mass flow of 205.08 mg/s. This generates 0.815 N of thrust and achieves a specific impulse of 405.3 s during a 1 second burn. These values are validated against Cantera and Rocket CEA simulations, showing agreement of and I_{sp}values within 2% of predicted results in Fig. 5.

Table 3: Thruster Performance vs. Electrolyzer Power (45 min accumulation)

Power [W]	p_{H2} [bar]	p_{O2} [bar]	$P_{c,eff}$ [bar]	Thrust [N]	I_{sp} [s]
3.96	2.16	2.16	2.46	0.372	166.3
5.87	3.29	3.29	4.72	0.713	318.9
7.78	4.46	4.46	6.00	0.815	405.3
9.70	5.67	5.67	6.00	0.815	405.3

Fig. 1,2, illustrates the relationship between effective chamber pressure $P_{c,\mathrm{eff}}$ and electrolyzer power under a fixed 45-minute accumulation period. At lower input power, less propellant is produced, resulting in lower tank and chamber pressures. As power increases, accumulated volumes of H_2 and O_2 rise, increasing chamber pressure. The pressure reaches the 6 bar design limit at approximately 7.15 W, beyond which it saturates due to nozzle constraints.

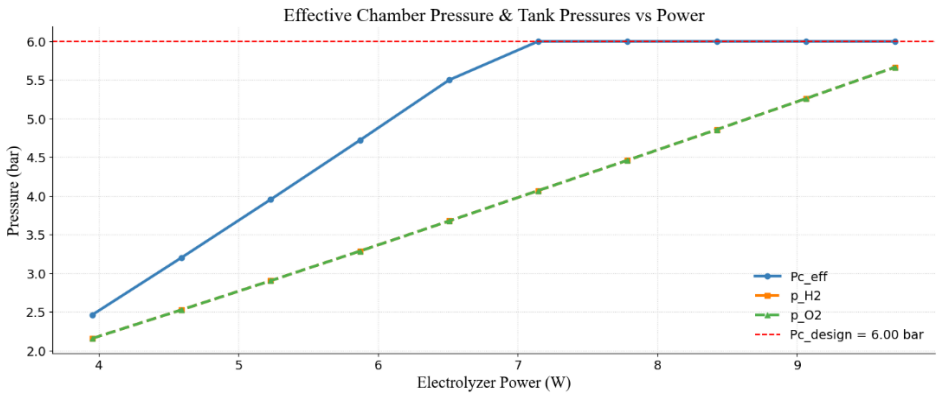


Figure 1: Effective chamber pressure Pc,eff vs. input power (45 min accumulation). Chamber pressure increases with power, saturating at 6 bar.

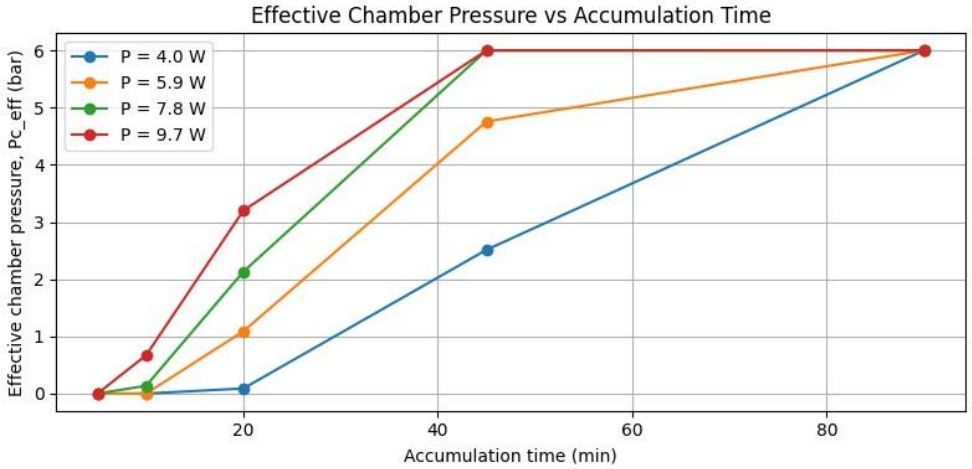


Figure 2: Tank and chamber pressures vs. input power. All pressures increase with power due to higher propellant generation.

This saturation behavior is further confirmed by the thrust and specific impulse trends shown in Table 3 and Fig. 4. Once P_c reaches the maximum limit, further increases in power do not yield higher thrust, indicating diminishing returns beyond 7.5 W.

A performance trade-off analysis shows that at 4 W, full pressurization takes up to 90 minutes. In contrast, systems operating between 7.8–9.7 W achieve optimal performance within 40–45 minutes—well within a typical CubeSat daylight orbit. This enables synchronization between solar charging and thrust execution, supporting flexible and energy efficient mission planning.

Materials Research Proceedings 69 (2026) 701-706 https://doi.org/10.21741/9781644904251-124

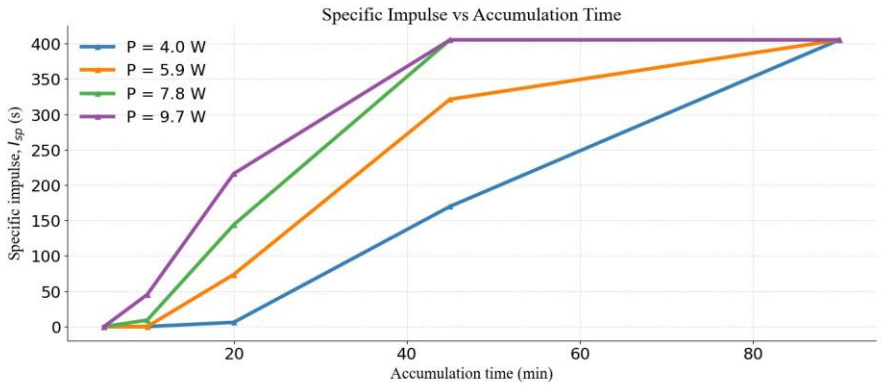


Figure 3: Specific Impulse vs. Accumulation time.

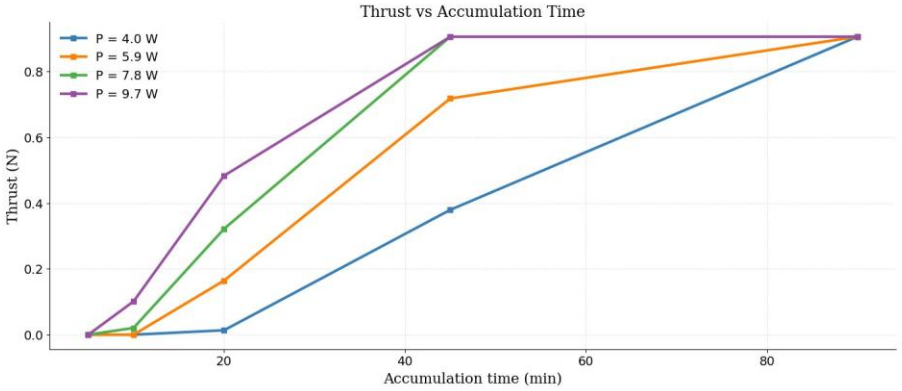


Figure 4: Thrust vs. Accumulation time.

Validation using Cantera and Rocket CEA:

The model was validated against Cantera (GRI-Mech 3.0) and Rocket CEA. At $P_c = 6$ bar and $\phi = 1.0$, the simulation predicted $T_c \approx 3300$ K and $I_{sp} \approx 405$ s, while Cantera predicts $T_c \approx 3320$ K and $I_{sp} \approx 410$ s, Rocket CEA yielded $T_c \approx 5359$ K and $I_{sp} \approx 351$ s. These deviations stemmed from differences in enthalpy and mixture assumptions. After adjusting combustion enthalpy and setting $\phi \approx 1.0$, the results aligned with actual T_c and I_{sp} values within 2% of Cantera values, confirming accurate integration of electrolysis, combustion, and nozzle flow in the simulation.

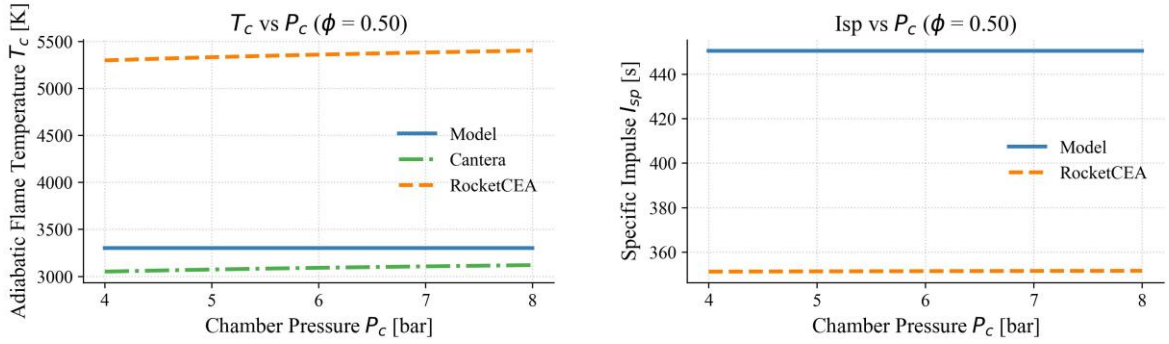


Figure 5: Comparison of I_{sp} and T_c vs. P_c for the model, Cantera, and Rocket CEA.

Conclusion and Future Work

This study presented the modeling and validation of a Water Electrolysis Propulsion (WEP) system for CubeSat scale applications. The integrated simulation—combining PEM electrolysis, gas storage, catalytic ignition, and nozzle flow—achieved 0.8 N thrust, 405 s specific impulse, and up to 76% efficiency at 10 W input, aligning with CubeSat mission requirements. Validation against Cantera and Rocket CEA showed less than 2% deviation with the actual adjusted final $T_c$and I_{sp}values, confirming model accuracy. A key outcome was the identification of a 6-bar chamber pressure cap, highlighting a performance saturation point critical for power and energy planning. Future efforts will include experimental hardware validation, regenerative fuel cell integration for water recycling, and exploration of plasma assisted ignition. Hybridization with vaporizing liquid micro thrusters (VLMs) also proposed to support dual mode, green micro propulsion for next-generation CubeSats.

References

[1] M. Hwang, T.-S. Rho, H. J. Lee, Conceptual design and performance analysis of water electrolysis propulsion system with catalytic igniter for CubeSats, Acta Astronautica, vol. 200, pp. 316–328, 2022. https://doi.org/10.1016/j.actaastro.2022.08.022

[2] A. Porter, M. Freedman, R. Grist, C. Wesson, M. Hanson, Flight qualification of a water electrolysis propulsion system. In: 35th Annual Small Satellite Conference, Utah, USA. SSC21-XI-06, 2021. https://doi.org/10.1016/j.actaastro.2016.11.001

[3] R. Pothamsetti and J. Thangavelautham, Photovoltaic Electrolysis Propulsion System for Interplanetary CubeSats, Proceedings of the IEEE Aerospace Conference, Big Sky, MT, 2016, pp. 1–10. https://doi.org/10.1109/AERO.2016.7500931

[4] K. James et al., Performance Characterization of the HYDROS™ Water Electrolysis Thruster, 2015. https://api.semanticscholar.org/CorpusID:56439844

Materials Research Proceedings 69 (2026) 707-712 https://doi.org/10.21741/9781644904251-125

Propeller Aerodynamics Under Non-Uniform Inflows

Sara MONTAGNER[1,a *], Manuel ZANNONE[1,b], Jacopo SERPIERI[1,c] and Gioacchino CAFIERO[1,d]

[1]Department of Mechanical and Aerospace Engineering, Politecnico di Torino, Corso Duca degli Abruzzi 24, Turin, Italy

[a]sara.montagner@polito.it, [b]manuel.zannone@polito.it, [c]jacopo.serpieri@polito.it, [d]gioacchino.cafiero@polito.it

Keywords: UAM, UAVs, Propeller, Non-Uniform Inflow, Aerodynamics

Abstract. Urban Air Mobility (UAM) is highly dependent on Unmanned Aerial Vehicles (UAVs) operating in complex urban environments, where propellers often encounter non-uniform inflows. These conditions can deteriorate the performance and stability of the vehicle, making standard uniform-inflow assumptions unrealistic and even dangerous for the prediction of the performance of UAVs. It is therefore of paramount importance to develop the capability to accurately reproduce in a repeatable manner such complex inflow conditions. This paper presents an experimental investigation of a propeller wake under controlled, non-uniform sheared inflow. Using Particle Image Velocimetry (PIV), the wake of a D=0.3 m propeller was characterized when operating in forward flight conditions. A modular fan array generated both uniform baselines and four linear shear rates. The results show that the sheared inflow creates an asymmetric wake with reduced vorticity magnitude and a radial streamtube expansion. Furthermore, Turbulent Kinetic Energy (TKE), highly localized in uniform flow, becomes significantly more diffused under sheared conditions, indicating altered turbulent mixing. These findings highlight the critical impact of the inflow conditions on the on the wake development.

Introduction

The viability of Urban Air Mobility (UAM) requires a step forward in the deployment of Unmanned Aerial Vehicles (UAVs), especially when operating in complex urban environments. Applications such as logistics and surveillance require low-altitude flight, where UAV propellers inevitably encounter non-uniform inflows, owing to the presence of unstructured environments, buildings and street canyons. These conditions significantly deviate from the ideal, uniform flow assumptions typically employed especially at a preliminary design stage. Operating in such perturbed aerodynamic environments can deteriorate propeller efficiency, induce unsteady loads, and compromise flight stability. Consequently, standard performance models, which assume uniform inflow, are often unrealistic. This discrepancy can lead to the underestimation of energy consumption and control effort required for stable flight, particularly in challenging scenarios like urban delivery, where adverse atmospheric disturbances are common [1].

Despite the clear operational need, many assessments of UAV propulsion systems and aerodynamics still rely on simplified inflow assumptions, potentially leading to overestimation of performance and reliability. Although the detrimental impact of non-uniform inflows is well-recognized, dedicated studies in the literature remain limited, particularly on the experimental side. Much of the available research relies on numerical simulations (CFD) to investigate the aerodynamic performance and forces on propellers subjected to wind fields [2]. Experimental work, in turn, has provided comprehensive force and flow-field datasets for propellers in steady non-axial (yawed) inflow conditions [4]. However, more complex simulations and experimental studies highlight that accurately modeling gust effects is crucial for predicting power consumption, as simplified aerodynamic models fail to capture performance degradation under high gust

Content from this work may be used under the terms of the Creative Commons Attribution 3.0 license. Any further distribution of this work must maintain attribution to the author(s) and the title of the work, journal citation and DOI. Published under license by Materials Research Forum LLC.

intensity [3]. Furthermore, accurately and repeatably simulating complex spat-temporal disturbances, such as the sheared inflows investigated in this work, remains a significant challenge for conventional wind tunnel facilities [3]. To address this gap, the present study takes a first step by experimentally characterizing the wake flow field of a propeller operating under controlled sheared inflow conditions.

Experimental setup

Experiments were performed in the indoor flight arena at Politecnico di Torino. The facility is equipped with a WindShaper modular fan array [5], which comprises an 8 × 6 matrix of modules with individually controllable fans. This setup creates a 2 m × 1.5 m active test section, enabling the generation of both uniform and precisely controlled non-uniform inflow profiles.

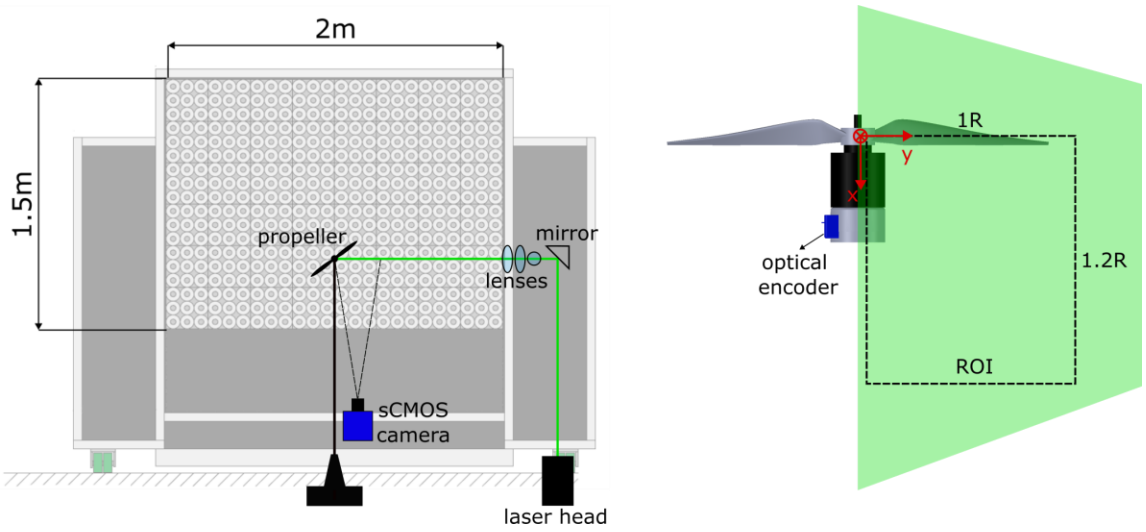


Figure 1: Schematic of the experimental setup.

The propeller used in the experiments was 3D-printed in resin with a diameter of D = 2R = 0.3 m, following the geometry from [6]. It was actuated by a brushless motor and an Electronic Speed Controller (ESC), controlled via an Arduino UNO board. An optical rotary encoder monitored the propeller's rotational speed, which was held constant at 2000 rpm for all tests. The propeller was positioned 1 m downstream from the fan array, with its rotation plane parallel to the fan wall to simulate forward flight. Particle Image Velocimetry (PIV) was employed to characterize the propeller's wake field; a schematic of the setup is shown in Figure 1. The flow was seeded with 1 µm diameter droplets generated by a Laskin nozzle. The region of interest was illuminated by a dual-pulse Nd:YAG laser (200 mJ/pulse) operating at 15 Hz. The laser beam was shaped into a 1 mm thick sheet, and the time separation between pulses was set to Δt =140 µs. PIV images were acquired using a 5.5 MP sCMOS camera (2560 × 2160 pixels) equipped with a 60 mm focal length lens set to $f_{\#}$=11. The imaged area covered approximately 1 R (radial, y) by 1.2 R (streamwise, x) downstream of the propeller, yielding a digital resolution of 13.5 px/mm. For each test case, 2200 image pairs were acquired. Raw images were pre-processed by subtracting the historical minimum to each acquired image in the dataset. Vector fields were computed using the PaIRS software [7] via a multi-step cross-correlation algorithm, using a final interrogation window of 32 × 32 pixels with 75% overlap. This resulted in a final vector spacing of 0.59 mm.

The experimental campaign focused on two primary inflow scenarios: uniform and non-uniform (shear flow). For the uniform inflow case, the advance ratio, defined as $J = U/(nD)$ was systematically varied over the range $0.2 \leq J \leq 0.7$. For the non-uniform cases, the WindShaper generated linear shear flow profiles across the propeller disk (in the y-direction). In these

Materials Research Proceedings 69 (2026) 707-712 https://doi.org/10.21741/9781644904251-125

configurations, the advance ratio, calculated using the velocity at the propeller hub ($y/R = 0$), was varied within the range $0.4 \leq J \leq 0.6$. Four distinct shear intensities were investigated, defined by the tip-to-tip velocity difference (ΔV_k) across the propeller: 1, 1.5, 2, and 3 m/s. These cases are hereafter denoted as SR_1 through SR_4, respectively.

Results

The analysis begins with the uniform inflow conditions, which serve as a baseline for the subsequent sheared cases. Figure 2 illustrates the normalized time-averaged flow fields of the streamwise component of the velocity, for three representative advance ratio $\boldsymbol{J} = 0.4$, 0.5 and 0.6. These baseline cases depict the classic propeller slipstream structure, where the influence of $\boldsymbol{J}$ on the flow acceleration behind the rotor and the subsequent wake development is clearly visible. In particular, as the advance ratio increases, we notice a lower slipstream contraction, as expected.

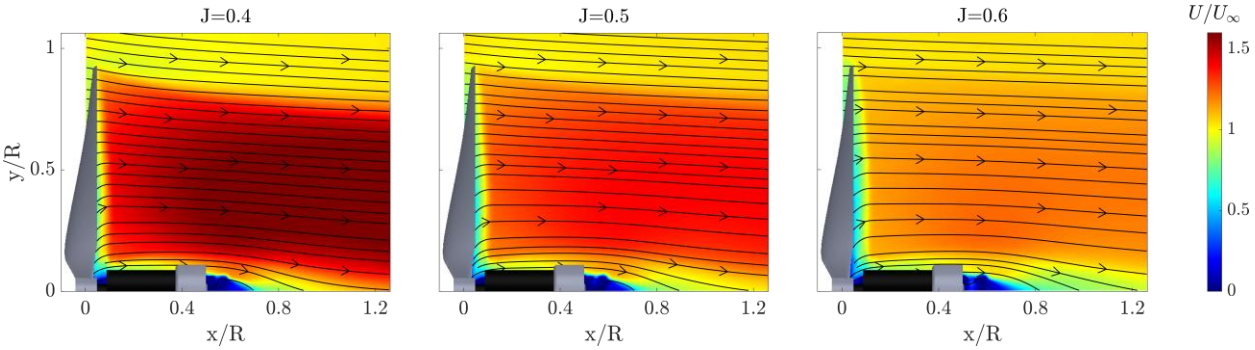


Figure 2: Time-averaged flow fields of the normalized streamwise velocity component. Cases of uniform inflow at J= 0.4, 0.5 and 0.6.

When introducing a sheared inflow, clear modifications in the wake topology are observed. This effect is highlighted in Figure 3, which displays the normalized out-of-plane vorticity (Ω_z) contours for the $J = 0.4$ case. The figure contrasts the baseline uniform inflow (a) against the four increasing shear rates, SR_1 to SR_4 (b-e). Two primary observations emerge. First, a progressive reduction in the overall vorticity magnitude is observed as the inflow shear rate increases. This distortion is an inevitable consequence of the inflow condition: a sheared flow imposes a non-uniform velocity U across the propeller disk. This, in turn, locally modifies the advance J and thus the aerodynamic loading on different sections of the blade, leading to an asymmetric and deformed wake structure.

Materials Research Proceedings 69 (2026) 707-712 https://doi.org/10.21741/9781644904251-125

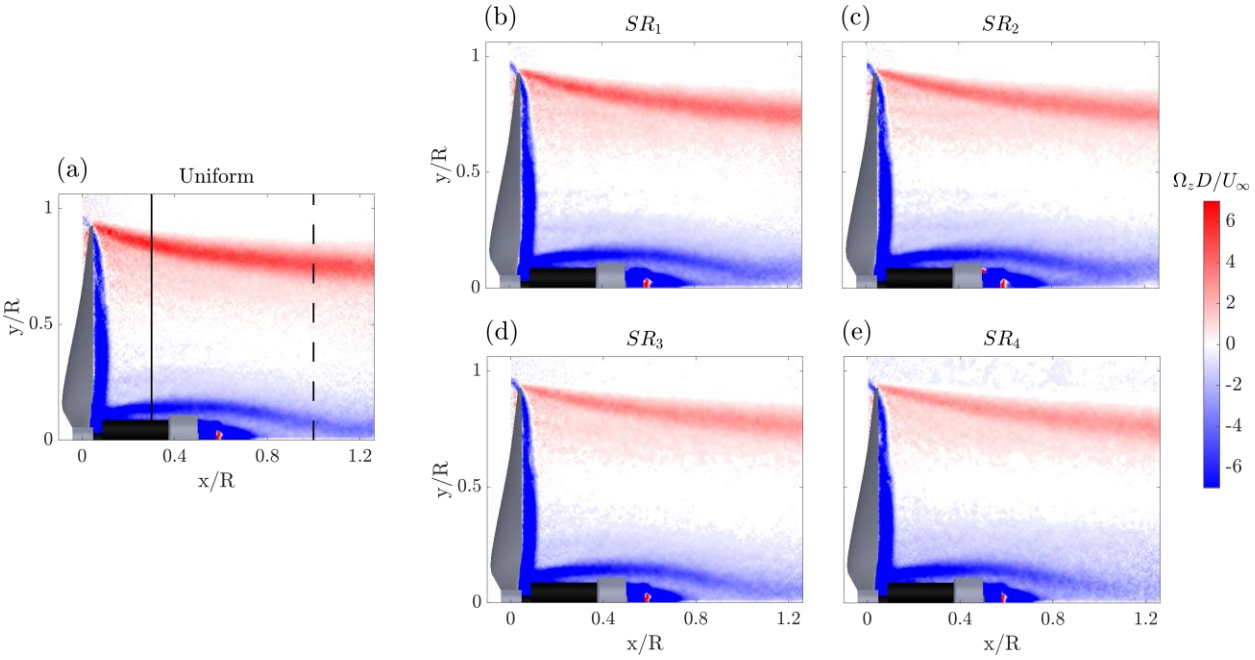


Figure 3: Time-averaged flow fields of the normalized out-of-plane vorticity $\boldsymbol{\Omega_z}$. Cases at $\boldsymbol{J = 0.4}$. (a) Uniform inflow. (b-e) Increasing sheared inflow from $\boldsymbol{SR_1}$ to $\boldsymbol{SR_4}$. The vertical solid ($\boldsymbol{x/R = 0.3}$) and dashed ($\boldsymbol{x/R = 1}$) lines in (a) indicate the reference stations selected for subsequent analysis.

To provide a more quantitative observation, Figure 4 shows the radial profiles of the normalized vorticity at the two reference stations identified by the two black lines in Figure 3(a). The results are presented for two advance ratios, $\boldsymbol{J} = 0.4$ and $\boldsymbol{J} = 0.6$. Within each plot, the solid lines refer to the station closer to the blades ($\boldsymbol{x/R} = 0.3$), while the dashed lines represent the station further downstream ($\boldsymbol{x/R} = 1$). The different colors distinguish the uniform inflow case from the four sheared conditions ($\boldsymbol{SR_1 - SR_4}$). Analyzing the near-wake station at $\boldsymbol{x/R} = 0.3$, two distinct peaks of opposite sign are evident. The negative peak at lower $\boldsymbol{y/R}$ corresponds to the mean trace of the hub vortices, which roll up near the motor, while the positive peak at higher$\boldsymbol{y/R}$ marks the mean trace of the tip vortices detaching from the blade tips and evolving along the wake. Focusing on this positive peak, it is clear that as the inflow shear rate increases, its intensity progressively decreases. Moreover, the location of the peak shifts at higher radial positions ($\boldsymbol{y/R}$), indicating an expansion of the streamtube in the analyzed region. By comparing the two plots, it is also evident that this combined effect (reduction in intensity and outward shift) is more pronounced at the lower advance ratio.

To further investigate the wake's turbulent characteristics, the velocity field is decomposed into its mean (U) and fluctuating (u') components using Reynolds decomposition. From the fluctuating parts, the Turbulent Kinetic Energy is computed as $TKE = {}^{1}/_{2}\left(\overline{u'^2} + \overline{v'^2}\right)$, considering only the measured components of the velocity fluctuations.

Materials Research Proceedings 69 (2026) 707-712 https://doi.org/10.21741/9781644904251-125

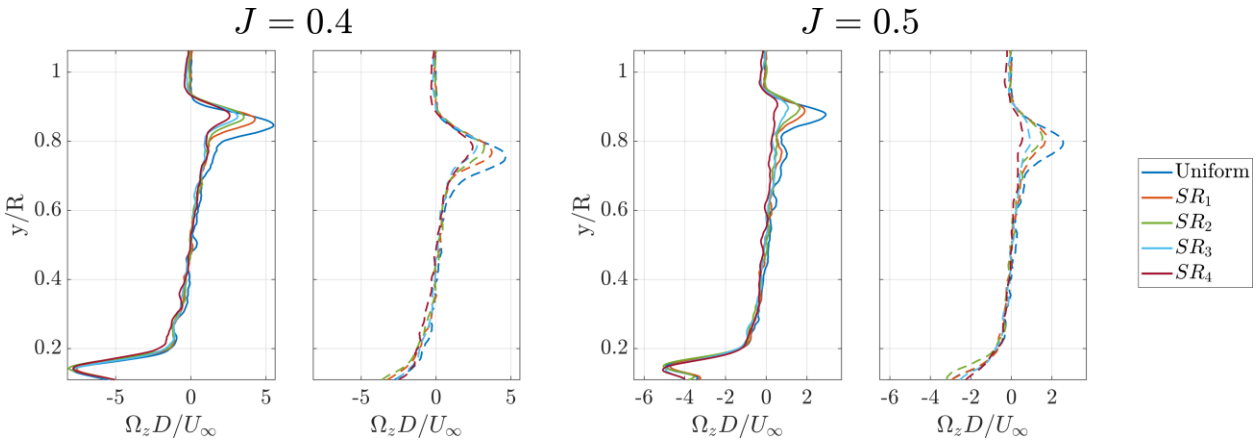


Figure 4: Radial profiles of normalized out-of-plane vorticity ($\boldsymbol{\Omega_z}$) for $\boldsymbol{J = 0.4}$ (left) and $\boldsymbol{J = 0.5}$ (right). Solid lines correspond to the near-wake station ($\boldsymbol{x/R = 0.3}$) and dashed lines to the far-wake station ($\boldsymbol{x/R = 1}$).

Figure 5 shows the radial profiles of the TKE at the same downstream stations ($x/R = 0.3$ and $x/R = 1$) and for the same advance ratios ($J = 0.4$ and $J = 0.5$) analyzed for the vorticity. A clear distinction emerges between the inflow conditions. For the uniform inflow cases, the TKE is highly concentrated, showing a sharp peak co-located with the mean tip vortex trace. This indicates that turbulence generation is primarily localized in that region. Conversely, in the presence of sheared inflow, the TKE is more diffused and spread out across the entire radial extent of the wake and is less localized in the tip region, suggesting that the incoming shear promotes a more widespread turbulence production and mixing.

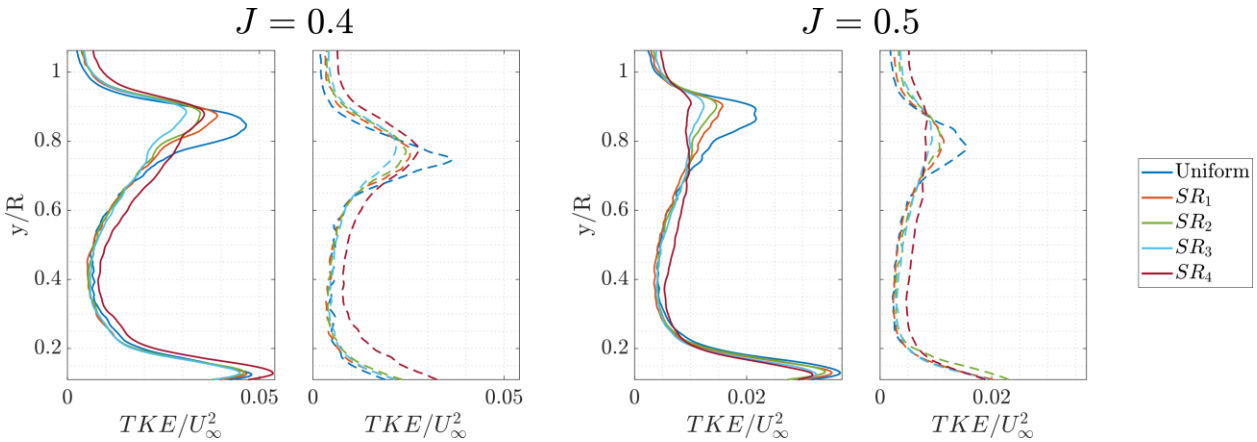


Figure 5: Radial profiles of normalized TKE for $\boldsymbol{J = 0.4}$ (left) and $\boldsymbol{J = 0.5}$ (right). Solid lines correspond to the near-wake station ($\boldsymbol{x/R = 0.3}$) and dashed lines to the far-wake station ($\boldsymbol{x/R = 1}$).

Summary and outlooks

This study presented an experimental PIV analysis of a propeller wake under both uniform and controlled sheared inflow conditions. The uniform inflow cases served as a baseline, exhibiting the expected slipstream contraction which diminished with increasing advance ratio $\boldsymbol{J}$. The introduction of a linear sheared inflow was shown to fundamentally alter the wake topology. The local changing of the operating conditions creates an asymmetric development of the wake, characterized by a reduction in the mean tip vortex vorticity and a radial expansion of the streamtube in the region under investigation. These effects are more pronounced at lower advance

ratios. Furthermore, the turbulence characteristics were significantly modified: while the TKE is highly localized in the tip vortex core for uniform flow, it becomes broadly diffused across the wake under shear, indicating enhanced turbulent mixing.

These results confirm that even in the simplest conditions of a linearly sheared inflow, the wake evolution is clearly affected, highlighting the limitations of uniform-inflow assumptions for UAM applications.

Acknowledgments
This study was carried out within the MOST – Sustainable Mobility National Research Center and received funding from the European Union Next-GenerationEU (PIANO NAZIONALE DI RIPRESA E RESILIENZA (PNRR) – MISSIONE 4 COMPONENTE 2, INVESTIMENTO 1.4 – D.D. 1033 17/06/2022, CN00000023). This manuscript reflects only the authors' views and opinions, neither the European Union nor the European Commission can be considered responsible for them. SM was supported by a scholarship funded through the WINDED Scalability Project, (PIANO NAZIONALE DI RIPRESA E RESILIENZA (PNRR) – MISSIONE 4 COMPONENTE 2, INVESTIMENTO 1.4 – D.D. 1033 17/06/2022, CN00000023**).**

References

[1] Betti Sorbelli, F. (2024). UAV-Based Delivery Systems: A Systematic Review, Current Trends, and Research Challenges. ACM Journal of Autonomous Transportation Systems, 1(3), Article 12. https://doi.org/10.1145/3649224

[2] Zhang, C., Xie, S. & Qin, T., Aerodynamic Analysis of Small Propeller in Wind Field Using CFD, 4th International Conference on Sustainable Energy and Environmental Engineering (ICSEEE 2015), 2015. https://doi.org/10.2991/icseee-15.2016.148

[3] Park, S., Lee, S., Im, B., Lee, D. & Shin, S., Improvement of a multi-rotor UAV flight response simulation influenced by gust, Aerospace Science and Technology, 134, 108156, 2023. https://doi.org/10.1016/j.ast.2023.108156

[4] Cerny, M. & Breitsamter, C., Investigation of small-scale propellers under non-axial inflow conditions, Aerospace Science and Technology, 106, 106048, 2020. https://doi.org/10.1016/j.ast.2020.106048

[5] Noca, F., Bujard, T., Visvaratnam, G., Catry, G., & Bosson, N. (2021). Flow Profiling in a Windshaper for Testing Free-Flying Drones in Adverse Winds. HES-SO University of Applied Sciences and Arts Western Switzerland, and WindShape, Geneva, Switzerland. https://doi.org/10.2514/6.2021-2577

[6] Casalino, D., Grande, E., Romani, G., Ragni, D., & Avallone, F. (2021). Definition of a benchmark for low Reynolds number propeller aeroacoustics. Aerospace Science and Technology, 113, 106707. https://doi.org/10.1016/j.ast.2021.106707

[7] Paolillo, G. & Astarita, T., PaIRS-UniNa: a robust and accurate free tool for digital particle image velocimetry and optical camera calibration, 21st International Symposium on Application of Laser and Imaging Techniques to Fluid Mechanics, 2024. https://doi.org/10.55037/lxlaser.21st.120

Materials Research Proceedings 69 (2026) 713-717 https://doi.org/10.21741/9781644904251-126

Thermo-structural Design of Composite Pressure Vessels for Hydrogen Aircraft

Luigi Maria CARDONE[1,a], Vittorio MEMMOLO[1,b*]

[1]Department of Industrial Engineering, University of Naples Federico II, Via Claudio 21, 80125 Naples, Italy

[a]luigimaria.cardone@unina.it, [b]vittorio.memmolo@unina.it

Keywords: Hydrogen Tanks, Sustainable Mobility, Aircraft Design, Composite Structure, Thermal Insulation

Abstract. Storage of liquid hydrogen in new generation aircraft is deemed crucial yet complex due to the cryogenic conditions involved. As a consequence, a multifunctional structure needs to be detailed design to meet the means of compliance for this kind of system. This paper showcases the pressure vessel design to equip a hydrogen fueled regional aircraft. The storing system is designed in detail considering different solutions. First a simplified model is used to study the trends of specific figure of merits while changing the stored mass. This shows the feasibility of the design when limited time duration is considered. Then, a high fidelity thermostructural analysis is carried out to verify local stresses and temperature of the system. Although, the capability of the pre-designed tank to withstand the operative conditions can be verified, the interlaminar stresses due to the multi-layered nature of the mechanical system become very high and need to be accommodated by a specific retaining system.

Introduction

On the way to sustainable mobility, aircraft design is experiencing a paradigm shift in the way propulsive technologies and architectures are conceived. Specifically, the new generation of aircraft requires electric powertrain to achieve net zero carbon emissions by 2050 [1]. In this context, green hydrogen is considered the energy carrier of the future as it can be conveyed to be burnt by turbofan or distributed to generate electricity to feed electric engines. However, despite the advancements in this sense, there is still a strong gap in the development of auxiliary systems which needs to be redesigned according to the new requirements.

One of the major concerns is the storing and deployment of fuel because the cryogenic temperatures play a critical role. Different possibilities in storing hydrogen are available, mostly including crystal confinement, compression and liquefaction. Among them, compressed and liquid forms can be carried on board. However, the former requires higher volumes, becoming unfeasible for flight. Instead higher energy density can be achieved in liquid form, making it attractive where weight limitations apply. However, hydrogen needs to be cooled down to extremely low temperatures until it becomes a liquid, opening a very challenge situation. As a matter of facts, improved storage methods are essential to realize the full potential of hydrogen as the new energy carrier in aviation [2]. In addition, to design appropriately hydrogen tanks, preliminary design of aircraft and its architecture need to be addressed. Afterward, the design of the tank can be performed with different degrees of fidelity [3].

There are several solutions to address these challenges, which have different strengths and drawbacks. Among these, the current paper presents the design of a multifunctional pressure vessel made of different structural and insulation layers coupled together with different solutions. Firstly, 50 passengers aircraft is preliminary conceived, returning that 492 kg of hydrogen is necessary to fulfill the considered flight mission [4]. The design carried out is then used to obtain a baseline

Content from this work may be used under the terms of the Creative Commons Attribution 3.0 license. Any further distribution of this work must maintain attribution to the author(s) and the title of the work, journal citation and DOI. Published under license by Materials Research Forum LLC.

Materials Research Proceedings 69 (2026) 713-717 https://doi.org/10.21741/9781644904251-126

tank model, whose geometrical and material properties can be varied to obtain the optimal configuration

Materials and Methods

The tank concept to store liquid hydrogen is reported in Figure 1. The multifunctional composite structure consists of four main layers aiming to deal with thermal exchange (insulation layers) and load bearing (structural layers). The inner tank (1) is made of carbon fiber reinforced polymer (CFRP) is the first structural layer and contain the liquid hydrogen. An open cell insulation layer (2) made of fiber reinforce aerogel is then used as first heat flux barrier. A second CFRP layer is used to withstand loads, specifically connected. Even though the material is the same, different layup and thickness is considered for the skirt (3) and the dome (4), as different stress levels arise due to the pressure loads. A closed cell insulation layer (5) made of PolyMethylMethAcrylate foam PMMA is finally wrapped to balance the external temperature. To keep simple the analysis, the tank shape factor is kept fixed in the geometrical configuration, with the same radius for cylindrical and spherical parts and the length of the tank is equal to three times the radius of the cylinder.

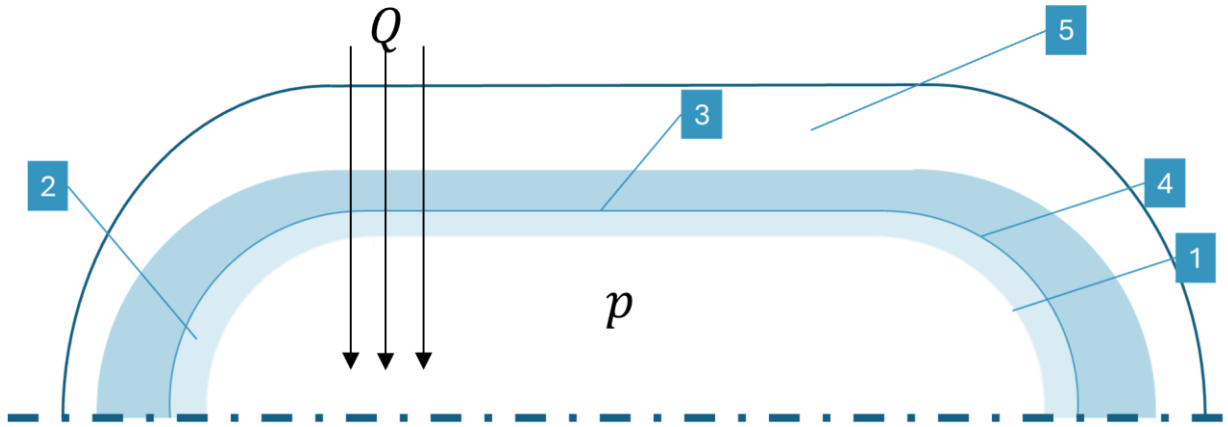


Figure 1. Preliminary LH2 Tank Configuration used for sizing.

Structural Analysis

To design the structural layers the ANSI/AIAA S-081B 2018 Standard for Space Systems Composite Overwrapped Pressure Vessels is considered to define the means of compliance. As to the static conditions, only pressure and thermal loads are accounted in this study. The Maximum Expected Operating Pressure (MEOP) is set equal to 6.5 bar with a stress safety factor equal to 2.0. The operation temperature is set as initial guess to be 218oK at layer 3-4 (flight temperature) and 90oK at layer 2. The design of the structural layers is carried out considering the temperature gradient and sizing the thickness to withstand either pressure or buckling. A carbon epoxy lamina is considered and stacked by filament winding as $[\pm 45,\pm 5,90]_s$, $[\pm 5, \pm 45, 90_3]_s$ or $[\pm 5, \pm 45, 90_2]_s$ according to the specific load. The resulting equivalent material properties are used to size the layer. The minimum thickness is obtained considering buckling due to temperature gradient

$$\sigma_{cr} = \frac{E}{3(1-\nu^2)}\left(\frac{t}{R}\right) \quad (1)$$

and limit stress along radial and longitudinal directions due to the pressure:

$$\sigma_r = \frac{pr}{2t}; \quad \sigma_l = \frac{pr}{t}; \quad (2)$$

Materials Research Proceedings 69 (2026) 713-717 https://doi.org/10.21741/9781644904251-126

Thermal Analysis

To size the insulation layers classical heat transfer mechanisms (conduction, convection, and radiation) are considered starting from the thicknesses sized through the structural configuration for the composite layers, which can be considered thermalized due to the temperatures involved. In particular, the tank system heat flux is set equal to the latent heat of vaporization of liquid hydrogen (Q = 447.60 kJ/kg), the evaporation rate is set equal to 8 kg/h, the temperature between the first insulation layer and the outer tank is set equal to 90 K, no structures acting as thermal bridges (piping, support systems, etc.) are considered. Starting from these assumptions, a first 2D modeling of the tank is made by considering its section only and omitting convective heat transfer with the external environment:

$$q = \frac{k\Delta T}{(s)}; \tag{3}$$

where k represents the thermal conductivity of the material, and (s) denotes the thickness of the layer under consideration. Afterwards a 3D Modeling is carried out heat flux was divided by the overall surface area of the structure, and the heat flux of the skirt and the dome are analyzed individually. At this stage, convective heat transfer with the external environment is also evaluated.

Thermostructural Analysis

A sequentially coupled thermostructural analysis is carried out in 3D Experience software. Only a section of the structure is considered, having in mind the simmetry of the problem, as depicted in Figure 2. The thermal analysis determine the thermal response by analyzing variables such as the temperature gradient and heat flow through time and space. The structural analysis takes the temperature map and determine the structural response by analyzing the imposed loads and temperatures.

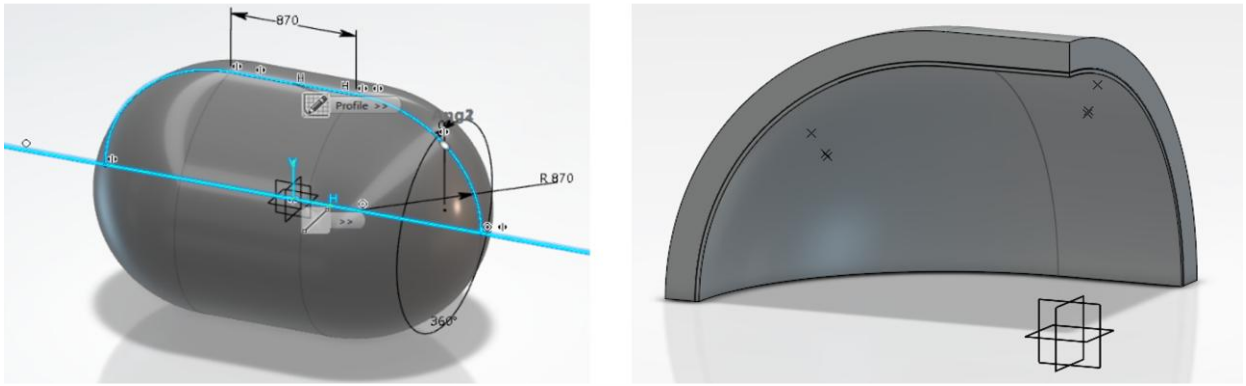
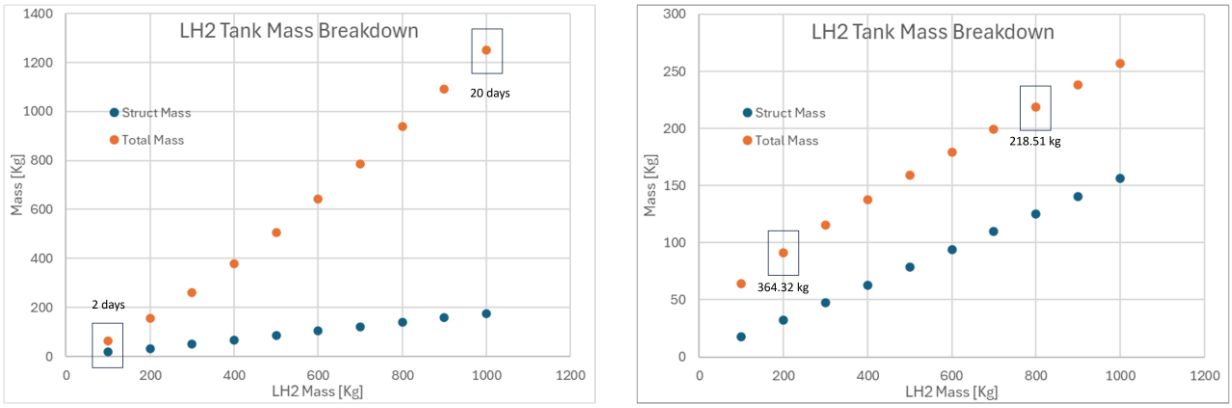


Figure 2. Virtual prototyping of the tank (left) and reduced model due to the symmetry of the problem (right).

Preliminary Sizing

The preliminary sizing carried out through the analytical framework returns a model used for the weight assessment of the whole system including thermal management and load bearing components (see Figure 3). Despite it returns qualitative results, the preliminary sizing shows shows relevant trends when increasing hydrogen volume. In particular, considering constant evaporation time rather than constant evaporation rate returns a feasible mass, which does not diverge while increasing hydrogen mass. In addition, it is important to maximize the volume and the ratio between volume and length (i.e.: using minimum number of tanks possible) to reduce weight and overall volume needed. Having in mind 800 Kg of hydrogen would require 218.51 Kg for a single tank configuration or 364.32 Kg for a 4 tank configuration.

Materials Research Proceedings 69 (2026) 713-717 https://doi.org/10.21741/9781644904251-126



(a) (b)

Figure 3. Mass breakdown of the tank obtained varying the liquid hydrogen mass under constant evaporation rate (a) and constant evaporation time (b).

High Fidelity Simulation

The high-fidelity analysis explored various design alternatives to optimize performance while connecting different layers at the interface. The thermal analysis confirmed the model's validity, showing that the temperature gradient and heat fluxes align with expectations and that the selected materials effectively maintain cryogenic conditions. Instead, structural results are affected by the interlaminar shear stresses and deformations arising between insulation and structural layers. The high deformation of the insulation materials, whose effect is neglected in the preliminary sizing, increases loads returing severe stresses at the structural layers, particularly at the outer dome. Thickening the structural layers reduced maximum stresses by 58.5%, ensuring they remained below the compression allowables for CFRP, but increased weight (142 kg to 287 kg). Despite the weight can be reduced resorting to stiffeners instead of increased thickness, the shear interlaminar stresses still remain high, resulting in unfeasible connection between structural and insulation layers, which requires for structural supports between inner and outer tank.

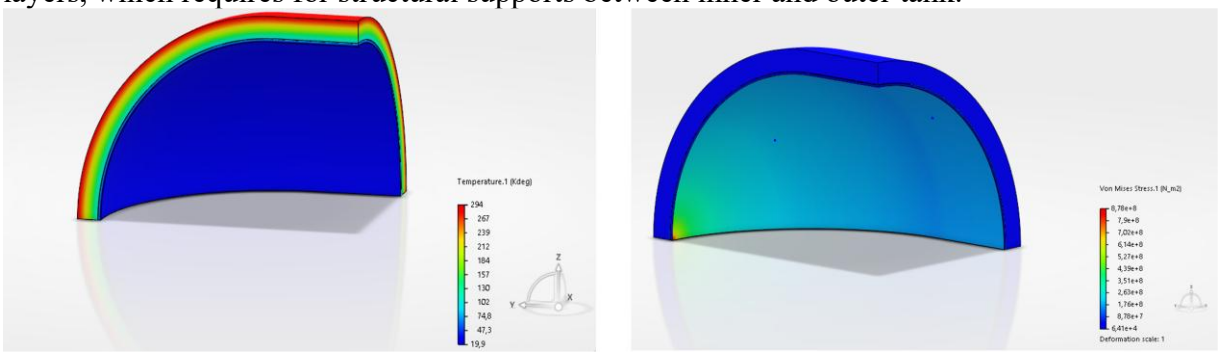


Figure 4. Temperature (left) and stress (right) distribution all over the tank due to hydrogen storage.

Conclusions

This paper showcases the pressure vessel design to equip a hydrogen fueled regional aircraft. Starting from a multi-disciplinary analysis and optimization of the air vehicle according the top level aircraft requirements, the hydrogen storing system is designed in detail considering different solutions. A further analysis shows the necessity to account the weight of the system versus its volume/surface ratio as a key parameter for preliminary design of such systems. In addition, the ratio between the actual volume of the tank and the volume of the hydrogen can give an overview of the system efficiency once the hydrogen rate is set to have a specific hydrogen duration. As a final study, a high fidelity multidisciplinary analysis is carried out to verify local stresses and

temperature of the system to validate the capability of the tank to withstand the operative conditions. Specifically, this last investigation shows the critical role of interlaminar stresses due to the multi-layered nature of the mechanical system.

Acknowledgement
This study was carried out within the MOST – Sustainable Mobility National Research Center and received funding from the European Union Next-GenerationEU (PIANO NAZIONALE DI RIPRESA E RESILIENZA (PNRR) – MISSIONE 4 COMPONENTE 2, INVESTIMENTO 1.4 – D.D. 1033 17/06/2022, CN00000023). This manuscript reflects only the authors' views and opinions, neither the European Union nor the European Commission can be considered responsible for them.

References

[1] D. Ciliberti, P. Della Vecchia, V. Memmolo, F. Nicolosi, G. Wortmann, F. Ricci, The Enabling Technologies for a Quasi-Zero Emissions Commuter Aircraft. Aerospace 2022, 9, 319. https://doi.org/10.3390/aerospace9060319

[2] L.M. Cardone, S. De Rosa, G. Petrone, F. Franco, C.S.. Greco, Review of the recent developments about the Hybrid Propelled Aircraft, Aerotecnica Missili e Spazio 103, 17–37 (2024). https://doi.org/10.1007/s42496-023-00173-6

[3] V. Memmolo, L.M. Cardone, G. Petrone, S. De Rosa, Design of hydrogen storage systems in new generation regional aircraft, Proceedings of ICAS 2024, 2024G.

[4] V. Marciello, M. Di Stasio, M. Ruocco, V. Trifari, F. Nicolosi, M. Meindl, B. Lemoine, P. Caliandro, P. (2023). Design Exploration for Sustainable Regional Hybrid-Electric Aircraft: A Study Based on Technology Forecasts. Aerospace, 10(2), 165. https://doi.org/10.3390/aerospace10020165

Materials Research Proceedings 69 (2026) 718-723 https://doi.org/10.21741/9781644904251-127

Configuration Analysis and Impeller Design for an Oxidizer Pump in Small Liquid Rocket Engines

Miłosz KOZYCZ[1]

[1]University of Science and Technology in Wrocław, Wrocław, Poland

miloszkozycz@gmail.com

Keywords: Oxidizer Pump, Liquid Propulsion, Sounding Rockets, Turbomachinery, CFD

Abstract. This article presents the design of an oxidizer pump impeller for experimental sounding rockets, based on the NOVA engine developed by the Scientific Student Association PWr in Space. The proposed methodology is applicable to other liquid-propelled engines in the 3–15 kN thrust range. The working fluid is nitrous oxide (N_2O), whose thermodynamic properties pose specific design challenges discussed in the paper. The model can also be adapted for other oxidizers, such as liquid oxygen (LOX). The paper begins with a comparison of engine cycles based on system mass and complexity, followed by an analytical impeller design approach grounded in established literature. Numerical validation was conducted using ANSYS Fluent and the BEM supercomputer at Wrocław University of Science and Technology. The study investigates optimal operating conditions, including pump operating parameters, selection of working fluid properties, and evaluation of pump-fed system influence on the total propulsion unit mass. An analytical procedure for impeller geometry design is proposed based on technical references. After defining the preliminary impeller geometry, further analysis focused on optimising selected parameters such as hydraulic efficiency, pressure head, and cavitation risk. The combination of analytical and CFD methods provides a foundation for the development of efficient oxidizer pump impellers. The findings are particularly relevant for small-scale, low-cost propulsion systems, where N_2O is often overlooked in favour of LOX.

Introduction

Pumps are rarely used in experimental sounding rockets, as their apogees are often limited to 10 km. However, for rockets targeting higher altitudes, where engines must deliver over 60,000 Ns of total impulse, their use becomes justified (see Section: System Configuration).

The pump was designed for the NOVA engine — a bipropellant liquid rocket engine developed in 2025 by the Student Scientific Association PWr in Space. The first version delivered 3.5,kN thrust and a specific impulse of approximately 16 000 Ns, using nitrous oxide and ethanol as propellants.

A new conceptual version of NOVA, intended for missions exceeding 20 km, required increased thrust and specific impulse. Design assumptions for the updated engine include estimated thrust of 5 kN, with N_2O mass flow rate of 2 kg/s and ethanol flow rate of 0.5 kg/s.

This paper presents the design process of an oxidizer pump impeller for NOVA, serving as a reference for small-thrust liquid engines in sounding rockets. It focuses on two main aspects: pump cycle configuration (as the rationale for pump use), and the impeller hydraulic design process, considered the most critical pump subsystem element. Structural design and material strength analysis are beyond the scope of this work.

System configuration

In rocket propulsion systems, several cycles involve pumps. Some of them are too complex to be considered at the initial stage of the project. After preliminary analysis, the following cycles were

Content from this work may be used under the terms of the Creative Commons Attribution 3.0 license. Any further distribution of this work must maintain attribution to the author(s) and the title of the work, journal citation and DOI. Published under license by Materials Research Forum LLC.

Materials Research Proceedings 69 (2026) 718-723 https://doi.org/10.21741/9781644904251-127

selected: pressure-fed (nitrogen as pressurant), oxidizer and fuel pump, and oxidizer pump with fuel pressurized by nitrogen.

In pump-based cycles, the pump was treated as an independent component; the type of pump power supply was not analysed here. According to [2], several engine work cycles can be identified. A comparison between turbine- and motor-driven pumps, as well as turbine based engine cycles, is beyond the scope of this paper. To simplify the analysis, the pump is assumed to be driven by an electric motor. The combined mass of the pump and motor was estimated at 12 kg for inertia calculations.

To estimate cycle efficiency, basic calculations were performed for pump parameters and propulsion subsystem mass. A simplified analytical model was prepared to justify the use of a pump for the oxidizer (and possibly also for the fuel). The model includes the mass of propellants, pressurant (nitrogen), pressure vessels, and tank structural components. Wall thicknesses were calculated according to [7].

Figure 1 compares system mass across three configurations: pressure-fed, oxidizer pump only, and both pumps.

The results clearly show that at higher total impulse, pump-fed cycles become more favourable. Therefore, since the second version of NOVA engine is intended for higher impulse missions, the pressure-fed configuration will not be further considered.

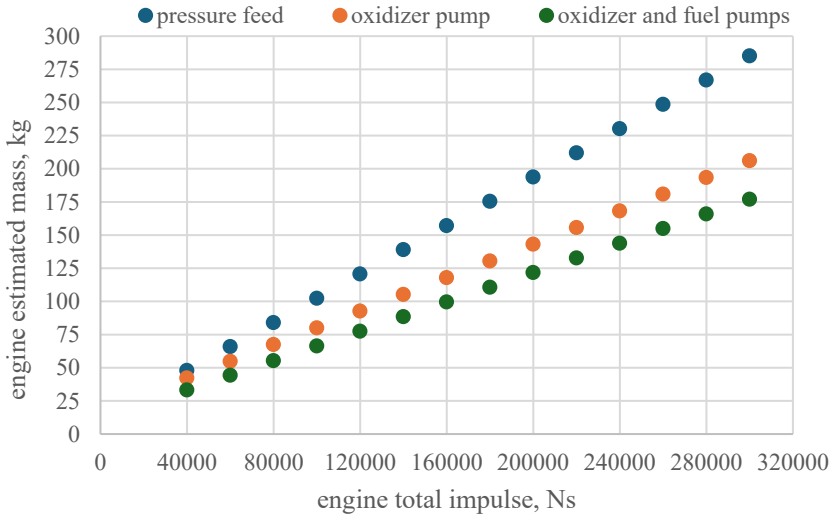


Figure 1: Estimated mass of propulsion system for three considered engine cycle configurations

The specific speed of pump n_q was calculated from formula 1

$$n_q = \frac{n \cdot \sqrt{\frac{Q}{k}}}{\left(\frac{H}{i}\right)^{\frac{3}{4}}} \tag{1}$$

Where: n_q-specific speed of pump, , n-rotation speed, Q-volumetric flow rate, H-total pressure head, k-number of channels, i-number of stages.

According to [5], the recommended range of specific speed values for centrifugal pumps with single-curved blades is between 15 and 30. Therefore, different pump configurations were compared based on their specific speed values. The considered options included single-stage and multi-stage pumps for both oxidizer and fuel, as well as the use of a pressurant gas for the fuel system. Ultimately, due to its lower complexity, a single-stage pump was selected as the most suitable option for the oxidizer. In contrast, designing a single-stage fuel pump is challenging due to the low flow rates involved, which typically necessitates a multi-stage configuration. This article

Materials Research Proceedings 69 (2026) 718-723 https://doi.org/10.21741/9781644904251-127

focuses primarily on the design of the impeller for the oxidizer pump; therefore, further analysis of the fuel pump is not included. However, for small-scale rocket engines, both multi-stage fuel pumps and pressurized fuel systems are viable options. If the manufacturing cost and complexity of a multi-stage pump are acceptable, it offers a more favourable solution from a mass balance perspective. For the oxidizer pump, the operating parameters were assumed, and the corresponding specific speed was calculated, from formula (1) for parameters listed below:

$$n = 35000\ RPM, Q = 0.0019\frac{m^3}{s}, i = 1, k = 1, H = 331m$$

As a result of iterative calculations, final value of specific speed, calculated from listed parameters is: $n_q = 19.43$.

Design methodology for an Impeller

Impeller geometry was based mostly on analytical code according [3] and [4].

Table 1presents the dimensions of the impeller, where: d_s – shaft diameter, d_{in} – inlet diameter. Other parameters follow the nomenclature presented in [3] and [4].

Table 1: Impeller dimensions

$d_s,[mm]$	$d_{in},[mm]$	$d_h,[mm]$	$d_1,[mm]$	$d_2,[mm]$	$b_1,[mm]$	$b_2,[mm]$
8	26.4	15	22	48	6	2

The blade was designed according to the point method [4].

The impeller geometry, represented as a 3D model, is shown in Figure 2.

The impeller geometry, represented as a 3D model and schema of meridional section of an impeller with marked the most significant dimensions are shown in Figure 2.

Numerical Calculation of Impeller Parameters

To verify velocity ranges and determine impeller performance, CFD simulations were conducted using Ansys Fluent 2023 R1. The Realizable *k-ε* turbulence model was applied, and the impeller region was modeled using the Moving Reference Frame (MRF) approach as the cell zone condition.

Boundary conditions were defined as follows: pressure inlet (Dirichlet) and mass flow rate outlet (Neumann). The Coupled algorithm was used as the solution method.

The simulations were carried out for four rotational speeds: 25,000; 30,000; 35,000; and 40,000 RPM. For each case, the pressure head H and hydraulic efficiency η_h were calculated.

The results of these calculations are presented in Table 2.

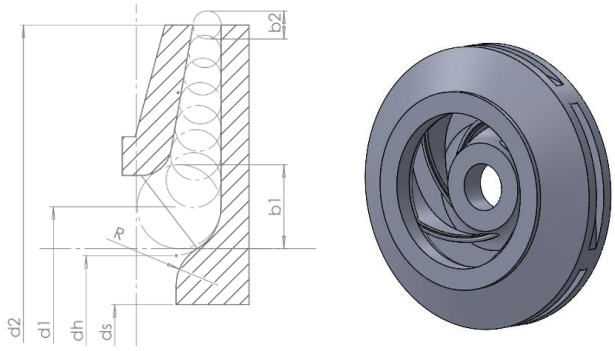


Figure 2: geometry of impeller, meridional section schema and 3D model

Materials Research Proceedings 69 (2026) 718-723 https://doi.org/10.21741/9781644904251-127

Table 2: Impeller parameters for different rotation speed

n	H	η_h
$[RMP]$	$[m]$	-
25000	167	0.82
30000	277	0.82
35000	422	0.82
40000	581	0.80

The highest hydraulic efficiency was observed at 35,000 and 40,000 RPM. However, 35,000 RPM was selected as the target rotational speed due to its proximity to the assumed pressure head value of $H_t = 331$ m.

Impeller parametric optimization

The current iteration of the impeller geometry revealed several areas with potential for improvement. The optimisation process focused on three main objectives: minimising regions susceptible to cavitation (defined as areas where the static pressure drops below the boiling pressure of nitrous oxide), enhancing hydraulic efficiency, and ensuring the required pressure head is achieved. The optimisation was conducted as a three-factor experimental design, with the selected variables being the inlet blade angle β_1, outlet blade angle β_2, and inlet region fillet radius R.

In order to reduce the number of geometry models, the range of selected factors was limited. As a result, the experimental plan was based on 18 different impeller geometries, divided into groups. The values of the considered factors are presented in Table 3. Each geometry was subjected to both qualitative and quantitative analysis. The qualitative analysis focused on identifying regions with potential cavitation risk, while the quantitative analysis included evaluation of impeller hydraulic efficiency and pressure head.

CFD results for impeller models.

Cavitation may occur in regions where the static pressure falls below the boiling pressure of nitrous oxide at the given temperature. The static pressure distributions for the selected impeller iterations are presented in Figure 3, showing the best-performing geometry in terms of cavitation risk from each group (iterations 1, 4, 8, 11, 14, and 16).

The results indicate that the impellers from group 5 (in particular, impeller 14) exhibit the smallest cavitation-prone areas on the blade surface. Conversely, the worst performance in this regard was observed for impellers from group 3 (impellers 8 and 11), which show significantly larger regions where cavitation may occur.

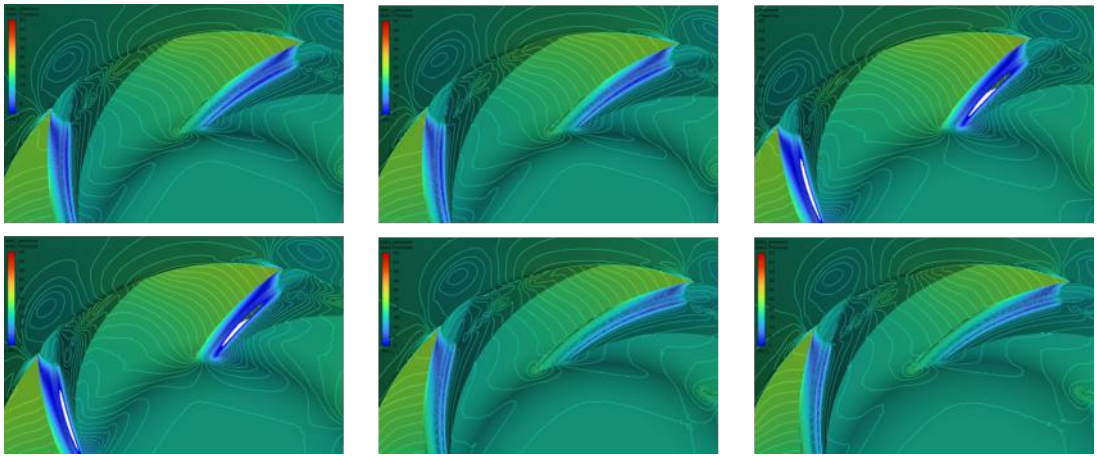


Figure 3: Static pressure on impeller blade for best cases in each group

Materials Research Proceedings 69 (2026) 718-723 https://doi.org/10.21741/9781644904251-127

The values of pressure head, mechanical efficiency, and hydraulic efficiency for all geometry iterations are presented in Table 3. From the perspective of pressure head, the best-performing impellers are iterations 2 and 3. In terms of efficiency, impellers 2 and 3 also achieve the highest values, although impellers from groups 5 and 6 demonstrate comparable performance.

Conclusions

From the quantitative perspective, the best-performing impellers are iterations 2 and 3. However, impellers from groups 5 and 6 show comparable results. Considering that, from the qualitative perspective, impellers from group 5 exhibit the lowest cavitation risk, they should be considered the most suitable option for the current configuration.

Further research will focus on validating the impeller geometry using a two-phase flow model and experimental verification. In the long term, the impeller is planned to be implemented in the pump of the second iteration of the NOVA engine, intended for higher-apogee flights.

Table 3: Impeller geometry variants with CFD results: hydraulic efficiency, pressure head and minimal static pressure

Iteration number	β_1, [°]	β_2, [°]	R, [mm]	Iteration group	η_h [mm]	H, [m]	p_{min}, [bar]
1	15	26	3	1	0.75	410.0	7
2	15	26	5		0.84	409.3	5
3	15	26	7		0.84	408.7	5
4	15	23	3	2	0.81	359.1	5
5	15	23	5		0.82	359.9	6
6	15	23	7		0.81	360.1	6
7	12	26	3	3	0.80	373.3	3
8	12	26	5		0.80	371.1	2
9	12	26	7		0.79	357.3	2
10	12	23	3	4	0.79	356.9	3
11	12	23	5		0.78	357.6	4
12	12	23	7		0.77	360.0	7
13	18	23	3	5	0.82	359.4	12
14	18	23	5		0.83	359.6	13
15	18	23	7		0.82	359.3	12
16	18	26	3	6	0.82	359.3	12
17	18	26	5		0.83	371.9	11
18	18	26	7		0.83	372.9	9

References

[1] Air Liquide, Gas Encyclopedia (2025), https://encyclopedia.airliquide.com. 2025-08-08

[2] W. Strunk Jr., E.B. White, Rocket Propulsion Elements, Wiley, New York 2017, section 6.6. Turbopump feed systems and engine cycles

[3] Alessandro de Iaco Veris, Fundamental Concepts of Liquid-Propellant Rocket Engines, 251-348, Springer, Rome 2021, https://doi.org/10.1007/978-3-030-54704-2

[4] Waldemar Jedral, Pompy Wirowe Odśrodkowe, ,Warsaw University of Technology Publishing House, Warsaw 2001, chapter 3-5

[5] Pumps and Pumping System https://ipumps.eu 2025-10-16
[6] E.W. Lemmon, M.L. Huber, and M.O. McLinden, NIST Reference Fluid Thermodynamic and Transport Properties Database (REFPROP), Version 10.0, National Institute of Standards and Technology, 2018.
[7] E.J. Bernier, Pressure Vessel Design Manual, Elsevier / Gulf Publishing Company, Houston 2013, Chapter 3

Materials Research Proceedings 69 (2026) 724-729 https://doi.org/10.21741/9781644904251-128

AI-Driven Inverse Constrained Design for Turbine Optimization

Francesco PORTA[1,a *] and Sergio LAVAGNOLI[2,b]

[1]Department of Turbomachinery and Propulsion, von Karman Institute for Fluid Dynamics, Rhode Saint-Genèse 1640, Belgium

[a]francesco.porta@vki.ac.be, [b]sergio.lavagnoli@vki.ac.be

Keywords: Turbomachinery, Multi-Objective Optimization, Kolmogorov-Arnold Networks

Abstract. This work presents an AI-driven framework for the inverse and constrained design of turbine blade sections, aimed at accelerating early-stage aerodynamic optimization. The methodology integrates automated database generation, surrogate modeling, and constrained multi-objective optimization within a unified process. A large set of high-Reynolds-number 2D uncooled blades is automatically generated and simulated through an in-house workflow, providing physically consistent data for model training. Kolmogorov–Arnold Networks are employed as surrogate models to establish a direct mapping between the aerodynamic duty parameters and the corresponding blade geometries and performance indicators. The surrogates are tuned through the Optuna optimization framework to ensure accuracy and robustness over the design space. Once trained, the models are coupled with a constrained optimization environment to identify the Pareto front between kinetic-energy losses and aero- dynamic loading while satisfying geometric feasibility requirements. The resulting framework enables rapid and physically informed exploration of turbine design alternatives without iterative CFD computations, offering a general and reproducible methodology for data-driven aerodynamic design.

Introduction

Conventional turbomachinery design follows an iterative, CFD-centered loop in which blades are iteratively modified and simulated. Although effective, this workflow is slow and computationally expensive, and success depends heavily on designer intuition. Early concepts often neglect physics that dominate performance, such as tip leakage, secondary and 3D flow structures, boundary layer development, and shock/boundary layer interaction, requiring expensive redesigns even in preliminary phases. Reliable early prediction of aerodynamic quantities and flow features is therefore essential to explore the design space broadly, preserve physical realism, and assess concepts before high-fidelity campaigns. Recent work integrates Machine Learning to accelerate aerodynamic design. Clark's [1] inverse design with radial basis functions maps the so-called aerodynamic duty/style to geometry for rapid, accurate profile generation. Bellucci et al. [2] couple automated CFD databases with Artificial Neural Networks (ANN) surrogates to include unsteady effects and deliver real-time performance and flow predictions. Petronio et al. [3] use Gaussian Process (GP) regression with Proper Orthogonal Decomposition (POD) to target informative samples, cutting CFD while accurately predicting losses and loading. Chen et al. [4] combine deep learning with multi-output GPs to automatically infer optimal turbine geometries without iterative optimization. Despite progress, broad adoption of AI in turbomachinery is limited by fragmented, case-specific workflows and the lack of a general, validated process for building, training, and testing models, especially for early-stage constrained design. This work addresses these gaps with a unified framework that systematizes database construction, model training/optimization, analysis, and constrained optimization. A physically consistent database spanning the aerodynamic design space is first constructed, after which machine-learning surrogates are trained and tuned to predict geometry and performances. The surrogates are then embedded in a constrained,

Content from this work may be used under the terms of the Creative Commons Attribution 3.0 license. Any further distribution of this work must maintain attribution to the author(s) and the title of the work, journal citation and DOI. Published under license by Materials Research Forum LLC.

Materials Research Proceedings 69 (2026) 724-729 https://doi.org/10.21741/9781644904251-128

multi-objective optimization, where model predictions of shapes and performance guide the search to satisfy target cost functions and feasibility requirements.

Numerical Methods

The workflow used to build the high Reynolds 2D uncooled blades database comprises three automated stages: blade geometry parametrization, target features definition, and flow computation and post-processing. Blade shapes are generated by combining a smooth camberline definition with a flexible thickness law. The camber line is represented by a 4th-order B-spline (five control points), ensuring up to C_3 continuity with low dimensionality. Its four design parameters are the inlet metal angle χ_1, the outlet metal angle χ_2, the x-location of the camber-line maximum x_p, and the value of the maximum y_p.

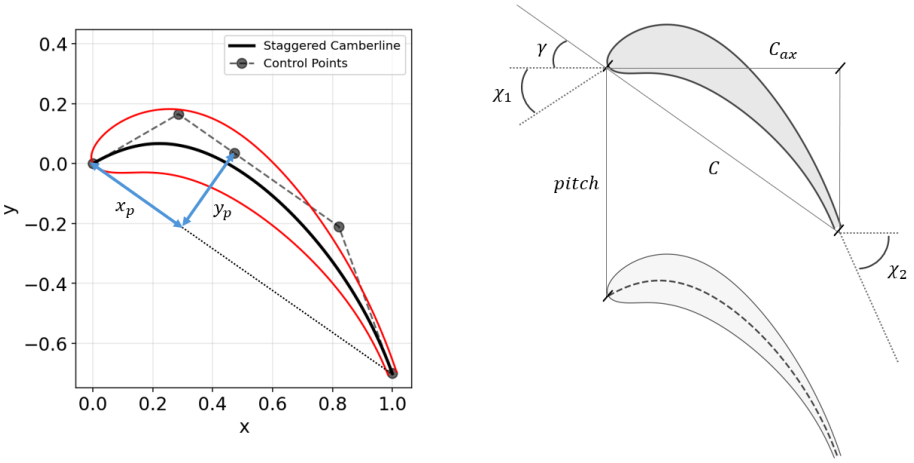


Figure 1: Camberline parametrization through 4-th order B-Spline using 5 control points.

The B-spline camber line is defined as follows:

$$\mathcal{C}(u) = \sum_{i=0}^{n} N_{i,p}(u)\mathcal{P}_i \tag{1}$$

where $p = 4$ is the degree, $N_{i,p}$ are the B-spline basis functions, and $\mathcal{P}_i$ are the control points. Thickness is modeled with Kulfan's modes [5]. Along the normalized chord $\psi \in [0, 1]$, the thickness distribution $\zeta(\psi)$ is:

$$\zeta(\psi) = C_{N_2}^{N_1}(\psi) \sum_{i=0}^{n} A_i \; S_{i,n}(\psi) \qquad S_{i,n}(\psi) = \binom{n}{i} \psi^i (1-\psi)^{n-i} \tag{2}$$

$$C_{N_2}^{N_1}(\psi) = \psi^{N_1}(1-\psi)^{N_2} \qquad \zeta_{TE}(\psi) = \psi \frac{R_{TE}}{c} \qquad R_{LE} = \frac{A_0^2 \, c}{2} \tag{3}$$

The coefficients N_1 and N_2 were set to 0.5 and 1, respectively, to generate a round leading edge and a pointed trailing edge, consistent with Kulfan's formulation. The first Kulfan's mode controls the leading-edge radius, while the last mode sets the wedge angle; coefficients can differ between suction and pressure sides for added flexibility. The final blade surface is obtained by superposing the thickness on the camber line along the local normal $\mathrm{n} = (\mathrm{n_x}, \mathrm{n_y})$. This parametrization achieves smooth, high-quality airfoils with limited parameters, enabling efficient exploration of large and diverse design spaces and supporting robust optimization and database generation. Blade design targets are defined through a combination of aerodynamic duty and aerodynamic style. The aerodynamic duty specifies boundary conditions: inlet flow angle α_1, outlet flow angle α_2, and

Materials Research Proceedings 69 (2026) 724-729 https://doi.org/10.21741/9781644904251-128

outlet Mach number M_2. The outlet Reynolds number Re_2 is derived from the inlet axial Reynolds number $Re_{1,ax}$, while specific heat coefficient γ and axial-velocity-density-ratio (AVDR) remain constant (respectively 1.4 and 1). The aerodynamic style parametrizes the surface Mach distributions using four control variables, namely the ratio of peak suction-side Mach to outlet Mach (M_{peak}), axial position of peak Mach on suction side (L_{peak}), the ratio of leading-edge pressure-side Mach to outlet Mach number (M_{ps}) and the ratio of leading-edge suction-side Mach to outlet Mach number (M_{ss}). Surface isentropic Mach numbers are normalized by the trailing-edge value (M/M_{te}) and plotted against non-dimensional surface length (L/L_{surf}) for better control over loading characteristics.

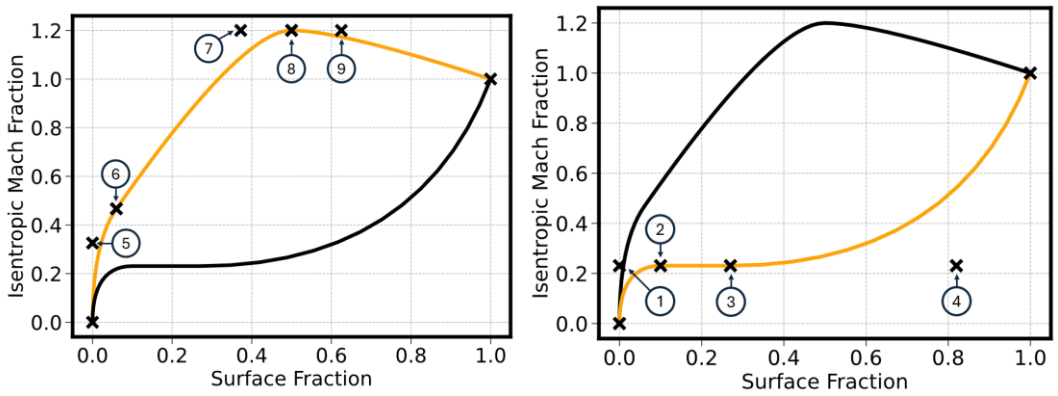


Figure 2: Loading parametrization for suction (left) and pressure (right) side.

The distributions are designed using a combination of linear functions and B-splines to ensure smoothness and derivability. The target Mach distribution and outlet flow angle guide the shape optimization process, aiming to align the real blade performance with the target input requirements. Flow computations are performed using MISES (Multiple blades Interacting Streamtube Euler Solver) [8] to obtain real flow angles and Mach distributions along blade surfaces. Boundary conditions include inlet flow angle, inlet axial Reynolds number, and outlet Mach number, with the real outlet Mach driven toward the target value. Turbulence intensity is fixed at 3.5\% with boundary layer tripping at 3\% axial chord, ensuring fully turbulent simulations throughout the design space. All simulations were executed on a dual-socket AMD EPYC 7551 machine. A single simulation required approximately 0.5 s of wall-clock time on a single CPU core. A total of 128 cores were used in parallel for the database creation of ~ 30.000 points over the course of 15 days.

Kolmogorov-Arnold Networks based model

A fast surrogate is developed to predict, with minimal cost, both blade-section geometries and key aerodynamic outputs for 2D, uncooled, high–Reynolds number profiles. The model delivers accurate estimates of kinetic-energy losses, Mach number distributions, outlet flow angles, and tangential force coefficient, enabling rapid screening of candidates and broad exploration of the design space in place of repeated CFD runs. The surrogate is built with Kolmogorov–Arnold Networks (KAN) [6], inspired by the Kolmogorov–Arnold representation theorem, which expresses multivariate functions as compositions of univariate functions and additions. Unlike Multi Layer Perceptron (MLP) that use fixed neuron activations, KAN employs learnable, edge-based activation functions parameterized by B-spline polynomials. These features provide fast, accurate predictions and immediate insight into geometry–performance couplings, accelerating early-stage turbomachinery design.

Materials Research Proceedings 69 (2026) 724-729 https://doi.org/10.21741/9781644904251-128

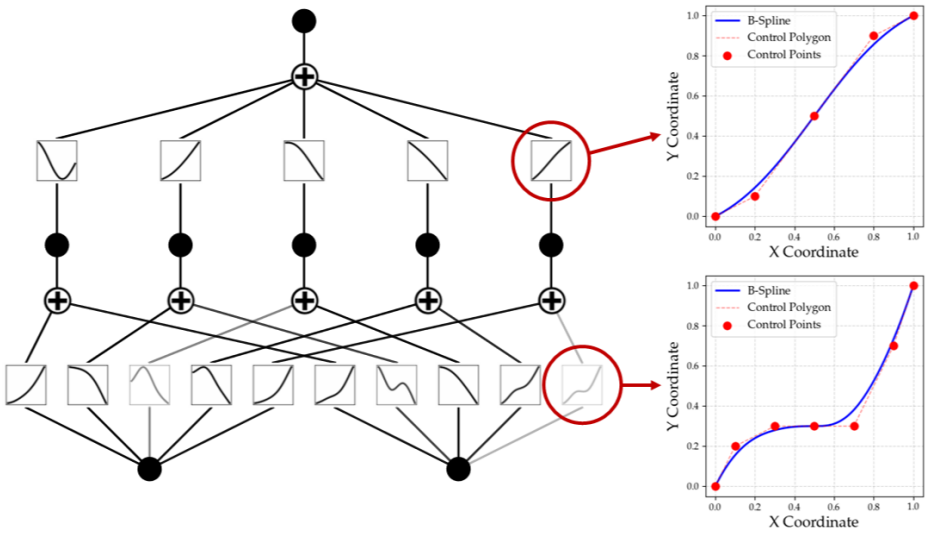


Figure 3: Example of KAN, with an highlight of the parametrization of the B-splines.

An initial trial-and-error sweep highlighted strong sensitivity to first-layer edge count, B-spline order k, number of multiplication subnodes, grid uniformity/size, and training steps; deeper networks frequently degraded performance, so a single-layer KAN was adopted. Four separate models were trained to predict: blade geometry, Mach RMS, outlet-angle error, and kinetic-energy loss. Hyperparameters were optimized with Optuna [7], while training employed Adaptive Moment Estimation (ADAM) with a learning rate set within the range $\in (0.0001, 0.005)$ and a spline grid size of 5. Validation monitoring indicated convergence after ~ 100 iterations. Compared with the initial setup, the optimized KAN markedly improved accuracy.

Constrained Optimization

In the following section, the framework for the constrained optimization is described. The trained models are used to predict the turbine's kinetic energy loss coefficient ξ and the tangential force coefficient C_y, which measures the circumferential turning effect of the cascade. The design target is defined by selecting the aerodynamic duty coefficients (α_1, α_2, M_2 and Re). The Pareto front is found by varying the aerodynamic style, defined by the aforementioned parameters M_{peak}, L_{peak}, M_{ss}, and M_{ps},. Additional geometric constraints can be introduced to control the blade design.

Materials Research Proceedings 69 (2026) 724-729 https://doi.org/10.21741/9781644904251-128

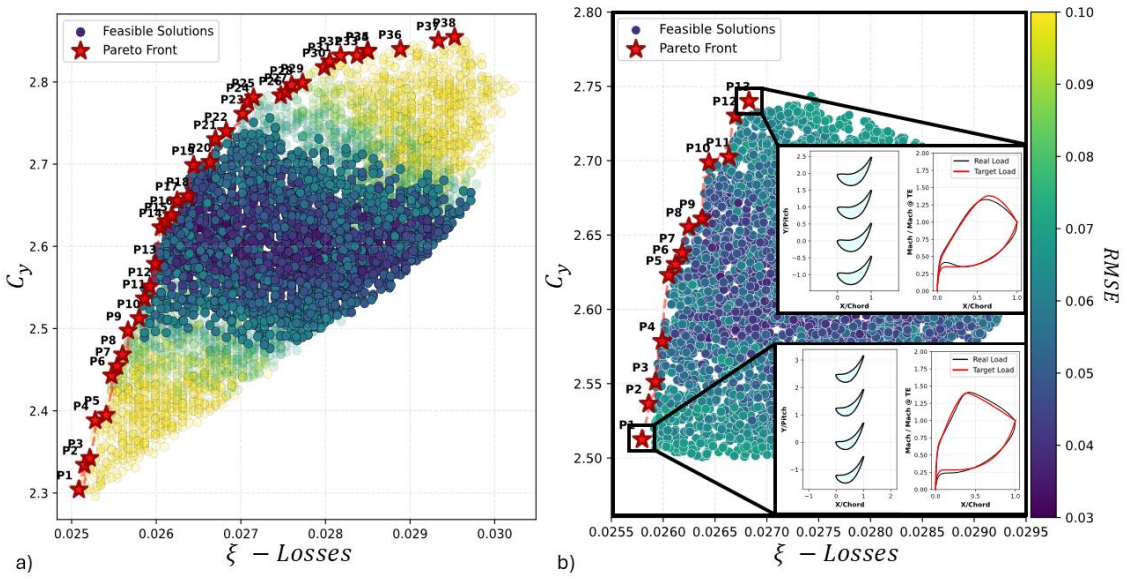


Figure 4: Tangential force coefficient versus kinetic energy loss coefficient. Figure (a) illustrates the entire population of solutions, while Figure (b) highlights the feasible subset with an RMSE below 0.06.

The optimization process was conducted with two objectives: minimizing the kinetic energy loss coefficient ξ while simultaneously maximizing the coefficient C_y. The example case study features to the following aerodynamic conditions: $\alpha_1 = -30°$, $\alpha_2 = 65°$ and $M_2 = 0.5$. The geometrical model was employed to rapidly populate the design space, while the performance models were used to evaluate each configuration in terms of loss characteristics and tangential force coefficient. However, the model exhibited difficulties in certain regions of the design space, leading to predictions that were not fully accurate or reliable. To assess and control these discrepancies, the root mean square error (RMSE) between the actual and target aerodynamic load distributions was evaluated. An acceptable threshold of 0.06 was defined in order to ensure that the predicted blade geometries remained physically consistent and representative of realistic performance. Figure 4.b presents the distribution of the acceptable solutions, highlighting the two extreme configurations. The results emphasize the evident trade-off between aerodynamic efficiency and blade loading.

Conclusions

A unified, automated framework for early-stage turbomachinery blade design is presented, integrating a physics-consistent database built through an automated workflow. The database (~30.000 2D high-Re uncooled blades) supports training of Kolmogorov-Arnold Network-based surrogate models that, after hyperparameter tuning, achieve accuracy sufficient to guide optimization at negligible evaluation cost. These models are integrated within an optimization framework to identify the optimal trade-off between minimizing kinetic energy losses and maximizing blade loading, while ensuring geometric feasibility (e.g., pitch-to-chord ratio and area constraints). An example case is discussed for operating conditions $\alpha_1 = -30°$, $\alpha_2 = 65°$ and $M_2 = 0.5$. The proposed AI-driven methodology enables reliable, CFD-free inverse and constrained aerodynamic design. The surrogates capture the nonlinear coupling between geometry and performance, reproducing the trade-off between efficiency and loading while preserving physical and geometric consistency. As a result, the proposed framework offers a fast, robust, and flexible solution for concept-level turbine design and provides a solid foundation for future extensions to fully three-dimensional and unsteady configurations.

References

[1] Christopher J. Clark, ”A step towards an intelligent aerodynamic design process”. ASME Turbo Expo 2019: Turbomachinery Technical Conference and Exposition, 2019.

[2] Bellucci, J.; Granata, A. A.; Silei, M.; Giovannini, M.; Spano, E.; Notaristefano, A.; Lengani, D. A Real Time AI-Based Strategy for the Design of a Low-Pressure Turbine Profile. In Volume 12D: Turbomachinery - Multidisciplinary Design Approaches, Optimization, and Uncertainty Quantification; Radial Turbomachinery Aerodynamics; Un-steady Flows in Turbomachinery; American Society of Mechanical Engineers: London, United Kingdom, 2024; p V12DT34A026. https://doi.org/10.1115/GT2024-128809.

[3] Petronio, D.; Paliotta, P.; Lengani, D.; Simoni, D. A ML Strategy for the Identification of Optimal LPT Design Region and Related Blade Shape. Aerospace Science and Technology 2024, 148, 109118. https://doi.org/10.1016/j.ast.2024.109118.

[4] Chen L, Zou L, Fan C et al (2020) Feature weighting network for aircraft engine defect detection. Int J Wavelets Multiresolut Inf Process 18(03):2050012. https://doi.org/10.1142/S0219691320500125

[5] Kulfan, B. M., 2008. “Universal parametric geometry representation method”. Journal of Aircraft, 45(1), pp. 142–158.

[6] Ziming Liu, Yixuan Wang, Sachin Vaidya, Fabian Ruehle, James Halverson, Marin Soljacic, Thomas Y. Hou, Max Tegmark. "KAN: Kolmogorov–Arnold Networks". https://arxiv.org/pdf/2404.19756, 2024.

[7] Takuya Akiba, Shotaro Sano, Toshihiko Yanase, Takeru Ohta, and Masanori Koyama. 2019. Optuna: A Next-generation Hyperparameter Optimization Framework. In KDD.

[8] Drela, M., and Youngren, H., 1998, “A User’s Guide to MISES 2.53, ”Massachusetts Institute of Technology, Cambridge, MA.

Materials Research Proceedings 69 (2026) 730-734 https://doi.org/10.21741/9781644904251-129

Enabling Aerospace Electrification by means of Scale-Resolved Battery Simulation

Max OKRASCHEVSKI[1,2,*], Janina DREWS[1,2], Steffen REHSE[3], Dana SCHONVOGEL[3], Ralf SCHMIDT[4], Tom BOENKE[4], Holger ALTHUES[4], Arnulf LATZ[1,2,5] and Timo DANNER[1,2]

[1]Institute of Engineering Thermodynamics, German Aerospace Center (DLR), 89081 Ulm, Germany

[2]Helmholtz Institute Ulm for Electrochemical Energy Storage (HIU), 89081 Ulm, Germany

[3]Institute of Engineering Thermodynamics, German Aerospace Center (DLR), 26129 Oldenburg, Germany

[4]Fraunhofer Institute for Material and Beam Technology IWS, 01277 Dresden, Germany

[5]Institute of Electrochemistry, University of Ulm, 89081 Ulm, Germany

*max.okraschevski@dlr.de

Keywords: Electrification, Batteries, Virtual Design, Scale-Resolved Simulation, Firedrake

Abstract. The decarbonization of the civil aviation sector is a challenging task which relies heavily on electrification. Independent of the concept and amount of electrification, e.g. more electric aircrafts (MEA) or even fully electric propulsion systems, the battery plays an important role. The latter are often criticized to be immature in terms of gravimetric energy density. But even if a high-energy cell with a value exceeding 750 Wh/kg on the pack level would be available [1], it is not guaranteed to fulfill corresponding power requirements. Batteries suffer from an energy-power-dilemma and, hence, call for design and optimization of the electrode structure. Inspired by the success of scale-resolved simulations for design and optimization in conventional jet engines, we present a scale-resolved methodology for batteries. The toolbox' potential to increase battery performance is showcased for a Lithium-Sulfur cell. The aforementioned chemistry is broadly anticipated as promising candidate for aerospace applications due to the exceptional high gravimetric energy density.

Introduction

Civil aviation is considered as part of the hard to abate sector [2]. Hence, several parallel technological routes are explored to reach decarbonization and emission goals set by regulatory frameworks [3]. On the commercially established side of the spectrum, optimized combustion-based propulsion is progressed, whereas on the other prospective side of the spectrum electric propulsion is under development.

For the first route it is broadly acknowledged that scale-resolved simulations, i.e. large eddy simulations (LES) [4,5], give invaluable insights to reach the full potential of novel technological adaptions. This concerns immediate short-term improvements through better flow understanding and control, e.g. [6,7], or potential long-term solutions based on sustainable fuels like hydrogen, even requiring a re-design of the injector [8,9]. These recent examples are also supported by the number of R&D codes with industrial relevance available in the community, e.g. AVBP, OpenFOAM, PRECISE-UNS, YALES2 and many more [10].

The second, perspectively more sustainable route of electric propulsion is currently approached by several hybridization concepts that usually involve batteries as key enablers [2,3]. This holds

Content from this work may be used under the terms of the Creative Commons Attribution 3.0 license. Any further distribution of this work must maintain attribution to the author(s) and the title of the work, journal citation and DOI. Published under license by Materials Research Forum LLC.

Materials Research Proceedings 69 (2026) 730-734 https://doi.org/10.21741/9781644904251-129

independent of the amount of electrification, from more electric aircrafts (MEA) to all electric aircrafts eventually. However, batteries are often criticized in the aerospace context to be immature because of their inherent energy-power-dilemma, i.e. high-energy cells suffer from insufficient power output and vice versa. Considering this battery bottleneck, which physically is an optimization problem of a multiscale reactor somewhat comparable to the traditional combustor, it is indeed surprising that scale-resolved simulations have much lower significance. The only R&D codes we are aware of are BEST/BLIR [11] and 4C [12].

Motivated by this deficiency and the potential to support aerospace electrification, we developed a performant, scale-resolving framework for Lithium-Sulfur batteries based on the open source solver Firedrake [13,14]. The aforementioned batteries are anticipated as a promising candidate for aerospace applications due to the exceptional high gravimetric energy density of 750 Wh/kg on pack level [1]. In [15], the framework was developed for traditional carbon-sulfur (C-S) composite cathodes, which lack significant power capability due to sluggish reaction kinetics. Here, we will show preliminary results for a polymeric cathode material, i.e. sulfurized polyacrylonitrile (SPAN), which eradicates these performance bottlenecks even without optimization measures derived from scale-resolved simulations, holing an untapped optimization potential.

Methods & Results

Our goal is to describe and optimize SPAN pouch cells currently under development in the BMFTR funded project SulForFlight (No. 03XP0491). The current rate performance on pouch cell level is shown and compared in Fig. 1 (a) to a traditional C-S system with similar sulfur loading and an idealized Li-Ion cell of a Boeing 787 MEA [16,17]. Obviously, the overall material system has a large influence on the energy-power-dilemma and the natural question is whether the slope of the SPAN cell, resulting from kinetic limitations at higher currents, can be flattened by structural design.

Therefore, we developed a coarse-grained continuum model (LES-like as in [15]) of the SPAN pouch cell that will be detailed elsewhere. Essentially, it physically describes electric charge and species mass transfer (i) in the SPAN cathode, (ii) in the novel electrolyte system and (iii) at the pristine Lithium anode interface. The developed base reaction scheme from [18] was slightly adapted (Fig. 1 (b)) and eventually, yet consistently, reduced to a one-step reaction

$$\frac{1}{6}\,\mathrm{PAN-S_4-PAN\,(S)} + \mathrm{Li^+\,(L)} + e^-\,\mathrm{(S)} = \frac{1}{3}\,\mathrm{PAN-S-Li\,(S)} + \frac{1}{3}\,\mathrm{Li_2S\,(S)}\,. \qquad (1)$$

This reduction to a one-step scheme allows us to construct a model, which in spirit very similar to usual Li-Ion battery models. The numerical solution is then obtained using Firedrake after discretization with a Discontinuous Galerkin (DG) approach and an implicit Euler time-stepping, which is embedded into a naive feedback controller [15]. Moreover, the resulting coarse-grained continuum model is calibrated by means of a fully homogenized 1D model (red lines) and experimental pouch cell data (grey lines) for discharge profiles as shown in Fig. 1 (c) with a near to perfect match. This is possible under species diffusion dominant scaling conditions [15,19].

Materials Research Proceedings 69 (2026) 730-734 https://doi.org/10.21741/9781644904251-129

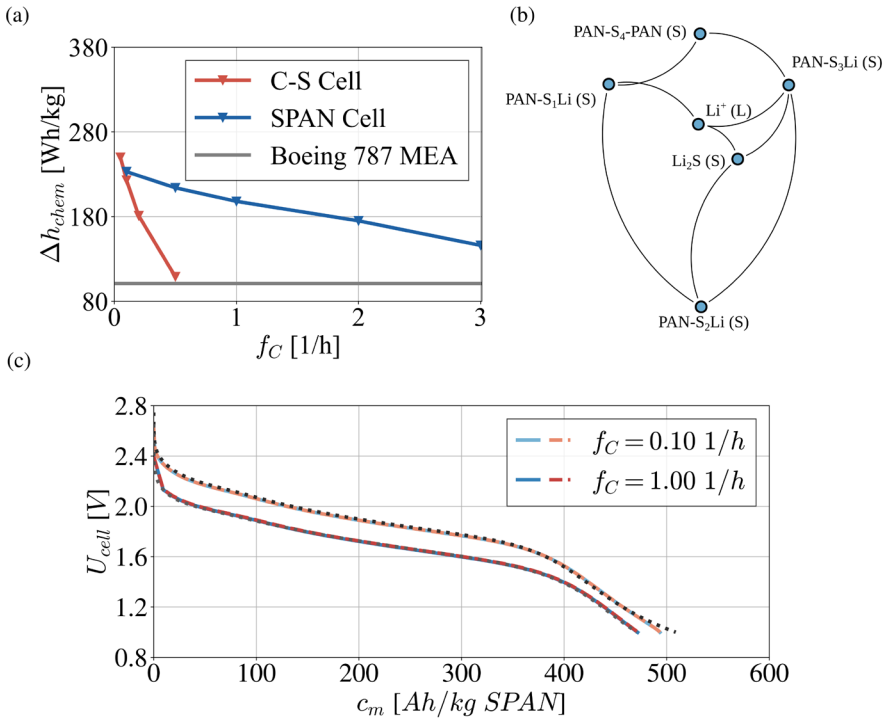


Figure 1: a) Rate performance comparison measured in gravimetric energy density over C-rate, (b) Considered base reaction mechanism for SPAN, (c) Discharge profiles for different C-rates measured in cell potential over discharge capacity.

Based on the resulting parametrization, 3D scale-resolved simulations (blue lines in Fig. 1 (c)) at the same operating conditions were performed. The underlying cathode structure was obtained from a computed tomography (CT) scan with a resolution of 0.6 µm and is highlighted in Fig. 2. The resulting discharge curves verify a posteriori that the assumption of species diffusion dominance on the coarse-graining scale above was justified. This manifests in an expected match of the global characteristics. Naturally, however, it prompts the question why one should perform such costly 3D simulations? A rather intuitive point can be made by looking at the Lithium distribution in the cathode material at the end of discharge (Fig. 2) for a C-rate of $f_C = 1.00\ 1/h$. Even if global characteristics between scale-resolved 3D models and fully homogenized 1D models are identical, the statistical information of inhomogeneous distributions are lost in 1D models by construction. This is not only relevant for degradation phenomena but also the reason why at higher currents, beyond the considered calibration range, fully homogenized 1D models are certain to give wrong predictions as the 3D structure starts to matter [15]. Then, 3D scale-resolved simulations are the only reliable way to tackle the energy-power-dilemma illustrated in Fig. 1 (c). Such simulations are currently a task at hand.

As a final note, we want to shortly comment on the computational cost of the considered 3D model in Fig. 2. Although it comprises only a part of the complete cathode, the emerging discrete problem possesses roughly 110 Mio. degrees of freedom (DoF) and inevitably requires high performance computing (HPC) capabilities. The virtual discharge in Fig. 2 was computed on the bwUniCluster3.0 located at the Scientific Computing Center (SCC) at Karlsruhe Institute of Technology (KIT) using 1536 cores. The virtual discharge took 1.5h, which requires the near to ideal strong scaling behavior of our approach up to 50000 DoF/process [15].

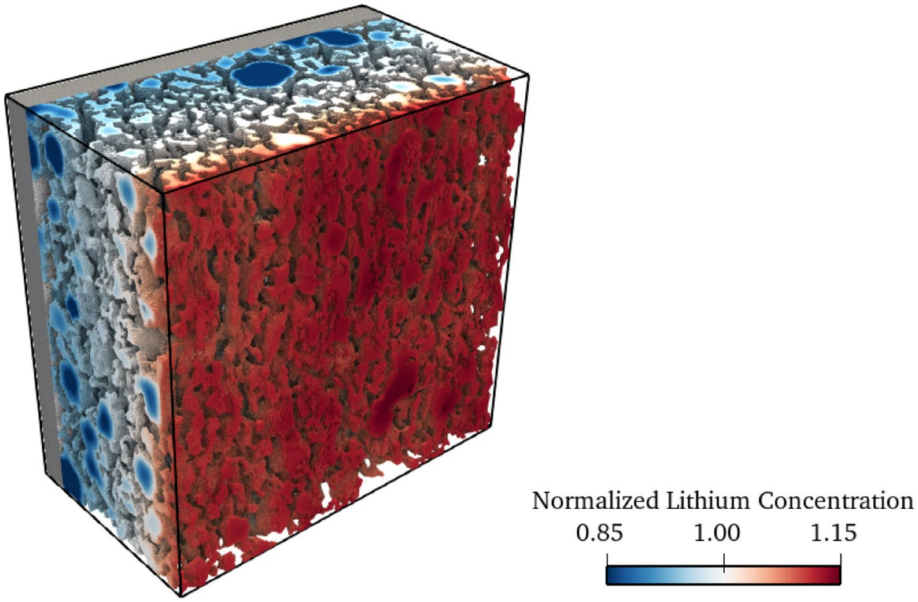


Figure 2: Normalized Lithium distribution in the SPAN cathode structure.

Summary

In this work, we presented preliminary results from scale-resolved simulations of a novel SPAN pouch cell developed in the BMFTR funded project SulForFlight (No. 03XP0491). Therefore, our recently developed 3D scale-resolved framework for Lithium-Sulfur batteries in Firedrake [15] was successfully applied for the first time to a model system similarly used for Lithium-Ion cells. This is as an important step to optimize this polymeric, next-generation Lithium-Sulfur cell in terms of the energy-power-dilemma in Fig. 1 (a). Hopefully, this enables us to tap the full potential of the SPAN cell and contributes to the electrification of the civil aviation sector.

References

[1] K. Kakiage, T. Yano, H. Uehara and M. Kakiage, Ultra-lightweight rechargeable battery with enhanced gravimetric energy densities >750 Whkg−1 in lithium–sulfur pouch cell, Commun. Eng. 3 (2024) 177. https://doi.org/10.1038/s44172-024-00321-1

[2] B. A. Adu-Gyamfi and C. Good, Electric aviation: A review of concepts and enabling technologies, Transp. Eng. 9 (2022) 100134. https://doi.org/10.1016/j.treng.2022.100134

[3] P. Su-ungkavatin, L. Tiruta-Barna and L. Hamelin, Biofuels, electrofuels, electric or hydrogen?: A review of current and emerging sustainable aviation systems, Prog. Energy Combust. Sci. 96 (2023) 101073. https://doi.org/10.1016/j.pecs.2023.101073

[4] P. Sagaut, Large Eddy Simulation for Incompressible Flows, Springer Berlin Heidelberg (2006)

[5] E. Garnier, N. A. Adams and P. Sagaut, Large Eddy Simulation for Compressible Flows, Springer Dordrecht (2009)

[6] M. Okraschevski, L. C. C. Mesquita, R. Koch, E. Mastorakos and H.-J. Bauer, A Numerical Study of Aero Engine Sub-idle Operation: From a Realistic Representation of Spray Injection to Detailed Chemistry LES-CMC, Flow Turbul. Combust. 111 (2023) 493–530. https://doi.org/10.1007/s10494-023-00443-0

[7] P. Koob, H. Nicolai, A. Lindenthal, F. A. Witkind Hirth, N. Bürkle, T. Soworka, R. L. G. M. Eggels, C. Clemen, R. Koch, T. Behrendt, M. Schroll and C. Hasse, Comprehensive Modeling of the Cause-and-Effect Chain in Aero-Engine Combustor Simulations: From Primary Breakup to Soot Formation, J. Eng. Gas Turbines Power 147 (2025) 121023. https://doi.org/10.1115/1.4069470

[8] S. Buro, R. Eggels, H. Nicolai and C. Hasse, Development and Assessment of Dual-Fuel Capabilities in Next-Generation Aero-Engine Injectors for Hydrogen and Liquid Fuels, Proc. ASME Turbo Expo. 2025, Memphis, Tennessee, USA. (2025). https://doi.org/10.1115/GT2025-152443

[9] M. Vilespy, A. Teixeira, Z. Al Hadi, S. Marragou, T. Guiberti, G. Magnotti, L. Selle, T. Schuller and T. Poinsot, Comparison of Large Eddy Simulation with local species, temperature and velocity measurements in dual swirl confined hydrogen flames, Combust. Flame 283 (2026) 114536. https://doi.org/10.1016/j.combustflame.2025.114536

[10] See https://coec-project.eu/codes/ (4th Nov. 2025)

[11] See https://www.math2market.com/industrial-solutions/batteries.html (5th Nov. 2025)

[12] See https://www.4c-multiphysics.org/capabilities/ (5th Nov. 2025)

[13] F. Rathgeber, D. A. Ham, L. Mitchell, M. Lange, F. Luporini, A. T. T. Mcrae, G.-T. Bercea, G. R. Markall and P. H. J. Kelly, Firedrake: Automating the Finite Element Method by Composing Abstractions, ACM Trans. Math. Softw. 43 (2016). https://doi.org/10.1145/2998441

[14] D. A. Ham, P. H. J. Kelly, L. Mitchell, C. J. Cotter, R. C. Kirby, K. Sagiyama, N. Bouziani, S. Vorderwuelbecke, T. J. Gregory, J. Betteridge, D. R. Shapero, R. W. Nixon-Hill, C. J. Ward, P. E. Farrell, P. D. Brubeck, I. Marsden, T. H. Gibson, M. Homolya, T. Sun, A. T. T. McRae, F. Luporini, A. Gregory, M. Lange, S. W. Funke, F. Rathgeber, G.-T. Bercea and G. R. Markall, Firedrake User Manual, Imperial College London and University of Oxford and Baylor University and University of Washington (2023). https://doi.org/10.25561/104839

[15] M. Okraschevski, T. Prill, P. Maidl, A. Latz and T. Danner, Structure Matters: A Scale-Resolved Numerical Operando Approach for Lithium-Sulfur Batteries arXiv:2511.05233 (2025). https://arxiv.org/abs/2511.05233

[16] See https://www.ntsb.gov/investigations/AccidentReports/Documents/Airworthiness_Factual_Addendum.pdf (06.11.2025)

[17] See https://liionbms.com/pdf/gsyuasa/LVP10-65.pdf (06.11.2025)

[18] E. K. Simanjuntak, T. Danner, P. Wang, M. R. Buchmeiser and A. Latz, A novel modeling approach for sulfurized polyacrylonitrile (SPAN) electrodes in Li metal batteries, Electrochim. Acta 497 (2024) 144571. https://doi.org/10.1016/j.electacta.2024.144571

[19] H. Arunachalam, S. Onori and I. Battiato, On Veracity of Macroscopic Lithium-Ion Battery Models, J. Electrochem. Soc. 162 (2015) A1940. https://doi.org/10.1149/2.07s71509jes

Materials Research Proceedings 69 (2026) 735-740 https://doi.org/10.21741/9781644904251-130

Experimental Flow Characteristics of Turbine Stator Well with Honeycomb and Labyrinth Structures

Jiahua LIU[1,a], Zeyu WU[1,b], Dongdong LIU[1,c], Nan CAO[2,d], and Xiang LUO[1,e*]

[1]Beihang University, No. 9 South Third Street, Shahe Higher Education Park, Changping District, Beijing, China

[2]Beijing Institute of Space Launch Technology,No. 1 Nandahongmen Road, fengtai District, Beijing, China

[a]buaa_ljh@buaa.edu.cn, [b]sxwzy@163.com, [c]ddliu@buaa.edu.cn, [d]caonan@buaa.edu.cn, [e]xiang.luo@buaa.edu.cn

Keywords: Honeycomb, Seal, Leakage, Pressure Loss, Turbine Stator Well

Abstract. The continuous improvement in aeroengine performance necessitates higher turbine inlet temperatures, presenting significant challenges to operational safety and imposing stricter requirements on secondary air system design. The high-temperature gas exiting the combustor subjects the high-pressure (HP) turbine to extreme conditions. To prevent ingress of this hot mainstream gas into the HP turbine disk cavity, a flow of coolant must be introduced into the secondary air system to seal the rotor-stator interface at the rim. The coolant supplied to the rim seal behind the first-stage HP turbine rotor blades is typically introduced below the second-stage nozzle guide vanes (NGVs) called turbine stator well. A portion of this coolant feeds the rim seal, while the remainder passes through the inter-stage seal located beneath the second-stage NGVs to reach the rim seal of the subsequent stage. Optimizing the flow allocation between the rim seal and the inter-stage seal within this configuration remains a critical design challenge. The goal is to achieve effective sealing with minimal total leakage flow by designing appropriate seal clearances and adjusting the rim seal coolant flow rate. However, during engine operation, seal clearances dynamically change due to centrifugal forces and thermal deformation causing rotor deflection, presenting a major challenge for seal design. To simulate the clearance variations induced by labyrinth tooth deformation under operating conditions, this paper presents an experimental investigation characterizing the flow and pressure behavior within a turbine rear cavity seal configuration. By systematically varying the seal clearance and rotor speed, the study examines the pressure across the inter-stage seal, along with the associated flow characteristics, under the effects of centrifugal deformation. Active, controllable abradable sealing techniques are commonly employed in aeroengine seal design. Honeycomb structures have seen increasing application in engine inter-stage seals in recent years. Incorporating a honeycomb layer onto the stator provides sufficient structural integrity while enhancing tolerance to high-speed rotor contact, minimizing damage during rub events. The inter-stage seal used in this experiment featured a hybrid design combining a honeycomb structure with labyrinth teeth. The experiment measured the pressure across inter-stage seal, along with the flow rates, under various inter-stage seal clearance settings. This yielded comprehensive data on flow allocation and pressure distribution for different clearances. Recognizing that honeycomb structures are prone to rub interactions with labyrinth teeth under engine operating conditions, the experiment deliberately induced deliberate and sufficient rub between the seal teeth and honeycomb at the minimum clearance setting and high rotational speed. Subsequent measurements revealed significant alterations in the sealing performance of the honeycomb structure following this rub event. Given that this experiment primarily focuses on flow allocation within the stationary turbine cavity and does not measure sealing efficiency, the turbine main gas path is simplified as a uniform HP plenum. Actual main

Content from this work may be used under the terms of the Creative Commons Attribution 3.0 license. Any further distribution of this work must maintain attribution to the author(s) and the title of the work, journal citation and DOI. Published under license by Materials Research Forum LLC.

Materials Research Proceedings 69 (2026) 735-740 https://doi.org/10.21741/9781644904251-130

flow blades are omitted, and HP air is supplied to the main flow region to simulate the core gas path pressure. Currently, many scholars have conducted research on turbine stator well. Feng Zhang,et al[1] established a two-stage main gas path model incorporating a turbine stator well, studying the effects of sealing flow rate, annular pressure ratio, and rotational speed on the flow characteristics of the rim cavity and sealing effectiveness. D.D. Coren,et al[2] employed a combined experimental and CFD approach to develop a turbine stator well structure, achieving improvements through geometric optimization, increased coolant delivery momentum, and strategic coolant injection positioning. A. Andreini,et al[3] utilized CFD simulations to examine several sealing air supply geometries, aiming to identify the impacts of coolant injection location, swirl number, and jet penetration depth on cavity sealing performance. D. Eastwood,et al[4] designed a two-stage turbine test rig to investigate hot gas ingestion phenomena in turbine stator wells under varying coolant flow rates. J.A. Dixon,et al[5] presented a high-fidelity experimental database for a two-stage turbine stator well and constructed corresponding CFD and FE models for the turbine test rig, achieving strong agreement with the experimental database. Previous studies have conducted extensive research on honeycomb seals. K.T. Han[6] introduced how to design and process honeycomb structures in aeroengines. Jun Li, et al[7] studied the flow characteristics of the through honeycomb seal by numerical simulation, and compared with the labyrinth seal, the dimensionless flow coefficient of the honeycomb seal is smaller than that of the labyrinth seal, because the leakage flow is divided into a smaller recirculation flow by the honeycomb seal than that of the labyrinth seal. Tony B. Sprowl, et al[8] studied the problem that the labyrinth seal is easily blocked by debris. The leakage flow rate of the blocked honeycomb seal increases, and the stiffness and dynamic stability also decrease. Thomas Zierer, et al[9] experimentally compared the leakage characteristics of standard membrane seal, flexible seal and honeycomb seal, in which honeycomb seal has stable and good performance under all pressure loads. Xin Yan, et al[10] studied the gap, element depth and element diameter of honeycomb seal by simulation. With the increase of gap, the leakage increases linearly, and with the increase of element depth, the sealing efficiency increases first, and then remains unchanged. The influence of element diameter is smaller than that of gap. Current research on inter-stage seals combining honeycomb and labyrinth structures within turbine stator well remains limited. This experiment measured pressure distribution inside the turbine stator well by varying seal clearances over a very small range , providing high-precision experimental data.

Test Rig

This experiment was conducted on a high-pressure rotor test rig, which was designed in a 1:1 scale with the actual engine. The inter-stage sealing structure between the second-stage guide vane and the rotor was simulated, with a honeycomb structure welded beneath the second-stage guide vane to mimic real engine conditions. To simulate rotor deformation caused by centrifugal force under engine operating conditions, different sealing gaps were designed.

The structure of the experimental bench is shown in Fig. 1. The air supply system of the experimental bench is as follows: atmospheric air is drawn into the air compressor and stored in the pressure regulating tank, which ensures stable airflow pressure. The pressure regulating tank provides stable airflow, which is dried by a filter and a drying tower, and the opening of the mechanical valve is controlled to adjust the supply pressure. Then, the flow rate is measured by a thermal flowmeter, and the air enters the shunt chamber, where it is divided into multiple paths to supply air to the experimental components.

The pressure in the experiment is measured by a Rosemount differential pressure sensor, and the flow rate is measured by an FCI thermal flowmeter. Both the flowmeter and the differential pressure sensor have analog signal output modules that can convert the measured values into 4-20mA analog signals. These signals are collected by an Adam analog signal acquisition module

Materials Research Proceedings 69 (2026) 735-740 https://doi.org/10.21741/9781644904251-130

and transmitted to the computer, where Labview software is used for programming and data acquisition.

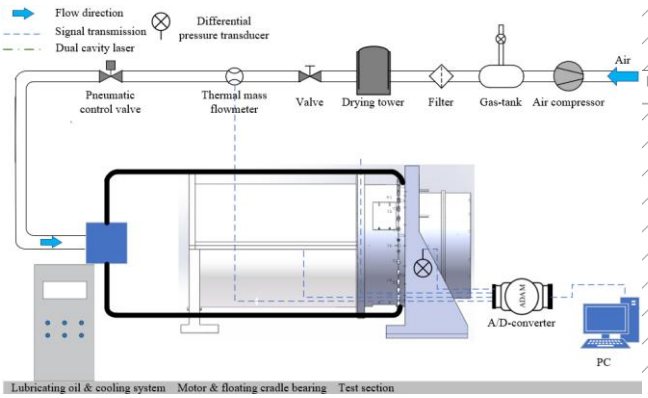


Figure 1:Test Rig

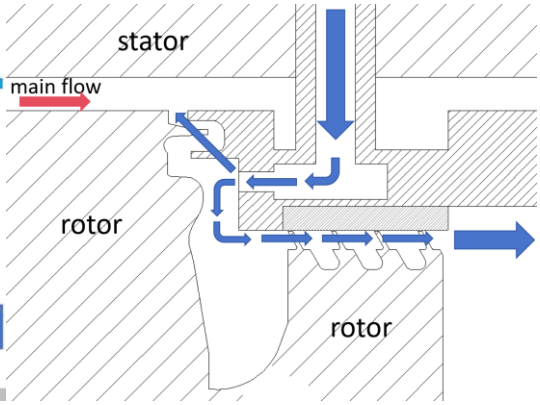


Figure 2:2-D detail of Test Part

The rotary static sealing test device is shown in Fig. 2. The airflow enters the test piece from the air supply pipe. The airflow then passes through the cavity below the second-stage guide vane and enters the cavity through the air supply hole. The honeycomb sealing structure is welded below the air supply cavity, and the honeycomb structure is followed by the rotor structure of the labyrinth seal.

The rotor is driven by a high-precision integrated motor with a rated power of 30 kW and a maximum speed of 10,000 rev/min. The motor's speed is precisely controlled by a frequency converter, achieving a control accuracy of 1%. The axial run out of the motor during operation is 0.03 mm.

The honeycomb is a thin ring structure with a diameter of 441mm, a width of 25mm, a height of 3.65mm, a single honeycomb grid of 1.6mm, and a thickness of 0.05mm. The material is Alloy HX.

Measurements and Parameter

The following are the experimental data measured in this experiment:

1)Mass flow through the honeycomb seal:m_1;
2)Mass flow through the rim seal:m_2;
3)Pressure of the honeycomb seal upstream:p_0;
4)Pressure of the honeycomb seal downstream:p_1;
5)Pressure of the main flow:p_2;
6)clearance between honeycomb and rotor:s;

The flow rate is measured using an FCI thermal flowmeter at the inlet of the experimental gas supply system (as shown in Figure 1). The flowmeter integrates a temperature and pressure calibration module inside, and the measured flow rate is the volumetric flow rate under standard conditions (20℃, 1atm). The uncertainty of flow measurement is ±3%.

The pressure is measured using a Rosemount differential pressure sensor, and the measurement location is shown in Fig. 3. The uncertainty of pressure measurement is ±1%.

measured the clearance with a thickness gauge in inter-stage seal. The uncertainty of flow measurement is 0~+0.05mm.

Materials Research Proceedings 69 (2026) 735-740 https://doi.org/10.21741/9781644904251-130

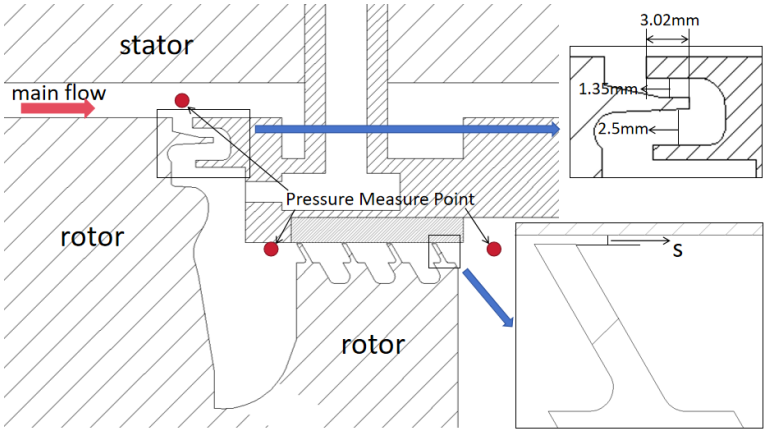


Figure 3:Honeycomb Sealing Clearance and Measure Point

Define the dimensionless parameters in this experiment:

Seal rotating Reynolds number:$Re_{\varphi} = \frac{\rho\omega r^2}{\mu}$; Seal flow Reynolds number:$Re_{\Phi} = \frac{m}{2\mu r}$; Pressure ratio before and after honeycomb seal:$\pi = \frac{p^0}{p^1}$.

The experimental conditions for this experiment are as follows:

1)Re_{φ}:$0\sim3.181\times10^6$;

2)π:1~1.7;

3)s:0.15mm-0.6mm.

To simulate the honeycomb cutting during engine operation, the honeycomb gap is set to the working clearance of 0.15mm when the engine is operating in a stationary state. With the honeycomb intact, the rotor rotational Reynolds number is set to aforementioned value, and the flow characteristics of the honeycomb seal are measured. Subsequently, the rotational speed is increased to 10000 rev/min, allowing the honeycomb to be fully worn out. The flow characteristics of the worn honeycomb are then tested at the same rotor rotational Reynolds number.

The deformation of the rotor labyrinth teeth Δs caused by rotation was obtained through strength simulation calculation, with a total of 4 labyrinth teeth. The average radial deformation value was taken, as shown in Table 1.

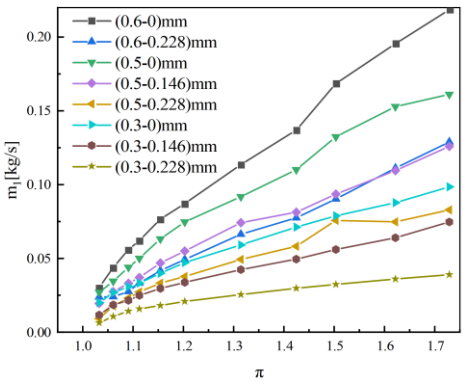
Table 1:Rotational Deformation Δs

Re_{φ}	1.909×10^6	3.181×10^6
Δs(mm)	0.146	0.228

Result And Discussion

Fig. 4 illustrates the flow characteristic curve of the honeycomb. It records the initial flow characteristics of the honeycomb seal at different rotational speeds, at which the honeycomb is not worn.Convert the rotation of the labyrinth teeth into clearance *s* changes and annotate them in the legend, for example:(0.6-0.228)mm,0.6 means design clearance,0.228 means rotational deformation when $Re_{\varphi} = 3.181\times10^6$, therefore actual clearance was 0.372mm.

Materials Research Proceedings 69 (2026) 735-740 https://doi.org/10.21741/9781644904251-130



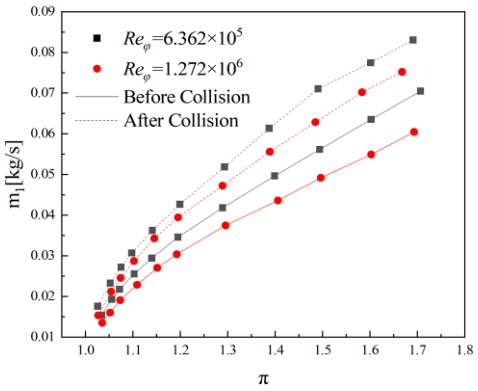


Figure 4:Flow Characteristic Before Collision *Figure 5:Flow Characteristic After Collision*

Under the same pressure ratio, the flow capacity of the seal decreases as the rotor rotation Reynolds number increases. This is because under the action of centrifugal force, the distance between the labyrinth seal on the rotor and the honeycomb decreases.This experiment was designed with different rotational speeds and clearances to obtain a wide range of flow characteristics.

When the static clearance is 0.15mm and the Re_φ is increased to 3.181×10^6, the honeycomb is fully worn, and the theoretical penetration depth of the honeycomb is 0.078mm.

Fig. 5 shows the comparison between the flow characteristic curve of the honeycomb after sufficient rubbing and before rubbing.

After the honeycomb is fully worn, the through-flow Reynolds number increases significantly under the same pressure ratio, especially for operating conditions with higher rotational Reynolds numbers. Fig. 6 will show the percentage increase in leakage before and after rubbing.

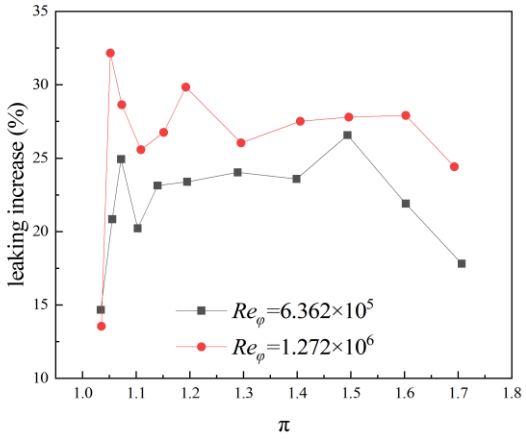


Figure 6:Leaking Increase After Collision

When the rotational Reynolds number is 6.362×10^5, the average leakage before and after honeycomb collision increases by approximately 22%. At a rotational Reynolds number of 1.272×10^6, the leakage rises by about 26%.

Summary

This experiment tested the flow characteristics under multiple gaps ranging from 0.15mm to 0.6mm. And the influence of wear on the leakage characteristics of the honeycomb was tested after

sufficient wear of the honeycomb. When the theoretical penetration depth of the honeycomb was 0.078mm, there was an increase of about 24% in sealing leakage at a gap of 0.15mm.

References

[1] Feng Zhang, Xinjun Wang, Jun Li, Daren Zheng,Computations on the flow characteristics and sealing performance of a stator well cavity for the second stage in gas turbine,Applied Thermal Engineering,Volume 125,2017,Pages 1300-1319,ISSN 1359-4311. https://doi.org/10.1016/j.applthermaleng.2017.07.078

[2] D.D. Coren, N.R. Atkins, C.A. Long, D. Eastwood, P.R.N. Childs, A. Guijarro-Valencia, J.A. Dixon, The Influence of Turbine Stator Well Coolant Flow Rate and Passage Configuration on Cooling Effectiveness, ASME Paper GT2011-46448. https://doi.org/10.1115/GT2011-46448

[3] A. Andreini, R. Da Soghe, B. Facchini,Turbine stator well CFD studies: effects of coolant supply geometry on cavity sealing performance,ASME J. Turbomach., 133 (2011), p. 021008 https://doi.org/10.1115/1.4000570

[4] D. Eastwood, D.D. Coren, C.A. Long, N.R. Atkins, P.R.N. Childs, T.J. Scanlon, A. Guijarro-Valenci,Experimental investigation of turbine stator well rim seal, re-ingestion and interstage seal flows using gas concentration techniques and displacement measurements,ASME J. Eng. Gas Turb. Power, 134 (2012), p. 082501 https://doi.org/10.1115/1.4005967

[5] J.A. Dixon, A. Guijarro-Valencia, A. Bauknecht, D.D. Coren, N.R. Atkins,Heat transfer in turbine hub cavities adjacent to the main gas path,ASME J. Turbomach., 135 (2013), p. 021025 https://doi.org/10.1115/1.4006824

[6] Han, KT. "Development of the Process of Honeycomb Seal for Gas Turbine." Proceedings of the ASME 2008 International Manufacturing Science and Engineering Conference collocated with the 3rd JSME/ASME International Conference on Materials and Processing. ASME 2008 International Manufacturing Science and Engineering Conference, Volume 2. Evanston, Illinois, USA. October 7-10, 2008. pp. 585-588. ASME. https://doi.org/10.1115/MSEC_ICMP2008-72561

[7] Li, J, Deng, Q, & Feng, Z. "Numerical Investigations of the Flow Characteristics in the Straight-Through Honeycomb Seal." Proceedings of the ASME 2005 Fluids Engineering Division Summer Meeting. Volume 1: Symposia, Parts A and B. Houston, Texas, USA. June 19-23, 2005. pp. 1565-1571. ASME. https://doi.org/10.1115/FEDSM2005-77064

[8] Sprowl, TB, & Childs, DW. "A Study of the Effects of Inlet Preswirl on the Dynamic Coefficients of a Straight-Bore Honeycomb Gas Damper Seal." Proceedings of the ASME Turbo Expo 2004: Power for Land, Sea, and Air. Volume 6: Turbo Expo 2004. Vienna, Austria. June 14-17, 2004. pp. 619-629. ASME. https://doi.org/10.1115/GT2004-53328

[9] Zierer, T, Bricaud, C, Escudero-Olano, M, McNally, J, & Mohammed, AP. "Experimental Analyses of a Static to Static Flex Seal and a Honeycomb Seal." Proceedings of the ASME Turbo Expo 2016: Turbomachinery Technical Conference and Exposition. Volume 5A: Heat Transfer. Seoul, South Korea. June 13-17, 2016. V05AT15A022. ASME. https://doi.org/10.1115/GT2016-57397

[10] Yan, X, Chen, X, & He, K. "Influence of Shroud Seal Dimensions on Aerodynamic Performance of Steam Turbine Stages: Part I — Honeycomb Seal." Proceedings of the ASME Turbo Expo 2016: Turbomachinery Technical Conference and Exposition. Volume 8: Microturbines, Turbochargers and Small Turbomachines; Steam Turbines. Seoul, South Korea. June 13–17, 2016. V008T26A018. ASME. https://doi.org/10.1115/GT2016-56917

Materials Research Proceedings 69 (2026) 741-746 https://doi.org/10.21741/9781644904251-131

Development and Characterization of Solid Propellants Based on Environmentally Friendly Sugar and Oxidants for Aerospace Applications

Gerardo Raúl CABALLERO MORALES[1,a *], Italo Paolo AMBROSIO HUANAY[1,b]

[1]Universidad Nacional de Ingeniería UNI, Lima, Peru

[a]gerardo.caballero.m@uni.pe, [b]italo.ambrosio.h@uni.pe

Keywords: Propellant, Small-Scale Rocketry, Low-Toxicity, Oxidizers, Bio-Based Energy

Abstract. The current commercial solid propellants for experimental rocketry are based on barium nitrate, ammonium perchlorate and black powder among others, all of which present potential toxicity. Besides, diphenylamine, an additive to avoid deterioration of nitrocellulose, is likely carcinogenic, and solid or liquid particles are deposited in the respiratory tract depending on their size, in addition to gaseous by-products such as SO_2 and NO_x that threaten environmental health. The main objective of this study was to develop a safe solid propellant, maintaining safety standards, aiming at sustainability by reducing the toxicity of solid propellant combustion. For our solid propellant SP1, we maintained a ratio of 65% anhydrous D-glucose to 35% potassium nitrate, with ferric oxide and calcium carbonate as oxidant. Thermochemical analysis was performed by Cantera simulation platforms, confirming that SP1 produces cleaner combustion than current commercial propellants, with CO_2, H_2O and N_2 as main products, as well as few NO_x emissions (< 5 %), and no halogenated by-products. Combustion temperature was between 1430 to 1730 °C, ignition temperature between 180 and 200 °C, specific impulse 120 and 140s, calorific value between 3.5 and 4.5 MJ/kg, and combustion velocity between 3 and 10 mm/s. Combustion simulation performed with ANSYS Mechanical, Open Rocket and MATLAB supported the predictions on fluid dynamics, structural integrity and flight. Laboratory tests were also performed to validate the results, calorimetry and combustion velocity. Data collection was performed on a static test bench, determining thrust and monitoring gas emissions. The propellant exhibited low sensitivity to impact and friction, moderate hygroscopicity, thermal stability at 180°C and a shelf life of 12 months without moisture. Thus, safe handling, low production cost and accessibility to raw materials make SP1 an interesting, secure and efficient alternative for experimental rocketry, CubeSat and aerospace platforms.

Introduction

Experimental rocket research is very useful for the evolution towards aerospace missions in the foreseeable future. Experimental vehicles can be launched from temporary sites throughout the country, can be used for remote field studies, and they can be used to develop and test new scientific instruments for measurement and observation [1].

Experimental rocketry is an effective tool for conducting scientific research [2]. Among the fields of application are biometeorology, photobiology, pollution monitoring and telecommunications [3]. It can also be applied to territory observation (security and defense) and aerial imaging, although aerial observation is increasingly and gradually being performed through drone technology. In addition to their contribution to science and technology, experimental rocket missions also provide excellent tools for scientific training [4, 5]. Experimental rocket research in Peru is a field where university initiatives and independent missions are gradually emerging, contributing to its growth. In particular, the National Institute for Research and Training in Telecommunications (INICTEL-UNI), the National University of Engineering (UNI), and the

Content from this work may be used under the terms of the Creative Commons Attribution 3.0 license. Any further distribution of this work must maintain attribution to the author(s) and the title of the work, journal citation and DOI. Published under license by Materials Research Forum LLC.

Materials Research Proceedings 69 (2026) 741-746 https://doi.org/10.21741/9781644904251-131

National University of San Marcos (UNMSM) have led efforts to create and test experimental rockets.

This study aims to promote experimental rocketry in Peru through the support of universities and research centers that demonstrate the country's interest and potential in this field, followed by the inauguration of the Aerospace Engineering degree program at the Faculty of Mechanical Engineering (FIM) of the UNI. On the other hand, the choice of propellant is key, as it directly influences the performance of the rocket. Globally, research into solid fuels has advanced significantly, particularly in relation to propellants based on perchlorates and other high-efficiency compounds that offer high specific impulse [6, 7, 8]. However, these compounds have significant disadvantages, such as high production cost and complex handling, and considerable risk due to their explosive and unstable nature due to micromechanical changes (cracks) [9]. Potassium nitrate (KNO_3), combined with fuels such as sucrose, is a viable option for experimental rocketry applications due to its low cost, wide availability, and greater relative safety [10]. In this context, it is essential to implement an efficient propellant design that minimizes risks during storage, transport, and ignition [11, 12].

Residual biomass from different sources such as potato (starch), is a promising option for application as propellant ingredient in rocketry in Peru, through biomass hydrolytic conversion into simple sugar molecules such as glucose. The development and optimization of a solid propellant based on potassium nitrate mixed with residual biomass as fuel source would not only benefit experimental rocketry projects in Peru, but could also position the country as an emerging competitor in aerospace research, given that there is a current project for construction of an aerospace port together with NASA in the city of Talara, in Peru, which would allow the launching of rockets in the near future [13].

Goal of this study was the design and optimization of formulation of a solid propellant composed of potassium nitrate and residual biomass, in order to improve its performance in propulsion systems, by means of a controlled combustion system that allows for uniform and efficient burning of the propellant, minimizing the generation of hot spots and preventing structural failures during the start-up of the propulsion system, ultimately reducing the environmental impact of the propellant.

Materials and methods

Solid propellant SP1 was prepared, with a mass ratio 65: 35 anhydrous D-glucose to potassium nitrate, 2% w/w ferric oxide and 3% w/w calcium carbonate as oxidant. D-glucose anhydrous $C_6H_{12}O_6$ (DGrace & ChJ, Lima) was used as pure powder; for the referential comparison propellant, commercial granulated refined sugar (sucrose) was employed. Table 1 shows the SP1 mixture content.

Table 1. *SP1 propellant composition. M_W = wet basis moisture content.*

D-glucose	7.00	$\xrightarrow{0.04\%}$	≈ 7.00
KNO_3	13.00	$\xrightarrow{0.04\%}$	≈ 13.00
Fe_2O_3	0.40	$\xrightarrow{0.04\%}$	≈ 0.40
$CaCO_3$	0.60	$\xrightarrow{0.04\%}$	≈ 0.60
• **Mixture (dry basis)**			≈ 21.00

Chemical reactions:

$$5\ C_6H_{12}O_{6\ (s)} + 24\ KNO_{3\ (s)} \xrightarrow{Fe2O3\ (s)} 18\ CO_{2\ (g)} + 30\ H_2O_{\ (g)} + 12\ K2CO_{3\ (s)} + 12\ N_{2\ (g)}$$

$$CaCO_{3\ (s)} + O_{2\ (g)} \xrightarrow{Fe2O3\ (s)} CO_{2\ (s)} + CaO_{\ (s)} + \text{energy}$$

Materials Research Proceedings 69 (2026) 741-746 https://doi.org/10.21741/9781644904251-131

$CaCO_{3\,(s)} \rightarrow CaO_{\,(s)} + CO_2$ (endothermic decarbonation)

Iron oxide FeO_3 acts as a catalyzer ingredient. It generates a homogenous chemical reaction through all the grain structure and releases heat (~2000 °C). Also, calcium carbonate $CaCO_3$ contributes to a longer but less intense combustion, which can improve ignition stability, although it decreases the brightness of the flame. It also facilitates self-ignition and reduces the delay time. The greater release of heat promotes faster expansion, which can increase thrust, but also the risk to be moistened if confinement is not controlled.

Pure KNO_3 has a high melting point (334 °C), but when mixed intimately with sucrose and heated, a eutectic mixture is formed. This mixture has a much lower melting point than its individual components, melting in the temperature range of sucrose (160-190 °C). KNO_3 dissolves in the molten sucrose. It should be noted that this does not mean that the components necessarily degrade or decompose to achieve the mixture.

Results and discussion

Figure 1 shows concentric cylindric grains of the SP1 propellant and the refined-sugar-based reference propellant. The SP1 propellant preparation resulted in a mass that had more homogeneity and less plasticity than the reference propellant.

The following simulation studies were conducted:

a. Thermochemical modelling and simulation of gas emission with stoichiometric balances was performed with MATLAB / Python. It was shown that SP1 produced cleaner combustion than current commercial propellants, with CO2, H2O and N2 as main products, as well as fewer NOx emissions (< 5 %), and no halogenated by-products.
b. Structure and grain design simulation was performed with SolidWorks to calculate thermal and structural stress that can lead to deformation and cracks.
c. Trajectory simulation was performed with OpenRocket to calculate maximum height, acceleration and stability.

(a)  (b) 

Figure 1. (a) *SP1 propellant.* ***(b)*** *Refined sugar-based propellant.*

Important parameters to consider are adiabatic flame temperature T_c at chamber pressure p_c. Equilibrium gas composition x_j, engine design parameters (average molecular weight M, specific heat ratio $\gamma = c_p/c_v$, characteristic speed c^* and specific impulse I_{sp}).

The simulation model was based on a closed combustion chamber, adiabatic, at constant pressure p_c in equilibrium. Ideal gas phase: CO_2, H_2O, CO, H_2, N_2. Solid phase: K_2CO_3, $CaCO_3$, CaO, Fe_2O_3.

The graphs obtained from the Cantera thermodynamic simulation platform of the green propellant reaction are shown below, analyzing how the energy released by the solid fuel is transformed into thermal energy from the combustion gases and, finally, into thrust.

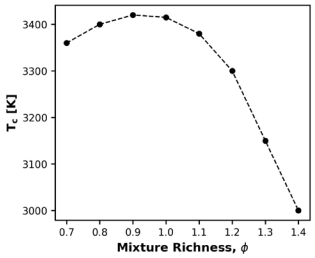


Figure 2. *Chamber temperature against mixture richness ϕ.*

Materials Research Proceedings 69 (2026) 741-746 https://doi.org/10.21741/9781644904251-131

Chamber temperature as a function of mixture richness ϕ as seen in Figure 2 shows that the maximum temperature obtained (3050 °C) of the sucrose-KNO_3 system is reached at ϕ = 0.9, i.e., for a mixture slightly rich in oxidant - and therefore not quite stoichiometric. At this point, the greatest release of energy per unit mass of mixture is achieved, which translates into a higher c^* and specific impulse, improving the overall performance of the engine. At the same time, the slight excess of oxidizer favors more complete combustion (less CO and carbonaceous residues).

Figure 3 shows that c^* of the sucrose–KNO_3 system is maximum (1600 m/s) at ϕ = 1.15, i.e., for a mixture slightly rich in fuel. At this point, the best compromise between T_c and M is achieved, so that the performance (and, consequently, I_{sp}) is maximized. For a green propellant, this operating range allows maximum thermodynamic performance to be extracted without resorting to more energetic but environmentally aggressive oxidizers.

The ideal specific impulse curve in vacuum, shown in Figure 4, indicates that the sucrose–KNO_3 propellant reaches its maximum performance at ϕ = 1.15, with I_{sp} = 320 s, showing that a slightly fuel rich mixture offers the best thermodynamic compromise for nozzle expansion.

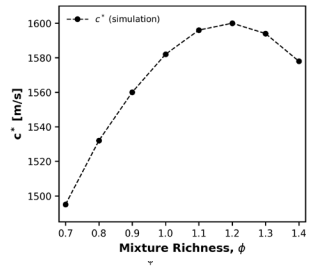


Figure 3. *Characteristic velocity c^* against mixture richness ϕ.*

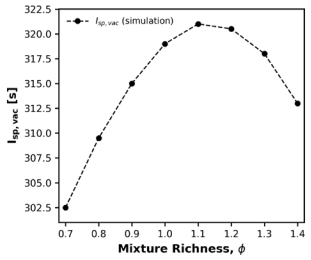


Figure 4. *Specific impulse I_{sp} against mixture richness ϕ.*

Table 2. *Molar composition of combustion gases for ϕ = 1.15.*

Species	X (mole exit, frozen)
H_2O	0.413
CO	0.198
H_2	0.121
N2	0.111
CO2	0.084
OH	0.035
H	0.025
O2	0.006
O	0.004
NO	0.004
HO2	2.215 e-05
HCO	8.233 e-06
N	5.490 e-06
H_2O_2	4.495 e-06
HNO	3.315 e-06
NH	3.140 e-06
NH_3	2.433e-06
NH_2	1.966 e-06

Values obtained from measurement of combustion temperature were between 1430 and 1730 °C, the ignition temperature between 180 and 200 °C, average specific impulse 130 s, calorific value between 3.5 and 4.5 MJ/kg, and combustion velocity between 3 and 10 mm/s. The structure design simulation result was expressed by the von Mises stress, which is shown graphically in Figure 5. As can be seen, a maximum stress of approx. 220 MPa takes place at the ignition ports; this value is lower than 290 MPa, which in turn represents the yield strength of AISI 316 stainless steel used as material for the rocket structure.

Materials Research Proceedings 69 (2026) 741-746 https://doi.org/10.21741/9781644904251-131

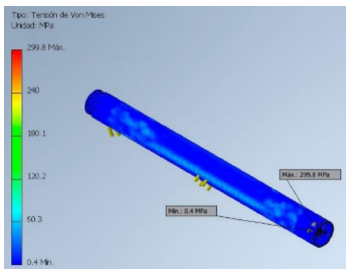
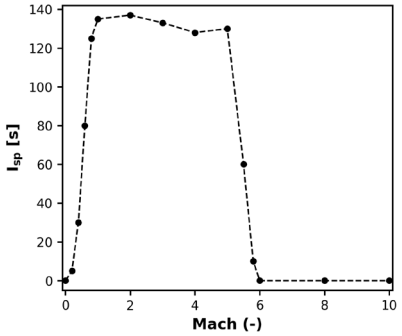


Figure 5. *Von Mises stress simulation results.*

In a Mach range from 1 to 5 an average specific impulse I_{sp} of approx. 130 s (sea level) was obtained Figure 6a shows the results of I_{sp} against Mach number. By comparison, Space X Merlin 1D engine (working with kerosene fuel) for Falcon 9 launch rocket vehicle has a I_{sp} = 310 s, while Ariane 6 launcher rocket booster engine P120C (working with solid fuel) has a I_{sp} = 278 s. A calorimetric test was also performed with the aid of a load cell to validate the calculations. Data collection was performed on a static test bench, determining thrust and monitoring gas emissions. Figure 6b shows a picture of the combustion test performed with SP1 propellant.

(a)



(b)

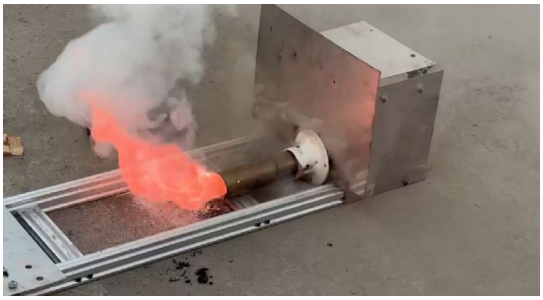


Figure 6. (a) *Specific impulse Isp for propellant SP1.* ***(b)*** *Combustion test SP1 propellant*

Conclusions and summary

The thermodynamic results show that the sucrose–KNO_3 mixture reaches its maximum performance at $\phi = 1.15$, where gas composition contains mostly H_2O, CO, and H_2, with significant fractions of N_2 and CO_2. At this point, the best compromise between chamber temperature, specific heat ratio, and molecular weight of the gases is obtained, so that the specific impulse and efficiency of chemical energy conversion into thrust are maximized for this solid propellant.

The presence of a lower environmental footprint compared to traditional propellants due to the gas plume consists mainly of H_2O, CO, H_2, N_2 and a moderate fraction of CO_2, with no presence of chlorinated species or halogenated compounds typical of perchlorate-based propellants. This means no subsequent generation of gaseous HCl, metal chloride particles or other highly corrosive and toxic products, significantly reducing the impact on the environment.

References

[1] Robayo-Salazar, R., Portocarrero-Hermann, J., Meneses-Suta, J., Salgado-Díaz, J., Martínez-Riaño, S., Delgado, F., Gómez-Ruge, A. (2021). Diseño, construcción y prueba estática experimental de un motor-cohete de combustible sólido. Escuela Militar de Aviación (EMAVI) – FAC.

[2] NASA Glenn Research Center. (2019). Chemical Equilibrium with Applications (CEA) Program. (2019). https://cearun.grc.nasa.gov/

[3] Marcado, V., Benítez, P., La Rosa, C., La Cruz, L., Parco, M., Ferrerira, J., Rojas, J. J. (2009). Progresos alcanzados en el proyecto universitario cohete sonda ULA. Universidad, Ciencia y Tecnología, 13(53), 305–316. https://doi.org/10.13140/RG.2.1.3286.5120

[4] Acosta Vasquez, E. A., Marin, L. E., & Jaimes, O. (2011). Cohetes hidráulicos. Diseño, construcción y experimentación, una experiencia integradora. 5° Congreso Nacional de Enseñanza de La Física, 229–231. Bogotá D.C.

[5] NA. Netzel, D. Strufaldi Batista, F. Granziera Jr., M. Carvalho Tosin. A versatile low-cost data acquisition system for small rocket engine test bench. HardwareX 23 (2025) e00686. https://doi.org/10.1016/j.ohx.2025.e00686

[6] G Ren , H Sun, C Hu, Y Yang, C. Li, Y. Xu, R. Xue, X. Hu. Historical trajectory, current status, and future challenges of powder engines and propellant supply technologies: A comprehensive review. Defence Technology 52 (2025) 142–183. https://doi.org/10.1016/j.dt.2025.06.005

[7] L Navarrete-Martin, P Krus. Sounding Rockets: analysis, simulation and optimization of a solid propellant motor using Hopsan. Transportation Research Procedia 29 (2018) 255–267. 10.1016/j.trpro.2018.02.023

[8] M Abbas, R Kumar, S Biswas. Effect on the performance of a hybrid rocket using AP in the PVC and HTPB-based hybrid fuel. FirePhysChem 5 (2025) 129–137. https://doi.org/10.1016/j.fpc.2024.08.004

[9] G.P. Sutton, O. Biblarz, Rocket Propulsion Elements (9th ed., 2016). Wiley. https://www.wiley.com/en-us/Rocket+Propulsion+Elements%2C+9th+Edition-p-9781118753651

[10] Kubota, N. (2007). Propellants and explosives: Thermochemical aspects of combustion. Wiley-VCH.

[11] European Space Agency (ESA), Green Propulsion Technologies – Status and Future Prospects.(2021). https://www.esa.int/Enabling_Support/Space_Transportation/Green_Propulsion_Technologies

[12] Y Hou, J Xu, C Zhou, X Chen. Microstructural simulations of debonding, nucleation, and crack propagation in an HMX-MDB propellant. Materials & Design 207 (2021) 109854. https://doi.org/10.1016/j.matdes.2021.109854

[13] Agencia de Promoción de la Inversión Privada PROINVERSION (2024). https://www.gob.pe/institucion/proinversion/noticias/904900-mindef-encargaria-a-proinversion-la-adjudicacion-para-la-construccion-de-un-puerto-espacial-en-talara-por-mas-de-s-1-000-mlls

Materials Research Proceedings 69 (2026) 747-750 https://doi.org/10.21741/9781644904251-132

Design of a Low Power Anode Layer Hall Thruster

Ivana SETTEMBRE[1,a *], Davide PICCIAU[1,b]

[1]Department of Civil and Industrial Engineering, University of Pisa, Largo Lucio Lazzarino, 56122, Pisa, Italy

[a]settembreivana@gmail.com, [b]picciaudav@yahoo.it

Keywords: Scaling Methodology, Anode Layer Hall Thruster, Low Power, Argon

Abstract. Electric propulsion (EP) has gained significant importance for space applications due to high specific impulse and increasing onboard power availability. This work focuses on the scaling and design of a low-power (~100 W) Anode Layer Hall Thruster (TAL) optimized for Argon propellant. Unlike conventional Stationary Plasma Thrusters (SPT), TALs feature metallic walls and a shorter acceleration channel, offering improved durability and compactness. A novel scaling methodology was developed by improving a phenomenological model to account for TAL-specific physics, including refined wall and anode loss relations. The methodology was validated against a performance database of 21 TAL thrusters, demonstrating excellent agreement. Two design configurations were derived, a baseline 100 W version and a 150 W version with a coaxial hollow cathode. Benchmarking shows promising performance metrics, establishing a robust framework for low-power TAL development.

Introduction

Electric propulsion generates thrust by accelerating ionized propellant via electromagnetic fields, offering superior efficiency over chemical propulsion for long-duration missions. Hall Thrusters (HTs) are widely used for station-keeping and orbit-raising due to their simplicity and adaptability [1]. Thrusters with Anode Layer (TALs) are a distinct category with a narrow acceleration zone and metallic channels biased at cathode potential. This configuration results in higher plasma densities and a stronger electric field compared to ceramic-channel SPTs Figure 1.

The shift toward small satellites has increased demand for compact, sub-500 W thrusters. Furthermore, the high cost of Xenon has driven interest in alternative propellants like Argon, which is abundant and affordable despite its higher ionization energy. This paper addresses the lack of unified scaling laws for low-power TALs by presenting a refined phenomenological model tailored for Argon operation.

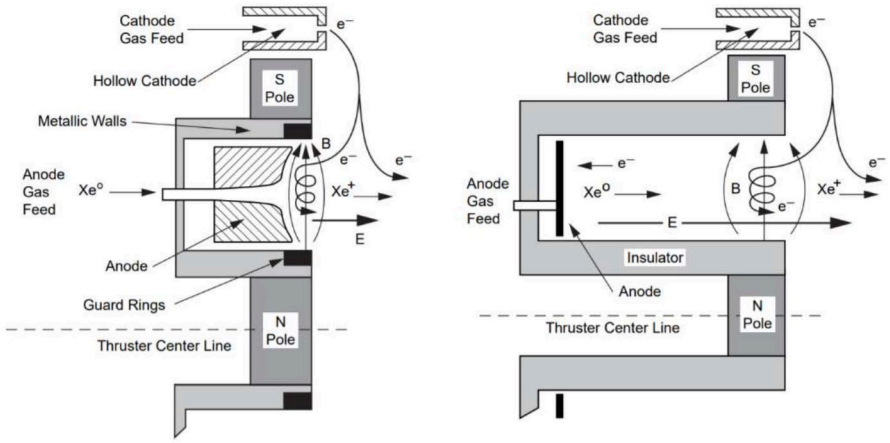


Figure 1 Comparison between SPT and TAL configuration

Content from this work may be used under the terms of the Creative Commons Attribution 3.0 license. Any further distribution of this work must maintain attribution to the author(s) and the title of the work, journal citation and DOI. Published under license by Materials Research Forum LLC.

Materials Research Proceedings 69 (2026) 747-750 https://doi.org/10.21741/9781644904251-132

Scaling Methodology

Scaling methods establish relationships between geometry and operating parameters to preserve performance at different power levels from a well-known thruster to the new one [2]. This work builds upon the flexible methodology developed at the University of Pisa [4], which utilizes a matrix-based approach to allow independent control of design parameters.

TAL-Specific Improvements. To adapt the general model for TALs, non-standard relations for loss mechanisms were introduced.

- *Wall Losses*: In TALs, the metallic walls are at cathode potential, eliminating the zero-net current condition found in SPTs. The wall loss coefficient ϵ_w is modeled as proportional to the ratio of channel length L to width b and the beam efficiency η_b:

$$\epsilon_w \propto \frac{L}{b}\eta_b \tag{1}$$

- *Anode Losses*: Representing the dominant loss in TALs, anode losses ϵ_a were modeled as a function of magnetic field B and discharge voltage V_D with two parametric coefficients (z & χ) which values were refined during the scaling procedure:

$$\epsilon_a \propto B^z V_D^{\chi-1} \tag{2}$$

- *Ionization Losses*: The power loss fractions are obtained by non-dimensionalizing the power losses with the discharge power. The ionization loss coefficient is obtained by using the power spent for propellant ionization, P_i:

$$\eta_i \propto \frac{\eta_b}{L_{ia}} \tag{3}$$

Design Objectives and Validation

The primary target was a 100 W class thruster with a discharge voltage of ~300 V using Argon. Key performance goals included a thrust efficiency $\boldsymbol{\eta > 0,3}$ and a specific impulse $\boldsymbol{I_{sp} > 1000s}$.

Model Validation. The scaling model was validated using a database of 21 TAL models (e.g., D-30, D-55, D-100). By scaling the D-55 reference thruster [3] to various operating points, the model demonstrated high accuracy in predicting thruster performances. Among the available solutions that maximized thrust efficiency, specific impulse and thrust, the ones that best balanced competitive dimensions, comparable to those of existing thrusters operating at similar power levels, with manufacturing considerations were selected. The results of the preliminary design are presented in Figure 2.

Proposed Configurations. Two designs were developed:

- *Standard TAL (100 W)*: Features an externally mounted cathode. The channel length was adjusted to enhance Argon ionization.
- *Coaxial cathode TAL (150 W)*: Incorporates central housing for a hollow cathode, improving compactness and beam neutralization.

Materials Research Proceedings 69 (2026) 747-750 https://doi.org/10.21741/9781644904251-132

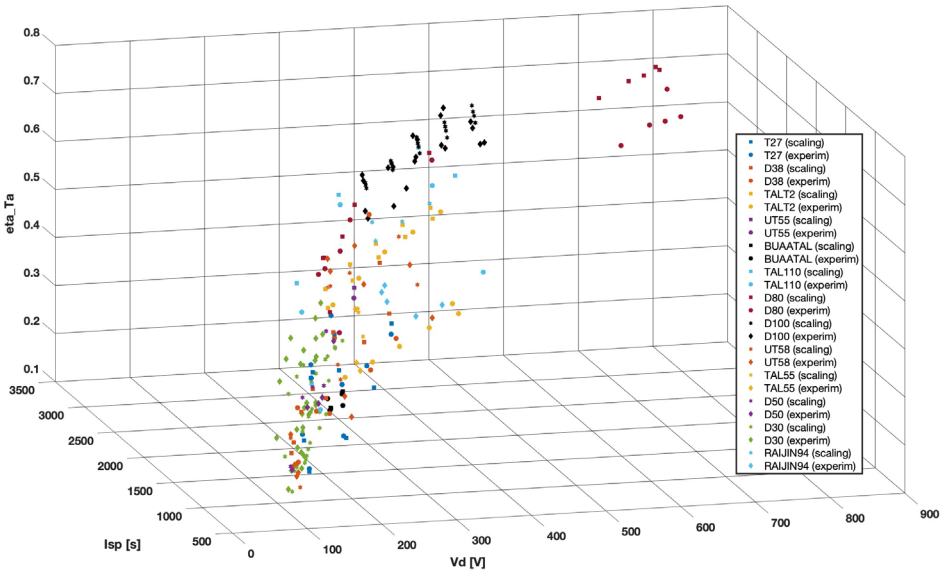


Figure 2 Scaling results: V_D - I_{sp} - η_{Ta}

Benchmarking and Conclusions

The final designs were benchmarked against current market HTs Figure 3. Despite the challenges of Argon (lower thrust efficiency compared to Xenon), the optimized TAL geometry and magnetic topology ensure performance suitable for CubeSat missions.

The proposed scaling methodology offers a robust tool for the preliminary design of TAL thrusters across various power levels. Future work will focus on experimental validation of the 100 W prototype and thermal-magnetic coupling simulations.

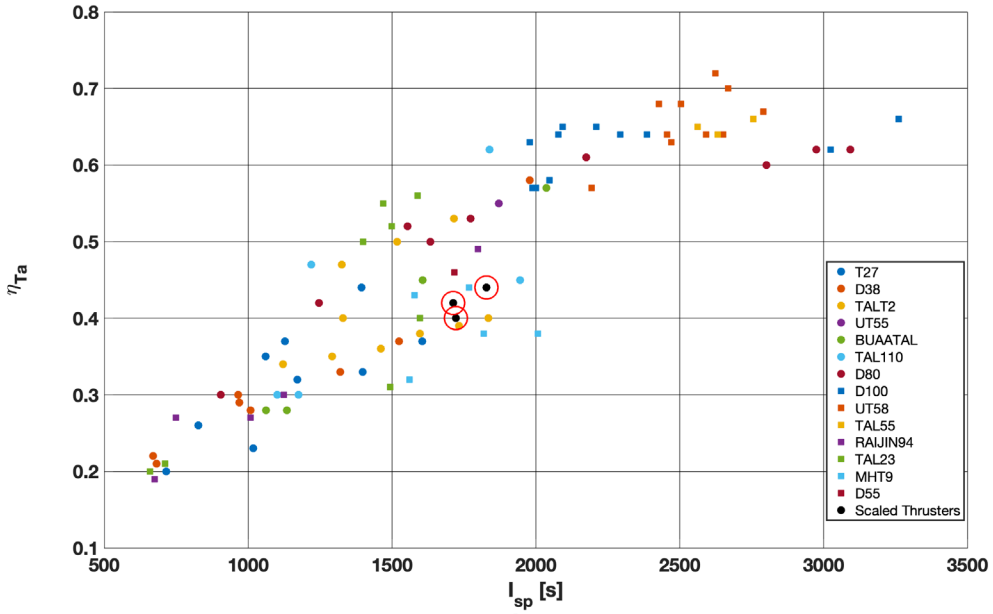


Figure 3 Comparison of the scaled thrusters models with the TAL database

References

[1] Goebel, D.M., Katz, I.: Fundamentals of electric propulsion: ion and hall thrusters. John Wiley and Sons, 79 (2008) https://doi.org/10.1002/9780470436448

[2] Morozov, A.I., Savelyev, V.V.: Fundamentals of stationary plasma thruster theory. Reviews of plasma physics, 203-391 (2000). https://doi.org/10.1007/978-1-4615-4309-1_2

[3] Sankovic, J., Haag, T., Manzella, D.: Operating characteristics of the Russian D-55. thruster with anode layer. 30th Joint Propulsion Conference and Exhibit., 3011 (1994). https://doi.org/10.2514/6.1994-3011

[4] Andrenucci, M., Battista, F., Piliero, P.: Hall thruster scaling methodology. The 29th Int. Electric Prop. Conf., Princeton University, 31 October-4 November 2005 (2005)

Materials Research Proceedings 69 (2026) 751-756 https://doi.org/10.21741/9781644904251-133

Comparative Analysis of Copper Hairpin Motors and Cryogenic Pure-Aluminum Litz-Wire Motors for Hybrid-Electric Aircraft Propulsion

Xinjun Liu[1,a*], Thomas Schriefer[1,b], Andreas Lindner[1,c], Maximilian Hofmann[1,d]

[1]Fraunhofer Institute for Integrated Systems and Device Technology IISB, Schottkystrasse 10, 91058 Erlangen, Germany

[a]xinjun.liu@iisb.fraunhofer.de, [b]thomas.schriefer@iisb.fraunhofer.de, [c]andreas.lindner@iisb.fraunhofer.de, [d]maximilian.hofmann@iisb.fraunhofer.de

Keywords: Hybrid-Electric Aircraft, Cryogenic Motor, Pure Aluminum, Litz-Wire Winding, Copper Hairpin, FEM Simulation, AC and DC Losses

Abstract. This paper compares an oil-cooled copper hairpin motor with a cryogenic pure-aluminum Litz-wire motor for hybrid-electric aircraft propulsion [1] under identical operating constraints. The study is motivated by fuel-cell architectures that enable winding temperatures near 70 K, where aluminum exhibits higher electrical conductivity than copper [2] and can therefore reduce stator direct-current (DC) losses and conductor mass. Finite-element models are employed to quantify electromagnetic behavior, including torque capability, DC and alternating-current (AC) winding losses, and efficiency. The results show that the aluminum concept achieves a lower total loss density despite slightly stronger proximity and eddy-current effects, because the Litz-wire configuration significantly mitigates AC losses. At the rated operating point of 750 kW and 21,000 rpm, peak efficiency reaches 99.0 % for the aluminum design versus 98.1 % for the copper reference. Mission-profile evaluation with a 750 kW rated load indicates up to 0.8 percentage-point higher instantaneous efficiency and an average improvement of about 0.65 percentage points over the cycle. These findings highlight the potential of cryogenic aluminum Litz-wire windings for lightweight, high-efficiency propulsion in future hybrid-electric aircraft.

Introduction

At Fraunhofer IISB, in collaboration with industrial partners and within the framework of European Clean Aviation AMBER project [3], a 12-phase, 750 kW copper hairpin motor operating at 21,000 rpm was previously designed and manufactured, demonstrating distributed windings, oil cooling, and a modular inverter interface as shown in Fig. 1. This design serves as the electromagnetic and geometric baseline for the present comparison.

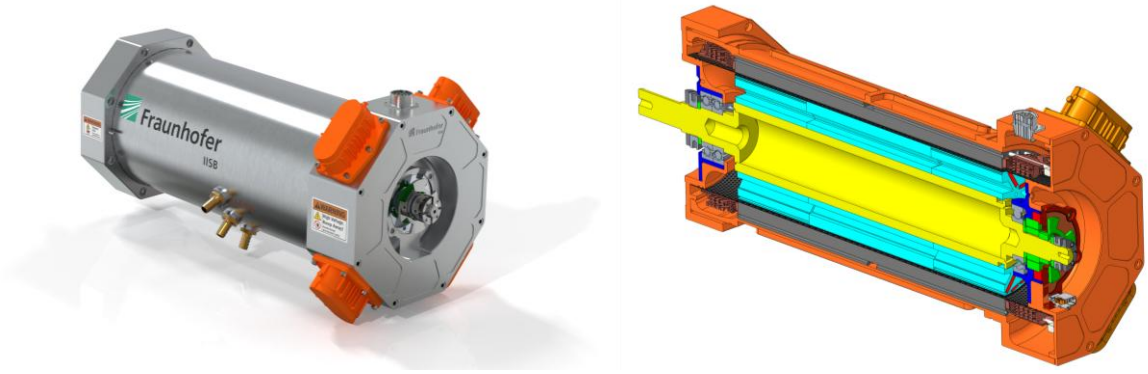


Fig. 1. Multi-phase (4x3) copper hairpin winding for hybrid-electric aircraft propulsion.

Content from this work may be used under the terms of the Creative Commons Attribution 3.0 license. Any further distribution of this work must maintain attribution to the author(s) and the title of the work, journal citation and DOI. Published under license by Materials Research Forum LLC.

Materials Research Proceedings 69 (2026) 751-756 https://doi.org/10.21741/9781644904251-133

Although copper hairpins offer excellent manufacturability and a high slot-fill factor, their rectangular conductors exhibit pronounced high-frequency losses caused by skin and proximity effects, and the high density of copper limits further mass reduction. Fuel-cell aircraft architectures can provide cryogenic cooling near 70 K, where aluminum surpasses copper in electrical conductivity. To address these limitations, this study develops a cryogenic pure-aluminum Litz-wire motor designed to reduce AC losses associated with high conductivity while maintaining identical constraints. Both concepts are evaluated and compared through finite-element modeling and a representative hybrid-electric aircraft mission profile. Mechanical integrity and insulation aspects are beyond the scope of this work and will be investigated in future studies.

Reference Multi-phase Copper Hairpin Winding Motor

The reference machine considered in this work is a high-speed, high-power-density copper hairpin motor, which was developed and manufactured at Fraunhofer IISB based on the overall system boundary conditions of the ATR 72-600 aircraft. The electrical specifications of the motor are listed in Table 1. The machine was specifically designed for hybrid-electric aircraft propulsion and represents a mature technological benchmark for the present comparative analysis. The detailed design process has been described in [4]. The manufactured stator is shown in Fig. 2, which demonstrates the realization of four magnetically decoupled inverter systems, providing independent and redundant operational behavior.

Table 1. Specification of the electric machines for hybrid-electric aircraft

Parameter	Specification Value
Machine type	PMSM
DC link voltage U_{DC}	825 V
Rated output power P_{mech}	750 kW
Target efficiency η_{motor}	95 %
Rated speed n_{r}	21 000 rpm
Rated torque T_{r}	341 Nm
Target power density	8 kW/kg
Thermal class	H (180°C)
Coolant system	Oil cooling

The 12-phase machine is supplied by four silicon carbide inverters. Four independent three-phase subsystems are implemented through a dedicated connector and winding layout, as detailed in [4]. This configuration with magnetically decoupled systems improves fault tolerance, harmonic suppression, and modularity, which are essential for aviation safety. The motor delivers 750 kW at 21,000 rpm and 341 Nm of torque with an efficiency above 95 percent. Direct oil cooling through ducts in each stator tooth ensures effective thermal management. The complete system, including cooling, weighs about 90 kilograms and achieves a specific power of 8.3 kW per kilogram. This validated copper hairpin motor serves as the electromagnetic baseline for the cryogenic aluminum Litz-wire design.



Fig. 2. Realized 12 phases stator with four magnetic decoupled systems and copper hairpin windings.

Materials Research Proceedings 69 (2026) 751-756 https://doi.org/10.21741/9781644904251-133

Cryogenic Pure-Aluminum Litz-Winding Motor

The cryogenic pure-aluminum Litz-wire motor was developed from the reference copper hairpin design while maintaining the same geometric, magnetic, and operational boundary conditions. The objective was to evaluate the electromagnetic performance of aluminum conductors under cryogenic operation and to quantify the influence of temperature-dependent conductivity on both DC and AC losses. The design assumes a cryogenic environment with a winding temperature below 70 K, where pure aluminum exhibits higher electrical conductivity than copper, which reduces DC losses but may increase AC losses in winding.

The stator winding was completely redesigned using a Litz-wire configuration in place of rectangular hairpins, which can reduce the AC losses in winding. Each phase comprises 144 parallel strands with a diameter of 0.3 mm, transposed over a defined pitch length to minimize skin and proximity effects at high frequency. The Litz-wire bundles were modeled as equivalent conductors in the finite-element domain, incorporating the strand count and twisting factor to ensure electromagnetic calculation. The strand diameter and the number of strands were chosen to match the effective cross-sectional area of the copper hairpin winding. The resulting stator and rotor configuration is illustrated in Fig. 3.

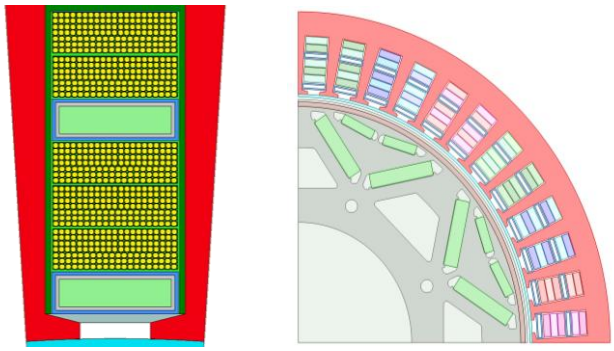
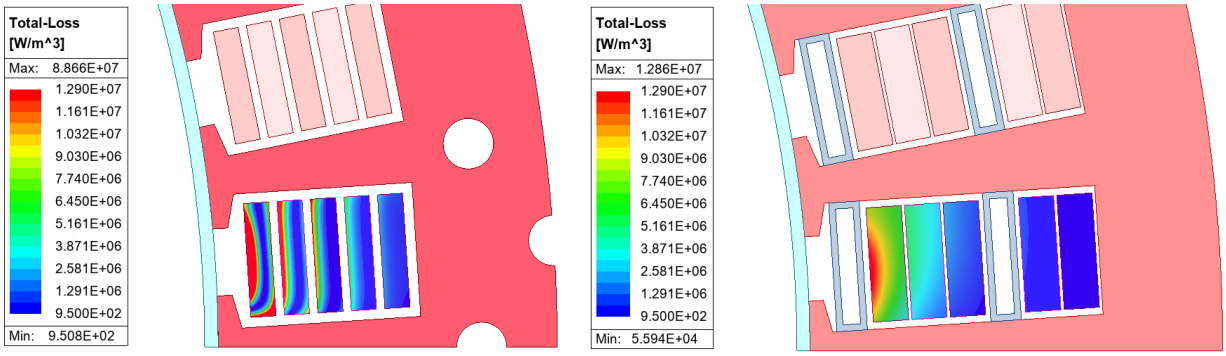


Fig. 3. FEM-model of the electric motor with cryogenic pure-aluminum Litz-wire winding.

Comparative Results

The finite element results of the total losses in the copper hairpin and aluminum Litz-wire windings are shown in Fig. 4. The aluminum Litz-wire concept incorporates a cooling channel within the stator slot, located close to the heat source, and supplied with gaseous helium to maintain a conductor temperature of approximately 70 K. The results indicate that the total loss density in each Litz-wire bundle is lower than that of the copper hairpin winding. Although pure aluminum exhibits higher electrical conductivity lower than 70 K, which increases the proximity and eddy-current effects, the overall loss density remains lower because the Litz-wire configuration effectively reduces AC losses.

Since the motor operates at cryogenic temperature, the ambient temperature of the permanent magnets must also remain within this range. Cryogenically rated magnets, VACODYM 131TP/DTP [5], were selected because they provide a remanent flux density between 1.57 T and 1.62 T from 77 K to 150 K, with 150 K considered as the worst-case design condition. Table 2 summarizes the main design and electromagnetic parameters of both motors. The cryogenic version maintains a geometry similar to the reference machine but incorporates several optimizations for low-temperature operation. The stator outer diameter increases from 195 mm to 206 mm to accommodate cooling channels and larger Litz-wire bundles, while the active length decreases from 429 mm to 352 mm due to the use of stronger cryogenic magnets. The rotor and magnetic circuit remain unchanged for consistent electromagnetic comparison.



a) b)

Fig. 4. FEM of total losses in a) copper hairpin winding and b) aluminum Litz-wires at time=0.011 ms.

FEM results confirm that both motors deliver the same average torque of 348 Nm at 21,000 rpm, demonstrating that the redesign preserves torque capability. The cryogenic aluminum Litz-wire motor achieves a significant reduction in losses. The DC losses in winding decrease from 5.1 kW to 0.27 kW, mainly due to the higher electrical conductivity of aluminum at 70 K. The AC losses also drop from 4.4 kW to 1.71 kW as a result of the Litz-wire configuration. As a consequence, efficiency at rated speed improves from 98.1 percent to 99.0 percent, and total power density increases from 8.1 kW/kg to 10.7 kW/kg.

Fig. 5 and Fig. 6 present the FEM-based efficiency maps and the winding losses distributions of both motors. In the copper hairpin motor, the loss density is concentrated near the slot openings, where strong proximity effects occur because of the rectangular conductor geometry.

These results confirm that the cryogenic Litz-wire concept maintains high electromagnetic performance while significantly improving efficiency and reducing total loss density compared with the copper reference design.

Table 2. Design parameters of the electric motor

Parameter	Value	
Winding type	Copper Hairpin-winding	Aluminum Litz-wire
Number of phases	4 x 3	4 x 3
Stator outer diameter	195 mm	206 mm
Stator bore diameter	154.6 mm	154.6 mm
Rotor outer diameter	147.0 mm	147.0 mm
Thickness of bandage	1.5 mm	1.8 mm
Active length	429 mm	352 mm
Rotor skewing	-3.6° / 0° /0° / -3.6°	-3.6° / 0° /0° / -3.6°°
Stator lamination	NO15	NO15
Rotor lamination	NO35-26Y500	NO35-26Y500
Magnet	48 EH	VACODYM 131 DP/TDP
Simulation temperature	393 K / 120 °C	70 K / -203 °C
Avg. Torque	348 Nm	348 Nm
Torque ripple	13.9 Nm	6.0 Nm
Max. Speed at 800 Vdc	21,000 rpm	22,300 rpm
Max. Voltage at 21,000 rpm	703 V	663 V
Max. Current density	12.02 A/mm^2	12.03 A/mm^2
Dimension of wires/bundle	- / 6.8 mm x 1.5 mm	0.3 mm / 7.1mm x 2.2 mm
Number of strands	1	144
Winding DC losses at 21,000 rpm	5.1 kW	0.27 kW
Winding AC losses at 21,000 rpm	4.4 kW	1.71 kW
Max. Efficiency at 21,000 rpm	98.1 %	99.0 %
Max. Total power density	8.1 kW/kg	10.7 kW/kg

Materials Research Proceedings 69 (2026) 751-756 https://doi.org/10.21741/9781644904251-133

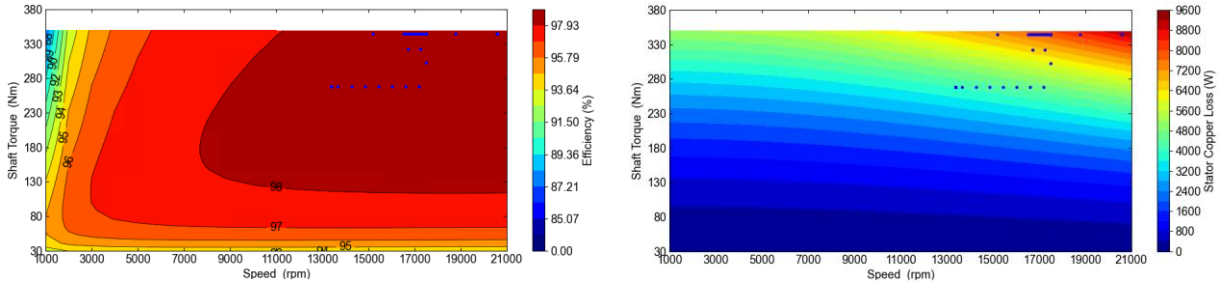


Fig. 5. Efficiency map and winding losses of copper hairpin winding in stator

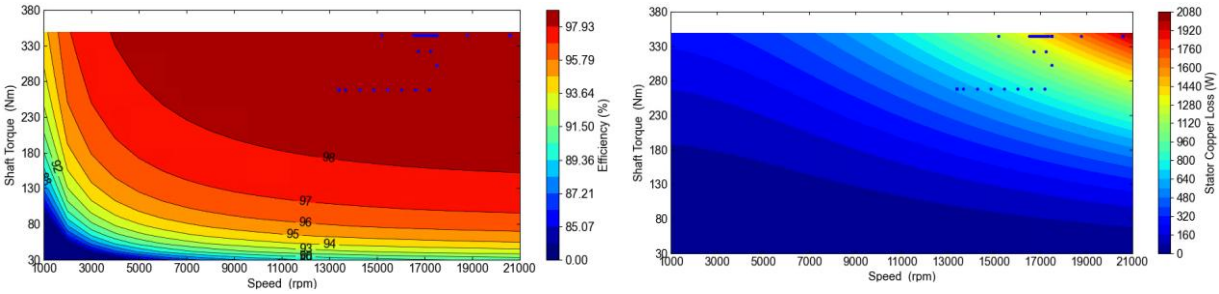


Fig. 6. Efficiency map and winding losses of pure-aluminum Litz-wire in stator

Load Profile Simulation

To evaluate overall propulsion-system efficiency, both the copper hairpin and cryogenic aluminum Litz-wire motors were analyzed under a representative hybrid-electric aircraft mission profile. The power and speed trajectories were derived from the operating cycle of an ATR 72-600-class regional aircraft. The original 850 kW peak load was scaled to 750 kW while maintaining the same speed envelope of 21,000 rpm, as shown in Table 3. The efficiency maps from Fig. 5 and Fig. 6 were combined with the mission load profile to calculate instantaneous machine efficiency throughout the cycle. Fig. 7 compares the mission efficiencies of both designs. During takeoff and climb, the aluminum Litz-wire motor achieves about 0.4 percent higher efficiency. In cruise, where torque demand increases, the efficiency advantage becomes more pronounced and remains in favor of the aluminum Litz-wire design. The maximum improvement over the mission reaches 0.8 percentage points, reflecting a measurable reduction in total losses.

Although the higher electrical conductivity exhibits slightly stronger proximity and eddy-current effects, the aluminum Litz-wire configuration significantly reduces AC losses, and the lower DC losses at cryogenic temperature yield a higher overall efficiency. The improved performance and reduced conductor mass demonstrate the potential of cryogenic aluminum windings for lightweight, high-efficiency hybrid-electric propulsion systems.

Table 3. Load profile of a hybrid-electric ATR 72-600 using a 750 kW electric machine

	START	TXOUT	TKO	CLB	CRZ1	CRZ2	DESC	APP	LAN	TXIN
Max. Power [kW]	375	375	750	750	750	750	556	556	556	375
Toque [Nm]	268	268	345	345	345	345	322	322	303	268
Cum Time [min]	0	14	16	33.4	33.4	62.9	75	77	78	85
Prop Speed [RPM]	780	780	1200	1200	1020	1020	960	960	1020	780
EM Speed [RPM]	13385	13385	20592	20592	17503	17503	16474	16474	17503	13385

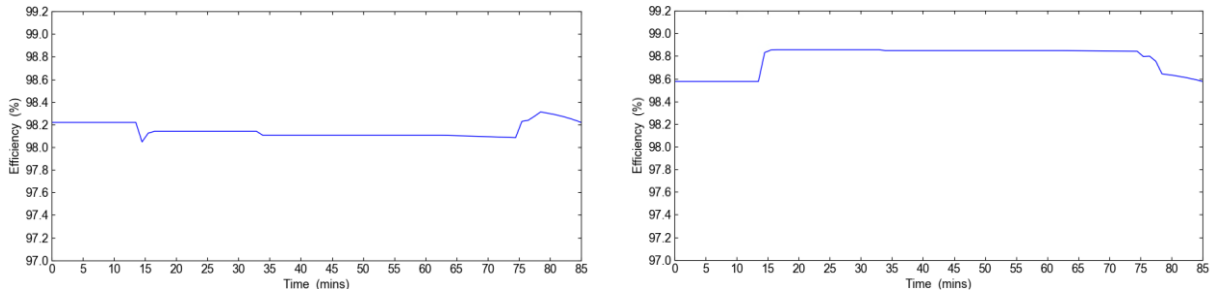


Fig. 7. Efficiency comparison between the concepts with a) hairpin winding and b) aluminum Litz-wire.

Summary

This paper presented a comparative electromagnetic analysis of a copper hairpin motor and a cryogenic pure-aluminum Litz-wire motor for hybrid-electric aircraft propulsion.

The results demonstrated that, although pure aluminum exhibits higher electrical conductivity at cryogenic temperatures, which enhances proximity and eddy-current effects, the use of Litz-wire conductors effectively suppresses these AC losses. As a consequence, the aluminum Litz-wire achieved a substantially lower total loss density and reduced winding losses compared with the copper hairpin winding. When evaluated over a representative hybrid-electric aircraft mission profile, the cryogenic aluminum Litz-wire motor delivered up to 0.8 percentage points higher efficiency and an average improvement of approximately 0.4 percentage points over the complete mission cycle. In addition to improved efficiency, the lower conductor density offers a meaningful reduction in total motor mass.

These findings confirm that cryogenic aluminum Litz-wire technology provides a promising path toward lightweight, high-efficiency electric propulsion systems. Future work will focus on thermal and mechanical validation, as well as experimental verification of the cryogenic prototype under representative operating conditions.

Acknowledgement

This contribution was supported by the European Clean Aviation “Innovative demonstrator for hybrid-electric regional application” (AMBER) project under grant agreement ID 101102020.

References

[1] F. F. Da Silva, J. F. P. Fernandes, and P. J. Da Costa Branco, "Barriers and Challenges Going from Conventional to Cryogenic Superconducting Propulsion for Hybrid and All-Electric Aircrafts," *Energies*, vol. 14, no. 21, p. 6861, 2021, doi: 10.3390/en14216861.

[2] H. Zhang *et al.,* "Electromagnetic Characterization of Hyperconducting Aluminum Litz Wires at Cryogenic Temperatures," *IEEE Access*, vol. 12, pp. 60234–60245, 2024, doi: 10.1109/ACCESS.2024.3391385.

[3] CORDIS - EU research results, Clean Aviation, *InnovAtive DeMonstrator for hyBrid-Electric Regional Application (AMBER).* [Online]. Available: https://cordis.europa.eu/project/id/101102020

[4] X. Liu, T. Schriefer, Maximilian Hofmann, and Bernd Eckardt, "Multi-phase Hairpin Winding Electric Machine for Hybrid Electrical Aviation Applications," *2025 2nd International Conference on Production Technologies and Systems for E-Mobility (EPTS)*, 2025.

[5] VAC, *VACODYM 131.* [Online]. Available: https://indico.cern.ch/event/682107/attachments/1560598/2465484/Vacodym_131_de.pdf

Materials Research Proceedings 69 (2026) 757-763 https://doi.org/10.21741/9781644904251-134

Retrofitting a Hairpin Stator Winding Aircraft Propulsion Motor with a Superconducting Rotor

Andreas Lindner[1,a*], Xinjun Liu[1,b], Daniel Walch[1,c]

[1]Fraunhofer Institute for Integrated Systems and Device Technology IISB, Schottkystr. 10, 91058 Erlangen, Germany

[a]andreas.lindner@iisb.fraunhofer.de, [b]xinjun.liu@iisb.fraunhofer.de, [c]daniel.walch@iisb.fraunhofer.de

Keywords: Superconducting Electric Motor, Permanent Magnet Machine, Electric Aircraft, Electric Excitation

Abstract. Currently, there are different future aircraft concepts considering hybrid electric and fully electric propulsion system. To achieve an electric aircraft there is the need for electric motors with a higher power density and lower weight than conventional solutions currently available [1]. Using hairpin stator windings increases the power density of the machine due to their high slot fill factor and good thermal properties. Furthermore, they enable automated manufacturing and decreasing costs. To achieve a further step regarding higher power densities, the use of superconductors in electric motors is proposed [2]. They have minor DC resistance in the superconducting state, which could minimize the motor losses and enable a generation of high flux density motors. Both stator and rotor could be realized using superconductors. A rotating magnetic field is generated in the stator, which is why AC currents are required. Consequently, AC losses still occur in machines with super-conducting stator (SC-stator) and must be considered to prevent quenching [3]. When using SC-rotors, an electrically excited synchronous machine is designed. Here, DC currents are used to generate a constant magnetic pole system. These AC losses are disregarded in the first place which simplifies the initial design process.

Introduction

In [4], a multi-phase electric motor for hybrid electrical aircraft applications is presented (Fig. 1, left). It uses a stator with hairpin winding and direct oil cooling and a permanent magnet excited rotor. The machine achieves a continuous power of 750 kW at a DC voltage of 800 V. A total power density of 8.33 kW/kg is realized including active and passive components such as bearings and housing. In this paper, the motor presented in [4] has been retrofitted with a superconducting rotor. For this, the same stator design and installation space is maintained. The new rotor design uses high temperature superconductor (HTS) winding for electrical excitation. Liquid hydrogen could be used as the cooling medium, which is on board as an energy storage anyway, depending on the aircraft design [5]. Different electromagnetic designs are presented, and the achievable power density is discussed. The maximal speed of the machine is 21000 rpm [4]. With the SC-technology the maximum torque could be increased by means of higher flux density values attained by an order of magnitude increased current density in the HTS-coils compared to conventional field windings in electrically excited synchronous machines (EESM). This would result in changes to the motor map and characteristics. To optimize the overall propulsion system, either the operating rotational speed can be changed, or the motor aspect ratio could be minimized.

Retrofitting of the machine

From the initial electromagnetic design presented in Fig. 1 on the left, the interior permanent magnet rotor (IPM-rotor) is replaced by a rotor with electrically excited coils while keeping the overall machine dimensions (Fig. 1, on the right).

Content from this work may be used under the terms of the Creative Commons Attribution 3.0 license. Any further distribution of this work must maintain attribution to the author(s) and the title of the work, journal citation and DOI. Published under license by Materials Research Forum LLC.

Materials Research Proceedings 69 (2026) 757-763 https://doi.org/10.21741/9781644904251-134

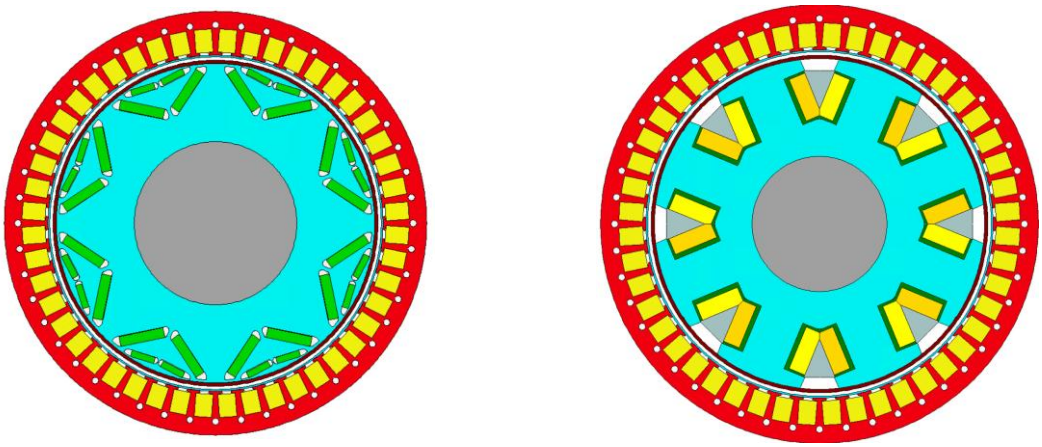


Fig. 1. Comparison of the machine designs of an interior permanent magnet rotor (left) and the superconducting rotor (right) in the same hairpin winding stator.

Then, the excitation current is adjusted to generate the same machine torque. This can be achieved using increased field current densities e.g. 23 A/mm^2 for which forced liquid rotor cooling in conventional technology already needs to be employed.

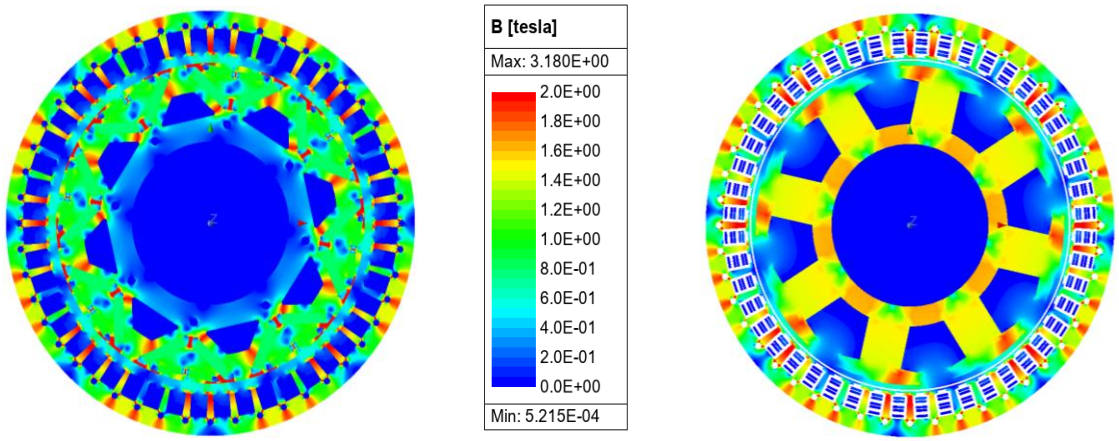


Fig. 2. Flux-density distribution of original (left) and electrically excited design (right) machine design at low current densities exhibiting the same torque behavior.

The resultant distribution of the magnetic flux density is presented in Fig. 2. The IPM shows some saturation particularly in the rotor iron bridges while the EESM is partly saturated within the stator teeth, in the tooth tip of the rotor and is generally magnetically more loaded (Fig. 2, on the right) than the IPM.

Employing super-conductivity

The EESM-design requires a continuous current flowing in the field-winding (FW) which creates the rotor pole system of the machine. To generate the same torque with the EESM-design the field-current densities are already very high. This was expected whereas the high energy rare-earth permanent magnets create a rotor excitation field which ampere-turns can only hardly be realized by a current driven field-winding. The magnetic energy density of rare-earth permanent magnets is generally unmatched in electrical machine design. Therefore, a more sophisticated technology needs to be employed to outperform the torque performance of the IPM-machine. This is

Materials Research Proceedings 69 (2026) 757-763 https://doi.org/10.21741/9781644904251-134

essentially achieved via super-conductivity exemplary in the rotor part. With this technology two orders of magnitude higher current-densities in the field-winding compared to conventional EESM-design are achievable without sacrificing the thermal limits of the FW [6]. However, the rotor of the partly SC-EESM must be held constantly at cryogenic temperatures by means of a special rotor cooling system.

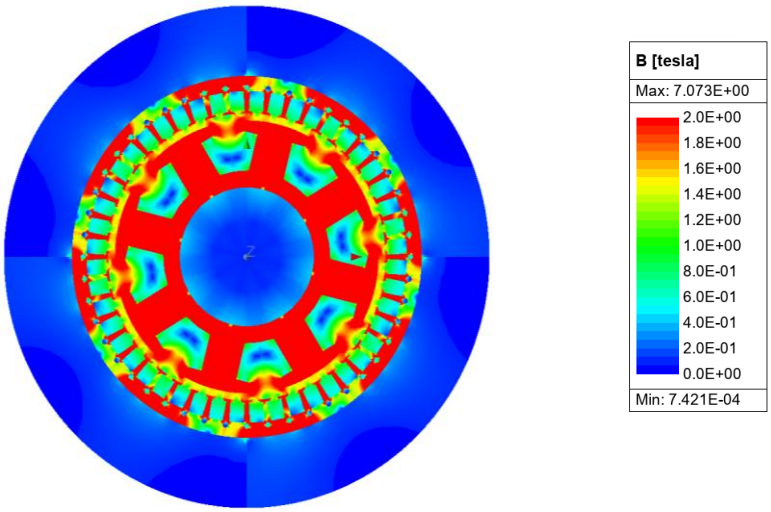


Fig. 3: Flux-density distribution of a partly SC-EESM

Depending on the used super-conductor, the employed cryogenic temperature and critical technical current densities for REBCO-tapes can range up to 3.3 kA/mm^2 [6]. However, to keep a sufficient distance to the critical current densities and magnetic field limits of the SC-tapes it is decided to use an intermediate engineering current density of $J = 300$ A/mm^2 for the SC-FW within EESM design. Fig. 3 shows the magnetic flux-density distribution of the machine showing large, saturated iron parts compared to Fig. 2 on the right. Due to the high magnetic saturation, the outer area is additionally magnetically modelled.

Rotor soft magnetic material

Three different motor variants of the partly SC-machine are magnetically simulated by exchanging the soft magnetic material of the rotor. For this, the magnetic properties of two different soft magnetic materials need to be examined in more detail.

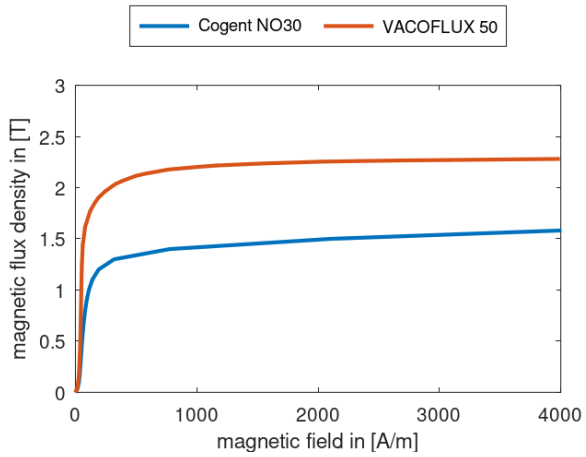


Fig. 4: Magnetization curve of conventional silicon-iron steel and cobalt-iron taken from Ansys MotorCad

Materials Research Proceedings 69 (2026) 757-763 https://doi.org/10.21741/9781644904251-134

Fig. 4 shows two different magnetization curves of a conventional silicon-iron steel (Fig. 4, Cogent NO30) and a high-performance cobalt-iron steel (VACOFLUX 50) exhibiting superior magnetization characteristics with saturation magnetization values of up to 2.4 Tesla. Both steels are now considered as rotor materials. Moreover, an air-cored rotor structure for the EESM will also be designed.

Torque development

From the saturation level displayed in Fig. 3 it is clear, that both soft magnetic materials will be highly saturated in terms of a partly SC-machine. However, it is expected that the cobalt-iron steel has more torque performance (Fig. 4, about +30%) even at high magnetic fields. Moreover, the flux guiding effect of the iron within the rotor of the EESM is not fully vanished.

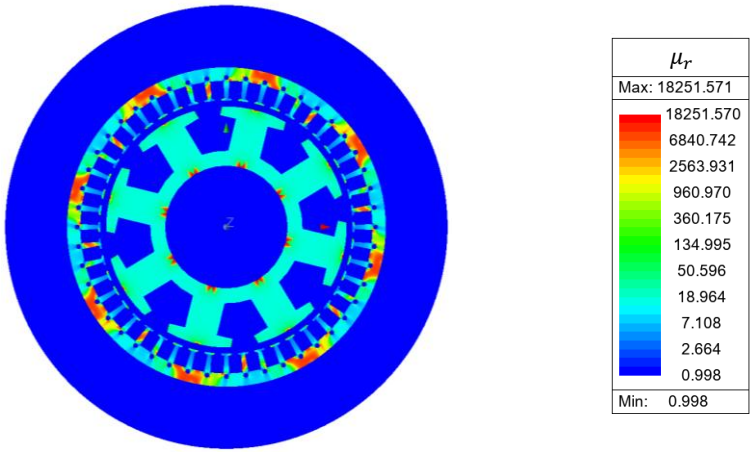


Fig. 5: Logarithmic relative magnetic permeability μ_r within a cobalt-iron SC-EESM rotor

Fig. 5 shows in this context the logarithmic distribution of the relative magnetic permeability μ_r of the machine which is several factors ($\mu_r \approx 15 \dots 20$, $\mu_r \approx 3 \dots 6$ for silicon-iron) above unity within the iron-cobalt rotor. To clarify this, the torque development of an air-cored rotor is also simulated.

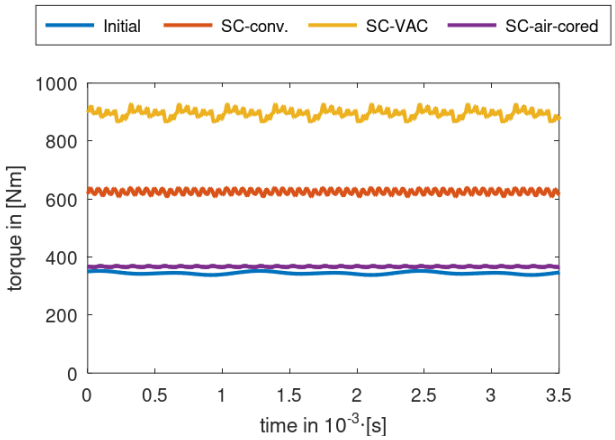


Fig. 6: Machine torque of different SC-configurations and the original torque

Fig. 6 illustrates a direct comparison of the machine design presented in Fig. 2 on the left and its equivalent SC-EESM design (Fig. 3) employing different magnetic rotor materials. From Fig. 5 and Fig. 6 it can be concluded, that the SC-rotor largely increases the torque of the machine whereby the torque of the NO30 conventional silicon steel is 43% lower than that of the iron-cobalt rotor presented in Fig. 5. A machine with an air-cored rotor has almost the same

Materials Research Proceedings 69 (2026) 757-763 https://doi.org/10.21741/9781644904251-134

performance as the non-superconducting machine. In this case the current density of the SC must be increased to achieve more performance as the magnetic flux in the rotor is not guided anymore. All partly SC-machine designs show an increased torque ripple.

Iron and solid losses

Partly SC-EESMs are highly magnetically loaded machines. For the core loss calculation the classical Bertotti equation [7] is used Eq. (1) where k_h, k_c and k_{exc} remark the coefficients for the hysteresis, classical eddy-current and excess losses, respectively.

$$p_v = k_h f \hat{B}^{\alpha} + k_c f^2 \hat{B}^2 + k_{exc} f^{\frac{3}{2}} \hat{B}^{\frac{3}{2}} \tag{1}$$

The magnitude of the flux-density $\hat{B}$ and the frequency f remark the time varying loss components. With the relation in Eq. (1), the loss density of the machine designs is calculated.

Table 1 : Iron loss coefficient and magnetization frequency for the evaluated machine designs

Motor design	α	k_h	k_c	k_{esc}	Frequency in [Hz]
IPM – NO30	2	7.6e-05	0.269	0	1400
SC-EESM-NO30	2	7.6e-05	0.269	0	773
SC-EESM-VAC	4.84	0.02096	2.86e-06	0.003557	540
Air-cored-rotor	2	7.6e-05	0.269	0	1315

Table 1 presents the iron loss coefficients of the magnetic materials displayed in Fig. 4. The air-cored machine has iron losses only in the stator. For the cobalt-iron rotor core the values of NO30 are applied in the stator. The different magnetization frequencies come from the power requirement of the machine (750 kW). Here, a proportional reduction of the rotational speed is possible because of the higher torque production of SC-machine designs.

Table 2: Overview over iron losses in the IPM and SC-EESM machine designs

Motor design	Rotor core losses in [W]	Stator core losses in 10^3·[W]
IPM – NO30	9	1.42
SC-EESM-NO30	6.4	3.38
SC-EESM-VAC	6e-3	2.55
Air-cored-aluminum rotor	1370	4.29

The evaluated iron losses are given in Table 2. The stator losses are the dominant part whereby the SC-EESMs incorporate more losses than the conventional machine design. In terms of an air-cored rotor made of aluminum massive eddy-current losses occur at the tooth tip of the rotor. The same effect will be present if a stainless-steel sleeve in the airgap is introduced to hermetically seal the rotating cryogenic part of the machine.

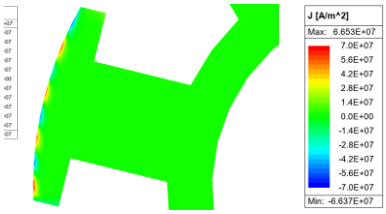


Fig. 7: Eddy-current distribution in SC-EESM ironless air-cored aluminum rotor

Fig. 7 shows the eddy-current distribution at the tooth tip of a rotor pole. Here, the slotting effect of the saturated stator teeth can clearly be seen. Moreover, as the stator teeth are highly saturated and very strong time varying magnetic proximity fields are present in the slot of the

machine. Simulations, which are not presented here, show that the proximity losses in the hairpin stator winding deteriorate efficiency in case of SC-rotor machines by several tens of percentage points. Therefore, the hair-pin winding is not applicable anymore in retrofit designs and the usage of stranded wires for the stator winding is obligatory.

Reduction of motor dimensions

In the previous chapter the iron losses are investigated with reduced rotational speed. Another way to use the high torque performance of the partly SC-EESM is to leave the rotor speed constant (21000 rpm) and reduce the axial machine dimension.

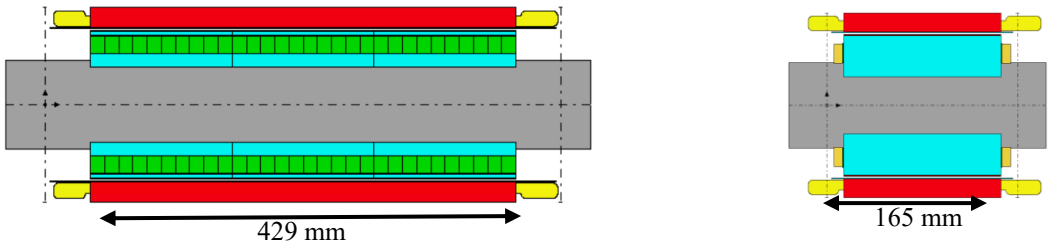


Fig. 8: Comparison of conventional IPM (left) and SC-EESM (right) having the same power

Fig. 8 shows a direct comparison of the axial dimension of conventional IPM-technology (Fig. 8, left) and its partly SC equivalent (Fig. 8, right). The machine volume and weight are more than two times reduced. The iron losses in the stator are four times higher due to the massive saturation (Fig. 3) and high frequency, which is approximately 0.8% of the machine efficiency. However, Fig. 8 shows the full potential of the SC-technology. The power density of an already highly utilized motor can be further increased to values above 20 kW/kg.

Summary

In this paper a retrofit design of a high-power electrical machine for hybrid aircraft propulsion is investigated. For this, a conventional IPM rotor is exchanged by a SC-EESM rotor carrying SC-field excitation coils. In this case one gets a highly saturated machine even when intermediate current densities are applied. Three machine designs with conventional, high-performance electrical steel and an air-cored rotor have been evaluated. Here, the application of iron within the rotor, even in high saturation state (Fig. 3), provides more torque than the air-cored machine variant (Fig. 6). If one can afford the losses in the cryogenic part (Fig. 7) a standard stator design can be used. Otherwise, a stator yoke in ring shape must be employed whereby losing 30 % torque in this case. Anyway, litz-wire is obligatory for the stator winding of SC-machines because high magnetic proximity fields.

References

[1] W. Cao, B. C. Mecrow, G. J. Atkinson, J. W. Bennett, and D. J. Atkinson, "Overview of Electric Motor Technologies Used for More Electric Aircraft (MEA)," *IEEE Trans. Ind. Electron.*, vol. 59, no. 9, pp. 3523–3531, 2012. https://doi.org/10.1109/TIE.2011.2165453

[2] P. Alvarez, M. Satrustegui, I. Elosegui, and M. Martinez-Iturralde, "Review of High Power and High Voltage Electric Motors for Single-Aisle Regional Aircraft," *IEEE Access*, vol. 10, pp. 112989–113004, 2022. https://doi.org/10.1109/ACCESS.2022.3215692

[3] R. Mellerud, M. Leandro, C. L. Klop, C. Hartmann, and J. K. Nøland, "Influence of Harmonic Distortion on AC Losses in Converter-Fed Superconducting Electrical Machines," *IEEE Trans. Appl. Supercond.*, vol. 35, no. 2, pp. 1–7, 2025. https://doi.org/10.1109/TASC.2024.3517669

[4] X. Liu, T. Schriefer, D. Walch, A. Lindner, M. Hofmann, and B. Eckardt, "Multi-phase Hairpin Winding Electric Machine for Hybrid Electrical Aviation Applications," *Production Technologies and Systems for E-Mobility (EPTS)*, 2025.

[5] R. Mellerud, C. Hartmann, C. L. Klop, S. Austad, and J. K. Nøland, Eds., *Design of a Power-Dense Aviation Motor With a Low-Loss Superconducting Slotted Armature*, 2023.

[6] H. S. Ruiz *et al.,* "Critical current density in advanced superconductors," *Progress in Materials Science*, vol. 155, p. 101492, 2026. https://doi.org/10.1016/j.pmatsci.2025.101492

[7] G. Bertotti, "General properties of power losses in soft ferromagnetic materials," *IEEE Transactions on Magnetics*, pp. 621–630, 1988. https://doi.org/10.1109/20.43994

UAV, UAM & Rotorcraft Systems



Materials Research Proceedings 69 (2026) 765-770 https://doi.org/10.21741/9781644904251-135

Shuttle Drone Control with Airflow Disturbance Compensation for Cooperative Target Capture

António S. Costa[1,a], Bruno J. N. Guerreiro[1,2,b*]

[1]DEEC, CTS-Uninova and LASI, NOVA University Lisbon, 2829-516 Caparica, Portugal

[2]ISR, LARSyS, Instituto Superior Técnico, Universidade de Lisboa, Portugal

[a]salvadorbouzaserrano@gmail.com, [b]bj.guerreiro@fct.unl.pt

Keywords: Drone Capture, Airflow Compensation, Nonlinear Control, Downwash Model

Abstract. This paper addresses the autonomous capture of a target drone by a shuttle drone in a cooperative scenario, focusing on modeling and compensating aerodynamic disturbances caused by environmental factors and proximity flight. The work integrates a nonlinear model of multirotor drones, incorporating aerodynamic effects such as rotor and frame drag, and designs a nonlinear controller to follow trajectories and mitigate disturbances. Additionally, a downwash model based on momentum theory is included to compensate for airflow disturbances during close-proximity capture maneuvers, enhancing stability and precision. Simulation results validate the proposed control strategies, demonstrating improved trajectory tracking and disturbance mitigation in various scenarios, including high-speed single drone operations and close-proximity two-drone maneuvers.

Introduction

Unmanned Aerial Vehicles (UAVs) have seen widespread adoption [1] across diverse applications including search and rescue operations,commercial package delivery,and precision agriculture. Recent advances have shifted focus toward cooperative multi-drone systems that share tasks, loads, or resources, enabling enhanced capabilities such as optimized search patterns and synchronized aerial displays.

Aerodynamic modeling research has identified critical factors affecting proximity flight, including frame drag impacts on trajectory tracking [2], rotor-air interactions in ground effect and formations [3], and downwash phenomena requiring safe operational regions [4]. While Momentum Theory applications enable modeling vehicles hovering beneath others [5] and differential flatness properties reduce tracking errors during agile maneuvers [6], existing studies primarily evaluate horizontal-plane interactions. Despite these advances, a critical gap exists in developing integrated control strategies that simultaneously address autonomous flight, vertical proximity aerodynamic effects, and cooperative capture execution.

This work addresses these gaps, within the CAPTURE project framework [7], by developing an integrated solution for cooperative capture maneuvers between quadrotors. The main contributions are threefold: (1) an integrated control framework that simultaneously handles autonomous flight and proximity aerodynamic effects, towards capture maneuver requirements, in a unified approach; (2) development of simple aerodynamic models and compensation strategies specifically addressing vertical proximity effects between quadrotors; and (3) validation through simulations, demonstrating effectiveness in managing environmental disturbances and inter-drone aerodynamic forces.

Vehicle Modeling and Control

Quadrotors are underactuated systems with six degrees of freedom, controlled by only four inputs, mapped to the rotor speeds. Motion control requires simultaneous speed variation.

Content from this work may be used under the terms of the Creative Commons Attribution 3.0 license. Any further distribution of this work must maintain attribution to the author(s) and the title of the work, journal citation and DOI. Published under license by Materials Research Forum LLC.

Materials Research Proceedings 69 (2026) 765-770 https://doi.org/10.21741/9781644904251-135

Two reference frames are essential for modeling: the world frame W, a fixed local tangent plane, considering North-East-Down coordinates, and the body frame B, attached to the vehicle's center of mass. The rotation matrix $R \in SO(3)$ transforms coordinates from frame B to frame W, whereas the position of B in W is denoted as $p \in \mathbb{R}^3$, the velocity of B described in W is $v \in \mathbb{R}^3$, and the angular velocity of B relative to W, described in B is denoted as ω.

Thus, the system state vector $x = [p^T \ \mathrm{vec}(R)^T \ v^T \ \omega^T]^T$, resulting in the vehicle kinematics, $\dot{p} = v$ and $\dot{R} = RS(\omega)$, with dynamics

$$\dot{v} = -gz_W + \frac{u_1}{m} z_B \tag{1}$$

$$\dot{\omega} = J^{-1}(-S(\omega)J\omega + u_\tau) \tag{2}$$

where g is gravitational acceleration, m is mass, J is the inertia matrix, $z_W = [0\,0\,1]^T$, $z_B = Rz_W$, and $S(\omega)$ is the skew-symmetric matrix of angular velocities, that also satisfies $S(a)b = a \times b$ for $a, b \in \mathbb{R}^3$. The control input vector to this model is defined as $u = [u_1 \ u_\tau^T]^T \in \mathbb{R}^4$, where $u_1 \in \mathbb{R}$ is collective thrust, $u_\tau \in \mathbb{R}^3$ represents torque inputs.

A nonlinear controller based on [8] can be designed to minimize tracking errors relative to a desired reference trajectory, defined by the desired yaw angle, ψ_d, position, p_d, velocity, v_d, and acceleration, a_d. Towards this end, a desired force vector is defined as

$$f_d = -K_p e_p - K_v e_v - K_{ip} e_{ip} + mgz_W + ma_d \tag{3}$$

where $e_p = p - p_d$ and $e_v = v - v_d$ are position and velocity errors, e_{ip} is the integral of the position error, whereas K_p, K_v, and K_{ip} are positive definite diagonal gain matrices. From this desired force, the thrust input is obtained through scalar projection, $u_1 = f_d^T z_B$, whereas the attitude control requires computing the desired rotation matrix $R_d = [x_{B,d} \, y_{B,d} \, z_{B,d}]$. The desired body z-axis aligns with the force direction, defining $z_{B,d} = f_d / ||f_d||$, and using the intermediate frame with $x_{C,d} = [\cos\psi_d \ \sin\psi_d \ 0]^T$, the remaining axes are defined as $y_{B,d} = (z_{B,d} \times x_{C,d}) / ||z_{B,d} \times x_{C,d}||$ *and* $x_{B,d} = y_{B,d} \times z_{B,d}$.

As such, the rotation error quantifies orientation discrepancy as $e_R = 1/2 S^{-1}(R_d^T R - R^T R_d)$ where $S^{-1}(\cdot)$ denotes the inverse operation of $S(\cdot)$. The desired angular velocities, ω_d are derived from the jerk (third derivative) of the trajectory, as detailed in [8], resulting in the torque control inputs $u_\tau = -K_R e_R - K_\omega e_\omega$, where $e_\omega = \omega - \omega_d$ is the angular velocity error, and K_R, K_ω are positive definite diagonal gain matrices.

Aerodynamic Modeling and Control

Rotorcraft vehicles motion is significantly influenced by aerodynamic forces opposing movement, formulated as $f_a = f_{rd} + f_{fd}$, where f_{rd} and f_{fd} represent rotor and frame drag forces respectively. A central concept in aerodynamic effects is the velocity of the air flow relative to the body frame B, expressed in B, here denoted as $v_{Bair} \in \mathbb{R}^3$. This accounts for the velocity of the vehicle and the velocity of the wind, which when described in the world frame W can be written as $v_{air} = Rv_{Bair} = v - v_w$.

Single vehicle aerodynamic forces modeling and compensation

Following [6], a simple model for the rotor drag force is defined as

$$f_{rd} = -RC_{rd} v_{Bair} \tag{4}$$

Materials Research Proceedings 69 (2026) 765-770 https://doi.org/10.21741/9781644904251-135

where C_{rd} is a diagonal matrix of rotor drag coefficients. Frame drag, modeled according to [2], represents air resistance due to the quadrotor shape, here defined as

$$f_{fd} = -\frac{1}{2}\rho C_d A v_{Bair} \odot |v_{Bair}| \tag{5}$$

where ρ is air density, C_d is the drag coefficient, $A = \mathrm{diag}(a_x.a_y, a_z)$ with a_i represents the projected area along axis i of the body frame, and the product $v_{Bair} \odot |v_{Bair}|$ denotes an element-wise multiplication between the two vectors, while a slight abuse of notation is used in $|v_{Bair}|$, denoting also the element-wise absolute value operator. The symmetry assumption simplifies modeling by using constant drag coefficients along body axes.

The complete velocity dynamics incorporating both effects becomes

$$\dot{v} = -g z_W + \frac{1}{m}(u_1 z_B + f_{rd} + f_{fd}) \tag{6}$$

Recalling the nonlinear controller presented above, which controls the attitude of the vehicle according to a desired force vector, with the addition of aerodynamic effects presented here, compensation is achieved through feed-forward control terms in the desired force as

$$f_d = -K_p e_p - K_{ip} e_{ip} - K_v e_v + m g z_W + m a_d - f_{rd} - f_{fd} \tag{7}$$

which can have both rotor-drag and frame-drag compensation, just one of these, or none, as will be explored in the results presented below.

Two-vehicle aerodynamic interactions

When two rotorcraft operate in proximity, the dynamics of the airflows of both vehicles might become coupled, possibly resulting in control authority loss. The scenario considered in this paper assumes a shuttle drone (drone 1) which generates downwash affecting the target drone (drone 2) flying below the shuttle drone, assuming identical vehicles.

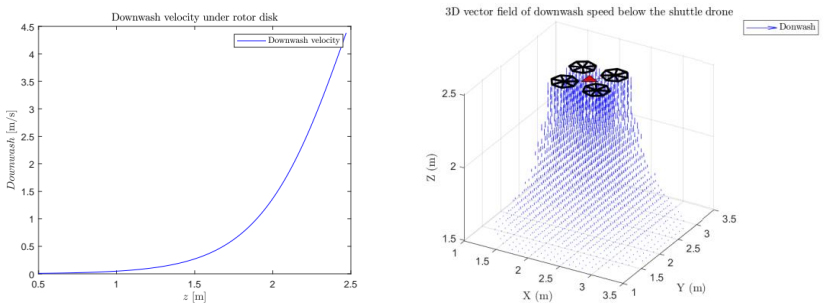
Using momentum theory [5], the induced air velocity of drone 1 is $V_{i_1} = \sqrt{T/(2\rho A_d)}$ where T is total thrust and A_d is rotor disk area. A possible estimate of the vertical air velocity $V_{d_1}(z)$, at a given vertical distance z (below the rotor height, z_r), can be defined as

$$V_{d_1}(z) = V_{i_1} + V_{i_1} \tanh\left(-k\frac{z_r - z}{h}\right) \tag{8}$$

where parameters h and k define the shape of the curve, as depicted in Fig. 1a.

Momentum theory assumes that $V_{d_1}(z)$ is uniform over the xy plane for a given z position. However, as the boundary of the downwash contracts due to acceleration, the radial condition

Materials Research Proceedings 69 (2026) 765-770 https://doi.org/10.21741/9781644904251-135



(a) 2-D plot (b) 3-D plot

Figure 1: Air flow beneath drone 1 analysis

for the vertical velocity reaching zero changes, expanding as the air goes down. Considering the radial distance $r_d(x, y)$ and the rotor radius r, the downwash velocity can be computed at any 3-D point, (x, y, z), below the rotor disc as

$$V_{dw_1}(x, y, z) = \begin{cases} V_{d_1}(z), & \text{if } r_d(x, y) < \frac{r}{\sqrt{1+\tanh\left(-k\frac{z_r - z}{h}\right)}} \\ 0, & \text{otherwise.} \end{cases} \tag{9}$$

This airflow can be seen in Fig. 1b, where 4 rotors for drone 1 are considered.

The downwash air flow velocity from drone 1 can be accounted for in drone 2 air flow velocity, by redefining

$$v_{air_2} = v_2 - v_w - v_{dw} \tag{10}$$

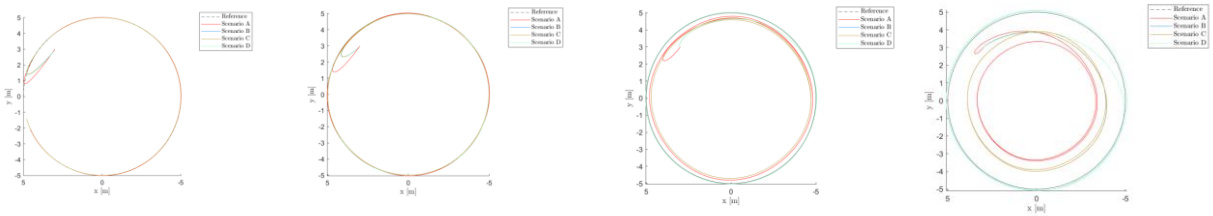
where v_{dw_1} represents the 3-D downwash velocity vector as $v_{dw_1} = [0\,0\,V_{dw_1}]^T$. This additional airflow component modifies both rotor and frame drag calculations for drone 2, according to the axpressions above, resulting also in a compensation of this factor in the controller.

Simulation Results

The proposed control strategies were implemented using MATLAB/Simulink, with separate modules for the quadrotor controller and dynamic model. The controller receives reference values for position, velocity, angular velocity, and rotation matrix, computing control inputs $u = [u_1\, u_\tau^T]^T$ that drive the quadrotor dynamics. Empirically tuned control gains were determined as: $K_p = \text{diag}(10, 10, 6)$, $K_v = 5I_3$, $K_R = 15I_3$, $K_\omega = I_3$, and $K_{ip} = 0.01I_3$.

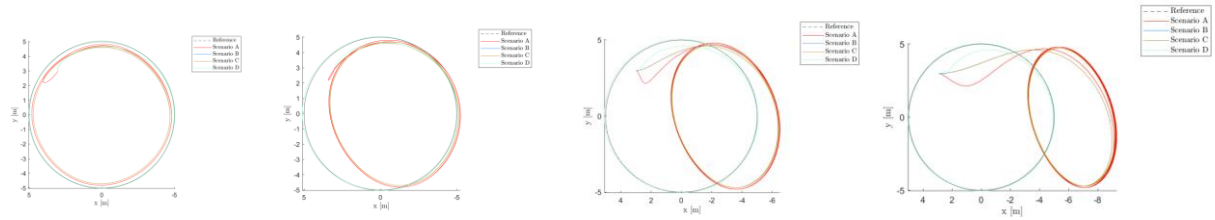
Four scenarios evaluated aerodynamic compensation effectiveness: (A) baseline without any feed-forward compensation, (B) with basic feed-forward terms (no aerodynamic terms), (C) with rotor drag compensation, and (D) with both rotor and frame drag compensation. Testing with circular trajectories ($x(t) = 5\cos(\omega_{ref}t)$, $y(t) = 5\sin(\omega_{ref}t)$, $z(t) = 3$) at varying speeds revealed significant performance improvements with compensation strategies, as presented in Figure 2, demonstrating progressive improvement from Scenario A to D. Wind disturbance analysis at different flight speeds demonstrates the controller effectiveness, as presented in Figure 3, showing how compensation strategies maintain tracking accuracy even under strong headwind conditions.

Materials Research Proceedings 69 (2026) 765-770 https://doi.org/10.21741/9781644904251-135



(a) $\|v\| = 1$ m/s (b) $\|v\| = 2$ m/s (c) $\|v\| = 5$ m/s (d) $\|v\| = 10$ m/s

Figure 2: Drone trajectories at different vehicle speeds.



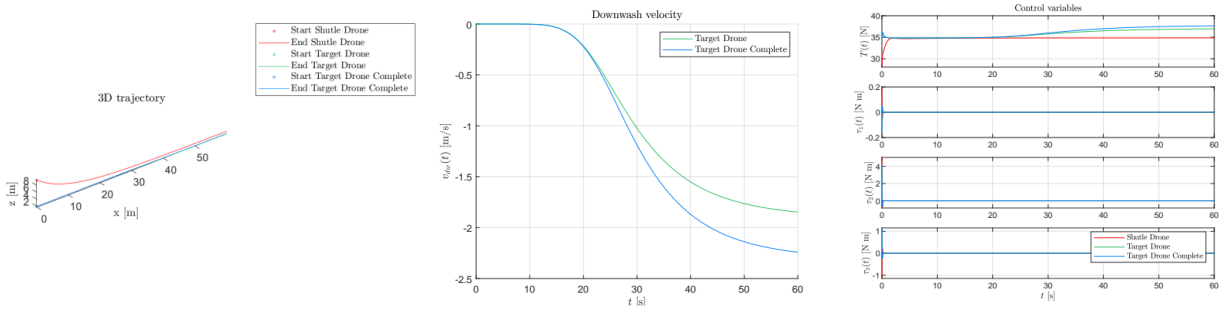
(a) No wind. (b) $v_{wx} = -5$ m/s (c) $v_{wx} = -10$ m/s (d) $v_{wx} = -15$ m/s

Figure 3: Drone trajectories under varying wind conditions.

These results indicate frame drag compensation provides the most significant improvement, reducing errors by approximately 50% for high-speed flight and nearly 10 times for extreme wind conditions. Feed-forward terms significantly reduced attitude oscillations, while complete compensation (Scenario D) maintained consistent performance across all conditions, with 89% and 91% RMSE error reduction when compared with no compensation (Scenario A), respectively, for 10 m/s vehicle velocity and for 15 m/s wind disturbances.

Two-drone proximity flight simulations evaluated downwash effects during capture operations. Drone 1 descended following $z(t) = 7\exp(-0.3t) + 2.00 + h$ while drone 2 maintained horizontal flight at $z = 2$ m, with identical horizontal trajectories, as shown in Figure 4a The downwash effects and corresponding control responses are visualized in Figure 4b.

These results show that downwash compensation reduced z-axis trajectory errors by 38\% at 0.5 m separation, with diminishing benefits beyond 1 m where aerodynamic interactions become negligible. The target drone required increased thrust (up to 37.65 N) to counteract downwash forces at close proximity, as illustrated in Figure 4c.



(a) 3-D visualization (b) Downwash velocity (c) Control inputs

Figure 4: Cooperative capture maneuver results.

Concluding Remarks

This paper presented a modeling and control framework for cooperative quadrotor capture maneuvers, focusing on aerodynamic interactions in close-proximity flight. Key contributions

include a nonlinear controller for accurate trajectory tracking, comprehensive aerodynamic modeling, and a novel downwash compensation approach enabling stable flight at close distances between drones. Simulations showed up to 89\% reduction in position RMSE at 10 m/s velocities and 91\% reduction in 15 m/s headwinds. Cooperative scenarios saw a 38\% error reduction at 0.5 m separation. Future work includes experimental validation and integration with realistic simulation environments.

Acknowledgements
This work was supported by the Fundação para a Ciência e a Tecnologia (FCT) through the research grants Capture [DOI: 10.54499-PTD-EEI-AU-173-2020], CTS [ref: CTS/00066], and LARSyS [DOI: 10.54499-LA-P-0083-2020, 10.54499-UIDP-50009-2020, 10.54499-UIDB-50009-2020].

References

[1] M. R. Polaris, "Commercial uav (unmanned aerial vehicle) market share, size, trends industry and analysis report," 2021. Accessed online: 2022-07-15.

[2] D. Di Bacco, M. Giurato, and M. Lovera, "Accurate positioning of multirotor uavs for civil infrastructure monitoring," in Proceedings of the 7th European Conference for Aeronautics and Space Sciences, 07 2017.

[3] C. Powers et al., "Influence of aerodynamics and proximity effects in quadrotor flight," pp. 289-302, 01 2013. https://doi.org/10.1007/978-3-319-00065-7_21

[4] J. A. Preiss et al., "Downwash-aware trajectory planning for large quadrotor teams," in 2017 IEEE/RSJ International Conference on Intelligent Robots and Systems (IROS), pp. 250-257, 2017. https://doi.org/10.1109/IROS.2017.8202165

[5] N. Sydney, B. Smyth, and D. Paley, "Dynamic control of autonomous quadrotor flight in an estimated wind field," pp. 3609-3616, 12 2013. https://doi.org/10.1109/CDC.2013.6760438

[6] M. Faessler, A. Franchi, and D. Scaramuzza, "Differential flatness of quadrotor dynamics subject to rotor drag for accurate tracking of high-speed trajectories," IEEE Robotics and Automation Letters, 2017. https://doi.org/10.1109/LRA.2017.2776353

[7] B. Guerreiro, "Project Capture - shuttle drone for launch and capture in cooperative and non-cooperative scenarios." Online : http://capture.isr.tecnico.ulisboa.pt (Accessed: 2025-08-04).

[8] D. Mellinger and V. Kumar, "Minimum snap trajectory generation and control for quadrotors," in 2011 IEEE International Conference on Robotics and Automation, pp. 2520-2525, 2011. https://doi.org/10.1109/ICRA.2011.5980409

Materials Research Proceedings 69 (2026) 771-776 https://doi.org/10.21741/9781644904251-136

Towards Cooperative Guidance in Air-Defense: Extending Weapon-Target Assignment into the Mid-Course Phase

Ole OSTERMANN[1,a *], Johannes AUTENRIEB[1,b] and Carsten SCHWARZ[1]

[1]DLR - German Aerospace Center, Institute of Flight Systems, 38108 Braunschweig, Germany

[a]ole.ostermann@dlr.de, [b]johannes.autenrieb@dlr.de

Keywords: Weapon-Target Assignment (WTA), Cooperative Guidance, Multi-Agent Systems, Online Task Assignment, Combinatorial Optimization, Missiles, Air-Defense

Abstract. As modern threats evolve through coordinated swarm attacks, static or pre-launch assignments for air-defense systems become outdated mid-engagement, necessitating in-flight reassignment. Therefore, cooperative guidance is introduced, extending dynamic Weapon-Target Assignment (WTA) from launch-time coordination into the mid-course flight phase. A decentralized architecture is proposed that couples WTA with trajectory guidance via informed cost functions. The information consensus-based WTA optimization procedure enables real-time adaptability under communication constraints. The Hungarian algorithm is chosen for its deterministic, low-complexity performance for the repeated optimizations. A simulation example illustrates mid-course reassignment triggered by target maneuvering, demonstrating the feasibility of collaborative flight-path adaptation.

Introduction

This work discusses cooperative guidance for air-defense systems, extending state-of-the-art launch coordination with dynamic Weapon-Target Assignment (WTA) in the mid-course phase. As modern threats evolve through coordinated swarm attacks [1, 2], we assume that static launch-time coordination becomes insufficient. While dynamic WTA improves responsiveness through sequenced launches [3, 4], a continuous in-flight cooperation is the next step. Enabled by network-centric warfare [5, 6], cooperative guidance allows effectors to jointly reassign targets in-flight, adapting to dynamic threats in real time. We propose a cooperative guidance concept for an onboard module, that integrates WTA and trajectory guidance via cost-informed assignments. It enables real-time adaptability with limited computational resources. The decentralized approach avoids single points of failure [7].

A dynamic optimization of assignments and collaborative adaption of intercept flight paths in real-time throughout the unpropelled mid-course of the missiles after their boost-phase, shall maximize intercept success probabilities. This cooperation allows to dynamically react to erratically evolving environments. The approach is expected to increase effectiveness for the air-defense while additionally saving on costly resources.

Background on Weapon-Target Assignment

The WTA problem can be approximated as a linear assignment problem. The best combination of all possible effector/target assignments is evaluated by a combinatorial optimization. To solve the linear assignment problem mathematically, scalar cost values c_{ij} for the assignment of each effector $i \in [\![1, N]\!]$ to each target $j \in [\![1, M]\!]$ are to be defined. This relationship is schematically shown in Fig. 1.

Content from this work may be used under the terms of the Creative Commons Attribution 3.0 license. Any further distribution of this work must maintain attribution to the author(s) and the title of the work, journal citation and DOI. Published under license by Materials Research Forum LLC.

Materials Research Proceedings 69 (2026) 771-776 https://doi.org/10.21741/9781644904251-136

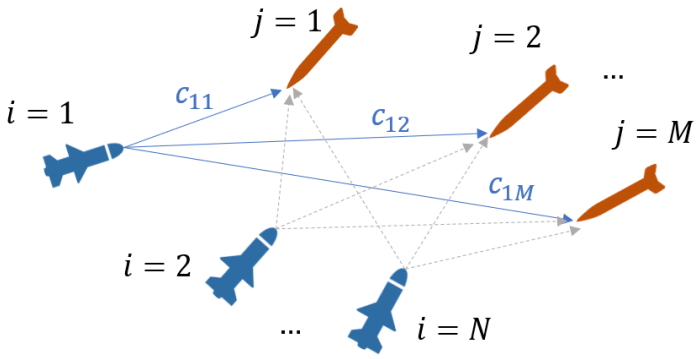


Fig. 1: Assignment Costs Illustration

The sum of these costs ought to be minimized by selecting an optimal assignment which is described by

$$\min_{x}\left(\sum_{i=1}^{N}\sum_{j=1}^{M} c_{ij}\ x_{ij_{,\tau}}\right), \tag{1}$$

where the binary variables x_{ij} represent the assignments of effectors to targets either at time τ or the previous timestep $\tau - 1$ (as in Eq. 3). This optimization shall be subject to the following constraints:

$$\begin{aligned}
&\text{C1 (binary assignment variables):} \quad \forall i \in [\![1,N]\!], \forall j \in [\![1,M]\!], \quad x_{ij} \in \{0,1\} \\
&\text{C2 (exactly one target assigned per effector):} \quad \forall i \in [\![1,N]\!], \quad \sum_{j=1}^{M} x_{ij} = 1 \\
&\text{C3 (bounds on effectors per target):} \quad \forall j \in [\![1,M]\!], \quad \left\lfloor \frac{N}{M} \right\rfloor \leq \sum_{i=1}^{N} x_{ij} \leq \left\lceil \frac{N}{M} \right\rceil
\end{aligned} \tag{2}$$

The first constraint (C1) enforces that the assignment variables x_{ij} are binary, indicating whether worker i is assigned to task j. The second constraint (C2) ensures that each worker is assigned to exactly one task. The third constraint (C3) limits the number of effectors assigned to any target between the floor and ceiling of the ratio $\frac{N}{M}$ for an even distribution of effectors across targets.

Cooperative Guidance Architecture

Cooperative guidance integrates WTA and trajectory guidance. While simultaneous optimization of assignment and trajectory is theoretically optimal, it is computationally prohibitive [8, 9] for onboard use. We instead adopt a separated approach: the trajectory guidance law is recognized in the cost function c_{ij} (e.g., via time-to-go estimates), enabling good performance with low complexity. A closed loop is created: the assignment defines the target for the mid-course guidance and in turn, guidance-relevant metrics feed into the cost function. A fully connected mesh enables decentralized cooperation (Fig. 2). Each effector exchanges state or cost estimates with peers (depending on the WTA algorithm selection in the next section), while receiving target data from a central node.

Materials Research Proceedings 69 (2026) 771-776 https://doi.org/10.21741/9781644904251-136

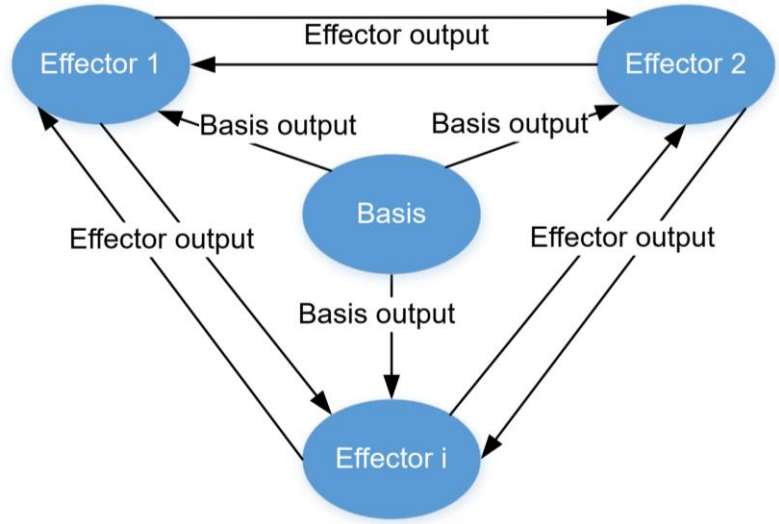


Fig. 2: Ideal Communication Scheme

Since cost function design bounds the decision quality for any optimization algorithm, the assignment optimization is assumed to be predominantly driven by a sound exploitation of flight mechanical and operational knowledge (e.g. regarding target/asset classification). As [10] outlines, WTA optimization objective is usually either based on minimization of target survivability or maximization of asset survivability. We suggest a multi-objective, cost-driven WTA optimization approach that achieves the following set of high-level objectives:

1) maximization of asset-survivability (e.g. by distance to predicted intercept area),
2) minimization of general threat level imposed by targets (e.g. via time-to-go) and
3) maximization of energy reserves (e.g. through predicted speed at intercept).

These objectives ought to be cast into combined cost parameters for any assignment of effectors to targets via a weighted sum, such that the WTA problem can be optimized by selecting a combination of assignments which minimize the overall costs. The systematic exploitation of domain-knowledge for the cost factors in order to achieve and balance these high-level objectives is not yet clear and should be investigated in future work. A manually tuned additional cost (i.e. switching cost) s can be added to the cost function (cf. Eq. 1) for previously not-assigned combinations as

$$\hat{c}_{ij} = c_{ij} + s\,(1 - x_{ij_{,\tau-1}}) \tag{3}$$

to penalize undesired high-frequency reassignments.

Weapon-Target Assignment Algorithm Selection

For the development from coordination to cooperation, some high-level requirements are derived for the WTA definition and its optimization algorithm. Due to the continuous evaluation, consistent solutions must be ensured in order to avoid wasteful perpetual swapping of assignments. Particularly for development, reproducibility is beneficial. This requires deterministic optimization algorithms. The optimization, including the calculation of a cost function as well as the solution, is time-critical. According to Eq. 2, the optimization algorithm must be able to ensure that every effector has exactly one target assigned to it (if targets are available) and every target can have different numbers of effectors assigned to it, depending on the symmetry of the number of participants.

Materials Research Proceedings 69 (2026) 771-776 https://doi.org/10.21741/9781644904251-136

In conjunction with the type of future connections and expected failures/limitations, a design decision needs to be made between information or assignment consensus. Fig. 3 illustrates a qualitative comparison of both approaches.

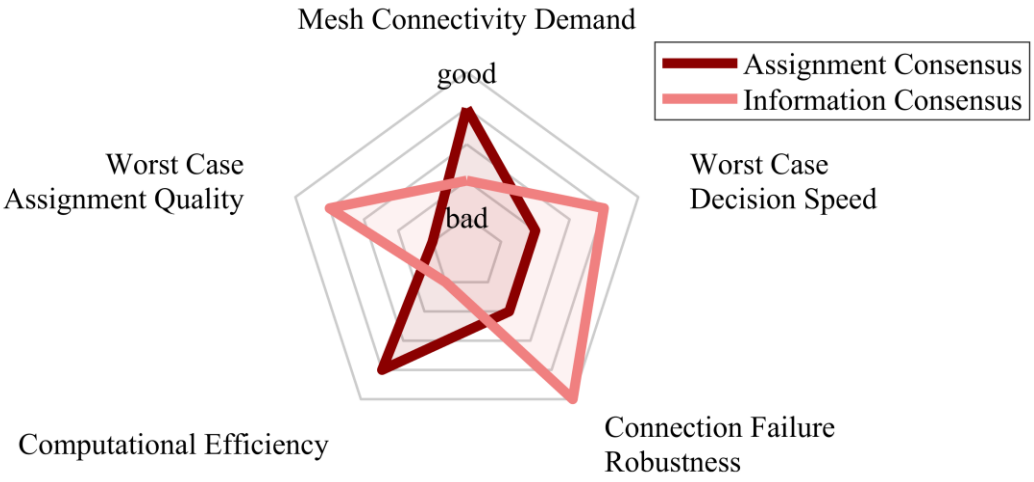


Fig. 3: Assignment vs. Information Consensus Trade-off

In scenarios with stable, short-range connections, assignment consensus methods operating on nearest-neighbor communication schemes can be effective [11]. Contrarily, information consensus tends to demand increased mesh connectivity. The required communication bandwidth varies between the two approaches. For information consensus, it depends on the cost function and its required information, whereas for assignment consensus, it depends on the specific framework used (e.g., transmitting entire bundles of bids simultaneously or one bid at a time, in turn requiring more communication iterations) [11].

However, when frequent connection failures are expected, information consensus enables compensation techniques like dead-reckoning (state estimation) on each effector, allowing to maintain a consistent assignment optimization plan [11]. Given the limited maneuverability of missiles, dead-reckoning techniques should work well for short durations. Particularly if flight dynamics and guidance are known for all effectors, well-informed predictions can then be made with continuous uplinks for target and asset information, reducing the requirements on effector-to-effector communication frequency. Reaching assignment consensus may be delayed due to communication latencies, potentially leading to decisions being made beyond a critical "point-of-no-return" in dynamic environments (worst case decision speed in Fig. 3). Information consensus combined with state estimation can make more up-to-date decisions. Nevertheless, solving the global assignment problem onboard every effector significantly increases computational demands. A simulation study comparing information vs. assignment consensus approaches with missiles under uncertainties and unstable connections should be pursued in future work.

Consulting survey papers on multi-robot task assignment such as [7] suggests that as long as communication network topology is not assumed as too restricted and computational demands are feasible, the simple Hungarian algorithm [12] (extended for rectangular cost matrices) for information consensus is the preferred choice. For cases of numerical superiority, the cost matrix has to be replicated to the right, such that the number of "virtual" (copied) targets is higher than the number of effectors to address C3 in Eq. 2. Computational demands remain feasible as long as no too complex simulations or trajectory optimizations for the WTA cost function are used and computational requirements are dominated by other subsystems (e.g. image processing in infrared seekers). Benefits of the Hungarian algorithm were previously demonstrated in similar multi-agent problems [13].

Materials Research Proceedings 69 (2026) 771-776 https://doi.org/10.21741/9781644904251-136

Simulation Test

The concept is exemplarily tested with a 3 effector vs. 3 targets simulation from launch until target interception (based on a simple proximity collision logic) in Fig. 4. Forward simulations with the model and guidance algorithms are performed in each iteration, to estimate the time-to-go for each effector/target combination as the only WTA cost parameter considered in this example. A simple Proportional Navigation Guidance (PNG) algorithm is used for trajectory guidance. The WTA is performed online with 1 Hz. Effector trajectories (in the back of the figure) are color-coded by assigned target. The effectors launch successively and allocate themselves such that each target is assigned to one effector. Mid-flight, the right-most (purple) target turns to the left. It is consecutively reassigned to effectors from right to left during the maneuver, such that the summed-up time-to-go for all effectors remains lowest. All computations are performed in each effector model. The entire simulation takes only a few seconds on a consumer laptop, demonstrating feasibility on embedded systems under real-time constraints.

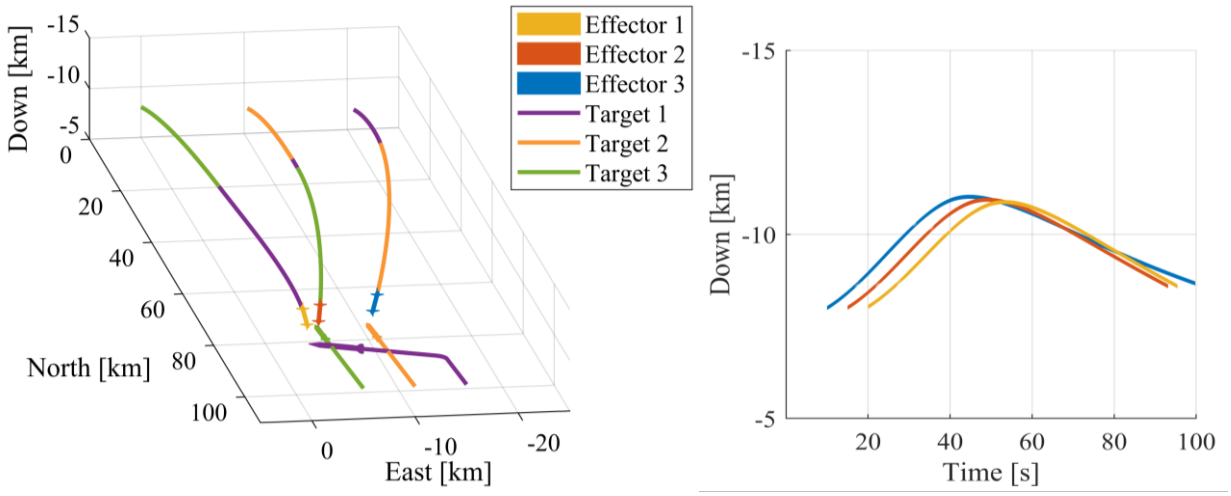


Fig. 4: Illustrative Scenario: Mid-Course Reassignment Triggered by Target Maneuver

Simulation Test

This paper introduces the concept of cooperative guidance for air-defense systems, extending WTA into the mid-course flight phase. We propose a decentralized, onboard architecture that tightly couples WTA with trajectory guidance through cost-informed feedback, enabling real-time adaptation to evolving threats. The integration of well-established components (e.g. Hungarian algorithm) into a lightweight, cooperative missile guidance loop represents a novel approach to adaptive air-defense. This work lays the conceptual foundation for future implementation and evaluation. Quantitative evaluation and cost function design will be presented in follow-up work. The framework paves the way for adaptive, resilient air-defense systems capable of countering next-generation swarm threats.

References

[1] P. van Hooft and L. Boswinkel, Surviving the Deadly Skies: Integrated Air and Missile Defense 2021-2035. The Hague Centre for Strategic Studies, 2021.

[2] R. Loss, "Welches Dach über Europa? Bodengebundene Luftverteidigung nach der Zeitenwende," in BAKS Arbeitspapiere, vol. 3/24, Bundesakademie für Sicherheitspolitik, 2024.

[3] A. Kline, D. Ahner, and R. Hill, "The weapon-target assignment problem," Computers & Operations Research, vol. 105, pp. 226-236, 2019. https://doi.org/10.1016/j.cor.2018.10.015

[4] G. Merkulov, E. Iceland, S. Michaeli, Y. Riechkind, O. Gal, A. Barel, and T. Shima, "Reinforcement learning based decentralized weapon-target assignment and guidance," in AIAA

SCITECH 2024 Forum, Reston, Virginia: American Institute of Aeronautics and Astronautics, 2024. https://doi.org/10.2514/6.2024-0125

[5] D. S. Alberts, J. Garstka, and F. P. Stein, Network centric warfare: The face of battle in the 21st century. CCRP publication series, Washington, DC: National Defense University Press, 1999.

[6] Bundesverband der Deutschen Luft- und Raumfahrtindustrie e.V., "Positionspapier zur Deutsch-Französischen Kooperation im Bereich Future Combat Air System," 2018.

[7] G. M. Skaltsis, H.-S. Shin, and A. Tsourdos, "A survey of task allocation techniques in MAS," in 2021 International Conference on Unmanned Aircraft Systems (ICUAS), pp. 488 497, IEEE, 2021. https://doi.org/10.1109/ICUAS51884.2021.9476736

[8] C. Kirches, "Mixed-integer optimal control," in Fast Numerical Methods for Mixed-IntegerNonlinear Model-Predictive Control, pp. 31-60, Wiesbaden, Germany: Vieweg+Teubner, 2011. https://doi.org/10.1007/978-3-8348-8202-8_3

[9] T. Jin, H.-S. Shin, A. Tsourdos, and S. He, "Integrated target assignment and trajectory optimization for many-to-many midcourse guidance," IEEE Transactions on Aerospace and Electronic Systems, p. 16, 2024. https://doi.org/10.1109/TAES.2024.3448408

[10] C. Leboucher, H.-S. Shin, S. Le Ménec, A. Tsourdos, A. Kotenkoff, P. Siarry, and R. Chelouah, "Novel evolutionary game based multi-objective optimisation for dynamic weapon target assignment," IFAC Proceedings Volumes, vol. 47, no. 3, pp. 3936-3941, 2014. https://doi.org/10.3182/20140824-6-ZA-1003.02150

[11] Luke B. Johnson, han-Lim Choi and Jonathan P. how, "The role of information assumptions in decentralized task allocation: A tutorial," IEEE Control Systems, vol. 36, no. 4,pp. 45-58, 2016. https://doi.org/10.1109/MCS.2016.2558419

[12] F. Bourgeois and J.-C. Lassalle, "An extension of the munkres algorithm for the assignment problem to rectangular matrices," Commun. ACM, vol. 14, no. 12, p. 802-804, 1971. https://doi.org/10.1145/362919.362945

[13] J. Autenrieb, N. Strawa, H.-S. Shin, and J.-H. Hong, "A Mission Planning and Task Allocation Framework For Multi-UAV Swarm Coordination," 2019 Workshop on Research, Education and Development on Unmanned Aerial Systems (RED-UAS), 2019, pp. 297-304. https://doi.org/10.1109/REDUAS47371.2019.8999708

Materials Research Proceedings 69 (2026) 777-781 https://doi.org/10.21741/9781644904251-137

Simulation-Based Development of a Forward-Motion Mid-Air Deployment System for Fixed-Wing UAVs from Quadrotor Platforms

Paul Olanifimihan OKE[1,a], Yingsong GU[2,b*]

[1]School of Aeronautics, Northwestern Polytechnical University, Xi'an, 710072, China

[2]National Key Laboratory of Strength and Structural Integrity, Xi'an 710065, China

[a]pauloke@mail.nwpu.edu.cn, [b]guyingsong@nwpu.edu.cn

Keywords: Fixed-Wing UAV, Quadrotor, Forward-Motion Release, Stability

Abstract. This work presents a detailed simulation framework for a novel aerial deployment system that enables mid-air release of a fixed-wing UAV from a quadrotor platform. Traditional launch systems for fixed-wing UAVs often rely on bulky infrastructure or manual intervention. This study proposes and simulates a more flexible and autonomous alternative tailored for constrained, tactical, or remote environments where conventional methods are impractical. The focus of this contribution is on modeling, simulating, and analyzing the system dynamics associated with forward-motion deployment, which adds complexity to the release dynamics and improves transition to autonomous flight post-deployment.

Introduction

Unmanned Aerial Vehicles (UAVs), particularly fixed-wing types, play a significant role in a variety of applications ranging from surveillance to disaster response. However, the launch of fixed-wing UAVs from platforms such as quadrotors faces considerable challenges due to the bulky infrastructure or manual intervention required in traditional launch systems. In constrained, tactical, or remote environments where conventional methods are impractical, an innovative solution is necessary. This study proposes and simulates a forward-motion mid-air deployment system, which enables the autonomous release of a fixed-wing UAV from a quadrotor platform.

Unlike previous studies that primarily focused on combination of both platforms into VTOL [1], this work introduces the novel concept of utilizing the quadrotor's forward motion during the deployment phase. By modeling and simulating the dynamics involved in forward-motion deployment, the proposed system provides initial aerodynamic lift and velocity to the fixed-wing UAV, thus enhancing the stability and transition to autonomous flight. This approach also reduces the risks associated with stall after the UAV's release [2].

The framework for this deployment system is developed using MATLAB Simulink, incorporating both Simscape Multibody and custom control blocks. The simulation includes three core subsystems: environment setup, plant setup for both the quadrotor and UAV, and a control system featuring several PID-based control loops. This method is validated by evaluating the system's performance under various deployment scenarios, including different payload weights, wind speeds, and forward velocities.

Numerical Background and Modelling Approach

The simulation framework in this study integrates key numerical models to simulate the dynamics of both the quadrotor platform and fixed-wing UAV during deployment. The methodology ensures that essential physical properties such as aerodynamics, control
dynamics, and payload interactions are accurately captured.

The quadrotor is modelled as a rigid body using Newton-Euler equations, Eq. 1, for both translational and rotational motion:

Content from this work may be used under the terms of the Creative Commons Attribution 3.0 license. Any further distribution of this work must maintain attribution to the author(s) and the title of the work, journal citation and DOI. Published under license by Materials Research Forum LLC.

Materials Research Proceedings 69 (2026) 777-781 https://doi.org/10.21741/9781644904251-137

$$M(q)\ddot{q} + C(q,\dot{q})\dot{q} + G(q) = u \quad (1)$$

where q includes position and orientation, M is the mass and inertia matrix, C is the Coriolis matrix, and G represents gravity, while u are the control inputs (thrust and torques). These equations model the quadrotor's response to forces generated by its motors, aerodynamics, and the payload during release.

The fixed-wing UAV is similarly modelled, with lift and drag forces calculated using:

$$F_L = \frac{1}{2}\rho v^2 C_L A \qquad F_D = \frac{1}{2}\rho v^2 C_D A \quad (2)$$

These equations, Eq. 2, predict the UAV's post-release flight dynamics and are crucial for determining its transition to level flight.

To model the interaction during release, a Force Interaction Model is used, Eq. 3. This model computes the forces acting on the payload at separation and estimates the resulting trajectory based on aerodynamic principles and initial velocity. A key factor is the change in the quadrotor's moment of inertia due to the payload release, defined in Eq. 3.

$$I_{\text{total}} = I_{\text{quadrotor}} + I_{\text{payload}} \quad (3)$$

This allows accurate prediction of how the release affects the quadrotor's stability and preserves pitch and roll stability.

A two-loop PID control system manages both trajectory and attitude during deployment. The position controller uses spline interpolation to ensure smooth path planning, avoiding sharp turns. These loops are built on basic PID control law, Eq. 4.

$$u(t) = K_p e(t) + K_i \int e(t)dt + K_d \frac{de(t)}{dt} \quad (4)$$

where $e(t)$is the error signal, and $K_p, K_i, K_d$are the control gains. This architecture helps maintain stability during UAV release and prevents destabilization from shifts in the center of gravity (CoG).

The payload release system's disengagement logic dynamically adjusts thrust at separation to prevent unwanted oscillations or instability in the quadrotor's trajectory. The release occurs when certain velocity and stability conditions are met, ensuring the UAV transitions smoothly to level flight.

The simulation framework is built in MATLAB Simulink 2023 with Simscape Multibody for accurate modelling of mechanical dynamics. SOLIDWORKS is used for CAD modelling, and Simscape Multibody Link imports the models into Simulink. Environmental factors, including wind speed and gravity, are incorporated to replicate real-world conditions as closely as possible.

Simulation Scenarios and Objectives

To evaluate the effectiveness of the proposed forward-motion UAV deployment system, a series of simulation scenarios were designed, varying key operational factors to assess the system's performance. These scenarios aimed to analyse the system's stability, level flight initiation, and transition to autonomous flight under different conditions, in comparison to prior work on UAV deployment [1][2].

The primary parameters tested include forward velocities (ranging from 0 to 15 m/s), payload weights (1.2 to 1.6 kg), and wind speeds (0 to 10 m/s). Each of these factors plays a

Materials Research Proceedings 69 (2026) 777-781 https://doi.org/10.21741/9781644904251-137

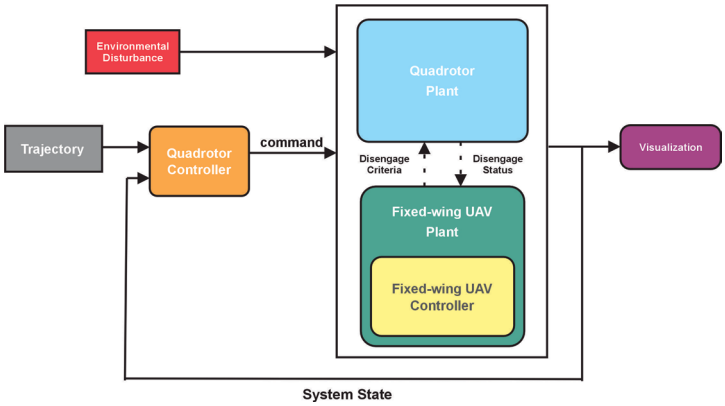


Figure 1 - Block diagram depicting the guidance and control architecture for quadrotor UAV deployment.



Figure 2 - Pre-release



Figure 3 - Post-release

crucial role in influencing the release dynamics. Forward velocity, for example, impacts the aerodynamic lift provided to the UAV during release, enhancing stability and glide performance [3]. Similarly, varying the payload weight allows for the examination of changes in the quadrotor's stability and control during release, as heavier payloads will affect the centre of gravity and moment of inertia. Environmental factors, such as wind speed, were included to assess how external disturbances affect both the quadrotor and UAV during deployment, with wind known to influence trajectory and stability [4].

The simulations aim to validate the system's ability to handle these variations while ensuring a smooth and stable transition to autonomous flight, optimizing the UAV deployment process in constrained or remote environments.

Results: Evaluation of Forward-Motion UAV Deployment System

The UAV deployment performance, influenced by factors like forward velocity, payload mass, and wind speed, reveals crucial insights into its stability, recovery time, and time to achieve level flight. In Figure 4, the relationship between recovery time and forward velocity shows that as the forward velocity increases, the recovery time decreases, especially for lighter payloads (e.g., 1.2 kg), where recovery time drops to as low as 2.5 seconds at 14 m/s. For heavier payloads (e.g., 1.6 kg), recovery times remain higher, reaching over 5 seconds, due to the increased inertia, which slows the UAV's ability to stabilize.

In Figure 5, we observe the time to achieve level flight, where lighter payloads, such as 1.2 kg, require approximately 1.5 seconds at 14 m/s. Heavier payloads take longer, with the 1.6 kg payload reaching 2.5 seconds under similar conditions. Wind speeds play a significant role here, as shown in Figure 6, where stronger winds (e.g., 10 m/s) lead to increased recovery times (over 7 seconds),

Materials Research Proceedings 69 (2026) 777-781 https://doi.org/10.21741/9781644904251-137

while higher forward velocities mitigate the wind's destabilizing effects, reducing the time to level flight.

Attitude deviation, analysed in Figure 7, shows a clear impact of payload mass and wind speed. For lighter payloads (1.2 kg), the attitude deviation is around 3 degrees at 10 m/s

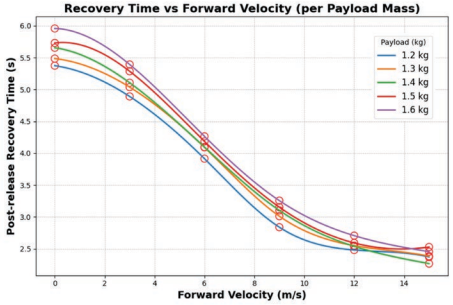


Figure 4 - Post-release Recovery Time

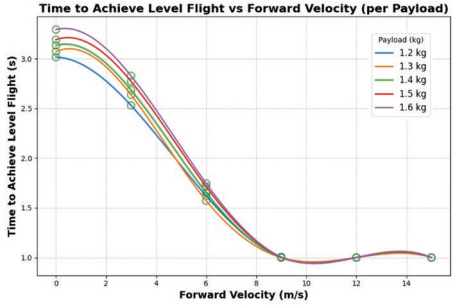


Figure 5 - Tim to Achieve Level Flight post recovery

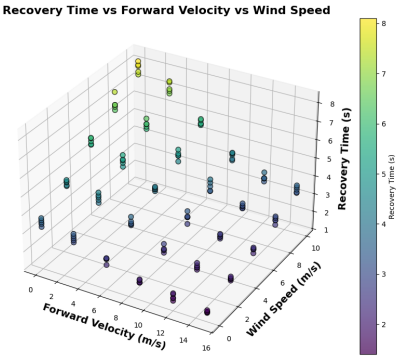


Figure 6 - Recovery Time as a Function of Forward Velocity and Wind Speed

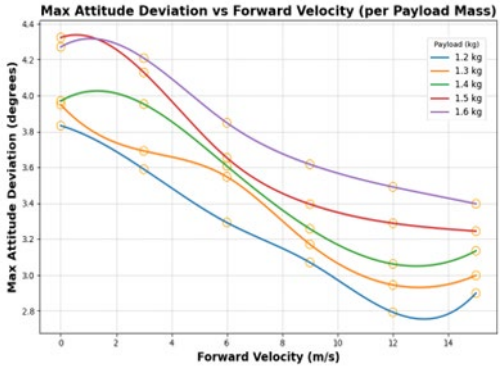


Figure 7 - Max Attitude Deviation with Recovery Time

wind speed, whereas heavier payloads (1.6 kg) exhibit larger deviations, up to 6 degrees. Wind speed further amplifies this effect, highlighting the importance of managing both payload and wind conditions to maintain stability.

Summary

The simulation results show that forward velocity, payload mass, and wind speed significantly affect UAV stability, recovery time, and time to level flight. Higher forward velocities improve stability and reduce recovery time, especially for lighter payloads, while heavier payloads lead to increased recovery times due to greater inertia. Compared to traditional vertical deployment, the forward-motion method enhances stability and reduces altitude loss, making it well-suited for tactical environments.

Optimizing forward velocity is critical for minimizing recovery time and time to level flight, especially with heavier payloads. Additionally, wind conditions should be considered, as they significantly impact recovery time and attitude stability, highlighting the importance of precise deployment strategies. This method could enable more flexible and autonomous UAV operations in constrained or remote areas, paving the way for real-world testing and validation.

References

[1] Gunarathna, Janith & Munasinghe, R. (2018). Development of a Quad-rotor Fixed-wing Hybrid Unmanned Aerial Vehicle. https://doi.org/10.1109/MERCon.2018.8421941

[2] Vijay Shankar Dwivedi, Hyo-Sang Shin, Antonios Tsourdos: Exploring the Concept of Air-runway for Fixed-wing UAVs. Proceedings of the 2024 CEAS EuroGNC conference. Bristol, UK. June 2024. https://doi.org/10.82124/CEAS-GNC-2024-046

[3] Ao, T., Zhang, K., Shi, H., Jin, Z., Zhou, Y., & Liu, F. (2023). Energy-Efficient Multi-UAVs Cooperative Trajectory Optimization for Communication Coverage: An MADRL Approach. Remote Sensing, 15(2), 429. https://doi.org/10.3390/rs15020429

[4] Geronel RS, Botez RM, Bueno DD. Dynamic responses due to the Dryden gust of an autonomous quadrotor UAV carrying a payload. The Aeronautical Journal. 2023;127(1307):116-138. https://doi.org/10.1017/aer.2022.35

Materials Research Proceedings 69 (2026) 782-787 https://doi.org/10.21741/9781644904251-138

Electric Powered Helicopter: From Concept to Feasibility

Elif Hazal ÇELİKCAN[1,a], Ahmad HAMMAD[1,b *] and Michail TSAGKARIS[2,c]

[1]Chair of eAviation, Department of Aerospace and Geodesy, Technical University of Munich, Germany

[2]Chair of Flight System Dynamics, Department of Aerospace and Geodesy, Technical University of Munich, Germany

[a]hazal.celikcan@tum.de, [b]ahmad.hammad@tum.de, [c]michail.tsagkaris@tum.de

Keywords: Electrical Helicopter, Battery-Powered Flight, Sustainable Aviation, Urban Air Mobility, eVTOL, Electric Propulsion

Abstract. The need to reduce aviation emissions is driving focus toward electric propulsion. While eVTOL (electric vertical takeoff and landing) designs face hurdles like system complexity and infrastructure deficits, the electrification of conventional helicopters through retrofitting remains underexplored. This study addresses this gap using a mission-driven approach, analyzing feasibility within realistic operational constraints. The profile specifies a cruise distance of 80 km, a speed of 185 km/h, and a maximum payload of 450 kg, plus an EASA-compliant reserve. The methodology involves: reviewing existing rotorcraft literature, designing a conceptual electric helicopter, and calculating power requirements based on the profile. Suitable electric propulsion configurations are then evaluated against current battery and motor technologies. The study concludes that although electric aviation in general, and electric helicopters in particular, show considerable promise, further advancements in battery energy density and component efficiency are still necessary to fully realize their operational potential.

Introduction

The need to reduce emissions in the aviation sector has led to a growing focus on alternative propulsion systems, with electric flight seen as a promising path toward more sustainable air transport. To support this shift, the EU's Flightpath 2050 targets a 75% reduction in CO2 and 90% in NOx emissions by mid-century [1], and similarly, NASA's N+3 goals aim for significant improvements in propulsion and efficiency.

Accounting for 95% of a helicopter's lifecycle emissions, propulsion is a critical area for carbon reduction [2]. Helicopters are essential for emergency and rescue missions, but their high fuel use and noise make them strong candidates for electrification, offering significant cuts in emissions and costs. Crucially, the retrofitting of existing, certified platforms is underexplored, despite avoiding the major hurdles affecting eVTOLs. Prototypes include the Sikorsky Firefly research demonstrator [3] and the more promising Tier 1 Engineering's e-R44, an electric conversion of the Robinson R44 [4].

Alongside these demonstrators, academic interest in electric rotorcraft design is growing. One study investigated configuration trade-offs for electric helicopters in urban air mobility, exploring single-main-rotor and lift-augmented compound layouts [5]. Another study conducted a preliminary and feasibility analysis of electrifying the conventional EC135 platform using a fuel-cell-based system and superconducting motor, emphasizing performance and energy system integration [6]. A conceptual all-electric retrofit of a lightweight helicopter, based on the Robinson R22, is presented in [7], evaluating several battery and fuel-cell configurations through performance and cost analyses. Existing technology and limitations were also reviewed [8].

Content from this work may be used under the terms of the Creative Commons Attribution 3.0 license. Any further distribution of this work must maintain attribution to the author(s) and the title of the work, journal citation and DOI. Published under license by Materials Research Forum LLC.

Materials Research Proceedings 69 (2026) 782-787 https://doi.org/10.21741/9781644904251-138

This study was developed in alignment with regulatory frameworks set by EASA, aiming to comply with CS-27 and SC E-19. These standards ensure the proposed electric configuration meets both certification and performance expectations.

Mission Profile

The mission profile is adapted from Archer Aviation's operational concept for the Midnight eVTOL. The mission, as illustrated in Fig. 1, encompasses a cruise distance of 80 km, a cruise speed of 185 km/h at an altitude of 2000 ft, and a maximum payload capacity of 450 kg. A 20-minute fuel reserve is added per EASA's Acceptable Means of Compliance (AMC) [9].

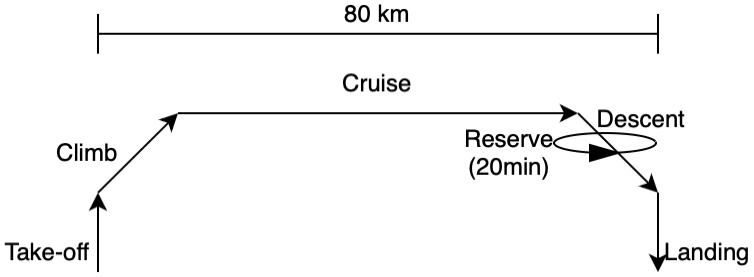


Figure 1. Mission profile for an electric helicopter

Power Calculation

In this work, rotor aerodynamic power is computed for each flight segment using standard momentum-disk relations and blade-element profile models [10]. The main-rotor power coefficient C_P consists of induced, profile, parasite, and climb contributions, expressed as

$$C_P = C_{P_i} + C_{P_o} + C_{P_p} + C_{P_c}, \tag{1}$$

where the non-dimensional power coefficients C_P relate to their dimensional counterparts by

$$P = \rho A(\Omega R)^3 C_P. \tag{2}$$

For hover calculations, only the induced and profile power components are considered. An induced power correction factor k of 1.10 is applied for hover, whereas for forward flight, in addition to induced and profile power, the parasite drag term also contributes, and the induced power factor is taken as $k = 1.25$. The tail-rotor contribution is obtained from the main-rotor mast torque,

$$Q_{MR} = \frac{P_i + P_o}{\Omega}. \tag{3}$$

The required anti-torque thrust follows from the tail-rotor moment arm about the mast,

$$T_{TR} = \frac{Q_{MR}}{l_{tr}}. \tag{4}$$

Parasite and climb terms do not contribute to mast torque and are therefore excluded from Q_{MR} but included in the total power. The data used to solve the power equations are presented in Table 1, and the resulting power curves with respect to the advance ratio μ are shown in Fig. 2. The total rotor power is:

$$P_{\text{rotors}} = P_{MR} + P_{TR}. \tag{5}$$

Materials Research Proceedings 69 (2026) 782-787 https://doi.org/10.21741/9781644904251-138

Table 1. Bell206B JetRanger III data used in power calculations

Quantity	**Main Rotor**	**Tail Rotor**
Angular Speed Ω [rad/s]	41.26	267
Radius R [m]	5.075	0.825
Chord c [m]	0.337	0.122
Solidity σ [-]	0.042	0.094
Number of blades [-]	2	2
Tail rotor moment arm about main rotor shaft l_{TR} [m]	5.94	
Maximum take-off weight (MTOW) m [kg]	1451	
Mean blade drag coeff. c_{d0} [-]	0.011	
Equivalent flat-plate area f [m^2]	0.604	

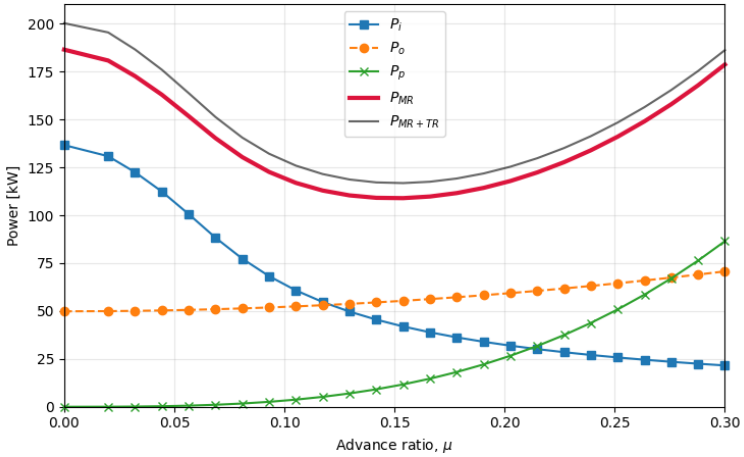


Figure 2. Main-rotor power components and total rotor power variation with advance ratio μ.

The battery power required for the electric retrofit is calculated considering transmission, motor, and inverter efficiencies, as well as auxiliary power demands, using the following equation:

$$P_{\text{batt}} = \frac{P_{\text{rotors}} + P_{\text{aux,shaft}}}{\eta_{\text{mech}}\eta_{\text{mot}}\eta_{\text{inv}}} + P_{\text{aux,elec}} \tag{6}$$

In this study, a slightly conservative mechanical efficiency of $\eta_{\text{mech}} = 0.96$ is adopted, based on technical data from NASA [11]. The motor and inverter efficiencies are taken as $\eta_{\text{mot}} = 0.96$ and $\eta_{\text{inv}} = 0.995$, respectively [12].

Electrically driven auxiliaries are based on Garmin's Electrical Load Analysis for the Bell 206A/B, which reports a typical bus usage of 24.8% of a 28–30 V, 105 A system (≈ 0.73 kW). Accordingly, a uniform auxiliary load of $P_{\text{aux,elec}} = 0.8$ kW is carried across all phases of flight [13].

Shaft-driven auxiliaries ($P_{\text{aux,shaft}}$) include the flight-control hydraulic pump and oil-cooler blower, both of which are mechanically driven by the main and tail-rotor transmissions. Bell technical data specify hydraulic pressures of around 600 psi and pump flows of 1.7–2.0 gpm, corresponding to 0.4–1.0 kW of hydraulic power via P=pQ, with an additional blower demand of comparable magnitude [14]. Accordingly, the shaft-driven auxiliary power is varied by flight phase, with $P_{\text{aux,shaft}} = \{2.0, 2.0, 1.5, 1.2, 1.5\}$ kW assigned to hover, climb, cruise, descent, and reserve, respectively, consistent with manufacturer data and typical light-helicopter operation. The total energy required for the mission is calculated as 145.59 kWh, and the results are summarized in Table 2.

Materials Research Proceedings 69 (2026) 782-787 https://doi.org/10.21741/9781644904251-138

Table 2. Pack-level power, energy, and duration summary for the selected mission profile.

Flight Segment	Power [kW]	Energy [kWh]	Δt [min]
Take-off hover	220.2	7.34	2
Climb	237.7	5.87	1.48
Cruise	160.4	69.37	25.95
Descent	51.5	1.72	2
Landing hover	220.2	7.34	2
Reserve	161.9	53.95	20

Battery Sizing

The state-of-the-art Tesla Panasonic 2170 lithium-ion NCA cell, with an energy density of 322 Wh/kg at the cell level, has been selected for this study [7] due to its high energy density, proven reliability in large-scale production, balanced energy-to-power characteristics, and efficiency in both energy storage and cost control. At the pack level, where structural and thermal components reduce usable energy density, an efficiency factor $\eta_{\text{pack}} = 0.65$ is applied [15]:

$$e_{\text{pack}} = \eta_{\text{pack}}\, e_{\text{cell}}. \tag{7}$$

The required battery pack mass becomes

$$m_{\text{bat}} = \frac{E_{\text{tot}}}{e_{pack}}.$$

With the values given above, this results in $e_{\text{pack}} = 209\ \text{Wh/kg}$ and $m_{\text{bat}} = 695.6\ \text{kg}$. (8)

After the nominal mission, when the reserve segment is not flown, the remaining state of charge is approximately 37%.

Weight Estimation

The baseline operational empty weight of the Bell 206B-3 is m_E = 785 kg, with a MTOW of 1451 kg. The removed and added components for the electric retrofit are detailed in Table 3. With the removed and added components to the electric retrofit helicopter, the new operational empty weight becomes 1419.6 kg, leaving a payload margin of 31.4 kg within the certified MTOW. From the analysis, with the selected mission profile and current battery technology, the maximum payload that can be carried is lower than what Archer's eVTOL promises to carry.

Table 3. Weight of the Removed and Added Components

Component	Removed [kg]
Engine (M250-C20J, dry)	71.7
Starter-generator	10.9
Fuel system hardware	26.0
Subtotal	108.6

Component	Added [kg]
Battery pack	695.6
Electric motor	11.2
Inverter	6.4
Balance-of-plant (HV/LV, cabling, cooling)	30
Subtotal	743.2

Trade-off Study

As a final step in this research, the trade-off study between payload and range is presented in Figure 3, as the intended mission of an 80 km cruise range renders the allowable payload insufficient to support a realistic application. However, for example, for a shorter mission with a 35 km cruise distance, the helicopter can carry approximately 218 kg of payload, which corresponds to two

people and essential equipment, representing a potential mission profile for an emergency service operation such as medical transportation.

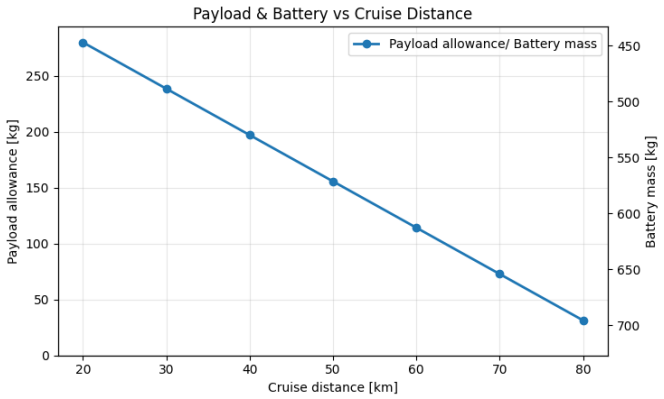


Figure 3. Payload vs Range Trade-off Plot

	eVTOL (Archer Midnight) [16]	**Conventional Helicopter (Bell 206B JetRanger III)**	**E-Heli (Electric retrofit of Bell 206B JetRanger III)**
Propulsion Type	Distributed Electric Propulsion	Turboshaft Engine	Battery Powered Electric Single Main Motor
Max. Payload [kg]	456	567	218
MTOW [kg]	3175	1451	1451
Range [km]	32-80	624 (no reserves)	35
Cruise Speed [km/h]	241	185	185
Certification Path	FAA Special-Class eVTOL	FAA Part27 / EASA CS-27	EASA CS-27 and CS-E-19 compliance

Conclusion

This study evaluated the feasibility of retrofitting a conventional helicopter, the Bell 206B, with an electric propulsion system using current lithium-ion battery technology. The analysis of rotor power requirements, mission energy demand, and overall mass distribution revealed that while electric propulsion can significantly reduce emissions and noise, current battery energy densities remain a major limitation.

For the defined 80 km mission, the retrofit results in a battery mass of approximately 696 kg, leaving only 31.4 kg available for payload within the maximum take-off weight. Reducing the mission range to 35 km increases the payload capacity to approximately 218 kg, allowing for limited applications such as short-range emergency or training operations. These results highlight that full electrification of existing rotorcraft is technically feasible but not yet operationally practical for typical missions.

Future research should focus on improving battery energy density, exploring hybrid-electric configurations, and optimizing weight distribution to enhance performance. Continued progress in certification standards and thermal management will be crucial to achieving broader adoption of electric-powered helicopters and advancing sustainable rotary-wing aviation.

References

[1] Flightpath 2050 – Europe's vision for aviation – Maintaining global leadership and serving society's needs, Publications Office, 2011, https://data.europa.eu/doi/10.2777/50266

[2] Airbus, Decarbonising Helicopters, Airbus, [Online]. Available: https://www.airbus.com/en/sustainability/our-approach-to-sustainability/decarbonisation/decarbonising-helicopters

[3] C.R. Russell, L.A. Young, G.K. Yamauchi, W. Johnson, D.D. Boyd, S.A. Gorton, C.A. Snyder, and L.W. Kohlman, Greener Helicopters, NASA, Washington, DC, USA, 2015.

[4] Vertical Flight Society, Tier 1 Engineering e-R44 3rd Generation, eVTOL News, June 20, 2023. [Online]. Available: https://evtol.news/tier-1-engineering-e-r44-3rd-generation

[5] J.A. Cole, L. Rajauski, A. Loughran, A. Karpowicz, and S. Salinger, Configuration Study of Electric Helicopters for Urban Air Mobility, Aerospace, vol. 8, no. 2, p. 54, February 2021. https://doi.org/10.3390/aerospace8020054

[6] I. Bolvashenkov, J. Kammermann, and H.-G. Herzog, Electrification of Helicopter: Actual Feasibility and Prospects, in: Proceedings of the 2017 IEEE Vehicle Power and Propulsion Conference (VPPC), IEEE, December 2017, pp. 1–6. https://doi.org/10.1109/vppc.2017.8330883

[7] J. Serafini, M. Cremaschini, G. Bernardini, L. Solero, C. Ficuciello, and M. Gennaretti, Conceptual All-Electric Retrofit of Helicopters: Review, Technological Outlook, and a Sample Design, IEEE Transactions on Transportation Electrification, vol. 5, no. 3, pp. 782–794, September 2019. https://doi.org/10.1109/TTE.2019.2919893

[8] P.J. Ansell, Review of Sustainable Energy Carriers for Aviation: Benefits, Challenges, and Future Viability, Progress in Aerospace Sciences, vol. 141, p. 100919, 2023.

[9] EASA, AMC and GM to Part-NCO – Issue 2, Amendment 12.

[10] W. Johnson, Helicopter Theory, Dover Publications, New York, 1980.

[11] T.L. Krantz, Experimental and Analytical Evaluation of Efficiency of Helicopter Planetary Stage, NASA Technical Publication 3063, NASA Lewis Research Center, Cleveland, OH, 1990

[12] T.C. Cano, I. Castro, A. Rodr´ıguez, D.G. Lamar, Y.F. Khalil and P. Kshirsagar, Future of Electrical Aircraft Energy Power Systems: An Architecture Review, IEEE Transactions on Transportation Electrification, Vol. 7, No. 3, pp. 1915-1929, 2021. https://doi.org/10.1109/TTE.2021.3052106

[13] Garmin International, Electrical Load Analysis G500H Bell 206A/B, Dwg. Number: 005-00577-20 Rev. 1, Garmin Ltd. or its subsidiaries, Olathe, KS, USA. [Online]. Available: https://static.garmin.com/pumac/005-00577-20.pdf

[14] Bell Helicopter Textron Inc., Technical Bulletin 206L-16-253: Hydraulic Fluid Conversion from MIL-PRF-5606 to MIL-PRF-87257, 14 December 2016. [Online]. Available: https://www.bellcustomer.com/Bulletins/Download?CategoryID=33&FileName=TB 206L-16-253.pdf

[15] T. Pattanayak and D. Mavris, Battery Technology for Sustainable Aviation: A Review of Current Trends and Future Prospects, Applied Energy, vol. 397, p. 126356, 2025. https://doi.org/10.1016/j.apenergy.2024.126356T. Pattanayak and D. Mavris, Battery Technology for Sustainable Aviation: A Review of Current Trends and Future Prospects, Applied Energy, vol. 397, p. 126356, 2025. https://doi.org/10.1016/j.apenergy.2025.126356

[16] Archer Aviation Midnight, Electric VTOL News by the Vertical Flight Society, Vertical Flight Society, Fairfax, VA, USA. [Online]. Available: https://evtol.news/archer/

Materials Research Proceedings 69 (2026) 788-793 https://doi.org/10.21741/9781644904251-139

Application of Control Barrier Functions to Avoid Vortex Ring State in Unmanned Helicopters

Emilia ISBONO[1,a], Mark SPILLER[2,b*] and Philipp SCHITZ[2,c]

[1]Technische Universität Berlin, Institute of Aeronautics and Astronautics, 10587 Berlin, Germany

[2]German Aerospace Center (DLR), Institute of Flight Systems, 38108 Braunschweig, Germany

[a]emilia.isbono@gmail.com, [b]mark.spiller@dlr.de, [c]philipp.schitz@dlr.de

Keywords: Constrained Control, Unmanned Helicopters, Vortex Ring State, Barrier Functions in Control

Abstract. In helicopter flight, the vortex ring state is a critical condition that can lead to a significant loss of lift, potentially resulting in a catastrophic accident. Recent developments in safety-critical control have led to formal methods which guarantee that dynamical systems remain within predefined safe conditions. Among these methods, control barrier functions offer a systematic framework to enforce safety constraints. In this contribution, we present a safety-critical control framework for unmanned helicopters using barrier function–based safety filters, which are integrated into a cascaded inner–outer loop flight control architecture. The safety filter is designed to prevent the occurrence of dangerous vortex ring state conditions, while accounting for external disturbances such as wind within the outer-loop control layer.

Introduction

Vortex ring state (VRS) is a hazardous flight condition that occurs under low forward speed with the vertical velocity approaching the wake-induced velocity [1]. In this state, additional vortices may develop near the rotor hub, resulting in a recirculating airflow that descends through the center of the rotor disk and then flows outward and upward around the edges, reinforcing the vortex ring. As a consequence, lift is significantly reduced, which can lead to a rapid loss of altitude.

Some VRS avoidance strategies for unmanned aircraft systems (UAS) have been published in the literature but, to the best knowledge of the authors, none of them apply control barrier functions (CBFs) for safety filter design. For instance, in [2], an avoidance scheme based on potential functions is proposed. The potential function defines a safety buffer around the region of vortex ring states. Depending on the value of the potential function, the nominal control law is modified. However, the design of the potential function and the altering of the nominal control input require tuning by the user and no safety guarantees are given. The VRS protection approach presented in [3] predicts the airspeed over a fixed time horizon to determine whether the predicted values violate the VRS conditions. In case of a violation, the set point of the controller is shifted to prevent entering the VRS conditions. As only the control reference is shifted, the method is unable to provide hard safety guarantees. In the work of [4], a monitor for early VRS detection and a recovery strategy based on increasing forward speed is introduced. The proposed avoidance concept is restricted to a descending spiral motion.

Control barrier functions, have emerged as a promising approach to formally guarantee that system states remain within defined safe sets. The CBF-based safety filters can be implemented on top of a nominal controller, modifying the control input only when necessary to ensure safety [5]. Original formulations of CBFs are limited to systems with a relative degree of one but recent advances have extended the framework to systems with higher relative degrees [6]. To make CBFs applicable to real world systems it is necessary to consider input constraints as well as disturbances.

Content from this work may be used under the terms of the Creative Commons Attribution 3.0 license. Any further distribution of this work must maintain attribution to the author(s) and the title of the work, journal citation and DOI. Published under license by Materials Research Forum LLC.

Materials Research Proceedings 69 (2026) 788-793 https://doi.org/10.21741/9781644904251-139

Several contributions have been proposed to handle the problem of CBF design under disturbances e.g. [7-11], under input constraints e.g. [12-16], or under input constraints and disturbances [17-19]. Another challenge in the application of CBFs is ensuring feasibility when multiple state and input constraints are present. Among other methods, a practical way to deal with the problem is to use prioritization schemes that may, however, lead to relaxation of the constraints [20], [21]. Also interesting is the reduction of conservativeness of CBFs in case of disturbances using adaptation techniques [22-24].

In this contribution, we consider the design of a CBF-based safety filter that manipulates the nominal helicopter controllers in order to avoid the dangerous vortex ring state conditions. Using the model of Johnson [1], we define the boundaries of our safe set as the complement of the unsafe region defined by the vortex ring state conditions. To enforce the bounds of the safe set, we apply input-to-state stable CBFs [7], which guarantee invariance of the safe set under input disturbances such as wind. A quadratic program (QP) is formulated to keep the deviation from the nominal control input minimal. In theory, we can avoid the VRS conditions by altering the horizontal or vertical speed or both. To regulate which input is predominantly used for avoidance, we introduce a weighting matrix into the QP. The analytic solution of the QP can be obtained using the Karush-Kuhn-Tucker (KKT) conditions.

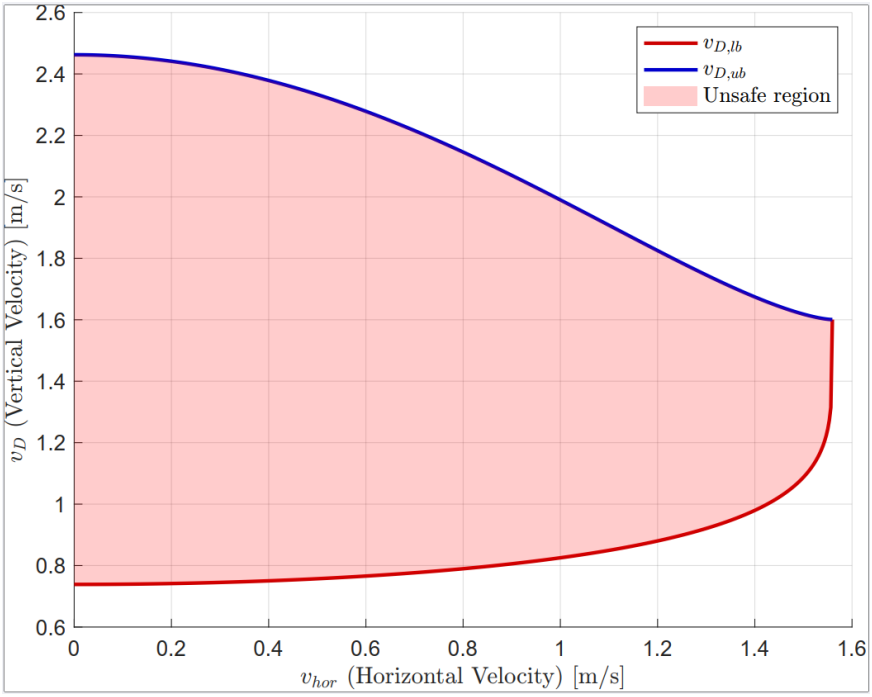


Figure 1: Visualization of unsafe region defined by vortex ring state conditions

Vortex Ring State Model

According to [1], the stability boundaries of VRS are defined by two equations. The upper and lower bounds $v_{D,\text{ub}}$ and $v_{D,\text{lb}}$ of the vertical velocity are given by

$$v_{D,\text{ub}} = v_{i,h}(0.5(V_{zN} + V_{zX}) - 0.5(V_{zN} - V_{zX})(1 - (V_x/V_{xM})^2)^{1.5}) \quad (1)$$

and

$$v_{D,\text{lb}} = v_{i,h}(0.5(V_{zN} + V_{zX}) + 0.5(V_{zN} - V_{zX})(1 - (V_x/V_{xM})^2)^{0.2}) \quad (2)$$

Materials Research Proceedings 69 (2026) 788-793 https://doi.org/10.21741/9781644904251-139

where $V_x = \frac{v_{hor}}{v_{i,h}}$ represents the horizontal flight velocity v_{hor}, normalized by the induced velocity $v_{i,h}$ during hover. The parameters V_{zN} and V_{zX} define the vertical descent region where instability can occur, while V_{xM} defines the boundary for stable horizontal flight. We use the parameter values defined by [1].
Based on the upper and lower bounds of (1) and (2), we define the unsafe state space region as the interior visualized in Figure 1.

Safety Filter Design
The bounds (1) and (2) define constraints on the vertical and horizontal velocities v_D, v_{hor}. Therefore, we implement the safety filter in the outer loop controller that controls position and velocity of the helicopter as shown in Figure 2.

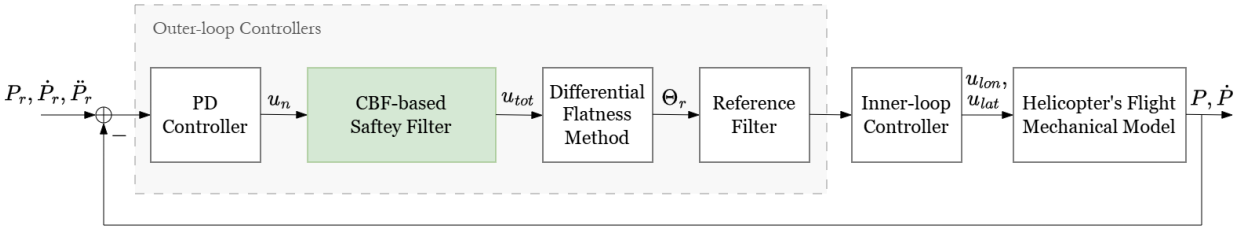


Figure 2: Implementation of the CBF-based safety filter in the outer-loop controller

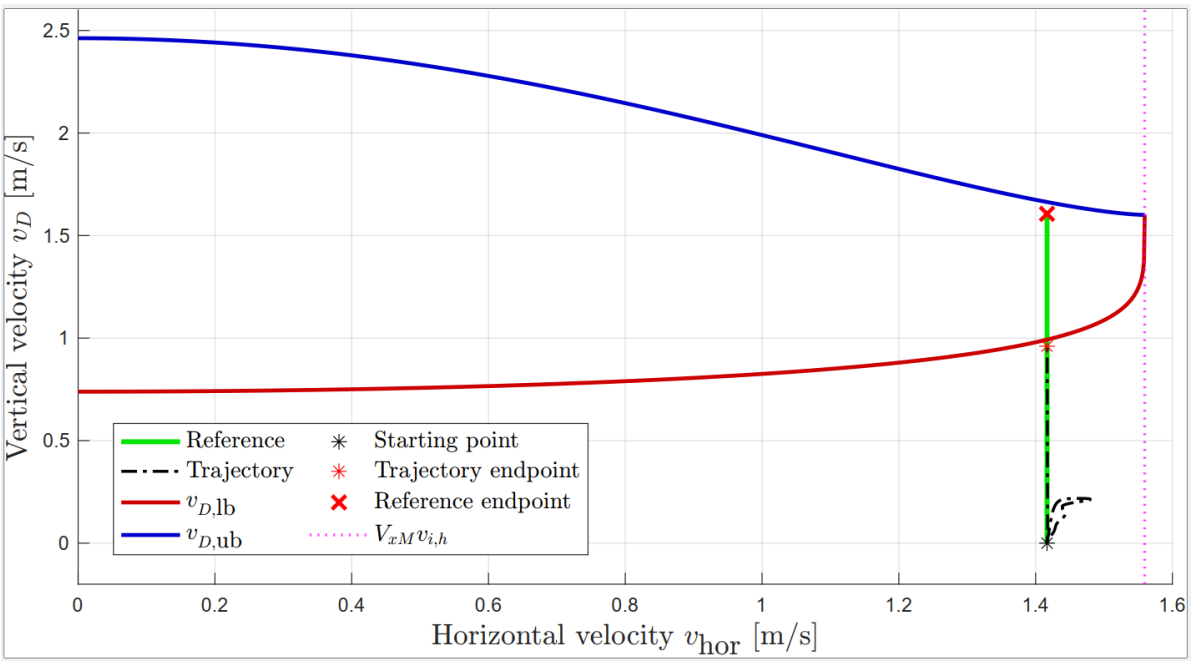
To avoid the VRS conditions we define the two constraint functions

$$h_{\text{ub}}(x) = v_D - v_{D,\text{ub}} \geq 0, \tag{3}$$
$$h_{\text{lb}}(x) = v_{D,\text{lb}} - v_D \geq 0 \tag{4}$$

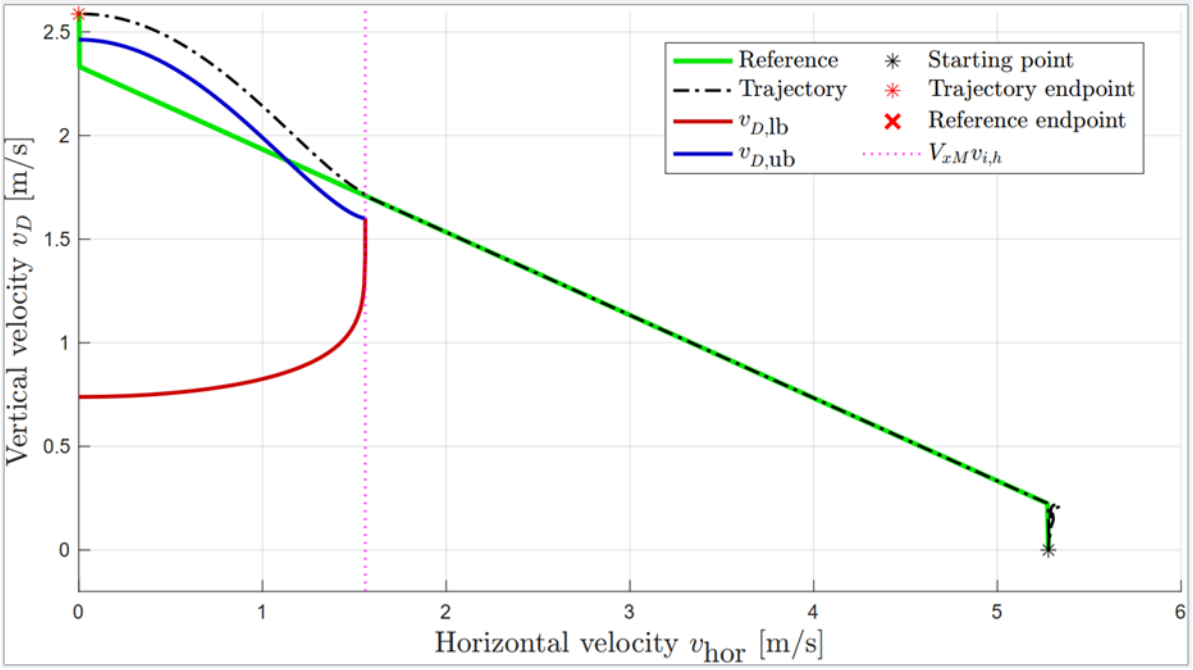
and the safe set $\mathcal{C} = \{x \in R^6 \mid h_{\text{ub}}(x) \geq 0 \vee h_{\text{lb}}(x) \geq 0\}$ as the complement of the unsafe region in Figure 1. By applying input-to-state safe CBFs, we solve for the QP

$$\min_{u_{\text{tot}} \in R^3} (u_{tot} - u_n)^T W (u_{tot} - u_n) \tag{5}$$
$$\text{s.t.} \quad L_g h_{ub}(x) u_{tot} \geq -\alpha h_{ub}(x) + \frac{||L_g h_{ub}(x)||^2}{\epsilon_0} \tag{6}$$
$$L_g h_{lb}(x) u_{tot} \geq -\alpha h_{lb}(x) + \frac{||L_g h_{lb}(x)||^2}{\epsilon_0} \tag{7}$$

where u_n and u_{tot} are the nominal and safety-filtered control inputs according to Figure 2, W is a positive definite weighting matrix, and ϵ_0 is a tuning parameter that accounts for the disturbances such as wind effects. The Lie derivatives $L_g h_{ub}(x)$ and $L_g h_{lb}(x)$ are determined based on the outer-loop dynamics of the helicopter following the model of [25]. We solve the QP case-dependent, meaning we consider (6) only if $v_D > v_{D,\text{ub}}$ and (7) only if $v_D \leq v_{D,\text{ub}}$.Therefore, we can derive analytical solutions of the QP using the KKT-conditions.



(a) Scenario I



(b) Scenario II

Figure 3: Prevention of VRS conditions by CBF-based safety filter. Nominal reference trajectory with VRS state violations (green line), true trajectory with VRS state prevention (dash-dotted black line), bounds of unsafe region (blue and red lines).

Simulation Results

The simulation results of the CBF-based safety filter are shown in Figure 3. Scenario I describes a descending during forward flight (vertical velocity increasing while horizontal velocity remains constant). Scenario II describes a descending while going from forward flight into hover (vertical velocity increasing while horizontal velocity decreases). In both scenarios, application of the

nominal controller following the reference trajectory would lead to VRS violations. The safety filter alters the applied control inputs in such a way that the helicopter states remain in the safe set, avoiding the VRS conditions. Based on the weighing matrix W, we emphasis the role of the vertical velocity component in order to achieve constraint satisfaction.

Conclusions

In this contribution, we apply the concept of control barrier function-based safety filters to helicopter UAS for prevention of dangerous vortex ring state conditions. The approach is embedded into a cascaded inner-outer loop controller structure with analytic solutions of the safety filter being obtained by solving the QP case-dependent based on KKT-conditions. The approach provides safety guarantees while minimizing deviations from the nominal control action.

References

[1] W. Johnson, "Model for vortex ring state influence on rotorcraft flight dynamics," NASA, TP-2005-213477, 2005.

[2] Y. Wang, A. Li, H. Tian and S. Yang, "Vortex ring state avoidance control scheme design for nonlinear autonomous helicopter," Journal of Guidance, Control, and Dynamics, vol. 45, no. 8, pp. 1546--1553, 2022. https://doi.org/10.2514/1.G006682

[3] B. Dang-Vu, "Vortex ring state protection flight control law," in 39th European Rotorcraft Forum, 2013.

[4] L. Chenglong, F. Zhou, W. Jiafang and Z. Xiang, "A vortex-ring-state-avoiding descending control strategy for multi-rotor UAVs," in 2015 34th Chinese Control Conference (CCC), 2015. https://doi.org/10.1109/ChiCC.2015.7260330

[5] A. D. Ames, S. Coogan, M. Egerstedt, G. Notomista, K. Sreenath and P. Tabuada, "Control barrier functions: Theory and applications," in 18th European control conference (ECC), 2019. https://doi.org/10.23919/ECC.2019.8796030

[6] W. Xiao and C. Belta, "Control barrier functions for systems with high relative degree," in IEEE 58th conference on decision and control (CDC), 2019. https://doi.org/10.1109/CDC40024.2019.9029455

[7] A. Alan, A. J. Taylor, C. R. He, G. Orosz and A. D. Ames, "Safe controller synthesis with tunable input-to-state safe control barrier functions," IEEE Control Systems Letters, vol. 6, pp. 908--913, 2021. https://doi.org/10.1109/LCSYS.2021.3087443

[8] J. Buch, S.-C. Liao and P. Seiler, "Robust control barrier functions with sector-bounded uncertainties," IEEE Control Systems Letters, vol. 6, pp. 1994--1999, 2021. https://doi.org/10.1109/LCSYS.2021.3136653

[9] M. H. Cohen, C. Belta and R. Tron, "Robust control barrier functions for nonlinear control systems with uncertainty: A duality-based approach," in IEEE 61st Conference on Decision and Control (CDC), 2022. https://doi.org/10.1109/CDC51059.2022.9992667

[10] E. Das and R. M. Murray, "Robust safe control synthesis with disturbance observer-based control barrier functions," in IEEE 61st Conference on Decision and Control (CDC), 2022. https://doi.org/10.1109/CDC51059.2022.9993032

[11] M. Jankovic, "Robust control barrier functions for constrained stabilization of nonlinear systems," Automatica, vol. 96, pp. 359--367, 2018. https://doi.org/10.1016/j.automatica.2018.07.004

[12] D. R. Agrawal and D. Panagou, "Safe control synthesis via input constrained control barrier functions," in 60th IEEE Conference on Decision and Control (CDC), 2021. https://doi.org/10.1109/CDC45484.2021.9682938

[13] J. Breeden and D. Panagou, "High relative degree control barrier functions under input constraints," in 60th IEEE Conference on Decision and Control (CDC), 2021. https://doi.org/10.1109/CDC45484.2021.9683705

[14] H. Dai and F. Permenter, "Convex synthesis and verification of control-Lyapunov and barrier functions with input constraints," in American Control Conference (ACC), 2023. https://doi.org/10.23919/ACC55779.2023.10156043

[15] P. Rabiee and J. B. Hoagg, "Soft-Minimum Barrier Functions for Safety-Critical Control Subject to Actuation Constraints," in American Control Conference (ACC), 2023. https://doi.org/10.23919/ACC55779.2023.10156245

[16] J. Breeden and D. Panagou, "Compositions of Multiple Control Barrier Functions Under Input Constraints," in American Control Conference (ACC), 2023. https://doi.org/10.23919/ACC55779.2023.10156625

[17] J. Breeden and D. Panagou, "Robust control barrier functions under high relative degree and input constraints for satellite trajectories," Automatica, vol. 155, pp. 111--109, 2023. https://doi.org/10.1016/j.automatica.2023.111109

[18] J. J. Choi, D. Lee, K. Sreenath, C. J. Tomlin and S. L. Herbert, "Robust control barrier--value functions for safety-critical control," in 60th IEEE Conference on Decision and Control (CDC), 2021. https://doi.org/10.1109/CDC45484.2021.9683085

[19] M. Spiller, E. Isbono and P. Schitz, "Feasibility of multiple robust control barrier functions for bounding box constraints," in American Control Conference (ACC), 2025. https://doi.org/10.23919/ACC63710.2025.11108097

[20] G. Notomista, S. Mayya, S. Hutchinson and M. Egerstedt, "An optimal task allocation strategy for heterogeneous multi-robot systems," in 18th European control conference (ECC), 2019. https://doi.org/10.23919/ECC.2019.8795895

[21] M. Srinivasan and S. Coogan, "Control of mobile robots using barrier functions under temporal logic specifications," IEEE Transactions on Robotics, vol. 37, no. 2, pp. 363--374, 2020. https://doi.org/10.1109/TRO.2020.3031254

[22] J. Autenrieb and A. Annaswamy, "Safe and stable adaptive control for a class of dynamic systems," in 62nd IEEE Conference on Decision and Control (CDC), 2023. https://doi.org/10.1109/CDC49753.2023.10383779

[23] J. Autenrieb, P. A. Fisher and A. Annaswamy, "Robust Safety Filters for Lipschitz-Bounded Adaptive Closed-Loop Systems with Structured Uncertainties," arxiv preprint.

[24] P. A. Fisher, J. Autenrieb and A. Annaswamy, "An Error-Based Safety Buffer for Safe Adaptive Control," arxiv preprint.

[25] T. J. Koo and S. Sastry, "Differential flatness based full authority helicopter control design," in Proceedings of the 38th IEEE Conference on Decision and Control, 1999. https://doi.org/10.1109/CDC.1999.830928

Materials Research Proceedings 69 (2026) 794-799 https://doi.org/10.21741/9781644904251-140

Anti-Windup Compensator Design for Fixed-Tilt Multirotors with Interaction Capabilities

Dharani JAYANNA[1,a *], Davide INVERNIZZI[1,b], Daniele MAGLIORE[2,c], Simone PANZA[2,d], and Marco LOVERA[1,e]

[1]Dipartimento di Scienze e Tecnologie Aerospaziali, Politecnico di Milano, Via La Masa 34, 20156 Milano, Italy

[2]ANT-X s.r.l., Via Davanzati 33, 20158 Milano, Italy

[a]dharani.jayanna@polimi.it, [b]davide.invernizzi@polimi.it, [c]daniele@antx.it, [d]simone@antx.it, [e]marco.lovera@polimi.it

Keywords: Anti-Windup Synthesis, Fully-Actuated UAVs, Aerial Physical Interaction, Actuator Saturation, Lateral Force Constraints

Abstract. This work addresses actuator saturation in fixed-tilt multirotor platforms used for aerial interaction. The fixed-tilt configuration imposes lateral force limitations, and exceeding these bounds under external disturbances can degrade performance and stability. To mitigate this, an anti-windup (AW) compensator is synthesized via an LMI-based convex optimization framework derived from the linearized closed-loop dynamics. An external wrench observer is integrated to estimate and counteract interaction and aerodynamic disturbances. The proposed AW augmented compensator structure preserves local stability during saturation, achieving improved transient behavior in simulation on the ARIES tiltrotor platform.

Introduction

The design of control strategies for aerial robots operating under constrained actuation has gained significant attention as unmanned aerial vehicles (UAVs) evolve from purely observational tasks to platforms capable of physical interaction for inspection and maintenance tasks [1]. Within this context, fully actuated multirotors have emerged as a promising class of vehicles capable of generating independent force and torque vectors in all degrees of freedom, enabling versatile interaction capabilities [2]. Among these, the fixed-tilt configuration stands out as one of the most structurally minimal designs, achieving full actuation through a non-coplanar arrangement of propellers. However, such a configuration introduces inherent lateral force constraints, since the available horizontal forces depend on the fixed cant and dihedral angles, which are typically chosen to satisfy nominal interaction requirements [2]. Under external influences such as contact interactions or wind disturbances, the controller may demand forces beyond the feasible envelope, leading to actuator saturation that degrades tracking performance and can compromise stability.

To address these limitations, this work presents the design of an anti-windup (AW) compensator providing stability guarantees under actuator saturation [3]. The compensator is synthesized through a convex optimization procedure based on linear matrix inequalities (LMIs), formulated from the linearized closed-loop dynamics of the system around a nominal equilibrium. The resulting design approximates the ideal unsaturated performance while maintaining stability within the feasible control region. In addition, an external observer is incorporated to reconstruct the forces and torques acting on the multirotor, thereby compensating for the reaction effects arising from contact interactions and aerodynamic disturbances. The synthesized AW compensator is integrated with both the dynamic feedback controller and the external observer to prevent wind-up phenomena. The proposed framework is validated in simulation, demonstrating effective suppression of wind-up and improved closed-loop behavior compared to the baseline controller.

Content from this work may be used under the terms of the Creative Commons Attribution 3.0 license. Any further distribution of this work must maintain attribution to the author(s) and the title of the work, journal citation and DOI. Published under license by Materials Research Forum LLC.

Materials Research Proceedings 69 (2026) 794-799 https://doi.org/10.21741/9781644904251-140

UAV Dynamics and Control Architecture

The experimental platform considered in this study is the ARIES tiltrotor, developed by ANT-X s.r.l. [4]. ARIES is a fixed-tilt hexarotor, as illustrated in Fig. 1, designed for aerial interaction and contact-based inspection tasks, capable of maintaining stable flight while exerting forces on the environment.



Figure 1: ARIES fixed-tilt hexarotor.

The motion of the hexarotor is described by the standard six-degree-of-freedom Newton-Euler equations. The translational dynamics are expressed in the inertial frame $\mathcal{F}_I = (O_I, i_1, i_2, i_3)$, while the rotational motion is represented in the body-fixed frame $\mathcal{F}_B = (O_B, b_1, b_2, b_3)$, centered at the platform's center of mass. Here, i_j and b_j $(j \in 1,2,3)$ denote right-handed orthonormal bases of the inertial and body frames, respectively, and O_I, O_B are their corresponding origins. The resulting dynamics are expressed as:

$$m\dot{v}_I = -mg\mathbb{e}_3 + R(f_{ca} + f_r), \quad J\dot{\omega}_B = -\omega_B \times J\omega_B + \tau_{ca} + \tau_r, \tag{1}$$

where $m \in \mathbb{R}_{>0}$ and $J = J^T \in \mathbb{R}^{3\times3}_{>0}$ denote the platform mass and inertia matrix, $R \in \mathrm{SO}(3)$ is the body-to-inertial rotation matrix, and v_I, ω_B are the translational and angular velocities defined in $\mathcal{F}_I$ and $\mathcal{F}_B$ frames respectively. The propeller generated wrench $w_{ca} = [f_{ca}^T \quad \tau_{ca}^T]^T$ acts on the vehicle, while the external wrench $w_r = [f_r^T \quad \tau_r^T]^T$ models aerodynamic and contact effects. The desired control wrench $w_c = [f_c^T \quad \tau_c^T]^T$ is mapped to the individual rotor thrusts through the constant input matrix $\mathbb{F}(\alpha, \beta) \in \mathbb{R}^{6\times6}$, defined by the geometry of the ARIES platform [5]:

$$\begin{gathered} w_c = \mathbb{F}(\alpha,\beta)\begin{bmatrix} k_f\omega_1^2 & \dots & k_f\omega_6^2 \end{bmatrix}^T, \qquad R_B^{R_i} = R_Y(\beta_i)R_X(\alpha_i)R_Y(\beta_a)R_Z(\psi_i), \\ \mathbb{F}_i(\alpha_i,\beta_i) = \begin{bmatrix} -R_{R_i}^B\mathbb{e}_3 \\ \left(-\left[x_{BR_i}^B\right]_\times + (-1)^{i-1}k_f^\tau \mathrm{I}_3\right) R_{R_i}^B\mathbb{e}_3 \end{bmatrix}, \end{gathered} \tag{2}$$

where α, $\beta \in \mathbb{R}^6$ are cant and dehidral angles of each propeller. Fully actuated multirotors allow independent force and torque control, enabling diverse feedback designs such as geometric or linear control [1, 6]. A hierarchical cascade structure is adopted, with outer position and attitude loops and inner velocity and rate loops. The translational controller computes f_c, while the attitude controller determines τ_c, yielding:

$$\begin{gathered} f_c = m\left(K_{vp}R\left(K_{pp}(p_r - p_I) + v_r - v_I\right) - K_{vd}R\dot{v}_I\right) - mgR\mathbb{e}_3 - \hat{f}_r, \\ \tau_c = K_{\omega p}\left(K_{\theta p}(\Theta_r - \Theta_B) + \omega_r - \omega_B\right) - K_{\omega d}\dot{\omega}_B - \hat{\tau}_r, \end{gathered} \tag{3}$$

where $K_{(\cdot)} \in \mathbb{R}^{3\times3}_{\geq0}$ are diagonal gain matrices and the vectors p_r, v_r, Θ_r, and ω_r represent the desired position, velocity, attitude, and angular rate setpoints, respectively. The observer-estimated wrench $\hat{w}_r = [\hat{f}_r^T \quad \hat{\tau}_r^T]^T$ compensates the external effects w_r in Eq. 1. The commanded wrench w_c is distributed through $\mathbb{F}(\alpha, \beta)$ in Eq. 2, ensuring accurate force and torque generation within the actuator range. When the compensated command exceeds feasible actuation, the applied wrench w_{ca} deviates from w_c, related by:

$$w_{ca} = \mathrm{sat}_{[u^-,u^+]}(w_c), \quad \mathrm{sat}_{[u^-,u^+]}(u) = \max\{\min\{u^+, u\}, -u^-\}, \tag{4}$$

where the saturation acts component-wise, with bounds $u^-, u^+ \in \mathbb{R}^{n_u}_{\geq0}$ and input dimension $n_u \in \mathbb{N}$. The next section introduces the external observer that estimates the acting wrench and integrates with the control framework.

Materials Research Proceedings 69 (2026) 794-799 https://doi.org/10.21741/9781644904251-140

External Wrench Observer

Accurate estimation of external forces and moments is crucial for safe aerial interaction, especially when direct sensing is impractical due to payload or hardware constraints. To reconstruct the external wrench acting on the platform, a model-based observer [6] is formulated using the UAV dynamics and onboard inertial measurements. The translational and rotational estimators are defined respectively as:

$$\begin{aligned} m\dot{\hat{v}}_I &= mg\mathbb{e}_3 + R^T\left(\mathbb{F}_f k_f \omega^2 + \hat{f}_r\right) + \Lambda_v(v_I - \hat{v}_I), \qquad \dot{\hat{f}}_r = \Lambda_f R(v_I - \hat{v}_I), \\ J\dot{\hat{\omega}}_B &= -\omega_B \times J\omega_B + \mathbb{F}_\tau k_\tau \omega^2 + \hat{\tau}_r + \Lambda_\omega(\omega_B - \hat{\omega}_B), \quad \dot{\hat{\tau}}_r = \Lambda_\tau(\omega_B - \hat{\omega}_B), \end{aligned} \tag{5}$$

where $\hat{v}_I$ and $\hat{\omega}_B$ are the estimated linear and angular velocities, and $\hat{f}_r$, $\hat{\tau}_r$ represent the estimated external force and torque. The positive definite gain matrices $\Lambda_{(.)} \in \mathbb{R}^{3\times3}_{\geq 0}$ govern estimator dynamics, balancing responsiveness and noise sensitivity. Matrices $\mathbb{F}_f$ and $\mathbb{F}_\tau$ map rotor speeds to translational and rotational components of the applied control wrench as mentioned in Eq. 1. This observer reconstructs external wrench in real time without dedicated sensors, enhancing disturbance compensation; however, when the estimated forces drive control inputs beyond actuator limits, an anti-windup compensator is augmented as discussed in the next section.

Anti-Windup Compensator Synthesis

The nonlinear dynamics of the multirotor, along with the baseline controller and external wrench observer, are linearized around the hovering equilibrium corresponding to zero attitude and steady thrust balancing gravity. The resulting augmented linear model captures the coupled behavior of the plant, controller, and observer, forming the basis for the AW synthesis. Following the methodology of [3], a fixed-structure AW compensator is introduced by embedding additional feedback gains within the controller to preserve stability under actuator saturation. The overall closed-loop system used for AW synthesis can be expressed in compact form as:

$$\begin{cases} \dot{\xi} = A\xi + B_q q_X, \\ z_e = C_z\xi + D_{zq} q_X, \\ y_c = C_y\xi + D_{yq} q_X, \end{cases} \tag{6}$$

Where $\xi = [x_a^T \quad x_{rm}^T \quad w^T]^T$ denotes the augmented closed-loop state, comprising the plant, controller, external wrench observer, and AW compensator states. The reference model represents the ideal system with unconstrained actuation, while w belongs to a specified class of reference inputs. The performance variable is $z_e = z - z_{rm}$, i.e., the deviation between the saturated response and the nominal reference-model output. The signal q_X denotes the AW interconnection term capturing the difference between the controller command and its saturated counterpart.

Based on this representation, the AW synthesis problem aims to determine the compensator gains that minimize the ℓ_2-norm of the performance output z_e, ensuring Lyapunov-based stability within a prescribed region of attraction. The resulting optimization problem is cast as a convex program subject to LMI constraints, whose solution directly yields the AW gain matrices. For detailed derivations and proofs, the reader is referred to [3].

Simulation Results

The closed-loop architecture of the ARIES platform incorporating the AW compensator is depicted in Fig. 2. The baseline controller generates the desired control wrench w_c from the reference signals y_r and w, while the external observer estimates the reaction wrench $\hat{w}_r$ using the measured states y and applied wrench w_{ca}. The control command is mapped through $\mathbb{F}^{-1}$, constrained by actuator limits via the saturation nonlinearity, and subsequently redistributed to the plant through $\mathbb{F}$. The AW compensator processes the input mismatch q_X between the pre and post

Materials Research Proceedings 69 (2026) 794-799 https://doi.org/10.21741/9781644904251-140

saturation signals to synthesize the corrective term v_{AW}, which is fed back to both the controller and observer to ensure consistent dynamic behavior and stability within the saturation region.

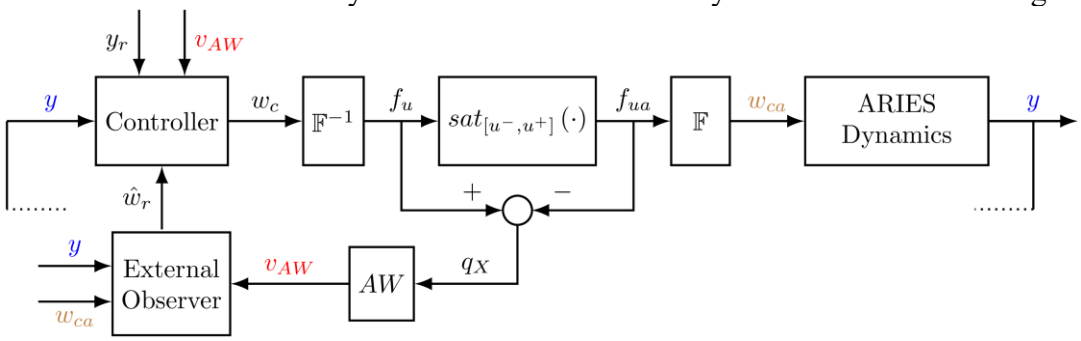


Figure 2: ARIES AW-augmented closed-loop system.

The proposed control framework is validated in simulation using the ARIES dynamic model, where the platform is commanded to maintain a hovering condition while subjected to a step-like external disturbance designed to induce actuator saturation. The simulations evaluate the capability of the AW-augmented controller to preserve stability and tracking accuracy under saturation, demonstrating the compensators effectiveness in mitigating windup effects and maintaining consistent closed-loop performance.

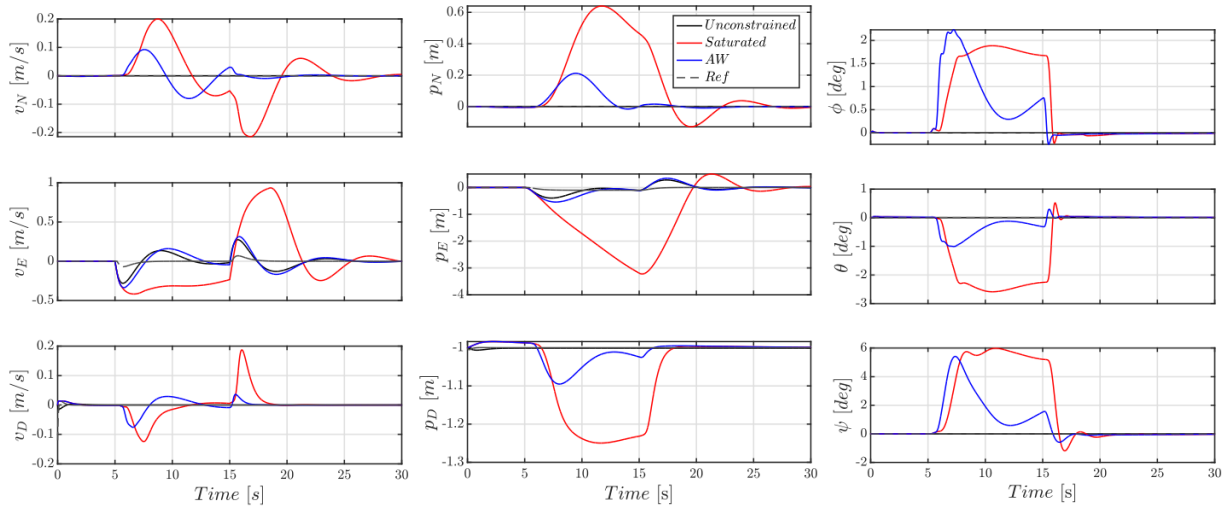


Figure 3: Position (left), velocity (middle), and attitude (right) tracking performance for fixed-tilt hexarotor under various controllers.

Fig. 3 illustrates the position, velocity, and attitude tracking performance of the fixed-tilt hexarotor under three configurations: the unconstrained nominal controller, the saturated controller without compensation, and the proposed AW-augmented controller. When saturation occurs, the nominal controller exhibits significant deviation and oscillatory behavior, particularly in the lateral and yaw dynamics, indicating loss of stability. In contrast, the AW-compensated response closely follows the nominal trajectory, achieving smooth transient behavior and faster recovery once the actuators re-enter the feasible region.

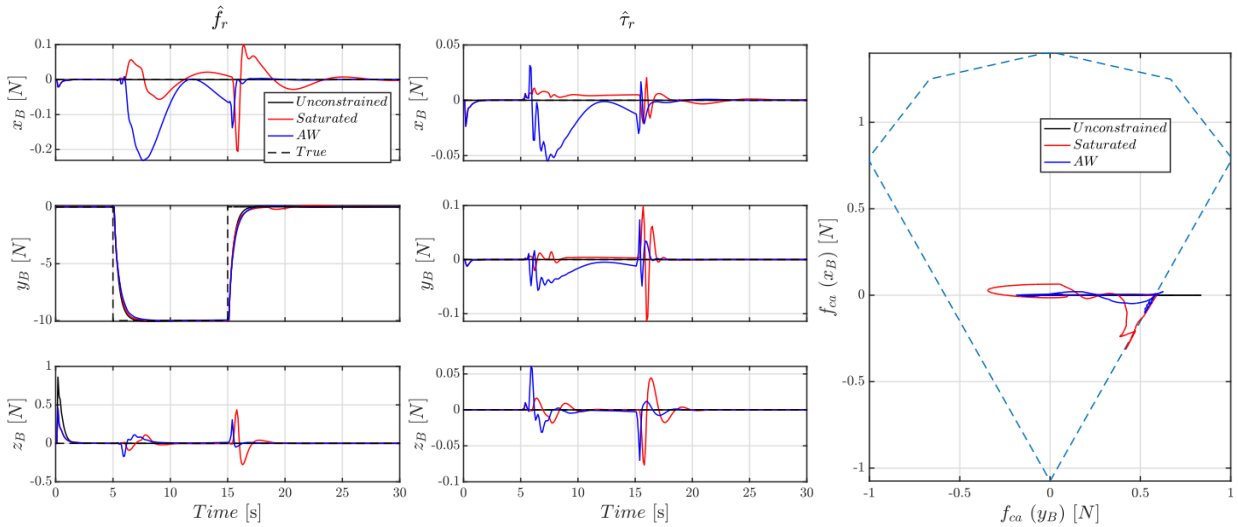


Figure 4: Estimated force (left), torque (middle), and applied force (right) with respect to available force envelope under various controllers (axes scaled for confidentiality).

Fig. 4 presents the estimated force and torque components, along with the applied force envelope in the lateral plane. The AW-compensated controller effectively limits the commanded forces within the feasible actuation range while maintaining consistent disturbance rejection. The force trajectories remain tangent to the saturation boundary, demonstrating how the compensator ensures stable recovery from saturation without inducing excessive overshoot or steady-state bias. These results confirm that the proposed anti-windup strategy effectively preserves nominal control performance within the feasible actuation region while ensuring stable and robust behavior under saturation-induced nonlinearities.

Summary

This work presents an anti-windup compensator for fixed-tilt multirotors operating under actuator saturation and external interaction forces. The framework integrates a model-based external wrench observer with a performance-oriented compensator synthesized through convex LMI optimization. Simulations on the ARIES hexarotor show that the AW-augmented controller mitigates windup, maintaining stability and near-nominal tracking under severe actuation limits. Future efforts will extend the approach to experimental validation for contact interaction scenarios.

Acknowledgement

This work is supported by the European Union - NextGenerationEU under the National Recovery and Resilience Plan (PNRR), Mission 4, Component 2 “From Research to Enterprise” - Investment 3.3, within the framework of the doctorate program activated under Ministerial Decree No. 352 of 9/04/2022.

References

[1] R. Rashad, J. Goerres, R. Aarts, J. B. Engelen, and S. Stramigioli, Fully actuated multirotor uavs: A literature review, IEEE Robotics and Automation Magazine, vol. 27, no. 3, pp 97-107, 2020. https://doi.org/10.1109/MRA.2019.2955964

[2] D. Kotarski, P. Piljek, J. Kasać, and D. Majetić, Performance analysis of fully actuated multirotor unmanned aerial vehicle configurations with passively tilted rotors, Applied Sciences, vol. 11, no 18, p. 8786, 2021. https://doi.org/10.3390/app11188786

[3] P. Ghignoni, N. Buratti, D. Invernizzi, and M. Lovera, Anti-windup design for directionality compensation with application to quadrotor uavs, IEEE Control Systems Letters, vol. 5, no. 1, pp. 331-336, 2020. https://doi.org/10.1109/LCSYS.2020.3001881

[4] ANT-X s.r.l., Aries - industrial drone for aerial interaction, https://antx.it/industrial-drones-antx/aries/, accessed: November 6, 2025.

[5] M. Ryll, H. H. Bülthoff, and P. R. Giordano, Modeling and control of a quadrotor uav with tilting propellers, in 2012 IEEE international conference on robotics and automation. IEEE, 2012, pp. 4606-4613. https://doi.org/10.1109/ICRA.2012.6225129

[6] M. Ryll, G. Muscio, F. Pierri, E. Cataldi, G. Antonelli, F. Caccavale, D. Bicego, and A. Franchi, 6d interaction control with aerial robots: The flying end-effector paradigm, The International Journal of Robotics Research, vol. 38, no. 9, pp. 1045-1062, 2019. https://doi.org/10.1177/0278364919856694

Materials Research Proceedings 69 (2026) 800-805 https://doi.org/10.21741/9781644904251-141

Ground Effect in Thrust-Lift Conversion using the Deflected Slipstream Concept in Martian Conditions

Wei HAN[1,a *], Manuel CARREÑO RUIZ[1,b] and Domenic D'AMBROSIO[1,c]

[1]Politecnico di Torino, Turin, Italy, 10129

[a]wei.han@polito.it, [b]manuel.carreno@polito.it, [c]domenic.dambrosio@polito.it

Keywords: Ground Effect, Martian UAS, Thrust-Lift Conversion, Deflected Slipstream

Abstract. As interest in Mars exploration grows, there is an increasing demand for versatile unmanned aerial systems (UAS) capable of vertical takeoff and landing (VTOL), driving the development of lightweight, high-lift configurations. Among these, the propeller–wing configuration with a deflected slipstream (DS) system, known as a DS-blown wing, enables efficient thrust–lift conversion. However, during VTOL, the ground effect can substantially alter the flow field and affect this conversion efficiency. Three-dimensional unsteady Reynolds-Averaged Navier–Stokes (URANS) simulations with fully resolved propeller-blade geometry were conducted to evaluate the thrust-lift conversion efficiency at various ground clearances and to examine the aerodynamic interactions among the propeller-induced flow, the deflected flap, and the ground surface. The results show that the DS-blown wing exhibits reduced efficiency in ground effect compared with out-of-ground-effect conditions, primarily due to a recirculation region beneath the wing that modifies the pressure distribution. When the wing operates in very close proximity to the ground, a rebound in thrust-lift conversion efficiency is observed. Moreover, at certain intermediate heights, a resonance phenomenon occurs, leading to large-amplitude lift fluctuations at the blade-passing frequency. This work enhances the understanding of DS-blown wing aerodynamics in ground effect under Martian conditions and provides valuable guidance for the design of future Mars UAS.

Introduction

Achieving efficient vertical takeoff and landing (VTOL) performance remains a significant challenge for unmanned aerial systems (UAS) operating on Mars, particularly when structural simplicity and low mass are required. Conventional rotorcraft can generate sufficient lift but suffer from poor aerodynamic efficiency in forward flight, whereas fixed-wing aircraft offer efficient cruise performance but face difficulties in achieving VTOL capability. To bridge this gap, the present study focuses on blown-wing configurations employing deflected slipstream (DS) systems, in which the high-momentum propeller slipstream is deflected by a flap to generate lift. This configuration has emerged as a lightweight and mechanically simple approach to achieving VTOL in fixed-wing UAS.

DS technology has been widely investigated and applied in aircraft designs aimed at achieving V/STOL performance [1]. Under Martian conditions, several studies have examined the interaction between propeller-induced flow and wing structures [2,3]. Other lift-augmentation concepts, such as the CoFlow Jet integrated into a DS-blown wing configuration, have also been explored [4]. During take-off and landing operations, the wing ground effect plays a crucial role in influencing aerodynamic performance, and it has been extensively investigated for various airfoils operating at low Reynolds numbers [5,6]. However, despite extensive research on blown wings and ground effect individually, the coupled influence of ground proximity on the deflected slipstream and its impact on thrust-lift conversion remains insufficiently understood. In particular, for DS-blown wing configurations, the interaction between the deflected jet flow and the ground significantly alters the overall flow behavior. In this study, we consider a blown wing with a 90° flap deflection,

Content from this work may be used under the terms of the Creative Commons Attribution 3.0 license. Any further distribution of this work must maintain attribution to the author(s) and the title of the work, journal citation and DOI. Published under license by Materials Research Forum LLC.

Materials Research Proceedings 69 (2026) 800-805 https://doi.org/10.21741/9781644904251-141

as shown in Fig. 1. Unlike the ground effect in a conventional isolated wing configuration, the DS-blown wing exhibits strong aerodynamic coupling among the slipstream, the wing, and the ground. On one hand, the ground blockage modifies the trajectory of the propeller slipstream, disturbing its deflection and consequently reducing the efficiency of thrust-lift conversion. On the other hand, varying levels of ground proximity lead to the formation of distinct recirculation regions, where the resulting bubble can alter the inflow conditions to the propeller blades.

Building on previous studies of DS technology and the wing ground effect, this work investigates how the flow physics of a DS-blown wing is modified when it operates near a solid surface under Martian conditions. Using computational fluid dynamics (CFD), we analyze the interaction between the propeller-induced flow and the deflected flap at various heights above ground. The ground effect, which arises from the proximity of the wing surfaces to the ground plane, can generally be categorized into two types: chord-dominated and span-dominated. The chord-dominated ground effect is characterized by the accumulation of ram pressure, a dynamic air cushion formed within the narrowed flow passage between the lower surface of the airfoil and the ground. In contrast, the span-dominated ground effect is associated with the breakdown or outward displacement of wingtip vortices [5]. In this study, periodic boundary conditions are applied to the spanwise boundaries; therefore, only the chord-dominated ground effect is considered.

The primary objective of this study is to quantify the influence of ground proximity on the aerodynamic characteristics of the DS-blown wing and to evaluate how these ground-induced effects modify the efficiency of thrust-lift conversion during low-altitude VTOL. Furthermore, the analysis reveals specific fluid interactions among the propeller-induced flow, the deflected flap, and the ground surface. The remainder of this paper is organized as follows: Section 2 describes the methodology and computational setup, Section 3 presents the main results and discussion, and Section 4 summarizes the key findings.

Methodology

In this study, we employed the commercial CFD software Simcenter STAR-CCM+ to perform three-dimensional unsteady Reynolds-averaged Navier–Stokes (URANS) simulations with fully resolved propeller-blade geometries using the sliding-mesh approach. Turbulence was modeled using the SST k-ω model developed by Menter, coupled with the γ-Reθ transition model to predict the laminar-to-turbulent flow transition under simulated Martian conditions.

The Ishii airfoil was selected for this investigation owing to its favorable aerodynamic performance at low Reynolds numbers [7]. An angle of attack (AOA) of 5° was adopted based on its good aerodynamic efficiency. The wing chord was set to 1 m. The flap, accounting for 25% of the chord length, was hinged at 75% of the wing chord and deflected by 90°. The chord-based Reynolds number was 25,500, with the reference velocity defined as the mean induced velocity. The employed propeller has a diameter of 0.4 m, and was optimized by Carreño Ruiz [8] for Martian conditions. The computational domain extended 80 chord lengths upstream and 80 chord lengths downstream of the wing to minimize boundary interference. A Cartesian grid consisting of approximately 5 million cells was employed, with prism layers refined to maintain a y+ value below 1, ensuring accurate resolution of strong wall-normal gradients, as shown in Fig. 2. The ground plane was modeled as a stationary no-slip wall, while periodic boundary conditions were applied in the spanwise direction. Simulations were conducted for different heights above the ground. The tested distances between the wing leading edge and the ground were 0.4 m, 0.6 m, 0.8 m, 1 m, 1.5 m, and an out-of-ground-effect condition.

Materials Research Proceedings 69 (2026) 800-805 https://doi.org/10.21741/9781644904251-141

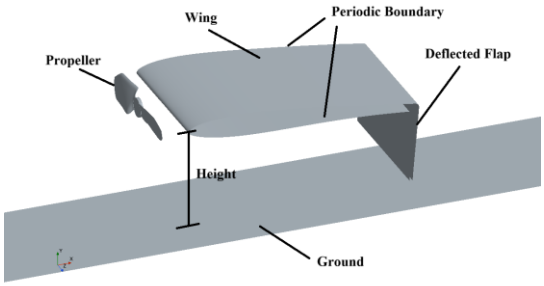


Figure 1: Blown wing with 90° deflected flap.

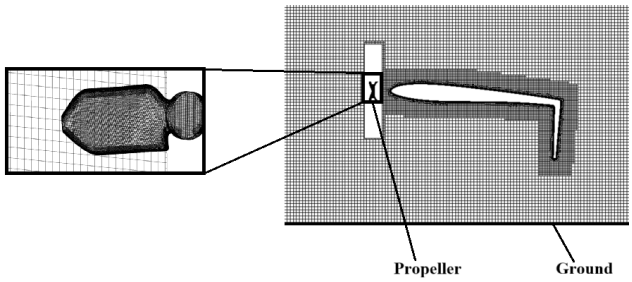


Figure 2: Cartesian grid of the DS-blown wing.

Results and Discussion

The simulation results demonstrate that the DS-blown wing operating in ground effect undergoes significant modifications in flow topology. Figure 3 presents the time-averaged pressure and velocity fields at the mid-span of the DS-blown wing. The main differences between the configurations operating in and out of ground effect are associated with the recirculation region beneath the wing and the high-pressure zone on the pressure side of the deflected flap. As the wing approaches the ground, the low-pressure region corresponding to the recirculation becomes compressed and constrained within the narrowing space between the wing's pressure surface and the ground. The lift-to-thrust ratio at different heights above the ground is summarized in Table 1. Unlike the typical lift enhancement caused by ram pressure beneath a conventional wing operating in ground effect, the DS-blown wing exhibits a reduction in thrust-lift conversion efficiency. This reduction can be attributed to ground-induced blockage which limits the effectiveness of the redirected slipstream. Interestingly, as the wing nears the ground, the lift-to-thrust ratio initially decreases but then rebounds when the airfoil is in very close proximity to the surface. The spanwise-averaged mean pressure coefficient distribution is shown in Fig. 4, where the blade-tip velocity is used as the reference velocity. This figure highlights how the lift varies with ground clearance. It is evident that, across the examined heights, the pressure distribution on the suction side remains nearly identical to that of the out-of-ground-effect case, whereas the pressure on the pressure side is noticeably altered.

Table 1: Lift–thrust ratio at different heights above ground

Height above ground [m]	Thrust-lift conversion efficiency	Thrust [N]
0.4	0.365	1.032
0.6	0.312	1.085
0.8	0.331	1.081
1.0	0.341	1.039
1.5	0.368	0.996
Out of ground effect	0.466	1.101

As the height decreases, a low-pressure recirculation region develops beneath the wing, which can be clearly observed in Fig. 3. Meanwhile, a local pressure increase appears near 60% to 70% chord region on the pressure side in the in-ground-effect cases, except for the H = 0.6 m case. However, this increase cannot compensate for the pressure loss generated by the recirculation region between 20% to 50% chord region. As the wing approaches the ground to a height equal to one propeller diameter (0.4 m), the recirculation bubble becomes increasingly compressed. The

Materials Research Proceedings 69 (2026) 800-805 https://doi.org/10.21741/9781644904251-141

intensified ram pressure on the pressure side extends over a broader region, leading to a rebound in lift compared with other in-ground-effect cases. Although a closer configuration could

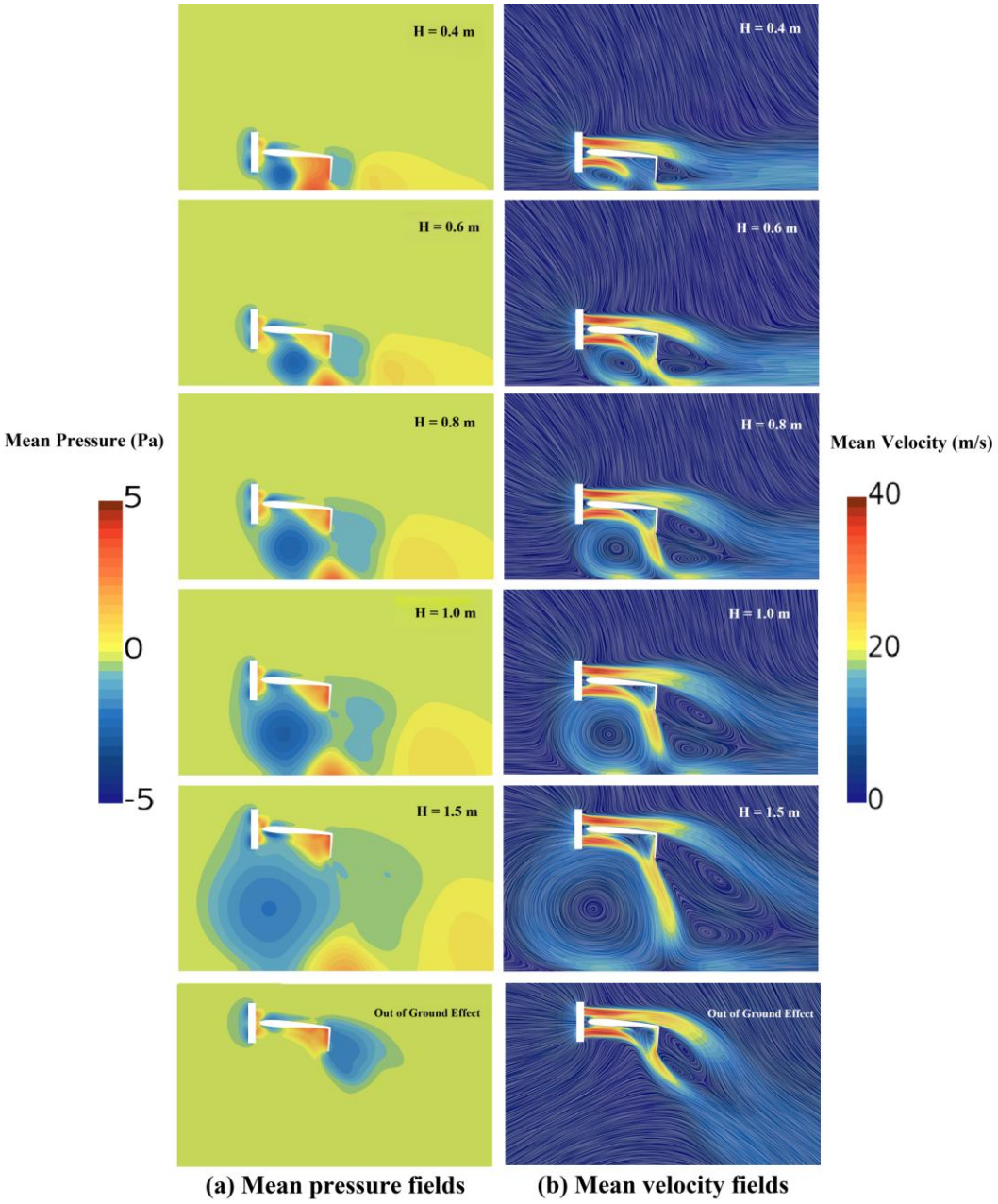


Figure 3: Time-averaged pressure and velocity fields at different wing heights above ground.

potentially enhance lift through stronger ram pressure, it has not been investigated here, as under realistic Martian conditions, a certain clearance between the flap and the ground is required due to the uneven and rocky terrain during VTOL operations.

In addition to quantifying the influence of ground proximity on thrust-lift conversion efficiency, we further examine the instantaneous behavior of lift and thrust. The lift force at different heights above the ground is shown in Fig. 5. As the DS-blown wing approaches the ground, the lift becomes increasingly unsteady, primarily due to the low-frequency vortex shedding behind the wing flap. Moreover, in the tested cases, the dominant low-frequency component of the vortex

Materials Research Proceedings 69 (2026) 800-805 https://doi.org/10.21741/9781644904251-141

shedding increases as the DS-blown wing moves closer to the ground. Another notable observation is that when the height falls below 0.8 m, the lift-force fluctuates at the blade-passing frequency (BPF) become more pronounced. The lift exhibits oscillations at the BPF with amplitudes reaching

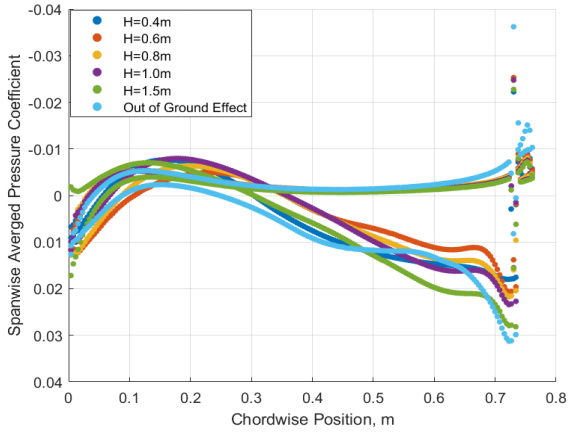


Figure 4: Mean pressure distribution at different heights above ground.

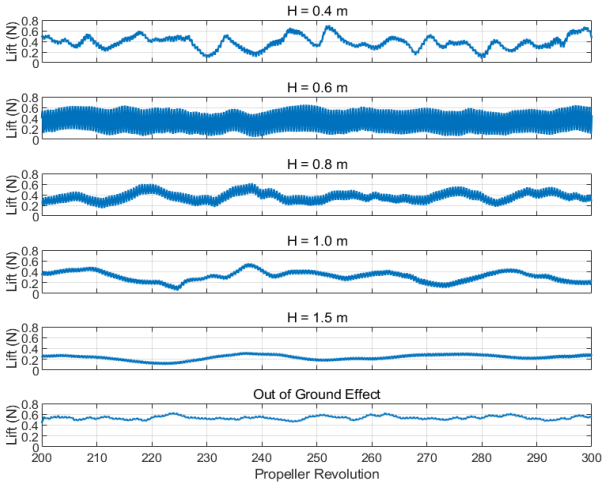


Figure 5: Lift force at different heights above ground.

approximately 50% and 100% of the mean lift at heights of 0.8 m and 0.6 m, respectively. However, these fluctuations decrease to roughly 15% of the mean lift when the height is reduced to 0.4 m, indicating that the resonance is amplified only for certain sizes of the recirculation bubble.

The observed fluctuations at the BPF are likely linked to a resonance phenomenon involving the propeller-induced flow, the recirculation region beneath the wing, and the propeller inflow. As seen in Fig. 3, the mean velocity fields reveal that cases exhibiting large-amplitude fluctuations share a common feature: the recirculation bubble is contained below the wing and shows a weakened interaction with the propeller's intake stream tube. In contrast, in other cases, the recirculation bubble feeds the rotor inflow. This observation is consistent with the thrust data presented in Table 1. When the propeller inflow is affected by the recirculation region, the local AOA decreases as the blade passes through this region, resulting in a reduction in thrust. In such

cases, the thrust loss ranges from 5% to 10%, whereas for cases with high-amplitude fluctuations, the thrust loss is less than 2% compared with the out-of-ground-effect condition.

Conclusions

This work studies the complex mechanisms governing the ground effect in the DS-blown wing configuration. The interactions among the propeller-induced flow, the deflected flap, and the ground have been preliminarily investigated. As the DS-blown wing approaches the ground, the thrust–lift conversion efficiency initially decreases and then rebounds; however, it remains lower overall under ground-effect conditions for the cases examined, unlike what happens with conventional wings in ground effect. In addition, a resonance phenomenon between the propeller-induced flow and the recirculation region beneath the wing has been observed, which may lead to potential instability and structural issues during VTOL operations. Understanding the relationship between thrust–lift conversion efficiency and height above ground is therefore essential for achieving smooth and stable VTOL and transition phases. This study provides valuable insights to guide the design and development of fixed-wing UAS for Mars, particularly regarding VTOL operations. Future work will consider different flap deflection angles and propeller positions to further enhance understanding of the ground effect in DS-blown wing configurations.

References

[1] W. D. Bertelsen, History of Deflected Slipstream VTOL Aircraft, American Helicopter Society 61st Annual Forum, 2005.

[2] F. Makino, H. Nagai, Propeller slipstream interference with wing aerodynamic characteristics of Mars airplane at low Reynolds number, 52nd Aerospace Sciences Meeting, AIAA, 2014. https://doi.org/10.2514/6.2014-0744

[3] W. Han, M. Carreño Ruiz, D. D'Ambrosio, Thrust–lift conversion in a fixed-wing vertical take-off and landing UAS in the Martian atmosphere, AIAA AVIATION Forum and ASCEND, AIAA, 2025. https://doi.org/10.2514/6.2025-3584

[4] J. Jeon, B. McBreen, G. Zha, Study of 3D flapped co-flow jet wings for ultra-high cruise lift coefficient, AIAA AVIATION Forum, AIAA, 2023.

[5] T. Lee and G. Lin, Review of experimental investigations of wings in ground effect at low Reynolds numbers, Front. Aerosp. Eng. 1 (2022) 975158. https://doi.org/10.3389/fpace.2022.975158.

[6] R.W. Schade, A study of ground interference effects on VTOL configurations, NASA Technical Report, 1974. https://ntrs.nasa.gov/

[7] M. Anyoji, Y. Inoue, S. Takahashi, T. Tanaka, T. Ishii, H. Asawa, Computational and experimental analysis of a high-performance airfoil under low-Reynolds-number flow conditions, J. Aircraft 51 (2014) 1864–1872. https://doi.org/10.2514/1.C032578

[8] M. Carreño Ruiz, D. D'Ambrosio, Aerodynamic optimization and analysis of quadrotor blades operating in the Martian atmosphere, Aerosp. Sci. Technol. 132 (2023) 108153. https://doi.org/10.1016/j.ast.2022.108153

Materials Research Proceedings 69 (2026) 806-811 https://doi.org/10.21741/9781644904251-142

Learning-Based Quadrotor Tracking Control Using Recursive Gaussian Processes

Alessandro LUPATINI[1,a*], Giovanni GOZZINI[1,b], Alessandro NAZZARI[1,c], Roberto RUBINACCI[1,d] and Marco LOVERA[1,e]

[1]Dipartimento di Scienze e Tecnologie Aerospaziali, Politecnico di Milano, Milano, 20156 ITA

[a]alessandro.lupatini, [b]giovanni.gozzini, [c]alessandro.nazzari, [d]roberto.rubinacci, [e]marco.lovera}@polimi.it

Keywords: Recursive Gaussian Process, Feedback Linearization, Reference Tracking, UAV

Abstract. High-precision UAV tracking is hindered by hard-to-model aerodynamic effects. We propose a *learning-based controller* for a simplified quadrotor that uses Feedback Linearization (FL), to cancel modeled dynamics, and a sparse Bayesian inference method called *Recursive Gaussian Process* (RGP), to learn and compensate residual nonlinearities in real time. Simulations and experiments conducted on a real 1D quadrotor platform demonstrate reduced tracking error and practical feasibility for *real-world implementation*.

Introduction

High-precision reference tracking for Unmanned Aerial Vehicles (UAVs) is one of the main challenges in the aerospace control community, primarily due to aerodynamics effects. These effects are difficult to model accurately and, therefore, are often neglected. As a result, model-based control methods frequently fail to achieve the desired performance. With the growing popularity of machine learning techniques, a promising research direction is the integration of model-based control with data-driven approaches.).

In this context, a popular model-based controller is *Feedback Linearization*, which employs the system model to cancel its nonlinear dynamics and render the system into a linear one. Past works used FL tuned with reinforcement learning [1] or combined with neural networks [2].

However, these approaches lack rigorous stability analysis. In contrast, Gaussian Processes (GPs) offer probabilistic guarantees and have therefore attracted significant attention within the control community. In fact, Greeff and Schoellig [4] demonstrated that using GPs online alongside FL substantially improves tracking performance and enhances robustness. Yet the approach was validated only in simulation and the computational constraints of onboard GP inference were not addressed.

In this paper, we propose a similar approach to control a 1-D quadrotor system. Specifically, we model the residual of the FL using a *sparse GP*, which significantly reduces the computational load of inference. We validate the approach on a real platform.

Baseline controller

Model assumptions. We consider a *SISO control-affine* system with state $x \in \mathbb{R}^n$ and input $u \in \mathbb{R}$:

$$\dot{x} = f(x) + g(x)u \tag{1}$$

Content from this work may be used under the terms of the Creative Commons Attribution 3.0 license. Any further distribution of this work must maintain attribution to the author(s) and the title of the work, journal citation and DOI. Published under license by Materials Research Forum LLC.

Materials Research Proceedings 69 (2026) 806-811 https://doi.org/10.21741/9781644904251-142

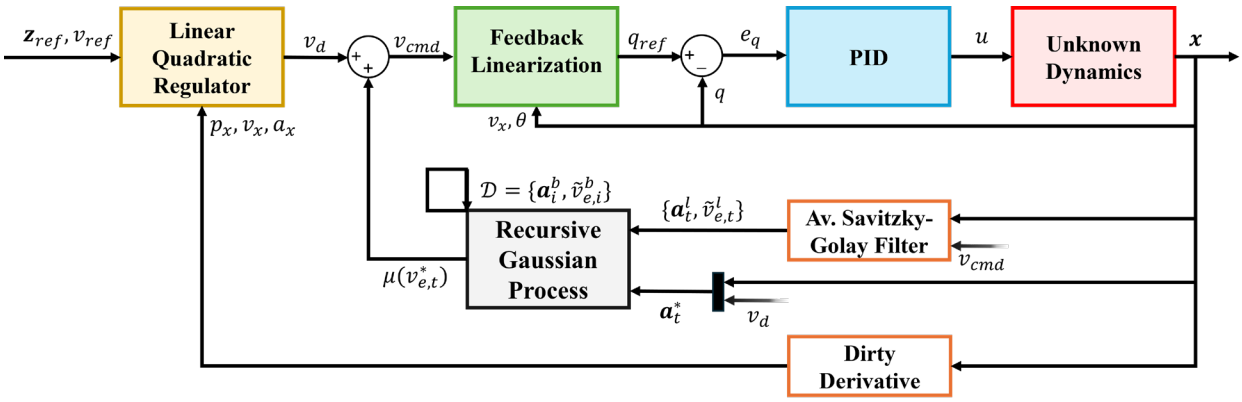


Figure 1: Controller scheme.

where $f(x)$ and $g(x)$ are unknown functions. *Assumption 1*: The system in 1 is differentially flat with respect to the known output $y = h(x) \in \mathbb{R}$. *Assumption 2*: A SISO nominal model of the system, also differentially flat in the output $y = h(x)$, is known:

$$\dot{x} = \hat{f}(x) + \hat{g}(x)u \tag{2}$$

Model specifications. The proposed controller (shown in Fig. 1) is formulated for a *2-DOF quadrotor system*, which dynamics is

$$\begin{cases} \dot{p}_x(t) = v_x(t) \\ \dot{v}_x(t) = -c v_x(t) - \bar{k} \sin(\theta(t)) \\ \dot{\theta}(t) = q(t) \\ \dot{q}(t) = -2\,\xi\,\omega_n q(t) - \omega_n^2 \theta(t) + \mu m_{c_x}(t) \end{cases} \tag{3}$$

where $c, \bar{k}, \xi, \omega_n$ and μ are obtained from grey-box identification. It is easy to show that the system is differentially flat. The angular velocity is controlled using a PID, which is a standard practice in quadrotor control. The resulting closed-loop is assumed fast enough to neglect it in the proposed control design. This allows us to consider the system a third-order one by approximating the pitch dynamics as

$$\dot{\theta} \simeq q_{ref} \tag{4}$$

where q_{ref} is the PID imposed dynamics.

Feedback Linearization and LQR. Using the above model, FL takes the form

$$\begin{aligned} q_{ref} &= \hat{\alpha}(\boldsymbol{z}) + \hat{\beta}(\boldsymbol{z}) v_{cmd} \\ &= \frac{c^2 v_x + c\,\bar{k} \sin\theta - v_{cmd}}{\bar{k} \cos\theta} \end{aligned} \tag{5}$$

where $v_{cmd} = \frac{u - \hat{\alpha}(\boldsymbol{z})}{\hat{\beta}(\boldsymbol{z})}$ is the imposed dynamics, *i.e.*, the third derivative of the output, and $\hat{\alpha}$ and $\hat{\beta}$ indicate approximations, obtained from the identified model, of the unknown true functions α and β. $\boldsymbol{z}$ is the states vector that contains the horizontal velocity v_x and acceleration a_x. $u = m_{c_x}$ is the system input, *i.e.*, the normalized pitch torque. The imposed dynamics v_{cmd}, *i.e.*, the desired third derivative, is calculated via the LQR from the setpoints and measurements.

Materials Research Proceedings 69 (2026) 806-811 https://doi.org/10.21741/9781644904251-142

Learning-based controller

We define the *nonlinear mismatch* v_e as the residual nonlinear dynamics that remain after the application of the FL, namely:

$$v_e(z,v) = v_{cmd} - v = \frac{\alpha(z) - \hat{\alpha}(z)}{\hat{\beta}(z)} + \frac{\beta(z) - \hat{\beta}(z)}{\hat{\beta}(z)} \tag{6}$$

Gaussian Process. The Gaussian Process is a Bayesian machine learning technique that approximates a function $f(x)$ at a new input x^*, using a dataset of stored observations $D = \{(x_i, \hat{y}_i) | i = 1, \dots, n\}$ [3]; this process is called inference and is performed under the assumption that all observations follow a multivariate Gaussian distribution. A GP is fully characterized by its prior distribution, which depends on the input values. This prior is specified by a mean function $m(x) = \mathbb{E}[f(x)]$ and a covariance function (or kernel) $k(x,x') = \mathbb{E}\big[\big(f(x) - m(x)\big)\big(f(x') - m(x')\big)\big]$. This structure makes GP a *nonparametric model*, offering a versatile and flexible properties.

Recursive algorithm. To reduce GP computational complexity for real-time implementation, a sparsity method introduced by Huber [5], called *Recursive Gaussian Process*, is used: this method completely *avoids inversion* of the data-points covariance matrix by fixing a priori a set of basis vectors, *i.e.*, the stored dataset inputs. Their outputs are updated iteratively as the new observations of v_e are obtained, using an algorithm which reminds the Kalman filter. This modification reduces the computational complexity of GP inference *from cubic to quadratic*.

Controller integration. The RGP operates in two phases: *running and update*.

In the running phase, using the states of the systems z and v_d, the RGP infers the nonlinear mismatch v_e from the RGP basis vectors dataset and adds it to v_d, *i.e.*, $v_{cmd} = v_d + v_e(z, v_d)$.

While in the update phase, previously collected observations of the input $[z, v]$ and the output $\tilde{v}_e$ are refined and used to update the RGP basis-vector outputs, improving the predictions. Refinement employs a *Savitzky–Golay filter* [6], a non-causal signal-processing technique that enables high-precision and efficient smoothing of signals.

The basis vectors are initialized in a *grid structure*, where the user defines for each input dimension x_i the number of samples n_i in the selected range $[x_{i,min}, x_{i,max}]$. The total number of basis vectors is $\prod n_i$.

To tune the kernel hyperparameters, for this application we choose the Squared Exponential (SE) kernel function, we use a gradient based minimization algorithm using data collected during a previous experiment, aiming at reducing the prediction error.

Implementation

The RGP part is run on a ground station that communicates via ROS1 with the drone during the experiments, providing also the setpoints for following the trajectory. This is done to limit the computational effort carried by the drone, which CPU and memory is very limited. The whole controller is running at $250Hz$, while the RGP component at $10Hz$ to avoid interference with the PID component that controls the angular velocity.

The experimental platform is the *ANT-X 2-DoF drone* (Fig. 2) produced by ANT-X (https://antx.it/about-us-antx/); a simulator that accurately mimics the behavior of the platform is also available. All experiments were performed in the Aerospace Systems Control Laboratory (ASCL) at Politecnico di Milano.

Parameters values. On the platform, the parameters useful for the FL control law are set to $c = 1.168\ \mathrm{s}^{-1}$ and $\bar{k} = 4{,}748\ \mathrm{m/s}^2$. To prove the efficiency of the controller, in the simulation

Materials Research Proceedings 69 (2026) 806-811 https://doi.org/10.21741/9781644904251-142

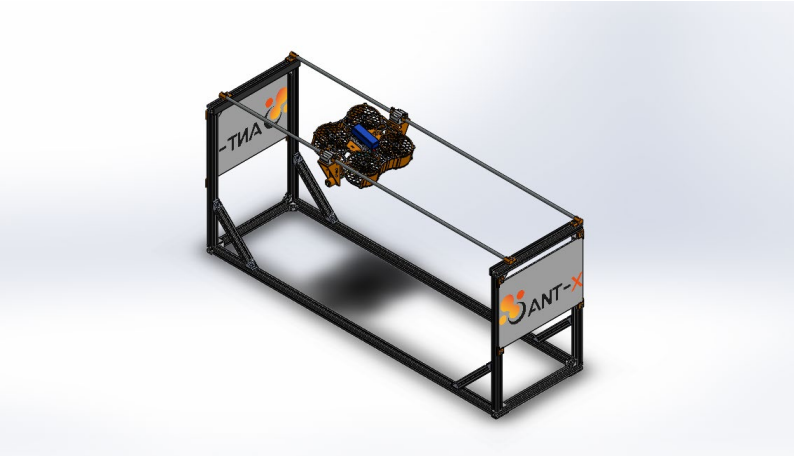


Figure 2: ANT-X 2-DoF drone.

moreover the measurement noise is added and in FL control action a slightly modified parameters respect to the identified model (*i.e.*, $\hat{c} = 2\ \mathrm{s}^{-1}$ and $\hat{\eta} = 12.5\ \mathrm{m/s}^2$) are used.
In both implementations, the grid of basis vector is initialized over the ranges $v_x \in [-0.3, 0.3]$, $\theta \in [-0.2, 0.2]$, and $v_{cmd}/v \in [-5, 5]$. For the physical platform, v_x, θ, and v_{cmd}/v are discretized into 4, 4, and 6 points, respectively, while for the simulator, they are discretized into 6, 6, and 8 points, respectively. The tuning algorithm produced different hyperparameter values for the RGP: for the platform, $l_{v_x} = 0.5\ \mathrm{m/s}$, $l_\theta = 0.5\ \mathrm{rad}$, $l_v = 1\ \mathrm{m/s}^3$, $\sigma_f = 1$, and $\sigma_n = 0.01$; for the simulator, $l_{v_x} = 0.4113\ \mathrm{m/s}$, $l_\theta = 0.4379\ \mathrm{rad}$, $l_v = 1.0272\ \mathrm{m/s}^3$, $\sigma_f = 0.9798$, and $\sigma_n = 0.016$.
The LQR parameters for the platform are set as $Q = [200, 1, 1]$ and $R = 1$, while for the simulation $Q = [100, 1, 1]$ and $R = 1$. The SGF parameter for the platform is $w_{size} = 51$; for the simulation $w_{size} = 21$.
The PID controller, pre-tuned by ANT-X, uses identical parameters for both the platform and simulation: $K_P = 0.009\ \mathrm{s/rad}$, $K_I = 0.21\ \mathrm{rad}^{-1}$ and $K_D = 0.0016\ \mathrm{s}^2/\mathrm{rad}$.

Results

To evaluate the performance, we used the *root-mean-square error (RMSE)* of the response with respect to the setpoint. The result shown for each reference signal is the *average of 5 experiments*. We performed two batches of simulated experiments: in the first batch the reference signal is a *sinusoid with constant amplitude* $r(t) = 0.2\sin(\omega t)$, while in the second one the signal is a *sinusoid with linear-varying amplitude* $r(t) = \frac{0.2}{60} t \sin(\omega t)$. The experiments are conducted varying the angular velocity: $\omega = 0.5, 0.8, 1, 1.5\ \mathrm{rad/s}$ for the first batch and $\omega = 1, 1.5\ \mathrm{rad/s}$ for the second one. We used sinusoidal signals because the time-domain results show the RGP's learning effect and the resulting reduction in error over time. Results in Fig. 3a and Fig. 3b show that *our proposed controller outperforms the baseline* (the same controller with no RGP contribution) with both types of signals.
In the real-world experiments, the reference signal is the *sinusoid with constant amplitude* $r(t) = 0.2\sin(\omega t)$ and the system is tested with angular velocities $\omega = 0.5, 0.8, 1.5\ \mathrm{rad/s}$. Improvements are significant in Fig. 3c at $\omega = 0.8\ \mathrm{rad/s}$, while at lower angular velocities the static friction can hinder the RGP's ability to accurately map v_e and at higher ones unmodeled nonlinear dynamics may adversely affect the RGP inference. In Fig. 4, a comparison between baseline and the full controller for reference tracking experiment with signal $r(t) = 0.2\sin(0.8\,t)$ is shown.

Materials Research Proceedings 69 (2026) 806-811 https://doi.org/10.21741/9781644904251-142

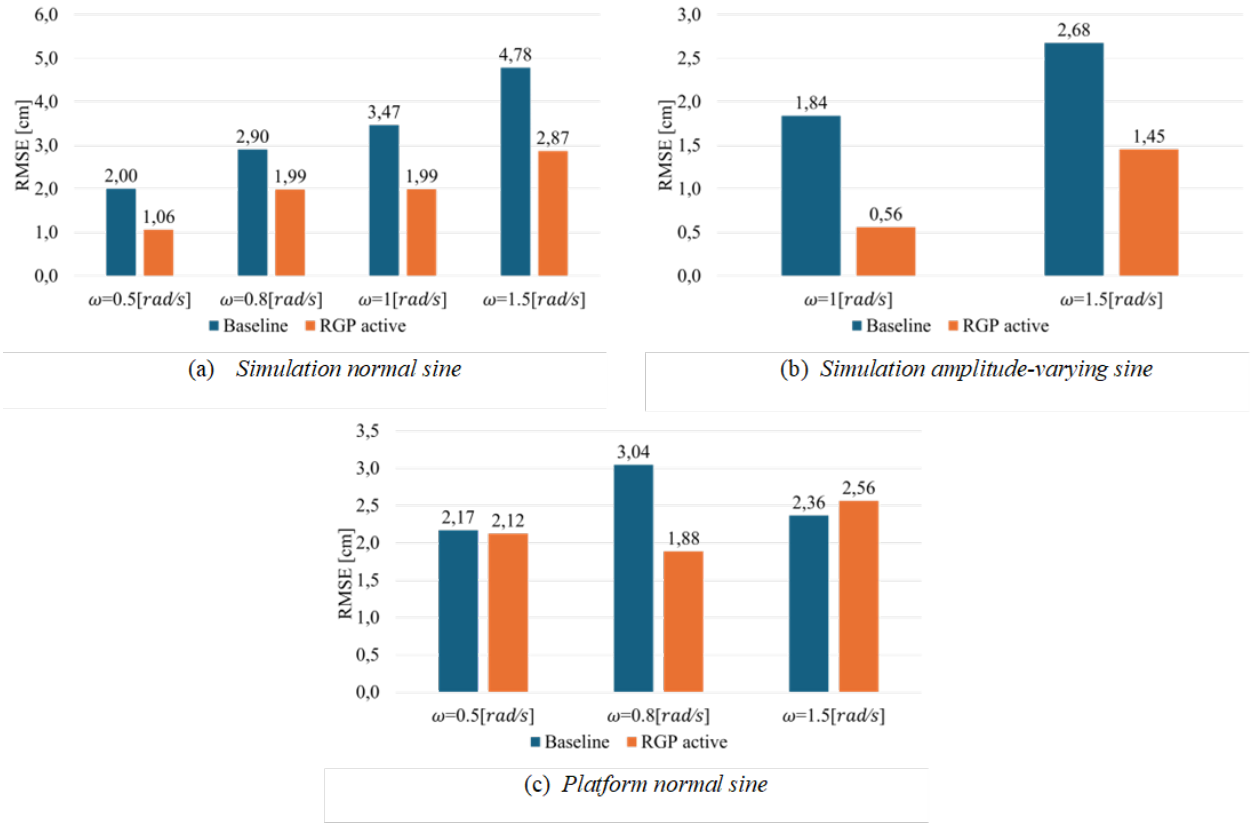


Figure 3: RMSE values for different angular velocities

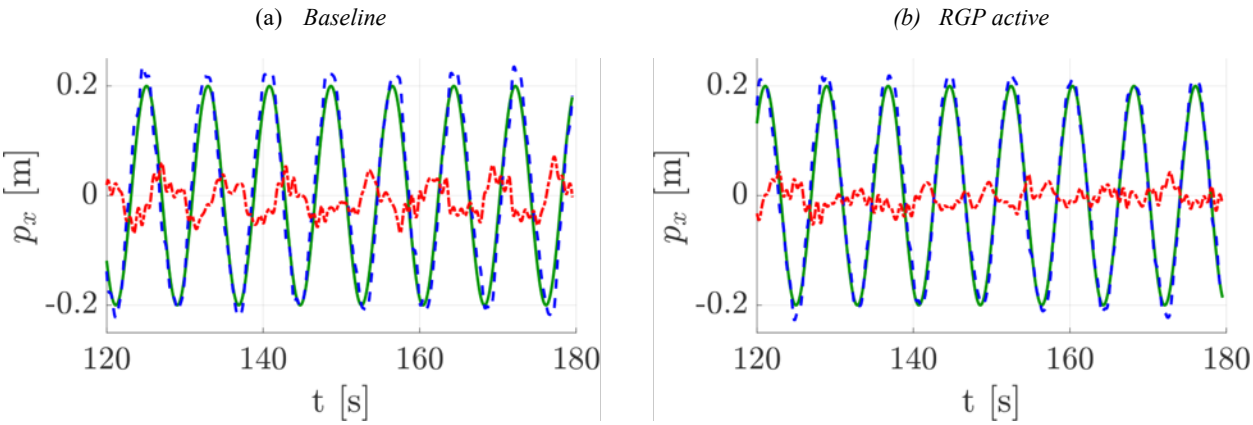


Figure 4: Platform tracking error for $r(t) = 0.2\,sin(0.8\,t)$

Conclusions

This paper aimed to design a learning-based tracking controller for a differentially flat system, which is proven to work effectively both in simulation and on the experimental platform. The computational issues associated with standard GP formulations were addressed using a sparsity method.

Future work includes the extension to an unconstrained drone, controlling all 3 axis, and the implementation of the RGP component directly onboard.

References

[1] T. Westenbroek, D. Fridovich-Keil, E. Mazumdar, S. Arora, V. Prabhu, S. S. Sastry, and C. J. Tomlin, "Feedback Linearization for Unknown Systems via Reinforcement Learning," Apr. 2020. arXiv:1910.13272 [math] https://doi.org/10.1109/ICRA40945.2020.9197158

[2] A. Yeşildirek and F. L. Lewis, "Feedback linearization using neural networks," Automatica, vol. 31, pp. 1659-1664, Nov. 1995. https://doi.org/10.1016/0005-1098(95)00078-B

[3] C. E. Rasmussen and C. K. I. Williams, "Gaussian processes for machine learning. Adaptive computation and machine learning", Cambridge, Mass.: MIT Press, 3. print ed., 2008.

[4] M. Greeff and A. P. Schoellig, "Exploiting Differential Flatness for Robust Learning-Based Tracking Control Using Gaussian Processes," IEEE Control Systems Letters, vol. 5, pp. 1121-1126, Oct. 2021. https://doi.org/10.1109/LCSYS.2020.3009177

[5] M. F. Huber, "Recursive Gaussian process: On-line regression and learning," Pattern Recognition Letters, vol. 45, pp. 85-91, Aug. 2014. https://doi.org/10.1016/j.patrec.2014.03.004

[6] R. Schafer, "What Is a Savitzky-Golay Filter? [Lecture Notes]," IEEE Signal Processing Magazine, vol. 28, pp. 111-117, July 2011. https://doi.org/10.1109/MSP.2011.941097

Materials Research Proceedings 69 (2026) 812-816 https://doi.org/10.21741/9781644904251-143

Perception Aware Quadrotor Control: An Experimental Evaluation

Lidia PEREZ[1,a *], Alessandro NAZZARI[1,b], Roberto RUBINACCI[1,c] and Davide INVERNIZZI[1,c]

[1]Dipartimento di Scienze e Tecnologie Aerospaziali, Politecnico di Milano, Via La Masa 34, 20156 Milano, Italy

[a]Lidia.perez@mail.polimi.it, [b]alessandro.nazzari@polimi.it, [c]roberto.rubinacci@polimi.it, [d]davide.invernizzi@polimi.it

Keywords: UAV, VIO, PAMPC, Perception Aware

Abstract. Accurate localization of an Uncrewed Aerial Vehicle (UAV) in GPS-denied environments remains a fundamental and unresolved challenge in robotics. Traditional approaches treat state estimation, trajectory planning, and control as separate modules, often assuming perfect state information. However, when visual sensors are used for localization, this assumption often breaks down under challenging conditions, such as poor lighting or textureless environments, resulting in significant drift and unreliable control decisions. Yet, perception performance can be significantly improved if the UAV's motion is planned with the constraints and capabilities of onboard vision in mind. In this context, Perception-Awareness (PA) emerges as a strategy to adapt a UAV's maneuvers based on the real-time perception of the environment. In this paper, we implement and evaluate a PA quadrotor controller through an extensive experimental campaign, demonstrating a reduction in odometry drift of up to 70% compared to a non-PA control approach.

Introduction

Perception-Awareness (PA) consists in adapting UAV's maneuvers based on the real-time perception of the environment. Previous works in PA control have focused on improving the performance of vision based odometry [1]. These efforts typically incorporate feature-based objectives such as:

1. Enforcing the visibility of a given set of landmarks.
2. Minimizing the reprojection error for certain landmarks.
3. Keeping the centroid of observed features centered in the image [1].
4. Minimizing the projected velocity of features to reduce motion blur.
5. Maximizing co-visibility across consecutive frames [2].

Depending on the formulation, PA strategies may influence only the timing of the trajectory, or they may directly affect the UAV's position [3], yaw angle, or both. A widely used method to incorporate such perception objectives into the control loop is Model Predictive Control (MPC). A notable example is PAMPC [1], which integrates perception objectives directly into the MPC optimization problem. This approach explicitly accounts for feature visibility within the camera's field of view (FOV) and penalizes motion that induces image blur.

The main contributions of the paper are the seamless integration of the PAMPC framework into a PX4-based quadrotor (equipped with a forward-looking stereo camera), and the comprehensive experimental evaluation of the resulting Visual Inertial Odometry (VIO) performance. We systematically compare PAMPC against a conventional, non-perception-aware MPC strategy, demonstrating the benefits of coupling perception and control in real world flight scenarios.

Content from this work may be used under the terms of the Creative Commons Attribution 3.0 license. Any further distribution of this work must maintain attribution to the author(s) and the title of the work, journal citation and DOI. Published under license by Materials Research Forum LLC.

Materials Research Proceedings 69 (2026) 812-816 https://doi.org/10.21741/9781644904251-143

Methodology

The perception-aware control problem is formulated as an Optimal Control Problem (OCP):

$$\min_{u(\cdot)} \int_0^T \big[L_a\big(x(t),u(t)\big) + L_p\big(z(t)\big)\big]\,dt \dot{x}(t) = f\big(x(t),u(t)\big), x(0) = x_0, x(t) \in \mathcal{X}, u(t) \in \mathcal{U}, \tag{1}$$

where, $x = [p_{WB}, v_{WB}, q_{WB}]^{\mathsf{T}}$ is the quadrotor state, including position, velocity and orientation of the body frame B with respect to the world frame W, expressed in world frame. The perception state $z = \left[s, \dot{s}\right]$ includes the image coordinates of the centroid of observed features, referred to as Point Of Interest (POI), expressed in pixel coordinates in the image plane, $s = (u, v)$, as well as its velocity on the image plane, $\dot{s}$. The cost L_a penalizes deviations from a reference trajectory, and L_p penalizes deviation from the null perception state $z = 0$, thus introducing perception objectives that keep the centroid of observed features centered in the image and minimize their projected velocity on the frame, a detailed derivation can be found in [1]. The optimized quadrotor control input is $u = [c, \Omega_B]$, where c is the mass-normalized thrust along the vertical axis in the body frame B, and $\Omega_B = \left[\omega_x, \omega_y, \omega_z\right]^{\mathsf{T}}$ is the angular velocity in body frame. The quadrotor state dynamics is described by:

$$\dot{p}_{WB} = v_{WB}, \dot{v}_{WB} = g + q_{WB} \odot c, \dot{q}_{WB} = \frac{1}{2}\Lambda(\Omega_B) \cdot q_{WB}, \tag{2}$$

where $\odot$ denotes the multiplication between a quaternion and a vector, and

$$\Lambda(\Omega_B) = \begin{bmatrix} 0 & -\omega_x & -\omega_y & -\omega_z \\ \omega_x & 0 & \omega_z & -\omega_x \\ \omega_y & -\omega_z & 0 & \omega_x \\ \omega_z & \omega_y & -\omega_x & 0 \end{bmatrix}. \tag{3}$$

The constraints imposed ensure the thrust, angular and linear velocities remain within feasible limits:

$$X = \{v_{WB} s.t. -v_{max} \le v_{WB} \le v_{max}\}, U = \begin{Bmatrix} c_{min} \le c \le c_{max} \\ -\Omega_{max} \le \Omega_B \le \Omega_{max} \end{Bmatrix}. \tag{4}$$

The POI coordinates in world frame are computed as follows: first, grayscale images from left camera are processed using an ORB feature detector to identify relevant landmarks, then, depth

Materials Research Proceedings 69 (2026) 812-816 https://doi.org/10.21741/9781644904251-143

information is used to map 2D frame coordinates to 3D space in the camera frame using the pinhole model; finally, camera pose information is utilized to transform this information into the 3D world frame. Figure 1(a) shows an example of the POI computed. The resulting OCP is discretized using Direct Multiple Shooting within ACADO and solved in a receding horizon fashion.

Experimental results

The solver runs in real time on the quadrotor companion computer at 50 Hz, the resulting velocity and acceleration commands are tracked by PX4's cascaded P-PID running at 250 Hz. Perception metrics (POI and s) are computed onboard using ORB feature detection and stereo triangulation. The experiments have been conducted inside the Flying Arena for Rotorcraft Technologies (FlyART) of the Aerospace System and Control Lab (ASCL). The FlyART is an indoor facility whose flight volume is $12 \times 6 \times 4$m. The quadrotor used in the experimental campaign is equipped with a forward-facing stereo camera, the ZED 2i and a Jetson Xavier NX. Communication between the various components is performed through Robot Operating System (ROS).

Experiments include straight-line flights at 0.3 m/s under both good and low-light conditions. Figure 2 shows the Experimental setup, while Figure 1(c) and 1(f) show the quadrotor's heading during the experiment. The Motion Capture system (MoCap) is used as the ground truth to evaluate the VIO performance. Figure 3 shows the odometry experimental result, with good illumination conditions PA reduced the in-plane drift rate from 0.49cm/s to 0.1cm/s. With low illumination conditions drift rate with and without PA are 0.20cm/s and 1.14cm/s, respectively.

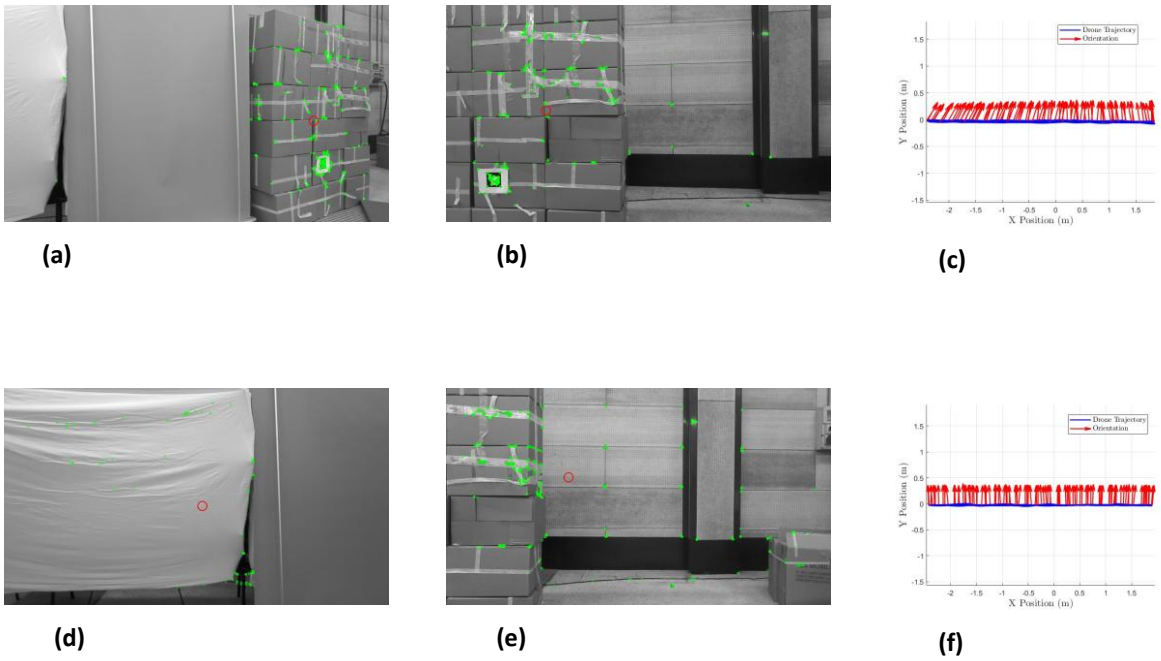
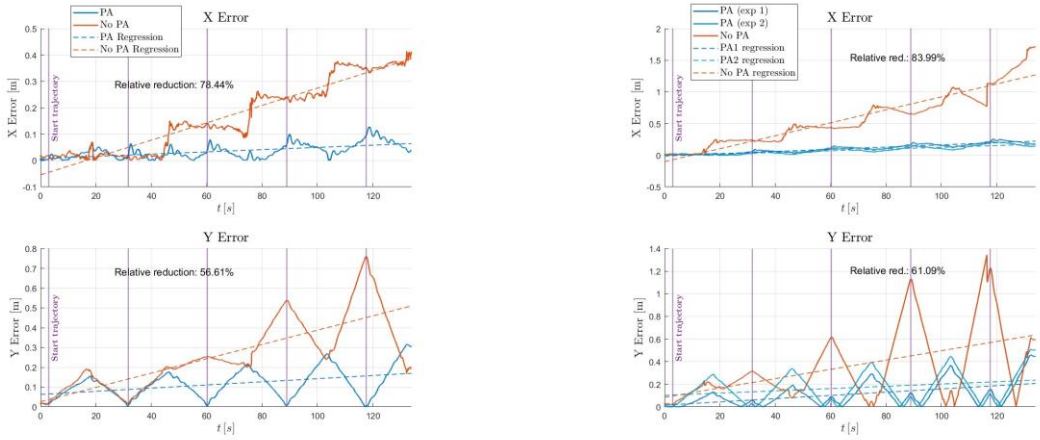


Figure 1. The top and bottom rows illustrate drone orientation with and without PA, respectively, during a linear trajectory. With PA, the quadrotor consistently adjusts yaw to keep the feature-rich region in the FOV. In contrast, without PA, the drone's camera captures mostly blank sheet (left bottom image).



(a) Good illumination (b) Low illumination

Figure 2. Experimental setup.



(a) Good illumination (b) Low illumination

Figure 3. Absolute x- and y-coordinate odometry error (w.r.t MoCap position estimate) in linear flight.

Conclusion

By integrating perception objectives, maximizing the visibility of the feature centroid and minimizing its projected velocity on the camera plane, into the control strategy, the resulting control actions enhance VIO performance. Experimental results demonstrate that the PA framework enhances overall VIO accuracy, even under challenging low-light conditions, ultimately leading to better decision-making based on visual information.

Acknowledgement

This study was carried out within the Agritech National Research Center and received funding from the European Union Next-GenerationEU (PIANO NAZIONALE DI RIPRESA E RESILIENZA (PNRR) – MISSIONE 4 COMPONENTE 2, INVESTIMENTO 1.4 – D.D. 1032 17/06/2022, CN00000022). This manuscript reflects only the authors' views and opinions, neither the European Union nor the European Commission can be considered responsible for them.

References

[1] D. Falanga, P. Foehn, P. Lu, and D. Scaramuzza, "PAMPC: Perception-Aware Model Predictive Control for Quadrotors," in IEEE International Conference on Intelligent Robots and Systems, 2018. https://doi.org/10.1109/IROS.2018.8593739

[2] V. Murali, I. Spasojevic, W. Guerra, and S. Karaman, “Perception-aware trajectory generation for aggressive quadrotor flight using differential flatness,” in Proceedings of the American Control Conference, 2019. https://doi.org/10.23919/ACC.2019.8814697

[3] X. Wu, S. Chen, K. Sreenath, and M. W. Mueller, “Perception-Aware Receding Horizon Trajectory Planning for Multicopters With Visual-Inertial Odometry,” IEEE Access, 2022. https://doi.org/10.1109/ACCESS.2022.3200342

Materials Research Proceedings 69 (2026) 817-821 https://doi.org/10.21741/9781644904251-144

eVTOLs in Inter-Hospital Medical Transport: A Simulation Based Scenario Analysis for Bavaria

Benedikt M. DREYER[1,3,a *], Sophie F. ARMANINI[2,b]

[1]Technical University of Munich, Department of Aerospace and Geodesy, Lise-Meitner-Str. 9, 85521 Ottobrunn

[2]Imperial College London, Department of Aeronautics, South Kensington Campus, SW7 2AZ London, UK

[3]ERC-System GmbH, Einsteinstraße 32, 85521 Ottobrunn, Germany

[a]benedikt.dreyer@tum.de, [b]s.armanini@imperial.ac.uk

Keywords: HEMS, eVTOL, Agent-based Simulation, Operational Cost

Abstract. With the ongoing hospital centralization in Germany, novel effective solutions for inter-hospital transport are required, a role mostly fulfilled by understaffed emergency ambulances. Electric vertical takeoff and landing (eVTOL) vehicles, promising fast and affordable transportation, have emerged as a potential solution for building up an effective patient transportation fleet. This work explores the feasibility and performance of eVTOL vehicles in inter-hospital patient transport, using Bavaria, Germany, as a real-world case study. An agent-based simulation framework was developed to compare ambulance, helicopter, and both battery-electric and hybrid eVTOL fleets as well as a combined hybrid eVTOL and ambulance fleet under realistic demand conditions. Simulation results show that a network with only 25 hybrid eVTOLs achieves 94% demand coverage with 41% fewer personnel and a 54% reduction in waiting time compared to a similar-performance ambulance network, at only a 33% increase in costs per patient kilometer. Compared to helicopters, the simulated eVTOL fleet offers significant cost savings, primarily in variable operational expenses. Battery-powered eVTOL vehicles offer locally emission-free operation at similar per-mission costs to hybrid eVTOLs, albeit at reduced demand coverage due to range limitations.

Approach

eVTOL vehicles present a significant opportunity to accelerate patient transport compared to road vehicles, while potentially requiring fewer personnel. With efficient wing-borne cruise, they provide a novel transport solution between ground ambulances and helicopters by offering a unique combination of fast, smooth and quiet rides. Inter-hospital transport furthermore presents a unique opportunity to rapidly develop functional eVTOL networks as it profits from existing helipad infrastructure that is otherwise not readily available.

The costs and benefits of aerial medical services have been widely discussed, as indicated by *[1]*, which systematically reviewed studies on helicopter emergency services. Studies specifically on eVTOL vehicle integration and operation in medical use cases have emerged only recently, such as by *[2]*, *[3]*, *[4]*, and *[5]*. Across prior work, a clear gap emerges: the lack of integration between real-world operational data and network-level assessments of eVTOL fleet performance. This study addresses that gap by combining specific operational patterns of medical transport with a simulation-based analysis approach.

An agent-based simulation framework was developed that enables the assessment of eVTOL utilization, cost efficiency, and time savings in patient transportation networks, with a focus on feasibility analysis. Given the computational complexity of the problem, the approach emphasizes

Content from this work may be used under the terms of the Creative Commons Attribution 3.0 license. Any further distribution of this work must maintain attribution to the author(s) and the title of the work, journal citation and DOI. Published under license by Materials Research Forum LLC.

comparative analysis rather than strict optimization, enabling insights into trade-offs between efficiency, cost, and service quality.

The simulation is based on the total real-world demand of 34,200 inter-hospital transport cases per year in Bavaria, Germany, and demand patterns obtained from *[6]*. Figure 1a illustrates the weekly demand pattern, Figure 1b depicts the simulated transport routes.

Four vehicle types are simulated and analyzed in detail: ambulances, helicopters, battery eVTOLs, and hybrid eVTOLs. The eVTOL aircraft specifications were obtained through sizing by the author following a configuration-agnostic point mass approach for lift and cruise eVTOLs, based on the required payload mass. Ambulance and helicopter data were obtained from the commercial vehicles Mercedes-Benz Sprinter 515 CDI and Airbus H135.

Operational assumptions were derived from interviews with 22 professionals including HEMS pilots, emergency physicians, nurses, operators, and industry experts, conducted across 17 sessions with a median duration of 51 minutes.

The simulation was validated by a Monte Carlo-based sensitivity analysis, using 20 random vehicle-to-base assignment and demand samples. Deviations in demand coverage and pickup waiting times showed median relative deviations from the reference simulation results of at most 2%, while cost per patient kilometer differed by less than 4%, confirming the robustness of the original results. The applicability of the findings is limited to Central European conditions; variations in infrastructure or vehicle allocation strategies could alter results.

Results & Discussion

Results were obtained in two steps. First, networks of varying fleet sizes were analyzed for all vehicle types. The results, shown in Figure 2, compare demand coverage, pickup waiting time, cost per patient kilometer, and vehicle utilization across fleet sizes. Hybrid eVTOLs show very good performance with high coverage and cost-efficiency. Helicopters offer slightly higher coverage at significantly higher cost, while battery eVTOLs are limited by range.

In addition to the single vehicle type networks, combined hybrid eVTOL and ambulance networks with varying fleet compositions were analyzed. Figure 3 highlights pickup waiting time, cost, and utilization across these fleet configurations, showing how integration of hybrid eVTOLs and ambulances improves overall network performance. A combined network of 20 ambulances and 10 hybrid eVTOLs was found to be particularly promising, offering 30% lower waiting times at only 10% increased costs compared to a purely ambulance-based network.

An assessment of network cost-effectiveness, judged by cost per patient kilometer plotted against the patient pickup waiting time in Figure 4, showed that the performance of a hybrid eVTOL fleet can be improved if combined with ground ambulances.

A fleet size of about 20 to 25 hybrid vehicles was found to be optimal based on the Bavarian hospital and transport demand structure. With a deployment of approximately one eVTOL vehicle per 500,000 inhabitants this implies a fleet of up to approximately 150 medical transport eVTOLs in Germany.

In a second step, the key performance metrics of the respective five most promising network configurations, specifically only 20 battery-electric eVTOLs, only 25 hybrid eVTOLs, a combined network of 10 hybrid eVTOLs and 20 ambulances, only 50 ambulances and only 25 helicopters, were analyzed in more detail. The combined hybrid eVTOL and ambulance fleet offers 41% reduced staff and 40% reduced median waiting times compared to the ambulance-only fleet at 11% increased cost per patient kilometer. Compared to helicopters, the combined hybrid eVTOL and ambulance fleet offers 32% reduced cost per patient kilometer at 28% longer median pickup waiting times. The hybrid eVTOL-only fleet offers similar waiting times as the helicopter-only fleet, at 18% reduced costs per patient kilometer. Hybrid eVTOL transport furthermore reduced simulated en-route transport time by about 80% compared to ambulances, significantly lowering transport strain on patients.

Materials Research Proceedings 69 (2026) 817-821 https://doi.org/10.21741/9781644904251-144

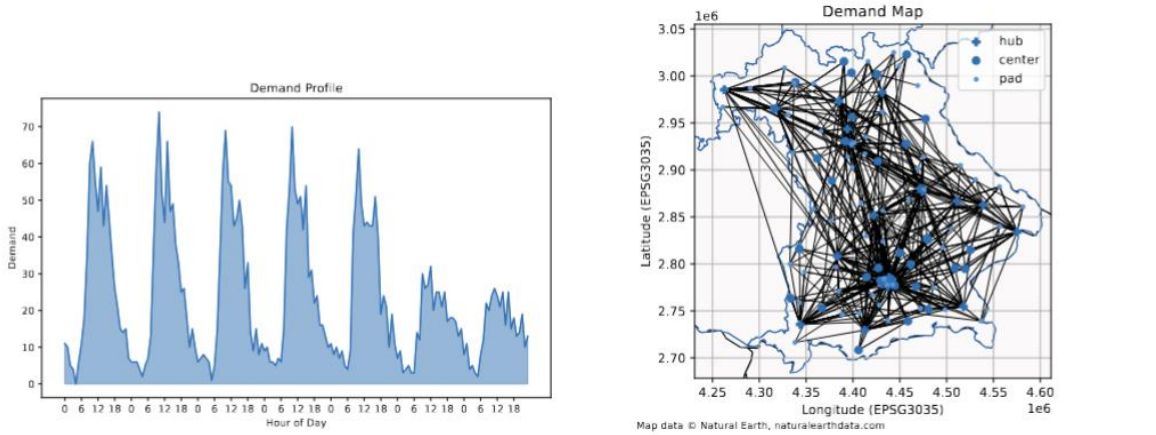
Detailed analysis of mission cost showed that the 18% operating cost reduction of hybrid eVTOLs compared to helicopters stems from a 41% reduction in variable costs per kilometer. Crew cost dominates the costs of operation of all fleets. Depreciation and maintenance costs exceed energy costs in eVTOLs, while helicopters' high energy consumption drives their expenses. The simulated hybrid eVTOL network consumed 2.3 times the amount of fuel as the ambulance-only fleet and 76% less fuel than the helicopter-only fleet. Respectively, the helicopter-only fleet showed a 4.16-fold increase in emissions over the hybrid eVTOL network. High utilization proved to be essential to realize the cost advantage of hybrid eVTOLs.

Regarding potential network congestion through additional aerial vehicles, it was found that 44% of hospitals were visited less than once per day on average, suggesting that shifting inter-hospital transport from ground to air with eVTOLs would not significantly block hospital landing pads for primary rescue missions.

Optimization potential in operational cost efficiency for future aerial patient transportation networks was identified mainly in reducing vehicle maintenance costs and enhancing patient loading and unloading processes, given that the cruise segment of hybrid eVTOL transport flights represents only 14.5% of the median mission.

Conclusion

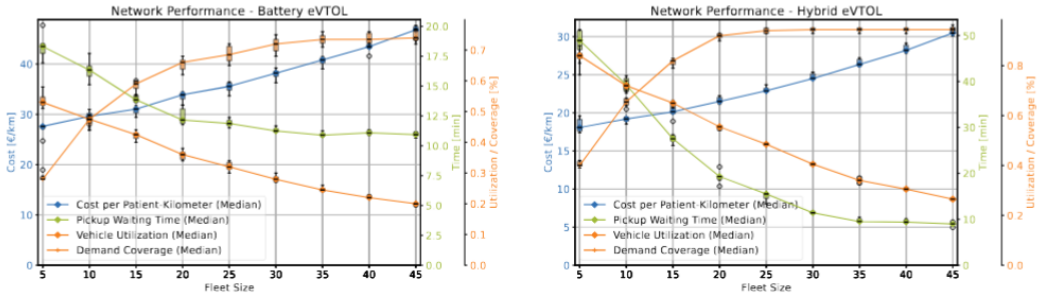
This study demonstrates the technical and economic feasibility of implementing eVTOL vehicles in Bavaria's inter-hospital patient transport system, supplementing previous studies by in-depth analysis with a novel comparative approach. The findings position hybrid eVTOLs as a viable and cost-effective alternative to helicopters and a high-performance complement to ambulance networks, offering tangible benefits for future medical transport.



(a) Demand for inter-hospital transport for the analysed time frame of one week, aggregated for 6 samples

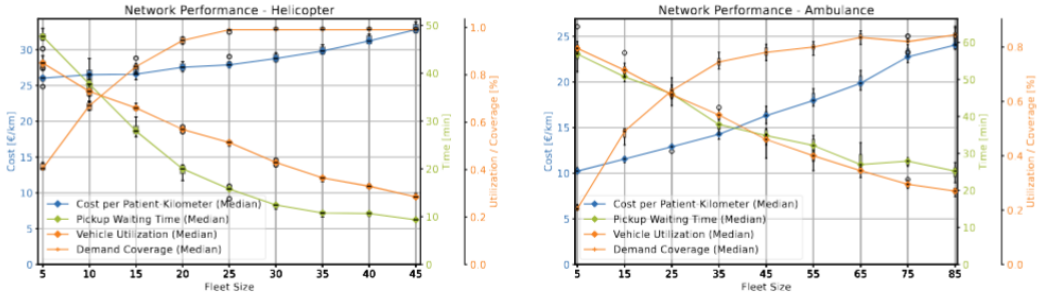
(b) Map of Bavaria, Germany, with the demand routes throughout one week for one of the six sample weeks

Fig. 1 Illustration of the modelled transport demand throughout the week as well as of the routes throughout Bavaria



(a) Battery-powered eVTOL network performance metrics depending on fleet size

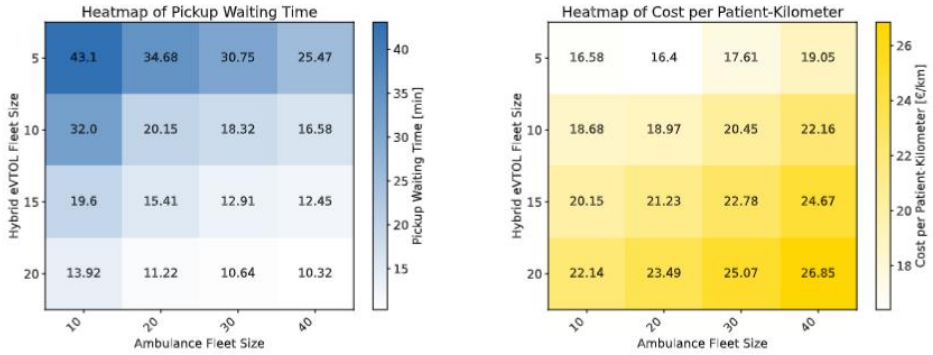
(b) Hybrid eVTOL network performance metrics depending on fleet size



(c) Helicopter network performance metrics depending on fleet size

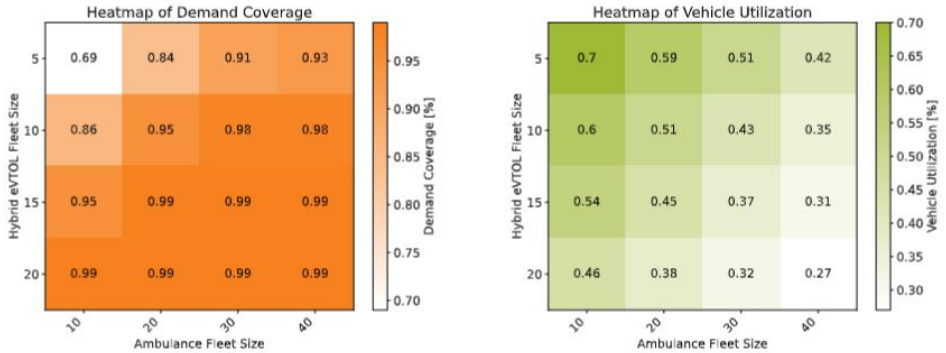
(d) Ambulance network performance metrics depending on fleet size

Fig. 2 Comparison of cost and time measures for various fleet sizes in Bavaria in networks employing a single type of vehicle



(a) Heatmap of network-wide pickup waiting time for combined ambulance and hybrid eVTOL fleets

(b) Heatmap of median mission costs for combined ambulance and hybrid eVTOL fleets



(c) Heatmap of network-wide demand coverage for combined ambulance and hybrid eVTOL fleets

(d) Heatmap of median vehicle utilization for combined ambulance and hybrid eVTOL fleets

Fig. 3 Comparison of cost, time and usage measures for various fleet sizes in Bavaria in networks employing a combination of hybrid eVTOL vehicles and road ambulances

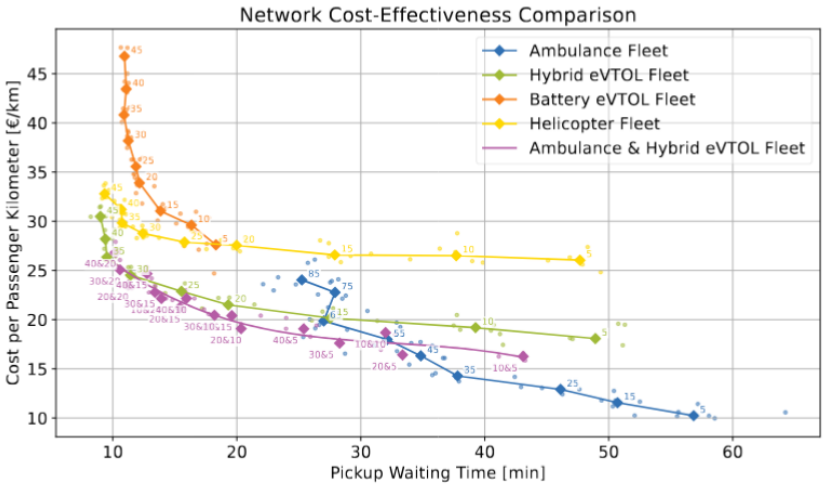


Fig. 4 Cost-Effectiveness of all vehicle types at various fleet sizes. Square markers define median values for specific fleet sizes. Points are individual simulation results of 6 simulations per fleetsize and vehicle type.

References

[1] Taylor, C. B., Stevenson, M., Jan, S., Middleton, P. M., Fitzharris, M., and Myburgh, J. A., A systematic review of the costs and benefits of helicopter emergency medical services, Injury, Vol. 41, No. 1, 2010, pp. 10-20., 2010. https://doi.org/10.1016/j.injury.2009.09.030

[2] Goyal, R., and Cohen, A., Advanced air mobility: Opportunities and challenges deploying eVTOLs for air ambulance service, Applied Sciences, Vol. 12, No. 3, 2022, p. 1183, 2022. https://doi.org/10.3390/app12031183

[3] Chappelle, C., Li, C., Vascik, P. D., and Hansman, R. J., Opportunities to enhance air emergency medical service scale through, Aviation Technology, Integration, and Operations Conference, p.2883, 2018. https://doi.org/10.2514/6.2018-2883

[4] Espejo-Díaz, J. A., Alfonso-Lizarazo, E., and Montoya-Torres, J. R., Improving access to emergency medical services using advanced air vehicles, Flexible Services and Manufacturing Journal, 2023, pp. 1-33., 2023.

[5] Karpstein, R., de Magalhaes, V. L., and Holzapfel, F., Agent-based Simulation of UAV based Logistics Networks with Real World Data, Vertical Flight Society 80th Annual Forum and Technology Display, Vertical Flight Society, Montreal, Canada,, 2024. https://doi.org/10.4050/F-0080-2024-1407

[6] (INM), Institut für Notfallmedizin und Medizinmanagement, «Rettungsdienstbericht Bayern 2024,» September 2024. Available: https://www.inm-online.de/de/aktuelles/405-rettungsdienstbericht-bayern-2024. [Accessed 11 03 2025].

Materials Research Proceedings 69 (2026) 822-826 https://doi.org/10.21741/9781644904251-145

An Extensible Drone Framework for In-flow Disturbance Analysis

Benedetta NOVELLI[1,2,a *], Stefano MELONI[1,b], Diego PENNINO[1,c], Alessandro TROTTA[1,c]

[1]Università degli Studi della Tuscia, Via Santa Maria in Gradi 4, Viterbo, Italy

[2]Scuola Marescialli Aeronautica Militare, Via Tuscanese 71/H, Viterbo, Italy

[a]benedetta.novelli@unitus.it, [b]stefano.meloni@unitus.it, [c]diego.pennino@unitus.it, [d]alessandro.trotta@unitus.it

Keywords: Drone, In-Flow Distorsions, Urban Mobility, Simulations

Abstract. The interaction between coherent turbulent structures across multiple scales and UAV dynamics is highly complex, particularly during maneuvering phases. In this context, the present study introduces a comprehensive simulation framework to model UAV quadcopter dynamics within urban wind environments. A key innovation of this approach is the integration of inflow distortion effects into the Gazebo Sim platform, which has already been validated for accurate representation of drone dynamics. In-flow distortions are implemented in Gazebo Sim through a custom Python script, following a progressive modeling strategy. The process begins with simplified analytical boundary layer profiles, specifically parabolic and logarithmic velocity versus altitude distributions, to evaluate the impact of canonical turbulent boundary layers on quadrotor performance. These foundational models are then enhanced by superimposing von Kármán and Rankine vortex structures, allowing the simulation of coherent turbulent features such as swirling gusts and vortex shedding generated by the urban canopy.

Introduction

The integration of Unmanned Aerial Vehicles (UAVs) into urban environments represents a transformative shift[1] in aerial mobility, offering new opportunities across various sectors, such as infrastructure inspection, emergency response, surveillance, and last-mile delivery. In particular, small multirotor drones provide unmatched operational flexibility due to their ability to maneuver in low-altitude, confined, and complex airspaces where manned aircraft cannot safely operate[2]. However, the deployment of UAVs in dense urban settings introduces a set of significant challenges that must be addressed to ensure safety, reliability, and environmental compatibility[3,4]. Among these challenges, in-flow distortions caused by complex urban aerodynamics play a critical role, as buildings and surface irregularities generate unsteady and spatially non uniform wind fields[5]. These perturbations can severely affect flight stability, control performance, and energy consumption, particularly for lightweight multirotor platforms[6,7]. In this context, the present study introduces a comprehensive simulation framework to model UAV dynamics within urban wind environments. A key innovation of this approach is the integration of in-flow distortion effects into the Gazebo Sim platform, which has already been validated for accurate representation of drone dynamics[8]. In-flow distortions are implemented in Gazebo Sim through a custom Python script, following a progressive modeling strategy. The process begins with simplified analytical wind profiles, specifically parabolic and logarithmic vertical distributions, to evaluate the impact of canonical turbulent boundary layers on quadrotor performance. These foundational models are then enhanced by superimposing von Kármán and Rankine vortex structures, allowing the simulation of coherent turbulent features such as swirling gusts and vortex shedding generated by the urban canopy. To ensure stable flight within these perturbed flow fields, a Python-based PID (Proportional–Integral–Derivative) controller was

Content from this work may be used under the terms of the Creative Commons Attribution 3.0 license. Any further distribution of this work must maintain attribution to the author(s) and the title of the work, journal citation and DOI. Published under license by Materials Research Forum LLC.

Materials Research Proceedings 69 (2026) 822-826 https://doi.org/10.21741/9781644904251-145

developed and integrated into the Gazebo environment. The controller actively compensates for trajectory deviations induced by the previously described aerodynamic disturbance models, adjusting motor thrust and torque. This closed-loop control system enables the UAV to maintain its desired flight path despite unsteady aerodynamic loads, while its modular Python implementation allows flexible tuning of control parameters and seamless interaction with the simulated urban wind environment.

Methodology

The foundation of this study is a comprehensive simulation framework developed in the Gazebo Sim platform, which provides a physics-based environment validated for accurate drone dynamic behavior. Inflow distortions are introduced through a custom Python script that interfaces with Gazebo using the topic-based communication mechanism. This setup enables the definition of spatially and temporally varying wind fields acting on the UAV model in real time. To represent the complex nature of urban airflow, a progressive modeling strategy was adopted. The first stage employs simplified analytical wind profiles, specifically parabolic vertical velocity distributions, to characterize the influence of canonical turbulent boundary layers on quadrotor dynamics. The parabolic boundary layer profile can be expressed as:

$$U(z) = \begin{cases} U_{\max}\left(\frac{z}{H}\right)\left(2 - \frac{z}{H}\right), & 0 \le z \le H \\ U_{\max}, & z > H \end{cases} \quad (1)$$

where U_{max} is the maximum horizontal velocity and H represents the height of the boundary layer. This formulation captures the quadratic velocity distribution typical of low-altitude urban flows, where wind velocity increases with height up to a maximum, then it remains constant. Subsequently, these baseline models are enriched by superimposing von Kármán and Rankine vortex structures, which enable the representation of coherent turbulent phenomena such as swirling gusts, shear layers, and vortex shedding generated by buildings and other urban obstacles. The tangential velocity magnitude of a single Rankine vortex, confined to the horizontal (x, y) plane, is expressed as:

$$v_\theta(r) = \begin{cases} \frac{\Gamma}{2\pi R^2}\, r, & r \le R \\ \frac{\Gamma}{2\pi r}, & r > R \end{cases} \quad (2)$$

where Γ indicates the circulation of the vortex, R is the radius of the vortex core, and r is the radial distance from the center of the vortex. This formulation ensures a smooth transition from a solid-body rotation inside the core to a potential vortex behavior in the outer region. To represent the unsteady and spatially varying structure of urban wind fields, the Rankine vortex model is extended to a multivortex configuration. Instead of a single vortex centered at (x_o, y_o), an array of N vortices is generated along the x axis, each separated by a distance D and with alternating circulation sign to emulate a counter rotating vortex street. For each vortex i, centered at (x_i, y_i) with circulation Γ_i, the tangential velocity field in polar coordinates is defined as:

$$v_{\theta,i}(r_i) = \begin{cases} \frac{\Gamma_i}{2\pi R_c^2}\, r_i, & r_i \le R_c \\ \frac{\Gamma_i}{2\pi r_i}, & r_i > R_c \end{cases} \quad (3)$$

where R_c is the core radius of the Rankine vortex and $r_i = \sqrt{(x - x_i)^2 + (y - y_i)^2}$. Since the Gazebo simulation environment operates in Cartesian coordinates, each tangential contribution is decomposed into horizontal components:

Materials Research Proceedings 69 (2026) 822-826 https://doi.org/10.21741/9781644904251-145

$$v_{x,i} = -v_{\theta,i}\frac{(y-y_i)}{r_i} \qquad v_{y,i} = v_{\theta,i}\frac{(x-x_i)}{r_i} \tag{4}$$

The total velocity field induced by the entire vortex array is then obtained as the superposition of every individual contribution:

$$v_x(x,y) = \sum_{i=1}^{N} v_{x,i}\,(x,y) \qquad v_y(x,y) = \sum_{i=1}^{N} v_{y,i}\,(x,y) \tag{5}$$

This formulation reproduces a spatially oscillating flow pattern, where regions of positive and negative circulation alternate along the streamwise direction, generating a simplified but physically consistent model of unsteady gusts and vortical disturbances. To reproduce periodic vortex shedding effects, a von Kármán vortex street configuration is introduced, consisting of an alternating array of counter rotating vortices positioned along the streamwise direction. The induced velocity v at each point (x, y) is obtained by the linear superposition of N vortices:

$$\mathbf{v}(x,y) = \sum_{i=1}^{N} \begin{bmatrix} -v_{\theta,i}(r_i)\frac{y-y_i}{r_i} \\ \\ v_{\theta,i}(r_i)\frac{x-x_i}{r_i} \end{bmatrix} \tag{6}$$

where (x_i, y_i) and Γ_i represent the position and circulation of each vortex, respectively, with alternating signs to mimic realistic wake structures. Finally, the complete inflow field is obtained by summing the contributions of the analytical boundary layer and the vortex-induced perturbations:

$$\mathbf{U}_{\text{total}}(x,y,z) = \begin{bmatrix} U(z) + \sum_i v_{x,i}\,(x,y) \\ \sum_i v_{y,i}\,(x,y) \\ 0 \end{bmatrix} \tag{7}$$

Details of the generated gust profiles are reported in Figure 1.

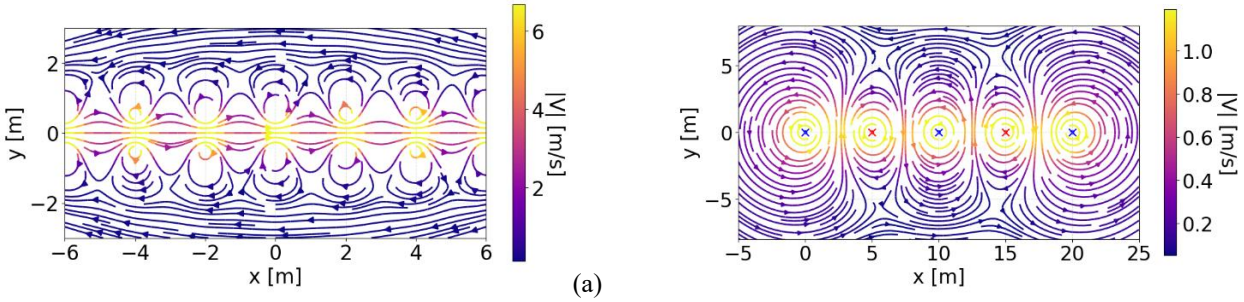


Figure 1:Streamlines of the perturbed velocity field: (a) Rankine vortices; (b) von Kármán wake.

Results

To assess the impact of coherent vortex structures on UAV dynamics, several simulations were conducted using the aforementioned methods to analyze their effects on the trajectory and stability of a quadrotor subjected to such inflow disturbances. In each simulation, the drone was controlled by a PID-based flight controller designed to achieve a stable hover at an altitude of 2 m before transitioning into a straight horizontal trajectory. By systematically varying the circulation strength, vortex core radius, and lateral offset of the UAV with respect to the vortex centers, it was possible to isolate the distinct dynamic effects produced by Rankine and von Kármán configurations, providing a clear basis for comparison across all test cases. The first set of simulations investigates the interaction between the UAV and a simplified gust field generated by

Materials Research Proceedings 69 (2026) 822-826 https://doi.org/10.21741/9781644904251-145

a pair of counter-rotating Rankine vortices (N = 2). Each vortex induces a tangential velocity field according to the formulation described in (3), with circulations of alternating sign (+Γ and −Γ), resulting in a symmetric flow pattern composed of two opposite swirling regions. The UAV is commanded to follow a straight trajectory along the x-axis, while the vortex field acts as a crosswind disturbance. To assess the sensitivity of the flight controller to the vortex-induced perturbations, three different lateral offsets were tested: y = 0 m, y = +1 m, and y = +2 m. Two different circulation strengths were considered, $\Gamma = 3$ m^2/s and $\Gamma = 7$ m^2/s, while keeping the vortex core radius constant at R = 0.1 m.

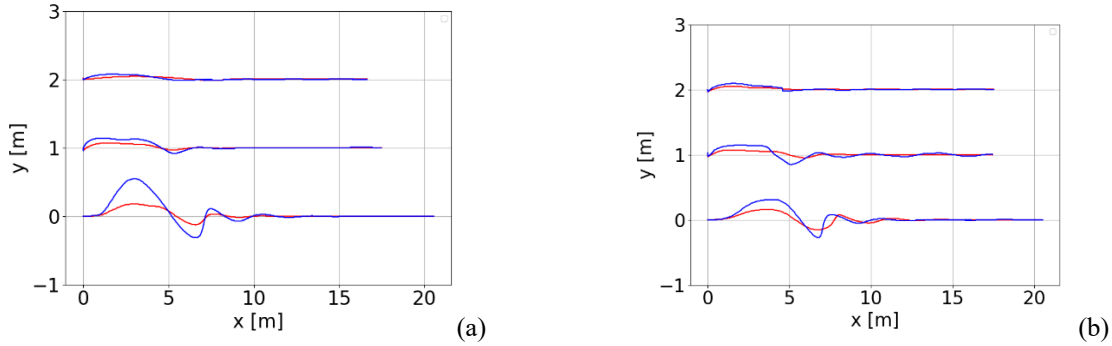


Figure 2: UAV trajectories under the influence of a pair of counter-rotating Rankine vortices. Blue ones are performed at Γ = 3, red ones at Γ = 7. (a) Simulations performed using Rankine vortices with vortex core radius R = 0.1; (b) vortex core radius R = 0.3.

Figure 2 (a) reports the resulting UAV trajectories. When the reference path lies at y = 0 m, the vehicle crosses the region of highest tangential velocity, directly intersecting the vortex cores. As a result, the quadrotor experiences stronger lateral accelerations, and the PID controller must generate larger corrective actions to maintain the desired trajectory. In contrast, when the flight path is shifted from y = 0 m, the vehicle moves through regions where the induced velocity decays with radial distance, leading to significantly milder perturbations and smoother trajectory corrections. A second set of simulations, shown in Figure 2 (b), was conducted with an increased vortex core radius of R = 0.3 m while keeping all other parameters identical. The resulting trajectories show only minor differences compared to the previous case, indicating that for the considered circulation magnitudes and vortex spacing, the flow structure outside the core region dominates the disturbance experienced by the UAV. The final set of simulations investigates the UAV response when flying through a von Kármán vortex street, generated by an alternating array of counter-rotating vortices. Again, the vehicle is commanded to follow a straight trajectory along the x axis, with a PID-based controller compensating for the flow-induced disturbances in real time. Three lateral offsets were tested (y = 0, 1, 2 m), and two circulation magnitudes were considered ($\Gamma = 10$ m^2/s and $\Gamma = 20$ m^2/s).

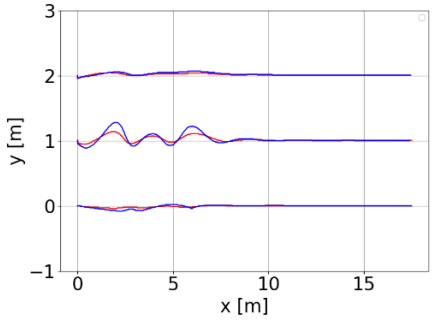


Figure 3: UAV trajectories under the influence of an alternating array of counter-rotating von Kármán vortices. Blue ones are performed at Γ = 10, red ones at Γ = 20.

The resulting trajectories, shown in Figure 3, reveal a markedly different behavior compared to the Rankine vortex cases. In this configuration, the strongest perturbations occur when the UAV flies at y = 1 m, while the paths at y = 0, 2 m experiences milder deviations. This inversion of the disturbance pattern is directly linked to the structure of the von Kármán wake. Unlike the Rankine configuration, where the velocity field is maximum along the vortex cores, the von Kármán vortex street generates alternating regions of high and low induced velocity that are displaced laterally from the symmetry axis of the wake.

Final Remarks

This study presented a comprehensive simulation framework for analyzing the interaction between small UAVs and complex urban wind environments. The approach integrates analytical aerodynamic models and vortex-based representations of coherent structures within the Gazebo Sim platform. A key contribution of this work lies in the incorporation of inflow distortion effects directly into a validated UAV simulation environment, along with the implementation of a Python-based PID controller capable of dynamically compensating for trajectory deviations induced by analytical flow perturbations.

References

[1] Huang Xun. 2025. “The Small-Drone Revolution Is Coming - Scientists Need to Ensure It Will Be Safe.” Nature 637: 29–30.

[2] Elbanhawi M., A. Mohamed, R. Clothier, J. L. Palmer, M. Simic, and S. Watkins. 2017. “Enabling Technologies for Autonomous MAV Operations.” Progress in Aerospace Sciences 91: 27–52. https://doi.org/https://doi.org/10.1016/j.paerosci.2017.03.002.

[3] Infra, Sofia Fraschini. 2021. “Droni e Nuova Mobilità Tra Sfide e Normativa.” https://www.infrajournal.com/it/w/droni-e-nuova-mobilit%C3%A0-tra-sfide-e-normativa.

[4] Aláez, D. X. Olaz, M. Prieto, J. Villadangos, and J. J. Astrain. 2023. “VTOL UAV Digital Twin for Take-Off, Hovering and Landing in Different Wind Conditions.” Simulation Modelling Practice and Theory 123.

[5] Pu Ou, Boqiu Yuan, Zhengnong Li, et al. 2023. “Research on the Characteristics of Urban Building Cluster Wind Field Based on UAV Wind Measurement.” Buildings 13, 3109.

[6] Petricelli Federico, Paruchuri Chaitanya, Sergi Palleja-Cabre, et al. 2023. “An Experimental Investigation on the Effect of in-Flow Distortions of Propeller Noise.” Applied Acoustics 214: 109682. https://doi.org/https://doi.org/10.1016/j.apacoust.2023.109682.

[7] Jawahar Hasan Kamliya, Liam Hanson, Stefano Meloni, and Mahdi Azarpeyvand. 2024. “A Multivariate and Wavelet-Based Analysis on the Wall Pressure Fluctuations for Propellers in Ground Effect.” International Journal of Aeroacoustics 23 (7-8): 763–84. https://doi.org/10.1177/1475472X241278651.

[8] Farley Andrew, Jie Wang, and Joshua A. Marshall. 2022. “How to Pick a Mobile Robot Simulator: A Quantitative Comparison of CoppeliaSim, Gazebo, MORSE and Webots with a Focus on Accuracy of Motion.” Simulation Modelling Practice and Theory 120: 102629. https://doi.org/https://doi.org/10.1016/j.simpat.2022.102629.

Materials Research Proceedings 69 (2026) 827-832 https://doi.org/10.21741/9781644904251-146

Aerodynamic Performance Characterization of UAV Propellers via Blade Element Momentum Theory including Post-Stall Behaviour

Marco LUCARINI[1,a *], Gianpietro DI RITO[2,b], Simone CAMARRI[2,c] and Marco NARDESCHI[1,d]

[1]UMBRAGROUP SpA, Via V. Baldaccini 1, 06034 Foligno, PG, Italy

[2]Department of Civil and Industrial Engineering, University of Pisa, Largo Lucio Lazzarino 2, 56122 Pisa, Italy

[a]mlucarini@umbragroup.com, [b]gianpietro.di.rito@unipi.it, [c]simone.camarri@unipi.it, [d]mnardeschi@umbragroup.com

Keywords: BEMT, Propellers, Post-Stall Modelling, Rotorcraft Design, Sustainable Propulsion, UAM, Aerodynamics

Abstract. This work deals with the development of a numerical code for the evaluation of aerodynamic performance of UAV propellers combining the Blade Element Momentum Theory (BEMT) with empirical corrections for the extension to the post-stall behaviour of blade sections. The formulation also takes into account low-Reynolds effects and starts from the aerodynamic data of blade airfoils in 2D flow. The results of the developed model are verified against manufacturer database for two types of fixed-pitch propellers, over a wide range of advance ratio, aiming to cover the flow conditions related to hovering and cruise phases of a reference VTOL UAV. The results stability is demonstrated by a discretization convergence analysis, assessing the influence of sectional resolution on blades. Owing to the fast convergence of the solver, the proposed approach is expected to be effectively employed as a starting point of propeller design optimization loops.

Introduction

The aerodynamic performance of propellers can be evaluated using models with different levels of fidelity and computational cost. Early formulations, such as the Froude's actuator disk theory, later extended by Betz and Joukowsky, idealized the rotor as a uniformly loaded disk imparting a pressure jump to the flow, establishing the theoretical efficiency limit of 59.3% [1].

A major improvement came with Glauert's Blade Element Momentum Theory (BEMT) [2], which coupled one-dimensional momentum conservation with sectional aerodynamics. By combining Joukowsky's momentum theory, Prandtl's tip-loss correction, and Drzewiecki's blade-element approach, the BEMT actually enabled accurate performance prediction with low computational requirements, laying the foundations of modern rotor analysis.

The increasing demand for electric Vertical Take-Off and Landing (eVTOL) aircraft and UAVs [3] has reinforced the need for fast and reliable aerodynamic modelling tools supporting the conceptual and preliminary design phases [4]. High-fidelity approaches, such as Computational Fluid Dynamics (CFD) or wind tunnel testing, remain indispensable for a final validation, but they are often impracticable in the early-stage design. Steady-state Reynolds-Averaged Navier–Stokes (RANS) simulations typically require hundreds of CPU hours per configuration [5], depending on mesh resolution and turbulence model. On the other hand, a reduced-order method based on BEMT, providing a favourable balance between accuracy and computational costs, is more suitable for preliminary optimization studies.

Experimental and numerical investigations have demonstrated the reliability of BEMT for small- and medium-scale propellers. Jdiobe et al. [6] validated BEMT predictions against wind-

Content from this work may be used under the terms of the Creative Commons Attribution 3.0 license. Any further distribution of this work must maintain attribution to the author(s) and the title of the work, journal citation and DOI. Published under license by Materials Research Forum LLC.

Materials Research Proceedings 69 (2026) 827-832 https://doi.org/10.21741/9781644904251-146

tunnel measurements of an APC propeller for a medium-sized eVTOL, reporting deviations below 10% across a wide range of advance ratios, and highlighting the influence of diameter and pitch variations. Moello and Liscouet [7] developed a coupled CFD–BEMT framework for propeller geometry definition, significantly reducing the number of fully CFD-based optimization iterations and halving the computational time. Andria et al. [8] employed a BEMT method for the design and rapid prototyping of fixed-pitch drone propellers, with experimental tests confirming the predicted thrust performance. Nevertheless, in most cases the BEMT methods disregard post-stall behaviours and low-Reynolds effects.

This work proposes an extension of conventional BEMT models, aiming at broadening the operational range of the underlying airfoil data. Empirical post-stall models and low-Reynolds penalization functions are thus combined with BEMT predictions in order to evaluate aerodynamic coefficients beyond the linear regime. These improvements permit to evaluate relevant trends on predictions extending their applicability over a wider range of operating conditions, including high angles of attack and low Reynolds numbers, quite common in small-size fixed-pitch propellers typically employed in lightweight eVTOL platforms. The results of the developed code are verified against the database of two propellers manufactured by APC, and a mesh-refinement analysis is performed to assess the numerical convergence of the code.

Materials and Methods

For a propeller with diameter $D=2R$ and number of blades B, rotating at angular speed Ω, and with an axial free-stream velocity V_∞, corresponding to an advance ratio $J=V_\infty/(\Omega D)$, the local tangential V_θ and axial V_x velocities on the blade element at a radial position r (Fig. 1), are defined in Equations (1) and (2). In these expressions, a and a' are the axial and tangential induction factors, respectively, and the actuator-disk theory speed induced by the thrust T on the propeller area $A=\pi R^2$ is used under hovering condition (i.e., $J=0$). The effective angle of attack $\alpha(r)$ is thus given by the difference between the local twist angle $\theta(r)$ and the calculated inflow angle $\phi(r)=\tan^{-1}(V_x/V_\theta)$ formed between the relative velocity V_{rel} and the propeller plane.

$$V_\theta(r) = \Omega\, r\, \left(1 + a'(r)\right) \tag{1}$$

$$V_x(r) = \begin{cases} V_\infty + 2\,a(r)\sqrt{|T|/2\rho A}\,, & J = 0 \\ V_\infty\left(1 + a(r)\right), & J \neq 0 \end{cases} \tag{2}$$

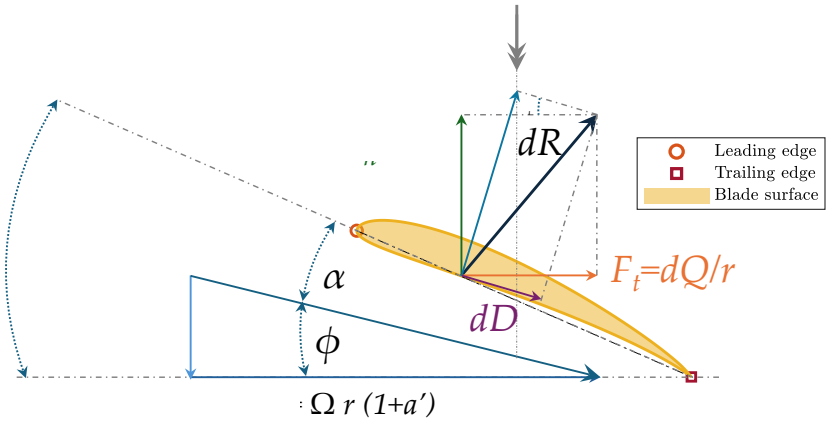


Figure 1. Velocity triangle and aerodynamic forces on a blade element at radial position r.

The aerodynamic coefficients have been derived from precomputed steady XFOIL simulations over a limited range of angles of attack [α_{min}, α_{max}] and discrete chord-based Reynolds numbers, resulting in 2-D lookup tables of lift $C_L(\alpha,Re)$, drag $C_D(\alpha,Re)$, and moment $C_m(\alpha,Re)$ coefficients. Intermediate values are instead obtained by applying cubic splines with respect to the angle of

Materials Research Proceedings 69 (2026) 827-832 https://doi.org/10.21741/9781644904251-146

attack and linear interpolation across the Reynolds number. In case that the Reynolds number of the blade section is calculated as lower than a pre-defined minimum value (5×10^4), empirical penalization functions are applied to reduce the maximum lift and increase drag, reproducing the degradation of aerodynamic performance observed in laminar flow regimes [9]. Beyond the stall angle, the lift and drag coefficients are then extrapolated using a modified Viterna–Corrigan model [10], while the moment coefficient is set to zero to represent fully separated flow. The original formulation has been actually refined to increase accuracy for the NACA 4412 wind-tunnel data reported in [11], as well as to enhance the numerical convergence of the BEMT solver. In the developed code, the post-stall lift and drag coefficients are thus reconstructed from the pre-stall boundary values ($C_L^{\alpha_{min}}$, $C_D^{\alpha_{min}}$) at α_{min} and ($C_L^{\alpha_{max}}$, $C_D^{\alpha_{max}}$) at α_{max}, using the sinusoidal relationships given in Equations (3-4), where α_0 denotes the zero-lift angle. The resulting global behaviour is illustrated in Fig. 2.

$$C_L = \begin{cases} -0.5\, C_L^{\alpha_{min}} \sin[2\,(\alpha-\alpha_0)], & \alpha < \alpha_{min} \\ 0.80\; C_L^{\alpha_{max}} \sin[2\,(\alpha-\alpha_0)], & \alpha > \alpha_{max} \end{cases} \tag{3}$$

$$C_D = \begin{cases} C_D^{\alpha_{min}} + 1.6\, \sin^2[2\,(\alpha-\alpha_0)], & \alpha < \alpha_{min} \\ C_D^{\alpha_{max}} + 1.6\, \sin^2[2\,(\alpha-\alpha_0)], & \alpha > \alpha_{max} \end{cases} \tag{4}$$

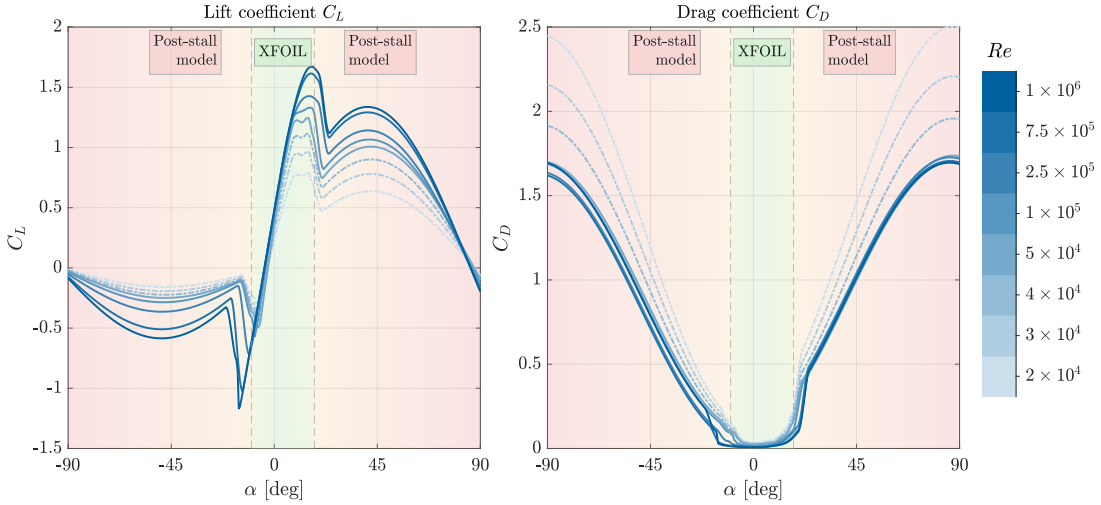


Figure 2. NACA 4412 lift and drag coefficients including post-stall and low-Reynolds effects

The aerodynamic forces per unit span (dr) are computed using Equations (5-6), where $c(r)$ is the local chord length and ρ is the air density; the corresponding elemental thrust dT and torque dQ are obtained from their projections, as expressed in Equations (7-8).

$$dL(r) = 1/2\,\rho V_{rel}^2 c(r) C_L(\alpha, Re) dr \tag{5}$$

$$dD(r) = 1/2\,\rho V_{rel}^2 c(r) C_D(\alpha, Re) dr \tag{6}$$

$$dT(r) = F_n = B(dL\cos\phi - dD\sin\phi) \tag{7}$$

$$dQ(r) = rF_t = Br(dL\sin\phi + dD\cos\phi) \tag{8}$$

The total thrust and torque, and consequently the power (P=QΩ), are obtained by spanwise integration. A parasitic drag component associated with the propeller hub is included by a constant drag coefficient $C_{D,h}$=0.55 referred to the hub frontal area.

Tip-loss effects are finally modelled through a modified Prandtl correction (Eq. 9), with the parameters and F_{min}=0.1 and $\varepsilon=10^{-4}$, preventing numerical instabilities.

$$F_{raw} = \frac{2}{\pi}\cos^{-1}\left[\exp\left(-\frac{B(R-r)}{2r(|\sin\phi|+\varepsilon)}\right)\right], \quad F = F_{raw} + (1 - F_{min})F_{raw} \tag{9}$$

The axial and tangential induction factors (a and a') are updated through the coupled momentum equations (10), where $\sigma=Bc(r)/2\pi r$ is the local blade solidity, while respectively, $C_n=C_L\cos(\phi)-C_D\sin(\phi)$ and $C_t=C_L\sin(\phi)+C_D\cos(\phi)$ are the normal and tangential forces coefficients.

$$a = \left[\frac{4F\sin^2\phi}{\sigma C_n} + 1\right]^{-1}, \quad a' = \left[\frac{4F\sin\phi\cos\phi}{\sigma C_t} - 1\right]^{-1} \tag{10}$$

To ensure robust convergence under hovering conditions, where the standard BEMT formulation may yield indeterminate induction factors as ϕ approaches zero, an iterative actuator-disk-based procedure is implemented. Starting from an initial thrust estimate, the induced axial velocity is computed according to Equation (2) at $J=0$, and the aerodynamic forces are iteratively updated until convergence. This approach enables stable initialization also in low-J simulations and ensures a continuous performance prediction from hover to forward flight.

A counter-based convergence criterion is adopted to ensure stable solutions of the induction factors. Convergence is achieved when the variation of a and a' between iterations remained below 10^{-4} for ten consecutive steps, preventing false positives due to transient oscillations. Under-relaxation by arithmetic averaging and a near-final safeguard are applied to enhance numerical stability, limiting global iterations at 1000. In the hovering iteration loop, convergence is monitored on both thrust and power to ensure consistency of the actuator-disk coupling.

Results and Discussion

Two APC propellers have been selected for the verification of the developed BEMT-based code: the APC 14×5.5MR, optimized for hovering flight, and the APC 14×10E, designed for cruise operation. The predictions of thrust (T), power (P), propulsive efficiency (η) and Figure-Of-Merit (FOM) are compared with the manufacturer data across the entire advance-ratio range and at three rotational speeds (4000, 8000, and 12000 rpm). As shown in Fig. 3 and Fig. 4, the model accurately reproduces the variation of the performances with the advance ratio. Relative errors remain consistently below 20% for all conditions, except where the reference quantity approaches zero. Minor discrepancies in power at the highest rotational speed are attributed to the neglect of compressibility effects, which slightly underestimates sectional drag at high Mach numbers at the blade tip. A residual bias also arises from the simplified assumption of a uniform distribution of NACA 4412 airfoil, whereas the APC blades employ Eppler E63 profiles near the hub.

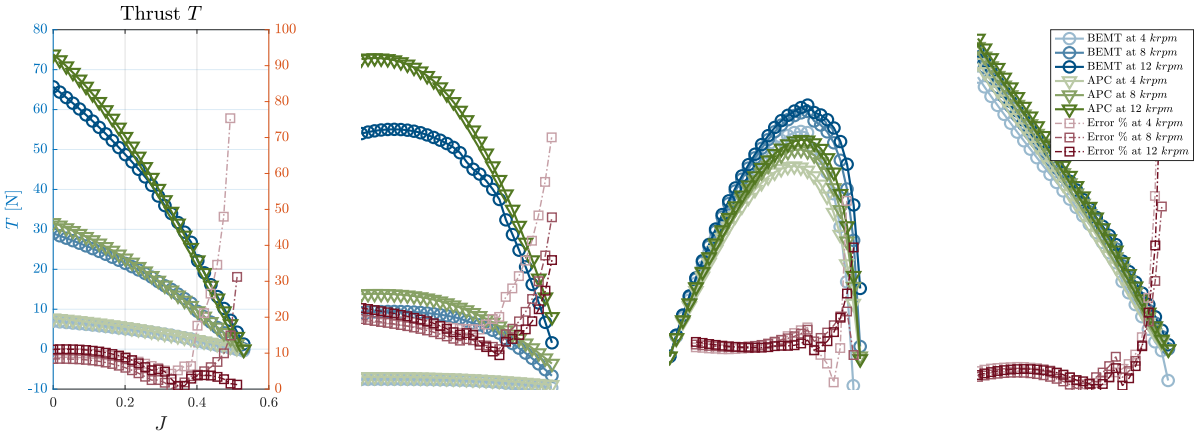


Figure 3. APC 14×5.5MR: comparison of manufacturer data and model results at 4000, 8000 and 12000 rpm

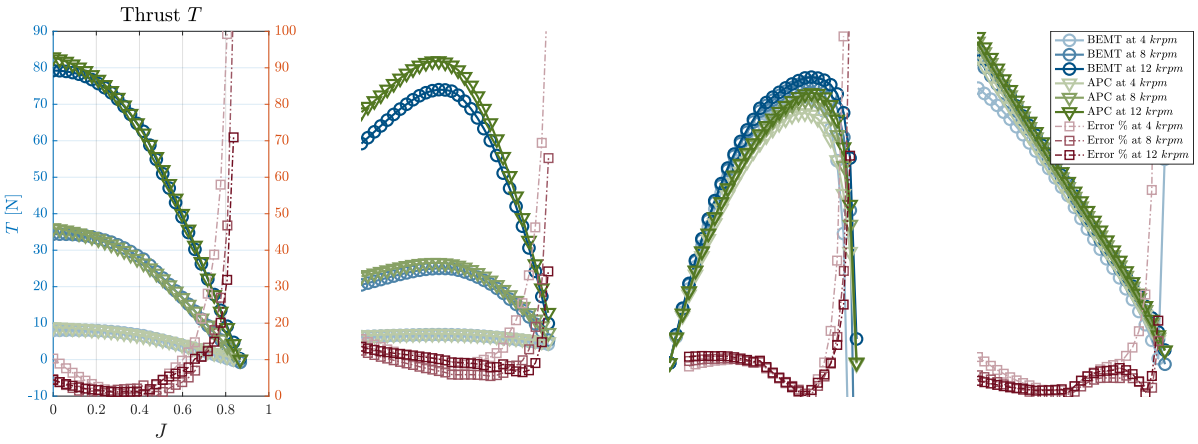


Figure 4. APC 14×10E: comparison of manufacturer data and model results at 4000, 8000 and 12000 rpm

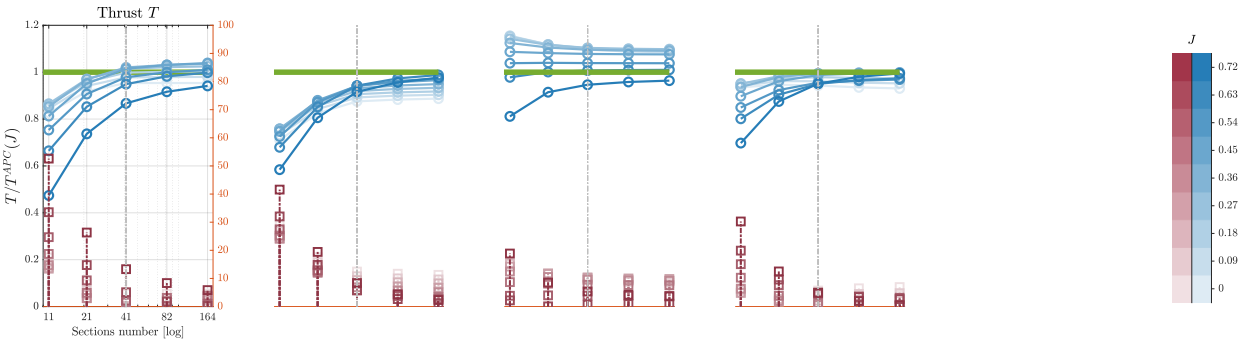


Figure 5. Performance sensitivity to the number of blade sections (simulations with APC 14×10E)

A mesh-refinement study on the APC 14×10E confirmed the numerical convergence of the BEMT-based code. As shown in Fig. 5, relative errors decreased monotonically with finer discretization, while the manufacturer's baseline mesh (41 sections) already ensured satisfactory accuracy. Further refinement yielded marginal gains, with runtime increasing almost linearly—from about 2 s to 6 s per operating point on a standard laptop PC.

Conclusions

The developed BEMT-based code represents an efficient tool for predicting the aerodynamic performance of small-size propellers for UAVs over a wide range of conditions, related to both hovering and cruise flight, by achieving satisfactory accuracy with respect to manufacturer data (maximum relative errors <20%). The inclusion of post-stall and low-Reynolds corrections enhances stability and extends the prediction trends. The solver generates complete performance maps within a few minutes, making it very suitable for preliminary design and optimization studies. Future developments will address multi-airfoil blades, compressibility effects, and the application to complex geometries such as toroidal propellers [12].

References

[1] V.L. Okulov, J.N. Sørensen, Maximum efficiency of wind turbine rotors using Joukowsky and Betz approaches, J. Fluid Mech. 649 (2010) 497-508. https://doi.org/10.1017/S0022112010000509

[2] H. Glauert, Airplane propellers, in: W.F. Durand (Ed.), Aerodynamic Theory, vol. IV, Springer, Berlin, Germany, 1935, pp. 169-360.

[3] European Union Aviation Safety Agency (EASA). Study on the societal acceptance of urban air mobility in Europe. Available online: https://www.easa.europa.eu/sites/default/files/dfu/uam-full-report.pdf, May 2021.

[4] Tripaldi, F., Vianello, S., & Bianchi, N. (2025). Emerging Trends in Urban Air Mobility: An Extensive Review. Energies, 18(6), 1426. https://doi.org/10.3390/en18061426

[5] Liu, Y., et al. (2023). Comparison studies on aerodynamic performances of a rotating propeller for small-size UAVs. Aerospace Science and Technology, 133, 108148. https://doi.org/10.1016/j.ast.2023.108148

[6] Jdiobe, M., Rouser, K., Paul, R., & Rouser, A. (2022). Validation of a wind tunnel propeller dynamometer for Group 2 unmanned aircraft. Applied Sciences, 12(17), 8908. https://doi.org/10.3390/app12178908

[7] Moello, N., & Liscouet, J. (2024, February). Multi-Fidelity Approach for Aerodynamic Optimization of Propeller Blades in VTOL UAVs. Paper presented at the More Electric Aircraft Conference, Toulouse, France.

[8] Andria, G., Di Nisio, A., Lanzolla, A. M. L., & Spadevecchia, M. (2018). Design and performance evaluation of drone propellers. In 2018 IEEE International Workshop on Metrology for AeroSpace (MetroAeroSpace) (pp. 407–412). IEEE. 10.1109/MetroAeroSpace.2018.8453604

[9] M.S. Genç, K. Koca, H.H. Açıkel, G. Özkan, M.S. Kırıcı, R. Yıldız, Flow characteristics over NACA 4412 airfoil at low Reynolds number, EPJ Web Conf. 114 (2016) 02029. https://doi.org/10.1051/epjconf/201611402029

[10] Viterna, L., and Corrigan, R. (1982). Fixed Pitch Rotor Performance of Large Horizontal Axis Wind Turbines. In DOE/NASA Workshop on Large Horizontal Axis Wind Turbines, Cleveland.

[11] C. Ostowari, D. Naik, Post-Stall Wind Tunnel Data for NACA 44XX Series Airfoil Sections, SERI/STR-217-2559, Solar Energy Research Institute (SERI), U.S. Department of Energy, Golden, CO, USA, 1985.

[12] Sebastian, T., & Strem, C. (2020). Toroidal propeller (U.S. Patent No. 10,836,466 B2). U.S. Patent and Trademark Office. https://patents.google.com/patent/US10836466B2

Materials Research Proceedings 69 (2026) 833-838 https://doi.org/10.21741/9781644904251-147

Assessing the Technical-Economic Feasibility of Unmanned Airships: Methodology and Case-Studies

Carlo E.D. RIBOLDI[1,a *] and Luca FANCHINI[1,b]

[1]Department of Aerospace Science and Technology, Politecnico di Milano, via La Masa 34, 20156 Milano, Italy

[a]carlo.riboldi@polimi.it, [b]luca1.fanchini@mail.polimi.it

Keywords: Lighter Than Air, LTA, Airship, Cost Analysis, Cost Estimation, Business Case, Competitors, Unmanned Airships, UAV, Helicopter, Drone, Design

Abstract. This paper outlines a comparative analysis of acquisition, operation & maintenance and overall mission costs carried out on three test cases, where existing flying machines currently flying operational missions (specifically, a multi-copter UAV, a fixed-wing UAV and a manned helicopter) are compared to a novelly designed unmanned airship. The analysis was carried out designing a specific airship for each mission by employing a well-proven technique implemented in the Morning Star suite at Politecnico di Milano. Furthermore, costs are evaluated through estimation relationships accounting for the specific features of an airship, in a fashion suggested by cost estimation methods available for fixed-wing aircraft. The results allow for interesting comparisons, and show where a small-scale unmanned LTA may reduce the cost associated to procurement and operation compared to other flying platforms, while successfully capturing the same mission target as current solutions.

Introduction

The recent development of lighter-than-air (LTA) platforms for low-altitude missions, witnessed by the growing number of new companies offering services based on this type of machine (like Kelluu [1], HyLight [2], Roboloon [3] or FloFleet [4] in Europe), has been fuelled by the advancement of some key enabling technologies. Among them, electric motors for powering propellers offer a higher power-to-weight ratio compared to internal combustion engines. The adoption of these motors is especially advantageous on airships, since they can supply thrust for both propulsion and attitude control when suitably positioned in a distributed fashion, at multiple locations in an airship layout [5], [6], [7], [8], [9]. Additionally, the comparatively low expenditure of energy for propulsion and the reduced peak power required even in terminal maneuvers, compared to either fixed-wing aircraft or rotor-craft, make the sizing of the batteries far less penalizing than heavier-than-air platforms, both in terms of battery mass for the mission, and corresponding battery volume. Similarly, fuelled by the boom of the market of multi-copter UAVs over the past decade [10], effective on-board electronics constitutes a key enabler for unmanned LTAs, especially since the removal of the crew and crew-related masses (e.g. a cockpit, physical control stick and related power lines, etc.) from an airship starkly saves on its buoyant volume as well.

The combined use of these technologies is making LTA technically-viable solutions, with clear performance advantages especially in terms of endurance in forward flight and time-over-target in hovering or station-keeping phases, compared to other flying machines like fixed-wing aircraft (incapable of hovering) and rotor-craft (dramatically limited in terms of endurance and time-over target). However, even for those missions where LTAs could be employed from a technical stand-point, their consideration by potential industrial end-users is still hindered by an uncertainty on the costs associated with procurement or operation & maintenance (O&M).

Content from this work may be used under the terms of the Creative Commons Attribution 3.0 license. Any further distribution of this work must maintain attribution to the author(s) and the title of the work, journal citation and DOI. Published under license by Materials Research Forum LLC.

Materials Research Proceedings 69 (2026) 833-838 https://doi.org/10.21741/9781644904251-147

In this regard, the present work aims to shed some light, by firstly introducing a simple analytic method for the most relevant components of the life cycle cost of a LTA platform for low-altitude use. Secondarily, this work provides a detailed analysis of three case studies, where the cost associated to flying machines currently operating a mission, namely a quadcopter UAV, a fixed-wing UAV and a manned helicopter, obtained as much as possible by processing relevant company data from actual operators, are compared to the outcome of a cost prediction made for an LTA capable of capturing the same mission target.

Methodology

Among the cost prediction methods [11], in the scenario at hand where practical realizations are still not many, a parametric estimation (PE) method [12] based on cost estimating relationships (CER) for sub-components of each major cost chapter has been adopted, trying to capture all major potential contributions to a specific cost. The advantage of a PE approach is that of binding cost estimation to quantities typically available at a preliminary design stage, like the break-down of take-off mass, the installed thrust, etc. [13], [14]. In order to feed CERs in the case of a LTA and obtain a cost prediction, it is possible to employ data on a LTA design solution obtained from a suitable preliminary design exercise (like volume, mass, etc.), considering a specific target mission. Such design exercise can be carried out in a largely automated fashion, thanks to consolidated procedures (Figure 1) available in the literature, bearing credible results once values pertaining to the mission at hand have been assigned [14], [15] [16], [8].

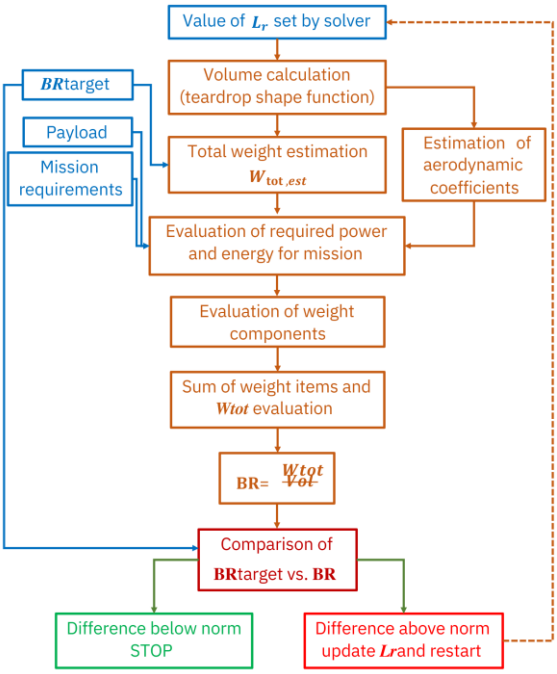


Figure 1 Schematic representation of the considered preliminary sizing algorithm for LTAs.

For some components of cost, a good commonality with respect to other applications in the industrial field can be expected (e.g. the cost of engineering). For components more typical to the LTA case, the build-up of simple CER has been attempted (especially for material cost), mostly based on current industrial data-sheets. Furthermore, CERs for research, development, test and engineering (RDTE) cost, as well as manufacture, have been considered for LTAs (Figure 2). Conversely, the estimation of O&M cost has been treated in a slightly different way for each case study at hand, on account of some specific features of each mission analysed, yielding the need for such customization.

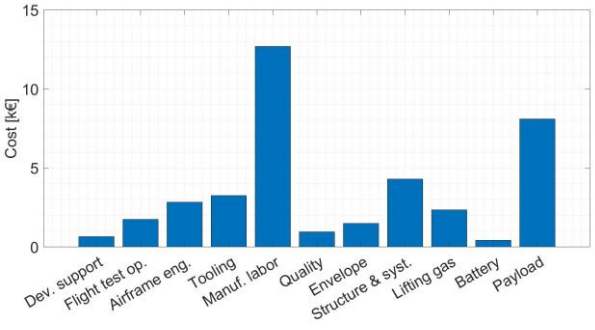


Figure 2 Example split of production cost for an LTA for solar plant inspection (for a production run of 50 exemplars).

Materials Research Proceedings 69 (2026) 833-838 https://doi.org/10.21741/9781644904251-147

Case studies and results

Three missions have been considered, among those currently flown by either UAV or manned machines (Figure 3), which could be flown by a low-altitude LTA at the current level of technology, and without the need for an unrealistically big sizing of the envelope. Care was taken to compare LTA solutions to existing ones flown only in fair weather, to increase the fairness of the analysis.



Figure 3 Competitors for LTA solutions: the DJI Matrice 210 RTK (left) employed for power-plant monitoring, the Tekever AR5 Evolution (center) for sea-life monitoring, and the Airbus AS350B3 (right) for pipeline inspection.

By knowing the target of the mission, a corresponding unmanned LTA UAV was designed for each of these missions, employing the design technique mentioned in the previous paragraph, implemented in the airship sizing suite Morning Star at Politecnico di Milano [15] [16].
Costs available from partners cooperating in this analysis was compared to values obtained from the methodology cited above, yielding the following results.

Solar power-plant inspection. This mission is currently carried out recurring to multi-copter UAVs, which overfly the plant from close distance with visual and infra-red sensors, looking for debris and dust accumulation and wear or damage to the cells. As a reference case for a quantitative analysis, the 87 MW plant of Trino Vercellese (VC) in Northern Italy has been selected. The corresponding LTA solution from the design method is reported in Table 1. The comparison of costs is portrayed in in Table 2. Here the cost per mission has been obtained from a depreciation scheme of 5 years for the quadcopter UAV (optimistic) and of 10 years for the LTA, corresponding to the life span of the envelope. It can be noted how the procurement cost is starkly in favour of the existing quadcopter solution. Yet the operation cost is much higher for that solution than for the LTA, on account of the much higher endurance of the latter. This in turns reduces the time for the mission from 4 days to 1 days, thus also significantly reducing the cost for the crew.

Sizing parameter	Value
Volume [m³]	20.74
Length [m]	9.24
Fineness ratio [-]	4.02
Battery mass [kg]	1.55
Battery energy [kWh]	209.25
Total mass [kg]	25.66

Table 1 Design parameters for LTA UAV for solar plant inspection

Cost component	Acquisition cost [EUR per item]	O&M cost [EUR per mission]	Overall cost [EUR per mission]
Quadcopter	22,005	2,031	2,091
Airship	44,655	813	825

Table 2 Cost comparison between as-is and LTA solutions for solar plant inspection.

Sea-life monitoring. This type of mission is nowadays flown with a fixed-wing UAV, which takes off from a suitable airstrip and flies to a monitoring area over high waters, where it spends most of the mission in a loiter, observing sea-life through electro-optical, infra-red or mirror-less digital camera sensors. As a reference case, the cetacean study mission carried out by a joint group including the Italian Coast

Materials Research Proceedings 69 (2026) 833-838 https://doi.org/10.21741/9781644904251-147

Sizing parameter	Value
Volume [m³]	49.36
Length [m]	12.34
Fineness ratio [-]	4.02
Battery mass [kg]	6.24
Battery energy [kWh]	805.95
Total mass [kg]	61.08

Table 3 Design parameters for LTA UAV for sea-life monitoring.

Guard near the Pelagos sanctuary in the Ligurian Sea in Northern Italy has been considered. The LTA solution designed for this case is significantly bigger than that for the previous one (Table 3). The LTA solution profits from the ability to take-off and land closer to the inspection target, thanks to the need for a reduced ground infrastructure. Furthermore, the lower emitted noise allows to capture good imagery while flying closer to the target (lower altitude) even when employing a cheaper and sensor suite *[17]*. In this specific analysis, the procurement cost of the fixed-wing UAV is extremely high compared to that of the LTA. Of course, such a rig may be very versatile and might be employed for additional missions than just the one considered here. The O&M cost for the LTA is low, thanks to the need for a minimal crew. Mixed with the lower overall mission range to be covered, as just commented, the overall cost per mission is starkly in favour of the LTA solution (Table 4).

Cost component	Acquisition cost [EUR per item]	O&M cost [EUR per mission]	Overall cost [EUR per mission]
Fixed-wing	1,460,000	4,642	5,042
Airship	96,241	826	852

Table 4 Cost comparison between as-is and LTA solutions for sea-life monitoring.

Pipeline inspection. This mission is currently flown typically with manned helicopters, crewed by two technicians with manual cameras, who inspect the pipeline in search of leaks and wear of the pipeline structure, while also checking the safety of the surroundings. The practical case of the Italian section of the Transalpine Oil Pipeline (TAL), linking Trieste (IT) to Ingolstadt (DE), has been considered for this analysis. The sizing results for an unmanned LTA solution on this mission are shown in Table 5. Notably, the overall sizing is generally similar to that obtained for the sea-life monitoring mission. The altitude on the target can be reduced with respect to that of a helicopter, on account of the lower noise emission of the airship *[18]*, *[19]*. Correspondingly, the quality (hence cost) of the optical sensors can be reduced. Table 6 shows the cost corresponding to the as-is and LTA solutions for the pipeline inspection mission. Similar to the previous test scenario, the acquisition cost is starkly in favour of the LTA (even though of course the helicopter can perform several more missions beside the one at hand). However, the LTA UAV is penalized by its low speed, which is inherent to a small-size LTA machine. For this reason, the LTA solution has been designed to cover only the outbound leg, which is flown in roughly one day. This saves on the cost of the pilot (which is hired for one day instead of two), but requires a rental truck to cover the return leg of the mission. The resulting O&M cost per mission, while keeping lower than for the helicopter case, is not so reduced as in other cases. The overall cost per mission is similarly penalized by this result.

Sizing parameter	Value
Volume [m³]	46.98
Length [m]	12.14
Fineness ratio [-]	4.02
Battery mass [kg]	6.07
Battery energy [kWh]	819.45
Total mass [kg]	58.13

Table 5 Design parameters for LTA UAV for pipeline inspection.

Cost component	Acquisition cost [EUR per item]	O&M cost [EUR per mission]	Overall cost [EUR per mission]
Helicopter	3,259,560	3,000	3,000
Airship	72,430	2,318	2,338

Table 6 Cost comparison between as-is and LTA solutions for pipeline inspection.

Conclusions

In this work we provided a first estimation of the acquisition, O&M and overall mission cost for innovative LTA UAVs, to be employed in replacement of existing flying solutions (specifically a multi-copter UAV, a fixed-wing UAV and a manned helicopter) on specific missions. A set of cost estimation relationships was established, based on the specific features of LTAs. The suite Morning Star was employed to preliminarily size a LTA for each specific mission. Interestingly, the comparison of cost showed a general advantage on the overall cost per mission of the LTA on these specific missions (selected on purpose as compatible with a LTA solution). However, procurement and O&M cost vary significantly from one case to another, and when considered separately, acquisition cost can be bigger for the LTA machine than for the existing platforms *[20]*. Future work should try to extend this approach further to include missions potentially flown by high-altitude airships (HAA).

Acknowledgements

The contributions of M. Perotti (EuroDrone), R. Basso (TAL), S. Airoldi (Tethys Research Institute), M. Bocken (Hylight), L. Braida and S. Dal Mas (EliFriulia), the Italian Coast Guard and the European Maritime Safety Agency are gratefully acknowledged. This work was partly funded by the IEC Pathfinder project IPROP under grant N. 101098900.

References

[1] Kelluu Oy, Metallimiehentie 4, 80330 Reijola, Finland - kelluu.com, accessed Jan. 2025.

[2] HyLight, 91220 Brétigny-sur-Orge, France - www.hylight.aero, accessed Jan. 2025.

[3] Roboloon, Nobelstraße 15, 70569 Stuttgart, Germany - www.roboloon.com, accessed Jan. 2025.

[4] FloFleet, Via Sebenico 24, 20124 Milan, Italy - www.flofleet.com, accessed Jan. 2025.

[5] C. E. D. Riboldi and A. Rolando, "Layout Analysis and Optimization of Airships with Thrust-Based Stability Augmentation," Aerospace, vol. 9, p. 393, 2022. https://doi.org/10.3390/aerospace9070393

[6] C. E. D. Riboldi and A. Rolando, "Thrust-based stabilization and guidance for airships without thrust-vectoring," Aerospace, vol. 10, n° 4, p. 344, 2023. https://doi.org/10.3390/aerospace10040344

[7] C. E. D. Riboldi and A. Rolando, "Autonomous flight in near hover and hover for thrust controlled unmanned airships," Drones, vol. 7, n° 9, p. 545, 2023. https://doi.org/10.3390/drones7090545

[8] C. E. D. Riboldi, M. Belan, S. Cacciola, R. Terenzi, S. Trovato, D. Usuelli and G. Familiari, "Preliminary sizing of a low-altitude airship including ion-plasma thrusters," in 34th Congress of the International Council of the Aeronautical Sciences (ICAS2024), 9-13 September 2024, Florence, Italy, 2024.

[9] IPROP - Ionic Propulsion in the Atmosphere - www.iprop-project.eu, Grant ID: HORIZON-EIC-2022-PATHFINDEROPEN-01, 2023-2027.

[10] J. Peksa and D. Mamchur, "A Review on the State of the Art in Copter Drones and Flight Control Systems," Sensors, vol. 24, p. 3349, 2024. https://doi.org/10.3390/s24113349

[11] R. Roy, "Cost Engineering: Why, What and How?," Cranfield, 2003.

[12] "NASA Cost Estimating Handbook (v4.0)," Washington, D.C., 2015.

[13] J. P. Large, H. G. Campbell and D. Cates, "Parametric Equations for Estimating Aircraft Airframe Costs," Santa, 1976.

[14] G. E. Carichner and L. M. Nicolai, Fundamentals of Aircraft and Airship Design, American Institute of Aeronautics and Astronautics, Inc., 2013. https://doi.org/10.2514/4.868986

[15] C. E. D. Riboldi, A. Rolando and G. Regazzoni, "On the feasibility of a launcher-deployable high-altitude airship: Effects of design constraints in an optimal sizing framework," Aerospace, vol. 9, p. 1-37, 2022. https://doi.org/10.3390/aerospace9040210

[16] C. E. D. Riboldi, M. Belan, S. Cacciola, R. Terenzi, S. Trovato, D. Usuelli and G. Familiari, "Preliminary Sizing of High-Altitude Airships Featuring Atmospheric Ionic Thrusters: An Initial Feasibility Assessment," Aerospace, vol. 11, n° 7, p. 590, 2024. https://doi.org/10.3390/aerospace11070590

[17] F. Salucci, C. E. D. Riboldi, L. Trainelli, A. Rolando and L. Mariani, "A noise estimation procedure for electric and hybrid-electric aircraft," in AIAA Scitech 2021 Forum, Online, 2021. https://doi.org/10.2514/6.2021-0258

[18] L. Trainelli, C. E. D. Riboldi and M. Bucari, "Observing the angle of attack of the tip-path plane from rotor blade measurements," in 41st European Rotorcraft Forum 2015 (ERF2015), Munich, Germany, 2015.

[19] L. Trainelli, M. Gennaretti, G. Bernardini, A. Rolando, C. E. D. Riboldi, M. Redaelli, L. Riviello and A. Scandroglio, "Innovative helicopter in-flight noise monitoring systems enabled by rotor-state measurements," Noise Mapping, vol. 3, no. 1, pp. 190-215, 2016. https://doi.org/10.1515/noise-2016-0014

[20] C. E. D. Riboldi and L. Fanchini, "Assessing the technical-economic feasibility of low-altitude unmanned airships: methodology and comparative case studies," Aerospace, vol. 12, p. 244, 2025. https://doi.org/10.3390/aerospace12030244

Materials Research Proceedings 69 (2026) 839-845 https://doi.org/10.21741/9781644904251-148

Identification of Airship Aerodynamic Models from Flight Data: Preliminary Investigation and Identifiability Analysis

Carlo E.D. RIBOLDI[1,a *], Stefano CACCIOLA[1,b], Yan POZHANKA[2,c] and Mostafa HASSANALIAN[2,d]

[1]Department of Aerospace Science and Technology, Politecnico di Milano, via La Masa 34, 20156 Milano, Italy

[2]New Mexico Institute of Mining and Technology, 801 Leroy Pl., Socorro, New Mexico, via La Masa 34, 20156

[a]carlo.riboldi@polimi.it, [b]stefano.cacciola@polimi.it, [c]yan.pozhanka@student.nmt.edu, [d]mostafa.hassanalian@nmt.edu

Keywords: Lighter Than Air, LTA, Airship, Aerodynamics, Aerodynamic Model, Dynamic Modeling, Simulation, Parameter Identification, Identifiability, Output Error

Abstract. In this research, a preliminary identification testing of some modelling parameters pertaining to the aerodynamic model proposed by Munk-Jones-DeLaurier for airships has been carried out. Identification trials have been carried out in virtual environment employing an output-error method, solving a non-linear optimization problem on the norm of the error between the output of an estimated model and that corresponding to a reference model, assumed as ground-truth. The practical results show how some of parameters in the aerodynamic model appear identifiable even employing a rather limited dataset also in presence of noise.

Introduction

The availability of accurate and reliable simulators represents a key-asset in the design, performance assessment and certification of any flying system. Lighter-than-air (LTA) flying vehicles are no exception. However, the substantial absence of well-validated and proven simulators accepted at an industrial level is just a result of complexity of embracing all airships via a simple unified theory (like the lifting line for slender wings, or BEM for rotors). Actually, the practical realization of LTA [1] may range significantly in terms of overall shape (including a larger or smaller fineness ratio, multi-lobed envelopes, multiple and freely positioned fins, etc. [2] [3] [4]) as well as in terms of the values of the Reynolds number, spanned in the typical speed domain of flight operations [5]. The latter, in combination with the relative bluntness of the envelope (which has to be compared in this regard to higher lift-to-drag bodies like a wing), provokes separation phenomena on the tail cone of the airship envelope. These are typically present also in standard forward flight for an airship, and their modelling is generally not trivial. Actually, where potential-flow-based theory, with corrections for cross-flow motion is still the reference for aerodynamic modelling (at least for computationally-fast flight dynamics simulators), the actual assignment of the parameters in that class of models is generally not easy to perform. In a similar fashion, the modelling alternative represented by aerodynamic specifications assigned as lumped coefficients (e.g. stability and control derivatives) is generally coupled for airships with CFD computational models, or data coming from experimental (i.e. wind tunnel) testing, which provide predictions not spared from a strict dependence on the specific geometry and flight regime (i.e. Reynolds number).

These considerations point out the need for model tuning procedures, which are especially required in the fine tuning phase of the setup of a virtual model for airship dynamics. For LTA flying vehicles, the employment of such techniques has been attempted only sporadically and with

Content from this work may be used under the terms of the Creative Commons Attribution 3.0 license. Any further distribution of this work must maintain attribution to the author(s) and the title of the work, journal citation and DOI. Published under license by Materials Research Forum LLC.

Materials Research Proceedings 69 (2026) 839-845 https://doi.org/10.21741/9781644904251-148

mixed results, in association primarily with the identification of lumped parameters in a simplified (linearized) dynamic formulation [6].

In the present work, the focus is moved to the tuning of a model based on the Munk-Jones-DeLaurier theory [7] [8], which basically mixes potential-flow aerodynamics with cross flow effects from cylinders and fins. The literature indicates that some coefficients in this formulation can be only guessed in a preliminary phase (for instance, when the airship is under design and no practical data is available), yet they need to be corrected when possible, by mixing experimental data and what is more accurately known of the model.

After shortly reviewing the features of the aerodynamic model of interest, the present paper shows a proposed application of a parameter estimation method which might be employed for the task. Finally, some preliminary results showing the potential of the proposed technique will be presented.

Methodology

A model capable of capturing the driving aerodynamic phenomena intervening on an airship in flight, with sufficient accuracy for flight dynamic computations, has been elaborated from the original theory of Munk [7] by Jones and DeLaurier [8]. Munk's theory has been developed from Lamb's solution of the potential flow around a generic ellipsoid [9], where the axis of the ellipsoid is misaligned with the prevalent direction of the flow. The contribution from Jones and DeLaurier has been the inclusion of separation phenomena, to supply the non-viscid (potential) theory with information of the separation effects taking place both on the envelope and on the tails on board an airship. This allows to correctly account for effects typically found at higher angles of attack or sideslip, which are typical to airships especially at low speed and in terminal maneuvers (i.e. close to hovering conditions). Besides the validation of the theory via fluid dynamics testing, including the experimental verification of effects bound to a rotary motion of a scaled test airship specimen (i.e. when the components of the rotational speed are not all zero) [8], the results of this aerodynamic modelling approach have been applied to the Lotte airship in the early 2000s [10]. In the latter case, experimental results in the wind tunnel have proven the generally very good likelihood obtained through this modelling approach, in that case in static flight conditions, yet considering the complete setup of the airship (i.e. including the tails) and flight at very high angle of attack, where separation phenomena are clearly intense [5].

An implementation of this aerodynamic model has been included in the Airship class of SILCROAD (SImulation Library for CRaft–Object Advanced Dynamics) [11] [12] [13] [14], an object-oriented flight simulation library working in Matlab®/Simulink, conceived for the computationally fast simulation of interacting flying objects.

Among the parameters that define the aerodynamic characteristics of the airship, according to this model, are the following related to the airship hull (including interference effects from the tail) [8]:

- $C_{D_0}^{hull}$, $C_{D_{cf}}^{hull}$. These represent the components of the hull drag coefficient accounting for viscosity in attached flow, typically modelled from a thin plate analogy, and cross-flow, obtained from the estimation of cylinder cross-flow.
- η_k^{hor}, η_k^{ver}. These represent an interference effect between the tail and the hull. In particular, in the original theory [8] only a single parameter was included for the entire fin, whereas in the SILCROAD implementation a slightly more refined model was introduced, allowing to split the two contributions, thus potentially allowing for a more elaborated and generic arrangement of the empennages in a specific design.
- k_1, k_2, k_3, k_3'. These represent the apparent inertia coefficients, and for the specific case of a slender body obtained as a solid of revolution have been tabulated by Munk starting from Lamb's solution of potential flow [7] [9].

Materials Research Proceedings 69 (2026) 839-845 https://doi.org/10.21741/9781644904251-148

Due to the uncertainties typically associated to the these quantities, they have been shortlisted as interesting candidates within a parameter estimation effort.

This work has been carried out in virtual environment (future developments will make use of data made available through the first flying demonstrator now available at Politecnico di Milano within project IPROP [15]). In this context, the virtual model of an airship test-bed has been assembled, and a preliminary estimation of the identifiability of these parameters has been carried out, perturbing one by one the candidate parameters for estimation, and employing a doublet on elevator and rudder controls. The results of this preliminary analysis have allowed assembling Fisher's information matrix. The latter confirmed the likely good identifiability of the parameters k_2, k_3, k_3' (notably, $k_2 = k_3$ for an axial-symmetric body), as well as η_k^{hor}, η_k^{ver}. Conversely, parameters $C_{D_0}^{hull}$, $C_{D_{cf}}^{hull}$ have tested harder to identify according to this analysis, possibly indicating that the proposed doublet on aerodynamic controls of the tail empennages (i.e., elevator and rudder controls) is not effective in stimulating the effect on dynamics of these two parameters.

In this work, after evaluating possible ways of carrying out parameter identification [16] [17] [18], an output-error approach was selected [19]. The parameters selected for identification have been collected in an array $\boldsymbol{p} = \{\eta_k^{hor}, \eta_k^{ver}, k_3, k_3'\}$. The output-error approach calls for the definition of an optimal problem, where parameters $\boldsymbol{p}$ are iteratively corrected by an optimal solver so as to obtain the best matching of the simulated system output and field data, when both the real machine and the simulated model are subject to the same input. In this case, the input was the same for which the analysis of Fisher's matrix had been carried out, i.e. a doublet of elevator and rudder.

In analytical terms, the response of the system $\boldsymbol{y} = g(\boldsymbol{p}, \boldsymbol{x}, \boldsymbol{u})$ is a function of the parameters, as well as of the system state $\boldsymbol{x} = \boldsymbol{x}(t)$ and controls $\boldsymbol{u} = \boldsymbol{u}(t)$. The time history of controls is assigned (i.e., the doublet on elevator and rudder, other controls are not stimulated), whereas the state solves the dynamic equilibrium equation $\dot{\boldsymbol{x}} = f(\boldsymbol{p}, \boldsymbol{x}, \boldsymbol{u})$. Assuming to know the output $\boldsymbol{z} = \boldsymbol{z}(t)$ from a test in the field, carried out subjecting the real machine to the same input as the value as the simulated system, it is possible to compute a quadratic norm of the error $\boldsymbol{e}(t) = \boldsymbol{z}(t) - \boldsymbol{y}(t)$, as

$$J = \frac{1}{t_f - t_0} \int_{t_0}^{t_f} \boldsymbol{e}(t)^T \boldsymbol{Q} \boldsymbol{e}(t) dt, \tag{1}$$

where the diagonal matrix $\boldsymbol{Q}$ is employed as a weight matrix, which might be set as the inverse of the squared covariance of the noise of each channel in array $\boldsymbol{e}(t)$. The identification of the parameters is then configured as the optimal problem

$$\min_{\boldsymbol{p}} J. \tag{2}$$

Working in virtual environment, the actual value of the coefficients, named $\boldsymbol{p}^*$, is known. Therefore, instead of employing data from the field, a simulation where $\boldsymbol{z} = g(\boldsymbol{p}^*, \boldsymbol{x}, \boldsymbol{u})$ is employed as a ground-truth dataset. For added realism, the channels in the so-obtained $\boldsymbol{z}(t)$ have been artificially polluted with random noise.

Results

In this work, a virtual model of the Lotte airship [5] has been employed as a test-bed. Reference values of the measures $\boldsymbol{z}(t)$ have been produced by running the simulation model in SILCROAD in forward, horizontal, steady and symmetric flight, at a reference horizontal speed of 8 m/s. A corresponding trimmed solution has been computed automatically. A time history $\boldsymbol{z}(t)$ extending from $t_0 = 0$ s to $t_f = 20$ s has been obtained running an integration over time on a model of the airship, with assigned values of the parameters $\boldsymbol{p}^* = \{1.0, 1.0, 0.86, 0.69\}$, corresponding to the Lotte airship.

The measures considered in the identification process are the three body velocities, the three body rotational rates, the attitude angles and the position of a point (center of buoyancy) with

respect to a ground observer (12 channels in total). All these quantities are realistically obtainable even from a relatively cheap, small-scale airship test-bed, like the one currently available within project IPROP [15].

The optimal problem in Eq. (2), based on the norm in Eq. (1), has been solved numerically, based on a gradient algorithm, starting from an initial guess artificially polluted so as to simulate an uncertainty in the values of the parameters. In particular, the initial guess $\boldsymbol{p_0} = \{1.05, 1.05, 0.93, 0.77\}$, where the latter two values, referring to k_3 and k_3' respectively, have been chosen from Munk's tabulated functions [7] so that they correspond to a higher fineness ratio of the hull than the actual one.

The period of the doublet on elevator and rudder controls have been selected so as to excite respectively the two oscillatory modes of the airship, namely the pendulum in the longitudinal domain (via the elevator control), and the roll mode in the lateral-directional domain (via the rudder control) [6]. For the test-bed at hand, the corresponding (positive) intervals of the doublet is 6.92 s for the elevator and 0.85 s for the rudder. A deflection amplitude (positive) of 1.0 deg has been employed for both controls, and the behaviour of the airship in flight was visually checked not to diverge towards unrealistic flight conditions over the duration of the simulations. In this regards, however, it should be remarked that, thanks to employing buoyancy as a lifting force, the range of flight dynamics states for an airship is generally much broader than for winged aircraft.

Several cases corresponding to different levels of artificial noise in the measures have been considered. Considering the different nature of the sensors providing the measures, the following reference noise levels have been considered:

- for velocity components (GPS differentiation), a $\sigma_V = 0.01$ m/s
- for rotational rate components (IMU), a $\sigma_\omega = 0.002$ rad/s
- for attitude angles (IMU), $\sigma_a = 0.001$ rad
- for position (GPS), $\sigma_P = 0.05$ m

The value of σ_P is comparatively higher on account of the low-value/low-accuracy of GPS sensors commonly employed on low-budget measurement units, like for scaled flying models [15].

Table 1 summarizes the results of the identification analysis, for changing values of the actual noise levels, artificially added to the measure channels in the reference simulation, and scaled by a same multiplier to simulate a generally higher or lower noise level in the measures. As it can be argued from Table 1, an identification of the selected parameters is indeed possible, and remarkably so even when employing (as done here) a very reduced dataset, corresponding to a single run on the reference test-bed. The most reduced error can be obtained in identifying Munk's parameters k_3 and k_3', even starting from a rather offset initial condition. A comparatively lower accuracy can be observed in the identification of the tail-to-hull interference parameters η_k^{hor}, η_k^{ver}, even though the change on the initial values computed by the solver is acting in most cases in the correct direction (i.e., the artificially-boosted initial values are changed by the algorithm towards the correct value).

Table 1 Results of identification runs, for changing values of the overall noise level multiplier.

Parameter ($\boldsymbol{p}$)	Real value ($\boldsymbol{p}^*$)	Init. Value ($\boldsymbol{p}^0$)	Estimated value ($\overline{\boldsymbol{p}}$) – No noise (0% of reference)		Estimated value ($\overline{\boldsymbol{p}}$) – Noise 1% of reference		Estimated value ($\overline{\boldsymbol{p}}$) – Noise 10% of reference		Estimated value ($\overline{\boldsymbol{p}}$) – Noise 100% of reference	
	Value		Value	Error [%]	Value	Error [%]	Value	Error [%]	Value	Error [%]
η_k^{hor}	1.0	1.05	0.9847	-1.5300	1.0022	0.2200	1.1082	10.8200	1.0571	5.7100
η_k^{ver}	1.0	1.05	0.9022	-9.7800	0.9694	-3.0600	1.0282	2.8200	1.0489	4.8900
k_3	0.86	0.93	0.8694	1.0930	0.8741	1.6395	0.7689	-10.5930	0.7999	-6.9884
k_3'	0.69	0.77	0.6808	-1.3333	0.7854	13.8261	0.7039	2.0145	0.7367	6.7681

Materials Research Proceedings 69 (2026) 839-845 https://doi.org/10.21741/9781644904251-148

To better interpret the results, it should be noted that the dataset (i.e., the simulations) with noise is only one for each overall noise scaling factor, hence the results just presented are not enough for a statistical analysis of correlation between the error on identification and the level of noise. They just serve to preliminary assess the general identifiability of the parameters in the problem at hand, and in this sense they look extremely promising.

As an example, the plot in Figure 1 show the time histories of longitudinal and lateral-directional states, and of controls, corresponding to the reference test-bed ($\boldsymbol{p} = \boldsymbol{p}^*$, in blue, barely visible under the green curves corresponding to estimations), the polluted initial condition ($\boldsymbol{p} = \boldsymbol{p_0}$, in amber), and the set of estimated parameters $\boldsymbol{p} = \bar{\boldsymbol{p}}$ (in green), corresponding to the result of the identification procedure. The figure is referring to a 1% of-reference-noise condition.

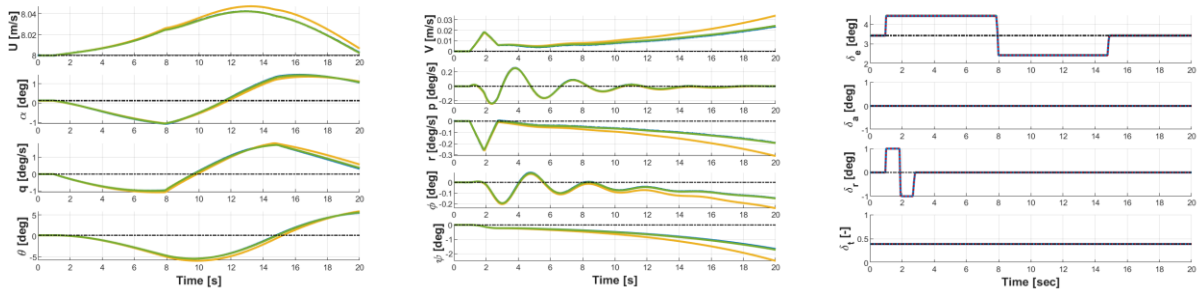


Figure 1 Time histories of longitudinal states (left), lateral-directional states (centre) and controls (right) for a simulation with a noise scaling factor of 1% in the reference test-bed. Blue: test-bed (barely visible under the green line). Yellow: starting point of identification. Green: result of identification.

As noted from Table 1, the result in the figure shows an a clear amelioration of the estimated parameters over the initial condition, with a very good likelihood of the output of the reference model corresponding to $\boldsymbol{p} = \boldsymbol{p}^*$ and the estimated one corresponding to $\boldsymbol{p} = \bar{\boldsymbol{p}}$.

Conclusions

A parameter identification method based on the output-error approach has been employed for the estimation of some parameters appearing in a mid-fidelity aerodynamic model of an airship. Following a shortlisting of the candidate identifiable parameters, and a preliminary synthesis of a time history of controls suitable for stimulating their expression in the dynamic response of the airship, the identification has been carried out employing as a test-bed the virtual model of the Lotte airship. Results obtained up to the present state of the research support the suitability of the technique selected for identification, which can easily work on the free response of the airship, taking advantage of the reduced tendency of barely stable or unstable airships to diverge fast from a trimmed condition even when non artificial stabilization is employed. The excitation input, based on doublets, appears to provide a dataset sufficiently rich for identification purposes, as far as the shortlisted parameters $\eta_k^{hor}, \eta_k^{ver}, k_3, k_3'$ are considered. The effect of noise has been preliminarily evaluated in view of an application of the proposed technique to the identification of parameters pertaining to an existing airship prototype, designed and built in Spring 2025 at DAER-Politecnico di Milano within project IPROP.

Future short-term developments will involve the investigation of additional maneuvers, such to allow the identification of the relevant drag-related coefficients $C_{D_0}^{hull}$, $C_{D_{cf}}^{hull}$, and possibly involving the use of thrusters instead of aerodynamic surfaces.

Acknowledgments

This work was partly funded by the IEC Pathfinder project IPROP under grant N.101098900.

References

[1] C. E. D. Riboldi and L. Fanchini, «Assessing the technical-economic feasibility of low-altitude unmanned airships: methodology and comparative case studies,» Aerospace, vol. 12, p. 244, 2025. https://doi.org/10.3390/aerospace12030244

[2] C. E. D. Riboldi, A. Rolando and G. Regazzoni, «On the feasibility of a launcher-deployable high-altitude airship: Effects of design constraints in an optimal sizing framework,» Aerospace, vol. 9, p. 1-37, 2022. https://doi.org/10.3390/aerospace9040210

[3] C. E. D. Riboldi, M. Belan, S. Cacciola, R. Terenzi, S. Trovato, D. Usuelli and G. Familiari, «Preliminary Sizing of High-Altitude Airships Featuring Atmospheric Ionic Thrusters: An Initial Feasibility Assessment,» Aerospace, vol. 11, n° 7, p. 590, 2024. https://doi.org/10.3390/aerospace11070590

[4] C. E. D. Riboldi, M. Belan, S. Cacciola, R. Terenzi, S. Trovato, D. Usuelli and G. Familiari, «Preliminary sizing of a low-altitude airship including ion-plasma thrusters,» in 34th Congress of the International Council of the Aeronautical Sciences (ICAS2024), 9-13 September 2024, Florence, Italy, 2024.

[5] B. Kämpf, «Flugmechanik und Flugregelung von Luftschiffen,» 2004.

[6] A. Kornienko, «System identification approach for determining flight dynamical characteristics of an airship from flight data,» 2006.

[7] M. M. Munk, «The aerodynamic forces on airship hulls,» 1926.

[8] S. P. Jones and J. D. DeLaurier, «Aerodynamic estimation techniques for aerostats and airships,» Journal of Aircraft, vol. 20, p. 120-126, 1982. https://doi.org/10.2514/3.44840

[9] H. Lamb, Hydrodynamics, Dover Publications, 1945.

[10] P. Funk, T. Lutz and S. Wagner, «Experimental investigations on hull-fin interferences of the Lotte airship,» Aerospace Science and Technology, vol. 7, pp. 603-610, 2003. https://doi.org/10.1016/S1270-9638(03)00058-0

[11] C. E. D. Riboldi and M. Tomasoni, «Formation Flight of Fixed-Wing UAVs: Dynamic Modeling, Guidance Design, and Testing in Realistic Scenarios,» Aerospace, vol. 12, n° 3, p. 260, 2025. https://doi.org/10.3390/aerospace12030260

[12] C. E. D. Riboldi and A. Rolando, «Thrust-based stabilization and guidance for airships without thrust-vectoring,» Aerospace, vol. 10, n° 4, p. 344, 2023. https://doi.org/10.3390/aerospace10040344

[13] C. E. D. Riboldi and A. Rolando, «Autonomous flight in near hover and hover for thrust controlled unmanned airships,» Drones, vol. 7, n° 9, p. 545, 2023. https://doi.org/10.3390/drones7090545

[14] C. E. D. Riboldi and A. Rolando, «Layout Analysis and Optimization of Airships with Thrust-Based Stability Augmentation,» Aerospace, vol. 9, p. 393, 2022. https://doi.org/10.3390/aerospace9070393

[15] IPROP - Ionic Propulsion in the Atmosphere - www.iprop-project.eu, Grant ID: HORIZON-EIC-2022-PATHFINDEROPEN-01, 2023-2027.

[16] L. Trainelli, M. Gennaretti, G. Bernardini, A. Rolando, C. E. D. Riboldi, M. Redaelli, L. Riviello and A. Scandroglio, «Innovative helicopter in-flight noise monitoring systems enabled by rotor-state measurements,» Noise Mapping, vol. 3, n° 1, pp. 190-215, 2016. https://doi.org/10.1515/noise-2016-0014

[17] L. Trainelli, C. E. D. Riboldi and M. Bucari, «Observing the angle of attack of the tip-path plane from rotor blade measurements,» in 41st European Rotorcraft Forum 2015 (ERF2015), Munich, Germany, 2015.

[18] S. Cacciola, L. Bottà, C. E. D Riboldi and L. Trainelli, «Identification of the impact of blowing on the aerodynamic model of an airplane with distributed electric propulsion,» 34th Congress of the International Council of the Aeronautical Sciences (ICAS2024), 9-13 September 2024, Florence, Italy, 2024.

[19] V. Klein and E. A. Morelli, Aircraft System Identification: Theory and Practice., AIAA (American Institute of Aeronautics & Astronautics), 2006. https://doi.org/10.2514/4.861505

Materials Research Proceedings 69 (2026) 846-849 https://doi.org/10.21741/9781644904251-149

Reinforcement Learning-Based Bezier Airship Hull Optimization: A Data-Driven Framework for Shape Adaptation Under Aerodynamic Constraints

Qian ZHAO[1,a *], and Carlo Emanuele Dionigi RIBOLDI[1,b]

[1]Department of Aerospace Science and Technology, Politecnico di Milano, via La Masa 34, 20156 Milano, Italy

[a]qian.zhao@polimi.it, [b]carlo.riboldi@polimi.it

Keywords: Airship Design, Bezier Curves, Reinforcement Learning, DDPG, Lift-to-Drag Ratio Optimization, Robust Design, Aerodynamic Efficiency, Data-Driven Optimization

Abstract. This paper proposes a data-driven reinforcement learning framework for aerodynamic optimization of airship hulls. It combines Deep Deterministic Policy Gradient (DDPG) with Bezier curve parameterization to adjust the shape of the classic airship ”Lotte” [1,2,3]. A volume-preserving constraint ensures buoyancy consistency. Different from previous studies focused solely on drag minimization, we target lift-to-drag ratio (L/D) and robustness [4,5]. Simulations in SILCROAD [6,7,8,9] demonstrate significant improvement in L/D while preserving volume and smoothness. The approach offers a modular, scalable framework for future multi-objective extensions..

Introduction

Airships are regaining attention for applications like surveillance, communication relay, and environmental monitoring [12]. A key design challenge is aerodynamic shape optimization of the hull, which affects drag, L/D, energy use, and mission range.

Traditional airship shapes often rely on empirical formulas or fixed parametric models, limiting flexibility for mission-specific designs. Prior aerodynamic optimization focused primarily on drag at constant angles, overlooking L/D, a critical factor for propulsion and endurance [11].

Reinforcement learning (RL) offers a flexible alternative for high-dimensional, constraint driven problems. Unlike gradient-based methods, RL learns from interaction and handles noisy evaluations.

This work introduces an RL framework integrating DDPG and Bezier parameterization for airship optimization [10]. The agent modifies control points to maximize L/D while preserving volume. Evaluation is performed using SILCROAD [6,7,8,9].

Main contributions include: (1) reinforcement learning with embedded physical constraints, (2) continuous shape control via Bezier parameters, and (3) performance improvements in L/D and robustness.

Methodology

The upper hull is modeled with a Bezier curve using $n + 1$ control points $\{P_0, \ldots, P_n\}$. The curve is:

$$R(x) = \sum_{i=0}^{n} B_{i,n}(x) P_i, \qquad B_{i,n}(x) = \binom{n}{i} (1-x)^{n-i} x^i \tag{1}$$

where x ∈ [0, 1] is the normalized axial coordinate. Endpoints P_0, P_n are fixed at zero and the agent adjusts the $n - 1$ interior points.

Content from this work may be used under the terms of the Creative Commons Attribution 3.0 license. Any further distribution of this work must maintain attribution to the author(s) and the title of the work, journal citation and DOI. Published under license by Materials Research Forum LLC.

Materials Research Proceedings 69 (2026) 846-849 https://doi.org/10.21741/9781644904251-149

Volume is maintained via scaling factor λ:

$$\lambda = \sqrt{\frac{V_0}{V'}}, \qquad P_i^{\text{scaled}} = \lambda P_i, \tag{2}$$

where V_0 is the volume of the original hull and V' is the volume of the perturbed shape, both computed via

$$V = \pi \int_0^L R(x)^2 dx \tag{3}$$

Here, L denotes the length of the hull.

RL formulation. The state is the set of current radii; the action is a perturbation vector on the interior control points. The reward is:

$$r = \omega_1 \left(\frac{L}{D}\right)_{avg} - \omega_2 \sigma_{\frac{L}{D}} - \omega_3 \|\Delta P\|_1 \tag{4}$$

The weights in (4) trade off performance and regularity. ω_1 scales the primary objective $(L/D)_{avg}$ (suggested range 0.5–1; we use $\omega_1 = 1$ to keep the natural scale and emphasize aerodynamic merit). ω_2 would penalize the variability $\sigma_{L/D}$ across α to promote robustness (typical 0–0.5), but is set to ω_2=0 here because our solver interface returns only the mean L/D. ω_3 regularizes shape smoothness via $\|\Delta P\|_1$ (implemented as the mean absolute first difference of control-point radii), for which 0.05–0.2 keeps the penalty one order below $(L/D)_{avg}$; we choose ω_3=0.1 as it curbs oscillatory updates without suppressing beneficial adjustments. Hence, (ω_1, ω_2, ω_3) = (1, 0, 0.1), matching the implementation $reward = AvgLD - 0.1 * smoothPenalty$.

Learning algorithm. Training uses MATLAB Reinforcement Learning Toolbox's rlDDPGAgent, the built-in implementation of the Deep Deterministic Policy Gradient (DDPG) algorithm—an off-policy, model-free actor–critic method for continuous-action control with a deterministic policy, experience replay, and target networks. Actor and critic networks are two-layer multilayer perceptrons. At each episode, the agent queries SILCROAD to compute the L/D curve over an angle-of-attack grid spanning 0°–30°; the resulting mean (and, when used, dispersion) of L/D across this range feeds the reward in (4).

Result and Discussion

Trained over 10,000 episodes, the agent consistently outperforms the baseline.

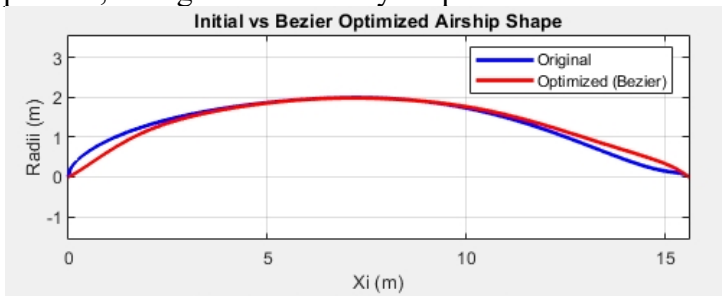


Figure 1: Original and optimized Bezier-based hull shapes.

Figure 1 shows original vs optimized shapes. The optimized hull has a smoother profile with gradual
tapering.

The shape preserves volume:

$$V_0 = V_{final} = 107.5273\ m^3, \quad \lambda = 1.16$$

Figure 2 shows the L/D improvement. Average values:

$$\left(\frac{L}{D}\right)_{\text{initial}} = 4.7766, \quad \left(\frac{L}{D}\right)_{\text{optimized}} = 5.3044, \qquad \text{Gain} = +11.05\%$$

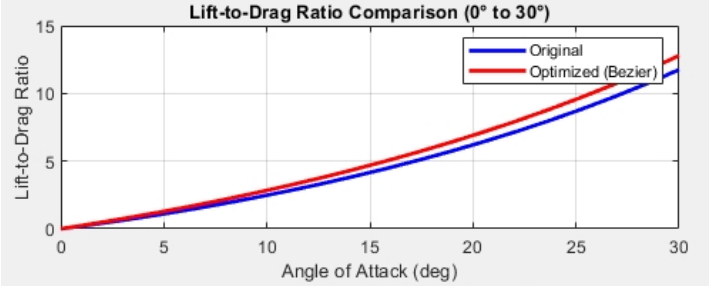


Figure 2: Lift-to-drag ratio comparison (0°–30° angle of Attack).

Perturbation tests showed reduced standard deviation in L/D. Shape smoothness was retained via $\|\Delta P\|_1$.

Conclusion

This study presented a reinforcement-learning-based framework for airship shape optimization. The DDPG agent adjusted Bezier control points while preserving volume. Evaluation in SILCROAD confirmed an 11.05% L/D improvement with retained robustness and smoothness [13]. The framework is modular, supporting future extensions such as tail design and stability control.

References

[1] A. K. Shakya, G. Pillai, and S. Chakrabarty, “Reinforcement learning algorithms: A brief survey,” *Expert Systems with Applications*, vol. 231, 2023, Art. no. 120495. https://doi.org/10.1016/j.eswa.2023.120495.

[2] P. Alfeld, M. Neamtu, and L. L. Schumaker, “Circular Bernstein–Bezier polynomials,” in *Mathematical Methods for Curves and Surfaces*, 1995, pp. 11–20.

[3] T. P. Lillicrap et al., “Continuous control with deep reinforcement learning,” arXivpreprint arXiv:1509.02971, 2015

[4] R. T. Jones, Classical Aerodynamic Theory. National Aeronautics and Space Administration, 1979.

[5] S. P. Jones and J. D. DeLaurier, “Aerodynamic estimation techniques for aerostats and airships,” Journal of Aircraft, vol. 20, no. 2, pp. 120–126, 1982.

[6] C. E. D. Riboldi, M. Belan, S. Cacciola, R. Terenzi, S. Trovato, D. Usuelli, and G.Familiari, “Preliminary sizing of a low-altitude airship including ion-plasma thrusters,”in Proc. 34th Congress of the International Council of the Aeronautical Sciences (ICAS),Florence, Italy, Sept. 9–13, 2024.

[7] C. E. D. Riboldi and A. Rolando, “Layout analysis and optimization of airships with thrust-based stability augmentation,” Aerospace, vol. 9, p. 393, 2022.

[8] C. E. D. Riboldi and A. Rolando, “Thrust-based stabilization and guidance for airships without thrust-vectoring,” Aerospace, vol. 10, 2023.

[9] C. E. D. Riboldi, A. Rolando, and G. Regazzoni, “On the feasibility of a launcher-deployable high-altitude airship: Effects of design constraints in an optimal sizing framework,” Aerospace, vol. 9, pp. 1–37, 2022.

[10] A. Kornienko, System Identification Approach for Determining Flight Dynamical Characteristics of an Airship from Flight Data. Ph.D. dissertation, University of Stuttgart, 2006

[11] T. Lutz and S. Wagner, “Drag reduction and shape optimization of airship bodies,”Journal of Aircraft, vol. 35, no. 3, pp. 345–351, 1998.

[12] C. E. D. Riboldi and L. Fanchini, “Assessing the Technical–Economic Feasibility of Low-Altitude Unmanned Airships: Methodology and Comparative Case Studies,” Aerospace,vol. 12, no. 3, p. 244, 2025.

[13] C. E. D. Riboldi and M. Tomasoni, “Formation Flight of Fixed-Wing UAVs: Dynamic Modeling, Guidance Design, and Testing in Realistic Scenarios,” Aerospace, vol. 12, no. 3, pp. 1–49, 2025.

Materials Research Proceedings 69 (2026) 850-855 https://doi.org/10.21741/9781644904251-150

CFD-Based Estimation of Added-Mass and Aerodynamic Derivatives in Heave Motion for a Hybrid Closed-Wing HAPS

Eleonora RICCIO[1,2 a *], Alessandro CERESA[1,b], Vincenzo Rosario BARANIELLO[1,c], Giuseppe PERSECHINO[1,d], Francesco TUFANO[1,e] and Domenico COIRO[2,f]

[1]Italian Aerospace Research Center – CIRA, Via Maiorise snc, Capua, 81043, Italy

[2]Department of Industrial Engineering - Aerospace Section, University of Naples Federico II, Via Claudio, Naples, 80125, Italy

[a]e.riccio@cira.it, [b]a.ceresa@cira.it, [c]v.baraniello@cira.it, [d]g.persechino@cira.it, [e]f.tufano@cira.it, [f]coirod@unina.it

Keywords: Hybrid HAPS, Added Mass, Dynamic Derivatives

Abstract. A CFD-based approach is proposed to estimate aerodynamic stability derivatives and added-mass coefficients of a hybrid High-Altitude Pseudo-Satellite (HAPS) with a closed-wing configuration. The combination of buoyant and aerodynamic lift makes the evaluation of added-mass effects crucial for accurate dynamic modelling. Unsteady Reynolds-Averaged Navier–Stokes (RANS) simulations in OpenFoam coupled with Fourier analysis were performed under prescribed harmonic oscillations; this paper focuses on the heave motion, showing the coupling between vertical acceleration and unsteady lift. The results confirm that the aerodynamic response is harmonic, matching the frequency of the imposed excitation, and highlight significant added-mass effects under stratospheric conditions, providing useful input for high-fidelity flight dynamics and control design of future hybrid HAPS platforms.

Introduction

HAPS and hybrid Heavier-Than-Air (HTA) platforms combine buoyant and aerodynamic lift to achieve long endurance, low fuel consumption, and operational flexibility for applications such as surveillance, environmental monitoring, and communications [1-4].

Their hybrid nature introduces specific challenges in flight dynamics due to the influence of added-mass effects, which occur when a moving body accelerates the surrounding fluid, effectively increasing its apparent inertia. These effects are particularly relevant for low-density vehicles such as airships and hybrid HAPS, and their accurate modelling is essential for reliable stability and control predictions [5].

Previous studies addressed this issue using high-fidelity numerical methods: unsteady RANS with Fourier analysis for airships [6], parametric sensitivity studies on geometry [7], and panel methods for full added-mass matrices [8].

Building upon these approaches, the present work applies an unsteady CFD method coupled with Fourier analysis to estimate aerodynamic stability derivatives and added-mass coefficients for a novel closed-wing hybrid HAPS configuration [4], shown in Fig. 1

Content from this work may be used under the terms of the Creative Commons Attribution 3.0 license. Any further distribution of this work must maintain attribution to the author(s) and the title of the work, journal citation and DOI. Published under license by Materials Research Forum LLC.

Materials Research Proceedings 69 (2026) 850-855 https://doi.org/10.21741/9781644904251-150

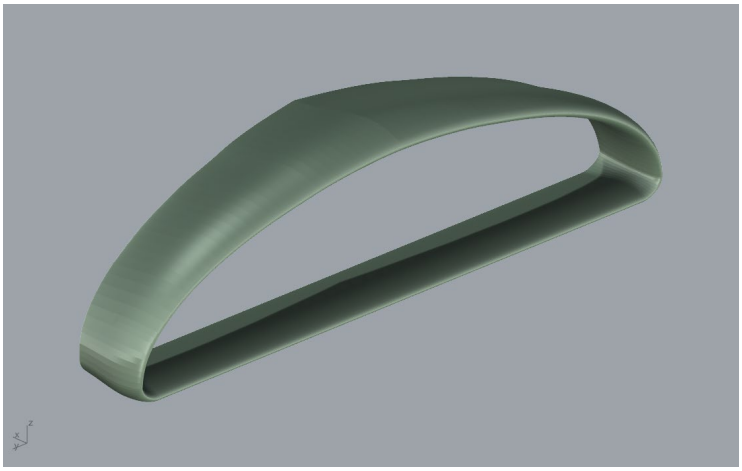


Fig. 1 Three-dimensional CAD model of the closed-wing HAPS configuration [4]

Methodology

Numerical simulations were carried out using the open-source CFD solver *OpenFoam*, solving the unsteady incompressible RANS equations with the $k-\omega$ SST turbulence model.

The computational setup, boundary conditions, and mesh parameters adopted in this study are consistent with those described in [4], to which the reader is referred for additional numerical details and grid-sensitivity assessment.

The computational domain was divided into three regions: an inner zone moving rigidly with the vehicle, an intermediate deforming zone managed through a spring-analogy mesh motion technique, and an outer fixed region extending far from the body and adjacent to the domain boundaries. This multi-zone strategy ensured grid quality and numerical stability during the imposed harmonic oscillations.

The configuration was subjected to prescribed sinusoidal motions representative of the relevant dynamic flight conditions. These motions are defined with respect to the stability-axis reference frame centered at the centre of gravity (CoG).

At the representative altitude of 20 km (air density ρ = 0.0889 kg/m³), these unsteady effects become more significant as aerodynamic damping decreases.

The main geometric and flight parameters of the hybrid platform are summarized in Table 1.

Table 1 Geometric and Flight Parameters of the Hybrid HAPS Platform

Parameter	Value
Wingspan	36 [m]
Maximum chord	7.8 [m]
Wing area	435 [m²]
Internal volume	288 [m³]
Cruise altitude	18–20 [km]
Cruise speed	16 [m/s]
Vehicle mass	127 [kg]

Longitudinal Dynamic Stability Derivatives

For the hybrid stratospheric platform featuring a closed-wing configuration, the longitudinal dynamic behaviour can be described by a reduced set of translational and rotational variables: the forward velocity u, the vertical velocity w, and the pitch rate q. The governing equations are derived under the assumptions of small perturbations and quasi-steady flow conditions.

The longitudinal dynamics of a hybrid vehicle, combining lighter-than-air (LTA) and heavier-than-air (HTA) characteristics, can be expressed as reported in Eqs. (1-3) [7,8], where D_a, L_a, and

Materials Research Proceedings 69 (2026) 850-855 https://doi.org/10.21741/9781644904251-150

M_a denote the aerodynamic drag, lift, and pitching moment, respectively. The terms D_{ext}, L_{ext}, and M_{ext} represent the external contributions due to buoyancy, gravity, or tether forces.

The parameters d_x and d_z represent the longitudinal and vertical distances between the vehicle's center of gravity (CG) and center of buoyancy (CB). These offsets introduce inertial coupling between translational and rotational accelerations, producing the additional moment terms md_x and md_z in the equations of motion.

$$(m - D_{\dot{u}})\,\dot{u} + (m\,dz - D_{\dot{q}})\,\dot{q} = D_a + D_{ext} \tag{1}$$

$$(m - L_{\dot{w}})\,\dot{w} - (m\,dx + L_{\dot{q}})\,\dot{q} = L_a + L_{ext} \tag{2}$$

$$(Iy - M_{\dot{q}})\,\dot{q} + (m\,dz - M_{\dot{u}})\,\dot{u} - (m\,dx + M_{\dot{w}})\,\dot{w} = M_a + M_{ext} \tag{3}$$

In these expressions, the subscripts u, w, and $q$refer to stability derivatives with respect to velocity perturbations, whereas the subscripts $\dot{u}$, $\dot{w}$, and $\dot{q}$ denote the corresponding acceleration-dependent terms, commonly referred to as added-mass derivatives.

The aerodynamic contribution to the longitudinal dynamics, for example the lift component L_a, can therefore be expressed as a combination of steady, velocity-dependent, and acceleration-dependent terms, as shown in Eq. (4).

$$L_a = L_e + L_u\,u + L_w\,w + (L_q - m_x\,U_e)\,q \tag{4}$$

Here, U_e is the steady axial velocity, L_e represents the equilibrium lift, L_u and L_w are the lift derivatives with respect to surge and heave velocities, respectively, and L_q is the lift derivative associated with the pitch rate. The acceleration-dependent (added-mass) derivatives $L_{\dot{u}}$, $L_{\dot{w}}$, and $L_{\dot{q}}$ appear in Eqs. (1-3) and are identified from the unsteady CFD simulations through Fourier analysis.

Pure Heave Motion

The heave motion corresponds to a vertical oscillation along the Z-axis, orthogonal to the freestream velocity vector (Fig. 2). This harmonic displacement induces variations in the effective angle of attack, generating unsteady aerodynamic forces and moments. Fig. 2 illustrates the configuration at the maximum upward ($z = +z_0$), equilibrium ($z = 0$), and maximum downward ($z = -z_0$) positions.

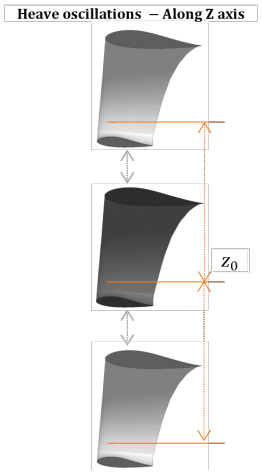


Fig 2 Schematic representation of the heave oscillation along the $\mathbf{Z}$*-axis. The amplitude* $\mathbf{z_0}$ *denotes the maximum vertical displacement from the equilibrium position.*

Materials Research Proceedings 69 (2026) 850-855 https://doi.org/10.21741/9781644904251-150

Assuming linear behaviour near the trimmed flight condition, the unsteady aerodynamic response to the imposed heave motion can be expressed as reported in Eq (5).

$$G(t) = G0 + G_w w + G_{\dot{w}} \dot{w} \tag{5}$$

where G_w and $G_{\dot{w}}$ are the aerodynamic stability and added-mass derivatives, respectively. Here, G denotes a generic aerodynamic quantity, which can refer either to a force (e.g., lift) or to a moment (e.g., pitching moment), evaluated separately.

A prescribed sinusoidal displacement is imposed in the CFD simulations, leading to the following kinematic relations: $z(t) = z_0 \sin(\omega t)$; $w(t) = \omega z_0 \cos(\omega t)$; $\dot{w}(t) = -\omega^2 z_0 \sin(\omega t)$.

The unsteady load history is approximated by a first-harmonic Fourier series, expressed in Eq. (6).

$$G(t) = \frac{1}{2} a_0 + a_c cos(\omega t) + a_s sin(\omega t) \tag{6}$$

By combining Eqs. (5) and (6), the aerodynamic derivatives can be obtained as: $G_w = \frac{a_c}{w_0}$; $G_{\dot{w}} = -\frac{a_s}{w_0 \omega}$. where $w_0 = \omega z_0$ is the velocity amplitude. These coefficients quantify the in-phase (velocity-dependent) and out-of-phase (acceleration-dependent) components of the unsteady aerodynamic response described by Eq. (5). The coefficients were obtained by performing a Fourier analysis of the time history of the aerodynamic force, retaining only the first harmonic of the force signal.

Results and Discussion

The unsteady aerodynamic response in heave was evaluated by prescribing a sinusoidal vertical displacement, producing a periodic variation of the angle of attack expressed as: $\alpha(t) = \alpha_m + \alpha_0 cos(\omega t)$; $\dot{\alpha}(t) = -\alpha_0 \omega sin(\omega t)$. In these equations, $\alpha_m = 4.5°$ and $\alpha_0 = 2.5°$ are the mean and oscillation amplitudes, respectively, and $\dot{\alpha}_0 = \alpha_0\, \omega$ is the peak angular velocity. A reference case was defined for $V = 16 \frac{m}{s}$ and $c = 7.8\ m$. The excitation frequency ω was chosen to keep the non-dimensional angular velocity close to 0.12. This quantity is defined in Eq. (7).

$$\widehat{\dot{\alpha}_0} = \frac{\dot{\alpha}_0}{\frac{2V}{c}} = \frac{(a_0\, \omega\, c)}{2V} \tag{7}$$

where $k = \frac{\omega c}{2V}$ is the reduced frequency ($k = \pi St$). With $a_0 = 2.5° = 0.0436\ rad$, this corresponds to $\omega = 11.40\ \frac{rad}{s}$ ($T = 0.551\ s$).

Fig. 3a shows that the unsteady CFD lift closely matches the first-harmonic Fourier reconstruction, confirming that the aerodynamic response remains linear within the investigated range. In Fig. 3b, the unsteady results describe an elliptical loop in the F_z–α plane, revealing a phase lag between lift and angle of attack that characterizes the non-stationary aerodynamic behavior. The loop remains narrow and nearly symmetric about the steady curve, indicating that the mean lift follows the steady trend and that the oscillation amplitude is small enough for the flow to remain within the linear unsteady regime.

Materials Research Proceedings 69 (2026) 850-855 https://doi.org/10.21741/9781644904251-150

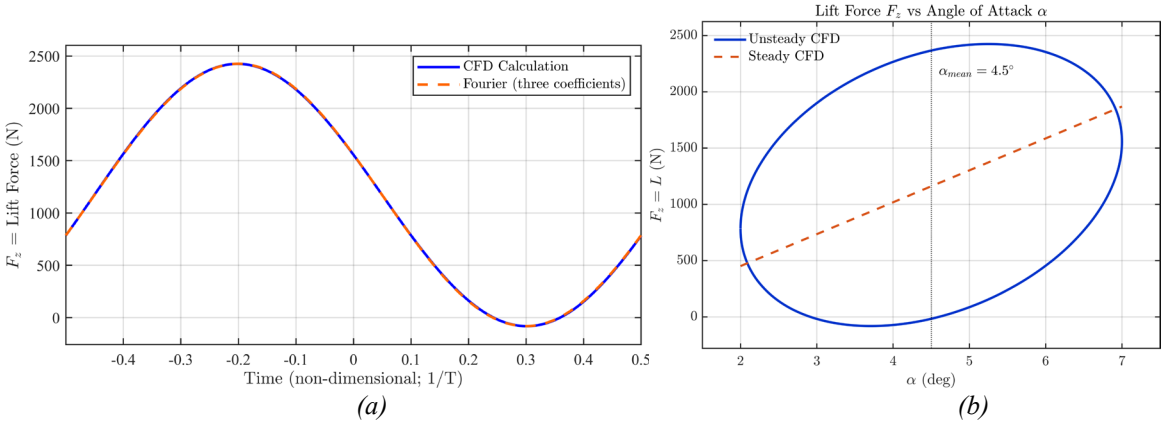


Fig. 3 (a) Time history of lift force $\boldsymbol{F_z(t)}$ and Fourier reconstruction; (b) Steady and unsteady CFD lift as a function of the instantaneous angle of attack $\boldsymbol{\alpha}$.

From the CFD-based heave analysis, the aerodynamic derivatives $L_w = -553.4\ Ns/m$ and $L_{\dot{w}} = -121\ kg$ were obtained, the latter arising from the fluid-inertial contribution. These coefficients were extracted from heave-type excitations, but they do not correspond to a pure heave condition.

Strictly speaking, the added-mass terms ($L_{\dot{w}}$, $M_{\dot{w}}$) are defined for zero forward velocity and non-lifting bodies, where they represent the inertia of the surrounding fluid at rest. For lifting configurations and finite forward velocity, the same physical mechanism gives rise to unsteady aerodynamic derivatives associated with $\dot{\alpha}$, which contribute to lift and pitch damping.

Accordingly, L_w and M_w correspond to the lift- and pitching-moment slopes (L_α, M_α), while $L_{\dot{w}}$ and $M_{\dot{w}}$ represent the unsteady aerodynamic derivatives ($L_{\dot{\alpha}}$, $M_{\dot{\alpha}}$). The resulting aerodynamic and added-mass derivatives obtained from the CFD analysis are summarized in Table 2.

Table 2 Aerodynamic and added-mass derivatives from heave-based CFD analysis.

Derivative	**Effect**	**Value**
L_w	Lift slope (equiv. L_α)	$553.4\ [\frac{Ns}{m}]$
$L_{\dot{w}}$	Unsteady Lift (equiv. $L_{\dot{\alpha}}$)	$121\ [kg]$
M_w	Pitching moment slope (equiv. M_α)	$113.6\ [N\ s]$
$M_{\dot{w}}$	Pitch-rate damping (equiv. $M_{\dot{\alpha}}$)	$-206.7\ [kg\ m]$

The relation $\alpha \approx w/V$ allows converting these quantities into the corresponding angle-of-attack derivatives, leading to the expressions: $L_\alpha = VL_w$; $L_{\dot{\alpha}} = VL_{\dot{w}}$; $M_\alpha = VM_w$; $M_{\dot{\alpha}} = VM_{\dot{w}}$. where V is the flight velocity. In the quasi-steady limit, the added-mass effects vanish, and the coefficients reduce to the static stability and pitch-damping derivatives.

Conclusion

A CFD-based methodology combined with Fourier analysis was applied to estimate aerodynamic stability derivatives and added-mass coefficients for a hybrid closed-wing High-Altitude Pseudo-Satellite (HAPS).

The results obtained from the heave motion analysis confirm that the aerodynamic response remains harmonic and follows the frequency of the imposed excitation. The analysis also highlights the relevance of added-mass effects under stratospheric operating conditions.

The extracted coefficients provide essential input for high-fidelity flight dynamics models and support the development of reliable stability and control strategies for future hybrid high-altitude platforms.

References

[1] J. Dolce, A. Colozza, High-altitude, long-endurance airships for coastal surveillance, NASA Tech. Rep., 2005.

[2] F.A. d'Oliveira et al., High-altitude platforms-present situation and technology trends, Journal of Aerospace Technology and Management 8 (3) (2016) 249-262. https://doi.org/10.5028/jatm.v8i3.699

[3] O. Abbasi et al., HAPS for 6G networks: Potential use cases, open challenges, and possible solutions, IEEE Wireless Communications 31 (3) (2024) 324-331. https://doi.org/10.1109/MWC.012.2200365

[4] E. Riccio et al., Preliminary conceptual design of a closed-wing high-altitude pseudo-satellite, Journal of Aircraft, in press (2025). https://doi.org/10.2514/6.2025-0461

[5] F. Fruncillo et al., Effects of comprehensive added masses modeling on airship equations of motion and dynamic stability, AIAA SciTech Forum, 2024. https://doi.org/10.2514/6.2024-2650

[6] X. Wang, CFD predictions of stability derivatives for airship, Journal of Aircraft 49 (3) (2012) 933-940. https://doi.org/10.2514/1.C031634

[7] A. Sasidharan et al., Stability derivatives of lighter-than-air vehicles: A CFD-based comparative study, Drones 6 (7) (2022). https://doi.org/10.3390/drones6070168

[8] M. Tuveri et al., Added masses computation for unconventional airships and aerostats, International Journal of Aeronautical and Space Sciences 15 (3) (2014). https://doi.org/10.5139/IJASS.2014.15.3.241

Materials Research Proceedings 69 (2026) 856-860 https://doi.org/10.21741/9781644904251-151

A Novel Approach to Quantify Counter-Drone System Effectiveness Against UAS Swarms

Dani HOTTERS[1,a*], Nikolaos KALLIATAKIS[1,b], Felix KUHNERT[1,c], Prajwal Shiva PRAKASHA[1,d], Ries VAN HEUR[2,e] and Buse KAYA[2,f]

[1]Hein-Saß-Weg 22, 21129 Hamburg, German Aerospace Center (DLR), GERMANY

[2]Kluyverweg 1, 2629 HS Delft, Delft University of Technology (TUDelft), THE NETHERLANDS

[a]dani.hotters@dlr.de, [b]nikolaos.kalliatakis@dlr.de, [c]felix.kuhnert@dlr.de, [d]prajwal.prakasha@dlr.de, [e]r.f.j.l.vanheur@student.tudelft.nl, [f]b.kaya-1@student.tudelft.nl

Keywords: Unmanned Aerial Systems, Drone Swarms, Agent-Based Simulation, Multi-Agent Systems, Requirements, System of Systems, Performance Analysis, Counter-UAS Systems, Defense

Abstract. Swarm attacks composed of *Unmanned Aerial System* (UAS) have rapidly evolved into a sophisticated and constantly evolving threat to modern air defense strategies. By exploiting overwhelming numbers, high agility, and a coordinated behavior, drone swarms are able to penetrate and overwhelm traditional, multi-layered, defense architectures. Recent conflicts have highlighted critical vulnerabilities and challenges in maintaining robust defense and deterrence postures against drone swarms. As counter-UAS technologies, systems, and *Concepts of Operations* (CONOPS) continue to evolve, a method to evaluate their effectiveness and to quantify their relative performance becomes crucial. This paper details the adaptation of an agent-based modeling and simulation environment, developed by the German Aerospace Centre (DLR), to assess the operational performance of counter-UAS architectures from a holistic *System of Systems* (SoS) perspective. To address the computational challenges of large-scale swarm engagements, the approach integrates surrogate models informed by *high-fidelity* (hi-fi) simulations, into *low-fidelity* (lo-fi) models to approximate the behavior of counter-UAS systems, thereby enabling scalability and simulation on the theater scale. Combined with well-defined *Measures of Effectiveness* (MoEs), this methodology provides a novel approach for comparing counter-UAS solutions. It provides stakeholders and decision-makers with the information needed to evaluate system performance and make informed decisions in shaping future air defense strategies and architectures.

Introduction

UAS swarms pose a rapidly escalating threat to military forces worldwide, both in increasing technological sophistication and operational scale [1]. For example, in 2019 the Houthi militant group used a swarm of 18 drones and 7 missiles in a coordinated strike on Saudi oil facilities. The incident demonstrated the challenges that traditional air defense systems can face when encountering swarm tactics [2,3]. More recently, during the Russian invasion of Ukraine, Russian forces repeatedly launched attacks involving hundreds of drones interlaced with cruise and ballistic missiles to overwhelm Ukrainian air defenses.

Traditional countermeasures - electronic warfare, *Anti-Aircraft Artillery* (AAA), and missiles - are effective against individual drones but are often costly or logistically unsustainable when facing large swarms [4]. As a result, research and development is increasingly focused on scalable, cost-effective counter-swarm strategies and systems.

Content from this work may be used under the terms of the Creative Commons Attribution 3.0 license. Any further distribution of this work must maintain attribution to the author(s) and the title of the work, journal citation and DOI. Published under license by Materials Research Forum LLC.

Materials Research Proceedings 69 (2026) 856-860 https://doi.org/10.21741/9781644904251-151

To support informed decision-making on fleet composition and system procurement for counter-UAS missions, it is essential to evaluate how different air-defense architectures perform against swarms with varying compositions and tactics. This paper proposes a novel framework that combines hi- and lo-fi simulation models to compare system performance against large-scale UAS swarm threats. The method provides a scalable and quantitative means to assess performance and interactions within the complex drone-warfare SoS.

Methodology

The proposed approach integrates hi- and lo-fi *Agent-Based Modeling and Simulati*on (ABMS) environments into a unified framework to evaluate the effectiveness of counter-UAS architectures. It is designed to balance fidelity and scalability, enabling engagements involving thousands of agents. This framework is demonstrated in Figure 1.

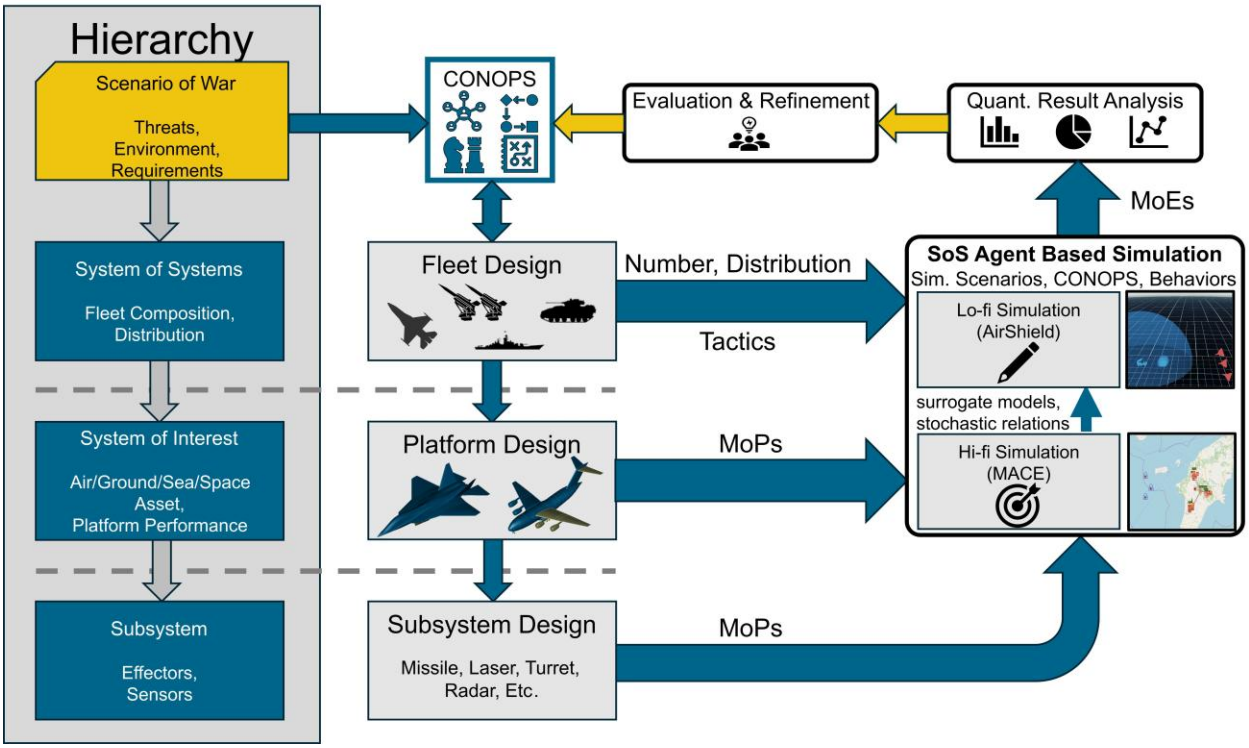


Figure 1: System-of-Systems framework to quantify counter-UAS system effectiveness

The implementation uses the off-the-shelf hi-fi ABMS environment *Modern Air Combat Environment* (MACE), developed by BSI[1], together with the *AirShield Simulation Environment*, as the lo-fi ABMS environment. The latter was developed by DLR to enable the evaluation of counter-UAS systems within a broader SoS context and to translate those evaluations into optimized system requirements and is based on the work shown in [5].

The two complementary simulation layers are:

1. **Hi-fi layer:** Detailed digital models represent threat and defensive systems, including the complex modeling of communication networks, electronic warfare, and C2. Engagement dynamics, sensor performance, and effector lethality are modeled deterministically by simulating the physics that govern them. Thus, these simulations effectively represent the complex interactions between individual drones and

[1] https://www.bssim.com/mace/

Materials Research Proceedings 69 (2026) 856-860 https://doi.org/10.21741/9781644904251-151

countermeasures. Due to the high complexity and computational demand, this layer is limited to engagement-level scenarios.

2. **Lo-fi layer:** This layer scales the analysis from engagement to theater level by using simplified digital surrogate models, allowing thousands of agents to interact. These surrogate models are generated to bridge the fidelity gap between the hi- and lo-fi layers. Engagement dynamics are modeled stochastically, informed by relationships derived from the hi-fi layer (e.g. rounds-to-kill as a function of target altitude, speed, and aspect) through one-on-one engagements.

To demonstrate the framework, a notional baseline scenario is created in the AirShield environment, as illustrated in Figure 2. In this scenario, 200 Shahed-like adversary drones conduct an attack at an altitude of 200 m—a noteworthy detail since both simulation layers operate in three dimensions and therefore account for line-of-sight effects, including Earth's curvature. The attack targets a layered air defense architecture consisting of a long-range air defense element protected by five short-range gun-based AAA units. This study evaluates variations in *Measures of Performance* (MoPs) of the AAA and translates the effects of these MoPs to SoS-wide MoEs. The influence of the altered MoPs on the kill dynamics of the AAA typically are based on running one-on-one engagement studies within the hi-fi environment. In the following analysis, this is not done, and instead the AAA's kill dynamics are modeled as a normal distribution around a mean *rounds-to-kill* (RTK) and its standard deviation. The values for the mean and standard deviation originate from preliminary analyses in the Hi-fi environment. However, they are also evaluated as sensitivities in this paper to illustrate the modularity of the design variables and the underlying models.

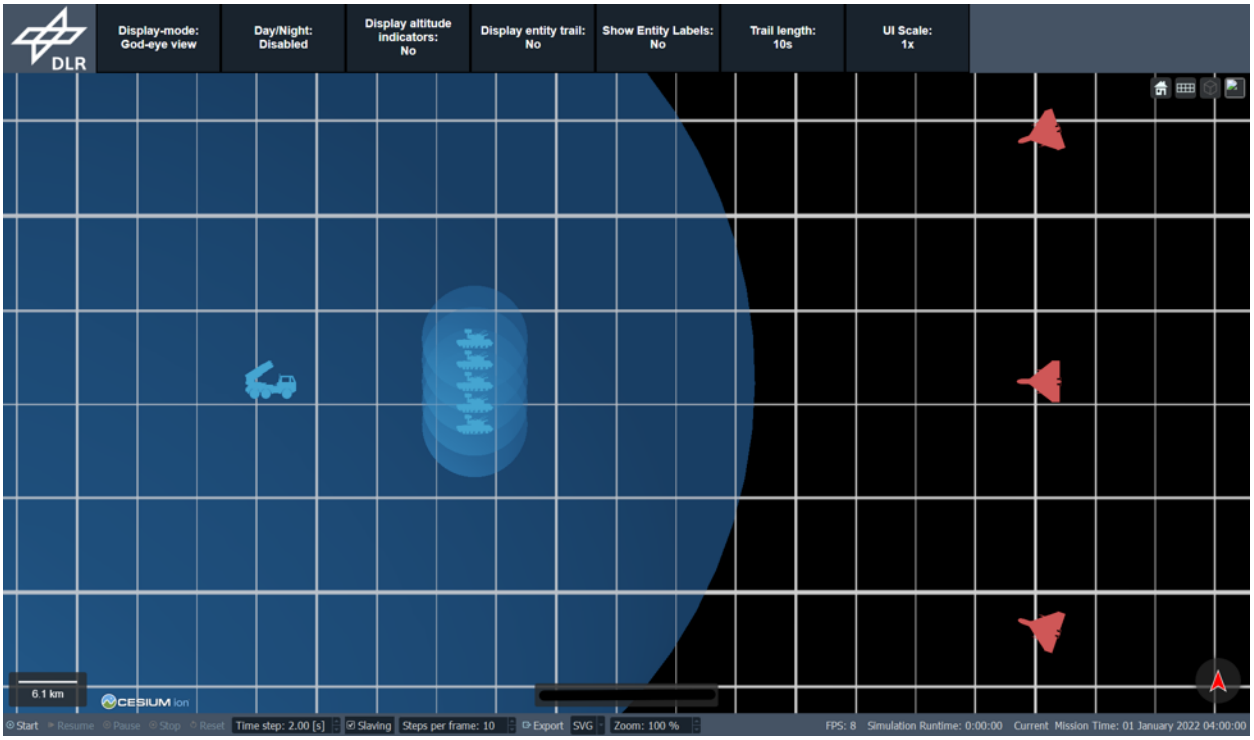


Figure 2: Baseline scenario in the AirShield user interface. Each cell width represents 6.1km. Blue zones show the engagement areas of counter-UAS systems, limited by Earth's curvature (not detection zones).

Materials Research Proceedings 69 (2026) 856-860 https://doi.org/10.21741/9781644904251-151

To evaluate the SoS effectiveness, a set of normalized MoEs is defined. Each MoE component - survivability (number of undamaged systems, $\hat{S}$), lethality (number of killed drones, $\hat{L}$), expended munition cost ($\hat{C}$), and infiltration rate (shortest distance to the drone's target, $\hat{I}$) - is normalized and averaged over multiple simulation runs for each data point. This weighted sum is shown in Eq. 1. The weights of the MoE variables originate from subject matter experts' opinions, a method detailed in [6].

$$MoE = 0.42\hat{S} + 0.36\hat{L} + 0.16\left(1 - \hat{C}\right) + 0.06(1 - \hat{I}) \quad (1)$$

Results

For the demonstration, variations in the AAA's turret slew rate and effective engagement range are investigated to understand their influence on overall SoS effectiveness. As previously noted, the hi-fi study is not conducted for this simplified scenario and therefore these parameters are not linked to the lo-fi kill dynamics. Instead, the mean RTK value and its standard deviation are incorporated into the analysis. Furthermore, to illustrate potential future offensives, the adversary swarm size is also included. The design space shown in Figure 3 is created and represents the MoE values for each data point using a color. The standard deviation of the mean RTK was found to have a negligible impact, likely due to the high number of rounds being fired by the AAA units, and is therefore excluded from this analysis. Instead, the plot shows values for varying the mean RTK at three standard deviations of spread.

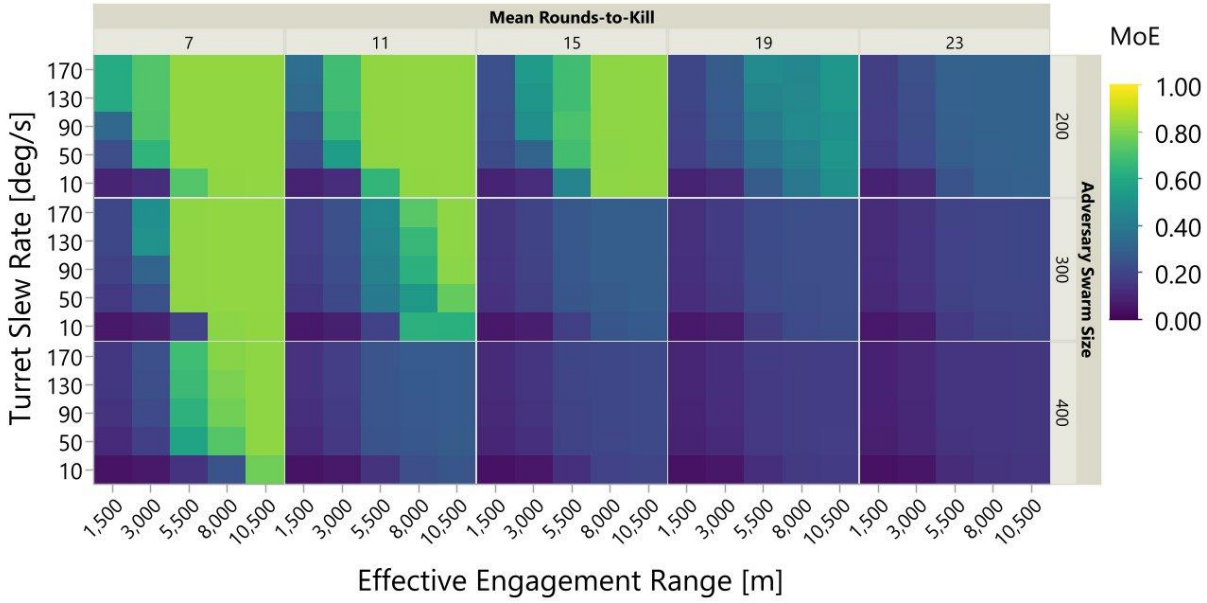


Figure 3: Design space exploration of the AAA system

Upon inspection of the results, three interesting patterns emerge:

Firstly, MoEs are highest when the AAA operates with large effective engagement ranges. This becomes apparent when the engagement range is increased beyond 5.5 km. However, it still requires that the mean RTK is low for the SoS to become effective. Thus, a combination of long engagement ranges with sufficient lethality (through low RTK) produces more desirable outcomes.

Secondly, for larger swarms, the system must possess a lower mean RTK for the SoS to remain effective. This dependency arises from a greater lethality, which logically increases the SoS effectiveness. Alongside this, reducing the mean RTK shortens required engagement lengths per

target, and thereby reduces ammunition expenditure. This enables longer sustainment and lethality, which is particularly interesting considering that one AAA caries only 640 rounds.

Lastly, the increase of turret slew rate has a positive but small influence. Increasing the slew rate increases the MoE, especially at the extreme low end (10 deg/s). With reduced slew rates, the system can only maintain effectiveness if the effective engagement range is large enough to compensate. This seems logical, as an increased mean RTK increases the *engagement time per UAS*, which reduces the distance between the UAS and the AAA, increasing relative angular velocities of the UAS. However, this secondary effect of the slew rate should be investigated further as in the baseline scenario the swarm spread is relatively limited.

Conclusion

This paper presented a scalable agent-based simulation framework for assessing counter-UAS architectures within a system-of-systems context. By coupling high- and low-fidelity simulation environments, the framework enables quantitative evaluation of counter-swarm performance while maintaining computational feasibility for large-scale scenarios. The demonstrated case study of a layered air defense architecture illustrated how variations in subsystem Measures of Performance propagate to system-wide Measures of Effectiveness.

The results of the simplified demonstration indicate that effective engagement range and lethality, expressed as mean rounds-to-kill, are the primary drivers of the system-of-systems effectiveness, while the turret slew rate plays a secondary role. The influence of mean rounds-to-kill becomes particularly dominant as the adversary swarm size grows, increasing combat sustainment and lethality. Based on the mock scenario, the framework was able to identify the system's most influential design traits that provided the most favorable operational effectiveness within the system-of-systems. Importantly, the model demonstrates that assessing different configurations of the same resource can reveal solutions that are more scalable than focusing solely on technological enhancements.

Although not explored in this study, operational strategy, such as defense system positioning/ placement and fleet combinations could be evaluated, garnering further insights to the system-of-systems, exemplifying the framework's capabilities in supporting informed decision making for system designers. Lastly, AI methods, drone design, and their dynamics could be applied to the framework to expand its application potential and utility.

References

[1] T. Ditter, E. Harvey, PRC Concepts for UAV Swarms in Future Warfare, CNA Corporation, 2025

[2] U. Azmi, Y. Ruyat, L.A. Affandi, Defence and Security System Against The Threat of Drone Weapons In The Oil and Gas Industry As a Vital National Object, The Republic of Indonesia defense University, 2024

[3] S. Crino, C. Dreby, Drone Attacks Against Critical Infrastructure: A Real and Present Threat, Atlantic Council, 2020

[4] O. Molloy, Drones in Modern Warfare: Lessons Learnt from the War in Ukraine, Australian Army Occasional Paper No. 29, 2024 https://doi.org/10.61451/267513

[5] S. Kilkis, N. Naeem, P.S. Prakasha, A Python Modelling and Simulation Toolkit for Rapid Development of System of Systems Inverse Design (SoSID) Case Studies, DLR, AIAA Aviation 2021 Forum https://doi.org/10.2514/6.2021-3000

[6] J. Seethaler, M. Strohal, P. Stütz, Finding Metrics For Combat Aircraft Mission Efficiency: An AHP-Based Approach, DLR, DLRK 2020

Guidance, Navigation & Control



Materials Research Proceedings 69 (2026) 862-867 https://doi.org/10.21741/9781644904251-152

Performance Assessment of a Multi-Step Guidance and Control Architecture for Approach and Capture of a Tumbling Space Target

Agostino MADONNA[1,a *], Giuseppe NAPOLANO[1,b], Alessia NOCERINO[1,c], Roberto OPROMOLLA[1,d], Giancarmine FASANO[1,e] and Michele GRASSI[1,f]

[1]Depertment of Industrial Engineering, University of Naples "Federico II", Piazzale Vincenzo Tecchio, 80, Naples, Italy

[a]agostino.madonna@unina.it, [b]giuseppe.napolano@unina.it, [c]alessia.nocerino@unina.it, [d]roberto.opromolla@unina.it, [e]giancarmine.fasano@unina.it, [f]michele.grassi@unina.it

Keywords: Close-Proximity Operations, Tumbling Target, Semi-Analytical Guidance, H-Infinity Control, Performance Assessment

Abstract. This paper assesses the performance of a Guidance and Control architecture designed to rendezvous with a tumbling space target. Specifically, it demonstrates its robustness against the uncertainties in the knowledge of the chaser parameters (including the actuators' mounting configuration), and the variability in the target initial conditions in terms of attitude and angular velocity. Finally, the impact on performance of failures in the actuation system is also analyzed.

Introduction

The increasing interest to In-Orbit Servicing (IOS) and Active Debris Removal (ADR) missions has highlighted the need to develop and demonstrate advanced technologies enabling autonomous Rendezvous and Proximity Operations (RPOs), particularly in scenarios involving non-cooperative space targets [1-3]. In such scenarios the autonomous Guidance, Navigation, and Control (GNC) system shall guarantee compliance with stringent accuracy and safety requirements, especially during the final approach phase, when the chaser must reduce its relative distance and align its attitude with the docking interface [4, 5].

Within the *Space It Up* (Spoke 1) project [6], two guidance strategies for the close-range rendezvous toward a tumbling target have been investigated: (i) an optimization-based method relying on the Sequential Convex Programming (SCP) algorithm [7]; (ii) a multi-step strategy, that combines analytical and optimization techniques [8]. Following this line of research, this work focuses on the latter methodology, due to its lower computational cost. Then, the trajectory generated by such guidance strategy is tracked using a coupled orbit–attitude H-infinity controller synthetized using a mixed-sensitivity, loop-shaping formulation [7]. A key point to validate the resulting G&C architecture is to demonstrate its capability to provide adequate control accuracy under highly variable conditions in terms of target's initial attitude and angular rate. Thus, an extensive campaign of numerical simulations is conducted in a virtual environment realistically reproducing target/chaser orbital and rotational dynamics, as well as sensors and actuators operations. The remainder of the paper is organized as follows. The section on reference frames and rendezvous phases introduces the problem formulation. Subsequently, the guidance and control algorithms are presented, followed by a description of the simulation environment and mission scenario. The numerical results are then discussed, and final remarks conclude the paper.

Notation and Reference frame

The following reference frames are adopted. The Spacecraft Centred Reference Frame (SCRF) and the Target Reference Frame (TRF) are body-fixed coordinate systems centered in the Centre of Gravity (CoG) of the chaser and target, respectively. The Grasping Reference Frame (GRF) is a coordinate system parallel to the TRF, centered at the target's berthing point. The Hill Reference

Content from this work may be used under the terms of the Creative Commons Attribution 3.0 license. Any further distribution of this work must maintain attribution to the author(s) and the title of the work, journal citation and DOI. Published under license by Materials Research Forum LLC.

Materials Research Proceedings 69 (2026) 862-867 https://doi.org/10.21741/9781644904251-152

Frame (HRF) is an orbiting coordinate system, centered at the target CoG, with the x axis in the radial direction, the z axis (cross-track) along the target orbital angular momentum vector, and the y axis (along-track) completing the right-hand triad.

Rendezvous Maneuver

The considered rendezvous scenario consists of two main phases. In the former (Close-range Rendezvous, CR), a translational maneuver is defined to drive the chaser to the entrance of the approach corridor while satisfying a keep-out zone (KOZ) constraint. At the same time, a slew maneuver synchronizes the chaser angular motion to the target one. Such maneuver is completed by a stabilization phase executed to perform health and safety checks before the final approach. In the latter phase (Final Approach, FA), the servicer moves along the approach corridor, while maintaining a constant relative attitude, up to the capture point. Again, this is followed by a stabilization step to meet a set of capture requirements.

Guidance Function

While details can be found in [8], the proposed guidance strategy is briefly recalled hereinafter.

During the CR Phase, the servicer maneuvers toward the approach axis while remaining outside a spherical KOZ. An original contribution of this work lies in the adaptive computation of the CR phase time duration (t_{CR}), which is derived from the current estimates provided by the navigation function, rather than being treated as a tuning parameter. This approach is conceived to improve the feasibility of the maneuver when considering targets with relatively high tumbling rates. Specifically, t_{CR} is determined so that the approach axis is aligned (at least with a certain margin) with the target-chaser line of sight, according to the following procedure. First, the target's rotational dynamics is propagated over the interval [t_{min}, t_{max}] and the angle φ between the two above-mentioned directions is evaluated. Then, t_{CR} is selected as the instant time corresponding to the minimum value of φ.

The translational reference trajectory is defined as the result of a set of ($N_{CR} - 1$) two-impulse rendezvous maneuvers, where N_{CR} is the number of corresponding impulsive nominal burns. The algorithm analytically ensures compliance with the KOZ constraint, modeled as a sphere of radius, r_{KOZ}, centered on the target. Then, a slew maneuver is defined via an iterative optimization that minimizes propellant consumption while also enforcing target visibility within the field of view (FOV) of a relative navigation sensor (i.e., a LIDAR in this work).

During the FA phase, the chaser moves along the approach corridor (i.e. the volume of a cone whose axis is normal to the target face hosting the berthing port), maintaining a constant relative attitude with respect to the target. The servicer proceeds from initial relative position along a straight line in TRF. The intermediate positions are computed using a modified Hablani algorithm [9] and are subsequently rotated into the HRF.

Control Function

The H-infinity controller provides the commanded force and torque required to nullify the deviation from the reference relative trajectory. The plant dynamics of the H-infinity controller, i.e., the coupled roto-translational dynamics of the satellite, is modeled using a first-order state space representation obtained by linearizing the nonlinear relative dynamics around a nominal operating point. The Clohessy–Wiltshire linear equations are employed to define the state matrix of the translational component, while details on the linearization of the relative attitude and rotational dynamics are provided in [7].

Simulation environment and scenario definition

Performance assessment is carried out within a numerical simulator reproducing the coupled translational and rotational dynamics of the target and chaser accounting for main environmental perturbations. A robotic arm is activated once the chaser is stabilized during the FA phase, in order

Materials Research Proceedings 69 (2026) 862-867 https://doi.org/10.21741/9781644904251-152

to demonstrate robustness against additional disturbances it induces in main body dynamics. The simulator includes a LIDAR-based relative navigation block to reproduce realistic relative state estimates and a dispatching function to account for non-idealities in the execution of control commands from the actuators [7, 8]. A typical Rendezvous mission toward a tumbling target is considered as an operational scenario. The chaser and target characteristics are taken from the e.Deorbit mission [8]. A statistical analysis of 100 Monte Carlo (MC) runs is performed considering uncertainties on the knowledge of chaser parameters, actuators mounting parameters and initial conditions (Table 1). For each run, the target mainly rotates around the direction of the approach axis (*-x TRF axis*) with small oscillations along the other two axis. Specifically, the target angular velocity varies in the range [-0.3 0.3] °/s for the second and third components, while the first component lies within the range [0.5 2] °/s. The initial attitude of the target is also randomized. Finally, an additional set of 100 simulations is carried out to account for thruster-failure scenarios. Specifically, in each run, one thruster is randomly selected and permanently disabled at a random time of the rendezvous maneuver. Consequently, the servicer must complete the run using the remaining thrusters.

Table 1. Uncertainties of MC analysis

Uncertainty	**3σ**	**Uncertainty**	**3σ**
Percentage of Chaser mass	1	Initial Position [cm]	30
Percentage of Chaser inertia	5	Initial Velocity [cm/s]	3
Chaser Centre of Gravity [mm]	3	Initial Attitude [°]	5
Displacement RCS [mm]	3	Misalignment RCS [°]	0.10

Results

The main results of the MC analysis are provided in this Section. Fig. 1 illustrates the reference relative position and velocity computed by the guidance function in the two phases, for a single random simulation. The minimum and maximum duration of the CR phase are set to 400 s and 1000 s, respectively. According to the procedure described previously, the resulting CR phase duration is 472 s. Therefore, the servicer moves from its initial position to the approach axis while staying outside the KOZ radius. In the FA phase, the servicer reaches the berthing point. In the CR phase, the largest nominal burns occur at the beginning and at the end, whereas in the FA phase the first two burns are the largest, while the final one has a lower magnitude (Table 2). Fig. 1 illustrates the reference relative attitude, angular velocity and the resulting nominal torque of the slew maneuver. In CR phase, the chaser maneuvers to reach the desired final relative attitude. Furthermore, this reference rotational trajectory is designed to ensure target visibility. Finally, the computational cost for guidance function execution is approximately 0.162 s. The algorithms are implemented on MATLAB/Simulink R2022b (×64) and tested on Intel(R) Core(TM) i510210U CPU @ 1.60GHz and 16.0 GB of RAM.

Regarding control performance, the control errors are defined as the deviations between the current true state of the chaser and the nominal state provided by the guidance function. The weights of the H-infinity controller are presented in [8]. Fig. 3 shows the control performance for the same random simulation. The peaks in relative position (with a maximum value of 1.20 m in the radial direction) are caused by the nominal burns which are not executed instantaneously by the chaser's actuation system. Nonetheless, the translational and rotational errors generated by the nominal burns are progressively corrected. At the end of the simulation, when the chaser reaches the berthing point, the relative position error is reduced to the centimeter level, and the relative attitude error is less than 0.2 degree for each component. In conclusion, Table 3 summarizes the performance of G&C architecture by reporting the control errors at the berthing point for all simulation. The results confirm the trend observed in Fig. 3. Specifically, position errors are below

Materials Research Proceedings 69 (2026) 862-867 https://doi.org/10.21741/9781644904251-152

50 cm for all components, and attitude errors remain within 2° for every component in 100% of runs. Computational cost for guidance function execution remains below one second (Table 4). Regarding thruster-failure case, only 4% of the simulations result in a position error greater than 1 m in any component, while the remaining simulations are consistent with the case in which all thrusters are operational (Table 5). Table 6 reports the propellant consumption statistics: a slight increase in mean under failure conditions, while the maximum value remains below 7 kg.

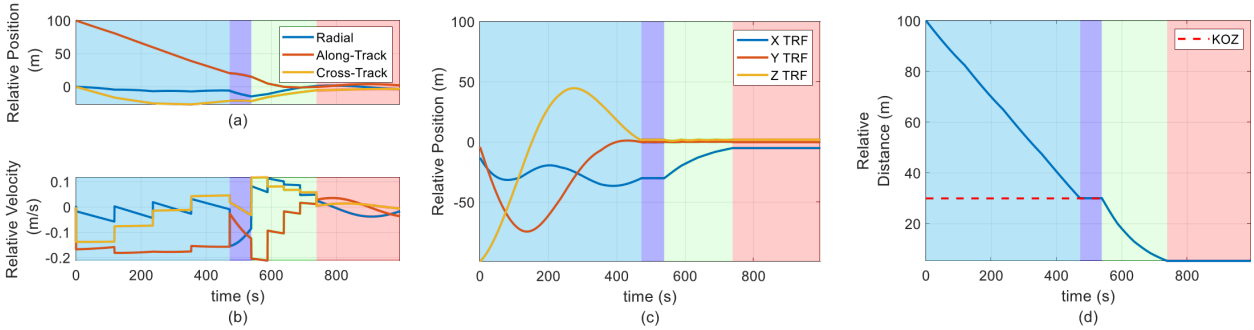


Fig. 1. Guidance results: (a) relative position in HRF; (b) relative velocity in HRF; (c) relative position in GRF; (d) KOZ constraint. Blue background represents CR phase, Green indicates FA phase, while Purple and Red correspond to stabilization phases.

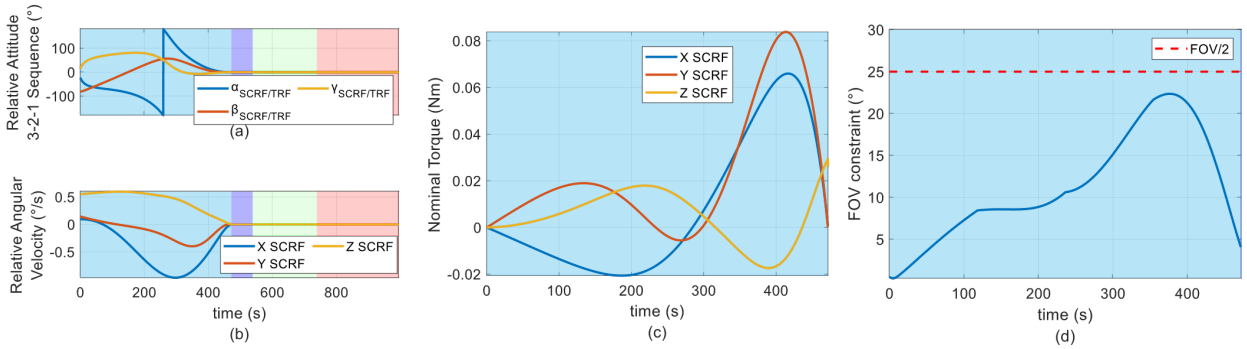


Fig. 2. Guidance results: (a) relative attitude (represented with a 3-2-1 Euler Sequence); (b) relative angular velocity; (c) nominal torque; (d) Target visibility constraint.

Table 2. Nominal impulsive burns computed by the guidance function during CR and Fa phases.

Nominal Impulsive Burns – CR [cm/s]						**Nominal Impulsive Burns – FA [cm/s]**				
	1st	2nd	3rd	4th	5th	1st	2nd	3rd	4th	5th
X HRF	-2.1	6.0	6.3	5.9	-14.7	15.8	5.4	-1.2	-3.9	-2.4
Y HRF	-16.5	-2.3	0.0	2.2	-13.5	-7.5	11.8	8.7	4.3	1.7
Z HRF	-13.7	6.1	5.9	5.4	-2.5	15.0	-3.7	-1.4	-1.0	-5.4

Materials Research Proceedings 69 (2026) 862-867 https://doi.org/10.21741/9781644904251-152

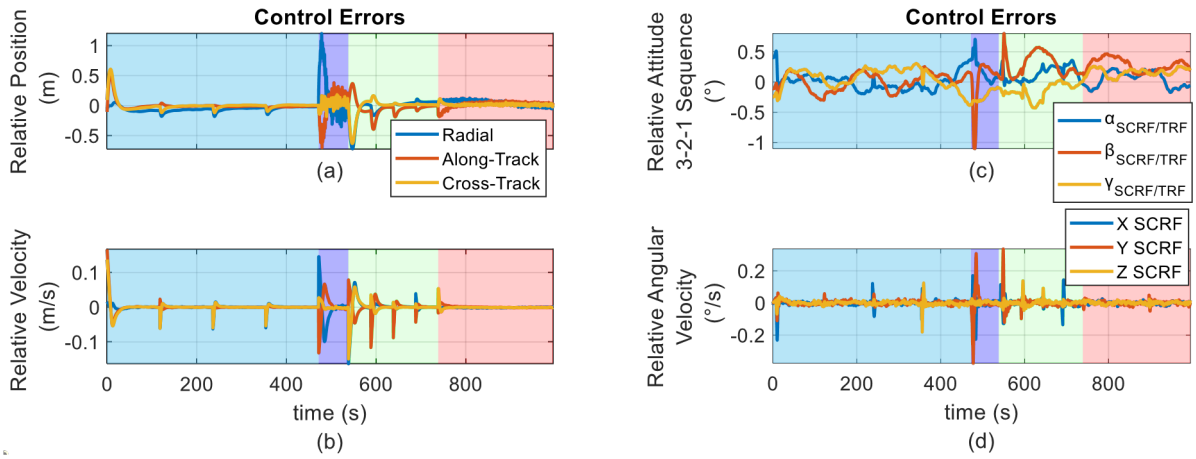


Fig. 3. Control Errors: (a) Relative Position and (b) Velocity; (c) Relative Attitude and (d) Angular Velocity.

Table 3. Performance of statistical analysis: mean, standard deviation (STD) and maximum

		STD	Mean	Max			STD	Mean	Max
Position [cm]	X - HRF	5.3	0.8	25.8	Attitude [°]	$\alpha_{SCRF/TRF}$	0.24	0.12	0.95
	Y - HRF	4.3	-0.3	17.9		$\beta_{SCRF/TRF}$	0.75	0.15	2.45
	Z - HRF	3.8	0.5	14.7		$\gamma_{SCRF/TRF}$	0.33	-0.05	1.09
Velocity [cm/s]	X - HRF	0.2	<0.1	1.3	Angular Velocity [°/s]	X SCRF	0.47	-0.08	1.26
	Y - HRF	0.2	<0.1	0.8		Y SCRF	0.65	-0.01	1.89
	Z - HRF	0.2	<0.1	0.8		Z SCRF	0.60	-0.07	2.07

Table 4. Performance of guidance function: duration of CR phase and computational cost for execution of the guidance function

	STD	Mean	Max
Duration CR phase [s]	220.16	720.36	1000.00
Computational Cost [s]	0.45	0.61	2.30

Table 5. Comparison of propellant consumption in the nominal thruster operation and thruster-failure cases.

Propellant Consumption [kg]	STD	Mean	MAX
Nominal Thruster Operation	1.27	3.56	8.40
One Thruster Failure	1.37	3.84	6.90

Table 6. Performance in thruster-failure cases: mean, STD and maximum of the relative position and attitude control errors at the berthing point.

		STD	Mean	Max			STD	Mean	Max
Position [cm]	X - HRF	59.8	-0.7	393.9	Attitude [°]	$\alpha_{SCRF/TRF}$	0.40	0.18	3.60
	Y - HRF	50.8	5.6	301.1		$\beta_{SCRF/TRF}$	0.68	0.15	1.90
	Z - HRF	54.3	2.0	301.8		$\gamma_{SCRF/TRF}$	0.34	-0.03	0.89

Conclusions

This paper presents a comprehensive analysis of the performance of G&C architecture, demonstrating its robustness with respect to variations in the target's initial attitude and angular rate, as well as actuator failures occurring during the maneuver. The guidance function is based on a semi-analytical approach [7], while a detailed description of the control function can be found in [7,8]. Numerical simulations show high accuracy of the proposed architecture. At the berthing point, the system consistently achieves position errors in the order of few centimeters and attitude errors below one degree. This level of precision can be considered adequate to enable successful rendezvous maneuvers. Similar results are obtained under thruster failure conditions.

Finally, computational cost of the guidance function generally remains below one second. Future work will focus on improving the efficiency of the guidance algorithm to reduce the computational cost and reformulating the guidance function to account for continuous (rather than impulsive) thrust, with the aim of reducing position and velocity control errors.

Acknowledgements

This work was carried out within the Space It Up! project funded by the Italian Space Agency (ASI) and the Italian Ministry of University and Research (MUR) under contract No. 2024-5E.0, CUP No. I53D24000060005.

References

[1] C. Petersen, R.J. Caverly, S. Phillips, A. Weiss, Safe and Constrained Rendezvous, Proximity Operations, and Docking, American Control Conference (ACC) (2023), 3645-3661. https://doi.org/10.23919/acc55779.2023.10155826

[2] B. Ma, Z. Jiang, Y. Liu, Z. Xie, Advances in space robots for on-orbit servicing: A comprehensive review. Advanced Intelligent Systems. (2023) 5(8), 2200397. https://doi.org/10.1002/aisy.202200397

[3] N. Fallahiarezoodar, and H.Z. Zheng. Review of autonomous space robotic manipulators for on-orbit servicing and active debris removal. Space: Science & Technology. 5 (2025), 0291. https://doi.org/10.34133/space.0291

[4] J. Gil-Fernandez, T. Prieto-Llanos, R. Cadenas-Gorgojo, M. Graziano, R. Drai. Autonomous GNC algorithms for rendezvous missions to near-Earth-objects. In AIAA/AAS Astrodynamics Specialist Conference and Exhibit. (2008) p. 7087. https://doi.org/10.2514/6.2008-7087

[5] W. Fehse. Automated Rendezvous and Docking of Spacecraft. Cambridge Univ. Press. (2003). https://doi.org/10.1017/cbo9780511543388.013

[6] Information on https://spaceitup.it/

[7] A. Madonna, G. Napolano, A. Nocerino, R. Opromolla, G. Fasano, M. Grassi. Guidance and control architecture for rendezvous and approach to a non-cooperative tumbling target. Aerospace. (2025) 12(8), 708. https://doi.org/10.3390/aerospace12080708

[8] A. Madonna, G. Napolano, A. Nocerino, R. Opromolla, G. Fasano, M. Grassi. A multi-step Guidance and Control strategy for autonomous rendezvous with a non-cooperative and tumbling spacecraft. EUCASS Proceedings Series. (2025). (pp. 1-15).

[9] H. B. Hablani, M. L., Tapper, and D. J. Dana-Bashian. Guidance and relative navigation for autonomous rendezvous in a circular orbit. Journal of guidance, control, and dynamics. (2002). 25(3), 553-562. https://doi.org/10.2514/6.2003-5355

Materials Research Proceedings 69 (2026) 868-873 https://doi.org/10.21741/9781644904251-153

Enhancing Incremental NDI Control with $\mathcal{L}_1$ Adaptive Augmentation in a Longitudinal Autopilot

Giorgio RAOS[1,a *], Giovanni GOZZINI[1,b] and Davide INVERNIZZI[1,c]

[1]Dipartimento di Scienze e Tecnologie Aerospaziali, Politecnico di Milano, Via La Masa 34, 20156 Milano, Italy

[a]giorgio.raos@polimi.it, [b]giovanni.gozzini@polimi.it, [c]davide.invernizzi@polimi.it

Keywords: Flight Dynamics, Autopilot, Flight Control System, Incremental Nonlinear Dynamic Inversion, Adaptive Control

Abstract. In this work the effectiveness of an adaptive control augmentation for high-performance fixed-wing aircraft is investigated. An Incremental Nonlinear Dynamic Inversion (INDI) pitch rate control loop is designed within the cascade of a longitudinal autopilot. A minimally invasive $\mathcal{L}_1$-adaptive controller is then designed to counteract system uncertainties and variations, with an hedging procedure that ensures bounded adaptation during saturation events. A time-domain performance analysis is performed, showing that the baseline INDI controller draws a clear benefit from the $\mathcal{L}_1$-adaptive augmentation.

Introduction

Most modern fixed-wing aircraft achieve stability through a Flight Control System (FCS) that relies on Gain-Scheduling (GS). In this method, the varying system dynamics is taken into account by switching the controller parameters in real time, based on some scheduling rules. Although there are techniques that can speed up the scheduling process [1], a significant effort in design and analysis is often required, and the full capabilities of the aircraft may not be exploited. In Incremental Nonlinear Dynamic Inversion (INDI) [2] architectures, a feedback linearization of the system dynamics allows for the desired response to be enforced in the complete flight envelope without the need for scheduling, in a modular and easily interpretable structure. However, the model-based implementations of INDI control laws suffer from model mismatches, whose effect on the response can be mitigated using an adaptive control augmentation. $\mathcal{L}_1$ adaptive control theory [3] offers a promising alternative to comparable architectures, as it avoids inducing the system into dangerous oscillatory behaviors resulting from fast adaptation. In this work we consider a nonlinear model for the longitudinal dynamics of an airframe, where a cascade autopilot controlling the climb angle is designed with a model-based INDI pitch rate control loop. Then, a minimally invasive $\mathcal{L}_1$ Piecewise Constant (PwC) adaptive [3] augmentation is designed to compensate for any uncertainty in the open-loop pitch rate dynamics. With a proposed hedging [4] method for the predictor in the adaptive controller, safe adaptation during actuator saturation events is ensured, which represents a step forward when compared to similar works [5].

Longitudinal Autopilot Baseline Design

Control Structure. A cascade architecture, visible in Fig. 1, is adopted to control a model for the longitudinal dynamics of the airframe shown in Fig. 2, using a tail elevator deflection δ, whose actuator is modeled through a second-order transfer function $G_{\mathrm{a}}(s)$ with position and rate limits δ_{M}, $\dot{\delta}_{\mathrm{M}}$. The two outer loops are closed with proportional gains K_{γ} and K_{az}, controlling respectively the climb angle γ and the vertical acceleration $a_z = \dot{w}$. The inner loop contains a model-based INDI controller, designed so that the pitch rate tracking error $e_q = q - q_{ref}$ remains small.

Content from this work may be used under the terms of the Creative Commons Attribution 3.0 license. Any further distribution of this work must maintain attribution to the author(s) and the title of the work, journal citation and DOI. Published under license by Materials Research Forum LLC.

Materials Research Proceedings 69 (2026) 868-873 https://doi.org/10.21741/9781644904251-153

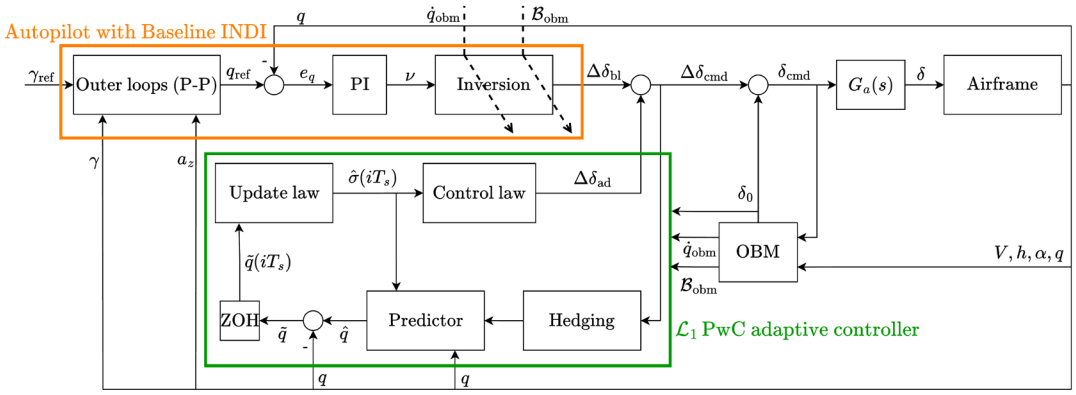


Fig. 1. Full autopilot structure with baseline INDI and $\mathcal{L}_1$-adaptive controllers.

Pitch dynamics. The second body-frame component of the Euler equations with the aerodynamic model adopted from [1] reads

$$\dot{q} = \frac{1}{J} q_\infty S_{\text{ref}} d_{\text{ref}} (C_{\mathcal{M}/q} q + C_{\mathcal{M},\alpha}(\alpha, V, M) + C_{\mathcal{M}/\delta}\delta), \tag{1}$$

where J is the moment of inertia of the airframe, q_∞ is the asymptotic dynamic pressure, S_{ref} and d_{ref} are the reference surface and length, $C_{\mathcal{M}/q}$ is the damping-in-pitch derivative, $C_{\mathcal{M},\alpha}(\cdot)$ is a nonlinear function depending on the angle of attack α, the airspeed V, and the Mach number M, while $C_{\mathcal{M}/\delta}$ is the elevator control derivative.

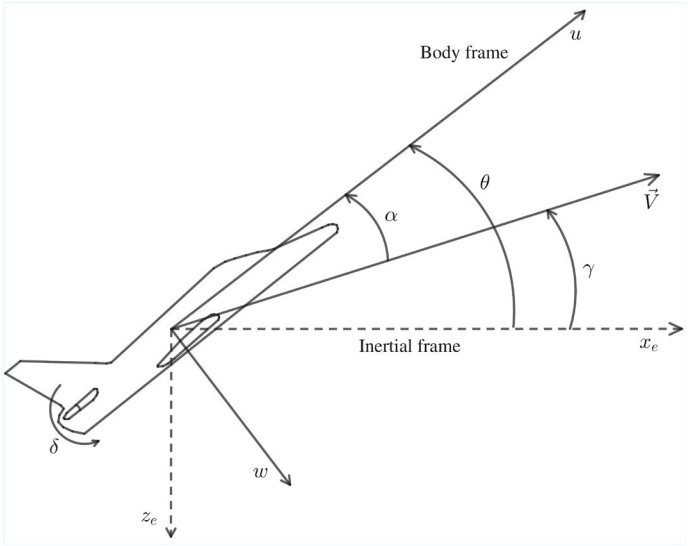


Fig. 2. The motion of the longitudinal airframe in the body and inertial frames.

INDI Baseline Controller. The first-order Taylor expansion of Eq. (1) is computed at each time step around the current condition, denoted by the subscript 0. The assumption of a separation in the timescales between (slow) rigid-body dynamics and (fast) actuator dynamics is adopted to simplify the obtained incremental dynamics [2] down to

$$\dot{y} \approx \dot{y}_0 + \mathcal{B}(\delta - \delta_0) \approx \dot{y}_0 + \mathcal{B}\Delta\delta_{cmd} \tag{2}$$

where $\mathcal{B} = \frac{1}{J} q_{\infty,0} C_{\mathcal{M}/\delta} S_{ref} d_{ref}$ is the control effectiveness and $\Delta\delta_{\text{cmd}}$ is the total incremental command. The baseline INDI incremental command $\Delta\delta_{\text{bl}}$ is then computed as

$$\Delta\delta_{\text{bl}} = \mathcal{B}_{\text{obm}}^{-1}(\nu - \dot{q}_{\text{obm}}) \tag{3}$$

with $\dot{q}_{obm}$ and $\mathcal{B}_{obm}$ representing estimates of $\mathcal{B}$ and $\dot{q}_0$, obtained from an On-Board Model (OBM) using nominal aerodynamics $\bar{C}_{\mathcal{M}/q}$, $\bar{C}_{\mathcal{M},\alpha}$, $\bar{C}_{\mathcal{M}/\delta}$. The total commanded input coming from

the baseline INDI controller is $\delta_{cmd} = \Delta\delta_{\mathrm{bl}} + \delta_0$, with δ_0 estimated with a model of the actuator $\bar{G}_{\mathrm{a}}(\mathrm{s})$. The pseudo control $\nu = K_P\big(q_{ref} - q\big) + K_I\int\big(q_{\mathrm{ref}} - q\big)$, with K_P, K_I positive constants, relates to the desired second-order pitch rate dynamics, achieved almost exactly within the whole flight envelope as long as the OBM estimates are sufficiently accurate.

$\mathcal{L}_1$-Adaptive Control Augmentation Design

In a practical scenario, model uncertainty and exogenous disturbances will affect the pitch rate dynamics of Eq. 1. These effects can be considered through a lumped uncertainty σ_m, matched inside the control channel of the open-loop pitch rate dynamics as

$$\dot{q} = \dot{q}_{\mathrm{obm}} + \mathcal{B}_{\mathrm{obm}}(\Delta\delta + \sigma_m). \tag{4}$$

Predictor. Within the $\mathcal{L}_1$-adaptive controller, the predictor is a dynamical system which computes an estimate of the pitch rate $\hat{q}$ according to:

$$\dot{\hat{q}} = \dot{q}_{\mathrm{obm}} + \mathcal{B}_{\mathrm{obm}}(\Delta\delta_{\mathrm{a}} + \hat{\sigma}_m) + L(q - \hat{q}), \qquad L > 0 \tag{5}$$

Hedging. In Eq. (4), $\Delta\delta_{\mathrm{a}}$ is obtained by estimating the incremental elevator deflection according to

$$\Delta\delta_{\mathrm{a}} = \bar{G}_{\mathrm{a}}(t) * \mathrm{sat}_{\delta_{\mathrm{M}}}\left\{\int_0^t \mathrm{sat}_{\dot{\delta}_{\mathrm{M}}}\left[\frac{d}{dt}(\delta_{\mathrm{cmd}}(\tau))\right]d\tau\right\} - \delta_0, \quad \delta_{\mathrm{cmd}} = \Delta\delta_{\mathrm{ad}} + \Delta\delta_{\mathrm{bl}} + \delta_0 \tag{6}$$

where $*$ is the convolution operator and $\mathrm{sat}_{\delta}(\cdot)$ is the symmetric saturation function. This modification guaranties that adaptation is not mistakenly driven during maneuvers or actuator saturation, avoiding potentially catastrophic events.

Update Law. The prediction error $\tilde{q} = \hat{q} - q$ is used to drive the parameter update law that estimates the uncertainty using a piecewise constant approximation according to

$$\hat{\sigma}_m(t) = K_{\mathcal{L}_1}(T_s)\tilde{q}(iT_s), \quad \forall\, t \in [iT_s, (i+1)T_s), \tag{7}$$

$$K_{\mathcal{L}_1}(T_s) = -\mathcal{B}_{\mathrm{obm}}^{-1}\left(1 - e^{-LT_s}\right)^{-1} L e^{-LT_s}, \tag{8}$$

where the adaptation speed is regulated through L and the sampling time of the controller T_s.

Control Law. The adaptive control law that compensates for the uncertainty is

$$\Delta\delta_{\mathrm{ad}} = -C(s)\,\hat{\sigma}_m(s), \qquad C(s) = \frac{\omega_{\mathrm{f}}}{s + \omega_{\mathrm{f}}}, \tag{9}$$

where s is the Laplace variable and $\omega_{\mathrm{f}} > 0$ adjusts the filtering action that prevents exciting the system at high frequencies.

Tuning remarks. The sampling period T_s should be selected as high as the available CPU allows. With $T_s \to 0$, and $F_\sigma(s)$ denoting the transfer function from σ_m to $\hat{\sigma}_m$ obtained by closing the loop in the prediction dynamics with Eq. 7 and Eq. 8, one gets that

$$F_\sigma(s) = -K_{\mathcal{L}_1}\left(s - (-L + \mathcal{B}_{\mathrm{obm}}K_{\mathcal{L}_1})\right)^{-1}\mathcal{B}_{\mathrm{obm}} = \frac{e^{-LT_s}}{1 + s(1 - e^{-LT_s}/L)}, \tag{10}$$

so that $\lim_{t\to\infty}[\hat{\sigma}_m(t) - \sigma_m(t)] \overset{L\to 0}{\to} 0$. The bandwidth of the filter ω_{f} should be as high as possible without exceeding the available bandwidth of the system.

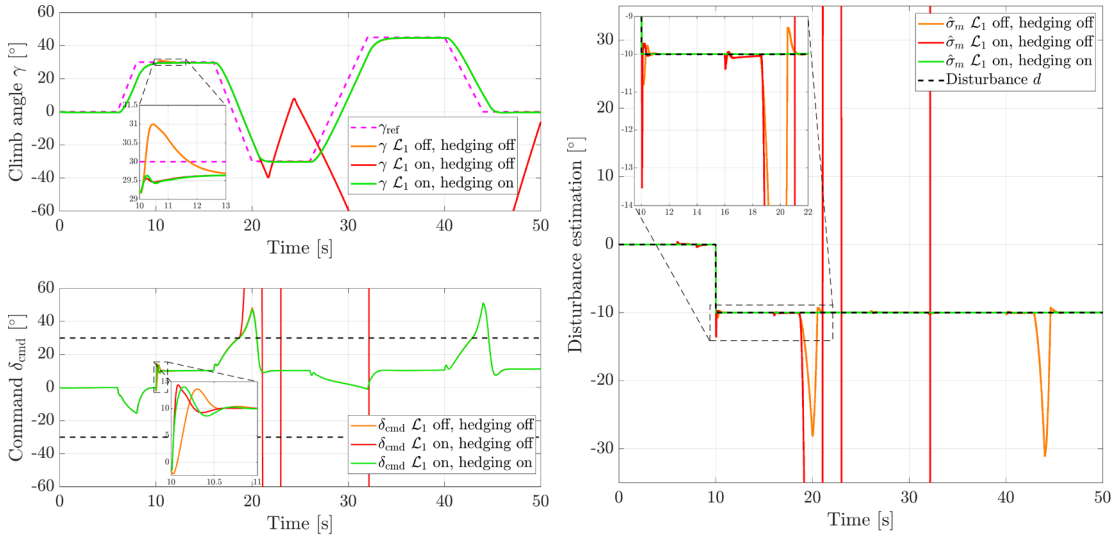
Materials Research Proceedings 69 (2026) 868-873 https://doi.org/10.21741/9781644904251-153

Performance Analysis

The controllers and the airframe model are implemented in MATLAB/Simulink®. The adopted controller parameters are shown in Table 1. The gains of the baseline controller were tuned with the MATLAB® function systune, while the adaptive controller was tuned conservatively using the guidelines described in the previous section.

Table 1. Tuned controller parameters

Parameter	Value
K_γ	-1324
K_{az}	-0.0093
K_P	18.55
K_I	67.58
T_s	0.01s
L	0.1
ω_f	50 rad/s



(a) Climb angle γ and commanded elevator deflection δ_{cmd}.

(b) Estimation performance in the adaptive controller with respect to disturbance d.

Fig. 3. Results of nonlinear simulations with injected disturbance d, comparing the baseline and $\mathcal{L}_1$-augmented controllers with and without predictor hedging.

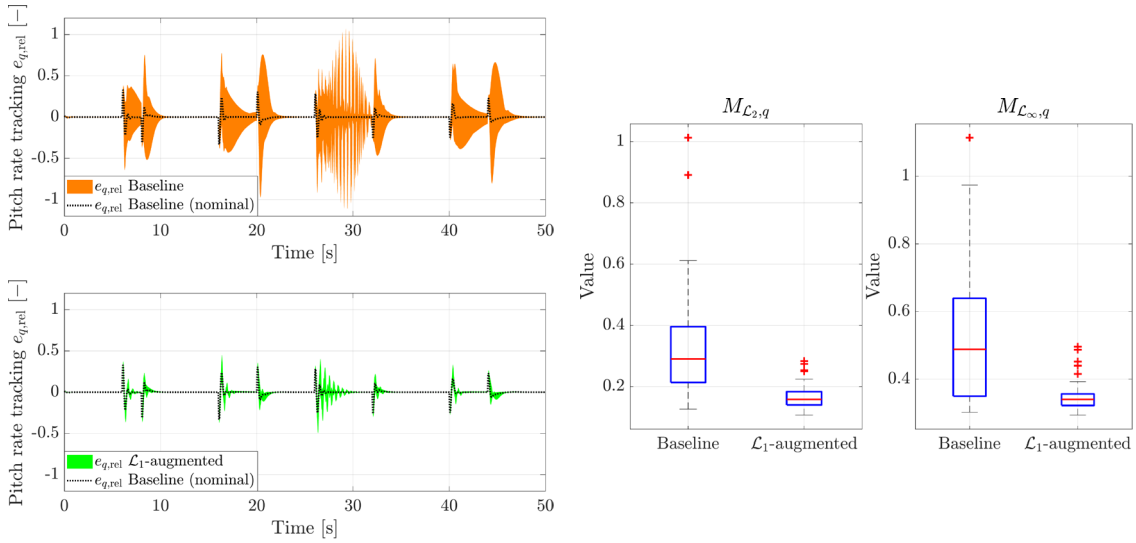
Disturbance Rejection. With a reference signal γ_{ref} that makes the system cross its envelope, a disturbance $d(t) = -10\text{step}(t-10)$ deg is injected in the control channel, with the objective of proving the effectiveness of adaptation and the importance of hedging. Fig. 3a shows the climb angle response and the corresponding total command, while Fig. 3b highlights the estimation performance of the adaptive controller. The $\mathcal{L}_1$ controller slightly increases the system responsiveness. However, with active adaptation, the proposed hedging methodology proves to be fundamental in avoiding instability and providing correct disturbance estimation. The baseline INDI controller also achieves an acceptable performance degradation, thanks to the integral action tuned by the gain K_I.

Monte Carlo Analysis. The following quantities are defined:

Materials Research Proceedings 69 (2026) 868-873 https://doi.org/10.21741/9781644904251-153

$$e_{q,\mathrm{rel}} = \frac{e_q}{\| q_{\mathrm{ref}} \|_{\mathcal{L}_\infty}}, \quad M_{\mathcal{L}_2,q} = \frac{\| e_q \|_{\mathcal{L}_2}}{\| q_{\mathrm{ref}} \|_{\mathcal{L}_2}}, \quad M_{\mathcal{L}_\infty,q} = \frac{\| e_q \|_{\mathcal{L}_\infty}}{\| q_{\mathrm{ref}} \|_{\mathcal{L}_\infty}}; \tag{11}$$

and a Monte Carlo study through nonlinear simulations is performed, considering parametric uncertainties. The relative pitch rate tracking error $e_{q,rel}$ is shown in Fig. 4a, comparing the baseline and the $\mathcal{L}_1$-augmented controllers to a nominal simulation. Undesirable pitch oscillations are greatly reduced by the adaptive augmentation when compared to the responses obtained with the baseline controller. The box plots in Fig. 4b highlight an improved consistency of performance under the varying conditions resulting from uncertainty.



(a) Time histories of the relative pitch rate tracking error

(b) Values for the pitch rate tracking performance metrics $M_{\mathcal{L}_2,q}$, $M_{\mathcal{L}_\infty,q}$.

Fig.4. Results of the Monte Carlo analysis comparing pitch rate tracking performance for baseline and $\mathcal{L}_1$-augmented controllers

Conclusions

The $\mathcal{L}_1$-adaptive augmentation of the INDI controller presented in this paper proved to be beneficial to the dynamic response of the airframe. Moreover, the proposed hedging method is fundamental to avoid inducing the system into unstable behavior in the case of actuator saturation events. Although the observations from time-domain simulations show an increase in tracking and disturbance rejection capabilities, a strict stability analysis would complete the evaluation of the architecture, which can potentially be extended to a complete aircraft model with multiple control channels.

References

[1] P. Gahinet, P. Apkarian, Automated tuning of gain-scheduled control systems, 52nd IEEE Conference on Decision and Control (2013) pp. 2740-2745. https://doi.org/10.1109/CDC.2013.6760297

[2] S. Sieberling, Q. P. Chu, J. A. Mulder, Robust flight control using incremental nonlinear dynamic inversion and angular acceleration prediction, Journal of guidance, control, and dynamics (2010) 33(6) pp. 1732-1742. https://doi.org/10.2514/1.49978

[3] N. Hovakimyan, C. Cao, L1 adaptive control theory: Guaranteed robustness with fast adaptation. Society for Industrial and Applied Mathematics, Philadelphia, 2010. https://doi.org/10.1137/1.9780898719376

[4] E. N. Johnson, A. J. Calise. Pseudo-control hedging: A new method for adaptive control. Advances in navigation guidance and control technology workshop (2000), Alabama, USA.

[5] P. Bhardwaj, V. S. Akkinapalli, J. Zhang, S. Saboo, F. Holzapfel, Adaptive augmentation of incremental nonlinear dynamic inversion controller for an extended f-16 model. AIAA Scitech 2019 Forum (2019) p. 1923. https://doi.org/10.2514/6.2019-1923

Materials Research Proceedings 69 (2026) 874-879 https://doi.org/10.21741/9781644904251-154

Adaptive Augmentation of Incremental NDI Laws with Systematic $\mathcal{H}_\infty$ Synthesis

Giulio FRANCESCHINI[1,a], Giorgio RAOS[1,b *], Giovanni GOZZINI[1,c] and Davide INVERNIZZI[1,d]

[1]Dipartimento di Scienze e Tecnologie Aerospaziali, Politecnico di Milano, Via La Masa 34, 20156 Milano, Italy

[a]giulio1.franceschini@polimi.it, [b]giorgio.raos@polimi.it, [c]giovanni.gozzini@polimi.it, [d]davide.invernizzi@polimi.it

Keywords: Flight Control System, Incremental Nonlinear Dynamic Inversion, Adaptive Control, Automatic Tuning

Abstract. Incremental Nonlinear Dynamic Inversion (INDI) is a promising control framework for systems characterized by significant nonlinearities and uncertainties, such as high-performance aircraft. However, the capabilities of INDI control are limited by its sensitivity to noise, delays, and modeling errors, which hinder its industrial adoption and certification. This paper presents an adaptive INDI extension with systematic synthesis capabilities, thereby enabling formal verification of performance and robustness, and paving the way toward certifiable INDI flight control systems.

Introduction

Given a control-affine nonlinear system $\dot{x} = f(x) + G(x)u$, the starting point of the INDI design is the linearization of the system about the previous time instant (x_0, u_0), obtaining

$$\dot{x} = \dot{x}_0 + F(x_0, u_0)\Delta x + G(x_0)\Delta u, \tag{1}$$

where $\Delta u = u - u_0$, $\Delta x = x - x_0$ are the input and state increments, respectively, $F(x_0, u_0) = \partial(f(x) + G(x)u)/\partial x$ evaluated at (x_0, u_0), $G(x_0)$ is the control effectiveness matrix and $\dot{x}_0 = f(x_0) + G(x_0)u_0$. The INDI control law is given by:

$$u = u_0 + \Delta u = u_0 + G^{-1}(x_0)(\nu - \dot{x}_0), \tag{2}$$

where ν is a virtual control input provided by an external controller [1] that achieves stable tracking of a reference signal x_{ref}.

When applied to the nonlinear plant, the control law approximately reduces the dynamics to a pure integrator, $\dot{x} = \nu$, which holds under the assumption of fast control update time and fast actuators, so that $\|F(x_0, u_0)\Delta x\| \ll \|G(x_0)\Delta u\|$. In the model-based INDI configuration, the On-Board Model (OBM)—a simplified dynamic model embedded in the flight control computer—is used to compute real-time estimates of the nominal state derivative, $\dot{x}_0$, and the control effectiveness matrix, $G(x_0)$. To enable this, both state and input feedback must be available from appropriate onboard sensors.

Content from this work may be used under the terms of the Creative Commons Attribution 3.0 license. Any further distribution of this work must maintain attribution to the author(s) and the title of the work, journal citation and DOI. Published under license by Materials Research Forum LLC.

Materials Research Proceedings 69 (2026) 874-879 https://doi.org/10.21741/9781644904251-154

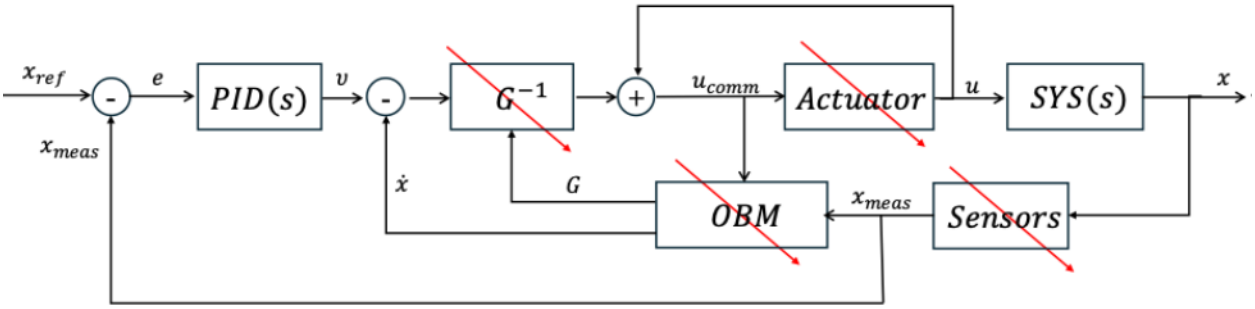


Fig. 1: Typical model-based INDI loop with uncertainty sources indicated with red arrows.

The combined effects of phase lag due to sensor dynamics, delays, actuator dynamics, and model estimation errors (Fig. 1) result in a deviation from ideal integrator behavior. The influence of these non-idealities on the INDI loop dynamics can be explicitly characterized by introducing perturbations in both the state function f and the control effectiveness G as follows:

$$\dot{x} = f(x) + \Delta f(x) + \big(G(x) + \Delta G(x)\big)u. \tag{3}$$

In [2], perturbations are matched in the actuator channel and compensated via an $\mathcal{L}_1$ adaptive controller in augmentation on the inner loop. This approach, however, results in a time-consuming tuning procedure, as the number of the adapted parameters equals the number of control channels. To overcome this issue, a novel adaptive architecture which augments the virtual control signal is presented, where an automatic tuning based on performance and robustness considerations is performed.

Adaptive Augmentation

The perturbation term of Eq. 3 is lumped into a single virtual disturbance $\sigma = \Delta f(x) + \Delta G(x)G^{-1}(x)\big(\nu - f(x)\big)$. Therefore, the INDI dynamics can be rewritten as $\dot{x} = \nu + \sigma$, i. e., a pure integrator with an input disturbance, recasting the whole problem into a classical linear disturbance rejection framework.

We solve the control problem via an adaptive augmentation approach by implementing an Extended State Observer (ESO) [3] that estimates the virtual disturbance and provides a control contribution ν_{ad} equal and opposite to its estimate $\hat{\sigma}$ (Fig. 2).

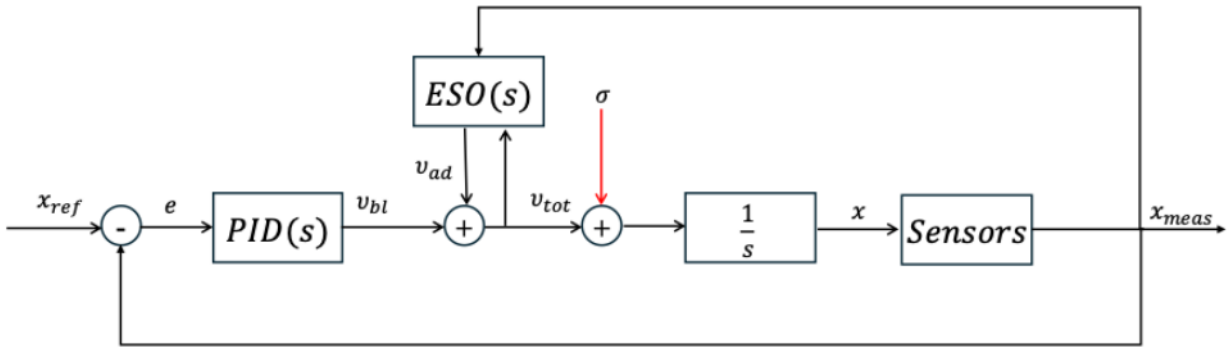


Fig. 2: Adaptive augmentation control architecture.

Materials Research Proceedings 69 (2026) 874-879 https://doi.org/10.21741/9781644904251-154

The considered ESO is described by

$$\dot{\hat{x}}(t) = \nu(t - \Delta T) + \hat{\sigma}(t) + L_1\big(x_{meas}(t) - \hat{x}(t)\big), \tag{4a}$$

$$\dot{\hat{\sigma}}(t) = Proj\big\{L_2\big(x_{meas}(t) - \hat{x}(t)\big)\big\}, \tag{4b}$$

$$\nu_{ad}(t) = -\hat{\sigma}(t), \tag{4c}$$

where x_{meas} is the state value measured by sensors, while L_1 and L_2 are positive definite ESO tunable gains. ΔT denotes a time shift applied to the predictor input. The inclusion of this term aims at compensating for the time misalignment between the predictor's state estimate $\hat{x}$ and the measured state x_{meas} introduced by sensor dynamics and delays. Numerical results show that this modification improves stability margins. Finally, a projection operator $Proj(\cdot)$ is applied to the virtual disturbance estimate to prevent drifting. One can prove that, with a proper tuning of the ESO gains, $\hat{\sigma}(t) \approx \sigma(t)$ and thus pure integral behavior of the INDI loop is approximately recovered.

Structured $\mathcal{H}_\infty$ Synthesis

The resulting proposed architecture (Fig. 2) is suitable for structured $\mathcal{H}_\infty$ synthesis [4] due to its simple structure and linearity in the parameters of the controller. Structured $\mathcal{H}_\infty$ solves a non-convex optimization problem to minimize the $\mathcal{H}_\infty$ norm of selected closed-loop transfer functions while respecting constraints on the controller's structure. These transfer functions represent key performance metrics such as tracking error, disturbance amplification, and control effort. Since the designer focuses on particular frequency ranges, it is common practice to weight each of these functions in the frequency domain. The designer can then tune the control system by adjusting these weighting functions to shape desired performance.

This tuning framework is more transparent and systematic for the designer than the standard manual tuning typically employed in the context of $\mathcal{L}_1$ adaptive control [2].

The presented approach is tested on a longitudinal autopilot of a nonlinear aircraft model in MATLAB/Simulink [5]. The autopilot consists of a cascade of three loops: the outer controls the climb angle γ, the middle the vertical acceleration a_z and the inner the pitch rate q (Fig. 3).

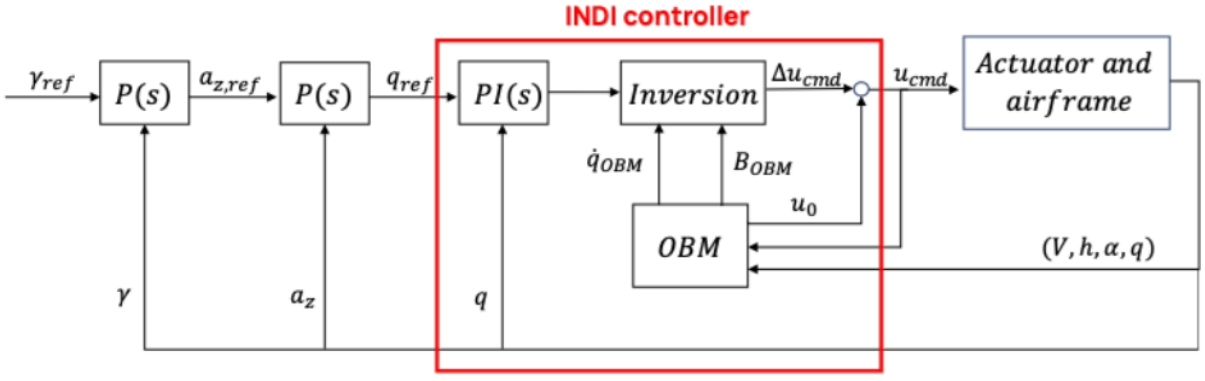


Fig. 3: Longitudinal autopilot baseline control system.

The baseline INDI controller adopted for the inner loop is augmented with the ESO architecture. Structured $\mathcal{H}_\infty$ synthesis is performed using three frequency-domain weighting functions, focusing on tracking performance, disturbance rejection capabilities, and control penalty:

$$W_{track}(s) = 0.1(s + 150\,)/(s + 1.5), \tag{5a}$$

Materials Research Proceedings 69 (2026) 874-879 https://doi.org/10.21741/9781644904251-154

$$W_{dist}(s) = 0.067(s + 15\ )/(s + 0.013), \tag{5b}$$

$$W_{act}(s) = 10(s + 0.15\ )/(s + 1500). \tag{5c}$$

The presented solution is then compared to the baseline INDI controller of Fig. 3 and to the $\mathcal{L}_1$ adaptive plant augmentation presented in [6].

The sensitivity functions in Fig. 4 show that the ESO augmentation retains most of the low-frequency disturbance rejection capability of the $\mathcal{L}_1$ augmentation presented in [6] while smoothing out the high-frequency peak.

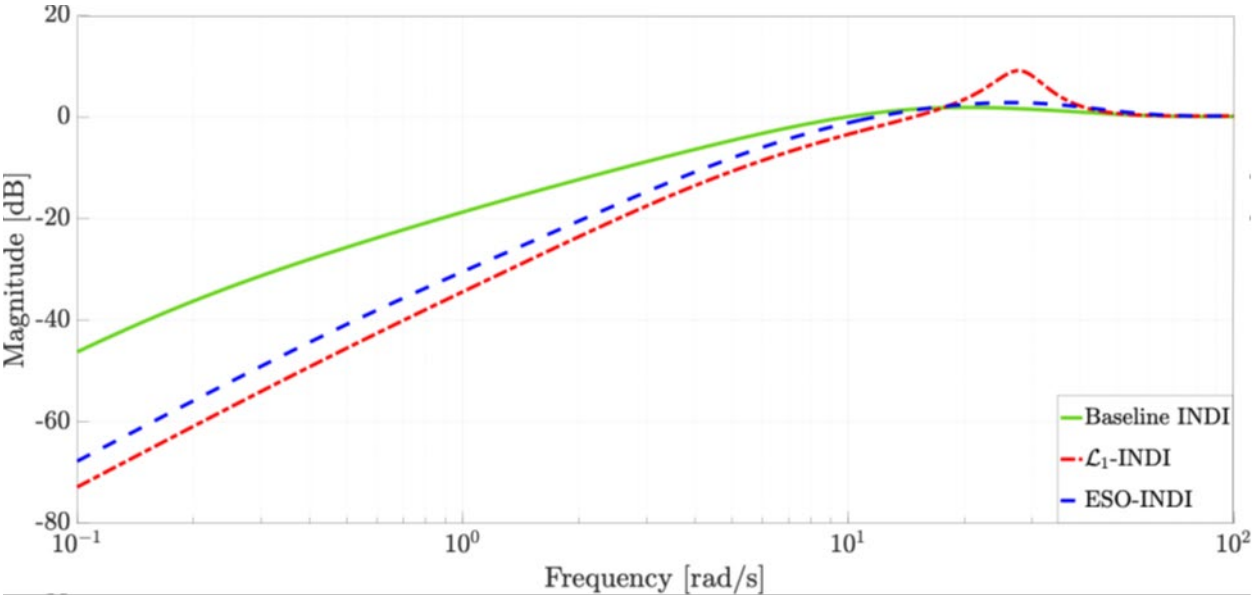


Fig. 4: Sensitivity functions of the INDI architectures.

Moreover, the Bode diagrams of the open-loop transfer function in Fig. 5 show that the ESO solution can recover and expand the stability margins of the baseline INDI controller of Fig. 3. Refer to Fig. 5: the light blue controller prioritizes an ample phase margin, while the dark blue controller prioritizes closed loop bandwidth. The designer can easily regulate the trade-off between the two by modifying the weighting functions of the $\mathcal{H}_\infty$ synthesis.

Materials Research Proceedings 69 (2026) 874-879 https://doi.org/10.21741/9781644904251-154

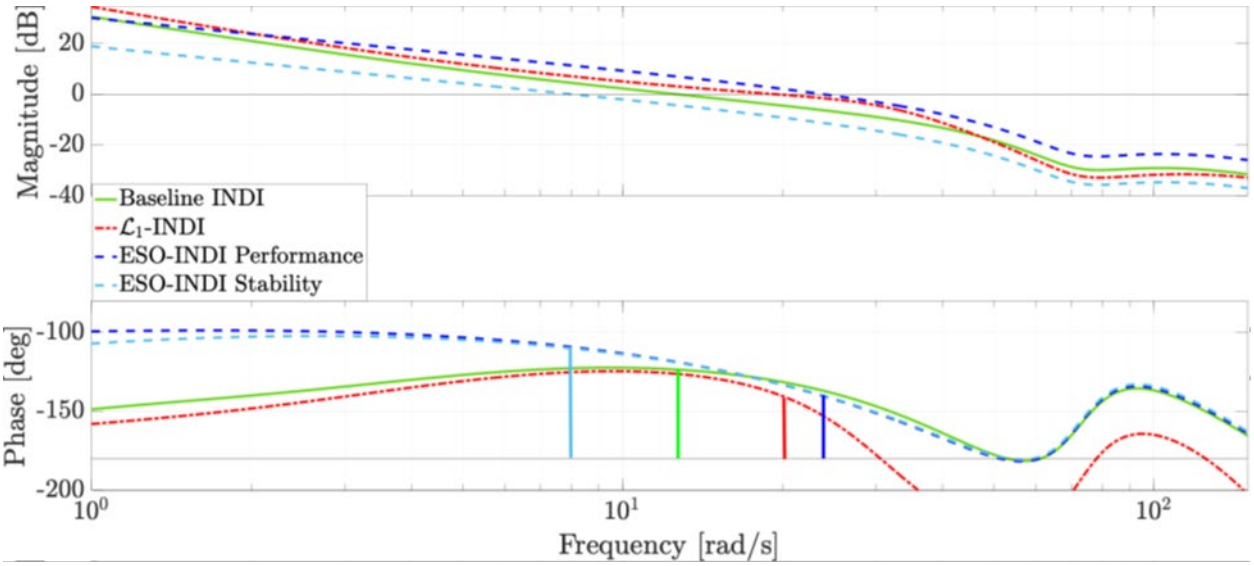


Fig. 5: Open-loop Bode diagrams.

Simulation Results

Performance of the adopted solution are evaluated under model uncertainties (inertia and aerodynamics), actuator degradation (−20% of effectiveness), sensor dynamics (with a bandwidth of 34 rad/s) and a sinusoidal external disturbance. As can be seen in Fig. 6, the ESO architecture shows sensibly improved performance compared to the baseline INDI controller of Fig. 3.

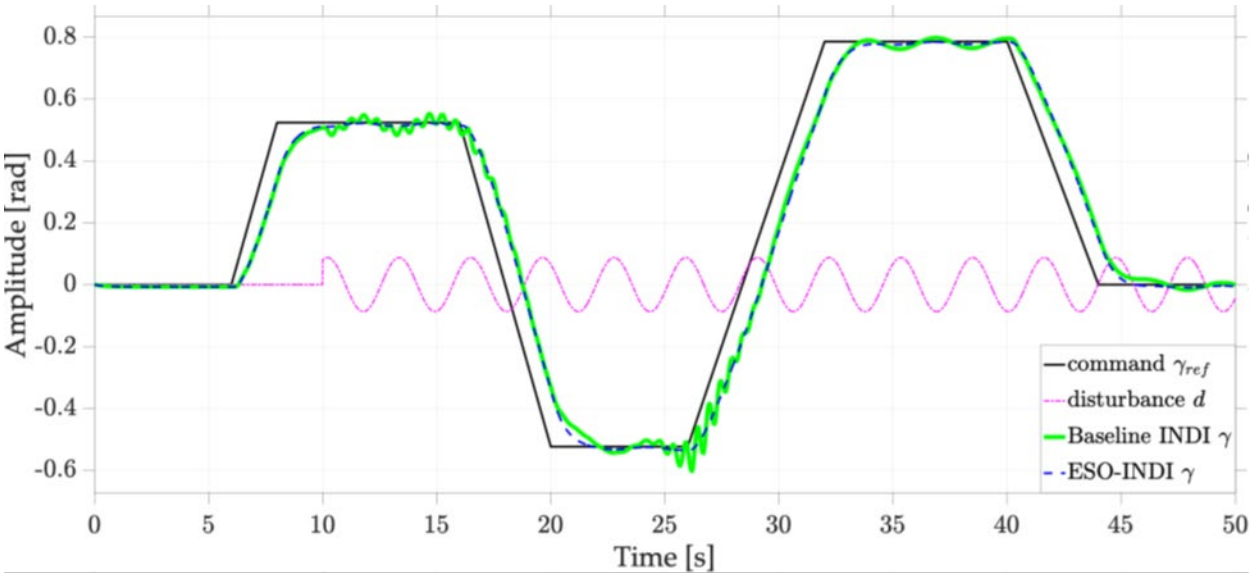


Fig. 6: Tracking of a reference climb angle.

Conclusions and Future Developments

Validation on a longitudinal autopilot case study shows that the $\mathcal{H}_\infty$-tuned INDI–ESO controller surpasses the performance and stability margins of a classical INDI or $\mathcal{L}_1$-adaptive scheme when sensor phase lag is present. The architecture also reduces manual tuning effort.

Several promising extensions can build on this foundation. First, disturbance estimation could be improved by incorporating Gaussian radial basis functions or neural network hybrids within the ESO, providing richer function approximation capabilities. Second, online delay identification algorithms could be embedded in the control loop to adaptively refine the ESO's delay estimate under variable computational or transmission latencies. Finally, a natural progression is to extend

the ESO–INDI framework to a multivariable flight control framework, developing vectorial disturbance observers and structured $\mathcal{H}_\infty$ controllers that explicitly handle pitch–roll–yaw coupling, enabling a unified autopilot for both longitudinal and lateral–directional dynamics.

References

[1] S. Sieberling, Q.P. Chu, J.A. Mulder, Robust Flight Control Using Incremental Nonlinear Dynamic Inversion and Angular Acceleration Prediction, Journal of Guidance, Control, and Dynamics, 33 (2010) 1732–1742. https://doi.org/10.2514/1.49978

[2] P. Bhardwaj, V.S. Akkinapalli, J. Zhang, S. Saboo, F. Holzapfel, Adaptive Augmentation of Incremental Nonlinear Dynamic Inversion Controller for an Extended F-16 Model, in: AIAA SciTech Forum, San Diego, CA, USA, 2019. https://doi.org/10.2514/6.2019-1923

[3] J. Han, From PID to Active Disturbance Rejection Control, IEEE-Transactions on Industrial Electronics 56 (2009) 900–906. https://doi.org/10.1109/TIE.2008.2011621

[4] P. Apkarian, D. Noll, Structured $\mathcal{H}_\infty$ Control of Infinite-Dimensional Systems, International Journal of Robust and Nonlinear Control 28 (2017) 3212–3238. https://doi.org/10.1002/rnc.4073

[5] MathWorks, Inc., Tuning of Gain-Scheduled Three-Loop Autopilot, MATLAB & Simulink Documentation, accessed November 9, 2025. Available: https://it.mathworks.com/help/slcontrol/ug/tuning-of-gain-scheduled-three-loop-autopilot.html

[6] G. Raos, Enhancing Incremental NDI Control with L1 Adaptive Augmentation in a Longitudinal Autopilot, M.Sc. thesis, Politecnico di Milano, Milan, Italy, 2024.

Materials Research Proceedings 69 (2026) 880-884 https://doi.org/10.21741/9781644904251-155

From Strain Measurements to Rotor Blade Shape and Loads Reconstruction: The BeSaME Project

Pierangelo MASARATI[1,a,*], Emanuele CASCIARO[1,b], Alessandro COCCO[1,c], Roman SUTOV[1,d], Paolo BETTINI[1,e], Alex ZANOTTI[1,f], Giovanni BERNARDINI[2,g], Francesco LIGUORI[2,h], Jacopo SERAFINI[2,i], and Claudio PASQUALI[2,l]

[1]Department of Aerospace Science and Technology, Politecnico di Milano, via La Masa 34, Milano, Italy

[2]Dipartimento di Ingegneria Civile, Informatica e delle Tecnologie Aeronautiche, Universita` degli Studi Roma Tre, Via Vito Volterra, 62, Roma, Italy

[a]pierangelo.masarati@polimi.it, [b]emanuele.casciaro@polimi.it, [c]alessandro.cocco@polimi.it, [d]roman.sutov@mail.polimi.it, [e]paolo.bettini@polimi.it, [f]alex.zanotti@polimi.it, [g]giovanni.bernardini@uniroma3.it, [h]francesco.liguori@ uniroma3.it, [i]jacopo.serafini@uniroma3.it, [l]claudio.pasquali@uniroma3.it

Keywords: Strain Measurements, Shape Sensing, Load Evaluation, Aerodynamic Testing

Abstract. The *BeSaME* (Helicopter Blade State and Loads Reconstruction Through Virtual Sensing for Health Monitoring and Performance Enhancement) project develops a virtual sensing framework for the real-time monitoring of helicopter rotor blades. Strain data from embedded fiber Bragg grating sensors are processed using inverse finite element methods and state estimation algorithms to reconstruct blade deformation and sectional loads. Aeroelastically scaled composite blades are manufactured and experimentally tested under static, dynamic, wind-tunnel, and rotating conditions, supported by a validated digital twin. The placement of the sensors is optimized to maximize the accuracy of reconstruction. Preliminary results show sub-percent shape estimation errors and load reconstruction errors below 5%.

Introduction

The *BeSaME* (Helicopter Blade State and Loads Reconstruction Through Virtual Sensing for Health Monitoring and Performance Enhancement) project aims to contribute to the ambitious ACARE SRIA and Flightpath 2050 targets—namely, an 80% reduction in rotor- craft accident rates and a 65% reduction in perceived noise emissions by 2050—by advancing structural health monitoring and performance optimization of helicopter rotors.

By leveraging fiber Bragg gratings (FBG), inverse finite element methods (IFEM), and augmented Kalman filtering, BeSaME seeks to deliver an experimentally validated real-time virtual sensing system capable of measuring axial and shear strains in rotating blades, reconstructing bending and torsional generalized strains, estimating blade shape, and inferring rotor states and aerodynamic loads under operational conditions.

The experimental program involves manufacturing aeroelastically scaled composite blades with embedded FBG sensors and intentionally introduced defects (delaminations, porosity) for damage-detection validation. Comprehensive testing includes static surveys, modal characterization under free and clamped conditions, aerodynamic and aeroelastic evaluation in a wind-tunnel, and trials on a rotating rig. Strain gauges and accelerometers provide cross- validation of optical sensor signals.

On the numerical side, a digital twin integrates detailed finite element structural models, multibody dynamics for full rotorcraft simulation, and comprehensive aeromechanics analysis to

Content from this work may be used under the terms of the Creative Commons Attribution 3.0 license. Any further distribution of this work must maintain attribution to the author(s) and the title of the work, journal citation and DOI. Published under license by Materials Research Forum LLC.

assess virtual sensor performance. Continuous model updating with experimental data ensures convergence and improves prediction fidelity.

The virtual sensing framework employs a hybrid strategy: inverse FEM for full-field deformation estimation, augmented Kalman filtering for spatially distributed load reconstruction, and neural networks for extracting critical load parameters and detecting anomalies indicative of damage. Sensor redundancy enhances resilience to individual failures while supporting accuracy validation with a minimal measurement network.

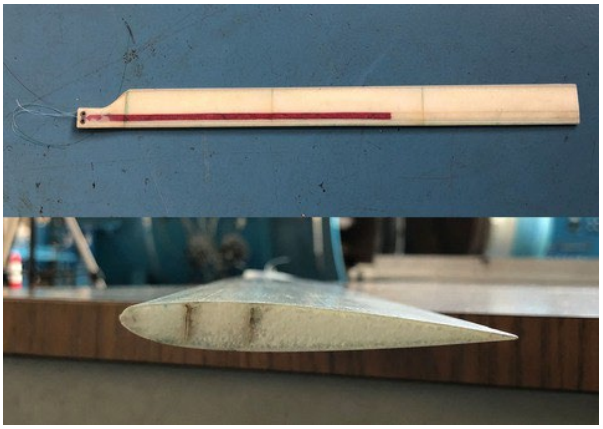


Figure 1: Example of blade specimen manufactured at POLIMI's technological lab.

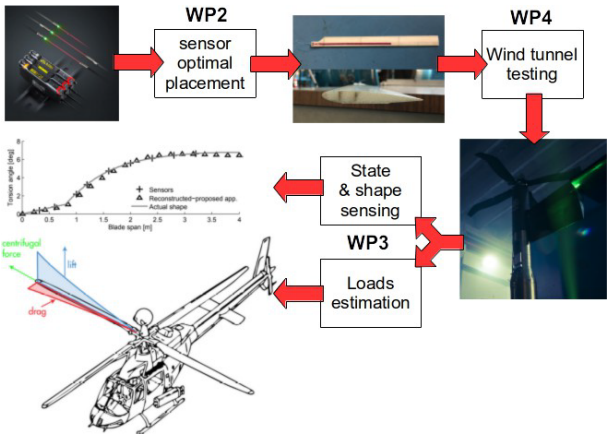


Figure 2: Block diagram of the project execution plan.

Expected outcomes include achieving TRL 5 (component/breadboard validation in relevant environment) for optical sensors in a rotating environment and TRL 4–5 (component/breadboard validation in laboratory or relevant environment) for virtual sensing algorithms, along with defining real-time and quasi-real-time metrics for blade health monitoring and control. The BeSaME system promises reduced maintenance costs, enhanced flight safety, and lower acoustic footprint, directly contributing to ACARE 2050 objectives and the Italian National Advanced Air Mobility (AAM) Strategic Plan.

The project, funded under the PRIN 2022 scheme and coordinated by Politecnico di Milano in collaboration with University Roma Tre, started in early 2025 and builds upon experience from earlier joint initiatives [1, 2, 3].

Shape and load sensing algorithm

The shape and load reconstruction approach is based on a modal method that leverages finite element analysis (FEA) to develop the blade monitoring algorithm. The algorithm consists of two main steps: first, the blade shape is reconstructed using a reduced set of eigenfunctions obtained from the FEM model; second, the loads are reconstructed using the computed displacement field along with the mass and stiffness matrices derived from the same model. Both shape and load reconstructions rely on strain measurements provided by FBG embedded sensors.

Preliminary analysis indicated that the algorithm is highly sensitive to sensor placement. Consequently, a bi-objective optimization is performed to determine the optimal sensor configuration, aiming to maximize reconstruction performance. The objective function combines the Fisher information factor and the conditioning of the reconstruction matrix. Figure 3 shows all the configurations obtained from the bi-objective optimizations, together with the corresponding Pareto front. The solution closest to the utopia point is selected as the optimal sensor layout.

The performance of the algorithm, based on the optimal sensor configuration, is evaluated using a three-dimensional beam model with an I-shaped cross-section. Reconstruction capabilities are assessed under both static and dynamic loading conditions chosen to reproduce the typical load

Materials Research Proceedings 69 (2026) 880-884 https://doi.org/10.21741/9781644904251-155

states experienced by a rotor blade in flight. In all cases, the results are consistent and satisfactory. For dynamic loads, the most demanding scenario, the mean percentage error in reconstructing the displacement at the tip of the beam along the elastic axis is 0.27%. For load reconstruction, the maximum error observed for the in-plane load component is 4.37%. Figure 4 shows an example of the reconstructed load distribution, where the precision in reproducing the FEM reference data can be inferred.

.

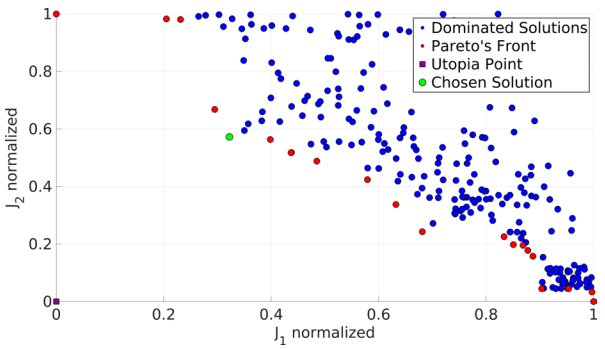


Figure 3: Optimal solutions from the bi-objective optimization, Pareto front, and selected optimal sensor configuration.

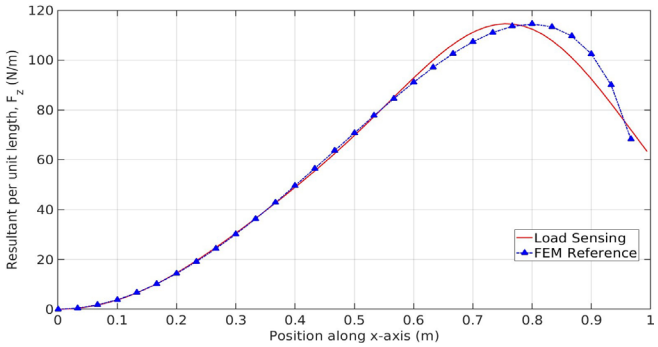


Figure 4: Comparison between reconstructed and FEM reference out-of-plane resultant per unit length.

Overall, the algorithm developed shows excellent capability to reconstruct the shape of the structure and good performance in identifying the section loads acting on it.

Blade manufacturing and testing

The current blade design is based on the one developed in [3], although minor modifications may be introduced to address issues and exploit improvement opportunities identified during the critical design review phase. The blade is constructed as a set of elements, each designed to perform a specific structural or functional role. The spar consists of two glass-reinforced unidirectional (UD) straps running along the entire span of the blade, with fibers oriented along the blade axis. These straps are designed to withstand axial forces from centrifugal loads and transfer them to the bearings around which the straps are wrapped. In the constant-section portion of the blade, each strap comprises four plies of 0.21 mm thickness, which split near the root to accommodate the bearings (Fig. 5).

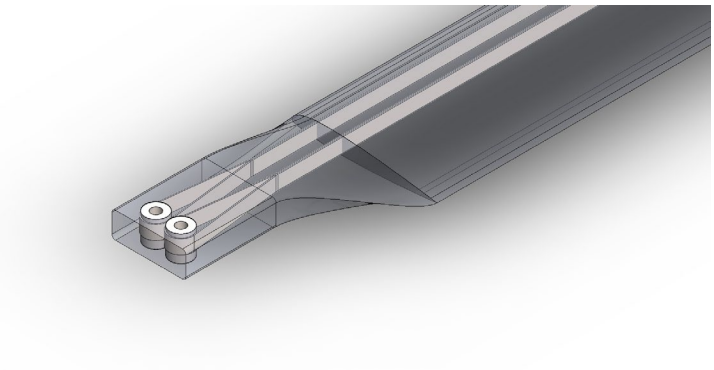


Figure 5: Detail of the root part of the blade, where straps split to wrap the bearings (adapted from [3]).

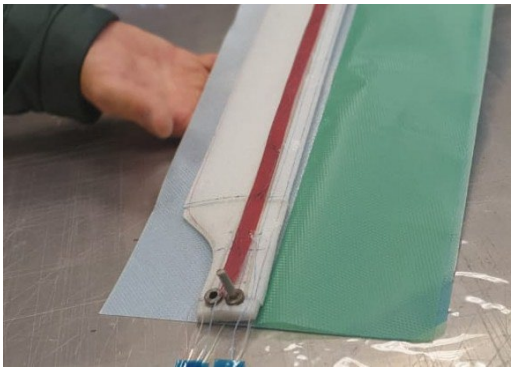


Figure 6: Final assembly of the blade (adapted from [3]).

Unlike more conventional designs, the ±45 deg wrapping that typically forms the torsional box is omitted to intentionally increase the blade's compliance and amplify torsional strains. A

Rohacell 51 WF polyurethane foam core provides the blade profile and the necessary support and pressure during manufacturing. The external skin consists of two plies of glass fabric, 0.12 mm thick, with fibers oriented at ±45 deg to ensure adequate torsional stiffness. A distinctive feature of this blade is the incorporation of two optical fibers that carry the torsion sensors. These fibers require special care to maintain proper orientation during assembly. To address this, an innovative technique called Quick-Pack (QP) is employed [4, 5]. The QP consists of a thin ribbon embedding a well-protected fiber optic along a predefined path (shown in red in Fig. 6). Its flexibility, enabled by the minimal thickness, allows it to adhere perfectly to curved surfaces, while the reinforced glass fiber protective layer ensures the integrity, functionality, and accurate orientation of the fiber optic.

Blade production involves three polymerization steps: fabrication of the UD straps, polymerization of the two QPs (one for the top and one for the bottom surface), and final curing of the external skins after assembly. Prior to polymerization, the Rohacell core is machined and the optical fibers positioned during assembly.

To evaluate the blade sensing capabilities under inertial and aerodynamic loads representative of a rotating rotor, a dedicated test rig is planned. It will feature a rigid mount for a pair of blades clamped at the root, with adjustable root pitch, actuated by an electric motor. Both blades will be instrumented, though limitations may exist in the number of optical channels that can be simultaneously acquired. This part of the project is currently under development.

Conclusions

The BeSaME project is developing a comprehensive framework for real-time virtual sensing of helicopter rotor blades, integrating fiber Bragg grating sensors, inverse finite element modeling, and augmented Kalman filtering. Preliminary numerical studies demonstrate excellent capability in reconstructing blade shape (sub-percent errors) and satisfactory performance in estimating sectional loads (errors below 5%).

The manufacturing and assembly of aeroelastically scaled composite blades with embedded sensors have been successfully designed, incorporating innovative techniques such as Quick-Pack for precise fiber placement. A dedicated test rig is currently under development to evaluate blade performance under representative inertial and aerodynamic loads.

Overall, the BeSaME framework shows strong potential to improve rotor blade health monitoring, support predictive maintenance, and enhance flight safety while reducing operational costs. Ongoing work will focus on experimental validation of the sensing algorithms, optimization of sensor networks, and extension to full rotorcraft systems.

Acknowledgements

This research is partially funded by MUR under the PRIN 2022 scheme.





Ministero dell'Università e della Ricerca



References

[1] Giovanni Bernardini, Roberto Porcelli, Jacopo Serafini, and Pierangelo Masarati. Rotor blade shape reconstruction from strain measurements. Aerospace Science and Technology, 79:580–587, August 2018. https://doi.org/10.1016/j.ast.2018.06.012

[2] Jacopo Serafini, Giovanni Bernardini, Roberto Porcelli, and Pierangelo Masarati. In-flight health monitoring of helicopter blades via differential analysis. Aerospace Science and Technology, 88:436–443, 2019. https://doi.org/10.1016/j.ast.2019.03.039

[3] Carmen Talamo, Roberta Cumbo, Daniela Rigamonti, Paolo Bettini, Daniel De Gregoriis, and Pierangelo Masarati. Blade load reconstruction from embedded strain measurements. In 78th Forum of the Vertical Flight Society, Fort Worth, TX, USA, May 20–22 2022. https://doi.org/10.4050/F-0078-2022-17521

[4] Giuseppe Sala, Luca Di Landro, Alessandro Airoldi, and Paolo Bettini. Fibre optics health monitoring for aeronautical applications. Meccanica, 2015. https://doi.org/10.1007/s11012-015-0200-6

[5] Daniela Rigamonti and Paolo Bettini. Enabling FO-based HUMS applications through an innovative integration technique: Application to a rotor blade mockup. In Piervincenzo Rizzo and Alberto Milazzo, editors, European Workshop on Structural Health Monitoring, pages 921–932, Cham, 2023. Springer International Publishing. https://doi.org/10.1007/978-3-031-07322-993

Materials Research Proceedings 69 (2026) 885-890 https://doi.org/10.21741/9781644904251-156

Hierarchical Task-Priority Tracking Control in Space Robots

Pietro BRUSCHI[1,a*] and Davide INVERNIZZI[1,b]

[1]Dipartimento di Scienze e Tecnologie Aerospaziali, Politecnico di Milano, Via La Masa 34, 20156 Milano, Italy

[a]pietro.bruschi@polimi.it, [b]davide.invernizzi@polimi.it

Keywords: Hierarchical Control, Space Robotics, GNC

Abstract. This paper extends a previously developed task-priority control algorithm for space robots to higher task dimensions, such that no degrees of freedom remain uncontrolled. The proposed design adopts an inner–outer loop paradigm and leverages a hierarchical formulation of the imposed tasks. This structure ensures modularity, robustness to singularities, and safe task execution in complex space operations.

Introduction

Space robotics has become a vital element of modern space missions, particularly in applications such as In-Orbit Servicing (IOS) and Active Debris Removal (ADR) [1]. These systems typically consist of a manipulator mounted on a satellite base, resulting in kinematic redundancy, where the number of actuated degrees of freedom (DoFs) exceeds those required to control the end-effector's pose. This redundancy provides flexibility to execute tasks in multiple ways—by moving either the base or the manipulator—while optimizing secondary objectives such as dexterity enhancement or joint-limit avoidance.

In many space scenarios, robots must perform multiple tasks simultaneously with different priorities. Redundancy can be exploited using the task-priority control framework, which assigns hierarchical importance to each control goal via nullspace projection [2]. A singularity-robust version of this method was developed in [3] and later generalized to multiple tasks in [4]. Building on this, in [5] we extended the approach to space robotic systems operating on nonlinear configuration manifolds, providing stability guarantees and demonstrating its effectiveness in an orbital capture scenario involving a tumbling target.

The present work advances the methodology introduced in [5] by extending the algorithm to tasks of higher dimension than the system dimension, thus fully exploiting all DoFs. This generalization leverages the methodology presented in [6], which utilizes a projection mechanism that activates a lower-priority task whenever a higher-priority one becomes singular.

The main contribution of this work is the extension of the approach of [6] to the case of space robots. Furthermore, the kinematic task-priority controller is embedded within a hierarchical inner–outer loop architecture that, following [7], ensures almost-global attitude tracking. This modular design enables independent tuning and stability analysis of each layer while maintaining task prioritization, unlike unified structure [6].

Furthermore, the inner loop incorporates a proportional–integral (PI) controller synthesized via H_∞ methods [8], which enhances robustness to spacecraft inertial uncertainties—a key requirement for future space operations.

Notation.

Readers may refer to [9] for a complete description of the spatial notation adopted. We recall here the definition of the pose matrix of a frame j with respect to a frame i, later used in the development of this work:

Content from this work may be used under the terms of the Creative Commons Attribution 3.0 license. Any further distribution of this work must maintain attribution to the author(s) and the title of the work, journal citation and DOI. Published under license by Materials Research Forum LLC.

Materials Research Proceedings 69 (2026) 885-890 https://doi.org/10.21741/9781644904251-156

$$ {}^{i}X_j := \begin{bmatrix} {}^{i}R_j & 0_3 \\ S({}^{i}p_j){}^{i}R_j & {}^{i}R_j \end{bmatrix} := X({}^{i}R_j, {}^{i}p_j). \tag{1} $$

The Euclidean norm is denoted by $\|\cdot\|$. We use the symbols $\bar{(\cdot)}$ and $\tilde{(\cdot)}$ to indicate errors and desired quantities, respectively. Given a matrix A, $\mathrm{skew}(A) := \frac{A-A^{\mathsf{T}}}{2}$.

The Weighted Moore-Penrose Inverse (WMPI) is compactly written as [6]:

$$ A^{\dagger} = \mathrm{WMPI}(A, W_1, W_2) = R_2^{-1}(R_1 A R_2^{-1})^{\dagger} R_1, \tag{2} $$

with $W_1 = R_1^{\mathsf{T}} R_1$, and $W_2 = R_2^{\mathsf{T}} R_2$ positive-definite weight matrices.

System Configuration

The scenario considered is the same as that presented in [5] and involves a space robot (a spacecraft equipped with an $N = 7$-link robotic manipulator) and a second satellite on which servicing operations are to be performed. The latter is referred to as the *target* and the former as the *chaser* throughout this work.

The system configuration is described using multiple Cartesian reference frames to represent the relative motion of the various bodies involved. Figure 1 provides a visual representation of the frames and the transformations along the kinematic chain. Readers may refer to [5] for a more detailed definition and description of the frames.

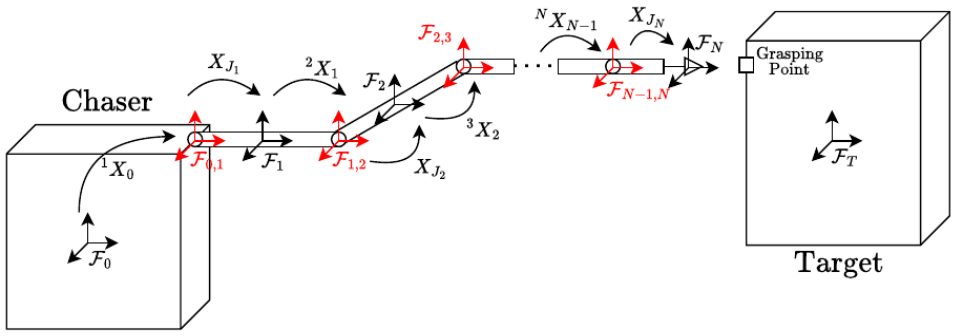


Figure 1: Geometric model of the space robot.

The attitude and position of the space robot base with respect to the target frame $\mathcal{F}_T$ are identified by the rotation matrix $R_0 \in \mathrm{SO}(3)$ and the position vector $p_0 \in \mathbb{R}^3$, respectively. Equivalently, using the spatial notation, the pose of the base frame is denoted $X_0 := X(R_0, p_0) \in \mathrm{SR}(6)$. The manipulator coordinates are described using joint angle variables, namely, as a set of angles collected in a vector $q = (q_1, q_2, \dots, q_N) \in \mathbb{T}^N := \mathbb{S}^1 \times \cdots \times \mathbb{S}^1$, where $\mathbb{S}^1$ is identified with $\mathbb{R}\,\mathrm{mod}(2\pi)$. These angles specify the relative rotation of the i-th joint frame, $\mathcal{F}_i$, with respect to the link frame $\mathcal{F}_{i-1,i}$. Given $n = 6 + N$ the number of total DoFs of the system, the configuration of the space robot is then uniquely and globally specified by the tuple (X_0, q), which is an element of the n-dimensional nonlinear manifold $\mathcal{M} := \mathrm{SR}(6) \times \mathbb{T}^N$.

The following system of nonlinear differential equations describes the kinematics of the multi-body system under consideration:

$$ \begin{cases} \dot{X}_0 = X_0 \nu_0^{\times} \\ \dot{q} = \Omega \end{cases} \tag{3} $$

Materials Research Proceedings 69 (2026) 885-890 https://doi.org/10.21741/9781644904251-156

where $\nu_0 := ({}^0\omega_{T0}, {}^0v_{T0}) \in \mathbb{R}^6$ is the base twist expressed in $\mathcal{F}_0$, while $\Omega \in \mathbb{R}^N$ represents the vector collecting the angular rates of the joints. For ease of notation, let us define $\mathrm{v} := (\nu_0, \Omega) \in \mathbb{R}^n$ as the system velocity.

The space robot dynamics is then given by the compact expression

$$H(q)\dot{\mathrm{v}} + C(\mathrm{v}, q)\mathrm{v} = u, \tag{4}$$

where $u := (\tau_0, f_0, \tau_q) \in \mathbb{R}^n$ collects the base torque, the base force, and the joint motor torque, respectively, while $H \in \mathbb{R}^{n\times n}$ is the generalized mass matrix and $C \in \mathbb{R}^{n\times n}$ is the Coriolis/centrifugal matrix (See, *e.g.*, [9], for a detailed derivation of these terms).

It is worth reporting the kinematics of the end-effector as well:

$$\dot{X}_N = X_N \nu_N^{\times}, \tag{5}$$

with $\nu_N := ({}^N\omega_{TN}, {}^Nv_{TN}) \in \mathbb{R}^6$ being the twist of the end-effector.

Multi-task priority control law design

Given the system (1)-(2), and a predefined number of tasks r, we remove the implicit assumption of [5] that the total task dimension $m = \sum_{k=1}^{r} m_k$, namely the overall number of DoFs requested by the tasks, is at most equal to the number of DoFs of the system n. Instead, we focus in the opposite case: we assume that the total task dimension is not less than the DoFs of the robot, *i.e.*, $m \geq n$, as done in [6].

As remarked in the introduction, the controller developed in this work relies on an inner–outer loop paradigm, where the outer loop commands to the inner one a virtual velocity input.

The commanded virtual velocity is determined based on the following process: a set of tasks is first established, after which the procedure outlined in [6] is applied. For each task, the dynamically consistent Jacobian matrix is computed starting from the actual Jacobian. According to the following routine:

$$\begin{aligned} \hat{J}_k &= J_k P_{k-1} \\ P_k &= P_{k-1}\left(I_N - \hat{J}_k^{\dagger}\hat{J}_k\right) \end{aligned} \tag{6}$$

where $k = 1, \dots, r$ and $\hat{J}_k^{\dagger} = \mathrm{WMPI}\left(\hat{J}_k, W_{1k}, W_2\right)$. The weight $W_{1k} = I_{m_k} \in \mathbb{R}^{m_k \times m_k}$ is chosen as an identity matrix of appropriate dimension, while $W_2 = H(q)$. Moreover, $P_0 = I_n$.

Using this definition, the Jacobian matrix of the first task remains unchanged. The recursive use of nullspace projectors will ensure that tasks are decoupled, since each lower-priority task will be applied only in directions that do not interfere with higher-priority tasks.

The pseudoinverses of the dynamically consistent Jacobian matrices may be compactly collected in a stack as well:

$$\hat{J}^{\dagger} = \begin{bmatrix} \hat{J}_1^{\dagger} & \cdots & \hat{J}_r^{\dagger} \end{bmatrix}. \tag{7}$$

The control law of the outer loop can now be explicitly stated:

$$\mathrm{v}^c = \hat{J}^{\dagger}\zeta. \tag{8}$$

The stack $\zeta = (\zeta_1 \cdots \zeta_r) \in \mathbb{R}^m$ collects the commanded tasks' velocities, which can be designed using different stabilizers, according to specific needs.

Materials Research Proceedings 69 (2026) 885-890 https://doi.org/10.21741/9781644904251-156

Then, the inner-loop controller computes the control input u to track the generalized velocity $\mathrm{v}^c \in \mathbb{R}^n$, provided by the outer loop to achieve the task objectives, according to the following law:

$$u = K_P\tilde{\mathrm{v}} + K_I x_I + H(q)\,\dot{\mathrm{v}}^c + C(q,\dot{q})\mathrm{v}^c, \tag{9}$$

where $\tilde{\mathrm{v}} = \mathrm{v} - \mathrm{v}^c \in \mathbb{R}^n$ is the control error, and $x_I \in \mathbb{R}^n$ is the integral state, defined such that $\dot{x}_I = \tilde{\mathrm{v}}$, which provides integral action on the twist error. The matrices $K_P \in \mathbb{R}^{n\times n}$ and $K_I \in \mathbb{R}^{n\times n}$ are gain matrices tuned using robust control techniques [8].

Numerical Results

In this section, we present the same scenario considered in [5], where a space robot must perform an orbital capture on a tumbling target. The control objectives are translated into two tasks: tracking the pose (position and attitude) of the end-effector and tracking the pose of the base spacecraft. In this work, we have added a third task, representing a safe joint configuration $\bar{q}$ [6]. Such a quantity is a set of joint angles that the arm has to track whenever the upper tasks become singular, *i.e.*, the corresponding Jacobian loses rank.

The three tasks considered can be specified as functions of the system state:

$$\begin{aligned} \xi &= (X_N, X_0, q) \\ \zeta &= (\nu_N^c, \nu_0^c, \Omega^c) \end{aligned} \tag{10}$$

where $\xi \in \mathbb{R}^m$ is the task specification vector.

Table 1: Selected Tasks.

Task #	Description	Jacobian	# of DoFs
1	Tracking EE's pose: X_N	$J_1 = [J_b \quad J_m]$	$m_1 = 6$
2	Tracking base pose: X_0	$J_2 = [I_6 \quad 0_{6\times 7}]$	$m_2 = 6$
3	Safe joint config.: q	$J_3 = [0_{7\times 6} \quad I_7]$	$m_3 = 7$

The three tasks, along with their Jacobians, are reported in Table 1.

The end-effector Jacobian J_1 is defined by

$$\begin{aligned} J_b &:= {}^N X_0 \\ J_m &:= \left[\cdots \; {}^N X_i X_{J_i}(q_i)\, s_r \; \cdots\right] \end{aligned} \tag{11}$$

with $s_r := [0\ 0\ 1\ 0\ 0\ 0]^\mathsf{T} \in \mathbb{R}^6$ being the motion constraint of the revolute joint.

Once the tasks have been specified, the problem may be solved by selecting the following commands:

$$\begin{aligned} \nu_N^c &= \gamma^X\left(\tilde{X}_N\right) + \tilde{X}_N^{-1}\bar{\nu}_N \\ \nu_N^c &= \gamma^0\left(\tilde{X}_0\right) + \tilde{X}_0^{-1}\bar{\nu}_0 \\ \Omega^c &= -K_q\tilde{q} \end{aligned}$$

The outer loop stabilizer is selected as in [5]. For $\kappa = 0, N$:

$$\gamma^\kappa = \left(\tilde{e}_\kappa, -\tilde{R}_\kappa K_\kappa^p \tilde{p}_\kappa\right),$$

where $\tilde{e}_\kappa = -S^{-1}\left(\mathrm{skew}\left(K_\kappa^R \tilde{R}_\kappa\right)\right)$ is the attitude error, and $K_\kappa^p \in \mathbb{R}^{3\times 3} > 0$, $K_\kappa^R \in \mathbb{R}^{3\times 3}$ and $K_q \in \mathbb{R}^{N\times N} > 0$ are symmetric gain matrices.

Materials Research Proceedings 69 (2026) 885-890 https://doi.org/10.21741/9781644904251-156

In the scenario considered, a reference trajectory is commanded to the end-effector to follow the grasping point on the target and perform an orbital capture. The base spacecraft is commanded to follow such a grasping point. The third task is commanded as a safe pose different from the one naturally obtained with the first two tasks active.

Two representative simulations are reported next.

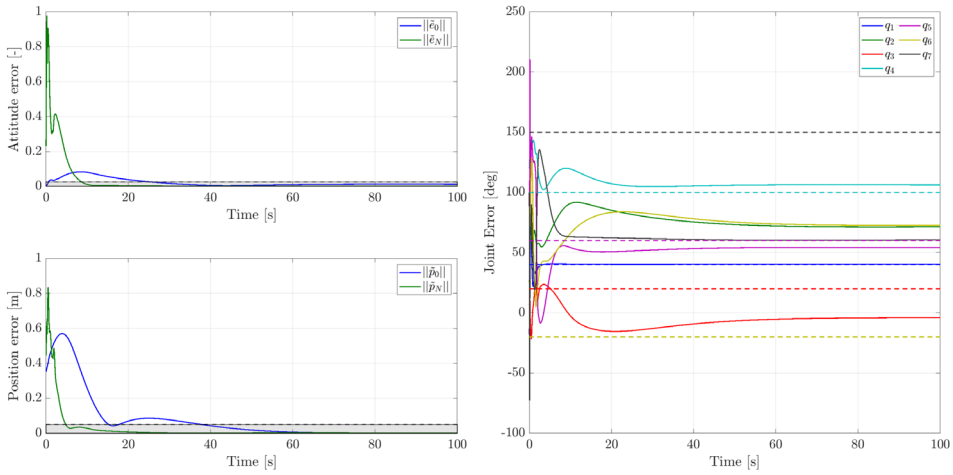


Figure 2: Pose errors of base and end-effector, and joint angles – non-singular ICs.

In the first simulation, the first two tasks are performed, as in both cases the position error norm and the attitude error norm converge below the threshold error (gray area in (Figure 2-left)) while the joint angles do not reach the safe configuration (dashed lines), except for the first joint q_1, that represents the only DoF not used by previous tasks (Figure 2-right).

In the second simulation (Figure 3), the initial conditions (ICs) of the manipulator are modified to make it start the maneuver in a singular configuration. In this way, the third task comes into action and the joints that result in critical positions (q_3 and q_5) reach the safe configuration. Then, the capture is performed nominally, after successfully exiting the singularity. The gray area in the joints plot marks the instant where the capture actually begins.

Conclusions

This paper has extended the hierarchical task-priority algorithm proposed in our previous work [5] to scenarios where the task dimension exceeds the DoFs of the system, while preserving modularity and robustness to kinematic singularities. Simulation results have proven the effectiveness of the proposed control scheme. By leveraging the safe pose at the end of the tasks stack, the system manages to escape from the singularity condition and subsequently performs the capture.

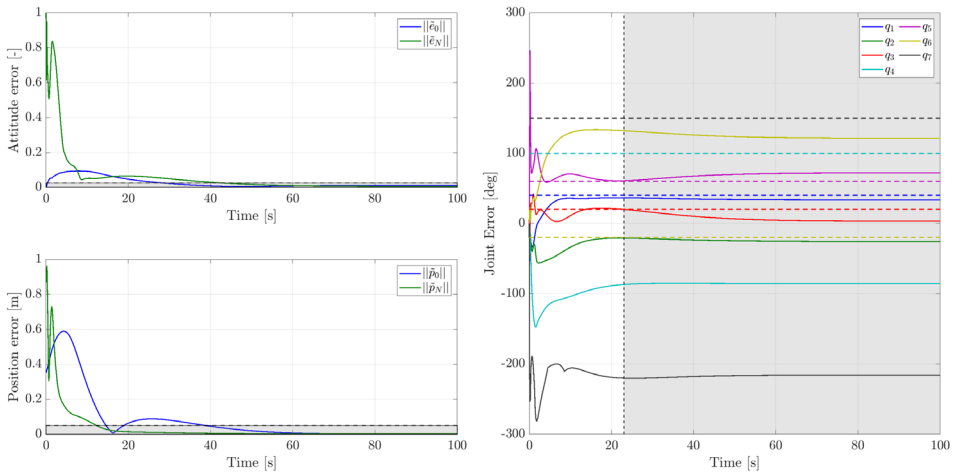


Figure 3: Pose errors of base and end-effector, and joint angles – singular ICs.

References

[1] P. Tsiotras, M. King-Smith, and L. Ticozzi, Spacecraft-mounted robotics, Annual Review of Control, Robotics, and Autonomous Systems, vol. 6, 2023. https://doi.org/10.1146/annurev-control-062122-082114

[2] Y. Nakamura, H. Hanafusa, and T. Yoshikawa, Task-Priority Based Redundancy Control of Robot Manipulators. The International Journal of Robotics Research, vol. 6, no. 2, pp 3-15, 1987. https://doi.org/10.1177/027836498700600201

[3] S. Chiaverini, Singularity-robust task-priority redundancy resolution for real-time kinematic control of robot manipulators, IEEE Transactions on Robotics and Automation, vol. 13, no. 3, pp. 398-410, 1997. https://doi.org/10.1109/70.585902

[4] G. Antonelli, Stability Analysis for Prioritized Closed-Loop Inverse Kinematic Algorithms for Redundant Robotic Systems, IEEE Transactions on Robotics, vol. 25, no. 5, pp. 985-994, Oct. 2009. https://doi.org/10.1109/TRO.2009.2017135

[5] P. Bruschi and D. Invernizzi, Singularity-free task-priority design for trajectory tracking in space robots, 2025 American Control Conference (ACC), Denver, USA, 2025, pp. 3825-3830. https://doi.org/10.23919/ACC63710.2025.11107894

[6] G. Garofalo and C. Ott, Hierarchical tracking control with arbitrary task dimensions: Application to trajectory tracking on submanifolds, IEEE Robot. Autom. Lett., vol. 5, no. 4, pp. 6153-6160, 2020. https://doi.org/10.1109/LRA.2020.3010449

[7] D. Invernizzi, M. Lovera and L. Zaccarian, Hierarchical dynamic control for robust attitude tracking, IFAC-PapersOnLine, vol. 53, no. 2, pp. 6171-6176, 2020. https://doi.org/10.1016/j.ifacol.2020.12.1701

[8] Apkarian, P., Gahinet, P., and Buhr, C., Multi-model, multi-objective tuning of fixed-structure controllers, 2014 European Control Conference (ECC), IEEE, Strasbourg, France, 2014, pp. 856-861. https://doi.org/10.1109/ECC.2014.6862200

[9] R. Featherstone, Rigid body dynamics algorithms. New York : Springer, 2008. https://doi.org/10.1007/978-1-4899-7560-7

Materials Research Proceedings 69 (2026) 891-896 https://doi.org/10.21741/9781644904251-157

Enabling Onboard Analytical Batch Filtering for Angles-Only Navigation to Non-Cooperative Space Targets

Alessandro SCALVINI[1,a *], Giacomo BORELLI[1,b] and Gabriella GAIAS[1,c]

[1]Department of Aerospace Science and Technology, Politecnico di Milano, Via La Masa 34, 20156 Milano, Italy

[a]alessandro.scalvini@polimi.it, [b]giacomo.borelli@polimi.it, [c]gabriella.gaias@polimi.it

Keywords: Angles-Only Relative Navigation, Sliding-Window LSQ, Analytical Batch LSQ

Abstract. Angles-only relative navigation enables autonomous operations with non-cooperative targets such as defunct satellites and orbital debris, which lack the means of communicating with other satellites or ground stations. In fact, this navigation paradigm relies on gathering information about the target only by means of passive cameras mounted on the chaser satellite. The camera provides a pair of bearing angles which are used by the navigation filter to estimate the relative orbit. As of today, sequential filters are typically employed for on-board applications due to their computational efficiency, whereas batch filters are mostly confined to ground-based operations, where their higher computational cost poses no limitation. In this work we revisit the semi-analytic batch least-squares (LSQ) filtering framework with the aim of bringing its on-board implementation closer to practical feasibility. The proposed LSQ filter preserves the analytical propagation required for real-time use while improving accuracy and observability through three key upgrades: (i) a closed-form propagation model including first-order J_2, J_4, J_6 and second-order Keplerian and J_2 effects; (ii) an exact measurement model with improved mean-to-osculating transformation; (iii) an efficient circular-buffer configuration. The proposed filter is tested in a high-fidelity 750 km sun-synchronous orbit simulation with realistic perturbations and is shown to achieve accurate relative state estimation without manoeuvre-induced observability.

Introduction

Angles-only relative navigation is a key technology for autonomous operations with non-cooperative resident space objects such as defunct satellites and debris lacking GNSS receivers, inter-satellite links or cooperative beacons. Missions such as on-orbit inspection, servicing, end-of-life disposal and active debris removal [1, 2, 3] must therefore rely on navigation systems capable of estimating relative states solely from onboard passive optical sensors [4]. Cameras are ideal due to their availability, low power, light weight and wide dynamic range. While sequential filters (extended/unscented Kalman filter) are the standard choice for onboard implementation [5], batch least-squares (LSQ) filtering may offer a robust complementary approach for onboard state estimation. Although traditionally used for precise ground-based orbit determination, an analytical formulation with a sliding observation window might enable computationally efficient onboard use, as suggested (but not demonstrated) by Ardaens [6]. In fact, these filters could serve as: (i) Cross-check mechanisms to reduce/eliminate outliers before they are used by the sequential filter. (ii) Re-initialisation in the event of filter divergence. (iii) Entirely novel hybrid batch-sequential architectures. This work extends the analytical LSQ framework by Gaias et al. [7], which used bearing angles and relative orbital elements (ROE) as states. Their inclusion of J_2 yielded weak observability compared to the completely unobservable Keplerian case studied in [8]. However, their relatively benign scenario characterised by high altitude, negligible differential drag (DD) and simplified propagation and measurement models limits applicability and estimation accuracy.

Content from this work may be used under the terms of the Creative Commons Attribution 3.0 license. Any further distribution of this work must maintain attribution to the author(s) and the title of the work, journal citation and DOI. Published under license by Materials Research Forum LLC.

Materials Research Proceedings 69 (2026) 891-896 https://doi.org/10.21741/9781644904251-157

Specifically, the J_2 model did not include effects induced by non-zero semimajor-axis. Moreover, the first-order mapping from relative orbital elements and line of sight (LoS) omitted the orbital curvature and mean-to-osculating transformations, reducing accuracy and observability. Nonetheless, the fully analytical nature proposed in [7] made the algorithm highly efficient. Here, the manoeuvre-free phase presented in [7] is revisited with the aim of improving estimation accuracy and observability while preserving analytical tractability. The proposed LSQ-based filter introduces the following improvements: (i) Enhanced propagation: analytical model including first-order J_2, J_4, J_6 and second-order Keplerian and J_2 effects [9]. (ii) Improved measurement: exact non-linear LoS transformation coupled with a refined mean-to-osculating transformation [10]. (iii) Circular-buffer implementation: the data batch is implemented as a sliding window, sized according to [11] and managed as a circular buffer to reduce memory operations. The LSQ filter is validated in a model-in-the-loop setup using a high-fidelity orbital simulator that accounts for higher-order gravity, third body effects, solar radiation pressure, and atmospheric drag. Camera noise, illumination, and shadowing are excluded in this first analysis and will be addressed in future work. The test scenario, consistent with [7], is inspired by the PRISMA mission and uses a 750 km sun-synchronous orbit. No manoeuvres is executed to avoid any observability enhancement. Preliminary results demonstrate good filter performance and a notable improvement in estimation accuracy compared to typical TLE-level initialization.

Propagation Model

Quasi-non-singular ROE provide an intuitive parametrisation of the relative motion of the target ("T") with respect to the chaser ("C"). Recalling the classical orbital elements (OE) vector $\boldsymbol{\alpha}=[a, e, i, \Omega, \omega, M]^\top$, the ROE are as a non-linear combination of the of $\boldsymbol{\alpha}_C$ and $\boldsymbol{\alpha}_T$ [9]. In particular, the dimensional (quasi-non-singular) ROE are defined as $a\delta\boldsymbol{\alpha} = a_C[\delta a, \delta\lambda, \delta e_x, \delta e_y, \delta i_x, \delta i_y]^\top$, where the components denote relative semi-major axis, mean relative longitude, eccentricity and inclination vectors. This representation gives a geometrically meaningful description of the motion in the Radial-Transversal-Normal frame (R) and separates the weakly observable range analogue $a\delta\lambda$ from the strongly observable components [7]. The GCL model [9] is selected for the LSQ filter since it accurately propagates $a\delta\boldsymbol{\alpha}(t_0)$ at initial time t_0 to time t, accounting for J_2, J_4, J_6, and second-order Keplerian and J_2 effects (DD is not modelled). The manoeuvre-free, analytical propagation model is:

$$a\delta\boldsymbol{\alpha}(t) = \mathbf{F}_{\mathrm{GCL}}(t_0, t, a\delta\boldsymbol{\alpha}(t_0), \boldsymbol{\alpha}(t_0)). \quad (1)$$

Measurement Model

In angles-only navigation, the chaser perceives the target solely through the bearing angles vector composed by a pair of azimuth (α) and elevation (ϵ) angles measured in the camera frame. In this article we follow the convention used in [5]. The camera frame (C) is oriented in anti-flight direction as in [7]. At time t, the navigation subsystem knows: the current knowledge of the ROE (from the filter), the chaser absolute OE (from external sources, e.g., GNSS) and the orientation of the inertial frame (I) relative to the camera ${}^{\mathrm{C}}\mathbf{R}_{\mathrm{I}}(t)$. The LoS vector is thus obtained using the exact fully non-linear transformation reported in [10]. By then the applying the definition of bearing angles, the resulting complete non-linear sequence of operations defines the modelled measurement:

$$\mathbf{y}(t) = [\alpha(t), \epsilon(t)]^\top = \mathbf{h}_{\mathrm{NL}}(a\delta\boldsymbol{\alpha}(t), \boldsymbol{\alpha}_C(t), {}^{\mathrm{C}}\mathbf{R}_{\mathrm{I}}(t)). \quad (2)$$

Circular Buffer Batch LSQ

In this work we implement an updated version of batch LSQ filter proposed in [7]. In fact, we use the more accurate [11] GCL analytical propagation model and, instead of relying on the

Materials Research Proceedings 69 (2026) 891-896 https://doi.org/10.21741/9781644904251-157

inaccurate ROE-to-LoS mapping presented in [7], we compute it numerically by taking the Jacobian of Eq. (2) with respect to $a\delta\boldsymbol{\alpha}(t)$. This results in a slightly higher computational cost which is however offset by the much higher accuracy [11]. The LSQ filter operates on a data structure composed of B data-points. The "batch size" B corresponds to the number of data-points available to the filter where the latter are *synchronous* collections of measurement time t_{meas} and corresponding observed bearing angles pair $\mathbf{z}(t_{\text{meas}})$, chaser absolute orbit $\boldsymbol{\alpha}_C(t_{\text{meas}})$ and camera attitude ${}^{\text{C}}\mathbf{R}_{\text{I}}(t_{\text{meas}})$. When a new measurement arrives, it is stored in a fixed, preallocated memory block together with the corresponding timestamp and the chaser absolute OE and camera attitude at that same instant. This operation effectively adds a new data point to the batch. This memory acts as a sliding window managed as a circular buffer, where the write position advances with each new entry and wraps around once the buffer is full, overwriting the oldest data to maintain a constant batch size (defined according to the guidelines of our previous work [11]). This strategy avoids physically shifting data in memory. Instead, only the read position is updated. When this index exceeds the buffer size, it is reset to the initial position. The process repeats, overwriting old data with a first-in, first-out logic. Once the buffer is fully updated, corresponding to a complete non-overlapping shift of the sliding window, the LSQ algorithm is executed using the current buffer contents as input. The selected algorithm also requires an *a priori* estimate of the $a\delta\boldsymbol{\alpha}$ and its associated uncertainty. During the first execution, this information is provided by external sources (e.g., NORAD TLE). For subsequent executions, the *a priori* information is derived from the previous estimate, propagated to the new estimation epoch. Additionally, the LSQ requires specifying the time instant at which the estimate is computed. In this work, it corresponds to the earliest measurement time within the buffer.

Preliminary Results

The LSQ filter undergoes model-in-the-loop validation by means of a high-fidelity simulation tool. The ground-truth simulation is obtained over 20 chaser orbital periods using a Dormand-Prince 5th-order integrator with a fixed step of 10 (s). The dynamical model includes the GGM03S gravity field up to degree and order 30, a cannonball drag model and atmospheric density computed from NRLMSISE-00. Camera noise, illumination and shadowing are excluded in this first analysis and will be addressed in future work. No manoeuvres are simulated to avoid artificial observability enhancement. Coherently with [7], the simulated case study is inspired by the PRISMA mission and uses a 750 km sun-synchronous orbit with LTAN = 9.5 hours for the chaser absolute orbit, whose spacecraft physical parameters can be found in [6]. The ground-truth initial conditions for the relative orbit are taken from Table 6 of [7] which also provide the initial guess for the batch LSQ filter with an error consistent with NORAD TLE accuracy, representing typical knowledge for debris or non-cooperative targets. The same level of uncertainty is the one used by the filter for the first call, in particular we assume that the *a priori* standard deviation vector $\boldsymbol{\sigma}_{a\delta\boldsymbol{\alpha}} = [20, 1000, 100, 100, 100, 100]^{\intercal}$. Moreover, for the successive calls, a minimum uncertainty is always enforced on the propagated uncertainty as suggested by [7]: $\boldsymbol{\sigma}_{a\delta\boldsymbol{\alpha}}{}^{\text{min}} = [3, 50, 10, 10, 10, 10]^{\intercal}$. Each time the circular buffer completes a full update, the LSQ algorithm receives the 120 data-points batch of data and performs the estimate. In this paper, the camera is assumed to output a valid measurement every 250 (s). Thus, with a circular buffer of 120 data-points, the measurements are uniformly spread over almost 5 full chaser orbit periods, as suggested in [11]. The results of the periodic estimation outcome are reported in Fig. 1 for the first run of the least square in Fig. 2 for the last run.

Materials Research Proceedings 69 (2026) 891-896 https://doi.org/10.21741/9781644904251-157

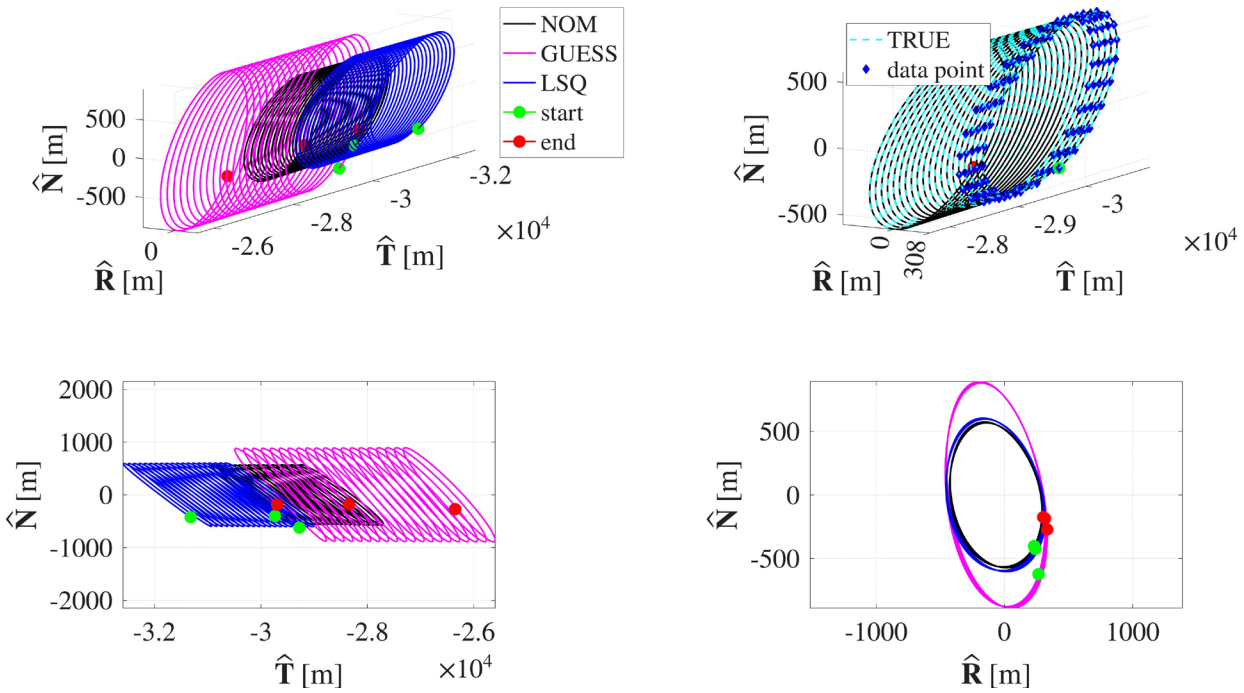


Figure 1: Results of the estimation procedure. Data collected over orbits 1 to 5.

Each figure consists of four plots. The top-left panel shows a 3D view of three relative orbits in the *R* frame, centred on the chaser spacecraft. The nominal (NOM) orbit, in solid black, is obtained by propagating the *true* initial conditions with the analytical model $\mathbf{F}_{\mathrm{GCL}}$. The initial guess (GUESS) orbit, in solid magenta, is propagated from the filter *a priori* guess, while the post-estimation (LSQ) orbit, in solid blue, uses the converged LSQ output. All orbits are propagated with the analytical model of Eq. 1, thus neglecting DD. The green and red markers indicate the start and end points, respectively. The second row presents the TN- and RN-plane projections (bottom-left and bottom-right plots). The top-right panel shows an additional 3D view, where the true (TRUE) orbit, obtained from the high-fidelity simulator, is superimposed on the nominal one with a dashed cyan line. The case study is inspired from PRISMA mission, where the high altitude orbit and almost equivalent ballistic coefficients of the two spacecraft [6] make DD effects negligible. Thus, given the high accuracy of the GCL model, NOM and TRUE orbits are practically equivalent. From the first figure, it is evident that the initial guess (derived from TLE) is significantly improved by the LSQ, despite the large uncertainty on $a\delta\lambda$. Recall that the authors of [7] had to impose an unrealistically small range uncertainty in the LSQ to ensure convergence, which in turn prevented meaningful updates of $a\delta\lambda$. The enhanced observability provided by the improved models allows this component to be accurately estimated.

Materials Research Proceedings 69 (2026) 891-896 https://doi.org/10.21741/9781644904251-157

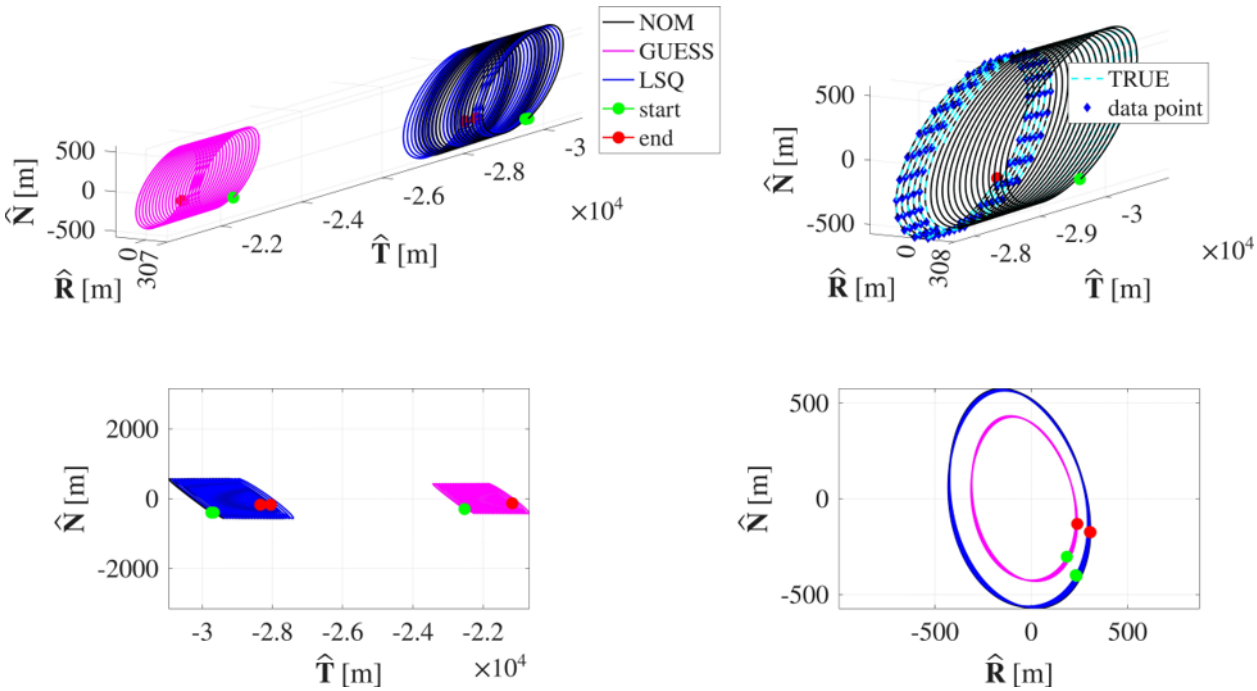


Figure 2: Results of the estimation procedure. Data collected over orbits 16 to 20.

The second figure illustrates two key aspects: first, that the previous LSQ runs degraded the estimate due to weak observability and the necessity to impose $\boldsymbol{\sigma}_{a\delta\boldsymbol{\alpha}}^{\min}$ to prevent filter stagnation [7]. Secondly, the filter successfully recovers and achieves an even more accurate relative orbit estimate. In general, it is observed that progressively running the LSQ as described in this work results in estimates oscillating around the true orbit. This behaviour arises partly from the weak observability of the problem and partly from the need to impose a minimum uncertainty to prevent filter stagnation [7]. In conclusion, this work enhances the batch LSQ framework of [7]. The refined analytical propagation and exact non-linear ROE-to-LoS transformation improve accuracy and observability in manoeuvre-free scenarios, enabling estimation of the weakly observable $a\delta\lambda$. The circular-buffer sliding window further advances the framework toward onboard implementation.

Acknowledgements

This research is funded by Infinite Orbits SAS, grant reference: UA.A.RRR.DAER.ELABS. AUTO.G8E4RICC00 PhD-GNC Rendezvous - RIF. 10/2024 GAIAS. The Authors would like to acknowledge GNC Engineers Daniel Opoka and Raffaele Tarone for their support.

References

[1] R. Biesbroek, S. Aziz, A. Wolahan, S. Cipolla, M. Richard-Noca, and L. Piguet. The clearspace-1 mission: Esa and Clearspace team up to remove debris. In Proceedings of the 8th European Conference on Space Debris, volume 8, pages 1-3. ESA Space Debris Office, 2021.

[2] S. Woicke, J. Jipp, C. Steimle, N. Pokrupa, and L. Metrailler. Adrios clearspace-1: In orbit demonstration of the removal of a non-cooperative spacecraft. In Proceedings of the 9th European Conference on Space Debris, volume 9. ESA Space Debris Office, 2025.

[3] A. Scalvini, A. Fois, A. Suarez, S. R. Nekoo, and A. Ollero. Adaptive state-dependent Riccati equation attitude control for rotation-flying dual-arm manipulators. In Proceedings of the 2024 International Conference on Space Robotics (iSpaRo), pages 372-379, Luxembourg, 2024. IEEE. https://doi.org/10.1109/iSpaRo60631.2024.10687494

[4] J. Sullivan, S. Grimberg, and S. D'Amico. Comprehensive survey and assessment of spacecraft relative motion dynamics models. Journal of Guidance, Control, and Dynamics, 40(8):1837-1859, 2017. https://doi.org/10.2514/1.G002309

[5] J. A. Sullivan. Nonlinear Angles-Only Orbit Estimation for Autonomous Distributed Space Systems. PhD thesis, Stanford University, 2020.

[6] J.-S. Ardaens. Angles-Only Relative Navigation in Low Earth Orbit. PhD thesis, Delft University of Technology, 2020.

[7] G. Gaias, S. D'Amico, and J.-S. Ardaens. Angles-only navigation to a noncooperative satellite using relative orbital elements. Journal of Guidance, Control, and Dynamics, 37(2):439-451, 2014. https://doi.org/10.2514/1.61494

[8] D. C. Woffinden and D.-K. Geller. Observability criteria for angles-only navigation. IEEE Transactions on Aerospace and Electronic Systems, 45(3):1194-1208, 2009. https://doi.org/10.1109/TAES.2009.5259193

[9] G. Gaias, C. Colombo, and M. Lara. Analytical framework for precise relative motion in low earth orbits. Journal of Guidance, Control, and Dynamics, 43(5):915-927, 2020. https://doi.org/10.2514/1.G004716

[10] G. Gaias, J.-S. Ardaens, and C. Colombo. Precise line-of-sight modelling for angles-only relative navigation. Advances in Space Research, 67(11):3515-3526, 2021. https://doi.org/10.1016/j.asr.2020.05.048

[11] A. Scalvini, G. Borelli, and G. Gaias. Towards robust angles-only relative orbit navigation: Assessing key modelling factors using batch least squares filtering. In Proceedings of the 11th European Conference for Aeronautics and Aerospace Sciences (EUCASS), 2025.

Materials Research Proceedings 69 (2026) 897-901 https://doi.org/10.21741/9781644904251-158

Hardware-in-the-Loop Implementation of a Fixed-Point Controller for Boresight Stabilization of Magnetorquer-Only Satellites

Emre SAYIN[1,a *], Stefano CARLETTA[2,b] and Fabio CELANI[2,c]

[1]Faculty of Aeronautics and Astronautics, Istanbul Technical University, Maslak, 34467, Istanbul, Türkiye

[2]School of Aerospace Engineering, Sapienza University of Rome, Via Salaria 851, 00138, Roma, Italy

[a]emre.sayin@itu.edu.tr, [b]stefano.carletta@uniroma1.it, [c]fabio.celani@uniroma1.it

Keywords: Boresight Stabilization, Magnetic Attitude Control, Hardware-In-The-Loop, FPGA

Abstract. In this work the implementation and hardware-in-the-loop testing of a boresight stabilization algorithm, based on the use of magnetorquers as actuators, is presented. The proportional-derivative controller, previously validated by numerical simulations, is here adapted to fixed-point arithmetic and discrete time, and implemented on a Field Programmable Gate Array. Optimal control gains are determined through particle swarm optimization and the resulting algorithm is tested hardware-in-the-loop, with the spacecraft attitude dynamics being simulated using Matlab/Simulink, through a Monte Carlo campaign. The results of this study confirm the suitability and performance of the boresight stabilization algorithm, even within limitations set by real flight hardware. The demonstrated hardware implementation bridges the gap between theoretical control design and embedded execution, offering a robust, low-cost solution for precise satellite pointing using minimal sensors and computational resources.

Introduction

Boresight stabilization represents a fundamental task of attitude control and it consists in pointing the bore axis of an onboard device (i.e. antenna, camera, etc.) towards a prescribed direction. Because the interest is related to the alignment of only one axis of the satellite, reduced attitude control techniques, with the pointing axis corresponding the boresight one, can be preferred to three-axis attitude control, leading to lower computational and energy requirements [1, 2, 3].

For satellites equipped with only magnetorquers as actuators, boresight stabilization towards an inertially-fixed reference direction has been developed and verified through numerical simulations [4, 5]. The resulting algorithm shows a proportional-derivative behavior, ensures stabilization without spinning around the boresight axis, and requires the measurements of the reference direction, the magnetic field induction, and the satellite angular rates, obtained by common on-board devices such as star-trackers, three-axis magnetometer and rate gyro. The result has been later extended to nadir pointing, that also requires determination of the full attitude [7].

In this paper, the effectiveness of the boresight stabilization algorithm developed in Refs [5,6] is verified after implementation on flight-proven hardware, a Artix-7 Field Programmable Gate Array (FPGA). The translation of the control algorithm from Matlab syntax to the Hardware Description Language (HDL) compatible with the use of finite-resolution sensors (i.e. star-tracker, three-axis MEMS magnetometer and gyroscope) requires two major adjustments: the transition from double-precision to fixed-point arithmetic and from variable-step to fixed-step. Indeed, this process produces a loss of accuracy of the attitude control algorithm, resulting in a larger pointing error and oscillation of the steady-state angular rates.

Content from this work may be used under the terms of the Creative Commons Attribution 3.0 license. Any further distribution of this work must maintain attribution to the author(s) and the title of the work, journal citation and DOI. Published under license by Materials Research Forum LLC.

Materials Research Proceedings 69 (2026) 897-901 https://doi.org/10.21741/9781644904251-158

To mitigate accuracy loss, adequate scale factors for the input measurements are identified, which guarantee the input never exceed the maximum representable value while maximizing the accuracy associated to the chosen fixed-point representation. Inasmuch, optimal gains are identified through particle swarm optimization (PSO) performed on Hardware-in-the-Loop (HiL) simulations, where the attitude dynamics is simulated on a host PC and the control algorithm is run onto the FPGA.

Finally, the performance of the algorithm is verified from a HiL Monte Carlo campaign, in which the initial attitude and angular rates are selected randomly within closed intervals. The results show good agreement with those obtained from numerical simulations and suggest the solution is effective to be used on real flight hardware.

Magnetic Boresight Stabilization Algorithm

The magnetic boresight stabilization algorithm can be described as follows. The spacecraft is modeled as a rigid body, and the body-fixed boresight axis is expressed by the constant column matrix of its body coordinates $\boldsymbol{a} \in S = \{\boldsymbol{v} \in R^3 : \boldsymbol{v}^T\boldsymbol{v} = 1\}$. The inertially-fixed reference axis is expressed by the constant column matrix $\boldsymbol{a}_r^i \in S$ of its coordinates along the standard Earth-Centered Inertial (ECI) frame. Let $\boldsymbol{R}$ be the rotation matrix that transforms a column matrix of ECI coordinates into the corresponding column matrix of body coordinates. Thus, the reference axis expressed in body-coordinates is given by $\boldsymbol{a}_r = \boldsymbol{R}\boldsymbol{a}_r^i$. The attitude kinematics is given by $\dot{\boldsymbol{R}} = -\boldsymbol{\omega}^{\times}\boldsymbol{R}$ where $\boldsymbol{\omega}^{\times}$ is a 3×3 skew-symmetric matrix that fulfills $\boldsymbol{\omega}^{\times}\boldsymbol{v} = \boldsymbol{\omega} \times \boldsymbol{v}$ for all $\boldsymbol{v} \in R^3$. The spacecraft attitude dynamics are given by $\boldsymbol{J}\dot{\boldsymbol{\omega}} + \boldsymbol{\omega} \times (\boldsymbol{J}\boldsymbol{\omega}) = \boldsymbol{T}_c$ where $\boldsymbol{J}$ is the spacecraft inertia matrix, $\boldsymbol{T}_c$ is the column matrix of body coordinates of the control torque. Disturbance torques are neglected throughout this work. The control torque is generated by three magnetorquers aligned with three orthogonal axes. Thus, it is given by $\boldsymbol{T}_c = \boldsymbol{m}_c \times \boldsymbol{b}$ where $\boldsymbol{m}_c$ is the column matrix of the body coordinates of the control magnetic dipole moment, and $\boldsymbol{b}$ is the column matrix of body coordinates of the geomagnetic induction at the spacecraft. The boresight stabilization law employed in this work is of the Proportional-Derivative (PD) type [5] and is given by

$$\boldsymbol{m}_c = \boldsymbol{b} \times \left[k_p(\boldsymbol{a} \times \boldsymbol{a}_r) - k_d\boldsymbol{\omega}\right] \tag{1}$$

where k_p and k_d are positive scalar gains. Its effectiveness is first validated by running numerical simulations employing a double precision variable-step solver. Tables 1 and 2 report the values of the parameters used in the simulations.

Table 1: Spacecraft parameters

$\boldsymbol{J}$ [kg m^2]	$m_{cx_{max}}$ [A m^2]	$m_{cy_{max}} = m_{cz_{max}}$ [A m^2]
diag ($9.2\cdot10^{-3}$ $4.44\cdot10^{-2}$ $4.486\cdot10^{-2}$)	0.097	0.151

Table 2: Orbital and boresight stabilization parameters

a [km]	e	i [deg]	Ω [deg]	$\boldsymbol{a} = \boldsymbol{a}_{ri}$	k_p	k_d
6971	0	98	235	[1 0 0]^T	218	$1.88\cdot10^5$

The spacecraft initial attitude, its initial argument of latitude, the initial angle of rotation of the Earth are all selected randomly with a uniform distribution over all of their possible values. The initial angular velocity is selected randomly with a uniform distribution over $\|\boldsymbol{\omega}(0)\| \leq 3$ deg/s. The IGRF model [8] is adopted for geomagnetic induction. A Monte Carlo (MC) campaign is carried out by running 30 simulations. The 30 time behaviors of the pointing error and of the norm

Materials Research Proceedings 69 (2026) 897-901 https://doi.org/10.21741/9781644904251-158

of the angular velocity are displayed in Fig. 1. They show that in all 30 simulation runs the law in Eq. (1) achieves boresight stabilization without spinning with very good accuracy.

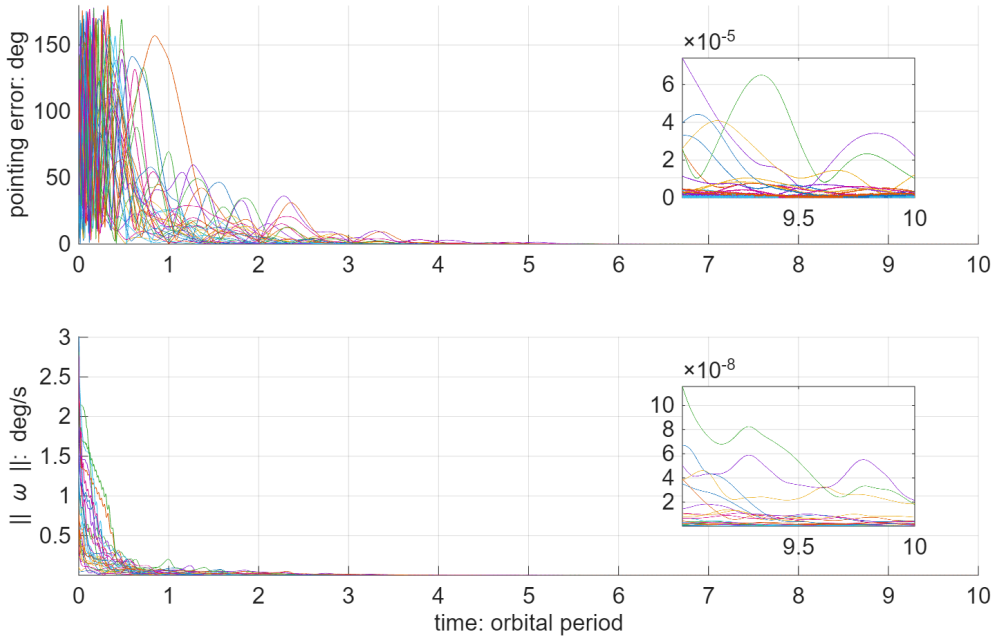


Figure 1: Time behaviors of pointing error and norm of angular velocity from the MC numerical campaign with double-precision variable-step solver.

Hardware-in-the-Loop Implementation and Testing

To validate the practical feasibility of the control law, the algorithm described in Eq. 1 was implemented on an AMD Artyx-7 FPGA and tested in a HiL configuration. This translation from the double-precision variable-step environment used for numerical simulation to a fixed-step fixed-point hardware implementation introduces several challenges that must be addressed.

First, the controller must operate at a fixed sample time T_s, which is chosen as 1 s for the HiL implementation. Additionally, the optimal behavior of FPGAs occurs under fixed-point operations, rather than floating-point operations. This conversion introduces quantization errors and carries the risk of numerical overflow or underflow. To overcome this, the input measurements (reference direction in body coordinates a_r, geomagnetic induction b, and angular velocity ω) and all intermediate variables were carefully scaled. The selection of these scale factors is a trade-off between maximizing the numerical precision (using the full fractional part of the fixed-point number) and maintaining sufficient integer part to prevent saturation during orbital variations or attitude maneuvers. To find the optimal gains for the controller, a PSO campaign has been conducted. The optimal parameters for the controller are indicated in Table 2.

Using the optimal control parameters as the reference, the fixed-point controller was designed. It was decided to use a 20-bit signed fixed-point arithmetic, with a fraction length of 16-bit to get the best accuracy as well as preventing the overflow. The units of the controller input parameters are subsequently arranged according to this fixed-point representation. Table 3 shows the unit conversions that are conducted to get the optimal controller input representation.

Materials Research Proceedings 69 (2026) 897-901 https://doi.org/10.21741/9781644904251-158

Table 3: Controller input ranges and conversions for fixed-point implementation

Variable	Numerical simulations	HiL simulations
Angular velocity $\boldsymbol{\omega}$	[-0.052, 0.052] rad/s	[-3 3] deg/s
Geomagnetic Induction	$[-5\ 5]\cdot 10^{-5}$ T	[-0.05, 0.05] mT

To validate the performance of the final fixed-point controller, the same Monte Carlo campaign was repeated using the HiL setup. The initial conditions for attitude and angular velocity were randomized identically to the double-precision variable-step numerical campaign. The results are presented in Fig. 2.

As shown in Fig. 2, the HiL results demonstrate the successful boresight stabilization in all 30 cases, showing strong agreement with the double-precision simulations in Fig. 1. A closer look to the steady-state performance (inset plots in Fig. 2) shows the expected effects of the fixed-point arithmetic. The pointing error stays in a bounded ``bouncing" region, with an amplitude of approximately 2 deg. Similarly, the norm of the angular velocity stays in a region with an amplitude of approximately $3\cdot 10^{-3}$ deg/s, indicating a minimal steady-state spin. This behavior is a direct and acceptable consequence of the quantization of sensor inputs and control outputs, and the performance remains well within acceptable limits for many nanosatellite missions.

To compare the pointing accuracy achieved in numerical simulations with HiL simulations, Table 4 reports the statistics of the maximum pointing error Θ_{max} and of the maximum norm of the angular velocity $|\omega|_{max}$ both in steady-state.

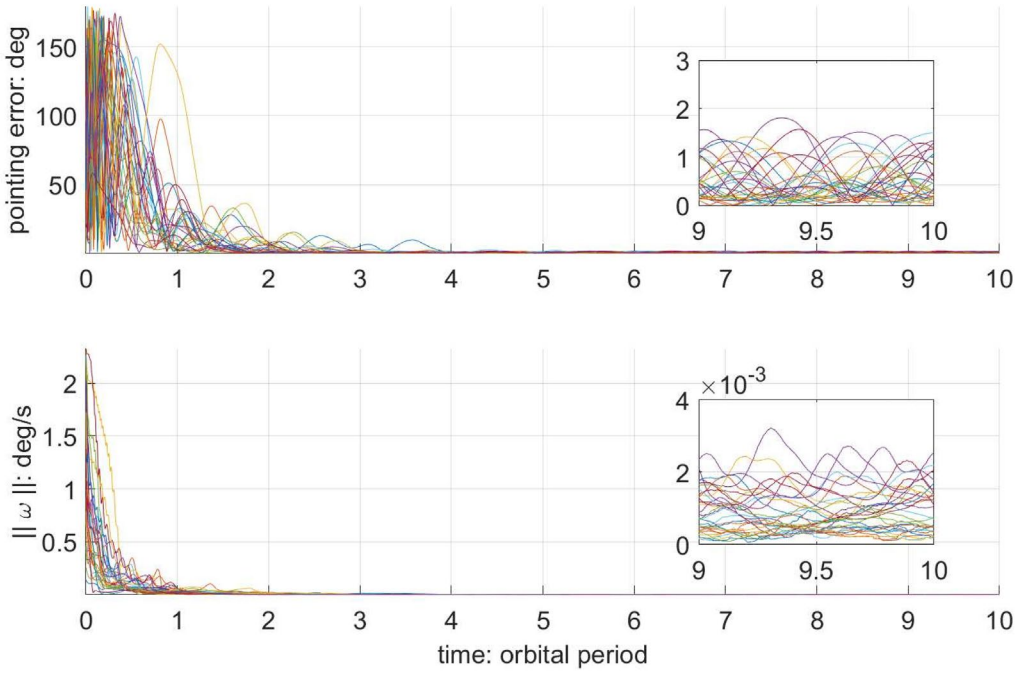


Figure 2: Time behaviors of pointing error and norm of angular velocity from the HiL MC campaign with 20-bit wordlength and 16-bit decimal resolution with fixed 1s time step.

Table 4: Statistics from the two MC campaigns ($\boldsymbol{\mu}(\boldsymbol{v})$ and $\boldsymbol{\sigma}(\boldsymbol{v})$ denote the mean and standard deviation of $\boldsymbol{v}$ respectively).

	Numerical	HiL	Unit
$\mu(\Theta_{max})$	$1.24 \cdot 10^{-5}$	0.94	deg
$\sigma(\Theta_{max})$	$1.95 \cdot 10^{-5}$	0.46	deg
$\mu(\|\omega\|_{max})$	$1.55 \cdot 10^{-8}$	$1.45 \cdot 10^{-3}$	deg/s
$\sigma(\|\omega\|_{max})$	$2.63 \cdot 10^{-8}$	$0.77 \cdot 10^{-3}$	deg/s

Discussion of the Results and Conclusions

The HiL experiments successfully demonstrated the capability of the proposed attitude control architecture to operate under realistic timing and quantization effects. The implemented fixed-point design maintained stable and accurate control performance within the expected operation, showing the suitability of the chosen numerical representation and scaling strategy. The results confirmed that the effects of fixed-step and fixed-point constraints remained acceptable for the test cases. Monte Carlo simulations performed in the HiL environment strengthened the controller's robustness against variations in initial conditions.

Overall, the obtained results verify the practical feasibility of the developed controller for real-time implementation on embedded hardware. The study emphasizes the importance of the fixed-point methodology, ensuring that the transition from simulation to hardware remains reliable. Future work will focus on extending the current HiL setup toward a full hardware-based validation environment. This will involve integrating a real magnetorquer and magnetometer within a Helmholtz cage to to test the behavior under controlled magnetic field, while the spacecraft simulator will be mounted on an air-bearing platform to emulate the friction-free rotational motion.

References

[1] D. Roldugin, A. Okhitina, U. Monakhova, and M. Ovchinnikov, Comparison of Feedback Three-Axis Magnetic Attitude Control Strategies, Aerospace 10 (2023). https://doi.org/10.3390/aerospace10120975

[2] P. Teofilatto, P. Testani, A. Nascetti, and M. Truglio, A nadir-pointing magnetic attitude control system for TigriSat nanosatellite, Proceedings of the International Astronautical Congress 2013, Beijing, China, 23-27 September 2013

[3] A. Drobysheva, S. Tkachev, D. Roldugin, One-axis magnetic attitude control for short-term high-accuracy pointing, Acta Astronautica 228 (2025) 675–685. https://doi.org/10.1016/j.actaastro.2024.12.047

[4] Y.-J. Cheon, S.-H. Lee, and J.-H. Kim, Fully Magnetic Devices-Based Control for Gyroless Target Pointing of a Spinning Spacecraft, IEEE Transactions on Aerospace and Electronic Systems 46 (2010) 1484-1491. https://doi.org/10.1109/TAES.2010.5545203

[5] F. Celani, Reduced-attitude stabilization for spacecraft boresight pointing using magnetorquers, Material Research Proceedings 37 (2023) 611–614. https://doi.org/10.21741/9781644902813-133

[6] F. Celani, Boresight stabilization for inertial pointing spacecraft using magnetorquers, Journal of Guidance Control and Dynamics (2026) accessed January 19, 2026. https://doi.org/10.2514/1.G009085

[7] F. Celani, Boresight stabilization of an Earth-pointing satellite using magnetorquers, Acta Astronautica, 239 (2026) 97-112. https://doi.org/10.1016/j.actaastro.2025.11.005

[8] P. Alken et al., International geomagnetic reference field: the thirteenth generation, Earth, Planets and Space 73 (2021) 1-25. https://doi.org/10.1186/s40623-020-01288-x

Materials Research Proceedings 69 (2026) 902-907 https://doi.org/10.21741/9781644904251-159

Single Agent On-Orbit Inspection: Energy-Awareness, Data Down-linking and Orbital Exploration via Deep-Q-Learning

Augustin DAY[1,a], Francesco Paolo SALZO[2,b,*], Gabriele GEMIGNANI[3,c,*], Stéphanie LIZY-DESTREZ[1,d], and Giordana BUCCHIONI[2,e]

[1]ISAE-SUPAERO, 31055 Toulouse, France

[2]University of Pisa, Department of Information Engineering, 56122 Pisa, Italy

[3]Polytechnic of Bari, Dept. of Electrical and Information Engineering, 70125 Bari, Italy

[a]augustin.day@student.isae-supaero.fr, [b]francesco.salzo@phd.unipi.it, [c]g.gemignani@phd.poliba.it, [d]stephanie.lizy-destrez@isae.fr, [e]giordana.bucchioni@unipi.it

Keywords: On-Orbit Inspection, Reinforcement Learning, Task Scheduling

Abstract. The increasing demand for autonomous space operations motivates lightweight AI-based approaches to Resident Space Objects (RSO) inspection, where spacecraft must balance trajectory optimization with strict onboard resource limitations in real-time. This paper presents a Deep Q-Network (DQN) for single-agent RSO inspection, combining fuel-efficient orbital exploration with battery management and data down-linking in a unified control policy. The environment features a discrete set of relative orbits, stochastic resource dynamics, and a closed-loop transfer method based on Relative Orbital Elements (ROEs). Results show how, across multiple training runs, the agent learns to accomplish the mission with a low number of transfers while efficiently handling battery and data processes.

Introduction

Inspection missions—particularly those targeting high altitude orbits—require spacecraft to autonomously manage multiple mission phases over extended durations. These missions involve coordinating several, competing objectives: maximizing information gain through optimal orbital path planning while preserving onboard resources for future operations. Resource management is crucial to prevent premature satellite failures and the resulting increase in space debris. This work specifically focuses on three critical constraints: fuel for orbital transfers, battery energy for sustaining operations and communications, and data storage capacity, which must be periodically cleared to enable near real-time data availability for ground stakeholders. Balancing these demands from ground stations in real-time is evidently unfeasible. In this paper, we do not address the problem of selecting the optimal set of orbits for inspection; instead, we assume a precomputed set. Unlike existing state-of-the-art approaches for on-orbit inspection [1-3], our primary focus is on the task allocation formulation rather than on optimizing the path to maximize information gain.

The main challenge in implementing scheduling methods on a spacecraft lies in computational complexity [4]. Being an NP-hard problem, classical optimization is impractical in high-variance, large-scale scenarios [5]. Therefore, this paper investigates AI-based approaches, focusing on Reinforcement Learning (RL) for real-time inspection mission planning. RL has shown promise in space applications such as Earth observation [6] and rendezvous [7], demonstrating its ability to learn complex, multi-objective policies without explicit mathematical models. This positions RL as a lightweight, onboard-deployable decision-making framework that can match the performance of traditional methods.

Follows a description of the system software architecture, comprehending the inspection environment simulator, the neural network acting on it, and the RL training algorithm. Then, we show the numerical results obtained in our training campaign and an exemplary simulation of the

Content from this work may be used under the terms of the Creative Commons Attribution 3.0 license. Any further distribution of this work must maintain attribution to the author(s) and the title of the work, journal citation and DOI. Published under license by Materials Research Forum LLC.

Materials Research Proceedings 69 (2026) 902-907 https://doi.org/10.21741/9781644904251-159

trained system. At the end of the manuscript, we draw summary conclusions based on our research work.

Reinforcement Learning Framework

We assume the close-distance inspection of a target orbiting circularly around the Earth, to meet the conditions imposed by the Hill-Clohessy-Wiltshire (HCW) relative frame [8] and thus relying on a well-established physical plant. We consider a fixed set of N orbits, assuming they were previously selected as suitable candidates for collecting image data around the target (see, for instance, [1]). The proposed single-agent inspection framework is formulated as a Markov Decision Process (MDP) and optimized via maximization of a *Reward* signal. An MDP can be interpreted as a sequential control loop running at fixed frequency, where an *agent* takes *decisions* based on feedback from the *environment*. The environment simulates the evolution of the surroundings and the agent's internal status (battery and data buffer) in response to actions.

Agent: The neural network is a Multi-Layer Perceptron (MLP) with four layers. The input layer matches the dimension of the observed state, followed by two hidden layers of 256 neurons each with ReLU activations. The output layer contains one neuron per action. Since the agent aims to explore the target from multiple viewing angles, it must perform an orbital transfer once the current relative orbit has been sufficiently explored. Moreover, to preserve the battery and data buffer states, the satellite can enter *Recharge* and *Downlink* modes, which are modeled here at a high level as a reset of the memory state and a fixed amount of battery recharged within a single timestep. We decided to keep a discrete action space by considering M fixed anomalies on each relative orbit as possible landing points of a transfer action. This way, we use an integer action set $\mathcal{A}$ that encloses both *inspection* and *transfer* actions as:

$$\mathcal{A} = \left\{ \underbrace{1, \dots,}_{\text{transfer}} \underbrace{(i-1) \times M + 1, \dots, i \times M,}_{\text{inspection arc}} \underbrace{i \times M + 1, \dots,}_{\text{transfer}} \underbrace{N \times M + 1,}_{\text{recharge}} \underbrace{N \times M + 2}_{\text{down-link}} \right\} \tag{1}$$

where $i \in \{1, \dots, N\}$ is the index of the currently visited orbit, passed as input to the agent.

Environment. Given the current anomaly ν on the current orbit i, the state space is composed of:

$$\mathcal{S} = \left\{ \underbrace{i, \nu}_{\text{Position onto current orbit}}, \underbrace{b, d}_{\text{Battery and Data level} \in [0,1]}, \underbrace{g_1, \dots, g_N}_{\text{Inspection Level} \in [0,1]} \right\} \tag{2}$$

with g the inspection level, namely the fraction of an orbit that has been explored. The objective of the mission is to maximize the inspection level, ideally $g_j = 1 \; \forall j \in \{1, \dots, N\}$. The action (1) taken by the agent modify the system's state (2) differently. While the transfer action moves the satellite to the given relative orbit at the given anomaly, the inspection arc results in a simple on-orbit propagation regardless of the chosen anomaly. The inspection level of the visited orbit is increased by a quantity μ, here modeled as a Gaussian variable to account for orbit and target heterogeneity. The data buffer is increased accordingly. The battery decay also follows a gaussian dynamics with a mean parameter $\beta_{a \in \mathcal{A}}$, whose value depends on the action taken. Both battery and data state are clipped to the interval [0,1].

Reward. The designed reward function (Table 1) seeks to achieve the full inspection of the relative orbits while minimizing the fuel expenditure Δv and ensuring the energy and data maintenance.

Materials Research Proceedings 69 (2026) 902-907 https://doi.org/10.21741/9781644904251-159

Table 1: Reward Function

Description	Value
Maneuver cost proportional to Δv	$-500 \cdot \Delta v$
Battery penalties	$\begin{cases} -5 & b < b_{th} \rightarrow \text{(battery threshold)} \\ -1 & a = N \times M + 1 \text{ (recharge)} \end{cases}$
Positive feedback for inspection	0.5
Full Inspection	$100 \quad \text{if } g_j = 1 \; \forall j \in \{1, \dots, N\}$

When a transfer occurs, the consumption Δv is computed through a closed-loop Artificial Potential Field (APF) controller [9], which stands on the Relative Orbital Elements (ROEs) theory [10].

Training Algorithm. We opted for the Deep Q-Network (DQN) [11] for its suitability to discrete action spaces. DQN approximates the cumulative discounted reward function for each action in a given state. Actions are selected using an ϵ-greedy policy, where ϵ decays from 1.0 to 0.01 over 4 million training epochs, trading off exploitation of learned strategies vs exploration of novel ones. Agent-environment interactions are stored in a replay buffer of size 100,000, and mini-batches of 256 samples are drawn to compute the loss, which is optimized with Adam (learning rate 10^{-4}). Training stability is ensured by maintaining a target network, updated every 3,000 steps.

Numerical Results

The architecture was tested for a target in a circular orbit around Earth with a mean motion of $n = 5 \times 10^{-4}$ s^{-1} (corresponding to a period of $T \simeq 200$ min and a semi-major axis of 11,600 km), considering the passive relative orbits shown on the left-hand side of Fig.1. The training results are also depicted on the right-hand side of Fig.1. Fig. 2 presents four different timestamps of the simulation, showing the trajectory of the satellite tasked with observing the debris from each orbit. Recharge and downlink operations are also indicated, along with the inspection level on the left and the amount of information gathered from each orbit. Fig. 3 shows the remaining battery and data storage levels throughout the inspection, as well as the ΔV expenditure. During the complete simulation, which lasts approximately 20 hours, the satellite performs three recharging operations and three data downlinks. It successfully avoids critical battery conditions, with the minimum battery level reaching around 30%, while the maximum data storage utilization reaches 94%.

Materials Research Proceedings 69 (2026) 902-907 https://doi.org/10.21741/9781644904251-159

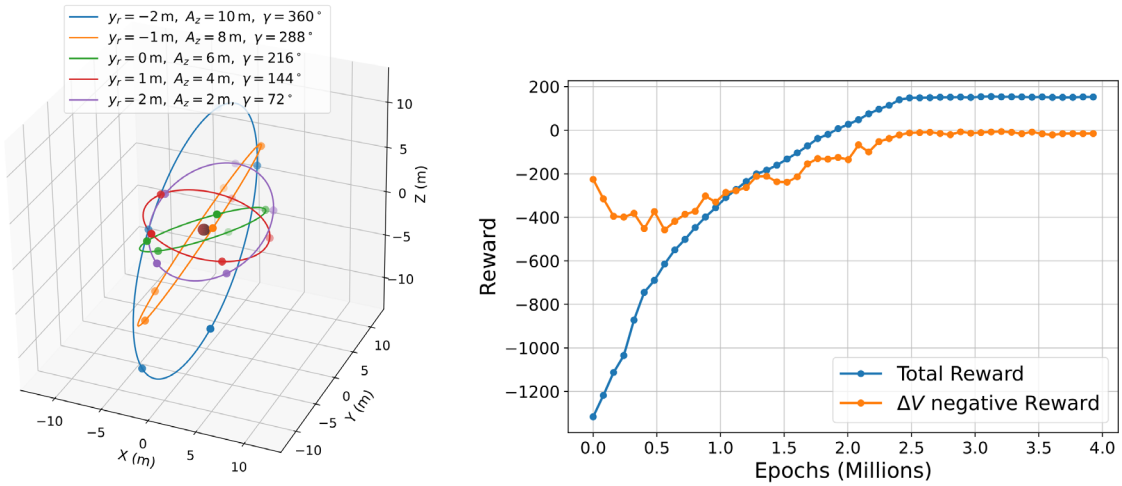


Figure 1: (Left) Simulation scenario (HCW frame) with N=5 relative orbits with their ROEs and M=5 landing anomalies on each. (Right) Reward signals over training.

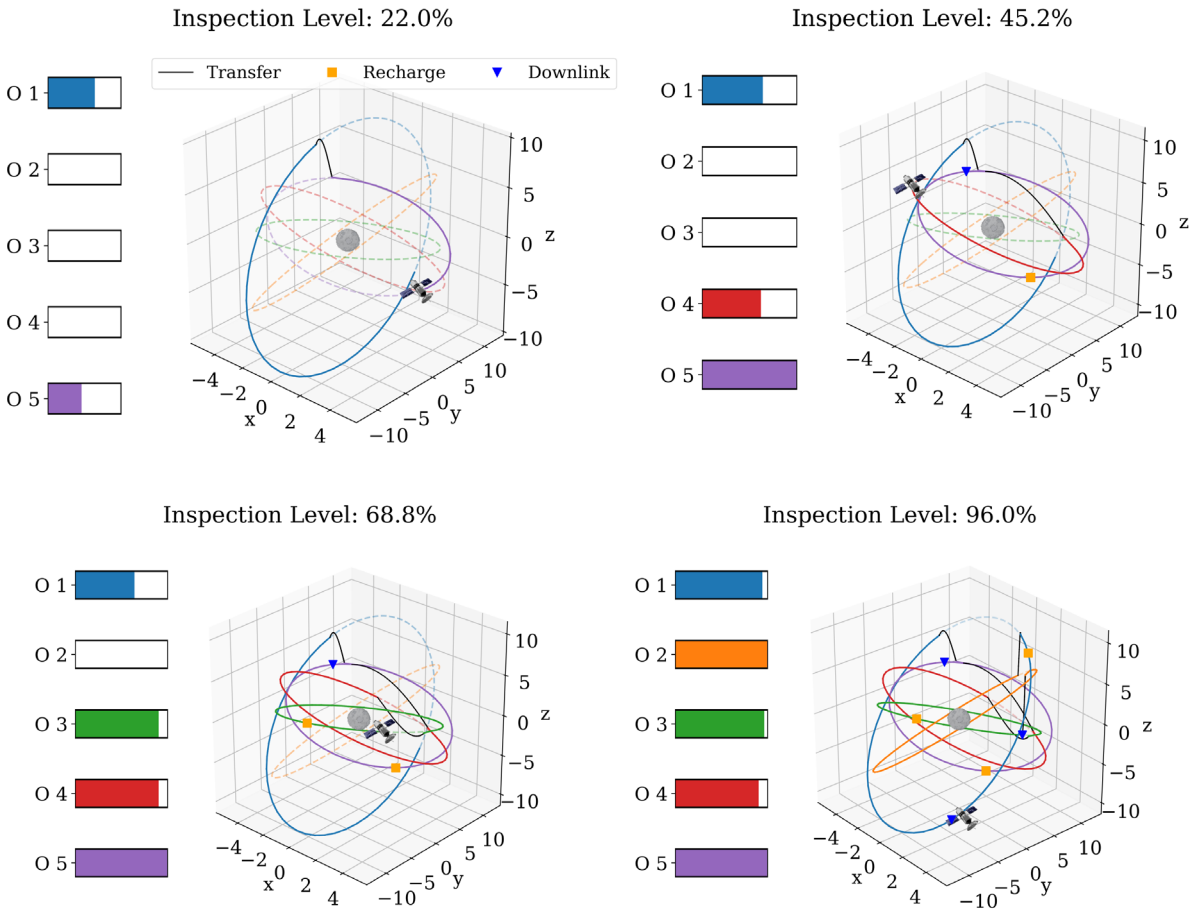


Figure 2: Comparison of simulations at different times. (Top left) 300 min. (Top right) 600 min. (Bottom left) 900 min. (Bottom right) 1300 min.

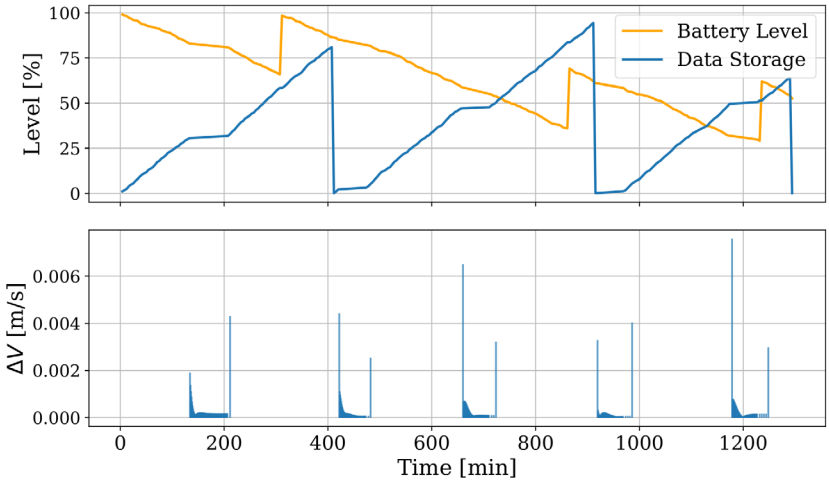


Figure 3: Battery level and data storage percentages over the entire simulation (top row), alongside fuel expenditure during orbital transfer maneuvers (bottom row).

Summary

This study represents an initial step toward developing energy-aware strategies for autonomous on-orbit inspection. In this preliminary scenario, the satellite successfully manages its resources while performing inspection tasks. Future work will focus on refining the modeling of resource dynamics and improving the inspection framework.

References

This project was partially supported by the Italian Ministry of University and Research (MUR) under the FoReLab project (Departments of Excellence) and by the European Union – Next Generation Eu - under the National Recovery and Resilience Plan (NRRP), Mission 4 Component 1 Investment 4.1 - Decree No. 118 (2nd March 2023) of Italian Ministry of University and Research - Concession Decree No. 2333 (22nd December 2023) of the Italian Ministry of University and Research, Project code D93C23000450005, within the Italian National Program PhD Programme in Autonomous Systems (DAuSy).

References

[1] Benjamin Bernhard, Changrak Choi, Amir Rahmani, Soon-Jo Chung, and Fred Hadaegh. Coordinated motion planning for on-orbit satellite inspection using a swarm of small-spacecraft. In 2020 IEEE Aerospace Conference, pages 1–13. IEEE, 2020. https://doi.org/10.1109/AERO47225.2020.9172747

[2] Yashwanth Kumar Nakka, Wolfgang H¨onig, Changrak Choi, Alexei Harvard, Amir Rahmani, and Soon-Jo Chung. Information-based guidance and control architecture for multi-spacecraft on-orbit inspection. Journal of Guidance, Control, and Dynamics, 45(7):1184–1201, 2022. https://doi.org/10.2514/1.G006278

[3] Francesco Capolupo and Pierre Labourdette. Receding-horizon trajectory planning algorithm for passively safe on-orbit inspection missions. Journal of Guidance, Control, and Dynamics, 42(5):1023–1032, 2019. https://doi.org/10.2514/1.G003736

[4] Jian Wu, Yuning Chen, Yongming He, Lining Xing, and Yangrui Hu. Survey on autonomous task scheduling technology for earth observation satellites. Journal of Systems Engineering and Electronics, 33(6):1176–1189, 2022. 10.23919/JSEE.2022.000141

[5] Xiaoyu Chen, Gerhard Reinelt, Guangming Dai, and Andreas Spitz. A mixed integer linear programming model for multi-satellite scheduling. European Journal of Operational Research, 275(2):694–707, 2019. https://doi.org/10.1016/j.ejor.2018.11.058

[6] Adam Herrmann and Hanspeter Schaub. Reinforcement learning for the agile earth-observing satellite scheduling problem. IEEE Transactions on Aerospace and Electronic Systems, 59(5):5235–5247, 2023. 10.1109/TAES.2023.3251307

[7] Qingyu Qu, Kexin Liu, Wei Wang, and Jinhu L¨u. Spacecraft proximity maneuvering and rendezvous with collision avoidance based on reinforcement learning. IEEE Transactions on Aerospace and Electronic Systems, 58(6):5823–5834, 2022. 10.1109/TAES.2022.3180271

[8] WH Clohessy and RS Wiltshire. Terminal guidance system for satellite rendezvous. Journal of the aerospace sciences, 27(9):653–658, 1960. https://doi.org/10.2514/8.8704

[9] Sylvain Renevey and David A Spencer. Establishment and control of spacecraft formations using artificial potential functions. Acta Astronautica, 162:314–326, 2019. https://doi.org/10.1016/j.actaastro.2019.06.024

[10] T. A. Lovell, D. A Spencer. Relative orbital elements formulation based upon the clohessy-wiltshire equations. The Journal of the Astronautical Sciences, 61(4):341–366, 2014. https://doi.org/10.1007/s40295-014-0029-6

[11] Volodymyr Mnih, Koray Kavukcuoglu, David Silver, Andrei A Rusu, Joel Veness, Marc G Bellemare, Alex Graves, Martin Riedmiller, Andreas K Fidjeland, Georg Ostrovski, et al. Human-level control through deep reinforcement learning. nature, 518(7540):529–533, 2015. https://doi.org/10.1038/nature14236

Materials Research Proceedings 69 (2026) 908-912 https://doi.org/10.21741/9781644904251-160

A Decentralized Cluster-based Approach for Multi-Agent On-Orbit Inspection

Francesco Paolo SALZO[1,a *], Pasquale FERRARA[2] and Giordana BUCCHIONI[1,b]

[1]University of Pisa, Department of Information Engineering, 56122 Pisa, Italy

[2]Leonardo S.p.A. – Artificial Intelligent Solutions, 21017 Samarate, Italy

[a]francesco.salzo@phd.unipi.it, [b]giordana.bucchioni@unipi.it

Keywords: On-Orbit Servicing, Inspection, Relative Orbital Elements, DBSCAN

Abstract. Close-range inspection of non-cooperative satellites is essential to assess their condition and support potential servicing or removal operations. This work considers targets with fixed attitude in the Local-Vertical Local-Horizontal frame, leveraging relative Clohessy-Wiltshire dynamics and six Relative Orbital Elements (ROEs). The best candidate orbits were found by means of a density-based clustering approach and assigned using a distributed best-response scheme balancing information gain and maneuver cost.

Introduction

The growing population of inactive satellites and orbital debris has made On-Orbit Servicing (OOS) and Space Situational Awareness (SSA) key priorities in modern space operations [1,2]. OOS aims to extend satellite lifetimes and support debris mitigation through actions such as refueling, repairing, or controlled disposal, while SSA focuses on monitoring and characterizing Resident Space Objects (RSOs). In both contexts, close-range inspection plays a fundamental role, enabling detailed observation and assessment of an RSO's condition to support servicing or removal activities. Both single- and multi-agent inspection strategies have been explored, with the latter offering improved efficiency, coverage, and robustness, though at the cost of greater coordination complexity. Multi-agent inspection can be approached through fixed formations, where each spacecraft maintains a predefined geometry, or via optimization-based frameworks that maximize information gain. In [3], optimal trajectories are obtained through continuous-time optimal control solved with pseudospectral methods, while [4] adopts a hierarchical scheme combining offline orbit selection with distributed onboard attitude planning. Similarly, in [5], satellites transition between intersecting orbits for more efficient target coverage. To enable real-time execution, such guidance strategies must remain computationally lightweight. This work addresses this need by considering the case of a target with a fixed attitude in the Hill frame. Exploiting natural relative dynamics, the inspection problem is reformulated geometrically using Relative Orbital Elements (ROEs) [6], and best orbits are identified through Density-based Spatial Clustering of Applications with Noise (DBSCAN) [7].

Problem Formulation

We consider an RSO orbiting the Earth and a group of N satellites assigned to perform its on-orbit inspection. The motion of an inspector satellite relative to the target is expressed in the Hill frame centered at the target's center of mass. Under the assumption of a circular reference orbit, the relative dynamics follow the well-known Clohessy–Wiltshire equations:

$$\ddot{x} - 3n^2x - 2n\dot{y} = 0, \quad \ddot{y} + 2n\dot{x} = 0, \quad \ddot{z} + n^2z = 0 \tag{1}$$

Content from this work may be used under the terms of the Creative Commons Attribution 3.0 license. Any further distribution of this work must maintain attribution to the author(s) and the title of the work, journal citation and DOI. Published under license by Materials Research Forum LLC.

Materials Research Proceedings 69 (2026) 908-912 https://doi.org/10.21741/9781644904251-160

where n is the mean motion of the target, and the relative position and velocity of the inspector are given by the vectors $[x, y, z]^T$ and $[\dot{x}, \dot{y}, \dot{z}]^T$ respectively. The free solutions of these linear dynamics can be written as:

$$x(t) = x_r - \frac{1}{2}a_r \cos E_r(t), \quad y(t) = y_r + a_r \sin E_r(t), \quad z(t) = A_z \sin(E_r(t) + \gamma) \tag{2}$$

where the ROE vector $\rho = [x_r, y_r, a_r, E_r, A_z, \gamma]$ uniquely defines the geometry and phase of the relative orbit, and provides a direct mapping between orbital parameters and Cartesian coordinates. The target's surface is discretized into M Points Of interest (POIs), each associated with a normal vector $\mathbf{n}_j$. Each POI has an inspection level $I_j \in 0,1$, where $I_j = 1$ if the point has been successfully observed and $I_j = 0$ otherwise. The global inspection level is defined as the fraction of observed points over the total number of POIs:

$$I = \frac{1}{M}\sum_{j=1}^{M} I_j \tag{3}$$

The inspection problem then consists of planning the motion of the inspecting satellites, selecting the most suitable relative orbits to maximize I, aiming to achieve complete coverage ($I = 1$) in the shortest possible time, while minimizing the propellant required for maneuvering.

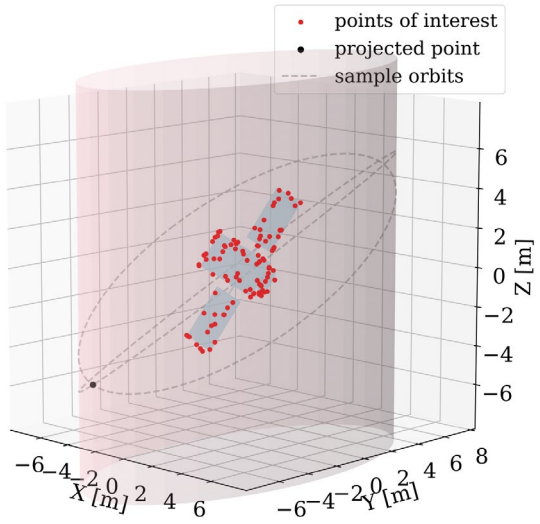


Figure 1: An illustrative satellite is selected as the inspection target. The red surface represents the space of all orbits, with two example orbits passing through a POI projected onto it.

In order to reach a geometric formulation of the problem, we restrict the set of admissible orbits to concentric ones with a fixed radial amplitude a_r. The family of all such trajectories spans a three-dimensional region $S \subset \mathbb{R}^3$, which corresponds to the lateral surface of a prism with elliptical base, as illustrated in Fig. 1. To evaluate which orbits provide the most information gain, each POI on the target surface is projected onto S along the direction of its surface normal $\mathbf{n}_j$. The intersection of this ray with the surface S defines the projected point $p_j \in S$. The resulting set of projected points makes it possible to identify candidate orbits from which the visibility of the largest number of POIs can be achieved. The remaining ROEs of the orbits passing through a projected point $p_j = (x_p, y_p, z_p)$ can be expressed as functions of its coordinates. In particular, the in-plane anomaly and the out-of-plane amplitude are given by:

$$E_r = \arctan\left(\frac{y_p}{-2x_p}\right), \quad A_z = \frac{z_p}{\sin(E_r+\gamma)} \tag{4}$$

Materials Research Proceedings 69 (2026) 908-912 https://doi.org/10.21741/9781644904251-160

Each projected POI thus defines a curve in the (A_z, γ) parameter space. The intersections of these curves correspond to orbits from which multiple POIs can be simultaneously observed. To identify the most informative orbits, i.e., those that enable the observation of the largest number of target points, we need to identidy the most dense regions in the (A_z, γ) space while discarding isolated or sparsely distributed points, with a density-based cluster algorithm. This allows us to extract a reduced set containing only the most effective orbits. The output of the clustering method is a set of K candidate orbits, each associated with m_k observable points, with $k = 1, \dots, K$, providing a guaranteed level of coverage. Then the orbit assignment is performed, taking into account the propellant required to reach the desired orbit, assuming a point-to-orbit ΔV-optimal bang-bang maneuver. This allocation problem can be modeled as a non-cooperative game, where each satellite independently selects an orbit from the available set based on its own knowledge. The decision process is governed by an individual utility function that balances inspection performance and fuel expenditure:

$$u_i = m_k - \lambda \Delta V_{ik}, \quad i = 1, \dots, N \tag{5}$$

where m_k is the number of observable points from orbit k, ΔV_{ik} is the required transfer cost for agent i, and λ is a weighting factor defining their trade-off. Each satellite updates its choice via Best Response Dynamics [8] to maximize its utility given the others' decisions. The process iterates until a Nash equilibrium is reached, where no agent can further improve its utility. Afterward, each satellite moves to its assigned orbit, performs the inspection, and broadcasts its observations to update the shared global map once all observable points have been covered.

Results

We now present the results of the proposed method. The algorithm was implemented in Python and tested in a realistic inspection scenario using an illustrative spacecraft model. The STL file was imported with a random attitude, and $M = 100$ surface POIs were uniformly sampled, as shown in Fig. 1.

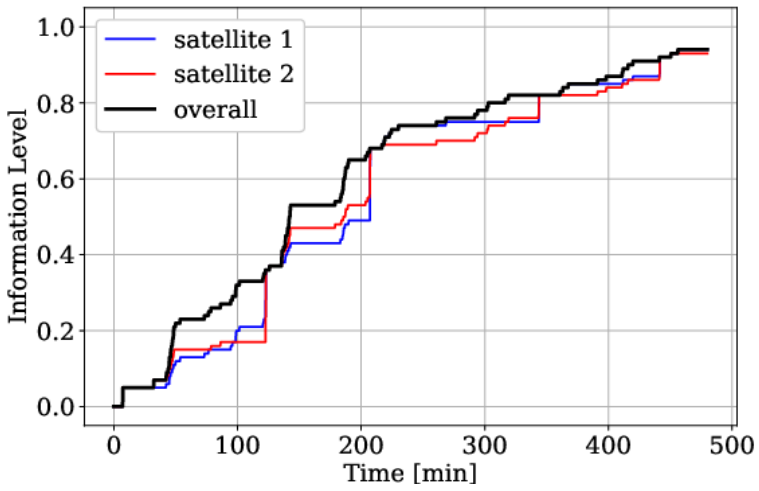


Figure 2: Inspection Level over time of both satellites and the overall level.

The algorithm was validated with $N = 2$ agents over a simulation time of $T_{sim} = 540$ min. As shown in Fig. 2, the system achieves 95% surface coverage. The two satellites inspect distinct POIs and update their information four times (at approximately 120, 200, 350, and 450 min), changing orbit after completing the observation of their current targets.

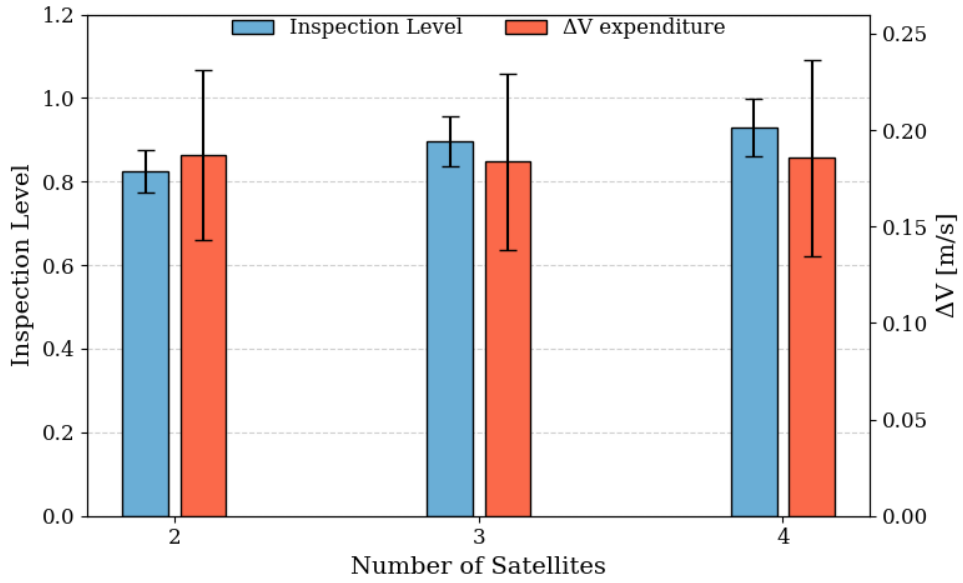


Figure 3: Mean and standard deviation of final inspection level reached and total ΔV expenditure for each configuration with 2, 3, and 4 satellites.

The algorithm was further validated through a Monte Carlo simulation with 2, 3, and 4 agents, demonstrating its scalability. For each case, 100 runs were performed with random initial agent states, spacecraft attitudes, and surface sampling. Each simulation lasted $T_{sim} = 360$ min. Fig. 3 reports the mean and standard deviation of the final overall inspection level and total ΔV expenditure. As expected, the inspection level increases with the number of agents, reaching nearly complete coverage with 4 satellites, while the ΔV remains approximately constant since each agent inspects a similar number of orbits within the same time window.

Summary

This work presents an initial framework for multi-agent satellite inspection that exploits clustering in the ROEs space to identify and select the most informative orbits. The resulting set of orbits effectively guides the agents toward configurations that ensure high levels of inspection coverage of the target. Future extensions will focus on refining the information gain function to account for attitude dynamics and on integrating a closed-loop controller.

Acknowledgement

This work was supported by the Italian National Recovery and Resilience Plan (PNRR, MUR Decree No. 117/2023), co-funded by Leonardo S.p.A. – Leonardo LABS. This work was also partially supported by the Italian Ministry of University and Research (MUR) under the FoReLab project (Departments of Excellence).

References

[1] European Space Agency. Esa space environment report 2024. https://www.esa.int/Space_Safety/Space_Debris/ESA_Space_Environment_Report_2024/, 2024. Accessed: October 14, 2025.

[2] NASA. Nasa to support darpa robotic satellite servicing program. https://www.nasa.gov/directorates/stmd/nasa-to-support-darpa-robotic-satellite-servicing-program/, April 4 2024. Accessed: October 14, 2025.

[3] M. Mercier, D. Curtis. A multi-agent guidance scheme for a cooperative inspection of an unknown space object. In 2023 IEEE Aerospace Conference, pages 1–9. IEEE, 2023. https://doi.org/10.1109/AERO55745.2023.10115546

[4] B. Bernhard, C. Choi, A. Rahmani, S.J. Chung, F. H. Coordinated motion planning for on-orbit satellite inspection using a swarm of small-spacecraft. In 2020 IEEE Aerospace Conference, pages 1–13. IEEE, 2020. https://doi.org/10.1109/AERO47225.2020.9172747

[5] Y. K. Nakka, W. Hönig, C. Choi, A. Harvard, A. Rahmani, S. J. Chung. Information-based guidance and control architecture for multi-spacecraft on-orbit inspection. Journal of Guidance, Control, and Dynamics, 45(7):1184–1201, 2022. https://doi.org/10.2514/1.G006278

[6] T. A. Lovell, D. A Spencer. Relative orbital elements formulation based upon the clohessy-wiltshire equations. The Journal of the Astronautical Sciences, 61(4):341–366, 2014. https://doi.org/10.1007/s40295-014-0029-6

[7] E. Schubert, J. Sander, M. Ester, H. P. Kriegel, X. Xu. Dbscan revisited, revisited: why and how you should (still) use dbscan. ACM Trans-actions on Database Systems (TODS), 42(3):1-21, 2017. https://doi.org/10.1145/306833

[8] B. Amiet, A. Collevecchio, M. Scarsini, Z. Zhong. Pure nash equilibria and best-response dynamics in random games. Mathematics of Operations Research, 46(4):1552–1572, 2021. https://doi.org/10.1287/moor.2020.1102

Materials Research Proceedings 69 (2026) 913-918 https://doi.org/10.21741/9781644904251-161

Nonlinear Simulation of Aircraft Terminal Maneuvers Including Gear Dynamics and Ground Effect

Stefano CACCIOLA[1,a *] and Andrea CALABRIA[1]

[1] Department of Aerospace Science and Technology, Politecnico di Milano, Milan, Italy

[a]stefano.cacciola@polimi.it

Keywords: Flight Dynamics, Terminal Phases, Simulation, Crosswind, Landing Gear, Nonlinear Aerodynamics, Ground Effect

Abstract. Due to ground proximity and limited time to react to possible issues, take-off and landing maneuvers represent the most critical conditions within the envelope of any airplane. In this context, accurate modeling of terminal maneuvers is essential to evaluate performance, identify possible issues, and assess the safety integrity of a design solution. This work focuses on the development of a nonlinear flight simulator capable of handling terminal maneuvers, including the impact of wind and ground effect on the aerodynamic characteristics of the aircraft. The proposed simulator is employed in different landing scenarios including crosswind conditions for evaluating the maximum wing-tip clearance.

Introduction

Terminal maneuvers represent the most critical conditions within an aircraft flight envelope. In the event of unexpected occurrences, pilots are given only a few seconds to assess the situation and respond appropriately, because of ground proximity [1, 2]. For this reason, accurate modeling of take-off, landing, and the associated airborne phases is essential to analyze the aircraft behavior in these conditions and identify potential safety concerns. This work focuses on the development of a nonlinear flight simulator tailored to terminal maneuvers, capable of handling both take-off and landing, as well as all airborne flight conditions. The simulator also accounts for the impact of wind and ground effect on the aerodynamic characteristics of the aircraft.

Although simple simulation methods relying on lumped elements are sufficient for many preliminary aircraft design applications to provide a general understanding of aircraft behavior during take-off and landing [3, 4, 5], a more sophisticated modeling approach is necessary when analyzing realistic terminal maneuvers, especially under windy conditions. Several factors must be considered. First, the airplane may touch down or lift off asymmetrically, such as one leg making contact first, so the kinematics of the aircraft movement must be accurately reproduced. Second, the contact between each leg and the ground requires consideration of the nonlinear dynamics of the landing gear and tires, including their interaction with the ground. Third, airplane aerodynamics are highly complex and must account for the variation in aerodynamic properties due to ground effects, affecting lift, drag, and moment coefficients.

This work focuses on the development of a nonlinear flight simulator tailored to terminal maneuvers, capable of handling both take-off and landing, as well as all airborne flight conditions. This simulator is an evolution of the one described in Ref. [6], utilizing standard rigid-body dynamics equations to model the aircraft motion, with its orientation parameterized using Cardan angles. The rigid-body dynamics is supplemented by the dynamics of the tires and landing gear, along with a specialized function to detect which leg, if any, has made contact with the ground. The aerodynamic angles are calculated while taking into account the presence of wind of generic magnitude and direction.

Additionally, the simulator includes a dedicated tool to model the aircraft aerodynamic characteristics, partially based on Digital Datcom [7], providing steady-state data and stability and

Content from this work may be used under the terms of the Creative Commons Attribution 3.0 license. Any further distribution of this work must maintain attribution to the author(s) and the title of the work, journal citation and DOI. Published under license by Materials Research Forum LLC.

control derivatives across the entire flight envelope, including the impact of ground effects on these characteristics. Due to certain limitations of the Datcom software, e.g. only one movable surface can be analyzed at a time, the derivation of the aerodynamic model is performed through multiple analyses in a prescribed process, which can also be applied to unusual configurations [8].

The paper is organized according to the following plan. In the section *Methodology*, the simulator will be described putting emphasis on the procedure based on Datcom to estimate the overall aerodynamic characteristic of a given airplane so as to create a large database which considers both longitudinal and lateral directional models and the impact of ground effect on both stability and control derivatives. Some examples of the possible use of the simulator will be reported in the section *Results*. This includes a comparison between landing performed with static aerodynamic model in which stability and control derivatives do not change as the airplane approaches the ground, and an evaluation of minimum wing-tip clearance and maximum lateral gear load during landing as functions of landing speed and crosswind velocity. Finally, section *Conclusions and outlook* concludes the paper by summarizing the main findings and the possible extension of this work.

Methodology

The simulator tailored to terminal maneuvers, which is the focus of this paper, is an evolution of the one described in Ref. [6]. It first relies on the standard rigid-body dynamics equations to model the aircraft motion, while Cardan angles are used for parameterizing the orientation of the airframe with respect to the navigational frame. The aerodynamic angles are calculated while taking into account the presence of wind with a specified magnitude and direction.

The rigid-body dynamics is supplemented by the dynamics of the tires and landing gear, along with a specialized function to detect which leg, if any, has made contact with the ground. In particular, a simplified tricycle landing gear geometry is implemented in which each gear leg consists of a tire and an oleo-pneumatic shock absorber. Tire behavior is rendered through a point-contact model, represented by a linear spring-damper system. The values of the equivalent tire spring and damper characteristics are chosen from literature to yield realistic deformations during simulations. Friction between tires and ground are formulated according to [9], which provides expressions for computing longitudinal and lateral friction coefficients. Braking is also simulated as an additional friction force.

The shock absorbers are modeled using basic physical nonlinear equations linking the elastic force to the stroke and the pressure inside the gas chamber, whereas the dissipative component is rendered through the usual damping arising from flow of the oil through an equivalent orifice. The forces generated at each landing gear contact point are integrated into the aircraft overall equations of motion. The landing gear dynamics is considered only when tire-ground contact is detected.

Additionally, the simulator includes a dedicated tool to model the aircraft aerodynamic characteristics, partially based on Digital Datcom [7], providing steady-state data and stability and control derivatives across the entire flight envelope, including the impact of ground effects on these characteristics.

Due to certain limitations of the Datcom software, and in particular that only one movable surface can be analyzed at a time, the derivation of the aerodynamic model is performed by simulating multiple analyses in a prescribed process.

First, the nominal aircraft is modeled in Datcom including flaps. The outcome of the analysis is the aerodynamic model of the airplane parameterized for different Mach numbers and different flap deflections. The model comprises steady characteristics (e.g. polar and steady moment coefficient) and dynamic stability derivatives.

The same analysis performed at point 1, is repeated including the deflection of the elevator. The outcome of this analysis consists in the variation of the lift $\Delta C_L(\alpha, M)$, drag $\Delta C_D(\alpha, M)$ and moment $\Delta C_{\mathcal{M}}(\alpha, M)$ coefficients entailed by the elevator deflectionδ_E as function of the elevator

Materials Research Proceedings 69 (2026) 913-918 https://doi.org/10.21741/9781644904251-161

deflection itself, the angle of attack α and Mach number M.Finally, $\Delta C_L(\alpha, M)$, $\Delta C_D(\alpha, M)$ and $\Delta C_{\mathcal{M}}(\alpha, M)$ should be then added to the polar obtained at point 1.

This analysis considers the ground effect. Since it is possible to analyze only one control surface at a time, the ground effect analysis is done in conjunction with multiple flap deflections, neglecting in this way the mutual impact of ground effect and elevator deflection. Datcom allows for the study of up to 9 deflections and 10 ground heights. Since the ground effect becomes essentially negligible for ground heights greater than the wingspan, the analyzed ground heights, normalized by the wingspan, range from a minimum value of 0.1 to a maximum value of 1. Digital Datcom performs the analysis for every combination of flap deflection and ground height. Additionally, no impact on the lateral-directional stability derivatives is considered.

In the fourth analysis, the ailerons are included in the Datcom model to estimate the aileron-related control derivatives, $C_{\mathcal{L}_{\delta A}}$ and $C_{\mathcal{N}_{\delta A}}$, which are given as functions of the aileron deflection δ_A and Mach, M.

The fifth analysis considers a model of the isolated fuselage to estimate the increment in the related drag caused by side-slip angle β. Since Digital Datcom does not support analyses varying with β, the approach is to rotate the fuselage by 90 degrees around the x-body axis. This way, when Datcom performs its standard analysis varying α on the rotated fuselage, it effectively analyzes the fuselage aerodynamic characteristics as a function of β.

This step considers the estimation of the control derivatives with respect to the rudder deflection and the increase in the drag entailed by the gears. Both tasks are accomplished using the approach described in [10]. The simulator is implemented in Matlab, and, for the discontinuity management, the model from Ref. [11] was used: as several discontinuous events occur during landings (contact with ground, rebounds, shock absorber motion), the simulation had to be segmented in between the events to avoid numerical problems due to integration of stiff systems.

Results

To demonstrate the capabilities of the simulator, a model of the Ryan Navion (a single-engine, propeller driven, four-seat aircraft) is considered. The digital Datcom was employed to characterize the aerodynamic modeling of the airplane as described in the Methodology section.

In the first scenario, we considered landing in calm air without the flare maneuver. In particular, the airplane was trimmed at a descending angle equal to 1 deg and the controls (deflection of control surfaces and throttle) are maintained fixed throughout the entire simulation. In order to show the importance to have a good characterization of the ground effect, two cases were simulated: one including the variation of the ground effect as function of the distance between the airplane center of gravity and the ground, and the other considering constant aerodynamic coefficients no matter the ground proximity.

Fig.1 shows the output of these simulations, respectively in terms of the airplane trajectory and flight angles as functions of the horizontal distance. The plots also compare two cases: one where the ground effect is considered (solid lines) and one where it is not (dashed lines).

In the considered scenario, due to the ground effect, resulting from the combined modification of the aerodynamics of the wing and tail, the aerodynamic pitch moment increases in magnitude while the airplane descends, causing a tendency to pitch the nose downward. This increase in pitching moment depends on many factors, including the location of the center of gravity and wing aerodynamic center, and is airplane-specific. This behavior is not new, as it was also observed in a paper by O'Leary on a de Havilland DH.106 Comet [12].

From the obtained outputs, although the approach angle is 1 deg, the airplane touches the ground at nearly 3 deg. Notably, this result would not have been obtained if the impact of the ground effect on the moment coefficient had not been considered.

Materials Research Proceedings 69 (2026) 913-918 https://doi.org/10.21741/9781644904251-161

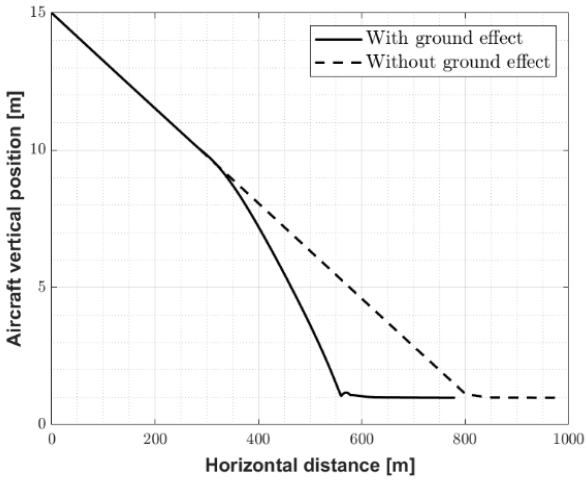


Figure 1: Example of the effect of ground effect on a landing simulation in calm air. Left plot: aircraft trajectory. Right plot: pitch angle (green line), climb angle (red line) and angle of attack (blue line). Solid lines: including ground effect; dashed lines: without ground effect.

In a second scenario, a crosswind is included in the simulations, as well as a dedicated automated control that models pilot's actions. Specifically, the pilot performs the flare before touching the terrain and, once the nose leg has touched the terrain, it also steers the nose wheel to align the trajectory of the airplane with the runway. A crosswind of 8 m/s blows from the left of the airplane, perpendicular to the runway direction. The landing simulation begins with the flapped aircraft in a trimmed configuration, with the nose aligned with the runway, yielding a sideslip approach, where the heading angle matches the flight path angle. Due to the crosswind, both the sideslip and roll angles are non-zero and touchdown occurs asymmetrically, with the left leg touching the ground first, followed by the right leg and, finally, by the nose leg. Fig. 2 shows the trajectory of the aircraft center of gravity during a landing with crosswind of 8 m/s coming from the left of the airplane. In the same plot, it is also possible to visualize the airplane trajectory on the runway after touchdown that follows the runway direction thanks to the nose wheel steering.

The same analysis was repeated multiple times for different values for the approach speed and the crosswind velocity in order to evaluate the impact of these quantities on minimum wing tip clearance. The maximum crosswind considered is 14 m/s, a value that is 50% higher than the maximum crosswind demonstrated in field for Navion aircraft. Fig. 4 shows the minimum wing tip clearance as a function of both approach and crosswind speed. It is possible to show that the worst case, referring to the approach speed equal to 45 m/s and crosswind equal to 15 m/s is associated with a minimum clearance of about 0.7 m. This value, although lower than the clearance for null crosswind, is still significantly positive, demonstrating the landing is still safe even in the presence of crosswind with severity significantly higher than that tested for certification.

Conclusions

A flight dynamics simulator has been developed, coupled with landing gear dynamics, capable of simulating any flight phase, including terminal maneuvers. The aerodynamic characteristics of the airplane are nonlinear and are obtained through a dedicated set of Datcom analyses to generate the aerodynamic dataset which also accounts for ground effect. The use of nonlinear aerodynamics, unlike linearized models, avoids introducing additional errors related to the deviation from the equilibrium point around which the linear model is built. A terminal phase control system has been also designed, to model the presence of the pilot acting on all control surfaces, throttle and nose wheel steer. The tool is effective in simulating terminal maneuvers also in presence of crosswind, without introducing significant simplifications to the dynamics and aerodynamics modeling. A

parametric study has been also performed to quantify the impact of crosswind on the minimum wingtip clearance to verify possible wingtip strikes. The analyses show that the reference aircraft can safely land even at crosswind speeds 50% higher than the maximum one demonstrated in field, without issues related to wingtip strikes.

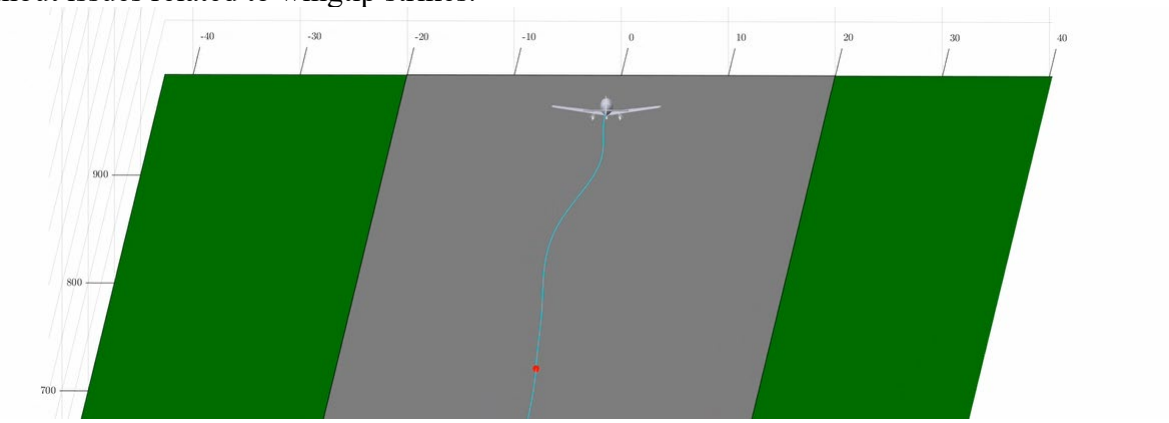


Figure 2: Airplane trajectory during landing with crosswind. Red mark: touchdown point.

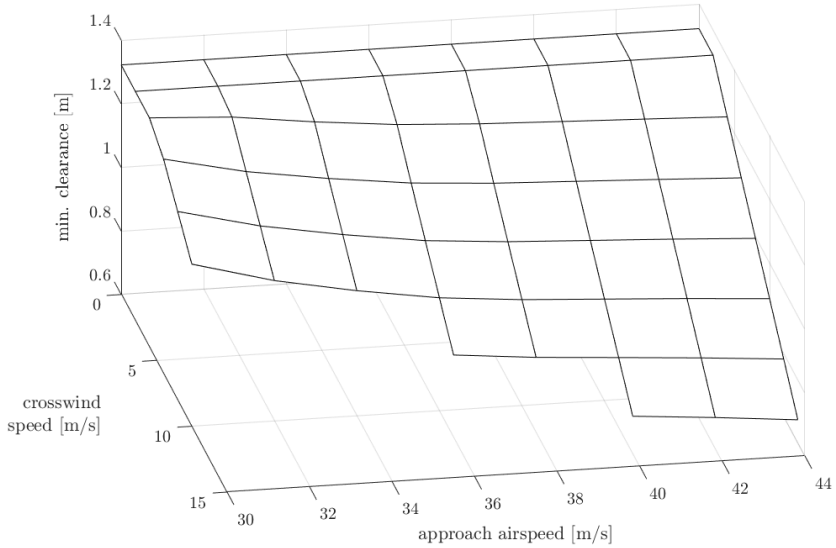


Figure 3: Minimum wingtip clearance as function of approach and crosswind speed

References

[1] Anonymous, A statistical analysis of commercial aviation accidents, 1958–2021. Technical Report (2021), Airbus, Blagnac, France, https://skybrary.aero/sites/default/files/bookshelf/34487.pdf (accessed on 06 November 2025).

[2] Anonymous, Statistical summary of commercial jet airplane accidents: World wide operations 1959–2015. Technical report (2015), Boeing Commercial Airplanes, Aviation Safety. https://www.boeing.com/content/dam/boeing/boeingdotcom/company/about_bca/pdf/statsum.pdf (accessed on 06 November 2025).

[3] M.E. Dreier. Introduction to Helicopter and Tiltrotor Simulation. AIAA Educational series (2007), Reston, VA, USA, 2007.

[4] P.E. Evans. Modeling and simulation of tricycle landing gear at normal and abnormal conditions. Master's thesis, West Virginia University (2010), Morgantown, WV, USA. https://researchrepository.wvu.edu/etd/2153. (accessed on 10 May 2023).

[5] C. Wang and F. Holzapfel. Modeling of the aircraft landing behavior for runway excursion and abnormal runway contact analysis. In Proceedings of the 2018 AIAA Modeling and Simulation Technologies Conference (2018), Kissimmee, FL, USA. https://doi.org/10.2514/6.2018-1166.

[6] S. Cacciola, C.E.D. Riboldi, E. Generali, Optimization of Airplane Landing in Crosswind Conditions for Minimum Tire Wear, Machines 11 (2023) 599-626. https://doi.org/10.3390/machines11060599

[7] R. Fink. USAF stability and control Datcom. Technical Report AFWAL-TR-83-3048 (1978), Mc-Donnell Douglas Astronautics Company.

[8] S. Cacciola, L. Testa, M. Saponi, A Procedure for Developing a Flight Mechanics Model of a Three-Surface Drone Using Semi-Empirical Methods, Aerospace 12 (2025) 515-1-19 https://doi.org/10.3390/aerospace12060515

[9] A. Barnes, T. Yager. Enhancement of ground handling simulation capability. Technical Report AGARD-AG-333 (1998) Advisory Group for Aerospace Research and Development, North Atlantic Treaty Organization, Neuilly sur Seine, France.

[10] J. Roskam. Airplane Design. Pt 4, (1989). Design Analysis and Research Corporation.

[11] Z. Lei, J. Hongzhou, and L. Hongren. Object-oriented landing gear model in a pc-based flight simulator. Simulation Modelling Practice and Theory, 16(9):1514–1532, 2008. https://doi.org/10.1016/j.simpat.2008.08.009

[12] C.O. O'Leary. Flight measurements of ground effect on the lift and pitching moment of a large transport aircraft (comet 3b) and comparison with wind tunnel and other data. Aeronautical Research Council Reports And Memoranda, 1968.

Materials Research Proceedings 69 (2026) 919-924 https://doi.org/10.21741/9781644904251-162

Precise Orbit Determination of Satellites with Low-Cost, Single Frequency Receivers in raPPPid

Hoor BANO[1,a *], Marcus Franz WAREYKA-GLANER[1,b] and Gregor MÖLLER[1,c]

[1]Department of Geodesy and Geoinformation, TU Wien, Wiedner Hauptstrase 8-10, 1040 Vienna, Austria

[a]hoor.bano@tuwien.ac.at, [b]marcus.glaner@tuwien.ac.at, [c]gregor.moeller@tuwien.ac.at

Keywords: raPPPid, Precise Orbit Determination, GNSS, Nanosatellites, Single frequency, Extended Kalman Filter

Abstract. Nanosatellites, particularly CubeSats, are being extensively used for Earth observation, scientific experimentation, atmospheric research, communication, and emerging LEO-based PNT (Positioning, Navigation, and Timing) missions. Hence, precise knowledge of satellite position and velocity is crucial to support both standalone CubeSat missions and large constellations. In this work, we present enhancements to the open source raPPPid software package to perform Precise Orbit Determination (POD) for LEO platforms using an Extended Kalman Filter (EKF). The state prediction is performed by incorporating the satellite's dynamical model, and observation correction is implemented by pseudo-range and carrier-phase measurements. Group and Phase Ionospheric Correction (GRAPHIC) Linear Combination (LC) method is implemented to mitigate the ionospheric delay, and Doppler measurements are used for robust cycle-slip detection to accurately estimate float ambiguities, in low-cost, single-frequency receivers. Observation weighting and exclusion are governed by elevation angle and boresight angle criteria. Boresight angle criterion improves orbit accuracy and performs efficient observation handling, especially, for satellites with rear-facing antennas. Validation is conducted on the Astrocast nanosatellite constellation, where low-cost receiver results yield a 3-D root mean square error (RMSE) of the post-fit residuals on the order of a few decimeters. As for high-quality geodetic receivers, such as the GNSS receiver onboard the Sentinel-3A satellite, the RMSE reduces to a few centimeters. The resulting ephemerids archive, formatted in SP3c, supports future space-based applications, e.g. measuring the dynamics of composition and density of Earth's upper atmosphere, and holds promise for real-time onboard application, e.g. by incorporating the Galileo High Accuracy Service (HAS) into orbit determination approach. These developments open the door for more autonomous, effective, and scalable navigation systems in future space missions, and highlight the possibility of low-cost GNSS-based POD for nanosatellites.

Introduction

Precise Orbit Determination (POD) is essential for modern satellite missions to provide positioning, navigation, and timing accuracy needed for both scientific and operational use. With the rise of nanosatellite constellations and CubeSats in low Earth orbit (LEO), achieving high-precision orbits using compact and cost-effective receivers has become a major challenge. Traditional differential techniques such as Real-Time Kinematics (RTK) provide high accuracy, but depend on dense ground networks and continuous communication links. In contrast, Precise Point Positioning (PPP) achieves comparable position accuracy using precise GNSS satellite orbit, clock and bias products, making it more suitable for autonomous space-borne applications.

raPPPid [1], an open-source MATLAB-based PPP software developed at TU Wien, provides a robust platform for PPP processing. For high quality receivers onboard geodetic missions, e.g. GRACE [2] and SWARM [3] etc., post processed results show enhanced accuracy and reliability of orbit determination solutions on the order of several millimeters to centimeters. Previous EKF-

Content from this work may be used under the terms of the Creative Commons Attribution 3.0 license. Any further distribution of this work must maintain attribution to the author(s) and the title of the work, journal citation and DOI. Published under license by Materials Research Forum LLC.

Materials Research Proceedings 69 (2026) 919-924 https://doi.org/10.21741/9781644904251-162

based POD studies have achieved sub-meter accuracy using single-frequency GRAPHIC combinations. For example, K.S. et al. [4] demonstrated 1 meter accuracy for missions such as GRACE and COSMIC, while the APOD nanosatellite [5] improved orbit precision from 67 cm to 31 cm by correcting for Code Residual Corrections (CRC). Real-time onboard POD remains challenging due to ionospheric effects, limited GNSS product accuracy, and receiver noise. Müller et al. [6] demonstrated 5–16 m real-time accuracy for low-cost receivers on the Astrocast satellites by NAVSOL.

Hence, it is observed that the performance of such low-cost receivers is often limited by poor observation handling. This work addresses these limitations by extending raPPPid, the PPP module of the Vienna VLBI and Satellite Software (VieVS PPP), for EKF-based POD of satellites with several novel processing strategies: (1) Boresight angle-based observation weighting and exclusion, which improves data handling for satellites with non-nadir or rear-facing antennas. (2) A Doppler-based cycle slip detection algorithm augmented with an acceleration term for high dynamic receivers. (3) An adaptive error covariance matrix tuning scheme for newly introduced ambiguities, maintaining solution continuity and improving filter stability for low-cost receivers. The raPPPid framework supports both low-cost and geodetic receivers, enabling comparative analysis under identical processing conditions.

The structure of this paper is organized as follows: Section 1 introduces the background, motivation, and related work. Section 2 describes the proposed POD methodology and EKF implementation within raPPPid. Section 3 presents the setup and results for the Astrocast and Sentinel-3A satellites. Section 4 concludes the paper with key findings, future recommendations and prospects for real-time onboard POD.

POD Methodology

Satellite Dynamical Model. A satellite's dynamical model is the mathematical representation of its motion, accounting for the dominant perturbing accelerations acting along its orbit. The model integrates the satellite's velocity and acceleration by summing the gravitational and non-gravitational forces acting on it, given in [7].

While gravitational accelerations such as Earth's central gravity and harmonics can be modeled with high precision, non-gravitational forces, such as atmospheric drag and solar radiation pressure, are more difficult to predict accurately. For example, the drag and solar coefficient may have to be estimated once per every orbit to account for varying environmental disturbances. For this research, they have been taken as constants. As a result, purely model-based orbit propagation gradually deviates from the true orbit over time. Hence, a GNSS receiver onboard nanosatellites offers a reliable and efficient way for POD, and helps correct modeling errors in the dynamical model.

Observation Handling. The quality of the GNSS observations plays a significant role in achieving accurate POD results. Hence, dedicated strategies for observation handling are implemented, including adequate cycle slip detection, observation weighting, and exclusion.

A Doppler-based cycle slip detection method is employed to ensure the continuity of carrier-phase measurements, tailored for high-dynamic receivers onboard satellites. Rapid motion can cause large phase variations, which is mitigated by including the acceleration term. The predicted phase measurement $L_{pred,k}$ based on Doppler measurements is given as:

$$L_{pred,k} = L_{k-1} - D_k dt + 0.5\left(\frac{D_k - D_{k-1}}{dt}\right) dt^2 \quad (1)$$

Here, L and D denote the phase and Doppler measurements, respectively, at time epoch k and $k-1$. dt is the time interval between the consecutive epochs. A cycle slip is flagged when the difference between $L_{pred,k}$ and the current measurement L_k exceeds a certain threshold.

Materials Research Proceedings 69 (2026) 919-924 https://doi.org/10.21741/9781644904251-162

Observation weighting and exclusion based on elevation and boresight angles, improve robustness by reducing the influence of low-quality or geometrically unfavorable measurements. In this research, we particularly mention boresight angle, which is the angle between the receiver antenna's pointing direction (antenna boresight) and the line of sight vector to the GNSS satellite, given as [8]:

$$\theta_{boresight} = \cos^{-1}\left(\frac{los_b \cdot r_{ant}}{\|los_b\| \, \|r_{ant}\|}\right) \quad (2)$$

Here, los_b is the line of sight vector between the GNSS satellite and the receiver in the body frame, while r_{ant} is the pointing vector of the antenna boresight. The boresight angle varies between [0, 180°]. For example, a cut-off value of 90° would mean that all the measurements outside of this 90° angular cone are assumed to be weaker and noisier, and will be excluded. Similarly, measurements with higher boresight angles can be given a lower weighting factor, and vice versa. A simple weighting function is given as:

$$W = 0.5\left(1 + \cos\left((\theta_{boresight}\right)\right) \quad (3)$$

Measurement Model: The measurement model is computed with the predicted states, accounting for receiver and satellite clock errors, atmospheric delays, and other measurement perturbations. The ionosphere is a major source of error in GNSS positioning. For single-frequency measurements, the first-order ionospheric effect can be mitigated using the GRAPHIC method, which utilizes the fact that the ionosphere affects code and phase measurements in opposite ways [9]. The combination G_1 is formed using single frequency pseudorange P_1 and carrier phase L_1 measurements as:

$$G_1 = \frac{P_1 + L_1}{2} \quad (4)$$

The combined GRAPHIC measurement G_1, after removal of the ionospheric effect d_{Iono}, is given as:

$$G_1 = \rho - c.dt^S - dt_{rel} + c.dt_R^{GPS} + \delta\rho_{PCO,PCV}^S - \frac{\delta\rho_R^{PCO,PCV}}{2} - \frac{\delta\rho_R^{CCO,CCV}}{2} + \frac{\delta\rho_{Wind-Up}}{2} + \frac{\lambda N}{2} \quad (5)$$

Here, ρ denotes the geometric distance between the receiver and GNSS satellite, which corresponds to the norm of los. $c.dt^S$ is the GNSS satellite clock offset correction, dt_{rel} is the relativistic correction, and $c.dt_R^{GPS}$ is the receiver clock error, with respect to GPS time. $\delta\rho_{PCO,PCV}^S$ is the correction for GNSS satellite antenna phase center offset and variation. $\delta\rho_R^{PCO,PCV}$ and $\delta\rho_R^{CCO,CCV}$ denote the corrections for receiver antenna phase center offset and variation, and code center offset and variation, respectively. $\delta\rho_{Wind-Up}$ represents the correction for the phase wind-up effect (phase rotation due to relative movement between the transmitter and receiver antenna), and λN is the carrier phase integer ambiguity term.

Extended Kalman Filter Tuning. The EKF framework is adopted for state estimation through prediction and correction steps, as commonly used in GNSS-based Precise Orbit Determination (POD) [4]. In this research, the focus is on its adaptive tuning to improve stability for low-cost receivers. To mitigate abrupt jumps in estimated states, and optimal handling of the observations when new satellites appear, an adaptive error covariance inflation strategy is applied on float ambiguities. The initial variance of a newly introduced ambiguity, $\sigma_{amb,0}^2$ is scaled according to its satellite "age" counter n as:

Materials Research Proceedings 69 (2026) 919-924 https://doi.org/10.21741/9781644904251-162

$$\sigma^2_{amb,0}(n) = max(1, f_0 - \alpha(n-1))\sigma^2_{amb,0} \quad (6)$$

Here, f_0 is the initial inflation factor and α is the decay rate. This gradual reduction of covariance smooths the transition when satellites enter or reappear. Hence, it improves filter stability and orbit solution for low-cost, single-frequency receivers which are subject to frequent constellation changes.

Results

Validation of satellite POD in raPPPid software was performed using GNSS data (GPS L1) from Astrocast satellite P03S04 and Sentinel-3A, to evaluate its performance for both CubeSat-class and high-quality geodetic receivers. These implementations are part of the public raPPPid Github repository. IGS Final precise orbit and clock products were used, and the ionospheric delay was corrected with the GRAPHIC-LC applied to GPS L1 measurements. An elevation cut-off of −15° was set, as the GRAPHIC combination mitigates most low-elevation ionospheric effects, while a boresight cut-off of 90° was applied. Boresight angle weighting was implemented for Astrocast P03S04 measurements due to its rear-facing antenna, whereas Sentinel-3A measurements employed an elevation angle weighting corresponding to its zenith-facing antenna.

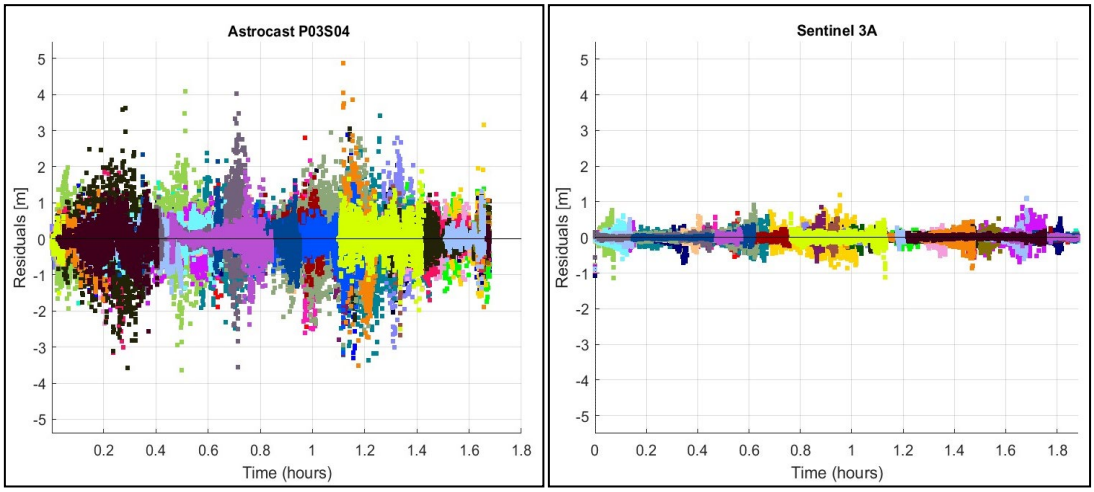


Figure 1: GRAPHIC post-fit residuals for Astrocast P03S04 and Sentinel-3A (GPS L1)

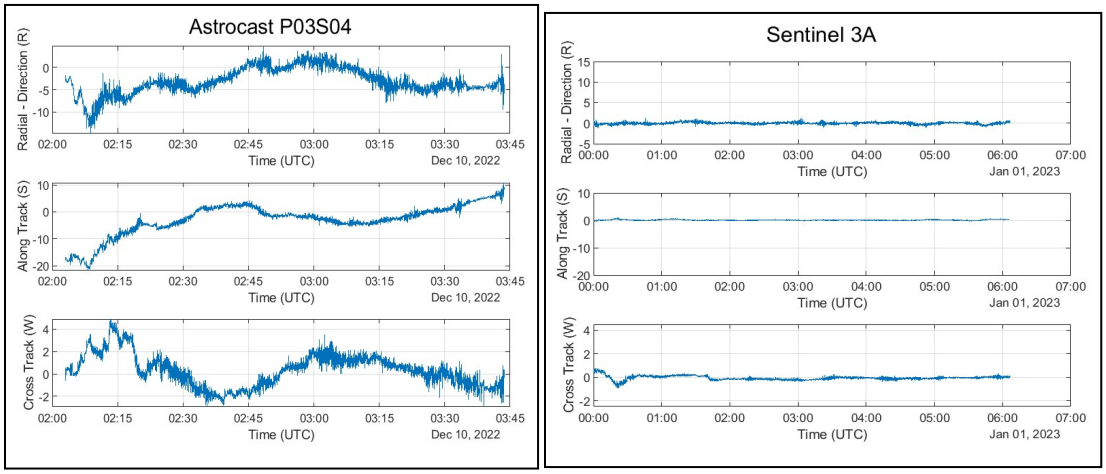


Figure 2: Difference in position for Astrocast P03S04 and Sentinel-3A (meters)

Fig. 1 shows the post-fit residuals between the observed and computed measurements for both satellites. The standard deviation of these residuals is 39 cm for the Astrocast P03S04 satellite and

9 cm for Sentinel-3A. Fig. 2 illustrates the differences in orbital positions for both satellites. For Astrocast P03S04, adaptive error covariance scaling was applied to newly introduced phase ambiguities, along with boresight angle weighting for observations. The improved solution, compared with the NAVSOL orbit [6], yields a 3D RMSE of 7.9 m, reduced from 8.7 m obtained without weighting and inflation. For Sentinel-3A, an elevation angle weighting was applied, increasing the influence of high-elevation measurements. As a result, the 3D RMSE improved from 52.5 cm to 47 cm, compared to its final SP3 orbit solution. These adaptive weighting strategies demonstrate a clear enhancement in orbit determination accuracy for both low-cost and high-quality GNSS receivers.

Conclusions

This work extends the open-source raPPPid software to perform Precise Orbit Determination (POD) for satellites using an Extended Kalman Filter with a dynamical model and GNSS observations. The GRAPHIC linear combination mitigates ionospheric delay, while an improved Doppler method effectively detects cycle slips. Adaptive error covariance tuning, and measurement weighting by elevation and boresight angle improve observation quality.

The achieved post-fit residuals are on the order of decimeters for low-cost receivers (e.g., Astrocast P03S04) and centimeters for geodetic receivers (e.g., Sentinel-3A), using L1 GPS measurements. The NAVSOL orbit is computed only with code measurements and without ionospheric correction, suggesting that our raPPPid solution may be more accurate. However, the results also highlight certain limitations of the GRAPHIC approach arising from code noise and unmodeled hardware effects. In the case of Sentinel-3A, multipath effects and unmodeled antenna code center corrections still remain present, whereas for Astrocast, both phase center and code center corrections are unknown, and therefore not applied.

Because raPPPid supports multiple precise orbit and clock products, it can also be used for near real-time POD by integrating correction streams such as the Galileo High Accuracy Service (HAS). All resulting orbits are stored in SP3-c format, enabling further applications such as atmospheric modeling etc. These findings demonstrate the potential of low-cost GNSS-based POD for autonomous and scalable nanosatellite missions.

References

[1] M. F. Glaner and R. Weber, "An open source software package for Precise Point Positioning: raPPPid," GPS Solutions, vol. 27, no. 3, 2023. https://doi.org/10.1007/s10291-023-01488-4

[2] B. D. Tapley, S. Bettadpur, M. Watkins and e. al., "The Gravity Recovery and Climate Experiment: Mission overview and early results," Geophysical Research Letters, vol. 31, no. 9, 2004. https://doi.org/10.1029/2004GL019920

[3] S. Macmillan and N. Olsen, "Observatory data and the Swarm mission," Earth, Planets and Space, vol. 65, pp. 1355-1362, 2013. https://doi.org/10.5047/eps.2013.07.011

[4] K. S., P. Mula, M. Kamat, N. S. and J. G. Manathara, "Extended Kalman filter-based precise orbit estimation of LEO satellites using GPS range measurements," IFAC Papers OnLine, vol. 55, no. 1, pp. 235-240, 2022. https://doi.org/10.1016/j.ifacol.2022.04.039

[5] D. Gu, Y. Liu, B. Yi, J. Cao and X. Li, "In-flight performance analysis of MEMS GPS receiver and its application to precise orbit determination of APOD-A satellite," Advances in Space Research, vol. 60, p. 2723-2732, 2017. https://doi.org/10.1016/j.asr.2017.08.023

[6] L. Müller, K. Chen, G. Möller, M. Rothacher, B. Soja and L. Lopez, "Real-time navigation solutions of low-cost off-the-shelf GNSS receivers on board the Astrocast constellation satellites," Advances in Space Research, vol. 73, pp. 2-19, 2024. https://doi.org/10.1016/j.asr.2023.10.001

[7] C. A. Kluever, Space Flight Dynamics, Missouri: John Wiley & Sons, 2018.

[8] G. Kim, C. Park and D. W. Lim, "Space Service Volume Augmented with Korean Positioning System at Geosynchronous Orbit," Journal of Positioning, Navigation, and Timing, vol. 9, no. 4, pp. 327-336, 2020.

[9] T. P. Yunck, "Coping with the Atmosphere and Ionosphere in Precise Satellite and Ground Positioning," Environmental Effects on Spacecraft Positioning and Trajectories, Geophysical Monograph Series, vol. 73, 1993.

Space Systems, GNC & Orbital Operations



Materials Research Proceedings 69 (2026) 926-929 https://doi.org/10.21741/9781644904251-163

GeoScout: Architecture for Piggyback Interplanetary CubeSats

Lorenzo OLIVIERI[1,a *], Alessandro FRANCESCONI[1,b], Matteo MASSIRONI[2,c]

[1]Department of Industrial Engineering, University of Padova, Via Venezia 1, 35131, Padova, Italy

[2]Department of Geosciences, University of Padova, Via Giovanni Gradenigo 6, 35131 Padova, Italy

[a]lorenzo.olivieri@unipd.it, [b]alessandro.francesconi@unipd.it, [c]matteo.massironi@unipd.it

Keywords: CubeSat, Piggyback, Interplanetary, Exploration, Architecture

Abstract. Deep-space exploration is rapidly evolving toward agile, distributed mission architectures that leverage miniaturized platforms to increase scientific return while reducing cost. GeoScout is a proposed 12-U CubeSat architecture designed to deploy as a piggyback payload on interplanetary motherships and perform short, very low-altitude flybys for high-resolution geological imaging. Building on heritage from pioneering interplanetary CubeSats and recent asteroid flyby demonstrators, GeoScout accepts higher mission risk in exchange for low cost and high scientific payoff. Key innovations include a battery-first operational mode for critical flyby phases, a compact cold-gas propulsion thrust system optimised for precision ΔV manoeuvres in deep space, and a mothership-relayed high-bandwidth short-range link that eliminates on-board high-gain radios. This paper introduces the architecture, subsystem choices, mission profile, and a comparative analysis with past small-sat demonstrations, highlighting the unique capability of GeoScout to acquire high-resolution surface observation data from very low-altitude encounters.

1. Introduction

Since the launch of the Soviet Venerea program [1], interplanetary exploration has been mostly performed with large, highly capable spacecraft. Data from NASA interplanetary missions [2] show that for a total of 35 spacecraft the average launch mass was above 1500 kg and the average cost (adjusted to fiscal Year 2022 equivalent dollars) well above 1 billion dollars.

The recent rise of CubeSats has changed this paradigm: small platforms have demonstrated viability beyond Low Earth Orbit, performing communications relays, targeted observations, and technology demonstrations. Among them, the Mars Cube One (MarCO) pair were the first CubeSats to operate successfully at interplanetary distances, relaying data during the InSight Mars landing and validating deep-space communication systems [3]. More recently, LICIACube achieved the first-ever asteroid flyby by a CubeSat, imaging the DART impact on Dimorphos and proving that compact imaging systems and autonomous operations can return valuable science despite the distance of tens of millions of kilometres from Earth [4,5]. In addition, cis-lunar (ArgoMoon [6]) and Hera mission (Juventas and Milani [7]) CubeSats are further demonstrating that deploying small satellites as secondary payloads on major missions is a viable opportunity to acquire additional scientifically relevant data.

In this context, GeoScout is a 12-U CubeSat architecture proposed to further extend the capabilities of piggyback CubeSats, enabling very low-altitude flybys for high resolution imaging.

2. Mission concept and operations

GeoScout is conceived as a 12-U CubeSat (size of about $10\times20\times60$ cm^3), designed for deployment from a mothership probe during cruise (e.g. for secondary targets investigation) or near-encounter phases to perform low-altitude fly-bys of the mission's primary target. The CubeSat design balances miniaturization with the minimum subsystem capability required for controlled, low-

Content from this work may be used under the terms of the Creative Commons Attribution 3.0 license. Any further distribution of this work must maintain attribution to the author(s) and the title of the work, journal citation and DOI. Published under license by Materials Research Forum LLC.

Materials Research Proceedings 69 (2026) 926-929 https://doi.org/10.21741/9781644904251-163

altitude flybys: a Cold-Gas propulsion system to provide the ΔV for at least a trajectory correction, enough power budget to perform the fly-by, a telecommunication system to relay data to the mothership, and a high-resolution imaging payload. This architecture trades a high margin of mission risk for low cost and simplicity: primary operations for the critical encounter phase are battery-powered, and communication relies on a short-range link instead of direct transmission to Earth. Among the critical subsystems, GeoScout will be also provided with a full 3-DoF attitude control system to satisfy pointing requirements.

A mission profile for GeoScout would be divided into three main phases:

1. Deployment from mothership and trajectory acquisition. In this phase, GeoScout will execute the necessary manoeuvres and corrections to enter the fly-by trajectory. This phase can be performed autonomously or with support from the mothership.
2. Low-altitude fly-by and scientific data acquisition. In this phase, GeoScout will acquire the images with its high-resolution payload and save it in its on-board memory. No data relay is expected in this phase, as the CubeSat will be pointed to the target body and all on-board resources will be dedicated to data acquisition.
3. Data relay and decommissioning. After the fly-by, GeoScout will relay the scientific data to the mothership. Post-encounter, the spacecraft may continue secondary science operations. Once the communication link will be lost, the CubeSat will deactivate all on-board systems entering in its decommissioned state.

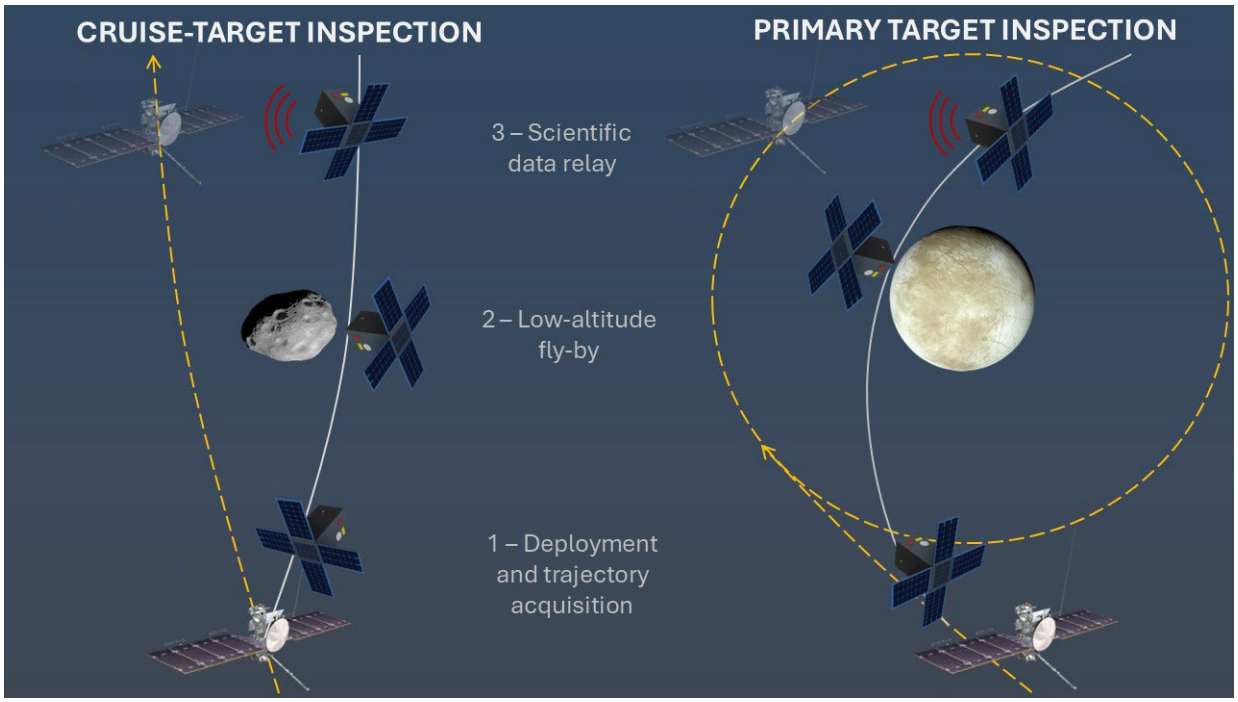


Figure 1: mission phases for targets fly-by during cruise (left) or for the primary target inspection (right)

3. Main systems design

In this section a first iteration of GeoScout design is presented, with details for the main CubeSat subsystem.

3.1 Propulsion

Achieving very low-altitude flybys requires a compact propulsion system capable of very precise thrust control. For GeoScout a Cold-Gas system has been selected as a trade-off between heritage,

Materials Research Proceedings 69 (2026) 926-929 https://doi.org/10.21741/9781644904251-163

safety, and system simplicity. In addition, the cold-gas choice mitigates propellant handling risks during launch and integration with a host spacecraft.

Such systems have been demonstrated in several small satellite missions and were installed on board of deep-space CubeSats; Table 1 shows a partial list of such missions, with reported CubeSat size, propellant, and estimated ΔV. It can be observed that for 6U CubeSat the average ΔV is about 40 m/s.

For a first iteration of the 12U GeoScout design, a scaled tank and thruster arrangement, as well as careful mass allocation, can provide ΔV budgets comparable to or exceeding those achieved by these missions.

Table 1: summary of Cold-Gas thrusters employed in deep-space CubeSat missions

Spacecraft	Size	Propellant	Estimated ΔV (m/s)	Reference
MarCO A / B	6U	R-236fa	~ 60 m/s	[8]
LICIACube	6U	R-236fa	~37–40 m/s	[9]
NEA Scout	6U	R-236fa	~37 m/s	[10]
ArgoMoon*	6U	R-236fa	~56 m/s	[6]
Juventas	6U	Butane	14 m/s	[11]
Milani	6U	Butane	~40 m/s	[12]

* equipped also with a monopropellant thruster

3.2 Power management and communications

GeoScout adopts a battery-first approach for the encounter phase: the spacecraft relies on rechargeable batteries charged during cruise (via body-mounted or deployable solar arrays when practical) but performs the short-duration, high-energy flyby and high-rate data transmission using the batteries alone. This approach was partially validated by CubeSats in previous deep-space operations that operated on battery during short critical phases when solar pointing was suboptimal [13].

To reduce mass and complexity, GeoScout uses a short-range high-bandwidth link to the mothership, rather than a large on-board high-gain antenna and DSN-class transmitter. This approach allows reducing the telecommunication system mass, allowing more volume for the other subsystems and the payload.

3.3 Scientific payload and data handling

GeoScout's primary payload is a high-resolution imager, capable of achieving resolutions below the meter from very low altitudes; its optical design will be based on state-of-the-art telescopes and off-the-shelf cameras. With this targeted resolution, GeoScout can resolve boulder distributions, stratigraphic layering, small-scale faulting, , pits accessing to underground voids, small landslides and granular flows, volcanic vents, rilles and small craters (including fresh and artificial ones) and candidate resource deposits. As reference, LICIACube achieved about 1.38 m/pixel imaging at about 60 km altitude during a flyby of Dimorphos, demonstrating that CubeSat optics can return valuable planetary imagery [9]; GeoScout aims to improve this by an order of magnitude in resolution through closer approach and larger aperture optics.

Supporting subsystems include an onboard data buffer sized to retain full-resolution data until transfer windows with the mothership, and a compact processing unit for compression and limited pre-processing.

Science return will depend on encounter geometry, surface slopes and photometric conditions, but even partial success provides datasets complementary to the broader, lower-resolution surveys of mothership instruments, and is particularly suitable for landing site reconnaissance and

characterization, geological and geomorphological investigations, and small-body surface process studies.

Conclusions

GeoScout represents a low-cost, high-gain architecture for piggyback interplanetary CubeSats focused on very low-altitude geological flybys. By combining a 12-U form factor, safe and validated cold-gas propulsion, battery-first encounter operations, and mothership-relayed communications, GeoScout enables high-resolution surface imaging at low incremental cost to host missions. Future work includes detailed trade studies of propellant sizing, cold-gas thruster arrangements, imaging system designs optimised for motion blur at close approach, and demonstration missions in cis-lunar or small-body contexts.

References

[1] Lund, Thomas. "Soviet Union Spacecraft That Explored Venus 1960–1980." Spacecraft that Explored the Inner Planets Venus and Mercury. Cham: Springer International Publishing, 2023. 35-89. https://doi.org/10.1007/978-3-031-29838-7_3

[2] NASA interplanetary mission (NIM) dataset, https://doi.org/10.5061/dryad.fj6q5745z

[3] Klesh, Andrew, et al. "MarCO: Early operations of the first CubeSats to Mars." Small Satellite Conference (2018).

[4] Scarpa, Eugenio, et al. "The First-Ever Asteroid Fly-By Performed by a CubeSat: Outcomes of the LICIACube Mission." Small Satellite Conference (2023).

[5] Gutierrez, Gabriel, et al. "LICIACube: Mission Outcomes of Historic Asteroid Fly-By Performed by a CubeSat." 2024 IEEE Aerospace Conference. IEEE, 2024. https://doi.org/10.1109/AERO58975.2024.10521222

[6] Lombardo, Marco, et al. "Design and analysis of the cis-lunar navigation for the ArgoMoon CubeSat mission." Aerospace 9.11 (2022): 659. https://doi.org/10.3390/aerospace9110659

[7] Felin, A., et al. "Hera cubesats operational mission analysis and trajectory design around binary asteroid for small bodies characterisation." 29th International Symposium on Space Flight Dynamics (ISSFD). 2024.

[8] Schoolcraft, Josh, Andrew Klesh, and Thomas Werne. "MarCO: interplanetary mission development on a CubeSat scale." Space Operations: Contributions from the Global Community. Cham: Springer International Publishing, 2017. 221-231. https://doi.org/10.1007/978-3-319-51941-8_10

[9] Dotto et al., LICIACube – the Light Italian Cubesat for Imaging of Asteroids, Planet. & Space Sci. https://doi.org/10.1016/j.pss.2021.105185

[10] Stiltner, Brandon C., et al. "Cold gas reaction control system for the near earth asteroid scout cubesat." AIAA SPACE and Astronautics Forum and Exposition. 2017. https://doi.org/10.2514/6.2017-5185

[11] Goldberg H., Karatekin Ö. “Development of the Juventas CubeSat for Hera”. iCubeSat 2019.

[12] PERSEUS Cold Gas Thruster: https://www.t4innovation.com/ianus-perseus-cold-gas/

[13] Krause, Frederick C., et al. "Implementation of commercial Li-ion cells on the MarCO deep space CubeSats." Journal of Power Sources 449 (2020): 227544. https://doi.org/10.1016/j.jpowsour.2019.227544

Materials Research Proceedings 69 (2026) 930-935 https://doi.org/10.21741/9781644904251-164

Mission Design and Enabling Technologies for a LEO-to-MEO Dual-Phase CubeSat Mission: The BOREALIS Platform

Lorenzo Nardi[1,2,a,*], Fabio Curti[2], Stefano Carletta[1], Parsa Abbasrezaee[1], Lorenzo Thomas Contessa[1], A. Di Serafino[1], Vahid Omrani[1], Domenico Caputo[3], Giovanni Palmerini[1], Nicola Lovecchio[3], Sahithi Sriramoju[1], VS Siva Sankaram Emani[1], Nunzio Burgio[3], Giulia Petrucci[3], Riccardo Mazzotti[1], Mara Mirasoli[4], Fabio Lorenzini[5], Matteo Mergé[6], and Augusto Nascetti[1]

[1]School of Aerospace Engineering, Sapienza University of Rome, Via Salaria 851, I-00138 Rome, Italy

[2]Department of Systems and Industrial Engineering,The University of Arizona,1127 E. James E. Rogers Way,Tucson AZ, USA

[3]Department of Information Engineering, Electronics and Telecommunications, Sapienza University of Rome, Via Eudossiana 18, I-00184 Rome, Italy

[4]Department of Chemistry "Giacomo Ciamician", Alma Mater Studiorum–University of Bologna, Via Piero Gobetti 85, I-40129 Bologna, Italy

[5]Kayser Italy S.r.l., Via di Popogna 501, I-57128 Livorno, Italy

[6]ASI, Italian Space Agency, Via del Politecnico, 00133 Rome, Italy

*lorenzo.nardi@uniroma1.it

Keywords: CubeSat, Orbit Transfer, Biofilm, Propulsion System, ADCS, Space Biology, LEO-to-MEO, Radiation Effects, Model-Based Design, Hardware-in-the-Loop

Abstract. BOREALIS – Biofilm Onboard Radiation Exposure Assessment Lab In Space – is a 6U CubeSat mission developed under the Italian Space Agency's ALCOR program. It introduces a dual-phase orbital profile enabling biological experimentation in both Low Earth Orbit (LEO) and Medium Earth Orbit (MEO), making BOREALIS one of the first CubeSat missions to attempt a LEO-to-MEO orbital transfer. This paper focuses on the mission's engineering innovations that make this transfer feasible, particularly the propulsion subsystem based on a water-fueled pulsed plasma thruster and the Attitude Determination and Control System (ADCS), validated through numerical and Hardware-in-the-Loop (HIL) experiments. Conducted in collaboration between the School of Aerospace Engineering of Rome and the University of Arizona, the tests demonstrated that a commercial ADCS can maintain sub-degree pointing during long-duration thrust operations when integrated within a closed-loop Simulink environment.

Introduction

BOREALIS (Biofilm Onboard Radiation Exposure Assessment Lab In Space) is a 6U CubeSat mission developed under the Italian Space Agency's ALCOR program through a consortium including the School of Aerospace Engineering (SIA) at Sapienza University of Rome, the Interdepartmental Centre for Industrial Aerospace Research (CIRI-Aerospace) of the University of Bologna, and Kayser Italia S.r.l. The mission pioneers a dual-phase orbital profile that enables biological experimentation in both Low Earth Orbit (LEO) and Medium Earth Orbit (MEO), representing one of the first CubeSats to attempt an autonomous orbit transfer between these regimes. The payload, a miniaturized lab-on-chip integrated with a fluorescence microscope, allows *in-situ* monitoring of microbial biofilms to study their survival, adaptation, and gene

Content from this work may be used under the terms of the Creative Commons Attribution 3.0 license. Any further distribution of this work must maintain attribution to the author(s) and the title of the work, journal citation and DOI. Published under license by Materials Research Forum LLC.

Materials Research Proceedings 69 (2026) 930-935 https://doi.org/10.21741/9781644904251-164

expression response to ionizing radiation, including the effects of a purpose-designed radiation shield.

The orbital architecture consists of an initial 650 km circular LEO phase dedicated to biological experiment activation and baseline environmental data collection, followed by a transfer to a 2050 km MEO orbit for exposure to an enhanced radiation environment. This profile enables comparative biological analysis across two distinct radiation regimes using a single payload, an uncommon capability within the CubeSat class. To achieve this ambitious goal, BOREALIS integrates two enabling technologies: a water-fed Pulsed Plasma Thruster (PPT) providing specific impulse around 4800 s and thrust of 37.5 mN, and a commercial Attitude Determination and Control System (ADCS) capable of maintaining sub-degree pointing during extended thrust operations.

The spacecraft design required a deep tradeoff between propulsion, power, and attitude control architectures. The adopted PPT allows incremental burns ranging from 600 to 3000 seconds, while the ADCS ensures stable boresight (i.e. thrust axis) stabilization and robust detumbling performance through quaternion-based feedback control and magnetorquer-assisted desaturation. The mission development followed a model-based systems engineering approach supported by MATLAB/Simulink simulations and GMAT trajectory analyses, incorporating higher order gravitational perturbations. This paper focuses on the engineering innovations behind the orbit-raising maneuver, highlighting the integrated propulsion-ADCS design and the test campaign performed using the HIL testbed developed at the School of Aerospace Engineering, accessed remotely from the University of Arizona.

Mission architecture and propulsion design

A model-based trade study was conducted to evaluate candidate propulsion architectures: cold-gas, monopropellant, and electric systems [1]. The selected water-based PPT provides ~37.5 mN thrust, specific impulse of ~4800 s, and total $\Delta v \approx 150$ m/s, enabling the orbit transfer in several burns of increasing duration (from 600 s to 3000 s). Orbit propagation and thermal analyses were performed using GMAT and MATLAB, including gravitational perturbations and aerodynamic drag. Table 1 summarizes the propulsion options.

Table 1. BOREALIS propulsion options during trade-off analysis [2].

Type	Thrust	Specific impulse	Max cont. firing time
Monopropellant thruster	1000 mN	215 s	600 s
Hall-effect thruster	5 mN	1000 s	900 s
RF ion-thruster	0.4 mN	2200 s	2500 s

ADCS architecture and simulation model

The BOREALIS ADCS is based on the CubeSpace CubeADCS 3-Axis unit [3], integrating three orthogonal reaction wheels (maximum torque 3.0 mN·m, inertia 1.3×10^{-6} kg·m², and maximum speed 6000 rpm) and three magnetorquers with dipole moments up to 0.2 A·m². The sensor suite includes fine and coarse sun sensors, a Nadir sensor, double-redundancy three-axis magnetometers, and a MEMS gyroscope, providing attitude estimation accuracy down to 0.1°. The ADCS can be accessed via UART interface. A HIL testbed, developed using Simulink and connected to the ADCS, was developed at the School of Aerospace Engineering and allows remote access from the University of Arizona for HIL testing. In this setup, Simulink runs on a host PC and it simulates the satellite attitude and orbital dynamics and commands the ADCS setup, that is monitored in real-time to provide a feedback on the actual torque produced over time, injected into

Materials Research Proceedings 69 (2026) 930-935 https://doi.org/10.21741/9781644904251-164

the Simulink model to close the loop. In the experiments discussed in this paper, telemetry and command exchange were achieved via a TCP/IP bridge from the University of Arizona, allowing real-time supervision from the U.S. laboratory during SIA-led control experiments.The attitude kinematics follow the quaternion differential equation [4]:

$$\dot{q} = ½\ \Omega(\omega)\ q$$

where q is the spacecraft quaternion and $\Omega(\omega)$ is the skew-symmetric angular rate matrix.

The control law is formulated using the quaternion error vector, which directly expresses the attitude error between the current spacecraft quaternion q_s and the target quaternion q_t. The quaternion error is defined as: [5]:

$$q_e = q_t^* \otimes q_s$$

where q_t^* is the conjugate of the target quaternion and $\otimes$ denotes quaternion multiplication.

Let $q_e = [\ q_{e4}\ \ q_{e1}\ \ q_{e2}\ \ q_{e3}\ ]^T = [\ s\ \ e^T\ ]^T$ where $s = q_{e4}$ is the scalar part and $e = [q_{e1} q_{e2}\ q_{e3}]^T$ is the vector part.
To ensure the shortest rotation path, the vector error is defined as:

$$\hat{e} = sign(s)\ \ e$$

The quaternion-based PD control torque can then be written as:

$$T_{cx} = 2K_p q_{e1} q_{e4} + K_d\ \omega_x$$

$$T_{cy} = 2K_p q_{e2} q_{e4} + K_d\ \omega_y$$

$$T_{cz} = 2K_p q_{e3} q_{e4} + K_d\ \omega_z$$

or, in compact vector form:

$$\tau_c = 2K_p\ \hat{e} - K_d\ \omega$$

with gain matrices K_p=0.12 $I_{3\times3}$ and K_d=0.015 $I_{3\times3}$. These values were tuned accounting for ±15% inertia uncertainty and disturbance torques below 2×10^{-6} N·m. The controller ensures robust pointing during thrusting maneuvers and stable detumbling following deployment.

Reaction wheel dynamics are modeled as first-order systems with a time constant of τ = 0.05 s, consistent with analytical formulations in REF [6]:

$$J_w\ \dot{\omega}_w = T_c - T_f$$

where T_f includes viscous and Coulomb friction terms. A continuous latent desaturation algorithm modulates the magnetic dipole mm to unload reaction wheel momentum via the cross-product interaction with the geomagnetic field [7]:

$$m = k_d\ (H_w \times B)$$

where H_w is the total wheel momentum and B the geomagnetic field vector. This approach follows the continuous momentum-dumping framework by Hogan and Schaub [8], enabling autonomous control without discrete unloading events.

The simulator uses ephemerides from GMAT, propagating position, velocity, and local field vectors along the orbit. Under nominal conditions, the model achieves <1° steady-state pointing error for detumbling, thrust-alignment modes, and maintains wheel momentum within ±5% during simulated PPT burns. Figure 1 illustrates the integrated Simulink–hardware communication and feedback loop scheme.

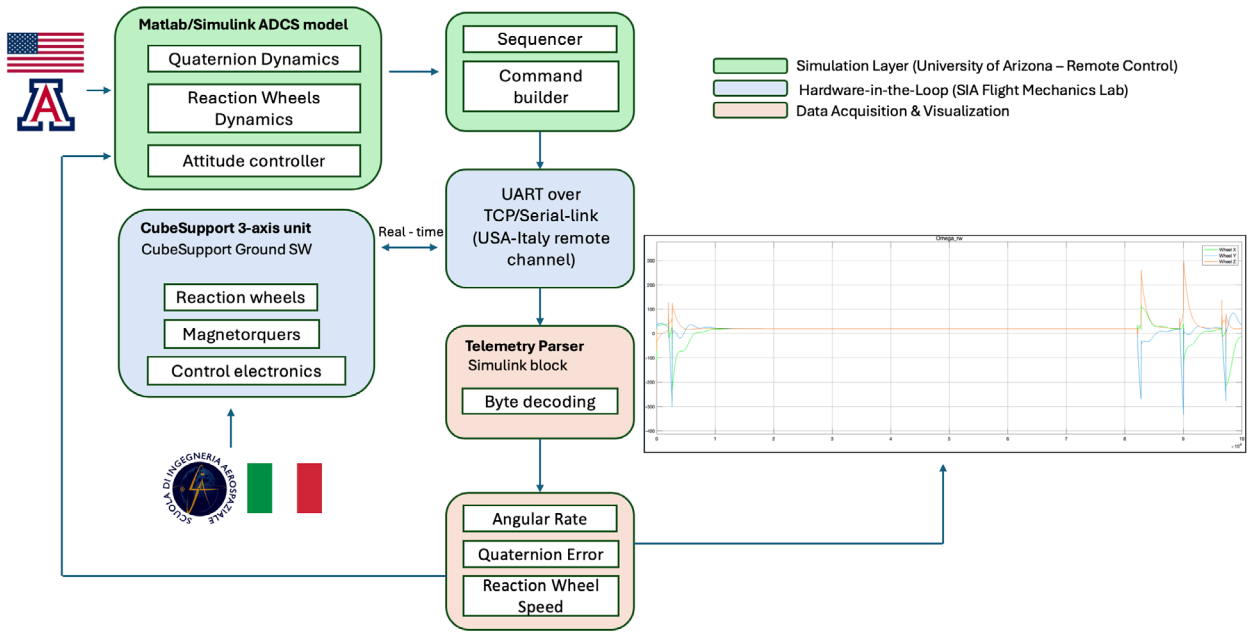


Figure 1. Integrated Simulink–hardware communication and feedback loop. The ADCS simulator developed at the University of Arizona exchanges real-time telecommands and telemetry with the ADCS testbed hosted at SIA Flight Mechanics Laboratory.

Hardware-in-the-loop experimental setup

The HIL campaign was performed collaboratively between the School of Aerospace Engineering (hardware site) and the University of Arizona (control and data processing). Using the remotely-controlled testbed discussed in a previous section the ADCS testbed located in Rome was commanded in real time from Tucson, ensuring data latency <100 ms via UART. Telemetry was parsed with a custom Simulink function compliant with the CubeSpace ICD, automatically updating wheel speed, torque, and magnetorquer current. Polling frequency was 2 Hz, and real-time command packets were generated every 0.5 s. The control loop managed mode transitions (enable, set-speed, poll, off) via a deterministic sequencer with time-indexed states. During thrust-mode simulation (3000 s equivalent burn), the reaction wheels reached ~4200 rpm while maintaining a pointing error below 2°. The magnetic desaturation loop executed every 250 s without oscillations. The revised telemetry parser with time-based watchdog successfully forced rpm reset within 1 s of wheel stop.

Materials Research Proceedings 69 (2026) 930-935 https://doi.org/10.21741/9781644904251-164

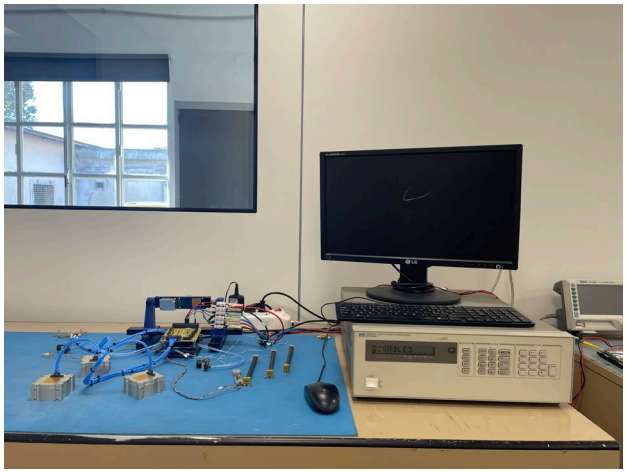


Figure 2. ADCS testbed and Host PC at SIA Flight Mechanics Lab connected to the control terminal at University of Arizona

Results and discussion

Simulink and HIL results exhibited good consistency, with less than 5% deviation in angular velocity profiles and torque command tracking. Table 2 summarizes key performance metrics. The experiment validated the stability of the attitude control algorithm under long-duration torque commands representative of low-thrust maneuvers.

Table 2 – ADCS performance metrics for preliminary tests.

Parameter	Simulation	HIL Test	Requirement
Pointing Error [max]	1.1	1.8	<2.0
Wheel Speed Max [rpm]	4300	4200	6000
Desaturation Period [s]	240	250	<300
Telemetry Latency [s]	0.5	0.6	<1.0

All parameters meet mission requirements with consistent margins between simulation and HIL results for the attitude control up to the burn moment (2000s into the simulation). Minor differences are due to hardware latency, sensor noise, and friction losses in the ADCS testbed unit. The pointing error refers to the maximum attitude deviation during thrust-pointing, and telemetry latency to the command–feedback delay. Overall, results confirm stable control and communication performance under representative LEO conditions. These findings confirm that a small-satellite-class ADCS can support orbit-raising maneuvers when tightly coupled with precise modeling and continuous ground verification. The combination of real-time telemetry, quaternion-based control, and remote HIL capability sets a precedent for distributed academic collaboration in spacecraft testing.

Conclusions

The BOREALIS CubeSat demonstrates how advanced ADCS and propulsion subsystems can extend the scientific reach of small spacecraft to inter-orbital research. Through the joint effort between the School of Aerospace Engineering of Sapienza University of Rome and the University of Arizona, the HIL testbed for BOREALIS ADCS and orbit control system was modeled, integrated, and validated in a cross-continental HIL campaign. Results confirm sub-degree pointing performance during simulated thrust operations and efficient desaturation management.

References

[1] CubeSpace, CubeADCS Gen 2 — Product Description, CubeSpace Satellite Systems (Pty) Ltd., Stellenbosch, South Africa, 2023. Available at: https://www.cubespace.co.za.

[2] Nardi, L., Carletta, S., Abbasrezaee, P., Omrani, V., Caputo, D., Palmerini, G., Lovecchio, N., Mirasoli, M., Lorenzini, F., Mergé, M., and Nascetti, A., "BOREALIS: A Dual-Phase LEO–MEO CubeSat for Space Biology and Radiation Shielding Experiments," International Astronautical Congress (IAC), IAC-24-A1.5.7, Milan, Italy, 2024. Available at: https://iafastro.directory/iac/paper/id/83842/summary/ (accessed Nov. 2025).

[3] Hogan, E. A., and Schaub, H., "Three-Axis Attitude Control Using Redundant Reaction Wheels with Continuous Momentum Dumping," Journal of Guidance, Control, and Dynamics, Vol. 38, No. 10, 2015, pp. 1865–1871. https://doi.org/10.2514/1.G000812 AIAA Journal

[4] Schaub, H., and Junkins, J. L., Analytical Mechanics of Space Systems, 2nd ed., AIAA Education Series, American Institute of Aeronautics and Astronautics, Reston, VA, 2009. https://doi.org/10.2514/4.867231 AIAA Journal+2.

[5] Crassidis, J. L., and Junkins, J. L., Optimal Estimation of Dynamic Systems, 2nd ed., Chapman and Hall/CRC, Boca Raton, FL, 2011. https://doi.org/10.1201/b11154 Taylor & Francis.

[6] Sidi, M. J., Spacecraft Dynamics and Control: A Practical Engineering Approach, Cambridge Aerospace Series 7, Cambridge University Press, Cambridge, U.K., 1997. https://doi.org/10.1017/CBO9780511815652 Cambridge University Press & Assessment.

[7] Steyn, W. H., "Comparison of Low-Earth-Orbit Satellite Attitude Controllers Submitted to Controllability Constraints," Journal of Guidance, Control, and Dynamics, Vol. 17, No. 4, 1994, pp. 795–804. https://doi.org/10.2514/3.21269 AIAA Journal+1.

[8] Hogan, E. A., and Schaub, H., "Continuous Momentum Management with Redundant Reaction Wheels," AIAA Guidance, Navigation, and Control Conference, 2015.

Materials Research Proceedings 69 (2026) 936-941 https://doi.org/10.21741/9781644904251-165

Autonomous Detection of Satellite Orbital Anomalies Through Statistical Behavioural Analysis

Pietro RUSSO[1,a *], Giorgio ISOLETTA[1,b], Roberto OPROMOLLA[1,c] and Giancarmine FASANO[1,d]

[1]University of Naples "Federico II", Piazzale Tecchio, 80, 80125, Naples, Italy

[a]pietro.russo2@unina.it, [b]giorgio.isoletta@unina.it, [c]roberto.opromolla@unina.it, [d]giancarmine.fasano@unina.it

Keywords: Anomaly Detection, Maneuver Detection, Pattern of Life, Space Situational Awareness, Space Surveillance & Tracking

Abstract. The proliferation of Resident Space Objects (RSOs) within the near-Earth orbital regime presents serious challenges for the sustainability and safety of space operations. Accurate tracking and cataloguing of RSOs are critical for Space Situational Awareness (SSA) and Space Traffic Management (STM). These tasks are hindered by unknown maneuvers of active satellites, which can lead to difficulties in correlating new observations with existing catalogued data. To address this issue, the study proposes a novel algorithm to detect satellite orbital anomalies based on a statistical analysis of its operational behaviour. Specifically, the algorithm is designed to detect anomalous or non-nominal satellite activities through the comparison of its most recent Pattern of Life with its current behaviour. The integration of statistical behavioural models into SSA pipelines provides a scalable solution for maintaining catalogue integrity in the increasingly congested orbital environment, by identifying satellite orbital anomalies.

Introduction

The proliferation of Resident Space Objects (RSOs) within the near-Earth orbital regime introduces substantial challenges to the long-term sustainability of space operations. As reported in the ESA Space Environment Report 2025 [1], population of debris larger than 1 cm exceeds one million, while only approximately 40000 objects are currently catalogued, including around 11000 active payloads. Tracking and cataloguing RSOs are crucial tasks for monitoring the space environment, understanding object behaviour, preventing collisions, predicting re-entries, and updating orbital states. Unknown maneuvers by active satellites introduce additional complexity to these activities. The correlation between new observations and catalogue objects can fail due to events such as fragmentations creating new unknown candidates, unknown maneuvers of catalogued objects, or the discovery of a new RSO. The detection and the estimation of maneuvers can cope with the second source of correlation errors, thus avoiding the duplication of objects and gaining a better understanding of their behaviour. Establishing a recurrent operational behaviour of satellites, called Pattern of Life (PoL), can help in predicting their maneuvers and facilitating their tracking, and enables the detection of anomalous or non-nominal activities. This work focuses on the development of an algorithm to detect anomalies in satellite behaviour through the comparison of the most recent PoL with the current satellite behaviour. The Pattern of Life provides a detailed characterization of a space object by capturing its typical behavioural patterns over time. Most applications in literature rely on Machine Learning techniques to generate PoL and detect maneuvers, but this requires a given amount of data that is not always available [2,3]. The alternative solution proposed in this study adopts a statistical approach to identify both maneuver and orbital parameter anomalies, enhancing scalability and broadening applicability. The remainder of the paper is structured as follows. Section 2 describes the architecture and the

Content from this work may be used under the terms of the Creative Commons Attribution 3.0 license. Any further distribution of this work must maintain attribution to the author(s) and the title of the work, journal citation and DOI. Published under license by Materials Research Forum LLC.

Materials Research Proceedings 69 (2026) 936-941 https://doi.org/10.21741/9781644904251-165

logic of the anomaly detection algorithm. Section 3 presents and discusses the achieved results. Final remarks and future works are reported in Section 4.

Methodology

The top-level architecture of the anomaly detection algorithm is reported in Fig. 1.

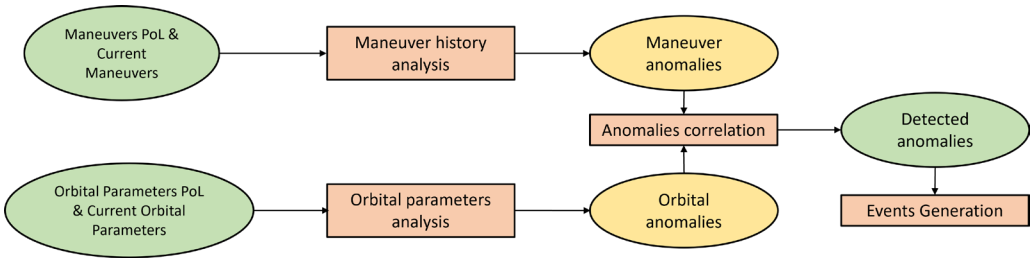


Fig. 1. Anomaly detection algorithm top-level architecture.

In order to identify deviations from the PoL that indicate an anomalous behaviour and avoid false anomalies, consistency between the PoL generation and the satellite behaviour analysis is required. To this end, the satellite behaviour subject to anomaly detection is organized in the same structure as the PoL to facilitate comparison and analysis, and the same logic to identify maneuvers is used for both PoL and anomaly detection. The PoL is constructed through the methodology introduced in [4], which is based on a statistical analysis of both the detected maneuvers [5,6] and the satellite orbital parameters. It includes the time history of the Keplerian orbital parameters of the satellite and information about the typical maneuvers, divided in four bins based on the intensity and distinguished according to the affected orbital parameter (Semi-Major Axis, Inclination, Right Ascension of Ascending Node, Argument of Latitude). The structure is represented in Fig. 2.

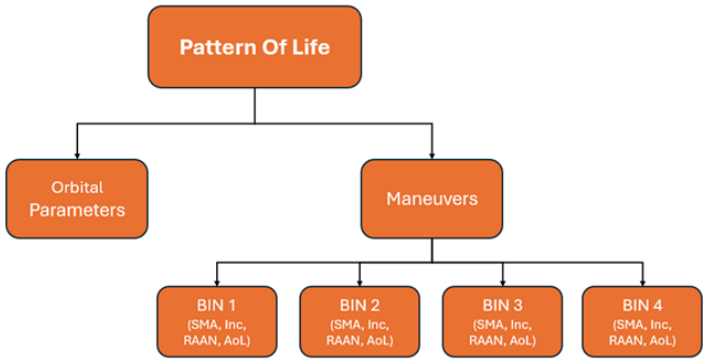


Fig. 2. Pattern of Life architecture.

The anomaly detection algorithm takes as input the list of maneuvers and the orbital state history of the object in the time interval of analysis *T*, organizes the input data in the same structure as the PoL and compares the object behaviour with its most recent Pattern of Life. Three main types of anomalies are defined:

- *orbital parameters anomaly*, which occurs when deviations in Semi-Major Axis and/or inclination exceed the admissible bounds defined by the nominal PoL variation envelope by more than the specified tolerance (*SMA tolerance* and *Inclination tolerance*). This kind of anomaly is the result of the orbital parameters analysis.
- *missed maneuvers anomaly*, that is caused by the absence of a maneuver within the expected time window. At each time instant, the time to last maneuver (TTLM) is computed in each bin of each parameter. If the TTLM is larger than the maximum time

Materials Research Proceedings 69 (2026) 936-941 https://doi.org/10.21741/9781644904251-165

between maneuvers reported in the PoL with a given tolerance (*Time-To-Last-Maneuver tolerance*), a missed maneuver anomaly occurs in that bin of that parameter for the entire time interval characterised by the absence of the expected maneuver.

- *out-of-scheme maneuver anomaly*, which is caused by an unexpected maneuver, because of intensity, if the maneuver magnitude exceeds the nominal bounds, or because of time, if it occurs with a significant temporal offset from the predicted time window. The algorithm analyses each maneuver detected in *T*. If the PoL does not contain any maneuver in the same bin of the same parameter as the detected maneuver, it is classified as an out-of-scheme maneuver of intensity. If the PoL contains maneuvers in the same bin of the same parameter as the detected maneuver, a temporal analysis is performed: the TTLM is computed and if it is smaller or larger than the minimum or maximum time between maneuvers with a given tolerance (*Time-Between-Maneuvers tolerance*), the maneuver is classified as an out-of-scheme maneuver of time.

Results

To evaluate the performance of the anomaly detection algorithm, three satellites were analysed: WorldView-1, COSMO-SkyMed-4, and Starlink-5481. For each of them, a long-term orbit maintenance simulation was carried out with the NASA open-source software General Mission Analysis Tool (GMAT). During the first six months, the nominal behaviour was simulated, after which artificial anomalies were randomly generated. The configuration parameters of the algorithm were the same for all the cases and are reported in Table 1.

Table 1. Anomaly detection algorithm configuration parameters.

Configuration Parameters	Value
SMA tolerance	± 0.1 [km]
Inclination tolerance	± 0.1 [°]
Time-To-Last-Maneuver tolerance	86400 $[sec]$
Time-Between-Maneuvers tolerance	± 86400 $[sec]$

Table 2 presents the four bins used for the PoL and to organize the maneuvers detected in the time interval of analysis *T*.

Table 2. Maneuvers bins intensity.

Maneuvers bins	
Bin 1	$[0, 0.1]$ $[m/s]$
Bin 2	$[0.1, 0.3]$ $[m/s]$
Bin 3	$[0.3, 50]$ $[m/s]$
Bin 4	> 50 $[m/s]$

WorldView-1. WorldView-1 is a commercial satellite for Earth observation operating on a Sun-Synchronous Orbit at about 500 km of altitude. During the 12 months following the nominal maintenance, 23 anomalies of different types were randomly introduced: 2 SMA anomalies; 8 missed maneuvers in the second bin of SMA; 8 out-of-scheme maneuvers of time in the second bin of SMA; 5 out-of-scheme maneuvers of intensity in the third bin of SMA. The SMA anomalies are clearly visible in Fig. 3, where SMA exceeds the PoL bounds twice.

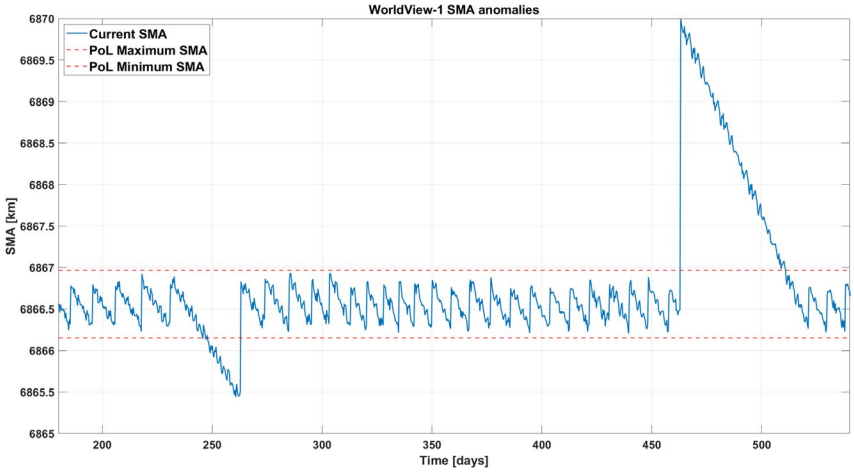


Fig. 3. WorldView-1 SMA anomalous behaviour.

The results of the anomaly detection algorithm are reported in Table 3. Following the comparison of the WorldView-1 behaviour in the time interval of analysis *T* with its most recent PoL, all the anomalies were correctly detected.

Table 3. WorldView-1 anomaly detection algorithm results.

WorldView-1 anomalies detected	
SMA anomaly	2/2
Missed Maneuer – SMA bin2	8/8
Time Out-Of-Scheme Maneuver – SMA bin2	8/8
Intensity Out-Of-Scheme Maneuver – SMA bin3	5/5

COSMO-SkyMed-4. CSK-4 is the unit of a constellation of four Earth observation satellites operated by the Italian Space Agency (ASI). It is placed on a Sun-Synchronous Orbit at an altitude of approximately 620 km. After six months of nominal maintenance, 10 anomalies were randomly generated: 1 SMA anomaly; 1 inclination anomaly; 2 missed maneuvers in the second bin of SMA; 2 missed maneuvers in the third bin of SMA; 2 out-of-scheme maneuvers of time in the second bin of SMA; 1 out-of-scheme maneuver of time in the third bin of SMA; 1 out-of-scheme maneuver of intensity in the third bin of inclination. Fig. 4 represents the anomalous behaviour of inclination with a sudden jump corresponding to the intensity out-of-scheme maneuver.

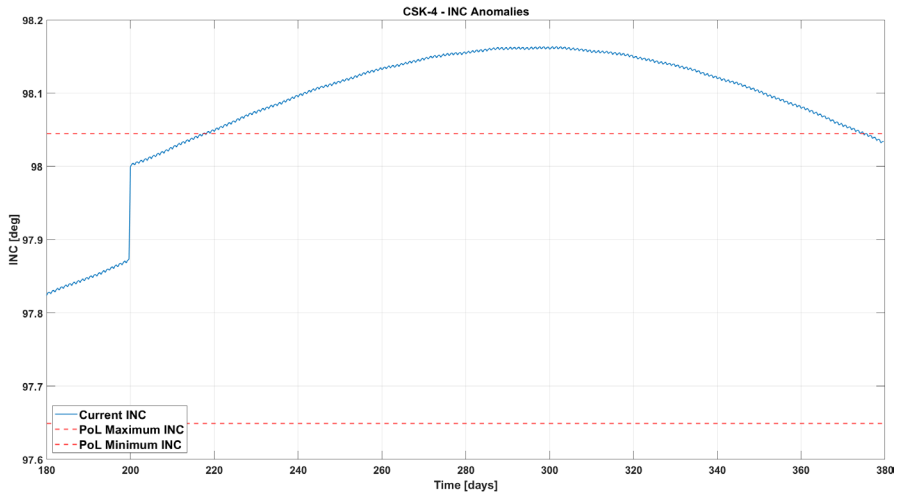


Fig. 4. CSK-4 inclination anomalous behaviour.

The results of the anomaly detection algorithm reported in Table 4 show that also in this case all the anomalies were correctly detected.

Table 4. CSK-4 anomaly detection algorithm results.

CSK-4 anomalies detected	
SMA anomaly	1/1
Inclination anomaly	1/1
Missed Maneuver – SMA bin2	2/2
Missed Maneuver – SMA bin3	2/2
Time Out-Of-Scheme Maneuver – SMA bin2	2/2
Time Out-Of-Scheme Maneuver – SMA bin3	1/1
Intensity Out-Of-Scheme Maneuver – Inclination bin3	1/1

Starlink-5481. Starlink-5481 is part of a mega-constellation providing internet services. Its orbit is quasi-circular, with an altitude of about 566 km and an inclination of 43°. Following a nominal maintenance of six months, 10 anomalies were randomly introduced: 2 SMA anomaly; 2 inclination anomalies; 2 missed maneuvers in the third bin of SMA; 1 out-of-scheme manuever of time in the second bin of SMA; 2 out-of-scheme maneuvers of time in the third bin of SMA; 1 out-of-scheme maneuver of intensity in the third bin of inclination. As it is reported in Table 5, all the anomalies were correctly detected.

Table 5. Starlink-5481 anomaly detection algorithm results.

Starlink-5481 anomalies detected	
SMA anomaly	2/2
Inclination anomaly	2/2
Missed Maneuver – SMA bin3	2/2
Time Out-Of-Scheme Maneuver – SMA bin2	1/1
Time Out-Of-Scheme Maneuver – SMA bin3	2/2
Intensity Out-Of-Scheme Maneuver – Inclination bin3	1/1

Conclusion and Future Works

The tool developed in this work aims to automate and speed up the anomaly detection process, generating an alert each time the satellite exhibits an anomalous behaviour, based on the statistical data derived from its Pattern of Life, which characterizes its nominal operations. Results demonstrate that this approach effectively detects anomalies in both orbital parameters and maneuvers in different scenarios. This functionality not only enhances situational awareness but also reduces the risk of errors in cataloguing activities and improves the reliability of space traffic management operations. In the framework of cooperative SSA, it is particularly relevant for uncooperative or non-collaborative objects, where external maneuver intent disclosures are unavailable. By integrating statistical behavioural models into SSA pipelines, the method provides a scalable solution for maintaining catalogue integrity in the increasingly congested orbital environment. Future work will focus on testing the methodology in a real operational environment.

Acknowledgments

The research grant of Mr. Pietro Russo is funded by the Italian Space Agency (ASI) through "Attività tecnico scientifiche di supporto a C-SSA/ISOC e simulazione di architetture di sensori per SST".

References

[1] ESA Space Debris Office, "ESA'S ANNUAL SPACE ENVIRONMENT REPORT," Mar. 2025.

[2] R. Mital, K. Cates, J. Coughlin, and G. Ganji, "A Machine Learning Approach to Modeling Satellite Behavior," in *Proceedings - 2019 IEEE International Conference on Space Mission Challenges for Information Technology, SMC-IT 2019*, Institute of Electrical and Electronics Engineers Inc., Jul. 2019, pp. 62–69. https://doi.org/10.1109/SMC-IT.2019.00013

[3] R. Cipollone, I. Leonzio, G. Calabrò, and P. Di Lizia, "An LSTM-based Maneuver Detection Algorithm from Satellites Pattern of Life," in *2023 IEEE 10th International Workshop on Metrology for AeroSpace, MetroAeroSpace 2023 - Proceedings*, Institute of Electrical and Electronics Engineers Inc., 2023, pp. 78–83. https://doi.org/10.1109/MetroAeroSpace57412.2023.10189993

[4] L. Perugino, G. Isoletta, and G. Fasano, "Statistical Approach for the Definition of Satellite Pattern of Life," in *IEEE 12th International Workshop on Metrology for AeroSpace (MetroAeroSpace)*, 2025.

[5] R. P. Patera, "Space event detection method," in *Journal of Spacecraft and Rockets*, American Institute of Aeronautics and Astronautics Inc., 2008, pp. 554–559. https://doi.org/10.2514/1.30348

[6] T. Kelecy, K. Hamada, and M. D. Stocker, "Satellite Maneuver Detection Using Two-line Element (TLE) Data."

Materials Research Proceedings 69 (2026) 942-947 https://doi.org/10.21741/9781644904251-166

Enhancing Space Manipulator Fault Tolerance for In-Orbit Servicing through Meta-Reinforcement Learning

Matteo D'AMBROSIO[1,a,*] and Michèle LAVAGNA[1,b]

[1]ASTRA Lab, Department of Aerospace Science and Technology, Politecnico di Milano, Via la Masa 34, 20156 Milan, Italy

[a]matteo.dambrosio@polimi.it, [b]michelle.lavagna@polimi.it

Keywords: Orbital Robotics, Failure Management, Deep Reinforcement Learning

Abstract. This study develops a data-driven motion planning framework for a 7-DoF robotic manipulator to enhance fault tolerance against joint failures during the pre-capture phase of In-Orbit Servicing missions. The system is trained using meta-Reinforcement Learning (meta-RL), exposing the agent to a wide range of randomized scenarios, including stochastic joint-locking. This process achieves two main goals: it equips the agent with strong generalization capabilities for conditions beyond its training domain, and it bypasses traditional inverse kinematics by learning a direct mapping from sensor data to joint-space commands. The meta-learning framework is shown to significantly improve the system's ability to autonomously manage unforeseen failure events. In non-critical scenarios, the agent successfully learns to repurpose redundant joints to complete its task. However, the system cannot recover from failures that cause an unrecoverable reduction of the manipulator's workspace. The results demonstrate that this approach leads to more predictable autonomous behavior during failures and, most importantly, shows how some unexpected anomalies may be overcome by simply reframing them as an operational constraint, before critical operations begin.

Introduction

In-Orbit Servicing (IOS) activities represent a transformative shift in space operations, demanding highly autonomous robotic systems for critical close-proximity tasks like satellite capture, maintenance, and disposal under strict safety constraints [1, 2]. Increasing the autonomy of Guidance, Navigation, and Control (GNC) pipelines for these missions remains challenging, as traditional methods struggle to adapt in real-time to environmental variability or unexpected system anomalies. Deep Reinforcement Learning (DRL) has emerged as a promising approach to enhance these GNC architectures [3], offering the ability to learn complex dynamics through simulated interactions with the environment [4, 5, 6].

Overview. This study, carried out within the ASTRA Lab at Politecnico di Milano, presents a DRL-based guidance framework for a 7-DoF space manipulator mounted on a free-flying satellite. Its specific goal is to synchronize the end-effector with a fixed point on a tumbling, uncooperative target object (Fig. 1) during the pre-capture operations. To achieve this, the proposed framework employs a meta-learning approach [7, 8, 9]. The agent is trained across a wide range of randomized nominal and off-nominal scenarios, including varied initial poses, target tumbling rates, and potential joint failures. This work specifically explores the agent's ability to leverage the system's kinematic redundancy to maintain performance under degraded conditions. The proposed guidance agent receives information from ideal sensors in the task space and directly produces joint-space trajectory references, and demonstrates that a learning-driven manipulator guidance architecture can inherently adapt to failures on-the-go under specific conditions.

Content from this work may be used under the terms of the Creative Commons Attribution 3.0 license. Any further distribution of this work must maintain attribution to the author(s) and the title of the work, journal citation and DOI. Published under license by Materials Research Forum LLC.

Materials Research Proceedings 69 (2026) 942-947 https://doi.org/10.21741/9781644904251-166

Space Robot Dynamics and GNC implementation

The robotic system is modeled through the open-source SPART toolkit [10], assuming a free-flying space robot model. The coupled equations of motion between base and manipulator are expressed in the compact form $\mathbf{H}(\mathbf{q})\ddot{\mathbf{q}} + \mathbf{C}(\mathbf{q}, \dot{\mathbf{q}})\dot{\mathbf{q}} = \boldsymbol{\tau}$ where $\mathbf{q}$ is the state variable (comprising the full state of the base and manipulator joints), and $\mathbf{H}$, $\mathbf{C}$ are the generalized inertia and convective inertia matrices. The implemented GNC system (Fig. 2) operates under the assumption of ideal navigation sensor outputs. These sensors feed information to the DRL-based guidance system, which in turn provides the desired manipulator trajectory.

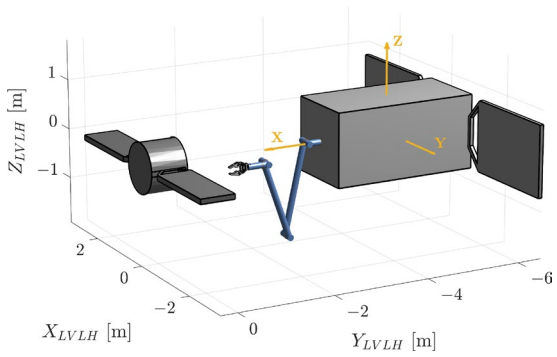


Figure 1: Satellite capture scenario.

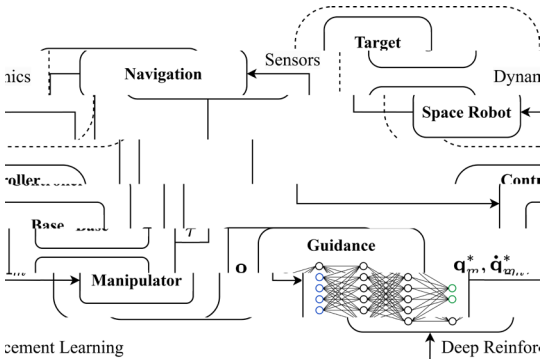


Figure 2: Space robot GNC architecture.

DRL agent guidance system. The core of the work regards the autonomous trajectory generation of the space manipulator, that is produced in real-time as each simulation progresses, based on the environmental perception of the agent at each instant. The inputs received by the agent correspond to the current state of the manipulator, and the errors between the current and target end-effector poses; the latter is ideally assumed as a known quantity for the scope of this work. The agent, implemented through a feedforward neural network, produces the desired joint angles and rates of the manipulator at each instant, bypassing the need for online optimization or inverse kinematics to produce a trajectory reference. A stochastic policy is applied during training to improve exploration of the action space, and consequently actions applied during training are sampled from a Gaussian distribution individually for each joint, encouraging the agent to avoid local minima during network optimization. The selected DRL algorithm is Proximal Policy Optimization [11], applying a reward function based on an Artificial Potential Field (Eq. 1), adapted from [12]. The value of U at each timestep k increases when the pose error of the end-effector decreases over time, such that the agent learns to guide the end-effector towards the desired pose. This goal-oriented reward is the core element of this formulation: the agent is motivated to move towards the desired goal, without directly prescribing how it should use the joint angles to achieve that. This is the crucial detail that makes the resulting trained policy adaptive, allowing it to autonomously decide how to exploit each of the joint angles, such that the final goal can be reached.

$$U_{\mathrm{k}} = -\tilde{r} + \frac{10}{(1+\tilde{r}_{ax})} + \frac{10}{(1+\tilde{r}_{tx})} + \frac{10}{(1+\tilde{\theta})} \qquad (1)$$

Training and results in nominal environment

As defined through the reward function, the goal is for the agent to synchronize the end-effector with a target pose, that is taken fixed to a target spacecraft, that follows a free tumbling dynamics. In the nominal training phase, the tumbling only happens around a single axis, without any failures encountered. In these conditions, each simulation starts with a different distance between chaser and target satellites, initial manipulator configuration, tumbling rate of the target, as well as final

Materials Research Proceedings 69 (2026) 942-947 https://doi.org/10.21741/9781644904251-166

end-effector goal on the circular face of the target (Fig. 1). Fig. 3 shows that the network optimization process in the randomized environment, under nominal (non-failure) conditions, converges in approximately 8000 episodes. To compute an episode's outcome, the time that the end-effector can reliably stay below specific thresholds $\bar{\boldsymbol{r}}$ and $\bar{\theta}$ is considered.

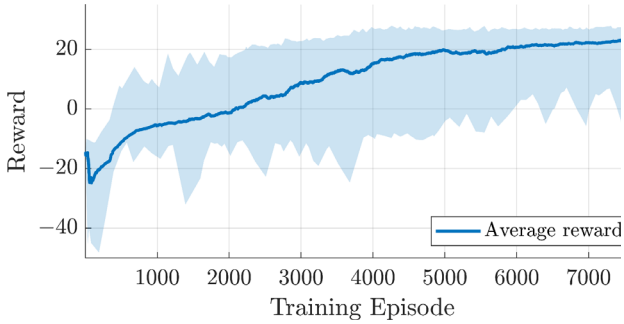


Figure 3: Training reward curve.

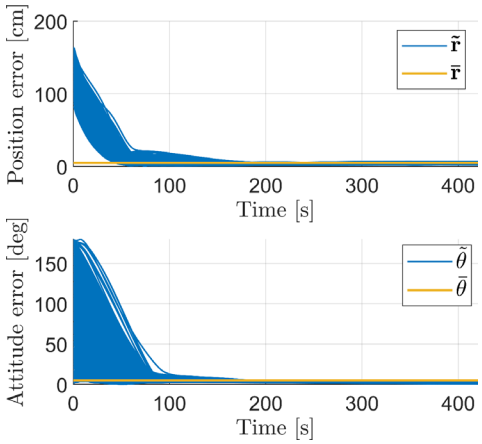


Figure 4: Montecarlo results.

A Monte Carlo analysis (Fig. 4) confirms the agent's ability to reliably synchronize its end-effector with a desired pose fixed to the tumbling target. In all simulations, the agent maintained a pose error below $\bar{r}$ = 1.5 cm and $\bar{\theta}$= 1° for at least 30 consecutive seconds, regardless of the randomized end-effector goal. This performance constitutes a 100% success rate, establishing the baseline used for comparison against non-nominal simulation scenarios.

Agent behavior under joint failures

This section explores how the agent manages the kinematic redundancy of the system, to maintain performance in degraded conditions where one of the joints is assumed failed, and is locked from the beginning of the simulation. The specific joint that is locked is chosen randomly at the beginning of each simulation: the joints are assumed ordered from 1 to 7, from base of the manipulator to end-effector. To evaluate the potential of the meta-reinforcement learning approach, three testing scenarios are considered: i) the baseline agent from the previous section is directly tested under degraded conditions, ii) additional training is conducted starting from the baseline agent, exposing it to a failure of any of the 7 joints, and iii) additional training is conducted with the baseline agent, exposing it to failures of only the joints deemed non-critical in terms of workspace reduction, i.e. joints 1, 5, 6, 7, based on the results from ii). The results in terms of synchronization success percentage are reported in Tab. 1. Despite the large performance decrease with respect to the nominal behavior of 100% synchronization success rate, it is clear that the failure of some specific joints is more critical than others. Through a deeper examination of the results, the unsatisfactory performance of the agent found consequently to the locking of joints 2-4, is due to the drastic reduction of the workspace and dexterity of the manipulator, that is unrecoverable.

Table 1: Testing results with failed joints for cases i), ii), iii).

Joint	1	2	3	4	5	6	7
Case i)	64%	5%	11%	0%	46%	54%	52%
Case ii)	57%	1%	9%	0%	35%	68%	65%
Case iii)	69%	N/A	N/A	N/A	40%	77%	51%

Materials Research Proceedings 69 (2026) 942-947 https://doi.org/10.21741/9781644904251-166

Regarding the non-critical joints, focusing specifically on iii), the performance with respect to nominal conditions is heavily impacted, with a percent reduction in the order of 23%-60%. Despite this, further analysis of the failure locations for each test case demonstrate that the proposed method leads to some important insight on the agent's behavior under failed conditions. An example is provided for joint 1 (Fig. 5), overlaying the randomized end-effector targets, together with the success/failure of each episode, on top of the target's circular face. While only the results from joint 1 are shown, the same behavior is found for the others deemed non-critical (5-7). While the percentage of failures itself does not improve through additional training that subjects the agent to joint failures, it can be seen in the results from case iii) (Fig. 5) that the region where failures are encountered becomes more predictable; in cases i) and ii), this region almost overlaps the whole surface of the target, demonstrating that the agent fails unpredictably. The greater predictability of failures in test case iii) is the primary benefit of the meta-training approach, demonstrating that for each joint there exist relative configurations between the servicer spacecraft and target, such that the agent can reliably provide a successful synchronization of the end-effector to the desired pose after encountering a manipulator failure.

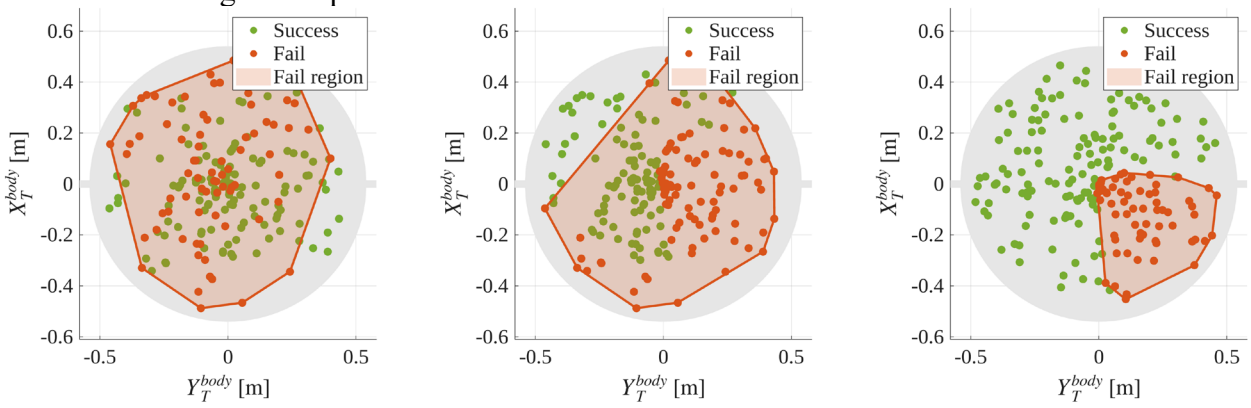


Figure 5: Joint 1 results for each testing case, i), ii), iii) (from left to right).

Overlaying the results from each of the non-critical joints (Figs. 6-7), it is clear that there are certain configurations between servicer spacecraft and target that allow the synchronization to be completed successfully, regardless of whether a non-critical joint is stuck in place at the beginning of the manipulator's motion. Indeed, by opportunely constraining the initial relative configuration between chaser and target, and maintaining it such that the grasping position falls outside of the failed-episode envelope, the 100% success rate of the agent can be fully retained even under failed conditions; this is achieved by autonomously repurposing the redundant joints. While a large reduction in success percent is obtained with respect to nominal conditions, the results show that a DRL-based manipulator guidance law trained through a meta-learning approach successfully improves the adaptability of the agent to unforeseen joint locks in the manipulator. This is a fundamental characteristic in safety-critical applications, and could be one of the main reasons to look into similar systems despite their novelty for space applications. By selecting an optimal relative configuration between chaser and target prior to the start of operations, together with an agent that can adapt to unforeseen failure events, the probability of a successful target capture can be increased even if a failure were to be encountered during operations.

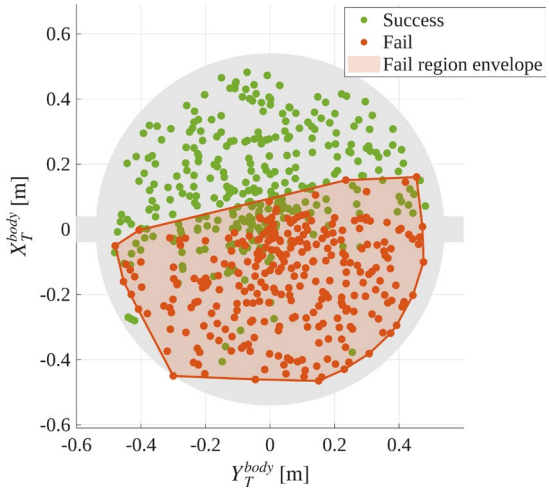


Figure 6: Fail region envelope.

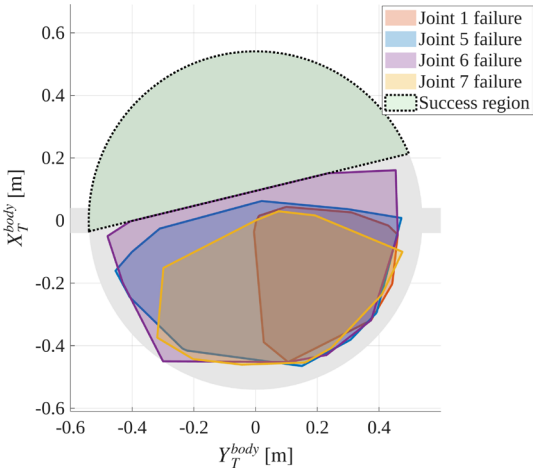


Figure 7: Fail regions overlayed.

Conclusion

This study demonstrates that meta-DRL approaches can significantly boost fault-tolerance capabilities of the space robot GNC system, that can be achieved by exposing the agent to targeted failures during the training phase. While overall performance still lags behind nominal conditions, the main outcome of the approach is the agent's ability to exploit the manipulator's kinematic redundancy to achieve its objective even under failed joint conditions, together with a much greater predictability of the agent's behavior during critical operations. Having similar knowledge of the agent's predictability consequently to failures is operationally invaluable, as it turns critical anomaly events into operational constraints.

Acknowledgments

The authors wish to express their gratitude to the ESA Academy Student Sponsorship Programme for supporting this work for presentation at the CEAS-AIDAA 2025 conference.

References

[1] A. Flores-Abad, O. Ma, K. Pham, S. Ulrich, A review of space robotics technologies for on-orbit servicing, Prog. Aerosp. Sci. 68 (2014) 1-26. https://doi.org/10.1016/j.paerosci.2014.03.002

[2] B.M. Moghaddam, R. Chhabra, On the guidance, navigation and control of in-orbit space robotic missions: A survey and prospective vision, (2021). https://doi.org/10.1016/j.actaastro.2021.03.029

[3] A. Al Ali, Z.H. Zhu, Reinforcement learning for path planning of free-floating space robotic manipulator with collision avoidance and observation noise, Front. Control Eng. 5 (2024). https://doi.org/10.3389/fcteg.2024.1394668

[4] S. Wang, X. Zheng, Y. Cao, T. Zhang, A multi-target trajectory planning of a 6-DoF free-floating space robot via reinforcement learning, in: Proc. IEEE, (2021) 3724-3730. https://doi.org/10.1109/IROS51168.2021.9636681

[5] J. Blaise, M.C.F. Bazzocchi, Space manipulator collision avoidance using a deep reinforcement learning control, Aerospace 10 (2023). https://doi.org/10.3390/aerospace10090778

[6] M. D'Ambrosio, L. Capra, A. Brandonisio, S. Silvestrini, M. Lavagna, Redundant space manipulator autonomous guidance for in-orbit servicing via deep reinforcement learning, Aerospace 11 (2024) 341. https://doi.org/10.3390/aerospace11050341

[7] B. Gaudet, R. Linares, R. Furfaro, Adaptive guidance and integrated navigation with reinforcement meta-learning, Acta Astronaut. 169 (2020) 180-190. https://doi.org/10.1016/j.actaastro.2020.01.007

[8] B. Gaudet, R. Linares, R. Furfaro, Terminal adaptive guidance via reinforcement meta-learning: Applications to autonomous asteroid close-proximity operations, Acta Astronaut. 171 (2020) 1-13. https://doi.org/10.1016/j.actaastro.2020.02.036

[9] M. D'Ambrosio, S. Silvestrini, M. Lavagna, Conditioned sequence models for warm-starting sequential convex trajectory optimization in space robots, Aerospace 13 (2026) 137. https://doi.org/10.3390/aerospace13020137. https://doi.org/10.3390/aerospace13020137

[10] J. Virgili-Llop, J.V. Drew II, M. Romano, SPART spacecraft robotics toolkit: an open-source simulator for spacecraft robotic arm dynamic modeling and control, (2016).

[11] J. Schulman, F. Wolski, P. Dhariwal, A. Radford, O. Klimov, Proximal policy optimization algorithms, arXiv:1707.06347 (2017).

[12] Y. Li, D. Li, W. Zhu, J. Sun, X. Zhang, S. Li, Constrained motion planning of 7-DoF space manipulator via deep reinforcement learning combined with artificial potential field, Aerospace 9 (2022). https://doi.org/10.3390/aerospace9030163

Materials Research Proceedings 69 (2026) 948-953 https://doi.org/10.21741/9781644904251-167

Estimating the Probability of Close Approaches Generated by an In-Orbit Fragmentation via Monte Carlo-Based Approach

Yeerang Lim[1,a *], and Camilla Colombo[1,b]

[1]Department of Aerospace Science Technology, Politecnico di Milano, Via La Masa 34, 20133 Milan, Italy

[a]yeerang.lim@polimi.it, [b]camilla.colombo@polimi.it

Keywords: Probability Estimation, Conjunction Assessment (CA), Monte Carlo Simulation, Line Sampling (LS), Subset Simulation (SS)

Abstract. Advanced Monte Carlo-based approaches are investigated for conjunction assessment with a breakup event, namely Line Sampling and Subset Simulation, which enable to detect the same extent of probability with fewer samples. The proposed approaches are applied to a hypothetical fragmentation and compared with the standard Monte Carlo approach.

1. Introduction

Probability estimation of Close Approaches (CAs) caused by a fragmentation is one of the key components for orbital neighbourhood awareness conjunction assessment. While the distribution of the fragments is often derived from the NASA Standard Breakup Model, a Monte Carlo simulation with large number of samples is required from such a model for a conjunction risk assessment, especially when the probability is small.

On the other hand, advanced Monte Carlo methods, namely line sampling and subset simulation can be used. Both approaches were originally developed to estimate structural failure [1,2], similar to the CA assessment, the system failure probability is the fraction of the number of samples which lead to the failure region. From its nature, a large number of samples are required for standard MC method to guarantee the accuracy of the estimated probability, which causes high computational cost. Both line sampling and subset simulation reduce this problem, by transforming it to a one-dimensional problem in the standard normal space, or by reformulating it as a combination of multiple conditional probabilities. Smaller number of samples will be required as a result, to achieve the same level of accuracy. The same approaches were applied later to the conjunction analysis of near-Earth objects for planetary projection as well [3].

In this work, we propose a line sampling and subset simulation approach to estimate the probability of close approach against debris fragments, to reduce the number of required samples and enhance computational efficiency and improve accuracy in the estimation of the collision probability. Instead of the uncertainty covariance of the initial condition, the probability distribution function from the breakup model can be treated in the same manner. The sample fragmentations are numerically propagated using high-fidelity gravity model implemented in ESA GODOT [4]. The performance of the proposed approaches is compared with the standard Monte Carlo simulation under the same condition, and the feasibility and the limitations of the proposed approaches are addressed by numerical simulations.

2. Advanced Monte Carlo-Based Approaches

Line Sampling

The line sampling (LS) method is a Monte Carlo-based approach for the estimation of small probabilities. It was originally developed for the reliability analysis of failure in complex structural systems [5,6], and later applied to risk estimation for orbital conjunction analysis in combination with differential algebra [3,7]. Both problems have very low probability (generally in the range of

Content from this work may be used under the terms of the Creative Commons Attribution 3.0 license. Any further distribution of this work must maintain attribution to the author(s) and the title of the work, journal citation and DOI. Published under license by Materials Research Forum LLC.

Materials Research Proceedings 69 (2026) 948-953 https://doi.org/10.21741/9781644904251-167

10^{-7} to 10^{-6}) and therefore require a large number of samples for probability estimation. The main feature of the Line Sampling method is the analytical estimation of the probability, obtained by reducing the multi-dimensional integration problem across the uncertainty domain to many one-dimensional integrals along lines following a reference direction that are used to sample the initial distribution; this direction is determined so that it points toward an impact region of the domain, and, if this is properly chosen, the method can considerably increase the accuracy of the solution or reduce the number of required system simulations with respect to a standard MC. It consists of four steps: 1) the mapping of random samples from the physical coordinate space into a normalized standard space; 2) the determination of the reference direction $\boldsymbol{\alpha}$; 3) the probing of the impact region along the lines following the reference direction; 4) the estimation of the impact probability [8].

The first step of the LS procedure is to map the physical coordinates $\mathbf{x} \in R^n$ onto the standard normal space $\boldsymbol{\theta} \in R^n$, whose components are all associated with a unit Gaussian distribution. The components of the vector $\boldsymbol{\theta}$ have the property of being independent and identically distributed random variables. In other words, each component has the same probability distribution as the others and all are mutually independent. Therefore, the joint PDF ϕ of these random parameters is equal to the product of all the single PDFs.

$$\phi(\boldsymbol{\theta}) = \prod_{j=1}^{n} \phi_j(\theta_j) \tag{1}$$

Thanks to this property, this transformation grants efficiency to the method, especially with high dimensions. It reduces the problem to a series of one-dimensional analytical evaluations, thus enabling a simplification of the computation of the probability. The direct and the inverse transformation, from the physical domain to the normalized one and vice versa, which preserve the joint cumulative distribution function (CDF) between the two spaces, are defined as below.

$$\begin{aligned} &\Phi(\boldsymbol{\theta}) = F(\mathbf{x}) \\ &\boldsymbol{\theta} = \Phi^{-1}\left[F(\mathbf{x})\right] \\ &\mathbf{x} = F^{-1}\left[\Phi(\boldsymbol{\theta})\right] \end{aligned} \tag{2}$$

Then the reference direction $\boldsymbol{\alpha}$ is determined, as the direction of a normalized “centre of mass” of the impact region in [3,8].

$$\boldsymbol{\alpha} = \frac{1}{N_s} \sum_{u=0}^{N_s} \frac{\boldsymbol{\theta}^u}{\left\|\boldsymbol{\theta}^u\right\|} \tag{3}$$

This region is approximated by applying the Metropolis-Hastings algorithm [9,10] as below, to generate a Markov Chain Monte Carlo (MCMC) lying entirely in the impact subdomain starting from an initial condition within it.

a. from the current element $\mathbf{x}_u$, $\boldsymbol{\xi}$ is generated by randomly sampling a user-defined "proposal" pdf $p^*(x_u)$;
b. compute the ratio $r = p(\boldsymbol{\xi}) / p(\mathbf{x}_u)$;
c. set $\tilde{\mathbf{x}} = \boldsymbol{\xi}$ with probability $\min(1, r)$ and set $\tilde{\mathbf{x}} = \mathbf{x}_u$ with the remaining probability $1 - \min(1, r)$, where $\tilde{\mathbf{x}}$ is the candidate for the next element of the chain;

Materials Research Proceedings 69 (2026) 948-953 https://doi.org/10.21741/9781644904251-167

d. check whether the candidate $\tilde{\mathbf{x}}$ lies in the region of interest I or not: if $\tilde{\mathbf{x}} \in I$, accept it as the next sample $\mathbf{x}_{u+1} = \tilde{\mathbf{x}}$; else, reject it and take the current sample as the next sample $\mathbf{x}_{u+1} = \mathbf{x}_u$.

After determining the reference sampling direction, N_T initial conditions $\mathbf{x}^k$ are randomly drawn from the nominal uncertainty distribution and then mapped to standard normal coordinates as $\boldsymbol{\theta}^k$ using the transformation above. For each sample in the standard normal space, a line starting from $\boldsymbol{\theta}^k$ and parallel to $\boldsymbol{\alpha}$ is defined according to the parameter c^k, such that

$$\begin{aligned} \boldsymbol{\theta}^k &= c^k \boldsymbol{\alpha} + \boldsymbol{\theta}^k{}_{\perp} \\ \boldsymbol{\theta}^k{}_{\perp} &= \boldsymbol{\theta}^k - \left\langle \boldsymbol{\alpha}, \boldsymbol{\theta}^k \right\rangle \boldsymbol{\alpha} \end{aligned} \tag{4}$$

where $\left\langle \boldsymbol{\alpha}, \boldsymbol{\theta}^k \right\rangle$ is the scalar product. In this way, the problem is reduced to a series of one-dimensional evaluations associated with each sample, with c^k also normally distributed in the standard space.

The standard domain is then explored along each line with the aim of identifying the impact region of an uncertainty set. For the problem under study, the occurrence of the events is expressed by the value of the non-dimensional performance function

$$g_\theta(\boldsymbol{\theta}(c)) = Y(c) \big/ R_{imp} - 1 \tag{5}$$

where Y is a function that maps the value of the parameter c to a performance index, an R_{imp} is the selected critical distance. By setting Y as the minimum distance from the body of interest in the given time of window, while R_{imp} as the radius around the body to define an impact, the performance can be written as

$$g_\theta(\boldsymbol{\theta}(c)) \begin{cases} < 0 \rightarrow & \text{Impact} \\ = 0 \rightarrow & \text{Limit condition} \\ > 0 \rightarrow & \text{No impact} \end{cases} \tag{6}$$

There will be a maximum of two intersections between each line and the impact region, meaning that two values of c^k exist for each standard normal random sample $\boldsymbol{\theta}^k$. Once the value $(\bar{c}_1^{\,k}, \bar{c}_2^{\,k})$ are known for all the sampling lines, the unit Gaussian CDF provides each random initial condition $\boldsymbol{\theta}^k$ with the conditional impact probability $\hat{P}^k(I)$, which can be computed as a one-dimensional integrals based on the properties of the normalized coordinate space.

$$\hat{P}^k(I) = \hat{P}\left[\bar{c}_1^{\,k} < N(0,1) < \bar{c}_2^{\,k} \right] = \int_{\bar{c}_1^{\,k}}^{\bar{c}_2^{\,k}} \phi(u) du = \Phi(\bar{c}_2^{\,k}) - \Phi(\bar{c}_1^{\,k}) \tag{7}$$

The total probability of the event $\hat{P}(I)$ can be approximated as follows.

$$\hat{P}(I) = \frac{1}{N_T} \sum_{j=1}^{N_T} \hat{P}^k(I) \tag{8}$$

Materials Research Proceedings 69 (2026) 948-953 https://doi.org/10.21741/9781644904251-167

Subset Simulation

The subset simulation (SS) method is an adaptive stochastic simulation method to compute efficiently small failure probabilities [3,7]. The approach was originally developed to address structural failure, but it was also used in different research areas in reliability, e.g. to address the failure probability of thermal-hydraulic passive system [5]. The basis of the method is to compute the probability as a product of larger conditional probabilities. Given a sequence of intermediate failure regions $F_1 \supset F_2 \supset \cdots \supset F_m = F$, the failure probability becomes

$$P(F) = P(F_m) = P(F_1)\prod_{l=1}^{m-1} P(F_{l+1}|F_l) \tag{9}$$

where $P(F_{l+1}|F_l)$ indicates the probability of F_{l+1} conditional to F_l. The method is initialized using a standard MC simulation to generate samples at conditional level 0. Once the failure region F_1 is determined and the probability $P(F_1)$ computed, a Monte Carlo Markov Chain (MCMC) algorithm is used to generate samples conditional to the failure region F_1. The next intermediate failure region F_2 is then located and other samples are generated with MCMC. The process can be repeated till the failure region corresponding to objects collision is identified. Similar to the LS method, the MCMC Metropolis-Hastings algorithm is to generate conditional samples in the new region [10]. The resulting SS algorithm can be performed through the following steps [7].

a. set $l = 0$ and generate N sample vectors $\mathbf{x}_0^{0,k}$ by standard MC simulation.
b. propagate each sample for the selected time window, and a list of possible target events is obtained. And compute the values of the performance function $g_x^{\,l}(\mathbf{x}_0)$ for the N samples $\mathbf{x}_0^{l,k}$.
c. sort the N samples in ascending order, according to their values of the performance function $g_x^{\,l}$. The samples closer to the failure region will be at the bottom of the list.
d. identify the intermediate threshold value D_{l+1} from the $(1-p_0)N$ th value of the sorted list. Define the $(l+1)$ th conditional level as $F_{l+1} = \left\{ d_{\Delta t_e} < D_{i+1} \right\}$. Considering how the threshold is defined, the associated conditional probability $P(F_{l+1}|F_l) = p_0$
e. if $D_{l+1} < D_{\lim}$, where $D_{\lim}$ is the target threshold distance, go to the last step. Otherwise select the last $p_0 N$ samples of the list. By definition, these samples belong to the $(l+1)$ th conditional level.
f. using MCMC, generate $(1-p_0)N$ additional condition samples starting from the previously selected seeds belonging to F_{l+1}. A sample is set to belong to F_{l+1} according to the following performance function.
g. set $l = l+1$ and return to step b.
h. stop the algorithm.

The total number of generates samples is

$$N_T = N + (m-1)(1-p_0)N \tag{10}$$

where n is the overall number of conditional levels required to reach the impact region. Since the conditional probability is equal to p_0 for each level, the impact probability becomes

Materials Research Proceedings 69 (2026) 948-953 https://doi.org/10.21741/9781644904251-167

$$\widehat{P}(F) = \widehat{P}(F_m) = P(F_m \left| F_{m-1} \right) p_0^{\,m-1} = p_0^{\,m-1} N_F / N \tag{11}$$

where N is the total number of samples at each conditional level and N_F is the number of samples at conditional level m, whose distance from the target is lower than D_{lim}.

3. Simulation Studies

The proposed LS and SS approaches are applied to a breakup scenario in Table 1, together with the standard Monte Carlo, for both explosion and non-catastrophic collision cases.

Table 1 Breakup simulation scenario

Parent orbit @ 2025-01-01 00:00:00					
SMA [km]	Ecc	Inc [deg]	RAAN [deg]	AoP [deg]	TA [deg]
8000.8008	0.0001	98.0	50.0	0.0	180.0
Target orbit @ 2025-01-01 00:00:00					
SMA [km]	Ecc	Inc [deg]	RAAN [deg]	AoP [deg]	TA [deg]
8248.307	0.03	80.0	50.0	0.0	188.0408

Conjunction assessment results after 2 hours from the breakup are summarized in Table 2. Taking into account the fact that each Monte Carlo simulation is different, it is noticeable that LS gives the same order of probability with a one hundredth of samples. If the standard deviations of the computed probabilities are considered, advanced Monte Carlo-based approaches provide smaller error covariances, meaning the LS is more reliable than the standard Monte Carlo when the number of samples is the same, or even smaller.

Table 2 Probability of close approach < 5 [km]

	Explosion	Collision
Standard MC ($N = 100,000$)	6.3282e-4	3e-5
LS ($N = 1000$)	2.5442e-4	2.7482e-5

A couple of points shall be added. First, the essential idea of the LS is based on the Gaussian distribution of the samples, which is the assumption used in the domain transformation. The distribution of the fragments from the breakup model, on the other hand, is not Gaussian, which explains the difference between two probabilities. Moreover, we suspect that this distribution becomes even less Gaussian along the propagation. It is expected the LS cannot find the $(\bar{c}_1^{\,k}, \bar{c}_2^{\,k})$ at a certain point. Second, we decided to discard the SS at the moment, not because it is not able to calculate the probability, but the value is strongly dependent on the distribution used in the MCMC, and it is not clearly figured out yet which distribution shall be used. The SS is still a considerable approach when the objective of the application is to detect possible close approaches, however the proposed distribution part should be investigated further for probability estimation.

4. Conclusion

Line sampling (LS) and subset simulation (SS) are applied to the conjunction assessment with a breakup event, which are alternatives to calculate a small probability with less random samples. While the approaches detect 1e-4 to 1e-5 probability of close approaches, we also notice some limitations, which are worth investigating further. One possible future work is the sensitivity analysis of the LS with respect to propagation time, to check when it starts not finding the roots in the standard normal domain. Another idea is to think of a way to keep the samples distribution Gaussian as possible, e.g. by introducing Gaussian mixture model. Last but not least, Markov

Chain in the SS could be examined further, to decide which proposed distribution provides the most realistic probability.

Acknowledgement
The research in this work has received funding from the European Space Agency, ESA Contract No. 4000146083/24/D/SR.

References

[1] G.I. Schuëller, H.J. Pradlwarter, P.S. Koutsourelakis, A critical appraisal of reliability estimation procedures for high dimensions. Probab. Eng. Mech. 19 (2004) 463-474. https://doi.org/10.1016/j.probengmech.2004.05.004

[2] S.-K. Au, J.L. Beck, Estimation of small failure probabilities in high dimensions by subset simulation. Probab. Eng. Mech. 16 (2001) 263-277. https://doi.org/10.1016/S0266-8920(01)00019-4

[3] M. Romano, M. Losacco, C. Colombo, P. Di Lizia, Impact probability computation of near-Earth objects using Monte Carlo line sampling and subset simulation. Celest. Mech. Dyn. Astr. 132 (2020) 42. https://doi.org/10.1007/s10569-020-09981-5

[4] Information on https://godot.io.esa.int/godotpy/

[5] E. Zio, N. Pedroni, Subset simulation and line sampling for advanced Monte Carlo reliability analysis, in Proceedings of the European Safety and RELiability (ESREL) Conference (2009).

[6] H. Pradlwarter, M. Pellissetti, C. Schenk, G. Schueller, A. Kreis, S. Fransen, A. Calvi, and M. Klein, Realistic and efficient reliability estimation for aerospace structures, Computer Methods in Applied Mechanics and Engineering. 194 (2005) 1597-1617. https://doi.org/10.1016/j.cma.2004.05.029

[7] A. Morselli, R. Armellin, P. Di Lizia, F.B. Zazzera. A high order method for orbital conjunctions analysis: Monte Carlo collision probability computation. Adv. in Space Research. 55 (2015) 311-333. https://doi.org/10.1016/j.asr.2014.09.003

[8] M. Romano, Orbit propagation and uncertainty modelling for planetary protection compliance verification, Doctoral thesis, Politecnico di Milano (2020). Supervisors: Colombo, C., and Sánchez Pérez, J. M.

[9] N. Metropolis, A. W. Rosenbluth, M. N. Rosenbluth, A. H. Teller, E. Teller, Equations of state calculations by fast computing machines, J. Chem. Phys. 21 (1953). 1087-1092. https://doi.org/10.1063/1.1699114

[10] W. K. Hastings, Monte Carlo sampling methods using Markov chains and their applications, Biometrika. 57.1 (1970). 97-109. https://doi.org/10.1093/biomet/57.1.97

Materials Research Proceedings 69 (2026) 954-959 https://doi.org/10.21741/9781644904251-168

Multidisciplinary Design and Optimization of Suborbital Transatmospheric Vehicles

Pierluigi DELLA VECCHIA[1,a *], Luca FALCONE[1,b], Agostino DE MARCO[1,c], Fabrizio NICOLOSI[1,d], Giulio AVANZINI[2,e], Mario DI RENZO[2,f], Donatella PASSIATORE[2,g], Danilo ZONA[2,h]

[1]Department of Industrial Engineering, University of Naples 'Federico II', Via Claudio, 21, Napoli, 80125, Italy

[2]Department of Engineering for Innovation, University of Salento, via per Monteroni, snc, Lecce, 73100, Italy

[a]pierluigi.dellavecchia@unina.it, [b]luca.falcone@unina.it, [c]agostino.demarco@unina.it, [d]fabrizio.nicolosi@unina.it, [e]giulio.avanzini@unisalento.it, [f]mario.direnzo@unisalento.it, [g]donatella.passiatore@unisalento.it, [h]danilo.zona@unisalento.it

Keywords: Multistage Suborbital Vehicles, Conceptual Design, Parametric Study

Abstract. Suborbital vehicles, which have the potential to drastically reduce the flight time of medium- and long-range missions to durations below one hour, are attracting increasing attention from the scientific community. The iConDeS (Integrated Conceptual Design Tools for Suborbital Vehicles) research project aims to develop advanced methodologies for the conceptual design and optimization of this class of vehicles. In this context, the present work investigates the influence of thrust-to-weight ratios on the design characteristics of a fully reusable two-stage launcher, with the objective of minimizing its liftoff mass.

Introduction

This work presents a multidisciplinary framework for the conceptual design and optimization of suborbital transatmospheric vehicles intended for space tourism and rapid global transportation of people and goods. The possibility of covering distances comparable to half of Earth's circumference in exceptionally short flight times would be a dramatic improvement for human society, and significant attention and investments have been drawn to this application. In recent years, private companies have developed suborbital vehicles for commercial use, notably in space tourism. Examples include Blue Origin's vertically launched New Shepard, Virgin Galactic's air-launched SpaceShipOne and SpaceShipTwo, and XCOR's Lynx, a rocket plane with conventional takeoff and landing. In parallel, major aerospace firms and research centers have focused on technology demonstrators for suborbital and hypersonic missions, such as Boeing X-37, Dream Chaser, CIRA's USV, and ESA's IXV. Research into fully reusable hypersonic aircraft continues, with key projects including SKYLON [1], LAPCAT A2, ZEHST, SpaceLiner [2], and HYPLANE [3]. The EU-funded STRATOFLY project further explores high-speed stratospheric flight [4]. Despite progress, integrated tools for efficient and safe suborbital vehicle design remain an active research need. This paper is based on the outcomes of the research program iConDeS (Integrated Conceptual Design Tools for Suborbital Vehicles) funded by the European Union through Next Generation EU (Project Identification Number P202272HBN). In this frame, a suborbital vehicle with a mission profile divided into four phases is considered: (i) an acceleration that brings the vehicle out of the atmosphere; (ii) a ballistic transfer covering most of the travel distance; (iii) an atmospheric re-entry close to the destination; (iv) a glide to the landing site. The methodology integrates sizing, aerodynamics, and trajectory analysis to design a minimum mass, fully reusable, two-stage vehicle tailored to specific mission scenarios. As a result, a multi-disciplinary technique

Content from this work may be used under the terms of the Creative Commons Attribution 3.0 license. Any further distribution of this work must maintain attribution to the author(s) and the title of the work, journal citation and DOI. Published under license by Materials Research Forum LLC.

Materials Research Proceedings 69 (2026) 954-959 https://doi.org/10.21741/9781644904251-168

is obtained that integrates all analysis tools [5, 6]. Building upon previous results, this study investigates the influence of the thrust-to weight ratios of both stages of the vehicle on its design characteristics at launch and on the overall mission profile, with the ultimate goal of analyzing and characterizing the design space to simplify and enhance the efficiency of the launcher's optimization process, which represents the final objective of the research project. The theoretical framework is complemented by numerical analysis to support the findings and ensure their validity.

Methodology

The conceptual design process, as shown in Fig. 1, follows a structured, iterative sequence of disciplinary modules. The design process begins with the definition of the Top-Level Requirements (TLR), which specify a fully reusable two-stage vehicle capable of transporting 50 passengers to the desired destination using liquid oxygen (LOX) and liquid methane (LCH4) as propellants. During the mission, the maximum acceleration must not exceed 4.5 g in either the ascent or descent of the flight, as higher values are considered hazardous for humans [5]. Initial data is generated using a statistical database and heuristic strategies (to estimate design velocity). The Weight and Sizing module, comprising HASA [7] for hypersonic orbiter and MARYLAND [8] for booster, iterates until mass convergence is reached. An embedded optimization minimizes fuel split while meeting acceleration limits. The design is then simulated in the Trajectory module, allowing the sizing of the Thermal Protection System (TPS), whose feedback refines velocity and mass. After convergence, the mass balance, the inertial properties, and the visual output are finalized. A detailed description of each disciplinary module and their integration within the design framework can be found in Ref. [6], where both stages were assumed to operate with fixed thrust-to-weight ratios, and the gross liftoff mass together with the optimal propellant distribution was determined to meet the mission objectives. In the present work, building on the results of previous studies, a design of experiments on the thrust-to-weight ratios for both stages is addressed. The goal is to identify the configuration that minimizes the total liftoff mass for a given mission, while fully complying with the Top-Level Requirements and the associated operational constraints.

Results

A design matrix was set up to assess the effects of varying the thrust-to-weight ratios of the booster ($(T/W)_1$) and the aircraft ($(T/W)_2$), ranging from 1.15 to 1.6 and from 0.9 to 1.2, respectively. The ranges of variation of the two ratios were selected to enable a comprehensive analysis of the strong relationships between these parameters and the characteristics of the vehicle at launch (gross mass, length, TPS ratio), as well as the trajectory flown to reach the target destination (acceleration, deceleration, heat flux profiles). Although no feasibility assessment of propulsion technologies was performed, the selected ranges still represent realistic scenarios for possible vehicle configurations. As a further remark, based on practical and technological considerations, the analysis was limited to configurations where the thrust-to-weight ratio of the first stag$(T/W)_1$) is always greater or, at most, equal to that of the second stage ($(T/W)_2$).

Materials Research Proceedings 69 (2026) 954-959 https://doi.org/10.21741/9781644904251-168

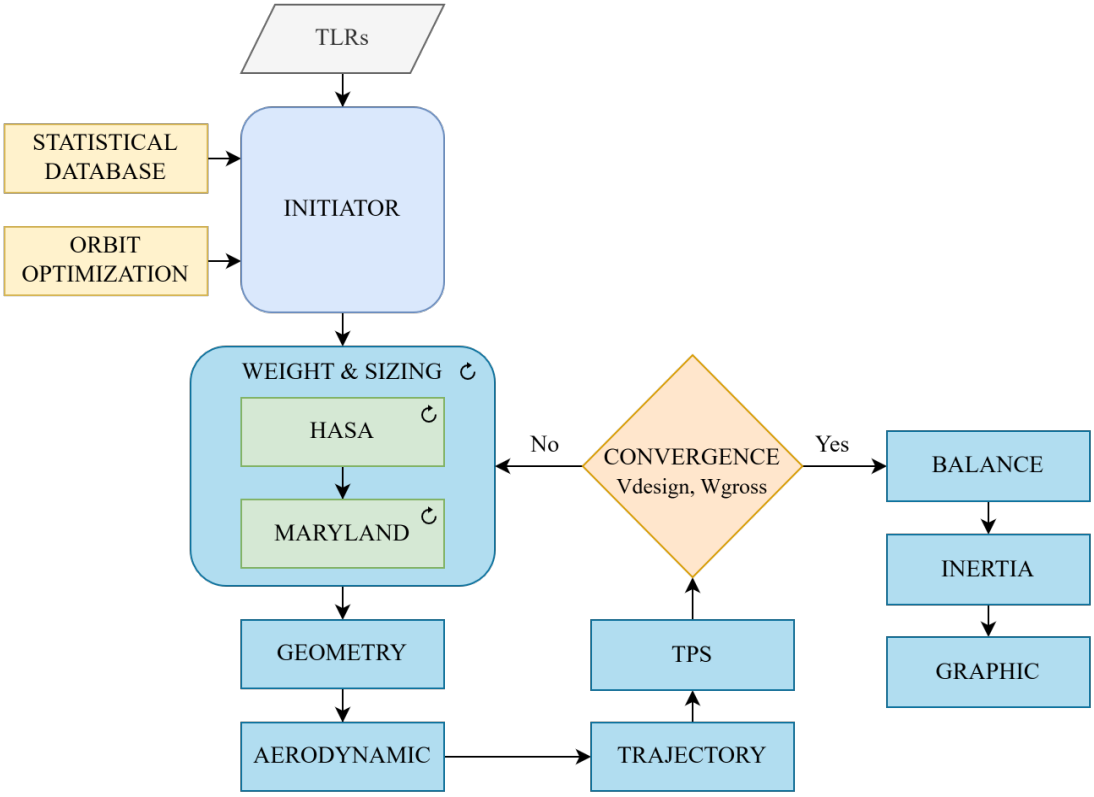


Figure 1: Workflow of the vehicle design methodology.

Fig. 2 shows a scatter plot of the results in terms of the gross mass of the entire vehicle at liftoff. Note that the graph includes some points that marginally exceed the maximum acceleration constraint (by less than 5%), and these points are marked with crosses. From this plot, it immediately emerges that the acceleration constraint poses an upper limit to the thrust-to-weight ratios, as excessive values of these parameters would bring the identified configuration to the bottom right corner of this plot, where all the crosses are distributed. The results shown in Figure 2 clearly indicate that the behavior of the gross mass at liftoff as a function of the two ratios is non-trivial, as it presents several local minima within the analyzed region. The global minimum can be identified at $(T/W)_1 = (T/W)_2 = 1.155$, corresponding to a total mass of 827.1 t. This point lies on the boundary delimiting the region of acceptable configurations and, importantly, the gradient of the gross mass is very steep in the vicinity of this minimum: a variation of only 4% in either parameter results in a change of approximately 10% in the gross mass.

Another region of interest can be observed around $(T/W)_1 = 1.25$ and $(T/W)_2 = 1.10$, corresponding to a total mass of 840.1 t. Unlike the previous case, the mass gradient in this region is milder with more gradual variations of the mass for the same variation in either parameter. Considering this region instead of that near the global minimum could therefore yield a more robust and less sensitive design solution.

Materials Research Proceedings 69 (2026) 954-959 https://doi.org/10.21741/9781644904251-168

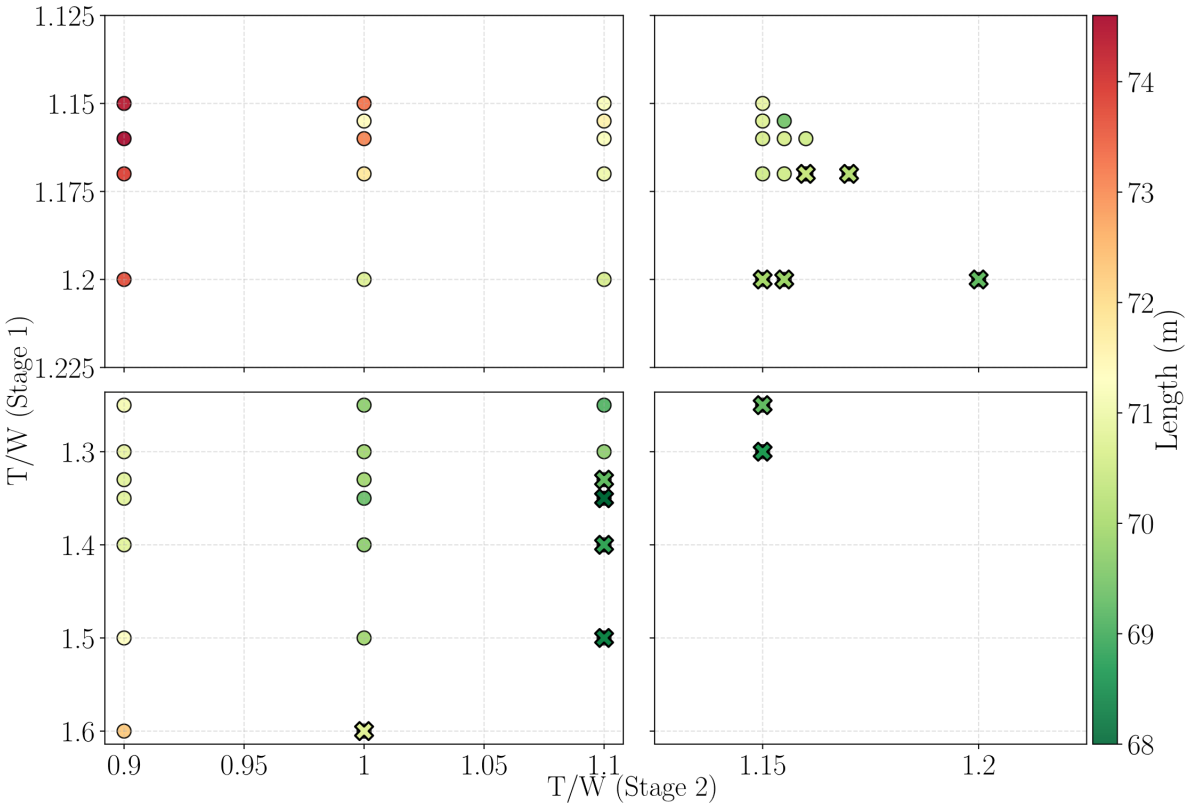


Figure 2: Scatter plot of considered points colored by gross mass. Circles represent configurations that comply with the maximum acceleration constraint, while crosses those that marginally exceed it. Axes are split and rescaled for clarity.

It is worth noting that, when including the solutions slightly violating the acceleration constraint, the global minimum corresponds to the configuration with $(T/W)_1$ = 1.35 and $(T/W)_2$ = 1.10, yielding a total mass of 812.5 t. This case achieves the mission with nearly 20 t less propellant compared to the configuration at $(T/W)_1 = (T/W)_2$ = 1.155, thus representing a significant design improvement while exceeding the acceleration limit by less than 1%. This small acceleration difference could be absorbed by considering control techniques of thrust and angle of attack in the launch and reentry phases, respectively, making this configuration fully acceptable.

Fig. 3 shows a scatter plot similar to that in Fig. 2 but with the points colored according to the total length of the vehicle instead of the gross mass. This quantity appears to qualitatively follow the same trend as the gross mass described previously. However, its variation with respect to the ratios is smaller, with a peak deviation of about 5% at $(T/W)_1$ = 1.15 and $(T/W)_2$ = 0.9 relative to the mean value across all configurations. This result indicates that variations in the thrust-to-weight ratios of the two stages have only a minor influence on the vehicle geometry, whose configuration at the acceptable global minimum is shown in Fig. 4 - 5.

Summary

A preliminary design of a suborbital vehicle capable of transporting 50 passengers from Naples to Port Moresby has been developed while satisfying, among other requirements, the acceleration constraints on the payload. The design optimization was conducted through a systematic design of experiments, varying the thrust-to-weight ratios of the two stages. The analysis revealed a nonlinear dependence of the vehicle gross mass on these parameters, with several local minima identified. Interestingly, the vehicle length remains nearly constant across all these minima, indicating a robust geometric configuration and suggesting that operational performance could be further optimized even after the vehicle's construction.

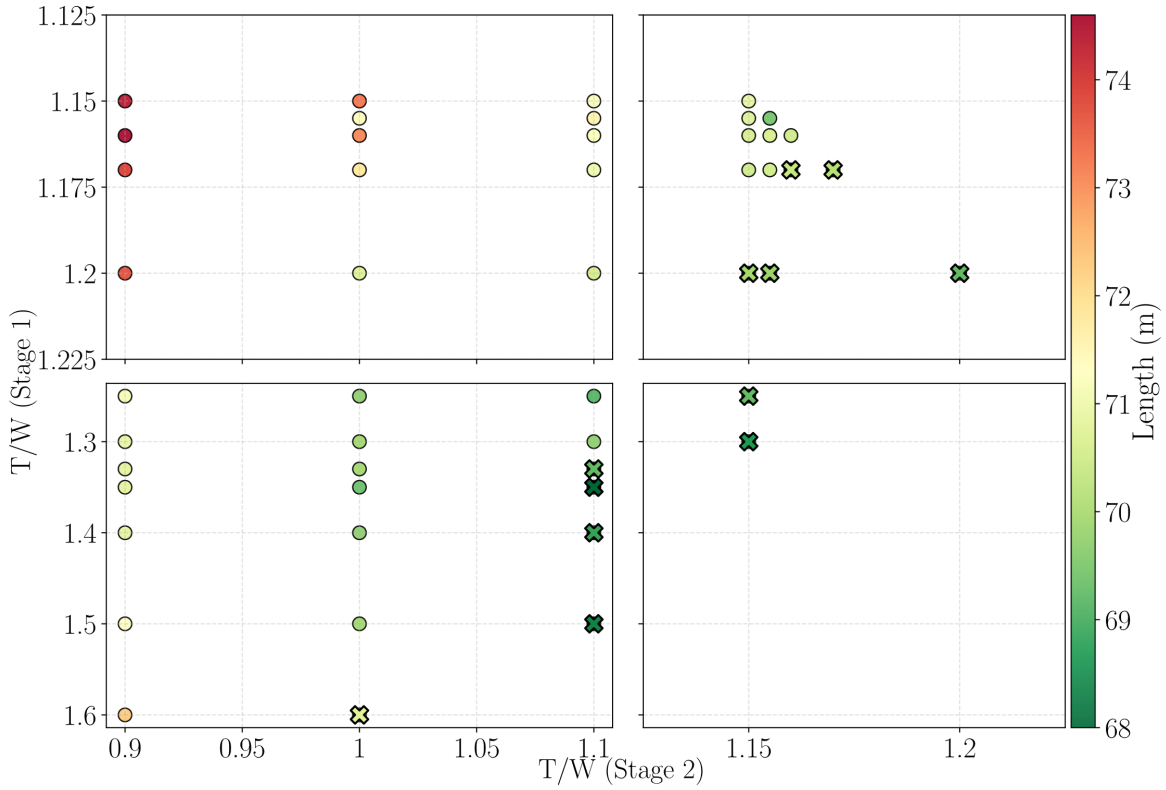


Figure 3:. Scatter plot of considered points colored by the total length of the vehicle. Circles represent configurations that comply with the maximum acceleration constraint, while crosses those that marginally exceed it. Axes are split and rescaled for clarity.

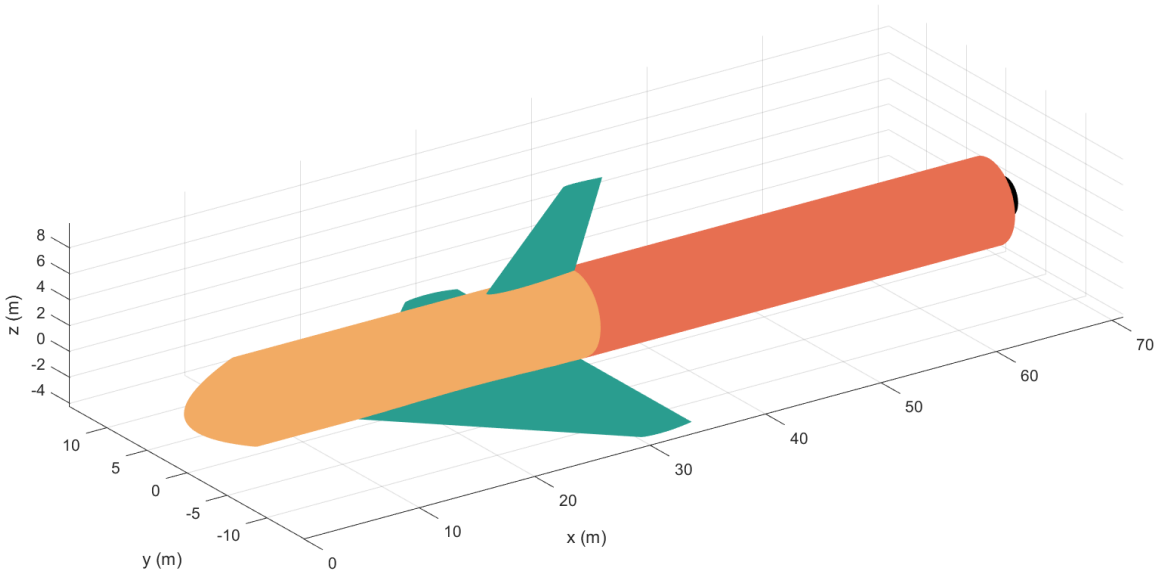


Figure 4: Three-dimensional view of the vehicle design.

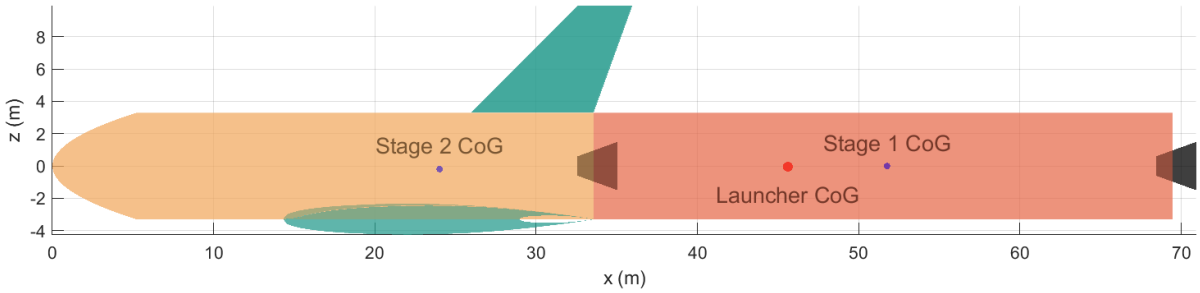


Figure 5: Lateral view of the vehicle design showing the center-of-mass positions at liftoff.

Reference

[1] Philippa Davies and Mark Hempsell, Progress on skylon and sabre, In 66th International Astronautical Congress (2015).

[2] Martin Sippel, Spaceliner technical progress and mission definition, In 20th AIAA International Space Planes and Hypersonic Systems and Technologies Conference (2015). https://doi.org/10.2514/6.2015-3582

[3] Gennaro Russo and Claudio Voto, Hyplane: a single-stage suborbital aerospaceplane, CEAS Space Journal, 15(6) 781-795 (2023). https://doi.org/10.1007/s12567-023-00494-z

[4] Nicole Viola, Roberta Fusaro, Bayindir Saracoglu, Christophe Schram, Volker Grewe, Jan Martinez, Marco Marini, Santiago Hernandez, Karel Lammers, Axel Vincent, Didier Hauglustaine, Bernd Liebhardt, Florian Linke, and Christer Fureby, Main challenges and goals of the h2020 stratofly project. Aerotecnica Missili & Spazio, 100(2) 95-110 (2021). https://doi.org/10.1007/s42496-021-00082-6

[5] G. Avanzini, M. Di Renzo, D. Passiatore, D. Zona, P. Della Vecchia, A. De Marco, F. Nicolosi, M. Capasso, L. Falcone, A conceptual design tool for preliminary sizing of suborbital transatmospheric vehicles, 75th International Astronautical Congress (IAC 2024), IAC-12-D2.IP.17x88991. https://doi.org/10.52202/078373-0092

[6] G. Avanzini, M. Di Renzo, D. Passiatore, D. Zona, P. Della Vecchia, A. De Marco, F. Nicolosi, M. Capasso, L. Falcone, A methodology for conceptual design of suborbital transatmospheric vehicles, 11th European Conference for Aeronautics and Aerospace Sciences (EUCASS 2025). https://doi.org/10.52202/078373-0092

[7] G. J. Harloff and B. M. Berkowitz, Hasa: Hypersonic aerospace sizing analysis for the preliminary design of aerospace vehicles, NASA-CR-182226 (1988).

[8] David L. Akin, Mass estimating relations, Lecture notes, Course ENAE 483/788D 2011, University of Maryland.

Materials Research Proceedings 69 (2026) 960-965 https://doi.org/10.21741/9781644904251-169

A Modular and Scalable Validation Framework for Planetary Rovers: Application to the ARDITO System

Amalia Dellacasa[1,a *], Gianmarco Polvani[1,b], Leonardo Maria Festa[1,c] and Fabrizio Stesina[1,d]

[1]STAR Lab, Department of Mechanical and Aerospace Engineering, Corso Duca degli Abruzzi 24, 10129, Torino, Italy

[a]amalia.dellacasa@studenti.polito.it, [b]gianmarco.polvani@studenti.polito.it, [c]leonardomaria.festa@polito.it, [d]fabrizio.stesina@polito.it

Keywords: Planetary Exploration, Aerospace Testing Principles, Autonomous Robotic Systems, System Validation, Modular Framework, Agile Methodologies, Reproducibility, Robotic System Testing

Abstract. Planetary exploration increasingly relies on autonomous robotic systems, yet the rigorous validation of end-to-end system behavior remains a significant bottleneck, par ticularly for small, multidisciplinary teams lacking the resources of large space agencies. This work addresses this challenge by tailoring established aerospace testing principles into a modular, scalable framework that balances thoroughness with agility. We demonstrate its application on the ARDITO rover, a platform developed by the DIANA student team at Po litecnico di Torino. Our approach provides a lean yet structured validation pathway, bridging the gap between ad-hoc laboratory tests and full-scale qualification campaigns governed by ECSS or NASA standards. The framework defines four distinct, interconnected testing layers: Design Validation (DEV), which focuses on component-level verification (e.g., finite-element analysis, bread board testing, test-driven development) within individual technical departments; Reduced Functional Tests (RFT), used as rapid control points to validate integrated subsystems after major events like transport or configuration changes; Full Functional Tests (FFT), which comprehensively evaluate the fully integrated rover under controlled laboratory conditions; and Mission Tests (MST), which simulate realistic task scenarios in environments like AL TEC Martian Terrain Simulator to evaluate performance under mission constraints. This hybrid agile-lean approach offers a clear academic and practical contribution for research groups and early-stage projects, ensuring reliable, mission-ready performance.

Introduction

Robotic systems with full or partial autonomy are becoming increasingly vital for planetary exploration. They are deployed to execute scientific, scouting, and support functions in remote, hazardous, poorly characterized locations (B. Hussain, 2025) (Ishigami, 2024). In the unforgiving space domain, where post-launch repair is impossible, Verification and Validation (V&V) are fundamental (R. C. Cardoso, 2021). Verification ensures a system is built according to its specifications, building the system right, while validation confirms it fulfills its intended purpose in its operational environ ment, building the right system. The state-of-the-art in V&V is polarized into two distinct paradigms based on mission scale and risk. The heavyweight standard, used for large-scale rovers, is exhaustive and requirements driven. Governed by NASA (Kapurch, 2010) and ECSS standards (ECSS, 2018), this multi-year process uses tiered f idelity testing, from simulations to hardware testbeds, consuming up to 80% of project timelines and creating a validation gap as system complexity outpaces testing capabilities. Conversely, the lightweight agile V&V for CubeSats is constraints-driven, prioritizing rapid schedules and fixed budgets. It relies on standardized tests and Commercial-Off-The Shelf (COTS) components. This polarization

Content from this work may be used under the terms of the Creative Commons Attribution 3.0 license. Any further distribution of this work must maintain attribution to the author(s) and the title of the work, journal citation and DOI. Published under license by Materials Research Forum LLC.

Materials Research Proceedings 69 (2026) 960-965 https://doi.org/10.21741/9781644904251-169

presents a significant challenge, particularly for the small, multidisciplinary teams in university and startup environments, which lack the resources for the heavyweight approach but cannot always afford the high risk of the lightweight model. The case study for this work is the rover ARDITO (Caraccio, 2025) (N. di Gruttola Giardino, 2024).

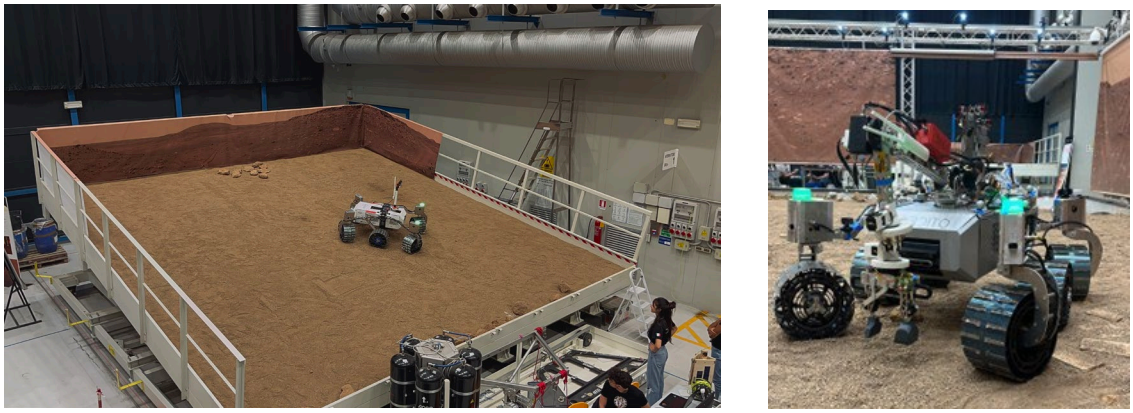


Figure 1: From left to right: ARDITO on the MTS Facility performing Science Mission Scenario. Ardito on the Tilting Platform . (These photos were taken at the ALTEC Mars Terrain Simulator - MTS Facility - which was developed for ESA ExoMars program under Thales Alenia Space Italy contract)

Layered Validation Framework

To bridge the gap between ad-hoc laboratory tests and full-scale qualification campaigns, we developed a modular, scalable validation framework tailored for resource-constrained robotic projects developed in an educational environment **(Corpino, IFAC Workshop on Aerospace Control Education WACE 2021)**. This framework is built on a progressive philosophy, systematically escalating the scope and complexity of testing from individual components to the fully integrated system operating under mission-like conditions. It provides a structured pathway to retire risk incrementally, ensuring that foundational elements are robust before they are integrate into more complex assemblies. The work starts with the system's functions prioritization coming from the European Rover Challenge (ERC) rules and some key core requirements identified in parallel by the team's board of directors. Aspecific functional analysis identifies which requirements and functions are relevant for the test plan, and consequently they are organized and divided by subsystems.

The framework is composed of four distinct yet interconnected layers: Design Validation (DEV), Reduced Functional Tests (RFT), Full Functional Tests (FFT), and Mission Tests (MST). Each layer serves a specific purpose, building confidence in the system's reliability and performance at critical stages of the development and operational lifecycle.

Layer 1: Design Validation (DEV). The foundational layer, Design Validation (DEV), focuses on component-level verification before any system integration occurs. This phase is executed internally by each technical departments, from mechanical subsystems designs **(Trentini, 2024)** to software autonomy modules creation **(Mustich, 2023)**. This allows for focused, discipline-specific analysis **(Festa L. M., 2022)** and testing. The primary goal of DEV is to confirm that each component meets its design requirements and specifications in isolation, preventing fundamental flaws from propagating to higher levels of assembly where they become more difficult and costly to diagnose and fix.

Layer 2: Reduced Functional Tests (RFT). RFTs serve as a crucial ”health check” on integrated subsystems. These are rapid, targeted tests designed to be executed after major events such as

Materials Research Proceedings 69 (2026) 960-965 https://doi.org/10.21741/9781644904251-169

hardware configuration changes, software updates, or transportation. The purpose of an RFT is to quickly validate essential functions with minimal external depen dencies, providing prompt feedback on the system's baseline health. This allows the team to confirm that a recent change has not introduced a critical failure before proceeding with more time-consuming tests. For example, a typical RFT, performed after transporting the rover to a test site, is a 10-minute procedure that involves powering on the main computer and drive system, commanding each wheel to spin for five seconds, and confirming a teleme try is received from all critical sensors. This simple test quickly verifies the integrity of the power system, drivetrain, and core communication pathways.

Layer 3: Full Functional Tests (FFT). FFTs are designed to comprehensively evaluate the fully integrated rover and its payloads under controlled laboratory conditions. Unlike RFTs, which are narrow in scope, FFTs execute pre-programmed, end-to-end mission routines to stress-test every operational mode and verify complex software logic and inter-system interactions. These tests are performed on a flat, predictable surface to isolate the system's performance from environmental challenges, focusing purely on functional correctness and integration stability. An example FFT for the ARDITO rover involved a 1-hour autonomous sequence that executed a full mission profile to validate the entire chain of operations from navigation to payload deployment, ensuring that all subsystems work cohesively as intended.

Layer 4: Mission Tests (MST). The final layer, Mission Tests (MST), evaluates the sys tem's end-to-end performance under realistic task scenarios and environmental constraints that closely recreate actual mission parameters. For this critical phase, we had the oppor tunity to perform tests in ALTEC S.p.A Martian Terrain Simulator (MTS Facility**) (Bramante, et al., 2019)** in Turin, Italy. ALTEC, a center of excellence for space logistics and engineering, operates the Rover Operations Control Centre (ROCC) for the ESA ExoMars mission, and its MTS provides a high-fidelity Martian analogue terrain for testing and verification activities. The MTS hosts a ground test model of the ExoMars rover and is designed to rehearse surface operations in a terrain with Mars-like morphology. Within this facility, the ARDITO rover was subjected to mission scenarios derived from the rules of the European Rover Challenge, including navigating uneven terrain with slopes and obstacles, and operating under simu lated communication constraints, such as limited bandwidth and command delays. These tests were essential for validating the rover's performance and robustness in conditions that could not be replicated in a standard laboratory.

To manage this campaign within tight schedules and with limited personnel, we integrated lean operational practices, using physical Kanban boards **(Bacea, Ciupe, & Meza, 2017)** for real-time task prioritization and checklist-based reports to ensure traceability and facilitate anomaly tracking.

Materials Research Proceedings 69 (2026) 960-965 https://doi.org/10.21741/9781644904251-169

Table 2: Mobility sub-system test summary

ID	Short Name	Test Description	Linked Reqs.
RFT			
RFT-M-01	MC&EL Steering	Steering	
RFT-M-02	MC&EL Feedback H7	Test H7	
RFT-M-03	MC&EL Feedback Webapp	Test Webapp	
RFT-M-04	Tracking	Test Tracking Service	
FFT			
FFT-M-N-01	WebApp Test	WebApp Feedback	R-GEN-060, R-OPS-110
FFT-M-N-03	Tracking	Tracking service	
FFT-M-N-04	POCO	Position Control mode	R-FUN-060, R-FUN-030
FFT-M-N-05	AUTONAV	Autonomous Mode	R-FUN-060, R-OPS-080, R-OPS-090
FFT-M-N-06	Performance Validation I	Precision in Velocity mode	R-GEN-060
FFT-M-N-07	Performance Validation II	Precision in Position Control mode	R-FUN-030
FFT-M-N-08	Performance Validation III	Precision in AUTONAV mode	R-FUN-250
FFT-M-N-09	Streaming	Streaming Cameras monitoring	R-OPS-110, R-FUN-170
FFT-M-N-10	Safety Button	Safety button does safely shut-off the rover	R-DES-020
MST			
MST-M-N-01	Navigation Task Test	Simulate Navigation Task	R-FUN-060, R-FUN-250
MST-A-M-01	Maintenance Task Test	Simulation of Maintenance Task	R-GEN-090
MST-A-P-01	Probing Task Test	Simulation of Probing Task	R-GEN-100
MST-A-S-01	Science Surface Sample Task	Simulation of Science Sample Task	R-FUN-150
MST-A-S-02	Science Construction Task	Simulation of Construction Task	R-DES-140

Methodology: Agile & Lean Process Management in the ARDITO project

To manage our complex four-layered validation campaign within a resource-constrained stu dent team, we adopted an agile-inspired approach. Our hybrid agile-lean methodology **(Festa G. P., 2025)** for the ARDITO project combines a high-level annual timeline with a dual-layered system built around major integration milestones called ”stable points” and two-week development cycles known as ”sprints.” The sprints were the engine of the project, where the low-level continuous work of the Design Validation (DEV) layer occurred. Within each sprint, techni cal groups focused on designing, building, and verifying their individual components through FEA, breadboarding, and test-driven development, ensuring quality was built in from the very beginning. The focus then shifted from the DEV layer to system-level verification, primarily using the Reduced Functional Test (RFT) and Full Functional Test (FFT) layers. This incremental approach was transformative for the project lifecycle; instead of a single, high-stakes integration event at the end of the year, we had multiple, lower-risk checkpoints. Each stable point provided a validated, reliable fallback

configuration, systematically miti gating risk and ensuring we always had a functional rover baseline. This structure creates a powerful feedback loop DEV − > RFT/FFT − > DEV. System-level failures found at a stable point are documented and feedback into the agile backlog to be resolved at the component level in the next sprint. This makes validation a continuous, iterative process, allowing us to manage complexity by progressively and thoroughly validating the system at every stage.

Conclusions

The novelty of our work lies in structuring these established methods into a tailored frame work guided by three core principles: modularity, scalability and feedback-driven iteration. By decoupling validation layers, defining adaptable templates and embedding agile feedback loops, the framework can be adopted or modified based on project scale and constraints. We have already begun applying this paradigm to other DIANA demonstrators, such as aerial companions, to further test its generalizability. In conclusion, this work presents a reproducible multi-layered testing framework that enables robust and resource-efficient validation of complex robotic systems. Its successful deployment on the ARDITO rover underscores its potential for broader adoption across academic and small-scale industrial contexts. Future work will formalise quantitative met rics, integrate software tools to replace physical boards and conduct cross-project studies to benchmark efficacy

Ackowledgments

The authors express their gratitude to the STAR Lab team and DIANA's students for their passion and continuous work, making this kind of work possible.

References

[1] B. Hussain, J. G. (2025). Robotics for space exploration: From mars rovers to lunar missions. International Journal of Ethical AI Application, vol. 1, 1-10. https://doi.org/10.64229/z94fvn06

[2] Bacea, I. M., Ciupe, A., & Meza, S. N. (2017). Interactive Kanban - Blending Digital and Physical Resources for Collaborative Project Based Learning. IEEE. https://doi.org/10.1109/ICALT.2017.68

[3] Bramante, L., Deffacis, M., Bussi, D., Barrera, M., Picco, C., & Franceschetti, P. (2019). The Mars Terrain Simulator: a high level measurement facility in support to the ExoMars mission. Turin, Italy: IEEE. https://doi.org/10.1109/MetroAeroSpace.2019.8869653

[4] Caraccio, L. a. (2025). ARDITO, a modular technology demonstrator for robotic planetary surface exploration and operational support: an overview. IEEE Aerospace and Electronic Systems Magazine, 1-10. doi:10.1109/MAES.2025.3564224 https://doi.org/10.1109/MAES.2025.3564224

[5] Corpino, F. S. (IFAC Workshop on Aerospace Control Education WACE 2021). Star laboratory at politecnico di torino: A facility to develop educational projects. IFAC-PapersOnLine, vol. 54, no. 12, , 80-87. https://doi.org/10.1016/j.ifacol.2021.11.013

[6] ECSS. (2018). Space engineering - Verification. ECSS (European Cooperation for Space Standardization).

[7] Festa, G. P. (2025). "Implementing agile management in space robotics university project: The ardito rover case study. IAC 2025, Sydney, Australia: IAF Astro.

[8] Festa, L. M. (2022). Advanced least weight design optimization of additive manufactured space rover steering brackets. IAC 2022. Paris, France: IAF Astro.

[9] Ishigami, R. T. (2024). Uncertainty-aware trajectory planning: Using uncertainty quantification and propagation in traversability prediction of planetary rovers. IEEE Robotics & Automation Magazine, vol. 31, no. 2, 89-99. https://doi.org/10.1109/MRA.2023.3341289

[10] Kapurch, S. J. (2010). NASA systems engineering handbook.

[11] Mustich, F. S. (2023). Point Cloud-Based Reinforcement Learning for Autonomous Navigation of a Robotic Rover on Planetary Surfaces. IAC 2023. Baku, Azerbaijan: IAF Astro.

[12] N. di Gruttola Giardino, F. F. (2024). A modular avionics architecture for a planetary rover demonstrator for human assistance. IFAC-PapersOnLine, vol. 58, no. 16, 2nd IFAC Workshop on Aerospace Control Education- WACE 2024, 181-186. https://doi.org/10.1016/j.ifacol.2024.08.483

[13] R. C. Cardoso, G. K. (2021). A review of verification and validation for space autonomous systems. Current Robotics Reports, vol. 2, no. 3, 273-283. https://doi.org/10.1007/s43154-021-00058-1

[14] Trentini, C. F. (2024). Design, validation and production of small-size rover elastic wheels: a solution to plastic deformations. IAC 2024. Milan, Italy: IAF Astro. https://doi.org/10.52202/078369-0037

Materials Research Proceedings 69 (2026) 966-971 https://doi.org/10.21741/9781644904251-170

Aerodynamic Characterization of Fin Configuration for VLEO Attitude Stabilization

Vincenzo Maria CANNAVALE[1,a*], Mattia ILLIANO[1,b], Tobia Armando LA MARCA[2,c], Maria Daniela GRAZIANO[1,d], Elisa CAPELLO[3,e] and Michele GRASSI[1,f]

[1]Department of Aerospace Engineering, Università degli Studi di Napoli Federico II Piazzale Tecchio 80, 80125 Napoli (NA), Italia

[2]Scuola Superiore Meridionale, Largo San Marcellino 10, 80138 Napoli (NA), Italia

[3]Department of Mechanical and Aerospace Engineering, Politecnico di Torino, C.so Duca degli Abruzzi 24, 10129 Torino (TO), Italia

[a]vincenzomaria.cannavale@unina.it, [b]mattia.illiano@unina.it, [c]tobiaarmando.lamarca-ssm@unina.it, [d]mariadaniela.graziano@unina.it, [e]elisa.capello@polito.it, [f]michele.grassi@unina.it

Keywords: VLEO, Aerodynamics, Drag Analysis, Surface Optimization, CubeSat

Abstract. This work proposes a hybrid tilt–twist fin configuration for CubeSat attitude control in Very Low Earth Orbit (VLEO), combining passive stability with potential control authority through two geometric parameters: tilt and twist angles. The aerodynamic forces and torques have been evaluated through a panel method in free molecular flow, across a parametric design space. Results demonstrate that hybrid configurations achieve lower drag than shuttlecock designs while providing superior control authority compared to feather configurations, establishing a crucial step for future dynamic deflection-based control laws in VLEO missions.

Introduction

The Very Low Earth Orbits (VLEOs), typically defined below 450 km, offers unique opportunities for future spacecraft missions by improving optical resolution, communication latency, and overall mission efficiency through lower-altitude operations. The denser atmosphere at these altitudes, however, introduces substantial aerodynamic forces and torques, which not only accelerate orbital decay but also dominate the disturbance environment affecting attitude dynamics. While traditional actuators, such as reaction wheels or magnetic torquers, may suffer from frequent saturation and limited lifetime under these conditions, the persistent aerodynamic environment can be exploited as a control resource rather than merely a disturbance [1]. The concept of aerodynamic attitude stabilization was initially formalized through analytical models linking geometrical parameters with stability derivatives, enabling the design of configurations that naturally keep the spacecraft's attitude around its aerodynamic equilibrium positions [2]. Subsequent studies demonstrated the feasibility of using deployable, fixed or multi-degree-of- freedom aerodynamic surfaces to achieve passive or active stabilization and control in VLEO [3,4]. Nonetheless, the integration of flexible elements can lead to complex nonlinear phenomena, including chaotic motion and coupled aero-elastic effects, which must be carefully modeled to ensure robust performance [5]. In this framework, the present work focuses on the aerodynamic characterization of fin-based configurations for CubeSats operating in VLEO, introducing a parametric design methodology that integrates geometric flexibility, with an aerodynamic analysis based on a panel method in free-molecular flow. The objective is to identify configurations that guarantee passive stabilization while preserving control authority and compatibility with CubeSat constraints, and to compare performances against shuttlecock and feather architectures. The paper is organized as

Content from this work may be used under the terms of the Creative Commons Attribution 3.0 license. Any further distribution of this work must maintain attribution to the author(s) and the title of the work, journal citation and DOI. Published under license by Materials Research Forum LLC.

Materials Research Proceedings 69 (2026) 966-971 https://doi.org/10.21741/9781644904251-170

follows: the Methodology section introduces the aerodynamic modeling approach and the parametric fin generation tool; the Results section presents the numerical outcomes and discusses the stability trends as a function of fin geometry; and the Conclusions section reports key findings and prospects for the integration of hybrid aerodynamic control architectures in future VLEO missions.

Methodology

This paper uses the following convention on aerodynamic angles, according to the defined Body Reference Frame (BRF) (Fig. 1): angle of attack (α, angle between X_{BRF} and the projection of the freestream vector on the XZ_{BRF} plane, positive in case of clockwise rotation about Y_{BRF}) and sideslip angle (β, angle between X_{BRF} and the projection of the freestream vector on the XY_{BRF} plane, positive in case of counterclockwise rotation about Z_{BRF}).

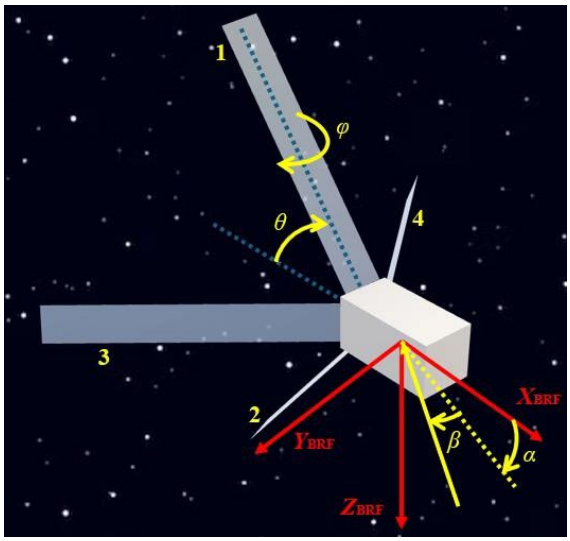


Fig. 1 Illustration of a 16U CubeSat with four deployable fins, the fin's geometric parameters (tilt angle θ and the twist angle φ) and the associated fin ID number, BRF and the aerodynamic angles (α, β).

The baseline spacecraft is a 16U CubeSat with four deployable fins attached to longitudinal edges (Table 1).

Table 1 Dimensions, mass, and material properties of the 16U CubeSat body and the deployable fins used for aerodynamic characterization.

Component	Parameter	Value
Body	Dimensions [mm]	400×200×200
	Mass[kg]	24
Fin	Dimensions [mm]	1000×130×0.5
	Mass [kg]	0.182

Each fin is characterized by two independent angular parameters: tilt angle θ (rotation about attachment edge, positive outward from X_{BRF}) and twist angle φ (rotation about spanwise axis, negative following right-hand rule) (Fig. 1), yielding an eight-dimensional design space $S = [\theta_1, \theta_2, \theta_3, \theta_4, \varphi_1, \varphi_2, \varphi_3, \varphi_4]$. Both parameters are discretized into $\theta \in [0°, 90°]$ and $\varphi \in [-90°, 90°]$, with

Materials Research Proceedings 69 (2026) 966-971 https://doi.org/10.21741/9781644904251-170

a 10-degree step each. For computational efficiency, the design space was subsequently reduced by imposing an axial symmetry with respect to X_{BRF} axis, coupling the parameters of opposing fin pairs ($\theta_1=\theta_2=\theta_3=\theta_4$; $\varphi_1=\varphi_2$; $\varphi 3=\varphi 4$). All configurations undergo geometric feasibility screening using intersection detection. The aerodynamic characterization employs the ADBSat computational framework for rarefied flow environments [6]. Aerodynamic forces and moments are computed using DRIA Gas Surface Interaction (GSI) with flight conditions specified in Table 2. Each configuration is evaluated under different wind conditions relative to the spacecraft. Specifically, α and β are varied within the range [−15°, 15°] with 3-degree increments, yielding 121 wind scenarios.

Table 2 Flight conditions and atmospheric parameters for aerodynamic characterization at 250 km altitude. The accommodation coefficient is computed according to [7].

Parameter	Value	Parameter	Value
Altitude [km]	250 km	Orbital velocity [km/s]	7.8
Latitude/Longitude [°]	40 N, 20 W	Atmospheric density [kg/m³]	~10^{-11}
Solar flux ($F_{10.7}$) [SFU]	140	Surface temperature [K]	300
Geomagnetic index (Ap)	14	Accommodation coef.	0.99
Knudsen number (Kn)	>> 10	Atm. Model	NRLMSISE-00

Among the 190 generated configurations, one optimal hybrid design is selected for comparison; this spacecraft architecture was derived from a Pareto optimization using the following objective weighting scheme: 0.2 for drag, 0.25 for torque magnitude, and 0.15 for each stability derivative.

Results

The aerodynamic characterization of this configuration demonstrates balanced performance in stability, controllability, and drag magnitude among the 190 candidate hybrid configurations. The optimal hybrid configuration, derived from Pareto analysis, features four fins with 10-degree tilt angle and asymmetric twist: $\varphi_1=\varphi_2=-20°$ and $\varphi 3=\varphi 4=+20°$. As shown in Fig. 2, the moment coefficients C_l, C_m, and C_n are close to zero at $\alpha=\beta=0$ (equilibrium), confirming trim conditions when the freestream aligns with -X_{BRF}. In this region, C_m and C_n are assumed to vary linearly with α and β, allowing the identification of static stability derivatives, according to [2].

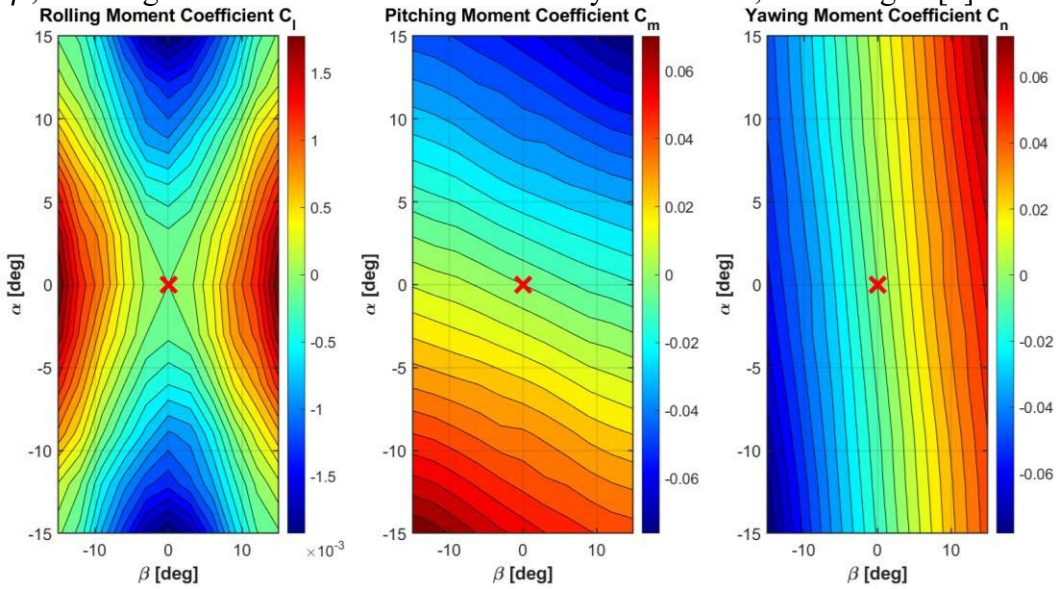


Fig. 2 Contour maps of the momentum coefficients as functions of the angle of attack and sideslip angle for the optimal hybrid fin configuration.

Materials Research Proceedings 69 (2026) 966-971 https://doi.org/10.21741/9781644904251-170

Fig. 3 indicates that $C_{m,\alpha}<0$ produces a restoring pitching moment as α increases, confirming pitch stability, while $C_{n,\beta}>0$ denotes yaw stability as β increases. In near-equilibrium region, the small magnitudes of $C_{l,\alpha}$ and $C_{l,\beta}$ suggest weak cross-axis coupling, ensuring nearly roll-independent pitch–yaw dynamics. The alternating sign of $C_{l,\alpha}$ reveals marginal roll stability, typical of symmetric aerodynamic layouts, yet acceptable for hybrid aerodynamic control schemes.

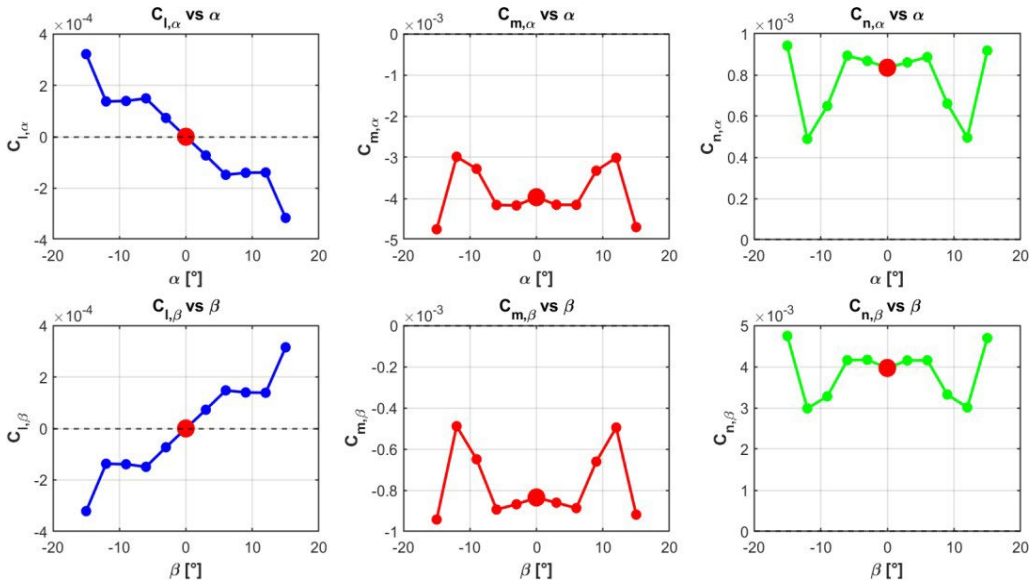


Fig. 3 Static aerodynamic derivatives as a function of incidence angles for the hybrid fin configuration.

For larger incidence angles, nonlinear variations of C_l, C_m, and C_n indicate increased torque generation, corresponding to reduced passive stability but improved control authority, especially along X_{BRF}. To validate the preliminary static performance of the hybrid configuration, a comparative analysis was conducted. In this study, the shuttlecock has 30-degree tilted fins with zero twist, promoting passive aerodynamic stabilization along the velocity vector, while the feather has 90-degree tilted and 90-degree twisted fins, minimizing drag and restoring torque [2]. Comparative results (Fig. 4) show that the shuttlecock offers stronger passive damping but with drag two orders of magnitude higher, while the feather minimizes drag but provides limited torque. The hybrid configuration effectively merges both behaviors, ensuring low drag and sufficient aerodynamic torque. The outperformance and trade-offs are further quantified in Table 3 by simulated semi-major axis decay over a single circular-orbit period using Gaussian Variation of Parameter (VOP) equations [8], where the shuttlecock's high drag leads to the highest decay, contrasting with the feather's minimal drag and lowest decay. The hybrid represents an optimized compromise, reducing the decay by approximately 83% compared to the shuttlecock.

Materials Research Proceedings 69 (2026) 966-971 https://doi.org/10.21741/9781644904251-170

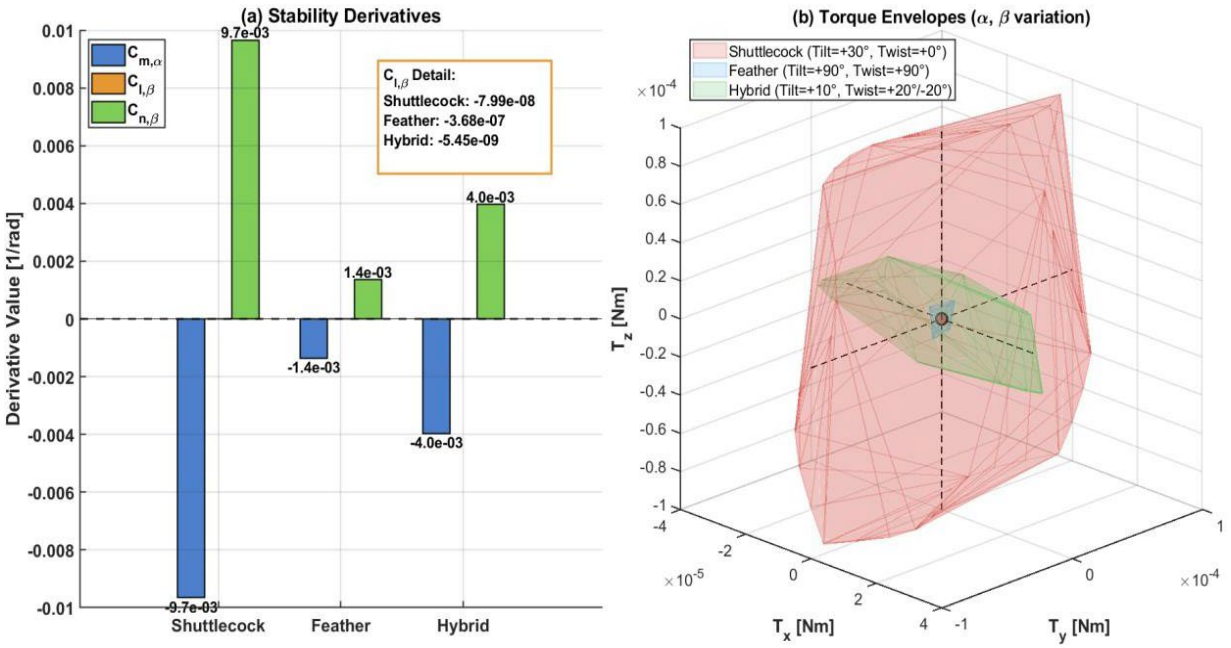


Fig. 4 Comparative analysis of the shuttlecock, feather, and hybrid fin configurations, showing (a) the stability derivatives at zero incidence, and (b) the resulting aerodynamic torque envelopes as a function of the aerodynamic angles.

Table 3 Comparative drag analysis and orbital decay for shuttlecock, feather, and hybrid fin configurations over one orbital period at 250 km altitude.

	Shuttlecock	Feather	Hybrid
Drag magnitude [N]	4.94×10^{-4}	1.45×10^{-5}	8.58×10^{-5}
1-orbit decay [m]	188	5.5	32.8

Conclusions

This work presents a parametric aerodynamic characterization of hybrid tilt–twist fin configurations for CubeSat attitude stabilization and control in VLEO. Panel-method free molecular flow simulations demonstrate that the selected optimal hybrid configuration achieves synergistic balance between passive damping and active control authority. The hybrid design exhibits negative pitch stability derivative and positive yaw stability derivative, confirming three-axis passive stability at trim conditions. Comparative analysis shows 83% reduction in orbital decay relative to the shuttlecock (32.8 m vs. 188 m per orbit) while maintaining superior control authority compared to the feather design.

Future work will extend this static aerodynamic characterization to dynamic attitude motion, validating the stability predictions through coupled rotational dynamics simulations. The parametric database established herein provides the foundation for developing control laws based on time-varying fin deflections. Control allocation algorithms will regulate fin deflections to achieve commanded torques while minimizing drag penalties.

Acknowledgements

This work was carried out within the *Space It Up!* project funded by the Italian Space Agency (ASI) and the Italian Ministry of University and Research (MUR) under contract No. 2024-5- E.0, CUP No. I53D24000060005.

References

[1] Muñoz, V. C., González, D., Becedas, J., Domínguez, R. M., Roberts, P. C. E., Crisp, N. H., Oiko, V. T. A., Edmondson, S., Worrall, S. D., Haigh, S., Smith, K., Lyons, R. E., Livadiotti, S., Huyton, C., Sinpetru, L. A., Rodriguez-Donaire, S., Garcia-Almiñana, D., Nieto, M., Muñoz, C., Sureda, M., Kataria, D., Herdrich, G. H., Romano, F., Binder, T., Boxberger, A., Fasoulas, S., Traub, C., Outlaw, R., Hanessian, V., Morsbøl, J., Villain, R., Perez, J. S., Conte, A., Belkouchi, B., Schwalber, A., and Heisserer, B., "Attitude Control for Satellites Flying in VLEO Using Aerodynamic Surfaces," Journal of the British Interplanetary Society, Vol. 73, 2020, pp. 103–112.

[2] Mostaza-Prieto, D., and Roberts, P. C. E., "Methodology to Analyze Attitude Stability of Satellites Subjected to Aerodynamic Torques," Journal of Guidance, Control, and Dynamics, Vol. 39, No. 3, 2016, pp. 437–449. https://doi.org/10.2514/1.G001481

[3] Chang, C., Breidenthal, R., Lin, B., and Yang, Y., "Aerodynamic Satellite Attitude Control in Very Low Earth Orbit," 2024.

[4] Riano-Rios, C., Sun, R., Bevilacqua, R., and Dixon, W. E., "Aerodynamic and Gravity-Gradient Based Attitude Control for CubeSats in the Presence of Environmental and Spacecraft Uncertainties," Acta Astronautica, Vol. 180, 2021, pp. 439–450. https://doi.org/10.1016/j.actaastro.2020.12.038

[5] Aslanov, V. S., and Sizov, D. A., "Chaos in Flexible CubeSat Attitude Motion Due to Aerodynamic Instability," Acta Astronautica, Vol. 189, 2021, pp. 310–320. https://doi.org/10.1016/j.actaastro.2021.08.055

[6] Sinpetru, L. A., Crisp, N. H., Mostaza-Prieto, D., Livadiotti, S., and Roberts, P. C. E., "ADBSat: Methodology of a Novel Panel Method Tool for Aerodynamic Analysis of Satellites," Computer Physics Communications, Vol. 275, 2022, p. 108326. https://doi.org/10.1016/j.cpc.2022.108326

[7] Pilinski, M. D., Argrow, B. M., and Palo, S. E., "Semiempirical Model for Satellite Energy-Accommodation Coefficients," Journal of Spacecraft and Rockets, Vol. 47, No. 6, 2010, pp. 951–956. https://doi.org/10.2514/1.49330

[8] Vallado, D. A., and McClain, W. D., "General Perturbation Techniques," Fundamentals of Astrodynamics and Applications, Microcosm Press, 2013, pp. 619–637.

Materials Research Proceedings 69 (2026) 972-993 https://doi.org/10.21741/9781644904251-171

GRIAL: A High-Fidelity Simulator of Orbital Forces and Torques

Valerio LEVI[1,2,a *], Adrián DE ANDRÉS TIRADO[1,b] and Miguel GUEREÑU MIRA[1,c]

[1]GMV Innovating Solutions, Madrid, Spain

[2]ISAE-SUPAERO, Avenue Edouard Belin, Toulouse, 31400, France

[a]vlevi@gmv.com, [b]adandres@gmv.com, [c]miguel.guerenu.m@gmv.com

Keywords: Orbital Forces Modelling, Orbital Torques Modelling, GPU-Powered Approach, In-Parallel Computation, SRP, Drag

Abstract. Precise orbit determination (POD) is essential for Earth observation missions and geodetic satellites operations. While current POD systems achieve centimetre-level accuracy, occasional residual discrepancies result from simplified spacecraft geometry models. Considering the true shape of the object, rather than relying on the typical box-wings approximation, can further increase the accuracy of the computation. Moreover, SST applications, such as collision risk assessment or re-entry predictions, can be enhanced by considering the real shape and attitude of space objects. In this regard, tools for attitude propagation and determination of tumbling objects are crucial, and require precise modelling of the torques affecting the satellite. This work presents GMV's GRIAL, a GPU-powered library for high-fidelity computation of force and torque perturbations acting on the surfaces of space objects of any complex shape in any attitude motion. In particular, the library models perturbations arising from solar radiation pressure (SRP), atmospheric drag, and Earth's albedo and infrared (IR) radiation. Utilizing the GPU enables highly efficient and precise calculations, allowing the forces and torques to be computed simultaneously at numerous points on the object's surface, and then summed using the CPU. Moreover, the incorporation of an OpenGL layer in the tool enables shadow casting, that efficiently accounts for the self-shadowing that occurs between different parts of the object, which is particularly significant for convex shaped features or protrusions such as dish antennas or solar arrays.

Introduction

The number of objects orbiting Earth has seen a rapid increase, particularly in the last decade. With the launch of mega-constellations and the advent of more affordable and accessible space technology, even for smaller entities, the density of satellites and debris in Low Earth Orbit (LEO) has significantly increased. Consequently, space traffic management has become a critical area of interest for satellite operations. Collision avoidance manoeuvres are becoming more and more essential, and their cost and effectiveness depend primarily on the precision of collision risk assessment. This precision relies mainly on accurate orbit prediction but can be further improved when the shape and attitude of the objects at the moment of closest approach are known. The same principle applies to other space applications, including re-entry predictions, Active Debris Removal (ADR) and In-Orbit Servicing (IOS), which rely on the real attitude of the object.

Consequently, a key step toward improving these applications is the ability to propagate the attitude motion of tumbling objects, which in turn requires accurate modelling of orbital torques acting upon them. It is important to highlight that determining the shape and surface properties of tumbling objects can represent a challenging task; the present work assumes that such information is available.

The accurate modelling of non-gravitational perturbations is a fundamental requirement for precise orbit and attitude prediction. Perturbations like SRP, atmospheric drag, and the Earth's albedo and infrared radiation can affect both orbital and rotational dynamics.

Content from this work may be used under the terms of the Creative Commons Attribution 3.0 license. Any further distribution of this work must maintain attribution to the author(s) and the title of the work, journal citation and DOI. Published under license by Materials Research Forum LLC.

Traditional POD tools typically rely on simplified geometries, such as box-wing or equivalent-area macromodels, in which more complex structures are reduced to a number of flat panels. While computationally efficient, these approximations neglect local variations in surface orientation and fail to capture self-shadowing effects that can arise between spacecraft components. As a result, the computed forces and torques may deviate from the true values, leading to systematic errors in orbit and attitude prediction.

Considering the actual three-dimensional geometry of a spacecraft allows a much finer description of the distribution of orbital forces and torques acting on its surfaces. However, computing sequentially the individual contributions of infinitesimal surface elements for complex geometries, while simultaneously considering self-shadowing effects, is computationally unfeasible.

This paper proposes a methodology for tackling these challenges by developing a high-fidelity, GPU-powered orbital forces and torques simulator, designed to handle complex-shaped objects in tumbling motion. The tool takes advantages of GPU-parallelization and OpenGL shadow-casting capabilities to increase its efficiency and the accuracy of the results.

For this purpose, the paper is organized as follows. First, the State-of-the-art Section presents current state-of-the-art POD software tools and GPU-based applications for orbital perturbations modelling. The Methodology Section illustrates the concept of GPU-based computation and presents the mathematical models used for orbital forces and torques of interest. The Results Section focuses on the validation of the work and on the discussion of the obtained results. Finally, all the results achieved are summarized in the Conclusions and Future Work Section and the possible focus points for future work are listed.

State-of-the-art

The state-of-the-art in POD software has seen significant advancements, driven by the growing complexity of space missions and the increasing need for high-precision satellite tracking. GEORB, an open-source software released in 2022, specializes in POD of Low Earth Orbiters and satellite gravity missions, supporting missions such as GRACE and GOCE [1]. It uses estimation techniques such as Kalman filtering and supports high-fidelity models for perturbation forces, including atmospheric drag, SRP, and third-body interactions.

On the other hand, OCEAN (Orbit/Covariance Estimation and ANalysis) is a comprehensive software suite for orbit determination and ephemeris propagation, employing high-fidelity models and classical estimation techniques such as least squares adjustment [2]. Its detailed covariance analysis is particularly useful for mission planning, satellite conjunction analysis, and risk assessment.

GMV employs its own POD software for satellite control of the ESA Copernicus constellation, called FocusPOD [3]. FocusPOD is powered by MAORI, a GMV Flight Dynamics and Geodesy library written in C++ and Python [3], highly efficient and accurate for box-wing-shaped satellites, whose attitude is controlled and known at all times. With extremely high-fidelity models for orbital perturbations, MAORI is capable of ensuring an accuracy on the order of centimetres for the satellite's estimated position.

However, all the aforementioned POD software tools rely on simplified macromodels of the satellite that do not account for its actual complex geometry or the self-shadowing effects between different components. To address these limitations, several studies have proposed higher-fidelity modelling of orbital perturbations, particularly SRP and atmospheric drag, through the explicit consideration of the object’s true three-dimensional shape. The advantages of GPU-based approaches have been explored by Zardaín [4] and, previously, by Tanygin [5]. Specifically, the first study [4] employs more traditional ray-casting and ray-tracing algorithms and it focuses exclusively on SRP. On the other hand, Tanygin [5] proposes in his study a similar OpenGL-based approach as the one used in this work, which relies on the GPU's native capabilities to perform

Materials Research Proceedings 69 (2026) 972-993 https://doi.org/10.21741/9781644904251-171

projections of a three-dimensional scene. The current research however expands the modelled perturbations, accounting for IR and albedo radiation (in addition to SRP and atmospheric drag), and it performs an extensive validation analysis against existing highly accurate POD tools.

Methodology

This section outlines the steps, methods and techniques used in the development of the GRIAL software for high-fidelity orbital forces and torques modeling. As previously mentioned, the work relies on GPU-powered computation to increase the performance and the accuracy of the software. The GPU-Powered Approach Section details the procedure behind this approach, explaining each step of the computation action both on the CPU and GPU sides.

Moreover, the Modelling Section details the equations and physics underlying the disturbance forces acting on the satellite. Each subsection will focus on a specific force, with the explanation of each individual model.

Finally, in the Torques Section the focus shifts towards GRIAL's torque computation capability, a feature critical for attitude propagation of tumbling objects.

GPU-Powered Approach. GPUs are designed to handle multiple operations concurrently, making them ideal for tasks that require parallel processing. In the context of orbital forces and torques simulation, this feature can be employed to perform simultaneous computations of vectorial forces and torques across numerous points on a satellite's surface. Traditional CPU-based methods for modelling orbital disturbances often involve sequential processing, which can be time consuming and computationally intensive, particularly for complex satellite shapes.

In the development of the GRIAL software, the parallel processing capabilities of GPUs were utilized through OpenGL to take advantage of its inherent automatic shadow-casting capability. The process begins with the definition of a detailed wavefront *.obj* file of the satellite using some open source 3D creation suite. This file describes the satellite's geometry. Alongside, a *mtl* file is created, which includes essential properties like optical characteristics (for radiation-related calculations, like SRP, albedo and IR), material temperature and air-interactions properties (for drag force computations, see the Atmospheric Drag Section).

Fig. 1 contains example snippets of a *.obj* and a *.mt* file. In summary, the *.obj* file defines:

- *Objects* (line starts with *o*). Object's parts are defined by their name and are composed of multiple triangular surface elements (facets).
- *Vertices* (line starts with *v*). Facets' vertices are defined by their position vectors in metres.
- *Normal Directions* (line starts with *vn*). Unit vectors defining the outwards normals to the facets of the part.
- *Textures* (line starts with *vt*). They are not used in the force and torque simulations.
- *Facets* (line starts with *f*). Each triangular facet of the part is defined by three triplets, each defining the index of the position vector, the index of the texture and the index of the outward normal direction at a vertex. They are grouped by materials.

The materials used by the facets of the *obj* file are defined in the *mtl* one. Each material is identified by a name and associated with the following data:

- Its specular and diffuse coefficients for visible light K_s and K_d necessary for SRP and albedo forces computation, as in the Solar Radiation Pressure and Albedo Reflected Radiation Sections.
- A wall temperature T_W used for drag force computation as will be explained in the Atmospheric Drag Section.
- Surface-air interactions parameters for drag computation σ_N and σ_T, as explained in the Atmospheric Drag Section.

Materials Research Proceedings 69 (2026) 972-993 https://doi.org/10.21741/9781644904251-171

- A reradiation index for visible light R_r, employed in the Solar Radiation Pressure and the Albedo Reflected Radiation Sections.
- Its specular and diffuse coefficients for IR radiation K_s^{ir} and K_d^{ir}, used for IR force computation, as in the Earth IR Radiation Section.
- A reradiation index for IR radiation R_r^{ir}, used in the Earth IR Radiation Section.

.obj

```
mtllib sentinel3A.mtl
o MainBody
v 2.205694 -0.894500 0.793500
v 2.205694 0.894500 0.793500
v 2.205694 -0.894500 -0.793500
[. . .]
vn 1.0000 -0.0000 -0.0000
vn -1.0000 -0.0000 -0.0000
vn -0.0000 -0.0000 1.0000
[. . .]
vt 0.625000 0.500000
vt 0.375000 0.750000
vt 0.375000 0.500000
[. . .]
s 0
usemtl PLUS_X
f 1/1/1 4/2/1 2/3/1
f 1/1/1 3/4/1 4/2/1
usemtl MINUS_X
[. . .]
o SolarArray 20
v -1.200000 3.646132 0.885685
[. . .]
usemtl SA
[. . .]
usemtl SA_2_SUN
[. . .]
```

.mtl

```
newmtl SA_2_SUN
Kd 0.0
Ks 0.18
Tw 273.15
Sn 0.914
St 0.914
Rr 0.0
KdIR 0.0
KsIR 0.31
RrIR 0.0

newmtl SA
Kd 0.19
Ks 0.0
[. . .]

newmtl PLUS_X
[. . .]

newmtl MINUS_X
[. . .]
```

Fig. 1 Examples of obj and mtl files

Once the *obj* file is loaded, an OpenGL scene is created each time a computation is executed. Depending on the force being calculated, the scene is projected in a specific direction (i.e. towards the Sun for SRP, along the velocity vector for atmospheric drag etc.). This projection simulates the casting of shadows on the model, ensuring that forces are computed only on the vertices directly exposed to the flow. This method represents a significant innovation and advantage over traditional approaches: without the need to perform any simplification or approximation of the satellite's shape, the software is capable of retrieving efficiently the set of "visible" points of the object.

The next step involves retrieving the material properties on the CPU side and passing them to the *vertex shader* as uniforms, which allows for dynamical modification of the properties if required. On the GPU side, the *vertex shader* executes the requested computations for each vertex exposed to the flow. The results of these calculations are stored as 3-dimensional force vectors in

Materials Research Proceedings 69 (2026) 972-993 https://doi.org/10.21741/9781644904251-171

an array of floats. The values are then normalized with a constant computed on the CPU, making each element fall between -1 and 1, and then passed as uniforms to the *fragment shader*.

Before reaching the *fragment shader*, OpenGL computes the interpolated normalized force vector on each visible pixel of the object, derived from the normalized forces of the vertices belonging to the facets where the pixel belongs. Then, in the customized *fragment shader*, each component of this normalized force vector is written to the red channel of a separate colour buffer (resulting in three buffers returned to the CPU), each stored as a 32-bit floating-point value. Since colour channels can only represent values between 0 and 1, a conversion of the form 0.5×(value+1) is applied prior to storage. Pixels that are not visible by the flux do not pass through the *fragment shader* and are directly assigned a zero value.

Finally, the CPU retrieves the three buffers and extracts the encoded normalized components of the force acting on each pixel. Pixels with a value exactly equal to zero are disregarded, as they correspond to areas not exposed to the incoming flux. After decoding and applying the inverse of the normalization factor, the forces from all pixels are summed, and the resulting vector is multiplied by the incident flux (e.g. radiation pressure or aerodynamic pressure) to obtain the total force acting on the object.

Traditional methods often rely on simplified satellite geometries, which can lead to inaccuracies in force and torque calculations. GRIAL can instead compute forces for detailed 3D models without approximation, even accounting for solar panel orientation. Specifically, the software is capable of continuously orientating the solar arrays of the satellite towards the Sun direction, optimizing at each instant the solar power generated and reflecting the behaviour of real-world satellites.

In the *mtl* file, the user can define solar panels and the Sun-lit face by naming the corresponding materials appropriately (name starting with "*SA_*"). This allows the software to recognize them as part of a moving solar array and autonomously rotate them in the optimal direction. To do so, the user has to define the rotation axis of the panel and its position in the body-fixed reference frame when loading the object model. Then, for every calculation, the software creates a rotation matrix $\underline{R}$, computed from the normal direction of the Sun-facing side of the panel, identified through the material name *SA_TO_SUN* in the *mtl* file. The matrix is then applied on the GPU side to the normal and the vertices of the panel, to account for its correct orientation. Let $\hat{n}_p$ be the projection of the panel normal vector $\hat{n}$ on the plane orthogonal to the rotation axis $\hat{r}$, defined as:

$$\hat{n}_p = \hat{r} \times (\hat{n} \times \hat{r}) \tag{1}$$

And $\hat{s}_p$ be the projection of the Sun direction in the satellite reference frame $\hat{s}$ on the same plane:

$$\hat{s}_p = \hat{r} \times (\hat{s} \times \hat{r}) \tag{2}$$

Then, $\underline{R}$ is defined as the rotation matrix that when applied to $\hat{n}_p$ returns s $\hat{s}_p$ with the smallest associated rotation angle around the $\hat{r}$ axis, as:

$$\hat{s}_p = \underline{R} \cdot \hat{n}_p \tag{3}$$

Modelling

The following Sections detail the characteristics of the mathematical models selected and implemented in GRIAL. The fidelity and the accuracy of the models is proved by their wide employment in POD applications.

Materials Research Proceedings 69 (2026) 972-993 https://doi.org/10.21741/9781644904251-171

Solar Radiation Pressure. SRP is a major perturbation factor for satellites in all orbital regimes. GRIAL makes use of a widely employed mathematical model for computing the force applied to the satellite by the solar radiation, defined and used by Zardaín [6] and Rodriguez [7]. The model, which corresponds to the one employed by MAORI, defines the SRP force $\vec{F}_{srp}$ on a flat surface to be a linear combination of the forces produced by the specular $\vec{F}_s$, absorbed $\vec{F}_a$ and diffuse $\vec{F}_d$ reflections, as:

$$\vec{F}_{srp} = K_s\vec{F}_s + K_a\vec{F}_a + K_d\vec{F}_d \tag{4}$$

Each force is defined as:

$$\vec{F}_a = P_{srp}A\cos\theta\,\vec{r}_s \tag{5}$$

$$\vec{F}_s = 2P_{srp}A\cos^2\theta\,\vec{n} \tag{6}$$

$$\vec{F}_d = P_{srp}A\cos\theta\left(\vec{r}_s + \frac{2}{3}\vec{n}\right) \tag{7}$$

Where:

- K_s, K_a, K_d are the material optical properties of the flat surface. Each coefficient is bounded between 0 and 1 and $K_s + K_a + K_d = 1$.
- A is the area of the flat surface.
- $\vec{n}$ is the unit vector normal to the surface.
- $\vec{r}_s$ is the unit vector that lies in the Sun-to-spacecraft direction.
- θ is the angle between incoming radiation and surface normal direction.
- P_{srp} is the solar radiation pressure at a given distance R from the Sun, computed as:

$$P_{srp} = P_{1AU}\left(\frac{\mathrm{AU}}{R}\right)^2 \tag{8}$$

Where $P_{1AU} = 4.57 \times 10^{-6}\ \mathrm{N/m^2}$ is the solar pressure at 1 Astronomical Unit (AU).

The total SRP force acting on the i-th surface element of a satellite is then defined by the sum of the three contributions as:

$$\vec{F}^i_{srp} = P_{srp}A_i\cos\theta_i\left[\left(1 - K_s^i\right)\vec{r}_s + 2\left(K_s^i\cos\theta_i + \frac{K_d^i}{3}\right)\vec{n}_i\right] \tag{9}$$

Finally, the model also allows for the user to require specific panels of the objects to re-radiate, as:

$$\vec{F}^i_{srp} = P_{srp}A_i\cos\theta_i\left[\left(1 - K_s^i\right)\vec{r}_s + 2\left(K_s^i\cos\theta_i + \frac{1-K_s^i}{3}\right)\vec{n}_i\right] \tag{10}$$

Atmospheric Drag. Aerodynamic drag is a significant force acting on satellites in LEO, where the residual atmosphere creates a drag effect that gradually reduces the satellite's altitude and affects its trajectory. This force arises from the interaction between the satellite's surface and the flow of atmospheric particles, leading to a deceleration that must be accurately modelled to predict the satellite's orbit over time.

Materials Research Proceedings 69 (2026) 972-993 https://doi.org/10.21741/9781644904251-171

The aerodynamic model selected for GRIAL is the one defined by Carná and Bevilacqua [8] in free molecular regime. The model uses the geometrical properties of the object and the atmospheric data to compute the aerodynamic coefficients. Breaking the spacecraft structure down into a series of panels, it is possible to express a pressure and a shear stress coefficient for each panel, as functions of the local inclination angle between the surface normal and the incoming flow direction. The coefficients, c_{P_i} and c_{τ_i} respectively, associated to the i-th surface of the body are expressed as:

$$c_{P_i} = \frac{1}{s^2}\left[\left(\frac{2-\sigma_N^i}{\sqrt{\pi}} s\cos\theta_i + \frac{\sigma_N^i}{2}\sqrt{\frac{T_w^i}{T_\infty}}\right) e^{-s^2\cos^2\theta_i} + \left(\left(2-\sigma_N^i\right)\left(\frac{1}{2}+s^2\cos^2\theta_i\right) + \frac{\sigma_N^i}{2}\sqrt{\frac{T_w^i}{T_\infty}}\sqrt{\pi}\, s\cos\theta_i\right)\right]\left(1+\mathrm{erf}(s\cos\theta_i)\right) \quad (11)$$

$$c_{\tau_i} = \frac{\sigma_T \sin\theta_i}{s\sqrt{\pi}}\left[e^{-s^2\cos^2\theta_i} + \sqrt{\pi}\, s\cos\theta_i\left(1+\mathrm{erf}(s\cos\theta_i)\right)\right] \quad (12)$$

Where θ_i is the angle between the incoming air flow direction and the panel surface normal ($\vec{n}_i$), σ_N and σ_T are the normal and the tangential momentum accommodation coefficients, dependent on the material of the body and on the incoming flow properties. These two parameters can be subject to parametric analysis to determine their optimal values for specific applications. A good agreement with experimental data is mentioned by Carná and Bevilacqua [8], considering $\sigma_N = \sigma_T = 0.9$ for aluminium-air interactions.

Also, s is the freestream molecular speed ratio:

$$s = \frac{V_\infty}{\sqrt{2RT_\infty}} \quad (13)$$

Where R=287 $\frac{\mathrm{J}}{\mathrm{kg}}$K is the ideal gas constant for air, T_∞ is the air temperature, T_w is the wall temperature of the panel.

Finally, the aerodynamic drag force acting on the i-th panel on the surface of the satellite is expressed as:

$$\vec{F}_{drag}^{\,i} = -\frac{1}{2}\rho v_i^2 A_i\left(c_{P_i}\vec{n}_i + c_{\tau_i}\vec{\tau}_i\right) \quad (14)$$

Where:

- ρ is the atmospheric density.
- v_i is the velocity of the panel with respect to the atmosphere.
- $\vec{n}_i$ is the unit vector in the direction normal to the surface.
- $\vec{\tau}_i$ is the unit vector tangent to the panel's surface and co-planar with respect to the velocity direction $\hat{v}_i$ and the normal $\vec{n}_i$, as:

$$\vec{\tau} = \frac{(\hat{v}\times\vec{n})\times\vec{n}}{\|(\hat{v}\times\vec{n})\times\vec{n}\|} \quad (15)$$

The minus sign is used so that the vector is opposed to the force direction, which is then accounted for with the other minus sign in front of the force definition.

Materials Research Proceedings 69 (2026) 972-993 https://doi.org/10.21741/9781644904251-171

It is important to observe that the angular velocity of the object also plays a role in the computation. Indeed, if the object is in tumbling motion, the incoming direction of the flow cannot be considered the same for all the surface points, as a relative air velocity vector $\vec{v}_{rel}$ must be added to the overall flow velocity in the body-fixed reference frame $\vec{v}_{air}$, as:

$$\vec{v}_i = \vec{\omega} \times \vec{r}_i + \vec{v}_{air} \tag{16}$$

where $\vec{\omega}$ is the object's angular velocity in the body-fixed reference frame, $\vec{r}_i$ is the considered vertex position with respect to the centre of mass. The flow velocity $\vec{v}_{air}$ is computed as the vectorial combination of the satellite velocity and the atmosphere velocity, assumed fixed to the Earth. Since GRIAL is designed to tackle uncontrolled tumbling satellites, this phenomenon has to be taken into account, as it affects the computation, in particular the drag-induced torque.

For its aerodynamic drag computation, MAORI employs a similar but slightly different model. In particular, MAORI takes into account all the elements in the atmosphere individually and computes their individual contribution to the total drag, taking into account each element's molar mass and its concentration, whereas GRIAL considers air as a unique mean. Moreover, while GRIAL employs the hypothesis of a free molecular regime and hyper-thermal flow, which means that any portion of the object not directly exposed to air flow does not contribute to the overall drag force computation, MAORI employs the front-back model developed by Smith [9].

As the first step in graphic computation of GRIAL is the projection and a shadow casting in the flow direction, the parts of the satellite which are not visible must be neglected, meaning that the assumption of hyperthermal flow is necessary for its implementation.

Albedo Reflected Radiation. Originating from the reflection of a fraction of the solar radiation on the Earth's surface, the albedo force mostly affects satellites in LEO. The albedo force is modeled exactly as the SRP one. As the radiation remains within the visible spectrum, the optical parameters K_s and K_d are the same as the ones employed for the SRP computation. The key difference between the two forces is the source of the radiation: unlike the SRP where the radiation arrives from the Sun, considered as a distant point, the albedo force comes from the radiation's reflection on Earth's surface. From the satellite's perspective, the Earth is a large entity and cannot be simplified to a point source as the Sun is in SRP calculations. To address this issue, the Earth's surface is divided into smaller areas, all of which contribute to the total computed force. Each surface element is associated to:

- The coordinates of its centre point (in *ITRF*).
- The area of the surface.
- An albedo coefficient. The albedo coefficient indicates how much of the incoming radiation is reflected towards the object. This value is not homogeneous across Earth's surface and is not constant over time. NASA's Space Weather website [10] provides data for surface elements of the Earth, subdivided into longitude–latitude grids and available for each month of the year.

As a result, a single force computation requires iterating over each visible portion of Earth's surface, performing a graphical computation for each element. Once computed, all the contributions are summed together to compute the total force. This process increases drastically the computation time compared to the SRP and atmospheric drag cases, which only require one graphical computation for each point.

The albedo force contribution produced by the i-th surface element is modelled similarly to the SRP case, described in Eq. 9 and Eq. 10, with the incoming flux direction being the Earth surface vector-satellite direction, instead of Sun-satellite, and the radiation pressure coming from the surface element, computed as:

Materials Research Proceedings 69 (2026) 972-993 https://doi.org/10.21741/9781644904251-171

$$P_{arp} = a_i \frac{L_\odot}{4\pi R^2} A_i \cos\alpha \frac{\cos\beta}{\pi} \frac{1}{d^2} \frac{1}{c} \quad (17)$$

Where:

- a_i is the albedo coefficient associated to the Earth's surface element.
- $L_\odot = 3.828 \times 10^{26}$W is the luminosity of the Sun.
- R is the distance of the Sun to the Earth's surface element.
- A_i is the area of the Earth's surface element.
- α is the angle of the Sun direction with respect to the normal to Earth's surface element. If $\alpha \leq 0$ the Sun is not visible from the surface element, thus the incoming radiation is zero.
- B is the angle of the satellite direction with respect to the normal to Earth's surface element.
- d is the distance between the satellite and the Earth's surface element.
- c is the speed of light.

Finally, the sum of each contribution results in the total albedo force acting on the satellite.

Earth IR Radiation. IR force is generated by the emission of thermal energy from Earth's surface, which impacts satellites in orbit. While typically weaker than solar radiation pressure, the IR force is still significant, especially for satellites in LEO. Unlike SRP and albedo, which become null during the eclipse phases, IR radiation applies a continuous force on satellites throughout the entire orbit.

As they are both Earth-emitted radiations, the IR force is modelled following the same approach as the albedo case, detailed in the previous section, with the only difference being in the use of the infra-red optical properties of the satellite, instead of visible light. Indeed, being an Earth-emitted radiation as well, the total force is the result of the sum of a set of individual contributions derived from all visible Earth's surface elements. The formulation for the force due to a single Earth surface element is identical to the expression for the SRP force (Eq. 9 and Eq. 10), with the direction of the Earth's surface element replacing the Sun direction, and the solar radiation pressure being replaced by the IR radiation pressure coming from the element, which is computed as:

$$P_{irp} = I_i A_i \frac{\cos\beta}{\pi} \frac{1}{d^2} \frac{1}{c} \quad (18)$$

Where:

- I_i is the irradiance of the Earth's surface element.
- A_i is the area of the Earth's surface element.
- β is the angle of the satellite direction with respect to the normal to Earth's surface element.
- d is the distance between the satellite and the Earth's surface element.
- c is the speed of light.

Finally, the sum of all the contributions results in the total IR pressure force.

Torques. Torque computation largely depends on the object shape and orientation. For example, satellites equipped with solar arrays that extend far from the centre of inertia of the object can be subject to non-neglectable torques, caused by forces acting on the surface of the panel (which can behave like a sail). Traditional algorithms are not capable of performing these point-wise computations efficiently and experimental data is limited.

In contrast, GRIAL represents a viable tool in this regard: its graphical, pixel-wise computation enables the calculation of the torque generated by any mentioned orbital disturbance. In OpenGL, the position of each pixel relative to the satellite's centre of mass (as defined in the *obj* model) is

Materials Research Proceedings 69 (2026) 972-993 https://doi.org/10.21741/9781644904251-171

known, allowing the torque around the centre of mass to be computed for any of the modelled forces presented in previous sections.

Moreover, using the OpenGL graphical approach (detailed in the *GPU-Powered Approach* subsection), the data transferred between the GPU and the CPU is not necessarily bounded to the three components of a 3-dimensional vector. Indeed, it is possible to transfer up to n colour buffers, where n varies depending on the hardware, with a typical value of n = 8. This means that the GPU can simultaneously compute up to two 3-dimensional vectors, which can be employed to evaluate each force and the corresponding torque by means of a single execution of the OpenGL computation.

In the vertex shader, for each vertex, the selected disturbance force is computed and stored. Then, from the knowledge of the position vector $\vec{r}_i$ of the vertex with respect to the center of mass of the object, the torque is computed as $\vec{T} = \vec{r}_i \times \vec{F}$. Finally, $\vec{F}$ and $\vec{T}$ are passed on to the vertex shader, where they are encrypted and transferred to the CPU side of the operations.

In addition to the torques produced by the orbital forces presented in the sections above, there are other common torques that do not depend on the surface of the object and are not computed by GRIAL: the gravity gradient torque, which directly depends on the inertia matrix (as described by Kasiri [11]) and the eddy currents torque, which depends on the eddy currents tensor (whose relevance is presented by Lin [12], and a mathematical model is presented by Gomez [13]). These two torques will however be considered in the analysis of orbital torques presented in the Torques Section for a relative comparison against the torques implemented by GRIAL and their mathematical models are presented in the Eddy Currents Torque and the Gravity Gradient Torque Sections.

Results

This section presents the results obtained from the implementation and testing of the GRIAL software for forces and torque simulation. The primary goal of this work was to evaluate the performance of GRIAL's GPU-powered orbital force computation against traditional CPU-based methods. The software chosen to perform the comparative analysis is MAORI.

The case study selected for the analysis is represented by the Sentinel-3A satellite. Sentinel-3A is the third satellite to be launched for Europe's Copernicus environmental monitoring program [14]. It is a 1200 kg satellite in a 800 km altitude Sun-synchronous orbit [15], whose shape is easily approximated to a box-wing structure. Given that MAORI is highly accurate in handling such geometries, it serves as an ideal benchmark to compare the results obtained from GRIAL.

Fig. 2 shows a comparison between the real Sentinel-3A satellite and its geometrical model from its *obj* file.



Fig. 2 Sentinel 3A satellite (left) and its geometrical model (right)

As mentioned, GRIAL is designed to handle both controlled and tumbling objects, both with simple and complex geometries. However, the lack of available data on disturbances acting on

Materials Research Proceedings 69 (2026) 972-993 https://doi.org/10.21741/9781644904251-171

uncontrolled objects limits the scope of this analysis to controlled targets. Therefore, the full range of GRIAL's capabilities, particularly for tumbling objects, cannot be fully explored in this study.

Forces. Sentinel-3A orbits Earth approximately every 90 minutes, completing around eight revolutions during the 12 hour long simulation period selected for the SRP and drag computation. The satellite orbit is a near-polar, sun-synchronous orbit, with 10:00h Mean Local Solar time [16].

Fig. 3 shows the comparison between the SRP and the drag forces acting on the Sentinel-3A satellite, as calculated by GRIAL and MAORI. The graph clearly shows the periodic repetition of illuminated and eclipse phases, corresponding to one complete orbital period. Notably, both tools account for the penumbra phase, during which only part of the Sun is visible, resulting in a partial but non-zero amount of radiation reaching the satellite. This phase has a short duration relative to the entire simulation, which is why it appears on the graph as a quasi-vertical line.

The accuracy of the results is also proven by the graph of Fig. 4, which shows the element-wise difference between the force vectors computed by both propagators. The graph allows to observe that that GRIAL has a margin of error relative to MAORI on the order of 10^{-7} N (approximately three orders of magnitude smaller than the force itself).

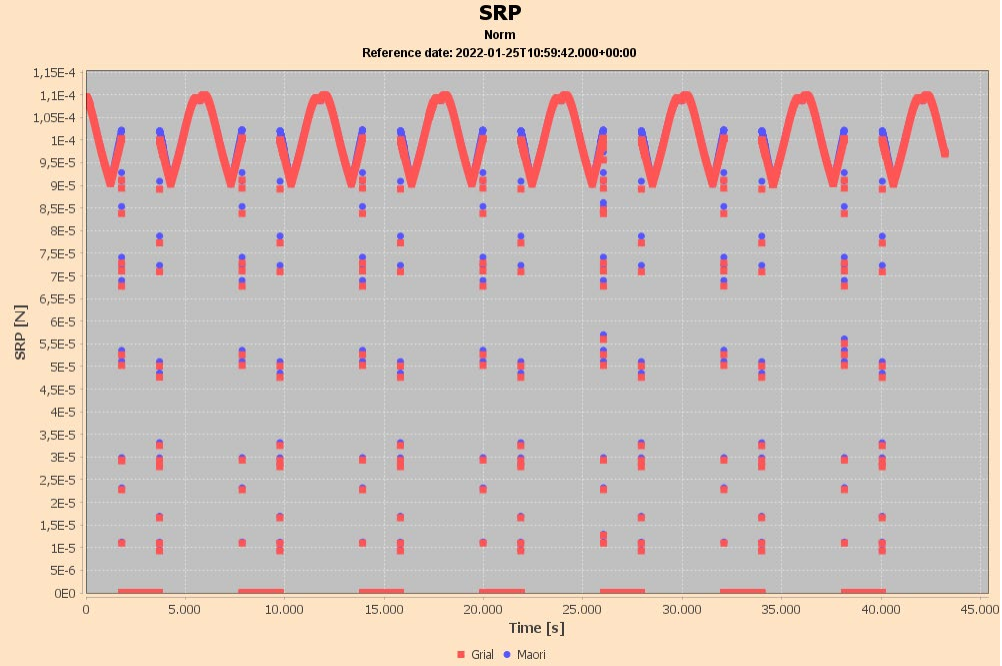


Fig. 3 SRP magnitude comparison between GRIAL and MAORI

Materials Research Proceedings 69 (2026) 972-993 https://doi.org/10.21741/9781644904251-171

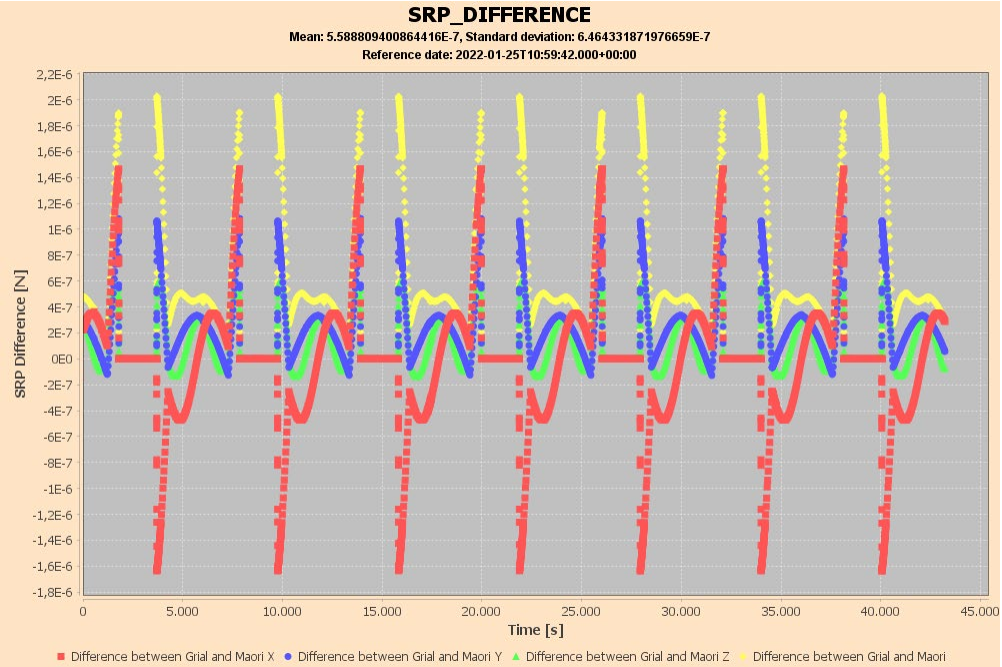


Fig. 4 SRP vector element-wise difference between GRIAL and MAORI

Similarly, Fig. 5 shows the magnitude of the drag force acting on the Sentinel-3A computed by GRIAL and MAORI. As the altitude of the satellite is not constant throughout the orbit (ranging between 811 km and 794 km), the drag force magnitude oscillates between 6.5×10^{-6} N and 10^{-6} N or below, with the peaks corresponding to the lower-altitudes instances (where the velocity and the air density are bigger).

Unlike the SRP case, the mathematical methods employed by GRIAL and MAORI for the computation of the aerodynamic drag are not the same, as explained in the *Atmospheric Drag* subsection. Nonetheless the simulations produce once again extremely similar results, as shown in Fig. 6, which illustrates the component-wise difference of the GRIAL and MAORI force vectors in the body-fixed reference frame.

The mean relative difference is once again in the order of 10^{-7} N, one order of magnitude below the force itself, despite the different models employed by the two tools, successfully validating GRIAL's method.

Materials Research Proceedings 69 (2026) 972-993 https://doi.org/10.21741/9781644904251-171

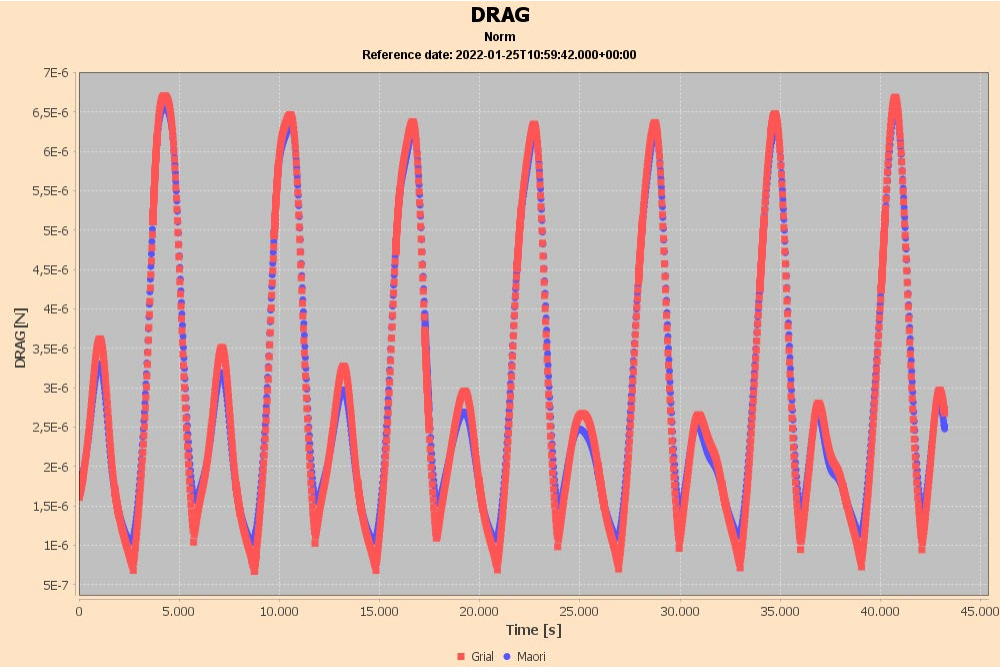


Fig. 5 Drag magnitude comparison between GRIAL and MAORI

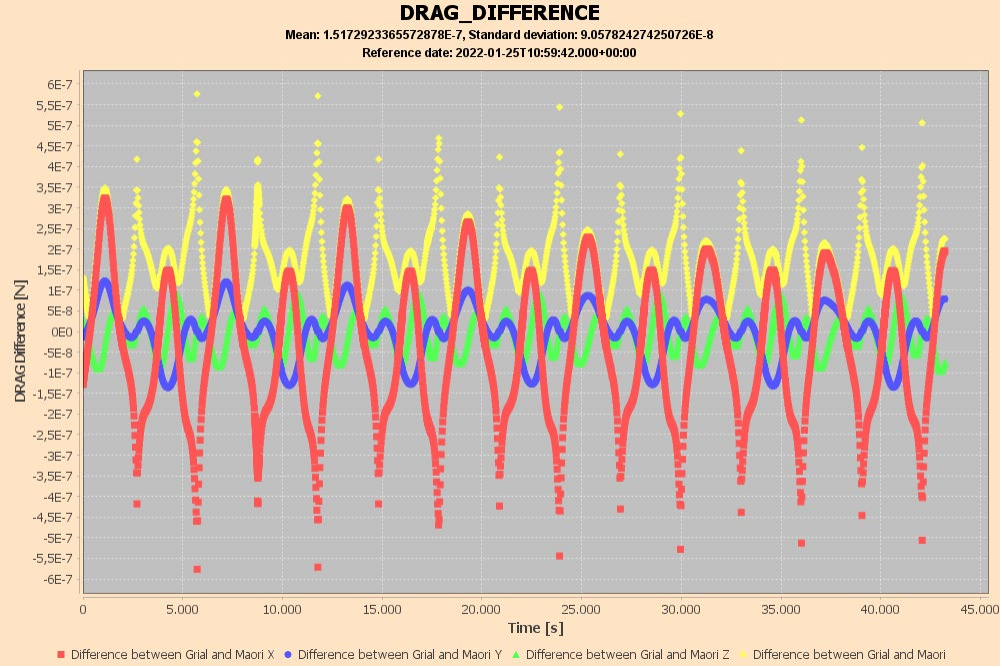


Fig. 6 Drag vector element-wise difference GRIAL and MAORI

Before performing the same analysis for the albedo and IR cases, it is necessary to make the following remark: the amount of radiation (reflected or emitted) is not constant around the surface of the Earth. For the albedo case, oceans and glaciers reflect more of the incoming solar radiation compared to trees and ground. Likewise, the IR radiation emitted varies depending on the temperature and radiative properties of the ground. With the seasonal changes in water levels, ice quantity and clouds presence, the amount of radiation reflected and emitted by any point of the surface is not quantifiable with absolute precision at every moment.

To tackle this issue, to each surface element of the 5°×5° longitude-latitude discretization of the Earth is assigned one reflective coefficient for each month of the year, for a total of 12 coefficients

Materials Research Proceedings 69 (2026) 972-993 https://doi.org/10.21741/9781644904251-171

per element. These grids have been generated for MAORI using monthly data from July 2002 to June 2020 from NASA's space weather website [10], and calculating the monthly average.

GRIAL follows exactly the same approach and it employs exactly the same coefficient as MAORI, allowing for a fair comparative analysis of the results. While the coefficients selected represent an accurate estimation of the real values, surface discretization introduces complexity and computational time problems for the algorithm. Being written on a pre-compiled language and performing all its computations on the CPU, MAORI is not expensively affected by this, whereas for GRIAL it represents an important performance limitation issue.

As mentioned in the *Albedo Radiation* and the *Infrared Radiation* subsections, the albedo and IR force calculation require to execute multiple times the graphic computation, one for each surface element into which the Earth has been divided visible from the satellite. Dividing the Earth's surface into a 72×36 grid across longitude and latitude (totaling to 2592 smaller surfaces), the Sentinel-3A satellite is visible from up to 400 of these surfaces at the time, with an average of around 250 surface elements per measurement. This means that to compute the Earth-radiation force in a single point of the orbit, hundreds of graphical computations must be performed (instead of just one, like in the SRP and drag cases). This heavy computational effort results in an exponential increase of computation time required to perform the calculation.

For computational time-related reasons, the results presented are computed over a reduced time interval of one single satellite orbital period, which corresponds to around 7500 seconds. This time span allows to fully observe the evolution and the behaviour of the forces over time, eclipse phases and most importantly the validity and accuracy of the results.

The comparison of Fig. 7 shows that the magnitude of the albedo force computed by GRIAL accurately matches the one computed by MAORI. Because of the resemblance to the SRP model, the accuracy of the results for the albedo calculation was expected. Moreover, both tools employ the same discretization of the Earth surface into smaller surfaces and the same albedo coefficients.

Fig. 8 shows the element-wise difference between the two solutions, with a mean difference between the results in the order of 10^{-7} N, which is two orders of magnitude below the force values. A possible source of discrepancy between the results are self-shadowing events that occur throughout the orbit caused by the solar panel, which MAORI cannot simulate.

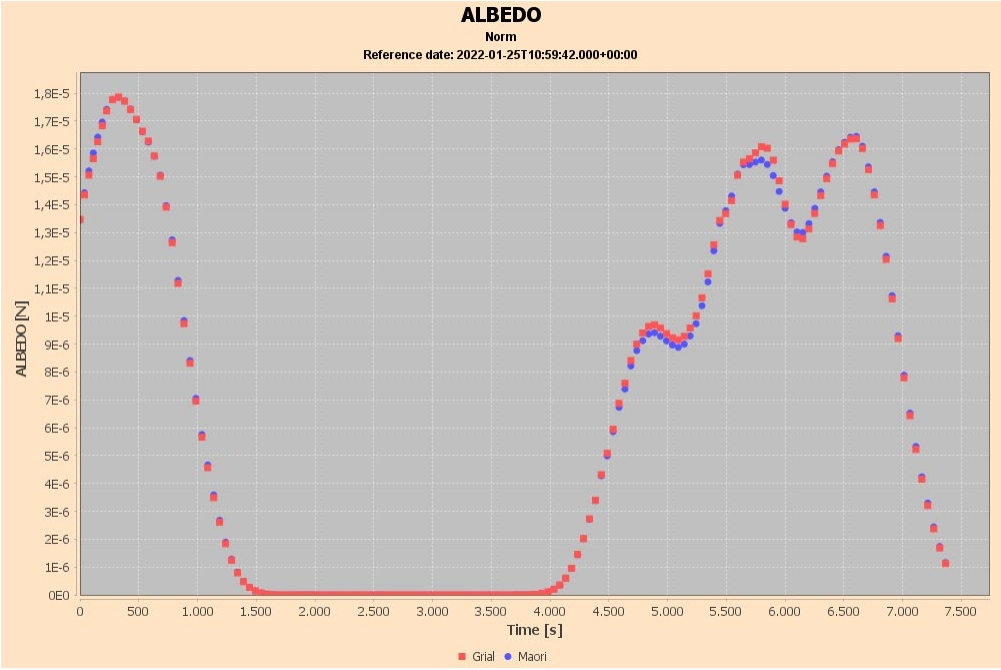


Fig. 7 Albedo force magnitude comparison between GRIAL and MAORI

Materials Research Proceedings 69 (2026) 972-993 https://doi.org/10.21741/9781644904251-171

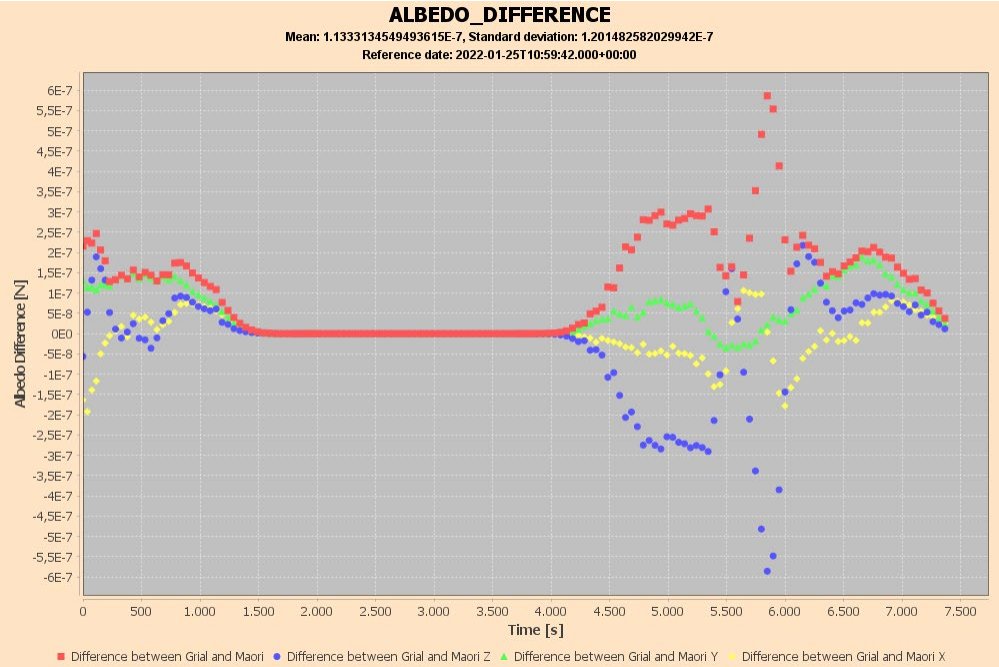


Fig. 8 Albedo force vector element-wise difference between GRIAL and MAORI

Finally, Fig. 9 shows the results of the same analysis applied to the IR radiation force case. The accuracy of the results was expected, given the similarity to the albedo radiation case, and it is further proved by the element-wise difference graph of Fig. 10. In particular, the mean difference between the two tools is found to be in the order of 10^{-8} N, which is three orders of magnitude lower than the force itself.

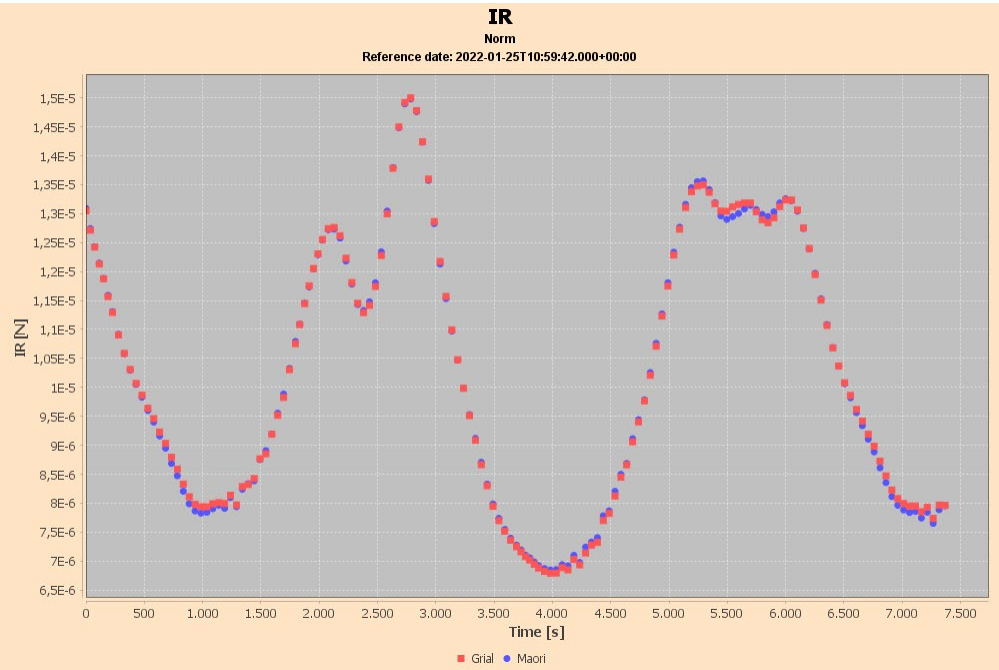


Fig. 9 IR force magnitude comparison between GRIAL and MAORI

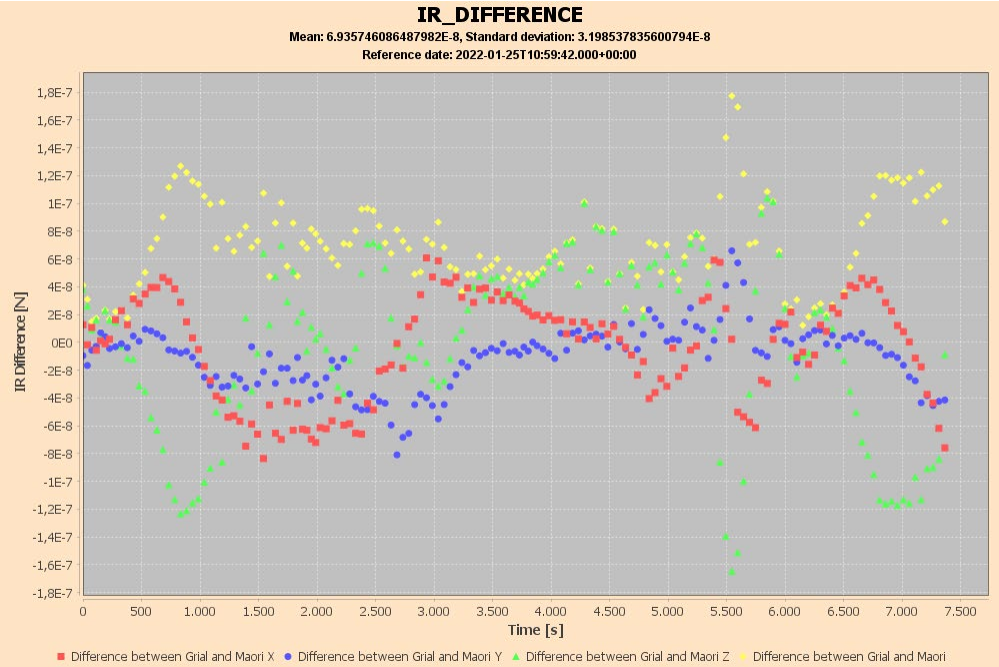


Fig. 10 IR force vector element-wise difference between GRIAL and MAORI

Computational Time. This section showcases GRIAL's computational efficiency for each of the force computations presented so far. As mentioned in the document, performance is a key driver for GRIAL. The graphic approach and the in-parallel computation enabled by the GPU aim at achieving high levels of accuracy without the need to compromise efficiency, even in the most complex scenarios. However, this method also introduces delays. Specifically, transferring data between processing units is the most time-costly operation of the algorithm. As this operation is performed once for every graphical computation, the number of times the GPU-powered methods are called directly affects the computational time of the entire operation. Table 1 shows the average time required to compute each force for different window resolutions.

The values in the table show that GRIAL is capable of efficiently performing complex calculations in acceptable durations. The main outtakes to retain from the table are:

- SRP and drag forces are computed fast because they only require executing the graphical computation once and they only perform one transfer of data between the GPU and the CPU.
- On the other hand, Earth radiation forces (albedo and IR) require much more time. This is due to the iteration over the visible smaller surfaces into which the Earth has been discretized (explained in the Albedo Reflected Radiation subsection). This repetition is particularly costly for GRIAL, as an asynchronous data transfer between the GPU and the CPU is performed for each graphical computation, which significantly increases computational time. The number of graphical computations is represented by the number of Earth surface elements visible from the satellite.
- GRIAL computes the albedo and IR forces simultaneously, optimizing a process which is time inefficient. The time required to compute them one at the time is the same as computing them together, as they can be transferred simultaneously to the CPU.
- The values do not depend on the satellite shape, but only on the desired resolution. Any geometry, regardless of its complexity, requires the same computational time, thanks to the graphical approach (GPU-Powered Approach subsection).

Materials Research Proceedings 69 (2026) 972-993 https://doi.org/10.21741/9781644904251-171

Table 1 Computational time (in ms) for each force computed over different window resolutions

	1000×1000 pixels per window	2000×2000 pixels per window
SRP	≈13 [ms]	≈90 [ms]
Drag	≈13 [ms]	≈90 [ms]
Albedo + IR	≈4000 [ms]	≈27000 [ms]

Torques. In addition to the torques implemented by GRIAL, there are two other main torques acting on space objects that do not depend on the surface geometry of the object: the gravity gradient torque and the eddy currents torque. These torques can directly be computed in the CPU and will be used in the analysis presented in this section to show the relative impact of all different torques in the case of Sentinel-3A.

Eddy Currents Torque. The electromagnetic interaction between a tumbling conductive satellite and Earth's magnetic field generates surface currents, known as eddy currents. These currents create a magnetic moment, which interacts with the magnetic field to produce a torque that alters the satellite's attitude. The eddy current torque mathematical model used is derived by Lin [12] and it is described by the following equation:

$$\vec{M}_{ec} = \vec{B} \times \left(\underline{L} \cdot \left(\vec{\omega} \times \vec{B} \right) \right) \tag{19}$$

Where:

- $\vec{M}_{ec}$ is the eddy current torque in the body-fixed reference frame.
- $\vec{B}$ is the geomagnetic field vector in body-fixed reference frame.
- $\vec{\omega}$ is the angular velocity of the object in the body-fixed reference frame.
- $\underline{L}$ is the eddy current tensor, defined in its general representation as:

$$\underline{L} = \begin{pmatrix} M_1 & -M_4 & -M_5 \\ -M_4 & M_2 & -M_6 \\ -M_5 & -M_6 & M_3 \end{pmatrix} \tag{20}$$

The coefficients M_1 to M_6 are constants which are determined by the geometry, conductivity, and material properties of the satellite. When the body-fixed reference frame is aligned with the eddy tensor eigenspace, the tensor reduces to a diagonal form, where $M_4=M_5=M_6=0$. Closed-form analytical solutions for the values of the parameters M_1 to M_3 exist only for simple geometries, such as a thin spherical shell. For general shapes, the coefficients must be experimentally determined or approximated. As the model indicates, eddy current torques act in opposition to the angular velocity of a tumbling object, thereby inducing rotational damping.

Gravity Gradient Torque. The gravity gradient torque arises from the gravitational potential acting on an extended rigid body in orbit, due to the difference in gravitational force acting on various parts of the satellite. For elongated or asymmetric spacecraft, this effect generates a restoring torque that tends to align the satellite's major axis with the local vertical (toward the Earth). This torque is particularly relevant in LEO, where the gravity gradient is strongest. The formulation used is extracted from Vallado [17]:

$$\vec{M}_{gg} = \frac{3|\vec{g}|}{|\vec{r}|} \hat{g} \times \left(\underline{I} \cdot \hat{g} \right) \tag{21}$$

Where:

- M_{gg} is the gravity gradient torque in the body-fixed reference frame.
- $\vec{r}$ is the satellite centre-of-mass (CoM) position vector relative to Earth attraction centre.

Materials Research Proceedings 69 (2026) 972-993 https://doi.org/10.21741/9781644904251-171

- $\vec{g}$ is the total gravity acceleration acting on the CoM of the object expressed in the body-fixed reference frame frame, with $\vec{g} = |\vec{g}|\hat{g}$.
- $\underline{I}$ is the inertia matrix of the spacecraft in the CoM of the object in body-fixed frame.

Magnitude of Torque Sources in Nominal Orbit. The external torques acting on a spacecraft are highly dependent on both the orbital environment and the rotational state of the satellite. For the Sentinel-3A satellite in a reference Sun-synchronous orbit (see Table 2), the sources considered in this study are albedo, atmospheric drag, eddy currents, gravity gradient, IR radiation and SRP. These torques are evaluated for the two (lower and upper) limits of analysed spin rates in the stable Z axis: Fig. 11a showcases an example with 0 rad/s while Fig. 11b shows a high-spin example at 1 rad/s.

Table 2 Orbital Information for Sentinel-3A

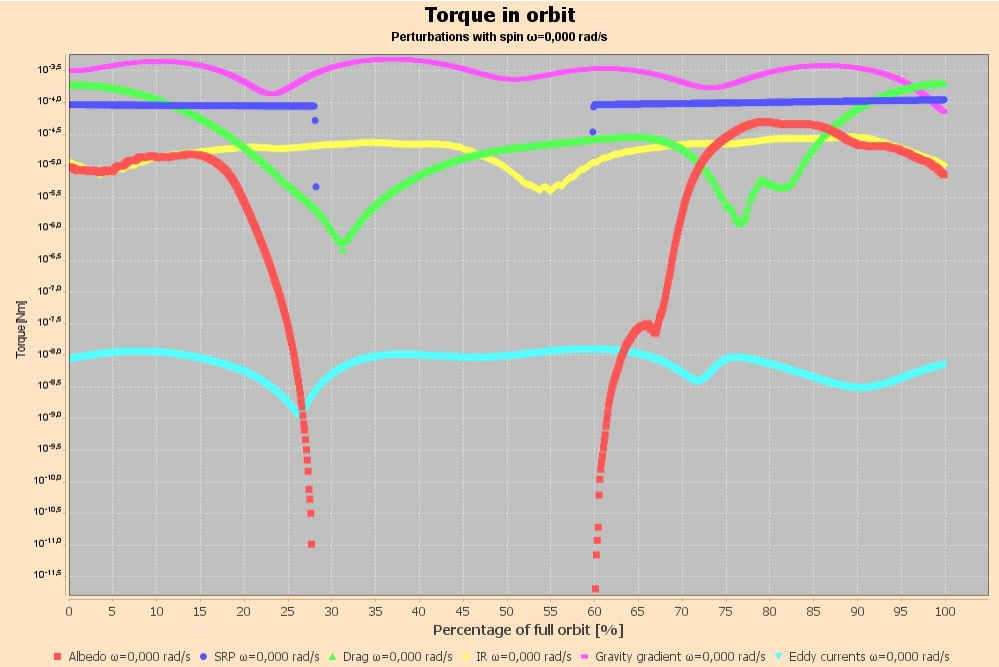
Altitude	Inclination	Period	Cycle	Ground-track deviation	Local time at descending node
814.5 km	98.65°	100.99 mins	27 days	±1 km	10:00 hours

Several phenomena that validate the implementation can be observed in Fig. 11, which simulates one orbital period of Sentinel-3A:

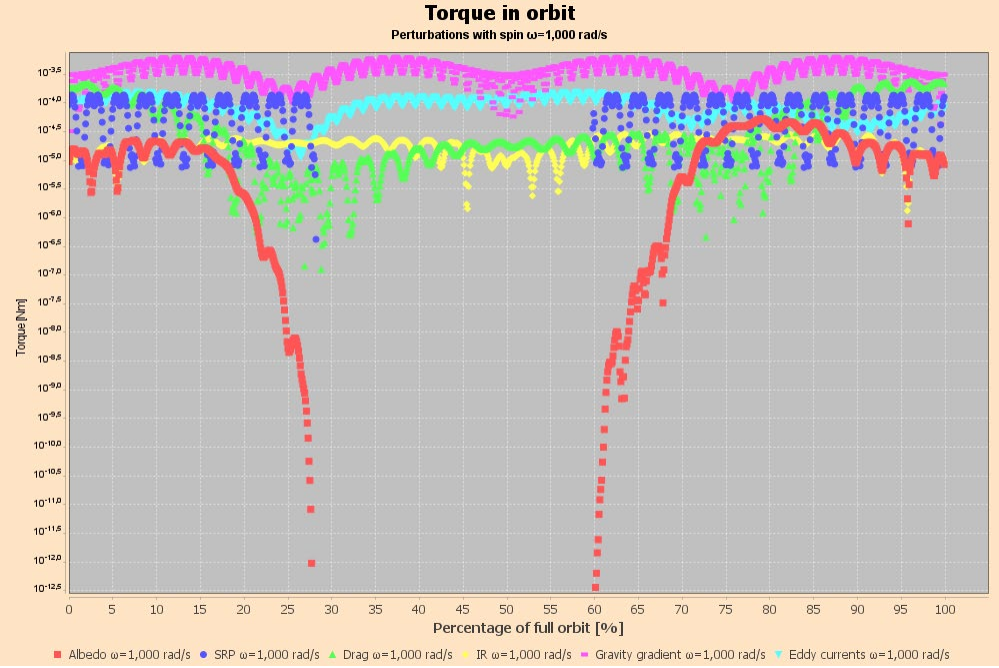
- During the eclipse (from around 28% to 60% of the orbit) there is no albedo or SRP torque on the object. Moreover, the transition for SRP takes place between less than two plotted points (each point represents 0.1% of the orbit) signalling a fast but not instantaneous transition to zero, coherent with the body's fast entrance to or exit from Earth's shade in the limits of the eclipse. In comparison, albedo diminishes at a lower rate, which is coherent with the progressive reduction of visible Sun-illuminated Earth tiles and their angle of reflection as the body approaches penumbra. All other perturbations are, as expected, not affected by Earth's shade.
- The spin rate barely affects the magnitude of the torques induced by Albedo, SRP, drag, IR or gravity gradient directly: instead, each rotational regime induces some level of oscillations around the same values which means that the attitude is the main driver for the change, not its derivative.
- For Eddy currents, the magnitude of the torque changes noticeably between the spin regimes: around $10^{-8.25}$ for 0 rad/s and around $10^{-4.25}$ for 1 rad/s, which is coherent with the proposed model. The eddy current tensor used for these simulations is:

$$\underline{L} = \begin{pmatrix} -1.8e5 & -2.0e4 & 1.5e4 \\ -2.0e4 & -2.5e5 & -1.8e4 \\ 1.5e4 & -1.8e4 & -3.5e5 \end{pmatrix}$$

A study by ESA [18] describes how for LEO objects the main torque-inducing disturbances are the gravity gradient, eddy currents (especially for fast rotating satellites) and SRP, in accordance with the results seen in Fig. 11, although atmospheric drag does reach their orders of magnitude for some configurations.



a) ω = 0 rad/s



b) ω = 1 rad/s

Fig. 11 Torques on Sentinel 3A during one orbital period.

When representing the average magnitude of each perturbation's torque over one orbit as a function of altitude (Fig. 12), using the shape of Sentinel-3A and a rotation period of 0.01 rad/s, the following conclusions can be drawn:

- The order of magnitude of the torques whose sources also provide a perturbation force evolve like the latter when varying altitude, that is: SRP stays constant and drives evolution at higher altitudes, drag decreases the fastest (it is not modelled after 1000 km with the atmospheric model employed in the work) and is the main perturbation at the lowest altitudes and IR and albedo decrease at the same ratio with altitude.

Materials Research Proceedings 69 (2026) 972-993 https://doi.org/10.21741/9781644904251-171

- Gravity gradient dominates the attitude from around 800 km to about 5500 km, and then follows an evolution like that of IR and albedo torques.
- Eddy current effects decrease at the highest rate when altitude increases due to the diminishing magnetic field ($\propto 1/r^3$) making the torque effect proportional to $1/r^6$. The plot was generated for a low spin case.
- The initial increase of SRP and albedo at low altitudes is due to the increase of Sun visibility, not an effect of higher order of magnitude per se. This effect depends on the mission orbit, specifically on inclination and local time at descending node, which define visibility and eclipses together with altitude. IR is somewhat indifferent to variables other than altitude.

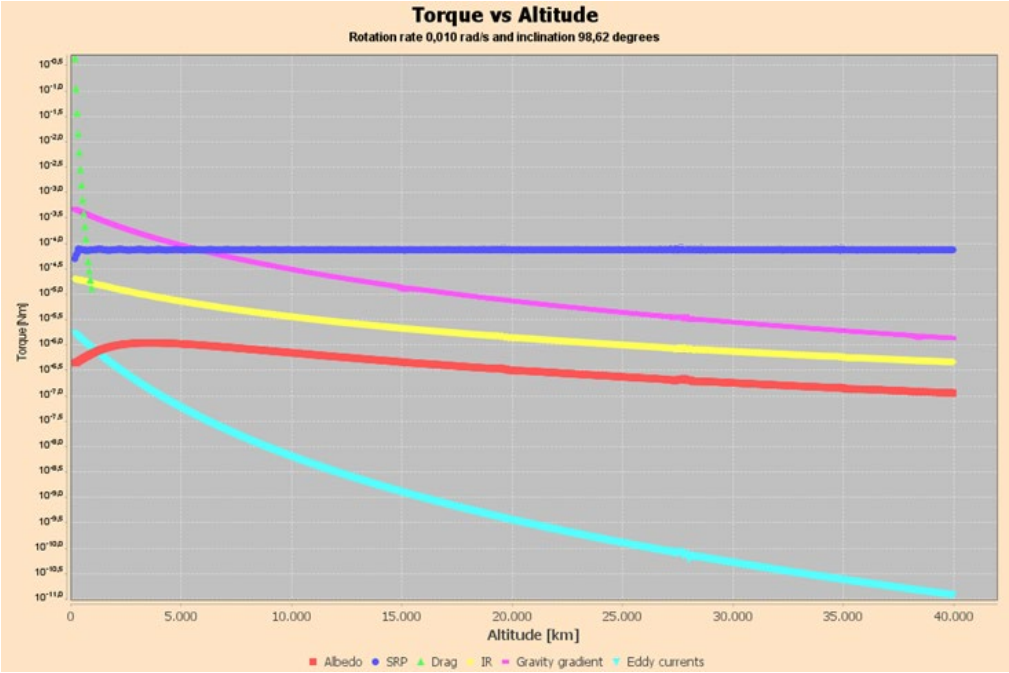


Fig. 12 Mean torque vs altitude at 98.62° inclination.

Conclusions and Future Work

High-fidelity orbital force computation is crucial for attitude propagation of tumbling objects and could improve POD operations on satellites orbiting Earth. High-fidelity mathematical models for the computation of aerodynamic drag, SRP, albedo and IR radiation forces have been successfully integrated into GRIAL for these purposes. Additionally, torque computation methods for these forces, along with gravity gradient and eddy current torques, have been modeled, enabling attitude propagation for tumbling objects.

The Sentinel-3A satellite case study was selected to perform the validation procedure against the forces obtained by the state-of-the-art POD software MAORI. The results were found to match the expected ones, consequently validating GRIAL.

A key aspect that could become the subject of future research is improving computational time. A possible solution to the issue is represented by the creation of grids of values of forces and torques of each orbital disturbance for an extensive number of possible incoming directions of the flux (e.g. solar radiation for the SRP, air flow for drag etc.). This discrete but extensive set of values computed by GRIAL can then be interpolated during the orbit or the attitude propagation procedure, to account for any incoming direction. Other than allowing for quick execution times, this approach would also enable any user to implement these tables in their own programming

language, without the imposition of using Java. Moreover, there is no requirement related to the presence of a GPU on the user's hardware, which GRIAL has.

Another possible improvement to the time-efficiency of the tool could be achieved by grouping together multiple pixels of the same window and summing their values together, instead of passing to the CPU the value associated to each individual pixel. As shown in Table 1, the computational time only depends on the number of pixels of the window, because of the delay in the GPU-CPU transmission. Lowering the number of values transmitted would lower the computational time, without affecting the accuracy.

Additionally, albedo and IR perturbations (which are the most time-consuming computations) could be enhanced by the use of a pool of CPUs, each associated to a copy of the object shape in the GPU.

Moreover, future studies should aim at refining and improving the mathematical models employed by the GRIAL algorithm. In particular, the atmospheric drag model has shown the greatest inaccuracy. A possibility of improvement could be represented by the use of a front-back model, which only requires the assumption of free molecular regime and accounts for forces acting on both the directly exposed surfaces and the rear-facing ones.

Further work also involves applying the software to other case-studies, to find out if it is possible to improve the efficiency of the POD analysis. In fact, the Sentinel-3A case study was selected because the satellite's structure can be easily approximated to a box-wing object, which is the structure usually employed by other tools to approximate satellites. GRIAL is instead capable of higher graphic computational capabilities, which allow to consider the real satellite shape. GRIAL is also capable of handling shapes of any complexity with the same efficiency, thanks to its GPU-powered parallel computation. Indeed, the real strength and novelty of GRIAL lies in scenarios with more complex satellite shapes, which cannot be approximated to simple box wing models, like the Sentinel-6, which represents the following trial ground for the software.

In conclusion, GRIAL proofs the efficiency and the potential of graphical approaches for orbital disturbances computation. The mathematical models it employs and its computational capabilities have been successfully validated against accurate results. The good performance and quality of the results highlight the software's potential for orbital and attitude propagation applications. Future analysis will demonstrate the tool's capabilities when employed in case studies with increasingly more complex-shaped satellites.

References

[1] T.L. Papanikolaou, GEORB: Release for precise orbit determination of low Earth orbiters and satellite gravity missions, Software Impacts 16 (2023) 100502. https://doi.org/10.1016/j.simpa.2023.100502

[2] B.N.C. Dalton, Orbit/Covariance Estimation and ANalysis (OCEAN).

[3] FocusPOD — GMV. Accessed: Sep. 03, 2024. https://www.gmv.com/en-es/products/space/focuspod

[4] L.I. Zardaín Rodríguez, Developing an efficient algorithm for computing solar radiation pressure, Master's thesis, Universitat Politècnica de Catalunya, 2019.

[5] S. Tanygin, G. Beatty, GPU-accelerated computation of SRP and drag forces and torques with graphical encoding of surface normals, 2016.

[6] Zardaín, L.: High-Fidelity Modeling and Visualizing of Solar Radiation Pressure: A Framework for High-Fidelity Analysis

[7] Rodríguez, Z., Iván, L.: Developing an efficient algorithm for computing solar radiation pressure. Master's thesis, Universitat Politècnica de Catalunya (2019). Accessed: Jul. 31, 2024. https://upcommons.upc.edu/handle/2117/176196

[8] S.F.R. Carnà, R. Bevilacqua, High fidelity model for the atmospheric re-entry of CubeSats equipped with the drag de-orbit device, Acta Astronautica 156 (2019) 134–156. https://doi.org/10.1016/j.actaastro.2018.05.049

[9] Smith, B.: A Comprehensive Examination of Low Earth Orbit Aerodynamic Accelerations for Satellite Formation Control (2019). https://doi.org/10.13140/RG.2.2.31390.89922

[10] CERES ERBE-like Time-Interpolated TOA Fluxes Terra and Aqua Crosstrack Edition4. Accessed: Sep. 30, 2024. https://asdc.larc.nasa.gov/project/CERES/CER_ES4_Terra+Aqua_Edition4

[11] A. Kasiri, F. Saberi, Agile multi-targeting spacecraft control via backstepping-sliding mode approach, in: Proceedings of the International Conference on Robotics and Mechatronics (ICRoM), 2019. https://doi.org/10.1109/ICRoM48714.2019.9071889

[12] Lin, H.-Y., Zhao, C.-Y.: Evolution of the rotational motion of space debris acted upon by eddy current torque. Astrophysics and Space Science 357(2), 167 (2015) https://doi.org/10.1007/s10509-015-2396-225

[13] Gómez, N.O., Walker, S.J.I.: Eddy currents applied to de-tumbling of space debris: Analysis and validation of approximate proposed methods. Acta Astro-nautica 114, 34–53 (2015) https://doi.org/10.1016/j.actaastro.2015.04.012

[14] Bergin, C.: Russian Rokot Launches Sentinel-3A. NASASpaceFlight.com. Accessed: Sep. 02, 2024. https://www.nasaspaceflight.com/2016/02/russian-rokot-sentinel-3a-launch/

[15] WMO OSCAR — Satellite: Sentinel-3A. Accessed: Sep. 02, 2024. https://space.oscar.wmo.int/satellites/view/sentinel_3a

[16] S3 Mission. Accessed: Sep. 26, 2024. https://sentiwiki.copernicus.eu/web/s3-mission

[17] Vallado, D.A., Wertz, J.: Fundamentals of Astrodynamics and Applications. Microcosm Press (2013)

[18] A. Vananti, Tumbling motion assessment for space debris objects, Technical report, ESA/ESOC, 2019. ESA/ESOC AO/1-9934/19/D/SR. https://nebula.esa.int/sites/default/files/neb_tec_studies/2745/public/GT17-152GR_EX.pdf

Materials Research Proceedings 69 (2026) 994-999 https://doi.org/10.21741/9781644904251-172

Forecasting a Complete Picture of Future Launches in Terms of Orbital Region and Physical Parameters

Wiebke RETAGNE[1,a*] and Camilla COLOMBO[1,b]

[1]Politecnico di Milano, Department of Aerospace Science and Technology, Via La Masa, 34, 20156 Milano, Italy

[a]wiebke.retagne@polimi.it, [b]camilla.colombo@polimi.it

Keywords: Launch Traffic, Launch Trends, Space Debris Evolution, Machine Learning, Historical Sampling

Abstract This paper provides a step-by-step guide to go from a given future number of launches to a complete picture in terms of orbital region and physical parameters. This paper only describes non-constellation launches. For these non-constellation launches distributions are built using historical data from DISCOS. Here, the orbital parameter distribution is built using Gaussian-Mixture Models. The object class is determined from a simple probability distribution. A special focus is given to the mass of the objects, since this is an important quantity to be considered when talking about the evolution of the space environment. For the mass, an XGBoost algorithm is employed, which uses the other object characteristics as an input. Finally, the area of the object is determined based on the mass.

Introduction

Forecasting the future launch traffic is not only a matter of determining the number of launches per year. To properly assess the effect of these launches on the space debris environment their orbital and physical parameters play a crucial role. Depending on these the orbital lifetime, collision risks and breakup probability differ drastically. This paper aims to develop a complete method to go from a number of launches to building a full picture of each single launch. This includes the distribution in the orbital parameters of the semi-major axis (sma), eccentricity (ecc) and inclination (inc) and the mass and area of each object, as well as their object type (Rocket Body, Payload, Mission-Related-Object (MRO)). The challenge here is that these parameters are all interconnected. Different orbital regions are used by different types of spacecrafts. This influences their area and mass. An earth observation satellite has significantly different characteristics than a GNSS satellite. Hence, the developed method must take this dependency of the orbital region into account. This paper only describes non-constellation launches. For the constellations information about the or-bit and physical characteristics are publicly available. Therefore, here it does not need to be determined statistically, but can be directly taken from the available information. This paper will give a step-by-step overview of the process at arriving at a complete picture of future non-constellation launches, starting from a given number of launches per year. To determine the distributions for each of the mentioned categories, the historical data coming from the ESA database DISCOS [1] is used. The available data is pre-processed by filtering out the debris objects. The data is then used to either create a distribution directly or as training data for models.

Object Class

The object class determines whether an object is a Rocket Body, Payload or Mission Related Object (MRO). This classification already exists in the historical data in DISCOS. Furthermore, depending on this category, parameters such as the explosion probability vary [2]. Therefore,

Content from this work may be used under the terms of the Creative Commons Attribution 3.0 license. Any further distribution of this work must maintain attribution to the author(s) and the title of the work, journal citation and DOI. Published under license by Materials Research Forum LLC.

Materials Research Proceedings 69 (2026) 994-999 https://doi.org/10.21741/9781644904251-172

the division of the launches into these categories will have a definite impact on space debris evolution.

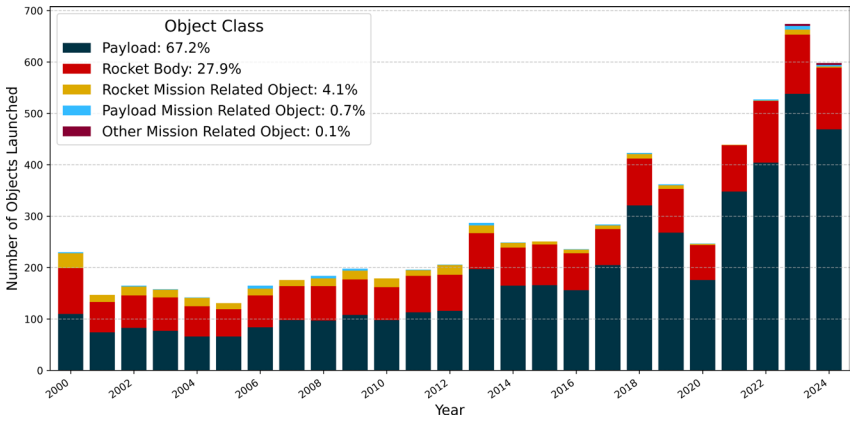


Figure 1: Number of non-constellation launches divided by object class and their total percentages since 2000.

To capture the recent trends in terms of object class distribution the historical data from 2000 to 2024 is considered. As seen in Fig. 1 the majority of launches is determined by Payload objects and Rocket bodies. The total percentages of the object categories in the years between 2000 and 2024 are used to create a categorical distribution. This categorical distribution is then randomly sampled.

Orbital Parameters

The orbital parameters are an important quantity when discussing the evolution of space debris. If the future launches are all concentrated in one orbital region the probability of collisions in that region increase greatly. The orbital parameters of interest are the semi-major axis [km], the eccentricity [-] and the inclination [◦]. To capture the recent trend towards the Low Earth Orbit (LEO), the historical data from 2000 to 2024 is used to create a distribution. The distribution is created by using Gaussian Mixture Models (GMMs). A Gaussian Mixture Model is a probabilistic model, which represents data as a combination of several Gaussian distributions. A more detailed explanation can be found in [3]. It is well suited for creating orbital distributions, since the orbital regions naturally cluster around different combinations of sma, ecc and inc. This method for determining future orbital regions was first presented in Wilson et. al. [4]. To ensure that only Earth related missions are considered, large orbital radius with sma $\geq 60,000$ km are filtered out. Before using the historical data to create the GMM clusters a few transformations are applied. These transformations are to make sure that the data samples stay in a realistic range. The eccentricity should always be between 0 and 1. The inclination between 0° and 180°. In the following the data pre-processing steps are described:

- Log transform the semi-major axis. This helps the model handle large numerical ranges.
- Logit transform the eccentricity to avoid infinites when approaching the bounds of 0 or 1.
- Represent the inclination in terms of sinus and cosinus. This ensures that angles that represent the same orientation such as 0° and 360° are treated in the same manner.
- Scale the entire dataset using the standard scaler which standardizes features by re-moving the mean and scaling to unit variance.

Materials Research Proceedings 69 (2026) 994-999 https://doi.org/10.21741/9781644904251-172

These transformations are only done to ensure a stable fit to the historical data. Before assigning each launch to its orbital parameters they are inverse transformed, so that the final launch data is again represented in the correct units. To determine the number of clusters and therefore the number of orbital regions which best fits the distribution in the historical data, the data from 2000 to 2025 is split into a test and train dataset. Different numbers of components are compared using the Bayesian Information Criterion (BIC) [5]. The best number of components was determined to be 8 orbital regions, with the characteristics represented in Tab. 1. The orbital regions span from Low Earth Orbit (LEO), Sun Synchronous Orbit (SSO) to Medium Earth Orbit (MEO), Highly Eccentric Orbit (HEO), Geostationary Orbit (GEO) and the Geostationary Transfer Orbit (GTO).

Table 1: Cluster orbital characteristics by region.

Region	n	sma_mean [km]	ecc_mean [-]	inc_mean [◦]
LEO (ISS orbit)	798	6762.8	0.0013	51.65
LEO (Mid inclined)	760	6908.8	0.0064	50.72
LEO (SSO)	2060	6951.2	0.0018	97.71
LEO (Polar)	367	7232.6	0.0133	90.19
MEO (Elliptical)	254	19568.5	0.2405	20.38
MEO/HEO (Inclined)	292	24224.7	0.3685	57.01
GTO	350	25099.1	0.7291	17.34
MEO	268	30777.1	0.1162	0.94
GEO	474	42163.4	0.0003	0.02

LEO is a highly populated region. GMMs tend to split dense clusters into multiple components, which is why the LEO clusters vary only slightly in their characteristics. For the future launches for each year the orbital distribution is sampled from these GMMs.

Distribution of Mass and Area

The mass is determined by using an XGBoost algorithm [6]. This is a machine learning algorithm which combines decision trees with gradient boosting. As an input the parameters determined so far are used: the object class, orbital region and type and the launch year. The classification of a satellite based on mass depends on the entity or agency. An overview can be found in A.S. Botelho et. al. [7]. For this work, a very simple classification is adapted. Depending on the mass, the average cross-section area (XSectAvg) also changes. The cross-section area intervals were determined based on the historical data available.

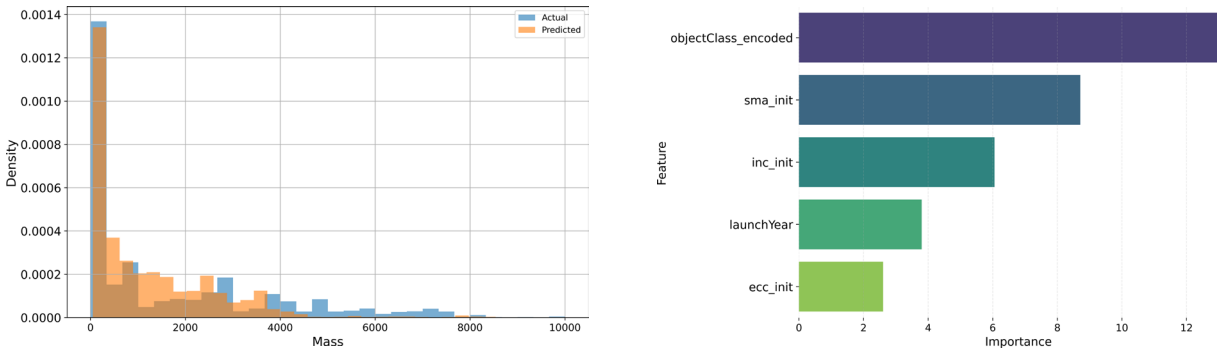
Table 2: Satellite classification by mass and the historical intervals for the average cross-section area.

Classification	Mass [kg]	XSectAvg [m^2]
Nanosatellites	≤10	[0.05, 1.83]
Microsatellites	10-100	[0.59, 13.93]
Minisatellites	100-500	[2.93, 22.10]
Small satellites	500-1000	[9.19, 28.8]
Large satellites	≥1000	[61.40, 1583.48]

When investigating the mass distribution of past launched satellites, it is clear that lower mass satellites are more frequent. In the historical data the biggest recorded mass is from the Discovery (STS-116) space shuttle mission [8]. This mission was launched in 2006 and had a mass of 132931 kg. Just 12 days after launch the shuttle returned to earth. This demonstrates

Materials Research Proceedings 69 (2026) 994-999 https://doi.org/10.21741/9781644904251-172

that the higher mass components in the launch data are more related to human space missions and not satellites that are representative for the space debris evolution. An example of a bigger satellite instead is the Envisat mission [9], launched in 2002, with a mass of 8140 kg. This satellite is characteristic of the mission trends at the time with the launch and operation of large satellites as true space laboratories serving a variety of applications. The XGBoost algorithm is trained for a mass ranging from 0 to 10,000 kg. The results are shown in Fig. 2.



(a) *Mass distribution in training vs. test data* (b) *Feature importance*

Figure 2: The XGBoost model for the mass determination tested against historical data and its feature importance

To train the XGBoost algorithm the full available data from 1957 to 2024 was split into a test and train dataset. The algorithm is validated against the test dataset. This validation can be seen in Fig. 2a. The actual distribution vs. the one predicted by the model is presented. There is good accordance between the two for the lower mass ranges, but the algorithm does not predict many higher mass objects. To correct this difference, in the future a few representative higher mass objects could be added manually. Furthermore, the feature importance can be investigated. Here, as seen in Fig. 2b, the object class drives the assignment of the mass. This is to be expected, since the mass between a Payload object or a Rocket Body might vary significantly. Based on the determined mass the average cross-section area is then assigned by randomly sampling the intervals corresponding to the mass classifications presented in Tab. 2.

Outlook and Conclusions

This paper presented an easy method to go from a given number of future launches to a full picture in terms of object class, orbital region, mass and area. These characteristics are just as important for space debris evolution as the number of launches itself. This method is independent from the model used to predict the future number of launches. The software structure is demonstrated in Fig. 3.

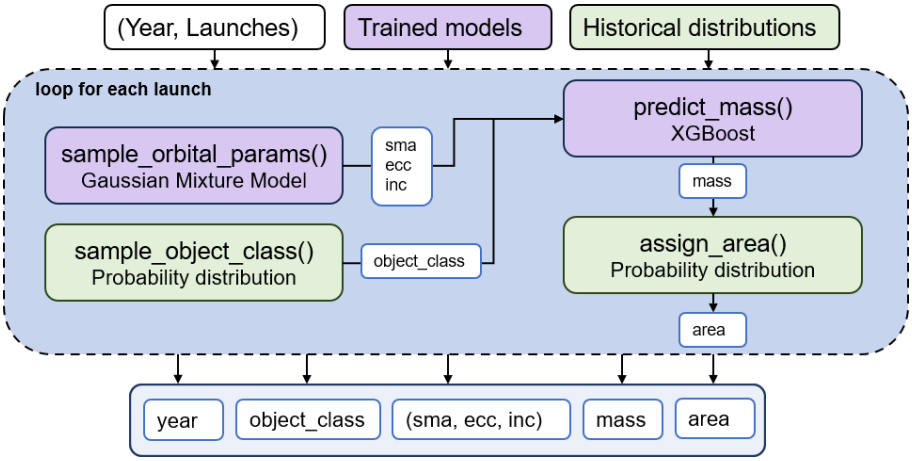


Figure 3: Software architecture to determine a full picture of future launches. The green modules represent historical distributions, and the purple modules describe trained models. The output of each module is marked with a blue border.

The software takes a file representing the future number of launches in the format (Year/Number of launches) and the trained models and distributions based on the historical data as an input. Then, for each launch the different modules are called. Firstly, the orbital parameters are determined using the GMMs, the object class is randomly drawn from the historical categorical distribution. Both of these results are then used as an input into the XGBoost model, to predict a mass based on orbital parameters and object category. The area is then sampled based on the mass classification. The final output file is a file containing the full information for each launch, including the launch year.

This file can then be used as an input into a space debris environment model to further investigate the effects that different launch scenarios can have on the environment as a whole.

Acknowledgments

This research received funding from the European Research Council (ERC) under the European Union's Horizon Europe research and innovation program as part of the GREEN SPECIES project (Grant agreement No - 101089265).

References

[1] European Space Agency. DISCOS: Database and Information System Characterising Objects in Space. https://discosweb.esoc.esa.int/, 2024. Accessed: 2025-07-21.

[2] Alyssa P. Manis, Mark J. Matney, Phillip D. Anz-Meador, and Andrew B. Vavrin. Time-dependent satellite explosion probabilities for long-term orbital debris environment mod-eling. Journal of Spacecraft and Rockets, 62(3):989-998, 2025. https://doi.org/10.2514/1.A36118

[3] Douglas Reynolds. Gaussian Mixture Models, pages 659-663. Springer US, Boston, MA, 2009. https://doi.org/10.1007/978-0-387-73003-5_196

[4] Callum J. Wilson, Massimiliano Vasile, Jinglang Feng, Keiran McNally, Alfredo Ant'on, and Francesca Letizia. Modelling future launch traffic and its effect on the leo operational environment. In AIAA SciTech 2024 Forum, Orlando, Florida, United States, 2024. American Institute of Aeronautics and Astronautics, AIAA. Peer-reviewed, accepted author manuscript. https://doi.org/10.2514/6.2024-1814

[5] Gideon Schwarz. Estimating the dimension of a model. The Annals of Statistics, 6(2):461-464, March 1978. https://doi.org/10.1214/aos/1176344136

[6] Tianqi Chen and Carlos Guestrin. Xgboost: A scalable tree boosting system. CoRR, abs/1603.02754, 2016. https://doi.org/10.1145/2939672.2939785

[7] A. S. Botelho and A. R. C. Xavier Jr. A unified satellite taxonomy proposal based on mass and size. Advances in Aerospace Science and Technology, 4:57-73, 2019. https://doi.org/10.4236/aast.2019.44005

[8] NASA. Sts-116 mission overview. https://www.nasa.gov/mission/sts-116/, 2006. Accessed: 2025-11-06.

[9] European Space Agency (ESA). Envisat mission overview. https://www.esa.int/Applications/Observing_the_Earth/Envisat/, 2002. Accessed: 2025-11-06.

Materials Research Proceedings 69 (2026) 1000-1005 https://doi.org/10.21741/9781644904251-173

Baseline Values and Sensitivity Analysis of the THEMIS Space Debris Index

Daniel LÜCK[1,a*], Andrea MUCIACCIA[1,b], Martina RUSCONI[1,c], Camilla COLOMBO[1,d]

[1]Politecnico di Milano, Department of Aerospace Science and Technology, Via La Masa 34, 20156 Milano, Italy

[a]daniel.luck@polimi.it, [b]andrea.muciaccia@polimi.it, [c]martina.rusconi@polimi.it, [d]camilla.colombo@polimi.it

Keywords: Space Debris, Space Debris Index, Space Sustainability

Abstract. Fragmentations caused by explosions or collisions contribute a significant share of the growing space debris population. These present a risk to active spacecraft and have caused collisions in the past. Each satellite has the potential to fragment and thereby threaten spacecraft in its vicinity. Politecnico di Milano developed a tool for Tracking health of environment and missions in Space (THEMIS) under a European Space Agency (ESA) project. It quantifies a mission's environmental impact using a space-debris index based on the Environmental Consequences of Orbital Breakups (ECOB) approach. In this approach, the probability and severity of a potential fragmentation are combined. THEMIS is undergoing beta testing and is being upgraded in a follow-up project. Since the approach is new, questions about interpreting the Index values have been raised. In this paper, reference values for selected missions in LEO and MEO, covering Earth observation, telecommunication and navigation applications are investigated. The sensitivities of index changes to orbital parameters, satellite properties and collision avoidance as well as post mission disposal strategies are estimated.

Introduction

The threat posed by space debris is increasingly recognised as a risk to active space missions. The number of objects in space has been rising steadily over the last years, and this trend is projected to continue [1]. Debris objects as small as 1 cm in size can damage or destroy satellites upon impact [2, 3]. The majority of space debris objects, and a large portion of the overall space object population, consists of fragments that originate from explosions or collisions of satellites and rocket stages [1]. Each mission has a risk of fragmentation, potentially increasing the risk for other satellites. Politecnico di Milano developed the Tracking health of environment and missions in Space (THEMIS) tool under an ESA project to quantify a mission's impact on the space environment [4]. Following the Environmental Consequences of Orbital Breakups (ECOB) approach, probability (p_c and p_e) and effect (e_c and e_e) of a potential collision (c) or explosion (e) of the spacecraft are estimated to calculate a space debris index I at a given instance via Eq. 1 [5].

$$I = p_c \cdot e_c + p_e \cdot e_e \tag{1}$$

Indices over all instances of a mission are aggregated to obtain the total Index of a mission. This Index quantifies the impact of the analysed mission on its environment as a measure of the increased risk to other satellites following a fragmentation of another mission. The probability of explosion pe is retrieved from statistical data [4], while the probability of a collision, significant enough to cause a catastrophic event, pc is estimated using ESA's MASTER software [6, 4]. For both explosions and collisions, the effect of the fragmentation (ec and ee) is estimated by propagating the fragment density and calculating the rate of impact on a set of representative

Content from this work may be used under the terms of the Creative Commons Attribution 3.0 license. Any further distribution of this work must maintain attribution to the author(s) and the title of the work, journal citation and DOI. Published under license by Materials Research Forum LLC.

Materials Research Proceedings 69 (2026) 1000-1005 https://doi.org/10.21741/9781644904251-173

targets [4, 7, 8, 12]. With the latest available reference population, only the impact of non-manoeuvrable objects is considered in the analysis. The analysed satellite can be modelled to be disposed at the end of its operational life or to decay naturally. Collision avoidance is modelled by removing a part of the collisions with trackable objects, proportional to the efficacy of the collision avoidance.

The THEMIS tool is now in the beta testing phase [9]. During the presentation of the tool to beta testers, questions on the interpretation of results were raised. Since the use of THEMIS and the underlying ECOB approach is not yet well established, this paper aims to provide reference values for a selected number of representative missions. Alongside those, the sensitivity of the index to certain design parameters, mass, area, orbit, Post-Mission-Disposal (PMD) and Collision Avoidance Manoeuvre (CAM) strategy are estimated.

Reference Objects

THEMIS can currently be used to estimate indices of objects in Low Earth Orbit (LEO), Medium Earth Orbit (MEO), Geostationary Transfer Orbit (GTO) and Geostationary Orbit (GEO). The calculation for GEO is being upgraded in the ongoing THEMIS 2 project and results may change in the near future. Therefore, this paper focuses on presenting results for LEO and MEO regions.

Satellites are selected to cover mission applications with the highest relevance, Earth observation, Telecommunication and Navigation. For LEO Earth observation, satellites similar to the ESA Envisat (OBS1) and Sentinel 1D (OBS2) satellites are selected. For LEO Telecommunication, one satellite similar to the ones of the Starlink constellation (COM1) and one similar to the Oneweb constellation (COM2) are used. In MEO, a satellite similar to the ones of the Galileo constellation (GNSS) and a satellite like the ones of the O3b constellation (COM3) are investigated. For each case, only one satellite is modelled, not the entire constellation. The launch epoch is set to November 2025 for all cases to show the impact of the launch of a new satellite of the given type.

Table 1 lists the reference input values. For all cases the eccentricity is assumed to be close to 0. For the baseline, reliability of both CAM and PMD is set to 90%. For missions representing Starlink, Galileo and O3b the latest satellite models of that constellation are used. Data on mass and area are retrieved from the ESA DISCOS database [11], while orbital data are retrieved from Space-Track [10]. For each case the index is first estimated using the settings described to get a baseline value.

Table 1 Reference settings

Mission	Mass/kg	Area/m²	SMA/km	Inc/°	Mission duration /years	PMD
OBS1	8110.0	74.39	7162	98.5	10	25 year eccentric
OBS2	2185.0	84.40	7064	98.2	12	25 year eccentric
COM1	730.0	33.88	6946	70.0	5	5 year circular
COM2	147.0	3.46	7571	86.4	7	5 year circular
GNSS	733.0	9.22	29601	57.2	15	graveyard disposal
COM3	1700.0	27.340	29601	0.0	15	graveyard disposal

Sensitivity is estimated for changes of: +1 kg mass, +1 m² area, +1 km SMA, +1° inclination and RAAN, +1 year PMD lifetime, and +1 percentage point in CAM/PMD reliability. Changes of this order may be possible during the design phase. The resulting changes are given both as absolute changes as well as percentage change with relation to the baseline value of the given mission $100 \cdot \frac{I_{sensitivity} - I_{baseline}}{I_baseline}$. For the relative values, the change in Index is given relative to a

Materials Research Proceedings 69 (2026) 1000-1005 https://doi.org/10.21741/9781644904251-173

1% change for mass, area and remaining lifetime. This is done to stay consistent across the varying masses, areas and lifetimes of the reference missions.

Results

The reference values for the evaluated missions are presented in Table 2. The heat maps in Figure 2 show both absolute changes (left) and relative percentage changes (right) in the index for design parameter modifications.

For the baseline values, Indices can vary by multiple orders of magnitude (8.84×10^{-5} to 3.43×10^{-8}), even in the same orbital region and the same application. The highest absolute value can be found for the first LEO observation mission. This is also the heaviest satellite placed in one of the most densely populated regions. The MEO communications constellation has the second highest value, only slightly lower. This is due to the fact that multiple satellites of the same constellation are placed in a narrow inclination band. The fragmentation of one of them would have a significant effect on the other satellites of the constellation. The second LEO Earth observation mission has a value around one order of magnitude lower than the first. The two communications satellites have similar values, around 2 orders of magnitude lower than that of OBS2. For COM1 this is due to the fast decay of satellites from low orbits, while for COM2 it is due to low mass, area and low density of objects at the altitude of the satellite. The lowest value overall is that of the GNSS mission, around half the value of that of the LEO communications satellites.

The sensitivity of the index to changes of the parameters varies between orbital regions and mission definitions. Regarding relative values, an increase in mass consistently increases the index. A 1% increase in mass increases the index by between 0.7 and 10%. An increase in area on the other hand increases the index by 0.6 to 2% for each percent of area change for the communications constellations in LEO and the first LEO observations satellite. It decreases the index significantly for the 2nd observation satellite. The reason for this is that, while the collision cross section is increased, the orbital decay is significantly sped up due to the higher area to mass ratio, reducing the impact over the satellite's lifetime. Similarly, increasing the SMA can either increase or decrease the index significantly depending on the orbit. In MEO changes to SMA or area have only little effect. Increasing the inclination by just one degree significantly lowers the index, in some cases by more than 20% for both Earth observation satellites and the constellation in MEO. It has little effect on the other missions though. Increasing PMD reliability and reducing PMD lifetime can significantly improve the index value for missions that are in densely populated regions and do not decay naturally. Increasing the reliability of the disposal by 1 percent point has an effect that is around 10 times larger than reducing the lifetime by 1%. For regions that are sparsely populated or where atmospheric drag is significant, changes in PMD have no effect. Increasing the reliability of CAM has a significant effect on objects in LEO but the effect is close to 0 in MEO.

Table 2 Baseline Index results

Mission	Index baseline value	Orbital Region
OBS1	8.84×10^{-5}	LEO
OBS2	7.84×10^{-6}	LEO
COM1	9.24×10^{-8}	LEO
COM2	7.03×10^{-8}	LEO
GNSS	3.43×10^{-8}	MEO
COM3	6.01×10^{-5}	MEO

Materials Research Proceedings 69 (2026) 1000-1005 https://doi.org/10.21741/9781644904251-173

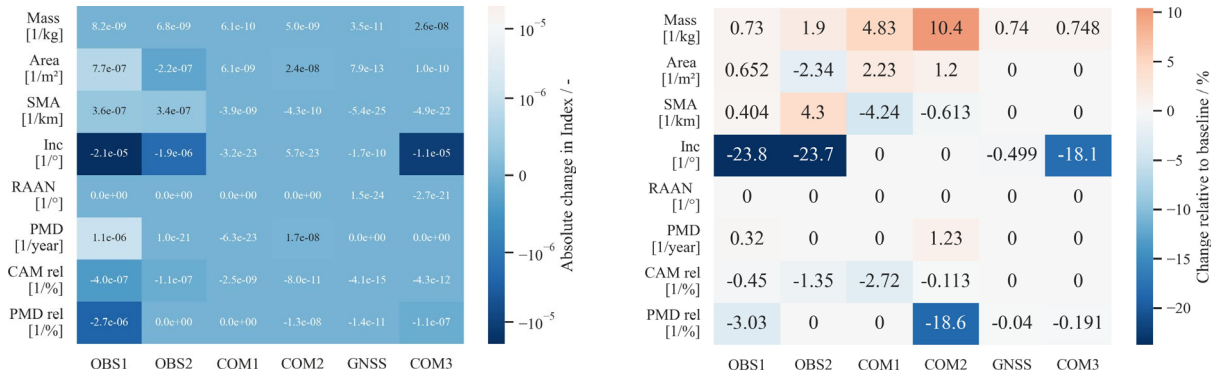


Figure 1: Absolute (left) and relative (right) sensitivity of index to changes in design parameters.

For a given mission, the sensitivity to mass, area, PMD and CAM parameters remain constant across values. For parameters related to the orbital region like SMA, inclination and RAAN however, the dependencies are more complex. Figure 2 shows the Index for an Envisat-like mission across different altitudes and inclinations. Multiple local maxima and minima can be identified. Depending on the location, the direction in which the index decreases switches. The exact location of extrema depends on other mission parameters like mass, area and PMD strategy. The index typically decreases with decreasing altitude below 800 km and with increasing altitude above 1500 km. The specific sensitivities have to be estimated individually for each case.

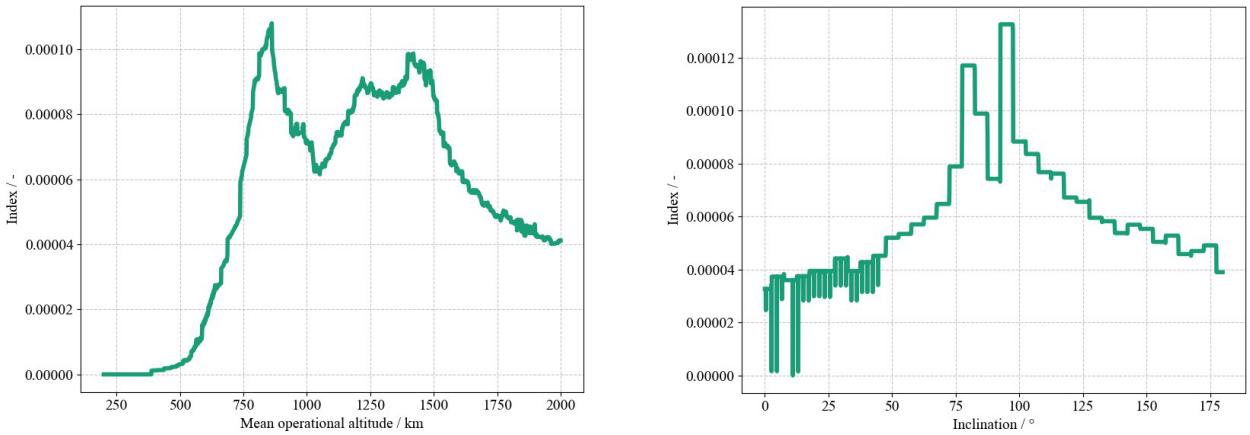


Figure 2: Sensitivity of relative index to changes in orbital altitude (left) and inclination (right) for Envisat-like mission.

Conclusion

Results of the Space Debris Index calculated with THEMIS were presented. The values can vary by multiple orders of magnitude depending on the orbit and spacecraft characteristics. Large satellites in densely populated Sun Synchronous Orbit (SSO) regions are found to have the highest index values but satellites in certain equatorial orbits can have similar values. The lowest indices are found in very low or very high LEO at the location of large communications constellations and for GNSS satellites.

The sensitivity of the index to design parameters also varies across missions. The most impactful changes to the index can be achieved via varying inclination or PMD reliability. Significant changes can also be made by changing mass, area, CAM reliability and SMA for some missions. Changes in RAAN and duration of PMD are small.

These results can be used as reference values to interpret the THEMIS index. The sensitivities can furthermore help to identify ways to effectively reduce the index of a mission during the design phase. In general, densely populated regions should be avoided when possible. If placed at an

altitude where orbital decay due to drag is slow, a high post-mission disposal reliability can decrease the index.

The results presented were obtained using a version of THEMIS that is currently under development. Changes in the implementation or the space environment like the deployment of a large constellation or significant space debris producing events can change those results.

Acknowledgements
The research in this work has received funding from the European Space Agency contract ESA Contract No. 4000145375/24/D/BL

References

[1] ESA, ”ESA’S ANNUAL SPACE ENVIRONMENT REPORT” 2025.

[2] H. Krag, M. Serrano, V. Braun, P. Kuchynka, M. Catania, J. Siminski, M. Schim-merohn, X. Marc, D. Kuijper, I. Shurmer, A. O’Connell, M. Otten, Isidro Mun˜oz, J. Morales, M. Wermuth, D. McKissock, A 1 cm space debris impact onto the Sentinel-1A solar array, Acta Astronautica, Volume 137, 2017, Pages 434-443, ISSN 0094-5765, https://doi.org/10.1016/j.actaastro.2017.05.010.

[3] Kelso, T.S., 2009. Analysis of the Iridium 33-Cosmos 2251 collision. Advances in the Astronautical Sciences, 135(2), pp.1099-1112.

[4] Colombo, C., Muciaccia, A., Giudici, L., Gonzalo Go´mez, J.L., Masat, A., Trisolini, M., Del Campo, B., Letizia, F. and Lemmens, S., 2023. Tracking the health of the space debris environment with THEMIS. In Aerospace Europe Conference 2023-Joint 10th EUCASS-9th CEAS Conference (pp. 1-8).

[5] Letizia, F., Colombo, C., Lewis, H.G. and Krag, H., 2018, February. Development of a debris index. In Stardust Final Conference: Advances in Asteroids and Space Debris Engineering and Science (pp. 191-206). Cham: Springer International Publishing.

[6] Braun, V., Horstmann, A., Lemmens, S., Wiedemann, C. and B¨ottcher, L., 2021, April. Recent developments in space debris environment modelling, verification and validation with MASTER. In 8th European Conference on Space Debris (p. 18). ESA Space Debris Office Darmstadt, Germany.

[7] Lorenzo Giudici, Juan Luis Gonzalo, Camilla Colombo, Density-based in-orbit collision risk model valid for any impact geometry, Acta Astronautica, Volume 219, 2024, Pages 785-803, ISSN 0094-5765, https://doi.org/10.1016/j.actaastro.2024.03.067.

[8] Andrea Muciaccia, Lorenzo Giudici, Francesca Letizia, Mirko Trisolini, Juan Luis Gonzalo, Camilla Colombo, Evaluating the environmental impact of space mis-sions, Acta Astronautica, Volume 236, 2025, Pages 239-250, ISSN 0094-5765, https://doi.org/10.1016/j.actaastro.2025.06.024.

[9] Camilla Colombo, Andrea Muciaccia, Martina Rusconi, Daniel Lu¨ck, Wiebke Retagne, Juan Luis Gonzalo, Marco De Pardi, Francisco Javier Simarro Mecinas, Diego Ramirez, Jack Ramshaw, Francesca Letizia, Emma Stevenson, Results of the beta testing by space-craft operators for THEMIS software for Tracking the Health of the Environment and Missions in Space, 2025, in IAC 2025

[10] Space-Track, ”Space-Track Catalog,” 2025. [Online]. Available: https://www.space-track.org/catalog. [Accessed: 05.11.2025].

[11] ESA, ”DISCOSweb” 2025. [Online]. Available: https://discosweb.esoc.esa.int/objects. [Accessed: 05.11.2025].

[12] Giudici, L., Trisolini, M., Colombo, C. (2023). Probabilistic multi-dimensional debris cloud propagation subject to non-linear dynamics. Advances in Space Research, 72(2), 129–151. https://doi.org/10.1016/j.asr.2023.04.030

Materials Research Proceedings 69 (2026) 1006-1011 https://doi.org/10.21741/9781644904251-174

Formation Flying Strategies for Small Distributed SAR Satellites: A Trade-Off between Stability and Performance

Maria SALVATO[1,a *], Antonio GIGANTINO[1], Gianluca COPPA[1], Francesca PELLICCIA[1], Maria Daniela GRAZIANO[1], Alfredo RENGA[1]

[1]Department of Industrial Engineering, University of Naples Federico II, Piazzale Vincenzo Tecchio 80, 80125, Napoli, Italy

[a]maria.salvato2@unina.it

Keywords: Formation Flying, DSAR, Small Satellites

Abstract. Formation flying techniques have enabled advanced interferometric and radar imaging capabilities for Earth observation missions in low Earth orbit (LEO). At one end of the possible geometries lies the safe ellipse configuration, widely adopted for its intrinsic passive safety. However, the continuously varying baseline complicates SAR data processing and may degrade image quality. At the opposite end, the train-like formation features a constant along-track geometry that simplifies SAR imaging and processing, with the downside of perturbations induced along-track drift. Although these performance versus stability trade-offs are well documented for large formation flying missions, their implications for small satellite constellations and distributed SAR (DSAR) realizations remain unexplored. This paper compares safe ellipse and train-like DSAR formations through orbital dynamics simulations, assessing relative motion stability, passive safety, and formation-keeping requirements to identify optimal and cost-effective architectures for small-satellite DSAR missions.

Introduction

The use of coordinated multi-satellite formations has become a recurring aspect of radar-based Earth observation missions, supporting increasingly demanding interferometric applications. For instance, the TanDEM-X [1] mission has demonstrated the potential of multi-satellite radar constellations for generating high-resolution and multi-baseline products. More recently, RODiO mission concept has explored the use of compact clusters of small satellites for distributed radar sensing [2, 3]. DSAR systems exploit the cooperation of multiple satellites flying in formation to synthesize a larger virtual aperture [4]. This approach enables platform miniaturization. Instead of a single large and complex spacecraft, a constellation of smaller and less expensive units, such as microsatellites, nanosatellites, and CubeSats, can achieve comparable imaging performance [5]. The achievable imaging quality depends on the spatial and temporal sampling of the received signals, governed by the satellites' relative geometry and motion [6, 7]. Ideally, the receivers should be displaced purely in the along-track direction, realizing uniform linear sampling of the equivalent phase centres [8]. In practice, perturbations and design constraints lead to non-uniform or even three-dimensional sampling distributions [7]. To represent these two scenarios, two configurations are analysed: the train-like formation, modelling the ideal linear case, and the safe ellipse formation, representing a more realistic three-dimensional geometry. The extension of these architectures to small satellites is still an open topic of research, particularly for DSAR missions. These systems are subject to severe resource limitations in terms of control effort [9], and the need to maintain precise relative geometry to preserve phase coherence further tightens the platform design margins. Therefore, understanding the dynamical behaviour of such formations is a necessary step toward the design of future small satellite DSAR missions. In this perspective, the present work focuses on formation stability and control effort, providing a quantitative assessment of the ΔV required to maintain both configurations under realistic orbital perturbations.

Content from this work may be used under the terms of the Creative Commons Attribution 3.0 license. Any further distribution of this work must maintain attribution to the author(s) and the title of the work, journal citation and DOI. Published under license by Materials Research Forum LLC.

Materials Research Proceedings 69 (2026) 1006-1011 https://doi.org/10.21741/9781644904251-174

Formation Design and Control

The design and control of satellite formations can be formulated either in terms of differential orbital elements or in Cartesian coordinates within the Hill Reference Frame (HRF) [10], reported in Fig. 1. Commonly, the former are adopted for formation design, while the latter are preferred for control applications. In this study, however, Cartesian coordinates are used as the starting point to derive the corresponding orbital element differences, ensuring a consistent link between geometry and control parameters. Subsequently, the formation keeping strategy, carried out in NASA's General Mission Analysis Tool (GMAT) [11], acts on the orbital elements to restore the desired separations defined in the Cartesian control framework.

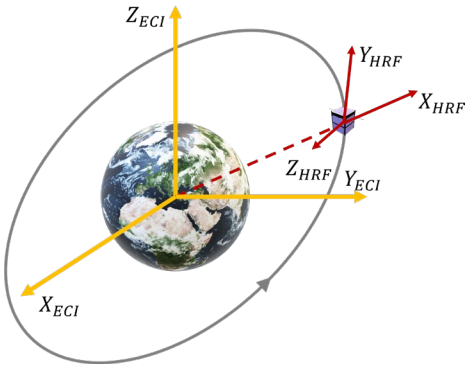


Fig. 1 HRF (in red) centred in the satellite with respect to Earth Centred Inertial reference frame (in yellow)

In the train-like formation satellites are placed along the same orbital path with along-track offsets from the chief, typically generated through variations in argument of perigee (AOP), δω, and mean anomaly, δM [10]. The adopted modelling approach introduces δM so as to produce the along-track offsets y_{off}, as per Eq. (1), while keeping all other orbital elements identical to chief.

$$y_{off} = a(\delta M_0). \tag{1}$$

The safe-ellipse configuration exploits the three-dimensional relative dynamics by introducing controlled differences to both in-plane and out-of-plane orbital elements: eccentricity, δe, δω, semi-major axis (SMA), δa, δM, inclination, δi, and right ascension of the ascending node, δΩ. The methodology detailed in [12] has been adopted for formation design. By tuning the differences in orbital elements, the deputies are placed on elliptical trajectories around the chief, with amplitude of radial oscillations A_x, minimum radial/cross-track separation $d_{xz,min}$, and cross-track separation at zero along-track $\tilde{z}$. The conditions described in Eq. (2) are imposed to ensure a slow variation of the radial/cross-track separations during the motion along the orbit and to suppress the secular drift induced by perigee precession.

$$A_x = d_{xz,min}, \quad \tilde{z} = 0, \quad x_{off} = \delta a = 0, \quad \delta i = 0. \tag{2}$$

For the following discussion, a case study has been considered as representative of a compact, LEO, DSAR mission, i.e., the RODiO cluster. The cluster comprises four 16U CubeSats equipped with an X-band antenna, one chief – RD_1 – and three deputies – RD_2, RD_3, RD_4 –. RD_1 shares the orbital parameters of PLT-1 [2]. The inter-satellite distance between chief and deputies is defined by separations of 0.18 km, 0.36 km, and 0.55 km in the along-track direction, with corresponding radial and cross-track offsets according to the chosen formation. The obtained configurations are reported in Fig. 2.

Materials Research Proceedings 69 (2026) 1006-1011 https://doi.org/10.21741/9781644904251-174

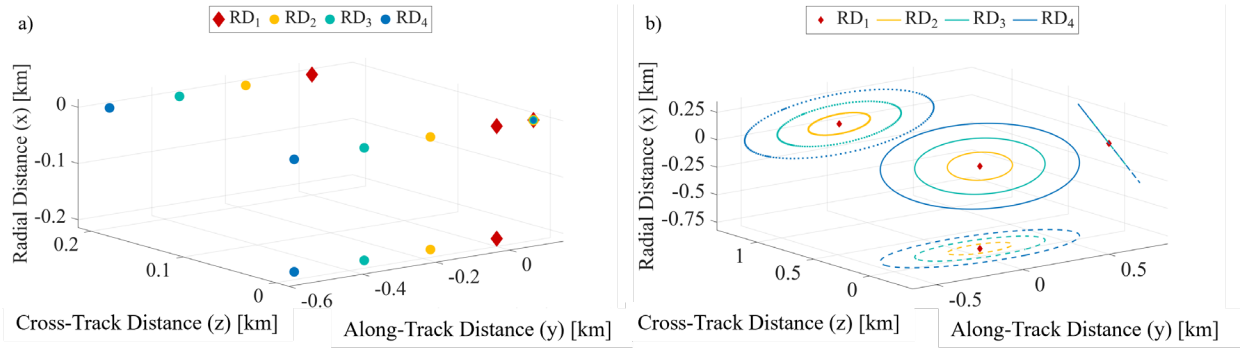


Fig. 2 RODiO cluster in a) Train-like formation and b) Safe ellipse formation

The conceived formation keeping strategy relies on the definition of a control volume, that is the allowable region of motion for each deputy around the chief. When a deputy reaches the boundary of its control volume, a corrective manoeuvre sequence is triggered to restore the nominal configuration. The geometry and size of this control volume depend on the characteristics of each formation. For the safe ellipse formation, the control concept is based on the definition of a safety tube within which the relative motion in all three directions is bound. The maximum along-track and cross-track/radial dimensions of the tube derive from DSAR performance requirements. Specifically, they are set as fractions (~5 to 10%) of the corresponding along-track and orthogonal critical values, following the relations in [5]. The resulting safety tube is characterised by maximum allowable separations of 0.6 km in along-track and 0.4 km in cross-track/radial directions. The same upper bounds are applied to the train-like formation. Additionally, since in this case the relative motion develops almost entirely in the along-track direction and is positive towards the chief, a minimum allowable distance needs to be defined to avoid undesired proximity among the deputies during the natural along-track drift. To this end, two alternative approaches have been considered. The first approach introduces a safe distance corresponding to the radius of the keep out zone sphere, which is defined in [13] as the worst-case sum of the physical radii of two neighbouring satellites with a 50% safety margin. For RODiO's cluster this distance equals to approximately 2 m and represents the minimum admissible separation among any two spacecraft, including the chief. The second approach defines a control window within which each deputy is allowed to drift up to a fixed fraction of its nominal separation from the chief. Since no strict requirement is imposed by the mission on the minimum along-track baseline, it is set to 90%. Until this threshold is reached, each deputy drifts freely. Then, when the first deputy violates this boundary, the entire cluster performs a correction manoeuvre sequence. This choice ensures that, even at the minimum limit of the control window, the residual inter-satellite distance is comparable with the control accuracy (~ 10 m).

Manoeuvring Strategy for Formation Keeping

The formation keeping logic differs between the two configurations. Concerning the safe ellipse, each deputy operates an independent (asynchronous) control, performing its manoeuvres individually as soon as its separation violates the control volume. In contrast, the train-like configuration adopts a coordinated and synchronised approach. Since the only existing separation is one-dimensional, the deputies' cluster performs the corrections once any satellite exceeds its boundary. Based on this operational logic, the manoeuvring strategy has been designed to restore the nominal along-track separations with a four-step sequence of impulsive in-plane burns. These manoeuvres act tangentially to the direction of motion and are carried out at the periapsis, apoapsis, and orbital nodes. The first two burns ΔV_1 and ΔV_2 constitute the phasing manoeuvre [14]. Subsequently, a third burn, ΔV_3, is applied at one of the orbital nodes to correct the rotation of the eccentricity vector using equinoctial elements H and K, whose formulation is detailed in [11]. This

Materials Research Proceedings 69 (2026) 1006-1011 https://doi.org/10.21741/9781644904251-174

manoeuvre restores the designed difference in the AOP between deputy and chief. Finally, two further burns, ΔV_4 and ΔV_5, are executed at the orbit apoapsis: the first compensates for the residual difference in eccentricity with respect to the chief's instantaneous state, and the second re-establishes the SMA. The complete sequence of manoeuvres is executed over a duration of three orbital periods, ensuring convergence of each deputy to its nominal along-track position and restoration of the designed in-plane formation geometry.

Simulation Setup and Results

The formation keeping logic has been simulated through GMAT [11]. The EarthMJ2000 reference frame and BrouwerMeanShort elements have been used to define and propagate the S/C's orbit. The initial simulation epoch is 01 January 2026 05:45:00 UTC. The perturbations included in the analysis are: i) Earth's gravitational potential series expanded up to degree and order 100; ii) the Moon and Sun's third body effect; iii) a reflectivity coefficient Cr = 1.8 for the solar radiation pressure modelling; iv) the Jacchia-Roberts atmospheric model. A chief-centred coordinate system is used to monitor and control the relative motion in the HRF and to evaluate violations of the control volume boundaries. This enables the derivation of the deputies' along-track coordinate behaviour with respect to the chief for both formations, as shown in Fig. 3. Here, the red lines identify the times at which a violation of the control volume occur, determining the scheduling of formation keeping manoeuvres. The corrections happen with a cadence that is in the order of days for the safe ellipse configuration and in the order of four-to-five months for the train-like formation. Consequently, the safe ellipse manoeuvring frequence is higher than the train-like one. As for the radial and cross-track coordinates, results from extended propagation periods, i.e., up to six months, indicate no violation of the control volume upper boundaries. Therefore, no out-of-plane manoeuvre is deemed necessary in this timeframe, and only in-plane manoeuvres are executed to restore the nominal along-track separations.

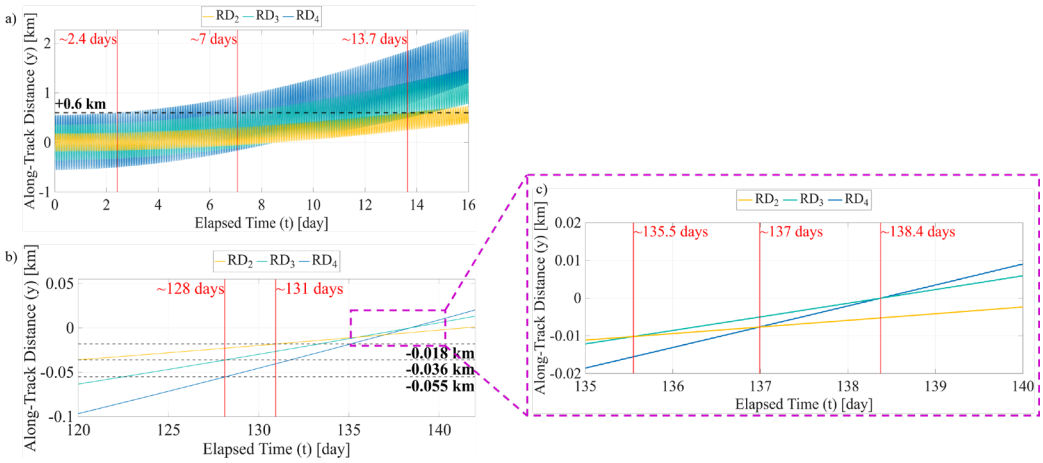


Fig. 3 Evolution of the deputies' along-track distances from the chief. a) safe ellipse formation, maximum along-track boundary of the control volume (black dashed line); b) train-like formation approach #2, minimum along-track boundaries of the control volume for each deputy (black dashed lines); c) zoomed view of Fig.3b) approach#1, collision times (red lines)

By applying the proposed manoeuvring strategy, the required ΔV budget for the safe ellipse and train-like configurations is computed and reported in Table 1. Given the difference in manoeuvring cadence, and to provide a common reference for comparison with the train-like configuration, the ΔV values reported in Table 1 for the safe ellipse formation are also expressed on a monthly basis, considering the violation times of each deputy from Fig. 3 a), b) and c). A first conclusion derivable from Table 1 concerns the comparison between the two approaches

considered for maintaining the train-like formation. The safe distance based approach results in a higher ΔV expenditure compared to control window one. This outcome is primarily due to the slight delay in violation times, which leads to longer drift times and thus larger corrective manoeuvres. Nevertheless, when comparing the two, the second approach proves to be more efficient and operationally preferable. As for the formations' comparison, a consistent trend is confirmed. The deputy with the largest relative orbit, RD_4, requires the highest ΔV for formation keeping, while control costs for RD_2 and RD_3 are smaller. Furthermore, despite the difference in manoeuvre frequency, the total ΔV required to maintain the train-like formation is approximately one order of magnitude lower than that of the safe ellipse case. This suggests that the train-like configuration, although less robust to the along-track drift, offers significantly reduced control effort and therefore represents a more cost-effective solution for small satellite DSAR missions.

Table 1 Formation keeping ΔV budget for the deputies of safe ellipse and train-like formations

	Safe ellipse formation			*Train-like formation*	
	ΔV_{tot} [m/s]	Manoeuvres per month	ΔV_{month} [m/s]	ΔV_{tot} [m/s] Approach #1	ΔV_{tot} [m/s] Approach #2
RD_2	1.27×10^{-1}	2.2	2.80×10^{-1}	2.09×10^{-2}	1.91×10^{-2}
RD_3	1.22×10^{-1}	4.3	5.18×10^{-1}	4.38×10^{-2}	3.94×10^{-2}
RD_4	5.96×10^{-2}	12.4	7.39×10^{-1}	6.58×10^{-2}	6.01×10^{-2}

Conclusions

This paper analysed two representative formation flying architectures for small satellite distributed missions: safe ellipse and train-like formations. Both have been modelled analytically in the HRF, linking their relative geometry to the corresponding orbital element differences. Subsequently, a dedicated formation keeping strategy has been implemented to evaluate the ΔV requirements under realistic perturbations, including J_2 effects, atmospheric drag, solar radiation pressure, and third-body interactions. Two control approaches have been tested for the train-like configuration and compared with the safety tube strategy adopted for the safe ellipse formation. As expected, the latter proves advantageous when collision risk mitigation is prioritised, but at the expense of more frequent corrective manoeuvres due to its varying geometry. Conversely, the former formation requires simpler control and lower fuel consumption, while remaining sufficiently stable over several months.

Acknowledgements

This study was carried out within the Space It Up! Project and received funding from the ASI and the MUR – Contract n. 2024-5-E.0 - CUP n. I53D24000060005. This manuscript reflects the views and opinions of the authors only; the funding bodies cannot be held responsible for them.

References

[1] G. Krieger, M. Zink, M. Bachmann, B. Bräutigam, D. Schulze, M. Martone, P. Rizzoli, U. Steinbrecher, A. J. Walter, F. De Zan, I. Hajnsek, K. Papathanassiou, F. Kugler, M. Rodriguez Cassola, M. Younis, S. Baumgartner, P. López-Dekker, P. Prats, A. Moreira, TanDEM-X: A Radar Interferometer with Two Formation-Flying Satellites, Acta Astronaut. 89 (2013) 83–98. https://doi.org/10.1016/j.actaastro.2013.03.008

[2] A. Gigantino, A. Renga, M. D. Graziano, C. Abbundo, F. Ravellino, A. Moccia, D. di Martire, M. Khalili, M. Ramondini, V. Pisacane, G. Lambitelli, R. Aurigemma, A. Fedele, R. Luciani, F. Tataranni, V. Martucci, S. Natalucci, Long-Baseline Multistatic and Bistatic SAR

Products: Application to the RODiO Mission, Acta Astronaut. 222 (2024) 314–324. https://doi.org/10.1016/j.actaastro.2024.06.019

[3] A. Gigantino, C. Vela, R. Opromolla, G. Fasano, A. Renga, M. D. Graziano, Effect of Formation Design on Azimuth Ambiguity Suppression Capability in a Spaceborne Distributed SAR, IGARSS 2024 - 2024 IEEE International Geoscience and Remote Sensing Symposium, IEEE. (2024) 10953–10957. https://doi.org/10.1109/IGARSS53475.2024.10640452

[4] G. Krieger, A. Moreira, Spaceborne Bi- and Multistatic SAR: Potential and Challenges, IEE Proceedings - Radar, Sonar and Navigation. 153 (2006) 184–198. https://doi.org/10.1049/ip-rsn:20045111

[5] P. López-Dekker, G. Krieger, A. Moreira, Multistatic Radar Systems, in: M. D'Errico (Ed.) Distributed Space Missions for Earth System Monitoring, Springer, New York, 2013, pp. 61–122. https://doi.org/10.1007/978-1-4614-4541-8_2

[6] G. Krieger, N. Gebert, A. Moreira, Unambiguous SAR Signal Reconstruction From Nonuniform Displaced Phase Center Sampling, IEEE Geoscience and Remote Sensing Letters. 1 (2004) 260–264. https://doi.org/10.1109/LGRS.2004.832700

[7] A. Renga, A. Gigantino, M. D. Graziano, Multiplatform Image Synthesis for Distributed Synthetic Aperture Radar in Long Baseline Bistatic Configurations, IEEE Trans Aerosp Electron Syst. 59 (2023) 9267–9284. https://doi.org/10.1109/TAES.2023.3316171

[8] N. Gebert, G. Krieger, A. Moreira, Digital Beamforming on Receive: Techniques and Optimization Strategies for High-Resolution Wide-Swath SAR Imaging, IEEE Trans Aerosp Electron Syst. 45 (2009) 564–592. https://doi.org/10.1109/TAES.2009.5089542

[9] R. M. Millan, R. von Steiger, M. Ariel, S. Bartalev, M. Borgeaud, S. Campagnola, J. Castillo-Rogez, R. Fléron, V. Gass, A. Gregorio, D. Klumpar, B. Lal, M. Macdonald, J. Park, V. Sambasiva Rao, K. Schilling, G. Stephens, A. Title, J. Wu, Small satellites for space science, Advances in Space Research.. 64 (2019) 1466–1517. https://doi.org/10.1016/j.asr.2019.07.035

[10] M. D'Errico, G. Fasano, Relative Trajectory Design, in: M. D'Errico (Ed.) Distributed Space Missions for Earth System Monitoring, Springer, New York, 2013, pp. 125–162. https://doi.org/10.1007/978-1-4614-4541-8_3

[11] NASA Goddard Engineering and Technology Directorate, General Mission Analysis Tool (GMAT) Documentation. Information on https://documentation.help/gmat/Preface.html

[12] R. Opromolla, G. Fasano, G. Rufino, M. Grassi, Design of Relative Trajectories for in Orbit Proximity Operations, Acta Astronaut. 145 (2018) 342–356. https://doi.org/10.1016/j.actaastro.2018.01.062

[13] J. Vasconcelos, S. Gaggi, T. Amaral, C. Bakouche, A. Cotuna, A. Friaças, Close-Proximity Operations Design, Analysis, and Validation for Non-Cooperative Targets with an Application to the ClearSpace-1 Mission, Aerospace. 12 (2025), 67. https://doi.org/10.3390/aerospace12010067

[14] D. A. Vallado, W. D. McClain, Fundamentals of Astrodynamics and Applications, 2nd Ed., Space Technology Library. 12 (2001). Microcosm Press.

Materials Research Proceedings 69 (2026) 1012-1017 https://doi.org/10.21741/9781644904251-175

Development of a Robotic Testbed and Initial Testing for Machine Learning-Based Spacecraft Pose Estimation

Alessandro LOTTI[1,a *], Dario MODENINI[1,2,b], and Paolo TORTORA[1,2,c]

[1]Department of Industrial Engineering, Alma Mater Studiorum - Università di Bologna, Via Montaspro 97 and Via Baldassarre Carnaccini 10-12, 47121, Forlì, Italy

[2]Interdepartmental Centre for Industrial Research in Aerospace, Alma Mater Studiorum - Università di Bologna, Via Baldassarre Carnaccini 10-12, 47121, Forlì, Italy

[a]alessandro.lotti4@unibo.it, [b]dario.modenini@unibo.it, [c]paolo.tortora@unibo.it

Keywords: Vision-Based Navigation, Spacecraft Pose Estimation, Hardware-In-The-Loop Validation, Proximity Operations

Abstract. Vision-based navigation is a key enabling technology for autonomous in-orbit operations. However, current deep learning-based pose estimation algorithms face a critical sim-to-real gap, where performance degrades significantly when transitioning from synthetic training images to real ones. This has driven the need for ground-based validation facilities to bridge this gap. This paper presents a robotic testbed installed at the Microsatellites and Space Microsystems Laboratory of the University of Bologna for hardware-in-the-loop validation of vision-based spacecraft pose estimation algorithms. The facility features a 7-DoF robotic system, an optical table with a spacecraft mockup, a sun simulator, and an RGB camera, all integrated within a controlled dark room environment. The software architecture is based on ROS 2, with custom nodes enabling coordinated control of all system components. An initial application demonstrates the facility's capability through the development of a dataset generation pipeline for the ALMASat spacecraft mockup. While designed within constrained budget and space requirements, the testbed provides high precision and supports both fundamental research and educational activities in vision-based spacecraft navigation.

Introduction

In-orbit operations are receiving growing attention within the space community due to their significant economic and scientific prospects for future space missions. Vision-based navigation is widely considered one of the most promising technologies to support autonomous navigation in this framework. Recent advances in deep learning have enabled significant progress in spacecraft pose estimation (i.e. relative chaser-target position and attitude) from images. Despite these advances, current methods face a critical challenge: the sim-to-real gap, where algorithms trained on rendered images achieve high accuracy on synthetic data but show degraded performance on real images [1]. This has led to two key developments: fundamental research at the intersection between space engineering and computer vision, and the establishment of ground-based validation as an essential step in the development pipeline.

This paper presents an ongoing research project at the University of Bologna developing a compact robotic testbed for validating vision-based navigation algorithms (see Fig. 1). While smaller in scale compared to large institutional facilities, the system is designed to provide high precision within a constrained footprint and budget, supporting both research activities and teaching in this field. The following sections first review the main educational facilities that inspired this work, then describe the system components and the design and control approach, briefly present a dataset generation pipeline, and finally discuss the final hardware integration currently underway to complete the testbed.

Content from this work may be used under the terms of the Creative Commons Attribution 3.0 license. Any further distribution of this work must maintain attribution to the author(s) and the title of the work, journal citation and DOI. Published under license by Materials Research Forum LLC.

Materials Research Proceedings 69 (2026) 1012-1017 https://doi.org/10.21741/9781644904251-175

Robotic Testbeds in Academic Institutions

Ground-based testbed facilities for hardware-in-the-loop validation can be broadly classified into two categories: robotic-arm systems and floating platforms. The former typically offer 6-Degrees-of-Freedom (DoF) motion control, though they are limited by the manipulator's reach. On the other hand, floating platforms provide more realistic free-floating dynamics but generally with fewer controllable DoF.

Among university-operated robotic facilities, Stanford's Robotic Testbed for Rendezvous and Optical Navigation [2] is specifically designed for validating vision-based navigation algorithms. It features two KUKA robotic arms: one mounted to a ceiling linear rail and one ground-based. The testbed includes Vicon motion-tracking cameras and light sources that emulate Earth albedo and sunlight.

Similarly, the Zero-G Lab [3] at the University of Luxembourg features two collaborative robots (UR10e) mounted on linear rails, designed to emulate proximity operations in orbit. The facility includes a sun simulator and a motion-tracking system within a 5×3 m workspace.

Other examples include Politecnico di Milano [4] operating a 7-DoF robotic arm, though primarily focused on planetary landing scenarios, the University of Würzburg [5] with two KUKA manipulators, and the Research Center of the Polish Academy of Sciences [6] with a compact 2-DoF robotic arm.

Overview of the Robotic Testbed

These facilities have inspired the design of the testbed presented in this paper, which also results from trade-offs accounting for available budget and space constraints.

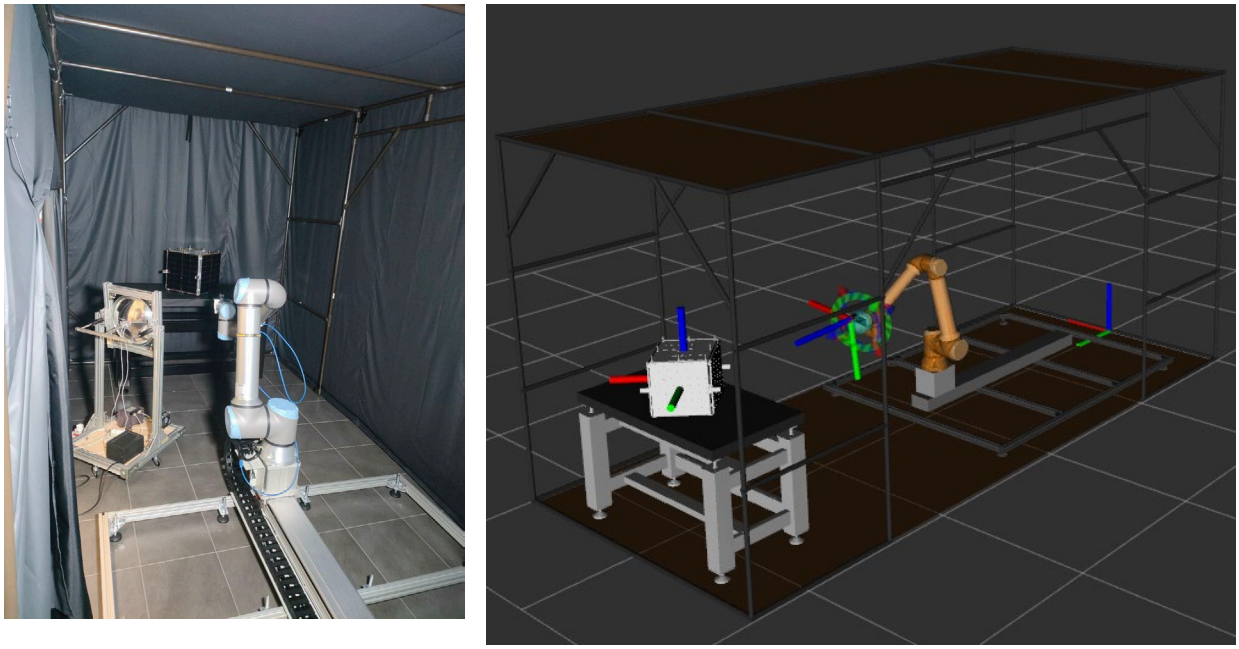


Figure 1: Overview of the robotic testbed: physical setup showing the UR10e cobot on linear rail, optical table with spacecraft mockup, and sun simulator within the dark room (left); RViz visualization displaying the main reference frames including camera frame, target body axes, and world frame (right)

The facility (see Fig. 1) features a 7-DoF robotic system, an optical table, a spacecraft mockup, a sun simulator, and an RGB camera, all integrated within a 4.4 × 2.0 m dark room. The room is enclosed by polyester blackout curtains, allowing fine control over lighting conditions, providing

Materials Research Proceedings 69 (2026) 1012-1017 https://doi.org/10.21741/9781644904251-175

a uniform background, and reducing secondary reflections to simplify image post-processing. A complete list of the current hardware is provided in Table 1.

Table 1: Main components of the robotic testbed

Component	Model	Specifications
Robotic arm	UR10e (Universal Robots)	6-DoF, 1.3 m reach, 12.5 kg payload, repeatability ±0.05 mm
7th axis (linear)	Slidekit 2.0 (Ewellix)	Ball screw drive, 1.8 m stroke, repeatability ±0.1 mm
Optical table	PFR60120-7 + B60120AX (Thorlabs)	1.2 × 0.6 × 0.76 m, high rigidity frame with damped optical surface
Mockup	ALMASat eng. model	33 × 33 × 31.5 cm
Sun simulator	Custom	Metal halide lamp (HMI), 400 W, 6200 K CCT
Camera	MER-231-41U3C (Daheng Imaging)	IMX249 CMOS sensor, 1920 × 1200 px
Dark room	Custom (OptoSigma)	4.4 × 2.0 × 2.2 m, polyester blackout curtain with acrylic backing

The sun simulator is a custom assembly of components originally used for characterizing hardware and numerical models for the CubeDyna ADCS testbed facility [7], developed by the Laboratory under ESA contract. The simulator features an HMI bulb and a parabolic reflector for light collimation, achieving an irradiance of 1000 to 1200 W/m^2.

The spacecraft mockup is a repurposed ALMASat engineering model [8]: a box-shaped spacecraft with side of 33 cm. The main bus is made of aluminum, while solar cells were emulated using glossy black vinyl, applied with a 3D-printed positioning mask that replicates the original cell geometry, over a copper backing. The mockup weighs approximately 8.5 kg, remaining within the cobot's payload envelope, and features a compatible mounting pattern, enabling installation on the end effector.

Software Integration and Control

The software stack controlling the robotic system is based on the Robot Operating System (ROS) 2 [9]. A workstation connects to the robotic arm's control box via Ethernet, the camera via USB 3.0, and the linear axis via a CAN-USB adapter. The seven joints are coordinated using MoveIt 2 [10], which handles inverse kinematics and collision-aware motion planning.

While the UR cobot integrates seamlessly into ROS workflows, the linear axis required a custom implementation leveraging the rail motor's support of the CANopen protocol. At the current deployment stage, the CAN connection is split between the workstation and the cobot's control box, as only target positions are currently controlled through ROS. Position control is performed in encoder counts. Dedicated ROS nodes bridge the low-level CAN communication, invoking the *cansend* and *candump* utilities for transmitting commands and reading responses and states, while interfacing with standard ROS and MoveIt interfaces. The software architecture can be conceptually organized into multiple layers:

- User interface and visualization: provides human-machine interface through RViz and live camera streaming, allowing the operator to monitor robot movements and camera view in real-time, as well as execute commands from the graphical interface.

Materials Research Proceedings 69 (2026) 1012-1017 https://doi.org/10.21741/9781644904251-175

- Motion planning and control: includes MoveIt 2 with three planning groups, one for the linear axis alone, one for the cobot alone, and one for joint control of both systems.

- Data integration and coordination: features custom rail nodes and a joint state merger that continuously collects joint states from the cobot and linear axis, republishing them for the 7-DoF MoveIt planning group.

- Drivers and device control: includes ROS nodes for each hardware component, managing device-specific protocols for the cobot, rail, and camera.

The cobot is always operated through ROS in remote mode. At system startup, a shell script powers on the robot, releases brakes, enables the linear axis motor by executing the CANopen state machine sequence, starts driver nodes, the joint state merger, MoveIt components, and finally launches RViz and camera streaming. After this startup sequence, the robotic system can be controlled through MoveIt move groups.

The main testbed components are modeled in the URDF file used by MoveIt for collision checking and kinematic chain reconstruction. However, discrepancies between actual component locations and the digital model are inevitable. Facility calibration is therefore crucial to reduce these drifts, specifically regarding hand-eye calibration (using OpenCV's *calibrateHandEye*), and determination of the mockup spacecraft position and orientation.

The latter is currently addressed by capturing an image of the mockup, setting a known pose for the robotic system, and manually selecting a set of landmarks matched to a CAD model of the spacecraft. The mockup pose relative to the camera is solved through PnP, while its absolute pose in the world frame is obtained through the robot's kinematic chain.

Towards the ALMASat Image Dataset

The first application of the testbed will be the development of a dataset for validating vision-based pose estimation algorithms. The ALMASat mockup, with its near-perfect symmetry, introduces additional complexity compared to existing datasets. To this end, a software pipeline has been developed with two main components. First, it enables the creation of a synthetic dataset using Blender, following a procedure closely aligned with the one illustrated in [11]. Second, it allows the collection of a real image dataset by separating pose planning and image acquisition steps.

The real dataset acquisition follows a multi-stage procedure. Initially, the working volume is discretized into a grid structure. For each cell center, the algorithm computes a look-at pose where the camera optical axis points towards the mockup's center. Using this target pose as reference, random variations are generated by adding small position jitter and randomly sampling rotation axes and angles. The script verifies pose reachability by sending inverse kinematics requests through MoveIt. If a solution is found, the corresponding joint values are exported for execution. A second script then executes the reachable poses, commanding joint positions with tolerances of 0.0046° for the cobot's joints and 0.1 mm for the linear guide. At the moment of image capture, the relative camera-mockup pose is recomputed to account for residual positioning errors arising from the difference between commanded and executed joint positions. The final step involves image post-processing through background removal using a Segment Anything Model [12]. The neural network is guided by a ground truth bounding box obtained by projecting the CAD wireframe model into the image using the known pose. Sample images from the dataset are illustrated in Fig. 2.

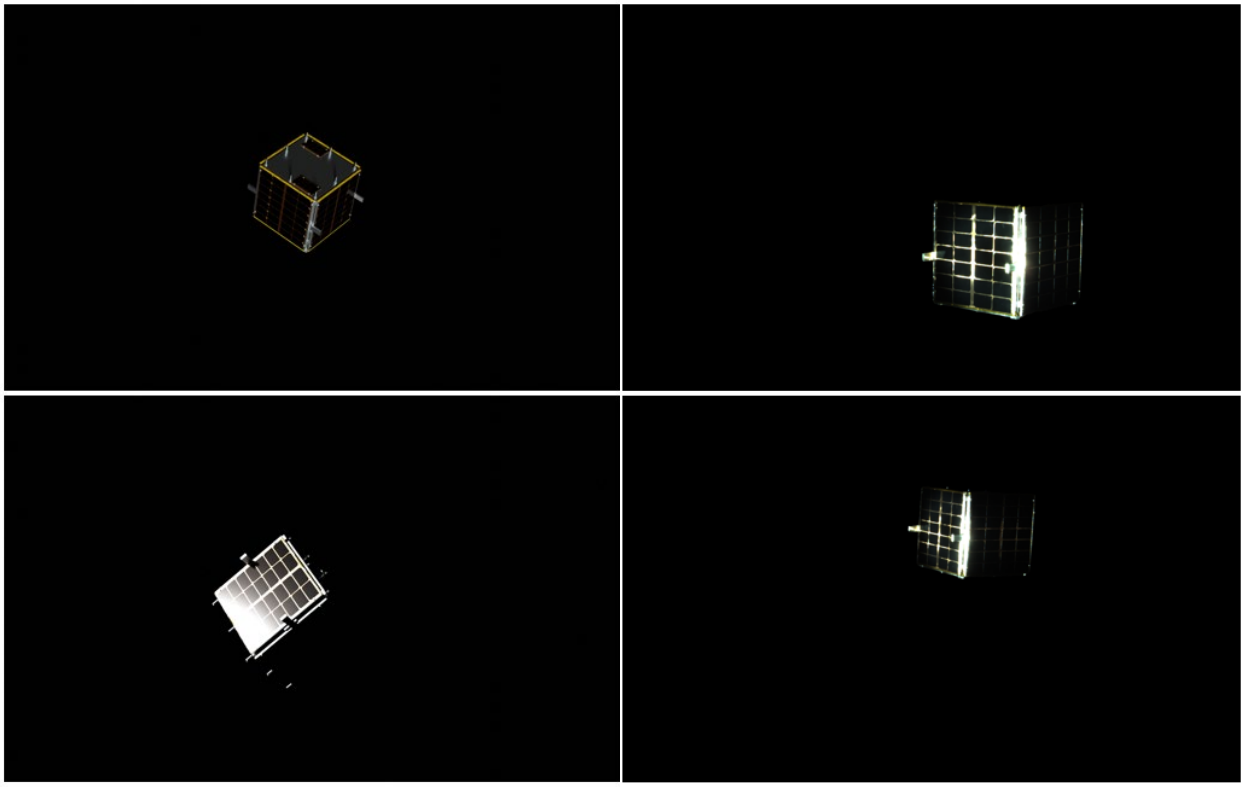


Figure 2: Representative samples from the ALMASat dataset: synthetic rendered images (left) and real images acquired with the testbed (right)

Conclusions and Future Work

This paper presented the development of a robotic testbed facility for hardware-in-the-loop validation of vision-based pose estimation algorithms at the University of Bologna. The main hardware and software components have been integrated and briefly described in the text, along with a dataset generation pipeline and initial samples demonstrating an early application of the facility.

However, the facility development is still ongoing. A set of four OptiTrack cameras has been installed and is being integrated into the ROS framework to provide an external pose reference. Additionally, new cameras and optics have been acquired to improve the depth of field compared to the current setup and to extend the facility with event cameras. These enhancements will further support algorithm validation and facilitate research and teaching activities in vision-based spacecraft navigation.

Acknowledgment

This work was carried out within the Space It Up! project funded by the Italian Space Agency (ASI) and the Italian Ministry of University and Research (MUR) under contract No. 2024-5-E.0, CUP No. I53D24000060005.

References

[1] T. H. Park, M. Märtens, M. Jawaid, Z. Wang, B. Chen, T.-J. Chin, D. Izzo, S. D'Amico, Satellite pose estimation competition 2021: results and analyses, Acta Astronautica 204 (2023) 640–665. https://doi.org/10.1016/j.actaastro.2023.01.002

[2] T. H. Park, J. Bosse, S. D'Amico, Robotic testbed for rendezvous and optical navigation: multi-source calibration and machine learning use cases, in: Proc. 2021 AAS/AIAA Astro-dynamics Specialist Conf., Big Sky, Virtual, 2021. https://doi.org/10.48550/ARXIV.2108.05529

[3] M. Olivares-Mendez, M. R. Makhdoomi, B. C. Yalçın, Z. Bokal, V. Muralidharan, M. Ortiz Del Castillo, V. Gaudilliere, L. Pauly, O. Borgue, M. Alandihallaj, J. Thoemel, E. Skrzypczyk, A. Rathinam, K. R. Barad, A. E. R. Shabayek, A. M. Hein, D. Aouada, C. Martinez, Zero-G Lab: A multi-purpose facility for emulating space operations, J. Space Saf. Eng. 10 (4) (2023) 509-521. https://doi.org/10.1016/j.jsse.2023.09.003

[4] P. Lunghi, M. Ciarambino, L. Losi, M. Lavagna, A new experimental facility for testing of vision-based GNC algorithms for planetary landing, in: Proc. 10th Int. ESA Conf. on Guidance, Navigation & Control Systems, 2017.

[5] L. Regoli, C. Herrmann, K. Ravandoor, K. Schilling, New testing facility for proximity operations in space, IFAC Proc. Vol. 46 (19) (2013) 353–358. https://doi.org/10.3182/20130902-5-DE-2040.00030

[6] T. Rybus, T. Barcinski, J. Lisowski, J. Nicolau-Kuklinski, K. Seweryn, M. Ciesielska, K. Grassmann, J. Grygorczuk, M. Karczewski, M. Kowalski, et al., New planar air-bearing microgravity simulator for verification of space robotics numerical simulations and control algorithms, in: Proc. 12th ESA Symposium on Advanced Space Technologies in Robotics and Automation (ASTRA), 2013

[7] A. Curatolo, D. Modenini, G. Curzi, A. Lotti, D. Pecorella, E. Strollo, A. Locarini, A. Hyslop, D. Oddenino, The nanosatellite-class attitude control facility at ESA-ESTEC, in: Proc. 10th EUCASS - 9th CEAS Aerospace Europe Conf., 2023. https://doi.org/10.13009/EUCASS2023-760

[8] P. Tortora, ALMASat-1 launch onboard the Vega maiden flight, in: Proc. 20th AIDAA National Congress, AIDAA, Milano, Italy, 2009, pp. 1–14.

[9] S. Macenski, T. Foote, B. Gerkey, C. Lalancette, W. Woodall, Robot Operating System 2: design, architecture, and uses in the wild, Sci. Robot. 7 (66) (May 2022). https://doi.org/10.1126/scirobotics.abm6074

[10] D. T. Coleman, I. A. Sucan, S. Chitta, N. Correll, Reducing the barrier to entry of complex robotic software: a MoveIt! case study, J. Softw. Eng. Robot. 5 (1) (2014) 3–16. https://doi.org/10.6092/JOSER_2014_05_01_P3

[11] A. Lotti, D. Modenini, P. Tortora, M. Saponara, M. A. Perino, Deep learning for real-time satellite pose estimation on tensor processing units, Journal of Spacecraft and Rockets 60 (3) (2023) 1034–1038. https://doi.org/10.2514/1.A35496

[12] A. Kirillov, E. Mintun, N. Ravi, H. Mao, C. Rolland, L. Gustafson, T. Xiao, S. Whitehead, A. C. Berg, W.-Y. Lo, P. Dollár, R. Girshick, Segment Anything, in: Proc. 2023 IEEE/CVF Int. Conf. on Computer Vision (ICCV), IEEE, Paris, France, 2023, pp. 3992–4003. https://doi.org/10.1109/ICCV51070.2023.00371

Materials Research Proceedings 69 (2026) 1018-1023 https://doi.org/10.21741/9781644904251-176

Chemical Emissions and Near-Field Dispersion of Suborbital Carriers in Conceptual Design

Fabrizio BORGNA[1,a *], Roberta FUSARO[1,b], Davide FERRETTO[1,c], Sara GNACCARINI[1,d] and Nicole VIOLA[2,e]

[1]Department of Aerospace Engineering, Politecnico di Torino, Corso Duca degli Abruzzi 24, 10129 Turin, Italy

[2]Department of Management and Production Engineering, Politecnico di Torino, Corso Duca degli Abruzzi 24, 10129 Turin, Italy

[a]fabrizio.borgna@polito.it, [b]roberta.fusaro@polito.it, [c]davide.ferretto@polito.it, [d]sara.gnaccarini@studenti.polito.it, [e]nicole.viola@polito.it

Keywords: Suborbital vehicles, Emission Estimation, Pollutants Dispersion, Local Air Quality, Environmental Impact

Abstract. As suborbital flights and space tourism move from promise to practice, quantifying their near-ground emissions is essential for responsible deployment and regulatory assessment. This study develops a reproducible, end-to-end methodology to quantify propulsive emissions and near-field plume dispersion for a suborbital carrier aircraft. The methodology is demonstrated on a representative point-to-point mission from the Italian Taranto–Grottaglie spaceport, transporting Virgin Galactic's SpaceShipTwo to approximately 15 km prior to release. Objectives are to generate phase-resolved emission source terms and translate them into site-specific ground concentrations to support early design and regulatory assessment. The methodology integrates high-fidelity mission simulations with the analytical BFFM2 emissions-estimation method to compute chemical source terms in an "idle-to-idle" approach, distinguishing fuel-proportional species (CO_2, H_2O, SOx), from power-dependent species (CO, NO_x, HC, PM). For each Landing and Take-Off (LTO) cycle phase, phase-averaged emission rates are represented as continuous elevated point sources and fed into an analytical Gaussian-plume model to compute spatially resolved concentrations C(x,y,z) of pollutants and greenhouse gases. The methodology is benchmarked against airport dispersion measurements and validated by cross-comparison with high-fidelity pollutant dispersion simulations. The proposed framework provides regulators and designers with a validated, transparent tool for early environmental evaluation of reusable suborbital operations, enabling informed decisions on site selection and operational constraints.

Introduction

Suborbital spaceflight is an emerging segment offering promising scientific and commercial opportunities, yet its environmental impacts remain poorly characterized. As air traffic and space tourism grow, rigorous evaluation of propulsive emissions has become critical, specifically for near-ground air-quality assessments [1,2,3,4]. In this regard, the present paper discloses a conceptual design methodology to quantify aircraft emissions and near-field plume dispersion for a suborbital launch system. In a representative point-to-point (A-to-A) mission from the Taranto-Grottaglie Italian spaceport - currently under evaluation by Italian and European authorities as a potential host site for Virgin Galactic's first European suborbital flights [5], chemical emissions from the WhiteKnightTwo (WK2) carrier aircraft are quantified and ground-level pollutant concentrations are estimated during transport of the SpaceShipTwo (SS2) suborbital vehicle to ~15 km altitude before release [6,7]. High-fidelity mission simulations provided time-resolved fuel flow, thrust and atmospheric data, which are combined with ICAO-certified emission indices [8]

Content from this work may be used under the terms of the Creative Commons Attribution 3.0 license. Any further distribution of this work must maintain attribution to the author(s) and the title of the work, journal citation and DOI. Published under license by Materials Research Forum LLC.

Materials Research Proceedings 69 (2026) 1018-1023 https://doi.org/10.21741/9781644904251-176

to derive fuel-flow-adjusted emission trends at altitude. Specifically, the BFFM2 [9,10] emissions estimation method is adopted to compute chemical emissions in a "idle-to-idle" approach. Then, local air quality impact assessment is carried out. A simplified Gaussian-plume model estimating NO_x dispersion from the aircraft near the runway is implemented [11,12]. The plume model computes the concentration field C(x,y,z) given emission rate Q and local meteorological conditions [13,14,15,16]. Crucially, this implementation is validated against published airport NO_x measurements and dispersion studies, showing reasonable agreement [17]. The presented conceptual design methodology integrates suborbital mission analysis with environmental assessment techniques, constituting a novel contribution to the field.

Methodology

The adopted methodology establishes a coherent and reproducible protocol that integrates high-fidelity mission simulations with analytical models for emissions estimation and atmospheric dispersion, as illustrated in Figure 1. The objective is to characterize the environmental footprint of the WK2 suborbital carrier aircraft during all operational phases.

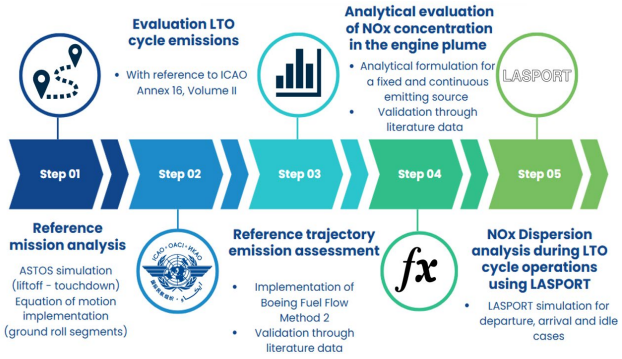


Fig. 1 - Air quality impact assessment methodology

The first step involves the simulation of the reference mission using a high-fidelity trajectory optimization environment. In this case, the authors selected the Analysis, Simulation and Trajectory Optimization Software for Space Applications (ASTOS) [18]. While ASTOS accurately models the airborne phases of flight, it does not explicitly simulate ground operations. To complement this, a dedicated simulation based on the equations of motion and Raymer's semi-empirical formulations was implemented to model the take-off and landing ground rolls, thereby enabling a complete "gate-to-gate" representation of the carrier mission [19]. This approach provides time-resolved outputs of fuel flow, thrust, engine operating conditions, and atmospheric parameters along the overall flight path. These data constitute the dynamic basis for the subsequent emission calculations. Chemical emissions are computed using a dedicated analytical model, namely the Boeing Fuel Flow Method 2 (BFFM2) [10]. This methodology relies on semi-empirical correlations documented in the literature, enabling the estimation of chemical emissions. To derive the Emission Indices (EI) of pollutants and greenhouse gases, expressed as grams of emitted species per kilogram of fuel burned, the BFFM2 procedure is applied as follows: (i) the flight-level fuel flow is corrected to an equivalent sea-level value; (ii) the corrected fuel flow is then used to infer sea-level emission indices through interpolation of tabulated data from the ICAO Engine Emissions Databank [8]; and (iii) the sea-level EIs are subsequently adjusted with altitude-dependent correction factors documented for each chemical species. This procedure yields altitude-corrected emission indices along the entire flight trajectory. For near-field air-quality evaluation, the disclosed methodology employs an analytical Gaussian-plume model to estimate pollutant dispersion and ground-level concentration fields [14,15,16]. Each LTO phase is modeled as a continuous elevated point source emitting a constant phase-averaged mass flow rate Q derived

Materials Research Proceedings 69 (2026) 1018-1023 https://doi.org/10.21741/9781644904251-176

from the emission calculations. The spatio-temporal concentration distribution $C(x, y, z, t)$ at any downwind location is given by the Gaussian-plume simplified formulation reported in Eq.1.

$$C(x,y,z,t) = \frac{Q}{(4\pi t)^{\frac{3}{2}}\sqrt{K_x K_y K_z}} \exp\left(\frac{(x-x')^2}{4K_x t} - \frac{(y-y')^2}{4K_y t} - \frac{(z-z')^2}{4K_z t}\right) \quad (1)$$

Where the K_i are the atmospheric turbulence coefficients calculated from the dispersion parameters obtained using Green's formulations [16]. The atmospheric dispersion model is based on the analytical solution of the advection-diffusion equation under the assumption of constant diffusion coefficients. However, to better reflect atmospheric conditions, the lateral and vertical diffusion parameters were treated as functions of distance, using the Pasquill-Gifford formulations [13]. This approach effectively adapts the Gaussian solution to account for atmospheric turbulence and stability variations. After defining a spatial grid in the vicinity of the emission points representing the LTO cycle phases, it is possible, for each grid node, to (i) calculate the concentration at each time step during the phase, and (ii) determine the mean concentration over the entire phase duration at each grid node. The spatial grid considered is 30 m wide in each direction and centered on the emission source, where the concentration values are the highest. Verification and validation represent the final step of the proposed workflow. Emission and dispersion results are benchmarked against published airport studies and compared with existing assessments of the WK2 aircraft and other large twin-fuselage carriers. Specifically, to validate the concentration results near the spaceport obtained with the simplified Gaussian plume model, high-fidelity dispersion analyses of WK2 NO_x emissions are performed using the commercial software LASPORT [20]. LASPORT represents the standard modeling tool adopted by the German Airport Association and has been applied in several national and international studies (e.g., [21,22]).

Results and Discussion

To address social acceptance concerns among communities surrounding Taranto-Grottaglie Airport, a comparative analysis was performed between the WK2 and the Boeing 747 LCF Dreamlifte, which operates weekly flights from Grottaglie to Charleston to transport fuselage sections of the Boeing 787 Dreamliner. Since LTO emissions and pollutants dispersion are the primary contributors to local air quality impacts, this comparison demonstrates that A-to-A suborbital operations could be integrated into conventional civil aviation without significant effects on nearby populations. Figure 2 compares the total mass of emissions produced by the two aircraft during their LTO cycles.

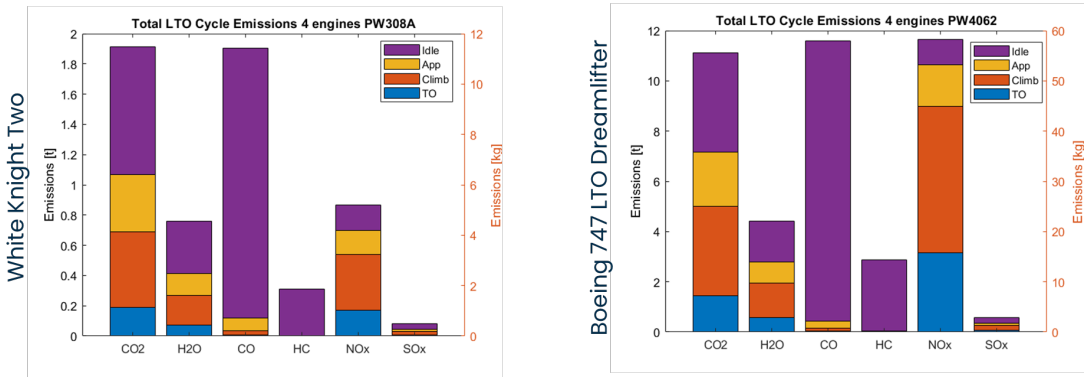
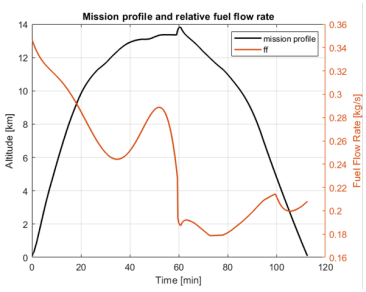


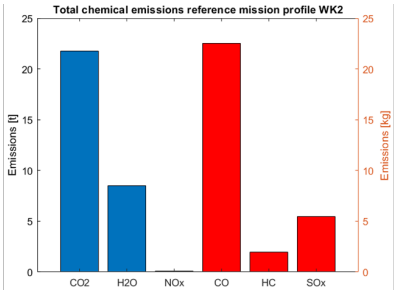
Fig. 2 - Total LTO cycle emissions, WK2 vs Dreamlifter

The Boeing 747 LCF Dreamlifter, equipped with four Pratt & Whitney PW4062 turbofan engines, exhibits similar emission distribution trends but considerably higher total emissions. For

Materials Research Proceedings 69 (2026) 1018-1023 https://doi.org/10.21741/9781644904251-176

both aircraft, CO_2, H_2O, CO, SO_x, and HC emissions are dominant during the idle phase, mainly due to its long duration, whereas NO_x emissions peak during the climb phase as a result of the combination of intermediate phase duration and higher engine power settings. This comparison highlights that suborbital A-to-A operations, such as those performed by WK2, would have a significantly smaller impact on local air quality than existing large transport aircraft activities, thereby supporting their social and environmental acceptability within civil aviation frameworks. Moreover, total aircraft emissions along the reference trajectory were calculated through the BFFM2 method for the WK2. The trajectory, simulated and validated in the ASTOS environment and complemented by analytically modelled ground phases (taxi, take-off, and landing rolls), is shown in Figure 3 together with emission trends compared with documented FAA estimates [17].





Emissions	Estimated Emissions	Documented (FAA) Emissions
CO_2[t]	21.746	22.962
H_2O [t]	8.477	9.12
NO_x [t]	0.088	0.091
CO [kg]	22.54	12.05
SO_x [kg]	5.47	9.43
HC [kg]	1.95	-

*Fig. 3 - Reference trajectory and total emissions comparison for the WK2 [**17**]*

The discrepancy between the two datasets stems from different mission assumptions: the present work considers idle-to-idle operations, including ground phases, and models variable fuel-flow rates during climb and approach instead of assuming constant power settings. Overall, BFFM2 results demonstrate good consistency. Finally, based on the LTO cycle emission results for both the WK2 and the Dreamlifter aircraft, air quality simulations were performed to assess NO_x dispersion in the Taranto-Grottaglie Spaceport area. The first stage of the analysis involved implementing a simplified analytical model to estimate the average NO_x concentration within the engine plume during the take-off phase. This concentration was calculated using the formulation reported in Eq. (1), derived from the simplified Gaussian plume model, assuming a constant emission mass flow rate Q from a single static source over a 1-minute period representing the take-off duration. The resulting concentrations were time-averaged across the defined spatial grid. The maximum point concentrations for both aircraft occur at the emission source, with corresponding values of 9.9 $\mu g/m^3$ for the WK2 and 153.7 $\mu g/m^3$ for the Dreamlifter. Since the LTO cycle emissions of the Dreamlifter are higher than those of WK2, it is expected and has been confirmed that NO_x concentrations are also higher during the take-off phase. The second stage of the air quality assessment validated the WK2 NO_x estimates from the simplified Gaussian plume model through high-fidelity dispersion simulations using the commercial software LASPORT. Three operational cases were simulated (departure, arrival, and idle) considering a headwind of 3 m/s for both departure and arrival. Near-ground concentrations averaged between 0 and 3 m above ground were computed with a 25 m horizontal resolution and recorded as consecutive 10-minute averages. Figure 4 presents NO_x concentration results for three consecutive 10-minute intervals following take-off. According to the EU Ambient Air Quality Directive 2008/50/EC [23], the annual mean NO_2 concentration must not exceed 40 µg/m³, and the hourly mean must remain below 200 µg/m³. The NO_x concentrations resulting from WK2 operations are well below these regulatory thresholds, further validating the simplified plume model results.

Materials Research Proceedings 69 (2026) 1018-1023 https://doi.org/10.21741/9781644904251-176

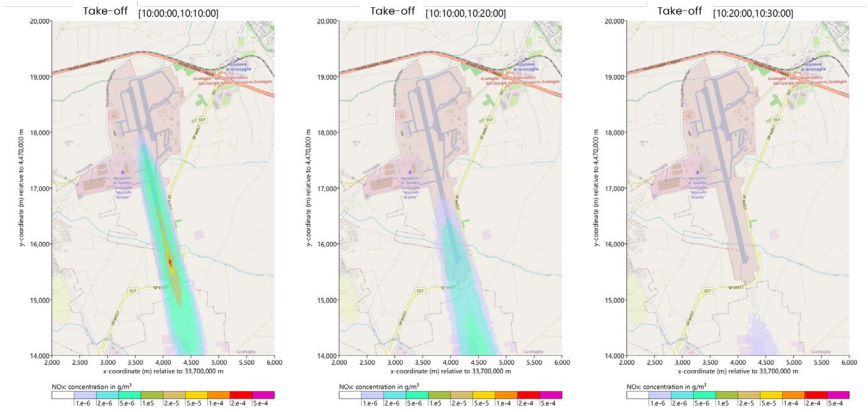


Fig. 4 - LASPORT NO_x concentration results for three consecutive 10-minute intervals following take-off

Conclusions

This work fits within the emerging European context of growing interest in suborbital flight. The study investigated the environmental impact of an A-to-A suborbital mission operating from Taranto-Grottaglie Airport, quantifying chemical emissions of the WK2 carrier enabling SS2's ascent to microgravity and assessing their influence on local air quality at ground level. The air-quality impact was found to be lower than expected, remaining below that of existing operations at the same airport. Consistently with LTO cycle overall emissions comparisons, the maximum NO_x concentration during the WK2 take-off phase is lower than that generated by the Dreamlifter, which performs weekly flights at the reference airport. To validate the concentration results obtained from the simplified Gaussian plume model, a subsequent dispersion analysis of the departure, approach, and idle phases were conducted using the LASPORT tool. The results describe the temporal evolution of NO_x concentrations over 10-minute intervals and constitute an initial step toward broader simulations that account for all airport-related traffic over a representative day at Taranto-Grottaglie Airport. In summary, this integrated workflow translates detailed flight-performance data into quantifiable environmental metrics through a combination of high-fidelity simulation, analytical emissions modelling, and Gaussian dispersion analysis. It provides an adaptable, transparent, and reproducible tool for assessing the atmospheric impact of suborbital carrier operations in mixed-traffic airspace. Beyond its application to the Grottaglie case study and aligned with emerging suborbital regulatory requirements in Italy and Europe, this work delivers a validated methodology for assessing the environmental footprint of reusable launch vehicles in mixed-traffic airspace., bridging the gap between aerospace design and environmental compliance.

References

[1] International Civil Aviation Organization, Local air quality. https://www.icao.int/environmental-protection/LAQ.

[2] J. Mettrop, 2019 World Radiocommunication Conference agenda item 1.6: Sub-orbital vehicles [white paper], FSMP WG17 / WRC-23 workshop materials, 2023. https://www.itu.int/dms_pub/itu-r/md/19/wshwrc23/c/R19-WSHWRC23-C-0023!!PDF-E.pdf.

[3] Intergovernmental Panel on Climate Change (IPCC), Aviation and the Global Atmosphere: A Special Report of IPCC Working Groups I and III, Cambridge University Press, Cambridge, UK, 1999.

[4] International Civil Aviation Organization, Annex 16 to the Convention on International Civil Aviation — Environmental Protection, Volume II: Aircraft Engine Emissions, 4th ed., ICAO, July 2017.

[5] Ente Nazionale Aviazione Civile (ENAC), Regolamento per le operazioni suborbitali e di accesso allo spazio (SASO), Ed. 0.0 Rev. 0, 20 November 2023.
[6] Virgin Galactic, WK2 Data Brochure, Oct. 2020.
[7] National Transportation Safety Board, In-Flight Breakup During Test Flight, Scaled Composites SpaceShipTwo, California, October 31, 2014, AAR-15/02, Washington, DC, 2015.
[8] European Union Aviation Safety Agency (EASA), ICAO Aircraft Engine Emissions Databank.
[9] D. DuBois, G. C. Paynter, "Fuel Flow Method 2 for Estimating Aircraft Emissions", SAE Technical Paper 2006-01-1987, SAE International, 2006. DOI: 10.4271/2006-01-1987.
[10] S. L. Baughcum, T. G. Tritz, S. C. Henderson, D. C. Pickett, Scheduled civil aircraft emission inventories for 1992: Database development and analysis, NASA Contractor Report (CR) 4700, NASA Langley Research Center, 1996.
[11] S. P. Arya, Air Pollution Meteorology and Dispersion, Oxford University Press, New York, 1999. ISBN: 9780195073980.
[12] D. B. Turner, Workbook of Atmospheric Dispersion Estimates (EPA–AP-26), U.S. Department of Health, Education, and Welfare / EPA, 1970.
[13] G. A. Davidson, A modified power law representation of the Pasquill–Gifford dispersion coefficients, Journal of the Air & Waste Management Association, 40(8), pp.1146–1147, 1990.
[14] F. A. Gifford, Turbulent diffusion-typing schemes: a review, Nuclear Safety, 17(1), pp.68–86 (1976).
[15] J. Yang, L. Li, X. Zheng, H. Liu, F. Li, and Y. Xiao, Pollutant dispersion of aircraft exhaust gas during the landing and takeoff cycle with improved Gaussian diffusion model, Atmosphere, 15(10) (2024) 1256. https://doi.org/10.3390/atmos15101256
[16] A. E. S. Green, R. P. Singhal, and R. Venkateswar, Analytic extensions of the Gaussian plume model, Journal of the Air Pollution Control Association, 30(7) (1980) 773–776.
[17] Federal Aviation Administration (FAA), Final Environmental Assessment for Mojave Air and Space Port and SpaceShipTwo; Final EA and FONSI (Office of Commercial Space Transportation), May 2012.
[18] dSPACE GmbH. Cooperating partners: Astos solutions.
[19] D. P. Raymer, Aircraft Design: A Conceptual Approach, 6th ed., American Institute of Aeronautics and Astronautics (AIAA), Reston, VA, 2018.
[20] Janicke Consulting, LASPORT: A Program System for the Calculation of Airport-Related Pollutant Emissions and Concentrations in the Lower Atmosphere, Technical Report, Version 2.3, Janicke Consulting, Überlingen, Germany, December 2018.
[21] U. Janicke, Application of effective conversion rates between NO and NO_2 in a standard airport dispersion model system, Atmosphere, 15(4) (2024) 431–447.
[22] U. Janicke, E. Fleuti, and I. Fuller, LASPORT – A model system for airport-related source systems based on a Lagrangian particle model, in: Proceedings of the 11th International Conference on Harmonisation within Atmospheric Dispersion Modelling for Regulatory Purposes, Cambridge, UK, 2007, pp. 352–356.
[23] European Commission, EU Air Quality Standards, 2024. Available from: https://environment.ec.europa.eu/topics/air/air-quality/eu-air-quality-standards_en.

Materials Research Proceedings 69 (2026) 1024-1029 https://doi.org/10.21741/9781644904251-177

Galileo Space Service Volume Analysis for Earth Orbit Rising Missions

Andrea PICCOLO[1,a *], Francesco MENZIONE[1,b]

[1]European Commission, Joint Research Centre (JRC), 21027 Ispra, Italy

[a]andrea.piccolo@ec.europa.eu, [b]francesco.menzione@ec.europa.eu

Keywords: Space Service Volume (SSV), Galileo, GNSS, Earth Orbit Rising (EOR), Electrical thrust, Spacecraft Manoeuvre, Orbit Determination

Abstract. Global Navigation Satellite Systems (GNSS) are becoming key enablers for autonomous operations beyond Low Earth Orbit (LEO). The Galileo Space Service Volume (SSV) offers strong potential for Earth Orbit Rising (EOR) missions, where spacecraft ascend from LEO to higher orbits using electric propulsion. This paper evaluates navigation performance achievable within the Galileo SSV for next-generation EOR missions using the JRC Integrated SSV Test Bench, which integrates realistic signal modelling, antenna patterns, and receiver dynamics. Two representative scenarios are analysed: a LEO–MEO transfer for a Galileo Second Generation satellite and a LEO–GEO transfer for a SATCOM platform. Results demonstrate that autonomous orbit determination is feasible with single-antenna configurations and moderate receiver sensitivity, confirming Galileo's readiness, either alone or in conjunction with GPS interoperability to support autonomous orbit raising and guide future receiver design.

Introduction

Global Navigation Satellite Systems (GNSS) has evolved from terrestrial navigation to an essential element of modern space operations. Beyond their widespread use in LEO, systems like Galileo and GPS now extend coverage into Medium Earth Orbit (MEO), Geostationary Orbit (GEO), and even cis-lunar regions. The operational domain supporting this is the Space Service Volume (SSV) [1]. Among emerging applications, Earth Orbit Rising (EOR)—the gradual ascent from LEO to higher orbits via low-thrust electric propulsion—represents a milestone toward fully autonomous space operations [2]. Electric propulsion provides flexibility, efficiency, and cost-effectiveness but also introduces new navigation challenges: weak GNSS visibility, prolonged thrusting, and frequent attitude steering. Autonomous GNSS-based navigation enables real-time manoeuvre planning and reduced ground dependency. While SSV applications have been studied for lunar or deep-space operations, less attention has been given to EOR missions using Galileo alone. Assessing Galileo-only performance within the SSV is essential for designing next-generation spaceborne GNSS receivers. This paper provides an updated Galileo SSV performance analysis using the European Commission's Joint Research Centre (JRC) Integrated SSV Test Bench (JRC-ISSVTB) environment [3], focusing on two reference cases: (i) a LEO to MEO transfer for a Galileo Second Generation satellite [4] , and (ii) a LEO to GEO transfer for a next-generation SATCOM platform [5].

Galileo Scenario Definition and Orbit Profiles

Scenario A – LEO to MEO Transfer (Galileo Second Generation)

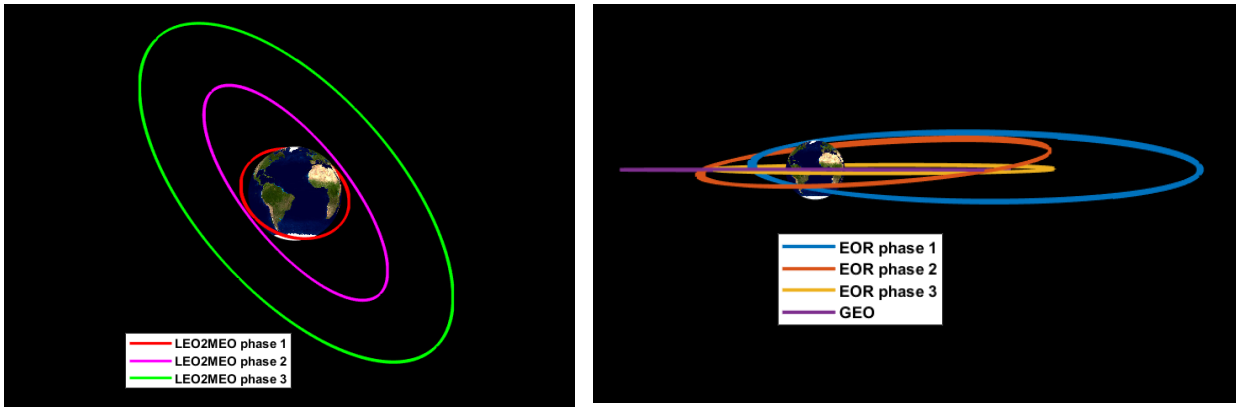
This scenario models a possible autonomous transfer of a Galileo Second Generation (G2G) satellite from a 1220 km, 56° circular parking orbit to its nominal MEO altitude of 23,222 km [4]. The spacecraft uses a single ion thruster (thrust 0.180 N, Isp 3829 s) to complete a one-year spiral transfer. The ascent is divided into three representative LEO to MEO (LEO2MEO) phases (Fig. 1a): a low-orbit phase (≈1220 km), an intermediate phase (≈11,860 km), and a high-altitude phase

Content from this work may be used under the terms of the Creative Commons Attribution 3.0 license. Any further distribution of this work must maintain attribution to the author(s) and the title of the work, journal citation and DOI. Published under license by Materials Research Forum LLC.

Materials Research Proceedings 69 (2026) 1024-1029 https://doi.org/10.21741/9781644904251-177

(≈21,813 km). Beyond 10,000 km altitude, GNSS visibility decreases, making spillover on the main lobe reception essential for continuous navigation—an ideal condition for assessing Galileo SSV coverage during orbit-raising operations.

Scenario B – LEO to GEO Transfer for a Next-Generation SATCOM Platform
This case represents an all-electric transfer of a geostationary communications spacecraft [2], [5], from a 700 km, 5° near-equatorial high elliptical Geostationary Transfer Orbit (GTO) to GEO at 35,786 km. The platform employs four Hall-effect thrusters (total thrust 0.35 N, Isp = 1700 s) operated in duty-cycled pairs over about 180-day transfer including eclipses and coasting phases. A sun-tracking attitude induces frequent slews and variable GNSS antenna pointing. Above 25,000 km, only a few Galileo satellites remain visible through side-lobes, yet multi-constellation (e.g. Galileo + GPS) reception and high-sensitivity front ends can sustain navigation continuity. Fig. 1b shows three main LEO to GEO transfer phases, namely EOR Phase 1, 2 and 3, up to the final equatorial GEO orbit.

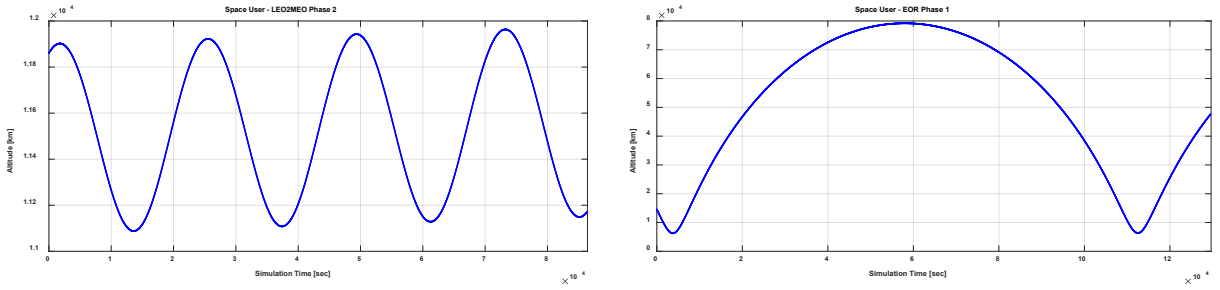


a) b)

Fig. 1 – Simulated EOR trajectories a) to MEO and b) to GEO

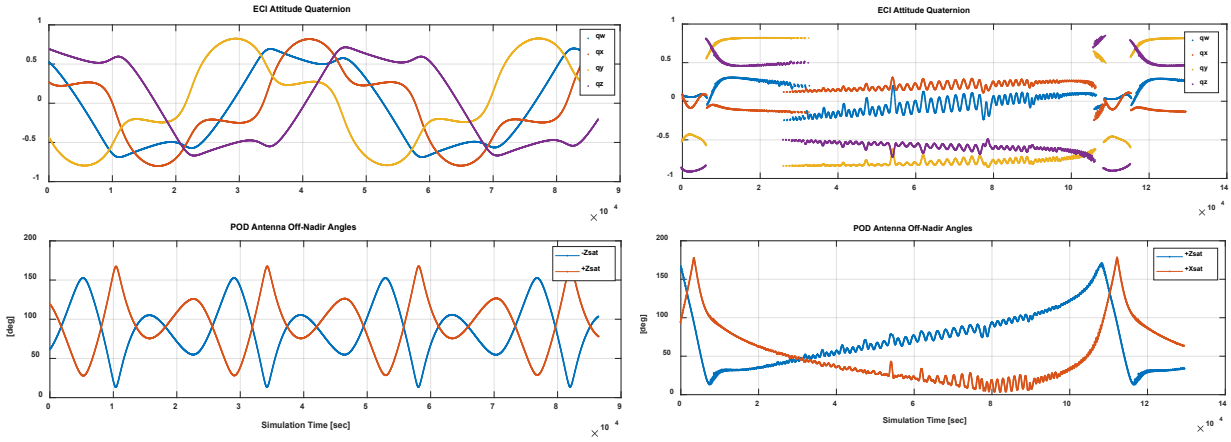
In both EOR scenarios, spacecraft traverse a wide range of altitudes, and the performance of GNSS-based navigation strongly depends on the geometry and visibility of transmitting satellites within the SSV. At LEO altitudes, direct line-of-sight to multiple satellites is ensured, while at MEO and GEO, only a limited number remain visible. The signal environment is characterized by two main reception mechanisms: main-lobe reception, from Earth-facing antennas, and side-lobe reception, from the residual energy radiated outside the nominal beam. As altitude increases beyond the GNSS constellation itself, users gradually move from the "Earth-facing" region (main lobe coverage) into the "above-the-constellation" region (side-lobe and back-lobe coverage). In this work the LEO2MEO phase 2 and EOR Phase 1 shown in Fig. 1 have been considered to evaluate the Galileo SSV performance under different manoeuvre planning, thrust control, and GNSS receiver antenna pointing configurations. The LEO–MEO Phase 2 represents the intermediate ascent segment toward the nominal Galileo MEO altitude, with an initial orbital altitude of approximately 11,860 km (Fig. 2a). The transfer follows a spiralling low-thrust trajectory (Fig. 3a), and both zenith ($-Z_{sat}$) and nadir ($+Z_{sat}$)-facing antennas are considered for signal reception [1]. The EOR Phase 1 case starts from a highly elliptical orbit with perigee and apogee altitudes of about 6,200 km and 79,300 km, respectively (Fig. 3b). A high-gain antenna is mounted on the $+Z_{sat}$ axis, complemented by a secondary along-track ($+X_{sat}$) antenna [5]. The spacecraft attitude is continuously adjusted according to thrust direction and power constraints, as shown in Fig. 3b. Fig. 3 shows the ECI J2000 attitude quaternions and the corresponding precise orbit determination (POD) antenna off-nadir behaviour for both orbital regimes.

Materials Research Proceedings 69 (2026) 1024-1029 https://doi.org/10.21741/9781644904251-177



a) b)

Fig. 2 – Space User Altitude: a) LEO2MEO case, b) EOR case



a) b)

Fig. 3 – Space User Attitude and POD antenna Off-Nadir: a) LEO2MEO case, b) EOR case

The off-nadir angle is monitored throughout the simulation to assess the impact of attitude steering on GNSS signal visibility and received power, a critical factor during electric-thrust phases where vectoring manoeuvres can significantly modify antenna orientation with respect to the GNSS constellation.

Simulation Environment and Configuration

JRC Integrated SSV Test Bench (JRC-ISSVTB)

Developed by the JRC, the JRC-ISSVTB integrates orbit and attitude dynamics, GNSS signal simulation, and receiver-level processing for SSV analysis [3]. It includes orbit propagation, realistic Galileo antenna patterns [6], and receiver modelling under weak-signal conditions. For this work, the software-only configuration was used, employing the same signal and geometry models as the hardware-in-the-loop (HIL) setup. Future work will extend to full hardware validation.

Galileo Constellation and Signal model

Galileo's operational constellation comprises 30 satellites (24 operational and 6 spares) distributed across three orbital planes at an altitude of 23,222 km [7]. This configuration provides stable geometry for terrestrial users and extends navigation service into higher altitudes through antenna side-lobe coverage. The Galileo transmit antennas [6] exhibit secondary lobes, which, although weak, remain detectable at GEO altitudes, supporting signal continuity during extended EOR operations. The simulation includes the Open Service (OS) Galileo Navigation Signals on the three frequency bands—E1, E5a, and E6 [7]. SSV performance is assessed in terms of received carrier-to-noise density ratio (C/N_0), computed from GNSS geometry, spacecraft antenna orientation, and

Materials Research Proceedings 69 (2026) 1024-1029 https://doi.org/10.21741/9781644904251-177

Earth disk obscuration. For each visible satellite, the JRC-ISSVTB simulator computes C/N_0 through a typical link budget model [3]:

$$C/N_0 = P_T + G_{T_x} + G_{R_x} - L_{FS} - L_{SVf} - L_{IL} - I_{IMP} - (K_B + T_{Sys}) \quad (1)$$

where P_T is satellite transmit power, G_{T_x} and G_{R_x} are the transmitting and receiving antenna gains respectively, L_{FS} is the free-space loss, L_{SVf} the filtering and modulation loss, L_{IL} the insertion loss, I_{IMP} the implementation loss, and K_B and T_{Sys} represent Boltzmann's constant and a system noise equivalent temperature, respectively.

Receiver model

The simulated receiver represents a high-grade spaceborne GNSS unit optimized for weak-signal operations within the SSV. The front-end thermal noise density is set to N_0 = –174 dBm/Hz, consistent with high-sensitivity L-band designs [3]. A C/N_0 acquisition threshold of 20 dB-Hz is used to assess signal availability across different sensitivity levels. Two antenna configurations are modelled [1], [3]: a ~5 dBi Low-Gain (LG) patch antenna, used in LEO to MEO transfers (zenith-pointing), and an 8–9 dBi High-Gain Antenna (HGA), used in MEO to GEO missions (nadir-pointing), where reception depends on spillover and side-lobe signals.

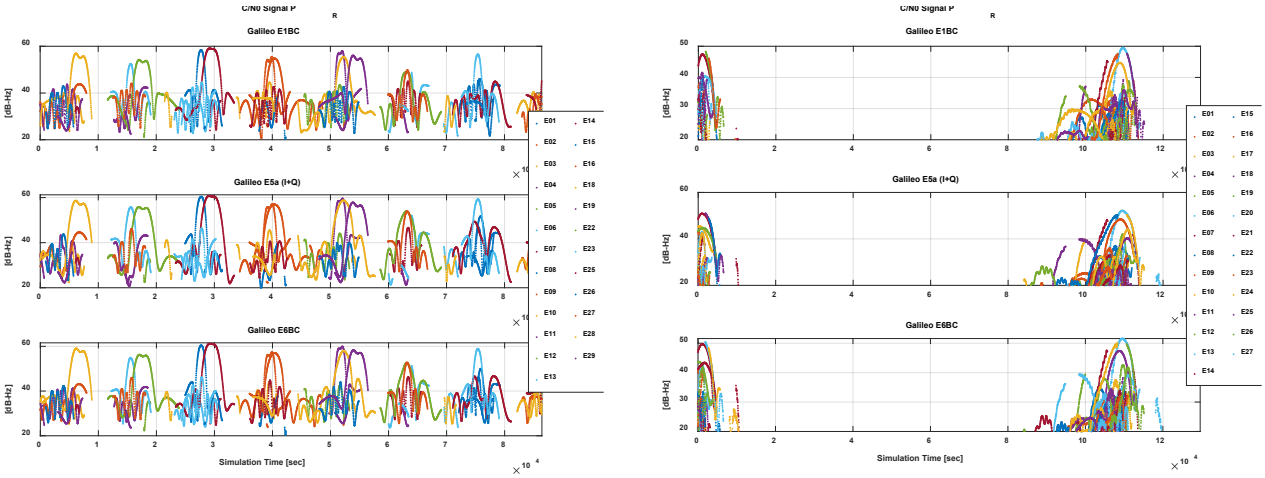
Results

The Galileo SSV performance for orbit transfer operations has been evaluated using Key Performance Indicators (KPIs) quantifying signal reception quality:

- **Received signal power (C/N_0)**: representing the effective carrier-to-noise density ratio at the receiver input, indicative of link margin and tracking robustness under weak-signal conditions [3].
- **Number of visible satellites:** reflecting instantaneous geometry and measurement redundancy, analysed for acquisition thresholds of 20, 25, and 30 dB-Hz.

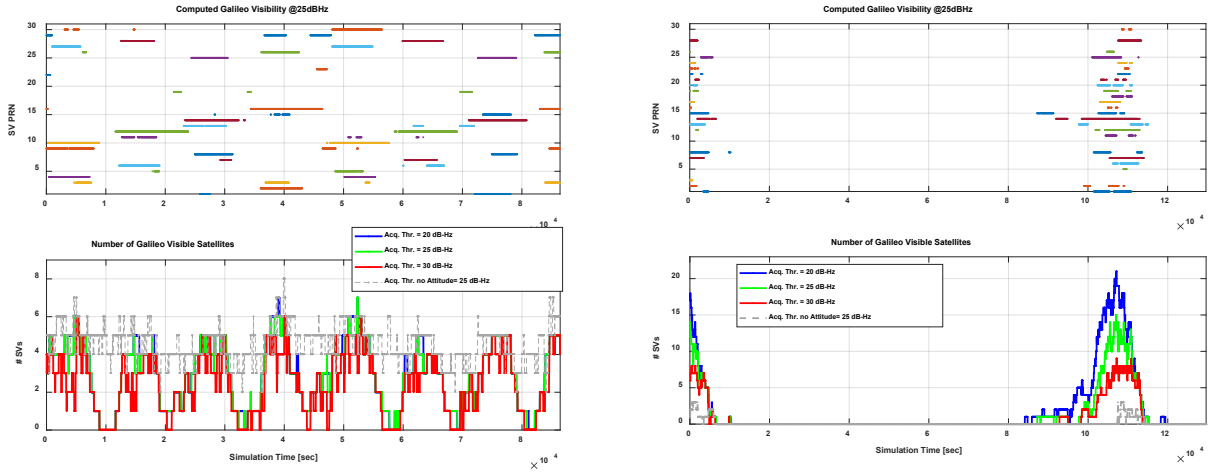
For the LEO–MEO scenario, a 24-hour simulation period has been analysed, while for the EOR Phase 1 high-eccentricity case, a 36-hour simulation has been performed to cover at least one full orbital period. Fig. 4 shows the simulated Galileo C/N_0 distributions for both scenarios at E1-BC, E5a (I+Q), and E6BC components. The plots highlight the correlation between signal strength and the POD antenna off-nadir angle (see Fig. 3). In the EOR Phase 1 case, extended signal outages—up to ~23 hours—are observed, as expected from mission geometry [5]. Hence, the usage of an Extended Kalman Filter (EKF) supporting signal outages can be a suitable implementation strategy to support autonomous navigation. Conversely, the LEO–MEO Phase 2 case exhibits improved visibility thanks to more favourable satellite geometry and reduced Earth blockage.

Fig. 5 illustrates the corresponding Galileo satellite visibility over time. The top panels show the visibility duration of each PRN (assuming 25 dB-Hz acquisition threshold), while the bottom charts report the total number of visible satellites under the three sensitivity thresholds. The comparison also includes a no-attitude-manoeuvre case at 25 dB-Hz acquisition threshold, highlighting the impact of attitude steering on GNSS signal continuity during orbit-raising. Overall, the simulations confirm that for single-antenna configurations, prolonged measurement gaps—up to 22–24 hours—can occur in high-altitude EOR phases, whereas continuous tracking is more feasible in intermediate MEO altitudes.



a) b)

Fig. 4 – Galileo C/No @E1-BC, E5a and E6-BC: a) LEO2MEO case, b) EOR case



a) b)

Fig. 5 – Galileo Visibility: a) LEO2MEO case, b) EOR case

Finally, Table 1 summarizes Galileo signal availability for each frequency band and antenna pattern region (main, secondary, and side lobes) at 25 dB-Hz acquisition threshold. Results show that while LEO–MEO operations primarily rely on secondary-lobe reception, EOR Phase 1 achieves a greater contribution from side-lobe signals, essential for maintaining navigation continuity beyond the Galileo constellation altitude.

Table 1 – Signal Availability vs Pattern lobe , Acq. Thr = 25 dB-Hz

Scenario	**LEO2MEO Phase 2 [%]**			**EOR Phase 1 [%]**		
Signal Component	**E1-BC**	**E5a (I+Q)**	**E6BC**	**E1-BC**	**E5a (I+Q)**	**E6BC**
Main lobe	26.0	26.9	26.9	45.5	58.8	50.5
Secondary lobe	74.0	73.1	73.1	43.9	36.4	37.8
Side lobes	0.0	0.0	0.0	10.6	4.8	11.8

Conclusion and Future Works

This study presented a simulation-based assessment of Galileo SSV performance for electric-propelled orbit transfer missions, focusing on two representative cases: LEO–MEO (Galileo Second Generation) and LEO–GEO (next-generation SATCOM). The analysis characterized

signal availability, geometry, and received power under realistic dynamics and antenna configurations. Results show that Galileo signals can sustain autonomous navigation throughout EOR phases, even beyond the constellation altitude, mainly through side-lobe reception. Although visibility gaps of several hours can occur for single-antenna configurations, the obtained link margins confirm the feasibility of GNSS-based orbit determination for long-duration, low-thrust transfers. Future work will extend this analysis to dual-antenna configurations, multi-constellation (Galileo + GPS) performance, and onboard navigation using an Extended Kalman Filter (EKF). Further validation within the JRC Integrated SSV Test Bench (HIL mode) will support the development of design guidelines for next-generation spaceborne GNSS receivers operating within the Galileo SSV.

References

[1] United Nations, The Interoperable Global Navigation Satellite Systems Space Service Volume, Second Edition. Vienna, 2021.

[2] J. A. Gonzalez del Amo and D. M. Di Cara, 'European Space Agency Electric Propulsion Activities', presented at the International Electric Propulsion Conference 2022, Boston, MA, US, June 2022.

[3] A. Piccolo and F. Menzione, 'GNSS Test Bench Calibration for Space Service Volume Applications', in 2024 11th International Workshop on Metrology for AeroSpace (MetroAeroSpace), June 2024, pp. 134–139. https://doi.org/10.1109/MetroAeroSpace61015.2024.10591570

[4] F. Menzione, A. Renga, and M. Grassi, 'On-board orbit determination for low thrust LEO-MEO transfer by Consider Kalman Filtering and multi-constellation GNSS', Acta Astronautica, vol. 138, pp. 242–254, Sept. 2017. https://doi.org/10.1016/j.actaastro.2017.05.029

[5] A. Ferrario et al., 'Autonomous, Low-Cost GNSS Positioning and Timing Function Under Electrical Propulsion Toward the Geostationary Orbit: A Novel Kalman Filtering Approach', presented at the 2018 9th ESA Workshop on Satellite Navigation Technologies and European Workshop on GNSS Signals and Signal Processing (NAVITEC), ESA-ESTEC, The Netherlands, Dec. 2018.

[6] F. Menzione and M. Paonni, '3D Galileo Reference Antenna Pattern for Space Service Volume Applications', Sensors, vol. 24, no. 7, 2024. https://doi.org/10.3390/s24072220

[7] European Union, 'European Union, Galileo Open Service Signal-In-Space Interface Control Document (OS SIS ICD)'. Nov. 2025. [Online]. Available: https://www.gsc-europa.eu/sites/default/files/sites/all/files/Galileo_OS_SIS_ICD_v2.2.pdf

Materials Research Proceedings 69 (2026) 1030-1035 https://doi.org/10.21741/9781644904251-178

Safe Reinforcement Learning for Autonomous and Constraint-Aware Earth Observation Satellite Scheduling

Fabio FAVARETTO[1,a], Claudio RONCHETTI[1,b] and Guido VOLPI[1,c *]

[1]Telespazio S.p.A., Via Tiburtina 965 00156 Rome, Italy

[a]fabio.favaretto@telespazio.com, [b]claudio.ronchetti@telespazio.com, [c]guido.volpi@telespazio.com

Keywords: Satellite Scheduling, Safe Reinforcement Learning, Autonomous Mission Planning, Constraint-Aware Optimization, Proximal Policy Optimization, Reward Reshaping, Lagrangian Relaxation, BSK-RL Framework, Space Operations, Intelligent Systems for Aerospace

Abstract. Satellite scheduling requires balancing dynamic tasking demands, limited resources, and real-time adaptability, conditions under which traditional rule-based and heuristic methods often fall short. This study explores Safe Reinforcement Learning (SRL) as a framework for autonomous, adaptive, and constraint-aware mission planning. We propose a frugal fine-tuning strategy that adapts a Proximal Policy Optimization (PPO) baseline to new operational domains within the BSK-RL simulation environment, leveraging soft constraints modeled through cost signals. Two SRL approaches are evaluated: (i) reward reshaping, which integrates constraint costs into the reward function, yielding stability improvements and an 8% reduction in actions per episode without sacrificing cumulative rewards; and (ii) Lagrangian-based Constrained Policy Optimization (CPO), which separately optimizes rewards and constraint costs, prioritizing constraint satisfaction and reducing actions by 20–28% at the expense of overall reward. Results demonstrate that SRL enhances both efficiency and constraint adherence in scheduling, while the proposed fine-tuning approach enables rapid transfer to new mission scenarios. These findings highlight SRL as a promising pathway toward scalable, safe, and adaptive satellite operations.

Introduction

Optimizing satellite scheduling remains a central challenge in aerospace mission operations, due to dynamic tasking, limited resources, and real-time constraints. Traditional scheduling methods, often based on rule-based logic or (meta)heuristic strategies, frequently lack the flexibility and efficiency required for modern satellite operations.

In recent years, satellite mission planning has seen a shift from traditional heuristic and meta-heuristic approaches, such as Genetic Algorithms (GAs), to modern AI-driven methods. GAs have long been valued for their robustness in solving multi-objective and constraint-rich scheduling problems, including ground station tasking [1,2]. However, their reliance on hand-crafted rules limits their scalability in dynamic, large-scale, and real-time multi-satellite scenarios [3].

In contrast, Deep Reinforcement Learning (DRL) offers a more flexible, learning-based paradigm. Algorithms such as Proximal Policy Optimization (PPO) [4], Deep Q-Networks (DQN) [5], and Shielded PPO (SPPO) [6] enable agents to learn complex scheduling and control strategies through interaction with high-fidelity simulators, such as [7,8]. Recent work has begun to explore hybrid and multi-stage DRL architectures, which combine heuristic or optimization layers with DRL-based policies to improve solution quality and robustness. For example, Rainbow DQN has been employed in a two-stage scheme to first resolve observation conflicts and then optimize task execution [9], while other methods integrate pointer networks or matrix-sorting with DRL agents to decompose sequencing and allocation, achieving higher responsiveness in dynamic scenarios [10,11].

Content from this work may be used under the terms of the Creative Commons Attribution 3.0 license. Any further distribution of this work must maintain attribution to the author(s) and the title of the work, journal citation and DOI. Published under license by Materials Research Forum LLC.

Despite these advancements, most of these recent approaches are not designed with explicit safety guarantees, particularly when operating under hard resource constraints, failures, or unpredictable task injections. While some modular architectures support replanning without retraining [11], and attention-based models improve decision granularity [12,13], they do not account for constraint adherence during learning itself. To address this, our work contributes to the emerging area of Safe Reinforcement Learning (SRL) [14] by integrating a variant of Constrained Policy Optimization (CPO) [15] and a cost-sensitive reward strategy. This promotes constraint-aware behavior during training, without relying on rigid enforcement or manual rule design—advancing the trustworthiness and adaptability of autonomous satellite schedulers in operational conditions.

A core innovation in our approach is its frugality and transferability: rather than retraining agents from scratch, we focus on fine-tuning an existing baseline policy to adapt efficiently to new mission domains or operational conditions. This is achieved within the high-fidelity BSK-RL simulation environment [16], using Proximal Policy Optimization (PPO) as the baseline. We implement soft constraints, which are not enforced through hard limits but modelled through cost signals that influence agent behavior via the learning process. These costs guide policies toward compliance without rigidly restricting exploration or solution space.

Problem formulation

We cast satellite task scheduling as a partially observable Markov decision process in which the full spacecraft–environment state is hidden, and the agent must act from telemetry and mission context. Each observation blends normalized spacecraft status—battery and memory fractions, reaction-wheel speeds, pointing errors, together with environmental cues (eclipse flag, normalized mission time) and planning context: up to thirty-two currently visible imaging opportunities annotated with priority and timing, plus the next ground-station downlink window. At each decision instant, the agent selects one discrete action: capture an image by choosing one of the currently visible targets; initiate a downlink to the next available ground station; switch to solar charging; execute a wheel desaturation; or drift (idle) to conserve resources.

The reward guides two operational goals: acquiring valuable imagery and managing storage through timely downlinks. When an image is successfully captured, the agent receives the target's priority as a positive reward; when a downlink is performed, it receives a utility proportional to the freed storage. Episodes terminate early with a large negative terminal reward if safety limits are violated, specifically, if the battery would drop below zero or reaction-wheel speeds exceed their bounds, so unsafe behavior is both discouraged and truncated. As a learning baseline we employ Proximal Policy Optimization (PPO), which updates a stochastic policy using a clipped surrogate objective with value-function fitting and an entropy bonus to balance exploitation and exploration. To introduce constraint awareness, we build on a common operational cost signal that grows when battery charge falls below a minimum fraction P_{min} or when memory usage exceeds a maximum fraction M_{max} (weights balance power vs. memory).

We study two strategies that use this cost differently. Reward reshaping subtracts the cost from the task reward at every step, yielding a single scalar objective that is simple to optimize but blends task performance and safety into one number. In contrast, a Lagrangian CPO-style variant keeps the original reward untouched and enforces the cost budget through an adaptive penalty: we extend the PPO backbone with a parallel cost-critic head that estimates cost returns, we compute a cost-advantage with cost-specific GAE, and we update a Lagrange multiplier λ online toward a target budget. As λ increases when violations persist and relaxes when behavior is safe, the policy learns to trade reward against constraint systematically without distorting the reward signal itself.

This formulation preserves a clear task objective, exposes resource limits as explicit constraints, and supports both a lightweight penalty (reward reshaping) and a principled safety mechanism (Lagrangian with a cost critic) within the same PPO architecture.

Materials Research Proceedings 69 (2026) 1030-1035 https://doi.org/10.21741/9781644904251-178

Experiment setup

The satellite and scenario configuration were defined through parameters governing data storage, power consumption, attitude control, orbital characteristics, and target generation variables. Several parameters were randomly initialized within realistic ranges to simulate diverse operational conditions, enabling the agent to adapt to varying real-world environments during both training and testing. Other parameters were held constant: data storage capacity of 8 GB, instrument data rate of 0.4 GB/s, transmitter rate of 0.2 GB/s, battery capacity of 720,000 W·s, and mode-dependent power consumption (–10 W·s idle, –30 W·s imaging, –25 W·s downlink, and –80 W·s thruster). The reaction wheels supported rotational speeds up to ±6000 RPM. The satellite operated in a 500 km altitude orbit with a 45° inclination. The scenario included 1000 randomly distributed Earth surface targets and seven predefined ground stations.

The PPO baseline agent was trained using a carefully tuned set of hyperparameters to ensure stable convergence and strong policy performance in the BSK-RL environment. The learning rate was set to 1×10^{-4}, with a discount factor γ of 0.99 and a GAE lambda λ of 0.85. A clipping range of 0.3 was applied to stabilize updates, while an entropy coefficient of 0.01 encouraged exploration. The value function loss was weighted with a coefficient of 1.0. Training used a batch size of 256 and a rollout horizon of 10,000 steps. Each PPO update was optimized over 10 epochs, with a total of 300 training iterations performed. The PPO agent reached stability after approximately 2.3 hours of training, achieving a mean return of about 41 and a mean episode length of around 260 steps.

The reward-reshaped agents, trained from scratch and fine-tuned from PPO, achieved rapid, stable convergence. In contrast, the L-CPO agents trained from scratch initially exhibited slower and less stable learning. However, fine-tuned L-CPO agents with a newly initialized cost head enabled reliable constraint learning and resulted in an approximate 28% reduction in mean episode length.

All training was performed on a virtual machine with 64 CPUs and 64 GB of RAM, leveraging the parallelization capabilities of Ray [17,18], an open-source distributed computing framework that scales Python applications efficiently from a single node to large clusters with minimal code modification.

Results

For a fair comparison, the initial conditions and random seeds were held constant across 100-episode evaluations. Each test began with the battery charged to 50%, data storage filled to 50%, and reaction wheels spinning at 1000 RPM. The orbital parameters—right ascension of the ascending node, argument of perigee, and true anomaly—were all set to zero degrees.

After the training, hyperparameter fine-tuning, and evaluation phases, the best-performing agents are selected: the PPO baseline (PPO), one reward-reshaped agent trained from scratch (RR_S), one reward-reshaped agent fine-tuned from PPO (RR_{FT}), and one Lagrangian agent fine-tuned from PPO ($L\text{-}CPO_{FT}$).

As shown in Fig. 1a, the PPO baseline exhibits higher costs and longer episodes, indicating less efficient operation. In contrast, reward-reshaped agents cluster at lower costs while maintaining longer trajectories, reflecting more cautious storage and power management behavior. The Lagrangian agent achieves the shortest episodes while maintaining costs below 5%, representing a safety-oriented operational regime.

Fig. 1b indicates that the RR variants maintain performance levels comparable to the PPO baseline in terms of cumulative reward, while enhancing policy stability and behavioral consistency. This method integrates constraint costs directly into the reward signal, encouraging a smoother trade-off between objective achievement and resource-aware behavior. Notably, it results in an 8% reduction in the number of actions taken per episode, reflecting more efficient and

Materials Research Proceedings 69 (2026) 1030-1035 https://doi.org/10.21741/9781644904251-178

stable decision-making. In contrast, the L-CPO approach treats the primary reward and constraint cost as separate optimization objectives, enabling a more explicit enforcement of constraint satisfaction. While this yields lower overall rewards compared to PPO and reward reshaping, it significantly emphasizes constraint adherence, resulting in a decrease in the number of actions taken in the episode (reduced by approximately 20–28%) and more conservative agent behavior. This separation of objectives offers greater interpretability and control over constraint tuning, in contrast to the blended reward-cost formulation in reward reshaping.

Fig. 2a (imaged-target distribution) and 2b (episode-length distribution) further characterize these dynamics. The PPO baseline yields higher throughput, but it is inefficient in terms of resource utilisation.

The reward-reshaped agent exhibits steadier and longer operational runs, whereas the Lagrangian agent maintains short, consistent episodes.

In conclusion, the baseline shows the largest variability, the reward-reshaped approach combines low cost with high return, and the Lagrangian method achieves the lowest cost with minimal dispersion but slightly reduced return.

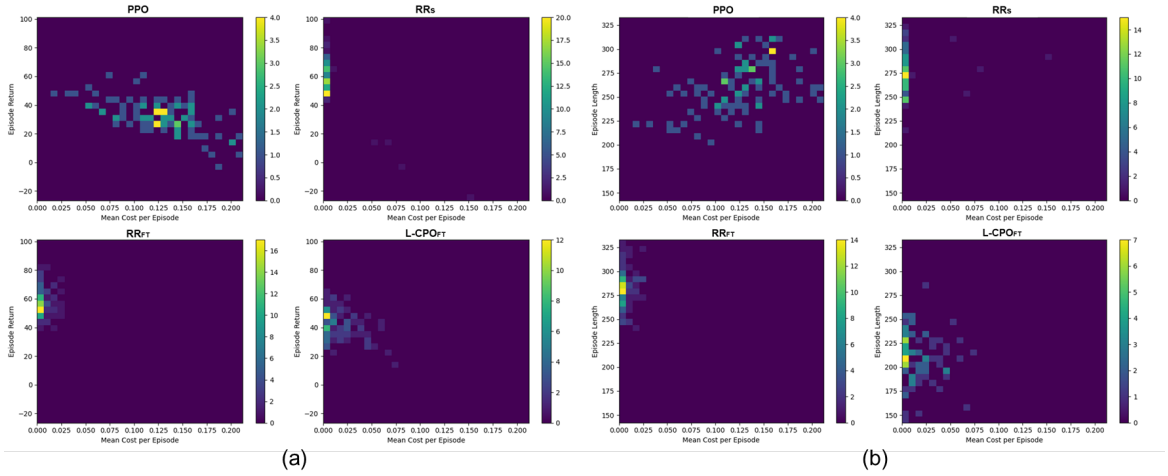


Figure 1. (a) Mean cost vs. episode length and (b) mean cost vs. episode return over 100 test episodes. The PPO baseline shows high-cost variability, often breaching the 10% safety threshold. Reward-reshaped agents (RRS and RRFT) achieve lower costs with longer, more structured episodes, while the Lagrangian-based agent (L-CPO) attains the shortest safe executions (<5% cost).

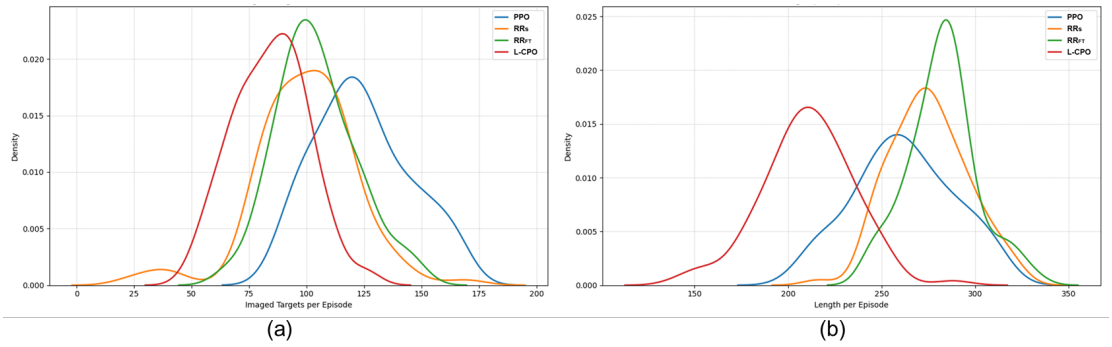


Figure 2. (a) Distribution of imaged targets per episode and (b) episode-length distribution. The PPO baseline achieves the highest throughput, but with inefficient energy and memory use. Reward-reshaped agents (RRS and RRFT) trade minor reductions in target count for longer, more stable operations, while the Lagrangian agent (L-CPO) maintains short, consistent episodes, reflecting efficient and constraint-aware behavior.

Conclusions

We investigated safe reinforcement learning for agile satellite scheduling in the BSK-RL environment, comparing a tuned PPO baseline with two constraint-aware variants: reward reshaping and a Lagrangian CPO-style approach. Our goal was twofold: (i) demonstrate that soft-constraint signals can steer policies toward operationally safe behavior, and (ii) show that frugal fine-tuning of a PPO baseline provides a practical path to rapid adaptation.

The comparative analysis of the PPO baseline, reward-reshaped agents, and the Lagrangian fine-tuned agent demonstrates distinct trade-offs between efficiency, stability, and constraint adherence. The PPO baseline, while achieving high throughput and reward, exhibits higher operational costs, longer and more variable episodes, and less resource-efficient behavior. In contrast, the reward-reshaped approaches—both trained from scratch (RR_S) and fine-tuned from PPO (RR_{FT})—achieve lower costs and enhanced stability without sacrificing overall performance. By embedding constraint information directly into the reward function, these agents demonstrate smoother policy behavior and a more balanced trade-off between performance and safety, reducing unnecessary actions and improving operational consistency. The Lagrangian fine-tuned agent ($L\text{-}CPO_{FT}$) further emphasizes constraint satisfaction, achieving the lowest operational costs and shortest, most consistent episodes. Although this comes with a modest reduction in cumulative reward, the resulting policy reflects a deliberate and safety-oriented operational strategy. Overall, the findings suggest that reward reshaping effectively enhances efficiency and stability while maintaining strong performance, whereas the Lagrangian method provides superior constraint control and interpretability, making it the most suitable approach for safety-critical or resource-constrained environments.

Funding

This work was supported by the European Defence Fund (EDF) under grant agreement No. 101103386, within the context of the FaRADAI (Frugal and Robust AI for Defence Advanced Intelligence) project.

Views and opinions expressed are, however, those of the authors only and do not necessarily reflect those of the European Union or the European Commission. Neither the European Union nor the granting authority can be held responsible for them.

References

[1] Xhafa, F., Herrero, X., Barolli, A., Barolli, L., & Takizawa, M. Evaluation of struggle strategy in genetic algorithms for ground stations scheduling problem. Journal of Computer and System Sciences, 2013, 79(7), 1086-1100. https://doi.org/10.1016/j.jcss.2013.01.023

[2] Xhafa, F., Sun, J., Barolli, A., Takizawa, M., & Uchida, K. Evaluation of genetic algorithms for single ground station scheduling problem. In 2012 IEEE 26th International Conference on Advanced Information Networking and Applications, 2012, pp. 299-306. https://doi.org/10.1109/AINA.2012.59

[3] Thangavel, K., Sabatini, R., Gardi, A., Ranasinghe, K., Hilton, S., Servidia, P., & Spiller, D. Artificial intelligence for trusted autonomous satellite operations. Progress in Aerospace Sciences, 2024, 144, 100960. https://doi.org/10.1016/j.paerosci.2023.100960

[4] Schulman, J., Wolski, F., Dhariwal, P., Radford, A., & Klimov, O. Proximal policy optimization algorithms (2017). arXiv preprint arXiv:1707.06347.

[5] Huang, Y. Deep Q-networks. In Deep reinforcement learning: fundamentals, research and applications. Singapore: Springer Singapore, 2020, pp. 135-160. https://doi.org/10.1007/978-981-15-4095-0_4

[6] Wang, H., Qin, J., & Kan, Z. Shielded planning guided data-efficient and safe reinforcement learning. IEEE Transactions on Neural Networks and Learning Systems, 36(2), 2024, 3808-3819. https://doi.org/10.1109/TNNLS.2024.3359031

[7] Maisonobe, L., Pommier, V., & Parraud, P. Orekit: An open source library for operational flight dynamics applications. In 4th international conference on astrodynamics tools and techniques, Paris: European Space Agency, 2010 May, pp. 3-6.

[8] Kenneally, P. W., Piggott, S., & Schaub, H. Basilisk: A flexible, scalable and modular astrodynamics simulation framework. Journal of aerospace information systems, 2020, 17(9), pp. 496-507. https://doi.org/10.2514/1.I010762

[9] Chen, X., Tian, T., Dai, G., Wang, M., Song, Z., Zheng, W., & Zhou, Q. A conflict Rainbow DQN-based two-stage optimization framework for multiple agile satellites scheduling. IEEE Transactions on Aerospace and Electronic Systems, 2025, 61(3). https://doi.org/10.1109/TAES.2025.3538476

[10] Liu, Z., Xiong, W., Jia, Z., & Han, C. Two-stage deep reinforcement learning method for agile optical satellite scheduling problem. Complex & Intelligent Systems, 2025, 11, 35. https://doi.org/10.1007/s40747-024-01667-x

[11] Xing, X., Wang, S., Liu, W., & Liu, C. A multi-satellite multi-target observation task planning and replanning method based on DQN. Sensors, 2025, 25(6), 1856. https://doi.org/10.3390/s25061856

[12] Chun, J., Yang, W., Liu, X., Wu, G., He, L., & Xing, L. Deep reinforcement learning for the agile earth observation satellite scheduling problem. Mathematics, 2023, 11(19), 4059. https://doi.org/10.3390/math11194059

[13] Liu, D., & Zhou, G. Deep reinforcement learning-based attention decision network for agile Earth observation satellite scheduling. Remote Sensing, 2024, 16(23), 4436. https://doi.org/10.3390/rs16234436

[14] Garcıa, J., & Fernández, F. A comprehensive survey on safe reinforcement learning. Journal of Machine Learning Research, 2015, 16(1), pp. 1437-1480

[15] Achiam, J., Held, D., Tamar, A., & Abbeel, P. Constrained policy optimization. In Proceedings of the 34th International Conference on Machine Learning, PMLR, 2017, pp. 22-31.

[16] Stephenson, M. A., & Schaub, H. BSK-RL: Modular, high-fidelity reinforcement learning environments for spacecraft tasking. 75th International Astronautical Congress, Milan, Italy, 2024. https://doi.org/10.52202/078372-0120

[17] Moritz, P., Nishihara, R., Wang, S., Tumanov, A., Liaw, R., Liang, E., ... & Stoica, I. Ray: A distributed framework for emerging {AI} applications. In 13th USENIX symposium on operating systems design and implementation (OSDI 18), 2018, pp. 561-577.

[18] Information on https://docs.ray.io/en/latest/ray-overview/getting-started.html

Materials Research Proceedings 69 (2026) 1036-1041 https://doi.org/10.21741/9781644904251-179

Rendezvous in Low-Lunar-Orbit from Gateway via Low-Thrust Nonlinear Control

Edoardo Maria LEONARDI[1,a *], Mauro PONTANI[1,b] and Paolo TEOFILATTO[1,c]

[1]Via Salaria 851, 00138, Rome, Italy

[a]edoardomaria.leonardi@uniroma1.it, [b]mauro.pontani@uniroma1.it, [c]paolo.teofilatto@uniroma1.it

Keywords: Rendezvous, Gateway, Moon Exploration, Low-Thrust, Nonlinear Control

Abstract. This research investigates low-thrust nonlinear control for rendezvous in lunar orbit, in a high-fidelity dynamical model and in the presence of nonnominal conditions. The feedback control law is based on Lyapunov stability theory and is capable of tracking time-varying orbital elements, including the true anomaly. Monte Carlo campaigns are run to assess the performance of the control strategy, with regard to both a controlled and an uncontrolled target vehicle (i.e. subject to free dynamics). Results show that the proposed low-thrust feedback controller is capable of driving the spacecraft to a safe distance from the target vehicle, with minimal residual velocity, without relying on any reference trajectory nor numerical integration, making it suitable for onboard implementation.

Introduction

The Artemis program led by NASA foresees the deployment of the space station Gateway along a Near-Rectilinear-Halo-Orbit around the collinear exterior point of the Earth-Moon system. Establishing a long-term human presence on the Moon will require the development of autonomous and reliable transportation systems between Earth, Moon and Gateway. As part of ESA's Explore 2040 strategy, the Argonaut spacecraft will carry cargo from and to the lunar surface, proving a versatile access to the lunar surface [1]. In this context, the development of efficient and lightweight guidance and control strategies for autonomous rendezvous in Low-Lunar-Orbit (LLO) is an area of doubtless interest among researchers.

The design of optimal trajectories in cislunar space usually leverages dynamical system theory or two-body approximations to generate initial guess solutions, to combine with differential corrections and optimization techniques. In this field, optimal trajectories from Gateway to LLO have been identified through either direct and indirect methods, with both high thrust and low thrust [2, 3]. Instead, other studies focus on guidance and control strategies for rendezvous in cislunar space. However approaches based on direct and indirect optimization methods [4, 5] involve a higher computational load. Recently, the application of machine learning has been investigated for efficient guidance schemes in rendezvous scenarios, though demanding extensive training. In contrast, nonlinear control does not require any offline design process, apart from tuning the control gains. The objective of this research is to assess low-thrust nonlinear control as a viable strategy for rendezvous in lunar orbit, in a high-fidelity dynamical framework and in the presence of nonnominal conditions. Specifically, the study case considers a spacecraft equipped with a low-thrust propulsion system that departs from Gateway and is directed toward a target vehicle in LLO, to rendezvous with minimal residual relative velocity. Modified Equinoctial Elements (MEE) are employed as state variables for dynamics modeling, which includes third-body perturbations from Earth and Sun, as well as the relevant harmonics of the selenopotential. The positions of Sun and Earth are taken from NASA ephemeris, which also provides the state of Gateway at initial time. To drive the spacecraft from Gateway toward the target, a nonlinear controller is being proposed. Specifically, the feedback control law at hand is based on Lyapunov

Content from this work may be used under the terms of the Creative Commons Attribution 3.0 license. Any further distribution of this work must maintain attribution to the author(s) and the title of the work, journal citation and DOI. Published under license by Materials Research Forum LLC.

Materials Research Proceedings 69 (2026) 1036-1041 https://doi.org/10.21741/9781644904251-179

stability theory and is capable of tracking time-varying orbital elements, including the true anomaly, while enjoying quasi-global stability [6]. Two different scenarios are being considered:

a) the target vehicle flies a circular and polar LLO at an altitude of 100 km, with constant orbital elements except for the true anomaly;
b) the target spacecraft is subject to an uncontrolled dynamics; its initial orbit is identical to case (a), but the orbital elements vary under the effect of perturbing accelerations.

Monte Carlo campaigns are intended to assess the performance of the control strategy in the high-fidelity model, in the presence of several nonnominal situations, namely (i) time delays on the departure from Gateway, (ii) thrust misalignment, (iii) temporary thrust unavailability and (iv) noise on the measured perturbing accelerations.

Orbit dynamics

In this research, Modified Equinoctial Elements (MEE) are adopted as state variables since they exhibit no singularities, apart from retrograde equatorial orbits [7], which are rarely encountered. The set of MEEs is denoted as $x = [x_1, x_2, x_3, x_4, x_5, x_6]^T$. Through MEEs, the dynamical equations of a spacecraft orbiting around a primary body (with gravitational parameter μ) can be expressed in a compact form,

$$\dot{\boldsymbol{x}} = \mathbf{G}(\boldsymbol{x})\boldsymbol{a} + \boldsymbol{f}, \tag{1}$$

Where $\boldsymbol{f} = \left[0_{1x5} \quad \sqrt{\mu/x_1^3}(1 + x_2 \cos x_6 + x_3 \sin x_6)^2\right]^T$, while $\mathbf{G}$ is a 6x3 matrix depending on the state $\boldsymbol{x}$. Finally, $\boldsymbol{a}$ collects the components of the vector $\vec{\boldsymbol{a}}$ of non-Keplerian accelerations in the Local-Vertical-Local-Horizontal frame [8]. This vector includes the contribution of (i) the perturbing acceleration $\vec{\boldsymbol{a}}_P$ and (ii) the thrust acceleration $\vec{\boldsymbol{a}}_T$.

Perturbing acceleration. The term $\vec{\boldsymbol{a}}_P$ includes the perturbing acceleration $\vec{\boldsymbol{a}}_g$ due to the harmonics of the gravitational potential (i.e. excluding the Keplerian term) and the gravitational acceleration $\vec{\boldsymbol{a}}_{3B}$ due to the third-body effects of both Earth and Sun. The acceleration $\vec{\boldsymbol{a}}_g$ can be expressed as the gradient of the gravitational potential, conveniently described in terms of multipole series of spherical harmonics functions. In this research, the corresponding coefficients are taken from the Lunar Prospector LP100K model for the lunar gravitational field [9]. However, only the relevant harmonics associated with coefficients $|J_{lm}| > 5 \cdot 10^{-6}$ are retained in the dynamical model. Instead, the gravitational acceleration $\vec{\boldsymbol{a}}_{3B}$ due to a generic third body can be expressed in terms of its gravitational parameter and position vector in the inertial frame [6], taken from NASA ephemeris.

Thrust acceleration. The spacecraft is equipped with a low-thrust engine, which is assumed to be steerable and throttleable, and provides the thrust acceleration $\vec{\boldsymbol{u}}_T = x_7\vec{\boldsymbol{a}}_T$, where x_7 is the mass ratio. The thrust acceleration magnitude $u_T = |\vec{\boldsymbol{u}}_T|$ can be modulated from 0 up to a maximum value u_{Tmax}. Therefore, the dynamical state of the spacecraft includes its mass ratio, whose time derivative is given by $\dot{x}_7(t) = -u_T/c$, where c is the effective exhaust velocity.

Nonlinear orbit control

Rendezvous is achieved through a nonlinear feedback control law, which in a previous work was proven to enjoy global asymptotic stability despite time-variable desired MEEs, including the true anomaly [6]. As a preliminary step, the state of the target vehicle is expressed in terms of MEEs, $\boldsymbol{x}_d = [x_{1d}, x_{2d}, x_{3d}, x_{4d}, x_{5d}, x_{6d}]^T$. Then, the target state is enforced as a nonlinear constraint,

Materials Research Proceedings 69 (2026) 1036-1041 https://doi.org/10.21741/9781644904251-179

$$\boldsymbol{\Psi}(\boldsymbol{x},t)=\begin{bmatrix}(1-\cos(x_6-x_{6d}))x_1\\(x_2-x_{2d})^2+(x_3-x_{3d})^2\\(x_4-x_{4d})^2+(x_5-x_{5d})^2\\(x_1-x_{1d})^2(1+x_2\sin x_6-x_3\cos x_6)\end{bmatrix}. \quad (2)$$

The formulation in Equation (2) allows to track all time-varying orbital elements of the virtual target, including the true anomaly. The instantaneous thrust acceleration is expressed as [6]

$$\boldsymbol{a}_T=-\frac{u_T}{x_7}\frac{\boldsymbol{b}+\boldsymbol{d}}{|\boldsymbol{b}+\boldsymbol{d}|},\qquad u_T=\begin{cases}x_7|\boldsymbol{b}+\boldsymbol{d}|, & \text{if } x_7|\boldsymbol{b}+\boldsymbol{d}|\le u_{Tmax}\\0, & \text{if } x_7|\boldsymbol{b}+\boldsymbol{d}|>u_{Tmax} \text{ and } \boldsymbol{b}^{\boldsymbol{T}}(\boldsymbol{b}+\boldsymbol{d})<0\\u_{Tmax} & \text{if } x_7|\boldsymbol{b}+\boldsymbol{d}|>u_{Tmax} \text{ and } \boldsymbol{b}^{\boldsymbol{T}}(\boldsymbol{b}+\boldsymbol{d})\ge 0\end{cases} \quad (3)$$

with $\boldsymbol{b}$ and $\boldsymbol{d}$ defined as

$$\boldsymbol{b}=\mathbf{A}^{\mathrm{T}}\boldsymbol{\Lambda}\boldsymbol{\Psi},\qquad \boldsymbol{d}=\boldsymbol{a}_P+\ \mathbf{A}^{\mathrm{T}}(\mathbf{A}\mathbf{A}^{\mathrm{T}})^{-1}\left(\frac{\partial\boldsymbol{\Psi}}{\partial\boldsymbol{x}}\boldsymbol{f}+\frac{\partial\boldsymbol{\Psi}}{\partial\boldsymbol{x}_d}\dot{\boldsymbol{x}}_d\right), \quad (4)$$

where $\mathbf{A}=\left(\frac{\partial\boldsymbol{\Psi}}{\partial\boldsymbol{x}}\mathbf{G}\right)$, while $\boldsymbol{\Lambda}$ is a diagonal and positive definite matrix, namely $\boldsymbol{\Lambda}=\mathrm{diag}\{\lambda_1,\lambda_2,\lambda_3,\lambda_4\}$.

Nonlinear orbit control

For each scenario, a Monte Carlo campaign comprising 100 simulations is run to assess the performance of the control strategy at hand in the high-fidelity model. The initial reference epoch is set to 25/05/2025 @14:06:08. The low-thrust propulsion system has effective exhaust velocity c = 30 km/s and maximum thrust acceleration $u_{Tmax}=4.91\cdot10^{-4}$ m/s^2. The control gains are tuned to $\lambda_1=10^2$, $\lambda_2=10^8$, $\lambda_3=10^8$, $\lambda_4=10^5$ and $\lambda_1=10^5$, $\lambda_2=10^{11}$, $\lambda_3=10^{10}$, $\lambda_4=10^{11}$ respectively for scenarios (a) and (b). Furthermore, canonical units are used throughout for numerical convenience: the distance unit (DU) is set to 10000 km, and the time unit (TU) is defined to yield a unit gravitational parameter.

The nonnominal conditions include (i) time delays on the departure from Gateway, (ii) thrust misalignment, (iii) temporary thrust unavailability, and (iv) noise on the measured perturbing accelerations. Further details on the modeling of these effects can be found in [6]. The integration is stopped when the final state corresponds to a safe distance $||\delta\vec{\boldsymbol{r}}||$ < 1.5 km from the target, where close-range rendezvous can be addressed as in recent contributions [10]. The performance of the strategy is analyzed in terms of final mass ratio (m_{Rf}), time of flight (ToF) and dispersions on $||\delta\vec{\boldsymbol{v}}||$, i.e. the magnitude of the spacecraft velocity relative to the target.

Table 1 collects the results of the Monte Carlo campaigns. The analysis of the results shows that the feedback control law drives the chaser to a safety distance from the target vehicle, with limited dispersion on the relative velocity, even when the spacecraft must rendezvous with the uncontrolled target. This is confirmed by inspection of Figure 1, which points out how the relative distance from the target is gradually reduced during each orbit. Rendezvous is achieved within an average of 65 days, with a modest fuel expenditure. Figures 2 and 3 show the time histories of the right ascension of the ascending node Ω, confirming the capability of the control law to track either constant or time-varying orbital elements. In particular, the zoom on the last days highlights the effectiveness of the feedback control law to track time-varying orbit elements induced by perturbations in the LLO environment.

Materials Research Proceedings 69 (2026) 1036-1041 https://doi.org/10.21741/9781644904251-179

Table 1: Results of the Monte Carlo campaign for scenarios (a) and (b).

Parameter	Scenario (a)		Scenario (b)	
	Mean value	Standard deviation	Mean value	Standard deviation
$\|\|\delta\vec{\boldsymbol{r}}\|\|$ [m]	1477.64	17.00	1471.96	22.03
$\|\|\delta\vec{\boldsymbol{v}}\|\|$ [m/s]	1.17	0.18	1.14	0.36
ToF [days]	65.26	5.37	64.60	0.99
m_{Rf}	0.897	$3.01 \cdot 10^{-3}$	0.912	$1.10 \cdot 10^{-3}$

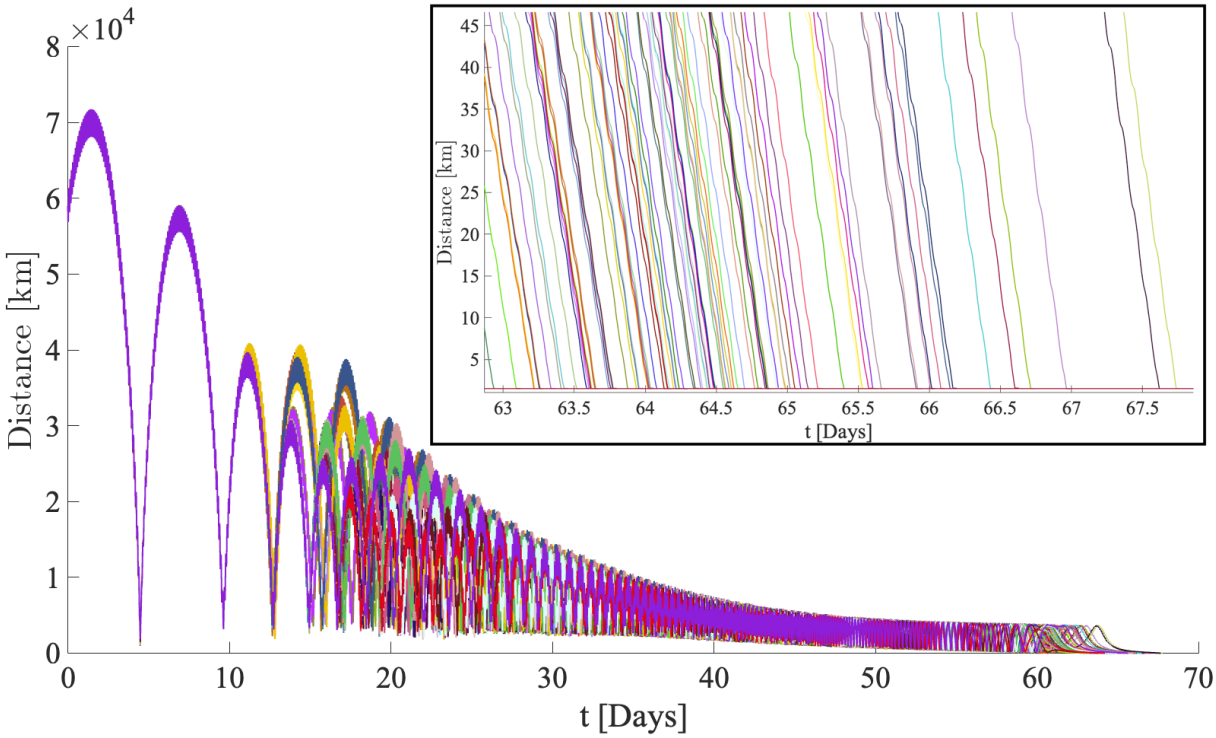


Figure 1: Scenario (b): time histories of the distance from the target across 100 Monte Carlo simulations with nonnominal conditions (in the insets, zoom on the last days).

Concluding remarks

The development of autonomous guidance and control techniques represents a key factor in ensuring the success of future lunar missions. This research addresses low-thrust nonlinear control as an effective guidance strategy for rendezvous from Gateway to LLO. A high-fidelity framework is employed for numerical simulations, including all relevant perturbations and nonnominal conditions associated with delays on the initial injection time, misalignment errors, thrust unavailability, and noise on measured accelerations. Moreover, low-thrust nonlinear control is employed to drive a spacecraft from Gateway toward rendezvous in LLO. The feedback law is capable to achieve rendezvous with either a controlled vehicle flying a Keplerian orbit or an uncontrolled target subject to natural (perturbed) dynamics. Remarkably, this strategy operates without the need for offline data or pre-computed trajectories, nor numerical integration, yielding a significantly lower computational cost compared to solutions based on optimal control theory. The low-thrust feedback controller requires only proper gain tuning, yet it is capable of autonomously generating trajectories online, making it suitable for onboard implementation.

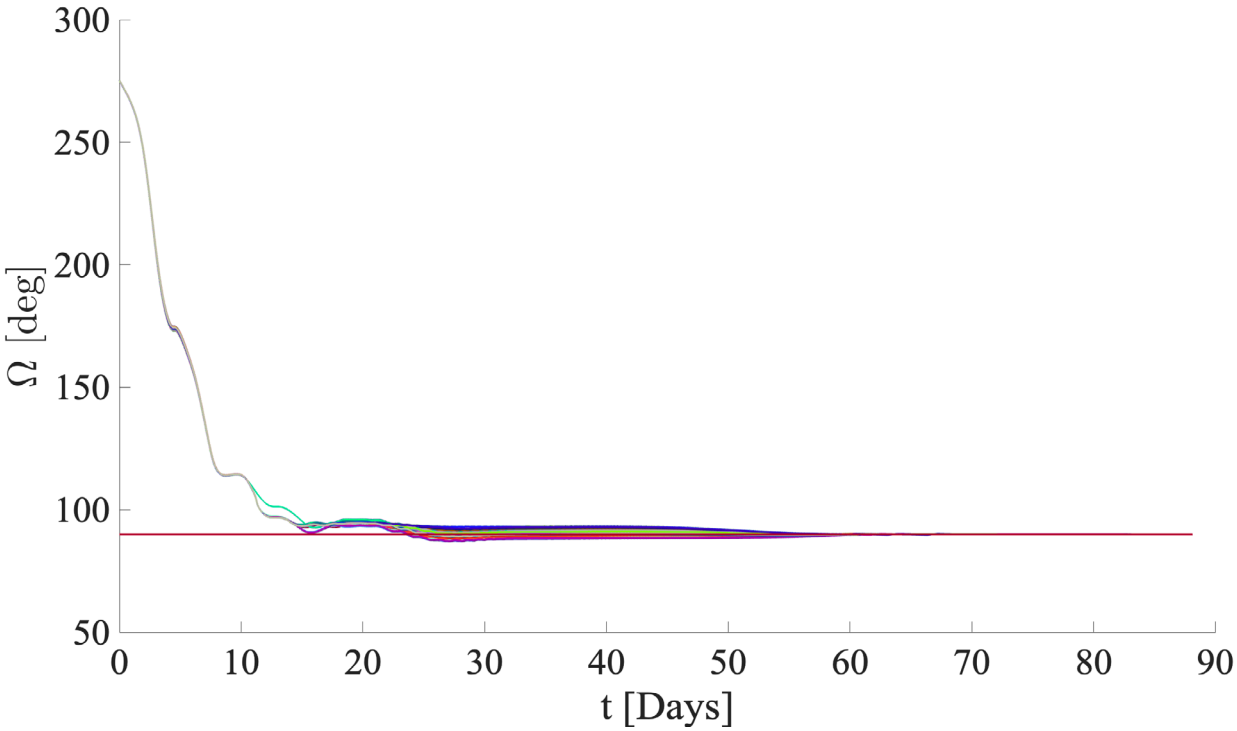


Figure 2: Scenario (a): time histories of Ω across 100 Monte Carlo simulations with non-nominal conditions.

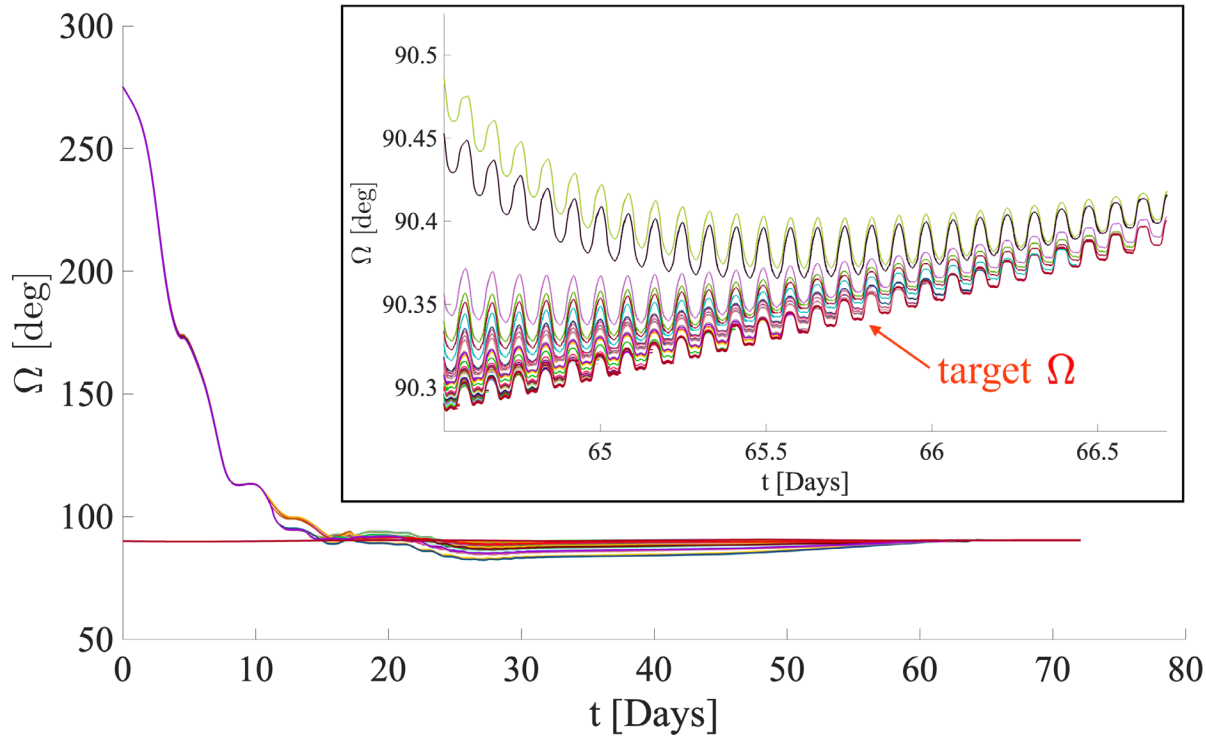


Figure 3: Scenario (b): time histories of Ω across 100 Monte Carlo simulations with non-nominal conditions (in the insets, zoom on the last days).

References

[1] ESA, Argonaut: Europe's lunar lander programme, 2025. Information on https://www.esa.int/Science_Exploration/Human_and_Robotic_Exploration/Exploration/Argonaut_Europe_s_lunar_lander_programme

[2] C. Pozzi, M. Pontani, A. Beolchi, E. Fantino, Optimization, guidance, and control of low-thrust transfers from the lunar Gateway to low lunar orbit," Acta Astronautica, 222 (2024), 39–51. https://doi.org/10.1016/j.actaastro.2024.05.036

[3] D. Sanna, E. M. Leonardi, G. De Angelis, M. Pontani, Optimal impulsive orbit transfers from Gateway to low lunar orbit, Aerospace, 11(6) (2024), 460. https://doi.org/10.3390/aerospace11060460

[4] A. Colagrossi, V. Pesce, L. Bucci, F. Colombi, M. Lavagna, Guidance, navigation and control for 6DOF rendezvous in cislunar multi-body environment, Aerospace Science and Technology, 114 (2021), 106751, 2021. https://doi.org/10.1016/j.ast.2021.106751

[5] M. Pagone, G. Bucchioni, F. Alfino, C. Novara, Autonomous lunar rendezvous trajectory planning and control using nonlinear MPC and Pontryagin's principle, IFAC Journal of Systems and Control, 30 (2024), 100282. https://doi.org/10.1016/j.ifacsc.2024.100282

[6] E. M. Leonardi, G. De Angelis, M. Pontani, Nonlinear orbit acquisition and maintenance of a lunar navigation constellation using low-thrust propulsion, Aerospace, 11(12) (2024), 1046. https://doi.org/10.3390/aerospace11121046

[7] R. A. Broucke, P. J. Cefola, On the equinoctial orbit elements, Celestial mechanics, 5(3) (1972), 303–310, https://doi.org/10.1007/BF01228432

[8] H. D. Curtis, Orbital mechanics for engineering students, third ed., Butterworth-Heinemann, 2019.

[9] A. Konopliv, S. Asmar, E. Carranza, W. Sjogren, D. Yuan, Recent gravity models as a result of the Lunar Prospector mission, Icarus, 150(1) (2001), 1–18. https://doi.org/10.1006/icar.2000.6573

[10] L. Russo, D. Sanna, D. P. Madonna, M. Pontani, and P. Gasbarri, "Autonomous guidance and control for rendezvous and mating with Gateway with collision avoidance maneuvering," Acta Astronautica, 232 (2025), 678–692, https://doi.org/10.1016/j.actaastro.2025.03.019

Materials Research Proceedings 69 (2026) 1042-1047 https://doi.org/10.21741/9781644904251-180

Conjunction Risk Reduction in LEO through Onboard Optical Processing

Giulio Campiti[1,a], Alessandra Colucci[1,b], Giuseppe Brunetti[1,c] and Caterina Ciminelli[1,d*]

[1]Optoelectronics Laboratory, Department of Electrical and Information Engineering (DEI), Politecnico di Bari, Via E. Orabona 4, Bari, Italy

[a]giulio.campiti@poliba.it, [b]alessandra.colucci@phd.poliba.it, [c]giuseppe.brunetti@poliba.it, [d]caterina.ciminelli@poliba.it

Keywords: Space Situational Awareness, Onboard Processing, Orbit Determination

Abstract. This work explores improving satellite collision prediction through autonomous optical observation and onboard orbit determination on at-risk LEO platforms. Potentially colliding objects pass near each other multiple times in the last orbits before a potential collision, allowing onboard sensors to collect especially timely data on secondary targets. A simulation framework combining multiple tools models these encounters, generating synthetic imagery and extracting astrometric measurements with uncertainties, which are then processed through sequential estimation filters. Results show how observation timing, sensor performance, and initial position/velocity uncertainty affect final accuracy. For debris at current uncertainty levels, most simulated sensors improve OD if detections succeed, while for accurately tracked satellites, achieving <15 arcsec total uncertainty is needed for noticeable gains.

Introduction

In Low Earth Orbit (LEO), potentially colliding objects generally pass close together multiple times during the orbits before the Time of the Closest Approach (TCA). These encounters, currently unexploited, present valuable opportunities for satellites equipped with optical sensors (including star trackers) to collect data on secondary objects. By processing this data onboard together with orbital estimates uplinked from the ground before TCA, meaningful refinement in positional knowledge of secondary objects can be achieved, enabling more informed manoeuvre decisions and reduced false alarm rates.

In previous studies, we established the feasibility of this approach from both orbital dynamics [1] and sensor detection performance perspectives [2]. In this work, we further implement an image-processing and orbit determination (OD) pipeline to assess the achievable reduction in positional uncertainties resulting from onboard processing of space-based observations, modeling sensors of varying quality. To this end, the simulation environment described in [2] is used to emulate the end-to-end operational concept in realistic conjunction scenarios based on actual events. The framework integrates a combination of commercial and open-source tools, such as MATLAB, Ansys's System Tool Kit (STK), and the Astrometry.net plate solver. Using this setup, space-based observation scenarios are simulated by incorporating various capabilities such as orbital dynamics, sensor optics and radiometric sensitivity, and space lighting conditions. Note that, as done in [2], object's trajectories are reconstructed starting from real-world data on historical at-risk objects. Particularly, Special Perturbations (SP) ephemerides are used to generate the "true" trajectories for each conjuncting pair. In parallel, for the secondary (uncooperative) object we retrieve Two-Line Elements (TLEs), which the simulated primary object uses both to predict observation windows and to initialize the OD process. This deliberate SP–TLE mismatch reflects operational reality, where the primary lacks high-fidelity knowledge of the secondary, and thus introduces realistic state and timing errors in the onboard analyses.

Content from this work may be used under the terms of the Creative Commons Attribution 3.0 license. Any further distribution of this work must maintain attribution to the author(s) and the title of the work, journal citation and DOI. Published under license by Materials Research Forum LLC.

Materials Research Proceedings 69 (2026) 1042-1047 https://doi.org/10.21741/9781644904251-180

A range of optical sensors is simulated using the same underlying model (STK's high-fidelity EOIR tool) but varying sensor parameters, including optical aperture, FoV, quantum efficiency, fill factor, readout noise and dark current. The set of simulated sensors, along with their specific parameters, matches that used in the detection-rate studies [2] and spans from low-quality star trackers to small imaging cameras for SmallSats.

Using STK's EOIR tool, synthetic imagery of the observed scenes is then generated. Such images are then post-processed to extract relevant target information for OD, as illustrated in Fig. 1. Specifically, after obtaining an astrometric solution with Astrometry.net [3], a free commercial plate solver, centroid detection algorithms implemented in MATLAB extract time-tagged angular measurements of detected targets, including right ascension (RA) and declination (DEC). Only extracting RA/DEC values from images is insufficient for meaningful OD in conjunction assessments; each RA/DEC pair must be accompanied by an uncertainty estimate. A tailored method is therefore applied to quantify the astrometric accuracy of angular measurements derived from optical observations. To follow, this method is described in more detail, since uncertainty characterization is a focus of the present work.

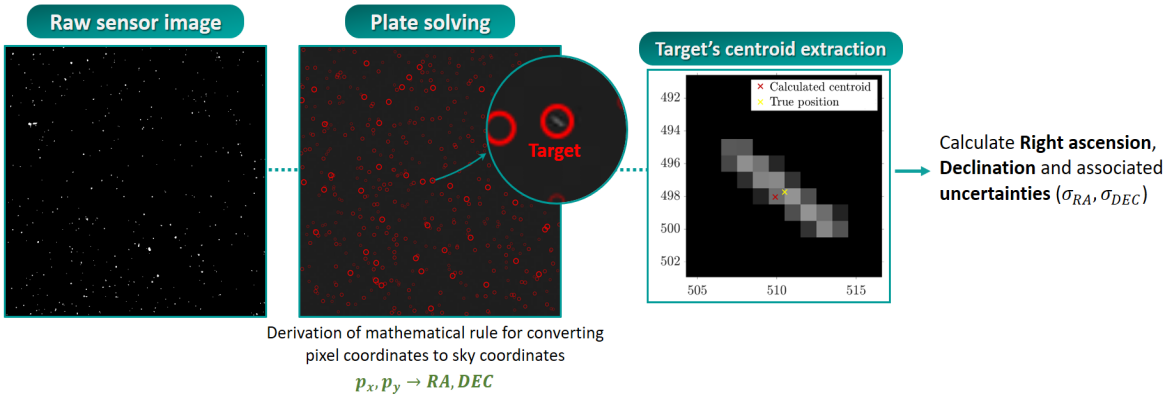


Fig. 1. *Main steps of the employed image processing pipeline.*

Estimation of Measurement Uncertainties

For space-based measurements, uncertainty arises from several independent sources, including coordinate fitting, centroiding, parallax, and timing errors. The total variance of a single observation is expressed as:

$$\sigma_{\text{tot}}^2 = \sigma_{\text{starfit}}^2 + \sigma_{\text{centr}}^2 + \sigma_{\text{par}}^2 + \sigma_{\text{timing}}^2 + \sigma_{\text{unknown}}^2 \quad (1)$$

where the terms are combined in quadrature, assuming uncorrelated errors. σ_{unknown}accounts for residual effects and is neglected here. All terms may be expressed in either pixels or arcseconds by applying the sensor's pixel scale. The general expression in Eq. 1 was originally introduced by [3] for quantifying the data quality of the Space-Based Visible sensor and it was later used for MOST satellite's observations [5] as well. The following discussion provides details on how each term in Eq. 1 is calculated here.

The Coordinate Fit Error (σ_{starfit}) represents the quality of the astrometric plate solution and depends primarily on the solver accuracy, the sensor's pixel scale, and star density in the field. To estimate σ_{starfit}, the residuals between measured and catalogued star positions from Astrometry.net are analyzed. The RMS residual in pixels is converted to arcseconds by multiplying by the pixel scale. Across multiple simulated images generated using EOIR, RMS errors ranged from 0.4–1.1 pixels. Comparing these values with those reported in the literature, they appear slightly higher than what can be reliably achieved with current solvers (0.01–0.2 px). This discrepancy is attributed to Astrometry.net's general-purpose nature, as it is not fine-tuned to specific optical

Materials Research Proceedings 69 (2026) 1042-1047 https://doi.org/10.21741/9781644904251-180

systems. For more realism, σ_{starfit} is modeled as a random value between 0.2–0.5 pixels, equally contributing to RA and DEC ($\sigma^2_{\text{starfit}} = \sigma^2_{\text{starfit, RA}} + \sigma^2_{\text{starfit, DEC}}$).

The Centroiding Error (σ_{centr}) quantifies the precision in locating the streak center and is here estimated as $\sigma_{\text{centr}} = 0.5 \cdot \text{FWHM}/\text{SNR}$ [6], where FWHM is the full width at half maximum of the source and SNR its signal-to-noise ratio. For elongated streaks, FWHM differs along and across the motion direction. As shown in Fig. 2, the procedure involves: 1) identifying the streak orientation via Principal Component Analysis (PCA) on the pixel coordinates; 2) rotating the Region of Interest (ROI) to align the streak horizontally; 3) extracting intensity profiles along and perpendicular to the streak; 4) computing FWHM values at half-maximum crossings. Although the uncertainties should ideally be projected into the inertial reference frame, for simplicity they are treated as isotropic. Thus, $\sigma_{\text{centr, RA}} = \sigma_{\text{centr, DEC}} = \text{FWHM}_{\parallel}/(2\sqrt{2} \cdot \text{SNR})$.

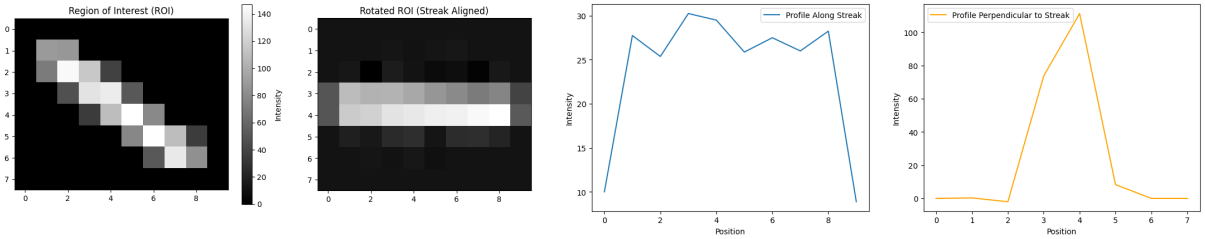


Fig. 2 *Steps for calculating the FWHM along and across the principal direction of an oblique streak*

Uncertainty in the observer's position introduces angular error due to parallax σ_{par}. For a platform position uncertainty σ_{eph} and target range R: $\sigma_{\text{par}} \approx \sigma_{\text{eph}}/R$, expressed in radians and converted to arcseconds by multiplying by 206,265. For GNSS-equipped satellites ($\sigma_{\text{eph}} < 15$ m) observing targets 300–800 km away, the parallax error ranges from 10.3 arcsec (300 km) to < 4 arcsec (800 km). Assuming no directional bias, $\sigma_{\text{par, RA}} = \sigma_{\text{par, DEC}} = \sigma_{\text{par}}/\sqrt{2}$.

Timing errors (σ_{timing}) arise from uncertainties in time-tagging observations. The resulting angular error is $\sigma_{\text{timing}} \approx \omega \cdot \sigma_t$, or equivalently, $\sigma_{\text{timing}} \approx \frac{v_{\text{FPA}}}{R} \cdot \sigma_t$, where v_{FPA} is the relative velocity projected onto the focal plane. Modern satellites synchronized via GNSS achieve $\sigma_t <$ 30ns, yielding sub-milliarcsecond errors (≈ 0.002 arcsec in worst cases), so σ_{timing} is neglected. Combining the three dominant terms and assuming error isotropy (i.e., $\sigma^2_{\text{i, tot}} = \sigma^2_{\text{i, RA}} + \sigma^2_{\text{i, DEC}}$), the total uncertainty per coordinate becomes:

$$\sigma_{\text{RA}} = \sigma_{\text{DEC}} = \frac{\sqrt{2}}{2}\sqrt{(rnd \cdot p_{\text{scale}})^2 + \left(\frac{\text{FWHM}_{\parallel} \cdot p_{\text{scale}}}{2 \cdot \text{SNR}}\right)^2 + \left(\frac{15}{R} \cdot 206{,}265\right)^2} \quad (2)$$

where rnd is a random value between 0.2–0.5 px and p_{scale} the pixel scale (arcsec/px).

Using Eq. 2, the total calculated angular error for the sensors simulated here ranges from ~8 to 51 arcsec. This estimate assumes that objects are detected at distances between 300 and 800 km with an SNR between 3 and 8, which is typical for the application at hand. Again, note that these angular error values do not solely reflect the intrinsic sensor resolution, which is included through p_{scale}. Deriving measurement uncertainty for optical observations requires accounting for the multiple factors in Eq. 2. Simply corresponding a sensor's resolution to its measurement accuracy in orbit is simplistic, as it neglects variable elements related to the observation strategy, specific application, and the accuracy of the platform's position and timing knowledge.

Materials Research Proceedings 69 (2026) 1042-1047 https://doi.org/10.21741/9781644904251-180

Orbit Determination

Once RA/DEC centroid coordinates and one-sigma uncertainties were collected for each simulated observation within a conjunction scenario, OD processing was performed using Ansys' ODTK, a comprehensive OD environment that seamlessly integrates with STK. Sequential estimation methods, and in particular the Extended Kalman Filter (EKF), were selected for their suitability to real-time applications such as the one considered here.

Each OD process begins by importing the RA/DEC measurements and one-sigma uncertainties into ODTK. The EKF is then initialized with an initial state derived from the secondary object's TLEs at the epoch of the last ground contact, denoted t_{LGC}. This instant represents the assumed final opportunity for the ground segment to upload an orbit solution to the primary before it must rely solely on its own onboard observations. In this analysis, t_{LGC} is varied between 1 and 10 hours before the TCA, while the simulated measurements typically occur within 40 to 120 minutes before TCA, when illumination and geometry are most favorable. EKF initialization also requires a covariance matrix for the secondary object, which should be representative of the orbit knowledge available at t_{LGC} from the ground. Since TLEs do not include uncertainty information, realistic covariance levels were derived from publicly available Vector Covariance Messages (VCMs). Accordingly, the simulated initial covariances were set between 0–200 m in position and 0–0.2 m/s in velocity, with components defined in the in-track, cross-track, and radial directions. Orbit propagation in ODTK was performed using the High Precision Orbit Propagator (HPOP), which numerically integrates the equations of motion considering gravitational harmonics, drag, and solar radiation pressure. The same propagator was used in STK to generate the reference trajectories, though with slightly different dynamic parameters to reflect the primary's imperfect knowledge of the secondary's physical properties and environment. Once initialized, the EKF processes the simulated onboard angular measurements to update the secondary's estimated state and covariance at each observation time.

Results

Figure 3 analyzes the sensitivity of OD performance to the initial position and velocity covariances. When the prior knowledge from the last ground update was poor—e.g., velocity uncertainties above 0.15 m/s or position uncertainties exceeding 150 m—onboard optical measurements from nearly all simulated sensors were able to reduce the final covariance magnitude in a meaningful way, often by 40–60%. However, enthusiasm for this result should be tempered by the fact that the smaller, lower-quality simulated sensors—although apparently effective from an OD standpoint—were rarely able to detect the target objects at all. In other words, between detection performance and measurement accuracy, the former emerges as the primary bottleneck preventing such sensors from being reliably used in operational contexts. As expected, for objects initialized with high-quality states, the gains became progressively smaller. While in recursive state-estimation filters every measurement, even one with high uncertainty, contributes information and cannot degrade the estimate [7], the achieved improvements were not significant enough to justify the operational adoption of most simulated sensors for already well-tracked objects. The only sensors providing both consistent detections and meaningful uncertainty reduction had apertures larger than 5 cm, narrow FoVs, and low electronic noise—comparable to high-performance star trackers or small imaging telescopes. Specifically, total angular errors exceeding 15 arcsec were found insufficient to improve the tracking of well-characterized active satellites.

Figure 4 illustrates the influence of the time elapsed between the last ground-based OD and the onboard measurement campaign. When ground-based OD can be performed within roughly one orbit (1–1.5 h) before TCA, the additional improvement provided by space-based observations becomes negligible. In all other cases, the total position uncertainty decreases by nearly an order of magnitude compared to uncorrected propagation. Currently, NASA takes final Go/No-Go

Materials Research Proceedings 69 (2026) 1042-1047 https://doi.org/10.21741/9781644904251-180

maneuver decisions about 12 hours before a potential collision, while ESA does so about 24 hours before TCA but preserves the option to cancel or refine the maneuver if additional ground-station accesses are available to upload updated commands. Other agencies adopt similar practices. This suggests that the operational concept proposed here, targeting observations in the last orbits before TCA, is generally effective.

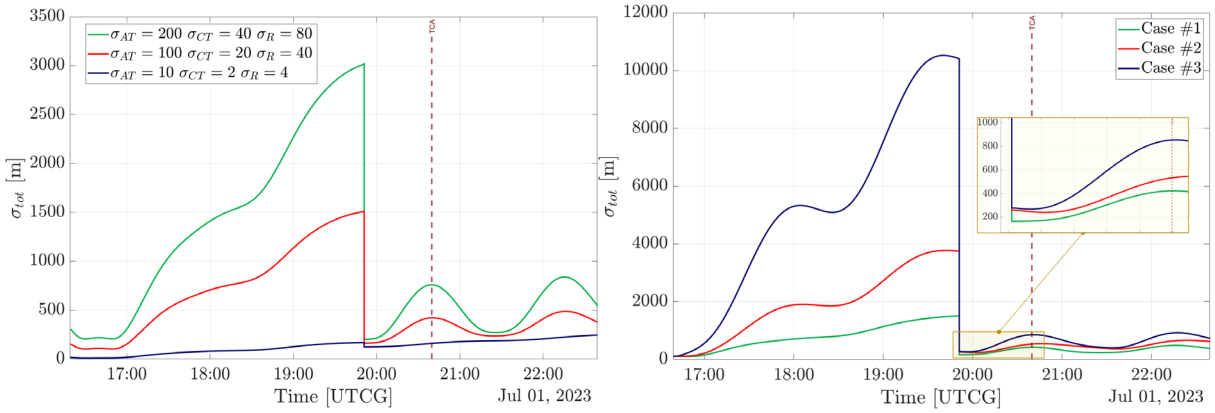


Fig. 3 *Impact of different initial positional uncertainties (left) and velocity uncertainties (right), with specific values reported in the legend*

Conclusion

This work analyzes the feasibility of using onboard optical sensors to refine conjunction risk estimates in LEO, by autonomously acquiring and processing astrometric measurements in the last orbits before TCA. The results show that for debris at current uncertainty levels, most simulated sensors yield meaningful uncertainty reduction if detections succeed, whereas for well-tracked active satellites only sensors achieving <15 arcsec total angular error provide tangible benefits. Operationally, these findings support hybrid schemes where modest onboard payloads complement ground networks, especially for poorly tracked objects and in late-warning regimes.

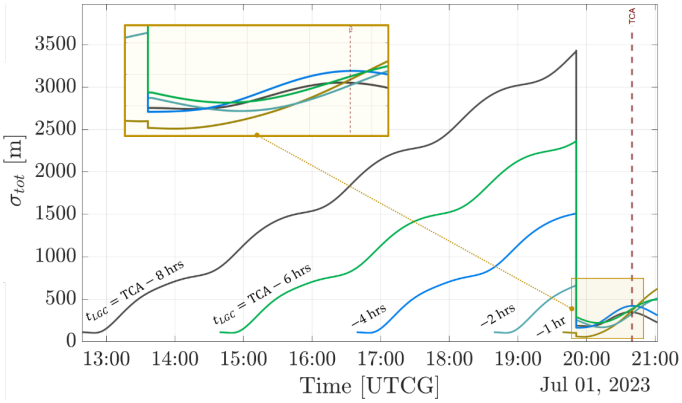


Fig. 4 *Total uncertainty evolution for different possible values of* t_{LGC}*: [8, 6, 4, 2, 1] hours.*

Acknowledgements

This work was supported by the "Space It Up!" project, funded by the Italian Space Agency and the Ministry of University and Research (Grant No. I53D24000060005).

References

[1] G. Campiti, G. Brunetti, V. Braun, E. Di Sciascio, C. Ciminelli, “Orbital kinematics of conjuncting objects in low-earth orbit and opportunities for autonomous observations,” Acta Astronautica, vol. 208, 2023, pp. 355-366, doi: https://doi.org/10.1016/j.actaastro.2023.04.032

[2] G. Campiti, G. Brunetti, C. Ciminelli, “Detectability of potentially colliding space objects through onboard cameras and star trackers, IEEE Transaction on Aerospace and Electronic Systems, doi: https://doi.org/10.1109/TAES.2025.3566681

[3] D. Lang, D. W. Hogg, K. Mierle, M. Blanton, S. Roweis, “Astrometry.net: blind astrometric calibration of arbitrary astronomical images,” The Astronomical Journal, vol. 139, 2010, pp. 1782–1800, doi: https://doi.org/10.1088/0004-6256/139/5/1782

[4] E. Andreis, P. Panicucci, F. Topputo, “An image processing pipeline for autonomous deep-space optical navigation,” arXiv online repository, 2023, doi: https://doi.org/10.48550/arXiv.2302.06918

[5] C. von Braun, J. Sharma, E.M. Gaposchkin, “Space-Based Visible metric accuracy,” Journal of Guidance, Control and Dynamics, vol. 23, no. 1, 2000, pp. 175-181, doi: https://doi.org/10.1016/10.2514/2.4508

[6] D. G. Monet, J. M. Jenkins, E. W. Dunham, S. T. Bryson, R. L. Gilliland, D. W. Latham, W. J. Borucki, D. G. Koch, “Preliminary astrometric results from Kepler,” in arXiv online repository, 2010, doi: https://doi.org/10.48550/arXiv.1001.0305

[7] G. T. Terejanu, P. Singh, T. Singh, and P. D. Scott, “Kalman Filtering with Uncertain Process and Measurement Noise Covariances,” Proceedings of the 2007 American Control Conference (ACC), New York, NY, USA, 2007, pp. 4842–4847

Materials Research Proceedings 69 (2026) 1048-1053 https://doi.org/10.21741/9781644904251-181

Trajectory Design, Stability, and Maintenance Analysis of Quasi-Satellite-Orbits in Martian Moons Environment

Enrico BELLONI[1,a *], Fabrizio Maccari[1,b] and Michèle LAVAGNA[1,c]

[1]Department of Aerospace Science and Technology, Politecnico di Milano, Via La Masa 34, 20156, Milano (MI), Italy

[a]enrico.belloni@polimi.it, [b]fabrizio.maccari@polimi.it, [c]michelle.lavagna@polimi.it

Keywords: Quasi-Satellite-Orbits, Trajectory Design, Sequential Convex Programming

Abstract. This paper presents advanced methods for designing scientific trajectories in the unique dynamical environment of the Martian moons, with a particular focus on stability analysis and station-keeping strategies. Such trajectories, aimed at deepening the understanding of Phobos and Deimos characteristics, have been proposed in different mission concepts over the past decade. The Japan Aerospace Exploration Agency's Martian Moons eXploration (MMX) mission, scheduled to visit Phobos in 2026, will mark the first practical implementation of these concepts. To build upon and complement the preparatory studies conducted for MMX, this work provides an in-depth analysis of orbital dynamics and long-term trajectory design specifically around Deimos. The results contribute to a broader framework for mission planning in irregular and weak-gravity environments, with implications for future exploration of small celestial bodies.

Introduction

Due to the strong gravity pull of Mars and the mass of Deimos being too small to capture a satellite, it is not possible to orbit the Martian moonlet in the usual two-body sense. Quasi-Satellite-Orbits (QSOs) [1] are a special kind of stable retrograde orbits in the restricted three-body problem that have gained attention as a viable candidate for future deep-space missions towards remote planetary satellites due to their mapping capabilities and high stability, coupled with low station-keeping costs.

These orbits can be found by iterative differential correction starting from a desired value of orbital radius. Additionally, out-of-plane motion can be also induced, in order to increase the surface coverage. However, the entity of the out-of-plane component must be limited, as it tends to destabilize the QSO, leading to an impact on Deimos or to an escape far from it. This work studies QSOs around Deimos, assessing their stability, their sensitivity to injection error and proposing a station-keeping strategy.

Dynamics

Due to the very low gravitational pull of Deimos, Hill's approximation of the Circular Restricted Three-Body Problem can be used to describe the dynamics [2], with the equations of motion that read:

$$\begin{aligned} \ddot{x} - 2\dot{y} &= g_x + 3x \\ \ddot{y} + 2\dot{x} &= g_y \\ \ddot{z} &= g_z - z \end{aligned} \qquad (1)$$

where g represents the gravitational acceleration of Deimos, computed accordingly to a high-fidelity polyhedron shape model. Indeed, at the distances of the chosen QSOs from the surface of the moonlet, the error between the simple spherical gravity approximation and the polyhedron

Content from this work may be used under the terms of the Creative Commons Attribution 3.0 license. Any further distribution of this work must maintain attribution to the author(s) and the title of the work, journal citation and DOI. Published under license by Materials Research Forum LLC.

Materials Research Proceedings 69 (2026) 1048-1053 https://doi.org/10.21741/9781644904251-181

model is up to 10-20%, as visible in Figure 1. The polyhedron approximation is computed as derived in [3] using the reference shape model of [4].

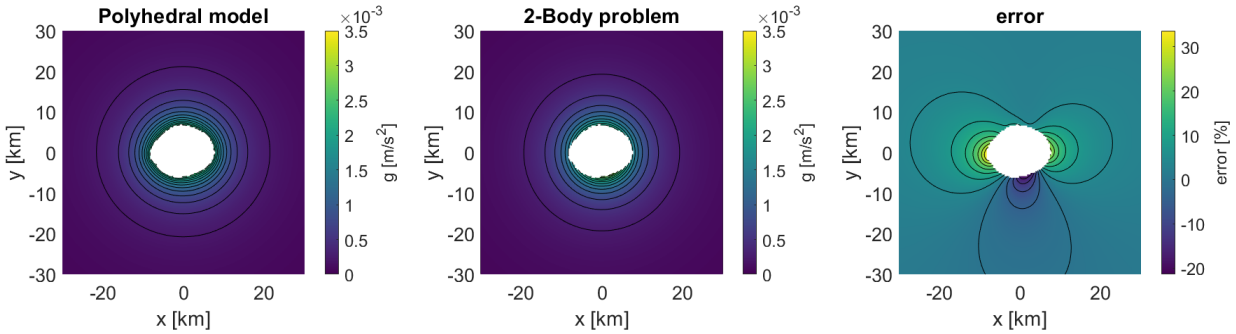


Figure 1: Difference between irregular and spherical gravity field models.

In addition, also a full ephemerides model should be considered to accurately describe the motion in the proximity of the small body. Consequently, two different dynamic models have been used in this work:

- A simplified model, in the Hill's reference frame, considering Martian gravity and a shape model to compute Deimos' gravitational attraction.
- A high fidelity model, propagated in an inertial reference frame centered at Mars. Here, Martian point mass and J_2 gravitational attraction are considered, together with Deimos shape model gravity. The motion of Deimos with respect to Mars is recovered using NASA spice ephemerides, with the mar097 and de432 kernels.

Stability analysis

The in-plane and out-of-plane periodicity of QSOs is assessed for a wide range of initial conditions. In particular, QSOs have been generated starting from an offset from Deimos on the x-axis of the Hill's reference frame ranging from 15 to 100 km. The prediction-correction is carried out in the simplified Hill model, with each orbit that is then re-propagated in full-ephemeris. More precisely, each QSO is computed considering only an in-plane initial velocity vector, then an out-of-plane component is included, progressively increasing the angle with respect to the x-y plane.

The objective of this analysis is to assess what is the limit on the out-of-plane component of the velocity vector, that tends to destabilize QSO motion as visible in Figure 2. Going further from Deimos the non-spherical gravitational attraction has a less important perturbing effect, with out-of-plane QSOs that are possible for higher inclinations of the initial velocity vector. This is outlined by Figure 3, in which the motion is bounded also for an out-of-plane angle of 20°.

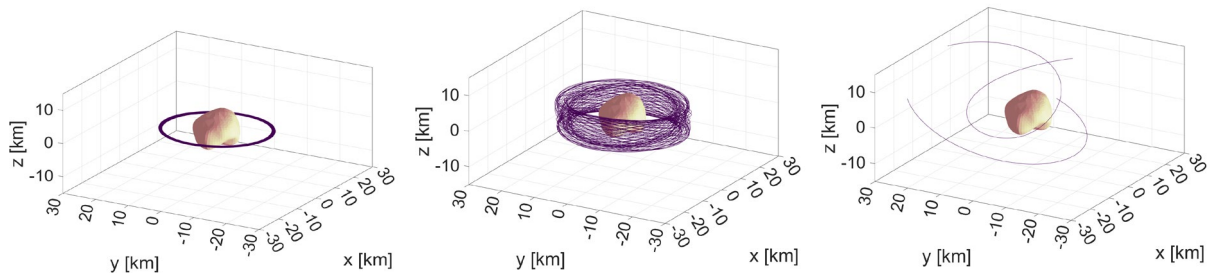


Figure 2: 60 km radius QSO. Motion computed with an in-plane initial velocity vector (left), and with a 10° (center) and 20° degree angle (right) with respect to the plane.

Materials Research Proceedings 69 (2026) 1048-1053 https://doi.org/10.21741/9781644904251-181

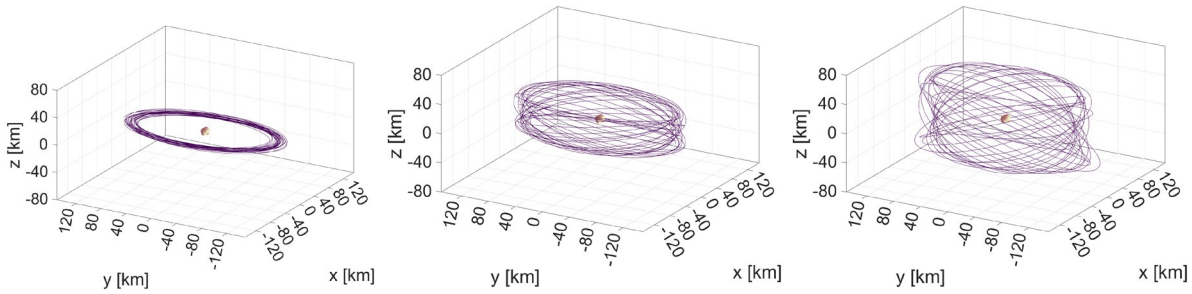
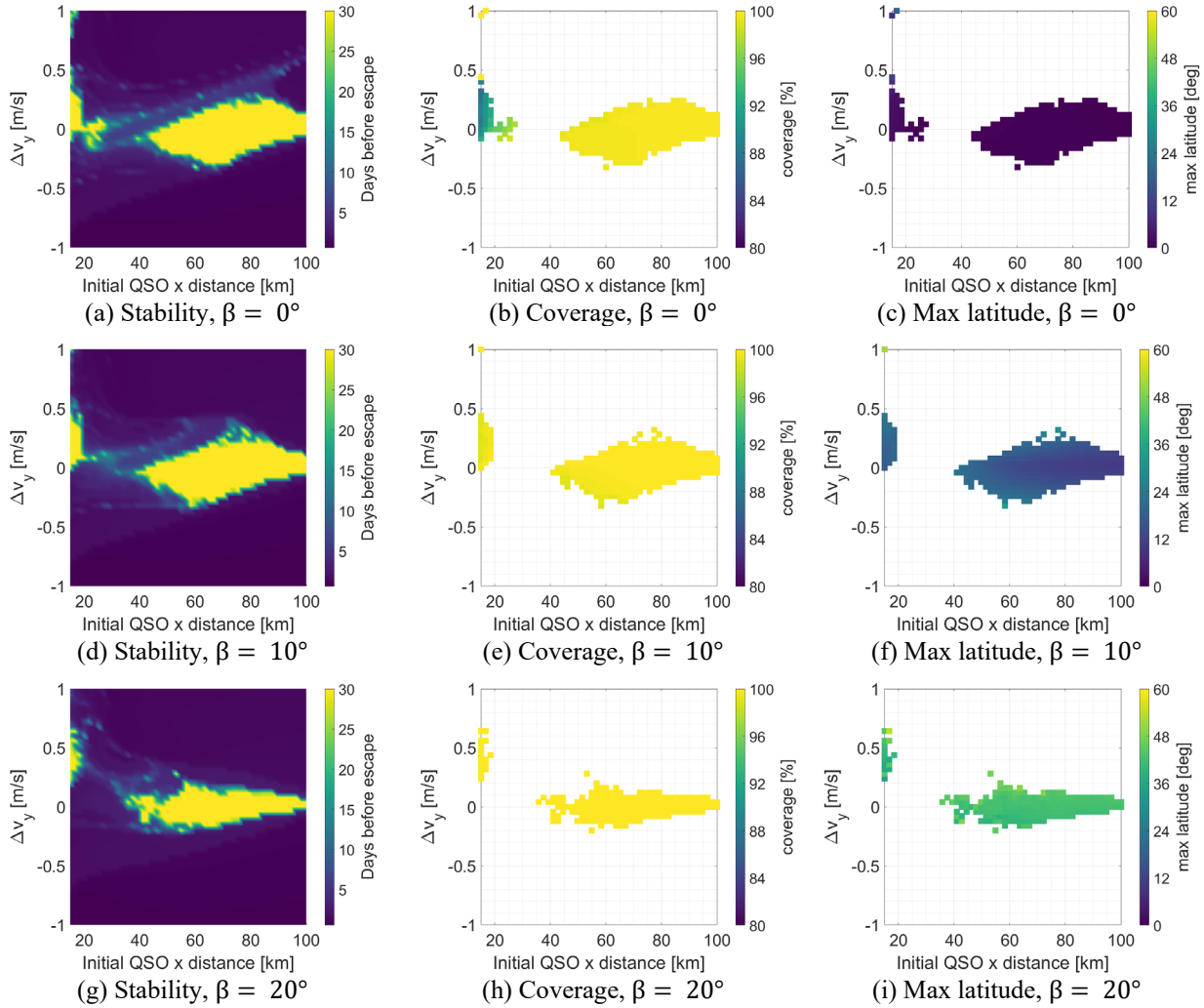


Figure 3: 60 km radius QSO. Motion computed with an in-plane initial velocity vector (left), and with a 10° (center) and 20° degree angle (right) with respect to the plane.

These results have then been generalized, by means of a sensitivity analysis of the stability of QSOs with respect to their initial distance and velocity with respect to Deimos. In this work, the stability analysis is carried out by propagating the orbit for a large number of revolutions in the high fidelity model, and by checking if the motion is bounded around Deimos or if the spacecraft escapes from the moonlet. Approaches based on the eigenvalues of the monodromy matrix are also possible [5], however, the necessity of using the full-ephemeris dynamics with non-spherical Martian moon gravity drove the choice towards a numeric approach for this work, with high-fidelity propagation.

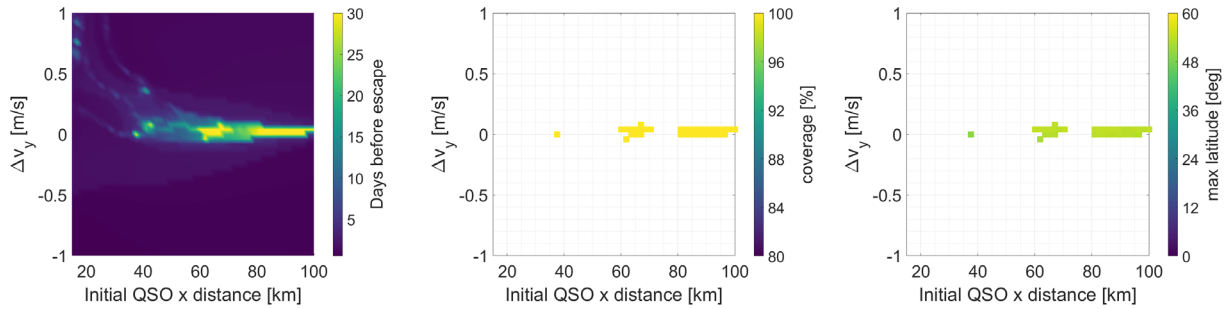


(a) Stability, β = 0° (b) Coverage, β = 0° (c) Max latitude, β = 0°

(d) Stability, β = 10° (e) Coverage, β = 10° (f) Max latitude, β = 10°

(g) Stability, β = 20° (h) Coverage, β = 20° (i) Max latitude, β = 20°

Materials Research Proceedings 69 (2026) 1048-1053 https://doi.org/10.21741/9781644904251-181



(j) Stability, β = 30° (k) Coverage, β = 30° (l) Max latitude, β = 30°

Figure 4: QSO stability and coverage analysis at different values of out-of-plane velocity component.

The result for in plane motion is shown in Figure 4a, which reports the days of bounded QSO motion over a maximum propagation interval of 30 days, in the full-ephemeris model. The plot presents the distance from Deimos along the Mars-Deimos line on the x-axis and possible tangential perturbations on the initial velocity on the y-axis. It can be noted that planar bounded QSO motion exists for almost the whole range of distances considered, with the exception of the region from 25 to 40 km. This difference with respect to the simplified Hill motion, for which bounded motion exists for all ranges, is probably due to the effects of the actual shape of Deimos' orbit around Mars, coupled with the highly irregular gravity field. Furthermore, it can be seen from the figures how the stability region shrinks for increasing value of initial out-of-plane velocity component.

Naturally, an additional limiting factor is the Δv_y perturbation on the initial velocity, that shall always remain within around 0.5 m/s to have a bounded QSO. Scientific performance of bounded orbits is also reported in Figure 4b, showing a percentage of visible surface up to 100%. This shows that from a sufficient distance almost the entire surface of Deimos can be covered, even with planar QSOs. The last plot on the right (Figure 4c) is the maximum latitude of the ground track of the spacecraft on Deimos. For planar motion it is obviously always zero. An exception arises for some perturbed low altitude orbits, that end up having an out-of-plane motion due to the non-symmetrical gravitational attraction of Deimos.

For out-of-plane QSOs the situation is similar, as visible from Figure 4d to Figure 4l. With the increase of the out-of-plane component of the initial velocity, the region of bounded motion in the $x - v_y$ plane tends to shrink and less QSOs are found for lower values of x offset. Again, this is due to the non-symmetrical shape of Deimos, that has a more important impact on the dynamics if the spacecraft is close to the moonlet.

Scientific orbit maintenance

In this Section, a station-keeping strategy for QSOs is explored, based on convex optimization techniques, which have found application in a wide variety of trajectory computation problems in the space domain [6, 7].

In this case, Sequential Convex Programming (SCP) techniques have been put in place, incorporating the effects of the irregular gravity field of the body in the trajectory generation. More in detail, an iterative station keeping algorithm is designed to compute the optimal control actions to maintain the nominal QSO, computed according to Hill three-body problem dynamics. In particular, each time the distance between the chosen QSO in the simplified model and the full-ephemeris propagation goes over 3 km, the GuSTO algorithm is used to bring the error to zero while minimizing $\boldsymbol{\Delta V}$, leaving a free maneuvering time. The example demonstrates the applicability of this strategy for a 30 km QSO with an initial velocity off-plane angle of 5°, which

would be unstable in the full ephemeris model. In particular, Figure 5 shows that the strategy is successful, being able to periodically correct the orbit for periods larger than one week with an average daily $\boldsymbol{\Delta V}$ equal to 1.12 m/s.

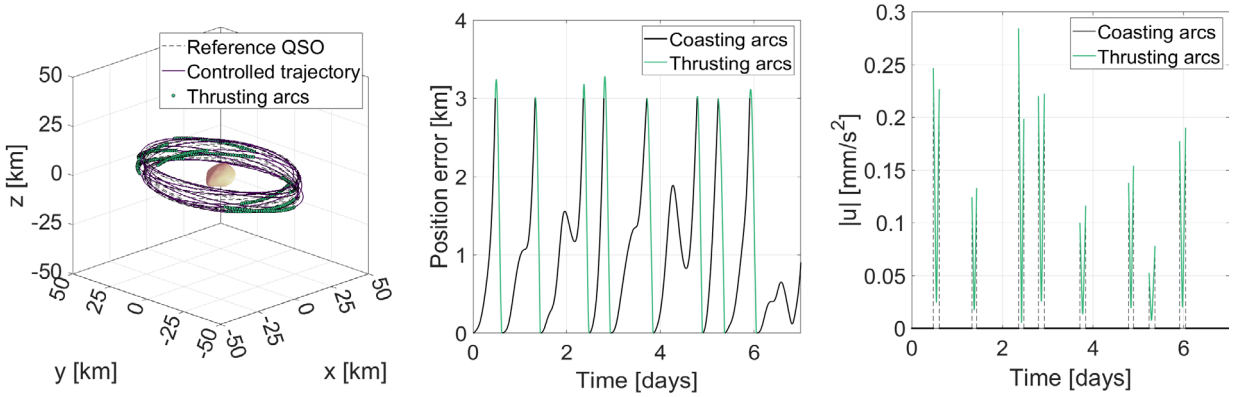


Figure 5: Results of station keeping analysis over a week of controlled motion in unstable 3D QSO region.

Conclusions

The analyses presented in this paper show that QSOs can be viable choices to meet high level requirements of typical scientific missions exploring Martian moon environment, while guaranteeing high orbital stability. Additionally, operational safety with respect to navigation and injection errors is also assessed for both planar and 3D orbit, in order to understand the applicability of the latter for high latitude observations. Finally, a SCP algorithm is proposed to iteratively compute dynamically feasible low-ΔV trajectory correction maneuvers to maintain periodic off-plane motion.

References

[1] Spiridonova, Sofya, et al. "Quasi-Satellite Orbits around Deimos and Phobos motivated by the DePhine Mission Proposal." (2017).

[2] Scheeres, Daniel J., Z. Olikara, and N. Baresi. "Dynamics in the Phobos environment." Advances in Space Research 63.1 (2019): 476-495. https://doi.org/10.1016/j.asr.2018.10.016

[3] Werner R, Scheeres D. Exterior Gravitation of a Polyhedron Derived and Compared with Harmonic and Mascon Gravitation Representations of Asteroid 4769 Castalia. Celestial Mechanics and Dynamical Astronomy, 1996, 65: 313-344, doi:10.1007/BF00053511. https://doi.org/10.1007/BF00053511

[4] Ernst CM, Daly RT, Gaskell RW, Barnouin OS, Nair H, Hyatt BA, Al Asad MM, Hoch KKW. High-resolution shape models of Phobos and Deimos from stereophotoclinometry. Earth, Planets Astrodynamics and Space, 2023, 75(103), doi:10.1186/s40623-023-01814-7. https://doi.org/10.1186/s40623-023-01814-7

[5] Chen, Hongru, et al. "Effective stability of quasi-satellite orbits in the spatial problem for phobos exploration." Journal of Guidance, Control, and Dynamics 43.12 (2020): 2309-2320. https://doi.org/10.2514/1.G004911

[6] Malyuta, Danylo and Reynolds, Taylor P. and Szmuk, Michael and Lew, Thomas and Bonalli, Riccardo and Pavone, Marco and Açıkmeşe, Behçet, Convex Optimization for Trajectory Generation: A Tutorial on Generating Dynamically Feasible Trajectories Reliably and

Efficiently, IEEE Control Systems Magazine, 2022, doi:10.1109/MCS.2022.3187542. https://doi.org/10.1109/MCS.2022.3187542

[7] Belloni, E. and Maccari, F. and Lavagna, M., ANIME Asteroid CubeSat Mission Concept and Rendezvous Phase: Progressive Hyperbolic ARCS Design for Radio-Science and Close Observation, 75th International Astronautical Congress (IAC) 2024. https://doi.org/10.52202/078368-0051

Materials Research Proceedings 69 (2026) 1054-1058 https://doi.org/10.21741/9781644904251-182

Remote sensing use in Insurance Companies to Manage Natural Disasters Policies – IRIDE Constellation Case Study

Ludovica LOCATELLI[1,a *], Giuseppe DI BELLA[1,b] and Franco BERNELLI-ZAZZERA[1,c]

[1]Politecnico di Milano, Milano, Italy

[a]ludovica.locatelli00@gmail.com, [b]giuseppedb2016@gmail.com, [c]franco.bernelli@polimi.it

Keywords: Earth Observation, Insurance, IRIDE, Natural Disasters, Remote Sensing

Abstract. The increasing frequency and severity of natural disasters pose significant challenges to the insurance industry, which requires innovative approaches to risk assessment and policy management. This paper explores the role of remote sensing in improving the ability of insurance companies to manage natural disaster policies, with a specific focus on the IRIDE constellation. Using services designed through satellite imagery and geospatial data, insurers can better understand risk exposure and improve their response strategies. Remote sensing technologies offer the advantage of monitoring large areas with high precision, detecting changes in land use, water levels, and atmospheric conditions that can influence insurance claims. This study aims to analyze how remote sensing helps insurers prepare for and respond to catastrophic events, focusing in particular on the use of IRIDE for the scope.

Introduction

The increasing frequency and intensity of natural disasters, coupled with the vulnerability of Italy's geographic and urban infrastructure, have created an urgent need for more effective disaster risk management strategies, particularly within the insurance sector. In 2023, global insured losses from natural disasters exceeded € 100 billion, a number expected to double within the decade due to climate change, according to the latest estimates from the Swiss Re Institute. Despite this, only about 25% of Italy's natural disaster losses are insured, the public finances absorbing most of the costs; approximately € 3.5 billion annually. This alarming trend confirms the need to apply innovative tools for risk assessment, monitoring, and post-event analysis. This project explores the application of remote sensing technologies, in this instance the Italian Earth observation constellation IRIDE, to improve the operational capabilities of insurance companies in handling policies for risks and catastrophes and risk modelling.

Use of Space Technologies by Insurance Companies

The use of satellite technology in the civil and commercial sectors is becoming more and more common and frequent. Therefore, many companies find themselves having to interface, along with its exponential development, with a scientific sector that is becoming less and less alien. The range of services that satellite technology can provide is becoming wider and more accessible, so the products that can be developed from it. Revenues from EO data in 2023 in the insurance and finance segment increase from approximately € 340 million to nearly € 900 million in 2033 [1].

In this context, a market analysis is conducted that highlights the strengths, weaknesses, opportunities, and threats of this business.

Several strengths of the adoption of space technologies in the insurance sector can be identified, including improved efficiency in pricing policies, the ability to offer more personalized policies at competitive prices, a reduction in insured and operational losses, and the development of new business opportunities, such as parametric insurance and community-based catastrophe insurance.

Content from this work may be used under the terms of the Creative Commons Attribution 3.0 license. Any further distribution of this work must maintain attribution to the author(s) and the title of the work, journal citation and DOI. Published under license by Materials Research Forum LLC.

Materials Research Proceedings 69 (2026) 1054-1058 https://doi.org/10.21741/9781644904251-182

Regarding opportunities, Italian companies are now required to obtain a Natural Catastrophe Insurance policy (CATNAT), which introduces, for the first time in the Italian regulatory framework, a mandatory insurance requirement for catastrophic risks, limited to the productive sector. This development requires insurance companies to be well prepared to manage these risks in the most efficient way. Another opportunity lies in the possibility for insurance companies to establish partnerships to bridge the knowledge gap regarding Earth observation and related services. Using the data, images, and services provided by the IRIDE constellation, they can enhance their capabilities in risk assessment and management.

However, there are also several threats and weaknesses in this market, such as the innovation inertia of the insurance sector, the lack of social awareness about the need to subscribe to policies, the requirement for big data management and highly specialized skills to handle Earth observation tools, and the still limited commercial adoption of EO techniques.

Chain of Acquisition of Data, Creation and Selling of Services

The current value creation model within the EO sector follows a multi-step value chain, which can be visualized in Figure 1. The initial stage includes the data providers, comprising entities that own and operate the space and ground segments responsible for acquiring raw EO data. Subsequently, the providers of products and services act as intermediaries, leveraging advanced data processing and analytics to transform raw data into customized solutions that address specific user requirements.

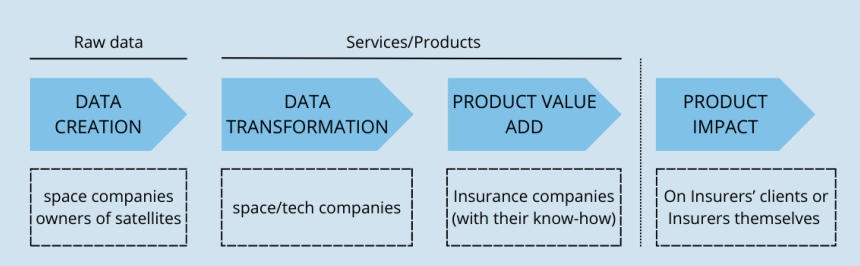


Figure 1: Value chain

Finally, in the context of this research, end users are represented by insurance companies, which use these refined data products to improve decision-making, optimize risk assessment, and streamline operational processes.

Satellite technologies can be considered a valuable investment in the insurance segment. Despite this, there are various ways to invest in this technology. In particular, companies can choose to invest in an internal team that processes raw data and transforms it into services, or they can form external partnerships with companies that have the resources and expertise to create semi-finished services to sell to insurance companies.

An Italian insurance company was interviewed, revealing the idea that it would be preferable to establish advanced partnerships, delegating the more complex aspects of satellite analysis to specialized partners. The current trend emerged leans toward integrating satellite technology into existing company processes without significantly disrupting the traditional insurance model.

Use of IRIDE Constellation

IRIDE is a satellite constellation for Earth observation initiated by the Italian Government, supported by resources from the National Recovery and Resilience Plan (PNRR). IRIDE will be completed by 2026 under the management of the European Space Agency (ESA), with the support of the Italian Space Agency (ASI). IRIDE satellites will offer 8 macro services for marine and coastal monitoring, air quality, ground motion monitoring, land cover analysis, hydro-meteorological and climate observation, water resource monitoring, emergency management, and

Materials Research Proceedings 69 (2026) 1054-1058 https://doi.org/10.21741/9781644904251-182

security. In total the constellation will be composed by 6 sub-constellations, placed in Low Earth Orbits to obtain more frequent and detailed images: HEO (Multi1) and EAGLET-2 (Multi2) have a multispectral sensor, NIMBUS-VHR (Opt) an optical one, NIMBUS-SAR (SAR1) and NOX (SAR2) have on-board a SAR sensor and PLATINOHYP (Iper) a hyperspectral sensor. Each constellation is defined by the orbital parameters of the satellites and the specifications of the sensors on board [2]. Some modifications and assumptions have been applied to obtain repeating ground tracks and improve coverage, following the system of equations 1 [3], which aims to obtain the new inclination (i) to respect the SSO requirement, and the new semi-major axis (a) to meet the periodicity constraint.

The propagation method used in the simulation is the SGP4 to compute satellites' positions and velocities; and to build a complete satellite simulation scenario, the Satellite Communications Toolbox in Matlab is adopted.

$$\begin{cases} i = cos^{-1}\left(\frac{-2\dot{\omega}_d a^{\frac{7}{2}}}{3\sqrt{\mu}J_2 R_e^2}\right) \\ P_\Omega = \frac{2\pi}{n+\frac{3nR_e^2 J_2\sqrt{1-e^2}}{4\left(a(1-e^2)\right)^2}(3sin^2 i-2)+\frac{2-3nR_e^2 J_2}{4\left(a(1-e^2)\right)^2}(4-5sin^2 i)} \\ k_{rep}P_\Omega\left(1-\frac{T_E}{T_y}\right) = k_{day}T_E \end{cases} \quad (1)$$

Coverage

To assess the performance of a constellation, it is crucial to analyze the number of days required to achieve meaningful coverage. The methodology used will take into account the exact area observed by each sensor type considering both the direction of the sensor and the acquisition mode [4].

Table 1 reports the percentages of coverage for each constellation reached in an interval of time of Italian territory. SAR1 results in being the most efficient constellation while the Optical is the least.

Table 1: Constellations' coverage

	Period [days]	**Coverage**
SAR1	6	98.93%
SAR2	15	76.87%
Opt	15	66.53%
Iper	15	83.59%
Multi1	10	82.23%
Multi2	6	94.97%

Revisit Time

Spatial coverage alone is insufficient without considering a temporal factor, which provides insights of how often and for how long the spacecraft is available within a given time frame. The goal of this analysis is to estimate and evaluate the revisit times of each constellation, ensuring that they meet the requirements of the end users.

All constellations are in Sun Synchronous Orbits (SSO) except from SAR1 which is in a Mid Inclination Orbit (MIO). For a given inclination of SSO, the revisit time decreases as the latitude increases, while SAR1 orbit is designed to have 6 satellites at 44 degrees inclination and the remaining 6 at 49 degrees, which results in having a lower revisit time around the latitude of 44

Materials Research Proceedings 69 (2026) 1054-1058 https://doi.org/10.21741/9781644904251-182

degrees, while only the 6 satellites with 49 deg inclination can access higher latitudes, resulting in less accesses to these areas.

Optical and SAR2 constellations have the highest revisit time due to their limited number of satellites. Additionally, the revisit time of each constellation depends much more on latitude than on longitude.

Ground Station Access

The primary purpose of Earth observation satellites is to collect data, such as imagery or environmental metrics. Ground stations receive this data via down-link for processing, analysis, and distribution. In the study of the link with ground stations, only those located within European territory are considered. It has been verified that satellites, after acquiring and processing images and data over Italy, can transmit and communicate with ground stations within Italian territory almost instantaneously (e.g. for the transmission of 1GB, see Equation 2, while remaining visible for the required duration. In fact, the duration of a typical communication session with a single satellite from one of the IRIDE constellations ranges between 6 and 8 minutes, which is sufficient for data transmission.

$$T = \frac{1GB(8Bit)}{400Mbps} = 20s \tag{2}$$

Requirements and IRIDE's adaptability for specific case studies of natural disasters

The events considered in this study are earthquakes, landslides, floods, fires, and critical infrastructure. For each event, the necessary requirements for their observation through remote sensing are investigated, as reported in Table 2 and retrieved from past literature. For each event, the most suitable IRIDE constellations are selected based on the requirements listed above. While resolution (Res) and sensor type are easily met, a more detailed analysis is conducted for revisit time (RT), identifying critical locations for each case study and evaluating them over a long time interval. When the use of the SAR1 constellation is required, it meets all requirements thanks to its high spatial and temporal efficiency. In contrast, the optical and hyperspectral constellations almost always require integration with external satellites due to their high revisit time, which does not meet the necessary requirements. Additionally, the combined use of MULT1 and MULT2 is sufficient for studying events requiring multispectral observation.

Table 2: Requirements for events' observation

	Sensor	**Res [m]**	**RT [days]**
Earthquakes	Optical SAR	5 20	1-7
Landslides	Optical Multi & InSAR	1 10	5
Floods	Optical SAR Multi	1-5 300 30	1-3 <1
Fires	Multi Hyper	10-500 ≥30	1-5 7
Critical In.	DinSAR (spotlight)	1-5	1-7

Conclusions

In conclusion, to scale EO for broader commercial use changes in data collection, sale and application are required. Despite EO can facilitate various industries, its commercial adoption has been slow, particularly in the insurance sector, due to technology inertia and financial barriers.

This research highlights the IRIDE program as a key solution, providing continuous and high resolution EO data for disaster monitoring and prevention. With the additional possibility of integrating IRIDE with other external constellations, insurance companies can improve risk assessment and develop advanced models such as parametric insurance. In addition, EO will complement, rather than replace, existing methods like in-situ sensors and drones, creating a comprehensive risk management approach.

As extreme weather events increase, creating partnerships between space agencies, insurers, and technologies providers will be crucial for maximizing EO's potential in disaster resilience.

References

[1] EUSPA. Wrapping up 2024: An unforgettable year for EUSPA, (2024). https://www.euspa.europa.eu/newsroom-events/news/wrapping-2024-unforgettableyear-euspa

[2] E. G. Cadau et al., The IRIDE Project: Satellites, Algorithms and Products of the New Italian Space Programme, IGARSS 2024 - 2024 IEEE International Geoscience and Remote Sensing Symposium, Athens, Greece, (2024), pp. 6763-6766, https://doi.org/10.1109/IGARSS53475.2024.10640855.

[3] D.A. Vallado, Fundamentals of Astrodynamics and Applications - Fifth Edition, Space Technology Library, Microcosm Press, (2022). ISBN: 978-1881883210 and 978-1881883227

[4] E. Resta. Coverage and revisit time estimation of the IRIDE mission. Master's thesis, Politecnico di Milano, (2024). https://www.politesi.polimi.it/handle/10589/219099

Materials Research Proceedings 69 (2026) 1059-1064 https://doi.org/10.21741/9781644904251-183

Experimental Validation of Initial Orbit Determination of Resident Space Objects Using Probabilistic Admissible Regions

Bart KIEBOOM[1,a *], Martin MICHEL[1,b] and Urs HUGENTOBLER[2,c]

[1]Airbus Defence and Space, Claude-Dornier-Straße, 88090 Immenstaad, Germany

[2]Technical University Munich, Arcisstraße 21/III, 80333 München, Germany

[a]bart.kieboom@airbus.com, [b]martin.michel@airbus.com, [c]urs.hugentobler@tum.de

Keywords: IOD, SST, SSA, Probabilistic Admissible Region, Tracklet Correlation, Space Surveillance, Space Debris, Astrodynamics, Gaussian Mixture Models

Abstract. This work considers the catalogue generation problem using ground-based passive optical data. In this context, surveillance observations often yield tracklets with very short arcs. These tracklets consist of a set of angular measurements closely spaced in time, covering only a small part of the object's orbit. This data is insufficient for conventional (Initial) Orbit Determination (IOD) and no full orbit can be derived. A different approach using the Admissible Region (AR), defined as the set of possible range and range-rate pairs consistent with the tracklet, is an effort to tackle this problem. Here we apply the Probabilistic Admissible Region, which is a probabilistic representation of the AR, to real-world optical data and use it to perform tracklet correlation and IOD to provide an experimental validation of the methodology.

Introduction

In the past decades the number of Resident Space Objects (RSO) has increased drastically. This trend is likely to continue and accelerate as more commercial and military activity in space is enabled by, among other things, the proliferation of launch capabilities accompanied by reduced cost, and increasingly favourable economics in satellite production. Moreover, these assets are widely integrated in civil and military systems and services, making the safety and operability of these assets a critical mission. A core activity in this mission is the generation and maintenance of a RSO catalogue. Catalogue generation is the process of finding new or previously lost RSO and determining their state, while catalogue maintenance is the process of maintaining the states of objects that are already in the catalogue.

This work considers the catalogue generation process using passive optical sensors. More specifically, it considers the data association problem for tracklets, sometimes called the tracklet-to-tracklet correlation or tracklet linking problem, using the Probabilistic Admissible Region.

A *tracklet* is a set of measurements of a single RSO closely spaced in time, and in the context of Initial Orbit Determination (IOD) often constitutes a *Too Short Arc* (TSA) [1, 2]. A TSA is too short in the sense that it has little geometric diversity, that is, it covers only a small part of the orbit. Such tracklets are insufficient for conventional IOD or OD processes and must be paired with other tracklets originating from the same object first. The challenge is that we do not know a priori which object a tracklet belongs to, and hence which tracklets should be paired. This is the essence of the tracklet correlation problem.

In the case of optical measurements, TSA tracklets capture only angular information, namely, the right ascension and declination and their rates, collectively referred to as the tracklet's *attributable*. In principle, any value for the remaining state components (range and range-rate) is consistent with the observations. However, we can constrain the space of possible values by making some reasonable or educated assumptions about the orbital state. The *Admissible Region* (AR) concept captures this approach. The AR was originally introduced for orbit determination of

Content from this work may be used under the terms of the Creative Commons Attribution 3.0 license. Any further distribution of this work must maintain attribution to the author(s) and the title of the work, journal citation and DOI. Published under license by Materials Research Forum LLC.

Materials Research Proceedings 69 (2026) 1059-1064 https://doi.org/10.21741/9781644904251-183

asteroids [1], and subsequently applied to space debris [2]. For Earth-orbiting objects, the AR is the set of admissible range and range-rate pairs under the assumption that the observed object is in fact in a bounded orbit about Earth. This requires the total energy to be negative and hence constrains the possible range and range-rate values. Additional constraints can be introduced, such as a minimum and maximum energy [3] and eccentricity value [4]. The extended concept is referred to as the *Constrained Admissible Region* (CAR). We can obtain a probabilistic representation of the CAR by assigning probabilities to admissible range / range-rate pairs, the resulting distribution is referred to as the *Probabilistic Admissible Region* (PAR). By assuming each admissible pair is equally probable, we arrive at a uniform distribution within the CAR [4]. Alternatively, one can assume that each semi-major axis / eccentricity pair within the given constraints is equally likely, this results in a non-uniform distribution within the CAR [5]. The PAR can be utilized to perform IOD [4] and/or tracklet correlation.

The main contribution of this work is an experimental validation of the utilization of the PAR for IOD and tracklet correlation using real-world optical data in the MEO regime. We present the full processing pipeline, from image data to (initial) orbital states and covariances of RSO, and its validation. While historically passive optical systems have been mostly utilized for cataloguing GEO objects, a growing number of telescope operators and space-based optical sensors calls for improved processing techniques for passive optical data for LEO and MEO. The data utilized in this work is obtained by the Airbus Robotic Telescope (ART) located in Extremadura, Spain, which is operated by the Space Situational Awareness team at Airbus Defence and Space, Friedrichshafen, Germany.

Method

ART is an optical telescope with an aperture of 40 cm and a focal length of 960 mm and is equipped with 150 megapixel back-illuminated CMOS sensor with a rolling shutter, giving it a field-of-view of $3.18° \times 2.38°$. ART is scheduled to either track satellites (using TLEs or ephemerides) or perform sidereal observations (inertial pointing). The resulting data are images in which the satellites and stars appear as point sources and streaks, respectively, for tracking observations, and streaks and point sources, respectively, for sidereal observations.

From the image data, an astrometric solution is obtained [6], resulting in a set of timed measurements of the sky coordinates, i.e., the right ascension α and declination δ. Measurements in consecutive images are then associated to form tracklets. Every measurement receives a rolling shutter, diurnal aberration, light-time and atmospheric refraction correction. The last two corrections require additional state information, and we refer the reader to the discussion and conclusion section for a discussion on this point.

If a tracklet is a TSA, no (traditional) IOD can be performed and we instead compute the attributable of the tracklet, which is composed of α and δ and the corresponding rates at the middle point of the tracklet, providing incomplete state information. It is computed by fitting a linear or quadratic motion model in α and δ to the measurement data [7].

From the attributable we compute the constrained admissible region (CAR) by imposing a minimum and maximum range, range-rate, semi-major axis and eccentricity. Next, we sample the CAR either uniformly in $(\rho, \dot{\rho})$ or uniformly in (a, e) (yielding a non-uniform distribution in $(\rho, \dot{\rho})$). The result is a set of 6-dimensional state vectors that provides an empirical probabilistic representation of the CAR, namely the PAR. The uncertainty in the attributable can be incorporated by sampling the Gaussian distribution derived from the least-squares fit, and computing the corresponding constraints for each sample separately. To obtain a more efficient representation of the distribution, we fit a 6-dimensional Gaussian Mixture Model (GMM) to the set of sampled states.

The tracklet correlation procedure is as follows. Given a pair of tracklets, the PAR associated with one of the tracklets is propagated to the epoch of the other. It is propagated using a random

Materials Research Proceedings 69 (2026) 1059-1064 https://doi.org/10.21741/9781644904251-183

sample of n^2m states, with n the state dimension and m the number of Gaussian components (e.g., for m = 50 we sample 1800 points). The large number of states necessitates a simple propagator, here an analytical J2 propagator is used [8]. Once propagated, we compute the product of the two distributions (a product of two GMMs, yielding another GMM). A simple criterion for establishing the correlation status is to consider the tracklets correlated if the distributions overlap and not correlated if they do not. A more reasonable and effective criterion can be found by looking at how similar the distributions are, quantified by the normalization factor obtained in computing the product of the distributions. This shall be described in more detail in the next section.

Note that the product of two PARs of a given tracklet pair gives an estimate of the orbit of an object that would have generated these tracklets at their respective epochs. More precisely, a (non-Gaussian) distribution of possible orbits is obtained, i.e., a covariance. We may assign the mean or the densest part of the distribution as the estimated orbit of the object.

Results

We consider a set of 194 tracklets obtained by tracking a set of 47 unique GNSS satellites over a period of approximately 82 hours, with the tracklets containing 3 to 22 measurements (mean 16.47) covering a time interval of 8.6 to 78.9 seconds (mean 68.9). The orbital period of these satellites ranges from 12 to 14 hours, hence these tracklets clearly constitute TSAs. Compared to accurate ephemeris data, the measurements have a bias of $(b_\alpha, b_\delta) = (-0.12'', 0.01'')$ and a standard deviation of $(\sigma_\alpha, \sigma_\delta) = (0.35'', 0.36'')$. For every tracklet we implement the described correlation procedure against every other tracklet. This means that for n tracklets we have n(n - 1) combinations, which in this case equates to 37442, of which 876 are correlated. To compute the PAR we sample 5000 pairs from a uniform (a, e) prior and use the following constraints: $\rho \in [350, 50000]$ km, $\dot{\rho} \in [-15, 15]$ km/s, $a \in [10000, 40000]$ km and $e \in [0, 0.1]$.

Fig. 1 shows the true positives (TP), false negatives (FN), true negatives (TN) and false positives (FP) for different number of Gaussian components used to represent the PAR. The basic criterion for correlation is used, i.e., whether or not there is overlap between the distributions. A low TP rate is observed for each case accompanied by a relatively high FP rate, especially for low number of Gaussian components.

We can improve the result by considering the sum of the normalization factors used to compute the product of the overlapping distributions, which provides a measure of similarity between the distributions, and shall be denoted with z. Note, this measure is only available for TPs and FPs, as the distributions do not overlap for the FNs and TNs. Fig. 2 shows the distribution of log z for the TP and FP rate using 100 Gaussian components. We observe a non-perfect separation of the TP and FP rates, but clearly a better correlation criterion can be determined. An optimal decision boundary can be computed given some fixed cost and reward for rejecting TPs and FPs, respectively. In practice, these values should reflect certain operational considerations. Here, we simply set the cost for rejecting TPs and FPs at 5 and -1, respectively, and compute the decision boundary that minimizes the cost. The decision boundary in Fig. 2 is shown as a dashed vertical black line and has a value of 25.88. This decision boundary provides a significant improvement over to the basic correlation criterion: 1214 FPs are rejected at the cost of rejecting only 23 TPs, resulting in a TP and FP rate of $\frac{848}{876}$ and $\frac{871}{36566}$, respectively.

For the cases where the PAR is represented using only a few Gaussian components, there is more overlap between the TP and FP distributions, resulting in more TP and/or less FP rejections. This highlights the (somewhat obvious) merit to accurately model the PAR.

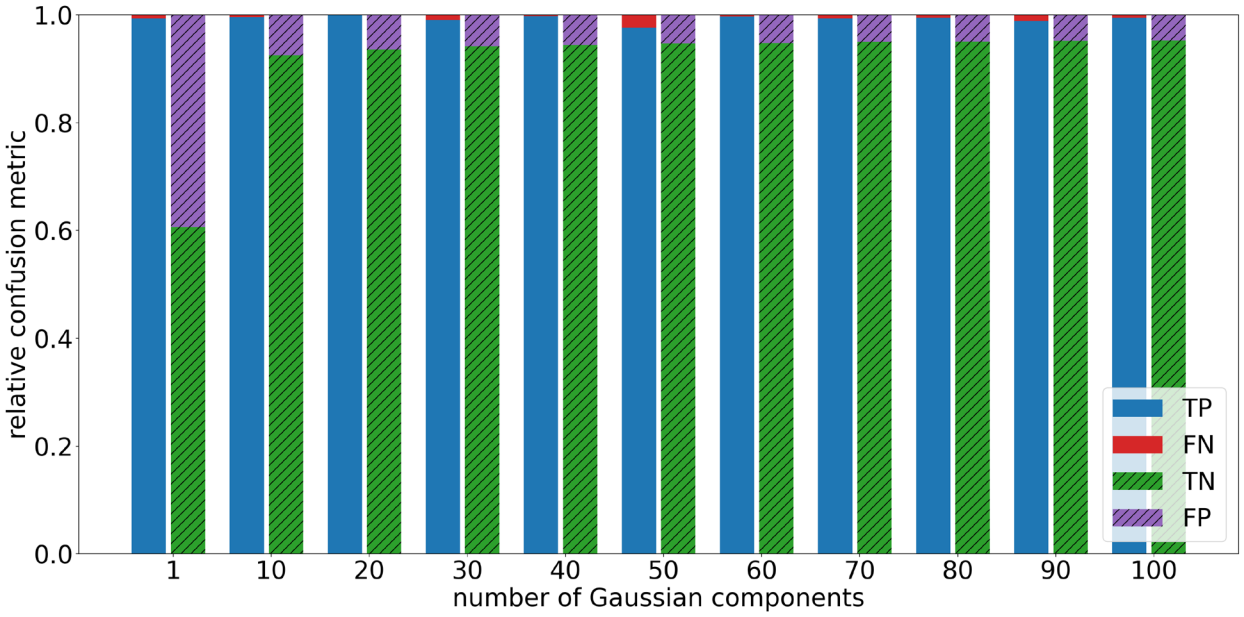


Figure 1: Tracklet correlation result for different number of Gaussian components, using the basic correlation criterion

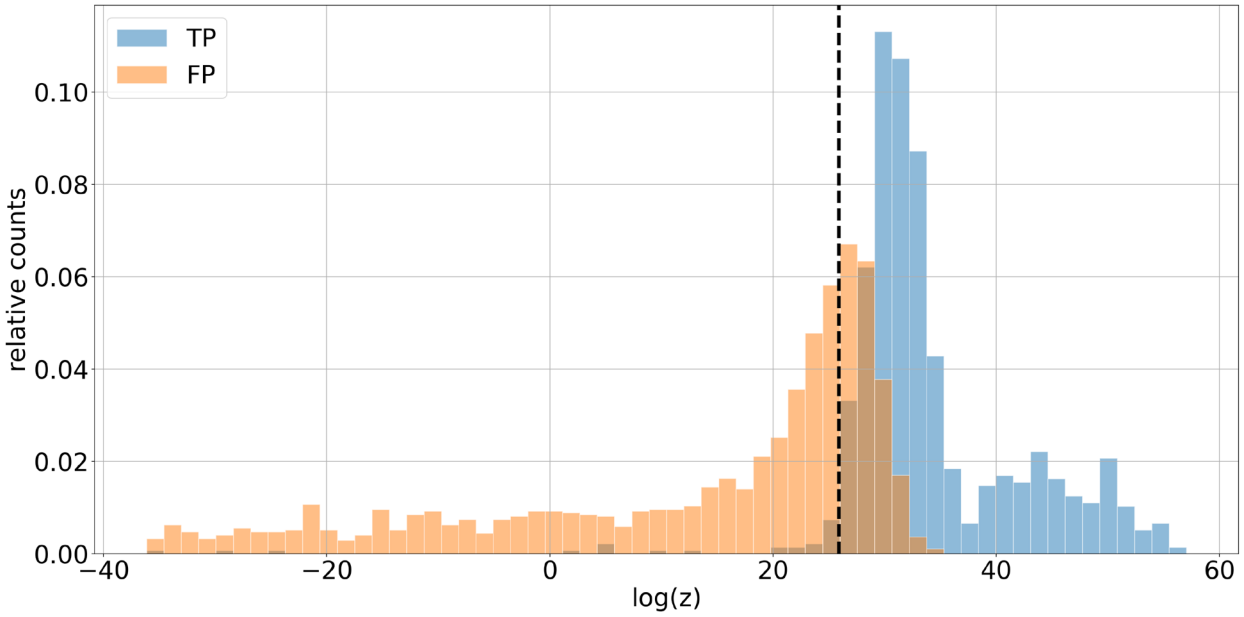


Figure 2: TP and FP rate distribution (100 Gaussian components) for the logarithm of the sum of the PAR products' normalization factors. The black horizontal line is the optimal decision boundary.

Next, for each TP pair, we compare its IOD solution (obtained by taking the mean of the PAR product of the two tracklets at the epoch of tracklet 2) to accurate external ephemeris data from the CDDIS database. Fig. 3 shows the IOD solution in terms of the RSW error (again using **100** Gaussian components) as a function of the angular separation between the tracklets. We see that the radial error (R) is generally larger than the along-track (S) and cross-track (W) error. Indeed, this is expected since it is the radial component that is not directly measured but inferred from the orbit instead. A reduction in the error is observed for increasing angular separation, which is most pronounced for the radial component. For sufficiently large angular separations (<70°), the radial error has a standard deviation in the range of 5 to 12 km, and the along-track and cross-track error

are around 2 km. Note that the accuracy of the IOD solution is in the end limited by the simplified models used in the correlation process. It is recommended to perform orbit determination on the combined tracklet data using more accurate models, with the PAR IOD solution as an initial guess.

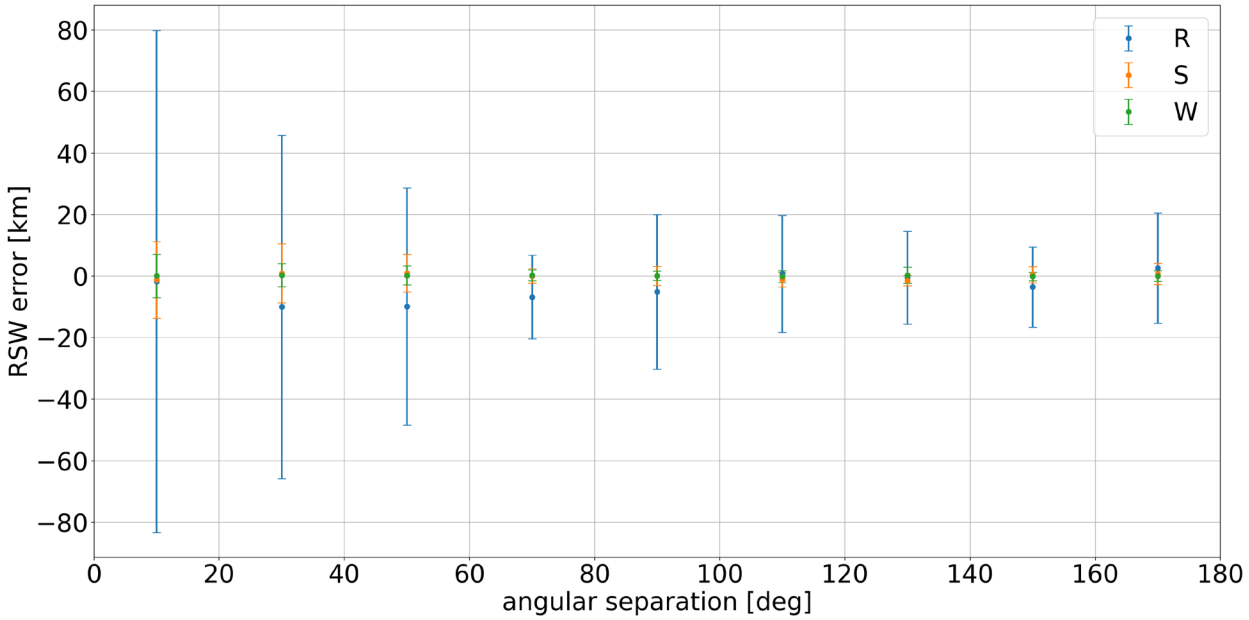


Figure 3: Mean RSW error for the PAR IOD solutions with 100 Gaussian components as a function of the angular separation between the correlated tracklets.

Discussion and conclusion

From the results we have seen that an accurately represented PAR can be used to effectively discriminate correlated from uncorrelated tracklets. A very small FN rate and FP rate is observed but in absolute terms a significant number of FP remain. The reason for this is the fact that many of the uncorrelated tracklets pairs are consistent with the observations under the given constraints. We can use the IOD solution to verify or reject the correlation result by associating it to an existing catalogue; or test it against a third tracklet; or schedule a follow-up observation in an attempt to reacquire the object. In the case of a high FP count, however, the last option may put an unnecessary high burden on the sensor network.

In the method section it was mentioned that a light-time and atmospheric refraction correction are applied, but in a true cataloguing generation scenario these cannot be directly computed. Instead, they need to be incorporated into the correlation process. We can compute these corrections once we have determined the set of admissible states and iterate as needed. This will influence the uncertainty in the attributable and its effect on the correlation process shall be considered in future work.

Another point of discussion is the selection of the constraints. In this work, the target population was in MEO and relatively loose constraints were chosen to capture this fact. How the choice of constraints affects the performance of the correlation process needs to be studied, and a structured method of choosing them is needed.

To conclude, the Probabilistic Admissible Region shows promise as tool in tracklet correlation and IOD for the catalogue generation of LEO and MEO objects. Future work aims to further improve and validate the methodology for LEO and space-based data.

References

[1] Andrea Milani et al. “Orbit Determination with Very Short Arcs. I Admissible Regions”. In: *Celestial Mechanics and Dynamical Astronomy* 90.1 (Sept. 2004), pp. 57-85. https://doi.org/10.1007/s10569-004-6593-5

[2] G. Tommei, A. Milani, and A. Rossi. ”Orbit Determination of Space Debris: Admissible Regions”. In: *Celestial Mechanics and Dynamical Astronomy* 97.4 (Apr. 2007), pp. 289-304. https://doi.org/10.1007/s10569-007-9065-x

[3] Kyle J. DeMars, Moriba K. Jah, and Paul W. Schumacher. “Initial Orbit Determination using Short-Arc Angle and Angle Rate Data”. In: *IEEE Transactions on Aerospace and Electronic Systems* 48.3 (July 2012), pp. 2628-2637. https://doi.org/10.1109/TAES.2012.6237613

[4] Kyle J. DeMars, Moriba K. Jah. “Probabilistic Initial Orbit Determination Using Gaussian Mixture Models”. In: *Journal of Guidance, Control, and Dynamics* 36.5 (2013), pp. 1324-1335. https://doi.org/10.2514/1.59844

[5] Islam I. Hussein et al. “Probabilistic Admissible Region for Multihypothesis Filter Initialization”. In: *Journal for Guidance, Control and Dynamics* 41.3 (2018), pp. 710-724. https://doi.org/10.2514/1.G002788

[6] Agnieszka Sybilska et al. “Astrometry24.NET – Precise Astrometry for SST and NEO”. In: *1st NEO and Debris Detection Conference*. Darmstadt, Germany: ESA Space Safety Programme Office, Jan. 2019.

[7] J. M. Maruskin, D.J. Scheeres, and K.T. Alfriend. “Correlation of Optical Observations of Objects in Earth Orbit”. In: *Journal of Guidance, Control and Dynamics* 32.1 (2009), pp. 194-209. https://doi.org/10.2514/1.36398

[8] David A. Vallado. *Fundamentals of Astrodynamics and Applications*. 4th ed. Hawthorne, CA, USA: Microcosm Press, 2013. ISBN 978-1881883203.

Materials Research Proceedings 69 (2026) 1065-1070 https://doi.org/10.21741/9781644904251-184

Impact assessment of perturbations on the orbit control in a Near-Zero Inclination Geosynchronous Synthetic Aperture Radar

Francesca PELLICCIA[1,a *], Alfredo RENGA[1], Matteo MONTI[2], Andrea MONTI-GUARNIERI[2], Giovanni Paolo BLASONE[3], Simona ZOFFOLI[3]

[1]Università degli Studi di Napoli Federico II, Dipartimento di Ingegneria Industriale, Piazzale Tecchio 80, 80125, Napoli, Italy

[2]Politecnico di Milano, Dipartimento di Elettronica, Informazione e Bioingegneria, Via Ponzio 34/5, 20133, Milano, Italy

[3]Agenzia Spaziale Italiana, Via del Politecnico, snc, 00133 Roma, Italy

[a]francesca.pelliccia@unina.it

Keywords: Synthetic Aperture Radar (SAR), Geostationary SAR, Orbit Control, Orbital Perturbations

Abstract. The Near-Zero Inclination Geosynchronous Synthetic Aperture Radar (NZI-GEOSAR) concept enables high-frequency observations with stable geometry for interferometric applications. However, orbit stability at GEO altitude is strongly affected by perturbative forces that challenge the control strategy efficiency. This work quantifies the relative contribution of lunisolar gravitational effects, solar radiation pressure, Earth's non-sphericity to the orbit maintenance of a NZI-GEOSAR mission implementing the Tangential-Normal (TN) control strategy proposed in [1]. Simulation results show that the lunar gravitational perturbation dominates the ΔV budget, accounting for about 85% of the total control effort, while solar and geopotential effects have minor influence. Moreover, a 14% ΔV increase between epochs is observed, driven by the 18.6-year lunar node regression cycle.

Introduction

Earth Observation missions increasingly rely on advanced spaceborne Synthetic Aperture Radar (SAR) systems to provide high-resolution, all-weather imaging for scientific and civil applications. Within this framework, the GEOSAR concept - proposed since 1978 in several configurations - offers the unique capability of wide-swath, near-persistent observation from geostationary orbit, enabling revisit intervals of 24 hours or less over continental scales due to its synchronicity with Earth's rotation. Recent developments confirm the growing interest in this architecture: China's Ludi-Tance 4-01 satellite, launched in August 2023 on a 16° inclined GEO orbit, represents the first operational GEOSAR mission [2], while ESA's Hydroterra+ concept, shortlisted under the Earth Explorer 12 call, envisions a C-band Near-Zero-Inclination (NZI) GEO system for twice-daily monitoring of Europe and the Mediterranean [3].

A key requirement for such systems - especially in NZI configurations - is the implementation of an orbit control strategy that preserves spatial and temporal coherence for interferometric SAR (InSAR) applications. Maintaining small cross-track baselines and stable Doppler bandwidth overlap is challenging at GEO altitude, where even small orbit deviations induce significant ground-projection errors. Perturbative accelerations due to Solar Radiation Pressure (SRP), Earth's oblateness, and lunisolar gravity can destabilize the orbit and degrade imaging performance even over short timescales. To meet these constraints, tailored control strategies have been proposed in [1], with the Tangential-Normal (TN) approach emerging as the most efficient trade-off between interferometric performance and propellant consumption. Such previous analyses, however,

Content from this work may be used under the terms of the Creative Commons Attribution 3.0 license. Any further distribution of this work must maintain attribution to the author(s) and the title of the work, journal citation and DOI. Published under license by Materials Research Forum LLC.

Materials Research Proceedings 69 (2026) 1065-1070 https://doi.org/10.21741/9781644904251-184

considered all perturbations simultaneously, without isolating their individual contributions. This limits the understanding of the physical origin of the ΔV demand in GEOSAR configurations.

The present work aims to identify and quantify the dominant perturbative sources affecting orbit stability and InSAR coherence in NZI-GEOSAR systems, clarifying how solar, lunar, and geopotential effects drive ΔV consumption over different epochs. The analysis compares multiple simulation scenarios in terms of ΔV budget and fuel usage, providing physical insight into orbital distortion mechanisms, useful for the optimization of control strategies for GEOSAR missions.

This paper is organized as follows. Section I explains the methodology behind the conducted orbit perturbation, Section II provides the simulation setting and the results, discussing the impact of them on the TN control strategy.

Orbit Perturbations Analysis

The efficient applicability of the Tangential-Normal control strategy [1] can be appreciated from two different perspective in Fig. 1 by comparing the drifting behaviour of the perturbed orbit and the stable behaviour of the controlled one. In the analyses that have been already conducted, the orbit control simulations are performed in totally perturbative orbit environments in GMAT software [4]. This implies that Earth gravitational potential up to 21 degree and order, Moon and Sun gravitational attractions, and SRP are activated in the orbit propagator to take into account all the perturbing accelerations acting on the system in the reference epoch (i.e., 15th March 2036 00:00:00 UTCG). Spacecraft mass is 2000 kg, the exposed area to the Sun is nominally 50 m^2, thus leading to 0.025 kg/m^2 of area to mass ratio A/m; the reflectivity coefficient C_r is 1.8. This simulation setting enabled the estimate of a realistic total ΔV budget that has to be allocated for orbit maintenance tasks.

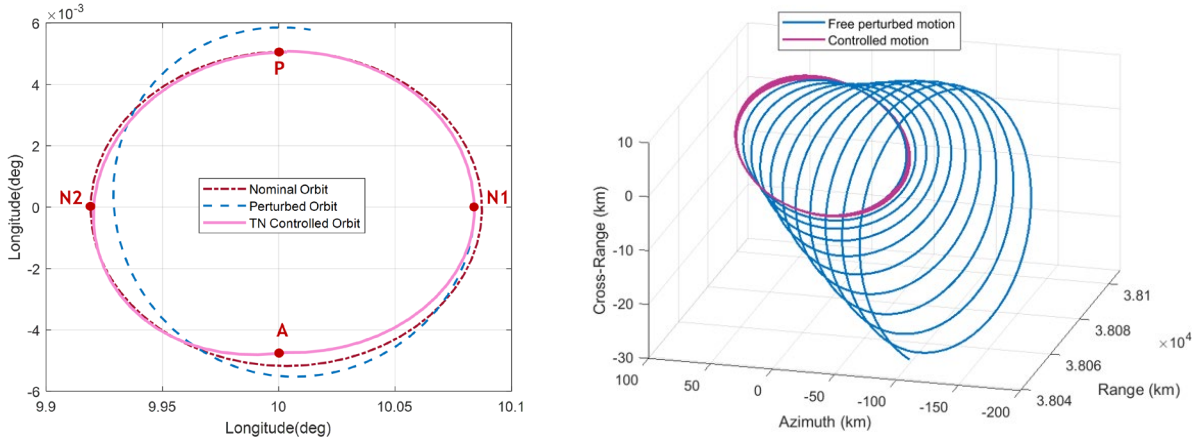


Figure 1 – Left: one-day comparison between the nominal orbit defined in [1], the perturbed orbit, and the TN controlled orbit from the ground-track point of view. P is perigee, A is apogee, N1 is the first orbit node, N2 is the second orbit node. Right: 10-days comparison between the free perturbed motion and the TN controlled motion in the topocentric Range-Azimuth-Cross-Range frame of a target placed at 16.75°E, 46°N, 0 km altitude

However, by switching to the analyses of the individual perturbations, it is possible to assess the impact of each force on the ΔV budget and the consequent fuel mass usage. Specifically, each perturbing force can be activated separately in the GMAT propagator so that its impact on the orbit stability and the maintenance cost can be properly appreciated and disentangled.

In general, the perturbative environment experienced by a GEOSAR satellite is governed by the complex gravitational interaction within the Earth-Moon-Sun system, which generates motions spanning a wide range of characteristic frequencies - from the daily Earth rotation to the lunar month, the solar year, and slow precessions of orbital planes and apsides extending up to tens of

Materials Research Proceedings 69 (2026) 1065-1070 https://doi.org/10.21741/9781644904251-184

thousands of years. Each of these perturbations acts, when isolated, with distinct frequency signatures and affects different orbital components, thus requiring specific orbit control actions to be counteracted. Among these phenomena, the most relevant long-term perturbation is linked to the regression of the lunar nodes, which completes a full cycle every 18.6 years, accompanied by an apsidal precession of approximately 8.85 years [5]. The lunar orbit, inclined by about 5.15° to the ecliptic, combined with the 23.44° tilt between the ecliptic and the Earth's equator, leads to a variable apparent inclination of up to ± 28.6° with respect to the equatorial plane. In general, the 18.6-year regression of the nodes periodically changes the direction and magnitude of the lunar gravitational acceleration acting on the GEO spacecraft, modulating the out-of-plane component of the perturbing force and, consequently, the ΔV required for North-South orbit maneuvers. When the Moon reaches higher declinations, the normal component of its gravitational force increases, leading to a higher ΔV demand for the spacecraft inclination control; conversely, when the Moon is near the equatorial plane, this requirement is minimized.

The Sun, although less variable in apparent motion, also contributes to the perturbative environment. Its declination range (± 23.44°) and distance to Earth vary only slightly throughout the year, making its influence on out-of-plane dynamics nearly constant over time. Additionally, this gravity contribution also determines in-plane oscillations, driving periodic variations in eccentricity and argument of perigee with annual frequency [6]. Another relevant aspect is that the interaction between solar and lunar perturbations can produce short-term beating patterns that slightly modulate the needed ΔV, particularly when their declinations align constructively or destructively. The different trend of the declination of these third bodies (i.e., Moon and Sun) can be appreciated in Fig.2, where a temporal window of 20 years is considered to confirm the peculiar periodicity of the relevant motions.

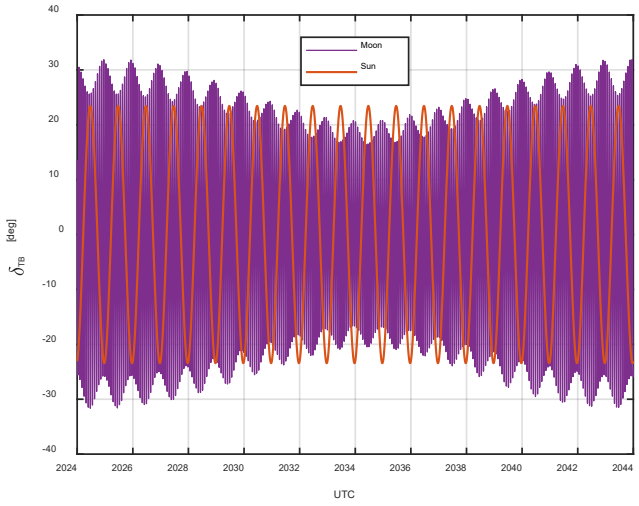


Figure 2 - Trend of the declination (δ_{TB}) of the involved third bodies (Moon, Sun) over a 20-year simulation period

The ephemerides of the Moon and the Sun are here generated through the JPL Horizons on-line solar system data calculator [7] considering the nominal fixed GEOSAR satellite point whose definition is provided in [1]. It is worth noting that, since the GEO observer is displaced from the Earth center, the apparent declination of the Moon reaches a maximum value that is slightly higher (± 31.7°) in absolute terms.

In addition to third-body effects, the Earth's non-sphericity - especially the equatorial asymmetry represented by the C_{22}, S_{22} geopotential spherical harmonics [8] - induces a longitudinal drift of the GEO point, causing an East-West motion that must be compensated by

Materials Research Proceedings 69 (2026) 1065-1070 https://doi.org/10.21741/9781644904251-184

tangential maneuvers. This perturbation is time-invariant and geometry-dependent, defining two stable (75°E, 255°E) and two unstable (165°E, 345°E) equilibrium longitudes. Finally, SRP acts primarily along the radial and tangential directions, depending on the spacecraft attitude and Sun-spacecraft geometry [8]. The main effects are small periodic eccentricity variations and minor diurnal oscillations in the ground track. Although the SRP long-term impact on orbit stability is limited, it can slightly perturb the along-track position, especially, for example, during spacecraft attitude transitions.

Simulations and Results

The impact of the perturbing forces can be appreciated looking at the orbit evolution in the topocentric reference frame centered in target B5, whose geodetic coordinates are 16.75°E, 46°N, 0 km altitude [1]. Fig. 3 depicts the controlled orbit evolution for a 30-days simulation under different propagator settings.

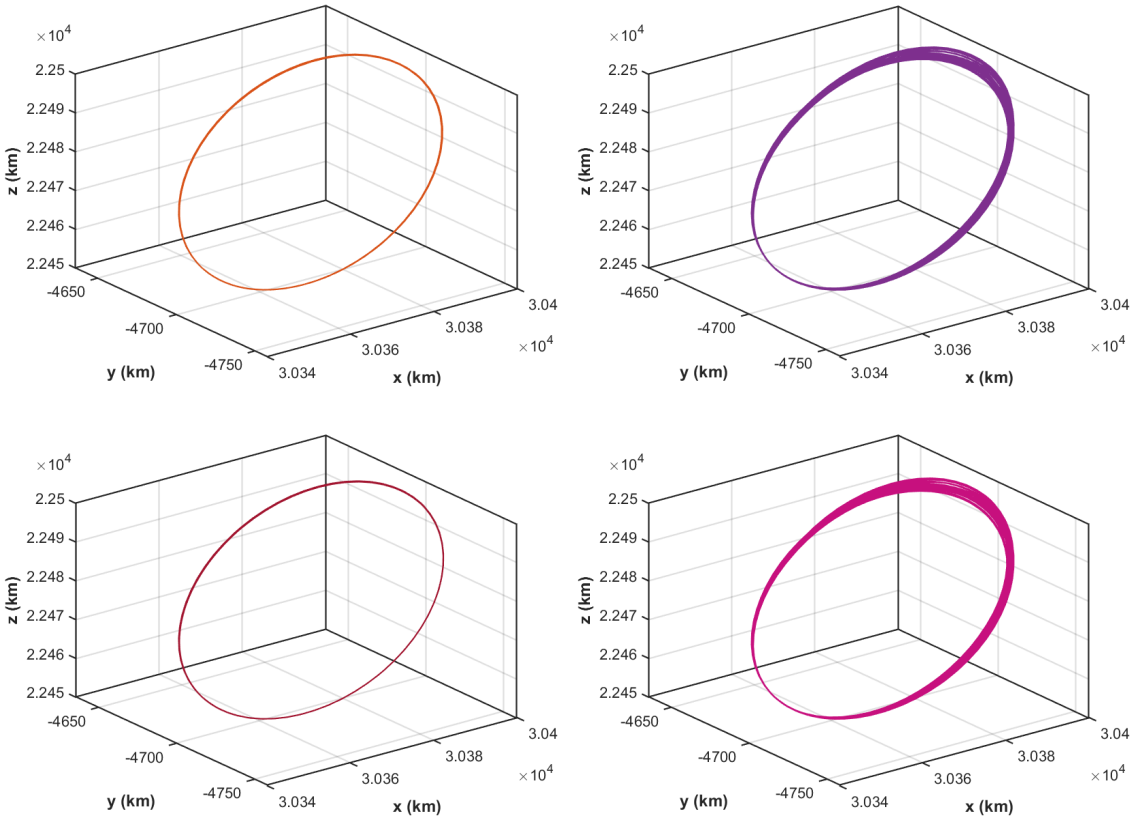


Figure 3 Controlled orbit evolution in the topocentric reference frame centered in beam B5, simulation of 30 days performed in GMAT activating different perturbing effects. Upper left: only Sun gravity is activated; Upper right: only Moon gravity is activated; Bottom left: only SRP and Earth non-sphericity are activated; Bottom right: all the perturbing forces are activated

The comparison among the different cases demonstrates that orbits propagated under lunar-only perturbations (Fig. 3 Upper right) closely reproduce the deviations observed when all perturbations are active (Fig. 3 Bottom right). This further confirms that lunar gravity is the primary driver of orbital plane distortion. Indeed, the Sun gravity contribution (Fig. 3 Upper left) is less impactful than the Moon one, causing smaller deviations of the orbit. When only SRP and Earth's non-sphericity are activated (Fig. 3 Bottom left), the orbit is very stable, remaining tightly bound around the nominal position, with very minor oscillations mostly confined to the along-track direction.

Materials Research Proceedings 69 (2026) 1065-1070 https://doi.org/10.21741/9781644904251-184

Beyond the geometric orbit representations, a quantitative comparison in terms of ΔV budget is performed to assess the effect of each perturbation source. Two distinct simulation epochs are selected to capture the temporal variability of the lunar gravitational influence, which - as previously discussed - is expected to dominate the long-term evolution of the orbital dynamics. Specifically, two epochs separated by approximately nine years are selected, corresponding to the phases of minimum and maximum lunar declination within the 18.6-year nodal regression cycle. According to the declination trends in Fig. 2, 15 March 2033 00:00:00 UTCG and 15 March 2042 00:00:00 UTCG are chosen as the initial epochs for one-year controlled simulations in GMAT.

Table 1 summarizes the resulting ΔV and propellant consumption (i.e., fuel mass usage, m_{fuel}), assuming a 2000 kg spacecraft equipped with a chemical propulsion system of specific impulse of 300 s. The results clearly indicate that the Moon's gravitational perturbation is the dominant source of instability for the NZI GEOSAR configuration, whatever the selected epoch is. When only the lunar attraction is active, the required ΔV accounts for approximately ~85 % of the total control effort, while the solar contribution remains below ~35 %. Additionally, the combined ΔV of the Sun and Moon acting separately slightly exceeds the total ΔV obtained when both perturbations are applied simultaneously. This behavior reveals a geometric partial compensation between the lunar and solar accelerations: depending on their relative phase and declination, the normal components of their perturbative forces can partially counteract each other, reducing the total control effort required. In contrast, when third-body effects are neglected, the ΔV requirement drastically drops to ~6 m/s, confirming that SRP and Earth's non-sphericity have a limited impact on long-term orbit stability.

Table 1 – ΔV budget and fuel usage comparison

Epoch	Active Perturbations	ΔV [m/s]	m_{fuel} [kg]
2033	ALL	87.55	61.11
	ONLY MOON	74.97	52.44
	ONLY SUN	32.45	22.86
	NO THIRD BODY	6.35	4.49
2042	ALL	102.15	71.13
	ONLY MOON	87.13	60.82
	ONLY SUN	32.41	22.84
	NO THIRD BODY	6.37	4.51

The comparison between the epochs reveals a ΔV increase of about 14%, in 2042 epoch, which can be directly attributed to the 18.6-year regression of the lunar nodes modulating the inclination of the Moon's orbital plane relative to the Earth's equator. In 2042, when the lunar declination reaches its maximum amplitude, the normal component of the perturbative acceleration is increased, leading to a larger ΔV associated with out-of-plane maneuvers. Conversely, in 2033, the smaller lunar declination corresponds to a dynamically favorable configuration requiring less control effort. As expected, the Sun's gravitational influence remains nearly constant across epochs due to the quasi-stationary geometry of the Earth-Sun system.

Conclusions

A detailed analysis of the perturbative accelerations on a NZI GEOSAR orbit has been conducted through high-fidelity GMAT simulations implementing the Tangential-Normal control strategy. Each perturbation source has been individually activated to quantify its contribution to orbit stability and control effort. Results confirm that the lunar gravitational attraction is the dominant disturbance, responsible for nearly 85% of the total ΔV required for orbit control. The comparison between 2033 and 2042 epochs shows a ΔV increase of about 14%, consistent with the 18.6-year

lunar node regression cycle that modulates the Moon's declination and strengthens its out-of-plane effect during maximum inclination phases. Overall, the study demonstrates that third-body geometry and epoch selection can relatively influence orbit-keeping efficiency. These results highlight the need for third bodies geometry-dependent control planning and propellant allocation strategies in future GEOSAR missions to ensure long-term interferometric performance with minimized fuel consumption.

References

[1] M. Monti, A. M. Guarnieri, F. Pelliccia and A. Renga, Geostationary Interferometric SAR: Orbit Design and Control Implementation, in IEEE Transactions on Geoscience and Remote Sensing, vol. 63, pp. 1-17, 2025, Art no. 5211017. https://doi.org/10.1109/TGRS.2025.3565889

[2] X. Chen, Z. Chen, Y. Li, C. Hu, X. Dong and S. Hobbs, Improving 2-D Resolution in Geosynchronous SAR via Spatial Spectrum Synthesis: Method and Verification, in IEEE Journal of Selected Topics in Applied Earth Observations and Remote Sensing, vol. 17, pp. 5847-5863, 2024. https://doi.org/10.1109/JSTARS.2024.3361165

[3] Information on https://www.esa.int/Applications/Observing_the_Earth/FutureEO/Preparing_for_tomorrow/ESA_selects_four_new_Earth_Explorer_mission_ideas

[4] General Mission Analysis Tool (GMAT), NASA, Washington, DC, USA, 2019

[5] A.J. Rosengren, E. M. Alessi, A. Rossi, G.B. Valsecchi, Chaos in navigation satellite orbits caused by the perturbed motion of the Moon, Monthly Notices of the Royal Astronomical Society. 449. 3522-3526. https://doi.org/10.1093/mnras/stv534

[6] G. E. Cook, Luni-Solar Perturbations of the Orbit of an Earth Satellite, Geophysical Journal International, Volume 6, Issue 3, April 1962, pp. 271–291. https://doi.org/https://doi.org/10.1111/j.1365-246X.1962.tb00351.x

[7] Information on https://ssd.jpl.nasa.gov/horizons/

[8] Vallado, D.A, Fundamentals of Astrodynamics and Applications. 3rd Edition, Springer, Berling, 2007

Materials Research Proceedings 69 (2026) 1071-1076 https://doi.org/10.21741/9781644904251-185

Digital Twins and Modelling for Spacecraft Science Operations: Application to Surface Interaction and Sampling on Small Solar-System Bodies

Iosto FODDE[1,a,*], Fabio FERRARI[1,b], and Franco Bernelli ZAZZERA[1,c]

[1]Department of Aerospace Science and Technology (DAER), Politecnico di Milano, Via La Masa 34, Milan, Italy

[a]iosto.fodde@polimi.it, [b]fabio1.ferrari@polimi.it, [c]franco.bernelli@polimi.it

Keywords: Space Exploration, Digital Twins, Small Solar-System Bodies

Abstract. The increasing number of space exploration missions presents a novel challenge with regards to planning and operations. Current architectures are composed of distinct teams and models performing separate tasks like navigation, planning, and science, which can lead to inefficiencies and delays. This work proposes a Digital Twin (DT) architecture which supports end-to-end mission design, operations, and scientific analysis. The proposed DT combines models of the spacecraft, its scientific payloads, and the target body, linked through a data processing layer that enables continuous monitoring, simulation, and decision support. A case study of a spacecraft exploring an asteroid and interacting with its surface through a lander and sampling arm is presented. This example specifically shows the importance of reduced order models (ROMs) to efficiently predict and interpret surface interactions. This approach highlights the potential of integrated DT architectures to enhance coordination, adaptability, and scientific return in future deep space missions.

Introduction

The number of missions exploring the solar system is increasing rapidly over time, from spacecrafts going to the Jovian system investigating the habitability of its moons, to mission improving our planetary defense capabilities by visiting near earth objects like Didymos and Apophis. These missions are complex, with various instruments that are necessary to meet science objectives, many different subsystems with intricate connections, and large ground teams that must analyse, plan, and operate these missions [7]. While miniaturization has driven down spacecraft manufacturing costs, the operational burden on the ground segment has not scaled down equivalently, in fact, the demands on mission planning and coordination are growing due to increasing number of deep space missions.

Currently, the planning and operation of these missions is performed by separate groups, e.g. hardware design, trajectory planning, navigation analysis, and science investigation groups. During all phases of the mission, decisions made by each group have a large influence on the other and require frequent iterations. This siloed approach leads to inefficiencies and repeated iterations, especially as small design or operational decisions can propagate significantly through the mission's architecture and affect science return. To address this challenge, this work proposes the integration of novel Digital Twin (DT) and modelling methodologies to improve operational efficiency and enhance scientific outcomes across all mission phases, from design to post-mission data analysis. DTs are virtual models of physical processes where data is exchanged (often real-time) to update the state of the virtual model. DTs have already been explored for individual subsystems of spacecrafts, like for example the EPS of Artemis [8]. However, here we propose to have a more holistic view of the mission Specifically, we envision a DT that encapsulates the spacecraft, its instruments, and the target planetary body. The central objective is not just

Content from this work may be used under the terms of the Creative Commons Attribution 3.0 license. Any further distribution of this work must maintain attribution to the author(s) and the title of the work, journal citation and DOI. Published under license by Materials Research Forum LLC.

Materials Research Proceedings 69 (2026) 1071-1076 https://doi.org/10.21741/9781644904251-185

engineering health monitoring, but mission science: continuously assessing whether science goals are being met, adapting operations in response to unexpected conditions, and extracting maximum insight from acquired data. In this work we present a general overview of this problem, and give an example related to a spacecraft trying to interact with the surface of a Small Solar-system Body (SSB) like an asteroid or small planetary moon.

Digital Twin

With an increase in computing power, larger numbers of spacecrafts, and more complex space systems the use of DTs in spaceflight has seen an increase in the last decades. Examples can be found for rover operations [10], spacecraft electrical power systems [8], and astronaut training [9]. For a more comprehensive overview, the reader is directed to [6]. There are many different definitions of what exactly a DT is, which also depend on the specific domain in which they are used. In general, there are two key characteristics that are common:

- It is a digital representation of a process/object/system in the physical world.
- There is a bidirectional exchange between the DT and the physical system.

In several cases there is also a (quasi) real-time aspect to the DT, as they are often used in critical processes like structural health monitoring where quick responses are required [5]. Due to the inherent delays present in deep space operations the real-time aspect is not considered for the DTs here.

Figure 1 shows the proposed architecture of the DT for science operations. It mainly consists of two blocks, representing the physical and digital environment. The physical environment consists of both the target objects (e.g. asteroid, moon, planet, etc.) and the spacecraft including all its scientific payloads, sensors, and actuators. The digital block consists of three sub-blocks: the spacecraft model, target model, and data processing blocks. The spacecraft model contains digital representations of the different subsystems and serves two purposes: interpreting incoming data from the physical spacecraft and simulating proposed commands sent from ground. The target block represents the current state of knowledge of the target. It can be used to understand the incoming observations, plan them based on the perceived lack of knowledge, and as a simulation tool for the simulated spacecraft. Finally, the data processing block contains all the decision making logic. It creates commands based on the current state of the spacecraft and target, it then performs predictive simulations using these commands, and finally decides on the actual command sent to the physical spacecraft (either human-in-the-loop or autonomously).

The individual spacecraft and target model blocks do not necessarily present novel ideas. Engineers have already implemented models and digital twins of the spacecraft itself during previous missions [8] and scientists have done the same for the target of interests of individual or combined missions [1]. The main novelty of the proposed architecture is to combine the different blocks into a single architecture and use the data processing block to monitor the system as a whole, perform scientific interpretation of the data, and plan the next steps. The advantages of this approach is the fact no long iterations between the different teams and their separate models/DTs are necessary, decreasing the turnaround time and making the mission more flexible to new observations. It also ensures that any unexpected events and faults in the spacecraft are propagated throughout the whole system, directly observing the consequences.

Materials Research Proceedings 69 (2026) 1071-1076 https://doi.org/10.21741/9781644904251-185

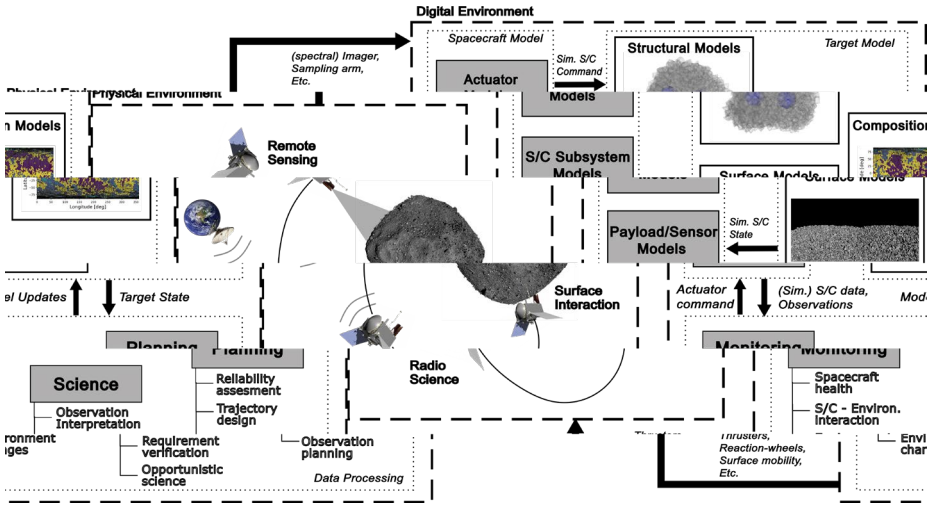


Figure 1 Schematical representation of the Digital Twin for space exploration and science

The main complexity of this architecture lies in the efficient modeling of the systems and efficiently using the sensors and instruments available on the spacecraft. For example, a large number of Small Solar System Bodies (SSBs) are thought to have a large amount of granular material, also known as regolith, and boulders on their surface. The interactions between the individual regolith particles, the boulders, and the spacecraft itself are governed by complex contact forces and are hard to model on Earth due to the low-gravity environment on these SSBs. Modeling SSBs thus requires complex discrete element models (DEMs), which have a high computational burden. Running many DEM simulations for interpreting continuously the novel observations and performing statistical predictions can take several days to weeks [4], thus reacting to these new observations becomes infeasible. Hence, reduced order models (ROMs) are needed that can be more efficiently used inside the DT. The focus for the following will be on how to generate these ROMs and how they can be used inside the DT framework. 3

Case Study: SSB landing and sampling

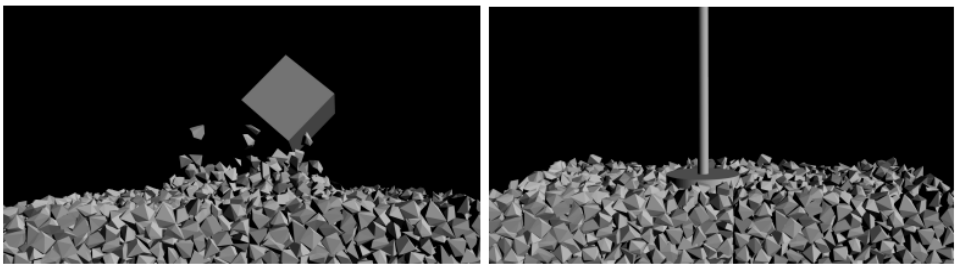
Many missions have attempted, or are planning to attempt, interactions with the surface of a SSB. For example, NASA's OSIRIS-Rex succesfully obtained a sample from the asteroid Bennu using its TAGSAM robotic arm, while JAXA's Martian Moons eXploration (MMX) will deploy a rover on the surface of the Martian moon Phobos. One of the main difficulties for these missions is the uncertainty related to the surface properties of SSBs. These properties are related to, for example, their size distribution, strength, contact parameters, and density. Determining these parameters not only serves to reduce the risk of an interaction, but also to improve our scientific knowledge as these parameters can tell us about the formation and evolution of these SSBs.

For this test case, a Hayabusa-2 like mission is used where first a lander is placed on the surface and afterwards a sampling manuever is performed. In this case, the DT architecture can help in interpreting the data from different instruments and the initial landing to inform the sampling strategy. First, the simulation setup is performed using a DEM code called GRAINS (more information regarding this code can be found in [2]). The surface conditions are first determined by observations from the optical and thermal imagers, which can obtain particle size and shape distributions (PSDs). Using these observations and the results from the radio science instrument to determine the local gravity level, the surface is created inside the DEM by generating a set of particles using the determined PSD and letting it settle under the local gravity level. This model can be continuously updated by new measurements of the imagers and/or the radio science

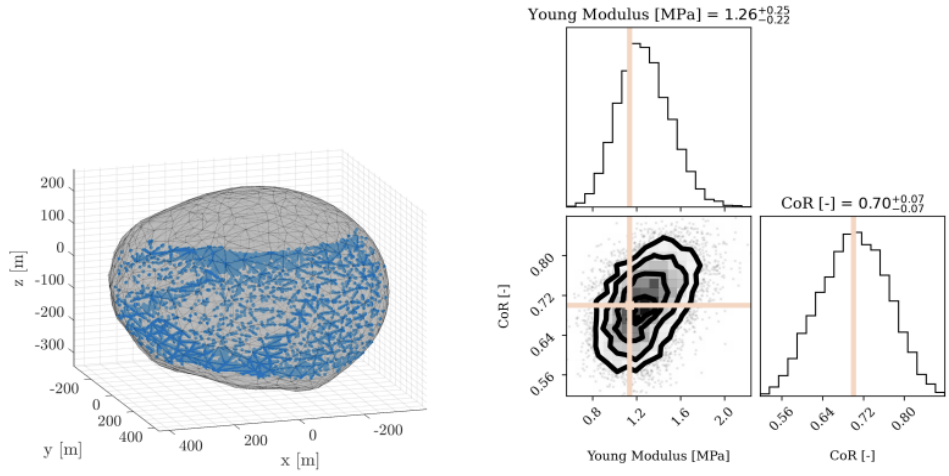
experiment. Once the surfaces are created, objects representing the lander and sampler can be incorporated, see Figures 2a and 2b.

As discussed before, a ROM of the surface interaction needs to be generated to perform statistically relevant reliability assessments and parameter estimation. This is achieved using a data-driven approach where a small number of DEM simulations are used to fit a ROM that can be more efficiently used. This ROM is created by a non-intrusive polynomial chaos method, which samples the initial conditions and system parameters in an optimal way, and takes the input-output relationship of these sample simulations to create a fit based on a family of orthogonal polynomials that represent the prior distribution of the input variables. A more detailed description of this method is given in [3].

It was found that the generated ROM for the landing has a maximum error of around 5 percent. Using this model, a reliability assessment was made for a hypothetical landing scenario on Didymos, show in Figure 2c. After the actual landing is performed, a Markov Chain Monte Carlo (MCMC) method was used to determine the contact parameters of the surface material. The MCMC method required 50000 samples to achieve an acceptable accuracy, using the original full order DEM model would take around 14.26 years to run. With the ROM this was reduced to around 6 minutes (excluding the one time cost of generating the ROM, requiring around 12 hours). This info can then be used for the sampling maneuver to derive a more robust maneuver. Similarly to before, after the sampling maneuver an MCMC method was performed to have a final estimate of the surface parameters, which are shown in Figure 2d.



(a) Lander. (b) Sampler.



(c) Distribution of landing locations. (d) Results of the model calibration.

Figure 2 Results for the test case of the landing and sampling of a SSB.

Having a combined DT of the spacecraft, the sampling arm, and the surface of the SSB will help in planning this operation, tracking the succesful execution of this maneuver, and interpret

the data for scientific purposes. The main difficulty here is the complexity of these types of simulations (requiring discrete element models (DEM) to simulate the motion of the surface particles, the spacecraft, and their interaction), and efficiently using the sensors and instruments available on the spacecraft. For both real-time tracking and post-processing the spacecraft data, reduced order models are needed that can be more efficiently run.

Conclusions

Here it was discussed how concepts from digital twins (DT) can be used in deep space missions, specifically looking at science operations. This DT serves multiple roles: (1) it supports pre-arrival parametric analysis, enabling assessment of operational feasibility and risk under different conditions; (2) it facilitates real-time mission support by quickly evaluating the implications of sensor data; and (3) it enables inverse modeling, where in-situ measurements are used to infer target properties, advancing scientific understanding of the Solar system. Concluding, this work highlights the potential of Digital Twin architectures to improve science operations for planetary missions. By integrating spacecraft dynamics, instrumentation, and environmental interaction into one model, decision-making can happen more efficiently, mission performance is optimised, and scientific return is maximised. Our SSB surface interaction case study gives an example of how this approach can be practically applied, from pre-mission design through to data interpretation, in one of the most complex and uncertain operational scenarios in planetary exploration.

Acknowledgments

This work was carried out within the Space It Up! project funded by the Italian Space Agency (ASI) and the Italian Ministry of University and Research (MUR) under contract No. 2024-5-E.0, CUP No. I53D24000060005.

References

[1] P. Bauer, T. Hoefler, B. Stevens, and W. Hazeleger. Digital twins of Earth and the computing challenge of human interaction. Nature Computational Science 2024 4:3, 4(3):154-157, 3 2024. https://doi.org/10.1038/s43588-024-00599-3

[2] F. Ferrari, M. Lavagna, and E. Blazquez. A parallel-GPU code for asteroid aggregation problems with angular particles. Monthly Notices of the Royal Astronomical Society, 492(1):749-761, 2 2020. https://doi.org/10.1093/mnras/stz3458

[3] I. Fodde, L. F. Civati, A. Cremasco, and F. Ferrari. Modelling and Estimation of Spacecraft Interactions with the Surface of Small Solar System Bodies. Submitted, 2025.

[4] I. Fodde and F. Ferrari. Dynamical modelling of rubble pile asteroids using data-driven techniques. Astronomy & Astrophysics, 695:A30, 3 2025. https://doi.org/10.1051/0004-6361/202452432

[5] S. Hassani and U. Dackermann. A Systematic Review of Optimization Algorithms for Structural Health Monitoring and Optimal Sensor Placement. Sensors 2023, Vol. 23, Page 3293, 23(6):3293, 3 2023. https://doi.org/10.3390/s23063293

[6] W. Liu, M. Wu, G. Wan, and M. Xu. Digital Twin of Space Environment: Development, Challenges, Applications, and Future Outlook. Remote Sensing 2024, Vol. 16, Page 3023, 16(16):3023, 8 2024. https://doi.org/10.3390/rs16163023

[7] P. Michel, M. K¨uppers, A. C. Bagatin, B. Carry, S. Charnoz, and others. The ESA Hera Mission: Detailed Characterization of the DART Impact Outcome and of the Binary Asteroid (65803) Didymos. The Planetary Science Journal, 3(7):160, 7 2022.

[8] G. J. Pierce, J. D. Heeren, and T. R. Hill. Orion SysML Model, Digital Twin, and Lessons Learned for Artemis I. INCOSE International Symposium, 33(1):290-304, 7 2023. https://doi.org/10.1002/iis2.13022

[9] O. Pi˜nal and A. Arguelles. Mixed reality and digital twins for astronaut training. Acta Astronautica, 219:376-391, 6 2024. https://doi.org/10.1016/j.actaastro.2024.01.034

[10] L. Pinello, L. Brancato, M. Giglio, F. Cadini, and G. F. De Luca. Enhancing Planetary Exploration through Digital Twins: A Tool for Virtual Prototyping and HUMS Design. Aerospace 2024, Vol. 11, Page 73, 11(1):73, 1 2024. https://doi.org/10.3390/aerospace11010073

Materials Research Proceedings 69 (2026) 1077-1082 https://doi.org/10.21741/9781644904251-186

The Legal Conundrum of Mega-Constellations: A Call for a Sustainable Space Governance Framework

Margherita PENNA[1,a *]

[1]Lungo Dora Siena, 100, 10153 Torino (TO)

[a]margherita.penna@unito.it / margherita.penna@unicasd.it

Keywords: Mega-Constellations, Harmful Contamination, Liability, Space Law, Environmental Law, Polluter Pays Principles, Remediation Fund

Abstract. The rapid deployment of mega-constellations in Low-Earth Orbit (LEO) exposes a critical failure in current International Space Law (ISL) to ensure sustainability and equitable access. Existing space *hard* and *soft law* is insufficient to curb the exponential growth of space debris, creating a significant negative environmental externality. This paper argues that International Environmental Law (IEL) principles, such as the polluter pays principle (PPP) should be integrated into the space legal sphere. Also, it proposes the establishment of some policy tools, which would be extremely in protecting space from a "tragedy of the commons".

Introduction

The New Space Economy (NSE), primarily driven by private actors, represents a vast shift from the initial era of the space race. Space has been transforming into a realm of commercially driven economic activities, extending well beyond traditional government-led missions. A robust and growing market for space ventures exists since space activities – from launching objects to operating them in orbit – generate economic value. At the core of NSE are mega-constellations, such as SpaceX's Starlink, which provide crucial services in the field of communication. However, these systems, composed of tens of thousands of satellites, pose significant risks, including near misses in orbit, interference with astronomical observations, and the looming threat of the Kessler Syndrome, which could render key orbital lanes unusable. Given the massive deployment of objects and private sector dominance, understanding the international rights and obligations regarding the sustainability and environmental impact of these complex infrastructures is a pressing matter. This work argues that International Space Law (ISL) lacks the specific binding norms necessary to govern the fallout of mega-constellations. The current legal framework fails to address the negative impacts of mass satellite launches, allowing operators to externalize environmental costs. To address this, principles of International Environmental Law (IEL) should be introduced into the legal discourse on space. A novel interpretative framework is needed for future space governance to ensure long-term sustainable use of outer space [1]. This paper proposes incorporating international environmental obligations, an updated licensing regime for mega-constellations, and establishing a dedicated fund for space debris remediation.

The Problem: Mega-Constellations.

Starting from the 2000s, a shift in the development of space systems has occurred, in particular in Low-Earth Orbit (LEO) – around 500 to 2000 km of altitude – and in relation to space communication systems. Indeed, most of the space objects now launched into space are communication satellites, deployed in LEO, in highly articulated connected systems. The reason behind the increased number of complex satellite systems lies in the fact that in LEO, a single satellite can cover a smaller fraction of Earth's surface. Therefore, to have a continuous service and full coverage a 'constellation' of communication satellites is required. Constellation projects need to be filed according to the international regime regulated by the International

Content from this work may be used under the terms of the Creative Commons Attribution 3.0 license. Any further distribution of this work must maintain attribution to the author(s) and the title of the work, journal citation and DOI. Published under license by Materials Research Forum LLC.

Telecommunication Union. Current or expected LEO constellations include SpaceX's Starlink (5,399 operational, 42,000 expected), EUTELSAT's OneWeb (636 operational), Amazon's Kuiper (2 deployed, 3,236 expected), China's Guowang (12,992 expected), and Rwanda's Cinnamon (337,320 expected) [2]. The upsurge in the number of constellations raises serious concerns about the sustainability of space activities. From a technical point of view, the LEO constellations aim to use a radio spectrum which is often already in use by satellites located in the Geostationary Orbit (GEO). Radio interferences may indeed occur when a mega-constellation flies over the beam of a GEO satellite, but also when two constellations interfere with each other in LEO. Also, mega-constellations raise issues at optical wavelengths, interfering with astronomical observation of the known Dark and Quiet Skies. It has been witnessed that Starlink is already creating "artifacts in astronomical observations", [3] impeding scientific investigation of the skies. Lastly, mega-constellations are exponentially augmenting the risk of collisions and near-misses among satellites (due to the high congestion of LEO) and consequently, the cascading risk of never-ending space debris creation, till the point feared by the Kessler Syndrome.

Technical risks are paired with political and environmental ones; first and foremost, inequality in the use of space between the owners of those constellations and new emerging and developing space actors. Such inequality is combined with a *de facto* discrimination in the allocation of radio frequency, following the first-come, first-served approach established by the International Telecommunication Union's Regulation. Indeed, even if art. 44 of the ITU Constitution recognizes radio spectrum as a "natural limited resource", it still partially regulates allocation of slots without considering an equitable and sustainable access to space [4]. Additionally, the development of mega-constellations raises concerns about their environmental impact, both in the short term and long term. The normative concerns pertain to issues of inequality in the access to space and use of radio frequency, in contrast with ISL principles, discrimination among the space actors, risks of harmful contamination of the environment and of harmful interference in the activities of others [5]. International space law has traditionally laid down the framework of analysis, even though it is argued, in the next paragraph, that is struggling to provide adequate answers.

What Is Missing in International Space Law

Historically, international space law has not specifically addressed sustainability, leaving environmental considerations on and in space on the side. There is no direct and enforceable obligation in the framework of the five space treaties [6,7,8,9,10] regarding the sustainability of space activities. Nevertheless, it is worth taking into consideration those norms from which environmental obligations may be inferred, starting from the Outer Space Treaty (OST) of 1967 [11]. Art. I OST codifies the freedom of access, use, exploration and scientific investigation of outer space and celestial bodies to all States, "for the benefit and in the interest of all countries" and on a basis of equality. These freedoms are inherent to sustainability and vice versa [12], particularly in relation to their equitable nature. Then, Art. IX OST does create an obligation to avoid "harmful contamination" (both forward and backward) and "adverse changes in the environment of the Earth", even though said interferences are considered in relation to the activities of other States Parties. Indeed, the provision obliges States to adopt appropriate measures for this purpose, but it fails to frame the obligation as a necessary protection to the space environment *per se*. Nonetheless, the reference to the prohibition of harmful contamination and the duty to consult may provide a basis for assessing the sustainability of space activities. A duty to consult is, in fact, also present among the principles of international environmental law, which will be addressed below. Some more hints can be drawn from the rules on responsibility and liability in ISL.

The OST establishes a framework of responsibility and liability for damages caused by both governmental and private space activities to which States shall respond. So, if the impact of mega-constellations on the space environment were to be framed as a harmful contamination interfering

with the free use of space by others, the concerned State Party could be found internationally responsible. Art. VI OST indeed establishes the international responsibility of States for all national activities. It adds, however, that all private activities shall undergo a process of authorisation and continuing supervision by "the appropriate State Party to the treaty". The prevailing interpretation of the norm recognizes States responsible for all national activities, not solely for authorising and supervising private ones [13]. Then, Art. VII OST considers the State that "launches or procures the launching of an object into outer space" or "from whose territory or facility a space object is launched" internationally liable for damage to another State Party or to its natural or judicial persons, caused by its space object [13]. The liability regime has been further elaborated in the Liability Convention [7]. However, the two regimes – responsibility and liability – do not seem to be connected. The Registration Convention [9] comes in handy in bringing the two regimes together.

The main controversy is that the liability of a State for damages subsists even in the absence of a wrongful act committed by the State itself or by a national private entity, but only in the presence of damages. While this differential nature with the general international responsibility regime underlines the importance of full compensation from space activities, several matters are left outside its scope of application. Indeed, mega-constellations are not *per se* wrongful, and, unless it is established that it produces damages to other space objects, natural or judicial persons, it does not raise questions of liability. Nevertheless, if the 'damages' were to include damages to the space environment *as such*, the liability regime of ISL could be leveraged in establishing a framework of environmental protection for space.

Amongst the five space treaties, the Moon Agreement [10] is the only one to incorporate a provision resembling an environmental obligation. Art. 7 establishes the obligation on State Parties to take all measures to avoid "disruption of the existing balance of [the Moon] environment, both by introducing adverse changes in that environment or by its harmful contamination". Despite the effort, the Moon Agreement has received a scarce number of ratifications, and it cannot be considered either binding over the international community or representative of a widespread State practice.

While the binding instruments regulating space activities lack provisions imposing environmental obligations over States, some non-binding instruments have addressed these *lacunae*. For instance, the UN General Assembly first endorsed the Inter-Agency Space Debris Coordination Committee (IADC) Space Debris Mitigation Guidelines (SDMG) in 2007 [14]. The SDMG – as more recently, the ESA Zero Debris Charter – aimed to curtail the production of short-term mission-related debris and limit long-term debris generation through end-of-life procedures. However, these guidelines lack references to constellations as an exacerbating factor, and most importantly, they are voluntary measures with no binding nature over States' activities, let alone private entities. Then the Committee on the Peaceful Uses of Outer Space (UNCOPUOS) adopted the Long-Term Sustainability Guidelines (LTSG) in 2019 [15]. Among these voluntary provisions, Guideline A.3 restates the centrality of continuous supervision of national space activities to assure their compliance with the aim of a long-term sustainability of outer space. Guideline A.4 stresses the importance of ensuring equitable, rational, and efficient use of spectrum and orbital regions. It also adds that end-of-life spacecraft should be removed from orbit or disposed of to avoid their long-term presence in LEO. For instance, the presence of mega-constellations' satellites in LEO – both functional and non-functional – has led to the impracticality of ensuring an equitable and rational use of space for all actors, resulting in the establishment of a *de facto* monopoly over the orbit. Notwithstanding the presence of some reference to sustainability, both *hard* and *soft* international space law seems to be insufficiently prepared to tackle the environmental legal sphere of space activities. Indeed, an intersection between environmental and space law is struggling to

Materials Research Proceedings 69 (2026) 1077-1082 https://doi.org/10.21741/9781644904251-186

be established, leading to a great deal of uncertainty on which environmental obligations States shall carry.

The Tools Offered by International Environmental Law

Art. III OST establishes that space law is not a self-contained regime and space activities shall be in conformity with international law and the UN Charter. Therefore, it has been recognised that international environmental law applies to space activities. Indeed, if mega-constellations are not *per se* unlawful economic activities according to international law, their effect on the space environment – and on Earth as well – might be in tension with several IEL principles, which apply alongside the above-mentioned ISL obligations. The implementation of environmental principles can reduce the risks of space debris creation, collisions and inequitable access to space. These principles appear in most of the environmental international treaties, as well as constituting parts of the States' environmental legal systems and are considered customary in nature [16]. Among these, the following are taken into consideration here: the principle of sustainable use; the principle of prevention; the precautionary principle; lastly, the polluter pays principle.

To start, the principle of prevention, firstly recognised in Principle 21 of the Stockholm Declaration (1972) [17], establishes that States are responsible to ensure that "activities within their jurisdiction or control do not cause damage to the environment of other States or of areas beyond the limits of national jurisdiction", i.e. outer space. In its current understanding, prevention entails a duty to both refrain from causing significant damages to the environment and pro-actively take measures in this direction; a duty to cooperate and consult; and lastly, a duty to conduct environmental impact assessments of potentially harmful activities [16]. The novelty embodied in this principle is that the focus has shifted from the liability for damages to other States onto the protection of the environment as such. To apply this principle in outer space would mean to impose over States to pro-actively assess national private activities environmental impact, for instance by evaluating the damages to the environment that mega-constellations may produce [18].

Secondly, it would be highly relevant to implement the precautionary principle into the regulatory space discourse. The space environment is characterised by a high-level of scientific uncertainties, due to the complex and mostly unknown nature of it. The precautionary principle states that "the lack of full scientific certainty shall not be used as a reason for postponing cost-effective measures to prevent environmental degradation", when there are threats of serious and irreversible damages (Principle 15 Rio Declaration) [19]. Even though the debate on the legal nature and limits of this principle is still on, it has been incorporated in treaty-law as well as been recognised in case-law of different supranational courts [16]. It can be at least concluded that if potential adverse effects of mega-constellations on LEO are not fully understood, the activities shall not proceed or at least States shall further investigate cost-effective measures on the matter.

Thirdly, considering the principle of sustainable development, it should be recognized once and for all that the sustainability of space activities is a critical issue to maintain long-term access to space, in light of the growing human dependency on it. The "Brundtland Report" firstly introduced the concept of sustainability [20], which in the space environment would be interpreted as the ability to conduct space activities indefinitely into the future in a manner that realises the objective of equitable access to the benefits of the exploration and use of outer space for peaceful purposes, in order to meet the needs of the present generations while preserving the outer space environment for future generations. Mega-constellations will likely occupy the whole LEO, rendering it inaccessible and unusable for upcoming space actors. In addition, future generations may not have the possibility to enjoy the benefit of exploring space, as it would inevitably be already occupied and exploited by present space actors.

Lastly, among environmental operational-oriented principles there is the polluter pays principle (PPP). The overarching idea is to balance environmental protection with other considerations. The polluter pays principle seeks to internalize the financial burden of pollution to the economic actors

Materials Research Proceedings 69 (2026) 1077-1082 https://doi.org/10.21741/9781644904251-186

who cause it, distributing the efforts among the various stakeholders involved. If indeed the damage caused to the environment remains within the limits of tolerability by the whole society it shall be internalized; otherwise, it is a matter of prevention of an intolerable damage to the environment. Considering the issue of mega-constellations, for the time being those who own such space infrastructures are externalizing over the whole community the costs – i.e., in terms of damages and pollution to the space environment – reinforcing the idea that space suffers from the "tragedy of the commons": the cost of the introduction of mega-constellations in the space environment is borne by the international community, while the benefits (at least in terms of economic profit) are advantageous only to the owners of such constellations. In light of this, it is argued that despite negotiating an *ad hoc* environmental space law treaty, it should be sufficient to enforce IEL principles in the current space legal framework.

Policy Recommendations to Address Negative Externalities

To bring environmental obligations into the space realm is a necessary step, but it is contended that it is insufficient if not paired with other actions of economic nature. Indeed, traditionally, a mere "command and control" approach is not sufficiently incentive for economic actors to shift their behaviour toward a more sustainable one. Firstly, an update to the current international license regime is considered necessary. The current regime, regulated by the ITU, is not equipped to face the expansion of mega-constellations [4]. The revised international license regime should pivot around an *a priori* planning (which already exists) while putting aside the first-come, first-served approach. In addition, there should be a fixed cap on the number of licenses that a State could grant to a single private actor, aiming at avoiding monopolistic behaviours. In addition, the licensing regime should introduce an internationally shared criterion of environmental impact assessments of proposed economic activities, as it has been advocated for on Earth.

Secondly, the basic interest of companies is profit maximization rather than loyalty toward an institutional actor; moreover, private space actors are not inclined to change their economic behaviour toward a sustainable one for the benefit of the space environment *per se* (which is a common good, both legally and economically speaking) if there is no incentive in doing so. Therefore, States should introduce incentives in the form of Pigou subsidies, for private actors who choose and implement sustainable technologies, offering an economically viable alternative. Some examples of financing sustainable behaviour in space have already been put into practice [21], but a definite and widespread environmental turn is needed, especially in light of the presence of massive satellite launches.

Thirdly, taking inspiration from proposals such as the Environmental Remediation Fund by the Nigerian Midstream Downstream Petroleum Regulatory Authority, a dedicated Space Debris Remediation Fund should be established. Participation in such a Fund would be a mandatory condition for launch authorization. This would internalize the cost of cleanup, ensuring that actors contribute to mitigating the debris they create. The Fund's primary duty would be to mitigate the negative impact of space activities when the licensees fail to do so.

To conclude, the increasing privatisation of space, often wrongly depicted as a "democratisation" process, is creating "in-groups" and "out-groups" in the space sector [22]. While this process has brought immense space innovation to the human population, it has failed to take into consideration the need to protect the space environment. Private space activities seem to have been undertaken not for the benefit of "humankind" but for "capitalistkind". Therefore, even if there is some industry acknowledgment of a sustainable use of space (i.e. the Space Safety Coalition group), it is the State's role to implement and enforce sustainable-oriented obligations over space activities. States shall take the lead in the protection of the space environment not only as a common good but as "the province of mankind" as established by the Outer Space Treaty.

References

[1] Y. Takeuchi, Y. Ishii, From Climate to Cosmos: The ICJ's Advisory Opinion and Its Implications for Sustainable Space Governance, EJIL:Talk! Blog, November 17, 2025.
[2] D. Daczi, Megaconstellations: Crowded, Contentious and Competitive, in B. Bartóki-Gönczy, G. Sulyok (Eds.), The New Space Age. Legal and Policy Perspectives, Ludovika University Press, Budapest, 2024, pp. 297-318. https://doi.org/10.36250/01208_00.
[3] M. Rawls, Megaconstellations Are Changing the Night Sky Forever, Forcing Astronomers to Adapt. Astronomy, March 1, 2023.
[4] J. A. Brobst, Role of the International Telecommunication Union in Regulating space Activities, in S. B. Bhat, D. Ukey, A. Variath (Eds.), International Space Law in the New Space Era, Oxford University Press, Oxford, 2024, pp. 205-229, doi: 10.1093/ 9780198909415.003.0011.
[5] A.C. Boley, M. Byers, Satellite mega-constellations create risks in Low Earth Orbit, the atmosphere and on Earth, Sci Rep 11, 10642, 2021. https://doi.org/10.1038/s41598-021-89909-7.
[6] Treaty on Principles Governing the Activities of States in the Exploration and Use of Outer Space, including the Moon and Other Celestial Bodies, 27 January 1967.
[7] Convention on International Liability for Damage Caused by Space Objects, 29 March 1972.
[8] Agreement on the Rescue of Astronauts, the Return of Astronauts and the Return of Objects Launched into Outer Space, 22 April 1968.
[9] Convention on Registration of Objects Launched into Outer Space, 12 November 1974.
[10] Agreement Governing the Activities of States on the Moon and Other Celestial Bodies, 18 December 1979.
[11] M. Williamson, Protection of the Space Environment Under the Outer Space Treaty. 48th IAF Congress, 1997, Turin, IISL-97-IISL.4.02.
[12] R. Navalgund, Reduce, Reuse and Recycle: An Environmental Law Approach to Long-Term Sustainability of Outer Space, Air & Space Law 45, no. 3, 2020, pp. 285–308.
[13] M. Pedrazzi, Outer Space, Liability for Damage, MPEPIL, May 2008, pp. 1-9.
[14] UN General Assembly, Resolution 62/217 of 22 December 2007, A/RES/62/217.
[15] Committee on the Peaceful Uses of Outer Space, Recommendations and Decisions, UN Doc A/AC.105/L.318/Add.6 (19 June 2019).
[16] P.-M. Dupuy, J. E. Viñuales, International Environmental Law, 2nd edition, Cambridge University Press, Cambridge, 2018.
[17] UN Conference on the Human Environment, Declaration of the United Nations Conference on the Human Environment, UN Doc. A/CONF.48/14 (June 16, 1972).
[18] Scott Millwood, The Urgent Need for Regulation of Satellite Mega-constellations in Outer Space, Springer Briefs in Law, 2023, https://doi.org/10.1007/978-3-031-19249-4.
[19] 1992 Rio Declaration on Environment and Development, UN Doc. A/CONF.151/26 (vol. I), 31 ILM 874 (1992).
[20] World Commission on Environment and Development, Our Common Future (Report, 1987).
[21] Christianna Reedy, Startup Gets Funding to Clean Up Our Orbital Space Junk, Futurism (accessed 6 June 2019), https://futurism.com/startup-gets-funding-to-clean-our-orbital-space-junk/.
[22] Shammas, V. L., & Holen, T. B. (2019). One giant leap for capitalistkind: Private enterprise in outer space. Palgrave Communications, 5, 10. https://doi.org/10.1057/s41599-019-0218-9.

Materials Research Proceedings 69 (2026) 1083-1088 https://doi.org/10.21741/9781644904251-187

Adaptive Sliding Mode for Agile Attitude Tracking in a High-Precision Modelled VLEO Environment

Pierantonio BERTUCCIO[1,a †*], Vincenzo Maria CANNAVALE[2,b †], Mattia ILLIANO[2,c †], Tobia Armando LA MARCA[3,d], Mauro MANCINI[1,e], Maria Daniela GRAZIANO[2,f], Elisa CAPELLO[1,g], Michele GRASSI[2,h]

[1]Department of Mechanical and Aerospace Engineering, Politecnico di Torino, Corso Duca degli Abruzzi 24, Torino, 10129, Italy

[2]Department of Industrial Engineering, University of Naples "Federico II", Piazzale Tecchio 80, 80125, Napoli, Italy

[3]Scuola Superiore Meridionale, University of Naples "Federico II", Largo San Marcellino 10, 80138, Napoli, Italy

[a]pierantonio.bertuccio@polito.it, [b]vincenzomaria.cannavale@unina.it, [c]mat.illiano@studenti.unina.it, [d]tobiaarmando.lamarca-ssm@unina.it, [e]mauro.mancini@polito.it, [f]mariadaniela.graziano@unina.it, [g]elisa.capello@polito.it, [h]michele.grassi@unina.it

† These authors contributed equally to this work

Keywords: VLEO, Spacecraft Attitude Control, Sliding Mode Control, Adaptive Control

Abstract. This paper presents a novel Sliding Mode Control (SMC) control formulated on the special orthogonal group SO(3) for spacecraft attitude control in Very Low Earth Orbit (VLEO). The approach addresses nonlinear rotation geometry and environmental disturbances without the singularities or redundancy of traditional attitude representations. A key innovation is the direct adaptive law that dynamically adjusts sliding manifold parameters, reducing reaching time and guiding the system toward desired dynamics once sliding is established. The controller is validated using the high-fidelity high-precision orbit propagator which accounts for the main environmental disturbances. Preliminary results demonstrate accurate attitude tracking performance in realistic maneuvering scenarios, confirming the controller's effectiveness for the challenging VLEO environment.

Introduction

The increasing interest in space missions operating in Very Low Earth Orbit (VLEO) has driven the development of advanced spacecraft attitude control strategies to ensure reliable performance in this challenging environment. In VLEO, perturbations arising from atmospheric drag become significant, requiring robust controllers to ensure precise pointing despite substantial uncertainties. In this context, a sliding mode–based attitude control law for VLEO spacecraft is proposed, designed to guarantee high pointing accuracy under severe disturbance and uncertainty conditions.

In this work, the attitude of the spacecraft is represented using rotation matrices defined on the Special Orthogonal Group SO(3). This choice provides a unique, global, and nonsingular representation of orientation, avoiding the well-known issues of singularities, redundancy, and normalization constraints associated with Euler angles and quaternions.

Sliding Mode Control (SMC) is a widely used nonlinear control technique, recognized for its robustness to parametric uncertainties and external disturbances. SMC operates through a two-phase mechanism: first, system trajectories are driven in finite time toward a subset of the system states named sliding surface. Then, the trajectories evolve on this surface, yielding reduced-order dynamics with strong disturbance rejection properties.

Content from this work may be used under the terms of the Creative Commons Attribution 3.0 license. Any further distribution of this work must maintain attribution to the author(s) and the title of the work, journal citation and DOI. Published under license by Materials Research Forum LLC.

Materials Research Proceedings 69 (2026) 1083-1088 https://doi.org/10.21741/9781644904251-187

Recent developments showed that a sliding surface can be defined directly on the Lie algebra associated with $\mathrm{SO}(3)$, thus preserving the intrinsic geometric structure of the attitude representation. This approach ensures global consistency and facilitates a systematic stability analysis [1,2].

Building upon these geometric formulations, this work introduces a time-varying SMC strategy that operates directly on $\mathrm{SO}(3)$. The proposed controller incorporates an adaptive mechanism that continuously adjusts the sliding manifold parameters in real time. During the reaching phase, this adaptation accelerates convergence by reshaping the manifold to align with the evolving system trajectories, while once sliding motion is achieved, the adaptive law steers the manifold toward the desired configuration, ensuring the intended closed-loop behavior [3].

Control framework on SO(3)

Attitude and velocity errors. Let $R(t) \in \mathrm{SO}(3)$ denote the current attitude of a rigid body and let $R_d(t) \in \mathrm{SO}(3)$ be a smooth, time-varying reference attitude. The corresponding body-fixed angular velocities are

$$\Omega = \left(R^\top \dot{R}\right)^\vee,\ \Omega_d = \left(R_d^\top \dot{R}_d\right)^\vee \in R^3, \tag{1}$$

where $(\cdot)^\vee : \mathfrak{so}(3) \to R^3$ is the vee operator and $\mathfrak{so}(3)$ is the Lie algebra of $\mathrm{SO}(3)$. The rotation error and angular velocity error are defined as

$$R_e = R_d^\top R \in \mathrm{SO}(3),\ \ \Omega_e = \Omega - R_e^\top \Omega_d \in R^3. \tag{2}$$

These errors quantify the geometric deviation of the current configuration from the desired trajectory directly on the manifold.

Kinematic Sliding Group and Control Law. Following the geometric sliding-mode design of [2,4], the sliding variable can be defined as follows:

$$s(R_e, \Omega_e) = \Omega_e + \lambda\, \Omega_u(R_e), \qquad \lambda > 0, \tag{3}$$

where log:$\mathrm{SO}(3) \to \mathfrak{so}(3)$ the matrix logarithm mapping the rotation error to the Lie algebra. Here, λ is a time-varying parameter according to the following adaptive law:

$$\dot{\lambda} = \mathrm{Proj}_{\lambda \in \Lambda}\left(-\gamma\, \mathrm{sign}(\langle J\Omega_u, s\rangle) - c\left(\lambda - \bar{\lambda}\right)\right), \tag{4}$$

where $\gamma > 0$ is an adaptation gain, and the Proj operator ensures λ remains in a feasible positive set $\Lambda \in R^+$. The adaptive law exhibits a two-term structure. The first term dominates when the system state is far from the sliding surface, accelerating convergence by dynamically steering the surface toward the system trajectories. As the sliding motion is established, this term vanishes, and the second term ensures that λ smoothly converges toward its desired nominal value $\bar{\lambda}$.

Finally, the control torque is designed as:

$$\tau_u = (J\Omega)^\wedge(\lambda\Omega_u(R_e) - \eta) - J\lambda\dot{\Omega}_u + J\dot{\eta} - Jk_s\langle Js, s\rangle^\sigma s + Jc\left(\lambda - \bar{\lambda}\right)\Omega_u(R_e), \tag{5}$$

where $k_s, > 0$ are control gains, $\bar{\lambda} > 0$ is final value reached by the λ parameter, η is the reference twist to be tracked expressed in the body frame, and $\langle\cdot,\cdot\rangle$ denotes the Euclidean inner product in R^3 and σ is a strictly positive value that varies between 0 and 0.5, in particular the latter

Materials Research Proceedings 69 (2026) 1083-1088 https://doi.org/10.21741/9781644904251-187

yields the discontinuous version of the controller. The resulting closed-loop system achieves almost-global stability on $SO(3)$, with finite-time reachability of the sliding manifold and exponential convergence in a neighborhood of the identity rotation matrix.

Simulation Environment

The spacecraft dynamics and control performance were evaluated using a high-fidelity six-degree-of-freedom numerical simulator developed in MATLAB/Simulink for VLEO operations. The simulator integrates coupled translational and rotational equations of motion in the Earth-Centered Inertial (ECI) reference frame, incorporating Earth's gravitational (EGM2008) and magnetic (IGRF-13) fields, atmospheric disturbances (NRLMSISE00), and solar radiation pressure (SRP). Attitude dynamics employ quaternion representation to avoid singularities, accounting for spacecraft inertia, environmental torques, control actuator torques, and momentum exchange with the reaction wheel (RW) assembly.

The simulation settings are reported in Table 1.

Table 1 Simulation settings including spacecraft properties, control hardware, sensor accuracy, initial conditions and space weather conditions.

	Parameter	Value
Spacecraft Mass Properties	Spacecraft Mass [kg]	29
	Inertia moments (I_{xx}, I_{yy}, I_{zz}) [kg/ m²]	1.117, 1.378, 0.508
	Residual Dipole (per axis) [Am²]	0.05
Control Hardware	RW Configuration	4-wheel pyramidal
	RW Tilt Angle [°]	26.57
	RW Saturation Momentum [Nms]	0.1
	RW Maximum Torque [mNm]	6
	Max. Magnetic Dipole [Am²]	2.6
Sensor Accuracy (1σ)	Position (X, Y) [mm]	1.5
	Position (Z) [mm]	1.25
	Velocity (X, Y) [mm/s]	0.015
	Velocity (Z) [mm/s]	0.03
	Angular Velocity [rad/s]	0.001
Initial Conditions	Epoch [UTC]	March 1, 2025, 10:00:00
	Position (ECI) [km]	[-2342.68, -6253.75, 0]
	Velocity (ECI) [km/s]	[-0.84, 0.32, 7.67]
	Euler Angles [°]	[0, 0, 0]
	Angular Velocity [°]	[0, 0, 0]
Space Weather Conditions (2001 Halloween storm)	$F_{10.7}$ (81-day-averaged, daily)	237
	Ap indeces	142

External disturbances encompass gravity gradient, magnetic, aerodynamic, and SRP torques. To minimize computational overhead, aerodynamic and SRP perturbations are pre-computed and stored in lookup tables rather than evaluated in real-time. The aerodynamic database, generated using the Cercignani–Lampis–Lord (CLL) gas–surface interaction model, combines data from a panel method in the free molecular flow regime [5] and high-fidelity Direct Simulation Monte Carlo (DSMC) runs in SPARTA [6] through a co-Kriging interpolation, increasing the accuracy of the aerodynamic force and torque coefficients parametrized by the angle of attack and sideslip angle relative to the body reference frame (BRF). The SRP database, computed via ray-tracing technique [7], contains force and torque distributions parametrized by solar azimuth and elevation angles with respect to the BRF. During propagation, disturbance forces and torques corresponding to instantaneous attitude configurations are retrieved through cubic spline interpolation of the lookup tables using the current relative orientation angles.

Materials Research Proceedings 69 (2026) 1083-1088 https://doi.org/10.21741/9781644904251-187

Results and Conclusions

The proposed control strategy enabled the spacecraft to successfully execute the complete multi-phase manoeuvre sequence, comprising slew, coast, and fine motion control phases, with smooth and stable dynamic behaviour.

Table 2 summarizes the time intervals associated with each manoeuvre phase, together with the selected convergence thresholds and the corresponding convergence times. The thresholds were chosen to both challenge the controller's performance and satisfy the mission requirements for fine pointing accuracy. The most stringent threshold corresponds to the onset of the fine motion phase, where the highest attitude precision is required.

The control frequency was set equal to the simulation integration step, i.e., 10 Hz, in accordance with the limitations of GNSS-based attitude measurements (here assumed to be available and aiding estimation) and the actuation bandwidth of the reaction wheels. Although higher control update rates are typically feasible, this frequency was assumed appropriate for the considered system constraints.

Despite the agility of the commanded profile, featuring pitch excursions of ±20° and angular rates on the order of 10^{-2} rad/s, the actuator torques remained unsaturated, Fig.2, exhibiting only brief peaks of less couple seconds during rapid slews. Across all phases, attitude convergence was achieved within a few seconds, as can be seen from Fig. 3, with steady-state errors consistently maintained below 0.01°.These results confirm the controller's effectiveness in achieving precise attitude tracking under the simulated dynamic and demanding VLEO conditions.

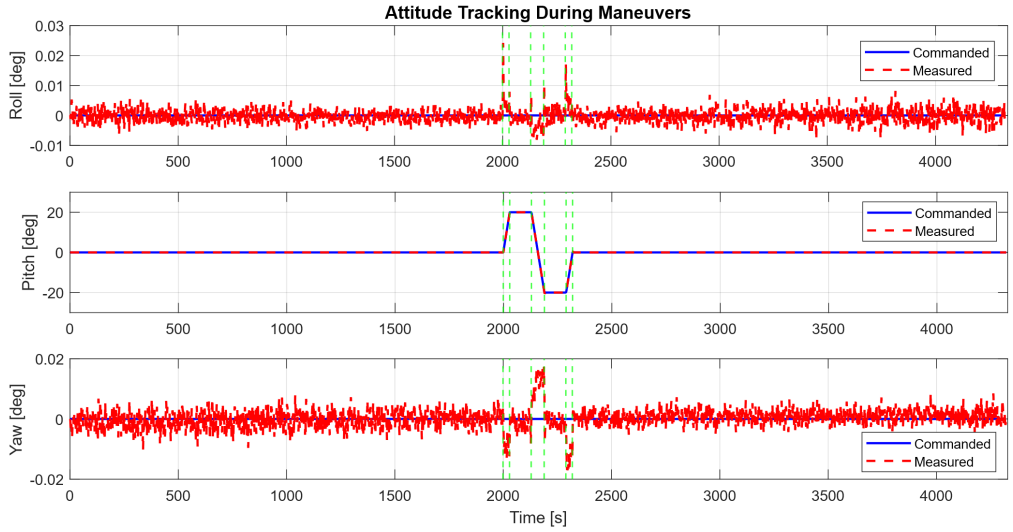


Figure 1. Commanded and measured Euler angles during the manoeuvre

Table 2. Time intervals of the different manoeuvre phases and respective convergence times and tolerances thresholds.

	Time interval [s]	Error threshold [°]	Convergence time [s]
Case 1	1998-2029	0.5	2.5
Case 2	2029-2129	0.5	2.1
Case 3	2129-2189	0.2	3.2
Case 4	2189-2289	0.5	2.2
Case 5	2289-2319	0.5	2.5
Case 6	2319-3000	0.5	2

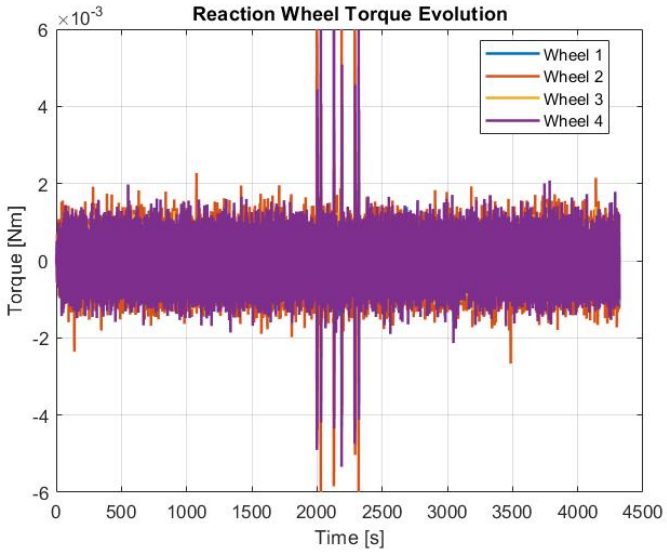


Figure 2. Distributed actuated torque on the RWs pyramidal configuration.

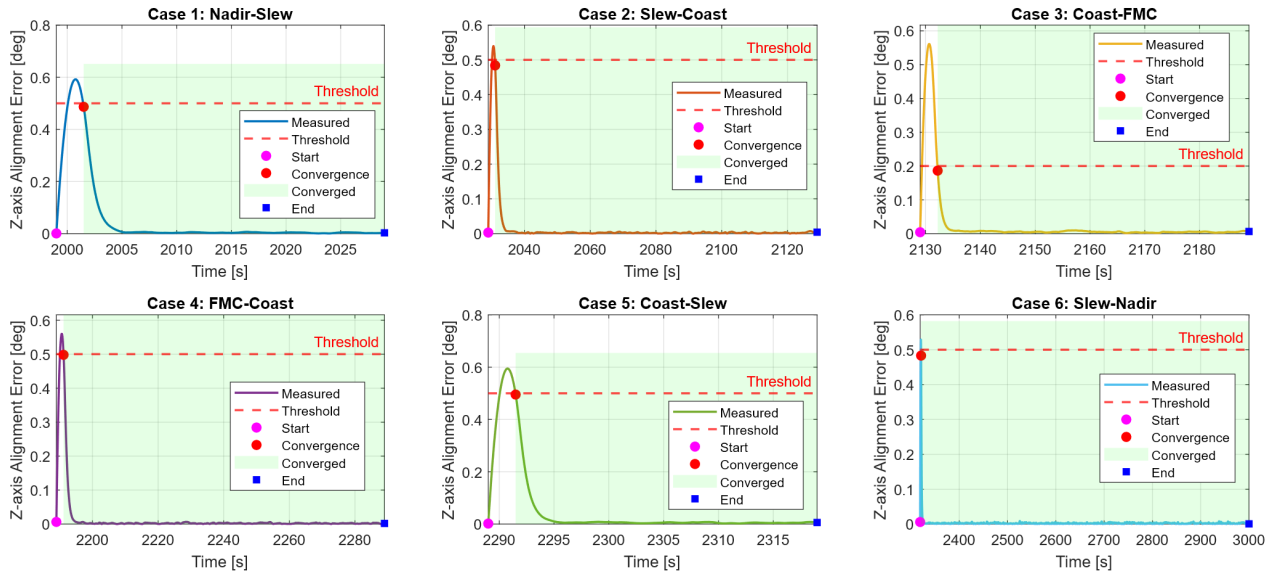


Figure 3. Convergence analysis for the separate phases of the manoeuvre.

Acknowledgements

This work was carried out within the *Space It Up!* project funded by the Italian Space Agency (ASI) and the Italian Ministry of University and Research (MUR) under contract No. 2024-5-E.0, CUP No. I53D24000060005.

References

[1] Francesco Bullo and Andrew D Lewis. Geometric Control of Mechanical Systems. Vol. 49. Texts in Applied Mathematics. Springer, 2004.

[2] Eduardo Espindola and Yu Tang. “Geometric sliding mode control of mechanical systems on Lie groups”. In: Automatica 177 (2025), p. 112346. issn: 0005-1098. doi:

https : / / doi . org / 10 . 1016 / j . automatica . 2025 . 112346

[3] M.Mancini. “Adaptive Variable Structure Control System for Attitude Spacecraft Applications”. PhD thesis. Politecnico di Torino, 2023.

[4] Qingkai Meng, Hao Yang, and Bin Jiang. “Second-order sliding-mode on SO(3) and fault-tolerant spacecraft attitude control”. In: Automatica 149 (2023), p. 110814. issn: 0005-1098. doi: https : / / doi . org / 10 . 1016 / j . automatica . 2022 . 110814.

[5] Sinpetru, L. A., Crisp, N. H., Mostaza-Prieto, D., Livadiotti, S., and Roberts, P. C. E., “ADBSat: Methodology of a Novel Panel Method Tool for Aerodynamic Analysis of Satellites,” *Computer Physics Communications*, Vol. 278, 2022, p. 108456. https://doi.org/10.1016/j.cpc.2022.108456

[6] Plimpton, S. J., Moore, S. G., Borner, A., Stagg, A. K., Koehler, T. P., Torczynski, J. R., and Gallis, M. A., “Direct Simulation Monte Carlo on Petaflop Supercomputers and Beyond,” *Physics of Fluids*, Vol. 31, No. 8, 2019. https://doi.org/10.1063/1.5108534

[7] Li, Z., Ziebart, M., Bhattarai, S., Harrison, D., and Grey, S., “Fast Solar Radiation Pressure Modelling with Ray Tracing and Multiple Reflections,” *Advances in Space Research*, Vol. 61, No. 9, 2018, pp. 2352–2365. https://doi.org/10.1016/j.asr.2018.02.019

Materials Research Proceedings 69 (2026) 1089-1094 https://doi.org/10.21741/9781644904251-188

A Heterogeneous Multi-robot Framework for Cooperative Lunar Exploration

Riccardo Caccavale[1,a *], Stefano Ciaravino[1,b], Alberto Finzi[1,c], Vincenzo Lippiello[1,d], Giuseppe Rauso[1,e]

[1]Università degli Studi di Napoli "Federico II", Dipartimento di Ingegneria, Elettrica e delle Tecnologie dell'Informazione (DIETI), Via Claudio 21, Napoli, Italy

[a]riccardo.caccavale@unina.it, [b]stefanociaravino96@gmail.com, [c]alberto.finzi@unina.it, [d]vincenzo.lippiello@unina.it, [e]giuseppe.rauso@unina.it

Keywords: Spaceflight Dynamics/GNC/Space Robotics, Space Exploration, In Situ Resource Utilization

Abstract We present a ROS 2-based multi-robot control framework for cooperative lunar exploration, designed to support heterogeneous rover teams operating in unstructured planetary environments. The framework integrates a novel gradient-based traversability plugin compatible with the Nav2 navigation stack, enabling terrain-aware path planning tailored to individual rover capabilities. Each agent is equipped with an executive system supporting local autonomy and reactive decision-making, allowing independent operation while enabling coordinated missions through minimal inter-agent communication. The system has been validated in a Gazebo Fortress simulation environment using realistic lunar terrain reconstructions and plausible physical parameters.

Introduction

Planetary rover missions demand robust exploration solutions to address the limitations of single-agent scenarios in mapping, sensing, and resource utilization. The pursuit of heterogeneous teams with differences in locomotion, perception, and scientific payload offers greater mission flexibility and resilience in unpredictable extra-terrestrial scenarios. A scalable, modular robotic framework must address three main challenges: (i) robust perception and localization, (ii) reliable terrain traversability analysis, and (iii) intelligent coordination among agents. Planetary rover exploration missions increasingly require fine-grained, large area mapping to detect resources, study geological features, or deploy distributed sensor networks. Single-robot solutions often fall short in efficiently covering wide areas or collecting multi-perspective data required for accurate modeling [1]. Multi-robot systems [2, 3] represent a significant advancement by enabling cooperative exploration strategies and distributed sensing. However, their success depends on robust navigation and coordination strategies, efficient communication, and intelligent task allocation. Furthermore, mobility in extraterrestrial environments, particularly on the Moon and similar planets, is severely constrained by rough terrain, steep slopes, and obstacles such as craters and boulders. Designing effective navigation systems for rovers thus requires not only precise perception and localization, but also reliable terrain analysis and traversability assessment. This work, conducted within the framework of the Italian project Space It Up (SIU) which promotes innovation in human and robotic space exploration envisions a team of heterogeneous, autonomous rovers cooperating to perform complex planetary missions such as searching for water or rare earth elements. Unlike other systems [4, 5], our approach addresses multiple levels of heterogeneity among agents. This includes not only differences in locomotion capabilities but also variations in scientific instrumentation, with agents equipped with complementary or redundant payloads tailored to specific mission goals. In this paper, we present a multi-robot control framework that enables a team of heterogeneous robots to safely navigate lunar-like environments and

Content from this work may be used under the terms of the Creative Commons Attribution 3.0 license. Any further distribution of this work must maintain attribution to the author(s) and the title of the work, journal citation and DOI. Published under license by Materials Research Forum LLC.

Materials Research Proceedings 69 (2026) 1089-1094 https://doi.org/10.21741/9781644904251-188

collaboratively perform exploration and inspection tasks by leveraging distributed sensing capabilities and diverse locomotion modalities. The framework is built upon the Robot Operating System 2 (ROS2) middleware and integrates a high-fidelity lunar simulation environment based on Gazebo Fortress. Our primary contributions include: (i) the architectural design of a scalable multi-robot system, in which each agent is equipped with an executive system [6] grounded in cognitive control and supervisory attention to support local autonomy and reactive decision-making; (ii) a rover-specific navigation module tailored to challenging lunar terrains; and (iii) a modular simulation environment for testing and validating multi-robot operations in realistic lunar scenarios, supporting a wide range of heterogeneous platforms. This architecture allows agents to perform independent and autonomous exploration tasks, while also enabling coordinated multi-robot missions through minimal and sparse inter-agent communication between the executive systems.

Related Works

Multi-robot exploration and coordination for planetary missions have been extensively investigated in recent years. The CADRE mission [5] introduces a cooperative autonomous distributed robotic exploration framework for lunar surface operations, employing a team of three rovers with dynamic leader election and centralized strategic planning. Although CADRE shares our focus on lunar multi-robot systems, our approach differs in its management of heterogeneity and in the integration of terrain-aware navigation directly within the costmap layer. Building upon the CADRE system, Nayak et al. [8] proposes a map partition-based exploration algorithm that divides unexplored space into non-overlapping regions assigned to individual robots. Similarly, our framework supports coordinated exploration through distributed executive systems, but it emphasizes autonomous single-agent capabilities with minimal inter-agent communication, avoiding the need for periodic centralized replanning. While their method prioritizes exploration efficiency, our approach integrates traversability assessment directly into the navigation planning process. Exploration efficiency is also the central focus of [9], where the authors introduce a distributed grid-based local planner (MGG) combined with a global sparse graph for frontier tracking. In their formulation, navigation constraints are natively incorporated into the overall planning process. In contrast, we adopt a more modular architecture in which 3D navigation is handled by a dedicated layer within the Nav2 costmap framework, allowing seamless integration with existing grid-based planners such as DWB, TEB, or A*.

System Architecture

The proposed architecture supports heterogeneous robotic platforms with diverse locomotion and perception capabilities (see Fig. 1, left). Each agent integrates an executive system that enables local autonomy, cognitive control, and supervisory attention; a perception subsystem supporting localization and mapping; and a planning and navigation module tailored to the locomotion characteristics of planetary rovers. The framework is built upon the ROS 2 middleware, where terrain-aware navigation is achieved through an extension of the standard Nav2 stack to incorporate traversability information into the planning process.

Materials Research Proceedings 69 (2026) 1089-1094 https://doi.org/10.21741/9781644904251-188

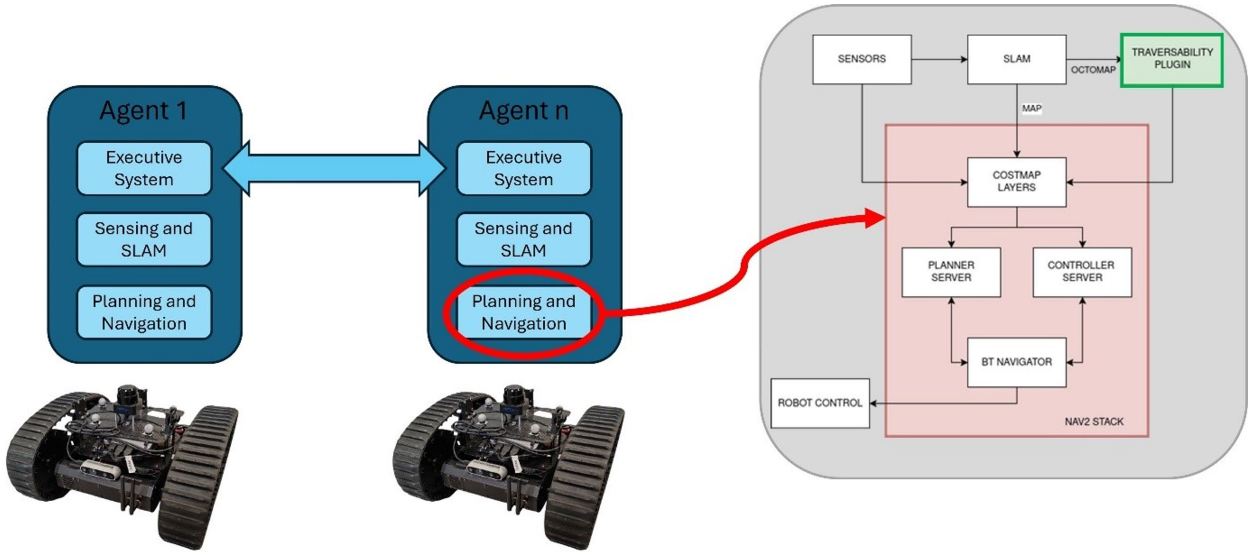


Figure 1: Multi-robot system architecture: executive layer, navigation module, perception subsystem.

Executive and Autonomy Layer. Each robot employs an executive system responsible for local task management and high-level decision making [6]. This system maintains a longterm repository of agent-specific, hierarchically organized skills, each defined by planning constraints such as preconditions and postconditions. Skills can be invoked at runtime and instantiated as hierarchical behaviors within a Working Memory (WM), where they are monitored and executed. When multiple skills or behaviors are simultaneously enabled, attentional regulation mechanisms resolve conflicts over shared resources [12, 13]. This cognitive control process enhances reactivity in dynamic lunar environments and ensures resilience to communication dropouts. Within this executive loop, collaborative multi-agent tasks are dynamically allocated, explicitly incorporating communication behaviors to support interagent synchronization.

Navigation and Traversability

We assume that each agent is equipped with 3D SLAM capabilities based on graph optimization, generating its own map referenced to the ground-station frame. To address terrainaware autonomous navigation in unstructured environments, we developed a gradient-based traversability plugin operating at the Nav2 costmap level. This approach seamlessly integrates with existing navigation stacks without modifying core planning algorithms, enabling terrain-aware path planning tailored to each rover's locomotion capabilities. The plugin processes 3D occupancy data to compute terrain traversability. An elevation map is first constructed by projecting OctoMap voxels onto a 2D grid, where each cell (i, j) stores the maximum elevation $h(i,j) = max_{v \in V_{ij}} z_v$, with V_{ij} being the set of occupied voxels within that cell and z_v the vertical coordinate of voxel v. Local terrain gradients are then computed using centered finite differences:

$$\left.\frac{\partial h}{\partial x}\right|_{i,j} \approx \frac{h(i+1,j) - h(i-1,j)}{2\Delta r}, \qquad \left.\frac{\partial h}{\partial y}\right|_{i,j} \approx \frac{h(i,j+1) - h(i,j-1)}{2\Delta r} \tag{1}$$

where $\partial h/\partial x$ and $\partial h/\partial y$ represent slopes in the horizontal (x) and lateral (y) directions, and Δr is the costmap resolution. The slope angle is computed by combining gradients, and traversability costs are assigned as:

Materials Research Proceedings 69 (2026) 1089-1094 https://doi.org/10.21741/9781644904251-188

$$\theta(i,j) = \arctan\left(\sqrt{\left(\frac{\partial h}{\partial x}\right)^2 + \left(\frac{\partial h}{\partial y}\right)^2}\right), \qquad C(i,j) = \begin{cases} C_{lethal}, & if\ \theta(i,j) \geq \theta_{max} \\ \alpha \cdot \theta(i,j), & otherwise \end{cases} \quad (2)$$

Where $\boldsymbol{\theta_{max}}$ is the rover's maximum traversable slope threshold and α normalizes costs to the Nav2 range $\mathbf{[0, 254]}$ accounting for rover locomotion characteristics. Spatial filtering further reduces computational overhead by processing only OctoMap voxels within a configurable radius of the robot, maintaining efficiency while preserving local terrain representation. The plugin integrates into the costmap pipeline between static/SLAM mapping and obstacle inflation layers, enriching global and local costmaps with terrain-aware traversability values while preserving compatibility with all Nav2-based planners.

Simulation and Validation

To validate the proposed system, a realistic simulation of the lunar surface was developed, based on reconstructions of the Apollo 14 landing site and plausible physical parameters. The Gazebo Fortress-based environment supports synchronized multi-robot scenarios and includes a variety of terrain features such as craters, slopes, and boulders (see Fig. 2). The framework provides full configurability for defining the number and initial placement of agents, the types of sensors they are equipped with, and the environment physical parameters (e.g., Earth or lunar gravity).



Figure 2: Snapshots of the simulated lunar environment, with representation of the perceived terrain and traversability costmap (upper-right window).

Experimental Workflow. To evaluate our system, we designed an experimental scenario inspired by the SIU case study, in which a team of two heterogeneous robots is tasked with exploring a designated area in search of traces of rare earth elements (REEs). Specifically, the first rover is equipped with a spectrometer (e.g., multispectral or gamma-ray) to remotely detect candidate regions where REEs may be present, while the second rover carries a hyperspectral camera to perform close-range analysis of these candidate areas. The experiments proceed as follows. At the beginning of each trial, the two robots are deployed in the virtual lunar environment at random initial poses, while n target spots are randomly distributed across the terrain. The robots are initially unaware of the positions of these target spots, which become detectable only when they fall within the sensing range of the spectrometer. The first rover is responsible for sweeping the area to identify potential target spots, whereas the second rover must approach and closely scan each detected location. The overall objective is to safely explore the area, identifying and analysing all target spots. An initial set of proof-of-concept trials was performed. Preliminary results,

obtained in scenarios covering approximately 50 m^2 and involving a small number of target sites ($n \in [3, 9]$), show that the robot team can successfully navigate the environment, avoid obstacle such as craters and rocks, and cooperatively detect and analyse the designated targets.

Conclusion

In this paper, we proposed a scalable multi-robot strategy that emphasizes heterogeneity and modularity to enable more robust and efficient lunar exploration. The system integrates a terrain-aware navigation module and an executive layer supporting local autonomy and cooperative behaviors through minimal inter-agent communication. The framework has been validated in a realistic lunar simulation environment, using plausible physical parameters and high-fidelity 3D reconstructions of the lunar surface, demonstrating effective performance across different rover configurations and terrains. Current efforts focus on validating the system on physical rovers and enhancing autonomous capabilities for multi-robot planetary exploration.

Acknowledgments

This work was supported by the SPACE IT UP project (PE15), funded by ASI and MUR under the Italian PNRR, NextGenerationEU.

References

[1] SA. Chien, G. Visentin, and C. Basich, “Exploring beyond earth using space robotics,” *Science Robotics*, vol. 9, no. 91, p. eadi6424, 2024. https://doi.org/10.1126/scirobotics.adi6424

[2] A. Torreno, E. Onaindia, A. Komenda, and M. Štolba, “Cooperative multi-agent planning: A survey,” *ACM Computing Surveys (CSUR)*, vol. 50, no. 6, pp. 1–32, 2017. https://doi.org/10.1145/3128584

[3] Y. Rizk, M. Awad, and EW. Tunstel, “Cooperative heterogeneous multi-robot systems: A survey,” *ACM Computing Surveys (CSUR)*, vol. 52, no. 2, pp. 1–31, 2019. https://doi.org/10.1145/330384

[4] F. Cordes et al., “Lunares: Lunar crater exploration with heterogeneous multi robot systems,” *Intelligent Service Robotics*, vol. 4, no. 1, pp. 61–89, 2011. https://doi.org/10.1007/s11370-010-0081-4

[5] J.-P. de la Croix, F. Rossi, R. Brockers, D. Aguilar, K. Albee, E. Boroson, A. Cauligi, J. Delaune, R. Hewitt, D. Kogan, G. Lim, B. Morrell, Y. Nakka, V. Nguyen, P. Proenca, G. Rabideau, J. Russino, M. S. da Silva, G. Zohar, and S. Comandur, “Multi-agent autonomy for space exploration on the CADRE lunar technology demonstration,” in *Proc. 2024 IEEE Aerospace Conf.*, 2024. https://doi.org/10.1109/AERO58975.2024.10521425

[6] R. Caccavale and A. Finzi, “A robotic cognitive control framework for collaborative task execution and learning,” *Topics in Cognitive Science*, vol. 14, no. 2, pp. 327–343, 2021. https://doi.org/10.1111/tops.12587

[7] S. Macenski, F. Martin, R. White, and J. Ginés Clavero, “The marathon 2: A navigation system,” in *Proc. IEEE/RSJ Int. Conf. on Intelligent Robots and Systems (IROS)*, 2020. https://doi.org/10.1109/IROS45743.2020.9341207

[8] S. Nayak, G. Lim, F. Rossi, M. Otte, and J.-P. de la Croix, “Multi-robot exploration for the CADRE mission,” *Autonomous Robots*, vol. 49, no. 2, p. 17, 2025. https://doi.org/10.1007/s10514-025-10199-3

[9] V. S. Varadharajan and G. Beltrame, “A multi-robot exploration planner for space applications,” *IEEE Robotics and Automation Letters*, vol. 10, no. 3, pp. 2446–2453, 2025. https://doi.org/10.1109/LRA.2025.3532158

[10] M. Saboia, F. Rossi, V. Nguyen, G. Lim, D. Aguilar, and J.-P. de la Croix, “CADRE MoonDB: Distributed database for multi-robot information-sharing and map-merging for lunar exploration,” in *Proc. MASSPACE24 Workshop*, 2024.

[11] M. Allan, U. Wong, P. M. Furlong, A. Rogg, S. McMichael, T. Welsh, I. Chen, S. Peters, B. Gerkey, M. Quigley, M. Shirley, M. Deans, H. Cannon, and T. Fong, “Planetary rover simulation for lunar exploration missions,” in *Proc. IEEE Aerospace Conf.*, NASA Ames Research Center, 2019. https://doi.org/10.1109/AERO.2019.8741780

[12] R. Caccavale and A. Finzi, “Learning attentional regulations for structured tasks execution in robotic cognitive control,” *Autonomous Robots*, vol. 43, pp. 2229–2243, 2019. https://doi.org/10.1007/s10514-019-09876-x

[13] G. Rauso, R. Caccavale, and A. Finzi, “Combined text-visual attention models for robot task learning and execution,” in *Advances in Artificial Intelligence. AIxIA 2024. Lecture Notes in Computer Science*, vol. 15450, A. Artale, G. Cortellessa, and M. Montali, Eds. Cham: Springer, 2025, pp. 228–240. https://doi.org/10.1007/978-3-031-80607-0_18

Materials Research Proceedings 69 (2026) 1095-1100 https://doi.org/10.21741/9781644904251-189

Integrated Active Vibration Control and Structural Health Monitoring of Flexible Spacecraft Panels

Muhammad Faisal NADEEM[1,a *], Sajid RAFIQUE[2,b]

[1]Aerospace Flight Vehicle Design,(School of Astronautics), Northwestern Polytechnical University, Xi'an, Shaanxi ,710072, China

[2]Faculty of Engineering and Sustainable Development, University of Gävle, 801 76 Gavle, Sweden

[a]mfaisaln@mail.nwpu.edu.cn, [b]sajid.rafique@hig.se

Keywords: Active Vibration Control, Offset Piezo Stack Actuators, H∞ Control, Finite Element Analysis, Eddy Current Sensor, Tip Deflection Measurement

Abstract. This paper presents an integrated active vibration control (AVC) and structural health monitoring (SHM) framework for flexible spacecraft panels using offset piezoelectric stack actuators (OPSA). A three-dimensional ANSYS finite-element model of a hub–panel assembly with eccentric OPSA mounting is reduced to a low-order state-space model retaining the first two bending modes. Based on this model, a mixed-sensitivity H_∞ controller is designed for robust vibration suppression and compared with an LQR baseline. For SHM, root delamination is represented as an equivalent stiffness loss at the clamp over a 0–40% damage range, and damage-sensitive features are extracted from the closed-loop impulse response, including modal frequency drops, RMS control voltage, residual tip vibration, and settling time. A physics-informed Gaussian process regressor trained on 200 virtual experiments accurately estimates the damage parameter, achieving $R^2 \approx 1.000$and an RMSE of about 0.25% damage. Over the investigated range, RMS control voltage increases from 48.2 V to 144.6 V, while residual tip amplitude rises from 0.315 mm to 0.633 mm, confirming strong monotonic sensitivity to structural degradation. The results demonstrate that the OPSA–H_∞ loop can provide both robust vibration suppression and a dual-use sensing channel for quantitative damage estimation without additional dedicated SHM hardware.

Introduction

Prior work has demonstrated the effectiveness of offset piezoelectric stack actuators (OPSA) for active damping of large flexible structures, and several authors have employed LQR, PPF, μ-synthesis, and smart-device concepts to suppress vibrations of solar arrays and similar appendages [1, 2, 3]. Recent studies further address optimal actuator/sensor placement and controller design using genetic algorithms and H∞ -based criteria [4, 5, 6]. Although well-established techniques including LQR, positive position feedback (PPF), and μ-synthesis have been widely applied, these approaches primarily focus on control performance, with comparatively little attention devoted to simultaneous structural health monitoring (SHM).

This paper proposes a compact dual-use framework in which an H_∞controller developed for active vibration suppression is also utilized for structural health monitoring of a flexible spacecraft panel with OPSA actuation. The main contribution is the integration of robust control and damage estimation within the same hardware and closed-loop architecture, allowing both frequency-based and control-derived features to be exploited for monitoring without additional dedicated SHM sensors. The study is limited to finite-element-based numerical validation, but it establishes a concise proof of concept for future experimental implementation and controller adaptation based on the estimated damage state.

Content from this work may be used under the terms of the Creative Commons Attribution 3.0 license. Any further distribution of this work must maintain attribution to the author(s) and the title of the work, journal citation and DOI. Published under license by Materials Research Forum LLC.

Materials Research Proceedings 69 (2026) 1095-1100 https://doi.org/10.21741/9781644904251-189

Mathematical Modeling

The hub–flexible panel idealized as cantilever shown in Fig. 1. Offset piezoelectric stack actuator (OPSA) is integrated on beam. The cantilever panel is modeled in ANSYS using SOLID186 elements for the aluminum structure and SOLID226 elements for the OPSA stacks. A reduced-order state-space model retaining the first two bending modes is derived from the FEA. The cantilever has dimensions of 1.1×0.25×0.002 m, and is discretized using a uniform mesh size of 5 mm.

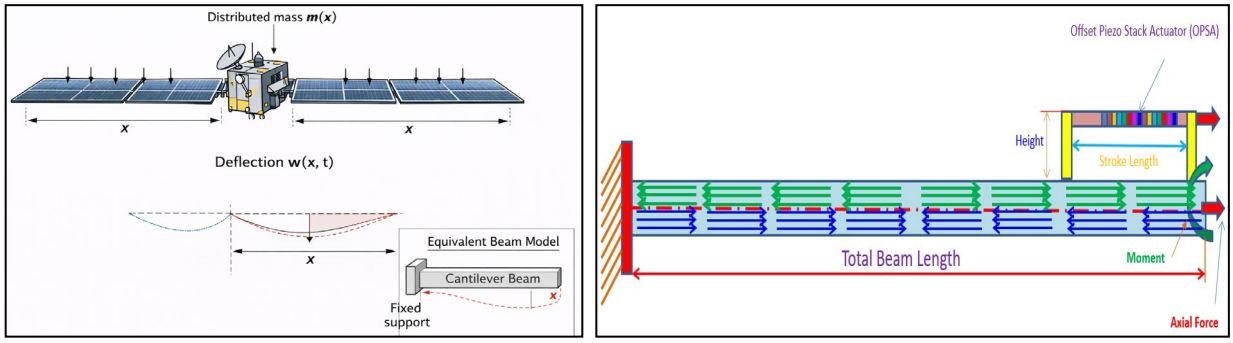


Figure. 1. Schematic of the flexible cantilever spacecraft panel with OPSA actuation and tip-response measurement used for integrated vibration control and damage monitoring

We model the coupled piezo-actuated structure using the FE formulation [3]:

$$M\ddot{u} + C\dot{u} + K_{\phi\phi}u + K_{u\phi}\phi = F + B_u v \tag{1}$$

where $\mathbf{M}, \mathbf{C}, \boldsymbol{K}$ are mass, damping and elastic stiffness matrices; $\mathbf{K}_{u\phi}$ piezoelectric coupling; $\mathbf{K}_{\phi\phi}$ dielectric stiffness; $\mathbf{u}$ structural DOFs; $\mathbf{F}_m$mechanical loads; v actuator voltages; ϕ denotes the lectric potential degree of freedom (DOFs) of the piezoelectric stacks; and $\mathbf{B}_u$ locate loads and actuators.

Root Delamination Modeling & Active Vibration Control (AVC)-Assisted Structural Health Monitoring (SHM)

Root delamination is modeled as an equivalent reduction in bending stiffness at the clamped end of the cantilever panel. A scalar damage parameter $d \in [0,0.4]$ is introduced, where $d = 0$ represents the pristine (healthy) structure and $d = 0.4$ corresponds to a 40% stiffness reduction. Root damage is therefore represented through a compact stiffness-loss parameter that preserves the dominant effect of localized delamination on the low-order bending dynamics. Since the present control problem is focused on the dominant flexible response, the full finite-element model is projected onto a reduced modal basis retaining the first two bending modes. This parameter is calibrated to reflect mode-dependent stiffness degradation, consistent with the characteristic behavior of flexible structures under localized root damage.

The integration of the H_∞ active vibration control (AVC) system with structural health monitoring (SHM) establishes a novel dual-use framework for non-invasive damage detection. By exploiting control-derived features—such as modal frequency shifts and actuator voltage demands—the damage parameter d can be accurately estimated using the existing control hardware alone. This approach provides a compact and computationally efficient damage indicator, eliminating the requirement for additional dedicated sensors and thereby reducing overall system cost and complexity.

Materials Research Proceedings 69 (2026) 1095-1100 https://doi.org/10.21741/9781644904251-189

Physics-Informed Damage Estimation Using Gaussian Process Regression

To estimate the damage level, we trained a Gaussian Process Regressor (GPR) on a dataset comprising control-derived features from the H_∞ loop. We define damage-sensitive SHM features as the first two frequency drops ($\triangle f_1$, $\triangle f_2$) , RMS control voltage V_{RMS} , residual tip displacement x_{res}, and settling time T_s, all extracted from the time-domain closed-loop response to a standardized impulse.

Mixed-sensitivity $\mathbf{H}_\infty$ Control Design

The OPSA-actuated panel, reduced to the first two bending modes, is written in the standard generalized plant form

$$\begin{bmatrix}\dot{x}\\ z\\ y\end{bmatrix} = \begin{bmatrix}A & B_1 & B_2\\ C_1 & D_{11} & D_{12}\\ C_2 & D_{21} & 0\end{bmatrix}\begin{bmatrix}x\\ w\\ u\end{bmatrix} \tag{2}$$

where x is the modal state, u is the OPSA control voltage, w collects exogenous inputs (reference and base disturbance), z stacks the performance outputs, and y is the measured tip signal. The matrices C_1, D_{11}, D_{12} embed the mixed-sensitivity weights W_1, W_2, W_3 so that

$$z \triangleq \begin{bmatrix}W_1(s)e\\ W_2(s)u\\ W_3(s)y\end{bmatrix},\ e = r - y \tag{3}$$

with r the tip reference, $S(s)$ and $T(s)$ the sensitivity and complementary sensitivity of the closed loop, and W_1, W_2, W_3 shaping vibration suppression, control effort, and high-frequency robustness, respectively.

A dynamic output-feedback controller is as in Eq. 4;

$$K(s):\ \begin{cases}\dot{x}_K = A_K x_K + B_K y,\\ u = C_K x_K + D_K y,\end{cases} \tag{4}$$

is sought such that the lower linear–fractional transformation $T_{zw}(s) = F_l(G, K)$ from w to z has bounded induced L2 gain,

$$\|T_{zw}(s)\|_\infty = \sup_{w\epsilon\mathbb{R}} \bar{\sigma}\left(\left(T_{zw}(jw)\right)\right) < \gamma \tag{5}$$

where $\bar{\sigma}(.)$ denotes the maximum singular value. In terms of the closed-loop maps

$$S(s) = (I + K(s)P(s))^{-1}, \qquad T(s) = I - S(s) \tag{6}$$

with $P(s)$ the nominal plant from u to y, this corresponds to the mixed-sensitivity optimization.

$$\left\|\begin{bmatrix}W_1(s)e\\ W_2(s)u\\ W_3(s)y\end{bmatrix}\right\|_\infty < \gamma \tag{7}$$

which enforces low sensitivity in the modal band, bounded OPSA voltages, and rapid loop roll-off at high frequency, jointly limiting spillover into truncated modes. The resulting H_∞controller

Materials Research Proceedings 69 (2026) 1095-1100 https://doi.org/10.21741/9781644904251-189

is computed using standard Riccati-based synthesis and provides robust performance across the family of plants generated by the root-stiffness (damage) parameter *d*.

In the present design, the mixed-sensitivity H_∞ framework is used to balance three objectives simultaneously: suppression of low-frequency flexible-mode vibration, limitation of actuator voltage demand, and attenuation of high-frequency amplification associated with truncated dynamics. The selected weighting functions therefore shape the closed-loop response to achieve robust disturbance rejection near the dominant bending modes while avoiding excessive control effort and spillover. This makes the controller suitable for flexible spacecraft structures, where reduced-order modeling and uncertainty in higher modes are unavoidable.

Integrated Results and Discussion

As shown in Fig. 2, the Bode diagram for Mode 1 indicates that both controllers substantially reduce the open-loop resonant peak, but the mixed-sensitivity H∞ design achieves the largest attenuation and a more favorable phase roll-off than LQR, implying stronger modal damping and improved phase margin. The corresponding Nyquist plot confirms closed-loop stability for both controllers, while the H∞ locus is more contracted and remains further from the-1 +0j point than the LQR curve, demonstrating superior robustness to gain and modeling uncer-tainties.

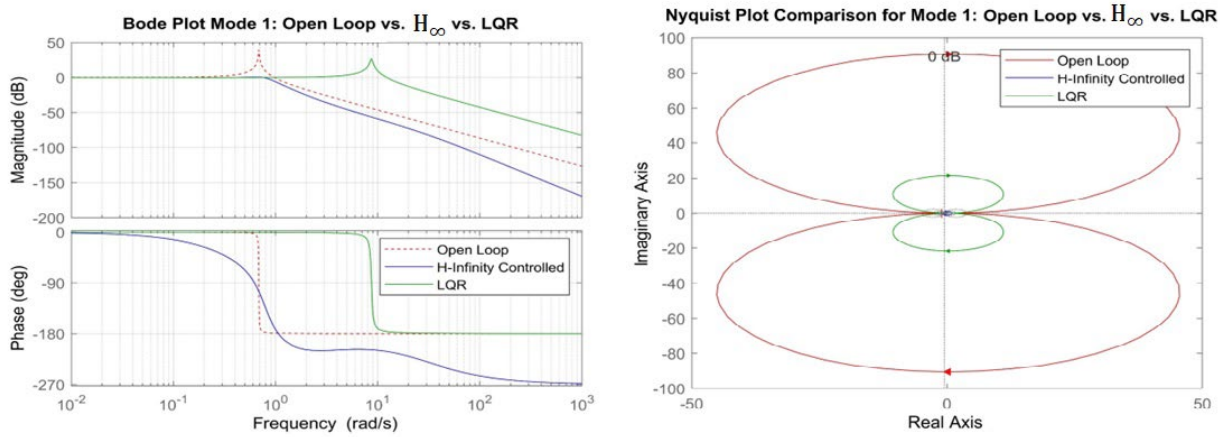


Figure. 2. Bode and Nyquist comparisons of the closed-loop response for the H∞ and LQR controllers, illustrating improved robustness and attenuation near the dominant flexible mode.

Table 1: Actual and predicted damage levels obtained from Gaussian process regression using selected vibration and control features.

Damage [%]	$\triangle f_1$ [Hz]	$\triangle f_2$ [Hz]	RMS Voltage [V]	Residual Amplitude [mm]	Settling Time (s)	Predicted Damage (%)
0	0	0	48.2	0.315	4.20	0.02
10	5.13	6.73	60.5	0.363	4.85	9.98
20	10.56	13.98	77.9	0.426	5.69	20.20
30	16.33	21.90	103.8	0.511	6.81	30.90
40	22.54	30.72	144.6	0.633	8.4	39.90

Table 1 and Fig. 3 jointly characterize that as the damage level increases from 0% to 40% stiffness loss, the first and second natural frequencies exhibit progressively larger drops, with the second mode consistently more affected, reflecting its higher sensitivity to root stiffness changes. In parallel, the RMS control voltage, residual tip amplitude, and settling time all increase monotonically, showing that the H_∞ controller must supply higher effort to stabilise a

Materials Research Proceedings 69 (2026) 1095-1100 https://doi.org/10.21741/9781644904251-189

progressively softer structure. The dual-feature SHM index constructed from RMS voltage and residual vibration follows the same smooth trend, further confirming the damage sensitivity of control-derived indicators.

The Gaussian-process regressor trained on these features reconstructs the scalar damage parameter with excellent accuracy, achieving a test-set coefficient of determination $R^2 \approx 1.000$ and a root-mean-square error of about 0.25% damage over the full 0–40% range. An ablation study shows that a control-only feature set (RMS voltage, residual vibration, settling time) attains nearly the same performance as the frequency-only set ($\triangle f_1$,$\triangle f_2$) confirming the strong monitoring value of control-derived features. A complementary boosted-tree feature-importance analysis identifies the fundamental frequency drop $\triangle f_1$ as the dominant predictor, in line with classical SHM, while the control-based features supply redundant but complementary information that is expected to become more valuable in experimental conditions with sensor noise and modelling errors. Overall, these results confirm the feasibility of the proposed unified AVC–SHM framework.

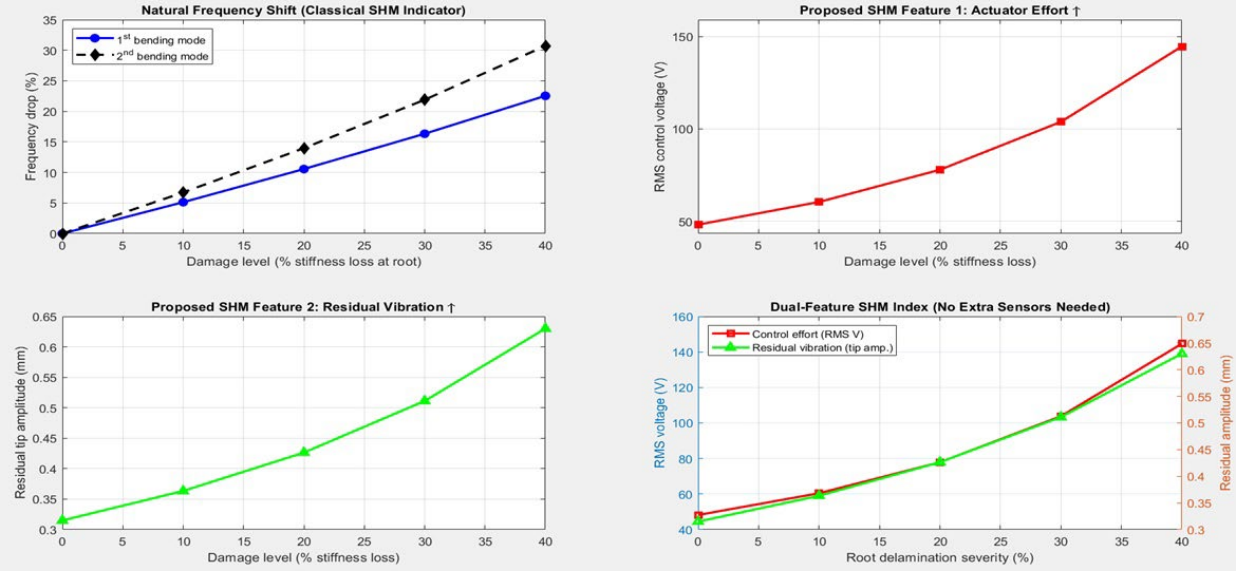


Figure. 3. Variation of frequency-based and control-derived features with increasing damage level, showing their monotonic sensitivity to root stiffness degradation.

The observed closed-loop trends are also consistent with the underlying structural mechanics. As root stiffness degrades, the effective rotational constraint at the clamped end weakens, reducing modal stiffness and increasing the dynamic compliance of the panel. This explains the progressive reduction in modal frequencies, together with the simultaneous increase in residual tip vibration and settling time. From the control viewpoint, the H∞ compensator must inject greater actuator voltage to maintain comparable vibration suppression as the structure becomes softer, which is why the RMS control effort rises monotonically with damage severity. The stronger sensitivity of the second bending mode further suggests that higher-order flexible dynamics are more influenced by localized root degradation, making Δf_2 a particularly informative damage feature.

These results also highlight the practical value of the proposed dual-use framework. While frequency-based indicators remain effective, the control-derived quantities $(V_{\mathrm{RMS}}, x_{\mathrm{res}}, T_s)$are directly available from the closed-loop response and therefore offer a convenient monitoring channel without dedicated additional SHM hardware. This is particularly attractive for spacecraft applications, where extra sensing hardware increases mass and integration complexity. The present results are based on finite-element-derived virtual experiments and should therefore be interpreted

as proof-of-concept performance prior to future experimental validation under broader uncertainty conditions.

Conclusion

This paper presented an integrated framework for active vibration control and structural health monitoring of flexible spacecraft panels using offset piezoelectric stack actuators. A reduced-order finite-element model was used to design a mixed-sensitivity H_∞controller, whose closed-loop performance showed improved robustness and stronger attenuation than an LQR benchmark around the dominant flexible modes. In addition, frequency-based and control-derived features extracted from the same closed-loop response exhibited monotonic sensitivity to increasing stiffness degradation, enabling accurate damage estimation through Gaussian process regression. These results support the feasibility of combining vibration suppression and damage monitoring within a single smart structural framework. The present study is limited to numerical validation, and future work will focus on experimental implementation and more realistic uncertainty conditions.

References

[1] Callipari, F., Sabatini, M., Angeletti, F., Iannelli, P., & Gasbarri, P. (2022). Active vibration control of large space structures: Modelling and experimental testing of offset piezoelectric stack actuators. Acta Astronautica, 198, 733-745. https://doi.org/10.1016/j.actaastro.2022.05.058

[2] Angeletti, F., Iannelli, P., Gasbarri, P., Gonzalez, J. P., Ellero, N., Wattrelot, T., ... & Palmerini, G. B. (2022). Robust collocated control of large flexible space structures. IFAC-PapersOnLine, 55(25), 85-90. https://doi.org/10.1016/j.ifacol.2022.09.328

[3] Khushnood, M. A., Xiaogang, W., & Naigang, C. (2018). A criterion for optimal sensor placement for minimizing spillover effects on optimal controllers. Journal of Vibration and Control, 24(8), 1469-1487. https://doi.org/10.1177/1077546316661471

[4] Li, D. X., Liu, W., & Fan, C. Z. (2018). Dynamic characteristics of satellite solar arrays under the deployment shock in orbit. Shock and Vibration, 2018(1), 6519748. https://doi.org/10.1155/2018/6519748

[5] Li, D., Jiang, J., Liu, W., & Fan, C. (2014). A new mechanism for the vibration control of large flexible space structures with embedded smart devices. IEEE/ASME Transactions on Mechatronics, 20(4), 1653-1659. https://doi.org/10.1109/TMECH.2014.2341664

[6] Wang, W., & Yang, Z. (2009). A compact piezoelectric stack actuator and its simulation in vibration control. Tsinghua Science and Technology, 14(S2), 43-48. https://doi.org/10.1016/S1007-0214(10)70029-8

Materials Research Proceedings 69 (2026) 1101-1106 https://doi.org/10.21741/9781644904251-190

Nonlinear Orbit Control for Small Satellite Missions with Hardware-In-The-Loop Testing

Virna SISTI[1,a], Stefano CARLETTA[2,b,*], Mauro PONTANI[3,c], Paolo TEOFILATTO[2,d]

[1]Department of Mechanical and Aerospace Engineering, Sapienza University of Rome, Via Eudossiana 18, 00184, Roma, Italy

[2]School of Aerospace Engineering, Sapienza University of Rome, Via Salaria 851, 00138, Roma, Italy

[3]Department of Astronautical, Electrical, and Energy Engineering, Sapienza University of Rome, Via Salaria 851, 00138, Roma, Italy

[a]sisti.1704866@studenti.uniroma1.it, [b]stefano.carletta@uniroma1.it, [c]mauro.pontani@uniroma1.it, [d]paolo.teofilatto@uniroma1.it

Keywords: Nonlinear Orbit Control, Hardware-In-The-Loop, FPGA

Abstract. This study presents the implementation and Hardware-In-The-Loop testing of a Lyapunov-based nonlinear orbit control algorithm. The controller, formulated in modified equinoctial elements, compensates for perturbations associated with aerodynamic drag and Earth oblateness, assuming steerable and throttlable low-thrust propulsion. The algorithm employs a scaling method to preserve numerical precision within limited memory resources. After implementation on an Artix-7 FPGA, a Monte Carlo Hardware-In-The-Loop campaign is performed simulating a LEO-GEO transfer with uncertain orbital parameters at departure. The results show good agreement with those from numerical simulations, which encourages further investigation of FPGA-based nonlinear control for satellite missions.

Introduction

Nonlinear orbit control techniques are attracting growing interest, but their use, particularly in low-cost missions based on the extensive use of commercial off-the-shelf (COTS) components, still raises some concerns. These are usually driven by (i) the greater complexity of implementing the nonlinear law, compared with the linear one, on flight hardware and (ii) the possibility of unstable control when processing low-resolution fixed-point measurements and parameters [1].

In this work, a Lyapunov-based nonlinear orbit control, extensively tested through double-precision numerical simulations in the past, is implemented on a commercial-grade Field Programmable Gate Array (FPGA) and tested through a Hardware-In-The-Loop (HiL) analysis. In particular, the feedback law is designed to compensate for aerodynamic drag and gravitational perturbations due to Earth oblateness, and provides real-time orbit control for a satellite equipped with a steerable and throttleable propulsion system [2].

After implementation on FPGA, the feedback law gains are selected for the case study of a non-coplanar LEO-GEO transfer. A HiL Monte Carlo campaign is performed, and the results are compared with those obtained from numerical simulations.

Nonlinear orbit control

Orbit dynamics is modeled using the modified equinoctial elements (MEE), which avoid singularities occurring when the orbit eccentricity or inclination approach zero, defined as [3]

Content from this work may be used under the terms of the Creative Commons Attribution 3.0 license. Any further distribution of this work must maintain attribution to the author(s) and the title of the work, journal citation and DOI. Published under license by Materials Research Forum LLC.

Materials Research Proceedings 69 (2026) 1101-1106 https://doi.org/10.21741/9781644904251-190

$$\begin{cases} p = a(1-e^2) \\ l = e\cos(\omega+\Omega) \\ m = e\sin(\omega+\Omega) \\ n = \tan(i/2)\cos\Omega \\ s = \tan(i/2)\sin\Omega \\ q = \Omega+\omega+\nu \end{cases} \tag{1}$$

where a, e, ω, Ω, i and ν are the classical orbital elements semi-major axis, eccentricity, argument of pericenter, right ascension of the ascending node (RAAN), inclination, and true anomaly.

Setting $\boldsymbol{z} = [x_1\ x_2\ x_3\ x_4\ x_5]^T = [p\ l\ m\ n\ s]^T$, the dynamics equations of motion can be represented in the following compact form [2]

$$\dot{\boldsymbol{z}} = G\boldsymbol{a} = \sqrt{\frac{x_1}{\mu_E}} \begin{bmatrix} 0 & 2\frac{x_1}{\eta} & 0 \\ sinx_6 & \frac{(\eta+1)cosx_6+x_2}{\eta} & -x_3\frac{x_4sinx_6-x_5cosx_6}{\eta} \\ -cosx_6 & \frac{(\eta+1)sinx_6+x_2}{\eta} & -x_2\frac{x_4sinx_6-x_5cosx_6}{\eta} \\ 0 & 0 & \frac{1+x_4^2+x_5^2}{2\eta}cosx_6 \\ 0 & 0 & \frac{1+x_4^2+x_5^2}{2\eta}sinx_6 \end{bmatrix} \boldsymbol{a}$$

$$\dot{x}_6 = \sqrt{\frac{\mu_E}{x_1^3}}(1+x_2cosx_6+x_3sinx_6)^2 + \sqrt{\frac{x_1}{\mu_E}}\frac{x_4sinx_6-x_5cosx_6}{1+x_2cosx_6+x_3sinx_6}a_h \tag{2}$$

$$\dot{x}_7 = -\frac{a_T}{c}x_7$$

where $\mu_E = 3.986 \cdot 10^5$ km^3/s^2 is the Earth gravitational parameter, $\eta = 1 + l\cos q + m\sin q$, $x_7 = m(t)/m(t_0)$ is the mass parameter, c is the characteristic velocity of the propulsion system, and $\boldsymbol{a} = \boldsymbol{a_T} + \boldsymbol{a_P} = [a_r\ a_\theta\ a_h]^T$ is the vector collecting the thrust ($\boldsymbol{a_T}$) and perturbation ($\boldsymbol{a_P}$) accelerations acting on the spacecraft, expressed in the local-vertical local-horizontal (LVLH) reference frame.

In the following analysis, the perturbation acceleration term includes the effect associated with (i) the main zonal harmonics term (J_2) of the Earth gravitational field and (ii) the aerodynamic drag, leading to

$$\begin{cases} a_r = \frac{3}{2}\frac{\mu_E}{(p/\eta)^4}J_2(-1+3\sin^2\nu\sin^2 i) - \frac{1}{2}\frac{\rho S c_D}{m(t_0)x_7}v_R\sqrt{\frac{\mu_E}{p}}e\sin\nu \\ a_\theta = -3\frac{\mu_E}{(p/\eta)^4}J_2(\sin\nu\sin^2 i\cos\nu) - \frac{1}{2}\frac{\rho S c_D}{m(t_0)x_7}v_R\left[\sqrt{\frac{\mu_E}{p}}(1+e\cos\nu) - \omega_E\frac{p}{\eta}\cos L\cos\zeta\right] \\ a_h = -3\frac{\mu_E}{(p/\eta)^4}J_2(\sin\nu\sin i\cos i) - \frac{1}{2}\frac{\rho S c_D}{m(t_0)x_7}v_R\omega_E\frac{p}{\eta}\cos L\sin\zeta \end{cases} \tag{3}$$

where $\boldsymbol{v_R} = \left[\sqrt{\frac{\mu_E}{p}}esin\nu\hat{r}\ \sqrt{\frac{\mu_E}{p}}(1+ecos\nu) - \omega_E\frac{p}{\eta}cosLcos\zeta\hat{\theta}\ \omega_E\frac{p}{\eta}cosLsin\zeta\hat{h}\right]^T$ is the relative velocity of the spacecraft with respect to the atmosphere rotating with the Earth at the rate $\omega_E = \frac{2\pi}{86164}$ s^{-1}, $\sin\zeta = \frac{\cos i}{\cos L}$, and L is the latitude.

The thrust acceleration is represented by the following feedback law derived in Ref. [2], obtained for the state vector $\boldsymbol{x} = [\boldsymbol{z}^T\ x_6\ x_7]^T$ and the control vector $\boldsymbol{u}_T = T/m(t_0)$, where T is the

Materials Research Proceedings 69 (2026) 1101-1106 https://doi.org/10.21741/9781644904251-190

thrust. The goal of the control is to set to zero the following vector function $\psi(\boldsymbol{z}) = [x_1 - p_d = 0\ x_2^2 + x_3^2 - e_d^2 = 0\ x_4^2 + x_5^2 - tan^2(i_d/2) = 0]^T$, hence establishing the desired orbital elements p_d, e_d and i_d

$$\boldsymbol{u}_T = -u_T^{max} \frac{x_7(\boldsymbol{b}+\boldsymbol{a_P})}{max(u_T^{max}, x_7\|\boldsymbol{b}+\boldsymbol{a_P}\|)} \tag{4}$$

With

$$\begin{cases} b_1 = \frac{2}{\eta}\sqrt{\frac{x_1}{\mu_E}}[k_1 x_1(x_1 - p_d) + k_2(x_2^2 + x_3^2 - e_d^2)(\eta^2 + x_2^2 + x_3^2 - 1)] \\ b_2 = -2k_2\sqrt{\frac{x_1}{\mu_E}}(x_3 cosx_6 - x_2 sinx_6)(x_2^2 + x_3^2 - e_d^2) \\ b_3 = \frac{k_3}{\eta}\sqrt{\frac{x_1}{\mu_E}}(x_4 cosx_6 + x_5 sinx_6)\left(x_4^2 + x_5^2 - tan^2(i_d/2)\right)(x_4^2 + x_5^2 + 1) \end{cases} \tag{5}$$

where the gains k_1, k_2 and k_3 are selected by the user.

Design of the Hardware-In-The-Loop test environment

A HiL setup, developed in Simulink, was used to test the nonlinear feedback law after implementation on flight hardware. For the analyses, the AMD Artix-7 XC7A35T-1CPG236C FPGA, integrated into the BASYS3 development board, was selected. The testbed, shown schematically in Figure 1, includes a host PC running a Simulink model connected to the FPGA: orbit propagation, using Eq. 2 and conversion of MEE to classical orbital elements, is performed in Simulink, while $\mathbf{u}_T$ is calculated by the FPGA and injected into the Simulink model via a JTAG interface.

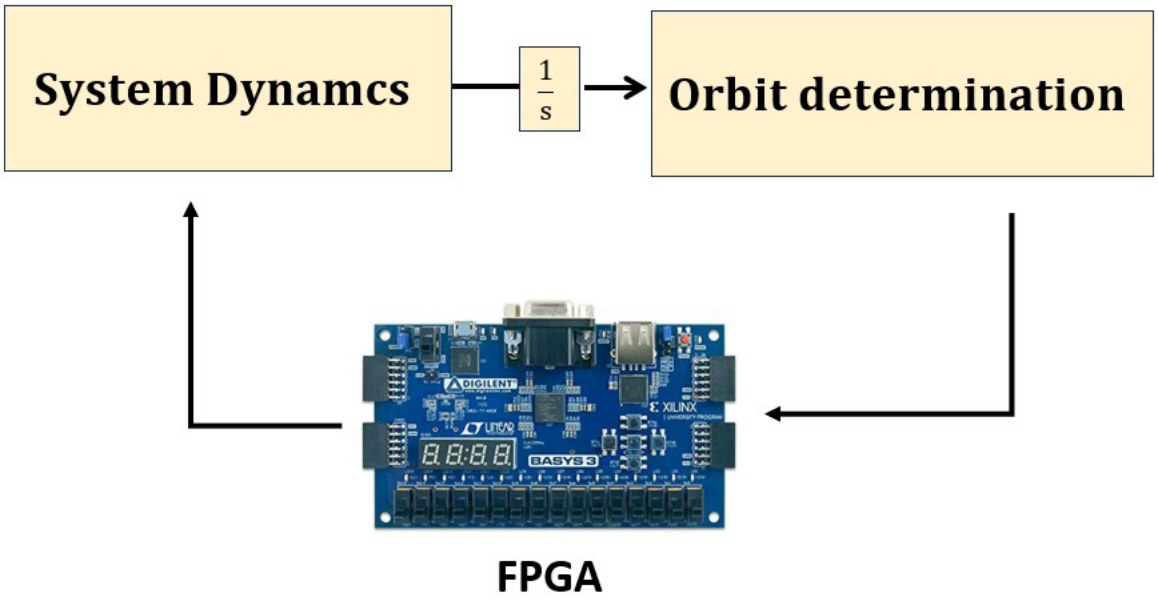


Figure 1: Scheme of the Hardware-In-The-Loop testbed including the AMD Artix-7 FPGA within the BASYS3 development board

Eq. 3-5 were converted to VHDL language using Simulink blocks of the *HDL Compiler* toolbox. The variables and parameters in the above-mentioned equations were converted from

Materials Research Proceedings 69 (2026) 1101-1106 https://doi.org/10.21741/9781644904251-190

floating-point double precision to fixed-point after selecting a word length and a resolution, defining the total number of bits used to represent a number and the fraction of the word length representing decimal values. Since the word length is limited by the memory resources available on the FPGA, the resolution cannot be arbitrarily selected, but must be determined from a tradeoff analysis.

The implementation of the nonlinear feedback law on the FPGA imposed a maximum word length of 18 bits. To increase the resolution for a fixed word length, the maximum representable value must be reduced and this was effectively obtained by scaling the variables and parameters in Eqs. 3-5. Distances and time were scaled by the factors DU$= R_E^{-1}$, where $R_E = 6378.136$ km is the mean Earth equatorial radius, and TU$= 806.8^{-1}$ 1/s, selected so that $\mu_E = 1$ DU^3/TU^2. Furthermore, noting that the variables $|x_i| < 1$ for $i = 2,3,4,5$, it is possible to set $k_s = \sqrt{2^{(\text{wordlength}-\text{resolution}-1)}} \geq 1$ and introduce the scaled factors

$$\begin{cases} \tilde{k}_i = \frac{k_i}{k_s} & i = 2,3 \\ \tilde{x}_i = x_i\sqrt{k_s} & i = 2,3,4,5 \end{cases} \tag{6}$$

To rearrange Eq. 5 as follows

$$\begin{cases} b_1 = \frac{2}{\eta}\sqrt{\frac{x_1}{\mu_E}}\left[k_1 x_1(x_1 - p_d) + \tilde{k}_2\left(\tilde{x}_2^2 + \tilde{x}_3^2 - \left(\sqrt{k_s}e_d\right)^2\right)(\eta^2 + x_2^2 + x_3^2 - 1)\right] \\ b_2 = -2\tilde{k}_2\sqrt{\frac{x_1}{\mu_E}}(x_3\cos x_6 - x_2\sin x_6)\left(\tilde{x}_2^2 + \tilde{x}_3^2 - \left(\sqrt{k_s}e_d\right)^2\right) \\ b_3 = \frac{\tilde{k}_3}{\eta}\sqrt{\frac{x_1}{\mu_E}}(x_4\cos x_6 + x_5\sin x_6)\left(\tilde{x}_4^2 + \tilde{x}_5^2 - \left(\sqrt{k_s}\tan(i_d/2)\right)^2\right)(x_4^2 + x_5^2 + 1) \end{cases} \tag{7}$$

Such that values of k_2 and k_3 larger than $2^{(\text{wordlength}-\text{resolution}-1)}$ and values of $|x_i| \leq 2^{-\text{resolution}}$, for $i = 2,3,4,5$, can be represented without affecting $\boldsymbol{b}$.

Together with the constraints on word length and resolution, the inputs to the FPGA from the Simulink model (i.e. MEE, x_i, $\tilde{x}_i$, etc.) have to be delivered at a constant frequency, actually limited by the sampling and processing frequencies of measurement sensors and orbit-determination devices that typically work in the range 1–100 Hz.

Monte Carlo Hardware-In-The-Loop test campaign

The FPGA implementation of the nonlinear feedback law was tested through a Monte Carlo (MC) HiL campaign, simulating an orbital transfer from a low-Earth orbit (LEO) to a geostationary orbit (GEO). The orbital elements for the two orbits are reported in Table 1, where the uncertainties for the LEO elements are selected as twice the orbit injection error of the Vega-C launch vehicle [4]. The selected satellite parameters are those of an ordinary 6U CubeSat, with wet mass at launch $m_0 = 15$ kg, $c_D = 2.2$, $A = 0.06$ m^2, equipped with a propulsion system providing a thrust $T = 5$ mN with $c = 32.361$ km/s [5].

Table 1: Initial and target orbit parameters

Orbit	p [km]	e	i [deg]
LEO	6778 ± 30	(5 ± 2.4)·10^-3	30 ± 0.3
GEO	42164	5·10^-3	0.5

Materials Research Proceedings 69 (2026) 1101-1106 https://doi.org/10.21741/9781644904251-190

According to Ref. [2], the gains k_2 and k_3, appropriately scaled for the thrust level considered in this study, should be approximately equal to 300, hence requiring 9 bits to be represented. It can be noted that the next larger value to be represented is $p_d = 42164$ km ≈ 6.6 DU, requiring just 3 bits for the integer part. Since a resolution of 10 bits is required to represent e and i, then the solution is not compatible with the maximum word length of 18 bits. To solve this issue, the scaling gain was selected by determining the minimum number of bits necessary to represent $\log_2(\sqrt{300}) < 5$, producing $k_s = 2^5 = 32$ and resulting in a resolution of $2^{-12} \approx 2.44 \cdot 10^{-4}$, compatible with the representation of e and i for the problem at hand.

A MC HiL campaign of 100 simulations was run by randomly selecting the initial orbital elements from Table 1 and setting a sampling frequency of 10 Hz. Simulink rates are treated as actual hardware rates with a target clock frequency of 100 MHz. The final time for the simulations is fixed to 15000 TU $\approx$ 140 days. The evolution in time for p, e, and i are shown in Figures 2–4. The mean error and standard deviation, computed using the values of p, i, and e over the last 1 TU are reported in Table 2, together with those obtained from the numerical simulations (64-bit double precision) run entirely in Simulink on the host PC.

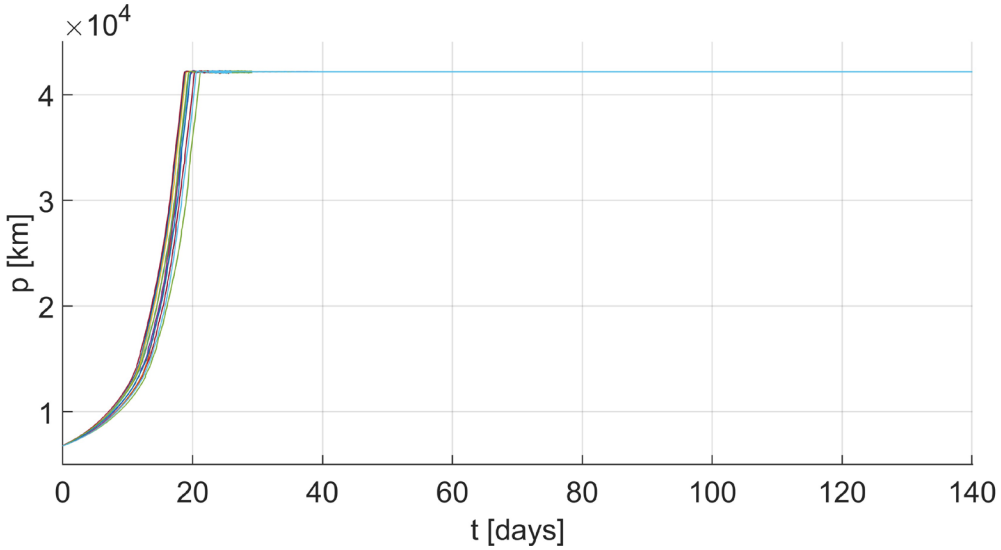


Figure 2: Results of the MC HiL campaign: p

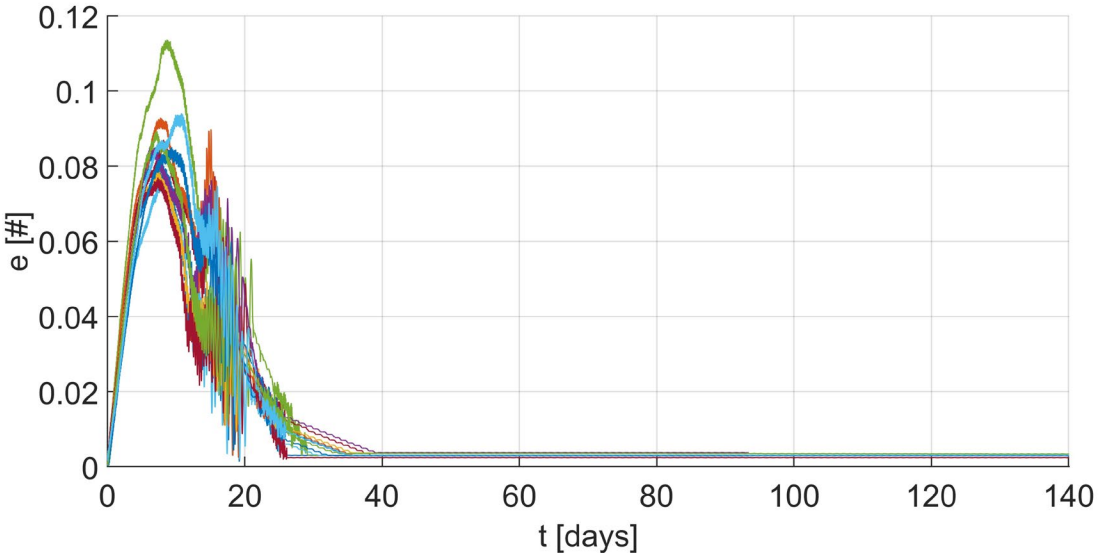


Figure 3: Results of the MC HiL campaign: e

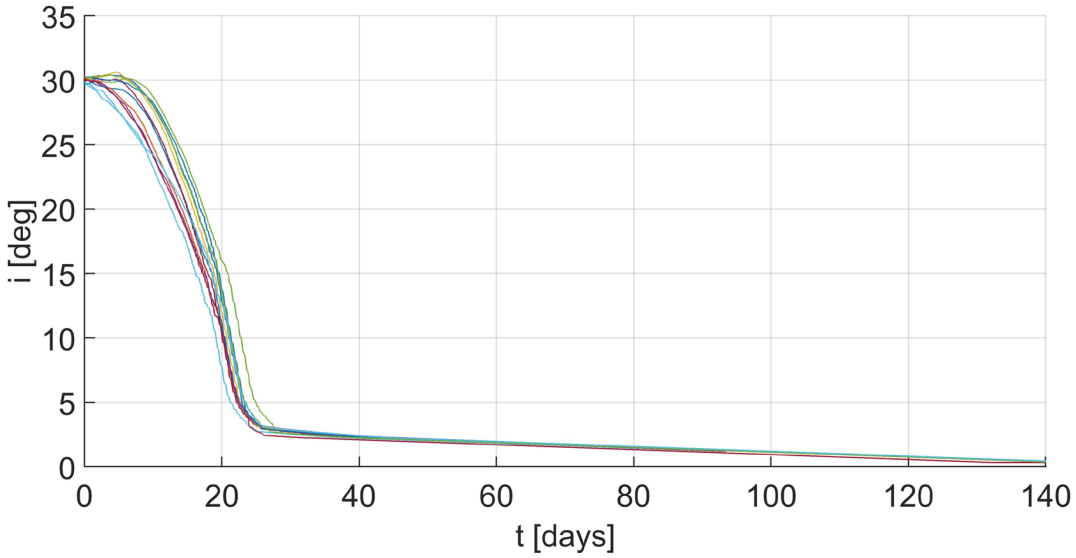


Figure 4: Results of the MC HiL campaign: i

Table 2: Mean error and standard deviation for the numerical and HiL simulations

Parameter	$p_f - p_d$ [km]	$e_f - e_d$	$i_f - i_d$ [deg]
Mean value MC numerical simulations	0.49	$1.17 \cdot 10^{-3}$	0.21
Mean value MC HiL simulations	0.68	$2.06 \cdot 10^{-3}$	0.33
St. deviation MC numerical simulations	0.54	$2.30 \cdot 10^{-4}$	0.003
St. deviation MC HiL simulations	0.71	$5.52 \cdot 10^{-4}$	0.031

Final remarks

The results of the MC HiL campaign show good agreement with those obtained from numerical simulations. In particular, the study demonstrates that the adequate selection of scaling factors allows preservation of the stability of the nonlinear feedback control law and suggests that it is suitable for use in future missions.

References

[1] B. Khusainov, E.C. Kerrigan, G.A. Constantinides, Multi-objective co-design for model predictive control with an FPGA, in: 2016 European Control Conference, IEEE, Aalborg, Denmark, 2016, pp. 110–115

[2] M. Pontani, M. Pustorino, Nonlinear Earth orbit control using low-thrust propulsion, Acta Astronautica 179 (2021) 296–310. https://doi.org/10.1016/j.actaastro.2020.10.037

[3] M. Pontani, Advanced Spacecraft Dynamics, Edizioni Efeso, 2023. ISBN 9788833814605

[4] Avio, Vega C User's Manual, Issue 1 Revision 0, September 2025

[5] Miles Space, Poseidon drop thruster. https://www.miles-space.com/#drop-thruster (accessed on 7 November 2025)

Materials Research Proceedings 69 (2026) 1107-1113 https://doi.org/10.21741/9781644904251-191

Tensor Modeling of Zero-Sum Games for In-Orbit Servicing Operations with Collision Avoidance

Stefano CARLETTA[1,a*], Alfonso FARINA[2,b], Giovanni B. PALMERINI[1,c], Francesco DE ANGELIS[1,d]

[1]School of Aerospace Engineering, Sapienza University of Rome, Via Salaria 851, 00138, Roma, Italy

[2]LFIEEE, FIET, Fellow of EURASIP

[a]stefano.carletta@uniroma1.it, [b]alfonso.farina@outlook.it, [c]giovanni.palmerini@uniroma1.it, [d]fr.deangelis@uniroma1.it

Keywords: In-Orbit Servicing, Collision Avoidance, Zero-Sum Games, Dynamic Game Theory, Nash Equilibrium, MLDS, Tensor Algebra

Abstract. In this work a tensor-algebra formulation of differential zero-sum games is applied to determine optimal control policies for multiple satellites performing simultaneous in-orbit servicing with collision avoidance constraints.

Introduction

Since the late 1980s, the term in-orbit servicing (IOS) has referred to a set of proximity or contact operations performed between satellites or their appendages to achieve specific mission objectives, such as assembly, refurbishing, debris removal and recognition [1]. As these operations become more complex and involve a growing number of spacecraft, the need to implement guidance and control laws capable of ensuring an adequate degree of autonomy and safety emerges.

In this work we propose the use of dynamic game theory to determine the optimal control policy for a set of N satellites simultaneously performing in-orbit servicing operations. Because the satellites operate simultaneously and in close proximity, an additional goal is to avoid collisions. This scenario can be represented as a collection of multi-agent differential games [2], resulting in a peculiar cooperative zero-sum game whose solution is a specific Nash equilibrium obtained when all the players implement an optimal control policy [3, 4].

Applications of zero-sum games in flight mechanics have been proposed since the 70s, when the limits in computational resources translated into simplified scenarios, often assuming planar motion or constant speed [5, 6]. As computer technology progressed, zero-sum game models are increasingly used also in complex scenarios, such as 3-dimensional dynamics, but are still limited in the number of players involved [7-9].

The method proposed here to solve the N-satellite zero-sum game, with N arbitrarily large, is based on tensor algebra and the differential game is modelled as a Multi-Linear Dynamical System. Each pair of satellites represents a couple of pursuer and evader and the solution of the game for all the pairs of satellites leads to the achievemnt of a shared goal for the formation. A visual example of the application proposed is shown in Figure 1. Each one of the 3 pairs of satellites play a pursuer evader game, with the pursuer satellite trying to get closer to the evader one and vice-versa. By solving the 3 competitive problems together and selecting an adequate cost functional, in case of loss of the initial triangular configuration the game as a whole leads to its restoration. In fact, it represents an extension to cooperative zero-sum games, applied to in-orbit servicing, of previous works developed by the authors, including the tensor Kalman filter and tensor linear quadratic Gaussian controller [10, 11]. Numerical simulations in Matlab are used to test the method at hand.

Content from this work may be used under the terms of the Creative Commons Attribution 3.0 license. Any further distribution of this work must maintain attribution to the author(s) and the title of the work, journal citation and DOI. Published under license by Materials Research Forum LLC.

Materials Research Proceedings 69 (2026) 1107-1113 https://doi.org/10.21741/9781644904251-191

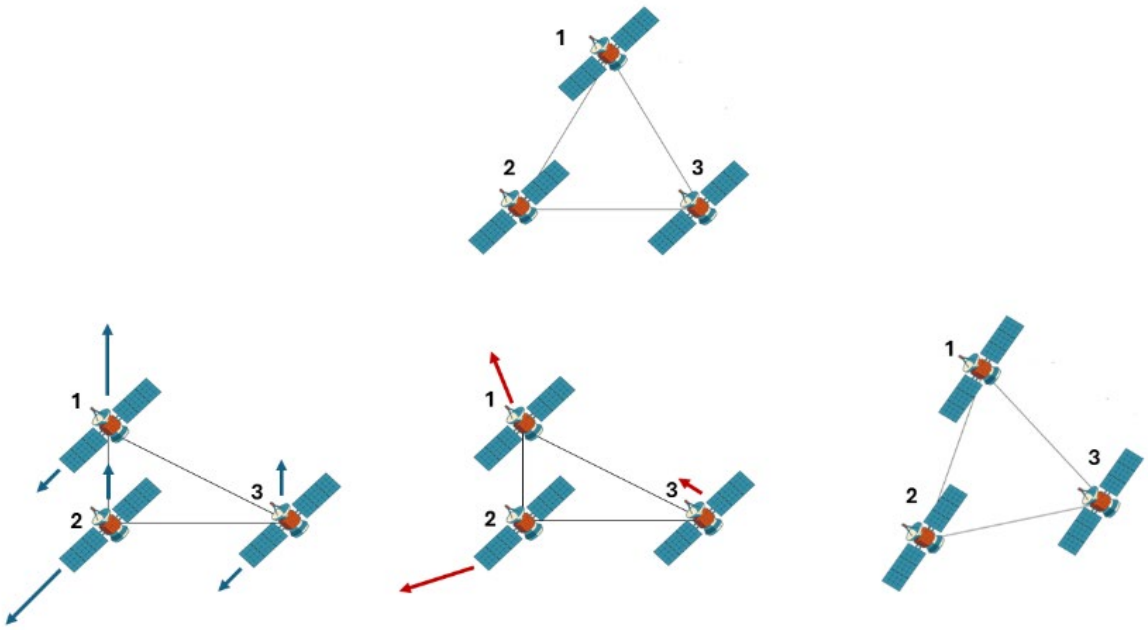


Figure 1: Scheme of a 3-satellite formation where each pair plays a competitive pursuer-evader game; the three competitive games correspond to a cooperative game among all the satellites: the formation recovers the initial triangle configuration while avoiding collision

Differential zero-sum games

Dynamic game theory offers the theoretical foundation for identifying the optimal control strategies of multiple agents that interact with one another—referred to as players in the game. In a dynamic game, each player's cost functional J depends not only on its own state and control variables but also on those of the other players. When the states and control policies of all players evolve over time according to differential equations, the game is referred to as a differential game.

Differential games can be categorized as competitive, where players have opposing interests (i.e., a reduction in the cost functional of one player results in an increase in that of another), or cooperative, where players adopt control strategies that jointly minimize each individual's cost functional. In a dynamic game, a Nash equilibrium is reached when no player can reduce their cost functional by unilaterally modifying their own control policy [12]. In other words, a player's cost can only be further minimized if the other players also adjust their control strategies.

An optimal equilibrium—and the corresponding optimal control policies for all players—can be determined under the assumption that the sum of the players' cost functionals equals zero, resulting in what is known as a zero-sum game.

The system dynamics and cost functional of a 2-party zero-sum game are provided below

$$\dot{\mathbf{x}} = f(\mathbf{x}, \mathbf{u}^P, \mathbf{u}^E, t) \tag{1}$$

$$J(\mathbf{x}, \mathbf{u}^P, \mathbf{u}^E, t) = \Phi(\mathbf{x}, t)\big|_{t_0}^{t_f} + \int_{t_0}^{t_f} L\,(\mathbf{x}, \mathbf{u}^P, \mathbf{u}^E, t)dt \tag{2}$$

where $\mathbf{x}$ is the relative state vector, collecting the relative position and velocity components between the two players, $\mathbf{u}^P$ and $\mathbf{u}^E$ are the control inputs of the pursuer and the evader, respectively the player that aims to minimize and maximize J, and t indicates time, with subscripts

0 and f referring to the initial and final values, Φ is a functional representing target initial and final conditions and L represents a cost to be minimized from t_0 to t_f.

The value of the cost functional correspoding to the optimal pursuer-evader game is given by

$$J(\mathbf{x}, \mathbf{u}^{P*}, \mathbf{u}^{E}) \leq J^*(\mathbf{x}, \mathbf{u}^{P*}, \mathbf{u}^{E*}) \leq J(\mathbf{x}, \mathbf{u}^{P}, \mathbf{u}^{E*})$$

$$\forall \mathbf{u^P} \in \mathcal{U}^P, \forall \mathbf{u^E} \in \mathcal{U}^E \tag{3}$$

where the symbol $*$ indicates the optimal value, and $\mathcal{U}^P$ and $\mathcal{U}^E$ are the sets of control inputs. For J^* continuously differentiable in t and $\mathbf{x}$, the optimal control $\mathbf{u}^P$ and $\mathbf{u}^E$ can be determined solving the following partial differential Isaacs' equations , and they represent a saddle point for J^*

$$\frac{\partial J^*}{\partial t} + \min_{\mathbf{u}^P} \max_{\mathbf{u}^E} \left\{ \frac{\partial J^*}{\partial \mathbf{x}} \dot{\mathbf{x}} + L \right\} = 0 \tag{4}$$

The solution of Eq. 4 can be simplified by the hypothesis of separable games

$$\begin{cases} \mathbf{u}^{P*} = f_P(\mathbf{x}^P, \mathbf{x}^E, t) \\ \mathbf{u}^{E*} = f_E(\mathbf{x}^P, \mathbf{x}^E, t) \end{cases} \tag{5}$$

where f_P and f_E are functions describing the evolution of $\mathbf{u}^{P*}$ and $\mathbf{u}^{E*}$ determined as solutions of the problem.

Tensor modeling of zero-sum games

A number m of pursuer-evader games of N players can be represented as a Multi-Linear Dynamical System (MLDS) based on tensor algebra [13]

$$\dot{\mathbf{x}} = A\mathbf{x} + B \bigotimes_{(2-5)}^{(1-4)} \mathbf{u} \tag{6}$$

where $\mathbf{x} \in \mathbb{R}^{n \times m}$ is the relative state tensor of n state variables, $\mathbf{u} \in \mathbb{R}^{s \times m \times p \times m \times m}$ is the control input tensor, collecting the s control actions for each player p ($p = 1$: pursuer, $p = 2$: evader) of the m games, $A \in \mathbb{R}^{n \times n}$ is the dynanic tensor, $B \in \mathbb{R}^{n \times m \times s \times m \times p}$ is the control tensor and the symbol $\bigotimes$ indicates the tensor product with respect to the dimensions indicated as super-and sub-scripts for, respectively, the first and the second factor. In this formulation of the MLDS $B_{(:,:,:,:,p=2)} = -B_{(:,:,:,:,p=1)}$.

The goal of the game is to minimize the cost functional given by

$$\frac{1}{2}\mathbf{x}_f \cdot (S\mathbf{x}_f) + \frac{1}{2}\int_{t_0}^{t_f} \left[\mathbf{x} \cdot (Q\mathbf{x}) + \mathbf{u} \cdot \left(R \bigotimes_{(4-6)}^{(1-3)} \mathbf{u} \right) \right] d\tau \tag{7}$$

where the symbol $\cdot$ indicates the scalar product, $S, Q \in \mathbb{R}^{n \times n}$, $R \in \mathbb{R}^{s \times m \times p \times s \times m \times p}$ and $R_{(:,:,:,:,:,p=2)} = -R_{(:,:,:,:,:,p=1)}$. Introducing the Lagrange multipliers tensor $\boldsymbol{\lambda} \in \mathbb{R}^{n \times m}$ and collecting Eqs. 6-7 it is possible to express the Hamiltonian for the problem by

$$H = \boldsymbol{\lambda} \cdot \dot{\mathbf{x}} + L = \boldsymbol{\lambda} \cdot \left(A\mathbf{x} + B \bigotimes_{(2-5)}^{(1-4)} \mathbf{u} \right) + \mathbf{x} \cdot (Q\mathbf{x}) + \\ + \mathbf{u} \cdot \left(R \bigotimes_{(4-6)}^{(1-3)} \mathbf{u} \right) \tag{8}$$

Eq. 8 allows deriving the optimal input tensor applying the Pontryagin minimum principle

$$\frac{\partial H}{\partial \mathbf{u}} = \boldsymbol{\lambda} \bigotimes_{(1-2)}^{(1-2)} B + R \bigotimes_{(4-6)}^{(1-3)} \mathbf{u}^* = 0 \rightarrow$$

$$R \bigotimes_{(4-6)}^{(1-3)} \mathbf{u}^* = -\boldsymbol{\lambda} \bigotimes_{(1-2)}^{(1-2)} B \tag{9}$$

After permuting the indices of R by $\begin{pmatrix} 1 & 2 & 3 & 4 & 5 & 6 \\ 1 & 4 & 2 & 5 & 3 & 6 \end{pmatrix}$ then $R^T \in \mathbb{R}^{s \times s \times m \times m \times p \times p}$ can be inverted and $\mathbf{u}$ can be explicited

$$R^T \bigotimes_{(2,4,6)}^{(1-3)} \mathbf{u}^* = -\boldsymbol{\lambda} \bigotimes_{(1-2)}^{(1-2)} B \rightarrow$$

$$\mathbf{u}^* = -\left(R^T\right)^{-1} \bigotimes_{(2,4,6)}^{(1-3)} \left(B \bigotimes_{(1-2)}^{(1-2)} \boldsymbol{\lambda}\right) \tag{10}$$

To determine the optimal input tensor, the Lagrange multipliers shall be determined from the Euler-Lagrange and boundary conditions

$$\begin{cases} \dot{\boldsymbol{\lambda}} = -\frac{\partial H}{\partial \mathbf{x}} = -A\boldsymbol{\lambda} - Q\mathbf{x} \\ \boldsymbol{\lambda}_f = \frac{\partial J}{\partial \mathbf{x}_f} = S\mathbf{x}_f \end{cases} \tag{11}$$

Assuming now $\boldsymbol{\lambda} = M\mathbf{x} + \boldsymbol{\nu}$ and applying the second of Eq. 11 the final values for the unknowns M and $\boldsymbol{\nu}$ are determined

$$\begin{cases} M_f = S \\ \boldsymbol{\nu} = 0 \end{cases} \tag{12}$$

And the following differential equation for the Lagrange multiplier tensor is determined

$$\dot{\boldsymbol{\lambda}} = \dot{M}\mathbf{x} + M\dot{\mathbf{x}} + \dot{\boldsymbol{\nu}} = -A\boldsymbol{\lambda} - Q\mathbf{x}$$

Introducing Eq. 6 into Eq. 10 leads to the following Tensor Differential Riccati Equations (TDRE) to be solved from the final conditions provided in Eq. 12

$$\begin{cases} \dot{M} = -MA + MB \bigotimes_{(2-5)}^{(1-4)} \left(R^T\right)^{-1} \bigotimes_{(2,4,6)}^{(2-4)} B \bigotimes_{(1)}^{(1)} M + \\ -A^T M - Q \\ \dot{\boldsymbol{\nu}} = MB \bigotimes_{(2-5)}^{(1-4)} \left(R^T\right)^{-1} \bigotimes_{(2,4,6)}^{(2-4)} B \bigotimes_{(1)}^{(1)} \boldsymbol{\nu} - A^T \boldsymbol{\nu} \end{cases} \tag{13}$$

Eq. 13 can be solved using the Tensor Runge-Kutta Integrator (T-RKI) and allows determining the optimal input tensor [10]

$$\mathbf{u}^* = K_x \bigotimes_{(5)}^{(1)} \mathbf{x} + k_v \tag{14}$$

where

$$\begin{cases} K_x = -\left(R^T\right)^{-1} \otimes_{(2,4,6)}^{(2-4)} B \otimes_{(1)}^{(1)} M \\ k_v = -\left(R^T\right)^{-1} \otimes_{(2,4,6)}^{(2-4)} B \otimes_{(1)}^{(1)} \mathbf{v} \end{cases} \tag{15}$$

Eqs. 14-15 allow determining the optimal control action for each player p of the m games. Applying $\mathbf{u}$, all the players attempt reaching the target state tensor $\mathbf{x}_f$ within the time interval $[t_0, t_f]$. Collision between players can be avoided selecting different values for the tensor R associated to different games.

Numerical study case

The formulation is studied considering $N = 5$ satellites operating in close proximity. For the sake of clarity, the simple problem of docking at a given set of coordinates is considered for the example. The MLDS for the problem is formulated extending to the tensor algebra the Hill–Clohessy–Wiltshire equations [14], as done in Ref [10].

The parameters for the problem at hand are the reference orbit angular speed $\omega = 0.00113\ rad/s$, the final time $tf = 2\pi/\omega$

$$Q = S \cdot 10^{-5} = \begin{bmatrix} I_{3\times3} & 0_{3\times3} \\ 0_{3\times3} & 0_{3\times3} \end{bmatrix}$$

and the components of R are selected such that the maximum thrust acceleration does not exceed $10^{-5}g$. The initial state tensor is selected randomly with position coordinates in the range $\pm 700m$ and velocity components in the range $\pm 7m/s$.

Figures 2-3 show, respectively, the variation in time of the Hill coordinates of satellites 2-5 with respect to the central satellite 1, and the change over time of the relative distances. Examining the figure it can be seen that all the satellites reach the target coordinates without collisions. In particular, the control operates such that the relative distance is kept high untile the relative configuration between the vehicles ensures that the target point can be reached without collisions.

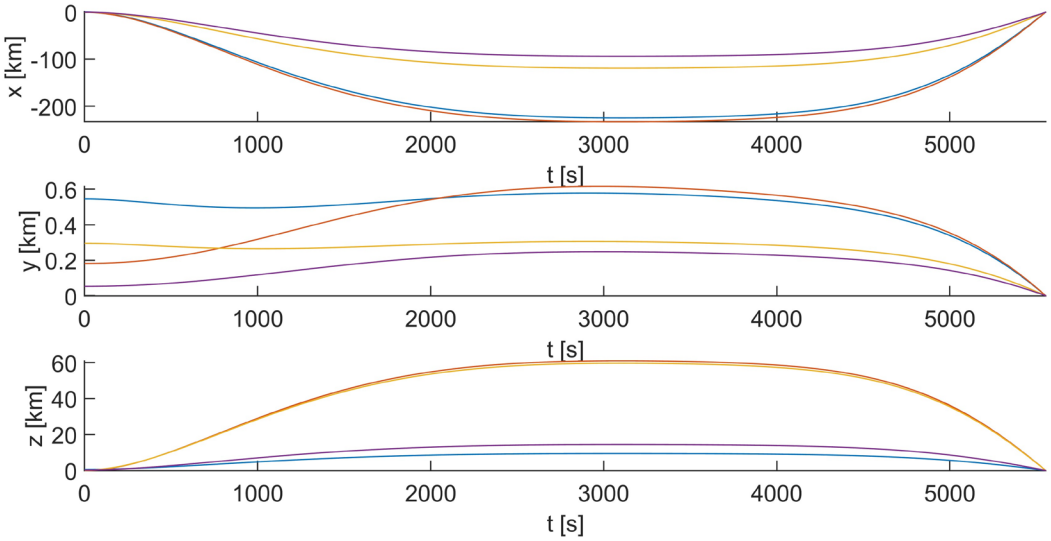


Figure 2: Relative coordinates of satellites 2-5 with respect to the central satellite 1

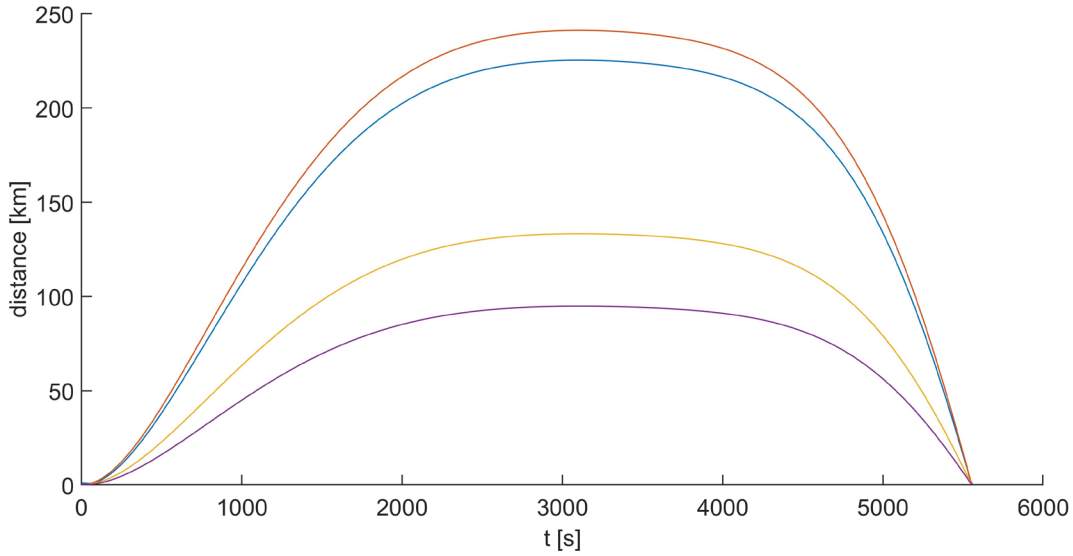


Figure 3: Relative coordinates of satellites 2-5 with respect to the central satellite 1

Final remarks

The tensor-based formulation of zero-sum games developed in this work provided encouraging results for applications in IOS missioons. Further advantages of model include: (i) exponential reduction (with N) of the computational time, (ii) inherent compatibility with parallel computing devices and (iii) the generation of synchronous control inputs.

References

[1] F.S. Wojtalik, Hubble Space Telescope Systems Engineering, IFAC Proceedings Volumes, Vol. 20, Is. 5(6), 1987, pp, 63-68. https://doi.org/10.1016/S1474-6670(17)55185-X

[2] P. J. Nahin, Chases and Escapes: The Mathematics of Pursuit and Evasion. Princeton University Press, Princeton (NJ), USA, 2007

[3] R. Isaacs, Differential Games. John Wiley and Sons, New York (USA), 1967

[4] J. Nash, Equilibrium Points in n-Person Games, Proceedings of the National Academy of Science, Vol. 36, 1950, pp. 48-49 https://doi.org/10.1073/pnas.36.1.48

[5] M. Athans, On Optimal Allocation and Guidance Laws for Linear lnterception and Rendezvous Problems, IEEE Transactions on Aerospace and Electronic Systems, Vol. 7, No. 5, 1971, pp. 843-853 https://doi.org/10.1109/TAES.1971.310324

[6] P. Hagedorn, J. V. Breakwell, A differential game with two pursuers and one evader, J Optim Theory Appl, Vol. 18, 1976, pp. 15-29 https://doi.org/10.1007/BF00933791

[7] P. K. A. Menon, E. L. Duke, Time-Optimal Aircraft Pursuit-Evasion with A Weapon Envelope Constraint, 1990 American Control Conference, San Diego, CA, USA, 1990, pp. 2337-2342 https://doi.org/10.23919/ACC.1990.4791146

[8] M. Pontani, B. A. Conway, Optimal Interception of Evasive Missile Warheads: Numerical Solution of the Differential Game, Journal of Guidance, Control, and Dynamics, Vol. 31, No. 4, 2008, pp. 1111-1122 https://doi.org/10.2514/1.30893

[9] S. Li, C. Wang, G. Xie, "Pursuit-evasion differential games of players with different speeds in spaces of different dimensions," 2022 American Control Conference (ACC), Atlanta, GA, USA, 2022, pp. 1299-1304 https://doi.org/10.23919/ACC53348.2022.9867329

[10] A. Farina, S. Carletta, G. B. Palmerini and F. De Angelis, Multilinear Dynamical Systems (MLDS): Applications to Tensor Kalman Filter and Tensor LQG, 2024 IEEE International Workshop on Technologies for Defense and Security (TechDefense), Naples, Italy, 2024, pp. 391-396 https://doi.org/10.1109/TechDefense63521.2024.10863198

[11] A. Farina, S. Carletta, G. B. Palmerini and F. De Angelis, Tensor formulation of Kalman Filter and Linear Quadratic Gaussian Controller for Applications on Multilinear Dynamical Systems, IET Radar, Sonar & Navigation: e70056.

[12] A. Heifetz, A. Nash equilibrium. In: Game Theory: Interactive Strategies in Economics and Management (pp. 65-84). Cambridge University Press, Cambridge (UK), 2012 https://doi.org/10.1017/CBO9781139049344.009

[13] S. Carletta, A. Farina, G. B. Palmerini and F. De Angelis, Tensor Modeling of Zero-Sum Games with Applications on N-Party Pursuer-Evader Games, 2025 IEEE International Workshop on Technologies for Defense and Security, Rome 5-7 November 2025

[14] J.A. Prussing, B.A. Conway, Orbital Mechanics; Oxford University Press: New York, NY, USA, 1993; pp. 139-152

Materials Research Proceedings 69 (2026) 1114-1119 https://doi.org/10.21741/9781644904251-192

Efficient Information Routing for Constellations with Satellite Clusters via Static Digraph

Giulio DE ANGELIS[1,a *], Matteo GUCCINI[2,b], Stefano CARLETTA[3,c], Mauro PONTANI[2,d] and Paolo TEOFILATTO[3,e]

[1]Thales Alenia Space Italia, Via Saccomuro 24, Rome, Italy

[2]Department of Mechanical and Aerospace Engineering (DIMA), Sapienza University of Rome, Via Eudossiana 18, Rome, Italy

[3]School of Aerospace Engineering, Sapienza University of Rome, Via Salaria 851, Rome, Italy

[a]giulio.deangelis@thalesaleniaspace.com, giulio.deangelis@uniroma1.it, [b]guccini.1883295@studenti.uniroma1.it, [c]stefano.carletta@uniroma1.it, [d]mauro.pontani@uniroma1.it, [e]paolo.teofilatto@uniroma1.it

Keywords: Satellite Constellations; Inter-Satellite Links; Communication Clusters; Static Digraph; Minimum Latency Routing

Abstract. Inter-satellite routing is key to enabling low-latency global connectivity in satellite constellations. Traditional models based on fixed topologies or discrete-time snapshots often overlook the geometric and temporal complexity of orbital motion, especially in sparse or heterogeneous systems. We introduce an event-based graph framework that captures all possible data exchanges within a constellation over a given time horizon. Each node represents a communication event—a finite interval during which one or more satellites can exchange data—while directed edges connect events that can be sequentially linked through shared satellites and overlapping time. The resulting structure is a static directed graph encoding all feasible routing paths based solely on mutual visibility. This compact formulation avoids redundancy typical of time-expanded graphs and naturally accommodates both permanent and temporary clusters, representing continuous or intermittent multi-satellite connectivity. Routing is performed on the event digraph using standard algorithms with latency- and hop-based metrics. Tests on LEO constellations demonstrate that the method efficiently identifies optimal paths and reveals key trade-offs between delay, hop count, and connectivity density, offering a scalable tool for constellation-level routing analysis.

Introduction

Satellite constellations are increasingly central to applications such as telecommunications, Earth observation, and navigation. Deploying multiple satellites enables data relaying strategies that reduce end-to-end latency: for instance, imagery acquired by one spacecraft can be forwarded through the constellation to another with earlier ground-station access. This capability relies on inter-satellite links (ISLs), traditionally implemented via radio-frequency (RF) communication and now evolving toward optical (laser) technologies offering higher data rates [1].

Effective routing in such constellations must account for the continuously changing network topology driven by orbital motion. Conventional routing methods based on static network snapshots [2, 3] perform well in dense or highly symmetric constellations but struggle to represent transient link opportunities in sparser systems. For example, Virtual Topology (VT) models divide operations into discrete snapshots [4, 5]. By discretizing time into fixed intervals, these approaches only partially capture the evolving connectivity, potentially overlooking routing opportunities with lower latency or hop count.

Content from this work may be used under the terms of the Creative Commons Attribution 3.0 license. Any further distribution of this work must maintain attribution to the author(s) and the title of the work, journal citation and DOI. Published under license by Materials Research Forum LLC.

Materials Research Proceedings 69 (2026) 1114-1119 https://doi.org/10.21741/9781644904251-192

This work extends our previously proposed static-graph routing approach based on instantaneous ISL contacts [6], introducing a cluster-based framework that shifts the modeling perspective from individual satellites to communication events. Each node in the proposed graph corresponds to a cluster event—a group of satellites remaining mutually connected over a finite or continuous time span—rather than to a single satellite. The resulting static directed graph compactly encodes all feasible communication paths within the considered time horizon, allowing standard algorithms such as Dijkstra's to identify optimal routes in terms of latency or hop count.

Cluster Identification

Constellation Configuration. The proposed routing framework is demonstrated on a low Earth orbit (LEO) constellation of 128 satellites in circular, repeating-ground-track orbits following a Walker-delta pattern. The repeating-ground-track condition accounts for the effect of Earth's oblateness (J_2), ensuring closure of each satellite's ground track after one nodal day and 14 orbits. For an inclination of 53°, the corresponding semimajor axis is 7210 km (altitude ∼832 km), yielding a nodal orbital period of 102 min [7]. The remaining Walker parameters—the number of orbital planes p and the phasing factor f—are specified later for each configuration considered [8].

Temporary Clusters. A *communication cluster* is a subset of satellites that remain mutually reachable—directly or via multi-hop relays—over a finite interval $[t_{start}, t_{end}]$. The constellation is first modeled as a time-varying graph $G(t)$, whose nodes are satellites and edges represent active ISLs, established whenever the inter-satellite distance stays below a maximum distance, d_{max}, for a continuous duration (see [9] for the method used to determine ISL contact windows). Each link appearance or disappearance defines a discrete epoch tk, at which the adjacency matrix $\mathbf{A}(t_k)$ is updated and its connected components are extracted.

Clusters are determined by chronologically scanning the sequence $\{\mathbf{A}(t_k)\}$. At each epoch, every connected component of two or more satellites is compared with existing clusters: if the composition matches, the cluster's lifetime is extended; if satellites join or leave, the current cluster is closed and a new one begins. This yields a complete, non-overlapping description of all clusters over time: $C_\ell = (S_{i1}, S_{i2}, \dots, S_{im}, [t^\ell_{start}, t^\ell_{end}])$, where S_{i1} denotes one of the satellites in the cluster. Two types are distinguished: (a) *permanent clusters*, persisting throughout the simulation horizon; (b) *temporary clusters*, active only over finite intervals.

This abstraction compactly encodes the evolving network topology and underpins the static digraph formulation for routing analysis. Although illustrated on a symmetric configuration, the method is general and applies to heterogeneous constellations.

Global Continuous Connectivity. A constellation exhibits *global continuous connectivity* when it remains fully connected at all times, meaning that any satellite can reach any other via multi-hop relays at every instant. Each snapshot $G(t_k)$ contains a single connected component, ensuring end-to-end reachability despite individual ISL variations.

Materials Research Proceedings 69 (2026) 1114-1119 https://doi.org/10.21741/9781644904251-192

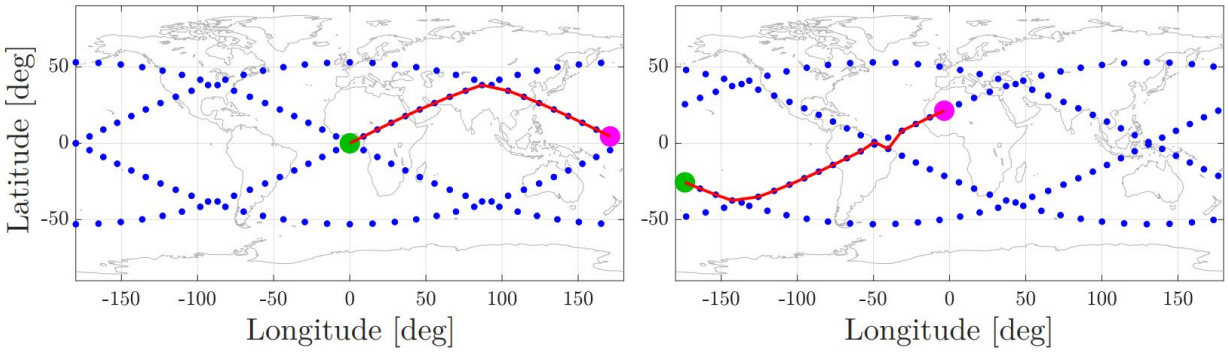


Figure 1. Global continuous connectivity for a 128-satellite constellation. Each panel shows a snapshot at (left) t = 0 s and (right) t = 3600 s, with satellites along their ground tracks (blue), source and destination (S_1, S_{128}) in green and magenta, and the routing path in red.

As an example, we consider a 128-satellite constellation with inclination 53°, arranged in p = 64 orbital planes with phasing factor f = 2, and maximum communication distance d_{max} = 2000 km. This configuration provides high inter-plane connectivity, with each satellite maintaining multiple cross-plane links throughout its orbit. Over one nodal orbital period (102 minutes), the cluster identification procedure yields a single permanent cluster containing all 128 satellites. While individual links appear and disappear as orbital geometry changes, global connectivity is maintained at every instant. This represents an ideal scenario where routing reduces to finding the shortest path without temporal coordination between communication events. Figure 1 shows two snapshots (t = 0 s and t = 3600 s) of routes between S_1 and S_{128}. Both routes consist of 17 hops, yet their satellite sequences differ due to orbital motion: some intermediate relays are replaced as the constellation geometry evolves, highlighting that even under continuous connectivity, optimal paths are time-dependent. To characterize constellation-wide connectivity, we compute the minimum hop-count paths between all satellite pairs. While global connectivity ensures that every pair is reachable, optimal routing paths change with orbital geometry. Because routing performance depends on satellites' instantaneous positions and ISL availability, we adopt a moving-window approach: the shortest-path analysis is repeated 100 times over one nodal orbital period, shifting the start time by 1/100 of the period at each iteration. Hop-count statistics show: mean 11.64, median 12, range [1–27], std 5.30, with the most frequent path length being 13 hops. The maximum of 27 hops occurs for nearly antipodal satellite pairs (e.g., separated by ∼180° in longitude and opposite hemispheres), where the shortest path must traverse approximately half the constellation circumference through sequential intra-plane and cross-plane links, each spanning at most d_{max} = 2000 km.

Static Digraph with Temporary Clusters

Definition and Design. Let $\mathcal{C} = \{C_1, \ldots, C_M\}$ be the set of identified clusters, and $\mathcal{S} = \{S_1, \ldots, S_N\}$ the satellites. We define a *static directed graph* $\mathcal{G} = (\mathcal{V}, \mathcal{E})$, where $\mathcal{V}$ includes both cluster nodes and satellite nodes, and $\mathcal{E}$ contains directed edges representing feasible information transfers. Each cluster C_k becomes a node active over its interval $[t^k_{start}, t^k_{end}]$. A directed edge $(C_k \rightarrow C_\ell)$ exists whenever (i) the two clusters *share at least one satellite* ($\exists\ S_i \in C_k \cap C_\ell$) and (ii) the transition respects *causality* ($t^\ell_{start} \geq t^k_{end}$), ensuring that data stored within C_k can be carried by the shared satellite(s) until C_ℓ becomes active. The edge weight reflects the full latency between the beginning of C_k and the beginning of C_l, $w(C_k \rightarrow C_\ell) = t^\ell_{start} - t^k_{start}$, thereby accounting for both the active duration of C_k and the waiting time until C_l starts. For hop-count optimization, all edges are assigned unit weights (w = 1). Each satellite S_i is also represented as a node connected to all clusters it belongs to via directed edges $S_i \rightarrow C_k$ and $C_k \rightarrow S_i$. This yields a single static digraph compactly

Materials Research Proceedings 69 (2026) 1114-1119 https://doi.org/10.21741/9781644904251-192

embedding both temporal and topological information, since each cluster aggregates extended intra-cluster communication periods.

Min-Latency Routing. Shortest-path algorithms such as Dijkstra's are applied to $\mathcal{G}$ using the weights $w(C_k \rightarrow C_\ell)$. The total latency along a path is the sum of these weights; when multiple paths yield identical latency, a modest penalty ϵ per edge favors shorter routes.

To illustrate this scenario, we consider a sparser 128-satellite constellation with the same inclination ($i = 53°$) and maximum distance ($d_{\max} = 2000$ km), but arranged in $p = 32$ orbital planes with phasing factor $f = 3$. Unlike the previous case, global connectivity is not maintained: multiple temporary clusters form and dissolve as satellites move along their orbits. Over one orbital period (102 min), the procedure identifies 2316 clusters. Cluster sizes range from 4 to 42 satellites (mean 20.5, median 6), with durations between 0.28 and 40 s (mean 22.5 s, median 14 s).

Dijkstra's algorithm on $\mathcal{G}$ yields the minimum-latency routes for each satellite pair, with hop count used as a tiebreaker. Three representative cases are reported for S_1 as source:

1. $S_1 \rightarrow S_2$: These satellites lie on adjacent planes and achieve direct visibility only after 15 minutes. However, both belong to an early cluster $C_{43} = (S_1, S_2, S_3, S_{19}, S_{20}, S_{21}, [76\text{ s}, 115\text{ s}])$, enabling relay through S_{19}. The minimum latency is therefore 76 seconds.
2. $S_1 \rightarrow S_3$: The same cluster enables multi-hop relay $S_1 \rightarrow S_{19} \rightarrow S_2 \rightarrow S_{20} \rightarrow S_3$, also with 76 s latency.
3. $S_1 \rightarrow S_4$: These satellites never communicate directly. The optimal path uses cluster C_{43} to route data from S_1 to S_3 (via S_{19}, S_2, S_{20}); then S_3 carries the data until cluster $C_{102} = (S_3, S_4, S_{121}), [258\text{ s}, 265\text{ s}])$ forms, completing the transfer through S_{121}. The total latency is 258 seconds (4.3 minutes), with 6 inter-satellite hops across 2 cluster transitions. The path is shown in Figure 2.

These examples illustrate how the cluster-based approach efficiently exploits both direct and multi-hop relay opportunities to minimize communication delay, even when satellites never share direct visibility.

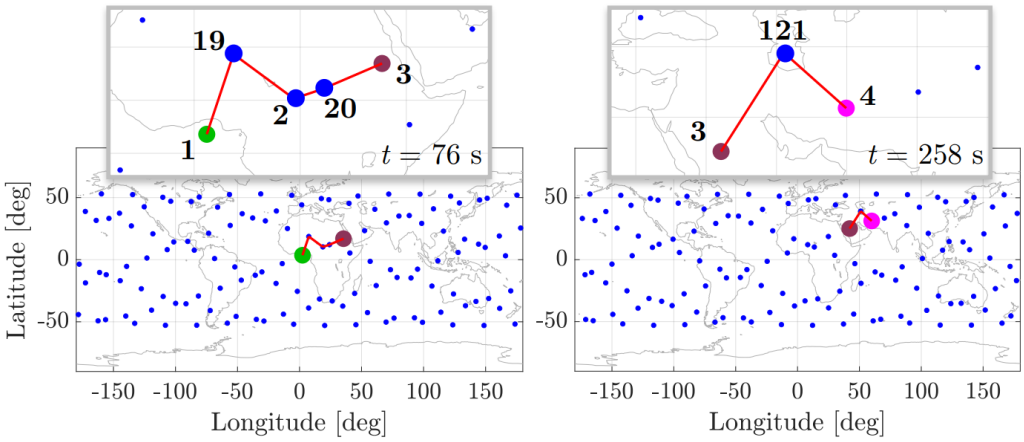


Figure 2. *Temporal routing for $S_1 \rightarrow S_4$. Left: data transfer within C_{43} at $t = 76$ s. Right: within C_{102} at $t = 258$ s, with S_3 linking the two clusters.*

Latency Matrix Computation. To characterize constellation-wide connectivity, we compute the minimum communication latency between all satellite pairs using the cluster-based routing framework. For each optimal cluster sequence identified by Dijkstra's algorithm, the corresponding hop count is computed as follows: within each cluster, a secondary shortest-path

search determines the minimum number of inter-satellite hops required to reach the shared satellite(s) connecting to the next cluster. The total hop count is the sum across all clusters in the sequence. Using the moving-window approach (100 runs, start time shifted by 1/100 of the nodal period), latency and hop-count values are computed for each realization and then averaged to obtain constellation-level statistics. The average latency is 5.01 minutes (median 5.67 min, std 3.49 min), ranging from immediate connectivity to 12.83 minutes. The average hop count is 11.87 (median 10, std 7.06), with a maximum of 38 hops observed. Figure 3 presents the mean latency and hop-count matrices side by side. Satellites are indexed sequentially by orbital plane (four per plane, for a total of 128).

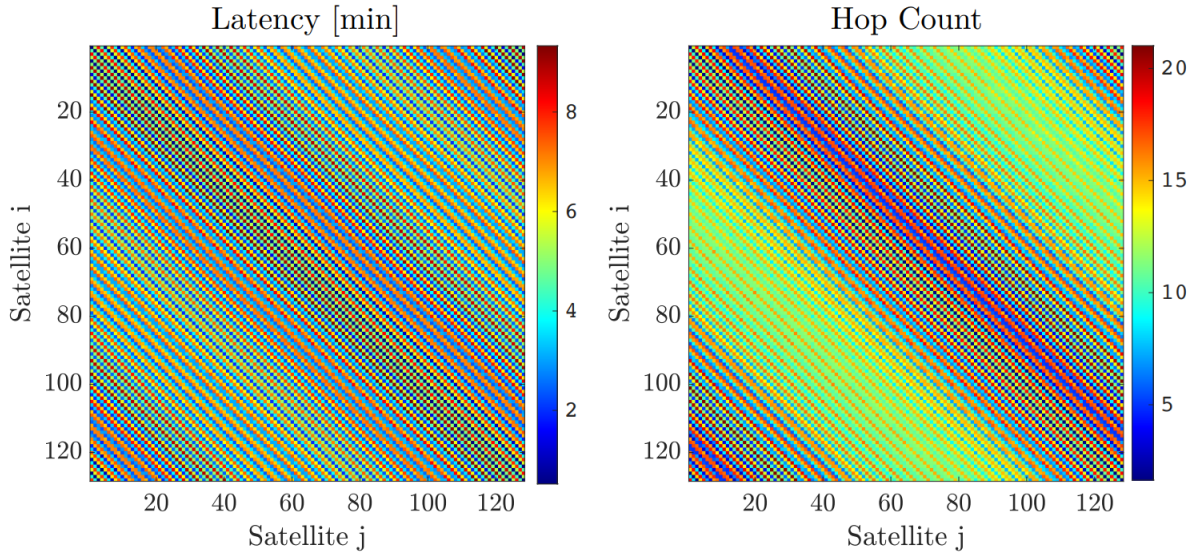


Figure 3. *Latency (left, in minutes) and hop count (right) between all satellite pairs, averaged over 100 realizations.*

Concluding Remarks

This work presents a cluster-based routing framework for satellite constellations that addresses the limitations of conventional snapshot-based methods. By shifting the modeling perspective from individual satellites to cluster communication events (groups of satellites that remain mutually connected over time intervals), the approach enables a compact static digraph representation that captures all feasible routing opportunities including short-lived connectivity windows that fixed-interval snapshots would miss. The framework was demonstrated on two configurations of a 128-satellite LEO constellation: one with global continuous connectivity and another with multiple temporary clusters. In the latter case, the cluster-based digraph enabled efficient minimum-latency routing through temporal coordination of communication events, achieving average latencies of approximately 5 minutes with typical hop counts around 12 satellites. The method is general and directly applicable to heterogeneous constellations with arbitrary orbital configurations, making it particularly suitable for sparse or asymmetric systems where traditional mesh-topology assumptions fail.

References

[1] Liz Martinez Marrero et al. “Architectures and synchronization techniques for distributed satellite systems: A survey”. In: *IEEE access* 10 (2022), pp. 45375–45409.

[2] Qi Xiaogang et al. “A Survey of Routing Techniques for Satellite Networks”. In: *Journal of Communications and Information Networks* 1.4 (2016), pp. 66–85. https://doi.org/10.11959/j.issn.2096-1081.2016.058

[3] Yixin Huang et al. “Reinforcement learning based dynamic distributed routing scheme for mega LEO satellite networks”. In: *Chinese Journal of Aeronautics* 36.2 (2023), pp. 284–291. issn: 1000-9361. https://doi.org/10.1016/j.cja.2022.06.021

[4] M. Werner. “A dynamic routing concept for ATM-based satellite personal communication networks”. In: *IEEE Journal on Selected Areas in Communications* 15.8 (1997), pp. 1636– 1648. https://doi.org/10.1109/49.634801

[5] Yanbo Liu et al. “An Improved Multi-path Routing Algorithm for Hybrid LEO-MEO Satellite Networks”. In: 2016 *IEEE Trustcom/BigDataSE/ISPA*. 2016, pp. 1101–1105. https://doi.org/10.1109/ TrustCom.2016.0181

[6] Giulio De Angelis et al. “Stereographic Projection and Static Digraph for Information Routing in Satellite Constellations”. In: *IAF Astrodynamics Symposium*. IAC 2024. International Astronautical Federation (IAF), 2024, pp. 924–941. https://doi.org/10.52202/078368-0078

[7] Mauro Pontani. *Advanced Spacecraft Dynamics*. 1st. Edizioni Efesto, 2023. isbn: 9788833814605.

[8] John G Walker. “Continuous whole-earth coverage by circular-orbit satellite patterns”. In: *Nasa Sti/recon Technical Report N* 78 (1977), p. 11169.

[9] Stefano Carletta et al. “Large constellations for fast acquisition and delivery of information: Design and analysis by stereographic projection onto the equatorial plane”. In: *International Journal of Satellite Communications and Networking* 42 (2023), pp. 134–164. url: https: //onlinelibrary.wiley.com/doi/10.1002/sat.1504

Materials Research Proceedings 69 (2026) 1120-1124 https://doi.org/10.21741/9781644904251-193

Orbit Data Analysis of LAGEOS and LARES 2 Space Missions

Ignazio CIUFOLINI[1,a *], Claudio PARIS[1,b], Darpanjeet DEKA[1,c], Emiliano ORTORE[1,d*], Antonio PAOLOZZI[1,e]

[1]Scuola di Ingegneria Aerospaziale, La Sapienza Università di Roma, Via Salaria 851, 00138 Rome, Italy

[a]ignazio.ciufolini@gmail.com, [b]claudio.paris@uniroma1.it, [c]darpanjeet.deka@uniroma1.it, [d]emiliano.ortore@uniroma1.it, [e]antonio.paolozzi@uniroma1.it

Keywords: LARES 2, LAGEOS, Precise Orbit Determination, General Relativity

Abstract. LARES 2 satellite has been launched on 13 July 2022 for testing general relativity and, in particular, the phenomenon known as Lense-Thirring effect or frame-dragging**.** In fact, Earth rotation drags spacetime and LARES 2 orbit with it. Precise Orbit Determination using laser-ranging data enables the accurate measurement of the orbital node shift. A key challenge is to isolate from this shift the contribution due solely to General Relativity, which is several orders of magnitude smaller than the one from the gravitational one. To solve this issue, orbital data from LARES 2 will be combined with the ones of LAGEOS satellite, along with state-of-the-art models of Earth's gravitational field. This paper describes the methodology which will be applied for the orbital analysis of the aforementioned satellite missions, which is essential to achieving the level of accuracy required by the scientific objectives of the LARES 2 space mission.

Lense-thirring effect and geodetic satellites

The relativistic effect consists in the dragging of space-time caused by the Earth rotation around its axis. A consequence of this phenomenon, defined as frame-dragging or the Lense-Thirring (LT) effect, is represented by the variation in the longitude of Earth satellites in the Earth Centred Inertial (ECI) reference frame, i.e. variation in Right Ascension of the Ascending Node (RAAN) **[1, 2]**.

Since for Earth satellites this variation in RAAN is millions of times smaller with respect to the one related to the perturbative effects of the gravitational field (the LT effect is large around a very massive body, in particular a black hole), in order to highlight it, it will be necessary to carry out an accurate process of orbit determination, called Precise Orbit Determination (POD) to be applied to geodetic satellites. In fact, this process must allow an extremely accurate estimate of all the other perturbing effects acting on the RAAN.

However, since the non-gravitational perturbations (atmospheric drag, solar radiation pressure, albedo) are intrinsically characterised by a greater uncertainty, due to the limited knowledge on the variability of the parameters involved in their modelling, they can be greatly reduced by considering satellites as spherical rigid bodies, with a very low surface-to-mass (A/m ratio). For example, LARES 2 satellite (launched in 2022) consists of a spherical monolithic piece made of nickel alloy with a diameter of 0.424 m and a weight of 294.8 kg. This design has already been tested on the LARES satellite (launched in 2012) that gave a measure of the LT effect in 2016 **[3]** The consideration of monolithic pieces reduces the thermal gradient on the surface, thereby further reducing the contribution to the solar radiation pressure related to absorption-emission phenomena on a spherical satellite. The spherical shape also guarantees an A/m ratio that is independent on the satellite attitude and cancels out the component of radiation reflected by the satellite in a specular manner **[4].**

Content from this work may be used under the terms of the Creative Commons Attribution 3.0 license. Any further distribution of this work must maintain attribution to the author(s) and the title of the work, journal citation and DOI. Published under license by Materials Research Forum LLC.

Materials Research Proceedings 69 (2026) 1120-1124 https://doi.org/10.21741/9781644904251-193

Precise orbit determination of geodetic satellites

The POD is a mathematical process that aims to gain accurate knowledge of the spacecraft's state vector, i.e. the position **r** and velocity **v** vectors, as a function of time **[5]**. This process is approached by implementing an iterative technique involving both the analysis of a large number of measurements performed by laser ranging ground stations (about 40 in the world) and the use of an accurate orbital propagator. To estimate the LT effect, the analysis is temporally subdivided into time intervals, whose duration can be either 7 or 14 days.

In fact, in each of these time intervals, the stations make a certain amount of measurements. These measurements, that are very accurate, are statistically processed by the station itself, so that they are reduced to a smaller amount (some hundreds) that is representative of that time interval. The statistical treatment eliminates erroneous measures and gives greater weight to the most accurate measurements. This is accomplished on the basis of the errors that are associated (a priori) with the measures themselves, identified by their standard deviations. These representative measurements will form a vector $\mathbf{M} = [m_1, m_2,...m_m]$, called vector of measurements, whose elements, called normal points, are the satellite's Cartesian coordinates (positions) at instants t_1, t_2,...t_m belonging to the time interval under consideration. Then, starting from an initial estimate of the state vector (at the beginning of the interval), a very accurate numerical propagation is carried out along the entire interval, realised by a program (e.g. Geodyn II orbit determination software) that integrates numerically the equations of motion of the satellite subjected to the Newtonian force due to the Earth and the orbital perturbations: asymmetries of Earth's gravitational field, gravitational attractions of other celestial bodies, solar radiation pressure,... The temporal evolution of the state vector (and consequently of the satellite orbit elements) over the entire interval is thus determined. Following this, the normal points for the interval under consideration are fitted using the least squares method **[5]**. The minimisation of the sum of the squares of the distances between the satellite coordinates, obtained by orbit propagation, and the points corresponding to the measurements, is achieved by making an appropriate modification to the initial conditions of the interval. This modification, called differential correction, involves not only the state vector but also some chosen characteristic parameters related to the orbital perturbation model (value of the reflectance coefficient C_R of the satellite, empirical accelerations, ...), which constitute a vector **F** defined as force model. In fact, at each iteration, in addition to the position and the velocity vectors, also these parameters can be changed in the neighbourhood of their initial conditions, in order to find their accurate values. As said, the procedure is iterative: with the initial conditions updated, a new orbital propagation is performed, leading to a new temporal evolution of the coordinates to be fitted again with the measurements in the interval, and so on. The process ends at a pre-established threshold, for which the determined initial state vector is sufficiently accurate; this occurs when the so-called Root Mean Square (RMS), given by the square root of the sum of the squares of the distances, becomes less than a given value (a few centimetres). Once the iterative cycle is completed, the next time interval is analysed, using as initial conditions the state vector related to the end of the previous interval (corresponding to the last numerical propagation performed in the previous interval).

As described, the POD allows the determination of the precise values of the state vector at the beginning of each interval. Thus, the set of all the initial states of the various intervals will provide the complete temporal evolution of the satellite orbit.

The purpose of this article is to illustrate the procedure that allows the LT effect to be estimated by appropriately applying the POD to geodetic satellites.

Computing the residual of right ascension of the ascending node

To estimate the LT effect, pairs of contiguous time intervals are used, following the procedure described below.

Materials Research Proceedings 69 (2026) 1120-1124 https://doi.org/10.21741/9781644904251-193

Let us consider a generic couple of contiguous intervals, and indicate the first one with Δ_{t-1} and the second with Δ_t. In the Δ_{t-1} interval, the POD is applied, leading to accurately estimate the initial conditions of this interval. At this point, the next interval is considered, taking as an initial estimate for such an interval Δ_t the final conditions of the previous interval (last propagation in Δ_{t-1}), indicated as $[\mathbf{r}, \mathbf{v}, \mathbf{F}]_{t-1}^{fin}$ (in fact, the final instant of the interval Δ_{t-1} coincides with the initial instant of arc Δ_t). Since the conditions $[\mathbf{r}, \mathbf{v}, \mathbf{F}]_{t-1}^{fin}$ derive from a numerical propagation, they will be affected by a small error linked to uncertainties in modelling the perturbative effects (coefficients J_{lm}, $C_{R,\ldots}$) and effects not included in the perturbing model (for us, the LT effect). At this point, starting from the initial conditions$[\mathbf{r}, \mathbf{v}, \mathbf{F}]_{t-1}^{fin}$, the POD is applied to the interval Δ_t, leading to accurately determine the initial conditions of this interval. These conditions, indicated here as $[\mathbf{r}, \mathbf{v}, \mathbf{F}]_t$, will differ from those related to the initial estimate $[\mathbf{r}, \mathbf{v}, \mathbf{F}]_{t-1}^{fin}$, since, as said, the state $[\mathbf{r}, \mathbf{v}, \mathbf{F}]_{t-1}^{fin}$ is affected by a small error. The difference between the states $[\mathbf{r}, \mathbf{v}, \mathbf{F}]_t$ and $[\mathbf{r}, \mathbf{v}, \mathbf{F}]_{t-1}^{fin}$ is then evaluated, and to this difference will correspond a specific variation for each orbit element, called residual. In particular, as mentioned, to estimate the LT effect, it is necessary to consider the residual of RAAN, which can be expressed as:

$$\delta\dot{\Omega} = \frac{\Omega_t - \Omega_{t-1}}{\Delta_{t-1}} = \frac{\Delta\Omega}{\Delta_{t-1}} \qquad (1)$$

As evidence shows, the difference between the states has to be divided by the duration of the time interval Δ_{t-1} because the propagation error has been "accumulated" during the last propagation over this interval; $\delta\dot{\Omega}$ represents indeed the error on the RAAN, averaged over the propagation time (thus the residual of the RAAN has the dimension of an angular velocity).

The process will then be repeated between the interval Δ_t and the next one (Δ_{t+1}), taking as initial conditions for the interval Δ_{t+1} the final conditions resulting from the last orbit propagation on Δ_t, and so on. Once obtained all the points over the entire interval of study, these points have to be fitted by the least square method to get the experimental time evolution of the RAAN. Finally, this evolution has to be compared with the theoretical one (equation (2) below), to test if the two temporal variations coincide.

The LT effect will be intentionally not included in the dynamic model and therefore in the propagations, so that it can be associated with the residual that remains after removing the other contributions. The most important contribution is represented by the systematic error due to the uncertainties in the knowledge of the Earth's gravitational coefficients related to the even zonal harmonics. The errors associated with the other gravitational harmonics, the gravitational attraction of the other celestial bodies, atmospheric effect, the solar radiation pressure and the albedo are instead small compared to the relativistic effect.

The contribution associated with the even zonal harmonics will then be "eliminated" using the supplementary orbit technique, based on processing orbital data from the geodetic satellites LAGEOS and LARES 2 satellites.

Orbits with supplementary inclinations

To improve the estimation of the LT effect, the RAAN residuals of LARES 2 satellite will be advantageously combined with those of LAGEOS satellite. LARES 2 has been, indeed, specifically placed in a circular orbit with the same orbit elements as LAGEOS, except for the inclination (about 70 deg), which is supplementary to that of LAGEOS (about 110 deg). This choice has been dictated by the fact that the secular variation of the RAAN due to the even zonal harmonics depends, as is well known, on the cosine of the orbit inclination (all variations of RAAN due to J_l, with $l = 2, 4, \ldots$ have this term). It follows that, while the nodal line of LAGEOS rotates counterclockwise, that of LARES 2 rotates clockwise at the same angular velocity. As a result, the

sum of the residuals of RAAN of the two satellites can be neglected, as it is much smaller than the sum of the errors due to the non-consideration of the relativistic effect in the orbital propagations of LARES 2 and LAGEOS. The modelling of the orbital perturbations due to the lunisolar Earth's tides perturbations **[6]** has to be carefully analyzed. The same occurs for the errors related to the modelling of all the other perturbing actions considered in the numerical propagations (other gravitational harmonics, gravitational attraction of other celestial bodies, atmospheric effect, solar radiation pressure, etc…) and to the errors deriving from the fact that the orbits are not perfectly supplementary and their semi-major axes and eccentricities are not exactly the same (all these effects will of course be included in the systematic error budget associated with the experimental estimate of the relativistic effect, here described). This will make it possible to verify experimentally the very small variation of RAAN due to the LT effect predicted by the theory of General Relativity (GR), which occurs in anti-clockwise direction regardless of whether the inclination is direct or retrograde:

$$\dot{\Omega}_{\text{LT}-\text{ THEORETICAL}} = \frac{2GJ}{c^2 a^3 (1-e^2)^{3/2}} \qquad (2)$$

In Eq. (2), G is the gravitational constant and *c* is the speed of light and J the angular momentum of the Earth.

Conclusions

LARES 2 has been launched in 2022 with the goal of increasing the accuracy of the results obtained by the LARES mission. The satellite is producing high quality ranging data that are being processed by the scientific team of the mission. This analysis will also involve the geodetic satellite LAGEOS. In fact, LARES 2 has been specifically positioned into an orbit having a supplementary inclination compared to that of LAGEOS, to allow a more accurate estimate of the relativistic effect. Accordingly, the procedure described in this article will lead to a very precise verification of the theoretical prediction coming from General Relativity theory by means of the exploitation of experimental Satellite Laser Ranging data.

Acknoledgements

The authors wish to thank the Italian Space Agency for having funded the design of the LARES 2 satellite under agreement n. 2017-23-H.0 and the orbital analysis of LARES 2 under the agreement "Attività di analisi dei dati scientifici della missione LARES 2", the European Space Agency and AVIO for the VEGA C inaugural flight.

References

[1] I. Ciufolini, A. Paolozzi, E.C. Pavlis, J.C. Ries, R. Matzner, C. Paris, E. Ortore, V. Gurzadyan, R. Penrose, The LARES 2 satellite, general relativity and fundamental physics, *European Physical Journal C*, Vol. 83, n. 1, Article number 87, pp.1-10, 2023. https://doi.org/10.1140/epjc/s10052-023-11230-6.

[2] I. Ciufolini, C. Paris, E.C. Pavlis, J.C. Ries, R. Matzner, A. Paolozzi, E. Ortore, G. Bianco, M. Kuzmicz-Cieslak, V. Gurzadyan, R. Penrose, First results of the LARES 2 space experiment to test the general theory of relativity, *European Physical Journal Plus*, Vol. 138, n. 11, Article number: 1054, pp. 1-6, 2023. https://doi.org/10.1140/epjp/s13360-023-04696-6. Part of the collection "Focus point on tensions in cosmology from early to late universe: Part II: New directions in the light of observations from the most modern astronomical facilities".

[3] I. Ciufolini, A. Paolozzi, E.C. Pavlis, et al., A test of general relativity using the LARES and LAGEOS satellites and a GRACE Earth gravity model: Measurement of Earth's dragging of

inertial frames, (2016) European Physical Journal C, 76 (3), art. no. 120. https://doi.org/10.1140/epjc/s10052-016-3961-8

[4] A. Paolozzi, I. Ciufolini, G. Sindoni, C. Paris, The LARES 2 satellite: new challenges for design and ground test, Aerotecnica, Missili e Spazio, 2018, Vol. 97, pp. 135-144

[5] O. Montenbruck, E. Gill, “Satellite Orbits - Models, Methods and Applications”, 2001 Springer, Section 8.1.

[6] B. Bertotti, M. Carpino, *Supplementary Satellites and Tidal Perturbations* in: *Measurement of the Gravitomagnetic Field Using a Pair of Laser Ranged Satellites*, ASI final report, Frascati, pp. 105-121, 1989.

Materials Research Proceedings 69 (2026) 1125-1130 https://doi.org/10.21741/9781644904251-194

Design of Responsive Space-Based Observation Systems with Integrated Collision Risk Consideration

Yifan CAI[1,a *] and Camilla COLOMBO[1,b]

[1]Politecnico di Milano, Via La Masa 52, Milan, Italy

[a]yifan.cai@polimi.it, [b]camilla.colombo@polimi.it

Keywords: Constellation Design, Multi-objective Optimisation, Collision Risk, Space Sustainability

Abstract. The rapidly increasing density of Low-Earth Orbit (LEO) space and the growing demand for time-critical Earth Observation (EO) tasks introduce new challenges for constellation design. Traditionally, optimisation efforts have prioritised coverage performance and system cost, while collision risk has been evaluated only at later operational stages. However, in an increasingly congested orbital environment, this separation is no longer sustainable. This paper addresses constellation design as a three-objective optimisation problem, where responsiveness, system cost, and orbit collision risk are treated as equally important objectives. A modelling framework is formulated, in which responsiveness is measured by the average revisit interval over a set of spatially distributed events, cost is approximated through a satellite-count-based linear model, and collision risk is estimated through a composite debris background and conjunction-based proxy. Two optimisation scenarios are examined: (i) responsiveness–cost optimisation while computing but not minimising risk, and (ii) full three-objective optimisation including risk as one of the objectives. Results demonstrate that explicitly optimising risk reshapes the Pareto frontier, favouring design configurations that provide comparable responsiveness and cost with substantially reduced collision risk. These findings support incorporating sustainability considerations at the conceptual design stage of future responsive EO constellations.

Introduction

Responsive Earth Observation (EO) has become fundamental to disaster assessment, emergency response, environmental monitoring, and security applications. Low-Earth Orbit (LEO) satellite constellations are particularly suitable for such missions due to their short orbital periods and high temporal revisit capability. However, the LEO environment is becoming increasingly congested. Collision risk, arising from both inter-constellation interactions and encounters with orbital debris, poses a growing challenge to long-term operational sustainability [1].

Conventional constellation design studies primarily optimise performance-driven metrics such as coverage, revisit time, and system cost [2-4]. In most cases, collision risk is considered only at later operational stages, for example during conjunction assessment and station-keeping planning [5,6]. This separation between early-stage architecture design and sustainability evaluation is increasingly problematic in an era of proliferating large constellations and escalating debris populations [7].

Recent discussions on the future of near-Earth space activities have emphasised the importance of evaluating collision probability in the context of orbital congestion. For instance, Rossi et al. highlight the challenges posed by debris accumulation and stress the need for systematic collision risk assessment [8]. The International Risk Governance Council similarly identifies the risks associated with new large satellite constellations as a central sustainability concern [9]. Meanwhile, Lucken et al. demonstrate the feasibility of modelling collision risk during constellation design, although their work does not directly address responsive observation missions [10].

Content from this work may be used under the terms of the Creative Commons Attribution 3.0 license. Any further distribution of this work must maintain attribution to the author(s) and the title of the work, journal citation and DOI. Published under license by Materials Research Forum LLC.

Materials Research Proceedings 69 (2026) 1125-1130 https://doi.org/10.21741/9781644904251-194

Taken together, these studies indicate that collision risk should be incorporated directly into constellation architecture design rather than treated as a downstream operational concern. Accordingly, we treat responsiveness, cost, and collision risk as co-equal design objectives and pose the central question: how does the Pareto-optimal trade space change when collision risk is promoted from a diagnostic output to an optimisation objective? To answer this, we compare two scenarios for responsive LEO constellations: Case A, where responsiveness and cost are optimised and risk is only reported, and Case B, where all three objectives are jointly optimised with no imposed priority. By analysing the resulting Pareto frontiers and representative constellation architectures, we characterise how risk-aware optimisation reshapes configuration choices and identify conditions under which sustainability can be improved without significant loss in performance or cost efficiency.

Problem Formulation and Method

The objective of this study is to investigate how incorporating collision risk as a co-equal optimisation objective reshapes the design space of responsive LEO satellite constellations. To this end, we formulate the constellation responsiveness measure, cost model, and collision risk representation in a unified multi-objective optimisation framework.

The Walker constellation is used and parameterised by:

$$x = [N, P, h, i], \tag{1}$$

where total satellite count N, orbital plane number P, altitude h, and inclination i define coverage geometry and debris exposure. The search is constrained to realistic LEO ranges. Each satellite is equipped one sensor to observe the events.

A set of spatially distributed observation-demand events is used to represent task locations. The system responsiveness is expressed as:

$$T_{\text{rev,avg}} = \frac{\sum_e \omega_e W_e}{\sum_e \omega_e n_e}, \tag{2}$$

where ω_e is the event relative importance weight, W_e is the observation time window length, and n_e is the number of times observed within that window, which output by sensor-tasking module [11]. $T_{\text{rev,avg}}$ reflects the effective revisit cadence across all events. This choice is representative rather than prescriptive: alternative responsiveness definitions (e.g., time-to-first-access, percentile revisit, or coverage-weighted measures) can be substituted without changing the optimisation structure.

Cost is approximated as:

$$\text{Cost} = c_{\text{unit}} \cdot N, \tag{3}$$

where c_{unit} is satellite unit cost (which may include manufacturing, launch, and operation costs). This keeps the optimisation interpretable and extendable. More detailed models (bus/payload mass-based costing, rideshare discretisation, ground segment) can be introduced in place of this proxy.

Collision risk over mission lifetime is represented as the union of background-flux for space debris and constellation self-induced collision for constellation [12]:

$$R_{\text{coll}} = 1 - \exp\left(-k_{\text{bg}}\rho(h)N\right)\exp\left(-k_{\text{cs}}\frac{2N(P\text{-}1)}{T}\right), \tag{4}$$

Materials Research Proceedings 69 (2026) 1125-1130 https://doi.org/10.21741/9781644904251-194

here, $\rho(h)$is altitude-dependent debris flux, $T$is orbital period, and k_{bg} and k_{cs} are scaling factors to adjust two risk unit. These are calibrated placeholders intended for concept studies and to be replaced with engineering-grade models.

Two scenarios are explored with the set as Table 1:

Table 1: Scenarios setting

Case	Objective Vector	Interpretation
A	$[T_{\mathrm{rev,avg}}, \mathrm{Cost}]$	R_{coll} reported but not optimised
B	$[T_{\mathrm{rev,avg}}, \mathrm{Cost}, R_{\mathrm{coll}}]$	R_{coll} is explicitly minimised

NSGA-II is employed to obtain Pareto fronts and population distributions [13]. To emphasise method rather than tooling, any competent multi-objective optimiser could be used. The problem setting intentionally adopts lightweight but physically interpretable proxies, allowing the analysis to focus on trade-space structure and decision implications, rather than on high-fidelity physical modelling. These proxies are designed to be directly replaceable with engineering-grade components without altering the optimisation structure.

Results and Discussion

This section compares the optimisation outcomes obtained under Case A (responsiveness–cost optimisation with risk computed but not minimised) and Case B (full three-objective optimisation), focusing on the structure of the resulting design trade-space.

Figure 1 presents the scatter matrix for average revisit interval, cost, and self-induced collision opportunity for Case A and Case B. Diagonal panels show marginal distributions, while off-diagonal panels depict pairwise correlations (x-axis: column variable; y-axis: row variable). Clear geometric couplings appear: shorter revisit times require more satellites, increasing both cost and collision opportunity. Case A exhibits wide spreads and a pronounced high-risk tail, reflecting unconstrained growth of large constellations. Case B yields markedly narrower clusters, suppressing high-cost/high-risk solutions and producing a more compact and sustainable design space.

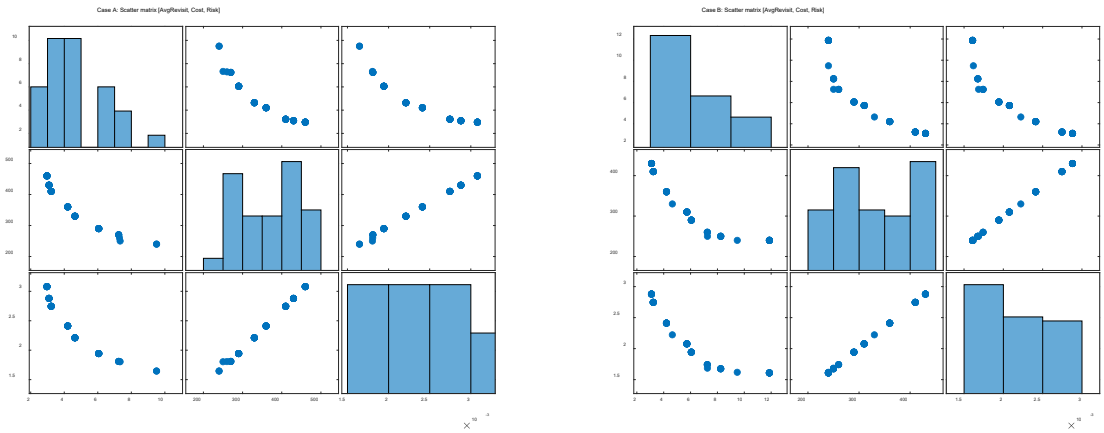


Figure 1: Scatter matrix of Case A and Case B.

In both cases, collision risk increases monotonically with (i) increasing satellite count (higher cross-sectional population density) and (ii) higher orbital altitude (higher debris flux in typical crowded LEO bands). This confirms the intended structural behaviour of the risk proxy: the model correctly captures macro-level variation in collision hazard.

Materials Research Proceedings 69 (2026) 1125-1130 https://doi.org/10.21741/9781644904251-194

For more details about differences between Case A and Case B distribution patterns. Case A retains many designs in high-cost / high-altitude regions where responsiveness is strong but risk is also significantly elevated. Case B suppresses these configurations, producing a population concentrated in lower-risk altitude bands (typically 420–500 km range) and with more moderate satellite counts. The optimisation pressure introduced by including risk does not eliminate high-performance solutions; instead, it filters out *imbalanced* designs that achieve responsiveness *only* through risk-intensive architecture choices.

Figure 2 compares the distributions of average revisit interval versus collision risk for Case A and Case B. For designs achieving comparable responsiveness, the solutions from Case B consistently exhibit lower collision risk than those from Case A. This indicates that, when risk is not explicitly controlled during optimisation, architectures with similar satellite counts may still display substantial variability and occasional escalation in risk. By contrast, incorporating collision risk as an optimisation objective drives the design space toward a more compact and systematically lower-risk region, even under similar cost constraints.

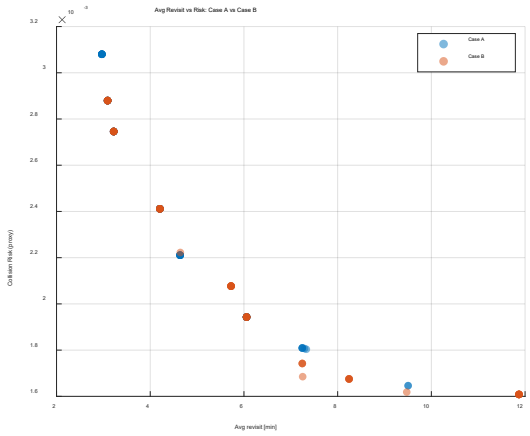


Figure 2: Avg Revisit and Risk of Case A and Case B.

The constellation design parameters obtained in the two cases are shown in Table 2. The optimisation outcomes highlight a clear structural shift when collision risk is treated as a co-equal design objective. Case A, which optimises responsiveness and cost alone, favours a 32-satellite constellation at 49° inclination. In contrast, Case B identifies a 24-satellite configuration with a significantly higher inclination (73.6°), achieving comparable revisit performance while reducing both cost and estimated collision probability. The higher inclination increases ground-track latitudinal coverage, enabling responsiveness to be maintained despite the reduced satellite count. Since the collision-risk proxy grows monotonically with constellation size, the reduction in N_{sat}directly yields a marked decrease in overall collision exposure. This illustrates that risk-aware constellation planning promotes architectural solutions that are simultaneously more sustainable and cost-efficient, without substantially degrading mission responsiveness.

Table 2: The constellation design parameters.

Case	N_{sat}	N_{planes}	h [km]	i [°]
A	32	8	400	49.3
B	24	8	405	73.6

The parallel coordinate plots for Case A and Case B (Figure 3) illustrate how the solutions distribute across the three objectives when normalised. A notable trend emerges in both scenarios:

Materials Research Proceedings 69 (2026) 1125-1130 https://doi.org/10.21741/9781644904251-194

cost and collision risk tend to vary in the same direction, reflecting their shared dependence on the constellation size.

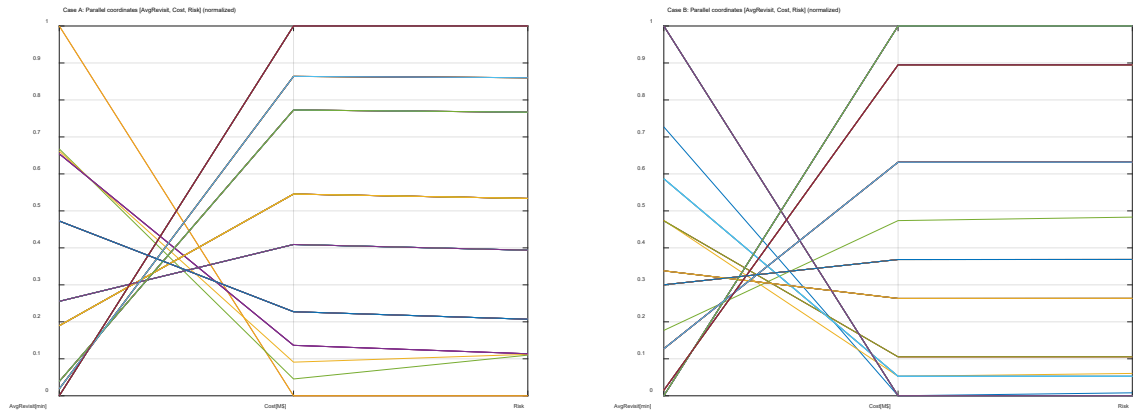


Figure 3: Parallel coordinates of Case A and Case B.

Since the cost proxy is proportional to the total number of satellites, $\mathrm{Cost} = c_{\mathrm{unit}}N$, and the collision risk proxy Risk includes both background flux exposure and an encounter-rate term that scale with N, increasing the constellation size simultaneously increases cost and elevates orbital exposure, thereby increasing the probability of conjunction or collision. As a result, the two quantities are positively correlated by construction, even before optimisation.

This structural correlation appears clearly in the Case A parallel coordinate plot, where several solutions achieving lower revisit intervals do so by increasing the satellite count, which in turn drives both cost and risk upwards. In this scenario, where risk is *not* included as an optimisation objective, the optimiser has no incentive to avoid these high-risk configurations; the design space therefore contains "high-performance but high-risk" constellations.

In contrast, in Case B, where risk is optimised jointly with cost and responsiveness, the parallel coordinate plot shows a visibly compressed range of collision risk across the final population. Solutions with high cost but also high risk are systematically excluded because they are dominated in the Pareto sense. This produces a frontier in which increasing satellite count no longer yields acceptable responsiveness gains, and the optimiser instead tends to explore constellations with fewer satellites but more favourable geometric factors, such as higher inclination and more efficient plane distribution, to preserve responsiveness without incurring excessive risk.

In other words, Case A can improve responsiveness primarily by adding satellites, but this pushes both cost and risk higher, which leads to wide spread in the "Risk" dimension. Case B avoids the part of the search space where both cost and risk increase together, encouraging structurally sustainable architectures, leading to narrower, lower band of risk values. This distinction directly explains why the best Case A and Case B solution settles at Table 2. This demonstrates that risk awareness reshapes the design strategy itself, rather than simply selecting among otherwise similar architectures.

Conclusion

This study demonstrates that treating collision risk as a co-equal design objective fundamentally reshapes the satellite constellation design trade space. When risk is only computed post-hoc, as in Case A, high-risk configurations may be incorrectly regarded as desirable due to their responsiveness–cost performance. However, when risk is explicitly included in optimisation (Case B), the resulting Pareto sets favour architectures that provide comparable responsiveness and cost while exhibiting significantly lower long-term collision risk. These findings highlight the

importance of incorporating sustainability and orbital safety considerations at the conceptual design stage, rather than deferring them to operations. The framework and insights presented here provide a basis for guiding responsible and resilient responsive EO system development.

References

[1] Johnson C D. The Legal Status of Mega LEO Constellations and Concerns About Appropriation of Large Swaths of Earth Orbit. Handbook of Small Satellites, 2020, 1-22. https://doi.org/10.1007/978-3-030-20707-6_95-1

[2] Colombi J M, Stern J L, Wachtel S T, et al. Multi-Objective Parallel Optimization of Geosynchronous Space Situational Awareness Architectures. Journal of Spacecraft and Rockets, 2018, 55(6): 1453-1465. https://doi.org/10.2514/1.A34043

[3] Wagner K M, Black J T. Genetic-Algorithm-Based Design for Rideshare and Heterogeneous Constellations. Journal of Spacecraft and Rockets, 2020, 57(5):1021-1032. https://doi.org/10.2514/1.A34527

[4] Ebrahimi B, Nadoushan M J, Roshanian J. Optimal Design and Reconfiguration of Flower Constellations: An Application to Global Disaster Management. Acta Astronautica, 2022, 198:550-563. https://doi.org/10.1016/j.actaastro.2022.06.043

[5] Petit A, Rossi A, Alessi EM. Assessment of the close approach frequency and collision probability for satellites in different configurations of large constellations. Advances in Space Research. 2021, 67(12):4177-92. https://doi.org/10.1016/j.asr.2021.02.022

[6] Zhang Y, Li B, Liu H, Sang J. An analysis of close approaches and probability of collisions between LEO resident space objects and mega constellations. Geo-spatial Information Science. 2022, 25(1):104-20. https://doi.org/10.1080/10095020.2022.2031313

[7] Huang S, Colombo C, Bernelli-Zazzera F. Multi-criteria design of continuous global coverage Walker and Street-of-Coverage constellations through property assessment. Acta Astronautica. 2021, 188:151-70. https://doi.org/10.1016/j.actaastro.2021.07.002

[8] Rossi A, Sánchez-Ortiz N, David E, Opromolla R, Grishko D. Future activities in the near-earth space in the face of ever-increasing space traffic. Acta Astronautica. 2024, 225:891-7. https://doi.org/10.1016/j.actaastro.2024.09.063

[9] Buchs R, Florin MV. Collision risk from space debris: Current status, challenges and response strategies. EPFL International Risk Governance Center. 2021.

[10] Lucken R, Giolito D. Collision risk prediction for constellation design. Acta Astronautica. 2019, 161:492-501. https://doi.org/10.1016/j.actaastro.2019.04.003

[11] Cai Y, Gonzalo Gomez JL, Colombo C. Efficient high-dimensional multi-objective optimisation method for large-scale sensor taskin. In 75th International Astronautical Congress. 2024. https://doi.org/10.52202/078360-0085

[12] Wertz, J. R., editor, Mission Geometry; Orbit and Constellation Design and Management, Microcosm Press and Kluwer Academic Publishers, 2001.

[13] Deb K, Pratap A, Agarwal S, Meyarivan TA. A fast and elitist multiobjective genetic algorithm: NSGA-II. IEEE transactions on evolutionary computation. 2002, 6(2):182-97. https://doi.org/10.1109/4235.996017

Materials Research Proceedings 69 (2026) 1131-1139 https://doi.org/10.21741/9781644904251-195

Estimation and Prediction of Long-duration Aerodynamic Drag Effect on Floating LEO Debris using the EDAC-adapted Model

Victor U. J. NWANKWO[1 *], Jens BERDERMANN[1], Timothy N. KODIKARA[1], Frank HEYMANN[1] and William DENIG[2]

[1]Institute for Solar-Terrestrial Physics, German Aerospace Center (DLR), Neustrelitz, Germany

[2]St. Joseph's College of Maine, Standish, ME 04084, USA

*Victor.Nwankwo@dlr.de

Keywords: Aerodynamic Drag, Ephemeris Data Assisted Calibration, LEO Debris, Orbital Decay

Abstract. The reliable estimation of atmospheric drag-induced orbital decay is quite challenging due to the limited representation of solar and non-solar forcing mechanisms in atmospheric density models and the complex operational dynamics of some spacecraft. Such uncertainties widen the gap between modelled estimates and actual orbital parameters and also hamper the ability of mission designers and/or operators to accurately estimate the remaining lifetime of spacecraft in orbit. Medium- to long-term estimation or prediction of a defunct spacecraft orbit is even more challenging when the object is no longer subject to ground commands. In this work, we present a robust atmospheric drag model adapted to the ephemeris data-assisted calibration (EDAC) simulation method, to improve the simulation and prediction of short-, medium- and long-term evolutions of the orbital decay of LEO objects, as functions of specific solar-geophysical indices. We show that the simulated long-term evolution of atmospheric drag-induced orbital decay compares well with the historical data of objects and confirms its validity using independent data. We present the EDAC-adapted model as a novel and effective approach to atmospheric drag prediction.

Introduction

The long-term estimation (or simulation) of atmospheric drag effects on spacecrafts in low Earth orbit (LEO) is particularly useful for satellite orbital prediction and maintenance, collision avoidance and debris tracking, re-entry estimations, mission plannings and constellation design, and space weather impact assessments [1-4]. The continuous long-term comparison between observed orbital decay and simulated drag can help to improve atmospheric density models and empirical drag coefficients (and vice versa), leading to improved predictive accuracy of space assets (e.g., [5, 6]). However, accurate modelling of drag over a long period is quite challenging due to a number of complex and interrelated factors such as unpredictable solar-geophysical events and the associated complex variability in atmospheric density models, complex spacecraft geometries and other perturbative forces [4,7-11]. The uncertainties introduced by these factors can widen the gap between observational data and simulated results – a scenario that can hamper the ability of mission designers and operators to estimate the lifetime of on-orbit spacecraft. Since the changing physical or orbital parameters of spacecraft (which is associated with their design evolution) requires a repetitive lifetime estimations for appropriate mission planning [1], a robust and scalable model is crucial for improved knowledg of atmospheric drag effects on their orbits.

Continuous developments in empirical, physical, and hybrid modeling methods have undoubtedly improved atmospheric drag estimations, including the integration of real-time space weather indices [12], data assimilation and machine learning techniques (e.g., [13, 14]), dynamic drag coefficient (Cd) modelling (e.g., [3,15,16]), probabilistic lifetime estimations [8] and hybrid

Content from this work may be used under the terms of the Creative Commons Attribution 3.0 license. Any further distribution of this work must maintain attribution to the author(s) and the title of the work, journal citation and DOI. Published under license by Materials Research Forum LLC.

Materials Research Proceedings 69 (2026) 1131-1139 https://doi.org/10.21741/9781644904251-195

physical-empirical comparative analyses [17]. However, many of these investigations have been focussed on active and/or controlled spacecraft with achievable stable flight configurations [1]; making the simulations less complex. The long-term estimation of a defunct and uncontrolled spacecraft orbit is more challenging, especially when the object is no longer responding to ground commands, which is the case for most space debris. In this work, we use a robust drag model that is adapted to the ephemeris data-assisted calibration (EDAC) simulation method, to improve the simulation and prediction of the evolution of orbital decay of LEO debris, as a function of solar-geophysical indices.

Data and method

In this work, we use a numerical integration method for orbital propagation using spherical coordinate system. The decay rate of the spacecraft orbital radius (r) or semimajor axis (a) is determined as a consequence of the rate of change of the satellite's radial velocity ($\dot{v}_r$). $\dot{v}_r$ is adapted to spacecraft ephemeris data-assisted calibration (EDAC) method by introducing a unitless normalisation coefficient (γ_{mod}) that minimizes the gap between the actual orbit decay (based on spacecraft ephemerides) and the modeled or simulated decay. Thus achieving a long-duration orbital decay rate (due to atmospheric drag) using the following set of coupled equations [4, 18]:

(1) $\dot{r} = v_r$

(2) $\dot{v}_r = -\dot{\emptyset} r^2 \rho \left(\frac{A_s C_d}{m_s}\right)$

(3) $\dot{\emptyset} = \frac{v_\emptyset}{r}$

(4) $\ddot{\emptyset} = -\frac{1}{2} r \rho \dot{\emptyset}^2 \left(\frac{A_s C_d}{m_s}\right)$

where v_r and $v_\emptyset$ are the radial and tangential velocity components, $\dot{v}_r$ and $\ddot{\emptyset}$ are the radial and azimuthal accelerations, respectively. A_s, C_d and m_s are, respectively, the projected area in the direction of motion, drag coefficient and mass of the spacecraft. ρ is the altitude-dependent atmospheric density, obtained from the Naval Research Laboratory Mass Spectrometer and Incoherent Scatter Extended (NRLMSISE) model [19]. To achieve long-duration orbital decay trajectories (that aligns closely with historical decay records of LEO objects) we applied a drag normalization coefficient (DNC) to the radial velocity component. The DNC is expressed as

(5) $\boldsymbol{\gamma}_{mod} = \frac{\Delta r_{act}}{\Delta r_{est}} = \frac{r_{at} - r_{af}}{r_{et} - r_{ef}}$

where Δr_{act} is the difference between the actual positions at time t (r_{at}), and some future time f (r_{af}), whereas Δr_{est} is the difference between the estimated positions r_{et} (r_{ef}) at the respective times $t(f)$. The goal of EDAC is to drive towards a unitary value of γ_{mod} (i.e, $\gamma_{mod} \sim 1$).

Applying DNC is important because simplified spherical coordinate drag models tend to over- or under-estimate long-term orbital decay when using nominal aerodynamic coefficients alone. In LEO, unmodelled effects such as attitude variations, complex geometry, atmospheric composition uncertainty, and along-track averaging tend to accumulate over thousands of orbits. The DNC acts as a physically motivated calibration factor that absorbs these unresolved processes without altering the governing dynamics. This approach is suitable for long-duration decay studies where reproducing observed semi-major axis evolution is more critical than resolving short-period oscillations. It also provides a realistic, validated bridge between simplified physics and historical orbital decay records.

This form of γ_{mod} (equation 5) have been previously used to simulate the orbital decay of selected LEO objects for long- and short-term regimes (e.g., [18]). However, the resulting γ_{mod} value sometimes require some adjustments to achieve a good drag estimate. The trends in the simulated mean height and orbit decay rate (ODR) have shown that γ_{mod} significantly depends on

Materials Research Proceedings 69 (2026) 1131-1139 https://doi.org/10.21741/9781644904251-195

solar activity and the spacecraft's orbital and ballistic parameters. To achieve an improved γ_{mod}, we leveraged these observed trends to develop and implement the equation for the DNC (γ_{mod}) in the long-term orbital decay simulations. The dimensionless normalization coefficient (γ_{mod}) that scales a spacecraft's drag-driven decay rate $\dot{\alpha}$ to a known reference condition based on the influencing factors of ballistic coefficients $B = A_s C_d/m_s$, atmospheric density $\rho(h)$ at the satellite altitude h and orbital eccentricity of the spacecraft can be expressed as:

$$(6) \quad \gamma_{mod}(h_p, B, e) = \frac{\dot{\alpha}(h_p,B,e)}{\dot{\alpha}(h_{ref},B_{ref},0)} \approx \left(\frac{B}{B_{ref}}\right).\left(\frac{\rho(h_p)}{\rho(h_{ref})}\right).\left(\frac{1-e}{1-e_{ref}}\right)$$

B_{ref}, h_{ref} and e_{ref} are the reference values for B, h and e, respectively. Our current implementation of the EDAC model assumes a satellite in a near-circular orbit where e ~ 0 such that the eccentricity factor, [(1-e)/(1-e$_{ref}$)], in equation 6 can be ignored. The mean effective atmospheric density of the spacecraft ($\bar{\rho}_{eff}$) at the spacecraft location can be used in place of the density at reference height ($\rho(h_{ref})$), which can be expressed as:

$$(7) \quad \bar{\rho}_{eff} = \frac{2(\sqrt{a_0}-\sqrt{a_1})}{B\sqrt{GM_e}(t_1-t_0)}$$

We selected 6 catalogued debris for this investigation, based on height (typically LEO) and the ability to be measured from the ground using the satellite laser ranging (SLR) technique via retro-reflectors. The orbital and ballistic parameters are provided in Table 1. All the listed objects have near circular orbits so that $a \sim r$ as noted above. Their historical orbital (and ballistic) data were obtained from a comprehensive satellite catalogue (https://in-the-sky.org/) and ESA's DISCOSweb (https://discosweb.esoc.esa.int/). The objects' drag coefficients (C_d) were based on the shape-dependent recommendations contained in [20-22]. Solar-geophysical indices for the solar radio flux (*F10.7*) and geomagnetic *Ap* are from GFZ Helmholtz Centre for Geosciences database (https://kp.gfz.de/en/data) and were used as inputs to the NRLMSISE to obtain the spacecraft local time (SLT) density profiles. Implicit in the reminder of this text is that the F10.7 is in solar flux units (1 sfu = 10^{-22} Watts per square meter per Hertz (W/m^2/Hz)) and Ap is in units of 2 nanoTesla (nT).

Table 1: The orbital and ballistic parameters of objects selected for investigation

	LEO Object	h (km)	m (kg)	A (m^2)	C_d	B (m^2/kg)	e	i (°)
1	1998-007A GFO-1	478.07	361.7	2.513	3.090	0.0214661	0.0800523	108.03
2	2005-031A OICETS	527.10	570.0	5.823	2.354	0.0240479	0.0078225	98.14
3	2011-076G ASAP-S	532.46	624.0	1.508	2.408	0.0058189	0.0048846	98.10
4	1999-064A HELIOS-1B	618.80	2544.0	9.274	2.200	0.0080196	0.0016220	98.27
5	1994-074A RESURS-O1	625.12	1900.0	11.656	3.253	0.0199562	0.0021570	97.75
6	2009-002E SOHLA-1	655.76	50.0	0.375	2.124	0.0159300	0.0058467	98.23

By incorporating Equation 6 with the appropriate space weather (density) and reference spacecraft parameters our drag model generates a suitable γ_{mod} for the long-duration propagation of a specific object's orbit. Table 2 shows the resulting γ_{mod} associated with each object. Using γ_{mod}, we simulated 6-month orbit decay evolution of the LEO objects (due to atmospheric drag effect) from January to June 2025.

Table 2: The γ_{mod} normalisation coefficient and the associated reference object parameters

	LEO Object	h_{ref} (km)	ρ_{ref} (kg/m^3)	A (m^2)	C_d	B_{ref} (m^2/kg)	e	γ_{mod}
1	1998-007A GFO-1	478.07	2.8260E-12	2.513	3.090	0.0214661	0.0800523	0.6618
2	2005-031A OICETS	527.10	1.6986E-12	5.823	2.354	0.0240479	0.0078225	0.6868
3	2011-076G ASAP-S	532.46	8.1800E-13	1.508	2.408	0.0058189	0.0048846	0.8590
4	1999-064A HELIOS-1B	618.80	2.1780E-13	9.274	2.200	0.0080196	0.0016220	0.8450
5	1994-074A RESURS-O1	625.12	3.3340E-13	11.656	3.253	0.0199562	0.0021570	0.5750
6	2009-002E SOHLA-1	655.76	1.3303E-13	0.375	2.124	0.0159300	0.0058467	0.8150

Results and discussion

Estimation of long-term aerodynamic drag effect

Figure 1 shows the actual mean height (*h-act*) obtained from the object's historical data and the simulated mean heights (*h-sim*) of satellites GFO, OICETS, ASAP-S, HELIOS, RESURS and SOHLA along with their corresponding orbit decay rates (ODR_act, ODR_sim), modeled as a function of the observed solar-geophysical indices during Jan-Jun 2025. The historical orbital data showed that the objects were orbiting Earth at the mean height of 478.1, 527.1, 532.46, 618.8, 625.12 and 655.8 km, respectively, on 1 January. Their respective actual and simulated mean heights (*h-act* and *h-sim*) after six months (on 30 June) are provided in Table 3. Their actual total orbit deviations (TOD_act) are 23.15, 12.7, 6.5, 2.8, 1.6, and 2.3 km, respectively, while their respective simulated total orbit deviations (TOD_sim) were 23.2, 13.3, 7, 2.8, 1.7, and 2.3 km, respectively. These values correspond to the standard deviation (σ) of 0.03, 0.25, 0.24, 0.02, 0.05 and 0.02 km, respectively, and a corresponding percentage error (δ) of 0.13. 1.93, 3.56, 0.89, 3.32 and 0.88%.

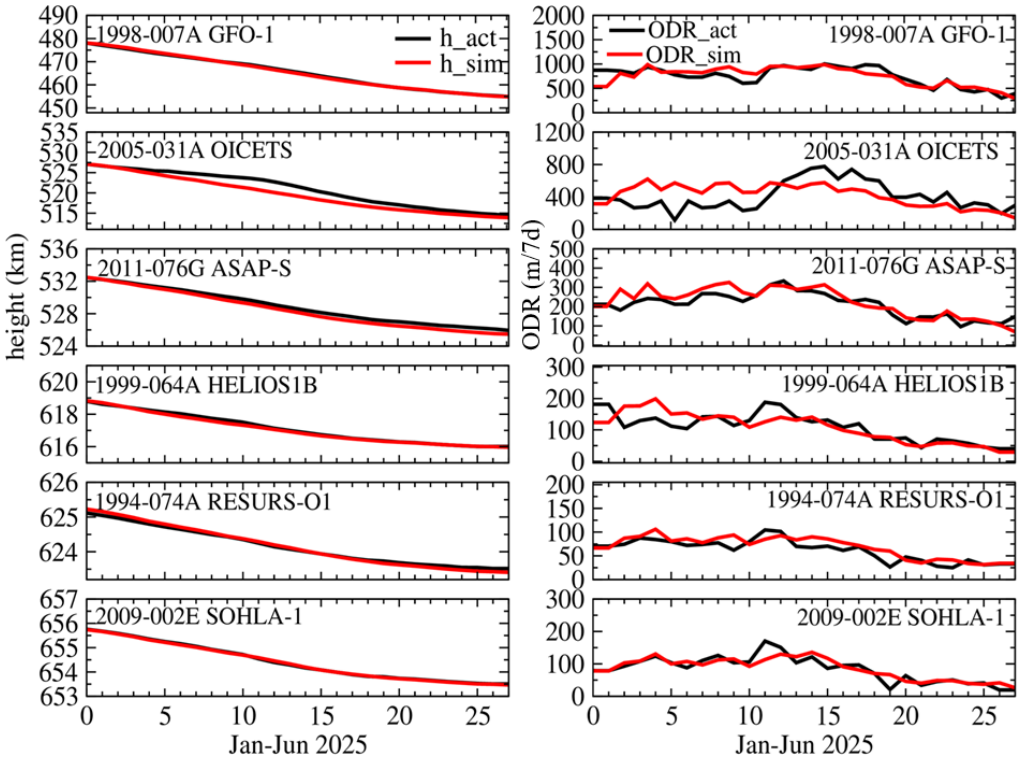


Fig. 1: Actual mean height (h-act) obtained from the object's historical data and the simulated mean heights (h-sim) of GFO, OICETS, ASAP-S, HELIOS, RESURS and SOHLA and their corresponding orbit decay rates (ODR_act, ODR_sim) during January - June 20025. The x-axes timelines are in weeks.

Materials Research Proceedings 69 (2026) 1131-1139 https://doi.org/10.21741/9781644904251-195

Table 3: The actual and simulated mean heights of the objects during Jan-Jun 2025

	Catalogued Object	**Actual mean *h* (km)**			**Simulated h-OSI (km)**	
	LEO Object	01.01.2025	30.06.2025	TOD	30.06.2024	TOD
1	1998-007A GFO-1	478.07	454.92	23.15	454.86	23.21
2	2005-031A OICETS	527.10	514.40	12.70	513.90	13.20
3	2011-076G ASAP-S	532.46	525.95	6.51	525.47	6.99
4	1999-064A HELIOS-1B	618.80	616.01	2.79	615.96	2.84
5	1994-074A RESURS	625.12	623.52	1.60	623.41	1.71
6	2009-002E SOHLA-1	655.76	653.51	2.25	653.47	2.29

In the present analysis, the mean σ and δ were 0.102 km and 1.79%, respectively. Four spacecraft show very small δ (0.13% (GFO), 0.89% (HELIOS), 0.88% (SOHLA), 1.93% (OICETS)), which are good fits for long-term decay modeling, whereas two spacecraft (having δ ≈ 3.56% (ASAP-S) and 3.32% (RESURS)) showed significantly larger deviations. There was also a very close agreement between the actual and simulated decay of three of the objects with low σ values of 0.02 (SOHLA), 0.03 (GFO) and 0.02 (HELIOS). The observed deviations in the *h-sim* and ODR_sim may be due to factors not well represented in the model such as poorly resolved normalization coefficients, unspecified differences in attitude or drag area histories, change in material or surface properties (affecting accommodation coefficients), questionable estimated mass or orientation assumptions (e.g., [1,8,23,24]). Nevertheless, the simulated mean altitudes (*h-sim*) and simulated orbital decay rates (ODR_sim) agree well with the historical orbital data of the objects and can be considered acceptable for mission purposes (such as lifetime planning and debris mitigation).

Prediction and validation of drag-induced orbital decay

We applied our model to predict the orbit decay of three LEO objects using NASA's estimate of solar-geophysical activity for the 25th solar cycle. (https://www.nasa.gov/solar-cycle-progression-and-forecast/). The predicted solar-geophysical indices (*F10.7* and *Ap*) represent the smoothed values for 13 months, based on a best estimate given as the 50th percentile value, along with the statistical 95th and 5th percentiles. The orbital decay was simulated according to the estimated levels of the indices and range of predicted values for each object. Figure 2 shows the model-based prediction of orbital decay evolution associated with the observed solar-geophysical indices for Jan-Mar 2025 and the predicted activity for Apr-July 2025. Details of the predicted decay are provided in Table 4. Based on the levels of estimated indices, the range of simulated mean height of the objects were 525.8 - 529.7, 617.51 - 618.25 and 716.89 - 717.71 km, respectively.

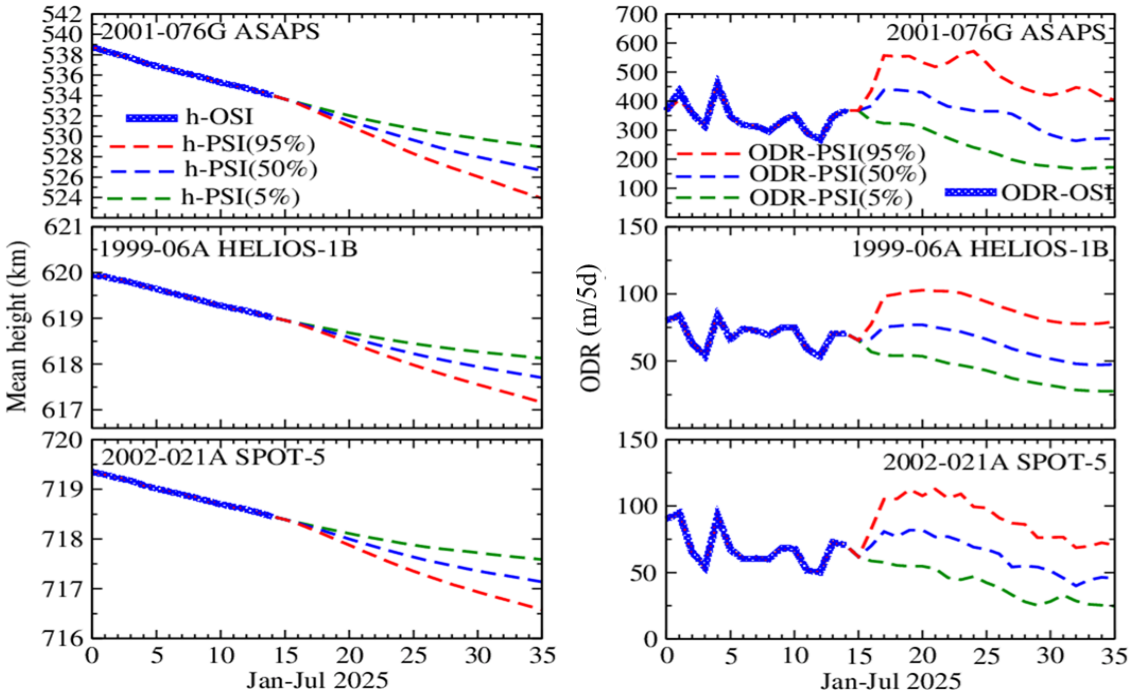


Fig. 2: The observed/predicted mean height (h) and orbit day rate (ODR) of 3 LEO objects, associated with the observed solar-geophysical indices (OSI) for Jan-Mar 2025 and the predicted solar-geophysical indices (PSI) for Apr-July 2025. The thick blue lines are the observed values, whereas the green, blue and red dashed lines are the predicted values.

Table 4: Predicted mean heights of the objects

	Mean height (*h*) analysis						
	Catalogued LEO object	**h-OSI (km)**			**predicted h-PSI (km)**		
	LEO object	**01.01.25**	**31.03.25 (ACT)**	**31.03.25 (SIML)**	**30.04.2025** F10.7=161.97 Ap=14.5	**31.05.2025** F10.7=179.47 Ap=14.77	**30.06.2025** F10.7=177.4 Ap=15.0
1	2011-076G ASAPS	538.77	533.52	534.01	531.31±0.58	529.31±1.32	527.75±1.95
2	1999-064A HELIOS-1B	619.93	619.02	619.02	618.54±0.12	618.17±0.26	617.88±0.37
3	2002-021A SPOT-5	719.34	718.46	718.45	717.95±0.13	717.58±0.28	717.30±0.41

To validate the predicted regime, we obtained and show in Fig. 3 and Table 5 the historical orbital data of the objects during Jan-Jun 2025. The actual heights of the objects at the end of June were 525.16, 617.11 and 717.52 km, respectively, which indicates that the actual mean heights of two (ASAP-S and HELIOS) of the objects lie slightly outside their error bar. This scenario may be unrelated to the model performance but on the predicted solar-geophysical indices for the interval. The predicted mean *F10.7*/*Ap* for April, May and June were 162/14.5, 179.5/14.8 and 177.4/15, respectively, while the respective observed mean values were 162.3/17.6, 135.3/17.3 and 131.3/20.5. The obvious difference between the predicted versus observed regimes is that the predicted values for *F10.7* were higher during the 3-month interval in contrast to the *Ap* predictions, which were lower than observed. Nonetheless, the predicted estimates were within an acceptable range and can potentially provide a testbed for the model improvement. As the results presented here are still in their preliminary stage, it would be premature to draw conclusions regarding the computational limitations of the model. However, the results of the model can be improved by; (i) diagnoses of observed outliers through the inspection of parameters such as attitude or area history, possible mass changes and exposure to uncaptured solar energetic events, (ii) use of precise orbit determination (POD) and accelerometer data (where available) to estimate satellite-specific drag coefficients, (iii) replacing a single global coefficient with a parametric

Materials Research Proceedings 69 (2026) 1131-1139 https://doi.org/10.21741/9781644904251-195

normalization or applying piecewise calibrations across altitude bands, and (iv) validating the approach using cross-validation and providing operational procedures for periodic recalibration after major solar events (e.g., [1,25,26]). Also, orbit propagation and/or prediction longer than 6-month duration (as done here) may require further refinement of the normalisation coefficients used here to conclusively assess the model's stability and predictive accuracy over the extended timescales that are typical of long-term orbit prediction.

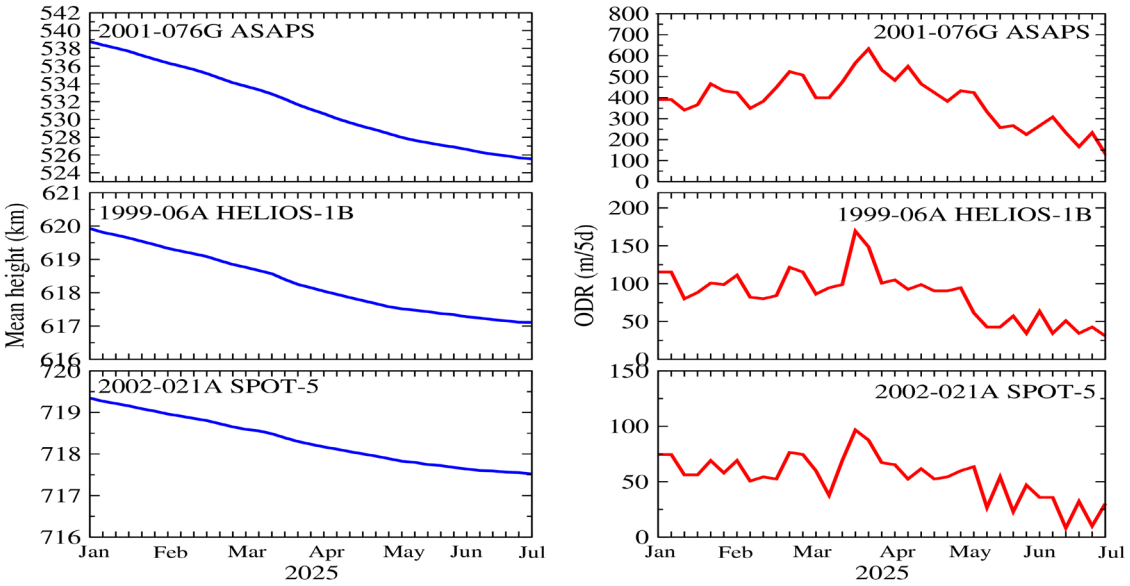


Fig. 3: Historical orbital data of the objects obtained for the period of Jan-Jun 2025 for validation of model-driven prediction of their orbital decay evolution.

Table 5: Observed mean heights of the LEO objects

	Historical orbital data analysis						
	Catalogued LEO Object	h-OSI (km)			Actual h (km)		
	LEO Objects	01.01.25	31.03.25 (ACT)	31.03.25 (SIM)	30.04.2025 F10.7=162.52 Ap=17.63	31.05.2025 F10.7=135.30 Ap=17.32	30.06.2025 F10.7=131.30 Ap=20.50
1	2011-076G ASAP-S	538.77	533.52	534.01	527.97	526.32	525.16
2	1999-064A HELIOS-1B	619.93	619.02	619.02	617.67	617.34	617.11
3	2002-021A SPOT-5	719.34	718.46	718.45	717.95	717.67	717.52

Conclusion

In this work, we simulated (and predicted) the orbital decay evolution of LEO debris with varying ballistic coefficients, as a function of solar-geophysical indices, using the ephemeris data-assisted calibration (EDAC) adapted model. The comparison between the actual and simulated decays yielded standard deviations (σ) ranging from 0.02 km to 0.25 km and percentage errors (δ) between 0.13% and 3.56%. These low deviations indicate strong consistency between the observed and modeled orbital decays, demonstrating the model's high suitability for long- and medium-term orbital prediction and decay trend estimation. The small dispersion of errors across spacecraft with different ballistic properties further suggests that the normalization coefficient effectively captures the altitude-dependent drag variability. Minor residuals were likely attributable to unmodeled spacecraft-specific parameters such as attitude, surface characteristics, or temporal density variations. The model's validation with independent data confirmed its predictive reliability and establishes a robust framework for further refinement. Overall, the performance of the model is good and consistent, supporting its application to both predictive and analytical orbit-decay studies.

Acknowledgements
This work was supported by the Impulsprojekt Orbitale Nachhaltigkeit (ION) of the German Aerospace Center (DLR). Authors acknowledge the data providers whose data were used for this work. The objects' mass, effective projected area, and shape were obtained from ESA DISCOSWeb. Their historical orbital data were obtained from In-the-sky.org satellite catalogue. The observed Ap and F10.7 were obtained from the database GFZ Helmholtz Centre for Geosciences, Germany and the predicted indices were obtained from NASA's estimate of the solar activity estimate for the 25th solar cycle (see, https://www.nasa.gov/solar-cycle-progression-and-forecast/).

References
[1] De Lafontaine, J. and Garg, S.C., 1982. A review of satellite lifetime and orbit decay prediction. Proceedings of the Indian Academy of Sciences Section C: Engineering Sciences, 5(3), pp.197-258. https://doi.org/10.1007/BF02897683
[2] Bigazzi, A., Cauli, C., and Berrilli, F., 2020. Lower-thermosphere response to solar activity: an empirical-mode-decomposition analysis of GOCE 2009-2012 data, Ann. Geophys., 38, 789-800, 2020. https://doi.org/10.5194/angeo-38-789-2020
[3] He, C., Yang, Y., Carter, B., Zhang, K., Hu, A., Li, W., Deleflie, F., Norman, R., & Wu, S. (2020). Impact of thermospheric mass density on the orbit prediction of LEO satellites. Space Weather, 18, e2020SW002336. https://doi.org/10.1029/2019SW002336
[4] Nwankwo, V. U. J., Denig, W., Ajakaiye, M. P., Akanni, J. F., Raulin, J.-P., Correia, E., Enoh, J. E., Fatokun, J., & Anekwe, P. I. (2021). Atmospheric drag effects on modelled low Earth orbit (LEO) satellites during the July 2000 Bastille Day event in contrast to an interval of geomagnetically quiet conditions. Annales Geophysicae, 39, 397-411. https://doi.org/10.5194/angeo-39-397-2021
[5] Chen, J., Du, J. and Sang, J., 2019. Improved orbit prediction of LEO objects with calibrated atmospheric mass density model. Journal of Spatial Science, 64(1), pp.97-110. https://doi.org/10.1080/14498596.2017.1371089
[6] Bernstein, V., Pilinski, M. and Sutton, E.K., 2021. Assessing thermospheric densities derived from orbital drag data. In Proceedings of the 31st AAS/AIAA Space Flight Mechanics Meeting. AAS Publications Office.
[7] Doornbos, E. and Klinkrad, H., 2006. Modelling of space weather effects on satellite drag. Advances in Space Research, 37(6), pp.1229-1239. https://doi.org/10.1016/j.asr.2005.04.097
[8] Vallado, D.A. and Finkleman, D., 2014. A critical assessment of satellite drag and atmospheric density modeling. Acta Astronautica, 95, pp.141-165. https://doi.org/10.1016/j.actaastro.2013.10.005
[9] Sagnieres, L. and Sharf, I., 2017, April. Uncertainty characterization of atmospheric density models for orbit prediction of space debris. In 7th European Conference on Space Debris (Vol. 1, pp. 18-21). ESA Space Debris Office Darmstadt, Germany.
[10] Kumar, R., Singh, R., Chinnappan, A.K. and Appar, A., 2022. Simulation of the orbital decay of a spacecraft in low Earth orbit due to aerodynamic drag. The Aeronautical Journal, 126(1297), pp.565-583. https://doi.org/10.1017/aer.2021.83
[11] Chen, X., Tang, C., Dai, W., Hu, X., Chen, L., Zhang, Z., Zhu, X. and Li, M., 2025. Modelling and prediction of atmospheric drag coefficients in LEO satellite orbit determination and prediction with Bi-LSTM approach. Advances in Space Research, 75(3), pp.2874-2888. https://doi.org/10.1016/j.asr.2024.10.063
[12] Oliveira, D.M., Zesta, E., Mehta, P.M., Licata, R.J., Pilinski, M.D., Tobiska, W.K. and Hayakawa, H., 2021. The current state and future directions of modeling thermosphere density

enhancements during extreme magnetic storms. Frontiers in Astronomy and Space Sciences, 8, p.764144. https://doi.org/10.3389/fspas.2021.764144
[13] Bruinsma, S. L., et al. (2021). The DTM-2020 thermosphere model: Evaluation with independent data. J. Space Weather Space Clim., 11, 1-20. https://doi.org/10.1051/swsc/2021032
[14] Cimmino, N., Opromolla, R. and Fasano, G., 2023. Machine learning-based approach for ballistic coefficient estimation of resident space objects in LEO. Advances in Space Research, 71(12), pp.5007-5025. https://doi.org/10.1016/j.asr.2023.02.007
[15] Pilinski, M.D., McNally, R.L., Bowman, B.A., Palo, S.E., Forbes, J.M., Davis, B.L., Moore, R.G., Kemble, K., Koehler, C. and Sanders, B., 2016. Comparative analysis of satellite aerodynamics and its application to space-object identification. Journal of Spacecraft and Rockets, 53(5), pp.876-886. https://doi.org/10.2514/1.A33482
[16] Wang, X., Ren, T., Wang, R., Luo, B., Aa, E., Cai, L., Li, M., Miao, J., Liu, S. and Gong, J., 2024. Estimates of spherical satellite drag coefficients in the upper thermosphere during different geomagnetic conditions. Space Weather, 22(11), p.e2024SW003974. https://doi.org/10.1029/2024SW003974
[17] Walterscheid, R.L., Chen, M.W., Chao, C.C., Gegenheimer, S., Cabrera-Guzman, J. and McVey, J., 2023. Comparative accuracies of models for drag prediction during geomagnetically disturbed periods: A first principles model versus empirical models. Space weather, 21(5), p.e2022SW003332. https://doi.org/10.1029/2022SW003332
[18] Nwankwo, V.U.J., Berdermann, J., Heymann, F., Kodikara, T.N. and Fernandez-Gomez I., 2025a. Model-driven assessment of space weather impact levels on the trajectory of floating debris in low earth orbit. Proceedings of the 9th ESA European Conference on Space Debris, Bonn, Germany.
[19] Picone, J. M., Hedin, A. E., Drob, D. P., & Aikin, A. C., 2002. NRLMSISE-00 empirical model of the 719 atmosphere: Statistical comparisons and scientific issues. J Geophys. Res.: Space Physics, 107(A12), SIA72015. https://doi.org/10.1029/2002JA009430
[20] Moe, M.M., Wallace, S.D. and Moe, K., 1995. Recommended drag coefficients for aeronomic satellites. The Upper Mesosphere and Lower Thermosphere: A Review of Experiment and Theory, 87, 349-356. https://doi.org/10.1029/GM087p0349
[21] Moe, K., Moe, M.M. and Wallace, S.D., 1998. Improved satellite drag coefficient calculations from orbital measurements of energy accommodation. J. Spacecr. Rockets, 35(3), 266-272. https://doi.org/10.2514/2.3350
[22] Moe, K. and Moe, M. M., 2005. Gas-surface interactions and satellite drag coefficients. Planet. Space Sci., 53(8), 793-801. https://doi.org/10.1016/j.pss.2005.03.005
[23] Pardini, C., Anselmo, L., Moe, K. and Moe, M.M., 2010. Drag and energy accommodation coefficients during sunspot maximum. Advances in Space Research, 45(5), pp.638-650. https://doi.org/10.1016/j.asr.2009.08.034
[24] Ray, V., Scheeres, D.J. and Alnaqbi, S., 2021. Decorrelating density and drag-coefficient through attitude variations. 2021 Advanced Maui Optical and Space Surveillance Technologies Conference (AMOS).
[25] Boniface, C. and Bruinsma, S., 2021. Uncertainty quantification of the DTM2020 thermosphere model. Journal of Space Weather and Space Climate, 11, p.53. https://doi.org/10.1051/swsc/2021034
[26] Mehta, P.M., Paul, S.N., Crisp, N.H., Sheridan, P.L., Siemes, C., March, G. and Bruinsma, S., 2023. Satellite drag coefficient modeling for thermosphere science and mission operations. Advances in Space Research, 72(12), pp.5443-5459. https://doi.org/10.1016/j.asr.2022.05.064

Materials Research Proceedings 69 (2026) 1140-1145 https://doi.org/10.21741/9781644904251-196

Reconfiguration and Optimization of Lunar Navigation Satellite Constellation Targeting South Hemisphere

Shuo YANG[1,a *], Rui ZHONG[2,b] and Franco BERNELLI ZAZZERA[1,c]

[1]Department of Aerospace Science and Technology, Politecnico di Milano, 20156 Milan, Italy

[2]School of Astronautics, Beihang University, 102206 Beijing, People's Republic of China

[a]shuo.yang@polimi.it, [b]zhongruia@163.com, [c]franco.bernelli@polimi.it

Keywords: Lunar Constellation, Constellation Reconfiguration, Multi-Objective Optimization

Abstract. The Lunar Navigation Satellite System (LNSS) is a critical initiative in response to the current surge in international lunar exploration. Compared to Global Navigation Satellite Systems (GNSS), the development of LNSS involves significantly higher costs and longer deployment cycles. As a result, optimizing constellation design to maximize the use of limited resources has become a popular topic. This work adopts two constellation reconfiguration strategies and a multi-objective optimization approach to extend the target area from the lunar South Pole to the whole Southern Hemisphere. First, Hohmann-type phasing maneuvers are applied to in-orbit satellites, with optimization of both fuel consumption and maneuver time, resulting in a notable improvement in dual coverage performance over the South Hemisphere. Second, new satellites are introduced to restore high-quality service in the South Pole region. Simulation results of coverage and navigation performance at the lunar South Pole confirm the effectiveness of the final constellation scheme.

Introduction

In 2005, NASA proposed six lunar communication architectures, regarding the resource-rich lunar south pole as the first exploration target [1]. In recent years, many studies have focused on the configuration design of lunar constellations. For example, Circi et al. used Halo orbits around L1 and L2 libration points to build a lunar constellation [2]. Zanotti et al. performed a multi-objective optimization of lunar orbits, targeting both low-altitude orbital missions and surface operations near the lunar South Pole [3].

The deployment of medium and large constellations usually involves reconfiguration operations, which are mainly applied in two scenarios. The first application scenario occurs when a satellite experiences an anomaly or a loss of functionality. Ferringer et al. simulated two failure scenarios and employed an evolutionary algorithm to optimize the reconfiguration process [4]. Arnas and Linares proposed a reconfiguration strategy considering the constraint of minimum inter-satellite safety distance [5]. The second scenario is the phased constellation deployment. Oliver et al. employed an Auction algorithm to derive the optimal assignment of satellites [6]. Alexandra et al. explored the design of a reconfigurable Earth observation satellite constellation, significantly improving detection rates for ground events [7].

In previous research, satellite constellations targeting the lunar South Pole have been optimized and analyzed [8]. This paper first presents the phase maneuvering methods, then the optimization models for two reconfiguration phases, followed by the results and conclusions.

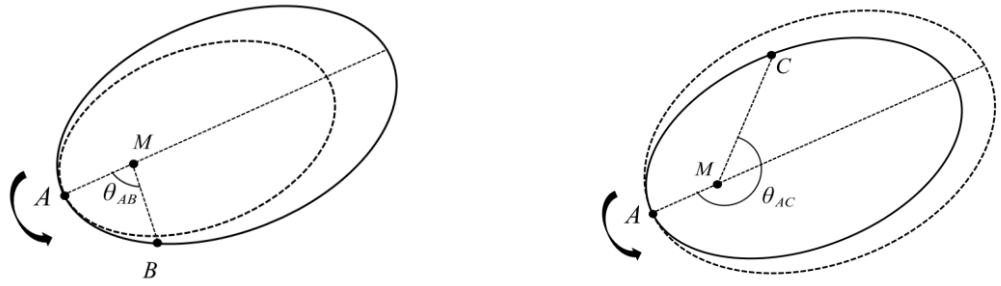
Orbital Phasing Maneuver

The first-phase reconfiguration is intended only as a temporary response to the urgent navigation demands in the Southern Hemisphere. Therefore, only orbital phase is adjusted. A Hohmann-type

Content from this work may be used under the terms of the Creative Commons Attribution 3.0 license. Any further distribution of this work must maintain attribution to the author(s) and the title of the work, journal citation and DOI. Published under license by Materials Research Forum LLC.

Materials Research Proceedings 69 (2026) 1140-1145 https://doi.org/10.21741/9781644904251-196

phasing maneuver is employed, including a sub- and a super-synchronous transfer, illustrated respectively in Fig. 1(a) and Fig. 1(b).



(a) *Sub-synchronous transfer* (b) *Super-synchronous transfer*

Figure 1: Phasing maneuver strategies. M denotes the Moon, A represents the perilune, and B and C indicate the target positions.

When the phase angle between the target position and the perilune satisfies $\theta_{AB} \leq 180°$, the sub-synchronous transfer is performed. The satellite enters a transfer orbit with lower attitude applying an impulse in the direction opposite the velocity at the perilune. After completing an integer number of revolutions, the satellite returns to original orbit using an equal impulse. Define t_{AB} as the time taken to move from A to B along the original orbit. Then the period of the transfer orbit can be calculated by

$$T_{sub} = T_0 - \frac{\Delta t_{AB}}{W} \tag{1}$$

where T_0 presents the period of the original orbit, and W represents the number of revolutions in the transfer orbit. The total velocity increment Δv_1 of two maneuvers can be given by

$$\Delta v_1 = 2|v_{Asub} - v_{A0}| \tag{2}$$

where v_{Asub} and v_{A0} represent the velocities of the perilune in the transfer orbit and the original orbit, respectively. The total duration of the transfer process is

$$\Delta t_1 = W \cdot T_{tran1} \tag{3}$$

When the phase angle satisfies $\theta_{AC} > 180°$, the super-synchronous transfer is employed. In this case, the satellite requires an accelerating impulse to change to a higher-altitude transfer orbit. Define t_{AC} as the time taken to move from A to C along the original orbit. Then, the period of the transfer orbit is

$$T_{super} = \frac{W+1}{W} T_0 - \frac{\Delta t_{AC}}{W} \tag{4}$$

The velocity increment Δv_2 and transfer duration Δt_2 can be determined in the same way as the previous case.

Materials Research Proceedings 69 (2026) 1140-1145 https://doi.org/10.21741/9781644904251-196

Optimization Model

Optimization Variables.

In the initial step of the reconfiguration, only the phases need to be adjusted. Therefore, the optimization variables and their bounds are

$$\begin{aligned} &x_{\mathrm{SH1}} = (\theta_i, W_i)^T, i = 1,2,\cdots, N_{\mathrm{SP}}, \\ &x_{\mathrm{SH1}lb} = (0° \times N_{\mathrm{SP}}, 1 \times N_{\mathrm{SP}})^T, x_{\mathrm{SH1}hb} = (360° \times N_{\mathrm{SP}}, 3 \times N_{\mathrm{SP}})^T \end{aligned} \tag{5}$$

where N_{SP} denotes the number of satellites in previous research [8].

In the second phase, the optimization focuses on orbital parameters of the new satellites. Consequently, both the orbital inclinations $incline_i$ and eccentricities e_i are considered as independent variables, and the allowable range for the perigee arguments ω_i is extended.

$$\begin{aligned} &x_{\mathrm{SH2}} = (incline_i, e_i, \omega_i, \Omega_i, \theta_i)^T, i = 1,2, \\ &x_{\mathrm{SH2}lb} = (0° \times N_{\mathrm{SH}}, 1 \times N_{\mathrm{SH}})^T, x_{\mathrm{SH2}hb} = (360° \times N_{\mathrm{SH}}, 3 \times N_{\mathrm{SH}})^T \end{aligned} \tag{6}$$

where Ω_i and θ_i represent the right ascension of the ascending node and the true anomaly, respectively.

Objective Functions.

Two coverage performance metrics $Cov2_i$, $Cov4_i$, and two navigation performance metrics $PerHDOP_i$, $PerGDOP_i$ are applied. Denote SP as the region spanning latitudes 70°S to 90°S, while SH as the region from 0°S to 70°S. In the phasing maneuver stage, the fuel consumption and reconfiguration time are also included as optimization objectives. As a result, there are seven optimization objectives for the first phase: $Cov4_{\mathrm{SP}}$, $PerHDOP_{\mathrm{SP}}$, $PerGDOP_{\mathrm{SP}}$, $Cov2_{\mathrm{SH}}$, $Cov4_{\mathrm{SH}}$, $\sum \Delta v_i$, $\max(\Delta t_i)$. The objective functions for the second phase are $Cov4_{\mathrm{SP}}$, $PerHDOP_{\mathrm{SP}}$, $PerGDOP_{\mathrm{SP}}$, $Cov2_{\mathrm{SH}}$, $Cov4_{\mathrm{SH}}$, $PerHDOP_{\mathrm{SH}}$.

Results

The optimization is based on two constellation schemes designed for lunar SP region in previous work, whose performance metrics are listed in Table 1.

Table 1: Performance metrics of constellation schemes targeting South Pole

Schemes	$Cov4_{\mathrm{SP}}$	$PerHDOP_{\mathrm{SP}}$	$PerGDOP_{\mathrm{SP}}$	$Cov2_{\mathrm{SH}}$	$Cov4_{\mathrm{SH}}$
SP_E	100%	91.03%	49.02%	61.23%	0%
SP_F	100%	94.91%	67.53%	80.73%	0%

The NSGA-II (Elitist Non-dominated Sorting Genetic Algorithm) method is used to optimize the model in last section. The sub-Pareto fronts are shown in Fig. 2. Compared to Table 1, most of the solutions in Fig. 2(a) and Fig. 2(b) no longer satisfy the continuous four-fold coverage over SP. Additionally, the navigation performance exhibit significant degradation. Solutions SH1_A and SH1_B in Fig. 2(c) achieve the highest $Cov2_{\mathrm{SH}}$ while maintaining 100% $Cov4_{\mathrm{SP}}$. However, the improvement in $Cov2_{\mathrm{SH}}$ compared to SP_E and SP_F is marginal, and the $PerGDOP_{\mathrm{SP}}$ deteriorates by over 15%. Similarly, solutions SH1_C and SH1_D in Fig. 2(d) reach the highest $Cov4_{\mathrm{SH}}$ while also ensuring 100% $Cov4_{\mathrm{SP}}$. But their $Cov2_{\mathrm{SH}}$ drops by more than 28%, and the navigation performances for SP are severely compromised. It is evident that none of these four representative points can be considered as the final solutions. Fig. 2(e) illustrates an inverse correlation between $Cov2_{\mathrm{SH}}$ and $Cov4_{\mathrm{SH}}$. Dual coverage is the most urgent requirement in the first

Materials Research Proceedings 69 (2026) 1140-1145 https://doi.org/10.21741/9781644904251-196

stage, so solution SH1_E with the highest $Cov2_{SH}$ is selected. As shown in Fig. 2(f), the velocity increment remains below 0.25 km/s, and the maximum maneuver duration does not exceed 83 hours, which is a positive outcome in terms of both efficiency and energy consumption.

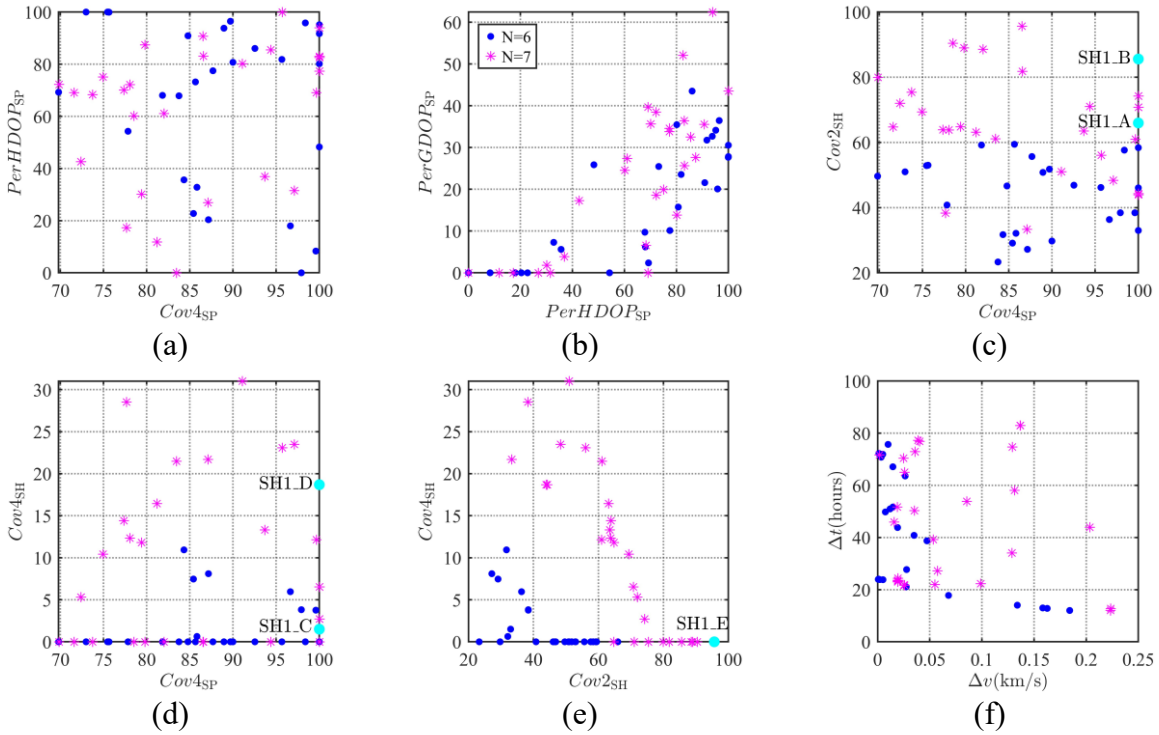
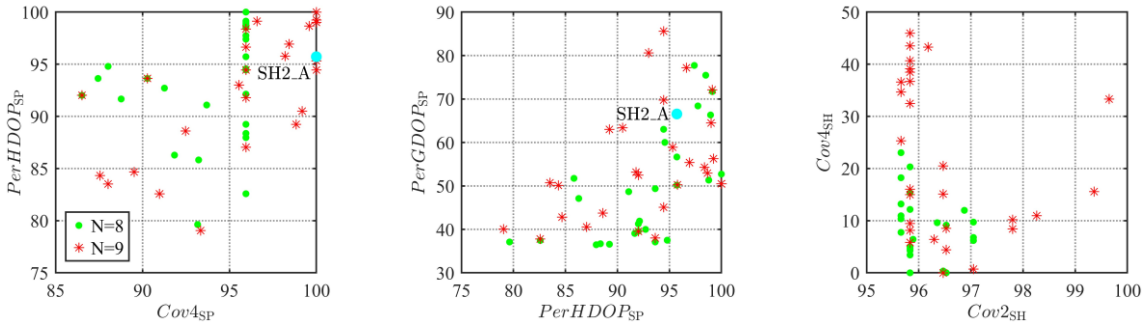


Figure 2: The Optimization Pareto fronts of the first stage of reconfiguration. N represents the number of the satellites.

The performance metrics of solution SH1_E $Cov4_{SP}$, $PerHDOP_{SP}$, $PerGDOP_{SP}$, and $Cov2_{SH}$ are 86.52%, 90.74%, 35.53%, and 95.66%, respectively. It can be observed that SH1_E exhibits performance decline over the SP region compared to SP_F. Therefore, in the second phase, the new satellites are added to restore the performance in SP regions. The second sub-Pareto fronts are illustrated in the Fig. 3. As seen in Fig. 3(a) and Fig. 3(b), significant improvements are observed in the performances for SP region. According to Fig. 3(c), the $Cov2_{SH}$ of all solutions maintains no lower than 95.66%. By comparing five candidate solutions satisfying 100% $Cov4_{SP}$ and better $PerHDOP_{SP}$ than SP_F, scheme SH2_A with highest $PerGDOP_{SP}$ and $PerHDOP_{SH}$ is chosen as the final solution.

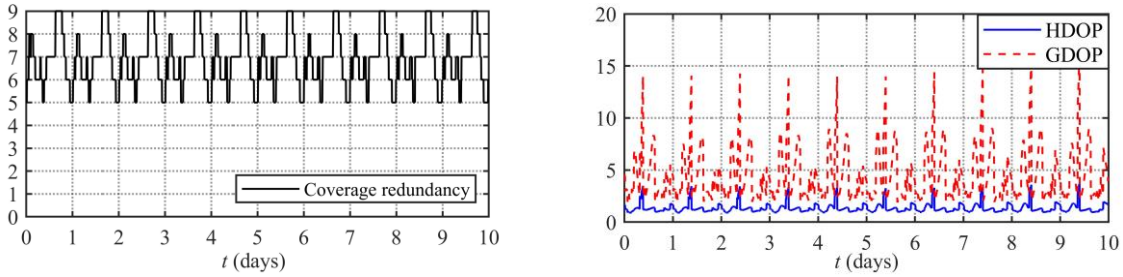
To evaluate the service capability, the coverage and navigation performance at the South Pole are shown in Fig. 4. From Fig. 4(a), it can be seen that the coverage redundancy at the south pole always exceeds five-fold, which implies superior navigation performance. This is further validated by Fig. 4(b). During the 10-day simulation period, the HDOP at the south pole remains below 5, while the GDOP stays below 10 for the most of time. These values indicate that scheme SH2_A can provide precise navigation support for most lunar missions at South Pole.

Materials Research Proceedings 69 (2026) 1140-1145 https://doi.org/10.21741/9781644904251-196



(a) (b) (c)

Figure 3: The Optimization Pareto fronts of the second stage of reconfiguration. Only three sub-Pareto fronts are shown here. N=8 and N=9 represent the addition of one or two satellites, respectively.



(a) *Coverage redundancy at South Pole.* (b) *HDOP and GDOP at South Pole.*

Figure 4: Coverage and navigation performance of SH2_A at South Pole. The simulation time is chosen as 10 days.

Conclusion

Based on the constellation schemes targeting the South Pole, this work applies the reconfiguration to extend the service area to the entire Southern Hemisphere. In the first stage, Hohmann-type phasing maneuvers are employed to adjust the phases of in-orbit satellites, with optimization for minimizing fuel and time consumption. Selected scheme SH1_E is able to achieve over 95% dual coverage across the Southern Hemisphere. In the second stage, one to two new satellites in non-frozen orbits are deployed to restore continuous four-fold coverage over the South Pole region.

Acknowledgments

This work was supported by the China Scholarship Council (CSC).

References

[1] K. Bhasin, A. Hackenberg, R. Slywczak, P. Bose, M. Bergamo, J. Hayden, Lunar relay satellite network for space exploration: architecture, technologies and challenges, in: 24th AIAA International Communications Satellite Systems Conference, AIAA, San Diego, California, 2006, p. 5363. https://doi.org/10.2514/6.2006-5363

[2] C. Circi, D. Romagnoli, F. Fumenti, Halo orbit dynamics and properties for a lunar global positioning system design, Monthly Notices of the Royal Astronomical Society. 442 (2014) 3511-3527. https://doi.org/10.1093/mnras/stu1085

[3] G. Zanotti, M. Ceresoli, A. Pasquale, J. Prinetto, M. Lavagna, High performance lunar constellation for navigation services to moon orbiting users, Advances in Space Research. 73 (2024) 5665-5679. https://doi.org/10.1016/j.asr.2023.03.032

[4] M. Ferringer, D. Spencer, R. Clifton, T. Thompson, P. Reed, Pareto-hypervolumes for the reconfiguration of satellite constellations, in: AIAA/AAS Astrodynamics Specialist Conference and Exhibit, AIAA, Honolulu, Hawaii, 2008, p. 6611. https://doi.org/10.2514/6.2008-6611

[5] D. Arnas, R. Linares, Uniform satellite constellation reconfiguration, Journal of Guidance, Control, and Dynamics. 45 (2022), 1241-1254. https://doi.org/10.2514/1.G006514

[6] O.L. De Weck, U. Scialom, A. Siddiqi, Optimal reconfiguration of satellite constellations with the auction algorithm, Acta Astronautica. 62 (2008), 112-130. https://doi.org/10.1016/j.actaastro.2007.02.008

[7] A.N. Straub, D.E. Hastings, D.W. Miller, O.L. De Weck, Deployment strategies for reconfigurable satellite constellations, in: ASCEND 2020, AIAA, VirtualEvent, 2020, p. 4246. https://doi.org/10.2514/6.2020-4246

[8] S. Yang, R. Zhong, Optimization method for lunar navigation satellite constellation targeting south pole, in: L. Yan, H. Duan, Y. Deng (Eds.), Advances in Guidance, Navigation and Control, Springer Nature Singapore, 2025, pp. 495-504. https://doi.org/10.1007/978-981-96-2248-1_48

Materials Research Proceedings 69 (2026) 1146-1152 https://doi.org/10.21741/9781644904251-197

Multi-Hitchhiking Strategies Using Advanced Tether Materials for Enhanced Deep Space Exploration

Valentina NASTI[1,2,a *], Giorgio ISOLETTA[3,b], Giancarmine FASANO[3,c] and Michele GRASSI[3,d]

[1]Scuola Superiore Meridionale SSM, Largo San Marcellino 10, 80138 Napoli (NA), Italy

[2]INFN Napoli, Via Vicinale Cupa Cintia, 26, 80126 Napoli (NA), Italy

[3]Department of Aerospace Engineering, Università degli Studi di Napoli Federico II, Piazzale Tecchio 80, 80125 Napoli (NA), Italia

[a]va.nasti@ssmeridionale.it, [b]giorgio.isoletta@unina.it, [c]g.fasano@unina.it, [d]grassi@unina.it

Keywords: Asteroid Exploration, Momentum Exchange, Advanced Tether Materials, Multi-Target Missions

Abstract. This study presents a comprehensive analysis of tether-assisted hitchhiking, an innovative propellant less technique that leverages momentum exchange through deployable tethers for asteroid and comet missions. Seven advanced materials are analyzed using the Space Hitchhike Equation framework, with multi-hop degradation modeling across radiation, thermal cycling, and micrometeoroid impacts. Results show that CNT150 provides 10.4 km/s ΔV capability, while Zylon offers near-term mission readiness at 1.9 km/s. Mission scenarios from Near-Earth Object tours (2 km/s) to Kuiper Belt exploration (10 km/s) validate scalability, demonstrating mass efficiency improvements over chemical propulsion.

Introduction

Conventional orbital maneuvering fundamentally relies on the rocket equation, where propellant mass fraction dominates mission architecture. For multi-target exploration requiring cumulative $\Delta V > 10$ km/s, propellant mass exceeds 90% of initial spacecraft mass, severely limiting payload capacity and mission scope. Space hitchhiking introduces a paradigmatic shift: momentum exchange with celestial bodies through temporary mechanical coupling via deployable tethers eliminates propellant dependency entirely[1]. During close approach to an asteroid or comet, a spacecraft deploys a high-strength tether that grapples the target body. Controlled differential velocity between spacecraft and body generates a tension force that decelerates the spacecraft thanks to tether retrieval. Elastic energy storage in the tether material is subsequently converted to electrical energy via a regenerative braking system, enabling propellantless ΔV accumulation across multiple encounters. Tether technology heritage includes several flight demonstrations: TSS-1, SEDS-1/2, YES2. However, these systems focused on single-use Earth-centric operations with Kevlar-class materials[2]. Recent advances in carbon nanotube (CNT) synthesis enable fiber production with tensile strengths exceeding 100 GPa in laboratory settings, though scalability challenges persist. While previous research has explored individual aspects of tether-based propulsion, no prior work comprehensively addresses the integration of multi-hop mission architectures with cumulative degradation modeling, regenerative energy harvesting systems, material trade-space analysis spanning candidates from TRL 4 through TRL 9[3], [4], and outer Solar System mission feasibility assessment. This study provides a comprehensive assessment of these aspects through physics-based modeling and performance simulation across mission scenarios ranging from Near-Earth Objects to Kuiper Belt Objects.

Content from this work may be used under the terms of the Creative Commons Attribution 3.0 license. Any further distribution of this work must maintain attribution to the author(s) and the title of the work, journal citation and DOI. Published under license by Materials Research Forum LLC.

Materials Research Proceedings 69 (2026) 1146-1152 https://doi.org/10.21741/9781644904251-197

Methodology

For this analysis, a uniform tether geometry is assumed, with L = 1000 m and A = 1×10^{-5} m² (1 cm² cross-section) across all materials, resulting in material-specific tether masses ranging from 13.5 kg (CNT-fiber) to 22.0 kg (Graphene), for the baseline 500 kg spacecraft configuration. The fundamental governing equation for achievable ΔV derives from energy conservation during tether-assisted braking. The analysis framework was implemented in Python using a modular library architecture, with numerical computations performed via *NumPy* and results visualized through *Matplotlib*. The code base includes dedicated modules for material characterization, tether dynamics, PMSG performance modeling, and degradation analysis across multi-hop mission profiles. For a spacecraft of mass m_0 (excluding tether) coupled via tether of mass m_t to an asteroid of mass $M_a \gg (m_0 + m_t)$:

$$\Delta V = \sqrt{\frac{\sigma}{\rho}} \cdot \sqrt{1 - \left(\frac{m_0}{M}\right)^2}. \quad (1)$$

where σ is material tensile strength [Pa], ρ is density [kg/m³], M = $m_0 + m_t$ is total system mass, and the term $\sqrt{\frac{\sigma}{\rho}}$ represents material-specific velocity—the theoretical maximum ΔV achievable as $m_t \to \infty$ [1]. During braking, kinetic energy converts to elastic potential energy stored uniformly across tether length L. For a uniform tether under maximum allowable stress σ_{max}/SF (SF = safety factor = 2.0)[5], integration yields Eq. 1. The mass efficiency factor in the Eq. 2

$$\eta_m = \sqrt{1 - \left(\frac{m_0}{M}\right)^2}. \quad (2)$$

quantifies the fraction of material-specific velocity achievable for a given tether-to-spacecraft mass ratio. Optimal performance occurs when $m_t \approx m_0$, yielding $\eta_m = 0.87$ (87% efficiency).
Seven candidate materials spanning TRL 4-9 were analyzed:

Table 1. Materials description and properties. [5], [6], [9], [10], [11], [12], [13], [14], [15].

Material	σ [GPa]	ρ [kg/m³]	ΔV_{max} [km/s]	TRL
Kevlar-49	3.0	1440	1.44	9
Zylon	5.8	1560	1.93	8
Graphene	3.54	1500	1.54	4
CNT-fiber	8.8	1450	2.46	6
MWNT	35	1450	4.91	5
SWNT	85	1400	7.79	4
CNT150	150	1400	10.35	4

- *Flight-Ready Materials*: Kevlar-49 represents baseline technology with extensive space heritage but limited ΔV capability (1.44 km/s). Zylon offers 34% performance improvement (1.93 km/s) with demonstrated Mars mission applications (airbag systems), positioning it as optimal near-term candidate. [7]
- *Developmental Materials*: Commercial CNT-fiber (TRL 6) offers intermediate performance between polymer and advanced nanotube options, achieving 2.46 km/s with 1 km production capability—sufficient for demonstration missions. Multi-wall (MWNT) and single-wall (SWNT) nanotubes provide 4.91 km/s and 7.79 km/s respectively, enabling Main Belt and

Materials Research Proceedings 69 (2026) 1146-1152 https://doi.org/10.21741/9781644904251-197

Centaur exploration but requiring production scalability development (current: 100 m and 10 m lengths) [8], [9].

CNT150 represents a laboratory-scale achievement with 150 GPa tensile strength in 1-meter samples, offering 10.35 km/s capability sufficient for Kuiper Belt missions. However, its TRL 4 status necessitates a 15–20-year development timeline[11]. A Permanent Magnet Synchronous Generator (PMSG) has been selected for kinetic energy conversion based on several advantages: elimination of excitation power requirements through permanent magnet design, high efficiency (92-97%), vacuum compatibility, and compact architecture with specific power of 50-100 W/kg for space-rated systems. The linear regenerative configuration with an insulated tether equipped with permanent magnets provides superior thermal management for critical high-ΔV maneuvers compared to induction-based alternatives. The generator produces back electromotive force opposing rotation, which creates electromagnetic braking torque[12]. The resulting power output scales with both stator current and angular velocity. Energy losses occur across multiple subsystems: copper losses in generator windings dominate at 40-50% of total dissipation due to resistive heating, iron losses contribute 10-20% through hysteresis and eddy currents, mechanical losses remain negligible (<1%) in vacuum, and power electronics inverter losses from switching transitions and conduction resistance account for 15-25%. The cascade of component efficiencies—generator (95%), inverter (97%), and energy storage (98%)—yields an overall system efficiency of 90.2%. Tether lifetime in multi-hop missions requires degradation analysis:

- *Radiation Exposure*: Cumulative dose varies by trajectory—Main Belt: 2 Mrad over 20 hops; Jupiter region: 10 Mrad (exceeds CNT tolerance limit of 10 Mrad but within Kevlar's 200 Mrad). Strength retention is modeled as in the Eq. 3:

$$\sigma(D) = \sigma_0 e^{-\frac{D}{D_0}}. \quad (3)$$

where D_0 is characteristic damage dose [19], [20].

- *Thermal Cycling*: Each hop induces thermal transient from ambient (300 K) to peak (400-600 K depending on braking duration and material). Polymer degradation: Kevlar retains 60% strength after 100 cycles; Zylon: 74%; CNT-fiber: 90%.
- *Micrometeoroid Impact*: modeled with probabilistic model in the Eq. 4

$$P_{impact}(t) = 1 - e^{-\lambda A t}. \quad (4)$$

where $\lambda = 10^{-6}$ m^{-2}yr^{-1} (Main Belt flux), A is the tether cross-sectional area [21].

Over a 20-year mission duration, impact probability is approximately 65% for Main Belt operations, compared with around 12% for Centaur and Kuiper Belt trajectories. Fig. 1 reveals a stark performance dichotomy. Polymer materials exhibit catastrophic UV-driven degradation, collapsing to <30% retention after 1-2 hops—rendering them non-viable for multi-hop architectures. In contrast, advanced CNT materials (MWNT, SWNT, CNT150) display gradual, predictable degradation at rates 6-7× slower, maintaining >60% strength retention over 15-20 hops. This fundamental material boundary defines the transition from single-encounter demonstrations to sustained deep-space exploration campaigns.

Materials Research Proceedings 69 (2026) 1146-1152 https://doi.org/10.21741/9781644904251-197

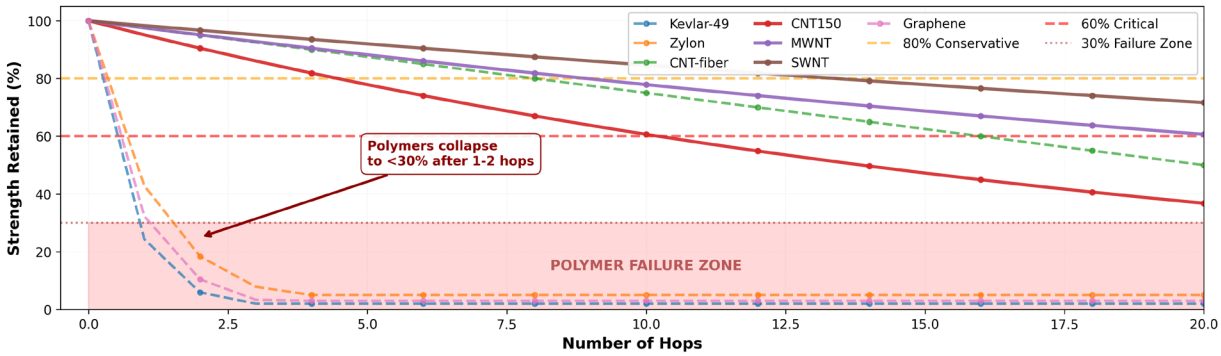


Fig. 1: Multi-hop degradation analysis.

Results

Fig. 2 presents Eq.1 performance across the mass ratio spectrum. CNT150 maintains >10 km/s capability until $m_0/M < 0.3$, while Kevlar-49 achieves ~ 1.44 km/s only for $m_0/M<0.5$.

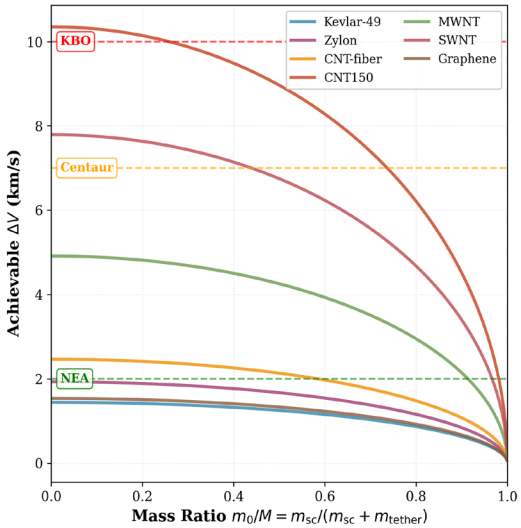


Fig. 2: Space Hitchhike Equation: achievable ΔV capabilities vs. mass ratio m_0/M for all materials, showing mission target thresholds (NEA, MBA, Centaur, KBO).

The computational analysis evaluates seven tether materials across 20 sequential hitchhike maneuvers, incorporating progressive strength degradation from radiation (dose-dependent exponential decay), UV exposure, thermal cycling, and micrometeoroid impacts. [15]
To be conservative, for each hop *i*, the strength retention factor, SRF_i, defined in Eq. 5

$$SRF_i(material) = min(SRF_{rad}, SRF_{UV}, SRF_{thermal}, SRF_{mmod}). \quad (5)$$

determines the degraded tensile strength, $\sigma_{degraded_i}$,

$$\sigma_{degraded_i} = \sigma_0 \times SRF_i. \quad (6)$$

which feeds into Eq.1 to calculate the available ΔV_i as

$$\Delta V_i = \sqrt{\frac{\sigma_{degraded_i}}{\rho}} \times \sqrt{\left[1 - \left(\frac{m_0}{M}\right)^2\right]}. \quad (7)$$

Cumulative ΔV budgets emerge from summation:

$$\Delta V_{total} = \sum_i^n \Delta V_i \, . \quad (8)$$

Results reveal critical material-dependent limitations driven by UV radiation: high-performance polymers (Kevlar, Zylon, Graphene) exhibit few or none viable hops due to catastrophic strength

Materials Research Proceedings 69 (2026) 1146-1152 https://doi.org/10.21741/9781644904251-197

loss (>50%) within the first hop cycle, despite adequate initial ΔV capacity (1.4-1.9 km/s). CNT-based materials demonstrate superior survivability [16]: CNT150 achieves 43.5 km/s cumulative over 20 hops (99+ hop theoretical maximum), MWNT delivers 24.2 km/s (22 hop limit), and SWNT provides 30.8 km/s (99+ hops), with radiation damage as the dominant long-term failure mechanism (D_{50} = 4-8 Mrad)[16].

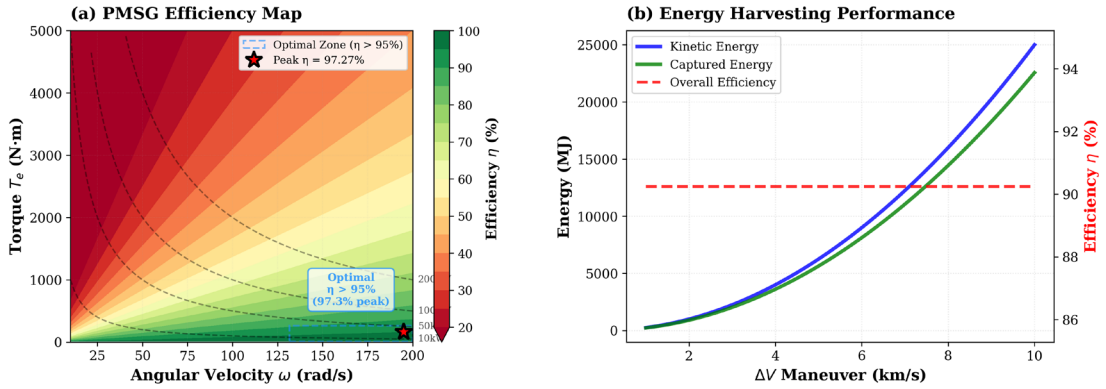


Fig. 3: PMSG regenerative braking system performance.

PMSG efficiency mapping identifies an optimal operating region at 125-200 rad/s and 200-1200 N·m (blue dashed zone, Fig. 3a), achieving peak efficiency of 97.3% with η > 95% throughout. Low-speed (<50 rad/s) and high-torque (>3000 N·m) regimes exhibit <60% efficiency due to fixed iron losses and excessive copper losses dominating, respectively. Energy harvesting maintains 90.2% overall efficiency across 1-10 km/s ΔV range, with captured energy scaling quadratically. The power-time trade-off demonstrates that extended braking strategies address both thermal management and mission operational requirements simultaneously, offering design flexibility across the mission complexity spectrum. TRL-performance scatter in Fig. 4 reveals critical trade-space: Kevlar-49, at TRL 9, offers immediate flight readiness, but its 1.4 km/s capability limits missions to NEA-class targets. Zylon (TRL 8, with 1.9 km/s capability) supports extension to MBA scenarios with minimal development risk. CNT-fiber (TRL 6, 2.5 km/s) requires 5-7 year maturation but enables comprehensive NEA campaigns. Advanced CNT materials (SWNT, CNT150) provide >7 km/s for Centaur/KBO missions but necessitate 10-20 year development timelines [3], [4], [17].

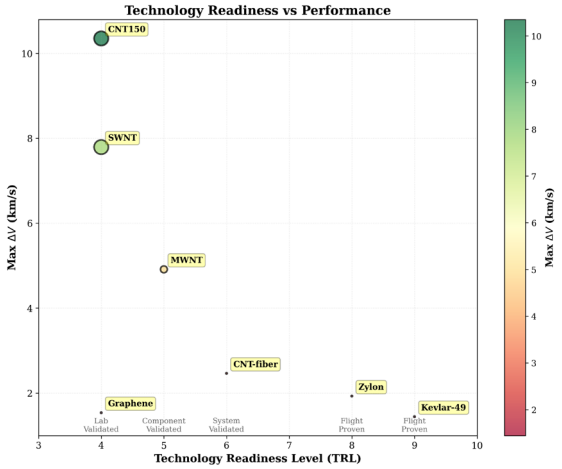


Fig.4: Technology readiness vs. performance: TRL assessment mapped against maximum achievable ΔV, with bubble size indicating max hops before 60% strength degradation threshold.

Conclusion

This analysis demonstrates that tether-assisted hitchhiking enables propellantless multi-target exploration through momentum exchange, with material selection critically determining mission scope. Flight-ready polymers (Kevlar, Zylon) support Near-Earth Object campaigns but exhibit UV-dominated degradation, limiting operational lifetime to <10 hops. CNT-based architectures unlock Main Belt and outer Solar System exploration with cumulative ΔV budgets exceeding 40 km/s over 20 hops, though thermal management and radiation tolerance remain critical design constraints. The identified TRL-performance trade-space provides mission planners with quantitative criteria for material selection aligned with scientific objectives, development timelines, and risk tolerance. Progressive PMSG efficiency validates the regenerative energy harvesting approach, establishing hitchhiking as a scalable paradigm for sustainable, long-duration exploration architectures that transcend conventional propellant limitations.

References

[1] M. Ono et al., Comet Hitchhiker NIAC Phase I Final Report, (2015). Information on https://www.nasa.gov/directorates/spacetech/niac/2015_Phase_I_Phase_II/Comet_Hitchhiker/

[2] M. Cosmo, E.C. Lorenzini, Smithsonian Astrophysical Observatory, Tethers in Space Handbook, third ed., 1997.

[3] Appendix G: Technology Assessment / Insertion, in: NASA (2012) Technology Readiness Assessment (TRA), Rev 2., vol. NASA/SP-2007-6105, 2012. Information on https://soma.larc.nasa.gov/SIMPLEx/pdf_files/NASA-SP-2016-6105-Rev2.pdf

[4] J.C. Mankins, Technology readiness assessments: A retrospective, Acta Astronaut. 65 (2009) 1216-1223. https://doi.org/10.1016/j.actaastro.2009.03.058

[5] NASA-STD-5001B, Structural Design and Test Factors of Safety for Spaceflight Hardware NASA Technical Standards System. Information on https://standards.nasa.gov/standard/NASA/NASA-STD-5001

[6] TOBOYO, TOBOYO MATERIAL SAFETY DATA SHEET. Information on https://www.toyobo-global.com/seihin/kc/pbo/zylon-p/bussei-p/sds.pdf

[7] DuPontTM, Kevlar® Properties. Information on https://www.dupont.com/news/kevlar-properties.html

[8] M. Zhang, K.R. Atkinson, R.H. Baughman, Multifunctional Carbon Nanotube Yarns by Downsizing an Ancient Technology, Science 306 (2004) 1358-1361. https://doi.org/10.1126/science.1104276

[9] M.-F. Yu, O. Lourie, M.J. Dyer, K. Moloni, T.F. Kelly, R.S. Ruoff, Strength and Breaking Mechanism of Multiwalled Carbon Nanotubes Under Tensile Load, Science 287 (2000) 637-640. https://doi.org/10.1126/science.287.5453.637

[10] B.G. Demczyk et al., Direct mechanical measurement of the tensile strength and elastic modulus of multiwalled carbon nanotubes, Materials Science and Engineering: A 334 (2002) 173-178. https://doi.org/10.1016/S0921-5093(01)01807-X

[11] M.F.L. De Volder, S.H. Tawfick, R.H. Baughman, A.J. Hart, Carbon Nanotubes: Present and Future Commercial Applications, Science 339 (2013) 535-539. https://doi.org/10.1126/science.1222453

[12] J.F. Gieras, M. Wing, Permanent magnet motor technology: design and applications, second ed., 2013.

[13] L.W. Townsend, Implications of the space radiation environment for human exploration in deep space, Radiat. Prot. Dosimetry 115 (2005) 44-50. https://doi.org/10.1093/rpd/nci141

[14] ESA/BISA, Space Environment Information System. Information on https://www.spenvis.oma.be/

[15] E.L. Christiansen, Meteoroid/Debris Shielding, in: NASA/TP-2009-214785, 2009. Information on https://www.researchgate.net/publication/24294569_MeteoroidDebris_Shielding

[16] A.V. Krasheninnikov, K. Nordlund, Ion and electron irradiation-induced effects in nanostructured materials, J. Appl. Phys. 107 (2010). https://doi.org/10.1063/1.3318261

[17] J.A. Dever, S.K. Miller, E.A. Sechkar, T.N. Wittberg, Space Environment Exposure of Polymer Films on the Materials International Space Station Experiment: Results from MISSE 1 and MISSE 2, High Perform. Polym. 20 (2008) 371-387. https://doi.org/10.1177/0954008308089704

Materials Research Proceedings 69 (2026) 1153-1157 https://doi.org/10.21741/9781644904251-198

A Compensation Strategy for Cases of Divergence in Angle of Arrival Measurements Due to Satellite Attitude

Marcello ASCIOLLA[1,a *], Angela CRATERE[1,b] and Francesco DELL'OLIO[1,c]

[1]Politecnico di Bari, Via Orabona 4, 70126, Bari, Italy

[a]m.asciolla@phd.poliba.it, [b]a.cratere@phd.poliba.it, [c]francesco.dellolio@poliba.it

Keywords: Angle of Arrival (AOA), Attitude Determination and Control System (ADCS), Attitude, Cramér-Rao Lower Bound (CRLB), Error Divergence, Error Compensation, Error Modelling, Satellite, Space Systems

Abstract. The study is on satellite systems for localization purposes. The platform of interest is a satellite system equipped with antenna array payload able to perform Angle of Arrival (AOA) measurements. The framework is on the possible interaction and mutual influence between two subsystems: the Attitude Determination and Control System (ADCS) and a payload composed of 3D antenna arrays. The paper wants to investigate the effects of the attitude of the satellite on the payload measurement and it focuses on the propagation of the attitude errors on the payload measurement error. In particular, it has been observed that in some relative configurations it is possible to have an unwanted divergence of the measurements: its prediction and compensation is of crucial interest both for Earth scanning operations and interplanetary missions. The methodology follows the analytical formulation of the problem of geolocation, through the measurement equation and performance metrics based on Cramér Rao Lower Bound (CRLB) for its variance. Then, combining the attitude of the satellite with the relative position of the emitter of signal with respect to the satellite platform, the reveal of cases of divergence is exposed. The novelty of the study is on the proposal of a scheme of compensation for such cases of divergence in order to obtain a reliable measurement considering only the data available onboard. The study is of interest for a set of future algorithms for miniaturized payload systems composed of sensors based on antenna arrays. Potential target satellite missions are on, but not limited to, search and rescue, telecommunication, and spectrum monitoring of jamming signals for civil aviation in E1/L1 GNSS band. The exemplary use-case scenario presented in the study involves an emitter of electromagnetic waves on the surface of the Earth and a satellite system with tri-axial antenna array as sensing equipment. Despite the toy model of the study is on Earth missions, the approach and results are generalizable and of interest also for any manned and unmanned interplanetary missions that have to deal with the influence of ADCS on 3D antenna array payloads.

Mathematical Model for Satellite-Based Geolocation

The starting point of the study is the problem of the geolocation of the position of a source of electromagnetic waves $\mathbf{x}_E$ by a satellite platform placed in $\mathbf{x}_S$ with Angle of Arrival (AOA) technology [1].

In order to perform this operation, the onboard algorithm must perform the workflow depicted in Figure 1; the operations are based on common representation of data in astrodynamics [2].

Content from this work may be used under the terms of the Creative Commons Attribution 3.0 license. Any further distribution of this work must maintain attribution to the author(s) and the title of the work, journal citation and DOI. Published under license by Materials Research Forum LLC.

Materials Research Proceedings 69 (2026) 1153-1157 https://doi.org/10.21741/9781644904251-198

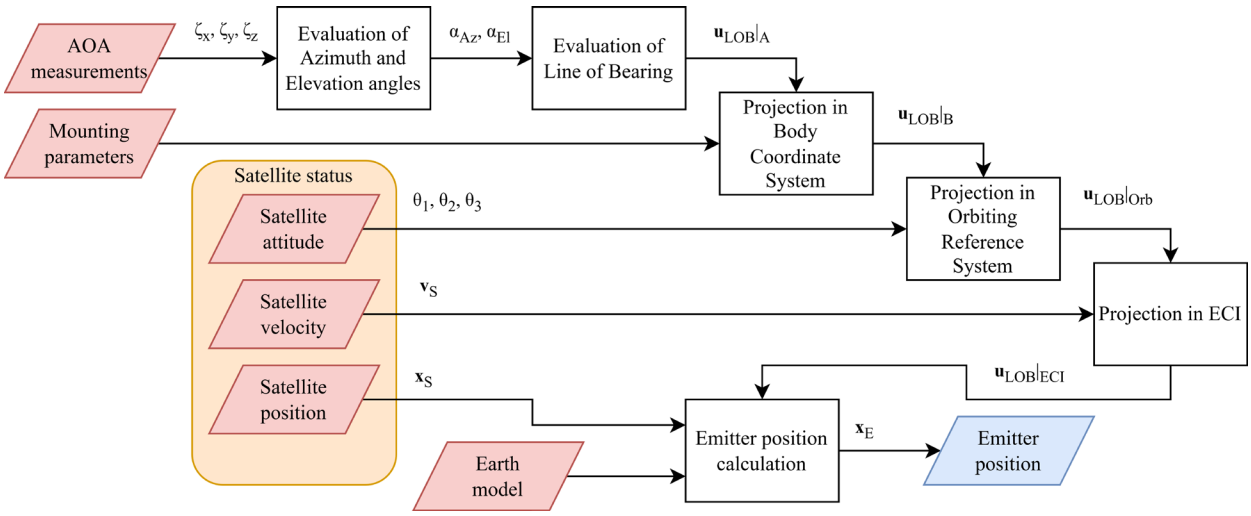


Figure 1 – Scheme of geolocation of the position an electromagnetic emitter of signal x_E from a satellite platform placed in x_S.

Each sensing array calculates its bearing angle ζ_x, ζ_y, ζ_z, which geometrically can be defined as the dot product between the Line of Bearing (LOB) $\mathbf{u}_{LOB}$ and the unit vectors of the arrays $\mathbf{u}_{Ar,x}$, $\mathbf{u}_{Ar,y}$, $\mathbf{u}_{Ar,z}$ as shown in (1).

$$\begin{cases} \cos(\zeta_x) = \mathbf{u}_{LOB} \cdot \mathbf{u}_{Ar,x} \\ \cos(\zeta_y) = \mathbf{u}_{LOB} \cdot \mathbf{u}_{Ar,y} \\ \cos(\zeta_z) = \mathbf{u}_{LOB} \cdot \mathbf{u}_{Ar,z} \end{cases} \tag{1}$$

Introducing [3] a local spherical coordinate system x_A, y_A, z_A, it is possible to define the (1) in terms of Azimuth angle α_{Az} and Elevation angle α_{El} as shown in (2).

$$\begin{cases} \cos(\zeta_x) = \mathbf{u}_{LOB}|_A \cdot \mathbf{u}_{Ar,x}|_A = \begin{pmatrix} \cos(\alpha_{Az})\cos(\alpha_{El}) \\ \sin(\alpha_{Az})\cos(\alpha_{El}) \\ \sin(\alpha_{El}) \end{pmatrix} \cdot \begin{pmatrix} 1 \\ 0 \\ 0 \end{pmatrix} = \cos(\alpha_{Az})\cos(\alpha_{El}) \\ \cos(\zeta_y) = \mathbf{u}_{LOB}|_A \cdot \mathbf{u}_{Ar,y}|_A = \begin{pmatrix} \cos(\alpha_{Az})\cos(\alpha_{El}) \\ \sin(\alpha_{Az})\cos(\alpha_{El}) \\ \sin(\alpha_{El}) \end{pmatrix} \cdot \begin{pmatrix} 0 \\ 1 \\ 0 \end{pmatrix} = \sin(\alpha_{Az})\cos(\alpha_{El}) \\ \cos(\zeta_z) = \mathbf{u}_{LOB}|_A \cdot \mathbf{u}_{Ar,z}|_A = \begin{pmatrix} \cos(\alpha_{Az})\cos(\alpha_{El}) \\ \sin(\alpha_{Az})\cos(\alpha_{El}) \\ \sin(\alpha_{El}) \end{pmatrix} \cdot \begin{pmatrix} 0 \\ 0 \\ 1 \end{pmatrix} = \sin(\alpha_{El}) \end{cases} \tag{2}$$

Unreliable Measurement and Attitude Role

A measurement of a broadside angle $\hat{\zeta}$ for a linear antenna array can be unreliable when the variance $\sigma_{\hat{\zeta}}^2$, predicted through the Cramér-Rao Lower Bound [4] and reported in (3), diverges.

$$\sigma_{\hat{\zeta}}^2 = \frac{12}{(2\pi)^2 SNR \frac{(M+1)}{(M-1)} M \left(\frac{fL}{c}\right)^2 \sin^2(\zeta)} \tag{3}$$

Materials Research Proceedings 69 (2026) 1153-1157 https://doi.org/10.21741/9781644904251-198

In the model SNR denotes the Signal-to-Noise ratio, c the speed of propagation of the signal, f the frequency of the signal. M and L denote the number of antenna elements and the length of the antenna array along the considered direction.

The divergence condition is $\sigma_{\hat{\zeta}}^2 \to \infty$ which corresponds to $1/\sin^2(\zeta) \to \infty$ or, equivalently, to $\sin(\zeta) \to 0$ and $\zeta \to 0 + k\pi$ with $k \in \mathbb{Z}$. Operatively, for models reported in (1) and (2), the condition of divergence written as $\cos(\zeta) \to \pm 1$ is of interest.

Given a certain relative configuration between the satellite position $\mathbf{x}_S$ and emitter position $\mathbf{x}_E$, this divergence can occur because the antenna array axis can be aligned to the LOB because of the satellite attitude, so it is possible to assume $\zeta = (\theta_1, \theta_2, \theta_3)$ as a first attempt of abstract model, where θ_1, θ_2, θ_3 denote the attitude angles of roll, pitch, and yaw of the satellite.

In particular, when $\hat{\zeta}_x$ results unreliable, then $\cos(\hat{\alpha}_{Az})\cos(\hat{\alpha}_{El}) \to \pm 1$ or, equivalently, $\hat{\alpha}_{Az} \to k_1\pi \cup \hat{\alpha}_{El} \to k_2\pi$ with $k_1, k_2 \in \mathbb{Z}$.

When $\hat{\zeta}_y$ results unreliable, then $\sin(\hat{\alpha}_{Az})\cos(\hat{\alpha}_{El}) \to \pm 1$ or, equivalently, $\hat{\alpha}_{Az} \to \frac{\pi}{2} + k_1\pi \cup \hat{\alpha}_{El} \to k_2\pi$ with $k_1, k_2 \in \mathbb{Z}$.

When $\hat{\zeta}_z$ results unreliable, then $\sin(\hat{\alpha}_{El}) \to \pm 1$ or, equivalently, $\hat{\alpha}_{El} \to \frac{\pi}{2} + k\pi$ with $k \in \mathbb{Z}$.

Possible Estimations of Azimuth and Elevation Angles

From the representation of data in (2) it is possible to conclude that for each pair of broadside angles an estimation of the Azimuth and Elevation angles is possible.

Given the measurements $\hat{\zeta}_x$ and $\hat{\zeta}_y$, the corresponding Azimuth and Elevation angles, denoted here with $\hat{\alpha}_{Az;x-y}$ and $\hat{\alpha}_{El;x-y}$ can be estimated through the ones reported in (4).

$$\begin{cases} \hat{\alpha}_{Az;x-y}(\hat{\zeta}_x, \hat{\zeta}_y) = \operatorname{atan2}\left(\cos(\hat{\zeta}_y), \cos(\hat{\zeta}_x)\right) \\ \hat{\alpha}_{El;x-y}(\hat{\zeta}_x, \hat{\zeta}_y) = \arccos\sqrt{\cos^2(\hat{\zeta}_x) + \cos^2(\hat{\zeta}_y)} \end{cases} \tag{4}$$

Given the measurements $\hat{\zeta}_x$ and $\hat{\zeta}_z$, the corresponding Azimuth and Elevation angles, denoted here with $\hat{\alpha}_{Az;x-z}$ and $\hat{\alpha}_{El;x-z}$ can be estimated through the ones reported in (5).

$$\begin{cases} \hat{\alpha}_{Az;x-z}(\hat{\zeta}_x, \hat{\zeta}_z) = \arccos\left(\dfrac{\cos(\hat{\zeta}_x)}{\cos\left(\arcsin\left(\cos(\hat{\zeta}_z)\right)\right)}\right) \\ \hat{\alpha}_{El;x-z}(\hat{\zeta}_z) = \arcsin(\hat{\zeta}_z) \end{cases} \tag{5}$$

Given the measurements $\hat{\zeta}_y$ and $\hat{\zeta}_z$, the corresponding Azimuth and Elevation angles, denoted here with $\hat{\alpha}_{Az;y-z}$ and $\hat{\alpha}_{El;y-z}$ can be estimated through the ones reported in (6).

$$\begin{cases} \hat{\alpha}_{Az;y-z}(\hat{\zeta}_y, \hat{\zeta}_z) = \arcsin\left(\dfrac{\cos(\hat{\zeta}_y)}{\cos\left(\arcsin\left(\cos(\hat{\zeta}_z)\right)\right)}\right) \\ \hat{\alpha}_{El;y-z}(\hat{\zeta}_y) = \arcsin(\hat{\zeta}_z) \end{cases} \tag{6}$$

Fusion of the Measurements in a Linear Model

When all the three measurements $\hat{\zeta}_x$, $\hat{\zeta}_y$, $\hat{\zeta}_z$ are reliable, then, in principle, it is possible to fuse all the estimations (4), (5), and (6). For simplicity and demonstrative purposes, in this paper a linear model with weights $w_{Az;x-y}$, $w_{Az;x-z}$, $w_{Az;y-z}$, $w_{El;x-y}$, $w_{El;x-z}$, and $w_{El;y-z}$ is assumed, as in (7).

Materials Research Proceedings 69 (2026) 1153-1157 https://doi.org/10.21741/9781644904251-198

$$\begin{cases} \hat{\alpha}_{\mathrm{Az}}(\hat{\zeta}_x, \hat{\zeta}_y, \hat{\zeta}_z) = w_{\mathrm{Az;x-y}}\hat{\alpha}_{\mathrm{Az;x-y}}(\hat{\zeta}_{\mathrm{x}}, \hat{\zeta}_y) + w_{\mathrm{Az;x-z}}\hat{\alpha}_{\mathrm{Az;x-z}}(\hat{\zeta}_{\mathrm{x}}, \hat{\zeta}_z) \\ \qquad\qquad + w_{\mathrm{Az;y-z}}\hat{\alpha}_{\mathrm{Az;y-z}}(\hat{\zeta}_y, \hat{\zeta}_z) \\ \hat{\alpha}_{\mathrm{El}}(\hat{\zeta}_x, \hat{\zeta}_y, \hat{\zeta}_z) = w_{\mathrm{El;x-y}}\hat{\alpha}_{\mathrm{El;x-y}}(\hat{\zeta}_{\mathrm{x}}, \hat{\zeta}_y) + w_{\mathrm{El;x-z}}\hat{\alpha}_{\mathrm{El;x-z}}(\hat{\zeta}_z) + w_{\mathrm{El;y-z}}\hat{\alpha}_{\mathrm{El;y-z}}(\hat{\zeta}_z) \end{cases} \tag{7}$$

The set of conditions on the weights are reported in (8).

$$\begin{cases} w_{\mathrm{Az;x-y}} + w_{\mathrm{Az;x-z}} + w_{\mathrm{Az;y-z}} = 1 \\ w_{\mathrm{El;x-y}} + w_{\mathrm{El;x-z}} + w_{\mathrm{El;y-z}} = 1 \\ 0 \le w_{\mathrm{Az;x-y}} \le 1 \\ 0 \le w_{\mathrm{Az;x-z}} \le 1 \\ 0 \le w_{\mathrm{Az;y-z}} \le 1 \\ 0 \le w_{\mathrm{El;x-y}} \le 1 \\ 0 \le w_{\mathrm{El;x-z}} \le 1 \\ 0 \le w_{\mathrm{El;y-z}} \le 1 \end{cases} \tag{8}$$

The reader can notice that $\hat{\alpha}_{\mathrm{El;x-z}}(\hat{\zeta}_z) = \hat{\alpha}_{\mathrm{El;y-z}}(\hat{\zeta}_z) = \hat{\alpha}_{\mathrm{El;z}}(\hat{\zeta}_z)$, so it is possible to consider $w_{\mathrm{El;x-z}} = w_{\mathrm{El;y-z}} = w_{\mathrm{El;z}}$, then the second equation of (7) can be rewritten as reported in (9).

$$\begin{cases} \hat{\alpha}_{\mathrm{Az}}(\hat{\zeta}_x, \hat{\zeta}_y, \hat{\zeta}_z) = w_{\mathrm{Az;x-y}}\hat{\alpha}_{\mathrm{Az;x-y}}(\hat{\zeta}_{\mathrm{x}}, \hat{\zeta}_y) + w_{\mathrm{Az;x-z}}\hat{\alpha}_{\mathrm{Az;x-z}}(\hat{\zeta}_{\mathrm{x}}, \hat{\zeta}_z) \\ \qquad\qquad + w_{\mathrm{Az;y-z}}\hat{\alpha}_{\mathrm{Az;y-z}}(\hat{\zeta}_y, \hat{\zeta}_z) \\ \hat{\alpha}_{\mathrm{El}}(\hat{\zeta}_x, \hat{\zeta}_y, \hat{\zeta}_z) = w_{\mathrm{El;x-y}}\hat{\alpha}_{\mathrm{El;x-y}}(\hat{\zeta}_{\mathrm{x}}, \hat{\zeta}_y) + 2w_{\mathrm{El;z}}\hat{\alpha}_{\mathrm{El;z}}(\hat{\zeta}_z) \end{cases} \tag{9}$$

An architectural representation of the linear fusion strategy of the model (9) is reported in Figure 2.

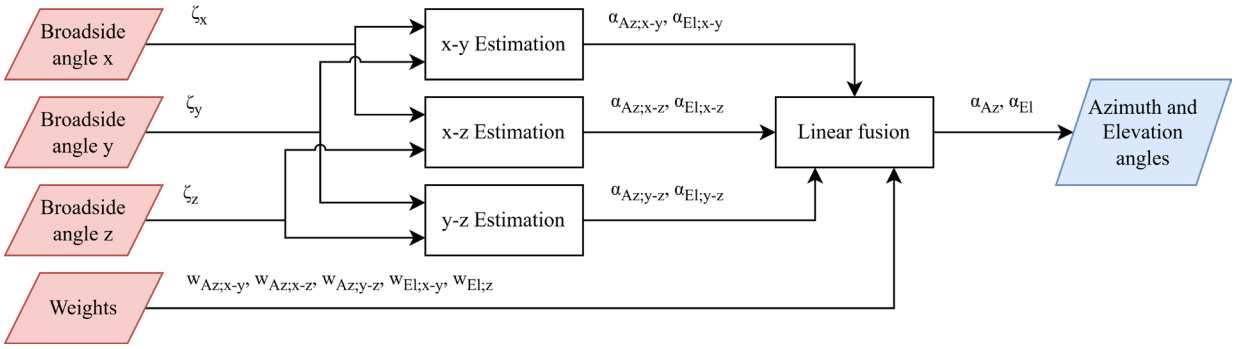


Figure 2 – Scheme of linear fusion of the measurements with weights for the calculation of Azimuth angle α_{Az} and Elevation angle α_{El}.

Management of Unreliable Measurements

Considering that an estimation of Azimuth angle and Elevation angle can be obtained even if one of the three broadside angles is unreliable, then it is possible to develop a simple scheme of reliability analysis with the selection of weights for the fusion of the measurements as reported in Figure 3. More generally, it is also possible to conceive the scheme considering the estimation of the position of the emitter of the signal as additional feedback information: in this latter case, the reliability analysis is performed considering the relative position between the satellite platform and the emitter of signal $\mathbf{x}_{\mathrm{E}} - \mathbf{x}_{\mathrm{S}}$ and the full state of the satellite.

Materials Research Proceedings 69 (2026) 1153-1157 https://doi.org/10.21741/9781644904251-198

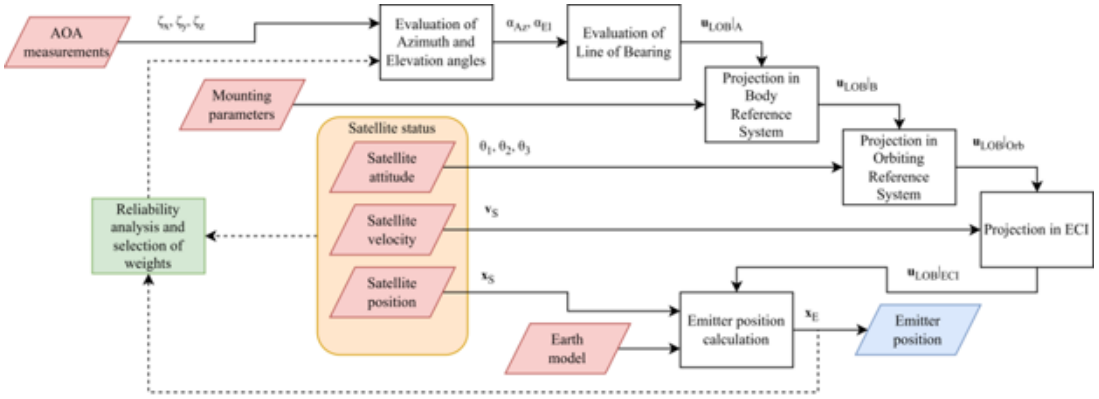


Figure 3 – Scheme of geolocation of the position an electromagnetic emitter of signal x_E from a satellite platform placed in x_S with a scheme of reliability analysis of the measurements and selection of weights for the fusion of the measurements.

Conclusions

The study presents a first level of theoretical analysis of cases of divergence of the dispersion of the measurements in space-based geolocation applications with tri-axial antenna arrays with AOA technology. The model shows that for this payload it is possible to predict and overcome the phenomenon of the divergence of the dispersion of the measurement if the current state of the satellite is available. Despite the study is restricted to a linear fusion model, an overall reliable measurement has been obtained and a compensation scheme has been presented. The validation of the method, its simulation and experimental implementation are left for future investigations.

References

[1] R. A. Poisel, Antenna Systems and Electronic Warfare Applications, Norwood, MA, USA: Artech House, 2012.

[2] V. A. Chobotov, Orbital Mechanics, Reston, VA, USA: AIAA Education Series, Cambridge University Press, 2002. https://doi.org/10.2514/4.862250

[3] G. B. Arfken and H. J. Weber, Mathematical Methods for Physicists, 30 Corporate Drive, Suite 400, Burlington, MA 01803, USA: Elsevier, Academic Press, 2005.

[4] S. M. Kay, Fundamentals of Statistical Signal Processing - Estimation Theory, Upper Saddle River, NJ, USA: Prentice Hall, Pearson, 1993.

Materials Research Proceedings 69 (2026) 1158-1163 https://doi.org/10.21741/9781644904251-199

A Multi-Constellation Approach to Space-Based RF Emissions Monitoring Through Opportunistic Satellite Cluster Collisions in LEO

Marcello ASCIOLLA[1,a *], Francesco MENZIONE[2,b], Angela CRATERE[1,c] and Francesco DELL'OLIO[1,d]

[1]Politecnico di Bari, Via Orabona 4, 70126, Bari, Italy

[2]European Commission (EC), Joint Research Centre, Space Sector, Via E. Fermi 2749, 21027, Ispra (VA), Italy

[a]m.asciolla@phd.poliba.it, [b]francesco.menzione@ec.europa.eu, [c]a.cratere@phd.poliba.it, [d]francesco.dellolio@poliba.it

Keywords: Angle of Arrival (AOA), Cramér-Rao Lower Bound (CRLB), Dilution of Precision (DOP), LEO satellites, multi-constellation, Radio Frequency Interference (RFI), RF emissions monitoring, space systems, Time Difference of Arrival (TDOA)

Abstract. The deployment of small Low Earth Orbit (LEO) satellites equipped with radio-frequency (RF) tracking sensors marks a transformative shift in global, space-based RF emissions monitoring. Leveraging cost-effective software-defined radio (SDR) technology and advanced micro-antenna arrays, these satellites – organized into tandems or clusters – can efficiently scan the Earth's surface. Their payload can generate Time Difference of Arrival (TDOA) or Angle of Arrival (AOA) observables that can be used to accurately detect and locate RF emitters. Applications range from identifying known distress signals for search and rescue operations to detecting unknown Radio Frequency Interference (RFI) sources that may disrupt protected bands, such as GNSS. Currently operational LEO satellite constellations already offer such data acquisition, with commercial providers offering varying performances based on the number of deployed satellites and revisit times. To achieve unparalleled monitoring coverage and responsiveness, this paper introduces the innovative concept of a multi-constellation approach, where a centralized RF monitoring service provider accesses data from multiple constellations. The cost-benefit of this more expensive solution hinges not on the sum of individual constellation capabilities but on the potential to capitalize on additional multi-constellation opportunistic events, termed 'collisions.' These occur when satellites from different constellations form new clusters, allowing simultaneous observation of the same area and enabling additional TDOA or AOA measurements not associated to a single constellation. The effectiveness of these collisions depends on relative geometry and other critical performance indicators, and not all events can be considered advantageous for a target RF detection and localization scenario. This paper develops a methodology to establish metrics that quantify the occurrence and utility of such interactions, providing collision frequency data. The methodology involves an analytical description of satellite constellations with varying orbit sizes, considering their relative kinematics to a reference signal emitter on Earth's surface, the Cramér-Rao Lower Bound (CRLB), Dilution of Precision (DOP), and incorporating constraints on the Line of Sight (LOS). Case studies in LEO mission applications, exemplary of search and rescue operations and spectrum monitoring in the E1/L1 GNSS frequency bands, are discussed. The proposed solution offers a crucial tool for monitoring service providers to evaluate the advantages of multi-constellation data access, assess the expected number of beneficial collisions, and optimize sensor acquisition scheduling to maximize multi-constellation RF detection and localization accuracy.

Content from this work may be used under the terms of the Creative Commons Attribution 3.0 license. Any further distribution of this work must maintain attribution to the author(s) and the title of the work, journal citation and DOI. Published under license by Materials Research Forum LLC.

Materials Research Proceedings 69 (2026) 1158-1163 https://doi.org/10.21741/9781644904251-199

Reference Context of the Study

The context of the study is within the macroscopic area related to the evaluation of the set of conditions that can guarantee a combined measurement for a set of constellations of satellites. For simplicity, the study is confined to a simpler case of two constellations $\mathcal{C}_1$ and $\mathcal{C}_2$. Each constellation is also supposed to be, more specifically, a cluster of satellites that orbit very close to each other: given two satellites $\mathbf{x}_{S_1} \in \mathcal{C}_1$ and $\mathbf{x}_{S_2} \in \mathcal{C}_2$, their distance is small compared to the total lengths $\mathcal{L}_{S_1}$ and $\mathcal{L}_{S_2}$ of their orbits, so condition $\|\mathbf{x}_{S_1} - \mathbf{x}_{S_2}\| \ll \mathcal{L}_{S_1} \cup \|\mathbf{x}_{S_1} - \mathbf{x}_{S_2}\| \ll \mathcal{L}_{S_2}$ holds for each couple of satellites within the same cluster.

The objective of the problem is to evaluate when the two constellations $\mathcal{C}_1$ and $\mathcal{C}_2$ are close enough to perform a combined measurement.

Without loss of generality and to have a first simpler approach to the problem, it is supposed that each constellation is composed of one single satellite, which is a representative for the whole cluster. The actors of the problem are then satellites $\mathbf{x}_{S_1} \in \mathcal{C}_1$ and $\mathbf{x}_{S_2} \in \mathcal{C}_2$

Each single satellite is supposed to have a generic payload composed of antenna array able to perform measurement with Angle of Arrival (AOA) technology and the combined presence of at least two satellites can perform a Time Difference of Arrival (TDOA) measurement [1].

These measurements can be used to geolocate an emitter of electromagnetic waves placed in $\mathbf{x}_E$ on the surface of the Earth for search and rescue operations or spectrum monitoring of jamming signals.

Relative Geometry and Intersection Points

Orbital kinematics of the satellites that orbit the Earth follow elliptic orbits that can be described by orbital parameters [2]: the semi-major axis a, the eccentricity e, the inclination i, the right ascension of the ascending node Ω, the argument of perigee ω, and the true anomaly ν. The true anomaly is the only parameter that depends on the time t, so $\nu = \nu(t)$.

For circular orbits $e = 0$, $\omega = 0$, and the semi-major axis is replaced by the radius of the orbit $a = r$. Given this further assumption, then $\mathbf{x}_{S_1}(r_1, i_1, \Omega_1, \nu_1(t))$ and $\mathbf{x}_{S_2}(r_2, i_2, \Omega_2, \nu_2(t))$.

In order to predict the moments in which a combined measurement is possible, a higher level of abstraction is required. More generally, for a satellite S it is possible to say that a circular orbit, described by a closed curve γ_S, lies completely in an orbital plane π_S.

By definition, an orbital plane π_S contains both the orbit γ_S and the centre of mass of the planet, which for the Earth is denoted by $\mathbf{x}_\oplus$ in this study.

Then, the intersection of the planes $\pi_{S_1} \cap \pi_{S_2}$ gives the line l_{S_1,S_2} in which the combined measurement of the two constellations $\mathcal{C}_1$ and $\mathcal{C}_2$ is supposed to be possible.

The set of points of the intersections I between this line and the orbits, formally

$$\begin{aligned} I &= \{\mathbf{x} \in \mathbb{R}^3 | (l_{S_1,S_2} \cap \gamma_{S_1}) \vee (l_{S_1,S_2} \cap \gamma_{S_2})\} \\ &= \{\mathbf{x} \in \mathbb{R}^3 | ((\pi_{S_1} \cap \pi_{S_2}) \cap \gamma_{S_1}) \vee ((\pi_{S_1} \cap \pi_{S_2}) \cap \gamma_{S_2})\} \end{aligned} \quad (1)$$

are of interest. If the orbital planes are not parallel $\pi_{S_1} \nparallel \pi_{S_2}$, the set of points I is finite and, in particular, it has two points (denoted here as A and B) for each orbit, $I = \{\mathbf{x}_{1,A}, \mathbf{x}_{1,B}, \mathbf{x}_{2,A}, \mathbf{x}_{2,B}\}$. Equivalently, this means that for each couple of orbital planes, two geometrical values of the true anomaly can be identified for each satellite; here, for two satellites S_1 and S_2 they are denoted with $\nu_{1,A}$, $\nu_{1,B}$, $\nu_{2,A}$, and $\nu_{2,B}$.

Materials Research Proceedings 69 (2026) 1158-1163 https://doi.org/10.21741/9781644904251-199

Intervals at Intersection Points

The position of each circular orbit is periodic with a period $T_k = 2\pi\sqrt{\frac{r_k^3}{\mu_\oplus}}$ with $k = 1,2$, where $\mu_\oplus$ is the standard gravitational parameter of the Earth. So also the passage of the satellites in each one of the intersection points is periodic with period T, so $\nu_{1,\mathrm{A}}(t) = \nu_{1,\mathrm{A}}(t + n_1T_1)$, $\nu_{1,\mathrm{B}}(t) = \nu_{1,\mathrm{B}}(t + n_1T_1)$, $\nu_{2,\mathrm{A}}(t) = \nu_{2,\mathrm{A}}(t + n_2T_2)$, $\nu_{2,\mathrm{B}}(t) = \nu_{2,\mathrm{B}}(t + n_2T_2)$ with $n_1, n_2 \in \mathbb{N}$.

A true anomaly of intersection $\nu_\mathrm{I} = \{\nu \in \gamma | \nu = \nu_\mathrm{A} \vee \nu = \nu_\mathrm{B}\}$ can be defined and considered to avoid the duplicated representation. In this representation, the periodicity is half of the orbital period: $\nu_{1,\mathrm{I}}(t) = \nu_{1,\mathrm{I}}(t + n_1T_1/2)$ and $\nu_{2,\mathrm{I}}(t) = \nu_{2,\mathrm{I}}(t + n_2T_2/2)$ with $n_1, n_2 \in \mathbb{N}$.

A measurement exists when the emitter of signal is within the line of sight of the satellite. Considering the geometry reported in Figure 1, the interval of true anomaly of visibility $\Delta\nu_\mathrm{v}$ can be calculated as in (2), where $R_\oplus$ is the radius of the Earth, assumed to be spherical for simplicity.

$$\Delta\nu_{\mathrm{v},k} = 2\arccos\left(\frac{R_\oplus}{r_k}\right), \quad k = 1,2 \tag{2}$$

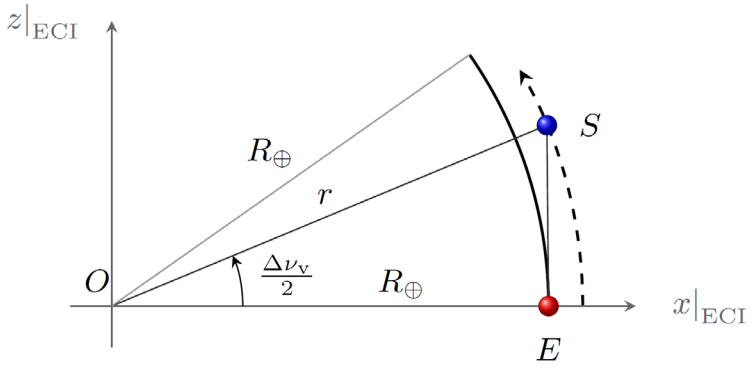


Figure 1 – Reference geometry to calculate the true anomaly of visibility from the Earth radius and satellite orbit radius.

The interval of time visibility ΔT_v is then

$$\Delta T_{\mathrm{v},k} = \frac{\Delta\nu_{\mathrm{v},k}T_k}{2\pi} = \frac{\arccos\left(\frac{R_\oplus}{r_k}\right)T_k}{\pi} = 2\arccos\left(\frac{R_\oplus}{r_k}\right)\sqrt{\frac{r_k^3}{\mu_\oplus}}, \quad k = 1,2. \tag{3}$$

The passage of the satellites at the intersection points can be modeled with a train of rectangular pulses f_1 and f_2 with periodicities $T_1/2$ and $T_2/2$, and widths $\Delta T_{\mathrm{v},1}$ and $\Delta T_{\mathrm{v},2}$, as shown in (4); $t_{0,1}$ and $t_{0,2}$ represent the initial starting times.

$$f_{\mathrm{v},k}(t) = \sum_{j=1}^{\infty}\Pi\left(\frac{\left(t - t_{0,k}\right) - j\frac{T_k}{2}}{\Delta T_{\mathrm{v},k}}\right) = \sum_{j=1}^{\infty}\Pi\left(\frac{\left(t - t_{0,k}\right)\sqrt{\frac{\mu_\oplus}{r_k^3}} - j\pi}{2\arccos\left(\frac{R_\oplus}{r_k}\right)}\right), \quad k = 1,2. \tag{4}$$

Superposition of Intervals

Once the intersection intervals have been defined and modelled it is possible to check their superposition in a certain instant of time.

Given starting instant of time $t_\mathrm{Start} = t_0 + nT$ with $n \in \mathbb{N}$ and ending instant of time $t_\mathrm{End} = t_0 + nT + \Delta T_\mathrm{v}$ with $n \in \mathbb{N}$, then the active interval for a satellite S can be defined as $I_{\mathrm{Act,S}}(n) = [t_\mathrm{Start}(n), t_\mathrm{End}(n)[$ with $n \in \mathbb{N}$; for satellites S_1 and S_2 they are as reported in (5).

Materials Research Proceedings 69 (2026) 1158-1163 https://doi.org/10.21741/9781644904251-199

$$\begin{aligned} I_{\mathrm{Act,S_1}}(n_1) &= \left[t_{0,1} + n_1 T_1\,, t_{0,1} + n_1 T_1 + \Delta T_{\mathrm{v},1}\right[\quad n_1 \in \mathbb{N} \\ I_{\mathrm{Act,S_2}}(n_2) &= \left[t_{0,2} + n_2 T_2\,, t_{0,2} + n_2 T_2 + \Delta T_{\mathrm{v},2}\right[\quad n_2 \in \mathbb{N} \end{aligned} \tag{5}$$

Formally, the set $\mathcal{T}_{\mathrm{Sup}}$ of instants of time of superposition of the intervals can be written as $\mathcal{T}_{\mathrm{Sup}} = \left\{t \in \mathbb{R}_{>0} \middle| \left(t \in I_{\mathrm{Act,S_1}}\right) \wedge \left(t \in I_{\mathrm{Act,S_2}}\right)\right\}$. Because the train of pulses defined in (4) have values of 1 if the interval is active and 0 if the interval is not active, so formally $f_{\mathrm{v},1}\left(t \in I_{\mathrm{Act,S_1}}\right) = 1$ and $f_{\mathrm{v},2}\left(t \in I_{\mathrm{Act,S_2}}\right) = 1$, then from an intuitive point of view, the set $\mathcal{T}_{\mathrm{Sup}}$ can be obtained evaluating the domain of the product function $f_{\mathrm{v},1} f_{\mathrm{v},2}$. To check if a superposition between two active intervals exists, the following situation must happen: both of the starting instants of time $t_{\mathrm{Start},1}$ and $t_{\mathrm{Start},2}$ must happen before of both the ending instants of time $t_{\mathrm{End},1}$ and $t_{\mathrm{End},2}$. This can be written formally as in (6).

$$\max\left(t_{\mathrm{Start},1}(n_1), t_{\mathrm{Start},2}(n_2)\right) < \min\left(t_{\mathrm{End},1}(n_1), t_{\mathrm{End},2}(n_2)\right), \quad n_1, n_2 \in \mathbb{N} \tag{6}$$

Counting the Intersections and Frequency of Collisions

Given the expected ending of the missions of a constellation in $T_{\mathrm{End},\mathcal{C}}$, then the scanning of the superposition of the intervals can happen within a maximum instant of time $T_{\mathrm{Max}} = \min\left(T_{\mathrm{End},\mathcal{C}_1}, T_{\mathrm{End},\mathcal{C}_2}\right)$, because it is supposed that it is not possible to exploit a combined measurement after the end of one of the two missions. From the evaluation of T_{Max}, then it is possible to obtain the total number of intervals for the satellites with $N_1 = 2\left(T_{\mathrm{Max}} - t_{0,1}\right)/T_1$ and $N_2 = 2\left(T_{\mathrm{Max}} - t_{0,2}\right)/T_2$.

With the aid of the condition in (6), it is possible to build an algorithm to predict and count the number of events with the aid of a counter N_{Events}, here denoted as collisions between constellations. When the total number of events have been calculated, then the frequency of collisions $f_c = N_{\mathrm{Events}}/T_{\mathrm{Max}}$ can be calculated. The metrics $f_c(\mathcal{C}_1, \mathcal{C}_1)$ can be useful to evaluate if two constellations $\mathcal{C}_1$ and $\mathcal{C}_2$ can be operatively exploited to perform combined measurements.

It is possible to filter the total number of events evaluating the quality of the collision with respect to local metrics, such as the position dilution of precision $PDOP$, which depends on the distribution of the satellites $\mathbf{x}_{\mathrm{S_1}}$, $\mathbf{x}_{\mathrm{S_2}}$ with respect to a local emitter of signal $\mathbf{x}_{\mathrm{E}}$. Furthermore, models for the variances of the measurements are required, which commonly can be estimated through the Cramér-Rao Lower Bound (CRLB); in particular, for two satellites, the variances of AOA $\sigma^2_{\mathrm{AOA},1}$, $\sigma^2_{\mathrm{AOA},2}$, and TDOA σ^2_{TDOA} can be employed. The details of the models are beyond the purposes of the study, dedicated literature on the topic can be found in [3], [4], [5], [6], [7].

Functional dependence is then in the form

$$PDOP = f\left(\mathbf{x}_{\mathrm{S_1}}, \mathbf{x}_{\mathrm{S_1}}, \mathbf{x}_{\mathrm{E}}, \sigma^2_{\mathrm{AOA},1}, \sigma^2_{\mathrm{AOA},2}, \sigma^2_{\mathrm{TDOA}}\right) \tag{7}$$

The algorithm is presented in Table 1.

Materials Research Proceedings 69 (2026) 1158-1163 https://doi.org/10.21741/9781644904251-199

Table 1 – Operative algorithm to calculate the frequency of collisions.

load $\mathbf{x}_{S_1}, \mathbf{x}_{S_1}, \mathbf{x}_E, \sigma^2_{AOA,1}, \sigma^2_{AOA,2}, \sigma^2_{TDOA}$ ▶Initial data
load $R_\oplus, \mu_\oplus$ ▶Earth model
set $t_{0,1}, t_{0,2}$ ▶Initial instants of time
set $T_{End,\mathcal{C}_1}, T_{End,\mathcal{C}_2}$ ▶Ending instants of time
$T_1 \leftarrow f(\mu_\oplus, r_1), T_2 \leftarrow f(\mu_\oplus, r_2)$ ▶Evaluate periods
$\Delta\nu_{v,1} \leftarrow f(R_\oplus, r_1), \Delta\nu_{v,2} \leftarrow f(R_\oplus, r_2)$ ▶True anomaly of visibility as in (2)
$\Delta T_{v,1} \leftarrow f(\Delta\nu_{v,1}, T_1), \Delta T_{v,2} \leftarrow f(\Delta\nu_{v,2}, T_2)$ ▶ Interval of time of visibility, as in (3)
$T_{Max} \leftarrow \min(T_{End,\mathcal{C}_1}, T_{End,\mathcal{C}_2})$ ▶ Time interval of scanning
$N_1 \leftarrow f(t_{0,1}, T_1, T_{Max})$, $N_2 \leftarrow f(t_{0,2}, T_2, T_{Max})$ ▶ Number of time intervals
for $n_1 \leftarrow 1$ to N_1 **do**
    Evaluate $t_{Start,1}(n_1)$, $t_{End,1}(n_1)$ ▶ Starting and ending instants of time for S_1
end for
for $n_2 \leftarrow 1$ to N_2 **do**
    Evaluate $t_{Start,2}(n_2)$, $t_{End,2}(n_2)$ ▶ Starting and ending instants of time for S_2
end for
initialize $N_{Events} = 0$
for $n_1 \leftarrow 1$ to N_1 **do**
    for $n_2 \leftarrow 1$ to N_2 **do**
        if inequality (6) is `true` **then** ▶ Check if superposition exists
            if evaluate $PDOP$ as in (7) **then** ▶ Filter results with local metrics
                $N_{Events} = N_{Events} + 1$ Update counter
            end if
        end if
    end for
end for
$f_c \leftarrow N_{Events}/T_{Max}$ ▶ Frequency of collisions
return f_c

Conclusions

The study presents a first level of theoretical analysis on the conditions that guarantee the possibility to perform combined measurements for multi-constellation systems, useful for space-based geolocation applications. Despite the study is restricted to two-constellation case and to satellites confined in a circular orbit, a first attempt of a formal framework to model and to build an operative algorithm to check and count the opportunities of such events, here denoted as collisions between constellations, has been obtained. The generalization of the model, e.g. to accommodate multiple constellations and elliptic orbits, its numerical simulation, and the validation of the approach in real-case operative scenarios are left for future investigations.

Credits

Activities of formal analysis and development of models and methods have been performed by the Politecnico di Bari. Motivations and possible application to real-case operative scenarios have been offered by the gentle consultancy of the EC Joint Research Center.

References

[1] R. A. Poisel, Antenna Systems and Electronic Warfare Applications, Norwood, MA, USA: Artech House, 2012.

[2] V. A. Chobotov, Orbital Mechanics, Reston, VA, USA: AIAA Education Series, Cambridge University Press, 2002. https://doi.org/10.2514/4.862250

[3] M. Asciolla and F. Dell'Olio, "Multi-satellite spatial optimization in geolocation algorithm via passive sensors onboard satellites," in 31st IAA Symposium on Small Satellite Missions, Milano, Italy, 2024. https://doi.org/10.52202/078365-0091

[4] M. Asciolla, R. Blázquez-García, A. Cratere, V. M. N. Passaro and F. Dell'Olio, "Satellite Constellation Optimization for Emitter Geolocalization Missions Based on Angle of Arrival Techniques," Sensors, vol. 25, no. 11, 2025. https://doi.org/10.3390/s25113376

[5] M. Asciolla, R. Blázquez-García, A. Cratere and F. Dell'Olio, "On the Optimum Update of Satellite Constellations with AOA Receivers: a Comparative Analysis," in 2025 IEEE 12th International Workshop on Metrology for AeroSpace (MetroAeroSpace), Napoli, Italy, 2025. https://doi.org/10.1109/MetroAeroSpace64938.2025.11114443

[6] M. Asciolla, R. Blázquez-García, A. Cratere and F. Dell'Olio, "On the Influence of the SNR on the Optimization of Two-Satellite Systems with AOA Receivers," in 2025 IEEE Sensors Applications Symposium (SAS), Newcastle, United Kingdom, 2025. https://doi.org/10.1109/SAS65169.2025.11105107

[7] M. Asciolla, R. Blázquez-García, A. Cratere, F. Menzione and F. Dell'Olio, "Optimization of multi-satellite constellations for GNSS spectrum monitoring applications via AOA-TDOA receivers in LEO," Progress in Engineering Science, vol. 2, no. 3, p. 100123, 2025. https://doi.org/10.1016/j.pes.2025.100123

Structures, Materials & Manufacturing



Materials Research Proceedings 69 (2026) 1165-1170 https://doi.org/10.21741/9781644904251-200

Open-Source Path Planning for Spot, Line, and Contour Strategies in E-PBF Additive Manufacturing

Anton Wiberg[1,a *], Pritwish Tarafder[1,b], Karin Wennersten[1,c], Jinghao Xu[1,d], Johan Moverare[1,e]

[1]Linköpings universitet, 591 83 Linköping, Sweden

[a]anton.wiberg@liu.se, [b]prithwish.tarafder@liu.se, [c]karin.wennersten@liu.se, [d]jinghao.xu@liu.se, [e]johan.moverare@liu.se

Keywords: Electron Beam Powder Bed Fusion, Open Source

Abstract. Electron Beam Powder Bed Fusion (E-PBF) enables the production of high-performance components by processing reactive alloys under vacuum with controlled microstructures. However, innovation in beam path development has been limited by proprietary software environments. This work introduces OBPlanner, an open-source Python package for slicing and generating beam path strategies for E-PBF. The framework supports spot and line melting, contouring, and localized preheating within a unified workflow and outputs paths in the open Open Beam Format (OBF) used by Freemelt systems. By enabling transparent and reproducible process strategy development, OBPlanner lowers the barrier to experimentation and accelerates open innovation in E-PBF research.

Introduction

Yet another 3D printing slicer? Why?

A fair question. While the market is saturated with commercial and open-source slicers, most are developed for polymer or laser-based additive manufacturing (AM) systems. These typically rely on simple path-planning routines that combine contour scanning with ordered infill lines (hatching). In contrast, Electron Beam Powder Bed Fusion (E-PBF) operates under a fundamentally different regime. The electron beam is magnetically controlled and contains no moving mechanical parts, allowing it to traverse the powder bed with exceptional speed and precision. This makes it possible to employ not only traditional line-based melting but also spot melting, where discrete points are rapidly melted and thermally managed across the layer [1].

Such unconventional beam path strategies offer new opportunities to control thermal gradients, tailor microstructures, and reduce distortion in high-performance alloys such as Ti-6Al-4V and nickel-based superalloys [1]. However, systematic exploration of these strategies has been hindered by proprietary software environments. Most existing E-PBF systems provide only a small set of predefined melting patterns, limiting researchers' ability to design, test, and share new process routes. This restricts reproducibility and slows innovation in a field that thrives on experimental creativity.

To address these limitations, we introduce OBPlanner [2], an open-source Python framework supporting spot and line melting, contouring, and local preheating. By enabling transparent, modifiable beam-path generation in the Open Beam Format (OBF), OBPlanner empowers researchers to experiment, share, and innovate in E-PBF strategy design.

Background and Related work

E-PBF is an AM process that uses a focused electron beam to selectively melt metallic powder under vacuum. Unlike laser-based systems, E-PBF employs electromagnetic lenses for beam deflection, providing non-mechanical, near-instantaneous control of beam position, focus, and power. This enables microsecond beam jumps and dynamic modulation of energy input, making

Content from this work may be used under the terms of the Creative Commons Attribution 3.0 license. Any further distribution of this work must maintain attribution to the author(s) and the title of the work, journal citation and DOI. Published under license by Materials Research Forum LLC.

E-PBF uniquely suited for advanced scan strategies such as discrete spot melting [1]. E-PBF builds typically combine several sequential heating stages to ensure process stability: spatter-safe preheating to minimize particle ejection, jump-safe preheating to stabilize the bed before melting, melting for material consolidation, and heat-balance heating to maintain interlayer temperature uniformity [1]. Recent research has shown that smart planning and thermal control enables microstructure engineering through beam path design, where variations in dwell time, overlap, or scan order can drastically affect local cooling rates and solidification behavior [3], [4], [5], [6]. In addition, studies have shown that ordered and random spot strategies can be used to promote different grain formation and reduce cracking demonstrating that beam motion itself can serve as a powerful process variable [6].

Recent developments in open-architecture research platforms, such as Freemelt's OBP [7] (instructions on how the beam should behave within a specific sequence in a layer) and OBF [8] (overall build process instructions). These open standards provide the foundation for programmable beam control, adaptive scanning, and microstructure-on-demand manufacturing. While these formats exist, there is a lack of open, easily extendable, and modifiable tools for creating such files.

The OBPlanner framework

The OBPlanner framework provides a modular, open-source environment for generating OBP and OBF files. Its architecture is founded on transparency and extensibility, enabling full access to each stage of beam-path generation, from geometric slicing to energy input specifications. At its core, OBPlanner combines two primary inputs: a user-defined JSON configuration file and a sliced 3D model. The configuration file defines which process strategies to apply, including parameters such as beam power, dwell time, and point spacing, while the sliced geometry constrains the beam path to the desired part contours. The output is written in the Open Beam Format (OBF), directly executable on Freemelt systems.

OBPlanner's software structure is organized around two major classes:

- Strategy: represents a process step, combining a pattern, beam parameters, and an execution movement strategy. Each strategy belongs to one of four categories (spatter-safe, jump-safe, melting, and heat-balance) and defines how energy is distributed across the layer.
- Pattern: generates the spatial distribution of exposure points according to a user-selected layout (square, triangular, HCP, or FCC). The pattern module governs spacing, rotation, and offset between layers, effectively defining the scan geometry.

This object-oriented design ensures that each function is self-contained yet interoperable, allowing users to extend or replace modules independently. For example, new pattern generators or ordering algorithms can be implemented by subclassing existing templates without modifying the rest of the code. This modularity makes OBPlanner both a practical research tool and a foundation for future adaptive process-control systems.

Computational Workflow

OBPlanner converts the combination of geometric and process definitions into ordered beam commands through six main stages (Figure 1):

Materials Research Proceedings 69 (2026) 1165-1170 https://doi.org/10.21741/9781644904251-200

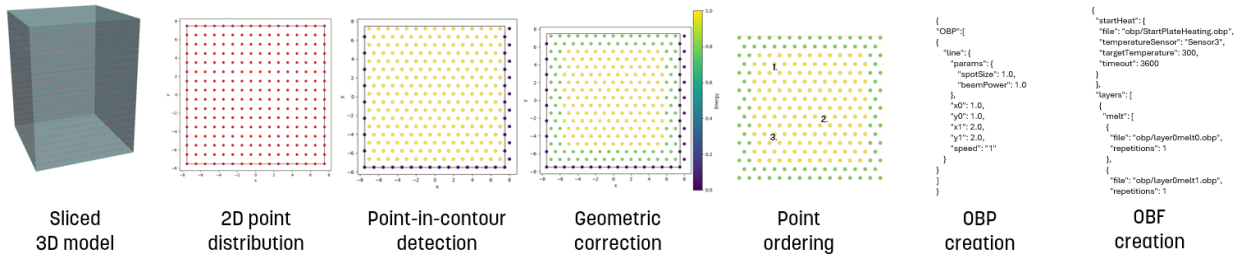
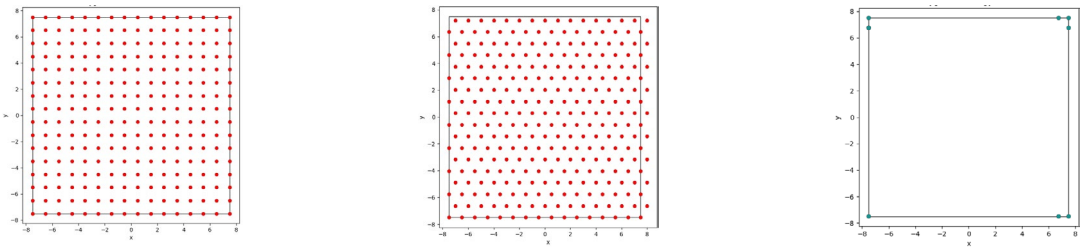


Figure 1. Overview of the OBPlanner workflow.

Sliced model input: The framework imports a sliced 3MF file containing the layer boundaries. This slicing can be performed using an external tool or with the py3mf_slicer Python package [9], which was developed in parallel with this work.
Point distribution: Candidate exposure points are generated according to the selected pattern type, with user-defined spacing and optional rotation between layers. Various filling strategies can be applied, including square and triangular fills, or contour-only exposure (see Figure 2). The package also supports advanced three-dimensional filling patterns, such as hexagonal and face-centered cubic (FCC) arrangements, which enable efficient 3D point packing.
Point-in-contour detection: The generated points are filtered using geometric inclusion tests to retain only those within the part contour. An optional offset parameter can be applied to modify the effective boundary size. This is useful, for example, when compensating for expected swelling during melting or when performing localized preheating slightly beyond the melt area.
Point-in-contour detection: Filter points using geometric inclusion tests to retain only those inside the part contour. In this step an offset setting can be applied to change the size of the boundary, this may be useful e.g. if the user expects swelling during melt or want to du local preheating a little bigger than the melt area.
Geometric correction: The local energy input can be adjusted to account for geometric features such as thin walls, edges, or overhangs, allowing targeted compensation for regions that require additional or reduced heat input.
Point ordering: The valid points are then arranged into optimized beam trajectories—such as random or ordered spot sequences, lines, or contour-following paths, according to user input (see Figure 3.). The code structure is intentionally modular, allowing users to easily integrate and test new path-planning strategies.
OBP/OBF creation: Finally, the ordered point data are converted into Open Beam Path (OBP) files containing position, power, and timing information. These are then assembled into a complete Open Beam Format (OBF) structure, ready for execution on compatible E-PBF systems.



(a) *(b)* *(c)*

Figure 2. Example of different 2D filling methods, (a) square filling, (b) triangular filling, and (c) contour filling.

Materials Research Proceedings 69 (2026) 1165-1170 https://doi.org/10.21741/9781644904251-200

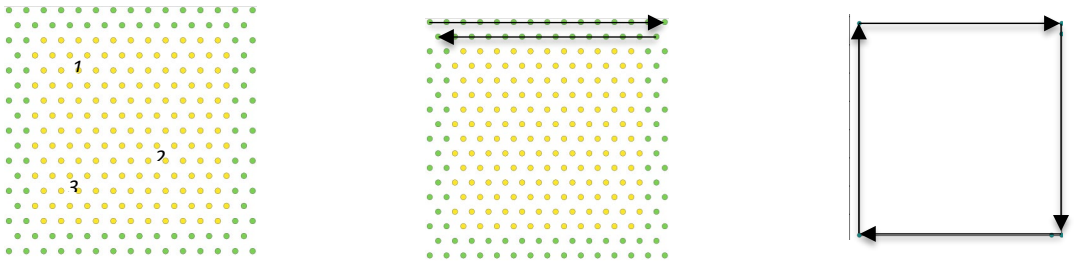


Figure 3. Example of different point ordering methods, (a) random spots, (b) connection of points to a snake line pattern, and (c) contour lines.

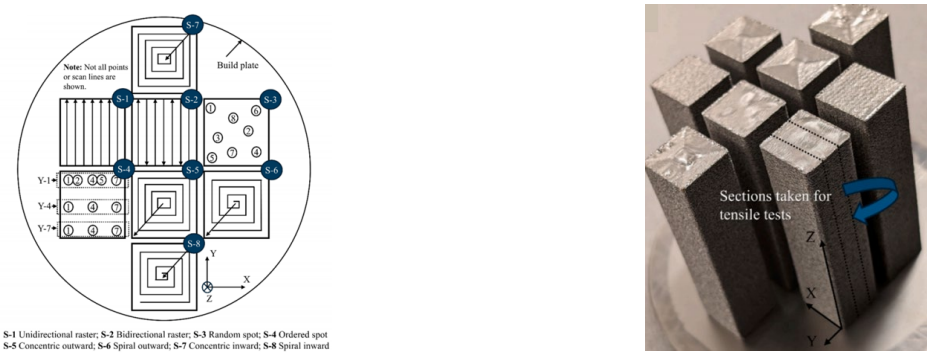
At runtime, OBPlanner reads the JSON configuration, initializes the output directory, and sequentially processes each layer according to the defined strategy hierarchy. For each strategy, the framework generates the spatial pattern, performs contour filtering, applies compensation (if defined), and exports ordered OBP elements. Additional OBF files and scripts (such as a lua script which controls what happens in the machine) are automatically generated to ensure full compatibility with Freemelt's open-architecture control environment.

Because every core operation is encapsulated in modular Python classes, OBPlanner can easily be extended with new patterns, compensation models, or adaptive algorithms. This flexibility encourages experimentation with feedback-based control, where beam parameters evolve dynamically in response to in-situ sensing or simulated temperature fields. By unifying these elements into a transparent and reproducible framework, OBPlanner bridges geometric design, thermal management, and process strategy. It provides a practical foundation for data-driven research on how beam path design influences local energy input, solidification behavior, and ultimately, microstructure formation in E-PBF.

Demonstration and usage

The OBPlanner package has been implemented and used to design and execute a wide range of beam path strategies for process evaluation and material development using a Freemelt ONE system. Its flexibility allows users to explore how variations in beam motion, energy distribution, and sequencing affect the resulting microstructures and material properties.

In the first demonstration, the package was used to generate eight distinct scan strategies for simple cubic samples. These included raster, spiral, concentric, and spot-based melting patterns. Each strategy produced a unique combination of thermal history and solidification behavior, resulting in visibly different microstructural morphologies and mechanical responses. The comparison between these strategies revealed that microstructure evolution in E-PBF is highly sensitive to local energy input and remelting cycles, showing that beam path design can be used as a deliberate control parameter for tailoring properties. The full study is presented in [6], see Figure 4.



(a) *(b)*

Figure 4. Test case one, (a) show the different strategies used for the cubes, (b) shows the printed specimens. Figure adapted from [6].

In the second case, the package was used to fabricate a scaled-down sand screen component representative of an industrial part, see Figure 5. Here, OBPlanner enabled the assignment of different scan strategies to specific regions of the geometry. The inner core was built with a raster strategy for uniform structure, while the outer rim employed a random spot strategy to increase hardness. The resulting component exhibited distinct microstructures and property gradients, demonstrating how spatially varying beam control can be used to locally tune mechanical performance within a single component [6].

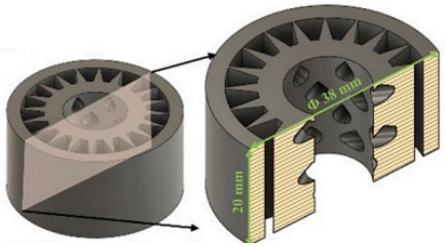


Figure 5. Sand screen component where one setting is applied on the outer ring and one is applied at the core structure. Figure adapted from [6].

Discussion and Outlook

The development of OBPlanner represents an important step toward openness and reproducibility in E-PBF research. By exposing the entire beam-path generation pipeline, from geometric slicing to executable beam commands, the framework gives researchers full control over parameters that are typically hidden in proprietary software. This transparency enables systematic investigation of how beam motion, energy input, and process strategy influence microstructure evolution and material performance. A central strength of OBPlanner is its accessibility and possibility to easy modify the process. All process definitions for the input is stored in human-readable JSON format and exported through the standardized OBF, allowing experiments to be easily replicated and shared across research groups. This open data structure supports the establishment of shared benchmarks for process parameters, thermal conditions, and resulting microstructures, facilitating truly comparable studies in E-PBF.

The framework's modular Python design also promotes collaborative research and education. It lowers the barrier for implementing custom scan patterns, compensation models, or control algorithms, making it a valuable platform for both industrial process development and academic instruction on beam-path design and solidification phenomena. While highly flexible, the current version remains focused on static, pre-defined strategies and relies on serial geometry operations. Future developments aim to integrate thermal simulation, process monitoring, and in-situ

feedback, enabling adaptive, closed-loop beam control. Such advancements would connect path planning directly with real-time process data, bridging the gap between design, monitoring, and microstructure control.

In summary, OBPlanner transforms beam-path generation in E-PBF from a closed, prescriptive task into an open, programmable, and reproducible research environment. By promoting transparency and collaboration, it provides a foundation for data-driven process optimization, functionally graded material design, and ultimately, microstructure-on-demand manufacturing.

Acknowledgements
This work has been co-funded by the European Union through the project IMA 3DAM (Project No. 20358491), supported by the European Regional Development Fund and administered by Tillväxtverket (the Swedish Agency for Economic and Regional Growth).

More information: https://innovativematerials.se/project/ima-3dam/

The full source code is available at GitHub (https://github.com/wiberganton/OBPlanner).

References

[1] Z. Fu och C. Körner, ”Actual state-of-the-art of electron beam powder bed fusion”, *Eur. J. Mater.*, vol. 2, nr 1, s. 54–116, dec. 2022. https://doi.org/10.1080/26889277.2022.2040342.

[2] Anton Wiberg, *wiberganton/OBPlanner*. (27 oktober 2025). Python. Åtkomstdatum: 10 november 2025. [Online]. Tillgänglig vid: https://github.com/wiberganton/OBPlanner

[3] A. R. Balachandramurthi, J. Olsson, J. Ålgårdh, A. Snis, J. Moverare, och R. Pederson, ”Microstructure tailoring in Electron Beam Powder Bed Fusion additive manufacturing and its potential consequences”, *Results Mater.*, vol. 1, s. 100017, aug. 2019. https://doi.org/10.1016/j.rinma.2019.100017.

[4] C. Körner, H. Helmer, A. Bauereiß, och R. F. Singer, ”Tailoring the grain structure of IN718 during selective electron beam melting”, *MATEC Web Conf.*, vol. 14, s. 08001, 2014. https://doi.org/10.1051/matecconf/20141408001.

[5] R.-H. Lu, S. Saptarshi, och O. Harrysson, ”The effect of scanning strategy on grain development of MAR-M247 in electron beam powder bed fusion”, *Prog. Addit. Manuf.*, okt. 2025. https://doi.org/10.1007/s40964-025-01376-y.

[6] P. Tarafder, J. Xu, A. Wiberg, och J. Moverare, ”Assessing the effect of scan strategies on the structure-property relationship in electron beam powder bed fusion processed 316L stainless steel”, *Mater. Des.*, vol. 253, s. 113837, maj 2025. https://doi.org/10.1016/j.matdes.2025.113837.

[7] Freemelt, ”Freemelt / Openmelt / OBPlib-Python · GitLab”, GitLab. Åtkomstdatum: 10 november 2025. [Online]. Tillgänglig vid: https://gitlab.com/freemelt/openmelt/obplib-python

[8] Freemelt, ”Freemelt / Openmelt / OBFlib-Python · GitLab”, GitLab. Åtkomstdatum: 10 november 2025. [Online]. Tillgänglig vid: https://gitlab.com/freemelt/openmelt/obflib-python

[9] Anton Wiberg, *wiberganton/py3mf_slicer*. (03 oktober 2025). Python. Åtkomstdatum: 10 november 2025. [Online]. Tillgänglig vid: https://github.com/wiberganton/py3mf_slicer

Materials Research Proceedings 69 (2026) 1171-1175 https://doi.org/10.21741/9781644904251-201

Low-Velocity Impact Analysis of Composite Plates using the Hashin 3D Criterion and Layer-Wise Models

Marco PETROLO[1,a *], Matteo FILIPPI[1,b], Erasmo CARRERA[1,c], Chiara FRANCESCHINI[1,d] and Elisa TORTORELLI[1,e]

[1]MUL2 Lab, Department of Mechanical and Aerospace Engineering, Corso Duca degli Abruzzi 24, 10129, Torino, Italy

[a]marco.petrolo@polito.it, [b]matteo.filippi@polito.it, [c]erasmo.carrera@polito.it, [d]chiara.franceschini@polito.it, [e]elisa.tortorelli@polito.it

Keywords: Carrera Unified Formulation (CUF), Low-Velocity Impact, Higher-Order Structural Modeling, Continuum Damage Mechanics, Delamination

Abstract. Numerical simulations are an essential tool for predicting structural response under low-velocity impact and for damage evolution. The present work investigates the low-velocity impact (LVI) response of composite laminate plates by applying the Carrera Unified Formulation (CUF) for structural modelling combined with a fully three-dimensional (3D) Hashin failure criterion for damage evaluation. Previous studies have employed two-dimensional (2D) Hashin criteria, combined with cohesive zone models, to detect intralaminar and interlaminar damage. However, such approaches neglect out-of-plane stress components, which are critical in impact scenarios. The methodology discussed overcomes this limitation by adopting the 3D Hashin criterion within each ply, thereby allowing all six stress components to be included and providing a more accurate prediction of intralaminar damage and interlaminar delamination activation. The numerical model is developed within the CUF framework, using higher-order structural theories based on Lagrange polynomial expansions and a layer-wise representation through the laminate thickness. The results highlight the accuracy of the proposed approach and its computational cost advantages.

Introduction

Impact response is one of the most critical loading cases for the lightweight, layered structures widely used in aerospace. LVI, in particular, are localized events that can introduce intralaminar and interlaminar damage that is difficult to detect visually. As a consequence, the residual strength of the structure is reduced. Numerical simulation helps reduce costly testing and enables rapid sensitivity studies to optimize the design. This, in turn, allows prediction of damage scenarios and stiffness degradation over time. Computational approaches for damage simulation are generally divided into two main categories. Discrete damage models, such as those based on cohesive zone methods (CZM) [1], provide detailed damage representation but are often computationally demanding. As an alternative, the continuum framework employed in [2] facilitates efficient damage simulation with reduced numerical overhead. This study is motivated by the need for a fast, computationally efficient tool to analyze impacts on composite structures. The advantages of using the Carrera Unified Formulation (CUF) in this context lie in achieving 3D fidelity at reduced computational cost. By coupling CUF with explicit dynamics and progressive damage models, it is possible to obtain a rapid, robust, and accurate simulation tool for impact problems.

Structural theories and damage model

The structural theories adopted in this paper are based on the Carrera Unified Formulation (CUF) [3], which employs higher-order Lagrange polynomial expansions and yields a layer-wise representation through the laminate thickness. CUF enables the derivation of 1D and 2D theories thanks to a compact notation by representing the displacement fields, over the cross-section for

Content from this work may be used under the terms of the Creative Commons Attribution 3.0 license. Any further distribution of this work must maintain attribution to the author(s) and the title of the work, journal citation and DOI. Published under license by Materials Research Forum LLC.

Materials Research Proceedings 69 (2026) 1171-1175 https://doi.org/10.21741/9781644904251-201

beams and through the thickness for plates and shells, as basic functions whose type and order are arbitrary. The three-dimensional displacements in the layer-wise 2D model adopted in this work can be expressed as:

$$u(x,y,z) = F_\tau(z)N_i(x,y)u_{\tau i}, \qquad \tau = 1,\dots,M, \qquad i = 1,\dots,N \tag{1}$$

That is, as the product of nodal displacements $u_{\tau i}$ for the expansion function $F_\tau(z)$ of M terms, which approximates the kinematics through the thickness of the plate, and for the 2D shape function $N_i(x,y)$.

The damage model [4,5] is divided into a criterion for which the damage is activated and a model for the evolution of this damage. The 3D Hashin criterion, which accounts for failure in both fibers and matrix, predicts damage initiation under compression and tension. Here, the 3D Hashin model is adopted for fiber tension and matrix and fiber compression. Only for matrix compression, the Puck criterion [6] is considered. Once the criterion for initiating failure is triggered, the subsequent progression of the damage follows a linear pattern, with the material stiffness decreasing until final failure. Using a unified subscript $P \in \{ft, fc, mt, mc\}$ to represent the four modes of damage, d_P is a parameter governing the evolution of damage in each mode. The constitutive elastic stress-strain relation during the damage evolution can be written as:

$$\sigma = C_{dam}\epsilon \tag{2}$$

where C_{dam} is the stiffness matrix in the damage state, function of damage parameters d_P.

Numerical examples

The first numerical example presents a multibody analysis of a spherical impactor (diameter 16 mm) striking a square, linearly elastic composite plate with a side length of 100 mm. The composite is modeled as a quasi-isotropic laminate with a stacking sequence $[90/45/0/-45]_{2s}$ and a total thickness of 2 mm. The material system is IM7/8552 CFRP; see Ref. [7], Table 1, for material properties. The plate is fully clamped along its edges, and the impactor hits the center with an initial velocity of 5 m/s.

Different CUF models are employed, characterized by increasing orders of Lagrange expansion through the thickness, denoted CUF-LE*x*, where *x* is the expansion order. In addition, a CUF model with multiple linear expansions per ply (CUF-3LE1/ply) is examined. Model details are provided in Model 1 (Table 1).

Figures 1 and 2 show the stress distributions from the CUF models near the center of the plate, benchmarked against a standard ABAQUS 3D FEA [7]. The numerical results indicate that in-plane stresses predicted by CUF are in excellent agreement with the ABAQUS solution (Fig. 1). By contrast, the interlaminar shear stresses (Fig. 2) are more challenging and require either higher-order through-thickness expansions or multiple linear expansions per ply to be captured accurately.

Materials Research Proceedings 69 (2026) 1171-1175 https://doi.org/10.21741/9781644904251-201

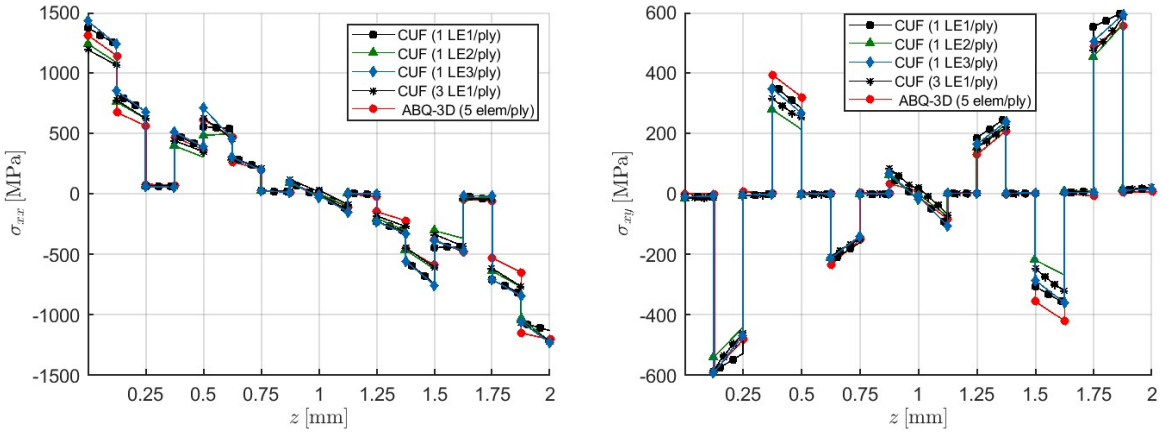


Figure 1: In-plane stress components through the thickness of the composite plate at the point (x,y)=(48 mm,48 mm).

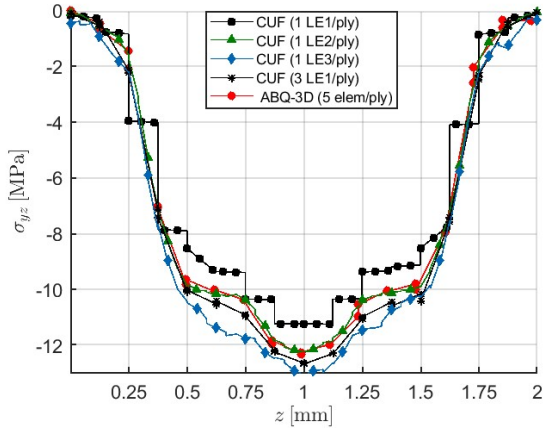


Figure 2: Interlaminar shear stress through the thickness of the square plate at the point (x,y)=(40 mm,40 mm).

Model 1	Discretisation of the laminate	DOF
CUF-LE1	400 Q9 (1 LE1/ply)	85,731
CUF-LE2	400 Q9 (1 LE2/ply)	166,419
CUF-LE3	400 Q9 (1 LE3/ply)	247,107
CUF-3LE1	400 Q9 (3 LE1/ply)	247,107
ABQ	512000 C3D8R (5 el./ply)	1,594,323
Model 2	**Discretisation of the laminate**	**DOF**
CUF-132Q9/LE2	132 Q9 (1 LE2/ply)	39,816
CUF-192Q9/LE1	192 Q9 (1 LE1/ply)	38,448
CUF-192Q9/LE2	192 Q9 (1 LE2/ply)	57,672
CUF-192Q9/LE3	192 Q9 (1 LE3/ply)	76,896
CUF- 260Q9/LE2	260 Q9 (1 LE2/ply)	77,832

Table 1: Model information

The second numerical study considers the impact of a rigid sphere on a circular composite plate with a stacking sequence of $[0/90]_{2s}$ and ply thickness 0.25 mm. The plate radius is 37.5 mm, thickness 2 mm, and is clamped at its boundary. The material is HTS40/9772 unidirectional CFRP. The impactor has a diameter of 15 mm, initial velocity 3.83 m/s, and kinetic energy 7.35 J. Delamination is modeled with cohesive elements inserted between adjacent plies. Material properties and cohesive parameters are taken from [7].

A mesh-convergence study on the peak impact force (Fig. 3) was performed using the same CUF LE2 expansion and varying in-plane discretizations of 132, 192, and 260 Q9 elements; see Model 2 in Table 1 for model and DOF details. The 192 Q9 mesh was chosen for subsequent analyses with different expansions. Force–time curves were denoised with MATLAB's smooth (centered moving average) using spans of 10–15%. Damage-variable contour maps for the 192 Q9–LE3 model are shown in Fig. 4, and the predicted inter-ply delamination is reported in Fig. 5 for each of the seven cohesive interfaces. The cohesive law triggers delamination once a relative displacement threshold is exceeded [8,9]. Experimental [10] and numerical results are compared.

Materials Research Proceedings 69 (2026) 1171-1175 https://doi.org/10.21741/9781644904251-201

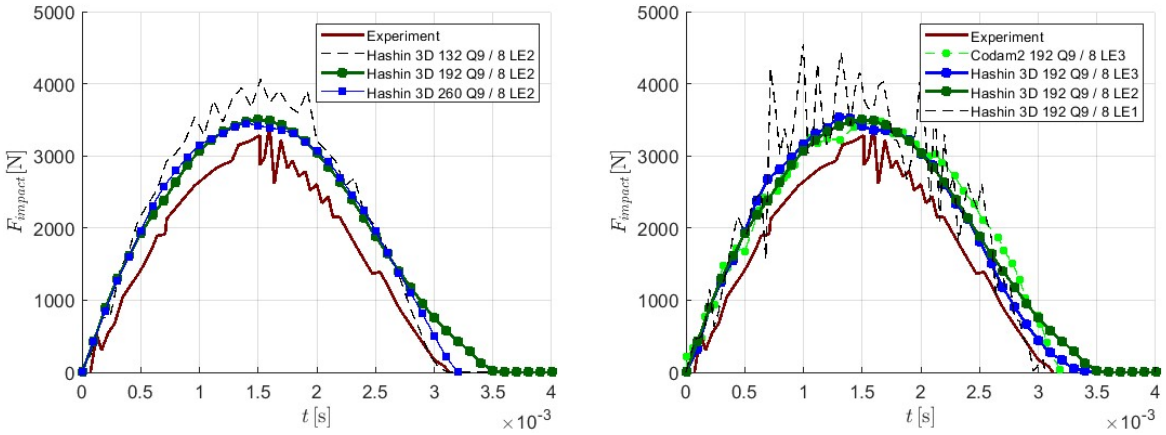


Figure 3: Impact force–time response; From left: (a) effect of in-plane mesh refinement; (b) effect of through-thickness expansion order. Reference experimental and numerical curves from [11].

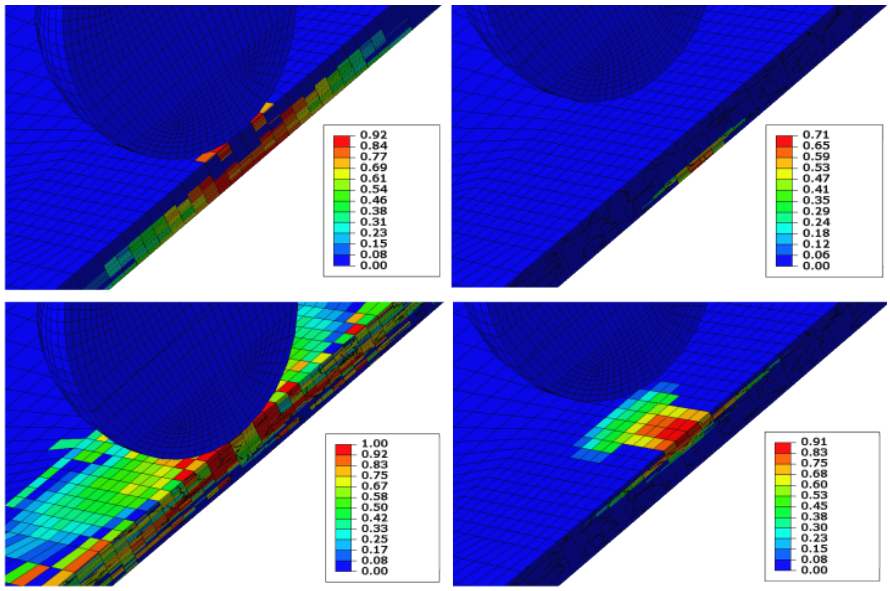


Figure 4: Damage in the impact region. Clockwise from the top-left: (a) Matrix tensile damage; (b) Fibre tensile damage; (c) Matrix compressive damage; (d) Fibre compressive damage.

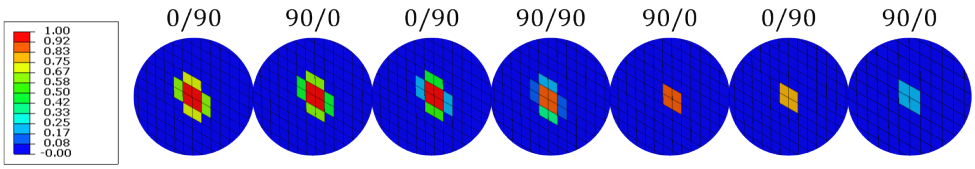


Figure 5: Predicted delamination at the ply interfaces ordered through-thickness from impacted surface (left) to back face (right).

Conclusions

In this study, the layer-wise 2D-CUF framework for impact analysis was extended from 2D damage criteria [11] to the 3D Hashin criterion, while retaining mixed-mode cohesive elements to model delamination. The proposed approach matches numerical and experimental results. The simulations indicate widespread, saturated matrix damage, while fiber damage remains partially unsaturated (see Fig. 4).

The 3D interlaminar stresses help calculate the extent and morphology of delamination, which more closely aligns with reference results [10]. In fact, slight back-face delamination is also

captured. Overall, the methodology resolves both intralaminar and interlaminar damage while preserving computational efficiency, as the present approach requires a fraction of 3D FEM DOF.

Acknowledgements
This study was carried out within the Space It Up!, funded by the Italian Space Agency, ASI, and the Ministry of University and Research, MUR, under contract n. 2024 - 5 -E.0 - CUP n. I53D24000060005.

References

[1] D. Xie, A. G. Salvi, A. M. Waas, and A. Caliskan, "Discrete cohesive zone model to simulate static fracture in carbon fiber textile composites", in Proc. 46th AIAA/ASME/ASCE/AHS/ASC Structures, Structural Dynamics and Materials Conf., Austin, Apr. 2005, AIAA Paper 2005-2320. https://doi.org/10.2514/6.2005-2320

[2] C. Zhao, B. N. Fedulov, C. Liu, K. Zhang, and H. Liu, "Establishment and development of an incremental constitutive model for CFRP considering the impact adiabatic effect", Aerotecnica Missili & Spazio, 2025. https://doi.org/10.1007/s42496-025-00261-9

[3] E. Carrera, M. Cinefra, M. Petrolo, and E. Zappino, "Finite Element Analysis of Structures through Unified Formulation", Hoboken, NJ, USA: Wiley, 2014. https://doi.org/10.1002/9781118536643

[4] M. Petrolo, E. Tortorelli, S. Saputo, and E. Carrera, "Tensile damage analysis of composite structures based on 3D Hashin failure criteria and 2D higher-order structural theories", Int. J. Non-Linear Mech., vol. 127, Art. no. 103591, 2020.

[5] M. Petrolo, E. Tortorelli, S. Saputo, "Compressive damage analysis of composite structures using 3D failure criteria and 2D higher-order structural theories", Mechanics of Advanced Materials and Structures, 2025. https://doi.org/10.1080/15376494.2025.2489138

[6] Y. Zhang, W. Van Paepegem, and W. De Corte, "An enhanced progressive damage model for laminated fiber-reinforced composites using the 3D Hashin failure criterion: A multi-level analysis and validation", Materials, vol. 17, no. 21, Art. no. 7681, 2024. https://doi.org/10.3390/ma17215176

[7] M. H. Nagaraj, E. Carrera, and M. Petrolo, "Progressive damage analysis of composite laminates subjected to low-velocity impact using 2D layer-wise structural models", Int. J. Non-Linear Mech., vol. 127, Art. no. 103591, 2020. https://doi.org/10.1016/j.ijnonlinmec.2020.103591

[8] I. Kaleel, E. Carrera, and M. Petrolo, "Progressive delamination of laminated composites via 1D models", Composite Structures, 235:111799, 2020. https://doi.org/10.1016/j.compstruct.2019.111799

[9] P.P. Camanho, C.G. Davila, and M.F. De Moura, "Numerical simulation of mixed-mode progressive delamination in composite materials", Journal of composite materials, 2003. https://doi.org/10.1177/0021998303034505

[10] Y. Shi, T. Swait, C. Soutis, "Modelling damage evolution in composite laminates subjected to low velocity impact", Composite Structures, Volume 94, Issue 9, 2012. https://doi.org/10.1016/j.compstruct.2012.03.039

[11] M. H. Nagaraj, J. Reiner, R. Vaziri, E. Carrera, and M. Petrolo, "Progressive damage analysis of composite structures using higher-order layer-wise elements", Compos. Part B Eng., vol. 200, Art. no. 107921, 2020. https://doi.org/10.1016/j.compositesb.2020.107921

Materials Research Proceedings 69 (2026) 1176-1180 https://doi.org/10.21741/9781644904251-202

Accuracy Prediction of Higher-Order Structural Theories for 1D Aerospace Structures Using Neural Networks

Marco Petrolo[1,a] *, Alfonso Pagani[1,b], Erasmo Carrera[1,c], and Giulio Candita[1,d]

[1]MUL2 Lab, Department of Mechanical and Aerospace Engineering, Corso Duca degli Abruzzi 24, 10129, Torino, Italy

[a]marco.petrolo@polito.it, [b]alfonso.pagani@polito.it, [c]erasmo.carrera@polito.it, [d]giulio.candita@polito.it

Keywords: Aerospace Structures, CUF, Higher-Order Theories, Neural Networks

Abstract. This study introduces a Machine Learning (ML) framework to assess the accuracy of higher-order structural theories for aerospace structures. Stiffened panels are modeled using one-dimensional elements and analyzed using refined theories based on the Carrera Unified Formulation (CUF). To evaluate accuracy, the framework compares the average error of the first ten natural frequencies with that of a reference model. An ML tool automatically predicts this error and identifies the most relevant generalized variables for each structural configuration. The dataset used to train the ML tool is generated using CUF and includes material properties, geometry, and the structural theory generalized variables. To process this information, two types of Neural Networks (NN) are employed: a Convolutional Neural Network (CNN) extracts geometric features from cross-section images, e.g., number and position of stiffeners, and a Deep Neural Network (DNN) combines these features with material and geometric data to predict the accuracy of each theory. As a result, the framework effectively predicts the most accurate and computationally efficient theories and their associated generalized variables.

Introduction

In structural mechanics, creating accurate reduced models is crucial to lowering the computational complexity of 3D analyses. Since they have fewer degrees of freedom than 3D models, 1D and 2D theories are frequently employed. However, depending on the specific problem, the accuracy of these theories can vary significantly. Classical theories such as the Euler–Bernoulli Beam Theory (EBBT) [1] and the Timoshenko Beam Theory (TBT) [2,3] are often unable to capture complex behaviors such as material anisotropy, shear deformability, or warping effects. To overcome these limitations, higher-order theories (HOT) [4,5] have been developed to address more complex structural problems, including composites [6] and thick beams [7, 8]. The Carrera Unified Formulation (CUF) [9] provides a general and systematic framework for defining structural theories of any order. The Axiomatic/Asymptotic Method (AAM) [10] can be applied to determine the most influential unknowns in higher-order theories, enabling the selection of the most efficient theory for a given problem. However, AAM requires multiple evaluations of generalized variables, leading to high computational costs. In recent years, Machine Learning (ML) techniques [11] have attracted increasing attention in structural mechanics and finite element analysis due to their predictive capabilities and reduced computational time. Their applications include stress prediction, structural health monitoring, and topology optimization. The present paper combines a fully connected Deep Neural Network (DNN) and a Convolutional Neural Network (CNN) to reduce the computational cost of AAM and improve the accuracy of error prediction. The proposed framework extends the authors' previous works [12,13] to stiffened structures for aerospace applications.

Content from this work may be used under the terms of the Creative Commons Attribution 3.0 license. Any further distribution of this work must maintain attribution to the author(s) and the title of the work, journal citation and DOI. Published under license by Materials Research Forum LLC.

Materials Research Proceedings 69 (2026) 1176-1180 https://doi.org/10.21741/9781644904251-202

CUF and FEM Formulations

The reference system adopted for beam structures is shown in Fig. 1. Here, the x-z plane lies on the cross-section Ω.

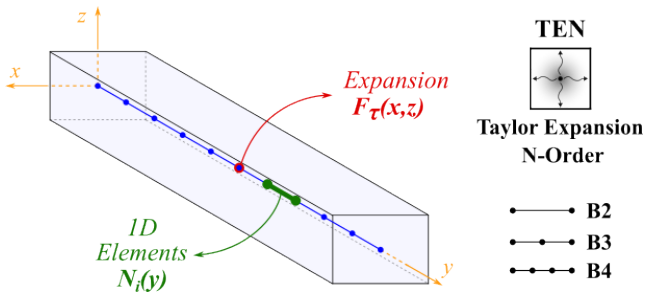


Figure 1: Reference coordinate system for beam models

The displacement field for beams can be expressed as:

$$\boldsymbol{u}(x,y,z) = N_i F_\tau(x,z)\boldsymbol{u}_{\tau i} \tag{1}$$

Where F_τ is the expansion function; τ=1,…, M, and M is the number of expansion terms. N_i is the shape function; $i = 1, \ldots, N_n$, where N_n is the number of FE nodes. $\boldsymbol{u}_{\tau i}$ is the vector of the nodal unknowns. For 1D theories, the expansion function F_τ acts on the cross-section x-z, while the shape function along the beam axis. For a second-order beam theory, the displacement field is:

$$\begin{aligned} u_x &= u_{x_1} + xu_{x_2} + zu_{x_3} + x^2u_{x_4} + xzu_{x_5} + z^2u_{x_6} \\ u_y &= u_{y_1} + xu_{y_2} + zu_{y_3} + x^2u_{y_4} + xzu_{y_5} + z^2u_{y_6} \\ u_z &= u_{z_1} + xu_{z_2} + zu_{z_3} + x^2u_{z_4} + xzu_{z_5} + z^2u_{z_6} \end{aligned} \tag{2}$$

With a total of eighteen nodal displacement variables. The Principle of Virtual Displacements is used to derive the governing equations for the free vibration problem,

$$\delta L_{int} = \delta L_{ext} - \delta L_{ine} \tag{3}$$

The work done by internal forces is δL_{int}, by external forces is δL_{ext}, and by inertial forces is δL_{ine}. In this free-vibration case, the governing equation is the following:

$$\delta \boldsymbol{u}_{sj}: \quad \boldsymbol{m}_{\tau sij}\ddot{\boldsymbol{u}}_{\tau i} + \boldsymbol{k}_{\tau sij}\boldsymbol{u}_{\tau i} = 0 \tag{4}$$

$\boldsymbol{k}_{\tau sji}$ and $\boldsymbol{m}_{\tau sji}$ are the 3x3 Fundamental Nuclei (FN), for the stiffness and mass matrix, respectively. By solving the eigenvalue problem, natural frequencies, ω_n, and modal shapes are obtained:

$$(\boldsymbol{K} - \omega_n^2\boldsymbol{M})\boldsymbol{U} = 0 \tag{5}$$

Neural Networks

The Neural Network (NN) has two components. The first is a CNN that takes as input real-scale images of the beam cross-sections used for training. The CNN, which works as a feature extractor, uses Sobel and Laplace filters to extract valuable geometric information from the images. For each structural case, the CNN output vector is concatenated with a vector containing the specific structural theory used, the slenderness ratio (L/h), and the beam material. Each structural theory is encoded as a sequence of 0s and 1s, where 1 represents an active generalized variable, e.g.,

Materials Research Proceedings 69 (2026) 1176-1180 https://doi.org/10.21741/9781644904251-202

$$u_x = u_{x_1} + xu_{x_2} + x^2u_{x_4} + z^2u_{x_6} = [1\ 1\ 0\ 1\ 0\ 1] \quad (6)$$

The resulting arrays are fed into a DNN trained on the average error of the first 10 natural frequencies with respect to the reference fourth-order theory for each structural case computed by AAM. The trained NN predicts the accuracy of a kinematic theory for a generic structural case, taking as inputs the image of the cross-section, the L/h ratio, and the beam material, see Fig. 2.

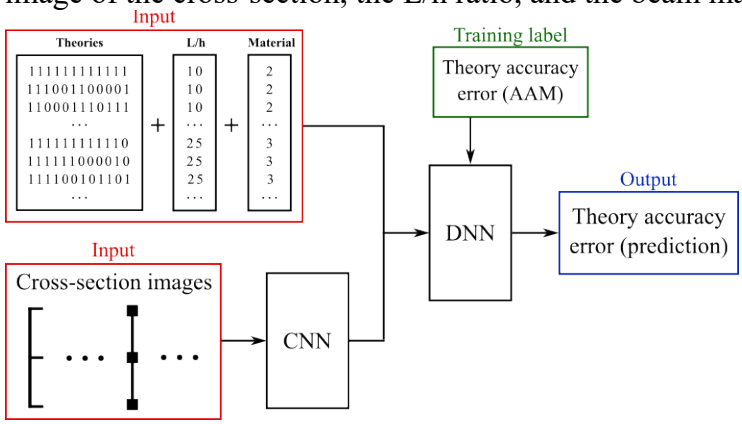


Figure 2: NN architecture

Numerical Results

The dataset consists of 1080 structural cases, each computed using AAM. Each AAM analysis comprises 4096 FEM modal analyses. To train the DNN, only 10% of these analyses were randomly selected and used. The results shown hereafter refer to two different beams, both clamped-free and made of titanium. The material properties are: E=115 GPa, ν=0.33, ρ=4500 kg/m^3. The first, whose cross-section is shown in Fig. 3, is a stiffened spar included in the network training. The length L is equal to 10m, the height of the cross section is 1m, the sides of the three equally spaced squared stiffeners are 4 cm, while the thickness of the web is 2 mm. The Best Theory Diagrams (BTD) computed by AAM and DNN are shown in Fig. 4, while Tables 1 and 2 report the best theories and their accuracies, from AAM and DNN, respectively. In these tables, the black triangle indicates that the generalized variable is active. The network's predictive capabilities were analyzed by testing different beams not used during network training. A stiffened spar not involved in the network training is shown in Fig. 5, with a length L of 8 m, a height "h" of the cross-section of 1 m, and the side of the squared stringer is 4 cm. The web thickness is 2 mm. The stringers are not equally spaced, with the middle stringer located at h/3 from the bottom of the cross-section. Figure 6 shows the BTD for this structural case, while Tables 3 and 4 report the best theories and their accuracies.

Figure 3: Stiffened spar cross-section included in the network training

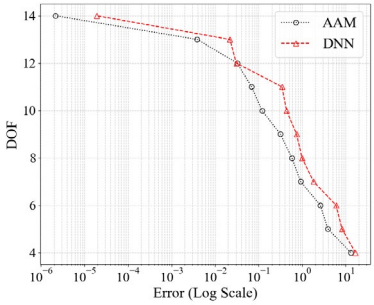


Figure 4: BTD of the stiffened spar included in the network training

DOF	*const.*	x	z	x^2	xz	z^2	x^3	x^2z	xz^2	z^3	x^4	x^3z	x^2z^2	xz^3	z^4	$\%E_{AVG}$
14	▲	▲	▲	▲	▲	▲	▲	▲	▲	▲	△	▲	▲	▲	▲	2.141E-06
13	▲	▲	▲	▲	▲	▲	△	▲	▲	▲	△	▲	▲	▲	▲	3.877E-03
12	▲	▲	▲	▲	▲	▲	△	▲	▲	▲	△	▲	△	▲	▲	3.216E-02
11	▲	▲	▲	▲	▲	▲	△	▲	▲	△	△	▲	△	▲	▲	6.892E-02
10	▲	▲	▲	▲	▲	▲	△	▲	▲	△	△	△	△	▲	▲	1.193E-01
9	▲	▲	▲	▲	▲	▲	△	▲	▲	△	△	△	△	▲	△	3.167E-01
8	▲	▲	▲	▲	▲	▲	△	△	▲	△	△	△	△	▲	△	5.798E-01
7	▲	▲	▲	▲	▲	▲	△	△	▲	△	△	△	△	△	△	9.229E-01
6	▲	▲	▲	▲	▲	▲	△	△	△	△	△	△	△	△	△	2.604E+00
5	▲	▲	▲	▲	▲	△	△	△	△	△	△	△	△	△	△	3.903E+00
4	▲	▲	▲	△	▲	△	△	△	△	△	△	△	△	△	△	1.305E+01

Table 1: Best theories from AAM of the stiffened spar included in the network training

DOF	*const.*	x	z	x^2	xz	z^2	x^3	x^2z	xz^2	z^3	x^4	x^3z	x^2z^2	xz^3	z^4	$\%E_{AVG}$
14	▲	▲	▲	▲	▲	▲	▲	▲	▲	▲	△	▲	▲	▲	▲	1.897E-05
13	▲	▲	▲	▲	▲	▲	△	▲	▲	▲	△	▲	▲	▲	▲	2.193E-02
12	▲	▲	▲	▲	▲	▲	△	▲	▲	▲	△	▲	△	▲	▲	3.064E-02
11	▲	▲	▲	▲	▲	▲	△	▲	▲	▲	△	△	△	▲	▲	3.443E-01
10	▲	▲	▲	▲	▲	▲	△	▲	▲	△	△	△	△	▲	▲	4.374E-01
9	▲	▲	▲	▲	▲	▲	△	△	▲	▲	△	△	△	▲	△	7.439E-01
8	▲	▲	▲	▲	▲	▲	△	△	▲	△	△	△	△	▲	△	9.949E-01
7	▲	▲	▲	▲	▲	▲	△	△	▲	△	△	△	△	△	△	1.820E+00
6	▲	▲	▲	▲	▲	▲	△	△	△	△	△	△	△	△	△	6.002E+00
5	▲	▲	▲	▲	▲	△	△	△	△	△	△	△	△	△	△	8.217E+00
4	▲	▲	▲	△	▲	△	△	△	△	△	△	△	△	△	△	1.665E+01

Table 2: Best theories from DNN of the stiffened spar included in the network training



Figure 5: Stiffened spar cross-section not included in the network training

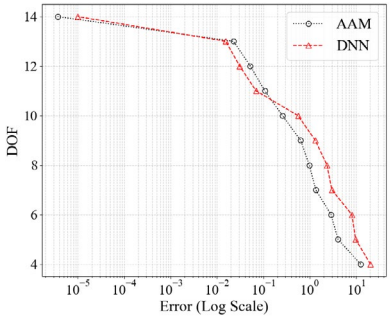


Figure 6: BTD of the stiffened spar not included in the network training

DOF	*const.*	x	z	x^2	xz	z^2	x^3	x^2z	xz^2	z^3	x^4	x^3z	x^2z^2	xz^3	z^4	$\%E_{AVG}$
14	▲	▲	▲	▲	▲	▲	▲	▲	▲	▲	△	▲	▲	▲	▲	3.664E-06
13	▲	▲	▲	▲	▲	▲	△	▲	▲	▲	△	▲	▲	▲	▲	2.275E-02
12	▲	▲	▲	▲	▲	▲	△	▲	▲	▲	△	△	▲	▲	▲	5.252E-02
11	▲	▲	▲	▲	▲	▲	△	▲	▲	▲	△	△	△	▲	▲	1.078E-01
10	▲	▲	▲	▲	▲	▲	△	▲	▲	△	△	△	△	▲	▲	2.586E-01
9	▲	▲	▲	▲	▲	▲	△	△	▲	△	△	△	△	▲	▲	6.384E-01
8	▲	▲	▲	▲	▲	▲	△	▲	▲	△	△	△	△	△	△	9.796E-01
7	▲	▲	▲	▲	▲	▲	△	△	▲	△	△	△	△	△	△	1.354E+00
6	▲	▲	▲	▲	▲	▲	△	△	△	△	△	△	△	△	△	2.882E+00
5	▲	▲	▲	▲	▲	△	△	△	△	△	△	△	△	△	△	4.086E+00
4	▲	▲	▲	△	▲	△	△	△	△	△	△	△	△	△	△	1.254E+01

Table 3: Best theories from AAM of the stiffened spar not included in the network training

DOF	*const.*	x	z	x^2	xz	z^2	x^3	x^2z	xz^2	z^3	x^4	x^3z	x^2z^2	xz^3	z^4	$\%E_{AVG}$
14	▲	▲	▲	▲	▲	▲	▲	▲	▲	▲	△	▲	▲	▲	▲	9.893E-06
13	▲	▲	▲	▲	▲	▲	△	▲	▲	▲	△	▲	▲	▲	▲	1.547E-02
12	▲	▲	▲	▲	▲	▲	△	▲	▲	▲	△	▲	△	▲	▲	3.097E-02
11	▲	▲	▲	▲	▲	▲	△	▲	▲	▲	△	△	△	▲	▲	6.975E-02
10	▲	▲	▲	▲	▲	▲	△	△	▲	▲	△	△	△	▲	▲	5.599E-01
9	▲	▲	▲	▲	▲	▲	△	△	▲	▲	△	△	△	▲	△	1.320E+00
8	▲	▲	▲	▲	▲	▲	△	△	▲	△	△	△	△	▲	△	2.359E+00
7	▲	▲	▲	▲	▲	▲	△	△	▲	△	△	△	△	△	△	3.007E+00
6	▲	▲	▲	▲	▲	△	△	▲	△	△	△	△	△	△	△	8.118E+00
5	▲	▲	▲	▲	▲	△	△	△	△	△	△	△	△	△	△	9.807E+00
4	▲	▲	▲	△	▲	△	△	△	△	△	△	△	△	△	△	2.041E+01

Table 4: Best theories from DNN of the stiffened spar not included in the network training

Conclusion

This work presents a methodology and a tool for the accuracy estimation of a beam theory and its generalized variables for a given problem. In addition, it assesses the minimum number of DOF required to obtain that level of accuracy. The proposed methodology uses NN to correlate structural theories, geometries, materials, and accuracy. The results show a strong correlation between AAM results and DNN predictions for the beams included in the network's training set. For those not included in the training, the results remain excellent for accuracy prediction, while the correlation slightly decreases for predicting the best theories. The results indicate that, in both cases, achieving errors below 10% requires at least two parabolic terms, while errors under 1% can only be ensured by using the complete parabolic expansion along with two or three additional higher-order terms. The results are highly problem-dependent, as the specific higher-order terms involved vary from case to case.

References

[1] Euler L. De curvis elasticis. Lausanne and Geneva: Bousquet, 1744.

[2] Timoshenko S.P. On the transverse vibrations of bars of uniform cross-section. The London, Edinburgh, and Dublin Philosophical Magazine and Journal of Science, 43(253):125-131, 1922. https://doi.org/10.1080/14786442208633855

[3] Timoshenko S.P. On the correction for shear of the differential equation for transverse vibrations of prismatic bars. The London, Edinburgh, and Dublin Philosophical Magazine and Journal of Science, 41(245):744-746, 1921. https://doi.org/10.1080/14786442108636264

[4] Carrera E. and Petrolo M. On the effectiveness of higher-order terms in refined beam theories. Journal of Applied Mechanics, 78(2):021013, 11 2010. https://doi.org/10.1115/1.4002207

[5] Carrera E., Pagani A., Petrolo M., and Zappino E. Recent developments on refined theories for beams with applications. Mechanical Engineering Reviews, 2(2):14-00298-14-00298, 2015. https://doi.org/10.1299/mer.14-00298

[6] Giunta G., Biscani F., Belouettar S, Ferreira A.J.M., and Carrera E. Free vibration analysis of composite beams via refined theories. Composites Part B: Engineering, 44(1):540-552, 2013. https://doi.org/10.1016/j.compositesb.2012.03.005

[7] Petrolito J. Stiffness analysis of beams using a higher-order theory. Computers & Structures, 55(1):33-39, 1995. https://doi.org/10.1016/0045-7949(94)00505-W

[8] Argyridi A.K. and Sapountzakis E.J. Higher order beam theory for linear local buckling analysis. Engineering Structures, 177:770-784, 2018. https://doi.org/10.1016/j.engstruct.2018.08.069

[9] Carrera E., Cinefra M., Petrolo M., and Zappino E. Finite element analysis of structures through unified formulation. John Wiley & Sons, 2014. https://doi.org/10.1002/9781118536643

[10] Petrolo M., Iannotti, P. Best Theory Diagrams for Laminated Composite Shells Based on Failure Indexes. Aerotec. Missili Spaz. 102, 199-218 (2023). https://doi.org/10.1007/s42496-023-00158-5 https://doi.org/10.1007/s42496-023-00158-5

[11] Thai H.-T., Machine learning for structural engineering: A state-of-the-art review. Structures, 38:448-491, 2022. https://doi.org/10.1016/j.istruc.2022.02.003

[12] Petrolo M., Pagani A., Carrera E., Candita G., Iannotti P. Mapping beam cross-section features to higher-order generalized variables using machine learning. Thin-Walled Structures, Volume 218, Part C, (2026). https://doi.org/10.1016/j.tws.2025.114108 https://doi.org/10.1016/j.tws.2025.114108

[13] Petrolo M., Pagani A., Candita G., Iannotti P., and Carrera E. Assessment of multi-fidelity structural theories for dynamic analyses using machine learning. In Proceedings of the ASME 2025 Aerospace Structures, Structural Dynamics, and Materials Conference SSDM2025, Houston, 2025. https://doi.org/10.1115/SSDM2025-152306

Materials Research Proceedings 69 (2026) 1181-1186 https://doi.org/10.21741/9781644904251-203

Adaptive Multi-Fidelity Framework for Defect and Damage Tolerant Composite Structures

Dario Zamani[1,a *], Chiara Franceschini[1,b], Marco Petrolo[1,c], Alfonso Pagani[1,d] and Erasmo Carrera[1,e]

[1]MUL 2 Lab, Department of Mechanical and Aerospace Engineering, Politecnico di Torino, Corso Duca degli Abruzzi 24, 10129 Turin, Italy

[a]dario.zamani@polito.it, [b]chiara.franceschini@polito.it, [c]marco.petrolo@polito.it, [d]alfonso.pagani@polito.it, [e]erasmo.carrera@polito.it

Keywords: Multi-Fidelity, Gaussian Process Regression, Carrera Unified Formulation, Uncertainty Quantification, Damage Tolerance

Abstract. This work presents an adaptive multi-fidelity framework for uncertainty quantification in defect-tolerant composite structures. The approach couples the Carrera Unified Formulation (CUF) for generating consistent low- and high-fidelity structural theories with an adaptive Gaussian Process Regression (GPR) surrogate that learns their correlation. High-fidelity simulations are selectively activated in regions of high uncertainty, minimizing computational cost while preserving accuracy. The framework enables probabilistic estimation of stresses and failure indices with confidence intervals and is validated against 3D Abaqus benchmarks.

Introduction

The increasing demand for lightweight and high-performance structures has driven the adoption of advanced composite materials, with manufacturing techniques like Automated Fiber Placement (AFP) enabling highly optimized and complex designs [1-2]. However, the reliability of these components is often compromised by the interplay of manufacturing defects, such as gaps, overlaps and fiber misalignment, and inherent material and load variability [3]. Designing defect and damage-tolerant components therefore requires a rigorous quantification of how these uncertainties shape local stress fields and drive damage evolution, including crack propagation. Traditional deterministic or single fidelity models are either prohibitively expensive for comprehensive probabilistic analysis or too simplistic to capture the governing physics, leaving a critical gap in robust composite design methodologies.

This work proposes a novel Multi-Fidelity (MF) probabilistic framework to overcome these limitations. The methodology is built upon the Carrera Unified Formulation (CUF) [4], which provides a consistent hierarchical basis for generating both computationally efficient Equivalent Single-Layer (ESL) models and highly accurate Layer-Wise (LW) models. An adaptive Gaussian Process Regression (GPR) [5-6] surrogate learns the correlation between these fidelity levels, drastically reducing the need for expensive High-Fidelity (HF) simulations. This intelligent learning process actively queries new HF data only in regions of high predictive uncertainty, maximizing information gain while minimizing computational cost. The conceptual workflow of this adaptive framework is illustrated in Fig. 1. This integrated framework enables an efficient and accurate uncertainty quantification for damage onset assessment, allowing for the direct calculation of key probabilistic metrics such as through-the-thickness stress profiles with confidence intervals, probability distributions of critical failure indices, and the overall probability of failure. To ensure methodological rigor, the framework's predictions are validated against benchmark analyses using high-fidelity 3D models in Abaqus.

Content from this work may be used under the terms of the Creative Commons Attribution 3.0 license. Any further distribution of this work must maintain attribution to the author(s) and the title of the work, journal citation and DOI. Published under license by Materials Research Forum LLC.

Materials Research Proceedings 69 (2026) 1181-1186 https://doi.org/10.21741/9781644904251-203

Furthermore, the framework extends to progressive damage [7] prediction by combining Low-Fidelity (LF) and high-fidelity models along the damage evolution path. The LF model efficiently captures the global structural response and damage progression, while the adaptive learning strategy selectively deploys HF simulations when approaching critical failure thresholds. A separable GPR surrogate corrects the entire damage history, enabling accurate reconstruction of high-fidelity crack-growth curves across the uncertainty space with minimal computational cost.

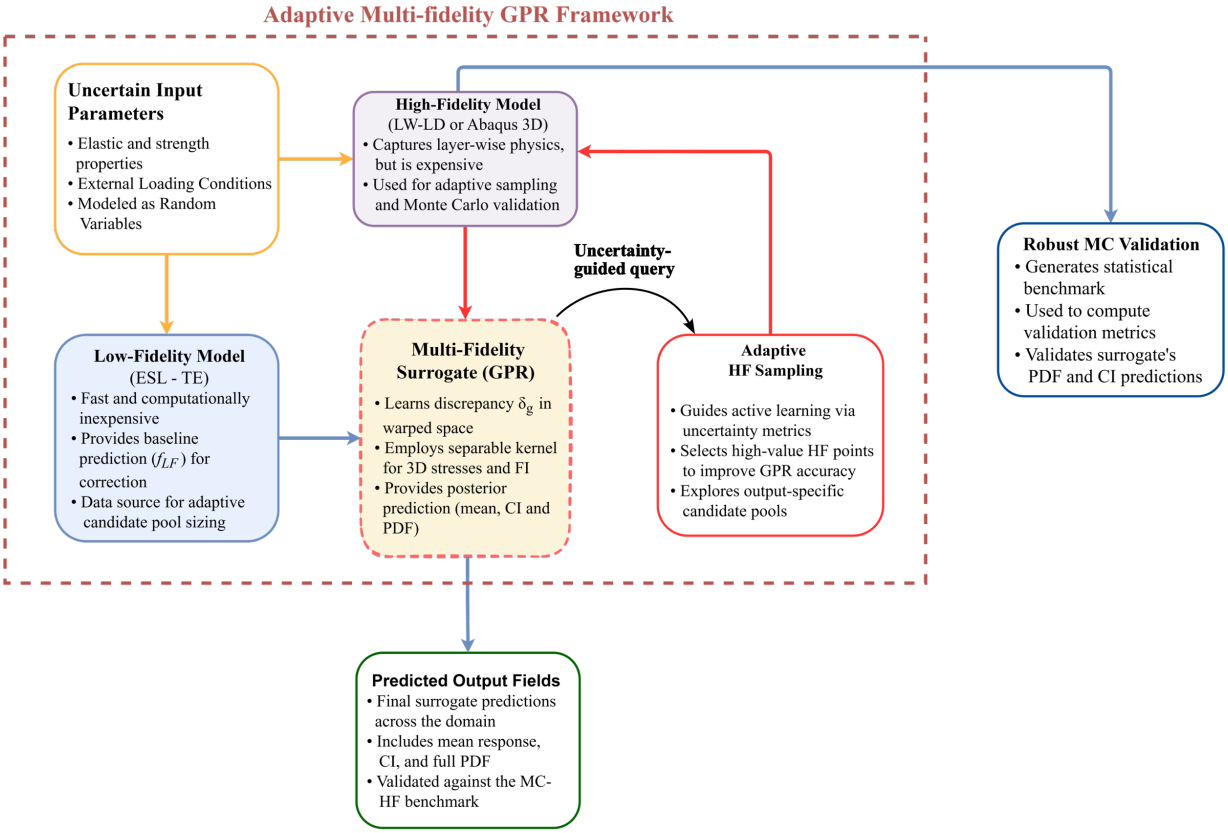


Figure 1. Adaptive multi-fidelity GPR framework combining low-fidelity predictions with selective high-fidelity corrections to provide probabilistic failure and stress predictions validated by Monte Carlo.

Unified finite elements

In this work, CUF formalism is used to implement 2D FE. The 3D displacement field can be expressed using arbitrary through-the-thickness expansion functions $\boldsymbol{F_\tau(z)}$ as follows:

$$\boldsymbol{u}(x,y,z) = F_\tau(z)\boldsymbol{u}_\tau(x,y).\ \tau = 1,\dots,M \tag{1}$$

The symbol M represents the number of expansion terms, and $\boldsymbol{u}_\tau(x,y)$ represents the vector containing the generalized displacements, with τ indicating summation. Examining multi-layered structures typically employs either an Equivalent-Single-Layer (ESL) or Layer-Wise (LW) approach. In this manuscript, ESL models utilize Taylor polynomials represented by $F_\tau(z)$; while LW employs Lagrange polynomials over individual layers and ensures the continuity of displacements at layer interfaces. Utilizing the FE and shape functions $N_i(x,y)$, the displacement field becomes:

$$\boldsymbol{u}(x,y,z) = N_i(x,y)F_\tau(z)\boldsymbol{q}_{\tau i}(x,y).\ i = 1,\dots,N_n \tag{2}$$

Materials Research Proceedings 69 (2026) 1181-1186 https://doi.org/10.21741/9781644904251-203

In Eq. (2), $\boldsymbol{q}_{\tau i}$ are the unknown nodal variables, with N_n denoting the number of nodes per element. This work employs 2D nine-node quadratic elements for the in-plane discretization.

The governing equations are derived using the Principle of Virtual Displacements (PVD), which asserts that the virtual variation of internal strain energy, $\delta\mathcal{L}_{int}$, equals the virtual work of external forces, $\delta\mathcal{L}_{ext}$, minus inertia forces, $\delta\mathcal{L}_{ine}$. Specifically, $\delta\mathcal{L}_{int}$ can be written as:

$$\delta\mathcal{L}_{int} = \delta\boldsymbol{q}_{sj}^{T}\left[\int_{V}\boldsymbol{D}^{T}(N_jF_s)\,\widetilde{\boldsymbol{C}}\boldsymbol{D}(N_iF_\tau)\,dV\right]\boldsymbol{q}_{\tau i} = \delta\boldsymbol{q}_{sj}^{T}\boldsymbol{k}_{0}^{ij\tau s}\boldsymbol{q}_{\tau i}, \tag{3}$$

where $\boldsymbol{k}_0^{ij\tau s}$ is the 3 × 3 Fundamental Nucleus (FN) of the stiffness matrix, invariant regardless of 2D shape function order and through-the-thickness expansion. $\boldsymbol{D}(\cdot)$ is the differential operator matrix with geometric relations, and $\widetilde{\boldsymbol{C}}$ is the material stiffness matrix in the global reference frame, i.e., $\widetilde{\boldsymbol{C}} = \boldsymbol{T}(x,y)^{T}\boldsymbol{C}\boldsymbol{T}(x,y)$. The global stiffness matrix, $\boldsymbol{K}$**,** is obtained by iterating over FN's with indices i, j, τ and s to compute element-level matrices, which are then assembled for the global structure.

MF - GPR framework

The approach integrates GPR with a multi-fidelity strategy combining LF (ESL) and HF (LW) simulations. Uncertainties stem from material properties and applied loads, as well as potential manufacturing defects such as fiber misalignments, gaps, overlaps, and resin-rich zones. Random samples are generated using Latin Hypercube Sampling (LHS) to ensure uniform coverage of the input space. GPR models the relationship between input parameters **x** and outputs f(**x**) as a Gaussian Process (GP) defined by a mean function μ(x) and a covariance function κ(x, x′):

$$f(x) \sim \mathcal{GP}(\mu(x), \kappa(x,x')) \tag{4}$$

$$\kappa(x,x') = \sigma_f^2 \exp\left(-\frac{\|x-x'\|^2}{2l^2}\right) \tag{5}$$

where σ_f^2 and l the kernel variance and length scale for each output. Using training data (X, y), the GP predicts outputs at new points by combining the mean and variance derived from the model. The multi-fidelity framework accounts for the discrepancy between low- and high-fidelity simulations. The high-fidelity response $\hat{f}_{HF}(x)$ is expressed as:

$$\hat{f}_{HF}(x) = f_{LF}(x) + \Delta(x) \tag{6}$$

where f_{LF} is the LF response and $\Delta(x)$ is the discrepancy between LF and HF modeled as a GP. This formulation enables accurate and efficient structural predictions under uncertainties by merging LF trends with corrections derived from high-fidelity data.

Damage model

The Hashin 3D criterion predicts the onset of fiber and matrix failure under tension and compression by evaluating stresses in three dimensions. When any failure index reaches unity, the corresponding damage mode is activated, initiating stiffness degradation through an evolution law. Hashin 3D criterion is adopted to evaluate three failure modes: fiber tension, fiber compression, and matrix compression.

$$F_{ft} = \left(\frac{\sigma_{11}}{X_T}\right)^2 + \alpha_f\left[\left(\frac{\sigma_{12}}{S_{12}}\right)^2 + \left(\frac{\sigma_{13}}{S_{13}}\right)^2\right]$$

Materials Research Proceedings 69 (2026) 1181-1186 https://doi.org/10.21741/9781644904251-203

$$F_{mt} = \left(\frac{\sigma_{22}+\sigma_{33}}{Y_T}\right)^2 + \frac{1}{S_{23}^2}(\sigma_{23}^2 - \sigma_{22}\sigma_{33}) + \left(\frac{\sigma_{12}}{S_{12}}\right)^2 + \left(\frac{\sigma_{13}}{S_{13}}\right)^2$$

$$F_{fc} = \left(\frac{\sigma_{11}}{X_C}\right)^2$$

F quantify the failure, the first subscript indicates whether the failure concerns the matrix (M) or the fiber (F), while the second whether it is tensile (T) or compressive (C). X is the strength of the fiber, if compressive X_C if traction X_T. S_{12}, S_{13} and S_{23} are the shear strengths. Y_T is the tensile strength of the matrix.

Only for matrix compression is considered the Puck criterion according to which the fracture of the matrix is due to stress σ_{nn}, σ_{nl}, σ_{nl}, which are respectively the normal, longitudinal shear and transverse stresses to the fracture plane.

$$F_{mc} = \left(\frac{\sigma_{nt}}{S_{23}^A - \eta_{nt}\sigma_{nn}}\right)^2 + \left(\frac{\sigma_{nl}}{S_{13} - \eta_{nl}\sigma_{nn}}\right)^2$$

η_{nt} and η_{nl} characterize the internal friction of the material while S_{23}^A is the transverse shear strength in the fracture plane.

Once the criterion for the initiation of failure is triggered, the progression of the damage is governed by a linear pattern of damage evolution, so that the stiffness of the material decreases until the final failure. The linear model is based on the equivalent displacements δ_{eq}. Using a unified subscript $P \in \{ft, fc, mt, mc\}$ to represent the four modes of damage, a parameter for the evolution of the damage is defined for each mode d_P,

$$d_p = \frac{\delta_{eq}^u(\delta_{eq} - \delta_{eq}^0)}{\delta_{eq}(\delta_{eq}^u - \delta_{eq}^0)}$$

$\delta_{eq}^0 = \delta_{eq,F=1}$ is the equivalent displacement at the beginning of the damage, while δ_{eq}^u is at the final failure.

The constitutive elastic stress-strain relation during the damage evolution can be written as

$$\sigma = C_{dam}\epsilon$$

where C_{dam} is the stiffness matrix in the damage state, function of damage parameters d_P.

Results

The case study analyzes a composite open-hole plate under tensile loading using the proposed multi-fidelity (MF) framework. The configuration follows a benchmark from Ref. [8] with a symmetric $[45°/90°/-45°/0°]_{3s}$ laminate. Material and load properties are modeled as normal or uniform random variables. LF analyses use an ESL-TE1 model, while HF analyses employ an LW model with one LD1 expansion per ply. Figures 2 and 3 show the probabilistic distributions of the Fiber Tension (FT) and delamination failure indices across the laminate thickness, comparing low-, high-, and multi-fidelity models with their 90% confidence intervals. The MF predictions accurately reproduce the HF trends with a fraction of the computational cost.

Materials Research Proceedings 69 (2026) 1181-1186 https://doi.org/10.21741/9781644904251-203

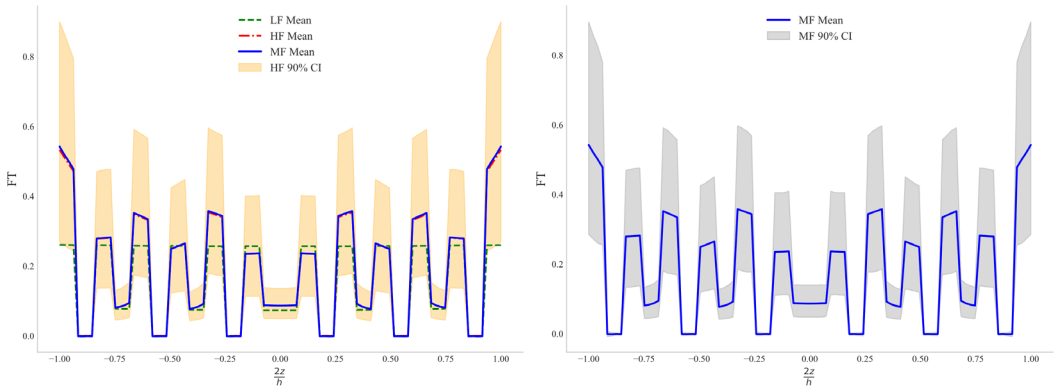


Figure 2. Fiber Tension (FT) failure index through the laminate thickness obtained from LF, HF, and MF models with corresponding 90% confidence intervals.

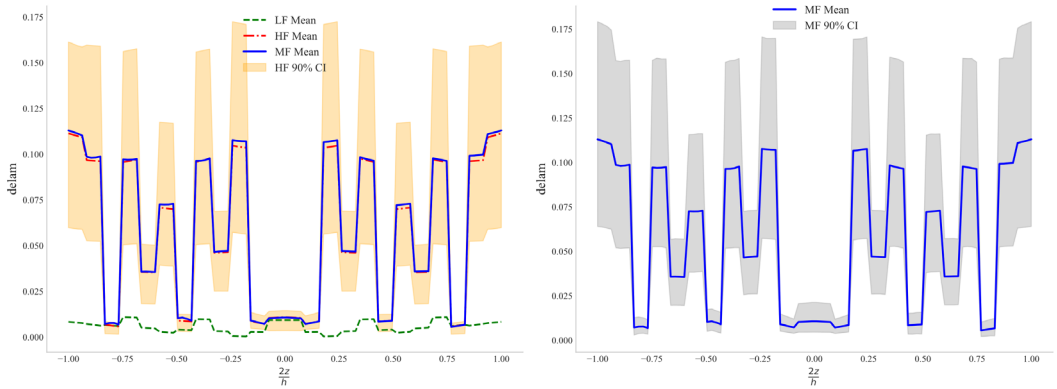


Figure 3. Delamination failure index through the laminate thickness obtained from LF, HF, and MF models with corresponding 90% confidence intervals.

Figure 4 presents the stress–strain response of a composite single element under tension with a symmetric laminate stacking sequence $\theta = [45,90,-45,0]^{\circ}_{4s}$. The uncertainties are applied to the material properties and strength allowables. The MF surrogate accurately reconstructs the high-fidelity (HF) reference using only a limited number of HF simulations (~10%), achieving close agreement with the deterministic curve and providing 90% confidence bounds on the predicted stress field.

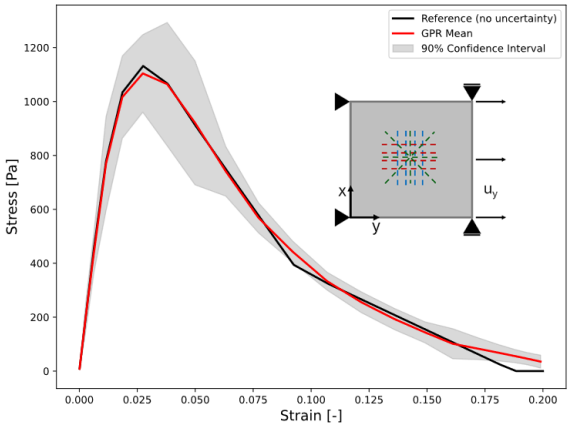


Figure 4. Multi-fidelity stress-strain curve under uncertainties

Conclusions

The proposed adaptive multi-fidelity framework effectively combines CUF-based structural models with Gaussian Process Regression to quantify the impact of material and manufacturing uncertainties on composite failure. By integrating low- and high-fidelity analyses within an active learning strategy, it achieves high accuracy with a fraction of the computational cost. These results demonstrate its potential for Reliability-Based Design Optimization (RBDO) of lightweight composite structures [9].

Acknowledgments

This study was carried out within the Space It Up project funded by the Italian Space Agency, ASI, and the Ministry of University and Research, MUR, under contract n. 2024-5-E.0 - CUP n. I53D24000060005. The support of the Italian Ministry of University and Research through the program FARE-III Edition (project LOUD, No. R20EENHZEJ) is also acknowledged.

References

[1] D. Zamani, A. Racionero Sánchez-Majano, A. Pagani. Mixed-integer, multi-objective layerwise optimization of variable-stiffness composites with gaps and overlaps. Struct Multidisc Optim 68, 107 (2025). https://doi.org/10.1007/s00158-025-04043-6

[2] A. Pagani, A. R. Sánchez-Majano, M. Petrolo: Influence of structural theories on optimal fiber distributions in tow-steered composites considering local strain and stress. Aerotecnica Missili e Spazio (2025). https://doi.org/10.1007/s42496-025-00275-3

[3] A. Pagani, A. R. Sánchez-Majano, D. Zamani, M. Petrolo, E. Carrera: Fundamental frequency layer-wise optimization of tow-steered composites considering gaps and overlaps. Aerotecnica Missili e Spazio (2024). https://doi.org/10.1007/s42496-024-00212-w

[4] E. Carrera, M. Cinefra, M. Petrolo, E. Zappino. Finite Element Analysis of Structures through Unified Formulation. Wiley & Sons, Hoboken, New Jersey, USA. 2014. https://doi.org/10.1002/9781118536643

[5] C. Rasmussen, C. Williams. Gaussian Processes for Machine Learning. MIT Press, Cambridge, Massachusetts, USA. 2005. https://doi.org/10.7551/mitpress/3206.001.0001

[6] M. Kanagawa, P. Hennig, D. Sejdinovic, B. K. Sriperumbudur. Gaussian Processes and Kernel Methods: A Review on Connections and Equivalences. arXiv preprint arXiv:1807.02582. 2018.

[7] M. H. Nagaraj, M. Petrolo, E. Carrera. A global-local approach for progressive damage analysis of fiber-reinforced composite laminates. Thin-Walled Structures, 169:108343, 2021. https://doi.org/10.1016/j.tws.2021.108343

[8] A. Catapano, M. Montemurro. Strength optimisation of variable angle-tow composites through a laminate-level failure criterion. Journal of Optimization Theory and Applications, 187:1-25, 2020. https://doi.org/10.1007/s10957-020-01750-6

[9] D. Zamani, A. Pagani, M. Petrolo, E. Carrera. Multi-patch hybrid optimization of composite wings. III ECCOMAS Thematic Conference on Multidisciplinary Design Optimization of Aerospace Systems (Lisbon, 22-24 April 2025).

Materials Research Proceedings 69 (2026) 1187-1191 https://doi.org/10.21741/9781644904251-204

Geometrically Non-Linear Thermo-Elastic Analysis of Variable Angle Tow Composite Plates Thorugh Layerwise Models

Francesca Bracaglia[1,a*], Alfonso Pagani[1,b], Enrico Zappino[1,c] and Erasmo Carrera[1,d]

[1]Mul2 Lab, DIMEAS, Politecnico di Torino, Corso Duca degli Abruzzi 24, Torino , Italy

[a]francesca.bracaglia@polito.it, [b]alfonso.pagani@polito.it, [c]enrico.zappino@polito.it, [d]erasmo.carrera@polito.it

Keywords: Thermo-Elastic Analysis, Geometrically Nonlinear Analysis, Variable Stiffness Composite, Thermal Stresses

Abstract. Composite materials are widely used in the engineering field due to their valuable specific properties and the adaptability of fiber orientation and lay-up to specific load conditions. The tailorability of composite materials is increased with Variable Angle Tows (VAT) composite materials, in which fiber deposition can follow a curved path. These properties lead to a higher anisotropy, and non-linear analyses are required to ensure a good description of the behaviour. The study focuses on the post-buckling configuration of the VAT model and examines the impact of curved fiber paths. The analyses are conducted to compare high-order theory for describing the nonlinear behaviour of the VAT composite structure. Additionally, the post-buckling shape of VAT plates is thoroughly explored, leading to the selection of the most accurate model for characterizing plate behaviour.

Introduction

Composite materials present valuable properties, such as high specific strength and stiffness, thermal stability, and the adaptability of lamination and lay-up to manage the mechanical and thermal properties of the structure [1]. Thanks to advanced manufacturing techniques, the capabilities of the constant-stiffness composite laminate are enhanced by the introduction of Variable Angle Tow (VAT) composite materials, which have been developed in recent years [2]. The VATs are characterized by the curvilinear path of the reinforced fibers. Consequently, the properties of VATs vary continuously within each lamina, depending on the curvature imposed on the fibers, opening a vast range of possibilities for the adaptability of the structures to the specific load conditions [3]. Due to their high tailoring capability, VATs are mainly studied in the field of optimization to adapt fiber orientation to different loads or geometric configurations.

Additionally, the remarkable stability under thermal and high-temperature conditions enables the use of this class of material in applications where temperature is a primary load factor. Among the key concerns in VAT plate analysis, thermal stability is a focal point, as demonstrated in [4]. Furthermore, this class of materials, which has been extensively studied in the field of linear or linearized analysis under mechanical and thermal loads, lacks studies in the nonlinear thermal field. The reported tailoring capabilities are suitable for adapting the fiber deposition to the load distribution. However, the post-buckling and high-deflection configurations can be significantly affected by the curved deposition. Under variation in the applied temperature, the presence of curved fibers can lead to unexpected phenomena, and nonlinear investigations are necessary to ensure a correct level of confidence in the results.

This paper utilizes the Carrera Unified Formulation (CUF) to develop a high-order plate theory within the finite element method framework, offering novel insights into the intricate three-dimensional phenomena exhibited by VAT structures [5]. The governing equations are obtained from the Principle of Virtual Displacement (PVD), and the nonlinear problem is solved through

Content from this work may be used under the terms of the Creative Commons Attribution 3.0 license. Any further distribution of this work must maintain attribution to the author(s) and the title of the work, journal citation and DOI. Published under license by Materials Research Forum LLC.

Materials Research Proceedings 69 (2026) 1187-1191 https://doi.org/10.21741/9781644904251-204

the Newton-Raphson procedure in conjunction with the arc-length constraint. The geometrical nonlinearity is described using the full Green-Lagrange strain tensor, and its accuracy is compared with that of the simplified von Kármán nonlinearities model. The analyses adopt a layer-wise approach, and a comparison to the equivalent single-layer model is also presented. It is demonstrated that the layer-wise model in combination with high-order theories provides an accurate description of the through-the-thickness primary unknowns, facilitating a detailed analysis of nonlinear thermal stresses within the component.

Non-linear thermal formulation

The thermo-mechanical field is expressed in a decoupled approach where the unknowns of the problem are the displacement components, which are expressed through the CUF and FEM as the combination of nodal displacements $\boldsymbol{q}_{i\tau}$, shape functions $\boldsymbol{N}_i(x,y)$, and expansion functions $\boldsymbol{F}_\tau(z)$, as reported in Eq. (1). More details about CUF can be found in [6].

$$\boldsymbol{u}(x,y,z) = \boldsymbol{F}_\tau(z)\,\boldsymbol{u}_\tau(x,y) = \boldsymbol{F}_\tau(z)\boldsymbol{N}_i(x,y)\,\boldsymbol{q}_{i\tau} \quad \tau = 1,2,\dots,M \quad i = 1,2,\dots,N_n \qquad (1)$$

Where the double indices mean sum, M and N_n are the number of expansion terms and the number of nodes respectively.

The VAT orientation is considered to vary linearly, following the notation by G*ü*rdal et al. [7]; the lamination is denoted as $[\Phi < T_0, T_1 >]$, where Φ is the reference system rotation angle from the x-axis, T_0 and T_1 are the fiber orientations in the center and at the edge of the plate, respectively.

It is possible to describe the strain and the stresses as the sum of the mechanical linear and non-linear terms and the thermal component, as reported in Eq.s (2), (3), where the nonlinearities are incorporated in the formulation using the full Green-Lagrange strain tensor, see [8].

$$\boldsymbol{\varepsilon} = \boldsymbol{\varepsilon}_m + \boldsymbol{\varepsilon}_\theta = (\boldsymbol{b}_l + \boldsymbol{b}_{nl})\boldsymbol{u} - \boldsymbol{\alpha}\,\Delta T \qquad (2)$$

$$\boldsymbol{\sigma} = \boldsymbol{C}\,\boldsymbol{\varepsilon} = \boldsymbol{C}[(\boldsymbol{b}_l + \boldsymbol{b}_{nl})\,\boldsymbol{u} - \boldsymbol{\alpha}\,\Delta T] = \boldsymbol{\sigma}_l + \boldsymbol{\sigma}_{nl} - \boldsymbol{\beta}\Delta T \qquad (3)$$

Where the vector $\boldsymbol{\beta}$ is the thermo-mechanical coupling coefficient. Due to the presence of VAT the fiber orientation vary from a point to another and consequently matrix $\boldsymbol{C}$ becomes a function of the position, $\boldsymbol{C}(x, \mathrm{y})$ as well as vector $\boldsymbol{\beta}\,(x,y)$.

The governing equations are obtained though the PVD as reported in Eq.s (4), (5).

$$\delta L_{int} = \int_V \delta\boldsymbol{\varepsilon}^T\boldsymbol{\sigma} = \int_V \delta\boldsymbol{\varepsilon}_m^T\boldsymbol{C}\boldsymbol{\varepsilon}_m dV - \int_V \delta\boldsymbol{\varepsilon}_m^T\,\boldsymbol{\beta}\Delta T\,dV = \delta\boldsymbol{q}^T\,\boldsymbol{K}_s\boldsymbol{q} - \delta\boldsymbol{q}^T\,\boldsymbol{F}_\theta = 0 \qquad (4)$$

$$\delta\boldsymbol{q} : \boldsymbol{K}_S\,\boldsymbol{q} - \boldsymbol{F}_\theta = 0 \qquad (5)$$

Where $\boldsymbol{K}_S$ is the secant stiffness matrix which depends only on the mechanical components and $\boldsymbol{F}_\theta$ is the nonlinear vector of thermal loads. Eq. (5) describes a nonlinear set of equations, and it is necessary to solve it in an iterative procedure. To use the Newton-Raphson method, the residual nodal force vector is defined as in Eq. (6). Furthermore, it is necessary to linearize the equation through a Taylor expansion about the known solution as reported in Eq. (7).

$$\boldsymbol{\varphi}_{res} = \boldsymbol{K}_S\,\boldsymbol{q} - \boldsymbol{F}_\theta \qquad (6)$$

$$\boldsymbol{\varphi}_{res}(\boldsymbol{q}+\delta\boldsymbol{q}, \Delta T + \delta\Delta T) = \boldsymbol{\varphi}_{res}(\boldsymbol{q}, \Delta T) + \left.\frac{\partial\boldsymbol{\varphi}_{res}}{\partial\boldsymbol{q}}\right|_q \delta\boldsymbol{q} + \left.\frac{\partial\boldsymbol{\varphi}_{res}}{\partial\Delta T}\right|_{\Delta T} \delta\lambda(\Delta T)_{ref} = 0 \qquad (7)$$

Materials Research Proceedings 69 (2026) 1187-1191 https://doi.org/10.21741/9781644904251-204

From Eq. (7) it is possible to define the tangent stiffness matrix as $\boldsymbol{K}_T = \frac{\partial \boldsymbol{\varphi}_{res}}{\partial \boldsymbol{q}}\Big|_q$ and the tangent load vector as $\widetilde{\boldsymbol{F}}_\theta = -\frac{\partial \boldsymbol{\varphi}_{res}}{\partial \Delta T}\Big|_{\Delta T} (\Delta T)_{ref}$ which is composed of a linear and a nonlinear part. Substituting these definitions into Eq. (7) it is possible to write Eq.s (8) and (9).

$$\boldsymbol{\varphi}_{res}(\boldsymbol{q} + \delta\boldsymbol{q}, \Delta T + \delta\Delta T) = \boldsymbol{\varphi}_{res}(\boldsymbol{q}, \Delta T) + \boldsymbol{K}_T\delta\boldsymbol{q} - \left(\widetilde{\boldsymbol{F}}_{l_\theta} + \widetilde{\boldsymbol{F}}_{nl_\theta}\right)\delta\lambda = 0 \quad (8)$$

$$\boldsymbol{K}_T\delta\boldsymbol{q} = \widetilde{\boldsymbol{F}}_\theta\delta\lambda - \boldsymbol{\varphi}_{res}(\boldsymbol{q}, \Delta T) \quad (9)$$

Here, the loading scaling parameter is introduced as a new variable; as a result, a constraint equation is needed to close the problem. The obtained system can be written as in Eq. (10).

$$\begin{cases} \boldsymbol{K}_T\delta\boldsymbol{q} = \widetilde{\boldsymbol{F}}_\theta\delta\lambda - \boldsymbol{\varphi}_{res} \\ c(\delta\boldsymbol{q}, \delta\lambda) = 0 \end{cases} \quad (10)$$

The path following method is adopted, where it is possible to act on both $\delta\boldsymbol{q}$ and $\delta\lambda$, see [9].

Numerical results

The study is conducted on a rectangular plate with lamination $[90 \pm < 60, 90 >]_{2s}$. The plate edges are $a = 300$ mm and $b = 150$ mm with a thickness of 1.0176 mm. The material properties are E_1=181GPa, E_2= E_3=10.27GPa, G_{12}= G_{13}=7.17GPa ν_{12}= 0.28, $\alpha_1 = -0.11$ x $10^{-6}/°C$, $\alpha_2 = \alpha_3 = 25.2$ x $10^{-6}/°C$. The plate is subjected to uniform thermal load. The edges are fixed against normal displacements, and they are allowed to translate in the tangential direction. A convergence analysis is conducted on the plate, for which a mesh of 5 x 10 Q9 elements is selected. A validation is presented in Fig. 1 comparing the displacement in the center of the plate. Present results are obtained with LE2 and TE2 models and are compared to reference [10].

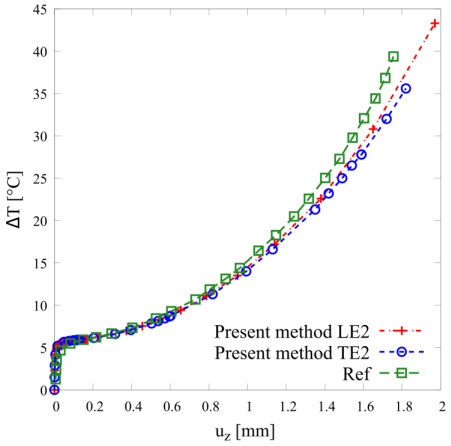


Figure 1: Displacement obtained through present method LE2 and TE2 compared to the reference [10].

From Fig. 1 it is possible to say that the displacements are in close agreement with the reference, which model is based on von Kármán-type nonlinearities and the Rayleigh-Ritz energy method. The discrepancy between the two results may be attributable to the differing formulations of the problem. In the present work the analysis is conducted to an higher level of temperature where the equilibrium curve change in shape due to the change of the post-buckling shape. From Fig. 2 it is possible to note the primary buckling and the secondary buckling of the plate.

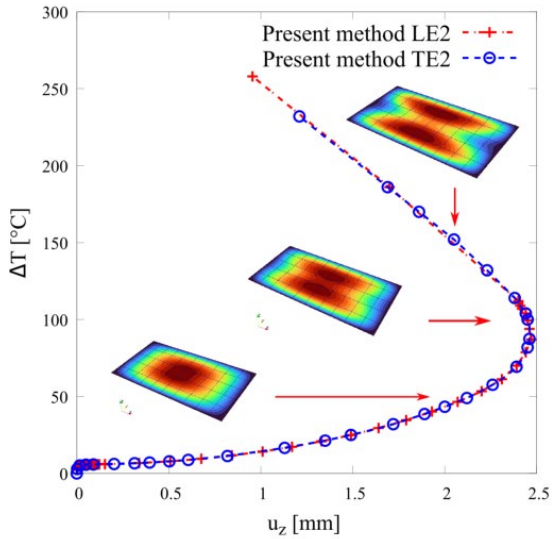


Figure 2: Displacement equilibrium curve obtained though the present method TE2 and LE2

Figure 3 shows the stress distribution for σ_x and σ_z along the thickness of the plate in Point A (75, 30) mm, considering the center of the plate as the origin of the reference system The results obtained demonstrate that, in the case of out-of-plane stresses, the interlaminar continuity is not guaranteed by the Taylor mode. Moreover, it is evident that a discrepancy in the results is present even when in-plane stresses are taken into consideration.

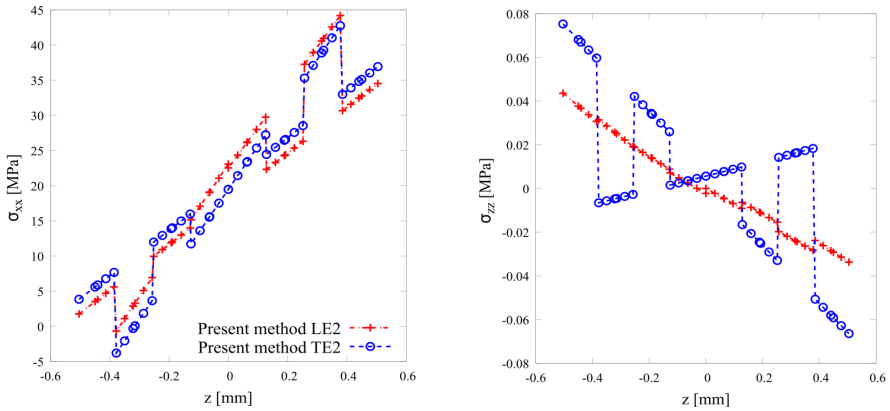


Figure 3: Stress distribution along the thickness Point A (75,30) mm. Comparison between LE2 and TE2 models.

Conclusions

The present work aims to show a nonlinear formulation for the post-buckling configuration of a rectangular plate made of a variable angle tow composite material. The governing equations are obtained from the principle of virtual displacement, and a comparison is conducted between the Lagrange and Taylor models for displacements and stresses. The findings indicate that the displacement description is accurate, even when the Taylor model is taken into consideration. However, to achieve optimal stress results, it is necessary to employ a Lagrange model in conjunction with the Layer wise description.

References

[1] Peters ST. Handbook of composites. 2nd ed. Boston, MA: Springer US; 1998. https://doi.org/10.1007/978-1-4615-6389-1

[2] Hyer MW, Charette RF. Use of curvilinear fiber format in composite structure design. AIAA J 1991;29(6):10115. https://doi.org/10.2514/3.10697

[3] A. Pagani, A. Racionero Sánchez-Majano & M. Petrolo. Influence of Structural Theories on Optimal Fiber Distributions in Tow-Steered Composites Considering Local Strain and Stress. Aerotecnica Missili & Spazio (2025). https://doi.org/10.1007/s42496-025-00275-3

[4] G. Manickam, M. Haboussi, M. D'Ottavio, V. Kulkarni, A. Chettiar, V. Gunasekaran. Nonlinear thermo-elastic stability of variable stiffness curvilinear fibres based layered composite beams by shear deformable trigonometric beam model coupled with modified constitutive equations. International journal of Non-Linear Mechanics, 148 (2023) 104303. https://doi.org/10.1016/j.ijnonlinmec.2022.104303

[5] F. Bracaglia, R. Masia, A. Pagani, E. Zappino, E. Carrera. Thermal buckling of variable stiffness composite laminates using high order plate finite elements. Composite Structures 345 (2024) 118393. https://doi.org/10.1016/j.compstruct.2024.118393

[6] E. Carrera, M. Cinefra, M. Petrolo, and E. Zappino. Finite Element Analysis of Structures through Unified Formulation. John Wiley & Sons, Chichester, West Sussex, UK, 2014. https://doi.org/10.1002/9781118536643

[7] Z. Gu¨rdal, B.F. Tatting, C.K. Wu. Variable stiffness composite panels: Effects of stiffness variation on the in-plane and buckling response. Composites Part A: Applied Science and Manufacturing, 39(5):911-922, May 2008. https://doi.org/10.1016/j.compositesa.2007.11.015

[8] P. Chiaia, A. Pagani, M. Cinefra and E. Carrera. Analysis of transversely isotropic compressible and nearly-incompressible soft material structures by high order unified finite elements. Mechanics of Advanced Materials and Structures. 2023: 31(27), 9451-9467. https://doi.org/10.1080/15376494.2023.2273962

[9] M. A. Crisfield. An arc-length method including line searches and accelerations. International Journal for Numerical Methods in Engineering, 19(9):1269-1289, September 1983. https://doi.org/10.1002/nme.1620190902

[10] X . Chen, G. Nie and X. Yang. Thermal postbuckling analysis of variable angle tow composite cylindrical panels. Journal of Thermal Stresses,(2021) 44:7, 850-882. https://doi.org/10.1080/01495739.2021.1923429

Materials Research Proceedings 69 (2026) 1192-1197 https://doi.org/10.21741/9781644904251-205

Multiscale Optimization of Composite Wings Through Global-Local High-Order Modeling

Spyridon KILIMTZIDIS[1,a *], Dario ZAMANI[2,b], Giuseppe PALAIA[2,c], Karim ABU SALEM[2,d], Alfonso PAGANI[2,e], Vassilis KOSTOPOULOS[1,f] and Spyridon PSARRAS[1,g]

[1]Applied Mechanics Laboratory, Mechanical Engineering & Aeronautics Department, University of Patras, Patras University Campus, Patras, GR-26504, Greece

[2]MUL2 Lab, Department of Mechanical and Aerospace Engineering, Politecnico di Torino, Corso Duca degli Abruzzi 24, 10129 Turin, Italy

[a]s.kilimtzidis@ac.upatras.gr, [b]dario.zamani@polito.it, [c]giuseppe.palaia@polito.it, [d]karim.abusalem@polito.it, [e]alfonso.pagani@polito.it, [f]TBD@ac.upatras.gr, [g]TBD@ac.upatras.gr

Keywords: Composite Aircraft Wings, Doublet Lattice Method (DLM), Finite Element Method (FEM), Aeroelastic Analysis, Neural Networks, Carrera Unified Formulation (CUF), Parametric Modeling, Global-Local Optimization

Abstract. This work presents a multiscale, global/local optimization framework for composite aircraft wings that integrates aeroelastic, strength, and stability constraints. Global-level analyses, including static aeroelasticity and flutter using the Doublet Lattice Method, provide the boundary conditions for local high-fidelity model based on the Carrera Unified Formulation. A neural-network surrogate enables rapid strength assessments, while a parametric FEM model supports geometry and thickness optimization. The framework establishes an efficient hierarchical methodology for integrating aeroelastic and structural design of composite wings.

Introduction

The structural optimization of composite aircraft wings remains a critical challenge in aerospace engineering due to the interplay between aeroelastic effects, buckling phenomena, and failure mechanisms at the ply level [1]. While global optimization frameworks efficiently handle stiffness and weight minimization, they often neglect the detailed stress fields and failure onset in layered composites. Conversely, local high-fidelity models capture these phenomena but are computationally prohibitive and rarely integrated into iterative optimization loops.

Recent advances in composite optimization have explored a wide range of formulations, from classical stacking-sequence and fiber-angle optimization [2,3] to topology-based approaches and reliability-based design optimization [4]. However, these methods typically operate at a single scale, limiting their capability to simultaneously address global performance metrics and local stress constraints. The multiscale nature of composite structures where interactions at lower scales influence the structural response at the macroscale, has motivated the development of hierarchical strategies capable of coupling global efficiency with local accuracy. Within this context, global/local frameworks have emerged as a promising approach, enabling the transfer of information from a global-level model to refined local domains [5,6]. The Carrera Unified Formulation (CUF) [7] offers an ideal foundation for this purpose, as it allows the automatic generation of refined structural theories, including higher-order shear deformation and Layer-Wise (LW) descriptions. By embedding CUF-based local analyses within a global optimization loop, a multiscale methodology can be established that preserves computational efficiency without compromising the accuracy of capturing the 3D stress field.

Content from this work may be used under the terms of the Creative Commons Attribution 3.0 license. Any further distribution of this work must maintain attribution to the author(s) and the title of the work, journal citation and DOI. Published under license by Materials Research Forum LLC.

Materials Research Proceedings 69 (2026) 1192-1197 https://doi.org/10.21741/9781644904251-205

Methodology

This work introduces a hierarchical global-local optimization framework that overcomes this gap, enabling minimum-mass design of composite wing structures under aeroelastic, buckling, and strength constraints. The global level relies on a fully parametric Finite Element Model (FEM), where geometric and thickness parameters are treated as design variables. Static aeroelastic loads and flutter boundaries are computed via the Doublet Lattice Method (DLM) [8], while structural stability is ensured through eigenvalue buckling analysis. All global analyses are automated through Patran Command Language (PCL) scripting and run in NASTRAN via MATLAB-controlled workflows, supporting efficient design-space exploration.

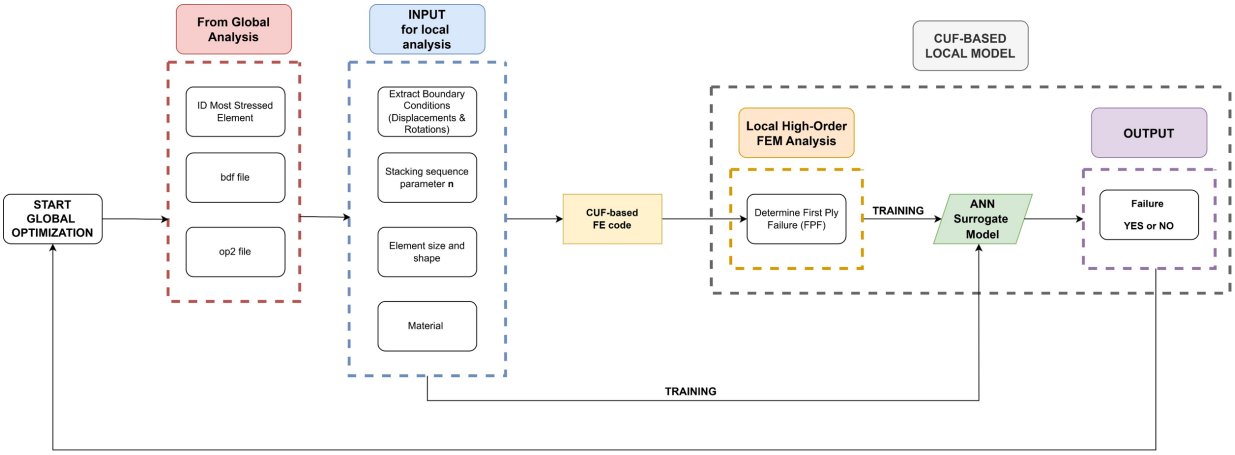


Figure 1. CUF-based local model integrated into the global optimization loop. Boundary conditions and laminate properties from the most stressed global element are used to perform high-fidelity CUF simulations. The results feed a neural network surrogate that predicts damage onset based on the 3D Hashin criterion.

The novelty of the framework lies in its local analysis strategy, which aims to provide accurate prediction of failure onset without compromising computational efficiency. A high-order two-dimensional Layerwise formulation based on the CUF is employed to capture the full three-dimensional stress distribution across the laminate thickness. Damage initiation is assessed via the 3D Hashin criterion, focusing on the most heavily stressed element of the global FEM model. The CUF model for the local domain adopts a displacement-based formulation, where only translational Degrees of Freedom (DOFs) are considered. Since the global model provides both translations $\left(\boldsymbol{u_x^0}, \boldsymbol{u_y^0}, \boldsymbol{u_z^0}\right)$ and rotations $\left(\boldsymbol{\theta_x^0}, \boldsymbol{\theta_y^0}, \boldsymbol{\theta_z^0}\right)$, a conversion procedure is required to express the latter as equivalent displacements. The Reissner–Mindlin displacement field in Eq. 1 is used to compute translational boundary displacements of the local model, written as:

$$u_x(x,y,z) = u_x^0(x,y) + z\theta_y^0(x,y) - y\theta_z^0(x,y)$$

$$u_y(x,y,z) = u_y^0(x,y) - z\theta_x^0(x,y) + x\theta_z^0(x,y) \quad (1)$$

$$u_z(x,y,z) = u_z^0(x,y) - y\theta_x^0(x,y) + x\theta_y^0(x,y)$$

Because repeated local evaluations using CUF-based models can be computationally expensive [9-10], a neural network-based surrogate model is trained to replace them within the optimization loop. The surrogate is constructed by sampling boundary conditions and material/laminate parameters, including stacking sequences and fiber properties, through Latin Hypercube Sampling.

Materials Research Proceedings 69 (2026) 1192-1197 https://doi.org/10.21741/9781644904251-205

Each configuration is simulated with high-fidelity CUF-based FE analysis and labeled according to the 3D Hashin criterion. The accumulated dataset is then used to train a neural network classifier. After testing several architectures involving principal component analysis (PCA), L2-regularized cross-entropy loss, and varying hidden-layer depths, the final network features three hidden layers (50, 30, and 10 neurons) trained via scaled conjugate gradient descent. Once trained, the surrogate enables real-time failure predictions based on the displacement field extracted from the global FEM model, as illustrated in Figure 1.

The optimization problem minimizes the structural mass, with constraints on buckling margin, flutter speed, and strength compliance. Colony Optimization (MIDACO) [11], based on Ant Colony Optimization, is used to explore the mixed-variable design space. At each iteration, the global model is updated, structural responses are computed, and the surrogate-based local model evaluates failure onset at the critical locations. The overall framework is presented in Figure 2. A representative composite wingbox configuration is optimized to demonstrate the methodology.

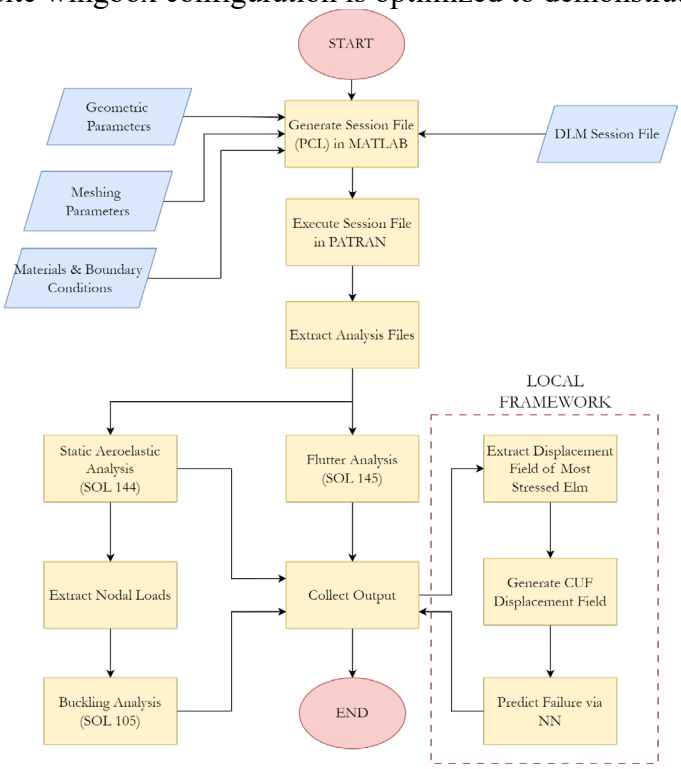


Figure 2. Workflow of the proposed global-local approach

Results and Verification

The optimization framework considers a semi-span composite wing box representative of a regional aircraft configuration. The model includes front and rear spars, ribs, stringers, and laminated skins. Design variables involve geometric parameters such as spar positions and stiffener spacing together with thicknesses of the structural components and ply orientations. The objective is to minimize the total structural mass subject to constraints on strength, stiffness, buckling, and dynamic behavior. Continuous and discrete variables are optimized simultaneously to achieve an efficient structural layout that satisfies all mechanical requirements.

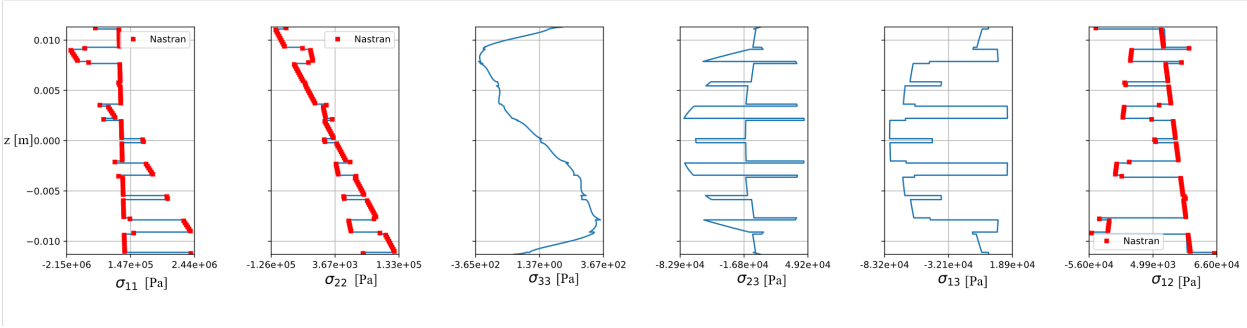


Figure 3. Local CUF-LW analysis of finite element ID 100 extracted from the global 2D finite element wing-box model. The through-thickness stress distributions $(\boldsymbol{\sigma_{11}, \sigma_{22}, \sigma_{33}, \sigma_{23}, \sigma_{13}, \sigma_{12}})$*are shown, comparing the present CUF-based results with the Nastran reference solutions for the in-plane stresses.*

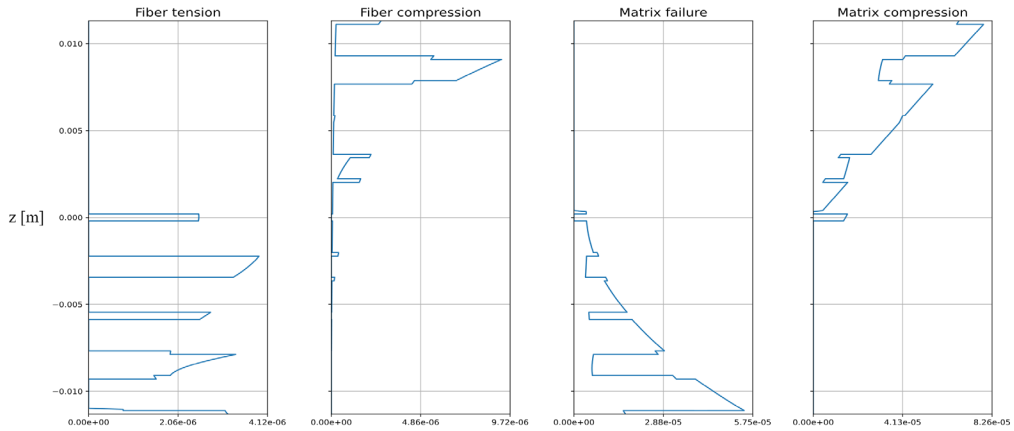


Figure 4. Through-thickness distribution of Hashin failure indices obtained from the local CUF-LW.

The structural constraints related to strength are evaluated through a global–local coupling procedure described, where local CUF-LW analyses are performed on the most stressed element identified in the global 2D wing-box model. Figure 3 shows the through-thickness stress distributions obtained from the local model, where the in-plane components are compared with the Nastran 2D global FE model, while the out-of-plane stresses are computed exclusively by the LW formulation. Figure 4 presents the corresponding Hashin failure indices for fiber tension, fiber compression, matrix tension, and matrix compression, which are used to evaluate the strength constraints within the optimization framework.

Additional verification analyses were carried out with the global optimization framework, which was executed for 300 iterations. The convergence of the objective function, the best feasible objective, and the aggregate constraint violation are depicted in Figure 5.

Materials Research Proceedings 69 (2026) 1192-1197 https://doi.org/10.21741/9781644904251-205

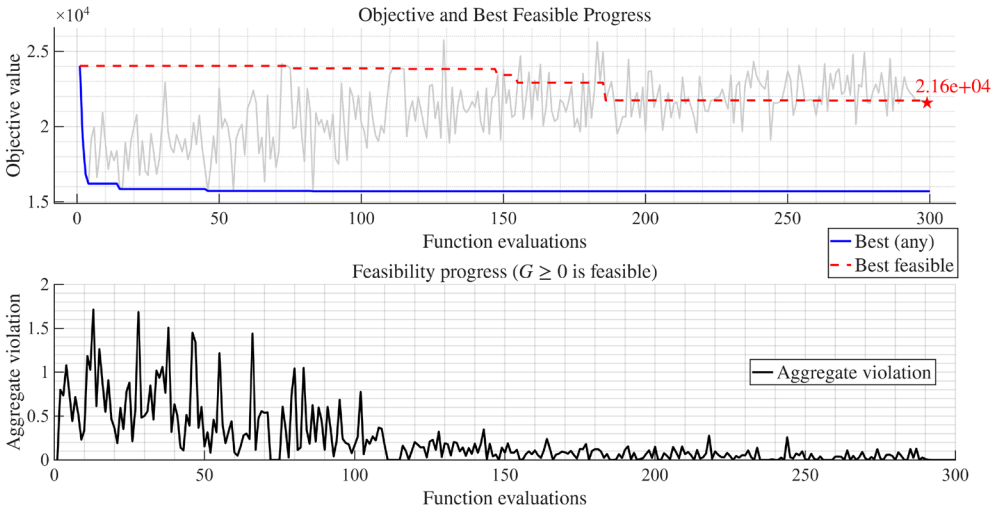


Figure 5 Convergence of objective function and aggregate violation

The optimized distribution of the design variables reflects a configuration consistent with the expected aeroelastic loading of a wing. The front and rear spar locations were adjusted toward the mid-chord region to efficiently react the maximum aerodynamic bending and torsional loads, providing an effective load path between the upper and lower skins. The relatively high skin thicknesses, particularly in the upper panel, correspond to regions of dominant compressive bending stresses, while thinner lower skins are associated with tensile-dominated regions. The spars and ribs exhibit moderately increased ply counts to enhance torsional stiffness and suppress local buckling, ensuring stability under combined bending and shear. In contrast, several beam-type components such as stringers and spar caps converge toward their lower bounds, indicating that their stiffness contribution beyond a certain threshold does not yield additional mass savings. Overall, the optimized configuration demonstrates a rational balance between stiffness, weight, and aeroelastic performance, with the structural reinforcements concentrated in load-critical regions.

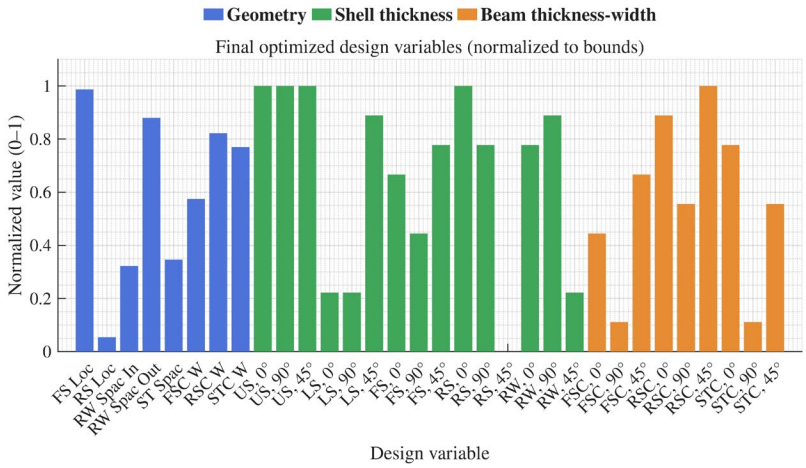


Figure 6 Final normalized values of the design variables obtained from the global optimization framework. Bars are color-coded by category: geometry (blue), shell thickness (green), and beam thickness-width (orange).

Conclusions

This research advances current methodologies by embedding surrogate-based local strength evaluations into a multiscale optimization process. The framework bridges efficient global-level aeroelastic design with detailed laminate-level failure modeling, providing a viable strategy for future composite wing development. Ongoing work will extend the approach to full aeroelastic tailoring and stacking sequence optimization for high-aspect-ratio wings.

Acknowledgments

The research presented in this paper has been performed within the framework of the HERA project (Hybrid Electric Regional Aircraft) and has received funding from the European Union Clean Aviation Program under grant agreement no. 101102007.

References

[1] S. Kilimtzidis, A. Kotzakolios, V. Kostopoulos, "Efficient Structural Optimisation of Composite Materials Aircraft Wings," Composite Structures, 303:116268, 2023. https://doi.org/10.1016/j.compstruct.2022.116268

[2] R. Le Riche, R. T. Haftka, "Optimization of laminate stacking sequence for buckling load maximization by genetic algorithm," AIAA Journal, 31(5):951-956, 1993. https://doi.org/10.2514/3.11710

[3] D. Zamani, A. Racionero Sánchez-Majano, A. Pagani. Mixed-integer, multi-objective layerwise optimization of variable-stiffness composites with gaps and overlaps. Struct Multidisc Optim 68, 107 (2025). https://doi.org/10.1007/s00158-025-04043-6

[4] D. Zamani, A. Pagani, M. Petrolo, E. Carrera: Multi-fidelity models for failure onset analysis of composites under uncertainties. Proceedings of the ASME 2025 Aerospace Structures, Structural Dynamics, and Materials Conference, Houston (TX, USA), May 5-7, 2025 https://doi.org/10.1115/SSDM2025-152303

[5] G. Guguin, O. Allix, P. Gosselet, S. Guinard, "Nonintrusive coupling of 3D and 2D laminated composite models based on finite element 3D recovery," International Journal for Numerical Methods in Engineering, 98:324-343, 2014. https://doi.org/10.1002/nme.4630

[6] J. B. Ransom, N. F. Knight, Jr., "Global/Local Stress Analysis of Composite Panels," NASA Technical Memorandum 101622, Langley Research Center, Hampton, Virginia, USA, 1989.

[7] E. Carrera, M. Cinefra, M. Petrolo, E. Zappino. Finite Element Analysis of Structures through Unified Formulation. Wiley & Sons, Hoboken, New Jersey, USA. 2014. https://doi.org/10.1002/9781118536643

[8] E. Albano, W.P. Rodden, "A Doublet-Lattice Method for Calculating Lift Distributions on Oscillating Surfaces in Subsonic Flows," AIAA Journal, 7(2):279-285, 1969. https://doi.org/10.2514/3.5086

[9] A. Pagani, A. R. Sánchez-Majano, D. Zamani, M. Petrolo, E. Carrera: Fundamental frequency layer-wise optimization of tow-steered composites considering gaps and overlaps. Aerotecnica Missili e Spazio (2024). https://doi.org/10.1007/s42496-024-00212-w

[10] M. Enea, R. Augello, A. Pagani, E. Carrera. Global/local models of composite laminated structures coupling classical 2D finite elements and arbitrarily large refined analysis subdomains. Computers & Structures 298 (2024): 107368. https://doi.org/10.1016/j.compstruc.2024.107368

[11] M. Schlueter, S. O. Erb, S. Kemble, M. Gerdts, and J.-J. Rueckmann. "MIDACO on MINLP Space Applications", Advances in Space Research, 51(7):1116-1131, April 2013 https://doi.org/10.1016/j.asr.2012.11.006

Materials Research Proceedings 69 (2026) 1198-1203 https://doi.org/10.21741/9781644904251-206

Experimental Study on Rotational Heat Transfer in Rib-pin Composite Trapezoidal Channels with Varied Rib Configurations

Chenghua ZHU[1,a], Hao LI[1,b], Jiale WANG[2,c], Jie WEN[1,d *]

[1]Research Institute of Aero-Engine, Beihang University, Beijing, P. R. China

[2]School of Energy and Power Engineering, Beihang University, Beijing, P. R. China

[a]zhuchenghua@buaa.edu.cn, [b]hao_li_@buaa.edu.cn, [c]by2104305@buaa.edu.cn, [d]wenjie@buaa.edu.cn

Keywords: Turbine Blade, Trailing Edge, Rotating, Heat Transfer, Pin-Fins, Ribs

Abstract. The current work conducts an experimental investigation of the heat transfer performance in a rib-pin composite trapezoidal channel. The channel employs ribs and pin-fins as turbulators, with the ribs arranged in two distinct configurations: forward-swept and backward-swept. The inlet Reynolds number (Re) and rotation number (Ro) respectively vary between 8000 and 24000 and from 0 to 0.83. The results indicate that under static conditions, forward-swept ribs enhance local heat transfer, but they provide no improvement in overall heat transfer within the low-radius region. Under rotating conditions, the heat transfer disparity between the leading and trailing walls progressively diminishes with increasing radius. When using backward-swept ribs, buoyancy forces influence the size of separation vortices induced by the ribs, which in turn reduces the overall heat transfer efficiency under rotation, especially when Ro > 0.5. This study demonstrates that in the trailing edge channel of turbine blades with lateral slots, within the commonly employed range of rotation numbers (Ro = 0 ~ 0.5), backward-swept ribs are more effective when combined with pin-fins, enabling optimal heat transfer performance.

Introduction

The continuous advancement of aero-engine technology is primarily marked by the progressive increase in turbine inlet temperature (TIT). High-performance aero-engines typically operate with TIT exceeding 2000 ℃, surpassing the thermal resistance capabilities of current high temperature alloys. Consequently, effective cooling strategies for turbine blades become indispensable [1]. The fundamental approach to turbine blade cooling involves introducing cooling air into internal channels to remove heat from the inner wall surfaces. Concurrently, a fraction of the cooling air is ejected through small holes on the blade surface, forming an insulating air film that covers the exterior and separates the metallic structure from the high-temperature gases. Due to the narrow and long geometric characteristics of the trailing edge of the turbine blade, the arrangement of internal turbulators is restricted [2]. Moreover, the lateral slots intensifies the flow loss of the cooling air [3]. All these factors jointly make the internal cooling of the trailing edge a weak link. Hence, achieving efficient cooling within the trailing edge is of critical importance for improving the overall thermal reliability of the blade cooling system.

The most commonly employed cooling enhancement structure in the trailing edge channel of turbine blades is the pin-fins [4], as it serves the dual purpose of enhancing turbulence intensity and maintaining structural integrity. Early research primarily concentrated on the arrangement [5,6], cross-sectional shape [7,8], and geometric characteristics [9,10] of pin-fins. Later, some researchers introduced ribs into the internal cooling design of the trailing edge to mitigate the high flow resistance associated with traditional pin-fins arrays [11], which led to a growing interest in investigating the heat transfer mechanisms of hybrid configurations combining ribs and turbulators

Content from this work may be used under the terms of the Creative Commons Attribution 3.0 license. Any further distribution of this work must maintain attribution to the author(s) and the title of the work, journal citation and DOI. Published under license by Materials Research Forum LLC.

[12,13]. Nevertheless, the integration of ribs and pin-fins remains somewhat empirical, and the coupling mechanisms under rotating conditions are still insufficiently explored.

This study experimentally examines the heat transfer mechanisms influenced by two different rib configurations under rotating conditions in a rib-pin composite channel, offering valuable insights for engineering applications to effectively leverage the individual advantages of ribs and pin-fins, thereby enabling more rational design of trailing edge cooling schemes.

Test Section and Measurement Method

The experimental facility comprises a power module, an air supply module, a support module, and a temperature measurement module, as shown in Fig. 1. The power module is centred around a 30 kW electric motor that drives the rotating shaft via a belt transmission system. The air source module provides compressed air at a maximum pressure of 0.8 MPa, serving as the coolant. The support module ensures stable mechanical support for the entire rotating assembly. In the temperature measurement module, the ADAM-4018 data acquisition module converts thermocouple signals from the test section into digital signals, which are then transmitted through a slip ring to the ADAM-4520 communication module. Subsequently, the RS-232 interface of the ADAM-4520 module transfers the data to the host computer for real-time monitoring and analysis. The test section is primarily composed of an aluminium cylinder, nylon frameworks, copper plate-based temperature measurement units, turbulators (including ribs and pin-fins), as shown in Fig. 2. The copper plate method [14] is employed as the measurement method. The fundamental principle of this method involves embedding copper plates within the nylon skeleton of the channel and applying thin-film heaters to the rear surfaces of the copper plates for controlled heating. Moreover, thermocouples are inserted into blind holes located on the back side of the copper plates to monitor their temperature (Fig 2(f)). Due to the high thermal conductivity of copper (approximately 400 W/(m·K)), the lumped parameter method can be applied, allowing the assumption that the temperature measured by the thermocouples accurately represents the temperature at the interface between the copper plates and the cooling air.

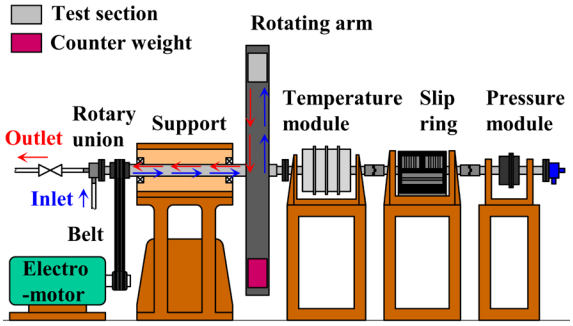


Fig. 1. Schematic illustration of the experimental facility configuration.

Data Reduction

The convective heat transfer coefficient (h) and the Nusselt number (Nu) on the wall of the channel are calculated using Eq. (1) and (2), respectively.

$$h = \frac{Q_{net}}{A\left(t_w - t_b\right)} \tag{1}$$

$$Nu = \frac{hD_h}{\lambda} \tag{2}$$

Materials Research Proceedings 69 (2026) 1198-1203 https://doi.org/10.21741/9781644904251-206

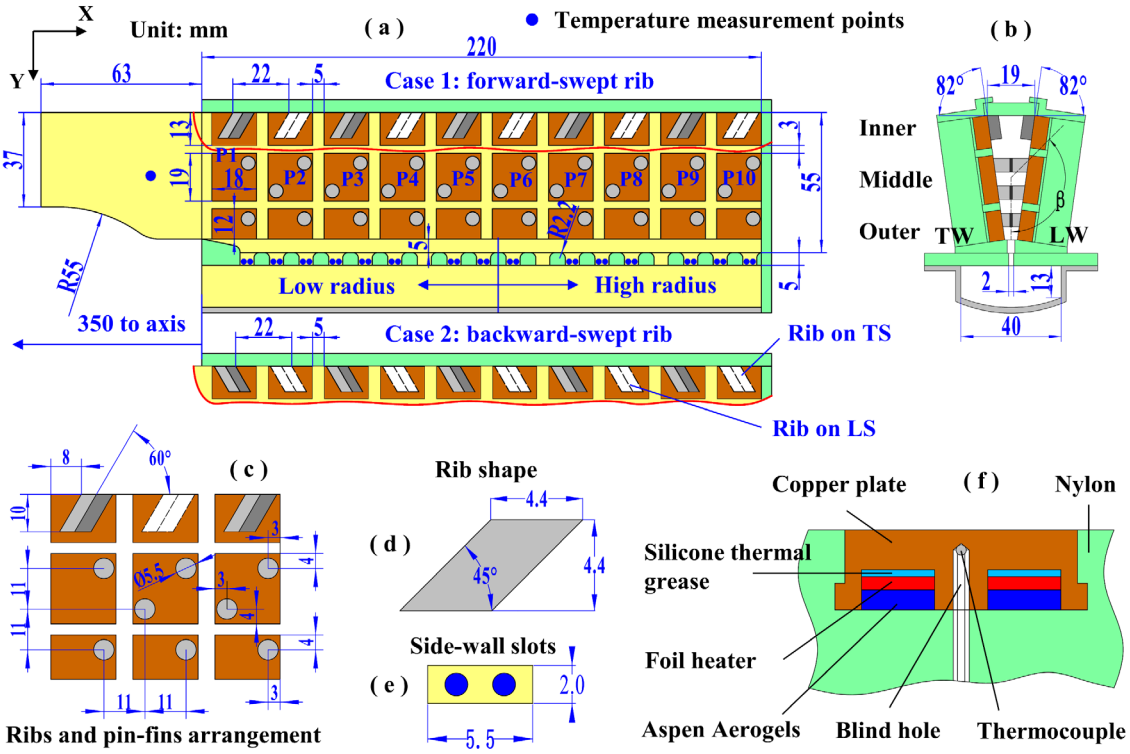


Fig. 2. Schematic illustration of the overall structure of the test section and the distribution pattern of turbulators within the channel.

Here, Q_{net} denotes the net heat flux applied to the copper plates, A represents the contact area between each copper plate and the cooling air, t_w indicates the temperature of the copper plate, t_b refers to the local mean bulk temperature, D_h signifies the hydraulic diameter at the channel inlet, and λ stands for the thermal conductivity of the cooling air.

The definition of net heat flux is as follows:

$$Q_{net} = I^2R - Q_{loss} = I^2R - \alpha\left(T_w - T_e\right) \tag{3}$$

$$\alpha = \frac{\left(I^2R\right)_{cond}}{T_w - T_e} \tag{4}$$

Here, α denotes the heat loss coefficient, which must be determined via a calibration experiment conducted in the absence of convective heat transfer. This experiment involves measuring the heat conducted to the surrounding environment ($\left(I^2R\right)_{cond}$), the wall temperature of the copper plate (T_w), and the ambient temperature (T_e).

The remaining dimensionless parameters to be controlled during the experiment are as follows:

$$Re = \frac{\rho_{in} U D_h}{\mu} = \frac{\dot{m}_{in} D_h}{\mu A_{in}} \tag{5}$$

$$Ro = \frac{\Omega D_h}{U} = \frac{\Omega \rho A_{in} D_h}{\dot{m}_{in}} \tag{6}$$

$$DR = \frac{\overline{T_w} - T_{in}}{\overline{T_w}} \tag{7}$$

Here, $\dot{m}_{in}$, μ, and ρ denote the inlet mass flow rate of the test section, the dynamic viscosity of the cooling air, and the coolant density, respectively. D_h and A_{in} represent the hydraulic diameter and the cross-sectional area at the inlet of the test section, respectively. Ω refers to the rotational speed,

Materials Research Proceedings 69 (2026) 1198-1203 https://doi.org/10.21741/9781644904251-206

T_w is the area-averaged wall temperature of the copper plates, and T_{in} denotes the inlet temperature. The range of experimental operating conditions for this study is presented in Table 1.

Table 1 Work conditions

Parameters	Values
Reynolds number (Re)	8000 ~ 24000
Rotation number (Ro)	0 ~ 0.83
Density ratio (DR)	0.07 ~ 0.14
Rotational speed [rpm]	0 ~ 800 (interval 100)
Back pressure [kPa]	around 500
Positional coordinates of the copper plates	X/D_h = 0.66, 1.78, 2.91, 4.03, 5.15, 6.27, 7.39, 8.51, 9.63, 10.75

Results and Discussion

The heat transfer characteristics of two configurations are examined under both static and rotating conditions. Under static conditions, the forward-swept rib scheme (Case 1) generated significantly larger separation vortices compared to the backward-swept rib scheme (Case 2). This resulted in a tortuous heat transfer distribution pattern in the inner region of Case 1, whereas such a phenomenon is absent in Case 2. However, in the low-radius middle and outer regions (Fig. 3(c)~(f)), heat transfer in Case 2 is stronger than in Case 1, indicating that the separation vortex induced by the forward-swept ribs under static conditions adversely affects spanwise heat transfer in adjacent regions, thereby diminishing the effectiveness of the pin-fins.

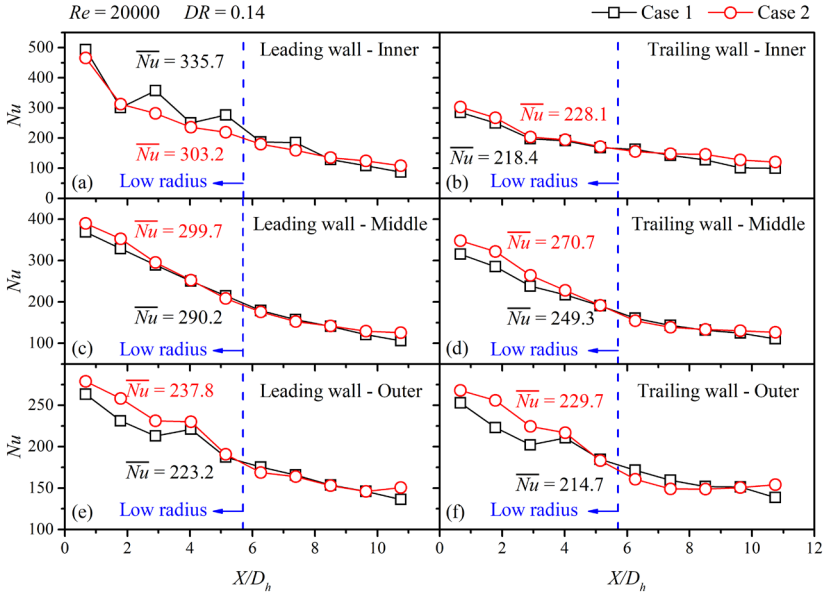


Fig. 3 Heat transfer distribution in the stationary channel under two different rib configurations.

Under rotating conditions, the differences in heat transfer distribution between the two configurations are minimal at low Ro. Overall, the effect of Re on rotational heat transfer can be decoupled, and heat transfer in the low-radius region exhibits greater sensitivity to rotation. A comparison of Fig. 4 and Fig. 5 reveals that, although the backward-swept rib channel shows a relatively small difference in heat transfer between the leading and trailing walls under rotating conditions, its heat transfer level declines significantly when Ro > 0.5, with a reduction exceeding 20%. This behaviour is attributed to the lower flow resistance of the backward-swept rib configuration, which allows a larger portion of cooling air to reach the high-radius region even under static conditions. At high Ro, the separation vortices generated by these ribs in the high-

Materials Research Proceedings 69 (2026) 1198-1203 https://doi.org/10.21741/9781644904251-206

radius downstream area are elongated due to the progressively increasing buoyancy force. This enlargement of the vortices adversely affects the heat transfer performance.

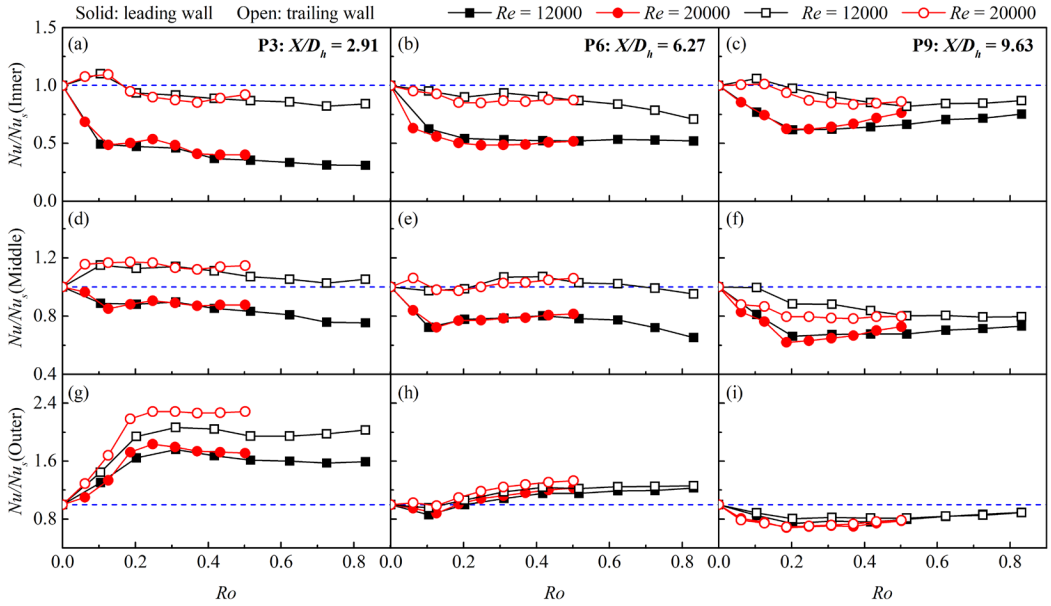


Fig. 4 Rotational heat transfer distribution in the channel with forward-swept ribs (Case 1).

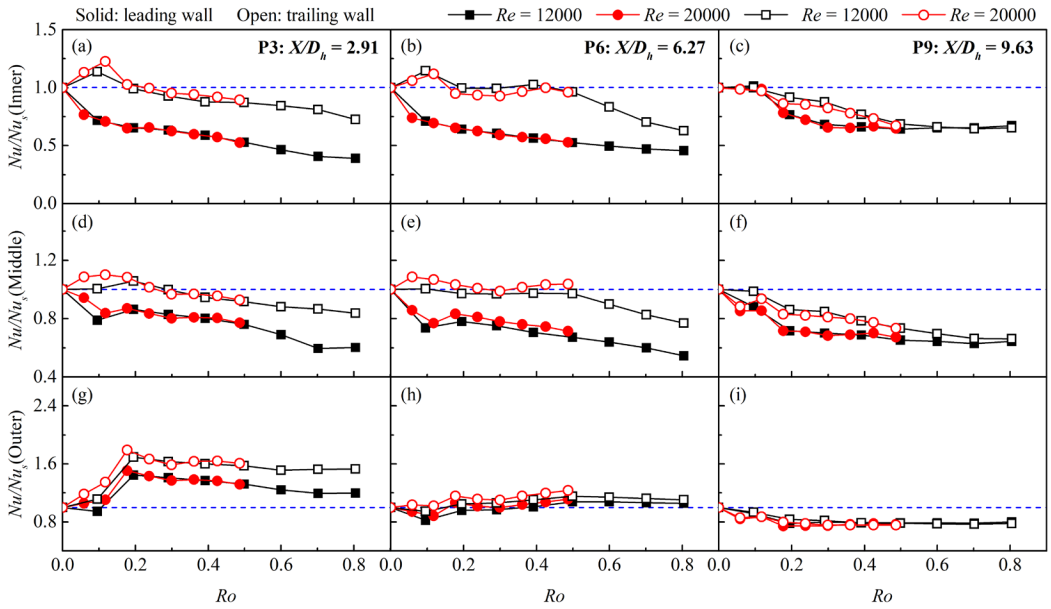


Fig. 5 Rotational heat transfer distribution in the channel with backward-swept ribs (Case 2).

Conclusion

Experimental investigations into the rotating heat transfer mechanisms of two rib-pin composite trapezoidal channels demonstrate that the coupling effect between ribs and pin-fins is primarily manifested through the separation vortices induced by the ribs. During rotation, the buoyancy force at the high-radius zone exerts a significant influence on the heat transfer distribution. The forward-swept rib configuration enhances local heat transfer. However, its adverse impact on heat transfer in adjacent regions is non-negligible. For operating conditions with Ro < 0.5, the backward-swept rib configuration is preferred. Otherwise, the forward-swept configuration becomes more advantageous.

References

[1] J.-C. Han, Advanced Cooling in Gas Turbines 2016 Max Jakob Memorial Award Paper, Journal of Heat Transfer 140 (2018). https://doi.org/10.1115/1.4039644.
[2] W. Du, L. Luo, Y. Jiao, S. Wang, X. Li, B. Sunden, Heat transfer in the trailing region of gas turbines – A state-of-the-art review, Applied Thermal Engineering 199 (2021) 117614. https://doi.org/10.1016/j.applthermaleng.2021.117614.
[3] Z. Tao, L. Qiu, H. Deng, Heat transfer in a rotating smooth wedge-shaped channel with lateral fluid extraction, Applied Thermal Engineering 87 (2015) 47–55. https://doi.org/10.1016/j.applthermaleng.2015.04.073.
[4] D.E. Metzger, R.A. Berry, J.P. Bronson, Developing Heat Transfer in Rectangular Ducts With Staggered Arrays of Short Pin Fins, Journal of Heat Transfer 104 (1982) 700–706. https://doi.org/10.1115/1.3245188.
[5] M.K. Chyu, Y.C. Hsing, T.I.-P. Shih, V. Natarajan, Heat Transfer Contributions of Pins and Endwall in Pin-Fin Arrays: Effects of Thermal Boundary Condition Modeling, Journal of Turbomachinery 121 (1999) 257–263. https://doi.org/10.1115/1.2841309.
[6] T.-M. Jeng, S.-C. Tzeng, Pressure drop and heat transfer of square pin-fin arrays in in-line and staggered arrangements, International Journal of Heat and Mass Transfer 50 (2007) 2364–2375. https://doi.org/10.1016/j.ijheatmasstransfer.2006.10.028.
[7] M.K. Chyu, C.H. Yen, S. Siw, Comparison of Heat Transfer From Staggered Pin Fin Arrays With Circular, Cubic and Diamond Shaped Elements, in: Volume 4: Turbo Expo 2007, Parts A and B, ASMEDC, Montreal, Canada, 2007: pp. 991–999. https://doi.org/10.1115/GT2007-28306.
[8] K.L. Kirsch, K.A. Thole, Heat Transfer Measurements of Oblong Pins, Journal of Turbomachinery 137 (2015). https://doi.org/10.1115/1.4029124.
[9] S.C. Siw, M.K. Chyu, T.I.-P. Shih, M.A. Alvin, Effects of Pin Detached Space on Heat Transfer and Pin-Fin Arrays, Journal of Heat Transfer 134 (2012) 081902. https://doi.org/10.1115/1.4006166.
[10] P. Narato, M. Wae-hayee, N. Kaewchoothong, C. Nuntadusit, Heat transfer enhancement and flow characteristics in a rectangular channel having inclined pin arrays mounted on the endwall surface, International Communications in Heat and Mass Transfer 122 (2021) 105162. https://doi.org/10.1016/j.icheatmasstransfer.2021.105162.
[11] W. Du, L. Luo, S. Wang, J. Liu, B.A. Sunden, Enhanced heat transfer in a labyrinth channels with ribs of different shape, HFF 30 (2019) 724–741. https://doi.org/10.1108/HFF-05-2019-0393.
[12] H.-W. Wu, H. Zirakzadeh, J.-C. Han, L. Zhang, H.-K. Moon, Heat Transfer in a Rib and Pin Roughened Rotating Multipass Channel With Hub Turning Vane and Trailing-Edge Slot Ejection, Journal of Thermal Science and Engineering Applications 10 (2017). https://doi.org/10.1115/1.4037584.
[13] S.W. Chang, C.J. Hsu, Effect of internal effusion on aerothermal performance of a three-pass channel roughened by angled ribs and pin-fins with lateral flow exit, INTERNATIONAL JOURNAL OF HEAT AND MASS TRANSFER 198 (2022). https://doi.org/10.1016/j.ijheatmasstransfer.2022.123387.
[14] J.-C. Han, L.M. Wright, Experimental Methods in Heat Transfer and Fluid Mechanics, 1st ed., CRC Press, 2020. https://doi.org/10.1201/9781003021179.

Materials Research Proceedings 69 (2026) 1204-1209 https://doi.org/10.21741/9781644904251-207

Understanding Strength reduction in Aerospace Composites Structures: The Role of Delamination

Abrar H. BALUCH[1,2,a *]

[1]Department of Aerospace Engineering, King Fahd University of Petroleum and Minerals, Dhahran, Saudi Arabia

[2]Interdisciplinary Research Center for Aviation and Space Exploration, King Fahd University of Petroleum and Minerals, Dhahran, Saudi Arabia

[a]abrar.baluch@kfupm.edu.sa

Keywords: Compression After Impact, Delamination, Composite Structures, Low Velocity Impact

Abstract. Composite materials possess excellent properties in terms of their high strength and stiffness. The use of CFRPs composites in aerospace and space applications is increasing exponentially due to their superior properties and usage in primary structures. Such structures because of their nature, if get impacted by external projectiles or debris can develop barely visible impact damage developing delamination within themselves. These delaminations become catastrophic when faced with additional compressive loads. These kinds of events are called compression after impact [CAI] events, and they are very critical for aerospace structures. These problems are solved by structural engineers either by experimentation or conducting computational studies by using commercially available tools or in-house developed codes. The experimental evaluation of CAI is quite expensive while the computational approach makes it a reasonable choice for engineers. In this study, the CAI event is computationally evaluated using commercially available ABAQUS software. Continuum shell modeling is utilized to make the geometry following the ASTM D7137 and Airbus AITM 1-0010 standard. Boundary conditions were provided according to the standard to mimic the failure behavior. Unidirectional AS4/8552 pre-preg material and its properties were used as material property. Structures with predefined delamination, which mimics impact events, were evaluated in this research and found that the simulated results were within ±10% difference, showing that Abaqus simulation helps researchers minimize experimental cost and can increase diversity in the profile of the results and composite laminates for CAI events. Local, mixed, and global buckling plays a critical role in CAI events.

Introduction

Composite materials are widely used in all engineering applications ranging from commercial structures to advanced aerospace / space structures including deep space exploration rovers. Their higher specific strength and stiffness make them distinctive in terms of their selection to their metallic counterpart. Despite their unique properties, their usage must be evaluated carefully because their failure mechanisms are different than that of metals [1]. Fiber breakage, matrix cracking, delamination, fiber kinking, in-plane and out of plane buckling are a few different failure mechanisms among many which used to happen in composites [2,3]. The behavior of composites towards damage also varies according to different loading scenarios. Tensile failure is different than that of compressive failure, impact loading is also different whenever categorized under high or low velocity impact loadings.

Low velocity impact (LVI) in composites needs to be evaluated critically. These kinds of impacts can damage the structures internally without leaving any traces on the surface. LVI are more critical for aerospace structures and their applications [3-5]. Externally the surface looks as

Content from this work may be used under the terms of the Creative Commons Attribution 3.0 license. Any further distribution of this work must maintain attribution to the author(s) and the title of the work, journal citation and DOI. Published under license by Materials Research Forum LLC.

Materials Research Proceedings 69 (2026) 1204-1209 https://doi.org/10.21741/9781644904251-207

clean as pristine but internally the damage has already happened. The LVI can be categorized where the effect is minimum unless crack growth takes place further that can be classified as barely visible impact damages (BVID). The term BVID is well known in composite/aerospace structure community. These BVIDs, because of low velocity impacts become even more critical if followed by compressive load which is usually called compression after impact (CAI) event [6-9].

CAI events have been investigated experimentally and computationally in an extensive way by different researchers in the aerospace community [10,11]. Experimentally it is extremely expensive, the best approach is to use commercially available tools and mimic those events computationally [12] and get reliable results. Among the available different tools, Abaqus is selected, being extensively used by the aerospace community and big companies.

In this computational work, the attempt was made to evaluate composite based structures for compression after impact events computationally by using commercially available software. The assumption was made that impact has happened already and investigated structure has already developed delamination with in it having different shapes. Afterwards compressive loads applied computationally and compared with available experimental data to validate.

Methodology

In this research, the commercially available FEM tool Abaqus is utilized for computational modelling of specimens. Within software Abaqus/Explicit module is utilized by adopting Continuum shell methodology technique. The FEM model is splitted into different zones. The area of interest, the central region is modelled by ply by ply or different laminates while the outer region is modelled by singly continuum shell elements by providing combined properties in the system. Unidirectional AS4/8552 pre-preg material and its properties were used as material property. Five diverse kinds of laminates were simulated as used by NASA and other researchers earlier in their research [13-15].

Table 1: Laminates as available in reference [9].

Laminate	# plies	t [mm]	Lay-up
181	16	2.944	[45, -45, 0, 45, 45, -45, -45, 90]s
181T	20	3.68	[45, -45, 0, 45, -45, 90, 45, -45, 45, -45]s
252	24	4.416	[45, 0, -45, 90, 45, 0, -45, 90, 45, 0, -45, 90]s
351	24	4.416	[45, 0, -45, 0, 45, 0, -45, 90, 45, 90, -45, 0]s
361	34	6.256	[45, 0, -45, 0, -45, 45, 0, -45, 90, 45, 45, 90, -45, 0]s

Different number of plies are there for different configurations. The ply properties were taken from earlier research available at [13]. Table is attached for reference here. In this research, meshing was done according to need, where we have more stress concentrations, there we have provided refine mesh while on the part with least interest, coarse mesh was provided as shown in figure 1. Boundary conditions and geometry configurations were provided as per ASTM standard D7137 and Airbus standard AITM 1-0010 [14,16]. Interested regions were modelled with finer mesh and multiple sub-laminates, while upper and lower parts were modelled with one element though the thickness of laminates.

Materials Research Proceedings 69 (2026) 1204-1209 https://doi.org/10.21741/9781644904251-207

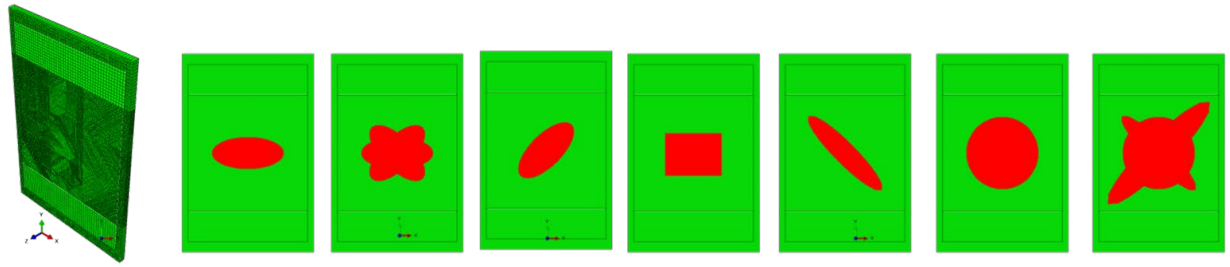


*Figure 1: FEM modelling in Abaqus (100 mm * 150 mm coupon size with central zone having finer mesh) and Different delamination's profiles in Abaqus for FEM.*

Multiple shapes were selected to provide delamination to mimic real time impact event within the laminate. These delamination's includes but not limited to Circle, Oval and Rectangular shapes. These delamination's were provided at various locations through the thickness of laminates. With these delamination's, the effect of delamination was studied with shape and location. For delamination behavior, Abaqus/explicit Cohesive zone modelling approach based on Surface based criterion were utilized. In comparison to Cohesive element approach, it was easier to define cohesive surface criterion and no of elements also reduced by its usage. After initiation, propagation was done by B-K law as available in Abaqus software.

Results and Discussion

Continuum shell modelling was adopted in this research by providing delamination at various locations with different shapes according to literature. Different delaminations and their different areas resulted in reduction in strength differently. Oval, circle, and square shapes with same areas resulted in different strength reduction as can be seen in figure 2 especially when the delamination was provided only one end and then on both end after third ply in series.

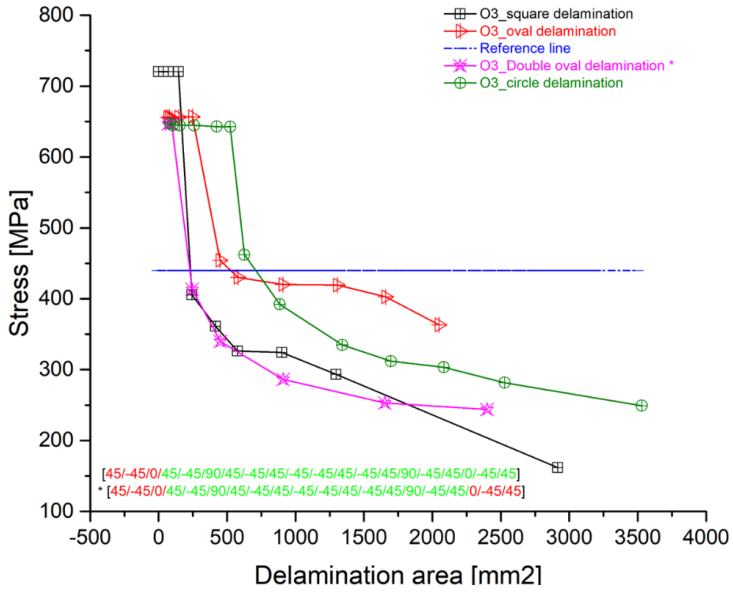


Figure 2: Reduction due to delamination area.

Afterwards multiple delamination's were provided to check how it affects the damage behavior. This multiple delamination was sorted out based on extensive literature [10-13] which suggests how strain energy is being accumulated and ply clustering plays a critical role in that. In addition

Materials Research Proceedings 69 (2026) 1204-1209 https://doi.org/10.21741/9781644904251-207

to this compression after an impact event initial depth of indent is the point where delamination moves towards the end, starting from back end delaminated piles.

The delamination can be seen in figure 3 below where it can be seen how the delamination propagates within the laminate after CAI loads.

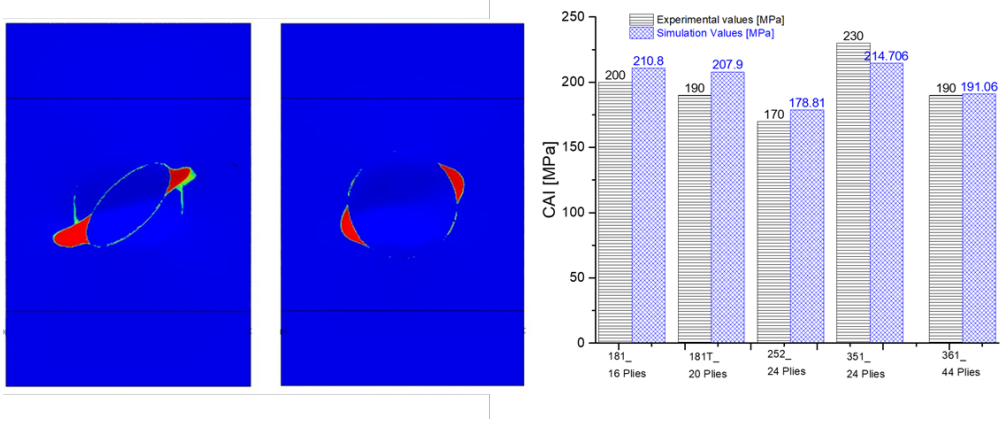


Figure 3: Delamination propagation in post-processor and Strength reduction due to delamination for different laminates (Experimental values taken from references [13,15,17]).

After applying multiple combinations for provided 5 different sets of plies, the analyses resulted in overpredicting most of the configurations by 5 to 10% while few of them resulted in under-prediction but all CAI simulated events resulted in ±10% of experimental known values from literature [15]. When laminate is thick its underpredict, while for thin laminate having ply less than 24, behavior shows over prediction. The interaction properties defined within the Abaqus also influenced the damage behavior.

In the figure 3, experimented values from reference [13,15] and simulated values, all are within ±10% variation. These results after further evaluation can be implemented to further unknown configurations and can get prediction without performing expensive experimentations. The buckling behavior observed in thin and thick laminates were also different.

Conclusion

Composite materials having exceptional engineering properties fail in a unique way which is different than that of conventional metals. These structures when used for aerospace applications need further care. They need to be evaluated critically if they are subjected to compressive load after an impact event, because internal delamination led to catastrophic effect. Structures with predefined delamination, which mimics impact events, evaluated in this research and found that simulated results were within ±10% difference, showing that Abaqus simulation help researchers to minimize experimental cost and can increase diversity in outcome and composite laminates profile for CAI events. Local, mixed, and global buckling plays a critical role in CAI events. This research is still going on by evaluating different delamination's profile by comparing real-time CSCAN data.

Acknowledgement

This work was supported by the Interdisciplinary Research Center for Aviation and Space Exploration, King Fahd University of Petroleum & Minerals (KFUPM) funded by the internal grants INAE 2505.

References

[1] S. Abrate, Modeling of impacts on composite structures, Composite Structures 51 (2001) 129 - 138. https://doi.org/10.1016/S0263-8223(00)00138-0

[2] D. J. Thomas, Complexity of understanding the failure of aerospace composite structures, Journal of Failure Analysis and Prevention (2016) 513-514. https://doi.org/10.1007/s11668-016-0141-y

[3] A. T. Rhead, R. Butler, G. W. Hunt, Compressive strength of composite laminates with delamination-induced interaction of panel and sublaminate buckling modes, Composite Structures 171 (2017) 326 - 334. https://doi.org/10.1016/j.compstruct.2017.03.011

[4] C. S. Lopes, O. Seresta, Y. Coquet, Z. Gurdal, P. P. Camanho, B. Thuis, Low-velocity impact damage on dispersed stacking sequence laminates. part i: Experiments, Composites Science and Technology 69 (2009) 926579- 936 https://doi.org/10.1016/j.compscitech.2009.02.009

[5] S. Hong, D. Liu, On the relationship between impact energy and delamination area, Experimental Mechanics 29 (1989) 115-120. https://doi.org/10.1007/BF02321362

[6] R. Craven, L. Iannucci, R. Olsson, Delamination buckling: A finite element study with realistic delamination shapes, multiple delaminations and fibre fracture cracks, Composites Part A: Applied Science and Manufacturing 41 (2010) 684 - 692. https://doi.org/10.1016/j.compositesa.2010.01.019

[7] M. Clarke, M. Pavier, Artificial damage techniques for low velocity impact in carbon fibre composites, Composite Structures 25 (1993) 113- 120 https://doi.org/10.1016/0263-8223(93)90157-L

[8] L. E. Asp, S. Nilsson, S. Singh, An experimental investigation of the influence of delamination growth on the residual strength of impacted laminates, Composites Part A: Applied Science and Manufacturing 32 (2001) 1229 - 1235 https://doi.org/10.1016/S1359-835X(01)00075-6

[9] Baluch AH, Kim CG. Effect of velocity variation on carbon/epoxy composite damage behavior. Journal of Composite Materials. 2015;50(15):2017-2024. doi:10.1177/0021998315598852 https://doi.org/10.1177/0021998315598852

[10] Z. Aslan, M. Sahin, Buckling behavior and compressive failure of composite laminates containing multiple large delaminations, Composite Structures 89 (2009) 382 - 390. https://doi.org/10.1016/j.compstruct.2008.08.011

[11] R. S. Choudhry, A. T. Rhead, M. W. Nielsen, R. Butler, A plate model for compressive strength prediction of delaminated composites, Composite Structures 210 (2019) 509 - 517. https://doi.org/10.1016/j.compstruct.2018.11.066

[12] E. Gonz'alez, P. Maim'ı, P. P. Camanho, A. Turon, J. Mayugo, Simulation of drop-weight impact and compression after impact tests on composite laminates, Composite Structures (2012) 3364 - 3378 https://doi.org/10.1016/j.compstruct.2012.05.015

[13] O. Falc'o, R. Avila, B. Tijs, C. S. Lopes, Modelling and simulation methodology for unidirectional composite laminates in a virtual test lab framework, Composite Structures 190 (2018) 137 - 159 https://doi.org/10.1016/j.compstruct.2018.02.016

[14] ASTM-D7136/D7136M-12., Standard test method for measuring the damage resistance of a fiber-reinforced polymer matrix composite to a drop-weight impact event., ASTM International standard; West Conshohocken PA, USA; (2012)

[15] P. P. Camanho, C. G. D'avila, Mixed-mode decohesion finite elements for the simulation of delamination in composite materials, NASA/TM-703 2002211737, pp. 137, 2002.

[16] AITM1-0010., Fibre reinforced plastics, determination of compression strength after impact., AITM, Airbus Test Method, Engineering directorate 31707 Blagnac Cedex France (2005).

[17] Abrar H. Baluch, Olben Falcó, José Luis Jiménez, Bas H.A.H. Tijs, Cláudio S. Lopes, "An efficient numerical approach to the prediction of laminate tolerance to Barely Visible Impact Damage, Composite Structures, Volume 225, 2019, 111017, ISSN 0263-8223. https://doi.org/10.1016/j.compstruct.2019.111017

Materials Research Proceedings 69 (2026) 1210-1214 https://doi.org/10.21741/9781644904251-208

Failure Analysis of Deployable Thin-Shell Space Structures Using Refined One-Dimensional Finite Elements

Daniele SCANO[1,a], Riccardo Augello[1,b], Erasmo CARRERA[1,c], Francesco LATINI[2,d] and Marco PETROLO[1,e *]

[1]MUL2 Lab, Department of Mechanical and Aerospace Engineering, Corso Duca degli Abruzzi 24, 10129, Torino, Italy

[2]Agenzia Spaziale Italiana, Via del Politecnico snc, 00133, Roma, Italy

[a]daniele.scano@polito.it, [b]riccardo.augello@polito.it, [c]erasmo.carrera@polito.it, [d]francesco.latini@asi.it, [e]marco.petrolo@polito.it

Keywords: Ultra-Thin Structures; One-Dimensional Refined Model; Carrera Unified Formulation; Failure Analysis

Abstract. This study investigates the failure of ultra-thin deployable composite structures. The analysis focuses on a laminated tape spring composed of three layers of glass fibre and carbon fibre reinforced polymers, subjected to opposing bending moments at its ends. The Carrera Unified Formulation (CUF) is employed for the numerical analysis within a geometrically nonlinear framework. This approach enables the accurate evaluation of the complete three-dimensional (3D) stress state at each equilibrium configuration. The Hashin 3D criterion is then applied to compute failure indices, allowing for the identification of critical points along the nonlinear equilibrium path. The results conclusively identify the mid-span section as the most critical region, with matrix-dominated failure modes being predominant.

Introduction

Deployable structures have gained prominence in space engineering due to their ability to reduce significantly mass, volume, and cost [1]. Typically fabricated from thin or ultra-thin materials, these structures are extensively used in applications such as satellite antennas [2]. Tape springs represent the most common type of deployable boom. While traditionally metallic, recent designs increasingly employ carbon fibre-reinforced plastic (CFRP) to achieve superior stiffness-to-mass ratios. These structures demand advanced analyses due to their nonlinear mechanical behaviour, including large deformations coupled with local and global instabilities, which can produce damages [3, 4]. Material nonlinearities present additional complexities, particularly when modelling composite or elastomeric components, where an accurate failure prediction is crucial and due to their propensity for multifaceted failure modes, making high-fidelity modelling both essential and challenging.

This study focuses on the accurate evaluation of three-dimensional (3D) stress fields and the failure mechanisms in space deployable structures by calculating the failure indices within the geometrical nonlinear framework. This study employs the one-dimensional version of Carrera Unified Formulation (CUF) [5, 6] for the structural modelling. CUF framework decomposes the three-dimensional displacement field into axial and cross-sectional components, enabling the implementation of higher-order theories that accurately capture cross-sectional deformation patterns. Specifically, Lagrange polynomial expansions are utilized to represent the kinematics. This refined beam formulation provides significant computational advantages over conventional 2D and 3D finite element approaches, particularly in terms of solution efficiency. The methodology maintains 3D solution accuracy while substantially reducing computational costs.

Content from this work may be used under the terms of the Creative Commons Attribution 3.0 license. Any further distribution of this work must maintain attribution to the author(s) and the title of the work, journal citation and DOI. Published under license by Materials Research Forum LLC.

Materials Research Proceedings 69 (2026) 1210-1214 https://doi.org/10.21741/9781644904251-208

CUF has been recently adopted for calculating the nonlinear behaviour of deployable space structures [7, 8].

This paper is organized as follows: (a) Section *Methodology* introduces the principles of CUF in the nonlinear scenario; (b) Section *Numerical Results* presents the main outcomes; and (c) Section *Conclusions* summarizes the key findings of the study.

Methodology

According to the CUF, the 3D displacement field can be expressed in the following unified form:

$$\mathbf{u}(x,y,z) = F_\tau(x,z)\mathbf{u}_\tau, \qquad \tau = 1,2,\dots,M \tag{1}$$

where $\mathbf{u}$ denotes the displacement vector with components defined in the global reference system (x,y,z). $F_\tau(x,z)$ represent the cross-sectional functions in-plane coordinates (x,z), τ is the summation index, and M is the number of terms used in the cross-sectional displacement expansion. In the present work, quadratic Lagrange polynomials (L9) are adopted to approximate the kinematic field; further details can be found in [5]. The use of Lagrange polynomials enables the discretization of complex cross-sectional geometries.

To approximate the displacement field along the beam axis, the Finite Element Method (FEM) is employed. Thus, the displacement vector $\mathbf{u}_\tau(y)$ may be now expressed as:

$$\mathbf{u}(x,y,z) = N_i(y)F_\tau(x,z)\mathbf{u}_{\tau i}, \qquad i = 1,2,\dots,N_n \tag{2}$$

where $N_i(y)$ denotes the i-th one-dimensional shape function, i indicates summation, and N_n is the number of finite element nodes per element, whereas $\mathbf{u}_{\tau i}$ is the vector of nodal parameters. In this formulation, one-dimensional finite Lagrangian elements are used along the y-axis.

Finally, the stress $\boldsymbol{\sigma}$ and strain $\boldsymbol{\epsilon}$ components are expressed in vectorial form as:

$$\boldsymbol{\sigma} = \{\sigma_{xx}\ \sigma_{yy}\ \sigma_{zz}\ \sigma_{yz}\ \sigma_{xz}\ \sigma_{xy}\}^T, \quad \boldsymbol{\epsilon} = \{\epsilon_{xx}\ \epsilon_{yy}\ \epsilon_{zz}\ \epsilon_{yz}\ \epsilon_{xz}\ \epsilon_{xy}\}^T \tag{3}$$

Regarding the geometric relations, the Green–Lagrange nonlinear strain components can be written as

$$\boldsymbol{\epsilon} = \boldsymbol{\epsilon}_l + \boldsymbol{\epsilon}_{nl} = (\mathbf{b}_l + \mathbf{b}_{nl})\mathbf{u} \tag{4}$$

where $\boldsymbol{\epsilon}_l$ and $\boldsymbol{\epsilon}_{nl}$ denote the linear and nonlinear strain components, respectively. The 6×3 linear and nonlinear differential operators, $\mathbf{b}_l$ and $\mathbf{b}_{nl}$, are defined in detail in [9]. As far as the constitutive relation is concerned, linear elastic structures are considered in this work. Consequently, the constitutive relation reads as:

$$\boldsymbol{\sigma}^k = \mathbf{C}^k\boldsymbol{\epsilon}^k \tag{5}$$

where $\mathbf{C}^k$ is the material elastic matrix of the k-th layer, whose explicit form can be found in [5].

In this study, the 3D Hashin failure criterion [10] is employed to assess material failure. This criterion identifies the predominant failure mode at the ply level based on the local stress state. Four distinct failure indices are considered: Fiber Tension (FT), Fiber Compression (FC), Matrix Tension (MT), and Matrix Compression (MC).

Numerical results

The analysed tape spring has a length of L = 577 (mm), a thickness of t = 80 (ìm), a radius of r = 11.25 (mm), and a subtended angle of α = 90°, see Fig. 1. The structure is simply supported and subjected to two applied moments at its ends. The boom consists of three layers made of Carbon

Materials Research Proceedings 69 (2026) 1210-1214 https://doi.org/10.21741/9781644904251-208

Fiber (CF) and Glass Fiber Plain Weave (GFPW), as shown in Fig. 1 and detailed in Tables 1 and 2, [11]. Its stacking sequence is [±45GFPW/0CF/±45GFPW]°.

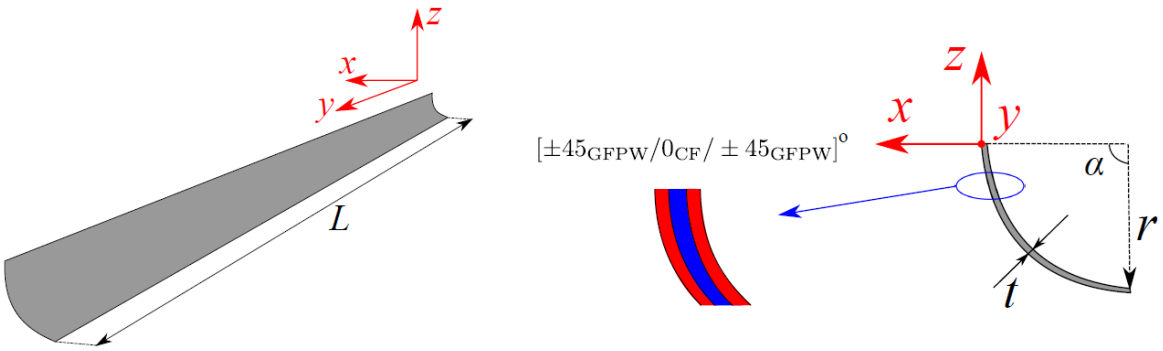


Figure 1: Geometrical details and stacking sequence of the tape-spring boom.

Table 1: Material characteristics of the tape-spring.

	E_1(GPa)	E_2(GPa)	G_{12}(GPa)	ν_{12}(-)	t(μm)
CF	128	6.5	7.6	0.32	
GFPW	23.8	23.8	3.3	0.17	

Table 2: Strength parameters for CF and GFPW in the tape-spring. Values in (MPa).

	X_T	X_C	Y_T	Y_C	S_{XY}	S_{XZ}	S_{XZ}
CF	2700	1650	55	225	100	100	32.26
GFPW	452.37	312.37	452.37	312.69	69.76	69.76	44.83

The structural model developed within CUF framework discretizes the cross-section into 30 L9 subdomains, enabling a piecewise parabolic approximation of the cross-sectional displacement field. Along the beam axis, two linear and eighteen cubic finite elements are employed, resulting in a total of 25,137 degrees of freedom (DOFs).

Figure 2 shows the equilibrium curve as a function of the angle θ, with the definitions of θ and the moment M provided for completeness. Point C (at $\theta = 6.8°$) marks the equilibrium state where the MC failure index reaches a critical value. A detailed distribution of the MC failure index at the equilibrium configuration C is provided in Fig. 3 (a). The plot clearly illustrates the variation of each failure index across the laminate's thickness at the mid-span. Fig. 3 (b) makes a comparison between configurations C and D.

Finally, Table 3 summarizes the maximum values of the four failure indices at the location of peak stress concentration for equilibrium states A, B, C, and D (see Fig. 2), along with their corresponding angles θ. All four failure indices reach their maximum values at the mid-span section, even though at distinct locations through the thickness. Specifically, the critical points for FT, MT, and MC are located within the GFWP layers, whereas the critical point for FC lies in the CF layer.

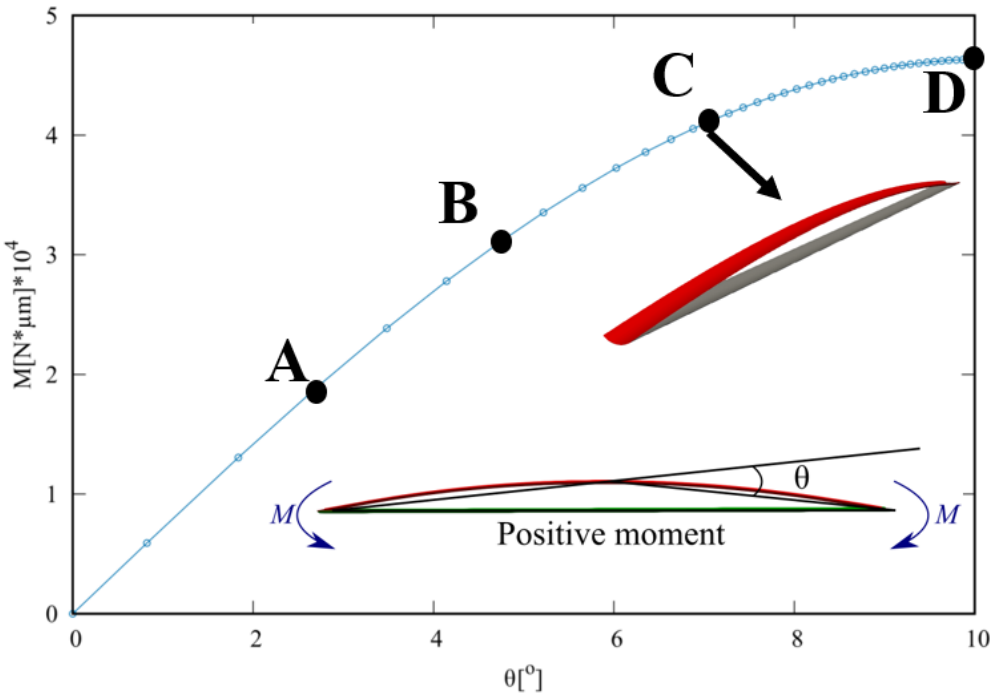


Figure 2: Equilibrium curve for the tape-spring boom.

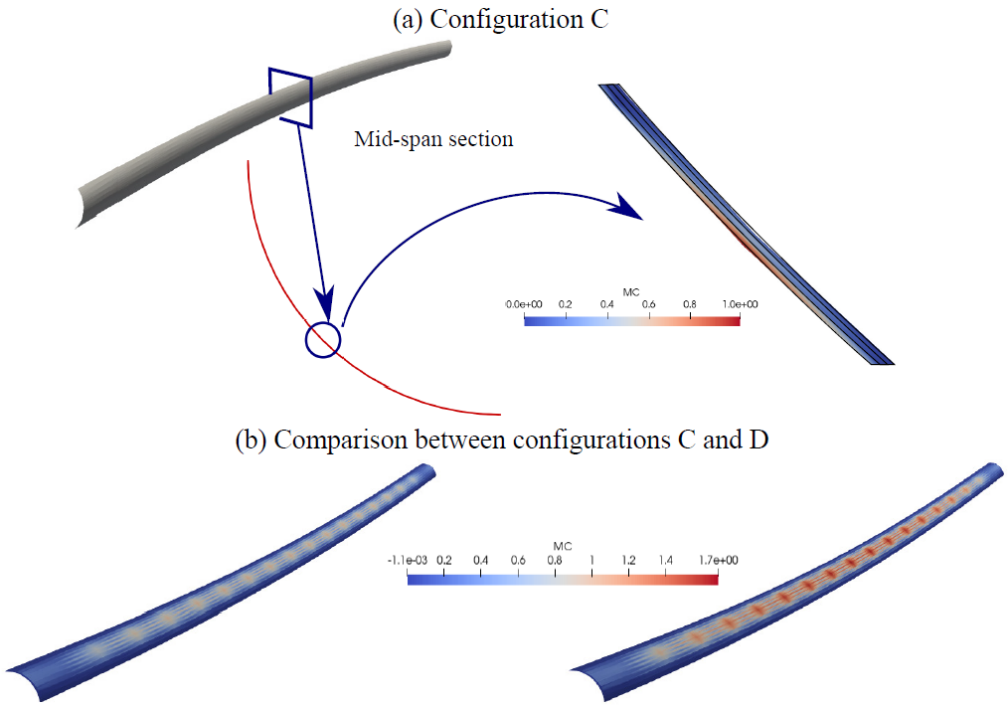


Figure 3: Failure indices for the equilibrium states C and D.

The results indicate that the structure may be susceptible to damage initiation even at relatively low angles of deformation. Among the considered failure indices, FT and FC, and MT are the least critical, whereas MC is significantly higher. The MC index, in particular, exhibits the most severe values, confirming it as the dominant failure mechanism. This analysis further reveals that the GFWP layers are the most prone to damage. Notably, the critical values for MC are reached during the nonlinear regime of the structural response.

Table 3: Failure indices for equilibrium points A, B, C, and D. (The locations are given in mm).

Configuration	θ[°]	FT (-0.0125,*L*/2,0)	FC (-3.51,*L*/2,-8.34)	MT (-4.22,*L*/2,8.94)	MC (-0.0125,*L*/2,-8.37)
A	2.7	0.000	0.000	0.010	0.16
B	4.7	0.002	0.000	0.026	0.44
C	6.8	0.006	0.002	0.031	1.03
D	9.9	0.009	0.002	0.050	1.69

Conclusions

This work has investigated the nonlinear behaviour of a tape-spring boom using a one-dimensional CUF framework. The Hashin 3D failure criterion was employed to assess the structure's failure state at various equilibrium points. It is important to note that the current model assumes a pristine, linear-elastic material response and does not incorporate damage progression. This simplification, the results clearly identify the mid-span region as the most critical area. Furthermore, the GFRP layers are identified as the most susceptible to damage initiation. Future work will focus on extending this analysis to include progressive failure modelling to accurately simulate damage initiation and evolution.

Acknowledgments

This study was carried out within the DISPCOMP funded by the Italian Space Agency, ASI, under contract n. 2024-38.I.0.

References

[1] P.A. Warren, Foldable member. U.S. Patent, 6: B1. (2002).
[2] F. Royer, S. Pellegrino, Ultralight ladder-type coilable space structures. In: 2018 AIAA Spacecraft Structures Conference, page 1200, 2018. https://doi.org/10.2514/6.2018-1200
[3] H.M.Y.C. Mallikarachchi, S. Pellegrino, Design of Ultrathin Composite Self-Deployable Booms, J. Spacecr. Rockets 51 (2014) 1811-1821. https://doi.org/10.2514/1.A32815
[4] K. Ubamanyu, D. Ghedalia, A.D. Hasanyan, S. Pellegrino. Experimental Study of Time dependent Failure of High Strain Composites. In: AIAA Scitech 2020 Forum, Orlando, FL, 6-10 January 2020. https://doi.org/10.2514/6.2020-0207
[5] E. Carrera, M. Cinefra, M. Petrolo, E. Zappino, Finite Element Analysis of Structures Through Unified Formulation, Wiley, Amsterdam, 2014. https://doi.org/10.1002/9781118536643
[6] D. Scano, E. Carrera, M. Petrolo, Use of the 3D Equilibrium Equations in the Free-Edge Analyses for Laminated Structures with the Variable Kinematics Approach, Aerotec. Missili Spaz. 103 (2024) 179-195. https://doi.org/10.1007/s42496-023-00177-2
[7] R. Augello, A. Pagani, E. Carrera, R. Masia, Virtual testing of folding and deployment of composite ultrathin tape spring hinges via unified 2D shell models. In: 73rd International Astronautical Congress (IAC), Paris, France, 18-22 September 2022.
[8] R. Augello, A. Pagani, E. Carrera, D.A. Iannotta, Stress and Failure Onset Analysis of Thin Composite Deployables by Global/Local Approach, AIAA J. 60 (2022) 5954-5966. https://doi.org/10.2514/1.J061899
[9] A. Pagani and E. Carrera, Unified formulation of geometrically nonlinear refined beam theories, Mech. Adv. Mater. Struct. 25 (2018) 15–31. https://doi.org/10.1080/15376494.2016.1232458
[10] Z. Hashin, Failure criteria for unidirectional fiber composites, J. Appl. Mech. 47 (1980) 329-334. https://doi.org/10.1115/1.3153664
[11] C. Leclerc, S. Pellegrino, Nonlinear elastic buckling of ultra-thin coilable booms, Int. J. Solids Struct. 202 (2020) 45–56. https://doi.org/10.1016/j.ijsolstr.2020.06.042

Materials Research Proceedings 69 (2026) 1215-1219 https://doi.org/10.21741/9781644904251-209

Virtual Modeling of The Curing Process of Composite Aerospace Components Using Coupled Multiphysics Models

M. SANTORI[1,a *], E. ZAPPINO[1,b], N. ZOBEIRY[2,c] and M. PETROLO[1,d *]

[1]MUL2 Lab, Department of Mechanical and Aerospace Engineering, Politecnico di Torino, 10129 Turin, Italy

[2]Department of Materials Science and Engineering, University of Washington, Seattle, WA, 98195, USA

[a]martina.santori@polito.it, [b]enrico.zappino@polito.it, [c]navidz@uw.edu, [d]marco.petrolo@polito.it

Keywords: Virtual Manufacturing, Carrera Unified Formulation, Multi-Field Model, Thermo-Chemo-Mechanical Analysis

Abstract. This work presents a multifield simulation approach using a higher-order one-dimensional model derived within the Carrera Unified Formulation framework to assess the impact of curing on the composite part's performance. The proposed approach enables coupled thermo-chemo-mechanical simulation and the simultaneous evaluation of temperature, degree of cure, process-induced deformations, and residual stresses in time and space. The advantage of this model is that it can generate a three-dimensional representation of the part while keeping computational cost low. Typical composite configurations in the aeronautical field, such as sandwich and stiffened structures, are analyzed. The results demonstrate the capability of the present numerical tool to simulate the behavior of the composite part during the process.

Introduction

The growing use of composite materials in the aerospace industry, owing to their excellent mechanical properties and high strength-to-weight ratio, has generated considerable interest in their curing processes. The complexity of the process and the stringent manufacturing specifications required to achieve high product quality have necessitated numerical modeling for the accurate and rapid study of the thermo-chemo-mechanical behavior of the composite part [1]. In recent years, more complex structural configurations, such as sandwich panels, have been increasingly used due to the excellent compromise between lightness and mechanical performance [2]. However, the presence of heterogeneous materials and complex interfaces makes the curing process even more challenging, requiring advanced numerical models that can realistically capture the three-dimensional distributions of temperature, degree of cure, and deformations.

The autoclave curing process is characterized by complex, coupled thermal, chemical, and mechanical interactions, further complicating its numerical simulation. The strong temperature and degree-of-cure gradients that develop within the laminate can lead to process-induced defects, such as residual stresses, warpage, and spring-in angles, which may significantly affect the final mechanical performance of the component [3,4]. In this context, numerical tools based on the finite element method (FEM) can be used to predict thermochemical behavior and process-induced defects; however, the inherently three-dimensional nature of the problem requires the use of solid elements, which significantly increases computational costs. For this reason, this work uses higher-order 1D models based on the Carrera Unified Formulation (CUF) [5] and finite elements to solve the coupled thermo-chemo-mechanical problem. In previous work, CUF-based models have been used to determine spring-in angles and stresses in L-shaped parts. Still, they have not accounted for the three-dimensional effects of thermal and chemical phenomena [6]. This variability is now introduced, enabling a more accurate solution for the part's temperature, degree of cure, and

Content from this work may be used under the terms of the Creative Commons Attribution 3.0 license. Any further distribution of this work must maintain attribution to the author(s) and the title of the work, journal citation and DOI. Published under license by Materials Research Forum LLC.

Materials Research Proceedings 69 (2026) 1215-1219 https://doi.org/10.21741/9781644904251-209

mechanical deformation. This work considers a typical aeronautical configuration of a stiffened honeycomb sandwich structure.

Thermo-chemo-mechanical model

To accurately describe the curing process, the thermochemical behavior of the composite is modeled using the 3D heat-conduction equation, coupled with the kinetic model governing the resin curing reaction [7]. The heat transfer equation is expressed as:

$$\rho C_p \frac{\partial T}{\partial t} = \nabla \cdot (\boldsymbol{\kappa} \nabla T) + \rho H_r \frac{d\alpha}{dt} \tag{1}$$

where ρ is the density, C_p is the specific heat and $\boldsymbol{\kappa}$ is the thermal conductivity tensor. $\partial T/\partial t$ and $d\alpha/dt$ are the two time derivatives of temperature and degree of cure, respectively, and ∇T is the gradient of temperature. H_r is the effective total heat of reaction. Curing kinetics depend on material type and are typically described by Arrhenius-type equations. For AS4 carbon fiber reinforced Hexcel 8552 resin, the cure rate is [8]:

$$\begin{aligned} &\frac{d\alpha}{dt} = \frac{K\alpha^m(1-\alpha^n)}{1+e^{C[\alpha-(\alpha_{C0}+\alpha_{CT}T)]}} \\ &K = Ae^{\frac{-\Delta E}{RT}} \end{aligned} \tag{2}$$

where A is the pre-exponential coefficient, ΔE is the activation energy, R is the universal gas constant, and the others are constant fitting parameters. The experimentally fitted cure kinetic parameters are given in [8].

During curing, the resin's mechanical properties and volumetric cure shrinkage depend on both the instantaneous temperature and the degree of cure. The fiber properties, on the other hand, are assumed to be constant and independent of the cure. Consequently, the composite's mechanical properties evolve in time and space in response to the local thermochemical behaviour. Micromechanical models, such as those presented in [8], are employed to relate the fiber and matrix properties and to derive the lamina's effective mechanical properties, thermal expansion coefficients, and cure shrinkage. The evolution of these quantities is then incorporated into the mechanical analysis to calculate the stiffness matrix and the external force vector, as described in [6].

Therefore, to solve for the unknown displacement field $\boldsymbol{u}$, a linear static mechanical equation is solved [6]:

$$\boldsymbol{k}_{uu}\boldsymbol{u} = \boldsymbol{p}_u \tag{3}$$

where $\boldsymbol{k}_{uu}$ is the [3x3] fundamental nucleus of the stiffness matrix, and $\boldsymbol{p}_u$ is the fundamental nucleus of the vector of external loads represented by the shrinkage and thermal strains. In this paper, the thermo-chemo-mechanical problem is solved using a higher-order 1D model based on CUF and finite elements. This model assumes that the displacement, temperature, and degree-of-cure fields in the cross-section are expressed as expansions of two-dimensional Lagrange functions. At the same time, along the y-axis of the beam, they are approximated using FEM, i.e., they can be written as:

$$\begin{aligned} \boldsymbol{u} &= N_i(y)F_\tau(x,z)\boldsymbol{u}_{i\tau}, \qquad \tau = 1,\dots,M; i = 1,\dots,N \\ T &= N_i(y)F_\tau(x,z)T_{i\tau}, \qquad \tau = 1,\dots,M; i = 1,\dots,N \\ \alpha &= N_i(y)F_\tau(x,z)\alpha_{i\tau}, \qquad \tau = 1,\dots,M; i = 1,\dots,N \end{aligned} \tag{4}$$

where $F_\tau(x,z)$ is the expansion function over the cross-section, $N_i(y)$ are the shape functions, and $\boldsymbol{u}_{i\tau}$, $T_{i\tau}$, and $\alpha_{i\tau}$ are the nodal unknowns of the displacement field, temperature, and degree of cure. M is the number of terms of the expansion function, and N is the number of nodes of the

Materials Research Proceedings 69 (2026) 1215-1219 https://doi.org/10.21741/9781644904251-209

finite element. By expressing the unknowns in terms of the CUF and finite elements and substituting them into the thermo-chemo-mechanical equations, the resulting system is obtained:

$$\begin{bmatrix} 0 & 0 & 0 \\ 0 & D_T & D_{T\alpha} \\ 0 & 0 & D_\alpha \end{bmatrix} \begin{Bmatrix} \dot{\boldsymbol{u}} \\ \dot{T} \\ \dot{\alpha} \end{Bmatrix} + \begin{bmatrix} \boldsymbol{k}_{uu} & 0 & 0 \\ 0 & K_T & 0 \\ 0 & 0 & 0 \end{bmatrix} \begin{Bmatrix} \boldsymbol{u} \\ T \\ \alpha \end{Bmatrix} = \begin{Bmatrix} \boldsymbol{p}_u \\ p_T \\ p_\alpha \end{Bmatrix} \tag{5}$$

whose terms are written as fundamental nuclei [5]. The problem is partially coupled, since thermal and chemical phenomena influence mechanics but not vice versa. Because the thermochemical problem requires more iterations than the mechanical problem, the heat-transfer and cure-kinetics equations are solved first using the Newmark method [9], yielding a 3D solution for temperature and degree of cure. Starting from the solution of α, the mechanical properties of the composite are evaluated and used as input for the mechanical analysis. The mechanical problem is solved iteratively using a CHILE approach [10,6]. In this way, an accurate solution can be obtained while limiting analysis time and computational costs.

Results

The higher-order 1D model introduced in this work is used to investigate the thermochemical behavior and process-induced deformations of a substructure representative of a stiffened honeycomb fuselage structure studied in [8]. The structure consists of two 12-layer AS4/8552 composite skins with symmetrical lamination $[45/90/-45/0/45/90]_s$. Between the two skins, there is a thick HEXCEL HRP-3/16-8.0 honeycomb core. The reinforcement, located on the top surface at the center of the sandwich panel, is a pre-cured resin-transfer molded J-frame. The tool used is made of aluminum, while the tool/part interface is simulated using a shear layer. All details on the materials used, geometric dimensions, and boundary conditions are given in [8]. In the reference, some properties of the composite and J-frame are temperature-dependent, whereas in this work, they are assumed constant and calculated using the maximum curing-cycle temperature. The curing cycle used in the numerical simulation is the one that most accurately reproduces the autoclave temperature measured experimentally in [8]. It involves two holding temperatures at 107 °C and 177 °C for 100 min and 116 min, respectively. The two heating ramps have heating rates of 1.85 °C/min and 0.7 °C/min, and a cooling rate of 2.3 °C/min. The FEM model consists of 3 quadratic beam elements, while 140 Lagrange elements with nine nodes (140L9) are used in the cross-section. The total number of degrees of freedom is 22085.

Figure 1 shows the temperature and degree of cure at the same points considered in [8], i.e., at the tool/part interface, on the top surface of the sandwich panel, and on the J-shaped reinforcement. A good match is obtained between the temperature obtained from the CUF model and those reported in the literature. Significant temperature and degree-of-cure gradients develop across the thickness of the sandwich panel due to the low thermal conductivity of the core. These variations can promote the formation of high residual stresses and induce deformations.

Materials Research Proceedings 69 (2026) 1215-1219 https://doi.org/10.21741/9781644904251-209

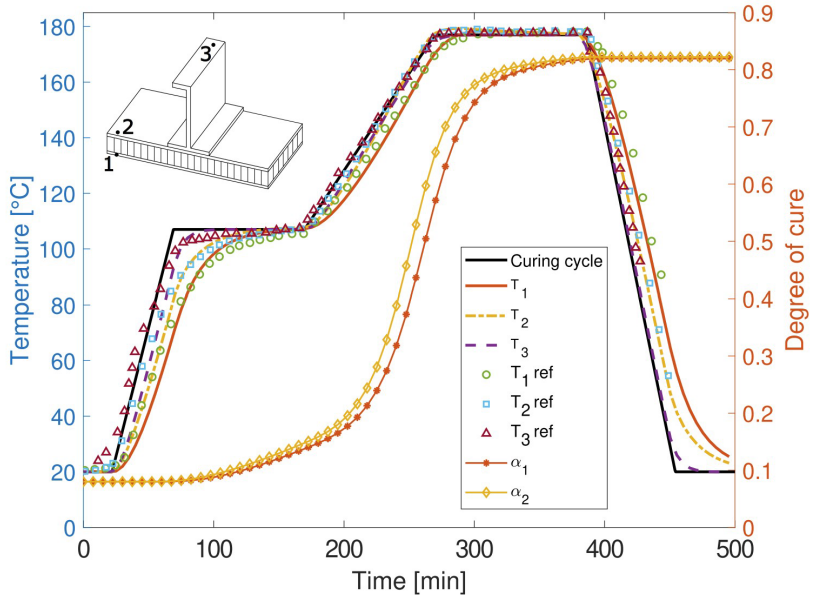


Figure 1: Temperature and degree of cure obtained using the present model and comparison with reference temperature solution [8] at points 1, 2, and 3 of the sandwich structure

Figure 2 shows the 3D deformation of the structure along the z-axis after tool removal. The structure exhibits warpage in the x–z plane. In the top plot of Fig. 2, the predicted warpage along the x-axis is compared with the fitted experimental results for three specimens reported in [8], showing good agreement.

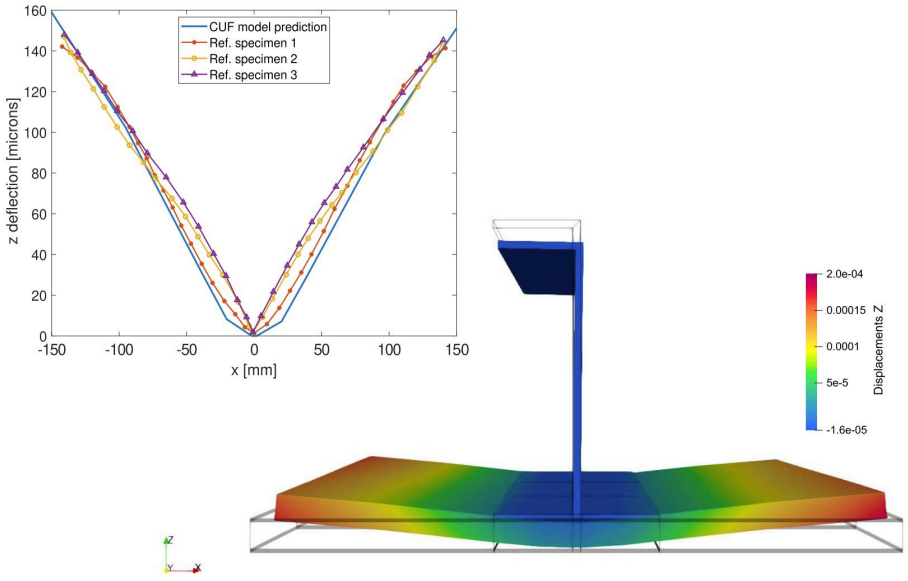


Figure 2: 3D distribution of the displacement in the z-direction (in mm) and comparison between the CUF model prediction and the experimental reference data taken from [8] of the warpage along the x-axis

Conclusion

This paper presents a numerical simulation to solve the coupled thermo-chemo-mechanical problem associated with the curing process of composite materials. The proposed model uses 1D finite elements along the beam axis and in the cross-section, higher-order distributions of temperature, degree of cure, and displacements using the Carrera Unified Formulation. The

advantage of the CUF model is that it can obtain 3D solutions for temperature, degree of cure, and displacements while maintaining a 1D formulation at low computational cost. A stiffened honeycomb sandwich panel is analyzed to validate the proposed numerical model. Comparing temperature measurements at different points on the part with the experimental data in the literature shows good agreement, confirming the accuracy of this approach.

Acknowledgement
This work was partly supported by the Italian Ministry of Foreign Affairs and International Cooperation, grant number US23GR12.

References

[1] E. Zappino, M. Santori, R. Masia, N. Zobeiry, M. Petrolo. Numerical Analysis of the Impact of Process Parameters on the Residual Stress of a Flat Composite Part, Aerotecnica Missili & Spazio 104(4), 277-291 (2025). https://doi.org/10.1007/s42496-024-00231-7

[2] G. Belingardi, M. Cavatorta, and R. Duella. Material characterization of a composite-foam sandwich for the front structure of a high speed train. Composite structures, 61(1-2):13-25 (2003). https://doi.org/10.1016/S0263-8223(03)00028-X

[3] Y. Li, A. Yang, Y. Liu, Y. Gao, J. Zhou, Y. Dong, S. Zhu. Analysis of warping defect formation mechanisms in hot molding of CF/PEEK thin-wall structures and their influence on mechanical properties. Thin-Walled Structures, 207, 112740 (2025). https://doi.org/10.1016/j.tws.2024.112740

[4] B. Wang, S. Fan, J. Chen, W. Yang, W. Liu, and Y. Li. A review on prediction and control of curing process-induced deformation of continuous fiber-reinforced thermosetting composite structures. Composites Part A: Applied Science and Manufacturing, 165:107321 (2023). https://doi.org/10.1016/j.compositesa.2022.107321

[5] E. Carrera, M. Cinefra, M. Petrolo, E. Zappino: Finite Element Analysis of Structures through Unified Formulation. John Wiley & Sons, 2014 https://doi.org/10.1002/9781118536643

[6] E. Zappino, N. Zobeiry, M. Petrolo, R. Vaziri, E. Carrera, A. Poursartip: Analysis of process-induced deformations and residual stresses in curved composite parts considering transverse shear stress and thickness stretching. Composite Structures, 241:112057 (2020). https://doi.org/10.1016/j.compstruct.2020.112057

[7] T. A. Bogetti. Process-induced stress and deformation in thick-section thermosetting composites. PhD thesis, University of Delaware (1989).

[8] A. A. Johnston. An integrated model of the development of process-induced deformation in autoclave processing of composite structures. PhD thesis, University of British Columbia (1997).

[9] K. J. Bathe. Finite Element Procedures. Klaus-Jurgen Bathe (2006).

[10] A. Johnston, R. Vaziri, and A. Poursartip. A plane strain model for process-induced deformation of laminated composite structures. Journal of Composite Materials, 35(16):1435-1469 (2001). https://doi.org/10.1106/YXEA-5MH9-76J5-BACK

Materials Research Proceedings 69 (2026) 1220-1224 https://doi.org/10.21741/9781644904251-210

A Multi-Fidelity Gaussian Process Framework for Predicting Process-Induced Deformations in Composites

K. JOHNSON[1,a], M. SANTORI[2,b], E. ZAPPINO[2,c], N. ZOBEIRY[1,d] and M. PETROLO[2,e *]

[1]Department of Materials Science and Engineering, University of Washington, Seattle, WA, 98195, USA

[2]MUL2 Lab, Department of Mechanical and Aerospace Engineering, Politecnico di Torino, 10129 Turin, Italy

[a]kaj1402@uw.edu, [b]martina.santori@polito.it, [c]enrico.zappino@polito.it, [d]navidz@uw.edu, [e]marco.petrolo@polito.it

Keywords: Multi-Fidelity Surrogate Models, Gaussian Process Regression, Bayesian Optimization, Carrera Unified Formulation, Process-Induced Deformations, Composite Design

Abstract. This work presents a multi-fidelity machine learning strategy for efficiently modeling the mechanical response of composite laminates during curing. A Gaussian Process Regression (GPR) framework is adopted to link the laminate stiffness parameters (B_{11}, D_{22}) to the stress component σ_{xx}, combining data from numerical models of different accuracy. High- and low-fidelity datasets are generated using Layer-Wise (LW) and Equivalent Single Layer (ESL) theories derived from the Carrera Unified Formulation (CUF) and finite-element analysis. The proposed approach employs Bayesian Optimization to adaptively select the most informative high-fidelity samples, thereby achieving accurate predictions at reduced computational cost. The model's predictive validity for stress distributions is demonstrated for L-shaped cross-ply composite laminates.

Introduction

Process-induced deformations and residual-stress development in composite laminates during curing pose significant challenges for ensuring structural performance and dimensional reliability in aerospace components [1]. Low-fidelity models provide fast, cost-effective estimates of deformation and stress distributions but often fail to capture detailed thickness variations. Conversely, high-fidelity simulations can resolve detailed stress fields across the laminate thickness but are computationally expensive, limiting their practicality for extensive design exploration of more complex part geometries.

For these reasons, there is growing interest in developing multifidelity simulation tools to analyze the composite manufacturing process [2]. The objective of this work is to minimize reliance on high-fidelity simulations by utilizing lower-fidelity data to train a surrogate model that accurately predicts stresses in composite components.

To bridge this gap, we propose a multi-fidelity surrogate modeling framework that combines two fidelity tiers: Equivalent Single Layer (ESL) theories and Layer-Wise (LW) simulations based on the Carrera Unified Formulation (CUF) [3]. A probabilistic surrogate model is then constructed using a Gaussian Process Regression (GPR) [2]. Two laminate stiffness parameters ($\mathbf{B_{11}}$, $\mathbf{D_{22}}$), derived from classical lamination theory, serve as GPR inputs and are mapped to the target stress. Bayesian Optimization (BO) is employed to allocate high-fidelity simulations to regions of high predictive uncertainty selectively.

Content from this work may be used under the terms of the Creative Commons Attribution 3.0 license. Any further distribution of this work must maintain attribution to the author(s) and the title of the work, journal citation and DOI. Published under license by Materials Research Forum LLC.

Materials Research Proceedings 69 (2026) 1220-1224 https://doi.org/10.21741/9781644904251-210

The effectiveness of the ML method is evaluated by predicting the stress $\boldsymbol{\sigma_{xx}}$ in L-shaped laminates made of AS4/8552 material.

Methodology

A multi-fidelity Gaussian Process Regression (GPR) framework was developed to model the relationship between laminate stiffness parameters B_{11} and D_{22} and the simulated stress component σ_{xx}. The goal was to quantify the amount of high-fidelity (HF) data required to achieve accurate predictions when abundant low-fidelity (LF) data are available. The GPR approach was chosen for its ability to provide both a mean prediction and an uncertainty estimate, enabling the model to use Bayesian optimization (BO) to identify regions where substitutive HF data would be most beneficial for improving model accuracy. The LF and HF datasets share the same inputs but differ in accuracy and computational cost. LF simulations are faster but less accurate, whereas HF simulations are more representative of the physical system but more computationally expensive to generate.

The distinction between fidelity levels arises from the structural modeling approach used to compute the training data. The high-fidelity (HF) data were obtained using Layer-Wise (LW) models, in which an independent kinematic expansion is used to describe each composite layer. This formulation enables a detailed through-thickness description, yielding a piecewise linear displacement field and a more accurate representation of interlaminar stress distributions. Conversely, the low-fidelity (LF) data are generated from Equivalent Single Layer (ESL) models, in which all layers share a single global kinematic expansion in the thickness direction. While each ply still retains its own material properties, the through-thickness displacement field in ESL models is linear and continuous. Both the ESL and LW datasets were generated using a higher-order model based on the Carrera Unified Formulation (CUF) combined with the finite element method (FEM) [4].

To appropriately represent the difference in accuracy between the two data sources, each fidelity level was assigned its own noise value (α). The noise term quantifies the uncertainty the model ascribes to each data point; larger values indicate that the model should place less trust in the data. Because LF simulations are less precise compared to HF simulations, the LF points were intentionally assigned higher noise levels. The optimal noise configuration was identified through a grid search over possible LF/HF combinations, ensuring that the LF-only model captures the general trends in the data without being overly optimistic. Once the baseline noise levels were established, the GPR model was iteratively trained using a composite kernel designed to capture both linear and nonlinear relationships between the stiffness parameters and stress response. The kernel combined a linear term, a Radial Basis Function (RBF), and a Rational Quadratic (RQ) component, along with a small fixed white noise term for numerical stability:

$$k(x,x') = C_1^2(x \cdot x') + C_2^2 RBF(L_1) + C_3^2 RationalQuadratic(\alpha, L_2) + C_4^2 WhiteNoise \quad (1)$$

$$k(x,x') = C_1^2(x \cdot x') + C_2^2\, exp\left(-\frac{\|x-x'\|^2}{2L_1^2}\right) + C_3^2\left(1+\frac{\|x-x'\|^2}{2\alpha L_2^2}\right)^{-\alpha} + C_4^2\delta(x,x') \quad (2)$$

where:

C_1^2 = Signal variance associated with the linear term
C_2^2 = Signal variance associated with the RBF term
L_1 = Characteristic length scale of the RBF term
C_3^2 = Signal variance of the RQ term
α = Shape parameter of the RQ term
L_2 = Length scale of the RQ term

Materials Research Proceedings 69 (2026) 1220-1224 https://doi.org/10.21741/9781644904251-210

C_4^2 = Noise variance
$\delta(x, x')$ = Kronecker delta function

Next, a BO framework was employed to determine which LF data points should be replaced with HF values to maximize model performance. The acquisition function utilized to accomplish this task was Expected Improvement (EI):

$$EI(x) = (\mu(x) - f^* - \xi)\Phi(z) + \sigma(x)\phi(z) \quad (3)$$

and

$$z = \frac{\mu(x) - f^* - \xi}{\sigma(x)} \quad (4)$$

where:
$\mu(x)$= Predicted mean of the Gaussian Process at candidate point x
$\sigma(x)$= Predicted standard deviation (uncertainty) of the Gaussian Process at x
f^*= Current best observed value of the objective function (here, validation R^2)
ξ= Small positive constant that controls exploration–exploitation balance
$\Phi(z)$= Cumulative distribution function (CDF) of the standard normal distribution
$\phi(z)$= Probability density function (PDF) of the standard normal distribution

At each iteration, BO ranks all candidate LF points by their potential contribution to model improvement. The LF samples with the greatest expected improvement are then replaced by their HF counterparts, and the GPR is retrained using the same kernel and noise configuration. This iterative substitution continues until the validation accuracy converges or all available HF data are used.

Results

The proposed approach was applied to an L-shaped composite structure comprising eight plies of unidirectional AS4/8552 material mounted on an Invar tool. The geometry, material properties, and curing cycle adopted are described in detail in [3]. Finite Element (FE) simulations based on the CUF higher-order model were conducted for all 256 possible cross-ply stacking sequences, employing both ESL and LW theories. The total degrees of freedom of the LW and ESL models of the L-shape structure were 21861 and 7455, respectively. The resulting dataset for the GPR analysis comprised 174 training points and 84 validation points. Initially, the GPR model was trained solely on the LF (ESL-based) dataset. In subsequent iterations, however, the 10 LF points with the greatest expected improvement are replaced with their corresponding HF counterparts. In Fig. 1 the updated GPR surface is evaluated over a grid to visualize how the predicted surface evolved as more HF data points are incorporated.

Materials Research Proceedings 69 (2026) 1220-1224 https://doi.org/10.21741/9781644904251-210

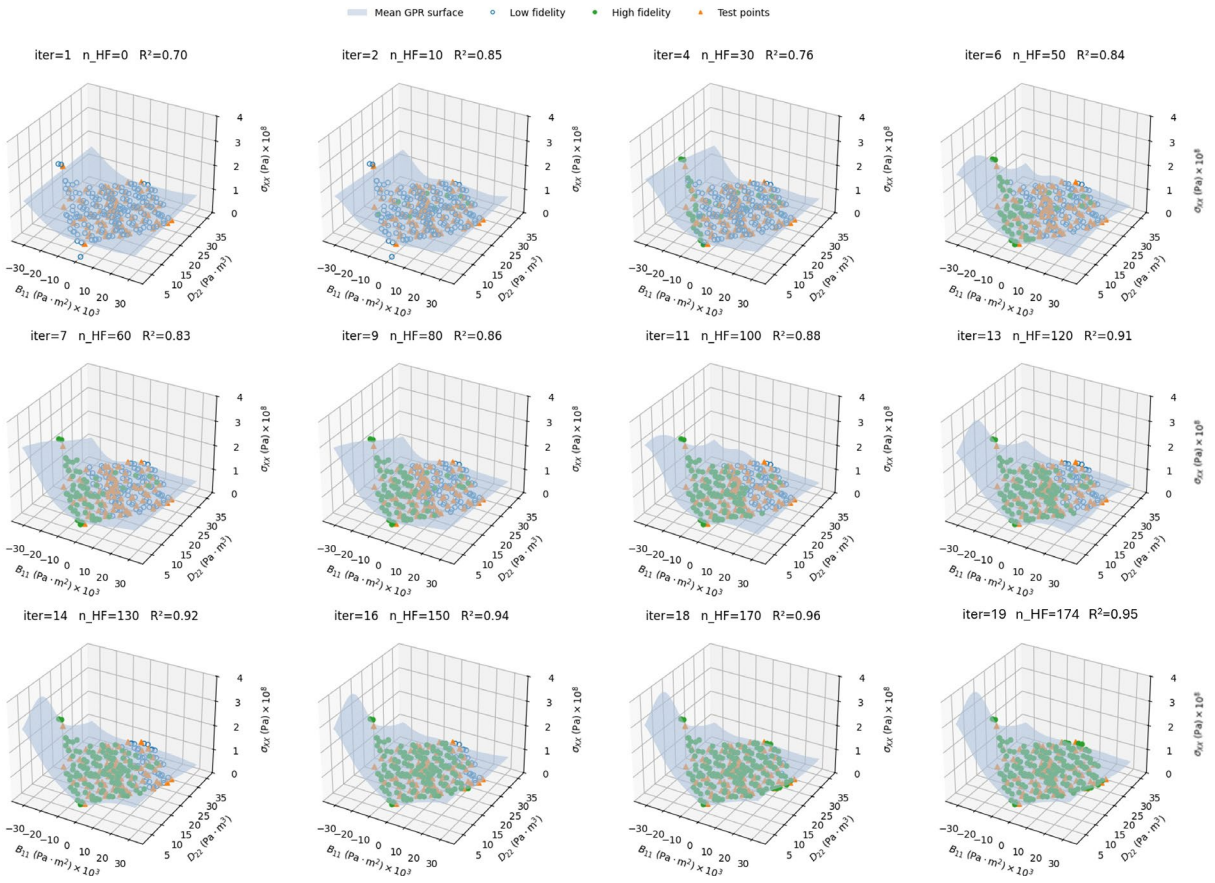


Figure 1: Evolution of the predicted GPR surface over the input parameter grid as high-fidelity data points $\boldsymbol{n_{HF}}$ are progressively incorporated

These results show the progressive refinement of the multi-fidelity GPR model as LF data points are gradually replaced with HF values. The term n_{HF} is representative of the number of HF points at a given iteration. At iteration 1 (iter = 1), the model trained only on LF data achieves a moderate accuracy (R^2 = 0.70), capturing general trends but missing finer variations in the 3D space. As additional HF points are incorporated, the predicted surface becomes smoother and more physically consistent with the observation data, and the validation accuracy steadily improves from roughly R^2 = 0.70 to R^2 = 0.95 by the final iteration. This also demonstrates that, within six iterations, the model increased accuracy by 14% and maintained that level for the remaining iterations. This means that, very quickly, it is possible to create an accurate machine learning model by replacing only 50 HF points (~29% of the total LF data). The results in Fig. 2 illustrate how the model evolves as HF data are selectively introduced through BO. At iteration 1, the GPR surface relies solely on LF data, producing a smooth but relatively uncertain trend with a moderate accuracy of R^2 = 0.70. By iteration 6, several strategically chosen LF points have been replaced by their HF counterparts, tightening the 95% confidence band and improving correlation to R^2 = 0.84. Evidence that the model is learning the actual stress distribution more effectively. Finally, at iteration 14, with 130 HF points now in training, the model achieves R^2 = 0.92, with the predictive surface aligning closely with the HF validation points and uncertainty collapsing in multiple zones of the domain.

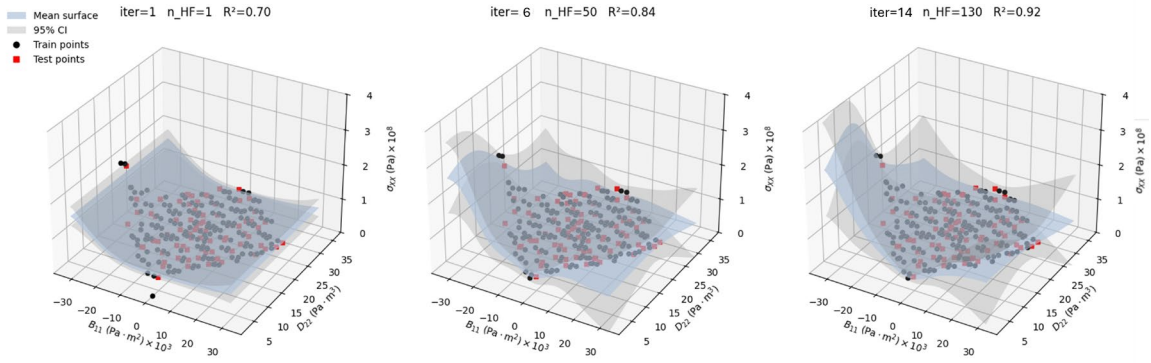


Figure 2: Multi-fidelity GPR predictive surface with iterative replacement of low-fidelity (LF) points by high-fidelity (HF) points, and comparison with the 95% confidence bands

Conclusion

In this work, a multi-fidelity GPR framework was applied to predict the stress field in composite laminates by combining data from models of different fidelity. The approach integrates low-fidelity (ESL) and high-fidelity (LW) simulations, formulated within the Carrera Unified Formulation (CUF), and solved using finite-element analysis. The results obtained for the L-shaped AS4/8552 composite structure show that, through Bayesian Optimization, a limited number of HF samples are sufficient to improve prediction accuracy significantly. After only a few iterations, the model achieved an accuracy $\mathbf{R^2}$ of 0.95, demonstrating that selective replacement of LF data is an effective strategy for balancing computational costs and accuracy.

Acknowledgement

This work was partly supported by the Italian Ministry of Foreign Affairs and International Cooperation, grant number US23GR12.

References

[1] E. Zappino, M. Santori, R. Masia, N. Zobeiry, M. Petrolo. Numerical Analysis of the Impact of Process Parameters on the Residual Stress of a Flat Composite Part. Aerotecnica Missili & Spazio (2025). https://doi.org/10.1007/s42496-024-00231-7

[2] C. Schoenholz, E. Zappino, M. Petrolo, N. Zobeiry. Efficient analysis of composites manufacturing using multi-fidelity simulation and probabilistic machine learning. Composites Part B: Engineering, Vol. 280, 111499 (2024). https://doi.org/10.1016/j.compositesb.2024.111499

[3] E. Zappino, N. Zobeiry, M. Petrolo, R. Vaziri, E. Carrera, A. Poursartip. Analysis of process-induced deformations and residual stresses in curved composite parts considering transverse shear stress and thickness stretching. Composite Structures, Vol. 241 (2020). https://doi.org/10.1016/j.compstruct.2020.112057

[4] E. Carrera, M. Cinefra, M. Petrolo, E. Zappino: Finite Element Analysis of Structures through Unified Formulation. John Wiley & Sons (2014). https://doi.org/10.1002/9781118536643

Materials Research Proceedings 69 (2026) 1225-1228 https://doi.org/10.21741/9781644904251-211

Numerical-Experimental Approach for Simplified Aerospace Structures' Testing Using the Eulerian Video Magnification Technique

Giusi MAGLIOCCO[1,a *], Salvatore MEROLA[1,b], Michele GUIDA[1,c], and Francesco MARULO[1,d]

[1]University of Naples Federico II – Dept. of Industrial Engineering, Naples, Italy

[a]giusi.magliocco@unina.it, [b]salvatore.merola@unina.it, [c]michele.guida@unina.it, [d]francesco.marulo@unina.it

Keywords: Testing in Aerospace, Eulerian Video Magnification, Video Processing, Finite Element Method, Modal Analysis

Abstract. This study presents a low-cost, non-contact experimental approach for structural dynamic testing of simplified aerospace components using Eulerian Video Magnification (EVM). Vibrations induced by a shaker are captured at 120 frames per second (fps), processed through a custom Python EVM algorithm, and compared with Finite Element (FEM) and analytical models. Results showed frequency deviations below 2% between EVM and FEM, validating the method's accuracy. The approach demonstrates that meaningful modal data can be obtained with consumer-grade equipment, enabling affordable, accessible, and non-invasive modal analysis for aerospace applications.

Introduction

Experimental Modal Analysis (EMA) is a key technique in structural dynamics used to determine the natural frequencies and mode shapes of mechanical and aerospace systems [1]. Conventional EMA approaches typically depend on costly and intrusive equipment, such as accelerometers, laser vibrometers, or high-speed cameras [2]. In this study, it is introduced and validated a low-cost, non-invasive experimental method that employs Eulerian Video Magnification (EVM) [3] using standard smartphone camera recordings to extract the vibrational characteristics of a simplified aerospace structure. EVM is a computational technique capable of amplifying subtle variations in motion and color within standard video recordings, analyzing pixel intensity variations over time, and applying temporal filtering to enhance imperceptible signals such as small vibrations or physiological changes. The method revealed versatility in applications, including the visualization of human pulse and the magnification of minute structural movements, marking a significant advancement in video-based motion analysis. This method is evaluated against both numerical (FEM) and theoretical analyses, providing a three-tier validation framework that integrates cost-effectiveness, computational modeling, and analytical accuracy. The study focuses on the dynamic characterization of a simplified structure (Fig. 1) through a detailed comparison between a numerical reference model and the results obtained from accessible measurement instruments. The structure is a simple beam-based model representative of aerospace components, excited by a shaker to produce broadband vibrations within the target frequency range, resulting in subtle oscillations that are often imperceptible to the human eye.

Content from this work may be used under the terms of the Creative Commons Attribution 3.0 license. Any further distribution of this work must maintain attribution to the author(s) and the title of the work, journal citation and DOI. Published under license by Materials Research Forum LLC.

Materials Research Proceedings 69 (2026) 1225-1228 https://doi.org/10.21741/9781644904251-211

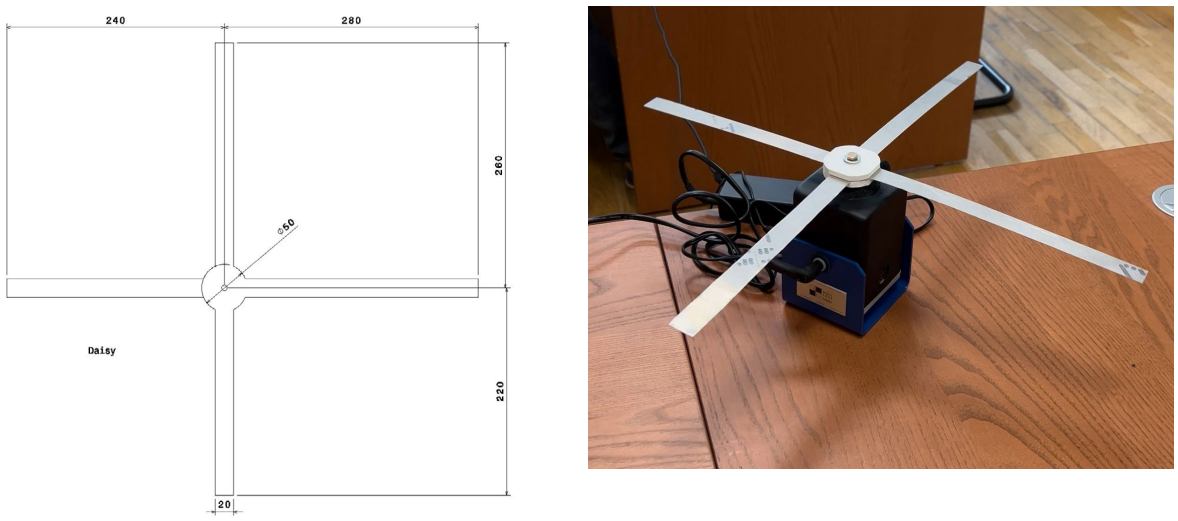


Figure 1 – Structure drawing (on left) and Experimental set-up (on right)

Methodology

To record these vibrations, an accessible approach is employed: a standard smartphone configured to capture video at 120 frames per second (fps). According to the Nyquist criterion, this sampling rate enables the detection of vibration frequencies up to 60 Hz, which is sufficient to capture the low-frequency vibration modes characteristic of the studied structure. Dedicated video recordings are obtained for the first and second vibration modes of each beam, ensuring full coverage of the relevant modal responses. This instrumental choice highlights the practicality of performing advanced dynamic analyses without relying on costly or specialized equipment [3]. Videos are recorded at both 60 frames per second (fps) and 120 fps using commercially available smartphones. A custom Python-based implementation of Eulerian Video Magnification is developed to process the video footage and extract the subtle motions associated with structural vibrations. The algorithm decomposes each video frame into multiple spatial scales using Gaussian and Laplacian pyramids, allowing the isolation of subtle motion components at different resolutions. Temporal intensity variations of pixels are then analyzed and filtered through a Butterworth bandpass filter, designed according to specified frequency bounds (low and high cutoffs) relative to the video frame rate. This enables selective amplification of vibrations within the frequency range of interest. For each pyramid level and color channel, temporal signals are detrended and transformed via Fast Fourier Transform (FFT) to identify dominant vibration frequencies and their spectral power. The filtered temporal signals are subsequently multiplied by a user-defined amplification factor, enhancing the magnitude of motion corresponding to the selected frequencies. The amplified Laplacian pyramid is then reconstructed into full-resolution frames, and the magnified video is saved in standard format. The code supports both grayscale and color processing, resizing videos to manageable dimensions (e.g., 640×360) for computational efficiency. It includes automatic frame reading, Laplacian pyramid generation, frequency-domain analysis, and result visualization through saved spectral plots. The resulting amplified videos allow for qualitative visualization and quantitative extraction of the mode shapes using frame differencing and pixel-based motion tracking techniques. In order to complement the experimental investigation and enable quantitative validation of the proposed method, a Finite Element Model (FEM) of the simplified structure is developed. The model serves as a theoretical benchmark for comparison with the experimental EVM results. The structure represents a simplified configuration of typical aerospace components, such as turbine blades.

Materials Research Proceedings 69 (2026) 1225-1228 https://doi.org/10.21741/9781644904251-211

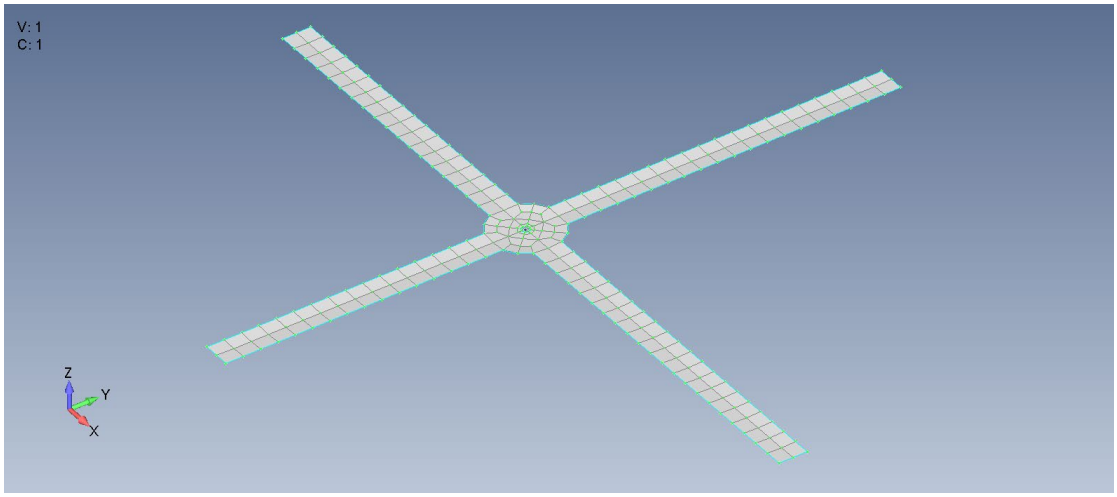


Figure 2 – FE Model of the Structure

The simulation used the SOL 103 solution for Normal Modes/Eigenvalue analysis [4]. The material properties are defined for Aluminum 3003 (Annealed Wrought). The model utilized SHELL elements and is constrained with a "Fixed" boundary condition at the center to simulate real conditions. Nastran input details included coordinate definitions and the EIGRL parameter to request the first 10 modes. The FEM successfully allowed for the determination of the frequencies and mode shapes of the first two vibration modes for each beam (petal) of the structure, providing the numerical benchmark for experimental comparison. The experimental setup is designed for efficiency and low cost. The simplified structure, representing aerospace components, is placed in the setup (Fig. 1). The structure is excited horizontally by a shaker, generating broadband vibrations within the target frequency range. These induced oscillations are described as subtle, often imperceptible to the human eye [1][5].

Results

The validation of the proposed approach relies on comparing the numerical (FEM) and experimental (EVM) results, supported by a theoretical analytical reference [6].The findings demonstrated high consistency across the estimated modal frequencies. For the first two vibration modes of the four analyzed beams, the frequency differences between EVM and FEM results are minimal.

Table 1 - Numerical-EVM Experimental Tests

Test	FPS	Beam	Mode	Freq. [Hz]	Num. Freq. [Hz]	EVM Freq. [Hz]	Err. % Num.	Err. % EVM
REC_001	120	1	1	6	5.47	6.03	9.69	0.5
REC_002	120	2	1	7	6.39	7.12	9.55	1.71
REC_003	120	3	1	8	7.74	8.14	3.36	1.75
REC_004	120	4	1	9	9.31	9.12	3.33	1.33
REC_005	120	1	2	35	34.18	35.4	2.4	1.14
REC_006	120	2	2	41	39.95	41.55	2.63	1.34
REC_007	120	3	2	49	47.72	49.64	2.68	1.31
REC_008	120	4	2	59	58.03	59.7	1.67	1.19

Conclusion

The EVM technique proved capable of handling moderate noise and suboptimal video resolution—factors typically expected to limit performance in high-precision applications. A key

contribution of this study is the demonstration that meaningful modal data can be extracted using ubiquitous and inexpensive hardware, such as smartphones, when combined with modern video processing techniques. This significantly lowers the entry barrier to experimental modal analysis, opening the door to practical applications in low-resource testing environments and preliminary engineering investigations.

Future work will focus on extending the proposed EVM-based approach to maintenance and testing activities in aerospace applications. In particular, the goal is to develop an integrated, video-based monitoring framework capable of supporting maintenance operations and in-field structural assessments with minimal instrumentation and setup complexity.

References

[1] Y. Yongchao, et al. Blind identification of full-field vibration modes from video measurements with phase-based video motion magnification. Mechanical Systems and Signal Processing, 2017, 85: 567-590. https://doi.org/10.1016/j.ymssp.2016.08.041

[2] M. Śmieja et al. Motion magnification of vibration image in estimation of technical object condition-review. Sensors, 2021, 21.19: 6572. https://doi.org/10.3390/s21196572

[3] J. G. Chen et al. Modal identification of simple structures with high-speed video using motion magnification. Journal of Sound and Vibration, 2015, 345: 58-71. https://doi.org/10.1016/j.jsv.2015.01.024

[4] K. Kilroy. MSC/NASTRAN Quick Reference Guide,1997.

[5] QIU, Qiwen; LAU, Denvid. Defect detection in FRP-bonded structural system via phase-based motion magnification technique. Structural Control and Health Monitoring, 2018, 25.12: e2259. https://doi.org/10.1002/stc.2259

[6] SHAO, Yanda, et al. Target-free 3D tiny structural vibration measurement based on deep learning and motion magnification. Journal of Sound and Vibration, 2022, 538: 117244. https://doi.org/10.1016/j.jsv.2022.117244

Materials Research Proceedings 69 (2026) 1229-1234 https://doi.org/10.21741/9781644904251-212

Experimental Investigation of Energy Dissipation in BCC and Wavy-BCC Lattice Structures under Drop-Weight Impact Testing

Giuseppe Iacolino[1,a *], Davide Tumino[1,b], Calogero Orlando[1,c], Giuseppe Mantegna[1,d], Giuseppe Catalanotti[1,e], Emilio V. González[2,f] and Andrea Alaimo[1,g]

[1]Department of Engineering and Architecture, Kore University of Enna, Cittadella Universitaria, 94100, Enna, EN, Italy

[2]AMADE, Polytechnic School, Universitat de Girona, Campus Montilivi s/n, Girona, 17071, Spain

[a]giuseppe.iacolino@unikorestudent.it, [b]davide.tumino@unikore.it, [c]calogero.orlando@unikore.it, [d]giuseppe.mantegna@unikore.it, [e]giuseppe.catalanotti@unikore.it, [f]emilio.gonzalez@udg.edu, [g]andrea.alaimo@unikore.it

Keywords: Lattice Structures, Wavy-BCC, PLA, Drop-Weight Impact Test, Experimental Study

Abstract. Additive manufacturing (AM), particularly fused deposition modelling (FDM), enables the precise fabrication of lattice structures with minimal material waste. This study investigates four polylactic acid (PLA) lattice geometries fabricated via FDM: two conventional body-centered cubic (BCC) configurations, BCC1.5 and BCC2, and two wavy-BCC (WBCC) counterparts, WBCC1.5 and WBCC2. The structures differ in strut diameter, set at either 1.5 mm or 2 mm, respectively. Each configuration was tested under identical low-velocity impact conditions using a 2 kg hemispherical impactor dropped from a height of 200 mm. The dimensionless index, D^*, was employed to relate the local indentation depth to the global maximum displacement. Results confirmed that BCC1.5 and WBCC1.5 exhibited higher energy dissipation (ED). Conversely, BCC2 and WBCC2 showed lower ED than their counterparts with smaller strut diameters. Notably, BCC2 yielded slightly lower ED than WBCC2 – yet with reduced indentation depth – indicating more favorable local deformation behavior.

Introduction

Cellular solids are a class of materials that continue to attract significant interest within the scientific community, due to their exceptional combination of low weight and excellent mechanical performance. These materials are frequently employed in sectors such as aerospace, automotive, and biomedical engineering [1]. Within this broad category, lattice structures – defined by the spatial repetition of unit cells organized in regular periodic patterns [2] – have demonstrated relevance for applications involving energy absorption [3].

Among lattice structures, the body-centered cubic (BCC) represents one of the most extensively studied topologies due to its favourable strength-to-weight ratio, and the relative simplicity with which it can be manufactured using both conventional and advanced techniques [4,5]. The latter are closely aligned with the principles of Industry 4.0, which integrates smart manufacturing and data for adaptive production [6]. In this regard, the rapid development of additive manufacturing (AM) technologies – ranging from powder bed fusion [7] to the fused deposition modelling (FDM) techniques – have further enhanced the feasibility of producing topology-optimized geometries [8] with high precision and minimal material waste.

While BCC structures have been extensively characterized in terms of their quasi-static mechanical response (e.g., see [9] and [10]), emerging research suggests that geometric

Content from this work may be used under the terms of the Creative Commons Attribution 3.0 license. Any further distribution of this work must maintain attribution to the author(s) and the title of the work, journal citation and DOI. Published under license by Materials Research Forum LLC.

Materials Research Proceedings 69 (2026) 1229-1234 https://doi.org/10.21741/9781644904251-212

modifications at the strut level can alter their global mechanical behavior. In this context, a modified BCC configuration has been introduced, featuring sinusoidal waviness along the struts [11]. This configuration, known as the wavy-BCC (WBCC), is based on the geometrical concept illustrated in Fig. 1. Particularly, it is characterized by curved struts defined by a non-zero amplitude a. The parameters Φ and L denote the strut's diameter and the characteristic side length of the unit cell, respectively.

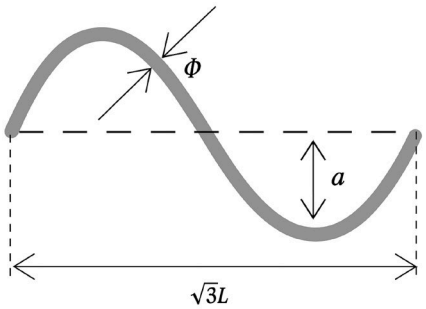


Fig. 1 Geometrical concept of strut waviness

Conversely, in explicit analyses, their local response may differ depending on the impact point. For this reason, a dimensionless index (D^*) [12] was previously defined to quantify the local indentation depth ($\bar{d}$) induced by the impact in relation to the global maximum displacement (δ_{max}), under a controlled drop height of 150 mm, in polylactic acid (PLA)-based lattices.

$$D^* = \frac{\bar{d}}{\delta_{max}} \quad \text{where} \quad \bar{d} = \frac{d_1 + d_2}{2}, \qquad \delta_{max} > 0 \tag{1}$$

In Eq. (1), d_1 and d_2 are the indentation depth values at the impact point, experimentally measured using a depth gauge in two perpendicular directions. Since the probe tip remains stationary and only the supporting base is repositioned along two perpendicular directions, both measurements refer to the same physical location. This accounts for surface irregularities resulting from the AM process.

Thus, the primary objective of this experimental campaign is to assess which BCC and WBCC structures, under the established impact conditions, demonstrate a lower energy dissipation (ED). This assessment is based on the hypothesis that increasing the strut diameter Φ from 1.50 mm to 2.00 mm may improve the structure's ability to withstand impact loads without undergoing catastrophic failure, thereby ensuring an efficient and stable energy response. This implies a higher fraction of energy stored elastically and released after impact, indicating improved structural resilience.

Experimental Setup and Results

The PLA periodic lattice specimens were manufactured at the Laboratory of Mechanical and Aerospace Engineering of the Kore University of Enna, Italy, using the Flashforge Adventurer M5 Pro 3D printer, following the ASTM D7136 [13] standard. To assess the mechanical properties of PLA, three additional dog-bone specimens were previously fabricated according to [14], with an average mass of 8.70 g (SD = 0.017 g). The tests yielded a Young's modulus (E) of 2427.67 MPa (SD = 19.75 MPa) and a maximum stress (σ_{max}) of 15.17 MPa (SD = 0.15 MPa).

The nominal dimensions of the BCC/WBCC samples along the x-y plane are 150 × 100 mm. Four lattice configurations were investigated, including BCC1.5 and WBCC1.5, featuring Φ = 1.5 mm, and BCC2 and WBCC2, with Φ = 2 mm. For each configuration, five samples were produced, resulting in a total of twenty specimens. All configurations feature top and bottom skins with a thickness of t = 1 mm and share the same nominal unit cell size (L = 10 mm), which enables the

Materials Research Proceedings 69 (2026) 1229-1234 https://doi.org/10.21741/9781644904251-212

impactor to strike the region between four nodes. For the WBCC categories, a was set at 1.5 mm. These dimensions were selected based on the manufacturing capabilities of the 3D printer and were defined according to practical constraints rather than through an optimization procedure. Fig. 2 shows a representation of the BCC1.5 (a), WBCC1.5 (b), BCC2 (c), and WBCC2 (d) unit cells.

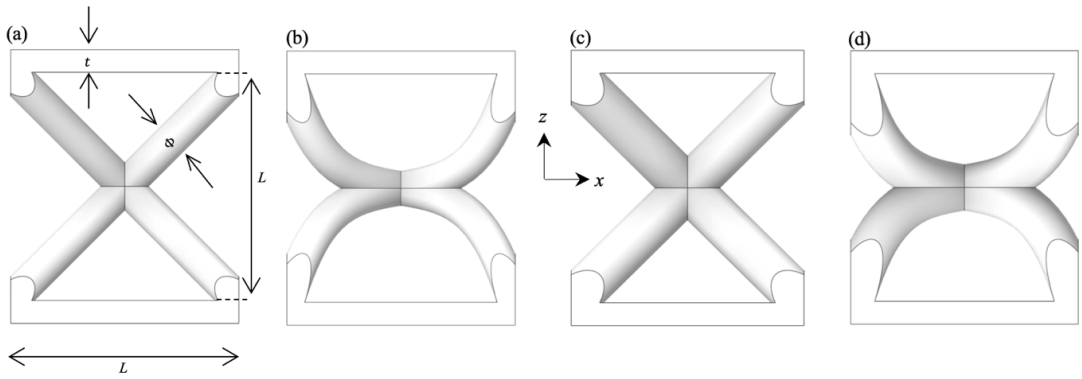


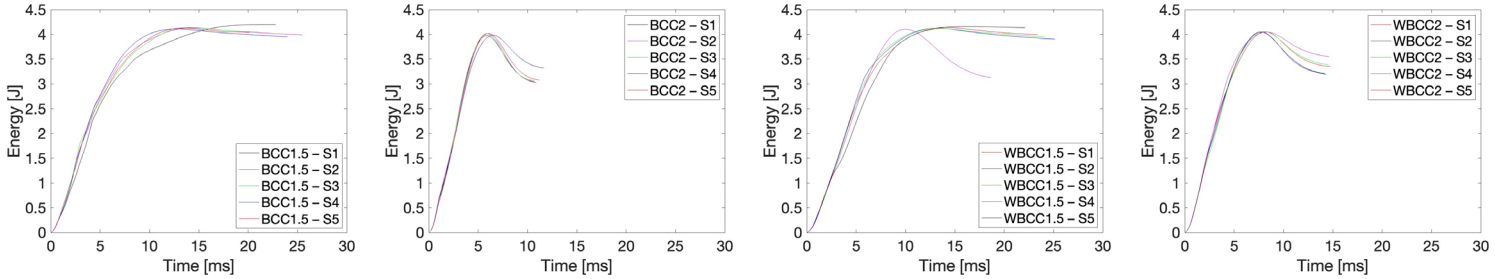
Fig. 2 Front view of the (a) BCC1.5, (b) WBCC1.5, (c) BCC2, (d) WBCC2 single-unit CAD models

The low-velocity impact tests were conducted at the Analysis and Advanced Materials for Structural Design (AMADE) research group at the University of Girona, Spain, utilizing a CEAST Fractovis Plus machine. All tests were conducted under identical conditions, employing a 2 kg hemispherical mass (Ø16 mm) dropped from a height of 200 mm, corresponding to an impact velocity of 1.98 m/s. After each individual test, dent depths d_1 and d_2 were measured using the Mitutoyo 547-217S ABS digital depth gauge to compute the D^* index.

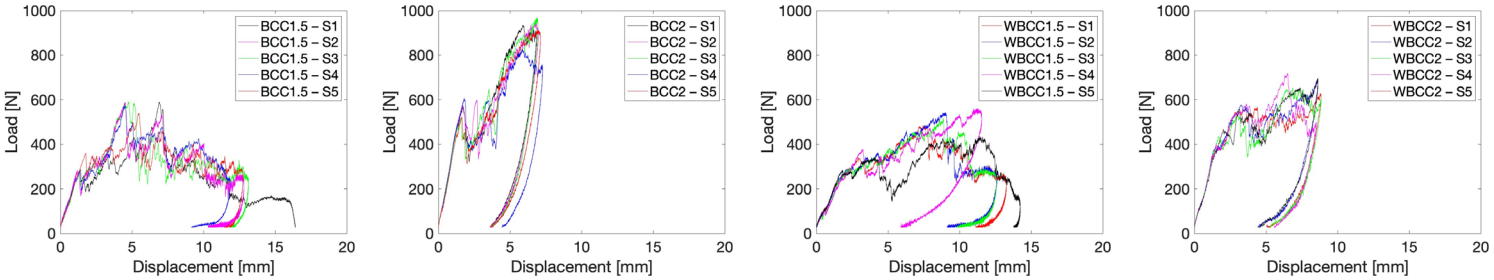
Figure 3 presents the energy-time and load-displacement diagrams for each configuration, whereas the averaged maximum values of each output are summarized in Table 1. Here, F_{mean}, δ_{mean}, $\bar{d}_{mean}$, ED_{mean}, and D^*_{mean} represent the mean values of the maximum load (F_{max}), δ_{max}, $\bar{d}$, ED, and D^* over all tested specimens within each sample category.

Table 1 Mean experimental values of $\boldsymbol{F_{max}}$, $\boldsymbol{\delta_{max}}$, $\boldsymbol{\bar{d}}$, $\boldsymbol{ED}$ and $\boldsymbol{D^*}$ after impact on each sample category

Sample Category	$F_{mean} \pm SD$ [N]	$\delta_{mean} \pm SD$ [mm]	$\bar{d}_{mean} \pm SD$ [mm]	$ED_{mean} \pm SD$ [J]	$D^*_{mean} \pm SD$
BCC1.5	577.02 ± 21.65	13.39 ± 1.75	7.33 ± 0.32	4.04 ± 0.09	0.55 ± 0.18
BCC2	918.68 ± 54.33	7.03 ± 0.17	2.05 ± 0.12	3.09 ± 0.12	0.29 ± 0.01
WBCC1.5	509.41 ± 49.62	12.85 ± 0.99	6.38 ± 2.22	3.82 ± 0.40	0.50 ± 0.16
WBCC2	679.55 ± 36.17	8.70 ± 0.14	2.73 ± 0.30	3.33 ± 0.14	0.31 ± 0.03



(a) (b) (c) (d)



(e) (f) (g) (h)

Fig. 3 Energy-time diagrams for BCC1.5 (a), BCC2 (b), WBCC1.5 (c) and WBCC2 (d) configurations; load-displacement diagrams for BCC1.5 (e), BCC2 (f), WBCC1.5 (g) and WBCC2 (h) configurations

According to Table 1, BCC2 exhibits the highest mean peak force (918.68 ± 54.33 N), while WBCC1.5 shows the lowest (509.41± 49.62 N). BCC1.5 reaches the highest δ_{max} (13.39 ± 1.75 mm), whereas BCC2 has the lowest (7.03 ± 0.17 mm). Similarly, BCC1.5 shows the largest $\bar{d}$ values (7.33 ± 0.32 mm), and BCC2 the smallest (2.05 ± 0.12 mm). ED_{mean} is highest in BCC1.5 (4.04 ± 0.09 J) and lowest in BCC2 (3.09 ± 0.12 J).

The BCC1.5 configuration – Figure 3(a) – recorded the highest ED_{mean} value, as the specimens exhibited low load-bearing capacity. Regarding the WBCC1.5 configuration – Fig. 3(c) – only one specimen (WBCC1.5 – S4) did not exhibit a failure mechanism. Fig. 4 presents a top-view comparison between specimen WBCC1.5 – S4 (a), and specimen WBCC1.5 – S1 (b), randomly selected among those presenting visible damage. The BCC2 and WBCC2 configurations demonstrated structurally efficient behavior, as evidenced by a clear plateau region in the energy-time domain – see Fig. 3(b) and 3(d). Notably, none of the tested specimens exhibited skin perforation. It is also worth noting that Fig. 3(e) and 3(g) reflect larger displacements, which are indeed associated with higher ED values. However, this does not apply to sample WBCC1.5 – S4, which showed lower displacement than the other specimens. Conversely, Fig. 3(f) and 3(h), representing the BCC2 and WBCC2 configurations, exhibit a more regular and progressive load-displacement behavior, with well-defined peak loads followed by gradual post-peak softening. These differences suggest that the higher ED observed in BCC1.5 and WBCC1.5 specimens is likely the result of sudden failure propagation rather than a more progressive damage, likely linked to a single failure mechanism. These observations are consistent with D^*, whose highest values were recorded for BCC1.5 (0.55 ± 0.18) and WBCC1.5 (0.50 ± 0.16).



(a) (b)

Fig. 4 Top view of (a) WBCC1.5 – S4 and (b) WBCC1.5 – S1 samples

Conclusions

In this experimental study, four PLA periodic lattice structures were subjected to low-velocity impact tests. A 2 kg mass was released from a height of 200 mm to evaluate which configuration exhibited lower ED. Despite BCC1.5 exhibiting the highest mean ED, its structural performance was poor due to sudden failure after impact. Similar behavior was observed in WBCC1.5, although only one out of five specimens showed minor denting. The increase in strut diameter in BCC2 and WBCC2 resulted in a general reduction in ED, likely due to the greater stiffness associated with the increased material volume. Notably, WBCC2 showed a 7.8% higher ED_{mean} and a 33.17% increase in $\bar{d}_{mean}$ compared to BCC2. This level of deformation may be considered acceptable in applications where limited localized damage is permissible. Conversely, BCC2 remains the optimal choice where even minimal indentations are critical.

Nevertheless, this study is subject to certain limitations. Firstly, only a single drop height was considered, limiting the validity of the results to the specific experimental conditions adopted. Moreover, the analysis was based on a limited sample size, with five specimens tested per configuration. Future work will examine alternative geometric configurations, including variations in skin thickness, as well as modified experimental conditions in which the impact load is applied directly to a node rather than in the area defined by four nodes.

Overall, the findings highlight the complex interplay between ED and geometric design in lattice structures under low-velocity impact, revealing how certain configurations may lead to sudden failure. The results provide valuable insights for the tailored design in applications where specific trade-offs between ED and structural preservation are required.

References

[1] W. Tao and M. C. Leu, “Design of lattice structure for additive manufacturing,” in *2016 International Symposium on Flexible Automation (ISFA)*, IEEE, Aug. 2016, pp. 325–332. https://doi.org/10.1109/ISFA.2016.7790182

[2] G. Mantegna, N. D. Cilia, C. Orlando, D. Tumino, C. R. Vindigni, and A. Alaimo, “1D Modelling of BCC Lattice Mechanical Behaviour Using Optimised Neural Networks,” *International Journal on Interactive Design and Manufacturing (IJIDeM)*, Jul. 2025. https://doi.org/10.1007/s12008-025-02361-z

[3] Z. Yu, R. Savinov, M. Matura, P. Zhang, and J. Shi, “Current research status on advanced lattice structures for impact and energy absorption applications: A systematic review,” *Thin-Walled Structures*, vol. 215, p. 113490, Oct. 2025. https://doi.org/10.1016/j.tws.2025.113490

[4] G. Marabello, M. Chairi, and G. Di Bella, “Optimising Additive Manufacturing to Produce PLA Sandwich Structures by Varying Cell Type and Infill: Effect on Flexural Properties,” *Journal of Composites Science*, vol. 8, no. 9, p. 360, Sep. 2024. https://doi.org/10.3390/jcs8090360

[5] D. T. Queheillalt and H. N. G. Wadley, “Cellular metal lattices with hollow trusses,” *Acta Mater*, vol. 53, no. 2, pp. 303–313, Jan. 2005. https://doi.org/10.1016/j.actamat.2004.09.024

[6] G. Mantegna *et al.*, “Representative volume element homogenisation approach to characterise additively manufactured porous metals,” *Mechanics of Advanced Materials and Structures*, vol. 30, no. 5, pp. 1073–1082, Mar. 2023. https://doi.org/10.1080/15376494.2022.2124002

[7] D. Tumino, A. Alaimo, C. Orlando, S. Valvano, and C. R. Vindigni, “Lattice Core FEM Simulation with a Modified-Beam Approach,” 2023, pp. 946–954. https://doi.org/10.1007/978-3-031-15928-2_83

[8] G. Mantegna, “Comparison of lattice core topologies in sandwich structures,” Dec. 2023, pp. 296–299. https://doi.org/10.21741/9781644902813-64

[9] C. Rodrigo, S. Xu, Y. Durandet, D. Fraser, and D. Ruan, “Quasi-static and dynamic compression of additively manufactured functionally graded lattices: Experiments and simulations,” *Eng Struct*, vol. 284, p. 115909, Jun. 2023. https://doi.org/10.1016/j.engstruct.2023.115909

[10] D. Wu *et al.*, “Quasi-static compression and fatigue performance of hybrid plate lattice metamaterial structures,” *Mechanics of Advanced Materials and Structures*, pp. 1–13, May 2025. https://doi.org/10.1080/15376494.2025.2502133

[11] D. Tumino, A. Alaimo, C. Orlando, and S. Valvano, “A Preliminary Study on the Effect of Strut Waviness on the Mechanical Properties of BCC Lattice Unit Cells,” in *Design Tools and Methods in Industrial Engineering II. ADM 2021*, C. Rizzi, F. Campana, M. Bici, F. Gherardini, T. Ingrassia, and P. Cicconi, Eds., Springer, 2022, pp. 431–441. https://doi.org/10.1007/978-3-030-91234-5_44

[12] G. Iacolino *et al.*, “Low-Velocity Impact Behavior of PLA BCC Lattice Structures: Experimental and Numerical Investigation with a Novel Dimensionless Index,” *Materials*, vol. 18, no. 19, p. 4574, Oct. 2025. https://doi.org/10.3390/ma18194574

[13] ASTM International, “ASTM D7136/D7136M-05. Standard test method for measuring the damage resistance of a fiber-reinforced polymer matrix composite to a drop-weight impact event.” 2005, *West Conshohocken, PA, USA*.

[14] “Test Method for Tensile Properties of Plastics,” Dec. 15, 2014, *ASTM International, West Conshohocken, PA*. https://doi.org/10.1520/D0638-14

Materials Research Proceedings 69 (2026) 1235-1239 https://doi.org/10.21741/9781644904251-213

Global-local Modelling with Node Dependent Kinematics and Arbitrary Displacement Fields for Plates

Daniele SCANO[1,a *], Erasmo CARRERA[1,b] and Enrico ZAPPINO[1,c]

[1]MUL2 Lab, Department of Mechanical and Aerospace Engineering, Corso Duca degli Abruzzi 24, 10129, Torino, Italy

[a]daniele.scano@polito.it, [b]erasmo.carrera@polito.it, [c]enrico.zappino@polito.it

Keywords: Finite Element Method, Higher-Order Theories, Kinematic Models, Unified Formulation, Node-Dependent Kinematics

Abstract. This paper introduces enhanced two-dimensional finite elements based on a node dependent kinematics method, which allows each node to adopt a unique thickness expansion. A key innovation of the proposed approach is the ability to independently select models for each of the three displacement variables, employing both Taylor-based and Legendre-based expansions for the cross-section. The formulation is developed within the framework of the Carrera Unified Formulation, which separates the three-dimensional displacement field into in-plane and cross-sectional components. The method is validated for a free-edge problem by comparison with results from the literature and highly refined benchmark solutions. The findings show that the optimal computational model for balancing accuracy and efficiency is problem specific.

Introduction

Laminated composite structures are extensively used in the aerospace and automotive industries for their lightweight and high-performance properties. However, their material inhomogeneity can cause complex behaviours, such as free-edge effects (i.e., stress concentrations at layer interfaces near discontinuities) that often serve as initiation sites for damage [1]. Refined theories, including those by Carrera based on Reissner's Mixed Variational Theorem and the Principle of Virtual Displacements (PVD) within the CUF framework [2, 3, 4], have improved upon classical models. Most existing studies use the Equivalent Single Layer (ESL) approach, which simplifies modelling by using variables independent of the number of layers. For more detailed and accurate stress analysis, the Layer-Wise (LW) approach is preferred, assigning separate variables to each layer.

While refined models improve accuracy, they also increase computational costs, especially when involving local phenomena like delamination [5]. To address this, hybrid modelling strategies have been developed, applying high-fidelity models only in critical regions and lower-fidelity models elsewhere, reducing computational load with minimal loss of accuracy. However, implementing such global–local approaches is complex, and numerous methods for integrating different structural theories have been proposed, as reviewed by Noor [6]. This work presents enhanced 2D finite elements based on the Node-Dependent Kinematics (NDK) method [7], which allows each node to adopt different section expansions and enables independent modelling of displacement variables without special coupling. As usual, the Lagrange (LW) and Taylor (ESL) polynomials are adopted as structural theories. The first step is the development of a unified method that isolates contributions of individual terms and avoids reformulating equations for each new theory, thereby balancing accuracy and computational efficiency. Building on Carrera's work [8, 9], the approach combines ESL and LW models within a consistent framework. The second step exploits the hierarchical nature of CUF to incorporate thickness-wise descriptions, assigning different structural theories to each node. Originally applied to plates and recently extended to plates [10], the NDK method provides flexibility in combining low- to high-order theories in 2D problems.

Content from this work may be used under the terms of the Creative Commons Attribution 3.0 license. Any further distribution of this work must maintain attribution to the author(s) and the title of the work, journal citation and DOI. Published under license by Materials Research Forum LLC.

Materials Research Proceedings 69 (2026) 1235-1239 https://doi.org/10.21741/9781644904251-213

Structure of the work. This paper is organized as follows. Section *Theoretical formulation* discusses the principles of the Unified Formulation and the mathematical details of the Node-Dependent Kinematics (NDK) approach, including the governing equations. Section *Numerical results* presents the outcomes for out-of-plane stresses. Finally, Section *Conclusions* summarizes the key findings of the work.

Theoretical formulation

In classical elasticity, the stress tensor, $\boldsymbol{\sigma}_k$, and the strain tensor, $\boldsymbol{\epsilon}_k$, can be conveniently expressed in vector form as:

$$\boldsymbol{\sigma}^k = \left\{\sigma_{xx}^k\ \sigma_{yy}^k\ \sigma_{zz}^k\ \sigma_{yz}^k\ \sigma_{xz}^k\ \sigma_{xy}^k\right\}^T, \quad \boldsymbol{\epsilon}^k = \left\{\epsilon_{xx}^k\ \epsilon_{yy}^k\ \epsilon_{zz}^k\ \epsilon_{yz}^k\ \epsilon_{xz}^k\ \epsilon_{xy}^k\right\}^T \tag{1}$$

The geometric relationships between strains and displacements are defined as:

$$\boldsymbol{\epsilon}^k = \mathbf{D}\mathbf{u}^k \tag{2}$$

where $\mathbf{D}$ is the matrix of differential operators, valid under the assumption of small displacements and small rotations [3]. For linear elastic orthotropic materials, the constitutive relation is given by

$$\boldsymbol{\sigma}^k = \mathbf{C}^k\boldsymbol{\epsilon}^k \tag{3}$$

where $\mathbf{C}^k$ denotes the matrix of material coefficients (see [11] for details).

Unified formulation. In this method, the concept of the Unified formulation and the FE method are used together. Furthermore, every FE node possesses its unique set of structural theories, and each displacement component can use a different theory. These concepts can be summarized mathematically as follows for the real system:

$$\begin{aligned} u_x^k(x,y,z) &= N_i(x,y)F_{u_x\tau}^{ki}(z)q_{x\tau i}^k,\ \ \tau = 1,\dots,M_{u_x}; i = 1,\dots,N_n \\ u_y^k(x,y,z) &= N_i(x,y)F_{u_y\tau}^{ki}(z)q_{y\tau i}^k,\ \ \tau = 1,\dots,M_{u_y}; i = 1,\dots,N_n \\ u_z^k(x,y,z) &= N_i(x,y)F_{u_z\tau}^{ki}(z)q_{z\tau i}^k,\ \ \tau = 1,\dots,M_{u_z}; i = 1,\dots,N_n \end{aligned} \tag{4}$$

where $F_{u_x\tau}^{ki}$, $F_{u_y\tau}^{ki}$, and $F_{u_z\tau}^{ki}$ denote the expansion functions associated with the generalized displacements $q_{x\tau i}^k$, $q_{y\tau i}^k$, and $q_{z\tau i}^k$, respectively. The index τ indicates summation, while M_{u_x}, M_{u_y}, and M_{u_z} represent the number of expansion terms for each displacement component. In this paper, seven-node Lagrange (LE7) expansions and Taylor functions are used. Moreover, N_i denotes the shape functions, with the repeated subscript i implying summation, and N_n the number of shape functions per element. For the numerical assessments carried out in this study, the classical nine-node Lagrangian element (Q9) is employed [11]. In the case of the virtual system, the indices i and τ are replaced by j and s, respectively.

Governing equations. By using the Principle of the Virtual Displacements:

$$\begin{aligned} &\delta L_{int} = \delta L_{ext} = \\ &\int_{Vk}\left(\delta\epsilon_{xx}^k\sigma_{xx}^k + \delta\epsilon_{yy}^k\sigma_{yy}^k + \delta\epsilon_{zz}^k\sigma_{zz}^k + \delta\epsilon_{yz}^k\sigma_{yz}^k + \delta\epsilon_{xz}^k\sigma_{xz}^k + \delta\epsilon_{zz}^k\sigma_{zz}^k\right)\mathrm{d}V^k = \\ &\delta u_x^k P_{u_x}^k + \delta u_y^k P_{u_y}^k + \delta u_z^k P_{u_z}^k \end{aligned} \tag{5}$$

It is possible to obtain three governing equations for each virtual displacement:

Materials Research Proceedings 69 (2026) 1235-1239 https://doi.org/10.21741/9781644904251-213

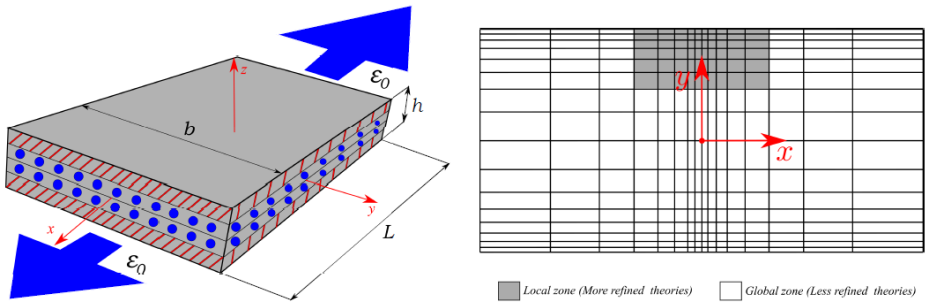
$$\begin{aligned}
\delta q^k_{x_{sj}}&: K^k_{u_x u_x s\tau ji} q^k_{x_{\tau i}} + K^k_{u_x u_y s\tau ji} q^k_{y_{\tau i}} + K^k_{u_x u_z s\tau ji} q^k_{z_{\tau i}} = P^k_{u_x sj} \\
\delta q^k_{y_{sj}}&: K^k_{u_y u_x s\tau ji} q^k_{x_{\tau i}} + K^k_{u_y u_y s\tau ji} q^k_{y_{\tau i}} + K^k_{u_y u_z s\tau ji} q^k_{z_{\tau i}} = P^k_{u_y sj} \\
\delta q^k_{z_{sj}}&: K^k_{u_z u_x s\tau ji} q^k_{x_{\tau i}} + K^k_{u_z u_y s\tau ji} q^k_{y_{\tau i}} + K^k_{u_z u_z s\tau ji} q^k_{z_{\tau i}} = P^k_{u_z sj}
\end{aligned} \tag{6}$$

The fundamental nuclei for the load vector are written in the followings:

$$\begin{aligned}
P^k_{u_x sj} &= N_j F^{kj}_{u_x \tau} P^k_{u_x} \\
P^k_{u_y sj} &= N_j F^{kj}_{u_y \tau} P^k_{u_y} \\
P^k_{u_z sj} &= N_j F^{kj}_{u_z \tau} P^k_{u_z}
\end{aligned} \tag{7}$$

Assembly. This work employs an innovative formulation of the Fundamental Nucleus (FN) that represents a significant departure from conventional CUF implementations. The key advancement lies in the treatment of FN components $K^k_{u_m u_l s\tau ji}$ and $P^k_{u_m sj}$ as single scalar elements rather than the traditional 3×3 matrix structure. The explicit expressions of $K^k_{u_m u_l s\tau ji}$ are not explicitly given for the sake of brevity. This streamlined approach requires only nine independent scalar parameters for complete stiffness characterization (and three for the load array), offering substantial computational advantages. The new formulation provides important theoretical and practical benefits compared to standard CUF implementations [2, 3]. Most notably, it eliminates the constraint requiring all variables to share the same expansion theory, a limitation that often forces unnecessary computational overhead in conventional approaches. See also [8,9]. The assembly across all displacement components, FE nodes, and elements results in the problem: $\mathbf{KU} = \mathbf{P}$.

Numerical results



(a) *Geometrical properties* (b) *NDK mesh*

Figure 1: Four-Layer composite plate. The study case is taken from [12] and [4].

The study investigates the free-edge behaviour of a symmetric composite plate (see Fig. 1a) with rectangular surface measuring L = 40 [mm], b = 20 [mm], and a thickness of h = 5 [mm]. The laminate has a stacking sequence of [45◦/−45◦]s, and its material properties are E_1 = 137.9 [GPa], $E_2 = E_3$ = 14.5 [GPa], $\nu_{12} = \nu_{13} = \nu_{23}$ = 0.21, and $G_{12} = G_{13} = \nu_{23}$ = 5.9[GPa]. The analysis, based on the works of Robbins and Reddy [12] and Scano et al. [4], applies a uniform axial strain ϵ_0 along the x-axis by imposing end displacements u at $x = \pm$L/2. This loading condition induces a constant strain field in the central region of the plate, provided that the plate length L is sufficiently large compared to the edge perturbed zones. In this problem, a finer mesh is required near the free edge; therefore, a non-uniformly distributed 16 × 16 finite element mesh is adopted. Figure 1b illustrates the mesh configuration, highlighting the local region with 208 FE nodes and the global region with 881 FE nodes, where more refined and less refined theories are employed, respectively. Shear, σ_{xz}, and transverse, σ_{zz}, stresses are calculated along the thickness of the plate near the

Materials Research Proceedings 69 (2026) 1235-1239 https://doi.org/10.21741/9781644904251-213

free-edge (at y/b = 0.998) in mid-plate (at x = 0). The results are reported in a scaled form as follows

$$\bar{\sigma}_{xz} = \frac{\sigma_{xz}}{\epsilon_0}, \quad \bar{\sigma}_{zz} = \frac{\sigma_{zz}}{\epsilon_0} \tag{9}$$

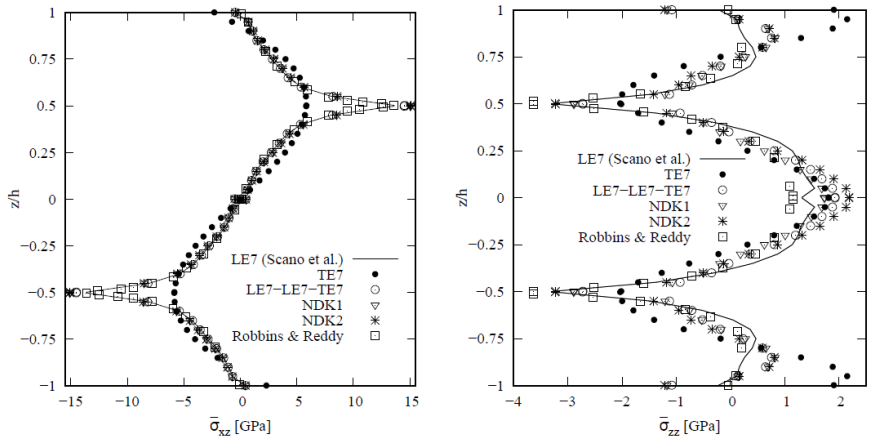
Table 1 presents the characteristics of the Unified Formulation models, including the adopted theories, the number of Degrees of Freedom (DOF), the corresponding DOF reduction, and the naming convention. Shear and transverse stresses along the thickness are studied, as displayed in Figs. 2a and 2b, respectively.

Table 1: Unified formulation models used for the angle-ply [45◦/−45◦]$_s$ laminate.

Global Model	Local Model	DOF	DOF Reduction [%]	Theory Definition
LE7-LE7-LE7	LE7-LE7-LE7	81675	—[a]	LE7 (Scano et al.)
TE7-TE7-TE7	TE7-TE7-TE7	26136	68.00	TE7
LE7-LE7-TE7	LE7-LE7-TE7	63162	22.67	LE7-LE7-TE7
TE2-TE2-TE2	LE7-LE7-TE7	19993	75.52	NDK1
TE1-TE1-TE2	LE7-LE7-TE7	18231	77.68	NDK2

(a): Taken as the reference solution.

The analysis reveals that lower-order models are sufficient for accurately representing the majority of the plate. However, when evaluating out-of-plane stresses, higher-order LW models are required to obtain accurate results for the u_x and u_y displacement components. Additionally, the two proposed NDK models demonstrate high efficiency, showing strong agreement with the reference results while achieving a degree-of-freedom reduction of over 75%, which is greater than that achieved with the TE7 model.



(a) *Shear stresses,* σ_{xz} (b) *Transverse stresses,* σ_{zz}

Figure 2: Out-of-plane stresses along **z** *of the angle-ply [45/-45]$_s$ laminate.*

Conclusions

The present work introduces an improved method for the analysis of two-dimensional structures within the framework of the CUF. The method is obtained by reformulating the traditional CUF approach and reorganizing the assembly of the FE matrices. The proposed framework relies on two main features: (1) Different expansions can be adopted for each displacement variable; in particular, Taylor- and Legendre-based expansions are employed. (2) The NDK approach is incorporated, allowing the adoption of a different model at each finite element node.

The paper demonstrates that the proposed method effectively joins different types of expansions and polynomial orders, allowing a significant reduction in the degrees of freedom through an accurate selection of expansions for each finite element node. It also enables the application of local kinematic refinements without altering the finite element mesh. Future work will focus on extending this approach to shell formulations and multifield analyses.

References

[1] J.N. Reddy, D.H. Robbins, Jr, Theories and computational models for composite laminates, Appl. Mech. Rev. 47(6) (1994) 147–169. https://doi.org/10.1115/1.3111076

[2] E. Carrera, Developments, ideas, and evaluations based upon Reissner's Mixed Variational Theorem in the modeling of multilayered plates and shells, Appl. Mech. Rev. 54(4) (2001) 301–329. https://doi.org/10.1115/1.1385512

[3] E. Carrera, M. Cinefra, M. Petrolo, E. Zappino, Finite Element Analysis of Structures Through Unified Formulation, Wiley, Amsterdam, 2014. https://doi.org/10.1002/9781118536643

[4] D. Scano, E. Carrera, M. Petrolo, Use of the 3D Equilibrium Equations in the Free-Edge Analyses for Laminated Structures with the Variable Kinematics Approach, Aerotec. Missili Spaz. 103 (2024) 179-195. https://doi.org/10.1007/s42496-023-00177-2

[5] A. Airoldi, A. Baldi, P. Bettini, G. Sala, Efficient modelling of forces and local strain evolution during delamination of composite laminates, Compos. B Eng. 72 (2015) 137–149. https://doi.org/10.1016/j.compositesb.2014.12.002

[6] A.K. Noor, Global-local methodologies and their application to nonlinear analysis, Finite Elem. Anal. Des. 2(4) (1986) 333–346. https://doi.org/10.1016/0168-874X(86)90020-X

[7] E. Zappino, G. Li, A. Pagani, E. Carrera, Global-local analysis of laminated plates by node-dependent kinematic finite elements with variable ESL/LW capabilities, Compos. Struct. 172 (2017) 1–14. https://doi.org/10.1016/j.compstruct.2017.03.057

[8] E. Carrera, D. Scano, Beam finite element models with node dependent kinematics and arbitrary displacement fields over the cross-section, Mech. Adv. Mater. Struct. (2025) 1-16. https://doi.org/10.1080/15376494.2024.2434198

[9] E. Carrera, D. Scano, E. Zappino, Plate finite elements with arbitrary displacement fields along the thickness, Finite Elem. Anal. Des. 244 (2025) 104296. https://doi.org/10.1016/j.finel.2024.104296

[10] D. Scano, E. Carrera, E. Zappino, Shell finite elements with arbitrary displacement fields along the thickness, Int. J. Solids Struct. 321 (2025) 113544. https://doi.org/10.1016/j.ijsolstr.2025.113544

[11] K.J. Bathe, Finite Element Procedure. Prentice hall, Upper Saddle River, New Jersey, USA, 1996.

[12] D.H. Robbins Jr., J.R. Reddy, Modelling of thick composites using a layerwise laminate theory, Int. J. Numer. Methods Eng. 36 (1993), 655–677. https://doi.org/10.1002/nme.1620360407

Materials Research Proceedings 69 (2026) 1240-1245 https://doi.org/10.21741/9781644904251-214

Global–Local Optimization of Composite Structures Using Unified High-Order Finite Element Models

Alex Pereira do Prado[1,2,3,a *], Dario Zamani[1,b], Alfonso Pagani [1,c], Erasmo Carrera[1,d], Saullo G. P. Castro[2,e], Roeland De Breuker[2,f], Pedro Higino Cabral[3,g]

[1]MUL 2 Lab, Department of Mechanical and Aerospace Engineering, Politecnico di Torino, Corso Duca degli Abruzzi 24, 10129 Turin, Italy

[2]Department of Aerospace Structures and Materials, Faculty of Aerospace Engineering, Delft University of Technology, Kluyverweg 1, 2629 HS Delft, The Netherlands

[3]R&D Department, Embraer S.A., Av. Brigadeiro Faria Lima 2170, 12227-901 São José dos Campos, Brazil

[a]A.PereiradoPrado@tudelft.nl, [b]dario.zamani@polito.it, [c]alfonso.pagani@polito.it, [d]erasmo.carrera@polito.it, [e]S.G.P.Castro@tudelft.nl, [f]R.DeBreuker@tudelft.nl, [g]pedro.cabral@embraer.com.br

Keywords: Structural Optimization, Composite Materials, Global–Local, Carrera Unified Formulation, Multi-Fidelity Modeling

Abstract. A global optimization framework with global–local verification is developed for composite wings by coupling a NASTRAN-based global finite element model with Carrera Unified Formulation (CUF)-based high-order local analyses. The proposed methodology enables the minimization of structural weight under stress and buckling constraints, while identifying critical zones of interest for multi-fidelity and hierarchical strategy. The global model based on first-order shear deformation theory identifies the critical regions where the CUF Equivalent Single Layer and Layer-Wise refinements should be introduced to provide detailed local buckling and stress analyses. This integrated global-local framework enables adaptive local fidelity global-local analysis, improving margins of accuracy while mapping the accessible design space and maintaining computational efficiency.

Introduction

The optimization of composite aircraft wings has long been a key challenge in aerospace structural design. Classical approaches have focused on minimizing mass or maximizing stiffness by tailoring stacking sequences and fiber orientations, often under constraints on strength, buckling, and aeroelastic performance [1–3]. These methods, implemented within commercial Finite Element (FE) solvers, have proven effective for global-level optimization but are typically limited by simplified structural theories, which are unable to represent local behaviors, especially in regions of complex stress or instability. In this regard, refined structural theories based on the Carrera Unified Formulation (CUF) [4] have been developed. CUF provides a hierarchical framework capable of generating both Equivalent Single Layer (ESL) and Layer-Wise (LW) FE formulations with Node-Dependent Kinematic (NDK). This enables an accurate representation of transverse shear effects, local buckling, and through-the-thickness stress distributions, which are critical in composite structures. CUF-based analyses have been successfully applied to a wide range of problems, including failure onset, progressive failure, and nonlinear postbuckling behavior, offering substantial improvements in accuracy over models based on Classical Laminated Plate Theory (CLPT) or First-Order Shear Deformation Theory (FSDT).

Content from this work may be used under the terms of the Creative Commons Attribution 3.0 license. Any further distribution of this work must maintain attribution to the author(s) and the title of the work, journal citation and DOI. Published under license by Materials Research Forum LLC.

Materials Research Proceedings 69 (2026) 1240-1245 https://doi.org/10.21741/9781644904251-214

Recent studies have explored global–local strategies that combine the efficiency of global FE models with the accuracy of CUF-based structural theories [5–6]. The global model captures the overall behavior of the structure and provides the boundary conditions for high-fidelity CUF submodels, enabling precise local stress evaluations where complex stress or instability phenomena occur. When integrated with an optimization process, this approach allows adaptive fidelity across automatically detected zone of interests (ZOI), ensuring accuracy only where needed while preserving computational efficiency [7]. The present work extends this concept to a fully integrated global–local analysis framework that couples NASTRAN global optimization analyses with CUF-based refinements for the weight optimization of composite wings under stress and buckling constraints.

Methodology

The framework developed in this work is presented in Figure 1. Its objective is to minimize structural weight while satisfying stress and buckling constraints, enabling automatic Global–Local (G–L) refinement on ZOIs. The approach integrates commercial and high-fidelity numerical tools, leveraging automatic multi-fidelity, multi-model and hierarchical strategy analysis for margin verification.

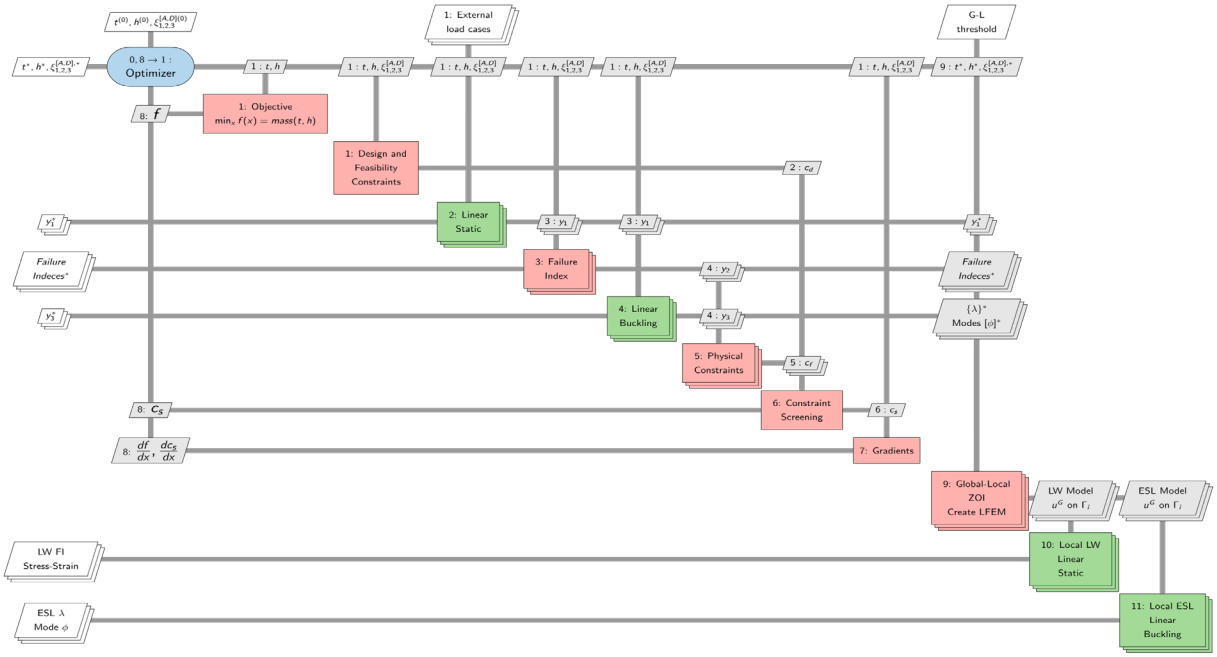


Figure 1- xDSM diagram of the novel global optimization framework with automatic global–local high-fidelity margins verification for composite structures.

In Figure 1, blocks along the diagonal represent processes, whereas off-diagonal blocks indicate the information exchanged among processes. Red blocks denote generic processes and green ones refer to FE and CUF solvers. Parallelograms represent data inputs and outputs; vertical lines indicate data-input and horizontal lines data-output. Stacked blocks denote parallel execution, and asterisks identifies optimal values.

Optimization Framework. First, a global FE model of the entire structure is built in NASTRAN using classical CQUAD4 shell elements based on FSDT. This global model serves as a computationally efficient baseline for the iterative optimization process using lamination parameters strategy [8–10]. The global optimization employs lamination parameters to map discrete stacking sequences into a continuous domain, enabling gradient-based SUMT optimization in NASTRAN MSCADS [11]. Design variables include laminate thicknesses, lamination parameters, and component shapes, while constraints comprise Angle-Minus-Loaded

(AML) failure indices [12-13], buckling loads, and laminate design and feasibility conditions [14-15]. Boundary conditions and multiple load cases are simultaneously applied to an idealized global model.

Global–Local Coupling. Second, once converged, the optimized model is automatically transferred to the G–L stage, which identifies ZOIs, extracts boundary conditions, approximates stacking sequences by minimizing AML values and ply-volume fractions using precomputed lookup tables, and generates corresponding high-fidelity CUF models.

Identification of Critical Regions. Third, ZOIs are selected through threshold criteria on AML failure indices for strength-critical elements and on global buckling-load factors followed by normalized buckling-mode displacement for buckling-critical panels. These metrics determine which regions require high-fidelity CUF analyses to verify margins and adjust the design, directly influencing final structural weight.

Local Analysis. Fourth, high-fidelity analyses are performed using the CUF, in the most critical subregions (ZOIs), allowing for an accurate evaluation of local stress and buckling behavior with an integrated G-L analysis. In the local CUF models, stress and strain distributions through the thickness, interlaminar behavior, and local buckling eigenmodes are evaluated for accurate failure-mechanism characterization.

The CUF model for the local domain adopts a displacement-based formulation, where only translational Degrees of Freedom (DOFs) are considered. Since the global model provides both translations $\left(\boldsymbol{u_x^0}, \boldsymbol{u_y^0}, \boldsymbol{u_z^0}\right)$ and rotations $\left(\boldsymbol{\theta_x^0}, \boldsymbol{\theta_y^0}, \boldsymbol{\theta_z^0}\right)$, a conversion procedure is required to express the latter as equivalent displacements. The Reissner–Mindlin displacement field in Eq. 1 is used to compute translational boundary displacements of the local model, written as:

$$\begin{aligned} u_x(x,y,z) &= u_x^0(x,y) + z\theta_y^0(x,y) - y\theta_z^0(x,y) \\ u_y(x,y,z) &= u_y^0(x,y) - z\theta_x^0(x,y) + x\theta_z^0(x,y) \\ u_z(x,y,z) &= u_z^0(x,y) - y\theta_x^0(x,y) + x\theta_y^0(x,y) \end{aligned} \tag{1}$$

The graphical representation of these transformations is shown in Fig. 2.

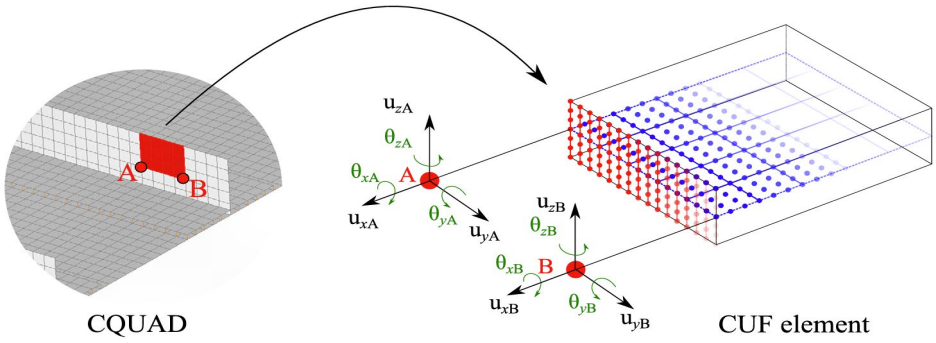


Figure 2. Schematic representation of the procedure adopted to transfer the rotational degrees of freedom from the global model into displacement-based boundary conditions for the local model.

In addition to the Element-Wise (EW) coupling strategy described above, a Patch-Wise (PW) formulation has been implemented to improve the accuracy of the boundary condition transfer between global and local models. In the EW approach, translational and rotational quantities are extracted from a single CQUAD4 element of the global model and employed to define the boundary displacements of the local CUF domain. Conversely, in the PW formulation, the interface displacements are evaluated over a larger region. This extended interpolation domain allows the contribution of all involved global nodes to be considered, resulting in smoother and

Materials Research Proceedings 69 (2026) 1240-1245 https://doi.org/10.21741/9781644904251-214

more consistent boundary conditions for the local problem. The PW procedure refines the displacement field without altering the geometry of the local region, providing higher fidelity in the transfer of boundary information. This enhancement leads to more accurate local stress predictions between the global and CUF-based submodels, particularly in zones characterized by high stress gradients or local instabilities.

Results

To demonstrate the proposed framework, a simplified composite wingbox segment was modeled in NASTRAN to represent a highly loaded wing section. The model consists of ten ribs (nine bays), two spars, and upper and lower reinforced skins with five blade-shaped stringers each. The main dimensions are 6.48 m span, 1.44 m chord, and 0.29 m height. The upper and lower skins are subdivided into 54 panels, and the spars into 9 panels, all designed as symmetric and balanced laminates. Stringer webs and feet are divided into nine segments with constant lamination parameters; only thicknesses and geometries are optimized. The stringers use a constant AML parameter of –10%, representing a "hard" laminate [12–13].

Material properties correspond to Hexcel 8552 IM7 unidirectional prepreg [16], using low-temperature dry (LTD) elastic data and open-hole tension/compression (OHT/OHC) allowable considering environmental variability.

The optimization problem comprises 1,072 design variables (thicknesses, lamination parameters, stringer shapes) and 3,554 constraints related to AML failure indices, buckling loads, and laminate feasibility. Two load cases, +2.5 G and –1.0 G, are applied by scaling the nominal distributed pressure and tip loads. Boundary conditions include a clamped root, 12,081 Pa pressure on the upper skin, and tip loads of 193,047 N and –581,201 Nm, representing the running loads of the adjacent wing segment for a MTOW of 62,500 kg.

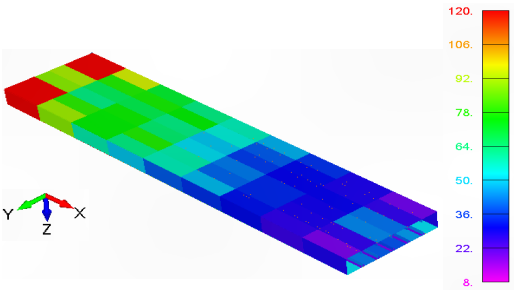


Figure 3. Optimized ply count.

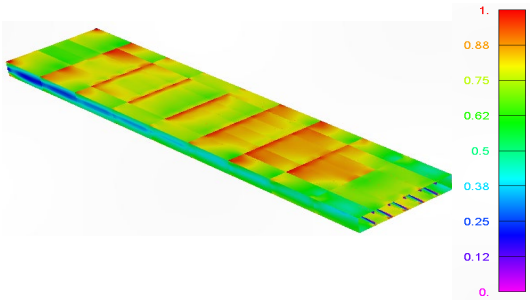


Figure 4. AML failure index.

As shown in Fig. 3, the optimization yields the number of layers, and Fig. 4 presents the corresponding AML failure indices. The optimized lamination parameters for each laminate— not shown here—contain information on fiber fractions for each lamination direction and the homogenized characteristics of the idealized optimal laminate using FSDT. This information is used to approximate stacking sequences by minimizing AML values and ply-volume fractions using precomputed lookup tables, as explained in the Methodology.

A higher number of layers improves the likelihood of obtaining a close approximation between the lamination parameters from continuous optimization and the discrete stacking sequence with similar characteristics. However, deriving an equivalent stacking sequence from idealized lamination parameters inherently introduces deviations. The effect of these deviations can be quantified by replacing panels represented by lamination parameters with discrete approximations that satisfy laminate-formation constraints and evaluating the model again.

Materials Research Proceedings 69 (2026) 1240-1245 https://doi.org/10.21741/9781644904251-214

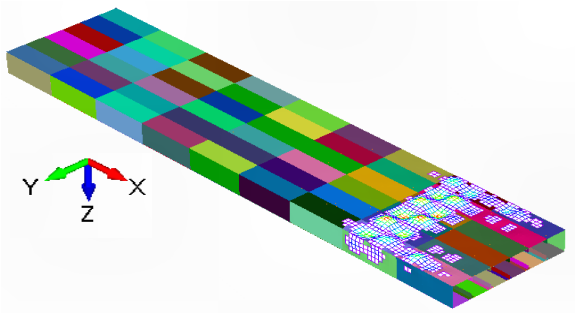


Figure 5. ZOI detection for buckled panels (5% threshold).

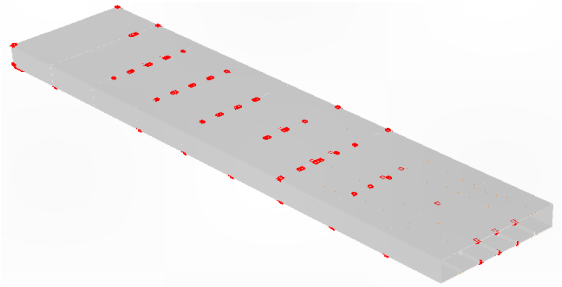


Figure 6. ZOI detection for LW stress analysis (1% FI threshold).

In this work, the G–L phase detected 25 panels out of 216 for CUF ESL buckling analysis above a 5% modal displacement threshold (Figure 5), and 191 ZOIs out of 18,900 elements for CUF LW stress analysis using a 1% AML failure index threshold (Figure 6). As an example, a critical panel with 28 layers exhibited differences of approximately 2.7% in critical buckling and 2.6% in the critical failure-index element.

Conclusions

The proposed framework integrates NASTRAN global analyses with CUF-based local refinements through a hierarchical two-level strategy for composite wing optimization. ESL models are used for local buckling assessment, while LW formulations enable detailed ply-level stress evaluation. The coupling between commercial and in-house solvers is fully automated thought ZOI detection, approximation from laminate variables to discrete stacking sequence while ensuring adaptive local fidelity during the design process. This multi-fidelity and hierarchical approach enhance constraint margins verification at two levels of local scale, explore the feasible design space with greater confidence, and maintains computational efficiency. The framework's modular architecture and high degree of automation make it suitable for integration into industrial design environments.

Acknowledgments

The authors would like to thank Daniele Scano and Professors Enrico Zappino and Riccardo Augello from the Politecnico di Torino MUL² Group for their support with the CUF formulation, modeling, and software application.

References

[1] G. Kennedy & J.R.R.A. Martins, A Comparison of Metallic and Composite Aircraft Wings Using Aerostructural Design Optimization, 12th AIAA Aviation Technology, Integration, and Operations (ATIO) Conference & 14th AIAA/ISSMO MDO Conference, 2012.

[2] D. Zamani, A. Pagani, M. Petrolo, E. Carrera. Multi-patch hybrid optimization of composite wings. III ECCOMAS Thematic Conference on Multidisciplinary Design Optimization of Aerospace Systems ,Lisbon, 22-24 April, 2025.

[3] A. Pagani, A. R. Sánchez-Majano, D. Zamani, M. Petrolo, E. Carrera: Fundamental frequency layer-wise optimization of tow-steered composites considering gaps and overlaps. Aerotecnica Missili e Spazio (2024).

[4] E. Carrera, M. Cinefra, M. Petrolo, E. Zappino. Finite Element Analysis of Structures through Unified Formulation. Wiley & Sons, Hoboken, New Jersey, USA. 2014.

[5] M. Enea, R. Augello, A. Pagani, E. Carrera. Global/local models of composite laminated structures coupling classical 2D finite elements and arbitrarily large refined analysis subdomains. Computers & Structures 298 (2024): 107368.

[6] E. Carrera, A. G. de Miguel, M. Filippi, I. Kaleel, A. Pagani, M. Petrolo, E. Zappino. Global-local plug-in for high-fidelity composite stress analysis in Femap/NX Nastran. Mechanics of Advanced Materials and Structures 28.11 (2021): 1121-1127.

[7] A. Pagani, A. R. Sánchez-Majano, M. Petrolo: Influence of structural theories on optimal fiber distributions in tow-steered composites considering local strain and stress. Aerotecnica Missili e Spazio (2025).

[8] H. Fukunaga and G. N. Vanderplaats, "Stiffness Optimization of Orthotropic Laminated Composites Using Lamination Parameters," AIAA Journal, vol. 29, no. 4, pp. 641–646, Apr. 1991. https://doi.org/10.2514/3.59931.

[9] H. Fukunaga, H. Sekine, M. Sato, and A. Iino, "Buckling design of symmetrically laminated plates using lamination parameters," Computers & Structures, vol. 57, no. 4, pp. 643–649, Nov. 1995. https://doi.org/10.1016/0045-7949(95)00050-Q.

[10] G. H. C. Silva, A. P. do Prado, P. H. Cabral, R. De Breuker, and J. K. S. Dillinger, "Tailoring of a Composite Regional Jet Wing Using the Slice and Swap Method," Journal of Aircraft, vol. 56, no. 3, pp. 990–1004, May 2019. https://doi.org/10.2514/1.C035094.

[11] MSC Software Corporation, "MSC Nastran 2023 Design Sensitivity and Optimization." 2023.

[12] H. Bau, D. Hoyt, and C. Rousseau, "Open Hole Compression Strength and Failure Characterization in Carbon/Epoxy Tape Laminates," in Composite Structures: Theory and Practice, P. Grant and C. Rousseau, Eds., 100 Barr Harbor Drive, PO Box C700, West Conshohocken, PA 19428-2959: ASTM International, 2001, pp. 273-273–20. https://doi.org/10.1520/STP14514S.

[13] W. J. Dorris, J. W. Hairr, J. T. Huang, J. E. Ingram, and B. M. Shah, "Advanced Composites Structural Concepts and Materials Technologies for Primary Aircraft Structures," p. 110.

[14] C. G. Diaconu and H. Sekine, "Layup Optimization for Buckling of Laminated Composite Shells with Restricted Layer Angles".

[15] J. L. Grenestedt and P. Gudmundson, "Layup Optimization of Composite Material Structures," in Optimal Design with Advanced Materials, Elsevier, 1993, pp. 311–336. https://doi.org/10.1016/B978-0-444-89869-2.50027-5.

[16] Kristin Marlett, "Hexcel 8552 IM7 Unidirectional Prepreg 190 gsm & 35% RC Qualification Material Property Data Report," Hexcel 8552 IM7 Uni Data Report Hexcel 8552 IM7 Uni Data Report CAM-RP-2009-015 Rev A, Apr. 2011.

Materials Research Proceedings 69 (2026) 1246-1249 https://doi.org/10.21741/9781644904251-215

Post-Buckling Behaviour of a Multi-Stable Composite Stiffened Specimen under Low-Cycle Fatigue – A Preliminary Study

Xi LI[1,a *] and Chiara BISAGNI[1,b]

[1]Department of Aerospace Science and Technology, Politecnico di Milano, Milano, Italy

[a]xi.li@polimi.it, [b]chiara.bisagni@polimi.it

Keywords: Buckling Mode-Switching, Composite Laminates, Compression, Digital Image Correlation

Abstract. This study experimentally investigates the effect of low-cycle fatigue loading on the evolution of buckling modes in a specimen consisting of a composite skin and four metallic stringers. The specimen was designed to achieve multiple stable configurations under compression through a tailored lay-up configuration that enables bucking to initiate in the thinner region and subsequently expand to the thicker region. The results indicate that the designed specimen was able of switching among different buckling modes under low-cycle fatigue loading. However, the skin-stringer separation was observed during high-amplitude fatigue loading.

Introduction

To meet the ambitious targets for clean aviation, weight reduction and efficiency increase are essential in structural design. Fibre reinforced composite materials are used in thin-walled aeronautical structures like wings and fuselages due to their light weight. By nature, they are susceptible to buckle under in-service loads, which can induce significant non-linear deformation and potentially complex failure mechanisms [1]. Consequently, a conservative no-buckling approach is often considered in the design phase. However, if buckling and post-buckling behaviour are allowed, provided they remain controlled, predictable, and confined to the elastic region, significant weight reduction can be achieved, even under fatigue loading. Furthermore, the potential to switch among different buckling modes could enable multiple stable configurations in aeronautical structures. Currently, there is a limited understanding on how aeronautical composite structures behave under fatigue loading with repeated buckling mode switches.

Buckling-driven composite design concepts for structural multi-stability are investigated in the NABUCCO project [2]. Studies to support such design concepts have been reported: Zhang and Bisagni [3] applied local displacement constraints to a simplified wing box, achieving changes in stiffness and buckling modes with redistributed load for twisting control; Gutiérrez Álvarez and Bisagni [4] combined mechanical and thermal loading in a flat, four-edge-clamped panel, which enabled buckling and subsequent mode switching under compression and heating; Bisagni and Gigliotti [2,5] designed multi-stiffness laminates with different number of plies and varying layups in local regions, which achieves changes in axial stiffness through local buckling at specific locations.

To further explore whether structural multi-stability induced by buckling can be controlled within the elastic region during repeated mode switching, this study investigates the post-buckling behaviour of a multi-stable stiffened specimen, achieved through a tailored layup configuration, under low-cycle fatigue loading.

Design, manufacturing and testing

As a preliminary study, the multi-stable design should be capable of switching among different buckling modes under compression and be suitable for easy hand laminating. To this end, a panel was designed from IM7/8552 material, incorporating four metallic stringers to create three distinct

Content from this work may be used under the terms of the Creative Commons Attribution 3.0 license. Any further distribution of this work must maintain attribution to the author(s) and the title of the work, journal citation and DOI. Published under license by Materials Research Forum LLC.

Materials Research Proceedings 69 (2026) 1246-1249 https://doi.org/10.21741/9781644904251-215

regions. The geometry of the design is detailed in Fig. 1. The central region (Region 1) is stacked in a sequence of [0/90/0], while the layup of the two lateral regions (Region 2) is [0/90/0/90/0]. The composite plate has a ply thickness of 0.125 mm, and the stringers are 1.5 mm thick. Buckling is expected to firstly occur in the thin region and subsequently expand to the thick region, enabling mode switching as the compressive load increases. Four aluminium 6061 T6 stringers were bonded to the composite plate. The top and bottom of the specimen were potted in metal-filled casting resin tabs.

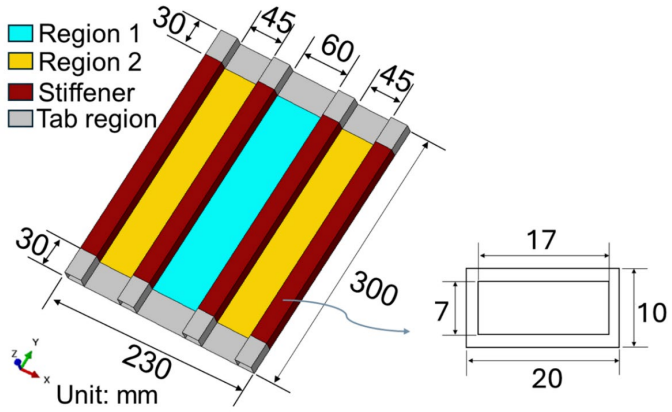


Fig. 1 Geometry of the multi-stable stiffened specimen.

A series of static tests were conducted to establish a baseline for the buckling and post-buckling behaviour of the specimen prior to fatigue testing. The tests were performed to different maximum loads, ranging from 3 kN to ~ 46 kN. During these tests, two digital cameras were positioned in front of the specimen to measure full-field deformation using digital image correlation (DIC) techniques, as shown in Fig. 2. The surface of the composite specimen was painted with a speckled pattern to assist DIC measurements. Then, a fatigue load profile was applied with a frequency of 1 Hz and a load ratio of 0.1. Each loading block consisted of approximately 10000 cycles at a constant amplitude. In total, four load blocks were applied with increasing maximum cyclic loads: Load Block 1 - 10 kN, Load Block 2 - 20 kN, Load Block 3 - 30 kN, Load Block 4 - 40 kN. To enable DIC image acquisition, the fatigue loading was interrupted every 1000 cycles to perform a static test at a loading rate of 10 kN/min.

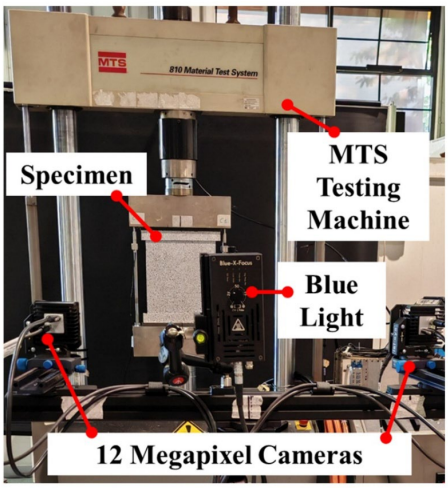


Fig. 2 Experimental set-up.

Materials Research Proceedings 69 (2026) 1246-1249 https://doi.org/10.21741/9781644904251-215

Results

The designed specimen exhibited a linear force-displacement relationship in the post-buckling regime under static loading, as shown in Fig. 3(a), which represents the final static test conducted prior to fatigue loading. The evolution of the buckling modes began in Region 1 with three half-waves and subsequently expanded to Region 2, forming a six half-wave pattern (Fig. 3(b)). As the applied force increased from 20 kN to 30 kN, the number of half-waves in the central region transitioned from three to four (Fig. 3(b)).

Fig. 4 presents the out-of-plane deformation fields of the specimen under a static load equivalent to the maximum cyclic load, both initially (0 cycle) and after 10000 cycles of Load Blocks 1-3. During Load Block 1, bucking primarily occurred in the central region with three half-waves, similar to the static baseline shown in Fig. 3. The low-cycle fatigue loading up to 10000 cycles evidently has a negligible effect on the post-buckling behaviour at this low load amplitude. When the maximum cyclic load was increased to 20 kN in Load Block 2, the buckling mode in the central region switched from three to four half-waves. This mode transition occurred at a static load higher than 20 kN. In Load Block 3, the buckling mode frequently changed between four and five half-waves in the central region. Meanwhile, visible local debonding between the composite skin and the stringers was observed at the top of the specimen. At the early stage of Load Block 4, local debonding propagated across the entire width of the specimen.

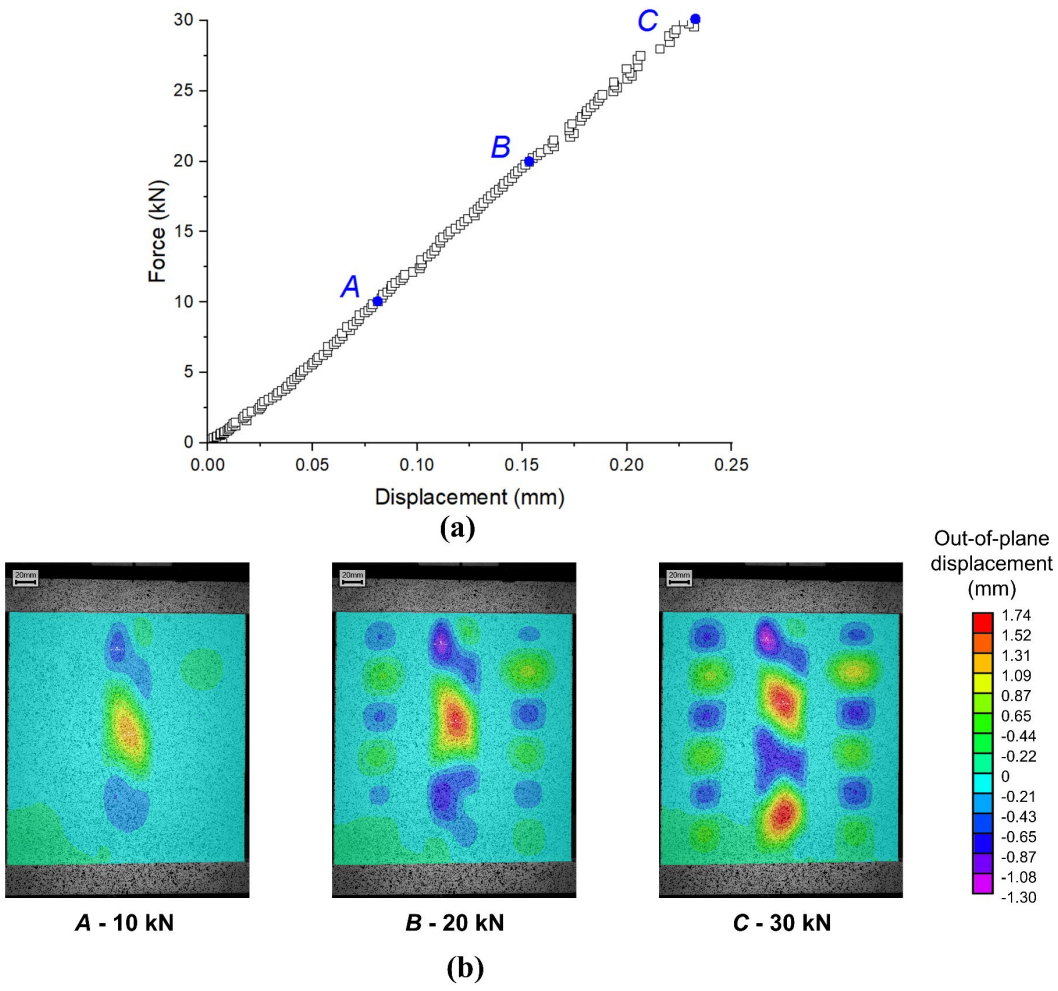


Fig. 3 Force-displacement response of the static test up to 30 kN (a), and evolution of buckling modes (b).

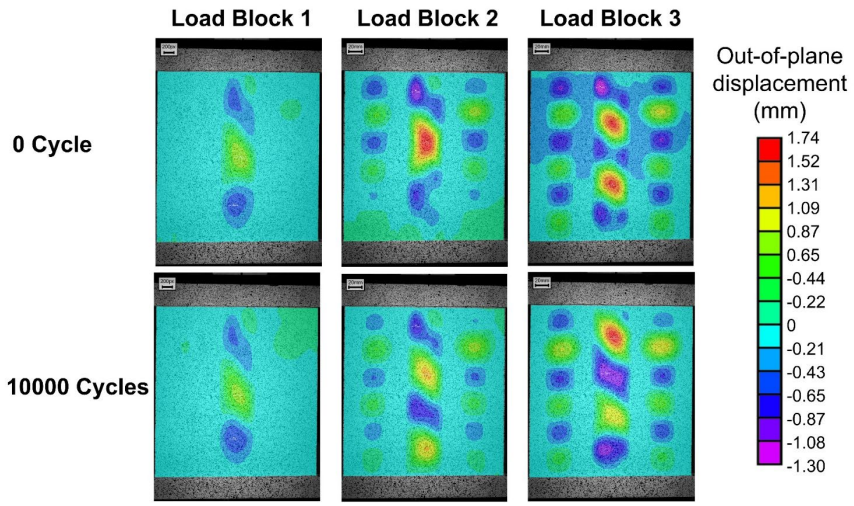


Fig. 4 Post-buckling mode at the maximum load of Blocks 1-3 at 0 and 10000 cycles.

Summary

Experimental work was carried out to design, manufacture and test a stiffened specimen with composite skin and metallic stringers under both static and fatigue loading conditions. The specimen was designed with variations in skin thickness, enabling to switch among different buckling modes as compressive load increases. Under low-cycle fatigue loading, the buckling mode in the central region changed as the load amplitude increased: it remained unchanged during the fatigue with 10 kN maximum load, transitioned from three to four half-waves during fatigue up to 20 kN, and switched frequently between four and five half-waves during fatigue up to 30 kN. Furthermore, local debonding between the composite skin and the stringers was observed under high-amplitude fatigue loading.

Acknowledgements

This study is partially funded by the European Union (ERC Advanced Grant, NABUCCO, project number 101053309). Views and opinions expressed are however those of the authors only and do not necessarily reflect those of the European Union or the European Research Council Executive Agency. Neither the European Union nor the granting authority can be held responsible for them. The first author would like to acknowledge the funding from the Italian Ministry of University and Research for young researchers, financed under the National Recovery and Resilience Plan as part of the European Union's NextGenerationEU program.

References

[1] J. Paz, A. Raimondo, and C. Bisagni, Experimental study of post-buckled single-stringer composite specimens under fatigue loads with different load levels and load ratios, Compos. Part B Eng., (2023) 255:110606. https://doi.org/10.1016/j.compositesb.2023.110606

[2] C. Bisagni, Nabucco take-off: multi-stable panels for an adaptive wing, in ICAS Proceedings, (2024) 1–9.

[3] J. Zhang and C. Bisagni, Buckling-driven mechanisms for twisting control in adaptive composite wings, Aerosp. Sci. Technol., (2021) 118: 107006. https://doi.org/ 10.1016/j.ast.2021.107006

[4] J. G. Álvarez and C. Bisagni, Investigation on buckling and mode jumping of composite plates under thermomechanical loads, Int. J. Non. Linear. Mech., (2021) 138:103837. https://doi.org/10.1016/j.ijnonlinmec.2021.103837

[5] G. Gigliotti, Design and analysis of buckling driven multi-stiffness panels for adaptive composite structures, Master thesis, Politecnico di Milano, (2024).

Materials Research Proceedings 69 (2026) 1250-1254 https://doi.org/10.21741/9781644904251-216

Evaluation of the Mechanical Properties of Ultrathin CNTs Reinforced Composites for Deployable Structures

Lorenzo MARTINAZZOLI[1,a], Flavia PALMERI[1,b] and Susanna LAURENZI[1,c] *

[1]Department of Astronautical Electrical and Energy Engineering, Sapienza University of Rome, Via Salaria 851-881, Rome, 00138, Italy, Europe

[a]lorenzo.martinazzoli@uniroma1.it, [b]flavia.palmeri@uniroma1.it, [c]susanna.laurenzi@uniroma1.it

Keywords: Ultrathin Composites, Deployable Structures, Carbon Nanotubes, Finite Elements

Abstract. The space industry continuously seeks lighter and higher-performance materials to improve the efficiency and reliability of spacecraft structures. This is particularly true for deployable boom structures, slender elements stowed during launch and extended in orbit to support antennas, solar panels, or sensors, where minimizing mass while maintaining sufficient stiffness and strength is essential for successful deployment and long-term stability. This study investigates the potential of incorporating carbon nanotubes (CNTs) into conventional carbon fiber reinforced polymers (CFRPs) for future application in deployable booms. Composite laminates were fabricated and characterized through tensile and column bending tests to evaluate their mechanical performance. The resulting material properties were then used in a buckling analysis of deployable booms, as buckling represents a critical design factor. The outcomes aim to assess whether CNT-enhanced CFRPs are a viable option for manufacturing next-generation space deployable boom structures.

Introduction

Advances in aerospace technology are driving spacecraft toward larger sizes and increasingly complex architectures. At the same time, the limited payload volume and mass capacity of launch vehicles pose significant challenges for integrating large-scale components such as solar sails, deep-space antennas, and high-capacity solar arrays. Space deployable structures offer an effective solution, allowing these components to be compactly stowed during launch and reliably deployed in orbit. Deployable booms can be efficiently stowed through coiling or folding and, once deployed, serve as structural elements in various space systems, including parabolic mesh antennas, solar sails, probes, and docking systems. Booms are typically classified based on the geometry of their cross-section; this work focuses on collapsible tubular masts (CTMs) with a double-omega cross-section [1]. The current trend in boom design is toward ultra-thin laminated composite materials, which provide high stiffness and strength at low mass while allowing for large deformations [2]. Booms manufactured from these composites have been fabricated and characterized experimentally [3], and the effects of ply number, fiber content, and fiber modulus on buckling behavior have been studied using free-end loading tests [4]. To date, laminates reinforced solely with continuous fibers have been employed, while the potential of hybrid composites, in which the polymer matrix is reinforced with both long fibers and carbon nanotubes (CNTs), remains largely unexplored. Such materials offer promising opportunities to enhance mechanical performance and enable multifunctional capabilities [5,6]. This study addresses this gap by manufacturing and mechanically characterizing CNT-reinforced CFRP laminates, which are subsequently used in finite element simulations to assess buckling behavior of a collapsible tubular mast (CTM), which is a critical design criterion for deployable structures.

Content from this work may be used under the terms of the Creative Commons Attribution 3.0 license. Any further distribution of this work must maintain attribution to the author(s) and the title of the work, journal citation and DOI. Published under license by Materials Research Forum LLC.

Materials Research Proceedings 69 (2026) 1250-1254 https://doi.org/10.21741/9781644904251-216

Materials and method

The material used is a based-spread tow carbon fiber reinforced polymer (CFRP). The reinforcement consists in TeXtreme 43 PW HS40 fabric. Before being woven, HS40 12K tows have been flattened by means of an airflow method to become spread [7]. The matrix is the bicomponent aerospace grade epoxy resin CYCOM®823 RTM. Two layers of spread tow plain weave fabric are embedded in an epoxy matrix with [0/90] lamination sequence and out-of-phase configuration [8]. Carbon nanotubes were added at a concentration of 0.7% of the total weight, dispersed in the resin using the centrifugal mixer/defuser THINKY MIXER ARE-250, as it's experienced to be the maximum concentration for mechanical properties improvement. The laminates for sample preparation are fabricated through vacuum bagging technique and pressed with a hydraulic hot press, with a pressure of 2.38 bar, to get lower thickness and facilitate nanotubes dispersion. Tensile tests are conducted on five samples of composite materials to measure the A_{11} and A_{12} components of their global stiffness matrix. Tensile tests are carried out using an AGS-X series Shimadzu machine with a tensile clamping. The experimental set-up and the tested specimen comply with ASTM d3039 [9], using a 10KN load cell and performing the test at 2 mm/min. The longitudinal and transversal strain, ϵ_1 and ϵ_2, respectively, are measured using a Digital Image Correlation (DIC) system. This optical equipment consists in a stereo camera system, able to observe micro displacements on the sample. An acquisition frequency of 4 Hz was selected. Then the A_{11} and A_{12} components are computed according to the followings:

$$A_{11} = \frac{F}{w}\frac{\epsilon_1}{\epsilon_1^2-\epsilon_2^2}\ ; \tag{1}$$

$$A_{12} = -\frac{\epsilon_2}{\epsilon_1}A_{11}\ ; \tag{2}$$

where w is the width of the sample.

To determine the bending properties of thin composite laminates, the Column Bending Test (CBT) method was adopted. Juan M. Fernandez et al. presented and validated the CBT mechanism design, optimized for thin-walled samples [10]. It consists in a counterweight-balanced CBT fixture adapted to the tensile test machine: bringing the pin close to each other, a bending behavior on the specimens is inducted. During the test, the curvature of the coupons has been approximated to a semi-circumference as Milinda et al. have already experienced to be a good choice for properties evaluation [11].

Material properties calibration

To populate the ABD matrix components which cannot be directly evaluated experimentally, the CLT has been used. Particularly, the experimental outcomes are used as reference for calibrating properties of the single phase in an iterative analysis such that the analytical results coming from the CLT best matched with the data from experiments. To obtain optimized values, a particle swarm optimizer (PSO) was implemented in Matlab. The cost function that compares experimental outcomes with properties coming from CLT is:

$$J = \left(\frac{A_{11}^{exp}-A_{11}^{CLT}}{A_{11}^{exp}}\right)^2 + \left(\frac{A_{12}^{exp}-A_{12}^{CLT}}{A_{12}^{exp}}\right)^2 + \left(\frac{D_{11}^{exp}-D_{11}^{CLT}}{D_{11}^{exp}}\right)^2\ ; \tag{3}$$

Here, normalized residuals were considered to give the same weight to each term in the evaluation of the minimum value of the cost function [12]. The calibration determined the complete global stiffness matrix of the composite material.

Materials Research Proceedings 69 (2026) 1250-1254 https://doi.org/10.21741/9781644904251-216

Buckling numerical model

The boom is modeled as two Ω-shaped shells, each 70 cm in length. The shells are bonded by interposing a ply that simulates the adhesive layer between their flat regions, while tie constraints are defined between each flat region and the adhesive. Multi-Point Constraints (MPCs) are applied to link the nodes at the tip and root cross-sections to reference points (RPs) located at the center of each cross-section. The RP at the boom root is fully constrained, whereas the RP at the boom tip is constrained in the x- and y-translations and in the x-, y-, and z-rotations. The load is a compressive load applied at the boom tip. The boom is discretized using S4R elements, which are 4-node, doubly curved thin shell elements with reduced integration and hourglass control. The simulation consists of a preliminary linear buckling analysis followed by a nonlinear Riks analysis [13,14]. The critical load and the deformed shapes corresponding to the first three buckling modes obtained from the linear buckling analysis are used to introduce initial geometric imperfections in the subsequent nonlinear analysis. The imperfections are scaled relative to the laminate thickness, with amplitudes of 1%, 0.5%, and 0.25% for the first, second, and third modes, respectively.

Material characterization results

Experimental tests allowed us to determine 3 of the components of the global stiffness matrix of the material.

$$A_{11} = 10607\ N/mm \tag{4}$$

$$A_{12} = 167.79\ N/mm \tag{5}$$

$$D_{11} = 7.86\ Nmm \tag{6}$$

While from properties calibration, the resulting ABD stiffness matrix is:

$$A_{0/90} = \begin{Bmatrix} 8511 & 81.53 & 0 \\ 81.53 & 8511 & 0 \\ 0 & 0 & 154.9 \end{Bmatrix}\ N/mm \tag{7}$$

$$D_{0/90} = \begin{Bmatrix} 8.819 & 0.049 & 0 \\ 0.049 & 1.407 & 0 \\ 0 & 0 & 0.093 \end{Bmatrix}\ Nmm \tag{8}$$

While matrix B results null due to lamination sequence.

Buckling numerical model

A mesh sensitivity analysis was performed through linear buckling simulations, determining asymptotic behaviour at 520 N starting from 20400 elements for each boom half and 1200 elements for each adhesive layer. The first three buckling modes, shown in Fig.1, results very close to each other, highlighting a local collapse at the boom root for a critical load of 518.9 N. This behaviour is replicated by the non-linear analysis, in which the boom shows a bulging effect near the root, determining buckling occurrence at critical load. A global and top side views are reported in Fig.2, to better explain the structural response to the compressive load.

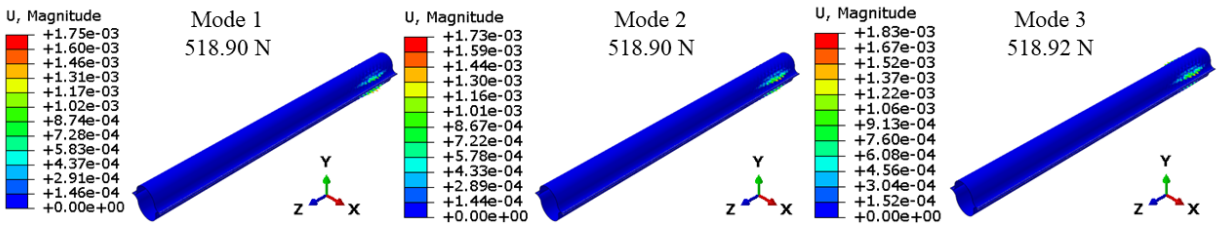


Figure. 1 Critical load of the first three buckling modes

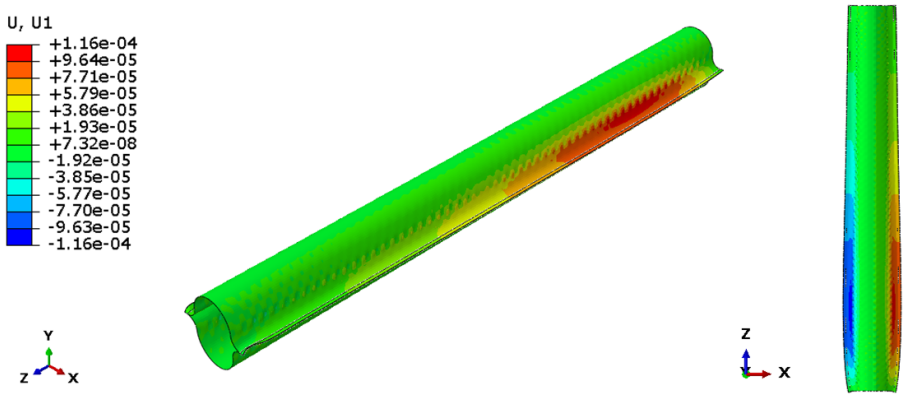


Figure. 2 Global (left side) and top (right side) view of the non-linear buckling outcome.

Conclusions

In this work, the mechanical characteristics of an ultra-thin composite material are determined, and the buckling behavior of a CTM boom is analyzed. Firstly, the composite material is selected and characterized through experimental tensile and bending tests. Specifically, an optimization process is performed to determine the ABD matrix providing reliable properties of such thin material. The second part of the study is focused on the numerical simulation of the buckling test. The aim was to realize a model that accurately describes the behavior of these ultra-thin structures under axial compression, accounting on reliable material properties. This work represents an initial step in the exploration of CNT-reinforced deployable composites. Beyond potential mechanical improvements, the introduction of CNTs could enable multifunctional capabilities, such as enhanced electrical conductivity, thermal management, or sensing, which warrant further investigation in future studies.

References

[1] Bruce B Rennie. "New closed tubular extendible boom". In: 2nd aerospace mechanisms symposium. Jet Propulsion Lab. Pasadena, CA. 1967, pp. 163- 170.

[2] Juan M Fernandez. "Advanced deployable shell-based composite booms for small satellite structural applications including solar sails". In: International Symposium on Solar Sailing. NF1676L-25486. 2017.

[3] Stohlman, Olive R., Martin E. Zander, and Juan M. Fernandez. "Characterization and modeling of large collapsible tubular mast booms." AIAA Scitech 2021 Forum. 2021. https://doi.org/10.2514/6.2021-0903

[4] Zheng Zhang et al. "Experimental study and numerical simulation of load-bearing/coiling characteristics of thin-walled lenticular composite booms".

[5] Georgantzinos, Stelios K., et al. "Design of laminated composite plates with carbon nanotube inclusions against buckling: Waviness and agglomeration effects." Nanomaterials 11.9 (2021): 2261. https://doi.org/10.3390/nano11092261

[6] Nicoletto, M., et al. "MWCNTs nanocomposites for space applications." 2015 IEEE International Symposium on Electromagnetic Compatibility (EMC). IEEE, 2015. https://doi.org/10.1109/ISEMC.2015.7256308

[7] Joel Galos. "Thin-ply composite laminates: a review". In: Composite Structures 236 (2020), p. 111920.[8] ASTM International. Standard Test Method for Tensile Properties of Polymer Matrix Composite Materials. 2002 https://doi.org/10.1016/j.compstruct.2020.111920

[8] Ö. Soykasap, "Micromechanical models for bending behavior of woven composites," Journal of Spacecraft and Rockets, vol. 43, no. 5, pp. 1093-1100, 2006, doi: 10.2514/1.18010. https://doi.org/10.2514/1.18010

[9] ASTM International, "ASTM D3039/D3039M - Standard Test Method for Tensile Properties of Polymer Matrix Composite Materials," ASTM D3039/D3039M-23, West Conshohocken, PA, 2023.

[10] Fernandez Juan M. and Murphey Thomas W. "A Simple Test Method for Large Deformation Bending of Thin High Strain Composite Flexures". In: (2018).[10] J. Gao et al. "Accuracy Analysis on Counterweight-Balanced Column Bending Test". In: Experimental Mechanics (2022). https://doi.org/10.2514/6.2018-0942

[11] Milinda Yapa Hamillage, Colin Leung, and Kawai Kwok. "Viscoelastic modeling and characterization of thin-ply composite laminates". In: Elsevier (2022). https://doi.org/10.1016/j.compstruct.2021.114901

[12] Zhiwei Cui and L. Catherine Brinson. "A combination optimization method for the estimation of material parameters for viscoelstic solids". In: Int. J. of Computing Science and Mathematics (2014).

[13] Christophe Leclerc and Sergio Pellegrino. "Nonlinear elastic buckling of ultra-thin coilable booms". In: Elsevier (2020), pp. 50-52. https://doi.org/10.1016/j.ijsolstr.2020.06.042

[14] Daniele Barbera and Susanna Laurenzi. "Nonlinear buckling and folding analysis of a storable tubular ultrathin boom for nanosatellites". In: Elsevier (2015). https://doi.org/10.1016/j.compstruct.2015.05.024

Materials Research Proceedings 69 (2026) 1255-1259 https://doi.org/10.21741/9781644904251-217

Regolith-Induced Abrasion as a Critical Challenge for Lunar Materials: Experimental Insights on Fiber Reinforced Composites and Polyethylene

Marta BALESTRA[1,a], Susanna LAURENZI[1,b*], Andrea DI BENEDETTO[2,c] and Antonia SIMONE[2,d]

[1]Department of Astronautical, Electrical and Energy Engineering, Sapienza University of Rome, Via Salaria 851-881, 00138 Rome, Italy

[2]Thales Alenia Space Italia, Strada Antica di Collegno 253, 10146 Turin, Italy

[a]balestra.1840527@studenti.uniroma1.it, [b]susanna.laurenzi@uniroma1.it, [c]andrea.dibenedetto@thalesaleniaspace.com, [d]antonia.simone@thalesaleniaspace.com

Keywords: Abrasion, Lunar Dust, Regolith, Taber Abraser, Grit Feeder, Wear Index

Abstract Abrasion caused by lunar regolith is a critical challenge for future exploration missions. The highly angular, sharp-edged particles of lunar dust can severely degrade mechanical systems, protective fabrics, and structural materials. This study focuses on the laboratory characterization of material degradation under three-body abrasion, which accurately represents the abrasive conditions caused by lunar regolith. Using a Taber Abraser equipped with a Grit Feeder and LHS-1 lunar highland simulant, the research compares the abrasion behavior of fiber-reinforced composites and polyethylene-based materials. By defining a Dust Wear Index (DWI) in terms of mass and thickness loss due to abrasion, the study establishes a framework for evaluating abrasion resistance of both classes of materials.

Introduction

The renewed global interest in lunar exploration, driven by programs such as NASA's Artemis and the development of permanent surface habitats is leading to new challenges in material engineering. Among these, lunar dust (i.e. regolith) remains one of the most mission-limiting factors. Its sharp, irregular particles adhere to surfaces establishing an abrasion mechanism followed by surface wear [1] as reported since the Apollo missions. Prolonged exposure can compromise the performance of materials used in life-support systems, seals, visors, and spacesuits [2,3].

Understanding and mitigating regolith-induced abrasion is thus essential to ensure astronaut safety, operational reliability, and lunar infrastructures sustainability. As future missions foresee prolonged surface operations [4], a systematic investigation of material degradation under realistic regolith–surface interaction scenarios becomes critical.

This study addresses the issue through controlled laboratory tests simulating three-body abrasion, a wear mechanism that best represents the lunar operating scenario [5]. By reproducing the interaction between regolith particles and material surfaces, it aims identifying suitable materials for lunar applications and to develop a quantitative Dust Wear Index (DWI) as a benchmark for abrasion resistance [6].

Materials and methods

Specimens

Specimens are square shaped measuring 10x10 cm with variable thickness in the range of mm, as this parameter is not critical for the test. Two material categories were tested: composite samples and polymer-based ones.

Content from this work may be used under the terms of the Creative Commons Attribution 3.0 license. Any further distribution of this work must maintain attribution to the author(s) and the title of the work, journal citation and DOI. Published under license by Materials Research Forum LLC.

Composites are realized starting from fiber fabric layers impregnated with epoxy resin Prime 37 with a mixing ratio of parts A to B of 100:29. The layers consist in a quasi-isotropic balanced layup sequence.

The curing process lasts 7 hours and occurs at a temperature of 65°C reached via a ramp of 4°C per minute, the specimen is placed in a vacuum bag inside a vacuum oven.
The Carbon/epoxy plate is manufactured using a 12K Prochima Carbon fiber fabric C-420/D, its fiber volume fraction is verified with a Thermogravimetric analysis to be 48.83%.

A second Carbon/epoxy plate, identical to the first one, is realized and then subjected to a chemical recycling treatment (solvolysis process) based on sulfuric acid at a concentration of 18.3 mol/l [7]. Its fiber volume fraction is verified with a Thermogravimetric analysis to be 55.58%.

The Glass/epoxy plate meets the same requirements of the Carbon/epoxy plates and underwent an additional 30 minutes post-curing phase to further relieve residual stresses.

Polymer based samples are manufactured starting from ultra-high modulus Polyethylene powder Aldrich. Samples are both in pure form and filled with 5% and 10% Biolit regolith simulant by weight. Biolite is a ultrafine basalt powder extracted from sites in Oberdorf, Austria [8].

The pure powder is placed in a metallic mold and then in a vacuum oven for 90 minutes at a temperature of 180°C while the filled ones were kept in the oven for 180 minutes at 220°C and 230°C. A higher temperature than that used for pure polyethylene samples was required to ensure proper mixing of Biolit and polyethylene.

Test methodology

All abrasion tests were carried out using a Taber Abraser (Model 5135) equipped with a Grit Feeder (Model 255) [9]. This configuration allows continuous and uniform deposition of abrasive particles between rotating wheels and specimen surface, thus reproducing three-body abrasion conditions.

The abrasive medium employed was LHS-1 (Lunar Highlands Simulant), it was oven-dried following the NASA standard [10] and sieved to ensure a representative grain size distribution of lunar regolith [11].

Before abrasion testing all specimens underwent a pre-conditioning phase in accordance with ASTM F510M-20 standard and a pre-characterization process in terms of mass, thickness and surface conditions. Mass was measured using a high-precision analytical balance (accuracy ± 0.1 mg), thickness using a digital micrometer (accuracy ± 1μm) and surface morphology was examined with an optical microscope. The thickness of each specimen was measured at five fixed points to account for possible non-uniformity.

The procedure is built starting from ASTM F510M-20 standard and consists of two sequential phases: reference and test, both lasting 1000 Taber cycles at 72 rpm.

In the *reference phase* specimens were abraded only with S-39 leather wheels without the introduction of regolith to quantify the wear only produced by the wheel–surface mechanical interaction.

In the *test phase*, the same setup was repeated with the Grit Feeder activated (feed rate set to 100), dispensing sieved LHS-1 on the specimen. The simulant particles act as the third body between the specimen and the surface, reproducing the lunar three-body abrasion mechanism.
After each phase, the specimens were cleaned with compressed air to remove residual dust.

Mass and thickness variations obtained in the reference phase are subtracted from the corresponding values measured after the test phase, where both wheels and regolith are present. This superposition of effects enables the isolation of the net contribution of regolith particles to the total abrasion, independent of the baseline mechanical wear.

Mass measurements exhibited a standard deviation less than 1 mg while thickness ones are reported using the standard error of the mean (SEM) as the representative uncertainty. The SEM

Materials Research Proceedings 69 (2026) 1255-1259 https://doi.org/10.21741/9781644904251-217

was computed to quantify the average thickness loss, over the five points, due to regolith abrasion for each specimen.

Based on the results, two *Dust Wear Indexes (DWI)* were defined as dimensionless quantities quantifying material degradation, expressed both in terms of mass by eq. 1 and thickness loss by eq. 2 allowing comparation of different materials.

$$DWI_m = \left|\frac{m_{pre\,ref} - m_{post\,ref}}{m_{pre\,test} - m_{post\,test}}\right| \cdot \frac{1}{N} \quad (1)$$

$$DWI_t = \left|\frac{t_{pre\,ref} - t_{post\,ref}}{t_{pre\,test} - t_{post\,test}}\right| \cdot \frac{1}{N} \quad (2)$$

Results and discussion

Composite specimens exhibited measurable mass and thickness loss after the standard test, confirming regolith's abrasive potential. Among the tested composites Carbon/epoxy showed the highest abrasion resistance, with minimal mass loss and moderate thickness one. Glass/ epoxy displayed intermediate performance, with localized thickness loss while recycled Carbon/epoxy was the most affected, showing the major mass and thickness losses. All results are shown in table 1.

A Differential Scanning Calorimetry analysis (DSC) was conducted on both the Carbon/epoxy and the recycled Carbon/epoxy plates, it revealed that the recycled plate underwent a less complete curing process showing residual polymerization. This highlights the key role of the curing cycle for composites, as improper curing can lead to a weaker matrix and increased susceptibility to abrasion.

Pure Polyethylene samples and filled ones behaved differently from composites. A mass gain occurred due to dust particles penetration in the porous surface of the specimens; the more the filler, the more the mass gain. This behavior was confirmed by the optical microscope analysis that shows dust particles entrapment on the specimens' surface.

The Dust Wear Index (DWI) provides a quantitative measure of materials' response to regolith-induced abrasion.

Since the DWI is inversely proportional to the measured losses during the test, lower DWI values indicate that the regolith exerts a stronger abrasive action on that material while higher DWI values correspond to a minor surface degradation.

However, in the case of polyethylene-based specimens, the interpretation of the DWI must be treated with caution. The combined action of two phenomena can be observed, on one hand the abrasive mechanism while on the other hand the penetration of regolith into surface porosities, which leads to an increase in the sample mass. Those two mechanisms need to be further addressed to better understand their combined action.

The observed mass gain and apparent lower DWI values do not reflect higher abrasion resistance but rather the penetration and entrapment of dust particles within the porous polymer surface.

This behavior results in apparent negative mass losses, the corresponding DWIs are mainly indicative of dust accumulation rather than true mechanical protection against regolith abrasion. A similar consideration can be applied to thickness measurements.

Materials Research Proceedings 69 (2026) 1255-1259 https://doi.org/10.21741/9781644904251-217

Table 1. Numerical results

Material	$\Delta_{m,reg}$ %	$DWI_m \cdot 10^{-4}$	$\Delta_{t,reg} \pm$ SEM	$\overline{\Delta}_{t,reg\%}$	$DWI_t \cdot 10^{-4}$
	[%]	[-]	[μm]	[%]	[-]
Carbon/epoxy	0.01	6.40	13.4 ± 4.7	0.38	5.78
Recycled carbon/epoxy	0.08	2.77	33.4 ± 7.7	1.45	2.48
Glass/epoxy	0.06	5.25	19.2 ± 6.0	0.48	3.90
Pure Polyethylene	-0.04	1.52	41.8 ± 7.2	0.41	3.96
Polyethylene + 5% Biolit	-0.15	0.96	11.0 ± 3.3	0.16	6.35
Polyethylene + 10% Biolit	-0.43	0.37	-9.6 ± 2.4	-0.14	15.45

Conclusions and future perspectives

The present study establishes a reproducible and standardized approach for assessing abrasion resistance of materials under lunar-like dust exposure.

Future research can expand this framework by testing under extended cycles to simulate prolonged missions, implementing thermal–vacuum conditions and exposure to ionizing radiations to replicate lunar atmospheric conditions and day–night temperature fluctuations, considering combined environmental factors and integrating the Dust Wear Index into design requirements.

Ultimately, understanding regolith-induced abrasion is not only a tribological issue but a crucial factor for the sustainability and safety of long-term lunar operations. Continued experimental research will enable the selection and engineering of materials capable of withstanding the unique challenges of the lunar environment.

References

[1] A.K. Sukumaran, Recent trends in tribological performance of aerospace materials in lunar regolith environment – A critical review, Adv. Space Res. (2024) (in press). https://doi.org/10.1016/j.asr.2023.10.039

[2] J.R. Gaier, et al., Abrasion of candidate spacesuit fabrics by simulated lunar dust, 39th Int. Conf. on Environmental Systems (ICES), No. E-16958-1 (2009). https://doi.org/10.4271/2009-01-2473

[3] A.V. Zakharov, L.M. Zelenyi, S.I. Popel', Lunar dust: Properties and potential hazards, Sol. Syst. Res. 54 (6) (2020) 455–476. https://doi.org/10.1134/S0038094620060076

[4] M. Smith, et al., The Artemis Program: An overview of NASA's activities to return humans to the Moon, 2020 IEEE Aerospace Conference, Big Sky, MT, USA (2020) 1–10. https://doi.org/10.1109/AERO47225.2020.9172323

[5] J.D. Gates, Two-body and three-body abrasion: A critical discussion, Wear 214 (1) (1998) 139–146. https://doi.org/10.1016/S0043-1648(97)00188-9

[6] R.L. Kobrick, D.M. Klaus, K.W. Street Jr., Defining an abrasion index for lunar surface systems as a function of dust interaction modes and variable concentration zones, Planet. Space Sci. 59 (2011) 1749–1757. https://doi.org/10.1016/j.pss.2010.10.010

[7] D. Tortorici, A. Adriani, S. Laurenzi, Development of a sustainable chemical recycling process of carbon fibers from epoxy-based composites, Compos. Sci. Technol. 111295 (2025). https://doi.org/10.1016/j.compscitech.2025.111295

[8] F. Zaccardi, et al., 3D printing of radiation shielding polyethylene composites filled with Martian regolith simulant using fused filament fabrication, Acta Astronaut. 190 (2022) 1–13. https://doi.org/10.1016/j.actaastro.2021.09.040

[9] Taber Industries, Taber Rotary Platform Abraser, 2025. Available at: https://www.taberindustries.com/taber-rotary-abraser (accessed 3 Oct 2025).

[10] K.K. John, C.E. Rogers, Classifications and requirements for testing systems and hard-ware to be exposed to dust in planetary environments, NASA Technical Report (2021). Available at: https://ntrs.nasa.gov/citations/20210025140

[11] J. Long-Fox, et al., Applicability of simulants in developing lunar systems and infras-tructure: Geotechnical measurements of lunar highlands simulant LHS-1, Earth and Space 2022 (2022) 76–85. https://ascelibrary.org/doi/abs/10.1061/9780784484470.007

Materials Research Proceedings 69 (2026) 1260-1265 https://doi.org/10.21741/9781644904251-218

Preliminary Design of a Platinum Wire Temperature Sensor for Martian Atmosphere Monitoring Using Additive Manufacturing Technologies

Elisabetta DOLEJSI[1,a*], Davide TONELLI[2,b], Bortolino SAGGIN[1,2,c], Francesca FERRI[1,d], Alessio ABOUDAN[1,e], Carlo BETTANINI[1,2,f], Giacomo COLOMBATTI[1,2,g]

[1]CISAS "Giuseppe Colombo" – Centre of Studies and Activities for Space, University of Padua, Via Venezia 1, 35131 Padova PD, Italy

[2]DII – Department of industrial engineering, University of Padua, Via Venezia 1, 35131 Padova PD, Italy

[a]elisabetta.dolejsi@unipd.it, [b]davide.tonelli.1@studenti.unipd.it, [c]bortolino.saggin@unipd.it, [d]francesca.ferri@unipd.it, [e]alessio.aboudan@unipd.it, [f]carlo.bettanini@unipd.it, [g]giacomo.colombatti@unipd.it

Keywords: Temperature Measurement, Temperature Sensors, RTD, 3D-Printing, Additive Manufacturing, Mars

Abstract. This work presents the development of a novel platinum wire Resistance Temperature Detector (RTD) designed for operation in the harsh Martian environment, within the "Space It Up" initiative. The current datasets of the Martian atmosphere measured parameters are limited in spatial and temporal coverage, highlighting the need for high-precision, robust sensors that can fill this gap. For this reason, accurate temperature measurements are essential to improve atmospheric models and support future human exploration missions and habitat design on Mars that require accurate thermal control. The proposed RTD uses a 700 mm length platinum wire of 60 μm diameter with a parylene insulation coating and a four-wire configuration. The preliminary designed sensor supporting structure has been produced using different Additive Manufacturing (AM) techniques, to enhance structural optimization through lightweight supports. Two prototypes have been developed and taken into consideration in this study: one in titanium via Direct Metal Laser Sintering (DMLS) and one in nanoceramic resin via Stereolithography (SLA). Due to the absence of geometric validation for the titanium specimen, the nanoceramic prototype demonstrated comparatively better structural geometry, as confirmed by FEM analyses and vibration testing. Also, to reduce production costs, AM techniques were selected after comparing different fabrication approaches. The sensor is suitable for integration into future rover, lander, and Entry-Descent-Landing (EDL) systems for Mars missions. As part of the characterization process, environmental qualification will be carried out through thermal-vacuum, calibration, and dust resistance tests.

Introduction

Human exploration of Mars requires in-depth knowledge of the Martian environment in order to accurately assess risks and operating conditions and, in general, to adequately prepare future missions to the Red Planet. Several atmospheric reference models are currently available [1,2], but the need to improve atmospheric measurements on Mars remains critical: current general circulation models rely on exiguous in situ datasets limited to specific locations and sometimes cannot be generalized to the entire planet due to local variations that come from altitude of the site, the presence of phenomena such as dust devils, the seasonality and the longitude and latitude. In order to effectively support future human exploration missions, particularly those aiming at the

Content from this work may be used under the terms of the Creative Commons Attribution 3.0 license. Any further distribution of this work must maintain attribution to the author(s) and the title of the work, journal citation and DOI. Published under license by Materials Research Forum LLC.

Materials Research Proceedings 69 (2026) 1260-1265 https://doi.org/10.21741/9781644904251-218

construction of human habitats, it is therefore necessary to expand and refine the in situ database of atmospheric parameters. An in-depth understanding of the environment could be a key resource for scientific activities such as boundary layer characterization, dust vortex studies, extended monitoring for integration into Martian global climate models, and it is also necessary to provide accurate and effective thermal control that is capable of handling the difficulties presented by future human systems.

Within the Space It Up initiative, a consortium funded by the Italian Space Agency (ASI) and the Ministry of University and Research (MUR), aimed at promoting innovation and collaboration in the field of space technologies, a specific research project is devoted to the "Development of prototypes for analysis of the external environment of potential extraterrestrial habitats". In this framework, a temperature sensor is specifically developed for collecting measurements during the atmospheric descent in the Martian atmosphere and for temperature evolution during surface operations.

Project requirement and operating environment

Mars has an extremely hostile and peculiar environment: the atmosphere is composed mainly of carbon dioxide (CO_2) with traces of other gases (N_2, Ar, O_2, CO, H_2O, NO), at very low pressures (approximately 70 - 1400 Pa), the environment is also characterised by a high presence of erosive dust, which can compromise the functioning of instruments, and by strong temperature gradients (from ~140 K to ~250 K) [1,2].

A sensor designed to operate in such conditions must guarantee high accuracy, rapid response and mechanical robustness. These requirements guided the definition of the design specifications and performance characteristics of the device, which include resistance to thermal shock, vibrations and, eventually, dust impacts and deposits.

Sensor design

The present study introduces a new platinum wire resistance temperature detector (RTD) design that is specifically studied to operate in the harsh Martian atmosphere. It represents the evolution of previous instruments, such as HASI TEM (Huygens Atmospheric Structure Instrument) from the Huygens mission [3], and MarsTem from ExoMars 2016 DREAMS package [4].

The new design is based on a high-purity platinum sensing element (99.9998% Pt) configured as a wire, a technologically advanced solution that offers high precision and stability. The structures of previous sensors were complex: HASI TEM used a platinum-rhodium structure with a glass coating [3], manufactured using high-precision techniques available at the time of its development, while MarsTEM used a monolithic titanium structure, carved from a single block. While these solutions demonstrated excellent compatibility with the project specifications and performance objectives, their implementation led to considerably high manufacturing costs, primarily due to the complexity of the fabrication processes and the precision required.

To achieve a balance between performance and manufacturability, this work explored the use of Additive Manufacturing (AM) techniques, which allow greater geometric freedom and rapid prototyping, with the added advantage of being able to use low-cost materials such as polymers and ceramics.

The sensor is based on a 700 mm long annealed platinum wire with a diameter of 60 μm, including the parylene coating of 0.01 mm thickness intertwined on a supporting structure. The coating guarantees electrical insulation from the metallic support, protects the sensitive element from external agents, assuring also chemical stability, and mechanical protection and thus increases reliability; still under investigation is the use of a noncoated wire in order to decrease further the time response of the sensor. The expected performance includes an accuracy of 0.2 K and a resolution of 0.05 K over the range of 150–300 K. The overall dimensions are approximately 75 × 20 × 25 mm^3, with a total mass of ~10 g for the titanium prototype and ~2 g for the

Materials Research Proceedings 69 (2026) 1260-1265 https://doi.org/10.21741/9781644904251-218

nanoceramic one, making it suitable for deployment on ground stations, rovers, and Entry-Descent-Landing (EDL) modules. The reading circuit configuration includes a four-wire setup, eliminating the interference caused by cable resistance to ensure high precision, and the possibility of post processing corrections. Specific shielded space-grade cables are employed, while a pulsed current of 1 mA is used to limit the phenomenon of self-heating. The sensor is designed to operate in wind speeds ranging from 0 to 50 m/s, and under pressures between 50 and 1500 Pa.

Mechanical design and additive manufacturing

The structure is designed to expose the sensing element to the atmospheric flow while minimizing spurious heat inputs, thereby ensuring a rapid response time. Several models were developed to optimize the RTD support structure and minimize both mass and manufacturing costs. Consequently, AM techniques were selected, as they provide high geometric freedom and allow the fabrication of complex prototypes [5].

Two main variants of the support structure were produced:

1. a titanium structure manufactured by Direct Metal Laser Sintering (DMLS)
2. a nanoceramic resin structure printed via Stereolithography (SLA), developed on the basis of the results present in the Master's thesis by Tonelli (2025) [Structural Design and Numerical–Experimental Validation of a 3D Printed Nanoceramic Structure for a Thermometer for Planetary Exploration, University of Padua].

The titanium version, conceived as an initial reference prototype, lacked sufficient geometric resolution to accurately reproduce the fine details conceived in the design. This was mainly due to the limited precision of the DMLS laser beam (±0.2 mm). As a result, several important features were not properly formed, including Ø 0.30 mm holes which were completely absent; threaded holes (M1.2), which proved difficult to tap due to their small size and the material hardness; and notches intended to the wire support, which could not be fabricated as their diameter (Ø 0.07 mm) was below the achievable resolution of the laser beam (Fig.1). Further optimisation will therefore be required to fully validate this manufacturing route. For future developments, it will be necessary to collaborate with a manufacturer equipped with a higher-precision laser system or willing to perform additional post-processing operations to achieve the required dimensional accuracy. The titanium prototype was not subjected to functional testing for the time of the study, but it is currently under test.

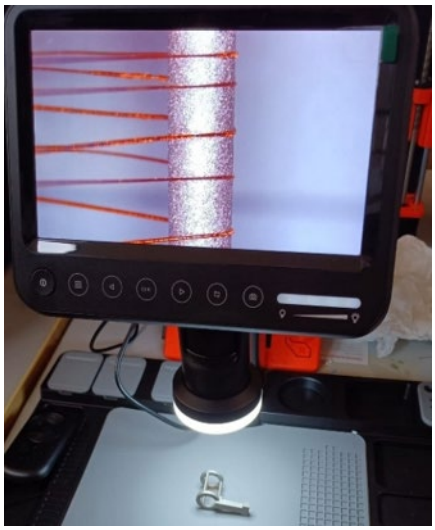


Fig. 1: Titanium prototype. Detail on the absence of the notches for the wire support

Materials Research Proceedings 69 (2026) 1260-1265 https://doi.org/10.21741/9781644904251-218

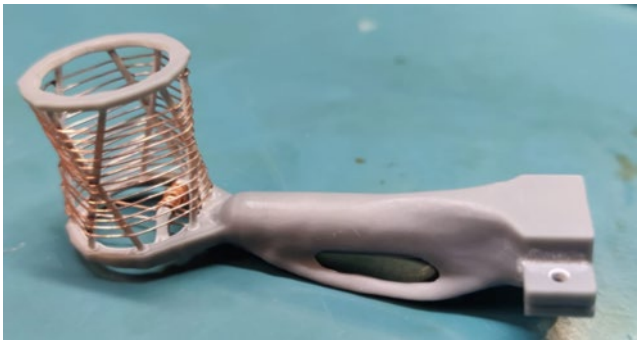


Fig. 2: ThermaDM570 material prototype

On the other hand, the nanoceramic resin prototype (Fig. 2) demonstrated superior performance in terms of geometric accuracy, design flexibility, and thermal insulation. The Therma DM570 material, which is a composite made of a polymeric matrix reinforced with nanometric ceramic particles, is compatible with SLA photopolymerization processes and characterised by low thermal conductivity (≈ 0.54 W/m·K at 30°C), density of 1730 kg/m³, Young's modulus of 6340 MPa, and tensile strength of 56 MPa after UV and thermal post-curing, was used for this specimen [6]. These properties make the material suitable for RTD structure, thanks to its low density, stiffness ratio and reduced heat transfer to the sensing element.

The mechanical design was conceived with the application of topology optimisation (TO) [7] using the finite element method (FEM) with the objective of compliance minimization, starting from the design of DREAMS MarsTem. The objective was to minimise mass while preserving the structural robustness required to withstand the launch loads, enforcing a minimum natural frequency of 100 Hz. For reference, the Falcon Heavy launcher loads were taken into consideration [8]. The resulting geometry achieved a more efficient structure and improved thermal isolation compared to the titanium version [6,9].

The numerical–experimental validation involved an extensive comparison between FEM analyses and laboratory tests, including tensile tests on post-cured resin specimens to characterise the mechanical properties, and vibration tests on 4:1 and 6:1 scale prototypes printed via Multi Jet Fusion (MJF) PA12 [10], using an electrodynamic shaker to evaluate the modal response and validate the numerical models. The scale prototypes were conceived to fully validate the models with minor influence of the measuring accelerometer mass. The results show (Fig. 3) a close correspondence between numerical and experimental data, with frequency discrepancies below 5%, validating the FEM model adopted in the real scale structure [11]. The structure proves to be adequate for the launch environment, with a worst case of 2 for the safety margins.

The only limitation observed concerns the anisotropic behaviour of the nanoceramic material in the printing directions (taken into account in the numerical validation): this could be mitigated through optimisation of printing parameters and post-curing cycles. Since the ThermaDM570 is conceived for high-temperature and high-pressure applications [6], it is essential to assess the performance of the nanoceramic resin under different thermal cycles, especially in low-temperature and low-pressure environments, such as those found on Mars.

Overall, the prototype of nanoceramic resin combines good mechanical performance, excellent thermal insulation, lightness and compatibility with high-precision additive manufacturing techniques to provide a technologically advanced and promising solution.

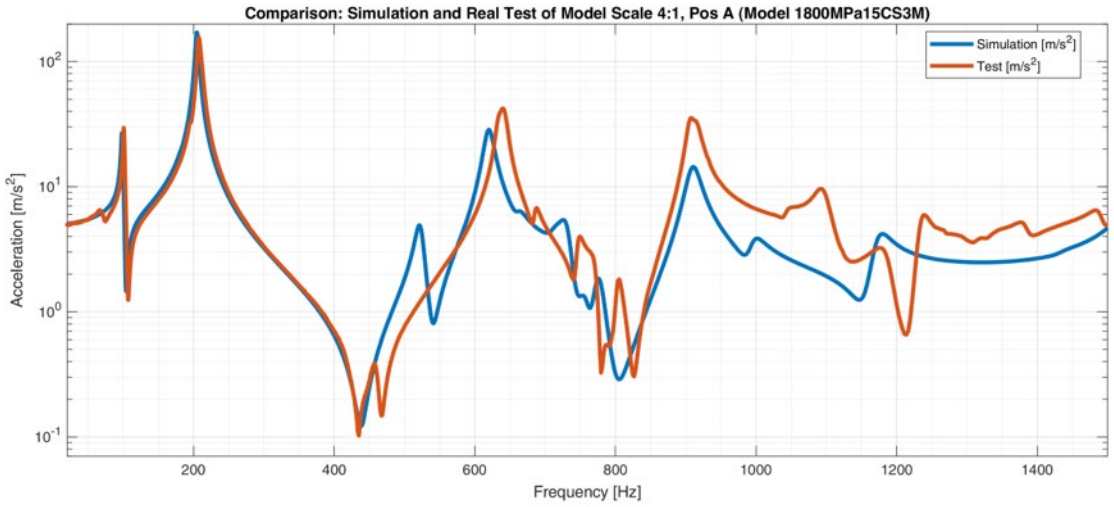


Fig. 3: Comparison between simulation and vibration test of model scale 4:1

Future developments

The following steps involve the production of a titanium version of the supporting structure of the sensing element (i.e. Pt wire) of the thermometer using higher precision additive manufacturing, followed by vibration and functional validation tests. In addition, thermal-vacuum tests and thermal cycling on the nanoceramic resin will be required to evaluate its behaviour under the Martian extreme environmental conditions. Accuracy, calibration, thermal shock, and dust resistance tests will also be necessary to reproduce Martian operating conditions. The experiments will be carried out in terrestrial analogue environments, such as the Moroccan Desert, or in specialized Martian simulation facilities, like the one at Aarhus University. Other test campaigns will include wind tunnel experiments to assess the sensor's survivability under Martian wind conditions and to evaluate the dynamic response of the sensor (e.g. time response).

Conclusions

Rapid prototyping has already been proven to be effective in the production of low-cost designs, even in space [12] and in addition it has shown significant advantages when it comes to geometric freedom, weight savings and time to develop.

More optimisation studies will still be needed, particularly on thermo-fluid dynamics and sensor response under extreme operating conditions for space qualification. Prototype validation goes on, and new configurations of the supporting frame are planned to be developed and tested. The scientific and engineering impact of the project lies in the possibility of obtaining lighter, and more adaptable temperature sensors, contributing to the advancement of measurement technologies for planetary exploration.

Acknowledgment

This study was carried out within the Space It Up project funded by the Italian Space Agency, ASI, and the Ministry of University and Research, MUR, under contract n. 2024-5-E.0 - CUP n. I53D24000060005.

References

[1] F. Forget, F. Hourdin, R. Fournier, C. Hourdin, O. Talagrand, M. Collins, S. R. Lewis, P. L. Read, and J.-P. Huot, Improved general circulation models of the Martian atmosphere from the surface to above 80 km, J. Geophys. Res., 104(E10), 24155–24175 (1999), https://doi.org/10.1029/1999JE001025.

[2] E. Millour, F. Forget, A. Spiga, T. Pierron, A. Bierjon, L. Montabone, M. Vals, F. Lefèvre, J.-Y. Chaufray, M. Lopez-Valverde, F. Gonzalez-Galindo, S. Lewis, P. Read, M.-C. Desjean, and F. Cipriani, and the MCD Team, The Mars Climate Database (Version 6.1), Europlanet Science Congress 2022, Granada, Spain, 18–23 Sep 2022, EPSC2022-786 (2022), https://doi.org/10.5194/epsc2022-786

[3] M. Fulchignoni, Ferri F., Angrilli F., et al., The characterisation of Titan's atmospheric physical properties by the Huygens Atmospheric Structure Instrument (HASI), Space Science Reviews 104, 395–431 (2002), https://doi.org/10.1023/A:1023688607077

[4] G. Colombatti et al., MarsTEM: The temperature sensor of the DREAMS package onboard Exomars2016, 2014 IEEE Metrology for Aerospace (MetroAeroSpace), Benevento, Italy, pp. 249-254 (2014), https://doi.org/10.1109/MetroAeroSpace.2014.6865929

[5] I. Gibson, D. Rosen, B. Stucker, Additive manufacturing Technologies, Springer, 2021, https://doi.org/10.1007/978-3-030-56127-7

[6] DWS S.r.l. Therma DM570 Technical Data Sheet, 12-2024.

[7] M.P. Bendsøe, O. Sigmund, Topology Optimization Theory, Methods and Applications, Springer, 2003, https://doi.org/10.1007/978-3-662-05086-6

[8] Space Exploration Technologies Corp., Falcon Payload User's Guide, Version 8, March 2025.

[9] S. Sartori, A. Bordin, L. Moro, A. Ghiotti, S. Bruschi, The Influence of Material Properties on the Tool Crater Wear When Machining Ti6Al4V Produced by Additive Manufacturing Technologies, Procedia CIRP, Volume 46, Pages 587-590, ISSN 2212-8271 (2016), https://doi.org/10.1016/j.procir.2016.04.032

[10] K.P.M. Lee, & M. Kajtaz, Experimental Characterisation and Finite Element Modelling of Polyamide-12 Fabricated via Multi Jet Fusion, Polymers, 14:5258 (2022), https://doi.org/10.3390/polym14235258

[11] NASA. Correlation of Finite Element Models and Shaker Test Data, NASA ™ 104187, 1992.

[12] A. Goulas, R. A. Harris, R. J. Friel, Additive manufacturing of physical assets by using ceramic multicomponent extra-terrestrial materials, Additive Manufacturing, Volume 10, Pages 36-42 , ISSN 2214-8604 (2016), https://doi.org/10.1016/j.addma.2016.02.002

Materials Research Proceedings 69 (2026) 1266-1271 https://doi.org/10.21741/9781644904251-219

Multifunctional Gels for Strain Sensing and Radiation Shielding in Space

Lucia LAMBERTINI[1,a], Maria Gabriella SANTONICOLA[2,b] and Susanna LAURENZI[1,c*]

[1]Department of Astronautical Electrical and Energy Engineering, Sapienza University of Rome, Via Salaria 851-881, 00138 Rome, Italy

[2]Department of Chemical Engineering Materials Environment, Sapienza University of Rome, Via del Castro Laurenziano 7, 00161 Rome, Italy

[a]lucia.lambertini@uniroma1.it, [b]mariagabriella.santonicola@uniroma1.it, [c]susanna.laurenzi@uniroma1.it

Keywords: Structural Health Monitoring (SHM), Flexible Sensors, Radiation Shielding

Abstract. This work investigates a novel class of multifunctional poly(vinyl alcohol) (PVA) gels incorporating multi-walled carbon nanotubes (MWCNTs) for combined radiation shielding and strain-sensing applications. The proposed PVA/MWCNT gels, crosslinked with boric acid, offer high flexibility, conductivity, and mechanical robustness. MWCNT dispersion was optimized by analyzing sedimentation behavior as a function of sonication temperature and PVA concentration. Experimental characterization, including compression tests (–60 °C to +60 °C) and tensile–impedance coupling, demonstrated excellent electromechanical stability. These findings confirm the suitability of PVA/MWCNT gels for flexible, radiation-resistant SHM sensors in space structures.

Introduction

Flexible, durable, and conductive materials have played a crucial role in the development of Structural Health Monitoring (SHM) systems [1]. Traditionally, they have been employed as strain sensors to track the mechanical deformation of structures under load, enabling the early detection of potential threats to structural integrity [2-4]. In the space sector, SHM techniques are widely used to monitor primary structures such as satellite solar panels and antennas. Strain sensors are typically fabricated by embedding conductive materials, such as carbon nanotubes (CNTs), graphene, metal powders, and conductive polymers, within the matrix of elastomers [5, 6]. This approach enables elastomer-based sensors to achieve significant stretchability while maintaining good electrical conductivity. However, the practical use of elastomers in space applications remains challenging because of their sensitivity to the harsh radiative environment.

In addition to elastomers, conductive gels heve also attracted considerable interest as alternative strain-sensing materials [7]. Due to their high water content, softness, and tissue-like mechanical properties, gels can conform to complex surfaces and detect even subtle deformations. Moreover, their conductivity, which can be further enhanced by incorporating conductive fillers, makes them suitable for flexible and stretchable sensor systems.

Results from the PErsonalized Robotics as SErvice Oriented applications (PERSEO) project have demonstrated that liquid water is highly effective in mitigating radiation damage in space environments [8]. Among the various candidate materials for radiation shielding, gels have gained particular attention in the medical and pharmaceutical fields due to their high water content, which provides superior shielding performance compared to conventional polymers. Being intrinsically rich in hydrogen, an essential element for attenuating ionizing radiation such as neutrons and protons, water-based gels represent a promising solution for multifunctional systems. Therefore,

Content from this work may be used under the terms of the Creative Commons Attribution 3.0 license. Any further distribution of this work must maintain attribution to the author(s) and the title of the work, journal citation and DOI. Published under license by Materials Research Forum LLC.

Materials Research Proceedings 69 (2026) 1266-1271 https://doi.org/10.21741/9781644904251-219

incorporating gels into SHM systems could simultaneously enable strain sensing and passive radiation shielding.

In this work, we propose a novel class of multifunctional gels designed for simultaneous radiation shielding and strain sensing applications. The gels are based on a polyvinyl alcohol (PVA) matrix incorporating 0.5, 1.0, and 2.0 wt% multi-walled carbon nanotubes (MWCNTs), which act as conductive fillers to enhance both mechanical robustness and electrical conductivity. Dispersion quality of MWCNTs was optimized by analyzing sedimentation times as function of sonication temperature and PVA concentration. The aqueous PVA–MWCNTs dispersions were then chemically crosslinked with boric acid (BA), aiming to leverage the well-established neutron absorption capabilities of the ^{10}B isotope for shielding applications [9]. To validate their multifunctionality, both experimental and numerical investigations were conducted. Compression tests across the temperature range typical of satellites (–60 °C to +60 °C) were performed using dynamic mechanical analysis, while quasi-static tensile tests coupled with impedance monitoring were used to evaluate electromechanical stability. Finally, radiation transport simulations using the On-Line Tool for the Assessment of Radiation in Space (OLTARIS) tool confirmed the gels' potential as lightweight shielding materials. These findings open new avenues for the development of smart, adaptive materials capable of withstanding extreme environments while providing real-time structural monitoring.

Fabrication of PVA/BA gels

The following materials were obtained from Sigma-Aldrich: poly(vinyl alcohol) (PVA, Mw = 30,000 Da, ρ = 1.3 g/cm³, product no. 8438680100), boric acid (BA, product no. B0394), and ethanol (ρ = 0.790 g/cm³ at 20 °C, product no. 02860-1L). Pristine multi-walled carbon nanotubes (MWCNTs, NC7000 series) supplied by Nanocyl S.A. (Belgium) were used as nanofillers in the gel matrix.

The dispersion of MWCNTs in water was optimized using poly(vinyl alcohol) (PVA) as dispersing agent. 0.03g of MWCNTs were dispersed in ultrapure water (12 mL) containing different PVA concentrations. The suspensions were magnetically stirred and sonicated for 1 hour at 60 °C. The investigated PVA-to-MWCNT weight ratios were 4:1 (denoted as PVA 1 wt%), 12:1 (PVA 3 wt%), 20:1 (PVA 5 wt%), 32:1 (PVA 8 wt%), 40:1 (PVA 10 wt%) and 60:1 (PVA 15 wt%). Sedimentation tests revealed that dispersions below 5 wt% PVA were unstable, while 5 - 15 wt% PVA at 60 °C ensured homogeneous, long-lasting dispersions. Further optimization identified 8 wt% PVA as the optimal concentration, maintaining full stability for at least eight days. After dispersing the MWCNTs in ultrapure water using the optimized PVA concentration, the PVA/BA–MWCNT gels were synthesized by chemical crosslinking. A 30 wt% aqueous PVA–MWCNT solution was prepared by magnetic stirring at 80 °C for 1 hour. Separately, a 10 wt/vol% boric acid (BA) stock solution in ethanol was prepared under the same conditions. Crosslinking was initiated by adding the BA solution to the PVA dispersion to obtain a final BA concentration of 4 wt/vol%. The resulting mixtures were cast into glass molds and conditioned in a climate chamber at 30 °C and 50% relative humidity for 48 hours.

Compressive behavior

Dynamic mechanical analysis (DMA) of PVA/BA–MWCNT gels revealed a strong dependence of viscoelastic behavior on MWCNT concentration (Fig. 1). The pristine gel showed the lowest storage modulus (Fig. 1a), indicating a weak polymer network. Introducing 0.5 wt% MWCNTs significantly increased the modulus, confirming efficient load transfer between polymer chains and dispersed nanotubes. At 1.0 wt%, the modulus plateaued, suggesting a percolation threshold and possible nanotube agglomeration. A minor improvement at 2.0 wt% indicated mechanical saturation. The loss modulus curves (Fig.1 b) displayed distinct glass transition peaks, with higher

Materials Research Proceedings 69 (2026) 1266-1271 https://doi.org/10.21741/9781644904251-219

MWCNT content enhancing energy dissipation. This increase reflects stronger polymer – nanotube interfacial interactions and reduced free water within the gel network.

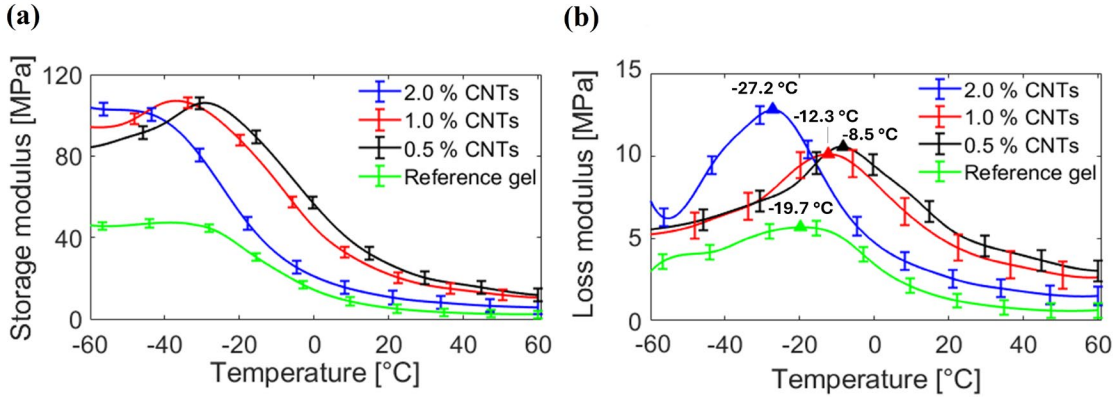


Fig. 1: DMA results of gels: (a) Storage and (b) Loss modulus with varying CNTs content.

SHM behavior through tensile-electrical tests

Tensile tests (ASTM D412-C) on PVA/BA gels with increasing MWCNT content (0–2 wt%) showed significant improvements in mechanical performance (Fig. 2a). The stress–strain curves shifted upward with higher filler content, indicating increased strength, elasticity, and energy absorption. The Young's modulus rose from 6.93 MPa for the reference gel to 18.41 MPa at 2 wt% MWCNTs, representing a threefold increase in stiffness. Additionally, the maximum strain at failure nearly doubled, demonstrating that MWCNT incorporation enhances both rigidity and toughness, allowing the gels to sustain larger deformations before failure.

Surface electrical conductivity measurements during tensile deformation (Fig. 2b) showed a clear increase in conductivity with higher MWCNT content, confirming the formation of interconnected conductive networks within the gels. Conductivity remained stable under strain, indicating good structural integrity of the network. As summarized in Table 11.5, conductivity rose by nearly three orders of magnitude—from 3.3×10^{-8} S/m for the reference gel to 2.4×10^{-5} S/m at 2 wt% MWCNTs.

Electrical conductivity describes how efficiently charge carriers move through a material, while conductance depends on geometry and deformation state. To evaluate the gels' sensing capability, conductance was derived from the real part of the admittance measured at 1 V and 1 kHz. As shown in Fig. 2c, the reference sample (0 wt% MWCNTs) and 0.5 wt% MWCNTs gels exhibited negligible conductance, indicating no percolating network. At higher filler contents, conductance increased markedly, reaching ~3×10^{-3} S for the 2 wt% MWCNT sample. This behavior confirms the formation of conductive pathways once the percolation threshold is achieved. From a Structural Health Monitoring (SHM) perspective, these conductance variations correlate with strain and integrity, providing a sensitive, non-destructive means to detect structural changes.

Materials Research Proceedings 69 (2026) 1266-1271 https://doi.org/10.21741/9781644904251-219

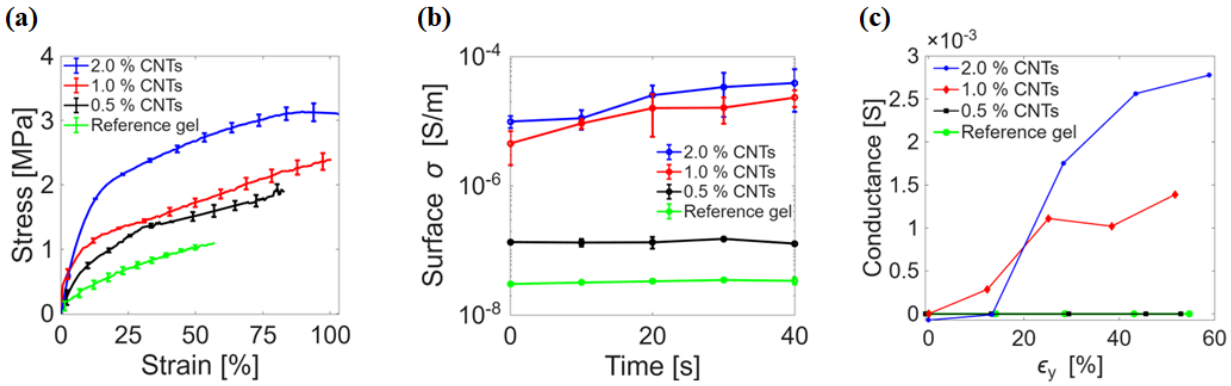


Fig. 2: Tensile-electrical results of PVA/BA-MWCNTs gels: (a) Engineering stress–strain curves of PVA/BA gels containing different weight fractions of MWCNTs (0, 0.5, 1.0, and 2.0 wt%); (b) Surface electrical conductivity (σ) of the gels as a function of time during tensile tests measured at frequency of 1 kHz; (c) Time evolution of the conductance at frequency of 1 kHz.

Numerical simulations

The radioprotective performance of gels was assessed through simulations using NASA's OLTARIS tool, developed at Langley Research Center [10]. In this study, the shielding effectiveness of PVA/BA gels was compared with standard liquid water investigated during PERSEO project. Simulations were carried out for a deep-space environment located at 1 astronomical unit (AU) from Earth, considering exposure to Galactic Cosmic Radiation (GCR) and Solar Particle Events (SPEs). The geometry consisted of a spherical shell with an inner void (radius 150 cm) and an external shielding layer of variable areal depth (0 – 5 g/cm²). This setup enabled a direct comparison between unshielded conditions (0 g/cm²) and progressively thicker protective layers. The Badhwar–O'Neill 2020 (BON2020) model was employed to represent the GCR spectrum, while the NUCFRG3 model was used for heavy-ion fragmentation processes. Historical SPE event of October 1989 was also simulated to evaluate solar proton exposure scenario. Materials of external layers were defined on the "Web Interface" using their density and elemental mass percentages reported in Table 1. Results were computed for the Male Adult voXel (MAX) human phantom modelt o assess radiation effects on human body.

Table 1: Input data for defining materials on OLTARIS tool.

Materials	Density [g/cm^3]	Elemental mass percentages []
PVA/BA (Ref. gel)	1.21	0.3436 C, 0.0931 H, 0.0029 ^{10}B, 0.0118 ^{11}B, 0.5486 O
PVA/BA-0.5 wt% CNTs	1.14	0.3730 C, 0.0909 H, 0.0031 ^{10}B, 0.0124 ^{11}B, 0.5206 O
PVA/BA-1.0 wt% CNTs	1.14	0.3577 C, 0.0912 H, 0.0029 ^{10}B, 0.0115 ^{11}B, 0.5367 O
PVA/BA-2.0 wt% CNTs	1.22	0.3550 C, 0.0903 H, 0.0027 ^{10}B, 0.0108 ^{11}B, 0.5412 O
H_2O (Liquid water)	1.00	0.1111 H, 0.8889 O

Fig. 3 illustrates the behavior of total effective doses equivalent as a function of areal depth for GCR and SPE environments. Results compare liquid water with PVA/BA gels incorporating different concentrations of carbon nanotubes (CNTs). In all cases, the effective dose equivalent decreases as depth increases, and the CNT-reinforced gels demonstrate shielding capabilities comparable to pure PVA/BA and water. These findings suggest that CNT reinforcement can be used to improve electrical and mechanical properties without compromising the radiation protection capability of PVA-based gels.

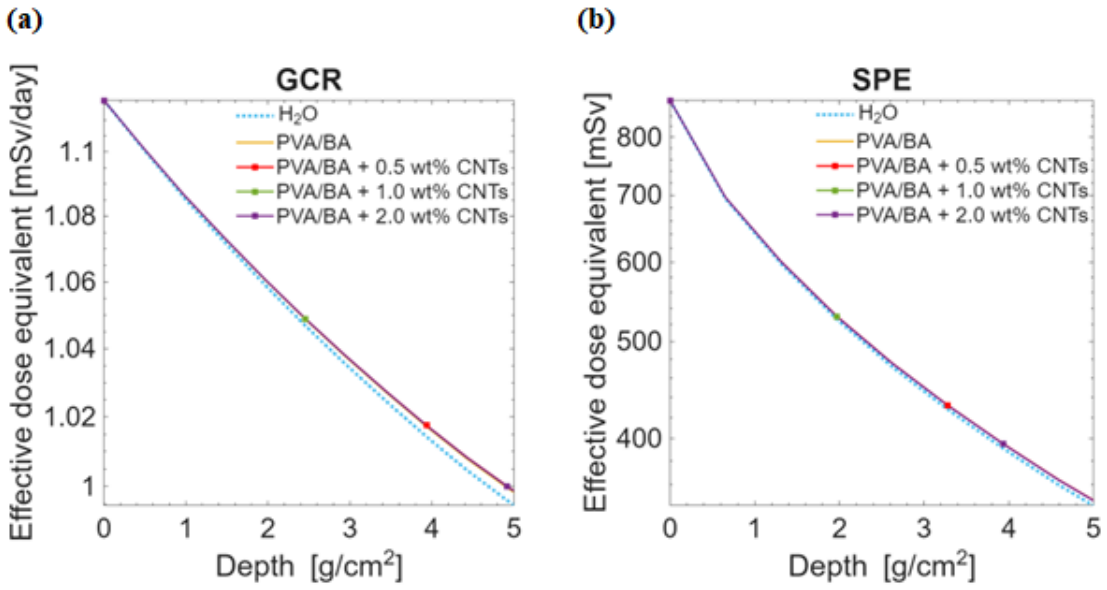


Fig. 3: Total effective dose equivalent as a function of depth for (a) GCR and (b) SPE scenarios.

Conclusions

PVA/BA–MWCNT gels were produced through an optimized nanotube dispersion process in water, ensuring uniform filler distribution within the polymer matrix. The resulting materials exhibited significant improvements in mechanical and electrical properties. DMA results showed that the storage modulus increased notably at 0.5 wt% MWCNTs, marking a mechanical percolation threshold between 0.5 and 1.0 wt%. The glass transition temperature displayed a non-monotonic trend, reflecting the balance between water plasticization and MWCNTs confinement. Electrical analysis revealed frequency-dependent conductivity enhancement, with a sharp rise between 0.5 and 1.0 wt% indicating conductive network formation. Tensile tests confirmed a threefold increase in stiffness (from 6.93 to 18.41 MPa) and nearly doubled strain at failure, while conductivity rose by three orders of magnitude. Overall, these gels combine mechanical strength and high conductivity, demonstrating strong potential for multifunctional sensing and structural health monitoring applications. Finally, numerical simulations confirmed that the incorporation of MWCNTs has a negligible impact on the radiation shielding capability of PVA-based gels, ensuring that the improvements in mechanical and electrical properties are achieved without compromising the protective behavior of pristine PVA/BA gels.

Acknowledgements

This study was carried out within the Space It Up project funded by the Italian Space Agency, ASI, and the Ministry of University and Research, MUR, under contract n. 2024-5-E.0 - CUP n. I53D24000060005.

References

[1] B. Cheng, Y. Li, H. Li, H. Li, S. Yang, P. Li, Y. Shang, An adhesive and self-healable hydrogel with high stretchability and compressibility for human motion detection, Composites Science and Technology, Vol. 213, 108948, 2021. https://doi.org/10.1016/j.compscitech.2021.108948

[2] Y. Park, M. Park, J. Lee, Reduced graphene oxide-based artificial synapse yarns for wearable textile device applications, Advanced Functional Materials, Vol. 28, 1804123, 2018. https://doi.org/10.1002/adfm.201804123

[3] Y. Liu, H. Fan, K. Li, N. Zhao, S. Chen, Y. Ma, X. Ouyang, X. Wang, Strain-isolation bridge structure to improve stretchability of highly sensitive strain sensors, Advanced Materials Technologies, Vol. 4, 1900309, 2019. https://doi.org/10.1002/admt.201900309

[4] M. Khatib, O. Zohar, W. Saliba, S. Srebnik, H. Haick, Highly efficient and water-insensitive self-healing elastomer for wet and underwater electronics, Advanced Functional Materials, Vol. 30, 1910196, 2020. https://doi.org/10.1002/adfm.201910196

[5] Y. Jung, K. K. Jung, D. H. Kim, D. H. Kwak, J. S. Ko, Linearly sensitive and flexible pressure sensor based on porous carbon nanotube/polydimethylsiloxane composite structure, Polymers, Vol. 12, 1499, 2020. https://doi.org/10.3390/polym12071499

[6] K. Kim, N. Jang, S. Ha, J. H. Cho, J. Kim, Highly sensitive and stretchable resistive strain sensors based on microstructured metal nanowire/elastomer composite films, Small, Vol. 14, 1704232, 2018. https://doi.org/10.1002/smll.201704232

[7] Y. Chen, Y. Zhang, A. Mensaha, D. Li, Q. Wang, Q. Wei, A plant-inspired long-lasting adhesive bilayer nanocomposite hydrogel based on redox-active Ag/Tannic acid-Cellulose nanofibers, Carbohydrate Polymers, Vol. 255, 117508, 2021. https://doi.org/10.1016/j.carbpol.2020.117508

[8] G. Baiocco, M. Giraudo, L. Bocchini, S. Barbieri, I. Locantore, E. Brussolo, D. Giacosa, L. Meucci, S. Steffenino, A. Ballario, The PERSEO Experience: A Water-Filled Garment Prototype for Personal Radiation Protection of Astronauts Successfully Tested on Board the International Space Station, Aerotecnica Missili & Spazio, Vol. 99, Pages 111-114, 2020. https://doi.org/10.1007/s42496-020-00048-0

[9] L. Lambertini, G. Coccarelli, E. Toto, M. G. Santonicola, S. Laurenzi, Poly(vinyl alcohol) gels cross-linked by boric acid for radiation protection of astronauts, Acta Astronautica, Vol. 221, Pages 142-154, 2024. https://doi.org/10.1016/j.actaastro.2024.05.020. https://doi.org/10.1016/j.actaastro.2024.05.020

[10] E. Toto, L. Lambertini, S. Laurenzi, M. G. Santonicola, Recent Advances and Challenges in Polymer-Based Materials for Space Radiation Shielding, Polymers, Vol. 16, 382, 2024. https://doi.org/10.3390/polym16030382

Materials Research Proceedings 69 (2026) 1272-1277 https://doi.org/10.21741/9781644904251-220

Flexible Poly(Vinyl Alcohol) Gels for Radiation Shielding in Next-Generation Spacesuits

Lucia LAMBERTINI[1,a], Maria Gabriella SANTONICOLA[2,b] and Susanna LAURENZI[1,c*]

[1]Department of Astronautical Electrical and Energy Engineering, Sapienza University of Rome, Via Salaria 851-881, 00138 Rome, Italy

[2]Department of Chemical Engineering Materials Environment, Sapienza University of Rome, Via del Castro Laurenziano 7, 00161 Rome, Italy

[a]lucia.lambertini@uniroma1.it, [b]mariagabriella.santonicola@uniroma1.it, [c]susanna.laurenzi@uniroma1.it

Keywords: Spacesuit Radiation Shielding, Poly(Vinyl Alcohol) Gels, Shielding Materials

Abstract. Protecting astronauts from radiation during space missions is a critical challenge. In the current context, where space agencies are working to establish permanent bases on the lunar surface, radiation shielding becomes an even more crucial issue. Indeed, as missions venture farther from Earth, crews lose the natural shielding provided by the Earth's magnetic field and atmosphere, resulting in high exposure to ionizing radiation**.** This study explores the integration of poly(vinyl alcohol) (PVA) gels as flexible intermediate layers in lunar spacesuits to enhance radiation shielding on lunar surface. Experimental tests demonstrated that PVA gels possess similar density and thermal conductivity to nylon but greater flexibility, denoted by their high strain at failure during tensile tests. Numerical simulations highlights that the gels' inclusion in spacesuits highly reduces total effective doses equivalent due to Solar Particle Events.

Introduction

Spacesuits have been designed primarily to ensure protection against extreme temperatures, micrometeoroids, and orbital debris [1, 2]. They consist of multiple specialized layers, each engineered for a specific function. The outermost layer, made of orthofabric composites, acts as a shield against micrometeoroids and space debris. Beneath this layer, an insulation system composed of aluminized mylar and dacron fabric provides thermal regulation. Finally, the innermost layers consist of the Pressure Bladder Garment (PBG), made of urethane-coated nylon, and the Liquid Cooling and Ventilation Garment (LCVG), made of nylon with embedded water tubes, designed to maintain a stable internal temperature.

Currently, polymer-based materials have been selected as promising solutions between innovative shielding techniques, due to their lightweight and excellent mechanical, thermal, and electrical properties. Their shielding performance has been further improved by incorporating specific fillers, including boron nitride, polyurethane, graphene, and carbon nanotubes [3 - 8]. However, their inherent rigidity and limited flexibility make them unsuitable for wearable systems such as spacesuits employed during Extravehicular Activities (EVAs). This limitation can be addressed by integrating ductile, hydrogen-rich, and flexible materials with high radiation stopping power directly into the suit's structure. As demonstrated by the PErsonalized Robotics as SErvice Oriented applications (PERSEO) project, hydrogen-rich materials, such as liquid water, are particularly effective in attenuating Galactic Cosmic Radiation (GCR) and Solar Particle Events (SPEs) [9]. However, the use of liquids in microgravity environments determines significant challenges, including increased system volume and complex fluid management. To overcome

Content from this work may be used under the terms of the Creative Commons Attribution 3.0 license. Any further distribution of this work must maintain attribution to the author(s) and the title of the work, journal citation and DOI. Published under license by Materials Research Forum LLC.

Materials Research Proceedings 69 (2026) 1272-1277 https://doi.org/10.21741/9781644904251-220

these constraints, gels have been proposed as innovative solution to enhance radiation protection inside spacesuits for missions beyond LEO [10].

This study examines the feasibility of enhancing radiation shielding for next-generation spacesuits during EVAs on the Moon without compromising their ergonomics by proposing the integration of poly(vinyl alcohol) (PVA) gels as an intermediate layer between the PBG and the LCVG of the spacesuit. Experimental tests were conducted to compare the physical properties of PVA-based gels with those of nylon, which is the primary material used in both the PBG and LCVG systems. The results show comparable density and thermal conductivity between the two materials. Moreover, the gels demonstrated higher flexibility, as evidenced by their local strain under tensile stress. Numerical simulations using the On-Line Tool for the Assessment of Radiation in Space (OLTARIS) confirmed the shielding potential of the gels. Indeed, integrating gel layers within the spacesuit resulted in reductions in both total effective dose equivalent and average organ dose equivalent.

Fabrication of PVA/BA gels

The following materials were purchased from Sigma Aldrich and used as received: PVA (Mw = 30,000 Da, ρ = 1.3 g/cm³, product no. 8438680100), BA (product no. B0394), and ethanol (ρ = 0.790 g/cm³ at 20 °C, product no. 02860-1L). Ultrapure water (resistivity 18.2 MΩ·cm) was produced using a Direct-Q3 UV purification system (Millipore, Molsheim, France).

PVA/BA gels were prepared via chemical crosslinking following a previously reported protocol [10]. Briefly, a 30 wt% aqueous PVA solution was prepared by magnetic stirring at 80 °C for 1 h. Separately, a 10 wt/vol% BA stock solution was prepared in ethanol under identical conditions. Crosslinking was initiated by adding the BA solution to the PVA solution to achieve a final BA concentration of 4 wt/vol%. The resulting mixture was poured into glass molds and conditioned in a climate chamber at 30 °C and 50% relative humidity for 72 h.

Comparison of Nylon and gel properties

The experimental results shown in Table 1 suggests that the PVA/BA gels possess a density (1.25 g/cm³) and thermal conductivity (0.27 W/m·K) comparable to those of Nylon 6 used in aerospace applications. However, the gels exhibit higher ductility compared to 9–25% for nylon, failing at about 65 % strain during tensile tests. Although the Young's modulus (12.75 MPa) is much lower than that of nylon, the gels demonstrate excellent flexibility due to their high water content (≈ 55 %), which also suggests potential benefits for radiation attenuation.

Table1: Comparison of physical and mechanical properties of PVA/BA gels and nylon.

Samples	PVA/BA gels	Nylon	Ref.
Density [g/cm³]	1.25*	1.14	[11]
Thermal conductivity [W/(mK)]	0.27*	0.10 ÷ 0.30	[12]
Strain at maximum elongation [%]	64.71*	9 ÷ 25	[13]
Young modulus [MPa]	12.75 ± 0.86	2450 ÷ 3100	[13]

* Standard deviation < 0.01.

Numerical simulations

Radiation exposure during lunar extravehicular activities (EVAs) was analyzed using NASA's OLTARIS platform [3], which employs the deterministic HZETRN transport code to solve one- or three-dimensional Boltzmann equations. Two primary lunar radiation environments were considered: Galactic Cosmic Radiation (GCR), including both free-space and albedo-reflected

Materials Research Proceedings 69 (2026) 1272-1277 https://doi.org/10.21741/9781644904251-220

components, and Solar Particle Events (SPEs), in which the external environment is negligible. For this study, GCRs were modeled during solar minimum, corresponding to maximum ionization, using a solar modulation parameter of 475 MV and the Badhwar–O'Neill (BON) 2020 model. SPEs were represented using the Tylka Bands Fitting for the October 1989 event. Material cross-sections were calculated with OLTARIS based on the chemical compositions and densities reported in Table 2.

Table 2: Input data used for defining materials on the OLTARIS tool.

Materials	Density [g/cm^3]	Elemental mass percentages []
Aluminized Mylar	1.40	0.624 C, 0.042 H, 0.332 O, 0.002 Al
Dacron	1.38	0.625 C, 0.042 H, 0.333 O
Neoprene coated Nylon	1.05	0.589 C, 0.077 H, 0.205 Cl, 0.060 N, 0.069 O
Nylon	1.14	0.637 C, 0.098 H, 0.124 H, 0.141 O
Orthofabric	1.80	0.470 C, 0.021 H, 0.380 F, 0.058 N, 0.071 O
Polycarbonate	1.20	0.706 C, 0.059 H, 0.235 O
S-glass composite	1.29	0.478 C, 0.046 H, 0.304 O, 0.022 N, 0.150 Si
Urethane coated Nylon	1.13	0.523 C, 0.077 H, 0.246 O, 0.154 N
PVA/BA gel	1.25	0.2147 C, 0.0999 H, 0.0018 ^{10}B, 0.0073 ^{11}B, 0.6763 O

Geometrical model

Simulations investigated the potential integration of gels within spacesuit structures modeled using NASA's Z2 CAD design [14] to assess possible enhancements in radiation protection during extravehicular activities (EVAs). The spacesuit model was oriented normal to the lunar surface and coupled with the MAX and FAX phantoms to assess human exposure. A MATLAB-based ray-tracing algorithm generated 512 rays from a central target and divided the CAD geometry into five anatomical regions aligned with the phantoms. For each region, material composition and thickness followed the Z2 configuration, with optional PVA/BA gel layers (0.5 – 3 cm) added between nylon and urethane-coated nylon. The resulting material profiles were compiled into an XML file compatible with OLTARIS for radiation transport simulations.

Results and discussion

Fig. 1 illustrates simulations in which a PVA/BA gel layer of varying thickness (0 – 3 cm) was incorporated into conventional spacesuit configurations. Under GCR conditions (Fig. 1a), initial Total Effective Dose Equivalents (TEDEs) were nearly identical for both sexes (288.1 mSv for the male and 286.1 mSv for the female phantom). At a 3 cm gel thickness, TEDEs decreased to approximately 260 mSv, corresponding to modest reductions of 9.7 % and 9.5 %, respectively. This limited improvement underscores the weak shielding capability of gels against highly penetrating GCR particles. In contrast, the SPE scenario (Fig. 1b) demonstrates a pronounced shielding effect. Without gel, TEDEs reach hazardous levels of 1313 mSv (male) and 1211 mSv (female). Introducing a 1 cm gel layer reduces these values by nearly 50 % (49.6 % and 47.1 %), while a 3 cm layer achieves dose reductions exceeding 60 % in both phantoms. The narrowing difference between male and female exposures with increasing gel thickness further indicates that effective shielding minimizes sex-based dose disparities. Overall, these results confirm that PVA/BA gels offer limited protection against GCR but are highly effective in mitigating SPE radiation, providing substantial reductions in TEDEs.

Materials Research Proceedings 69 (2026) 1272-1277 https://doi.org/10.21741/9781644904251-220

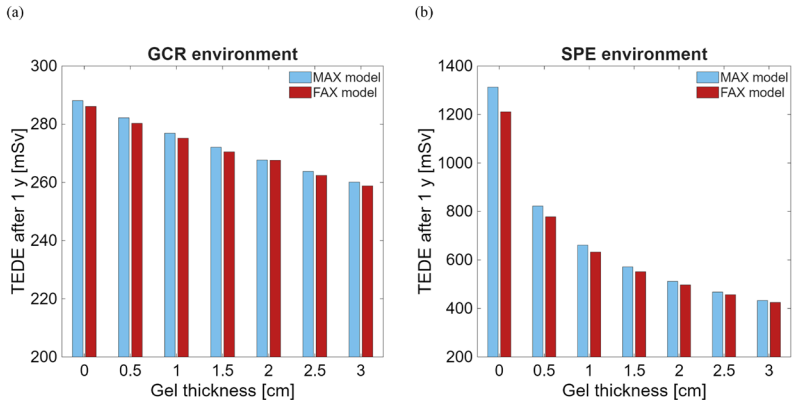


Fig.1: Total Effective Doses Equivalent (TEDEs) after 1 y for MAX (male) and FAX (female) models as a function of gel layer thickness (0 – 3 cm) under (a) Galactic Cosmic radiation (GCR) and (b) Solar Particle Event (SPE) environments.

Fig. 2 and 3 illustrate a comparative analysis of the average organ doses equivalent in male and female phantoms during a 1-year mission. Under GCR conditions (Fig. 2), the skin receives the highest doses (~ 500 mSv in FAX and ~ 450 mSv in MAX), followed by the lens and salivary glands. Increasing the protective gel layer thickness yields only minor reductions, highlighting the limited effectiveness against GCR particles. In contrast, during SPE (Fig. 3), the high skin doses (> 10^5 mSv) decrease sharply with increasing gel thickness, confirming the attenuation capability of gels against solar protons.

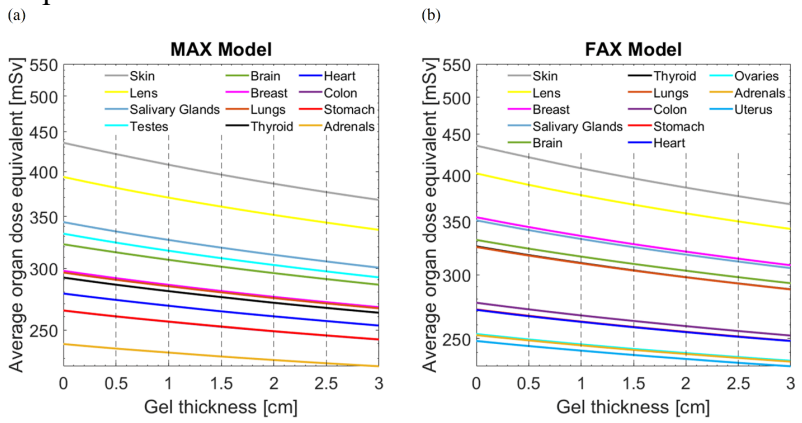


Fig. 2: Average organ dose equivalent as a function of gel thickness integrated into the spacesuit under Galactic Cosmic Radiation (GCR) exposure, for MAX (a) and FAX (b) phantoms.

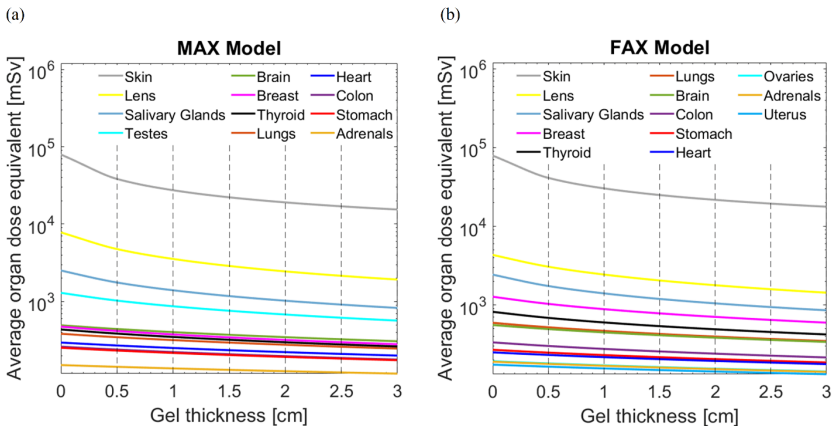


Fig. 3: Average organ dose equivalent as a function of gel thickness integrated into the spacesuit under Solar Particle Events (SPE) exposure, for MAX (a) and FAX (b) phantoms.

Conclusions

This study demonstrates that PVA/BA gels are promising materials for improving personal radiation protection in astronaut spacesuits. Experimental characterization showed that the gels have physical properties comparable to nylon, including similar density and thermal conductivity, but with much higher flexibility (Young's modulus = 12.75 MPa; strain ≈ 65 %). Numerical simulations using OLTARIS tool confirmed the gels' radiation-shielding potential when positioned between the PBG and LCVG. A 1 cm gel layer was identified as the optimal configuration, balancing protection and added mass (~ 21 %). Under GCR exposure, dose reductions were modest (≈ 4 %), while under SPE conditions, reductions reached nearly 50 % for both male and female phantoms.

Acknowledgements

This study was carried out within the Space It Up project funded by the Italian Space Agency, ASI, and the Ministry of University and Research, MUR, under contract n. 2024-5-E.0 - CUP n. I53D24000060005.

References

[1] C. Paige, D. Newman, S. J. H. Lombardo, An Integrated Innovative 3D Radiation Protection Fabric for Advanced Spacesuits and Systems, 2020 IEEE Aerospace Conference, Big Sky, MT, USA, Pages 1-11, IEEE, 2020. https://doi.org/10.1109/AERO47225.2020.9172794

[2] J. M. Waller, K. Rojdev, K. Shariff, D. A. Litteken, R. A. Hagen, A. J. Ross, Simulated Galactic Cosmic Ray and Solar Particle Event Radiation Effects on Inflatable Habitat, Composite Habitat, Space Suit and Space Hatch Cover Materials, 2020.

[3] E. Toto, L. Lambertini, S. Laurenzi, M. G. Santonicola, Recent Advances and Challenges in Polymer-Based Materials for Space Radiation Shielding, Polymers, Vol. 16, 382, 2024. https://doi.org/10.3390/polym16030382

[4] W. Zhang, Y. Feng, J. T. Althakafy, Y. Liu, H. M. Abo-Dief, M. Huang, L. Zhou, F. Su, C. Liu, C. Shen, Ultrahigh molecular weight polyethylene fiber/boron nitride composites with high neutron shielding efficiency and mechanical performance, Advanced Composites and Hybrid Materials, Vol. 5, Pages 2012-2020, 2022. https://doi.org/10.1007/s42114-022-00539-7

[5] F. Zaccardi, E. Toto, S. Rastogi, V. La Saponara, M. G. Santonicola, S. Laurenzi, Impact of proton irradiation on medium density polyethylene/carbon nanocomposites for space shielding applications, Nanomaterials, Vol. 13, Article 1288, 2023. https://doi.org/10.3390/nano13071288

[6] Y. Shang, G. Yang, F. Su, Y. Feng, Y. Ji, D. Liu, R. Yin, C. Liu, C. Shen, Multilayer polyethylene/hexagonal boron nitride composites showing high neutron shielding efficiency and thermal conductivity, Composites Communications, Vol. 19, Pages 147-153, 2020. https://doi.org/10.1016/j.coco.2020.03.007

[7] P. R. De Oliveira, A. K. Sukumaran, L. Benedetti, D. John, K. Stephens, S.-H. Chu, C. Park, A. Agarwal, Novel polyimide-hexagonal boron nitride nanocomposites for synergistic improvement in tribological and radiation shielding properties, Tribology International, Vol. 189, Article 108936, 2023. https://doi.org/10.1016/j.triboint.2023.108936

[8] V. Pavlenko, N. Cherkashina, R. Yastrebinsky, Synthesis and radiation shielding properties of polyimide/Bi_2O_3 composites, Heliyon, Vol. 5, Article e02890, 2019. https://doi.org/10.1016/j.heliyon.2019.e01703

[9] G. Baiocco, M. Giraudo, L. Bocchini, S. Barbieri, I. Locantore, E. Brussolo, D. Giacosa, L. Meucci, S. Steffenino, A. Ballario, The PERSEO Experience: A Water-Filled Garment Prototype for Personal Radiation Protection of Astronauts Successfully Tested on Board the International Space Station, Aerotecnica Missili & Spazio, Vol. 99, Pages 111-114, 2020. https://doi.org/10.1007/s42496-020-00048-0

[10] L. Lambertini, G. Coccarelli, E. Toto, M. G. Santonicola, S. Laurenzi, Poly(vinyl alcohol) gels cross-linked by boric acid for radiation protection of astronauts, Acta Astronautica, Vol. 221, Pages 142-154, 2024. https://doi.org/10.1016/j.actaastro.2024.05.020

[11] H. Mahfuz, V. Rangari, M. Hasan, S. Jeelani, W. Wright, S. Deteresa, Enhancement of strength and stiffness of Nylon 6 filaments through carbon nanotubes reinforcement, Appl. Phys. Lett. 88 (2006) 083119-083119. https://doi.org/10.1063/1.2179132

[12] D. Murphy, B. Tucker, D. Sykes, Advanced Liquid Cooling and Ventilation Garment Using Thermally Conductive Tubing, in: 49th International Conference on Environmental Systems, 2019.

[13] DuPont Performance Polymers, DuPont™ Zytel® 101L BKB080 Nylon Resin: Technical Data Sheet, E.I. du Pont de Nemours and Company, Wilmington, Delaware, USA, 2015. https://www.dupont.com/products-and-services/plastics-polymers-resins/thermoplastics.html.

[14] Information on https://nasa3d.arc.nasa.gov/detail/nmss-z2.

Materials Research Proceedings 69 (2026) 1278-1282 https://doi.org/10.21741/9781644904251-221

Conceptual Structural Design of a Pressurized Inflatable and Deployable Habitat Optimized for Lunar Surface Missions

Alfonso CAIAZZO[1,a *], Giuseppe PETRONE[1,b], Alessandro CASABURO[1,c], Sergio DE ROSA[1,d], and Francesco FRANCO[1,e]

[1]Department of Industrial Engineering, University of Naples Federico II, Naples, Italy

[a]alfonso.caiazzo@unina.it, [b]giuseppe.petrone@unina.it, [c]calessandro.casaburo@unina.it, [d]sergio.derosa@unina.it, [e]francesco.franco@unina.it

Keywords: Inflatable Structures, Deployable Structures, Structural Design, Static Analysis, Dynamic Analysis, Flexible Materials

Abstract. Inflatable and deployable structures are increasingly recognized as a promising solution for long-duration missions on the Moon and beyond. This study addresses the conceptual design and preliminary assessment of a pressurized habitat intended for lunar surface deployment. Three geometric configurations have been evaluated in terms of mass efficiency, stress distribution, and habitability. The fabric restraint shell, made of aluminized Kapton Kevlar (AKK) and sized with a safety factor of four, was combined with a carbon-fiber-reinforced floor designed to support astronaut loads and internal equipment. The cylindrical configuration proved the most suitable option due to its reduced structural mass, modularity, and ease of deployment. A finite element model was developed to investigate static pressurization and thermal loads, confirming structural adequacy with acceptable stress and displacement levels. A digital habitability analysis using anthropometric mannequins further validated the spatial configuration. Finally, a dynamic inflation analysis with LS-DYNA has been done to capture the stress-strain evolution.

Introduction

In recent years, the colonization of celestial bodies has evolved from a distant goal to a tangible objective. The Moon, as a stepping stone toward Mars, serves as a testbed for life-support technologies and infrastructure. Inflatable and deployable habitats have already proven feasible and reliable in orbit: NASA's TransHab concept, Genesis I and II, and the Bigelow Expandable Activity Module (BEAM) on the ISS [1].

Unlike orbital environments, surface habitats must withstand extreme thermal cycles (from –233°C up to +127°C on the moon), leading to thermally induced stresses. Additional challenges include radiation from galactic cosmic rays and solar flares, and the abrasive, contaminant nature of lunar regolith. The low-density atmosphere requires full pressurization, while lunar gravity (17% of Earth's) influences both structure and human physiology. This study presents the conceptual design and structural assessment of a pressurized, inflatable, and deployable lunar habitat. The design emphasizes the membrane maintaining internal pressure of the restraint layer, sized with a safety factor of four, in compliance with NASA habitability standards NASA-STD: 3000 [2] and 3001 [3].

Geometric Conceptual Design

Three continuous-curvature geometries were selected to ensure uniform stress distribution under internal pressurization, reducing local stress concentrations that may cause fatigue or collapse [4]. The analyzed configurations are: (i) hollow torus, (ii) hollow hemisphere, and (iii) hollow cylinder [1]. For the toroidal and cylindrical cases, a reference internal radius of 1.6 meters was adopted, consistent with existing designs such as HALO (Habitation and Logistics Outpost) [5] and CYGNUS [6].

Content from this work may be used under the terms of the Creative Commons Attribution 3.0 license. Any further distribution of this work must maintain attribution to the author(s) and the title of the work, journal citation and DOI. Published under license by Materials Research Forum LLC.

Materials Research Proceedings 69 (2026) 1278-1282 https://doi.org/10.21741/9781644904251-221

A MATLAB code was developed to dynamically link the internal habitable volume (V_{int}) with the geometric parameters of each configuration. The user specifies the habitable volume and the fabric thickness (t); the algorithm then computes the corresponding structural dimensions, ensuring that the required internal volume is maintained.

An analysis was conducted to optimize the floor placement for circular-section habitats such as the cylinder and the torus. The optimization cost parameter (η), shown in Eq. 1, represents a trade-off between the habitable volume and the storage capacity beneath the floor.

$$\eta = \frac{V_{stow}}{V_{int}} \times 100\ (\%). \tag{1}$$

Based on a reference internal diameter of 3.2 meters, the floor position in circular-cross-section habitat varied to maximize habitability, minimize structural clutter, and consequently reduce mass. The optimal floor height was found at approximately 21% of the internal diameter, providing a balanced configuration in terms of usable space and stowage efficiency. Defining the habitable volume as the space above the floor, the cylindrical habitat was chosen for detailed analysis among the three configurations due to its lower mass, modular design, and ease of deployment.

Stiffened Cylinder Sizing

The structural complexity of pressurized extraterrestrial inflatable habitats required resilience against a broad range of loads, primarily including pressurization, thermal, radiation loads, and micrometeoroid impact [1]. The restraint layer sizing focuses on pressurization and thermal loads. In adherence to NASA-STD-3001 [3], a pressurized lunar habitat must maintain an internal condition of 101325 Pa and 20°C and therefore be capable of sustaining a pressure differential (Δp) of 101325 Pa and a thermal differential (ΔT) of approximately 200°C with the external lunar environment. A safety factor (c) of four is applied.

The flexible shell material selected is aluminized Kapton-Kevlar (AKK), which has a yield stress (σ_y) of 3000 MPa and a Poisson's ratio (ν) of 0.36. The combined stress condition for a thin-walled shell under pressure (σ_p) and thermal (σ_T) loading is expressed as follows:

$$\frac{\Delta p \cdot r}{t} + \frac{E \cdot \alpha \cdot \Delta T}{1-\nu} \leq \frac{\sigma_y}{c} \tag{2}$$

From Eq. 2, a wall thickness of 0.8 mm is selected. The reinforced cylindrical shell has two open ends: one interfaces with a docking system connected to a main structure (rover, base, or launcher), while the opposite end can connect modularly to other habitats or terminate with an endcap. According to Niu [7], three endcap types are possible: flat, hemispherical ($\varphi = 90^{\circ}$), and semi-spherical ($\varphi < 90^{\circ}$).

The flat configuration causes stress concentrations, whereas curved geometries ensure smoother load transfer. Owing to deployability, the hemispherical endcap with tangential continuity to the cylindrical body offers the most efficient stress distribution and compact stowage. The total external restraint layer mass of the cylinder connected to the endcap is 107 kg. The floor placement analysis identified an optimal position at 21% of the habitat diameter, providing a 2.5 m width, an efficiency factor (η) of 17%, and a maximum habitable height of 2.56 m. For a two-astronaut pressurized habitat, an internal volume (V_{int}) of 50 m^3 was imposed, yielding to 7 m in length.
The floor was sized for two occupants from the 95th percentile of the ANSUR database: a 101 kg male and a 79 kg female; with an additional 1400 kg representing equipment and furnishings. The load was modeled as uniformly distributed over a 2.5 m × 7 m area. A carbon fiber/epoxy prepreg (T700/epoxy) was selected for its foldability under both equal or opposite-sense methodologies [8].

Materials Research Proceedings 69 (2026) 1278-1282 https://doi.org/10.21741/9781644904251-221

The sizing resulted in a 3.6 mm laminate of 12 plies (0.3 mm each) with stacking sequence $[0/90/0/90/0/90]_s$ and a total mass of 103 kg. Eight circular supports for membrane deployment and eight supports for the floor yielded a preliminary total habitat mass of 219 kg.

Habitability Analysis

The CAD model of the pressurized, inflatable, and deployable habitat in its fully deployed configuration was created in CATIA and subsequently imported into Siemens NX to perform a preliminary habitability assessment.

Two digital human mannequins were positioned within the habitat, both representing the 95th percentile of the ANSUR anthropometric database: a male subject weighing 101 kg and standing 187 cm tall, and a female subject weighing 79 kg and standing 174 cm tall.

The mannequins were placed in a virtual environment populated with volumetric placeholders simulating operational equipment and material usage.

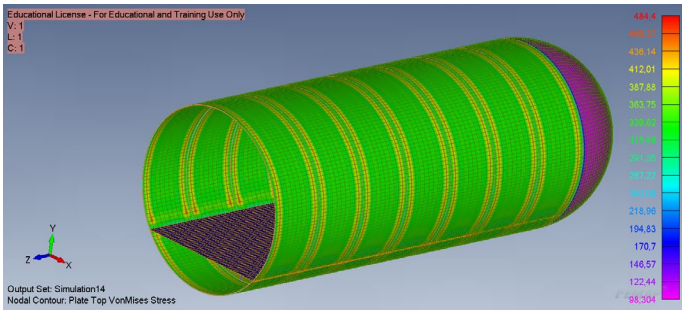


Figure 1: Isometric rendering of the fully deployed pressurized inflatable habitat, showing two digital mannequins and operational equipment placeholders.

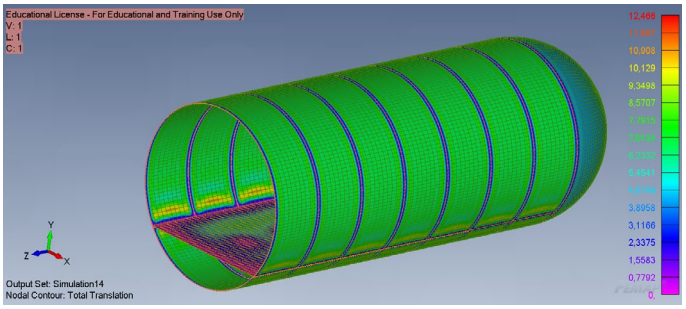
As shown in Fig. 1, the analysis indicates that the dimensions of the habitat are found to be suitable for the designated purpose, thereby confirming that the internal spatial configuration is adequate to meet the requisite habitability criteria.

Static Analysis

Based on the geometric information obtained from the conceptual design and sizing phases, a finite element model (FEM) of the habitat was developed in FEMAP. The model includes plate elements for the cylindrical membrane and the hemispherical endcap, beam elements of various sizes and shapes for the telescopic linear guides and supports, and laminated plate elements for the floor. Thermal loads of 200 °C and a pressure load of 0.101325 MPa were applied to the membrane, while a pressure load of 0.0013 MPa was applied to the floor.



(a) Plate Von Mises stress



(b) Total displacement

Figure 2: Results of the preliminary static analysis for the fully deployed pressurized inflatable habitat: (a) Von Mises stress distribution on plate elements and (b) total displacement field.

The resulting stress analysis indicates a pressure accumulation at the cylinder-endcap interface corresponding to 22.62% of the AKK yield strength (σ_y) when evaluated using elemental contour data.

For the nodal contour representation, shown in Fig. 2a, the corresponding value is 16.14%. Stress concentrations are primarily observed near the circular and linear stiffeners, while the membrane region exhibits a nearly uniform distribution with lower values on the hemispherical endcap, confirming the effectiveness of its geometry.

The maximum displacement is 12.466 mm on the flexible cylindrical membrane mainly occurring between the circular frames and near the linear stiffener and 9.345 mm on the stiffened floor. The observed stress and displacement increments are not sufficient to warrant additional stiffening, and in real configurations they are expected to be further reduced due to the non-perfectly rigid interaction between the structural frames and the membrane.

Conclusion

This study presented the conceptual design and preliminary structural and habitability assessment of a pressurized, inflatable, and deployable lunar habitat. Among the configurations analyzed, the cylindrical geometry proved most efficient in terms of mass, modularity, and stress distribution. Finite element simulations confirmed the structural adequacy of the membrane and floor under combined pressurization and thermal loads. The habitability evaluation validated the internal configuration for a two-astronaut crew. Future work will focus on dynamic simulations using LS-DYNA, experimental tensile testing of fabric materials to derive stress-strain curves to insert in numerical solvers, and experimental validation on scaled prototypes.

References

[1] Caiazzo, Alfonso, et al." Structures for Extraterrestrial Habitat: A Review". Acta Astronautica Vol. 238, pp. 471-493, 2026. ISSN: 0094-5765. https://doi.org/10.1016/j.actaastro.2025.10.029

[2] Connolly, J. H. and Arch, M., 2005, "NASA Standard 3000 Human Systems Integration Standards (HSIS) Update," Proceedings of the Human Factors and Ergonomics Society Annual Meeting, Vol. 49, SAGE Publications Sage CA: Los Angeles, CA, Paper No. 23, pp. 2018-2022. https://doi.org/10.1177/154193120504902304

[3] Whitmore, M., Boyer, J., and Holubec, K., 2012, "NASA-STD-3001, spaceflight human system standard and the human integration design handbook," Industrial and systems engineering research conference, 19-23 May 2012, Paper No. JSC-CN-25695.

[4] Naser, M. Z., Redmond, L., Chen, Q., and Rangaraju, P. "Habitats for Space Exploration: Construction Materials, Design Concepts, and Future Directions." In The Planning and

Execution of Human Missions to the Moon and Mars, Chapter 8, pp. 229-266, AIAA, 2023. https://doi.org/10.2514/5.9781624106545.0229.0266

[5] Smith, Marshall, et al." The Artemis program: An overview of NASA's activities to return humans to the moon." IEEE Aerospace Conference, 7-14 March 2020. IEEE, 2020. https://doi.org/10.1109/AERO47225.2020.9172323

[6] Davis, Chad L., and Ken Peek." Feasibility study for using Cygnus as a habitat in deep space exploration." AIAA SPACE, 13-16 September 2016, Long Beach, California. eISBN: 978-1-62410-427-5.

[7] Niu, M. C. Y. "Airframe Stress Analysis and Sizing." Adaso/Adastra Engineering Center (2011): ISBN 978-9627128083.

[8] Liu, Tian-Wei, et al." Folding behavior of thin-walled tubular deployable composite boom for space applications: Experiments and numerical simulation." Acta Astronautica, 209, (2023): 159-171. https://doi.org/10.1016/j.actaastro.2023.05.010

Materials Research Proceedings 69 (2026) 1283-1286 https://doi.org/10.21741/9781644904251-222

Non-Equilibrium Thermochemical Models for the Characterization of Titan Atmospheric Entry Under Hypersonic Conditions

Antonio NARRACCI[1,a *], Francesco BONELLI[1,b], Davide NINNI[1,c], Gianpiero COLONNA[2,d], Annarita LARICCHIUTA[2,e] and Giuseppe PASCAZIO[1,f]

[1]DMMM & CEMeC, Politecnico di Bari, Via Re David 200, Bari, 70125, Italy

[2]Istituto per la Scienza e Tecnologia dei Plasmi, Bari section, Via Amendola, 122/D, 70126 Bari, Italy

[a]a.narracci1@phd.poliba.it, [b]francesco.bonelli@poliba.it, [c]davide.ninni@poliba.it, [d]gianpiero.colonna@cnr.it, [e]annarita.laricchiuta@cnr.it, [f]giuseppe.pascazio@poliba.it

Keywords: Titan, Hypersonic Flows, Thermochemical Non-Equilibrium, Multi-Temperature, State-to-State

Abstract. This work shows the development and verification of a model for the simulation of an atmospheric entry on Titan in non-equilibrium conditions. Park's and Nelson's multi-temperature approaches are tested on a literature test case for a neutral mixture and Park's model is also verified for a charged mixture to evaluate the effects of ionization. Finally, a state-to-state model is used for further verification on the neutral mixture.

Introduction

Titan, Saturn's largest moon, has a dense atmosphere characterized by the presence of organic compounds, making it a key target for exploration. Atmospheric entry, however, remains a fundamental problem since the hypersonic entry speed, together with the extreme pressure and heat generated, may exceed material limits. To predict heating and behavior of the vehicle, the developed hypersonic non-equilibrium flow must be characterized.

An accurate model should account not only for gas dynamics but also for processes like dissociation, vibrational and electronic excitation, ionization and radiation [1] and for imbalances in translational, rotational, vibrational and electronic temperatures. For this reason, a thermochemical model is introduced, such as the multi-temperature (mT) or the state-to-state (StS) models: the first characterized by high efficiency, the second by accuracy [2]. In particular, the State-to-State model provides an accurate description of vibrational and electronic excitation by treating each internal state of the most relevant particles as a pseudo-species and formulating a continuity equation for each of them, while the multi-temperature model considers each molecule globally and represents the internal energy distribution using different characteristic temperatures, adding a vibro-electronic energy transport equation for each particle in the mixture [3, 4].

As regards the solver, the multi-GPU code developed by Politecnico di Bari in collaboration with the Istituto per la Scienza e Tecnologia dei Plasmi (ISTP) of CNR in Bari was employed [5]. The finite volume solver applies a second order Runge Kutta scheme to the system of equations, while space discretization is performed by a Steger and Warming flux vector splitting, together with a second order MUSCL reconstruction.

To verify the model and its applicability to atmospheric entry applications, simulations carried out by NASA [6] were used as test case.

Test Case

Simulations were performed on a two-dimensional geometry reproducing half of an axisymmetric, 3.75 m wide, capsule profile entering the atmosphere at an altitude of 269 km.

Content from this work may be used under the terms of the Creative Commons Attribution 3.0 license. Any further distribution of this work must maintain attribution to the author(s) and the title of the work, journal citation and DOI. Published under license by Materials Research Forum LLC.

Materials Research Proceedings 69 (2026) 1283-1286 https://doi.org/10.21741/9781644904251-222

In the case of a neutral mixture, 12 species have been considered (N, N_2, C, C_2, H, H_2, CN, NH, CH, CH_2, CH_3, CH_4), whereas 18 species (N_2^+, CN^+, C^+ N^+, H^+, e^- in addition to the neutral mixture) have been included for the ionized mixture. In both cases the freestream flow is composed of molecular nitrogen at 95% and methane at 5%. Capsule velocity and atmosphere characteristics are shown in Table 1 together with the estimated Mach number.

Table 1 Test case flow characteristics

Velocity [m/s]	Pressure [Pa]	Temperature [K]	Density [kg/m^3]	Mach
5761	6.91	152.7	1.491 x 10^{-4}	22.7

A super catalytic wall condition was imposed to replicate the configuration of the NASA test case where the gas composition on the wall is set exactly equal to the freestream mixture composition. This was done by imposing recombination of N_2 and CH_4 at wall and solving mass balance to evaluate catalysis source terms.

Results

Code verification was carried out by considering the neutral mixture for both Park's and Nelson's multi-temperature models, with the resulting profiles compared against literature data. The main difference between the two models for the neutral mixture lies in the dissociation-recombination reactions of Nitrogen: where Nelson's model considers collisions with any species in the mixture, Park's reactions only consider collisions with N_2 and N. Regarded as the most consistent with the underlying physics [6], only Park's model was used to simulate the ionized mixture. Finally, to verify the model against the state-to-state model, given the high concentration of nitrogen in the mixture, the test was carried out on a pure nitrogen mixture N_2-N to ease calculations.

Fig. 1 shows a temperature contour plot, providing a good overall agreement with the reference solution [6], especially in terms of shock standoff distance.

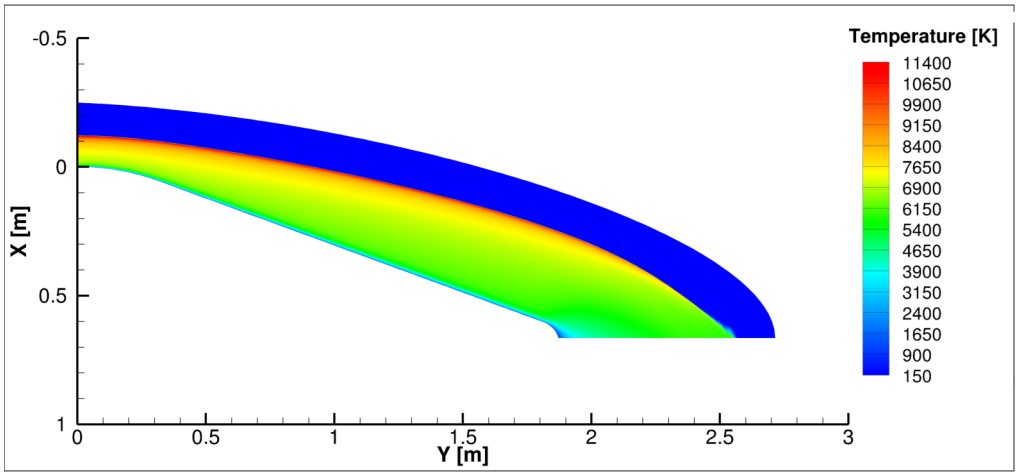


Figure 1 Temperature contour obtained using Park's model with the neutral mixture

This is confirmed by the temperature profiles on the stagnation line of Fig. 2 (left). The higher mesh resolution used in this work at the location of the shock wave allows for a better capture of the discontinuity and thus justifies the difference in heat flux between the simulated models and the reference, in Fig. 2 (right). Furthermore, the temperature relaxation zone downstream the shock is in good agreement with the reference data showing an overall goodness of the model.

Materials Research Proceedings 69 (2026) 1283-1286 https://doi.org/10.21741/9781644904251-222

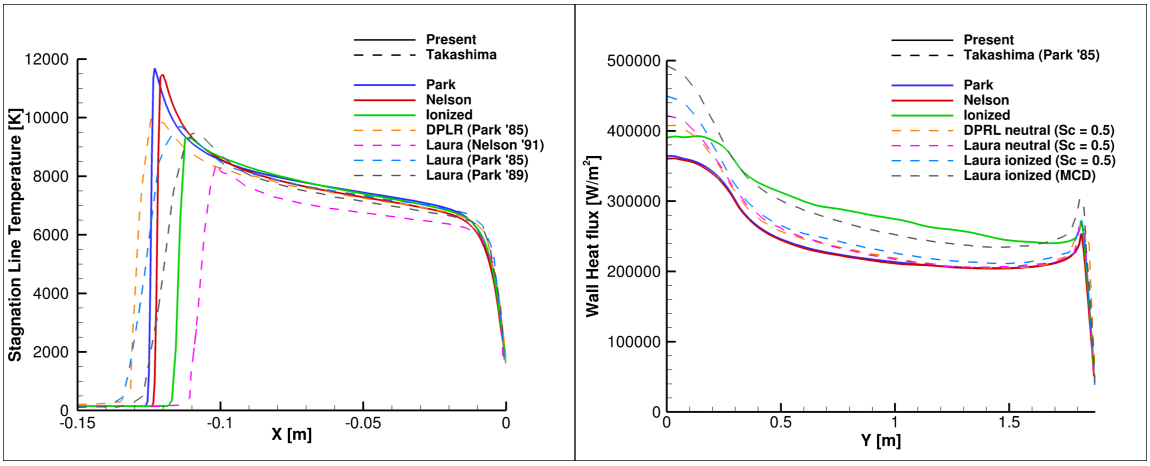


Figure 2 Comparison in terms of stagnation line temperature profile (left) and wall heat flux (right) with the reference [6]

The neutral mixture shows a higher peak temperature and a lower heat flux with respect to the ionized mixture, due to the major absorption of energy in the ionization reactions and the energy release on the wall during recombination.

Results demonstrate an overall agreement between Nelson's and Park's model, with a slight reduction in shock standoff distance, while the reference profiles show a much more significant difference. However, given the high concentration of nitrogen in the mixture, the agreement between the two models is considered consistent, since nitrogen collisions with other species have a lower statistical impact.

Fig.3 shows the comparison between results obtained with Park's model by considering both the twelve species mixture and the binary N_2-N mixture. This was mainly intended to analyze the influence of the species other than molecular and atomic nitrogen on the flow development, and to verify the feasibility of the subsequent test using the state-to-state model with the binary mixture.

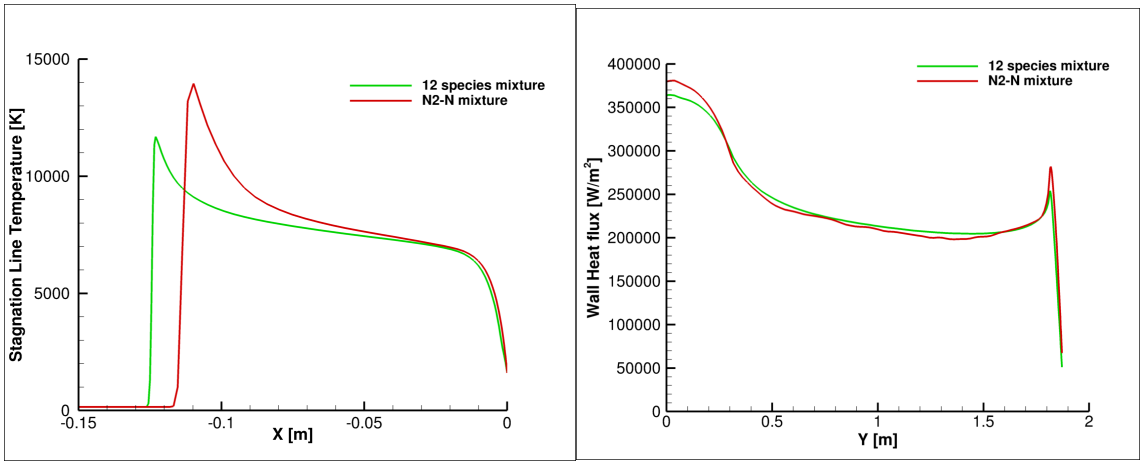


Figure 3 Comparison between the twelve species mixture and the N_2-N mixture

Fig. 4 shows the same quantities, for the binary mixture, comparing the multi-temperature and the state-to-state models, both in case of no wall catalysis. A good overall agreement is shown, although the different approach of the StS to non-equilibrium results in a small difference in terms of shock standoff distance (3%) and wall heat flux (7.5%) since the latter is strongly influenced by shock position and reactions involved.

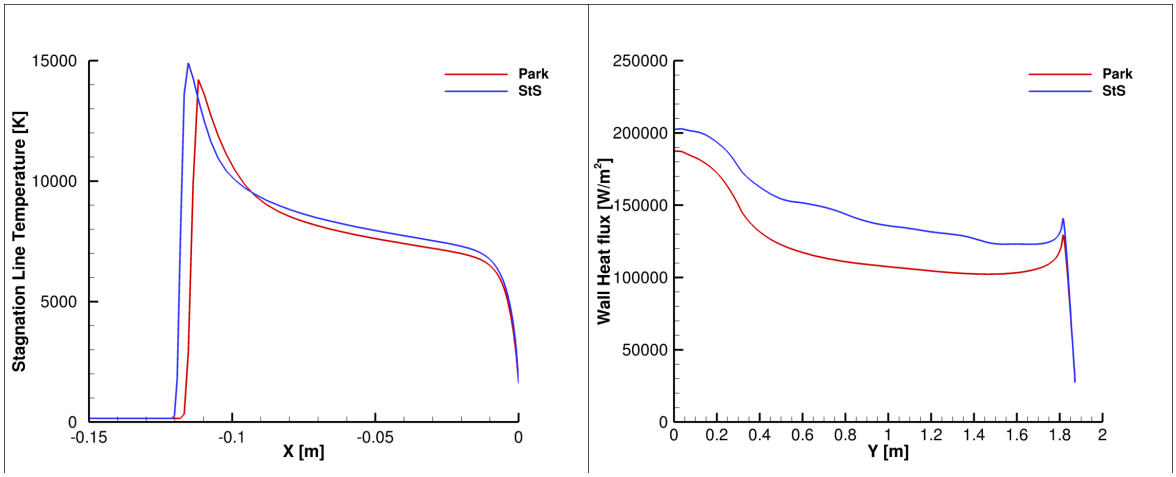


Figure 4 Comparison between Park's and the StS models using the N_2-N mixture

Conclusions

In this work, the implemented multi-temperature model was verified by simulating the atmospheric entry of a capsule into Titan's atmosphere, demonstrating its capabilities to handle realistic two-dimensional cases under complex scenarios, in hypersonic and thermochemically non-equilibrium conditions.

Ionization effects were also considered, and the implemented Park's model was further compared against the reaction rates proposed by Nelson. Finally, additional verification was performed using the results from the state-to-state model.

References

[1] J. D. Anderson, Hypersonic and High-Temperature Gas Dynamics, second edition, American Institute of Aeronautics and Astronautics, Inc., Virginia, 2006. https://doi.org/10.2514/4.861956

[2] M. Capitelli, R. Celiberto, G. Colonna, F. Esposito, Fundamentals aspects of Plasma Chemical Physics: Kinetics, Springer, NewYork, 2016. https://doi.org/10.1007/978-1-4419-8185-1

[3] G. Pascazio, D. Ninni, F. Bonelli, G. Colonna, Hypersonic flows with detailed state-to-state kinetics using a GPU cluster, in Plasma modeling: methods and applications, Second Edition, Institute of Physics Publishing, 2022, p. Chapter 10. https://doi.org/10.1088/978-0-7503-3559-1ch10

[4] F. Bonelli, D. Ninni, A. Narracci, G. Colonna, G. Pascazio, Assessment of a consistent multi-internal-temperature kinetic model for hypersonic neutral air flows using a finite volume solver, Computers and Fluids, 301, 2025, https://doi.org/10.1016/j.compfluid.2025.106796

[5] G. Colonna, F. Bonelli, G. Pascazio, Impact of fundamental molecular kinetics on macroscopic properties of high-enthalpy flows: The case of hypersonic atmospheric entry, Phys. Rev. Fluids 4, 033404, 2019. https://doi.org/10.1103/PhysRevFluids.4.033404

[6] N. Takashima, B. Hollis, E. Zoby, K. Sutton, J. Olejniczak, M. Wright, D. Prabhu, Preliminary Aerothermodynamics of Titan Aerocapture Aeroshell. 2006. https://doi.org/10.2514/6.2003-4952

Materials Research Proceedings 69 (2026) 1287-1291 https://doi.org/10.21741/9781644904251-223

Toward Vibration-Based Damage Detection: Nonlinear Modal Damping Estimation in Delaminated Structures

Shabnam KIASAT[1,a *], Ali SALEHZADEH NOBARI[2,b*], Matteo FILIPPI[1,c] and Erasmo CARRERA[4,d]

[1]Mul[2], Department of Mechanical and Aerospace Engineering, Politecnico di Torino, 10129 Torino, Italy

[2]Aeronautics Engineering Department, Imperial College London, London, United Kingdom

[a]shabnam.kiasat@polito.it, [b]ali.salehzadeh-nobari@imperial.ac.uk, [c]matteo.filippi@polito.it, [d]erasmo.carrera@polito.it

Keywords: Vibration-Based Monitoring, Modal Damping, Delamination, Structural Health Monitoring, Nonlinear Dynamics

Abstract. This study presents a nonlinear vibration-based framework for early damage identification in viscoelastic sandwich structures with interfacial delamination. Unlike conventional frequency-based indicators, the proposed approach exploits changes in modal damping, which exhibit higher sensitivity to small and localized defects. Both global damping effects arising from the viscoelastic core and local dissipation due to frictional contact at delaminated interfaces are modeled within a combined time–frequency domain analysis. Nonlinear phenomena, including superharmonic responses, are explicitly captured to improve agreement with experimentally observed behavior. The results demonstrate that pseudo-modal damping parameters provide a robust and reliable indicator for detecting early-stage interfacial damage.

Introduction

In vibration-based structural health monitoring (VHM), traditional global dynamic features such as shifts in natural frequencies are commonly used as damage indicators [1,2]. Frequency shifts usually result from localized reductions in stiffness caused by damage mechanisms such as delamination or cracking. However, these indicators exhibit limited sensitivity to small damage sizes. This reduced sensitivity depends not only on the severity of the defect but also on its location relative to the mode shape. In particular, sensitivity is significantly diminished in regions of low strain energy or near nodal points [3]. As a consequence, damage may remain undetected until it progresses to a more advanced stage, thereby reducing the reliability of frequency-based indicators. These limitations are even more pronounced in sandwich structures, where interfacial damage often induces negligible changes in natural frequencies during the early stages of degradation.

Sandwich structures typically consist of viscoelastic (VE) cores bonded between stiff composite or metallic face sheets and are widely used in aerospace engineering due to their high stiffness-to-weight ratios, excellent damping characteristics, and high flexural rigidity [4,5]. The combination of a soft, energy-dissipating core and high-modulus outer layers provides optimized performance under both dynamic and static loading conditions, making these structures particularly suitable for lightweight panels, control surfaces, and vibration-sensitive components [6]. Nevertheless, their structural performance can be severely affected by interfacial delamination, which is one of the most common damage mechanisms in such systems. Delamination alters both local and global dynamic characteristics, while nonlinear behavior arising from frictional contact within the delaminated regions further complicates the prediction and assessment of the dynamic response.

Content from this work may be used under the terms of the Creative Commons Attribution 3.0 license. Any further distribution of this work must maintain attribution to the author(s) and the title of the work, journal citation and DOI. Published under license by Materials Research Forum LLC.

Materials Research Proceedings 69 (2026) 1287-1291 https://doi.org/10.21741/9781644904251-223

In comparison with frequency shifts, modal damping has recently attracted increasing attention as a more damage-sensitive feature, particularly for the detection of early-stage defects [7, 8]. Even small delaminations or localized interfacial damage can lead to significant changes in damping behavior by modifying the mechanisms through which energy is dissipated. This makes damping a promising parameter for vibration-based condition assessment. However, the reliable estimation of modal damping remains challenging, especially in the presence of nonlinear effects. In delaminated sandwich structures, localized mechanisms such as interfacial friction introduce nonlinear phenomena that often manifest as superharmonics or amplitude-dependent responses [9]. These effects complicate the interpretation of vibration data and frequently prevent standard numerical models from accurately reproducing experimentally observed damping trends. Most conventional simulations rely on linear assumptions and therefore fail to capture the complexity of dissipation mechanisms in damaged layered systems.

This paper presents a numerical framework for modeling both global damping effects associated with the viscoelastic behavior of the core and local damping effects induced by frictional contact at delaminated interfaces. To this end, a combined time–frequency domain workflow is developed that accounts for the nonlinear behavior resulting from contact and friction. The proposed approach enables damage identification through modal parameters such as damped natural frequency and pseudo-modal damping, evaluated for the fundamental mode and its first two superharmonics.

Finite Element Model and Numerical Validation

To demonstrate the proposed approach, the sandwich structure shown in Fig. 1 was selected as the case study. The specimen consists of two elastic face sheets bonded to a viscoelastic core, forming a typical sandwich beam configuration with clamped–free boundary conditions. The geometric dimensions and mechanical properties of the beam are summarized in Table 1 [10].

Table 1: Beam Dimensions and Material Properties.

Property	Unit	Elastic Faces (Metal)	VE Core (3M ISD112)
Young's Modulus (E)	GPa	69	0.1523
Density (ρ)	kg/m³	2766	1600
Poisson's Ratio (ν)	–	0.30	0.49
Length (L)	mm	177.8	177.8
Width (b)	mm	12.7	12.7
Thickness (h)	mm	1.524	0.127

Figure 1 illustrates the schematic representation of the sandwich beam subjected to an applied sweep force, along with a detailed cross-sectional view of its layered construction. The face sheets are assumed to behave elastically, while the core exhibits viscoelastic behavior. The viscoelastic properties of the core were incorporated into the model through Prony series coefficients associated with the frequency-dependent shear modulus. A finite element model of the pristine beam was developed and validated by computing its damped natural frequencies using the numerical workflow proposed in [10]. The obtained results were then compared with available analytical solutions and previously reported numerical and experimental studies, showing good agreement and confirming the accuracy of the modeling approach.

Materials Research Proceedings 69 (2026) 1287-1291 https://doi.org/10.21741/9781644904251-223

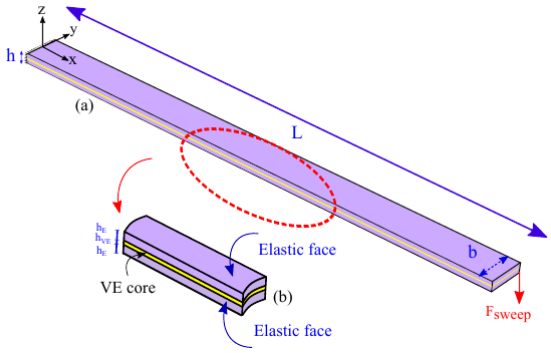


Fig. 1: (a) Schematic of the sandwich beam under the applied sweep force with clamped-free boundary conditions (BCs). (b) The cross-sectional view detailing the layered construction consists of elastic face sheets and a V E core [10]

Numerical Results

Debonding was modeled by decoupling the FE nodes in the delaminated region while maintaining their coincident spatial positions. This allows relative motion be tween the separated substructures, effectively simulating frictional contact. As shown in Fig. 2, 20% of the core-face interface is debonded (highlighted in color). By varying the lamination thickness and the damage offset from the neutral axis, the effects on the frequency response function (FRF) peaks and hysteresis loop area were investigated. A time-varying sinusoidal force covering the first five natural frequencies was applied to the structure. By varying the lamination thickness and the offset of the damaged region from the neutral axis, the effects on the frequency response function (FRF) peaks and the hysteresis loop area were systematically investigated.

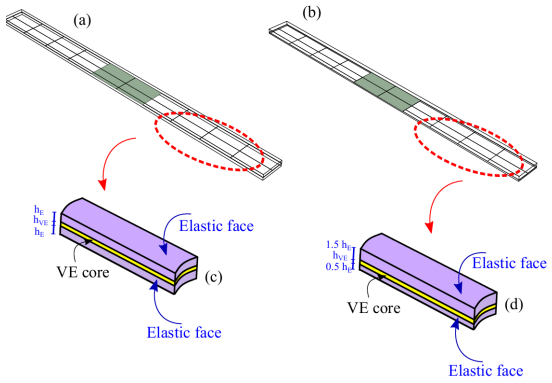


Fig. 2: Beam layup and delamination pattern for the (a,c) symmetric and (b,d) asymmetric configurations

Figure 3 presents the point FRFs of the pristine and delaminated configurations. The results indicate that symmetric delamination mainly affects the third and fourth resonant peaks, which is consistent with its location near the turning points of the corresponding mode shapes. In contrast, the asymmetric delamination, due to its off-center position, exhibits a broader influence across the resonant peaks. This observation highlights the critical role of delamination location in assessing structural integrity and dynamic behavior.

Figure 4 illustrates the force–displacement hysteresis loops for the first three superharmonics and the corresponding percentage change in loop area when the delamination is shifted away from the mid-axis. At lower frequencies, an increase in the hysteresis loop area indicates the dominance of frictional damping mechanisms. Conversely, at higher superharmonics, namely the second and third for the symmetric configuration and the third for the asymmetric configuration, the observed

Materials Research Proceedings 69 (2026) 1287-1291 https://doi.org/10.21741/9781644904251-223

reduction in loop area suggests that motion constraints induced by delamination limit the overall damping, despite the presence of frictional effects. Furthermore, off-center (asymmetric) delamination tends to sustain contact-induced damping at higher frequencies due to increased interfacial slip and more complex modal interactions. In contrast, symmetric delamination exhibits stronger motion constraints in these frequency ranges.

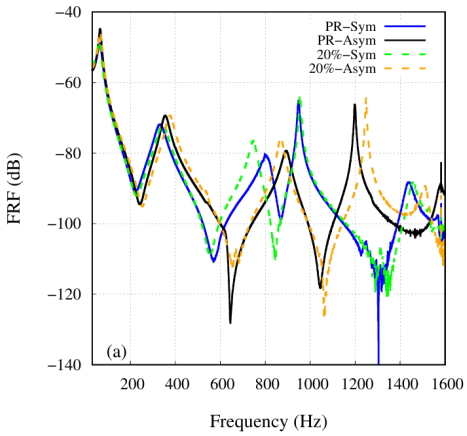


Fig. 3: Point-FRF of the structure symmetric and asymmetric layup, relative to the neutral axis for 20% delamination along the width in the interface (shown in highlighted in Fig. 2)

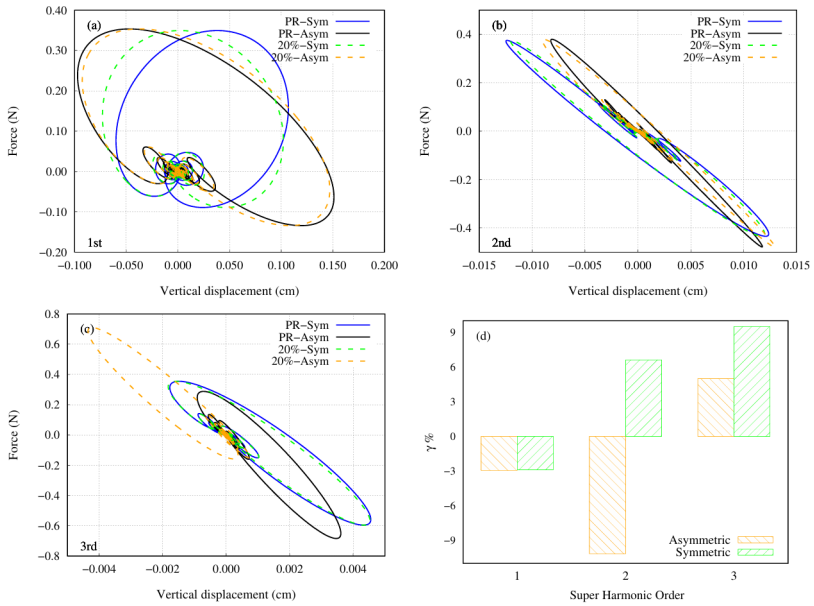


Fig. 4: Force-displacement loops at the excitation point for the first three superhar monics (a-c), comparing pristine, asymmetric, and symmetric layups. The percent age change in the hysteresis loop area (γ) for the reference case with the pristine state is shown in (d).

Overall, the offset of the delamination from the mid-axis plays a crucial role in determining the balance between frictional damping and motion-restricting mechanisms within the structure.

Conclusion

This study introduced a numerical framework for modeling modal damping induced by nonlinear mechanisms such as contact and friction, thereby overcoming the limitations of conventional linear-based approaches. The results demonstrate that these nonlinear interactions generate

distinctive dynamic features, including superharmonics, and produce clearer dissipation-related signatures in the fundamental frequency range. The findings further confirm that modal damping is significantly more sensitive to damage than traditional modal parameters, such as natural frequency. In summary, the proposed framework highlights the strong potential of modal damping as a reliable indicator for the detection of early-stage damage in delaminated structures.

References

[1] F. Dipietrangelo, F. Nicassio, G. Scarselli, SHM implementation on an RPV airplane model based on machine learning for impact detection, Aerotecnica Missili & Spazio 103(4) (2024) 363–375.

[2] A.V. De Nunzio, G. Faraco, N.I. Giannoccaro, A. Messina, Sensitivity analysis of a damage detection method through high-resolution photos on various statically deflected beams, Aerotecnica Missili & Spazio 103(2) (2024) 129–135.

[3] S. Kiasat, A.S. Nobari, M. Filippi, E. Carrera, Characterization of viscoelastic damping mechanism in a delaminated structure, Mechanical Systems and Signal Processing 219 (2024) 111600. https://doi.org/10.1016/j.ymssp.2024.111600

[4] J.R. Vinson, Sandwich structures: past, present, and future, in: Sandwich Structures 7: Advancing with Sandwich Structures and Materials, Springer, Dordrecht, 2005, pp. 3–12. https://doi.org/10.1007/1-4020-3848-8_1

[5] S. Kiasat, M. Filippi, A.S. Nobari, E. Carrera, Layer-wise dynamic analysis of a beam with global and local viscoelastic contributions using an FE/Laplace transform approach. Acta Mechanica, Vol. 233, pp. 4747–4761, 2022. https://doi.org/10.1007/s00707-022-03349-6

[6] J. Xue, H.-W. Ma, L.-Q. Chen, Vibration localization and reduction in plates via lightweight soft acoustic black hole and vibration absorbers, Acta Mechanica Sinica 41(6) (2025) 524141. https://doi.org/10.1007/s10409-024-24141-x

[7] M. Khazaee, A.S. Nobari, M.H.F. Aliabadi, Experimental investigation of delamination effects on modal damping of a CFRP laminate, in: Vibration-Based Techniques for Damage Detection and Localization in Engineering Structures, World Scientific, 2018, pp. 75–103.

[8] S. Kiasat, Novel approach to damage detection in laminated structures: modal damping as a damage indicator, Materials Research Proceedings, Vol. 42, pp. 31–37, 2024, https://doi.org/10.21741/9781644903193-8

[9] M. Müller, Clapping in delaminated sandwich-beams due to forced oscillations, Computational Mechanics 39(2) (2007) 113–126. https://doi.org/10.1007/s00466-005-0013-x

[10] S. Kiasat, A.S. Nobari, M. Filippi, Time-domain analysis of delaminated sandwich structures: Viscoelastic and frictional damping effects, Mechanics of Advanced Materials and Structures, 2025. https://doi.org/10.1080/15376494.2025.2535741

Materials Research Proceedings 69 (2026) 1292-1297 https://doi.org/10.21741/9781644904251-224

Comparative Analysis of Nonlinear Effects in Debonded Structures under Deterministic and Stochastic Excitations

Shabnam KIASAT[1,a*], Matteo FILIPPI[1,b*], Ali SALEHZADEH NOBARI[2,c], and Erasmo CARRERA[4,d]

[1]Mul[2], Department of Mechanical and Aerospace Engineering, Politecnico di Torino, 10129 Torino, Italy

[2]Aeronautics Engineering Department, Imperial College London, London, United Kingdom

[a]shabnam.kiasat@polito.it, [b]matteo.filippi@polito.it, [c]ali.salehzadeh-nobari@imperial.ac.uk, [d]erasmo.carrera@polito.it

Keywords: Debonded Structures, Nonlinear Vibration, Deterministic Excitation, Stochastic Excitation, Structural Dynamics

Abstract. Interfacial debonding in layered composite structures introduces localized nonlinearities that can significantly alter their dynamic response. This study investigates the vibrational behavior of debonded structures under sine-sweep and random excitations, with particular emphasis on contact and friction effects between separated layers. Statistical indicators such as root mean square, along with energy-based measures, are employed to characterize response variability and dissipation mechanisms. The results highlight the influence of excitation type on revealing nonlinear damage signatures and provide insights for improved modeling and structural health monitoring of bonded composite systems.

Introduction

Composite panels and adhesively bonded joints are widely used in aerospace engineering due to their high stiffness-to-weight and strength-to-weight ratios. A key challenge in such structures is interfacial debonding, which occurs when bonded layers separate because of manufacturing defects, cyclic fatigue, or impact [1]. Even small debonded regions can alter the mechanical and dynamic behavior of the structure, introducing nonlinear effects primarily through local contact and friction between the separated layers [2–4]. These effects can change stiffness, damping, and energy dissipation, and may significantly influence the overall vibratory response, complicating both analysis and damage detection.

Understanding these nonlinearities requires studying structural responses under both deterministic and stochastic excitations. Deterministic inputs, such as sine sweeps, are commonly used in modal testing to track resonance frequencies and mode shapes [5], while stochastic excitations better represent real operational environments dominated by turbulence, engine noise, and aerodynamic fluctuations [6].

In this study, we compare the dynamic response of layered structures with interfacial debonding under sine-sweep and random excitations. The analysis focuses on the role of contact and friction between separated layers, using statistical measures such as crest factor (CF) and root mean square (RMS) to characterize amplitude variations and response quality [7]. Energy parameters, including strain energy and frictional dissipation, are also examined to assess how excitation type influences energy flow and system stability.

The goal is to clarify how different excitations reveal local nonlinear effects in debonded regions and to quantify the differences in response. These insights can guide the development of predictive models and monitoring strategies for high-performance layered structures.

Content from this work may be used under the terms of the Creative Commons Attribution 3.0 license. Any further distribution of this work must maintain attribution to the author(s) and the title of the work, journal citation and DOI. Published under license by Materials Research Forum LLC.

Materials Research Proceedings 69 (2026) 1292-1297 https://doi.org/10.21741/9781644904251-224

Excitation Methods and Signal Characterization

Two types of excitations were applied to the delaminated structure: a logarithmic sine sweep and a broadband random force. Both were applied as time-dependent point loads at the tip for 2 s, sampled at 5000 Hz, ensuring 8000 discrete steps. The spectral content and RMS level of the random signal were matched to the sine sweep (0–2500 Hz), allowing a fair comparison of their effects on the nonlinear dynamic response. Sine Sweep Excitation. A logarithmic sine sweep was used to systematically excite the structure across a wide frequency range. This deterministic excitation effectively activates fundamental and harmonic modes, revealing nonlinear responses such as amplitude-dependent stiffness and damping [8]. Random Excitation. Aband-limited Gaussian random signal was generated to match the spectral and RMS properties of the sine sweep. By providing equivalent energy input, differences in structural response can be attributed to the deterministic versus stochastic nature of the excitations rather than to power or frequency content [9, 10]. Figure 1 compares the power spectral densities and integrated energy of the two excitations, showing equivalent bandwidth and energy levels, which ensure a consistent basis for evaluating nonlinear effects.

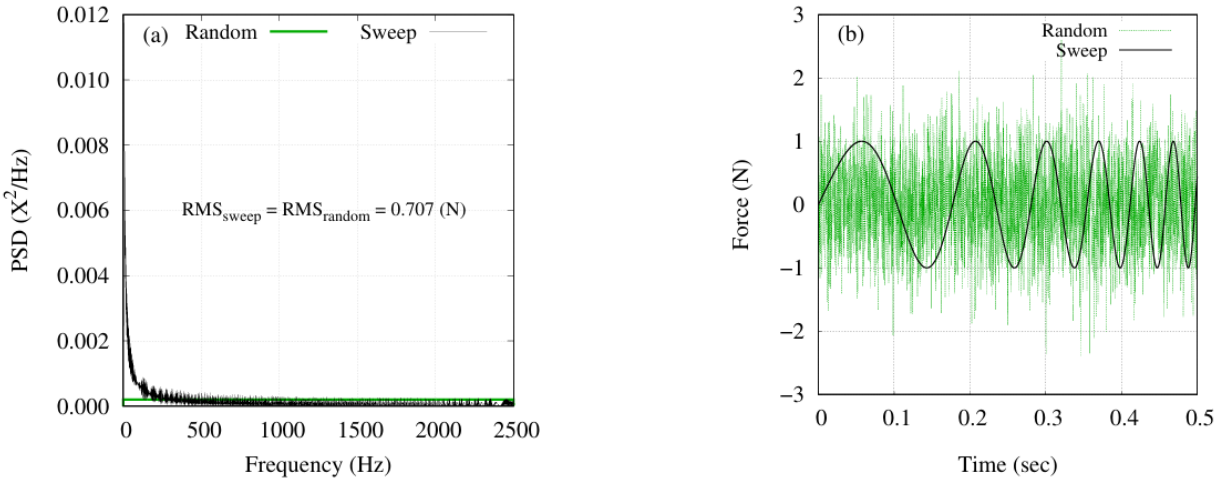


Fig. 1: (a) PSD comparison of sine-sweep and random excitations with equal RMS level. and integrated energy (b) of the sine sweep and RMS-matched random excitation signals. (b) Zoomed-in view of the two signals over 0.5 seconds

Finite Element Model and Numerical Validation

Finite Element Model and Numerical Validation In this work, a simple two-layer finite element (FE) model with clamped-free boundary conditions was developed to study the behavior of laminated beams undergoing debonding. To capture the detailed structural response, the beam was modeled as a three-dimensional solid and discretized using linear hexahedral (C3D8) elements, with small deformation assumed, as illustrated in Fig. 2.

Materials Research Proceedings 69 (2026) 1292-1297 https://doi.org/10.21741/9781644904251-224

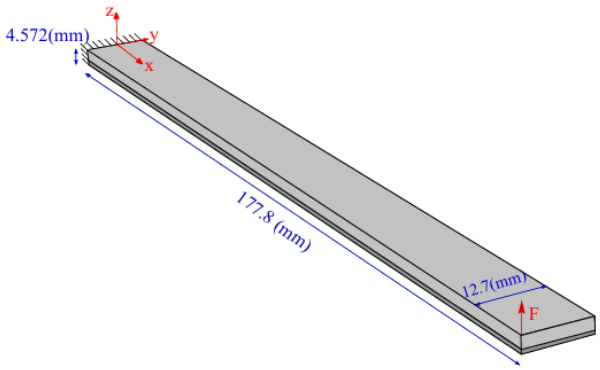


Fig. 2: Two-layered beam, boundary conditions (BCs) and excitation point [11].

The material and geometric parameters follow those used in [4], from which the time–frequency algorithm and overall computational workflow were also adapted. Interfacial debonding was simulated by separating coincident nodes in the debonded area, allowing for relative motion and frictional interaction between the layers. Having established the modeling approach, we now present results for the pristine structure. Figure 3 compares FRF1 and FRF2 for the pristine structure under sweep and random excitations. The FRF peaks in Fig. 3 coincide with the natural frequencies obtained from the FE modal analysis. This coincidence confirms the validity of both the numerical model and the solution workflow described in the authors' prior research [4].

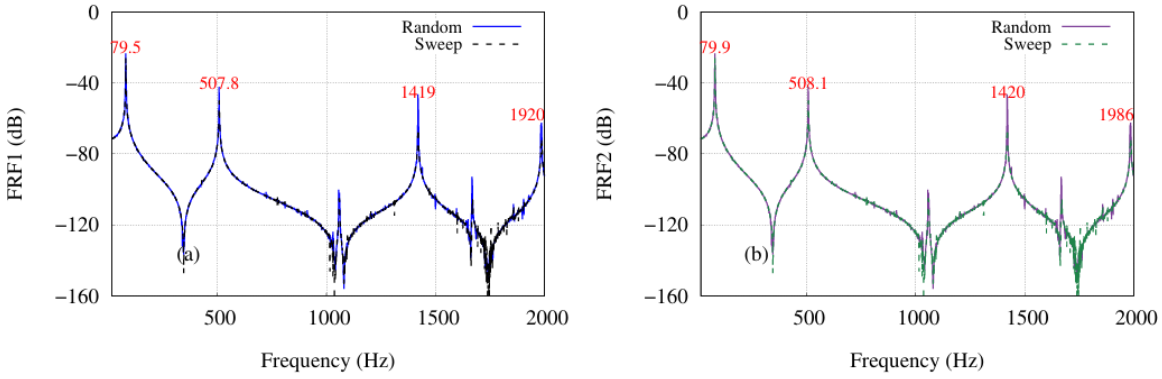


Fig. 3: Point FRF1 and FRF2 of the pristine structure under random and sine-sweep excitations [11].

Figure 4 shows the amplitude spectrum of the vertical displacement (a) and the relative frictional slip (b) of a node located at the center of the damaged region. To assess the frictional nonlinearity [12] at the delaminated interface, one-period friction–slip loops were extracted at the instant of maximum friction for the fundamental frequency and its superharmonics. These loops were consistently extracted at the same instant of maximum friction, enabling a direct comparison between random and sweep excitations. The resulting loops are shown in Fig. 5.

Materials Research Proceedings 69 (2026) 1292-1297 https://doi.org/10.21741/9781644904251-224

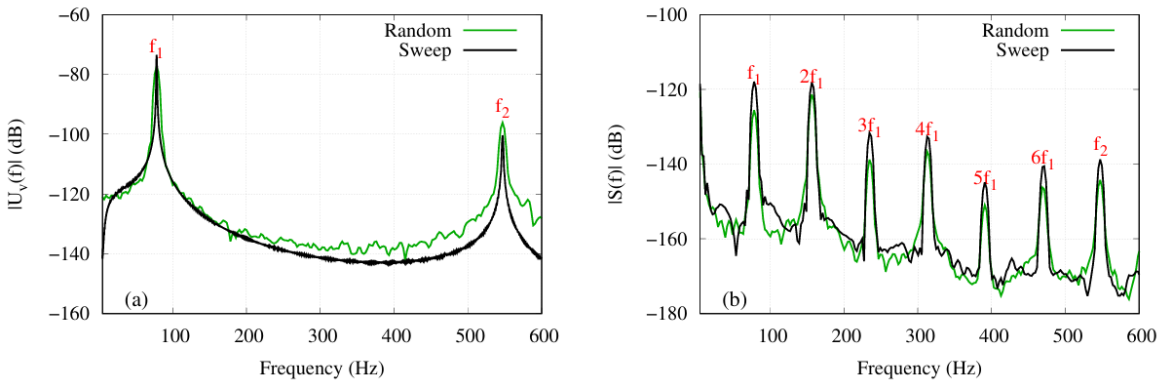


Fig. 4: amplitude spectrum of the vertical displacement (a) and the relative frictional slip (b) of a node located at the center of the damaged region. To assess the frictional nonlinearity at the delaminated interface.

At the fundamental frequency, the loops obtained under both excitation types are almost identical. This indicates that the system behaves nearly linearly and that only a small amount of microslip occurs at the interface. When moving to the first superharmonic ($2f_1$), the slip amplitude becomes noticeably larger; however, the loops corresponding to random and sweep excitations still overlap closely. This suggests that the interface has already entered a saturation-like state in which friction is fully engaged, rendering the response insensitive to how the input energy is distributed across frequencies, even though both excitations have the same RMS level.

Conclusion

This study aims to compare the ability of stochastic and deterministic excitation signals to reveal local nonlinearity effects due to damage. The results demonstrate that even when random and deterministic excitations have the same RMS energy, their responses begin to differ once higher harmonics are examined. At these harmonics, the broadband nature of the random input makes it more effective at exposing localized frictional and slip-related nonlinearities than a sweep signal. When the slip becomes large, however, the difference between the two excitations diminishes, meaning the response is governed mainly by the interface properties themselves. Overall, the way the two excitation types diverge and converge across harmonics provides a clear indicator of damage-related nonlinearities and highlights why excitation choice matters for detecting and characterizing delaminated interfaces.

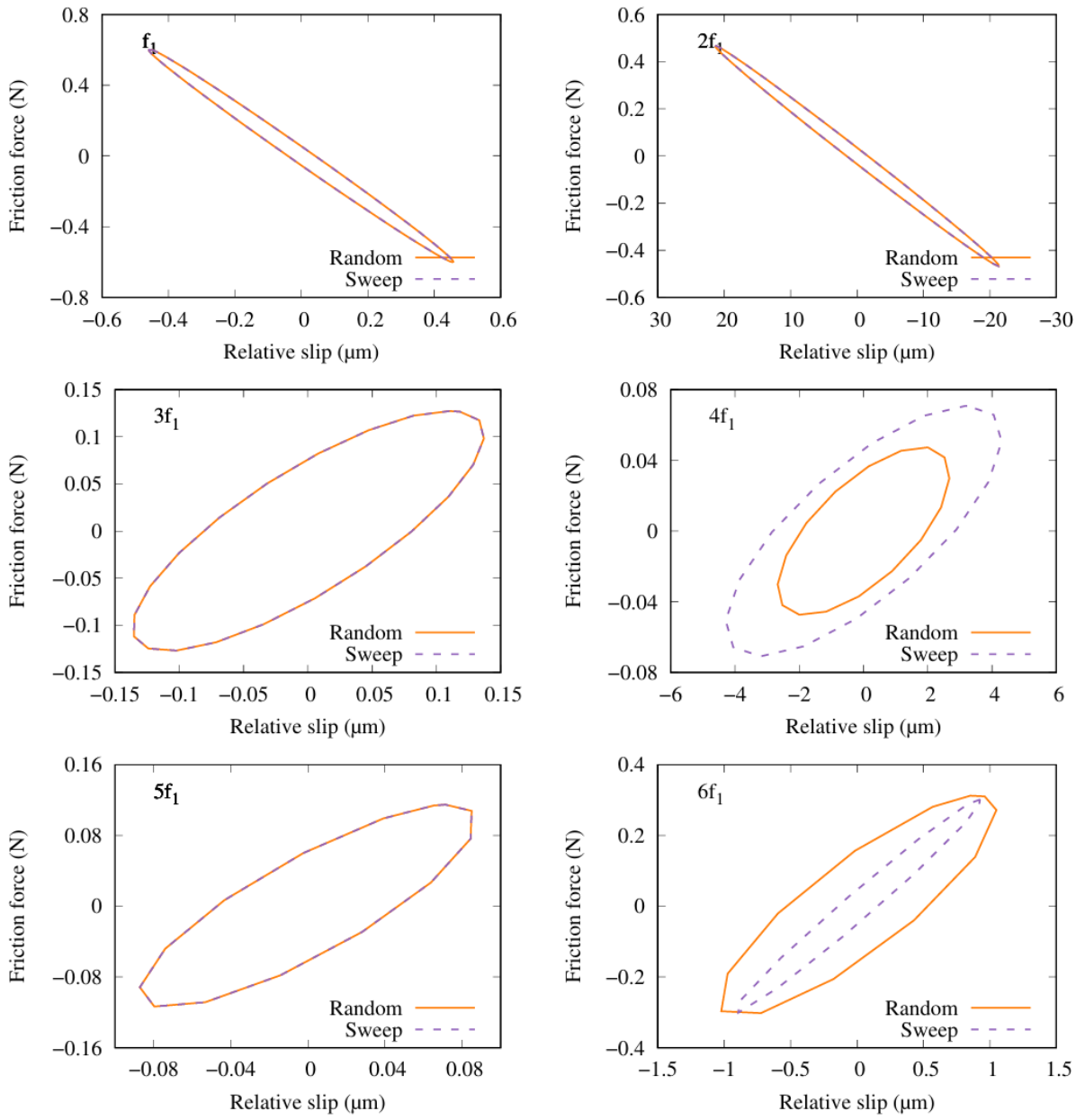


Fig. 5: One-period max friction–slip loops for the fundamental frequency and its harmonics.

References

[1] M. Lo Cascio, A. Milazzo, Free vibrations of composite cylindrical panels with cutouts of general shape, Aerotecnica Missili & Spazio (2025). https://doi.org/10.1007/s42496-025-00266-4

[2] R. Castaldo, A. Russo, Skin-stringer debonding growth in composite structures, in: Dynamic Response and Failure of Composite Materials – DRAF 2024: Perspectives on Innovative Manufacturing Technologies for Dynamic Response Improvement, Springer Nature, 2025, p. 39. https://doi.org/10.1007/978-3-031-81284-2

[3] S. Kiasat, A.S. Nobari, M. Filippi, E. Carrera, Characterization of viscoelastic damping mechanism in a delaminated structure, Mechanical Systems and Signal Processing 219 (2024) 111600. https://doi.org/10.1016/j.ymssp.2024.111600

[4] S. Kiasat, A.S. Nobari, M. Filippi, Time-domain analysis of delaminated sandwich structures: Viscoelastic and frictional damping effects, Mechanics of Advanced Materials and Structures (2025). https://doi.org/10.1080/15376494.2025.2535741

[5] [6] PCB Piezotronics, The Fundamentals of Modal Testing, Application Note 243-3, PCB Group Inc., Depew, NY, USA, 2002.

[6] J.B. Roberts, P.D. Spanos, Stochastic averaging: An approximate method of solving random vibration problems, International Journal of Non-Linear Mechanics 21(2) (1986) 111–134. https://doi.org/10.1016/0020-7462(86)90025-9

[7] A.V. Oppenheim, R.W. Schafer, Discrete-Time Signal Processing, 3rd ed., Prentice Hall, 2009.

[8] T. Dossogne, L. Masset, B. Peeters, J.P. Noël, Nonlinear dynamic model upgrading and updating using sine-sweep vibration data, Proceedings of the Royal Society A 475(2229) (2019) 20190166. https://doi.org/10.1098/rspa.2019.0166

[9] T. Irvine, Sine sweep testing, in: enDAQ Technical Reference Series, enDAQ Inc., Woburn, MA, 2023.

[10] A.U. Mange, J. Zhao, Sine sweep in high frequency range, in: Sentek Dynamics Technical Articles, Sentek Dynamics Inc., Irvine, CA, USA, 2021.

[11] S. Kiasat, A.S. Nobari, M. Filippi, E. Carrera, A study of frictional contact effects on modal dissipation characteristics in a debonded structure, under review (2026).

[12] K. Worden, Nonlinearity in Structural Dynamics: Detection, Identification and Modelling, CRC Press, Boca Raton, 2001.

Materials Research Proceedings 69 (2026) 1298-1303 https://doi.org/10.21741/9781644904251-225

Preliminary Fatigue Life Prediction of Composite Wing under Gust Spectrum Loads Using a CUF-Based Approach

Elisa TORTORELLI[1,a *], Marianna VALENTE[1,b], Giuseppe PALAIA[1,c] and Erasmo CARRERA[1,d]

[1]MUL2 Lab, Department of Mechanical and Aerospace Engineering, Corso Duca degli Abruzzi 24, 10129, Torino, Italy

[a]elisa.tortorelli@polito.it, [b]marianna.valente@polito.it, [c]giuseppe.palaia@polito.it, [d]erasmo.carrera@polito.it

Keywords: Fatigue Life, Composite Structures, CUF, Gust

Abstract. This work presents a framework for predicting the fatigue life of a composite aircraft wing under von Kármán gust spectrum loads. The approach integrates the Carrera Unified Formulation (CUF) for high-fidelity structural modeling with Dirlik's frequency-domain method for fatigue estimation. The influence of turbulence intensity and scale on fatigue life is examined, demonstrating that the proposed CUF-based method offers an accurate and computationally efficient tool for early-stage design of composite aerospace structures.

Introduction

Fatigue failure remains a major concern in aerospace structures due to the complex and stochastic nature of in-flight loading [1]. Aircraft wings are continuously subjected to random aerodynamic excitations from turbulence and gusts, leading to variable stress histories and cumulative damage. With the increasing use of lightweight composite materials, accurate and efficient fatigue life prediction methods are becoming essential.

Atmospheric turbulence, influenced by climate variability, can alter its intensity and spatial characteristics [2], affecting the fatigue load spectra experienced during flight. Hence, fatigue models must account for a broad range of stochastic gust environments.

Traditional time-domain fatigue analyses, though accurate, are computationally demanding for broadband random loads [3]. Frequency-domain methods, such as Dirlik's approach [4], offer a more efficient alternative by relating fatigue damage directly to the power spectral density (PSD) of the load.

In this study, a CUF-based framework [5] is proposed to predict the fatigue life of a composite aircraft wing subjected to von Kármán gust spectrum loads. The methodology includes: (i) definition of the case study and loading condition, (ii) structural modeling via CUF, (iii) evaluation of the PSD of the most stressed region following [6], and (iv) application of Dirlik's method for fatigue life estimation.

Structural theories: Carrera Unified Formulation

The one-dimensional (1D) model employed in this study is formulated within the Carrera Unified Formulation (CUF) framework. The three-dimensional displacement field of a solid plate can be represented as a general expansion of the generalized displacements, expressed as the product of a one-dimensional shape function, $N_i(y)$, and a two-dimensional expansion function, $F_\tau(x,z)$.

$$\mathbf{u}(x,y,z) = F_\tau(x,z) N_i(y) \mathbf{u_{\tau i}} \qquad \tau = 1,\ldots,M \qquad i=1,\ldots, p \qquad (1)$$

where $F_\tau(x,z)$ is the expansion function modelling the displacement field over the cross section, and its order depends on the parameter M. The vector $\mathbf{u_{\tau i}}$ is the nodal displacement unknown vector, and p is the number of nodes of each element. The results of this work are obtained using

Content from this work may be used under the terms of the Creative Commons Attribution 3.0 license. Any further distribution of this work must maintain attribution to the author(s) and the title of the work, journal citation and DOI. Published under license by Materials Research Forum LLC.

Materials Research Proceedings 69 (2026) 1298-1303 https://doi.org/10.21741/9781644904251-225

both Lagrange (LE) and Taylor (TE) expansion allowing different levels of kinematic refinement to be achieved according to the desired balance between model accuracy and computational efficiency.

Methodology

The proposed methodology for fatigue life estimation is organized in two main stages: (i) load assessment, where the aerodynamic load spectrum induced by turbulent wind is determined, and (ii) fatigue estimation, where the structural stress response and the resulting fatigue life are evaluated. The full workflow is shown in Fig. 1.

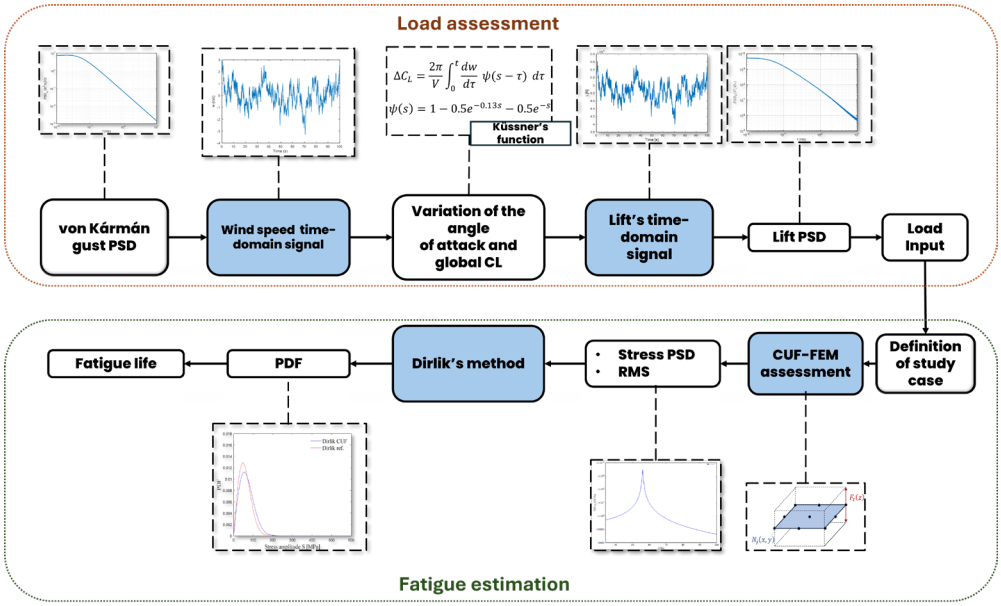


Figure 1. Methodological framework for load assessment and fatigue life estimation.

The gust PSD is defined according to the von Kármán turbulence model, which depends on two key parameters: σ, the root mean square of the gust velocity representing the intensity and L, the turbulence scale length, representing the characteristic size of the gust. The von Kármán spectrum is expressed as:

$$PSD_{vk}(f)=\frac{\sigma^2 L}{\pi V}\frac{1+\frac{8}{3}\left(1.339\frac{2\pi L}{V}f\right)^2}{\left[1+\left(1.339\frac{2\pi L}{V}f\right)^2\right]^{\frac{11}{6}}} \tag{2}$$

Once the gust PSD is defined, a time-domain gust velocity signal can be obtained by applying the inverse Fourier transform. To evaluate the unsteady aerodynamic response of the wing to this gust, Küssner's model is employed [7]. Specifically, it describes the time-dependent lift response of a two-dimensional airfoil to a vertical gust of arbitrary shape. The corresponding expression for the variation of the lift coefficient is given by:

$$\Delta c_L=\frac{2\pi}{V}\int_0^s \frac{dv_g}{d\tau}\psi(s-\tau)\ d \tag{3}$$

Materials Research Proceedings 69 (2026) 1298-1303 https://doi.org/10.21741/9781644904251-225

where V is the undisturbed free-stream velocity, v_g is the vertical component of the gust velocity, $\psi(s-\tau)$is the Küssner function, representing the aerodynamic lag response. s is the reduced time, defined as $s = \frac{Vt}{c}$ with t being the physical time and c the airfoil chord length. The derivative $\frac{dv_g}{d\tau}$ represents the rate of change of the gust velocity, which drives the unsteady lift response, while $\psi(s-\tau)$ acts as a weighting function describing how past gust inputs influence the instantaneous lift through aerodynamic memory effects. The Küssner function is typically approximated using the expression:

$$\psi(s)=-0.5e^{-0.13s}-0.5e^{-s} \quad (4)$$

By applying this formulation, it is possible to compute the time history of the lift coefficient variation induced by the gust and, consequently, to derive the corresponding lift PSD. It is worth noting that Eq. 3 is valid for the single airfoil, so to derive the lift coefficient variation of the entire wing, the geometrical (e.g. aspect ratio) and aerodynamic parameter (e.g. Oswald factor) of the wing has to be known in advance. In this case, we considered that same variation of the lift coefficient for both airfoil and wing, aware that a reduction factor should be considered.

The structural response of the component to the aerodynamic loading is evaluated using a CUF–FEM model. The lift load obtained in the first step is applied to the structural model to compute the dynamic stress response. The power spectral density (PSD) function of the stress $\boldsymbol{G}_{\sigma_j}(f)$ is computed by using lift input PSD function $\boldsymbol{G}_{\boldsymbol{F}}(f)$ and the system transfer function $\boldsymbol{H}(f)$:

$$\mathbf{G}_{\boldsymbol{\sigma_j}}(f)=\overline{\mathbf{H}_{\boldsymbol{\sigma_j}}}(f)\mathbf{G}_{\mathbf{F}}(f)\mathbf{H}^{\mathbf{T}}_{\boldsymbol{\sigma_j}}(f) \quad j=1,\ldots,6 \quad (5)$$

where$\overline{\boldsymbol{H}_{\sigma_j}}(f)$ and $\boldsymbol{H}^{\boldsymbol{T}}_{\sigma_j}(f)$ are the complex conjugate and the transpose of this function. By using the Tsai-Hill criterion is used to provide a satisfactory description of the relationship between multiaxial stresses and to compute $G_{\sigma_{eq}}(\omega)$, as described in [8].

The next step involves the use of Dirlik's method, which provides an analytical estimate of the probability density function (PDF) p(S) of stress range amplitudes directly from the stress PSD:

$$p(S)=\frac{1}{\sqrt{m_0}}\left[\frac{B_1}{Q}e^{-Z}+\frac{B_2 Z}{T^2}e^{-\frac{Z^2}{2T^2}}+B_3 Z e^{-Z^2}\right] \quad (6)$$

where $m_i=\int_0^\infty f^i G_\sigma(f)\,df$ are the spectral moments, as described in [9]. Finally, the stress range PDF is combined with the material S–N (Wöhler) curve to evaluate the fatigue life T:

$$T=\frac{1}{\nu\int_G^\infty \frac{p(S)}{N(S)}\,dS} \quad (7)$$

where $\nu=\frac{1}{2\pi}\sqrt{\frac{m_2}{m_0}}$ is the number of the stress cycles in a unit of time and N(S) is the S-N curve of material.

Results

Fatigue life analysis is performed on a clamped-free composite box beam structure that approximates a wing model of the Pilatus PC-12 aircraft (8 × 0.80 × 0.13 m, thickness of 0.01016

Materials Research Proceedings 69 (2026) 1298-1303 https://doi.org/10.21741/9781644904251-225

m), as illustrated in Fig. 2. The material properties are derived from [6], in which a unidirectional (0°) composite is under consideration.

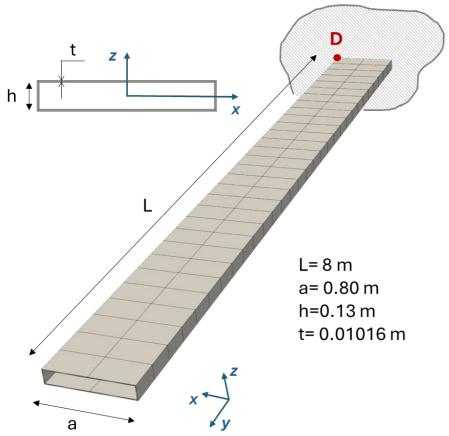
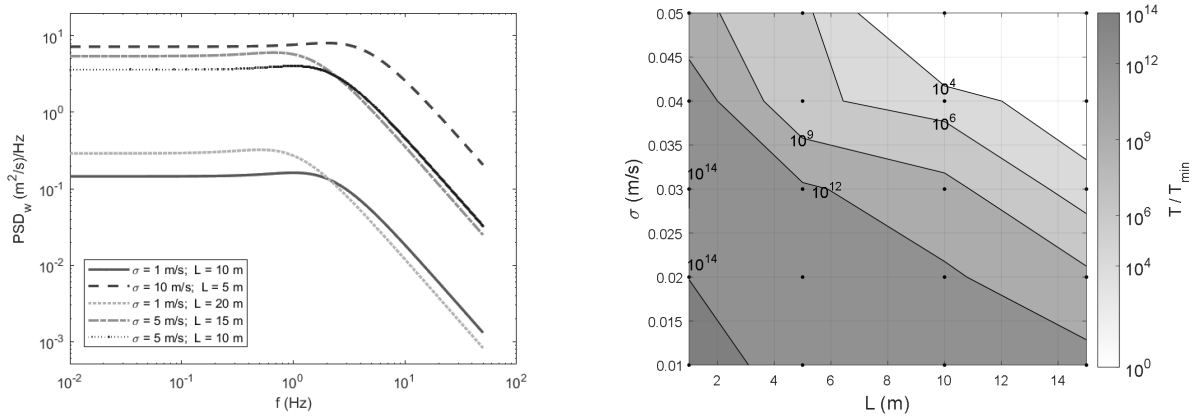


Figure 2. Geometry and mesh of box beam.

Firstly, a modal analysis identified the TE7 expansion as the most suitable CUF model, ensuring good agreement with FEMAP/NX results, as in Table 1. Along the longitudinal direction, 30 four-node beam elements are employed. Across the cross-section, the displacement field is expanded using TE1, TE3, TE6, TE7, TE8, and 12-LE9 functions. In Fig. 3a, the von Kármán gust PSDs are shown as function of turbulence intensity σ and the integral scale length L. These represent the load inputs employed to obtained the fatigue response depicted in Fig. 3b, where the iso-curves of the normalized fatigue life T/T_{min} as function of the von Kármán turbulence parameters σ and L are plotted: lighter shades denote longer life, darker shades shorter life. The contour map shows that the normalized fatigue life T/T_{min} is primarily governed by the turbulence intensity σ, with higher leading to a drastic reduction in life over several orders of magnitude. The influence of the integral scale length L is weaker and non-monotonic: for low turbulence levels, the longest lives are obtained for small scales ($L < 4$ m), while increasing L beyond this range results in a progressive decrease of T/T_{min}.

Table 1. First five natural frequencies for the composite box beam with different expansion functions for CUF and comparison with 2D FEMAP/NX model

Model	f_1 (Hz)	f_2 (Hz)	f_3 (Hz)	f_4 (Hz)	f_5 (Hz)
CUF 12-LE9	5.6	16.4	22.3	24.7	31.4
CUF TE1	6.2	22.9	36.7	41.9	91.4
CUF TE3	5.9	22.3	22.1	28.4	63.2
CUF TE6	5.6	20.2	22.3	24.9	52.1
CUF TE7	5.5	18.6	22.3	23.8	41.6
CUF TE8	5.5	18.6	22.3	23.2	40.7
FEMAP/NX	5.4	19.1	22.3	22.5	47.7



(a) Gust PSD varying parameters (b) Fatigue life varying gust parameters

Figure 3. Effect of the von Kármán gust parameters on a) gust PSD and b)the iso-curves in logarithmic scale of the normalized fatigue life T/T_{min}.

Conclusions

The CUF-based framework accurately predicts the fatigue life of composite wings under von Kármán gust loads. Results show that turbulence intensity strongly affects fatigue life, while the scale length has a secondary, non-monotonic influence. As future developments, the proposed approach will be refined and extended to improve its applicability and robustness for early-stage fatigue assessment of composite aerospace components.

Acknowledgements

This work was partially financed by the European Union- NextGenerationEU (National Sustainable Mobility Center CN00000023, Italian Ministry of University and Research Decree n. 1033- 17/06/2022, Spoke 11- Innovative Materials {\&} Lightweighting). The opinions expressed are those of the authors only and should not be considered as representative of the European Union or the European Commission's official position. Neither the European Union nor the European Commission can be held responsible for them.

References

[1] P. D. Williams, Increased light, moderate, and severe clear-air turbulence in response to climate change, Advances in Atmospheric Sciences, 34 (2017) 576–586. https://doi.org/10.1007/s00376-017-6268-2

[2] M. Muñiz-Calvente, A. Álvarez-Vázquez, F. Pelayo, M. Aenlle, N. García-Fernández, and M. J. Lamela-Rey, A comparative review of time- and frequency-domain methods for fatigue damage assessment, International Journal of Fatigue, 163 (2022) 107069. https://doi.org/10.1016/j.ijfatigue.2022.107069

[3] A. Halfpenny, A Frequency Domain Approach for Fatigue Life Estimation from Finite Element Analysis, Key Engineering Materials, 167–168 (1999) 401–410. https://doi.org/10.4028/www.scientific.net/KEM.167-168.401

[4] E. Carrera, M. Cinefra, M. Petrolo, and E. Zappino, Finite element analysis of structures through unified formulation, John Wiley & Sons, 2014.

[5] D. Y. Gao, W. X. Yao, W. D. Wen, and J. Huang, Equivalent Spectral Method to Estimate the Fatigue Life of Composite Laminates Under Random Vibration Loadings, Mechanics of Composite Materials, 57 (2021) 101–114. https://doi.org/10.1007/s11029-021-09937-2

[6] S. Zhou, Y. Sun, and L. Guo, Random fatigue life prediction of carbon fibre-reinforced composite laminate based on hybrid time-frequency domain method, Advanced Composite Materials, 26 (2016) 181–195. https://doi.org/10.1080/09243046.2016.1158935

[7] T. Dirlik and D. Benasciutti, Dirlik and Tovo-Benasciutti Spectral Methods in Vibration Fatigue: A Review with a Historical Perspective, Metals, 11 (2021) 1333. https://doi.org/10.3390/met11091333

[8] G. Sedky, A. Gementzopoulos, I. Andreu-Angulo, F. D. Lagor, and A. R. Jones, Physics of gust response mitigation in open-loop pitching manoeuvres, Journal of Fluid Mechanics, 944 (2022). https://doi.org/10.1017/jfm.2022.509

[9] G. Di Giorgio, Safety and Accidents Involving Aircraft Manufactured from Polymer Composite Materials: A Review, Aerotecnica Missili & Spazio, 102 (2023) 337–353. https://doi.org/10.1007/s42496-023-00170-9

Materials Research Proceedings 69 (2026) 1304-1309 https://doi.org/10.21741/9781644904251-226

Novel Curvilinear 2|3D Unified Finite Element Formulations for the Analysis of Complex Shell Structures

Piero CHIAIA[1,a *], Maria CINEFRA[2,b] and Erasmo CARRERA[3,c]

[1]Department of Mechanical and Aerospace Engineering, Polytechnic of Turin, Corso Duca degli Abruzzi 24, 10129 Torino, Italy

[2]Department of Mechanics, Mathematics and Management, Polytechnic of Bari, Via Edoardo Orabona 4, 70126 Bari, Italy

[a]piero.chiaia@polito.it, [b]maria.cinefra@poliba.it, [c]erasmo.carrera@polito.it

Keywords: Curvilinear Models, Shell Models, Variable Thickness, Variable Curvature

Abstract. In this paper, a detailed locking analysis of novel curvilinear finite element models for the analysis of shells is proposed. In the introduced methodology, novel higher-order shell models are proposed in a non-orthogonal reference frame, recovering the classical Cartesian description via a consistent transformation law. The shell models are defined within the well-established Carrera Unified Formulation (CUF) framework, by which Lagrange-based theory of structures are merged with classical finite element interpolation of the reference mid-surface, obtaining novel shell elements with enhanced three-dimensional geometrical modeling capabilities. By exploiting the computational efficiency of 2D models, these novel 2|3D elements are now being adopted in locking investigations to assess the accuracy and capabilities of the proposed approach when complex structural problems are addressed. The methodology is validated by analyzing classical numerical benchmarks and patch tests proposed in the literature.

Introduction

Modern aeronautical structures, increasingly complex due to performance, weight, and material innovations, demand advanced numerical modeling techniques [1] since numerical simulations have become essential in aerospace structural analysis [2]. Generally, conventional finite element formulations are used to model thick, curved, and variable-thickness components typical of aircraft structures [3]. To overcome the limitations of classical approaches, such as the limited superimposed theory of structures or hexahedral models' aspect-ratio constraints, novel shell models incorporating geometric variation and complex boundary conditions are being developed to improve accuracy and efficiency in modeling components [4]. This work presents a novel class of 2|3D fully curvilinear shell finite elements derived within the framework of Carrera Unified Formulation (CUF) [5], under the Node-Dependent Kinematics (NDK) approach [6]. The proposed framework integrates the three-dimensional shell description into the element formulation within a rigorous differential-geometry framework, thereby generalizing the accurate modeling of variable geometrical features while mitigating numerical locking through higher-order kinematic descriptions [7]. Under this approach, each reference mid-surface node can adopt its own through-the-thickness kinematics description, accounting for local higher-order refinements, in a resulting pure displacement-based numerical approach. The use of the Fundamental Nuclei (FN), the key feature of the CUF formalism, allows for the definition of the governing equations in curvilinear coordinates, exploiting basic elementary units, invariants of the reference mid-surface finite element modeling, and the theory of structural approximation adopted [8]. The curvilinear 2|3D elements, under an isoparametric approach, can represent arbitrary 3D geometries without any superimposed assumption of the geometry. The capabilities of the present modeling strategy have recently been assessed in [8] and are now being extended to comprehensive

Content from this work may be used under the terms of the Creative Commons Attribution 3.0 license. Any further distribution of this work must maintain attribution to the author(s) and the title of the work, journal citation and DOI. Published under license by Materials Research Forum LLC.

Materials Research Proceedings 69 (2026) 1304-1309 https://doi.org/10.21741/9781644904251-226

convergence and patch test analyses to assess the robustness of the present methodology and the effective mitigation of locking phenomena. This work proposes validation by analyzing classical benchmark problems in locking investigations for shell models [9]. Overall, the proposed formulation significantly advances FE modeling for aerospace applications, offering a powerful and efficient tool for the design and optimization of high-performance structural components.

Curvilinear 2|3 shell models

To address these challenges, novel non-conventional finite elements have recently been developed based on purely displacement-driven formulations [10], which can effectively handle complex geometries while preserving the accuracy and computational efficiency typical of classical 2D models [11]. This advancement allows complex shell configurations to be represented accurately within a unified three-dimensional higher-order framework. Moreover, the proposed modeling strategy also accounts for the use of different polynomial orders of approximation along different directions, thereby enhancing accuracy without sacrificing computational efficiency. Within this methodology, the node-dependent kinematic approach is exploited by means of a rigorous coupling between the finite element interpolation and theory of structure approximation, specifically between the specific FE node of the mid surface and is specific through-the-thickness kinematics under a coupled recursive index formalism:

$$\boldsymbol{u}(\alpha^1,\alpha^2,\alpha^3) = F_\tau^i(\alpha^3)N_i(\alpha^1,\alpha^2)\boldsymbol{u}_{\tau i} = L_{\tau i}(\alpha^1,\alpha^2,\alpha^3)\boldsymbol{u}_{\tau i} \quad \tau = 1,..,\mathrm{M}^i, \quad \mathrm{i} = 1,..,\mathrm{N_n} \quad (1)$$

where $\boldsymbol{M^i}$ is the related to the order of the node-wise structural theory considered, $\boldsymbol{F_\tau^i(z)}$ is the set of the through-the-thickness expansion functions, representing the theory of structure approximation, $\boldsymbol{N_i(x,y)}$ is the set of 2D shape functions of the discrete $\mathrm{N_n}$ finite nodes along the reference mid-surface, and finally $\boldsymbol{u_{\tau i}}$ is the vector of generalized displacements. In the present work, the set of 1D Lagrange's polynomials will be adopted in the z-direction [5]. Starting from these three-dimensional extensions of a classical 2D model, geometric quantities and finite element matrices are evaluated in a general 3D sense in the covariant reference frame, enabling the straightforward inclusion of geometrical feature variations within the element itself [11]. One of the key features of the proposed methodology is that no additional unknowns are added into the global system of equations, as it employs the same set of variables used in classical CUF shell models under an isoparametric approach, where the geometry is also discretized and interpolated by the same formal definition:

$$\boldsymbol{X}(\alpha^1,\alpha^2,\alpha^3) = L_{\tau i}(\alpha^1,\alpha^2,\alpha^3)\boldsymbol{X}_{\tau i} \quad \tau = 1,..,\mathrm{M}^i, \quad \mathrm{i} = 1,..,\mathrm{N_n} \quad (2)$$

Under this formalism, all geometrical quantities required for the computation of finite element matrices are straightforwardly computed from the discretized expression of the geometrical description of the shell, such as co- and contra-variant basis and metric tensor, as well as the transformation law between covariant and Cartesian reference frames [8]. The robustness of the present modeling strategy is ensured by adopting higher-order methods, which naturally mitigate numerical limitations. Figure 1 depicts the proposed curvilinear shell model in a non-orthogonal reference frame, focusing on the possibility to arbitrary model the through-the-thickness kinematics for each finite node.

Materials Research Proceedings 69 (2026) 1304-1309 https://doi.org/10.21741/9781644904251-226

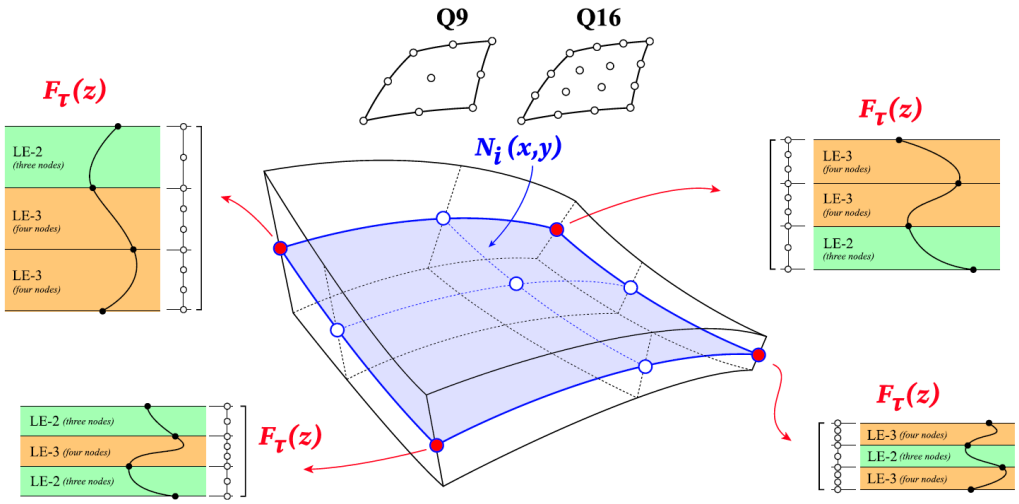


Figure 1: Curvilinear shell model with node-dependent through-the-thickness kinematics, including curvature and thickness variation.

Governing equations

The equilibrium equations for the linear static analysis are derived from the Principle of Virtual Displacements (PVD):

$$\delta\mathcal{L}_{int} = \delta\mathcal{L}_{ext} \tag{3}$$

where $\boldsymbol{\mathcal{L}_{int}}$ and $\boldsymbol{\mathcal{L}_{ext}}$ are the internal strain energy and external work, respectively, and $\boldsymbol{\delta}$ denotes the virtual variation. Adopting the index notation introduced in Eq. (1)-(2) for the displacement field and geometrical interpolation, one can derive the expression of strain and stress tensor in curvilinear coordinates [8] and expressing it in terms of Cartesian components by means of a transformation law. In this way, starting from the definition of involved energetic contributions, the FN (Fundamental Nuclei) of the linear stiffness matrix and external force vector can be derived:, obtaining the matrix form of the governing equation.

$$\delta\mathcal{L}_{int} = \delta\hat{\boldsymbol{u}}_{sj}^{T}\left[\int_{\Omega} \boldsymbol{B}_{curv}^{sj\,T}\boldsymbol{J}_{c2c}\boldsymbol{C}\boldsymbol{J}_{c2c}\boldsymbol{B}_{curv}^{\tau i}\,|\boldsymbol{J}|dV\right]\hat{\boldsymbol{u}}_{\tau i} = \delta\hat{\boldsymbol{u}}_{sj}^{T}\boldsymbol{K}^{\tau sij}\hat{\boldsymbol{u}}_{\tau i} \tag{4}$$

$$\delta\mathcal{L}_{ext} = \delta\hat{\boldsymbol{u}}_{sj}^{T}\left[\int_{\Sigma} L_{sj}(\alpha^1,\alpha^2,\alpha^3)\,\boldsymbol{f}\,|\boldsymbol{J}_{\Sigma}|dV\right] = \delta\hat{\boldsymbol{u}}_{sj}^{T}\boldsymbol{P}^{sj} \tag{5}$$

where $\boldsymbol{B}_{curv}^{\tau i}$ and $\boldsymbol{B}_{curv}^{sj}$ are the algebraic matrices of derivative operators applied to shape functions in curvilinear coordinates, $\boldsymbol{J}_{c2c}$ is the transformation matrix from covariant and Cartesian reference frame, $|\boldsymbol{J}|$ and $|\boldsymbol{J}_{\boldsymbol{\Sigma}}|$ are respectively the Jacobian from curvilinear and natural reference frames for integral evaluation computed in the Gauss-Point of the Ω closed 3D domain or Σ 2D surface for load boundary applications, $\delta\hat{\boldsymbol{u}}_{sj}$ are the Cartesian components of the virtual displacements and finally $\hat{\boldsymbol{u}}_{\tau i}$ are the Cartesian components of the final, unknown, displacement field. The quantities $\boldsymbol{K}^{\tau sij}$ and $\boldsymbol{P}^{sj}$ are the FN of the stiffness matrix and external force vector, independent of the chosen FE implementation models, allowing for a flexible implementation of any arbitrary shell model. More details about the derivation can be found in [8].

Numerical results

The proposed approach is applied to the analysis of a pinched shell supported by rigid diaphragms at both free ends. This case study has been extensively analyzed in the literature to investigate locking phenomena in the shell finite element formulation, as analyzed by Bathe *et al.* [12] and

Materials Research Proceedings 69 (2026) 1304-1309 https://doi.org/10.21741/9781644904251-226

later by Cinefra *et al.* [9]. The addressed case study involves the analysis of a thin shell with a total length L = 600 in, a constant radius of curvature R = 300 in, and a thickness t = 3 in. The shell is loaded with two equal forces acting at two diametral points of value P = 1 lb, as shown in Fig. 1. Thanks to the symmetry of the structure, only one eighth of the shell is discretized by applying symmetry boundary conditions. The material properties considered for the isotropic materials are $E = 3 \times 10^6$ psi and $\nu = 0.3$. The structure is discretized using curvilinear 2|3 models, as introduced, to investigate locking phenomena in this novel finite element approach. The results proposed are compared against available literature references, where the transversal displacement of the point "A" reported in Fig. 2 is computed with classical thin shell theories. Table 1 presents a comparison between higher-order curvilinear 2|3 models and the available literature. Both parabolic and cubic models are consistently adopted in the present case to analyze how higher-order models can mitigate locking phenomena, both along the reference mid-surface and in through-the-thickness kinematics, and to examine the influence of the theory of structures on the solution as well as the polynomial order in the reference mid-surface interpolation. The relative percentage difference between the available reference and the results obtained via the present higher-order curvilinear models is also reported. According to [], the transversal displacement obtained adopting higher-order models is expected to be higher than the reference value, since it is computed with classical shell theories for thin structures, whereas higher-order models take into account shear effects, leading to higher values. This is also demonstrated by the results obtained adopting 15×15 or 20×20 cubic finite elements along the reference mid-surface. Figure 3 presents the results of the convergence analysis, which investigates the convergence ratio of the solution. Regarding the adoption of parabolic models along the mid-surface, larger relative errors and inconsistencies are found, and refined discretization is necessary to obtain consistent solutions. Instead, adopting cubic models yields results in excellent agreement with the reference solution, even for coarser discretizations.

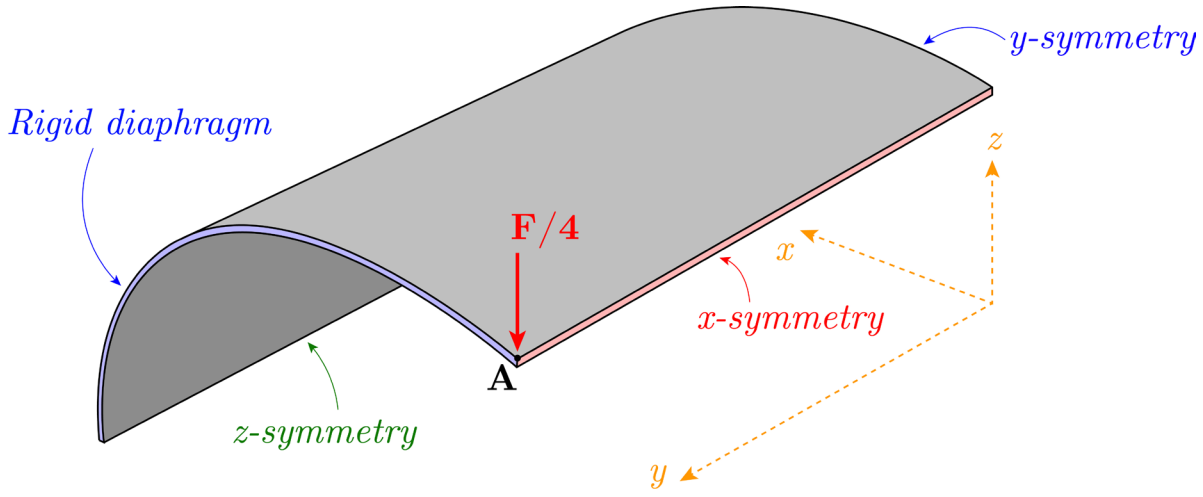


Figure 2: Isotropic pinched shell: geometrical features and boundary conditions considered.

Materials Research Proceedings 69 (2026) 1304-1309 https://doi.org/10.21741/9781644904251-226

Table 1: Isotropic pinched shell: convergence analysis for various FE approximations and theory of structure approximations. Transversal displacement u_z measured at point "A" [in]. Comparison between curvilinear 2D CUF shell results and available literature results.

		Parabolic Q9 mesh		Cubic Q16 mesh	
Mesh	**Expansion**	$u_z(A) \cdot 10^5$ [in]	**DOFs**	$u_z(A) \cdot 10^5$ [in]	**DOFs**
5 × 5	1 LE-2	-0.7608$^{58.31\%}$	1353	-1.3411$^{26.51\%}$	2304
	1 LE-3	-0.7679$^{57.92\%}$	1980	-1.3620$^{25.36\%}$	3072
10 × 10	1 LE-2	-1.2790$^{29.91\%}$	3969	-1.7903$^{1.89\%}$	8649
	1 LE-3	-1.2993$^{28.80\%}$	5292	-1.8118$^{0.72\%}$	11532
15 × 15	1 LE-2	-1.6132$^{11.60\%}$	8649	-1.8345$^{0.53\%}$	19044
	1 LE-3	-1.6312$^{10.61\%}$	11532	-1.8408$^{0.88\%}$	25392
20 × 20	1 LE-2	-1.7282$^{5.30\%}$	15129	-1.8423$^{0.96\%}$	33489
	1 LE-3	-1.7288$^{5.26\%}$	20172	-1.8327$^{0.43\%}$	44652
Ref [1]	-	-1.8248	-	-1.8248	-

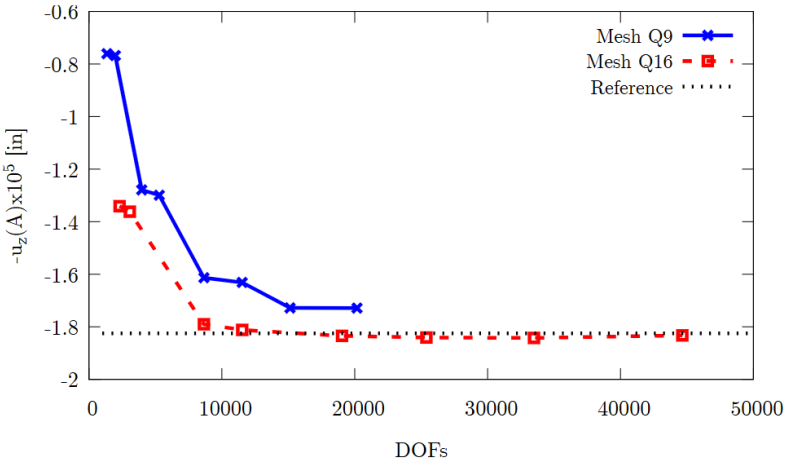


Figure 3: Isotropic pinched shell: convergence analysis for various FE approximations and theory of structure approximations.

Conclusions

This manuscript discusses the implementation of curvilinear higher-order shell models for the linear static analysis of complex geometries. The capabilities of the present approach are demonstrated by a severe patch test available in the literature for the locking investigation of shell finite element approaches. The model is formulated fully in curvilinear coordinates, including straightforwardly the geometrical features variation within the element definition, under a rigorous differential geometry framework The governing equations for the linear static analysis are defined via numerical procedures based on higher-order CUF-based finite element, an efficient tool for the generation of any arbitrary shell model, here extended to the definition of variable thickness and variable curvature shell structures. The proposed results suggest the robustness and consistency of the proposed approach, where the adoption of higher-order models mitigates numerical effects such as locking in thin shell formulations.

References

[1] R J. N. Reddy. “Finite Element and Finite Volume Methods for Heat Transfer and Fluid Dynamics”. Cambridge University Press, 2022

[2] Addessi D., Di Re P., and Cimarello G. “Enriched beam finite element models with torsion and shear warping for the analysis of thin-walled structures”. Thin-Walled Structures, 159:107259, 2021. https://doi.org/10.1016/j.tws.2020.107259

[3] Patni M., Minera S., Weaver P.M., and Pirrera A. “Efficient modelling of beam-like structures with general non-prismatic, curved geometry”. Computers & Structures, 240:106339, 2020, https://doi.org/10.1016/j.compstruc.2020.106339

[4] Cinefra M. and Rubino A. “Assessment of New Adaptive Finite Elements Based on Carrera Unified Formulation for Meshes with Arbitrary Polygons”. Aerotecnica Missili & Spazio, Vol. 102, 279–292 (2023).. https://doi.org/10.1007/s42496-023-00165-6

[5] Carrera E., Cinefra M., Zappino E., and Petrolo M. “Finite Element Analysis of Structures Through Unified Formulation”. Wiley, Chichester, West Sussex, UK, jul 2014.

[6] Li G., Carrera E., Cinefra M., de Miguel A.G., Pagani A., and Zappino E. “An adaptable refinement approach for shell finite element models based on node-dependent kinematics”. Composite Structures, 210:1–813 19, February 2019. https://doi.org/10.1016/j.compstruct.2018.10.111

[7] Cinefra M. Formulation of 3D finite elements using curvilinear coordinates. Mechanics of Advanced Materials and Structures, 29(6):879–888, July 2020. https://doi.org/10.1080/15376494.2020.1799122

[8] Chiaia P., Cinefra M. and Carrera E. “Curvilinear 2|3D finite elements for the analysis of shells with arbitrary curvature and variable thickness”, Computers & Structures, Vol 317, October 2025, 107911. https://doi.org/10.1016/j.compstruc.2025.107911

[9] Cinefra M., Chinosi C. and Della Croce L. “MITC9 Shell Elements Based on Refined Theories for the Analysis of Isotropic Cylindrical Structures”. Mechanics of Advanced Materials and Structures, 20:2, 91-100. https://doi.org/10.1080/15376494.2011.581417

[10] Cinefra M. Non-conventional 1D and 2D finite elements based on CUF for the analysis of non orthogonal geometries. European Journal of Mechanics - A/Solids, 88:104273, July 2021. https://doi.org/10.1016/j.euromechsol.2021.104273

[11] Moruzzi M.C., Cinefra M., and Bagassi S. Free vibration of variable-thickness plates via adaptive finite elements. Journal of Sound and Vibration, 577:118336, May 2024. https://doi.org/10.1016/j.jsv.2024.118336

[12] Bathe K.J. and Ho L.W. “A simple and effective element for the analysis of general shell structures”. Computers & Structures, Vol. 13, pp. 673-681, 1981. https://doi.org/10.1016/0045-7949(81)90029-8

Materials Research Proceedings 69 (2026) 1310-1313 https://doi.org/10.21741/9781644904251-227

Functionally Graded TPMS Structures for Boundary Layer Suction on a Swept Wing

Jan KUBE[1,a *], Lajos FOHLMEISTER[2,b], Rolf RADESPIEL[2,c] and Christian HÜHNE[1,d]

[1]Technische Universität Braunschweig, Institute of Mechanics and Adaptronics, Langer Kamp 6, 38106 Braunschweig, Germany

[2]Technische Universität Braunschweig, Institute of Fluid Mechanics, Hermann-Blenk-Straße 37, 38108 Braunschweig, Germany

[a]jan.kube@tu-braunschweig.de, [b]lajos.fohlmeister@tu-braunschweig.de, [c]rolf.radespiel@tu-braunschweig.de, [d]christian.huehne@tu-braunschweig.de

Keywords: TPMS, Gyroid, Additive Manufacturing, HLFC

Abstract. Reducing aerodynamic drag via laminar flow on wings offers significant energy savings compared to common, mostly turbulent wings. At TU Braunschweig, an extended Hybrid Laminar Flow Control (xHLFC) concept has been developed, combining a laminar front-wing design with active suction panels in the rear upper shell of the wing [1]. To avoid heavy metal suction skins and panel structures and a complicated assembly, this concept implements a fully integrated, polymer 3D-printed panel employing a sandwich-like structure: a micro-perforated skin with printed perforations on a Triply Periodic Minimal Surface (TPMS) based core. Next to being lightweight, the TPMS core mechanically supports the suction skin and enables internal transport and pressure control of the suction air flow. This study focuses on Gyroid structures with their channel-like inner structure and adaptability through functional grading. To validate the approach, a complete suction panel with a specifically graded Gyroid core was integrated into a swept wing and tested in a laminar low-speed wind tunnel, showing up to 25 % longer laminar boundary layers at 60 m/s.

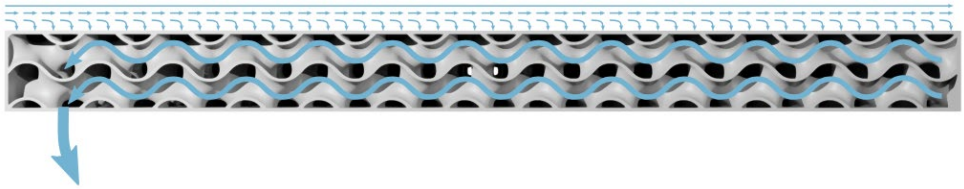


Figure 1: Concept of the core structure for the suction panel. Left: Schematic of the suction panel concept. The air is drawn in from perforations on top of the panel and then transported through the Gyroid structure

Introduction

As aviation moves towards more sustainability, significant gains in aerodynamic efficiency are required to reduce both fuel consumption and emissions. A key lever is the reduction of aircraft drag. Especially the viscous drag as one component is significantly higher for turbulent wings in comparison to wings with a laminar boundary layer. Studies show that laminarization of the wings can reduce the total drag by up to 18 % [2]. Therefore, much research has been conducted in the area, resulting in applications for wind tunnel tests on wings and fins and the implementation in different structural concepts [3]. The implemented concepts mostly focus on the front section of the wing around the leading edge and separately develop the suction skin and core structure which are joined afterwards. This results in structural complexity and high weight, as mostly metals are used.

Content from this work may be used under the terms of the Creative Commons Attribution 3.0 license. Any further distribution of this work must maintain attribution to the author(s) and the title of the work, journal citation and DOI. Published under license by Materials Research Forum LLC.

Materials Research Proceedings 69 (2026) 1310-1313 https://doi.org/10.21741/9781644904251-227

To address these issues, this study presents a fully integrated, additively manufactured suction panel concept. As the suction panels are located at the upper rear section, additive manufacturing (AM) with polymers is used, enabling much lower weight than using metals. The panels employ a sandwich construction featuring a micro-perforated, printed skin [4] and a core based on triply periodic minimal surfaces (TPMS). TPMS structures offer nearly isotropic mechanical properties and multidirectional channels. The concept is shown in Fig. 1 with a Gyroid as the chosen core structure. As the air is sucked in, it runs through the Gyroid structure with its multiple channels and curvatures that lead to a pressure drop. By specifically adjusting the main cell parameters, which are the wall thickness and the unit cell size, this pressure drop can be determined for different flow rates.

The presented approach is designed and tested for a new laminarization approach called *extended* Hybrid Laminar Flow Control (xHLFC). Therefore, an airfoil was designed at TU Braunschweig for natural laminar flow on the front region of the upper wing to allow for the suction panel to be beneficial in the rear area. Wind tunnel tests on this airfoil with the printed suction panel successfully show a downstream shift of laminar-turbulent transition.

Materials and Methods

A major design objective of using TPMS structures as the panel core is fitting a tailored pressure distribution within the core, as wing profiles have a pressure distribution that is not constant. To achieve the right pressure difference from this outer distribution to the panel core structure and thereby the right suction rate, this must be matched with the core design.

To investigate the correlation between pressure drop characteristics and geometry, multiple flat specimens (comparable to Fig. 1) have been manufactured. The specimens vary systematically in unit-cell size and wall thickness, including fully graded Gyroid cores, and represent sections of the sandwich-like suction panels. All specimens were tested with a flow meter recording the volumetric flow rate, while pressure taps along the core measure the internal pressure distribution. For cases with low flow rates, the structures are densified locally by a strong increase in wall thickness, while still keeping the channel structure and flow inside of the Gyroid core. This can increase the pressure drop strongly and is also investigated in this study. Methods for this have been implemented at the Institute of Mechanics and Adaptronics [5].

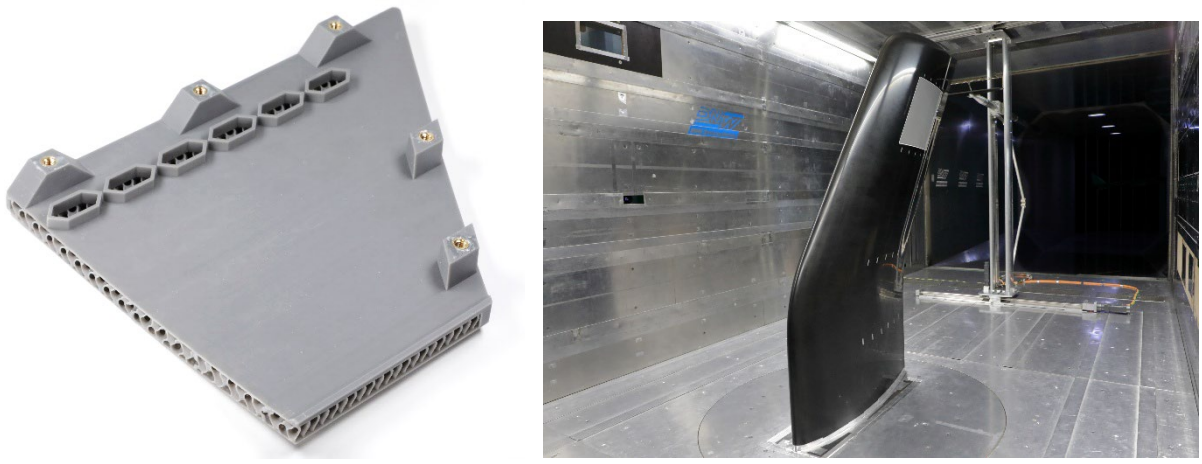


Figure 2: Wind tunnel test of the integral suction panel employing a Gyroid core. Left: Panel section with the core structure, threaded inserts for assembly and suction air outlets. Right: The sickle wing in the DNW-NWB wind tunnel with the integrated suction panel

Materials Research Proceedings 69 (2026) 1310-1313 https://doi.org/10.21741/9781644904251-227

At the Institute of Fluid Mechanics of TU Braunschweig, a special sickle-shaped wing has been designed and manufactured that allows to investigate multiple influences on the transition from laminar to turbulent boundary layers. The model has a cut area where the suction panel can be integrated (grey area in Fig. 2). Based on the pressure-drop results, a suction panel with a graded Gyroid core is integrated and tested in the swept wing area. This is shown in Fig. 2. The Gyroid panel core has a unit cell length of 12 mm and a core wall thickness of 1 mm. The perforation size is 250 µm with square holes with a design porosity of 1 %. There are six densifications in 50 mm distance over the LE-normal length of the panel to increase the pressure drop in the core to the required level. The panel consists of six segments printed in a stereolithography process. Each one combines hull, brackets for threaded inserts, core and perforations in one integral part, as can be seen in Fig. 2. After cleaning in IPA and post-curing, the panel sections are joined together and then built into the wing. The panel dimensions are 450 mm in spanwise direction, going from 35 to 80 % chord length. Surface finishing by sanding is applied as the suction panel is placed in the cut. With this, a high surface quality, matching curvature and a smooth interface between wing and panel can be ensured.

The wing with the panel was then installed in the wind tunnel and tested at different conditions. With applied suction at different suction rates, the wind tunnel speed was varied between 30 and 75 m/s under different angles of attack. With infrared cameras, the transition from laminar to turbulent was observed for different flow conditions and suction rates. Pressure taps in the wing and the panel core allow for measurement of the pressure distributions. The tests were conducted in the Low-Speed Wind Tunnel Braunschweig of the German-Dutch Wind Tunnels (DNW).

Results

The test in the wind tunnel has shown a significant influence of the built-in suction panel on the transition behavior. Because of the polymer base material of the panels, the transition can be detected by IR cameras directly on the suction panel. This is another advantage of the material choice, especially for research applications. Without applied suction, the panel causes a forward shift of the transition compared to the natural transition line. This can be explained by the induced roughness from the holes and blow-out from the front region of the suction panel due to the pressure gradient.

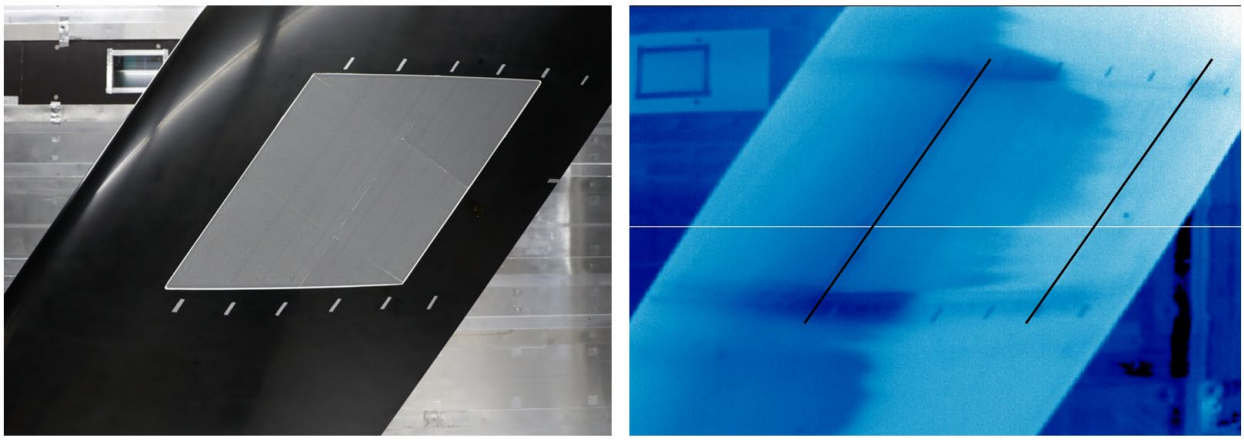


Figure 3: Infrared measurements results. Left: Image of the suction panel in the swept area of the wing. Right: Infrared image at 60 m/s wind tunnel speed and applied suction with the darker laminar area extended by the panel

With applied suction, the transition can be shifted downstream significantly. This was successfully demonstrated at wind tunnel speeds of 45 to 60 m/s, with an extension of the laminar

region by 20 to 25 % compared to the natural flow with a smooth surface, visible in Fig. 3. At 45 m/s, the flow could be kept laminar over almost the whole suction panel area, which can be considered the optimum. Suction rates were varied from zero to up to 40 m^3/s. After the optimum, oversuction leads to a decrease in the length of the laminar boundary layer. The joint between the panel sections and also between the panel and the surrounding wing skin exhibited no visible influence on the transition.

Pressure measurements in the core structure of the suction panel reveal an actual pressure gradient due to the design of the core structure, going in the direction of the aimed pressure distribution. This exhibits the potential of using TPMS structures as a core structure. The trend also matches the results from the flow meter measurements, showing the strong increase in pressure drop due to the densifications in the structure. A uniform TPMS structure yields a near-linear pressure drop, functional grading enables spatially tailored gradients or strong increases.

Summary

The study showed the applicability of additive manufacturing for the implementation of suction panels for xHLFC application. A micro-perforated skin was printed together in one integral part with a Gyroid core structure that supports the suction skin as well as controls the inner pressure distribution for a designed suction rate. The use of polymers makes the concept lightweight and enables transition measurement through IR thermography directly on the suction panels. For future applications, challenges are expected in the manufacturing of bigger panel structures, as the current process involves many joints that have to be precisely shaped to not cause laminar-turbulent transition. With the current progress in printing quality and size, this appears feasible. Together with additional research on mechanical properties and modelling currently conducted, the whole process chain from panel design and dimensioning to implementation can be realized.

Acknowledgements

We would like to acknowledge the funding by the Deutsche Forschungsgemeinschaft (DFG, German Research Foundation) under Germany's Excellence Strategy – EXC 2163/1- Sustainable and Energy Efficient Aviation – Project-ID 390881007.

References

[1] H. Traub, J. Wolff, S. Jose, L. Lobitz, M. Schollerer, and C. Hühne, "Concept and design of extended hybrid laminar flow control suction panels," *Scientific Reports*, 2021. https://doi.org/10.21203/rs.3.rs-924184/v1.

[2] N. Beck, T. Landa, A. Seitz, L. Boermans, Y. Liu, and R. Radespiel, "Drag Reduction by Laminar Flow Control," *Energies*, vol. 11, no. 1, p. 252, 2018. https://doi.org/10.3390/en11010252.

[3] K. Krishnan, O. Bertram, and O. Seibel, "Review of hybrid laminar flow control systems," *Progress in Aerospace Sciences*, vol. 93, pp. 24–52, 2017. https://doi.org/10.1016/j.paerosci.2017.05.005.

[4] H. Traub, J. Kube, S. Jose, A. Prasannakumar, and C. Hühne, "Structural and Aerodynamic Characteristics of Micro-Perforated Porous Sheets for Laminar Flow Control," in *ASME 2024 Aerospace Structures, Structural Dynamics, and Materials Conference*, Renton, Washington, USA, 2024. https://doi.org/10.1115/SSDM2024-121620.

[5] D. Lohuis, H. Traub, and C. Hühne, "Mechanical testing of threaded inserts for additively manufactured sandwich panels with Gyroid core structures," *Results in Materials*, vol. 21, p. 100543, 2024. https://doi.org/10.1016/j.rinma.2024.100543.

Materials Research Proceedings 69 (2026) 1314-1318 https://doi.org/10.21741/9781644904251-228

High-Order Kinematic Coupling of Embedded Fiber and Matrix Ensembles Using a Unified Variational Approach

Alberto RACIONERO SÁNCHEZ-MAJANO[1,a *] and Alfonso PAGANI [2,b]

[1]Department of Aerospace Engineering, Universidad Carlos III de Madrid, Av. de la Universidad, 28911, Leganés, Spain

[2]MuI2 Lab, Department of Mechanical and Aerospace Engineering, Politecnico di Torino, Corso Duca degli Abruzzi 24, 10129, Turin, Italy

[a]alracion@ing.uc3m.es, [b]alfonso.pagani@polito.it

Keywords: Embedded Finite Elements, High-Order Models, Unified Formulation, Textile Composites

Abstract. This work presents a framework for simulating fiber–matrix assemblies using an Embedded Finite Element (EFE) approach, where the matrix and fibers are modeled as host and embedded bodies, respectively. One-dimensional beam finite elements represent both constituents, with distinct kinematic models defined through the Carrera Unified Formulation (CUF). Displacement compatibility is enforced via the Lagrange multiplier method, augmented with a perturbation term to prevent stiffness matrix singularity. Furthermore, the variational principle includes a corrective term accounting for the volume redundancy of the embedded elements. The proposed methodology demonstrated high accuracy and computational efficiency, showing strong potential for the analysis of fiber–matrix assemblies and the modeling of complex textile composite geometries.

Introduction

Micro- and mesoscale simulation of composite materials is a challenging task that often requires computationally intensive methods to accurately represent the three-dimensional (3D) stress state. Among these models are tetrahedral and hexahedral solid finite elements (FEs), which adapt to the geometry of the matrix and fibers. However, this approach leads to the generation of highly refined and cumbersome meshes to accurately capture the fiber geometry [1]. An alternative method to reduce the pre-processing effort required for mesh generation is the voxel-based FE approach, where the geometry is subdivided into parallelepiped partitions. Nevertheless, voxel-based meshes cannot accurately capture the mechanical behavior near the fiber–matrix interface [2].

In recent years, Embedded Finite Element (EFE) methods have been proposed to reduce mesh generation times and avoid voxel-based meshes. However, these approaches still rely on 3D solid models [3] to resolve stress distributions with sufficient accuracy, which introduces additional challenges related to element aspect ratios and skewness. As a result, achieving acceptable accuracy often requires a large number of elements. Furthermore, commercial EFE strategies allow for embedding truss, beam, or plate elements into 3D solids, but they suffer from two main limitations: (i) they couple only translational degrees of freedom, leaving rotational ones unconstrained, and (ii) they do not account for volume redundancy [4]. The first limitation has been addressed in geotechnical engineering through the modeling of pile–soil interaction, where piles are modeled as Timoshenko beams with circular cross-sections and the soil as a 3D solid, and the coupling was achieved through Lagrange multipliers and penalty methods [5,6]. Nevertheless, this approach lacks generality for arbitrary cross-sections and higher-order beam models.

Content from this work may be used under the terms of the Creative Commons Attribution 3.0 license. Any further distribution of this work must maintain attribution to the author(s) and the title of the work, journal citation and DOI. Published under license by Materials Research Forum LLC.

Materials Research Proceedings 69 (2026) 1314-1318 https://doi.org/10.21741/9781644904251-228

The present manuscript aims to overcome these limitations. The proposed EFE framework introduces a novel coupling strategy that accounts for both higher-order kinematic fields and volume redundancy. The former is achieved by employing the Carrera Unified Formulation (CUF) [7,8] to generate low- to high-order beam theories, integrated into a perturbed Lagrangian formulation to enforce kinematic compatibility [9]. The latter is addressed by introducing a corrective term to the internal virtual work in the variational principle. A previous version of CUF-based EFE was proposed by the authors in [10]. The main difference with the present approach is that the previous one only permitted the coupling between 1D FE employing Lagrange expansion for the host and embedded element, while the present one permits the use of arbitrary expansions for both constituents.

The results presented herein demonstrate strong agreement with benchmark solutions from the literature, while achieving a significant reduction in computational cost. This approach paves the way for cost-effective virtual testing of composite parts through accurate mesoscale modeling, among other potential applications.

Unified formulation of embedded one-dimensional finite elements

When combining the Carrera Unified Formulation (CUF) with FEM, the 3D displacement field of a beam-like structure in a Cartesian reference frame can be written as:

$$\boldsymbol{u}(x,y,z) = F_\tau(x,z)N_i(y)\boldsymbol{u}_{\tau i} \qquad \tau = 1,\dots,M \quad i = 1,\dots,N \tag{1}$$

where F_τ are the expansion functions dependent on the beam's cross-sectional coordinates, N_i are the shape functions along the beam axis, and $\boldsymbol{u}_{\tau i}$ are the nodal generalized displacements. The parameter M denotes the number of expansion terms defining the beam's kinematic field, while N is the number of nodes per finite element. The choice of F_τ determines the order and type of the kinematic approximation; in CUF literature, Taylor (TE) and Lagrange (LE) expansions are the most commonly employed [7]. This combined CUF–FEM framework enables the analysis of structures with arbitrary material properties, loading conditions, and boundary configurations.

In the CUF–FEM framework, the system of equations for a static problem, $\boldsymbol{Ku} = \boldsymbol{F}$, is derived from the Principle of Virtual Displacements (PVD), and the assembly of the stiffness matrix is performed through the τ, s, i, and j indices of the so-called Fundamental Nucleus. For brevity, this process is not detailed in this manuscript; further information regarding the assembly procedure can be found in [7].

Kinematic coupling between host and embedded bodies

The kinematic coupling between the host and embedded bodies is achieved by introducing additional terms into the PVD statement, namely the volume redundancy term and the traction $\boldsymbol{\lambda}$ on the physical interface between the host and embedded bodies. In the following, the superscripts h and e denote quantities associated with the host and embedded domains, respectively. The modified PVD statement reads as:

$$\delta\boldsymbol{u}_{sj}^{h^T}\int_{V^h}\boldsymbol{D}^T\left(N_j^hF_s^h\right)\boldsymbol{C}^h\boldsymbol{D}\left(N_i^hF_\tau^h\right)dV^h\boldsymbol{u}_{\tau i}^h + \delta\boldsymbol{u}_{sj}^{e^T}\int_{V^h}\boldsymbol{D}^T\left(N_j^eF_s^e\right)\boldsymbol{C}^e\boldsymbol{D}(N_i^eF_\tau^e)dV^e\boldsymbol{u}_{\tau i}^e$$

$$-\delta\boldsymbol{u}_{sj}^{e^T}\int_{V^h}\boldsymbol{D}^T\left(N_j^eF_s^e\right)\boldsymbol{C}^e\boldsymbol{D}(N_i^eF_\tau^e)dV^e\boldsymbol{u}_{\tau i}^e + \int_{S_c}\delta\boldsymbol{u}_{sj}^{h^T}N_j^hF_s^h\boldsymbol{\lambda}dS_c - \int_{S_c}\delta\boldsymbol{u}_{sj}^{e^T}N_j^eF_s^e\boldsymbol{\lambda}dS_c =$$

$$\delta\boldsymbol{u}_{sj}^{h^T}\int_{V^h}N_j^hF_s^h\boldsymbol{b}dV^h + \delta\boldsymbol{u}_{sj}^{h^T}\int_S N_j^hF_s^h\boldsymbol{t}dS \tag{2}$$

Materials Research Proceedings 69 (2026) 1314-1318 https://doi.org/10.21741/9781644904251-228

where the first term on the second line corresponds to the redundant volume of the embedded body. This term must be subtracted to avoid introducing additional stiffness into the overall system, as discussed in [3]. In the above equation, $\boldsymbol{D}$ is the differential operator relating strains and displacements, $\boldsymbol{C}$ is the matrix version of the fourth-order material stiffness tensor, and $\boldsymbol{b}$ and $\boldsymbol{t}$ are the body and traction forces acting on the host domain, respectively.

The previous equation is complemented by the weak form of the displacement continuity condition on the interface between the two domains, S_c, expressed as:

$$\int_{S_c} \delta\boldsymbol{\lambda}^T(\boldsymbol{u}^h - \boldsymbol{u}^e)dS_c - \frac{1}{\alpha}\int_{S_c} \delta\boldsymbol{\lambda}^T\boldsymbol{\lambda}dS_c = 0 \tag{3}$$

where the second term is introduced to prevent zero diagonal entries in the system matrix, leading to a perturbed Lagrangian formulation of the displacement continuity condition. Here, α is a large penalty parameter.

By discretizing the interface traction as $\boldsymbol{\lambda} = N_i^{\lambda}F_{\tau}^{\lambda}\boldsymbol{\lambda}_{\tau i}$, substituting into the above equations, and expanding over the τ, s expansion, and i, j FE indices, the following system of equations is obtained:

$$\begin{bmatrix} \boldsymbol{K}^h & \boldsymbol{0} & \boldsymbol{B}^{\lambda,h} \\ \boldsymbol{0} & \boldsymbol{K}^e & \boldsymbol{B}^{\lambda,e} \\ \boldsymbol{B}^{\lambda,h^T} & \boldsymbol{B}^{\lambda,e^T} & \boldsymbol{B}^{\lambda,\lambda} \end{bmatrix} \begin{Bmatrix} \bar{\boldsymbol{u}}^h \\ \bar{\boldsymbol{u}}^e \\ \bar{\boldsymbol{\lambda}} \end{Bmatrix} = \begin{Bmatrix} \boldsymbol{F} \\ \boldsymbol{0} \\ \boldsymbol{0} \end{Bmatrix} \tag{4}$$

where $\boldsymbol{K}^h$ and $\boldsymbol{K}^e$ are the assembled stiffness matrices of the host and embedded bodies; $\boldsymbol{B}^{\lambda,h}$ and $\boldsymbol{B}^{\lambda,e}$ are the kinematic coupling matrices; and $\boldsymbol{B}^{\lambda,\lambda}$ is the assembled perturbed Lagrangian matrix. The vector $\boldsymbol{F}$ contains the external loads, which, in this work, are assumed to act only on the host body, while $\bar{\boldsymbol{u}}^h$, $\bar{\boldsymbol{u}}^e$, and $\bar{\boldsymbol{\lambda}}$ denote the vectors of host and embedded displacements and the Lagrange multipliers, respectively. For brevity, the procedure used to compute the coupling matrices is not reported here and can be found in Granitzer et al. [6].

Numerical results

The square-pack unit cell subjected to a uniform transverse displacement, as presented by Tabatabaei et al. [3], was used to verify the proposed methodology. The material properties, unit cell dimensions, and boundary conditions are detailed in the referenced work. The host matrix body employs an LE expansion consisting of 49 bi-quadratic subdomains, while the embedded fiber adopts a first-order TE (TE1) model, a Timoshenko-like beam formulation, to represent the beam cross-section. Both constituents utilize one-dimensional cubic shape functions for the FE discretization. In total, the simulation of the unit cell comprises 2772 degrees of freedom.

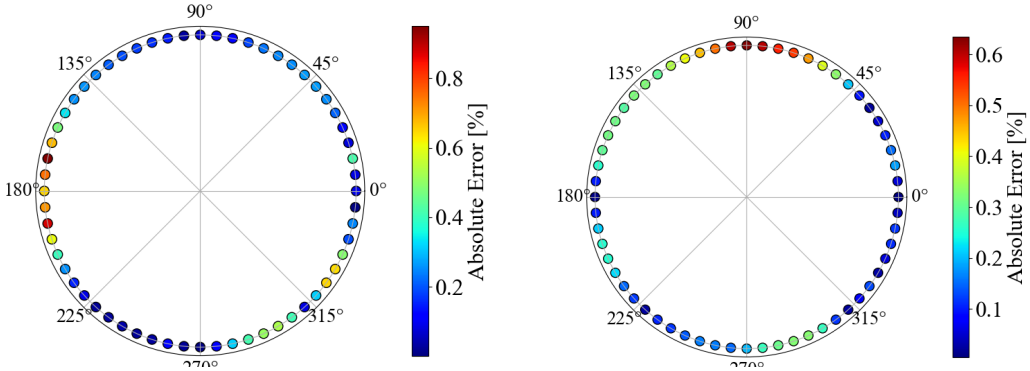


Figure 1. Absolute error in radial and hoop displacements at the fiber-matrix interface.

Materials Research Proceedings 69 (2026) 1314-1318 https://doi.org/10.21741/9781644904251-228

Figure 1 demonstrates the displacement continuity at the fiber–matrix interface. The figure shows the absolute difference between the predicted displacements in the radial and hoop directions. The results indicate excellent continuity across the interface, with weighted mean errors of 0.36% and 0.28% for the radial, u_r, and hoop, u_θ, displacement components, respectively. Similarly, Fig. 2 presents the σ_{yy} and σ_{xx} stress contours for the matrix and fiber domains. These results are consistent with those reported by Tabatabaei et al. [3], where the peak values of σ_{yy} in the matrix and σ_{xx} in the fiber were 0.33 and 0.70, respectively. Note that these quantities are dimensionless. Minor discrepancies can still be observed at the interface, where stress gradients between the fiber and matrix are not fully captured due to the use of a regular host cross-sectional discretization. Although a structured mesh would improve accuracy, it would also increase pre-processing complexity, thereby compromising the simplicity and generality of the proposed methodology for analyzing square-pack unit cell geometries.

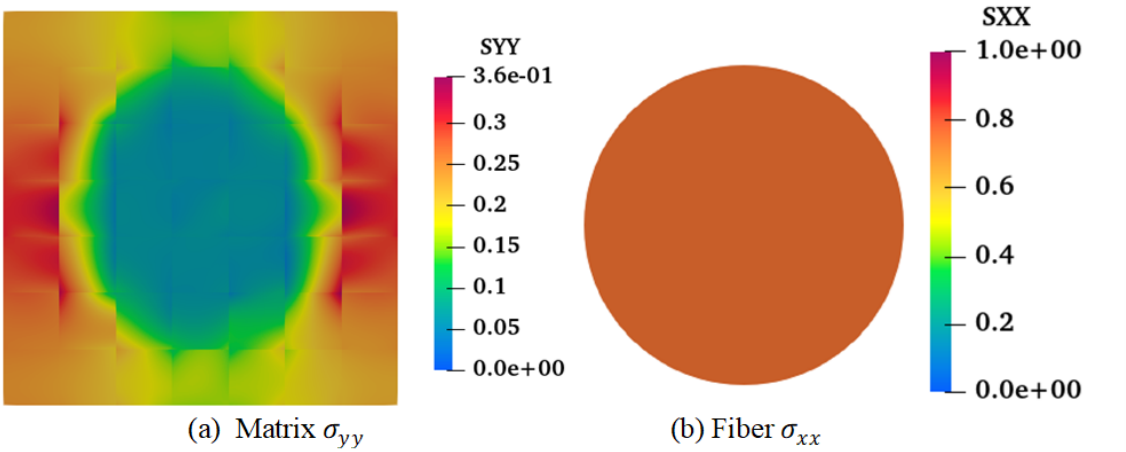


Figure 2. Stress contours for the matrix and fiber. A total of 322 points were used to discretize the fiber-matrix intergace, where the coupling matrices were computed. A 49L9 host cross-section and a TE1 embedded structural model were employed.

Conclusions

This study presented a Carrera Unified Formulation–Embedded Finite Element (CUF–EFE) framework for simulating fiber–matrix assemblies. The matrix and fiber of a square-pack unit cell were modeled as host and embedded bodies using one-dimensional beam elements with distinct CUF-based kinematic models. Displacement compatibility was enforced through Lagrange multipliers, with perturbation and corrective terms addressing stiffness singularity and volume redundancy. The results confirmed the accuracy and efficiency of the proposed approach, demonstrating its strong potential for more intricate fiber-matrix assemblies like those found in textile, 3D printed discontinuous composites, and tow-matrix interactions in variable stiffness composites [11].

References

[1] S. Green, M. Matveev, A. Long, D. Ivanov, and S. Hallett, Mechanical modelling of 3D woven composites considering realistic unit cell geometry, Composite Structures, 118 (2014), 284 – 293. https://doi.org/10.1016/j.compstruct.2014.07.005

[2] H. J. Kim, and C. C. Swan, Voxel-based meshing and unit-cell analysis of textile composites, International Journal for Numerical Methods in Engineering, 56(7) (2003), 977–1006. https://doi.org/10.1002/nme.594

[3] S. A. Tabatabaei, S. V. Lomov, and I. Verpoest, Assessment of embedded element technique in meso-FE modelling of fibre reinforced composites, Composite Structures, 107(2014), 436–446. https://doi.org/10.1016/j.compstruct.2013.08.020

[4] Abaqus Analysis User's Guide on Embedded Elements: http://130.149.89.49:2080/v2016/books/usb/default.htm?startat=pt08ch35s04aus138.html

[5] D. F. Turello, F. Pinto, and P. J. Sánchez, Embedded beam element with interaction surface for lateral loading of piles, International Journal for Numerical and Analytical Methods in Geomechanics, 40(2016), 568-582. https://doi.org/10.1002/nag.2416

[6] A. Granitzer, F. Tschuchnigg, S. Hosseini, and S. Brasile, Insight into numerical characteristics of embedded finite elements for pile-type structures employing an enhanced formulation, International Journal for Numerical and Analytical Methods in Geomechanics, 48(2024), 223-249. https://doi.org/10.1002/nag.3641

[7] E. Carrera, M. Cinefra, M. Petrolo, and E. Zappino, Finite element analysis of structures through unified formulation. John Wiley \& Sons, 2014. DOI: 10.1002/9781118536643

[8] I. Kaleel, M. Petrolo, and E. Carrera, Elastoplastic and progressive failure analysis of fiber-reinforced composites via an efficient nonlinear microscale model, Aerotecnica Missili & Spazio, 97(2018), 103-110. https://doi.org/10.1007/BF03405805

[9] O. C. Zienkiewicz, R. L. Taylor, and J. Z. Zhu, The finite element method: Its basis and fundamentals. Elsevier, 2013. https://doi.org/10.1016/C2009-0-24909-9

[10] A. Racionero Sánchez-Majano, and A. Pagani. High-order embedded finite elements for the component-wise analysis of composite laminated structures. Proceedings of the American Society for Composites - 38th Technical Conference, 2023. DOI: 10.12783/asc38/36543

[11] A. Pagani, A. Racionero Sánchez-Majano, and M. Petrolo. Influence of Structural Theories on Optimal Fiber Distributions in Tow-Steered Composites Considering Local Strain and Stress. Aerotecnica Missili & Spazio, (2025). https://doi.org/10.1007/s42496-025-00275-3

Materials Research Proceedings 69 (2026) 1319-1324 https://doi.org/10.21741/9781644904251-229

Damage Localization Accuracy in Probabilistic Imaging Techniques based on Guided Ultrasonic Waves

Francesco GASPERINI[1,a], Vittorio MEMMOLO[1,b *], Fabrizio RICCI[1,c]

[1]Department of Industrial Engineering, University of Naples Federico II, Via Claudio 21, 80125 Naples, Italy

[a]fr.gasperini@studenti.unina.it, [b]vittorio.memmolo@unina.it, [c]fabrizio.ricci@unina.it

Keywords: Structural Health Monitoring, Lamb waves, Aerospace Structures, Stiffened Composite, Damage Detection

Abstract. The assessment of hidden flaws in composite structures is crucial for aircraft safety and requires accurate detection and localization. Conventional damage tolerance relies on design margins and scheduled inspections, resulting in costly maintenance. Structural Health Monitoring (SHM) provides a cost-effective alternative, enabling continuous assessment through guided-wave–based damage imaging. When ultrasonic waves interact with defects, signal variations can be quantified through scalar features related to damage severity and position. This work presents a probabilistic multi-parameter imaging approach to evaluate localization accuracy under varying input parameters and post-processing conditions. Using the open-access *Open Guided Waves* dataset, results show high sensitivity to damage location when energy- and correlation-based indicators are employed. In addition, the findings show that excitation frequency is a key parameter to improve localization accuracy.

Introduction

The widespread use of fiber-reinforced composites in aerospace structures demands advanced Structural Health Monitoring (SHM) methods for detecting internal flaws such as delaminations, matrix cracks, or debonding. Ultrasonic guided waves are particularly effective, as their interaction with defects produces measurable waveform variations from which damage-sensitive features can be extracted [1].

Among imaging techniques, the *Reconstruction Algorithm for Probabilistic Inspection of Damage* (RAPID [2] estimates a spatial probability map of damage occurrence from signal deviations and sensor geometry, providing an efficient and robust localization approach. However, despite its extensive use, a systematic characterization of the method under varying input parameters—such as excitation frequency, feature type, and post-processing strategy—is still lacking. Understanding how these factors influence localization accuracy is essential to ensure reproducibility and reliability of the results.

In this work, RAPID is applied to the open-access *Open Guided Waves* dataset [3], including ultrasonic measurements on composite panels with various artificial damages. The study examines the influence of input parameters and feature selection on localization accuracy, contributing to the development of reliable probabilistic imaging methods for SHM.

Materials and Methods

The tested structure is a quasi-isotropic CFRP plate (550 × 550 mm^2, 2 mm thick) with layup $[45/0/-45/90/-45/0/45/90]_s$. An omega-shaped stringer bonded on the upper surface introduces geometric discontinuities that promote guided-wave scattering and mode conversion.

Artificial damages were simulated by bonding elliptical steel masses at three locations (D1–D3, Fig. 1), each with thirteen size levels obtained by progressively increasing the bonded area. Baseline signals were first recorded on the pristine plate.

Content from this work may be used under the terms of the Creative Commons Attribution 3.0 license. Any further distribution of this work must maintain attribution to the author(s) and the title of the work, journal citation and DOI. Published under license by Materials Research Forum LLC.

Materials Research Proceedings 69 (2026) 1319-1324 https://doi.org/10.21741/9781644904251-229

Twelve surface-mounted PZTs were used for actuation and sensing along multiple paths. Excitation consisted of 5-cycle Hanning-windowed tone bursts with central frequencies between 40 kHz and 260 kHz. For each frequency, all damage and baseline states were measured, with five repetitions for repeatability. Further details are provided in [3].

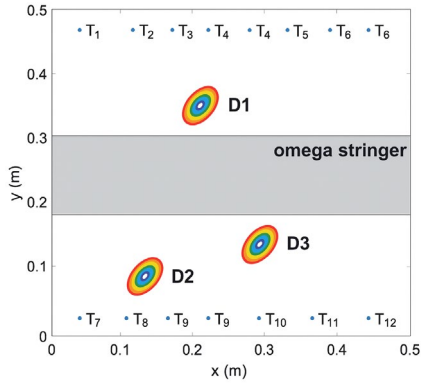


Figure 1: CFRP plate geometry and damage locations, adapted from [3].

RAPID Algorithm

The *Reconstruction Algorithm for Probabilistic Inspection of Defects* (RAPID) [2] was used to estimate the most probable damage location from the actuator–sensor network. The method is applied independently to each configuration, using path-wise damage indicators as input features.

A defect primarily perturbs guided-wave propagation along the direct transmitter–receiver path, with its influence decaying away from the path centerline. For each pair, an elliptical spatial weighting function is defined with the transducers at the foci, representing the probability that a signal deviation originates from any point (x, y) within the inspected area.

The overall probability map is computed as:

$$P(x,y)=\sum_{i=1}^{N_x}\sum_{j=1}^{N_y} A_{ij}\left[\frac{\beta-R_{ij}(x,y)}{\beta-1}\right], \qquad (1)$$

where A_{ij} is the damage indicator of the $i-j$ path, and $R_{ij}(x, y)$ the normalized distance ratio within the ellipse of influence. The factor decreases linearly from the path centerline ($R_{ij} = 1$) to zero at the boundary ($R_{ij} = \beta$), where ($\beta > 1$) (typically 1.05–1.2) defines the ellipse size. The ratio is expressed as:

$$R_{ij}=\frac{\sqrt{(x-x_i)^2+(y-y_i)^2}+\sqrt{(x-x_j)^2+(y-y_j)^2}}{\sqrt{(x_j-x_i)^2+(y_j-y_i)^2}} \qquad (2)$$

In this formulation, A_{ij} quantifies the deviation of each signal from its baseline along path i - j. The full set of metrics is reported in [4]; here, focus is given to the *Energy Difference* and *Pearson Correlation*, which yielded the most consistent performance.

After superimposing all path contributions, the resulting map P(x, y) exhibits a dominant peak near the actual defect. Post-processing (normalization, smoothing, clustering) improves localization robustness and mitigates spurious responses. Fig. 2 illustrates the elliptical influence region of each actuator–sensor path.

Materials Research Proceedings 69 (2026) 1319-1324 https://doi.org/10.21741/9781644904251-229

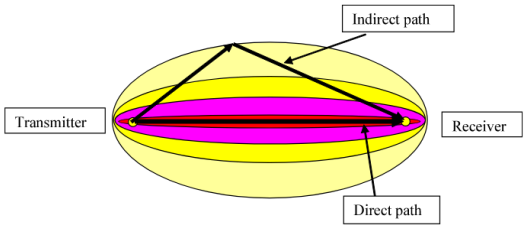


Figure 2: Elliptical spatial weighting function in the RAPID algorithm, showing direct and indirect wave paths [2].

Signal Processing and Feature Extraction

All guided-wave signals were imported and, for each excitation frequency, the five repetitions were averaged to obtain a representative waveform, then filtered and cross-talk removed to enhance signal quality. The damage indices (*DI*) defined in [4] were subsequently extracted, generating a database of interchangeable features for RAPID processing. Each DI's performance was assessed through the Euclidean distance between the real damage position and the estimated *damage centroid* from RAPID imaging.

Fig. 3 presents the tomographic reconstruction for damage location 2, size 13, using *Energy Difference* at 40 kHz, illustrating the offset between the RAPID peak and the actual damage position.

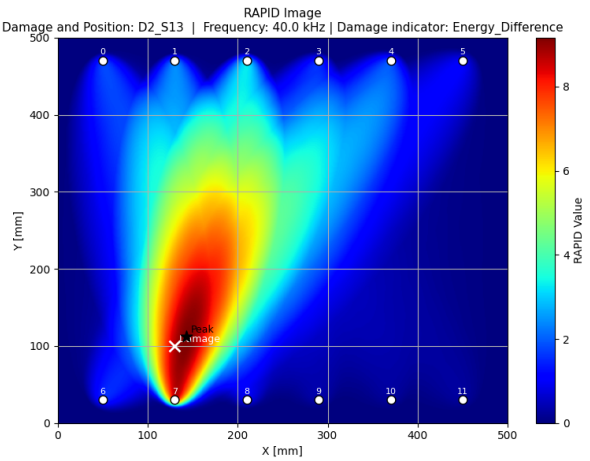


Figure 3: RAPID reconstruction for damage location 2, size 13 at 40 kHz using Energy Difference as damage index.

Effect of Damage Size and Burst Frequency on Localization Error

The Euclidean distance between the RAPID peak and the actual defect position was analyzed as a function of defect size and excitation frequency. As shown in Fig. 4, for damage location D1 the localization error decreases with increasing defect size, indicating that larger damages produce stronger and more distinct signal deviations. In contrast, the frequency trend shows an initial rise up to about 220 kHz, followed by a decrease at higher frequencies. This behavior agrees with guided-wave studies [5, 6], which highlight the trade-off between wavelength, scattering sensitivity, and spatial resolution.

These results confirm that the largest damage size (size 13) and the lowest burst frequency (40 kHz) provide the most reliable conditions for feature-based classification.

Materials Research Proceedings 69 (2026) 1319-1324 https://doi.org/10.21741/9781644904251-229

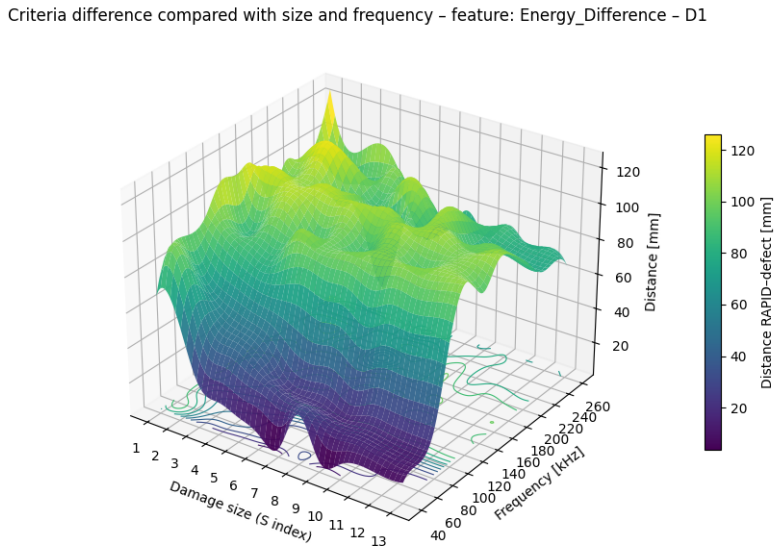


Figure 4: Variation of the Euclidean distance between the RAPID peak and the actual defect position for damage location D1 as a function of damage size and excitation frequency.

Feature Ranking

Table 1 reports the Euclidean distance between the RAPID peak and the actual defect position for the three damage locations (D1–D3) at 40 kHz and damage size 13. Among all features, *Energy Difference* and *Pearson Correlation* yielded the lowest localization errors, confirming their robustness in capturing waveform variations induced by damage. In contrast, amplitude-based features such as *Peak* and *Peak-to-Peak* showed higher sensitivity to noise and scattering, resulting in less accurate localization. These findings highlight the relevance of energy- and correlation-based indicators for reliable RAPID imaging in composite structures.

The best localization result was obtained for damage location D3 using *Pearson Correlation*, with an error of only 0.52 mm. Fig. 5 shows the corresponding RAPID reconstruction, confirming the close match between the estimated and actual defect positions.

Table 1: Euclidean distance between the RAPID peak and the actual defect position (mm) for the best-performing features at 40 kHz and damage size 13..

Feature	D1	D2	D3
Energy Difference	12.58	18.05	18.55
Pearson Correlation	19.33	19.47	0.52
Peak	38.32	59.10	45.53
Peak-to-Peak	38.32	59.10	45.53
RMS	60.36	60.35	48.42

Materials Research Proceedings 69 (2026) 1319-1324 https://doi.org/10.21741/9781644904251-229

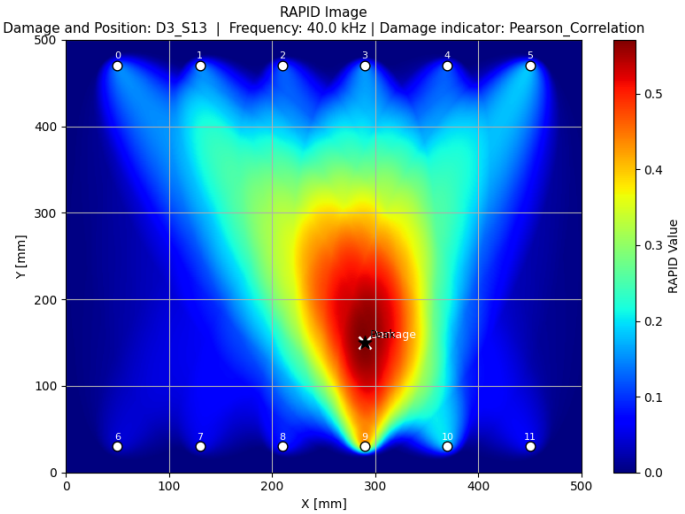


Figure 5: RAPID reconstruction for damage location 3, size 13 at 40 kHz using Pearson Correlation as damage index.

Influence of Environmental Conditions

An additional analysis was performed across all burst frequencies, best-performing features, and damage locations to assess the effect of environmental conditions on RAPID localization accuracy. As an example, Fig. 6 shows results for damage location D1 at 40 kHz using *Energy Difference* as indicator. A localized anomaly occurs for damage size 8 during the first repetition, producing a temporary increase in Euclidean distance and a deviation from the expected decreasing trend (see Fig. 4). This irregularity is attributed to external factors affecting acquisition, confirming the sensitivity of guided-wave measurements to ambient variations.

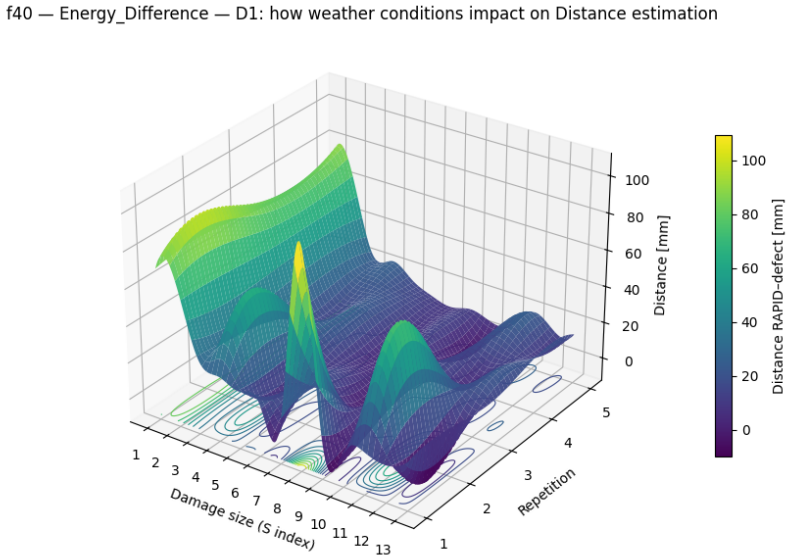


Figure 6: Effect of environmental conditions on the Euclidean distance for damage location D1 at 40 kHz using Energy Difference as damage indicator.

Conclusions

This work assessed the performance of the RAPID algorithm for damage localization in composite structures using guided-wave features. Results demonstrated that energy and correlation-based indicators provide the highest accuracy, with localization errors below 1 mm in optimal conditions. The analysis across frequencies, defect sizes, and repetitions highlighted the influence of both excitation parameters and environmental variability, confirming the robustness and limitations of RAPID imaging for reliable SHM applications. In addition, considering different damage locations did not affect the results significantly.

References

[1] F. Ricci, E. Monaco, N. D. Boffa, L. Maio, and V. Memmolo, Guided waves for structural health monitoring in composites: A review and implementation strategies, Progress in Aerospace Sciences 129 (2022) 100790. https://www.sciencedirect.com/science/article/abs/pii/S0376042121000920

[2] X. Zhao, H. Gao, G. Zhang, B. Ayhan, F. Yan, C. Kwan, and J. L. Rose, Active health monitoring of an aircraft wing with embedded piezoelectric sensor/actuator network: I. Defect detection, localization and growth monitoring, Smart Materials and Structures 16(4) (2007) 1208–1217. https://doi.org/10.1088/0964-1726/16/4/032

[3] J. Moll, C. Kexel, J. Kathol, C.-P. Fritzen, M. Moix-Bonet, C. Willberg, M. Rennoch, M. Koerdt, and A. Herrmann, Guided Waves for Damage Detection in Complex Composite Structures: The Influence of Omega Stringer and Different Reference Damage Size, Applied Sciences 10(9) (2020) 3068. https://www.mdpi.com/2076-3417/10/9/3068

[4] F. Gasperini, Prognostics methodologies based on guided wave propagation for residual useful life estimation in composites, Master's Thesis, University of Naples Federico II, Naples, Italy, 2025.

[5] V. Memmolo, E. Monaco, and F. Ricci, Damage localization in composite structures using a guided waves based multi-parameter approach, Aerospace 5(4) (2018) 111. https://doi.org/10.3390/aerospace5040111

[6] F. Ricci, E. Monaco, and V. Memmolo, Frequency and time domain analysis of guided waves for damage detection, in: Proceedings of the Structural Health Monitoring 2025 Conference, Destech Publications, 2025. https://doi.org/10.32604/shm2025.37444

Materials Research Proceedings 69 (2026) 1325-1330 https://doi.org/10.21741/9781644904251-230

Preliminary Study on the Design of a Fragmentation Warhead and Damage Simulation using FEM Models

Francesco GASPERINI[1,a *], Matteo GIANNITTI[1,b], Michele GUIDA[1,c], Simone GUBBIONI[2,d] , Emanuele COFANI[2,e]

[1]University of Naples Federico II, Department of Industrial Engineering, Naples, Italy

[2]MBDA, Lethality Section, Rome, Ital

[a]fr.gasperini@studenti.unina.it, [b]m.giannitti@studenti.unina.it, [c]michele.guida@unina.it, [d]simone.gubbioni@mbda.it, [e]emanuele.cofani@mbda.it

Keywords: Fragmentation Warhead, Finite Element Method (FEM), Lethality Assessment, Impact Dynamics, Explosive Simulation, Missile, Counter-UAS, Penetration Mechanics (THOR Law), Gurney Model

Abstract. The design and assessment of fragmentation warheads are key to the effectiveness of modern defense systems, particularly in counter-drone applications where unmanned aerial vehicles are increasingly employed. This work presents a preliminary study combining empirical formulations and finite element modeling (FEM) to support early-stage warhead design and lethality evaluation. Gurney and THOR formulations are first used to estimate fragment acceleration and penetration, providing the theoretical baseline for subsequent simulations. Two complementary numerical strategies are then developed: a simplified fragment-to-plate configuration for rapid analytical validation, and a full detonation model resolving the explosive–fragment interaction and impact on a target plate. The simplified model enables a quick assessment of penetration capability, while the full-scale simulation reproduces the acceleration and dispersion of a 225-fragment array. Results show good agreement with theoretical expectations, with ejection velocities around 1500~m/s and residual velocities consistent with the analytical framework. The integrated approach combines fast preliminary evaluation with high-fidelity physical insight, supporting early optimization of warhead design parameters and demonstrating the value of FEM in modeling fragmentation dynamics.

Introduction

The rapid proliferation of unmanned aerial vehicles (UAVs) has profoundly transformed modern warfare, enabling new capabilities in surveillance, intelligence, and precision strikes. Recent conflicts have highlighted the increasing dominance of small, low-cost, and agile drones, which allow rapid deployment, swarm tactics, and persistent reconnaissance at minimal expense. However, their affordability and widespread availability pose growing security challenges, as hostile UAVs can be employed for espionage or explosive delivery with limited financial risk.

This shift towards inexpensive UAVs requires an evolution in counter-drone systems. Traditional high-cost defense solutions are often unsuitable for neutralizing large numbers of small threats [1,2]. Affordable anti-drone missile systems have therefore become essential to modern defense strategies [3]. Countering UAVs remains complex due to their variable size, speed, and flight profiles, demanding advanced detection, tracking, and interception technologies.

Within the *Aerospace Design Project* course at Federico II of Naples, conducted in collaboration with MBDA Roma, the *SAGITTARIUS* missile (Fig. 1) was developed as a ground-to-air system. The project focused on the integration of precision, reliability, and adaptability in modern missile design. This paper concentrates on the preliminary design of the warhead and its lethality assessment, with particular attention to the fragmentation dynamics determining

Content from this work may be used under the terms of the Creative Commons Attribution 3.0 license. Any further distribution of this work must maintain attribution to the author(s) and the title of the work, journal citation and DOI. Published under license by Materials Research Forum LLC.

Materials Research Proceedings 69 (2026) 1325-1330 https://doi.org/10.21741/9781644904251-230

effectiveness against aerial targets. The analysis examines how the detonation shockwave accelerates fragments toward a representative aluminum plate, providing insight into dispersion and energy transfer mechanisms.

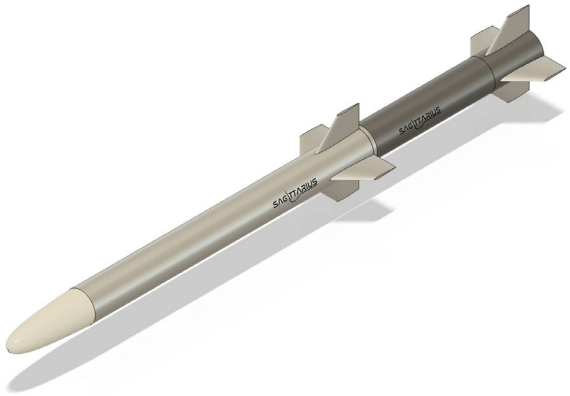


Figure 1: SAGITTARIUS Missile Design.

Preliminary Design and Theoretical Analysis

A cylindrical fragmentation warhead was selected, as this configuration efficiently directs the explosive energy outward, imparting a radial velocity to the fragments and maximizing the impact probability against fast-moving targets.

The radial velocity, a key parameter for lethality, was estimated through the G*urney formula* [4], which relates fragment velocity to the mass and energy distribution of the explosive:

$$V_r=\sqrt{2E}\sqrt{\frac{c/m}{1+0.5(c/m)}} \quad (1)$$

where E is the energy per unit mass of explosive and c/m the charge-to-mass ratio. This radial component, combined with the missile and target velocities (V_a), defines the total after-detonation velocity V_{ae}.

Fragment penetration capability was assessed using the *THOR model* [5], considering an AISI 4340 steel fragment impacting a 7075 aluminum alloy plate of thickness t:

$$V_{res} = V_{imp} - 0.3048\cdot10^{c_{11}}(61023.75\ t\ A)^{c_{12}}(915432.1m_{sf})^{c_{13}}\left(\frac{1}{\cos\alpha}\right)^{c_{14}}(3.28084)^{c_{15}}\ V_{imp} \quad (2)$$

$$M_{res} = m_{sf}-6.48\cdot10^{c_{31}-5}(61023.75\ t\ A)^{c_{32}}\ (915432.1m_{sf})^{c_{33}}\left(\frac{1}{\cos\alpha}\right)^{c_{34}}(3.28084)^{c_{35}}\ V_{imp} \quad (3)$$

where V_{imp} and V_{res} are the impact and residual fragment velocities, M_{res} the residual mass, A the contact area, and c_{ij} the material coefficients for the aluminum target.

TNT was selected as explosive (density 1.6 kg/mm^3, detonation velocity 6780 m/s), with pre-cut spherical steel fragments of radius 5 mm and a charge-to-mass ratio c/m = 0.5. Given the short travel distance, aerodynamic drag was neglected, assuming:

$$V_{ae} = V_{imp} = 1714.6\ m/s \quad (4)$$

Applying the THOR model to a 10 mm aluminum plate yields:

$$V_{res} = 763.9\ m/s, \quad M_{res} = 2.6\ m/s \quad (5)$$

Materials Research Proceedings 69 (2026) 1325-1330 https://doi.org/10.21741/9781644904251-230

Considering missile constraints, the warhead length and diameter were set to L_w = 150 mm and D_w = 77 mm (L/D ≈ 2), which allows for an accurate estimation of the velocity using the Gurney formula [4]. Each ring contains n_{fr} = 15 spherical fragments, giving n_f = 225 in total. The fragment mass is m_f = 0.9189 kg, with m_e = 0.4595 kg of explosive for c/m = 0.5. Assuming fragments and explosive account for 70% of the total mass:

$$m_w=\frac{m_e+m_f}{0.7}=1.97 \text{ kg} \quad (6)$$

Given ρ_e = 1600 kg/m^3, the explosive diameter is:

$$d_e=2\sqrt{\frac{m_e}{L_w\rho_e\pi}}= 0.0486 \text{ m} \quad (7)$$

The final geometry, including fragment distribution and explosive core, is shown in Fig. 2.

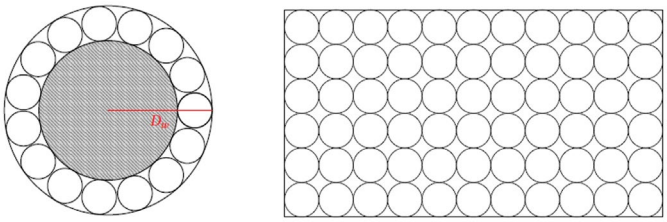


Figure 2: Schematic representation of the warhead geometry.

Simulation Modeling

Two finite element models are developed to reproduce the main physical mechanisms of detonation and fragment impact: a simplified *fragment-to-plate configuration* and a *full explosion-driven warhead model*. Both share the same geometry and materials defined in the preliminary design, differing only in the physical detail represented.

The first model (Fig. 3) isolates the impact phase to analyze the penetration mechanics of a single steel fragment against an aluminum plate. The fragment is assigned an initial velocity equal to the theoretical ejection speed obtained from Eq. 4. This setup allows direct validation of the THOR law by comparing impact and residual velocities, neglecting the influence of the detonation front.

The second model (Fig. 4) reproduces the complete detonation event. The explosive expansion generates a transient pressure field described by the Jones–Wilkins–Lee (JWL) equation of state [6]. This pressure wave transfers momentum to the surrounding fragments, producing their radial acceleration and dispersion. The model captures the coupled behavior between explosive gases, casing confinement, and fragment ejection, offering a physically consistent description of the early fragmentation stage.

Together, these two configurations provide complementary insight: the fragment-to-plate model addresses localized impact response, while the explosion-driven model resolves detonation-induced acceleration and dispersion, enabling a complete representation of the warhead lethality process.

Materials Research Proceedings 69 (2026) 1325-1330 https://doi.org/10.21741/9781644904251-230

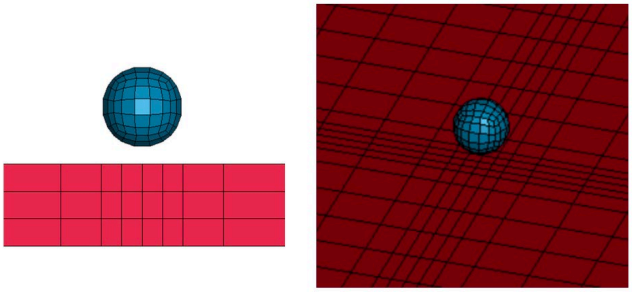


Figure 3: Simplified fragment-to-plate configuration.

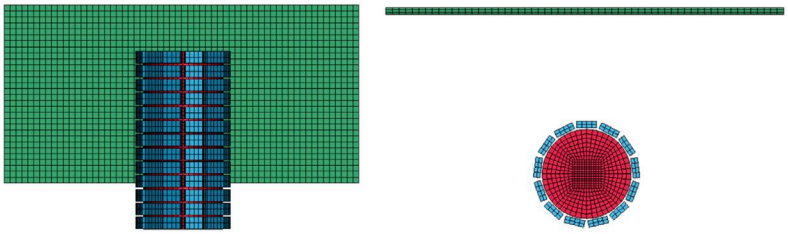


Figure 4: Full explosion-driven model showing the warhead mesh configuration.

Results and Discussion

The analyses carried out for both configurations allow a direct comparison between analytical predictions and finite element (FEM) results in terms of fragment velocity, kinetic energy, and penetration behavior.

For the fragment-to-plate configuration, Fig. 5 shows the time histories of velocity, which exhibits a sharp drop within the first microsecond, corresponding to the impact and energy transfer to the target. The final velocity stabilizes around 760 m/s, in close agreement with the analytical prediction (Eq. 5), with a residual kinetic energy of about 730 J. This confirms the simplified model's accuracy in capturing local deformation and penetration dynamics.

In the full explosion-driven simulation, the TNT detonation generates a transient pressure field through the casing, accelerating 225 fragments outward. The pressure peak reaches about 21 GPa, followed by a rapid expansion phase leading to fragment dispersion. The first impacted fragment achieves an ejection velocity of approximately 1500 m/s and a residual velocity near 760 m/s, in good agreement with the Gurney and THOR formulations. This consistency is notable given that, in the full-scale FEM model, fragments were idealized as rectangular elements to reduce computational cost, introducing only a minor geometric simplification. The corresponding velocity evolution is reported in Fig. 6.

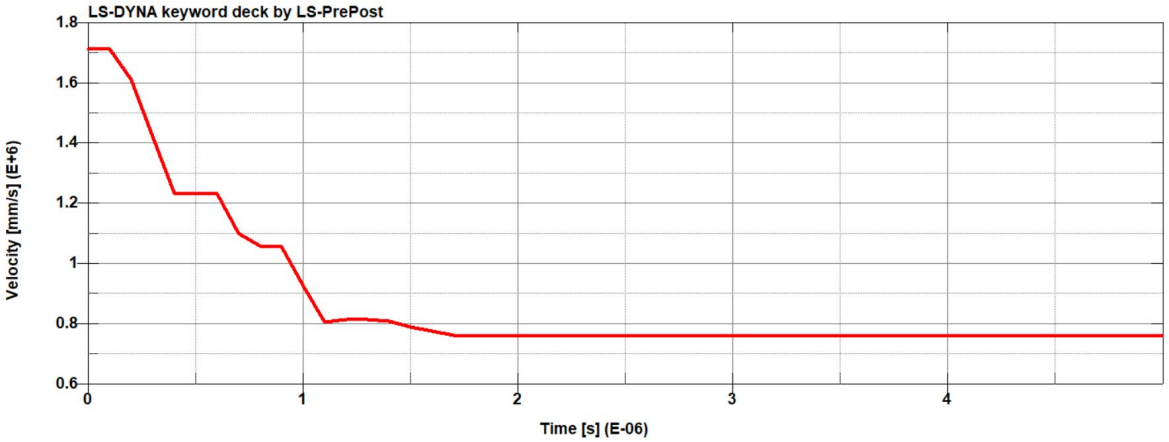


Figure 5: Velocity evolution for the fragment-to-plate configuration.

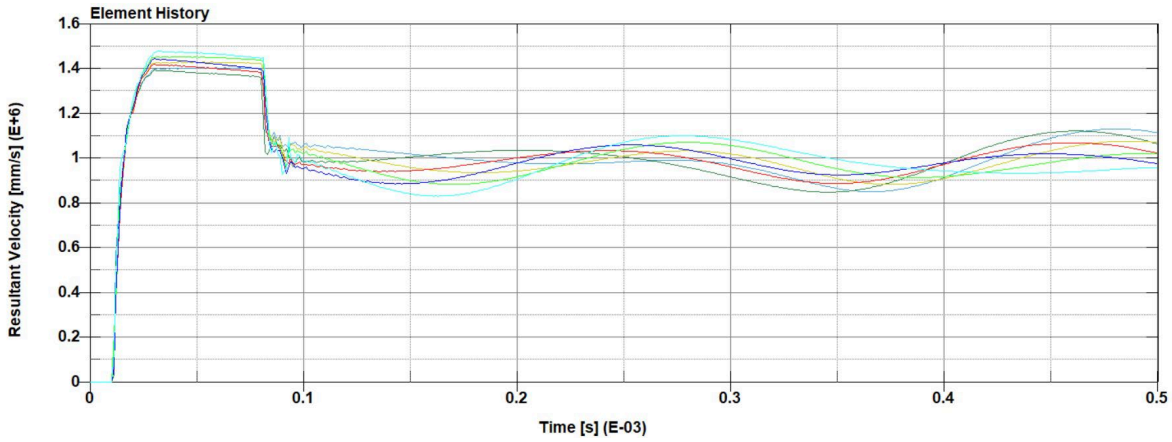


Figure 6: Velocity history of the first impacted fragments in the full explosion-driven model.

The comparison summarized in Table 1 highlights the strong agreement between analytical and FEM results, confirming the reliability of the proposed modeling approach for preliminary design assessment.

Table 1: Comparison between analytical and FEM results.

Parameter	FEM	Empirical (THOR/GURNEY)
Residual kinetic energy	730 J	761 J
Residual velocity	760 m/s	764 m/s
Residual mass	2.6 g	2.6 g
Average ejection velocity	1500 m/s	1715 m/s
Pressure peak	21 GPa	21 GPa

The consistency across all parameters demonstrates that analytical laws offer accurate first-order estimates, while the FEM provides deeper insight into the transient pressure field and fragment dispersion mechanisms.

Conclusions

The combined use of the two FEM simulations — the simplified fragment-to-plate model and the full explosion-driven configuration — enabled an effective validation of the empirical framework provided by the Gurney and THOR formulations. The consistency between analytical predictions

and numerical results confirms the reliability of these models for early-stage warhead design and demonstrates that finite element simulations can accurately capture the physical phenomena governing fragment acceleration and penetration.

Fig. 7 illustrates the final damage state of the aluminum target, showing perforation caused by fragments.

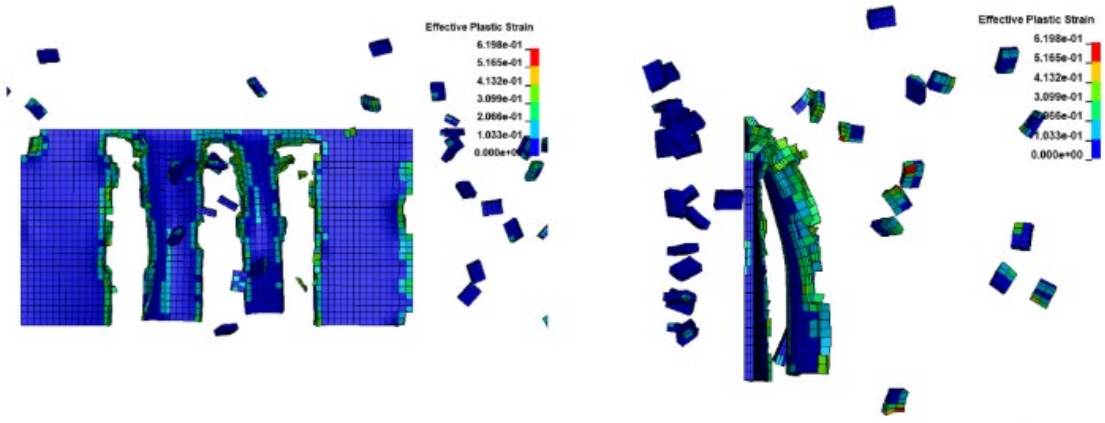


Figure 7: Simulated damage pattern on the aluminum target.

References

[1] O. Molloy, How are drones changing modern warfare?, Australian Army Research Centre, Land Power Forum, 2024. https://researchcentre.army.gov.au/library/land-power-forum/how-are-drones-changing-modern-warfare

[2] C. Marino, Send in the drones, Army AL&T Magazine, 2024. https://www.army.mil/article/280609/

[3] H. González Jorge, E. Aldao, G. Fontenla Carrera, F. Veiga López, E. Balvís, and E. Ríos Otero, Counter Drone Technology: A Review, Preprints, 2024, 10.20944/preprints202402.0551.v1.

[4] U.S. Army Materiel Command, Engineering Design Handbook: Warheads – General, Alexandria, VA, 1964. https://apps.dtic.mil/sti/tr/pdf/AD0501329.pdf

[5] J. Wang, Y.-C. Wang, S.-Q. Zhu, W.-H. Ren, and T.-L. Niu, Improvement and Simulation of THOR Formula with Yaw Angle, Journal of Engineering Science and Technology Review 7(2) (2014). https://jestr.org/downloads/Volume7Issue2/fulltext167214.pdf

[6] G. Baudin, C. Baudoin, A. Soufflet, and L. Champion, Review of Jones–Wilkins–Lee Equation of State (JWL), EPJ Web of Conferences 10 (2010). https://doi.org/10.1051/epjconf/20101000021

Materials Research Proceedings 69 (2026) 1331-1335 https://doi.org/10.21741/9781644904251-231

Maintaining Multistability in Cured Shapes of Series-Connected Unsymmetrical Laminates with Clamped Edges

P. R. MANU[1,a *], B. N. RAO[1,b], and P. M. ANILKUMAR[2,c]

[1]Structural Engineering Division, Department of Civil Engineering, Indian Institute of Technology Madras, 600 036 Chennai, Tamil Nadu, India

[2]Institute of Structural Analysis, Leibniz University Hannover, Appelstraße 9A, 30167 Hannover, Germany

[a]ce23d028@smail.iitm.ac.in, [b]bnrao@iitm.ac.in, [c]a.nair@isd.uni-hannover.de

Keywords: Finite Elements, Boundary Conditions, Morphing, Multistability

Abstract. Adaptive structures are designed to undergo controlled shape changes in response to varying functional requirements, making them highly versatile for advanced engineering applications such as aerospace and space structures. Within this domain, unsymmetrical laminates have gained considerable attention due to bistability arising from residual thermal stresses generated during the curing process. However, the practical applications of the cured shapes of unsymmetrical laminates are often restricted due to the possibility of only two room-temperature equilibrium states. By connecting multiple bistable laminates in series, it becomes possible to realize surfaces with a high degree of multistability. The degree of multistability of such connected laminates is strongly influenced by boundary conditions, which play a critical role in shaping the stability landscape. While most theoretical models in the literature assume simplified center-fixed boundary conditions, such idealized constraints are rarely representative of real-world applications. This study aims to bridge this gap by investigating the influence of boundary constraints on the multistability of series-connected composite laminates. Specifically, a one-end-fixed boundary configuration is analyzed, in which one end of the laminate is clamped. The study shows that the clamped edge imposes significant mechanical constraints that limit bending parallel to the clamped edge. A solution to retain multistability could be the use of a transition region, ensuring that a laminate can recover its original multistable state even when one edge is clamped. Such a transition region helps preserve the multistability of the connected laminate. The results offer new insights into how fixed boundary conditions affect the design space, thereby deepening the understanding of multistable laminates and advancing their application potential in morphing systems.

Introduction

Adaptive structures are designed to alter their shape in response to varying external conditions, making them highly valuable in applications such as aerospace and wind energy systems. Multistable components form a crucial part of these structures due to their ability to maintain multiple stable shapes without the need for continuous energy input to retain those shapes. The potential of unsymmetrical laminates to exhibit multistability, owing to their cured shapes, has attracted considerable attention since the pioneering studies by Hyer [1,2]. When multiple bistable laminates are integrated or interconnected within a structure, they enable continuous and controllable shape transformations. By arranging these bistable laminates in series or parallel, higher-order multistable systems can be achieved. Theoretically, a system composed of n bistable elements in series can exhibit up to 2^n distinct stable states [3]. Transitions between these stable configurations can be realized through appropriate actuation strategies [4].

Content from this work may be used under the terms of the Creative Commons Attribution 3.0 license. Any further distribution of this work must maintain attribution to the author(s) and the title of the work, journal citation and DOI. Published under license by Materials Research Forum LLC.

Materials Research Proceedings 69 (2026) 1331-1335 https://doi.org/10.21741/9781644904251-231

Several studies have explored the behavior of connected multistable laminates [5,6]. Although series-connected laminates have successfully demonstrated the maximum theoretical number of stable configurations [3,7], these investigations predominantly employed a center-fixed boundary condition, which is not representative of most practical scenarios. To move toward more realistic configurations, it is essential to investigate clamped boundary conditions, which can retain the multistability [8,9,10]. Research by Boddapati et al. [11] on clamped bistable laminates demonstrated that clamped boundaries significantly influence the strain energy profile of prestressed laminates and established criteria for the minimum length required to preserve bistability under edge clamping. However, these findings are still limited to bistable laminates, while the behavior of multistable laminates remains unexplored. Understanding how clamped boundaries affect the multistability of series-connected laminates is, therefore, of practical importance.

In the present study, one end of the series-connected unsymmetrical laminates is clamped to reflect a fixed boundary condition. The existence or potential loss of multistability under such clamped configurations is examined by introducing a specially designed transition region. Furthermore, the influence of the stacking sequence on the required transition region length is systematically analyzed.

Methodology and results

In this study, square laminates with dimensions of $L_x = L_y = 135$ mm are considered. The material properties used for the analysis are listed in Table 1. Finite element analysis is performed using the commercial software ABAQUS, employing a four-node, reduced-integration, general-purpose shell element (S4R) for modeling. An initial curing temperature of 180 ºC is applied to the entire assembly, which is subsequently cooled to room temperature (20 ºC), resulting in the first stable configuration. The actuation strategy adopted follows the approach reported in the literature for series-connected laminates with center-fixed boundary conditions [7]. Nonlinear geometric effects are included in the analysis by enabling the NLGEOM option, which is essential for accurately capturing large deformations and snap-through behavior.

Theoretically, up to four stable states are possible for series-connected laminates when their centers are fixed, as illustrated in Fig. 1 (a). However, when one end of the laminate is directly clamped, the curvature in the clamping direction (i.e., the $\boldsymbol{y}$-direction) is restricted. As a result, all configurations involving curvature in the $\boldsymbol{y}$-direction are suppressed, and only the state exhibiting curvature solely in the $\boldsymbol{x}$-direction remains stable. Consequently, the laminate becomes monostable, as shown in Fig. 1 (b).

Table 1: Properties of laminate selected in the present study

Component	E_{11} (GPa)	E_{22} (GPa)	G_{12} (GPa)	$\boldsymbol{\nu}_{12}$	$\boldsymbol{\alpha}_{11}$ (10^{-6}/ ºC)	$\boldsymbol{\alpha}_{22}$ (10^{-6}/ ºC)	$\boldsymbol{t}$ (mm)
Lamina	164	6.8	3.4	0.28	-0.02	33	0.140

Materials Research Proceedings 69 (2026) 1331-1335 https://doi.org/10.21741/9781644904251-231

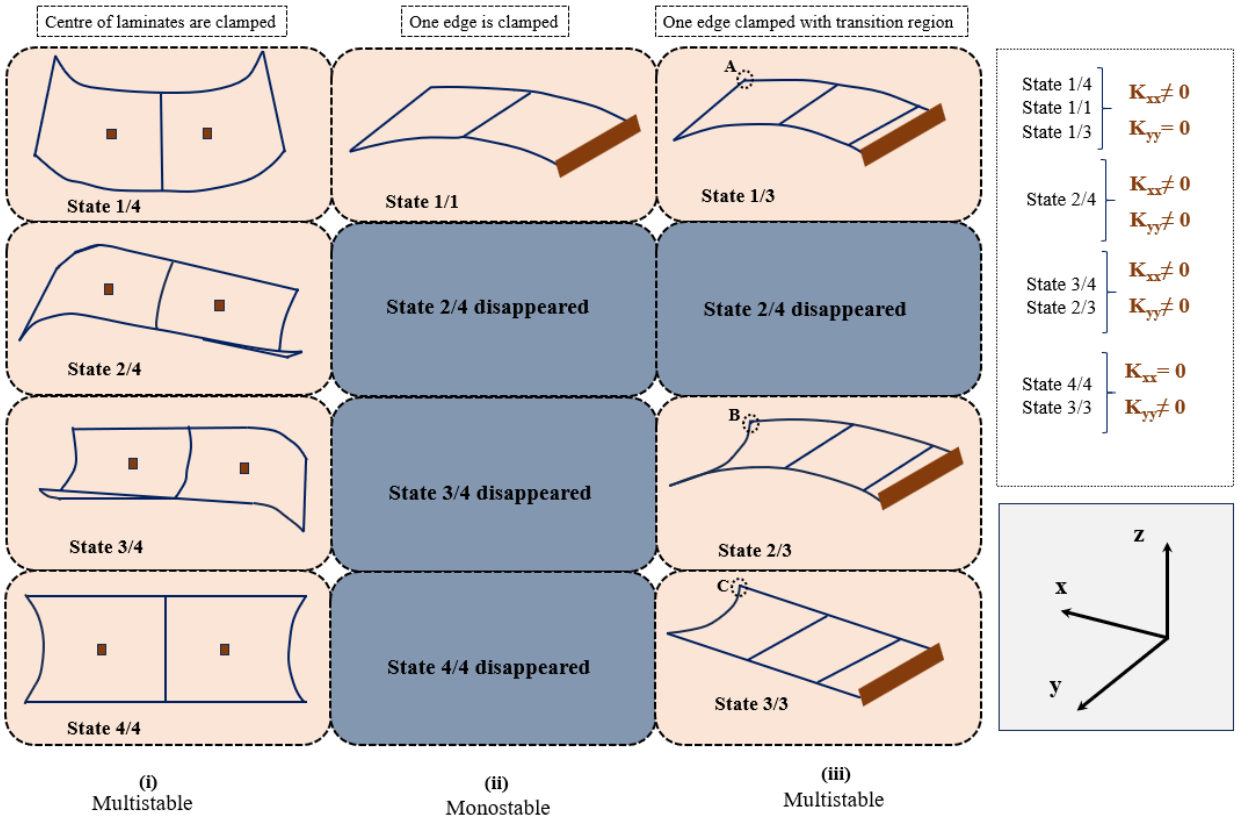


Figure 1. Schematic representation of (i) mathematically possible configurations of series connected laminates when the center of the laminates are fixed, (ii and iii) the effect of clamped boundary on the multistability when the edge is clamped, and the significance of transition plate in regaining the lost states

A transition region is introduced between the laminate and the clamped support. One edge of the transition plate is clamped, and no other boundary conditions are imposed on the assembly. The length of the transition plate is denoted by T_x, and the width of the transition plate is taken to be equal to L_y, since it must be attached to the laminate edge. The transition ratio ($\boldsymbol{TR} = \frac{T_x}{L_x}$) is defined as the ratio of the length of the transition plate to the length of one laminate plate (both laminate plates have the same dimensions). Different stacking sequences are used for the transition region, with the transition ratio varied from 0.05 to 0.5 in increments of 0.05. The transition ratio at which the $\boldsymbol{y}$-direction curvature is maintained, or bistability/multistability exists, is then identified.

The addition of a transition region facilitates the regaining of multistability. A maximum of three stable states is regained by introducing the transition region, as shown in Fig. 1(c). However, the extent of this recovery depends on the stacking sequence of the transition region, as shown in Fig. 2. For a stacking sequence of [0/90], bistability or multistability reappears at a $\boldsymbol{TR}$ of 0.2, whereas for the [0/0] and [90/90] configurations, it occurs at $\boldsymbol{TR}$ = 0.25. In the case of [90/0], bistability is regained only at $\boldsymbol{TR}$ = 0.5. Conversely, the [-45/45] stacking sequence exhibits monostable behavior across all transition ratios considered. Specific examples of the multistable configurations identified in Fig. 2 are summarized in Table 2. The corresponding out-of-plane displacements measured at the laminate corner for state 1, state 2, and state 3 are also provided in Table 2.

Materials Research Proceedings 69 (2026) 1331-1335 https://doi.org/10.21741/9781644904251-231

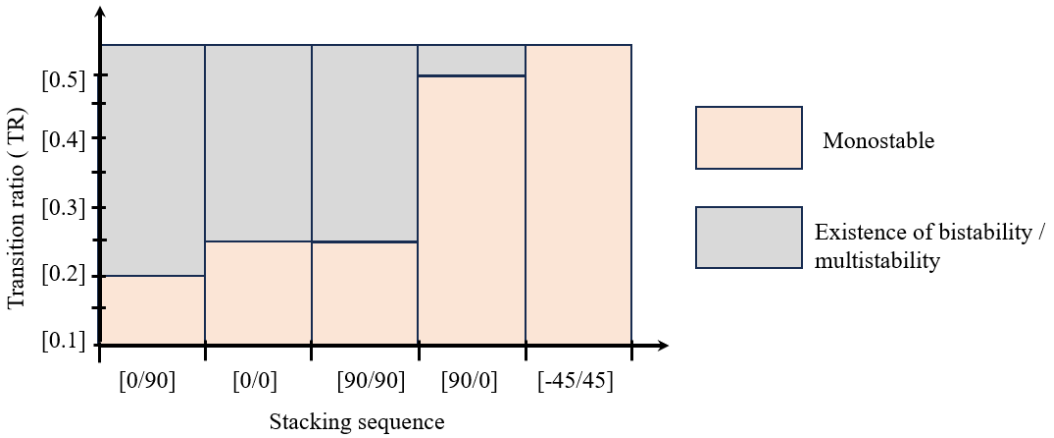


Figure 2. Representation of regaining of bistability/multistability for change in transition ratio for different stacking sequences

Table 2: Out-of-plane displacement values (A, B and C) at the corner for different states for the successful multistable cases depicted in the Fig. 1(c)

Transition ratio	Stacking sequence	Out-of-plane displacement (mm)		
		State 1 (A)	State 2 (B)	State 3 (C)
0.25	[90/90]	174.03	292.84	159.97
0.25	[0/90]	216.34	286.37	173.58
0.30	[90/90]	173.44	299.33	279.96
0.35	[0/90]	182.44	199.77	123.64
0.50	[0/90]	151.83	274.64	210.22

Summary and conclusions

The multistable behavior of series-connected laminates under clamped boundary conditions is investigated in this study. It is observed that clamping leads to a loss of multistability, resulting in a monostable configuration. However, introducing a transition region between the clamped support and one edge of the laminate restores the lost stable configurations, enabling the existence of three stable shapes. The restriction imposed by the clamped edge suppresses curvature in the y-direction, which is the primary cause of the loss of multistability. The addition of the transition region alleviates this restriction, allowing the laminates away from the clamped edge to regain curvature in the y-direction, thereby recovering multiple stable states. The influence of different stacking sequences on the multistability of laminates with a transition region is also examined. However, laminates directly connected to the clamped edge through the transition region are unable to exhibit significant curvature in the y-direction. This investigation holds considerable practical relevance, as it represents a step toward boundary conditions commonly encountered in real-world applications.

References

[1] Hyer, Some observations on the cured shape of thin unsymmetric laminates, Journal of Composite Materials 15 (2) (1981) 175–194. https://doi.org/10.1177/002199838101500207

[2] Hyer, The room-temperature shapes of four-layer unsymmetric cross-ply laminates, Journal of Composite Materials 16 (4) (1982) 318–340. https://doi.org/10.1177/002199838201600406

[3] Y. Cui, M. J. Santer, Adaptive multistable flexible composite surfaces, in: Spacecraft Structures Conference, 2014, p. 0671. https://doi.org/10.2514/6.2014-0671

[4] D. Bashir, P. M. Anilkumar, S. Scheffler, A. Haldar, B. N. Rao, R. Rolfes, A review of the dynamic behavior of thermally induced bistable configurations of unsymmetrical composite laminates and their applications, Archives of Computational Methods in Engineering (102024). https://doi.org/10.1007/s11831-024-10192-6

[5] F. Mattioni, P. Weaver, M. Friswell, Multistable composite plates with piecewise variation of lay-up in the planform, International Journal of Solids and Structures 46 (2009)151–164. https://doi.org/10.1016/j.ijsolstr.2008.08.023

[6] F. Dai, H. Li, S. Du, Design and analysis of a tri-stable structure based on bi-stable laminates, Composites Part A: Applied Science and Manufacturing 43 (9) (2012) 1497–1504. https://doi.org/10.1016/j.compositesa.2012.03.018

[7] A. Kumar, P. M. Anilkumar, A. Haldar, S. Scheffler, O. Dorn, B. N. Rao, R. Rolfes, Investigations on the multistability of series-connected unsymmetric laminates, Composites Science and Technology (2022) 109635. https://doi.org/10.1016/j.compscitech.2022.109635

[8] A. Mukherjee, M. I. Friswell, S. F. Ali, A. Arockiarajan, Modeling and design of class of hybrid bistable symmetric laminates with cantilever boundary configuration, Composite Structures 239 (2020) 112019. https://doi.org/10.1016/j.compstruct.2020.112019

[9] M. Brunetti, S. Vidoli, A. Vincenti, Bistability of orthotropic shells with clamped boundary conditions: An analysis by the polar method, Composite Structures 194 (2018)388–397. https://doi.org/10.1016/j.compstruct.2018.04.009

[10] Z. Zhang, Y. Li, X. Yu, X. Li, H. Wu, H. Wu, S. Jiang, G. Chai, Bistable morphing composite structures: a review, Thin-walled structures 142 (2019) 74–97. https://doi.org/ 10.1016/j.tws.2019.04.040

[11] Boddapati, J. C. Osorio, A. F. Arrieta, On the loss of stability of bistable laminates due to clamping, in: AIAA SCITECH 2024 Forum, 2024, p. 1333. https://doi.org/10.2514/6.2024-1333

Materials Research Proceedings 69 (2026) 1336-1340 https://doi.org/10.21741/9781644904251-232

Constrained Surrogate-based Optimisation for Finite Element Model Updating

Eduardo LARREA HERRANZ[1,a] and Gabriele DESSENA[1,b *]

[1]Department of Aerospace Engineering, Universidad Carlos III de Madrid, Av. de la Universidad 30, 28911 Leganés, Madrid, Spain

[a]100510548@alumnos.uc3m.es, [b]gdessena@ing.uc3m.es

Keywords: Surrogate-Based Optimisation, Finite Element Model Updating, Constrained Optimisation, Kriging, Modal Analysis

Abstract. Finite element model updating represents a pivotal process in civil aircraft development, enabling the reconciliation of numerical models with experimental data obtained from static or ground vibration testing. Traditional surrogate-based optimisation methods, particularly Efficient Global Optimization through Kriging modelling, often lack robust constraint handling mechanisms, which are essential for real-world aerospace applications. This study presents the development and validation of a Constrained refined Efficient Global Optimisation (CrEGO) framework that addresses this limitation by integrating a Probability of Feasibility-penalised Expected Improvement acquisition function into the refined EGO methodology. The CrEGO algorithm constructs Kriging surrogate models for both objective and constraint functions, enabling rapid feasibility assessment without costly evaluations. Validation on the eXperimental BearDS 2 high-aspect-ratio wing spar demonstrates remarkable performance improvements, reducing the Modified Total Modal Assurance Criterion from 0.214 to 0.006 (97% improvement) whilst maintaining strict mass constraints, using only 829 expensive finite element evaluations.

Introduction

The evolution of modern aeronautical design has been characterised by the increasing reliance on high-fidelity numerical simulations, including Computational Fluid Dynamics and Finite Element Methods (FEM), which provide essential insights for structural analysis and certification processes. However, discrepancies between numerical predictions and experimental observations necessitate systematic model updating procedures to ensure accurate representation of real-world behaviour.

Finite element model updating (FEMU) has evolved from its foundations in the 1980s to become an indispensable tool in the study of structural dynamics, with a strong influence on aircraft development [1], allowing for the numerical models to reconcile with the experimental data obtained, either by static or ground vibration testing. The discipline encompasses both direct methods, including matrix updates, optimal matrix and error matrix, and eigenstructure assignment; and indirect methods that use experimental data through modal parameters or frequency domain information. Modal parameters, particularly natural frequencies (ω_n) and mode shapes ($\boldsymbol{\phi_n}$) [2], have emerged as preferred choices due to their stability compared to damping ratios.

Though many optimisation strategies have been proposed, most are predominantly classified as evolutionary, gradient- or local search-based, and surrogate-assisted approaches, a category now also including artificial intelligence-driven methods. Nevertheless, the primary objective of any optimisation technique is to address the specific problem with maximum efficiency [3]; therefore, in most practical applications, it is rarely necessary to employ exceedingly intricate or data-intensive models.

Content from this work may be used under the terms of the Creative Commons Attribution 3.0 license. Any further distribution of this work must maintain attribution to the author(s) and the title of the work, journal citation and DOI. Published under license by Materials Research Forum LLC.

Materials Research Proceedings 69 (2026) 1336-1340 https://doi.org/10.21741/9781644904251-232

Traditional optimisation approaches face significant challenges when applied to the FEMU procedure. Gradient-based methods struggle with non-linear, noisy objective landscapes where direct numerical derivatives lose accuracy and optimisers become prone to local minima stagnation, unless very good initial parameter estimates are available. Conversely, evolutionary algorithms, whilst providing a more global search and being more robust to derivative noise, require prohibitively high evaluation budgets incompatible with expensive numerical simulations inherent in FEMU applications.

Surrogate-based optimisation techniques have emerged as powerful solutions by constructing efficient approximation models from limited, expensive function evaluations. The Efficient Global Optimisation (EGO) framework [4], with Kriging modelling and Expected Improvement criteria, has demonstrated remarkable success in balancing exploration and exploitation. Enhanced variants such as refined Efficient Global Optimisation (rEGO) [5] have further improved performance through hybrid global-local search strategies and adaptive domain reduction. Despite these advances, a critical limitation persists for rEGO: the absence of robust constraint handling mechanisms essential for real-world aerospace applications. Practical FEMU problems invariably involve constraints related to performance requirements, manufacturing restrictions, and regulatory guidelines. This study addresses this gap by developing the Constrained refined Efficient Global Optimisation (CrEGO) framework.

Methodology

CrEGO extends the rEGO algorithm by integrating non-linear constraint handling capabilities whilst preserving its improved characteristics. The framework constructs Kriging surrogate models for both objective and constraint functions, represented as Gaussian processes, approximating the functions with the model:

$$\mathrm{Y}(\mathrm{x}) = \mu + \epsilon(\mathrm{x}) \tag{1}$$

where μ represents the average of the stochastic process and $\epsilon(\mathrm{x})$ is the error term distributed with zero mean and variance $\sigma(\mathrm{x})$. The constraint handling mechanism is based on variations of the Expected Improvement (EI) acquisition function, representative of the Kriging modelling [6]. The full expression becomes:

$$\mathrm{EI}(\mathrm{x}) = \left(\mathrm{f_{min}} - \mu(\mathrm{x})\right) \cdot \Phi\left(\frac{\mathrm{f_{min}} - \mu(\mathrm{x})}{\sigma(\mathrm{x})}\right) + \sigma(\mathrm{x}) \cdot \phi\left(\frac{f_{min} - \mu(x)}{\sigma(x)}\right) \tag{2}$$

where $\Phi(\cdot)$ and $\phi(\cdot)$ represent the cumulative distribution function and probability density function of the standard normal distribution, respectively, and $\mathrm{f_{min}}$ is the current minimum solution found. The EI is modified to penalise the acquisition function through the product of the Probability of Feasibility (PoF) for each constraint [7]:

$$\mathrm{EI}_{mod}(x) = \mathrm{EI}(x) \prod_{i=1}^{m} min(2 \cdot \mathrm{PoF}(g_i(x) \leq 0), 1) \tag{3}$$

being m the total number of constraints and having the PoF for the i-th constraint calculated using the Kriging model parameters:

$$\mathrm{PoF}(g_i(x) \leq 0) = \Phi\left(-\frac{\mu(x)}{\sigma_i(x)}\right) \tag{4}$$

Algorithm Enhancement.

CrEGO refines rEGO for constraint management: Latin hypercube sampling is used to verigy feasibility within $(\mathrm{d} \times 50)$ samples; constraints use individual Kriging models at the objective sample sites to evaluate PoF at low cost; if $(\mathrm{EI_{mod}})$ returns unfeasible points, the genetic algorithm enforces feasibility during EI maximisation; stopping combines an EI threshold with a minimum

Materials Research Proceedings 69 (2026) 1336-1340 https://doi.org/10.21741/9781644904251-232

Euclidean distance between successive feasible candidates. CrEGO is implemented in MATLAB R2024b and it is based on the DACE toolbox[1] for Kriging and data declustering.

High Aspect Ratio Wing Case Study

The CrEGO framework is applied to the eXperimental BeaRDS 2 (XB-2) high-aspect-ratio wing spar [8] for validation. The spar, shown in Fig. 1, geometry consists of a St. George's cross-shaped cross section, which changes proportions along the span, and a rectangular cross section in the root section, where the spar can be clamped. It is constructed from aluminium alloy 6082-T6 with a density $\rho = 2700$ kgm^{-3}, Young's modulus $E = 70$ GPa and a total mass $M_{\text{spar}} = 1.225$ kg.

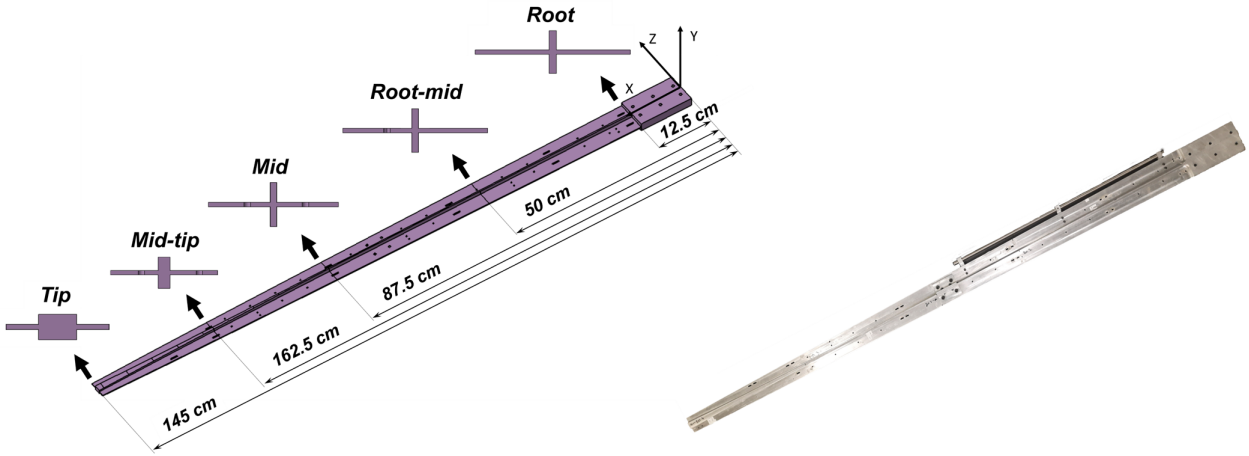


Figure 1 Spar CAD model (on the left), with the interested sections divisions and position, next to the real spar image (on the right), retrieved from [9].

The optimisation scenario involved tuning sectional density and Young's modulus parameters across the four taper segments of the spar described in Fig. 1, considering a fixed root section corresponding with the area where the spar is clamped. Limit bounds to the parameter variations are set to [0.7, 1.3] relative to baseline values of 1, constituting eight design variables total. The complement of the Modified Total Modal Assurance Criterion (MTMAC) [10] served as the objective function.

As per the main constraint, a critical mass restriction was imposed to maintain structural resemblance to the original configuration:

$$g(x) = \left(\mathrm{M}_{\mathrm{FEM}}(x) - \mathrm{M}_{\mathrm{spar}}\right)^2 - \left(\gamma \cdot \mathrm{M}_{\mathrm{spar}}\right)^2 \leq 0 \tag{5}$$

where $\mathrm{M}_{\mathrm{FEM}}$ represents the Finite Element Model (FEM) mass as a function of design variables, $\mathrm{M}_{\mathrm{spar}}$ denotes the baseline spar mass and γ stands for the maximum variation allowed between the previous masses. This formulation ensures the optimised configuration remains within $\pm$5% of the original mass, $\gamma = 0.05$.

Ground vibration testing (GVT) data [9] for the first three vertical bending modes provided experimental reference values for model updating. Modal measurements were extracted at strategically positioned nodes corresponding to accelerometer locations used in experimental testing, ensuring consistent comparison between numerical and experimental modal data. The optimisation used ANSYS Mechanical APDL for finite element analysis, with automated model parameter extraction integrated within the MATLAB CrEGO workflow.

Results are presented as a comparison between the experimental data [9], the Baseline FEM model analysis and the CrEGO FEMU procedure. Starting from a Baseline MTMAC value of 0.214, the CrEGO algorithm achieved a final value of 0.006, representing a 97% improvement in

[1] The DACE toolbox is available at https://orbit.dtu.dk/en/publications/dace-a-matlab-kriging-toolbox/

Materials Research Proceedings 69 (2026) 1336-1340 https://doi.org/10.21741/9781644904251-232

modal correlation. This enhancement was accomplished using 829 finite element evaluations whilst strictly maintaining the imposed mass constraint. The final optimised spar mass of 1.164 kg remained within the allowable ±5% deviation from the baseline 1.225 kg, consistently identifying the constraint boundary as optimal.

The parameter optimisation revealed consistent density reductions across spar elements, particularly concentrated in the third element, where the scaling factor reached the lower bound. Conversely, Young's modulus parameters generally approached upper bounds. Notably, during the GVT in [9], plastic deformation near the spar root was spotted, leading to enhanced resistance to further deformation in the area. The optimisation procedure captured this material stiffening through high E values in the first (closest to the root) spar element.

In terms of modal behaviour, the results presented in Tab. 1 and Fig. 2 show a clear enhancement with respect to the Baseline analysis. MAC values increased significantly, where the biggest effect was found in the 3rd bending mode, changing from 0.988 to 0.995.

Table 1 Modal natural frequency values for the Experimental, Baseline, and CrEGO updated model with percentage difference w.r.t. experimental values.

Natural Frequency [Hz] – (Difference in %)			
Mode	**Experimental**	**Baseline**	**CrEGO**
1st Bending	4.855	5.563 (14.58)	4.855 (0.00)
2nd Bending	26.966	31.193 (15.68)	26.965 (0.00)
3rd Bending	76.851	92.012 (19.73)	76.861 (0.01)

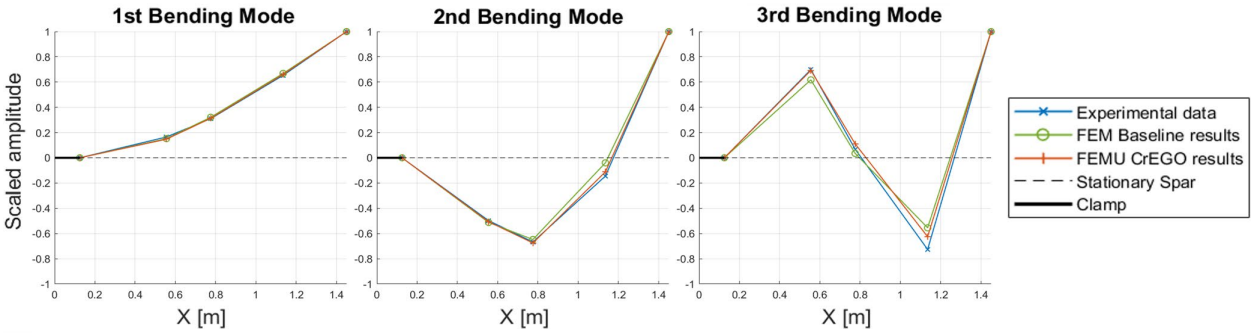


Figure 2 Mode shapes identified from the experimental data, the Baseline FEM and the Baseline FEM and the CrEGO FEMU procedure for the spar.

Conclusions

This study successfully developed and validated the Constrained refined Efficient Global Optimisation (CrEGO) framework, addressing a critical gap in surrogate-based optimisation for aerospace applications. By integrating Probability of Feasibility-penalised Expected Improvement into the refined EGO methodology, CrEGO enables effective constraint satisfaction whilst efficiently exploring the design space, making it practical for real-world FEMU problems. The framework's robust constraint handling mechanisms, incorporating Kriging surrogate models for both objective and constraint functions, enable efficient feasibility assessment without expensive constraint evaluations. This represents a significant advancement over traditional penalty methods. The adaptive stopping criteria combining Expected Improvement thresholds with explicit feasibility checks ensured reliable convergence whilst preserving computational efficiency throughout the optimisation process. Validation on the eXperimental BearDS 2 high-aspect-ratio wing spar demonstrated exceptional performance. The algorithm achieved a 97% improvement in modal correlation, reducing the MTMAC from 0.214 to 0.006 whilst maintaining strict mass constraints using only 829 expensive finite element evaluations. The final optimised spar mass of

1.164 kg remained well within the allowable ±5% deviation from the baseline. Modal correlation analysis revealed substantial improvements across all considered modes. Maximum modal frequency deviation decreased from 19.73% to 0.01%, whilst MAC values increased significantly, approaching 1.

These findings establish CrEGO as a powerful tool for aerospace FEMU problems where computational efficiency and constraint satisfaction are paramount. The framework contributes to more efficient, accurate, and reliable structural analysis methodologies essential for future aviation developments.

Aknowledgements
This work is supported by the grants for research activity of young PhD holders, part of the Universidad Carlos III de Madrid Own Research Program (TOMA - Tangential interpolation for Operational Modal Analysis project).

References

[1] Marwala T, Sibisi S. Finite Element Model Updating Using Bayesian Framework and Modal Properties. J Aircr 2005;42:275–8. https://doi.org/10.2514/1.11841.

[2] Rosati I, Fabbrocino G, Rainieri C. A discussion about the Douglas-Reid model updating method and its prospective application to continuous vibration-based SHM of a historical building. Eng Struct 2022;273:115058. https://doi.org/10.1016/j.engstruct.2022.115058.

[3] Raviolo D, Civera M, Zanotti Fragonara L. A Comparative Analysis of Optimization Algorithms for Finite Element Model Updating on Numerical and Experimental Benchmarks. Buildings 2023;13:3010. https://doi.org/10.3390/buildings13123010.

[4] Jones DR, Schonlau M, Welch WJ. Efficient Global Optimization of Expensive Black-Box Functions. J Glob Optim 1998;13:455–92. https://doi.org/10.1023/A:1008306431147.

[5] Dessena G, Ignatyev DI, Whidborne JF, Zanotti Fragonara L. A global–local meta-modelling technique for model updating. Comput Methods Appl Mech Eng 2024;418:116511. https://doi.org/10.1016/j.cma.2023.116511.

[6] Forrester AIJ, Sóbester A, Keane AJ. Engineering Design via Surrogate Modelling. Wiley; 2008. https://doi.org/10.1002/9780470770801.

[7] Bagheri S, Konen W, Allmendinger R, Branke J, Deb K, Fieldsend J, et al. Constraint handling in efficient global optimization. Proc. Genet. Evol. Comput. Conf., New York, NY, USA: ACM; 2017, p. 673–80. https://doi.org/10.1145/3071178.3071278.

[8] Yusuf SY, Hayes D, Pontillo A, Carrizales MA, Dussart GX, Lone MM. Aeroelastic Scaling for Flexible High Aspect Ratio Wings. AIAA Scitech 2019 Forum, Reston, Virginia: American Institute of Aeronautics and Astronautics; 2019, p. 1–14. https://doi.org/10.2514/6.2019-1594.

[9] Dessena G, Ignatyev DI, Whidborne JF, Pontillo A, Zanotti Fragonara L. Ground vibration testing of a flexible wing: A benchmark and case study. Aerospace 2022;9:438. https://doi.org/10.3390/aerospace9080438.

[10] Perera R, Torres R. Structural Damage Detection via Modal Data with Genetic Algorithms. J Struct Eng 2006;132:1491–501. https://doi.org/10.1061/(ASCE)0733-9445(2006)132:9(1491).

Materials Research Proceedings 69 (2026) 1341-1346 https://doi.org/10.21741/9781644904251-233

Smart Composite for Structural Health Monitoring: Using Copper Wires for Strain Sensing

Antonio Paolo Fontanella[1,a *], Matteo Febo[1,b], Ester D'Accardi[1,c], Davide Palumbo[1,d], Umberto Galietti[1,e], Francesco Ciampa[1,f] and Maria Cinefra[1,g]

[1]Department of Mechanics, Mathematics and Management, Politecnico di Bari, Via Edoardo Orabona 4, 70126 Bari, Italy

[a]a.fontanella1@phd.poliba.it, [b]matteo.febo@poliba.it, [c]ester.daccardi@poliba.it, [d]davide.palumbo@poliba.it, [e]umberto.galietti@poliba.it, [f]francesco.ciampa@poliba.it, [g]maria.cinefra@poliba.it

Keywords: Structural Health Monitoring, Smart Composite, Passive Sensors, Copper Wires, Strain Sensing

Abstract. This study presents a multifunctional Carbon Fiber Reinforced Polymer (CFRP) composite integrating embedded copper wires for Structural Health Monitoring (SHM) through strain-induced resistance variation. The monitoring principle relies on the linear relationship between mechanical strain and the change in electrical resistance of the copper wires. A preliminary feasibility test was carried out through a three-point bending experiment up to failure, with real-time resistance acquisition managed by an Arduino Giga R1 WiFi controller. A complementary Finite Element Method (FEM) analysis in Ansys was employed to predict wire deformation and corresponding resistance change. The first correlation between the experimental and numerical results confirms the effectiveness of the proposed sensing approach as a continuous, non-invasive, and cost-efficient strain monitoring technique for advanced composite structures.

1. Introduction

Carbon Fiber Reinforced Polymers (CFRPs) are widely used in aerospace, automotive, civil, and marine engineering due to their superior mechanical performance, lightweight, and design flexibility. The growing demand for reliability and structural safety has driven the development of multifunctional composites that can integrate self-sensing and damage monitoring capabilities, known as Structural Health Monitoring (SHM) systems [1,2].

Conventional inspection methods typically rely on periodic or post-damage evaluation, limiting their applicability for real-time monitoring. Embedding passive sensors directly within the composite matrix offers a practical solution for continuous structural assessment at low cost and with minimal additional weight.

In this work, copper wires are integrated within CFRP laminates to serve as in-situ strain sensors. The sensing mechanism is based on monitoring the electrical resistance variations resulting from mechanical elongation during loading. The resistance increases proportionally with the strain-induced length change of the wire [3−5]. While wire rupture provides a discrete damage indicator (loss of electrical continuity), this study aims to achieve continuous strain monitoring throughout the entire deformation process. Copper was selected for its high electrical conductivity and ductility, ensuring good compatibility with the composite matrix. The embedded longitudinal and transverse copper wires allow for localized deformation monitoring, and the first correlation between numerical and experimental results supports the feasibility of the proposed sensing approach.

Content from this work may be used under the terms of the Creative Commons Attribution 3.0 license. Any further distribution of this work must maintain attribution to the author(s) and the title of the work, journal citation and DOI. Published under license by Materials Research Forum LLC.

Materials Research Proceedings 69 (2026) 1341-1346 https://doi.org/10.21741/9781644904251-233

2. Materials and Methods

Rectangular CFRP specimens (100 mm × 20 mm) were fabricated via the Vacuum Assisted Resin Transfer Molding (VARTM) process, ensuring uniform resin infiltration and void-free consolidation. The composite consisted of ten woven carbon-fiber plies, each approximately 0.2 mm thick. Copper wires (diameter 0.2 mm) were embedded as passive strain sensors between specific layers.

Two distinct wire arrangements were implemented: Transverse sensors (20 short wires placed between the 3rd and 4th plies) and Longitudinal sensors (4 long wires positioned between the 7th and 8th plies). The wires were embedded 2.5 mm from the specimen edges, with 5 mm spacing between adjacent wires (Figure 1).

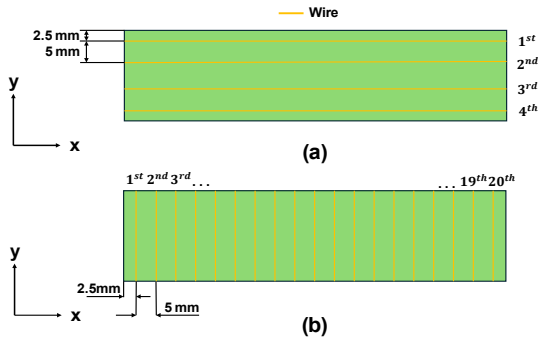


Figure 1. Schematic in plane representation of the embedded copper wire network in the CFRP: a) Longitudinal and b) Trasversal wires

Table 1 summarizes the mechanical and physical properties of the composite constituents.

Table 1. Mechanical and Physical Properties of Constituent Materials

	CFRP laminate	Copper
Young's Modulus E [GPa] (in Plane)	60	110
Young's Modulus E [GPa] (out of Plane)	3	
Poisson's ratio v (in Plane)	0.04	0.34
Poisson's ratio v (out of Plane)	0.3	
Shear Modulus G [GPa] (in Plane)	1	-
Shear Modulus G [GPa] (out of Plane)	2	-
Electrical resistivity ρ [Ω × m]	-	1.68×10^{-8}

3. Finite Element Modeling

A linear static Finite Element Analysis (FEA) was performed in Ansys to predict the mechanical strain and elongation of the embedded copper wires. The model reproduced the geometry, material properties, and boundary conditions of the tested specimens.

A high-resolution mesh with 20-node solid elements (SOLID 186) and element size of approximately 0.25 mm was used. Local mesh refinement was applied at the copper–matrix interface to capture high strain gradients (Figure 2). To enforce perfect bonding between the CFRP layers and the embedded copper wire, a node merge technique was implemented at the interfaces.

Materials Research Proceedings 69 (2026) 1341-1346 https://doi.org/10.21741/9781644904251-233

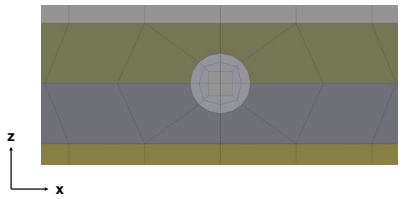


Figure 2. Finite Element Mesh detail of the copper wire cross-section

The resistance variation was estimated from the classical resistence formula:

$$\Delta R = \rho \frac{\Delta L}{S_0}. \tag{1}$$

where ρ is the electrical resistivity of copper, S_0 is the initial cross-sectional area of the copper wire and ΔL is elongation computed from the deformed nodal coordinates.

To obtain ΔL,the deformed length L_{def} of the wire's centerline axis is computed by summing the lengths of all elemental segments in the final, loaded configuration.

If the wire's centerline is defined by a sequence of nodal coordinates $\boldsymbol{X}_i^{def} = (x_i^{def}, y_i^{def}, z_i^{def})$ for node i, the length of the segment between node i and node $i+1$ in the deformed state is found using the Euclidean distance:

$$L_{def} = \sum_{i=1}^{N-1} \sqrt{\left(x_{i+1}^{def} - x_i^{def}\right)^2 + \left(y_{i+1}^{def} - y_i^{def}\right)^2 + \left(z_{i+1}^{def} - z_i^{def}\right)^2}. \tag{2}$$

$$\Delta L = L_{def} - L_0. \tag{3}$$

where N is the total number of nodes along the wire axis. The initial undeformed length L_0 is calculated similarly using the initial nodal coordinates $\boldsymbol{X}_i^0$.

Numerical results were obtained for Longitudinal Wires 1 and 2, with symmetry assumed for Wires 3 and 4. The predicted ΔR–displacement curves for both wires showed nearly identical nonlinear trends, confirming a uniform strain field near the specimen mid-plane (Figure 3**)**

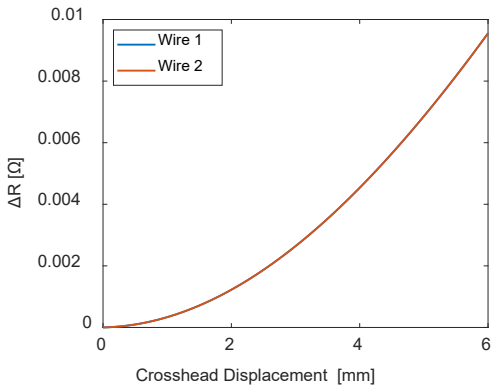


Figure 3. Numerical prediction of $\Delta \boldsymbol{R}$ *for Longitudinal Wires 1 and 2*

4. Experimental Setup for Resistance Measurement

The resistance measurement system was built around an Arduino Giga R1 WiFi microcontroller connected to a set of parallel voltage divider circuits. Each channel consisted of a fixed resistor ($R = 100\ [\Omega]$) in series with the variable resistance of the copper wire (R_i).

The output voltage V_{out} of each divider is given by:

Materials Research Proceedings 69 (2026) 1341-1346 https://doi.org/10.21741/9781644904251-233

$$V_{out} = \frac{R}{R+R_i} V_{in}. \quad (4)$$

and the resistance of each wire is calculated as:

$$R_i = \left[\left(\frac{V_{in}}{V_{out}}\right) - 1\right] \times R, i = 1,2, \dots N. \quad (5)$$

where V_{in} is the input voltage of the circuit, typically 5 [V] for the Arduino system. This relationship was implemented in the Arduino code to compute real-time resistance changes (ΔR) for all sensing channels (Figure 4).

It is important to note that the electrical resistivity (ρ) of copper increases with temperature according to its positive temperature coefficient. During the tests, a slight thermal rise was observed in the wires connected to the Arduino board due to Joule heating and continuous current flow. This thermal effect contributes to a baseline drift in the measured resistance, which was subsequently compensated during signal post-processing.

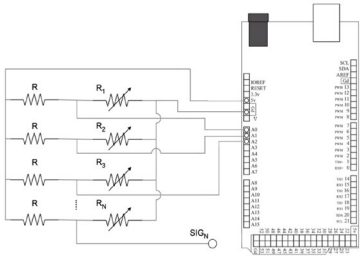


Figure 4. Arduino Giga R1 Wifi connected to the designed system with N denoting the number of channels on the structure [1]

4.1. Experimental Procedure

The sensor-reinforced composite specimens were subjected to three-point bending tests until failure. The experimental setup involved a central load application, with the supports placed between the 4th and 5th transversal wires and between the 16th and 17th transversal wires. This setup (Figure 5) allowed for the analysis of the resistance change under a controlled and localized stress state.

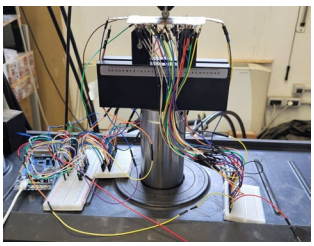


Figure 5. Experimental setup for the three-point bending test and real-time resistance measurement

Transverse wires exhibited negligible resistance changes due to their orientation and proximity to the neutral axis, making them unsuitable for quantitative correlation. Therefore, the analysis focused exclusively on the four longitudinal wires, which provided, strain-dependent resistance variations.

The specimen failed at a maximum load of 640 N and a crosshead displacement of 6 mm, defining its ultimate flexural capacity.

The raw electrical signals were filtered using a two-step procedure: a moving median filter to remove high-frequency spikes and a zero-phase Butterworth low-pass filter to extract the underlying trend. Additionally, to compensate for the thermal drift caused by resistivity increase

at higher temperature, each filtered curve was corrected by subtracting a reference baseline obtained from a separate "no-load" experiment, in which the system was powered and allowed to reach its steady-state thermal condition without mechanical loading.

Figure 6 illustrates the recorded ΔR profiles for longitudinal Wire 1 and Wire 2.

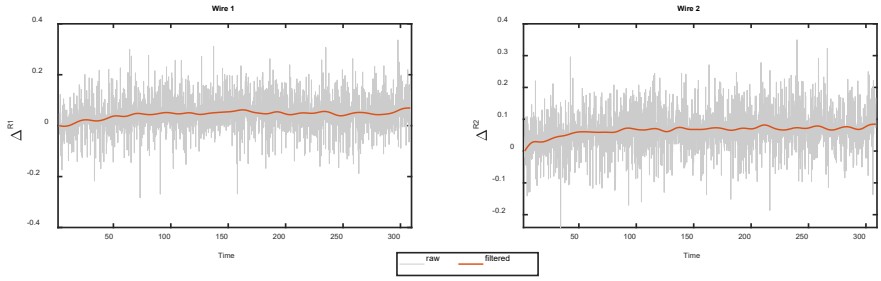


*Figure 6. Experimental resistance variation (Δ**R**) over time for the four longitudinal copper wires (Wire 1 to Wire 4) during the three-point bending test*

The filtered curves exhibit a smooth, nonlinear increase in ΔR consistent with progressive structural deformation.

5. Results and Discussion

During the bending test, longitudinal wires exhibited clear strain-dependent resistance increases, while transverse wires showed minimal variations masked by electrical noise. The ultimate load and displacement at failure were 640 N and 6 mm, respectively, consistent with the expected flexural strength for the tested laminate.

Figure 7 illustrates the feasibility of the proposed sensing approach through a comparison between the numerically predicted and experimentally measured ΔR curves for the longitudinal wires. Both trends exhibit a gradual increase in resistance variation with increasing displacement, as expected from strain-induced effects. The overall variations remain very small – on the order of 0.02 at most – making them difficult to discern experimentally. Despite this, the model successfully captures the general evolution of ΔR and provides a reasonable estimate of the magnitude, strongly supporting the feasibility and reliability of the proposed method.

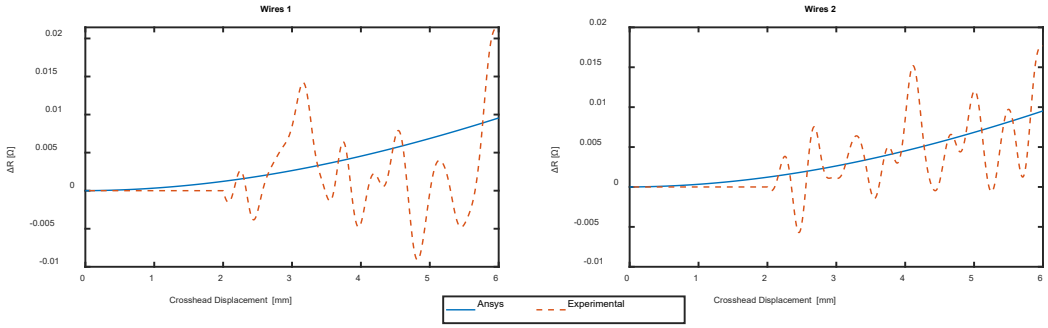


*Figure 7. Comparison of predicted vs. experimental Δ**R** for the longitudinal copper wires*

6. Conclusion

This work demonstrated the feasibility of embedding copper wires as passive strain sensors within CFRP composites for real-time SHM applications.

- Sensing Mechanism Validation: The Arduino-based monitoring system successfully acquired resistance changes during deformation, revealing strong correlation with mechanical strain.

- Numerical–Experimental Correlation: FEM simulations accurately reproduced experimental resistance variations by computing the strain-induced wire elongation.

The correlation between experimental and numerical data confirms the reliability of the proposed approach as a low-cost, integrated, and non-invasive strain monitoring solution. Future developments will focus on extending this methodology to multi-sensor networks for distributed SHM and dynamic loading conditions.

Acknowledgments
Authors acknowledges support by the European Union - NextGenerationEU (National Sustainable Mobility Center CN00000023, Italian Ministry of University and Research Decree n. 1033 – 17/06/2022, Spoke 11 – Innovative Materials & Lightweighting). The opinions expressed are those of the authors only and should not be considered as representative of the European Union or the European Commission's official position. Neither the European Union nor the European Commission can be held responsible for them.

References:

[1] W. Adeyemi, W. Khor, F. Ciampa, Material-Enabled Impact Detection and Damage Localisation System Using Shape Memory Alloy Tufted Composites. Sensors 2023, 23, 9565. https://doi.org/10.3390/s23239565

[2] H. Rocha, C. Semprimoschnig, J.P. Nunes, Sensors for process and structural health monitoring of aerospace composites: A review,Engineering Structures, 2021, https://doi.org/10.1016/j.engstruct.2021.112231

[3] E.R. Cosau, V. Goanta, I. Blanari, L. Alkisswani, F. Samara, Determination of Tensile Characteristics and Electrical Resistance Variation of Cables Used for Charging Electric Vehicles. Polymers fammi , 17, 1317. https://doi.org/10.3390/polym17101317

[4] J.-W. J.-P. Song, Hong, Y.-J. An, S.-H. Son, J.-S. Park, S.-H. Kim, S.-H. Kang, J.-H. Kang, Evaluation of the Mechanical and Electrical Properties of Multistage Drawn Copper-Clad Aluminum Wire After Annealing Process. Metals 2024, 14, 1386. https://doi.org/10.3390/met14121386

[5] G. Uribe-Riestra, P. Ayuso-Faber, M. Rivero-Ayala, J. Cauich-Cupul, F. Gamboa, F. Avilés. Structural health monitoring of carbon nanotube-modified glass fiber-reinforced polymer composites by electrical resistance measurements and digital image correlation. Structural Health Monitoring. 2023; https://doi.org/10.1177/14759217231173439

Materials Research Proceedings 69 (2026) 1347-1352- https://doi.org/10.21741/9781644904251-234

Nonlinear Post-Buckling Analysis of Variable Cross-Section Beams Using the Carrera Unified Formulation

Antonio Paolo Fontanella[1,a*], Tommaso Sironi[1,b], Piero Chiaia[2,c], Maria Cinefra[1,d] and Alfonso Pagani[2,e]

[1]Department of Mechanics, Mathematics and Management, Politecnico di Bari, Via Edoardo Orabona 4, 70126 Bari, Italy

[2]Mul2 Lab, Department of Mechanical and Aerospace Engineering Politecnico di Torino, 10129 Turin, Italy

[a]a.fontanella1@phd.poliba.it, [b]t.sironi@phd.poliba.it, [c]piero.chiaia@polito.it, [d]maria.cinefra@poliba.it, [e]alfonso.pagani@polito.it

Keywords: Carrera Unified Formulation, Non-linear Analysis, Buckling, Tapered Beam

Abstract. Variable cross-section beams are highly susceptible to instability phenomena, and traditional 3D Finite Element (FE) methods are often computationally demanding for slender members. This work proposes a refined, fully nonlinear one-dimensional (1D) beam model for tapered and twist geometries, developed within the Carrera Unified Formulation (CUF) framework. The element directly accounts for cross-sectional variation by performing a three-dimensional integration of of approximating function in the Jacobian matrix. The nonlinear governing equations, derived via the Principle of Virtual Work, are solved using a Newton-Raphson linearization scheme coupled with an arc-length path-following method. The formulation's effectiveness is validated through numerical applications, including the buckling of a tapered steel C-section beam.

1. Introduction

The structural analysis of tapered beams, members with continuously varying cross-sections, is crucial for high-performance structures in engineering [1]. Although analytical solutions exist for prismatic beams, tapered geometries typically require computationally expensive 3D Finite Element (FE) models., particularly for thin-walled slender structures where fine meshes are needed to capture nonlinearities.

To address this, we present a novel, fully nonlinear 1D beam element for tapered geometries, developed within the Carrera Unified Formulation (CUF) framework [2]. This formulation systematically derives hierarchical models with 3D capabilities, thus overcoming the inherent limitations of conventional 1D beam theories..

The proposed element directly incorporates cross-section variation through a three-dimensional integration of the approximation functions and the Jacobian [3,4]. This approach enables a consistent representation of non-uniform geometries while preserving accuracy. The nonlinear governing equations, derived via the Principle of Virtual Work, are solved using a Newton-Raphson linearization scheme combined with an arc-length constraint path-following method [5-7].

The effectiveness is validated through numerical applications, including the buckling of a tapered steel C-section benchmark [8]. Comparisons with experimental data available in the literature and conventional 3D FE simulations confirm the model's high fidelity and significant improvement in computational efficiency in predicting the nonlinear buckling response of variable cross-section beams.

Content from this work may be used under the terms of the Creative Commons Attribution 3.0 license. Any further distribution of this work must maintain attribution to the author(s) and the title of the work, journal citation and DOI. Published under license by Materials Research Forum LLC.

Materials Research Proceedings 69 (2026) 1347-1352- https://doi.org/10.21741/9781644904251-234

2. Theoretical Framework and Numerical Methodology

The finite elements employed here are an extension of the Carrera Unified Formulation (CUF) [9]. CUF allows for the consistent derivation of one-dimensional (1D) beam theories with arbitrary kinematic hypotheses by approximating the three-dimensional displacement field $\boldsymbol{u}(x,y,z) = (u_x(x,y,z), u_y(x,y,z), u_z(x,y,z))$ as a generalized expansion. This field is approximated by combining the CUF expansion functions (F_τ) along the cross-section/thickness with the standard Finite Element (FE) shape functions (N_i) along the beam axis, leading to the combined displacement formulation:

$$\boldsymbol{u} = F_\tau(x,z)N_i(y)Q_{\tau i} = L_{\tau i}(\xi,\eta,\nu)Q_{\tau i}. \tag{1}$$

where $q_{\tau i}$ represents the generalized nodal degrees of freedom, and (ξ,η,ν) are the natural coordinates corresponding to (x,y,z). In this expression, $L_{\tau i}(\xi,\eta,\nu)$ represents a new 3D shape function in which the order of expansion can be different along one of the spatial directions. Considering this formalism, the volume integrals involved in the governing equations will be not split in 1D and 2D integrals as usual, but the functions $(N_i F_\tau)$ will be handled as regular 3D shape functions; consequently, the Jacobian matrix relative to the transformation from natural coordinates (ξ,η,ν) to global coordinates (x,y,z) will be computed in 3D form. However, a formal separation of the coordinates as in Eq. (1) is still possible and the choice CUF FE approximations follows the same principles as in conventional beam and plate elements based on CUF, that is functions with higher polynomial order are employed along the larger directions.

The resulting elements, including the novel formulations [3,4], are specifically designed to consistently model non-orthogonal geometries. This is achieved by explicitly treating the element as a full 3D domain for the integration of stiffness and mass matrices, ensuring geometric consistency and improved accuracy compared to classical 1D formulations.

Figure 1 illustrates the modeling approach, which depicts the combination of 2D cross-section discretization (four node plate element Q4, nine node plate element Q9, sixteen node plate element Q16) and 1D beam elements (two nodes beam element B2, three node beam element B3, four node beam element B4) in a tapered geometry.

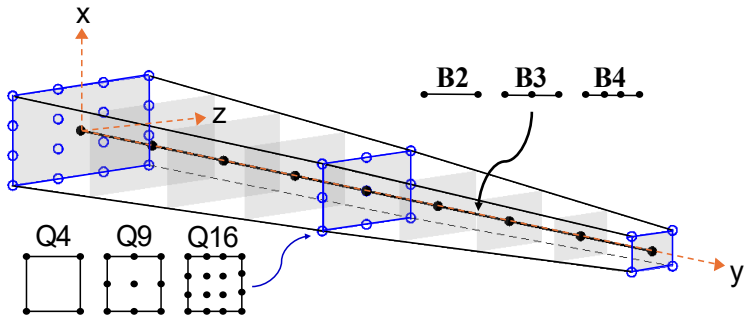


Figure 1. Conceptual representation of the Tapered CUF element showing the coupling of 2D cross-section discretization and 1D through-the-thickness expansion in a tapered geometry.

2.1 Geometrically Nonlinear Solution Strategy

The structural analysis is conducted in the geometrically nonlinear regime adopting a finite element procedure based on the Total Lagrangian formulation. The large displacement behavior is described adopting the Full Green-Lagrange strain tensor, defined as:

$$\boldsymbol{E}_{ij} = \frac{1}{2}\left(\boldsymbol{u}_{i,j} + \boldsymbol{u}_{j,i} + \boldsymbol{u}_{k,i}\boldsymbol{u}_{k,j}\right). \tag{2}$$

Materials Research Proceedings 69 (2026) 1347-1352- https://doi.org/10.21741/9781644904251-234

where $\boldsymbol{u}_{i,j}$ represents the displacement gradient $\partial \boldsymbol{u}_i / \partial x_j$. The last term, $\boldsymbol{u}_{k,i}\boldsymbol{u}_{k,j}$ is essential for capturing large displacements, rotations, and buckling phenomena.

The nonlinear equilibrium equations, derived from the Principle of Virtual Work ($\delta L_{int} = \delta L_{ext}$), are solved using an incremental-iterative procedure based on the Newton-Raphson scheme. Linearization around the non-trivial equilibrium state leads to the definition of the Tangent Stiffness Matrix $\mathbf{K_T}$:

$$\delta L_{int} = \delta Q^T(\mathbf{K_0} + \mathbf{K_{T1}} + \mathbf{K}_\sigma)\Delta Q = \delta Q^T \mathbf{K_T} \Delta Q. \quad (3)$$

Here, ΔQ is the vector of incremental degrees of freedom, $\mathbf{K_0}$ is the linear stiffness matrix, $\mathbf{K_{T1}}$ is the nonlinear contribution to the tangent stiffness matrix coming from the linearization of the constitutive law, and $\mathbf{K}_\sigma$ is the geometric stiffness matrix (or initial stress matrix), which accounts for the influence of pre-stressed effects for predicting the critical buckling load.

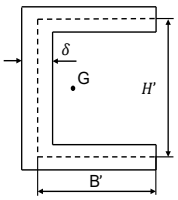
To trace the equilibrium path, especially beyond limit points (instability regions), a path-following method (such as the Arc-Length method [5]) is implemented, allowing for the stable and accurate calculation of the post-buckling response.

3. Case Study I: Lateral Buckling of a Variable C-Beam

This initial case study validates the proposed formulation by reproducing the post-buckling behavior of a variable cross-section steel C-beam, benchmark against the experimental results of Mascolo et al. [8].

The C-beam is tapered along the -axis; dimensions for the initial and final cross-sections are documented in Table 1. A compressive load, F, is applied along the line connecting the cross-section centroids (G). The beam has a length $L = 0.9\ m$ and is modeled with simply supported boundary conditions (Section A: u_x and u_z constrained; Section B: u_x, u_y, u_z constrained)(Figure 2.a). The equilibrium path is traced using the displacement measured at mid-length (Figure 2.b).

Table 1 - End cross-sections (A and B) details.

	$Section\ A$: $B' = 28.5\ mm;\ H' = 87.0\ mm;$ $\delta = 3\ mm;\ A = 642\ mm^2$
	$Section\ B$: $B' = 18.5\ mm;\ H' = 177.0\ mm;$ $\delta = 3\ mm;\ A = 432\ mm^2$

The material properties correspond to S420 steel grade, utilizing a Young's Modulus of 210 GPa and Shear Modulus of 80.77 GPa. The setup includes two elastic transverse plates (diaphragms) located at $z = 0.3\ m$ and $z = 0.6\ m$, with a thickness of $3\ mm$, modeled using B3 elements and 32 Q9 elements in the cross-section (Figure 2. c). The remainder of the beam employs B4 elements along the axis and 14 Q9 elements in the cross-section, ensuring a robust discretization suitable for thin-walled structures.

3.1 Results and Validation

The numerical analysis using the tapered CUF elements and the arc-length path-following technique yielded a critical load of 51.6 kN. This result demonstrates excellent agreement with the experimental critical buckling load of 53.6 kN reported in the reference paper.

Materials Research Proceedings 69 (2026) 1347-1352- https://doi.org/10.21741/9781644904251-234

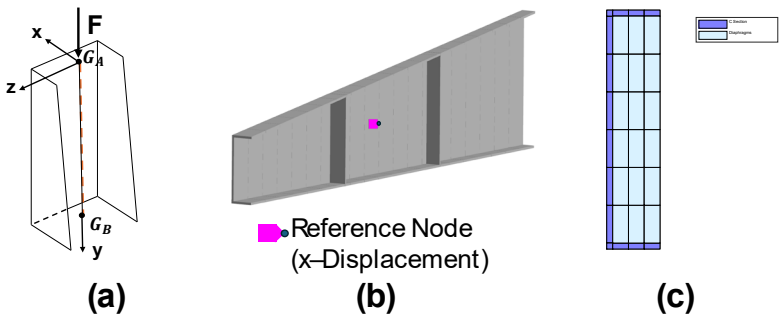


***Figure 2**. a) Schematic of the analyzed beam and basic notation, b) Reference node (used to build the equilibrium curve), c) Diaphragms section, CUF expansion detail*

Furthermore, the equilibrium path (F vs. u_y) obtained from the CUF analysis showed a consistent trend when compared against a full geometrically nonlinear structural analysis performed with the commercial FE software Ansys. This consistency confirms the reliability of the CUF formulation in capturing the complex instability mode (Figure 3.a) and resulting deformed shape (Figure 3.b) for thin-walled tapered structures.

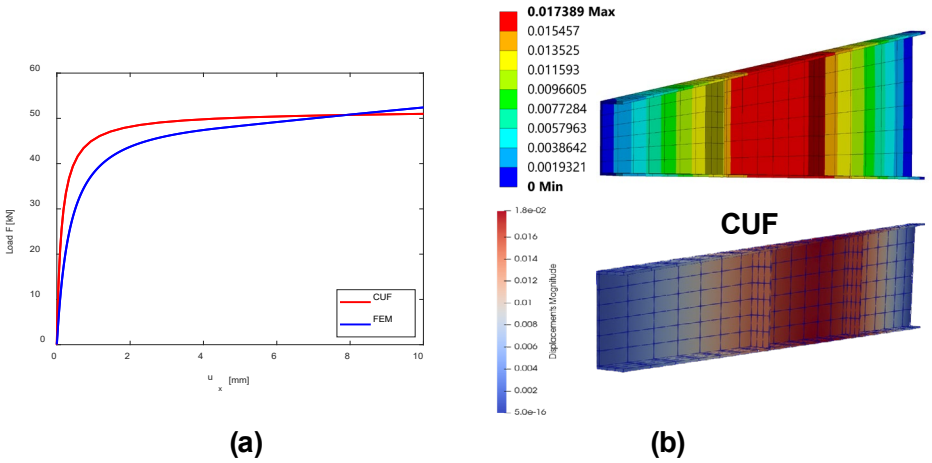


Figure 3. a) Equilibrium curve F vs u for the variable C-beam. Comparison between CUF and Ansys results. b) Deformed shape of the variable C-beam at critical load

4. Case Study II: Post-Buckling of a Tapered and Twisted Beam

This second case study provides a purely numerical comparison designed to test the model's performance under geometric non-uniformity. It analyzes a simply-supported beam of length $L = 1\ m$, subjected to an axial compressive load, F, and made of S420 steel. The geometry presents a double geometric complexity:

1. Tapering: The dimensions (height and width) of the final section B are two times those of the initial section A. The initial section dimensions are 5 mm (height) and 25 mm (width).
2. Twist: the final cross-section is subjected to an anticlockwise twist of one full turn (2π) relative to the initial section along the beam axis.

A visual representation of the geometry and loading conditions is provided in Figure 4. The mesh discretization consists of 30 B4 elements along the axis and a cross-section discretized with a 2×8 array of Q16 elements (height × width).

This combination of tapering and twist aims to test the element's performance under geometric variation and its capability to capture instability in highly non-conventional structures.

Materials Research Proceedings 69 (2026) 1347-1352- https://doi.org/10.21741/9781644904251-234

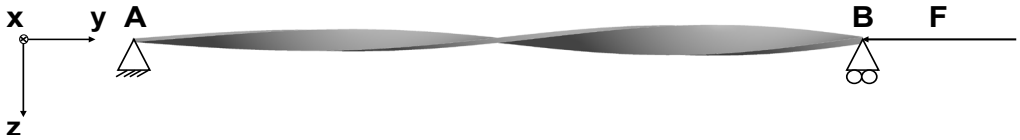


Figure 4. Schematic of the analyzed beam and basic notation

4.2. Results and Discussion

The critical load and post-buckling response were obtained using the nonlinear CUF model and compared against a full 3D structural nonlinear simulation in Ansys. The CUF formulation demonstrated remarkable computational efficiency, achieving results comparable to the 3D model with a significant reduction in computing time, while accurately capturing the entire post-buckling trend (Figure 5.a). This confirms the model's robustness and efficiency even under severe geometric variation and axial twist (Figure 5.b).

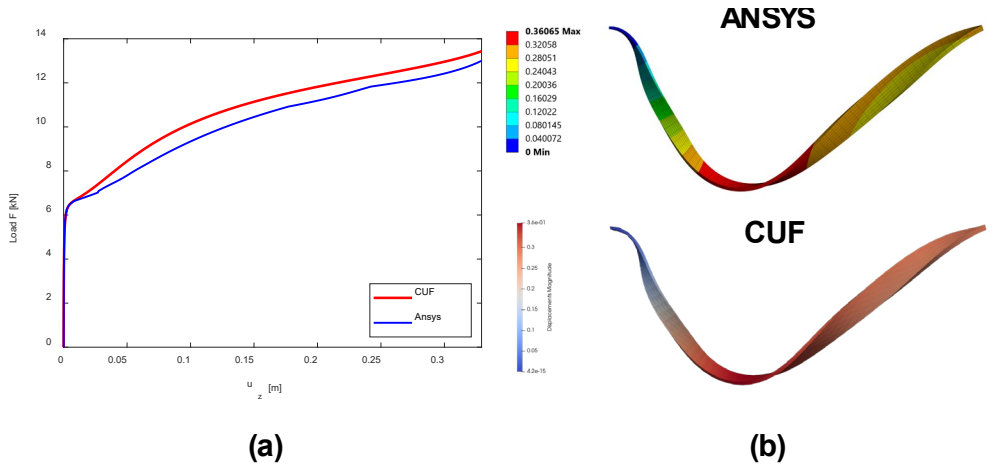


Figure 5. a) Equilibrium curve F vs $\boldsymbol{u_x}$ for the variable rectangular beam. B) Deformed shape (axial buckling mode)

5. Conclusions

This paper successfully introduced and validated a novel class of Tapered Finite Elements developed within the Carrera Unified Formulation (CUF) framework for the geometrically nonlinear buckling analysis of variable cross-section beams. The key contribution of the formulation lies in the consistent incorporation of cross-sectional variation directly into the element matrices through three-dimensional integration, coupled with a path-following method for tracing highly nonlinear equilibrium paths.

The method's reliability was demonstrated through two rigorous benchmarks. A comparison against experimental data for the lateral-torsional buckling of a clamped C-beam showed a good correlation with the critical load reported in the literature. Furthermore, a numerical benchmark involving an extremely complex, twisted geometry successfully captured the entire nonlinear post-buckling trend when compared against full 3D simulations. In summary, the proposed CUF tapered elements are an accurate, robust, and computationally effective alternative to conventional 3D Finite Element models, offering a powerful tool for the high-fidelity analysis and design of complex non-prismatic components.

Acknowledgments

Authors acknowledges support by the European Union - NextGenerationEU (National Sustainable Mobility Center CN00000023, Italian Ministry of University and Research Decree n. 1033 –

17/06/2022, Spoke 11 – Innovative Materials & Lightweighting). The opinions expressed are those of the authors only and should not be considered as representative of the European Union or the European Commission's official position. Neither the European Union nor the European Commission can be held responsible for them.

References:

[1] V. Mercuri, F. Greco, and R. Luciano, Three-Dimensional Beam Element with Continuous Variation of the Cross-Sectional Area, Computers & Structures, Vol. 88, No. 21–22, 2010, pp. 1261–1269. https://doi.org/10.1016/j.compstruc.2010.07.00

[2] E. Carrera; M. Cinefra; M. Petrolo; E. Zappino; Finite Element Analysis of structure through unified Formulation, John Wiley & Sons, 2014

[3] M. Cinefra, Non-conventional 1D and 2D finite elements based on CUF for the analysis of non-orthogonal geometries, European Journal of Mechanics - A/Solids, Volume 88, 2021, 104273, ISSN 0997-7538, https://doi.org/10.1016/j.euromechsol.2021.104273

[4] P. Chiaia, M. Cinefra, E. Carrera, Curvilinear 2|3D finite elements for the analysis of shells with arbitrary curvature and variable thickness, Computers and Structures, 2025, https://doi.org/10.1016/j.compstruc.2025.107911

[5] E. Carrera, "A Study on Arc-Length-Type Methods and their Operation Failures Illustrated by a simple model", Computers & Structures (1994), Vol. 50, n° 2, pp. 217-229, https://doi.org/10.1016/0045-7949(94)90297-6

[6] A. Pagani; E. Carrera, (2018) Unified formulation of geometrically nonlinear refined beam theories, Mechanics of Advanced Materials and Structures, 25:1, 15-31, https://doi.org/10.1080/15376494.2016.1232458

[7] B. Wu; A. Pagan; M. Filippi; W.Q. Che; E. Carrera; Large-deflection and post-buckling analyses of isotropic rectangular plates by Carrera Unified Formulation, International Journal of Non-Linear Mechanics, Volume 116, 2019, Pages 18-31, ISSN 0020-7462, https://doi.org/10.1016/j.ijnonlinmec.2019.05.004

[8] I. Mascolo; M. Modano; A. Fiorillo; M. Fulgone; V. Pasquino; F.Fraternali, Experimental and Numerical Study on the Lateral-Torsiona Buckling of Steel C-Beams with Variablea Cross-Section, Metals 2018, 8, 941; https://doi.org/10.3390/met8110941

[9] E. Carrera, G. Giunta, M. Petrolo, Beam Structures: Classical and Advanced Theories, John Wiley & Sons, 2011.

Materials Research Proceedings 69 (2026) 1353-1357 https://doi.org/10.21741/9781644904251-235

Fatigue Cracking Analysis by Coupled 3D Peridynamics and 1D High Order Refined Elements

Qiang ZHANG[1,2,a *], Alfonso PAGANI[2,b], Xiang LIU[1,c], Wei ZHOU[1,d], and Jiahui SHEN[2,e]

[1]Key Laboratory of Traffic Safety on Track, Ministry of Education, School of Traffic & Transportation Engineering, Central South University, Changsha, China

[2]Mul2 Team, Politecnico di Torino, Corso Duca degli Abruzzi 24, Torino, Italy

[a]csu_zhangqiang@csu.edu.cn, [b]alfonso.pagani@polito.it, [c]xiangliu@csu.edu.cn, [d]gszx_zhouwei@csu.edu.cn, [e]jiahui.shen@polito.it

Keywords: Carrera Unified Formulation, Higher-Order Beam Theories, Peridynamic Fatigue Model

Abstract. Previous studies have demonstrated that coupling three-dimensional Peridynamics (PD) with one-dimensional high-order refined elements via the Lagrange multipliers method ensures physical consistency at the PD–FE interface [1]. This coupling strategy has also been applied to quasi-static crack propagation analyses of brittle materials [2]. Building upon this framework, the present work extends the approach by incorporating a peridynamic fatigue model, providing an efficient framework for fatigue crack analysis, especially in three dimensional cases [3]. The accuracy of the proposed model has been verified by reproducing the S–N and Paris curves of the 7075–T651 aluminum alloy. It demonstrates a promising method for fatigue crack analysis in aeronautical structures.

Introduction

Peridynamics (PD) is a nonlocal theory of continuum mechanics that uses integral equations to model material behavior, making it particularly well suited for simulating the initiation and propagation of fracture and damage [4]. Beyond the original formulation by Silling, PD has been effectively used for discontinuous structural problems and fracture modeling in aerospace contexts [5]. This PD theory has been extended to simulate fatigue by incorporating damage accumulation laws into the nonlocal formulation, allowing the explicit prediction of crack initiation and propagation under cyclic loading [3]. However, peridynamic fatigue analysis faces a significant challenge in its high computational cost, which often becomes prohibitive due to the nonlocal interactions and the large number of loading cycles required. To mitigate this computational burden, many researchers have proposed hybrid modeling strategies that couple peridynamics with more efficient methods, such as the Finite Element Method (FEM), restricting the computationally intensive peridynamic domain to critical regions where damage is expected to occur [6]. The present work follows this approach. In particular, the one-dimensional high-order refined elements employed here are based on the well-known Carrera Unified Formulation (CUF), a hierarchical framework that enables refined structural modeling with reduced computational cost. Recent advances in CUF-based analysis have further demonstrated its capability to efficiently handle complex composite and anisotropic structures [7]. Building upon these foundations, the present study extends the existing CUF–PD coupling framework by incorporating a peridynamic fatigue model to achieve unified simulation of fatigue crack initiation and growth under cyclic loading.

Bond-Based Peridynamics (BBPD)

In the linear elastic and static case, the bond-based peridynamic equilibrium of a material point $\mathbf{x}_i$ is expressed as

Content from this work may be used under the terms of the Creative Commons Attribution 3.0 license. Any further distribution of this work must maintain attribution to the author(s) and the title of the work, journal citation and DOI. Published under license by Materials Research Forum LLC.

Materials Research Proceedings 69 (2026) 1353-1357 https://doi.org/10.21741/9781644904251-235

$$\sum_{j=1}^{N_{H_i}} \mathbf{C}(\mathbf{x_j} - \mathbf{x_i})\,(\mathbf{u_j} - \mathbf{u_i})\,V_j = \mathbf{0} \tag{1}$$

Where. $\mathbf{C}(\boldsymbol{\xi}) = c\frac{\boldsymbol{\xi}\boldsymbol{\xi}^{\mathbf{T}}}{|\boldsymbol{\xi}|^3}$ is the micromodulus tensor and V_j is the nodal volume. By assembling the contributions of all interacting pairs, the discrete peridynamic formulation can be written compactly as

$$\mathbf{K}^{\mathrm{PD}}\mathbf{K}^{\mathrm{PD}} = \mathbf{F}^{\mathrm{PD}} \tag{2}$$

which is formally analogous to the global stiffness equation in the finite element method.

High-Order 1D Theories Based on Classical Elasticity

In the framework of CUF, the 3D displacement field of a beam with main axis along y is expressed as a generic expansion of the generalized displacements $u_\tau(y)$:

$$u_\alpha(x,y,z) = \sum_{\tau=1}^{M} F_\tau(x,z)\,u_{\alpha\tau}(y), \qquad \alpha = x,y,z \tag{3}$$

Where $F_\tau(x,z)$ are expansion functions over the cross-section and M denotes the number of terms adopted in the expansion. The choice of F_τ defines the class of 1D CUF models: for instance, Taylor Expansion (TE) models employ polynomial terms, whereas Lagrange Expansion (LE) models use Lagrange-type shape functions to capture cross-sectional variations.

Along the beam axis, the generalized displacements are discretized by finite elements as

$$u_{\alpha\tau}(y) = \sum_{i=1}^{p+1} N_i(y)\,u_{\alpha\tau i} \tag{4}$$

Where $N_i(y)$ are the 1D FE shape functions and $u_{\alpha\tau i}$ are the nodal unknowns. Substituting the kinematic expansion (3) and the FE approximation (4) into the virtual work principle leads to the discrete equilibrium equation:

$$\mathbf{K}^{FE}\mathbf{K}^{FE} = \mathbf{F}^{FE} \tag{5}$$

Where $\mathbf{K}^{FE}$ is the global stiffness matrix obtained from the integration of the 3D constitutive relations over the cross-section and beam axis, $\mathbf{U}^{\mathrm{FE}}$ is the vector of nodal unknowns, and $\mathbf{F}^{\mathrm{FE}}$ is the external force vector.

Coupling of PD and CUF via Lagrange Multipliers

The coupled domain is divided into a 3D peridynamic (PD) region and a 1D high-order refined element region based on the Carrera Unified Formulation (CUF). Neglecting interface constraints, the two subdomains can be independently assembled as

$$\mathbf{KU} = \mathbf{F}, \text{ i.e. } \begin{bmatrix} \mathbf{K}^{\mathrm{PD}} & 0 \\ 0 & \mathbf{K}^{\mathrm{FE}} \end{bmatrix} \begin{bmatrix} \mathbf{U}^{\mathrm{PD}} \\ \mathbf{U}^{\mathrm{FE}} \end{bmatrix} = \begin{bmatrix} \mathbf{F}^{\mathrm{PD}} \\ \mathbf{F}^{\mathrm{FE}} \end{bmatrix} \tag{6}$$

To ensure displacement compatibility along the PD–FE interface Γ_I, Lagrange multipliers λ are introduced, see Fig.1. The interface constraint is enforced by requiring $\mathbf{u}_k^{PD} = \mathbf{u}^{FE}(\mathbf{x}_k)$ for each particle k located on Γ_I. This leads to the weak form of the coupled problem:

$$\begin{cases} \mathbf{KU} + \mathbf{B}^{\mathrm{T}}\boldsymbol{\lambda} = \mathbf{F} \\ \mathbf{BU} = \mathbf{0} \end{cases} \tag{7}$$

or equivalently, in matrix form,

$$\begin{bmatrix} \boldsymbol{K} & \boldsymbol{B}^{\mathrm{T}} \\ \boldsymbol{B} & \boldsymbol{0} \end{bmatrix} \begin{bmatrix} \boldsymbol{U} \\ \boldsymbol{\lambda} \end{bmatrix} = \begin{bmatrix} \boldsymbol{F} \\ \boldsymbol{0} \end{bmatrix} \tag{8}$$

where **B** is the coupling matrix assembled from the interface kinematic relations. This formulation guarantees full displacement continuity between the PD and CUF regions while preserving the nonlocal nature of the peridynamic model.

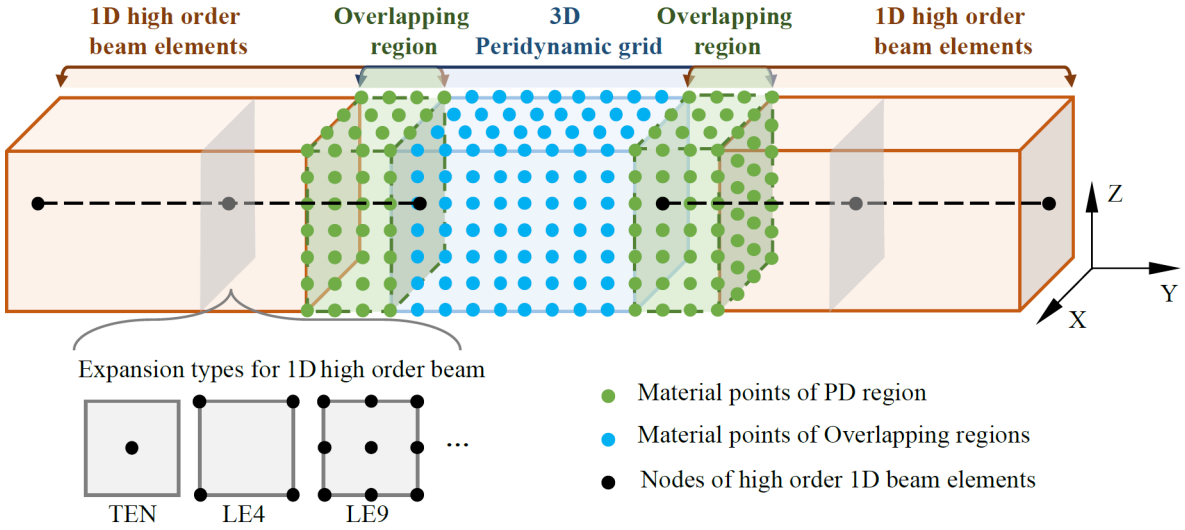


Figure 1: CUF-PD Coupling Scheme

Peridynamic Fatigue Model (Silling, 2014)

The peridynamic fatigue model proposed by Silling introduces a history-dependent damage law in which each bond is assigned a remaining life variable $\lambda = (\mathrm{x}, \boldsymbol{\xi}, \mathrm{N})$ evolving with the number of load cycles N as

$$\frac{d\lambda}{dN} = -A\varepsilon^{m}, \qquad \lambda(0) = 1 \tag{9}$$

where ε is the cyclic bond strain, and A, m are material parameters calibrated from S–N or Paris law data. A bond irreversibly fails when $\lambda \leqslant 0$, enabling spontaneous nucleation and growth of fatigue cracks without introducing additional crack-growth criteria. The model distinguishes between the nucleation phase (parameters A_1, m_1) governed by strain–life relations and the growth phase (parameters A_2, m_2) calibrated to the Paris law, ensuring consistency with experimental $da/dN - \Delta K$ curves. This formulation naturally captures fatigue crack initiation, coalescence, and propagation within the peridynamic framework while preserving its nonlocal and mesh-independent character.

Numerical Results

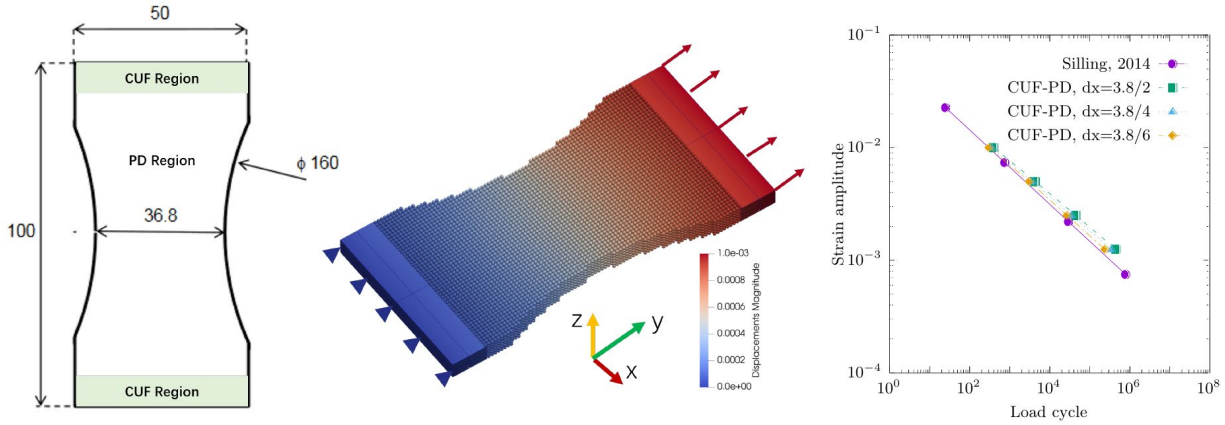
The proposed CUF–PD coupled framework has been applied to reproduce the fatigue behavior of 7075–T651 aluminum alloy, following the benchmark study of Silling (2014). The peridynamic fatigue law defined in Eq.(9) was integrated within the coupled BBPD–CUF formulation described above, enabling the simultaneous treatment of 3D peridynamic regions and 1D refined finite elements under cyclic loading. The model successfully reproduced both the S–N curve and the Paris law crack growth rate observed experimentally for this alloy. Table 1 summarizes the reduction in the total number of degrees of freedom achieved by the CUF–PD model compared

with the full-PD approach for both specimens, highlighting the significant gain in computational efficiency.

Table 1: Illustrative DOF reduction of CUF–PD(B2+L4) versus full-PD

Specimen	Model	PD-DOFs	FE-DOFs	Total DOFs	Reduction
Hourglass	Full-PD(dx = 3.8/6)	77,462	–	77,462	–
	CUF–PD(dx = 3.8/6)	49,287	1,188	50,475	34.8%
CT	Full-PD(dx = 3.8/8)	145,487	–	145,487	–
	CUF–PD(dx = 3.8/8)	26,532	2,328	28,860	80.2%

As shown in Fig.2 and Fig.3, the numerical predictions demonstrate close agreement with the reference data, capturing the slope of the S–N relation, and the linear trend in the $\log(da/dN) - \log(\Delta K)$ domain. This confirms the capability of the coupled CUF–PD formulation to accurately describe fatigue crack initiation and propagation within a unified nonlocal framework. The demonstrated consistency with experimental fatigue behavior highlights the potential of the CUF–PD approach for reliable fatigue assessment in complex structural components.



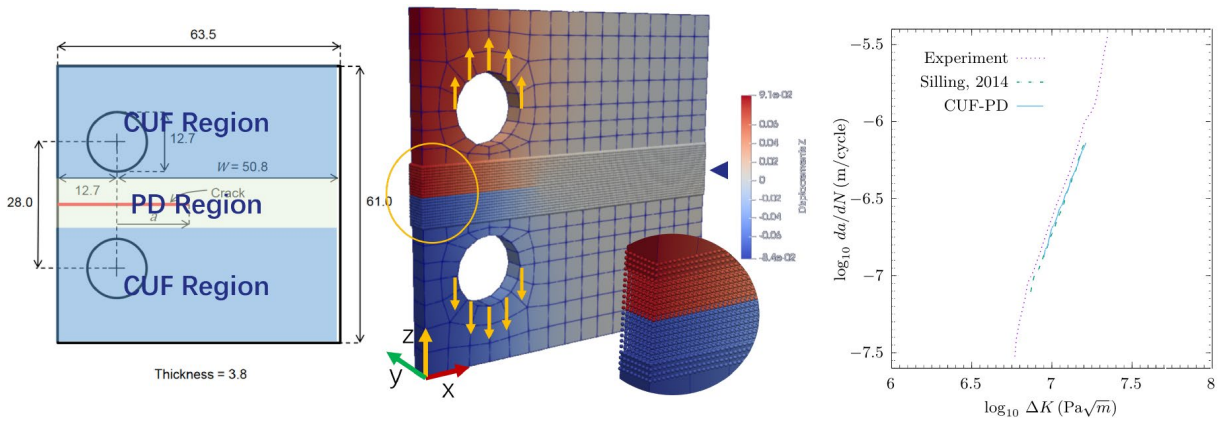
(a) Hourglass specimen geometry and boundary conditions

(b) S–N curves from Silling's and CUF–PD models.

Figure 2:Phase I verification of the CUF–PD fatigue model (crack nucleation).

Summary

This work extends the CUF–PD coupling framework by incorporating Silling's peridynamic fatigue model, enabling unified simulation of fatigue crack initiation and propagation. The proposed approach accurately reproduces the S–N and Paris law curves of 7075–T651 aluminum alloy, demonstrating its effectiveness for fatigue life prediction in aeronautical structures.



(a) CT specimen geometry and boundary conditions.

(b) Paris law curves from Silling's and CUF–PD models.

Figure 3 Phase II verification of the CUF–PD fatigue model (crack propagation).

References

[1] A. Pagani and E. Carrera. Coupling three-dimensional peridynamics and high-order one-dimensional finite elements based on local elasticity for the linear static analysis of solid beams and thin-walled reinforced structures. International Journal for Numerical Methods in Engineering, 121(22):5066-5081, November 2020. https://doi.org/10.1002/nme.6510

[2] Alfonso Pagani, Marco Enea, and Erasmo Carrera. Quasi-static fracture analysis by coupled three-dimensional peridynamics and high order one-dimensional finite elements based on local elasticity. International Journal for Numerical Methods in Engineering, 123(4):1098-1113, February 2022. https://doi.org/10.1002/nme.6890

[3] Stewart Andrew Silling and Abe Askari. Peridynamic model for fatigue cracking. Journal of Elasticity, 12 2013. https://doi.org/10.2172/1160289

[4] S. A. Silling. Reformulation of elasticity theory for discontinuities and long-range forces. Journal of the Mechanics and Physics of Solids, 48(1):175-209, 2000. https://doi.org/10.1016/S0022-5096(99)00029-0

[5] M. Zaccariotto, G. Sarego, D. Dipasquale, A. Shojaei, S. Bazazzadeh, T. Mudric, M. Duzzi, and U. Galvanetto. Discontinuous mechanical problems studied with a peridynamics-based approach. Aerotecnica Missili & Spazio, 96:44-55, 2017. https://doi.org/10.1007/BF03404736

[6] Ugo Galvanetto, Teo Mudric, Arman Shojaei, and Mirco Zaccariotto. An effective way to couple FEM meshes and Peridynamics grids for the solution of static equilibrium problems. Mechanics Research Communications, 76:41-47, September 2016. https://doi.org/10.1016/j.mechrescom.2016.06.006

[7] Alfonso Pagani, Alberto Racionero S'anchez-Majano, Dario Zamani, Marco Petrolo, and Erasmo Carrera. Fundamental frequency layer-wise optimization of tow-steered composites considering gaps and overlaps. Aerotecnica Missili & Spazio, 104:135-151, 2025. Published online: 22 April 2024. https://doi.org/10.1007/s42496-024-00212-w

Materials Research Proceedings 69 (2026) 1358-1363 https://doi.org/10.21741/9781644904251-236

High-Order Multiscale Thermo-Elastic Analysis of a Triangular Sub-Array with Dielectric Patches

Rebecca MASIA[1,a*], Irene IZZO[1,b], Alfonso PAGANI[1,c], Enrico ZAPPINO[1,d], Ryo HIGUCHI[2,e], Xin LU[2,f] and Erasmo CARRERA[1,g]

[1]Politecnico di Torino, Corso Duca degli Abruzzi 24, Torino, Italy

[2]Department of Aeronautics and Astronautics, The University of Tokyo, 7-3-1 Hongo, Bunkyo-ku, Tokyo 113-8656, Japan

[a]rebecca.masia@polito.it, [b]s319906@studenti.polito.it, [c]alfonso.pagani@polito.it, [d]enrico.zappino@polito.it, [e]higuchi@aastr.t.u-tokyo.ac.jp, [f]xinlu@g.ecc.u-tokyo.ac.jp, [g]erasmo.carrera@polito.it

Keywords: Phased-Array Antennas, Multiscale Modelling, Thermo-Elastic Deformations, Carrera Unified Formulation

Abstract. Current trends in space observation require lightweight phased-array antennas capable of electronic beam steering from geostationary orbit. In this work multiscale numerical framework is developed, combining thermo-elastic micromechanical and macroscopic analyses, both formulated within the Carrera Unified Formulation (CUF). The Variational Asymptotic Method (VAM) is employed to derive effective properties at the microscale, while the Principle of Virtual Displacement (PVD) is employed for thermo-mechanical predictions at the structural level. Validation against commercial tools confirms the reliability and computational efficiency of the proposed approach, demonstrating its suitability for future space antenna design.

Introduction

Modern spaceborne observation and communication missions increasingly employ phased-array antennas, which enable electronic beam steering with high precision and adaptability [1]. Unlike mechanically steered systems, these arrays consist of dense networks of radiating elements, each individually controlled in phase, delay, and amplitude to achieve real-time beam reconfiguration and enhanced resolution, essential for geostationary radar applications [2]. Typically, these antennas are designed as ultra-light planar composite structures with dielectric patches and embedded electronics, combining high stiffness and low mass. However, their continuous solar exposure in geostationary orbit, interrupted only by brief eclipse phases, generates severe thermal gradients. These gradients induce thermo-elastic deformations caused by mismatched Coefficient of Thermal Expansion (CTE) among composite layers, potentially degrading antenna performance [3]. To accurately capture such behavior, a multiscale and multifield modelling approach is required, since the critical thermo-elastic phenomena are strongly scale dependent [4]. Establishing this micro–macro link efficiently, without the excessive computational cost of conventional commercial multiscale analyses, is a key challenge [5].

The present study introduces a strategy combining micromechanical and macroscopic analyses within the unified framework of the Carrera Unified Formulation (CUF). At the microscale, the analysis is based on the Mechanics of Structure Genome (MSG), which employs the Variational Asymptotic Method (VAM) to extract effective thermo-elastic properties directly from material characteristics and geometry, without explicit load application. The microstructural model is constructed using high-order, geometrically accurate beam finite elements derived within CUF, where Hierarchical Legendre Expansions (HLE) describe the cross-sectional fields, ensuring efficiency and accuracy [6].

Content from this work may be used under the terms of the Creative Commons Attribution 3.0 license. Any further distribution of this work must maintain attribution to the author(s) and the title of the work, journal citation and DOI. Published under license by Materials Research Forum LLC.

Materials Research Proceedings 69 (2026) 1358-1363 https://doi.org/10.21741/9781644904251-236

At the macroscale, the antenna structure is modeled using high-order CUF-based plate finite elements. The in-plane domain is discretized through two-dimensional elements, while the through-the-thickness behavior is represented using high-order expansion functions. These can be formulated following either the Equivalent Single Layer (ESL) approach, typically employing Taylor expansions (TE), or a Layer Wise (LW) approach based on Lagrange expansions (LE) [7].

The comparison between results obtained from the developed CUF-based framework and those from commercial software demonstrates the robustness, reliability, and computational efficiency of the proposed methodology for the analysis of complex space structures.

Carrera Unified formulation for high order theories

CUF is employed to model the structural behavior of the antenna component. Within the CUF framework, the three-dimensional (3D) unknown field for beam (1D) and the plate (2D) models are defined as:

$$\begin{aligned} \boldsymbol{q}_{1D}(x,y,z) &= F_\tau(x,z)N_i(y)\boldsymbol{q}_{\tau_i} \\ \boldsymbol{q}_{2D}(x,y,z) &= F_\tau(z)N_i(x,y)\boldsymbol{q}_{\tau_i} \end{aligned} \qquad \tau = 1,\dots,M \qquad i = 1,\dots,N \tag{1}$$

where F_τ are expansion functions, N_i are shape functions. M is the number of expansions, τ denotes summation and N is the number of beam/plate nodes. Note that $\boldsymbol{q}$ denotes nodal unknowns: in micromechanics it corresponds to the fluctuation field $\boldsymbol{\chi}$, while in macroscopic thermo-elastic analysis it represents the displacement $\boldsymbol{u}$.

At the microscale, the 1D model uses $F_\tau(x,z)$ to discretize the cross-section into multiple expansion subdomains and $N_i(y)$ to represent the beam axis. RUC constituents are modeled by enforcing displacement compatibility at their interfaces so $\boldsymbol{\chi}$ remain continuous. Subdomains are described with HLE, and accuracy improves by adding higher-order polynomials. HLE subdomains match the geometry of microstructural constituents via non-isoparametric mapping. Blending functions parameterize arbitrary geometries for direct inclusion in the numerical model. These CUF capabilities enable a Component Wise (CW) description of the RUC.

At the macroscopic scale, the structure is represented by a 2D model. The in-plane domain is discretized with $N_i(x,y)$, while the through-thickness response is captured by $F_\tau(z)$. Two strategies are compared: in ESL, laminate stiffness is derived by homogenizing layer properties, producing a kinematically uniform model that neglects interlaminar effects. TE functions are usually employed in this approach. In LW, each layer is assigned an independent displacement field with interface continuity enforced, enabling an explicit description of interlaminar stress transfer and delamination; LE are typically employed in this approach.

Microscale modeling

In micromechanical analyses the size of RUC is assumed to be much smaller than the global structure. It is assumed that geometry, loading and boundary conditions at the macroscale do not affect the effective properties obtained at the microscale, and that the local solutions, averaged over the RUC volume, correspond to the global macroscopic solution:

$$\bar{\boldsymbol{u}}(\boldsymbol{x}) = \frac{1}{V}\int_V \boldsymbol{u}(\boldsymbol{x};\boldsymbol{y})\, dV \tag{2}$$

where $\bar{\boldsymbol{u}}$ denotes the global displacement components and V the RUC volume.

According to the VAM, by minimizing the difference between the heterogeneous and homogeneous strain energy, one can compute the solution to the stationary value problem as:

$$\boldsymbol{\Pi} = \frac{1}{2}\left\langle \boldsymbol{\varepsilon}^T\boldsymbol{C}\boldsymbol{\varepsilon} - 2\boldsymbol{\beta}\boldsymbol{\varepsilon}\theta + c_v\frac{\theta^2}{T_0}\right\rangle - \frac{1}{2}\left(\bar{\boldsymbol{\varepsilon}}^{\boldsymbol{T}}\boldsymbol{C}^*\bar{\boldsymbol{\varepsilon}} - 2\boldsymbol{\beta}^*\bar{\boldsymbol{\varepsilon}}\theta + c_v^*\frac{\theta^2}{T_0}\right) \tag{3}$$

where $\langle\cdot\rangle$ denotes the volume average, $\mathbf{C}$ is the elasticity matrix, $\boldsymbol{\beta}$ is the thermal stress tensor defined as $\boldsymbol{\beta} = \mathbf{C}\boldsymbol{\alpha}$, with $\boldsymbol{\alpha}$ being CTE, the superscript * denotes the same quantities in the homogenized material. $\mathbf{T_0}$ is the reference temperature, $\mathbf{c_v}$ is the specific heat, and θ is the variation

Materials Research Proceedings 69 (2026) 1358-1363 https://doi.org/10.21741/9781644904251-236

of temperature with respect of $\mathbf{T_0}$. With $\boldsymbol{\varepsilon} = \bar{\boldsymbol{\varepsilon}} + \boldsymbol{D\chi}$, $\boldsymbol{\chi}$ must satisfy the constraint $\langle \boldsymbol{\chi} \rangle = 0$; under periodic boundary conditions applied in the three directions of the RUC, this is automatically fulfilled. In CUF-FEM framework the functional in Eq. (3) can be expressed in terms of the Fundamental Nuclei (FN) to be assembled over the four indices of the problem. After some mathematical passages the $\boldsymbol{\chi}$ are obtained through a linear system and finally the effective properties are obtained as:

$$\boldsymbol{C}^* = \frac{1}{\Omega}\left(\boldsymbol{\chi}_0^T \boldsymbol{D}_{h\varepsilon} + \boldsymbol{D}_{\varepsilon\varepsilon}\right) \qquad \boldsymbol{\beta}^* = \frac{1}{\Omega}\left[\frac{1}{2}\left(\boldsymbol{\chi}_0^T \boldsymbol{D}_{h\theta} - \boldsymbol{D}_{h\varepsilon}^T \boldsymbol{\chi}_\theta\right) + \boldsymbol{D}_{\varepsilon\theta}\right] \qquad c_v^* = \frac{1}{2\Omega}\left[\frac{D_{\theta\theta}}{T_0} - \boldsymbol{\chi}_\theta^T \boldsymbol{D}_{h\theta}\right] \tag{4}$$

In the case of a 3D macroscopic model, **C*** corresponds to the full 3D elasticity matrix, whereas for a 2D macroscopic model it reduces to the matrices **A**, **B**, and **D**, representing membrane stiffness, coupling stiffness and bending stiffness, respectively.

After the structural analysis, the global strain response $\bar{\boldsymbol{\varepsilon}}$ can be used to recover the local stress field over the RUC volume based on Hooke's law:

$$\boldsymbol{\sigma} = \boldsymbol{C}\bar{\boldsymbol{\varepsilon}} - \boldsymbol{\beta}\theta \tag{6}$$

Thermo-elastic problem

The Principle of Virtual Displacements (PVD) yields the governing equations of the thermo-elastic problem. In the decoupled setting, the temperature field is prescribed. Equilibrium holds when internal and external virtual work are equal, with the virtual internal work given by the sum of mechanical and thermal parts:

$$\delta L_{int} = \int_V \delta \boldsymbol{\varepsilon}_m^T \boldsymbol{\sigma} dV = \int_V \delta \boldsymbol{\varepsilon}_m^T (\boldsymbol{\sigma}_m + \boldsymbol{\sigma}_\theta) dV = \int_V \delta \boldsymbol{\varepsilon}_m^T \widetilde{\boldsymbol{C}} \boldsymbol{\varepsilon}_m dV - \int_V \delta \boldsymbol{\varepsilon}_m^T \theta \widetilde{\boldsymbol{\alpha}} dV \tag{7}$$

where $\widetilde{\boldsymbol{C}}$ the constitutive matrix. When the structure is subjected only to a thermal profile, the virtual external work, which refers to mechanical loads, vanishes. FN of the stiffness matrix can be identified as $\boldsymbol{K}^{\tau s i j}$, while the thermal load vector nucleus is defined as $\boldsymbol{\Theta}^{sj}$:

$$\boldsymbol{K}^{\tau s i j} \boldsymbol{u}_{\tau i} = \boldsymbol{\Theta}^{sj} \tag{8}$$

The complete system matrices are assembled through CUF automatic building process, independent of the selected expansion theory.

Antenna model

The antenna considered here is adapted from [3]. The macroscopic configuration is a finite plate with multiple surface-mounted patches, as shown in the right part of Fig. 1, with a 200 mm base and 100 mm height. The length of the square patch is 8 mm, while the thickness of the plate is 0.1 mm and that of the patch is 0.5 mm. The plate is made of conventional fabric composite with E = 50 GPa, a Poisson's ratio of 0.2, and a CTE of 1.44×10^{-7} K^{-1}. In contrast, the patch, representing a dielectric layer, exhibits a substantially lower E = 0.9 GPa, a Poisson's ratio of 0.3, and a much higher CTE of 4.00×10^{-5} K^{-1}. The macroscopic numerical model imposes a clamped constraint at the center patch along the thickness direction.

In this preliminary multiscale study, the antenna is idealized in the microscopic part as RUC shown on the left of Fig. 1, with the patch embedded in the host plate to reflect its slender geometry. These models are illustrative only, and no rigorous scale separation is enforced at this stage; the work should therefore be read as a preliminary step toward a fully validated workflow.

Materials Research Proceedings 69 (2026) 1358-1363 https://doi.org/10.21741/9781644904251-236

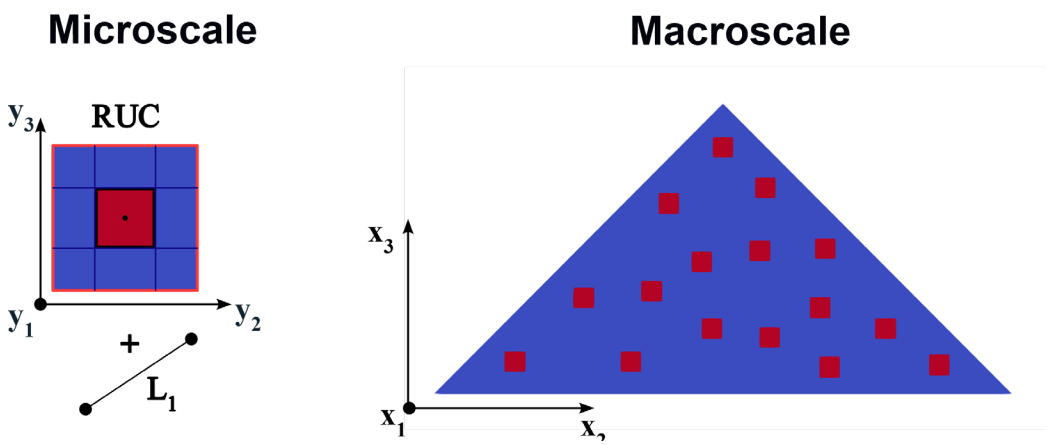


Figure 1. Micro- and Macroscale model of antenna.

Numerical results

Micromechanics. The first step of the multiscale analysis is the homogenization of the thermo-elastic properties. The RUC is modeled with two sections in the y_2–y_3 plane, connected through 2 two-nodes beam elements (B2), placed along the y_1 direction. Linear Lagrange shape functions are employed along the beam direction, whereas the cross-section is discretized using HLE functions of varying order. Table 1 reports the results of the 3D homogenization obtained with HLE of order 4, 6, and 8. It is observed that increasing the HLE order leads to the convergence of the results.

Table 1. Effective 3D thermo-elastic properties.

HLE order	E_1 (Pa)	E_2=E_3 (Pa)	G_{12}=G_{13} (Pa)	G_{23} (Pa)	ν_{12}=ν_{13}	ν_{23}	α_1 (1/K)	α_2=α_3 (1/K)
4	4.418 E10	3.999 E10	1.687 E10	1.666 E10	0.192	0.184	2.784E-07	3.206E-07
6	4.414 E10	3.952 E10	1.654 E10	1.641 E10	0.191	0.185	2.795E-07	3.253E-07
8	4.412 E10	3.9421 E10	1.642 E10	1.633 E10	0.191	0.185	2.799E-07	3.265E-07

Now, the localization of stresses due to a uniform temperature variation of 100 K applied over the structure, is performed on the RUC. Figure 2 shows the in-plane stress distribution at the interface between the two components. Due to the mismatch between the constituents' CTEs, thermal stresses develop. The in-plane stress components σ_{22} and σ_{33} exhibit a compressive character. Whereas, for the out-of-plane shear stresses σ_{13}, opposite regions of the patch are subjected to tension and compression along the y_3-direction. Finally, for the in-plane transverse shear component, σ_{23}, a doubly antisymmetric distribution is observed.

Materials Research Proceedings 69 (2026) 1358-1363 https://doi.org/10.21741/9781644904251-236

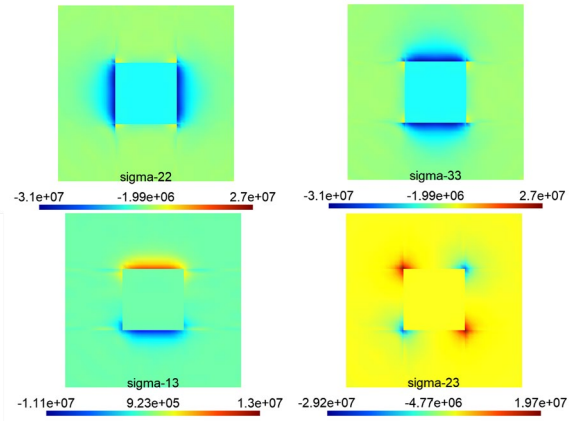


Figure 2. Stress state [Pa] due to the application of $\theta = 100$ K.

Evaluation of macroscopic thermal deformation. Lastly, the thermo-elastic analysis of the complete model is performed to assess the macroscopic thermal deformation. The comparison involves both the ESL and LW approaches, considering TE and LE models of different orders. The obtained CUF results demonstrate a good correlation with the Abaqus reference solution, accurately reproducing the global deformation trend under thermal loading. CUF-based models achieve this accuracy with a substantially lower number of DOF, thus ensuring a remarkable reduction in computational cost.

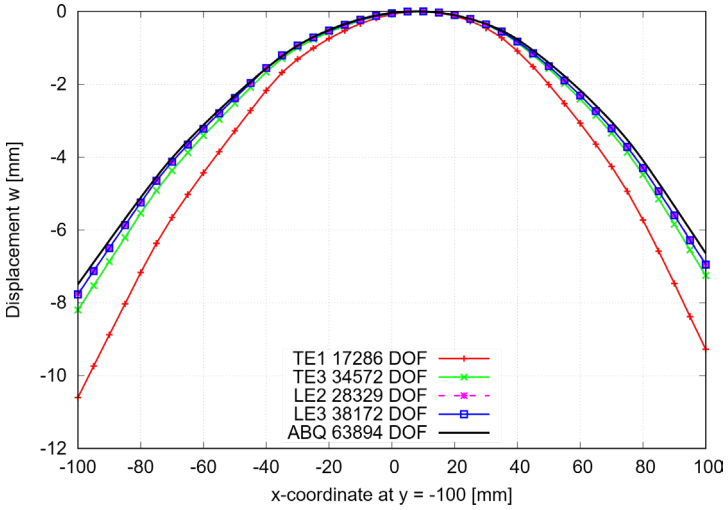


Figure 3. Out-of-plane displacement under a thermal load of 100 K: comparison between TE, LE, and Abaqus results with respective DOF.

Conclusions

This work presented a multiscale thermo-elastic analysis of a patch-mounted antenna within the Carrera Unified Formulation (CUF). At the microscale, the MSG/VAM approach using high-order CUF beam elements with HLE, provided accurate effective properties and local stress distributions. At the macroscopic CUF-based analysis, both ESL and LW models successfully reproduced the global thermal deformation. The CUF results showed excellent agreement with Abaqus while requiring far fewer DOF, confirming the efficiency and accuracy of the proposed method. Overall, the framework proves suitable for a future reliable and computationally efficient multiscale framework of lightweight space structures such as phased-array antennas.

References

[1] A. Canabal, R.P. Jedlicka, A.G. Pino. Multifunctional phased array antenna design for satellite tracking. Acta Astronautica, 2005, https://doi.org/10.1016/j.actaastro.2005.03.072

[2] J. Taylor, A. Okazaki, T. Honda, S. Kotsuki, M Yamaji, T. Kubota, R, Oki, T. Iguchi, T. Miyoshi. Oversampling Reflectivity Observations from a Geostationary Precipitation Radar Satellite: Impact on Typhoon Forecasts Whitin a Perfect Model OSSE Framework. James, 2021, https://doi.org/10.1029/2020MS002332

[3] I. Hayashy, R. Higuchi, T. Yokozeki, T. Aoki. Analytical study on the thermal deformation of ultralight phased array antenna. Acta Astronautica, 2021, https://doi.org/10.1016/j.actaastro.2021.08.009

[4] Nagaraj, M.H., Kaleel, I., Carrera, E. et al. Elastoplastic Micromechanical Analysis of Fiber-Reinforced Composites with Defects. Aerotec. Missili Spaz. 101, 53–59 (2022). https://doi.org/10.1007/s42496-021-00103-4

[5] A.R. Sanchez-Majano, R. Masia, A. Pagani, E. Carrera. Microscale thermo-elastic analysis of composite materials by high-order geometrically accurate finite elements, Composite Structures, 2022, https://doi.org/10.1016/j.compstruct.2022.116105

[6] A. Pagani, E. Zappino, F. Bracaglia, R. Masia, E. Carrera, Thermal stress analysis of variable angle tow composite plates through high-order structural models, Elsevier, Composite structures, 2023. https://doi.org/10.1016/j.compstruct.2023.117668

[7] A. Racionero Sanchez-Majano, R. Azzara, A. Pagani, E. Carrera. Accurate stress analysis of variable angle tow shells by high-order equivalent-single-layer and layer-wise finite element models. Materials, 2021, https://dx.doi.org/10.3390/ma14216486

Materials Research Proceedings 69 (2026) 1364-1368 https://doi.org/10.21741/9781644904251-237

Variational Asymptotic Micromechanics of Piezoelectric Composites Using Carrera Unified Formulation

Alfonso PAGANI[1,a], Rebecca MASIA[1,b*] and Enrico ZAPPINO[1,c]

[1]Politecnico di Torino, Corso Duca degli Abruzzi 24, Torino, Italy

[a]alfonso.pagani@polito.it, [b]rebecca.masia@polito.it, [c]enrico.zappino@polito.it

Keywords: Piezoelectricity, Variational Asymptotic Method, Carrera Unified Formulation, Micromechanics, Composite Materials

Abstract. Piezoelectric composite materials are increasingly used in sensors, actuators, ultrasonic imaging probes, and radar systems as they efficiently convert electrical energy into mechanical deformation. However, the variety of configurations complicates the evaluation of effective properties and the prediction of performance, requiring robust and high-fidelity design tools. This study introduces a micromechanics model based on the Variational Asymptotic Method (VAM) to determine the effective piezoelectric properties of composites. The structural formulation follows the Carrera Unified Formulation (CUF) with high-order beam elements representing the Repeatable Unit Cell (RUC) and Hierarchical Legendre Expansions (HLE) describing cross-sectional kinematics. Numerical studies on PZT-epoxy composites verify the model, showing accurate homogenized elastic, piezoelectric, and dielectric properties compared with reference data. The proposed CUF micromechanics framework is established to be inherently multifield and suitable for hierarchical multiscale analyses, enabling rigorous design, optimization, and reliability assessment of advanced piezoelectric composites.

Introduction

Piezoelectric composite materials have gained growing attention for their wide range of applications in sensors, actuators, ultrasonic imaging devices, and radar systems, owing to their ability to efficiently convert electrical energy into mechanical deformation. Embedding the piezoelectric active phase within a lightweight matrix mitigates the weight and shape limitations of bulk ceramics and enables the design of tailored composite architectures [1]. Driven by the increasing demand for intelligent systems and Industry 4.0 applications, smart components based on materials such as lead zirconate titanate (PZT) can produce an electric response under mechanical loading, providing direct feedback on structural stress and strain for adaptive and self-aware systems [2].

However, the wide variety of possible microstructural configurations poses significant challenges in accurately predicting the effective electromechanical properties and overall performance of these composites. To facilitate their design and optimization, reliable and efficient modelling tools are essential. Traditional analytical approaches are limited to simplified geometries and cannot capture the complex interactions occurring within heterogeneous architecture. Numerical micromechanical homogenization methods provide greater accuracy but often at a high computational cost.

In this work, a novel micromechanics model based on the Variational Asymptotic Method (VAM) is proposed for the homogenization of the Repeating Unit Cell (RUC) of piezoelectric composites [3]. The formulation combines VAM with the Carrera Unified Formulation (CUF) to derive a computationally efficient high-fidelity description of composite behavior [4]. The micromechanical problem is discretized using the Finite Element Method (FEM), enabling the treatment of complex boundary conditions and heterogeneous materials. The CUF framework

Content from this work may be used under the terms of the Creative Commons Attribution 3.0 license. Any further distribution of this work must maintain attribution to the author(s) and the title of the work, journal citation and DOI. Published under license by Materials Research Forum LLC.

Materials Research Proceedings 69 (2026) 1364-1368 https://doi.org/10.21741/9781644904251-237

employs high-order, geometrically exact beam elements and Hierarchical Legendre Expansions (HLE), ensuring full three-dimensional (3D) accuracy with reduced computational effort [5].

The proposed method is verified through numerical case studies involving unidirectional PZT-epoxy composites with varying fiber volume fractions V_f. The homogenized elastic, piezoelectric, and dielectric properties are benchmarked against the literature and commercial finite element homogenization tools, demonstrating excellent accuracy and efficiency.

Micromechanics for the piezoelectric problem within CUF framework

The fundamental idea of micromechanical analysis is that the size of RUC is much smaller than the global structure. Assuming **y** and **x** as local and global reference systems of the RUC, respectively, the relation **y** = **x**/δ defines the link between the two scales, where δ is a small scaling parameter, as shown in Fig. 1.

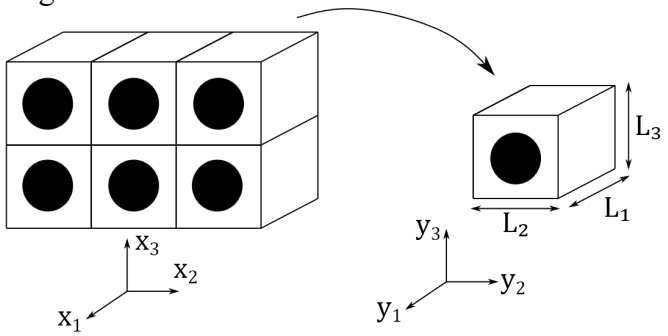


Figure 1. Coordinate reference systems of a periodic heterogeneous material and its RUC.

It is assumed that geometry, loading and boundary conditions at the macroscale do not affect the effective properties obtained at the microscale, and that the local solutions, averaged over the RUC volume, correspond to the global macroscopic solution:

$$\bar{\boldsymbol{u}}(\boldsymbol{x}) = \frac{1}{V}\int_V \boldsymbol{u}(\boldsymbol{x};\boldsymbol{y})\, dV$$
$$\bar{\boldsymbol{\psi}}(\boldsymbol{x}) = \frac{1}{V}\int_V \boldsymbol{\psi}(\boldsymbol{x};\boldsymbol{y})\, dV \tag{1}$$

where $\bar{\boldsymbol{u}}$ denotes the global displacement components, $\bar{\boldsymbol{\psi}}$ is the global electric potential and V the RUC volume.

In piezoelectric materials, the elastic and dielectric responses are coupled: the mechanical variables of stress and strain are related not only to each other but also to the electric field and the electric displacement. This electromechanical interaction is governed by the piezoelectric coefficients, and the linear coupled constitutive equations can be written in indicial notation as:

$$\sigma_{ij} = C_{ijkl}\varepsilon_{kl} - e_{ijk}E_k$$
$$T_i = e_{ikl}\varepsilon_{kl} + k_{ij}E_j \tag{2}$$

where σ_{ij} is the stress tensor, ε_{kl} the strain tensor, E_i the electric field vector, T_i the electric displacement vector, C_{ijkl} the fourth-order elasticity tensor (at constant electric field), k_{ij} is the second-order dielectric permittivity tensor (at constant strain), and e_{ijk} is the third-order piezoelectric coupling tensor.

According to the VAM, by minimizing the difference between the strain energy between the heterogeneous and the homogenized material, one can compute the solution to the stationary value problem as:

$$\Pi = \frac{1}{2}\langle \boldsymbol{\epsilon}^T\, \boldsymbol{G}\, \boldsymbol{\epsilon}\rangle - \frac{1}{2}(\bar{\boldsymbol{\epsilon}}^T \boldsymbol{G}^* \bar{\boldsymbol{\epsilon}}) \tag{3}$$

Materials Research Proceedings 69 (2026) 1364-1368 https://doi.org/10.21741/9781644904251-237

where $\boldsymbol{G}$ is the 9 × 9 constitutive matrix, including the elastic coefficients **C**, the piezoelectric coefficients **e**, and the dielectric coefficients **k**, and $\boldsymbol{\epsilon} = \bar{\boldsymbol{\epsilon}} + \boldsymbol{D}\boldsymbol{\chi}$ contains both strain field $\boldsymbol{\varepsilon}$ and the electric field **E**. **D** is the 9 × 4 differential operator matrix and $\boldsymbol{\chi}$ is the fluctuation vector containing both the elastic and the fluctuations associated with the electric potential. The * refers to the correspondent homogenized quantity. These fluctuation functions must satisfy the constraint $\langle \boldsymbol{\chi} \rangle = 0$, which, in the case of periodic boundary conditions applied over the three directions of the RUC, is automatically satisfied.

According to CUF, the 3D RUC can be reduced to a high-order beam model, where the beam axis is aligned with the fiber direction y_1, and the y_2–y_3 plane defines the beam cross-section Ω. The fluctuation unknowns, $\boldsymbol{\chi}$, can be expanded over the cross-section by means of arbitrary functions F_τ depending on the local coordinates y_2 and y_3, along the y_1, the problem is discretized using FEM with Lagrange shape functions N_i:

$$\boldsymbol{\chi}(\boldsymbol{x};\boldsymbol{y}) = F_\tau(y_2, y_3)\, N_i(y_1)\, \boldsymbol{\chi}_{\tau i}(x) \qquad \tau = 1, \dots, M \quad i = 1, \dots, N \tag{4}$$

where M is the number of expansions, τ denotes summation and N is the number of the beam nodes. To represent generic microstructural cross-section geometries, the domain can be discretized into multiple expansion subdomains. HLE functions are used to describe the subdomains, exploiting their hierarchical features. The accuracy of the unknowns is improved by adding higher-order polynomials.

By rewriting the fluctuation functions in the CUF-FEM framework and substituting into the functional of Eq. (3), the functional can be expressed in terms of the Fundamental Nuclei (FN) to be assembled over the four indices of the problem. Therefore, the strain functional becomes:

$$\Pi^* = \frac{1}{2}(\boldsymbol{\chi}_{sj}^T \boldsymbol{H}^{\tau sij} \boldsymbol{\chi}_{\tau i} + 2\boldsymbol{\chi}_{sj}^T \boldsymbol{D}_{h\epsilon}^{sj} \bar{\boldsymbol{\epsilon}} + \bar{\boldsymbol{\epsilon}}^T \boldsymbol{D}_{\epsilon\epsilon} \bar{\boldsymbol{\epsilon}}) \tag{5}$$

By minimizing the functional in Eq. (5), the following linear system is obtained:

$$\boldsymbol{H}\boldsymbol{\chi} = -\boldsymbol{D}_{h\epsilon}\bar{\boldsymbol{\epsilon}} \quad \text{with} \quad \boldsymbol{\chi} = \boldsymbol{\chi}_0 \bar{\boldsymbol{\epsilon}} \tag{6}$$

where $\boldsymbol{\chi}_0$ is the fluctuation solution vector. Finally, the effective constitutive matrix $\boldsymbol{G}^*$ of the homogenized piezoelectric medium is obtained as:

$$\boldsymbol{G}^* = \frac{1}{V}(\boldsymbol{\chi}_0^T \boldsymbol{D}_{h\epsilon} + \boldsymbol{D}_{\epsilon\epsilon}) \tag{7}$$

Numerical results

The present procedure provides a unified framework for general 3D RUC problems using high-order beam models. First, the proposed homogenization methodology is benchmarked against results from the literature; then, a novel microstructure comprising SiC fibers and PZT-7A inserts in a Epoxy matrix is investigated.

The piezoelectric composite analyzed here consists of circular PZT fibers embedded in an epoxy matrix. The epoxy matrix is considered isotropic, whereas the fiber properties are orthotropic and taken from [3]. The RUC is modeled as a square-pack arrangement (Fig. 1). V_f is varied from 10% to 70%, using fifth-order HLE. The results in Fig. 2 compare the present outputs with VAMUCH and an ANSYS FEM model reported in [3].

Materials Research Proceedings 69 (2026) 1364-1368 https://doi.org/10.21741/9781644904251-237

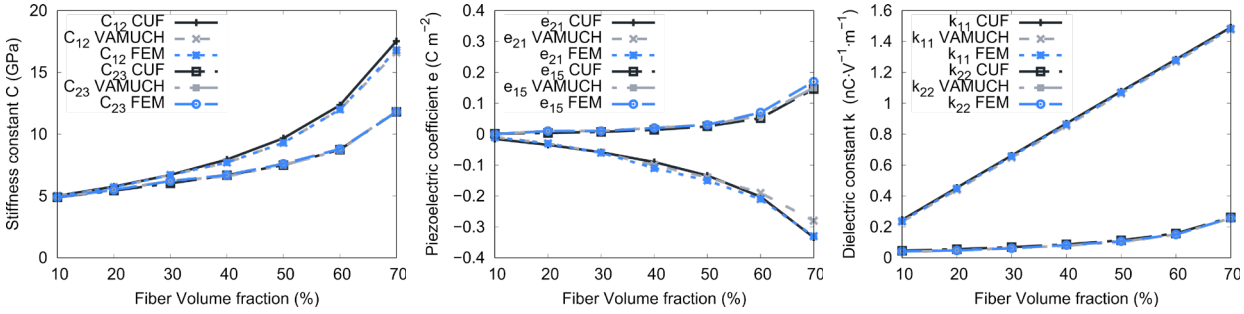


Figure 2. Effective coefficients for the square-pack model as a function of V_f: elastic (a), piezoelectric (b), and dielectric (c), compared with VAMUCH and ANSYS FEM [3].

It can be observed that CUF predictions show excellent agreement with both reference approaches. In the case of component e_{21}, the results are particularly close to the FEM outcomes.

The second case study considers a modified hexa-pack structure, shown in Fig. 3(a), comprising Epoxy matrix, SiC fibers and PZT-7A inserts. V_f is computed by parameterizing the fiber radius and the half-length of the piezoelectric insert. Figures 3(b–d) report the effective elastic, piezoelectric, and dielectric coefficients, respectively, as V_f varies. The results confirm that, for all effective properties, longitudinal and transverse quantities tend to coincide at lower V_f.

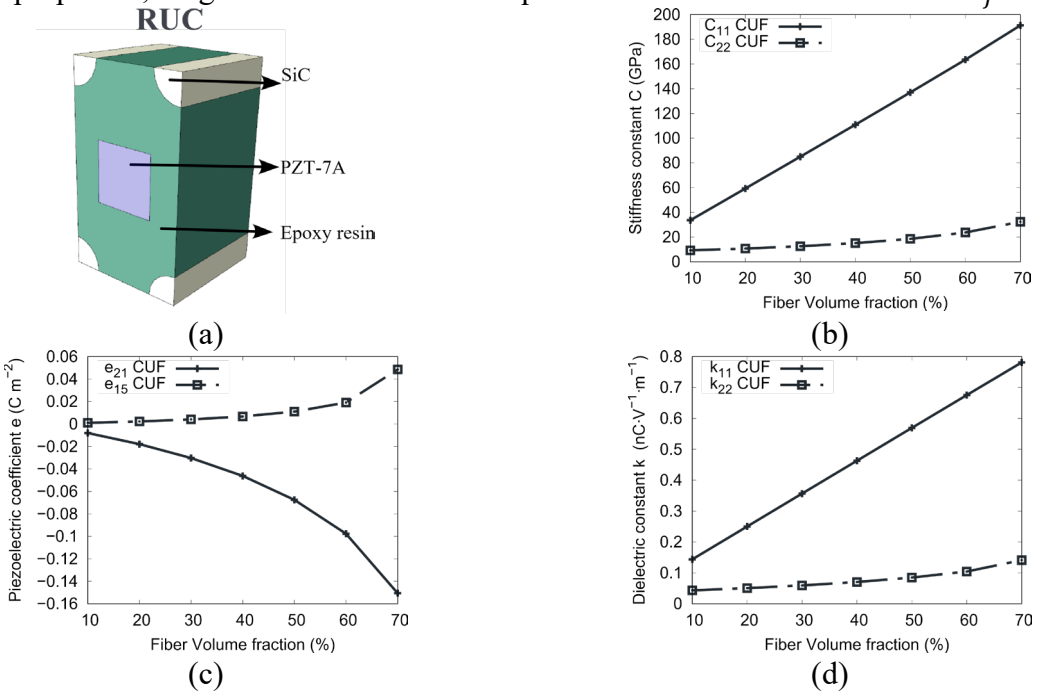


Figure 3. Novel microstructure with multiple materials (a), effective coefficients of the novel model as a function of V_f: elastic (b), piezoelectric (c), and dielectric (d).

Conclusions

This work presented a micromechanical framework that integrates the Variational Asymptotic Method (VAM) with the structural analysis capabilities of the Carrera Unified Formulation (CUF) to compute homogenized piezoelectric properties in an accurate and efficient scheme. The formulation was verified against VAMUCH and an ANSYS finite-element model, showing close agreement for elastic, piezoelectric, and dielectric tensors. These results build confidence in applying the method to more complex, multiphase RUC while reliably predicting effective

properties. The CUF–VAM approach is naturally suited to hierarchical multiscale analyses and supports design, optimization, and reliability assessment of advanced piezoelectric composites.

Acknowledgments
This research was carried out within the project PRE-ECO: A new paradigm to re-engineering printed composites, funded by the European Research Council under the European Union's Horizon 2020 research and innovation programme (Grant Agreement No. 850437).

References

[1] M. Habib, I. Lantgios, K. Hornbostel, A review of ceramic, polymer and composite piezoelectric materials. Journal of Physics D: Applied Physics, 2022. https://doi.org/10.1088/1361-6463/ac8687

[2] G. Graterol Nisi, M. Eugeni, V. Cardini, S. Atek, L. Pollice & P. Gaudenzi. Basic Technology for Smart Multifunctional Components with Embedded Electronics using Fused Filament Fabrication. Aerotecnica Missili & Spazio, 2019. https://doi.org/10.1007/s42496-019-00015-4

[3] T. Tang, W. Yu, Variational Asymptotic Micromechanics Modeling of Heterogeneous Piezoelectric Materials. Mechanics of Materials, 2008. https://doi.org/10.1016/j.mechmat.2008.04.007

[4] R. Masia, A. R. Sanchez-Majano, A. Pagani. Hygro-elasticity and moisture diffusivity analysis of periodically heterogeneous materials by hierarchical microscale models. International Journal of Solids and Structures, 2023. https://doi.org/10.1016/j.ijsolstr.2023.112231

[5] E. Carrera, A. G. de Miguel, A. Pagani. Hierarchical theories of structures based on Legendre polynomial expansions with finite element applications. International Journal of Mechanical Sciences, 2017. https://doi.org/10.1016/j.ijmecsci.2016.10.009

Materials Research Proceedings 69 (2026) 1369-1373 https://doi.org/10.21741/9781644904251-238

Thermal and CUF-Based Decoupled Thermo-Elastic Analysis of a Microstrip Patch Antenna Circuit for Radar Applications

Rebecca MASIA[1,a], Federico ZOPPI[1,b], Alfonso PAGANI[1,c *], Enrico ZAPPINO[1,d], Erasmo CARRERA[1,e]

[1]Politecnico di Torino, Corso Duca degli Abruzzi 24, Torino, Italy

[a]rebecca.masia@polito.it, [b]federico.zoppi@studenti.polito.it, [c]alfonso.pagani@polito.it, [d]enrico.zappino@polito.it, [e]erasmo.carrera@polito.it

Keywords: Microstrip Patch Antennas, Geostationary Radar Applications, Thermal Loads, Higher-Order Theories, Thermo-Elasticity, CUF

Abstract. This paper presents a method for a thermo-mechanical analysis of ultra-thin multilayered structures for space applications. A geostationary radar microstrip patch antenna circuit is designed using a simulated annealing algorithm. Material properties are determined from literature, and preliminary thermal analyses are performed with ESATAN-TMS. The application of the Carrera Unified Formulation (CUF) in the Finite Element Method (FEM) framework enables decoupled thermo-elastic analyses to identify deformations, stresses, and critical areas. Results demonstrate that the method reduces computational cost via high order theories, while accurately identifying specific regions most affected by thermal stress.

Introduction

The concept of microstrip patch antennas gains attention at the beginning of the 1970s. Its basic geometry consists of a flat conducting patch mounted on a dielectric substrate which is then backed by a plate. Compared with conventional microwave antennas, microstrip patch antennas provide a more compact profile, lower weight, ease of integration into circuits and higher power efficiency [1]. In addition to the benefits mentioned, the ability of the design to be arranged in large, ultra-lightweight phased array antennas accounts for its effectiveness in geostationary radar applications [2]. During orbital operations, extreme conditions in space may irreversibly alter the proper functioning of a large, ultra-thin planar antenna. Excessive thermal loads can compromise the maintenance of the antenna's proper temperature range and cause excessive thermal stress and deformation. The underlying issue is not only the risk of structural integrity being compromised, but also the loss of flatness requirements, which leads eventually to severe degradation of the radiation pattern and overall electromagnetic performance. Thermo-mechanical analyses have a fundamental role in predicting the overall response in space, particularly when composite materials are employed. With regard to multilayer structures, the CUF [3] proves to be suited for performing these analyses as it allows the description of all the kinematic models, from classical to high order theories. Moreover, it reduces the computational cost associated with 3D models.

In the present work, a square patch circuit is studied. The circuit serves as the fundamental unit of the ultra-lightweight phased array radar antenna. Following the explanation of the theoretical aspects involved, the second section presents the geometry of the circuit and its characteristics in terms of materials. Subsequently, on-orbit thermal analysis is displayed, while, in the last section, the CUF is used both with Equivalent Single Layer (ESL) models and Layer Wise (LW) models. This study assumes homogeneous thermal loads, as its primary objective is to validate the effectiveness of the proposed methodology. Future analyses will address the implementation of spatially varying thermal loads.

Content from this work may be used under the terms of the Creative Commons Attribution 3.0 license. Any further distribution of this work must maintain attribution to the author(s) and the title of the work, journal citation and DOI. Published under license by Materials Research Forum LLC.

Materials Research Proceedings 69 (2026) 1369-1373 https://doi.org/10.21741/9781644904251-238

Thermo-mechanical Problem and Theoretical Framework of the approach

CUF is a well-established theory that enables the hierarchical development of structural theory through the use of an extensive index notation and generalized expansions of the primary mechanical variables from lower to higher orders.

By using CUF, the 3D displacement field $\mathbf{u}(x, y, z)$, which can be seen in Eq. 1, is expressed through a condensed notation. In the 2D case, the formulation combines expansion functions $F_\tau(z)$, that describe the through-thickness displacement component, and the general 2D displacement vector $\mathbf{u}_\tau(x, y)$ (Eq. 2)[3,4].

$$\mathbf{u}^T(x, y, z) = (u_x \; u_y \; u_z) \tag{1}$$

$$\mathbf{u}(x, y, z) = F_\tau(z)\mathbf{u}_\tau(x, y) \qquad \tau = 1,2,\dots N \tag{2}$$

Where N represents the order of expansion function. It is worthwhile to mention that within this theory, the formulation remains invariant when the order of expansion is changed.

In the present study, Lagrange Expansion (LE) [5] with Layer Wise theory (LW) [3,6] and Taylor Expansion (TE) [7], with Equivalent Single Layer theory (ESL) [3,6], are used as expansion functions.

The CUF can be applied to the FEM framework, which if included in Eq. 2 allows us to obtain:

$$\mathbf{u}(x, y, z) = F_\tau(z)N_i(x, y)\mathbf{q}_{\tau i} \tag{3}$$

where $\mathbf{q}_{\tau i}$ and N_i are the nodal displacement and the shape function, respectively.

The governing equations can be obtained by applying the Principle of Virtual Displacements (PVD), which, in the absence of mechanical loads, can be expressed as:

$$\delta L_{int} = \int_V \delta\boldsymbol{\varepsilon}^T\boldsymbol{\sigma}dV = \int_V(\delta\boldsymbol{\varepsilon}_m + \delta\boldsymbol{\varepsilon}_\theta)^T\boldsymbol{\sigma}dV = \int_V \delta\boldsymbol{\varepsilon}_m^T\boldsymbol{\sigma}dV \tag{4}$$

The term $\delta\boldsymbol{\varepsilon}_\theta$ is zero when decoupled analyses are considered, as it is done in this work. Introducing CUF and FEM formulations, Eq. 4 becomes:

$$\delta L_{int} = \delta\mathbf{q}_{sj}^T\mathbf{K}^{\tau sij}\mathbf{q}_{\tau i} = \boldsymbol{\Theta}^{sj} \tag{5}$$

By means of the indices i, j, τ, s the stiffness matrix can be decomposed and represented through 3×3 matrices known as Fundamental Nuclei (FN). Moreover, $\boldsymbol{\Theta}$ is a 3×1 matrix, which represents the fundamental nucleus of the thermal load matrix. Details and additional information on the aforementioned matrices and their derivation procedure can be found in [3].

Microstrip Patch Antenna Circuit

The studied circuit is composed of 16 patches. The position of their center of mass is determined by a simulated annealing algorithm [7], which is written with connection length between patches as the only parameter to be minimized and optimized. No additional initial considerations on the circuit are made since the aim of the work is to validate the suitability of the adopted methodology. In Fig. 1(a) the final structure can be seen. The proposed structure consists of four layers, arranged from bottom to top as follows: a CFRP support plate (10 cm × 10 cm) fabricated using IM600/133 composite, a copper foil layer serving as the ground plane, where a reduction in area occurs relative to the support plate, an RT/duroid® 5880 laminate acting as the dielectric substrate, and a second copper foil layer for the implementation of the patches and feed lines. Comparing the patches layer with the duroid laminate, a further reduction in area is present.

On-orbit Thermal Analysis

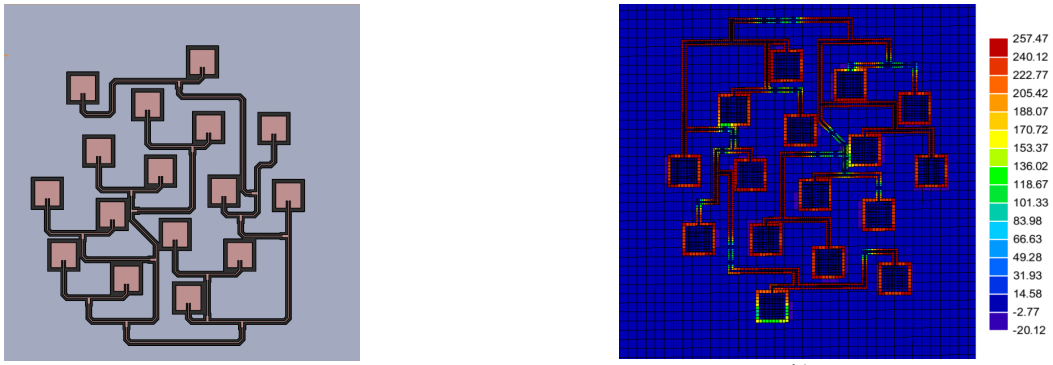
To conduct on-orbit thermal analysis, the software ESATAN-TMS is used. Material properties are determined after conducting a meticulous literature review. The geostationary orbit is discretized

Materials Research Proceedings 69 (2026) 1369-1373 https://doi.org/10.21741/9781644904251-238

into 11 timesteps, at each of which the temperatures of the 44,841 thermal nodes in the model are computed. A set of three nodes per layer is used in the thickness direction of the model. Nodes are positioned at the top, bottom, and mid-plane of each layer.

In Fig. 1(b) the most critical timestep, which corresponds to the timestep 25920 s in the 86400 s orbit, is depicted. It should be noted that the temperature range exceeds the survival range of spacecraft components.

As has previously been stated, the purpose of this work is to validate the analysis methodology. Consequently, the analyzed structure does not correspond to a real application. The obtained results serve as the basis for justifying the load assumptions adopted in the subsequent thermoelastic evaluation.



a) b)

Fig. 1: a) Microstrip patch antenna circuit, b) critical timestep (degree Celsius).

CUF-based Thermo-mechanical Analysis

The mechanical model is implemented in Abaqus and is composed of 3078 elements. More specifically, Q9 elements are used and a constant thermal load of 100 °C is imposed over the whole structure. This step serves to verify the results before proceeding to variable thermal loads in space. The following boundary condition is selected for the following analyses: constraint along the thickness of four points in the vicinity of the central point. The rationale for the choice lies in the possibility of evaluating a more complex displacement field. Regarding the LW theory, the following analyses are conducted for each layer of the structure: 1 LE1, 2 LE1, 3 LE1, 4 LE1, 1 LE2, 2 LE2, 1 LE3, and 2 LE3, whereas for the ESL approach, TE from order 1 up to order 6 are implemented.

Fig. 2 shows the comparison with Abaqus in terms of out-of-plane displacement. In particular, 21 points were selected along a line passing through the center of the structure and parallel to the x-axis, and an additional 21 points were taken along another line, also passing through the center and parallel to the y-axis. Fig. 3(a) and Fig. 3(b) show the overall out-of-plane displacement field obtained from Abaqus and from the 1 LE3 analysis, respectively.

To assess which of the two High Order Theories is more appropriate for the study of the structure, convergence analyses via normal and shear stresses through thickness are performed. Stress distribution is evaluated at the central point of the northernmost patch. Data shows that the same stress distribution is consistently obtained with 2 LE2, 1 LE3 and 2 LE3 analyses, while convergence is not equivocally attained from TE analyses. Furthermore, the LE stress field through thickness is consistent with the literature.

Conclusions

The study employed the CUF within FEM framework to investigate the decoupled thermo-mechanical response of ultrathin multilayer structures. Results demonstrate the validity of the

Materials Research Proceedings 69 (2026) 1369-1373 https://doi.org/10.21741/9781644904251-238

model with respect to commercial software and a complete stress characterization is obtained. High Order Theories allow to reduce the computational cost, still providing overall accuracy in predicting the mechanical response to the applied load.

Among these, LW approach with Lagrange expansion function proved to be most suitable to the case under study as it allows to describe the discontinuity of mechanical properties along the thickness with high accuracy. Future analysis will address the implementation of spatially varying thermal loads.

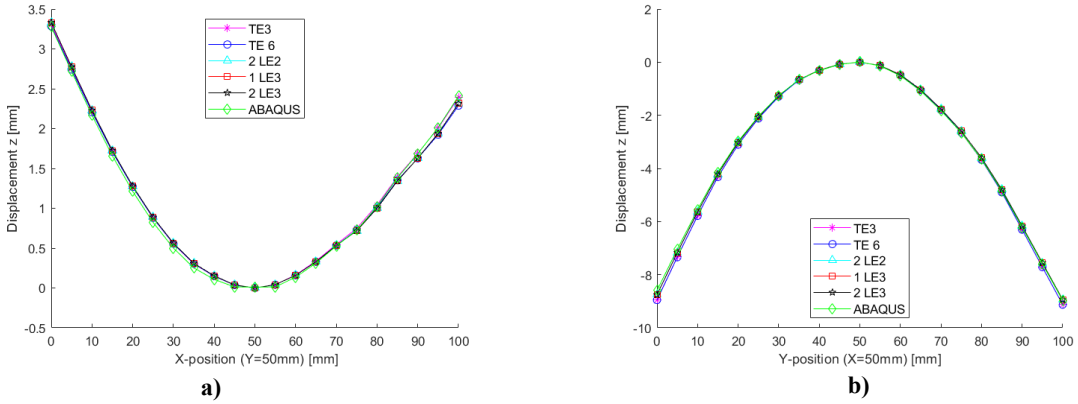


Fig. 2: Out-of-plane displacement field at 42 output points: comparison between CUF and Abaqus. a) displacement of the 21 points in the x direction, b) displacement of the 21 points in the y direction.

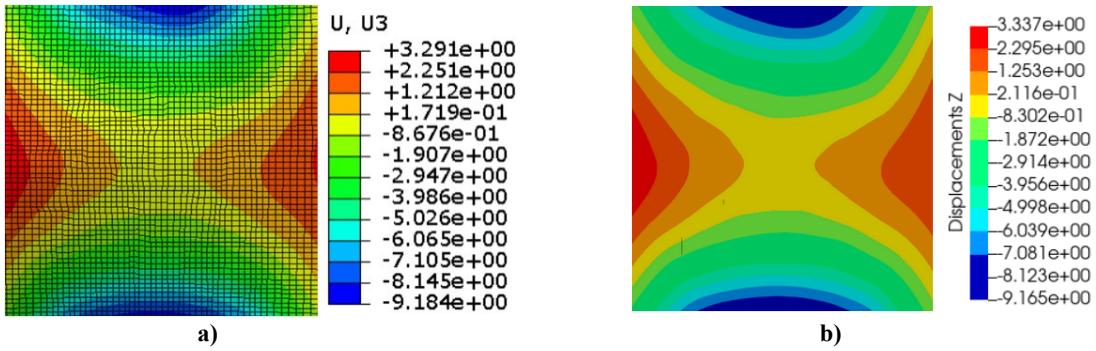


Fig. 3: Overall out-of-plane displacement field of the structure. a) Abaqus results, b) CUF (1 LE3) results. The unit of measurement is millimetres.

Acknowledgements

This study was carried out within the Space It Up!, funded by the Italian Space Agency, ASI, and the Ministry of University and Research, MUR, under contract n. 2024 - 5 -E.0 - CUP n. I53D24000060005.

References

[1] K.F. Lee, K.F. Tong, Microstrip Patch Antennas, in: Z. Chen (Ed.), Handbook of Antenna Technologies, 1st ed., Springer, 2016, pp.1-55. https://doi.org/10.1007/978-981-4560-44-3_29

[2] A. Okazaki, T. Honda, S. Kotsuki, M. Yamaji, T. Kubota, R. Oki, T. Iguchi, T. Miyoshi, Simulating precipitation radar observations from a geostationary satellite, Atmos. Meas. Tech. 12 (2019) 3985–3996. https://doi.org/10.5194/amt-12-3985-2019

[3] E. Carrera, M. Cinefra, M. Petrolo, E. Zappino, Finite Element Analysis of Structures Through Unified Formulation, Wiley, Chichester, 2014. https://doi.org/10.1002/9781118536643

[4] E. Carrera, M. Cinefra, M. Petrolo, E. Zappino, Comparison between 1D (Beam) and 2D (Plate/Shell) Finite Elements to Analyze Thin Walled Structures, Aerot. Miss. Spaz. 97 (2018) 41-50. https://doi.org/10.1007/BF03404671

[5] A. Pagani, E. Carrera, R. Augello, D. Scano, Use of Lagrange polynomials to build refined theories for laminated beams, plates and shells, Compos. Struct. 276 (2021) 114505. https://doi.org/10.1016/j.compstruct.2021.114505

[6] A. Pagani, A. Racionero Sánchez-Majano, M. Petrolo, Influence of Structural Theories on Optimal Fiber Distributions in Tow-Steered Composites Considering Local Strain and Stress. Aerotec. Missili Spaz. 104 (2025) 1-15. https://doi.org/10.1007/s42496-025-00275-3

[7] E. Carrera, M. Petrolo, Guidelines and recommendations to construct theories for metallic and composite plates, AIAA J. 48(12) (2010) 2852–2866. https://doi.org/10.2514/1.J050316

[8] R.A. Rutenbar, Simulated Annealing Algorithms: An Overview, IEEE Circuits Devices Mag. 5 (1989) 19–36. https://doi.org/10.1109/101.17235

Materials Research Proceedings 69 (2026) 1374-1378 https://doi.org/10.21741/9781644904251-239

Magnetically Targeted Microcapsules to Enhance Self-Healing Behaviour of High-Performance Polymers Designed to Withstand Moondust Environment

Guido SACCONE[1,a*], Elisa TOTO[2,b], Nunzia FAVALORO[1,c], Marianna RINALDI[3,d], Maria Gabriella SANTONICOLA[2,e]

[1]Italian Aerospace Research Centre (CIRA), Via Maiorise snc, 81043, Capua (CE), Italy

[2]Department of Chemical Engineering Materials Environment, Sapienza University of Rome, Via del Castro Laurenziano 7, 00161 Rome, Italy

[3]Italian Space Agency, Via del Politecnico snc, 00133, Rome, Italy

[a]g.saccone@cira.it,[b]elisa.toto@uniroma1.it, [c]n.favaloro@cira.it, [d]marianna.rinaldi@asi.it, [e]mariagabriella.santonicola@uniroma1.it

Keywords: Moon, Microcapsule Self-Healing, Dust Mitigation Technology, Innovative High-Performance Polymers, Space Exploration

Abstract. Lunar regolith dust poses a critical challenge for sustained surface operations, as its highly abrasive, sharp-edged, and electrostatically charged particles readily adhere to surfaces, degrading optical, thermal, and mechanical systems and posing health hazards to astronauts. To address this issue, the SELENE project, led by CIRA with contributions from Sapienza Università di Roma under ASI financial support, aims to develop lightweight, high-performance fluorinated co-polyimide composites engineered for passive dust mitigation and durability. The material integrates dual self-healing mechanisms: (i) an extrinsic system based on microcapsules containing UV-curable healing agents released upon mechanical damage, and (ii) an intrinsic supramolecular component capable of reversible non-covalent bonding to autonomously repair microcracks. An innovative feature of SELENE project is the magnetic manipulation of microcapsules containing Fe_3O_4 nanoparticles, enabling targeted positioning before thermal imidization to enhance crack interception and surface damage protection. This multifunctional approach aims to significantly enhance longevity, survivability, wear resistance and reliability of lightweight, high-performance materials for building lunar infrastructures and allows human long-term settlement.

Introduction

The growing international interest in space exploration and colonization has long underscored the need to develop and raise to an adequate Technology Readiness Level (TRL), technologies capable of supporting both robotic and crewed missions through systems that are increasingly compact, efficient, and cost-effective. Numerous lunar and Martian exploration missions are planned for the coming years, including, but not limited to, Artemis, ExoMars, Mars Sample Return, and Terrae Novae.

Future lunar and Martian missions must overcome a range of technological challenges to ensure human survival in such hostile environments [1]. Indeed, the surfaces of both the Moon and Mars are characterized by extreme thermal fluctuations, minimal or absent atmospheric pressure, micrometeorite bombardment, and intense exposure to electromagnetic radiations, all of which can cause severe and irreversible damage to both biological tissues and electronic systems. In addition, the presence of micrometric regolith dust particles, sharp-edged, abrasive, irregularly shaped, chemically reactive, electrostatically charged, highly adhesive, and in some cases magnetic, poses a further major threat.

Content from this work may be used under the terms of the Creative Commons Attribution 3.0 license. Any further distribution of this work must maintain attribution to the author(s) and the title of the work, journal citation and DOI. Published under license by Materials Research Forum LLC.

Materials Research Proceedings 69 (2026) 1374-1378 https://doi.org/10.21741/9781644904251-239

These fine dust particles, highly toxic if inhaled, can interfere deleteriously with numerous mechanical, optical, photovoltaic, and electronic components, e.g., by reducing solar panel efficiency through surface darkening and accumulation, disrupting sensors and measuring instruments, and degrading the thermal performance of radiators and heat exchangers. Moreover, lunar and Martian dust can adhere strongly to astronauts' suits and visors, causing a wide range of critical operational and safety issues during both exploration and long-term habitation missions (see Figure 1) [2-3].



Figure 1. Examples of lunar dust issues.

In this context, SELENE project aims to design and synthesize an innovative multifunctional polymeric material exhibiting low surface adhesion to lunar regolith microparticles, high thermo-mechanical performance, and self-healing capability to autonomously repair microcracks and abrasions induced by the sharp and abrasive dust particles typical of the lunar environment [4].
At the core of the SELENE project lies the development of a dual-mode self-healing strategy embedded within a fluorinated co-polyimide matrix, specifically engineered to exhibit low surface energy and superior dust-repellent properties belonging to the category of passive dust mitigation technologies in agreement with an international accepted [3].

Methodology

One of the core functionalities of the SELENE project's Proof of Concept (PoC) is the ability to autonomously repair microcracks generated by the abrasive action of sharp and angular lunar regolith particles. Structural integrity recovery is achieved through an extrinsic, autonomous self-healing mechanism enabled by the homogeneous dispersion of polymeric microcapsules with diameters ranging from a few to several hundred micrometres within the polymeric matrix and containing a UV-curable monomer and crosslinking photo-initiators, as schematically illustrated in Figure 2.

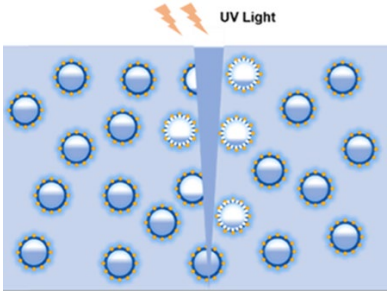


Figure 2. Conceptual representation of UV triggered microcapsule self-healing

Microencapsulation is a process in which solid particles, liquid droplets, or gas bubbles are enclosed within an inert spherical or ellipsoidal shell that isolates and protects the internal phase from the surrounding environment. In its simplest configuration i.e., mononuclear, a microcapsule consists of a single-core structure enclosed by a uniform shell, where the core contains the active monomers i.e., healing agents, and the shell generally acts only as the protective barrier. Instead, in the SELENE project to the external layer of the microcapsule is provided also the fundamental function to improve the dust mitigation capacity of the final material. This has been achieved by the advantageous use of innovative and specifically selected poly dimethyl siloxanes (PDMS).

Materials Research Proceedings 69 (2026) 1374-1378 https://doi.org/10.21741/9781644904251-239

In self-healing polymers, microcapsules are primarily used as microscopic reservoirs of reactive monomers or oligomers, which are released when the capsule ruptures due to crack propagation. The released healing agents diffuse toward the crack tip through capillary forces and react with the catalysts, initiating polymerization or crosslinking reactions that seal the crack and restore the original mechanical integrity.

This extrinsic self-healing approach offers significant advantages e.g., simpler fabrication, faster healing kinetics, and no need for chemical modification of the host matrix, although it cannot be used multiple times due to its inherent configuration. The process involves three main stages as depicted in Figure 3 [8]:

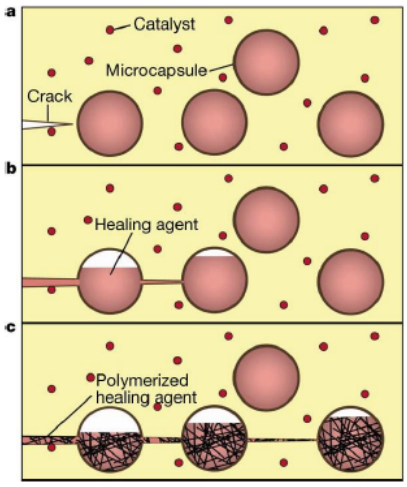


Figure 3. Schematic illustration of the three fundamental steps of the crack induced microcapsule self-healing mechanism [8].

a. Activation: initiation of capsule rupture upon damage occurrence;
b. Transport: diffusion of the healing agent toward the damage site;
c. Repair: polymerization or crosslinking reaction, whose kinetics depend on temperature and catalyst concentration.

The overall healing efficiency depends on the balance between the crack propagation rate and the healing kinetics of the released agents. Although this mechanism enables effective and rapid crack closure, it remains limited to a single healing event per site, since the local supply of healing agents cannot be replenished. Moreover, due to the heterogeneous nature of the microcapsule-based approach, it may be incompatible with optically transparent components where high transmittance is required.

One of the most critical challenges hindering the efficient implementation of the microcapsule-based self-healing mechanism lies in achieving a homogeneous dispersion of the healing agent reservoirs within the co-polyimide matrix during the intermediate stage of polymerization. This difficulty arises from the intrinsically high viscosity of the polyamic acid precursor, which exhibits substantial drag resistance to particle diffusion and dispersion. Conventional mechanical stirring techniques cannot be employed, as they would inevitably induce the formation of gaseous bubbles and other forms of contamination within the sensitive and highly reactive co-polyamic solution.

Results and Discussion

Instead, a distinctive innovation of SELENE project consists of the magnetically controlled positioning of microcapsules [9-10]. Each capsule contains superparamagnetic Fe_3O_4 nanoparticles, allowing their directed migration within the polyamic acid precursor under an

external magnetic field. By precisely controlling their spatial arrangement before curing, this approach ensures targeted reinforcement, enhanced crack interception, and a homogeneous distribution of the healing system across the matrix as shown in Figure 4.

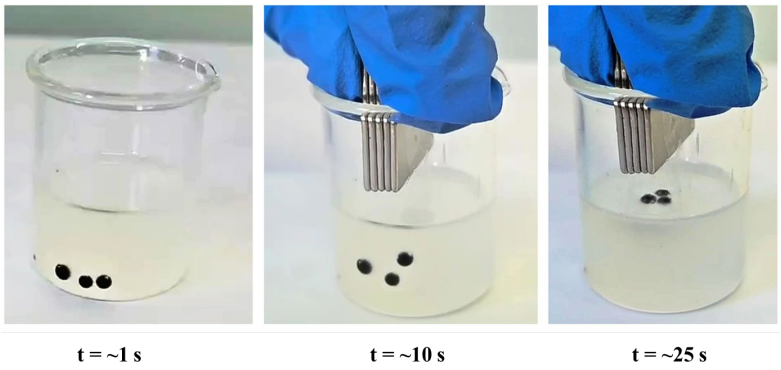


Figure 4. Sequence of successive frames illustrating the magnetically induced migration of microcapsules containing magnetic nanoparticles

The core–shell microcapsules feature a PDMS-based shell compatible with the polyimide host, and a liquid core comprising a photo-activated healing agent premixed with a UV initiator, taking advantage of the intense solar UV radiation on the lunar surface. Upon crack formation and subsequent UV exposure, the released agent polymerizes in situ, restoring the composite's mechanical continuity and integrity.

Beyond its smart healing functionality, the SELENE material is tailored to endure lunar environmental extremes, providing abrasion resistance, thermal endurance, and low dust adhesion, which mitigate the degradation of critical systems. The magnetically guided healing network further increases protection in high-stress regions, extending operational life.

This multifunctional composite is envisioned for space-critical components, including rovers, landers, habitats, solar panels, optical systems, radiators, and astronaut gear, where micrometric, abrasive lunar regolith represents a persistent threat. Its high *abhesivity*, resilience, and autonomous repair capability make it a promising solution for durable, reliable, and sustainable materials in future lunar surface operations.

Summary

In essence, SELENE introduces an adaptive polymer platform that combines passive dust mitigation with active self-repair, paving the way for a new generation of smart materials for long-duration extra-terrestrial missions.

References

[1] Favaloro, N., Saccone, G., Piscitelli, F., Volponi, R., Leoncini, P., Catalano, P., Visingardi, A., Noviello, M.C., Enabling technologies for space exploration missions: The CIRA-TEDS program roadmap perspectives, Aerotecnica Missili & Spazio, 2023, https://doi.org/10.1007/s42496-023-00159-4

[2] Cannon K.M., Dreyer C.B., Sowers G.F., Schmit J., Nguyen T., Sanny K., Schertz J., Working with lunar surface materials: Review and analysis of dust mitigation and regolith conveyance technologies, Acta Astronautica 196, 259-274 (2022), doi.org/10.1016/j.actaastro.2022.04.037

[3] Saccone, G., Favaloro, N. Dust Mitigation Strategies Enabling Moon Exploration Missions. Aerotec. Missili Spaz. (2024), https://doi.org/10.1007/s42496-024-00225-5

[4] Wohl, C.J., Atkins, B.M., Belcher, M. A., Connell, J.W., Copoly(imide siloxane) Abhesive Materials with Varied Siloxane Oligomer Length, International SAMPE Symposium and Exhibition (Proceedings), (2010).

[5] Toto, E., Laurenzi, S., Pellegrini, R.C., Cavallini, E., Santonicola, M.G., Eco-friendly synthesis of high-performance polyimide materials using bio-based greener solvents: Towards sustainable technologies in space environment. Materials Today Sustainability, 25, 100657, (2024). https://doi.org/10.1016/j.mtsust.2023.100657

[6] Toto, E., Santonicola, M.G., Laurenzi, S., Circi, C., Pellegrini, R.C., Cavallini, E., Serra, E., Scaglione, S., Zola, D., UV–VIS-NIR optical properties of micrometric-thick polyimide membranes for lightweight devices in space, Optical Materials 146, 114604, (2023). https://doi.org/10.1016/j.optmat.2023.114604

[7] Périchaud, A.A., Iskakov, R.M., Kurbatov, A., Akhmetov, T.Z., Prokohdko, O.Y., Razumovskaya, I.V., Bazhneov, S.L., Apel, P.Y., Voytekunas, V.Y., Abadie, M.J.M., Auto-Reparation of Polyimide Film Coatings for Aerospace Applications Challenges & Perspectives, Chapter 11, Intech Abadie et al. (2012), http://dx.doi.org/10.5772/46005

[8] Roy, N., Buhler, E., Lehn, J-M., The Tris-Urea Motif and Its Incorporation into Polydimethylsiloxane-Based Supramolecular Materials Presenting Self-Healing Features, Chem. Eur. J., (2013), https://doi.org/10.1002/chem.201203518

[9] Gwon, K., Dharmesh, E., Nguyen, K.M., Shornack, A.M.R., de Hoyos-Vega, J.M., Ceylan. H., Stybayeva, G., Peterson, Q.P., Revzin, A., Designing magnetic microcapsules for cultivation and differentiation of stem cell spheroids, Microsystems & Nanoengineering 10:127, (2024), https://doi.org/10.1038/s41378-024-00747-9

[10] Chauhan, R., Usman, H., Minocha, N., Molaei, M., Niepa, T.H.R. and Singh, M.R., Predictive Modeling and Experimental Validation of Magnetophoretic Delivery of Magnetic Nanocultures, ACS Materials Lett. 7, 2679−2685, (2025), https://doi.org/10.1021/acsmaterialslett.5c00753

Materials Research Proceedings 69 (2026) 1379-1383 https://doi.org/10.21741/9781644904251-240

Novel Modeling Technique of Metamaterials Using One-Dimensional Finite Elements

Riccardo Augello[1,a *], and Erasmo Carrera[1,b]

[1]MUL2 Lab, Department of Mechanical and Aerospace Engineering, Politecnico di Torino, Corso Duca degli Abruzzi 24, 10129 Torino, Italy

[a]riccardo.augello@polito.it, [b]erasmo.carrera@polito.it

Abstract. Geometry-driven metamaterials offer negative Poisson's ratios, vanishing shear stiffness, and programmable multi-stability, but their slender struts and large rotations overwhelm conventional finite-element meshes. A streamlined framework that couples classical finite elements with the Carrera Unified Formulation (CUF) resolves cross-sectional deformation through higher-order beam expansions, reproducing three-dimensional behaviour while retaining a one-dimensional model. Contrary to the conventional beam definition, in this study the structural beam axis is aligned with the thickness of the sandwich panel, while the cross-section extends across its width. This particular application is useful to highlight the flexibility of CUF in modelling any structural configuration as an advanced 1D element. Representative static linear analyses are presented of the hexagonal metamaterial design.

Introduction

In the past decade, lattice-based metamaterials have risen to prominence as engineered architectures whose macroscopic behaviour is dictated far more by geometry than by chemistry. Built from periodically replicated unit cells (UCs), these structures are meticulously tuned to deliver unprecedented mechanical responses. For instance, by judiciously sculpting the UC, targeted properties can be achieved—from auxetic systems with a negative Poisson's ratio [1, 2] to pentamodes that suppress shear almost entirely [3], or non-linear responses can be elicited through large bending deformations and elastic instabilities. Because the global behaviour of a lattice hinges on its microscopic architecture, many studies have sought closed-form links between UC geometry and effective properties. Pioneering work based on Bernoulli–Euler and Timoshenko theories yielded analytical expressions for the elastic moduli and Poisson's ratio of cuboid microlattices [4].

Transitioning to three dimensions unlocks richer behaviours: 3D NPR lattices have been conceived through both additive manufacturing [5] and mechanical assembly. Li's 3-D re-entrant lattice, experimentally validated in compression [6], and its augmented counterpart with extra struts, capable of wide-range tunability [7], are prime examples. The interlocking-assembly route further reduces fabrication overheads compared to layer-wise printing [8]. Accurately simulating the rich mechanics of such structures requires numerical tools capable of resolving rigid-body rotations, large strains, and steep stress gradients without prohibitive cost. Conventional FEM, though ubiquitous, struggles: reproducing the fine architectural details typically forces excessively dense meshes and long runtimes. A general solution is presented by integrating classical FEM with the Carrera Unified Formulation (CUF) [9]. CUF enriches one-dimensional finite elements through tailored expansion functions that faithfully recover cross-sectional deformation modes. When Lagrange expansions are employed, the method accommodates arbitrarily intricate cross-sections—making it especially suited to the convoluted geometries of metamaterials [10].

Metamaterial structure

A metamaterial structure is used as a benchmark to demonstrate the CUF-based modelling capabilities. The geometry of a generica metamaterial is reported in Fig. 1. In this study,

Content from this work may be used under the terms of the Creative Commons Attribution 3.0 license. Any further distribution of this work must maintain attribution to the author(s) and the title of the work, journal citation and DOI. Published under license by Materials Research Forum LLC.

Materials Research Proceedings 69 (2026) 1379-1383 https://doi.org/10.21741/9781644904251-240

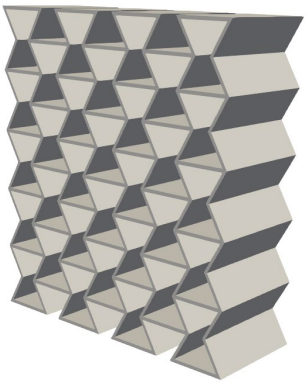


Figure 1: Re-entrant metamaterial structure.

exploiting CUF capabilities, the whole structure is modelled as 1D beam elements. The beam axis is aligned with its width, leaving the conventional beam definition, as reported in Fig. 2. The cross-sections of the metamaterial is discretized using high-order Lagrange polynomials;

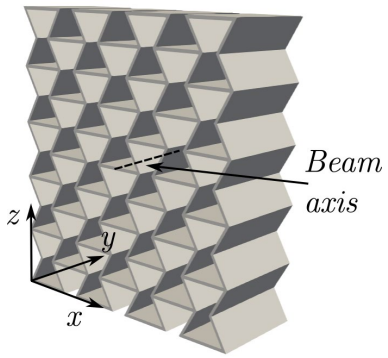


Figure 2: CUF model of the re-entrant metamaterial structure.

this discretization ensures detailed representation of geometry and its mechanical behaviour. To maintain displacement continuity between the domains, shared Lagrange points are defined at their interfaces, as reported in Fig. 3. The precise alignment of shared Lagrange points eliminates any potential discontinuities at the interfaces, enabling an accurate representation of the coupling the elements. The use of high-order Lagrange polynomials enables

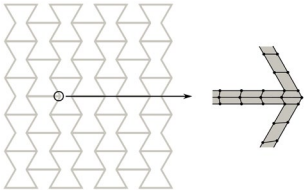


Figure 3: Lagrange elements for the discretization of the re-entrant metamaterial structure.

enhanced cross-sectional resolution, capturing thoroughly the displacement field. This is achieved by significantly reducing DOFs without compromising accuracy with respect to the high fidelity 3D FEM simulations, as widely discussed in the following. To perform comparisons, the same metamaterial structure has been analysed by means of commercial FEM

software, i.e. Abaqus. In CUF, the displacement field u(x, y, z) for a 1D beam is represented as:

$$\boldsymbol{u}(x,y,z) = F_\tau(x,z)N_i(y)\boldsymbol{u}_{\tau i} \qquad \tau = 1,2,\dots,M \quad i = 1,2,\dots,N_n$$

Materials Research Proceedings 69 (2026) 1379-1383 https://doi.org/10.21741/9781644904251-240

where $F_\tau(x,z)$ denotes the expansion functions in the cross-sectional plane, $N_i(y)$ the shape functions along the beam axis, and $\boldsymbol{u}_{\tau i}$ the nodal unknowns. As earlier mentioned, Lagrange polynomials are used as $F_\tau(x,z)$.

Numerical results

The numerical study focuses on a metamaterial with hexagonal topology (Fig. 4). Three modeling strategies are considered: (i) a 2D Abaqus model discretized on the surface (inplane section), (ii) a 2D Abaqus model discretized across the width (transverse section), and (iii) a 3D model based on the Carrera Unified Formulation (CUF), which explicitly represents the metamaterial's three-dimensional geometry. The structure is subjected to a uniform transverse pressure and is clamped along one boundary, with all remaining edges free. For each model, a mesh-refinement study was performed. Table 1 reports the total number of degrees of freedom (DOFs) together with the lateral displacement values evaluated at a selected control point. The entries that achieved mesh convergence are highlighted in blue in the table. Compared with the 2D Abaqus reference discretizations, the CUF model reaches the converged response with roughly 20% of the DOFs, indicating a substantial reduction in problem size for a comparable accuracy. This reduction in DOF count translates into lower memory requirements and shorter solution times, while preserving the fidelity needed to capture the characteristic deformation mechanisms of the hexagonal architecture. Finally, Fig. 5 illustrates the deformed configurations (plotted with an exaggerated scale for clarity). The three modeling approaches yield consistent global deformation patterns and confirm the expected stiffness trends under transverse loading, further validating the efficiency and accuracy of the CUF-based 3D representation for this class of metamaterials.

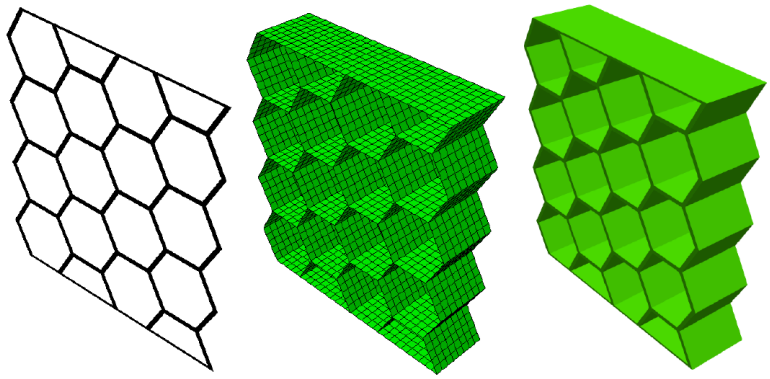


Figure 4: Numerical models of the hexagonal metamaterial. 2D Abaqus models (left and center), CUF 1D model (rigth)

Materials Research Proceedings 69 (2026) 1379-1383 https://doi.org/10.21741/9781644904251-240

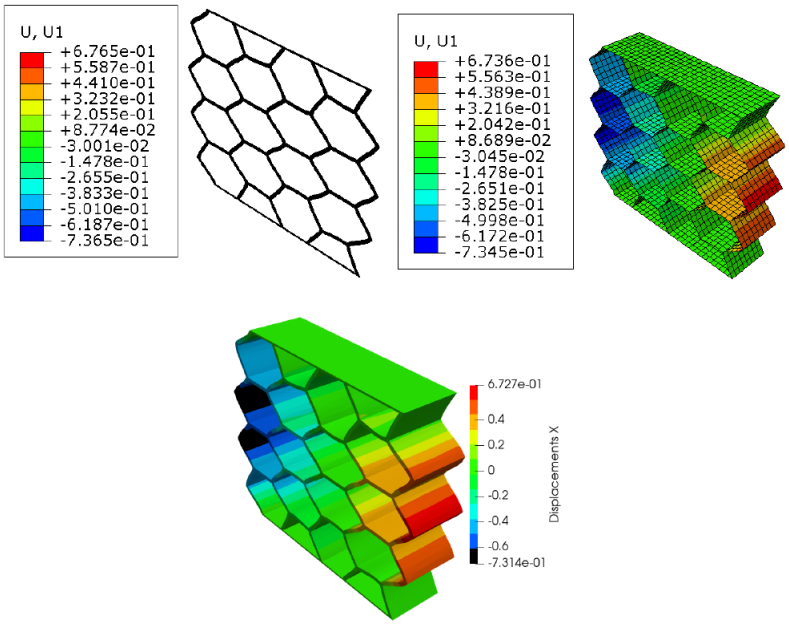


Figure 5: Numerical results of the hexagonal metamaterial. 2D Abaqus models (top), CUF 1D model (bottom)

Table 1: DOFs and lateral displacement of the considered analysis. In blue the converged models.

Model	DOFs	Lateral displacement
Abaqus 2D (Fig. 4 left)	16902	0.6234
	98154	0.6765
	291930	0.6769
Abaqus 2D (Fig. 4 center)	34830	0.6521
	95724	0.6736
	677538	0.6731
CUF 1D (Fig. 4 rigth)	19674	0.6727
	29511	0.6725
	118434	0.6724

Conclusions

This work presented a numerical study of a hexagonal metamaterial structure using the Carrera Unified Formulation (CUF) to achieve accurate and efficient modeling. The key findings and contributions of this research are summarized as follows.

- The use of CUF enabled the development of enhanced one-dimensional finite elements with three-dimensional capabilities. This allowed for precise detection and prediction of deformations across the structure's cross-section, providing a robust framework for analyzing future complex mechanical behaviors.
- The proposed model accurately captured the static behavior of the hexagonal metamaterial, comparing the results with Abaqus results. The gain in terms of number of DOFs is high.
- Metamaterial structures, featuring any cross-sectional geometry across their width, can be modeled easily using CUF. This capability opens up possibilities for adapting the model to further investigate three-dimensional metamaterials.

The findings of this study provide a robust foundation for future research into the design and optimization of metamaterial structures.

References

[1] Changfang Zhao. Multi-plateau auxetic metamaterials with intra-and inter-cellular gradients for energy absorption. Aerotecnica Missili & Spazio, pages 1-9, 2025.

[2] L Ai and X-L Gao. Metamaterials with negative poisson's ratio and non-positive thermal expansion. Composite Structures, 162:70-84, 2017. https://doi.org/10.1016/j.compstruct.2016.11.056

[3] Muamer Kadic, Tiemo B¨uckmann, Nicolas Stenger, Michael Thiel, and MartinWegener. On the practicability of pentamode mechanical metamaterials. Applied Physics Letters, 100(19), 2012. https://doi.org/10.1063/1.4709436

[4] Evangelos Ptochos and George Labeas. Elastic modulus and poisson's ratio determination of micro-lattice cellular structures by analytical, numerical and homogenisation methods. Journal of Sandwich Structures & Materials, 14(5):597-626, 2012. https://doi.org/10.1177/1099636212444285

[5] J Schwerdtfeger, P Heinl, RF Singer, and C K¨orner. Auxetic cellular structures through selective electron-beam melting. physica status solidi (b), 247(2):269-272, 2010. https://doi.org/10.1002/pssb.200945513

[6] Li Yang, Ola Harrysson, Harvey West, and Denis Cormier. Compressive properties of ti-6al-4v auxetic mesh structures made by electron beam melting. Acta Materialia, 60(8):3370-3379, 2012. https://doi.org/10.1016/j.actamat.2012.03.015

[7] Xiang Li, Zixing Lu, Zhenyu Yang, and Chen Yang. Directions dependence of the elastic properties of a 3d augmented re-entrant cellular structure. Materials & Design, 134:151-162, 2017. https://doi.org/10.1016/j.matdes.2017.08.024

[8] Xin-Tao Wang, Xiao-Wen Li, and Li Ma. Interlocking assembled 3d auxetic cellular structures. Materials & Design, 99:467-476, 2016. https://doi.org/10.1016/j.matdes.2016.03.088

[9] E. Carrera, G. Giunta, and M. Petrolo. Beam structures: classical and advanced theories. John Wiley & Sons, New York, USA, 2011. https://doi.org/10.1002/9781119978565

[10] R Augello and E Carrera. Nonlinear dynamics and band gap evolution of thin-walled metamaterial-like structures. Journal of Sound and Vibration, 578:118329, 2024. https://doi.org/10.1016/j.jsv.2024.118329

Materials Research Proceedings 69 (2026) 1384-1386 https://doi.org/10.21741/9781644904251-241

Component-Wise Beam Modelling of Sandwich Panels with Arbitrary Core Topologies

Erasmo Carrera[1,a], Karim Abu Salem[1,b*], and Riccardo Augello[1,c]

[1]Polytechnic of Turin, Corso Duca degli Abruzzi 24, 10129, Torino, Italy

[a]erasmo.carrera@polito.it, [b]karim.abusalem@polito.it, [c]riccardo.augello@polito.it

Keywords: Sandwich, CUF, Component-Wise, Layer-Wise, Stress, Failure

Abstract. This paper presents a Component-Wise (CW) 1D beam formulation within the Carrera Unified Formulation (CUF) [1] to model and simulate the mechanical behaviour of sandwich panels. The approach treats skins and cellular cores as distinct sub-domains in a single one-dimensional element. By representing the true cross-sectional geometry with high-order Lagrange polynomials, the model achieves high three-dimensional accuracy [2], including the capture of localized deformations and through-thickness stresses, while significantly reducing the degrees of freedom (DoFs) with respect to 3D FEM simulations. This paper provides evidence that this single refined 1D beam is easy to model, numerically efficient and mechanically accurate for any sandwich/metamaterial cores, from classic honeycomb to novel butterfly lattices, thereby enabling parametric studies and precise failure-onset assessment.

Sandwich and lattice-core metamaterials represent advanced and efficient lightweight structures for aerospace sector thanks to their high stiffness-to-mass ratio and multifunctionality [3]. Their architectural complexity, however, challenges traditional modelling processes. Homogenised Layer-Wise (LW) models are not able to detect the actual mechanical behaviour of the complex core geometry, whereas detailed 3D solids elements explode the number of DoFs and therefore the design-space exploration time. A modelling and simulation framework that is simultaneously efficient, accurate, and local-effect resolving is thus essential.

CUF allows to model complex sandwich structures with a single 1D beam element. The beam reference axis does not follow the panel length, as in the canonical beam descriptions, but aligns to the thickness direction, see Figure 1; the full cross-section is represented by arbitrary-order Lagrange polynomials describing independently skins and core. This CW discretisation preserves representation of actual structure geometry, including local variations, allowing to overcome core homogenisation while reaching 3D FEM accuracy. The polynomial order of Lagrange expansion is user-tunable, allowing trade-offs between level of resolution and number of degrees of freedom. Continuity across skin-core interfaces is guaranteed through shared Lagrangian nodes, producing reliable displacement and stress fields in critical interface regions.

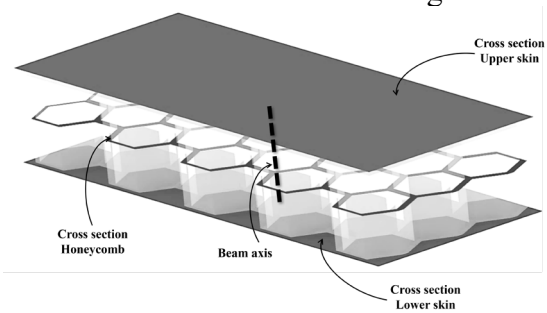


Figure 1. CW representation of the 1D beam model of a sandwich panel

Content from this work may be used under the terms of the Creative Commons Attribution 3.0 license. Any further distribution of this work must maintain attribution to the author(s) and the title of the work, journal citation and DOI. Published under license by Materials Research Forum LLC.

Materials Research Proceedings 69 (2026) 1384-1386 https://doi.org/10.21741/9781644904251-241

This approach is extremely flexible, as it allows the modelling of any core geometry for sandwich panels. To provide quantitative results, six different core topologies were simulated under several static load cases: butterfly, large and small unit cell hexagonal honeycomb, large and small unit cell square, and triangular lattice, see Figure 2.

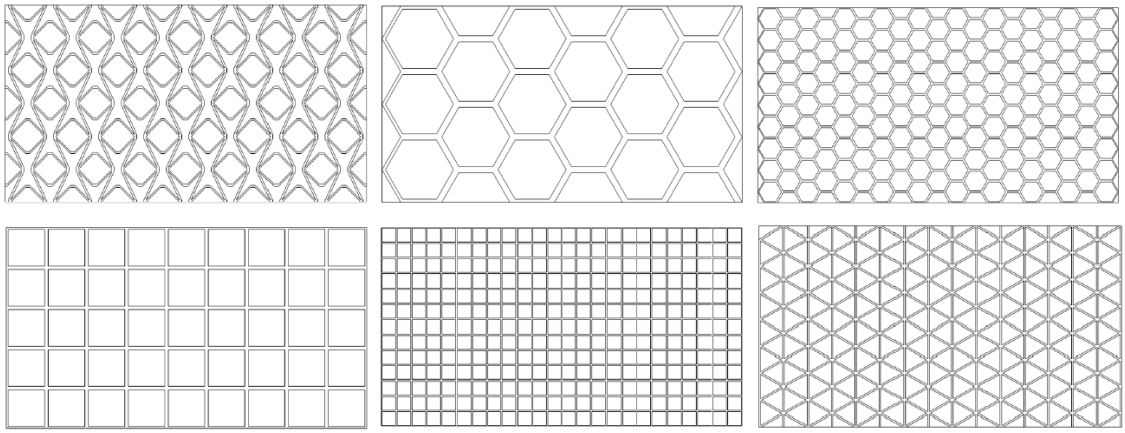


Figure 2. Cross sections of the different core geometries considered

Focusing on the large-cell honeycomb, several static load scenarios representative of service loads were applied: concentrated load on specific cells, uniform pressure, torsion, concentrated forces on skins edge, core inflection, and single-cell crushing. Each case was modelled and simulated with both CW and LW model whose core is homogenised [4].

Considering a case of sandwich panel clamped on both edges and with groups of concentrated forces on some selected cells, the potential of CW representation and the limitations of the LW model appear evident. Results in terms of deformed shape and Von Mises stress contour map comparisons are provided in Figure 3 and Figure 4, respectively. The CW model resolves the three distinct indentations in the upper skin, each corresponding to a loaded honeycomb cell. In contrast, the LW counterpart exhibits a smooth global inflection produced by bending; no local indentations appear because the core is represented as an equivalent continuum. This clearly anticipates major differences in the quantitative fields. Indeed, considering Von Mises stress distributions, in the CW model the stress field forms pronounced circular bands around each indented cell, with steep gradients that quickly decay into the surrounding webs, representing localised load transfer at skin-core interfaces. The LW displays an almost uniform distribution with only mild variations in the acting areas of the concentrated forces; the distinct zones evident in the CW analysis are entirely smoothed out. This proves that homogenised formulations prevents the identification of critical stress areas that the CW approach allows to detect, underscoring its superiority to capture failure-relevant local effects.

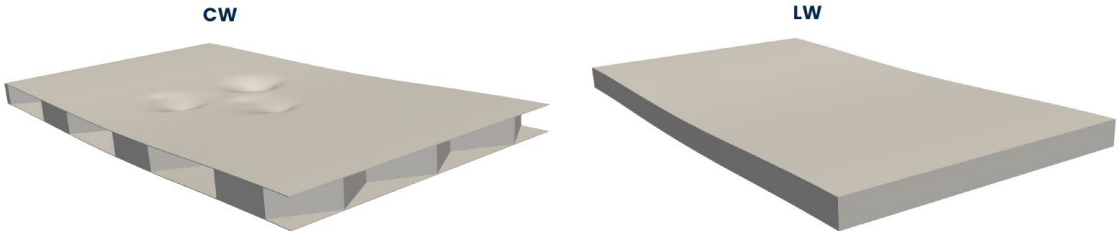


Figure 3. CW vs LW sandwich panel deformed shapes

Materials Research Proceedings 69 (2026) 1384-1386 https://doi.org/10.21741/9781644904251-241

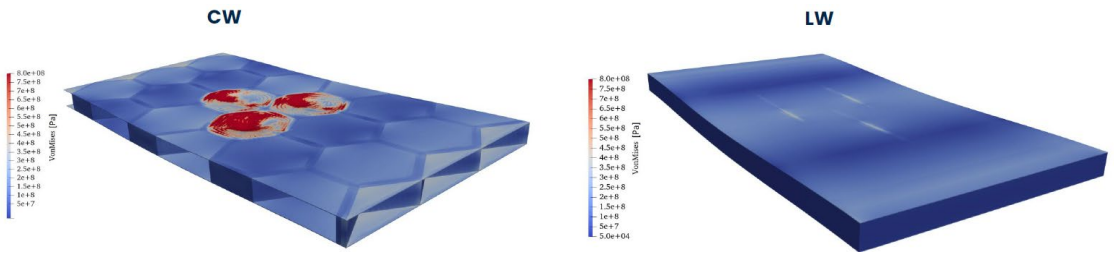


Figure 4. CW vs LW Von Mises stress distributions

The resolution of CW reveals how bending of individual hexagonal cell drives skin indentation; the homogenised LW model, lacking geometric detail, ignores these local kinematics and cannot identify the onset points for face-sheet wrinkling or local core stress peaks. These results highlight the indispensable role of CW kinematics when failure-critical local fields are required. Results provided in ref. [5] proved the accuracy of the approach, comparable to that of 3D FEM models, and its efficiency, as CW model reduces the number of DoFs up to six times compared to the 3D FEM counterpart.

The component-wise CUF beam element forms a unified and flexible tool for high-fidelity yet computationally efficient analysis of sandwich and metamaterial panels. By integrating exact geometrical and mechanical descriptions with high-order kinematics, it bridges the gap between oversimplified LW homogenized model and prohibitively heavy 3D solids FEM models. The framework not only provides an excellent framework for parametric design or structural optimization, but also provides a reliable tool for the local stress assessment indispensable for accurate failure-onset assessment, paving the way for accurate design of next-generation lightweight structures.

References

[1] E. Carrera, M. Cinefra, M. Petrolo, and E. Zappino, Finite Element Analysis of Structures through Unified Formulation, John Wiley & Sons, West Sussex, United Kingdom, 2014.

[2] D. Scano, E. Carrera, and M. Petrolo,. Use of the 3D equilibrium equations in the free-edge analyses for laminated structures with the variable kinematics approach. Aerotecnica Missili & Spazio, 103(2), pp.179-195, 2024

[3] J.K. Paik, A.K. Thayamballi, and G.S. Kim, The strength characteristics of aluminum honeycomb sandwich panels, Thin Walled Structures, vol. 35, no. 3, pp. 205–231, 1999. https://doi.org/10.1016/S0263-8231(99)00026-9

[4] Kumar, A., Muthu, N., Narayanan, R. G., Equivalent orthotropic properties of periodic honeycomb structure: strain-energy approach and homogenization. International Journal of Mechanics and Materials in Design, 19(1), 137-163, 2025, https://doi.org/10.1007/s10999-022-09620-x

[5] K. Abu Salem, R. Augello, E. Carrera, Component-wise modelling of core and skin in sandwich structures using a single refined beam finite element, Mechanics of Advanced Materials and Structures, 2025, https://doi.org/10.1080/15376494.2025.2458237

Materials Research Proceedings 69 (2026) 1387-1390 https://doi.org/10.21741/9781644904251-242

Folding Simulation of Flat Arrays Using Refined Beam Finite Elements

Riccardo Augello[1,a *], and Erasmo Carrera[1,b]

[1]MUL[2] Lab, Department of Mechanical and Aerospace Engineering, Politecnico di Torino, Corso Duca degli Abruzzi 24, 10129 Torino, Italy

[a]riccardo.augello@polito.it, [b]erasmo.carrera@polito.it

Keywords: Deployable Structure, Carrera Unified Formulation, Foldable Flat Array

Abstract. The shift toward smaller satellites has sparked growing interest in deployable booms that can stow compactly and extend to full length once on-orbit [1]. These booms are typically rolled into a coil and, when released, unroll into slender rods made of thin-walled composite shells, releasing stored strain energy in the process; such mechanisms are common in spaceborne telescopes and other large-aperture payloads [2,3]. Tape springs, thin elastic strips, remain the most prevalent deployable boom. The introduction of carbon-fibre-reinforced-plastic (CFRP) tape springs has further improved stiffness-to-mass ratios [4]. A related concept, the Triangular Rollable and Collapsible (TRAC) boom, links two tape-spring "flanges" along a common "web," forming a triangular cross-section that offers markedly higher bending stiffness. First developed at the Air Force Research Laboratory by Murphey and Banik [5], metallic TRAC booms flew on NASA's NanoSail-D solar sail [6]; more recent work has shifted to composite TRAC designs to mitigate temperature-gradient problems seen in metal versions. One high-profile application is Caltech's Space Solar Power Project (SSPP), which envisions a modular lattice of TRAC longerons and rectangular CFRP battens that supports arrays of multifunctional tiles. These tiles harvest solar energy, convert it to RF power, and beam it to Earth [7]. The SSPP structure consists of bending-stiff trapezoidal strips, arranged in four identical quadrants. The two edges of each strip are formed by composite TRAC longerons, connected by carbon fiber rectangular battens. Accurate simulation is vital for sensitivity studies and for minimizing costly hardware tests. Conventional finite-element analysis often relies on 2-D shell elements to model slender booms, a choice that struggles to capture out-of-plane responses and local effects, especially critical in composite laminates [8]. To overcome these shortcomings, this work employs a Carrera Unified Formulation (CUF)–based finite-element model [9]. CUF enriches one-dimensional beam elements with high-order cross-sectional expansions, allowing three-dimensional and localized behaviours to appear within a low-degree-of-freedom framework. The method has already proven effective for buckling and post-buckling studies of deployable booms [10]; here, it is extended to simulate the full folding and deployment sequence of the SSPP flat-array module.

Refined one-dimensional finite element

For the numerical model, a Cartesian reference system is used, so that the y direction is placed in the length direction, and the x,z identify the cross-sectional domain as shown in Fig. 1.

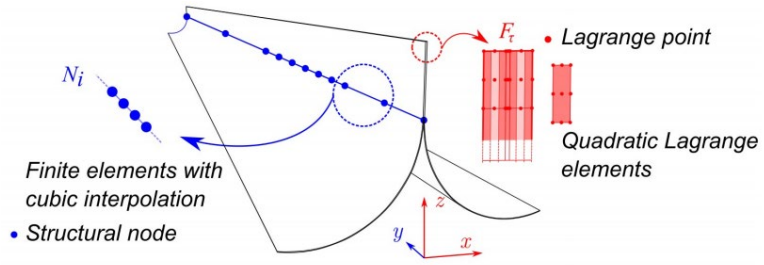


Figure 1 - Model of the TRAC longeron based on the Carrera unified formulation.

Content from this work may be used under the terms of the Creative Commons Attribution 3.0 license. Any further distribution of this work must maintain attribution to the author(s) and the title of the work, journal citation and DOI. Published under license by Materials Research Forum LLC.

Materials Research Proceedings 69 (2026) 1387-1390 https://doi.org/10.21741/9781644904251-242

According to the Carrera Unified Formulation (CUF), the three-dimensional displacement field can be written in the following unified manner:

$$\boldsymbol{u}(x,y,z) = F_\tau(x,z)\boldsymbol{u}_\tau(y) \qquad \tau = 1,2,\dots,M \tag{1}$$

where $\boldsymbol{u}(x,y,z)$ is the displacement vector, whose components are expressed in the general reference system (x,y,z), $F_\tau(x,z)$ represent the cross-sectional functions depending on the x,z coordinate, τ is the sum index and M is the number of terms of the expansion in the cross-section plane assumed for the displacements. The proposed work adopts quadratic Lagrange polynomials (L9) as $F_\tau(x,z)$ to approximate the kinematics of the theory.
To approximate the displacement field over the beam axis, the Finite Element Method (FEM) is adopted. The generalized displacement vector $\boldsymbol{u}_\tau(y)$ is expressed as follows:

$$\boldsymbol{u}_\tau(y) = N_i(y)\boldsymbol{u}_{\tau i} \qquad \tau = 1,2,\dots,N_n \tag{2}$$

where N_i stands for the i-th one-dimensional shape function, i indicates summation and N_n is the number of the FEs nodes per element. Finally, $\boldsymbol{u}_{\tau i}$ is the following vector of the FE nodal parameters:

$$\boldsymbol{u}_{\tau i} = \{\boldsymbol{u}_{x_{\tau i}}, \boldsymbol{u}_{y_{\tau i}}, \boldsymbol{u}_{z_{\tau i}}\}^T \tag{3}$$

Here, 1D finite Lagrangian elements are used along the y-axis.

Methodology

The deployable structure analyzed in this study is a complex structure made of longerons, transverse battens, and hinges. A simple version is shown in Fig. 2(a), and it is referred to as a double-strip due to its composition of two sub-structures connected by two hinges.

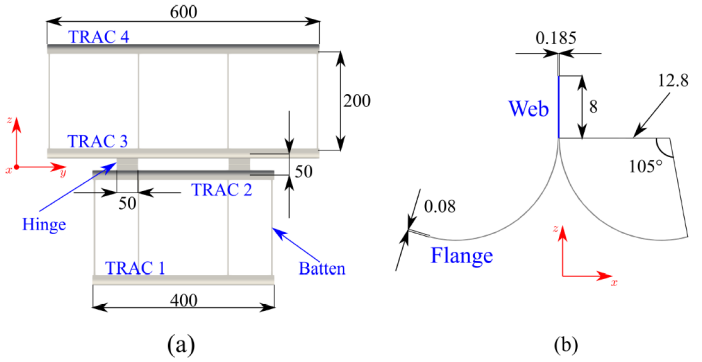


Fig. 2 (a) double-strip structure (b) one TRAC longeron cross-section. The dimensions are given in mm.

Each strip consists of two TRAC longerons and four battens. The cross-section of the longerons is shown in Fig. 2(b), with all dimensions provided in millimeters. As far as the material properties are concerned, the composite layup in the flanges of the longeron is [± 45 GFPW/ 0 CF/ ± 45 GFPW]°, and the layup of the web region is [± 45 GFPW/ 0 CF/ ± 45 GFPW/ 0 CF/ ± 45 GFPW]°, where CF represents a thin ply with unidirectional carbon fibers and GFPW stands for plain weave scrim glass. Both plies are impregnated with resin. In this case, six different cross-sections are utilized, as illustrated in Fig. 3(b).

Materials Research Proceedings 69 (2026) 1387-1390 https://doi.org/10.21741/9781644904251-242

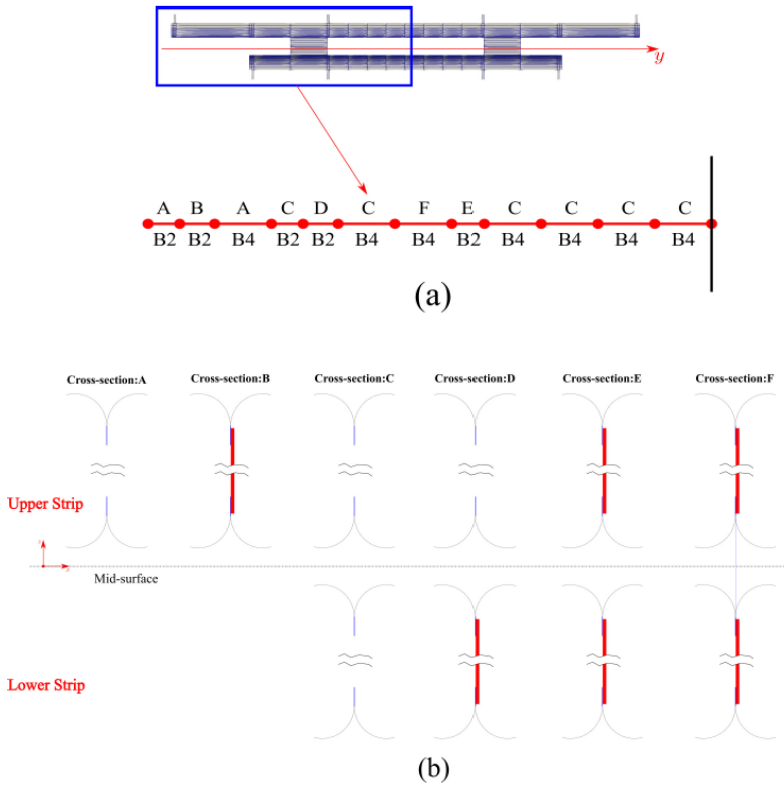


Fig. 3 Mesh discretization for the double-strip structure. (a) Beam finite element used along y-axis. (b) Representation of the six cross-sections.

Finally, Fig. 4 shows a four-strip structure that the will be also analysed in the full paper. It involves four strips joined together with hinges and both transverse and diagonal battens. The structure is modeled using a single axis refined beam, using the same approach described above.

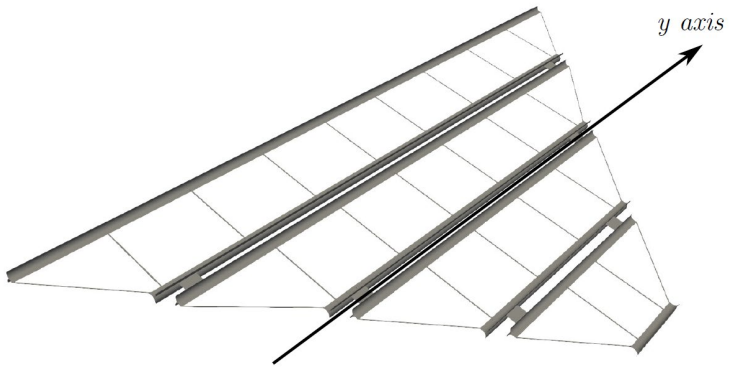


Fig. 4 Model of the elastically foldable flat array.

The full paper will deal with the folding of the elastically foldable flat array.

References

[1] Warren, P., "Foldable member. USA Patent. 6:B1," , 1969.

[2] Mungiguerra, S., Gardi, R., Savino, R., Vernillo, P., Ferracina, L., Punzo, F., Ruggiero, M., Aurigemma, R., Dell'Aversana, P., Gramiccia, L. and Ianelli, S., 2024. Mini-IRENE, a

successful re-entry flight of a deployable heatshield capsule. Aerotecnica Missili & Spazio, pp.1-16. https://doi.org/10.1007/s42496-024-00237-1

[3] Sun, T., Gasbarri, P., Du, L. and Deng, Z., 2024. Dynamic modelling and performance analysis of deployable Telescopic Tubular Mast. Aerotecnica Missili & Spazio, pp.1-13. https://doi.org/10.21203/rs.3.rs-4741721/v1

[4] Yee, J. C. H., Soykasap, O., and Pellegrino, S., "Carbon fibre reinforced plastic tape springs," 45th AIAA/ASME/ASCE/AHS/ASC Structures, Structural Dynamics & Materials Conference, Vol. 5234, 2004, p. 1819. https://doi.org/10.2514/6.2004-1819

[5] Murphey, T., and Banik., J., "Triangular rollable and collapsible boom. USA Patent 7,895,795," , 2011.

[6] Whorton, M., Heaton, A., Pinson, R., Laue, G., and Adams, C., "Nanosail-D: the first flight demonstration of solar sails for nanosatellites," 22nd Annual AIAA/USU Conference on Small Satellites, 2008, pp. 1-6.

[7] Arya, M., Lee, N., and Pellegrino, S., "Ultralight structures for space solar power satellites," 3rd AIAA Spacecraft Structures Conference, 2016, p. 1950. https://doi.org/10.2514/6.2016-1950

[8] Hirwani, C., Mishra, P., and Panda, S., "Nonlinear steady-state responses of weakly bonded composite shell structure under hygro-thermo-mechanical loading," Composite Structures, Vol. 265, 2021, p. 113768. https://doi.org/10.1016/j.compstruct.2021.113768

[9] Carrera, E., Cinefra, M., Petrolo, M., and Zappino, E., Finite element analysis of structures through unified formulation, John Wiley & Sons, Hoboken, New Jersey, USA, 2014. https://doi.org/10.1002/9781118536643

[10] Pagani, A., Augello, R., and Carrera, E., "Numerical simulation of deployable ultra-thin composite shell structures for space applications and comparison with experiments," Mechanics of Advanced Materials and Structures, Vol. 30, No. 8, 2023, pp. 1591-1603. https://doi.org/10.1080/15376494.2022.2037173

Materials Research Proceedings 69 (2026) 1391-1396 https://doi.org/10.21741/9781644904251-243

The Effect of TVAC Cycles on Physical Properties and Morphology of Alumina Coated AA7075 via Hard Anodization and Pulsed Laser Deposition: A Comparative Study for Space Applications

Andrea SEMERARO[1,6,a *], Luca GIULIANI[2,6,b], Emanuele Nicolò PIZZO[1,6,c], Federico PICCAGLI[1,5,d], Diego SCACCABAROZZI[3,e], Chiara MARTINA[3,f], Marco G. BEGHI[4,g], Fabio DI FONZO[5,h] and Nicola CEFIS[2,i]

[1]Politecnico di Milano, Department of Chemistry, Materials and Chemical Engineering, Piazza Leonardo Da Vinci 32, 20133 Milano, Italy

[2]Politecnico di Milano, Department of Civil and Environmental Engineering, Piazza Leonardo Da Vinci 32, 20133 Milano, Italy

[3]Politecnico di Milano, Department of Mechanical Engineering, Via Previati 1c, 23900 Lecco, Italy

[4]Politecnico di Milano, Department of Energy, Via Lambruschini 4a, 20156 Milano, Italy

[5]X-nano S.r.l., Via Rubattino 81, 20134 Milano, Italy

[6]PoliSpace, Via Monte Grappa 1, 21050 Lonate Ceppino (VA), Italy

[a]andrea.semeraro@polispace.it, [b]luca.giuliani@polispace.it, [c]emanuelenicolo.pizzo@polispace.it, [d]federico.piccagli@polimi.it, [e]diego.scaccabarozzi@polimi.it, [f]chiara.martina@polimi.it, [g]marco.beghi@polimi.it, [h]fabio.difonzo@x-nano.it, [i]nicola.cefis@polimi.it

Keywords: Hard Anodization, PLD, Space Applications, Aluminum, TVAC, SEM, Brillouin Spectroscopy, Elastic Properties

Abstract. Aluminium alloys used in space structural applications are exposed to extreme environmental conditions. To preserve the integrity of structural materials in such environments, various surface treatments have been developed with the goal of forming thin films of hard oxides. Traditionally, the standard surface treatment for space applications has been hard anodization, which produces aluminium oxide layers through an electrochemical reaction between the substrate and an electrolyte. As an alternative to this well-established technique, thin film deposition via Pulsed Laser Deposition (PLD) has been explored. This study compares the traditional hard anodization method with PLD to evaluate their respective strengths and weaknesses and assess the potential of PLD as a viable alternative to coat AA7075-T6, a widely used alloy in the space industry. This work examines the effects of Low Earth Orbit (LEO) conditions on the morphology and on the interface between the aluminum substrate and the deposited alumina. The LEO environment experienced by the "6S CubeSat" of the PoliSpace project [1] is simulated through thermal cycling in a Thermal Vacuum Chamber (TVAC), in accordance with the "ECSS-E-ST-10-03C" standard. The samples underwent a tailored thermal cycle, in which the maximum and minimum temperatures represent limiting conditions selected to prevent damage to sensitive components, such as the structural batteries. A high vacuum level was ensured during each test to fully simulate the space environment. The physical and elastic properties of both coatings were evaluated employing Brillouin spectroscopy, offering insights into how the fabrication method influences the final characteristics of the deposited films. Visual tests confirmed the different nature of the two interfaces and the expected higher compactness of the PLD-deposited alumina with respect to the anodic one.

Content from this work may be used under the terms of the Creative Commons Attribution 3.0 license. Any further distribution of this work must maintain attribution to the author(s) and the title of the work, journal citation and DOI. Published under license by Materials Research Forum LLC.

Materials Research Proceedings 69 (2026) 1391-1396 https://doi.org/10.21741/9781644904251-243

Introduction

Structures working in space environments are exposed to a complex environment, which can affect their integrity in different ways. To avoid their failure under these conditions, a common solution for aluminium components is to coat them by hard anodization, which generates a thick, columnar and porous outer layer of aluminium oxide (Al_2O_3) [2].

However, alternative coating techniques have been proposed to replace the previous method. A particularly innovative and promising approach is pulsed laser deposition (PLD), in which a laser ablates a target to deposit a layer of Al_2O_3 onto the substrate. This process offers several advantages, including thinner alumina layers that reduce component volume [3], lower average power consumption, minimal impurity incorporation due to the high vacuum environment, and the ability to tailor the deposition pattern as needed [4].

In this study, both hard anodize and PLD coatings are produced on AA7075-T6 substrate and then characterized with scanning electron microscopy. After being subjected to cycles inside a thermal vacuum chamber (TVAC) to simulate space conditions, the effect of this treatment on the elastic properties of the coatings is evaluated via Brillouin spectroscopy, estimating the variation in their Young's moduli and Poisson's ratios.

Materials and Methods

Thermal Vacuum Chamber (TVAC). This study is based on the "6S CubeSat" project of the PoliSpace association of Politecnico di Milano, a cubic satellite designed to operate in a Low Earth Orbit environment [1]. To reproduce the effects of this environment, a TVAC test session was designed for both coatings, consisting of one non-operative cycle followed by three operative cycles. The threshold temperatures were determined from a thermal study on the CubeSat and the tests were conducted in accordance with the "ECSS-E-ST-10-03C" standard. In a medium-high vacuum and starting from +25 °C, the samples first underwent a non-operative thermal cycle with temperatures ranging from -20 °C to +40 °C. Then three operative cycles followed, ranging from +50 °C to -40 °C. For all these cycles, each threshold temperature was held for 15 minutes.

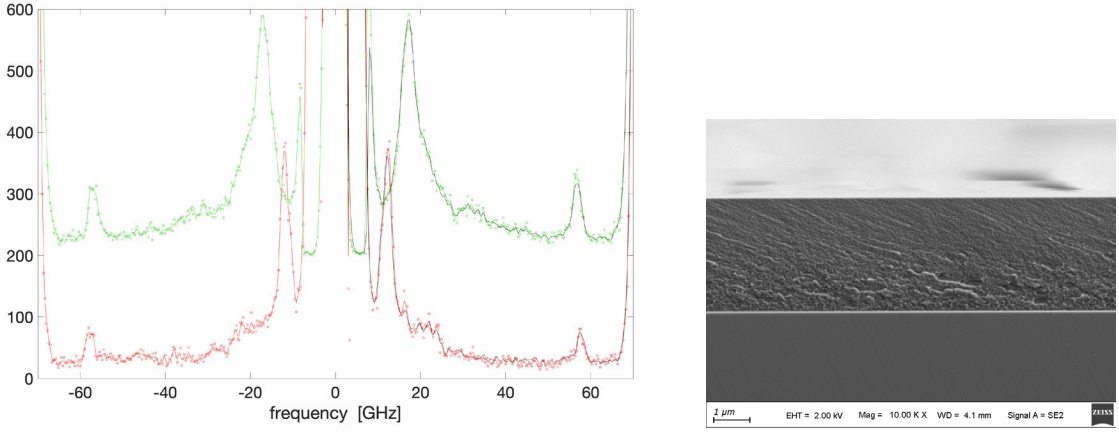
Brillouin Spectroscopy. Brillouin scattering techniques rely on spontaneous thermal fluctuations in the acoustic modes, namely phonons, and on their detection by local inelastic scattering of light. The probing light is therefore not responsible for the thermal vibrations, but it is the medium through which the measurement is performed, and since the beam is in the visible, the probed frequencies are on the order of tens of GHz. However, given the weak fluctuations investigated, the measurements are typically time-consuming. A laser beam in the visible range is focused onto the sample at an incidence angle θ from the surface normal. Scattered light is collected and its spectrum is analysed by a tandem multi-pass Fabry-Perot interferometer. The scattering geometry and the laser wavelength select the probed acoustic wavevector.

Spectral peaks (Fig. 1a) show the frequencies of the acoustic modes which propagate at the selected wavevector. In the bulk the probed wavevector scales as the refractive index n, and the acousto-optical interaction is mediated by the acoustically induced modulation of n. Bulk waves can be longitudinal or transversal, respectively at higher and lower frequencies, and characterized by a medium-to-low intensity. At the surface, scattering involves only the wavevector component parallel to the surface, which scales as $\sin(\theta)$ but does not depend on n, and the acousto-optical interaction is mediated by the acoustically induced corrugation of the surface. These surface wavevectors, or Rayleigh waves, give intense lower frequency peaks. In both cases, from frequencies and wavevectors the velocities of the acoustic modes are obtained, from which derived constants can be obtained if mass density is known. [5]

Materials Research Proceedings 69 (2026) 1391-1396 https://doi.org/10.21741/9781644904251-243

Results

Spectra analysis and mathematical model for PLD samples. Fig.1a shows measured spectra on PLD untreated and treated samples.



(a) *(b)*

Figure 1: (a) PLD spectra for untreated sample at an incident angle equal to 40° (red curve) and treated sample at an incident angle equal to 70° (green curve); (b) Cross-section of PLD-coated samples.

Three different peaks can be distinguished at around 15, 20 and 55 GHz respectively. For the first peak, associated with the Rayleigh wave, its velocity and frequency can be related as follows:

$$f = \frac{2v_R}{\lambda} \cdot sin(\theta) \tag{1}$$

where f is the frequency, v_R is the velocity of the Rayleigh wave, θ is the angle between the incident light and the sample surface and λ is the wavelength of the incident light, in this study 532 nm. This dependence justifies the relevant shift of the first peak for the two curves, which are obtained at two different incident angles. The peak at 55 GHz is associated with the bulk longitudinal wave, for which, by means of solid-state physical considerations, the relation between frequency and velocity can be expressed as:

$$v_L = \frac{f\lambda}{2n} \tag{2}$$

where v_L is the velocity of the longitudinal wave and n is the refractive index of the coating, which, in this study, was considered equal to 1.65 [6].

The last peak at 20 GHz normally represents the bulk transversal acoustic mode, but in this case it does not depend on n: in addition, the peak also appears at lower frequency than expected, suggesting the possibility of an indirect scattered bulk mode, i.e. the propagating wave inside the bulk is scattered by a phonon with a wavevector parallel to the surface [5]. As previously described for the Rayleigh wave, the velocity is governed by the θ angle as described in Eq. 1. To verify the

Materials Research Proceedings 69 (2026) 1391-1396 https://doi.org/10.21741/9781644904251-243

indirect scattering in the bulk, the following relation between the frequencies and the velocities of the indirect bulk and Rayleigh acoustic modes must be verified:

$$\frac{v_b}{v_R} = \frac{f_b}{f_R} \tag{3}$$

Eq. 3 is verified allowing the determination of the refractive index without further tests, showing accordance with the values found in literature. A similar consideration can be made for the middle peak in the spectrum obtained after TVAC (green curve), from which it is possible to extract a similar value for the refractive index. However, to completely confirm the presence of the indirect bulk scattering and that the refractive index is not affected by the treatment, further tests are required to provide a statistical validity.

Fig. 1b shows that the PLD coating appears to be amorphous and homogeneous: hence, an isotropic behaviour can be validly assumed. Moreover, the thickness of the coating (3 μm) is enough for Brillouin spectroscopy to be considered a semi-infinite material, meaning that no influence of the substrate is expected. From these considerations it is possible to relate the frequencies and the velocities extracted from the peaks in the spectra to the elastic properties of the coating through a simplified model. Therefore, the Young's modulus (E) and the Poisson's coefficient (ν) are sufficient to fully characterize the material, since the two parameters are linked to the velocities and the frequencies of the spectral peaks through the C_{11} and C_{44}, ij-th components of the stiffness matrix. The following relations can be used [6]

$$v_l = \sqrt{\frac{C_{11}}{\rho}}, \qquad v_t = \sqrt{\frac{C_{44}}{\rho}}, \qquad v_R \approx v_t \frac{2.87C_{11} - 4C_{44}}{3C_{11} - 4C_{44}} \tag{4}$$

where v_l and v_t are the bulk longitudinal and bulk transversal velocities respectively, v_R is the velocity of the Rayleigh (surface) wave and ρ is the density of the coating which is equal to 3470 Kg/m^3. The expression for v_R is an approximate solution of the cubic equation relating v_R to v_t. From the two components of the stiffness matrix, E and ν can be obtained via the following equations [6]:

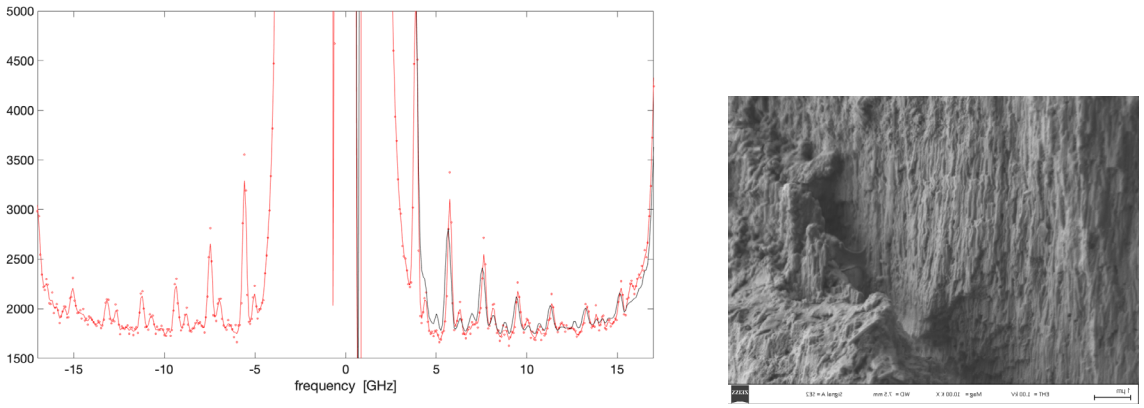
$$C_{11} = \frac{E(1-\nu)}{(1+\nu)(1-2\nu)} \qquad C_{44} = \frac{E}{2(1+\nu)} \tag{5}$$

Observing the Brillouin spectra, it is possible to notice an invariance in the significant peaks analysed for the extraction of the elastic properties, which reflects also to the final elastic constants.

However, due to the limited number of analysed samples, further investigation is required to understand whether the two populations are statistically different.

Materials Research Proceedings 69 (2026) 1391-1396 https://doi.org/10.21741/9781644904251-243

Hard Anodized Samples. Fig.2a shows measured spectra on untreated hard anodized sample.



(a) ***(b)***

Figure 2: (a) Untreated Hard Anodized spectrum; (b) Cross-section of hard anodized coated samples.

Fig. 2a shows numerous peaks which, however, are not of the type mentioned before. In fact, for high frequencies no bulk peaks are observed, while a series of small peaks are present for very low frequencies, with a dependence on the refractive index, behaviour typical of bulk waves. This excludes the possibility that the slowest wave is the Rayleigh one. Moreover, the columnar nature of the anodic film (Fig. 2b) invalidates the homogeneous and isotropic hypotheses, thus requiring a dedicated model for anisotropic materials for which Eq. 1 and Eq. 2 are no longer valid. Nevertheless, the porous structure of the coating may create a series of collective/stationary waves that, being non-propagating, will not contribute to the characterization of the elastic properties of the coating, and changes given by the TVAC cycling.

Conclusion and future activities

Overall, the measurements obtained for the PLD samples following the TVAC cycles show no discernible alteration in their properties, indicating that the microstructure of the coating remains amorphous, with no evidence of sporadic crystalline domain formation [6]. Confirmation of this hypothesis will require additional characterization, including XRD and SEM analyses. Conversely, the observed behaviour of the hard anodized samples may be attributable to collective motions inherent to the porous structure of the coating. Both phenomena necessitate more detailed studies and will be the focus of subsequent investigations.

Acknowledgments

The authors would like to thank Dr. C. Martina and Prof. D. Scaccabarozzi from the MetroSpace Lab for providing the TVAC facility, and Prof. M.G. Beghi for his supervision in Brillouin spectroscopy. Acknowledgments are also due to Dr. F. Piccagli and Dr. F. Di Fonzo at X-nano Srl (Milan, Italy) for their assistance with PLD equipment access, coating deposition and preliminary characterization. Furthermore, the authors acknowledge YDF (Carimate, Italy) for the aluminum laser cutting, Al Ti Color (Piazzola sul Brenta, Italy) for the electropolishing of the substrates, and Argos ST (Opera, Italy) for the hard anodization process

References

[1] Botti, F., Dowell, M., Raymond, A., Mazzotti, L., Piunti, M., Bianchini, G., Bernasconi, L., Raveane, M., Biella, A., Maconi, E., Fascendini, D., Festa, L., Serlini, M., Platano, G., Sportelli, L., Curti, G., Vescovi, P., Malandra, A., Bedoya, J., . . . Schembri, F. (2024). Structural and Thermal Model testing campaign of a 1U CubeSat. https://doi.org/10.52202/078376-0001

[2] Sano, T., Wakabayashi, Y., & Asoh, H. (2023). Formation of hard anodic films on the 7075-T6 aluminum alloy by anodization in sulfuric acid and ethylene glycol. Surface and Coatings Technology, 459. https://doi.org/10.1016/j.surfcoat.2023.129399

[3] Yu, J., Han, W., Suleiman, A. A., Han, S., Miao, N., & Ling, F. C. C. (2024). Recent Advances on Pulsed Laser Deposition of Large-Scale Thin Films. In Small Methods (Vol.8, Issue 7). John Wiley and Sons Inc. https://doi.org/10.1002/smtd.202301282

[4] Horwitz, J. S. (2018). Pulsed-Laser Deposition. In Surface Engineering (pp. 621–626).

ASM International. https://doi.org/10.31399/asm.hb.v05.a0001294

[5] Kundu, T. (Ed.). (2013). Ultrasonic and Electromagnetic NDE for Structure and Material Characterization: Engineering and Biomedical Applications (1st ed.). CRC Press. https://doi.org/10.1201/b12268

[6] García Ferré, F., Bertarelli, E., Chiodoni, A., Carnelli, D., Gastaldi, D., Vena, P., Beghi, M. G., & di Fonzo, F. (2013). The mechanical properties of a nanocrystalline Al2O 3/a-Al2O3 composite coating measured by nanoindentation and Brillouin spectroscopy. Acta Materialia, 61(7), 2662–2670. https://doi.org/10.1016/j.actamat.2013.01.050

Materials Research Proceedings 69 (2026) 13971401- https://doi.org/10.21741/9781644904251-244

The Effect of TVAC Cycles on Mechanical Properties of Coated AA7075 via Hard Anodization and Pulsed Laser Deposition: A Comparative Study for Space Applications

Emanuele Nicolò PIZZO[1,7,a *], Luca GIULIANI[2,7,b], Andrea SEMERARO[1,7,c], Andrea RAYMOND[3,7,d], Federico PICCAGLI[1,6,e], Diego SCACCABAROZZI[4,f], Nora LECIS[5,g], Chiara MARTINA[4,h], Fabio DI FONZO[6,i] and Nicola CEFIS[2,j]

[1]Politecnico di Milano, Department of Chemistry, Materials and Chemical Engineering, Piazza Leonardo Da Vinci 32, 20133 Milano, Italy

[2]Politecnico di Milano, Department of Civil and Environmental Engineering, Piazza Leonardo Da Vinci 32, 20133 Milano, Italy

[3]Politecnico di Milano, Department of Aerospace Science and Technology, Piazza Leonardo Da Vinci 32, 20133 Milano, Italy

[4]Politecnico di Milano, Department of Mechanical Engineering, Via Previati 1c, 23900 Lecco, Italy

[5]Politecnico di Milano, Department of Mechanical Engineering, Via La Masa 1, 20156 Milano, Italy

[6]X-nano S.r.l., Via Rubattino 81, 20134 Milano, Italy

[7]PoliSpace, Via Monte Grappa 1, 21050 Lonate Ceppino (VA), Italy

[a]emanuelenicolo.pizzo@polispace.it, [b]luca.giuliani@polispace.it, [c]andrea.semeraro@polispace.it, [d]andrea.raymond@polispace.it, [e]federico.piccagli@polimi.it, [f]diego.scaccabarozzi@polimi.it, [g]nora.lecis@polimi.it, [h]chiara.martina@polimi.it, [i]fabio.difonzo@x-nano.it, [j]nicola.cefis@polimi.it

Keywords: Hard Anodization, PLD, Space Applications, Aluminium, TVAC, Mechanical Performance, Tribological Tests

Abstract. In the space environment, aluminum alloys used in structural applications are exposed to severe conditions such as debris impacts and extreme temperature fluctuations. These phenomena can significantly compromise surface integrity, leading to increased wear, reduced mechanical performance, and premature failure of components. To address these challenges, various surface treatments have been developed to form protective oxide films on aluminum surfaces. Hard anodization is the traditional and widely adopted method, producing thick, hard and columnar aluminum oxide through an electrochemical reaction. Recently, Pulsed Laser Deposition (PLD) has emerged as a potential alternative, offering the possibility of depositing dense, uniform thin films with strong adhesion to the substrate. The aim of this work is to assess the reliability of both coating techniques when samples are subjected to TVAC cycling. To achieve this objective, AA7075-T6 coated samples underwent both thermal cycling in vacuum and tribo-mechanical tests. To simulate the Low Earth Orbit (LEO) exposure, the environment in which the "6S CubeSat" of the PoliSpace project is subjected, a Thermal Vacuum Chamber (TVAC) was used, following "ECSS-E-ST-10-03C" standard. By maintaining a high vacuum level, the samples underwent a specifically designed thermal cycle, with the maximum and minimum temperatures chosen based on the thermal study of the cited project. These temperatures were the ones at which premature

Content from this work may be used under the terms of the Creative Commons Attribution 3.0 license. Any further distribution of this work must maintain attribution to the author(s) and the title of the work, journal citation and DOI. Published under license by Materials Research Forum LLC.

failure of some components of the CubeSat was observed [1]. Subsequently, the mechanical behaviour of the coatings was characterized both before and after TVAC exposure, focusing on properties critical to in-orbit durability. Vickers and Berkovich tests were conducted to monitor changes in surface hardness for hard anodized and PLD coatings, respectively. Vickers micro-hardness tests followed the procedures outlined in "ISO-4516-2002", while Berkovich nano-hardness tests were selected for the PLD coatings due to their limited thickness. The friction coefficient and coating wear must be considered for the CubeSat rails, as these components are critical for the satellite's release from the rocket's storage chamber. To assess the performance of our coatings in relation to these factors, a pin-on-disk wear test was conducted under dry conditions. Coating adhesion, a crucial factor for the stability of space structures in the presence of sliding space debris, was evaluated through scratch tests following "ASTM-C-1624-05". These tests provided insights into interface stability, coating adhesion under increasing applied load, and the failure mechanism. A quasi-static load ramp was applied to avoid impact-like loading conditions.

Introduction

Structures operating in the space environment are subjected to various phenomena of different natures. This study is based on the "6S CubeSat" project developed by the Politecnico di Milano student association PoliSpace, where the combined effects of thermal and mechanical loads create a highly demanding environment for the materials employed. In this context, hard anodization is the most common and ECSS-recommended coating technique for protecting aluminum structures by producing a thick, columnar, and porous layer of alumina (Al2O3) on the substrate [2]: the oxide layer obtained in this study is 40 μm thick. However, recent advancements in coating technologies have enabled the deposition of thinner and compact oxide layers on various substrates. In this study, the pulsed laser deposition (PLD) technique, a physical vapour deposition (PVD) method that deposits Al2O3 from a target onto the substrate, is investigated as a promising alternative to traditional hard anodization; this deposition technique allowed us to obtain 3 μm thick coatings [2]. The primary objective of this preliminary study is to evaluate the tribo-mechanical properties of both coatings applied on square samples of AA7075-T6 substrate through hardness, wear, and scratch tests, under conditions representative of the Low Earth Orbit (LEO) environment, with the final aim of mitigating issues such as excessive wear during the launch of the CubeSat. To simulate LEO conditions, cycles in a thermal vacuum chamber (TVAC) were performed on both coatings.

Materials, methods and results

TVAC. To replicate the effects of the LEO environment on both coatings, a TVAC cycle, consisting of one non-operative cycle and 3 operative ones, was designed for both coatings, following "ECSS-E-ST-10-03C". Under medium-high vacuum, the samples underwent a thermal cycle with a temperature range from –40 °C to +50 °C for the operative cycles, and from –20 °C to +40 °C for the non-operative one, limits identified by the thermal design on the components of the CubeSat [1]. For all the cycles, the initial temperature was +25 °C and, for all the boundary temperatures, a holding time of 15 minutes was applied, as shown in Fig. 1.

Materials Research Proceedings 69 (2026) 13971401- https://doi.org/10.21741/9781644904251-244

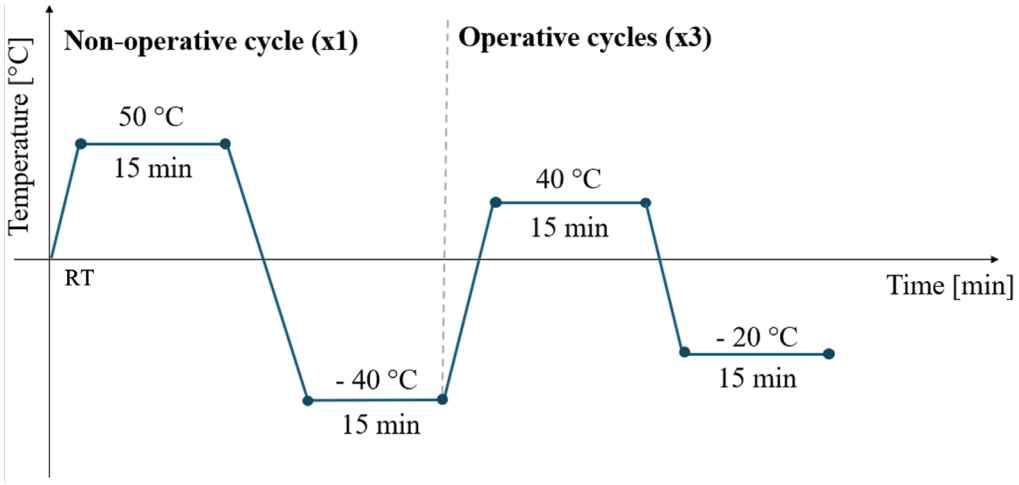


Figure 1: Applied TVAC cycles: the starting temperature (RT) is 25 °C, heating/cooling rate of 0,1 °C/min.

Hardness test. Vickers micro-hardness tests were performed on hard anodized samples at four different loads (3 N, 5 N, 10 N and 20 N) to evaluate the field of influence of the substrate [4]. A preliminary set of micro-hardness tests on the hard anodized samples shows that the actual value of hardness depends on the applied load, highlighting the growing influence of the substrate. However, this phenomenon is also affected by the microstructure: with smaller loads the actual values have a stronger dependence on the position of the indentation since the porosities will have a major effect (Fig. 2a). Moreover, after TVAC cycles, a reduction in hardness is observed. As shown in Fig. 2b the effect of the TVAC treatment is less relevant at higher loads, probably due to the interference of the substrate. Still, this variation in hardness suggests a possible effect of the TVAC cycles on the microstructure of the coating.

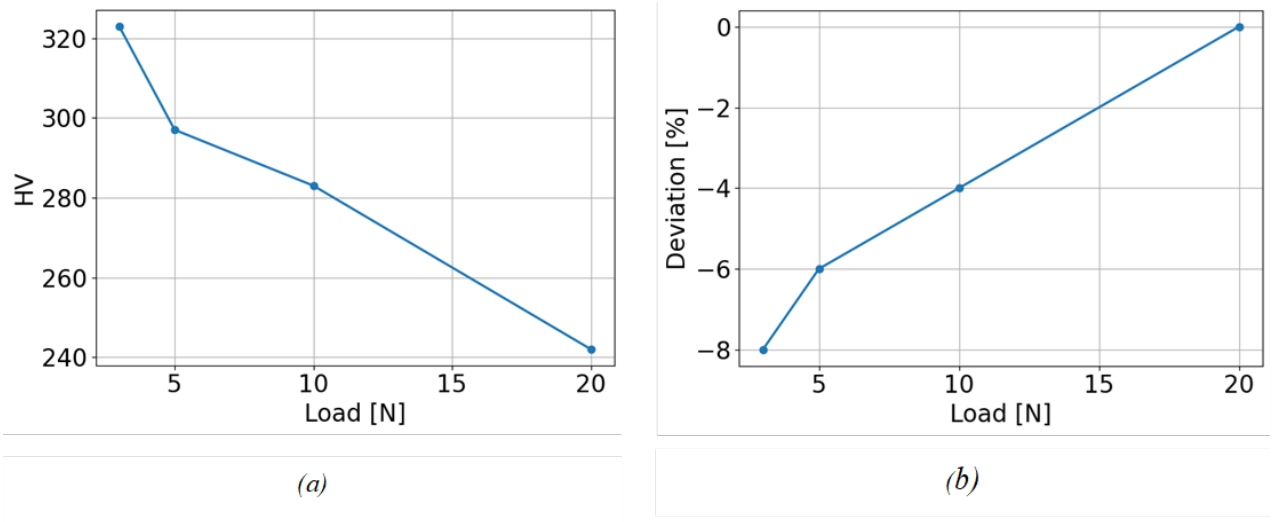


Figure 2: Vickers micro hardness change on hard anodized samples [4] (a) varying the load, (b) after TVAC cycles

On the other hand, PLD samples could not be tested the same way because the thickness of the coating is not at least ten times greater[1]. For this reason, the study of the hardness variation in PLD samples after the TVAC cycles needs to be conducted based on future Berkovich nanoindentation tests.

Materials Research Proceedings 69 (2026) 13971401- https://doi.org/10.21741/9781644904251-244

Scratch test. In both PLD and hard anodized samples, after TVAC, no relevant differences were found in terms of the load needed to start fracture and the friction coefficient. Hard anodized samples break by arc tensile cracking, while PLD samples break by wedging spallation, as shown in Fig. 3.

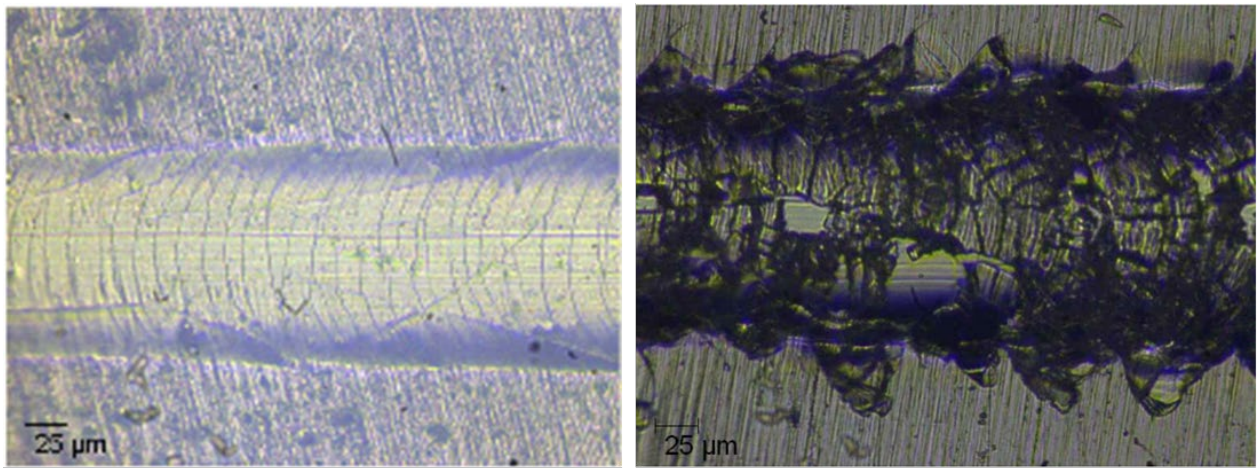


Figure 3: Scratch trace on (a) hard anodized and (b) PLD samples taken at 20 N

A preliminary investigation of Fig. 3[2], highlights a radically different fracture mode between the two coatings: the hard anodized samples present cracks only inside the scratch trace, meaning that the inherent cohesion of the coating is lower with respect to its adhesion to the substrate, possibly because the process transforms the base metal into the coating material. On the other hand, PLD samples present cracks also outside the scratch trace: this may be due to a higher cohesive strength with respect to the adhesive one.

Wear test. From a preliminary analysis, it is possible to observe a difference in the wear behaviour of the two coatings, perhaps due to dissimilar active wear mechanisms, which would be supported by the diverse fracture mechanisms highlighted with the scratch tests. Moreover, after TVAC, both hard anodized [5] and PLD samples show a reduction in the friction coefficient and seem to change in their wear trend (Fig. 4a - Fig. 4b). However, this characteristic is still under investigation and further mechanical testing is essential to assess the reliability of the previous hypothesis.

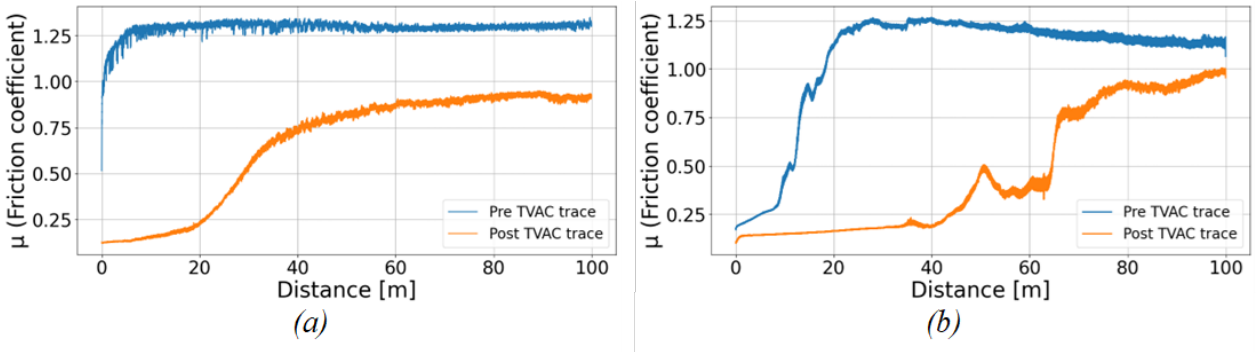


Figure 4: Wear traces for (a) hard anodized components, (b) PLD components before and after TVAC cycling

Future prospects

While the results are still under evaluation, further analysis is required to confer statistical validity to the work and to give a deeper insight of the implications of the detected changes. Firstly, a more comprehensive understanding of the wear mechanisms of both anodic and PLD coatings is necessary: specifically, profilometry measurements and SEM imaging will be conducted to assess wear trace depth and identify peculiar microstructural features that may influence coating behaviour. Moreover, TVAC cycling did not significantly affect the adhesion of either coating, as evidenced by scratch test results. However, hardness values changed by approximately 8% after TVAC cycling, suggesting a potential effect on hard anodized samples; consequently, nanoindentation will be performed to verify if PLD samples are similarly affected. Nevertheless, amorphous alumina produced by PLD appears promising for space applications. Its superior control over film composition, density, and purity compared to hard anodization offers distinct advantages for protective coatings, such as those for solar panels. Furthermore, by eliminating the use of acid electrolytes, PLD enables a safer and more sustainable waste management process.

Acknowledgments

The authors express their gratitude to Dr. C. Martina and Prof. D. Scaccabarozzi of the MetroSpace Lab for their valuable assistance and for providing the TVAC facility for thermal- vacuum testing. We also thank Dr. F. Piccagli and Dr. F. Di Fonzo at X-nano Srl (Milan, Italy) for their assistance with PLD equipment access, coating deposition and preliminary characterization. Appreciation is extended to Prof. N. Lecis for granting access to the laboratory equipment for tribological characterization. Finally, the technical contributions of YDF (Carimate, Italy) for laser cutting, Al Ti Color (Piazzola sul Brenta, Italy) for substrate electropolishing, and Argos ST (Opera, Italy) for the hard anodization process are gratefully acknowledged.

References

[1] Botti, F., Dowell, M., Raymond, A., Mazzotti, L., Piunti, M., Bianchini, G., Bernasconi, L., Raveane, M., Biella, A., Maconi, E., Fascendini, D., Festa, L., Serlini, M., Platano, G., Sportelli, L., Curti, G., Vescovi, P., Malandra, A., Bedoya, J., ... Schembri, F. (2024). Structural and Thermal Model testing campaign of a 1U CubeSat. https://doi.org/10.52202/078376-0001

[2] Lerner, L. M. (2010). Hard anodising of aerospace aluminium alloys. Transactions of the Institute of Metal Finishing, 88(1), 21–24. https://doi.org/10.1179/174591909X12614823458038

[3] Garc´ıa Ferr´e, F., Bertarelli, E., Chiodoni, A., Carnelli, D., Gastaldi, D., Vena, P., Beghi, M. G., & di Fonzo, F. (2013). The mechanical properties of a nanocrystalline Al2O3/a-Al2O3 composite coating measured by nanoindentation and Brillouin spectroscopy. Acta Materialia, 61(7), 2662–2670. https://doi.org/10.1016/j.actamat.2013.01.050

[4] Sarhan, A. A. D., Zalnezhad, E., & Hamdi, M. (2013). The influence of higher surface hardness on fretting fatigue life of hard anodized aerospace AL7075-T6 alloy. Materials Science and Engineering: A, 560, 377–387. https://doi.org/10.1016/j.msea.2012.09.082

[5] SERT, Y. (2020). Determining Optimum Anodic Oxidation Parameters for Hardness and Wear Properties of AA7075-T6 Alloys Using Taguchi Design. Brilliant Engineering, 2(1), 10–18. https://doi.org/10.36937/ben.2021.001.003

Materials Research Proceedings 69 (2026) 1402-1406 https://doi.org/10.21741/9781644904251-245

A Simplified Modelling Strategy for the Analysis of Lattice Structures with Manufacturing Defects

Davide Lorenzo CAPPA[1,a *], and Riccardo VESCOVINI[2,b]

[1]Dipartimento di Scienze e Tecnologie Aerospaziali, Politecnico di Milano, Via la Masa 34, 20156 Milano, Italy

[a]davidelorenzo.cappa@polimi.it, [b]riccardo.vescovini@polimi.it

Keywords: Lattice Structures, Manufacturing Defects, Additive Manufacturing

Abstract. The response of additively manufactured lattices is strongly affected by manufacturing induced imperfections. This work presents a numerical framework to model and assess these imperfections effectively. A simplified beam model is developed starting from accurate three-dimensional finite element analyses carried out on struts where the imperfections are modeled explicitly. The results show that the simplified models proposed here are capable of obtaining good matching with 3D simulations in terms of stiffness and strength, while requiring significantly lower computational cost.

Introduction

Lattice structures present attractive features for space applications. They are characterized by high structural efficiency and their cost is limited even for low production volumes [1, 2]. Furthermore, their production via additive manufacturing (AM) allows innovative configurations to be designed. So peculiar requirements of space structures can be met with larger flexibility. However, the AM process inevitably introduces dimensional inaccuracies, surface defects, and porosity [3]. Several studies have investigated these issues, particularly geometric defects in selective laser melting (SLM) of metallic parts [4, 5, 6]. The waviness and radius variation of struts have been analyzed with several models, including variable elliptical cross-sections [7], imperfect beams [8], and FEM incorporating scan-based data [9].

Despite the relatively vast literature on the topic, the modelling of defects is often based on costly analyses, which are unsuitable for preliminary assessments, where multiple configurations need to be analyzed. In particular, typical geometrical defects due to AM can have a drastic impact on both the linear and nonlinear structural response of lattices. Therefore, an effective modelling technique is crucial to simplify and speed-up the preliminary design phase, fully exploiting the potential of these structures.

In this paper, geometrical defects are modelled referring to the strategy proposed in Ref. [10], the KRK model: the struts are represented as the union of multiple spheres, each characterized by random variation in radius, axial offset, and penetration between adjacent spheres. Previous studies proved the impact of these features on the mechanical response of imperfect lattice structures.

Simplified beam models are developed to represent the structural behavior of lattice panels, using the KRK model to extract the constitutive laws for imperfect struts from three-dimensional finite element analyses. These models enable a rapid assessment of the non-linear response of complete lattice structures, making them particularly suitable for exploring different configurations and performing preliminary optimization.

Modelling of imperfections

Due to the relevance of manufacturing-induced defects, their explicit modelling is first addressed using 3D finite elements. With this purpose, a code has been developed to create either single struts or lattice configurations with multiple struts using Abaqus with Python scripting. The geometry is

Content from this work may be used under the terms of the Creative Commons Attribution 3.0 license. Any further distribution of this work must maintain attribution to the author(s) and the title of the work, journal citation and DOI. Published under license by Materials Research Forum LLC.

Materials Research Proceedings 69 (2026) 1402-1406 https://doi.org/10.21741/9781644904251-245

generated automatically by assigning random distributions to the model parameters. Specifically, the parameters of the model are associated with a normal distribution whose average value and deviation can be determined from CT images [5, 10, 11]. Multiple struts are then merged together to form lattice cells. Once the geometry is generated, the component is meshed with tetrahedral C3D4 elements.

In addition to geometric imperfection, porosity caused by unmelted powder is modelled by generating spheres with diameters between 30 − 40 μm, uniformly distributed along the strut axis, radial offset, and angular coordinate. To avoid excessive mesh refinement, the elements located within these porosity spheres are identified, and their Young's modulus is reduced by a factor of one thousand with respect to the nominal material. This approach greatly simplifies the meshing process.

Simplified models

The 3D models just presented provide a refined description of the manufacturing imperfections. However, the large number of degrees of freedom resulting from the generation restricts the applicability of this approach. For this purpose, a simplified modelling strategy based on 1D beam elements is proposed herein. Two different techniques are investigated to capture the initial stiffness of the structure, the critical load, and the post-critical behavior of the structure under compressive loading.

The first class of simplified models relies on a 1-element-per-strut modelling. In this case, both the material and geometric nonlinearities are embedded in the constitutive law, which is defined by the force–displacement response of an imperfect strut under tension or compression. Two different strategies are investigated in this context: one using truss elements and the other using beam elements. To determine the section properties of the beam elements, a reduced section is considered. Specifically, it is obtained as the equivalent circular section of a perfect beam that undergoes the same deflection u of the imperfect strut in a cantilever bending test. The equivalent radius Req is obtained by inverting the formula from the vertical displacement of a linear elastic beam:

$$R_{eq} = \left(\frac{FL^3}{3\pi Eu}\right)^{\frac{1}{4}} \quad (1)$$

A second class of beam models considers multiple elements per strut. In these models, the constitutive law of the elements is obtained from a traction test. The presence of multiple elements allows a more accurate representation of the compressive deformation. Two of these models are analyzed: one includes regions near the nodes with artificially increased Young's modulus to account for local material accumulation, as in [10], while the other neglects these regions. The section of the beam elements is assigned with the equivalent radius Req of Eq. 1.

Numerical results

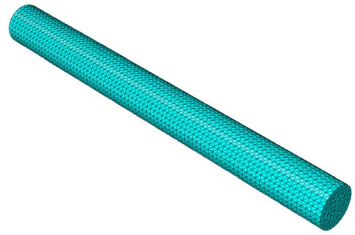
A set of analyses is conducted on both the single strut and the periodic octet cell. This latter is a cell composed by 24 struts merged at their intersection. The aim of the analyses is to evaluate the influence of imperfections and to assess the predictive capabilities of the simplified models. A bilinear constitutive law is adopted for the material, with Young's modulus E = 70000 MPa, yield strain ε = 0.002, Poisson's ratio ν = 0.33 and plastic modulus Ep = E/50.

To illustrate the impact of AM-induced defects, three FE models of a single strut with nominal radius R = 0.1 mm and length 2 mm, are analyzed, consistent with the dimensions of the CT data. In the first case, Fig. 1a, a strut is generated with the ideal geometry. In the second, Fig. 1b, the defects are introduced by considering a typical distribution with radius average R_{avg}= 0.1 mm and deviation R_{dev}= 0.028 R_{avg}, offset from the axis average $A_{d,avg}$ = 0.01 mm and deviation $A_{d,dev}$

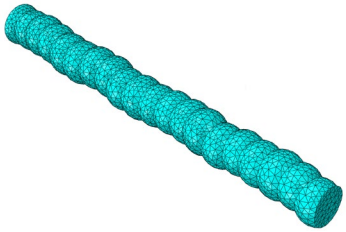
Materials Research Proceedings 69 (2026) 1402-1406 https://doi.org/10.21741/9781644904251-245

= 0.012 R_{avg}, penetration average $L_{p,avg}$ = $R_{avg}$and deviation $L_{p,dev}$ = R_{dev}. An even clearer representation of the imperfect strut is provided in Fig. 1c, where the defects are introduced with the offset from the center $A_{d,avg}$ and all deviations doubled, hence leading to an even rougher surface.

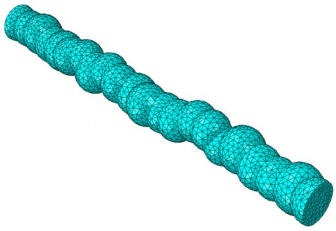
A compression analysis is performed for all three struts. The introduction of geometric imperfections significantly reduces the critical load, which shows a reduction of 20% and 29% for the two defective cases shown in Figs. 1b and 1c, respectively.



(a) *Ideal strut.*



(b) *Strut with typical defects.*



(c) *Strut with larger defects.*

Figure 1: Comparison of struts with different imperfections.

The effect of porosity is evaluated by a set of traction tests on single struts from 0% to 10% of volumetric porosity. For each percentage, 10 different struts are generated and the mean force-displacement curve is obtained. As expected, increasing porosity leads to lower yield and plastic loads.

The influence of strut length is also investigated, as imperfections affect both the stress– strain response in tension and the equivalent section properties in bending. A set of 100 3 struts is generated varying the length in the range of L = 0.2 − 10 mm. Each strut is clamped at one end and subjected to a prescribed displacement u = 0.18L on the opposite side. The stress is reconstructed for a circular section of radius R_{avg}. From the results is clear how longer struts are characterized by smaller yield stress. This effect is ascribed to the more extensive role played by imperfections. For the assessment of the equivalent section, each strut is fixed at one end and loaded transversely at the other end with a force F. The equivalent radius is then obtained with Eq. 1. The results of these analyses show that the equivalent radius stays in the range of R_{eq}= 0.5 − 0.65 R_{avg}, noticeably lower than the nominal radius.

Materials Research Proceedings 69 (2026) 1402-1406 https://doi.org/10.21741/9781644904251-245

Finally, a compression analysis of the periodic octet cell is performed to assess the performance of the simplified models. The cell consists of 24 struts with the typical defect distribution. A reference point is associated with the nodes at each exterior intersection to impose the periodic boundary conditions. Each pair of reference points on opposite faces is constrained to have equal in-plane displacements. Along the compression axis, a shortening Δ is applied. Free displacements are allowed along the remaining two axes, with identical values for each face.

The results of the compression analysis are presented in Fig. 2. As shown, for the single element-per-strut models, the initial stiffness and maximum load are captured accurately. However, the post-critical deformation is not represented correctly, as the model is inherently limited by the adoption of a single element per strut. The truss model performs particularly well, as expected for a stretch-dominated cell. Among the multi-element-per-strut models, only the configuration with a stiffer region near each vertex reproduces the initial stiffness accurately. Both multi-element models, however, capture the post-critical deformation with good agreement to the 3D solid-element model. For comparison, results from an ideal beam model with the nominal material and section properties are also reported; this model clearly overestimates the overall structural strength.

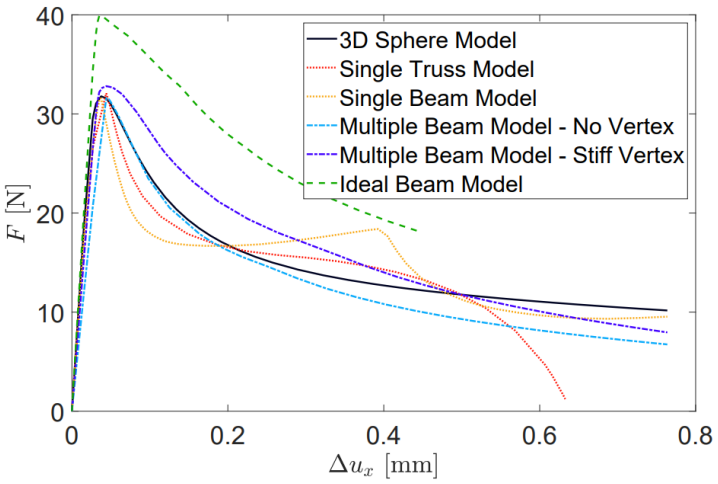


Figure 2: Comparison of struts with different imperfections.

Conclusions

The results demonstrate that geometric imperfections significantly reduce the critical load under compression, while porosity lowers the yield point of the material. The mechanical response is also affected by the strut length: longer members exhibit larger sensitivity to defects and lower yield stresses. The equivalent radius obtained from bending tests was found to be significantly lower than the nominal value.

The simplified 1D models reproduced the overall compression behavior of the octet cell in good agreement with high-fidelity 3D solid models, while requiring drastically lower computational cost. Therefore, the proposed approach is a promising way to account for manufacturing-induced defects, while preserving computational effectiveness.

Acknowledgments

This work was carried out within the Space It Up! project funded by the Italian Space Agency (ASI) and the Italian Ministry of University and Research (MUR) under contract No. 2024-5-E.0, CUP No. I53D24000060005.

References

[1] O. Rehme, C. Emmelmann, Rapid manufacturing of lattice structures with selective laser melting. Laser-based Micropackaging 6107 (2006) 192-203. https://doi.org/10.1117/12.645848.

[2] E. Atzeni, A. Salmi, Economics of additive manufacturing for end-usable metal parts. The International Journal of Advanced Manufacturing Technology 62 (2012) 1147–1155. https://doi.org/10.1007/s00170-011-3878-1.

[3] I. Echeta, X. Feng, B. Dutton, R. Leach, S. Piano, Review of defects in lattice structures manufactured by powder bed fusion. The International Journal of Advanced Manufacturing Technology 106 (2020) 2649–2668. https://doi.org/10.1007/s00170-019-04753-4.

[4] X. Cao, Y. Jiang, T. Zhao, P. Wang, Y. Wang, Z. Chen, Y. Li, D. Xiao, D. Fang, Compression experiment and numerical evaluation on mechanical responses of the lattice structures with stochastic geometric defects originated from additive manufacturing. Composites Part B: Engineering 194 (2020) 108030. https://doi.org/10.1016/j.compositesb.2020.108030.

[5] L. Liu, P. Kamm, F. García-Moreno, J. Banhart, D. Pasini, Elastic and failure response of imperfect three-dimensional metallic lattices: the role of geometric defects induced by Selective Laser Melting. Journal of the Mechanics and Physics of Solids 107 (2017) 160-184. https://doi.org/10.1016/j.jmps.2017.07.003.

[6] R. Gümrük, R.A.W. Mines, Compressive behaviour of stainless steel microlattice structures. International Journal of Mechanical Sciences 68 (2013) 125-139. https://doi.org/10.1016/j.ijmecsci.2013.01.006.

[7] B. Lozanovski, M. Leary, P. Tran, D. Shidid, M. Qian, P. Choong, M. Brandt, Computational modelling of strut defects in SLM manufactured lattice structures. Materials & Design 171 (2019) 107671. https://doi.org/10.1016/j.matdes.2019.107671.

[8] M. Smith, Z. Guan, W.J. Cantwell, Finite element modelling of the compressive response of lattice structures manufactured using the selective laser melting technique. International Journal of Mechanical Sciences 67 (2013) 28-41. https://doi.org/10.1016/j.ijmecsci.2012.12.004.

[9] H.D. Carlton, N.A. Volkoff-Shoemaker, M.C. Messner, N.R. Barton, M. Kumar, Incorporating defects into model predictions of metal lattice-structured materials. Materials Science and Engineering A 832 (2022) 142427. https://doi.org/10.1016/j.msea.2021.142427.

[10] M.R. Karamooz Ravari, M.A. Kadkhodaei, Computationally efficient modelling approach for predicting mechanical behavior of cellular lattice structures. Journal of Materials Engineering and Performance 24 (2015) 245–252. https://doi.org/10.1007/s11665- 014-1281-4.

[11] S. Tsopanos, R.A.W. Mines, S. McKown, Y. Shen, W.J. Cantwell, W. Brooks, C.J. Sutcliffe, The influence of processing parameters on the mechanical properties of selectively laser melted stainless steel microlattice structures. Journal of Manufacturing Science and Engineering 132 (2010) 041011. https://doi.org/10.1115/1.4001743.

Materials Research Proceedings 69 (2026) 1407-1411 https://doi.org/10.21741/9781644904251-246

Dynamic Characterization of Compliant Wheel for Martian Rover: ARDITO

Enrico SABBATINI[1,a *], Damiano CARRA[2,b], Enrico ZAPPINO[2,c]

[1]STAR Lab, Department of Mechanical and Aerospace Engineering, Corso Duca degli Abruzzi 24, 10129, Torino, Italy

[2]MUL2 Lab, Department of Mechanical and Aerospace Engineering, Corso Duca degli Abruzzi 24, 10129, Torino, Italy

[a]enrico.sabbatini@stuenti.polito.it, [b]damiano.carra@studenti.polito.it, [c]enrico.zappino@polito.it

Keywords: Experimental Modal Analysis, Finite Element Method, Modal Correlation, Martian Rover, Compliant Wheels, Team DIANA, ARDITO

Abstract. This work presents the dynamic characterization of a compliant wheel [1] designed for ARDITO [2] a modular Martian rover. The wheel is composed of two main structures: a rigid Al2024 hub made from a single milled raw aluminum block and the external spring steel structure. The outer structure is made from twenty cylinders, an external skin and forty grousers, all made from C67 spring steel. This material ensures wheels' elastic behavior, essential to navigate and adapt in different conditions, while keeping the design mechanically reliable. This study aims to compare a FEM [3] model of the compliant wheel, used to perform structural analyses, with an Experimental Modal Analyses (EMA) [4] through a vibrational test of both the internal hub and the elastic part. Since the materials are very different the central hub and the outer compliant structure were analyzed and compared separately but the same methodologies were applied to both structures. This combined study is a start to understanding the dynamic behavior of the locomotion system and pave the way to many more analyses in order to better understand the system and how it interacts with other structures. A key objective is to ensure that the wheel's resonance modes do not couple with operational excitations, preventing unwanted dynamic amplification during planetary missions specially for what regards launch operations, where it is imperative to ensure that launch vibrations don't resonate with the structure's natural frequencies in order to prevent damages. This work was developed within the DIANA student team at Politecnico di Torino, which participated in competitions such as the Rover Challenge Series, bringing together student teams worldwide and individuals from various engineering disciplines to design a working space rover prototype.

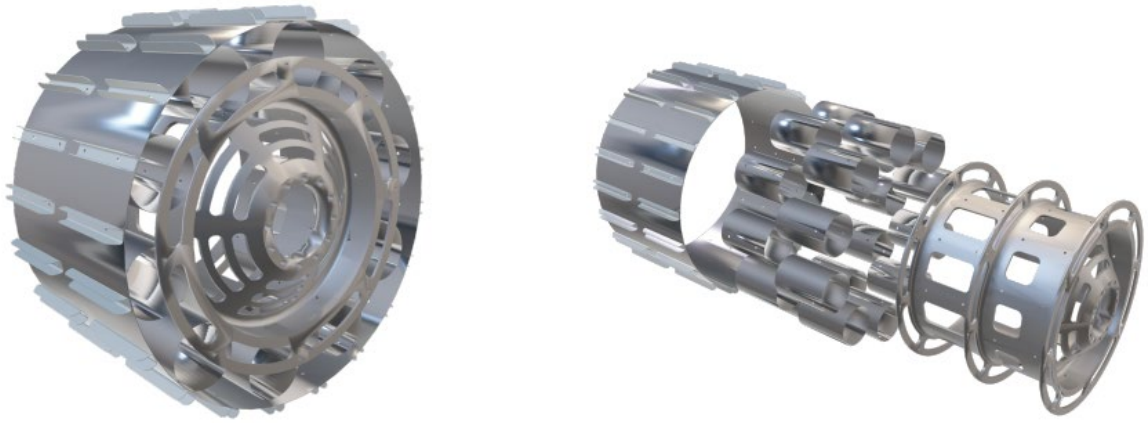
Introduction

Exploring extraterrestrial environments, like Mars, demands the rovers' mobility systems to handle uneven terrain in extreme conditions such as: irregularities, drastic temperature changes and reduced gravity. This environment place severe constraints on how the rover moves and maintains traction, that is why wheel design is a critical factor for mission success. Traditional rigid wheels, while mechanically simple, struggle to provide the adaptability required in such conditions. This has led to growing interest in compliant wheels architectures, capable of elastically deforming to overcome terrain deformations without relying on active suspension systems. The combination of flexibility and strength help maintain the rover's contact with the ground and distribute its load more evenly, thereby improving stability and durability. The ARDITO rover embraces this approach with a modular and adaptable mobility system. A new compliant wheel has been developed and optimized for small-scale planetary rovers. The design integrates a rigid Al2024 aluminum hub with an external C68 spring steel structure composed of multiple cylinders,

Content from this work may be used under the terms of the Creative Commons Attribution 3.0 license. Any further distribution of this work must maintain attribution to the author(s) and the title of the work, journal citation and DOI. Published under license by Materials Research Forum LLC.

Materials Research Proceedings 69 (2026) 1407-1411 https://doi.org/10.21741/9781644904251-246

grousers, and an outer skin. This design ensures both mechanical reliability and the elastic response necessary for navigating uneven terrain. This paper focuses on the dynamic characterization of the compliant wheel. In the following section, the experimental setup and the FEM analyses are described in order to understand how its modal shapes can effect the overall structure. This study lays the foundation for future research aimed at gaining a deeper under-standing of the ARDITO rover's behavior. Characterizing the modal shapes of the wheel components is essential to understanding how they influence each other and whether these vibrations can be transmitted to the rover, potentially affecting its precision during operation.



(a) Exploded view (b) Compliant wheel

Figure 1: Render of ARDITO's wheel

Test campaign

Two test campaigns were conducted, the first focused on the dynamic characterization of the central part of the hub while the second on the elastic part of the whole wheel, with the objective of identifying the modal frequencies of the structure. Since the number of measured point were conspicuous, we relied on the DEWESoft company and the Mul2 Laboratory. The experimental setup was composed of the following elements:

- DAQ SIRIUSie-8xUNI+
- Instrumented hammer PCB 086C03
- Accelerometer PCB 356BA43
- Foam to simulate an unconstrained environment
- A protoype of the rover's wheel
- Software DEWESoft X with the following plugin:
  - plug-in Modal Testing.
  - plug-in Modal Analysis.

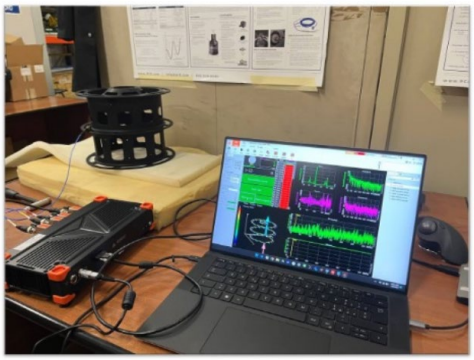


Figure 2: *EMA Setup*

Due to the complexity of the component, measurement points were defined and strategically distributed over the structure. Installing a large number of accelerometers wouldhave required excessive setup time, so the reciprocity principle [8] of modal analysis wasapplied. This approach made it possible to characterize the entire structure using a singleaccelerometer.To further simplify the measurement process, data acquisition was limited to a singleaxis. This choice was based on preliminary FEM analyses.To simulate a free-free boundary condition [9], the component was placed on a polyurethanefoam support. This setup eliminated the need for rigid support while ensuring accurate dynamic measurements.

Materials Research Proceedings 69 (2026) 1407-1411 https://doi.org/10.21741/9781644904251-246

FEM Analysis of the hub

Regarding the hub, two numerical analyses were carried out using finite element models developed in MSC Apex and MSC Patran/Nastran. The first model was discretized with a standard three-dimensional tetrahedral mesh, consisting of approximately 145,000 nodes and about 868,000 degrees of freedom. This configuration allowed for an accurate representation of the structural behavior.

The second model used a two-dimensional mesh with planes placed at mid-thickness to reduce computational effort while maintaining a good approximation of the structural response. This approach made it possible to assess which modeling strategy provided a more accurate discretization of the structure and a closer representation of the real component. To enable a direct comparison with the experimental setup, the nodes that best matched the measurement points were selected. The analyses were performed using the SOL103 solver, with the structure left unconstrained and no external forces applied. This produced 28 mode shapes within the 100–1600 Hz range. The first six rigid-body modes were excluded, as they are not relevant to the dynamic analysis of the component.

The results from both FEM analyses show a difference in modal frequencies ranging from 16 to 100 Hz. This demonstrates how the discretization method affects the outcomes. The variations come from differences in stiffness between the two models. In Figures 3 and 4, CrossMac results are shown.

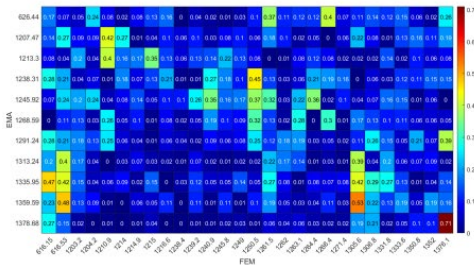


Figure 3: *CrossMAC between the 3D-Mesh Model and the experimental data*

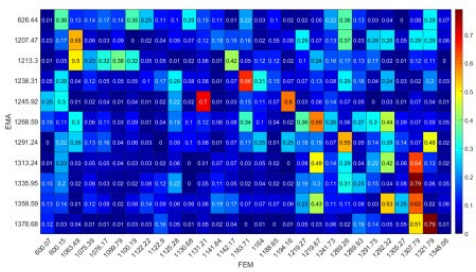


Figure 4: *CrossMAC between the 2D-Mesh Model and the experimental data*

After a visual comparison, the first mode shape at around 620 Hz involves the overall structure and can potentially transmit vibrations to the rover. The second global mode, at around 3000 Hz, concerns the interface between the hub and the rover. This mode showed good correlation between the experimental and numerical results, indicating that the numerical model represents it accurately. The remaining modes are local, mainly located in the three radial flanges of the hub, and are not relevant to the overall behavior of the system.

Elastic part

The second test campaign focused on the elastic outer part of the wheel, the goal was to correlate the experimental measurements of natural frequencies to the ones obtained by a mathematical analyses.

In order to do so, three progressively refined 2D models were developed using Patran to better capture the dynamics of the full assembly and a SOL103 was made to extract natural frequencies and modal shapes. The first and more basic model simulated the outer structure using surface elements. The second model had thicker surfaces to approximate the real wheel's weight as closely as possible. The third and more accurate was composed of surfaces to mimic the cylinders, coupled with all 40 grousers distributed equally along the wheel. Analyses show that the second one can be used with no problem, it's less computationally demanding and the results are comparable to those of the full wheel with grousers. The model used during analyses had a rigid hub, contact between surfaces was added and rivets were simulated trough node equivalence. Regarding testing,

the accelerometer was mounted radially along the skin of the wheel, and 40 nodes were identified for characterization between the grousers to avoid signal noise as much as possible.

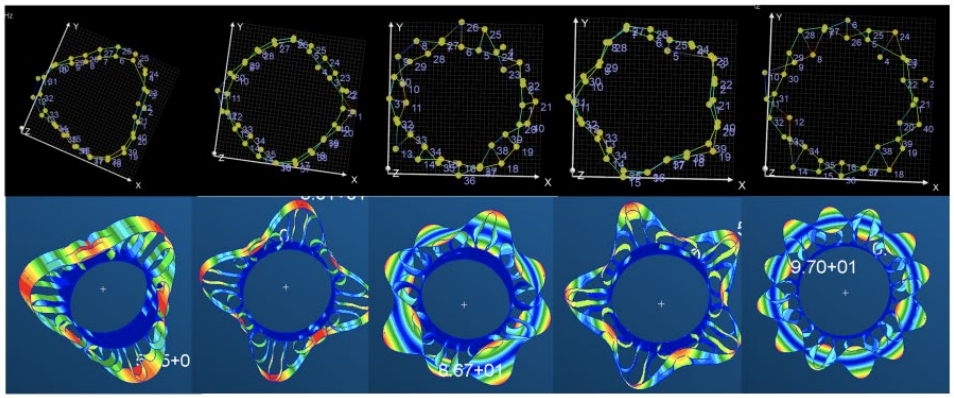


Figure 5: *Comparison between EMA and FEM analyses*

In the picture you can see a visual correlation of some of the modal shapes obtained by the DewesoftX software (on top) and the ones obtained by Patran (on the bottom). As shown on the picture we obtained the same shapes trough both of the methods and the frequencies associated differ by a margin of less than 10%.

Conclusion and future developments

This work represents a fundamental step towards assuring that mathematical models can closely simulate the behavior of mechanical components. Understanding and accurately identifying the natural frequencies of rover components is essential in space-related projects because dynamic loads encountered during launch, landing, and surface operations can excite structural vibrations. If these vibrations coincide with the component's natural frequencies, resonance can occur, leading to amplified stresses, reduced performance, or even structural failure. The correlation between FEM predictions and Experimental Modal Analysis provides confidence in the wheel's dynamic performance and informs future design refinements. Overall, the study of natural frequencies is a crucial step in developing robust, efficient, and safe mobility systems for planetary exploration. Future work on this matter may consist of a deep analysis of the wheel under operational conditions with different structural stresses and scenarios. This, correlated to a series of test campaigns, would allow us to deeply understand the behavior of not only the wheel
sub-system but also the mobility system as a whole.

Acknowledgement

This work was conducted within the environment of the student team DIANA from Poltecnico di Torino. The authors express their gratitude to the whole team for their hard work and to the Politecnico di Torino's funding commission for allowing us to work on and develop the project.

References

[1] M. Trentini, G. Candita, L.M. Festa, A. Dellacasa, A. Pagani, F. Stesina, Design, validation and production of small-size rover elastic wheels: a solution to plastic deformations,

2024. https://doi.org/10.52202/078369-0037

[2] L. Caraccio, A. Dellacasa, N. di Gruttola Giardino, L.M. Festa, T. Galliano, G. Gorgerino, A. Meloni, F. Mustich, F. Stesina, ARDITO, a modular technology demonstrator

for robotic planetary surface exploration and operational support: an overview, IEEE

Aerosp. Electron. Syst. Mag., 2025. https://doi.org/10.1109/MAES.2025.3564224

[3] J.N. Reddy, Introduction to the Finite Element Method, fourth ed., McGraw-Hill Education, New York, 2019.

[4] D.J. Ewins, Modal Testing: Theory and Practice, John Wiley & Sons, Inc., 2000.

[5] Dewesoft, DewesoftX, https://dewesoft.com/, [Online]. Available: https://dewesoft.com/it/prodotti/dewesoftx. [Accessed: July 31, 2025].

[6] Hexagon MSC Software, MSC Patran, https://hexagon.com/it/products/patran. [Online]. Available: https://www.mscsoftware.com/product/msc-patran. [Accessed: July 31,

2025].

[7] Hexagon MSC Software, MSC Apex, https://hexagon.com/it/products/productgroups/computeraided-engineering-software/msc-apex. [Online]. Available: https://www.mscsoftware.com/product/msc-apex. [Accessed: July 31, 2025].

[8] Pete Avitabile. ”Can you describe reciprocity? It just doesn’t make sense to me.” In:

SEM Experimental Techniques (2008)

[9] Pete Avitabile. ”Will the support mechanism have any effect on FRFs?” In: SEM Experimental Techniques (2010)

Materials Research Proceedings 69 (2026) 1412-1415 https://doi.org/10.21741/9781644904251-247

A Multiscale Approach for the Thermo-Hydraulic and Structural Performance Prediction of Compact Cross Flow Heat Exchangers

Girindra RAMGOBIN[1*], Harvey THOMPSON[2], Amirul KHAN[3], Martin MUIR[4], and Gregory de BOER[2]

[1]EPSRC Centre for Doctoral Training in Fluid Dynamics, School of Computer Science, University of Leeds, LS2 9JT, UK

[2]School of Mechanical Engineering, University of Leeds, LS2 9JT, UK

[3]School of Civil Engineering, University of Leeds, LS2 9JT, UK

[4]Airbus Central Research and Technology, Bristol, BS34 7PA, UK

* scgr@leeds.ac.uk

Keywords: Heat Exchangers, Multiscale Modelling, Conjugate Heat Transfer, Homogenisation

Abstract. The design of compact heat exchangers (HXs) for hydrogen fuel cell and battery-electric aircraft presents unprecedented challenges in terms of thermal management and structural integration. This study introduces an open-source multiscale–multiphysics framework for predicting the thermo-hydraulic and structural performance of cross-flow HXs based on repeated unit cells. The framework combines detailed microscale conjugate heat transfer simulations with macroscale modelling through two complementary reduced-order strategies: upscaling and homogenisation. The reduced-order models are benchmarked against fullscale, high fidelity simulations. Results demonstrate good agreement of both the upscaled and homogenised models with full-scale CFD simulations, particularly deviations below 4 % for fluid temperatures, with the upscaled model performing consistently better.

Introduction

The design methodologies for HXs have evolved significantly over recent decades, transitioning from traditional empirical correlations to advanced numerical simulation and multiscale modelling techniques. Multiscale approaches are particularly relevant for aircraft-scale systems, where sustainable propulsion architectures such as battery-electric and hydrogen fuel cells generate large quantities of low-grade heat that must be rejected efficiently. As direct high-fidelity analysis of fullscale configurations is computationally prohibitive, performance evaluation and optimisation down to the microscale can deliver significant system-wide gains, particularly in the case of additively manufactured periodic HX cores. While previous studies have applied multiscale methods to compact HXs in automotive applications [1, 2], they have primarily focussed on thermo-fluidic performance. More recently, researchers have adopted high-fidelity CFD to study novel configurations enabled by additive manufacturing [3]. On the structural side, Imediegwu et al. [4] used a multiscale approach for thermo-structural coupling to improve thermal performance in a heat sink. On the thermo-hydraulic side, porous flow modelling and homogenisation techniques have also emerged as promising alternatives means to accurately characterise complex, periodic geometries [3]. Despite these advances, the explicit coupling of multiphysics effects combining thermofluidic and structural responses, which are particularly important in aerospace applications, remains rare.

Content from this work may be used under the terms of the Creative Commons Attribution 3.0 license. Any further distribution of this work must maintain attribution to the author(s) and the title of the work, journal citation and DOI. Published under license by Materials Research Forum LLC.

Materials Research Proceedings 69 (2026) 1412-1415 https://doi.org/10.21741/9781644904251-247

Methodology

Overview. A novel open-source framework is introduced for multiscale and multiphysics analysis of a compact cross-flow HX with repeating unit cells (RUCs). The framework starts with a parametric model for a microscale unit cell of the HX core, as seen in Figure 1a, generating a multi-region mesh that can then be used for thermofluid and structural analysis. As part of the multiscale strategy, two reduced order models (ROMs) are considered, namely upscaling and homogenisation. The performance of these ROMs is evaluated against high-fidelity macroscale simulations to determine their accuracy and efficiency.

Microscale. A conjugate heat transfer (CHT) model is first solved using the multi-region mesh by means of the continuity, momentum and energy equations. The structural domain is solved using Cauchy's momentum equation for solids using combined mechanical loading and thermal stresses.

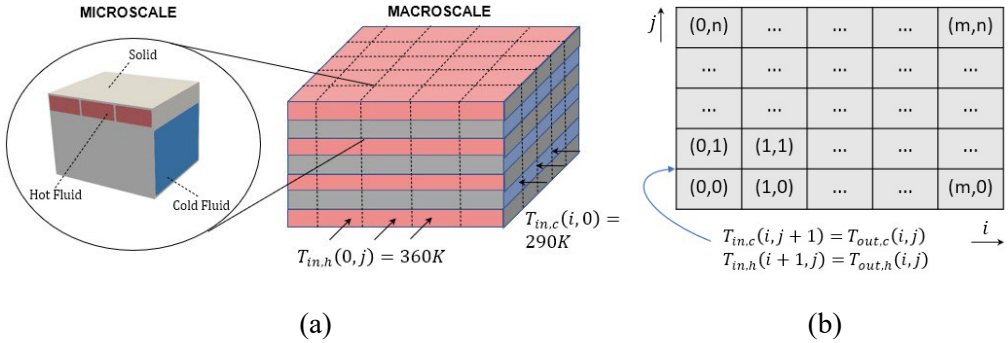


Figure 1: (a) The microscale and macroscale HX multi-region domain (b) boundary conditions transfer using the upscaling algorithm.

Macroscale. For the upscaling procedure, the algorithm originally proposed by Ciuffini et al. [2] is first implemented in a single layer of the HX block consisting of RUCs, and later adapted to a 3-dimensional framework. Each RUC represents a fully resolved microscale CHT simulation. The coupling between neighbouring RUCs is achieved through a sequential mapping procedure, defined by the boundary transfer relationships shown in Figure 1b, with the initial conditions of the hot and cold fluids defined as shown in Figure 1a.

Subsequently, homogenisation is employed as an alternative reduced-order approach to predict the effective thermo-mechanical behaviour of the HX. This method enables two-scale coupling, where heat-transfer and structural properties are first evaluated at the microscale and then averaged to define equivalent parameters at the macroscale. While upscaling relies on cell-to-cell coupling, homogenisation replaces detailed local variations with averaged quantities that preserve the overall physical response.

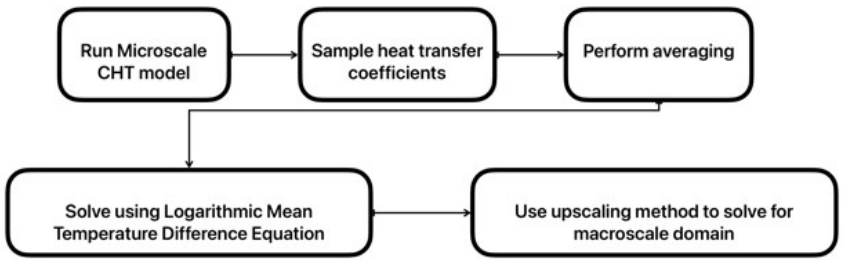


Figure 2: Homogenisation steps to reconstruct the macroscale temperature distribution from microscale simulations using LMTD equation and upscaling

Materials Research Proceedings 69 (2026) 1412-1415 https://doi.org/10.21741/9781644904251-247

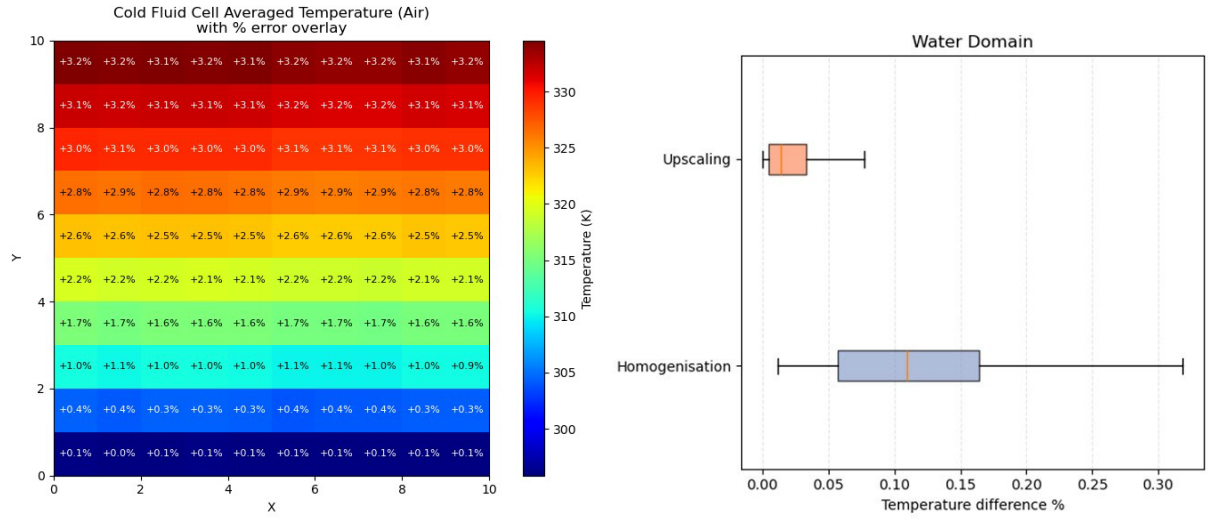
The procedure for reconstructing the macroscale temperature distribution using homogenisation is highlighted in Figure 2. For the structural characterisation, the unit cell is evaluated under six independent loading cases to determine the uniaxial and shear components of the effective stiffness matrix. The resulting properties, which are orthotropic because of the geometric configuration of the RUC used, are subsequently used to solve a macroscale model of homogenised material with equivalent overall dimensions.

Results and Discussion

The upscaling algorithm from Ciuffini et al. [2] is implemented on a two-dimensional 10×10 RUC array representing a layer of the compact cross-flow HX and is subsequently benchmarked against full-scale CFD results with the same configuration. A direct error comparison between the upscaling and homogenisation approaches is performed to assess their predictive accuracy. As shown in Figure 3a, the upscaling method achieves excellent agreement with the full-scale solution, with deviations below 4% for the cold-fluid domain. Figure 3b further confirms that the upscaling approach outperforms homogenisation for the hot fluid region. Future work will focus on integrating surrogate models to reduce the number of microscale simulations required for homogenisation, thereby extending the framework's applicability to a wider range of inlet flow and thermal conditions.

Conclusion

This work presented an open-source multiscale–multiphysics framework for predicting the thermo-hydraulic and structural performance of cross-flow HXs. The upscaling and homogenisation approaches were benchmarked against full-scale CFD, with the upscaling method achieving higher accuracy at reduced computational cost. The framework's consistent use of a single multi-region mesh enables efficient extraction of coupled thermal and structural properties, providing a foundation for future optimisation and design of lightweight, multifunctional HXs for sustainable aircraft.



(a) (b)

Figure 3: (a) Temperature distribution and cell percentage deviation of the cold fluid domain using upscaling (b) Comparison of the reduced order models against fullscale CFD for the hot fluid domain

Acknowledgement
This work was supported by the Engineering and Physical Sciences Research Council (Grant No. EP/S022732/1).

References

[1] G. Starace, M. Fiorentino, M. Longo, and E. Carluccio, "A hybrid method for the cross flow compact heat exchangers design," Applied Thermal Engineering, vol. 111, p. 1129-1142, Jan. 2017. https://doi.org/10.1016/j.applthermaleng.2016.10.018

[2] A. Ciuffini, A. Scattina, F. Carena, M. Roberti, G. Toscano Rivalta, E. Chiavazzo, M. Fasano, and P. Asinari, "Multiscale computational fluid dynamics methodology for predicting thermal performance of compact heat exchangers," Journal of Heat Transfer, vol. 138, no. 7, p. 071801, Jul. 2016. https://doi.org/10.1115/1.4032980

[3] A. Chiodi, A. Alaia, E. Lombardi, M. Cisternino, K. Gkaragkounis, and S. Shahpar, "Multidisciplinary optimisation of additive manufactured heat exchangers for aeronautical applications," in Volume 13: Heat Transfer: General Interest / Additive Manufacturing Impacts on Heat Transfer; Wind Energy. London, United Kingdom: American Society of Mechanical Engineers, Jun. 2024, p. V013T13A026. https://doi.org/10.1115/GT2024-126786

[4] C. Imediegwu, R. Murphy, R. Hewson, and M. Santer, "Multiscale thermal and thermostructural optimization of three-dimensional lattice structures," Structural and Multidisciplinary Optimization, vol. 65, no. 1, p. 13, Jan. 2022. https://doi.org/10.1007/s00158-021-03087-8

Materials Research Proceedings 69 (2026) 1416-1421 https://doi.org/10.21741/9781644904251-248

Assessment of CUF-Based Variable-Section 1D Finite Elements for the Nonlinear Analysis of a Wingbox Structure

Francesco Mario Antonio MITROTTA[1*], Antonio Paolo FONTANELLA[2], Maria CINEFRA[2], and Rauno CAVALLARO[1,3]

[1]Department of Aerospace Engineering, Universidad Carlos III de Madrid, Leganés, Spain

[2]Department of Mechanics, Mathematics, and Management, Politecnico di Bari, Bari, Italy

[3]Barcelona Supercomputing Center, Barcelona, Spain

*francesco.mitrotta@uc3m.es

Keywords: Carrera Unified Formulation, Finite Element Analysis, Nonlinear Analysis, Wingbox Structure

Abstract. The integration of postbuckling behavior into aeroelastic optimization frameworks faces a critical barrier in the computational cost of nonlinear finite element analyses with traditional shell-based wingbox models. This study investigates whether variable-section 1D finite elements based on the Carrera Unified Formulation (CUF) can replicate the nonlinear response of wingbox structures with reduced computational cost. Nonlinear analyses of the Simple Transonic Wing benchmark are performed using MSC Nastran shell elements and two CUF models with different mesh refinements. While the CUF models achieve comparable or better computational efficiency, the approaches predict substantially different onset points for geometric nonlinearity: the Nastran model exhibits softening behavior at the linear buckling load of 133 kN, whereas the CUF models maintain nearly linear response until approximately 264–272 kN. Importantly, the close agreement between the two CUF mesh refinements demonstrates that this discrepancy cannot be attributed to insufficient CUF discretization. These findings raise a critical question about the minimum fidelity required to accurately capture global nonlinear postbuckling behavior, whose answer is essential for including nonlinear structural stability analysis in aeroelastic optimization.

Introduction

The aviation industry is facing unprecedented challenges as it strives to achieve net-zero carbon emissions by 2050, as targeted by the Air Transport Action Group (ATAG) [1]. While sustainable aviation fuels (SAF) have been identified as a cornerstone for meeting these climate goals, recent trends indicate that SAF development is progressing at a pace insufficient to deliver the ambitious emissions reduction targets within the required timeframe [2]. In parallel, radical technological solutions such as hydrogen propulsion and unconventional aircraft configurations have encountered significant uncertainties and program suspensions, as highlighted by the recent delays and pauses in major initiatives like Airbus' ZEROe hydrogen-powered aircraft program and Boeing's X-66 truss-braced wing flight demonstrator.

Given these uncertainties, maximizing the structural efficiency of conventional airframes has become increasingly critical. One promising avenue is the exploitation of the load-carrying capacity of aeronautical structures in their elastic postbuckling regime [3], thereby enabling lighter, more efficient wing designs. However, integration of postbuckling behavior into preliminary design and modern aeroelastic optimization processes remains a major challenge. Traditionally, global aeroelastic optimization frameworks have relied on linear buckling constraints, whereas advanced postbuckling analyses, capable of demonstrating safe operation beyond linear buckling limits, have largely been confined to detailed panel-level studies and have remained isolated from the overall wing design process.

Content from this work may be used under the terms of the Creative Commons Attribution 3.0 license. Any further distribution of this work must maintain attribution to the author(s) and the title of the work, journal citation and DOI. Published under license by Materials Research Forum LLC.

Materials Research Proceedings 69 (2026) 1416-1421 https://doi.org/10.21741/9781644904251-248

Recent work has attempted to bridge this gap by proposing a paradigm shift for the assessment of structural stability in aeroelastic optimization [4]. Rather than viewing stability through the binary lens of buckling and postbuckling, this approach continuously monitors the structural stability through path-following continuation and enforces the positivedefiniteness of the tangent stiffness matrix to impose a stable deformation of the structure. This methodology enables wingbox optimization with nonlinear structural stability constraints, potentially unlocking significant weight savings while maintaining structural integrity.

However, a key barrier is the computational intensity of nonlinear Finite Element (FE) analyses with typical shell-based wingbox models, which can be prohibitive in optimization problems with many design variables. To address this challenge, the present study investigates whether variable-section 1D FEs based on the Carrera Unified Formulation (CUF) [5] can replicate the nonlinear response of a wingbox structure with reduced computational cost. Using the benchmark Simple Transonic Wing (STW) [6] as a test case, the nonlinear response from a CUF-based model is compared to a shell-based analysis in MSC Nastran.

CUF Methodology

The CUF provides a systematic framework for developing FE models with enhanced kinematic descriptions. The three-dimensional displacement field $u(x, y, z)$ of the variable-section 1D FEs employed in this work is expressed through a generalized expansion that combines expansion functions (F_τ) over the cross-sectional domain with conventional FE shape functions (N_i) along the beam axis [5]:

$$\boldsymbol{u}(x, y, z) = F_\tau(x, z) N_i(y) \boldsymbol{Q_{\tau i}} = L_{\tau i}(\xi, \eta, \nu) \boldsymbol{Q_{\tau i}} \tag{1}$$

where $\boldsymbol{Q_{\tau i}}$ denotes the generalized nodal degrees of freedom, and ξ, η, ν represent the natural coordinates[1]. The quantity $L_{\tau i}(\xi, \eta, \nu)$ defines a three-dimensional shape function in which the expansion order can vary independently along different spatial directions. The volume integrals appearing in the governing equations are evaluated directly in three dimensions rather than being decomposed into separate 1D and 2D integrals. The Jacobian matrix for the transformation from natural to global coordinates is therefore computed in full 3D form. Nevertheless, the formal coordinate separation shown in Eq. (1) remains valid, and higher-order polynomial functions can still be assigned to directions with larger geometric extent.

This formulation enables finite elements that accurately represent variable-section beamlike structures while potentially maintaining significantly fewer degrees of freedom compared to shell-based discretizations. The modeling approach is illustrated in Fig. 1.

For nonlinear analyses, the structural response is computed using a Total Lagrangian formulation with the Full Green-Lagrange strain tensor. The nonlinear equilibrium equations are solved through an incremental-iterative Newton-Raphson scheme, with the tangent stiffness matrix decomposed into linear, material nonlinear, and geometric components. The arc-length method is employed to trace the equilibrium path.

[1] The natural coordinates are dimensionless coordinates that represent the physical coordinates over the interval $[-1, +1]$, either along the cross-sectional dimensions of the beam or along its length.

Materials Research Proceedings 69 (2026) 1416-1421 https://doi.org/10.21741/9781644904251-248

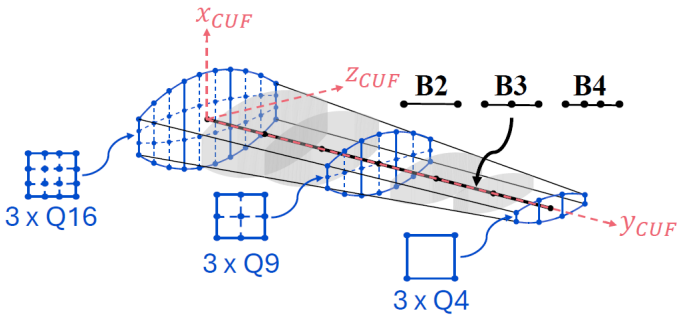


Figure 1: Conceptual illustration of variable-section CUF elements with coupling of 2D cross-sectional discretization and 1D beam-wise expansion. Each beam element can use a different formulation, and for each beam node it is possible to choose a different CUF expansion.

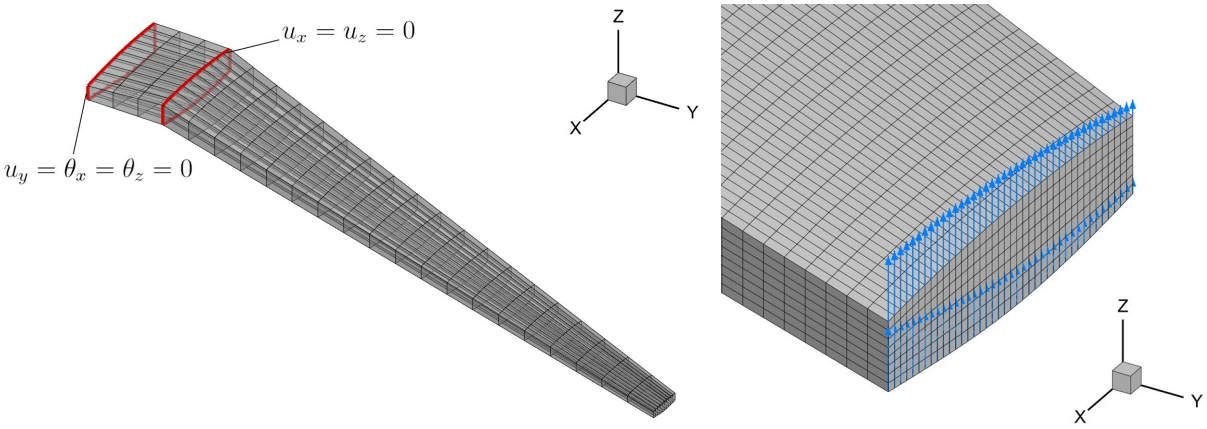


Figure 2: Overview of the STW model showing the wingbox geometry and loading conditions. Left: STW wingbox with boundary conditions. Right: Applied load distribution.

STW Description

The STW is a benchmark model for aeroelastic optimization [6]. Its structural design consists of a 14 m semispan wingbox comprising upper and lower skins, leading and trailing edge spars, and 23 ribs. The version used in this work is a modification of the original model employing an aluminium structure and 9 blade stiffeners for each skin [7]. All stiffeners span root to tip with constant 50 mm height. The baseline wingbox features uniform thickness of 6.5 mm for ribs, skins, and spars, and 6.0 mm for stiffeners.

The Nastran model uses four-node quadrilateral shell elements with six degrees of freedom per node, employing Mindlin-Reissner theory. Two CUF models are constructed: CUF 2-B4 employs two B4 elements between each rib pair, while CUF 3-B4 employs three B4 elements for increased refinement. Both use one B3 element across each rib thickness and 540 Q16 elements for each beam node expansion.

The load case consists of distributed forces in the positive z-direction over tip nodes of both skins, as illustrated in Fig. 2. Each row of nodes experiences linearly varying forces from 4P on the rear spar node to P on the front spar node, simulating the nose-down tip twist typical of backward-swept wings. Boundary conditions include symmetry at the centerline and constraints in chordwise (x) and vertical (z) directions at the side-of-body (SOB) break located at y = 1.5 m.

Materials Research Proceedings 69 (2026) 1416-1421 https://doi.org/10.21741/9781644904251-248

Table 1: Computational characteristics of the nonlinear analyses.

	Nastran	CUF 2-B4	CUF 3-B4
DOFs	271,995	249,936	324,384
Wall time, h	24.8	24.0	22.0
Arc-length steps	500	185	280
Processor	i7-8700 (3.20 GHz)	i9-13900K (3.00 GHz)	-

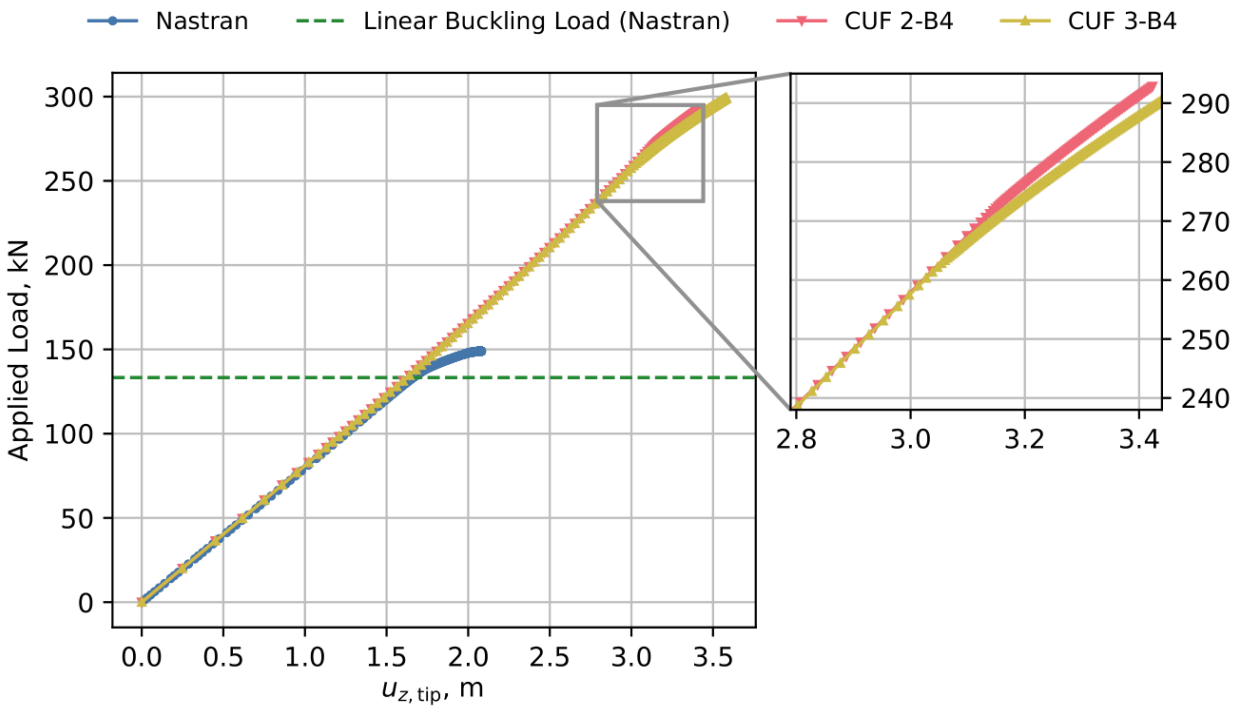


Figure 3: Load-displacement diagram for tip displacement.

Results

Three nonlinear analyses of the baseline STW wingbox are executed: one using MSC Nastran's SOL 106 arc-length method, and two using CUF methodology with different mesh refinements. All employ a 10−5 tolerance on the respective load and displacement convergence criteria. Table 1 summarizes the computational characteristics. The coarser CUF 2-B4 model exhibits 8% fewer degrees of freedom than Nastran and achieves comparable wall-clock time, while the refined CUF 3-B4 model has 19% more degrees of freedom but completes 11% faster. It should be noted that analyses were performed on different processors and no mesh tailoring was performed for the CUF models, which could further improve computational efficiency.

Figure 3 compares the load-displacement response for tip displacement, indicating global structural behavior. The horizontal dashed line shows the linear buckling load predicted by Nastran (approximately 133 kN). All models exhibit identical initial stiffness, evidenced by the coincident linear regime at low loads. However, they predict substantially different onset points for geometric nonlinearity. The Nastran model shows characteristic softening near the linear buckling load. In contrast, the CUF models maintain nearly linear response until approximately 272 kN (CUF 2-B4) and 264 kN (CUF 3-B4).

Materials Research Proceedings 69 (2026) 1416-1421 https://doi.org/10.21741/9781644904251-248

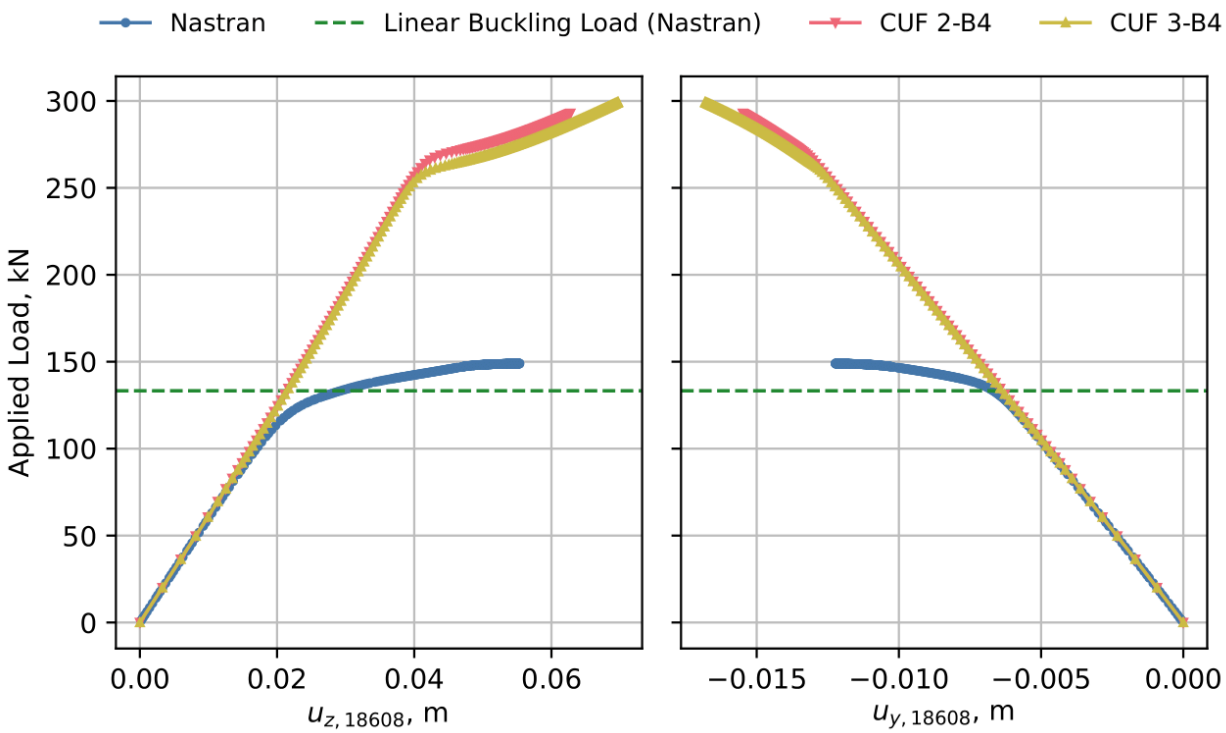


Figure 4: Load-displacement diagrams of node 18608.

The minimal difference between the two CUF mesh refinements demonstrates that the discrepancy with Nastran cannot be attributed to insufficient CUF discretization. Finally, the nonlinear stiffness reduction magnitude in both CUF models is noticeably smaller than in Nastran. To examine local response, Fig. 4 presents load-displacement diagrams for node 18608, which experiences maximum displacement in the first linear buckling mode. This node is located approximately at the center of the second top skin panel outboard of the SOB break. Two displacement components are shown: z-displacement and y-displacement, the latter indicating panel shortening. For the CUF models, equivalent displacements are obtained by interpolating surrounding nodes. The local response exhibits trends consistent with global tip displacement: identical initial stiffness, followed by nonlinear behavior onset at the linear buckling load for Nastran, while in the CUF models nonlinearity appears at higher loads. The magnitude of the stiffness variation is once again more pronounced in the Nastran model.

The discrepancy between Nastran and CUF models is obtained despite the Nastran mesh convergence having been verified in a previous work [7], and the employed 1D CUF elements having been validated for nonlinear postbuckling analyses of variable cross-section beam structures [8]. Two potential sources of this discrepancy have been identified and are currently under investigation. First, the stringer-rib intersections are modeled with independent nodes in Nastran, leaving these junctions essentially free as in a real wingbox with mouseholes, whereas the CUF models enforce shared nodes at these intersections, potentially adding artificial rigidity. Second, the sectional expansion in CUF builds thickness outward from the reference geometry, effectively increasing the cross-sectional area and moment of inertia compared to Nastran's symmetric thickness assignment. Both effects could contribute to the increased stiffness observed in the CUF models. At the same time, establishing a definitive ground truth remains challenging: the STW is a purely numerical benchmark without experimental data, and a reference three-dimensional solid element model has not yet been developed.

Conclusions

These findings raise a critical question: what level of model fidelity is minimally required to accurately capture global nonlinear postbuckling behavior of wingbox structures? Answering this question is a prerequisite for realizing the nonlinear structural stability paradigm shift that seeks to bridge the gap between high-level aeroelastic optimization frameworks and detailed component-level postbuckling analyses. The observed discrepancy between traditional shell-based and CUF-based approaches highlights the importance of carefully accounting for modeling assumptions, particularly regarding structural connectivity at component intersections and thickness reference planes. Future work will address the development of a three-dimensional finite element model of a simplified wingbox structure to provide an independent reference for validating both approaches, as well as more consistent Nastran and CUF models that more accurately replicate modeling assumptions regarding stringer-rib connectivity and thickness assignment.

References

[1] Air Transport Action Group. Waypoint 2050: Balancing growth in connectivity with a comprehensive global air transport response to the climate emergency. Technical report, Geneva, Switzerland, 2021.

[2] P. Bardon and O. Massol. Decarbonizing aviation with sustainable aviation fuels: Myths and realities of the roadmaps to net zero by 2050. Renewable and Sustainable Energy Reviews, 211:115279, 2025. https://doi.org/10.1016/j.rser.2024.115279

[3] G. Zhang, Y. Hu, B. Yan, M. Tong, and F. Wang. Buckling and post-buckling analysis of composite stiffened panels: A ten-year review (2014-2023). Thin-Walled Structures, 205:112525, 2024. https://doi.org/10.1016/j.tws.2024.112525

[4] F.M.A. Mitrotta, A. Pirrera, T. Macquart, J.E. Cooper, A. Pereira do Prado, and P. Higino Cabral. Proof of concept of a nonlinear structural stability constraint for aeroelastic optimisation. The Aeronautical Journal, 129(1335):1237-1264, 2025. https://doi.org/10.1017/aer.2024.151

[5] M. Cinefra. Non-conventional 1d and 2d finite elements based on cuf for the analysis of non-orthogonal geometries. European Journal of Mechanics - A/Solids, 88:104273, 2021. https://doi.org/10.1016/j.euromechsol.2021.104273

[6] A.C. Gray and J.R. Martins. A proposed benchmark model for practical aeroelastic optimization of aircraft wings. In AIAA SCITECH 2024 Forum. https://doi.org/10.2514/6.2024-2775

[7] F.M.A. Mitrotta, A. Pirrera, and J.E. Cooper. Preliminary aeroelastic optimization of the simple transonic wing with nonlinear structural stability constraints. In AIAA SCITECH 2025 Forum. https://doi.org/10.2514/6.2025-2811

[8] A.P. Fontanella, T. Sironi, P. Chiaia, M. Cinefra, and A. Pagani. Nonlinear post-buckling analysis of variable cross-section beams using the carrera unified formulation. In CEASAIDAA Joint Conference 2025.

Materials Research Proceedings 69 (2026) 1422-1426 https://doi.org/10.21741/9781644904251-249

Peridynamic Modeling of Nearly-Incompressible Soft Materials for Aerospace Systems

Francesco SCABBIA[1,a,*], Vito DIANA[2,b], Francesca FANTONI[3,c], Mirco ZACCARIOTTO[1,d] and Ugo GALVANETTO[1,e]

[1]Department of Industrial Engineering, Università degli Studi di Padova, Italy

[2]Department of Civil, Chemical and Environmental Engineering, Università degli Studi di Genova, Italy

[3]Department of Civil Engineering, Architecture, Territory, Environment, and Mathematics, Università degli Studi di Brescia, Italy

[a]francesco.scabbia@unipd.it, [b]vito.diana@unige.it, [c]francesca.fantoni@unibs.it, [d]mirco.zaccariotto@unipd.it, [e]ugo.galvanetto@unipd.it

Keywords: Correspondence Model, Fracture Mechanics, Hyperelastic Constitutive Model, Volumetric Locking, Large Deformations

Abstract. Soft materials are increasingly integrated into modern aerospace systems due to their unique ability to deform, adapt, and absorb energy under extreme conditions. Applications such as morphing wing skins, soft robotic components for extraterrestrial exploration, and impact-absorbing systems in UAVs and space capsules, to cite a few, rely on soft polymers and elastomers subjected to large deformations. A major concern in these applications is the initiation and evolution of cracks, which can arise from cyclic loading, environmental exposure, or sudden impacts, possibly leading to failures like tearing or puncture. Predicting such damage with advanced numerical tools is essential for ensuring structural integrity, reliability, and mission success. Peridynamics, a nonlocal continuum mechanics theory, is particularly well-suited to modeling discontinuities due to fracture phenomena as the integral formulation of the internal forces allows to easily remove interactions between points across the crack surface. Therefore, cracks are not required to propagate along predefined paths, but can evolve along the most energetically favorable paths. Furthermore, peridynamic correspondence models allow to embed into the peridynamic framework hyperelastic constitutive laws used in classical continuum mechanics to describe the behavior of soft materials. Correspondence models require a stabilization technique to avoid zero-energy modes, which can undermine numerical accuracy. However, when modeling nearly-incompressible soft materials, stabilized correspondence models exhibit a numerical issue which leads to unrealistically stiff responses and an incorrect reproduction of the strain energy density for non-homogeneous deformations. Therefore, we propose a robust yet simple method to mitigate this issue and validate it through numerical examples of benchmark problems involving hyperelastic materials.

Introduction

Soft and compliant materials (typically soft polymers, elastomers, and composite hydrogels) are increasingly being used in advanced aerospace and robotic systems due to their unique mechanical capabilities, including large reversible deformations and exceptional energy absorption under extreme mechanical or environmental conditions. Notable applications include morphing aircraft wing skins, which alter aerodynamic profiles in response to flight conditions [1,2], soft robotic actuators designed for extraterrestrial exploration or manipulation in uncertain environments [3,4], impact-absorbing and adaptive landing systems used in unmanned aerial vehicles (UAVs),

Content from this work may be used under the terms of the Creative Commons Attribution 3.0 license. Any further distribution of this work must maintain attribution to the author(s) and the title of the work, journal citation and DOI. Published under license by Materials Research Forum LLC.

Materials Research Proceedings 69 (2026) 1422-1426 https://doi.org/10.21741/9781644904251-249

planetary landers, and space capsules [5]. In all of these systems, soft materials experience large nonlinear deformations and are often subjected to complex, multiaxial, and cyclic loading regimes.

A critical concern in the long-term performance of such systems is the initiation, propagation, and coalescence of cracks due to repeated cyclic loading, aggressive thermal or ultraviolet environments, or high-velocity impacts. Accurately predicting these failure mechanisms is essential to ensure structural integrity, durability, and mission reliability in demanding aerospace applications. Traditional finite element methods (FEM) based on classical continuum mechanics often face challenges when simulating crack evolution because the formation and progression of discontinuities require either complex remeshing or predefined crack paths.

To address these limitations, a nonlocal reformulation of continuum mechanics, i.e. the peridynamic (PD) theory, has emerged as a powerful computational framework for modeling fracture and damage evolution. Unlike classical differential-based continuum formulations, peridynamics represents internal forces through integrals over a finite horizon, allowing natural handling of discontinuities without the need for additional criteria or remeshing [6]. In this model, interactions (bonds) between material points across newly forming crack surfaces can be simply removed, enabling cracks to evolve spontaneously along energetically favorable directions without prior assumptions on crack path.

Correspondence models [7] allow to embed constitutive models from classical continuum mechanics, such as hyperelastic laws (e.g., Neo-Hookean or Mooney–Rivlin models), into the peridynamic framework. These models require a stabilization technique, such as the bond-associated approach [8], to prevent numerical instabilities due to zero-energy deformation modes. Nonetheless, when simulating nearly-incompressible hyperelastic materials, stabilized correspondence models may exhibit artificial stiffening and distort the representation of strain energy density under non-homogeneous deformation fields, similarly to volumetric locking in FEM models. Therefore, the selective bond-associated approach was proposed in [9] to avoid locking phenomena by stabilizing only the deviatoric part of the strain energy density.

The selective bond-associated correspondence model was validated for nearly-incompressible materials whose deviatoric strain energy density can be described with invariant-based hyperelastic models, such as Neo-Hookean or Mooney-Rivlin laws. However, the Ogden constitutive law offers superior flexibility and accuracy compared to the Mooney–Rivlin formulation because it expresses the strain energy density as a function of the principal stretches raised to non-integer exponents, rather than as low-order polynomials of the invariants of the deformation tensor. This allows the Ogden model to capture both the strain-stiffening behavior observed at large stretches and the asymmetric tension-compression responses typical of many soft materials [10]. In this work, the selective bond-associated correspondence model applied to a nearly-incompressible material described with the hyperelastic Ogden law is validated by means of the benchmark problem of Cook's membrane.

Ogden hyperelastic model for nearly-incompressible materials

Ogden proposed in [10] to express the hyperelastic strain energy density in the form

$$\psi = \sum_{p=1}^{N} \frac{\mu_p}{\alpha_p} \left(\lambda_1^{\alpha_p} + \lambda_2^{\alpha_p} + \lambda_3^{\alpha_p} - 3 \right), \tag{1}$$

where λ_1, λ_2, and λ_3 are the principal stretches, and α_p and μ_p are the constitutive parameters of the material. Principal stretches can be computed as the square roots of the eigenvalues of the left Cauchy-Green strain tensor $\mathbf{C} = \mathbf{F}^{\mathrm{T}}\mathbf{F}$, with $\mathbf{F}$ being the deformation gradient tensor. Note that Neo-Hookean and Mooney-Rivlin constitutive models can be obtained as a particular case of Eq. 1.

Several materials, such as the unfilled elastomers, can be regarded as incompressible since volumetric deformations (even in regions with high strains) are negligible. Perfect incompressibility assumes that $\lambda_1\lambda_2\lambda_3 = 1$, but the constitutive equations are often regularized by

Materials Research Proceedings 69 (2026) 1422-1426 https://doi.org/10.21741/9781644904251-249

modeling incompressible materials as slightly compressible and assigning a large value to the bulk modulus k:

$$\psi = \psi_{\text{dev}} + \psi_{\text{vol}} = \sum_{p=1}^{N} \frac{\mu_p}{\alpha_p} [(\lambda_1^*)^{\alpha_p} + (\lambda_2^*)^{\alpha_p} + (\lambda_3^*)^{\alpha_p} - 3] + \frac{1}{2} k(J-1)^2 \,, \tag{2}$$

where $J = \det(\mathbf{F})$ and λ_1^*, λ_2^*, and λ_3^* are the deviatoric principal stretches computed as the square roots of the eigenvalues of $\mathbf{C}_{\text{dev}} = J^{-2/3}\mathbf{C}$. Note that, as k increases, the function used for ψ_{vol} penalizes the volumetric deformation of the material ($J \to 1$).

Selective bond-associated correspondence model

Peridynamic correspondence models are based on the nonlocal definition of the deformation gradient tensor ($\bar{\mathbf{F}}$ in the original version [7] and $\tilde{\mathbf{F}}$ in the stabilized version [8]), which can be used into classical continuum mechanics constitutive laws. The peridynamic deformation gradient at a point $\mathbf{x}$ is defined as

$$\bar{\mathbf{F}} = \mathbf{I} + \left[\int_{H_\mathbf{x}} (\mathbf{u}' - \mathbf{u}) \otimes \boldsymbol{\xi}\, dV_{\mathbf{x}'}\right] [\bar{\mathbf{K}}(\mathbf{x})]^{-1}, \tag{3}$$

where $\mathbf{I}$ is the identity tensor, $H_\mathbf{x}$ is the neighborhood of $\mathbf{x}$ (sphere in 3D or circle in 2D, centered at $\mathbf{x}$, with radius δ called the horizon size), $\mathbf{u}'$ and $\mathbf{u}$ are the displacement vectors respectively of $\mathbf{x}'$ (material point within the neighborhood $H_\mathbf{x}$) and $\mathbf{x}$, $\boldsymbol{\xi} = \mathbf{x}' - \mathbf{x}$ is the bond vector (the relative position between the interacting points), $dV_{\mathbf{x}'}$ is the volume associated to $\mathbf{x}'$, and $\bar{\mathbf{K}}$ is the shape tensor given as

$$\bar{\mathbf{K}} = \int_{H_\mathbf{x}} \boldsymbol{\xi} \otimes \boldsymbol{\xi}\, dV_{\mathbf{x}'}, \tag{4}$$

To avoid zero-energy modes, the stabilized deformation gradient can be defined for each bond $\boldsymbol{\xi}$ as

$$\tilde{\mathbf{F}} = \mathbf{I} + \left[\int_{H_\mathbf{x} \cap H_{\mathbf{x}'}} (\mathbf{u}' - \mathbf{u}) \otimes \boldsymbol{\xi}\, dV_{\mathbf{x}'}\right] \left[\tilde{\mathbf{K}}(\mathbf{x})\right]^{-1}, \tag{5}$$

where the difference with the original version lies in the integration region, which is the intersection of the neighborhoods of $\mathbf{x}$ and $\mathbf{x}'$ in the bond-associated model. The stabilized shape tensor can be determined accordingly as

$$\tilde{\mathbf{K}} = \int_{H_\mathbf{x} \cap H_{\mathbf{x}'}} \boldsymbol{\xi} \otimes \boldsymbol{\xi}\, dV_{\mathbf{x}'}. \tag{6}$$

The integrands of all these equations can also be multiplied by an arbitrary influence function, which is chosen to be unitary here.

To avoid locking phenomena in the peridynamic correspondence model, the deviatoric and volumetric part of the first Piola-Kirchhoff stress tensor are separately computed using the deformation gradient in Eq. 3 and Eq. 5, respectively:

$$\tilde{\mathbf{P}}_{\text{dev}}(\boldsymbol{\xi}) = \frac{\partial \psi_{\text{dev}}(\tilde{\mathbf{F}})}{\partial \tilde{\mathbf{F}}}, \qquad \bar{\mathbf{P}}_{\text{vol}}(\mathbf{x}) = \frac{\partial \psi_{\text{vol}}(\bar{\mathbf{F}})}{\partial \bar{\mathbf{F}}}, \tag{7}$$

Therefore, in the selective bond-associated correspondence model, the force state (force in the bond per unit volume squared) can be computed as

$$\hat{\mathbf{T}}\langle\boldsymbol{\xi}\rangle = \left(\tilde{\mathbf{P}}_{\text{dev}}(\boldsymbol{\xi}) + \bar{\mathbf{P}}_{\text{vol}}(\mathbf{x})\right)[\bar{\mathbf{K}}(\mathbf{x})]^{-1}\boldsymbol{\xi}. \tag{8}$$

Finally, the peridynamic equation of motion at point $\mathbf{x}$ is given as

$$\rho\ddot{\mathbf{u}} - \int_{H_\mathbf{x}} \left(\hat{\mathbf{T}}\langle\boldsymbol{\xi}\rangle - \hat{\mathbf{T}}\langle-\boldsymbol{\xi}\rangle\right) dV_{\mathbf{x}'} = \mathbf{b}. \tag{9}$$

where ρ is the density of the material, $\ddot{\mathbf{u}}$ is the acceleration of $\mathbf{x}$, and $\mathbf{b}$ is the volume force density at $\mathbf{x}$. The numerical implementation of this model is similar to that illustrated in [9].

Numerical example

To validate the selective bond-associated correspondence model with the use of the hyperelastic Ogden law for nearly-incompressible materials, we numerically solved the problem of Cook's membrane with the presented method and with FEM using high-order elements (so that volumetric locking does not affect the solution). The geometry, boundary conditions, and the numerical results are shown in Fig. 1. The membrane is made of neoprene rubber which is modeled with a one-term Ogden law with $\mu_1 = 2.29$ MPa and $\alpha_1 = 2.23$ [11]. The imposed force, uniformly distributed on the free edge at the left-hand side of the membrane, is equal to $f = 3$ N.

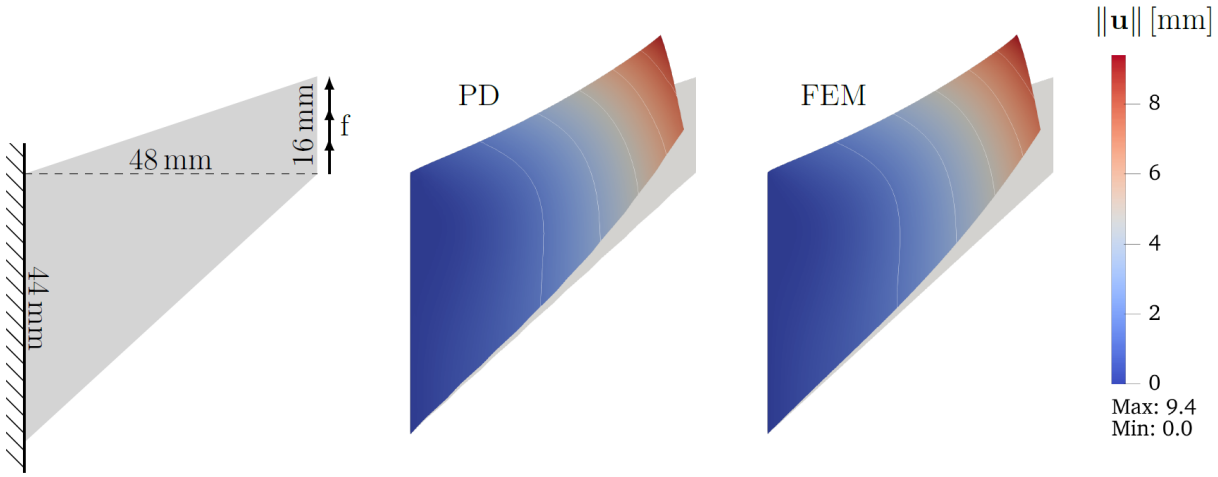


Figure 1. Geometry and boundary conditions for Cook's membrane problem and its numerical solution obtained with peridynamics (PD) and classical continuum mechanics discretized with the finite element method (FEM).

The numerical results show that the magnitudes of PD and FEM displacements are in excellent agreement. Therefore, the selective bond-associated correspondence model is suitable for modeling elastomeric nearly-incompressible materials with Ogden-like constitutive laws based on principal stretches.

Conclusions

In this work, the recently proposed selective bond-associated correspondence model within the peridynamic framework has been validated for the modeling of nearly-incompressible soft materials with the use of the Ogden hyperelastic constitutive law. This development represents an important advancement in modeling the complex mechanical response of soft polymers and elastomers that exhibit strain-stiffening and nonlinear tension-compression asymmetry, features that simpler constitutive models such as Neo-Hookean or Mooney–Rivlin cannot accurately reproduce. The selective bond-associated stabilization effectively avoids the artificial stiffening typical of volumetric locking while preserving numerical stability of the peridynamic correspondence models. The validation through the benchmark problem of Cook's membrane confirms that the model can accurately reproduce the expected deformation field, demonstrating its robustness and suitability for simulating nearly-incompressible soft materials used in advanced aerospace and soft-robotic applications.

Acknowledgements

The authors acknowledge support from the European Union - Next GenerationEU under the call PRIN 2022 PNRR of the Italian Minister of University and Research (MUR); Project P2022HLHHB (PE - Physical Sciences and Engineering) *A digital framework for the cutting of soft tissues: A first step towards virtual surgery* (National coordinator V. Diana). U. Galvanetto

and M. Zaccariotto acknowledge the financial support of the University of Padova through the projects BIRD237212/23 and BIRD232492/23.

References

[1] C. Thill, J. Etches, I. Bond, K. Potter, P. Weaver, Morphing skins, The Aeronautical Journal, 112 (2008) 117-139. https://doi.org/10.1017/S0001924000002062

[2] S. Barbarino, E.S. Flores, R.M. Ajaj, I. Dayyani, M.I. Friswell, A review on shape memory alloys with applications to morphing aircraft, Smart Materials and Structures, 23 (2014) 063001. https://doi.org/10.1088/0964-1726/23/6/063001

[3] D. Rus, M.T. Tolley, Design, fabrication and control of soft robots, Nature, 521 (2015) 467-475. https://doi.org/10.1038/nature14543

[4] D. Trivedi, C.D. Rahn, W.M. Kier, I.D. Walker, Soft robotics: Biological inspiration, state of the art, and future research, Applied Bionics and Biomechanics, 5 (2008) 99-117. https://doi.org/10.1080/11762320802557865

[5] H. Yin, X. Wang, L. Wu, W. Zhang, T. Zhao, G. Wen, J. Liu, Review on soft landing buffer systems for planetary exploration, Acta Astronautica, 228 (2024) 561-594. https://doi.org/10.1016/j.actaastro.2024.12.028

[6] S.A. Silling, Reformulation of elasticity theory for discontinuities and long-range forces, Journal of the Mechanics and Physics of Solids, 48 (2000) 175-209. https://doi.org/10.1016/S0022-5096(99)00029-0

[7] S.A. Silling, M. Epton, O. Weckner, J. Xu, E. Askari, Peridynamic states and constitutive modeling, Journal of Elasticity 88 (2007) 151-184. https://doi.org/10.1007/s10659-007-9125-1

[8] H. Chen, Bond-associated deformation gradients for peridynamic correspondence model, Mechanics Research Communications 90 (2018) 34-41. https://doi.org/10.1016/j.mechrescom.2018.04.004

[9] F. Scabbia, V. Diana, F. Fantoni, M. Zaccariotto, U. Galvanetto, Peridynamic correspondence model for nearly-incompressible finite elasticity, Computer Methods in Applied Mechanics and Engineering, 447 (2025) 118350. https://doi.org/10.1016/j.cma.2025.118350

[10] R.W. Ogden, Large deformation isotropic elasticity–on the correlation of theory and experiment for incompressible rubberlike solids, Proceedings of the Royal Society of London A, Mathematical and Physical Sciences, 326 (1972) 565-584.

[11] A.R. Trivedi, C.R. Siviour, A simple rate-temperature dependent hyperelastic model applied to neoprene rubber. Journal of Dynamic Behavior of Materials 6 (2020) 336-347. https://doi.org/10.1007/s40870-020-00252-w

Materials Research Proceedings 69 (2026) 1427-1431 https://doi.org/10.21741/9781644904251-250

Computationally Efficient Fracture Modeling Using a Hybrid Peridynamic Formulation

Mirco ZACCARIOTTO[1,a,*], Sebastiano GALEAZZO[1,b], Francesco SCABBIA[1,c], Ugo GALVANETTO[1,d]

[1]Dep. of Industrial Engineering, University of Padova, Padova, Italy

[a]mirco.zaccariotto@unipd.it, [b]sebastiano.galeazzo@studenti.unipd.it, [c]francesco.scabbia@unipd.it, [d]ugo.galvanetto@unipd.it

Keywords: Crack propagation, Peridynamics, Fast Convolution Based Method

Abstract. The accurate prediction of failure in structural components is a crucial requirement in modern aerospace applications, particularly with the rise of reusable launch systems. Traditional finite element methods, based on Classical Continuum Mechanics, are limited when it comes to modelling discontinuities such as cracks. Peridynamics (PD) theory overcomes these limitations by using integral equations which allow describing a natural and autonomous damage evolution. However, PD suffers from high computational costs, particularly when solved using the commonly adopted mesh-free method with one-point Gaussian quadrature. The Fast Convolution Based Method (FCBM) exploits the convolutional structure of PD equations and the Fast Fourier Transform to critically reduce the computational time. However, it can compromise accuracy in the simulation of crack propagation, due to the damage model adopted. This work presents a novel Hybrid PD method (developed for both the Bond-Based and Ordinary State-Based formulations) that combines the accuracy of PD mesh-free formulation with the efficiency of FCBM, achieving a significant reduction in computational time.

Introduction

The peridynamic (PD) theory, proposed by S.A. Silling [1], is an alternative (nonlocal) framework to the (local) theory of Classical Continuum Mechanics. The mathematical formulation is based on integral equations, rather than spatial derivatives, and it allows modelling long-range interactions between material points within a limited domain with a size defined by a length-scale called *horizon*. Therefore, since discontinuities in the displacement field do not affect the validity of integral operators, Peridynamics is able to *naturally* simulate propagating cracks in an *autonomous* way. Once discretized, peridynamic equations are usually solved through a meshfree method with one point Gaussian quadrature (MM) [2], characterized by a computational complexity $\mathcal{O}(N^2)$ (with N the number of nodes).

Many strategies have been developed to reduce the computational cost of peridynamic simulations [3, 4]. One of the most promising methods is the Fast Convolution Based Method (FCBM) [5, 6], which rewrites PD equations as linear combination of circular convolutions and exploits the FFT algorithm to scale as $\mathcal{O}(N\log_2 N)$.

However, the applicability of this method to crack propagation problems depends on a modified damage model, which is formulated on the basis of a material-point removal approach, as opposed to the standard MM framework, where damage evolution is governed by the progressive breakage of bonds. As a consequence, mass losses are introduced in the regions close to the propagating crack and, sometimes, the crack paths differ from those obtained with MM.

The present work proposes a new hybrid method (Hybrid PD) [7], which combines the FCBM and the MM with the aim of reducing the computational cost while preserving the accuracy of the crack paths predicted by the MM. The method is based on the subdivision of the problem domain into two regions, limiting the application of MM to the points close to the propagating crack (MM

Content from this work may be used under the terms of the Creative Commons Attribution 3.0 license. Any further distribution of this work must maintain attribution to the author(s) and the title of the work, journal citation and DOI. Published under license by Materials Research Forum LLC.

region) and analyzing the remaining part of the domain with the FCBM (FC region). The combination is realized within an overlap region between MM and FC domains, enabling the consistent exchange of peridynamic quantities computed by the two methods. The hybrid method has been developed for the linearized Bond-Based (BB-PD) and Ordinary State-Based (OSB-PD) formulations.

Fast Convolution Based Method

The Fast Convolution Based Method [5], rewrites PD equations as linear combination of circular convolutions to exploit the relation between the Discrete Fourier Transform (DFT) and the circular convolution (for details see [5]). This allows using the optimized FFT algorithm, reducing the computational complexity from $\mathcal{O}(N^2)$ to $\mathcal{O}(N\log_2 N)$.

As an example, consider the i-th component of the internal force density according to the BB-PD formulation [1]:

$$L_i(\mathbf{x},\mathbf{x}',t) = \int_{\mathcal{H}_x} \mu\,(\mathbf{x},\mathbf{x}',t)\mathbf{C}(\boldsymbol{\xi})\boldsymbol{\eta}(\mathbf{x},\mathbf{x}',t)\,dV_{x'}, \quad \mathbf{C}(\boldsymbol{\xi}) = c\;\omega(\|\,\boldsymbol{\xi}\,\|)\frac{\boldsymbol{\xi}\otimes\boldsymbol{\xi}}{\|\,\boldsymbol{\xi}\,\|^2} \tag{1}$$

where μ is the history-dependent integrity function of the bond $\boldsymbol{\xi} = \mathbf{x}' - \mathbf{x}$, $\boldsymbol{\eta} = \mathbf{u}(\mathbf{x}',t) - \mathbf{u}(\mathbf{x},t)$ is the relative displacement, c is a material dependent constant called *micromodulus*, ω is the *influence function* and $\otimes$ denotes the tensorial product.

Following the procedure explained in [5] and exploiting the Einstein's notation, the final convolutional form of Eq. 1 can be written as follows:

$$L_i(\mathbf{x},\mathbf{x}',t) = \chi_B(\mathbf{x},\mathbf{x}')\lambda(\mathbf{x})\{\big[C_{ij}\circledast\big(\chi_B\lambda u_j\big)\big](\mathbf{x},t) - u_j(\mathbf{x},t)\big[C_{ij}\circledast(\chi_B\lambda)\big](\mathbf{x},t)\} \tag{2}$$

where $\circledast$ denotes the circular convolution, χ_B is the characteristic function of the body B defined as follows (see Fig. 1b):

$$\chi_B(\mathbf{x}) = \begin{cases}1 & \mathbf{x}\in B\\ 0 & \mathbf{x}\in\Lambda = \mathbb{T}^d\backslash B\end{cases} \tag{3}$$

and λ is the *integrity index*:

$$\lambda(\mathbf{x},t) = \begin{cases}1 & W(\mathbf{x},t) < W_c\\ 0 & W(\mathbf{x},t)\geq W_c\end{cases}, \quad W_c = \frac{G_0}{2\delta} \tag{4}$$

where W_c is the critical strain energy density and G_0 is the critical energy release rate.

A similar procedure can be employed to obtain the equations of the FCBM according to the OSB-PD formulation [5].

The characteristic function χ_B allows excluding the undesired nonlocal interactions between the material points inside the extension region Λ and the points inside the body domain B (Fig. 1b). The extension region Λ is necessary to build the periodic box $\mathbb{T}^d$ (where d is the spatial dimension of the considered problem) represented in Fig. 1b, which allows exploiting the relation between the circular convolution and DFT, after a proper discretization [5].

The product $\lambda(\mathbf{x})\lambda(\mathbf{x}')$, which is implicitly present in Eq. 2, replaces the standard history-dependent function μ of Eq. 1, which does not have a structure suitable to be expressed as convolution [5]. However, the definition of λ (Eq. 4) implies the removal of fully damaged material points, which inherently results in a reduction of the system mass and may lead to crack paths differing from those predicted by the MM [5].

Hybrid PD

The Hybrid PD method [7] has been developed to restore the "original" damage evolution and crack propagation criterion of the standard damage model and overcome the issues related with the mass loss introduced by the modified damage model of FCBM.

Materials Research Proceedings 69 (2026) 1427-1431 https://doi.org/10.21741/9781644904251-250

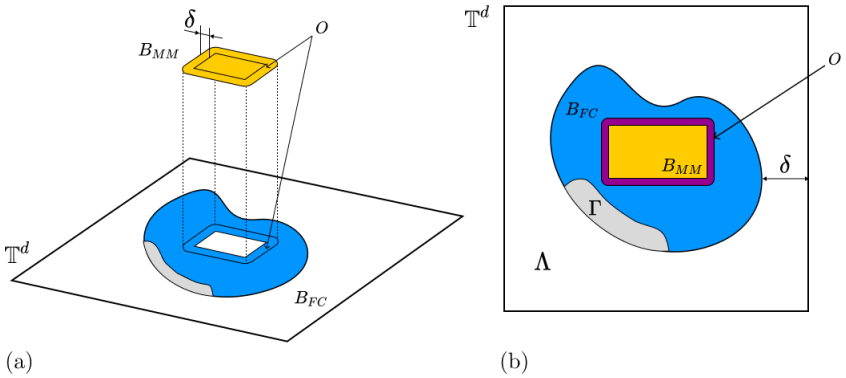


Figure 1: Domains subdivision of periodic box $\mathbb{T}^d$ according to Hybrid PD: the yellow region is analyzed through the MM, while the blue one is analyzed through the FCBM. The purple region is the overlap region.

To apply the hybrid approach, the body domain is split into two regions (see Fig. 1): one analyzed through the MM approach (called *MM region*, B^{MM} and defined by the masking function μ_{MM}) and the other one through the FCBM approach (called *FC region*, B^{FC} and defined by the masking function μ_{FC}). To guarantee the correct application of the method, it must be also ensured that the MM and FC regions share a layer of points of width δ, called *overlap region* and defined by the masking function μ_O, as shown in Fig. 1. Furthermore, the bonds with both ends inside the overlap region must be excluded from the integrals of MM to avoid the introduction of an "overstiffened" zone. This can be achieved with the complementary masking function of the overlap region defined as:

$$\overline{\mu_O}(\mathbf{x}, \mathbf{x}') = 1 - \mu_O(\mathbf{x}, \mathbf{x}') \tag{5}$$

To describe the damage evolution with the standard damage model of the MM, it is necessary to ensure that all points of the FC region are enough away from the propagating crack. This can be achieved by ensuring that the MM region has a minimum width of δ around the crack path in the BB-PD formulation, and a minimum width of 2δ in the OSB-PD formulation.

Based on the BB-PD definition of internal force density, the masking functions introduced above enable a linear combination of the quantities from the MM and FC regions [7]:

$$\begin{aligned} L_i &= L_i^{FC} + L_i^{MM} = \\ &= \chi_{FC}\chi_B\{[C_{ij} \circledast (\chi_{FC}\chi_B u_j)] - u_j[C_{ij} \circledast (\chi_{FC}\chi_B)]\} + \\ &+ \int_{\mathcal{H}_x} \overline{\mu_O}\,\mu_{MM}\mu\; C_{ij}\eta_j\; dV_{x'} \end{aligned} \tag{6}$$

A similar procedure can be applied to derive the hybrid approach equations within the OSB-PD framework, following a careful algebraic reformulation of the peridynamic quantities [7].

Numerical examples

To show the capabilities of the proposed approach, a crack propagation test is carried out on the model depicted in Fig. 2. The model consists of a 0.1×0.04 m^2 rectangular plate of soda-lime glass discretized into a uniform grid 400×160, resulting in a grid spacing $\Delta = 0.25$ mm. A horizon size of 0.75 mm has been adopted, with $\overline{m} = \delta/\Delta = 3$.

Materials Research Proceedings 69 (2026) 1427-1431 https://doi.org/10.21741/9781644904251-250

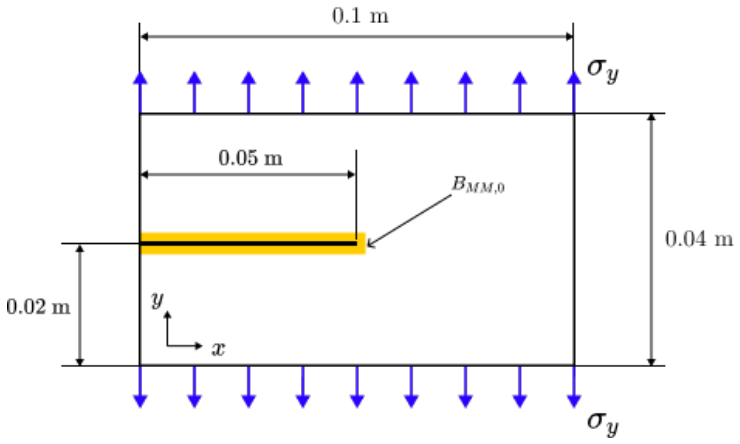


Figure 2: 2D Hybrid BB-PD model for the crack propagation test. $B_{MM,0}$ denotes the initial extension of the MM region.

The material properties of the soda-lime glass are [4]: $E = 72$ GPa (elastic modulus), $\nu = 1/3$ (Poisson's ratio), $\rho = 2440$ kg/m^3 (mass density), $G_0 = 3.8$ J/m^2 (critical energy release rate).

The model has been analyzed through the three methods: MM, FCBM and Hybrid PD. The Hybrid PD simulation has been run with an adaptivity energy threshold of 0.7 W_c. The expected MM region maximum extension is chosen to match the entire domain. A vertical traction load $\sigma_y = 8$ MPa has been used.

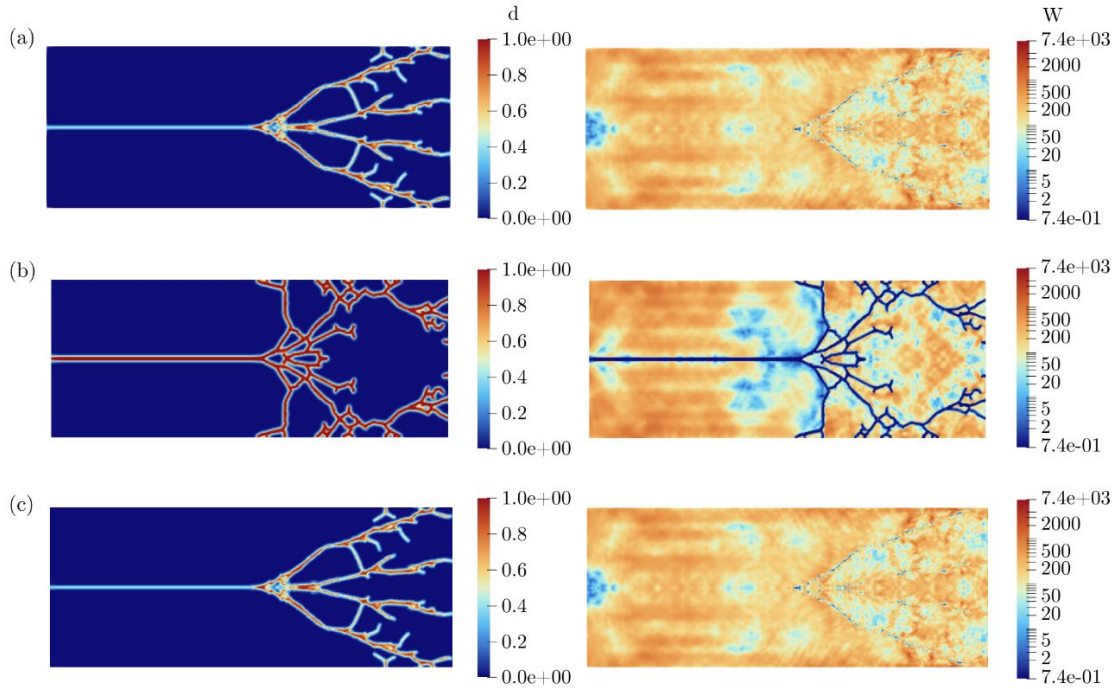


Figure 3: Results of the 2D crack propagation test at $t = 30$ μs, with an externally applied load of 8 MPa. From top to bottom: MM (a), FCBM (b), Hybrid PD with adaptivity (c).

As shown in Fig. 3, the Hybrid PD method reproduces the crack paths and strain energy distribution of the MM, even in the presence of multiple branching features. On the contrary, the FCBM is not able to capture well the branching phenomena. On a laptop computer equipped with 11th Gen Intel Core i3-1115G4 3 GHz dual-core processor and 32 GB of RAM, the MM simulation takes 240 s, while the FCBM and the Hybrid PD method require 40 s and 60 s respectively, with

the Hybrid PD method reducing the computational time by 75% compared to MM for the studied example.

Conclusions

The paper presents a new hybrid approach (Hybrid PD) to combine the FCBM and MM. The method has been developed for the Bond-Based and Ordinary State-Based formulations. The body domain is subdivided into two regions which overlap within a layer of nodes of width equal to δ. The MM application is limited to the MM region located close to the damaged area, while the FCBM is applied to the remaining part of the body.

The Hybrid PD method allows implementing the standard damage model of the MM near the damaged area, restoring the original bond breakage feature of the MM. The size and location of the MM region is adapted throughout the whole simulation through an adaptive strategy. This allows minimizing the extent of the MM application region and analyzing the remaining part of the domain through the FCBM, which significantly reduces computational time thanks to the application of the Fast Fourier Transform algorithm.

Acknowledgements

U.G., M.Z. acknowledge the support received from: Next Generation EU under the call PRIN 2022 PNRR of the Italian Minister of University and Research (MUR); Project P2022HLHHB: A digital framework for the cutting of soft tissues: A first step towards virtual surgery. The Space It Up project funded by the Italian Space Agency, ASI, and the Ministry of University and Research, MUR, under contract n. 2024-5-E.0 - CUP n. I53D24000060005. The University of Padova, Italy under the research projects BIRD2023 NR.237212/23 and NR.232492/23

References

[1] Silling, S.A.: Reformulation of elasticity theory for discontinuities and long-range forces, Journal of the Mechanics and Physics of Solids 48(1), 175-209 (2000). https://doi.org/10.1016/S0022-5096(99)00029-0

[2] Silling, S.A., Askari, E.: A meshfree method based on the peridynamic model of solid mechanics, Computers and Structures 83(17), 1526-1535 (2005). https://doi.org/10.1016/j.compstruc.2004.11.026

[3] Ni, T., Zaccariotto, M., Zhu, Q., Galvanetto, U.: Matrix-based implementation and GPU acceleration of linearized ordinary state-based peridynamic models in MATLAB (2023). https://arxiv.org/abs/2309.11273

[4] Zaccariotto, M., Mudric, T., Tomasi, D., Shojaei, A., Galvanetto, U.: Coupling of fem meshes with peridynamic grids, Computer Methods in Applied Mechanics and Engineering 330, 471-497 (2018). https://doi.org/10.1016/j.cma.2017.11.011

[5] Jafarzadeh, S., Mousavi, F., Larios, A., Bobaru, F.: A general and fast convolution-based method for peridynamics: Applications to elasticity and brittle fracture, Computer Methods in Applied Mechanics and Engineering 392, 114666 (2022). https://doi.org/10.1016/j.cma.2022.114666

[6] Jafarzadeh, S., Mousavi, F., Wang, L., Bobaru, F.: Perifast/dynamics: A matlab code for explicit fast convolution-based peridynamic analysis of deformation and fracture, Journal of Peridynamics and Nonlocal Modeling 6(1), 33-61 (2024). https://doi.org/10.1007/s42102-023-00097-6

[7] Galeazzo, S., Scabbia, F., Galvanetto, U., Zaccariotto, M. A novel hybrid approach for employing the fast convolution-based method in peridynamics with standard peridynamic damage criterion. Submitted for publication.

Materials Research Proceedings 69 (2026) 1432-1437 https://doi.org/10.21741/9781644904251-251

Structural Batteries for Aeronautical Applications: A Multidisciplinary Analysis of Integration and Multifunctional Performance

M. MANGONE[1,a]*, S. MALLARDO[2], C. B. NIUTTA[3], A. CIAMPAGLIA[3], M. GUIDA[1], P. RUSSO[2], G. SANTAGATA[2], R. CIARDIELLO[3], F. MARULO[1], G. BELINGARDI[3]

[1]University of Naples Federico II – Dept. of Industrial Engineering, Naples, Italy

[2]Istituto per i Polimeri, Compositi e Biomateriali (IPCB), Consiglio Nazionale delle Ricerche (CNR), Naples, Italy

[3]Politecnico di Torino - Dipartimento di Ingegneria Meccanica e Aerospaziale, Turin, Italy

[a]mtt.mng98@gmail.com

Keywords: Structural Batteries, Multifunctional Materials, Electrochemical Performance, Experimental Characterization

Abstract. The transition toward electric aviation demands energy storage technologies that overcome the weight limitations of conventional lithium-ion batteries. Structural batteries, capable of simultaneously carrying load and storing electrical energy, offer a promising route toward lighter and more efficient aircraft systems. This work presents the development and experimental evaluation of a type-III structural battery cell concept tailored for aeronautical integration. A multifunctional cell demonstrator was manufactured and tested to assess its electrochemical behavior and verify its feasibility as an energy-storing composite. Considerations on manufacturing scalability and material reclamation further highlight the potential of this approach for sustainable aerospace applications.

Introduction

This paper deals with the manufacturing of a prototype of a cell-like type III core for a laminated structural battery. A type III [1] SB integrates both load-bearing and electrochemical functions within a single multifunctional composite, where carbon fibers act simultaneously as structural reinforcement and active electrodes, and a solid polymer electrolyte serves as both the ionic conductor and matrix material. A key aspect of this study is to prove the multifunctional performance, highlighting the energy storage capability of the cell-like core structure of the SB. An additional focus of this study is the end-of-life management of the multifunctional composite. Unlike conventional crosslinked polymer matrices, the selected solid polymer electrolyte forms reversible physical bonds that can be disrupted through mild mechanical or ultrasonic agitation. This enables the recovery of carbon fibers, glass fibers, and active electrochemical constituents.

Manufacturing of the Cell-like Core of the SB

The complete structural battery (SB) will ultimately be realized through the stacking of multiple lithium-ion cell layers. Each cell is bonded within a tailored stacking sequence designed to meet the specific mechanical and electrical requirements of the intended application. This paragraph explains the details of the manufacturing process of the SB cell.

Content from this work may be used under the terms of the Creative Commons Attribution 3.0 license. Any further distribution of this work must maintain attribution to the author(s) and the title of the work, journal citation and DOI. Published under license by Materials Research Forum LLC.

Materials Research Proceedings 69 (2026) 1432-1437 https://doi.org/10.21741/9781644904251-251

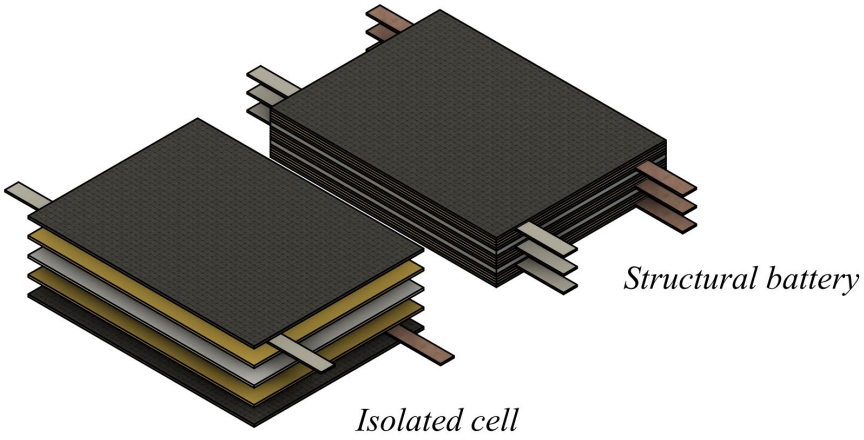


Fig. 1 - structural battery laminate

Cells are manufactured by layering two SPE films (SPE), two carbon fibers twill plies (CF), a glass fiber ply (GF) and the current collectors (cc) though the following stacking sequence (Eq. 1).

$$[CF_{anode}/cc(Cu)/SPE/GF/SPE/cc(Al)/CF_{cathode}] \quad (1)$$

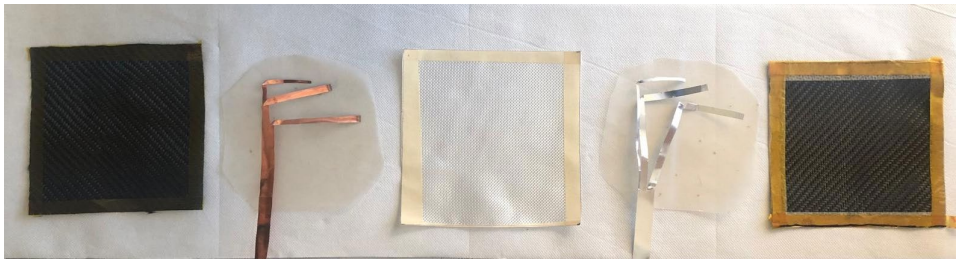


Fig. 2 - cell layup

Material and Methods

The two carbon fiber plies act as cathode and anode. While as anode an untreated ply of carbon fiber can be utilized, the ply acting as cathode is required to be exposed to an active material ($LiFePO_4$) through the process of functionalization [2]. The functionalization is obtained by distributing a solution of $LiFePO_4$**,** nitric acid (65% v/v)**,** hydrochloric acid (35% v/v) and **s**ulfuric acid (pure) onto a plasma treated ply of carbon fiber. The plasma treatment improves the wettability of the carbon fiber surface through cycles of ionized gas injections at high-frequency voltage within a controlled very low-pressure chamber (Diener Pico). The solid polymer electrolyte (SPE) films are manufactured through a one-pot preparation technique. A mixture of polyethylene glycol (PEG), sepiolite (SEP), polyethylene oxide and Lithium triflate (LiTfr), was prepared as follows. In a 400 mL erlenmeyer flask, SEP (1,75 g) was suspended in demi water (250 mL) and 2,63 g of PEG1000 was added. A dispersion/homogenization device (Ultraturrax, IKA T25) was used at 12000 rpm for 15 minutes to obtain a homogenous suspension. The suspension was organo-modified sepiolite (SEPmod) with PEG. The second step was to add in the same flask 87,5 g of polyethylenoxide (PEO) and 8,13 g of lithium triflate (LiTfr) and a dispersion/homogenization device was used at 12000 rpm for 15 minutes more. The resulting suspension was washed 3 times with demineralized water and centrifuged. The precipitate was collected and dried in an oven at 40°C under vacuum overnight (14 hours). The solid polymer electrolyte (SPE), was obtained through their mass solvent mixing (water solvent). To erase stratification effect after solvent evaporation and to uniformize composition, the obtained

Materials Research Proceedings 69 (2026) 1432-1437 https://doi.org/10.21741/9781644904251-251

compound was chopped in very small parts and dried at 40°C for 24 hours, under vacuum, so to remove the moisture. Finally, the SPE films (Fig. 3) were prepared by using a table hydraulic hot-press (Collin Press Model P100) at 130°C and subjected to 0 bar (thermal ramping) for 5 minutes, 20 bar for 3 minutes, 40 bar for three minutes, followed by a rapid quenching phase.

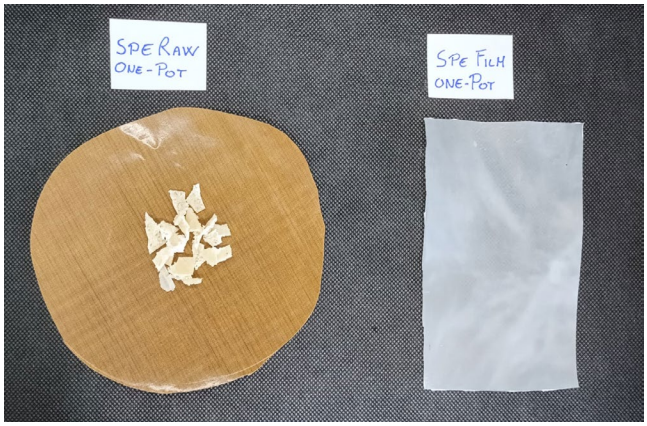


Fig. 3 - raw and film state of SPE

For energy storage characterization, a 300x300 mm cell was manufactured (Fig. 4). The assembly of the laminate was conducted following a tuned thermal-pressure cycle, allowing for the correct flow of the SPE within the carbon fiber bundles, acting as matrix and fixing the structure of the cell. The stacked unbound components (Fig. 2) were inserted in the table hydraulic hot-press (Collin Press Model P100) at 60°C and subjected to the same pressure and quenching profile followed for the SPE manufacturing.



Fig. 4 - assembled structural battery cell

To avoid the carbon fibers layers to be in contact at the cell border, and the consequential short-circuiting, the glass fiber separator was extended beyond the cell edges and polyimide film (Kapton) tape was added to those critical areas. All the processes employed in the fabrication of the SPE and the full cell are meant to be easily scalable for mass production.

Table 1 - cell geometry and physical properties

Plan view dimensions [mm]	300x300
Thickness [mm]	0.855
Mass [kg]	0.140

Materials Research Proceedings 69 (2026) 1432-1437 https://doi.org/10.21741/9781644904251-251

Energy Storage Characterization of the Structural Battery Cell

An enabling step for the development of the full laminate SB is the characterization of the isolated cell energy storage performance. A CC/CV bench power supply tailored for lithium-ion batteries was used for charging the cell to its estimated maximum capacity. Due to the experimental nature of the cell, a 0.1C charging current was employed. In order to properly estimate the current to supply, as a first assumption, weight-specific capacity was assumed identical to already proven similar specimen found in literature [3], equal to 8.55 Ah/kg. Due to testing on previous iterations of the cell [4], a 2.7 V maximum voltage was selected for the CC/CV switch activation. The charging cycle was terminated once the absorbed current reached 60 mA, equal to C/20, following industry standard. To avoid the formation of metallic dendrites and consequential internal short-circuiting, a 2.1 V lower cut-off voltage was considered when discharging the cell. From the resulting discharging curve (Fig. 5), it was possible to extrapolate the energy storage capabilities of the cell.

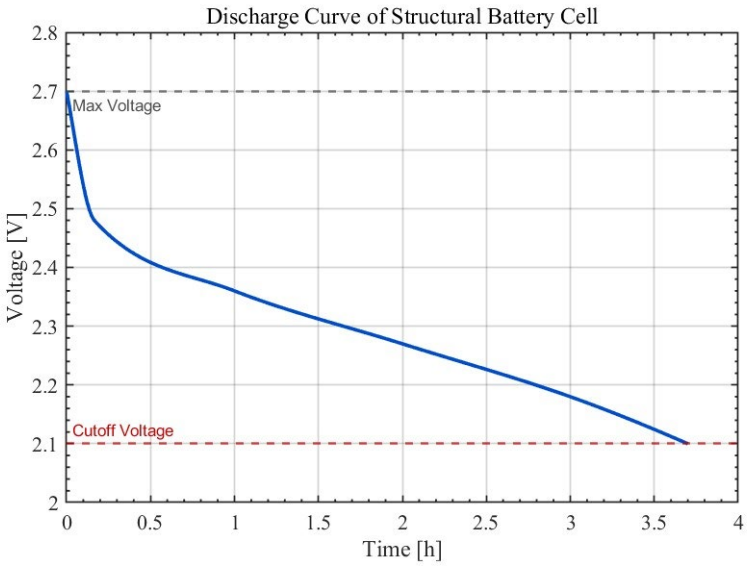


Fig. 5 - discharge curve of structural battery cell

Table 2 - cell energy storage performances

Specific capacity [Ah kg^{-1}]	2.69
Energy density [Wh kg^{-1}]	6.19
Specific average power [W kg^{-1}]	1.67
Cell mass [kg]	0.140

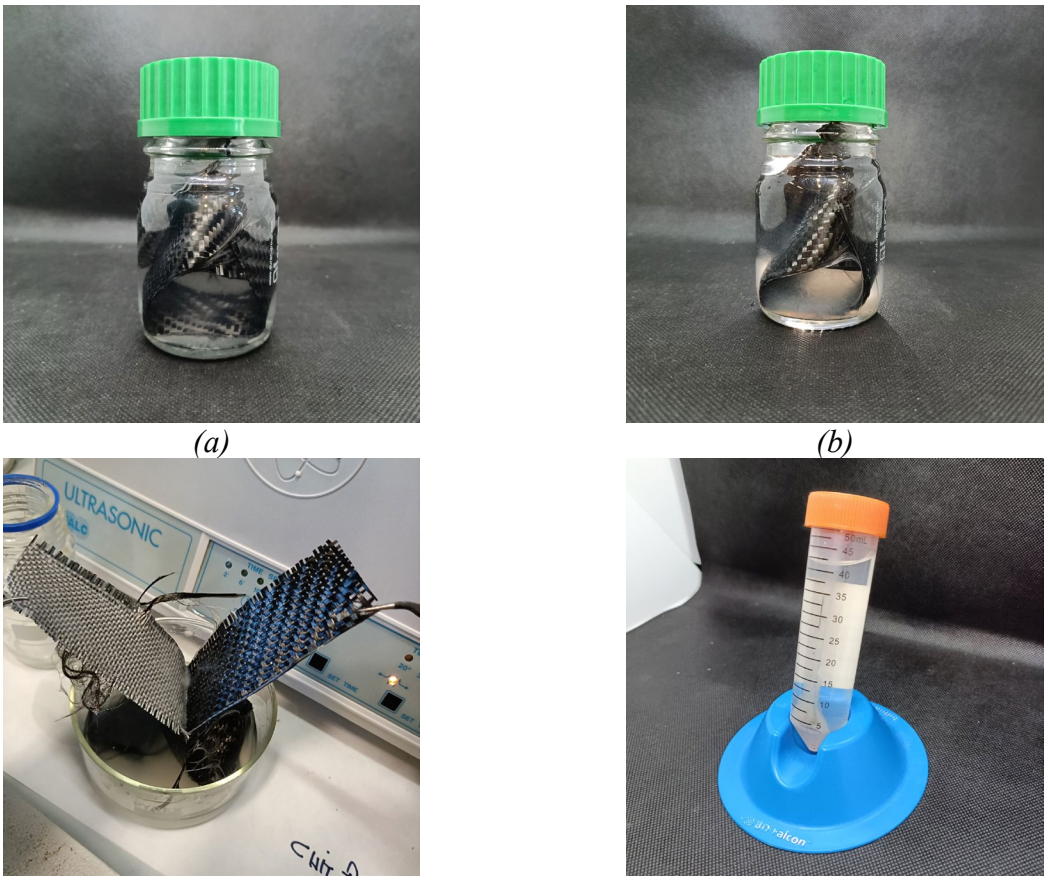
SB Laminate

To enhance the energy storage performance per unit area of the proposed structural battery (SB), multiple cells will be stacked (Fig. 1). A secondary material will be employed to bond the cells, serving as an interface matrix and improving the overall mechanical integrity of the assembly. Future studies will address the selection of this interfacial material and the mechanical characterization of the resulting laminate. The matrix is required to provide electrical insulation between adjacent cells. Potential aeronautical applications of such SB laminate include non–structurally-critical secondary components [5,6] where multifunctionality can provide tangible mass and volume savings without imposing excessive certification burden. Examples include access panels and cabin interior panels. The adoption of SB laminates in these zones would enable progressive validation within a reduced regulatory envelope, serving as a stepping-stone toward

future integration in higher-criticality composite structures. Further studies will be conducted once a full laminated SB specimen will be manufactured.

Material Reclamation

A defining feature of the proposed structural battery (SB) is its intrinsic disassemblability (Fig. 6), which enables efficient end-of-life recovery and reuse of its constituent materials. The SPE matrix provides physical bonding between the carbon and glass fiber plies without forming irreversible chemical crosslinks. As a result, the laminate can be mechanically dissociated. Preliminary experiments show that an ultrasonic bath (Falc Ultrasonic, 22 min at 30 °C) effectively disrupts the polymer matrix, allowing the separation of the carbon fiber and glass fiber layers. The resulting suspension contains Sepiolite, $LiFePO_4$, lithium triflate, PEO, and PEG. Subsequent centrifugation (Hermle Z326K, 15 min at 6000 RPM) enables selective precipitation of Sepiolite, $LiFePO_4$, and lithium triflate, yielding distinct solid fractions suitable for direct recovery or reprocessing. The remaining polymer-rich aqueous phase, composed primarily of hydrated PEO and PEG, can be dried to obtain a reusable polymer mixture with potential applications in various industrial sectors, particularly where low-molecular-weight polyethylene oxides are required.



(a) *(b)* *(c)* *(d)*

Fig. 6 – material reclamation process (a): preparation for ultrasonic water bath (b): SPE dispersed in water solution (c): fiber recovery (d): precipitation of constituents

Summary

This work demonstrates the fabrication and characterization of a type-III structural battery cell. Carbon fibers act as both structural reinforcement and active electrodes, while a solid polymer electrolyte ensures ionic conduction and laminate cohesion. A functionalized $LiFePO_4$ cathode, a

controlled hot-pressing cycle, and a scalable manufacturing route enabled the production of a 300×300 mm demonstrator. Electrochemical testing confirmed the cell's ability to store and deliver energy, validating the multifunctional concept. A preliminary end-of-life recovery process was also established, showing that the cell can be disassembled and its constituent materials reclaimed through mild mechanical treatments. More sustainable replacements for the acid solution required for the functionalization phase will be investigated.

References

[1] Adam T. J., Liao G., Petersen J., Geier S., Finke B., Wierach, P. & Wiedemann M., Multifunctional composites for future energy storage in aerospace structures (2018) https://doi.org/10.3390/en11020335

[2] Hagberg J., Leijonmarck S. & Lindbergh G, High precision coulometry of commercial PAN-based carbon fibers as electrodes in structural batteries, Journal of The Electrochemical Society, 163(8), A1790 (2016) https://doi.org/10.1149/2.0041609jes

[3] Asp L. E., Bouton K., Carlstedt D., Duan S., Harnden R., Johannisson W. & Zenkert D., A structural battery and its multifunctional performance, Advanced Energy and Sustainability Research, 2(3), 2000093 (2021) https://doi.org/10.1002/aesr.202170008

[4] Di Mauro Gennaro (2024), A multidisciplinary approach for Structural Batteries integration in Aeronautical Applications, Doctoral Thesis (2024)

[5] Di Mauro Gennaro, Guida Michele & Gomez L. Olivares Gerardo, Safety Design Approach for Structural Batteries Integration in Composite Structures by Means of Multiphysics Analysis (2024) https://doi.org/10.1007/978-3-031-77697-7_19

[6] Di Mauro Gennaro, Guida Michele, Olivares Gerardo & Gomez Luis, Structural batteries challenges for emerging technologies in aviation (2023) https://doi.org/10.21741/9781644902813-88

Materials Research Proceedings 69 (2026) 1438-1443 https://doi.org/10.21741/9781644904251-252

Design and Prototyping of a Lunar Rover Wheel Using Additive Layer Manufacturing

Gaetano IPPOLITO[1,a *], Rosario BORRELLI[1,b], Stefania FRANCHITTI[1,c], Marco RUSSO[1,2,d], Nunzia FAVALORO[1,e]

[1]Italian Aerospace Research Centre (CIRA), Via Maiorise 1, 81043, Capua, Italy

[2]Department of Chemical, Materials and Production Engineering, University of Naples Federico II, Piazzale Tecchio 80, 80125, Naples, Italy

[a]g.ippolito@cira.it, [b]r.borrelli@cira.it, [c]s.franchitti@cira.it, [d]marco.russo8@unina.it, [e]n.favaloro@cira.it

Keywords: Space Exploration, Technologies, Rover, Wheel, FEM, ALM, DfAM, EB-PBF

Abstract. The continued global interest in human and robotic Moon exploration has ramped up the demand for innovative engineering solutions that can overcome the challenges of the harsh lunar environment. These challenges include extreme temperature fluctuations, abrasive regolith particles, ionising radiation, low gravity, and the constraints of transporting equipment or spare parts from Earth. In this context, the development of robotic systems and components requires a careful balance among structural performance, weight efficiency, and manufacturability. This paper presents a case study, performed in the framework of the *CIRA-TEDS Program* [1], on the design and manufacture of a lunar mini rover's wheel prototype, using *additive layer manufacturing* (ALM) and *design for additive manufacturing* (DfAM) techniques. Starting from high-level mission and environmental requirements, a reverse integration process ensures alignment between system objectives and wheel design. A hybrid design approach combining *Topological Optimisation* (TO) and *Generative Design* (GD) was applied, supported by *Finite Element Method* (FEM) analysis to evaluate structural behaviour and guide iterative improvements. The wheel was manufactured in Ti6Al4V using *Electron Beam Powder Bed Fusion* (EB-PBF). Although physical testing is planned, current results show that GD outperforms conventional designs in stress distribution and weight reduction. The study proposes a replicable framework integrating system-level requirements, DfAM, and ALM to accelerate the development of space-ready hardware for future lunar and planetary missions.

Introduction

Designing mobility systems for lunar rovers involves overcoming challenges posed by the Moon's harsh surface and environment. Lunar regolith is abrasive, electrostatically active, and offers low traction, making traditional wheel designs ineffective. Specialized wheels with flexible structures and grousers have been developed to enhance mobility, load distribution, and energy efficiency [2]. Wheel failure risks include entanglement, sinkage, and traction loss [3]. Therefore, wheel design is critical to mission success. Rover design begins with mission requirements, which guide subsystem specifications and design drivers through a structured engineering process [4]. To this end starting from a preliminary design, a hybrid approach combining topological optimisation (TO) and generative design (GD) was employed. These two tools offer complementary capabilities, TO identifies the most efficient material distribution based on constraints and applied loads [5], while GD explores different configurations that can be adapted to various manufacturing technologies [5]. Recent studies [6, 7] have demonstrated that integrating these two techniques yields superior design optimisation and efficiency. The software used to perform topological optimisation and generative design was Autodesk Fusion 360®. To evaluate structural behaviour

Content from this work may be used under the terms of the Creative Commons Attribution 3.0 license. Any further distribution of this work must maintain attribution to the author(s) and the title of the work, journal citation and DOI. Published under license by Materials Research Forum LLC.

and support iterative improvements during the design process, Finite Element Method (FEM) analysis was conducted using Abaqus® software.

A prototype for the virtual model validation means experimental testing

In the context of lunar exploration missions, the development of mechatronic systems, such as planetary rovers, demands extremely stringent requirements in terms of reliability and predictability of operational behaviour. Space systems are launched in their final configuration, with no possibility of post-deployment intervention or correction. This constraint makes it essential to build robust numerical models capable of simulating lunar environmental conditions. The accuracy of the model is directly related to the system's ability to operate autonomously and safely in unpredictable environments [8], and the validation of the numerical model must be performed using rigorous methods, as it is the only tool available to anticipate the behaviour of the system once in mission. Representative prototype enables this correlation, particularly in the presence of complex interactions such as wheel-ground dynamics, where phenomena such as slippage, sinkage, and soil compaction significantly affect mobility performance [9]. The validation of virtual models through experimental testing is a cornerstone in the development of reliable engineering systems. Physical prototypes serve as tangible benchmarks to assess the accuracy of simulations, especially in complex domains such as aerospace, robotics, and engineering. One of the most revolutionary factors in this validation process is the ALM, which is particularly valuable in space applications [10]. In conclusion, experimental testing supported by manufacturing through ALM provides a solid framework for validating virtual models, bridging the gap between simulation and reality, and innovation through iterative design.

From the High-Level Robotic System Requirements to the Component

In the development of space robotic systems, the transition from high-level system requirements to individual components is a critical phase that ensures traceability, consistency, and technical integrity throughout the engineering process. According to ECSS-E-ST-10C, system engineering shall implement a structured requirements breakdown process to establish a validated technical framework for system-level requirements into subsystem and component-level. To formalize this derivation, a tree procedure is defined that maps system-level mobility requirements to wheel geometry parameters. For instance, the Lunar Rover Optimization Platform (LROP) developed at NASA Glenn Research Center [11] demonstrated how variations in wheel geometry and center-of-gravity positioning directly affect slope ascent capability and obstacle negotiation. Similarly, it has been demonstrated that grouser configuration significantly influences terrain deformation and traction performance, validating the reverse integration methodology through simulation and experimental testing [12]. Through reverse engineering, rover platforms are analysed to extract the needed subsystem performance and interactions. This information allows to understand the capabilities that the wheel as a component should have, such as locomotion efficiency on granular regolith, maximum permissible slope before tilting, thermal resistance during prolonged exposure to the lunar day, structural resilience during launch, landing, and soil reaction loads. From these inputs, component-level requirements for the wheel are released, such as rolling resistance, maximum drawbar-pull force, slippage, and mass and volume constraints to maintain rover stability and minimize energy consumption. Starting from the System Technical requirements, the rover classification is focused on Sub-R range [13], the procedure used incorporates Terramechanics models [14], such as Bekker’s pressure-sinkage equation, Wong-Reece shear stress models, and wheel-soil interaction model dynamic constraints as slip ratio, normal load, and soil mechanical properties, enabling parametric optimization of Wheel geometry as reported in Table 1. Titanium alloy has been selected as the wheel material, in accordance with the design heritage and performance requirements observed in both recent and planned lunar exploration missions.

Materials Research Proceedings 69 (2026) 1438-1443 https://doi.org/10.21741/9781644904251-252

Table 1. Wheel Geometrical Parameters and Boundary Conditions

Preliminary Geometrical Parameters			*Boundary Conditions*	*FEM*		*GD*	
Diameter	50	[mm]	Wheel load	0,406	[N]		
Width	10	[mm]	Gravitational Acceleration	1,625	[m/s^2]		
Grousers Height	5	[mm]	Translational velocity	0,02	[m/s]	-	
Number of Grousers	12		Rotational Wheel Velocity	1	[rad/s]	-	
Number of Spokes	6		Slip ratio	20	[%]	-	
			Axial Torque	-		0,01	[Nm]

Design for Additive Manufacturing

The wheel was re-designed using the Design for Additive Manufacturing (DfAM) approach to refine the preliminary geometry defined through reverse engineering of the rover architecture and maximise the advantages offered by ALM. The objective was to determine the optimal number of spokes and the best material distribution along them. The initial stage of the topology optimisation analysis involved the identification of the design space. This region was confined to the volume between the Central Hub and the Outer Rim, with the Central Hub excluded from the optimisation process in order to preserve its structural and functional integrity. This was implemented by defining it as Preserve Region. Subsequently, to ensure uniform deformation distribution in all directions, two orthogonal symmetry planes intersecting at the wheel axis were assigned. The applied load conditions were configured to simulate the operational conditions of the wheel on the lunar surface (*Table 1*). The ground-wheel tread contact was simulated by constraining the faces of the Outer Rim and Grousers over an angular sector of ±34°. The material assigned as described in the previous section is Ti6Al4V alloy. The optimization criteria adopted were the strategy proposed by the software, in particular, the maximization of stiffness and a target mass set to automatic. The decision not to set a target mass value was because the objective of topological optimization is to provide only an efficient preliminary design. The solution obtained proposed a preliminary design involving four spokes connecting the Central Hub to the Outer Rim, with a spatial distribution more concentrated towards the side of the wheel corresponding to the Central Hub assembly interface, which is the area expected to experience higher stress concentration. The preliminary configuration yielded substantial data on material distribution, which was then assessed to verify structural efficiency. Analysis revealed extremely low stress levels (a maximum Von Mises stress of 0.137 MPa) and a high safety factor of around 6500, indicating that the design was considerably oversized. These results highlighted the potential for further optimisation, leading to the development of a lighter three-spoke configuration in the subsequent Generative Design phase. Following the results obtained from topological optimization, a Generative Design study was performed with the aim of developing a geometry that would satisfy the wheel design constraints and that could be manufactured through additive manufacturing. Prior to the implementation of the generative study setup, it was necessary to prepare the functional geometries in the Autodesk Fusion Design environment. In particular, three groups of functional geometries were modelled. First, the *Preserve Geometries,* included the Central Hub and the Outer Rim with the Grousers, which were kept unaltered due to functional and interface constraints. Second, the *Obstacle Geometries,* represented the volumes in which material generation is not allowed. Specifically, an internal axial cylinder was modelled inside the Central Hub to ensure mechanical coupling, while an external cylinder concentric to the Outer Rim prevented the generation of material in the Wheel Tread and Grousers areas. Two additional lateral cylinders were also modelled on the outer faces of the wheel with the aim of limiting the growth of material along the axial direction. Finally, the *Starting Shape* was modelled on the qualitative results obtained in the topological optimization phase. This initial configuration consisted of a wheel with three solid cylinders, representing the spokes positioned radially at 120° to the axis of rotation. To ensure a

Materials Research Proceedings 69 (2026) 1438-1443 https://doi.org/10.21741/9781644904251-252

structurally balanced and symmetric outcome, three symmetry planes were defined into the model. Specifically, a primary reference plane at 0°, aligned with the vertical diameter of the wheel, and two additional inclined planes at ± 120°, introduced to further constrain material distribution along the spokes. The boundary and load conditions were assigned in the same manner as in the topological optimization analysis. The generation objective was set to minimize mass, with the production method specified as Additive Manufacturing. The Additive Manufacturing method requires the definition of a series of parameters, including the growth direction of the component (in this case, all directions were permitted), the minimum wall thickness set at 2 mm, and the overhang angle set at 45°. As in the previous phase, the material assigned for the study was Ti6Al4V. All the solutions generated by the Generative Design study followed the predefined constraints and reflected the design intent of maximising spatial efficiency. While the shapes of the spokes were different, they always kept the same connection to the areas to be preserved, respected symmetry conditions, and met the manufacturability requirements imposed by additive manufacturing technologies. Furthermore, no material was generated within the volumes defined as obstacles, ensuring clean integration with the functional zones. The new configuration obtained allowed for significant improvements in material distribution. The selected geometry features three symmetrical spokes arranged radially at 120°, connecting the Central Hub to the Outer Rim. The resulting design achieved a total mass of 23.402 grams, representing a mass reduction of 21% compared to the preliminary wheel design configuration. The wheel obtained through generative design has been referred to for the rest of the document as 3-Spoke GD wheel.

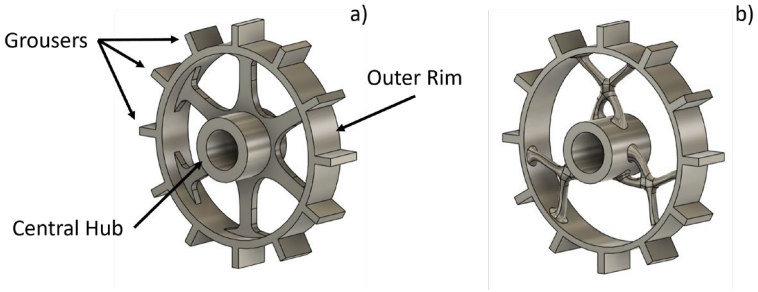


Figure 1. Preliminary Wheel Design vs GD Wheel Design

Numerical Validation of the Generative Design Prototype

The use of the FEM is of fundamental importance in the design of mobility systems for the lunar surface, where unique environmental conditions such as low gravity, vacuum, and the mechanical behaviour of the lunar regolith pose significant challenges to experimental validation. The virtual analysis strategy employed is applicable to the lunar exploration wheels and is inspired by the work done in [15]. The virtual structural assessment of the rover wheel on the lunar surface involves four steps: *Initial Step* where soil conditions are set using predefined fields, initializing vertical and horizontal stresses based on material properties and void ratio; *Gravity Step* were gravity is activated and internal soil stresses are balanced; *Attitude Step* where the wheel load is applied, establishing static equilibrium and contact patch; finally the *Rolling Step* where wheel motion is simulated with constant vertical load and ramped velocity, capturing dynamic wheel-soil interaction and footprint formation. In the initial phase of wheel design, a traditional six-spoke configuration was selected for its symmetry and structural reliability. However, applying generative design techniques, as shown in *Figure 1,* led the algorithm to converge on a three-spoke solution, which met the same mechanical and functional performance criteria. This outcome demonstrated a higher structural efficiency, challenging conventional assumptions by optimizing load paths and material distribution. Despite the radical change in geometry, both designs were developed to endure identical operational loads and conditions. The generative design maintained attitude and rolling performance while achieving a 21% mass reduction, a critical advantage in

Materials Research Proceedings 69 (2026) 1438-1443 https://doi.org/10.21741/9781644904251-252

space robotic applications due to its impact on energy consumption and inertial response. From a structural standpoint, stress analysis revealed that during the attitude step, the equivalent von Mises stress increased by 303% (*Figure 2*), attributed to a worst-case loading condition not supported by a spoke. Nevertheless, the design remained within acceptable safety margins for lunar use.

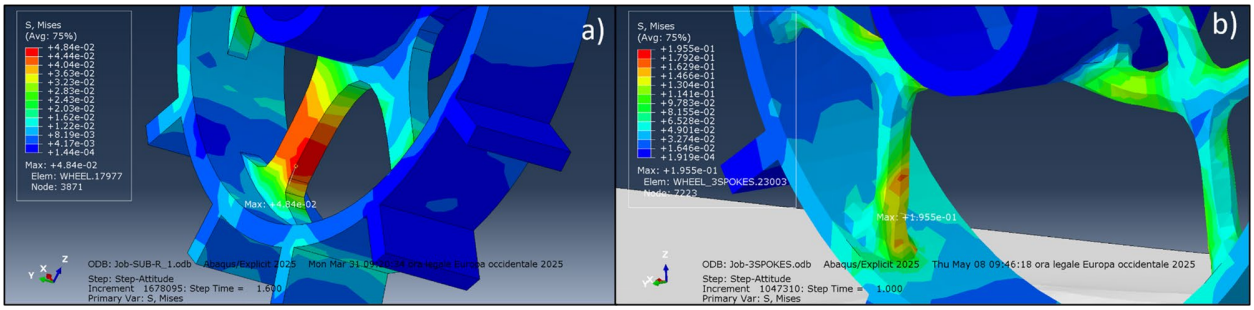


Figure 2. Wheel Stress State during Attitude Step. a) Preliminary Design; b) Generative Design

During the Rolling step, stress increased by about 30%, still within structural limits, confirming the generative design's mechanical integrity under nominal dynamic conditions (*Figure 3*). Overall, the comparison underscores how algorithm-driven approaches can reduce material usage and refine engineering assumptions, offering optimized structures without compromising performance, and paving the way for further structural innovation.

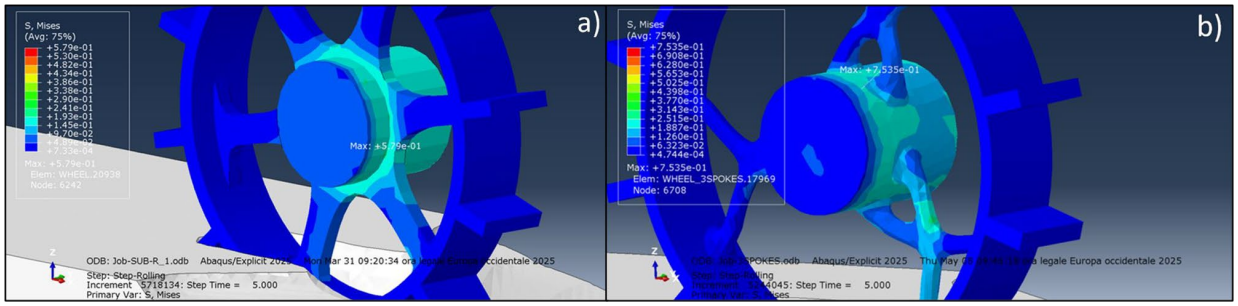


Figure 3. Wheel Stress State during Rolling Step. a) Preliminary Design; b) Generative Design

Conclusions and Perspectives

This paper presents a replicable framework for designing and manufacturing lightweight lunar rover components, integrating system-level requirements with DfAM principles and ALM technologies to optimize performance and adaptability. A conventional six-spoke wheel design was initially adopted for structural symmetry and load handling. However, generative design algorithms, through constraint-based optimization and iterative simulation, proposed a structurally compliant three-spoke configuration, minimizing mass without compromising integrity. This challenges traditional design paradigms and highlights the potential of computational design exploration. Future validation through FEM analysis and physical testing will ensure feasibility under lunar conditions.

References

[1] N. Favaloro, G. Saccone, F. Piscitelli, R. Volponi, P. Leoncini, P. Catalano, A. Visingardi and M. C. Noviello, "Enabling Technologies for Space Exploration Missions: The CIRA-TEDS Program Roadmap Perspectives," Aerotecnica Missili & Spazio, vol. 102, no. 3, pp. 187-197, 2023. https://doi.org/10.1007/s42496-023-00159-4

[2] J. L. Wong, Theory of Ground Vehicles, John Wiley and Sons Inc., 2008.

[3] Y. Wang, Space Robotics, Springer, 2021.

[4] G. Puleo, G. I. N. Favaloro e M. Grassi, «Preliminary Design of Mini-Rovers in Swarm Configuration for a Moon In-Situ Resource Utilization Mission,» in 75th International Astronautical Congress (IAC), Milan, Italy, 2024, https://doi.org/10.52202/078357-0201

[5] J. Srivastava e H. Kawakami, «Systematic Review of Difference Between Topology Optimization and Generative Design,» IFAC-Papers online, vol. 56, n. 2, pp. 6561-6568, 2023, https://doi.org/10.1016/j.ifacol.2023.10.307

[6] O. Lkadi, M. Nassraoui and O. Bouksour, "Optimization of Lightweight Components through Hybrid Topology Optimization and Generative Design in Additive Manufacturing," Key Eng Mater, vol. 1018, p. 67–76, 2025. https://doi.org/10.4028/p-jWOR8x

[7] L. Zhang, Z. Li and H. Ying, "Lightweight Design Process Combining Generative Design and Topology Optimization Based on Fusion 360 and ANSYS: A Case Study of a Biped Robot's Arch Component," International Journal of Precision Engineering and Manufacturing, vol. 26, p. 1775–1788, 2025. https://doi.org/10.1007/s12541-025-01226-5

[8] K. Iagnemma and S. Dubowsky, Mobile Robots in Rough Terrain: Estimation, Planning and Control with Application to Planetary Rovers, Springer Tracts in Advanced Robotics, Vol. 12, 2004. https://doi.org/10.1007/b94718

[9] A. Aboubakar, R. Alhammadi, Y. Zweiri and L. Seneviratne, "Advance Simulation Method for Wheel-Terrain Interactions of Space Rovers: A Case Study on the UAE Rashid Rover," in 21st ICAR, Abu Dhabi, UAE, 2023. https://doi.org/10.1109/ICAR58858.2023.10406669

[10] I. Gibson, D. Rosen and B. Stucker, Additive Manufacturing Technologies - 3D Printing, Rapid Prototyping, and Direct Digital Manufacturing, New York: Springer, 2014.

[11] K. Zhang, Y. Zhang, J. Shi and W. Kong, "Modeling of Lunar Rover Vehicle Wheel-Soil Interaction Using Fem-Dem Method," in 11th ISTVS, 2022. https://doi.org/10.56884/OTLT5367

[12] J. Kamohara, V. Ares, J. Hurrell, K. Takehana, A. Richard, S. Santra, K. Uno, E. Rohmer and K. Yoshida, "Modeling of Terrain Deformation by a Grouser Wheel for Lunar Rover Simulation," in 12th ISTVS, Yokohama, Japan, 2024.https://doi.org/10.56884/fryx2uhe

[13] M. Conroy, "Florida Space Institute - Rover Classification," [Online]. Available: https://fsi.ucf.edu/wp-content/uploads/sites/4/2021/07/FSI-Rover-Classification-Details.pdf

[14] M. G. Bekker, Introduction to Terrain-Vehicle Systems, The University of Michigan Press, 1969.

[15] J. Pruiksma, J. Teunissen, G. Kruse and M. Van Winnendael, "Tractive Performance Modelling of the Exomars Rover Wheel Design on Loosely Packed Soil Using the Coupled Eulerian Lagrangian Finite Element Tecnique," 2011.

Materials Research Proceedings 69 (2026) 1444-1449 https://doi.org/10.21741/9781644904251-253

Numerical Modeling and Fabrication of Hybrid Metal-Ceramic Structures for Space Applications Using FDM Additive Manufacturing

Enrico ZAPPINO[1,a *], Matteo FILIPPI[1,b] and Alfonso PAGANI[1,c]

[1]MUL2 Lab, Department of Mechanical and Aerospace Engineering, Corso Duca degli Abruzzi 24, 10129, Torino, Italy

[a]enrico.zappino@polito.it, [b]matteo.filippi@polito.it, [c]alfonso.pagani@polito.it

Keywords: Additive Manufacturing, Fused Deposition Modeling, Metal–Ceramic Co-sintering, Thermal Protection Systems

Abstract. This study explores the fabrication of hybrid metal–ceramic structures for space applications using Fused Deposition Modeling (FDM) additive manufacturing. Combining metals and ceramics enables components with both high strength and thermal resistance, but property mismatches at interfaces cause stress and deformation. Numerical simulations were conducted to design optimized interfaces that minimize these effects. A three-step process involving printing, debinding, and sintering was developed for 316L steel and zirconia. Results demonstrate that engineered interfaces significantly improve bonding and mechanical reliability, offering a viable route for advanced aerospace components.

Introduction

The growing demand for materials capable of withstanding extreme environments in aerospace and propulsion systems has intensified research on advanced hybrid structures. Components exposed to re-entry or combustion conditions must resist steep temperature gradients and large thermal stresses [1]. Ceramic materials exhibit outstanding thermal stability and oxidation resistance, but their brittleness and low fracture toughness limit structural reliability. Metals, conversely, provide ductility and strength but degrade at high temperatures. Combining both in metal–ceramic hybrids could, in principle, merge their advantages; however, mismatches in thermal expansion, sintering shrinkage, and elastic modulus generate severe interfacial stresses, often causing cracking, delamination, or residual deformation [2–4].

Functionally Graded Materials (FGMs) were conceived to overcome these issues by introducing a continuous or stepwise variation in composition or microstructure between dissimilar materials. This gradual transition reduces property discontinuities and redistributes stresses generated during fabrication or thermal loading [5]. Several studies have demonstrated the feasibility of such systems—for instance, multilayer ZrO_2–NiCr composites fabricated through shrinkage-matching sintering [6] or zirconia–steel laminates optimized for compatible densification and thermal expansion [7]. Despite these results, traditional FGMs remain largely restricted to research activities. Their production is technically complex, costly, and difficult to scale. Conventional methods such as tape casting, lamination, and powder metallurgy require precise control of particle packing, sintering rates, and geometry; small mismatches can induce warping or fracture. These limitations have hindered the industrial deployment of FGMs, confining them to academic prototypes or specialized demonstrators [2,5]. The advent of Additive Manufacturing (AM) has revitalized interest in functionally graded and multi-material structures. By depositing material layer by layer, AM enables unprecedented geometric freedom and localized composition control. Among AM techniques, Fused Deposition Modeling (FDM) has attracted attention for its simplicity, scalability, and compatibility with thermoplastic feedstocks loaded with ceramic or metallic powders [8,9]. This process allows the fabrication of hybrid parts with tailored interfaces, where the local material composition can be precisely adjusted within the same build.

Content from this work may be used under the terms of the Creative Commons Attribution 3.0 license. Any further distribution of this work must maintain attribution to the author(s) and the title of the work, journal citation and DOI. Published under license by Materials Research Forum LLC.

Materials Research Proceedings 69 (2026) 1444-1449 https://doi.org/10.21741/9781644904251-253

Recent developments in thermoplastic extrusion-based AM have extended these capabilities further. By employing paraffin- or wax-based binders with high powder loading (up to 50 vol%), it is now possible to co-deposit different materials—such as metals and ceramics—within a single printing process [10]. Careful tuning of feedstock rheology, deposition parameters, and sintering schedules enables co-sintered components that are dense, homogeneous, and free of cracks. Studies on stainless steel and zirconia composites have shown that such hybrid parts can be sintered successfully when the shrinkage and thermal behavior of both materials are properly matched [10,11]. Moreover, graded architectures combining dense and porous regions have been demonstrated, highlighting the potential of thermoplastic AM to produce lightweight and multifunctional components [12].

Alongside experimental advances, numerical modeling has become essential for understanding the thermo-mechanical behavior of such systems. Early viscous and viscoelastic formulations by Green and colleagues [3,4] demonstrated that small mismatches in densification rate can induce tensile stresses sufficient to cause warping or cracking in layered ceramics. Building on these concepts, recent finite element (FE) simulations have incorporated phase transformation, plastic deformation, and cohesive interfaces to capture the evolution of stress, deformation, and delamination in hybrid laminates [13]. These models provide predictive tools for optimizing interface design and processing parameters before experimental trials.

The present study combines thermo-mechanical modeling with extrusion-based AM to design and fabricate metal–ceramic hybrid structures suitable for aerospace applications. The objective is to exploit the geometric and compositional control of additive manufacturing to engineer graded or architected transition zones—flat, wavy, or lattice-like—that minimize residual stresses after sintering. Through the integration of modeling and experimental validation, this approach demonstrates a viable pathway to overcome the long-standing manufacturing difficulties that have limited FGMs to academic research, paving the way for structurally reliable, thermally resistant multi-material components for next-generation space systems.

Printing process

The fabrication process is based on Fused Deposition Modeling (FDM) using a Mingda MD-400D 3D printer equipped with dual extrusion and temperature-controlled nozzles and build plate. The feedstock materials are Zetamix filaments (Nanoe, France), thermoplastic compounds containing fine 316L stainless steel or 3Y-TZP zirconia powders uniformly dispersed in a polymeric binder. After printing, the green parts undergo chemical debinding in acetone using a ultrasonic bath.

Final densification of the green part is performed in a Zetasinter tube furnace, providing precise temperature and atmosphere control. According to the literature [5–7,13], 316L stainless steel and zirconia are among the most compatible pairs for co-sintering, exhibiting similar shrinkage behavior and comparable coefficients of thermal expansion (≈10–11 × 10^{-6} K^{-1}). These characteristics reduce interfacial stresses and improve bonding, enabling the production of dense and crack-free hybrid structures.

Sintering Chemo-Thermal Kinematic Model

The evolution of densification during sintering was described using an Arrhenius-type kinetic law that links temperature and time to the change in relative density. The material was considered a porous continuum in which the diffusion rate controls the reduction of porosity according to

$$\dot{\rho} = A \exp(-\frac{Q}{RT}) (1-\rho)^n,$$

where A is a pre-exponential constant, Q the apparent activation energy, R the universal gas constant, T the absolute temperature, and n an empirical exponent that accounts for the slowdown of densification as pores close. This expression, originally formulated for viscous and grain-

Materials Research Proceedings 69 (2026) 1444-1449 https://doi.org/10.21741/9781644904251-253

boundary diffusion sintering, captures the fundamental temperature sensitivity of the process [3,14].

From the calculated density evolution, the corresponding shrinkage was obtained through isotropic mass conservation, while the total deformation over the thermal cycle was determined by combining the densification-induced contraction with the integrated thermal expansion. Mechanical properties were updated stepwise as functions of density using empirical power-law and exponential relationships, which link stiffness and strength to porosity reduction.

Although simplified, assuming homogeneous and isotropic densification, the model effectively reproduces the densification and shrinkage trends observed in sinter-based additive manufacturing of both metallic and ceramic feedstocks [15].

CUF-Based Layer-wise Residual Deformation Analysis

The residual deformations induced during sintering are evaluated through a Carrera Unified Formulation (CUF) framework combined with a layer-wise modeling strategy. The thermo-mechanical problem is solved incrementally as a sequence of quasi-static states, each corresponding to a discrete time or temperature step of the sintering cycle. The approach has been developed at first for the virtual manufacturing of composite material [16] and is here extended to the sintering of metallic materials. At every instant, the stiffness matrices of the individual layers are updated according to their instantaneous elastic properties and thermal expansion coefficients. The total residual deformation is then obtained as the cumulative sum of these incremental static states over the entire thermal history.

Numerical results

The mechanical and thermal properties of zirconia (3Y-TZP) and 316L stainless steel were defined according to the model developed for this study. The resulting curves, shown in Figure 1, illustrate the progressive increase in stiffness and density as the porosity decreases during processing, while the thermal expansion coefficient remains relatively stable for both materials.

Starting from these data, the process induced deformation behavior was evaluated for a standard cantilever beam with a length of 40 mm and a width of 6 mm. The baseline configuration (Base) was modeled with a total thickness of 5 mm, composed of 4 mm of 316L steel and 1 mm of zirconia bonded at the interface. Symmetry constraints were applied on one short and one lateral face, so that the model effectively represents one-quarter of a beam twice as long and twice as wide, preserving the correct curvature and deformation behavior.

In parallel, four alternative interface configurations were analyzed to investigate the influence of geometric transitions on the global deformation:

- INT-1: interface with a zig-zag profile preserving the same volume ratio as the baseline case (4 mm metal / 1 mm ceramic).
- INT-2: zig-zag interface with an enlarged transition region, redistributing the two materials without maintaining the original thickness ratio.
- INT-3: introduction of a lamellar interlayer (4mm) between the metal and ceramic layers, composed of vertical lamellae designed to redistribute local shrinkage.
- INT-4: same lamellar interlayer (4mm) configuration as INT-3, but with the lamellae inclined at 45°, providing an oblique load transfer path during sintering.

These configurations allow direct comparison between the effect of interface morphology and the global curvature of the beam.

Materials Research Proceedings 69 (2026) 1444-1449 https://doi.org/10.21741/9781644904251-253

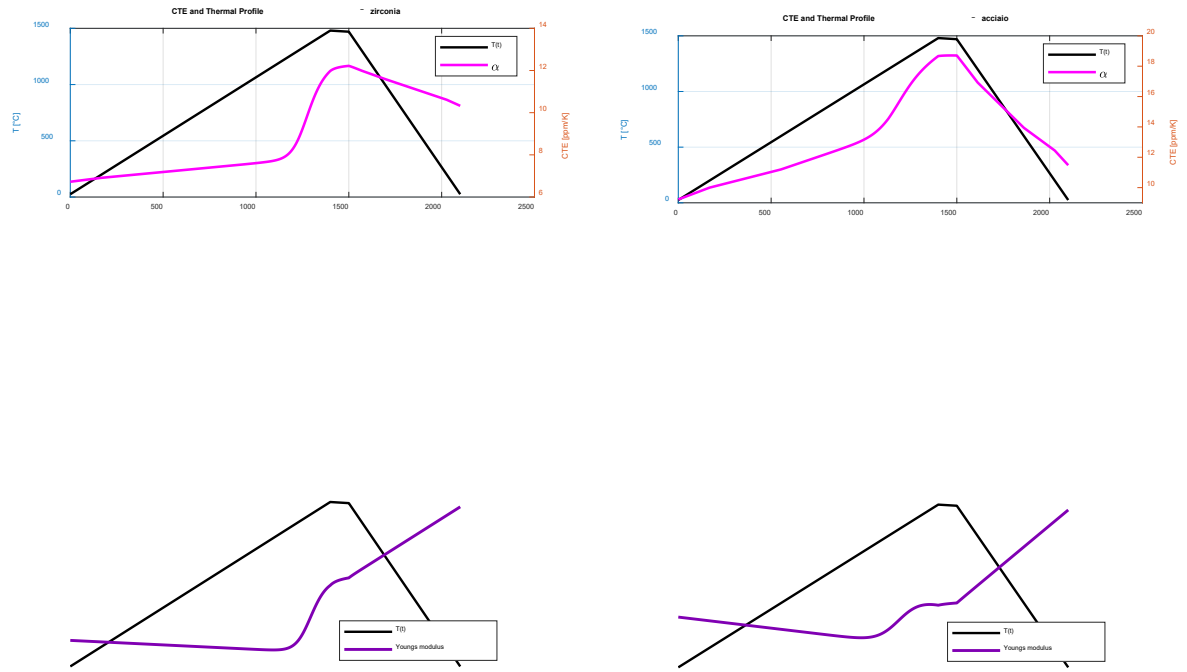


Fig. 1 Evolution of the main thermo-mechanical properties (E, α, ρ) of 316L stainless steel (right) and 3Y-TZP zirconia (left) during the sintering process.

Figure 2 compares the maximum deflection for the five interface configurations. The Base model shows the highest curvature (4.15 mm) and serves as the reference. The INT-1 zig-zag interface slightly reduces the deflection (−4.6%), while INT-2, with a wider transition zone, produces a small increase (+1.7%). The best results are achieved with the lamellar structures: INT-3 with vertical lamellae and INT-4 with 45° inclined lamellae reduce the deflection by 40.7% and 35.2%, respectively. These results confirm that introducing a lamellar interlayer is the most effective strategy for mitigating shrinkage mismatch and improving dimensional stability during co-sintering.

Conclusions

This study demonstrates that FDM additive manufacturing can effectively be combined with numerical modeling to design hybrid metal–ceramic components with improved dimensional stability. The results show that the geometry of the interface plays a crucial role in controlling the deformation generated during co-sintering. By exploiting the design flexibility of 3D printing, it is possible to tailor the interface morphology to redistribute shrinkage and thermal mismatch between materials, significantly mitigating global curvature. Although based on simplified material assumptions, the proposed approach provides a reliable framework for predicting deformation trends and guiding interface design before experimental validation. Overall, this work confirms that additive manufacturing enables functional control of metal–ceramic interfaces, opening the way to optimized, thermally stable structures for aerospace and high-temperature applications.

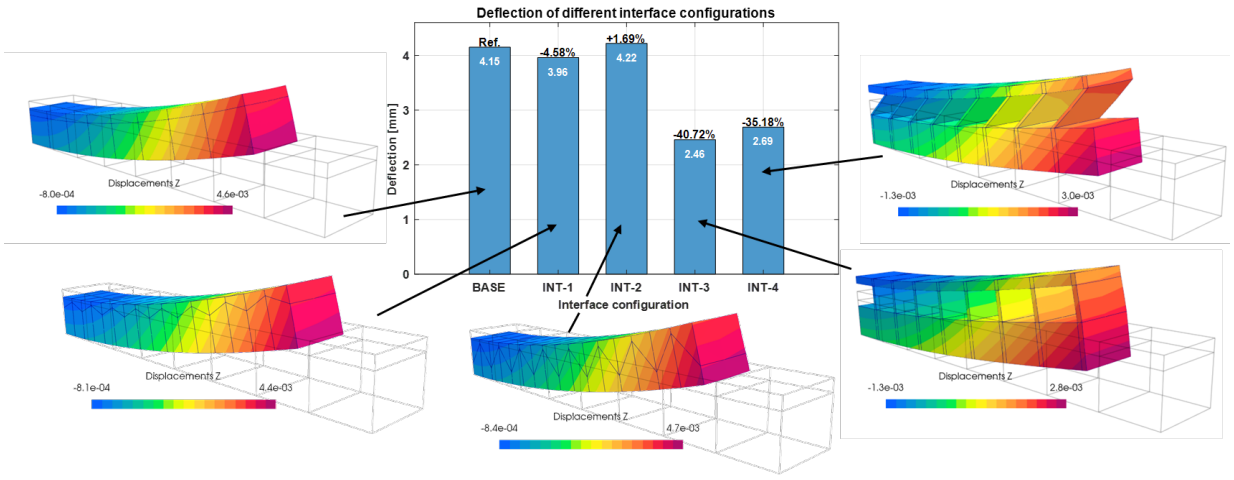


Fig. 2 Comparison of the maximum deflection for the five interface configurations: Base, INT-1, INT-2, INT-3, and INT-4. The bars show the absolute deflection values, while the percentage labels indicate the variation with respect to the Base model.

References

[1] Uyanna, O., & Najafi, H. (2020). Thermal protection systems for space vehicles: A review on technology development, current challenges and future prospects. Acta Astronautica, 176, 341-356. https://doi.org/10.1016/j.actaastro.2020.06.047

[2] Naebe, M., & Shirvanimoghaddam, K. (2016). Functionally graded materials: A review of fabrication and properties. Applied Materials Today, 5, 223-245. https://doi.org/10.1016/j.apmt.2016.10.001

[3] Green, D. J., Cai, P. Z., & Messing, G. L. (1999). Residual stresses in alumina-zirconia laminates. Journal of the European Ceramic Society, 19, 2511-2517. https://doi.org/10.1016/S0955-2219(99)00103-X

[4] Ravi, D., & Green, D. J. (2006). Sintering stresses and distortion produced by density differences in bi-layer structures. Journal of the European Ceramic Society, 26, 17-25. https://doi.org/10.1016/j.jeurceramsoc.2004.10.032

[5] Wu, K., Scheler, S., Park, H.-S., & Willert-Porada, M. (2013). Pressureless sintering of ZrO_2-$ZrSiO_4$/NiCr functionally graded materials with a shrinkage matching process. Journal of the European Ceramic Society, 33, 1111-1121. https://doi.org/10.1016/j.jeurceramsoc.2012.11.026

[6] Slawik, T., Günther, A., Moritz, T., & Michaelis, A. (2016). Co-sintering behaviour of zirconia-ferritic steel composites. AIMS Materials Science, 3(3), 1160-1176. https://doi.org/10.3934/matersci.2016.3.1160

[7] Scheithauer, U., Slawik, T., Schwarzer, E., Richter, H.-J., Moritz, T., & Michaelis, A. (2015). Additive manufacturing of metal-ceramic composites by thermoplastic 3D printing (3DTP). Journal of Ceramic Science and Technology, 6(2), 125-132.

[8] Scheithauer, U., Bergner, A., Schwarzer, E., Richter, H.-J., & Moritz, T. (2014). Studies on thermoplastic 3D printing of steel-zirconia composites. Journal of Materials Research, 29(17), 1931-1938. https://doi.org/10.1557/jmr.2014.209

[9] Srivastava, M., Maheshwari, S., & Kundra, T. K. (2015). Virtual modelling and simulation of functionally graded material components using FDM technique. Materials Today: Proceedings, 2, 3471-3480. https://doi.org/10.1016/j.matpr.2015.07.323

[10] Moritz, T., Michaelis, A., & Richter, H.-J. (2015). Thermoplastic feedstocks for additive manufacturing of ceramics and metals. Journal of Ceramic Science and Technology, 6, 133-141.

[11] Scheithauer, U., Weingarten, S., Johne, R., Schwarzer, E., Abel, J., Richter, H.-J., & Michaelis, A. (2017). Ceramic-based 4D components: Additive manufacturing of functionally graded materials by thermoplastic 3D printing (T3DP). Materials, 10(12), 1368. https://doi.org/10.3390/ma10121368

[12] Slawik, T., Scheithauer, U., Schwarzer, E., & Moritz, T. (2018). Metal-ceramic hybrid structures produced by additive manufacturing. Journal of the European Ceramic Society, 38(9), 3191-3200.

[13] Liu, C., Deng, Y., Gruner, D., Kaletsch, A., Gestrich, T., & Broeckmann, C. (2024). Densification, deformation, and delamination during co-sintering of metal-ceramic laminates. Journal of the American Ceramic Society, 108, e20190. https://doi.org/10.1111/jace.20190

[14] Bordia, R.K. & Scherer, G.W.,(1988) On constrained sintering- II. Comparison of constitutive models. Acta Metallurgica 36(9), pp.2399-2409. https://doi.org/10.1016/0001-6160(88)90190-3

[15] Gözüküçük, F., Telgkamp, J., Scharowsky, T., & Tenelsen, C. (2025). Sintering simulation and validation for the sinter-based fused filament fabrication process route. Progress in Additive Manufacturing, 10, 10091-10109. https://doi.org/10.1007/s40964-025-01229-8

[16] Zappino, E., Santori, M., Masia, R. Zobeiry N., & Petrolo M., (2025) Numerical Analysis of the Impact of Process Parameters on the Residual Stress of a Flat Composite Part. Aerotecnica Missili Spazio 104, 277-291. https://doi.org/10.1007/s42496-024-00231-7

Materials Research Proceedings 69 (2026) 1450-1454 https://doi.org/10.21741/9781644904251-254

Fatigue Life Estimation in Frequency-Domain of Composite and Metallic Structures via CUF and Dirlik's Method

Elisa TORTORELLI[1,a *], Giuseppe PALAIA[1,b] and Erasmo CARRERA[1,c]

[1]MUL2 Lab, Department of Mechanical and Aerospace Engineering, Corso Duca degli Abruzzi 24, 10129, Torino, Italy

[a]elisa.tortorelli@polito.it, [b]giuseppe.palaia@polito.it, [c]erasmo.carrera@polito.it

Keywords: CUF, Fatigue, Composite

Abstract. This work presents a framework for predicting the fatigue life of composite and metallic structures under random excitations. The framework combines the Carrera Unified Formulation (CUF), Dirlik's frequency-domain approach, and the Tsai–Hill criterion to evaluate fatigue damage from stress power spectral densities. Results for various laminate configurations show good agreement with FEMAP/NX simulations, demonstrating the accuracy and efficiency of the proposed CUF-based fatigue assessment.

Introduction

Fatigue is a significant contributor to the failure of structural and mechanical components. Its assessment requires evaluating stress or strain distributions resulting from the loading history and predicting the stress response under random excitations, which is crucial for estimating fatigue life. In the aerospace sector, where aircraft and spacecraft are exposed to random atmospheric loads [1], fatigue is commonly evaluated using a damage tolerance approach, focusing on the growth of existing cracks [2]. Similar strategies based on fracture mechanics under Gaussian random loading are also applied in other fields, such as mooring systems [3].

The increasing use of composite materials introduces new challenges due to their anisotropic behavior and damage mechanisms, including matrix cracking, delamination, and fiber breakage [4]. Predicting the fatigue life of composites requires advanced modeling techniques that can capture both stochastic loading and progressive damage [5]. Traditional time-domain simulations are accurate but computationally expensive, whereas frequency-domain methods, such as Dirlik's approach [6], provide efficient alternatives for fatigue estimation under random vibrations [7].

This work proposes a framework combining the Carrera Unified Formulation (CUF) [8] with Dirlik's frequency-domain method. CUF enables high-fidelity finite element modeling of multilayered laminates, capturing stress distributions across plies. Stress responses are computed in the frequency domain, with aluminum fatigue assessed via the critical stress PSD component and composite fatigue evaluated using the Tsai–Hill failure index. Dirlik's method then estimates fatigue life from the stress PSD through spectral moments, PDF evaluation, and S-N curve integration. The assessment considers the computation of fatigue life for different laminations of composite specimens under random loading via the CUF model and compares the results with those from FEMAP/NX commercial software.

The following work summarizes in the first two sections the methodology, in the third section the main results, and in the last section the conclusions.

Carrera Unified Formulation

The two-dimensional (2D) model adopted in this study is developed within the framework of the Carrera Unified Formulation (CUF). CUF enables the derivation of the governing equations for any refined structural theory using a limited set of Fundamental Nuclei (FNs). The three-dimensional displacement field of a solid plate can be represented as a general expansion of the

Content from this work may be used under the terms of the Creative Commons Attribution 3.0 license. Any further distribution of this work must maintain attribution to the author(s) and the title of the work, journal citation and DOI. Published under license by Materials Research Forum LLC.

Materials Research Proceedings 69 (2026) 1450-1454 https://doi.org/10.21741/9781644904251-254

generalized displacements, expressed as the product of an in-plane two-dimensional shape function, $N_i(x,y)$, and a one-dimensional expansion function, $F_\tau(z)$.

$$\mathbf{u}(x,y,z) = F_\tau(x,z)N_i(y)\mathbf{u_{\tau i}} \qquad \tau = 1,\ldots,M \qquad i=1,\ldots,p \tag{1}$$

Where $F_\tau(z)$ is the expansion function modelling the displacement field, the order of the expansion function depends on the parameter M, $\mathbf{u_{\tau i}}$ is the nodal displacement unknown vector, and p is the number of nodes of each element. The results of this work are obtained using bi-quadratic (Q9) elements as shape functions $N_i(x,y)$ to discretize the in-plane geometry.

Fatigue life estimation in frequency domain

Starting from the general equation of motion and using the modal reduction strategy to reduce the computational effort, the frequency-domain formulation becomes:

$$\mathbf{X^T q_k}(\omega) = \left[-\omega^2\left(\mathbf{X^T M X}\right) + i\omega\left(\mathbf{X^T C X}\right) + \left(\mathbf{X^T K X}\right)\right]^{-1}\mathbf{X^T F_k^*} \tag{2}$$

where the modal generalized matrices of mass, damping and stiffness are $\boldsymbol{X^T M X}$, $\boldsymbol{X^T C X}$, $\boldsymbol{X^T K X}$, respectively. $\boldsymbol{F_k^*}$ is the generalized force vector; $\boldsymbol{q_k}$ is the vector that collects the degree of freedom (DOF) of the FE model and $\boldsymbol{X}$ is the matrix that collects the eigenvectors.

The power spectral density (PSD) function of a signal provides a quantitative representation of the distribution of power in the frequency domain. In the event of a given force input PSD function $\boldsymbol{G_F}(f)$, the system's transfer function can be utilised to calculate the stress output response $\boldsymbol{G_{\sigma_j}}(f)$:

$$\mathbf{G_{\sigma_j}}(f) = \overline{\mathbf{H_{\sigma_j}}}(f)\mathbf{G_F}(f)\mathbf{H_{\sigma_j}^T}(f) \quad j=1,\ldots,6 \tag{3}$$

Where $\boldsymbol{H}(f)$ is the system transfer function, i.e. a function which describes how a linear time invariant system responds (output signal) to a specific input and, in particular, $\overline{\boldsymbol{H_{\sigma_j}}}(f)$ and $\boldsymbol{H_{\sigma_j}^T}(f)$ are the complex conjugate and the transpose of this function.

The Tsai–Hill criterion has been experimentally validated for predicting failure in composite laminates under multiaxial static loading. Although fatigue may involve the same damage mechanisms observed under static loading, including matrix cracking, fiber breakage, interfacial debonding, and delamination, fatigue failure results from progressive damage accumulation rather than instantaneous failure. The Tsai–Hill criterion is therefore used here to condense the multiaxial stress state into an equivalent PSD function as in [9], which can then be used within the fatigue framework.

$$G_{\sigma_{eq}}(\omega) = \frac{\frac{1}{2X^2} + \frac{1}{2X^2}G_{\sigma_1-\sigma_2}(\omega) + \frac{2X^2 - Y^2}{2X^2Y^2}G_{\sigma_2}(\omega) + \frac{1}{S_\tau^2}G_{\tau_{12}}(\omega)}{\frac{1}{2X^2} + \frac{1}{Y^2} + \frac{1}{S_\tau^2}} \tag{4}$$

Fatigue life estimation can be computed introducing the Probability Density Function (PDF) of the equivalent stress using the Dirlik's method:

$$p(S) = \frac{1}{\sqrt{m_0}}\left[\frac{B_1}{Q}e^{-Z} + \frac{B_2 Z}{T^2}e^{-\frac{Z^2}{2T^2}} + B_3 Z e^{-Z^2}\right] \tag{5}$$

Materials Research Proceedings 69 (2026) 1450-1454 https://doi.org/10.21741/9781644904251-254

where the spectral moments are involved $m_i = \int_0^\infty f^i G_\sigma(f)\, df$. More details on the parameters are given in [6].
Finally, the fatigue life T of a composite laminate under random vibration loading is computed as

$$T = \frac{1}{\nu \int_G^\infty \frac{p(S)}{N(S)}\, dS} \tag{6}$$

where $\nu = \frac{1}{2\pi}\sqrt{\frac{m_2}{m_0}}$ is the number of the stress cycles in a unit of time and N(S) is the S-N curve of material.

Results

To validate the proposed approach, numerical results obtained via CUF-based modeling are compared with simulations performed in Femap/NX Nastran commercial software. The fatigue life is estimated for several composite laminates with different stacking sequences: $[90/-45/45/0]_s$, $[0/45/-45/90]_s$, $[0/90/0/90]_s$, and $[-45/45/-45/45]_s$. The specimen is clamped-free with geometry dimensions as in [10] and subjected to a bending excitation corresponding to a constant base acceleration PSD of 0.5 g^2/Hz. The same methodology is applied to an aluminum specimen as an isotropic reference case, which, as expected, exhibits a significantly shorter fatigue life. In Fig. 1, the root mean square (RMS) of the specimen with lamination of $[90/-45/45/0]_s$, showing that the fatigue hotspot of the composite specimen is near the hole in point P.

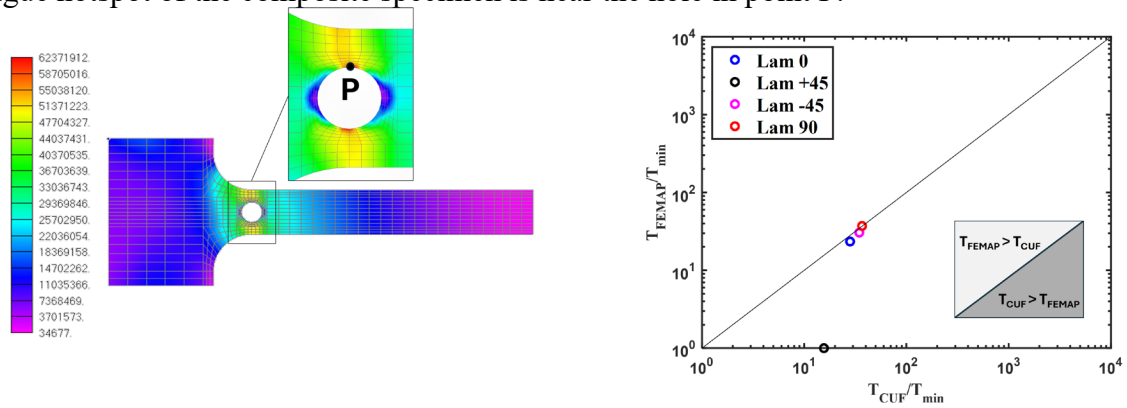


Figure 1. Root mean square (RMS) of global structure at left. Evaluation and comparison of fatigue life of specimen in point P for laminate $[0/45/-45/90]_s$ at right.

The fatigue life estimation of laminate $[0/45/-45/90]_s$ for each layer is shown in Fig. 2. In Table 1, the fatigue life and RMS of four different laminates are shown and compared with the aluminum specimen, which shows shorter fatigue life. For the metallic structure, the Von Mises criteria is applied to evaluate G_{eq}. It is important to notice that the RMS value alone is not fully representative of the fatigue life, as the PDF also plays a crucial role. This is evident from the Fig. 2, where the specimen with the lowest RMS value, corresponding to the $[0/90/0/90]_s$ laminate, does not exhibit the highest fatigue life. This highlights that the PDF has a fundamental influence on the fatigue response.

Materials Research Proceedings 69 (2026) 1450-1454 https://doi.org/10.21741/9781644904251-254

Table 1. Fatigue life and RMS stress for different laminates and aluminium specimens

Specimen	T_{CUF} (s)	RMS_{CUF} (Pa)
[90/-45/45/0]	5.67E+17	5.37E+13
[0/45/-45/90]	1.17E+18	8.79E+12
[0/90/0/90]	2.01E+18	1.59E+12
[-45/45/-45/45]	3.78E+18	8.48E+12
Al	7.99E+07	2.59E+14

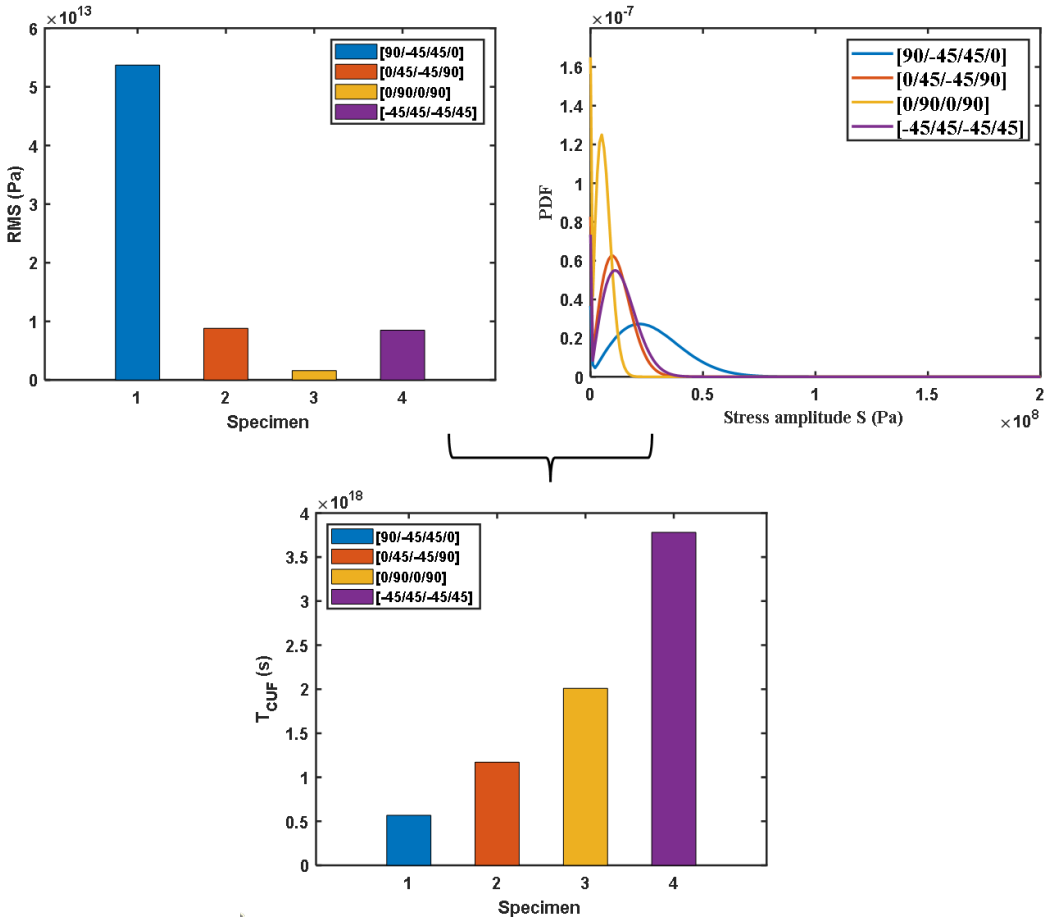


Figure 2. RMS, PDF, and fatigue life using the CUF model of composite with four different laminations $[90/-45/45/0]_s$, $[0/45/-45/90]_s$, $[0/90/0/90]_s$, and $[-45/45/-45/45]_s$.

Conclusions

This paper investigates the use of the CUF-FEM approach combined with the Tsai–Hill failure criterion to predict the fatigue life of composite structures under random excitation. The results are presented in terms of power spectral density, probability density function, and estimated fatigue life. The numerical study considered four composite specimens with different stacking sequences and compared them with an aluminum specimen. The results show good agreement with those obtained using commercial software and demonstrate that the proposed methodology, combining CUF with the frequency-domain approach based on the equivalent stress model, can be effectively applied to multi-axial fatigue analysis.

Acknowledgements

This work was partially financed by the European Union- NextGenerationEU (National Sustainable Mobility Center CN00000023, Italian Ministry of University and Research Decree n. 1033- 17/06/2022, Spoke 11- Innovative Materials & Lightweighting). The opinions expressed are

those of the authors only and should not be considered as representative of the European Union or the European Commission's official position. Neither the European Union nor the European Commission can be held responsible for them.

References

[1] T. Reytier, C. Bes, P. Marechal, M. Bianciardi, and A. Santgerma, Generation of correlated stress time histories from continuous turbulence Power Spectral Density for fatigue analysis of aircraft structures, International Journal of Fatigue, 42 (2012) 147–152. https://doi.org/10.1016/j.ijfatigue.2011.08.013

[2] R. Talreja and N. Phan, Assessment of damage tolerance approaches for composite aircraft with focus on barely visible impact damage, Composite Structures, 219 (2019) 1–7. https://doi.org/10.1016/j.compstruct.2019.03.052

[3] X. Xue and N. Chen, Fracture mechanics analysis for a mooring system subjected to Gaussian load processes, Engineering Structures, 162 (2018) 188–197. https://doi.org/10.1016/j.engstruct.2018.02.040

[4] I. M. Daniel and O. Ishai, Engineering mechanics of composite materials, vol. 3, Oxford University Press, New York, 1994.

[5] C. Caprile and G. Sala, Fatigue behaviour of CFRP jointed specimens, Aerotecnica Missili & Spazio, 65 (1986) 176–185.

[6] A. Halfpenny, A Frequency Domain Approach for Fatigue Life Estimation from Finite Element Analysis, Key Engineering Materials, 167–168 (1999) 401–410. https://doi.org/10.4028/www.scientific.net/KEM.167-168.401

[7] T. Dirlik and D. Benasciutti, Dirlik and Tovo-Benasciutti Spectral Methods in Vibration Fatigue: A Review with a Historical Perspective, Metals, 11 (2021) 1333. https://doi.org/10.3390/met11091333

[8] E. Carrera, M. Cinefra, M. Petrolo, and E. Zappino, Finite element analysis of structures through unified formulation, John Wiley & Sons, 2014.

[9] S. Zhou, Y. Sun, and L. Guo, Random fatigue life prediction of carbon fibre-reinforced composite laminate based on hybrid time-frequency domain method, Advanced Composite Materials, 26 (2016) 181–195. https://doi.org/10.1080/09243046.2016.1158935

[10] D. Y. Gao, W. X. Yao, W. D. Wen, and J. Huang, Equivalent Spectral Method to Estimate the Fatigue Life of Composite Laminates Under Random Vibration Loadings, Mechanics of Composite Materials, 57 (2021) 101–114. https://doi.org/10.1007/s11029-021-09937-2

Human Factors, Cockpit & Operations



Materials Research Proceedings 69 (2026) 1456-1459 https://doi.org/10.21741/9781644904251-255

Application of Random Forest and HRV Analysis for Real-Time Pilot Mental Workload Monitoring: Toward an Intelligent Cockpit Support System

Carmelo Rosario VINDIGNI[1,a *], Giuseppe IACOLINO[1,b], Antonio ESPOSITO[1,c], Calogero ORLANDO[1,d], and Andrea ALAIMO[1,e]

[1]Department of Engineering and Architecture, Kore University of Enna, 94100, Enna, Italy

[a]carmelorosario.vindigni@unikore.it, [b]giuseppe.iacolino@unikorestudent.it, [c]antonio.esposito@unikore.it, [d]calogero.orlando@unikore.it, [e]andrea.alaimo@unikore.it

Keywords: Mental Workload Monitoring, Heart Rate Variability, Random Forest Classification, Aviation Human Factors

Abstract. In aviation, continuous monitoring of pilots' mental workload is vital to ensure safety and performance, as cognitive overload or underload can affect decision-making and situational awareness. This study explores the use of heart rate variability, a physiological marker linked to mental effort, for real-time MW assessment using wearable bio-sensors. A Random Forest machine learning algorithm is applied to classify workload levels, exploiting its robustness, interpretability, and ability to model complex feature interactions. The study evaluates RF performance across different settings to find the best configuration for the development of an embedded cockpit support system. Results are evaluated against a Kriging model to assess comparative effectiveness.

Introduction

In the high-risk aviation environment, the continuous assessment of pilots' Mental Workload (MW) is critical for maintaining operational safety and performance. Mental overload or underload can compromise decision-making, situational awareness, and reaction times. Recent advances in wearable bio-sensing technologies have opened new possibilities for non-intrusive, real-time monitoring of physiological signals, which can be used to infer cognitive states [1]. Among these signals, Heart Rate Variability (HRV) has emerged as a promising indicator due to its established links with autonomic nervous system activity and mental effort. The present study investigates the application of the Random Forest (RF) machine learning algorithm [2] to HRV data for the classification of mental workload levels in pilots, aiming at the development of a real-time, embedded system for intelligent cockpit support. This work focus on exploiting the strengths of the Random Forest algorithm, namely robustness, interpretability, and the capacity to handle complex feature interactions, to obtain a reliable classifier capable of distinguishing between multiple workload conditions. A key objective is to evaluate the algorithm's performance across various settings and identify optimal configurations for real-world deployment. The results obtained through the RF are also compared with Kriging model ones [3].

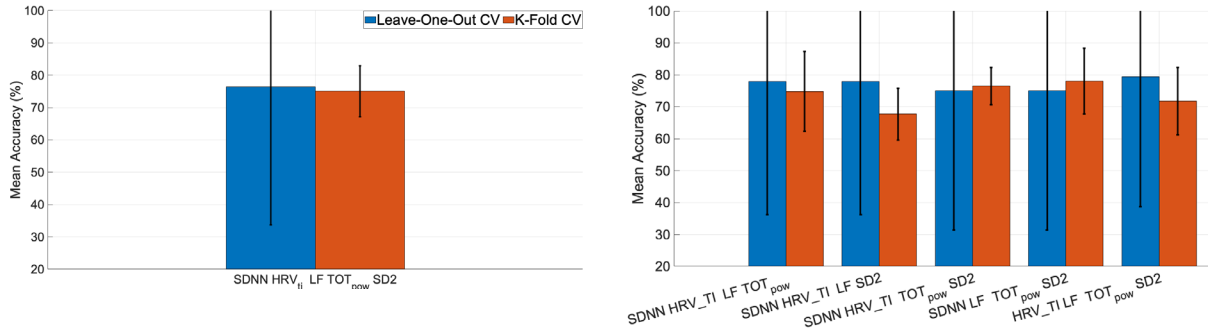
Materials and method

The RF model has been exploited in literature for pilot's MW analysis. For instance, in [4] the Electrocardiogram (ECG) signals collected for 18 pilots subjects were processed and classified in order to estimate if the pilot is in a distracted state or not. Different classification algorithms were employed, namely, the K- Nearest Neighbour (KNN), Decision Tree(DT), Random Forest (RF), Naive Bayes (NB), and Gradient Boosting Machine (GBM). The results reported by the authors have demonstrated an accuracy of the RF model of the 90 %. In [5] electroencephalogram (EEG) data were collected from ten collegiate aviation students during a live-flight scenario in a single-

Content from this work may be used under the terms of the Creative Commons Attribution 3.0 license. Any further distribution of this work must maintain attribution to the author(s) and the title of the work, journal citation and DOI. Published under license by Materials Research Forum LLC.

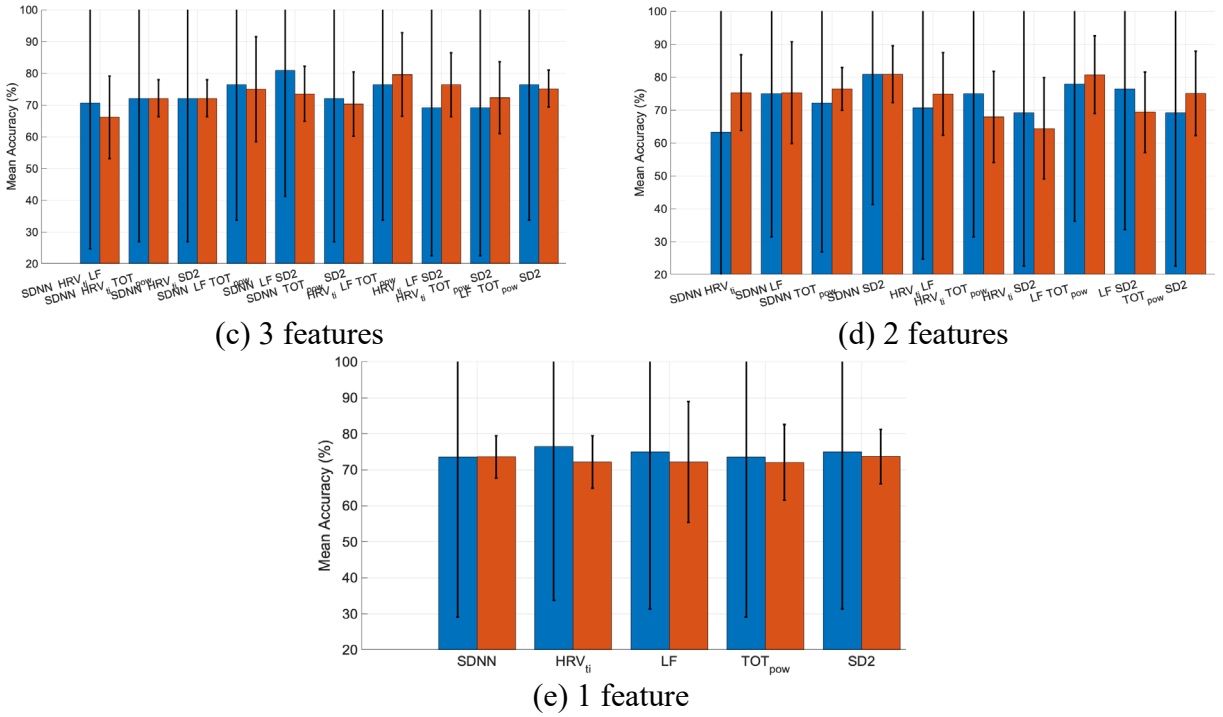
engine aircraft. The data were then processed using a stacking model algorithm in which the first level was implemented by a RF algorithm. Moreover, in [6] the feasibility of a headset-based system for pilots MW has been studied. Twenty-one male pilot cadets participated in the experiment, and their EEG data were recorded and processed using different classifiers, including three SVM-based models, one KNN, and an RF classifier. The RF model has shown an accuracy of the 86.5 %. Given the promising results obtained in literature for pilot's MW analysis using RF models, in this work the application of RF purely based on HRV data is studied to preliminary assess the application of this tool in real time scenarios. The dataset for training and test of the RF was collected in a controlled environment simulating aviation tasks with varying cognitive demands. Participants were subjected to task conditions designed to induce different levels of mental workload. During these tasks, physiological data were recorded using wearable ECG devices. From the raw signals, a set of HRV features was extracted, namely SDNN, HRV_{TI} , LF, TOT_{Pow}, and SD2 [7]. First, the analyses focused on determining whether specific combinations of features can enhance the predictive accuracy of the Random Forest algorithm. To investigate this, all possible combinations of the 5 features were systematically generated and evaluated. For each combination two procedures have been explored and compared, i.e. Leave-One-Out Cross-Validation (LOOCV) and Stratified k-fold cross-validation [8].The results in Figure 1 show that among the feature combinations, the best performance was achieved using SDNN and SD2 features while the worst performance came from the combination of SDNN and HRV_{TI} .

After refining the dataset, performance studies were performed. Specifically, it has been investigated how the number of trees in the forest and the proportion of training and test data affect performance, using a stochastic approach. The evaluation was carried out using standard performance metrics: Out-Of-Bag (OOB) error, Precision, Recall, and F1-score [9]. Moreover, being defined the best combination of training percentage and number of trees in the forest the hyper-parameters maximum depth and minimum samples per split were investigated. From the analyses carried out it has been found that the best RF configuration involved 300 trees, a trees depth equal to 2, and minimum 8 samples per split. Last, the best average performance metrics obtained from the parametric studies are summarized in Table 1 and compared with those achieved using a Kriging model, highlighting that the Random Forest algorithm outperforms the Kriging one.



(a) 5 features (b) 4 features

Materials Research Proceedings 69 (2026) 1456-1459 https://doi.org/10.21741/9781644904251-255



(c) 3 features (d) 2 features

(e) 1 feature

Figure 1: Features combination study results

Table 1: Performance metrics

Model	Class	Precision	Recall	F1 Score	Test Accuracy
Random Forest	Low	0.80	0.80	0.79	83%
	High	0.77	0.75	0.74	
Kriging	Low	0.77	0.65	0.65	70.6%
	High	0.69	0.82	0.71	

Conclusions

This study explored HRV features from non-invasive ECG signals as indicators of pilots' mental WL during flight. Data were collected from certified pilots in a fully controlled flight simulator experiment. Results showed that a RF classifier outperformed a Kriging-based model in distinguishing low and high WL. The combination of SDNN and SD2 features achieved the highest accuracy (83%), demonstrating RF's robustness and reliability in capturing autonomic responses to cognitive demands.

Funding

The study was financially supported by the Italian Ministry of University and Research M.U.R. under the TWINCRAFT project (CUP J53D23002230008).

References

[1] G. Iacolino, A. Esposito, C. Orlando, and A. Alaimo, "A brief review of pilots' workload assessment using flight simulators: subjective and objective metrics," Materials Research Proceedings, vol. 37, 2023. https://doi.org/10.21741/9781644902813-161

[2] L. Breiman, "Random forests," Machine learning, vol. 45, no. 1, pp. 5-32, 2001. https://doi.org/10.1023/A:1010933404324

[3] A. Esposito, G. Iacolino, C. Orlando, and A. Alaimo, "Metamodelling of the workload assessment in simulated flights using the kriging method," in ICAS Proceedings, 2024.

[4] A. Rajendran, P. M. Kebria, N. Mohajer, A. Khosravi, and S. Nahavandi, "Machine learning based prediction of situational awareness in pilots using ecg signals," in 2021 IEEE Symposium Series on Computational Intelligence (SSCI), pp. 1-6, IEEE, 2021. https://doi.org/10.1109/SSCI50451.2021.9660076

[5] H. Taheri Gorji, N. Wilson, J. VanBree, B. Hoffmann, T. Petros, and K. Tavakolian, "Using machine learning methods and eeg to discriminate aircraft pilot cognitive workload during flight," Scientific Reports, vol. 13, no. 1, p. 2507, 2023. https://doi.org/10.1038/s41598-023-29647-0

[6] C. Liu, C. Zhang, L. Sun, K. Liu, H. Liu, W. Zhu, and C. Jiang, "Detection of pilot's mental workload using a wireless eeg headset in airfield traffic pattern tasks," Entropy, vol. 25, no. 7, p. 1035, 2023. https://doi.org/10.3390/e25071035

[7] P. Wang, R. Houghton, and A. Majumdar, "Detecting and predicting pilot mental workload using heart rate variability: a systematic review," Sensors, vol. 24, no. 12, p. 3723, 2024. https://doi.org/10.3390/s24123723

[8] T. Wong, "Performance evaluation of classification algorithms by k-fold and leave-one-out cross validation," Pattern recognition, vol. 48, no. 9, pp. 2839-2846, 2015. https://doi.org/10.1016/j.patcog.2015.03.009

[9] G. Naidu, T. Zuva, and E. M. Sibanda, "A review of evaluation metrics in machine learning algorithms," in Computer science on-line conference, pp. 15-25, Springer, 2023. https://doi.org/10.1007/978-3-031-35314-7_2

Materials Research Proceedings 69 (2026) 1460-1465 https://doi.org/10.21741/9781644904251-256

Data-Driven Detection of Pilot-Induced Oscillations using Principal Component Analysis

André L. A. PALADINI[1,2,a *], Raghu Chaitanya MUNJULURY[1,4,b], Daniel DREWIACKI[3,c], Petter KRUS[1,d], and Jorge Henrique BIDINOTTO[2,e]

[1]Department of Management and Engineering, Division of Fluid and Mechatronic Systems, Linköping University, Linköping, Sweden

[2]Department of Aeronautical Engineering, University of São Paulo, São Carlos, Brazil

[3]Embraer SA, São José dos Campos, Brazil

[4]SAAB Aeronautics, Linköping, Sweden

[a]andrepaladini@usp.br, [b]raghu.munjulury@liu.se, [c]daniel.drewiacki@embraer.com.br, [d]petter.krus@liu.se, [e]jhbidi@sc.usp.br

Keywords: Pilot-Induced Oscillations, Principal Component Analysis, Convolutional Neural Network, Wavelet Transform, Flight Simulators

Abstract. This study proposes a PIO detection algorithm based on a convolutional/fully connected regression neural network that processes PCA-reduced flight data from wavelet-transformed signals. The model achieved a correlation of 0.88, according to the modified Pearson Correlation Coefficient, with Principal Component Analysis enabling a two-order-of-magnitude dataset reduction and improved training efficiency.

Introduction

Pilot-induced oscillations (PIO) remain a persistent and safety-critical challenge in the field of aircraft handling qualities. These undesired and potentially destabilizing oscillations arise from closed-loop interactions between the pilot and the aircraft, particularly during high-precision control tasks or in the presence of time delays. Despite extensive research leading to various prediction methodologies, PIOs are still difficult to detect and diagnose objectively, whether in real flight tests, operational missions, or simulator-based evaluations.

Traditionally, the detection and evaluation of PIOs have relied on the Pilot-Induced Oscillation Rating Scale (PIOR), a subjective metric assigned by test pilots during handling qualities assessments. The PIOR spans from Grade 1 (no PIO tendencies) to Grade 6 (sustained, hazardous PIOs), offering a standardized framework for severity classification [1]. However, because it depends on human perception, it introduces variability and limits reproducibility across different evaluators and test conditions [2]. To address these limitations, some objective, data-driven identification methods have been developed [3]. These techniques use control input and aircraft response signals to detect the onset of PIO. However, aligning their outputs with pilot assessments remains a significant challenge due to differences in sensitivity, interpretability, and underlying assumptions.

Machine learning techniques have also been investigated for PIO detection. In a previous study [4], a Convolutional Neural Network (CNN) was proposed to identify patterns associated with PIO within stick deflection and pitch rate signals. These signals were represented in the time–frequency domain using the Wavelet Transform. Although this approach produced outputs in the same framework of the PIOR scale, it exhibited limitations in classification accuracy and faced challenges during training due to the substantial computational time, complex network architecture, and memory requirements imposed by the dataset size.

Content from this work may be used under the terms of the Creative Commons Attribution 3.0 license. Any further distribution of this work must maintain attribution to the author(s) and the title of the work, journal citation and DOI. Published under license by Materials Research Forum LLC.

Materials Research Proceedings 69 (2026) 1460-1465 https://doi.org/10.21741/9781644904251-256

To address these limitations, Principal Component Analysis (PCA) presents a promising complementary technique when integrated with CNNs. PCA transforms the data into a set of orthogonal components, reducing feature correlation and dimensionality, which simplifies the dataset and can enhance model efficiency and performance [5].

Accordingly, this work introduces a CNN-based method for PIO detection, leveraging a flight dataset in which stick deflection and pitch rate signals are processed using the Wavelet Transform followed by Principal Component Analysis (PCA).

The Dataset

The dataset used in this study was collected during a flight test campaign conducted in a fixed-base flight simulator. In this campaign, ten formally trained test pilots, all familiar with the PIOR scale, participated in eight variations of a pitch-angle tracking task. The task was presented as a moving target on a simulated artificial horizon. To track the target, the pilots used a centrally positioned, right-hand joystick to control a linear aircraft model representative of a FAR 25 aircraft in cruise flight at 40,000 feet and Mach 0.8. Fig. 1 illustrates the flight simulator setup used in this campaign.

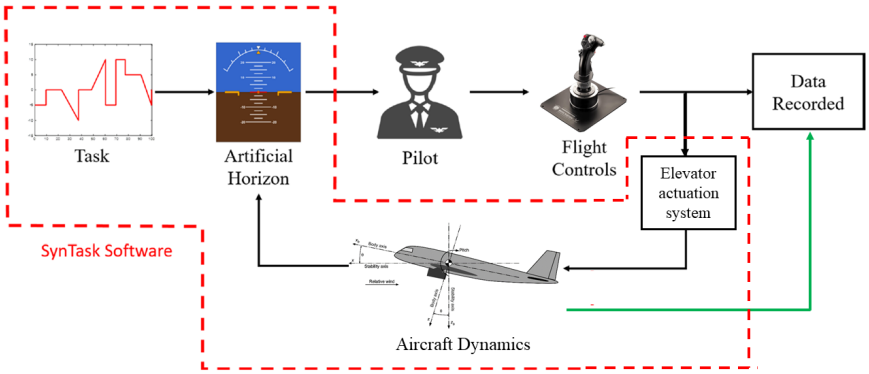


Figure 1: Flight Simulator campaign schematics [4].

Six variations of the aircraft model were generated by arbitrarily modifying the $C_{m\dot{\alpha}}$ stability derivative. These modifications allowed the pilots to experience six levels of PIO proneness, ranging from the least prone (baseline) to the most critical condition (unstable short-period) [4].

The flight test campaign thus comprised a total of 480 simulation runs. For each run, the stick deflection and corresponding pitch rate time series were recorded, together with a PIOR scale assessment assigned by the pilot at the end of the simulated flight. From a machine learning perspective, the raw dataset consists of samples comprising two-channel inputs (stick deflection and pitch rate) each associated with a corresponding PIOR label.

The Wavelet Transform

One way to enrich the information contained within time-series data is through the application of the Wavelet Transform. This is a multi-scale time-frequency transform particularly suited for non-stationary signals, which are common in piloting scenarios, including those involving PIO [4]. The Wavelet Transform was therefore applied to both the stick deflections and pitch rate time-series, generating an expanded dataset to be used by the PIO detection algorithm.

The definition of the Wavelet Transform is given by Eq. 1:

$$W(\tau, f) = \sqrt{f} \int_{-\infty}^{\infty} x(t) \Psi^*\big(f(t-\tau)\big) dt \quad (1)$$

Materials Research Proceedings 69 (2026) 1460-1465 https://doi.org/10.21741/9781644904251-256

where x and Ψ^* are the analysed signal and the complex conjugate of the wavelet function, respectively. For this analysis, the Morlet wavelet function was employed. The parameters τ and f correspond to the time and frequency axes of the transform output, respectively.

Following the transformation, each time-series produced an output matrix of dimensions 512x941. In this representation, the rows correspond to the discrete frequency axis, while the columns correspond to the discrete time axis. The absolute value of each element was then computed to represent the magnitude of the transformation.

At this stage of preprocessing, the dataset consisted of 480 samples represented as two-channel magnitude matrices, rather than time-series, with a total size of approximately 1.8 GB. As mentioned previously, this dataset format and size posed challenges during the PIO detection algorithm training process, increasing training time and constraining the network architecture in terms of complexity and efficiency [4].

Principal Component Analysis

The resulting wavelet matrices, also referred to as scalograms, were subsequently processed using Principal Component Analysis (PCA) [5]. In this analysis, each PCA sample (not to be confused with a dataset sample) corresponds to a scalogram row representing the frequency axis, while each PCA feature corresponds to a scalogram column representing the time axis.

This preprocessing stage began by calculating the mean value across the rows of each scalogram and subtracting it from the original matrix, yielding the centralized scalogram (S). The covariance matrix (C) was subsequently derived in accordance with Eq. 2.

$$C = S^T S \tag{2}$$

The next step involved computing the eigenvalue and eigenvector matrices associated with the covariance matrix. The eigenvalues indicate the proportion of variance (or influence) each component contributes when the scalogram is projected onto its corresponding eigenvector. Based on this analysis, the 31 most significant eigenvectors were selected to form the reduced eigenvector matrix ($V_{reduced}$). The scalograms were then transformed to the reduced coordinate space through a coordinate change operation, as described in Eq. 3.

$$S_{reduced} = (V_{reduced}^T S^T)^T \tag{3}$$

The new dataset, composed of the reduced scalograms ($S_{reduced}$), has a total size of approximately 60 MB, representing a reduction of two orders of magnitude compared to the wavelet data, without losing the most relevant information potentially associated with PIO signatures.

The PIO Detection Algorithm

The PIO detection algorithm was designed as a neural network that processes the PCA-transformed dataset as a two-channel input, representing the stick deflection and pitch rate signals in their PCA-reduced forms, and produces a PIOR scale grade as output. The architecture integrates a Convolutional Neural Network with seven convolutional layers, followed by a Fully Connected Network composed of three layers, as represented in Fig. 2.

Materials Research Proceedings 69 (2026) 1460-1465 https://doi.org/10.21741/9781644904251-256

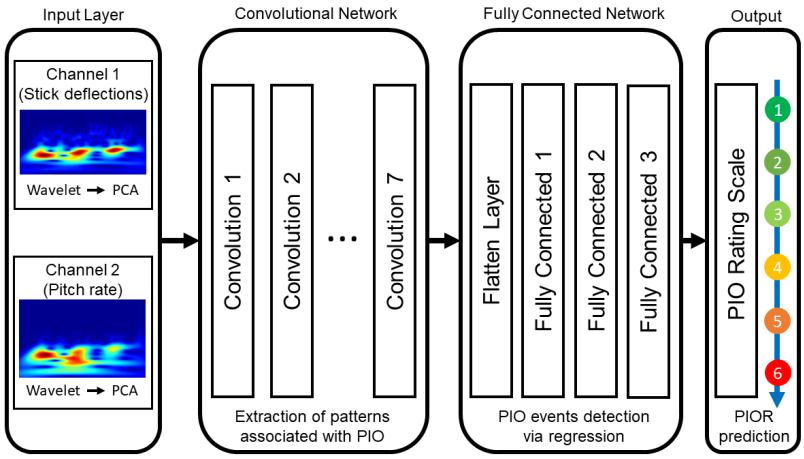


Figure 2: The PIO detection algorithm architecture.

The algorithm was trained by comparing the predicted PIOR output value with the corresponding true PIOR label for each PCA data sample. Consequently, the network functions as a regression model. Training was conducted using the Huber loss function and the Weighted Adaptive Moment (AdamW) optimization algorithm.

Before the training process, 20% of the samples were separated from the dataset to form the test set. The remaining data were used for model training through a stratified K-fold cross-validation procedure, in which the dataset was divided into training and validation folds. A total of nine folds were employed, resulting in nine independent training iterations, each performed with a distinct configuration of training and validation data.

Results

Accordingly, each model version produced a PIOR grade prediction (Y_k) for each dataset sample. The final ensemble prediction ($Y_{ensemble}$) was obtained by averaging the outputs of all model versions, as defined in Eq. 4, where n is the number of folds. This ensemble approach reduces the variance among each model version predictions and enhances the robustness of the overall estimation.

$$Y_{ensemble} = \frac{1}{n}\sum_{k=1}^{n} Y_k \tag{4}$$

To compare the ensemble predictions with the true PIOR labels ($Y_{observed}$), which were provided by the pilots in the simulator campaign, the R_{match} metric was employed [6]. This metric, defined in Eq. 5, is a modified version of the Pearson Correlation Coefficient that quantifies the degree of linear correlation between the predicted and observed PIOR grades. In essence, it evaluates the regression accuracy of the ensemble model.

$$R_{match} = \sqrt{1 - \sqrt{\frac{\sum(Y_{observed} - Y_{ensemble})^2}{\sum Y_{observed}^2}}} \tag{4}$$

Fig. 3 illustrates the PIO detection performance on the best validation set, yielding an R_{match} value of 0.95. This result demonstrates that the network effectively captured PIO-related features and established a strong correlation with the corresponding PIOR labels. For the test set, the R_{match} value decreased to 0.88, indicating mild overfitting, as this subset remained unseen throughout the training process.

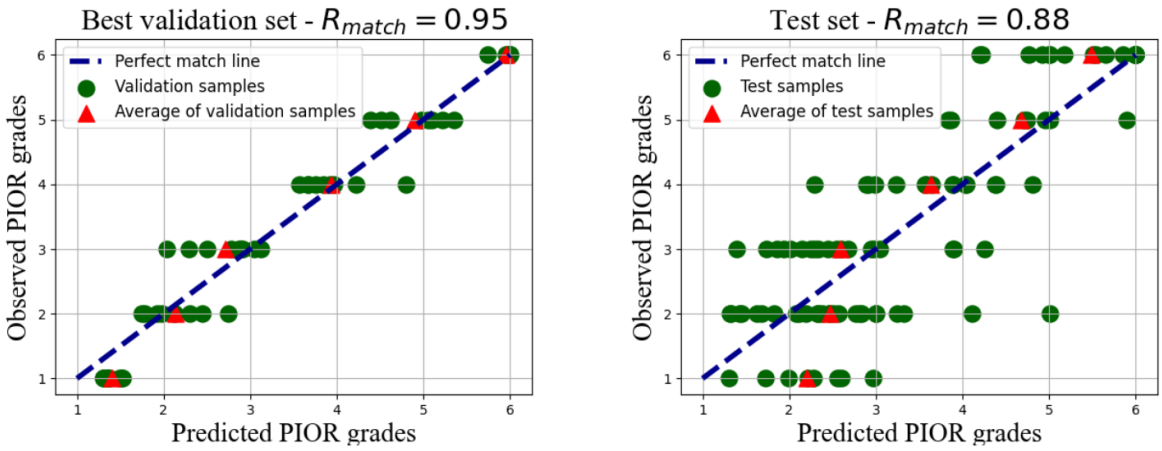


Figure 3: PIO detection results obtained from the best validation set and the test set.

It can be observed that the individual test samples exhibited larger deviations from their corresponding true PIOR labels, whereas these deviations were considerably smaller for the validation samples. However, the average predicted PIOR values for the test set were very close to the perfect match line, which explains the high R_{match} value, with the notable exception of PIOR 1. For this grade, the mean predicted value was higher than that of PIOR 2, indicating that the algorithm was unable to clearly distinguish between these two ratings. According to results obtained from pilot behaviour models reported in the literature [6], this lack of distinction between PIORs 1 and 2 is expected for datasets collected using a fixed-base flight simulator. This suggests that the accuracy of the PIO detection algorithm could be improved if real flight data were used during the training process.

The use of PCA preprocessing in this study enabled an increase in the complexity of the proposed algorithm, allowing the implementation of seven convolutional layers—compared to the four used in the previous study [4], as well as the addition of an extra fully connected layer. Because the PCA-processed dataset is two orders of magnitude smaller than the wavelet-based one, more epochs per fold could be executed during training. This reduction in data size made it feasible to employ a regression model rather than a classification model, as regression models typically require slower convergence.

Conclusion

It can be concluded that the algorithm was capable of providing moderate to high accuracy in PIO identification, with the exception of PIOR 1. As suggested in the literature, this limitation may be attributable to the nature of the dataset (fixed-base flight simulator) rather than the methodology itself, although further investigation is necessary. The PCA preprocessing offered several advantages, including enhanced model convergence during training and increased network complexity, enabling the inclusion of additional layers to more effectively extract PIO-related features.

Acknowledgments

The authors would like to acknowledge the Conselho Nacional de Desenvolvimento Científico e Tecnológico (CNPq) – Brazil, and the Swedish-Brazilian Innovation Center (CISB) for their financial support through the scholarship MCTI/CNPq CISB SAAB AB 37/2023 200932/2024-1.

References

[1] J. Hodgkinson, Aircraft Handling Qualities, 1st. Reston, VA: AIAA Education Series, 1999, p. 517.

[2] A. L. A. Paladini, D. Drewiacki, and J. H. Bidinotto, “Aeroelastic effects in PIO occurrences: A dual approach on flight simulator tests”, Aerospace Science and Technology, p. 109337, 2024. https://doi.org/10.1016/j.ast.2024.109337

[3] D. Mitchell, A. Arencibia, and S. Munoz, “Real-time detection of pilot-induced oscillations”, in AIAA Atmospheric Flight Mechanics Conference and Exhibit, 2004, p. 4700.

[4] A. L. A. Paladini, D. Drewiacki, R. Munjulury, et al., “Convolutional neural network for detection and quantification of pilot-induced oscillations”, in Swedish Aerospace Conference, FT2025, vol. 215, 2025. https://doi.org/10.3384/wcc215.1194

[5] G. James, D. Witten, T. Hastie, R. Tibshirani, et al., An introduction to statistical learning. Springer, 2013, vol. 112.

[6] E. Bachelder, E. Bjorkman, and B. Aponso, “PIO and handling qualities prediction using the USAFTPS Bjorkman PIO data set”, in Vertical Flight Society’s 80th Annual Forum & Technology Display, Montreal, Canada, 2024.

Materials Research Proceedings 69 (2026) 1466-1470 https://doi.org/10.21741/9781644904251-257

Integrated Rotorcraft Stability through Pilot Biomechanics: A Human Factors Perspective

Andrea ZANONI[1,a] and Pierangelo MASARATI[1,b,*]

[1]Department of Aerospace Science and Technology, Politecnico di Milano, via La Masa 34, Milano, Italy

[a]andrea.zanoni@polimi.it, [b]pierangelo.masarati@polimi.it

Keywords: Pilot Biomechanics, Rotorcraft-Pilot Couplings, Stability

Abstract. Aircraft- and Rotorcraft-Pilot Couplings remain a critical concern for handling qualities and flight safety. Pilots play a central role, yet fully understanding their contribution and the factors that govern it remains an open challenge. Awareness of adverse couplings and their potential impact on operations is essential for testing protocols and training syllabi.

Introduction

Aircraft- and Rotorcraft-Pilot Couplings (APCs and RPCs), undesirable interactions between pilot biomechanics and vehicle dynamics, continue to challenge handling qualities and flight safety [1, 2]. Over the past fifteen years, research has focused on modeling pilot biodynamic feedback and assessing its influence on vehicle stability and control. Building on these contributions, this paper aims at reframing RPCs from a human-centered perspective, examining how pilot biomechanics, transmitted through biodynamic feedthrough (BDFT), shape handling qualities.

Early studies showed that involuntary pilot body motion, particularly of the arm and torso, closes a biomechanical feedback loop that affects control inceptor inputs and vehicle response. For example, Quaranta et al. [3] used robust control techniques to treat pilot biodynamics as model uncertainty, quantifying proneness to RPC under collective-bounce excitation. Gennaretti et al. [4] explicitly examined BDFT in RPC onset, identifying mechanisms by which pilot body dynamics degrade damping and excite resonance modes.

Subsequent work deepened biomechanical modeling. In [5], multibody models of the spine, torso, and limbs were calibrated against experimental input data collected in passive (involuntary, control-unrelated) tasks, while [6] extended this to bioaeroservoelastic modeling, formalizing pilot body impedance contributions across flight axes. Masarati et al. [7] further investigated the role of muscular activation, showing how co-contraction patterns influence transmissibility and phase lag.

These developments, along with contributions such as [8, 9, 10]), emphasized the relevance of biomechanical modeling for pilot-vehicle system stability and handling qualities, and revealed task-dependent variability driven by posture, muscle tone, and workload.

Quaranta et al. [11] provided a comprehensive overview of aeroelastic RPC phenomena, consolidating modeling approaches, validation strategies, and classification schemes. Numerical studies of specific RPC events, such as collective bounce [12] and lateral oscillations [13], used simplified yet representative rotorcraft models, incorporating the participating rotor states and highlighting the most influential parameters.

More recently, Zanoni et al. [14] introduced a conceptual-design methodology embedding handling qualities and pilot response variability, motivating the inclusion of biomechanics early in design. This view of RPC-informed flight simulation was reinforced in simulation-focused studies such as [15].

Content from this work may be used under the terms of the Creative Commons Attribution 3.0 license. Any further distribution of this work must maintain attribution to the author(s) and the title of the work, journal citation and DOI. Published under license by Materials Research Forum LLC.

Materials Research Proceedings 69 (2026) 1466-1470 https://doi.org/10.21741/9781644904251-257

Pilot Biomechanics as a Rotorcraft Control Subsystem

Building on these foundations, the present study treats pilot biomechanics as an active subsystem within rotorcraft control dynamics [16], with direct implications for human factors. Instead of representing the pilot purely as a command source, we model biodynamic feedthrough—anatomical impedance shaped by resonances and reflexive dynamics—as an integral component of the closed-loop response, affecting both stability and perceived handling qualities.

Pilot biomechanical models derived from experimental data and detailed multibody simulations are integrated into pilot-in-the-loop simulation campaigns that use mid-fidelity rotorcraft models of medium-lift utility helicopters and tiltrotor aircraft. Experimental data collected using the RPC testbed (Fig. 1) and robust modeling methods support an evaluation of performance metrics (RMS control input, task performance, workload) across hover, low-speed maneuvering, and obstacle-avoidance tasks inspired by ADS-33 [17] (Fig. 2). Following [14, 18], we explicitly incorporate pilot biomechanics into these investigations.

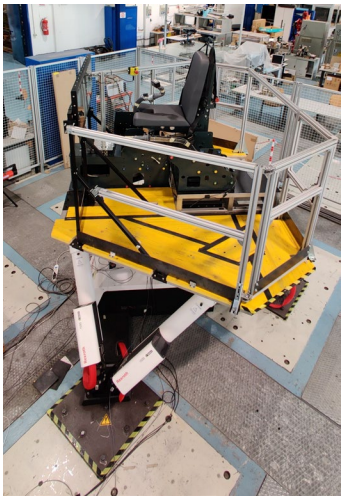


Figure 1: RPC testbed.

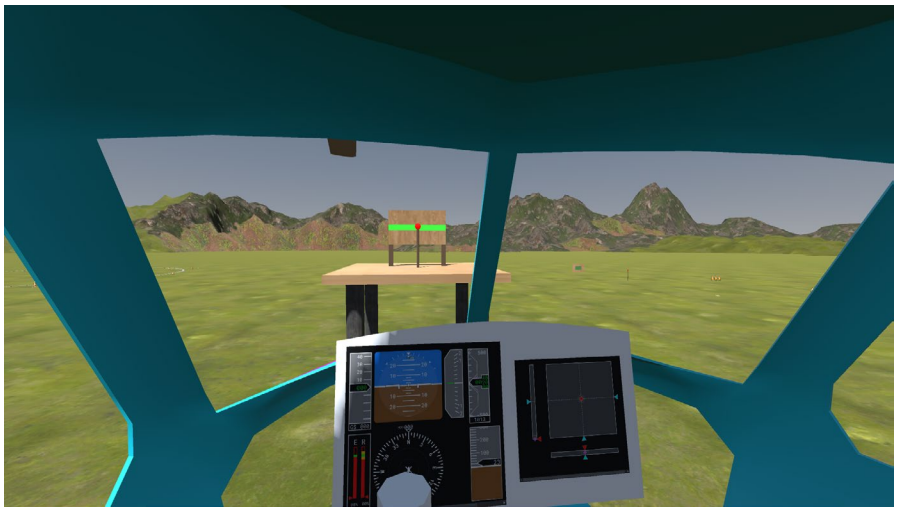


Figure 2: VR pilot view for ADS 33 vertical positioning.

A biomechanical sensitivity analysis was performed based on experimental data (Figs. 3 and 4). Key where pilot body parameters (stiffness, damping, mass distribution, reflex latency) were varied to emulate different postures and neuromuscular states. Stability margins, phase lag, axis coupling, and limit-cycle tendencies were evaluated under both linear and nonlinear control laws. Resonant modes were typically found in the 3–7 Hz range, overlapping rotor excitation frequencies (e.g., coning and slow cyclic lag modes in the non-rotating frame), thus influencing control fidelity.

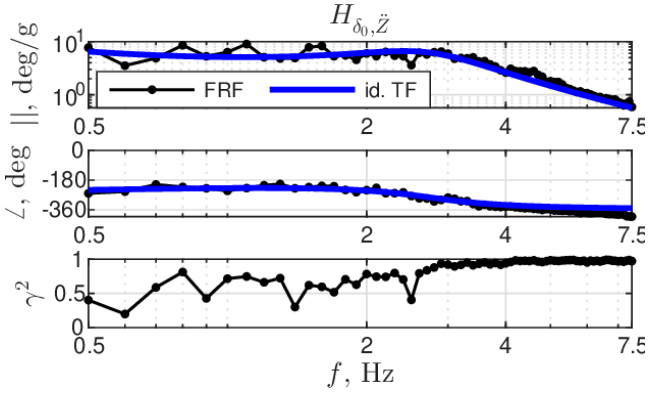


Figure 3: example BDFT identification of collective rotation due to vertical acceleration.

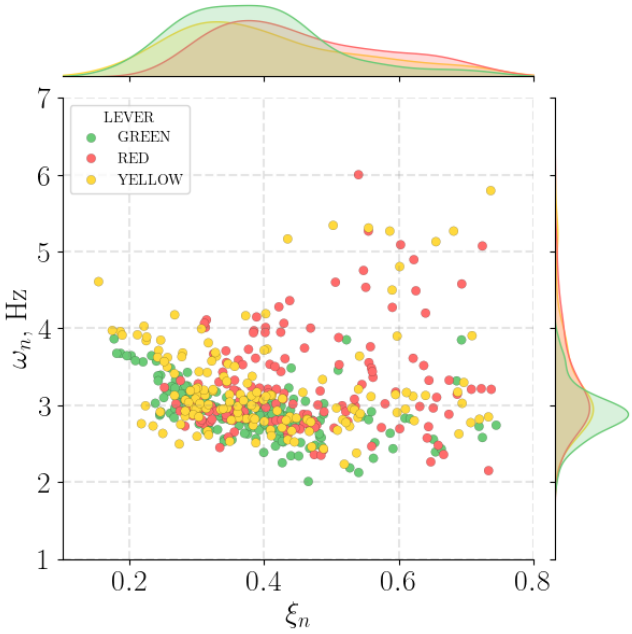


Figure 4: example of experimental distribution of BDFT dominant pole frequency ω_n and damping ξ_n for 15 subjects and 3 different collective levers.

The results indicate that anatomical resonance can reinforce lightly damped rotorcraft modes, potentially inducing instability or limit cycles, particularly under collective bounce conditions. Inter-pilot variability (e.g., BMI, posture, muscle co-contraction level) can qualitatively alter system behavior. Incorporating biomechanical modeling in early handling-qualities assessment reveals vulnerabilities not captured by conventional methods. Adaptive mitigation strategies, including seat damping, inceptor-response tuning, and control-law augmentation, can mitigate feedthrough-induced degradation while maintaining pilot authority.

The Way Forward

This perspective motivates revisiting both training and certification practices. Several questions remain open, such as:

- How do individual physical characteristics influence pilot control strategy?
- Can simulators meaningfully emulate posture-dependent biomechanical effects for training?
- Should aeromechanical stability clearance (and eventually certification) include robustness margins across a population of biomechanical models?

Introducing biodynamic sensitivity analysis into handling-quality frameworks may offer more robust design criteria by extending traditional bandwidth/phase-delay requirements. Simulator testing and pilot training should likewise incorporate posture- and stiffness-dependent modeling into protocols and syllabi, respectively, to raise awareness of involuntary control coupling.

References

[1] D. T. McRuer. Aviation Safety and Pilot Control: Understanding and Preventing Unfavourable Pilot-Vehicle Interactions. Washington DC: National Research Council, National Academy Press, 1997.

[2] Marilena D. Pavel, Michael Jump, Binh Dang-Vu, Pierangelo Masarati, Massimo Gennaretti, Achim Ionita, Larisa Zaichik, Hafid Smaili, Giuseppe Quaranta, Deniz Yilmaz, Michael Jones, Jacopo Serafini, and Jacek Malecki. Adverse rotorcraft pilot couplings — past,

present and future challenges. Progress in Aerospace Sciences, 62:1–51, October 2013. https://doi.org/10.1016/j.paerosci.2013.04.003.

[3] Giuseppe Quaranta, Pierangelo Masarati, and Joost Venrooij. Impact of pilots' biodynamic feedthrough on rotorcraft by robust stability. Journal of Sound and Vibration, 332(20):4948–4962, September 2013. https://doi.org/10.1016/j.jsv.2013.04.020.

[4] Massimo Gennaretti, Jacopo Serafini, Pierangelo Masarati, and Giuseppe Quaranta. Effects of biodynamic feedthrough in rotorcraft-pilot coupling: Collective bounce case. J. of Guidance, Control, and Dynamics, 36(6):1709–1721, 2013. https://doi.org/10.2514/1.61355.

[5] Pierangelo Masarati, Giuseppe Quaranta, and Michael Jump. Experimental and numerical helicopter pilot characterization for aeroelastic rotorcraft-pilot couplings analysis. Proc. IMechE, Part G: J. Aerospace Engineering, 227(1):124–140, January 2013. https://doi.org/10.1177/0954410011427662.

[6] Pierangelo Masarati and Giuseppe Quaranta. Bioaeroservoelastic analysis of involuntary rotorcraft-pilot interaction. J. of Computational and Nonlinear Dynamics, 9(3):031009, July 2014. https://doi.org/10.1115/1.4025354.

[7] Pierangelo Masarati, Giuseppe Quaranta, and Andrea Zanoni. Dependence of helicopter pilots' biodynamic feedthrough on upper limbs' muscular activation patterns. Proc. IMechE Part K: J. Multi-body Dynamics, 227(4):344–362, December 2013. https://doi.org/10.1177/1464419313490680.

[8] Marilena D. Pavel, Pierangelo Masarati, Massimo Gennaretti, Michael Jump, Larisa Zaichik, Binh Dang-Vu, Linghai Lu, Deniz Yilmaz, Giuseppe Quaranta, Achim Ionita, and Jacopo Serafini. Practices to identify and preclude adverse aircraft-and-rotorcraft-pilot couplings — a design perspective. Progress in Aerospace Sciences, 76:55–89, 2015. https://doi.org/10.1016/j.paerosci.2015.05.002.

[9] J. Venrooij, D. A. Abbink, M. Mulder, M. M. van Paassen, and M. Mulder. Biodynamic feedthrough is task dependent. In 2010 IEEE International Conference on Systems Man and Cybernetics (SMC), pages 2571–2578, Istanbul, Turkey, October 10–13 2010. https://doi.org/10.1109/ICSMC.2010.5641915.

[10] Andrea Zanoni, Matteo Zago, Rita Paolini, Giuseppe Quaranta, Emanuela Galli, and Pierangelo Masarati. On task-dependence of helicopter pilot biodynamic feedthrough and neuromuscular admittance. an experimental and numerical study. IEEE Transactions on Human-Machine Systems, 51(5):421–431, 2021. https://doi.org/10.1109/THMS.2020.3044971.

[11] Giuseppe Quaranta, Pierangelo Masarati, Jacopo Serafini, and Massimo Gennaretti. Aeroelastic rotorcraft-pilot couplings: Problems and methods. l'Aerotecnica Missili e Spazio, 95(3):176–187, 2016. https://doi.org/10.1007/BF03404726.

[12] Vincenzo Muscarello, Giuseppe Quaranta, and Pierangelo Masarati. The role of rotor coning in helicopter proneness to collective bounce. Aerospace Science and Technology, 36:103–113, July 2014. https://doi.org/10.1016/j.ast.2014.04.006.

[13] Vincenzo Muscarello, Pierangelo Masarati, Giuseppe Quaranta, Georges Tod, Julien Gomand, François Malburet, and Marilena D. Pavel. Instability mechanism of roll/lateral biodynamic rotorcraft-pilot couplings. Journal of the American Helicopter Society, 63:022004, 2018. https://doi.org/10.4050/JAHS.63.022004.

[14] Andrea Zanoni, Giacomo Gerosa, Luigi Di Lallo, and Pierangelo Masarati. Handling qualities in rotorcraft conceptual design. l'Aerotecnica Missili e Spazio, 101(1):95–108, 2022. https://doi.org/10.1007/s42496-022-00107-8.

[15] Marilena D. Pavel, Deniz Yilmaz, O. Stroosma, Binh Dang-Vu, Pierangelo Masarati, Giuseppe Quaranta, Massimo Gennaretti, Michael Jump, Linghai Lu, Michael Jones, Hafid Smaili, and Larisa Zaichik. Practices for identifying and precluding adverse aircraft- and rotorcraft-pilot couplings events — a ground simulator perspective. Progress in Aerospace Sciences, 77:54–87, August 2015. https://doi.org/10.1016/j.paerosci.2015.06.007.

[16] Davide Marchesoli, Andrea Zanoni, and Pierangelo Masarati. A meta-model for comprehensive pilot modeling. In 80th Vertical Flight Society Forum, Montreal, Canada, May 7–9 2024. https://doi.org/10.4050/F-0080-2024-1272.

[17] Anonymous. Performance specification, handling qualities requirements for military rotorcraft. ADS 33-E-PRF, US Army AMCOM, Redstone Arsenal, Alabama, USA, 2000.

[18] Qiuyang Xia, Davide Marchesoli, Meng Liu, and Pierangelo Masarati. Sensitivity of pilot biodynamic feedthrough to boundary avoidance tracking task complexity. Journal of Aerospace Information Systems, 22(7):523–540, 2025. http://doi.org/10.2514/1.I011566.

Materials Research Proceedings 69 (2026) 1471-1474 https://doi.org/10.21741/9781644904251-258

DLR Project NICo – Feasibility Study of an Alternate Airport Assistant for Pilots Deciding Where to Divert

Joan Iñaki GONZÁLEZ CABEZA[1,a *], Sören PETERSEN[1,b], Jan-Philipp BUCH[1,c], Dominik NIEDERMEIER[1,d], Matthias WIES[2,e], and Anne PAPENFUß[2,f]

[1]German Aerospace Centre, Institute of Flight Systems, Lilienthalplatz 7, 38108 Braunschweig, Germany

[2]German Aerospace Centre, Institute of Flight Guidance, Lilienthalplatz 7, 38108 Braunschweig, Germany

[a]joan.gonzalezcabeza@dlr.de, [b]soeren.petersen@dlr.de, [c]jan-philipp.buch@dlr.de, [d]dominik.niedermeier@dlr.de, [e]matthias.wies@dlr.de, [f]anne.papenfuss@dlr.de

Keywords: Single Pilot Operations, Electronic Flight Bag, Flight Deck, Human-Machine Interface

Abstract. Recently, industry has worked on concepts for reducing active flight crew in cruise while one crew member is resting (extended Minimum Crew Operations, eMCO). The project Next generation Intelligent Cockpit (NICo) of the German Aerospace Centre (DLR) aimed to develop assistance systems in the context of single pilot operations (SiPO) to support and relieve pilots in phases of high workload. To assist pilots with considering options for an alternate airport in case of urgent diversions, DLR has designed an electronic flight bag (EFB) application that calculates in-flight and landing performance and provides a ranking of suitable airports. Four criteria comprising distance, fuel on arrival, stop margin and crosswind defined suitability. In a previous pilot survey, these criteria were identified as important when deciding where to divert. The aims of a simulator study were to assess the functionalities of the EFB application and to gain pilot feedback on its usability and suggestions for further development. Focus was laid on investigating whether the equal weightings are consistent with the pilots' reasoning. Seven crews of two pilots with current or past Airbus A320 type rating performed a scenario in the DLR AVES full-motion A320 simulator. In this study, crews had to decide whether they would divert to an alternate airport when encountering a non-time-critical malfunction in adverse meteorological conditions. The pilots made use of the EFB application during their FORDEC process resting importance on its comprehensible ranking mechanism. In a preliminary analysis of results, it became evident that pilots rated the EFB application favourably and would consider using it in real operations when faced with the need to divert from the planned destination. Pilots experienced little workload throughout the scenario which shows that the EFB application is intuitive, helpful and lowers the workload in a potentially stressful situation.

Introduction

As global air traffic is forecast to grow significantly in the future and qualified aircrew is becoming scarce [1], concepts of reduced crew operations (RCO) have been investigated [2]. In recent times, the industry has been focussing on developing ideas to minimise the number of active crew members during cruise while one crew member is resting (extended Minimum Crew Operations, eMCO) [3]. Further reductions would lead to single pilot operations (SiPO) albeit neither concept is yet certified for EASA CS-25 aircraft. The project Next generation Intelligent Cockpit (NICo) of the German Aerospace Centre (DLR) aimed to develop assistance systems in the context of SiPO to support and relieve pilots in phases of high workload [4]. These systems should not only be of use for SiPO but also for common multicrew operations.

Content from this work may be used under the terms of the Creative Commons Attribution 3.0 license. Any further distribution of this work must maintain attribution to the author(s) and the title of the work, journal citation and DOI. Published under license by Materials Research Forum LLC.

Materials Research Proceedings 69 (2026) 1471-1474 https://doi.org/10.21741/9781644904251-258

Pilots are trained to adhere to the FORDEC or similar decision-making schemes. The mnemonic acronym FORDEC abbreviates the steps of collecting Facts, generating Options, analysing Risks and benefits, making a Decision, Executing it and Checking its adequacy over time [5]. According to recent expert interviews, pilots would welcome additional support, particularly with the FORDEC decision-making steps [6]. However, the experts emphasised that the final decision and its execution must remain the responsibility of the human crew or pilot, not an automated system.

DLR has created an electronic flight bag (EFB) application to support pilot's decision-making bearing in mind the FORDEC process. It should assist mainly with the categories Facts, Options, and Risks of FORDEC when exploring alternatives for a diversion. The application calculates and evaluates in-flight and landing performance to suggest suitable airports. The suitability of airports was determined by four key factors: distance, fuel on arrival, stop margin, and crosswind. Initially, these factors were given equal weight using the multi-criteria decision-making approach TOPSIS [7]. Findings from a previous pilot survey confirmed the importance of these criteria in determining where to divert [8]. The aims of the present study were thus to assess the feasibility of the EFB application and to get pilot feedback on its usability.

Methods

Fourteen pilots which hold or held an Air Transport Pilot Licence (ATPL) and were rated on the Airbus A320 were recruited to participate in the research study. The mean age of the participants was 49.36 (standard deviation, SD = 12.38) years. The average hours of flying experience were 14740 (SD = 10870). Seven pilots were first officers or captains, respectively. Categorised by their most recent operations, five were flying long-range while nine were flying short-range flights.

For each experiment run, a crew of two pilots was seated in the Airbus A320 replica as part of the Air Vehicle Simulator (AVES) and was provided with the application under research on both EFB. After a familiarisation scenario, the main scenario flight was performed with both crew on the simulator flight deck. The pilots were free to choose who would be pilot flying (PF) and pilot monitoring (PM). Shortly after take-off upon retracting the slats and flaps, the crew would encounter a malfunction as the flaps would not fully retract but remained stuck between their 0 and 1 position. The effects of the failure included higher fuel consumption because of increased drag, and longer distance required to land the aeroplane. Due to adverse weather conditions at several airports, the pilots needed to consider carefully where to divert.

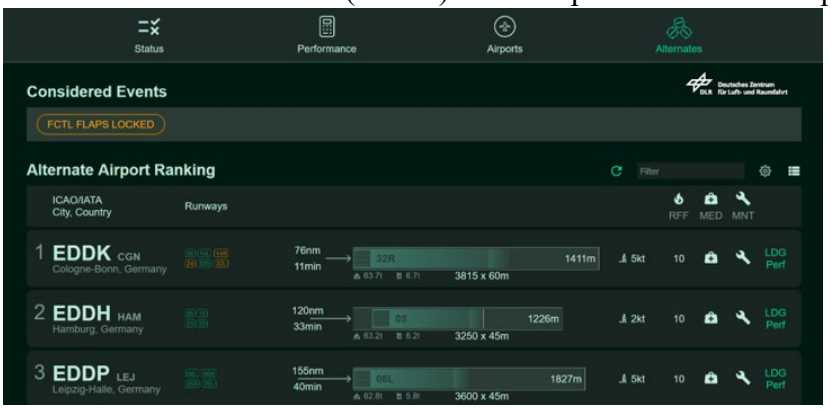


Figure 1. Alternates page

The EFB app features four main pages, i.e. a status page, a performance page, an airports page and an alternates page. The most important page is the alternates page where a ranking of airports suitable for a diversion is provided (cf. Figure 1). Suitability is defined by the four aforementioned criteria comprising distance, fuel on arrival, stop margin and crosswind. These are weighted equally by default using the multi-criteria decision-making method TOPSIS. Pilots are able to modify the weightings relatively. The status page informs the pilots about the effects of a detected failure and its influence on the app's calculations, e.g. increased fuel consumption. Also, considered Notices to Airmen (NOTAM) are shown. The other pages present the performance

Materials Research Proceedings 69 (2026) 1471-1474 https://doi.org/10.21741/9781644904251-258

calculations for each runway of a selected airport and a list of airports with prevailing weather conditions.

The underlying calculations provide the distance and remaining flight time to each airport, as well as estimates of landing performance, i.e. required landing distances and speeds that are computed failure-dependent. In the given scenario, the flaps locked fault led to higher approach speeds and increased distances needed at landing. The system also considers any predicted crosswind and potentially higher fuel consumption. On the performance page, pilots can adapt input values like the runway condition and wind speed, or indicate the use of reverse thrust. Both pilots were provided the application on their respective EFB devices that were mounted to the side-wall panels of the flight deck. The EFB were not synchronised but allowed for individual use.

The questionnaires employed in the research included one about demographics (i.e., age, gender, nationality, position, aircraft types, flight hours), one about the different features of the EFB app, one about ergonomics (i.e., situational awareness, trust, task sharing), and the NASA Task Load Index (NASA-TLX) [9].

During the scenario flight, data from the simulator as well as video and audio were recorded. The former included flight dynamics parameters, and aircraft system states, while the latter two comprised a view of the flight deck, screencasts from instruments, and communication between flight crew, simulated ATC, and researchers.

Results

The NASA-TLX questionnaire was administered upon concluding the experiment. Figure 2 shows the average weighted scores of twelve of the subjects across the dimensions mental demand (MD), physical demand (PD), temporal demand (TD), performance (PE), effort (EF), and frustration (FR), as well as the aggregate task load index (TLX). Two participants did not fill out the questionnaire and are thus not included in the results. On average, the pilots indicated a TLX of 7.41 which is fairly low on a scale from zero to 100. Partial scores of mental demand were the highest and those of frustration the lowest.

Valuable feedback on features and user interface of the application was received, including suggestions to increase button size, include a map, and provide a return button. All pilots indicated that the app's pages were intuitive to use. Many pilots affirmed that its features were useful.

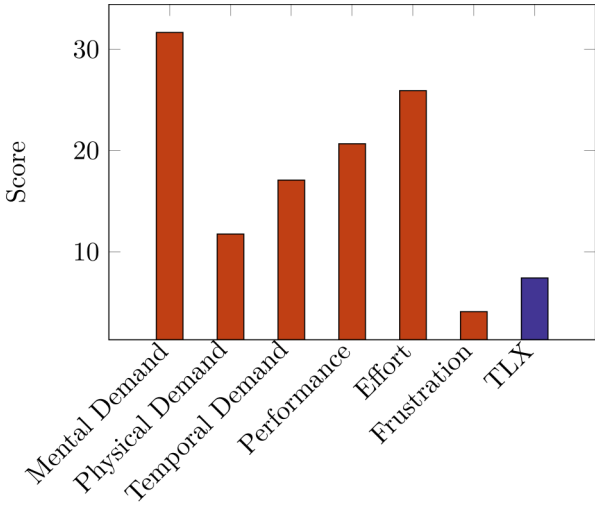


Figure 2. NASA-TLX average weighted scores

Discussion

The research aimed to assess the feasibility of a newly developed EFB application that should support pilots' decision-making when considering options where to divert. The results revealed that pilots rated the app favourably and found its features useful, particularly the alternates ranking which is based on a multi-criteria decision-making method. Pilots rested importance on the comprehensibility of the ranking mechanism.

Pilots experienced low workload throughout the scenario and were on average little demanded nor frustrated. This supports the statement that the EFB app is not an additional burden on them. For a different scenario where pilots operated spatially separated and without the EFB app, Niedermeier et.al. [4] reported that pilots felt rather overwhelmed and not able to deliver their full performance. Especially in such scenarios with high workload, the app could be of use.

The results need to be interpreted within the confines of the research. All participants volunteered, potentially leading to self-selection bias and the sample was relatively small (14 pilots). This limited number of participants does not allow any generalisation of the study results.

Conclusion

Within the project NICo, an exploratory simulator study was performed to assess the feasibility of a newly-developed EFB app in a failure scenario. Although only seven crews took part in the experiments, interesting qualitative results based on questionnaires and crew comments were obtained. Crew comments showed the app's potential for use in commercial operations.

References

[1] D. Hulst. „Boeing Commercial Market Outlook.“ [Online]. Available: https://www.boeing.com/content/dam/boeing/boeingdotcom/market/assets/downloads/2024-cmo-executive-presentation.pdf

[2] R. E. Bailey, L. J. Kramer, K. D. Kennedy, C. L. Stephens, and T. J. Etherington, „An assessment of reduced crew and single pilot operations in commercial transport aircraft operations,“ in 2017 IEEE/AIAA 36th Digital Avionics Systems Conference (DASC), 2017, pp. 1–15. [Online]. Available: https://ieeexplore.ieee.org/abstract/document/8101988

[3] D. Ziakkas, A. Plioutsias, and K. Pechlivanis, „Artificial Intelligence in aviation decision making process.The transition from extended Minimum Crew Operations to Single Pilot Operations (SiPO),“ in Artificial Intelligence and Social Computing, 2022, doi: 10.54941/ahfe1001452.

[4] D. Niedermeier, A. Papenfuß, and M. Wies, „Simulator Study on a Spatially Separated Airline Crew in a Complex Decision-Making Scenario,“ in AIAA AVIATION 2023 Forum, San Diego, CA and Online, 2023, doi: 10.2514/6.2023-3474.

[5] H. Soll, S. Proske, G. Hofinger, and G. Steinhardt, „Decision-Making Tools for Aeronautical Teams: FOR-DEC and Beyond,“ Aviation Psychology and Applied Human Factors, vol. 6, no. 2, pp. 101–112, 2016, doi: 10.1027/2192-0923/a000099.

[6] F. Zinn, J. della Guardia, and F. Albers, „Pilot‘s Perspective on Single Pilot Operation: Challenges or Showstoppers,“ Lecture Notes in Computer Science, vol. 14018, pp. 216–232, 2023. [Online]. Available: https://elib.dlr.de/194502/

[7] B. Uzun, M. Taiwo, A. Syidanova, and D. Uzun Ozsahin, „The Technique For Order of Preference by Similarity to Ideal Solution (TOPSIS),“ in Application of Multi-Criteria Decision Analysis in Environmental and Civil Engineering (Professional Practice in Earth Sciences), D. Uzun Ozsahin, H. Gökçekuş, B. Uzun, and J. LaMoreaux, Eds., Cham: Springer International Publishing, 2021, pp. 25–30.

[8] G. Schmitz and J.-P. Buch, „DLR-Projekt NICo: Vorläufige Auswertung einer Online-Pilotenstudie zur Entscheidungsfindung bei der Auswahl eines Ausweichflughafens,“ 2024, doi: 10.25967/610107.

[9] S. G. Hart and L. E. Staveland, „Development of NASA-TLX (Task Load Index): Results of Empirical and Theoretical Research,“ in Human Mental Workload (Advances in Psychology), Elsevier, 1988, pp. 139–183.

Materials Research Proceedings 69 (2026) 1475-1480 https://doi.org/10.21741/9781644904251-259

Visual Monitoring Behavior in Dual- and Reduced-Crew Configurations During Abnormal Events

Nicola PUCA[1,a *], Marco POGLIANO[2,b], Gabriele LUZZANI[3,c], Giorgio GUGLIERI[1,d], and Danilo DEMARCHI[2,e]

[1]Department of Mechanical and Aerospace Engineering, Politecnico di Torino, Turin, Italy

[2]Department of Electronics and Telecommunications, Politecnico di Torino, Turin, Italy

[3]Department of Aerospace Engineering, University of Maryland College Park, MD, 20740, USA

[a]nicola.puca@polito.it, [b]marco.pogliano@polito.it, [c]gluzzani@umd.edu, [d]giorgio.guglieri@polito.it, [e]danilo.demarchi@polito.it

Keywords: Cockpit Monitoring, Scanpath Analysis, Reduced-Crew Operations, Attention, A320 Flight Simulator

Abstract. The proposed reduction in commercial flight crew sizes, together with evolving cockpit operational concepts, introduces significant human factors challenges related to attention management, workload allocation, and pilot–automation interaction. Although such scenarios may be confined to specific flight phases, they highlight the continued importance of robust cockpit monitoring and have intensified interest in digital assistants to support task execution and decision-making. This study presents a comparative assessment of eye-tracking metrics and visual scanning strategies adopted by two professional pilots operating an A320 full-flight simulator. A representative short-haul mission was performed under nominal and abnormal conditions, including a hydraulic failure, in both dual- and single-pilot configurations. Gaze data were collected using Tobii Pro Glasses 3 and analyzed through an area-of-interest–based approach to characterize scanning pattern complexity. Preliminary results indicate distinct monitoring behaviors across conditions, largely influenced by the presence and modality of assistance.

Introduction

Visual monitoring is essential for commercial piloting, as it enables the continuous construction and maintenance of situational awareness through structured scan patterns, selective attention, and systematic cross-checking of cockpit information. [1] Persistent shortcomings in monitoring performance, however, continue to contribute to major incidents and crew-related operational errors. [2] This is partly attributable to the vulnerability to fatigue, which can degrade scanning strategies and impair the timely detection of safety-critical events. [3] These observations extend across diverse operational domains, with eye-movement behavior shown to reflect operators' supervisory functions and cognitive states. [4] Concerning aviation, pilots' scanpath organization varies systematically across flight phases, while different expertise levels can affect fixation distributions and visual strategy structures. [5, 6]

Recent advances in eye-tracking technology [7] have enabled precise and largely unobtrusive measurement of gaze behavior in both operational settings and high-fidelity simulation environments. [8] Consequently, these tools are now widely employed for workload assessment, training evaluation [9], and predictive modelling in human–machine interaction [10].

As flight decks progress toward higher levels of automation, the potential transition to reduced crew operations [11] is expected to redistribute attentional resources that currently benefit from cooperative scanning and shared mental models. This shift raises concerns regarding increased attentional demands on the remaining pilot, thereby motivating renewed interest in monitoring behaviors and in the potential contribution of intelligent aiding systems. Despite the valuable

Content from this work may be used under the terms of the Creative Commons Attribution 3.0 license. Any further distribution of this work must maintain attribution to the author(s) and the title of the work, journal citation and DOI. Published under license by Materials Research Forum LLC.

Materials Research Proceedings 69 (2026) 1475-1480 https://doi.org/10.21741/9781644904251-259

insights provided, the correspondence between eye movements and attention is not perfect, as attentional shifts and peripheral information processing may occur without direct fixation. Accordingly, eye-based measures are most informative when triangulated with complementary data sources.

Experiment and Data Analysis

An experimental campaign was conducted using an Airbus A320 FNPT II MCC simulator at KKtoFly (Collegno, Italy). Two A320 type-rated male pilots each flew the same short-haul mission from Torino Caselle (LIMF) to Rome Fiumicino (LIRF) under dual- and single-pilot configurations, with a qualified co-pilot included when required. For each configuration, two scenarios were tested: (i) a nominal baseline and (ii) a Green + Yellow (G+Y) hydraulic system low-pressure failure, requiring early landing preparation, degraded flight-envelope protections, reduced system redundancy, and predominantly manual control via ECAM-directed procedures. All missions included variable weather and standard ATC interactions, handled by a dedicated operator.



Figure 1 *Single-crew configurations employed for the two pilots.*

As a starting point for single-pilot operations, tasks normally assigned to the co-pilot are assumed to be performed by the captain, although the target scenario involves collaboration with intelligent assistive entities. Two experimental variants were therefore implemented (see *Figure 1*). The first corresponds to an unassisted "all-alone" condition, in which higher workload and monitoring demands are intentionally imposed on the pilot (Pilot 2) to stress and test his condition. By contrast, the second condition provides the pilot (Pilot 1) with a custom software tool on the Electronic Flight Bag that replicates selected overhead-panel functions, executes predefined routines (e.g., overhead configuration and ECAM procedures), and provides continuous feedback. Readers can refer to the left-hand side of *Figure 2*. This assisted mode redistributes task allocation and is expected to influence monitoring strategies and eye-movement behavior.

Materials Research Proceedings 69 (2026) 1475-1480 https://doi.org/10.21741/9781644904251-259

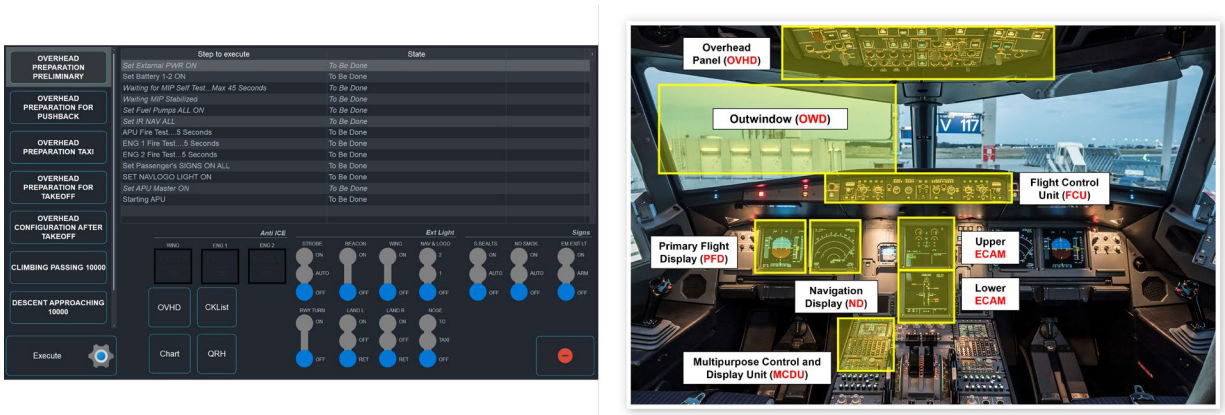


Figure 2 *On the left – A sketch from the Virtual Assistant landing page. On the right – AOI definition inside the A320 cabin.*

Pilot gaze was recorded using Tobii Pro Glasses 3 at 50 Hz and processed using Tobii Pro Lab software. Gaze samples were classified into fixations and saccades. In accordance with established eye-tracking standards [12], fixations were identified using a minimum duration threshold of 120 ms.

The cockpit was partitioned into eight Areas of Interest (AOIs) corresponding to the primary operational displays and interaction zones of the Airbus A320 (*Figure 2*). In the assisted single-pilot condition, a ninth AOI was introduced to capture gaze directed toward the tablet-based Virtual Assistant. AOI definitions were spatially consistent across participants, and samples falling outside predefined regions were excluded. Fixations were assigned to AOIs, and consecutive fixations within the same region were aggregated into dwells.

The analysis focused on a short, operationally relevant flight segment surrounding the failure event, spanning from failure onset to completion of all ECAM actions required to minimally secure the aircraft (i.e., transition to the Status page). This interval captures the critical phase requiring immediate diagnostic and procedural responses.

Results and Discussion

Two complementary analyses were conducted. The first examined scanpath dynamics via gaze transitions between AOIs to characterize the structure and temporal organization of visual scanning. The second quantified attentional allocation using fixation-based metrics, namely Total Fixation Duration (TFD) and Mean Fixation Duration (MFD). TFD reflects overall visual workload, whereas MFD captures the depth of visual processing. As shown in *Figure 3*, scanpaths are analyzed at the AOI level, whereas TFD and MFD are aggregated into functional and thematic AOI clusters to support workload interpretation in terms of general piloting functions. Analyses were conducted both across configurations and between pilots, given the fixed single-pilot condition of interest. Although the overall time window spans only a few minutes, it was sufficient to reveal meaningful differences between conditions. The pilots under analysis always acted as pilot flying, thereby retaining primary control of the aircraft and responsibility for communications.

Analysis of Pilot 2's visual behavior indicates a strong dependence on the crew configuration. In Dual-Pilot Operations (DPO), Pilot 2 directs most visual attention to the Primary Flight instruments, with a dynamic scanpath marked by frequent transitions and short fixations, consistent with shared workload and continuous monitoring on the PFD. No gaze directed toward OVHD was observed during this condition, as these tasks are typically performed by the co-pilot. Under Single-Pilot Operations (SPO), by contrast, attention shifts markedly to the Systems cluster, which dominates both TFD and MFD. Once the failure has happened, PFD monitoring becomes

Materials Research Proceedings 69 (2026) 1475-1480 https://doi.org/10.21741/9781644904251-259

sporadic, and long system-focused dwell periods emerge, especially on ECAM-UPPER and OVHD. FCU involvement decreases sharply, suggesting reduced capacity for flight-control adjustments. The mayday call was observed to occur sooner during SPO, reflecting the absence of cross-checking or probably the latent need to accelerate operations. Overall, Pilot 2's scanpath shifts from broad, high-frequency monitoring with DPO to a system-focused pattern characteristic of increased workload and reduced situational awareness (for SPO).

The same analysis can be done for Pilot 1. In DPO, attention is primarily divided between Systems and Control/Mode, with substantial engagement of Primary Flight instruments. The scanpath remains rich and continuous, supported by effective task sharing. In SPO, Systems monitoring increases—as observed for Pilot 2, yet Pilot 1 maintains recurrent transitions to PFD and ND even after the failure, preserving a more balanced monitoring loop. Scanpaths remain diversified, with short-to-medium dwell times indicative of active management of both flight-path monitoring and diagnostic tasks. The Virtual Assistant appears to redistribute, rather than intensify, workload by supporting ECAM interpretation and procedural structuring, thus reducing prolonged system-focused fixations. A notable drawback is the reduced outside-window scanning, which, although mitigated in this scenario by benign cruise-phase conditions, would not be desirable in other phases of flight. It is also relevant to remember that the pilot received minimal training with the assistant; increased familiarity may further enhance monitoring stability.

Conclusion

This preliminary study examined changes in pilot gaze behavior during abnormal event management across dual- and single-pilot configurations. Despite the limited sample, eye tracking revealed consistent shifts in visual strategies associated with increased workload and changes in monitoring responsibilities. Future work will extend the analysis to more pilots, flight phases, and failure scenarios, and integrate gaze data with performance and workload measures. Beyond reduced-crew operations, this approach may also inform cockpit interface design, assistive tool evaluation, and training for effective monitoring.

Materials Research Proceedings 69 (2026) 1475-1480 https://doi.org/10.21741/9781644904251-259

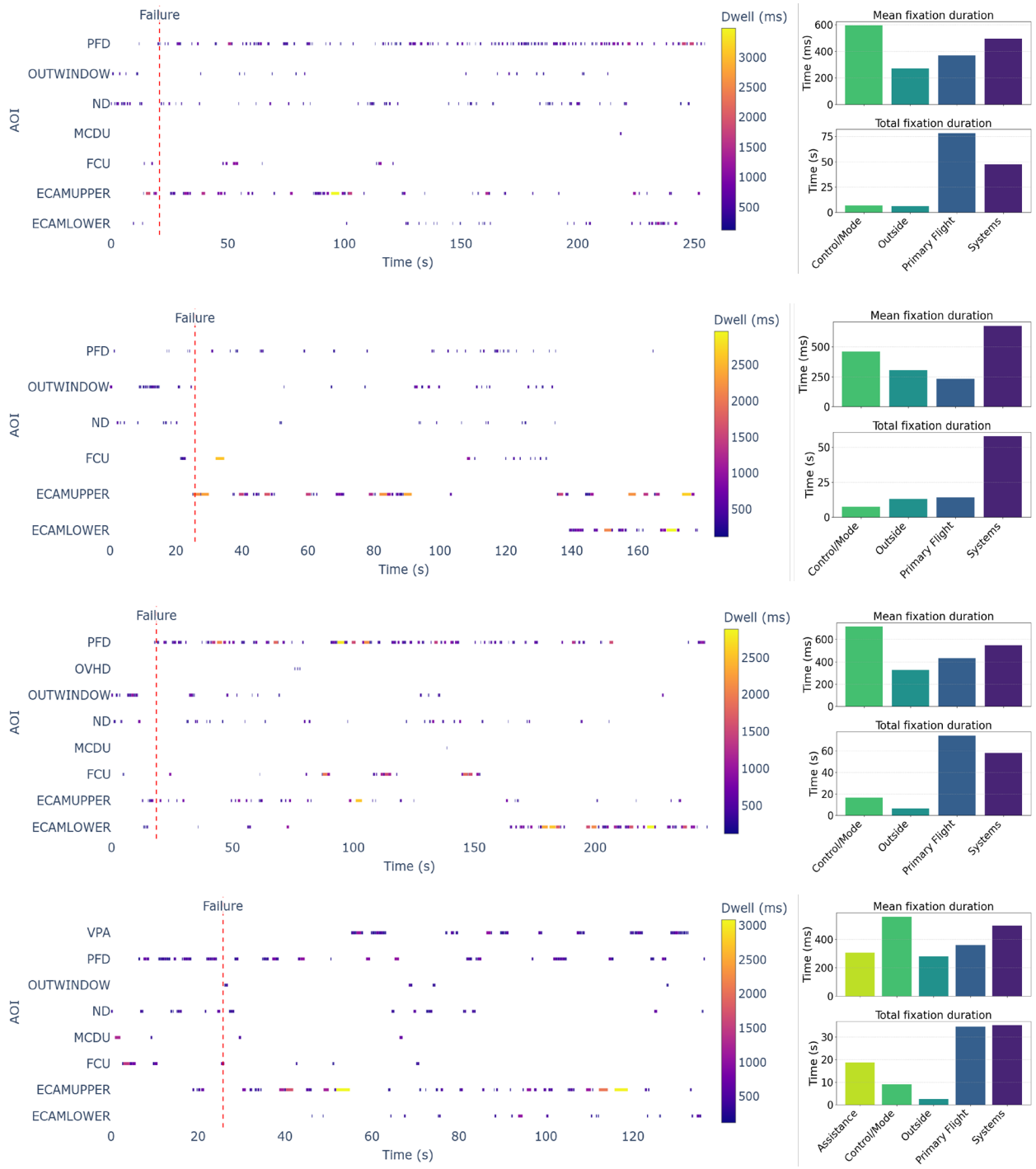


Figure 3 *On the left of each panel, the scanpath is shown, where small rectangles denote individual fixations on the corresponding AOI over time; the red vertical line marks the moment of failure onset. On the right, histograms report fixation metrics aggregated into thematic clusters, each grouping multiple AOI: Primary Flight (PFD, ND), Systems (ECAM UPPER, ECAM LOWER, OVHD), Control/Mode (FCU, MCDU), Assistance (VPA), and Outside (OUTWINDOW).*

References

[1] Loss of Control Action Group, "Monitoring Matters: Guidance on the Development of Pilot Monitoring Skills," Civil Aviation Authority (CAA), London, UK, CAA Paper 2013/02, 2013.

[2] R. \ Dismukes Key and B. Berman, "Checklists and Monitoring in the Cockpit: Why Crucial Defenses Sometimes Fail," National Aeronautics and Space Administration, Ames Research Center, Moffett Field, CA, USA, NASA Technical Memorandum (TM) NASA/TM-2010-216396, Jul. 2010. [Online]. Available: https://ntrs.nasa.gov/citations/20110011145

[3] X. Wu, X. Wanyan, and D. Zhuang, "Pilot's Visual Attention Allocation Modeling Under Fatigue," *Technol. Health Care*, vol. 23, no. Suppl.\;2, pp. S373–S381, 2015. https://doi.org/10.3233/THC-150974.

[4] U. S. D. of Defense, "Crew Systems Analysis: A Review of Aircrew Performance, Attention, and Monitoring," Defense Technical Information Center, AD1000097, 2010. [Online]. Available: https://apps.dtic.mil/sti/tr/pdf/AD1000097.pdf

[5] C. Lounis, V. Peysakhovich, and M. Causse, "Visual scanning strategies in the cockpit are modulated by pilots' expertise: A flight simulator study," *PLOS ONE*, vol. 16, no. 2, p. e0247061, 2021. https://doi.org/10.1371/journal.pone.0247061.

[6] M. Friedrich, S. Y. Lee, P. Bates, W. Martin, and A. K. Faulhaber, "The influence of training level on manual flight in connection to performance, scan pattern, and task load," *Cogn. Technol. Work*, vol. 23, pp. 715–730, 2021. https://doi.org/10.1007/s10111-020-00663-8.

[7] K. Holmqvist, M. Nyström, R. Andersson, R. Dewhurst, H. Jarodzka, and J. van de Weijer, *Eye Tracking: A Comprehensive Guide to Methods and Measures*. Oxford: Oxford University Press, 2011.

[8] L. Mengtao, L. Fan, X. Gangyan, and H. Su, "Leveraging eye-tracking technologies to promote aviation safety-a review of key aspects, challenges, and future perspectives," *Saf. Sci.*, vol. 168, p. 106295, 2023.

[9] O. Lefrançois, N. Matton, and M. Causse, "Improving Airline Pilots' Visual Scanning and Manual Flight Performance through Training on Skilled Eye Gaze Strategies," *Safety*, vol. 7, no. 4, 2021. https://doi.org/10.3390/safety7040070.

[10] L. Wang, Z. Zhang, W. Tan, and Z. Yang, "A Real-Time Measurement Model of Attention-Allocation Level and Its Application in Simulated SPO Task," *Int. J. Aerosp. Eng.*, vol. 2024, 2024. https://doi.org/10.1155/2024/3901699.

[11] N. Puca and G. Guglieri, "Enabling Civil Single-Pilot Operations: A State-of-the-Art Review," *Aerotec. Missili Spaz.*, vol. 104, pp. 187–212, 2024. https://doi.org/10.1007/s42496-024-00223-7.

[12] D. D. Salvucci and J. H. Goldberg, "Identifying fixations and saccades in eye-tracking protocols," in *Proceedings of the Eye Tracking Research & Applications (ETRA'00)*, 2000, pp. 71–78. https://doi.org/10.1145/355017.355028.

Materials Research Proceedings 69 (2026) 1481-1486 https://doi.org/10.21741/9781644904251-260

Continuous Time Estimation of Pilot Biodynamic Response for Vertical Bounce Coupling Assessment

Tommaso ARESI[1,a *], Andrea ZANONI[1,b] and Pierangelo MASARATI[1,c]

[1]Via La Masa, 34, 20156 Milan, Italy

[a] tommaso.aresi@polimi.it, [b]andrea.zanoni@polimi.it, [c]pierangelo.masarati@polimi.it

Keywords: Rotorcraft–Pilot Coupling RPC, Pilot-Assisted Oscillations PAO, Time-Varying Parameters, Kalman Filter, Parameter Identification

Abstract. This work addresses the estimation of time-varying pilot parameters within Rotorcraft–Pilot Couplings. An analytical, physics-based model with the minimum number of degrees of freedom represents the coupled pilot–helicopter dynamics. Parameter tracking uses sigma-points filtering to capture time-varying parameter characterization. Simulations under diverse conditions accurately reconstruct the trajectories of states and parameters in real time. The approach provides a practical basis for robust online identification and control strategies to mitigate Pilot-Assisted Oscillations.

Introduction

The helicopter's vibrations, inherent to rotor–airflow interactions, degrade controllability and overall safety. Pilots experience these effects as reduced control authority. Pilots' performances decrease while workload increases [1,2].

In the context of interactions between pilot biomechanics and helicopter vibratory dynamics, known as (adverse) Rotorcraft–Pilot Couplings (RPCs) [1,3], this work is focused in the 2–8 Hz range, which lies outside the pilot's intentional control bandwidth; in this regime, the pilot's biomechanical response becomes the driver of a closed-loop behavior.

Following Venrooij's framework [4], the input-output relation is defined as Biodynamic Feedthrough (BDFT). This specific case studies the vertical collective bounce [3], an RPC where vertical excitation couples with collective-lever motion through pilot biomechanics, forming a feedback loop. Since the collective lever controls the main rotor thrust, this loop can enter a self-excited limit cycle, making it one of the critical RPC phenomena to be mitigated.

Several pilot–helicopter models have been developed to capture RPC dynamics [4,5]. An analytical, physics-based approach is adopted in [6], with the minimum number of degrees of freedom and parameters, and benchmarked against prior studies and validated references. These models aim to provide interpretable representations without any loss of information about the phenomenon. The objective is to clarify how physics and geometry non-linearities shape the dynamic response.

These models simplify the parameters' tuning relative to higher order models and preserve a direct link between parameter modifications and system response. The reduced parameters set helps the deployment in control and estimation frameworks with efficient real-time execution; moreover, the provided kinematic models can be exploited for inference even in the absence of input information.

Problem

Biomechanical systems exhibit intrinsic time variance due to fatigue or sudden events. Accordingly, their parameters cannot be assumed constant over time [7]. The governing laws are not known a priori, and such variability may trigger Pilot-Assisted Oscillations (PAOs).

Content from this work may be used under the terms of the Creative Commons Attribution 3.0 license. Any further distribution of this work must maintain attribution to the author(s) and the title of the work, journal citation and DOI. Published under license by Materials Research Forum LLC.

Materials Research Proceedings 69 (2026) 1481-1486 https://doi.org/10.21741/9781644904251-260

The goal is to identify parameters' evolution without an explicit model or direct measurements, selecting at each instant the most plausible parameters set to enable interpretation and mitigation via informed and robust control schemes, without sacrificing controllability.

Estimating time-varying parameterization is widespread across disciplines. Among others, see the work by [8, 9].

The task is inherently complex: online parameter evolution requires simultaneous state and parameter estimation. Even a simple relation $\dot{x} = w(t)\, x(t)$ becomes nonlinear here, since both w(t) and x(t) are jointly unknown and must be estimated [8]. , a probabilistic and optimization approach is adopted. The helicopter-focused literature remains limited [7], especially on sigma-point framework, which uses deterministic sampling for statistically robust linearization [9]. Two approaches are considered [8, 9], with the latter's core scheme presented.

Algorithm 1. Sigma-points Parameter Filter

Require prior $\hat{\mathbf{w}}_0 = \mathrm{E}[\mathbf{w}]$, $\mathbf{P}_{w,0} = \mathrm{E}[(\mathbf{w} - \hat{\mathbf{w}}_0)(\mathbf{w} - \hat{\mathbf{w}}_0)^\intercal]$
for k = 1, 2, … **do**
  $\hat{\mathbf{w}}_k^- \leftarrow \hat{\mathbf{w}}_{k-1}$, $\mathbf{P}_{w,k}^- \leftarrow \mathbf{P}_{w,k-1} + \mathbf{R}_{k-1}^w$
  $\mathbf{S}_{w,k} \leftarrow \mathrm{chol}(\mathbf{P}_{w,k}^-)$
  $\mathcal{W}_{k|k-1} = [\hat{\mathbf{w}}_k^-,\ \hat{\mathbf{w}}_k^- \pm \gamma\, \mathbf{S}_{w,k}]$
  $\mathcal{D}_{k|k-1} \leftarrow \mathrm{G}(\mathrm{x}_k, \mathcal{W}_{k|k-1})$
  $\mathbf{d}_k \leftarrow \sum_i \mathbf{W}_i^{(m)}\, \mathbf{D}_{i,k|k-1}$
  $\mathbf{P}_{dd,k} \leftarrow \sum_i \mathbf{W}_i^{(c)}\, (\mathbf{D}_{i,k|k-1} - \mathbf{d}_k)(\mathbf{D}_{i,k|k-1} - \mathbf{d}_k)^\intercal + \mathbf{R}_k^e$
  $\mathbf{P}_{wd,k} \leftarrow \sum_i \mathbf{W}_i^{(c)}\, (\mathbf{W}_{i,k|k-1} - \hat{\mathbf{w}}_k^-)(\mathbf{D}_{i,k|k-1} - \mathbf{d}_k)^\intercal$
  $\mathbf{K}_k \leftarrow \mathbf{P}_{wd,k}\, \mathbf{P}_{dd,k}^{-1}$
  $\hat{\mathbf{w}}_k \leftarrow \hat{\mathbf{w}}_k^- + \mathbf{K}_k(\mathbf{d}_k - \mathbf{d}_k)$, $\mathbf{P}_{w,k} \leftarrow \mathbf{P}_{w,k}^- - \mathbf{K}_k\, \mathbf{P}_{dd,k}\, \mathbf{K}_k^\intercal$
end for

The problem is decoupled [8]: a state estimation step and a parameter identification step are executed separately at each time step. This strategy lowers computational cost, and often allows each sub-problem to be treated as linear, unlike the joint formulation, [8]. In the absence of a known parameter-evolution model, each parameter follows a random walk, enabling probabilistic exploration of the parameter's space at every step. Future work will consider richer dynamics while addressing hyperparameter selection. In general, the problem can be written as:

$$\begin{cases} \dot{x} = f\big(x(t), u(t); w(t)\big) + v_x(t), \\ \dot{w} = g\big(x(t), w(t)\big) + v_w(t), \\ y = h\big(x(t), w(t)\big) + v_y(t). \end{cases}$$

Here f is the state dynamics of x, g is the parameter dynamics of w, h is the observation map for y, and v_x, v_x, v_γ are the process and measurement noise. Multiple formulations were considered: first, a second-order system to estimate both physical parameters and the state-space entries of A (a simple black-box setup).; subsequently, a formulation from prior work [6] was adopted, reported below:

$$\big[\ell^2\big(\eta^2 m_e + m_p\big) + J_\ell\big]\ddot{\theta} + \big[c_p \ell^2 cos^2\dot{\theta} + c_o\big)\dot{\theta} + \big[\ell g\big(m_e + m_p\big) - \ell^2 k_p sin\theta\big)cos\theta + \ell^2 k_p sin\theta cos\theta + k_o\theta - k_o\hat{\theta} = -\ell\big(m_e + m_p\big)cos\theta\ddot{z}$$

Materials Research Proceedings 69 (2026) 1481-1486 https://doi.org/10.21741/9781644904251-260

Where θ is the angle between the collective axis and the floor, [θ, θ̇] are the states; ℓ the lever length; η the Center of Mass relative position; m_l, $m_p(t)$ the lever and pilot equivalent mass; J_l the lever inertia; $c_p(t)$, c_o the equivalent damping; $k_p(t)$, k_o the equivalent stiffness; $\hat{\theta}$, $\bar{\theta}$ the spring preloads; and $\ddot{z}$ the base vertical acceleration. Parameters to be identified: $[m_p, c_p, k_p]$.

Simple linear systems are modeled as mass–spring–damper equivalents and can be written in two standard forms:

$$\begin{bmatrix}\dot{\theta}\\ \ddot{\theta}\end{bmatrix} = \begin{bmatrix}0 & 1\\ -\frac{k}{m} & -\frac{c}{m}\end{bmatrix}\begin{bmatrix}\theta\\ \dot{\theta}\end{bmatrix} + \begin{bmatrix}0\\ 1\end{bmatrix}\ddot{z}$$

The goal is to estimate both state-space coefficients $[a_{21}(t), a_{22}(t), b_{21}(t)]$ and physical parameters $[m_p(t), c_p(t), k_p(t)]$, which enter the equations through nonlinear terms. Despite its simplicity, the single Degree of Freedom (1-DOF) model yields a statistically grounded linearization at each step, enabling effective use of measurements, unlike purely deterministic differentiation. Equation (2), though the simplest in [6], already embeds the key nonlinearities, making it a suitable benchmark for parameter identification. Future work will extend to 2-DOF (linear and nonlinear) models as proxies for complex multibody systems, enabling rigorous model-mismatch tests. The observation model is a direct state measurement [8]; future work will include richer sensor dynamics. Algorithms from [8] (a Dual Extended Kalman Filter with recursive state-parameter coupling) and from [9] (a sigma-points Kalman filter) were tested. The latter proved to be more robust via implicit statistical linearization; therefore, the square-root Central Difference Kalman Filter (additive-noise form) of [10] is adopted. To drive parameter covariance, two options are used: Robbins–Monro adaptation and annealing of a preset constant matrix. Future work will estimate process and measurement noise online, reducing reliance on offline tuning, following [11].

Results

Several systems with distinct dynamics were simulated via an Euler–Maruyama step for stochastic dynamics and excited with inputs ranging from simple accelerations of the base to identification-oriented force signals. Noise was varied in both the process and the measurement channels.

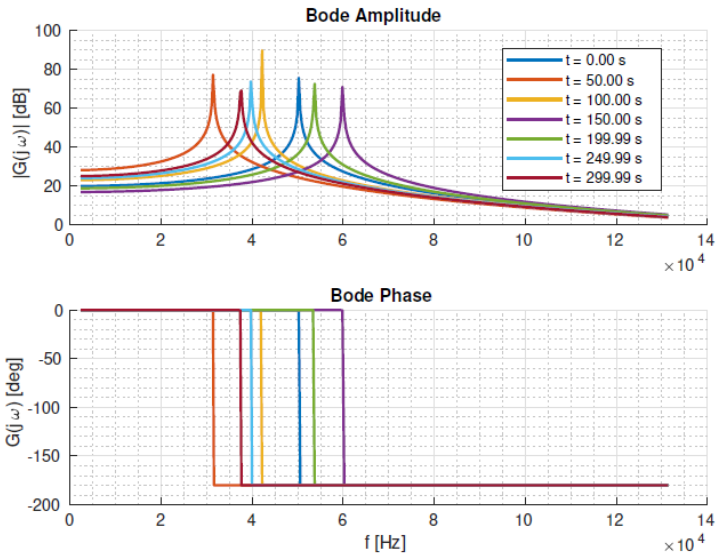


Figura 1: Time Variant Bode Graphs.

Materials Research Proceedings 69 (2026) 1481-1486 https://doi.org/10.21741/9781644904251-260

Evolving parameter dynamics produce distinct frequency-domain responses. Identifying the transfer function through linear or physics-based models enables characterization of system behavior and detection of deviation from nominal dynamics, informing control strategies to maintain robust stability (object of future work).

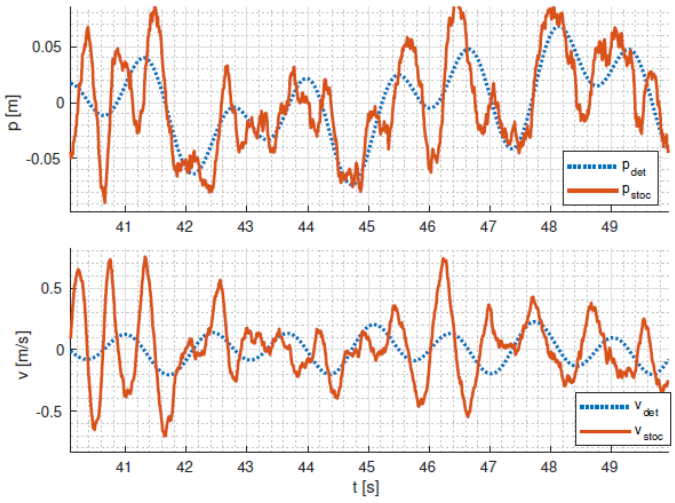


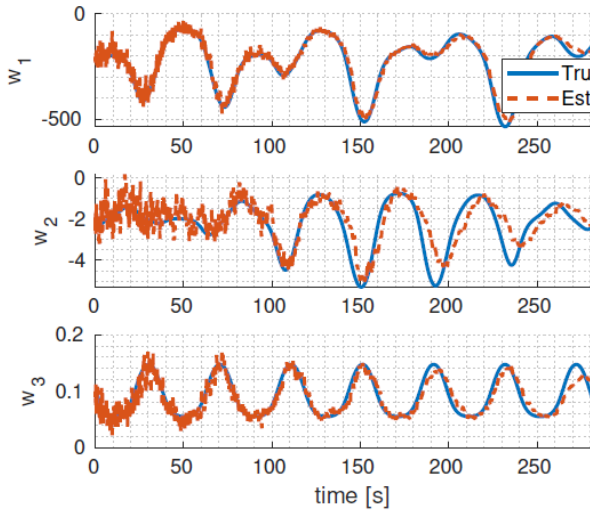
Figura 2: Linear System Process Noise.

Here, the excitation profiles and the corresponding simulations of the system dynamics are shown

Results for selected noise levels show simultaneous reconstruction of the state and time-varying parameters. The main challenge is the lack of a direct measurement map for parameters such as equivalent mass, damping, and stiffness, which are not directly measurable.

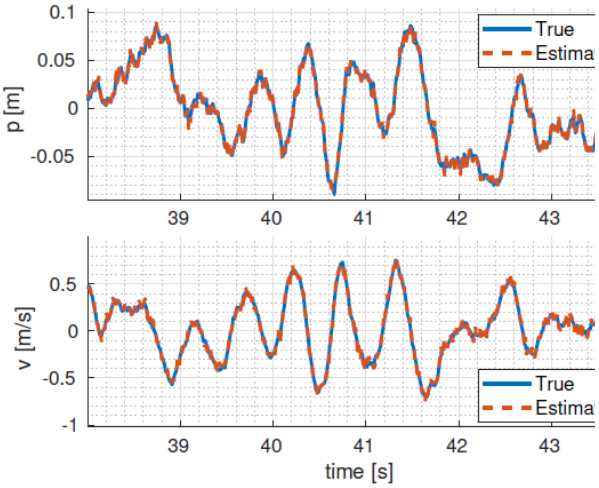
Nevertheless, the approach is effective: it is equivalent to Recursive Least Squares in linear cases or (in general) to an optimization-based method (Modified Gauss Newton [8,9], but it is implemented as a Kalman filter on parameters rather than on states.

These results are illustrative. Further refinements and a broader analysis will follow.



(a) *Parameters Reconstruction.*

Figura 3: Linear Parameters Reconstruction



(b) *State Reconstruction.*

Figura 4: Linear State Reconstruction.

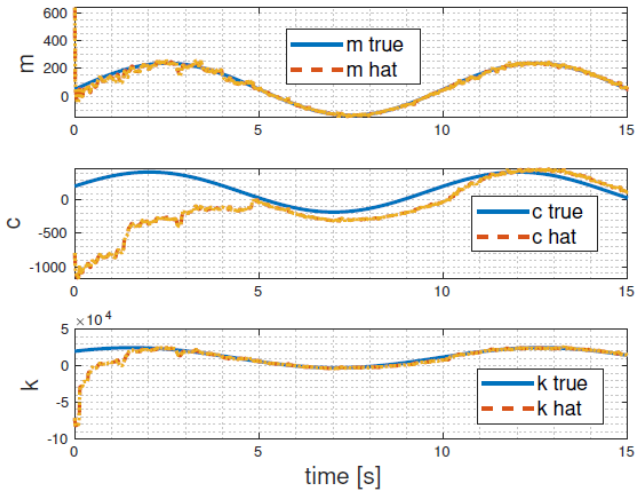


Figura 5: Nonlin Parameters Identification.

Conclusions and Future Work

The work demonstrates reconstruction over time of previously unknown pilot parameters' trajectories, from simple linear equivalents to more complex models, leveraging concise, physically consistent formulations from prior work [6] with the aim to support mitigation strategies [12] and gain better knowledge of the phenomenon. Complex, computationally demanding models can be handled by allowing time-varying components to capture unmodeled dynamics: at each instant, the simplest consistent model (e.g., mass–spring–damper harmonic oscillator) represents the system, while residual effects are absorbed by probabilistic time-adaptation of the parameter

The study is not exhaustive: limits due to process/measurement noise and parameter-rate bounds will be analyzed. Diverse parameter trajectories and increasing model mismatch will be explored and compared. The filter will be made agnostic to initial tuning by implementing methods from [11] and drawing on optimization results [8,9] also following the Linear Mean Square (LMS) approach in [12]. Upcoming work includes progressively complex tests and real-world experiments to map the method limits and define the most suitable operating range.

References

[1] M. D. Pavel, M. Jump, B. Dang-Vu, P. Masarati, M. Gennaretti, A. Ionita, L. Zaichik, H. Smaili, G. Quaranta, D. Yilmaz, M. Jones, J. Serafini, and J. Malecki. Adverse rotor-craft pilot couplings - past, present and future challenges. Progress in Aerospace Sciences, 62:1-51, 2013. https://doi.org/10.1016/j.paerosci.2013.04.003

[2] Duane T. McRuer. Aviation Safety and Pilot Control: Understanding and Preventing Unfavourable Pilot-Vehicle Interactions. National Academy Press, Washington, DC, 1997.

[3] V. Muscarello, G. Quaranta, and P. Masarati. The role of rotor coning in helicopter proneness to collective bounce. Aerospace Science and Technology, 36:103-113, 2014. https://doi.org/10.1016/j.ast.2014.04.006

[4] J. Venrooij. Measuring, Modeling and Mitigating Biodynamic Feedthrough. PhD thesis, Delft University of Technology, 2014.

[5] A. Zanoni, A. Cocco, and P. Masarati. Multibody dynamics analysis of the human upper body for rotorcraft-pilot interaction. Nonlinear Dynamics, 102(3):1517-1539, 2020. https://doi.org/10.1007/s11071-020-06005-7

[6] T. Aresi, A. Zanoni, P. Masarati, and G. Cassoni. Simplified models of pilot biomechanics for rotorcraft vertical bounce analysis. In Proc. 34th Congress of the International Council of the Aeronautical Sciences (ICAS), Florence, Italy, 2024. Sept. 9-13, 2024.

[7] M. Olivari, J. Venrooij, F. Nieuwenhuizen, L. Pollini, and H. Bülthoff. Identifying time-varying pilot responses: a regularized recursive least-squares algorithm. In AIAA Scitech 2016, 2016. https://doi.org/10.2514/6.2016-1182

[8] A. T. Nelson. Nonlinear Estimation and Modeling of Noisy Time Series by Dual Kalman Filtering Methods. PhD thesis, Oregon Graduate Institute of Science and Technology, 2000.

[9] R. van der Merwe. Sigma-Point Kalman Filters for Probabilistic Inference in Dynamic State-Space Models. PhD thesis, Oregon Health & Science University, 2004.

[10] K. Ito and K. Xiong. Gaussian filters for nonlinear filtering problems. IEEE Transactions on Automatic Control, 45(5):910-927, 2000. https://doi.org/10.1109/9.855552

[11] A. H. Mohamed and K. P. Schwarz. Adaptive kalman filtering for ins/gps. Journal of Geodesy, 73:193-203, may 1999. https://doi.org/10.1007/s001900050236

[12] Stephen J. Elliott. Signal Processing for Active Control. Signal Processing and its Applications. Academic Press, London, 2001. https://doi.org/10.1016/B978-012237085-4/50012-0

Materials Research Proceedings 69 (2026) 1487-1492 https://doi.org/10.21741/9781644904251-261

Navigating the New Frontier: The EU Space Act and its Impact on the European Aerospace Sector

Cecilia NOTA[1,a *]

[1]Lungo Dora Siena, 100, 10153 Torino (TO), Italy

[a]cecilia.nota@unito.it

Keywords: EU Space Act, European Space Policy, Space Safety, Space Resilience, Space Sustainability, Art. 114 TFEU, Regulatory Harmonisation

Abstract. The proposed EU Space Act aims to harmonise the Union's space governance under a single regulatory framework centered on safety, resilience, and sustainability. The Proposal introduces a system for authorisation and supervision of space activities, addresses protection of space infrastructure through a sector-specific cybersecurity regime, and mandates operators to calculate the environmental footprint of their activities as part of authorisation procedures. The Proposal marks a step forward for the European space framework, but its ultimate success will depend on balanced implementation and the EU's ability to maintain global competitiveness.

1. Introduction

The European space sector is undergoing a profound transformation, driven by the rapid commercialisation of space, the rise of "New Space" actors, and intensifying geopolitical competition [1]. This environment presents opportunities for economic growth and innovation, but it is hindered by a significant challenge: a fragmented regulatory landscape across the European Union (EU), as, currently, only 13 Member States have enacted national space laws, with others in the process of drafting their own [2]. Their varied approaches to safety, liability, and sustainability create legal uncertainty, distort competition, and erect barriers to a truly integrated single market for space services and products [3]. This fragmentation impedes the competitiveness of the EU space industry and undermines the goal of achieving strategic autonomy in a critical domain [4].

In response to these challenges, the European Commission has introduced in 2025 a Proposal for a Regulation of the European Parliament and of the Council on the safety, resilience and sustainability of space activities in the Union, the so-called EU Space Act (hereinafter referred to as 'the Proposal') [2]. This long-awaited regulation represents the first comprehensive attempt to govern the European space economy at a supranational level, aiming to create a harmonised, predictable, and competitive framework for all space operators within the EU [5]. This contribution explores the legal architecture and impact of this legislative initiative on the European aerospace ecosystem.

2. The Legal Architecture of the EU Space Act

Under the Lisbon Treaty, space is a shared parallel competence, meaning both the EU and the Member States may regulate space activities, with the latter retaining the freedom to pursue national policies alongside EU action. Indeed, Art. 189 of the Treaty on the Functioning of the European Union (TFEU), while establishing that the EU shall draw up a European space policy to promote scientific progress and industrial competitiveness, explicitly excludes the "harmonisation of the laws and regulations of the Member States" [6,7]. This caveat has historically prevented the EU from creating a unified legal framework for space activities [8,9], and it reflects the reluctance of Member States to cede sovereignty over a sector seen as strategic [10,11].

Content from this work may be used under the terms of the Creative Commons Attribution 3.0 license. Any further distribution of this work must maintain attribution to the author(s) and the title of the work, journal citation and DOI. Published under license by Materials Research Forum LLC.

The Commission addresses this limitation by grounding the Proposal on Art. 114 TFEU, the legal basis for measures concerning the establishment and functioning of the internal market [12]. Diverging national standards [13] create obstacles to the free movement of space services and distort competition, necessitating Union-level action to ensure a level playing field [2,14]. In this sense, the Proposal entails a genuine form of harmonisation, as it defines uniform technical and operational standards and introduces coordinated governance mechanisms to ensure their implementation. This legal strategy, previously employed in other sectors such as data protection with Regulation (EU) 2016/679 (GDPR) and environmental protection with Regulation (EC) 1907/2006 (REACH), represents a significant evolution in EU space governance [15]. The Commission's reasoning behind the use of Art. 114 TFEU is based on the grounds that a genuine internal market for space services and products is emerging within the Union, encompassing satellite communication, Earth observation data, and downstream applications integrated into the broader digital and industrial ecosystem. In this context, the choice of a regulation reinforces the internal market rationale because, pursuant to Art. 288 TFEU, regulations are directly applicable and binding in their entirety, ensuring uniform application across Member States [16], a necessary condition to eliminate legal fragmentation and guarantee equal market access for all operators.

It is important to note, however, that the EU Space Act has not yet entered into force. Proposed by the Commission in June 2025, the regulation is scheduled to become applicable on 1 January 2030, with the intervening period allocated for stakeholder adaptation and institutional preparation [2]. At this stage, the text remains open to amendments, as the Proposal is still in the initial phase of the ordinary legislative procedure and subject to modifications by the European Parliament and the Council, meaning that certain provisions may yet be redefined. Nevertheless, the regulatory architecture already envisioned demonstrates the Commission's intent to transcend the constraints of Art. 189 TFEU's prohibition on harmonisation by establishing binding technical and operational standards applicable across the entire EU space market through the direct applicability of regulation. This approach enables the Commission to project EU regulatory authority by conditioning participation in the EU space market on the basis of compliance with EU standards. That is to say that all operators must meet the same regulatory requirements if they wish to provide space services within the Union, thereby ensuring uniform compliance.

The Proposal's application extends beyond EU operators to non-EU operators providing space services in the Union, employing a marketplace criterion similar to the GDPR and the Digital Services Act [14]. This approach reflects the Commission's ambition to establish the Union as a global standard setter for space activities. However, this strategy carries a critical caveat for European aerospace competitiveness: the regulatory advantage depends on whether major space-faring states and global private operators voluntarily adopt or are compelled to adopt equivalent standards. If competitors operating under different regulatory regimes can undercut European manufacturers' compliance costs without losing EU market access through equivalent recognition, the competitive gains promised by harmonisation may evaporate [17].

The success of the regulation thus hinges not merely on internal EU alignment, but on whether the Union can sustain global regulatory leadership in space [2,14]. In this sense, the Proposal reflects the ambition to replicate the "Brussels effect" intended as the EU's capacity to export its regulatory standards globally through market access conditionality [18]. However, this is not without tension and the Proposal envisages a mechanism allowing the Commission to recognise third-country legal frameworks as equivalent to EU requirements (Art. 105 Proposal), facilitating international cooperation but potentially diluting the regulatory leverage the Union seeks to assert.

3. The Three Pillars of the EU Space Act and Their Implications for the European Aerospace System

The proposed EU Space Act is built on three pillars: safety, resilience, and sustainability. These pillars entail a broad regulatory transformation reshaping technical requirements and governance

structures across the space value chain [19]. This overhaul reconfigures institutional roles and establishes a harmonised framework for the authorisation and supervision of space activities (Art. 6 Proposal). The Proposal distinguishes between activities involving Union-owned space assets and those relating to non-EU assets. In the former case, authorisation and supervision powers rest with the Commission, which is supported by the European Union Agency for the Space Programme (EUSPA) in carrying out technical assessments and certification tasks (Arts. 11-13 Proposal). In the latter case, competence lies with the Member States, which must designate a National Competent Authority (NCA), eventually aided by the EUSPA, endowed with powers of supervision, investigation, and sanctioning to ensure compliance (Arts. 28-30 Proposal).

(i) The safety pillar addresses orbital congestion by setting binding rules requiring operators to ensure object trackability and reduce space debris. It introduces harmonised safety and operational standards applicable to all categories of operators carrying out space activities in the EU (Art. 6 Proposal). All operators, including non-EU entities and intergovernmental organisations, must register in the Union Register of Space Objects (URSO) to obtain EU compliance certification (Arts. 24-25 Proposal). Launch operators must implement debris control measures, fragmentation prevention, and end-of-life disposal procedures (Art. 61 Proposal), while spacecraft operators must subscribe to EU collision avoidance services (Art. 64 Proposal).

This shift from voluntary guidelines to enforceable safety protocols will affect mission design and operational procedures across the European aerospace sector; the Commission, in its impact assessment, notes that shifting from individual to constellation authorisation is projected to save operators EUR 68 million over the next decade, while extending satellite lifespans from 5 to 6 years could yield EUR 1.3 billion annually. However, these benefits must be weighed against increased manufacturing and compliance costs, with satellite operators potentially facing a 10% increase in manufacturing costs depending on mission requirements, and launch service providers incurring in additional expenses of EUR 1.5 million for heavy launchers and EUR 200,000 for small and medium sized enterprises (SMEs). Compliance will require redesign of mission architecture, enhanced engineering protocols for debris mitigation, and investment in collision avoidance systems.

(ii) The resilience pillar addresses the protection of space infrastructure from growing threats by establishing a sector-specific cybersecurity regime. Unlike the general cybersecurity frameworks established by Directive (EU) 2022/2555 (Network and Information Security - NIS2) and Directive (EU) 2022/2557 (Critical Entities Resilience - CER), which do not cover all segments of space infrastructure, the Proposal is intended to function as *lex specialis* [2], creating a bespoke resilience baseline applicable to all EU space operators (Art. 75 Proposal). In particular, the NIS2 Directive establishes cybersecurity obligations for medium and large providers of public electronic communications networks as well as for certain ground-segment operators. However, it notably excludes significant components of the space sector, most importantly space constellations owned by the Union. In addition the CER Directive is not applicable to Union-owned space infrastructures that fall within the scope of the EU Space Programme [20]. To remedy this gap, the Proposal stipulates that, for any operator already designated as “essential” or “important,” its space-specific provisions take precedence over the more general rules laid down in the NIS2 and the CER Directives (Art. 75 Proposal). Operators must implement risk management across all mission stages and conduct mission-specific risk assessments (Arts. 76-78 Proposal), enforce strict access control protocols (Arts. 81-82 Proposal), and report incidents (Art. 93 Proposal). The Proposal also creates a Union Space Resilience Network to coordinate responses to major cyber incidents (Art. 94 Proposal).

For the European aerospace sector, this represents a fundamental reorientation towards security-by-design principles, requiring aerospace manufacturers and operators to embed cybersecurity considerations into hardware, software, and communication protocols from the inception of the

Materials Research Proceedings 69 (2026) 1487-1492 https://doi.org/10.21741/9781644904251-261

design phase (Arts. 31, 58, and 73 Proposal). Risk management costs for companies are estimated by the Commission at 10% of their IT budgets, with authorisation requirements per product line costing approximately EUR 100.000, particularly affecting supply chain management, as EU space operators must establish frameworks aimed at reducing risks through software integrity controls and cybersecurity provisions (Art. 92 Proposal). Conversely, the implementation of these standards across the EU market is expected to provide significant competitive advantages; manufacturers potentially stand to save EUR 320 million per year through cybersecurity standards that reduce cyber-related risks.

(iii) The sustainability pillar introduces environmental requirements aligned with the European Green Deal objectives requiring operators to calculate the environmental footprint of their space activities as part of their authorisation applications (Art. 96 Proposal). This mandate covers all lifecycle stages, and relies on assessment methods aligned with the Commission Recommendation of Environmental Footprint (Arts. 97-98 Proposal). The requirement applies to all EU space operators except small-sized enterprises (Art. 5(26) Proposal) and research and education institutions until 31 December 2031 (Art. 96(8) Proposal). Additionally, the regulation mandates that spacecraft maintain a specific visual magnitude throughout their lifetime, including design requirements to limit pollution and minimise impact on astronomical observations, while establishing plans to reduce radio frequency disruptions (Art. 72 Proposal).

For the European aerospace industry, these sustainability requirements will drive substantial innovation in green propulsion technologies, sustainable materials, and eco-design methodologies. Implementing product environmental footprint rules is estimated by the Commission to cost EUR 4.000-9.000 per company, yet the creation of a unified environmental assessment framework provides European companies with opportunities to establish themselves as leaders in sustainable space technologies in a global market increasingly prioritising environmental responsibility. The centralised EU database for environmental footprint data, coupled with mandatory reporting of aggregated and disaggregated datasets, will facilitate informed decision-making, potentially positioning European manufacturers as pioneers in environmentally conscious space operations (Arts. 96(6) and 99 Proposal).

4. Enforcement Framework and Structural Challenges

Beyond these three substantive pillars, the EU Space Act's enforcement architecture carries significant implications for European operators.

As already mentioned, to mitigate regulatory friction with third countries, the Proposal grants the Commission discretionary power to recognise third-country legal frameworks as equivalent to EU requirements (Art. 105 Proposal). While this mechanism promotes international cooperation and reduces barriers, it also creates potential loopholes that could undermine enforcement consistency. Non-EU operators whose home countries receive equivalence decisions may bypass stringent EU compliance requirements, creating an uneven competitive landscape where some foreign competitors face lighter regulatory burdens than European manufacturers operating under domestic supervision. For the European aerospace sector, the breadth and flexibility of equivalence determinations will directly impact whether compliance costs translate into genuine competitive advantage.

Additionally, the regulation establishes a dual supervisory system: Member States supervise EU-based space operators through designated national authorities, while the Commission and EUSPA directly supervise non-EU operators, with power to impose penalties up to 2% of annual turnover (Arts. 48-56 Proposal). This division creates asymmetrical compliance pressures. European aerospace manufacturers and operators must navigate both EU standards and domestic Member State oversight, accumulating compliance costs through both levels. Conversely, foreign competitors may face Commission supervision alone, or, if their home state obtains equivalence recognition, potentially lighter oversight entirely (Art. 105 Proposal). For European SMEs, already

Materials Research Proceedings 69 (2026) 1487-1492 https://doi.org/10.21741/9781644904251-261

facing 10% manufacturing cost increases, this fragmented enforcement regime risks exacerbating competitive disadvantage relative to larger, globally-diversified competitors less dependent on EU market access.

Additionally, critical gaps and ambiguities threaten to undermine the objectives of the Proposal. First, the regulatory burdens imposed regarding compliance and certification procedures (Arts. 6-19, 41 and 46 Proposal) risk placing disproportionate strain on SMEs, the backbone of European space innovation. Although the Proposal acknowledges supportive measures (Arts. 109-111 Proposal), it provides insufficient concrete specifications, raising the prospect that under-resourced operators may be forced to curtail their activities [20]. Second, the Proposal remains notably silent on space resource exploitation, a critical omission given that certain Member States have already pursued unilateral legislative initiatives in this domain [21], potentially fragmenting the legal landscape further. Third, persistent ambiguity surrounds the dual-use character of space assets, as the preservation of Member States prerogatives on national security creates potential friction between supranational technical harmonisation and sovereign security determinations (Art. 4 Proposal).

5. Conclusion

The EU Space Act is an important step in the evolution of the Union's space governance, seeking to consolidate a unified regulatory environment underpinning EU strategic autonomy [22]. Through the three pillars, the Proposal aspires to replicate in the space domain the already mentioned "Brussels effect" [14,18]. Yet, as discussed, systemic limitations may hinder this ambition. The disproportionate compliance burdens for SMEs, the persistent legal vacuum surrounding space resource exploitation, and the unresolved tension between supranational harmonisation and Member States' security prerogatives risk constraining the reach of the Act.

Ultimately, the EU Space Act embodies both the promise and the problem underlying European integration in space: it projects regulatory authority on a global scale while remaining bound by the structural asymmetries of EU competence and enforcement capacity. Its success will, therefore, depend not only on the internal coherence of its governance architecture but also on whether the Union can translate its normative ambition into effective global influence.

References

[1] D. Fiott, Strategic Domains: Developing the EU's Capabilities and Enablers for a Free and Secure Global Order, Future Europe Journal 5(2) (2024).

[2] European Commission, Proposal for a Regulation of the European Parliament and of the Council on the safety, resilience and sustainability of space activities in the Union, COM(2025) 335.

[3] C. Evroux, A. Heflich, and J. L. Saulnier, Towards EU leadership in the space sector through open strategic autonomy, European Parliamentary Research Service (2023).

[4] European Commission, Joint Communication to the European Parliament and the Council on a European Union Space Strategy for Security and Defence, JOIN(2023) 9.

[5] European Parliament, EU space law in "A new plan for Europe's sustainable prosperity and competitiveness", Legislative Train Schedule.

[6] S. Garben, Article 189 TFEU, in: M. Kellerbauer, M. Klamert and J. Tomkin (Eds.), The EU Treaties and Charter of Fundamental Rights: A Commentary (2nd Edition), Oxford University Press, Oxford, 2024.

[7] M. Klamert, 2024, Article 4 TFEU, in: M. Kellerbauer, M. Klamert and J. Tomkin (Eds.), The EU Treaties and Charter of Fundamental Rights: A Commentary (2nd Edition), Oxford University Press, Oxford, 2024.

[8] D. Stefoudi, EU Space Law - Three reasons against, three reasons in favour, Blog of the European Journal of International Law (2025).

[9] J. Wheeler, The Space Law Review: Europe, Law Reviews (2023).

[10] F. Mazurelle, J. Wouters and W. Thiebaut, The Evolution of European Space Governance: Policy, Legal and Institutional Implications, Leuven Centre of Global Governance Studies' Working Papers (25) (2009). https://doi.org/10.1163/157237409X464233

[11] F. Von der Dunk F., Legal Challenges in the Context of the European Space Policy, in: T. Hoerber and S. Lieberman (Eds.), A European Space Policy: Past Consolidation, Present Challenges and Future Perspectives, Routledge/Taylor & Francis Group, London, 2009.

[12] M. Kellerbauer, Article 114 TFEU, in: M. Kellerbauer, M. Klamert and J. Tomkin (Eds.), The EU Treaties and Charter of Fundamental Rights: A Commentary (2nd Edition), Oxford University Press, Oxford, 2024. https://doi.org/10.1093/law/9780198913689.003.0490

[13] I. Marboe, The Lack of National Space Legislation in EU Member States and the Role of the EU as a New Responsible (?) Actor in Outer Space, in: P.J. Blount, T. Masson-Zwaan and R. Moro-Aguilar (Eds.), Proceedings of the International Institute of Space Law, Eleven International Publishing, The Hague, 2022, 405-418. https://doi.org/10.5553/IISL/2022065006002

[14] A. Miglio, The EU Space Act proposal: A GDPR for outer space?, European Law Blog (2025). https://doi.org/10.21428/9885764c.f26cb1fa

[15] B. Jacobs, Understanding the EU's Competence to Harmonize Space Law Amid Publication Delays, Air & Space Law 49 (4&5) (2024) 477-504. https://doi.org/10.54648/AILA2024030

[16] M. Klamert and P.-J. Loewenthal, Article 288 TFEU, in: M. Kellerbauer, M. Klamert and J. Tomkin (Eds.), The EU Treaties and Charter of Fundamental Rights: A Commentary (2nd Edition), Oxford University Press, Oxford, 2024.

[17] G. Ünüvar, The EU Space Act: Internal Harmonisation and External Influence, European Law Blog (2025).

[18] A. Bradford, The Brussels Effect, Northwestern University Law Review 107(1) (2012).

[19] G. Pavesi and J. Wouters, The final frontier? The European Union and the governance of outer space, Journal of European Integration (2023) 1199-1217. https://doi.org/10.1080/07036337.2023.2274885

[20] T. Pham and F. Casaril, Regulating the Final Frontier: Why the EU Space Act Matters, CELIS Blog (2025).

[21] Luxembourg, Loi du 20 juillet 2017 sur l'exploration et l'utilisation des ressources de l'espace, Journal Officiel du Grand-Duché de Luxembourg, Mémorial A, No. 674, 28 July 2017.

[22] C. Cellerino, EU Space Policy and Strategic Autonomy: Tackling Legal Complexities in the Enhancement of the 'Security and Defence Dimension of the Union in Space', European Papers 8(2) (2023) 487-501.

Systems Engineering, Digital Twins & Simulation



Materials Research Proceedings 69 (2026) 1494-1499 https://doi.org/10.21741/9781644904251-262

From Flight Test to a Simulator Model - System Identification of the ISTAR Research Aircraft

Christian RAAB[1,a *], Anton DILCHER[2,b]

[1]DLR (German Aerospace Center) – Institute of Flight Systems, Lilienthalplatz 7, D-38108 Braunschweig, Germany

[2]DLR (German Aerospace Center) – Flight Experiments, Lilienthalplatz 7, D-38108 Braunschweig, Germany

[a]Christian.Raab@dlr.de, [b]Anton.Dilcher@dlr.de

Keywords: Flight Test, Data Analysis, Modelling, System Identification, Simulation

Abstract. The German Aerospace Centre (DLR) acquired a Dassault Falcon 2000LX research aircraft, designated ISTAR (In-flight Systems & Technology Airborne Research), to support research in variable stability, advanced flight control concepts and pilot assistance systems. A high-fidelity flight dynamics model of the ISTAR is essential for the development of these systems and for simulator-based flight control testing. The model is based on an aerodynamic model identified through system identification (SysID) techniques using flight test data. The modular design of the aerodynamic modelling software enabled seamless integration of the identified model into the ISTAR simulator. This paper gives an overview of the model development process and an example for the application of the simulator model for the design and implementation of a yaw controller is presented.

Introduction

The development of a flight dynamics model for a simulator is a complex and time-consuming task, particularly during the design phase of new aircraft. Initially, the model relies heavily on wind tunnel measurements and computational fluid dynamics (CFD) calculations, which are later refined and validated using flight test data. The accuracy of the flight dynamics model is crucial, as it directly impacts the design of flight control functions and performance models. Furthermore, the model is an integral component of flight training devices, which are typically developed in parallel with or subsequent to the aircraft development process.

This paper provides an overview of the flight dynamics model development process for ISTAR, which is being designed as a platform for testing novel guidance, navigation and control systems. In the forthcoming years, the aircraft's control system will undergo substantial modifications, enabling researchers to integrate and test custom flight control software [1]. To facilitate this development, a cockpit simulator has been established at the DLR AVES (Air Vehicle Simulator) simulation centre, supporting the development and validation of flight control software prototypes. Consequently, an accurate flight dynamic model is essential to demonstrate to regulatory authorities that the implemented modifications and safety measures are based on a realistic model.

A key strategy for accelerating the model development process was the direct reuse of software components created during the system identification (SysID) process in the AVES simulator software. The aerodynamic model was verified through software validation during the SysID process, where model outputs were directly compared to flight data measurements. Additionally, the flight dynamics model was validated using an automated process, which enables rapid updates to the simulator model in response to significant modifications to the aircraft or to new flight test data. This approach ensures that an up-to-date 6-degrees-of-freedom model of the ISTAR flight dynamics can be maintained at all times.

Content from this work may be used under the terms of the Creative Commons Attribution 3.0 license. Any further distribution of this work must maintain attribution to the author(s) and the title of the work, journal citation and DOI. Published under license by Materials Research Forum LLC.

Materials Research Proceedings 69 (2026) 1494-1499 https://doi.org/10.21741/9781644904251-262

Aircraft and Instrumentation

The ISTAR aircraft is a modified Dassault Falcon 2000LX with a wingspan of 21.38 m and a maximum takeoff weight of 19.4 t. The standard avionic system features two independent Air Data Systems (ADS) that measure atmospheric parameters and calculate airspeed, Mach no. and barometric altitude. To obtain more accurate air data measurements, a nose boom installation is utilized, which enables the collection of data in the relatively undisturbed airflow ahead of the aircraft nose. Three independent and one experimental inertial reference systems measure acceleration along and rotational rates around the body axis. Position sensors installed on the aircraft control surfaces record the deflections of the elevator, ailerons, and rudder. A data acquisition system is integrated into the cabin, enabling the processing and storage of all flight parameters. The aircraft cabin features two stations, allowing the flight test engineer and an experimenter to monitor flight parameters in real-time during flight operations. This configuration facilitates direct communication with the test pilots, permitting the repetition or adaptation of manoeuvres as required by the experimenter.

Flight Manoeuvres and Test Points

A comprehensive flight test campaign was conducted to gather data for the development of a model representing the flight dynamics throughout the operational envelope. The test program comprised 9 flights, performed between February and May 2022, during which a total of 26 test points were completed. These test points spanned various altitudes, speeds, and aircraft configurations, including different slat/flap settings and landing gear states. Details about the test points are shown in Table 1. The flight test campaign involved a range of SysID manoeuvrers designed to excite the aircraft's motion modes independently. Longitudinal motion was excited through multi-step elevator inputs, small step inputs, and double step inputs to the thrust lever and horizontal stabilizer. Lateral manoeuvrers included bank-to-bank turns, aileron and rudder doublets, and steady heading sideslip manoeuvrers. Additionally, level accelerations and decelerations were performed at altitudes of 30000 ft and 45000 ft. The collected dataset, which spans over 6.5 hours, includes more than 590 manoeuvres. Notably, the flight test campaign was impacted by nose boom vibration issues at speeds above 290 kt indicated airspeed (IAS), which precluded the completion of test points 5, 6, 7, and 9. These test points will be revisited once the vibration issues have been resolved. Overall, the gathered flight data provided a solid foundation for the development of an accurate flight dynamics model of the ISTAR aircraft.



Fig 1. *The DLR ISTAR research aircraft. Source: DLR*

Data Post-Processing and Compatibility Check

Accurate flight data measurements were crucial for developing a high-quality flight dynamics model. To ensure data consistency and accuracy, a data compatibility check (DCC) was performed [2]. The DCC is a higher-level process that detects and corrects measurement errors, and develops sensor models that provide adequate agreement between reference and measured airflow signals. A key component of the DCC is the flight path reconstruction (FPR) method, which uses inertial measurements to calculate reconstructed air data.

Materials Research Proceedings 69 (2026) 1494-1499 https://doi.org/10.21741/9781644904251-262

***Table 1**. Flight test points used for system identification manoeuvrers.*

TP	Altitude [ft]	IAS [kt]	Ma
1a	11000	120	0.22
1b	11000	135	0.25
1c	11000	145	0.27
1d	11000	150	0.28
2	11000	170	0.32
3	11000	220	0.41
4	11000	270	0.50
5	11000	320	0.59
6	20000	320	0.69

TP	Altitude [ft]	IAS [kt]	Ma
7	27000	320	0.79
8	27000	220	0.56
9	33000	300	0.84
10	37000	260	0.80
11	37000	240	0.75
12	37000	220	0.69
13	37000	190	0.60
14	37000	160	0.51
15	45000	210	0.78

We applied the DCC method to our flight data measurements to ensure their accuracy and consistency [3]. Another aim of the DCC is to develop models for the aircraft air data and inertial sensors, representing the dynamic sensor characteristics. Accurate sensor models were essential for the SysID process and simulator model development, as control system designs must account for sensor characteristics such as time delays, bias, and factor errors. In preparation for the SysID process, the flight data were augmented with additional aircraft properties, including current weight, centre of gravity (CG) position and moments of inertia. These parameters were derived using a manufacturer's weight and balance model, which accounted for the zero-fuel weight and the current fuel content in each tank. Additionally, a manufacturer-provided engine model was employed to compute the thrust force as a function of Mach number, altitude and engine speed (N1).

System Identification

A crucial component of the flight dynamics simulation is the aerodynamic model, which determines the aerodynamic forces and moments acting on the aircraft. This model typically consists of equations for each aerodynamic force and moment coefficient, with each term comprising a derivative parameter multiplied by an influence variable. To estimate the aerodynamic parameters, the output error method was applied, which operates in the time domain and compares the model outputs with the measured flight data [2]. The procedure is illustrated in Fig. 2: The measured control deflections, engine thrust and current weight and balance properties were used as inputs to the model. Utilizing these inputs and the rigid body model states, the aerodynamic model calculated the forces and moments acting on the aircraft. The necessary state variables, such as flight speed, were determined using the equations of motion. Numerical integration of the equations of motion yielded the resulting model states, which served as inputs for the sensor models. The sensor models, which were previously validated through a DCC, remained fixed, and their outputs were compared with the measured flight data. An iterative process was used to minimize the calculated model error by optimizing the model parameters. This involved adjusting the structure and parameters of the aerodynamic model accordingly. The SysID process was performed using the MATLAB tool FITLAB [4] developed by the DLR Institute of Flight Systems. The kinematic model, aerodynamic model and sensor model were integrated as modular software components into a C++ library for use with the SysID process. The models and identified parameters, denoted by hatched blocks in Fig. 2 are the software components that are reused for implementing the flight dynamics model in the simulator. The results of a successful match between the flight data and the identified flight dynamics model are presented in Fig. 3. This figure displays time series plots of a sequence of lateral manoeuvres, including two bank-to-bank and two rudder doublets, followed by a steady heading sideslip and a rudder release. The input signals of the ailerons and rudder control surfaces are shown in the first two subplots, while

Materials Research Proceedings 69 (2026) 1494-1499 https://doi.org/10.21741/9781644904251-262

the subsequent subplots illustrate the corresponding responses in terms of angle of sideslip, roll rate, yaw rate, bank angle and yaw angle. A comparison between the measured flight test data (blue lines) and the simulated model responses (red lines) reveals only minor discrepancies, indicating that the model accurately captures the flight dynamics of the ISTAR aircraft. A more detailed description of the system identification procedure and an assessment of the current model quality can be found in a companion technical report [5].

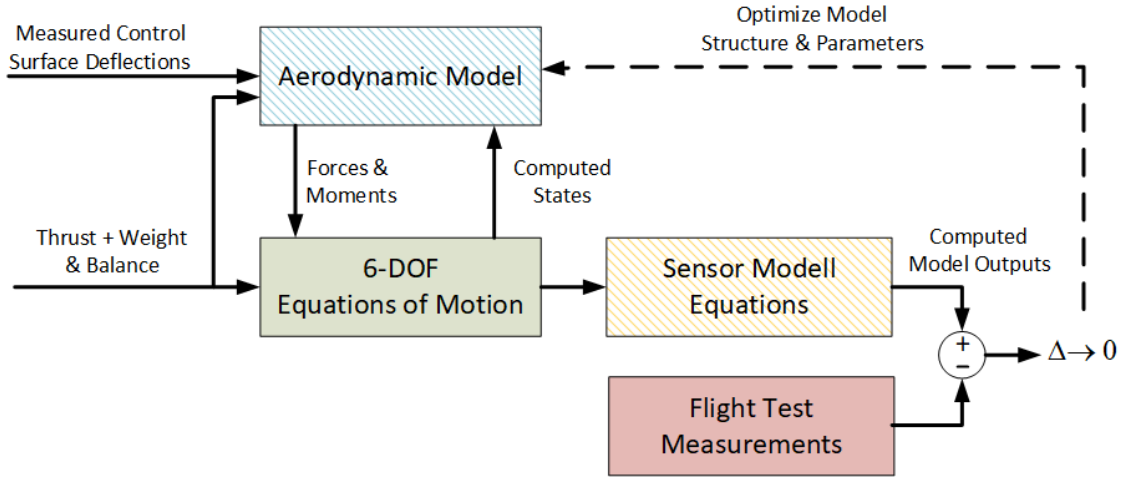


Fig. 2. *System identification process for the aerodynamic model.*

ISTAR Flight Simulator

The ISTAR cockpit simulator at the DLR AVES simulation centre is a combination of actual aircraft and reproduced hardware. All software necessary for operating the simulator is being developed completely in-house at the DLR Institute of Flight Systems. A central interface system, based on TCP/UDP communication protocols, connects the different cockpit simulator parts, like pilot control, display, vision and motion systems. The ISTAR simulation model is implemented in MATLAB/Simulink. The core of the simulation model comprises the equations of motion, supplemented by a set of sub-models for aerodynamics, sensors, weight and balance, landing gear and engine. Leveraging existing code, the aerodynamics and air data sensor models, previously employed in the SysID process, are integrated into the simulation framework via corresponding C++ S-Functions, promoting code reusability and efficiency. This extensive simulation model is being extended to include the unmodified aircraft's automatic flight control system (AFCS). As ISTAR undergoes modification to its flight control system, these changes will also be reflected in the simulation model. In order to run in real-time within the simulator, the model is compiled using Simulink Coder. When modifications are complete, the ISTAR simulator will be used to test experimental flight control software prior to flight tests. This also allows the flight test crew to gain experience with the expected flight control behaviour before flying. As the transfer between experimental flight controls and the unmodified aircraft is important from a safety perspective, relevant aircraft systems such as the AFCS must also be sufficiently simulated. Initially basic autoflight functions, such as the yaw damper and the heading and flight path angle modes, have been implemented in the ISTAR simulator, with provisions for the future implementation of more advanced capabilities [6]. As specifics of the Falcon 2000 AFCS, such as system gains or control loop structure, are not known, these needed to be estimated or inferred based on flight test data and limited system descriptions.

Materials Research Proceedings 69 (2026) 1494-1499 https://doi.org/10.21741/9781644904251-262

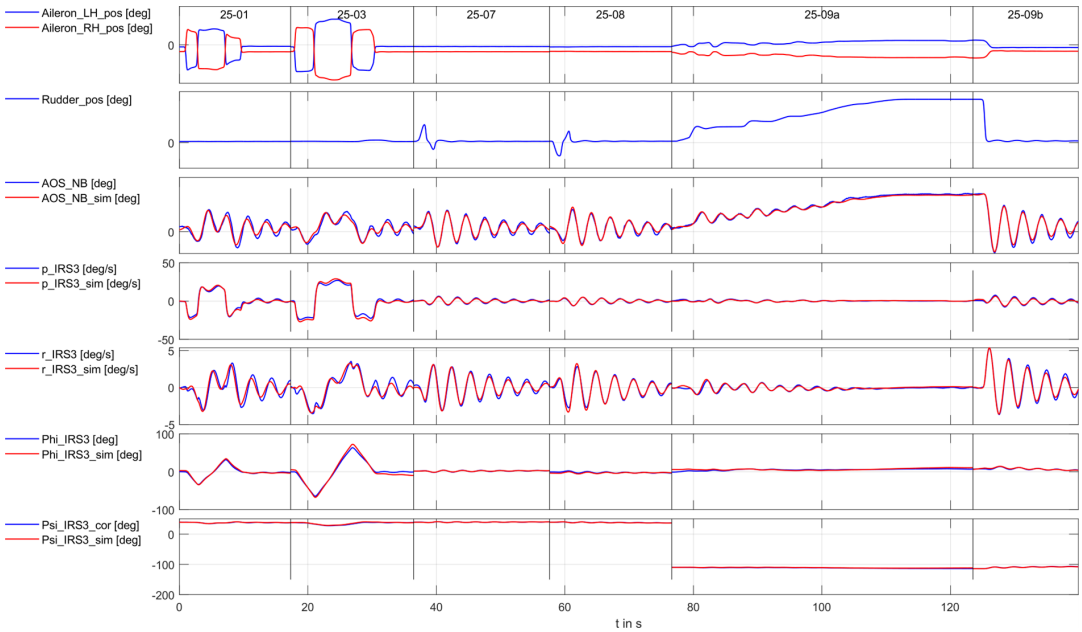


Fig. 3. *Time series plots for excitation manoeuvres in the lateral motion with measured flight data (blue) and model response (red).*

Yaw Damper Implementation

The yaw damper is the most basic form of stability augmentation found in the Falcon 2000 and is used to illustrate how the ISTAR simulation model can be used to develop flight controllers. The yaw damper was implemented using a root locus method and tuned with flight test data. Only very limited information about the yaw damper is available from the aircraft manufacturer. The functioning of the yaw damper was essentially reverse engineered using flight test data. The implementation is conventional using yaw rate feedback to the rudder and a washout filter. An offline version of the SysID determined flight dynamics model is available in Simulink. With a trimming script a state-space model of the linearized aircraft motion around a trim point of 220 kt IAS at 12000 ft was computed. This condition was chosen, because SysID test points were performed with and without the yaw damper engaged. Using a state-space model of the lateral-directional motion at this trim point, a root-locus analysis of yaw rate feedback to rudder was performed. With the yaw rate feedback and the washout filter implemented in the offline simulation, their effects were tuned to the aircraft motion measured during flight test. Figure 4 shows the effect of the yaw damper implementation on the dutch roll poles. At the trim point, a yaw rate feedback gain of 1.3 s and a washout filter time constant of 1.5 s, caused the dutch roll damping ratio to increase from 0.1 to apx. 0.4, while the natural frequency decreased (refer to Table 2) closely resembling aircraft motion. With the exception of a pole from the washout filter, located near the origin at -2.6e-3 on the real axis, the roll and spiral modes are both stabilized by the yaw damper. Particularly the spiral mode pole moves from very close to the origin further to the left along the real axis. For this yaw damper implementation to be suitable for the entire flight envelope and not just the chosen trim point, gain scheduling will be required. Subsequently, a coordinated-turn controller incorporating feedback of the lateral acceleration n_y is implemented. This leads to a marginal increase in the natural frequency of the dutch roll mode, while maintaining high damping levels.

Table 2. *Comparison of the dutch roll properties with and without the yaw damper implemented.*

Yaw Damper	Damping	Frequency [Hz]
Not Implemented	0.10	0.270
Implemented	0.38	0.073

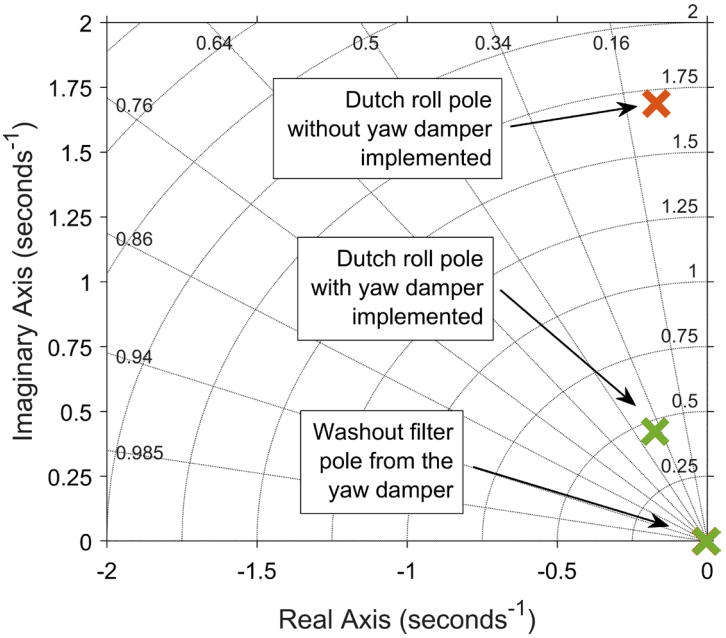


Fig. 4. *Location of the dutch roll poles with (green) and without (red) the yaw damper implemented.*

Conclusion and Outlook

In conclusion, we have successfully developed and implemented a simulation model for the ISTAR research aircraft, utilizing extensive flight test data and system identification techniques. This model has demonstrated its value in flight preparation, testing and development of control systems, such as the yaw damper controller. Future work will focus on enhancing the ISTAR research aircraft by enabling direct access to the flight control system. Additionally, the simulation model will be refined to capture a broader range of operational conditions, including high- and low-speed regimes, such as stalls, through a series of supplementary flight tests.

References

[1] D. Niedermeier, K. Giese, and D. Leißling, “The new research aircraft ISTAR – experimental flight control system,” 33rd ICAS Congress, 4. - 9. Sept. 2022, Stockholm, no. 0439, 2022.

[2] R. V. Jategaonkar, Flight vehicle system identification. Reston: American Institute of Aeronautics and Astronautics, Jan. 2015. https://doi.org/10.2514/4.866852

[3] C. Raab, “Practical examples for the flight data compatibility check,” CEAS Aeronautical Journal, October 2023. [Online]. Available: https://elib.dlr.de/198066/. https://doi.org/10.1007/s13272-023-00687-6

[4] S. Seher-Weiss, “Fitlabgui - a versatile tool for data analysis, system identification and helicopter handling qualities analysis,” English, 42nd European Rotorcraft Forum 2016, Vol. 2, p.1503–1521, 2016.

[5] C. Raab, “Dassault Falcon 2000LX ISTAR System Identification - Part I Process and Aerodynamic Model Description V1.0,” DLR - Institut für Flugsystemtechnik, Tech. Rep., 2024. [Online]. Available: https://elib.dlr.de/206264/

[6] A. Dilcher, “Development of flight control functions for the simulation model of the Dassault Falcon 2000LX ISTAR,” TU Braunschweig, Tech. Rep., Apr. 2025. [Online]. Available: https://elib.dlr.de/214607/

Materials Research Proceedings 69 (2026) 1500-1504 https://doi.org/10.21741/9781644904251-263

Another F-16 Simulation? A User-Friendly Julia, MATLAB, and Simulink Flight Simulation Package Suitable for Undergraduate Teaching

Duc NGUYEN[1,a *] and Mark LOWENBERG[1,b]

[1]University of Bristol, Queen's Building, University Walk, Bristol, BS8 1TR, United Kingdom

[a]duc.nguyen@birstol.ac.uk, [b]m.lowenberg@bristol.ac.uk

Keywords: Flight Simulation, Aircraft Dynamics, Education, Julia, MATLAB, Simulink

Abstract. We present a compact and user-friendly simulation package of the F-16 aircraft, which is based on aerodynamic data from the 1979 report by NASA. Developed across Julia, MATLAB, and Simulink, the package was designed for education and early research training. Priorities were given for clarity and ease-of-use over advanced functionality while preserving the full six-degree-of-freedom equations of motion and nonlinear aerodynamics. Three model variants are provided: 4th-, 8th-, and 12th-order, each progressively expanding the simulated dynamics. In addition to solving the nonlinear equations of motion, some common functions for flight dynamics analysis are provided, including trimming and linearisation, parameter sweep using parallel simulations, 3D trajectory display, and a unique real-time plotting capability in Julia. Benchmarking demonstrates excellent performance, particularly for Julia, which achieves sub-millisecond runtimes for typical time-integration tasks. The package enables learners to explore core flight-dynamics principles and nonlinear behaviours such as spins and deep stalls within a minimal coding structure. This work aims to lower the entry barrier to flight-simulation education and provide a flexible platform for undergraduate teaching and introductory research.

Introduction

The nonlinear 6-degree-of-freedom (DoF) aircraft equations of motion are a challenging topic to teach. Based on the author's experience, the reason can be attributed to the large jump from simple linear representation (transfer function and state-space) to nonlinear equations with complex coupling terms and lookup tables. Rather unfortunately, many students consider linear feedback control as one of the harder units in an aerospace engineering degree. This reduces the number of students choosing to explore aircraft dynamics further – typically as an optional unit or via a final-year research project. Students who choose this topic typically go through an 'adjustment period' of transitioning from solving handwritten equations to complex and (often) closed-source flight simulations. These software are typically constructed for a research environment that prioritises functionalities and expandability, but not necessarily user friendliness. This results in a steep learning curve and requires major effort for onboarding new lab members. Similarly, experienced control engineers from other sectors may also run into the same challenges when first introduced to atmospheric flight systems.

To address the bottleneck problem above, we propose a 'lightweight' flight simulation that prioritises simplicity over functionality – one that preserves the full 6 DoF equations of motion without advanced features that can overwhelm newcomers. This means omitting additional control surfaces (flaps, spoilers, etc.), actuator and engine modelling, atmospheric modelling, and a complex coding structure with multiple nested functions. The focus is on helping learners grasp the fundamentals behind the equations of motion for aircraft and the structure of an aircraft flight dynamics simulation—including elements such as lookup tables, time integration, and initial conditions. Other key features, such as trajectory visualisation, trimming, and linearisation, should

Content from this work may be used under the terms of the Creative Commons Attribution 3.0 license. Any further distribution of this work must maintain attribution to the author(s) and the title of the work, journal citation and DOI. Published under license by Materials Research Forum LLC.

Materials Research Proceedings 69 (2026) 1500-1504 https://doi.org/10.21741/9781644904251-263

still be included, ideally in a way that does not overwhelm the learners. This is the opposite approach to some existing open-source flight simulations, most famously the University of Minnesota F-16 simulation [1], its recent update by one of the original authors [2], and the reduced model described in the textbook by Stevens and Lewis [3]. Furthermore, we do not favour the block-diagram approach as seen in a few Simulink examples [4], as they tend to be complex visually and may impede the user's understanding of the nonlinear equations of motion (especially if 'lazy' black box blocks are used, such as those provided in Simulink's Aerospace Blockset package [4]).

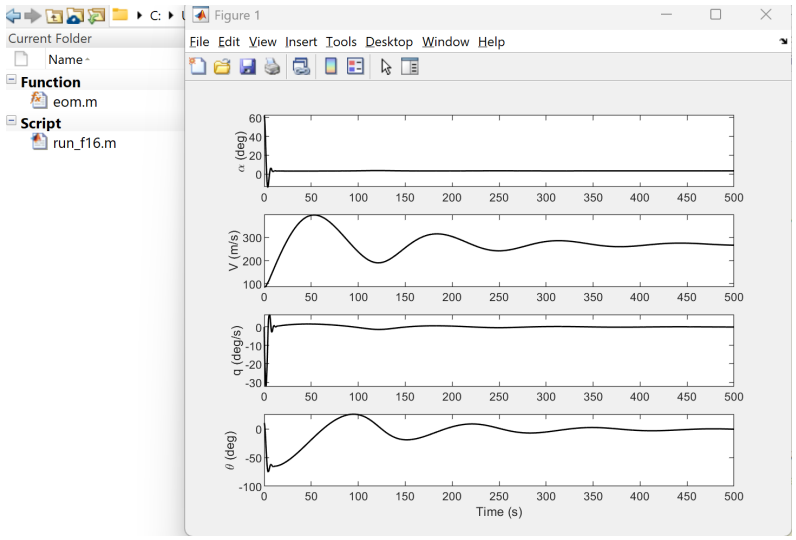


Fig. 1. 4th-order MATLAB simulation, showing the simple simulation structure with only 2 files totalling 96 lines of code.

Key features

Our simulation package, which can be downloaded from GitHub [5], is based on the F-16 aerodynamic data published in the 1979 NASA report [6]. Some well-known MATLAB/Simulink packages based on this database have been published, most notably those from the University of Minnesota [1, 2]. The package presented in this paper is a collection of 4 x 3 = 12 small simulations, which are built around the 4 coding environments used (MATLAB, Simulink, MATLAB with C-code generation, and Julia) and 3 levels of complexity in the equations of motion (4th, 8th, and 12th-order). The choice of multiple simulation environments covers a wide range of user bases. Regarding the 3 variants of the equations of motion, our rationale is:

- 4th-order: limits the aircraft motion to the longitudinal plane only. This is the ideal starting point for newcomers because the model contains all elements of a nonlinear aircraft simulation (coupled states, force and moment coefficients, and lookup table) while still being significantly simpler than the full 6 DoF equations. The 4 states modelled in the simulation are angle of attack, velocity, pitch rate, and pitch angle. The code to run the 4th-order time integration in MATLAB (including nonlinear aerodynamic tables) has only 96 lines, split between two files (see Fig. 1).

- 8th-order: expands the dynamics to include full 6 DoF. This implementation omits the 4 uncoupled equations: three representing the aircraft's location in the flat-Earth XYZ axes, plus the heading angle.

- 12th-order: contains the 4 coupled states mentioned above, along with an aircraft trajectory plotting routine.

All models assume that the air density is constant, with the default value set to 0.458 kg/m^3 (30,000 ft altitude). This assumption removes the coupling between air density and the aircraft Z-axis coordinate, thereby preventing an additional coupling term in the equations of motion. In

Materials Research Proceedings 69 (2026) 1500-1504 https://doi.org/10.21741/9781644904251-263

almost all entry-level flight dynamics texts, only the short-term dynamics is considered, which does not involve significant changes in air density. If a different altitude is desired, users can easily change the air density constant in the code.

In addition to time integration of the flight dynamics equations of motion, a few additional features are included:

- Trimming and linearisation routines to facilitate some basic open-loop analysis.
- Parallel simulation routine to run a parameter sweep. The included example determines the trim point at different stabilator deflections by running multiple simulations for a long duration, then collecting the aircraft states at the end of each simulation.
- For the 12th-order model in Julia, the code includes a plotting routine that displays the result while the differential equation solver is still running (see Fig. 2). This is similar to the 'scope' blocks in Simulink. Visualising the solutions in real-time could be useful for detecting simulations that diverge or encounter numerical instability, which tend to result in unreasonably long or infinite run time with no easy way to alert the user. To the best of the authors' knowledge, this code is the first flight visualisation package for Julia in the public domain.

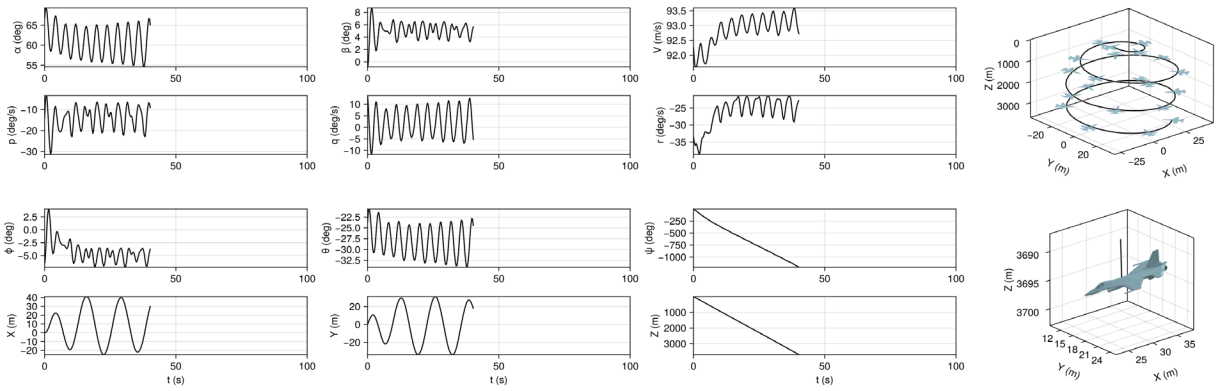


Fig. 2. 12th-order Julia simulation with plot-while-simulating feature, showing the aircraft in a spin at high angle of attack. The lower-right trajectory plot is drawn to scale.

Another notable feature is that the equations of motion are written in the wind axes instead of the typical body axis (i.e., using α, β, and V instead of body-axis velocities u, v, and w). The wind-axis representation provides an alternative reference to other simulations available. Regarding the orientation equations, we use Euler angles instead of quaternions to provide a closer link to the typical textbook equations of motion. Experienced users can easily convert the simulations to a body-axis system and/or quaternions.

Performance

Coding best practices were employed to create a light code base with high speed. The run times of two 500-second simulations (one 4th- and one 8th-order) with variable steps and 1e-4 relative tolerance are shown in Table I. Results were obtained on a laptop with a 24-core Intel i9-13950HX processor and 32 GB of RAM.

Table I. 500-second simulation run times in seconds.

ENVIRONMENT	4TH-ORDER	8TH-ORDER
MATLAB	1.14	18.3
Simulink	0.776	0.702
MATLAB with C-code generation	0.0616	0.108
Julia	0.00209	0.0194

Materials Research Proceedings 69 (2026) 1500-1504 https://doi.org/10.21741/9781644904251-263

Table II shows the run times of a parameter sweep using parallel simulation, which involves 7826 simulations of duration 500 seconds split between 23 parallel workers. The same solver settings as above were used.

Table II. Parallel simulation run times in sec., excluding overheads and post-processing.

ENVIRONMENT	4TH-ORDER
Simulink	81.8
Julia	18.3

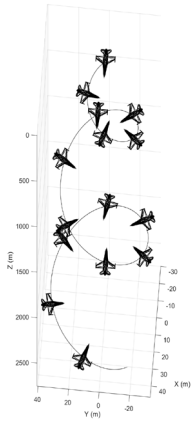
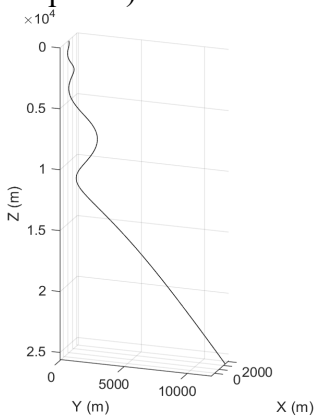
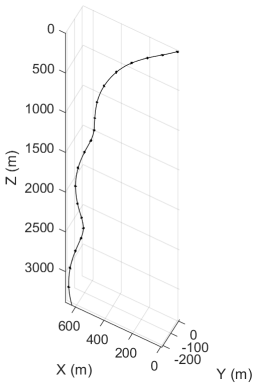
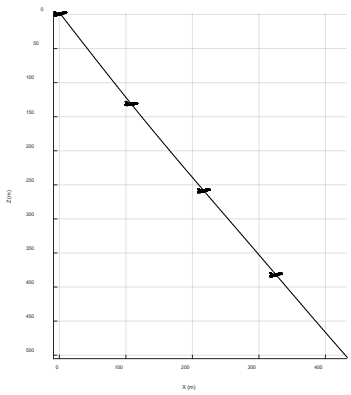
Key results

The 8th- and 12th-order simulations contain a set of control inputs (CI) and initial conditions (IC) that demonstrate some well-known nonlinear dynamics behaviours of the F-16. Most of these arise from the combination of nonlinear aerodynamics and aft centre-of-gravity placement. Table III summarises those cases. The airframes displayed are drawn to scale at 2-second intervals.

Acknowledgements

This work was supported by the UK Engineering and Physical Sciences Research Council, grant number EP/Y014545/1.

Table III. Nonlinear dynamics demonstrations in the 8th- and 12th-order simulations.

	CI 1	CI 2
IC 1	Fully developed spin 	Spin self-recovery (back to deep stall) 
IC 2	Spin entry from deep stall 	Deep stall 

References

[1] Balas, G. "Non-Linear F-16 Aircraft Model", dept.aem.umn.edu/~balas/darpa_sec/SEC.Software.html [retrieved 21 July 2025].

[2] Bhattacharya, R. "F16-Model-Matlab", github.com/isrlab/F16-Model-Matlab [retrieved 31 July 2025].

[3] Stevens, B. L., Lewis, F. L., and Johnson, E. N., Aircraft Control and Simulation: Dynamics, Controls Design, and Autonomous Systems, Wiley, 2015. https://doi.org/10.1002/9781119174882

[4] MathWorks. "Fly the De Havilland Beaver", uk.mathworks.com/help/aeroblks/fly-the-dehavilland-beaver.html [retrieved 21 July 2025].

[5] Nguyen, D. H., and Lowenberg, M. H. "F-16_Bristol", github.com/duchn7/F-16_Bristol.git [retrieved 8 November 2025].

[6] Nguyen, L. T., Ogburn, M. E., Gilbert, W. P., Kibler, K. S., Brown, P. W., and Deal, P. L. "Simulator Study of Stall/Post-Stall Characteristics of a Fighter Airplane with Relaxed Longitudinal Static Stability," NASA Technical Paper 1538. NASA, Langley Research Center, Hampton, Virginia, 1979.

Materials Research Proceedings 69 (2026) 1505-1511 https://doi.org/10.21741/9781644904251-264

Integrated Model-Based Systems Engineering methodology for design, analysis and simulation of an Environmental Control and Life Support System for an Analog Habitat

Giacomo LUCCISANO[1,a *], Loris GIANNINI[1,b], Nicole VIOLA[2,c] and Roberta FUSARO[1,d]

[1]Department of Mechanical and Aerospace Engineering (DIMEAS), Politecnico di Torino, 10129, Turin, Italy

[2]Department of Management and Production Engineering (DIGEP), Politecnico di Torino, 10129, Turin, Italy

[a]giacomo.luccisano@polito.it, [b]loris.giannini@studenti.polito.it, [c]nicole.viola@polito.it, [d]roberta.fusaro@polito.it

Keywords: Analog Habitat, ARCADIA, Capella, Environmental Control and Life Support System, Human Spaceflight, Model-Based System Engineering

Abstract. In the context of human space exploration, the Environmental Control and Life Support System (ECLSS) plays an essential role in ensuring that space habitats provide and maintain life-sustaining conditions for astronauts. A long-duration human spaceflight mission necessitates the development of a highly reliable and sophisticated ECLSS, for which traditional Systems Engineering (SE) approaches, being primarily document-based, are likely to be inadequate in addressing the intrinsic complexity of developing such systems. To overcome these limitations, this work explores the applicability of Model-Based Systems Engineering (MBSE) models and tools, and discloses an integrated MBSE approach that establishes a link between the system model and analysis and simulation tools to support the iterative evaluation and refinement of the system model throughout the design process. To validate the proposed approach, the methodology is applied to the preliminary design of an ECLSS for an Analog Habitat. The results highlight several advantages, including early validation and verification of concepts, improved detection of design inconsistencies, rapid evaluation of design changes, and enhanced robustness, traceability, and efficiency of the design process.

Introduction

The Environmental Control and Life Support System (ECLSS) is a mission-critical element for human spaceflight: it supplies and regulates atmosphere, water, waste handling and, ultimately, habitability across spacecraft and surface habitats. Decades of research and flight experience have consolidated baseline functions and architectures for ECLSS and clarified their tight coupling with other onboard systems [1]. As exploration shifts from short sorties to longer campaigns, reliability, resource closure and integration constraints become the dominant drivers of systems and subsystems architecture definition and technology selection. Standards and agency practices (e.g., ECSS E-34 [2]) further frame the design space and verification needs.

Traditional Systems Engineering (SE) approach for ECLSS design has been predominantly document-centric: requirements, interfaces and verification artifacts are captured in dispersed specifications whose dependencies are difficult to maintain as complexity grows. The resulting friction (weak traceability, delayed defect discovery, and high maintenance overhead) is well documented in SE literature and practice [3]. Model-Based Systems Engineering (MBSE) addresses these limits by making a coherent model the authoritative source for requirements, design, analysis, verification and validation throughout the life cycle; this is reflected in the

Content from this work may be used under the terms of the Creative Commons Attribution 3.0 license. Any further distribution of this work must maintain attribution to the author(s) and the title of the work, journal citation and DOI. Published under license by Materials Research Forum LLC.

Materials Research Proceedings 69 (2026) 1505-1511 https://doi.org/10.21741/9781644904251-264

INCOSE definition and subsequent studies on MBSE value [4]. Moreover, economic/operational analyses indicate that earlier validation, automated consistency, and faster change propagation provide tangible benefits on complex programs.

This paper adopts the ARCADIA methodology implemented in Capella – a MBSE tool well diffused in both Industry and Academia [5] – to structure an ECLSS architecture and its engineering data, leveraging the method's viewpoints and traceability to manage requirements, functions, interfaces and physical architecture. Capella add-ons are used to parameterize the model and expose data to analysis/simulation. In the proposed approach, an analysis and a simulation paths are complementary to provide quantitative estimations at first and then to validate the concept's performance: (i) a quantitative analysis path computing Equivalent System Mass (ESM) [6] and reliability metrics [7] – standard figures for mass, power, volume, crew-time consolidation and risk assessment – based on NASA and common practice, and (ii) a dynamic simulation path via Virtual Habitat (V-HAB) [8] to capture closed-loop interactions and operational envelopes.

The scientific contribution of this work is threefold: (i) to formalize an MBSE workflow that binds ARCADIA/Capella models to external analysis and simulation artifacts through a parameterized bridge; (ii) to demonstrate on an Analog Habitat ECLSS how ESM/reliability analytics and dynamic simulations can be executed directly from the authoritative model to inform trades, check requirements, and iterate the architecture; and (iii) to discuss the impacts on verification & validation timing and configuration control relative to document-centric baselines (NASA SE handbook framing).

The paper is structured as follows: Section 2 outlines the integration approach and model parametrization; Section 3 applies it to the Analog Habitat use-case; Section 4 synthesizes benefits and limitations and identifies extensions to later design phases.

Proposed Integrated MBSE Approach for ECLSS Design

The proposed integrated MBSE approach, described in this paper, aims to support the development of an ECLSS architecture for an Analog Habitat application throughout the entire design process. Fig. 1 provides a comprehensive overview of the main steps that constitute the proposed framework.

The approach relies on the connection between the system model and analysis & simulation tools, enabling engineers to evaluate system performance and iteratively refine the model in an automated and traceable way. In the integration process detailed in this section, the system model is initially connected to engineering analysis tools, which are particularly relevant in the early ECLSS design phases.

The proposed framework consists of four main steps: (i) model definition and parametrization, (ii) automated data extraction and tools interoperability, (iii) simulation and analysis activities, and (iv) results evaluation and requirements validation. In the proposed approach, the system model is progressively defined throughout the process using the ARCADIA methodology [5], exploiting information on the system coming from the integrated analysis and simulation tools, in an iterative process. The integration method relies on the use of the Capella's add-on Property Values Management Tools (PVMT) [9], which enables the parametrization of the model. This allows designers to generate data that can be addressed to the elements of the model, enriching it with information that support the execution of relevant analyses and definition of the system architecture.

Materials Research Proceedings 69 (2026) 1505-1511 https://doi.org/10.21741/9781644904251-264

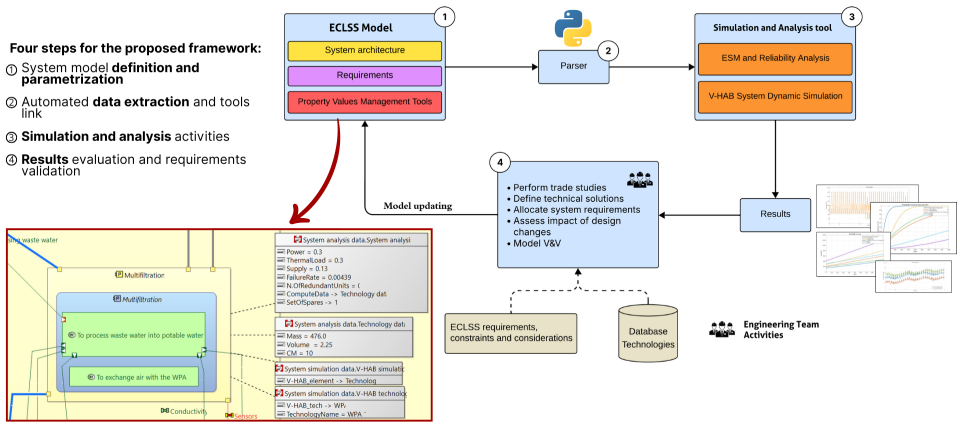


Fig. 1: Integrated MBSE approach.

The integration of the model with the analysis and simulation tools is achieved through a Python-based parser implemented in-house. This library enables the access to model elements and diagrams, as well as the extraction and manipulation of the parameters created through the PVMT. The system data that are extracted are then used to perform analyses or simulations, linking the extracted data with the appropriate external tools. This approach enables the automatic execution of system analysis and simulation, with the objective of obtaining insights into the system's characteristics and behavior. In this work, two different tools are integrated into the model to provide useful information about the system during the early design phases: an Equivalent System Mass (ESM) and reliability analysis tool, as well as the above-mentioned V-HAB simulator. The first tool, based on the parameters extracted from the model, computes two metrics that are fundamental for understanding the characteristics of an ECLSS: the system's ESM and the Probability of Loss of Crew *Pr(LOC)*.

The second tool that is integrated into the model is V-HAB, a simulation tool that simulates the dynamic behavior of an ECLSS for a specified mission scenario. In this work, a Python code is created to convert the system architectural and parametric models from Capella into the corresponding V-HAB ECLSS model. This approach enables the automatic generation of the V-HAB model and the execution of a simulation of the system for the specified mission. Each Python script that enables the extraction of system model information and the subsequent execution of analyses and simulations is imported into Capella using the *Python4Capella* add-on [9]. Once a system configuration is defined, designers can execute the scripts directly from the model, automatically obtaining the results for the system represented in Capella. Designers can exploit these results to perform trade studies, define technical solutions, verify requirements, assess the impact of design changes, and conduct continuous verification and validation of the model. Therefore, the proposed integrated approach supports the iterative evaluation and definition of the system model through the design process.

ECLSS Design for an Analog Habitat

To validate the proposed approach and obtain a more comprehensive understanding of its key advantages, the integrated approach is applied for the preliminary design of the ECLSS for an Analog Habitat. They provide a controlled, Earth-based proxy to test architectures, procedures, and human-system interactions under realistic operational constraints before flight, while offering cost and risk reduction, TRL maturation for ECLSS technologies, and high-fidelity study of human factors. An Analog Habitat campaign therefore constitutes an appropriate proving ground for an MBSE-driven ECLSS design loop: mission durations are shorter, safety can rely on terrestrial contingencies, and rapid iteration is feasible – yet the same drivers (closure vs. logistics, reliability vs. mass, ops complexity vs. robustness) still govern architecture quality [10].

Materials Research Proceedings 69 (2026) 1505-1511 https://doi.org/10.21741/9781644904251-264

The Analog Habitat is modeled with ARCADIA/Capella across its Operational, System, Logical, and Physical layers; mission objectives and requirements derive from stakeholder analysis and drive the ECLSS functions and interfaces used downstream. The Physical Architecture level (of which an example is shown in Fig. 2) serves as the authoritative source for technology choices and links (e.g., Atmosphere Control & Supply (ACS), Water Recovery & Management (WRM), Temperature & Humidity Control (THC) sub-systems), enriched with PVMT properties to capture masses, volumes, power, heat loads, consumables/expendables/spares, failure rates, redundancy/spares counts, set-points, and scenario data.

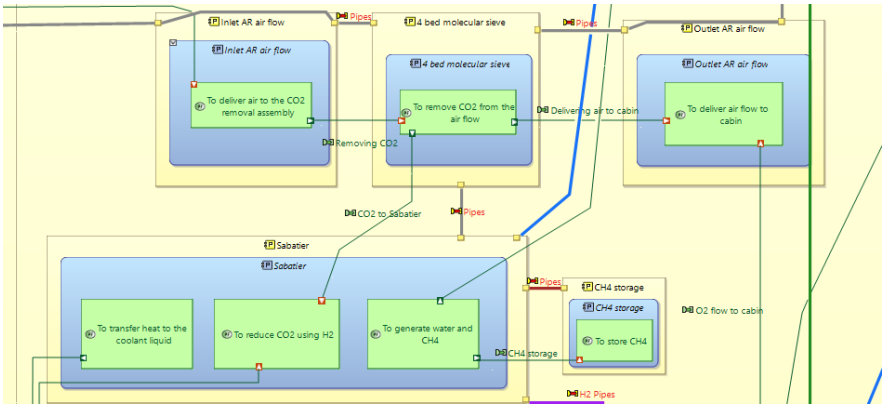


Fig. 2: Portion of the initial ECLSS architecture as represented in the PAB diagram.

A Python bridge (Python4Capella/capellambse) extracts components, links, PVMT properties (i.e., masses, flow-rates, power consumptions, simulation data, etc.), requirement links for the two tools: (i) an ESM & reliability calculator; (ii) a V-HAB model generator/runner. Execution inside Capella keeps analyses coherent with the checked-in model state.

The baseline ECLSS emphasizes the adoption of regenerative P/C technologies appropriate for long duration (eventhough in the analog they are assessed here over shorter analog missions). ESM aggregates mass, power, volume, heat rejection, and crew-time via mission-specific conversion factors per [6]; reliability uses constant-rate components with spares/redundancy treatment to estimate Probability of Loss of Crew *Pr(LOC)* [7].

The initial configuration (no spares/redundancy), results – as per Fig. 3 and Fig. 4 – show approximately linear ESM growth with duration (driven by time-dependent terms) and an unacceptably high Pr(LOC) even at ~10 days – highlighting the classic mass–reliability tension of recycling-heavy systems. The analyses show how storage-heavy architectures tend to be more reliable for short missions but incur higher ESM at longer durations; closing loops reduces ESM at longer durations but increases failure exposure unless mitigated by spares/redundancy.

Materials Research Proceedings 69 (2026) 1505-1511 https://doi.org/10.21741/9781644904251-264

The V-HAB generator creates a model equivalent to the Capella component-level model (at PA level): compartments, storages, technology instances, and controllers, with boundary conditions from PVMT (e.g., phasing, crew planners, initial inventories).

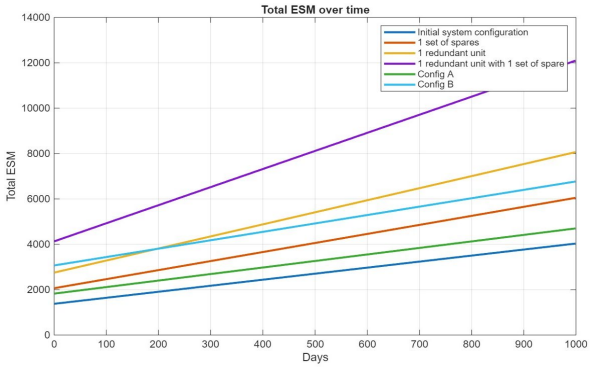


Fig. 3: Pr(LOC) over mission duration.

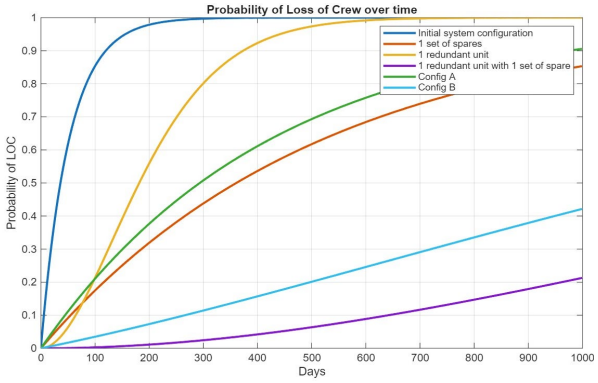


Fig. 4: ESM over mission duration.

The simulator runs closed-loop simulations (cabins, species, inventories, power) to verify requirement bounds and probe sensitivities/failure responses. Typical checks include: cabin pressure and major constituent partials recovery after disturbances; WRM throughput under crew metabolic loads; power/thermal margins; controller robustness under off-nominal inflows or component outages. Results – of which an example is shown in Fig. 5 and Fig. 6 – are fed back to requirement elements (Reviewed/WIP) to maintain traceable closure.

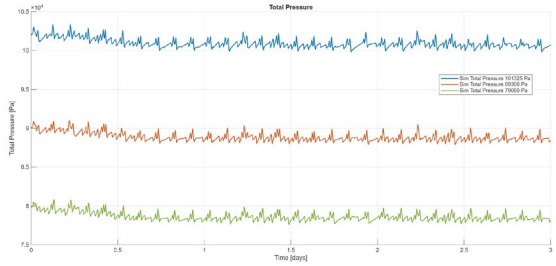


Fig. 5: Total cabin pressure over the mission duration for three different scenarios.

Materials Research Proceedings 69 (2026) 1505-1511 https://doi.org/10.21741/9781644904251-264

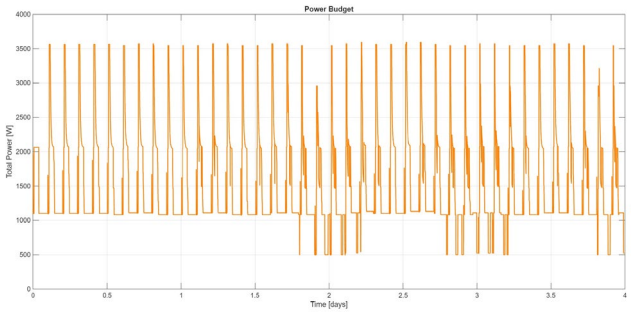


Fig. 6: ECLSS Power budget for a specified mission.

As illustrated in this section, this integrated MBSE approach establishes the model as the central source of truth for data across the entire design process, serving as a unified repository that guides requirement traceability, architecture development, analysis, and simulation throughout all phases of the ECLSS design.

Conclusion

The proposed integrated MBSE approach was developed to support the ECLSS design process. Its application to a real-world project enabled the identification of the key advantages of this approach, thereby overcoming the main limitations of the traditional methodology and leveraging the full potential of MBSE. This work demonstrated that any kind of analysis or simulation tool can be effectively integrated into a standard MBSE methodology. Indeed, a successful connection was established between Capella and an external simulation tool, as well as a custom-made analysis.

The characteristics of the proposed approach ensure consistency between the system model in Capella and the analysis and simulation tools. This guarantees that simulations and analyses are always consistent with the system model established in Capella, ensuring they consistently reflect the latest version of the model. The automatic execution of integrated tools from the model also contributes to a reduction in time and errors involved in creating the simulation each time it is required. In this integrated environment, once a system configuration has been established, analyses and simulations can be conducted rapidly, thereby providing insights into the system and enabling the rapid evaluation of the effects of design changes.

Moreover, this integrated approach facilitates the early detection and resolution of design issues by enabling verification and validation of the system from the initial stage of the design process. Furthermore, it facilitates the assessment of requirements since the initial design stages. Consequently, the proposed approach is expected to enhance the management of complexity in designing systems like the ECLSS, improving the overall robustness, traceability, and efficiency of the design process.

Future work will aim to integrate the system model with advanced engineering tools to assess the effectiveness of the approach in later design phases and further consolidate its applicability to other mission-critical systems.

Acknowledgements

G.L. work has been conducted within the Space It Up project funded by the Italian Space Agency (ASI) and the Italian Ministry of University and Research (MUR), under contract n. 2024-5-E.0 - CUP n. I53D24000060005.

References

[1] P. Eckart. Spaceflight life support and biospherics. Space technology library. Microcosm Press, Torrance, CA, US, 1996. ISBN 978-90-481-4659-8.

[2] ECSS-E-ST-34C – ECLS. 2018. Available online. url: ecss.nl/standard/ecss-e-st-34c-environmantal-control-and-life-support-ecls (accessed on 30 Oct 2025).

[3] P. O. Wieland. Designing for human presence in space: an introduction to environmental control and life support systems. NASA, Marshall Space Flight Center, Huntsville, AL, US, 1994.

[4] A. M. Madni and M. Sievers. Model-based systems engineering: Motivation, current status, and research opportunities. *Systems Engineering*, *21(3)*: 172–190, 2018. https://doi.org/10.1002/sys.21438

[5] Thales Group. Arcadia method overview, 2005. Available online. url: mbse-capella.org/arcadia.html (accessed on 01 Jul 2025).

[6] J. A. Levri, D. A. Vaccari and E. Alan. Theory and Application of the Equivalent System Mass Metric. *SAE Technical Paper Series, vol. 1*. 2000. https://doi.org/10.4271/2000-01-2395.

[7] H. Jones. Design and Analysis of a Flexible, Reliable Deep Space Life Support System. In *42nd International Conference on Environmental Systems*, 15-19 Jul 2012, San Diego, CA, US. 2012. https://doi.org/10.2514/6.2012-3418

[8] M. Czupalla, A. Zhukov, J. Schnaitmann, C. Olthoff, M. Deiml, P. Plotner, and U. Walter. The virtual habitat – a tool for dynamic life support system simulations. *Advances in Space Research, 55(11)*: 2683–2707, 2015. ISSN 0273-1177. https://doi.org/10.1016/j.asr.2014.12.029

[9] Eclipse Inc. Capella MBSE Add-On. 2025. Available online. url: https://mbse-capella.org/addons.html (accessed on 3 Nov 2025).

[10] C. Heinicke and M. Arnhof. A review of existing analog habitats and lessons for future lunar and Martian habitats. *REACH, vol. 21-22*: 100038. 2021. https://doi.org/10.1016/j.reach.2021.100038

Materials Research Proceedings 69 (2026) 1512-1517 https://doi.org/10.21741/9781644904251-265

Integrating Scenario-Based Life Cycle Assessment into Model-Based Systems Engineering for Space Exploration Systems Design

Giacomo LUCCISANO[1,a *], Fabrizio BORGNA[1,b *], Roberta FUSARO[1,c] and Nicole VIOLA[2,d]

[1]Department of Mechanical and Aerospace Engineering (DIMEAS), Politecnico di Torino, 10129, Turin, Italy

[2]Department of Management and Production Engineering (DIGEP), Politecnico di Torino, 10129, Turin, Italy

[a]giacomo.luccisano@polito.it, [b]fabrizio.borgna@polito.it, [c]roberta.fusaro@polito.it, [d]nicole.viola@polito.it

Keywords: Model-Based Systems Engineering, Life Cycle Assessment, Space Exploration Systems, Space Mission Design, Modeling & Simulation

Abstract. Ambitions for sustained human presence beyond Earth are accelerating, while environmental accountability and long development timelines expose limits of document-centric systems engineering approach. Crewed mission architectures integrate propulsion, communications, life support, and habitats under tight safety, performance, and sustainability constraints; decisions propagate across technologies and phases, and their impacts unfold over space and time under uncertainty. Model-Based Systems Engineering (MBSE) can manage architectural complexity, but it rarely embeds life cycle sustainability reasoning with sufficient fidelity or timeliness. This paper introduces the concept of a framework that unifies MBSE and Scenario-Based Life Cycle Assessment (SB-LCA) to perform continuous, traceable, time- and location-aware sustainability evaluation as systems' designs evolve. The framework consists of two layers: (i) a process-based LCA that quantifies the environmental impact of technologies to drive architecture trades; (ii) a transportation layer that selects payload-feasible launcher classes and partitions their footprint into static (manufacture, propellants, end-of-life) and variable (trajectory-resolved operations) contributions. Within this second layer, mission analysis couples emissions and atmospheric-response models to generate a geo-referenced inventory. Hetero-functional graphs capture interdependencies and enable reuse of SB-LCA modules across phases. The proposed approach is envisioned to identify dominant drivers, quantify sensitivities to payload growth, vehicle choice, and trajectory design, and iteratively guide lower-impact configurations – providing measurable environmental targets for responsible human space exploration.

Introduction

Designing crewed space exploration systems represents a complex system-of-systems problem: various subsystems – propulsion, communications, life support, etc. – must function coherently under harsh environments, long development timelines, and stringent safety and performance constraints [1]. Traditional, document-centric Systems Engineering (SE) has struggled to provide timely, traceable decision support across these tightly coupled design spaces. Model-Based Systems Engineering (MBSE) advances the state of practice by shifting to model-centric artifacts that improve consistency, collaboration, and lifecycle traceability [2]. Yet, even MBSE workflows rarely embed environmental sustainability with sufficient fidelity to influence early trades, despite the growing imperative to account for life-cycle impacts of space infrastructures. Life Cycle Assessment (LCA) and its broader sustainability formulations have recently been proposed to inform mission design, but adoption remains fragmented and often decoupled from architecture

Content from this work may be used under the terms of the Creative Commons Attribution 3.0 license. Any further distribution of this work must maintain attribution to the author(s) and the title of the work, journal citation and DOI. Published under license by Materials Research Forum LLC.

models and design iteration [3]. Moreover, launcher footprint and the chemical emissions produced throughout a space mission have emerged as potentially dominant contributors to climate and atmospheric impacts, reinforcing the need to co-design payload architectures with transportation choices. Recent studies quantify large climate impacts tied to rocket exhaust and compare environmental burdens across launcher architectures [4][5], while analyses of rapidly expanding space infrastructures highlight prospective greenhouse-gas footprints at constellation scale [6]. These insights motivate sustainability assessments that are (i) scenario-aware, (ii) time- and location-resolved, and (iii) natively integrated within systems models and mission analyses. Scenario-Based LCA (SB-LCA) offers a principle-based language to represent uncertainty in future technologies, operations, and policies, enabling structured comparison of plausible pathways [7]. However, practical integration of SB-LCA into MBSE remains limited by representational gaps (how to bind LCA elements to system architecture and behavior), data gaps (how to reuse and update inventories as designs evolve), and analytical gaps (how to propagate mission analysis, emissions, and atmospheric responses into life-cycle metrics). Closing these gaps is especially important in early phases of crewed missions, where small architectural changes – mass growth, interface choices, duty cycles – can cascade into different launcher classes, trajectories, and, ultimately, different environmental profiles.

This paper addresses these gaps by introducing an MBSE ARCADIA/Capella-based Modeling & Simulation (M&S) framework [8], enriched with SB-LCA, for human exploration architectures, demonstrated on a notional Lunar Habitat mission. The framework embeds LCA constructs directly into system and mission models, enabling continuous, traceable sustainability evaluation alongside performance and safety considerations. It enforces a two-layer architecture: (i) a process-based LCA layer quantifies sustainability metrics for habitat technologies to drive architecture trades; and (ii) a transportation layer that, after preliminary habitat sizing, supports the user in selecting feasible launcher classes from payload-driven macro-categories and partitions their footprint into static (manufacturing, propellants, end-of-life) and variable (trajectory-resolved operations) contributions. The variable contribution is quantified by coupling mission analysis with emissions and atmospheric-response models to produce a geo-referenced inventory along the prescribed trajectory, which is then integrated with habitat delivery impacts for a mission-level footprint [4][5]. In doing so, it turns MBSE from a passive container of sustainability results into an active co-simulation environment where environmental objectives can be traced to architecture choices, requirements, and operational concepts [2][3].

Proposed methodology

First layer. The first layer of the proposed methodology presents as main baseline a ARCADIA/Capella-based workflow [9], with the model acting as the authoritative source for requirements, behavior, interfaces, and physical architecture. Specific Capella add-ons for creating parametric extensions (PVMT) and Python bridges (Python4Capella) [10] enable the automatic extraction of model data, the execution of external analyses and simulations, and the write-back of results, thereby maintaining configuration coherence and traceability throughout iterative trade studies and early V&V. This integration pattern has been demonstrated in previous Capella applications to quantitative assessment and dynamic simulation, establishing a reliable path for analysis-in-the-loop [8]. An example of the framework structure is presented in Fig. 1.

Within this baseline, the lifecycle and the Concept of Operations (ConOps) with associated Operating Modes are modeled as co-equal artifacts and tightly linked to the evolving architecture. Mission phases and mode logic structure the full sequence of activities from early development and verification through commissioning to nominal operations, providing the temporal scaffold required for scenario-aware assessments and allowing performance and behavior to be evaluated consistently from the earliest stages [8].

Materials Research Proceedings 69 (2026) 1512-1517 https://doi.org/10.21741/9781644904251-265

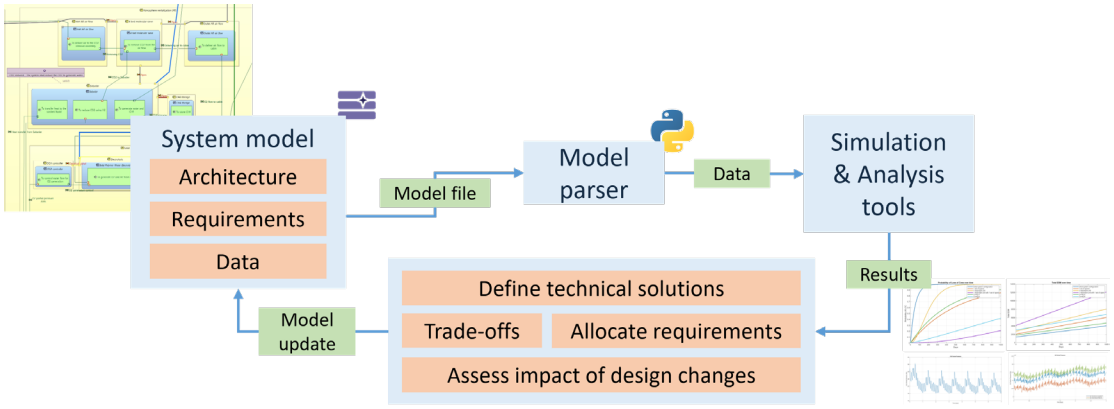


Fig. 1: First layer and M&S framework structure.

Scenario-Based Life Cycle Assessment (SB-LCA) is embedded in this environment to transform the modeled lifecycle and ConOps into quantified sustainability evidence. For a selected configuration and scenario, the Capella bridge composes the pre-operational and operational activity set from the lifecycle and ConOps, projects each activity to its planned execution year, aggregates inventories, and computes characterized impacts that are written back to the model as figures of merit alongside mass, power, reliability, and other metrics. In this way, environmental performance becomes a peer objective in model-driven trades rather than an external report, consistent with the two-layer methodology in which process-based LCA supports technology decisions at habitat level while transportation impacts are assessed separately and merged to produce a mission-level footprint. A practical bottleneck lies in building the life-cycle inventory for every component and every modeled activity. To avoid out-of-model information spread, LCA metadata are authored directly in Capella – leveraging PVMT and domain extensions – so that materials, energy, logistics, facility usage, consumables, and end-of-life assumptions are attached to components and to lifecycle/ConOps activities within the same authoritative model. This approach reuses the proven data plumbing employed for quantitative analyses and enables consistent queries by configuration, phase, or scenario; Ecodesign4Capella add-on [10] supports this in-model inventory capture and governance.

Second layer. The second layer of the framework enables the selection of a launch vehicle using outputs from the first layer – payload mass, volume, and sustainability-feasible habitat configurations – and evaluates the chosen vehicle's environmental performance on a life-cycle basis. Vehicles are drawn from a predefined pool grouped by lift capacity; once a candidate is identified, its impacts are quantified across production and operations and decomposed into: (i) a static contribution covering manufacturing of hardware and propellants and end-of-life treatment, sourced from referenced impact databases and industrial inventories [5][6][11][12]; and (ii) a variable contribution covering mission operations along the trajectory, including atmospheric responses to pollutant and greenhouse-gas emissions generated during flight [4][13][14]. The aggregation of static and variable parts yields a comprehensive, LCA-based environmental profile that supports comparative assessment and sustainability-driven trade-offs within mission design. Inputs comprise payload descriptors and a candidate set characterized by class (medium, heavy, super-heavy), stage configuration, propulsion type, propellant mass, and fairing dimensions. A selection algorithm matches requirements to a class and vehicle, within a scenario-based LCA structure that separates modeling, scenario definition, and impact evaluation for transparency and reuse [3][5][6].

Each launcher is parameterized in the MBSE environment so that mass breakdowns, propellant demand, and geometry propagate automatically to downstream assessments. This modularity enables rapid substitution of vehicles or mission scenarios with immediate updates to impacts. For

Materials Research Proceedings 69 (2026) 1512-1517 https://doi.org/10.21741/9781644904251-265

the static life-cycle portion, cradle-to-gate and launch-to-grave costs of rocket hardware and propellants are quantified and split into manufacturing/upstream propellant production and end-of-life processes; reported evidence indicates manufacturing/upstream dominates the overall footprint of launch systems [5]. Hardware inventories for structures, engines, tanks, avionics, and subsystems are taken from industry LCA studies and validated databases [15], while propellant chains (oxidizer and fuel synthesis, cryogenic processing, storage) use literature emission factors [16]. Static LCA modules are implemented as reusable elements linked to the parametric launcher model so that changes in mass, materials, or configuration are reflected automatically, preserving traceability between design parameters and impact indicators.

The variable contribution is derived from mission operations by coupling a mission-analysis tool with an emissions module that produces a time-resolved, geo-referenced exhaust profile for the selected launcher, as shown in Fig. 2. Mission analysis generates the trajectory from thrust requirements, propellant mass flow, and aerodynamic characterization. The emissions module thermodynamically characterizes the engine via a simplified propulsion model and, from propellant mass, temperature, and pressure profiles, estimates time-resolved chemical outputs using combustion-kinetic formulations. Tracked species include CO_2, H_2O, NO_x, CO, and soot (black carbon). Species-specific, altitude-dependent impact coefficients from atmospheric chemistry and radiative-transfer models capture the differing climate and ozone effects across atmospheric layers [16], with high-altitude releases receiving enhanced forcing factors to reflect disproportionate radiative and chemical effects relative to surface emissions [4]. Geospatial and temporal multipliers convert emitted masses into standardized impact units (e.g., CO_2-equivalents, ozone-depletion equivalents). Resulting inventories feed impact-assessment functions (global-warming potential, ozone effects, etc.) to yield the variable share of the launcher footprint [13][14].

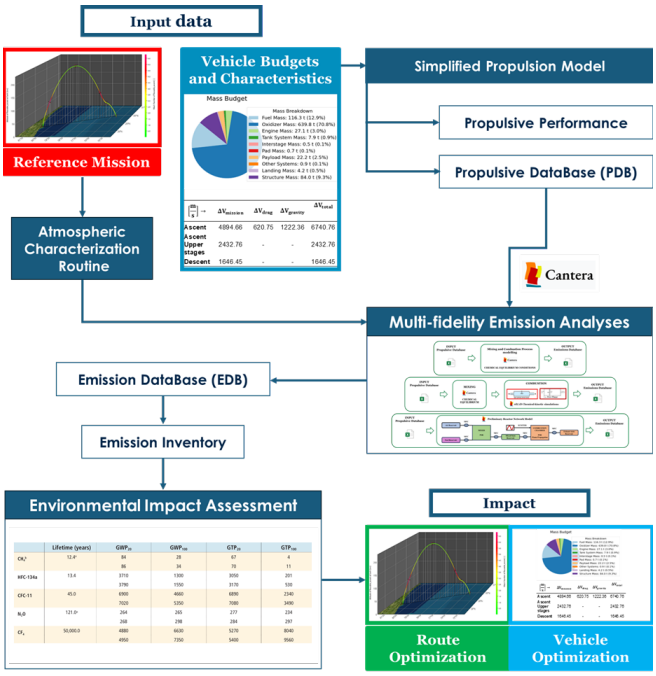


Fig. 2: Second layer dynamic contribution.

Static and dynamic contributions are then aggregated to provide the total environmental footprint of the selected transport vehicle, per mission or per kilogram of delivered habitat, expressed in standardized metrics that can be directly compared with habitat subsystem impacts from the first layer. Embedded within an MBSE/SB-LCA backbone, the process is inherently iterative: alternative vehicles, profiles (timing, trajectory), and reuse assumptions can be introduced as new scenarios, each producing updated, scenario-consistent impacts for quantitative trade-off analyses. SB-LCA principles allow systematic exploration of launch cadence, reusability rate, and technological evolution on environmental outcomes [3][5][6], while the MBSE backbone ensures consistent, traceable data flows across design iterations, inventories, and analyses [11][12][15][16].

By applying SB-LCA principles, the approach allows decision-makers to systematically evaluate how variations in key assumptions – such as launch cadence, reusability rate, or technological evolution – affect environmental outcomes, while the MBSE backbone ensures that data flows remain consistent, traceable, and fully integrated across design iterations.

In this configuration, calculated environmental impacts – time-located and scenario-consistent – serve as decision-quality figures of merit for technology selection and scheduling, while end-to-end traceability is preserved across requirements, architectural choices, lifecycle/ConOps definitions, and quantitative analyses executed from the model.

Conclusions

The presented integrated framework embeds Scenario-Based Life Cycle Assessment within an ARCADIA/Capella Modeling & Simulation workflow for crewed space systems. Lifecycle and Concept of Operations are modeled as first-class artifacts, while life-cycle inventories are authored in-model via PVMT and Ecodesign4Capella, making environmental assessment continuous, traceable, and time-located.

A two-layer formulation couples Scenario-Based Life Cycle Assessment for technology trades with a transportation layer that partitions launcher impacts into static (manufacturing, propellants, end-of-life) and variable (trajectory-resolved operations) components, ensuring delivery and pre-operational flights are captured in the mission footprint. Impact metrics are written back to the authoritative model alongside performance and safety figures of merit. The proposed approach, co-locating Scenario-Based Life Cycle Assessment with lifecycle and operating-mode models can thus expose dominant drivers early, quantify sensitivities to payload evolution, subsystem choices, launcher macro-class, and trajectory design, and support iterative convergence toward lower-impact architectures.

Current limitations center on inventory completeness, database representativeness, and uncertainty propagation across coupled analyses. Future work will emphasize uncertainty and sensitivity quantification, standardized data schemas and connectors, validation against test/flight evidence, and extensions to logistics, reuse/refurbishment, and in-situ resource utilization. With these enhancements, the framework provides a decision-grade backbone for setting – and demonstrating progress toward – measurable environmental targets in complex crewed mission design.

Acknowledgements

G.L. work has been conducted within the Space It Up project funded by the Italian Space Agency (ASI) and the Italian Ministry of University and Research (MUR), under contract n. 2024-5-E.0 - CUP n. I53D24000060005.

References

[1] Larson, W. J.; Pranke, L. K. (Eds.). Human Spaceflight: Mission Analysis and Design 5th ed. *Space Technology Series*, McGraw-Hill: New York, NY, 2007.

[2] INCOSE. Systems Engineering Vision 2020. 2007. Available online. url: ccose.org/media/upload/SEVision2020_20071003_v2_03.pdf (accessed on 1 Jul 2025).

[3] Wilson, A. R.; Vasile, M.; Maddock, C.; Baker, K. Implementing life cycle sustainability assessment for improved space mission design. *Integrated Environmental Assessment and Management, 19(4)*: 1002-1022, 2023. https://doi.org/10.1002/ieam.4722

[4] Domínguez Calabuig, G. J.; Wilson, A.; Bi, S.; Vasile, M.; Sippel, M.; Tajmar, M. Environmental life cycle assessment of reusable launch vehicle fleets: large climate impact driven by rocket exhaust emissions. *Acta Astronautica, 221*: 1-11. 2024. https://doi.org/10.1016/j.actaastro.2024.05.009

[5] Fischer, J.-S.; Fasoulas, S.; Brun-Buisson, C.; Del Olmo, E. Comparison study on the environmental impact of different launcher architectures. In *Aerospace Europe Conference 2023 - 10th EUCASS - 9th CEAS*, 9-13 Jul 2023, Lausanne, CH. https://doi.org/10.13009/EUCASS2023-274

[6] Kukreja, R.; Oughton, E. J.; Linares, R. Greenhouse Gas (GHG) emissions poised to rocket: modeling the environmental impact of LEO satellite constellations. *Preprint*, 2025. https://doi.org/10.31223/X5CF09

[7] Fukushima, Y.; Hirao, M. A structured framework and language for scenario-based Life Cycle assessment. *International Journal of Life Cycle Assessment, 7*: 317-329, 2002. https://doi.org/10.1007/BF02978679

[8] Campioli, S.; Luccisano, G.; Ferretto, D.; Stesina, F. Towards a Unified Modeling and Simulation Framework for Space Systems: Integrating Model-Based Systems Engineering with Open Source Multi-Domain Simulation Environments. *Aerospace, 12(8)*: 745. 2025. https://doi.org/10.3390/aerospace12080745

[9] Voirin, J.-L. Model-Based System and Architecture Engineering with the ARCADIA method. *Implementation of model based system engineering set*, ISTE Press, London, UK. 2018. https://doi.org/10.1016/C2016-0-00862-8

[10] Eclipse Inc. Capella MBSE Add-On. 2025. Available online. url: mbse-capella.org/addons.html (accessed on 3 Nov 2025).

[11] Chanoine, A; Duvernois, P.A.; Le Guern, Y. Environmental impacts of launchers and space missions. 2017.

[12] Gallice, A.; Maury, T.; Del Olmo, E. Environmental impact of the exploitation of the Ariane 6 launcher system. 2018.

[13] Voigt, C.; Schumann, U.; Graf, K.; Gottschaldt, K.-D. Impact of rocket exhaust plumes on atmospheric composition and climate – an overview. *Progress in Propulsion Physics,* 4: 657-676. 2013. https://doi.org/10.1051/eucass/201304657

[14] Larson, E. J. L.; Portmann, R. W.; Rosenlof, K. H.; Fahey, D. W.; Daniel, J. S.; Ross, M. N. Global atmospheric response to emissions from a proposed reusable space launch system. *Earth's Future, 5(1)*: 37-48. 2017. https://doi.org/10.1002/2016EF000399

[15] El-Shawa, S.; Cattani, B. M.; Innocenti, L.; Delaval, J. From cradle to grave: ESA Clean Space's approach to space sustainability, In *72nd International Astronautical Congress (IAC)*, Dubai, UAE, October 2021.

[16] Myhre, G.; Shindell, D.; Bréon, F.M.; Collins, W.; Fuglestvedt, J.; Huang, J.; Koch, D.; Lamarque, J. F.; Lee, D.; Mendoza, B. *et al.* Anthropogenic and natural radiative forcing. IPCC (Ed.), *Climate Change 2013: The Physical Science Basis. Contribution of Working Group I to the Fifth Assessment Report of the Intergovernmental Panel on Climate Change*, Cambridge University Press, Cambridge, UK and New York, NY, US. 2013.

Materials Research Proceedings 69 (2026) 1518-1523 https://doi.org/10.21741/9781644904251-266

iDREAM 2.0: A Paradigm Shifts Towards Reusable Space Systems

Antonio GREGORIO[1], Roberta FUSARO[1,a *], Nicole VIOLA[2,b], Davide FERRETTO[1,c], Giuseppe NARDUCCI[1], Valeria BORIO[1], Giacomo LUCCISANO[1], Marco VERRASCINA[1] and Giuseppe DE BARI[1]

[1]Department of Mechanical and Aerospace Engineering (DIMEAS), Politecnico di Torino, 10129, Turin, Italy

[2]Department of Management and Production Engineering (DIGEP), Politecnico di Torino, 10129, Turin, Italy

[a]roberta.fusaro@polito.it, [b]nicole.viola@polito.it, [c]davide.ferretto@polito.it

Keywords: Reusable Space System, Multidisciplinary Design Analysis, Flight Vehicle Design, Technology Roadmaps, Cost Estimation

Abstract. The design of next-generation flight vehicles for space access and in-orbit operations requires agile and modular tools that can support the rapid prototyping of expendable and reusable vehicles. Since 2020, Politecnico di Torino has been developing the iDREAM methodology and toolset within the framework of the GSTP program under the supervision of the European Space Agency (ESA). In its initial iteration, iDREAM focused on two case studies: a Micro Launcher (ML) and a Human Landing System (HLS). The toolset is composed of three main modules to: (i) support conceptual design activities through ASTRID-H, (ii) enable early-stage assessment of economic viability via HyCost and, (iii) analyze technology sustainability through TRIS, the dedicated technology roadmapping module. Moreover, a unified and upgraded database, supported by an in-house developed Database Management Library, supports the operation of all modules within the integrated toolset. The ongoing second phase (iDREAM 2.0) marks a paradigm shift by extending the methodology to support reusable flight systems, including first and/or second stage vertical and/or horizontal landing launch vehicles (RLV), reusable re-entry vehicles (RREV), and hypersonic use cases and introducing a highly modular environment. A key innovation lies in the integration of reusable systems modelling within existing expendable-focused routines, reducing redundancy and maximizing tool adaptability. The adopted approach focuses on minimizing the number of routines required for design and analysis while maximizing the coverage of reusable configuration combinations. Following a detailed trade-off analysis, the final architecture includes six routines for ASTRID-H, three for HyCost, and a single unified routine for the technology roadmapping TRIS module. This paper presents the current status of the ongoing iDREAM 2.0 project, which is currently in the development phase and undergoing validation through a set of reference vehicles. These include reusable launch systems, with vertical and horizontal recovery, reusable re-entry capsules, and hypersonic vehicle, demonstrating the framework's versatility in supporting the design of future reusable space systems.

Introduction

The contemporary space sector faces compressed timelines, heterogeneous missions, and rising cost pressure. Early decisions must therefore couple performance, affordability, and technology maturity – yet these dimensions are still too often treated in separate loops. Multidisciplinary Design Optimization (MDO) enables fast, coupled performance trades, but mainstream practice rarely integrates cost and technology roadmapping in the same decision cycle [1]. Concurrent design teams demonstrate that time-boxed, integrated studies accelerate iteration and improve

Content from this work may be used under the terms of the Creative Commons Attribution 3.0 license. Any further distribution of this work must maintain attribution to the author(s) and the title of the work, journal citation and DOI. Published under license by Materials Research Forum LLC.

Materials Research Proceedings 69 (2026) 1518-1523 https://doi.org/10.21741/9781644904251-266

traceability, but economic and maturation analyses are typically handed off to downstream tools [2].

Within performance, high-fidelity mission/trajectory tools (e.g., ASTOS [3]) assess launcher and re-entry feasibility but are not designed to co-evolve with cost or roadmap logic in early trades. In parallel, cost estimation spans agency and commercial traditions – from TRANSCOST and NAFCOM [4] to subsystem-level CERs for small-launcher markets [5] – yet these models are seldom wired directly to the conceptual sizing variables that drive mass and configuration sensitivities. Subsystem-granular CERs and "theoretical first unit" logic are most useful when fed by design data rather than spreadsheets; classic systems texts (e.g., SMAD [6]) similarly argue for considering affordability from day one.

On the technology side, roadmapping aligns stakeholder needs, capabilities, and enabling technologies. Phaal et al. [7] frame it as a flexible planning method. Building on this literature and ESA practice, TRIS introduced a rational, systems-engineering process that prioritizes technologies, quantifies schedule/cost implications, and plans maturation activities – moving beyond purely expert-driven roadmaps [8].

What was missing was a single, modular environment that (a) makes design, cost, and roadmapping talk natively; (b) keeps stakeholder needs in the driver's seat; and (c) preserves consistent data across loops. iDREAM 1.0 addressed this gap within ESA's GSTP framework (with ASI support), unifying ASTRID-H (conceptual/preliminary design), HyCost (early life-cycle cost), and TRIS (technology roadmapping) on a shared HyDat database and in-house management library [9].

This paper presents iDREAM 2.0, which generalizes that baseline for reusability and hypersonic missions. The architecture embeds recovery and operations within the same loop as sizing, cost, and roadmaps, while minimizing routine duplication. Concretely, it consolidates six ASTRID-H routines, three reuse-aware HyCost flows, and a single unified TRIS routine, all backed by an upgraded HyDat for traceable, one-source-of-truth parameters and automatic exchange of mass, cost, and roadmap evidence.

The paper is organized as follows: §2 summarizes iDREAM 1.0; §3 details the iDREAM 2.0 architecture and reusable-system extensions; §4 concludes with key findings and future work.

iDREAM 1.0 toolset and capabilities

iDREAM 1.0 integrates three pillars – ASTRID-H for conceptual/preliminary design, HyCost for early life-cycle cost assessment, and TRIS for technology roadmapping – on top of a shared database (HyDat) and an in-house Database Management Library, as shown in Fig. 1. ASTRID-H extends a decade of multi-fidelity sizing research at Politecnico di Torino from aircraft into microlaunchers and lunar landers, retaining a structured workflow that supports both *"sizing from scratch"* and assessment of existing configurations. It exchanges mission analysis data with ASTOS to refine closure: preliminary sizing (mass, dimensions, aerodynamics, propulsion) is iterated with an internal mission design routine, then re-optimized in ASTOS, and reintegrated into ASTRID-H to sharpen propellant and payload allocation. The microlauncher workflow implements both a restricted staging algorithm for feasibility checks and an optimal Lagrange-multiplier staging

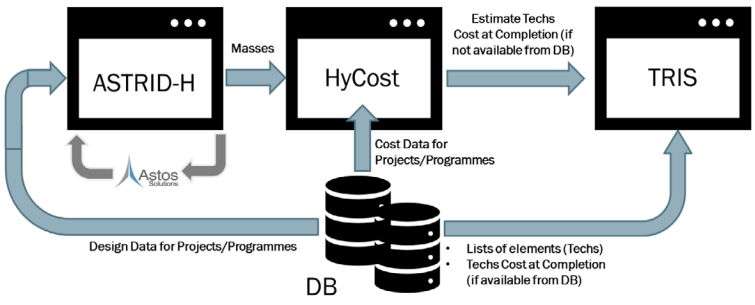


Fig. 1: iDREAM 1.0 structure.

scheme to minimize mass given payload and burnout velocity, with structural-ratio ranges linked to propellant type.

HyCost complements ASTRID-H by estimating development, manufacturing, and operating costs – as well as cost and price per flight – directly from design variables and performance outputs or from user databases. At its core are subsystem-level cost-estimation relationships, tuned with reduction factors for commercial applications and learning curve options for innovative manufacturing. The adopted approach builds on an ESA methodology for small and commercial launch vehicles based on *"recurring first unit"* logic and linear factors at subsystem/equipment level, extended in iDREAM to include process/manufacturing considerations so that estimates remain transparent and updateable as new commercial data emerge. HyCost also aggregates results by technology families to provide cost-at-completion inputs for TRIS.

TRIS closes the loop by converting the coupled design–cost view into a rational, stakeholder-driven roadmap. The methodology proceeds through five steps – (i) stakeholder analysis, (ii) elements definition (operational capabilities, technologies, building blocks, and mission concepts/activities), (iii) prioritization, (iv) planning, and (v) results evaluation – implemented with mathematical and logical models and supported by database-curated lists and resource estimates for TRL transitions. Recent updates improve allocation of budget/time in the planning algorithm and enable "non-ideal" roadmaps under constrained scenarios, reflecting ESA practice across hypersonic, re-entry, and exploration contexts.

These modules operate on a common data backbone. HyDat – a MySQL database originally developed with ESA to support technology roadmapping for hypersonic transportation and reusable access-to-space systems – now feeds and records parameters across design, cost, and roadmaps through a dedicated Database Management Library. The entire stack is implemented in Python with an integrated GUI; each module can be used stand-alone or in the fully coupled flow, ensuring traceable, bidirectional data exchange and repeatable studies.

With such structure, iDREAM 1.0 enables rapid *"what-if"* exploration where a design change immediately propagates to affordability and maturation plans – and vice versa. A validation on Rocket Lab's Electron [10] illustrates the approach: starting from public mission and configuration data, ASTRID-H/ASTOS converge on masses and dimensions within ~10% of reported values – consistent with conceptual-design expectations – while HyCost produces a subsystem breakdown aligned with reference costs and TRIS organizes a time- and budget-aware development path to TRL 9 over the program timeline. Methodologically, iDREAM sits alongside MDO/PIDO integration frameworks but takes a deliberately domain-opinionated stance: aerospace-specific routines and a shared database minimize setup friction and brittle file hand-offs while preserving the agility of early-phase trades. That foundation proved particularly useful as reusability became mainstream – where recovery constraints, refurbishment, and cadence-driven operations tightly couple trajectory, structures, and cost – setting the stage for the generalized, modular extensions presented in §3.

iDREAM 2.0 updated toolset and capabilities

iDREAM 2.0 generalizes the 1.0 framework to cover reusable systems and hypersonic use cases while deliberately minimizing the number of routines needed to span a wide configuration space. The guiding principle is to embed reuse logic inside the same expendable-focused workflows wherever possible, avoiding duplicate code paths and brittle hand-offs. After a trade-off on alternative decompositions, the architecture converged into six routines for ASTRID-H, three for HyCost, and a single, unified routine for TRIS. This structure keeps data consistent across modules and concentrates model complexity where it adds coverage rather than redundancy.

ASTRID-H. As shown in Fig. 2, the ASTRID-H module now supports both expendable and reusable configurations through four core routines – Expendable/Reusable Vertical Launcher (ER-

Materials Research Proceedings 69 (2026) 1518-1523 https://doi.org/10.21741/9781644904251-266

VT), Expendable/Reusable Horizontal Take-Off (ER-HT), Re-entry Vehicle (REV), and Human Landing System (HLS) – augmented by two supplementary landing routines for Vertical Landing (VL) and Horizontal Landing (HL).

1. Take-Off and Landing Strategies: Module Definition

	ASTRID-H					
	Configuration (T/O)			Landing		Case Study
Categories	Winged	Vertical Launcher	Lifting Body	HL	VL	
Micro Launcher		1		N/A	N/A	ML
Medium Launcher		1		N/A	N/A	MED L
Heavy Launcher		1		N/A	N/A	HEA L
Reusable Launch Vehicle 1st stage		1			4	RLV1 VTVL
		1		5		RLV1 VTHL
	2				4	RLV1 HTVL
	2			5		RLV1 HTHL
Expendable Vehicle 1st stage		1		N/A	N/A	EXP1 VT
	2			N/A	N/A	EXP1 HT
Reusable Launch Vehicle 2nd stage	2			5		RLV2 HL
		1			4	RLV2 VL
Expendable Vehicle 2nd stage		1		N/A	N/A	EXP2
Exp. Re-entry*			3	N/A	N/A	EREV
Reusable Re-Entry Vehicle *			3	5		RREV HL
					4	REV VL
Hypersonic Vehicle	2			5		HYPER
Lunar Lander		6			6	HLS

Combining the stage from Table 1 shows that the routine methodologies (ASTRID-H, HyCost) can be combined in the same way of vehicle stages.

2. Potential Vehicle Combinations (RLV - EXP): Module Blend

First Stage	Second Stage: EXP2	Second Stage: RLV2 VL	Second Stage: RLV2 HL	Combination	Name	Reference vehicle
RLV1 VTVL				RLV1 VTVL - EXP2	RLV1 VTVL	RETALT 1 [1]
				RLV1 VTVL - RLV2 VL	Fully Reusable VTVL	Starship [2]
				RLV1 VTVL - RLV2 HL	Fully Reusable	
RLV1 VTHL				RLV1 VTHL - EXP2	RLV1 VTHL	ENTRAIN (DLR) [3]
				RLV1 VTHL - RLV2 VL	Fully Reusable	
				RLV1 VTHL - RLV2 HL		
RLV1 HTVL				RLV1 HTVL - EXP2	RLV1 HTVL	
				RLV1 HTVL - RLV2 VL	Fully Reusable	
				RLV1 HTVL - RLV2 HL		
RLV1 HTHL				RLV1 HTHL- EXP2	RLV1 HTHL	Sanger II (1st stage) [4]
				RLV1 HTHL - RLV2 VL	Fully Reusable	
				RLV1 HTHL - RLV2 HL	Fully Reusable HTHL	Saenger II [4]
EXP1 VT				EXP1 VT - EXP2	MED L, HEA L	Ariane 62 - 64 [5]
				EXP1 VT - RLV2 VL	RLV2 VTVL	Starship (2nd stage) [2]
				EXP1 VT - RLV2 HL	RLV2 VTHL	
EXP1 HT				EXP1 HT - EXP2	EXP HT	
				EXP1 HT - RLV2 VL	RLV2 HTVL	
				EXP1 HT - RLV2 HL	RLV2 HTHL	

Fig. 2: iDREAM - ASTRID-H routines modularity overview.

The landing routines compute propellant consumption and the additional equipment/mass required for controlled descent, then feed those increments back into the sizing loop. This structure lets a single vehicle study switch from expendable to reusable assumptions by toggling landing logic rather than swapping entire design flows; it also keeps hypersonic, wing-assisted take-off cases within the same ER-HT backbone. Complementing this architecture, the modularity approach was derived from a survey of target categories – RLV first/second stages (VTVL/VTHL/HTHL or VL/HL), E/REVs, hypersonic vehicles, and medium/heavy launchers – so common take-off/landing strategies and reuse features are handled by shared sub-models rather than case-specific branches.

Methodologically, ASTRID-H retains the multi-fidelity conceptual/preliminary design stack established in 1.0 and continues to exchange mission analysis data with ASTOS for closure. The same design estimation logic and mass estimation workflow used for expendable microlaunchers is now re-used for RLVs, with landing increments and recovery constraints injected through the VL/HL supplements before trajectory re-optimization. This preserves the tight ASTOS-ASTRID-H loop that proved effective for 1.0 while expanding coverage to reuse-driven constraints.

HyCost. To parallel the generalized design layer, HyCost consolidates early-phase LCC into three approaches: (i) an Expendable Launchers (EXP) flow; (ii) a Reusable Space & Point-to-Point Transportation and Re-entry (RST) flow covering reusable first/second stages, HTHL/VTHL concepts, and E/REVs; and (iii) a tailored Human Landing System (HLS) routine. The RST logic introduces refurbishment, inspection/maintenance, turnaround assumptions, and cadence effects while preserving the subsystem-granular CER philosophy adopted in 1.0 so estimates remain transparent and updateable as new commercial data emerge. All three flows ingest ASTRID-H outputs directly (masses, counts, propellants, equipment) to keep architectural sensitivities intact.

TRIS. In 2.0, TRIS operates through a single roadmapping routine applied uniformly across case studies. It keeps the five-step, systems-engineering process while incorporating the recent upgrades to time/budget estimation and to resource-constrained planning that allow realistic, non-ideal roadmaps. Technologies tied to reuse (e.g., Thermal Protection System (TPS) durability, landing systems, rapid turnaround operations) can therefore be prioritized and scheduled with budget/time constraints and demonstration-asset logic, consistently across RLVs, RREVs, and hypersonic cases.

HyDat. All modules share an upgraded HyDat-backed database accessed through the in-house Database Management Library, ensuring one-source-of-truth parameters and automatic exchange of mass, cost, and roadmap evidence across studies. The same backbone that linked ASTRID-H, HyCost, and TRIS in 1.0 now anchors reuse-specific fields (e.g., landing equipment, refurbishment tasks, inspection intervals) without fragmenting the schema, which is crucial for rapid, cross-module *"what-if"* iterations.

Validation set and current status. iDREAM 2.0 is being validated against a reference vehicle set spanning vertical and horizontal recovery launchers, a reusable re-entry capsule, and a hypersonic vehicle. These cases exercise the combined ER-VT/ER-HT/REV/HLS workflows and the VL/HL landing supplements, while the corresponding EXP/RST/HLS cost flows and the unified TRIS routine are used to verify consistent propagation of design changes into affordability and maturation plans. This staged validation is intended to demonstrate that the *"few routines, broad coverage"* strategy yields AGILE prototyping across reusable and expendable regimes.

Conclusions

This paper has presented iDREAM 2.0, an integrated methodology and toolset that brings conceptual design, early cost assessment, and technology roadmapping into a single, data-consistent environment, extending the scope of iDREAM 1.0 to reusable launch systems, reusable re-entry vehicles, and hypersonic applications. The core architectural choice – few routines, broad coverage – keeps early-phase studies agile while introducing the hooks required by reusability. Concretely, ASTRID-H now organizes sizing and mission analysis through four core routines (expendable/reusable vertical launcher, expendable/reusable horizontal take-off, re-entry vehicle, and lunar lander) complemented by two landing supplements (vertical and horizontal) that inject recovery physics and landing equipment into the loop. HyCost offers three reuse-aware flows (expendable, reusable/point-to-point/re-entry, and a tailored HLS routine) to keep subsystem sensitivities visible as assumptions evolve. TRIS operates through a single, unified methodology that prioritizes and schedules maturation activities using the same evidence base as design and cost. All modules exchange parameters through an upgraded HyDat database and the in-house management library, ensuring traceability and rapid *"what-if"* propagation across the stack.

The result is a domain-opinionated environment that maintains the speed of conceptual trades while reflecting operational realities – landing increments, refurbishment and turnaround, reuse-dependent reliability and maintenance, and cadence-sensitive economics – without multiplying bespoke tools or brittle hand-offs. Current limitations are those inherent to early-phase modeling: bounded fidelity for certain subsystems, uncertainty in commercial cost data, and the need for richer representations of refurbishment policies and inspection intervals. Near-term development will focus on uncertainty propagation across design-cost-roadmap strands, deeper reliability and maintenance modeling for reusable elements, tighter links to trajectory optimization and aero/thermal pre-design and expanded sustainability metrics. With these enhancements, iDREAM 2.0 offers a practical foundation for fast, defensible decisions across a broader class of future reusable space systems.

References

[1] J. Hugues, M. Perrotin, T. Tsiodras, Using MDE for the rapid prototyping of space critical systems. In *19th IEEE/IFIP International Symposium on Rapid System Prototyping*, 2-5 Jun 2008, Monterey, CA, US, pp. 10-16. https://doi.org/10.1109/RSP.2008.19.

[2] D. Knoll, C. Fortin, A. Golkar. Review of Concurrent Engineering Design practice in the space sector: state of the art and future perspectives. In *2018 IEEE International Systems Engineering Symposium (ISSE)*, 1-3 Oct 2018, Rome, IT, pp. 1-6. https://doi.org/10.1109/SysEng.2018.8544387.

[3] Astos Solutions GmbH. ASTOS (Analysis, Simulation and Trajectory Optimization Software for Space Applications). 2025. Available online. url: astos.de/products/astos (accessed on 6 Nov 2025).

[4] D. E. Koelle. Handbook of cost engineering for space transportation systems with TRANSCOST 8.2: statistical-analytical model for cost estimation and economical optimization of launch vehicles (Rev. 4). TRANSCOST Systems: Ottobrunn, DE. 2013.

[5] V. Vercella. Cost-effective and sustainable scenarios for future reusable space transportation and re-entry systems. PhD Thesis, Politecnico di Torino. 2023.

[6] J. R. Wertz, D. F. Everett, J. J. Puschell (Eds.). Space Mission Engineering: The New SMAD. *Space Technology Library*, Microcosm Press: Torrance, CA, US. 2018.

[7] R. Phaal, C. Farrukh, D. Probert. Fast-Start Roadmapping Workshop Approaches. In *Technology Roadmapping for Strategy and Innovation*, Springer: Berlin/Heidelberg, DE, pp. 91-106, 2013. https://doi.org/10.1007/978-3-642-33923-3_6.

[8] G. Narducci, R. Fusaro, N. Viola. Technology Roadmap Methodology and Tool Upgrades to Support Strategic Decision in Space Exploration. *Aerospace, 12(8)*: 682. 2025. https://doi.org/10.3390/aerospace12080682.

[9] N. Viola, R. Fusaro, G. Narducci, G. Governale, J. Rimani, D. Ferretto, S. A. Chiusano, A. Fiori, O. Cohen, E.-M. Dupuy. iDREAM: a multi-disciplinary methodology and integrated toolset for flight vehicle engineering. In *73rd International Astronautical Congress (IAC)*, 18-22 Sep 2022, Paris, FR.

[10] Rocket Lab. ELECTRON. 2025. Available online. url: rocketlabcorp.com/launch/electron/ (accessed on 7 Nov 2025).

Materials Research Proceedings 69 (2026) 1524-1529 https://doi.org/10.21741/9781644904251-267

Digital Twinning for Onboard Health Monitoring of Solar Panels for Space Exploration Missions

Sachin SOLANKI[1,a *], Francesco DI FIORE[1,2,b] and Laura MAININI[1,2,c]

[1]Department of Aeronautics, Imperial College London, London, United Kingdom, SW7 2AZ

[2]Brahmal Institute for Sustainable Aviation, Imperial College London, UK, SW7 2AZ

[a]sachinksolanki02@gmail.com, [b]f.difiore@imperial.ac.uk, [c]l.mainini@imperial.ac.uk

Keywords: Spacecraft Health Monitoring, Solar Panels Incipient Damage Identification, Onboard Fault Diagnosis, Signals Compression, Bayesian Inference

Abstract. Spacecraft solar panels are among the most failure-prone subsystems, requiring onboard health monitoring to ensure reliable operation in harsh space environments. This work demonstrates and validates the FREEDOM digital twin for onboard near real-time health management of spacecraft solar arrays under limited computational resources. The twin is trained offline through a two-stage data-assimilation process, and operates online to predict degradation via inverse Bayesian optimization. Validation performed on a solar panel integrating AZUR SPACE 3C44 cells under incipient damages across a ten-year geostationary-orbit mission scenario yielded a mean damage-prediction error of 5.2 % with a computational time of 62 s.

Introduction

Spacecraft solar panels represent the dominant source of unrecoverable faults within the electrical power system (EPS) [1]. Fault detection and isolation (FDI) for these systems remains particularly challenging due to their coupled electrothermal dynamics, limited sensing capability, and continuous exposure to the harsh space environment [2]. Solar panels are subjected throughout their operational life to radiation, micrometeoroid and debris impacts, and ultraviolet (UV) darkening, which induce gradual and often coupled degradation in the photovoltaic materials and interfaces [3]. These effects alter the current–voltage response in subtle ways, producing variations in telemetry that remain within nominal limits until significant power loss occurs [2]. The detection of such incipient degradations is further complicated by the need for near real-time monitoring in geostationary and deep-space missions, where long communication delays prevent continuous ground supervision [4].

State-of-the-art FDI methods for spacecraft solar panels are not yet capable of meeting these requirements. Hardware redundancy and threshold-based limit checking [5] lack sensitivity to progressive incipient degradation, while analytical model-based approaches [6] rely on high-fidelity physics models whose computational cost exceeds the capabilities of flight-qualified processors. Moreover, the scarcity of in-orbit fault data limits the applicability of purely data-driven methods, which typically depend on extensive labeled datasets to generalize effectively [7]. These constraints highlight the need for data-efficient FDI frameworks able to operate autonomously onboard, extract fault-relevant information from sparse telemetry, and detect early degradation before functional losses become critical.

In recent years, digital twin technologies have emerged as a promising alternative for health monitoring of complex engineering systems [8]. By maintaining a dynamic virtual counterpart of the physical asset that evolves in parallel with flight operations, digital twins enable continuous synchronization between measured and simulated responses to infer system health and predict degradation trends [9]. To address the challenges of fault diagnosis in spacecraft solar panels, this work demonstrates the FREEDOM digital twin - Fast Reliability Estimate and incipient fault

Content from this work may be used under the terms of the Creative Commons Attribution 3.0 license. Any further distribution of this work must maintain attribution to the author(s) and the title of the work, journal citation and DOI. Published under license by Materials Research Forum LLC.

Materials Research Proceedings 69 (2026) 1524-1529 https://doi.org/10.21741/9781644904251-267

Detection Of Multiphysics aerospace systems-, a computational framework tailored for onboard near real-time health monitoring of complex multiphysics systems subject to incipient damages [10]. The FREEDOM digital twin combines offline data assimilation and online inference in a unified, computationally efficient architecture. Offline, it employs Dynamic Mode Decomposition and Self-Organizing Maps to compress high-dimensional telemetry into a fault-informative representation; online, it assimilates new data and predicts evolving degradation states via inverse Bayesian optimization, continuously updating the virtual counterpart of the physical system. The twin is validated for a spacecraft solar panel composed of AZUR SPACE 3C44 triple-junction cells operating in a 10-year geostationary-orbit mission scenario, and considering multiple concurrent incipient damages.

Digital Twins Requirements for FDI of Spacecraft Solar Panels

Extending the digital twin concept to spacecraft solar panels presents unique challenges arising from the panels' coupled electrothermal behavior and limited sensing capability. Their electrical response depends on complex interactions between environmental and material effects, yet only a few low-rate telemetry channels - typically voltage, current, and temperature - are available for monitoring. At the same time, onboard processors impose strict computational limits, and the scarcity of in-orbit fault data restricts the use of supervised learning approaches. To operate effectively under these conditions, a digital twin for spacecraft solar arrays must meet three key requirements:

1. *Efficient data assimilation and compression*: extract and compress fault-relevant features from sparse low-rate telemetry while retaining sensitivity to early degradation signatures.

2. *Incipient fault prediction*: accurately predict multiple co-occurring early-stage degradation mechanisms whose effects are weakly observable in the measured signals.

3. *Computational tractability*: ensure near real-time operation within the strict processing and memory constraints of flight-qualified onboard hardware.

Methodology

The FREEDOM digital twin enables near real-time onboard health monitoring of spacecraft solar arrays by maintaining a continuously updated virtual representation of the physical subsystem. The framework is organized into two complementary phases: an offline efficient data assimilation and compression stage, and an online prediction stage, in which the twin operates onboard assimilating telemetry to predict the evolving degradation state. The division between offline and online stages ensures that the computationally demanding tasks are performed on the ground, while the flight implementation remains lightweight and data-efficient. Fig. 1 illustrates the conceptual interaction of the FREEDOM digital twin with the real solar panel. In the following, we outline the mathematical foundations of the FREEDOM framework. A complete description of the digital twin is provided in [10].

Materials Research Proceedings 69 (2026) 1524-1529 https://doi.org/10.21741/9781644904251-267

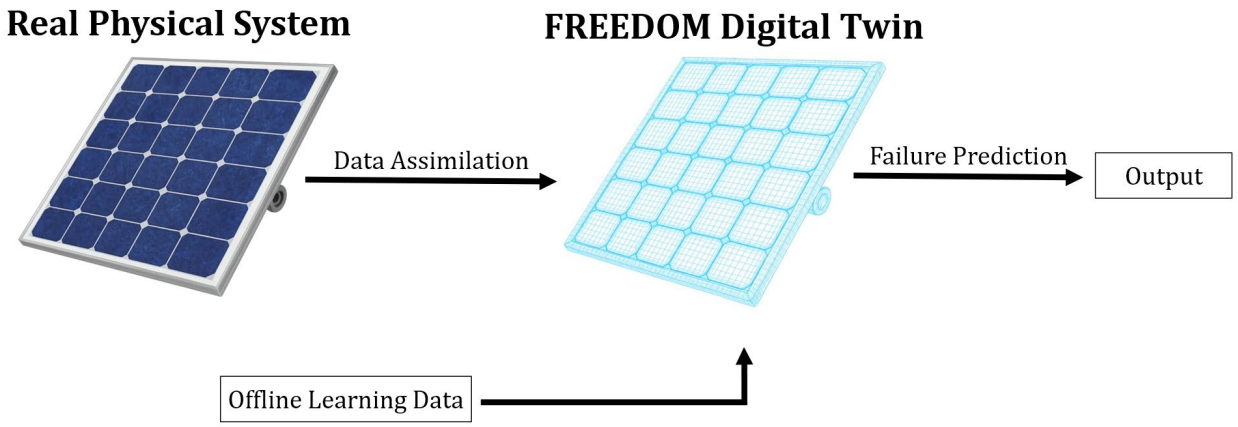


Figure 1: FREEDOM digital twin conceptual interaction with the real physical system

Offline Learning. In the offline phase, FREEDOM learns a reduced-order representation of the system encoding the essential system dynamics and fault sensitivity in a compressed form that minimizes onboard computational requirements. Time-series voltage signals $v(t,k)$ are generated from a high-fidelity model of the solar array under varying degradation parameters k. The first stage applies Dynamic Mode Decomposition (DMD) to extract the dominant temporal modes of the system response: $v(t+\Delta t) \approx A\, v(t)$, where A is the best-fit linear operator capturing the system's coherent dynamics. The DMD decomposition yields modal structures and eigenvalues (ϕ_i, λ_i) that form a reduced basis:

$$v(t) \approx \sum_{i=1}^{r} b_i\ \phi_i e^{\omega_i t}, \tag{1}$$

where r is the retained rank determined by the cumulative energy criterion, and $\omega_i = \ln(\lambda_i)/\Delta t$ represents the modal frequency content. The resulting modal amplitudes are processed using a Self-Organizing Map (SOM) to cluster similar degradation signatures, and identifies the most informative temporal points $\hat{x}$ defining a compression mask that preserves diagnostic information. The outcome of this stage is a mapping function $\mathcal{C}: v(t) \rightarrow \hat{v}(\hat{x})$, where $\hat{v}$ is the low-dimensional fault-informative projection of the original signal. This compression significantly reduces the dimensionality of the inverse problem to be solved during onboard operation.

Online Prediction. During the mission, the FREEDOM digital twin operates continuously updating its internal state based on incoming telemetry. The objective is to predict the current health status k^* of the solar panel. The health estimation problem is formulated as an inverse optimization task:

$$k^* = \arg\min_{k} \delta\left(\hat{\boldsymbol{v}}_{meas}, \hat{\boldsymbol{v}}_{sim}(\boldsymbol{k})\right) \tag{2}$$

where $\hat{\boldsymbol{v}}_{meas}$ is the compressed voltage measurement obtained from telemetry, $\hat{\boldsymbol{v}}_{sim}(\boldsymbol{k})$ is the corresponding twin-predicted signal. Eq. (2) is addressed through Bayesian Optimization (BO) with a Gaussian Process (GP) surrogate model [11] to approximate the discrepancy function, $\delta(k) \sim \mathcal{GP}\left(\mu(k), \sigma^2(k)\right)$, where μ and σ^2 represent the mean and uncertainty of the GP model prediction. The next query point k_{n+1} is selected by maximizing a non-myopic acquisition function $k_{n+1} = \arg\max_{k} \alpha(\boldsymbol{k}; \mu, \sigma)$ [10]. This iterative process converges to the optimal degradation vector k^* while minimizing the number of model evaluations. The resulting k^* defines the twin's current health state, which is continuously updated as new telemetry becomes available.

Materials Research Proceedings 69 (2026) 1524-1529 https://doi.org/10.21741/9781644904251-267

Experimental Setup

We simulate a representative mission scenario to validate FREEDOM using a detailed solar cell model subjected to multiple evolving degradation mechanisms. The model employs the AZUR SPACE 3C44 triple-junction GaAs solar cell, widely used in geostationary and deep-space missions [12]. Implemented in the Simulink/Simscape Electrical environment, it reproduces the electrical behavior of a solar panel element through an equivalent-circuit (EC) representation. We estimate the EC parameters - photocurrent, series resistance, shunt resistance, diode saturation current, and ideality factor - from manufacturer datasheet values, defining the nominal healthy condition of the system. We model three primary degradation mechanisms: micrometeoroid and debris impacts (k_1), radiation damage (k_2), and ultraviolet (UV) darkening (k_3). We simulate (i) radiation-induced effects using ESA's SPENVIS toolkit [13], (ii) micrometeoroid and debris impacts using empirical relations from NASA's Handbook for Designing MMOD Protection [14], and (iii) UV darkening with an empirical factor that reduces photocurrent over time [15]. These effects combine into a time-dependent parameter set that captures realistic in-orbit degradation over a ten-year GEO mission. In particular, we focus on modeling and predicting incipient damages define as $k_i < 0.1$ for the k normalized damage variable. Within this range, damages generate subtle and hardly detectable variations in the current–voltage curve, providing a challenging test of FREEDOM's sensitivity to early fault signatures. We generate the input measurement set for the FREEDOM offline learning phase by running 10000 high-fidelity simulations, each corresponding to a unique degradation vector $k = [k_1, k_2, k_3]^T$ determined using a scaled Latin hypercube design with a scaling exponent of 1.5.

Results and Discussion

Fig. 2(a) shows thirty informative temporal points identified for data assimilation by the offline learning phase over a representative voltage signal. The density of informative points increases toward the end of the simulated mission, where the dominant dynamic modes extracted by DMD exhibit greater divergence between health states, indicating that FREEDOM allocates computational resources to the temporal regions carrying the highest degradation informative content. Fig. 2(b) reports the evolution of the mean Relative Parameter Error (RPE) over twenty runs for each degradation mechanism during online inference. The FREEDOM digital twin accurately tracks the evolution of incipient degradations across all modes. Radiation-induced damage (k_2) is estimated with negligible error, while micrometeoroid and debris impacts (k_1) and ultraviolet (UV) darkening (k_3) show consistently low RPE values. The overall mean estimation error of 5.2% demonstrates the accurate prediction of multimodal failures under realistic mission conditions. All evaluated cases fall within the incipient degradation regime targeted for prediction by FREEDOM during operation. The high accuracy achieved in this range demonstrates the framework's ability to capture the subtle electrical signatures of early-stage damage, well before measurable power loss occurs. In addition, FREEDOM completes the entire prediction phase in 62s, confirming its computational efficiency.

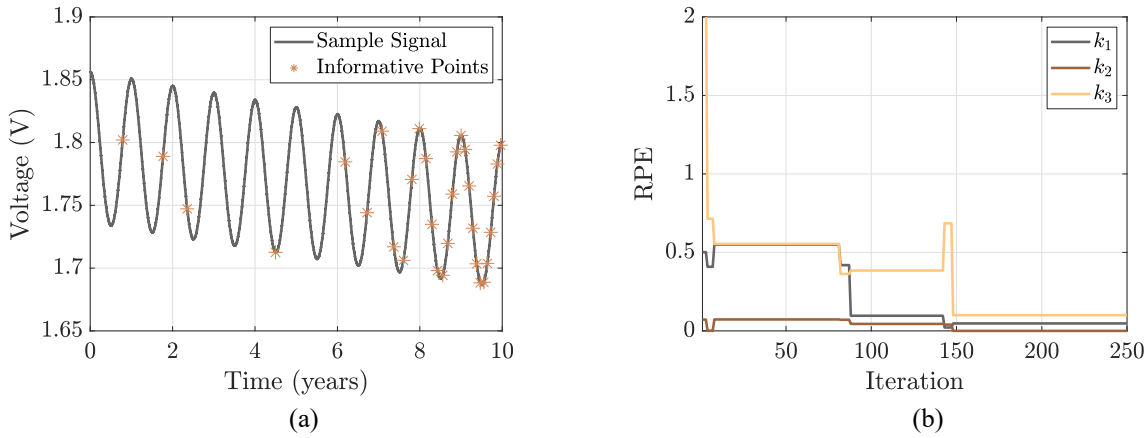


Figure 2: (a) Offline learning output showing the informative temporal points extracted by the DMD-SOM compression. (b) Online predictive performance showing the mean Relative Parameter Error of the damage prediction.

Concluding Remarks

This work demonstrated the FREEDOM digital twin for autonomous health monitoring of spacecraft solar arrays, addressing the challenges of data efficiency, incipient fault prediction, and onboard computational limits. FREEDOM combines offline data assimilation through Dynamic Mode Decomposition and Self-Organizing Maps with online Bayesian inference to identify multiple degradation mechanisms in near real-time. Validation on a solar panel composed of AZUR SPACE 3C44 cells over a ten-year geostationary-orbit scenario achieved a mean relative parameter error of 5.2% with a runtime of 62s, confirming its capability for accurate, data-efficient, and computationally tractable onboard degradation diagnosis.

References

[1] S.Y. Kim, J.F. Castet, J.H. Saleh, Spacecraft electrical power subsystem: failure behavior, reliability, and multi-state failure analyses, Reliability Engineering & System Safety. 98 (2012) 55-65. https://doi.org/10.1016/j.ress.2011.10.005

[2] M.R. Patel, O. Beik, Spacecraft Power Systems, second ed., CRC Press, Boca Raton, 2023. https://doi.org/10.1201/9781003344605

[3] M. Hadrami, L. Roubi, M. Zazoui, J. Bourgoin, Relation between solar cell parameters and space degradation, Solar Energy Materials and Solar Cells. 90 (2006) 1486–1497. https://doi.org/10.1016/j.solmat.2005.10.013

[4] R.S. Bokulic, C.C. DeBoy, Spacecraft Subsystems IV - Communications and Power, in: J.R. Wertz, D.F. Everett, J.J. Puschell (Eds.), Space Mission Engineering: The New SMAD, Microcosm Press, 2011, pp. 627-662.

[5] M.A. Carbone, K.A. Loparo, Fault Detection and Diagnosis in Spacecraft Electrical Power Systems, J. of Aerospace Information Systems. 20 (2023). https://doi.org/10.2514/1.I011136

[6] R. Fonod, C. Charbonnel, E. Bornschlegl, Position and Attitude Model-Based Thruster Fault Diagnosis: A Comparison Study, J. of Guidance, Control and Dynamics. 38 (2015) 1012-1026. https://doi.org/10.2514/1.G000309

[7] T.S. Abdel Aziz, G.I. Salama, M.S. Mohamed, S. Hussein, Spacecraft fault detection and identification techniques using artificial intelligence, J. of Physics: Conference Series. 2616 (2023) 012025, 2023. https://doi.org/10.1088/1742-6596/2616/1/012025

[8] R. Van Dinter, B. Tekinerdogan, C. Catal, Predictive maintenance using digital twins: A systematic literature review, Information and Software Technology. 151 (2022) 107008. https://doi.org/10.1016/j.infsof.2022.107008

[9] AIAA Digital Engineering Outreach and Integration Committee, Digital twin: Definition & value, AIAA and AIA Position Paper. (2022)

[10] F. Di Fiore, P.C. Berri, L. Mainini, FREEDOM: Validated Method for Rapid Assessment of Incipient Faults of Aerospace Systems, AIAA Journal. 62 (2024) 776–790. https://doi.org/10.2514/1.J062911

[11] P.I. Frazier, Bayesian Optimization, in: D. Shier (Ed.), Recent advances in optimization and modeling of contemporary problems, Informs, 2018, pp. 255–278. https://doi.org/10.1287/educ.2018.0188

[12] Information on https://azurspace.com/index.php/en/products/products-cpv

[13] SPENVIS. (v4.6.13), European Space Agency. (2025). https://www.spenvis.oma.be/

[14] J. Arnold, E.L. Christiansen, A. Davis, J. Hyde, D. Lear, J. Liou, F. Lyons, T. Prior, G. Studor, M. Ratliff, S. Ryan, F. Giovane, B. Corsaro, Handbook for Designing MMOD Protection, NASA, Johnson Space Center, 2009. https://ntrs.nasa.gov/citations/20090010053

[15] A. Sinha, J. Qian, S.L. Moffitt, K. Hurst, K. Terwilliger, D.C. Miller, L.T. Schelhas, P. Hacke, UV-induced degradation of high-efficiency silicon PV modules with different cell architectures, Progress in Photovoltaics. 31 (2023) 36–51. https://doi.org/10.1002/pip.3606

Materials Research Proceedings 69 (2026) 1530-1536 https://doi.org/10.21741/9781644904251-268

Temporal Decoupling of Weakly Coupled Systems in Hybrid Co-Simulation

Erik ROSENLUND[1,2,a *], Robert HÄLLQVIST[1,2,b], Robert BRAUN[2,c] and Petter KRUS[2,d]

[1]Saab Aeronautics, Linköping, Sweden

[2]Fluid and Mechatronic Systems, Linköping University, Sweden

[a]erik.rosenlund@saabgroup.com, [b]robert.hallqvist@saabgroup.com, [c]robert.braun@liu.se, [d]petter.krus@liu.se

Keywords: Cyber-Physical Systems, Parallel Co-Simulation, Functional Mock-up Interface, Information/Temporal Decoupling, Directed Acyclic Graph Scheduling, Logical Execution Time, Transmission Line Modeling

Abstract. Cyber-Physical Systems—such as aerospace systems—increasingly rely on multi-physics co-simulation, yet data exchange and orchestration strategies across black-box FMUs can erode accuracy and wall-time performance. This work exploits physical and logical delays—captured through Transmission Line Modeling insights and Logical Execution Time semantics—to segment model coupling graphs into temporally independent sub-system groups. Benchmarks of weakly coupled groups show that an increased macro time step, while respecting signal delays, can preserve system dynamics while reducing model invocations and enabling parallelization without breaking causality.

Introduction and Background

Modern Cyber-Physical Systems (CPS) in aerospace, automotive, and infrastructure integrate multi-physics, embedded computers, and communication networks. Their scale and tight coupling create demands for sophisticated modeling and simulation techniques for design, verification, and validation [1, 2, 3, 4, 5, 6, 7]. Co-simulation has emerged as the dominant solution, enabling the coupling of sub-system models from diverse disciplines and tools through black-box encapsulation [6, 8, 1, 9, 10, 11]. However, this approach introduces significant challenges, particularly concerning accuracy, numerical stability, and performance, especially in hybrid systems—integrating both continuous-time and discrete events—that may demand real-time or faster-than-real-time execution for hardware-in-the-loop integration or large design-space exploration [5, 12, 2, 3, 13, 14, 9, 6, 15, 16].

A critical limitation in achieving credible and wall-time efficient co-simulation originates from data exchange and orchestration strategies. The black-box nature of many sub-system models, for example Functional Mock-up Units (FMUs), restricts the visibility of internal dynamics, sometimes hindering the design of optimal orchestration algorithms necessary for reliable execution [11, 17, 14, 18]. Current approaches often rely on time-triggered communication with Zero-Order Hold (ZOH) sampling strategies that can introduce artificial delays and unwanted high frequency dynamics [12, 19, 3, 17, 4, 20]. These effects can significantly degrade results when dealing with weakly coupled sub-systems that naturally function semi-independently over extended periods [2, 3, 16, 4, 13].

Content from this work may be used under the terms of the Creative Commons Attribution 3.0 license. Any further distribution of this work must maintain attribution to the author(s) and the title of the work, journal citation and DOI. Published under license by Materials Research Forum LLC.

Materials Research Proceedings 69 (2026) 1530-1536 https://doi.org/10.21741/9781644904251-268

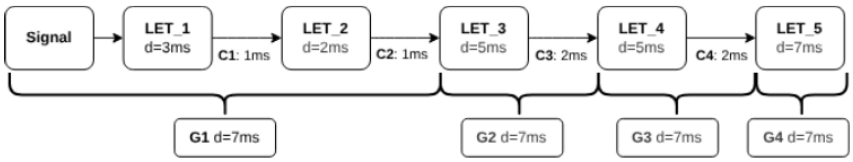


Figure 1: Temporal decoupling of sub-system group G1, G2, G3 and G4. Arrows show information propagation within the system. *d* shows the sub-system or connections signal delay.

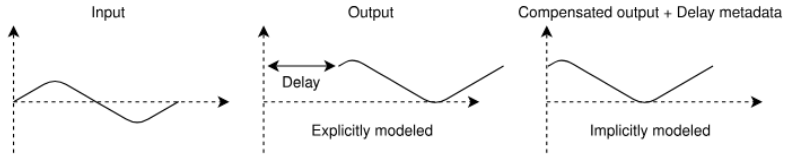


Figure 3: Comparison between *explicit* and *implicit* modeled delay

Structured segmentation of systems into weakly coupled sub-systems enables information-dependent yet temporally independent operations to be executed concurrently without violating causality [21]. This capability is crucial for multi-rate co-simulations, where different sub-systems are allowed to operate at different communication steps and therefore demand sophisticated synchronization for correct data exchange [22, 6]. Two paradigms are utilized as a basis for enabling this: first, the Logical Execution Time (LET) paradigm [23, 24, 25], which decouples a model from its actual execution time; and second, Transmission Line Modeling (TLM), which utilizes physically motivated information delays (e.g., control signal latencies, sensor sampling periods, component response times, or fluid propagation speed) between sub-systems to decouple them for stability [12, 21, 26].

The criterion for safe decoupling is whether the chosen macro/communication time step exceeds the propagation delay across a sub-system. When this condition holds, the sub-system behaves temporally independent within a step, eliminating algebraic constraints and enabling robust parallel scheduling; if the step exceeds the effective delay, discretization can introduce a numerical error that manifests as phase distortions and system instability. In TLM it is common that the temporal independence that can be utilized for parallelization within a system is equal to the smallest delay that is present between a system's models [26]. By introducing a grouping mechanism of signal delays, the temporal independence between groups can be increased without sacrificing validity and independent groups can be simulated in parallel, see Figure 1.

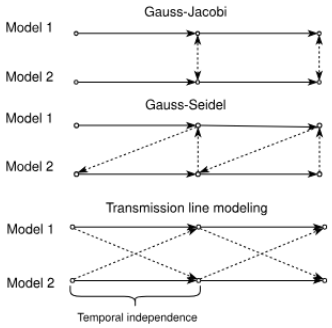


Figure 2: Comparison between orchestration methods, Dashed lines are information propagation.

Signal delays can either be explicitly or implicitly modeled. When delays are explicit, the model itself compensates for the phase shift introduced by the intrinsic delay, see Figure 3 for minimal overview of the concept. When delays are implicit, and not represented in the model, the co-simulation layer must compensate to ensure the system's true propagation characteristics, in this case by introducing an artificial phase shift. Utilizing the known phase shift allows the co-simulation engine to map the information into the future, thereby creating weakly coupled—and temporally independent—sub-systems as long as the time step does not exceed the model delay; Figure 2 illustrates how TLM applies this insight.

Contributions. This paper advances delay-aware co-simulation beyond established TLM and LET practices through three contributions:

1. Delay-aware grouping scheduler, a method that fuses LET semantics with TLM-style delays to execute groups of weakly coupled subsystems in parallel without violating causality.

2. FMI 2.0 orchestration workflow, a deterministic orchestration algorithm, based on (1.), that utilizes implicit signal delays to increase parallelization of Functional Mock-up Interface (FMI) 2.0 components while emulating FMI 3.0 Intermediate Update Mode (IUM) via sub-stepping (Algorithm 1).

3. Quantitative evaluation, a controlled benchmark that quantifies phase shift for common orchestration algorithms, and for the proposed approach, using first zero-crossing metrics (Figures 5a–5).

Scope and Limitations. This short paper targets delay-aware scheduling for weakly coupled CPS co-simulations. The requirements are originating from aeronautical systems with tightly integrated mechanical, hydraulic, and control subsystems. The scope is limited to systems where intrinsic signal delays can be removed from the models and replaced by metadata. This initial study intentionally scopes the evaluation to a single, well-understood benchmark to isolate the interaction between explicit and implicit delays and a comparison between a custom, tailored scheduler and the two commonly used master algorithms, Gauss-Jacobi and Gauss-Seidel.

Methodology

A controlled benchmark composed of sub-systems with predefined information delays, see Figure 1, is realized as a monolithic system in the Modelica tool Dymola [27] to establish a reference that is free from co-simulation emergent behavior. The system is designed to enable grouping of sub-systems and connections and to enable testing at a predefined “large” macro time step. The signal passed through the system is a sine wave with constant frequency and amplitude; the models contain only a pure phase shift to enable easy visualization of changes. Using this monolithic realization as ground truth ensures that any deviations observed after export are attributable to the co-simulation strategy and implementation rather than to modeling or coupling inconsistencies. From the monolithic reference, the system is exported as a System Structure & Parameterization (SSP) where each sub-system and connection is an FMU to enable utilization within the co-simulation environment.

To verify the export and coupling of the system, a co-simulation applying both Gauss–Jacobi and Gauss–Seidel master algorithms with a small (relative to the test system dynamics) communication step (0.01ms) is used to replicate the monolithic results. Both the sub-systems and the connections remain explicitly modeled just as in the reference system. The same configuration is then simulated using larger time steps (1ms, 2ms, and 3ms) to observe signal characteristics and the phase shift caused by the orchestration method. Because the benchmark introduces only phase shifts (no amplitude distortion), the resulting phase shift is computed by locating the time of the first zero crossing of each signal and subtracting the corresponding reference time.

Finally, to validate that temporally independent groups can be executed concurrently without degrading validity, the sub-systems are clustered into the groups defined in Figure 1 and advanced with a 7ms macro step tailored to the system delays. Enabling the grouping and concurrent execution requires removing phase shifts from the sub-system models, making the delays implicit; metadata describing the delay characteristics is provided to the tooling. FMI 3.0 offers Intermediate Update Mode (IUM) to mitigate effects from sparse model invocation by exposing data between communication points [12, 28]. Because the experiments rely on FMI 2.0, which lacks equivalent functionality, each model executes repeated sub-steps internally to emulate richer data propagation of IUM; the complete orchestration algorithm is shown in Algorithm 1.

Materials Research Proceedings 69 (2026) 1530-1536 https://doi.org/10.21741/9781644904251-268

Algorithm 1: Grouping orchestration Pseudocode

```
in sequence foreach macro step H do
    in parallel foreach Group G_k do
        in sequence foreach Model M in G_k in signal dependency order do
            // Emulate intermediate updates inside the macro step
            t ← 0
            while t < H do
                Execute M for a sub-step h
                t ← t + h
```

Result

To observe distortion caused by orchestration algorithm selection and step size, the accumulated phase shifts of the signals are visualized. In Figure 4, the resulting signals corresponding to the commonly used master algorithms Gauss–Jacobi and Gauss–Seidel are compared across step sizes. For small steps, both algorithms closely match the Dymola monolithic reference, while larger steps introduce increasing distortion. Figure 5a summarizes the resulting accumulated phase shifts for both master algorithms; the results indicate that system design influences how phase shift scales with the time step, complicating general conclusions in regard to phase shift and step-size increases. Figure 4 also highlights the zero-order-hold staircase effect, where the plateau length equals the macro time step, in effect degrading signal quality.

Figure 5 shows the system simulated using emulated IUM. Gauss–Jacobi does not benefit from IUM because the algorithm is inherently parallel, meaning information can only be exchanged deterministically at communication points. Gauss–Seidel, on the other hand, benefits from the serial execution order, which allows intermediate updates to reduce phase shift. Both Gauss–Seidel and the proposed approach (temporally independent sub-systems), when combined with emulated IUM, yield higher signal quality without staircase artifacts. Compared to Gauss–Seidel, the proposed approach maintains parallel execution while keeping the resulting phase shift small and enabling larger macro time steps.

Discussion and Conclusion

This work is intentionally limited as a proof of concept. Future work should extend the comparison to other solutions, for example adaptive step-size co-simulation and other decoupling techniques. Additional benchmarks are needed to evaluate how the concept scales to more realistic systems in terms of accuracy and stability. These comparisons will quantify how delay-aware grouping may complement existing FMI master algorithms and highlight opportunities for hybrid schedulers. A key requirement for applying the grouping mechanism to high-fidelity models is the ability to externalize delays from the sub-systems; how broadly this assumption holds must be evaluated.

To enable usage and adaptation of these principles, since delay information is seldom included explicitly in FMU or SSP metadata, it should be considered how to identify system delays post-export through data-driven estimation or optimization. That said, estimating delay information is only the first step: selecting an effective graph segmentation and step size is non-trivial and likely depends on factors such as system design, model design, operating system scheduling, background load, and hardware. A limitation of the current solution is that it accounts only for static delays

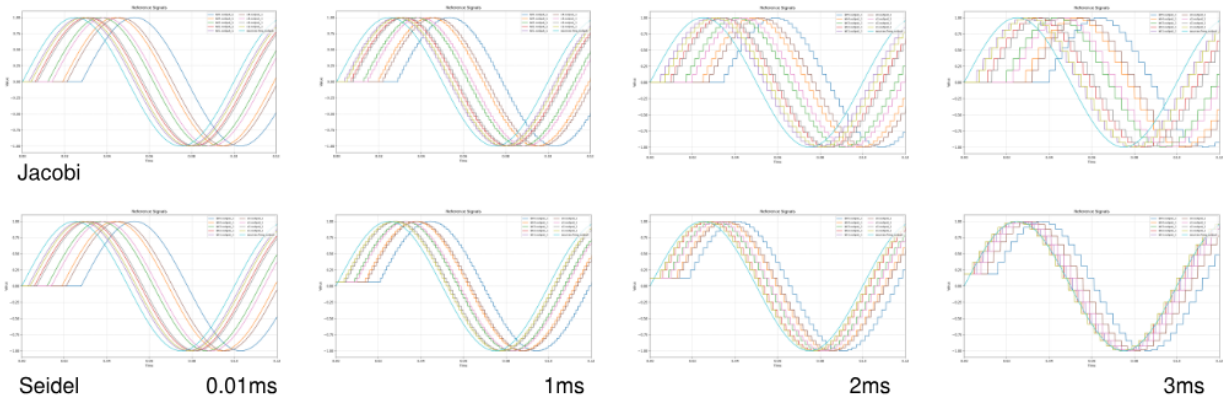
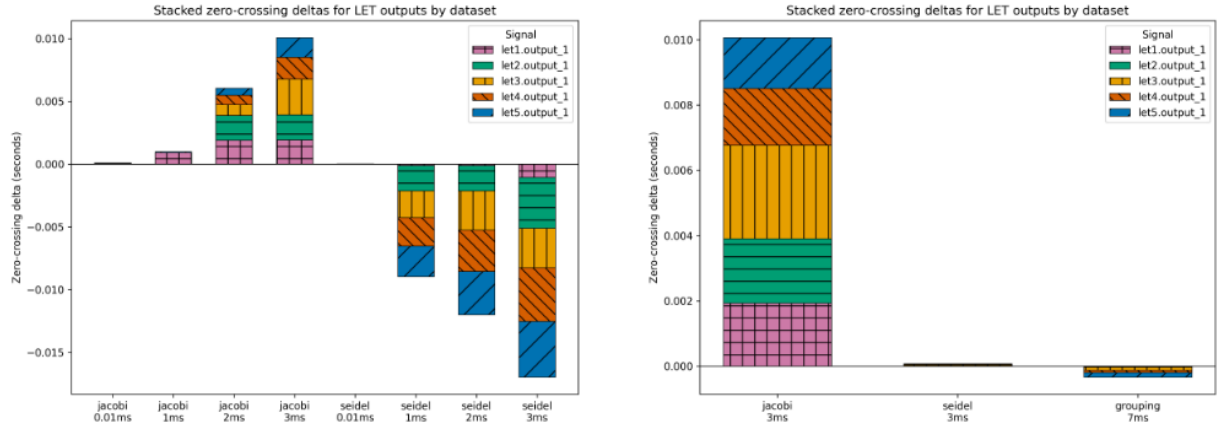


Figure 4: Comparison between Jacobi and Seidel phase shift depending on time step



(a) Accumulated phase shift depending on time step

(b) Comparison of phase shift utilizing intermediate variable access

Figure 5: Reference simulation results and phase shift comparison across orchestration strategies and step sizes.

within the system. Extending the approach to dynamic attributes, for example using model Jacobians to estimate online delay variations, could unlock additional optimization opportunities such as adaptive loop breaking during execution.

As a side note, explicitly defining information delays may also provide benefits to commonly used orchestration algorithms. For example, on how to break loops in the signal dependency graph with minimal impact, prioritizing the slowest (largest-delay) links as cut points to minimize artificial decoupling, or to ensure that the step size does not break the Nyquist–Shannon sampling theorem by providing guidance to where step refinement could be applied locally along the most restrictive links.

Acknowledgments

This research was conducted within the scope of the Advanced digitization ERATO (grant 2024-02521) and the ITEA4 OpenSCALING (grant 2023-00969) project, funded by Vinnova and Saab AB.

References

[1] Salah Eddine Saidi, Nicolas Pernet, and Yves Sorel. “Automatic parallelization of multi-rate FMI-based co-simulation on multicore”. 2017.

[2] Fabio Cremona et al. “Hybrid co-simulation: it’s about time” (2019). https://doi.org/10.1007/s10270-017-0633-6.

[3] Cláudio Gomes et al. “Co-simulation: State of the art” (2017). https://doi.org/10.48550/arXiv.1702.00686

[4] Giovanni Liboni and Julien Deantoni. “CoSim20: An Integrated Development Environment for Accurate and Efficient Distributed Co-Simulations”. 2020. https://doi.org/10.1145/3437075.3437101

[5] Nicolai Pedersen. “Co-Simulation of Cyber-Physical System with Distributed Embedded Control”.

[6] Jarkko Rahikainen et al. “On the cosimulation of multibody systems and hydraulic dynamics” (2020). https://doi.org/10.1007/s11044- 020-09727-z

[7] Salah Eddine Saidi, Nicolas Pernet, and Yves Sorel. “A method for parallel scheduling of multi-rate co-simulation on multi-core platforms” (2019). https://doi.org/10.2516/ogst/2019009

[8] Salah Eddine Saidi. “Automatic parallelization and scheduling approaches for co-simulation of numerical models on multi-core processors”. 2018.

[9] Simon Thrane Hansen et al. “Synthesizing Co-Simulation Algorithms with Step Negotiation and Algebraic Loop Handling”. 2021. https://doi.org/10.23919/ANNSIM52504.2021.9552073

[10] Tamas Kalmar-Nagy and Ilinca Stanciulescu. “Can complex systems really be simulated?” (2014). https://doi.org/10.1016/j.amc.2013.11.037

[11] G. Schweiger et al. “An empirical survey on co-simulation: Promising standards, challenges and research needs” (2019). https://doi.org/10.1016/j.simpat.2019.05.001

[12] Robert Braun and Dag Fritzson. “Numerically robust co-simulation using transmission line modeling and the Functional Mock-up Interface” (2022). https://doi.org/10.1177/00375497221097128

[13] Cláudio Gomes et al. “Co-Simulation: A Survey” (2018). https://doi.org/10.1145/3179993

[14] Cláudio Gomes et al. “Co-simulation: The Past, Future, and Open Challenges”. Ed. by Tiziana Margaria and Bernhard Steffen. 2018. https://doi.org/10.1007/978-3-030-03424-5_34

[15] Salah Eddine Saidi et al. “Acceleration of FMU Co-Simulation On Multi-core Architectures”. 2016. https://doi.org/10.3384/ecp16124106

[16] Casper Thule et al. “Towards the Verification of Hybrid Co-simulation Algorithms”. Ed. by Manuel Mazzara, Iulian Ober, and Gwen Salaün. 2018. https://doi.org/10.1007/978-3-030-04771- 9_1

[17] Simon Thrane Hansen et al. “Co-simulation at different levels of expertise with Maestro2” (2024). https://doi.org/10.1016/j.jss.2023.111905

[18] Bentley James Oakes et al. “Hint-Based Configuration of Co-simulations with Algebraic Loops”. Ed. by Mohammad S. Obaidat, Tuncer Ören, and Helena Szczerbicka. 2021. https://doi.org/10.1007/978-3-030-55867-3_1

[19] Giovanni Liboni. “Complex systems co-simulation with the CoSim20 framework: for efficient and accurate distributed co-simulations” (2021).

[20] Iacopo Tamellin et al. “Eigenstructure assignment and compensation of explicit co-simulation problems” (2022). https://doi.org/10.1016/j.mechmachtheory.2022.105004

[21] Abir Ben Khaled et al. “Multicore simulation of powertrains using weakly synchronized model partitioning” (2012). https://doi.org/10.3182/20121023-3-FR-4025.00018

[22] Claudio Gomes and Hans Vangheluwe. “Co-Simulation of Continuous Systems: A Hands-on Approach”. 2019. https://doi.org/10.1109/WSC40007.2019.9004704

[23] Tobias Dorr et al. “A Behavior Specification and Simulation Methodology for Embedded Real-Time Software”. 2022. https://doi.org/10.1109/DS-RT55542.2022.9932069

[24] Rolf Ernst et al. The Logical Execution Time Paradigm: New Perspectives for Multicore Systems (Dagstuhl Seminar 18092). Schloss Dagstuhl – Leibniz-Zentrum für Informatik, 2018. https://doi.org/10.4230/DAGREP.8.2.122

[25] Edward A. Lee and Marten Lohstroh. “Generalizing Logical Execution Time”. Ed. by Jean-François Raskin et al. 2022. https://doi.org/10.1007/978-3-031-22337-2_8

[26] Petter Krus et al. Distributed Simulation of Hydromechanical Systems. 1990.

[27] Dag Brück et al. “Dymola for Multi-Engineering Modeling and Simulation” (2002).

[28] Robert Braun et al. “TLM-Based Asynchronous Co-simulation with the Functional Mockup Interface” (2017). https://doi.org/10.1007/978-3-030-14883-6_2

Materials Research Proceedings 69 (2026) 1537-1543 https://doi.org/10.21741/9781644904251-269

An Experimental Co-Simulation Engine for Advanced Cyber-Physical Systems (CPS) Scheduling and Digital Twin Evaluation

Erik ROSENLUND[1,2,a *], Robert HÄLLQVIST[1,2,b], Robert BRAUN[2,c] and Petter KRUS[2,d]

[1]Saab Aeronautics, Linköping, Sweden

[2]Fluid and Mechatronic Systems, Linköping University, Sweden

[a]erik.rosenlund@saabgroup.com, [b]robert.hallqvist@saabgroup.com, [c]robert.braun@liu.se, [d]petter.krus@liu.se

Keywords: Cyber-Physical Systems, Co-simulation, Functional Mock-up Interface (FMI), System Structure and Parameterization (SSP), Scheduling Algorithms, Orchestration Algorithm, Digital Twin, Hardware-in-the-Loop (HiL)

Abstract. This paper presents an experimental co-simulation engine designed to study scheduling strategies and performance trade-offs in complex Cyber-Physical Systems (CPS). The engine offers a modular, graph-based architecture with deterministic execution semantics, lightweight configuration, and built-in measurement. These features enable fair comparisons across orchestration algorithms and parallelization strategies. We outline the design, document determinism and performance mechanisms, and benchmark against a reference setup to support rigorous evaluation and future digital-twin deployments.

Introduction

The escalating complexity of modern Cyber-Physical Systems (CPS)—ranging from nuclear power plants to aerospace—necessitates more advanced design, operation, and maintenance methodologies [1, 2, 3, 4, 5, 6]. These systems couple physical processes with software and electronics, often with some computation controlling dynamics via feedback loops [4, 7, 5]. Traditional monolithic simulation struggles with CPS heterogeneity, where sub-systems often are developed by different teams, or even sub-contractors, using disparate tools and formalisms [8, 9, 10].

Co-simulation addresses these challenges by coordinating multiple sub-systems to reproduce the behavior of a coupled system [5, 11, 8, 12, 13, 14, 15, 16, 17]. It lets domain experts work in their preferred tools while maintaining a holistic system view [5, 18]. The Functional Mock-up Interface (FMI) [19] has become the de facto standard for tool-independent model exchange and co-simulation, packaging models as black-box Functional Mock-up Units (FMUs) [3, 5, 8, 20, 21, 22, 23, 24, 25].

In addition to FMI, the System Structure and Parameterization (SSP) standard [26] complements co-simulation workflows by describing the architecture of a system-of-systems, including how FMUs are interconnected, their parameters, and configurations. SSP separates concerns by defining system topology, parameter sets, and simulation settings independently of the FMUs themselves, enabling modular, tool-independent reuse and configuration of co-simulation setups. This standard facilitates exchange of system designs between different engineering tools and supports scalable system integration, versioning, and automation in CPS development pipelines [27, 28].

Despite broad adoption, co-simulation still faces challenges in numerical stability, accuracy, and performance, especially for strongly coupled and hybrid systems [1, 8, 29, 14, 10, 16, 5, 17, 30]. Achieving credible results [31] depends strongly on the orchestration/master algorithm, its

Content from this work may be used under the terms of the Creative Commons Attribution 3.0 license. Any further distribution of this work must maintain attribution to the author(s) and the title of the work, journal citation and DOI. Published under license by Materials Research Forum LLC.

role to dictate signal exchange strategies [25, 10, 15]. Selecting an appropriate algorithm is context dependent and hinges on the characteristics and implementations of the individual simulation units [10].

Table 1: Comparison of simulation engines over characteristics relevant for the presented work

Software	Open	FMI	SSP	RT/HiL
OMSimulator [32]	Yes	Yes	Yes	Soft RT
FMI Go! [33]	Yes	Yes	Yes	Soft RT
Notes: strong focus on distributed simulations.				
Open Simulation Platform [34]	Yes	Yes	Partial	Soft RT
Notes: strong focus on maritime.				
FmPy [35]	Yes	Yes	Partial	No
Maestro2 [36]	Yes	Yes	No	Partial
DACCOSIM NG [37]	Yes	Yes	No	Partial
Mosaik [38]	Yes	Yes	No	Partial

A focused experimentation co-simulation engine that combines the transparency and modularity of lighter simulation engines with determinism, SSP model management, and HiL readiness would provide a base for reproducible multi-domain experiments, transparent orchestration semantics, and the ability to integrate into real-time hardware campaigns and would fit into aerospace digital twin development at Saab [28]. Table 1 compares open-source engines over attributes relevant for the presented work. The top entries provide full compliance with both FMI and SSP standards as well as support soft real-time execution modes. The lower portion illustrates complementary engines: such as FmPy, Maestro2, DACCOSIM NG, and Mosaik, that address specific application areas but only cover subsets of the FMI/SSP stack and rarely extend beyond partial real-time requirements.

Across these products, there is limited focus on determinism, real-time constraints or Hardware-in-the-Loop (HiL) integration. Many of the products both support Model Exchange (ME) and Co-Simulation (CS), inferring architectural limitations that could be avoided in a pure co-simulation engine with the added benefit of limiting code base size and complexity. Adapting an existing platform is possible, but the two that look most promising out of the box (OMSimulator and FMI Go!) are both large and mature projects and would require substantial effort to tailor and adapt. Thus the decision was made to design and implement a small, purpose-built experimental engine for testing and evaluation of CPS co-simulation orchestration methods leveraging FMI and SSP. Its primary goals are:

- A lightweight and simple experimentation platform for credible co-simulation of CPS models that provides a basis for scheduling experimentation and enable comparison of established orchestration methods such as Gauss–Jacobi and Gauss–Seidel [12, 30], alongside novel, tailored algorithms [15] to study impacts on accuracy, stability, and performance.
- Enable deterministic co-simulation with controlled propagation of information between models [14, 29, 39, 5] of physical, logical, and software models, reflecting the multi-domain nature of CPS.
- Enable evaluation of multi-core parallelization methods [17, 40, 23, 41], variable step sizes and adaptive scheduling [42, 24, 7, 17], and efficiency techniques such as advanced algebraic loop handling [10, 15, 43, 17], creating enablers for extensive design space exploration and HiL integration, both vital for industrial applications and digital-twin development [23].

Materials Research Proceedings 69 (2026) 1537-1543 https://doi.org/10.21741/9781644904251-269

Scope and Contributions. Compared to OMSimulator, FMI Go!, and related applications, the proposed engine purposefully narrows scope to pure co-simulation with SSP-managed composition and real-time optimized execution paths. The design emphasizes (1.) determinism via explicit data selection and integer time, (2.) transparency of orchestration semantics for comparisons, and (3.) a compact codebase that lowers the barrier for implementing and testing scheduling variants. Its main contributions are:

- An open-source modular, simple, graph-based simulation engine that enables comparison of orchestration algorithms, SSP4SIM.
- An open source SSP and FMI XML parsing library for C++, SSP4CPP.
- A benchmark against OMSimulator to quantify correctness and performance under standard Gauss–Jacobi orchestration utilizing an environmental control reference system.

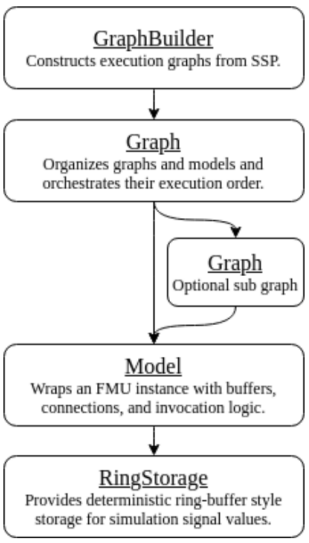


Figure 1: Solution architecture

Simulation Engine Architecture

This section introduces the overall layout of the simulation engine. The architecture emphasizes modularity, repeatability, and performance, enabling comparisons across orchestration algorithms and different degrees of parallelism.

Modularity. The implementation separates the workflow into clear assembly stages. The first step (Figure 1) interprets SSP metadata and produces an intermediate dependency graph closely aligned with the SSP representation. The intermediary graph is then processed into a ”simulation graph” specialized for efficient execution and traversal. In this representation both models and graphs are nodes that can be connected and nested, where each layer may employ different orchestration algorithms, see Figure 3. To further simplify testing and evaluation of strategies, orchestration algorithms and analysis passes are handled in separate layers to ensure they do not interfere with FMU integration or storage layers.

Determinism. The runtime enforces repeatable execution through two mechanisms. First, a small but essential solution, time is represented as integer nanoseconds (seconds in int64_t) instead of floating-point, avoiding comparison pitfalls. Second, each model maintains a ring-buffered data store (RingStorage) for its outputs, see Figure 2, to enable access to a number of past outputs. This allows orchestrators to select data to propagate deterministically between models, thus avoiding hidden race conditions in parallel and multirate execution. This strictness incurs one extra copy of all data passed between models but allows different orchestration algorithms to select data according to their requirements or data interpolation/extrapolation. The buffer size is selected to fit with the algorithm selected, certain algorithms may require several iterations of output values to be stored while simple ones like Gauss–Jacobi need only a small set. Together, these two mechanisms improve the possibilities for deterministic results even under parallel and multirate execution.

Materials Research Proceedings 69 (2026) 1537-1543 https://doi.org/10.21741/9781644904251-269

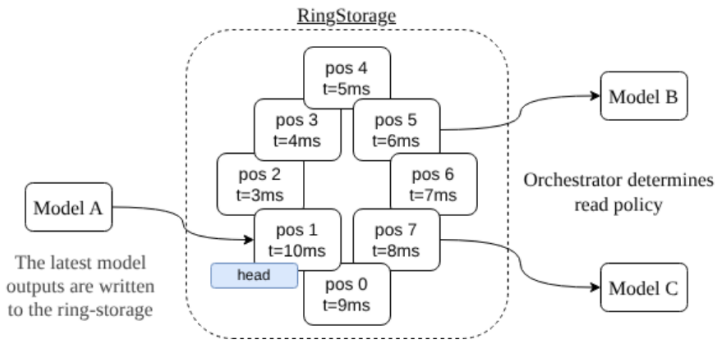


Figure 2: Schematic overview of the output ring buffer solution

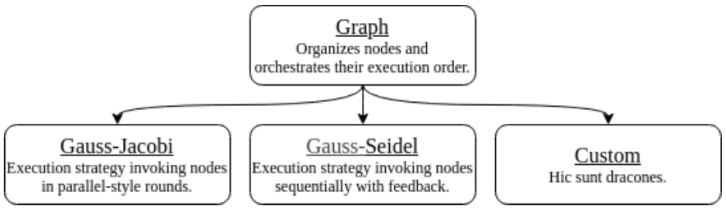
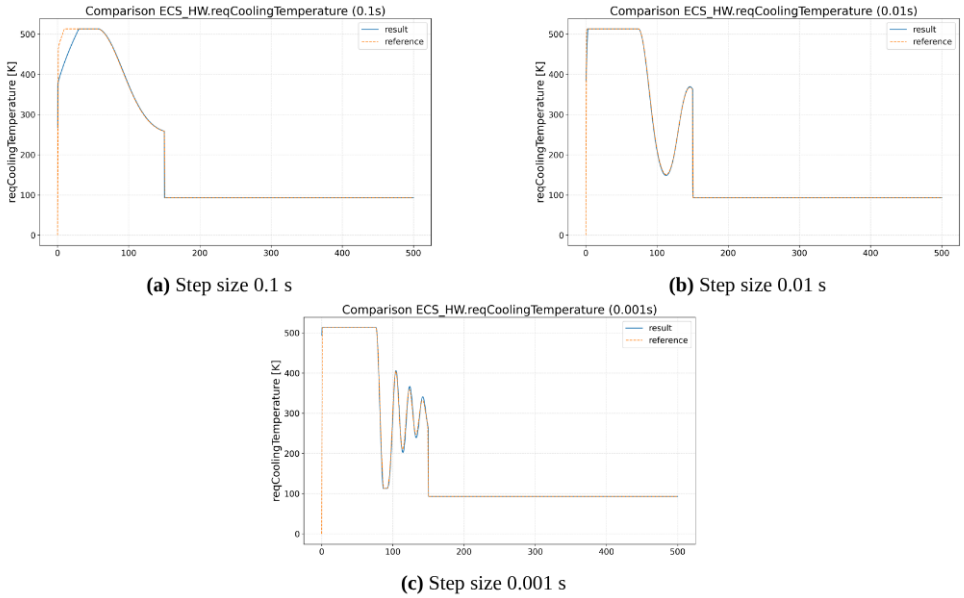


Figure 3: Execution algorithms

Performance. To meet demanding performance constraints, (1.) precomputing and deferring work away from time-critical simulation loops minimize repeated operations. As shown in Figure 1, the GraphBuilder parses and evaluates the SSP System Structure, establishes model connections, and streamlines the Graph and Models for inexpensive execution. (2.) separating the simulation path from result recording ensures that slower disk read/write does not bottleneck execution. A dedicated worker thread continuously samples results from signal ring buffers and writes them to disk, independent of the critical simulation path. A note here is that there is a trade-off for this speed increase, even if the internal simulation is fully deterministic, the externally recorded data may vary slightly between runs depending on how the operating system schedules the recorder. (3.) the runtime embeds quantitative feedback via timers around experiments and critical components, collecting cumulative statistics to provide the evidence needed to compare scheduling variants, assess parallel scaling, and validate HiL readiness to identify bottlenecks and enable further optimization.

Configuration and Logging. Other noteworthy attributes are: (1.) A lightweight JSON-backed configuration service provides a single source of truth for runtime options. Core components query this service for model selection, timing, solver tolerances, orchestrator selection, and various toggles, enabling simple scenario changes by switching profiles. (2.) A dedicated logging utility supplies thread-safe, severity-filtered diagnostics that logs to file or network target using an established JSON format compatible with common viewers.

Benchmark results. The initial benchmark compares against OMSimulator (OMS) using an open reference system [44] for simple benchmarking: an environmental control loop with a heat source, a heat sink, and a controller [45]. Since OMS uses Gauss–Jacobi for co-simulation the comparison will utilize the same algorithm. Three different time step sizes are compared using the same reference system to see if behaviors are overlapping. There behaviors between the two engines is very similar, Figure 4a, 4b, and 4c, and to a large extent the verification of the implementation is successful, there is a slight diff in the initial stages of Figure 4a that need to be evaluated further.



(a) Step size 0.1 s **(b)** Step size 0.01 s

(c) Step size 0.001 s

Figure 4: Reference vs result responses under different macro step sizes.

Conclusion and Future Work

To support further verification of the simulation engine, future work includes: (i) completing further comparisons across multiple SSPs against multiple reference engines, (ii) expanding the set of scheduling policies and parallel executors, and (iii) quantifying determinism trade-offs under mixed real-time loads. We will use these results to guide robust digital-twin deployments in safety-critical CPS.

Acknowledgments

This research was conducted within the scope of the Advanced digitization ERATO (grant 2024-02521) and the ITEA4 OpenSCALING (grant 2023-00969) project, funded by Vinnova and Saab AB.

References

[1] Cláudio Gomes et al. “Co-simulation: The Past, Future, and Open Challenges”. Ed. by Tiziana Margaria and Bernhard Steffen. 2018. https://doi.org/10.1007/978-3-030-03424-5_34.

[2] Simon Thrane Hansen et al. “The FMI 3.0 Standard Interface for Clocked and Scheduled Simulations” (2022). https://doi.org/10.3390/ electronics11213635

[3] Simon Thrane Hansen, Cláudio Gomes, and Zahra Kazemi. “Synthesizing Orchestration Algorithms for FMI 3.0” (2023).

[4] Edward A. Lee. “Cyber Physical Systems: Design Challenges”. 2008. https://doi.org/10.1109/ISORC.2008.25

[5] Nicolai Pedersen. “Co-Simulation of Cyber-Physical System with Distributed Embedded Control”.

[6] Salah Eddine Saidi et al. “Fast Virtual Prototyping of Cyber Physical Systems using SystemC and FMI: ADAS Use Case”. 2019. https://doi.org/10.1145/3339985.3358488

[7] Robert Braun, Robert Hällqvist, and Dag Fritzson. “Transmission line modeling co-simulation with distributed delay-size control using steady-state identification” (2023). https://doi.org/10.1007/ s00366-023-01791-1

[8] Robert Braun and Dag Fritzson. “Numerically robust co-simulation using transmission line modeling and the Functional Mock-up Interface” (2022). https://doi.org/10.1177/00375497221097128

[9] Claudio Gomes, Levi Lucio, and Hans Vangheluwe. “Semantics of Co-simulation Algorithms with Simulator Contracts”. 2019. https://doi.org/10.1109/MODELS-C.2019.00124

[10] Simon Thrane Hansen et al. “Verification and synthesis of co-simulation algorithms subject to algebraic loops and adaptive steps” (2022). https://doi.org/10.1007/s10009-022-00686-8

[11] Mehrdad Moradi and Claudio Gomes. “Optimizing Fault Injection in FMI Co-Simulation through Sensitivity Partitioning” (2019).

[12] Claudio Gomes and Hans Vangheluwe. “Co-Simulation of Continuous Systems: A Hands-on Approach”. 2019. https://doi.org/10.1109/WSC40007.2019.9004704

[13] Cláudio Gomes et al. “Co-simulation: State of the art” (2017). https://doi.org/10.48550/arXiv.1702.00686

[14] Cláudio Gomes et al. “Co-Simulation: A Survey” (2018). https://doi.org/10.1145/3179993

[15] Simon Thrane Hansen et al. “Synthesizing Co-Simulation Algorithms with Step Negotiation and Algebraic Loop Handling”. 2021. https://doi.org/10.23919/ANNSIM52504.2021.9552073

[16] Tamas Kalmar-Nagy and Ilinca Stanciulescu. “Can complex systems really be simulated?” (2014). https://doi.org/10.1016/ j.amc.2013.11.037

[17] Salah Eddine Saidi, Nicolas Pernet, and Yves Sorel. “A method for parallel scheduling of multi-rate co-simulation on multi-core platforms” (2019). https://doi.org/10.2516/ogst/2019009

[18] Robert Hällqvist et al. “Heterogenous System Modelling in Support of Incremental Development”. 2022.

[19] FMI development group. Functional Mock-up Interface. https: //fmi-standard.org.

[20] Jose Evora-Gomez et al. Daccosim NG: co-simulation made simpler and faster. 2019. https://doi.org/10.3384/ecp19157785

[21] Virginie Galtier et al. “FMI-based distributed multi-simulation with DACCOSIM” (2015).

[22] Simon Thrane Hansen et al. “Co-simulation at different levels of expertise with Maestro2” (2024). https://doi.org/10.1016/j.jss.2023. 111905

[23] Salah Eddine Saidi. “Automatic parallelization and scheduling approaches for co-simulation of numerical models on multi-core processors”. 2018.

[24] Tom Schierz, Martin Arnold, and Christoph Clauss. “Co-simulation with communication step size control in an FMI compatible master algorithm”. 2012. https://doi.org/10.3384/ecp12076205

[25] G. Schweiger et al. “An empirical survey on co-simulation: Promising standards, challenges and research needs” (2019). https://doi.org/10.1016/j.simpat.2019.05.001

[26] SSP development group. System Structure and Parameterization. https://ssp-standard.org

27] Jochen Köhler et al. “Modelica-Association-Project ”System Structure and Parameterization” - Early Insights”. 2016. https://doi.org/10.3384/ecp1612435

[28] Robert Hällqvist et al. “Engineering Domain Interoperability Using the System Structure and Parameterization (SSP) Standard”. 2021. https://doi.org/10.3384/ecp2118137. [

29] David Broman et al. “Requirements for hybrid cosimulation standards”. 2015. https://doi.org/10.1145/2728606.2728629

[30] Casper Thule et al. “Towards the Verification of Hybrid Co-simulation Algorithms”. Ed. by Manuel Mazzara, Iulian Ober, and Gwen Salaün. 2018. https://doi.org/10.1007/978-3-030-04771- 9_1

[31] National Aeronautics and Space Administration. Standards for Models and Simulations, NASA STD-7009. 2008.

[32] https://github.com/OpenModelica/OMSimulator/. OpenModelica/OMSimulator. Ed. by Linköping university. 2022.

[33] http://www.fmigo.net/. FMIGo!

[34] https://opensimulationplatform.com/. Open Simulation Platform.

[35] https://github.com/CATIA-Systems/FMPy. CATIA-Systems/FMPy. 2025.

[36] https://github.com/INTO-CPS-Association/maestro. INTO-CPS-Association/maestro.

[37] https://www.edf.fr/en/the-edf-group/inventing-the-future-of-energy/r-d-global-expertise/our-offers/simulation-softwares/daccosim-ng. DACCOSIM NG | EDF FR. 2021.

[38] https://github.com/OFFIS-mosaik/mosaik. OFFIS-mosaik/mosaik. 2025.

[39] Edward A. Lee. “The Past, Present and Future of Cyber-Physical Systems: A Focus on Models” (2015). https://doi.org/10.3390/s150304837

[40] Abir Ben Khaled et al. “Multicore simulation of powertrains using weakly synchronized model partitioning” (2012). https://doi.org/10.3182/20121023-3-FR-4025.00018

[41] Salah Eddine Saidi et al. “Acceleration of FMU Co-Simulation On Multi-core Architectures”. 2016. https://doi.org/10.3384 / ecp16124106

[42] Emin Oguz Inci, Wim Desmet, and Cláudio Gomes. “Error Estimators for Adaptive Scheduling Algorithm for Serial Co-Simulation” (2023).

[43] Bentley James Oakes et al. “Hint-Based Configuration of Co-simulations with Algebraic Loops”. Ed. by Mohammad S. Obaidat, Tuncer Ören, and Helena Szczerbicka. 2021. https://doi.org/10.1007/978-3-030-55867-3_1

[44] Robert Hällqvist and Erik Rosenlund. Reference Envionmental Control System (SSP). 2025. https://doi.org/10.5281/zenodo.17288988

[45] Robert Hällqvist et al. “Validation Techniques Applied on the Saab Gripen Fighter Environmental Control System Model”. 2015. https://doi.org/10.3384/ecp15119

Materials Research Proceedings 69 (2026) 1544-1548 https://doi.org/10.21741/9781644904251-270

Communication Architectures for System-of-Systems Engineering

Jorge L. LOVACO[1,a *], Karl ZUBER[1,b *], Raghu Chaitanya MUNJULURY[1,2,c], and Petter KRUS[1,d]

[1]Department of Management and Engineering, Linköping University, Olaus Magnus väg, Linköping, Sweden

[2]Saab Aeronautics, Bröderna Ugglas gata, Linköping, Sweden

[a]jorge.lovaco@liu.se, [b]karl.zuber@liu.se, [c]raghu.munjulury@liu.se, [d]petter.krus@liu.se

Keywords: System-of-Systems Engineering, System-of-Systems Architecture, Communication, Software Architecture, Agent-Based Modelling and Simulation

Abstract. System-of-Systems Engineering (SoSE) studies how independent constituent systems interact to generate emergent capabilities. However, it is challenging linking the study operations and SoSE to software implementation and agent-based simulations. This paper considers communication as the primary architectural concern and examines how software architectures can improve SoS modelling and simulation. In particular, by relating software architectures to Observe–Orient–Decide–Act (OODA) loops, which are a promising structure for aligning communication, decision logic, and agent interactions with modular and traceable agent architectures. The goal of this work is to explore how communication within SoS architectures can be better structured, represented, and analysed through software engineering and agent-based modelling frameworks in the context of hierarchical and cooperative operational environments, where information exchange directly influences system performance and emergent outcomes.

Background

System of Systems Engineering (SoSE) studies the methodologies for developing assemblies of systems in such a way that the collective brings new capabilities [1]. These systems operate independently but also as a part of an overarching System of Systems (SoS) architecture designed to form a collaborative and communicative network. The communication and interaction between systems are what makes the new capabilities emerge [1]. It is difficult, however, to provide an architecture for the SoS without being aware of the emergent capabilities beforehand, for that reason, modelling and simulation is used for finding these unforeseen capabilities. However, when using software for implementing a simulation tool for the SoS, not knowing the overall architecture represents a challenge that could make the models diverge from reality. The present work proposes the use of communication as the starting point for proposing a software architecture that could be easily relatable when considering options for the SoS architecture. By considering communication early in the process, issues related to communication in the form of delays, scalability, traceability, or interoperability can be addressed so they do not become an issue later.

Systems Engineering as Starting Point

There have been attempts to connect the Systems Engineering (SE) Vee Model to SoSE [2], but SE design and analysis assumptions are not always suitable for every SoS case [1]. There are accepted heuristics for architecting an SoS that can be found in the literature [3], being considered the correct modelling of interactions as the most critical one for capturing emergence. A very interesting approach for defining system architectures is heuristic extrapolation [4]. This method is particularly relevant as it is context sensitive and abstraction is removed iteratively in the design representation. The heuristic extrapolation method takes a general descriptive heuristic to derive domain-specific heuristics and rationale for decisions.

Content from this work may be used under the terms of the Creative Commons Attribution 3.0 license. Any further distribution of this work must maintain attribution to the author(s) and the title of the work, journal citation and DOI. Published under license by Materials Research Forum LLC.

Materials Research Proceedings 69 (2026) 1544-1548 https://doi.org/10.21741/9781644904251-270

Adopting Software Engineering

The process of modelling and analysis of SoS architectures is inherently iterative. For SoSE studies, the development of a simulation model is going to depend on the software architecture chosen for representing interactions during an operation. However, the goal of implementing such model to be used during SoSE processes is to be able to make decisions for defining the SoS architecture and interactions. Moreover, for a proper analysis, if the decided software architecture is representative of the SoS architecture, obvious parallelisms between them will rise, and engineers should be able to extrapolate from one another more easily and intuitively. This coupling usually requires an iterative process with numerous trade-off discussions. For parallelisms, considering similar architectures that are already in use simplifies the process. Shown in Fig. 1 is a simplified hierarchy for wildfire suppression operations, and by using these established structures, it is possible to choose amongst the already defined software architectures. Many of them are well-known [5] and provide guidance for implementing the models required for SoS analysis. Moreover, many of these software architectures have well-defined layers, a clear structure of how the information is propagated, and whether a layer can access resources from other layers. Using these software architectures as a starting point for discussing SoS architectures is considered optimal, as they are well defined and they can be used directly for the implementation of models while keeping traceability of the reasoning behind the decisions taken. To improve the process, one of the most recent methods proposed combines mathematical formulations with model theory, which has been validated and used for system and software design bringing numerous advantages [6].

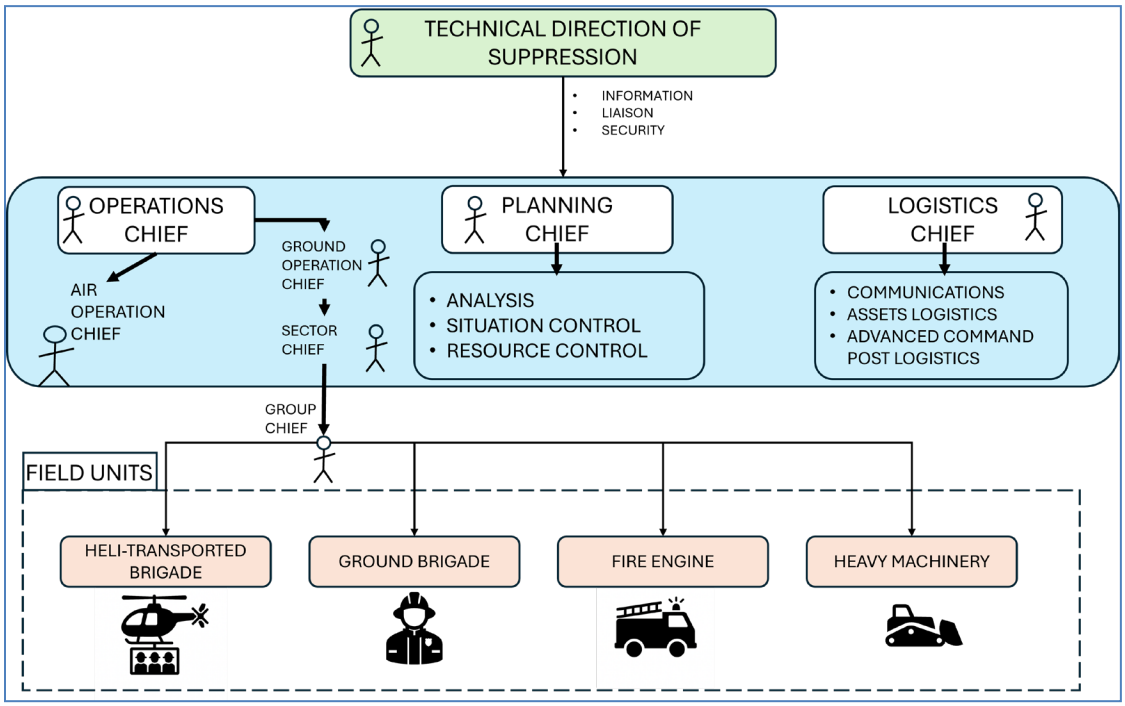


Figure 1: Incident Command Structure for Wildfire Suppression. Adapted from [10].

In terms of modelling and simulation for SoSE, agent-based models are usually used [1]. They focus on the interactions of agents, both between them and with their environment, for finding emergent behaviours or missing capabilities that could define requirements for designing new constituent systems. A traditional high-level software architecture of an agent separates the functions for observation of the environment and the functions for acting upon the environment [7], as shown in Fig. 2. However, this architecture is insufficient when trying to represent agents

Materials Research Proceedings 69 (2026) 1544-1548 https://doi.org/10.21741/9781644904251-270

with more advanced interaction capabilities, such as an incident commander agent in a wildfire suppression operation whose interactions are roughly represented in Fig. 3.

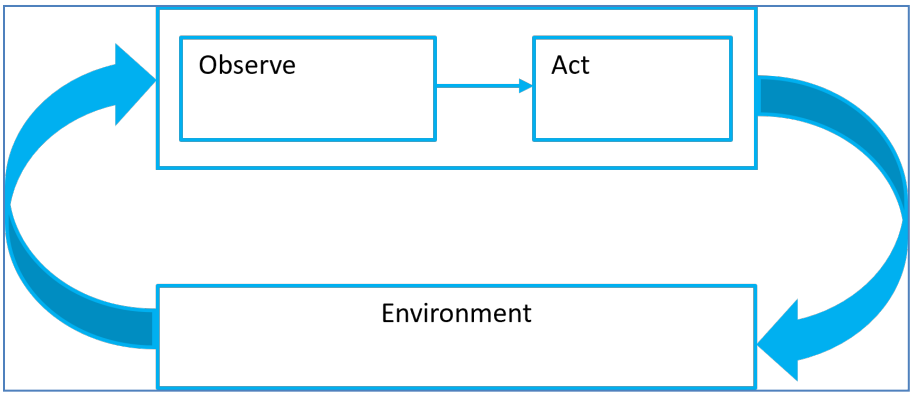


Figure 2: High-level agent architecture.

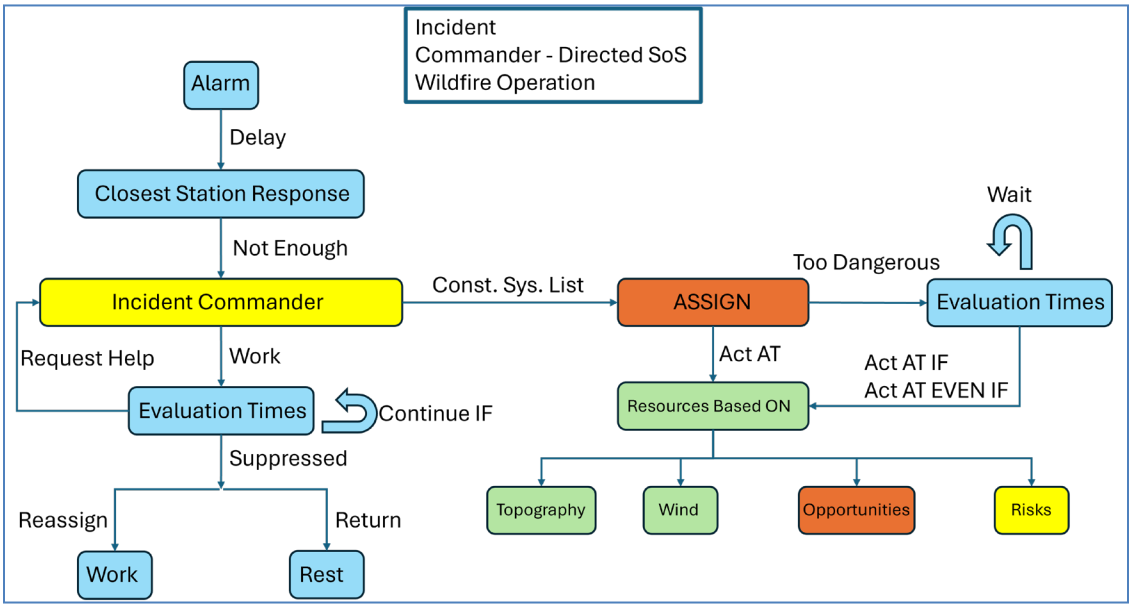


Figure 3: Figure 3: Incident commander agent interactions.

The goal behind these agent architectures and agent-oriented programming is to perform all the coding considerations as if they were mental states [9], being the difference with object-oriented programming that agents can choose whether to perform a task, and objects cannot. The agent could also be implemented with beliefs and commitment rules.

Agents then could be defined in terms of being communicative or not [7]. For the specific case of SoS, an interesting option for implementing agents would be to adopt an architecture based on Observe-Orient-Decide-Act (OODA) loops, which would allow to compartmentalise the implementation of the agents' behaviour in each part of the loop, define clear flows of information and how it is shared, and include interactions in the Decide and Act steps of the loop. This architecture could include forms of artificial intelligence and even be extended with agent intentions [8].

Conclusion

Despite the ongoing research about SoSE and software architectures, there seems to be no method considered standard for linking SoS architectures and software implementation, especially through

communication logic. The method of extrapolating heuristics and the consideration of software structures do not fully relate to how information flows, transforms, and supports decisions during an SoS operation. Software architectures have well-defined communication layers, but those layers do not fully represent SoS decision dynamics. To address this disconnection, this paper has proposed communication-centred architectures as the starting point, considering OODA loops particularly relevant, as they can relate system behaviour during real operations directly to agent implementations in simulation models. The OODA loops have structured information flow and a traceable and modular separation of concerns, which maps in a straightforward manner to both software implementation and SoS interactions, and how information evolves into decisions. These reasons make the loop valuable for SoSE applications where coordination and communication fidelity are necessary to find any emergent system performance. While OODA loops alone do not solve all SoSE challenges, their simplicity, modularity, and operational clarity provide a framework for agent-based models.

Future work should therefore focus on implementation and verification of an OODA-based framework with special attention to the communication layer for SoS simulation. Particularly relevant topics for future research are the definition of messaging (to represent human communication), evaluate the scalability and interoperability in a model with heterogeneous agents, and verify that the OODA loops do indeed improve traceability between SoS architecture decisions and software implementations.

Acknowledgements
The research presented in this paper has been performed in the framework of the COLOSSUS project (Collaborative System of Systems Exploration of Aviation Products, Services and Business Models) and has received funding from the European Union Horizon Europe programme under grant agreement No. 101097120. The Swiss participation in the Colossus project is supported by the Swiss State Secretariat for Education, Research and Innovation (SERI) under contract number 22.00609. The authors would also like to acknowledge the Swedish Innovation Agency (VINNOVA) and The Swedish Defence Materiel Administration (FMV) for financial support through the grant 2019-05371.

References

[1] D. A. M. K. &. G. C. DeLaurentis, System of systems modeling and analysis., CRC Press., 2022. https://doi.org/10.1201/9781003231011

[2] O. Hoehne, The SoS-VEE Model: Mastering the Socio-Technical Aspects and Complexity of Systems of Systems Engineering (SoSE)., INCOSE International Symposium, vol. 26, n° 11, https://doi.org/10.1002/j.2334-5837.2016.00241.x

[3] M. W. Maier, Architecting principles of system-of-systems, Systems Engineering, vol. 1, n° 14, pp. 267-274, 1998. https://doi.org/10.1002/(SICI)1520-6858(1998)1:4<267::AID-SYS3>3.0.CO;2-D

[4] Maier, M. W. (1994, August). Heuristic extrapolation in system architecture. In INCOSE International Symposium (Vol. 4, No. 1, pp. 486-493). https://doi.org/10.1002/j.2334-5837.1994.tb01747.x

[5] Bass, L., Clements, P., & Kazman, R. (2021). Software architecture in practice. AddisonWesley Professional.

[6] Dickerson, C. E., Wilkinson, M., Hunsicker, E., Ji, S., Li, M., Bernard, Y., ...& Denno, P. (2020). Architecture definition in complex system design using model theory. IEEE Systems Journal, 15(2), 1847-1860. https://doi.org/10.1109/JSYST.2020.2975073

[7] M. Wooldridge, An Introduction to Multiagent Systems, John Wiley & Sons, LTD., 2002.

[8] Silvander, J., & Angelin, L. (2019). Introducing intents to the OODA-loop. Procedia Computer Science, 159, 878-883. https://doi.org/10.1016/j.procs.2019.09.247

[9] Y. Shoham, Agent-oriented programming, Artificial intelligence, vol. 60, n° 11, pp. 51-92, https://doi.org/10.1016/0004-3702(93)90034-9

[10] C. d. L. C. I. Forestales, ESTRUCTURA ORGANIZATIVA DEL SISTEMA DE GESTION DE EMERGENCIAS EN INCENDIOS FORESTALES, Gobierno de España, 2008.

Materials Research Proceedings 69 (2026) 1549-1553 https://doi.org/10.21741/9781644904251-271

Extended Reality Technologies for enhanced Public Acceptance of Urban Air Mobility: insights on the State of the Art

Millene GOMES ARAUJO[1,a *], Francesca DE CRESCENZIO[1,b], Francesca STARITA[2,c] and Giuseppe DI PELLEGRINO[2,d]

[1]Department of Industrial Engineering, University of Bologna, Via Fontanelle 40, Forlì, Italy

[2]Department of Psychology, University of Bologna, Viale Berti Pichat, 5, Bologna, Italy

[a]millene.gomesaraujo@unibo.it, [b]francesca.decrescenzio@unibo.it, [c]francesca.starita2@unibo.it, [d]g.dipellegrino @unibo.it

Keywords: Public Acceptance, Extended Reality (XR), Urban Air Mobility (UAM), Human Factors (HF)

Abstract. The aviation sector is currently moving towards the integration of Urban Air Mobility (UAM), a new, safer and more sustainable aerial domain. UAM uses electric vertical take-off and landing (eVTOL) technology and Unmanned Aerial Systems (UAS) to transport goods and people at very low altitudes. However, technological and social sustainability challenges still need to be addressed before it can be fully developed. One of the main challenges is public acceptance of UAM and how to assess levels of acceptance. Acceptance frameworks that have already been successfully exploited in the aviation field can be implemented in the UAM context to investigate such social acceptance of UAM services. Since these methodologies are largely based on subjective perceptions, Extended Reality (XR) technologies have the potential to increase public acceptance of UAM systems, as they offer an immersive visualization of the relevant aspects. In this context, this work presents insights from a literature review on the state of research into the application of XR technologies to public acceptance of UAM. Previous studies have identified future users of UAM as clients of services and infrastructures, air taxi passengers, and pedestrians. Some of the use cases conducted include the development of operational concepts and the design of vertiports and air taxi interiors, as well as visual and auditory perception. Understanding how different aspects of acceptance are addressed can help us to appreciate the potential of XR to enhance such applications.

Introduction

UAM leverages the use of electrical take-off and landing (eVTOL) aircraft and UAS, also called drones, to very-low airspace level aerial applications such as package delivery, air taxis, traffic monitoring, surveillance and emergency [1]. Being an innovative transportation technology, there are still some implementation and operational challenges to be considered before its full deployment. Thus, a holistic and collaborative approach is required to address technological aspects such as propulsion systems, vehicle design and network connection, ground and air infrastructure development, services and policies development [2]. Beyond technical challenges, social factors play an important role in the deployment of UAM services [3]. Within the aviation context, acceptance methodologies such as Technology Acceptance Model (TAM) have already been exploited to address aviation risk assessment methods [4], to evaluate students' acceptance of AR instructions in aviation maintenance training [5] and to assess costumers' experience in the context of airport self-services [6]. In 2019, EASA ser the foundational brick for human stakeholders in UAM by investigating, at European level, public opinion and acceptance of UAM missions, with results demonstrating that 83% of respondents have a positive attitude towards such innovative aerial transportation system, with 71% ready to try out its services [7]. In the next

Content from this work may be used under the terms of the Creative Commons Attribution 3.0 license. Any further distribution of this work must maintain attribution to the author(s) and the title of the work, journal citation and DOI. Published under license by Materials Research Forum LLC.

Materials Research Proceedings 69 (2026) 1549-1553 https://doi.org/10.21741/9781644904251-271

sections, a preliminary view on the State of the Art of XR applied to the Public Acceptance of UAM will be presented, with a special focus on the identification of potential users of such systems and what aspects of XR Technology have been employed to assess social acceptance.

Public Acceptance of UAM services

Studies founded on TAM and applied to UAM have been extensively conducted, with results reflecting positive perceptions and attitudes towards UAM services [8-10]. However, these studies are mostly conducted via surveys, online questionnaires and telephone interviews, lacking in offering realistic perceptions of the addressed concepts. While such traditional methods allow for rapid dissemination and completion of data acquaintance, they lack realistic visualization of the users' experience. Thus, the results are mainly based on the subjective opinion of participants. When thinking about understanding public perceptions of UAM, it is fundamental to expose citizens to realistic environmental conditions that replicate real features considering future UAM scenarios. Therefore, simulation platforms capable of enabling such requirements are utmost required. Immersive simulations can facilitate the involvement of stakeholders in the development and implementation of UAM services by providing realistic UAM experiences.

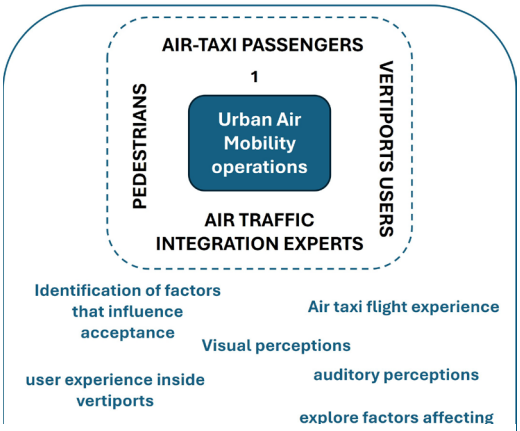


Fig. 1 Overview of Social Acceptance applications identified in the literature review. (1) Users addressed in existing studies. (2) Use-cases implemented.

Preliminary Literature review on XR Technologies and acceptance of UAM services

XR is a promising technology for facilitating stakeholders involvement in UAM deployment. In order to understand how the intersection between XR Technologies and acceptance of UAM services has been addressed, a preliminary comprehensive literature review has been conducted on existing works. A combination of keywords such as *"UAM"*, *"Acceptance"*, *"Public Acceptance"*, *"XR Technologies"*, *"Virtual Reality"*, *"Augmented Reality"*, *"Mixed Reality"* and *"drones"* as input in major scientific databases was used, with a total of 11 works selected. The use-cases addressed, technologies used and which part of acceptance is targeted in such works are summarized in Table 1. By understanding how different aspects of social acceptance are addressed, we can better appreciate the potential of XR to enhance such applications.

Table 1 Collection of works considered for the present study.

Reference	XR Technology	UAM social stakeholders	Aim of work conducted	Country and sample size
[11]	VR	Pedestrians	Identify factors affecting public acceptance of drones in cities.	Germany, 10
[12]	VR and AR	Pedestrians, Airspace Integration Experts and future users	Public requirements on UAM operational concepts, to understand the acceptance of different drone mission types and to explore the perception of drone flights in an urban scenario.	Germany, 20
[13]	VR	Future air taxi passengers/users	Influence of media conditions (VR, video and photo-based presentations) on the acceptance of air taxis.	Germany, 191
[14]	VR	Pedestrians	Participants' reaction to an air taxi landing nearby and the effects of drone flight height, its noise and visual density have on acceptance.	Germany, 47

[15]	VR	Future air taxi passenger and UAM user	Factors that influence acceptance of UAM services and passenger experience.	Germany, 294
[16]	VR	Air taxi passengers	Factors influencing adoption intentions of autonomous UAM services, specifically the effects of affective and cognitive considerations in adoption intentions.	Germany, 261 and 345
[17]	MR	Air taxi passengers	How information needs, maneuvers and crew members influence acceptance.	Germany, 30
[18]	VR	Vertiport user experience	User Experience inside urban airports (vertiports).	United Kingdom, 20
[19]	VR	Pedestrians	Subjective annoyance rates of drone noise.	The Netherlands, 11
[20]	VR	Pedestrians	Human perception and noise annoyance of UAM vehicles.	The Netherlands, 30
[21]	MR	Air taxi passenger	Passengers' acceptance aspects of air taxi operations	Germany, 12 and 30

Conclusion

UAM is an innovative and growing concept in the aviation field and, before its full integration, some aspects such as social acceptance of these systems should be addressed. Acceptance frameworks such as TAM have been successfully applied to different aviation areas, allowing for its transversal application to address acceptance in UAM. Since such traditional methods rely on two-dimensional visualization, XR Technologies comes as an enabling technology to address acceptance since it offers immersive simulation interfaces. In this context, this paper highlights a literature study on XR technologies applied to Public Acceptance of UAM systems aiming at identifying main aspects addressed. Some of the use-cases identified were vertiport and aircraft interior design, visual and auditory perceptions, operational concepts development, and exploratory studies on underlaying acceptance factors. The users addressed in previous studies are pedestrians, future UAM and vertiport users and air taxi passengers.

Acknowledgment

This study was carried out within the MOST – Sustainable Mobility National Research Center and received funding from the European Union Next-Generation EU (PIANO NAZIONALE DI RIPRESA E RESILIENZA (PNRR) – MISSIONE 4 COMPONENTE 2, INVESTIMENTO 1.4 – D.D. 1033 17/06/2022, CN00000023). This manuscript reflects only the authors' views and opinions, neither the European Union nor the European Commission can be considered responsible for them.

References

[1] EASA - What is UAM on https://www.easa.europa.eu/en/domains/drones-air-mobility/drones-air-mobility-landscape/basics-explained. Last accessed: 30/10/2025.

[2] J. Pons-Prats, T. Živojinović, J. Kuljanin, On the understanding of the current status of urban air mobility development and its future prospects: Commuting in a flying vehicle as a new paradigm, in: Transportation Research Part E: Logistics and Transportation Review, 166 (2022) https://doi.org/10.1016/j.tre.2022.102868

[3] Wang, Leilei, et al. "A review of urban air mobility-enabled intelligent transportation systems: Mechanisms, applications and challenges." Journal of Systems Architecture 141 (2023): 102902. https://doi.org/10.1016/j.sysarc.2023.102902

[4] Mhangami, Washington, Stephen King, and David Barry. "Accepting Technology in Aviation Safety Risk Management: an extension of the technology acceptance model." Annual Conference of the PHM Society. Vol. 16. No. 1. 2024. https://doi.org/10.36001/phmconf.2024.v16i1.3922

[5] Wang, Yu, Amadou Anne, and Tim Ropp. "Applying the technology acceptance model to understand aviation students' perceptions toward augmented reality maintenance training instruction." International Journal of Aviation, Aeronautics, and Aerospace 3.4 (2016): 3. https://doi.org/10.15394/ijaaa.2016.1144

[6] Wongyai, Phutawan Ho, et al. "Self-service technology in aviation: A systematic literature review." Journal of the Air Transport Research Society 2 (2024): 100016. https://doi.org/10.1016/j.jatrs.2024.100016

[7] EASA, "EASA - Full report on UAM acceptance," European Union Aviation Safety Agency, on: https://www.easa.europa.eu/sites/default/files/dfu/uam-full-report.pdf. Last Accessed: 14/04/2025.

[8] Yao, Enjian, et al. "The role of technology belief, perceived risk and initial trust in users' acceptance of urban air mobility: An empirical case in China." Multimodal Transportation 3.4 (2024): 100169. https://doi.org/10.1016/j.multra.2024.100169

[9] Kim, Young Woo, Cherin Lim, and Yong Gu Ji. "Exploring the user acceptance of urban air mobility: extending the technology acceptance model with trust and service quality factors." International Journal of Human-Computer Interaction 39.14 (2023): 2893-2904. https://doi.org/10.1080/10447318.2022.2087662

[10] Hu, Sangen, et al. "Modeling the adoption of urban air mobility based on technology acceptance and risk perception theories: A case study on flying cars." Multimodal Transportation 4.2 (2025): 100200. https://doi.org/10.1016/j.multra.2025.100200

[11] Stolz, Maria, et al. "See it, hear it, feel it: an explorative virtual reality study to identify factors determining public acceptance of drones in different city environments." CEAS Aeronautical Journal 16.1 (2025): 119-139. https://doi.org/10.1007/s13272-024-00785-z

[12] Stolz, Maria, et al. "A mixed-method approach to investigate the public acceptance of drones." CEAS Aeronautical Journal 14.4 (2023): 835-855. https://doi.org/10.1007/s13272-023-00693-8

[13] Bagratuni, Mikael, et al. "Media immersion and acceptance of technologies: Exploring the influence of virtual reality, video, and photo-based presentations using the case of air taxis." Transportation Research Interdisciplinary Perspectives 29 (2025): 101317. https://doi.org/10.1016/j.trip.2024.101317

[14] Stolz, Maria, and Tim Laudien. "Assessing social acceptance of urban air mobility using virtual reality." 2022 IEEE/AIAA 41st Digital Avionics Systems Conference (DASC). IEEE, 2022. https://doi.org/10.1109/DASC55683.2022.9925775

[15] Janotta, Frederica, and Jens Hogreve. "Understanding user acceptance of air taxis-Empirical insights following a flight in virtual reality." (2021). https://doi.org/10.31219/osf.io/m62yd

[16] Janotta, Frederica, and Jens Hogreve. "Ready for take-off? The dual role of affective and cognitive evaluations in the adoption of Urban Air Mobility services." Transportation Research Part A: Policy and Practice 185 (2024): 104122. https://doi.org/10.1016/j.tra.2024.104122

[17] Papenfuss, Anne, et al. "Experiencing urban air mobility: how passengers evaluate a simulated flight with an air taxi." CEAS Aeronautical Journal (2025): 1-19. https://doi.org/10.1007/s13272-025-00823-4

[18] Birrell, Stewart, et al. "Urban air mobility infrastructure design: Using virtual reality to capture user experience within the world's first urban airport." Applied Ergonomics 105 (2022): 103843. https://doi.org/10.1016/j.apergo.2022.103843

[19] Aalmoes, Roalt, and Naomi Sieben. "Noise and visual perception of Urban Air Mobility vehicles." Delft International Conference on Urban Air Mobility (DICUAM), virtual. 2021.

[20] Aalmoes, Roalt, and Naomi Sieben. "Visual and audio perception study on drone aircraft and similar sounds in an Urban Air Mobility setting." INTER-NOISE and NOISE-CON Congress and Conference Proceedings. Vol. 263. No. 4. Institute of Noise Control Engineering, 2021. https://doi.org/10.3397/IN-2021-2160

[21] Ernst, Johannes Maria, et al. "How does it feel to fly in an air taxi? Exploring modern head-mounted display capabilities for mixed reality flight simulation." CEAS Aeronautical Journal (2025): 1-17. https://doi.org/10.1007/s13272-025-00820-7

Materials Research Proceedings 69 (2026) 1554-1558 https://doi.org/10.21741/9781644904251-272

Urban Air Mobility: Trends and Economic Perspective in Europe and Italy

Gabriele LECIS[1,a], Leonardo CORBO[1,b *], Francesca DE CRESCENZIO[2,c], Millene GOMES ARAUJO[2,d]

[1]Department of Management, University of Bologna, Via Capo di Lucca 34, 40126 Bologna, Italy

[2]Department of Industrial Engineering, University of Bologna, Via Fontanelle, 40, Forlì, Italy

[a]gabriele.lecis2@unibo.it, [b]leonardo.corbo@unibo.it, [c]francesca.decrescenzio@unibo.it, [d]millene.gomesaraujo@unibo.it

Keywords: Urban Air Mobility, Advanced Air Mobility, Business Models, Sustainable Mobility

Abstract. This paper provides an overview of the emerging trends and business models in the Advanced Air Mobility (AAM) sector, with a particular focus on the Urban Air Mobility (UAM) segment [5] in the European and Italian contexts. The work presents a multidimensional analysis aimed at identifying the main demographic, technological, industrial and regulatory trends. After that, it examines the current Italian scenario, the main recognizable business models, and offers some considerations on UAM's ability to create, capture and distribute value.

Introduction

UAM generally refers to an innovative transportation segment that uses aerial vehicles such as drones and electric vertical take-off and landing (eVTOL) aircraft for both passenger and cargo transport within urban and suburban environments [9]. The purpose of this transportation system is to enhance safety, sustainability and accessibility [14] through the use of renewable energy sources, automation and digital infrastructure [1]

Scenarios

In order to understand the context and economic potential of UAM, this study identifies the main demographic, technological, industrial and regulatory trends. From a demographic perspective, UAM is driven by rapid urbanization in both developed and developing countries [13]. It is estimated that by 2050, more than 70% of the European population and more than 80% of the North American population will live in urban areas [11]. This urban growth is expected to exacerbate traffic congestion and pollution [11], [12]. In this scenario, UAM emerges as key solution to mitigate these issues, with the potential to reduce emissions by up to 80% compared to traditional cars [14].

Table 1. Summary of main UAM trends

Demographic	*Technological*	*Industrial*	*Regulatory*
Urbanizations driving UAM demand	Innovations in eVTOL and drone technologies	Initiatives by major companies (Boeing, Airbus, etc.)	FAA and EASA as major authorities
Impact of urban congestion and pollution	Advancements in battery technology	Initiatives by major delivery companies (Amazon, UPS, etc.)	European Green Deal

Content from this work may be used under the terms of the Creative Commons Attribution 3.0 license. Any further distribution of this work must maintain attribution to the author(s) and the title of the work, journal citation and DOI. Published under license by Materials Research Forum LLC.

Economic implication of traffic congestion	Integration of 5G for communication	European Drone Regulation
Factors influencing public acceptance	Autonomy and AI in UAM systems	

From a technological standpoint, the main trends involve innovations in vehicle design, electric or hydrogen propulsion, autonomous flight and advanced communication systems [11]. These technologies enable UAM applications for both cargo and passenger transport [19].

At the industry level, UAM promises to generate a new market, with projections reaching up to $9 trillion by 2050 [10]. The sector is also anticipated to have a significant impact on employment, particularly in fields such as engineering, aviation, software development, and logistics.

At the regulatory level, the Federal Aviation Administration (FAA), in collaboration with NASA, is leading the development of operational standards in the United States [9]. In China, the regulatory framework relies largely on existing civil aviation regulations [11]. In Europe, the European Union Aviation Safety Agency (EASA) has published special conditions for authorizing the use of VTOLs, with the aim of positioning the European industry as a global first mover [6]. These efforts align with the European Union's broader strategy to foster smart and sustainable mobility [2], [7].

Business models

As with technology, business models in the UAM industry are evolving rapidly, reflecting the potential and challenges of a fast-growing market. These models are generally classified into three categories, each with their own specifications and dynamics [15]: passenger transport; cargo; hybrid solutions. The latter includes models that do not fully fall into the first two categories, such as the concept of overhead warehouses.

Within the UAM landscape, passenger transport represents one of the most promising areas, with several emerging business models that aim to revolutionize urban mobility. Unlike what is observed in the automotive and traditional aviation sectors, passenger UAM vehicles do not yet adhere to standard designs, as demonstrated by wide variety of eVTOL configurations. Initially, these services are likely to target high-income users due to high costs. However, from an economic point of view, technological maturation and computational advances are expected to drive economies of scale, reducing production costs and gradually increasing the affordability and accessibility of these services [16].

Based on the types of consumers targeted, three main business models for UAM passenger transport can be identified [4], [8]:

- *Air taxis*. Urban Air Mobility promises to significantly alleviate congestion in urban areas through a non-stop on-demand flight service that allows citizens to move from one landing pad to another within a defined area. This service will operate over short distances, typically between 15 and 50 km, covering the diameter of the entire urban center.
- *Airport shuttles*. Airport shuttles are designed to cover similar and longer distances than air taxis. These flights would operate between various landing pads distributed throughout the city and the main airport. In this context, flights would not be on demand but regular.
- *Intercity flights*. Intercity flights are designed to operate between cities that are too close to justify traditional flights, but far enough away to benefit from air travel. The distance covered will vary between 50 and 250 km [4].

UAM technologies have also found important applications in the cargo sector [3]. For over a decade, several companies have been developing cargo models that rely on drones for so-called

last-mile deliveries [18], [3]. Unmanned aerial vehicles (UAVs), which include drones, are extremely versatile tools with applications across various domains. The drone-based *delivery of goods and food* items represents the first major frontier in aerial cargo. In recent years, many companies – such as Amazon - have invested significant resources in the developing services for the delivery of goods and groceries. Cargo in the context of UAM also includes the distribution of critical *medical supplies and healthcare equipment*. The ability to reduce delivery times and operational costs presents a substantial advantage for the healthcare sector. Drones, capable of flying autonomously and covering long distances, provide a solution to geographic accessibility challenges, particularly in remote or underserved areas. As healthcare systems face rising labor costs and fluctuating fuel prices, the automation of transport processes becomes an effective strategy to reduce costs and minimize delays typically associated with traditional delivery services [17].

The Italian market. The Italian UAM market is still in its early development phase. It is estimated that the entire AAM sector, which includes UAM, could reach a market value of € 1.8 billion by 2030, with a compound annual growth rate (CAGR) of about 20.6% between 2025 and 2030. The segment with the greatest growth potential is passenger transport, with a growth of 36% by 2030, followed by cargo with a growth of 18.5% [12]. Investments in research and development are expanding. In 2022 they amounted to € 16 million in cargo and € 8 million in passenger transport, with a projected CAGR in 2030 of 11% and 30% respectively [12]. The Italian industrial landscape is currently dominated by startups, with limited involvement from medium and large companies. In fact, only 1% of companies operating in the AAM sector in Italy report an annual turnover exceeding € 5 million [12].

Value creation. In the Italian context, value creation through the UAM sector is still in its early stages. Italy has begun laying the groundwork for future positioning, particularly in cargo segment, with a focus on medical logistics. In this segment, value is primarily created through improved efficiency, speed and reduced lead times for critical deliveries. In the passenger transport segment, value creation is similarly driven by efficiency and speed, in particular for air taxi services and airport-to-city connections. However, significant additional opportunities could emerge in the tourism sector, leveraging the silent and environmentally friendly nature of electric UAM vehicles. This could enable unique air tours over historic cities such as Rome, offering a new, sustainable form of experiential tourism.

Value capture. Value capture in the Italian UAM sector is currently limited by a fragmented regulatory environment. Most companies are still in the investment phase and have yet to establish commercial services. At present, revenue streams are largely limited to the cargo segment, including drones and software sales for specific industrial applications. Initial business models are expected to rely primarily on B2B partnerships, which offer more predictable revenue streams than B2C approaches. For instance, UAM companies could establish partnerships with airports and other operators to provide regular and scheduled services. Additionally, companies involved in the development of UAM infrastructure may capture value through take-off and landing fees, as well as ancillary passenger services. However, the introduction of such innovative and advanced technologies must be carefully managed to ensure they remain inclusive and accessible to the broader public.

Value delivery. Effective value delivery in the UAM sector depends on two key strategic priorities: regulatory and institutional collaboration, and the development of supporting infrastructure. In Europe, unlike the approaches taken in America and Asia, regulation often acts

as a barrier to rapid technological development, largely due to stringent safety standards and rigorous certification processes. However, regulation is a key aspect in ensuring that UAM services are safe, reliable and socially accepted. This highlights the importance of limited, step-by-step pilot projects to demonstrate the practical benefits of UAM and gradually build public trust. The goal is not simply to convince the public of the value of UAM, but to actively engage them in the development of a sector with significant societal and economic potential.

Contribution

The study is presented as a review of the current economic scenario of the UAM, contributing to enriching the UAM literature, which is still limited. In particular, it places a greater focus on the European and Italian contexts, moving from a multidimensional framework and the use of updated data. The work thus highlights the main trends, challenges and opportunities in the sector, offering a useful basis for policy makers and other stakeholders.

Acknowledgments

This study was carried out within the MOST – Sustainable Mobility National Research Center and received funding from the European Union Next-Generation EU (PIANO NAZIONALE DI RIPRESA E RESILIENZA (PNRR) – MISSIONE 4 COMPONENTE 2, INVESTIMENTO 1.4 – D.D. 1033 17/06/2022, CN00000023). This manuscript reflects only the authors' views and opinions, neither the European Union nor the European Commission can be considered responsible for them.

References

[1] AGOURIDAS V., BIERMANN F., CZAYA A., RICHTER D., STEMMLER J., STĘCHŁY J., WITKOWSKA KONIECZNY A., KUMAR R., PATATOUKA E. (2021). Urban Air Mobility and Sustainable Urban Mobility Planning - Practitioner Briefing. UIC2 - UAM Initiative Cities Community, EU's Smart Cities Marketplace.

[2] ALAVERDYAN, D., KUČERA, F., & HORÁK, M. (2018). Implementation of the smart city concept in the EU: importance of cluster initiatives and best practice cases. International Journal of Entrepreneurial Knowledge, 6(1). https://doi.org/10.37335/ijek.v6i1.67

[3] BAUR, S. (2022). Cargo drones: A potential gamechanger in the logistics industry, Roland Berger.

[4] BAUR, S., SCHICKRAM, S., HOMULENKO, A., MARTINEZ, N., & DYSKIN, A. (2018). Urban air mobility: The rise of a new mode of transportation. Roland Berger Focus.

[5] COHEN, A. P., SHAHEEN, S. A., & FARRAR, E. M. (2021). Urban air mobility: History, ecosystem, market potential, and challenges. IEEE Transactions on Intelligent Transportation Systems, 22(9), 6074-6087. https://doi.org/10.1109/TITS.2021.3082767

[6] EASA, N. (2021). Study on the societal acceptance of urban air mobility in Europe.

[7] GUERRA, C., MUZZOLON, E., & SIMONI, C. (2024). Guida alla discussione: 28 giugno 2024. Centro Nazionale per la Mobilità Sostenibile MOST.

[8] HADER, M., BAUR, S., KOPERA, S., SCHÖNBERG, T., & HASENBERG, J. P. (2020). Urban air mobility, USD 90 billion of potential: how to capture a share of the passenger drone market. Roland Berger.

[9] HAMILTON, B. A. (2018). Urban air mobility (UAM) market study: Final Report. National Aeronautics and Space Administration (NASA). Available online: https://ntrs. nasa. gov/citations/20190001472 (accessed on 2 June 2020).

[10] MORGAN STANLEY RESEARCH. (2021). eVTOL/Urban Air Mobility TAM Update: A Slow Take-Off, But Sky's the Limit. Morgan Stanley.

[11] PONS-PRATS, J., ŽIVOJINOVIĆ, T., & KULJANIN, J. (2022). On the understanding of the current status of urban air mobility development and its future prospects: Commuting in a flying vehicle as a new paradigm. Transportation Research Part E: Logistics and Transportation Review, 166, 102868. https://doi.org/10.1016/j.tre.2022.102868

[12] PWC STRATEGY&. (n.d.). Advanced Air Mobility (AAM) Italian market study: Recommendations for a national ecosystem. PwC.

[13] PWC STRATEGY&. (2021). The path towards a mobility in the third dimension: How to create a National ecosystem for Advanced Air Mobility. PricewaterhouseCoopers Business Services Srl.

[14] RAGHUNATHA, A., LINDKVIST, E., THOLLANDER, P., HANSSON, E., & JONSSON, G. (2023). Critical assessment of emissions, costs, and time for last-mile goods delivery by drones versus trucks. Scientific Reports, 13(1), 11814. https://doi.org/10.1038/s41598-023-38922-z

[15] SHAHEEN, S. A., COHEN, A. P., BROADER, J., DAVIS, R., BROWN, L., NEELAKANTAN, R., & GOPALAKRISHNA, D. (2020). Mobility on demand planning and implementation: current practices, innovations, and emerging mobility futures (No. FHWA-JPO-20-792). United States. Department of Transportation. Intelligent Transportation Systems Joint Program Office.

[16] STRAUBINGER, A., MICHELMANN, J., & BIEHLE, T. (2021). Business model options for passenger urban air mobility. CEAS Aeronautical Journal, 12(2), 361-380. https://doi.org/10.1007/s13272-021-00514-w

[17] ZIPLINE. (n.d.) The Essential Guide to Implementing Drone Delivery in Healthcare. FlyZipline. Available at: https://www.flyzipline.com/solutions/healthcare/healthcare-guide.

[18] Information on https://www.aboutamazon.com/search?q=drone+delivery

[19] Information on https://www.leonardo.com/en/focus-detail/-/detail/advanced-air-mobility

Materials Research Proceedings 69 (2026) 1559-1562 https://doi.org/10.21741/9781644904251-273

An Extended Reality-based Platform for Digital Twin applications in Urban Air Mobility and Advanced Air Mobility: Framework proposed within MOST Project

Francesca DE CRESCENZIO[1,a] , Millene GOMES ARAUJO[1,b *], Sara BAGASSI[1,c], Fabrizio LAMBERTI[2,d], Filippo Gabriele PRATTICO'[2,e], Domenico ACCARDO[3,f], Claudia CONTE[3,g], Lorenza SABATINO[4,h] and Marco BAZZANI[4,i]

[1]Department of Industrial Engineering, University of Bologna, Italy

[2]Department of Control and Computer Engineering, Polytechnic of Turin, Italy

[3]Department of Industrial Engineering, University of Naples Federico II, Italy

[4]Teoresi Group, Italy

[a]francesca.decrescenzio@unibo.it, [b]millene.gomesaraujo@unibo.it, [c]sara.bagassi@unibo.it, [d]fabrizio.lamberti@polito.it, [e]gabriele.prattico@polito.it, [f]domenico.accardo@unina.it, [g]claudia.conte2@unina.it, [h]lorenza.sabatino@teoresigroup.com, [i]marco.bazzani@teoresigroup.com

Keywords: Digital Twin Platform, Extended Reality, Urban Air Mobility, Advanced Air Mobility, Unmanned Aerial Systems

Abstract. Urban Air Mobility (UAM) is currently emerging as innovative mobility solution for urban transport. To ensure its seamless integration into existing systems, advanced simulation frameworks are strongly needed. Extended Reality (XR) technologies offer powerful tools to support such simulations. This paper presents a suite of Extended Reality-based integrated simulation and interaction platforms for multipurpose testing of UAM through Digital Twins of missions and scenarios. The platforms combine various hardware and software infrastructures and components, including the IRIS Cave Automatic Virtual Environment (CAVE), an eVTOL passenger simulator, and an Augmented Reality application for drone-based aircraft maintenance. Developed within the framework of the MOST – Sustainable Mobility Project, these platforms aim to support diverse use cases and contribute to the safe and efficient integration of UAM systems.

Introduction

In the context of rapid technological advancements and increasing digitalization of systems, the airspace domain is moving towards new solutions such as Advanced Air Mobility (AAM) and Urban Air Mobility (UAM). AAM is enabled by electric take-off and landing (eVTOL) aircraft and Unmanned Aerial Systems (UAS) and UAM refers to its implementation in urban scenarios [1]. These innovative aerial operations are expected to enhance the overall efficiency and sustainability of airspace systems. However, their integration into existing environments poses significant challenges related to safety, infrastructure development, and public acceptance. To address these challenges, a collaborative approach among the various stakeholders involved in this emerging transportation ecosystem is essential for achieving full-scale deployment. One key aspect of this process involves sharing information and data within realistic visualization and interactive environments. In this regard, the use of Extended Reality (XR) technologies for visualizing Digital Twins (DT) of aircraft and/or operational scenarios offers a promising path to support stakeholders, providing comprehensive, high-fidelity environments for prediction,

Content from this work may be used under the terms of the Creative Commons Attribution 3.0 license. Any further distribution of this work must maintain attribution to the author(s) and the title of the work, journal citation and DOI. Published under license by Materials Research Forum LLC.

Materials Research Proceedings 69 (2026) 1559-1562 https://doi.org/10.21741/9781644904251-273

monitoring, and decision-making [2]. In the aerospace domain, DT applications have already been carried out across different areas such as aircraft design and development, manufacturing, operation and maintenance [3]. Further applications have been proposed in the context of Urban Air Mobility, such as exploring ground infrastructure location and aerial corridors [4] and supporting airspace management [5]. Although there exists no consensus on the formal definition of a DT, most reputable research shares the commonality that a DT is a cyber-physical system consist of at least three components: a physical system, a virtual model and their interactions [2][6][7]. Extended Reality (XR) Technologies, including VR (Virtual Reality), AR (Augmented Reality) and MR (Mixed Reality), enable seamless human–Digital Twin interaction by blending real and digital content, integrating high-fidelity simulation modules, and fostering collaboration among users [9]. Building upon these concepts, this work presents a modular and collaborative XR-based platform for Digital Twin visualization and interaction, developed through close cooperation between academic and industrial partners within the framework of the MOST – Sustainable Mobility Project.

XR-based Simulation Platform for Digital Twin applications in AAM and UAM

In the MOST Project, an XR multisensory simulator supports the need of a convergence place for safe AAM and UAM simulation and interaction and has ultimately two main goals: i. to integrate multi-layered DT capabilities in three-dimensional DT models of UAM and AAM missions; ii. To enable a realistic, collaborative and interactive user experience through simulation platforms designed to the analysis of DTs. The proposed simulation framework has been deployed, in both software and hardware infrastructure, to different facilities of project partners and has the capability to support and simulate multiple use-cases including eVTOL passenger transport, AR drone-enhanced aircraft maintenance and public acceptance. The overall hardware-software architecture of the XR multisensory simulator is depicted in *Figure 1*.

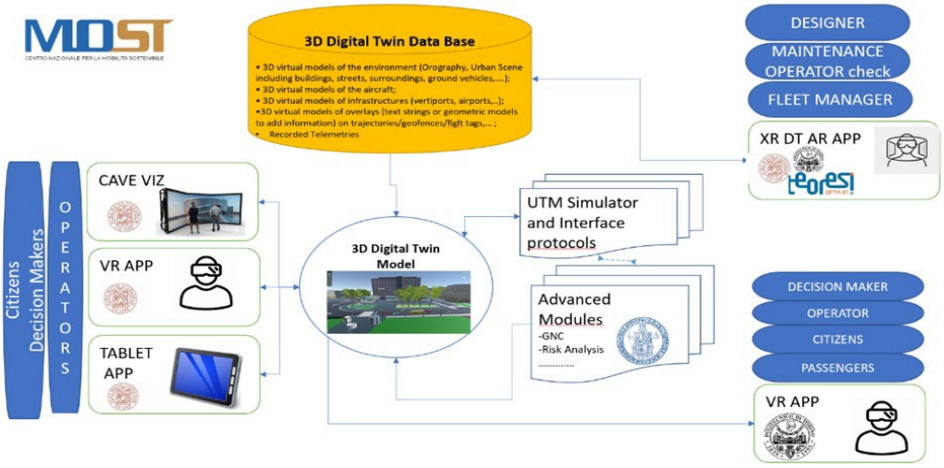


Figure 1 *The overall suite XR-based simulation platforms for Digital Twin visualization and interaction developed in the framework of MOST - Sustainable Mobility Project.*

The architecture of such XR Platform follows a modular design and is built upon the creation of a virtual scene composed of different data layers that can be combined between themselves and deployed according to the desired application. These layers are the Digital Twin Model layer, in which the three-dimensional models of the individual objects for each layer are integrated, including high-fidelity 3D models of eVTOLs and drones, urban environments and its components (e.g. buildings, streets, ground vehicles, terrain data), infrastructure dedicated to UAM (known as *vertiports*), overlays (text strings or geometric models to add information) and the recorded trajectories and paths database; The XR Visualization layer, that provides the XR Human Machine

Materials Research Proceedings 69 (2026) 1559-1562 https://doi.org/10.21741/9781644904251-273

Interface through which the application will be experienced and interacted to by the user and the Integration and Simulation Engine layer: responsible for managing layer interaction logics and data communication with external simulators or telemetry sources.

The MOST XR Platform modules

IRIS – Immersive Reconfigurable Innovative System is a unique cutting-edge immersive simulation infrastructure that allows users to experience Virtual Reality applications within an environment projected onto the walls of a room-sized cube (See Figure 2). The facility installed at the University of Bologna site in Forlì, leverages key features such as *immersion*, enabled by multiple projectors displaying high-resolution three-dimensional environments and *interaction*, enabled by input devices (e.g. tracking systems). A simulator aiming at replicating onboard flight experience from the point of view of passengers was developed by the Polytechnic of Turin (See Figure 3). The simulator reproduces an autonomous or piloted UAS mission under different visibility conditions (e.g. clear daylight, clear nighttime, cloudy with rain and foggy scenarios), during which other UAM traffic is visible to the user.



Figure 2 Immersive Reconfigurable Innovative System (IRIS) Cave platform in its open configuration displaying the Digital Twin model of Fuorigrotta, Naples, developed within MOST Project.



Figure 4 Passenger view from the UAV Passenger Simulator.

Aircraft maintenance activities can benefit from Augmented Reality interfaces due to the high level of interaction intrinsic of such procedures [10]. An AR interface to enhance drone-based maintenance and inspection procedures was proposed by Teoresi (See Figure 4*)*. The system primarily focuses on enhancing real-time situation awareness by leveraging Augmented Reality to display telemetry data (e.g. battery status, aircraft position and key metrics) to remote drone operators while executing predefined aircraft inspection activities. As the operator can visualize key information to support efficient and informed decisions. The ultimate goal is to boost precision, responsiveness and overall effectiveness of airport inspection and maintenance tasks through AR-enabled workflows. To demonstrate the capability of supporting the smooth integration of AAM and UAM into the current airspace scenario, the various infrastructures and components of the XR framework were tested through a series of pilot cases integrating advanced simulation modules, such as and the risk analysis framework developed by the University of Naples and the Unmanned Traffic Management simulator provided by TopView through Cascade Funding. A further module is the Simultaneous XR simulator for airport scenarios immersive experience provided by TXT through cascade fundings.

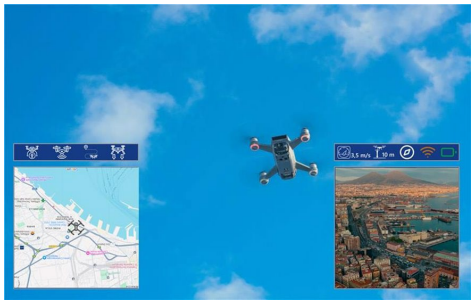


Figure 3 The AR for AR-enhanced aircraft maintenance.

Conclusion

AAM and UAM are promising concepts for the future of aerial transportation; however, further efforts are still required to ensure their effective integration into existing airspace systems. To this end, this paper has presented an XR-based platform designed for Digital Twin (DT) applications in UAM and AAM simulation. Three hardware components have been developed: the IRIS immersive system, the eVTOL passenger simulator, and an AR enhanced, drone-based maintenance application. The proposed simulation framework demonstrates the potential of bridging XR technologies and DTs, not only as tools for visualization and interaction but also as a foundation for informed decision-making among UAM and AAM stakeholders.

Acknowledgments

This study was carried out within the MOST – Sustainable Mobility National Research Center and received funding from the European Union Next-Generation EU (PIANO NAZIONALE DI RIPRESA E RESILIENZA (PNRR) – MISSIONE 4 COMPONENTE 2, INVESTIMENTO 1.4 – D.D. 1033 17/06/2022, CN00000023). This manuscript reflects only the authors' views and opinions, neither the European Union nor the European Commission can be considered responsible for them.

References

[1] EASA Pro – European Union Aviation Safety Agency on htpp://www.easa.europa.eu/en/what-is-uam. Accessed on: 25/10/2025.

[2] Liu, Y.K., Ong, S.K. & Nee, A.Y.C. State-of-the-art survey on digital twin implementations. Adv. Manuf. **10**, 1–23 (2022). https://doi.org/10.1007/s40436-021-00375-w

[3] Z, H. & Wang, L.. (2020). Application and Development Prospect of Digital Twin Technology in Aerospace. IFAC-PapersOnLine. 53. 732-737. https://doi.org/10.1016/j.ifacol.2021.04.165

[4] Brunelli, M.; Ditta, C.C.; Postorino, M.N. A Framework to Develop Urban Aerial Networks by Using a Digital Twin Approach. Drones 2022, 6, 387.

[5] K. Namuduri, "Digital Twin Approach for Integrated Airspace Management With Applications to Advanced Air Mobility," in IEEE Open Journal of Vehicular Technology, vol. 4, pp. 693-700, 2023.

[6] F. Tao, H. Zhang, A. Liu and A. Y. C. Nee, "Digital Twin in Industry: State-of-the-Art," in IEEE Transactions on Industrial Informatics, vol. 15, no. 4, pp. 2405-2415, April 2019.

[7] Roland Rosen, Georg von Wichert, George Lo, Kurt D. Bettenhausen,About The Importance of Autonomy and Digital Twins for the Future of Manufacturing, IFAC-PapersOnLine, vol. 48, 3, 2015, pp567-572.

[8] Qinglin Qi, Fei Tao, Tianliang Hu, Nabil Anwer, Ang Liu, Yongli Wei, Lihui Wang, A.Y.C. Nee, Enabling technologies and tools for digital twin, Journal of Manufacturing Systems, vol. 58, Part B, 2021, pp 3-21.

[9] Lorenzo Stacchio, Alessia Angeli, Gustavo Marfia, Empowering digital twins with eXtended reality collaborations, Virtual Reality & Intelligent Hardware, vol. 4, 6, 2022, pp 487-505.

[10] Eschen, Henrik & Kötter, Tobias & Rodeck, Rebecca & Harnisch, Martin & Schüppstuhl, Thorsten. (2018). Augmented and Virtual Reality for Inspection and Maintenance Processes in the Aviation Industry. Procedia Manufacturing. 19. 156-163. https://doi.org/10.1016/j.promfg.2018.01.022

Materials Research Proceedings 69 (2026) 1563-1567 https://doi.org/10.21741/9781644904251-274

FORTUNA: Design, Integration and Testing of a Technology Demonstrator for Space Exploration Rover

Enrico SABBATINI[1,a *], Ludovica GIACCONI[1,b], Fabrizio STESINA[1,c], Stefano GIULIANELLI[1], Damiano CARRA[1], Massimiliano MORELLI[1], and Federico FANTASTICO[1]

[1]STAR Lab, Department of Mechanical and Aerospace Engineering, Corso Duca degli Abruzzi 24, 10129, Torino, Italy

[a]enrico.sabbatini@stuenti.polito.it, [b]ludovica.giacconi@teamdiana.it, [c]fabrizio.stesina@polito.it

Keywords: Technological Demonstrator, Modular Rover, Space System Design, System Engineering, Planetary Exploration

Abstract This paper introduces the design of FORTUNA, a modular rover aimed at enabling robotic operations and exploration on planetary surfaces. The work entirely developed by students of team DIANA from Politecnico di Torino. FORTUNA's goal is to explore the planetary surface by interacting with other platforms (forming a fleet of rovers) and surviving the environment. The project is part of an ever-growing vision of an established presence on the moon, which would require many robotic platforms to perform various tasks, from maintenance to exploration. The rover, developed following the experience gained on the team's previous rover ARDITO [1], it is designed to be smaller, faster, and more cost effective. These improvements are achieved through its high degree of modularity and its capability to host different payloads. In September 2025, FORTUNA took part to the European Rover Challenge (ERC) in Poland, where the platform accomplished all competition tasks achieving a 4th place overall. In May 2026 the platform will compete in the University Rover Challenge (URC) in the Mars Desert Research Station The Fortuna rover offers a lightweight and cost-effective platform specifically designed to support maintenance operations at lunar base as well as exploration missions on the Moon and Mars. Its modular architecture and advanced autonomous[2] system enable adaptability to diverse mission requirements, from routine infrastructure inspection to complex surface exploration. By integrating a 6-DOFrobotic arm and supporting both autonomous and remote-controlled modes, Fortuna enhances operational flexibility while reducing mission costs. This combination of features makes Fortuna an optimal candidate for sustainable surface exploration and long-term human presence on planetary surfaces.

Introduction

DIANA (Ducti Ingenio Accipimus Naturam Astrorum) was born in 2008, in Politecnico di Torino, prompted by the AMALIA project, a space-grade rover, aiming at participating in the Google Lunar X-Prize and land on the Moon.

In 2015, the team shifted its focus to student competitions, with project TO-RO the team had the opportunity of participating in its first rover series competition. In 2019 a new rover, TRINITY, was presented and from 2021 to 2024 ARDITO was built but it had reached it's operational limit, taking into consideration past experiences and valuable advices given by the judges, DIANA has decided to design a brand new rover.

FORTUNA (Fortuna Operans Res Terrarum Universi Navigatio Astrorum) is DIANA's latest prototype of a robotic space rover aimed at student competitions. It is a brand new concept of rover for the team, being a lightweight and agile platform, able to quickly overcome obstacles and manipulate objects, rocks, and regolith.

Content from this work may be used under the terms of the Creative Commons Attribution 3.0 license. Any further distribution of this work must maintain attribution to the author(s) and the title of the work, journal citation and DOI. Published under license by Materials Research Forum LLC.

Materials Research Proceedings 69 (2026) 1563-1567 https://doi.org/10.21741/9781644904251-274

FORTUNA is an end-to-end project developed in STARLab [3], the team was required to design a full platform of a space rover prototype while following ERC requirements. This approach is consistent with the team's philosophy of using as much in-house solutions as possible and keeping a close eye to the space industry. The whole project is being followed by a group of system engineers that ensures the compliance of the project with all requirements and performs functional analysis based on ERC tasks.

Design Approach

From an early stage, a V-Model [4] approach was adopted for the FORTUNA project. This model describes a clear representation of the sequence of steps that have been taken during the project life-cycle development. At the beginning of the year, a project timeline has been defined to schedule the major project tasks, outlining the progression from the design phases to integration and testing. Following the ECSS Standards [5] (ECSS-M-ST-10C Rev. 1), several milestones have been set to monitor the progress of the main activities and their completion: the Preliminary Design Review (PDR) for the evaluation of consistency between the preliminary design and system requirements, the Critical Design Review (CDR) to confirm that the design is at stable point meeting the technical requirements in order to proceed to the manufacturing phase, the Qualification Review (QR) for the system validation under specific operational conditions and the Operational Readiness Review (ORR) to determine the readiness of the Rover for operations and mission execution.

Throughout all the project phases, a dedicated group of System engineers is responsible for ensuring the compliance with the requirements defined at the beginning and conducting a first assessment of the risk analysis. Due to time constraints and a strict timeline the V-model was adopted without much possibility for many iterations. A dedicated group of system engineers followed the project from its early-phase, using ERC Appendix 3 and rule-book as stakeholder needs to write all Rover requirements following the ECSS Standards.

FORTUNA's requirements have been divided into:

- Mission
- Functional
- Interface
- Physical
- Environmental
- Operational
- Design
- Configuration
- Human Factors

FORTUNA Design

Together with requirement definition a Concept of Operations (ConOps) study and a Functional Tree were developed. The functional analysis aimed to create a list of every function the rover must perform in order to complete all the assigned tasks. A function-equipment matrix was also made, which assigns to each rover function its assigned equipment. This approach is crucial to identify mission critical equipments and to enable the early implementation of redundancy where needed. All system engineering work was done during concurrent engineering sessions during which Functional Table, ConOps and requirements were updated simultaneously.

FORTUNA's mobility system is based on a double-bogie configuration composed of four independent driving wheels made of a TPU outer skin and an aluminum alloy outer plate. The system is composed of two mirrored structures made of carbon tubes profiles joined with aluminum plates and structural glue. At both ends of each mobility are placed steering BLDC MyActuator motors with an integrated control board. The two halves of the mobility system are linked together through a differential system that allows the rover to safely overcome obstacles up to 250 mm while maintaining the stability of the rover. The two bogies are connected through a dual-pivot differential system, increasing the available volume within the avionics module while significantly reducing the overall system mass. To ensure the rover's capacity to overcome obstacles the whole system has been validated and simulated through various runs on HEXAGON ADAMS [6] software. COSMOS is the software module responsible for managing the rover's

Materials Research Proceedings 69 (2026) 1563-1567 https://doi.org/10.21741/9781644904251-274

mobility, receiving as input a target linear velocity and steering angle and processing them through algorithms that calculate, in real time, the optimal velocity and steering angle for each actuator. Since each wheel is powered by independent motors, COSMOS can assign different commands to each wheel, enabling complex and adaptive maneuvers. The system supports multiple operational modes designed for specific locomotion scenarios. The Idle mode sets the rover in a static state, while the new Translation mode allows motion in any direction with fixed orientation, enhancing maneuverability. For curved paths, COSMOS implements Ackermann and Double Ackermann modes based on Ackermann steering geometry. The single Ackermann mode replicates car dynamics, while the Double Ackermann mode, with all four wheels steerable, improves precision; the Spinning mode allows rotation in place. COSMOS ensures full and flexible mobility control by selecting the proper mode and calculating individual wheel commands.

The Avionics bay [7] is designed to pack all the main platform avionics into a single compact structure. All the control logics are fitted into a 9U CubeSat form factor box, designed with handles to be easily swappable in case of malfunctions, with two identical avionics bays prepared to hot-swap if needed. The battery is placed under the avionics bay to lower the center of mass, and a payload interface plate at the back provides power, data, and structural connections. The structure, made from folded aluminum sheets (Al5754), ensures strength and lightness, while the PMU controls all subsystems, allowing remote shutdowns through the CAN-bus line. The Raspberry Pi 5 and Jetson ORIN Nano handle communication, control, and AI tasks, with STM32 H7 boards running FreeRTOS for a more robust firmware system.

DIANArm Mk2 is FORTUNA's six-degrees-of-freedom robotic arm, enabling interactions such as grabbing objects, using tools, and collecting samples. It is made from carbon fiber tubes joined by aluminum plates and 3D printed parts, with each joint actuated by BLDC Cubemars motors with integrated control boards and mechanical reduction for torque and precision. The control logic is stored in the avionics bay, all boards and motors communicate through CAN-bus, and the total weight has been reduced to 8 kg, with improved accuracy for manipulation and autonomy. The Arm Control Unit runs FreeRTOS and the GrippyGrabby logic offers four control modes, while AUTOGrabby and SISMA provide autonomous operation through AI-based detection and trajectory planning with fail-safe mechanisms. The End Effector, made of CNC-machined aluminum plates, includes sensors, camera, TOF sensor, and Dynamixel motor driving a differential mechanism, with modular TPU fingertips for grasping and tactile feedback.

The main structure of a Deep Sampler consists of a precision linear guide with a worm screw actuated by a stepper motor, allowing the sampling mechanism to rise and lower by activating the screw. Collected sand is stored and weighted in a separate 3D printed container at the bottom of the structure, enabling safe deep sampling operations up to 30 cm. The payload is mounted on the back of the rover using aluminum profiles, with an additional thicker 20x40 mm profile added for structural integrity and stress reduction. As with all other rover payloads, the Soil Sampler carries its own control logics and connects to the Main On-Board Computer through CAN-bus communication as defined in the interface document.

Materials Research Proceedings 69 (2026) 1563-1567 https://doi.org/10.21741/9781644904251-274

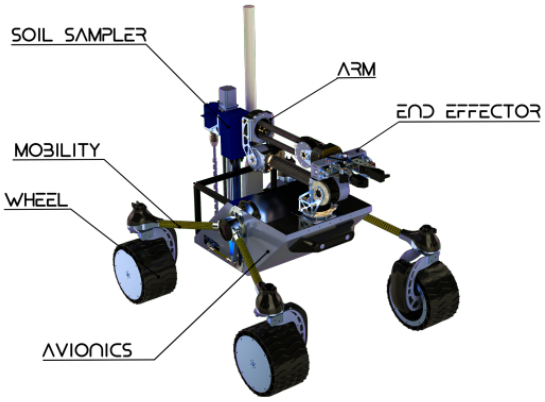


Figure 1: FORTUNA Rover

Test Approach

A well-structured test verification plan employs a layered approach. Four types of test have been defined in order to cover each phase of the FORTUNA project. After the Design Validation team undergoes a temporary reorganization into cross-functional groups focused on integrating and testing specific systems.

FORTUNA Design (DEV): This first layer is the Design Validation, conducted internally by each department. During the development stages, each component is verified independently, with a different strategy according to its nature: mechanical structures are mainly validated through FEM analysis and discussions with our suppliers; electrical hardware undergoes analyses and breadboard testing; software is tested during development, following a test-driven development approach. This kind of verification is crucial, but it is not formally included in the test plan, which accounts system and sub-system, leaving the departments dealing with components validation. This approach ensures a more balanced distribution of validation responsibilities among technical development leaders and the test manager.

Reduced Functional Tests (RFT): This kind of tests have a threefold function:

- Validate the system once integrated;
- Acting as a control point, verifying essential functions before proceeding with more extensive testing;
- Verify rover state after a system upgrade or a transportation.

This test has to be performed once the Rover has been integrated and the components are already verified. To understand the status of each system tests are performed excluding as much as possible dependencies from other part of the Rover. The goal of this layer is to obtain full knowledge regarding the system's operative status.

Full Functional Tests (FFT): Full Functional Tests will be performed once the Rover is stable to assess the correct integration of FORTUNA and its payloads in each configuration. These tests can be performed in non-operative conditions and has to cover every function of the Rover.

Mission Test (MST): Finally, mission-oriented tests simulate real task scenarios, providing a comprehensive check of the system's performance under realistic conditions. These tests will be conducted both in a simulated martian scenario in collaboration with ALTEC S.p.A [8].

(Aerospace Logistics Technology Engineering Company), a sponsor of the Team which grants the access to their facilities, and on the newly developed SimVISION simulator.

Acknowledgement
This work was conducted within the environment of the student team DIANA from Poltecnico di Torino.The authors express their gratitude to the whole team for their hard work and to the Politecnico di Torino's funding commission for allowing us to work on and develop the project.

References

[1] L. Caraccio, A. Dellacasa, N. di Gruttola Giardino, L.M. Festa, T. Galliano, G. Gorgerino, A. Meloni, F. Mustich, F. Stesina, "ARDITO, a modular technology demonstrator for robotic planetary surface exploration and operational support: an overview," in IEEE Aerospace and Electronic Systems Magazine.

[2] F. Mustich, L. M. Festa, F. Stesina, and R. Camoriano, "Point cloud-based reinforcement learning for autonomous navigation of a robotic rover on planetary surfaces," in IAC 2023, Baku, Azerbaijan: IAF Astro, 2023.

[3] F. Stesina and S. Corpino, "Star laboratory at politecnico di torino: A facility to develop educational space projects," IFAC-PapersOnLine, vol. 54, no. 12, pp. 80-87, 2021, IFAC Workshop on Aerospace Control Education WACE 2021. https://doi.org/10.1016/j.ifacol.2021.11.013

[4] G. Polvani and L. M. Festa, "Implementing agile management in space robotics university project: The ardito rover case study," in IAC 2025, Sydney, Australia: IAF Astro, 2025. https://doi.org/10.52202/083102-0047

[5] ECSS. (2018). Space engineering - Verification. ECSS (European Cooperation for Space Standardization)

[6] Hexagon MSC Software, MSC ADAMS, https://hexagon.com/it/products/productgroups/computer-aided-engineering-software/adams

[7] N. di Gruttola Giardino, F. Fantastico, L. M. Festa, G. Gorgerino, F. Mustich, F. Stesina, and E. Vacchetto, "A modular avionics architecture for a planetary rover demonstrator for human assistance," IFAC-PapersOnLine, vol. 58, no. 16, pp. 181- 186, 2024, 2nd IFAC Workshop on Aerospace Control Education - WACE 2024. https://doi.org/10.1016/j.ifacol.2024.08.483

[8] L. Bramante, M. Deffacis, D. Bussi, M. Barrera, C. Picco, and P. Franceschetti, "The mars terrain simulator: A high level measurement facility in support to the exomars mission," Turin, Italy: IEEE, 2019. https://doi.org/10.1109/MetroAeroSpace.2019.8869653

Materials Research Proceedings 69 (2026) 1568-1573 https://doi.org/10.21741/9781644904251-275

Ontology-Assisted Aircraft Cabin Design: A Data-Driven Approach Using Language Models

Raghu Chaitanya MUNJULURY[1,2,a *], Jorge LOVACO[1,b], Ludvig KNÖÖS FRANZÉN[1,c], Petter KRUS[1,d]

[1]Department of Management and Engineering, Linköping University, Olaus Magnus väg, Linköping, Sweden

[2]Saab Aeronautics, Bröderna Ugglas gata, Linköping, Sweden

[a]raghu.munjulury@liu.se, [b]jorge.lovaco@liu.se, [c]ludvig.knoos.franzen@liu.se, [d]petter.krus@liu.se

Keywords: Large Language Models, Ontology, Aircraft Conceptual Design, Cabin Design, Geometrical Design, CAD, Knowledge-based Engineering, Singular Value Decomposition

Abstract. A method for generating an aircraft cabin from Large Language Models (LLM), ontology, and Singular Value Decomposition is presented in this paper. An initial aircraft outer geometry from previous work is used as a starting point for the concept generation of the cabin design. ChatGPT, Claude, and Copilot were used to generate the initial ontology of the aircraft cabin along with requirements, functions, and design alternatives. The ontology is refined through chain-of-thought prompting and later modified to obtain the required ontology. The data of the aircraft cabin was also collected similarly and used in the Singular Value Decomposition (SVD). Because ontology representations have limited numerical computation capabilities, the collected data are processed with SVD to obtain quantitative estimations. Statistical analysis further enriches the knowledge extracted from the ontology. A case study validates the proposed methodology by generating a cabin configuration that satisfies the stated requirements.

Introduction

Passenger aircraft design is a complex and multidisciplinary task that involves the integration and consideration of numerous systems, requirements, and constraints. The need for tools that can manage such complexity grows together with the demand to find more efficient and sustainable solutions. The recent rise of LLMs, as well as an increasing interest in semantic technologies, introduces new opportunities for improving and evolving the existing procedures of today in the search for new solutions.

Among the many subsystems involved in the design of large passenger aircraft, the cabin plays an important role that often determines the required fuselage dimensions and influences the aircraft layout. The cabin is often one of the very starting points in an aircraft sizing procedure [1] and involves considering the trade-offs while balancing regulatory requirements with spatial constraints and passenger-centered considerations. The purpose of this paper is to present a method that utilises LLMs, ontology, and statistical SVD analyses for ultimately generating aircraft cabin design concepts. The method thereby enables quick evaluations and trade-off analyses of different aircraft cabin concepts.

A case study for the cabin design of a conventional large passenger aircraft is used to illustrate the various steps of the presented method. Finally, an outlook on possible future improvements of the said method is presented.

Content from this work may be used under the terms of the Creative Commons Attribution 3.0 license. Any further distribution of this work must maintain attribution to the author(s) and the title of the work, journal citation and DOI. Published under license by Materials Research Forum LLC.

Materials Research Proceedings 69 (2026) 1568-1573 https://doi.org/10.21741/9781644904251-275

Theoretical Background

This section gives a brief theoretical background for the foundational principles used in the proposed method of this paper. The presented work is an extension of the work performed in [2], which describes a method by which an ontology description can be used to generate a geometrical representation of a concept aircraft. Consequently, this previous work forms the foundation for the present study; therefore, background related to Ontology, Matrix of alternatives, Interactive Reconfigurable Matrix of Alternatives (IRMA) and SVD, Effective Parameterisation for Geometry Build-up can be referred to the previous paper [2].

Aircraft and Cabin Design

Aircraft Interiors are a major component of the Aircraft Design process. Cabin space should be used intelligently to maximise its potential, to identify and incorporate factors that contribute to passenger comfort, and to accommodate the required maximum number of passengers. The design of the cabin complies with FAR 25 regulations.

Large Language Models

Based on advanced forms of Statistical Language Models, Large Language Models the estimated likelihood of words appearing in a given sequence [3]. Different forms of machine learning have been used over the years, including recurrent neural networks or reinforcement learning [4]. The result is a Large Language Model that undergoes training with feedback, reducing the output error to a value close to, but never equal to, zero, in accordance with the *Universal Approximation Theorem*.

Method

This section introduces and explains the method for generating aircraft cabin concepts based on the foundational principles mentioned in the previous section. An illustration of the method and corresponding steps is shown below in Figure 1. The method is intended to apply to domains other than just aircraft cabin design and has therefore been kept agnostic to promote reuse in other engineering endeavours. LLM is used to generate an initial ontology with entities and relationships from the desired domain. The ontology can, from there, be expanded or modified based on the initial requirements to give a desired and correctly structured knowledge representation. Description logic reasoning can help ensure that the ontology is consistent and logically sound. Once the desired ontology is established, information about, for example, functions and design alternatives can be extracted and used to create more common and condensed conceptual design tools for added decision support, such as a matrix of alternatives, or a more advanced IRMA as shown in [2]. The outcome of the ontology part in Figure 1 is a qualitative description of the generated concept's characteristics.

As ontologies are limited in terms of numerical calculation capabilities, a parallel track with numerical data generated through an LLM and later processed with SVD is seen in Figure 1. The SVD model is used on the numerical data to give initial quantitative estimations of the intended concept based on the most important requirements for the design in question. Here, Quality Function Deployment (QFD) is a means for prioritising requirements if needed. Ultimately, the outcome from the SVD analysis is numerical estimations for the intended concept properties based on statistical data. The qualitative estimations from the ontology and the quantitative estimations from the SVD analysis can be synthesised into a complete initial estimate of the concept. The concept must be verified against the requirements and adjusted or negotiated if it does not meet them.

Materials Research Proceedings 69 (2026) 1568-1573 https://doi.org/10.21741/9781644904251-275

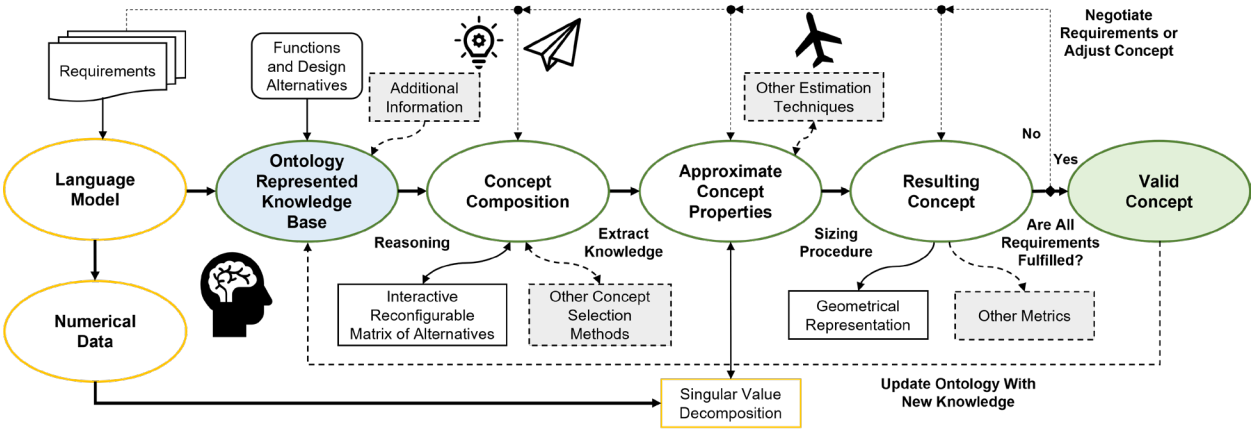


Figure 1 An illustration of the presented method and its corresponding steps.

Use Case: Aircraft Cabin Design

This section describes how the proposed method from Figure 1 is used to generate an initial aircraft cabin design based on basic requirements.

LLM-based Ontology Creation and Usage

The ontology used in this case study was initially generated with LLM. The ontology has thereafter been refined in the Protégé ontology editing software [5] to include proper relationships between cabin design functions and their potential design alternatives. The ontology also includes a hierarchy of general cabin design considerations and components. These range from basic considerations such as cabin seating arrangements to amenities such as potential entertainment systems. Figure 2 shows an extract of the used ontology. As shown on the right-hand side of Figure 2, the Seating Alternatives individual has three object property assertions linking it to three different design alternatives through the hasAlternative relationship. A similar structure is applied to all function individuals within the ontology to establish the connections to their respective design alternatives. Consequently, the ontology acts as an overarching knowledge base for the cabin design procedure and may also include potential incompatibilities between design alternatives.

LLM-based Numerical Data Collection

The numerical dataset was generated through data retrieval using state-of-the-art models (GTP-5 and Claude). The input prompt used with both models was: “Make a table of Figure 2 – The ontology class hierarchy (left) and the definition for a Seating Alternatives individual (right). Aircraft name, Manufacturer, Passenger capacity, No. of seating classes, No. of seats in First, Business and Economy classes, No. of lavatories, No. of galleys, No. of aisles and No. of exists for the following aircraft” followed by a list of aircraft available from a single manufacturer. It was noticed, during the process that mixing manufacturers in the prompt led to misleading data due to the issues of hallucination that these kinds of models still experience even after their latest improvements [6]. The data generated when requesting a single manufacturer in the prompt was of good quality, yet not completely correct and still requires human review.

Materials Research Proceedings 69 (2026) 1568-1573 https://doi.org/10.21741/9781644904251-275

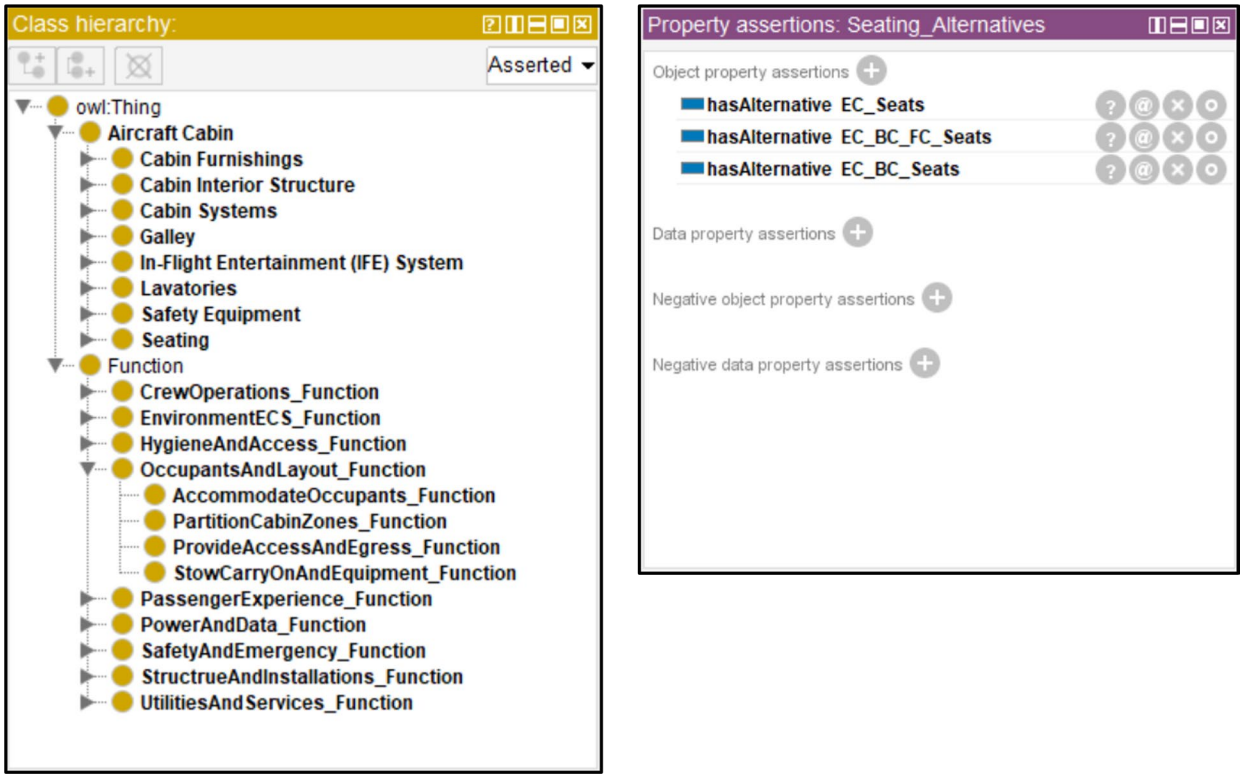


Figure 2 The ontology class hierarchy (left) and the definition for a Seating Alternatives individual (right).

Singular Value Decomposition Analysis

The generated numerical data was converted into logarithmic values to gain a more linear model structure for the SVD analysis [7]. The analysis itself, and the required matrix operations, were performed using an Excel-implemented macro. The outcome of this macro is an SVD model with determined SVD-variables [2]. If the model is used to predict the values for an Airbus A220 by using only 2 variables (3rd-rightmost column for reference), and the model inputs are respectively 132 passengers and 2 seating classes, it can be seen in Figure 3 that the predictions show a relative error of 63% (2nd-leftmost column) with respect to the estimated values by the model (4th-leftmost column). This is due to the higher number of 3-class aircraft in the dataset, which skews the prediction. If the same procedure is done again but only using 2-class aircraft for generating the SVD model, the relative error is drastically reduced to 37% as shown in Figure 4.

	Rel error	A220-300	Estimate	Adjusted	Result	Average										SVD variables	w-diagonal
Passenger Capacity	0.05	132.00	125.80	2.10	-0.22	2.32	-0.159	0.211	-0.041	0.012	0.012	0.000	-0.003	-0.004	0.000	3.00	43.51
No. of Seating Classes	0.02	2.00	1.95	0.29	-0.17	0.46	-0.055	-0.002	0.000	0.000	0.000	-0.001	0.000	0.000	0.000	1.22	4.31
First Class Seats	0.00	0.00	0.00	-15.81	-15.28	-0.53	-5.079	-0.035	0.000	0.000	0.000	0.000	0.000	0.000	0.000	0.00	1.29
Business Class Seats	0.63	12.00	19.52	1.29	-0.26	1.55	-0.170	0.203	0.049	0.059	-0.003	0.000	-0.017	-0.002	0.006	0.00	0.69
Economy Class Seats	0.07	120.00	111.27	2.05	-0.14	2.19	-0.141	0.227	-0.115	-0.007	-0.006	0.000	-0.001	0.001	0.008	0.00	0.12
No. of Lavatories	0.03	3.00	2.90	0.46	-0.25	0.71	-0.169	0.212	0.043	-0.042	-0.001	0.000	-0.021	-0.010	-0.035	0.00	0.01
No. of Galleys	0.14	2.00	2.28	0.36	-0.19	0.55	-0.148	0.210	0.044	-0.007	-0.001	0.000	0.036	-0.025	0.011	0.00	0.43
No. of Aisles	0.32	1.00	1.32	0.12	-0.01	0.13	-0.050	0.118	0.041	-0.029	0.001	0.000	-0.008	0.028	0.049	0.00	0.50
No. of Exits	0.04	6.00	5.79	0.76	-0.05	0.81	-0.061	0.114	0.011	0.009	0.000	0.000	0.020	0.044	-0.033	0.00	0.60
	0.63																

Figure 3 Model for prediction of aircraft cabin using two variables.

Materials Research Proceedings 69 (2026) 1568-1573 https://doi.org/10.21741/9781644904251-275

	Rel error	A220-300	Estimate	Adjusted	Result	Average						SVD variables	w-diagonal
Passenger Capacity	0.00	132.00	132.00	2.12	0.25	1.87	0.123	-0.161	0.005	-0.014	0.000	0.73	18.34
No. of Seating Classes	0.00	2.00	2.00	0.30	0.10	0.20	0.142	0.003	0.001	0.001	0.000	-1.01	0.83
Business Class Seats	0.16	12.00	10.10	1.00	5.42	-4.42	7.483	0.010	0.000	0.000	0.000	0.00	0.37
Economy Class Seats	0.01	120.00	121.74	2.09	0.24	1.84	0.105	-0.164	0.009	-0.012	0.000	0.00	0.06
No. of Lavatories	0.11	3.00	2.67	0.43	0.28	0.15	0.110	-0.194	0.056	0.014	0.000	0.00	0.00
No. of Galleys	0.37	2.00	2.73	0.44	0.18	0.26	0.080	-0.117	-0.136	0.006	0.000		
No. of Aisles	0.00	1.00	1.00	0.00	0.00	0.00	0.000	0.000	0.000	0.000	0.000		
No. of Exits	0.11	6.00	6.65	0.82	0.14	0.68	0.058	-0.098	0.030	0.007	0.000		
	0.37												

Figure 4 Unbiased model for prediction of aircraft cabin using two variables.

Concept Geometry Layout

The resulting concept is thoroughly evaluated against the requirements, ensuring its validity. The values of Passenger Capacity and Number of Seating classes obtained from the SVD are used in PreSTo (Figure 5 - Top) along with the previous values from outer geometry design [2]. The values for cabin layout from PreSTo are then imported to the Enhanced User Interface (Figure 5 - middle) and later exported to the Knowledge Based Engineering (KBE) tool RAPID [9] (Figure 5 - Bottom). Insights from the SVD analysis and geometrical sizing will be used to update the ontology and the corresponding individual with new data properties.

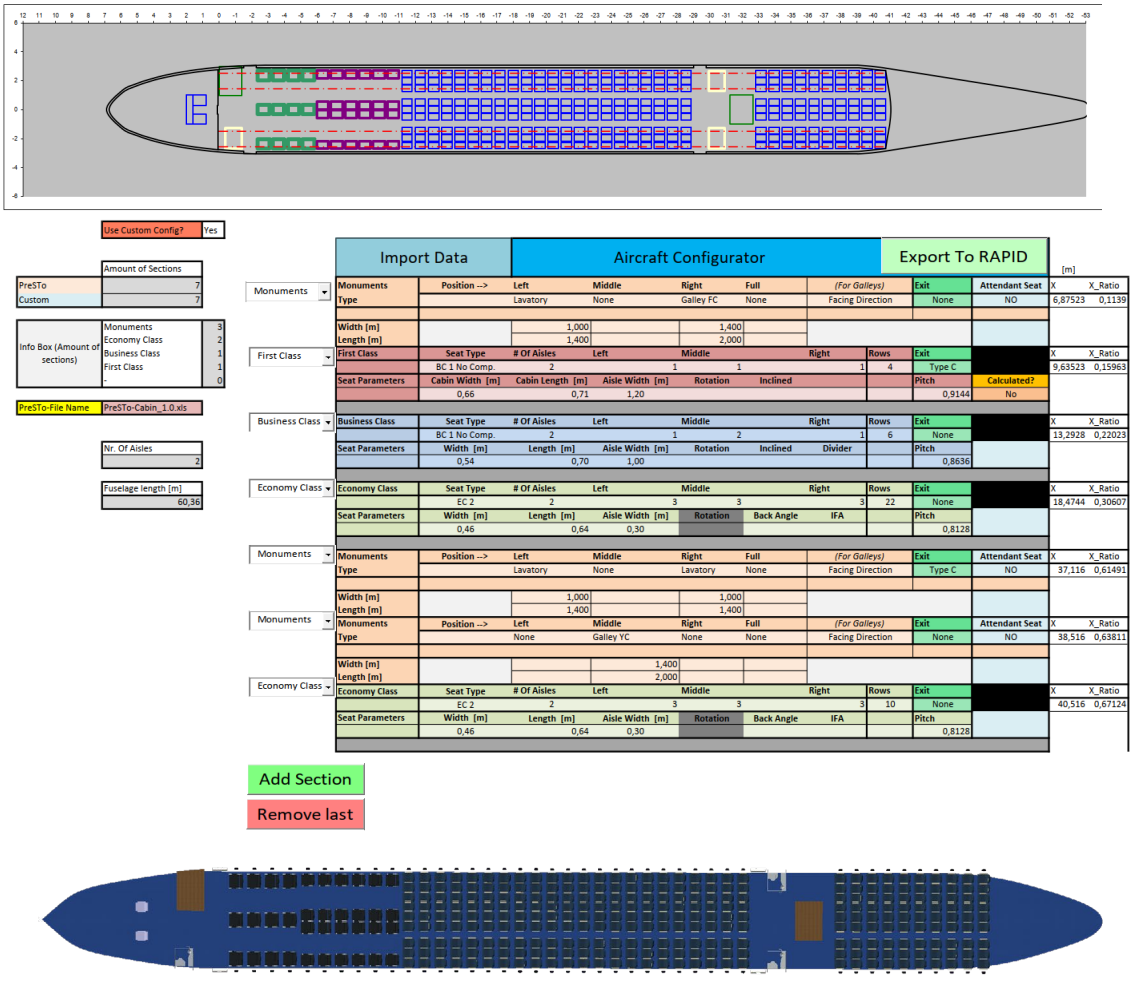


Figure 5 Representation of the results along with the flow process for a 3-Seating classes. Top to Bottom, Preliminary Sizing Tool (PreSTo), Enhanced user interface [8] and generated concept in Robust Aircraft Parametric Interactive Design (RAPID) [9], [10].

Conclusions and Outlook

In this paper, a method for generating an aircraft cabin using LLM, ontology, and SVD is presented. The extraction and enhancement of relevant information using approaches such as a statistical SVD analysis have narrowed down the number of parameters needed for estimation. The resulting information was used as input for an initial geometric sizing step that generated initial-sized versions of selected concepts using PreSTo and finally representing the 3-dimensional model of the aircraft in RAPID. The initial ontology generation produced difficulties in capturing the requirements, functions, and design alternatives, necessitating additional manual refinement. Further manual work was needed in updating the same. Knowledge graphs, combined with an AI agent, could replace much of the current manual effort. An AI agent specifically trained for Aircraft Concept generation and Cabin Design, would be valuable for both in research and academic applications.

References

[1] L. R. Jenkinson, P. Simpkin, and D. Rhodes, Civil Jet Aircraft Design. Reston, VA: AIAA Education Series, 1999. https://doi.org/10.2514/4.473500

[2] L. Knöös Franzen, R. C. Munjulury, and P. Krus, "Ontology-assisted aircraft concept generation", in 33rd Congress of the International Council of the Aeronautical Sciences, ICAS 2022, Stockholm, Sweden, 4-9 September 2022.

[3] C. E. Shannon, "A mathematical theory of communication", The Bell system technical journal, vol. 27, no. 3, pp. 379-423, 1948. https://doi.org/10.1002/j.1538-7305.1948.tb01338.x

[4] W. De Mulder, S. Bethard, and M.-F. Moens, "A survey on the application of recurrent neural networks to statistical language modeling", Computer Speech & Language, vol. 30, no. 1, pp. 61-98, 2015. https://doi.org/10.1016/j.csl.2014.09.005

[5] M. A. Musen, "The protégé project. a look back and a look forward", AI Matters. Association of Computing Machinery Specific Interest Group in Artificial Intelligence, vol. 1, no. 4, 2015. doi: 10.1145/2557001.25757003. https://doi.org/10.1145/2757001.2757003

[6] M. Leon, "Gpt-5 and open-weight large language models: Advances in reasoning, transparency, and control", Information Systems, p. 102 620, 2025. https://doi.org/10.1016/j.is.2025.102620

[7] J. Mandel, "Use of the singular value decomposition in regression analysis", The American Statistician, vol. 36, no. 1, pp. 15-24, 1982. https://doi.org/10.1080/00031305.1982.10482771

[8] F. Prokic, C. Eriksson, and R. C. Munjulury, "Design and visualization of a knowledge based aircraft cabin in virtual reality", in 34th Congress of the International Council of the Aeronautical Sciences, ICAS 2024, Florence, Italy, 2024, 2024.

[9] R. C. Munjulury, I. Staack, P. Berry, and P. Krus, "A knowledge-based integrated aircraft conceptual design framework", CEAS Aeronautical Journal, vol. 7, no. 1, pp. 95-105, 2016. https://doi.org/10.1007/s13272-015-0174-z

[10] R. C. Munjulury, Knowledge-based integrated aircraft design: An applied approach from design to concept demonstration. Linköping University, 2017, vol. 1853. https://doi.org/10.3384/diss.diva-137646

Materials Research Proceedings 69 (2026) 1574-1579 https://doi.org/10.21741/9781644904251-276

Development of a Flexible Flight Simulation Design and Test Environment

Peter THOMAS[1,a *] and Joanna RAWSKA[1,b]

[1]Department of Engineering, University of Hertfordshire, Hatfield, UK, AL10 9AB

[a]p.thomas5@herts.ac.uk, [b]j.rawska@herts.ac.uk

Keywords: Flight Simulation, Aircraft Design, Pilot Studies, Aircraft Modelling

Abstract. This paper describes the development and use of a new, flexible flight modelling and simulation environment based on Alsim's engineering pack simulation tool with their AL250 simulators, recently installed at the University of Hertfordshire. This capability provides the necessary performance and flexibility to support the university's aerospace engineering and pilot studies programmes, along with supporting the breadth of ongoing research activities. Two key developments are highlighted: pilot studies assessment, and a modelling framework for general fixed wing aircraft for design testing. Examples of research activities currently in planning and development are also briefly presented, including work on emission modelling for general aviation aircraft. The outcomes from these activities have had notable improvements on previous facility capabilities in all areas.

Introduction

Access to increasingly high-quality and higher-fidelity flight simulation environments is crucial for universities running aerospace degree programmes to be able to provide effective laboratories for active learning. A great amount of flexibility is often required to be able to utilise the same simulator for multiple different learning objectives and avoid the cost and space requirements of multiple specialised systems. This flexibility is also crucial for supporting research and development activities that could encompass investigations in topics ranging from human factors studies to flight control design and testing. The technical performance of many affordable flight simulators is now at the point where they are ubiquitous in most universities running aviation, pilot studies, or aerospace engineering degree programmes [1]. However, not all simulator offerings provide the necessary flexibility for all of these, in addition to requirements for research activity.

As part of a recent upgrade to new facilities the University of Hertfordshire (UH) has recently invested in three Alsim AL250 flight simulators. The AL250 is a reconfigurable single and twin engine piston FNPT II[1] aircraft simulator, designed to meet the training requirements of PPL/CPL/IR/MEP[2]. The cockpit multi-function displays can be switched between traditional instrumentation in a T arrangement and a conventional electronic flight instrument system (EFIS). The base flight models are notably accurate and whilst the simulators can be certified, of more interest to the university is the engineering design and analysis capabilities afforded by its 'engineering pack' (E-Pack) software. These features make it an increasingly attractive tool for many other universities. Waterloo University has used its AL250 extensively for eye tracking, cognitive load, and human factor studies since 2023 [2–5]. A variety of applications in taught programmes have already been explored at Nottingham [6] whilst Portapas [7], also at Nottingham, has used the AL250 with the E-Pack to implement a model of an eVTOL for both teaching and research applications. Such applications are similarly planned at UH throughout the undergraduate and postgraduate programmes. These activities have previously been achieved using a Merlin

[1] Flight and Navigation Procedural Trainer, Level II.

[2] Private Pilot License/Commercial Pilot License/Instrument Rating/Multi-Engine Piston (rating).

Content from this work may be used under the terms of the Creative Commons Attribution 3.0 license. Any further distribution of this work must maintain attribution to the author(s) and the title of the work, journal citation and DOI. Published under license by Materials Research Forum LLC.

Materials Research Proceedings 69 (2026) 1574-1579 https://doi.org/10.21741/9781644904251-276

MP520 and X-Plane based simulators. The greater flexibility and accuracy of the AL250 enhances these activities through the integration with MATLAB/Simulink which is also taught throughout the degree programme.

System overview

Two of three AL250 simulators recently installed at the university, shown in Fig. 1, can send and receive data to and from a MATLAB/Simulink client operating from a networked computer running the E-Pack software. This is achieved with a network datastore that acts as a CAN bus to share and push data between each of the simulator's subsystems. This includes, when connected, the client running the MATLAB/Simulink E-Pack software. The E-Pack is implemented as MATLAB and Simulink toolboxes that facilitate the communication with an AL250 unit and its various subsystems. As many of the data variables driving the simulator can be read from and/or sent to the simulator a substantial variety of applications is possible: from simple data logging to flying completely new, bespoke aircraft flight and systems models. Administrators access the simulator configuration controls through an instructor station whilst pilots may access similar controls, particularly for flight data recording, via a tablet device in the flight deck which also serves as an electronic flight bag (EFB).

The simulators have three primary use cases: i) pilot studies training and assessment, ii) aircraft design simulation, iii) research applications. Each of these is briefly discussed in the subsequent sections.

Pilot studies assessment

A pilot studies pathway of aerospace engineering is offered to undergraduate students who, in addition to core modules on all aerospace engineering pathways, undertake specialised pilot studies modules in topics such as air law, navigation, meteorology, planning, communications, flight performance, avionics, and human factors. Graduating from the programme requires completion of 20 hours of flying (instructed or solo). The flight simulation facilities at the university have long been used to allow students to develop confidence and skills to support this, in addition to more authentic sessions and assessments. This is enhanced with the new flight simulators which provides a highly accurate flight model, high-fidelity flight deck and controls, and easier access to data logging commands through the EFB.

An example of one of the more complex assessments on the programme is a flight planning exercise requiring students to plan a route via multiple local waypoints, including two short-stop landing/takeoffs, avoiding class D airspace (Fig. 2). Students must then fly a minimum 20 nautical



Figure 1. Alsim AL250 simulators.

Materials Research Proceedings 69 (2026) 1574-1579 https://doi.org/10.21741/9781644904251-276

mile portion of this route to demonstrate sufficient flight control and navigation skill. A significant enhancement with the AL250 compared to previous simulators is an integrated, physical GPS navigation unit for the students to use.

Other notable enhancements with the AL250 simulators are greater weather setting controls and a higher fidelity flightdeck which provides a more realistic environment for radio communication lessons and tests (Fig. 3). This enables both the actual flight and radio equipment to be used as part of the assessment to enhance the training transfer.

Aircraft design tool

Many aerospace degree courses will incorporate some form of aircraft design capstone project [8–11]. One of the fundamental aims of this kind of project is to replicate the industrial working environment of (and subsequently build students' skills and confidence in) cooperative design and systems integration. Consequently, these projects are typically undertaken as group work which reflects the nature of industrial work. An important element of the design process, or more generally as part of the feedback loop for developing students' knowledge and understanding, is for students to quickly generate a flight model of their design to analyse and evaluate it.

Fast generation of flight models from preliminary design parameters is a relatively mature topic owing to the wealth of knowledge and information on this topic. As such, there is a wide variety of methodologies that can be programmed to generate these flight models (Fig. 4), which trade accuracy for complexity and timeliness. The requirements of a tool for student-focused aircraft design activities are:

1. Fast generation of flight models from a basic geometry and mass specification.
2. Generation of simulated flight data to support performance, stability, and control analysis.

High fidelity models are not crucial for this task so analytical and semi-empirical models for computing the aerodynamic and stability parameters can be readily computed in MATLAB/Simulink for easy implementation with the E-Pack software. This is being done using methods from DATCOM, ESDU datasheets, and various well-known texts [12,13] to create a general template to model a generic fixed wing aircraft.

For example, Fig. 5 shows an electric-powered acrobatic aircraft designed by one group of students on the final year capstone group design module. In previous years we have used parametric modelling tools using a Merlin MP520 two-axes motion simulator and/or X-Plane software, both requiring some geometric data as well as propulsion performance data. Propulsion

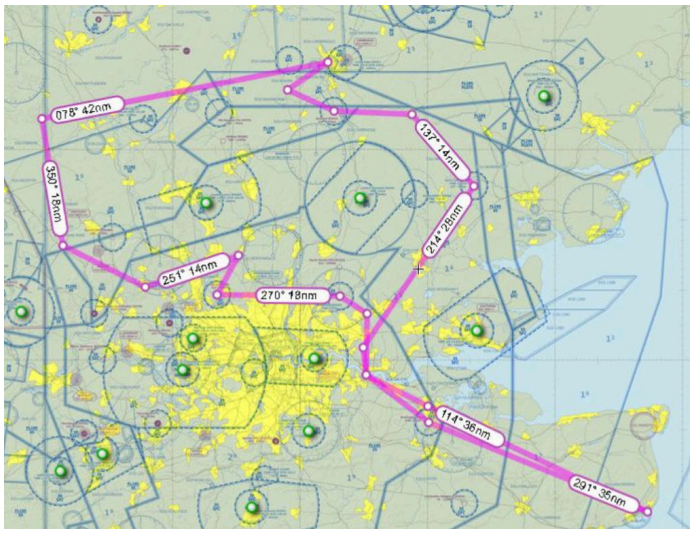


Figure 2. Example flight planning exercise.

Figure 3. Radio communication test.

Materials Research Proceedings 69 (2026) 1574-1579 https://doi.org/10.21741/9781644904251-276

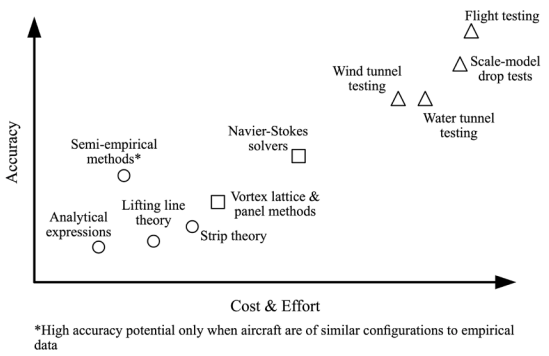


Figure 4. Aerodynamic model estimation methodologies.



Figure 5. Example design from the capstone aircraft design module: A two-seat sport electric aircraft.

system models with these systems were limited to conventional types (piston and gas turbine-based), with limited capability of electric propulsions systems in X-Plane. With the flexibility offered by the MATLAB/Simulink environment detailed models of more modern and advanced propulsion systems can now be explored and implemented. This includes more comprehensive modelling for batteries and hydrogen-based fuel cell systems for a variety of electric and hybrid propulsion models. This is in addition to the capability of modelling more complex systems, e.g., variable cycle engines.

The use of MATLAB/Simulink also means that higher fidelity models and different vehicle configurations with the design tool can be supported with an inherent modularity in its implementation. Additional functionality is planned as future module updates.

Research applications

Research capabilities with the new AL250 simulators include:

1. Nonlinear and unconventional configuration flight dynamics modelling.
2. Control inceptor evaluation.
3. Human-machine interaction studies.
4. Flying and handling qualities evaluation.
5. Flight control design and analysis.
6. Designing flight recovery techniques.

Most of these rely on the flexible modelling and data-reading functionality provided by the E-Pack software. The use of the simulators to enhance two example research projects are described below.

In the first example, an autonomous take-off system is implemented as an assistive autopilot. Such a system has potential applications in autonomous short takeoff/landing aircraft and in single pilot operations. A section of the system is presented in the Stateflow state machine of Fig. 6. This is combined with a low-level attitude autopilot as well as a thrust asymmetry control law which regulates the lateral deviation in engine-out scenarios. This system has been assessed in a purely software environment but the added benefit of running it on the AL250 simulator, via the E-Pack, means the human interaction with the system can be evaluated through the representative flight deck and autopilot panel controls.

The second example relates to the modelling of aircraft emissions of fixed wing aircraft to support a research project in the decarbonisation of general aviation airports. The project aims to define the exemplar framework for small airfields to approach and achieve decarbonisation and sustainability targets through a variety of approaches. One approach is better understanding and management of airfield emissions from the aircraft that operate from it, which are predominately

training school flights. One approach to emission modelling is to consider the fuel consumption multiplied by the specified emission species index. To achieve a baseline model a set of simulated training sorties are flown in the AL250 simulator, with the fuel consumption extracted and recorded through the E-Pack. In particular, the fuel consumption at different phases of flight is obtained from the simulated aircraft and used to obtain flight phase benchmarks for the emissions. Fig. 7 illustrates the simulated fuel consumption and mass of various emission species (carbon monoxide, CO; carbon dioxide, CO_2; Hydrocarbons, HC; Nitrogen oxides, NO_x) throughout a circuit for a twin-engine aircraft flight model, using emissions factors derived from [14]. The trends are consistent with experimental measurements from literature [14,15]. The data is also useful to compare the accuracy of metamodels that rely solely on flight hour date from trainer flights.

Conclusions

An overview of recent developments and uses with Alsim AL250 flight simulators in university taught and research programmes has been presented. These simulators provide improvements and capabilities for the three key uses: i) pilot studies assessments, ii) modelling for aircraft design activities, and iii) a wide range of research activities. Examples of these have been presented. The greater fidelity of the simulated flight deck environment, along with the wide-ranging capabilities from the MATLAB/Simulink E-Pack, has enabled more authentic piloting assessments, more

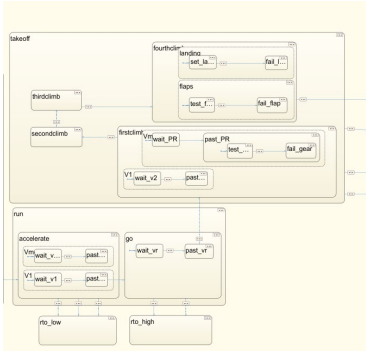


Figure 6. Section of a Stateflow model for the autonomous takeoff system.

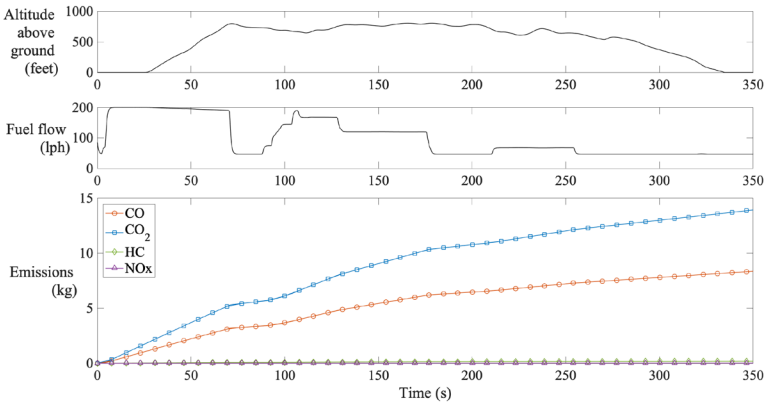


Figure 7. Estimated emission profile during simulated flight (fully rich mixture).

detailed aircraft system modelling capabilities, and more accurate simulation environments for research, compared to previous facilities. This is achieved in a smaller footprint than previously possible due to the flexibility of the Alsim simulators.

References

[1] D. J Allerton, The impact of flight simulation in aerospace, The Aeronautical Journal, 114(1162), 2010, pp. 747–756. https://doi.org/10.1017/S0001924000004231

[2] N. Ayala, D. Mardanbegi, A. T. Duchowski, E Niechwiej-Szwedo, S. Cao, S. Kearns, E. Irving, On The Visibility of Fiducial markers For Mobile Eye Tracking, Symposium on Eye tracking Research and Applications, 2023, 30 May–02 June, Tubingen, Germany, pp. 1–7. https://doi.org/10.1145/3588015.3588413

[3] N. Ayala, S. Kearns, S. Irving, C. Cao, E. Niechwiej-Szwedo, Investigating the role of flight phase and task difficulty on low-time pilot performance, gaze dynamics and subjective situation

awareness during simulated flight, Journal of Eye Movement Research, 17(1), 2024, pp. 1–27. https://doi.org/10.16910/jemr.17.1.6

[4] C. M. Calderon, J. Bae, S Cao, M. Barnett-Cowan, Navigating simulator sickness: The effect of flight maneuvers in fixed-base flight simulators. Proceedings of the Human Factors and Ergonomics Society Annual Meeting, 68(1), 2024, pp. 1674–1679. https://doi.org/10.1177/10711813241260681

[5] N. Ayala, A. Lynch, E. Irving, S. Kearns, S. Cao, E. Niechwiej-Szwedo, M. Barnett-Cowan, Towards real-time assessment of cognitive demands using gaze dispersion in an aviation landing task. Symposium on Eye tracking Research and Applications, 2025, 26–29 May, Tokyo, Japan, pp. 1–7. https://doi.org/10.1145/3715669.3726852

[6] F. Biertunmpfel, C. Annon, H. Pfifer, Hands-on flight dynamics and controls teaching using flight simulators, IFAC PapersOnLine 58-16, 2024, pp. 241–246. https://doi.org/10.1016/j.ifacol.2024.08.493

[7] V. Portapas, Developing Alsim AL250 based eVTOL flight simulator, Aviation, 29(1), 2025, pp. 39–47. https://doi.org/10.3846/aviation.2025.23167

[8] S. J. D'Urso, An Example of Industrial Interaction with Undergraduate Aircraft Design Program, AIAA Aircraft Design Systems and Operations Meeting, 1991, 23-25 September, Baltimore, Maryland, USA, pp. 1-18. https://doi.org/10.2514/6.1991-3116

[9] R. M. Cummings and D. W. Hall, STOL Aircraft Design for Undergraduates, Biennial International Powered Lift Conference and Exhibit, 2002, 5–7 November, Williamsburg, Virginia, USA, pp. 1–5. https://doi.org/10.2514/6.2002-5998

[10] C. Jouannet, P. Berry, and P. Krus, Aircraft design education at Linköpings University, Proceedings of the Institute of Mechanical Engineers, Part G: Journal of Aerospace Engineering, 221(2), 2007, pp. 217–224. https://doi.org/10.1243/09544100JAERO131

[11] S. Esteban and M. R. Arahal, Project Based Learning Methodologies Applied to Large Groups of Students: Airplane Design in a Concurrent Engineering Context, IFAC-PapersOnLine 48-29, 2015, pp. 194-199. https://doi.org/10.1016/j.ifacol.2015.11.236

[12] F. O. Smetana, Computer-assisted analysis of aircraft performance stability and control, McGraw-Hill, 1984.

[13] M. V. Cook, Flight dynamics principles: A linear systems approach to aircraft stability and control (3rd ed.), Butterworth-Heinemann, 2013.

[14] T. Rindlisbacher, Aircraft Piston Engine Emissions Summary Report, Federal Department of the Environment, Transport, Energy and Communications DETEC Federal Office of Civil Aviation FOCA Aviation Policy and Strategy Environmental Affairs. 0/3/33/33-05-033.022, 2007.

[15] J. Markowski, J. Pielecha, R. Jasiński, Model to assess the exhaust emissions from the engine of a small aircraft during flight, Procedia Engineering, 192, 2017, pp. 557–562. https://doi.org/10.1016/j.proeng.2017.06.096

Keyword Index

3D Modeling 9
3D Printing 106, 1260

A320 Flight Simulator 1475
AAM 314
Abrasion 1255
Absorption Coefficient 335
AC and DC Losses 751
Acoustic Liner 281, 325, 335
Acoustic Metacontinuum 54
Acoustic Metamaterial 293, 341
Acoustics Analogy 308
Acoustics 275
Active Flow Control 154
Active Vibration Control 1095
Actuator Saturation 794
Adaptive Control 366, 868, 874, 1083
Adaptive Geometry 418
Adaptive Weighting 42
ADCS 930
Added Mass 850
Additive Manufacturing 1260, 1310, 1402, 1444
ADS-B 2
Advanced Air Mobility (AAM) 94, 425, 1554, 1559
Advanced Tether Materials 1146
Advection Boundary Law 325
Aerial Physical Interaction 794
Aero Engines 583
Aeroacoustics 112, 281, 287, 308, 564
Aerodynamic Coefficients 418
Aerodynamic Drag 475, 846, 1131
Aerodynamic Model 839
Aerodynamic Performance 414
Aerodynamic Prediction 84
Aerodynamic Testing 880
Aerodynamics 100, 106, 119, 154, 221, 244, 260, 707, 827, 839, 966
Aeroelastic Analysis 1192
Aeroelasticity 352, 362, 370, 396, 402, 493
Aero-Propulsive Coupling 457
Aero-Propulsive Interaction 650
Aerospace Structures 1176, 1319
Aerospace Testing Principles 960
Ageing 572
Agent-Based Modelling and Simulation 88, 1544
Agent-based Simulation 94, 817, 856
Agile Methodologies 960
AI-Based Control 15
Air Injection System 275
Air Taxi 319
Air Traffic 522
Aircraft Capability Enhancing 431
Aircraft Concepts 442
Aircraft Conceptual Design 558, 1568
Aircraft Design 463, 469, 481, 487, 607, 666, 713, 1574
Aircraft Dynamics 1500
Aircraft Electrification 689
Aircraft Maintenance 21, 37
Aircraft Modelling 1574
Aircraft Navigation 2
Aircraft Noise 308
Aircraft Noise 346
Aircraft Operations 540
Aircraft Preliminary Design 504
Aircraft Separation Minima 199
Aircraft Sizing 448
Aircraft Subsystems 589
Aircraft Surface Inspection 37
Aircraft System Design 552
Aircraft Technologies 442

Aircraft 100, 106
Air-Defense 771
Airflow Compensation 765
Airfoil Performance 84
Airplane 100
Airport Infrastructure 662
Airship Design 846
Airship 833, 839
ALM 1438
Aluminium 1397, 1391
Analog Habitat 1505
Analytical Batch LSQ 891
Angle of Arrival (AOA) 1153, 1158
Angles-Only Relative Navigation 891
Anhedral Angle 331
Anode Layer Hall Thruster 747
Anomaly Detection 936
Anti-Windup Synthesis 794
ARCADIA 1505
Arc-Heated Wind Tunnel 177
Architecture 926
ARDITO 1407
Argon 747
Art. 114 TFEU 1487
Artificial Intelligence 558
Asteroid Exploration 1146
Astrodynamics 1059
Astronaut Training 9
Attention 1475
Attitude Determination and Control System (ADCS) 1153
Attitude 1153
Auralisation 346, 319
Automated Flight Test Procedures 457
Automated Flight Testing 650, 656
Automatic Architecture Generation 469
Automatic Tuning 874
Autonomous Mission Planning 1030
Autonomous Robotic Systems 960
Autopilot 868
Aviation Human Factors 1456
Aviation 510

Barrier Functions in Control 788
Batteries 730
Battery 589
Battery-Powered Flight 782
Bayesian Inference 1524
Bayesian Optimization 1220
BCC Lattice 384
BEMT 827
Bezier Curves 846
Bio-Based Energy 741
Biofilm 930
Blade Collectors 638
Blade-Vortex Interaction (BVI) 331
Boeing Fuel Flow Method 540
Booster Recovery 522
Boresight Stabilization 897
Boron-Containing Compounds 620
Boundary Conditions 1331
Boundary Layer Separation 112
Box-Wing 463
Breguet 666
Brillouin Spectroscopy 1391
BSK-RL Framework 1030
Buckling Mode-Switching 1246
Buckling 1347
Business Case 833
Business Models 1554
BVI Noise 331
BVI 287

CABARET Method 564
Cabin Design 346, 1568
CAD 1568

Calibration 130
Capella 1505
Carbon Nanotubes 1250
Carrera Unified Formulation (CUF) 267, 1171, 1181, 1192, 1210, 1215, 1220, 1240, 1347, 1353, 1358, 1387, 1416
Carreraâ€™s Unified Formulation 341, 1364
Certification By Analysis 493
CFD Validation 418
CFD 244, 314, 493, 534, 718
Chase Model 60
Chevron Nozzles 275
Circular Cylinder 211
Clean Aviation 516, 577
Climate Impact Assessment 481
Close-Proximity Operations 862
CO_2 Emissions 546
Cockpit Monitoring 1475
Code-Minus-Carrier 42
Collaborative AI 88
Collision Avoidance 1107
Collision Risk 1125
Combinatorial Optimization 771
Communication Clusters 1114
Communication 1544
Competitors 833
Compliant Wheels 1407
Component-Wise 1384
Composite Aircraft Wings 1192
Composite Design 1220
Composite Laminates 1246
Composite Materials 1240
Composite Structure 713
Composite Structures 713, 1204, 1298
Composite 1450
Compositeâ€¯Materials 1364
Compressible Flows 233, 375
Compressible Turbulence 239
Compression After Impact 1204
Compression 1246
Computational Analysis 125
Computational Fluid Dynamics (CFD) 66, 154, 205, 227, 260, 431
Computational Methods 112
Computer Vision 21, 72, 177
Comsol Multiphysics 335
Conceptual Design 954
Concurrent Engineering 499
Conjugate Heat Transfer 1412
Conjunction Assessment (CA) 948
Constellation Design 1125
Constellation Reconfiguration 1140
Constrained Control 788
Constrained Optimisation 1336
Constraint-Aware Optimization 1030
Continuum Damage Mechanics 1171
Control Loops 672
Convective Metasurfaces 54
Convolutional Neural Networks (CNN) 66, 1460
Cooperative Guidance 771
Copper Hairpin 751
Copper Wires 1341
Corona Discharge 632
Correlation Analysis 558
Correspondence Model 1422
Co-simulation 1537
Cost Analysis 546, 833
Cost Estimation 833, 1518
Counter-UAS Systems 856
Counter-UAS 1325
Counter-UAV Systems 499
Crack propagation 1427
CramÃ©r-Rao Lower Bound (CRLB) 1153, 1158
Cremer Impedance 325
Crosswind 913

Cryogenic Motor 751
CubeSat 701, 926, 930, 966
CUF 1176, 1298, 1369, 1384, 1450
Curvilinear Models 1304
Cyber-Physical Systems 1530, 1537

Damage Detection 1319
Damage Tolerance 1181
Data Analysis 1494
Data Augmentation 21
Data-Driven Optimization 846
DBSCAN 908
DC-3 352
DDPG 846
Debonded Structures 1292
Deep Learning 25, 37, 60
Deep Reinforcement Learning (DRL) 15, 942
Deep-Learning 48
Defense 856
Deflected Slipstream 800
Delamination 1171, 1204, 1287
Demand Estimation 94
Dent Detection 37
Deployable Structures 453, 1250, 1278, 1387
Design of Experiments (DOE) 436
Deterministic Excitation 1292
DfAM 1438
Differentiable Programming 78
Differential Flap Setting 136
Digital Image Correlation 1246
Digital Optics 21
Digital Twin Platform 1559
Digital Twin 9, 493, 1071, 1537
Dilution of Precision (DOP) 1158
Directed Acyclic Graph Scheduling 1530
Discontinuous Galerkin Method 390
Distorted Similitude 298
Distributed Electric Propulsion 457, 650, 656
Distributed Propulsion 564
Double Ailerons Wing 366
Double-Level Collectors 638
Doublet Lattice Method (DLM) 1192
Downwash Model 765
Drag Analysis 966
Drag Decomposition 254
Drag Reduction 119, 260
Drag 972
Drone Capture 765
Drone Swarms 856
Drone 822
Drones 314
Drop-Weight Impact Test 1229
Dry Wing 402
DSAR 1006
Dust Mitigation Technology 1374
Dynamic Analysis 303, 1278
Dynamic Derivatives 850
Dynamic Game Theory 1107
Dynamic Modeling 839
Dynamic Response 244
Dynamic Stall 418

EAD Thruster 632
Earth Observation 1054
Earth Orbit Rising (EOR) 1024
EB-PBF 1438
Eco-Design 677
Eddy Current Sensor 1095
Education 1500
EHD Atmospheric Propulsion 638
Elastic Properties 1391
Electric Aircraft 577, 757
Electric Excitation 757
Electric Propulsion 672, 782

Electric Vertical Take-Off and Landing (eVTOL) 331
Electrical Energy Storage System 589
Electrical Helicopter 782
Electrical Thrust 1024
Electrification 730
Electrochemical Performance 1432
Electron Beam Powder Bed Fusion 1165
Electronic Flight Bag 1471
Embedded Finite Elements 1314
Emission Estimation 1018
Energetic Assessment 481
Energy Analysis 250
Energy Decomposition 187
Energy Management 644
Ensemble Modelling 84
Entropy Conservative Fluxes 239
Environmental Control and Life Support System 1505
Environmental Impact 540, 546, 1018
Environmental Law 1077
Environmental Performance Improvement 442
Ephemeris Data Assisted Calibration 1131
Equivalent Sources 287
Error Compensation 1153
Error Divergence 1153
Error Modelling 1153
EU Space Act 1487
Eulerian Video Magnification 1225
European Space Policy 1487
eVTOL (Electric Vertical Take-Off and Landing) 94, 572, 782, 817
Exergy Decomposition 187
Exergy-Balance 254
Experimental Characterization 1432
Experimental Modal Analysis (EMA) 362, 1407
Experimental Structural Dynamics 380
Experimental Study 1229
Experimental Testing 595
Exploration 926
Explosive Simulation 1325
Extended Kalman Filter 919
Extended Reality (XR) 1549
Extended Reality 1559
Extended-Kalman-Filter 72
External Compression Inlet 626
Extreme Accelerations 211

FADEC 672
Failure Analysis 1210
Failure Management 942
Failure 1384
Falkner-Skan Boundary Layer 250
Far-Field 187
Fast Convolution Based Method 1427
Fatigue Life 1298
Fatigue 1450
Fault Tolerance 366
FDM Technology 106
Feedback Linearization 806
FEM Simulation 751
FEM 1438
Field Reconstruction 66
Finite Element Analysis 1095, 1416
Finite Element Method (FEM) 370, 1192, 1225, 1235, 1325, 1407
Finite Element Model Updating 1336
Finite Elements 1250, 1331
Fire Fighting 431
Firedrake 730
Firefighting 463
Fixed-Wing Aircraft Control 15
Fixed-Wing UAV 777
Flag Flutter 370

Flame Stability 695
Flexible Aircraft 390
Flexible Materials 1278
Flexible Sensors 1266
Flexible Wings 380
Flight Control System 656, 868, 874
Flight Deck 1471
Flight Dynamics 868, 913
Flight Profile Optimization 448
Flight Simulation 1460, 1500, 1574
Flight Test 1494
Flight Testing Optimization 431
Flight Testing 475, 534
Flight Vehicle Design 1518
FlightStream 534
Floquet Method 358
Flow Control 31
Flow Measurements 164
Fluid Dynamics 148
Fluid Mechanics 260
Fluid-Structure Interaction 158, 172, 267
Flutter Suppression System 366
Flutter 352
Flywheel 589
Foldable Antennas 453
Foldable Flat Array 1387
Formation Flying 1006
Forward-Motion Release 777
FPGA 897, 1101
Fractional Change 481
Fracture Mechanics 1422
Fragmentation Warhead 1325
Free Edge 267
Free-Wake 142
Full-Scale Flight Validation Data 493
Fully Electric Aircraft 558
Fully-Actuated UAVs 794
Functional Hazard Analysis 689
Functional Mock-up Interface (FMI) 1537, 1530
Fused Deposition Modeling 1444

Galileo 1024
Gardon Gauge 130
Gateway 1036
Gaussian Mixture Models 1059
Gaussian Process Regression 1181, 1220
General Relativity 1120
Generalized Flight Control 15
Generalized Lifting Line Theory 142
Generative AI 21, 37
Geometrical Design 1568
Geometrically Nonlinear Analysis 1187
Geostationary Radar Applications 1369
Geostationary SAR 1065
Globalâ€“Local 1240
Global-Local Optimization 1192
GNC 885
GNSS Interference 2
GNSS Positioning 42
GNSS 919, 1024
GPU-Accelerated CFD 239
GPU-Powered Approach 972
Grazing Waves 293
Green Aviation 666
Green Propellant 601, 701
Green Propulsion 638
Grid Collectors 638
Grit Feeder 1255
Ground Effect 800
Ground Effect 913
Ground Resonance 358, 408
Gurney Model 1325
Gust Loads 352
Gust 1298
GVA 2

Gyroid 1310
Gyroplane 106

H Control 1095
Hard Anodization 1391, 1397
Hardware-in-the-Loop (HiL) 1537
Hardware-In-The-Loop Validation 1012
Hardware-In-The-Loop 897, 1101
Harmful Contamination 1077
Heart Rate Variability 1456
Heat Exchangers 583, 1412
Heat Flux 130
Heat Transfer 1198
Helicopter Rotor 408
Helicopters 683
HEMS 817
Hierarchical Control 885
High Deformable Wings 375
High enthalpy 177
Higher-Order Beam Theories 1353
Higher-Order Models 303
Higher-Order Structural Modeling 1171
Higher-Order Theories 1176, 1235, 1369
High-Order Accuracy 193
High-Order Finite Elements 267
High-Order Methods 239
High-Order Models 1314
H-Infinity Control 862
Historical Sampling 994
HLFC 1310
Holistic Systems Approach 425
Homogenisation 1412
Honeycomb Structures 335
Honeycomb 735
Hub Vibratory Loads 331, 414
Human Factors (HF) 1549
Human Spaceflight 1505
Human-Machine Collaboration 552
Human-Machine Interface 1471
Humidity 632
Hybrid HAPS 850
Hybrid Propulsion 689
Hybrid Rocket Propulsion 601
Hybrid-Electric Aircraft 469, 558, 607, 644, 751
Hydrogen Aircraft 402
Hydrogen Conditioning 583
Hydrogen Enrichment 695
Hydrogen Tanks 713
Hydrogen 666
Hydrogen-Powered Aircraft 662
Hydrogen-Rich Polymers 620
Hyperelastic Constitutive Model 1422
Hyperelasticity 390
Hypersonic Flow 250, 1283

IAM 25
IDDES 254
Identifiability 839
Immersed Boundary 158, 172
Immersive Simulation 9
Impact Dynamics 1325
Implicit-Mesh Discontinuous Galerkin Method 193
In Situ Resource Utilization 1089
Incompressible Navier-Stokes Equations
Incremental Nonlinear Dynamic Inversion 868, 874
Inflatable Structures 1278
In-Flow Distorsions 822
Information/Temporal Decoupling 1530
Initial Design Point (IDP) 436
Innovative High-Performance Polymers 1374
In-Orbit Servicing 1107
In-Parallel Computation 972
Inspection 908

Insurance 1054
Interblade Damper 408
Interplanetary 926
Inter-Satellite Links 1114
IOD 1059
IRIDE 1054
Isotropic Plates 298

Jet Noise 287
Julia 1500

KÃssner-Schwarz 142
Kalman Filter 1481
Kill Probability (Pk) 499
Kinematic Models 1235
Kinetic Energy Preserving Schemes 239
Knowledgeâ€‘based Engineering 1568
Kolmogorov-Arnold Networks 724
Kriging 1336

Lab-Testing 72
Labyrinth 293
LAGEOS 1120
Lagrange Polynomials 267
Lagrangian Relaxation 1030
Lamb waves 1319
Landing Gear 913
LARES 2 1120
Large Deformations 1422
Large Eddy Simulation 158, 172, 239, 564
Large Language Models 552, 1568
Laser 130
Lateral Force Constraints 794
Lattice Boltzmann 158, 172
Lattice Structures 1229, 1402
Launch Traffic 994
Launch Trends 994
Layer-Wise 1384
Leakage 735
Lean Blowout 695
LEO Debris 1131
LEO Satellites 1158
LEO-to-MEO 930
Lethality Assessment 1325
Liability 1077
Lid-Driven Cavity Problem 193
Life Cycle Assessment 487, 546, 1512
Lifting-Line Theory 370
Lift-Offset 414
Lift-to-Drag Ratio Optimization 846
Lighter Than Air 833
Lighter Than Air 839
Limit Cycle 396
Line Sampling (LS) 948
Linear Stability Analysis 250
Linear Time-Periodic Systems 358
Li-Po Battery Pack 572
Liquid Propulsion 718
Liquid-Hydrogen 528
Litz-Wire Winding 751
Load Analysis 402
Load Evaluation 880
Loads Kernel 352
Local Air Quality 1018
Logical Execution Time 1530
Low Power 747
Low Velocity Impact 1204
Low-Thrust 1036
Low-Toxicity 741
Low-Velocity Impact 1171
LTA 833, 839
LTI Harmonic Decomposition 358
LTO Cycle 540
Lunar Constellation 1140
Lunar Dust 1255

Lunar Exploration Missions 614
Lunar Landing 48
Lunar Pressurized Rover 9
Mach Stem 217
Machine Learning 31, 84, 177, 271, 994
Magnetic Attitude Control 897
Maneuver Detection 936
Maneuver Loads 352
Maneuver Simulation 493
Manufacturing Defects 1402
Mars 1260
Martian Rover 1407
Martian UAS 800
Matching Pursuit 221
Match-Range Operation 448
Mathematical Model 577
MATLAB 1500
MDO 463
Mechanical Performance 1397
Mega-Constellations 1077
Mental Workload Monitoring 1456
Mesh Topology 418
Metalâ€“Ceramic Co-sintering 1444
Metamaterials 54
Metasurfaces 54
Methane-Hydrogen Flames 695
Micro Propulsion 701
Microcapsule Self-Healing 1374
Microjet Prototypes 595
Micromechanics 1364
Microstrip Patch Antennas 1369
Minimum Energy 78
Minimum Latency Routing 1114
Missile 1325
Missiles 771
Mission Design 601
Mission Simulation 644
MLDS 1107
Modal Analysis 380, 1225, 1336
Modal Assurance Criterion 267
Modal Correlation 1407
Modal Damping 1287
Model Identification 457, 650, 656
Model Reproducibility 84
Model-Based Design 930
Model-Based System Engineering 1505, 1512
Modeling & Simulation 1512
Modelling and Simulation 683
Modelling 1494
Modular Design 100, 106
Modular Framework 960
Modular Rover 1563
Momentum Decomposition 187
Momentum Exchange 1146
Monte Carlo Simulation 948
Moon Exploration 1036
Moon 1374
Moonlight 48
More Electric Aircraft 589
Morphing Airfoil 418
Morphing Wings 370
Morphing 1331
Moving Reference Frame 418
Multi-Agent Systems 771, 856
Multi-Constellation 1158
Multidisciplinary Design Analysis 1518
Multidisciplinary Design Optimization (MDO) 436
Multi-Disciplinary Optimization 504
Multidisciplinary 463
Multi-Fidelity Modeling 1240
Multi-Fidelity Surrogate Models 1220
Multi-Fidelity 1181
Multifidelity 66
Multi-Field Model 1215
Multifunctional Materials 1432

Multi-objective Optimisation 724, 1125, 1140
Multipath Mitigation 42
Multiscale Modelling 1358, 1412
Multistability 1331
Multistage Suborbital Vehicles 954
Multi-Target Missions 1146
Multi-Temperature 1283

NACA 13112 418
Nanosatellites 919
Nash Equilibrium 1107
Natural Disasters 1054
Neural Networks 1176, 1192
Node-Dependent Kinematics 1235
Noise Control 325
Noise Robustness 271
Noise 275, 314
Nonlinear Aerodynamics 913
Nonlinear Analysis 1347, 1416
Nonlinear Control 765, 1036
Nonlinear Dynamics 1287
Nonlinear Orbit Control 1101
Nonlinear Trim 390
Nonlinear Vibration 1292
Nonlocal 325
Non-Uniform Inflow 707
Nose Spike 119
Nowcasting 25
Numerical Simulation (CFD) 211, 620, 626
Oblique Shock Reflection 217
Off-Design Performance 607
Off-Design 136
Offset Piezo Stack Actuators 1095
Offset Rocket Fins 260
Onboard Fault Diagnosis 1524
Onboard Processing 1042
One-Dimensional Refined Model 1210
Online Task Assignment 771
On-Orbit Inspection 902
On-Orbit Servicing 908
Ontology 1568
OODA Loop 88
Open Source 1165
OpenFOAM 148
Operational Cost 817
Operational Modal Analysis (OMA) 362
Operational Modal Analysis 380
Optimization 463
Orbit Control 1065
Orbit Determination 1024, 1042
Orbit Transfer 930
Orbital Decay 1131
Orbital Forces Modelling 972
Orbital Perturbations 1065
Orbital Robotics 942
Orbital Torques Modelling 972
Orchestration Algorithm 1537
Origami 341
Overall Aircraft Design 528
Oxidizer Pump 718
Oxidizers 741

PAMPC 812
Panel Method 396
Paper Flutter 370
Paraffin/HTPB Fuel Blends 601
Parallel Co-Simulation 1530
Parameter Identification 839, 1481
Parametric Modeling 1192
Parametric Study 954
Passive Sensors 1341
Pattern of Life 936
Pazy Wing 396
Penetration Mechanics (THOR Law) 1325

Perception Aware 812
Perceptual Noise Assessment 319
Performance Analysis 856
Performance Assessment 862
Performance Testing 572
Performance 632
Peridynamic Fatigue Model 1353
Peridynamics 1427
Permanent Magnet Machine 757
Phased-Array Antennas 1358
Piezoelectricity 1364
Piggyback 926
Pilot Biomechanics 1466
Pilot Studies 1574
Pilot-Assisted Oscillations PAO 1481
Pilot-Induced Oscillations 1460
Pin-Fins 1198
Pitch-Link Vibratory Loads 414
PLA Filament 106
PLA 1229
Planetary Exploration 960, 1563
Plasma-Assisted Combustion 695
PLD 1391, 1397
Plug and Play Architecture 436
Pollutant Emissions 540
Pollutants Dispersion 1018
Polluter Pays Principles 1077
Poly(Vinyl Alcohol) Gels 1272
Polygonal Cylinders 158
Polyimide 614
Polymer Blends 620
Pose 72
Post-Stall Modelling 827
Potential Flows 375
Power Balance Method 187
Power Management Systems 689
Precise Orbit Determination 919, 1120
Preliminary Design 516
Preliminary Missile Design 499
Pressure Loss 735
Pressure 632
Principal Component Analysis 1460
Probabilistic Admissible Region 1059
Probability Estimation 948
Process-Induced Deformations 1220
Propellant 741
Propeller 707
Propeller-driven Vibration Testing 380
Propellers 827
Proper Orthogonal Decomposition (POD) 504
Propulsion System 930
Propulsion 572
Proton Exchange Membrane (PEM) Electrolysis 701
Proximal Policy Optimization 1030
Proximity Operations 1012
Pseudo-Random Number Generator 84
Public Acceptance 1549
Pure Aluminum 751

Quadrotor UAV 78
Quadrotor 777
Quasi-Satellite-Orbits 1048

Radar Cross Section (RCS) 436
Radial Vane 384
Radiation Effects 930
Radiation Shielding 1266
Radio Frequency Interference (RFI) 1158
Ramjet Propulsion 626
Random Forest Classification 1456
Random Seed Initialization 84
raPPPid 919
Raw-Riblets 125
Reacting Flows 183
Recursive Gaussian Process 806

Reduced Order Model (ROM) 287, 504
Reduced-Crew Operations 1475
Redundant Longitudinal Control 534
Reference Tracking 806
Regolith 1255
Regulatory Harmonisation 1487
Reinforcement Learning 846, 902
Relative Orbital Elements 908
Reliability 689
Remediation Fund 1077
Remote Sensing 510, 1054
Rendezvous 1036
Reproducibility 960
Requirements 856
Residence Time 583
Response Time 583
Reusable Launcher 522
Reusable Space System 1518
Reward Reshaping 1030
RF emissions monitoring 1158
Ribs 1198
Rigid Coaxial Rotor 414
Rigid-Body Dynamics 148
Roadmaps 442
Robotic System Testing 960
Robust Design 846
Rocket Wave Drag 260
Rotary Wing 142
Rotating Meshes 564
Rotating 1198
Rotor Aerodynamics 142
Rotorcraft Design 827
Rotorcraft Stability 358
Rotorcraft-Pilot Couplings 1466, 1481
Rover 1438
RTD 1260

Safe Reinforcement Learning 1030
Safety 469, 689
Sandwich Panel 303
Sandwich 1384
Satellite Constellations 1114
Satellite Drag Mitigation 271
Satellite Scheduling 1030
Satellite 510, 1153
Scale-Resolved Simulation 730
Scaling Methodology 747
Scanpath Analysis 1475
Scheduling Algorithms 1537
Seal 735
Seed Sensitivity 84
Self-Healing Properties 614
SEM 1391
Semi-Analytical Guidance 862
Sensor 130
Separated Flows 227
Sequential Convex Programming 1048
Shape Memory Ability 614
Shape Sensing 880
Shell Models 1304
Shielding Materials 1272
Shock Wave-Boundary Layer Interaction 205
Shock-Combustion Interaction 183
Signals Compression 1524
Sim2Real 72
Simply-Supported Boundary 267
Simulation and Off-Design Analysis 499
Simulation 100, 839, 913, 1494
Simulation-Based Certification 493
Simulations 822
Simulink 1500
Single frequency 919
Single Pilot Operations 1471
Singular Value Decomposition (SVD) 558
Singular Value Decomposition 1568

Slepian Sequences 78
Sliding Mode Control 1083
Sliding-Window LSQ 891
Slosh Dynamics 148
Small Satellites 1006
Small Solar-System Bodies 1071
Small-Scale Rocketry 741
Smart Composite 1341
Software Architecture 1544
Solar Cycle Prediction 271
Solar Panels Incipient Damage Identification 1524
Sonic Boom 211
Sounding Rockets 718
Space Applications 1391, 1397
Space Biology 930
Space Debris Evolution 994
Space Debris Index 1000
Space Debris 1000, 1059
Space Exploration Systems 1512
Space Exploration 1071, 1089, 1374, 1438
Space Law 1077
Space Mission Design 1512
Space Operations 1030
Space Radiation Shielding 620
Space Resilience 1487
Space Robotics 885
Space Safety 1487
Space Service Volume (SSV) 1024
Space Situational Awareness 936, 1042
Space Surveillance & Tracking 936
Space Surveillance 1059
Space Sustainability 1000, 1150, 1487
Space System Design 1563
Space Systems 1153, 1158
Space Weather Forecasting 271
Spacecraft Attitude Control 1083
Spacecraft Control 148
Spacecraft Health Monitoring 1524
Spacecraft Manoeuvre 1024
Spacecraft Pose Estimation 1012
Spaceflight Dynamics/GNC/Space Robotics 1089
Spacesuit Radiation Shielding 1272
Spacetime 54
Spectral Analysis 510
Spectral Method 250
Spoofing 2
SRP 972
SSA 1059
SST 1059
Stability Augmentation 475
Stability 777, 1466
Stabilizer 100
Stacked Ensemble 271
STAR CCM+ 187
State-Space 370
State-to-State 1283
Static Analysis 1278
Static Digraph 1114
Steady-State Approximation 577
Steering 244
Stiffened Composite 1319
Sting Software 100
Stochastic Excitation; Structural Dynamics 1292
Strain Measurements 880
Strain Sensing 1341
Stress 1384
Strong Oblique Shock Wave 626
Structural Batteries 1432
Structural Design 1278
Structural Dynamics 595
Structural Health Monitoring (SHM) 1266, 1287, 1319, 1341
Structural Optimization 1240
Structural Sizing 402

Structure-Preserving 233
SU2 217
Suborbital vehicles 1018
Subset Simulation (SS) 948
Suitability Analysis 589
Supercapacitor 589
Superconducting Electric Motor 757
Super-Resolution 66
Supersonic Aircraft 119
Supersonic Inlet 626
Supersonic/Hypersonic Flows 205
Supramolecular Interactions 614
Surface Optimization 966
Surface Pattern 125
Surrogate-Based Optimisation 1336
Sustainable Aviation Fuel 487
Sustainable Aviation Fuels 546
Sustainable Aviation 589
Sustainable Aviation 782
Sustainable Mobility 1554
Sustainable Mobility 713
Sustainable Propulsion Systems 644
Sustainable Propulsion 683, 827
Sustainable Space Propulsion Systems 677
Symbolic Regression 271
Synthetic Aperture Radar (SAR) 1065
Synthetic Dataset 72
System Architecture 469
System Context Input 552
System Design 425
System Engineering 1563
System Identification 221, 1494
System Integration 431
System of Systems 856
System Structure and Parameterization (SSP) 1537
System Validation 960
System-of-Systems Architecture 1544
System-of-Systems Engineering 1544
System-of-Systems 88

Taber Abraser 1255
Tailless Aircraft 475
Tapered Beam 1347
Task Scheduling 902
Taylor Expansion 267
Team DIANA 1407
Technological Demonstrator 1563
Technologies 1438
Technology Roadmaps 1518
Temperature Measurement 1260
Temperature Sensors 1260
Tensioning System 453
Tensor Algebra 1107
Terminal Phases 913
Test Stand 275
Testing in Aerospace 1225
Testing 683
Textile Composites 1314
Thermal Insulation 713
Thermal Loads 1369
Thermal Protection Systems 1444
Thermal Stresses 1187
Thermally Perfect Gases 233
Thermalmechanical Analysis 384
Thermochemical Non-Equilibrium 1283
Thermo-Chemo-Mechanical Analysis 1215
Thermodynamic Methods 187
Thermo-Elastic Analysis 1187
Thermo-Elastic Deformations 1358
Thermo-Elasticity 1369
Thin Membranes 453
Three-Surface Airplane 534
Thrust-Lift Conversion 800
Thunderstorms 25

Tiltrotor 331
Time Difference of Arrival (TDOA) 1158
Time-Varying Parameters 1481
Tip Deflection Measurement 1095
Titan 1283
Total Pressure Recovery 626
TPMS 1310
Tracklet Correlation 1059
Trailing Edge Flap 418
Trailing Edge 1198
Trailing-Edge Serrations 564
Trajectory Design 1048
Trajectory Optimization 78
Transformers 60
Transient Modelling 583
Transient Performance Estimation 577
Transition Criteria 217
Transmission Line Modeling 1530
Transmission Loss 293
Transportation Economics 94
Tribological Tests 1397
Truss-Braced-Wing Open-Rotor 528
Tumbling Target 862
Turbine Blade 1198
Turbine Stator Well 735
Turbomachinery 718
Turbomachinery 724
Turbulence Modelling 205
Turbulent Boundary Layer 60
Turbulent Flows 281
Turbulent Jet 164
TVAC 1391, 1397

UAM 707, 827
UAS 314
UAV Propulsion 683
UAV 164, 572, 707, 806, 812, 833
Ultra Efficient Regional Aircraft 516
Ultrathin Composites 1250
Ultra-Thin Structures 1210
Uncertainty Quantification 1181
U-Net 66
Unified Formulation 1235, 1314
Unmanned Aerial Systems 856, 1559
Unmanned Aerial Vehicle 475
Unmanned Airships 833
Unmanned Helicopters 788
Unsteady Aerodynamics 142, 370
Unsteady CFD 187
Urban Air Mobility (UAM) 319, 564, 782, 1549, 1554, 1559
Urban Mobility 822
Use Case Analysis 425

Variable Camber 136
Variable Curvature 1304
Variable Stiffness Composite 1187
Variable Thickness 1304
Variationalâ€¯Asymptoticâ€¯Method 1364
Various Angles of Attack 106
Ventilated Brake Disc 384
Venturi Intake 595
Vertical Stabilizers 106
Vibration-Based Monitoring 1287
Vibroacoustic Analysis 303
Vibroacoustics 267, 298
Video Processing 1225
VIO 812
Virtual Design 730
Virtual Flight Testing 493
Virtual Manufacturing 1215
Virtual Modelling 431
Virtual Reality 9, 346
Viscous Drag 125
Vision-Based Navigation 48, 1012
Visual Check 37

VLEO 966, 1083
Volumetric Locking 1422
Vortex Induced Vibration 158, 172
Vortex Lattice Method 390
Vortex Lattice 396
Vortex Ring State 788
Vortex Shedding 112, 254
VPM 314

Wake Turbulence 199
Wake Vortex Encounter 199
Wake Vortex 199
Wall Thermal Inertia 583
Wall Turbulence 31
Wall-Bounded Flows 233
Wall-Pressure Fluctuations 60
Wankel Engine 683
Water Electrolysis Propulsion (WEP) 701
Water Electrolysis 677
Wave Finite Element Method 341
Wavelet Transform 1460
Wavenumber Space 298
Wavy-BCC 1229
WBCC Lattice 384
Weapon-Target Assignment (WTA) 771
Wear Index 1255
Wedging Angles 100
Wheel 1438
Whirl Flutter 362
Wildfire Suppression 88
Wind Tunnel Blockage 227
Wind Tunnel 100
Wing Aeroelasticity 375
Wingbox Structure 1416

YOLO 72

Zero-Sum Games 1107
ZND Detonation 183